

AD-A279 448



AFFDL TR 70-144

10

DTIC  
ELECTE  
MAY 20 1994  
S F D

0

**PROCEEDINGS  
OF THE  
AIR FORCE CONFERENCE  
ON  
FATIGUE AND FRACTURE  
OF  
AIRCRAFT STRUCTURES AND MATERIALS**

**Proceedings of the Conference held at  
Miami Beach, Florida, 15-18 December 1969**

*TECHNICAL EDITORS:*

*H. A. WOOD, R. M. BADER, W. J. TRAPP, R. F. HOENER, R. C. DONAT*

91120

94-15201



This document has been approved for public release and sale.  
Its distribution is unlimited.

DTIC QUALITY ASSURED 3

Sponsored by  
Air Force Flight Dynamics Laboratory  
and  
Air Force Materials Laboratory  
Air Force Systems Command

**Best  
Available  
Copy**

## FOREWORD

The Air Force Conference on Fatigue of Aircraft Structures and Materials, sponsored by the Air Force Flight Dynamics Laboratory (AFFDL) and the Air Force Materials Laboratory (AFML), Air Force Systems Command, was held on 15-18 December 1969 at the Carillon Hotel, Miami Beach, Florida. The purpose of the Conference was to discuss technological advancements in fatigue and fracture theory.

The Conference was comprised of ten technical sessions (including two panel discussions) entitled "The Role of Materials in Structures"; "Fundamentals I & II"; "Criteria"; "Fracture I & II"; "Phenomena I & II"; "Analysis"; "Design and Service Experience". A total of fifty-six technical papers were presented.

The members of the Technical Committee, who also served as the Technical Editors, express their appreciation to the authors, session chairmen, panel members, and attendees for their contributions toward a successful conference. Special appreciation is extended to General James Ferguson, Commander, Air Force Systems Command\* for his excellent keynote address. Wholehearted thanks are also offered to Professor A.M. Freudenthal, The George Washington University, for delivering the opening technical paper.

Grateful acknowledgement is made to the staff of University of Dayton Research Institute, for their assistance in conference arrangements and in particular to Mr. Dart Peterson, Assistant to the Director, for his efforts in preparing these Proceedings for publication.

*September, 1970*  
*Wright-Patterson Air Force Base, Ohio 45433*

*\*Now Retired.*

*The Technical Editors*

Accession For	
NTIS CRA&I	<input checked="" type="checkbox"/>
DTIC TAB	<input type="checkbox"/>
Unannounced	<input type="checkbox"/>
Justification	
By _____	
Distribution /	
Availability Codes	
Dist	Avail and/or Special
A-1	

## TABLE OF CONTENTS

### OPENING SESSION

Opening Remarks	3
<i>Dr. A.M. Lovelace</i>	4
<i>Col. J.R. Myers</i>	5
Keynote Address	5
<i>Gen. J. Ferguson</i>	9
Fatigue Mechanisms, Fatigue Performance and Structural Integrity	9
<i>A.M. Freudenthal</i>	

### SESSION 1

#### THE ROLE OF MATERIALS IN STRUCTURES

The Material Selection and Structural Development Process for Aircraft Structural Integrity Under Fatigue Conditions	17
<i>J.P. Butler</i>	

### SESSION 2A

#### FUNDAMENTALS I

Fatigue Mechanisms and the Development of Fatigue-Resistant Materials	47
<i>J.C. Grosskreutz</i>	
A Micromechanic Theory of the Effect of Mean Stress on Fatigue Crack Nucleation	63
<i>T.H. Lin and Y.M. Ito</i>	
Subcritical Crack Growth Criteria for Inconel 718 at Elevated Temperatures	71
<i>H.G. Popp and A. Coles</i>	
The Effects of Microstructure on the Strength and Fracture of 18% Ni (250 Grade) Maraging Steel	87
<i>A.M. Adair and J.A. Roberson</i>	
Fatigue Performance of High Strength Steels as Related to Their Transformation Mechanism	99
<i>M. Ronay</i>	

### SESSION 2B

#### CRITERIA

Miner's Law: What Price Conformity?	113
<i>H.A. Lipsitt, D.F. Frank, and G.C. Smith</i>	

Application of the Residual Strength Concept to Fatigue Design Criteria	117
<i>D.J. Trent and I. Bouton</i>	

Fatigue Loadings on Commercial Transport Airplanes	123
<i>T.L. Coleman and P.A. Hunter</i>	

On the Analytical Basis for Fatigue Life Predictions	131
<i>S.C. Saunders</i>	

The Application of the Scratch Strain Gage in a Total Fleet Fatigue Damage Monitoring System	137
<i>T.L. Haglage and H.A. Wood</i>	

Airframe Environment Design Considerations - The Shape of the Turbulence Spectrum and Probabilities of Encountering Given Peak Gusts and RMS Values	159
<i>J.W. Jones</i>	

### SESSION 3A

#### FRACTURE I

Three-Dimensional Stress-State in a Cracked Plate	175
<i>G.C. Sih</i>	

Buckling in Thin Cracked Sheets	193
<i>R.L. Carlson, G.F. Zielsdorff, and J.C. Harrison</i>	

The Effect of Riveted and Uniformly Spaced Stringers on the Intensity Factor of a Cracked Sheet	207
<i>C.C. Poe, Jr.</i>	

Stress Intensity Factor for a Straight Crack Approaching a Circular Hole	217
<i>A.S. Kobayashi and D.E. Maiden</i>	

An Effective Strain Concept for Crack Propagation and Fatigue Life with Specific Applications to Biaxial Stress Fatigue	225
<i>E.K. Walker</i>	

Fracture and Fatigue Growth of Partially Embedded Flaws	235
<i>L.R. Hall and R.W. Finger</i>	

TABLE OF CONTENTS (Continued)

**SESSION 3B  
FUNDAMENTALS II**

On the Criterion of Low-Cycle Shear Fracture  
*F.D. Ju, J.T.P. Yao, and T.T. Liu* 265

The Effect on the Surface Layer and Environment on Cyclic Behavior and Fatigue of Metals  
*I.R. Kramer* 271

Mechanisms of Fatigue in Filament-Reinforced Metals  
*J.R. Hancock* 295

The Effect of Frequency on High-Temperature, Low-Cycle Fatigue  
*L.F. Coffin, Jr.* 301

A Kinetic Model for Crack Growth Predictions  
*P.H. Graham* 313

**SESSION 4A  
FRACTURE II**

Statistical Variation in Fracture Toughness Data of Airframe Materials  
*A.F. Liu* 323

Fatigue and Fracture of Metal-Matrix Composites  
*I.J. Toth and K.D. Shimmin* 343

The Effect of Strain Rate on the Fracture of Advanced Fiber-Reinforced Composites  
*F.Y. Soliman and J.S. Wallace* 377

Fracture Toughness Studies Using Thick Acrylic Materials  
*H.L. Smith, F.R. Stonesifer, and K.R. McKinney* 395

**SESSION 4B  
PHENOMENA I**

Review of Theories and Laws of Fatigue Crack Propagation  
*R.M. Pelloux* 409

A Model Study of the Characteristics of Fatigue Crack Extension  
*W.G. Fleck and R.B. Anderson* 417

Experiments on the Nature of the Fatigue Crack Plastic Zone  
*G.T. Hahn, M. Sarrate, and A.R. Rosenfield* 425

Fatigue Crack Growth and the Strain Intensity Factor  
*A.J. McEvily* 451

Prediction of Fatigue Lifetime by Combined Mechanics and Acoustic Emission Techniques  
*D.O. Harris, H.L. Dunegan, and A.S. Tetelman* 459

**SESSION 5A  
PHENONEMA II**

The Prediction of Fatigue Life in Random Vibration Environments  
*J.C. Bowman* 475

Impending Fatigue Failure Detection by Optical Correlation  
*E. Marom and R.K. Mueller* 493

Use of Damping to Reduce Vibration Induced Failures in Aerospace Systems  
*D.I.G. Jones, J.P. Henderson, and A.D. Nashif* 503

Effects of Corrosive Environments on Fatigue Life of Aluminum Alloys Under Maneuver Spectrum Loading  
*J.J. Gruff and J.G. Hutcheson* 521

Correlation of Residual Strength of Ballistically Damaged Panels with Fracture Toughness Theory  
*M.D. Campbell, J.E. Jensen, and J.F. Haskins* 539

Combined Environment Sonic Fatigue Test of the Aft Fuselage Panels for a Fighter Bomber Aircraft  
*O.F. Maurer and R.M. Shimovetz* 557

**SESSION 5B  
ANALYSIS**

Structural Reliability Through Detail Design and Development Testing  
*M. Stone* 579

Application of Fracture Mechanics for Fatigue Life Prediction  
*R.V. Sanga and T.R. Porter* 595

Fatigue Crack Propagation Behavior and Residual Strength of Bonded Strap Reinforced, Lamellated and Sandwich Panels  
*S.H. Smith, T.R. Porter, and W.L. Engstrom* 611

TABLE OF CONTENTS (Continued)

**SESSION 5B (Continued)**

Vulnerability Considerations in the Design  
of Rotary Wing Aircraft Structures  
*M.J. Rich*

635

Damage Tolerant Design-Analysis Methods  
and Test Verification of Fuselage Structure  
*T. Swift and D. Y. Wang*

653

A Re-definition of Endurance  
Life Design Strength Criteria  
by Statistical Methods  
*E.B. Haugen and J.A. Hritz*

685

**SESSION 6  
DESIGN AND SERVICE EXPERIENCE I**

Some Developments in the Air Force  
Aircraft Structural Integrity  
Program (ASIP)  
*T.T. King*

701

The F-100 Aircraft Structural Integrity  
Program (ASIP)  
*G.E. Fitch, Jr., R.E. Jackman,  
and W.P. Horsfall*

723

The B-52G-H Wing Cyclic Test Program  
*D.F. Bryan*

755

Results of Analysis, Fatigue Testing and Usage  
of a High Speed Aircraft Subjected to  
Combined Peacetime and High Combat  
Environments  
*A. Merkin*

779

The Development and Implementation of  
a Fatigue Monitoring Program for a  
Transport Aircraft

*A.P. Shewmaker and J.A. Wagner*

833

B-58 Fleet Life Monitoring and Usage  
Evaluation by Cumulative Fatigue  
Damage Method

*D.H. Whitford and R.J. Dominic*

847

**SESSION 7  
DESIGN AND SERVICE EXPERIENCE II**

Comparison of Air Force Fatigue Problems  
with Problems on Similar  
Commercial Aircraft

*R.O. Schwake*

867

Parametric Fatigue Analysis  
Models for Fighter Aircraft

*B.S. West and G.J. Roth*

877

F-111 Service Usage Recorder Program  
*W.P. Dunn*

889

Aircraft Structural Integrity  
Program in AFLC

*Col. H.B. Morrison, Jr.*

899

**INDEX OF AUTHORS**

903

**CONFERENCE COMMITTEES**

904

**OPENING SESSION**

**OPENING REMARKS**

Dr. A.M. Lovelace, Director  
Air Force Materials Laboratory

Col. J.R. Myers, Commander  
Air Force Flight Dynamics Laboratory

**KEYNOTE ADDRESS**

Gen. J. Ferguson, Commander  
Air Force Systems Command

**OPENING TECHNICAL PAPER**

A.M. Freudenthal

## OPENING REMARKS

Dr. A.M. Lovelace

Director  
Air Force Materials Laboratory

On behalf of the Air Force Materials Laboratory, I would like to welcome you to this important conference. The general subject which will receive our attention during the next few days is probably, in the final analysis, the single most critical one in the operational performance of aircraft weapon systems and it cannot be over-emphasized.

Despite many decades of awareness of the problem, the last twenty or so years of which have seen an intensification of study, fatigue still remains today as one of our most perplexing difficulties. Though often incorrectly classified as a "nuisance" in earlier aeronautical operations, it now commands the major attention it warrants. The fracture of components, often occurring when least expected, also remains a serious problem of growing proportions. It took a long time, with many debates and some reconciliation among various schools of thought before we were able to appreciate the extremely elusive and complicated nature of fatigue. Our research in recent years, for example, has clarified the fact that an immensely large array of environmental and loading conditions can individually or collectively influence the initiation and propagation of fatigue and fracture, whether in a simple material specimen or complicated structure. As aeronautical structures become more complex and operating conditions more severe, the number of specific sets of design and usage circumstances which can lead to trouble will certainly increase. Under such conditions, it should be obvious that the "solution" of fatigue and fracture problems will most likely take the form of minimizing the causes and maximizing the control of the causing factors. The more sophisticated we can make this process, the greater reliability we can introduce into the system.

We in the Materials Laboratory are strongly motivated by the philosophy of this conference which, among several things, refers to the inter-relationship between

structural design and materials development with regard to fatigue and fracture behavior. The makeup of the conference technical program indeed attests to the relative inseparability of the two. It is certainly appropriate that the Air Force Flight Dynamics and Materials Laboratories, representing in essence these two disciplines should jointly sponsor this conference to consider the fatigue and fracture problems in structures and in materials in a single context.

In a very real sense, the materials man performs primarily a supporting function for the materials user, in this case, the structures designer and fabricator. While some idealists in the materials community might wish to argue that point, it nevertheless remains our most important responsibility to polarize our efforts toward specific systems requirements and be guided by them. The development of a general purpose structural alloy is now a less likely goal than before; rather, the achievement of a particular set of performance goals dictated by future design requirements, can set narrow development objectives. And the measure of success in the tailoring job is established only after extensive characterization is completed wherein every facet of the material's physical and mechanical behavior is explored in order to provide the designer with all available facts with which to exercise his design options, maximize structural configurations and predict performance. In fact, the establishment of methods of predicting materials behavior in pertinent environments, and of translating such behavior into the structural situation, are just as important as the basic materials development task itself.

The subjects of fatigue and fracture, the causes and the methods of prediction have in the past and will in the future command major attention in the Materials Laboratory as well as throughout the Air Force. Your participation in this conference is ample evidence of the importance of the subject to all of us.



## OPENING REMARKS

Col. J.R. Myers

Commander  
Air Force Flight Dynamics Laboratory

Thank you, Al. Good morning General Ferguson, gentlemen. May I extend a welcome to you from members of the Air Force Flight Dynamics Laboratory.

As Dr. Lovelace has emphasized, fatigue is the most critical phenomenon affecting the operational status of our aircraft today. It is the cancer of the fleet -- it strikes without warning, too often with fatal results. I can think of no weapon system that has been produced in quantity that has not been affected by fatigue problems at some time during its operational lifetime. We can all think of examples: F105 fuselage, C-130 wing, KC-135 tail, T-37 wing, B-52 wing, F-100 wing carry-through structure. In each situation, aircraft were grounded or their performance was curtailed.

Yet, we feel that we know many of the symptoms of this "cancer" such as tool marks, improper machining, material inclusions, sharp radii . . . Fresh analytical approaches, such as fracture mechanics, offer further insight into the problem. Progress is being made and we hope that this Conference will stimulate further activity toward a better understanding of fatigue. Certainly, the challenge exists to improve our flight vehicle safety and operational readiness with maximum structural efficiency. I urge you to actively participate in the technical sessions of this conference and information discussions during your stay here.

We are fortunate to have as our keynote speaker Gen. James Ferguson. General Ferguson began his Air Force career in 1934. He commanded a fighter-bomber group and participated in various campaigns in Europe during World

War II. He served in several Air Force command positions in Korea during that conflict. Following services as Deputy Commander of the 9th Air Force, Gen. Ferguson began a series of assignments that have kept him in the Washington, D.C. area since 1955. These included the Director of Requirements, Office of the Deputy Chief of Staff for Development, Headquarters, USAF, Vice Commander of the Air Research and Development Command -- the predecessor of the Air Force Systems Command, and Deputy Chief of Staff for Research and Development, Headquarters, USAF where he directed the total research and development of the Air Force.

In 1966, he assumed command of the Air Force Systems Command. His command has the responsibility for providing the weapon systems and meeting the technology needs of the total Air Force mission. It includes laboratories (such as the co-sponsors of the Conference -- the Flight Dynamics Laboratory and Materials Laboratory) that have responsibilities for the exploratory and advanced development programs, product divisions for development and acquisition of military systems and test centers to insure the capability of these systems prior to their use by Air Force operational commands.

Gen. Ferguson is no stranger to the cockpit. He brings to us a wealth of past experience and accomplishments from the operational commands as well as the research and development area.

Gentlemen, it is my pleasure to present the Commander, Air Force Systems Command, General James Ferguson.

## KEYNOTE ADDRESS

General James Ferguson

Commander  
Air Force Systems Command

It is a great pleasure to be here, and to have a part in this Air Force Conference on Fatigue and Fracture of Aircraft Structures and Materials. I also welcome the opportunity to get away from Washington, where all of us who work on military matters at the Seat of Government have been badly fatigued and fractured for most of this past year.

I would like, with your indulgence, to devote my keynote to a brief exploration of this current trend, and what it will mean to all of us here in the particular context of defense research, development, and systems acquisition. That approach, I think, should be of more use to this very expert gathering than my demonstrating -- in fifteen minutes -- how much less I know than all of you about structural fatigue and fracture theory.

Which is not to say, however, that I do not have a deep appreciation for the excellent work you are doing in this field. I have, on the contrary, a deep and abiding interest in this area, both from my perch at Systems Command and as an unreconstructed fighter pilot. Old fighter pilots, you know, do not always just fade away; they sometimes go out rather dramatically as a result of structural failure directly attributable to fatigue. Not in the pilot -- in the airframe or engine.

You have, of course, helped to minimize that sort of thing, which has been known to ruin a pilot's entire day. Improvements in the Basic Aircraft Structural Integrity Program (ASIP) over the past several years have been many and exceedingly worthwhile. But, consider this: When we held the first Air Force Symposium on Fatigue of Aircraft Structures in Dayton ten years ago, the future of manned aircraft for military purposes seemed to many to be awfully dim. In fact, as you may recall, the future Air Force was being characterized as "the silent silo sitters of the 60s."

Well, since those days we've seen what amounts to a virtual revolution in aeronautics. Thanks in great part to what our laboratories -- military in-house, university, and industrial -- have achieved in materials, structures, flight dynamics, propulsion, guidance, avionics, and other disciplines, we have what really amounts to a renaissance in aircraft. The YF-12, SR-71, F-111, C-141, and C-5 are only a few examples of the advances that have already been accomplished. Each represented an entirely new order of capability over previous tactical, strategic and airlift aircraft. And now we have started to develop the F-15 air superiority fighter, the B-1 advanced bomber seems to be

getting off the ground at last, and approval for such advanced programs as AWACS, the A-X, and a Light Intra-theater Transport seems favorable.

All of these types, whether in production, test, development, or the exploratory stage, will make greater demands upon you than anything within previous experience. These aircraft will be either faster, higher flying, longer ranged, increased in carrying capacity, operating in extremes of environment, extremely maneuverable, or any combination of these. The engines, similarly, will operate in a wide variety of pressure, temperature, and altitude regimes.

So it is quite obvious that considerations of fracture and fatigue will be increasingly more vital. In that connection, Air Force Systems Command is charged with implementing Aircraft Structural Integrity Program requirements as an integral part of the total weapon system R&D and acquisition cycle, from contract definition right through to final procurement.

In order to fulfill this responsibility, we'll have to have a good deal of technological advancement in the areas of materials development, service loads, structural analysis, reliability, testing, and nondestructive inspection, to name only a few.

So you see, your work is really cut out for you; you will certainly find no lack of challenge in the years ahead.

I would like to be able to assure you, then, that you will also find no lack of resources with which to meet that challenge. That, unfortunately, is not very likely to be the case, which brings me to the theme I mentioned: current trends, and their probable effect on the entire defense R&D community.

The causes for the present anti-military climate are numerous, divergent, and sometimes only marginally related. Nonetheless, military and military-related activities present such a large and obvious target that all sorts of diverse dissatisfactions converge upon the man in uniform and all those in any way associated with him. This situation underlies a number of very curious ironies.

First, if nothing succeeds like success, success in the case of military R&D would appear to have succeeded a

little too well. Certainly, a strong case can be made that the so-called "military/industrial complex" has helped the United States to survive, and to grow and prosper in a hostile world. But the very essence of art, it is said, is to hide the labor that went into its creation. And so, having succeeded so well in countering every threat to our national security, we have perhaps made it seem that there is no threat -- or that we are eternally immune from any external threats. Thus, a large part of the American people would seem to feel that external pressures have been relieved, and they turn more attention to the internal pressures in our society.

That very situation was well underscored, I think, in *Newsweek* magazine's Gallup poll of "middle Americans" a few months ago. In an unusually wide sampling of public opinion, as reported by the magazine: "Only two percent of the sampling thought to mention nuclear war as a problem facing the country; fewer than one percent listed Russia or Red China."

Which brings up the second irony. In the years when the people were very sensitive to the dangers of nuclear war, and of the threat from the USSR and China, our nuclear superiority was overwhelming. Technologically, we were far ahead of the Soviets, and Red China had no means of posing any threat to the United States.

So we have, as I say, perhaps succeeded too well. We made it seem almost too easy to be superior and safe. And just at the time when that safety and superiority are most threatened, the people seem to have turned their backs on the danger. They cry for the scalps of the military and industrial elements that together provide a genuine safeguard against the very real danger we face. And among these elements under attack are the military, academic and industrial research laboratories.

As one result, at a time when the Soviets are expanding in every area of research, development, and production of weapon systems, and Red China is testing missiles to deliver its nuclear warheads, many elements in the United States are turning against defense research and development. We find, for example, Cornell University preparing to sell the Cornell Aeronautical Laboratories, and MIT ready to divorce itself from or convert the Lincoln and Instrumentation Labs.

This, too, is ironical -- in its own way as ironical as the anti-ROTC activities on a number of our campuses. Both types of agitation, taken to a logical conclusion, could force the military to turn inward upon itself -- for both officer procurement and R&D -- and to become, in fact, the sort of closed society we are accused of being.

Dr. John Foster, Director of Defense Research and Engineering expressed a very possible outcome in a speech last Summer. "Now here is my concern:" he said, "Research and development funds may well be reduced and then confined for the foreseeable future to some lower level. This

trend faces us just as the Soviet Union has pulled roughly even with the United States in the amount of effort put into defense-related research and development. Furthermore, the Soviet Union is increasing its efforts at a disturbing rate. Therefore, the United States in the future may well see superiority in defense technology pass to the Soviet Union."

As it developed, Dr. Foster was not whistling up phantoms. Later in his address, for example, he said this:

"A logical national decision would be to increase our research and development effort in order to continue our insurance against technological surprise. The new administration wants to do this. The President is requesting an increase in defense R&D of almost seven percent over last year, despite a two-billion dollar overall decrease in the Defense budget recommended by the previous administration."

That, of course, was encouraging. But the hope, as you are probably aware, did not live very long. First, the military authorization bill was debated an unprecedented ten weeks in the Senate -- as against the usual two or three days of previous years. And this, of course, was only for *authorization*, not for the appropriation of any actual funds.

The House of Representatives moved a little more quickly and was somewhat more liberal with the figures. But, when the two houses received the compromise conference bill, R&D authorizations for all the Services had been cut 11% below the level requested by the administration. In addition, Title II, Section 203 of the bill reads:

"None of the funds authorized to be appropriated by this Act may be used to carry out any research project or study unless such project or study has a direct and apparent relationship to a specific military function or operation."

That provision, I am afraid, is so open to divergent interpretation as to be, potentially, severely restricting. While it would seem to apply more to basic than applied research, it *could* very well result in limiting a good many of our R&D projects. It would be very interesting, in fact, to track back and see how many of today's operational or near-operational developments originated in studies and projects that, at their inception, appeared to have *very little*, if any, direct military application.

In any event, we see that Dr. Foster's fears have been realized. Nor can we take any genuine comfort from the fact that, on the whole, the Congress dealt rather kindly with the military procurement authorizations. Many of the Senate votes, you will recall, were uncomfortably close. There is every indication that the years ahead will see the momentum build up. At the same time, we know with reasonable certainty that the administration will be requesting a lower level of funding for defense. So the pressures for reduction will be coming from both the Executive and Legislative branches.

I can only promise you, then, that we all face some lean years into the foreseeable future. Yet our responsibilities will not diminish; if anything, they are increasing, and particularly in view of the pace at which the Soviets are pursuing technological progress.

The supreme irony, however, is this: After ten years of centralized management and control in the Office of the Secretary of Defense, with the military Services having very little to say about their own programs, and with very few new starts in major weapon systems, the entire picture has changed. Detailed management of systems programs -- with the necessary authority and responsibility -- is being given back to the Services. In the case of the Air Force, for example, the focal point for managing R&D and systems acquisition is back at the Air Force Systems Command. And, as I mentioned earlier, we have been given the go-ahead for a large number of new starts -- an advanced interceptor, the LIT, AWACS, the A-X, the F-15, and the B-1, among others.

But -- and this is the irony -- while we have an embarrassment of riches in approved programs, we are more than likely to suffer an embarrassment of poverty in the resources necessary to carry them out.

I think you can see, then, what the climate is today, and what it will most probably be for some time to come. The President has set the tone and supplied the dominant themes -- decentralization of authority, more *selectivity* among technological possibilities, and better defined goals and priorities. He has pointed out a new way of doing business, but it is very clear that both he and the Congress expect it to be done with less money.

Secretary Laird, his deputy, Mr. Packard, and Dr. Foster have pledged, in turn, that there will definitely be less risk-taking in the acquisition and production of major systems; and that development and production will be decoupled, with meaningful milestone decision points acting as the buffers.

This means that risk-taking on large systems and large expenditures is going to be at a minimum. The base line of exploratory development -- even though six to fifteen years from initial inventory -- is going to have to be narrowed. In advanced development, we will be called upon to demonstrate *feasibility* of certain subsystems to a much greater degree than ever before, in order to reduce the risks on systems that may take advantage of such technology. Each of these "high order" demonstrations, in turn, will consequently require more resources than we might normally expect to apply to an advanced development program. We know, therefore, that fewer items will be able to reach the demonstration stage.

As far as the labs are concerned, I feel that our Technology Needs program, and our greater emphasis on sound mission and systems analyses, will help us to achieve the long-range foresight that will be necessary to put our diminishing resources on the right items.

Those of you in the laboratories -- whether our own Air Force labs or those university and commercial facilities with which we contract -- obviously have your work cut out for you. *Realism, selectivity, feasibility* -- these are the characteristics of the operative environment for some time to come.

My long years in the management of military R&D have convinced me completely of the necessity and value of the labs; they have impressed me with the caliber of the people and the superb quality of the work; and, above all, they make me wish that I could give free rein to the creative and innovative spirits that have made our laboratories great.

Unfortunately, for the many reasons I have outlined here today, this is not possible. Along with the scientific and engineering disciplines in which each of you works, there is now the added discipline of increasingly limited means. I would particularly ask, therefore, specifically of those of you in the AFSC laboratories, that you enter into a broadened and continuing dialogue with the Systems Division -- ASD, ESD, and SAMSO -- and especially with the Systems Program Offices. And again, your relationship must be carried out in terms of *realism* and *selectivity*.

There is also a need, as you are probably aware, to be especially *articulate* in communicating with the program managers -- in justifying your projects and the need for them. After all, they are faced with a very definite ceiling on expenditures, and in this climate of *realism* and *selectivity* you might naturally expect them to place more value on the "bird in hand" than those "in the bush." The burden, then, is upon you, to *convince* them that you offer something measurably superior to what is already in hand. This is no small burden, because without the ability to be convincing in this respect, the very genuine value of your basic work might be only academic.

In summary, the future promises to be difficult. Our potential adversaries are pushing on all the frontiers of technology. We cannot safely do less, and yet we must achieve our technological goals with less in the way of money, manpower, and facilities. This is the ultimate challenge to our ingenuity, our creativeness, our sense of realism, and our managerial competence.

One thing we can clearly predict: With the small force structure we know is ahead, and with all resources limited, each of our aircraft will have to be better, more capable, stronger, more durable, and preferably less costly. That's a huge order. The more we can learn and apply concerning fatigue and fracture of aircraft structures and materials, the better our chance of filling that order.

I wish you every success in your conference. A great deal depends upon what all of us can learn here from each other.

Thank you.

## FATIGUE MECHANISMS, FATIGUE PERFORMANCE AND STRUCTURAL INTEGRITY

by

A.M. Freudenthal

The George Washington University

To present the opening paper at this distinguished conference imposes on the speaker the obligation to attempt to correlate its specific objectives, as outlined in the invitation, in the light of its over-all purpose, in order to establish the unity of purpose in this interdisciplinary research and development effort in fatigue and fracture of aircraft structures and materials. Since the individual objectives are pursued by research at different levels of "observational resolution", the correlation of objectives will provide the correlation between those levels, so that the designer or stress-analyst viewing the airframe as a progressively cracking elastic structure, can be made to understand on the one hand the approach of the metallurgist who is attempting to control the initiation and propagation of the crack in the micro-structure of the metal, and on the other that of the reliability statistician for whom the individual airframe in a fleet is nothing more than a member of a statistical population defined by the distribution function of the time to failure or to a specified "damage". At all three levels the principal concern is with progressive damage in the form of structural defects, with its rate or probability of growth and with the possibilities of its control by material selection and/or by design. Thus the difference in the research approach at the three levels is only one of emphasis; however, the differences in the professional training and background of research workers at the different levels of approach cannot fail to produce the idiosyncrasies that make effective communication, which has to precede any attempt at correlation, rather difficult.

The problem of fatigue and of structural reliability under conditions leading to fatigue has grown in importance with demands for longer operational lives of aircraft and with the increasing use of high-strength structural alloys resulting from rapid rise in weight and increasing severity of operational conditions. The problem of fatigue arose almost immediately with the use of metals in structures subject to dynamic loading, beginning with the introduction of coach service on the roads of France, and continuing with the development of railroad bridges and locomotive axles in England about 100 years ago, with the manufacture of cars, welded ships and other structures, pressure vessels and, finally, aircraft. At every step in the development of new structural types of forms, a similar sequence of events has been repeated: introduction of a new material to meet new performance requirements was followed by a sudden incidence of fatigue failures, a flare-up of fatigue research and

a gradual accommodation to the new conditions by improvements in design, in testing and in fabrication. The metal producing industry, whose approach to improvement of structural materials has always been in terms of static tensile strength, usually blames the designer or the fabrication process for inadequate fatigue performance and resists pressure for improvement of this performance as long as the produced material can be sold in quantity, unless such improvement is specially paid for by the prospective user. Even then, if the industry undertakes this task at all, it is with considerable reluctance simply because, up to the present time, reliable guiding principles for the development of metals of superior fatigue performance are lacking.

Fatigue research by the metal producing industry, when existing at all, is minimal. There is, at best, some half-hearted conventional fatigue testing for not clearly specified purposes. In spite of the fact that more than 95 per cent of all reported structural failures are fatigue failures, the industry appears to have convinced the users that the principal approach to improved fatigue performance is through design, fabrication, and testing rather than through the specific development of fatigue resistant materials. The emphasis, in recent years, on crack propagation as the principal fatigue research topic illustrates this fact quite convincingly: materials evaluation for fatigue performance is based on crack-propagation rates in metals developed, produced and accepted on the basis of static strength properties that are not or are only vaguely related to fatigue performance.

Fracture mechanics has, in fact, been a boon to the metal producing industry: it has made the finite crack in a structure reputable and even fashionable. To raise the question of the possibility of developing and of producing a reasonably high-strength metal of commensurately high resistance to fatigue damage before the initiation of a propagating crack seems, at present, somewhat old-fashioned and may even raise the suspicion that the questioner does not know enough fracture mechanics. Nevertheless, and in spite of the fact that under current conditions of material development the structural designer has to live with cracked structures and therefore with fracture mechanics, the control of progressive damage under cyclic straining preceding crack propagation is the key problem in the development of fatigue resistant materials.

The stage of fatigue crack propagation, to the analysis

of which concepts of fracture mechanics are applicable, extends in a well designed structure roughly over the last 40 to 60 per cent of its expected fatigue life. The significance of fracture mechanics based on continuum theory arises directly from the fact that, at this stage of fatigue damage, metallurgical microstructure is not of major significance. This can be inferred from the general form of the well-known and experimentally verified relation between the rate of crack propagation per cycle ( $dc/dN$ ) and certain relevant material and design parameters

$$\frac{dc}{dN} \sim (G \cdot \gamma \cdot \sigma_y^2 \cdot H)^{-1} \cdot K^\alpha \quad (1)$$

where the elastic shear modulus  $G$ , the strain-hardening modulus  $H$ , the yield stress  $\sigma_y$ , the surface energy  $\gamma$  and the exponent  $2 < \alpha < 5$  are material parameters that depend on microstructure, while the stress-intensity factor  $K$  is essentially a design parameter.

Considering that a faulty design of some critical structural detail can easily raise  $K$  by a factor of two, leading, for the usual values of  $\alpha$ , to a premature crack propagating at about 10 to 100 times the expected rate, it is easily seen that such increase cannot be compensated within the practical range of variation of the micro-structure-dependent material parameters in competitive structural metals, even if  $\alpha$  is substantially reduced towards the range of  $2 < \alpha < 3$ . Such a reduction of  $\alpha$ , however, is not achieved by modification of the microstructure of a particular type of metal, but requires the selection of a material with a basically different mechanism of crack-propagation and thus of a basically different type of microstructure. Since a drastic reduction of  $\alpha$  is usually accompanied by a reduction of  $\sigma_y$ , even the substitution of a different microstructure may not adequately compensate for faulty design, once the crack-propagation stage is attained. Fatigue crack propagation rates in a structure with fatigue sensitive details are therefore much more effectively controlled by careful design and development testing of details, and by the incorporation in the design of crack-stopping or crack-retarding elements, than by materials selection on the basis of the evaluation of expected fatigue performance by S-N diagrams or by fracture-toughness.

The very weak dependence on microstructure of the crack-propagation process in fatigue is further confirmed by the existence of the almost material-independent approximate relation between the plastic cyclic strain range  $\epsilon_p$  and the number  $N$  of cycles to failure of unnotched metal specimens in "low-cycle" fatigue in which a large fraction of the fatigue life  $N$  is crack-growth

$$\epsilon_p N^n = \text{Const. for } N < 10^5 \quad (2)$$

where  $0.5 < n < 0.8$  shows a weak dependence on microstructure. This equation can also be applied to crack propagation through the plastically strained material by assuming that, in rough approximation the rate of crack propagation

$$\frac{dc}{dN} \sim \frac{c}{N} \quad (3)$$

and therefore, from Eq. (2)

$$\frac{dc}{dN} \sim c \epsilon_p^{1/n} \quad (4)$$

It should be pointed out that all of the above relations and conclusions do not necessarily apply to high-strength steels. The recent development of these steels has emphasized high tensile strength at reasonably high toughness with respect to fracture under unidirectional straining rather than cyclic straining. The fact that "fracture toughness" is not a direct measure of fatigue performance cannot be over-emphasized. Particularly in the non-homogeneous microstructures characteristic of low carbon high-strength steels the strain-concentrating effect of the hard phases under reversed cyclic strain, as well as of the diffusionless transformation processes, damages the fatigue performance without affecting fracture toughness.

In view of the weak effect of microstructure on the crack-propagation process, an improvement in the fatigue life of a well-designed structure subject to a spectrum of forces of a certain intensity can only be expected from

- (a) use of a material with the lowest possible value of  $\alpha$  at the highest possible yield stress;
- (b) reduction of the cyclic plastic strain produced by the specified intensity of the spectrum;
- (c) retardation of the damage initiation process in the microstructure so as to delay the start of the process of crack-propagation.

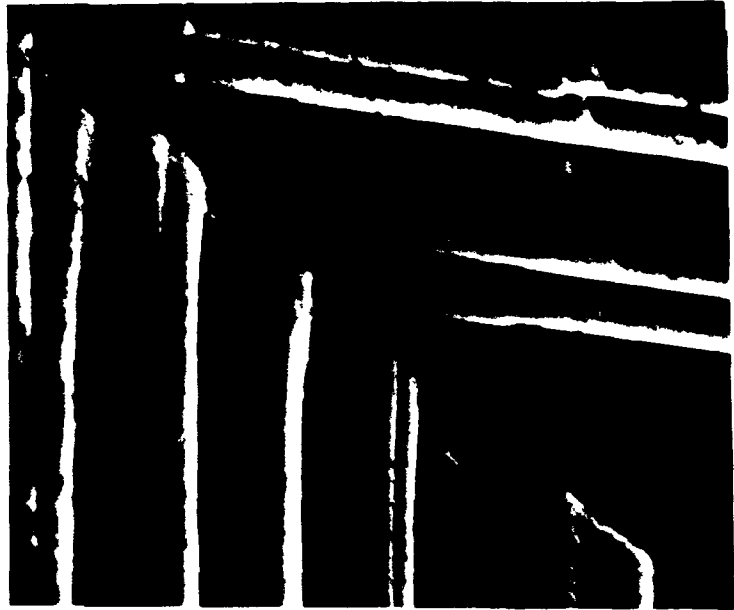
Of these three possibilities, it is the last which is likely to produce the most substantial improvement, the first two being concerned only with the crack-propagation stage.

Nuclei of fatigue damage develop very early in the course of cyclic straining as the result of the incompatibility of the locally anisotropic, incompletely reversed slip processes in the heterogeneous polycrystalline microstructure with the deformational restraints imposed by grain boundaries as well as with the continuity of the macroscopic strain field.<sup>1</sup>

In uni-directional straining local incompatibility centers are smoothed out by widely dispersed slip, while the concentration of reversed slip in striations intensifies rather than relieves existing centers and creates new ones. In the course of cyclic straining such incompatibility centers become damage nuclei the severity of which increases with the number of applied strain cycles at a rate that depends on the extent of local micro-slip per cycle<sup>2</sup>. The momentary fatigue damage in the material is determined by the severity of existing damage nuclei and their volume or surface

**Figure 1. Interfering Slip Motions under Reversed Torsion (Strain Amplitude 0.8%) on Surface in Pure Copper Tubular Specimen, Producing Incompatibility Center in the Form of Micro-hole at Boundary Between Adjacent Grains.<sup>3</sup>**

**(a) Magnification x6000**



**(b) Magnification x24,000**

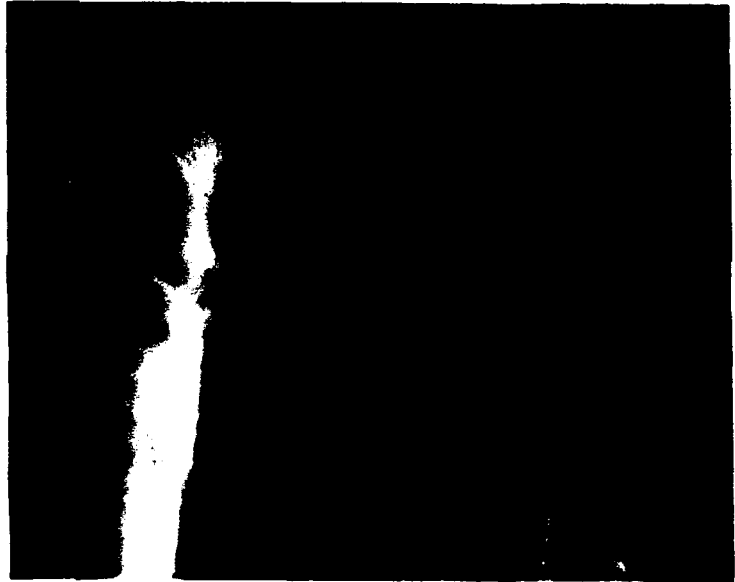


**Figure 2. Surface Folding Produced by Reversed Shear (Strain Amplitude 0.8%) and Extrusion of Metal Flake in Pure Copper Tubular Specimen (Magnification x5000).<sup>3</sup>**



Figure 3. Local Surface Disruption Produced by Reversed Shear (Strain Amplitude 0.8%) in Pure Copper Tubular Specimen (Magnification  $\times 2250$ ).<sup>3</sup>



concentration. Severity of individual damage nuclei depends on microstructure, strain-amplitude and number of strain-reversals, while their concentration is also affected by the inhomogeneity of the strain field.

In polycrystalline metals, damage nuclei develop both in the grain or cell boundaries and within the grains. Cell boundary nuclei are the result of incompatibility of adjoining active slip system as indicated on Fig. 1, while damage nuclei inside the crystal develop from the penetration of the surface by concentrated reversed slip accompanied by ridges, grooves, and small extrusions (Fig. 2) into local material eruptions from a completely shattered surface (Fig. 3). These observations on the scanning electron microscope on copper in reversed torsion are made at strain amplitude  $\pm 0.0075$  in the life range of  $10^5$  cycles at 250 and 1000 cycles respectively, that is within less than one per cent of the expected fatigue life.<sup>3</sup> It is interesting to note that the shattering of the surface is visible only in oblique illumination. In vertical illumination, only the slip traces appear, producing the apparent regularity of the slip deformation characteristic of the optical microscope and the replica technique of the electron microscope.

The relative importance of crystal slip and of grain or cell boundary restraints on the development of incompatibility centers depends necessarily on the mobility of the boundaries. Since the fatigue life of single crystals is much less affected by elevated temperature than that of the polycrystalline aggregate, and since elevated temperatures affect the boundary mobility much more than transcrystalline slip, it might be assumed that at room temperature the more severe fatigue damage nuclei develop as the result of transcrystalline slip and surface shattering, while boundary nuclei become increasingly significant as the temperature increases. The cell structure itself, which is associated with a metastable "cyclic state" and is a function of strain-amplitude and temperature, has no direct relation to the damage

process other than that of producing a deformed microstructure in which, by a yet unknown mechanism, micro-cracks are progressively developing.

It seems therefore convenient to keep the deformation phenomena under cyclic straining of the microstructure separated from "fatigue damage". Changes in the microstructure as well as changes in the stress-strain relation associated with deformation under cyclic straining is reasonably well understood; the mechanism of fatigue damage initiation is still not quite clearly understood, although very recent observations provide clear evidence of the intensification of the regions of incompatibility of reversed slip (Fig. 4) in adjacent crystals of different orientation which finally leads to a local break-up of the microstructure accompanied by microcracks. The few observations presented here seem to suggest, however, that the initiation of fatigue damage by the formation of damage nuclei from deformation incompatibility centers, and their coalescence into microcracks, cannot be realistically dealt with either on the lattice defect scale or on a (elastic or plastic) continuum scale. Neither the concept of formation of atomic vacancies by intersection of moving dislocations and their coalescence into clusters, nor that of cracking produced by dislocation pile-ups have any apparent relation to what appears to be the process of fatigue initiation reflected by the observations. Clusters of atomic defects are hardly stable enough to form damage nuclei of the order of magnitude of  $10^{-5}$  to  $10^{-4}$  mm that appear to delineate the start of the fatigue initiation process. On the other hand, the shattered microstructure around a number of dispersed damage nuclei cannot be reasonably well represented by an elastic continuum in which a single crack propagates at a velocity that depends on its elastic stress-intensity factor. The concept of a perforated sheet in which the damage nuclei ("pores") represent the perforations, and crack propagation proceeds between preferentially aligned nuclei, which has been suggested by Wood<sup>2</sup> for the H-stage, seems to provide the most reasonable model of the fatigue crack initiation process. It seems justi-



Figure 4. Microcrack at the Boundary Between Three Grains in Pure Copper Tubular Specimen under Reversed Torsion Resulting from the Incompatibility of the Deformation in the Adjacent Grains (Magnification  $\times 11,750$ ).<sup>3</sup>



fied to assume that an applied or a residual tensile mean stress will significantly facilitate this process by reducing the energy release rate associated with crack extension between nuclei.

From the designers' point of view, fatigue resistance in the H-stage is the significant property for effective material selection. Once it is admitted that the initiation of a fatigue crack *cannot* be prevented, the effect of materials selection is secondary to that of reduction of crack-propagation rate by design and development testing of fatigue sensitive details. Only under the assumption that crack-initiation in these critical locations *can* be prevented does selection of a fatigue resistant material become significant, not only with respect to structural safety, but still more with respect to economy of maintenance coupled with improved fleet readiness. The development of fatigue resistant materials in which crack-initiation is significantly retarded is the only certain way to a drastic reduction of maintenance costs and of the uncertainty of life prediction associated with highly fatigue sensitive materials.

Intensity and concentration of damage nuclei are obviously most severe at the location of the largest strain-amplitudes. In the case of a long range transport the most damaging strain cycles are produced by the ground-air-ground cycle; with an assumed average time between landings of 3 hours and 30,000 hours design service life, their number is of the order of magnitude of  $10^4$ . Considering that the associated nominal strain amplitudes in the critical members may attain values of 0.1 to 0.15 per cent (which would be in the F-range), the magnification of these values by local stress concentrations might easily reach 0.5 per cent with an associated fatigue life at the upper limit of the H-range ( $N \sim 10^5$ ). Considering that in this range observations show development of severe damage nuclei at less than 10 per

cent of this limit, it would appear that fatigue damage initiation in aircraft structures arises from interaction, at the critical locations, of the effects of the multitude of flight induced strain-cycles (that are either in the F or the S range) with the damage nuclei that are gradually intensified by the almost periodically induced ground-air-ground cycles and other less frequent but more damaging accidental cycles arising from thunderstorm gusts or clear-air turbulence. This interpretation is supported by results of spectrum fatigue tests in which the ground-air-ground cycles produce a highly disproportionate amount of damage, a result that should completely shatter any remaining belief in the usefulness of Miner's uncorrected rule. If therefore this damage accumulation in the H-range could be significantly retarded, the total fatigue life might be increased by several orders of magnitude.

Improvement of the fatigue resistance by retardation of the formation of damage nuclei in the H-range would require a drastic reduction of the extent of slip in this range which could be achieved by grain-refinement that remains stable under reversed straining. A very fine-grained structure stabilized by a finely dispersed alloying element is obviously associated with a high elastic limit that is the result of stable pinning of the structural defects by the dispersed particles. However, in metals elasticity up to high stress levels under uni-directional *and* reversed straining is an anomaly that can be expected only if the pinning of the defect structures is reasonably stable under all conditions of straining. The rate of fatigue damage initiation will depend on the *rate of loss* of this stability under *reversed* cyclic straining as a function of strain amplitude and of frequency.

Such loss will be most pronounced in pure torsion where the stabilizing effect of a hydrostatic stress component does not exist. Instability can therefore be demonstrated

best by the superposition of an axial load on cyclic torsion, since this load magnifies the instability effect by producing the "cyclic creep" which is a manifestation of the microstructural instability.

In a recent study of the fatigue performance of some high yield low-carbon ferrous metal alloys<sup>6</sup>, the desirability of a very fine-grained, homogeneous, stabilized microstructure has been demonstrated by the truly outstanding performance of the quenched and tempered 5 Ni-Cr-Mo-V (HY130) steel.

In another study<sup>7</sup>, the normally neglected effect of the frequency of cyclic straining on the stability of dislocation pinning has been demonstrated by exciting low-carbon iron specimens at ultrasonic frequency. While no indication of any change in microstructure could be discovered at strain amplitudes up to  $13 \times 10^{-4}$  and conventional frequencies (1700 cpm), isolated slip was intense

at ultrasonic frequency (17,000 Hz) already at amplitude of  $2 \times 10^{-4}$ , microcracks appearing at amplitude  $4 \times 10^{-4}$ , which is less than one third of the "safe" limit at conventional frequencies. These observations support the interpretation that fatigue damage initiation depends on the level of the stable elastic limit that can be produced by dislocation pinning. The stability of this pinning prevents the breakaway of dislocations at low frequencies of cyclic straining and within a certain range of strain-amplitudes. At ultrasonic frequencies resonance of dislocation loops oscillating about the pinning points may lead to local break-away at points at which the applied energy will concentrate and produce intense slip followed by microcracks.

The close interrelation between the fatigue performance of the airframe and the changes in the microstructure of the metal are illustrated by these examples, which thus demonstrate the necessity of the interdisciplinary approach to fatigue to which this conference is devoted.

#### REFERENCES

1. A.M. Freudenthal, *Proc. Symp. Internal Stresses and Fatigue*, p.428, Elsevier Publishing Co., New York (1959).
2. M. Ronay, "On Strain Incompatibility and Grain Boundary Damage in Fatigue," *Acta Tech. Acad. Sci. Hung.*, 54(1-2):199-218 (1966).
3. W.A. Wood, *Fatigue Crack Initiation as Viewed by Scanning Electron Microscope*, TR-1, George Washington University, Washington, D.C. (1970).
4. W.A. Wood, "Systematic Microstructural Changes Peculiar to Fatigue Deformation," *Acta Met.*, 11:643 (1963).
5. W.A. Wood, "Yield and Second Order Effects Induced by Cyclic Torsion in Copper Under Tension," *Acta Met.*, 15:841-846 (1967).
6. M. Ronay, *Fatigue Performance of High Strength Steels as Related to Their Transformation Mechanism*. Presented at the Air Force Conference on Fatigue and Fracture of Aircraft Structures and Materials, Miami Beach, Florida, December 1969.
7. W.A. Wood and W.P. Mason, "Fatigue Mechanism in Iron at Ultrasonic Frequency," *J. Appl. Phys.*, 40:4514 (1969).

**SESSION 1**

**THE ROLE OF MATERIALS IN STRUCTURES**

*Moderator*

Dr. H. M. Burte  
Air Force Materials Laboratory

# THE MATERIAL SELECTION AND STRUCTURAL DEVELOPMENT PROCESS FOR AIRCRAFT STRUCTURAL INTEGRITY UNDER FATIGUE CONDITIONS

by

Joseph P. Butler

The Boeing Company  
Commercial Airplane Group  
Renton, Washington

## I. INTRODUCTION

Since man first glanced at the unbounded sky above him and noted the grace and the ease of flight by the birds about him, he has conjured schemes to sever his bonds to earth. Mimicry and materials of the day gave Daedalus and Icarus the freedom of flight in mythology. However, Icarus, a venturesome test pilot overcome with the ecstasy of flight, ignored the operational placard limits and soared too close to the sun, as mythology would have it. As a result, his bird-like wing structure, perhaps the first composite or bonded structure, be it only feathers and wax, lost its structural integrity as the wax melted in the heat of the sun and Icarus plunged into the sea. Stone, clay or paper have since recorded man's endeavor to break the gravity barrier and enter into the realm of flight. These recorded configuration studies of man's fantasy and fascination with flight were quite heavily guided by successful vehicles of the day; i.e., the birds, and in the light of today's technology, would be put in a category for the birds!

Nevertheless, in these records of man's yearning for flight status, he was faced with the choice and limits of materials around him. Earned knowledge of fabricating and joining structures from materials around him led to resolution of the lack of naturally grown flight structures. Man had to synthesize and identify the essential characteristics of flight structures as he saw them. On paper man's imagination was free to soar in that two-dimensional world. And, perhaps there are certain advantages to this constriction. Certainly, there are no paper airplane failures or coincident, premature fatigue damage. Only with the choice and the fabrication of materials into real structures do difficulties appear.

In today's world, the frustrations of reality can be illustrated by Fig. 1. This is a summary chart of the various fatigue incidents recorded in the FAA Airworthiness Directives pertaining to large aircraft. It should be self-evident that these incidents are not planned but rather reflect the interaction of real materials, their application and their environment. Somewhere in the archives of nineteenth-century literature is recorded a pertinent philosophic observation that may aptly summarize the situation. This observation is "It ain't the things we don't know that get us into trouble. It's the things we know that ain't so."

Certainly during the design process we "know" or define a solution with certainty or resolution but only gain positive knowledge of its reliability through experience.

## II. THE STRUCTURAL TASK

In the subsequent remarks, the nature of the task for material selection and structural development for structural integrity under fatigue conditions will be reviewed. A first cursory look is directed at the structural task and the developmental testing requirements. The share that operational environment, fatigue crack initiation, fatigue crack propagation and material and structural configuration residual strength characteristics play in the process is then considered in relation to the selection and developmental phase. The aspects of inspection control, fatigue variability and fatigue damage containment are reviewed and the material selection and structural development process summarized.

Taking some liberties with the tools of systems analysis, Fig. 2 has been created to highlight the path the struc-

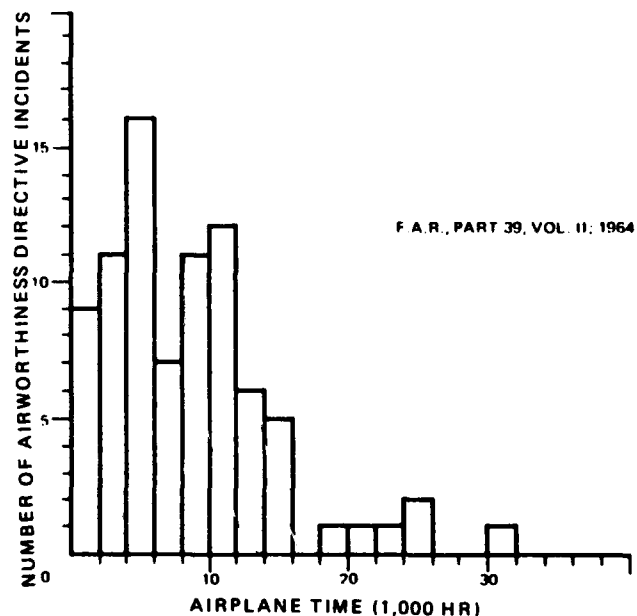


Figure 1. Structural Fatigue Performance of Aircraft Structures.

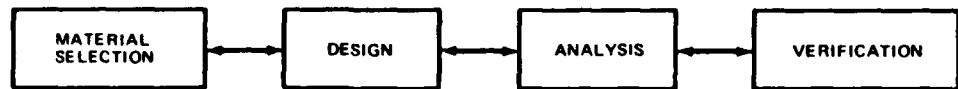
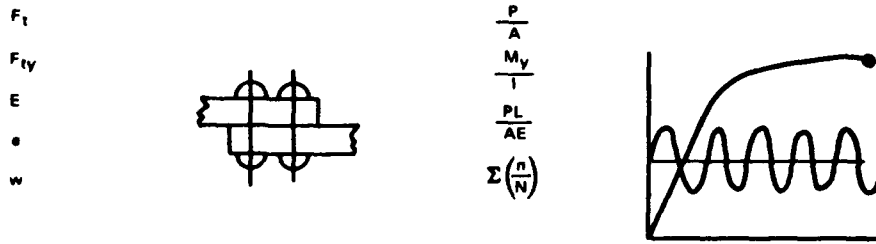


Figure 2. The Structural Task for Materials.



tural engineer essentially follows in resolving his task. Without question, material selection is the first step towards structural design. However, the shape and/or function elements of design are closely tied to a material's behavior. Ultimate strength,  $F_{tu}$ , the elastic behavior such as the yield stress,  $F_{ty}$ , and the stiffness, as defined by the modulus of elasticity,  $E$ , are the first important characteristics. Also, a part of this evaluation process is the yielding behavior of the material, as indicated by the total elongation capability of the material,  $e$ . Unit weight or material density is obviously an important element in the selection process for both structural efficiency and dollars per pound evaluation. The design function is simply illustrated in Fig. 2 as a joint. Configuration and function such as load transfer are the key elements in this part of the critical path in structural design.

With determination of the product shape and necessary function, the task becomes one of analysis to substantiate the likelihood of successful operational performance. Loads and material properties must be matched as a first task. In this stage, consideration must be given to the problem of survival of the structure under the varied conditions of usage, which may be known, defined or even unknown in detail. Fatigue is one element of this task. Its cumulative effect is summed up by the Palmgren-Miner Cumulative Damage Rule and the variable load cycles must be pertinent to the actual operational use of the structure. Unstated but a parallel consideration is the calendar time problem and the associated physical environment, like corrosion, which likewise may have a cumulative effect on the service behavior of the structure. So far the materials selection problem is likely to be a paper operation. Now the designer is faced with the verification or demonstration stage. Here structural testing of materials and their designed structures must be accomplished to assure successful interaction of design and analysis functions.

Where the structural designer's path leads through an area of both new materials and design, the need and objectives of materials and structural testing are found as both initial and final verification stages of the design task. In Fig. 3, three major stages of the structures task are presented. The first stage is concerned with the ascertaining of the strength and stiffness of the structure for its envelope of total usage. This first stage defines the likelihood of building a device or structure at all. Next, if the structure func-

tions, will it survive it's intended operational or service usage? Both cumulative exposure to its total load environment and its likely survival as measured by fatigue performance and the probable or improbable initiation and detection of fatigue cracking in the structure are the main factors of this goal. The actual reliability of the structure, an after the fact event, makes itself known only after operational exposure and long after the design and verification stages. In fact, reliability in terms of structural performance is the response to a sometimes nightmarish kaleidoscope of conditions. Surviving the exposure to the total environment of mechanical loads and physical exposure is probably the primary hurdle for success in meeting practical reliability. The likely appearance of fatigue damage after exposure to the environment is not an absolute measure of the structural reliability. Fatigue crack propagation or growth in the structure and its containment are attenuating factors. Structural maintainability, repairability or replaceability of the structure and most impor-

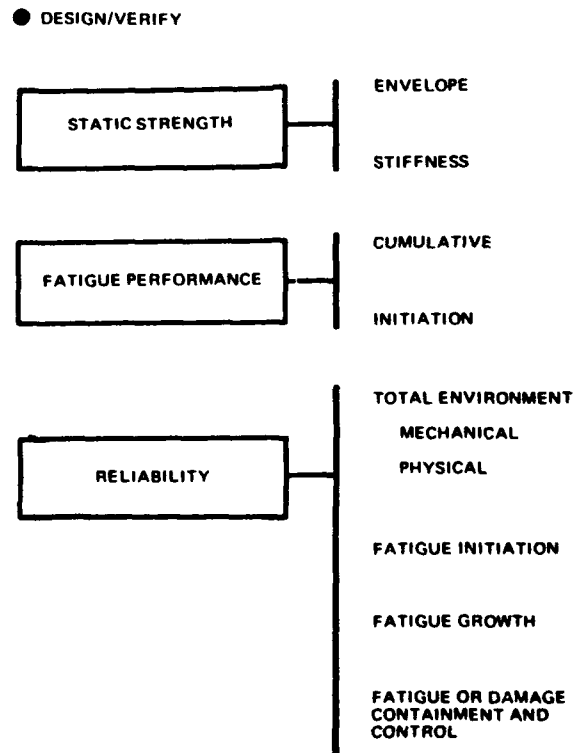


Figure 3. Objectives of Materials and Structural Testing.

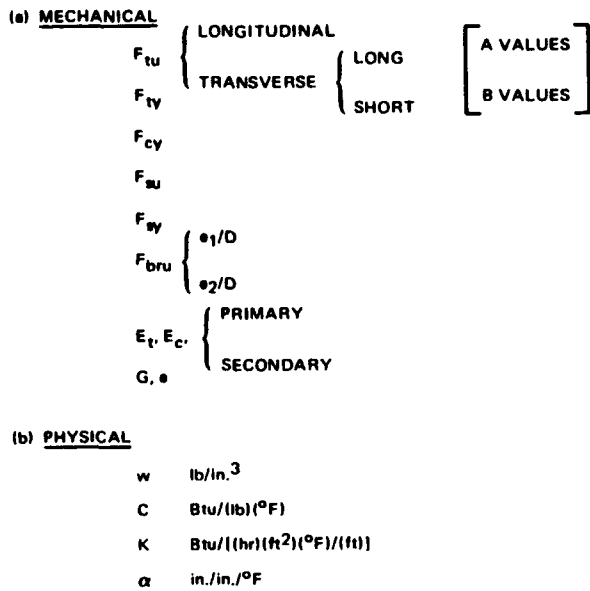


Figure 4. Material Properties for Design.

tantly the safety of the structure under conditions of operation with undetected or unexpected fatigue damage or other likely damage place fatigue damage initiation into its frame of reference. It is suggested that the indeterminate or premature, unplanned appearance of catastrophic fatigue damage or the untenable grounding of a fleet of aircraft because of suspected fatigue damage are key factors in the evaluation of fatigue damage initiation.

In essence, then, the task of material selection and the definition of structures of the selected material is a process of directed testing and associated analysis to cope

with the uncertainties of the problem. Accordingly, the testing process is really a specific design data development and verification process rather than just something to do. Usable and useful information is the desired output.

The use of materials in structural elements or components needs the knowledge of material behavior under its expected structural environment. Both mechanical and physical behavior of materials are well documented for the aeronautical designer in such tomes as MIL-HDBK-5.<sup>1</sup> Ultimate tensile strength, tensile and compressive yield stress, shear properties, stiffness properties like the moduli under direct or shear loadings are the basic properties that only experiment can define. Unfortunately materials are not homogeneous and fabrication processes affect these properties in various directions. Longitudinal grain, transverse grain, edge margin and stress level affect the measured quantity. Figure 4 sums up these necessary mechanical properties and physical constants.

Variability is found in any one property. Hence, material strength is a statistical quantity and the designer is faced with the task of recognizing probabilistic levels of performance. Strength properties are generally established at a 95% level of confidence for which an "A" value is equalled or exceeded 99 percent of the time. A "B" value property has the same confidence level for equalling or exceeding a defined value with a probability of only 90 percent. Physical properties or other unidentified levels of certainty are usually only average values. Hence, the engineer is faced with not only an experimental process but a significant sampling effort to define even the simplest of properties. For instance, the tensile ultimate and tensile yield stress (i.e., 0.002 in./in. offset) properties and mod-

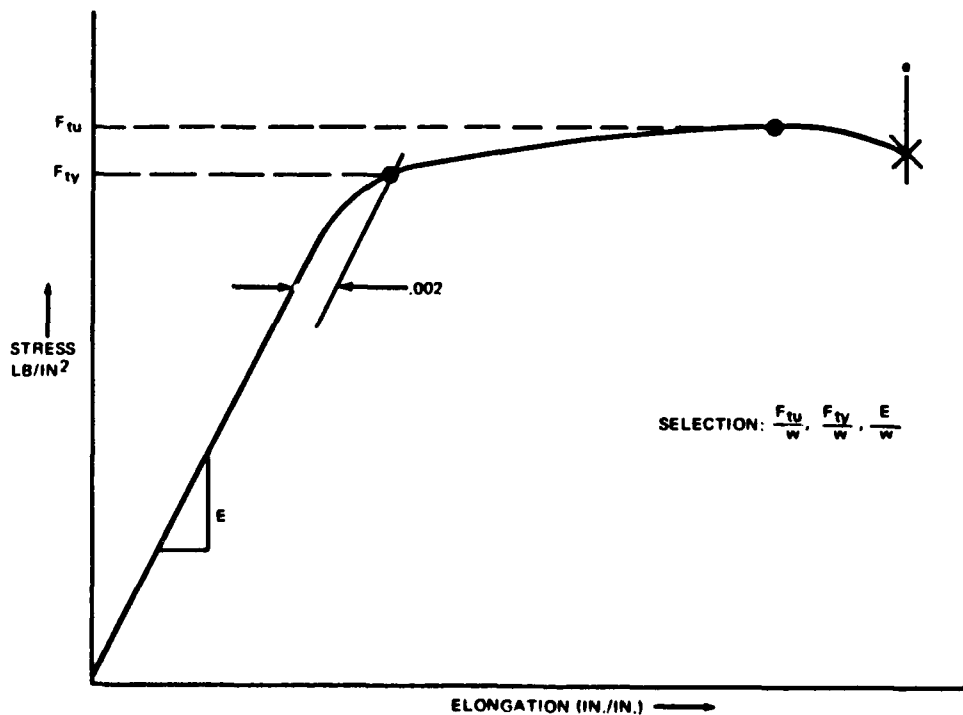


Figure 5. Material Properties.

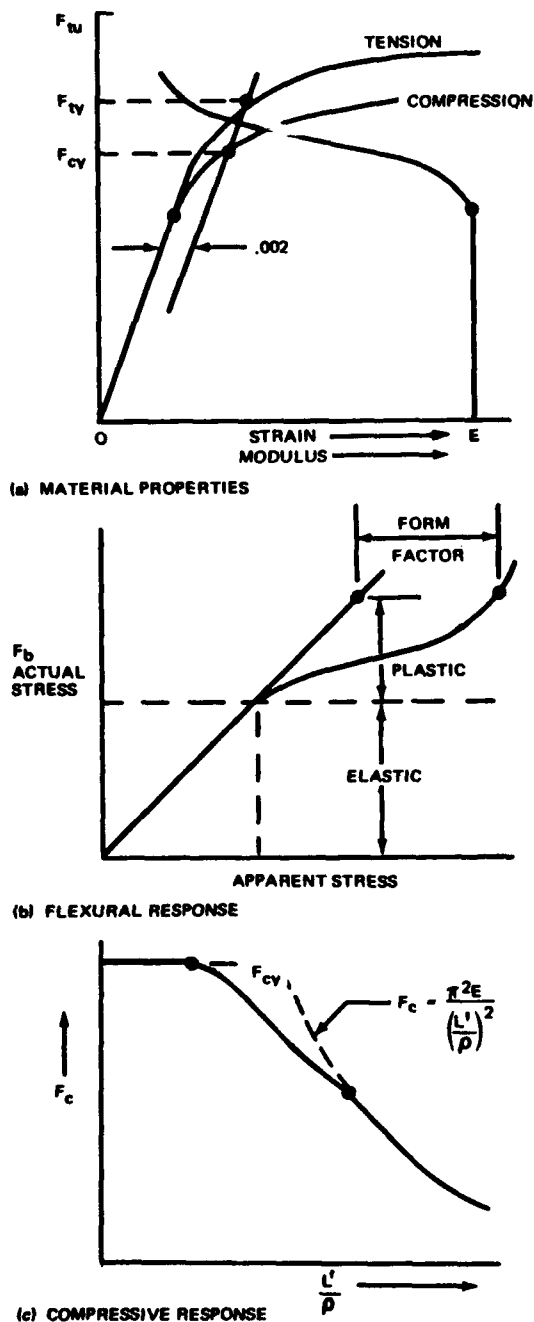


Figure 6. Material Properties and The Structural Response.

ulus are derived from a load-strain curve of a rather arbitrarily defined specimen and gage length on that specimen. This measurement, as illustrated in Figure 5, provides the first step in sizing the material for a structural element. The choice of material requires formation of an efficiency parameter that measures strength or stiffness per unit weight. In Figure 6(a), the stress-strain characteristics for tensile and compressive properties are shown to be different with the nature of the stress. Furthermore, the modulus is shown to depart from a fixed value at the proportional limit. Use of

the material in a structural element also requires further definition of the material's behavior. In Figure 6(b), the flexural response of a material to the more complicated stress fields of an element under bending forces is typified. Both the cross-sectional shape and the stress level indicate departures from the satisfying or peaceful world of elasticity and its comfortable formulations. Figure 6(c) outlines the problem of the compressive exploitation of materials in structural elements. As may be inferred from Figure 6(a), the stability of the elastically formulated Euler column equation needs modification by use of the local or tangent modulus as well as a cut-off usually associated with the compressive yield of the material.

So far, the preoccupation has been with ultimate strength. Aircraft structures have a long history of design development derived upon the strength properties of materials defined by specific test and analysis of internal stresses of the structure. Likewise, in considering the resolution of fatigue and fracture oriented problems, specific and purposefully directed testing is necessary to design and verify the structural behavior of materials and their structural element or component deployment. In Figure 7, some of these considerations are enumerated. Basic strength and stiffness have already been discussed. The local stress field, as created by the actual shape of the structure or element, adds complications. A change of section shape along the load path does nothing but add duress to the state of stress. In simple terms, such a section change is a notch and results in local distortion of the nominal stress as the load flows through the member and becomes a point or area of stress. In a broader sense the transition of a structure from a single element to a built-up structure poses some of the same problems as the notch. In this latter sense, careful selection of the structural configuration may minimize the stress field distortion.

### III. OPERATIONAL ENVIRONMENT INFLUENCE

Actual structures have a real exposure from two viewpoints. Strength must match not only the envelope of loads found during the actual use of the structure but also all the cumulative and variable loads. Another significant part of this exposure is the coincident physical environment of the structure. Some materials, loosely speaking, seem to have a certain degree of water solubility when exposed to certain gases (e.g., hydrogen in the case of steel), or fluids as well as stress. Notches or fatigue cracks provide the high local stresses that promote this material behavior identified as stress corrosion or embrittlement.

- BASIC STRENGTH
- STIFFNESS
- NOTCH
- CONFIGURATION
- LOADING-EXPOSURE

Figure 7. Material Selection Test Configurations.

As indicated earlier, the operational behavior of materials is sensitive to not only the level of load but also the cumulative experience of load changes. In a structural development program it obviously behooves one to ascertain the probable load history of the structure. In the case of aircraft structures two essentially different load regimes are experienced. Of course, there is some interaction but typically aircraft structures have flight loads and ground loads. In Figure 8(a), the flight regime is shown in the usual terms of structural accelerations versus the flight velocity. With such an envelope, there is associated a given vehicle configuration status including such items as flaps

down or up, load and fuel distribution, altitude, etc. A horizontal cutoff line is shown for both the positive and the negative maneuver bounds of the structure. Superimposed upon the maneuver envelope is illustrated a positive gust limit load. For simplicity the gust ultimate load envelope has been omitted. However, it would enclose the limit load envelope with a separation equal to the ultimate strength factor of safety. Obviously, the shape of the gust envelope is dependent upon the aerodynamic characteristics of the airplane structure as it meets the selected gust velocities normal to its flight path. In Figure 8(b), the ground load exposure regime is illustrated with just the 1-g steady state condition and an arbitrary ultimate strength cutoff shown. Ground conditions are chosen to reflect the velocity regime from zero to the takeoff speed. A myriad of conditions are found in the ground operational regime. Landing and takeoff roll, braking, turning, towing and other likely handling conditions and loading conditions are to be found in the ground phase of the aircraft's structural existence.

Figure 9, shows an operational loading envelope for flights in terms of the incremental acceleration and the equivalent airspeed. A typical gust strength envelope has been superimposed for both limit and ultimate load design conditions. This data is the output of a simple V-g recorder and truly represents only an envelope of accelerations experienced by the aircraft. Nevertheless, it is important to note that the actual boundary of encountered gust accelerations is different from the estimated design envelope for the estimated flight conditions. With a little more sophisticated instrument, the VGH recorder, not only can the discrete acceleration be identified with its coincident velocity and altitude but some distinction of the nature of the acceleration (i.e., gust or maneuver) can be made. Hence, a summation of discrete loads can be derived from the measured accelerations as shown in Figure 10. It is particularly important to note and to recognize that the load experience of an aircraft is not a fixed or precise relationship but rather is a random affair which does tolerate an averaging process and resultant smoothing of the data as sample size increases.

Structural practice has characterized the loading experience of aircraft in terms of C.G. accelerations. Translation of such data to the strength and fatigue yardstick of stress experience is an interesting and necessary task. The flexible nature of aircraft structures and the dynamic character of the applied loads, such as gusts in flight, make the stress response for a component like a large wing structure differ from the statically calculated stress reflecting C.G. acceleration. In Figure 11, an illustrative plot of the occurrences of accelerations versus the equivalent incremental wing bending moment for both the measured C.G. accelerations and the measured incremental bending moments for a specific wing station at the same level of occurrence. Two points are to be observed. First, the local measured stress experience differs from the C.G. acceleration estimated stress experience, being greater in

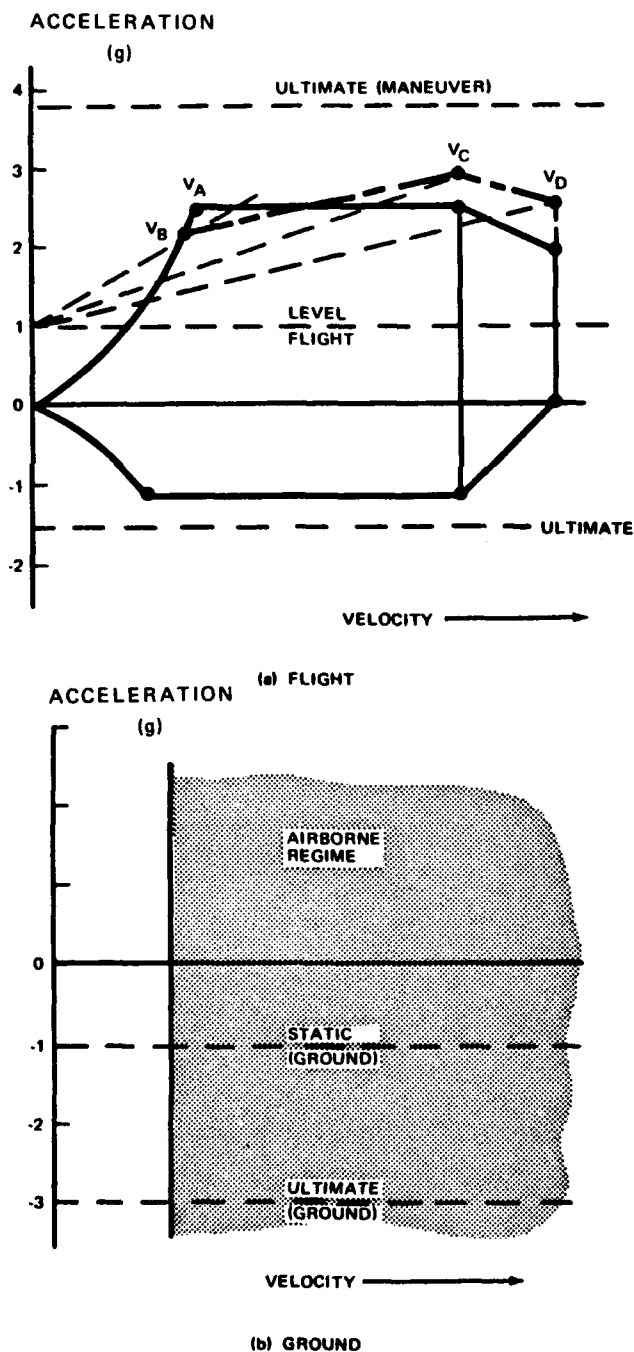


Figure 8. Airplane Structural Operating Limits.



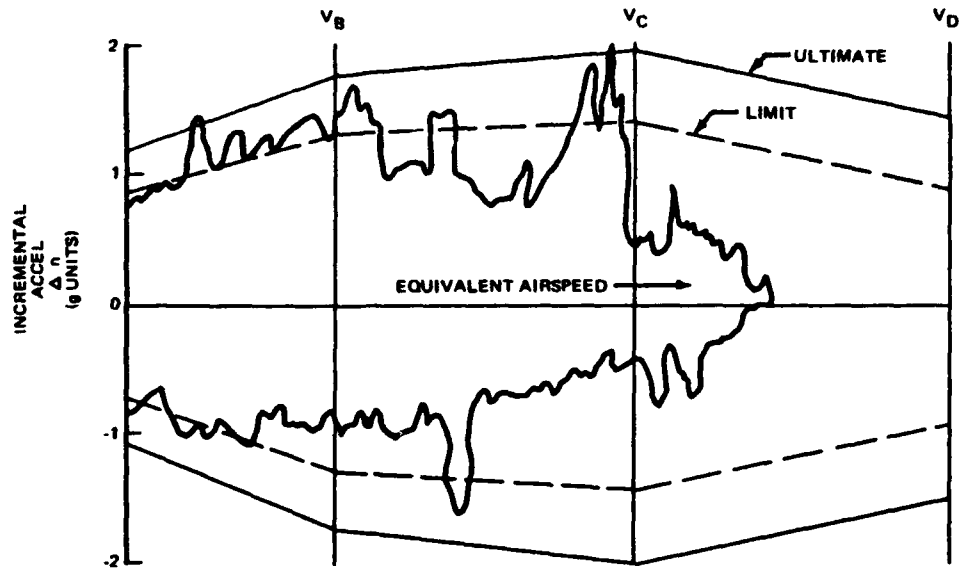


Figure 9. Operational Loading Envelope in Flight (V-G Data).

magnitude. Second, the measured stress levels coincident with the C.G. acceleration were not a direct or discrete relationship but rather had some unidentified statistical correlation. In this case, the variability was just assigned an average value with no particular twinge of engineering conscience. Sophisticated analysis techniques, such as the power spectral density analysis procedures and large electronic computers, provide some insight to this problem in a statistical sense. However, there still is a need for correlation with flight behavior that links the atmospheric turbulence with the resultant dynamic response of the flight structure.

The duress of materials in aircraft structures, while responsive to accelerations, is really a function of the resultant stresses. A representation of this relationship is shown in Figure 12. Superimposed upon a typical transport type aircraft V-n diagram for positive flight maneuver and gust conditions is a stress-strain curve for the material of construction. With design direction emphasizing maximum structural efficiency, there is not much reserve between a material's capability and its load exposure. With ultimate stress as a focal point, the usual design ultimate gross stress must be adjusted to account for net section and the notched strength behavior of the material. In the case of structure fabricated from a ductile material like 2024 aluminum alloy and assembled by fasteners, the developed net section average stress at a fastener row with load transfer demonstrates a reduction from the actual smooth specimen tensile properties. At limit load stress conditions, the gross operating stress is probably within the elastic behavior region of the material. Only the peak local stresses of notches or stress concentrations serve to confound the behavior of the structure. It is also of interest to note that operating 1-g stresses are likely to be less than the strength envelope 1-g stress. Nevertheless, stress levels in excess of the proportional limit or even yield stress can be experienced locally at severe notches, stress concentrations, or loaded fastener

locations. Such influences can precipitate early fatigue damage in structure.

Relative to the question of the notched strength of materials, Figure 13 illustrates the effect of notch severity on the static net tensile strength of two aluminum alloys. Two important material behaviors are illustrated in this figure. First, there are distinct differences in the structural response of the two materials over a range of machined notches. The 7000-series alloy apparently equals or exceeds its unnotched strength for notches having a theoretical stress concentration factor of 5 or less. On the other hand, the 2000-series alloy has less static strength at that range of notch severity. Second, at the limit of notch severity, a fatigue crack, both alloys develop fracture stresses less than the ultimate strength of the unnotched material. However, the 7075-T6 alloy has less relative residual strength than the 2024-T3 alloy. Both alloys have some variability in their residual strength behavior. A likely range in the fracture strength of the 7075-T6 material is indicated by the shaded area. Relative to material strength property testing and subsequent material selection, it is important to note the possible significant difference caused in mechanical behavior by the severe notch of a fatigue crack. The presence of humidity and moisture or fluids at the site of a crack tip may also cause measurable deterioration in strength. Elevated temperatures tend to reduce material sensitivity to fracture in the presence of a crack but the resultant ductility may lead to creep at the high stress region of the crack tip and subsequent crack growth under the relatively lower steady state loads. Along this same line, toughness of metal alloys generally has been characterized by impact testing with a machined-notch specimen such as the Izod or Charpy type specimen. However, as discussed above, this type of testing does not distinguish the relative merit of an alloy under fatigue conditions. Realistic assessment of the integrity of materials under fatigue conditions points toward testing specimens

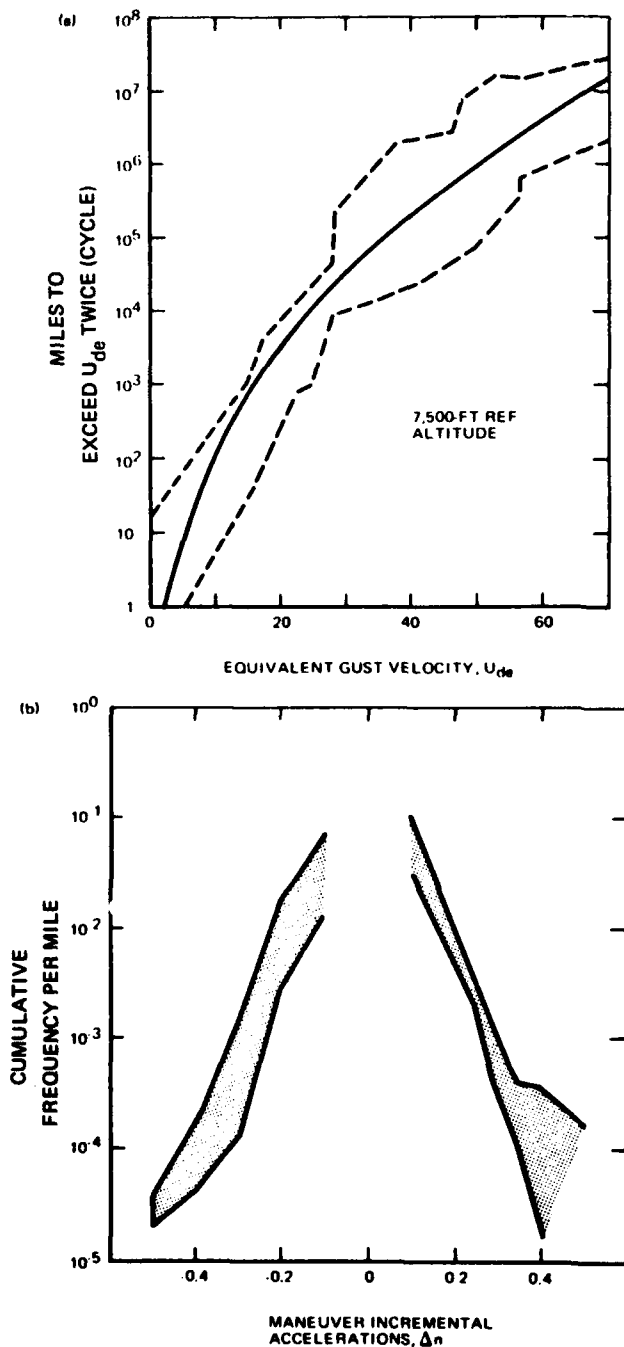


Figure 10. Environmental Loads for Fatigue Analysis.

in the presence of the fatigue crack.

#### IV. FATIGUE DAMAGE INITIATION CONSIDERATIONS

Under fatigue conditions, it should be evident that material structural behavior is keyed to the phenomena of fatigue crack initiation, the subsequent crack growth and ultimate level of strength in the presence of the fatigue crack. The S-N curve or Wohler curve has been the characteristic display of fatigue performance. Repeated load

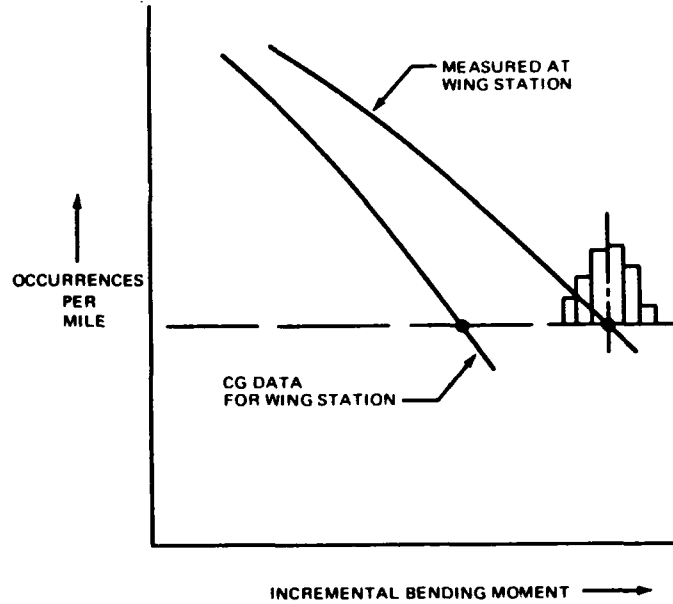
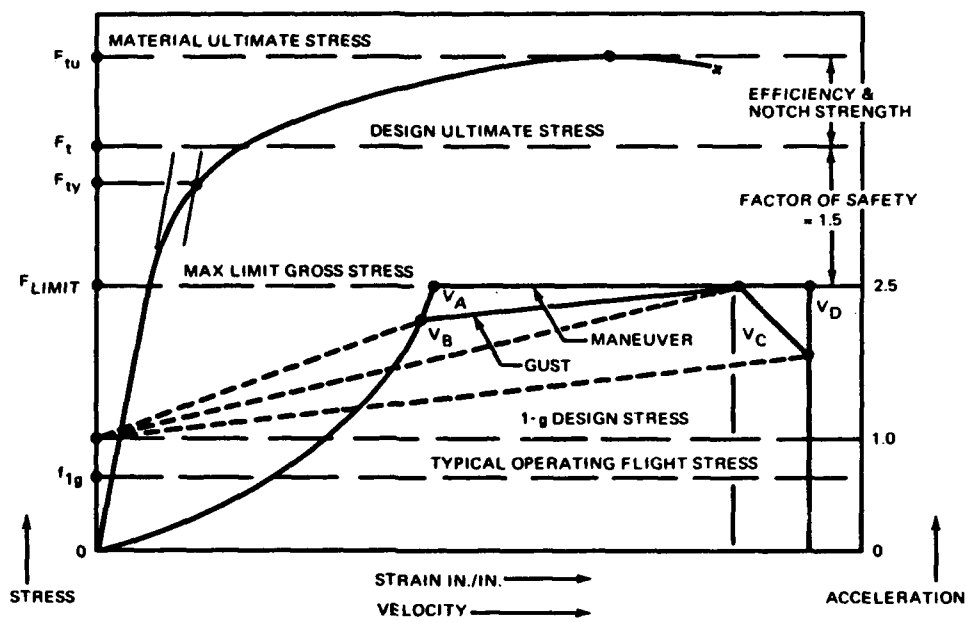


Figure 11. Characterization of Structural Response to Dynamic Loads.

testing to failure provides the data to develop this behavior under variable loading. Figure 14 typifies the presentation of fatigue data. The ordinate is usually some measure of the variable loading in terms of an alternating stress,  $f_a$ , when testing at a mean stress,  $f_m$ . Testing is also done at a constant ratio,  $R$ , of the minimum stress to the maximum stress. The data may be plotted on either semi-log or log-log coordinates. In figure 14, semi-log coordinates have been chosen. The curve represents fatigue performance usually measured in cycles at a given variable loading to failure of the specimen. Usually in large structures such as panels, components, or the assembled aircraft, the cycles to first detectable crack at a detail are the measure of fatigue performance. With detection of the first crack in a large specimen, steps are taken to repair the detected fatigue crack and pursue the testing to ferret out other critical locations. Hence, each location would have its own unique fatigue performance.

The test loadings to develop the S-N curve are obviously variable in nature. Sinusoidal or similar regular constant amplitude loading is used. Sometimes test equipment or operational loading conditions provide or demand a variation of the sinusoidal loading such as a "square" wave. In a complex loading situation, a programmed loading, which may be a series or blocks of constant amplitude loads in sequence, is applied. A complete randomization of loads may also be used. The selection of either style of loading should, of course, be guided by the probable fatigue exposure of the aircraft structure. Whatever the nature of the test loads applied to determine or verify the fatigue performance of the detail, the S-N curve merely presents those results. Constant amplitude testing is the simplest test and combined with the Palmgren-Miner Cumulative Damage Rule provides an analysis method and an estimate of the probable per-

Figure 12. Material Strength and Service Loads.



formance under a spectrum of loads. As suggested in earlier remarks, the operational exposure of structure, the response of the structure to that environment, and the allowable fatigue performance, as defined by simulating specimens, are real contributors to the adequacy of any cumulative damage fatigue analysis method. Looking further at the S-N curve, there are several other interesting observations to be made. First, the static strength of a structure or detail can be identified as one terminus of the S-N curve. Next, stresses of the order of the ultimate strength can be applied a number of times without low-cycle fatigue and fracture occurring. This fact is historically well demonstrated in the static testing of aircraft structures wherein nearly design ultimate load is applied several times during the ap-

plication of the envelope of loads defined by the V-n diagram for the operational regime of the aircraft. Next, fatigue performance is truly not a unique, singular value under even simple constant amplitude loads. In the finite life region, there is a statistical variation in the cyclic life. At the extreme, high-cycle life or endurance regime, there is also a statistical element to the allowable, applied variable stress to achieve a certain cyclic life.

While considering the fatigue evaluation process, a look at the fatigue damage incubation process is suggested. In the data of Figure 15, the cyclic life of these test specimens is found to consist of several phases. These phases and their cyclic detection period are identified into milestones

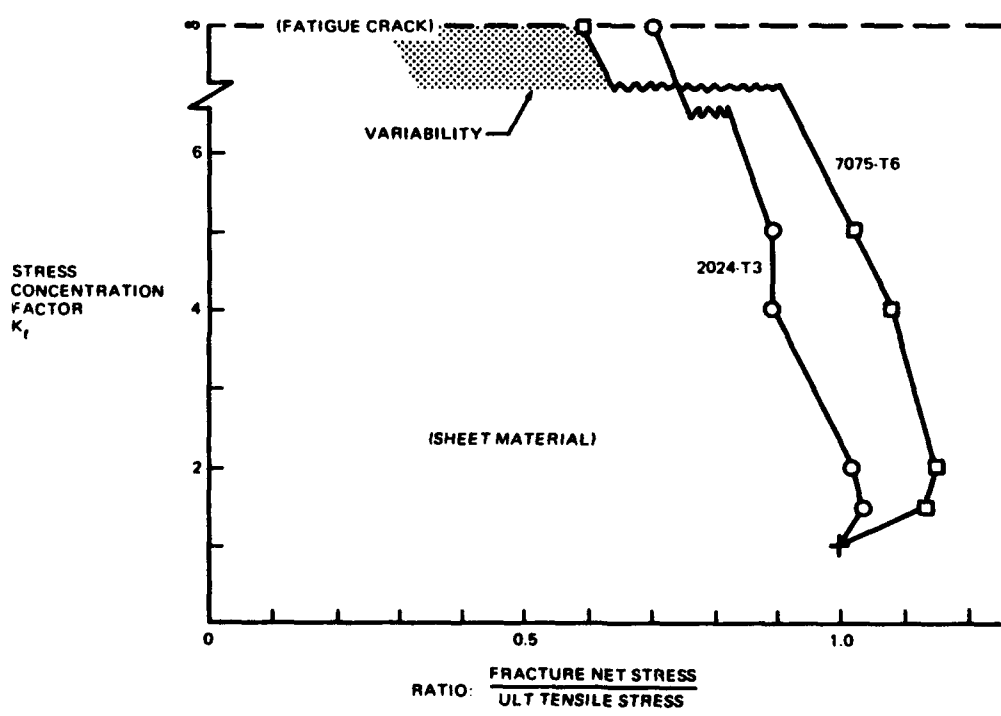


Figure 13. Notched Strength of Materials.

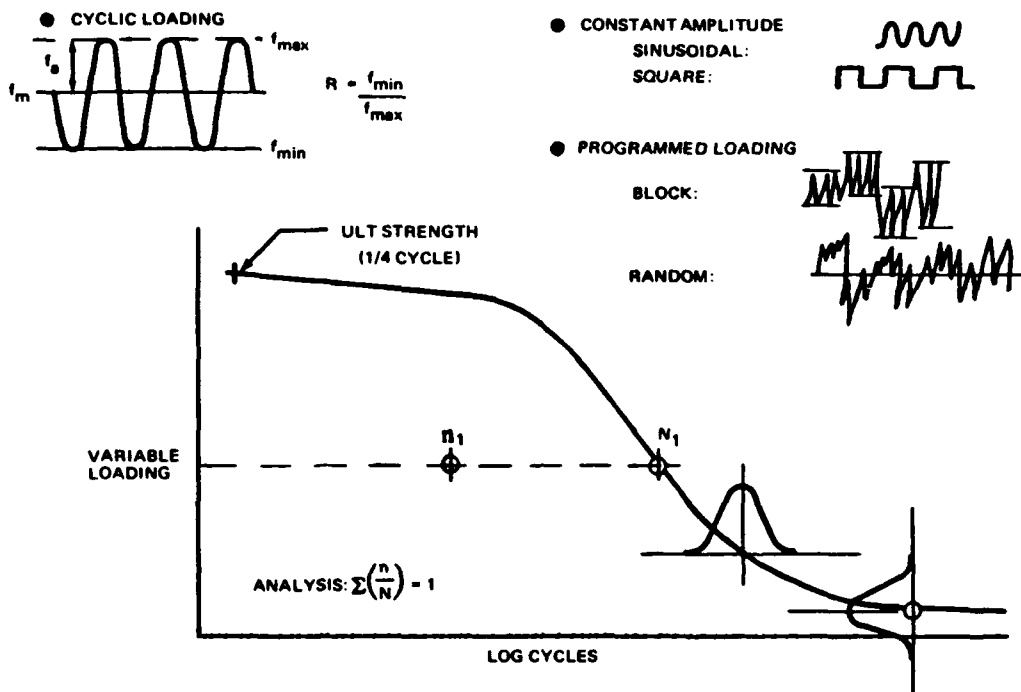


Figure 14. Fatigue Performance Testing and Analysis.

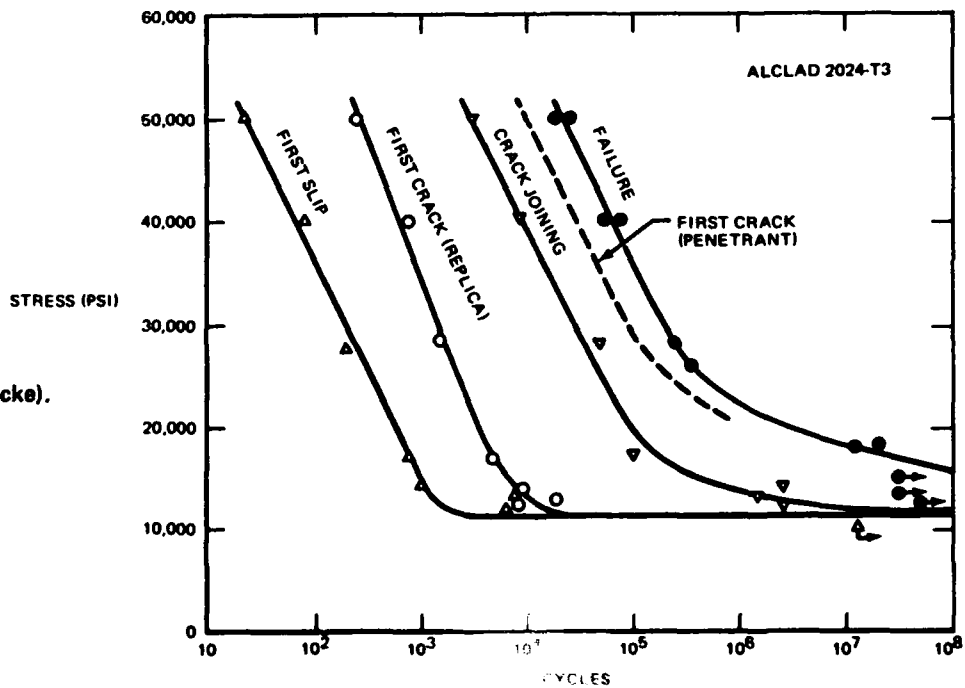


Figure 15. Fatigue Damage Incubation (Per Hunter and Fricke).

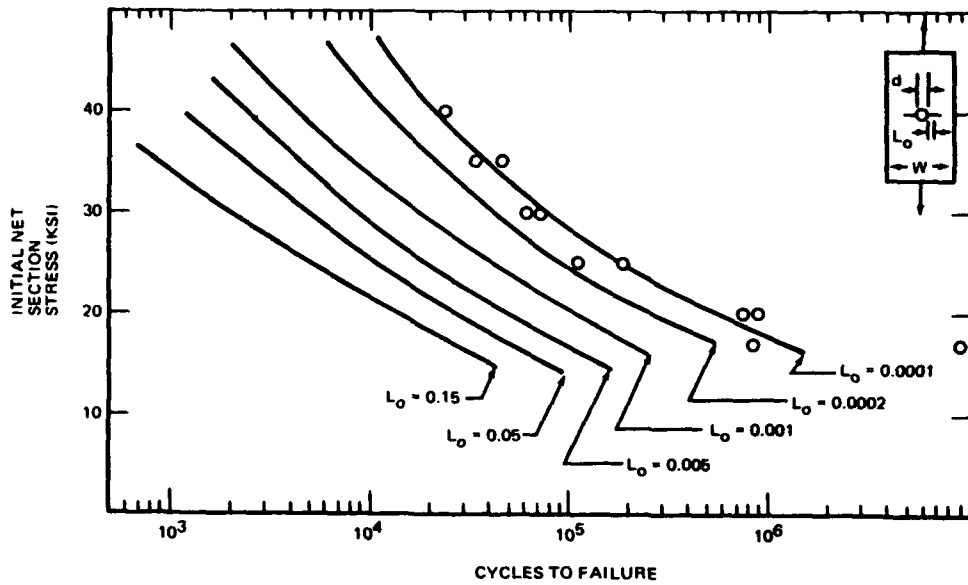


Figure 16. Fracture Mechanics in Fatigue Performance (Material 2024-T3,  $W=4.0$ ,  $d=1/8$ ,  $r=0.091$ ,  $R=0$ , NACA TN 3631).

of fatigue behavior as follows: first slip, first crack by replica techniques, microscopic crack joining, first crack detectable by penetrant inspection and finally failure. The fatigue damage process is found to be a continuous process and the probable fatigue performance is related to the level

local peak stress region of a stress concentration or stress field. Such damage is removable and the part may continue in service to the degree dictated by the nature of the rework. Be that as it may, it is possible to treat the fatigue process as a cumulative fatigue crack growth process. In Figure 16 are shown the results of examining in this fashion a simple specimen notched with a central hole. Fracture mechanics principles, using the stress-intensity-factor concepts and available crack growth rate data, were used to predict the likely growth of an arbitrary through-the-thickness type of fatigue crack. Several initial crack lengths are considered. The cyclic life is taken as merely equivalent to the number of cycles required to grow the initial crack to the estimated critical crack length. For this specimen, the net section yield stress was selected to define the critical crack length for fracture.

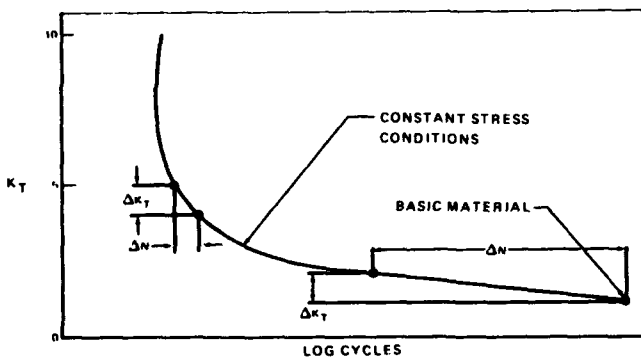


Figure 17. Effect of Notches.

of detectable damage. Furthermore, fatigue damage in structure is typically a local phenomenon, originating in the

Another consideration in the fatigue assessment task concerns the nature of the test specimen and its likely laboratory response and subsequent service behavior. A great deal of material evaluation fatigue testing has been done with small structural simulators, like lap joints or other con-

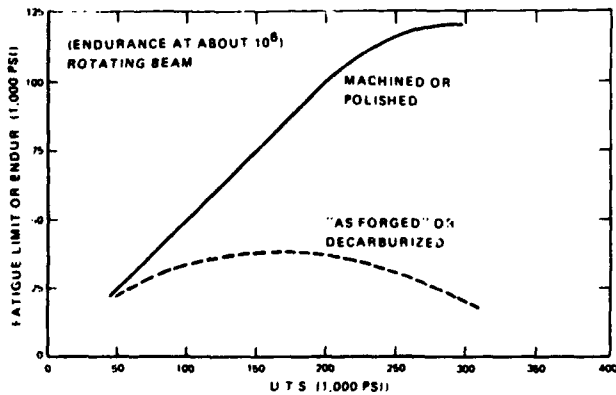


Figure 18. Manufacturing Process Effect on Fatigue Performance (J.Y. Mann).

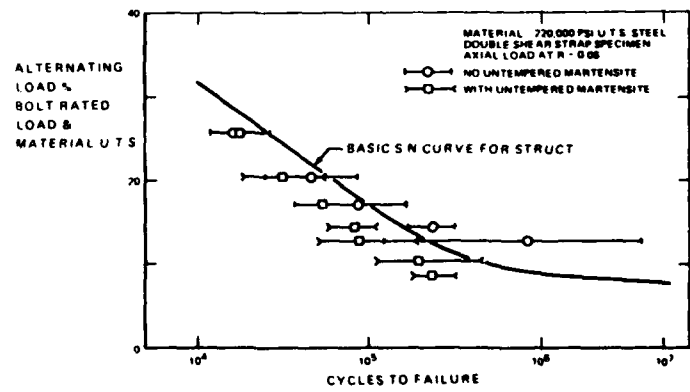


Figure 19. Effect of Fabrication Process on Fatigue Performance of Drilled Holes.

figurations and monolithic specimens. In either case there is a critical location or surface, as the case may be, where fatigue damage will initiate at the peak stress location or root of a notch. Fatigue behavior of notched structures is illustrated in Figure 17. Materials in the "as-received" condition or unnotched condition have considerable variation in their fatigue performance. Furthermore, as the severity of the notch increases the cycles to failure reduce until increases in practical notch severity have no further deleterious effect on cyclic life under constant amplitude test loads. Accordingly, at low variable-stress levels and low notch stress concentrations, any slight increase in effective notch severity can mean large changes in fatigue performance. Conversely, severe notches may not have their response significantly affected by such changes. However, there is one interesting facet of this last observation. Probably wherever low local stress levels exist at a fatigue critical detail, regardless of notch severity, superposition of damage at that locality may introduce a deleterious effect on fatigue performance.

In the assessment of material testing for fatigue testing, the condition of the material is quite important. For example, the forming or thermal treatment process of steel alloys may cause a decarburized surface, particularly in the case of the usual low alloy heat-treatable steels. Figure 18 illustrates such a response. While fatigue performance potential for the machined or polished surface steel will increase with heat treatment, the actual decarburized steel has no significant improvement as ultimate strength increases. In a similar fashion, as illustrated in Figure 19, improper fabrication processes in the drilling of holes in 220,000 psi heat-treated steel degrades fatigue performance. Both a reduced finite life and a reduced endurance limit seem to result. Laboratory and production processing can have differences in fatigue performance.

Likewise, application of a protective finish such as chrome plating can significantly reduce fatigue performance. The addition of residual compressive surface stresses by shot peening, in the case of steel alloys, can minimize or eliminate the detrimental fatigue influence of chrome plating, as illustrated in Figures 20(a) and (b).

One other phase of the materials' fatigue testing problem concerns a calendar time or physical environment condition. A corrosive environment has a practice of breaking through the finish barrier selected for protection. As a result, the structural material can suffer in fatigue performance as well as the actual strength. In Figure 21 is shown the effect of outdoor exposure on the fatigue performance of bare and clad 2024 and 7075 aluminum alloys. Several interesting points are observable from this set of tests. Apparently the calendar time and outdoor exposure tends to reduce the spread in the cyclic life of the test specimens. Secondly, the protective cladding material was effective on 2024 but not on the 7075 material. Probably the character of the cladding in these two alloys provides the clue in this behavior. Another incidental ob-

servation relative to this corrosion story is the likelihood of making inconclusive observations from limited sample sizes. For instance, it would be quite simple to observe practically no or an extreme influence of exposure on the relative cyclic life with just the chance selection of a few test specimens, say 3 or 4 specimens, out of either end of the scatter band for the total lot tested.

## V. FATIGUE CRACK PROPAGATION CHARACTERISTICS

So far this discussion has focussed on the structural characteristics of materials and the associated load exposure. The task of estimating fatigue damage initiation has also been highlighted. Also, as stated earlier, experience indicates that there is an ever-present risk of unexpected or premature fatigue damage initiation. There are probably a number of reasons for this situation. Such factors as material quality or condition, detail design, fabrication, structural response to the operational environment or differences between the predicted environment and the actual service

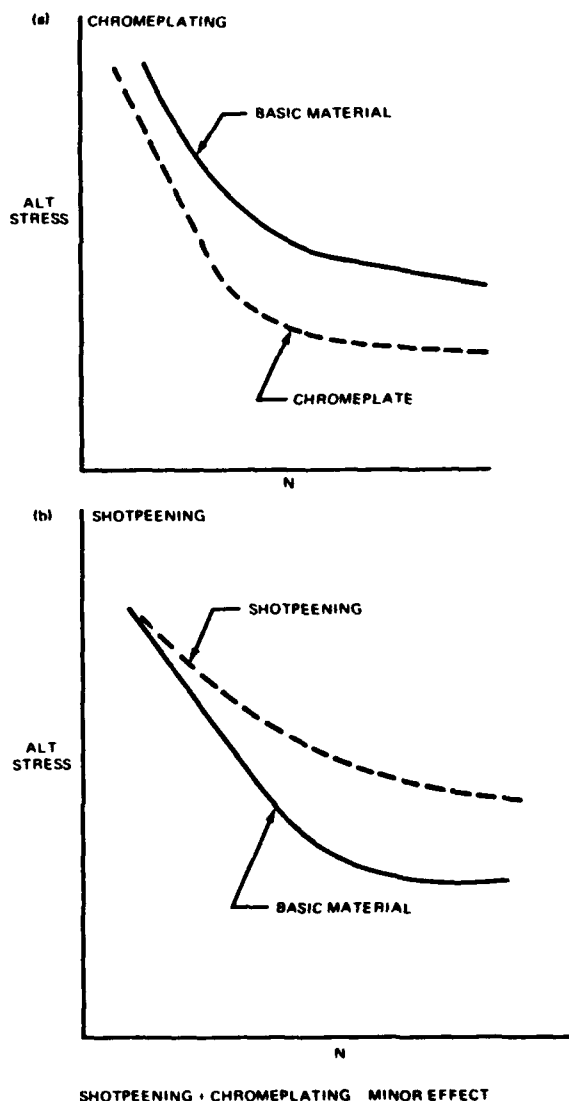
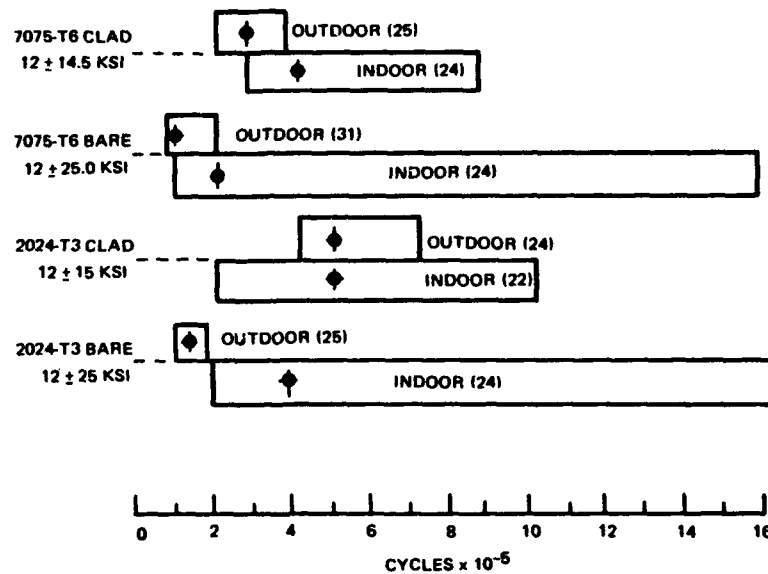


Figure 20: Material Finish Effect on Fatigue Performance.

MATERIAL CYCLIC LIFE COMPARISON UNDER ATMOSPHERIC EXPOSURE  
& STRESS

Figure 21. Effect of Corrosion on Fatigue Performances.



conditions, could lead or share as the source for the precipitation of fatigue damage. With the presence of fatigue damage, the structural integrity is dependent upon the resultant fatigue crack growth rate and the residual strength of the structure in the presence of the fatigue cracks. In relation to the very necessary and continuous structural integrity assessment of aircraft structure, this dual behavior of material and its structure are vital parts of the experimental development work of design and the inspection control for the operational aircraft. Incidentally, it is not the intent to propose flying of aircraft with the presence of fatigue cracks in the structure but rather to provide the opportunity to detect and correct the condition. This is a primary tenet of fail-safe or damage tolerant design philosophy for fatigue-exposed structure.

The task of determining fatigue crack growth and coincident residual strength of materials and their structures is outlined in Figure 22. The first element of this program is graphically outlined in Figure 22(a). Material of the type form and condition intended for the structure, is tested under variable loads with a fatigue crack whose growth is monitored. Usually, a flat sheet is the structural form of interest and crack growth measurements made on a centrally initiated crack. The physical environment is also an important element in this test. The presence of moisture or other ambient physical environment at the growing fatigue crack can accelerate fatigue crack growth at a most alarming rate. The cyclic life of the test panel can be a fraction of the normal laboratory atmospheric conditions. One important point of interpretation of this type of data, mainly a question of semantics, is that the environmental effect on the material's behavior is relative to the crack growth. The residual strength and fast crack growth leading to total fracture is a consistent property of the material. Its character will be further discussed in subsequent remarks. Accordingly, in Figure 22(a) the same critical crack length

is noted for both conditions of environment. The crack-length/cycles data is defined and interpreted in terms of the growing field of fracture mechanics and its yardstick of fracture toughness, the stress intensity factor,  $K$ . Reference should be made to the current literature, References 3-10, for the details of its concepts.

The appeal of fracture mechanics is in its tie to the theoretical and elastic description of the stress field around the crack and the experimental determination of a materials fracture behavior which is an individualistic quantity for any given material. The principles of fracture mechanics are directly and best applicable to brittle or elastic material as well as real material whose ductility does not significantly cause any divergence in the crack stress field of the real material and the theoretical stress field. As an extraneous remark, it is to be noted that ductility has not been a hindrance to the application of elastic analysis concepts to ductile failures such as found in beam bending of stable structural elements. Also, there are other methods of analysis, for example, References 11 and 12, which direct themselves to the residual strength phase of the problem.

From the crack-length/cycles curve of Figure 22(a), crack growth rates,  $\Delta 2a / \Delta N$ , can be calculated in terms of  $K_{max}$  or a  $\Delta K$  at a given test load condition at stress ratio,  $R$  or  $\beta$ , with  $\beta$  being the reciprocal of  $R$ . The character of this curve is material dependent and isn't necessarily linear over the whole range of crack growth rates. Aside from the intermediate range of crack growth rate behavior of materials, there are two significant structural limitations. Obviously, at rapid fracture, or total crack length leading to instantaneous failure of the part, there is an extremely high rate of growth. In fact, this point is bounded by the critical  $K$  and the crack growth curve becomes asymptotic to the critical  $K$  as suggested in Figure 22(b). At the lower bound an opposite behavior is

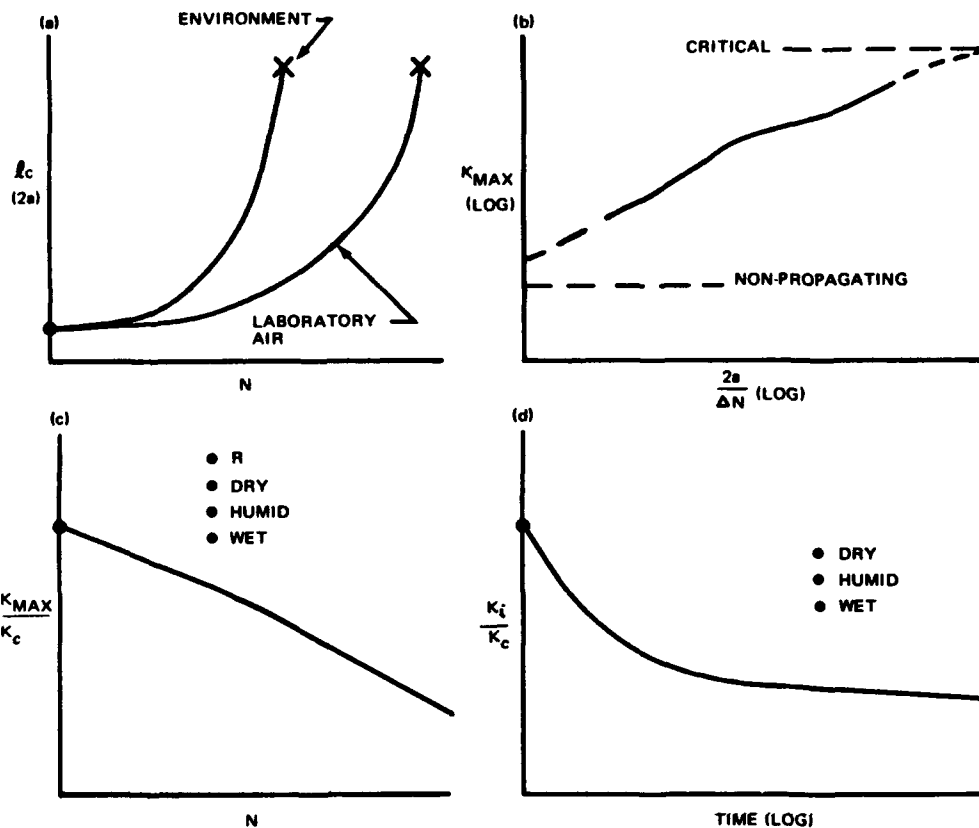


Figure 22. Inspection and Fail-Safe Test Data Collection.

found. There is a  $\Delta K$ -range or maximum  $K$  value under variable loads that forms an asymptotic lower limit to the curve. Thus the general behavior of the curve over the whole range of crack growth is likened to an S-curve.

Another useful bit of crack growth data is the number of fracture resistant cycles remaining in a structural element with a given crack size. This data is presented in terms of the ratio,  $K_{\max}/K_c$ , versus the number of cycles to initiate rapid fracture of the detail as shown in Figure 22 (c). The application of such data is in proof-testing of structure. For example, if a structure passes a proof load of a given magnitude, it is assumed that the material had contained a critical flaw size compatible with the applied proof stress. Hence, a successive number of cycles at some fraction of the proof load could be sustained without fracture. This data is dependent upon the stress-ratio and the ambient physical environment such as a dry or humid atmosphere or a fluid.

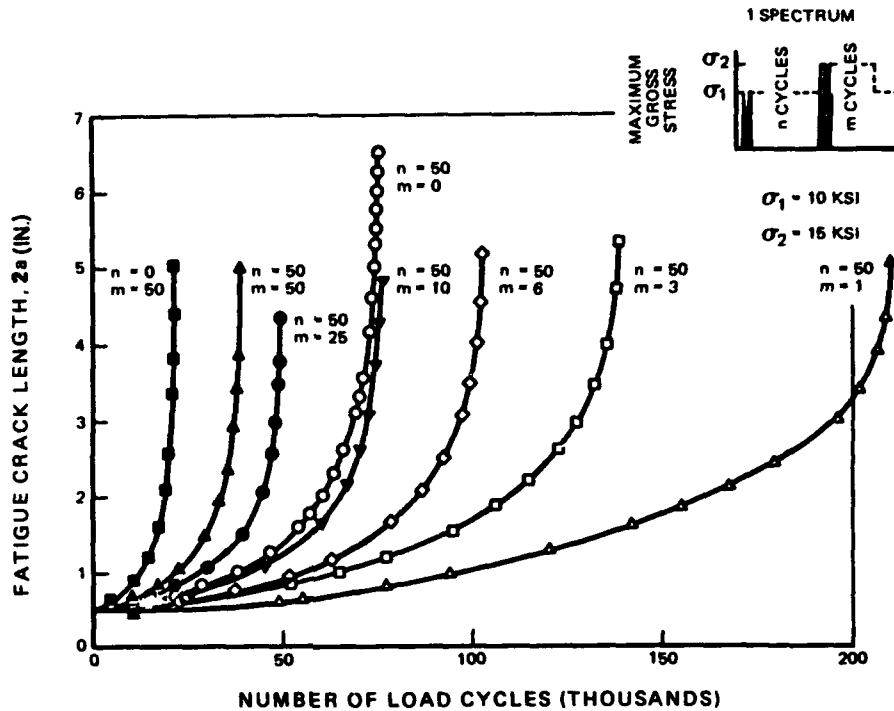
So far fatigue crack growth rates have been consid-

ered in the terms of variable loading and its magnitude. Unfortunately materials have a fracture response to merely a static state-of-stress and ambient physical environment. For example, hydrogen embrittlement of steel can be taken as one form of this behavior. Testing for such embrittlement is usually done with a smooth specimen under a steady state of stress. However, the presence of a fatigue crack and an ambient environment of gas, humidity or fluid accentuates this form of crack behavior. Stress corrosion cracking behavior of materials is an important material fracture behavior characteristic because it significantly effects the integrity of a structural element in the presence of a flaw, notch or a fatigue crack and a residual, installation or operational stress. In essence, this material behavior is similar to the S-N for fatigue performance curve but it compares constant loading at an exposure to time rather than a variable loading to cycles of that loading. Figure 22(d) illustrates such material behavior.

Interaction of load levels is another important element in the propagation of fatigue cracks through ma-



Figure 23. Variable-Amplitude Fatigue-Crack Growth Behavior of 0.16-In. 7075-T6 Aluminum Alloy in 12-In. Wide Transverse Grain Panels.



materials and their structures. Sequence and magnitude do affect the rate of crack growth through a panel. Any material with natural ductility, as found in the non-linear strain hardening phase of the stress-strain curve, as typically illustrated in Figure 5, has some response for this condition. In Figure 23 are shown the crack growth curves for various relations of stress levels and cycles in a two-step loading. Both crack growth delay and acceleration are shown to occur in relation to the single level loading. Another illustration of this behavior is found in Figure 24. Analysis of this loading spectrum with but one high load between every 29 low load cycles, indicates some consistency in the number of delay cycles relative to the ratio of the high

load to the lower load level.

So far the question or property of material crack growth has been presented as a nice, precise engineering curve. Likewise, there has been some inference of little variability because of the severe notch or stress concentration coincident with the stress field around a fatigue crack in an element. However, Figure 25 illustrates the variability found in different tests on the same alloy at a fixed cyclic test rate of 3000 cpm and other conditions of longitudinal grain, 0.080 in. thick, laboratory air, stress ratio of  $\beta=2.11$  with the crack at half-panel width. Applying the same conditions of reliability assessment as used for the static

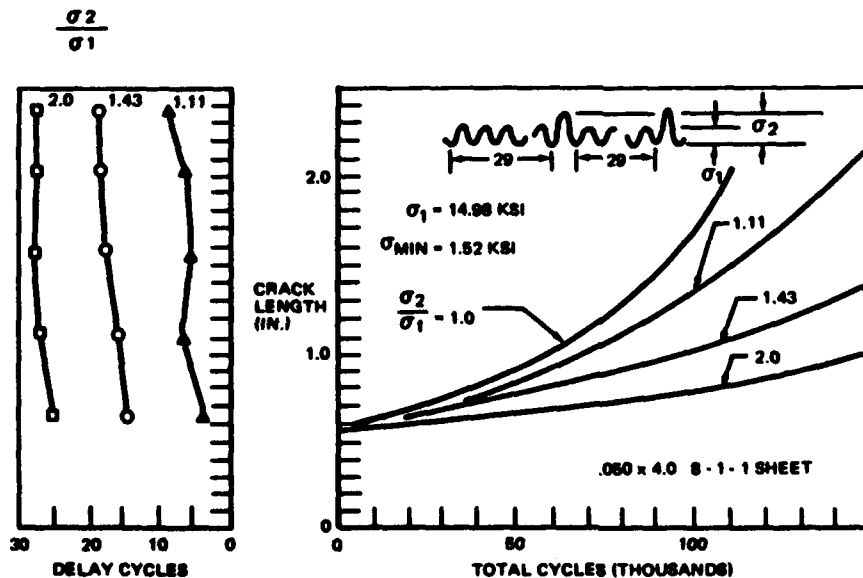
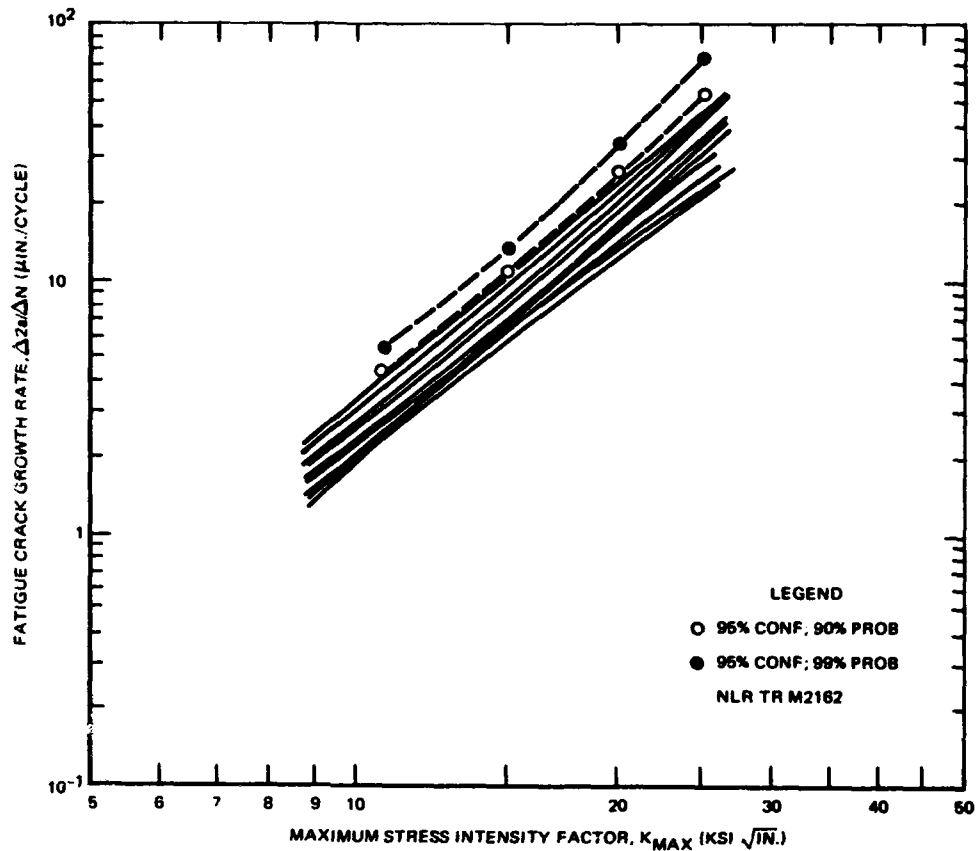


Figure 24. Crack Propagation with Single Intermittent Loads.

Figure 25. Tolerance Limit Levels for Maximum Fatigue Crack Growth Rate in 2024-T3 Material.



material strength properties, the corresponding "A" and "B" values (i.e., 99 and 90 percent probability at 95 percent confidence) differ significantly from the mean or the lowest rate of crack growth measured in this specific test program.

Crack propagation through built up structure is also of concern in the task of material selection and structural design. In Figure 26 are shown the crack growth curves for a three-ply bonded skin with a crack in the surface layer. The structural configuration has served to contain the

growth of the fatigue curve and linearize the crack-length/cycles curve from its usual somewhat parabolic shape.

Structural configuration and its influence on crack propagation characteristics are factors to consider in any developmental program. In Figure 27, the crack growth is shown for a simple honeycomb sandwich panel with 2.81 in. wide straps located 18 inches on centers. These straps represented about 15 percent stiffening in terms of the face skin bay area. With a sawcut in the skin to initiate crack growth under cyclic load, the crack-length-cycles

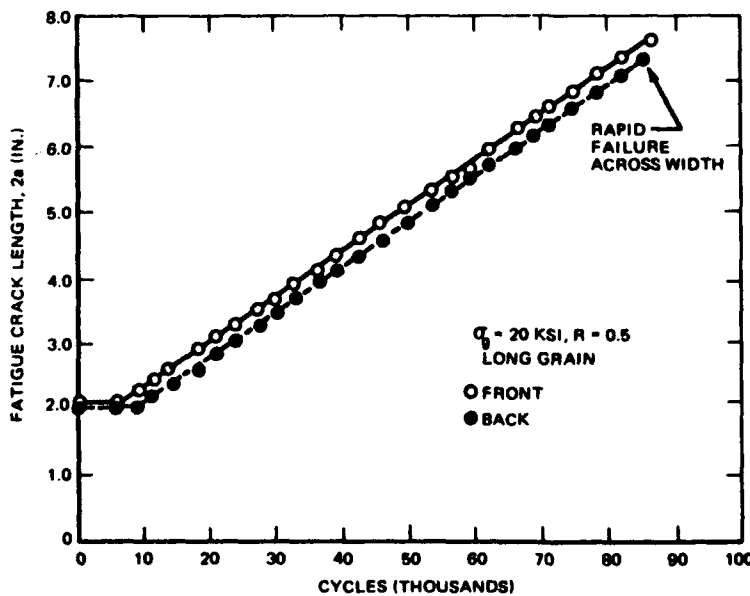
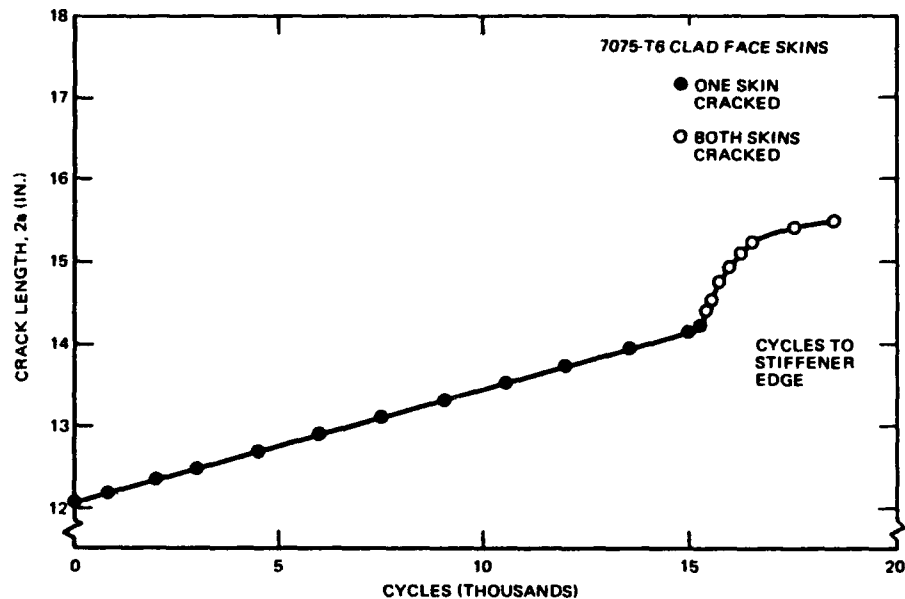


Figure 26. Surface Fatigue Crack Length Behavior of Three-Ply 0.063-In. 7178-T6 Skins, Honeycomb Sandwich.

Figure 27. Fatigue Crack Growth Behavior of Honeycomb Sandwich Panel with Strap-Type Bonded Stiffeners.



curve is linear instead of parabolic in shape. With the two faces cut, the crack growth rate immediately jumps but then slows down as it reaches the strap, to less than the initial single face crack. Such behavior is naturally traced to the structural configuration and the local stress/strain field at the crack tip region.

## VI. RESIDUAL STRENGTH EVALUATION

Evaluation of the fracture or residual strength properties of materials with fatigue cracks have a basic similarity with their usual strength properties. A mechanical test of the material is made. Material form and condition are similarly important parameters. However, in the case of fracture properties, material thickness or size has a significant influence. Two effects are present. One consists of the material condition just due to processing or the reduction in mass from the ingot to finished product, like in the case of sheet. Another factor is the state of stress due to size of the cracked part. Thus thin sheet is considered as responsive to plane stress conditions and thick plate or bars have a plane strain condition and respond in a brittle fracture manner. In Figure 28(a), the residual strength of a material is presented in terms of the stress intensity factor  $K$  versus the thickness of the material. Experience indicates materials do have a likely unique critical thickness or an asymptotic value of the stress intensity factor associated with the plane strain fracture condition. Much attention has been focused on this regime of fracture toughness.

One element of the experimental process for defining fracture toughness is the identification of the crack geometry. Through-the-thickness cracks in thin sheet have their initial dimensions established easily by pre-fracture measurement and subsequent fracture face examination. However, this process is really positive only for the initial crack size. Most structural materials have some ductility that allows crack extension as the fracture load builds up to

its critical magnitude. Here, high speed (e.g., 1000 frames per second) photography of the specimen fracture process is one means to determine the critical crack length. With cross correlation of test load and crack length, the definition of the critical crack length is obtained as indicated in Figure 28(b). Surface flaws in thick sections pose more of a problem and fatigue markings interpreted after fracture are about the only clue to the critical crack length and  $K_{IC}$  determination. Yielding in the specimen load-strain curve of a thick section with either a surface flaw or a through-the-thickness type of crack describes the phenomenon of "pop-in" and provides a clue for estimating the plane-strain stress-intensity-factor measure of toughness,  $K_{IC}$ . Extensive ground rules for the experimental determination of the plane strain fracture toughness have been established by the ASTM. These criteria do provide some consistency in methods for determining a very complex property, the fracture of thick materials.

As yet the plane stress fracture properties are even more complicated in nature by virtue of voids in the theoretical understanding of the fracture process. However, such analytical problems do not void the engineering or practical solution of the problem. Figure 28(c) illustrates the type of information a few tests can generate for specific geometry wherein brittle fracture analysis techniques may be inadequate. At the risk of heresy to the fracture mechanist, it is suggested that the primary goal of the designer is fatigue damage containment in an actual structure regardless of validity questions in theory.

Somewhere in the structural development process experimental verification should be done to conditions reflective of the operational envelope for the vehicle. Interesting potential complications to the fracture process in sheet materials are illustrated in Figure 28(d). As a central crack spreads to the total width of the flat sheet, one finds a minimum net area fracture stress and a corresponding lack

$$K = \sigma_0 \sqrt{\pi a} \quad \Omega(2a, W, L, t)$$

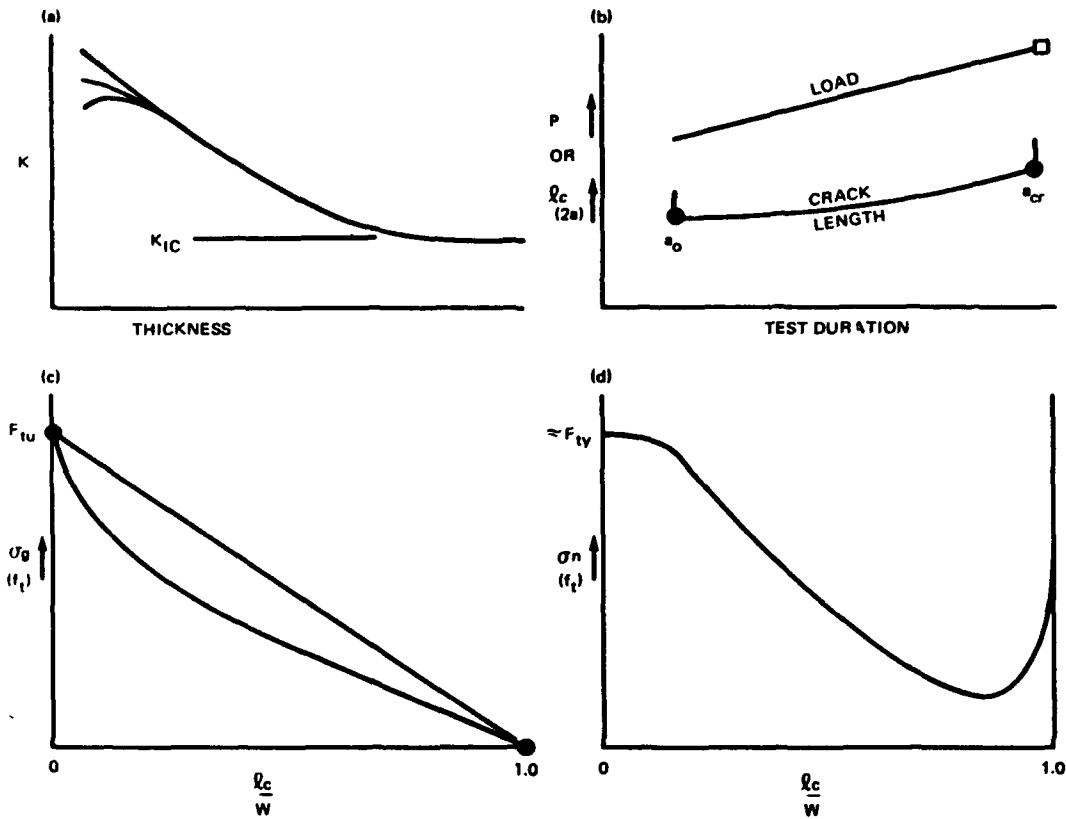


Figure 28. Residual Strength Test Data Collection.

of uniqueness in its value on either side of the minimum.

Some of these complications of analytical interpretation of the fracture behavior of materials merit further review. For instance, in Figure 29 the slow growth definition of the fatigue crack in a very simple bonded, strap-reinforced structural panel is shown as derived from high speed photography. Only the last fraction of a second of the panel's structural integrity is plotted in terms of time versus crack length. The initial preloaded crack length,  $2a_0$ , and the analysis selected critical crack length,  $2a_{cr}$ , are identified. There is clear and unmistakable evidence that identify the unstability of the crack. However, the crack length could be followed across the panel. In contrast to this behavior, Figure 30 presents the slow yielding of the crack from an initial, preloading size of 7.2 inches to its final failure length of 16.2 inches. Considerable non-linearity is shown in the crack length as the fracture load approaches failure. The selection of the critical

crack length is subject to some conjecture and one assessment of the critical crack length is identified. Figure 31 illustrates a crack behavior intermediate between the two previous figures.

Still dwelling on the identification of the fracture toughness of a given material, Figure 32 sums up a series of reasonably consistent tests of aluminum alloy flat sheet. Width effects and plastic zone size were considered in the conversion of the data to the plane stress intensity factor measure of toughness. Most revealing is the variability in the fracture toughness of this material.

There is about a 20 to 50 percent difference between the median and the 90 and 95 percent probability levels in that order. Hence, it is evident that fracture analysis on the basis of one or two tests may not reflect a reliable or proper identification of the fracture toughness of the material and its structure. In contrast, the allowable ultimate strengths of materials are usually identified by

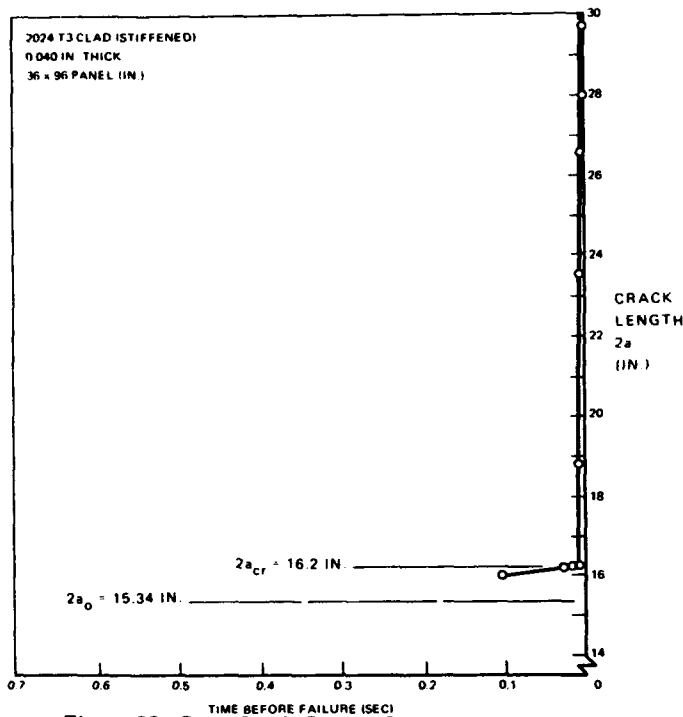


Figure 29. Slow Crack Growth Measurements Under "Brittle" Fracture Conditions.

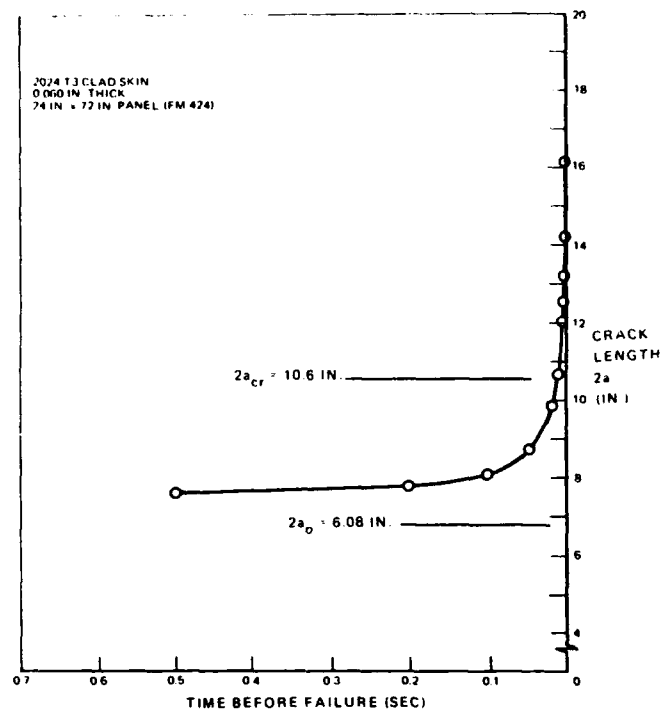


Figure 31. Slow Crack Growth Measurements Under Semi-Ductile Fracture Measurements.

ten specimens from ten different heats of the material.

### VII. INSPECTION CONTROL AND FATIGUE VARIABILITY

Structural integrity of aircraft structure is of major concern to the designer. The analysis and demonstration

of the potential fatigue-worthiness of a structure is truly a more complex process than strength, as generally practiced for the latter. The solution is not only confounded by the primary fatigue behaviors of crack initiation, crack propagation, and residual strength of a material in the presence of a fatigue crack, but also the geometry or configuration of the structure and its physical exposure. As pointed out earlier (e.g., Fig. 1), there is a real risk of fatigue damage initiation in a structure. Continual surveillance of the struc-

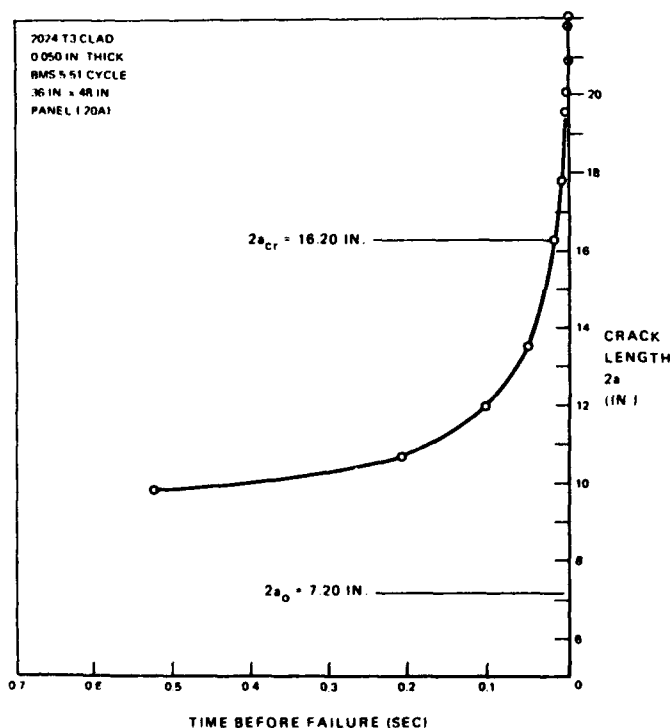


Figure 30. Slow Crack Growth Measurements Under Ductile Fracture Conditions.

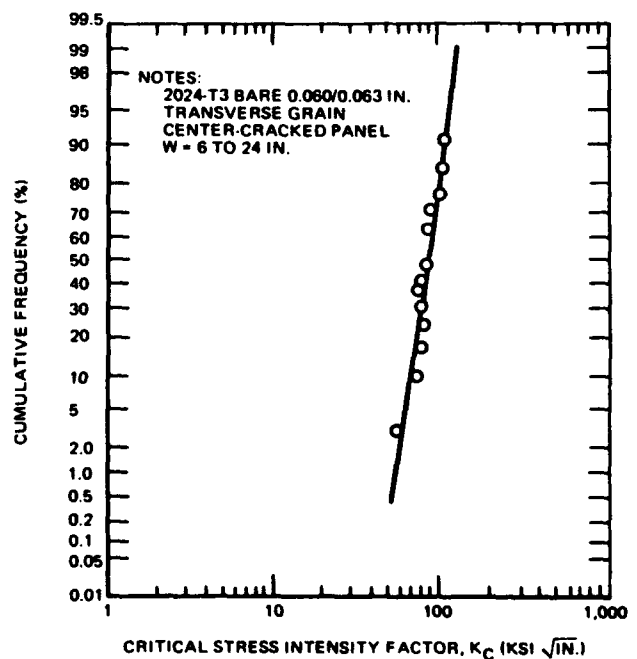


Figure 32. Variability of Critical Stress Intensity Factor (Log-Normal Distribution).

ture is an important element of maintaining structural integrity. In Figure 33, an illustration of this process and its key features are identified. Crack initiation and its propagation control are the main points of focus. Any structure has some level of detectable crack size to identify the time of fatigue damage initiation and service limit of that structure. This length is dependent upon inspection techniques that may range from some sophisticated means as X-ray, penetrant, or eddy current to visual external detection by sight or feel. The maximum or total possible fatigue performance is, of course, limited by the critical crack length. The intermediate range between the detectable level to the residual strength level provides a time zone where detection should be accomplished to maintain structural integrity. Identifying and demonstrating this capability of the structure is a necessary plan for structural integrity.

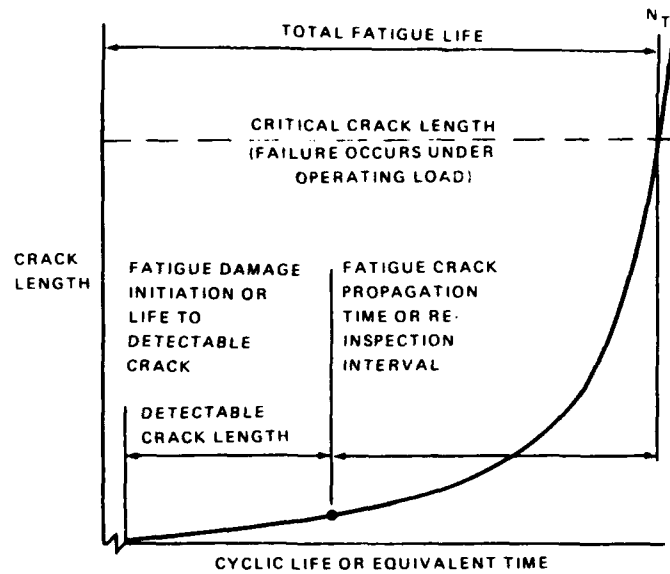


Figure 33. Relationship of Fatigue Performance and Reinspection Interval.

In Figure 34, there is reproduced some crack initiation and propagation data for a C-46 wing tested by

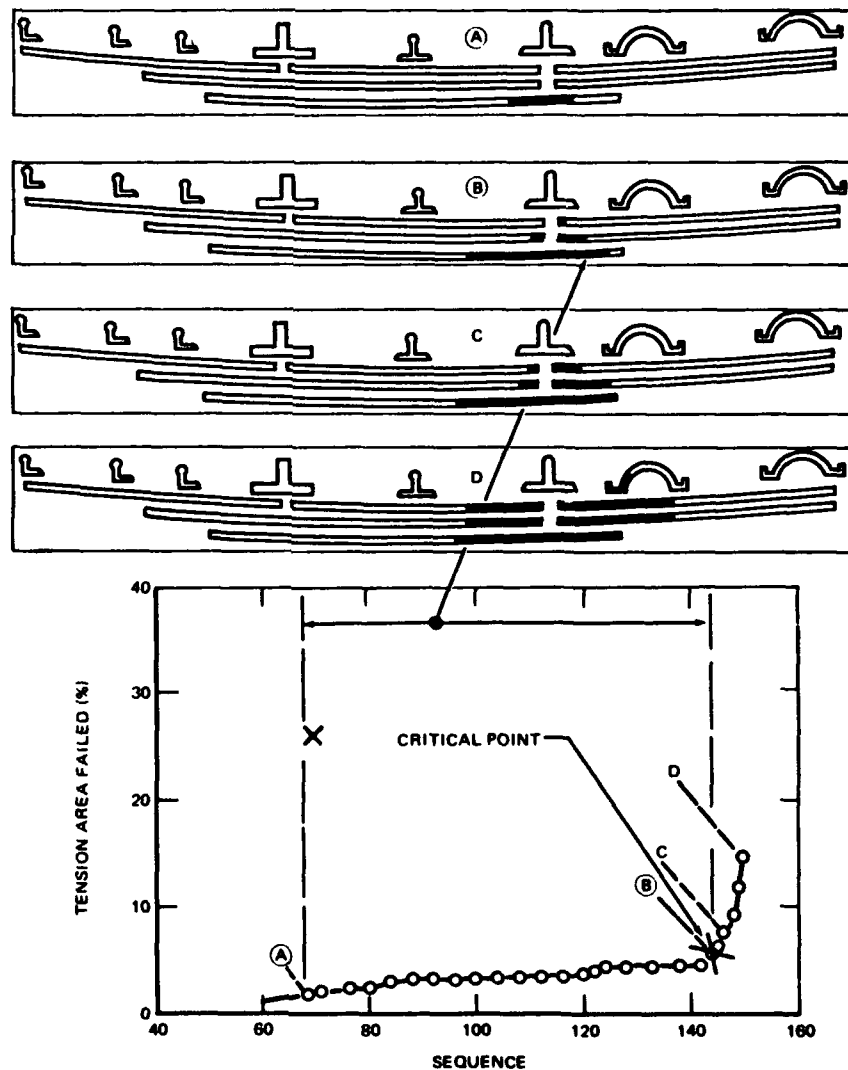


Figure 34. Crack Initiation and Propagation in Doubler of Wing Section.

NACA a couple of decades or so ago. Initial detection and the critical point are identified on the graph. A similar presentation is shown in Figure 35 for a different section. This latter section illustrates the typical propagation and arrest characteristics of a multiple load path structure as the crack develops through the buildup section.

So far the discussion has been related to the nature of fatigue performance and its dependency on both mechanical and physical environment. Notation has also been made of its variability for any one type of structural exposure. Laboratory verification or determination of that fatigue behavior has been the primary point of view. However, a fleet in operation is also a test bed for the potential fatigue performance of the structure. The problems of environmental test conditions can be automatically circumvented by fatigue results gained from an operational fleet. The important elements for interpretation of this

fleet data include the following: (a) an assumption of a shape for the statistical distribution for fatigue variability; (b) a knowledge of the distribution of times on the individual airplanes within a fleet; and (c) an acceptance of the condition that operational usage of all airplanes in the fleet are practically the same. As illustrated in Figure 36, a tabular histogram of the distribution of individual times is constructed. These data are transcribed to a frequency distribution and its cumulative distribution with the latter's shape factor selected to match the cumulative service failures. This result provides a forecast of the likely development of fatigue damage in the fleet as well as an estimate of the probable median life. With the collection of a significant number of a specific type of incident, a graphical plot of the ordered data on probability paper (say log-normal in time) will produce similar information at that time it may be just an academic question.

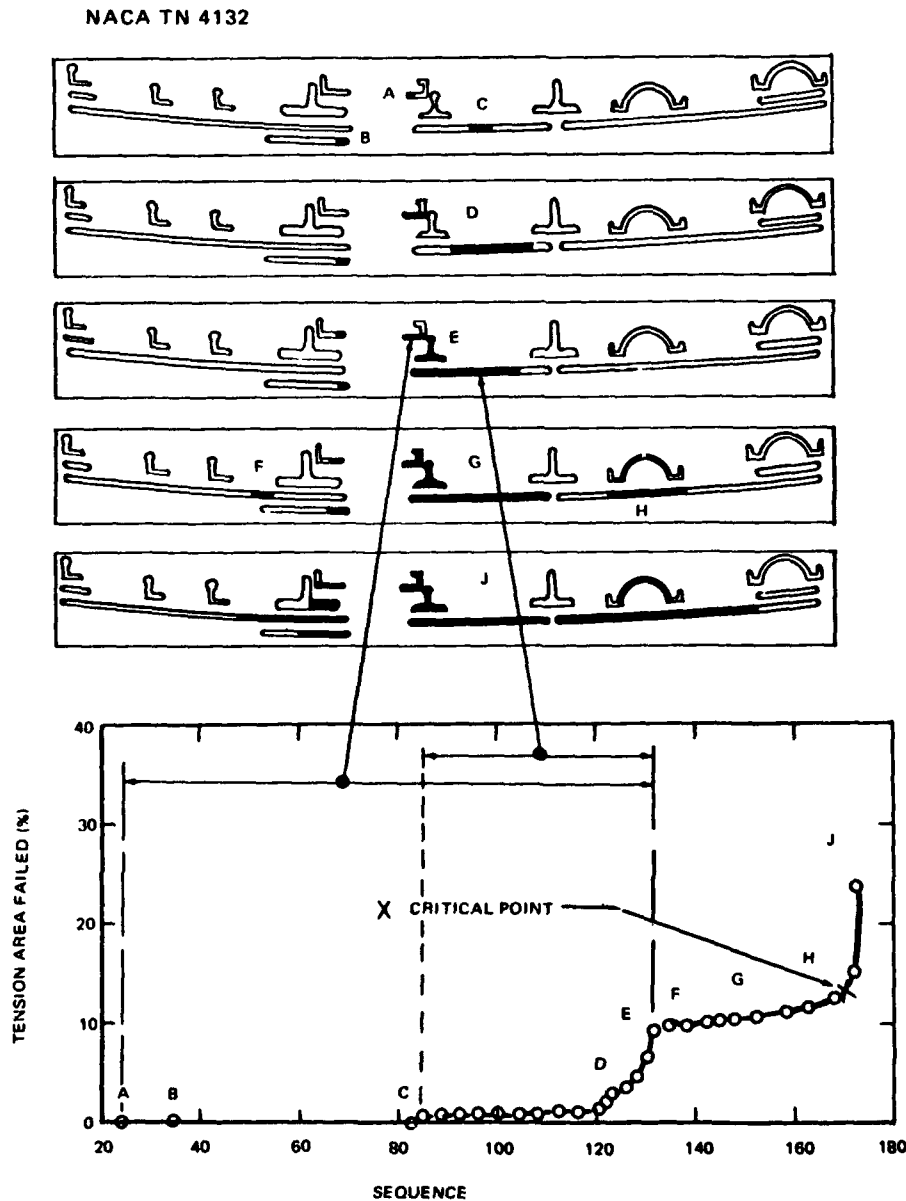


Figure 35. Crack Initiation and Propagation in Elements of Wing Section.

A/P INTERVAL (HR)	FLEET STATUS								PROB FAIL FORX
	M	J	S	D	M	J	S	D	
	31	30	30	31	31	30	30	31	
0-999	1	1							
1000-1999	15	5	3						
2000-2999	32	19	9	4					
3000-3999	3	27	20	13	6				
4000-4999	6	2	20	24	16	8	3		
5000-5999		6	4	11	25	21	13	6	
6000-6999			4	8	7	22	21	14	
7000-7999					6	3	14	19	
8000-8999						6	5	12	
9000-10000							4	8	

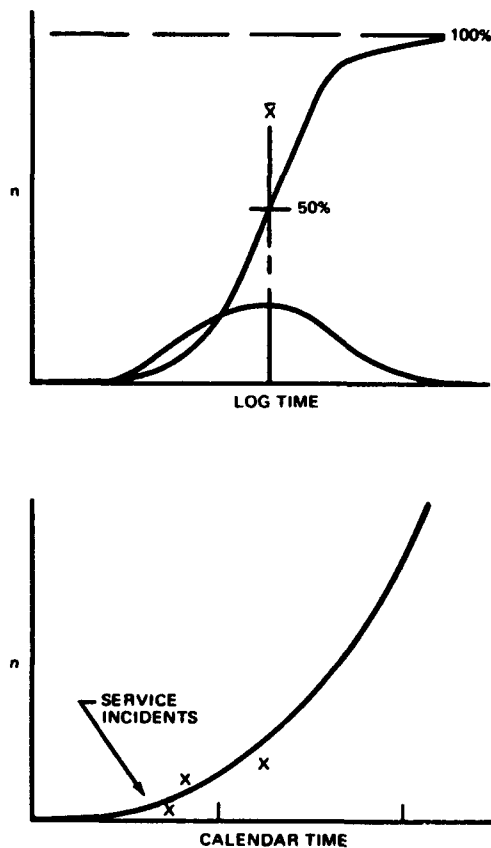


Figure 36. Fleet Fatigue Performance Prediction.

Going back to the task of laboratory verification of fatigue performance there are several options available to demonstrate the level of fatigue performance. The output of the usual laboratory testing program are usually median, average or some other characteristic life. An S-N curve can be constructed or developed from limited test data, like one specimen plus other available data that may provide instruction to extrapolate the specific laboratory data. From such average or median data, an estimate of the required fatigue performance to meet service goals can be made. Then, as illustrated in Figure 37, two options are available to verify the probable fatigue performance reliability. Qualifying tests may be set up to match the service

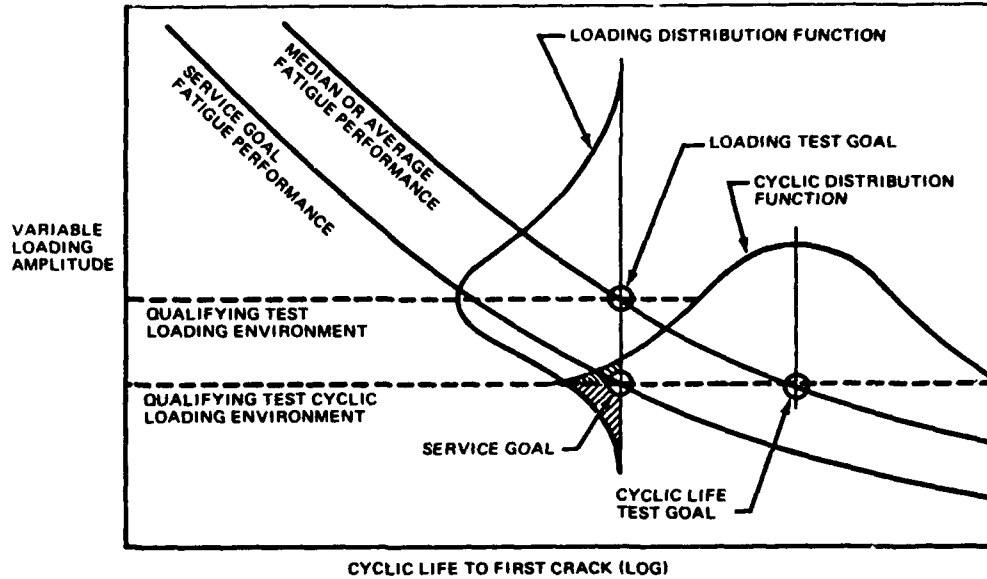
goal by either an extended test to the defined service loading exposure or a test at an increased loading level which is the equivalent of the cyclic goal. The savings in cycling time by the use of increased loads may be a benefit. However, in a complicated structure some knowledge of the influence of increased load levels on the stress exposure of various elements of that structure is needed. At least under high loads there is good assurance of at least detecting most fatigue critical details. Testing at the exactly expected service load environment has some hazards if the environment does increase.

The selection of the test spectrum to develop or demonstrate fatigue performance is still an argumentative process at best. Exact prediction of actual service cumulative loading experience is still a matter of development. Obviously each new aircraft system offers advances that will be exploited or even allow penetration into operational regimes that are only identifiable by monitoring the usage long after the design has been established. Hence any verification process has the requirement of extrapolation from test conditions to the actual conditions. As mentioned earlier, the Palmgren-Miner Cumulative Damage Rule and constant amplitude testing offers a practical solution to this task. Furthermore, examination of the predicted loading exposure and flight profiles will identify likely load levels. For instance a ground-air-ground cycle is a cyclic load envelope assured for each flight of an aircraft. The other loading experience is supplemental to the ground-air-ground cycle and can be bracketed in its likely extent. Local stress experience and dynamic response to the environment probably are major stumbling blocks in the reliability path to fatigue performance.

As noted earlier, variability in fatigue damage initiation and fatigue crack propagation is a common behavior to both characteristics of materials under a fatigue environment. In relation to the inspection control process, fatigue damage initiation identifies a point in time when a structure approaches either a limit to its operational life or a period of increased surveillance and structural maintenance. To identify the time at which fatigue crack initiation becomes a likelihood, median or average estimated fatigue performance is reduced by a factor. Judgment and guidance from statistical assessment of the variability provide definition of this factor. In Figure 38, there is presented the variability found in the fatigue performance of variously sized groups of identical laboratory test specimens having from 2 to 25 specimens in each group. The data is normalized in terms of the logarithmic average cyclic life of each group of specimens. It is readily noted from this summarized data that 50 percent (i.e., the median) to 95 percent of each size of group has its ratio of logarithmic average cyclic life from about 1.5 to 4 times the minimum life except for the data having 11 to 15 specimens in each group. For some unidentified reason this size of group has an unusually large range between the median and 95 percent ratios. In Figure 39, three methods of identifying the scatter between the logarithmic average fatigue perfor-



Figure 37. Test Verification of Fatigue Reliability.



mance and some level of minimum life. These three methods or approaches are identified as follows: (a) the engineering approach; (b) the statistical approach and (c) the order statistic approach. In the first approach to identifying the scatter between the logarithmic average life,  $\bar{Y}$ , and the safe or no-fatigue-damage life,  $\bar{Z}$ , is taken to be between 2:1 to 4:1. Using statistical concepts to identify the nature of the fatigue performance variability, some further qualification of the scatter factor can be made. First, the scatter factor can be assigned some level of confidence to identify the sampling uncertainties of group size for fixing the logarithmic average fatigue performance. Next a probable value of equalling or exceeding a minimum cyclic life can be identified. In this particular chart a confidence level of 95 percent on the lower limit of

the mean life,  $\bar{Y}_R$ , is shown for the range of one to three specimens in the test sample. This same value of probability level was taken to show the likely minimum life,  $\bar{Z}_R$ . The order statistic approach adds one more refinement to the estimation of the likely minimum fatigue performance. Recognition is made of the likelihood of there being one, two or more incidents of fatigue damage in a fleet or group of parts exposed to a fatigue environment. A group of 1000 parts and a 95 percent level of confidence and probability were selected to guide the illustration. One to three specimens were also considered to identify the magnitude of the confidence input. In Figure 40, the influence of selecting either a log-normal or two-parameter Weibull distribution is illustrated for the conditions of one and two failures in variously sized fleets. With the use of the ordered

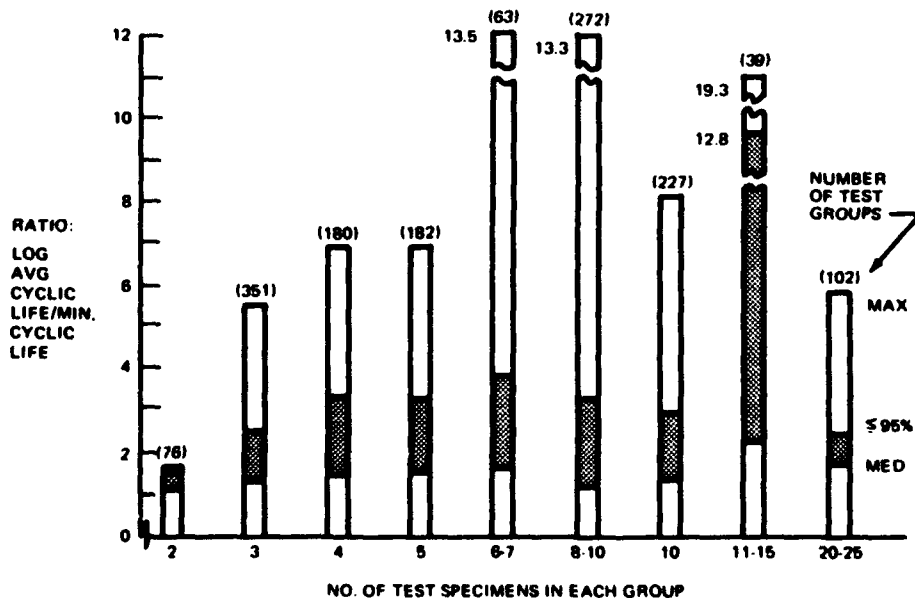
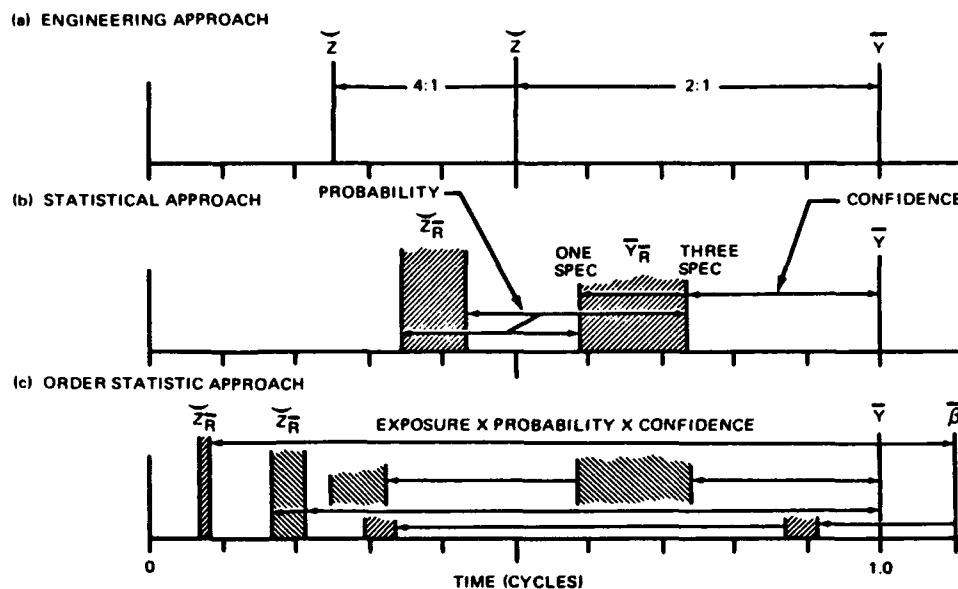


Figure 38. Fatigue Variability in Laboratory Test Data.

**Figure 39. Comparison of Reliability Analysis Development in Fatigue Performance Evaluation.**



statistic approach, an assessment can be made of the time for likely appearance of the first or early fatigue initiation in a fleet. Furthermore, some guidance may be gained to define reinspection intervals at the critical initiation time to assure minimum fatigue damage penetration into a fleet.

The principles of fracture mechanics also provide some means to control the possible loss of structural integrity in aircraft. As illustrated earlier in Figure 33, crack growth is a vital element of inspection requirements. In Figure 41(a), the shaded band indicates the cyclic life range wherein an undetected fatigue crack has little effect on structural integrity. This band can be approximated by calculating fatigue crack growth by fracture mechanics principles. In Figure 41(b), calculated crack-length versus cycles curves are shown for a range of alternating stresses and a constant  $\beta$  with an arbitrary initial crack length. The critical crack length cutoffs are also indicated for

either the plane stress critical crack length, based on  $K_{IC}$ , or the plane strain critical crack size, based on  $K_{IC}$ . The cyclic life between the initial crack length and the critical stress-intensity-factor cutoff length define the safe detection period for an unidentified fatigue damage location. The ratio of calculated cycles in this period to the total cycles to failure of the detail provide an estimate of the reinspection period for assuring control of undetected damage at any time during the usage of the structure. Tabulated data for this specific example is given in the table included in Figure 41. It is noted that the percent of crack growth cycles is larger for short cyclic life than long cyclic life.

### VIII. FATIGUE DAMAGE CONTAINMENT TASK

With the likelihood of undetected fatigue cracks present in a structure, attention must be given to their

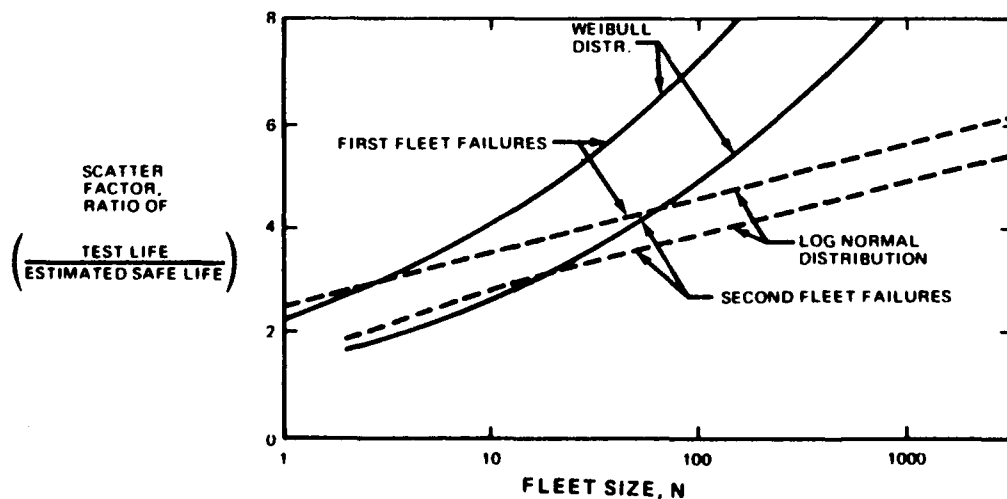
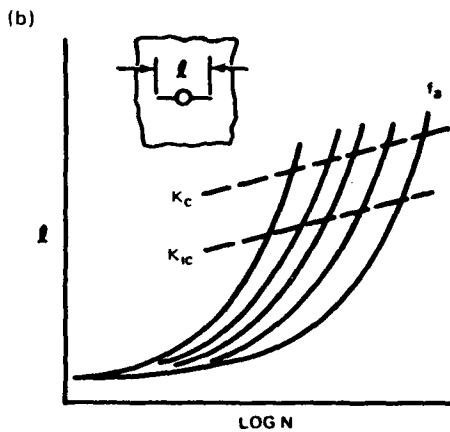
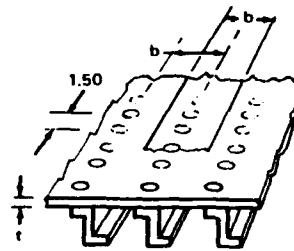
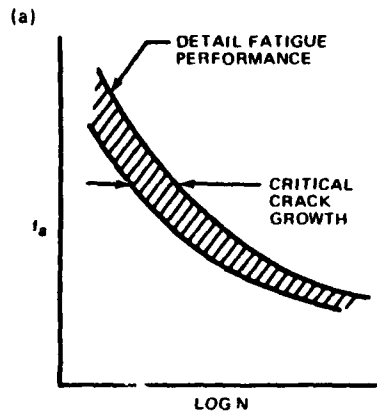
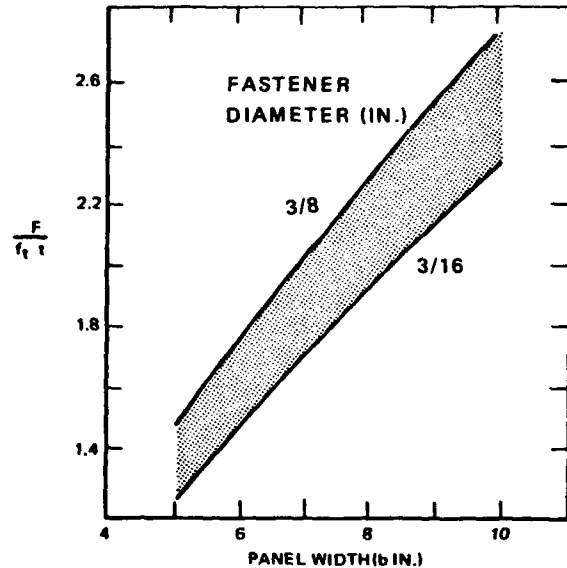


**Figure 40. Influence of Fleet Size on Scatter Factor at 0.90 Reliability with 0.95 Confidence for First and Second Fleet Failures (Test Sample Size  $n = 1$ ;  $\sigma = 0.14$  and  $\alpha = 4.0$ ).**



FIRST FASTENER LOAD PARAMETER



ALT STRESS KSI	CRACK GROWTH CYCLES	TOTAL FAILURE CYCLES	GROWTH CYCLES/FAILURE CYCLES
10.0	1,800	9,000	20%
8.0	3,500	19,000	18%
6.0	7,300	45,000	16%
4.0	18,000	125,000	14%
2.0	100,000	650,000	15%

Figure 41. Inspection Intervals - Stress Intensity Concepts.

containment. The crack initiation crack propagation and residual strength definition and verification process or considerations in materials and their structures have been touched upon in the preceding notes. It has been shown (Figure 27) that multiple-member or builtup panels like bonded sandwich panels with separate reinforcing straps do contain the growth of fatigue cracks under cyclic load. An important element of this capability is load transfer from the cracked member to the crack by-passing, undamaged reinforcing member. The capability of the selected fastening between the two members to transfer load is an item for selection and development or verification in maintaining the structural integrity of the structure. Conventional structure has mechanical fasteners while composites and bonded structure utilize an adhesive. In Fig-

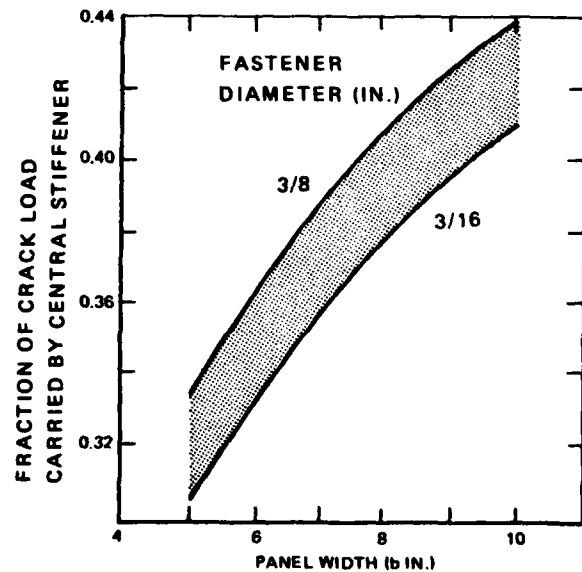
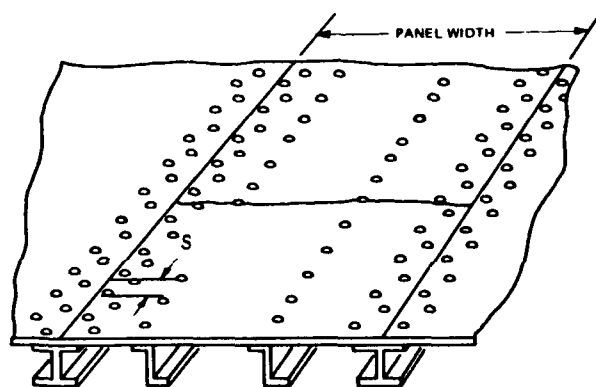


Figure 42. Load Transfer from Crack to Central Stiffener for Fail-Safe Analysis.

ure 42, an illustration is given of load transfer considerations for mechanical fasteners where a fatigue crack is centered over a stiffener. Two important factors are identified. First, in the upper graph of the figure, the estimated load

parameter for the first fastener load on either side of the fatigue crack is plotted for a range of stiffener spacings and fastener diameters. The load parameter consists of the fastener load,  $F$ , the gross stress,  $f_t$ , and the skin thickness,  $t$ . An arbitrary crack equal to the stiffener spacing,  $b$ , has been used in developing this chart for a fixed stiffener-to-skin area ratio and rigid fastener. The installed fastener flexibility crack length and stiffener area are significant parameters whose response to load need identification and evaluation by appropriate testing. The lower graph indicates the percentage of load transferred from the cracked skin to the adjacent stiffeners. Similar information for design or verification in the material selection and structural development process is given in Figure 43.

With such information, as outlined above, the load distribution in a typical structural panel can be calculated.



FASTENER SPACING - 1.50 IN  
 FAIL SAFE STIFFENER AREA -  $0.15 B \times T$

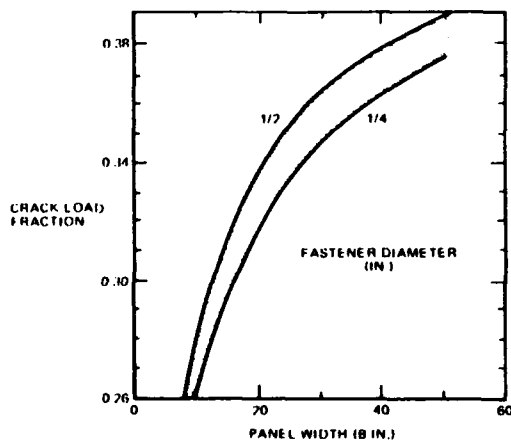


Figure 43. Load Transfer from Cracked Panel To Both Fail - Safe Stiffeners.

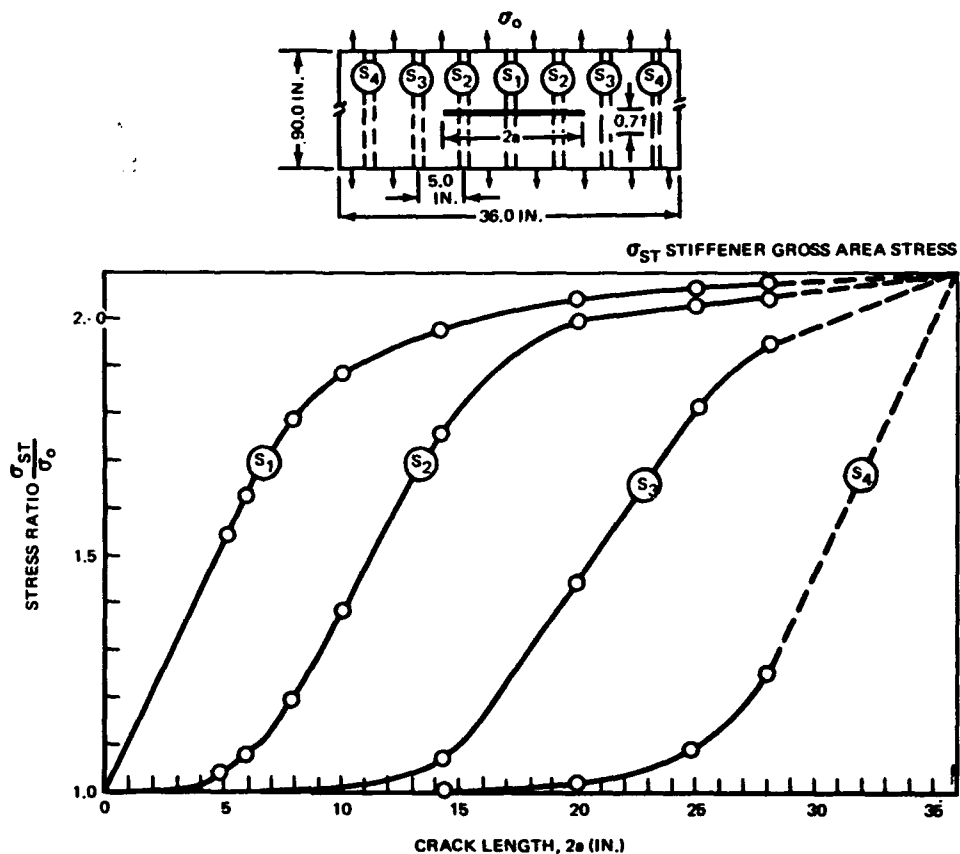
Figure 44 illustrates the manner in which stiffeners pick-up load as the fatigue crack propagates across the panel from its central point of initiation. The significance of fastener flexibility in this load transfer task is further emphasized in Figure 45. With perfectly rigid connections in this example of doubler to skin fastening, the load transfer is very high and the doubler and skin work at the same stress. However as fastener flexibility increases, the load distribution on fasteners tends to equalize and, finally, with very soft fastening, no significant load is diverted from the continuous element to the doubler.

## IX. THE DEVELOPMENT PROCESS AND CONCLUDING REMARKS

Structural integrity in aircraft structures is gained through detail attention to a multiplicity of material and its structure's behavioral characteristics. Static strength in itself is a complicated process in which material properties under load and geometry must be measured and defined. Statistical assessment of experimental strength data is done to obtain some probabilistic assurance that the material will perform its structural function. On the other hand structural integrity under fatigue conditions is not only dependent upon the load response of the material in its structural form but also needs to match the maximum load envelope of the cumulative variable load experience in the presence of fatigue damage. Of course, like in the static strength definition, a limit to the residual strength envelope is generally set. For example, the critical service loads under fatigue conditions are set at values of 80 percent of limit load or limit load itself. Nevertheless strength under fatigue conditions must recognize the initiation and propagation of fatigue damage through the structure. To demonstrate or develop structural integrity under fatigue conditions particular attention must be given to a greater variety of structural effects on materials than demanded by static strength. However, there are some overlap of requirements. The following paragraphs review in detail the summarized items of Figure 46.

1. *Loading.* Structural integrity cannot be separated from the response to the loading environment of the structure. To survive fatigue conditions a material or structure must match the variable load response without suffering fatigue damage initiation, critical fatigue crack growth and subsequent fracture. Characterization of a material and its structure to an all-encompassing range of variable loads is not a practical approach. Hence it is suggested that the operating load environment of the structure be considered. The nature and magnitude of expected loads and coincident stresses need identification or estimation and elimination to make the task tractable. Previous experience or definition of the fatigue environment is the first step in the procedure. Particular attention must be given to the operational use of the structure. Certainly the stress range of a flight from ground conditions to flight conditions at expected operating conditions is a most important range to explore a material's or its

Figure 44. Stiffener Stress Versus Crack Length 2a in a 6A1-4V Titanium Skin-Stiffener Panel (0.04-Inch Sheet, 93.5% Stiffening, 5/32-In. dia. Fasteners at 0.71 In).



structure's behavior. Next steady state loads and their character like tensile, compressive, etc., need consideration and definition. Wings, fuselages, vertical tail surfaces, horizontal tail surfaces and landing gears are all major components of concern in the integrity assessment task. Thus the nature, magnitude and frequency of the variable loading

environment must be identified. Tests and testing equipment should match this exposure or capability available or developed to equate laboratory rates with service rates. For instance the pressure cycle on a pressurized fuselage has a significantly different load change rate than the usual laboratory fatigue test machine. Also fuselage skin pressure

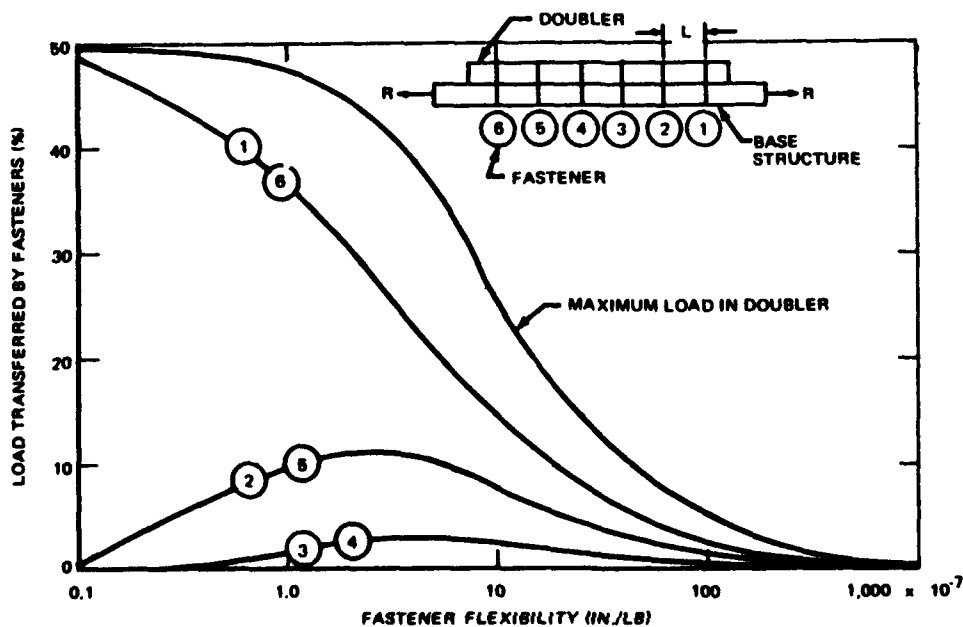


Figure 45. Variation in Load Transfer with Fastener Flexibility.

- **LOADING**  
STEADY STATE AND INCREASING  
CYCLIC
- **ENVIRONMENT (PHYSICAL)**
- **SPECIMEN CONFIGURATION**  
BASIC MATERIAL  
GEOMETRY
- **MECHANICAL PROPERTIES**  
 $F_{tu}$ ,  $F_{ty}$ ,  $F_{cy}$ ,  $E$ ,  $e$ ,  $w$
- **FRACTURE PROPERTIES**  
 $K$   
 $\sigma_n$  or  $\sigma_g$  AT  $2a_{cr}$

**Figure 46. Material Selection and Structural Development Process**

loads behave as a steady state load with superimposed variable loads of maneuver and gust. Accordingly, the first stage in the material selection and structural development process needs definitive action in these areas:

- a. Flight profiles
- b. Cumulative loading experience
- c. Variable load magnitudes
- d. Mean load conditions
- e. Cyclic loading frequency (ground, flight, acoustic, impact, etc.)
- f. Ground-air-ground cycles
- g. Effective test loads

2. *Environment.* The physical environment of a structure can be more meaningful than even fatigue performance. The process of corrosion has a habit of attacking materials to some degree in an unanticipated manner. Hence material selection needs guidance or definitive action in these areas:

- a. Corrosion resistance in the operating environment
- b. Dissimilar metal problems
- c. Stress corrosion
- d. Embrittlement
- e. Protective finish effects

Simple tests can at least identify relative sensitivity of an alloy to a physical environment.

3. *Specimen Configuration.* Particular care must be given to the selection of a fatigue test specimen for identifying the actual or relative fatigue performance of a given material or its structure. Some of the considerations relative to simulation concern the following:

- a. Stress field
- b. Stress magnitude
- c. Load transfer
- d. Simulation
- e. Fatigue crack initiation data
- f. Fatigue crack growth data
- g. Fatigue crack residual strength or fracture data (material or structure)
- h. Process effects

4. *Mechanical Properties.* In a fatigue environment, static mechanical properties have some application. A major step towards sizing the structure is taken with this type of data as well as definition of the maximum strength of the structure where fatigue damage hasn't had any deleterious effects. Of interest in determination of these material behaviors are the following properties:

- a. Tensile
- b. Compressive
- c. Shear
- d. Bearing
- e. Modulus or stiffness
- f. Fastener flexibility and load transfer

5. *Fracture Properties.* Under fracture properties the whole gamut of fatigue behavior is considered. Fatigue damage initiation, fatigue crack propagation and residual strength in the presence of fatigue cracks provide both material selection and structural assessment data. The development and use of fracture mechanics principles has been a major step forward in developing structural integrity for structures subject to a fatigue environment. The essential steps in assessing the fatigue damage resistance and containment are proposed as follows:

- a. Plane stress fracture toughness,  $K_{Ic}$
- b. Plane strain fracture toughness,  $K_{IIc}$
- c. Fracture stresses
- d. Crack growth rates
- e. Loading rates
- f. Environmental crack growth response
- g. Structural configuration for damage containment
- h. Dynamic loading rates
- i. Variability and reliability

## REFERENCES

1. *Metallic Materials and Elements for Aerospace Vehicle Structures*, MIL-HDBK-5A, Department of Defense, Washington, D.C. (1966).
2. *Summary of Airworthiness Directives for Large Aircraft*, Federal Aviation Regulation, Vol. II, Pt. 39, U.S. Government Printing Office, Washington, D.C.
3. A.A. Griffith, "The Phenomena of Rupture and Flow in Solids," *Phil. Trans. Roy. Soc. London*, 221A (1920).
4. G.R. Irwin, "Analysis of Stresses and Strains Near the End of a Crack Transversing a Plate," *J. Appl. Mech.*, 24/3:361-364 (1957).
5. G.R. Irwin, *Plastic Zone Near a Crack and Fracture Toughness*. Presented at the 7th Sagamore Army Materials Research Conference, Raquette Lake, New York, August 1960.
6. J.R. Low, Jr. et al., "Fracture Testing of High-Strength Sheet Materials: A Report of a Special ASTM Committee," *ASTM Bull.*, No. 243:29-40 and No. 244:18-28 (1960).
7. J.R. Low, Jr. et al., "Screening Tests for High-Strength Alloys Using Sharply Notched Cylindrical Specimens: Fourth Report of a Special ASTM Committee," *Mater. Res. Stand.*, 2/3:196-203 (1962).
8. J.R. Low, Jr. et al., "Progress in Measuring Fracture Toughness and Using Fracture Mechanics: Fifth Report of a Special ASTM Committee," *Mater. Res. Stand.*, 4/3:107-119 (1964).
9. *Fracture Toughness Testing and Its Applications*, ASTM-STP-381, American Society for Testing and Materials, Philadelphia, Pennsylvania (1965).
10. *Plane Strain Crack Toughness Testing of High-Strength Metallic Materials*, ASTM-STP-410, American Society for Testing and Materials, Philadelphia, Pennsylvania (1967).
11. P. Kuhn, "Observations on Strength Calculations for Sheet Metal Parts with Cracks," *Mater. Res. Stand.*, 8/9:21-26 (1968).
12. W.J. Crichlow, "The Ultimate Strength of Damaged Structure-Analysis Methods with Correlating Test Data," pp. 149-209, *Full-Scale Testing of Aircraft Structures*, Pergamon Press, London (1961).

**SESSION 2A**  
**FUNDAMENTALS I**

*Chairman*

**Dr. S.W. Tsai**  
**Air Force Materials Laboratory**



# FATIGUE MECHANISMS AND THE DEVELOPMENT OF FATIGUE-RESISTANT MATERIALS\*

by

J.C. Grosskreutz

Midwest Research Institute  
Kansas City, Missouri

## I. INTRODUCTION

In general, research into the nature of fatigue mechanisms has tended to be qualitative. That is, the objective has been to *describe* in detail the sequence of events which culminate in fatigue failure. To achieve this description, it has been necessary to employ microscopic examination of the test specimen - to identify cracks at the earliest possible stage and to follow their growth in detail. Not satisfied with these results, many investigators have examined the microstructure of materials and the ways in which it is altered by fatigue stressing, thereby hoping to establish the nature of fatigue damage. The results of all these studies have unavoidably been couched in terms of microscopic entities and their interactions: e.g., dislocations, vacancies, inclusions, second-phase precipitates, environmental attack, etc. Although mechanisms research has been able to provide a fairly accurate picture of the fatigue sequence in terms of these microscopic entities, it has been very difficult to construct a quantitative theory of fatigue which contains the familiar and useful macroscopic variables, nominal stress, strain and cycles to failure. These difficulties are gradually being overcome, however, and the first generation of fatigue crack-growth theories have appeared during the past two years - theories which were derived from crack-growth models based on qualitative observations.

Despite the lack of quantitative results, much has been accomplished by mechanisms research. To begin with, the greatest contribution has been an intangible one: the "mystery" has been removed from catastrophic fatigue failure. We know now that failure is the certain result of the nucleation and growth of highly localized microcracks, and that general degradation of the material does not occur except for fatigue softening of some previously hardened materials. This knowledge has freed both the designer and operator to think positively in terms of cracks as the only meaningful indicator of impending failure. The application of fracture mechanics to structures subject to fatigue stresses is based entirely on the knowledge that residual strength depends on the size and location of microcracks.

A second major contribution of mechanisms research has been the identification of those parameters which

are important to fatigue failure. A listing of these would include: the surface as the most likely site for crack nucleation; inhomogeneous plastic deformation, e.g., slip bands, grain boundary rumpling, etc., as the precursors of crack initiation; inclusions and other second-phase particles as micro stress-concentrators which aid and abet crack nucleation; the plastic strain amplitude as the important variable in the fatigue of materials at high loads; and the material response at the tip of the growing fatigue crack, e.g., plastic zone size and shape, hardening/softening, plastic relaxation as the controlling agent for crack growth rates. Each of these parameters, have been identified as relevant to fatigue, has provided new areas of research and development on the fatigue problem; surface coatings, slip homogenization, removal of inclusions, low-cycle fatigue and the cyclic stress-strain curve, and the application of fracture mechanics to fatigue-crack growth.

Finally, the prospects are bright for the translation of mechanisms knowledge into practical guidelines for the materials developer. The task of relating microstructure to macroparameters is under way, and the expression of crack growth rates in terms of physical properties has already been accomplished.<sup>1</sup> It is the objective of this paper to show how this interaction between mechanisms research and materials development is being achieved. Although it is tempting to begin such a paper with a state-of-the-art summary of the mechanism of crack initiation and growth,<sup>2</sup> a more useful purpose will be served if several very practical questions are first raised and the answers then supplied from the background of current mechanisms knowledge. In this way, the interaction becomes much more apparent, and the language of the two fields can be interfused.

## II. RELEVANT QUESTIONS FOR DEVELOPMENT OF FATIGUE-RESISTANT MATERIALS

Many of us tend to ask too global a question to begin with, such as "why do metals fail in fatigue?" Or, "what is the best microstructure to resist fatigue?" A more fruitful approach is to ask subquestions, all of which add finally to make the global question. A materials designer might well pose the following questions to obtain the guidelines for fatigue-resistant materials:

\* Supported by the Air Force Materials Laboratory, Wright-Patterson Air Force Base, Ohio.

1. How can high static yield stresses be maintained under cyclic loading?
2. How can crack initiation be suppressed?
3. How can crack growth rates be reduced?
4. How do temperature and environment affect answers to the above questions?

(We shall assume that the materials developer is aware of the fact that in the final analysis, his material must have good fracture toughness to resist catastrophic tensile failure in the presence of small flaws and cracks.)

In what follows, an attempt will be made to provide answers to these questions based on the current mechanisms knowledge. Attempts will also be made to find macroscopic, mechanical properties (easily measurable) which can be related to the microscopic entities which are used to describe much of mechanisms research. In this way, the task of the materials designer can be alleviated and the amount of sophisticated microscopic examination can be reduced.

## II. MAINTENANCE OF MONOTONIC FLOW STRESS

The flow stress of a material undergoing cyclic straining is represented by the *cyclic stress-strain curve*.<sup>3,4</sup> This curve is generated by plotting, for a given temperature and initial material condition, the steady-state saturation stress  $\sigma$  versus  $\Delta\epsilon_p/2$ , where  $\Delta\epsilon_p$  is the applied cyclic plastic strain range. In other words, this curve is the locus of the tips of all steady-state cyclic hysteresis loops of width  $\Delta\epsilon_p$ . Figure 1 illustrates this point and displays schematic cyclic stress-strain curves as well as the more familiar tensile (monotonic) curves for comparison purposes. Feltner and Laird<sup>4</sup> have shown that wavy-slip-mode materials<sup>†</sup> possess a unique cyclic stress-strain curve independent of prior strain history. The cyclic stress-strain curve for most materials can be fitted approximately with a power law relation:

$$\sigma_s = \sigma_0 (\Delta\epsilon_p / 2)^n \quad (1)$$

where  $\sigma_0$  is a material constant proportional to the fracture stress and  $n$ ' is the cyclic strain hardening exponent.

<sup>†</sup> Slip mode, as characterized by the appearance of the surface slip markings which accompany plastic deformation, can be classed as either wavy or planar depending on the ease with which plastic deformation spreads from one crystallographic plane to another. Materials in which screw dislocations cross-slip easily displays a wavy-slip mode. Most materials can be classed somewhere in the range between the two extremes of "wavy" and "planar". Some simple examples are:

WAVY SLIP	
Copper	Nickel
Aluminum	Silver
Iron	Low-carbon steels

PLANAR SLIP	
$\alpha$ -brass	Nickel-base super alloys
Magnesium	Stainless steel
Titanium	

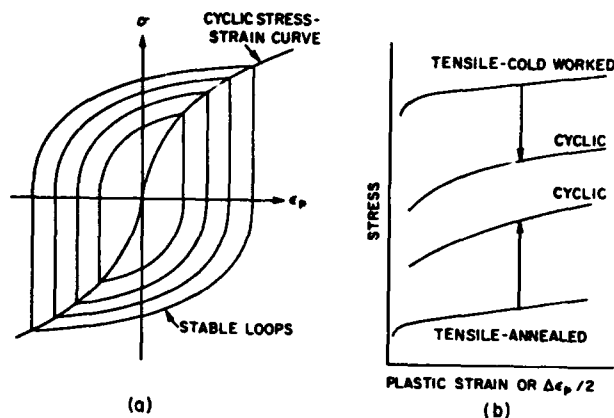
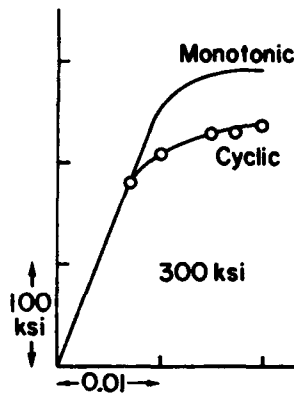


Figure 1. Schematic Illustration of Cyclic Stress-Strain Curves. (a) Construction from Steady-State Cyclic Loops; (b) Comparison of Tensile and Cyclic Stress-Strain Curves on same Diagram. (After C.E. Feltner and C. Laird, Ref.4).

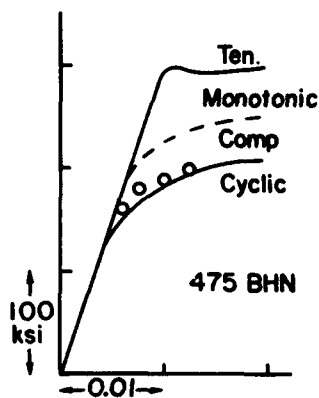
Raising the flow stress of annealed material by fatigue stressing will be beneficial in most structural applications, but the softening which occurs for some previously cold-worked or hardened material can be potentially dangerous, especially if the structures designer is unaware of this phenomenon. Admittedly, many structures are designed to operate at nominal stresses below the elastic limit where general fatigue softening does not occur; however, the very existence of fatigue failure proves that *localized* plastic deformation does indeed occur. Hence, the degradation of monotonic yield properties has significance for the entire fatigue sequence. In this sense, fatigue softening represents fatigue damage which is different in kind from the older concept of a general strength degradation which, in fact, does not usually occur.<sup>5</sup>

Two important examples of high-strength commercial materials which fatigue soften appreciably are given in Figure 2. The 0.2% offset yield strength measured under monotonic and cyclic loading conditions for the 18% Ni maraging steel are 280 ksi and 215 ksi, respectively, and for the 4142 steel, 275 ksi and 160 ksi. These examples show that the effect is not trivial!

At present there are no quantitative rules for predicting the amount of hardening or softening that will occur under a given set of conditions. However, Manson et al.<sup>7,8</sup> have proposed a rule which allows one to predict, from



(a) 18% Nickel Maraging Steel



(b) Quenched and Deformed 4142 Steel. (Ref. 6.)

Figure 2. Cyclic and Monotonic Stress-Strain Curves

monotonic stress-strain properties, whether hardening or softening will occur. The rule states that if the ratio of the ultimate tensile strength to the 0.2% offset yield strength is  $\sigma_u/\sigma_{0.2\%} > 1.4$ , then hardening will occur. If  $\sigma_u/\sigma_{0.2\%} < 1.2$ , then softening will occur. For values of the ratio between 1.2 - 1.4, the behavior is not certain, but the material should be fairly stable. Feltner and Landgraf<sup>9</sup> have applied this rule to 35 different materials, with successful results in all but two cases.

The task here is to use knowledge of the mechanisms of fatigue hardening/softening to produce guidelines for designing materials to withstand cyclic degradation of the monotonic flow stress. We begin by observing that the majority of research has been directed at understanding the mechanism of fatigue hardening in materials.<sup>10-14</sup> This emphasis is understandable in terms of the earlier and parallel development of research into monotonic work hardening. But, from the viewpoint of the materials designer, an investigation of the mechanisms of fatigue softening of various microstructures would have been more helpful. Fortunately, a few papers do exist in the literature which pertain to fatigue softening which can be utilized to illuminate our discussion.

To begin with, it will be convenient to list those microstructures, or mechanisms, commonly employed to provide high static strength in materials.

#### A. Microstructures Which Produce High Static Yield Stresses

*Strain hardening*, in which dislocations are blocked and pinned by their own substructure.

*Martensitic hardening*, in which a diffusionless transformation produces a very fine grain structure together with the dislocation networks created by the martensitic shear displacements.

*Precipitation hardening*, in which constituents of the alloy are allowed to precipitate from solid solution to form tiny second-phase particles, sometimes coherent with the matrix, which act as obstacles to dislocation motion.

*Dispersion hardening*, in which hard, noncoherent, second-phase particles are dispersed throughout the matrix by powder metallurgy methods, internal oxidation, etc., to provide dislocation barriers.

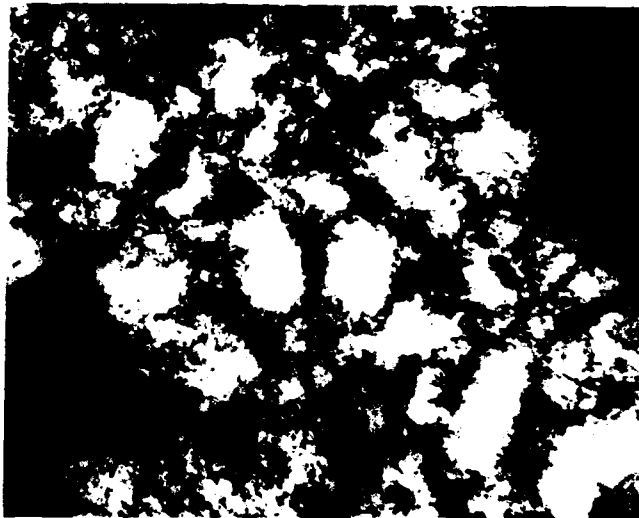
*Solid-solution hardening*, in which substitutional solute atoms create an obstacle to dislocation motion by virtue of a number of possible mechanisms, including misfit stress fields, long- and short-range order.

*Filament reinforcement*, in which very fine fibers of high strength are embedded in the matrix to produce a composite material whose mechanical properties are some mean value between that of the filament and of the matrix.

#### B. Fatigue Softening

The majority of the observations which have been made on fatigue softening have utilized materials originally strengthened by cold work (strain hardening). If  $\sigma_u/\sigma_y < 1.2$ , then softening will occur provided the plastic strain is actually reversed, i.e., the sample is driven into plastic compression.<sup>10</sup> Transmission electron microscopy has shown that this softening is accomplished by altering the original tensile-induced dislocation morphology into one more nearly characteristic of the cyclic strain level. In wavy-slip-mode materials, where cross-slip is active, the softening occurs rapidly and a dislocation structure unique to the given strain amplitude is formed.<sup>10</sup> An example is shown in Figure 3. It is generally agreed that the destruction of the original strain-hardened dislocation network is accomplished by the cumulative action of dislocations cutting back and forth through the network. The fatigue softening of a low-carbon martensitic steel occurs by a similar mechanism,<sup>15</sup> in which the dislocations introduced by the martensitic transformation are rearranged.

Precipitates in age-hardened structures, especially the Al alloys, have been the subject of several fatigue-



(a) After Initial Cold Work  
(5% Reduction in Diameter).



(b) After Fatigue Softening (Ref. 10).

Figure 3. Dislocation Structure in Copper.

softening studies. Some controversy still exists over the mechanism in aluminum alloys, but it appears that in the high-purity systems Al-Cu and Al-Zn-Mg, softening occurs by repeated shearing of the precipitate particles by oscillating dislocations.<sup>16,17</sup> Figure 4 illustrates the process schematically. After being reduced below a certain minimum size, the particles revert into solid solution. This process begins in concentrated slip bands and then spreads as the bands widen and multiply. The situation in commercial aluminum alloys of the same basic composition, 2024-T4 and 7075-T6, is entirely different. No evidence of reversion has been observed, even at the tips of fatigue cracks where the strain concentration is highest.<sup>18</sup> These observations are further confirmed by the fact that both alloys are observed to harden under reversed cyclic strain.<sup>19</sup>

The reason for this marked difference between high-purity and commercial alloys of the same type is most likely due to the presence of dispersoid particles in the commercial alloys which act as hard obstacles to cyclic dislocation motion. These particles are intermetallic compounds composed of aluminum and the additional elements (Mn, Mg, Cr) found in commercial alloys. An example of the fatigue-hardened structure in 2024-T4 is shown in Figure 5 where the dispersoid particles are identified by arrows. Tangled dislocations around these particles are clearly evident.

Reversion by shearing of carbide precipitates in low-carbon steels<sup>20</sup> and  $\gamma'$  precipitates in nickel-base superalloys<sup>21</sup> has also been observed to occur during fatigue. The marked fatigue softening of maraging steels is most likely a combination of dislocation rearrangement in the martensitic structure and reversion of the aged carbide precipitate.

Solid-solution-hardened alloys apparently soften only when long-range order is present and then only at high plastic strain amplitudes.<sup>22</sup> The mechanism involves a reduction in antiphase domain size by repeated slip.

Dispersion-hardened materials contain small particles which are usually too hard to be sheared by moving dislocations. Therefore, they should be stable against fatigue softening. Starting with as-received thoria-doped nickel ( $\sigma_y \sim 77$  ksi), Ham and Wayman<sup>23</sup> showed that some fatigue softening occurred at room temperature, but that the dispersed microstructure remained stable. Leverant<sup>24</sup> used a recrystallized thoria-doped nickel ( $\sigma_y \sim 35$  ksi) and observed considerable fatigue hardening. The conclusion is that the dispersion strengthening is stable and unaffected by cyclic straining, and that the fatigue strain hardening/softening occurs in the nickel matrix.

Fiber-reinforced composite materials have not yet been studied for their fatigue-softening characteristics, but unpublished work by Hancock<sup>25</sup> indicates that the situation may be analogous to the dispersion-hardened materials. No degradation of the filament-matrix structure occurs, and any fatigue hardening or softening observed must be due to strain hardening in the matrix.

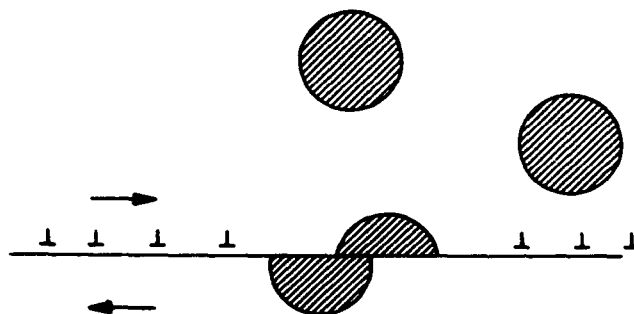


Figure 4. Schematic Representation of Dislocation Shearing a Precipitate.

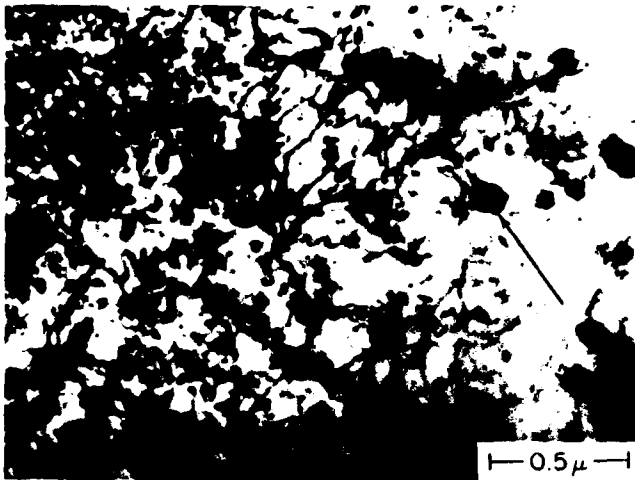


Figure 5. Transmission Electron Micrograph of Fatigued 2024-T4 Aluminum Showing Dispersoid Particles (arrows) and Tangled Dislocations Around Them.

### C. Generalizations on the Mechanisms of Fatigue Softening

What characteristics do the various softening mechanisms described above have in common? Clearly, the dominant feature is the to-and-fro motion of dislocations through the original hardening microstructure. The amount of softening is determined by the ability of these dislocations to alter, or annihilate the basic hardening structure which consists of pinning points and obstacles. The unique feature of fatigue softening is its accumulation; that is, given enough cycles of strain reversal, the small contribution of each oscillating dislocation can be summed over the entire dislocation array to produce a measurable effect. The contribution of vacancies produced in fatigue to the softening of initial structure is not clear. They certainly can play a role, but, in the special case of strain-hardened materials, their contribution is not necessary for softening to occur, as shown by experiments conducted at 78°K on copper.<sup>47</sup>

What hardening structures are most susceptible to fatigue softening? Although it is not possible to make a quantitative ranking, it appears that strain-hardened and precipitate-hardened structures, particularly with a wavy-slip mode matrix and with ratio  $\sigma_u/\sigma_y < 1.2$ , rank highest in susceptibility. Because of the nature of their hardening mechanism, martensitic and maraging steels would also have to be included. The least susceptible are dispersion-hardened fine-grain-size, and filament-reinforced materials, wherein the strengthening microstructure is not affected by repeated dislocation motion.

For those materials in which  $\sigma_u/\sigma_y > 1.2$ , softening does not generally occur, and if the ratio is greater than 1.4, hardening will occur. These values of the ratio simply reflect an increasing ability of the material to work-harden. Another index for stating the same thing is the cyclic work-hardening exponent,  $n'$ . The larger  $n'$ , the more likely the material will cyclically harden rather than soften. That is, the internal microstructure is such that it *allows* to-and-fro

dislocation motion to occur without annihilation of structure, and by self-interaction, to produce typical fatigue-hardening structures.

### D. Guidelines for Maintaining High Static Yield Stress

Our discussion so far has indicated that while there is still much to learn about fatigue softening, enough is known to sketch some guidelines for the prevention of softening.

1.  $\sigma_u/\sigma_y > 1.2$ . Whether this guideline holds for all of the different hardening microstructures mentioned above is not yet known.

2.  $n'$  should be as large as possible.

In addition to these two quantitative guidelines, a number of qualitative ones can be stated. It is obvious that increases in static yield strength must be achieved by microstructures which are not annihilated, or whose rate of annihilation by cyclic dislocation motion is low.

3. To achieve high yield by strain hardening, planar-slip-mode materials should be used.

4. To achieve high yield by precipitate hardening, the precipitate must be stable against re-solution (or growth); or, lacking that, other stable dispersoid particles must be added to inhibit long-range dislocation motion (as in 2024 and 7075 aluminum).

5. To utilize wavy-slip-mode materials, the best mechanisms for achieving a stable high yield stress are dispersion hardening, filament reinforcement, and small grain size. Of course, these strengthening mechanisms are equally good for planar-slip-mode materials.

### IV. SUPPRESSION OF CRACK INITIATION

A major contribution of mechanisms research has been to isolate the *site* of fatigue crack initiation in a variety of materials. In otherwise uncracked material, cracks always begin at concentrations of plastic strain, and because plastic deformation begins at free surfaces, most fatigue cracks have their origins at a surface. The sites of crack initiation can be listed as follows:

*Slip bands*, which are concentrations of plastic deformation intersecting the surface of a material. They are important as crack initiation sites in most pure fcc and bcc materials and in a number of alloys such as brass, Cu-Al, high-purity aluminum alloys and steels, and some titanium alloys.

*Twin boundaries* are important sites in hcp materials, such as titanium and some of its alloys.

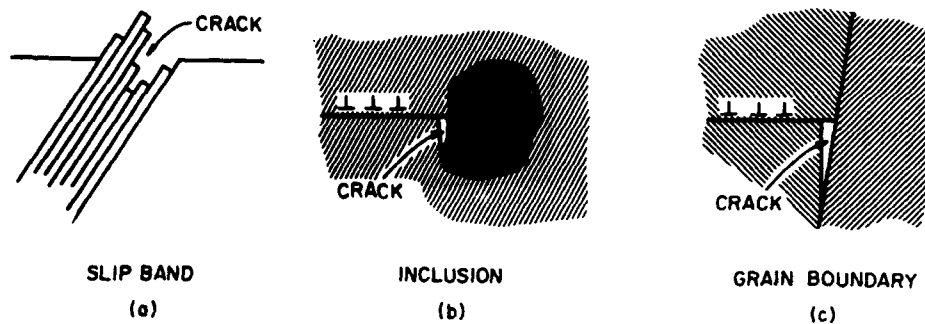


Figure 6. Schematic Illustration of Crack Initiation Caused by Nonreversible Displacements at (a) Slip Bands, (b) Inclusions, and (c) Grain Boundaries.

*Inclusions* and undissolved second-phase particles dominate crack initiation in many commercial-purity alloys, including some of the important aluminum alloys and high-strength steels.

*Grain boundaries* become important at high-strain amplitudes and at temperatures,  $T > 0.5 T_m$ , where  $T_m$  is the melting temperature, or in the presence of impurities which embrittle the boundary ( $O_2$  in Fe). In some martensitic steels, previous austenitic grain boundaries are the sites of crack initiation,<sup>26</sup> but this site does not appear to be a common one.

The mechanism of crack initiation at these sites varies, of course, but in the sub-creep region ( $T/T_m < 0.5$ ) two things are shared in common. First, these sites are all regions where enhanced, localized plastic deformation occurs. In fact, comparison of dislocation microstructures at these sites with those in the matrix always reveals a structure which is characteristic of high-strain amplitude cycling of bulk materials regardless of the nominal, applied load amplitude.<sup>1,2</sup> If fatigue softening is possible in the particular material, then the concentration of plasticity will be regenerative, and the initiation of the crack accelerated. Second, nonreversible slip at these sites gives rise to permanent offsets or displacements which serve as crack nuclei. Figure 6 illustrates this point schematically. If slip were completely reversible, cracking would either not occur, or be tremendously delayed. But all materials of technical interest are subject to oxidation in our usual environment, so nonreversibility of slip at surfaces is insured.

Without going further into the details of crack-nucleation mechanisms, it is possible to suggest several means for delaying or suppressing the start of fatigue cracking.

1. Slip, and hence plastic deformation, should be homogenized to prevent localized accumulation of plastic deformation. An obvious way of doing this is to employ planar-slip-mode materials, a point which has already been demonstrated for single crystals.<sup>27</sup>

2. The surface yield stress should be raised to prevent

the onset of plastic deformation there. The time-honored way of achieving this is shot peening, which introduces a residual compressive stress. A more sophisticated method is to produce surface alloying which raises the yield. Case carburizing of steels is a good example. More recently, surface diffusion coatings have been utilized in an attempt to achieve high yield, but with only scattered success. Examples are shown in Figure 7 where the S/N curves for Ti 8A1-1V-1Mo with a surface layer of diffused Be are compared with the untreated sample, and pure Al with a surface diffused layer of copper is compared with an untreated sample.<sup>28</sup> This method still requires considerable research to identify the optimum properties of a surface alloyed layer to suppress fatigue. In many other cases which have been tried, the effect has been to produce either no improvement, or an actual degradation of fatigue properties.<sup>29</sup>

3. The density of inclusions (defects) should be reduced so that cracks will not nucleate at these sites. There is a growing body of evidence that such an approach will pay excellent dividends, not only for suppressing crack initiation but for inhibiting crack growth and increasing fracture toughness. The effects were first demonstrated for steels,<sup>30</sup> and recently aluminum alloys have been prepared with very low inclusion densities. Figure 8 illustrates the improvement obtained for 2024-T4 Al in which the volume fraction of undissolved second phase was reduced from 0.09% to 0.00016%.<sup>31</sup> Crack nucleation no longer occurred at inclusions in this alloy, and the number of cycles to initiate a microcrack was extended by a factor of 1.6. Fracture toughness increases of 60% have recently been reported for a 2024-T4 inclusion-free alloy.<sup>32</sup>

4. Materials should be chosen which resist cyclic softening to further suppress the nucleation rate of fatigue cracks. If this is not possible, surface treatments which will help to resist softening should be employed.

Mechanisms research has definitely shown that the fraction of fatigue life to nucleate a fatigue crack,  $N_o/N_f$ , increases as the load amplitude decreases. Hence, the guidelines and treatments suggested above should be expected to

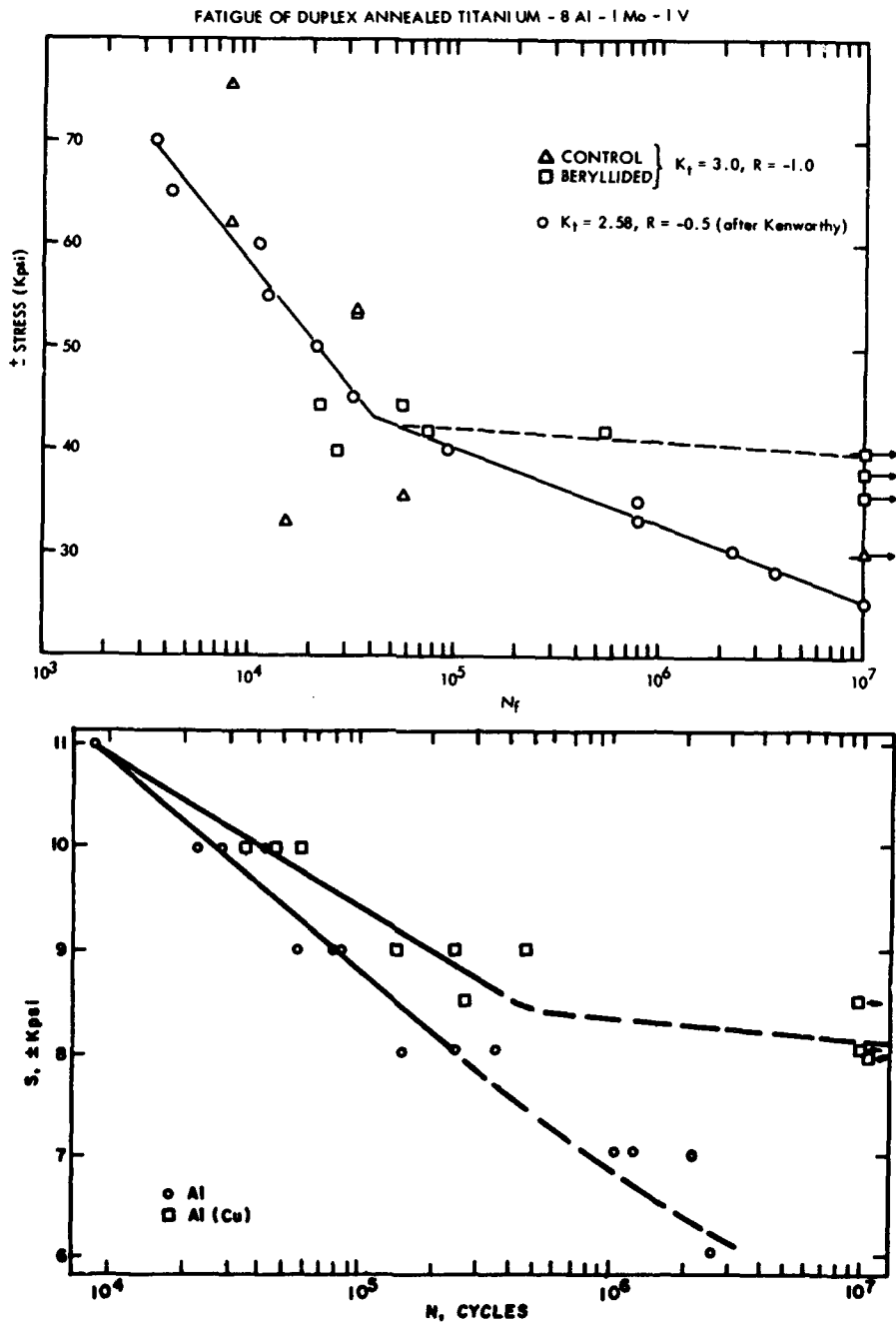


Figure 7. The Effect of Surface Diffusion Coatings on Fatigue Lives.

produce their greatest effects in the long-life regime. The curves in Figure 7 illustrate this point very well.

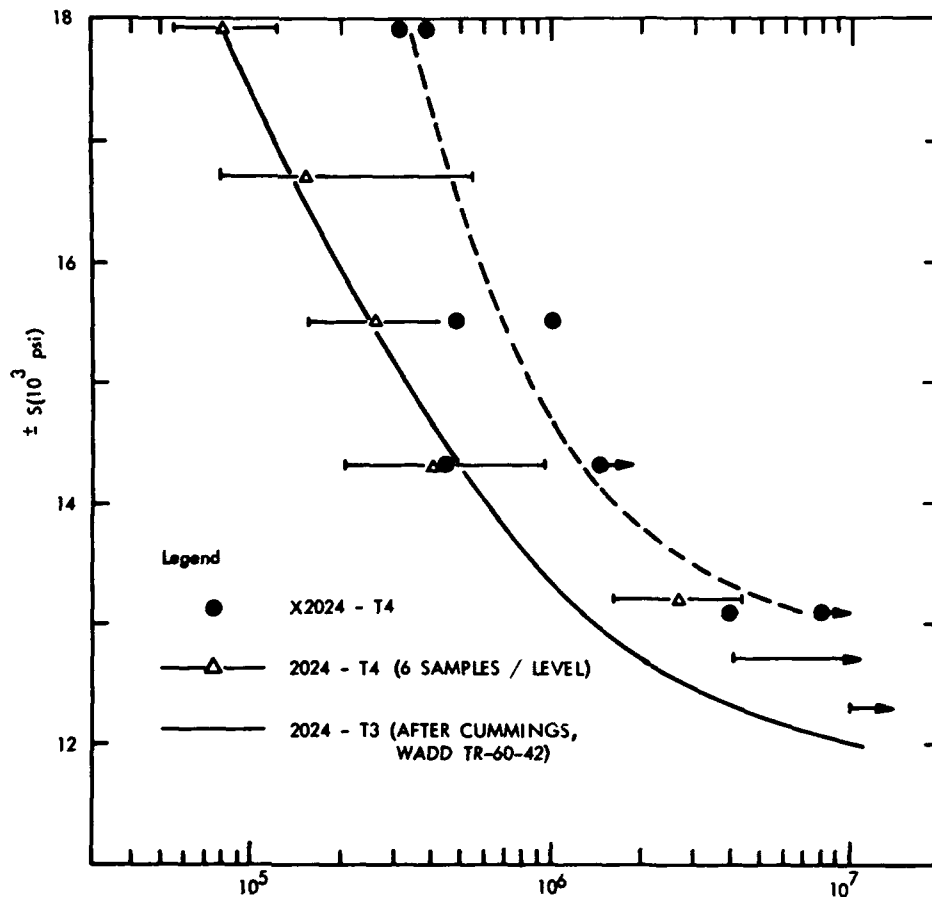
**V. REDUCTION OF CRACK PROPAGATION RATES**

At high-load amplitudes, a major fraction of fatigue life is occupied with growing a crack.<sup>33</sup> If the sample is notched, the fraction becomes even higher. And, for a great many "real" structures, the existence of flaws and other defects make crack propagation the only mechanism of importance in fatigue, regardless of load amplitude. Therefore, it is highly important to consider the manner in which

these cracks grow and the way this knowledge can be used to design materials to resist crack growth.

Several good reviews of the mechanisms of fatigue crack propagation exist,<sup>34,35</sup> and only the relevant highlights will be listed here. Cracks start in a crystallographic shear (Stage I) mode, penetrate a few tenths of a millimeter, and then propagate perpendicular to the tensile axis in a tensile (Stage II) mode (see figure 9). The stress concentration at the crack tip causes local plastic deformation in a zone extending ahead and on either side of the crack. As the crack grows, this plastic zone increases in size until it becomes comparable to the thickness of the specimen. As

Figure 8. The Effect on Fatigue of Reducing the Concentration of Undissolved Second-Phase Particles in 2024-T4 Aluminum. Volume Percent of "Inclusions": X2024,  $1.6 \times 10^{-4}$ ; Commercial 2024,  $9 \times 10^{-2}$ .



this occurs, the plane-strain conditions ahead of the Stage II crack no longer hold, and the crack rotates into a final plane-stress, shear mode (see figure 10). Microscopic studies of the Stage II fracture surface have shown that

crack growth occurs for each load cycle. Although growth striations have been observed on some Stage I surfaces, there is no direct evidence of growth *each* cycle in this stage.

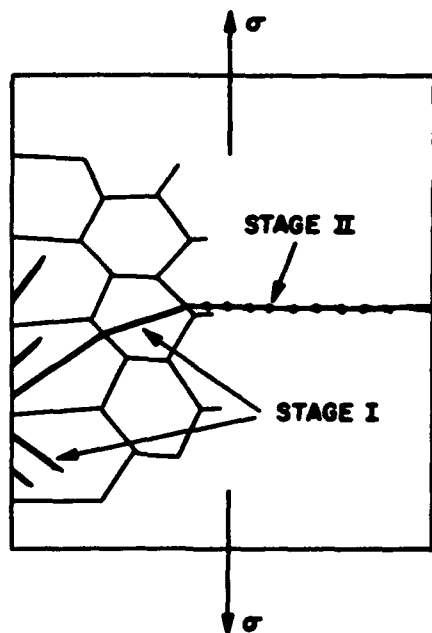


Figure 9. Schematic Illustration of Stage I and Stage II Crack Growth (Ref. 34).

The rate of fatigue crack growth,  $da/dN$  ( $a$  is crack length,  $N$  the number of cycles), is controlled by the local events which occur at the crack tip and in the plastic zone immediately ahead. Because fatigue is a repetitive process, understanding the mechanism of crack extension during any one cycle allows one to describe the growth during an entire stage. Most attention has been focused on the Stage II mode at relatively high-load amplitudes where observation is simplest.<sup>34,37</sup> In this stage, the crack grows by repetitive blunting and sharpening of the crack tip. The sequence of events is shown in Figure 11. During the tensile part of the load cycle, large plastic strains at the crack tip cause localized slip on the planes of maximum shear. Reversal of the load forces the crack faces together, and the new surface created during tension is not completely rehealed by reversed slip. Depending on the material and the environment, much of the slip during compression occurs on new planes and the crack tip takes on a folded appearance with "ears". After completion of the compressive half-cycle, the crack tip is resharpened and the sequence can begin all over again. There is good evidence<sup>34,36</sup> that Stage I cracking occurs in much the same way, but with only one set of  $45^\circ$  slip planes operative.

Examination of the material immediately adjacent



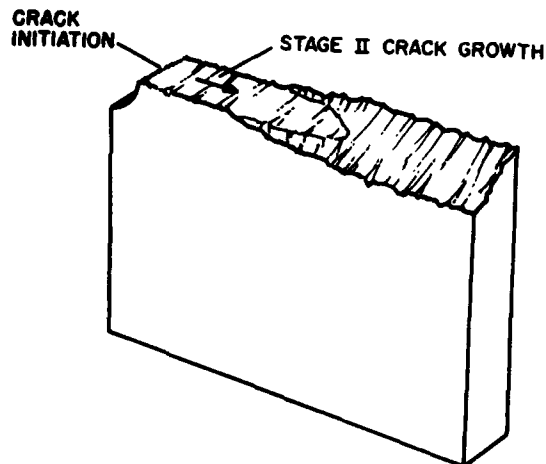


Figure 10. Schematic Illustration of Fatigue Fracture Surface. Plane Strain Crack Growth Occurs at  $90^\circ$  with Respect to the Tensile Axis Near the Point of Crack Initiation. Propagation under Plane Stress Conditions Begins at Later Stage and Crack Continues in a  $45^\circ$  Shear Mode.

to and ahead of fatigue cracks by transmission electron microscopy<sup>18,38</sup> has revealed the dislocation morphology characteristic of high-strain fatigue cycling of bulk specimens. Particularly dense dislocation arrays are observed just beneath the growth striations<sup>39</sup> (see figure 12), which indicate the presence of the active slip zones shown in Figure 11. Nothing in these observations would indicate that a unique microstructural change accompanies fatigue crack growth other than the concentration of plastic strain. Therefore, an important conclusion can be drawn, namely, that crack growth in homogeneous materials can be treated by elastic-plastic continuum theory without fear of omitting some unique feature. These observations also bring to mind that all of the possibilities for fatigue softening discussed in Section III

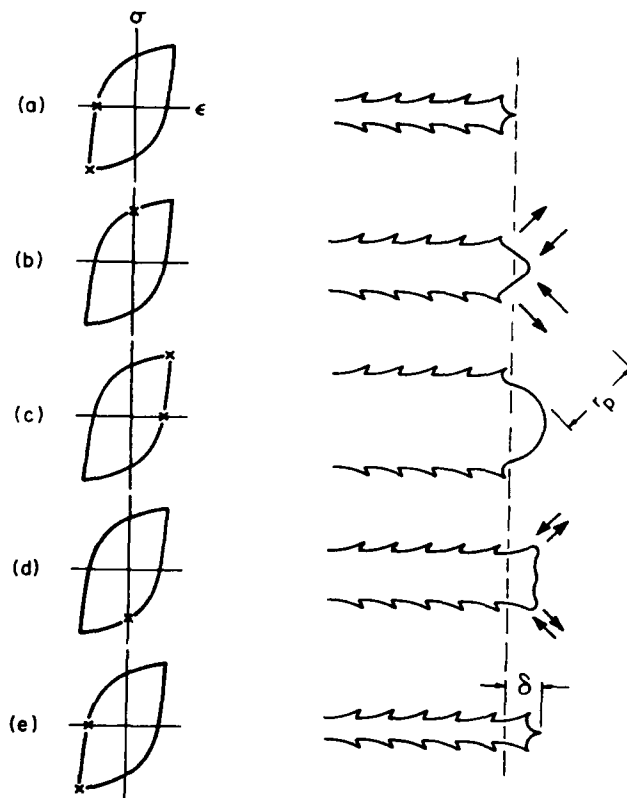


Figure 11. Fatigue Crack growth by the Plastic Blunting Mechanism. Drawings at Left Indicate Points on the Cyclic Hysteresis Loop for Which Crack-Tip Geometry Obtains  $r_p$  = Plastic Zone Size Along Planes of Maximum Shear.

exist in concentrated form at the tip of a growing fatigue crack.

From the above description of crack growth, it is quite clear that inclusions or undissolved second-phase particles can have an important effect on the events occurring

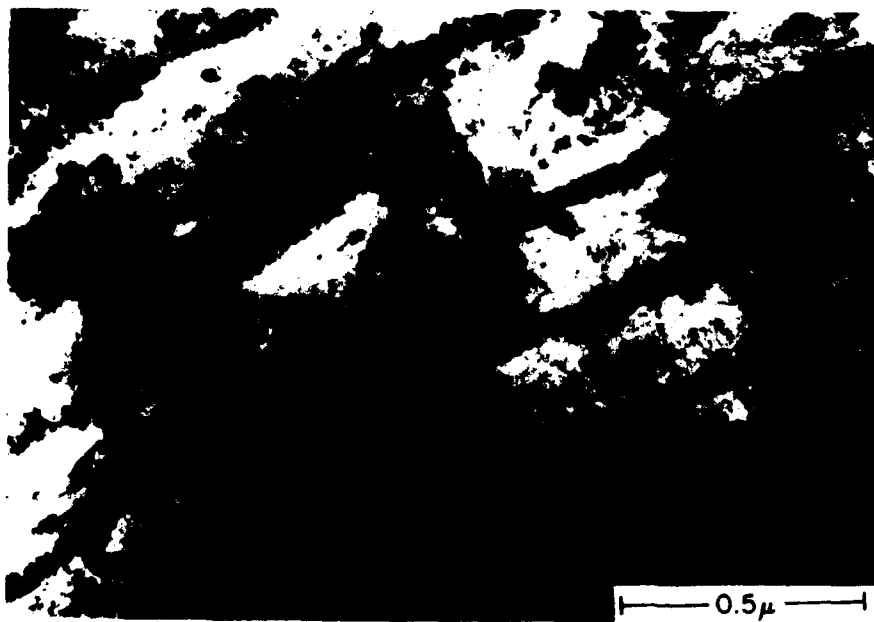


Figure 12. Transmission Electron Micrograph of the Fracture Surface of Fatigued 7075-T6 Al. Dense Dislocation Patches Occur Regularly at Successive Positions of the Crack Front. (Ref. 39.)

**TABLE I**  
**FATIGUE CRACK GROWTH LAWS**

AUTHOR	TYPE OF TEST	GROWTH LAW
McClintock <sup>42</sup>	Constant stress, $\Delta\sigma$	$da/dN = \frac{4\alpha}{E\sigma_u} (\Delta\sigma)^2 a$
Lardner <sup>43</sup>	Constant stress, $\Delta\sigma$	$da/dN = \frac{\pi(1-\nu)}{4G\sigma_u} (\Delta\sigma)^2 a$
Tomkins <sup>44</sup>	Constant stress, $\Delta\sigma$	$da/dN = \frac{\pi^2(\Delta\sigma)^{2n'}}{32(\sigma_o)^{1/n'}\sigma_y^2} a$
	Constant plastic strain, $\Delta\epsilon_p$	$da/dN = \frac{\pi^2}{32} \left(\frac{\sigma_o}{\sigma_y}\right)^{2n'+1} \Delta\epsilon_p a$

$\sigma_u$ = ultimate tensile strength	E, G = elastic moduli
$\sigma_y$ = yield stress	$\nu$ = Poisson's ratio
$\sigma_o, n'$ = defined by cyclic stress-strain relation, page 6, Eq.(1)	$\alpha$ = number less than 1

at the crack tip. At high-load amplitudes, such particles could cause ductile fracture or microfatigue crack initiation ahead of the crack tip, thus accelerating  $da/dN$ . Broek<sup>40</sup> has reported this effect in aluminum alloys at high stresses, but finds no effect at low stresses.

Laird<sup>34</sup> has reviewed the influences of metallurgical structure on crack growth rates and concludes that at high-load amplitudes, the effect of microstructure is minimal. Most fatigue cracking in the sub-creep range

$$(T/T_m < 0.5)$$

is transcrystalline, with intergranular cracking becoming important only as mean stress is added. The effects of grain size are minimal for wavy-slip-mode materials at high-load amplitudes,<sup>33</sup> but at lower loads, the effect is to lower  $da/dN$  as grain size is decreased for planar-slip materials.<sup>41</sup>

Considerably more insight into the design of crack-resistant materials can be obtained by using the results of recent crack-growth theories. These theories are the result of mechanisms research which showed that continuum elastic-plastic theory could be applied to crack extension and provided workable models (e.g., Figure 11) from which to derive the theory. The results of three derivations which use the plastic-blunting model are given in the table above.

The first two laws were derived assuming a perfectly plastic material (no work hardening), and hence contain only elastic material constants plus an ultimate tensile strength. The third derivation was made assuming the material to obey a cyclic stress-strain hardening law, Eq. (1). Note that the first two expressions call for high elastic

modulus, and high ultimate for best fatigue-crack-growth resistance.

Tomkins' derivation illustrates the sensitivity of  $da/dN$  to the cyclic-strain-hardening exponent,  $n'$ , which appears in the exponent of  $\Delta\sigma$  and  $\Delta\epsilon_p$ . His analysis also illustrates that optimum material properties for crack-growth resistance depend on whether one wants to resist stress or strain cycling.<sup>9</sup> In either case, a high value of the yield stress,  $\sigma_y$ , will produce low  $da/dN$ . The value of  $\sigma_o$  is approximately equal to the fracture strength of the material, and plays a different role in the two expressions. Increasing  $\sigma_o$  actually increases the crack growth rate under constant  $\Delta\epsilon_p$ .

The most interesting parameter in Tomkins' equations is  $n'$ . For constant  $\Delta\epsilon_p$ , increasing  $n'$  will decrease  $da/dN$ , all other things being equal ( $\sigma_o, \sigma_y$ ). For constant  $\Delta\sigma$  tests, the opposite holds: decreasing  $n'$  will decrease  $da/dN$ . To appreciate the effect of  $n'$ , consider the crack extension per cycle,  $\delta$ . From Tomkins,<sup>44</sup>

$$\delta = \Delta\epsilon_p \cdot r_p \quad (2)$$

where  $r_p$  is the extent of the plastic zone (Figure 11).

Now,  $r_p = \text{constant} \times (\Delta\sigma)^2 a$ , therefore,

$$\delta = \text{constant} \times \Delta\epsilon_p (\Delta\sigma)^2 a \quad (3)$$

Use the cyclic stress-strain relation to convert Eq. (3) to either stress or strain. For stress control,

$$\delta = \text{constant} \times \left(\frac{\Delta\sigma}{\sigma_o}\right)^{1/n'} (\Delta\sigma)^2 a \quad (4)$$

As  $n'$  is decreased, the fraction  $\Delta\sigma/\sigma_0$  raised to the  $1/n'$  power will decrease. So, for a given  $\Delta\sigma$ , and from Eq. (3),  $\delta$  decreases.

For the case of strain control,

$$\delta = \text{constant} \times (\Delta\epsilon_p)^{2n'+1} \quad (5)$$

Because  $\Delta\epsilon_p$  is always less than unity, increasing  $n'$  will decrease the amount of crack advance per cycle. Physically, increasing the work hardening capacity means a smaller  $\Delta\sigma$  for a given  $\Delta\epsilon_p$ ; hence, the plastic zone decreases in size, and similarly,  $\delta$  (Eq. (2)).

How does one control the value of  $n'$ ? There are very little data from which to answer this question. Feltner and Laird<sup>4</sup> found that  $n'$  tended to be larger for wavy-slip-mode materials compared to planar-slip-mode materials. Hence, to resist stress cycling, one should employ planar slip; to resist strain cycling, wavy slip. A few results exist to test this conclusion. McEvily and Boettner<sup>45</sup> found that increasing the planarity of slip in  $\alpha$ -brass alloys generally decreased  $da/dN$  under constant stress cycling, as predicted. On the other hand, Miller et al.,<sup>46</sup> investigating a series of Cu-Al alloys, obtained similar results under constant strain cycling, contrary to the prediction. But Feltner and Beardmore<sup>1</sup> have plotted total fatigue life under constant plastic strain versus  $n'$  and find  $N_f$  to increase as  $n'$  increases, as predicted. Hence, the situation is not entirely clear for strain-controlled tests, and additional work is necessary.

To summarize, resistance to fatigue crack growth can be achieved as follows:

#### *High-Amplitude, Constant-Stress or Plastic-Strain Tests*

1. Reduce inclusion density.

#### *Constant Plastic-Strain Tests*

1. High cyclic-strain-hardening coefficient - wavy-slip-mode material (needs further confirmation).
2. Low value of ratio  $(\sigma_0/\sigma_y)$ .

#### *Constant-Stress Tests*

1. Low cyclic-strain-hardening coefficient - planar-slip-mode material.
2. High elastic modulus.
3. High ultimate tensile strength.
4. High yield stress.
5. Small grain size (at low stress amplitudes) in planar-slip-mode materials.

## VI. EFFECTS OF TEMPERATURE AND ENVIRONMENT

Above  $T/T_m \sim 0.5$ , the mechanisms of fatigue change from slip-assisted crack initiation and stable elastic-plastic crack growth to mechanisms in which vacancy-assisted diffusion and creep interact strongly with the normal fatigue sequence. It is beyond the scope of this paper to discuss temperature effects in this regime. However, there are several important temperature effects in the sub-creep range which should be taken into account when considering fatigue-resistant materials. In this section, these effects will be summarized briefly with no attempt at in-depth discussion.

Fatigue softening of work-hardened copper has been found to occur more rapidly and the final flow stress to be lower when the temperature is raised.<sup>4</sup> Furthermore, the temperature dependence of softening in copper is consistent with the thermal activation of cross-slip.<sup>47</sup> It seems reasonable to extend these observations and conclude that thermally activated dislocation processes will in general promote greater fatigue softening as temperature is raised. The conclusion applies not only to work-hardened structures, but to precipitate-hardened<sup>48</sup> and solid-solution-hardened structures as well. The strain-hardening coefficient is also affected by temperature, decreasing as the temperature is raised.<sup>4</sup> The temperature dependence of the cyclic flow stress in wavy-slip-mode materials is greater than that of the monotonic flow stress, and equal or less in materials of planar-slip mode.<sup>4</sup>

Crack initiation and growth processes are generally accelerated as temperature is increased. In many instances grain-boundary cracking occurs at elevated temperatures, and these cracks grow at a faster rate and with a different mechanism than transcrystalline cracks. The greater plasticity which accompanies higher temperatures affects the plastic-blunting growth process of Stage II cracks. Greater crack-tip displacements will occur which will increase  $da/dN$  and the decrease in  $n'$  at elevated temperatures will also increase  $da/dN$  under strain-cycling conditions. As a final note on temperature effects, Buch<sup>49</sup> has surveyed many materials and found that at a given temperature  $T$ , the fatigue ratio is highest for those materials with the lowest homologous temperature,  $T/T_m$ .

The effects of normal operating environments on fatigue processes are almost always deleterious. Although fatigue-softening mechanisms are not affected by environment, the initiation and growth of cracks can be severely affected. These effects are a continuing subject of study, and they are not well understood from a mechanisms viewpoint. The formation of oxides on freshly exposed surfaces can prevent reversed slipping which results in accelerated crack initiation and propagation. In some instances, aggressive environments may embrittle the material at a crack tip, thus causing brittle crack advance, which can be very fast. Achter<sup>50</sup> has recently reviewed the effects of environment on the mechanisms of fatigue-crack growth, and concludes

that embrittling or weakening of metallic bonds at the crack tip is the mechanism most consistent with experimental results. Thus, in the development of new, fatigue-resistant materials the important criterion is to reduce the chances for corrosive attack in highly stressed regions. This is precisely the problem of preventing stress-corrosion cracking (SCC) and the ranking schemes for SCC resistance<sup>51</sup> should apply to fatigue as well.

## VII. THE IDEAL FATIGUE-RESISTANT MATERIAL

This final section is devoted to a summary of the guidelines which have been developed in this paper and a final synthesis into the "ideal" fatigue-resistant material.

To maintain the original static yield strength, the microstructures by which the strength is achieved must not be annihilated by cyclic dislocation motion. This situation can be achieved by either providing a very stable strengthening microstructure, or by suppressing the ease with which dislocations can oscillate to-and-fro during fatigue, or both. The most stable microstructures are dispersion-hardened and filament-reinforced metals; restricting cross-slip by use of planar-slip-mode materials will help to reduce dislocation traffic. A combination of these two should produce the optimum structure; however, less stable structures such as work-hardened and precipitate-hardened materials can be partially stabilized by the use of planar-slip-mode matrices, and small grain size. Useful quantitative guidelines are that the ratio  $\sigma_u/\sigma_y$  should be greater than about 1.2, and that the cyclic-strain-hardening exponent,  $n'$ , should be large.

To suppress crack initiation, local concentrations of nonreversible slip (usually at surfaces) must be avoided. If cyclic softening, which usually starts on a very localized scale, is avoided, then some suppression of crack initiation is already achieved. The two most common sites for crack initiation, surface slip bands and inclusions (including undissolved second phases), can be reduced by dispersing slip with planar-slip-mode materials and by removing the inclusions. The plastic deformation which leads to cracking can be further suppressed by raising the yield strength of a thin (0.003-0.005 in.) surface layer, either by coating, mechanical, or metallurgical treatments. Care must be taken to keep the fracture strain,  $\epsilon_f$ , of the coating high enough to avoid brittle fracture during fatigue loading.

To suppress crack propagation, one must first decide on whether the material is to resist cyclic strain or cyclic stress. In the former case, a high value of  $n'$  is desirable, along with a low value of  $\sigma_u/\sigma_y$ . These two requirements are mutually exclusive in the extreme, so that a compromise is necessary. To resist crack growth under cyclic

stress requires high values of  $E$ ,  $\sigma_u$ , and  $\sigma_y$ , a low value of  $n$  and small grain size. For either application, resistance is improved at high loads if inclusions are removed from the material. In fact, significant improvement in both crack initiation and growth resistance could be achieved in many alloys simply by improving mill practices to eliminate impurities, defects, undissolved second phases, and undesirable (tensile) residual stresses.

The "ideal" material, synthesized from the above guidelines, has the following properties:

### *Metallurgical Structure*

1. Dispersion-hardened, or filament-reinforced planar-slip-mode material. (Good interfaces are assumed.)
2. Small grain size in the matrix.
3. Low inclusion density in the matrix.
4. Surface treatment to produce high yield stress and sufficiently high fracture strain to avoid brittle fracture of the surface under normal fatigue loading.

### *Mechanical Properties*

1.  $(\sigma_u/\sigma_y)$  matrix  $> 1.2$  (to prevent softening of work-hardened structure in matrix).
2. Cyclic strain applications.
  - a.  $\sigma_u/\sigma_y$  low, consistent with 1, above.
  - b.  $n'$  high, consistent with a, above.
3. Cyclic stress applications.
  - a.  $E$ ,  $\sigma_y$ ,  $\sigma_u$ , high, but consistent with 1, above.
  - b.  $n'$  low, consistent with 1, above.

Finally, the material should have a low homologous temperature ( $< 0.2$ ) at the temperature of application, and possess resistance to stress corrosion in the environment of application.

This idealization should be considered exactly that, but it should also serve to illustrate the considerable contribution of fatigue-mechanisms research to a definition of the most desirable properties for high fatigue resistance. As more research is performed, with the specific goal of refining these guidelines, we shall arrive at yet higher fatigue strengths.

## REFERENCES

1. C.E. Feltner and P. Beardmore, "Strengthening Mechanisms in Fatigue," *Achievement of High-Fatigue Resistance in Metals and Alloys*, ASTM-STP-, American Society for Testing and Materials, Philadelphia, Pennsylvania (in press).
2. J.C. Grosskreutz, "Fatigue Mechanisms in the Sub-Creep Range," to be published.
3. J. Morrow, "Cyclic Plastic Strain Energy and Fatigue of Metals," p. 45, *Internal Friction, Damping and Cyclic Plasticity*, ASTM-STP-378, American Society for Testing and Materials, Philadelphia, Pennsylvania (1965).
4. C.E. Feltner and C. Laird, "Cyclic Stress-Strain Response of FCC Metals and Alloys - I," *Acta Met.*, 15:1621 (1967).
5. N. Thompson and N. Wadsworth, "Metal Fatigue," *Advan. Phys.*, 7:72 (1958).
6. R.W. Landgraf, *Cyclic Deformation and Fatigue Behavior of Hardened Steels*, T/AM-320, University of Illinois, Urbana, Illinois (1968).
7. S.S. Manson and M. Hirschberg, *Fatigue: An Interdisciplinary Approach*, p. 133, Syracuse University Press, Syracuse, New York (1964).
8. R. Smith, M. Hirschberg, and S.S. Manson, *Fatigue Testing of Metals and Alloys - Strain Cycling in Low and Intermediate Life Range*, NASA-TN-D-1574, National Aeronautics and Space Administration, Washington, D.C. (1963).
9. C.E. Feltner and R.W. Landgraf, *Selecting Materials to Resist Low-Cycle Fatigue*, ASME Paper 69-DE-59, American Society of Mechanical Engineers, New York (1969).
10. C.E. Feltner and C. Laird, "Cyclic Stress-Strain Response of FCC Metals and Alloys - II," *Acta Met.*, 15:1633 (1967).
11. R.L. Segall, "Fatigue Hardening in FCC Metals," *Advan. Mater. Res.*, 3:109 (1968).
12. J.R. Hancock and J.C. Grosskreutz, "Mechanisms of Fatigue Hardening in Copper Single Crystals," *Acta Met.*, 17:77 (1969).
13. P.O. Kettunen, "Fatigue Hardening of Copper Single Crystals at Low-Stress Amplitudes," *Acta Met.*, 15:1275 (1967).
14. S.J. Basinski, Z.S. Basinski, and A. Howie, "Early Stages of Fatigue in Copper Single Crystals," *Phil. Mag.*, 19:899 (1969).
15. P. Beardmore and C.E. Feltner, "Cyclic Deformation and Fracture Characteristics of a Low Carbon Martensitic Steel," p. 607, *Proc. 2nd Int. Conf. Fracture*, Chapman and Hall, London (1969).
16. C.A. Stubbington and P.J.E. Forsyth, "Some Observations on Microstructural Damage Produced by Fatigue of an Al (7.5%) Zn (2.5%) Mg Alloy at Temperatures Between Room Temperature and 250°C," *Acta Met.*, 14:5 (1966).
17. A. Abel and R.K. Ham, "The Cyclic Strain Behavior of Crystals of Al (4%) Cu - II. Low-Cycle Fatigue," *Acta Met.*, 14:1495 (1966).

## REFERENCES (Continued)

18. J.C. Grosskreutz and G.G. Shaw, "Microstructure at the Tips of Growing Fatigue Cracks in Aluminum Alloys," p. 226, *Fatigue Crack Propagation*, ASTM-STP-415, American Society for Testing and Materials, Philadelphia, Pennsylvania (1967).
19. T. Endo and J. Morrow, "Cyclic Stress Strain and Fatigue Behavior of Representative Aircraft Metals," *J. Mater.*, 4:159 (1969).
20. J.T. McGrath and W.J. Bratina, "Interaction of Dislocations and Precipitates in Quench-Aged Iron-Carbon Alloys Subjected to Cyclic Stressing," *Acta Met.*, 15:329 (1967).
21. C.H. Wells and C.P. Sullivan, "The Low Cycle Fatigue Characteristics of a Nickel-Base Superalloy at Room Temperature," *ASM Trans. Quart.*, 57:841 (1964).
22. R.K. Ham, *The Metallurgy of Fatigue*, RD/L/M-149, Central Electricity Research Laboratories, England (1967).
23. R.K. Ham and M.L. Wayman, "The Fatigue and Tensile Fracture of TD-Nickel," *Trans. Met. Soc. AIME*, 239:721 (1967).
24. G.R. Leverant, "The Fatigue Behavior of a Dispersion Strengthened Metal," *Trans. Met. Soc. AIME*, 239:1992 (1967).
25. J.R. Hancock, Midwest Research Institute, Kansas City, Missouri.
26. B.Z. Weiss, S. Niedzwiez, and E. Rozovski, "The Influence of Previous Austenitic Grain Size on Initiation and Propagation of Fatigue Cracks in Silicon-Manganic Steel," *J. Iron Steel Inst. (London)*, 205:1246 (1967).
27. D.H. Avery and W.A. Backofen, "Nucleation and Growth of Fatigue Cracks," p. 339, *Fracture of Solids*, John Wiley, New York (1963).
28. J.C. Grosskreutz and D.K. Benson, "The Effects of the Surface on the Mechanical Properties of Metals," p. 61, *Surfaces and Interfaces*, Vol. II, Syracuse University Press, Syracuse, New York (1968).
29. R.D. Weltzin and G. Koves, "Surface Treatment of Ti-6Al-4V for Impact-Fatigue and Wear Resistance," p. 283, *Applications Related Phenomena in Titanium Alloys*, ASTM-STP-432, American Society for Testing and Materials, Philadelphia, Pennsylvania (1968).
30. W.E. Duckworth, "The Achievement of High Fatigue Strength in Steel," *Met.*, 9:63 (1964).
31. J.C. Grosskreutz, G.G. Shaw, and D.K. Benson, *The Effect of Inclusion Size and Distribution on Fatigue of 2024-T4 Aluminum*, AFML-TR-69-121, Air Force Materials Laboratory, Wright-Patterson AFB, Ohio (1969).
32. C.M. Carman et al., "Crack Resistance Properties of High-Strength Aluminum Alloys," p. 995, *Proc. 1st Int. Conf. Fracture*, Vol. II, Japanese Society for Strength and Fracture of Materials, Sendai, Japan (1965).
33. R.C. Boettner, C. Laird, and A.J. McEvily, "Crack Nucleation and Growth in High Strain Low Cycle Fatigue," *Trans Met. Soc. AIME*, 233:379 (1965).

## REFERENCES (Continued)

34. C. Laird, "The Influence of Metallurgical Structure on the Mechanisms of Fatigue Crack Propagation," p. 131, ASTM-STP-415. (See Ref. 18)
35. J. Schijve, "Significance of Fatigue Cracks in Micro-Range and Macro-Range," p. 415, ASTM-STP-415. (See Ref. 18)
36. M. Gell and G.R. Leverant, "The Characteristics of Stage I Fatigue Fracture in a High-Strength Nickel Alloy," *Acta Met.*, 16:553 (1968).
37. B. Tompkins and W.D. Biggs, "Low Endurance Fatigue in Metals and Polymers," *J. Mater. Sci.*, 4:544 (1969).
38. M. Klesnil and P. Lukas, "Dislocation Structure Associated with Fracture Surface of Fatigued Copper Single Crystals," *Phil. Mag.*, 17:1295 (1968).
39. C.Q. Bowles and D. Broek, "The Microstructure of Fatigue Fracture Surfaces," *Int. J. Fracture Mech.*, 5/4:350 (1969).
40. D. Broek, "The Effect of Intermetallic Particles on Fatigue Crack Propagation in Aluminum Alloys," p. 754, *Proc. 2nd Int. Conf. Fracture*, Chapman and Hall, London (1969).
41. P.G. Forrest and A.E. Tate, "The Influence of Grain Size on the Fatigue Behavior of 70/30 Brass," *J. Inst. Metals*, 93:438 (1965).
42. F.A. McClintock, "On the Plasticity and Growth of Fatigue Cracks," p. 65, *Fracture of Solids*, John Wiley, New York (1963). (Note: See also discussion at end of Ref. 34).
43. R.W. Lardner, "A Dislocation Model for Fatigue Crack Growth in Metals," *Phil. Mag.*, 17:71 (1968).
44. B. Tompkins, "Fatigue Crack Propagation - An Analysis," *Phil. Mag.*, 18:1041 (1968).
45. A.J. McEvily and R.C. Boettner, "On Fatigue Crack Propagation in FCC Metals," *Acta Met.*, 11:725 (1963).
46. G.A. Miller, D.H. Avery, and W.A. Backofen, "Fatigue Crack Growth in Some Copper Base Alloys," *Trans. Met. Soc. AIME*, 236:1667 (1966).
47. R.K. Ham and T. Broom, "The Mechanism of Fatigue Softening," *Phil. Mag.*, 7:95 (1962).
48. K. Erhardt and N.J. Grant, "Behavior of 2024 Aluminum in Low-Cycle Fatigue at Low Strain Rates as a Function of Temperature," p. 702, *Proc. 2nd Int. Conf. Fracture*, Chapman and Hall, London (1969).
49. A. Buch, "Fatigue Properties of Pure Metals," *Int. J. Fracture Mech.*, 3:145 (1967).
50. M.R. Achter, "Effect of Environment in Fatigue Cracks," p. 181, ASTM-STP-415. (See Ref. 18)
51. B.F. Brown, "A New Stress-Corrosion Cracking Test for High-Strength Materials," *Mater. Res. Stand.*, 6:129 (1966).

# A MICROMECHANIC THEORY OF THE EFFECT OF MEAN STRESS ON FATIGUE CRACK NUCLEATION

by

T.H. Lin and Y.M. Ito

School of Engineering and Applied Science  
University of California, Los Angeles

## INTRODUCTION

Answers to the question of how fatigue cracks in metals nucleate under stresses far below the static fracture strength have been sought by many investigators. However this question is far from being solved. The present study attempts to answer this question by showing a quantitative mechanism of how the local plastic strain can build up under cycles of loading, and then to evaluate the effect of mean stress on fatigue failure.

The development of the present theory<sup>1</sup> of fatigue crack nucleation is guided by experimental observations.<sup>2-8</sup> These observations have been reviewed in a previous paper<sup>1</sup> and only a summary of the conclusions drawn from them is presented here. Since fatigue crack nucleation has been observed at 1.7°K, it appears that the *mechanics of purely geometrical deformation of the surface is responsible for fatigue crack nucleation*. The formation of fatigue cracks is associated with slip. Slip depends on the resolved shear stress and is independent of the normal pressure on the sliding plane. *Reverse loading produces slip lines which are close to, but not coincident with, the lines formed during the forward loading*. Plastic strain is concentrated in the localized slip bands, and in some cases marked changes occur in contour leading to the monotonic rising of "extrusions" and deepening of "intrusions." A number of theories previously proposed for fatigue crack initiation are based on the clue of extrusions and intrusions.<sup>9-11</sup>

Based on these conclusions drawn from experimental observations, the present theory is developed as follows. Lattice imperfections exist in all metals and give rise to an initial heterogeneous microstress field. It has been experimentally observed that two distinct closely located slices slide such that one slice slides during the forward loading and the neighboring slice slides during the reversed loading.<sup>3,4</sup> The initial stress field favorable for this sequence of slip is clearly one having positive resolved shear stress in one slice and negative resolved shear stress in the other.<sup>12</sup>

Referring to Figure 1, let  $x_1$  and  $x_2$  be a set of rectangular coordinates on a longitudinal section of polycrystalline metal subject to a fluctuating stress along the

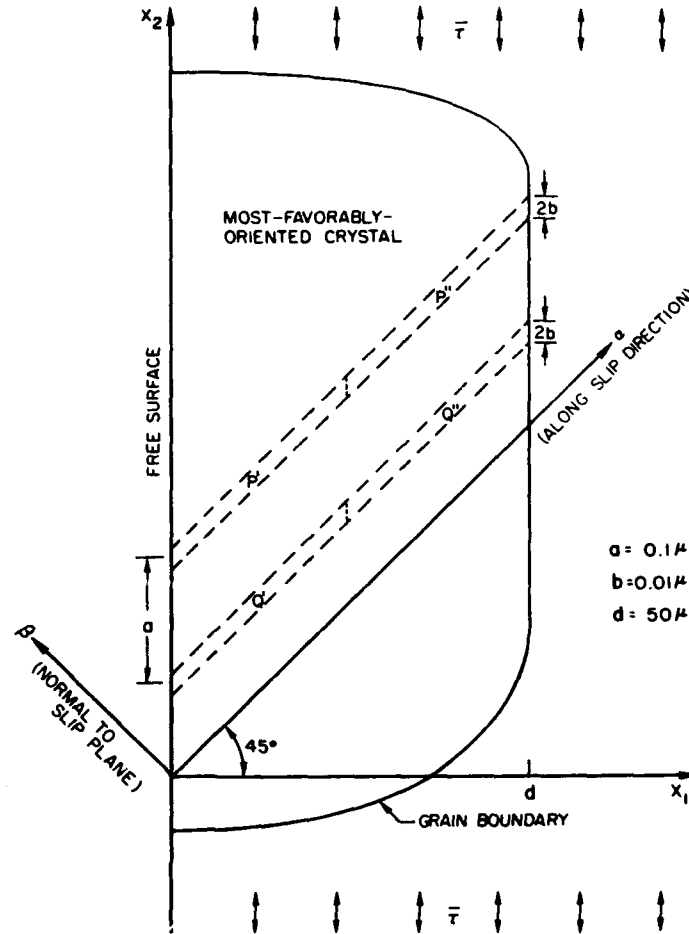
$x_2$ -direction. Let  $\alpha$  and  $\beta$  be another set of rectangular coordinates with  $\alpha$  along the slip direction and  $\beta$  normal to the slip plane of a most-favorably-oriented crystal. The elastic constants of the individual crystals are assumed to be isotropic, so that the polycrystal is elastically isotropic and homogeneous. Both the slip direction and the normal to the slip plane of the most-favorably-oriented crystal make 45° angles with the loading axis and the free surface. The two thin slices are parallel to the slip plane and are denoted as P (P' for the half slice near the free surface and P'' for the other half) and Q (Q' for the half slice near the free surface and Q'' for the other half).

The initial resolved shear stress is assumed to vary linearly from +5 psi at the free surface to -5 psi at the interior end of slice P and from -5 psi at the free surface to +5 psi at the interior end of slice Q. The initial resolved shear stress is positive in P' and Q'' but negative in Q' and P''. The initial resolved shear stress is assumed to vanish everywhere except in slices P and Q.

Under the applied tensile loading the applied resolved shear stress is positive. Because of the initial resolved shear stress the positive critical shear stress is attained in P' and Q''. The plastic strain which occurs in P' and Q'' produces a residual stress field. This residual stress field is *continuous* and relieves the positive resolved shear stress in both slices and helps to keep Q' and P'' from reaching the positive critical shear stress during the tensile loading. Under the subsequent reversed loading the applied resolved shear stress is negative. Because of the initial and residual resolved shear stresses the negative critical shear stress is attained in Q' and P''. The plastic strain which occurs produces another residual stress field. This residual stress field relieves the negative resolved shear stress in both slices and helps to keep P' and Q'' from reaching the negative critical shear stress during the reversed loading. Similarly this process of alternating slip will be repeated during every loading cycle. Hence, no special gating mechanism, such as certain Lomer-Cottrell barrier movement as proposed by Kennedy,<sup>13</sup> is necessary. The sequence of slip in slices P and Q tends to push out the region between them as the start of an extrusion. The interchange of the sign of the initial resolved shear stress in P and Q tends to initiate an intrusion.



Figure 1. Two Thin Slices of a Most-Favorably-Oriented Crystal at the Free Surface of a Polycrystal.



The present mechanism<sup>1</sup> explains how the local plastic strain can be built up and why extrusions and intrusions grow monotonically with cycles of loading. This theory seems to explain the monotonic growth of extrusions and intrusions better than the previous theories. With the mechanism of fatigue crack initiation clear, the effect of mean stress on the build-up of local plastic strain is readily calculated.

#### MATHEMATICAL FORMULATION AND NUMERICAL CALCULATIONS

The metal considered is assumed<sup>1</sup> to be a semi-infinite solid under plane deformation. The analogy<sup>14</sup> between plastic strain and an equivalent force, similar to Duhamel's analogy<sup>15</sup> in thermoelasticity, is used to calculate the residual stress field caused by the plastic strain. For numerical calculations the two thin slices are divided along their length into thin parallelogram regions  $R_n$  where  $n = 1, 2, \dots, 2N$  (see Figure 2). The surface enclosing  $R_n$  is denoted by  $S_n$ . The plastic shear strain  $e''_{\alpha\beta n}$  in each region  $R_n$  is assumed to be constant. From the plane strain

solution<sup>16,17</sup> of a point force in a semi-infinite elastic medium the residual resolved shear stress  $\tau_{\alpha\beta R}$  caused by a given distribution of plastic strain has been represented as<sup>18</sup>

$$\tau_{\alpha\beta R}(x_1, x_2) = 2G \sum_{n=1}^{2N} e''_{\alpha\beta n} \oint_{S_n} K_i(x'_1, x'_2; x_1, x_2) \nu_i dS' - 2Ge''_{\alpha\beta}(x_1, x_2), \quad (1)$$

where  $(x_1, x_2)$  denotes the field point,  $(x'_1, x'_2)$  denotes the slip point,  $G$  is the shear modulus and  $\nu_i$  is outward unit normal. The functions  $K_i$  ( $i = 1, 2$ ) are given as:

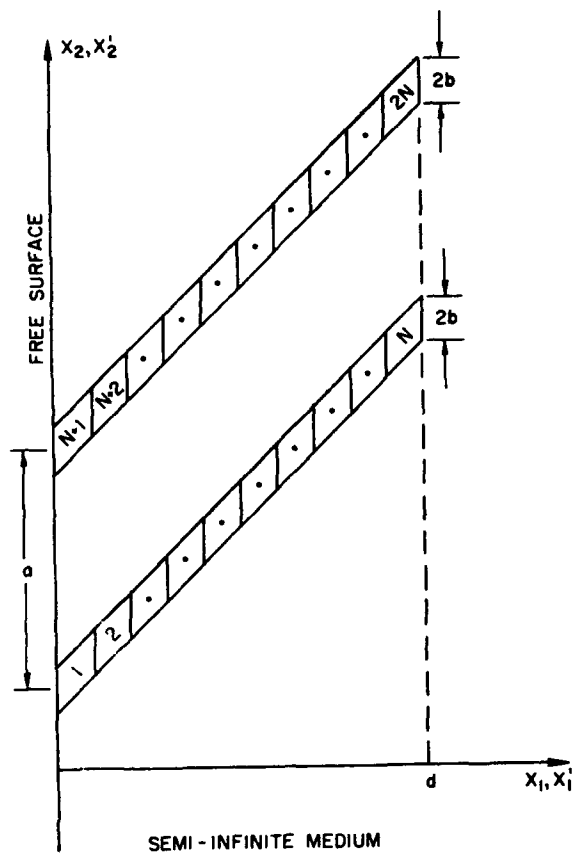


Figure 2. Grids of the Two Sliding Slices.

$$K_1(x_1', x_2'; x_1, x_2) =$$

$$\left\{ \begin{aligned} & -k \frac{(x_1 - x_1') [(x_1 - x_1')^2 - (x_2 - x_2')^2]}{\rho^4} \\ & + \frac{(x_1 - x_1') [(x_1 + x_1')^2 - (x_2 - x_2')^2] + 4x_1 x_1' (x_1 + x_1')}{r^4} \\ & - \frac{16x_1 x_1' (x_1 + x_1') (x_2 - x_2')^2}{r^6} + (1-2\sigma) \left[ \frac{x_1 - x_1'}{\rho^2} \right. \\ & \left. + \frac{x_1 - x_1'}{2} - \frac{4x_1 (x_2 - x_2')^2}{r^4} \right] \end{aligned} \right\} \quad (2)$$

$$K_2(x_1', x_2'; x_1, x_2) =$$

$$\left\{ \begin{aligned} & k (x_2 - x_2') \frac{(x_1 - x_1')^2 - (x_2 - x_2')^2}{\rho^4} \\ & + \frac{(x_1 - x_1')^2 - (x_2 - x_2')^2}{r^4} - \frac{8x_1 x_1' [(x_1 + x_1')^2 - (x_2 - x_2')^2]}{r^6} \\ & - (1-2\sigma) \left[ \frac{1}{2} + \frac{1}{r} - \frac{4x_1 (x_1 + x_1')}{r^4} \right] \end{aligned} \right\} \quad (3)$$

where  $\sigma =$  Poisson's ratio,

$$k = \frac{1}{4\pi(1-\sigma)},$$

$$\rho^2 = (x_1 - x_1')^2 + (x_2 - x_2')^2,$$

$$r^2 = (x_1 + x_1')^2 + (x_2 - x_2')^2.$$

The initial resolved shear stress  $\tau_{\alpha\beta I}$  is assumed such that  $\tau_{\alpha\beta I}(x_1, x_2) = 5 \left(1 - \frac{2x_1}{d}\right)$  psi in P,

$$\tau_{\alpha\beta I}(x_1, x_2) = -5 \left(1 - \frac{2x_1}{d}\right) \text{ psi in Q,} \quad (4)$$

$$\tau_{\alpha\beta I}(x_1, x_2) = 0 \text{ elsewhere.}$$

The applied resolved shear stress  $\tau_{\alpha\beta 0}$  due to the mean tensile stress  $\bar{\tau}_M$  and the alternating tension-compression stress  $\bar{\tau}_A$  is

$$\tau_{\alpha\beta 0}(x_1, x_2) = \frac{1}{2} (\bar{\tau}_M + \bar{\tau}_A) \equiv \frac{1}{2} \bar{\tau} \quad (5)$$

After slip occurs, there is a residual resolved shear stress as given by Eq. (1). The resolved shear stress  $\tau_{\alpha\beta}$  is the sum of the applied, initial, and residual resolved shear stresses. Therefore, the resolved shear stress is:

$$\tau_{\alpha\beta}(x_1, x_2) = \frac{1}{2} \bar{\tau} + \tau_{\alpha\beta I}(x_1, x_2)$$

$$+ 2G \sum_{n=1}^{2N} e''_{\alpha\beta n} \oint_{S_n} K_i(x_1', x_2'; x_1, x_2) v_i dS'$$

$$- 2G e''_{\alpha\beta}(x_1, x_2). \quad (6)$$

Since the resolved shear stress and slip strain are referred to the  $\alpha\beta$ -slip system, the subscript  $\alpha\beta$  of  $\tau$  and  $e''$  are hereafter deleted and the resolved shear stress of the grid  $R_q$  is given as

$$\tau_q = \frac{1}{2} \bar{\tau} + \tau_{Iq}$$

$$+ 2G \sum_{n=1}^{2N} e''_n \oint_{S_n} K_i(x_1', x_2'; x_{1q}, x_{2q}) v_i dS'$$

$$- 2G e''_q, \quad (7)$$

where  $q = 1, 2, \dots, 2N$ .

$$\tau_q \equiv \tau_{\alpha\beta}(x_{1q}, x_{2q}),$$

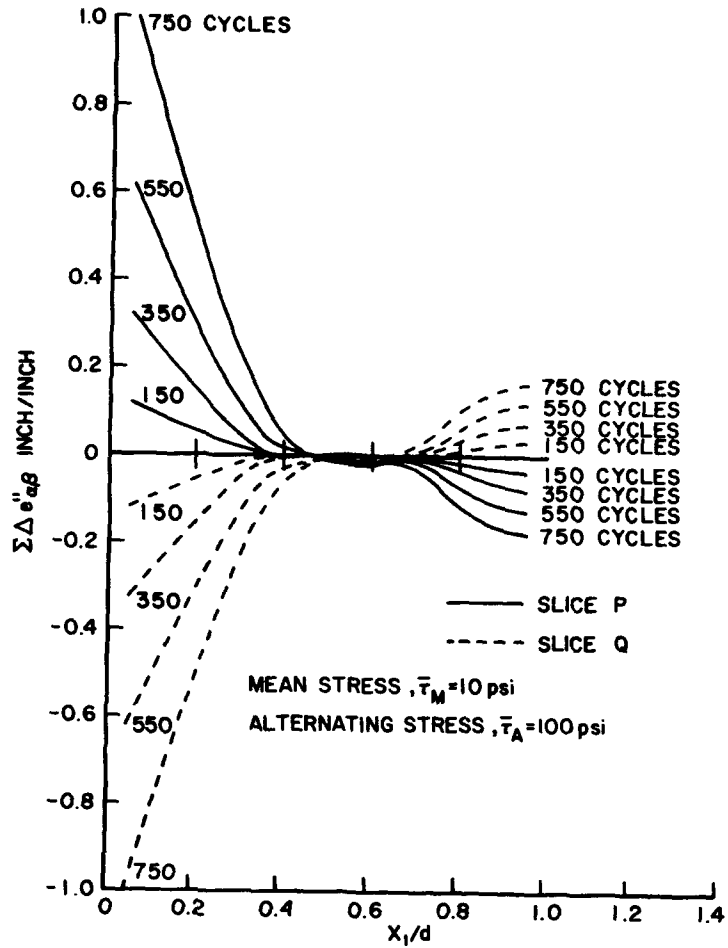
$$\tau_{Iq} \equiv \tau_{\alpha\beta I}(x_{1q}, x_{2q}),$$

$$e''_q \equiv e''_{\alpha\beta}(x_{1q}, x_{2q}).$$

$$(x_{1q}, x_{2q}) = \text{center point of } R_q.$$

The initial stress field does not change with loading, so that  $\Delta\tau_I = 0$ . The incremental resolved shear stress of the grid  $R_q$  during loading is then

Figure 3. Plastic Strain Build-up in Sliding Slices.



$$\Delta\tau_q = \frac{1}{2} \Delta\bar{\tau}$$

$$+ 2G \sum_{n=1}^{2N} \Delta e''_n \oint_{S_n} K_i(x'_1, x'_2; x_{1q}, x_{2q}) v_i dS'$$

$$- 2G \Delta e''_q \quad (8)$$

To simplify the calculations, the local strain hardening is assumed<sup>1</sup> to be zero. The critical shear stress of the crystal is denoted by  $\tau_C$ . For those grids where the magnitude of the resolved shear stress as given by Eq. (7) is less than the critical shear stress, sliding will not occur. If  $R_p$  is one of these grids, it follows that

$$|\tau_p| < \tau_C, \Delta e''_q = 0. \quad (9)$$

But in those grids where the magnitude of the resolved shear stress equals the critical shear stress, slip occurs. If  $R_m$  is one of these grids, we have that

$$|\tau_m| = \tau_C, |\Delta e''_m| > 0, \quad (10)$$

and since the local strain hardening is assumed to be zero,

$$\begin{aligned} \Delta\tau_m &= \frac{1}{2} \Delta\bar{\tau} \\ + 2G \sum'_n \Delta e''_n \oint_{S_n} K_i(x'_1, x'_2; x_{1m}, x_{2m}) v_i dS \\ - 2G \Delta e''_m &= 0, \end{aligned} \quad (11)$$

where  $\sum_n'$  indicates the summation of the active grids only.

The thickness  $2b$  of grid  $R_n$  is much smaller than the length. For this case, the residual resolved shear stress Eq. (1) has been shown<sup>19</sup> to vary linearly with  $b$ . Hence, for slip in a very thin slice, the residual resolved shear stress is directly proportional to the plastic strain and the slice thickness  $2b$ . Equation (11) is a set of linear equations with as many unknown  $\Delta e''_n$  as there are equations. The plastic strain increment  $\Delta e''_n$  in the sliding grids for an increment of applied stress  $\Delta \bar{\tau}$  can readily be determined from Eq. (11).

The extrusion thickness has been observed to be about  $0.1\mu$ . Hence for numerical calculations the distance 'a' between the two slices is taken to be  $0.1\mu$ . The thickness '2b' of the slices is very small and is assumed to be  $0.02\mu$ . The linear dimension 'd' of the sliding crystal is taken to be  $50\mu$ . The critical shear stress  $\tau_C$  is 53.5 psi, Poisson's ratio,  $\sigma = 0.3$ , and the shear modulus,  $G = 3.85 \times 10^6$  psi. These values correspond to the properties of commercially pure aluminum. An aluminum crystal has four sliding planes, but in the present calculations the sliding crystal is assumed to have only one active sliding plane. The initial resolved shear stress is given by Eq. (4).

The effect of a mean tensile stress  $\bar{\tau}_M$  superimposed on an alternating stress  $\bar{\tau}_A$  is evaluated numerically. The calculated build-up of the local plastic shear strain distribution under a mean tensile stress of

10 psi and an alternating stress of 100 psi is shown in Figure 3. The sum of the local plastic shear strain increments reaches 100 per cent at the free surface in about 750 cycles. This large plastic strain in the slices (positive in P' and negative in Q') indicates the start of an extrusion of the material between the slices. The interchange of the sign of the initial stress in P and Q causes the start of an intrusion. Local plastic shear strain of 100 per cent is used as the criterion of fatigue crack initiation. Figure 4 shows that increasing the amount of mean tensile stress decreases the number of cycles to initiate a crack for a constant value of alternating stress.

The fatigue strength of a material under fluctuating stresses can be represented<sup>20</sup> on a diagram in which the ratio of the alternating stress to the alternating fatigue strength  $(\bar{\tau}_A/\bar{\tau}_{A_0})$  is plotted against the ratio of mean stress to tensile strength  $(\bar{\tau}_M/\bar{\tau}_U)$ . The straight line and the curve shown in Figure 5 represent two widely used empirical relations. The straight line joining the alternating fatigue strength to the tensile strength is the modified Goodman law. The top curve is a parabolic relation and this is known as Gerber's parabola. The relationships may be written mathematically as follows<sup>20</sup>:

Modified Goodman Law,

$$\left(\frac{\bar{\tau}_A}{\bar{\tau}_{A_0}}\right) = 1 - \left(\frac{\bar{\tau}_M}{\bar{\tau}_U}\right)$$

Gerber's Law,

$$\left(\frac{\bar{\tau}_A}{\bar{\tau}_{A_0}}\right) = 1 - \left(\frac{\bar{\tau}_M}{\bar{\tau}_U}\right)^2$$

where  $\bar{\tau}_A$  is the alternating stress associated with a mean stress  $\bar{\tau}_M$ ,  $\bar{\tau}_{A_0}$  is the alternating fatigue strength (zero mean stress) and  $\bar{\tau}_U$  is the tensile strength (zero alternating stress). The calculated results for the present theory lie between Gerber's parabolic law and the modified Goodman linear law as shown in Figure 5. Approximating these results by a mathematical relationship we have the following:

$$\text{Present Theory, } \left(\frac{\bar{\tau}_A}{\bar{\tau}_{A_0}}\right) = 1 - \left(\frac{\bar{\tau}_M}{\bar{\tau}_U}\right)^{1.2}$$

## CONCLUSIONS

The build-up of local plastic strain with cycles of loading is calculated. With a small initial resolved shear stress two closely spaced slices slide in opposite directions under the effect of a mean stress superimposed on an alternating stress. The sum of the local plastic shear strain increments reaches a magnitude of 100 percent in a few hundred cycles. The mechanics of the build-up of large local plastic strains clearly cause the start of an extrusion or intrusion and the nucleation of a fatigue crack. The continuity of the stress field caused by plastic strain in the slices clearly causes the alternate sliding of the two closely located thin slices in forward and reversed loadings. No special gating mechanism like Lomer-Cottrell barrier movement proposed by Kennedy<sup>13</sup> is necessary.

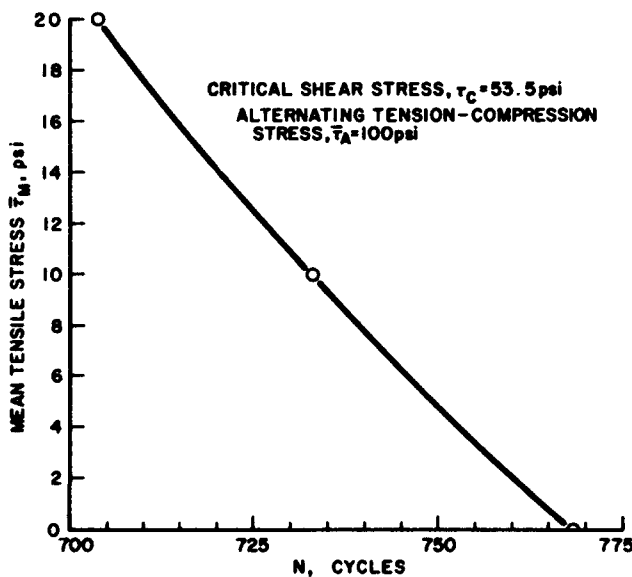
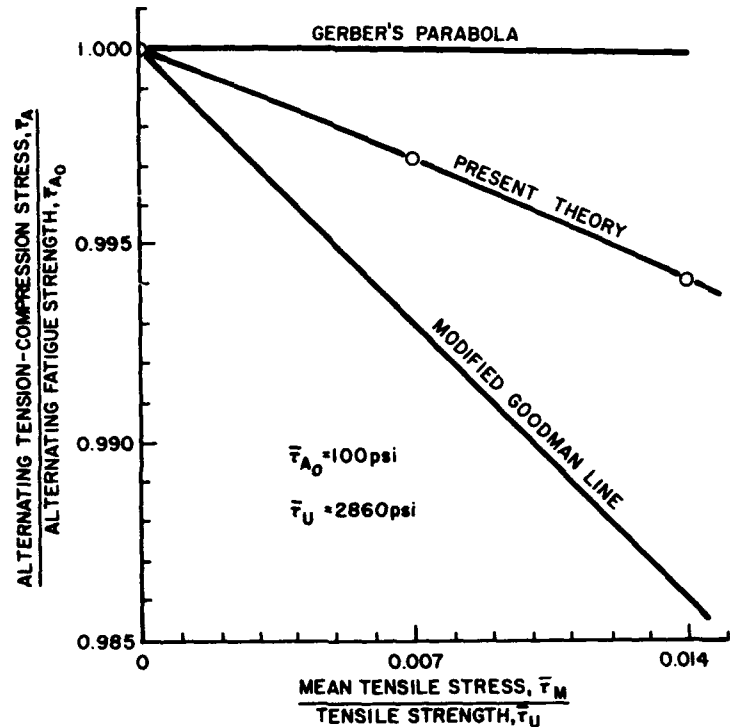


Figure 4. Variation of Cycles with Mean Stress to Give 100 Per Cent Local Plastic Strain.

Figure 5. Alternating Tension-Compression Stress versus Mean Tensile Stress to Give 100 Per Cent Local Plastic Strain in 768 Cycles.



The calculated results of the present theory lie between Gerber's parabolic law and the modified Goodman linear law for fatigue failure. This compares well with a majority of the experimental data<sup>20</sup> which fall between the Goodman line and the Gerber parabola.

The slip distributions calculated by the present method satisfy the conditions of compatibility and equilibrium and the relation between slip and resolved shear stress throughout the metal of all stages of fluctuating loads. Local strain-hardening is assumed to be zero. Sim-

ilar calculations may be made for cases where the strain-hardening is not zero.

#### ACKNOWLEDGEMENT

This research was sponsored by the National Science Foundation under a grant GK 2198 to the University of California, Los Angeles. The authors express their gratitude to the Campus Computing Network of the University of California at Los Angeles, for the use of the IBM 360 computer.

#### REFERENCES

1. T.H. Lin and Y.M. Ito, "Mechanics of a Fatigue Crack Nucleation Mechanism," *J. Mech. Phys. Solids*, 17:511 (1969).
2. J.A. Ewing and J.W.C. Humphrey, "The Fracture of Metals Under Repeated Alternations of Stress," *Phil. Trans. Roy. Soc. London*, 200A:241 (1903).
3. P.J.E. Forsyth, "Some Further Observations on the Fatigue Process in Pure Aluminum," *J. Inst. Metals*, 82:449 (1954).
4. P. Charsley and N. Thompson, "The Behavior of Slip Lines on Aluminum Crystals Under Reversed Stresses in Tension and Compression," *Phil. Mag.*, 8:77 (1963).

## REFERENCES (Continued)

5. R.K. MacCrone, R.D. McCammon, and H.M. Rosenberg, "The Fatigue of Metals at 1.7°K," *Phil. Mag.*, 4:267 (1959).
6. G.I. Taylor, "Plastic Deformation of Metals," *J. Inst. Metals*, 62: 307 (1938).
7. H.J. Gough, "Crystalline Structure in Relation to Failure of Metals, Especially by Fatigue," *ASTM Proc.*, 33:3 (1933).
8. P.J.E. Forsyth and C.A. Stubbington. "The Slip Band Extrusion Effect Observed in Some Aluminum Alloys Subjected to Cyclic Stresses," *J. Inst. Metals*, 83:395 (1955).
9. W.A. Wood, "Mechanism of Fatigue," p. 1; A.M. Freudenthal, Ed., *Fatigue in Aircraft Structures*, Academic Press, New York (1956).
10. A.H. Cottrell and D. Hull, "Extrusions and Intrusions by Cyclic Slip in Copper," *Proc. Roy. Soc. London*, 242A:211 (1957).
11. N.F. Mott, "Origin of Fatigue Cracks," *Acta Met.*, 6:195 (1958).
12. T.H. Lin and Y.M. Ito, "Fatigue Crack Nucleation in Metals," *Proc. Natl. Acad. Sci. U.S.*, 62:631 (1969).
13. A.J. Kennedy, *Process of Creep and Fatigue in Metals*, pp. 331-341, John Wiley, New York (1963).
14. T.H. Lin, *Theory of Inelastic Structures*, Chapter 2, John Wiley, New York (1968).
15. Y.C. Fung, *Foundations of Solid Mechanics*, p. 393, Prentice-Hall, Princeton, New Jersey (1965).
16. T.K. Tung and T.H. Lin, "Slip Strains and Stresses in Polycrystalline Aggregates Under Cyclic Load," *J. Appl. Mech.*, 29:523 (1966).
17. E. Melan, "Der Spannungszustand der Durch Eine Einzelkraft in Innean Beansprochten Halbschibe," *Z. Angew. Math. Mech.*, 12:343 (1932).  
Corrections, 20:368 (1940).
18. T.H. Lin and Y.M. Ito, "Slip Distribution in a Thin Slice of a Crystal at a Free Surface," *J. Appl. Phys.*, 38:775 (1967).
19. T.H. Lin and Y.M. Ito, "Mechanism of Fatigue Crack Nucleation Based on Microstresses Caused by Slip," UC-DE-R68-19, University of California, Dept. of Engineering, Los Angeles, California (1968).
20. P.G. Forrest, *Fatigue of Metals*, p.93, Addison-Wesley, Reading, Massachusetts (1962).

# SUBCRITICAL CRACK GROWTH CRITERIA FOR INCONEL 718 AT ELEVATED TEMPERATURES

by

Herbert G. Popp and Anton Coles

Aircraft Engine Group  
General Electric Company  
Cincinnati, Ohio

## INTRODUCTION

Continuing demand for higher performance and lighter weight jet engines coupled with the trend for much longer operating lives with improved reliability have re-emphasized the need for maximum efficient usage of materials. The requirement for longer lives with improved reliability are particularly challenging to the designer. Improved materials cyclic life prediction is a prime criterion to success since fatigue cracking is usually the limiting consideration. Until recently, the advantages of the subcritical crack growth design concept have not been fully exploited for application to jet engine hardware. Because most components operate at elevated temperatures, a major limitation has been the lack of high temperature fracture mechanics technology. A prime question in the application of fracture mechanics concepts to elevated temperature situations is whether basic

elastic principles are or are not violated when creep and relaxation are encountered. Investigations to determine the usefulness of fracture mechanics techniques at elevated temperatures have been conducted at the Aircraft Engine Group of the General Electric Company.

The emphasis for lightest weight at reasonable cost on all components has resulted in the widespread use of welded sheet fabricated static structures in jet engines. Even with precise processing and quality control, small defects in the welds cannot always be avoided and allowances must be made for them in design. Although good design practice requires welds be placed in area of relatively low stress and low stress concentrations and avoid areas of high constraint, a thorough understanding of the defect tolerance of the weld material is mandatory if excessively low stresses and overly conservative, heavy designs are to be avoided.

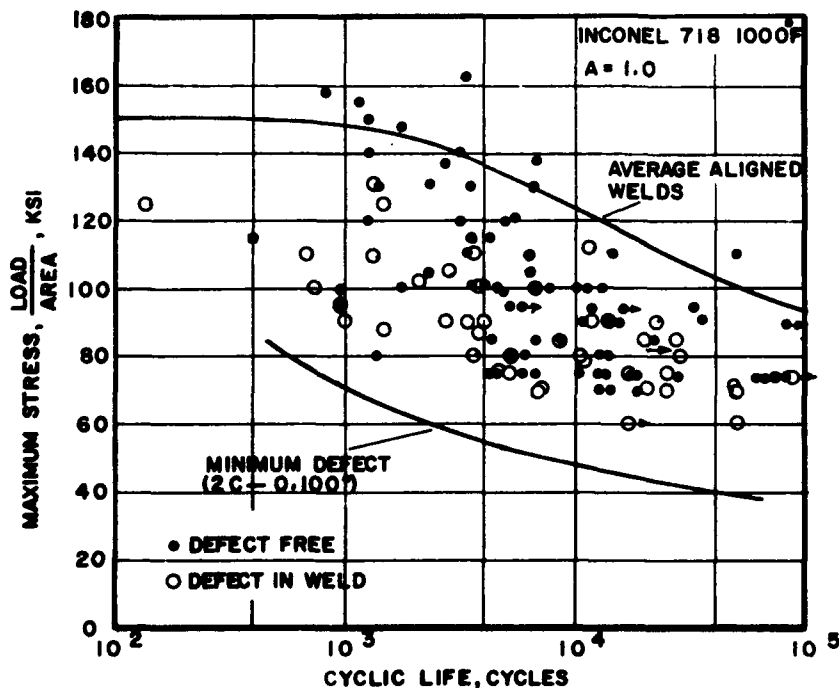


Figure 1. Cyclic Life Variation in  
Production Quality TIG Welds.

Welded Inconel 718 sheet is a major mainstay material for many high temperature statically loaded jet engine parts such as frames and casings. Generally, it welds very well but as with any material, weld defects can occur. Since welds are used typically without removing the metal build up formed during fusion, cracking on the fusion line at the weld bead intersection with the sheet surface is of major concern.

Life limits of current jet engine frames and casings require that they survive between 5000 and 50,000 load pressure cycles. Large variations in cyclic life can be encountered in good quality production welds, particularly when expressed in terms of nominal applied stress. Figure 1 demonstrates the range of cyclic behavior of nominally-aligned, reinforced Inconel 718 welds with inspection limits to insure defects less than one tenth of an inch in length. In the life range of  $5 \times 10^4$  cycles there is a factor of about 2.5 between average and minimum stress for constant life. Obviously, a closer understanding of the factors contributing to this variation is needed. Major considerations are the defect state and defect tolerance of the welded material since defects cannot always be avoided in practical production welds. Fracture mechanics methods, if applicable to the high operating temperature range, offer a rigorous design approach to cyclic life prediction. This paper is a discussion of the observed behavior of subcritical crack growth and the fracture toughness behavior of parent metal and welded Inconel 718 at temperatures to 1200°F and suggests a design approach for welded high temperature structures.

#### APPROACH

The purpose of this investigation was to determine if fracture mechanics methods are suitably accurate to predict the defect tolerance of Inconel 718 welds at temperatures up to 1200°F in the cyclic conditions typically encountered in jet engine frames and casings. Studies were directed mainly at the cyclic crack growth response in the low cycle fatigue regime of this material under stress, temperatures, hold times, and defect state typical of these components. Basic static and cyclic fracture toughness data were generated at temperatures in the creep regime and compared to the expected behavior as described in the literature for purely elastic con-

ditions. Basic properties included rising load fracture toughness, time dependent fracture and cyclic crack growth data. By superposition of models available in the literature, an analysis was developed for predicting subcritical crack growth under cyclic conditions in the creep regime. Verification tests were conducted using this analysis and the basic materials crack resistance data.

#### MATERIAL

The material used for this investigation was Inconel 718 sheet, a high-strength, corrosion resistant nickel base superalloy which depends on precipitation hardening for its strength. In the sheet form, useful jet engine applications are made to 1150°F. Inconel 718 differs from other superalloys in that (1) columbium is substituted for much of the aluminum and titanium hardeners, and (2) it has a higher percentage of iron. These differences provide a high strength material with reduced temperature capabilities compared to some nickel base superalloys but greatly enhance welding characteristics. Table I lists chemical composition and Table II shows the heat treatments used. A number of heats of material were used in the investigation and each met the requirements of applicable General Electric Specifications. Typical properties taken from one of these heats are shown in Figure 2. Creep deformation becomes a consideration at temperatures about 800°F for high stress cases, as in areas adjacent to sharp stress concentration such as cracks or defects.

#### TEST SPECIMENS AND METHODS

The data generated in this investigation were part of a more extensive program in which a number of sheet thicknesses between 0.028 and 0.135 inches were examined. Accordingly, specimen thicknesses sometimes varied between portions of this program. This factor is considered in more detail and reported with the test results.

Four types or geometries of specimens were necessary for the different properties considered. Important aspects of each are shown in Figures 3 and 4. Similarly, different

TABLE I.  
CHEMICAL COMPOSITION BY WEIGHT PERCENT OF INCONEL 718

Carbon .....	0.02-0.08	Molybdenum .....	2.80-3.30
Manganese .....	0.35 Max.	Columbium	
Silicon .....	0.35 Max.	+ Tantalum .....	4.75-5.50
Sulfur .....	0.015 Max.	Titanium .....	0.75-1.15
Phosphorus .....	0.015 Max.	Aluminum .....	0.30-0.70
Chromium .....	17.00-21.00	Boron .....	0.006 Max.
Iron .....	16.50-20.50	Copper .....	0.30 Max.
Cobalt .....	1.00 Max.	Nickel .....	Remainder



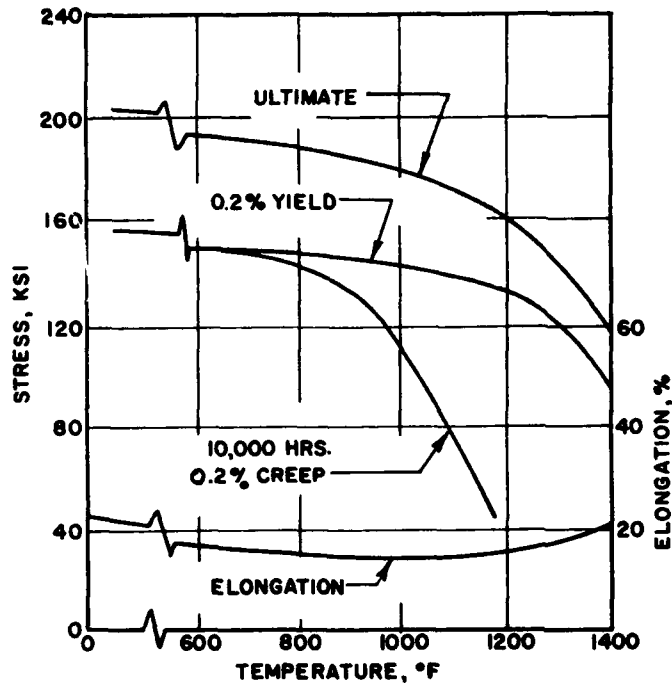


Figure 2. Typical Inconel 718 Sheet Properties.

test arrangements were necessary for the static and fatigue experiments. Specimens and test details are discussed below.

Rising load fracture toughness and time-dependent fracture testing on both parent metal and welded material used the relatively standard center-notched sheet specimen shown in Figure 3. The three-inch wide specimen was used for the evaluation of sheet thickness and weld metal versus parent metal effects. Wider specimens were used when panel width effects on mixed mode fracture toughness was the variable being studied. Precracking of the panel was accomplished by initiating and extending a fatigue crack from an EDM center slot. ASTM recommendations relating to precracking of compact fracture toughness specimens were interpreted for the geometry used in this study in the selection of stress intensity ranges. Precracking of welded specimens followed weld bead removal by hand grinding until bead was nearly flush with the sheet surface.

Closed-loop servo-hydraulic testing systems were used to perform the rising load fracture toughness tests. Stress intensity increase rates converted to load rates followed the ASTM recommendations as translated to the geometry used. Heating of the three inch specimens was by induction heaters while the wider specimens were heated by radiation from quartz lamps. Fracture toughness calculations were based on maximum loads, since plane strain analyses were inapplicable.

Time-dependent fracture testing was conducted in rupture machines equipped with resistance-wound furnaces, using the three-inch wide specimen described in Figure 3. Precracking procedures were identical to those used for the rising load tests. Initial crack lengths on these specimens were selected as approximately one inch or 1/3 of the width unless dictated by tester loading capacity. Test results were reported as the time to fracture as a function of the initial

TABLE II . HEAT TREATMENTS FOR INCONEL 718 SPECIMENS

PARENT METAL	
Mill Anneal	
1700°F - 1 Hour - Air Cool	
1325°F - 8 Hours - Furnace Cool to 1150°F at 100°F per hour, Air Cool to R.T.	
WELDED MATERIAL	
Mill Anneal	
Weld (Tungsten Inert Gas)	
1700°F - 1 Hour - Air Cool	
1325°F - 8 Hours - Furnace Cool to 1150°F at 100°F per hour, Air Cool to R.T.	

rising load toughness. Constant loads were maintained throughout the tests.

Cyclic crack growth tests both with and without hold times up to 90 seconds at the peak loads were conducted in the closed-loop servo hydraulic systems with load the control mode. Tests with hold times in excess of 5 minutes were conducted in rupture test machines which were modified to cycle load. Specimens subjected to 5-minute hold times were tested in both types of equipment. Optical measurement of crack extension during the tests was accomplished by using 40X scopes during periodic interruptions after cooling to room temperature. Cyclic rates on continuously cycling tests were selected to be between 15 and 60 cpm. For hold time cyclic tests loading and unloading was accomplished in 10 seconds or less. In all crack growth

testing, the A-Ratio (alternating to mean stress) was equal to 0.95. Precracking of all cyclic crack growth specimens was at a rate between 1 and 30 cps at room temperature. Cyclic load levels applied to the EDM slot during precracking resulted in stress intensity range after the crack initiated equal to that planned in the subsequent elevated temperature crack growth tests.

Verification or model testing employed the specimens shown in Figure 4. These three configurations coupled with imposed load methods simulated the stress situation encountered in production butt welds used in some jet engine static hardware. Although weldments are usually loaded in a tension stress field, unavoidable mismatch between mated sheets can superimpose very high bending stresses. Specimen A in Figure 4 has a pure tensile stress field and simulates a semi-elliptical surface crack in a perfectly aligned weld loaded in tension. Specimens B and C duplicate the stress situation when typical production mismatches are encountered. With 20% mismatch, bending stresses equal to the tension field are often attained locally on reinforced welds. Since this investigation was to verify a potential material property design practice, bending stresses equal to those resulting from the maximum sheet mismatch expected in hardware were studied. The condition selected was that the imposed bending stress was equal to the tensile stress. Specimen B achieved these conditions by incorporating a mismatched welded specimen in an uniaxial stress field. In the specimen C configuration the service conditions were simulated by applying an off-center axial load which generated the axial stress and bending moment components on an aligned welded specimen.

Semi-elliptical surface cracks were obtained by precracking the specimen at room temperature from a small EDM slot on the surface. Precracking cyclic loading conditions at room temperature were identical to subsequent high temperature testing conditions. Verification testing was conducted at 15 cpm in closed-loop servo-hydraulic systems with induction heating of the test area.

## TEST RESULTS AND DISCUSSION

### Fracture Toughness

An investigation was conducted, as described earlier, to evaluate the influence of both geometric and test variables on the rising load fracture toughness of Inconel 718 sheet and weldments. The stress intensity (K) relationship for axially loaded through-the-thickness center cracked panels is given by:

$$K = \sigma (a)^{1/2} f \left( \frac{a}{w} \right) \quad (1)$$

where  $\sigma$  = applied stress, ksi

K = elastic stress intensity factor, ksi (in.)<sup>1/2</sup>

w = panel width, ins.

a = crack semi-length, ins.

and  $f \left( \frac{a}{w} \right)$  = K - calibration curve for center-cracked specimens, as suggested by Forman et al<sup>1</sup>.

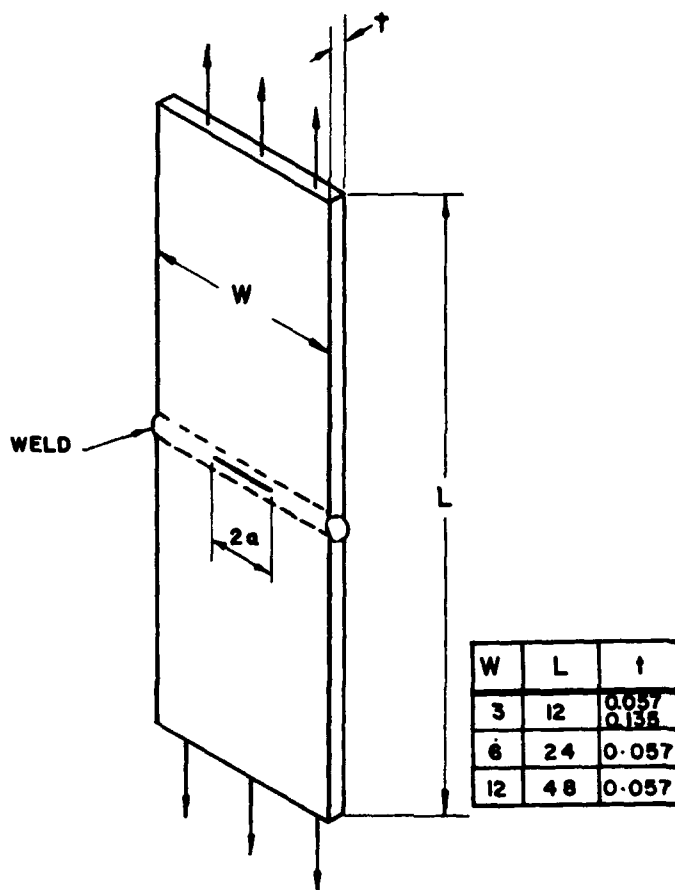
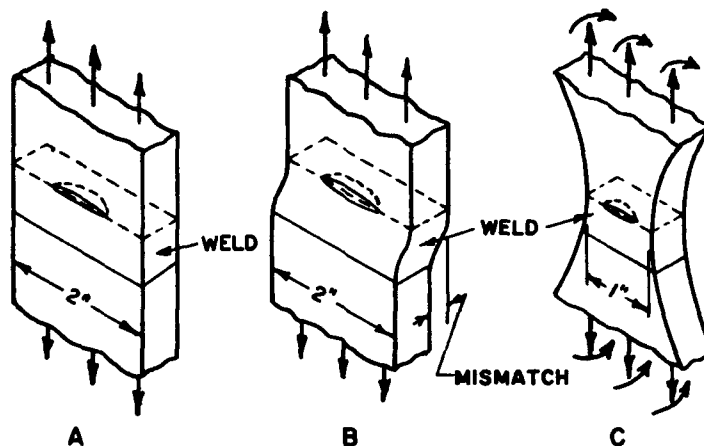


Figure 3. Fracture Toughness and Crack Growth Specimen.

Figure 4. Verification  
Test Specimens.



For mixed mode testing described herein, fracture is defined as  $\sigma \rightarrow \sigma_{\max}$ , and  $K \rightarrow K_{\text{critical}} = K_c$ . At fracture instability, plasticity at the crack tip becomes significant, effectively increasing the crack semi-length by the plastic zone radius. For  $K_c$  calculations, the plastic zone adjustment was made in the form shown in Eq. (2).

$$K_c = \sigma_{\max} (a + r_y)^{1/2} f \left( \frac{a}{W} \right) \quad (2)$$

where  $K_c$  = (mixed mode) fracture toughness, ksi (in.)<sup>1/2</sup>

$\sigma_{\max}$  = Maximum stress, ksi

$\sigma_{ys}$  = yield stress, ksi (3)

$$r_y = \frac{1}{2\pi} \left( \frac{K_c}{\sigma_{ys}} \right)^2 = \text{plastic zone size, ins.}$$

Experiments were conducted, as described earlier, to evaluate the influence of both geometric and test parameters on the rising load fracture toughness of Inconel 718 sheet. The toughness of parent material, weldments and weld fusion area material at 1000°F was examined in 3-inch width center-cracked specimens (Figure 3) with crack-length to width ratio of  $\sim 0.3$ . As shown in Figure 5, relatively small toughness reductions were noted. When precracked in the weld nugget, fracture toughness  $K_c$  was approximately 10% less than the parent metal. When precracked along the fusion zone, toughness was 10 to 15% less than parent metal. Accordingly, detailed investigation of geometric influence on the mixed-mode toughness was confined to parent material specimens.

Fracture toughness values, based on maximum load, measured from 3-inch wide, 0.057-inch thick center-cracked sheet specimens at 1000°F, were noted to be a function of relative crack length,  $\frac{2a}{W}$ , in a range 0.2 to 0.55, increasing from 146 to 162 ksi (in.)<sup>1/2</sup>, as shown in Figure 6. Analysis of results from geometrically identical specimens ( $\frac{L}{W} = 4$ ) in-

dicated similar trends for 6-inch and 12-inch wide panels, for crack length ratio ranges 0.1 to 0.3 and 0.1 to 0.2, respectively. Reductions in toughness observed for greater relative crack lengths were attributed to buckling instabilities, which are currently being investigated. Prior to the onset of buckling, substantially increased toughness is indicated for both the 6 and 12-inch wide panels compared to the 3-inch wide specimens.

The fracture resistance of the center-cracked panels was also found to depend on sheet thickness. Results of 1000°F toughness tests on 3-inch wide specimens with relative crack lengths of about 0.35, are shown in Figure 7 as a function of sheet thickness. Toughness values increased about 35% with increasing thickness in the range 0.029 to 0.102 inches. As indicated the increased  $K_c$  with thickness tends to a maximum. Further thickness increase would likely result in reduced toughness as plane strain conditions are approached.

The influences of the experimental parameters temperature and loading rate were evaluated on 3-inch wide center-cracked specimens, 0.056 inch thick. Fracture tough-

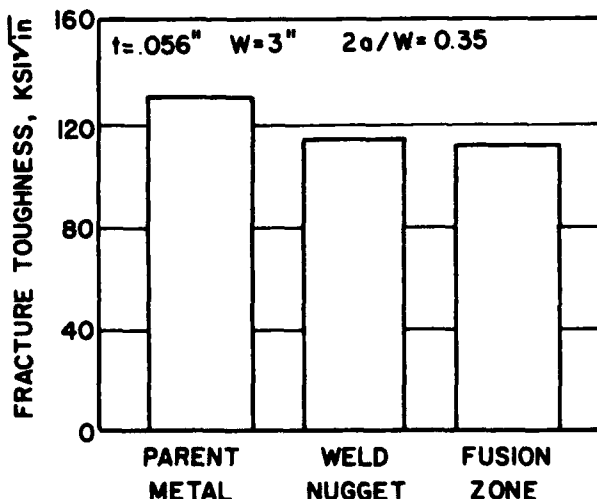
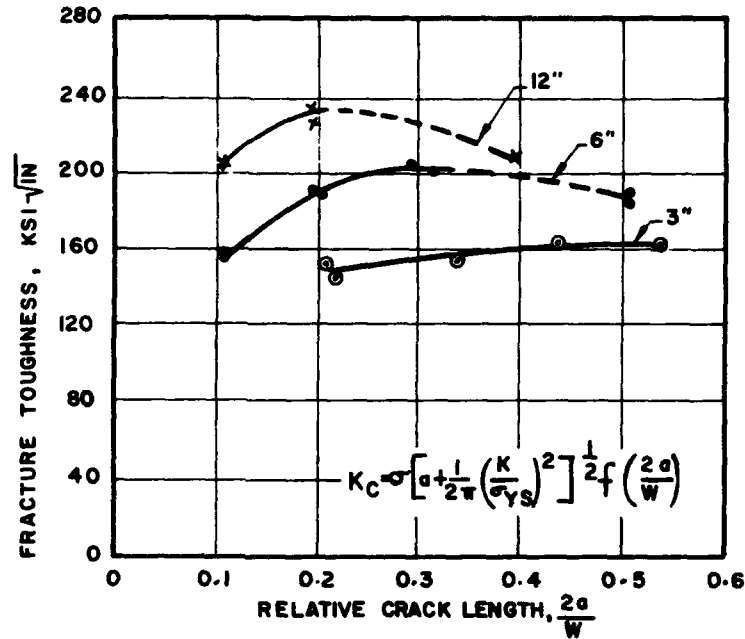


Figure 5. Relative Toughness of Three Material Conditions in Inconel 718 Welds.

Figure 6. Fracture Toughness of  
56 MIL Inconel 718 Sheet at 1000°F.



ness was found to decrease with increase temperature (Figure 8); the ratio of  $\frac{K_C}{\sigma_{YS}}$  remaining approximately constant over the temperature range 70° to 1400°F (Ref. Figures 2 and 8). The effect of loading rate on fracture toughness at 1000°F was found to be negligible for strain rates of 0.005 in./in./min. and 0.5 in./in./min.

Time-dependent fracture was studied and the results are shown in Figure 9. The effect of time-on-load was to significantly lower the load bearing capacity, hence the apparent  $K_C$ . Pre-fatigue cracked 3-inch wide center cracked specimens, 0.057 inch thick, were loaded at 1000°F to particular elastic (no plastic zone correction) stress intensity

levels and held on load until fracture occurred. An apparent 30% toughness reduction is indicated for a 100 hour load cycle. The strength reduction is not attributed to a degradation of toughness, per se, but rather to the process of stable crack growth and consequent increase in stress intensity during the course of the test. Toughness values calculated from final crack dimensions, approached the rising-load fracture toughness.

#### Crack Growth Behavior

Results of continuously cycling crack growth tests are shown in Figure 10. Crack growth rates, inches of crack

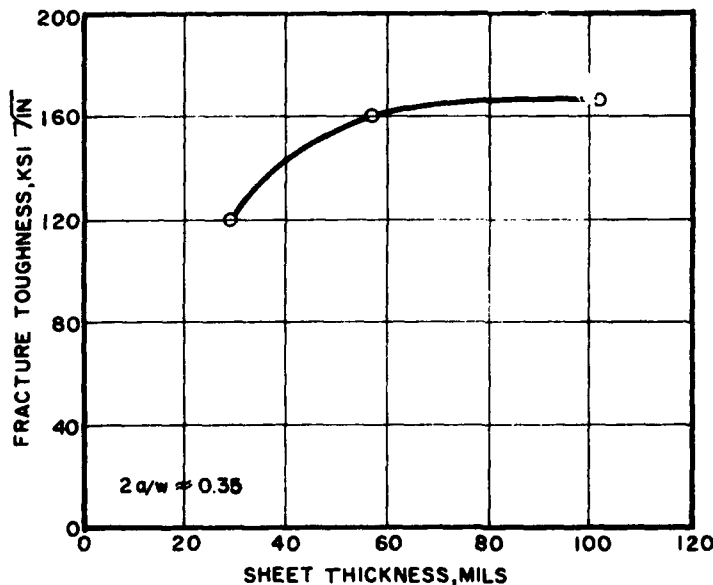
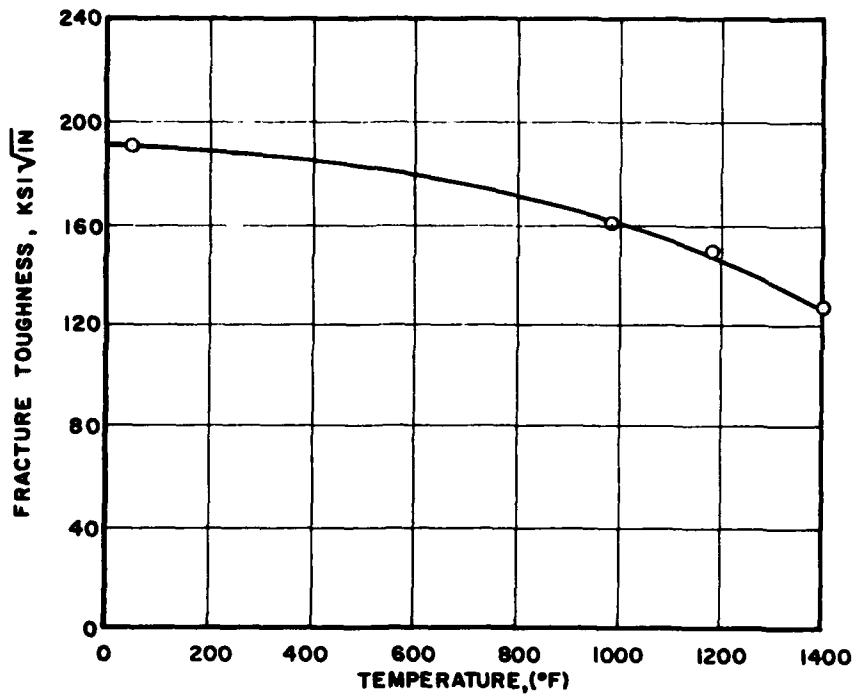


Figure 7. Fracture Toughness of  
Inconel 718 Sheet at 1000°F.

Figure 8. Effect of Temperature on Fracture Toughness of 56 MIL Inconel 718 Sheet.



extension ( $\Delta a$ ) per load cycle ( $\Delta N$ ) are plotted versus the applied cyclic stress intensity range ( $\hat{K}$ ).  $\hat{K}$  is the range of  $K$  (see equation 1) for the maximum and minimum applied load. Data are shown for the three conditions that can be encountered in Inconel 718 welded structures. The three are: Crack growth in the parent metal, in the weld nugget, and along the fusion zone between the weld nugget and parent metal. Within the bounds of the observed scatter for any one group of data, there is no significant difference in the cyclic growth behavior of these three conditions.

The slope of the log  $da/dN$  versus log stress intensity range,  $K$ , curve is 4.3, which agrees well with the value of 4.0

observed for many materials at low temperatures.

As indicated previously, these crack growth specimens were 3 and 12 inches in width. Although data up to the mid-range of stress intensity range showed no effect of specimen width on crack growth rate, effects are expected as the stress intensity range  $\hat{K}$  approaches the  $K_c$ . Crack growth data for  $K \geq 100 \text{ ksi } \sqrt{\text{in}}$ , were generated on 12 inch width panels which displayed  $K_c (r_y=0)$  of 190-200  $\text{KSI } \sqrt{\text{in}}$ . For cases where three-inch panels were used,  $da/dN$  showed an acceleration as the  $K_c$  (120  $\text{ksi } \sqrt{\text{in}}$ ) was approached. Similarly, sheet thickness would affect  $da/dN$  as  $\hat{K}$  approached the relative  $K_c$  value. Any crack growth

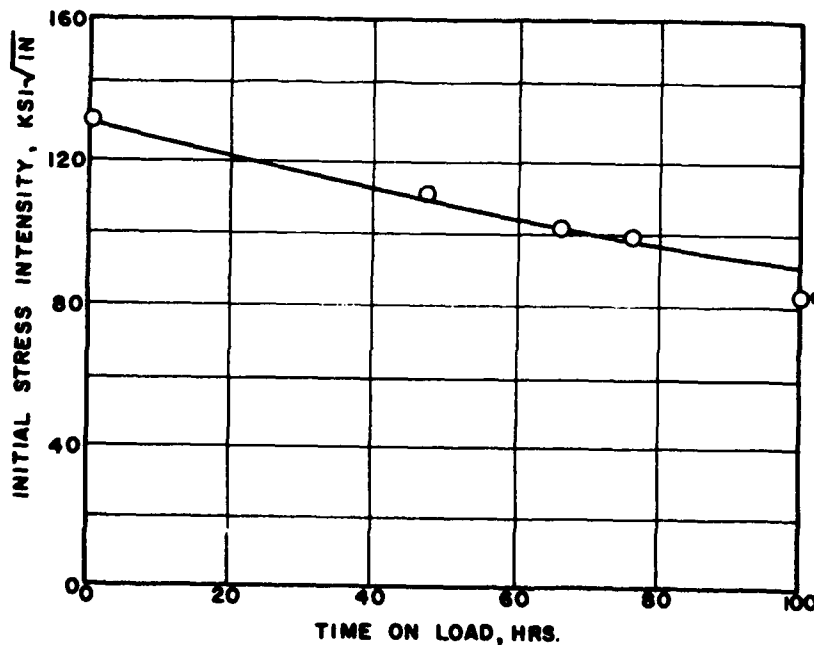
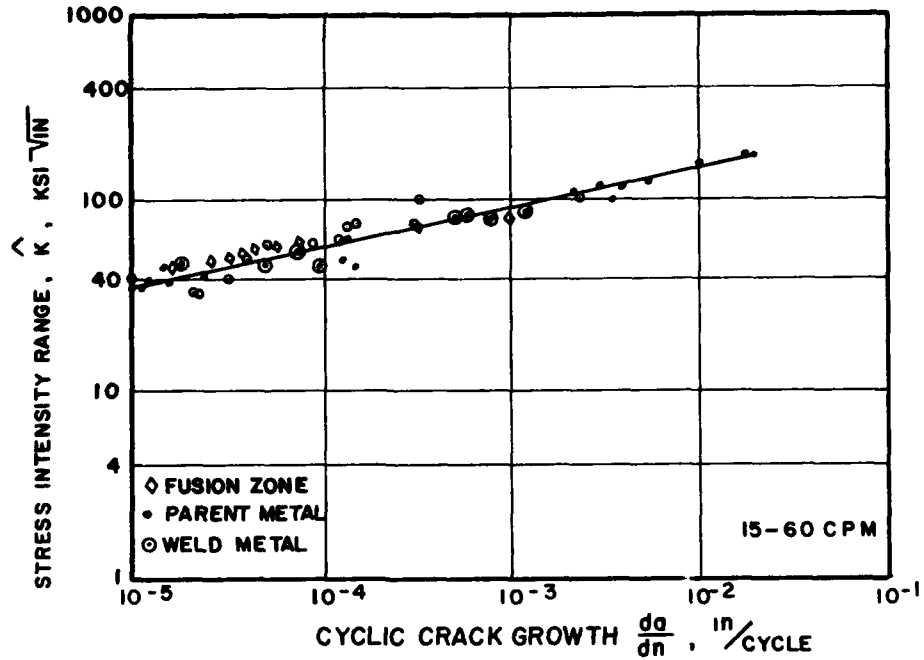


Figure 9. Time Dependent Fracture of Inconel 718.

Figure 10. Crack Growth Rates in Inconel 718 Weld Components at 1000°F.



analysis to final fracture must recognize the geometric dependence of  $K_c$ .

Typical operations of static components of jet engines are such that hold times under peak stresses are encountered. A viable defect tolerance design criteria must allow for any hold time acceleration of the crack growth behavior. As discussed previously, subcritical crack growth in Inconel 718 is time dependent under static loading conditions. Studies were conducted to evaluate to what extent combination of hold times with cyclic loading would affect crack growth behavior. Test results are shown in Figure 11 for

zero to two hours hold time during each load cycle. As shown, hold times greatly affected crack growth behavior, expressed in inches per cycle. Analysis of two-hour hold period data demonstrated a 100 fold increase in cyclic growth rates compared to continuously cycling data. Shorter hold times induced smaller, but still significant, crack growth accelerations.

It is interesting to note that the slopes of all cyclic crack growth rate curves remained sensibly constant at a value of 4.3 regardless of hold time. Similar parallel behavior was observed by Sinclair and Rolfe.<sup>2</sup> Program limit-

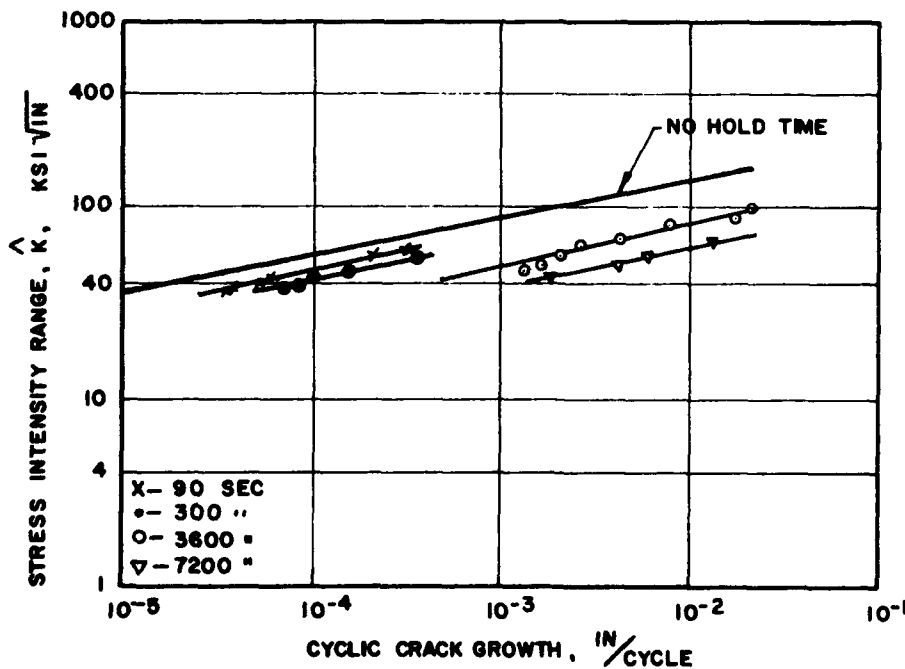
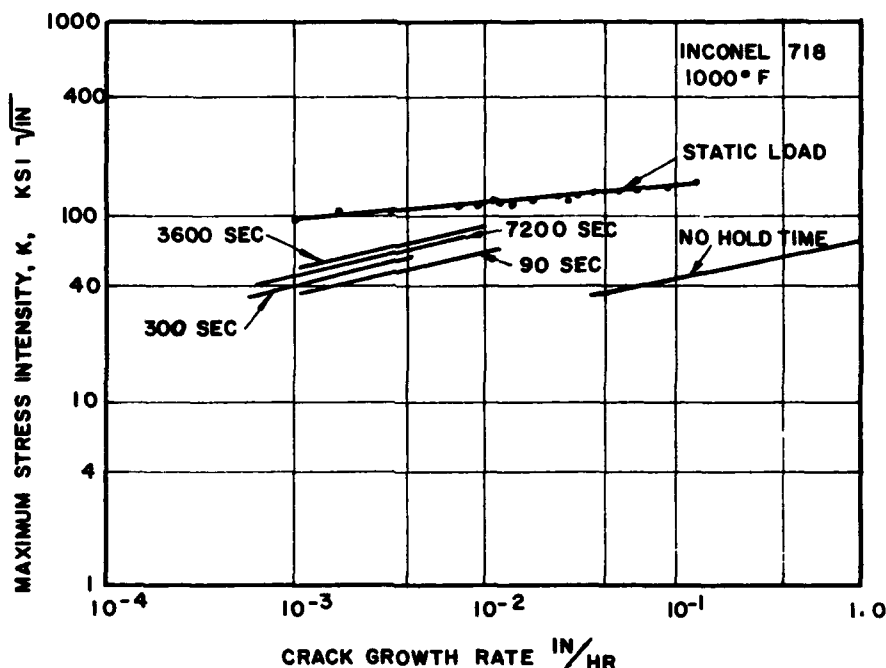


Figure 11. Hold Time Effects on Crack Growth at 1000°F.

Figure 12. Hold Time Effects on Crack Growth in Terms of Time Rate.



ations prevented exploration of hold time effects at the two extremes of the  $\hat{K}$ ; that is, the threshold stress intensity for crack growth,  $\hat{K}^*$ , and values approaching  $K_c$ . Near the threshold values ( $da/dN < 10^{-6}$  in/cycle) little is known about hold time effects. However, at the other extreme, the static time dependent fracture tests did indicate that regardless of the time to failure from a starting stress intensity, the crack extended until the effective  $K$  equalled  $K_c$ . This observation would imply no hold time effect at the upper limit of the cyclic crack growth curve which approaches the fracture toughness  $K_c$  as a limit.

The effects of hold time are shown in terms of crack growth per unit time in Figure 12. Cyclic crack growth data were converted to time units by multiplying the observed rates by the cycles per hour. In this manner, static subcritical crack growth observations from time-dependent fracture toughness testing can be plotted as a limit of cyclic time data ( $t_h \rightarrow \infty$ ). The other limit is the no hold time behavior ( $t_h = 0$ ). As expected all data were bounded by these limits. It is interesting to note that the hourly crack growth rate approaches a minimum at about one hour hold period per each cycle. Although the two-hour data show an apparent slight increase in rate, this is probably within the scatter of the data and may not be real.

Hold-time cyclic growth data are difficult to obtain because of pedestrian rates at which cracks grow in the important stress intensity range levels. A reliable prediction method is therefore needed. In order to develop a systematic method of interpolation and extrapolation of growth rates, an attempt was made to apply a time-temperature parameter to describe the data. As noted in Figures 11 and 12, the data are represented by parallel lines. This indicates that within the bounds of the data, the effect of hold

times on crack growth rates is a single multiplier for each hold period. A single relationship at any constant level of stress intensity range would then describe the behavior at all levels.

The Larson-Miller parameter<sup>3</sup> has been used with good results on other time-dependent phenomena in metals' behavior and it offers potential to describe time-temperature effects on crack growth rate. The data displayed in Figure 11 plus additional crack growth data at other temperatures and hold times were applied to a parameter ( $P$ ) where:

$$P = (T + 460) (C + \log t_h) \quad (4)$$

where  $T$  = temperature, °F

$t_h$  is the hold time per cycle, hours

$C$  is a material constant determined by regression analysis.

Figure 13 displays the fit of this parameter to the data at a stress intensity range of 45 ksi (in.)<sup>1/2</sup> for hold time and temperature ranges, 0-2 hours and R.T.-1200°F, respectively. Continuously cycling data, generated as part of this investigation, had a triangular wave loading function and the  $t_h$  was judged as the time increment at which the applied load was above 90% of the peak stress. Hudson<sup>4</sup> did not indicate exact cyclic rates for individual experiments, only ranges that include extremes in testing conditions.

Figure 13. Parametric Fit of Crack Growth Data at Constant  $\hat{K}$ .

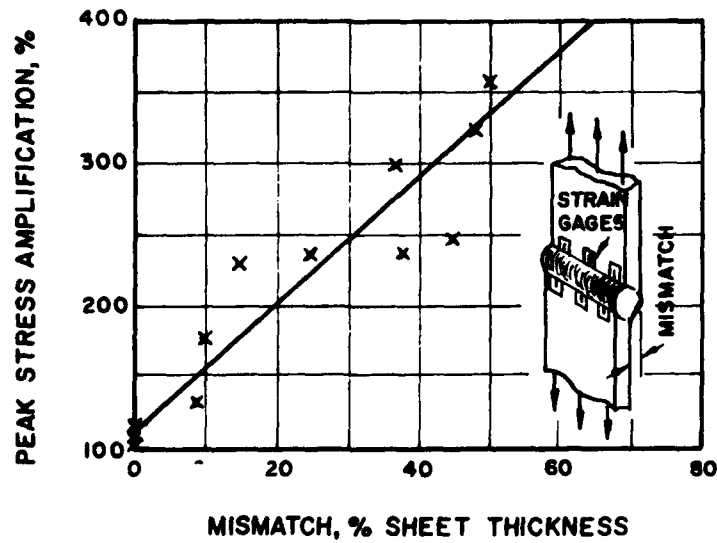
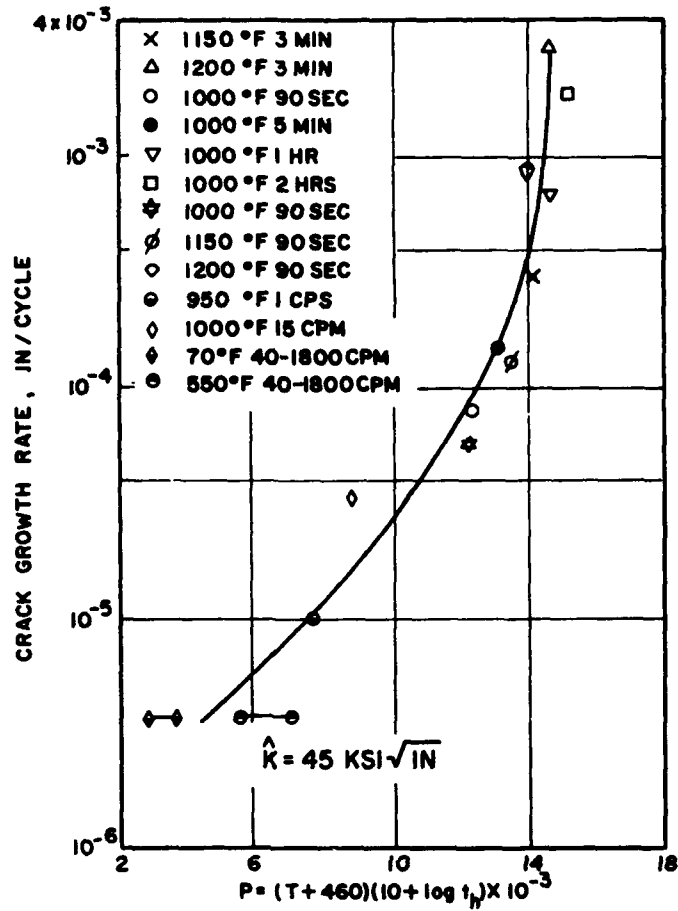


Figure 14. Strain Gage Evaluation of Misaligned Reinforced Weldments.



Accordingly, his data were considered as ranges in the analysis using the same 90% criteria for estimated hold times. The fit of the data to the parameter is quite acceptable. The maximum deviation of observed to calculated data is a factor of two in rate, and these deviations occur for continuously cycling conditions. Where definite hold times (90 sec. or more) are involved excellent agreement was observed.

### LIFE ANALYSIS APPROACH

The scatter observed in the low cycle fatigue properties of welded Inconel 718 (Figure 1) reflects the difficulty in life prediction on an applied nominal stress basis. It emphasizes the importance of developing a life prediction analysis which considers the sources of variation. Major concerns in Inconel 718 welds are misalignment between welded panels and any small occasional defects.

As shown in Figure 1, even without significant defects, gross scatter was observed in cyclic life. Stress concentration at the weld bead intersection with the surface, resulting from the discontinuity of the weld bead and localized bending caused by mismatch were identified as major contributors to the scatter. Studies using very small gage length (1/32 inch) strain gages, indicated significant stress concentrations at the weld bead. Results of strain measurements are shown in Figure 14. As shown the stress intensification can be large due to sheet misalignment. With production welds, reasonable tolerances permit up to 10% mismatch on relatively thin walled jet engine structures. Stress peaks can reach twice the nominal stresses. Even with perfect alignment, stress concentrations of 20% (Figure 14) are possible due to the geometric discontinuity at the weld. Because of the finite length, strain gages cannot measure peak stress exactly at the intersection of bead and sheet. Therefore, even higher local values are probable.

The results of low cycle fatigue tests on defect free welds of Inconel 718 with the stress measured at the point of crack initiation are shown in Figure 15. Much better agreement was noted between life and the applied stress than when life was expressed in terms of nominal stresses (Figure 1).

Similarly, accurate prediction of defect tolerance in welds depends on a thorough understanding of the factors governing crack growth. Materials toughness data discussed previously have been studied in terms of the elastic fracture mechanics singularity of stress intensity (K) at the crack tip. Generally, under these simplified conditions, analysis of K is well established. Even so, the validity of K as a singularity to describe high temperature defect tolerance has not been substantiated. The following is a discussion of a stress intensity analysis model to describe the cyclic crack growth in a typical welded jet engine static structure which operates at temperatures in the creep regime.

The most troublesome defects that occur in Inconel 718 TIG welds are surface cracks along the fusion line between the parent metal and the weld nugget. Detection of these defects is difficult because the naturally occurring line at the intersection confounds both X-ray and penetrant type inspection procedures. Furthermore, these fusion line defects are potentially of greater concern because of the local stress concentrations in this area (see Figure 14). Accordingly, the analysis was developed for this type of defect though other defects can be handled in a similar fashion. Although naturally occurring surface defects or cracks in Inconel 718 welds could be of any configuration, for analytic potential, a simple semi-elliptical crack front was selected as the most appropriate form based on examination of cracks at weldment fusion lines.

The major requirements of a model analysis for this

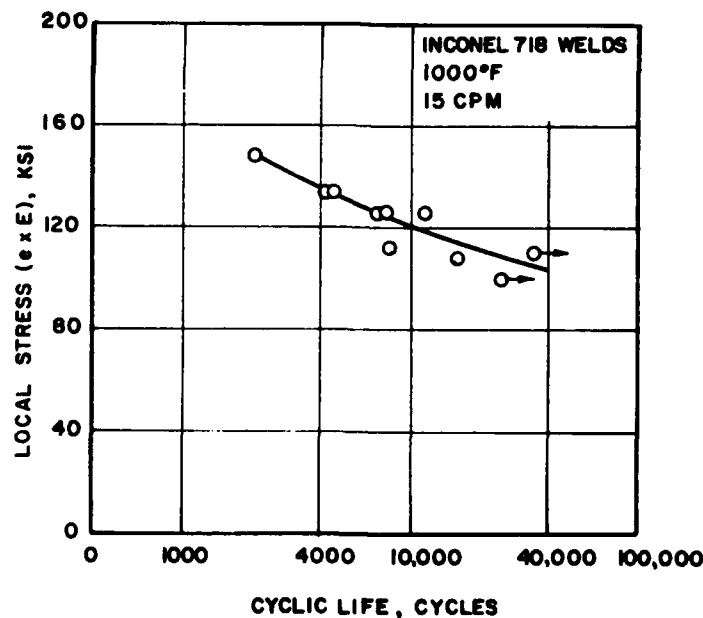


Figure 15. Fatigue Behavior of Defect-Free Welds When Plotted Versus Local Stress Conditions.

application are that:

1. Cyclic growth can be predicted as a surface semi-elliptical crack which penetrates the back surface and then grows as a through-the-thickness crack.

2. Cyclic crack growth can be predicted for stress gradients across the thickness ranging from the pure tension case to a bending situation, where the bending stress equals the tensile stress field.

3. Crack front elliptical aspect ratios can vary between 1 and  $\infty$ .

4. Sheet thickness can be a variable.

5. Peak stress hold time effects on crack growth rates are included.

These requirements were met by incorporating the following features into the analysis as suggested and developed by W.L. Knaus and J.R. Giard of the General Electric Company.

1. Stress intensity analyses from the literature for semi-elliptical crack fronts in a pure tensile field or pure bending field were superimposed for conditions of combined tension and bending.

2. Criteria for crack front shape after the semi-elliptical crack penetrated the thickness were developed.

3. Parametric modification of the crack growth curve was incorporated to account for temperature and hold time effects on cyclic growth rate.

Details of the Analysis are discussed.

#### Model Development

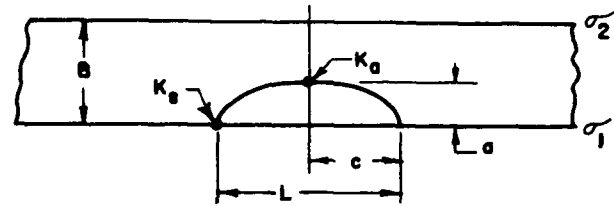
As indicated above, a semi-elliptical, surface crack case was selected as the most appropriate crack configuration. The stress intensity for an elliptical surface crack,  $(2c)$  long,  $(a)$  deep, is given by

$$K = \frac{\sigma \sqrt{\pi a}}{\Phi} (F_i) \quad (5)$$

where  $\sigma$  = unperturbed stress,

$\Phi$  = elliptical integral and

$(F_i)$  represent modifying factors relating to free surface correction, stress gradients through-the-thickness, and back surface correction. The selected crack model and analytic stress intensity factor expressions are shown in Figure 16 where modifying factors  $F_1$ ,  $F_2$  and  $F_3$  are associated with  $K$



#### STRESS INTENSITIES:

$$K_a = \frac{\sigma_1 \sqrt{\pi a}}{\Phi} F_1 F_2 F_3$$

$$K_b = \frac{\sigma_1 \sqrt{\pi a}}{\Phi} F_4 F_5$$

Figure 16. Stress Intensifiers for Semi-Elliptical Surface Cracks.

at the maximum crack depth location and  $F_4$  and  $F_5$  modify surface crack tip  $K$  calculations.

#### Stress Intensity Factor at Maximum Crack Depth

The assumption was made that the expression for stress intensity at maximum crack depth ( $K_a$ ) was of the form:

$$K_a = \frac{\sigma \sqrt{\pi a}}{\Phi} F_1 F_2 F_3 \quad (6)$$

$F_1$  is a free surface correction factor which accounts for variation in stress intensity as the crack gets deeper relative to its surface length. Information from References 5 and 6 suggests the following expression for its magnitude:

$$F_1 = 1.1 - 0.07 (a/c) \quad (7)$$

where  $a$  = crack depth

$c$  = surface crack semi-length

$F_2$  is a stress gradient or bending modifying factor to reduce the stress intensity as the unperturbed stress diminishes through the section thickness. The relationships observed in References 2 and 6 were used in graphical form to determine the  $F_2$  modifying factor. A specific example of this relationship for semi-circular surface crack shape is:

$$F_2 = 1 - 0.73 \left(\frac{a}{B}\right) \left(1 - \frac{\sigma_2}{\sigma_1}\right) + 0.04 \left(\frac{a}{B}\right)^2 \left(1 - \frac{\sigma_2}{\sigma_1}\right)^2 \quad (8)$$

where  $B$  = sheet thickness

$\sigma_1$  = stress magnitude on surface containing defect

and  $\sigma_2$  = stress magnitude on back surface

The  $(1 - \frac{\sigma_2}{\sigma_1})$  factors were added to treat the combined tension plus bending stress rather than pure bending as cited by the authors of References 2 and 6.

$F_3$  is a factor to account for the influence of the back surface on stress intensity as the back surface is approached by the crack. The following expression was developed to describe the relationships suggested by the work of Shah, Tiffany and Lorenz<sup>5</sup>:

$$F_3 = 1 + 10.8 \left(\frac{a}{B}\right)^{2.5} e^{+4.9(a/c)} \quad (9)$$

#### Stress Intensity Factor at Surface Crack Tip

The stress intensity factor expression used for determining  $K_s$  at the surface crack tip was essentially similar to Eq. (1)

$$K_s = \frac{\sigma\sqrt{\pi a}}{\Phi} \cdot F_4 \cdot F_5 \quad (10)$$

$F_4$  and  $F_5$  are stress gradient and free surface correction factors, respectively, for the stress intensity at the surface. From the concepts observed in References 6 and 5, respectively, the following expressions were formulated:

$$F_4 = 1 - 0.16 \left(\frac{a}{B}\right) \left(1 - \frac{\sigma_2}{\sigma_1}\right) \quad \text{Reference 6} \quad (11)$$

and

$$F_5 = 0.38 + 0.85 (a/c) \quad \text{Reference 5} \quad (12)$$

A computer program was developed to calculate progressive crack depth, surface length and respective stress in-

tensity factors for various increments of cyclic life, based on the expressions (6) and (10) and actual crack growth data. The crack growth process is such that the elliptical surface crack extends along the free surface and through the sheet thickness. At some stage a transition occurs changing the surface crack into a through-the-thickness crack with a curved crack front. No fully acceptable analysis for such a situation is available in the literature. A typical crack front after back surface penetration is shown in Figure 17. For the analysis described the crack front was assumed to be straight but at an acute angle to the sheet surfaces. The angle of the crack front was assumed to remain constant after back surface penetration. Furthermore, the through-the-thickness stress intensity calculation was based on an effective semi-crack length ( $c_e$ ), where  $c_e$  is defined as:

$$c_e = C - 0.5 C_p \quad (13)$$

$C$  = actual semi-surface crack length

and

$C_p$  = semi-surface crack length at penetration of back surface

Transition of the surface crack to through-the-thickness crack was taken when the plastic zone ahead of the crack tip reached the free surface i.e., when

$$B - a = \frac{1}{4\pi} \left(\frac{K_a}{\sigma_{ys}}\right)^2 \quad (14)$$

for cyclic loading cases.

For combined bending-tension stress cases with a through crack, an effective tensile stress was calculated as

$$\sigma = \frac{\sigma_1 + \sigma_2}{2} + 0.4 \frac{\sigma_1 - \sigma_2}{2} \quad (15)$$

**N FRACTURE = 18,048 CYCLES**

Figure 17. Typical Crack Propagation Contours Under Axial - Bending Loading.

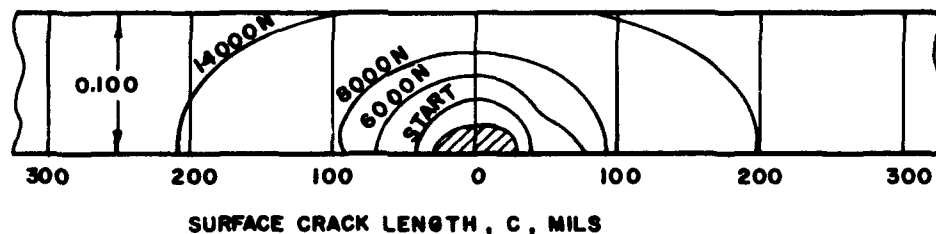
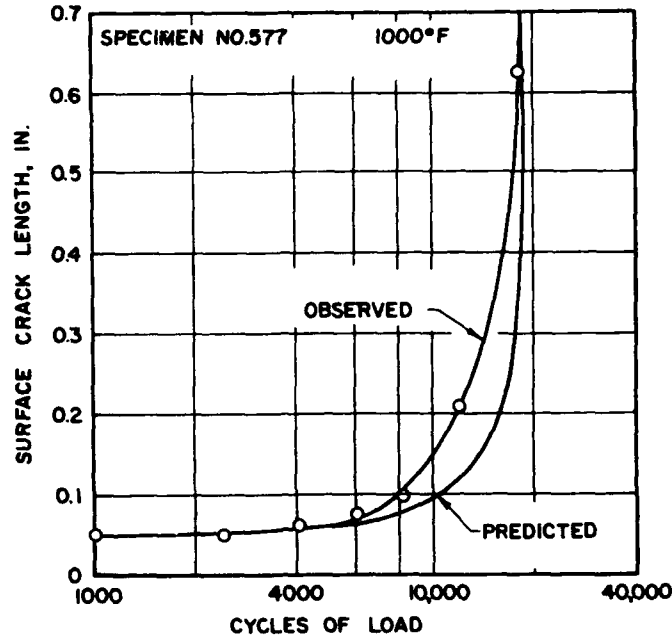


Figure 18. Observed Versus Predicted Crack Growth .



where the constant  $0.4 =$

$$\frac{1 + \mu}{3 + \mu}$$

is that suggested by Paris and Sih<sup>7</sup> and  $\mu$  is Poisson's Ratio.

The computer program calculated cyclic lives by successive integration of the striation density (reciprocal of crack growth rate) as a function of crack length. Striation density was determined by calculation of the local stress intensities at the two critical points ( $K_a$  and  $K_b$ ) on the crack front and comparing these to the crack growth rates. For part-through cracks, the integration variable is  $da$  and, changes to  $dc$  for through-the-thickness cracks. The Larson Miller parametric relationship, discussed previously, was embodied in the program to predict life for cyclic stress

with superimposed hold time at temperature ranges relevant to jet engine conditions.

The program was arranged to print a tabulation of  $N$ ,  $a$ ,  $K_a$ ,  $c$  and  $K_c$  at selected intervals of  $N$ , for given initial crack dimensions and stress conditions, thus allowing contours of crack front shape to be analyzed as a function of cyclic life and compared to test observations. The program terminates when the fracture toughness of the material is exceeded.

#### Verification Tests

A series of cyclic crack growth tests were conducted to verify the applicability of the fracture mechanics approach to predict defect tolerance of Inconel 718 welds under jet

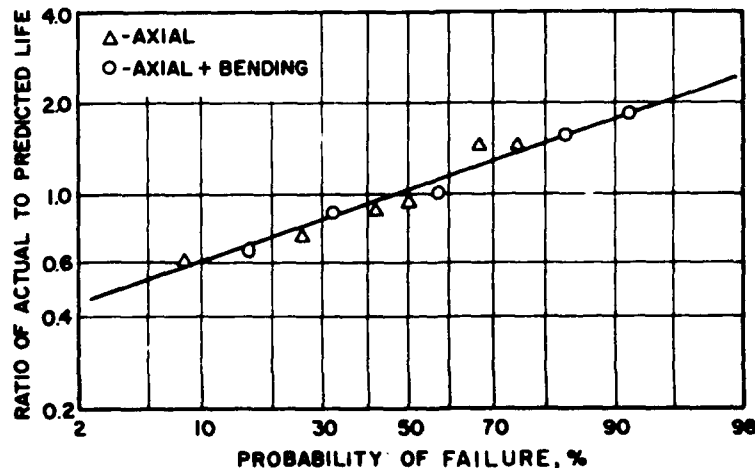
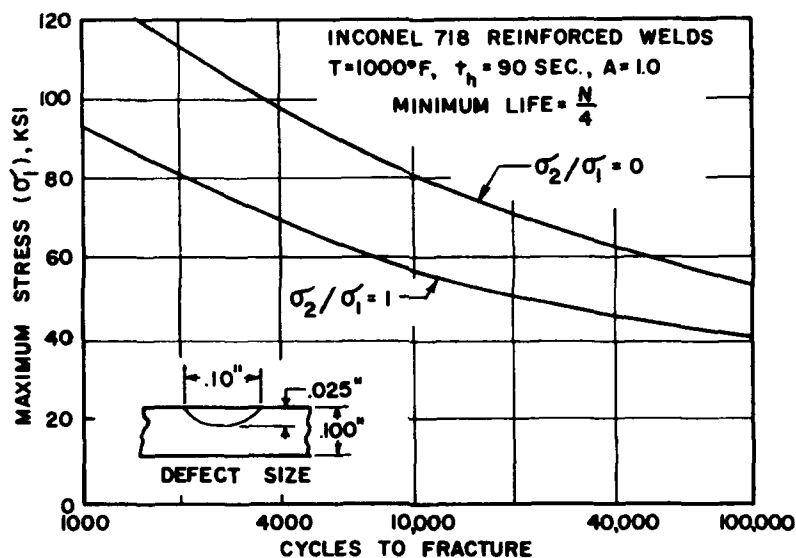


Figure 19. Correlation of Predicted Crack Propagation Lives to Observed Test Results.

Figure 20. Predicted Inconel 718 Defect Tolerance.



engine component conditions. Three configurations of specimens (Figure 4) with semi-elliptical surface defects were tested at 1000°F under loading conditions from pure tension to tension plus equal bending at cyclic rates of 15 cpm. Observations of surface crack length were made at regular intervals and cyclic lifetimes to fracture recorded. Correlation of observed and predicted surface crack length provided good agreement. A typical comparison is shown in Figure 18. The shape of the crack growth curves agree quite well. Particularly good fit was observed during the part-through-thickness portion of the crack growth life.

A summary of results of these tests is in Table III. Listed are the observed or test lives compared to the predicted lifetimes from the computer program, and the ratios of actual to predicted lives. These values are plotted against the normal probability of failure in Figure 19. As seen, a straight line relationship resulted within the extremes of 0.61 and 1.86 ratio-range obtained. Perfect agreement corresponds to a ratio of unity. A factor of less than two on individual lives compared to the average is considered excellent agreement for cyclic life prediction. Furthermore, the fact that more than a factor of two was observed in the crack growth scatter of simple specimens (see Figure 10) makes the agreement even more convincing. The predicted lives as shown are for average behavior. To insure a safe design, from a life prediction standpoint, it would be necessary to reduce the calculated life by some factor to gain the high probability of survival required. For instance, a factor of 4 on predicted lives would provide better than 99.9% chance of survival.

Using the above methods, viable materials design cyclic life curves can be prepared for unavoidable defects in Inconel 718 welds. The results of a typical design exercise where residual life properties of Inconel 718 reinforced weldments containing defects were required is shown in Figure 20. The load-time profile being considered included a 90 second hold, the temperature 1000°F and initial defects taken as semi-elliptical with 0.100 inch length and 0.025 inch depth. The curves shown are for both uniform stress fields and zero to maximum stress gradients and represent average properties. As an example, from the curves it is seen that for the uniform stress case, a 40 ksi maximum stress cycle would correspond to 25,000 cycle minimum life.

## CONCLUSIONS

1. Elastic fracture mechanics methods can be applied at temperatures in the creep regime with reasonable accuracy for Inconel 718.
2. A fracture mechanics model was developed to predict the residual cyclic life of Inconel 718 weldments containing surface defects. Cases of axial and combined axial and bending stress fields were treated.
3. The utility of a time-temperature parameter to predict cyclic crack growth rates at particular stress intensity was demonstrated. The parameter  $P = (T - 460) / (10 + \log t_h)$  provided reasonably accurate description of crack growth rate data for temperatures ranging from 70-1200°F and peak stress hold times of one second to two hours.

TABLE III.

## VERIFICATION TEST RESULTS FOR SEMI-ELLIPTICAL SURFACE CRACKED SPECIMENS

SPEC NO.	STRESS, KSI		W in.	B in.	a* in.	2c* in.	LIFE CYCLES		RATIO ACTUAL/ PREDICTED
	$\sigma_1$	$\sigma_2$					ACTUAL	PREDICTED	
43	80	80	2	.073	.035	.050	28,000	20,197	1.39
47	73	73	2	.074	.050	.080	24,800	17,514	1.42
48	78	78	2	.076	.050	.050	12,000	19,652	0.61
11	86.5	86.5	2	.078	.055	.160	3,800	4,105	0.92
46	90	90	2	.080	.040	.040	11,400	13,105	0.87
49	78	78	2	.080	.030	.070	13,600	18,766	0.73
42	110	0	1	.078	.065	.130	16,125	10,435	1.55
50	110	0	1	.078	.030	.065	22,000	25,270	0.87
559	110	0	2	.102	.081	.170	13,865	7,459	1.86
516	110	0	1	.101	.020	.051	22,555	33,281	0.68
577	110	0	2	.100	.038	.081	18,048	18,009	1.0

\* Initial Crack Size.

## REFERENCES

1. W.F. Brown, Jr. and J.E. Srawley, *Plane Strain Crack Toughness Testing of High Strength Metallic Materials*, ASTM-STP-410, American Society for Testing and Materials, Philadelphia, Pennsylvania (1967).
2. G.M. Sinclair and S.T. Rolfe, *Analytical Procedures for Relating Subcritical Crack Growth to Inspection Requirements*. Presented at the ASME Conference on Environmental Effects in Failure of Engineering Materials, April 1969.
3. F.R. Larson and J. Miller, "A Time-Temperature Relationship for Rupture and Creep Stresses," *Trans. ASME*, 74:765 - 775 (1952).
4. C.M. Hudson, *Studies of Fatigue Crack Growth in Alloys Suitable for Elevated Temperature Applications*, NASA-TN-D-2743, National Aeronautics and Space Administration, Washington, D.C. (1965).
5. R.C. Shah, C.F. Tiffany, and P.M. Lorenz, *Extended Loading of Cryogenic Tanks*, NASA-CR-72252, National Aeronautics and Space Administration, Washington, D.C. (1967).
6. A.F. Emery, A.S. Kobayashi, and F.W. Smith, *Stress Intensity Factors for Penny Shaped Cracks*, ASME Paper 67-WA/APM-2. Presented at the Winter Annual Meeting, Pittsburgh, Pennsylvania, November 1967.
7. P.C. Paris and G.C. Sih, "Stress Analysis of Cracks," pp. 30-81, *Fracture Toughness Testing and Its Applications*, ASTM-STP-381, American Society for Testing and Materials, Philadelphia, Pennsylvania (1965).

# THE EFFECTS OF MICROSTRUCTURE ON THE STRENGTH AND FRACTURE OF 18% Ni (250 Grade) MARAGING STEEL

by

A.M. Adair

and

J.A. Roberson

Air Force Materials Laboratory  
Wright-Patterson AFB, Ohio

Aerospace Research Laboratories  
Wright-Patterson AFB, Ohio

## INTRODUCTION

The maraging steels offer a very desirable combination of high strength, high toughness and dimensional stability. The high strength level is achieved primarily through precipitation hardening<sup>1</sup>, with contributions from solid solution hardening<sup>2</sup>, and substructure hardening<sup>3</sup>. Cold working can also be quite effective in strengthening these alloys, as was shown by Decker, Eash, and Goldman<sup>4</sup>, Kula and Hickey<sup>5</sup>, Nolan and Davidson<sup>6</sup>, and Roberson and Adair<sup>7</sup>. The high toughness of these alloys has been reported to be as a result of the absence of brittle grain boundary precipitates<sup>8</sup>, low carbon contents, and the fact that the matrix is a massive martensite rather than a twinned martensite<sup>9</sup>. One of the problems in the processing of these alloys from ingot to plate has been a tendency to develop laminations in the microstructure parallel to the rolling plane<sup>10,11</sup>.

Salmon-Cox, Reisdorf, and Pellissier<sup>12</sup> have reported that the plane strain fracture toughness of a 250 grade maraging steel containing a laminated microstructure depends on the orientation between the main crack growth direction and the laminations. They observed the highest  $K_{Ic}$  value when the main crack growth direction was perpendicular to the plane of the laminations, i.e. a crack-arresting orientation.

They observed the lowest value of  $K_{Ic}$  when both the main crack growth direction and the notch were parallel to the laminations. Kula and Hickey report values of  $K_{Ic}$  just under the highest value reported by Salmon-Cox, et al.

Previous investigators have observed that annealing maraging steel above a temperature of about 2000°F has resulted in severe embrittlement, as measured by a loss of Charpy impact strength in aged samples<sup>13</sup>. Attempts to reduce the thermal embrittlement by annealing treatments at intermediate temperatures prior to aging were generally unsuccessful and in some cases led to further embrittlement. The cause of the embrittlement was found to be the precipitation of Ti (C,N) compounds on prior austenitic grain boundaries. Pellissier<sup>14</sup> reports that hot work

which causes sufficient motion of austenitic grain boundaries may provide enough nucleation sites so that the effects of the Ti (C,N) precipitate are minimized.

Banerjee and Hauser<sup>11</sup> report that the Ti (C,N) precipitates occur in continuous networks. In addition to the Ti (C,N) grain boundary precipitates, they found that titanium tends to segregate in regions of reverted austenite during aging. These regions tend to be lamellar and parallel to the rolling plane. Their steel was observed to delaminate during Charpy impact testing.

Bush<sup>15</sup> also investigated the effects of rolling on impact strength. He observed that hot rolling was much more beneficial than either warm or cold rolling.

The present work was undertaken to determine the effects of thermal and thermomechanical treatments on the structure and properties of a 250 grade 18% Ni maraging steel. The as-received material contained laminations parallel to the rolling plane. It seemed reasonable to believe that the laminations might serve as crack arresters if favorably oriented.

## EXPERIMENTAL PROCEDURE

Sheet type tensile specimens were machined with their length in the rolling direction and their width in the long transverse direction (X type) or with their width in the short transverse direction (L type). They were annealed at selected temperatures for one hour to promote grain growth and then cooled to room temperature. All tensile specimens were re-annealed at 1500°F for one hour to minimize variations other than variations in grain size. They were subsequently aged at 900°F for three hours. The tensile gauge length was one inch; the width and thickness were approximately 0.185 and 0.100 inches respectively. All tensile specimens were electropolished prior to testing and all tests were conducted at an engineering strain rate of 0.02 per minute.

Standard size Charpy V-notched specimens were prepared for  $K_{Ic}$  tests in slow bending from plate which had been annealed and cold rolled. These specimens were aged

## RESULTS AND DISCUSSION

### Microstructure

A typical banded microstructure of this 250 grade maraging steel given the standard heat treatment is shown in Fig 2. The area shown is from a section through a Charpy specimen (X type) which had been annealed at 1500°F for one hour and aged three hours at 900°F. In Fig 2, one can distinguish both dark and light etched bands and second phase particles strung out in the rolling direction. The dark etched bands are martensite as is the matrix and the light etched bands are retained austenite, as described in detail by Salmon-Cox, et al.

### Tensile Behavior

The yield stress and tensile stress of this 250 grade maraging steel are affected by annealing temperature and cold rolling prior to aging as shown in Figures 3 and 4, respectively. The prior austenitic grain size begins to enlarge upon annealing above 1700°F. There is no apparent change in the banded microstructure for one-hour anneals at any temperature. A surprisingly different behavior was observed for X type tensile specimens given the same thermal treatments as the L types. The alignment of the banded microstructure with respect to the tensile axis is the same for both X and L types; however, the bands are perpendicular to the wider dimension in the L type and parallel to it in the X type.

The volume fraction of the light and dark bands in our rectangular design specimens was independent of specimen orientation, as was the total interfacial area between the matrix and the bands. However, the fraction of the interfacial area which could offer constraint during axial extension was different. The L-type specimens had the greater fraction of constrained internal surface area,

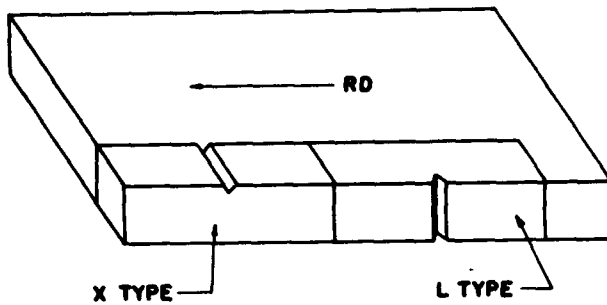


Figure 1. Sketch of 250 Grade Maraging Steel Plate Showing the Orientation of X and L Type Charpy Specimens.

three hours in a neutral salt bath, and then they were pre-cracked by fatigue. Two specimen orientations were used as shown in Fig. 1. In one case the notch was in the rolling plane perpendicular to the rolling direction and the crack propagated in the short transverse direction (X type). In the other orientation the notch was in the short transverse direction, and the crack propagated in the long transverse direction (L type).

Standard size Charpy V-notched specimens that had been fully machined were held at various temperatures in vacuum for one hour to promote grain growth. They were then reheated to 1500°F for one hour and air cooled before aging in order to minimize variations other than variations in prior austenitic grain size. They were then aged for three hours at 900°F in a neutral salt bath. Both orientations were used for impact testing. All tests were conducted at room temperature. The composition of this steel was the following: in wt percent, 18.1 Ni; 8.6 Co; 5.3 Mo; 0.4 Ti; 0.07 Mn; 0.05 Cr; 0.05 Si; 0.002 B; 0.1 Cu; 0.05 Al; 0.002 Zr; 0.016 C; Balance Fe.



Figure 2. Section Through a 1500°F-One Hour X Type Slow Bend Specimen. Nital Etch. 200X.



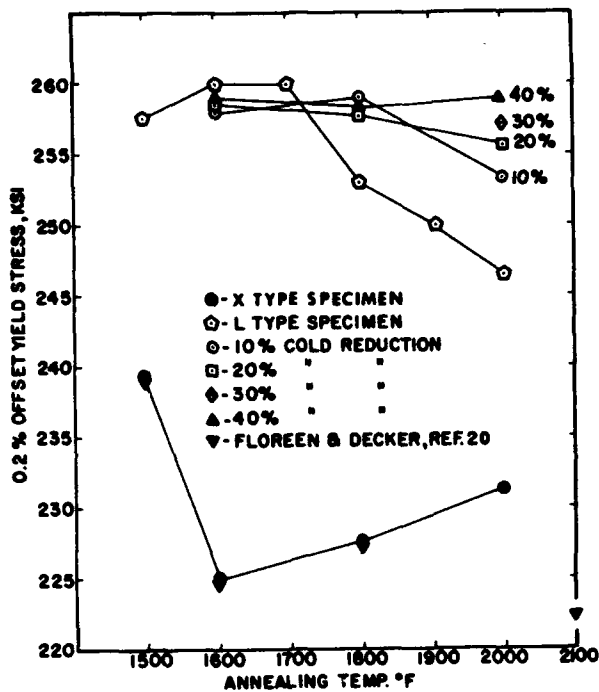


Figure 3. Yield Stress Versus Annealing Temperature for X and L Orientation Specimens of 250 Grade Maraging Steel. All Annealing times are 1 hour followed by a solution treatment and aging. Percent cold rolling as indicated was performed on X orientation material after solution treatment prior to aging.

and they had higher tensile properties. Therefore, the variation of tensile properties with specimen orientation is believed to be a result of this difference in the relative amount of constrained internal surface area.

Material that had been annealed one hour at 1600°, 1800° and 2000°F was rolled various amounts at room temperature prior to aging. Cold rolling prior to aging was reasonably effective in increasing the yield strength of annealed material, although the increase which was observed in the strength of aged specimens was not especially sensitive to the amount of cold work. The variation of aged strength with percent reduction was systematic only at the highest annealing temperature employed. The ultimate tensile stress follows somewhat the same pattern as the yield stress for both the annealed and the rolled material. The percent elongation was about 5% for all specimens.

The increased strength properties resulting from cold rolling this alloy prior to aging are considered to result from the combined effect of the aging reaction and the strain hardening resulting from the stable dislocation struc-

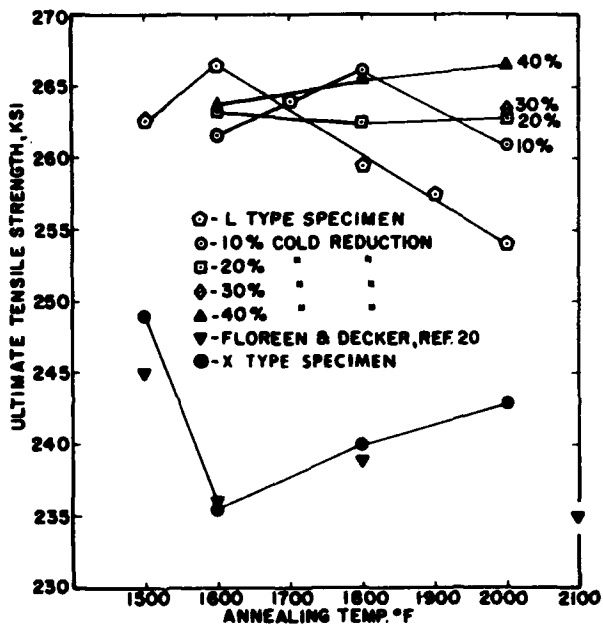


Figure 4. Ultimate Tensile Strength Versus Annealing Temperature for X and L Orientation Specimens of 250 Grade Maraging Steel. All Annealing times are 1 hour followed by a solution treatment and aging. Percent cold rolling as indicated was performed on X orientation material after solution treatment prior to aging.

ture (surviving the 900°F-3 hour age) introduced by the deformation. Also, the deformation was observed to cause transformation of retained austenite which could allow more efficient aging. Previous experience<sup>7</sup> indicates that interactions between the dislocation structures produced by the deformation and the precipitates from the aging reaction become significant above 40% reduction, which was the highest amount used in the present work.

#### Fracture Toughness Behavior

The plane strain fracture toughness was determined from slow bend tests at room temperature using fatigue precracked specimens of standard Charpy geometry. The yield stress of this alloy in the aged condition is high enough that the  $K_{Ic}$  values determined from this type of specimen are considered to be valid. In Figure 5, the  $K_{Ic}$  values are plotted against the yield stress (.2% offset, L type specimens) for material subjected to various thermal treatments. Average values (at least 2 and sometimes 3 tests) are shown for both X and L orientations. Two data points in Figure 5 are for other than one-hour

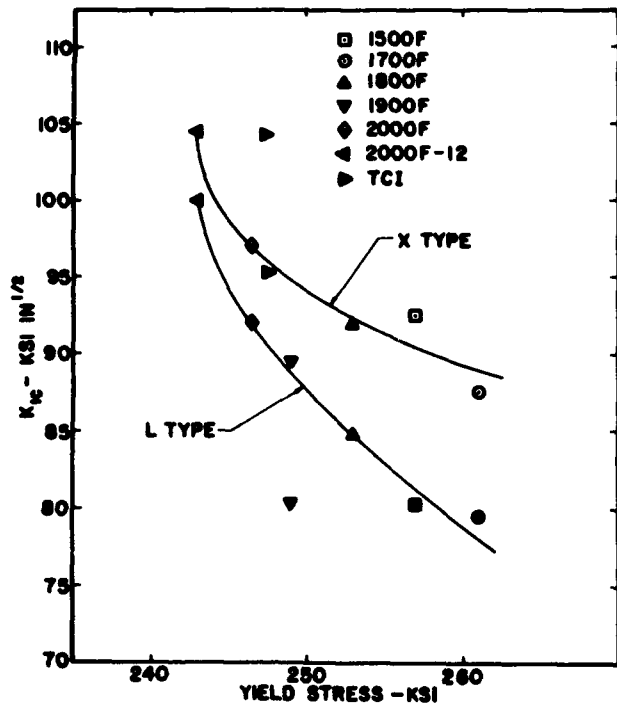


Figure 5.  $K_{Ic}$  Values for X and L Orientations Versus the Yield Stress (L orientation) for the Indicated Thermal Treatments. Specimens 2000-12 were annealed 12 hours at 2000°F. TC1 specimens were annealed 12 hours at 2000°F and cycled five times between 1700°F and room temperature. All other annealing times were one hour.

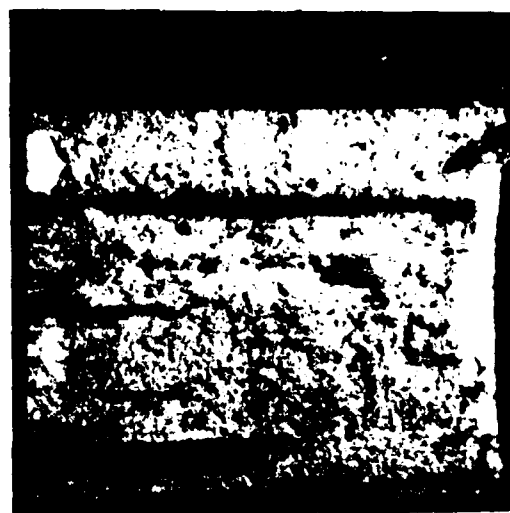
anneals - one for specimens annealed 12 hours at 2000°F and the other for specimens TC1, which were thermally cycled 5 times between room temperature and 1700°F after a 12-hour anneal at 2000°F. This thermal cycling effected a reduction in prior austenite grain size from ASTM 1 to 7, and the process is described in detail by Saul, Roberson, and Adair<sup>16</sup>.

As shown in Fig. 5, in general, the yield stress decreases and the toughness increases as annealing temperature is increased or as the annealing time is increased at the highest annealing temperature. The X or crack-arresting orientation specimens have higher values of  $K_{Ic}$  than the L or crack-dividing orientations for all conditions, although the difference between them becomes less at the higher toughness levels. The TC1 specimens have a higher yield stress than the 12-hour 2000°F annealed ones; however the toughness decreases only for the L orientation. The 1900°F, one-hour specimens are considerably below the trend for both orientations. This temperature may be optimum for a form of thermal embrittlement for the composition of this alloy. The  $K_{Ic}$  values of X and L type specimens given the 1500°F, one-hour thermal treatment are about the same as those reported by Salmon-Cox, et al, although the yield strength of the L type specimens in the present work is considerably higher.

Delamination occurred during fracture of the X type specimens which were annealed one hour. Figure 6 shows fracture surfaces for 1800° and 2000°F, one-hour specimens and they are considered to be typical. The delaminations result when the main crack is split along the banded microstructure, generally associated with retained



1800-1 X  
92-253



2000-1 X  
97-247

Figure 6. Typical Fracture Surface of X Type Slow Bend Specimens Annealed One Hour. The lower numbers are average  $K_{Ic}$  and L orientation yield stress (KSI) values, respectively.



Figure 7. Section Through an 1800°F One Hour X Type Slow Bend Specimen. The main crack growth direction is from top to bottom at the left of the field of view. A diverted crack along the banded structure is shown. Nital etch. 200X.

austenite. Figure 7 shows a section through an 1800°F, one-hour  $K_{Ic}$  specimen; the main crack is to the left of the field of view. Figure 8 shows a section through an X type 1500°F, one-hour  $K_{Ic}$  specimen for which the bend test was stopped prior to complete failure. The splitting of the crack away from the main crack growth direction is apparent. X type specimens of TC1 and 2000°F, 12-hours, on the other hand, exhibited very little tendency toward delamination, as shown in Figure 9. Typical fracture surfaces for L type specimens annealed one hour are shown in Figure 10, where the crack dividing influence of the banded microstructure is apparent. As was true for the X orientation, the L type specimens of TC1 and 2000°F, 12-hours do not have the same fracture appearance as the one-hour annealed samples. It is evident from these results that the additional annealing time at 2000°F resulted in increased homogenization; however, there is still a measurable difference in toughness between the X and L specimens.

Average values of  $K_{Ic}$  versus yield stress for X type specimens deformed prior to aging are plotted in Fig 11. The thermal treatment curve and the 1500°F, one-hour (STD) data point from Fig 5 are included for comparison. For all conditions except the 40% reduction, 1600°F data point, there is a significant improvement in toughness gained from the cold rolling, especially for the 2000°F specimens. In general, the microstructures of these samples after rolling and aging contained less retained austenite

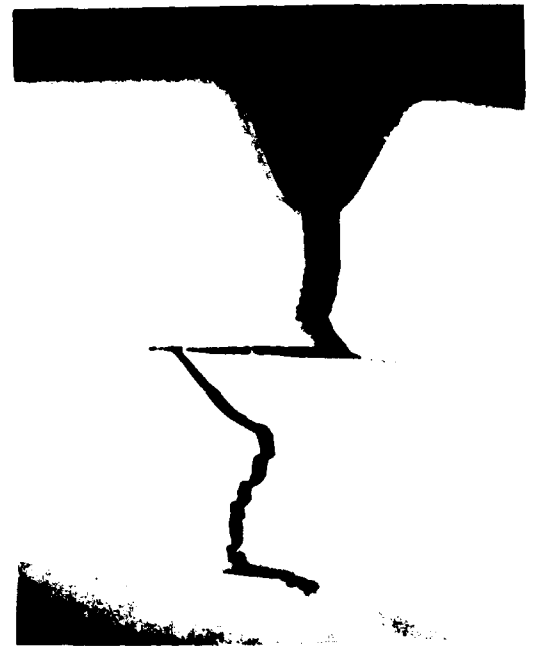
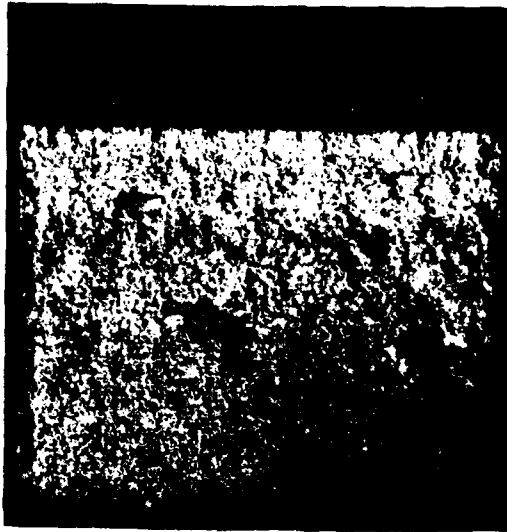


Figure 8. Section Through a 1500°F One Hour X Type Slow Bend Specimen Which Was Not Tested to Failure. Unetched. Approximately 10X.



TC1 X  
104-248



2000-12 X  
105-243

Figure 9. Fracture Surfaces of TC1 and 2000-12 Specimens With the X Orientation. Lower numbers are average  $K_{Ic}$  and L orientation yield stress (KSI) values, respectively.



1800-1 L  
85-253



2000-1 L  
92-247

Figure 10. Typical Fracture Surfaces of L Type Slow Bend Specimens Annealed One Hour. The lower numbers are average  $K_{Ic}$  and yield stress (KSI) values, respectively.

in the bands, and the 2000°F, 40% reduction specimen showed very little retained austenite at all. However, the delamination tendencies of the rolled specimens, as shown in Fig 12, are somewhat greater than for the thermally treated once.

The influence of cold rolling prior to aging on the yield stress-toughness relationship for L type specimens is shown in Figure 13. The thermal treatment curve and the 1500°F, one-hour (STD) data point from Fig. 5 are included for comparison. Rolling prior to aging has a more erratic effect on the L type specimens, where only the 2000°F annealed and worked specimens lie above the thermal treatment curve for all reductions. The  $K_{Ic}$  values of the 1600° and 1800°F annealed and worked samples are very low for samples with a 40% reduction.

### Charpy Impact Behavior

The Charpy impact strength of the X type and L type specimens is shown in Fig. 14. It may be observed in these figures that the impact strength of aged samples was not very sensitive to annealing temperature. The prior austenitic grain sizes were determined by metallographic examination of fractured specimens. From these results it may be inferred that the Charpy impact strength of this steel, when fully heat treated, is not particularly sensitive to prior austenitic grain size. Since each austenite grain

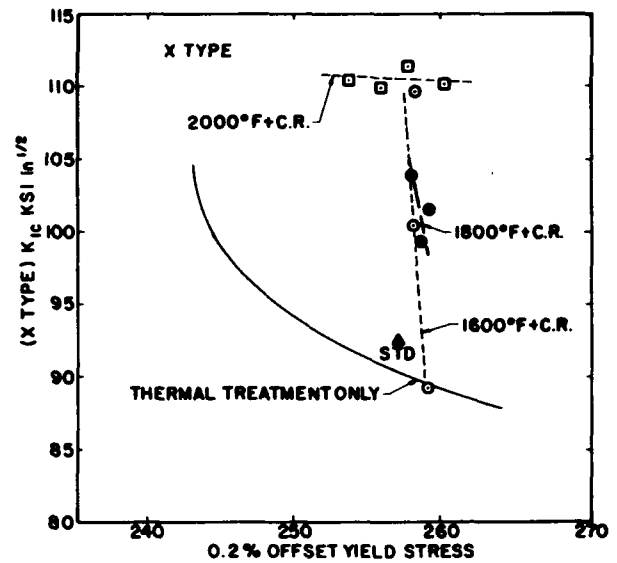
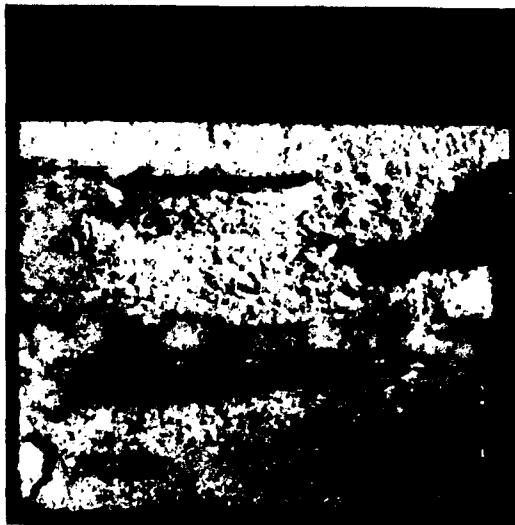


Figure 11.  $K_{Ic}$  Values for X Orientation Slow Bend Specimens Versus Yield Stress for Material Annealed at the Temperatures Indicated and Rolled Prior to Aging.



2000-40% X  
110-260



1600-40% X  
89-259

Figure 12. Fracture Surfaces of X Type Slow Bend Specimens From Material Cold Rolled Prior to Aging. The annealing temperature and percent reduction are indicated. Lower numbers are average  $K_{Ic}$  and yield stress (KSI) values, respectively.

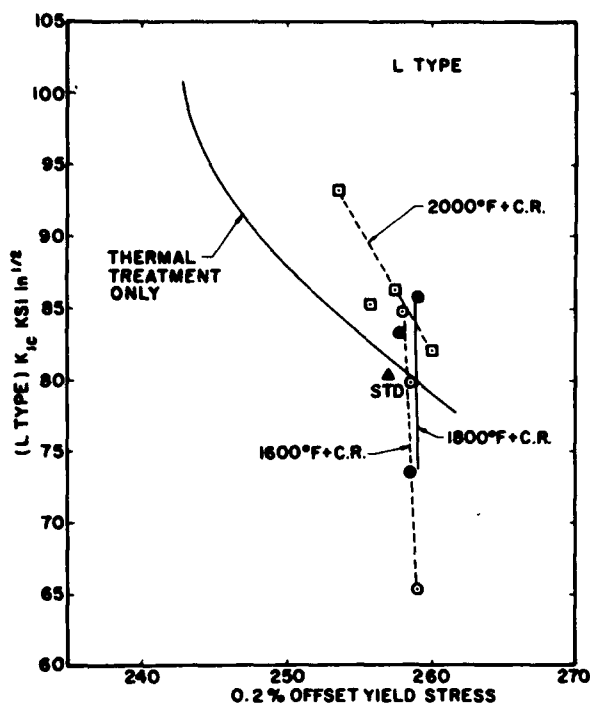


Figure 13.  $K_{Ic}$  Values for L Orientation Slow Bend Specimens Versus Yield Stress (X Orientation) for Material Annealed at the Temperatures Indicated and Rolled Prior to Aging.

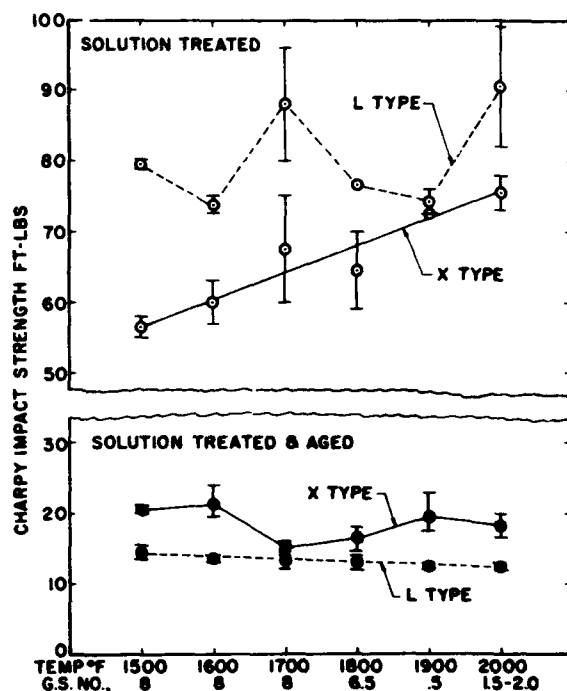


Figure 14. The Effect of Annealing Temperature on the Charpy Impact Strength of 250 Grade Maraging Steel. All annealing times are one hour. Prior austenite grain sizes (ASTM Nrs.) resulting from each annealing treatment are indicated.

transforms to a number of martensite plates during cooling, one might not expect a strong effect of austenitic grain size on impact strength, unless thermal embrittlement has occurred at prior austenite grain boundaries as reported by previous investigators. This does not seem to have occurred in the present work, although segregation at these boundaries was clearly evident in some cases. These results are in general agreement with those of Brikle, Dabkowski, Paulina, and Porter<sup>17</sup>. They reported that the effects of grain size on the impact strength of maraging steel were frequently obscured by other factors.

The effect of prior austenitic grain size on the impact strength of samples in the solution annealed condition was found to be more significant. Fracture in solution annealed samples was accompanied by large amounts of plastic flow. Laminations could be seen in the fracture surfaces, but the effects of delamination seem unimportant (see Fig. 15). It may also be observed in Fig. 14 that the impact strength of the X type specimen is lower in the solution annealed condition and higher in the aged condition than the comparable strength of L type specimens. The fracture strength of solution treated X type specimens in-

creases with annealing temperature, even when the temperature is too low to promote grain growth.

The effects of laminations on fracture path in aged samples are much greater than in solution treated samples. Delamination occurs to a larger extent in both L type and X type specimens. The appearances of the fracture surfaces are quite similar to those previously shown in Figs. 10 and 12. The laminations in X type specimens do serve as crack arresters. A considerable amount of fracture surface is produced which is perpendicular to the nominal direction of crack propagation in these specimens. The laminations in L type specimens cause the crack to advance along an irregular front, but do not necessarily cause crack blunting.

The measured value of fracture energy was not very high with either orientation for aged specimens. This observation tends to indicate that fracture may proceed along the laminations with very little energy loss with any specimen orientation.

In some specimens, cracks were found to propagate

along the lamination even when there was no applied stress acting in the direction which would be required to cause the fracture. The laminations are subject to plastic constraint by the adjacent martensite, and because of the Poisson effect, the laminations were subjected to a transverse tensile stress in the required direction. It seems reasonable to believe that the triaxiality of the stress thus imposed on the lamination is sufficient to suppress plastic deformation and promote low energy fracture.

The fractures observed in the matrix of this steel were always ductile. Fracture in the aged Charpy samples seemed to occur by the nucleation and growth of voids. Floreen<sup>9</sup> reports that this behavior is typical in maraging steels. This process is illustrated in Fig. 16, which was taken from the area at the root of a Charpy notch. In many cases, fracture seems to originate at the interface between the matrix and an unidentified salmon-colored particle. Ten such particles with associated voids are shown in Fig. 16. The area at the upper right of the figure is the root of the Charpy notch. The whole area covered is within a radius of 0.02 inches of the notch tip. In some cases, the particles were fractured, but the usual mode of fracture initiation was interface separation. Voids such as these were never observed in unfractured specimens. These particles were observed throughout the matrix of the steel, and they were also found to be concentrated

in or near the laminations discussed previously. Microprobe analysis indicated that the particles were rich in Ti and that some of them were rich in S.

Previous workers<sup>11,13</sup> have reported the occurrence of  $Ti_2S$  in maraging steels of similar composition.

### GENERAL DISCUSSION

It is important to keep in mind the relative merit of banded structures when considering the fracture behavior of high strength materials. There is no doubt that more energy is absorbed during crack propagation when a crack splits along laminations, is reinitiated to propagate in the main growth direction, splits again, etc. McCartney, Richard and Trozzo<sup>18</sup> observed that a Charpy specimen of high strength AISI 4337M steel, containing two equally spaced nickel plate laminates beneath the notch (crack-arresting) failed to fracture when tested at room temperature, i.e., the specimen absorbed the 120 ft-lbs capacity of the machine. A homogeneous specimen of the same steel absorbed only 13 ft-lbs of energy. Embury, Petch, Wraith and Wright<sup>19</sup> studied the effect of the orientation of laminates in mild steel on the ductile to brittle transition temperature. They found substantial reductions in the transition temperature for crack-arresting Charpy specimens, and less of a reduction for laminated specimens with crack-dividing orientations.

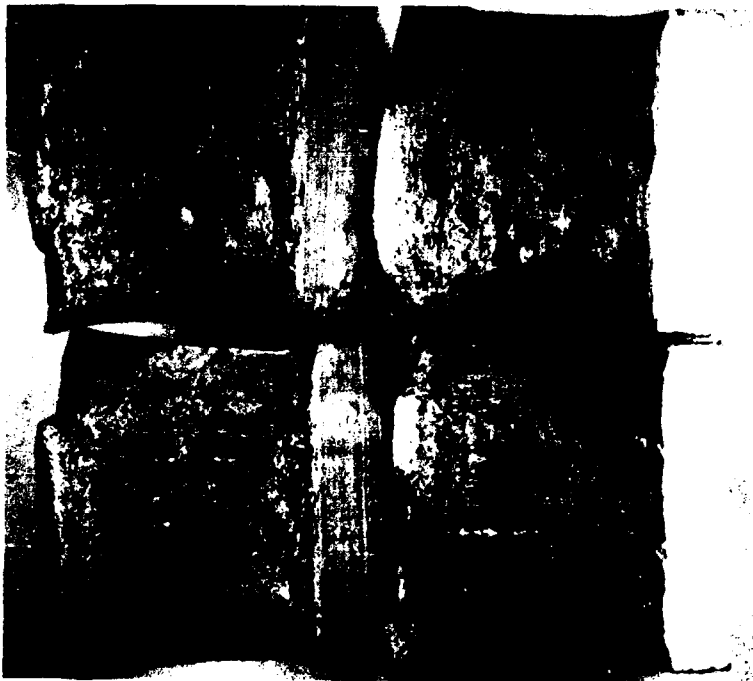


Figure 15. Charpy Impact Specimens Fractured in the Solution Treated Condition. Annealing temperature: left, 2000°F; right, 1500°F. Orientation: top, X type; bottom, L type. 5X.

**Figure 16. Cross Section of Broken Charpy Impact Specimen. Root of Charpy notch is at top right. Fracture initiates at interface of second phase particles. Unetched. 400X.**



The TC1 samples, which showed very little tendency toward delamination, had higher  $K_{IC}$  values for both orientations than did the 2000°F, one-hour annealed samples which delaminated considerably. TC1 and 2000°F, one-hour samples both have about the same yield stress. Working prior to aging was extremely beneficial in increasing the toughness of the 2000°F, one-hour annealed samples, but working was less effective for the 1600°F, one-hour annealed samples. Both the 2000°F, one-hour and the 1600°F, one-hour worked samples showed extensive delamination tendencies.

Thus, the degree of benefit in toughness attributable to a laminated structure is not a simple relationship, but strongly depends on the characteristics of the bulk material, the laminate, and the properties of the interfaces. For a material such as maraging steel with a high inherent toughness, the uniformity of composition and dislocation content and distribution prior to aging may overshadow direct benefits of crack arresters in the structure.

The variation of tensile properties with annealing treatment is also more complex than was originally believed. Floreen and Decker<sup>20</sup> have reported tensile properties for a similar maraging steel as a function of annealing temperature. Their results are compared to the present results in Figures 3 and 4. The agreement is excellent for tensile specimens taken parallel to the rolling plane, but there is a striking difference between these specimens and those with their width perpendicular to the rolling plane (L type). In general, the austenitic grain size increases with annealing temperature and the degree of homogeneity increases slightly with annealing temperature.

If one considers the width perpendicular specimens only, there is a reasonable correlation between yield stress and prior austenitic grain diameter (the Hall-Petch relationship), but this relationship does not exist for specimens taken from the rolling plane (X type). The  $K_{IC}$  results for specimens thermally treated only were plotted against the yield stress for the width perpendicular specimens because their yield stress varied in a more reasonable fashion. The disparity between the tensile properties for specimens with different orientations is not fully understood, but there can be no doubt that this effect is a result of the inhomogeneous microstructure and the geometry of our sheet type tensile specimens.

#### **SUMMARY AND CONCLUSIONS**

1. The tensile and fracture behavior of maraging steel with a banded microstructure is strongly influenced by prior history and is very sensitive to specimen orientation with respect to the rolling plane. Higher fracture toughness and higher Charpy impact values result when specimens are of the crack-arresting type rather than the crack-dividing type. The increased toughness results in part from splitting of the main crack along the banded structure but the orientation dependence persists even when the material is homogenized to the extent that delamination no longer occurs during fracture.
2. Cold working this alloy in the solution treated condition following a 2000°F, one-hour anneal results in an optimum combination of high yield stress and fracture toughness.
3. The yield stress of this alloy is more strongly affected by specimen orientation with respect to the banded microstructure than it is affected by prior austenitic grain size alone.



## REFERENCES

1. I.L. Cheng and G. Thomas, *ASM Trans. Quart.*, 61: 14-25 (1968).
2. M.J. Roberts and W.S. Owen, *ASM Trans. Quart.*, 60: 687-692 (1967).
3. G.R. Speich and P.R. Swann, *J. Iron Steel Inst. (London)*, 203: 480-485 (1965).
4. R.F. Decker, J.T. Eash, and A.J. Goldman, *ASM Trans. Quart.*, 55: 58-76 (1962).
5. E.B. Kula and C.F. Hickey, Jr., *Trans. Met. Soc. AIME*, 230: 1707-1712 (1964).
6. C.J. Nolan and T.E. Davidson, *ASM Trans. Quart.*, 62: 271-277 (1969).
7. J.A. Roberson and A.M. Adair, *Trans. Met. Soc. AIME*, 245: 1937-1941 (1969).
8. S. Floreen and G. R. Speich, *ASM Trans. Quart.*, 57: 714-726 (1964).
9. S. Floreen, *Met. Rev.*, 13/126: 115-128 (1966).
10. *Fourth Maraging Steel Project Review*, AFML-TDR-64-225, Vol. I, Air Force Materials Laboratory, Wright-Patterson AFB, Ohio (1964).
11. B.R. Banerjee and J.J. Hauser, AFML-TR-66-166, Air Force Materials Laboratory, Wright-Patterson AFB, Ohio (1966).
12. P.H. Salmon-Cox, B.G. Reisdorf, and G.E. Pellissier, *Trans. Met. Soc. AIME*, 239: 1809-1817 (1967).
13. C.J. Barton, B.G. Reisdorf, P.H. Salmon-Cox, J.M. Chilton, and C.E. Oskin, Jr., *Investigation of Thermal Embrittlement in 18% Ni (250) Maraging Steel*, AFML-TR-67-34, Air Force Materials Laboratory, Wright-Patterson AFB, Ohio (1967).
14. G.E. Pellissier, *Eng. Fracture Mech.*, 1: 55-75 (1968).
15. R.H. Bush, *ASM Trans. Quart.*, 56: 885-887 (1963).
16. G. Saul, J.A. Roberson, and A.M. Adair, *Trans. Met. Soc. AIME*, 1: 383-387 (1970).
17. A.J. Birkle, D.S. Dabkowski, J.P. Paulina, and L.F. Porter, *ASM Trans. Quart.*, 58: 285-301 (1965).
18. R.F. McCartney, R.C. Richard, and P.S. Trozzo, *ASM Trans. Quart.*, 60: 384-394 (1967).
19. J.D. Embury, N.J. Petch, A.E. Wraith, and E.S. Wright, *Trans. Met. Soc. AIME*, 239: 114-118 (1967).
20. S. Floreen and R.F. Decker, *ASM Trans. Quart.*, 55: 518-530 (1962).

# FATIGUE PERFORMANCE OF HIGH STRENGTH STEELS AS RELATED TO THEIR TRANSFORMATION MECHANISM

by

Maria Ronay

Columbia University \*  
New York, New York

## INTRODUCTION

The endurance limit of quenched and tempered high strength steels generally increases with tensile strength. For tensile strength up to 200 ksi, the ratio of endurance limit to tensile strength is about one half. Above 200 ksi the increase of endurance limit with increasing tensile strength becomes gradually less and less. As fatigue failure in such materials starts at stress concentrations inherent in the material (or in the engineering structure) it is generally believed that the increasing sensitivity to stress concentrations with increasing material strength, thus decreasing toughness, provides sufficient explanation for this phenomenon. According to this concept the major trend in improving the fatigue performance of high strength steels is to reduce by vacuum melting processes the number and size of inclusions that initiate fatigue failure.

The development of high toughness, high strength, maraging type steels has provided steels with a decreased sensitivity to stress concentrations and a very low inclusion content; therefore the fatigue performance of these steels was expected to be superior to that of the quenched and tempered high strength, low toughness, air melted steels. As these expectations were not fulfilled, in fact the fatigue performance of maraging steels is inferior to that of the quenched and tempered steels of the same strength<sup>1</sup>, reasons other than sensitivity to inclusions must be considered. In the work to be reported here the fatigue performance is related to the mechanism of phase transformation that statically strengthen these materials. The testing conditions were such as to be relevant to aircraft fatigue.

## MATERIAL

Fatigue tests were conducted on an 18 Ni 300 grade maraging steel. The steel was supplied in the solution-annealed condition (1500°F) as 1.2 in. x 7 in. flats having

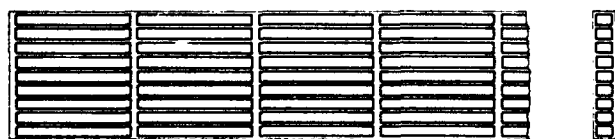


Figure 1. Machining of fatigue specimens from the flats.

\* Presently at IBM Thomas J. Watson Research Center, Yorktown Heights, New York.

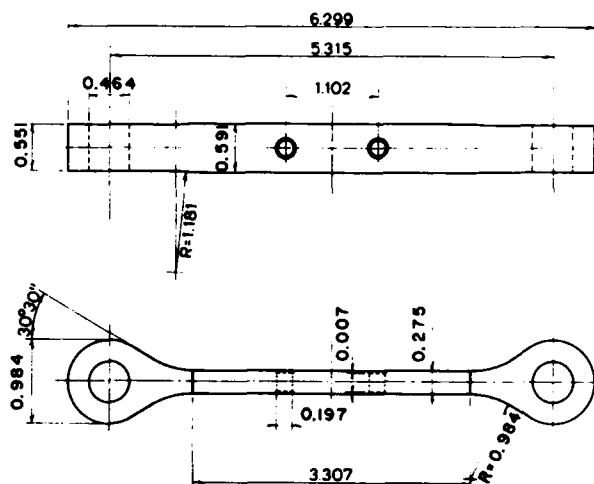


Figure 2. Notched fatigue specimen<sup>2</sup>.

the analysis shown in Table I. The mechanical properties as measured on 0.32 in. diameter specimens after aging at 900°F for 3 hours are given in Table II.

## FATIGUE TESTS

The fatigue specimens were machined from the flats as shown in Figure 1 with consecutive numbering of specimens. The fatigue tests were conducted on notched specimens, the geometry of which is given in Figure 2. This

TABLE I  
ACTUAL AND STANDARD CHEMICAL COMPOSITION  
OF 18 NI (300) MARAGING STEEL.

	ACTUAL	STANDARD
C (wt pct)	0.011	0.03 max
Mn	0.03	0.10 max
Si	0.01	0.10 max
P	0.003	0.010 max
S	0.004	0.010 max
Ni	18.56	18.50
Co	9.21	9.00
Mo	4.82	4.80
Al	0.10	0.10
Ti	0.65	0.60
B	0.003	0.003
Zr	0.010	0.02
Ca	0.05	0.05

**TABLE II**  
**ACTUAL AND STANDARD MECHANICAL PROPERTIES OF SOLUTION –**  
**ANNEALED AND AGED 18 NI (300) MARAGING STEEL.**

DIRECTION		0.2 PCT YS KSI	UTS KSI	R.A. PCT	ELONGATION $\delta_5 = 5.65\sqrt{A}$
actual	long.	270	279	39.5	8.0
actual	long.	272	283	48.8	7.7
actual	trans.	263	273	39.8	7.7
standard requirement (SNV-L 419.4)	long. trans.	252–294	259–301	(45)	5

fatigue specimen shape resembles closely enough frequently occurring construction parts in airplanes<sup>2</sup>. The ready specimens were aged at 900°F for 3 hours.

The specimens were tested on a six-bar fatigue test bed developed, designed and built in the Swiss Federal Aircraft Establishment.

This testing machine was developed to apply history loading simultaneously to 6 specimens in order to obtain a scatter band in one test, eliminating scatter caused by machine or loading program deviations. Description of the testing facility can be found in Reference 2.

The specimens were tested with VENOM History Program II<sup>2</sup>. History program is a fatigue loading program which simulates the fatigue history of an aircraft. The first such program developed by Branger is the VENOM Program<sup>3,4</sup>. This fatigue program simulates the service history of one particular fighter plane (VENOM) under the particular service and gust conditions of Switzerland. It is im-

portant to note that the actual sequence of loads is strictly observed. A schematic representation of history loading is given in Figure 3<sup>2</sup>.

The specimens were tested in axial loading. The ratio R of compressive to tensile load amplitudes was equal to  $R = -0.3$ , an important assumed amplitude ratio in aircraft design. The tests were run at 240 cpm. One of each 6 specimens was electropolished for subsequent metallographical investigation.

The results of the fatigue tests are represented in Figure 4.<sup>†</sup> The abscissa gives the number of periods of the history program leading to fatigue failure. One period of the history program is defined as the return period of the peak load. It represents 350 different flights; the number of load cycles in one period is about 39,000, from which about 1,700 cycles are equal or higher than 50% of the peak load<sup>2</sup>. The ordinate of Figure 4 gives the absolute magnitude of the peak stress in the history program. It is the measure of the severity of loading within the application of a certain pro-

Scheme of History Loading

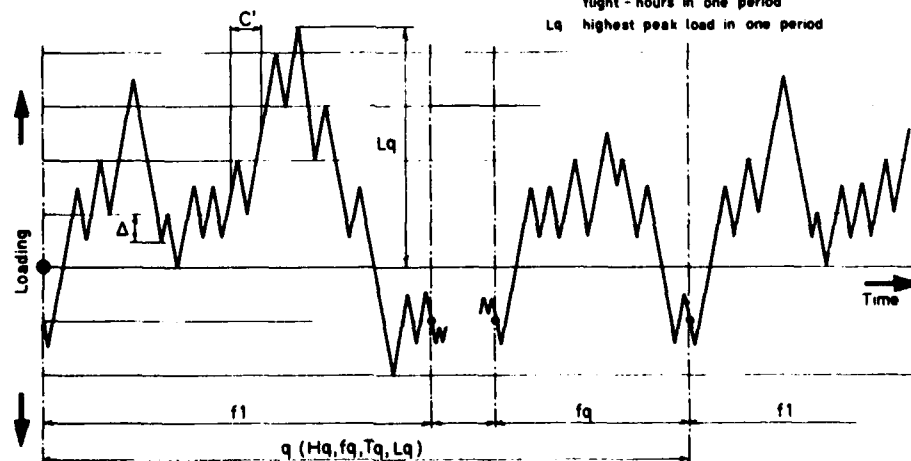


**Figure 3. Schematic representation of history loading<sup>2</sup>.**

<sup>†</sup> Fatigue lives of electropolished specimens are not included in this diagram as they were not cycled until failure.

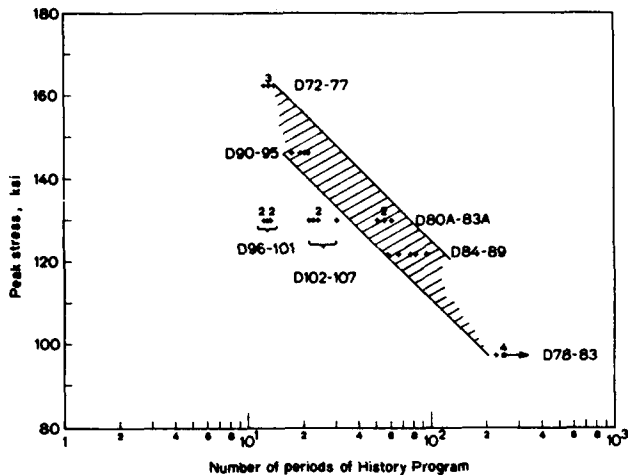


Figure 4. Fatigue lives of 18 Ni (300) Maraging Steel specimens under history program fatigue.

gram and also defines the magnitude of the other (smaller) load cycles.

The fatigue lives of specimens D 96-101 were very short in relation to lives at other stress levels; therefore tests at this stress level (128 ksi) were repeated. This resulted in fatigue lives still too short (D 102-107) to fit an assumed S-N relation. For the third repetition of this test specimens were not taken with further increasing numberings (Figure 1) but from the other end of the flat. The specimens of this third test (D 80 A - 83 A) fractured at lives falling in the middle of the bounded S-N relation with a scatter than can be considered small for a high strength steel. It must be noted that the scatter in fatigue lives is relatively small at every stress level except for specimens D 96-107.

The reason for the distribution of fatigue lives

seemed to be a local heterogeneity in the microstructure.

### THE MICROSTRUCTURE OF MARAGING STEEL

The microstructure of fatigue specimens that failed within the bounded S-N relation was the one that is considered normal in 18 Ni maraging steels (Figure 5). Specimens D 96-107 were however a more or less pronounced mixture of two different microstructures: a light etching and a dark etching one.

The structure of specimen D 102 is represented in small magnification in Figure 6. It consists of dendrites, a remainder of the cast structure. The dendrites are of the light etching structure while the interdendritic space is filled with the dark etching structure.

At a larger magnification it can be seen that the dark etching microstructure is made up of packets of parallel plates, (also called "laths")<sup>5</sup> which are oriented at an angle of about 60° to each other, forming occasionally an equilateral triangle (Figure 7).

The light etching microstructure as revealed by a larger magnification is a massive or granular structure, the same as the normal structure of maraging steel. Figure 8 shows a mixture of the light etching and of the dark etching microstructures in specimen D 96.

A detailed study of the same maraging steel reported elsewhere<sup>6</sup> revealed that the composition of this steel is such that by air cooling it is on the boundary of two microstructures: bainite and martensite. The dark etching microstructure was identified as martensite and the light etching microstructure as granular bainite.



Figure 5. Microstructure of fatigue specimens failing within the bounded S-N relation. Etchant Marble's reagent. (500X.)

**Figure 6. Dendritic structure of specimen D 102. Marble's reagent. (8X.)**



**Figure 7. The dark etching microstructure of specimen D 96 consisting of packets of parallel plates oriented at 60° to each other. Marble's reagent. (500X.)**

**Figure 8. Mixture of the dark etching and of the light etching microstructure, the later being a massive or granular structure. Specimen D 96. Marble's reagent. (500X.)**



A very interesting phenomenon was observed in these mixed bainitic-martensitic structures, and is demonstrated in Figure 9. As the bainitic transformation takes place first in the course of cooling, the parallel plates of martensite are reflected at the boundaries of the already existing bainitic islands. They are also partly reflected at the boundaries of previously formed packets of martensite plates, partly penetrate them, similar to the behavior of waves. As a result of this reflection and the crystallography<sup>6</sup> of this transformation, the martensite plates form equilateral triangles in any little region left untransformed by the bainitic transformation as can further be seen in Figure 10.

Surface shears on prepolished specimens have shown



**Figure 9. The packets of parallel plates of the dark etching martensitic microstructure are reflected at the boundaries of the already existing light etching bainitic microstructure. They are partly reflected at the boundaries of previously formed packets of parallel martensite plates, and partly penetrate them, similar to the behavior of waves. Specimen D 96. Marble's reagent. (1000 X.)**

that frequently the formation of these triangular shapes takes place in a way that the martensite plates go without interruption around three sets of parallel crystallographic planes inscribing a family of equilateral triangular shapes as it is presented in Figure 11.

#### **ON THE FORMATION OF MARTENSITE AS RELATED TO FATIGUE**

During the martensitic transformation of Fe-30 Ni alloy, pronounced mechanical vibration of the sample was observed, induced apparently by the strain waves generated during transformation<sup>7,8</sup>. The rate of propagation of martensite has been measured by the resistance change during transformation, and Bunshah and Mehl<sup>9</sup> reported a

Figure 10. The dark etching martensite forms equilateral triangles at any little region left untransformed by the light etching bainite. Specimen D 96. Marble's reagent. (1000 X.)



velocity of about one-third of the velocity of (elastic) shear waves in the austenite matrix. Recent experiments of Mukherjee<sup>8</sup> confirmed this result. Of the theories describing the formation of martensite plates, the only theory that yields explanations consistent with the observations is a mechanism based on propagation of the transformation strain as a shear wave<sup>10</sup>.

We assume that in the case of lath (massive) martensite the propagation of the transformation is by reflection of this strain wave.

The transformation strain wave is most frequently reflected at the austenite grain boundary. If the austenite

grain contains three of the energetically equivalent  $\{111\}_A$  planes<sup>†</sup>, the reflected strain wave can go around along three sets of parallel planes inscribing a family of equilateral triangular shapes as shown in Figure 11 and schematically in Figure 12a. Of course later in the course of propagation not a neighboring grain but an already existing neighboring martensite plate serves as the reflecting boundary. (This was also demonstrated in Figure 9.)

More frequently the orientation of a crystallite is such that less than three sets of octahedral planes provide the potential path for the reflected strain wave. In the case of formation of a "packet" of parallel plates which is very characteristic of lath (massive) martensite, reflection is



Figure 11. Surface shears on prepolished specimen D 102. The martensite plates go around three sets of parallel crystallographic planes inscribing a family of equilateral triangular shapes. Dark field illumination. (2300 X.)

† The crystallography of martensitic transformation in 18 Ni (300) maraging steel is discussed in Reference 6.

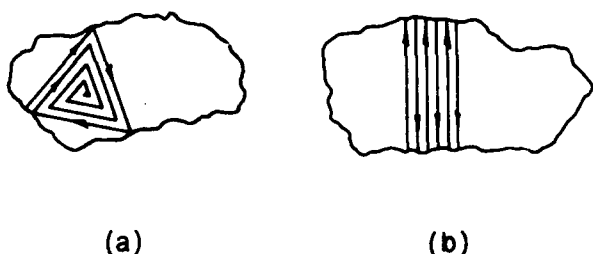


**Figure 12. Schematic representation of two cases of transformation strain wave reflection in lath (massive) martensite: (a.) If the austenite grain contains three sets of the energetically equivalent  $\{111\}_A$  planes, the reflected strain wave can go around along these planes inscribing a family of equilateral triangular shapes. (b.) In the case of formation of a "packet" of parallel plates, reflection is confined to one set of parallel planes so that the reflection of the transformation strain wave results in reversed shearing of alternate plates.**

confined to one set of parallel planes so that the reflection of the transformation strain wave results in reversed shearing of alternate plates as shown schematically in Figure 12b. Thus the "lateral" growth of martensite packets takes place by the addition of new plates resulting from reversed shear in a direction perpendicular to the "lateral growth". This is quite well demonstrated though not recognized in the microphotographs of Yeo<sup>11</sup> and Marder<sup>12</sup>.

It may be assumed that the energetically favorable martensitic transformation by reflected waves of reversed homogeneous shearing of alternate plates proceeds with relatively little resistance because the Bauschinger effect reduces the critical yield stress in reversed shear.

Either of the two mechanisms of shear wave reflection illustrated in Figure 12, or a combination of both, will lead to a stabilization with proceeding transformation of the microstructure by dissipation through slip of the elastic strain energy stored in the crystal lattice. However, some of the elastic strain energy will be transferred to the incompatibility centers that are being build up along the reflecting grain boundary due to localized unresolved slip processes, a concept to which we return later.

With reference to the proposed mechanism of shear wave reflection, mechanism a (Figure 12a) is demonstrated in Figures 9, 10, and, particularly in Figure 11. For the existence of reversed shear, mechanism b (Figure 12b) the following evidence is presented:

1. In the martensitic transformation of indium-thallium alloys both the first and the second shear occur in alternating opposite senses<sup>13</sup>, reversed shear has thus been found in at least one martensitic transformation.

Figure 13a shows the prepolished surface of specimen

D 102 after the martensitic transformation; Figure 13b shows the prepolished surface of annealed O.F.H.C. copper after  $10^5$  cycles of  $\pm 45 \times 10^{-4}$  reversed surface shear<sup>14</sup>. The similarity of the two microstructures, the existence of concentrated slip bands - a characteristic consequence of reversed shear - on the surface of maraging steel suggests that the martensitic transformation proceeds by reversed shearing.

2. After the martensitic transformation, the surface contour of the prepolished surface of specimen D 102 was taken by the Microcorder. This is an electro-mechanical instrument which drives a tracer over the surface being tested. The tracer translates the surface irregularities into voltage changes. The voltage change is being fed after amplification to the recorder, producing a chart. Such a chart is presented in Figure 14. It shows notches and peaks characteristic of reversed shearing clearly different from the surface contour resulting from unidirectional straining. This phenomenon is widely discussed in the fatigue literature.

3. Floreen has found very coarse, localized slip on the polished surface of an iron-18 percent nickel binary alloy after applying as little as 2.0 percent unidirectional strain<sup>15</sup>. On the other hand the experiments of Kemsley on high-conductivity copper showed that coarse and localized slip bands were found on the polished surface after and around a hardness impression if the previous deformation of the sample was either very large (30 percent unidirectional strain) or small but reversed<sup>16</sup>. The propensity for slip to be concentrated in localized bands characteristic of the deformation of 18 percent nickel binary lath (massive) martensite suggests that the transformation strain was reversed.

The characteristic dislocation cell structure of lath (massive) martensite is also characteristic of fatigued metals. While strains as small as  $\pm 0.002$  (0.2 percent) are sufficient to develop a cell structure in fatigue<sup>17</sup>, similarly well-developed cell structure was observed after 35 percent unidirectional straining<sup>18</sup>; both authors using 99.99 percent aluminum and transmission electron microscopy. As the martensitic transformation strain is in the range of microplasticity, the cell structure established by such small strains suggests that they are reversed.

## DISCUSSION

If we assume that the massive martensitic transformation in many locations proceeds by the transformation strain being reversed then this martensitic structure is similar to the structure of fatigued metals. Such similarity has been observed<sup>2</sup> and pointed out in this paper with respect to both the microstructure and the dislocation structure. A consequence of reversed shearing in fatigue is the accumulation of strain incompatibilities at the strain reflecting boundaries, and these unresolved incompatibilities were assumed to be one of the reasons for failure initiation in fatigue<sup>14</sup>. Similar incompatibility centers are possibly built up along



Figure 13a. Prepolished surface of specimen D 102 after the martensitic transformation; (1000 X.)

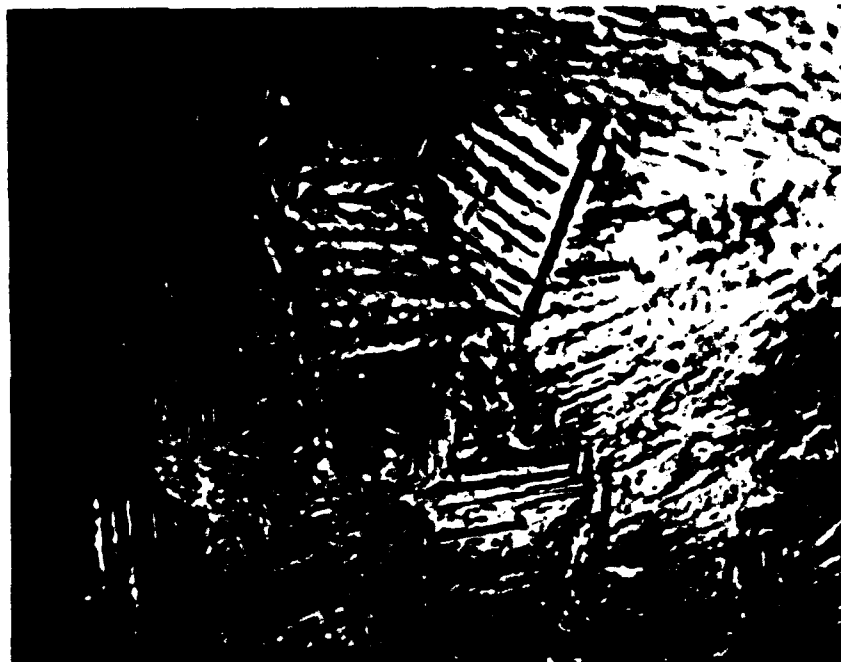


Figure 13b. Prepolished surface of annealed pure copper after  $10^5$  cycles of  $\pm 45 \times 10^{-4}$  reversed surface shear<sup>14</sup>. (500 X.)



the reflecting boundaries due to reflected reversed transformation strain waves, and it is conceivable that such a structure has not much resistance to subsequently applied reversed shearing, as the capacity of the structure to accommodate microstrains has been exhausted by the transformation. This mechanism would explain the relative low fatigue resistance of massive martensitic steels.

The results of fatigue tests on a heterogeneous maraging steel reported here proved only that a mixture of martensite with granular bainite is inferior in fatigue to gran-

ular bainite alone. To prove that martensite formed by reflected, reversed shear waves has a poorer resistance to fatigue than a granular microstructure, one should compare the fatigue performance of these microstructures alone.

Figure 15 shows the microstructure of quenched and tempered 4335 steel. It consists of martensite transformed by reflected and reversed shear waves, and no other microstructures have been found in this steel.

Figure 16 shows the microstructure of quenched and

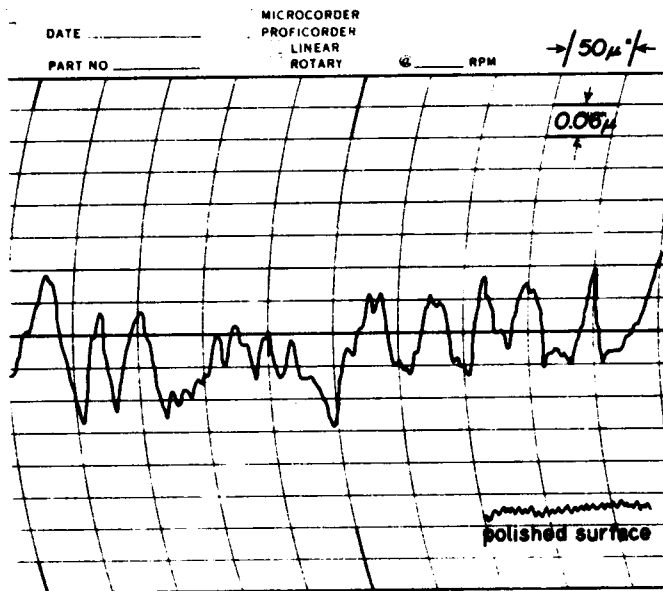


**Figure 14. Surface contour of the prepolished surface of specimen D 102 after the martensitic transformation as taken by the Microcorder.**

tempered 5 Ni-Cr-Mo-V (HY 130). The special etching revealed a very fine homogeneous granular microstructure.

Both steels were tested in the Swiss Federal Aircraft Establishment under the same conditions as the ones reported here. 4335 failed after 14 periods of the history program with a peak load that was 80 percent of the statically permissible limit load, while HY 130 failed after 80 periods with a peak load that was 107 percent (!) of the statically permissible limit load.

While the fine granular HY 130 proved to be so ex-

cellent in fatigue that the phenomenon of fatigue can be neglected in design, in 4335, the macroscopic crack propagation started already after the first period, showing the lack of any resistance against reversed loads. This happened in spite of the fact that the steel was melted in vacuo, displaying a very low inclusion content. Details of this research will be reported elsewhere<sup>19</sup>.

The most important thing to stress is that the 4335 steel is tempered at 480°F - a temperature too low to permit a structural change in martensite. HY 130 however was tempered at 1130°F, and at this temperature it seems that a recrystallization or at least polygonization of martensite took place, resulting in the formation of superfine grains. The fine granular structure of tempered steels was related in the past to the precipitation of spheroidal carbides. This view can not be held for steels of very low carbon content, where fine grains are formed by the matrix rather than by carbide precipitates.

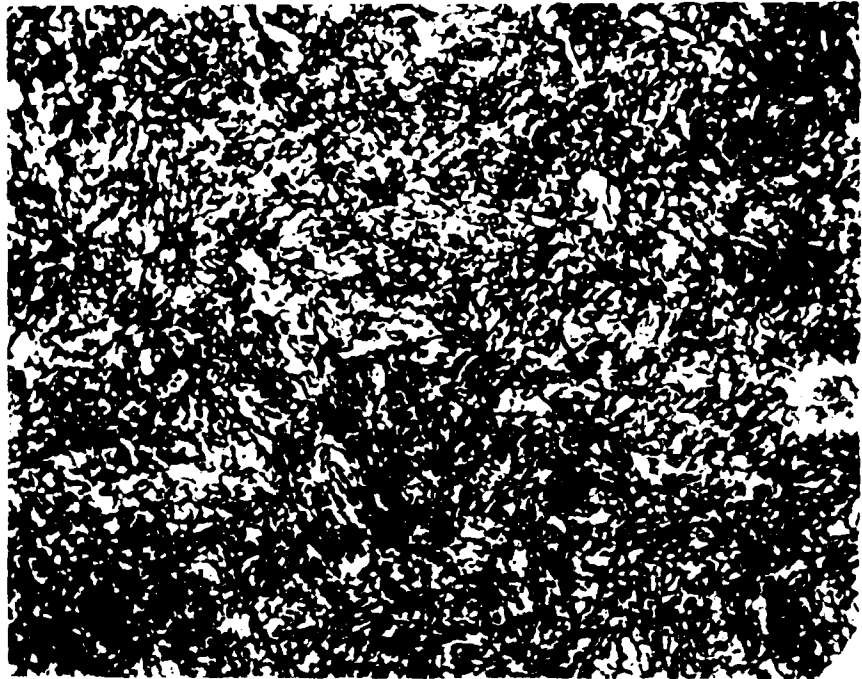
If a recrystallization of martensite is the prerequisite of good fatigue performance then the decay of relative fatigue strength from 200 ksi tensile strength on may easily be related to tempering temperatures too low to decompose martensite, since tempering temperatures are decreased in order to increase tensile strength. As the temperature of recrystallization as well as polygonization depends on alloy content, tempering of steels of a very high alloy content at relatively high temperatures may still preserve the martensite.

It is suggested that steels developed for good fatigue performance should not have the untempered martensitic microstructure formed by reflected reversed shear waves. As the extent of shear wave reflection is possibly dependent

**Figure 15. Microstructure of quenched and tempered 4335 steel. Etchant 5 percent Nital. (1000X.)**



Figure 16. Microstructure of quenched and tempered 5 Ni- Cr-Mo- V (HY 130). Etchant modified Marble's reagent, afterwards 5 percent Nital. (1000 X.)



on austenite grain size, this effect should also be considered.

Steels developed for good fatigue performance, however, should have a superfine granular structure. To this end the process of high temperature tempering of low carbon martensites should be reexamined, particularly with respect to the formation of a superfine granular structure.

It seems that the mechanism of martensitic transformation and the mechanism of tempering of martensite are important in establishing a resistance to reversed loads, and improvement of fatigue performance should be sought along these lines rather than along the lines of reducing inclusion content.

#### ACKNOWLEDGEMENT

The fatigue tests reported in this paper were done in the Swiss Federal Aircraft Establishment, Emmen, under the Exchange Agreement between Columbia University and the Eidgen. Technische Hochschule (Federal Institute of Technology) in Zurich, in which both the Eidgen. Flugzeugwerk (Federal Aircraft Establishment) and the Eidgen. Material-prufungs und Versuchsanstalt (Federal Materials Testing and Research Center) participate.

The author is deeply indebted to chief engineer J. Branger of the Federal Aircraft Establishment, who planned the research program on the fatigue performance of high strength steels in aircraft structures, in the framework of which present work was done. Mr. Branger developed the unique testing facilities and was in charge of the fatigue tests reported here. Many thanks are due to him for many illuminating discussions, for his continuous support and encouragement.

## REFERENCES

1. G.P. Contractor, *Kobalt*, No. 33:163-175 (1966).
2. J. Branger and M. Ronay, *Investigation of High Strength Steels Under History Program Fatigue, Part 1*, TR-56, Institute for the Use of Fatigue and Reliability, Columbia University, New York (1968).
3. J. Branger, *Second Seminar on Fatigue and Fatigue Design*, TR-5, Institute for the Use of Fatigue and Reliability, Columbia University, New York (1964).
4. J. Branger, *The VENOM Program*, S-197, Swiss Federal Aircraft Establishment, Emmen, Switzerland.
5. A.B. Greninger and A.R. Troiano, *Trans. AIME*, 140:307-336 (1940).
6. M. Ronay, *Study of a Heterogeneous 18 Ni, 300 Maraging Steel*, TR-64, Institute for the Use of Fatigue and Reliability, Columbia University, New York (1969).
7. E.S. Machlin and M. Cohen, *Trans. AIME*, 191:746-754 (1951).
8. K. Mukherjee, *Trans. Met. Soc. AIME*, 242:1495-1501 (1968).
9. R.F. Bunshah and R.F. Mehl, *Trans. AIME*, 197:1251-1258 (1953).
10. E.S. Machlin and M. Cohen, *Trans. AIME*, 191:1019-1029 (1951).
11. R.B. Yeo, *ASM Trans. Quart.*, 57:48-61 (1964).
12. J.M. Marder and A.R. Marder, *ASM Trans. Quart.*, 62:1-11 (1969).
13. J.S. Bowles and C.S. Barrett, "Crystallography of Transformations," pp. 1-41; B. Chalmers, Ed., *Progress in Metal Physics*, Vol. III, Interscience, New York (1952).
14. M. Ronay, *Acta Tech. Acad. Sci. Hung.*, 54 (1-2):199-218 (1966).
15. S. Floreen, *Trans. Met. Soc. AIME*, 230:842-849 (1964).
16. D.S. Kemsley, *Phil. Mag.*, 2:1103-1104, Pl. 43 (1957).
17. J.C. Grosskreutz, *J. Appl. Phys.*, 34:372-379 (1963).
18. R.L. Segall and P.G. Partridge, *Phil. Mag.*, 4:912-919, Pl. 100-104 (1959).
19. J. Branger and M. Ronay, to be published.

**SESSION 2B**

**CRITERIA**

*Chairman*

Lt. Col. C.K. Grimes  
Air Force Flight Dynamics Laboratory

*Co-Chairman*

W.J. Mykytow  
Air Force Flight Dynamics Laboratory

## MINER'S LAW: WHAT PRICE CONFORMITY?

by

H.A. Lipsitt and D.F. Frank

and

G.C. Smith

Aerospace Research Laboratories  
Wright-Patterson AFB, Ohio

Department of Metallurgy  
University of Cambridge  
Cambridge, England

### INTRODUCTION

Miner's Law<sup>1</sup> for cumulative damage accumulation in fatigue was written to describe the stages of multi-stress fatigue up to the time a visible crack appeared in a material in which no work hardening occurs. It is obvious that this rule does not strictly apply to many of the situations for which it has been used. However, it has come into wide and continuous usage to describe the whole of fatigue life for a great many materials because its predictions are, on the whole, conservative. Because of its obvious simplicity and slightly conservative predictions, its limitations have been first overlooked and then forgotten.

Lipsitt<sup>2</sup> has previously presented results aimed at rationalizing the failures of Miner's Law. It was shown that a linear damage rule was inadequate because:

- a. The number of cycles required to initiate a crack of a given length is not a linear function of stress.
- b. The rate of crack growth at constant engineering stress increases exponentially with crack length; crack growth rate is also a complex function of stress in a multi-stress situation.
- c. It is possible that discontinuities in crack growth rate may occur with each stress change.
- d. More total crack penetration can be tolerated prior to fracture as the (engineering) stress is lowered.

Laird and Smith<sup>3</sup> have shown that it is possible to achieve linear crack growth rates by maintaining a constant stress at the tip of a propagating fatigue crack. Thus, it appeared possible to achieve the conditions necessary for cumulative fatigue damage to be linearly related to both stress and the number of cycles applied.

This research was an attempt to validate Miner's Law for fatigue crack propagation. It was also possible to ascertain the nature and magnitude of any discontinuities in crack growth rate which might accompany a stress change. The conditions employed were:

a. To use a metallurgically stable, well work hardened material so that almost none of the applied work would be used to alter the microstructure.

b. To precrack the specimen sufficiently so that all the fatigue damage was Stage II crack propagation (by ripple growth). This is necessary to eliminate both crack nucleation and Stage I (or slip plane) propagation.

c. To maintain constant stress at the crack tip by decreasing the applied load proportionately as the crack propagates. It has been shown<sup>3</sup> that in this event the Stage II ripple width, and therefore the crack propagation per cycle, remains constant.

d. To employ a simple high-low or low-high load cycle so as to reduce any disturbances in crack growth rate which may accompany the stress changes.

### EXPERIMENTAL MATERIAL AND METHOD

This experiment was performed with a fairly high purity unalloyed aluminum. The material was obtained through the courtesy of Major P.C. Varley of the British Aluminium Company as a 1-1/2" diameter rod which had been hot extruded from an 8" diameter billet. The rod was then cold rolled to a 13/16" square cross-section through the courtesy of Mr. A. Cibula of the British Non-Ferrous Metals Research Association. A chemical analysis of the barstock indicated that the major impurities were 35 ppm Cu, 20 ppm Si, 40 ppm Fe, 20 ppm Mg, 10 ppm S, and 8 ppm Zn. The material in the cold-rolled condition exhibited a yield stress (at 0.1% offset) of 10,100 psi, an ultimate tensile strength of 11,400 psi and, at fracture, 26% elongation and 95% reduction in area.

Edge notched specimens, as shown in Figure 1, were machined from the barstock and tested in the cold-rolled condition. Testing was performed in an Instron machine using a load cycling device to apply a sinusoidal load function and an area compensating device to maintain nearly constant stress on the remaining net section. Reverse stressing, usually at 9500 or 10,000 psi, was used to allow a Stage II crack to form at the notch root. When a single crack was propagating nicely the

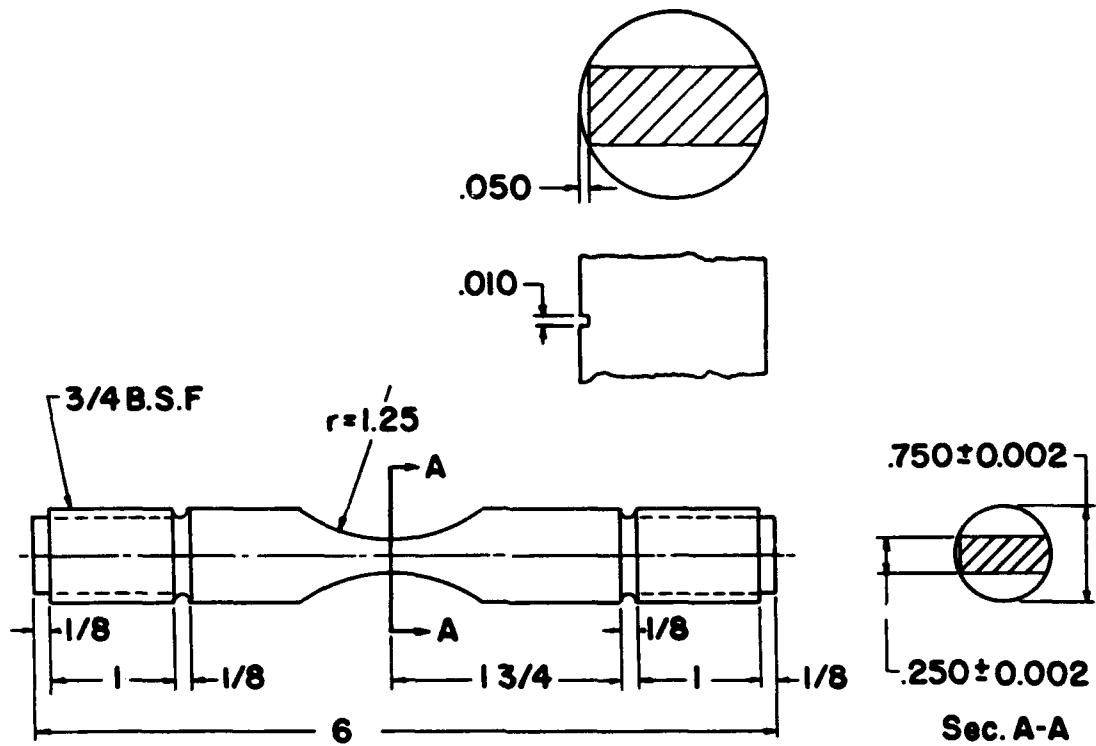


Figure 1. Fatigue Specimen.

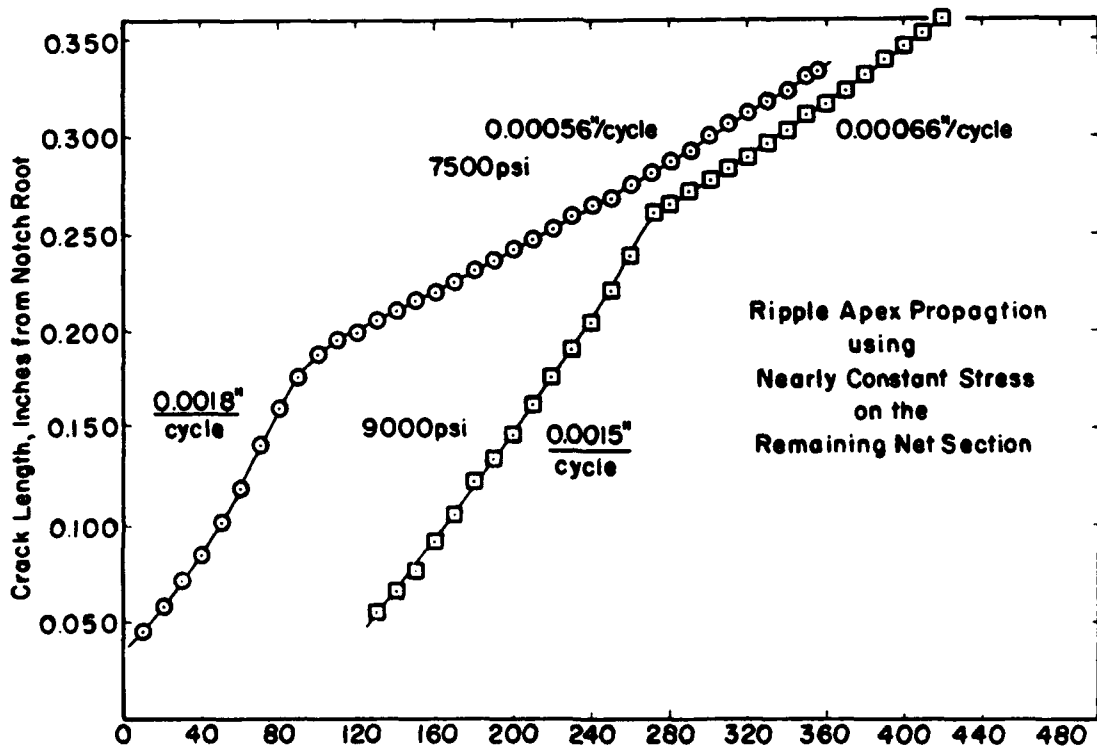


Figure 2. Cycles of Crack Growth (Arbitrary Zero).



**Figure 3. Fracture Surface of High-Low Specimen (64X).**



stress was suddenly reduced to 9,000 psi on the remaining net section. The area remaining was determined by following the crack growth with a traveling micrometer microscope. The net stress was readjusted after each 0.004" of crack propagation for which the area change was computed to be about 0.001 sq. in. When essentially linear crack propagation had been observed for about 100 cycles, the stress was suddenly lowered to a computed 7,500 psi on the remaining net section. This condition was usually maintained for several hundred cycles until the area compensating device arrived at the end of its adjustment. At this time, the crack length was about 0.330", or, including the notch, about half way across the specimen diameter. At this point, the stress was again increased to 9,000 psi (to provide a demarcation line on the fractured surface) and the specimen was allowed to fail in the normal way.

Following the fatigue test the specimen fracture surface was photographed at 50x, and the ripples counted and measured. Early experiments in this program showed ripple markings which were sensibly straight across the specimen. However, for some undiscoverable reason, the specimens discussed here did not behave as expected: the crack fronts were convex in the direction of motion. This introduces two errors into the stress control calculations. There is a stress error due to the presence of the convex crack front and another arising from its movement. For a typical specimen this meant that the actual stress, when cycling, increased from about 9,400 to 9,700 psi as cycles were accumulated at the nominal stress of 9,000 psi. On making the transition to a nominal 7,500 psi the actual stress dropped to about 8,000 psi, and increased with continued cycling to about 8,300 psi. These errors cause the ripple width to increase slightly as the crack length increases.

## RESULTS

The initial results in this program are shown in Figure 2. Other data for this high-low sequence have been obtained using a manually controlled Losenheim machine. These are qualitatively similar to those in Figure 2, but are not presented here because they show considerably greater scatter due to the uncertainties of manually reducing the load by small increments. One test in Figure 2 has been made to accentuate propagation at the

high stress and the other to show greater linear growth at the lower stress. Those latter data actually continue linearly beyond the graph to a length of 0.400".

Figure 3 shows the ripples on a fracture surface just before, during, and just following a high-low stress transition. Figures 2 and 3 taken together show several things. It may be seen that, at least under these conditions of testing, there are no spurious effects occurring immediately following the stress change. This has also been shown previously<sup>3</sup>. It may also be noted that there is a very slight increase in ripple width as the crack grows at nearly constant stress. It is most likely that this is due to the fact that it was not possible to hold the stress absolutely constant, and that the slow increase in stress is reflected in the slowly changing ripple width.

## DISCUSSION AND CONCLUSIONS

The data show that fatigue damage under these conditions is essentially linear at each stress. Thus, Miner's Law has been validated for the first time.

But at what price? The conditions and precautions necessary for this experiment are vastly different than those encountered in actual service. The obvious conclusion, then, is the same as that from our previous research; Miner's Law should not be applied to a cumulative damage situation involving crack formation and propagation under the usual conditions of engineering service.

"But, Miner's Law works," you might say, "and more, it is usually even a shade conservative which provides aircraft designers with a much-needed margin of safety." We would certainly agree. "Well, then," you might say, "Why on earth did you do this research?"

This research has been done because it is known that Miner's Law is only fortuitously valid. However, it has worked so well that many of its flaws have been glossed over. These results merely serve as a reminder of the fortuitous nature of the agreement found in cumulative damage fatigue data. In addition, the constraints necessarily applied to achieve this complete agreement pinpoint the exact areas where new information could lead to the formulation of a much more precise cumulative damage rule.

## REFERENCES

1. M.A. Miner, "Cumulative Damage in Fatigue," *J. Appl. Mech.*, 12: A159 (1945).
2. H.A. Lipsitt, "Crack Propagation in Cumulative Damage Fatigue Tests," *Proc. 11th AF Sci. Eng. Symp.* (1964).
3. C. Laird and C.G. Smith, "Crack Propagation in High Stress Fatigue," *Phil. Mag.*, 7: 847 (1962).

# APPLICATION OF THE RESIDUAL STRENGTH CONCEPT TO FATIGUE DESIGN CRITERIA

by

D. J. Trent\* and I. Bouton\*\*

Space Division, North American Rockwell Corporation  
Downey, California

## INTRODUCTION

A new concept of the fatigue problem was developed during a recent USAF/AFFDL study contract.<sup>1</sup> The approach involves considerations that are fundamentally different from those used in most other fatigue analysis procedures. The principal difference is that residual strength, rather than life, is used as the significant fatigue parameter. In fatigue analysis, life is not a physically meaningful concept. Freudenthal has noted that "fatigue failure is, in essence, an ultimate load failure, but one involving a fatigue-damaged structure, and therefore, occurring under a terminal load of considerably lower intensity...."<sup>2</sup> No structure ever failed mechanically simply because it exceeded some number of operational hours. Fatigue failure in an aerospace structure occurs only when a static load is applied that exceeds the residual strength of the structure. Although residual strength is primarily influenced by repeated low-magnitude loads, the life at failure usually depends on the occurrence of an infrequent high load. For example, consider a fighter airplane that has experienced significant fatigue damage as it approaches its design life. If low loads are being experienced when the life is exceeded, as in a navigational training flight,

the structure will not fail. However, if a high load is experienced at any time near the supposed end of life, the structure will fail. Failure must always be the result of a load, at a particular instant of time, which exceeds the strength at that particular instant of time.

The residual strength approach to fatigue allows a new look at the statistical aspects of the fatigue problem. Just as the initial strength in a group of similar structures will vary, so will the residual strengths of these same structures vary at a later time during the life of the structure. The probability of fatigue failure in service can be assessed in terms of the statistics of the strength distribution and the load distribution, with either or both a function of time. A similar analysis can be made of test failures, and their relationship to service failures can be established. If the required statistics can be obtained, the residual strength approach may prove to be the means of achieving practical fatigue design criteria.

Very little data are available to indicate the shape of a curve of residual strength as a function of time. A few static tests of fatigue-damaged structures and material coupons, and some basic reasoning, lead us to expect a

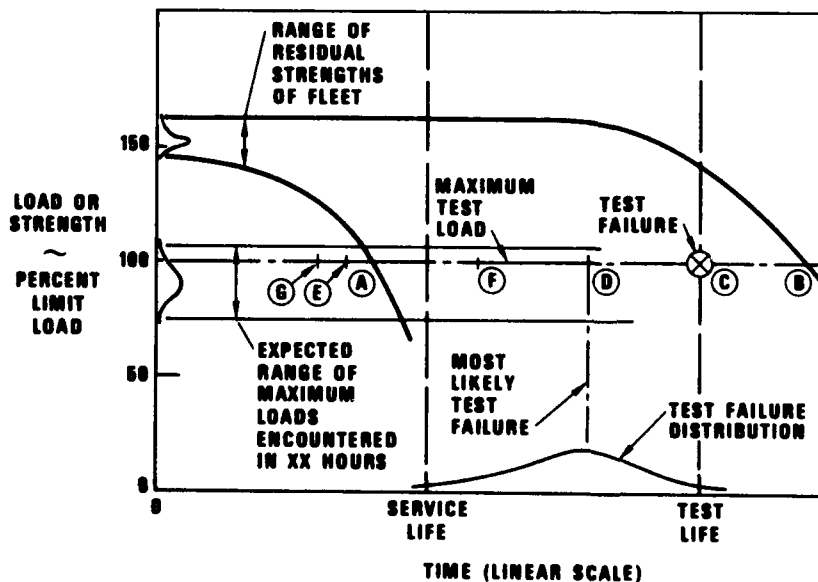


Figure 1. Typical Residual Strength Distribution.

\* Now with Martin Marietta Corp., Denver Div.; Denver, Colorado.

\*\* Now with Technology Incorporated, Information Systems Div.; Dayton, Ohio.

large amount of statistical variation in the strength of structures that have experienced fatigue damage. If these statistical variations can be defined, the probability of fatigue failure can be expressed in terms of the statistics of the residual strength distribution and of the loading distribution.

## DISCUSSION

### Strength Scatter and Life Scatter

The scatter in residual strength of fatigue-damaged structure is closely related to, but is not the same as, the large life scatter typical of fatigue data. If a structure at the high (low) extreme of the static strength distribution is assumed to also be at the high (low) extreme of the fatigue strength distribution, curves may be drawn describing strength percentiles throughout the life of the structure. Figure 1 shows schematically the range of the residual strength distribution of a structure subjected to a prescribed fatigue loading spectrum. In this example, the basic loading spectrum consists of repeated blocks of loads, each representing XX hours of service loading. The number XX is arbitrary but usually represents 1 to 10 percent of the design life.

The 1-percent-exceed and the 99-percent-exceed curves of a structure's residual strength are represented by the two curves of Figure 1. If the highest load in each loading block is limit load, the points A and B on Figure 1 define the range of life wherein most test failures occur. The distribution of times to failure will be approximately as shown on Figure 1 by the curve labeled "test failure distribution." Since the test failure will occur under the maximum repeated test load, the distribution of test failures is closely related to the maximum load. On the other hand, the strength degradation function is more the result of the greater numbers of loads of lesser magnitude. It is generally recognized that the maximum load, which

is repeated only a few times, will have little effect on the fatigue damage.

The failure distribution in actual service may be different from that experienced in testing, even though the test is an exact representation of the strength degradation produced by service loading. This is because high loads are distributed differently in the two cases. The test loading distribution is always truncated at the maximum load applied during the test, while the service loading spectrum contains a finite probability of loads higher than the maximum test load. This is illustrated in Figure 1.

The purpose of the fatigue test is to disclose those designs whose residual strength range is such that the vehicle will too often fail in service before the desired service life is achieved. This concept of testing has been advanced for static tests in previous papers.<sup>3,4</sup>

### Probability of Failure

If the load and strength distributions are known during any small time interval, the probability of failure during the interval can be computed by well-known mathematical procedures. Figure 2 presents a typical curve showing the increase in failure probability with increasing time. From Figures 1 and 2, it is seen that most of the early failures contributing to the failure probability must occur at loads corresponding to the lower boundary of the strength distribution.

The curve in Figure 2 represents service failures. In a testing program, no failure will occur until the strength of the test article is degraded to the magnitude of the highest test load. Because loads in service will sometimes exceed the maximum test load, however, some service failures will occur before the first test failure is expected. In

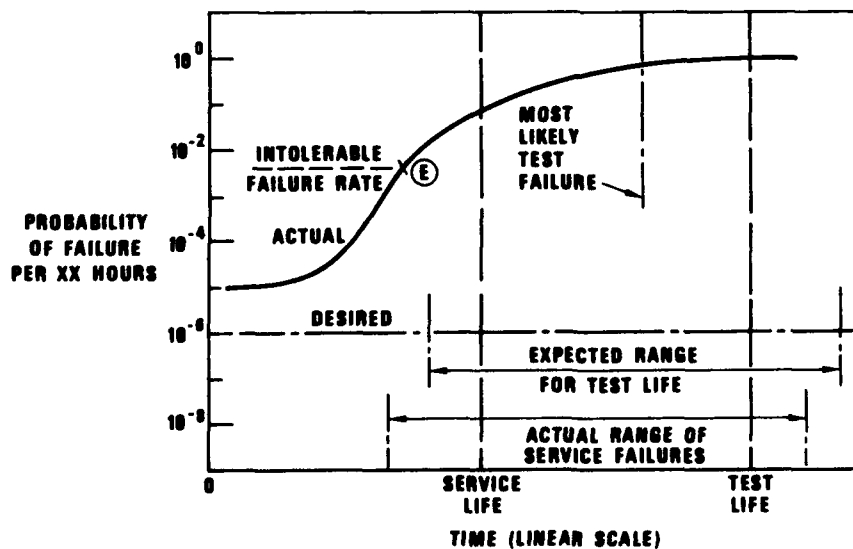
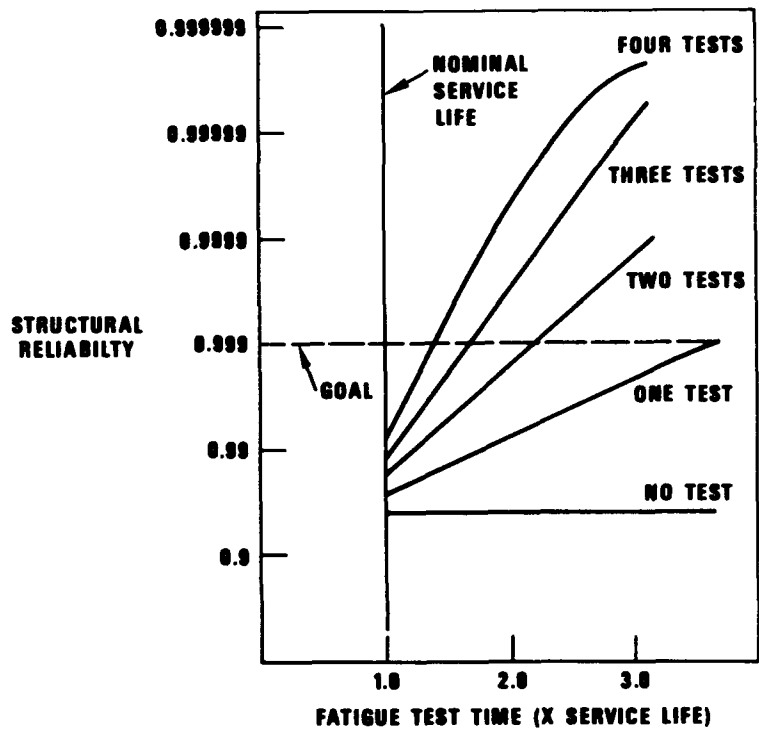


Figure 2. Hypothetical Failure Probability vs. Time.

Figure 3. Effect of Number of Fatigue Tests on Structural Reliability.



fact, an ordinary fatigue test failure usually occurs at a time corresponding to a period in service when the failure rate has already reached an intolerable level.

The exact magnitude of the intolerable failure rate depends upon the circumstances. For example, if the fleet size is 1000 and the failure probability exceeds  $10^{-3}$ , the failure rate will certainly be intolerable. If, in the fleet of 1000, one failure occurs every XX hours, it will not take many XX periods before one, two, or five failures occur. Clearly, this represents an intolerable rate for the fleet. As shown in Figure 2, the time when the failure rate becomes intolerable may be somewhat below the range for expected test failures. Recognizing this fact, we have in the past required the test life to be some multiple of the service life (typically 2X to 4X).

#### Limitations of Available Procedures

In the decade since the 1957 Fatigue Symposium,<sup>5</sup> the record of fatigue failures indicates that available analytical and test procedures are as yet insufficient to solve the fatigue problem. This is due to the complexity of fatigue phenomena and to the lack of testing procedures that can reliably eliminate weak designs. This is illustrated by Figures 1 and 2. Figure 1 shows a typical time for test failure at C. This is somewhat higher than the most likely value at D. However, any value between A and B cannot be considered unexpected. Figures 1 and 2 show a permissible service life which is one half of the test life. As previously described, the life at which the failure rate, E, is intolerable

(Figure 2) is less than the permissible service life in this hypothetical example. The test failure at time C might be considered to be a random success where an unacceptable design was falsely accepted.

On the other hand, if the test failure occurs as far below the mean test life as C is above, there will be no such problem. A test failure at F will result in a permissible service life G (one half of F) which is below the time at which the failure rate is intolerable. Thus, the permissible service life resulting from either of two failures in the expected range will be acceptable in one case and unacceptable in the other.

The relationship between A and B, the range of expected test failure times, and E, the time when the failure rate becomes intolerable, depends on the characteristics of the residual strength distribution. When the uncertainty of this distribution is coupled with the wide range of expected test failures, there is a large uncertainty in the magnitude of the ratio between the permissible service life (E or less) and the time of the test failure. The question is: how can we define the separation between the time of test failure C (or F) and the time for intolerable failure rate E so that the permissible service life can be designated as a value that will always be less than E?

#### Effect of Testing Procedures

The effect of various testing procedures on the reliability of structures was studied<sup>1</sup> and some typical re-

sults computed. These results, presented in Figures 3 and 4, are for a particular set of parameters described in Reference 1. Although the figures illustrate the relative value of various types of tests, the actual reliability numbers are useful only for purposes of illustration.

Figure 3 shows the conditional reliability of the structure resulting from various combinations of test life and number of independent fatigue tests. For example, if the structural reliability goal is 0.999, a design is acceptable if the test article survives to a test life 3.7 times the specified service life. If two articles are tested independently, the test life can be reduced to 2.2 times the service life. For four test articles, the test life needs to be only 1.5 times the service life.

The required testing time can be reduced if the fatigue-damaged structure is tested statically to failure. The advantage of this type of test is that the load-carrying ability of the structure is measured under conditions that correspond more closely to service failure conditions than those provided by the conventional fatigue test. Figure 4

shows the conditional reliability of the example structure resulting from combinations of test life and number of independent fatigue tests, with each fatigue test followed by a static test to failure. For a structural reliability goal of 0.999, a design is acceptable if it sustains ultimate load following a fatigue test to 1.2 times the service life.

## SUMMARY

The residual strength concept is presented as a new approach to the fatigue design problem. The ideas and examples developed to date indicate that the approach has merit because it leads to fatigue criteria that are more closely related to the load-carrying ability of the structure than are conventional criteria. Much work remains to be done before such criteria can be developed and the advantages of the residual strength concept exploited. The objective of this paper has been to stimulate thinking in this direction. Continued development of the residual strength concept could be the key to improved fatigue criteria.

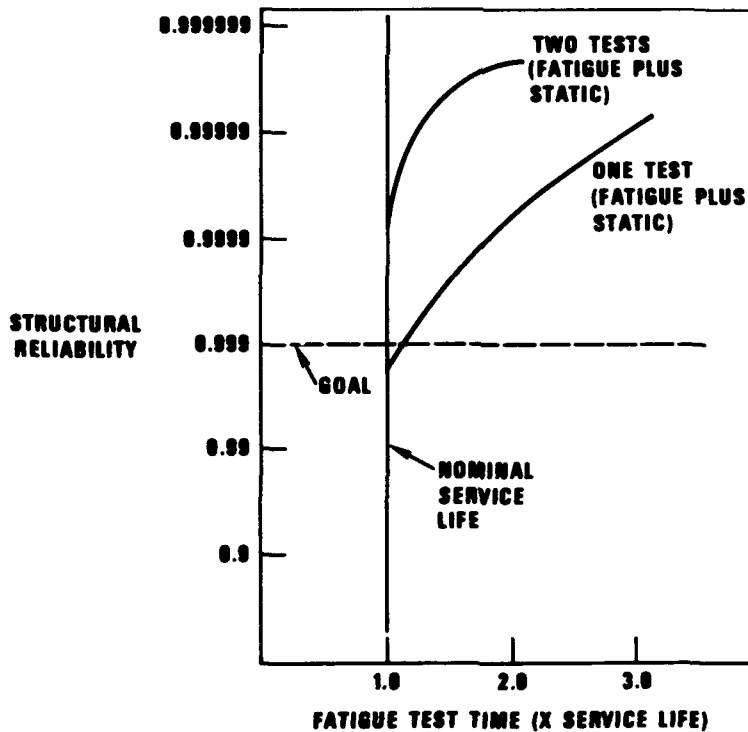


Figure 4. Effect on Structural Reliability of Static Test at End of Fatigue Test.

## REFERENCES

1. I. Bouton, D. J. Trent, M. Fisk, and A. H. McHugh, *Quantitative Structural Design Criteria by Statistical Methods*, AFFDL-TR-67-107, Vols. I-III, Air Force Flight Dynamics Laboratory, Wright-Patterson AFB, Ohio (1968).
2. A. M. Freudenthal, *Life Estimate of Fatigue Sensitive Structures*, AFML-TDR-64-300, Air Force Materials Laboratory, Wright-Patterson AFB, Ohio (1964).
3. I. Bouton and D. J. Trent, *Test Factor of Safety: A New Means for Proving Compliance With Structural Reliability Requirements*. Presented at the 8th AIAA Structures, Structural Dynamics, and Materials Conference, Palm Springs, California, March 1967.
4. I. Bouton and D. J. Trent, *The Unreliability of Structural Reliability*, ASM-TR-P9-12.4. Presented at the ASM Materials Engineering Congress, Philadelphia, Pennsylvania, October 1969.
5. *Proceedings of the Symposium on Fatigue of Aircraft Structures*, WADC-TR-59-507, Aeronautical Systems Division, Wright-Patterson AFB, Ohio (1959).

# FATIGUE LOADINGS ON COMMERCIAL TRANSPORT AIRPLANES

by

Thomas L. Coleman and Paul A. Hunter

NASA Langley Research Center  
Langley Station, Hampton, Va.

## INTRODUCTION

The judicious provision of adequate fatigue strength in commercial transport airplanes requires reliable data on the repeated loads likely to be experienced during many years of operations. One of the major sources of such data is the NASA operational data collection program which is conducted in cooperation with manufacturers and airlines. This program provides statistical data on the normal acceleration experience and the airspeed and altitude practices of commercial transport airplanes. For each successive generation of airplanes, analyses of the data have provided information on the magnitude and frequency of occurrence of accelerations (which can be related to loads) due to various sources, such as gusts and maneuvers, and on the effect of airplane characteristics and operating practices on the loads.

The most recent summaries of the repeated loads on transport airplanes are those given in References 1 and 2. Reference 1 summarized the statistical loads data collected on piston- and turbine-powered transports from 1947 to 1965 and provided information on the trends in the repeated loads spectra with the evolution of the transports. Reference 2 updated the summary of loads data given in Reference 1 primarily by the inclusion of some initial data samples collected on light jet transports. Subsequent to the Reference 1 and Reference 2 studies, additional data samples on 2-, 3-, and 4-engine jet transports have been obtained.

In this paper, all of the statistical loads data which are available from turbojet and turboprop transports will be discussed. The data to be presented pertain to the repeated loads resulting from atmospheric turbulence, maneuvers, landing contact, and ground operations. The primary aims of the discussion are: (1) to show the variation of the repeated loads among several types of 2-, 3-, and 4-engine jet transports and (2) to show the effect of operator on the repeated loads of given types of transports. In addition, selected data samples are presented to illustrate the variability of fatigue loads among airplanes of a given type operated by a single airline. Also, the effect of sample size on the data is shown.

## INSTRUMENTATION AND RECORD EVALUATION

The data were obtained with the NASA VGH recorder which is described in detail in Reference 3. Consequently, only a brief description of the recorder and the type of record obtained is given. A picture of the VGH recorder is shown in Figure 1. The recorder consists of three major components: the recorder base, the attached film recording drum, and the acceleration transmitter. The transmitter is usually installed within 5 feet of the center of gravity of the airplane, whereas the recorder base may be mounted at any convenient location within the airplane. The installed weight of the VGH recorder is 20 to 25 pounds.

An illustrative VGH record is shown in Figure 2. It is a time-history record of indicated airspeed, pressure

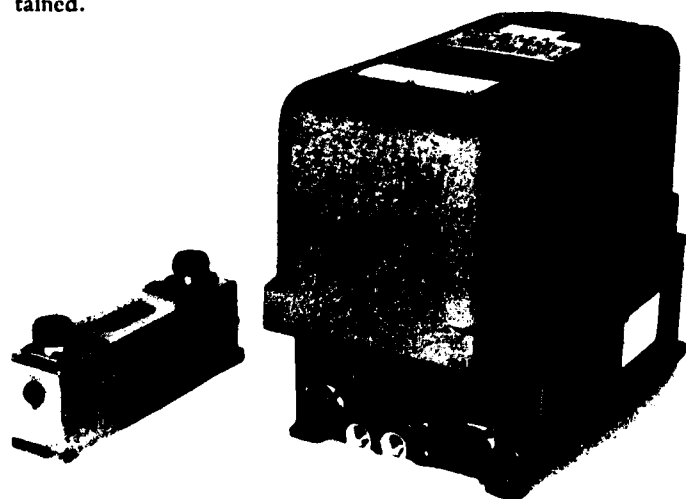


Figure 1. Instrumentation.

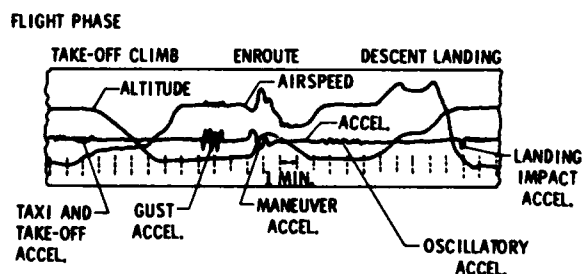


Figure 2. Illustrative VGH Record.

TABLE I.  
AIRPLANE CHARACTERISTICS

AIRLINE SERVICE	AIRPLANE TYPE	PROPULSION	MAX. GROSS WEIGHT, LB.	WING AREA, FT <sup>2</sup>	WING LOADING, LB/FT <sup>2</sup>
SHORT HAUL	A	2-engine turbofan	76,500	980	78.1
	B	2-engine turbofan	90,700	925	98.1
	C	2-engine turbojet	110,231	1579	69.8
	D	3-engine turbofan	152,000	1650	92.1
LONG HAUL	E	4-engine turbojet	184,500	2000	92.3
	F	4-engine turbofan	239,200	2250	106.3
	G	4-engine turbojet	249,000	2433	101.5
	G-1	4-engine turbofan	257,000	2433	105.6
	H	4-engine turbojet	276,000	2773	99.5
	H-1	4-engine turbojet	310,000	2773	111.8
	G-2	4-engine turbojet	312,000	2892	107.9
	G-3	4-engine turbofan	312,000	2892	107.9

altitude, and normal acceleration. From this record, it is possible to make detailed counts of the normal acceleration peaks caused by various sources such as gusts, maneuvers, and ground operations and to determine the associated airspeeds and altitudes.

The manner of evaluating the VGH records is illustrated in Figure 3. The steady flight position of the acceleration trace is used as a reference from which to read the incremental acceleration peaks which equal or exceed a selected threshold value. Only the maximum value of the acceleration is read for each crossing of the reference. (Other methods of evaluating accelerations from time-history records - such as counting each reversal of the trace as a peak - have been employed by some investigators. The method employed herein, however, has been used from the inception of the VGH program, is simple, and gives an adequate representation of the repeated loads for the purposes of this report.) The selected threshold values range from  $\pm 0.05g$  to  $\pm 0.30g$ , depending upon the airplane type and the source of the accelerations being evaluated. For each acceleration peak evaluated, the corresponding values of airspeed and altitude are also evaluated. In addition, the airspeed and altitude are read at 1-minute intervals to provide data on the airspeed operating practices and the altitudes flown.

#### SCOPE

##### Types of Airplanes

Some of the general characteristics of the airplanes on which the data were collected are shown in Table I. As shown in the table, the data were obtained from three types of 2-engine jet transports, one type of 3-engine transport, and four basic types of 4-engine jet transports. In addition to the basic types of airplanes, data from several models of two of the airplane types were obtained as denoted by the dash-numbered suffix after the basic airplane designation. In total, eight basic airplane types plus an additional four

models (G-1, G-2, G-3, and H-1) are represented. Both turbojet and turbofan powered airplanes are included.

As shown in the table, the maximum gross weights of the airplanes ranged from 76,500 pounds (type A) to 312,000 pounds (type G-3). The maximum wing loadings ranged from about 70 pounds per square foot for airplane type C to 112 pounds per square foot for type H-1.

Airplane types A through D may be broadly described as having been used in short-haul airline service for which the average flight lengths ranged from about 250 to 560 miles. The remaining airplane types were used in long-haul airline service (average flight lengths from 660 to 1758 miles). All the airplanes except types A and C were of United States manufacture.

In order to show some of the operational features of the airplanes, the average true airspeeds (from takeoff to landing) and the average cruise altitudes of the airplanes are shown in Figure 4. For comparison, similar information taken from Reference 1 for piston and turboprop transports

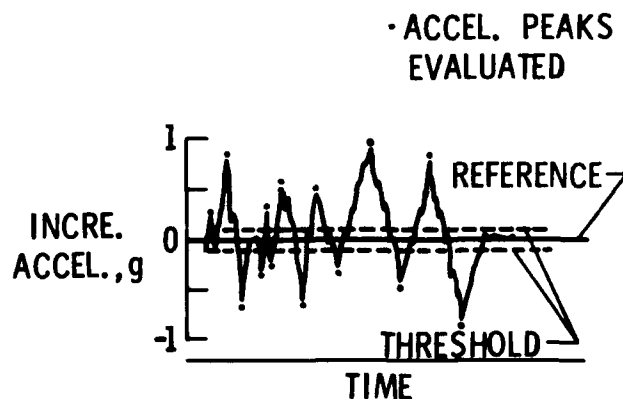


Figure 3. Method of Evaluating Accelerations.



are also shown. The figure shows that the average cruise altitudes for both the short-haul and the long-haul jet transports ranged from approximately 22,000 to roughly 34,000 feet. The average true airspeeds of the short-haul transports ranged from 340 knots to 430 knots, whereas the long-haul transports had average airspeeds of approximately 430 to 460 knots. Both the cruise altitudes and the true airspeeds for the jet transports are significantly higher than those of the previous airline operations of piston and turboprop airplanes.

### Sample Sizes

The sizes of the data samples in terms of the number of airplanes instrumented, the number of airlines represented, and the number of flight hours of VGH data are shown in Table II. The VGH sample sizes for the various types of airplanes range from 537 flight hours for airplane type F to 4916 hours for airplane type G-2.

In general, the data sampling program has been aimed at obtaining about 1000 flight hours of VGH data from each airline operation. (As used herein, an airline operation consists of a given airplane type in service on a given airline. Thus, the data for a given operation reflect the combined effects of the operating procedure of the particular airline, the airplane characteristics, and any influences of the airline routes on the repeated loads.) In order to minimize bias due to possible seasonal effects, the sampling period for each operation usually covered a period of 1 to 3 years.

The data were collected on United States and foreign airlines engaged in domestic and international operations.

## DISCUSSION

### In-Flight Accelerations

Typical examples of the data on the in-flight ac-

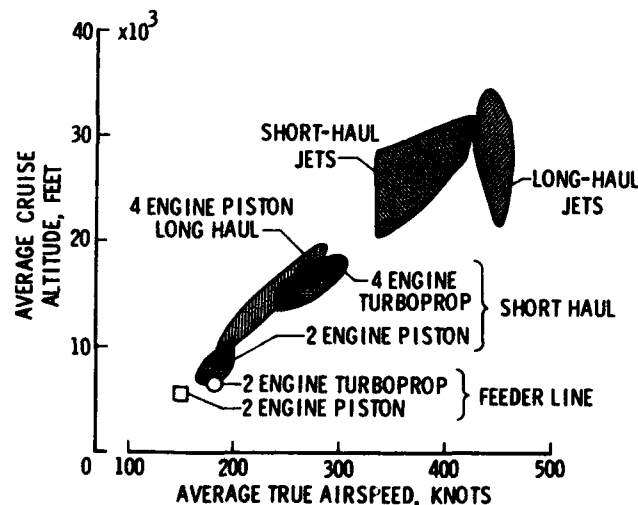


Figure 4. Flight Environment.

TABLE II.  
SCOPE AND SIZES OF VGH DATA SAMPLES

AIRPLANE TYPE	AIRPLANES	NUMBER OF AIRLINES	FLIGHT HOURS
A	1	1	1,156
B	2	1	1,509
C	1	1	723
D	4	4	2,076
E	2	1	3,766
F	1	1	537
G	2	2	2,409
G-1	1	1	1,324
H	2	1	2,464
H-1	2	2	2,151
G-2	2	2	4,916
G-3	3	1	4,152
<b>TOTALS</b>	<b>23</b>	<b>18</b>	<b>27,183</b>

celeration experience for two airline operations are shown in figure 5. The data denoted by the circular symbols are for an operation of a 2-engine jet transport and the square symbols are for a 4-engine transport. Each of the four plots in the figure gives the cumulative frequency distribution of accelerations per mile of flight. The upper left plot presents gust acceleration data; the upper right plot pertains to accelerations caused by maneuvers performed during routine operational passenger-carrying flights; and the lower left plot shows the acceleration distributions caused by maneuvers performed during pilot training or airplane check flights. By adding the gust, operational maneuver, and check-flight maneuver distributions for each operation, the cumulative frequency distributions representing the total in-flight acceleration experiences, as shown in the lower right plot, are obtained. All of the ordinate values in Figure 5 are based on the total flight miles represented by the data sample for the particular operation.

The results shown in Figure 5 are used herein to il-

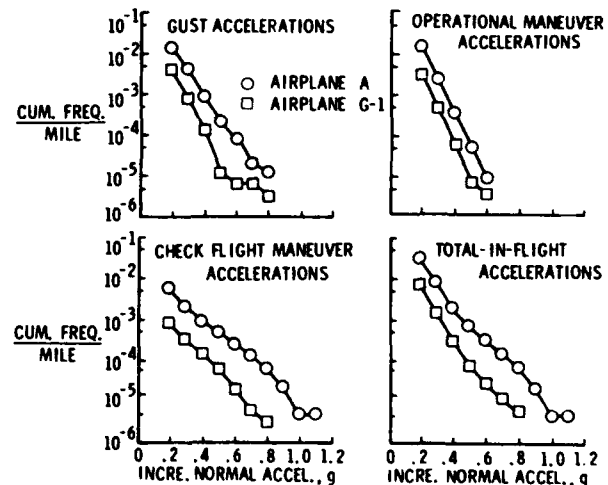


Figure 5. Illustrative Acceleration Distributions.

illustrate several general features of the in-flight acceleration data for jet transports and to form a basis for subsequent discussions aimed at summarizing data from all the jet transport operations. For the two operations shown in Figure 5, an order of magnitude difference exists between the acceleration experience due to each acceleration source and also for the total in-flight acceleration experience. For the most part, corresponding results for other jet transports fall within the range of the results for these two operations. Also, the slopes of the distributions for the other operations are comparable to those of the distributions shown in the figure. In view of these similarities among the data from the various operations and to facilitate presentation of results, the in-flight acceleration data for all the operations will be discussed in terms of the cumulative frequency of occurrence of accelerations greater than 0.3g. This value is selected because it is in the range of accelerations which produce a substantial portion of fatigue damage and because it is in the most reliable range of the distributions.

**Gust Accelerations.** The gust acceleration experience for the various airplanes and operations are compared in Figure 6. Each data point represents a particular airline operation involving the airplane type indicated below the symbol. The ordinate is the cumulative frequency of occurrence of gust accelerations  $\geq 0.3g$  per mile of flight.

Several points of interest are shown by the results in Figure 6. First, the gust acceleration experience for the various airplane types differ by factors as high as 20 to 1. Second, the gust acceleration experience for the 4-engine jet transports is, in general, less severe than that for the lighter 2- and 3-engine jet transports. There are exceptions to this trend, however, as evidenced by the operations involving airplanes E and H. Third, among operations involving a given airplane type, the gust acceleration experience varies by factors of about 5 to 1 based on the results for airplane D and airplane H-1. The differences among the gust acceleration experiences for the various airplane types and operations shown in Figure 6 are due to differences in airplane response characteristics to turbulence, effect of route on the turbulence environment, and to airline operating practices as regards turbulence.

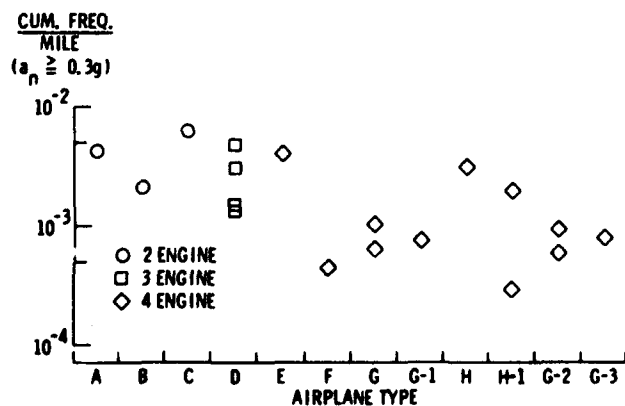


Figure 6. Comparison of Gust Acceleration Frequency.

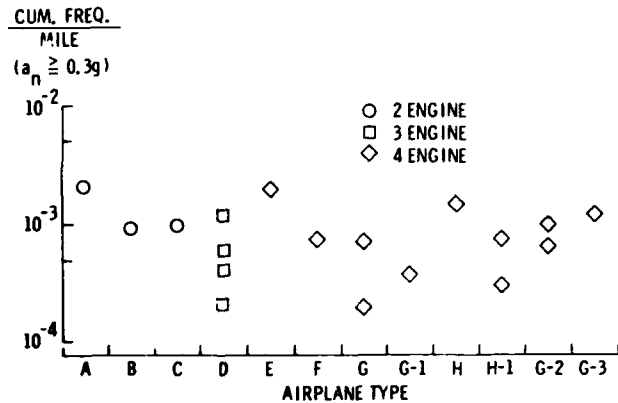


Figure 7. Comparison of Operational Maneuver Acceleration Frequency.

**Operational maneuver accelerations.** Figure 7 compares the operational maneuver acceleration experience for the various operations. The manner of presentation of the results is identical to that used in the previous figure. The results show that the operational maneuver acceleration experience for the various airplane types differ by as much as 10 to 1. The severity of the maneuver accelerations do not appear to be a function of airplane type. Based on the results for airplanes D, G, and H-1, the maneuver acceleration experience for a given airplane type may vary by factors as large as 5 to 1 among different operators.

**Check-flight maneuver accelerations.** The results pertaining to the acceleration experience due to check flight maneuvers are shown in Figure 8. Again, the manner of presentation follows that of the previous two figures. The results show differences as high as two orders of magnitude among the check-flight maneuver acceleration experiences for the different airplane types. No significant effect of airplane type on the severity of the acceleration experience is evident. For a given airplane type, the acceleration experience varies by as much as two orders of magnitude among

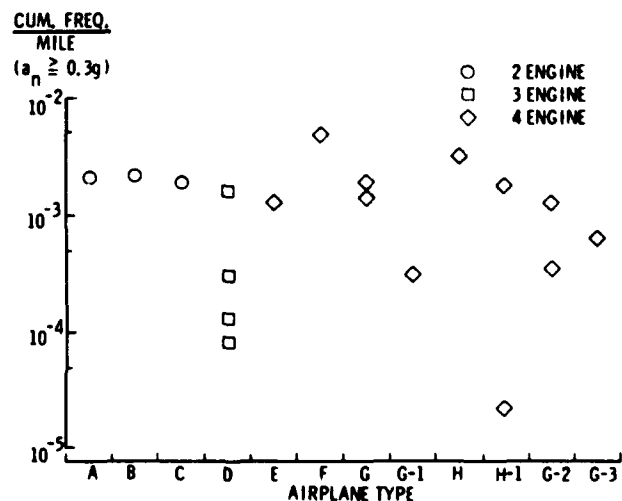


Figure 8. Comparison of Check-Flight Maneuver Acceleration Frequency.

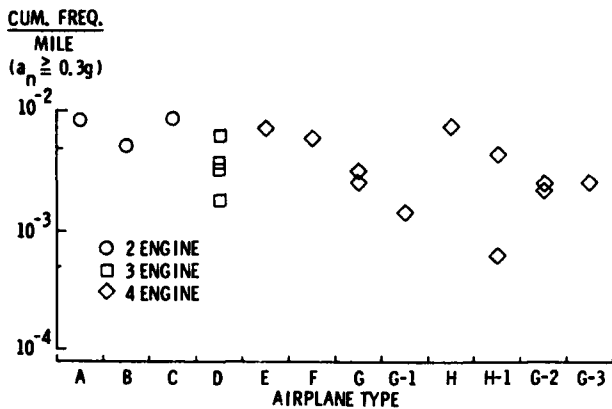


Figure 9. Comparison of Total Acceleration Frequency.

different operators as shown by the results for airplane types D and H-1.

The results in Figure 8 indicate that significant and, for the most part, unpredictable differences exist among the check-flight maneuver experiences of individual airplanes. There are probably two main reasons for the large differences among the check-flight maneuver experiences. First, there are apparently significant differences between airlines in regard to the amount of check-flight flying required and to the number and types of maneuvers performed. Second, the percent of the total flight time which is spent in check flights varies by an order of magnitude between individual airplanes. For the operations reported herein, the percent of total flight time which was spent in check flights ranged from approximately 0.7 percent to 12 percent.

**Total in-flight accelerations.** The total in-flight acceleration experiences for the various operations are shown in Figure 9. The data show the cumulative frequency of occurrence per mile of flight of accelerations greater than 0.3g caused by gusts, operational maneuvers, and check-flight

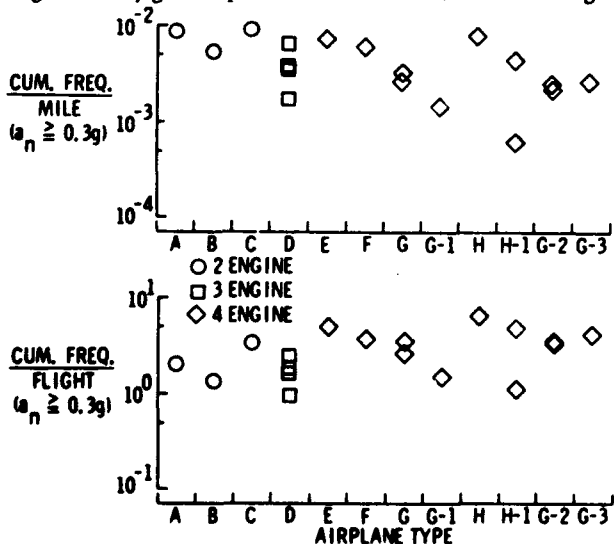


Figure 10. Comparison of Total Acceleration Frequency per Mile and per Flight.

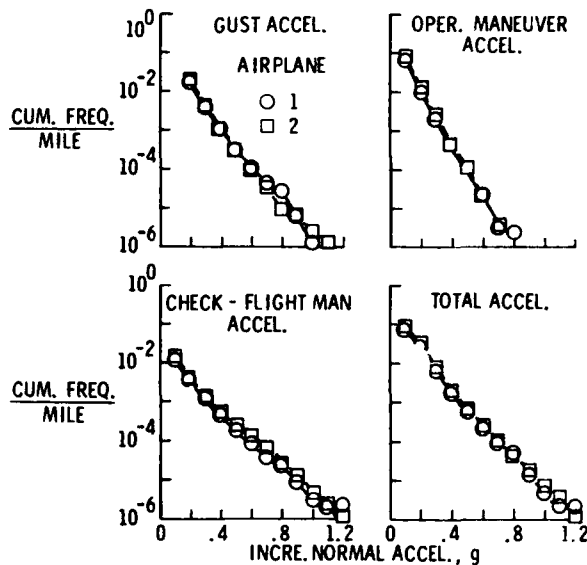


Figure 11. Variation Between Data from Individual Airplanes.

maneuvers. The results indicate maximum differences of about 15 to 1 among the total in-flight acceleration experiences for the various airplanes. With the exception of one operation involving airplane H-1, however, the differences among the operations are about 6 to 1. Among the four operations of airplane D, the acceleration experience varied by about 4 to 1, and for the two operations of airplane H-1, by about 8 to 1.

An analysis of acceleration data from piston, turbo-prop, and three types of 4-engine jet transports reported in Reference 1 showed that the in-flight acceleration histories exhibited less variation among airplane type when viewed on a per-flight rather than a per-mile basis. In order to show how the present results compare on the per-flight and the per-mile bases, the total in-flight acceleration data are plotted in figure 10 on both bases. The upper plot shows the cumulative frequency of in-flight accelerations per mile, whereas the lower plot shows the cumulative frequency of in-flight acceleration per flight. Comparison of the two sets of results shows three points of interest. First, the maximum difference between the acceleration experience on the "per-flight" basis is about 6 to 1 as compared to about 15 to 1 on the "per-flight-mile" basis. Second, some reduction in the variations among operations of a given airplane type is achieved by viewing the results on a per-flight basis as shown by the results for airplanes D and H-1. Third, from the overall viewpoint, the total in-flight acceleration experiences for the various types of airplanes are relatively consistent when viewed on the per-flight basis. These results tend to support the Reference 1 findings that frequency per flight is a more consistent and appropriate basis for assessing in-flight fatigue loadings than the frequency-per-flight-mile basis.

**Variation within an airline fleet.** In connection with certain aspects of aircraft fatigue, it is of interest to con-

sider the variation among the repeated loads experienced by individual airplanes within an airline's fleet of a given type of transport. For this purpose, figure 11 shows the cumulative frequency distribution of accelerations per mile of flight for two individual type E airplanes operated by a particular airline. These results are based on 1949 and 1817 flight hours of VGH data for airplanes 1 and 2, respectively. The results show that the gust, operational maneuver, check-flight maneuver, and the total in-flight acceleration experiences for these two airplanes were very similar. These results are typical of those which have been obtained for two other types of airplanes (Refs. 4 and 5). Although the data samples available for comparison are too few to be conclusive, it appears that there is substantial consistency among the in-flight acceleration experiences for individual airplanes of a given type within an airline's fleet

*Effect of sample size.* The in-flight acceleration data discussed in the preceding sections were obtained from VGH data samples representing from about 500 to 4100 flight hours of operations. The statistical reliability of data samples of these sizes have been the subject of continual study. The results of one such study are shown in Figure 12. The data show the cumulative frequency distributions of in-flight accelerations for one operation involving airplane E. The data shown by the square symbols are based on the total data sample of 1949 flight hours. The data shown by the circular symbols are based on 475 flight hours taken from the total data sample by arbitrarily selecting each fourth VGH record.

The results in Figure 12 show that there is very close agreement between the results based on the two data samples insofar as gust and operational maneuvers are concerned. Differences of about 2 to 1 are evident between the check-flight maneuver acceleration distributions for the two data samples. The differences between the total in-flight accel-

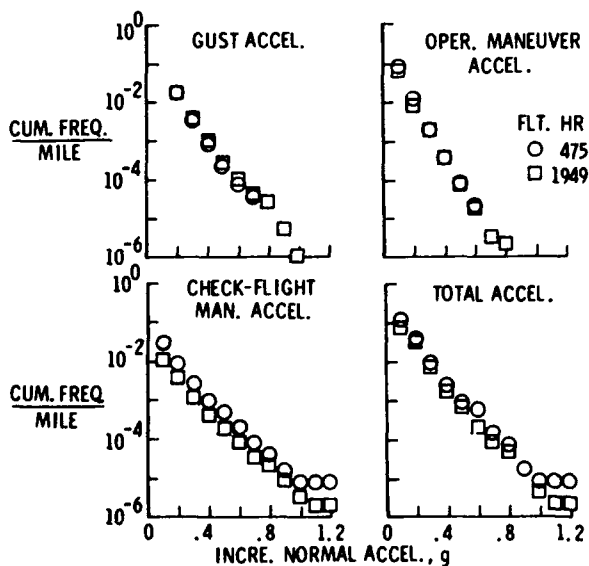


Figure 12. Effect of Sample Size.

eration distributions are less than 2 to 1 over most of the range of measured accelerations.

The results shown in Figure 12 are typical of those obtained for other data samples. In general, it has been found that good estimates of the gust and operational maneuver acceleration distributions can be obtained with relatively small (about 400 flight hours) data samples, provided operations in each of the four seasons are about equally represented. As previously noted, the check-flight maneuver distributions exhibit the most variability and data samples of 1000 or more flight hours are usually required to obtain acceptable statistical reliability.

### Landing Impact Accelerations

Two data samples of the accelerations caused by landing impact are shown in Figure 13. The ordinate is the probability per flight that a given value of the abscissa, the maximum positive acceleration increment due to initial landing impact, will be exceeded. Mathematical probability curves were fitted to each set of data and are shown by the solid lines.

The results in Figure 13 show large differences between the landing impact acceleration experiences for the two types of 4-engine jet transports. The mean values of the accelerations are about 0.2g and 0.3g for airplanes G-1 and F, respectively. To compare the relative severity of the landing impact accelerations for all the operations for which data are available, the mean values of the distributions are shown in Figure 14.

The results in Figure 14 show that the mean values of the landing impact accelerations range from 0.2g for one operation of a 4-engine jet transport (airplane G-1) to 0.3g for the operation of a 2-engine transport (airplane B). Con-

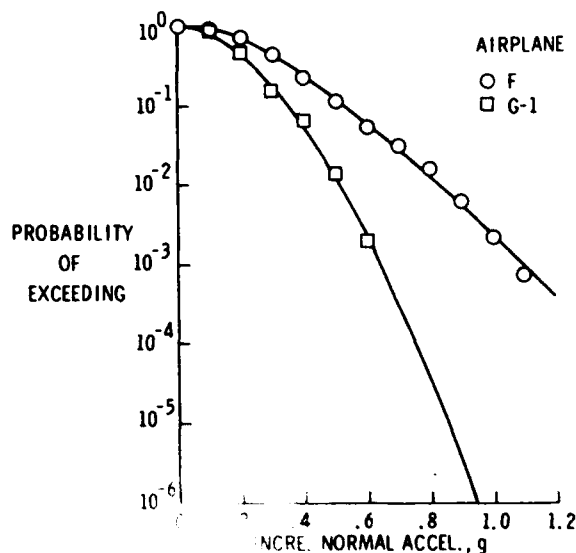


Figure 13. Landing Impacts for Two Operations.

sidering the data for the 4-engine transports, the mean values range from 0.20g to 0.32g. Also, large differences between the mean values are shown for the three 2-engine transports. For the two airplane types for which data from more than one operator is available (types D and H-1), little effect of operator on the landing impact accelerations is evident. This suggests that the variations in landing impact accelerations shown in Figure 14 is more a reflection of the effect of airplane characteristics than of operator.

### Accelerations During Ground Operations

The available data on accelerations experienced during ground operations are summarized in Figure 15. The data show the cumulative frequency distributions of accelerations per flight for a 2-engine jet transport and for three types of 4-engine jet transports. Each of the four data samples represent from 666 to 827 flights.

For accelerations up to about 0.4g, there is little difference among the distributions for the four airplane types. For higher accelerations, the data for airplane H-1 show higher and more frequent accelerations than are shown by the data for the other three airplanes. Whether this difference is real or is due to variability of the data at the higher acceleration levels is not known. From the overall viewpoint, however, the results in Figure 15 indicate a large measure of consistency among the ground acceleration experience for the four airplane types for which data are available.

### CONCLUDING REMARKS

A review of the repeated loads data collected by NASA on commercial jet transports has been made. This review has served to summarize the available data on repeated loads caused by gusts, operational maneuvers, check-flight maneuvers, landing impact, and ground operations according to airplane type. Based on the analysis, which encompassed about 27,000 flight hours of data from 18

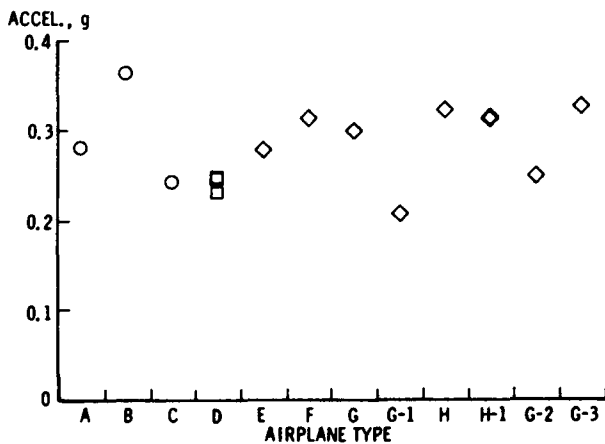


Figure 14. Mean Values for Landing Impacts.

airline operations of 12 types of 2-, 3-, and 4-engine jet transports, the following observations are made:

1. The frequency of accelerations per mile of flight due to gusts and operational maneuvers varies by an order of magnitude among different airplane types. Among different operations of a given type of airplane, differences of about 5 to 1 exist in the gust and operational maneuver acceleration frequency.

2. The frequency of accelerations per mile of flight due to check-flight maneuvers varies by as much as two orders of magnitude between airplane types and between different operations of a given airplane type.

3. The combined in-flight acceleration experience due to gusts, operational maneuvers, and check-flight maneuvers varies by about 15 to 1 among airplane types and about 8 to 1 among operations of a given airplane type when viewed on a per-flight-mile basis. The variations are substantially reduced, however, by expressing the results in terms of frequency per flight.

4. The severity of the landing impact accelerations varies significantly among the different airplane types. This variation is apparently more of a function of the airplane characteristics than of the operator.

5. Based on limited comparisons, it appears that there is close agreement among the in-flight acceleration experience for individual airplanes of a given type within an airline's fleet.

6. In general, VGH data samples of about 400 flight hours, distributed among operations during the four seasons, provide reliable estimates of the gust and operational maneuver acceleration distributions. Data samples of 1000 flight hours or larger are required to obtain good estimates of check-flight maneuver acceleration experiences.

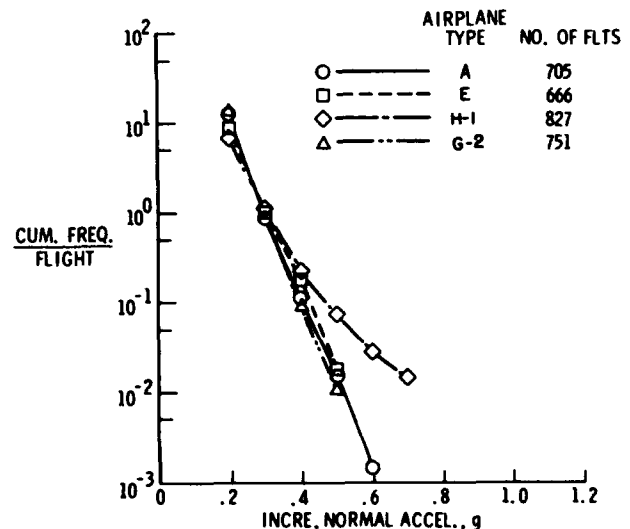


Figure 15. Total Ground Run Accelerations.

## REFERENCES

1. T.L. Coleman, *Trends in Repeated Loads on Transport Airplanes*, NASA-TN-D-4586, National Aeronautics and Space Administration, Washington, D.C. (1968).
2. P. Donely, J.W. Jewel, Jr., and P.A. Hunter, *An Assessment of Repeated Loads on General Aviation and Transport Aircraft*, Presented at the 5th ICAF Symposium, Melbourne, Australia, May 1967.
3. N.R. Richardson, *NACA VGH Recorder*, NACA-TN-2265, National Aeronautics and Space Administration, Washington, D.C. (1951).
4. P.A. Hunter, *An Analysis of VGH Data from One Type of Four-Engine Turbojet Transport Airplane During Commercial Operations*, NASA-TN-D-4330, National Aeronautics and Space Administration, Washington, D.C. (1968).
5. P.A. Hunter and W.G. Walker, *An Analysis of VG and VGH Operational Data from a Twin-Engine Turboprop Transport Airplane*, NASA-TN-D-1925, National Aeronautics and Space Administration, Washington, D.C. (1963).

# ON THE ANALYTICAL BASIS FOR FATIGUE LIFE PREDICTIONS

by

Sam C. Saunders

Boeing Scientific Research Laboratories  
Seattle, Washington

## INTRODUCTION

The basis for the calculation of fatigue life has required knowledge of the fatigue strength of the component, the loading spectrum, and the imposed scatter factors. The early methods of analysis established the fatigue strength from a limited number of fatigue tests at various constant stress levels, then obtained flight measurements from which a vibratory load spectrum was derived. Then scatter factors were applied to the test results and a safe life was calculated by means of some rule, usually Miner-Palmgren, using the load spectrum.

In the past, the scatter factors used were somewhat arbitrary and neither the stochastic nature of fatigue strength nor the statistical requirements for adequate testing were fully understood; moreover, there was considerable argumentation about which fatigue life rule should be used. Nevertheless, the determinations made were in the main successful in reducing catastrophic failures to an acceptable level.

The reasons for this success may lie in the adoption of considerable conservatism either in the flight spectrum, in the scatter factors or in the fatigue life rule. But knowledge, both experimental and theoretical, is necessary to illuminate the exact reasons. If this knowledge could be obtained, a refinement of the design process would be possible through the elimination of the conservatism which is now necessitated by our uncertain knowledge and theory. What is needed is to make use of the knowledge of load order influence acquired in programmed load studies, taking into account the influence of sample sizes in the statistical analysis of failure data and the fact that the actual loading environment is stochastic in nature in the calculation of the safe fatigue life.

In the following pages we hope to present a synopsis of some recent work on the important statistical questions which arise in problems of fatigue analysis.

## A FORMULA FOR EXPECTED LIFE

By the early sixties there had been such a proliferation of mutually incompatible theories for the calculation of fatigue life that several comprehensive studies were undertaken to compare them. Two of these were sponsored

by the Air Force. One, in 1963, was of a theoretical nature<sup>1</sup>, and the other, completed in 1962<sup>2</sup>, was an engineering evaluation of the extant methods for the prediction of fatigue life. The conclusion of the second report contained the statement: "The statistical nature of many facets of the fatigue problem precludes hope of any specific fatigue life prediction of a single article. The best that can be achieved is broad comparisons of the expectations of new structures compared with current and past fleet performance . . . From this study the use of the Linear Cumulative Damage Hypothesis (Miner's Rule) is recommended as best qualified from the standpoint of simplicity, versatility and of sufficient accuracy (in view of other intangibles in the problem) for use in design."

The words "Miner's Rule" and "Linear Cumulative Hypothesis" referred to a result in a paper published in 1945 by M.A. Miner<sup>3</sup>. This was in fact an independent derivation of a formula given earlier by A. Palmgren in 1924<sup>4</sup>.

A disadvantage of a "rule" is that the conditions under which it can be used are not stated, usually because they are not known, whereas a mathematical theorem has an explicit hypothesis which always gives sufficient and sometimes necessary conditions for the conclusion.

The original assumptions, under which Miner proved the rule, became known as the Linear Cumulative Damage Hypotheses:

- I. a) Each specimen can absorb the same amount of fatigue damage and when that amount is attained failure occurs.
- b) The amount of damage absorbed by the material in any one cycle is determined only by the load during that cycle.
- c) The total damage absorbed by the specimen under a sequence of load cycles is equal to the sum of damages absorbed in each cycle during the sequence.

**Theorem 1:** (Miner<sup>3</sup>)

If hypotheses I hold and there are only  $k$  possible load cycles where  $\nu_i$  equals the number of cycles to failure

under repetition of the  $i^{\text{th}}$  load cycle, then a loading spectrum which contains  $n_i$  applications of the  $i^{\text{th}}$  cycle can be repeated  $\nu$  times until failure where

$$\nu = \frac{1}{\sum_{i=1}^k \frac{n_i}{\nu_i}} \quad (1.1)$$

The contumely which has been heaped upon Miner's Rule, as expressed in (1.1), has been based on the simplistic and unrealistic nature of the hypotheses I. The obvious question is: How can it be that such a rule is in some average sense good (in fact, best of those compared), by empirical verification as in Reference 2, when the hypotheses are known to be false? The answer is just as obvious: The conclusion must be true under weaker conditions.

In 1965 a study was begun to try to replace all of the deterministic assumptions of Miner in hypotheses I with stochastic ones which were more realistic. This alternative, published in 1968 in the *SIAM Journal*<sup>5</sup>, was:

- II. a) Fatigue failure, due to the growth and extension of a dominant failure crack, occurs when a (random) initial length  $W$  is reached.
- b) The (random) incremental crack extension  $Z_i$  during the  $i^{\text{th}}$  cycle has a distribution depending only upon that cycle.
- c) For each  $i=1,2,\dots$  the random variable  $Z_i$  is non-negative and has a distribution with an increasing failure rate. Moreover, the partial sums

$$S_n = \sum_{i=1}^n Z_i$$

are statistically independent of  $W$  for all  $n=1,2,\dots$

We now state

**Theorem 2:** (Birnbaum, Saunders<sup>5</sup>)

If hypotheses II hold and we let  $N_i$  be the (random) number of cycles to failure under repetition of the  $i^{\text{th}}$  cycle with finite mathematical expectation  $\nu_i = EN_i$  for  $i=1,\dots,k$ , then the random number of times a spectrum, containing  $n_i$  repetitions of the  $i^{\text{th}}$  cycle, can be applied until failure has finite expectation  $\nu$  bounded by

$$\frac{1}{\sum_{i=1}^k \frac{n_i}{\nu_i}} - 1 \leq \nu \leq \frac{1}{\sum_{i=1}^k \frac{n_i}{\nu_i + 1}} \quad (1.2)$$

The point is that the expression for  $\nu$  given in (1.1)

lies between the bounds given in (1.2). Moreover, one can begin to see that if Miner's Rule did in fact predict only the mean, statistical variation in measurements would naturally occur about this value but on the average it would be correct. Also, we could expect a contribution to dispersion because of sample fluctuation in estimating the  $\nu_i, i=1,\dots,k$ .

There are only two points that I wish to discuss about hypotheses II. The first is that the assumption of crack extension being functionally independent of the preceding loads could only be an approximation to reality in the early stages of crack initiation and growth. It is known to be false at later stages<sup>6</sup>. The second point of possible contention, namely increasing failure rate (IFR), was justified in Reference 5 by the "rip in the screen door" model which we now repeat.

Consider a macroscopic crack within a material which, to fix ideas, we picture as shown in Figure 1.

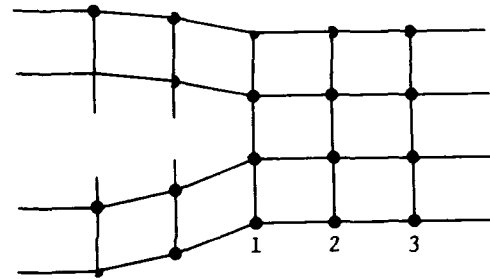


Figure 1. Macroscopic Crack Model.

For a given stress imposed let  $U$  be the (random) number of bonds broken. Let  $q_i$  be the probability that the  $i^{\text{th}}$  bond is broken given that the  $(i-1)^{\text{st}}$  bond is broken.

It is intuitively clear that for a given stress the probability of rupture, given the preceding bond is broken, should decrease the further away the bond is from the crack tip. But it can be shown (see Ref. 5) that the  $q_n$  are decreasing if and only if the random variable  $U$  is IFR. Thus we conclude that the IFR assumption is intrinsically a natural condition.

We now turn to some results, reported in Reference 8, which require more careful definition and somewhat more mathematical sophistication.

A load function is a continuous piecewise linear function on the positive real line, the value of which at any time gives the stress imposed by the deflection of the specimen. Moreover, the slope of such a function changes sign exactly once at the midpoint of each interval of unit length at  $(j,j+1)$  for  $j=0,1,2,\dots$ . An oscillation of a load is the function restricted to an interval of unit length on half of which the function is increasing. (This definition is due



to metallurgical opinion that crack growth occurs only during the tension portion of the cycle.) A *load spectrum* is a load function which takes the value zero except on some interval of the form  $(0, m)$  where the integer  $m$  is called the *duration*. A *programmed load*  $\underline{\lambda}$  is the repetition of a spectrum  $\lambda$ , of duration  $m$  say,  $\underline{\lambda} = (\lambda_1, \lambda_2, \dots)$  where  $\lambda_j$  is the  $j^{\text{th}}$  repetition of the spectrum load  $\lambda$  and defined for  $t > 0, j=0, 1, \dots$  by

$$\lambda_{j+1}(t) = \lambda(-jm+t).$$

By a *load history* (or partial spectrum) of length  $i$ , denoted by  $\lambda^i$ , we mean  $\lambda$  restricted in domain to the interval  $(0, i)$ , with or without subscripts on  $\lambda$ .

A non-negative random variable  $X$  is said to be "new better than used in expectation" (NBUE) whenever

$$E[X - x | X > x] \leq EX \quad \text{for all } x > 0.$$

This concept was introduced in reliability studies in 1964<sup>7</sup>. Using this concept we can formulate a third set of hypotheses:

- III. a) Fatigue failure, due to the initiation and growth of a dominant fatigue crack, occurs when a (random) critical size  $W$  is reached.
- b) The  $i^{\text{th}}$  incremental extension during the last oscillation of the history  $\lambda_j^i$  is a non-negative random variable  $Z_j^i(\lambda_j^i)$  depending only upon  $\lambda_j^i$ . The  $Z(\lambda)$  for all affixes  $i, j$  are mutually independent random variables independent of  $W$ .
- c) The incremental growth random variable  $Z(\lambda)$  for all affixes is an NBUE random variable.
- d) There exists a finite set of loading oscillations, say  $\Omega = \{\omega_0, \dots, \omega_k\}$ , such that for any admissible loading history  $\lambda$  we have an equivalent  $\omega_j \in \Omega$ , written  $\lambda \approx \omega_j$ , for which in distribution

$$Z(\lambda) = Z(\omega_j).$$

In particular,  $\omega_0$  is the oscillation such that  $Z(\omega_0) = 0$ .

Let us comment on the degree of generality we have postulated. The incremental crack extension may depend upon all the loads previously imposed during that spectrum's repetition as well as the actual propagating load. The incremental growth random variables are assumed to satisfy the very weak NBUE criterion, which is more general than the IFR class. This means that for a given load, knowing the fatigue damage exceeds a given amount, we

conclude that the expected residual fatigue damage from that load is less than the expected damage was from the load before it was applied initially. This would seem to be virtually undeniable. We also assume that there exists a resolving set of loading oscillations  $\Omega$  to which we refer for fatigue damage assessment.

We can now state a result from Reference 8 concerning programmed loads.

**Theorem 3:** If the hypotheses III are satisfied, then each programmed repetition of the spectrum  $\lambda$  results in a sequence of independent replications of the random crack growth

$$Y(\lambda) = \sum_{i=1}^m Z^i(\lambda^i)$$

which are NBUE. If  $N_{Y(\lambda)}$  is the random number of spectra which can be sustained until failure, it has finite expectation bounded by

$$\frac{1}{\sum_{j=1}^k \frac{n_j(\lambda)}{v_j}} - 1 \leq EN_{Y(\lambda)} \leq \frac{1}{\sum_{j=1}^k \frac{n_j(\lambda)}{v_j + 1}} \quad (1.3)$$

where for  $j = 1, 2, \dots$

$$n_j(\lambda) = \sum_{i \geq 1} \{ \lambda^i \approx \omega_j \}, \quad v_j = EN_{Y(\omega_j)}$$

and  $\{ \pi \}$  is the indicator function of the relation  $\pi$  being one if true and zero otherwise.

Let  $\Lambda$  denote a random function taking values in the space of admissible load functions  $\mathcal{L}$ . Assume a *random load*  $\underline{\Lambda} = (\Lambda_1, \Lambda_2, \dots)$  where each  $\Lambda_j$  is an independent replication of the random spectrum  $\Lambda$ .

We now state another result given in Ref. 8 which concerns random spectra.

**Theorem 4:** If hypotheses III are satisfied, then the expected number of random spectra which can be sustained until failure, is bounded below and

$$\frac{1}{\sum_{j=1}^k \frac{En_j(\Lambda)}{v_j}} - 1 \leq EN_{Y(\Lambda)} \quad (1.4)$$

To obtain an upper bound, analogous to that given

in (1.3), appears to be mathematically difficult. In fact we found it necessary to make additional assumptions.

The incremental damage  $Z(\lambda)$  during the last oscillation of the spectrum  $\lambda$  has a complementary distribution (unity minus the distribution) we label  $R(x:\lambda)$  for  $x > 0$ . We now make the assumption:

- e) For any  $x > 0$ ,  $R(x:\lambda)$  is a convex function of  $\lambda$  over the convex space  $\mathcal{L}$ .

The physical plausibility of this assumption is discussed in Ref. 8. We obtain an upper bound in

**Theorem 5:** If III and e) are satisfied, then we have, in the notation of Theorem 4,

$$EN_{Y(\Lambda)} \leq \frac{1}{\sum_{j=1}^k \frac{n_j(E\Lambda)}{v_j + 1}} \quad (1.5)$$

For the usual situation where each oscillation of stress would cause failure in between  $10^2$  and  $10^6$  repetitions, we conclude that the expected number of times the spectrum  $\Lambda$ , formed from such oscillations, can be repeated is given with virtual equality by

$$EN = \frac{1}{\sum_{j=1}^k \frac{En_j(\Lambda)}{v_j}} \quad (1.6)$$

We shall, in what follows, assume that (1.6) holds exactly.

As a final comment, it well may be that the probabilistic structure of  $\Lambda$  which arises in practical applications may contain a form of symmetry so that  $En_j(\Lambda)$  is virtually equal to the actual count of oscillations of a particular type and thus would appear to be independent of order. This would account for the closeness of Miner's Rule in the original form to the true value of the expected life. Moreover, the inequality given in (1.4) accounts for conservative tendency in practice. And lastly, we note the formula (1.6) is almost identical to the one given by Freudenthal and Heller<sup>9</sup> where instead of  $En_j(\Lambda)$  they have utilized what they termed "empirical interaction factors".

### A CONNECTION WITH SERVICE LIFE

Fatigue tests for life length are recorded in number of cycles to failure. The distinction between the discrete random variable number of cycles and the continuous random variable life time is not usually maintained since it is often assumed that there is a known relationship of cycles per unit time in service. Let us assume that the fatigue life variability exhibited for a given detail under any load-

ing regime and environment is a non-negative random variable which can be described by the following general class:

- A<sup>0</sup> The observed fatigue life  $X$  has an unknown distribution within the two-parameter family, defined for given  $F$ , by

$$P[X \leq x] = F[(x/\beta)^\alpha] \quad \text{for } x > 0$$

where  $\alpha > 0$  is the shape parameter and  $\beta > 0$  is the scale parameter (often called the characteristic life).

Note that this formulation includes many of the usual models including the log-normal and the Weibull by proper specification of  $F$ .

Of course, we could formulate a model with unknown scale and location parameters by considering  $\log X$  as the observable variate, and because of the extreme variability in fatigue life observations it is frequently the logarithm which is used in engineering study. However, we prefer to use the former model and there is an easy transformation from one to the other.

Let  $X_0$  be the random variable with distribution  $F$ , then

$$X = \beta X_0^{1/\alpha}, \quad \ln X = \ln \beta + \frac{1}{\alpha} \ln X_0 \quad (2.1)$$

We now make assumption

- B<sup>0</sup> The shape parameter  $\alpha$  for the distribution of  $X$  remains fixed within the family.

Thus we see the variance of the logarithm of service life depends only upon  $\alpha$  and the choice of  $F$ .

The whole point of this discussion is, one should choose statistical procedures which do not depend strongly upon the choice of  $F$ . One should make estimates and reach conclusions which are the same for a rather wide class of the choices of  $F$  at which nature may arrive (and of which we must ultimately remain ignorant).

The verification of B<sup>0</sup> represents a non-trivial engineering and statistical task. A document which represents a start in this direction is Reference 10. It provides specific statistical methods for the treatment of the type of data obtained in fatigue tests for the estimation of  $\alpha$ . It also classifies from prior data the conditions of practical concern under which  $\alpha$  may be considered constant and then determines this value.

Thus it is possible to determine a model so that sound statistical prediction can be based on one observation which can be used to estimate  $\beta_1$ . We shall be concerned here only with A<sup>0</sup>, B<sup>0</sup> in so far as they relate to the assumptions of the previous section. Recall  $\Lambda$  denotes a

random spectrum (of random duration M) where all the oscillations were assumed to be of the same duration. For the representation of service life this is, of course, mathematically convenient but it is fiction.

Let  $U_i$  be the (random) time between the  $i-1$ st and  $i$ th oscillations defined in some systematic way. The usage process then is defined by

$$U(t) = \sum_{i=1}^{\infty} \left[ \begin{matrix} V_{i+1} \geq t \geq V_i \\ \left[ i + \frac{t-V_i}{U_{i+1}} \right] \end{matrix} \right] \quad \text{for } t > 0$$

where  $V_n = \sum_{i=1}^n U_i$ . Hence,  $\Lambda [U(t)], t > 0$

represents an actual random loading as encountered in service with changes in both amplitude and frequency. The service time to complete the spectrum  $\Lambda$  is random and is expressed by

$$L = \sum_{i=1}^M U_i$$

Let T denote the total service life under usage  $\Lambda(U)$ , then

$$T = \sum_{j=1}^N L_j$$

where  $L_j$  for  $j=1,2,\dots$ , are independent and identically distributed independent of N. That is to say, failure is a result of the number and type of oscillations and not of the length of time between (at least for the range of frequencies we are considering). Hence from Theorem 4

$$ET = (EN)(EL) = \frac{EL}{\sum_{j=1}^k \frac{En_j(\Lambda)}{v_j}} \quad (2.2)$$

But from (2.1),  $ET = \beta g(\alpha)$  where  $g$  is a functional of F. But also from  $A^0$  and  $B^0$  we see  $v_j = \beta_j g(\alpha)$  is the expected life and  $\beta_j$  is the characteristic life under repetition of oscillations of type  $j$ . Thus it is that Miner's Rule allows the

computation of characteristic life under a random usage spectrum  $\Lambda(U)$  as

$$\beta = (EL) / \sum_{j=1}^k \frac{En_j(\Lambda)}{\beta_j} \quad (2.3)$$

This conclusion has been pointed out previously in a less general context<sup>11</sup>.

The great utility of the modified Miner's Rule, as expressed in (1.6), coupled with assumptions  $A^0$  and  $B^0$  is the statistical quantification of scatter factor. Suppose that  $\beta$  as calculated by (2.3) is determined, then with  $\alpha$  estimated from prior data by the methods presented in Ref. 10 we set the safe life  $t_\epsilon$  at 100  $(1-\epsilon)\%$  confidence where we take  $\epsilon$  to be small. Thus  $t_\epsilon$  is the life before which failure will occur with probability  $\epsilon$  and is given by

$$t_\epsilon = \beta [F^{-1}(\epsilon)]^{1/\alpha} \quad (2.4)$$

Hence the reciprocal of the scatter factor in (2.4) is  $[F^{-1}(\epsilon)]^{1/\alpha}$  which value can be determined for many choices of F and the most stringent one taken. Or alternatively, the usually applied scatter factor can be assessed as to the implied level of confidence by the use of (2.4).

#### CONCLUSION

In this expository note we have tried to point out the ubiquity of the Miner-Palmgren Rule for the calculation of fatigue life by showing that from a rather general and plausible, mathematical and probabilistic framework it appears as the expected value of stochastic fatigue life. These results explain its empirically verified utility and the difficulty of supplanting it with other "rules". We also show how such a result fits nicely in theory into any two-parameter shape and location model for the calculation of safe service life.

Lastly, we do not pretend that any particular theory, such as this, can be the final word or that it is impossible that further knowledge of the physics of material could vitiate the model we have employed. However, we do think that it does indicate that deterministic models for fatigue should be reassessed.

## REFERENCES

1. L. Kaechele, *Review and Analysis of Cumulative-Fatigue-Damage Theories*, RM-3650-PR, Rand Corporation, Santa Monica, California (1963).
2. W.J. Crichlow et al., *An Engineering Evaluation of Methods for the Prediction of Fatigue Life in Airframe Structures*, ASD-TR-61-434, Aeronautical Systems Division, Wright-Patterson AFB, Ohio (1962).
3. M.A. Miner, "Cumulative Damage in Fatigue," *J. Appl. Mech.*, 12: A159-A164 (1945).
4. A. Palmgren, "Die Lebensdauer von Kugellagern," *Z. Ver. Deut. Ing.*, 68:339-341 (1924).
5. Z.W. Birnbaum and S.C. Saunders, "A Probabilistic Interpretation of Miner's Rule," *SIAM J. Appl. Math.*, 16:637-652 (1968).
6. J.C. McMillan and R.M. Pelloux, "Fatigue Crack Propagation under Program and Random Loads," pp. 505-532, *Fatigue Crack Propagation*, ASTM-STP-415, American Society for Testing and Materials, Philadelphia, Pennsylvania (1967).
7. R.E. Barlow and F. Proschan, "Comparison of Replacement Policies and Renewal Theory Implications," *Ann. Math. Statist.*, 35:577-589 (1964).
8. S.C. Saunders, "A Probabilistic Interpretation of Miner's Rule - II," *SIAM J. Appl. Math.*, 19:251-265 (1970).
9. A.M. Freudenthal and R.A. Heller, "Accumulation of Fatigue Damage," in *Fatigue in Aircraft Structures*, A.M. Freudenthal, Ed., Academic Press, New York (1956).
10. I.C. Whittaker and P.M. Besuner, *A Reliability Analysis Approach to Fatigue Life Variability of Aircraft Structures*, AFML-TR-69-65, Air Force Materials Laboratory, Wright-Patterson AFB, Ohio (1969).
11. S.C. Saunders, "Some Comments on Miner's Rule," in *Proc. Int. Conf. Struct. Safety Reliability*, Washington, D.C. (1969).

# THE APPLICATION OF THE SCRATCH STRAIN GAGE IN A TOTAL FLEET FATIGUE DAMAGE MONITORING SYSTEM

by

T.L. Haglage and H.A. Wood

Flight Dynamics Laboratory  
Wright-Patterson Air Force Base, Ohio

## I. INTRODUCTION

Individual aircraft within a fleet may accumulate damage at widely different rates due to variations in operational usage. It has been shown that total damage is not necessarily proportional to the number of flight hours<sup>1</sup>. Calculation of fatigue damage for sensitive areas of individual aircraft on a regular programmed basis, usually flight by flight, requires knowledge of damage accumulation rates in terms of basic mission parameters (gross weight, velocity, stores configuration, load level, etc.) for mission segments (taxi, take-off, cruise, weapon release, etc.). Mission parameter input for the fatigue analysis is derived from structural flight load recorder programs measuring operational usage. The recorders are installed on only a small percentage of the total fleet. Cost and timely data reduction usually preclude instrumenting every aircraft. Current practice provides the capability of calculating damage through a parametric fatigue analysis. Such an analysis depicts damage accumulation rates in terms of basic environmental mission parameters (gross weight, velocity, stores configuration, load level, etc) for various mission segments (taxi, take-off, cruise, etc).

The results of Reference 1 suggest that for fighter aircraft it is necessary to monitor only the normal load factor during the combat phase of the mission. Knowledge of this single parameter in combination with store, gross weight, and appropriate flight log data would lead to an accurate assessment of the major portion of the damage accumulated during the total mission. This implies, also, that a simple sensing device such as an accelerometer or strain gage could, economically, be utilized in an individual aircraft life monitoring program.

This study presents a tail number damage monitoring system adaptable to maneuvering load sensitive aircraft such as fighters and trainers. The heart of the system is the commercially available Prewitt Scratch Strain Gage. This device is a self-contained mechanical extensometer capable of measuring and recording total deformation and thus average strain cycles over the effective installed gage length of the member to which it is attached.

In service, the most effective use of a device such as the Prewitt Scratch Gage would be in a tail number fatigue

damage monitoring program. In this role, individual aircraft would be equipped with one or more strategically located gages installed to monitor strain continuously. With correct placement, information from numerous flights could be contained on one target since disc capacity is merely a function of the total number and magnitude of strain occurrences sensed by the gage.

## II. IN-HOUSE LABORATORY EVALUATION PROGRAM

### 2.1 Evaluation Parameters

An in-house laboratory evaluation program for the scratch gage has been completed with favorable results<sup>2</sup>.

The following significant parameters were evaluated through a series of axial load cyclic tests:

- (a) Recording sensitivity - maximum and minimum
- (b) Sensitivity to strain range - including compression
- (c) Sensitivity to mean strain level
- (d) Target (disc) capacity
- (e) Trace repeatability

Due to the wide variation in strain magnitude, it was decided to test the three commercially available sizes of gages, three, six, and 12 inches, simultaneously. Initial system checkout and gage sensitivity was accomplished primarily with a series of varying constant amplitude block loadings. A tactical fighter mission stress profile provided a means to further investigate recording capability and was utilized to estimate target capacity.

The gage was found to be capable of recording strain comparable to an electric resistance strain gage, and its sensitivity is directly dependent on its length.

### 2.2 Gage Description

As is indicated in Figure 1, the gage consists of

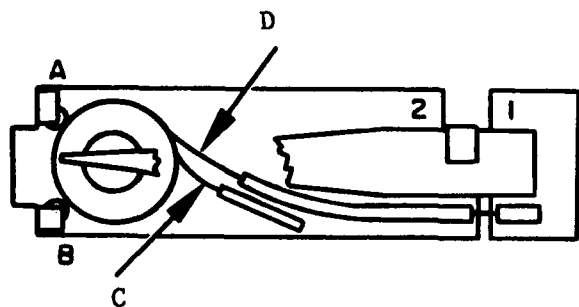
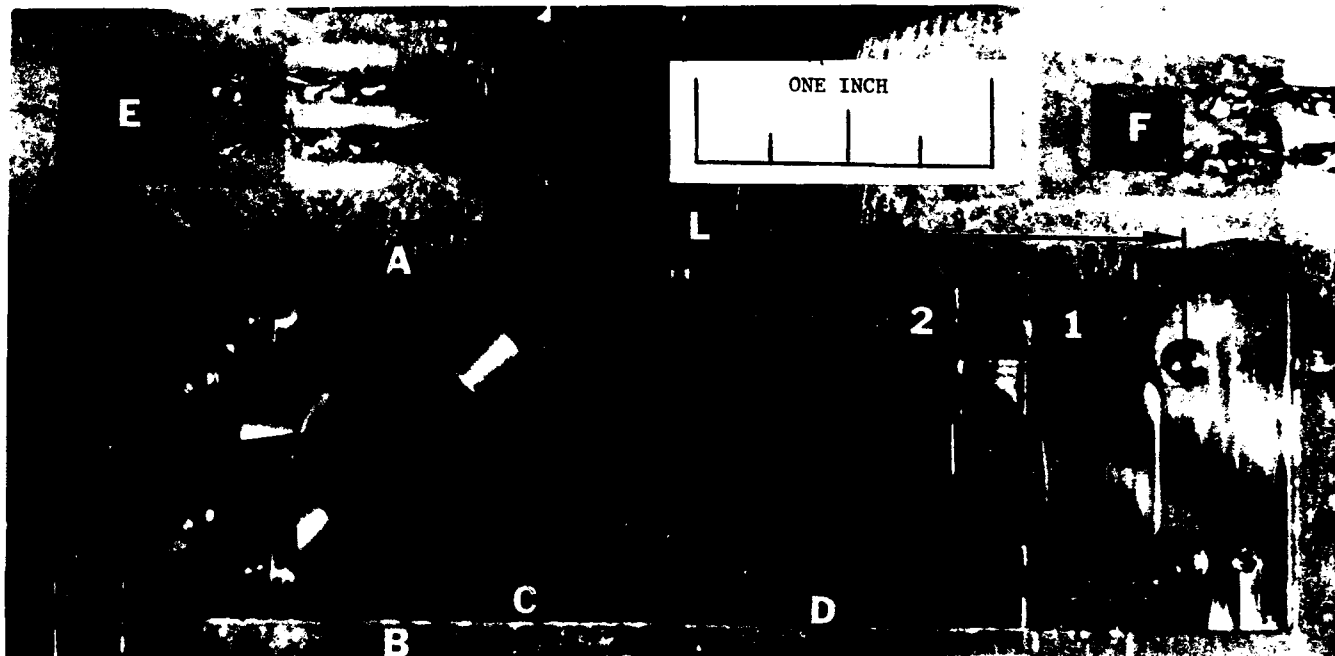


Figure 1. Three-Inch Prewitt Scratch Strain Gage.



two steel base plates (1) and (2), with (1) containing a recording stylus, and (2) the brass recording disc. Physical attachment of the gage assembly to the structure is achieved by either bonding, clamping, or screwing the ends of each base plate.

The outer periphery of the disc is grooved so as to accommodate two rollers (A and B, Figure 1) and encased steel wire brushes (C and D, Figure 1) used to hold the disc in place.

As the structure is strained, the two base plates move relative to each other causing the stylus to scratch the disc and record the total movement. Automatic rotation of the disc occurs under cyclic straining allowing separation of each strain excursion. The counterclockwise rotation is accomplished during gage contraction by the tangential force of the longer brush, D on the circumference of the disc. The shorter brush, C, is used merely to prevent reverse rotation. A typical recorded trace can be seen in Figure 2. Trace characteristics are explained in greater detail in the following section.

To obtain a reference scratch on the recording brass disc, the disc should be rotated manually a small amount in a counterclockwise direction, (about 5 degrees or an arc of

1/16 inch), while it is seated in its position in the gage and at a time when the structure is being strained at a known value. This method is used to zero-in the gage after installation.

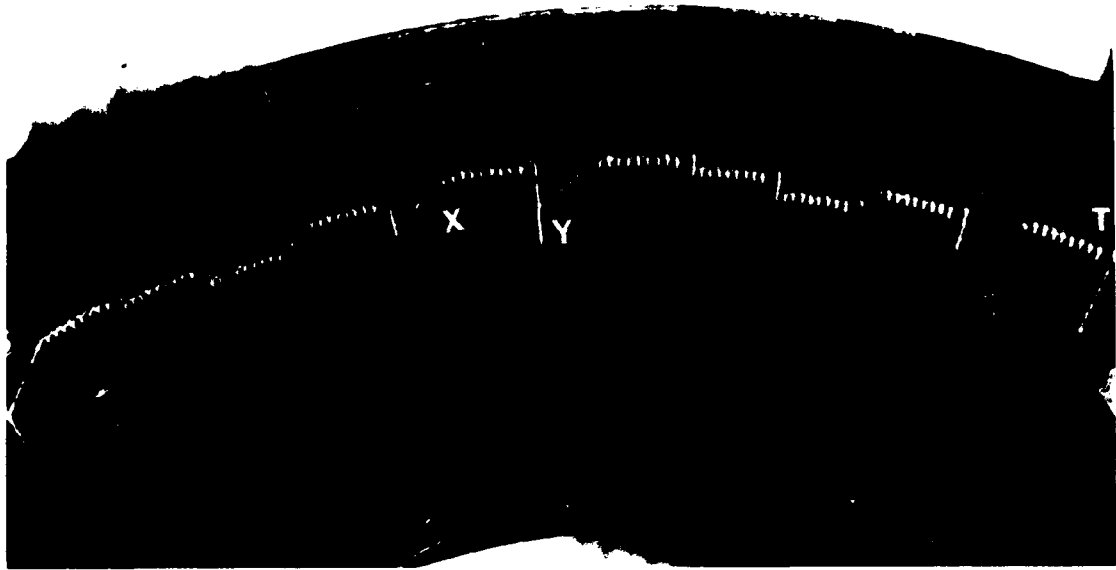
Three standard lengths, three-, six-, and 12-inch, are available. However, longer gages can be obtained.

### 2.3 Scratch Description

The scratch on the disc, as shown on Figure 2 and the sketch, Figure 3, follows a specific pattern. The vertical part, A-B, (solid line in sketch) or that portion which is perpendicular to the disc tangent, is made by an elongation or a tensile strain. The slanted part, B-C, (dotted line in sketch) is made by a contraction or a compressive strain. The arc S-T is used as a reference line to separate and directly measure tensile and compressive strains. The actual edge of the disc can also be used as this reference.

Special note should be taken of the scratch (X, Figure 3). This is apparently due to a built-in tolerance within the gage assembly. A small amount of the gage contraction is needed for the wires (D, Figure 1) to become seated in the disc groove before producing rotation. This

Figure 2.  
Actual  
Scratch  
on the  
Brass  
Disc.



amount of contraction is estimated to be approximately 0.002 inch.

Any additional overlapping of the scratch (Y, Figure 2 and Figure 3) is a consequence of the gage gap being set too great. In other words, the elongations experienced are so large that the wire tension in the disc groove is reduced to such an extent that the wires are unable to rotate the disc during the initial contraction.

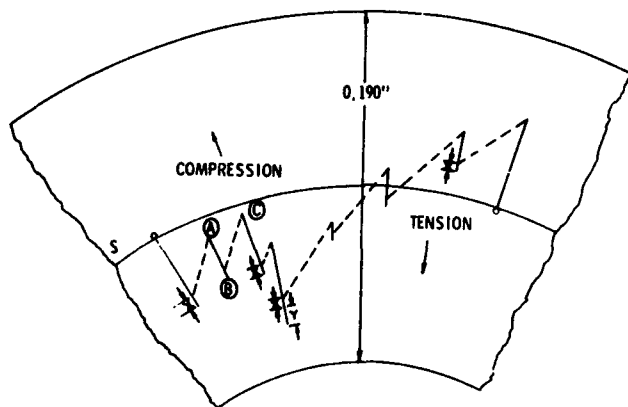


Figure 3. Typical Scratch Representation.



Figure 4. Gage Being Pressed In Place.

## 2.4 Gage Installation

The basic installation and operation of the gage is quite simple. However, certain precautions, must be taken when installing the gages. (1) The direction of principal strain to be measured should coincide with the longitudinal axis of the gage (Figure 4). (2) The free or spanning length of the gage (L, Figure 1) must be accurately known. When mechanical fasteners are used for installation, there is no problem. However, when an adhesive bonding is utilized, a barrier or dam should be used to restrict the area which is being bonded thus having an accurate dimension for the spanning length. In this program the six- and 12-inch gages were bonded and a piece of aluminum foil taped in place, as shown in Fig 5, accomplished the desired effect. The two taped-on aluminum foil patches (A & B, Figure 6) were used as frictionless buckling restraints for the longer 12-inch gage, since the longer unsupported length has a tendency to bow away from the structure.

After the gage is fastened to the structure to be tested, the brass disc is placed in position under the stylus,



Figure 5. Aluminum Foil Barrier Taped in Place.



Figure 6. Taped-On Aluminum Foil Buckling Restraints On the Twelve-Inch Gage.

making certain that each of the rotating wires is guided into the groove of the disc. The stylus is then allowed to rest on the brass disc. Slight mention will be made at this point of the gage installation gap, dimensions X and Y (Figure 7). These dimensions are critical because they control the rotation capabilities of the gage at various strain levels. This will be explained in greater detail in the following paragraph.

For the purpose of an expedient evaluation, all three gages, three-, six-, and 12-inch, were mounted on the same specimen, as shown in Figure 8. Since these mountings



Figure 7. Scratch Gage with Dimensional Gage Gap.

were to be somewhat permanent, epoxy glue was used to install the 12-inch and the six-inch gages. The three-inch gage was installed with self-tapping screws.

Electrical resistance strain gages were also mounted to monitor the strain application (E & F, Figure 1). A permanent oscillograph record of each test was used for direct correlation with the disc traces.

## 2.5 Test Program

All tests were conducted with a 7075-T6 ( $E = 10.3 \times 10^6$  PSI) aluminum alloy sheet specimen with dimensions as indicated in Figure 9.

With the gages (scratch and electric) installed as indicated in Figure 8, the specimen was mounted in a 50,000 lb. capacity hydraulic test fixture. Cyclic loading was controlled either manually or with magnetic tape. A nominal loading rate of 0.5 CPS was maintained throughout the test.

Three separate types of loading conditions were applied throughout this program. Condition No. 1 (Figure 10) was a series of constant amplitude load applications and was used for initial system checkout. Condition No. 2 (Figure 11) was a taped stress profile for a typical tactical fighter training mission which included three low level runs, three bombing runs, three strafing runs, and the return flight. Condition No. 3 (Figure 12) was a series of constant amplitude cyclic loads with constant stress range and decreasing mean stress level.

Specimen geometry precluded the possibility of applying axial compressive loads during this investigation. In order to record and observe compressive strains, the beam was manually deflected in bending. Trace characteristics in compression are similar to those in tensile elongation and

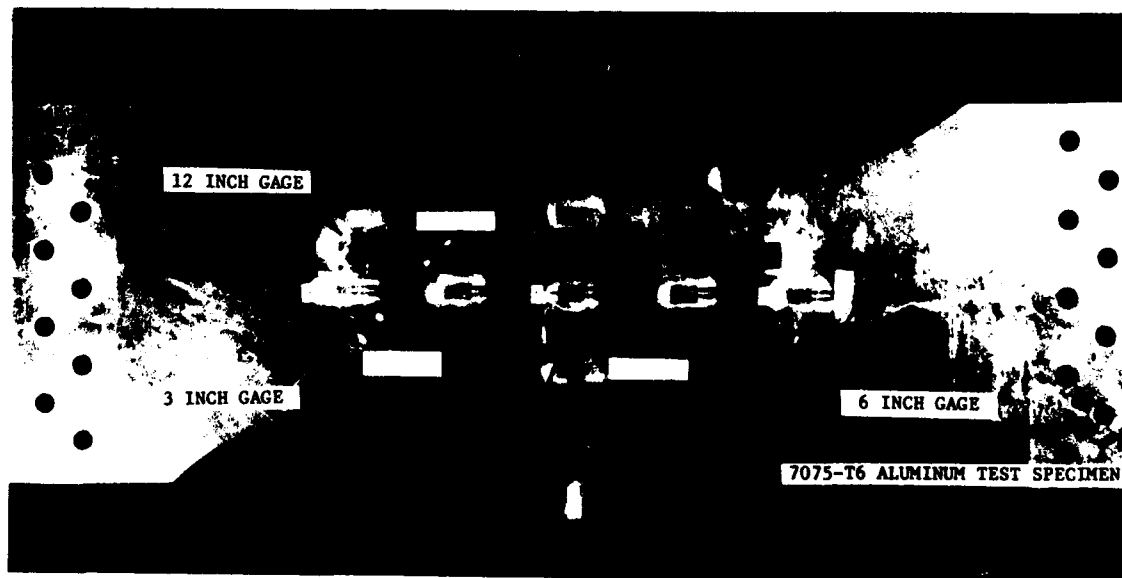


Figure 8. Scratch Gages (Three-, Six-, and Twelve-Inch) Mounted on the Test Specimen.



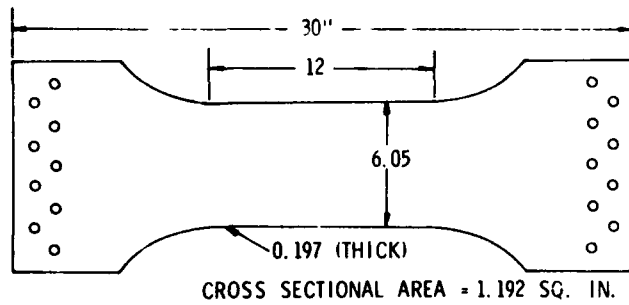


Figure 9. 7075-T6 Aluminum Test Specimen.

have been further described in Section 2.3. No quantitative measurements of compressive strains have been included in this summary.

### 2.6 Test Results

To initiate the testing program, loading conditions numbers 1 and 2 were applied to the specimen with all three gages actively recording. Upon completing one set of loads, the discs were removed, examined, and the traces photographed through a 50X microscope. Correlations with the output of the two electrical resistance strain gages were made.

Under normal operation, strain sensitivity and total disc rotation would be expected to increase with increased gage length. However, during the initial test phase the following observations were made:

- (1) The three- and six-inch gages operated well and recorded strains lower than anticipated or advertised by the manufacturer. (0.004 inch/gage length, Reference 2).
- (2) The six-inch gage disc rotated more than either the three- or 12-inch for the same strain levels and number of cycles.
- (3) Under improper installation, certain malfunctions would occur.

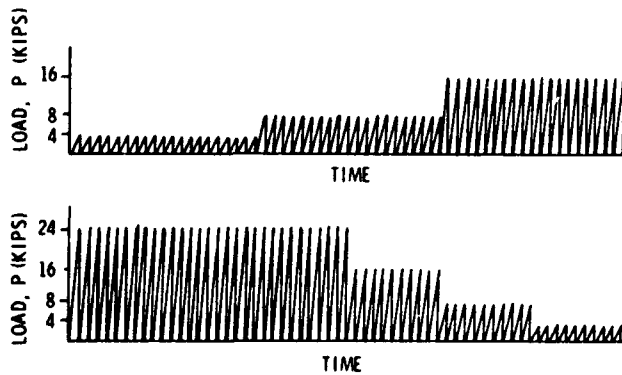


Figure 10. Condition No. 1 Loading Profile.

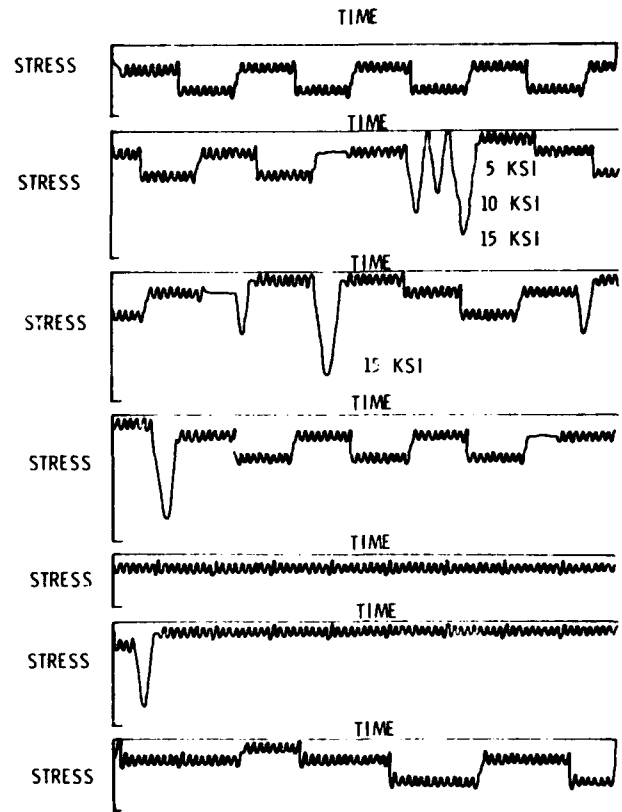


Figure 11. Condition No. 2 Stress Profile.

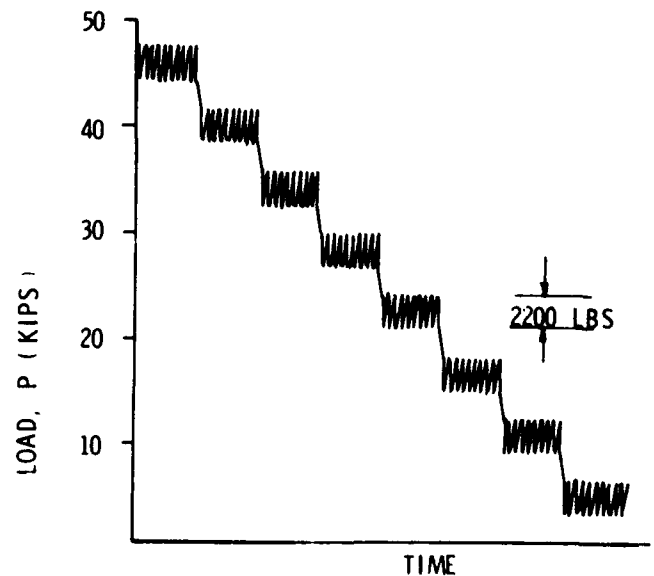


Figure 12. Condition No. 3 Loading Profile.

**TABLE I**  
**GAGE GAP INSTALLATION COMPARISON**

L IN.	X IN.	Y IN.
3	0.043	0.043
6	0.032	0.031
12	0.071	.048

(4) The 12-inch gage disc rotated only at strain levels greater than 160 micro-strain and less than 400 micro-strain.

(5) At strain levels outside the range of 160  $\mu\epsilon$  – 400  $\mu\epsilon$  the stylus of the 12-inch gage remained in the same vertical groove and required either a much greater or a much smaller strain to allow the stylus to escape and the disc to rotate.

The last observation was caused by improper installation. Examination of the gage installation gap (Figures 7 and 13) revealed that the 12-inch gage had been installed in a "cocked" position as indicated in Table I.

The 12-inch gage was removed and reinstalled, setting both X and Y equal to 0.040 inch. Again, the variable stress profile, loading condition number 2 was applied; once as per Figure 11 and then repeated with all loads increased by 50%. The results were more favorable since an improved sensitivity to individual strains was noted (the lowest being 190 micro-strain), as well as an increased revolution of the disc. The disc capacity was exceeded with less than two complete condition number 2 programs applied. This is indi-

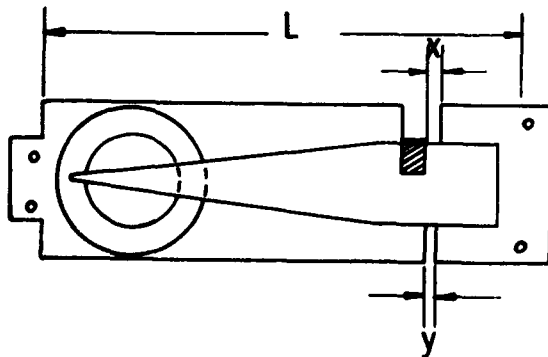


**Figure 13. Gage Gap Illustration.**

cated in Figure 14 which is a photograph of the recording disc utilized in this sequence. The portion of the trace which overlapped is discernible and can easily be read with the microscope.

To examine the effect of mean strain on gage sensitivity, the third loading program was applied with all three gages in operation. The sequence of loads of Condition No. 3 produced eight sets of constant strain range with seven reductions in the mean strain level.

The three- and six-inch gages recorded the variation in mean strain levels but failed to record the ten cycles of superimposed  $\Delta P$  (2200 lbs) alternating about the mean. The 12-inch gages failed to separate the first four mean strain reductions, but did separate the last three. It also recorded each individual cycle of  $\Delta P$  during the last three variations in mean load.

To examine these observations, the 12-inch was reinstalled with a reduced gage gap of 0.020 inch (dimensions X and Y, Figure 7). Loading condition number 3 was re-applied and the gage recorded and separated all strain values less than 3000 micro-strain. However, about this limit the disc would not rotate because the wire brush tension was reduced to a small portion of that required for effective rotation. The increase in tensile mean strain thus effectively increases the installation gage gap and reduces the gage rotation sensitivity.

Upon comparing the results of two separate installation gaps, a pattern is seen to evolve. With an installation gap of 0.040 inch, the maximum rotating tensile strain is 1750 micro-strain. With a gap of 0.020 inch, this maximum increases to 3000 micro-strain or within 500 micro-strain of being twice that of the first installation. At 3000 micro-strain, an increase in elongation of 0.036 inch on the 12-inch gage is experienced which at this maximum point increases the total gage gap 0.020 inch to 0.056 inch. The maximum strain of 1750 micro-strain recorded with the first installation is produced by an elongation of 0.021 inch which increases the gap from 0.040 inch to 0.061 inch. Thus it is apparent that the 12-inch gage disc fails to rotate when the total gap becomes greater than  $\approx 0.056$ . Therefore, if an estimate is made of the maximum value of strain to be recorded, the proper installation gap can be estimated by multiplying the maximum strain by the gage length (12-inch in this case) and subtract the constant, 0.056 inch.

Although the preceding values were derived for the 12-inch gage which was examined, the same relationship should hold for any gage length so long as loading is always tension-tension. A typical gage gap installation curve might be constructed on Figure 15.

If compressive strain is to be measured, gage installation techniques should account for the possibility of completely closing the gap. Observance of the compressive recording region of Figure 15 will preclude this possibility.

START OF CONDITION II  
STRAIN RECORD

END OF 50% INCREASE OF  
CONDITION II STRAIN RECORD

1/8      1/4      3/8

1/2 inch TO SCALE

END OF CONDITION II STRAIN RECORD

START OF 50%  
INCREASE OF  
CONDITION II  
STRAIN RECORD

Figure 14. Brass Disc Containing the Strain Recording of Loading Condition No. 2 and 1.5 Times Loading Condition No. 2 Application.

### III. IN-HOUSE FLIGHT TEST EVALUATION PROGRAM

#### 3.1 Evaluation Program

An in-house flight test program has been completed with favorable results<sup>3</sup>. Three scratch gages were installed on a USAF trainer aircraft for the purpose of determining sensitivity, capacity, and overall recording capabilities of the gage under actual flight conditions.

The aircraft used for this program was especially suited for scratch gage instrumentation in that it was a flight loads survey aircraft involved in a flight test to determine stress levels in the lower front spar cap and lower front spar root fitting. Thirty-four electrical resistance strain gages were installed on the right wing in the area just described. An accelerometer was installed at the aircraft center of gravity. The scratch gages were installed in the critical spar region close to the electrical strain gages so that data correlation between the two types of gages could be made. The spar geometry is especially suited for the scratch gage installation because of the flat exposed flange which is of adequate width to accommodate the gage. High positive and low negative g (acceleration of the center of gravity of the aircraft) loadings were experienced during eight individual flights of approximately one hour duration each.

#### 3.2 Installation of Gages

Scratch gages were installed on both main spars at the locations indicated in Figure 16. The mid point of the gage spanning length was coincident with W.S. 64 in all locations. At the time of installation, the aircraft fuel tanks were empty.

The spar cap flange (Figure 17) was buffed with emery cloth at the point of the gage attachment to remove any paint or oxide coating on the surface in order to insure adequate bonding. Each gage was then fastened to the exposed flange of the spar cap using epoxy adhesive. Pressure was applied to the gage ends on the upper wing surface during the curing period with metal "duck" weights as seen in Figure 18. Wooden props, shimmed up from the hangar floor, were used for the lower wing surface installation. (Figures 19 and 20).

All of the above installation procedures for the three gages were performed in approximately one hour after the aircraft was rolled into the hangar. The adhesive was allowed to cure overnight.

During installation, the gage gap of all gages was set at 0.025 inches. This value was predetermined based on an estimate of maximum strain expected and the equation  $\epsilon_{max} = (0.056 - G.G.) / L$ . (Ref. 2).

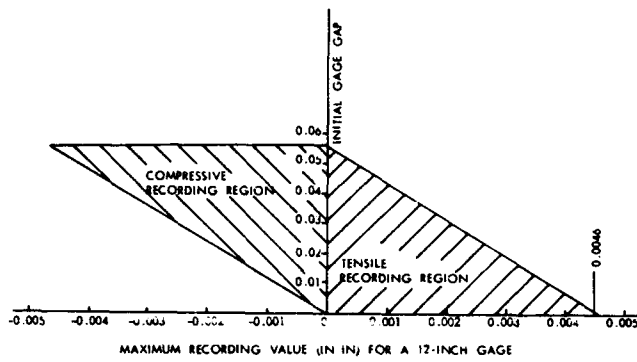


Figure 15. Gage Gap Installation Curve.

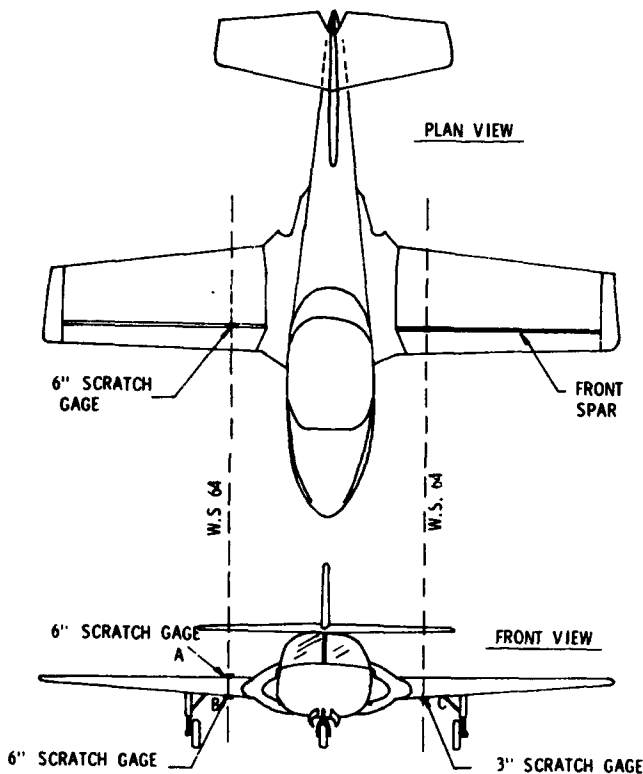


Figure 16. Plan View of and Front View of a Jet Trainer Aircraft Illustrating Scratch Gage Locations.

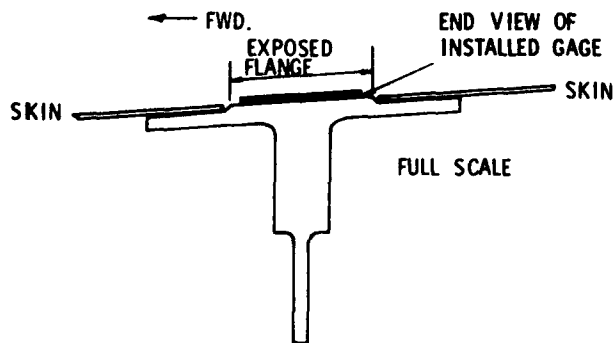


Figure 17. Upper Spar Cap Cross Section.



**Figure 18. Six-Inch Scratch Gage Being Mounted on Upper Spar Cap.**

To complete the gage installation, the brass recording discs were inserted and the stylus allowed to rest on the recording surface. Before each flight, the disc was manually rotated counter-clockwise through a small angle to produce an arc (A, Figure 21) which could later be used as a reference data point for strain measurement. This arc also provided an index to separate data on a flight-by-flight basis.

The final step of the installation procedure was the fastening of a prefabricated cover over each gage (Figure 22). The covers were shaped from 0.020" aluminum sheets and were provided with a plexiglass window directly above the brass disc in order that the gage disc could be observed without removing the cover. Strips of 3" wide adhesive tape were used to hold the covers in place, thus allowing easy removal for the purpose of gage inspection and flight indexing. The covers were required to protect the gages from foreign object damage during taxi, take-off, and landing; and in addition, provided moisture-proofing protection since any ice formation could be detrimental to the gage operation. The covers projected approximately  $\frac{1}{4}$ " above the wing surface but caused no apparent aerodynamic effects on this aircraft. They did provide the desired protection of the gages during the entire flight program which lasted about 3 weeks. No de-bonding of the gages or covers occurred at any time during the program.

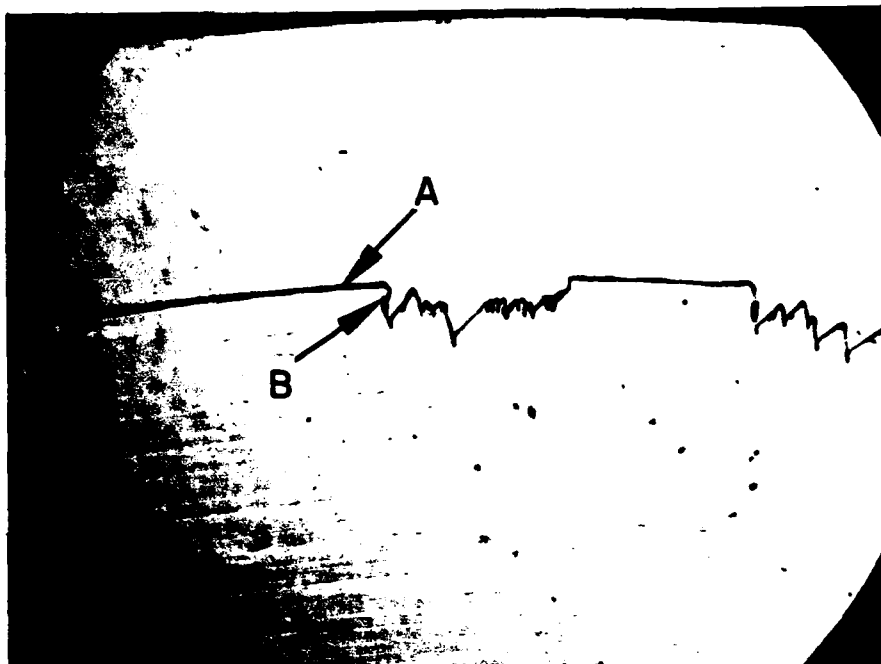


**Figure 19. Installation of Six-Inch Scratch Gage on Lower Spar Cap.**



**Figure 20. Pressure Application Using Wooden Props.**

**Figure 21. Photomicrograph of Flight No. 2, Scratch Strain Record.**



### 3.3 Flight Program

The flight program<sup>4</sup> was composed of two phases. Phase I consisted of various low g and high g maneuvers. The following is a list of Phase I flight maneuvers.

- |   |  |
|---|--|
| <ul style="list-style-type: none"> <li>(1) Level flight cruise</li> <li>(2) Positive maneuvers             <ul style="list-style-type: none"> <li>(a) Approximately 4.0, 5.0, and 6.0 g's at minimum airspeed.</li> <li>(b) Approximately 4.0, 5.0, and 6.0 g's at minimum airspeed of 370 knots.</li> </ul> </li> <li>(3) Negative maneuvers at approximately -1.0 and -2.0 g's.</li> <li>(4) High speed LH and RH rolling pullout at approximately 4.5 g's.</li> <li>(5) Landing impact at a sink rate greater than 5 ft./sec. (at high gross weight).</li> </ul> | <ul style="list-style-type: none"> <li>(8) Spin prevention</li> <li>(9) Simulated single-engine pattern and landing</li> <li>(10) Maximum performance climbing turn</li> <li>(11) Lazy eight</li> <li>(12) Aileron roll</li> <li>(13) Loop</li> <li>(14) Immelmann</li> <li>(15) Clover leaf</li> <li>(16) Barrel roll</li> <li>(17) Cuban eight</li> <li>(18) Split "S"</li> <li>(19) Power on stalls</li> <li>(20) Secondary stalls</li> </ul> |
|---|--|

Phase II of the flight program consisted of individual maneuvers taken from the Air Training Command flight syllabus. The following is a list of these flight maneuvers.

- (1) Runaway trim
- (2) Recovery from vertical flight
- (3) Recovery from inverted flight
- (4) High speed dive recovery
- (5) Slow flight
- (6) Traffic pattern stalls
- (7) Spin recovery



**Figure 22. Gage Cover.**

Nine flights were required to complete Phases I and II with a total of 9 hours and 35 minutes of actual flight time logged. Visual Flight Rule Conditions prevailed at all times, with outside temperature approximately 31°F. Flight No. 1 (70 minutes duration) and flight No. 2 (45 minutes) were instrumentation check flights. Various adjustments and corrections were needed for several of the electrical resistance strain gages and/or their oscillograph channels. The three scratch gages required no adjustment after the initial installation. Flight No. 3 (75 min.) included all of the maneuvers from Phase I with the exception of the individual impact landings. Flights No. 4 (80 min.), No. 6 (80 min.), and No. 7 (65 min.) consisted of the maneuvers from Phase II. Flights No. 8 (45 min.) and No. 9 (35 min.) accomplished the individual impact landings. The oscillograph traces for Flight No. 8 were unsatisfactory due to malfunctioning of electrical recording equipment, but the scratch gages functioned satisfactorily at all times.

### 3.4 Results

#### 3.4.1 Disc Capacity

The capacity of the brass recording disc for any specific installation is dependent on the amplitude of the strains which it records, the frequency of which they occur, and the length of the gage. For the entire Phase I and II flight program described, the 3" gage disc rotated approximately 1/3 of a revolution. (Including the small flight index arcs). The 6" gage discs each rotated almost 1½ revolutions producing a trace overlap of about ½ revolution. More will be said concerning this overlapped portion later in this section.

It is obvious from the above discussion that the length of the gage does influence the amount of rotation of the discs indirectly, in that the smaller gust loads are not sensed by

the shorter 3" gage, consequently there is no rotation. However, with the longer 6" gage, all load ranges of ½ g or more are recorded.

Based on these observations, it would be expected that the 3" gage disc would make one full revolution with 30 hrs. of flight time similar to the flight program used herein. For similar usage, the 6" gage disc should rotate completely with approximately 7 hours of flight time. These time capacity estimates do not account for the manual indexing of the recording disc. In actual operation, flight separation would normally not be necessary unless an indication of the maximum strain range (ground-air-ground) for each flight was desired.

#### 3.4.2 Trace Characteristics

The minimum strain range value recorded by the 3" scratch gage was 600  $\mu\epsilon$  (Ref. 2). This is more sensitive than the response level stated by the manufacturer. In terms of center of gravity g loading, this is equivalent to individual occurrences of approximately 1.5  $\Delta$  g. This means that all vibrations and even small gust accelerations were not sensed by the gage.

The 6" scratch gage on the lower right spar cap (B, Fig. 16) had a minimum threshold strain range sensitivity of 250  $\mu\epsilon$  (Ref. 2) and was capable of recording all  $\Delta$  g loading occurrences of ½g and greater. Thus, some gust loads and small secondary g ranges in between primary peaks were sensed and registered. All gages performed equally well during the negative g maneuvers as during the positive regions. Individual sensitivity remained the same.

Figure 23 is a photomicrograph of the 3" gage recording of the entire flight No. 5 (80 minutes). The large excur-

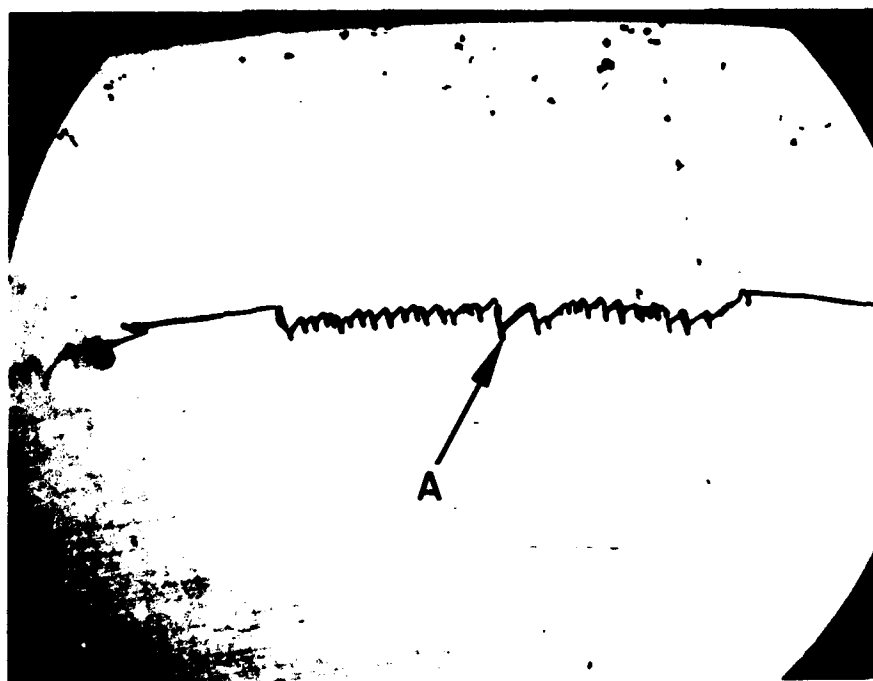


Figure 23. Three-Inch Gage Recording of Flight No. 5.

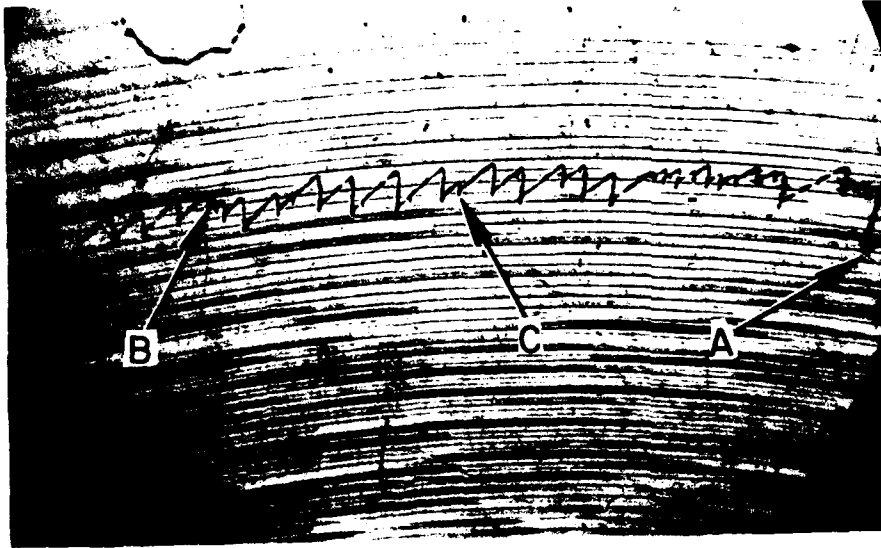


Figure 24. Six-Inch Gage Recording of the First Half of Flight No. 5.

sion in the center of the trace (A, Figure 23) represents a strain of  $2340 \mu\epsilon$  or an acceleration of the center of gravity of approximately 6 g's. After examining the pilot's log, it was discovered that this high load factor was produced during a recovery from a high speed dive. For the purpose of a visual comparison, Figure 24, a photomicrograph of the first half of flight No. 5 recorded by the 6" gage, is presented, and includes the same large 6 g load recording (A, Figure 24). (The magnification is the same for both photomicrographs, 25X). The recording of various small maneuver and gust loads (B and C, Fig. 24) are apparent in the 6" gage trace but are not present in the 3" gage trace.

The index arc, (A, Fig 21) which has been mentioned previously in this report, was made after each flight by a flight technician who manually rotated the disc a small amount in a counter-clockwise direction. The disc will rotate in this direction only. It had been intended that this arc serve as a zero strain reference for calibration purposes. However, this method was not acceptable as can be seen in Figure 21. Upon examination of the scratch trace, it was noted that each strain excursion returned to the same strain level. This, by definition, is the trim stress level or the stress level caused by a 1 g flight configuration. Calibration was accomplished by using point B, (Fig 21) as the true reference zero strain level. This strain level is considerably different than the strain level A, (Fig 21), produced during rotation; one possible reason being that the disc was not rotated with a pure torque motion, but was pulled slightly away from the rollers. Another possibility is that the stylus arm moved laterally a small amount with the rotation of the disc and then sprang back. This motion produced the hook in the scratch from A to B (Fig 21).

Means of alleviating this problem are under further investigation at the present time by the gage manufacturer. One solution which has been used is a complete circumferential scratch manufactured on the disc which is used as a reference strain level.

#### IV. STRAIN MEASUREMENT

The stylus makes a permanent record of total axial deflection over the gage length. Conversion to strain requires accurate measurement of the effective gage length and scribed trace amplitude. Effective gage length is dependent upon the method of installation, and this item was discussed in Section II.

##### 4.1 Laboratory Investigation

Two methods of measuring trace amplitude were attempted:

- (1) Measurement from a photomicrograph of the disc.
- (2) Direct measurement of the trace with a calibrated microscope.

Measurements obtained by each method were divided by effective gage length to obtain average strain and the results compared with electrical resistance strain gage readings. Tables II and III include comparative values obtained by each method encompassing nearly the entire range of strain values employed in this study.

Figure 25 includes a portion of the disc obtained from the six-inch gage with magnification of 25X. The magnification value was obtained by measuring a portion of the arc and chord length from the photograph and comparing this measurement with the known true dimension of the disc. Even with this relatively simple and crude method, accuracy is noted to be quite good.

The variation in readings between the photographs and the strain gage was usually less than 100 micro-strain (Table II).

The second method of measuring the trace amplitudes requires a great amount of care, especially at the



**TABLE II**  
**COMPARISON OF SCRATCH GAGE STRAIN READINGS TO**  
**ELECTRIC GAGE STRAIN READINGS**

Photograph Comparator Method

3-INCH SCRATCH $\mu\epsilon$	ELECTRIC $\mu\epsilon$	6-INCH SCRATCH $\mu\epsilon$	ELECTRIC $\mu\epsilon$	12-INCH SCRATCH $\mu\epsilon$	ELECTRIC $\mu\epsilon$
667	680	236	280	355	320
1000	1080	675	600	710	680
1450	1400	1015	1000	1340	1400
2000	1880	1350	1320	1770	1800
2140	2040	2840	2780	1940	2040

**TABLE III**  
**COMPARISON OF SCRATCH GAGE STRAIN READINGS TO**  
**ELECTRIC GAGE STRAIN READINGS**

Calibrated Microscope Method

3-INCH SCRATCH $\mu\epsilon$	ELECTRIC $\mu\epsilon$	6-INCH SCRATCH $\mu\epsilon$	ELECTRIC $\mu\epsilon$	12-INCH SCRATCH $\mu\epsilon$	ELECTRIC $\mu\epsilon$
430	350	250	300	166	217
1000	920	930	920	242	289
1100	1120	1133	1120	1075	1120
1300	1360	1310	1360	1766	1850
1830	1860	2700	2780	1850	1920

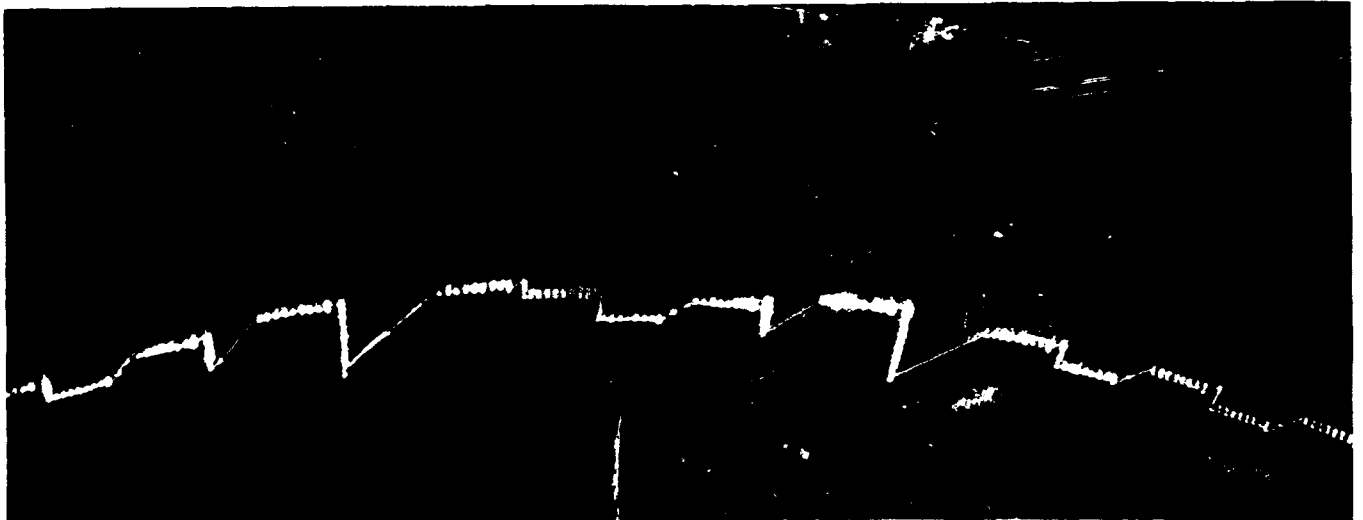


Figure 25. Photomicrograph of Six-Inch Gage Disc.

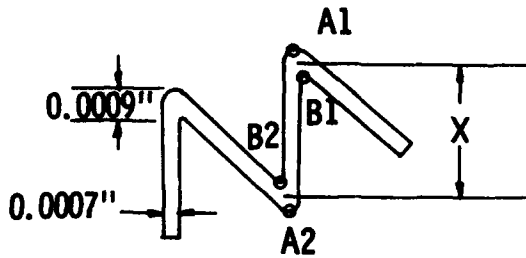


Figure 26. Typical Dimensioned Scratch.

lower strain levels, due to errors which may occur in the determination of the actual path of the trace and the center of the scratch. The scratch itself is 0.0007 wide, and the vertex or peak dimension, 0.0009 inch. (Figure 26). Consequently, if distances A1-A2 or B1-B2 are read instead of the true value, X, a significant error will be introduced. Readings for this investigation were obtained with a 100X microscope with a traveling table capable of reading 0.0001-inch increments. Measurements were made from a reference zero point to the estimated center of the scratch. The comparative results are summarized in Table III. The precision of this method is on the same order as method one which is usually less than 100 micro-strain.

#### 4.2 Flight Test Investigation

Two procedures were used to reduce the scratch data. Both were manual and employed different visual measuring techniques. The first method involved a closed circuit television camera which projected a magnified image of the scratch (2000 to 1 maximum) onto a 12" x 12" screen. As seen in Fig. 27, the resolution of the scratches was of good enough quality to permit measurement with a calibrated scale affixed to the television screen. The passing of the trace under the microscope was accomplished using a target rotating mechanism. An entire trace was processed by this method using a level crossing count method. This task was accomplished in a few minutes with a reading tolerance of less than  $50 \mu\epsilon$  for the 6" gages. Incremental counting levels of  $100 \mu\epsilon$  were used.

The data reduction technique termed the level-crossing count method is one of the various counting methods which can be applied for the purpose of analyzing load-time histories. By this method, a count is made each time the trace or scratch with a negative slope crosses a prescribed load level and these counts can be restricted to certain minimum and maximum load levels. This is illustrated in (Figure 28).

As was stated earlier, the trace on the brass circular disc in the six inch gage did overlap. A photomicrograph of

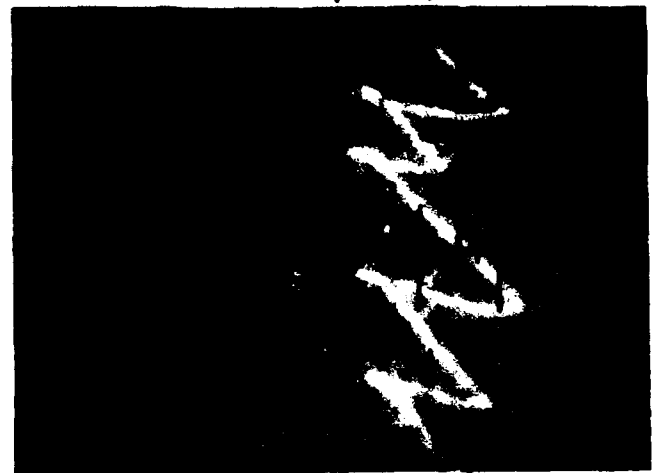
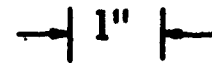
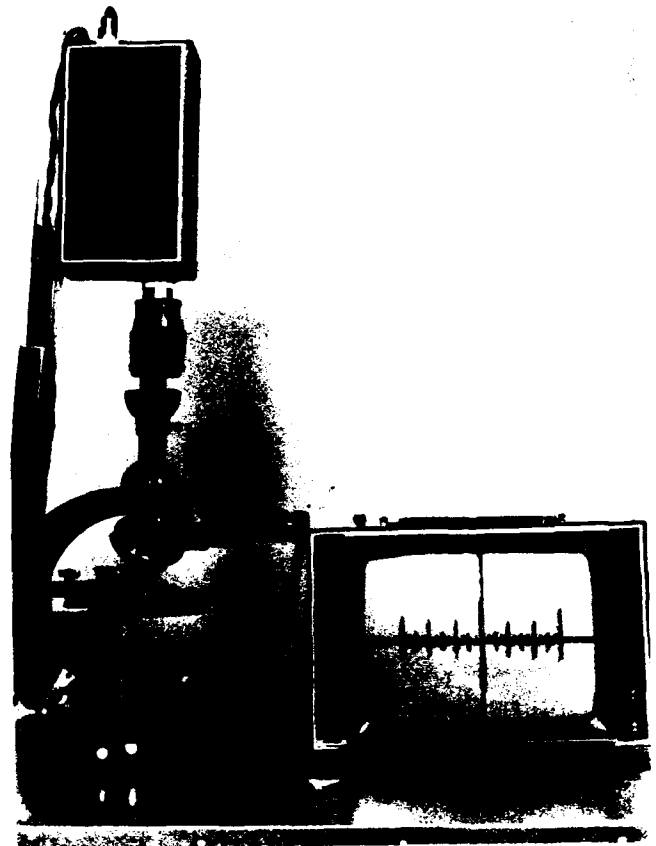


IMAGE OF SCRATCH

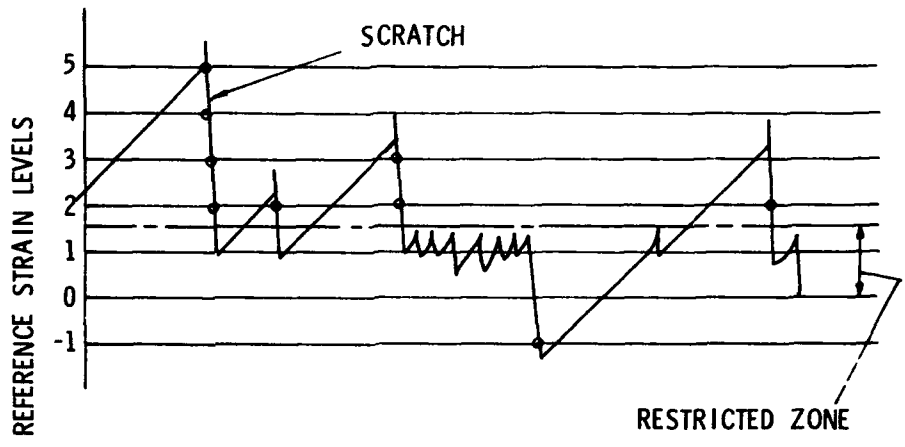
Figure 27. Television Camera Data Reduction System.

the overlapped portion is seen in Figure 29. It is evident that the path of one individual scratch is difficult and sometimes impossible to follow. Since this problem exists, the occurrence data of an individual flight cannot be reduced but rather the data reduction must be based on the disc as a whole. The overlapped trace would not be detrimental to

RESULTS OF COUNTS	
€ LEVEL	OCCURRENCE
-1	1
2	4
3	3
4	1
5	1

◦ DENOTES A COUNT

Figure 28. Level Crossing Count Method.



the level crossing counting method as long as the counting was restricted to levels above or below the 0 to +1.5 g recording zone, since this might be obscure as seen in Figure 29. The values of 0 and 1.5 were chosen since all small maneuver and gust loads occur within these boundaries. The level crossing counting procedure was utilized on an overlapped recording on a disc from the 6° lower surface gage. The results of this data retrieval are seen in Figure 30.

A single trace would be necessary for other types of counting methods, especially those involving strain ranges, since a critical and very meaningful range might extend from a positive value to a negative value or through the obscure region of the trace. Also, an overlapped trace should be avoided if automated data reduction techniques are used. These possible techniques will be presented in more detail later in the report.

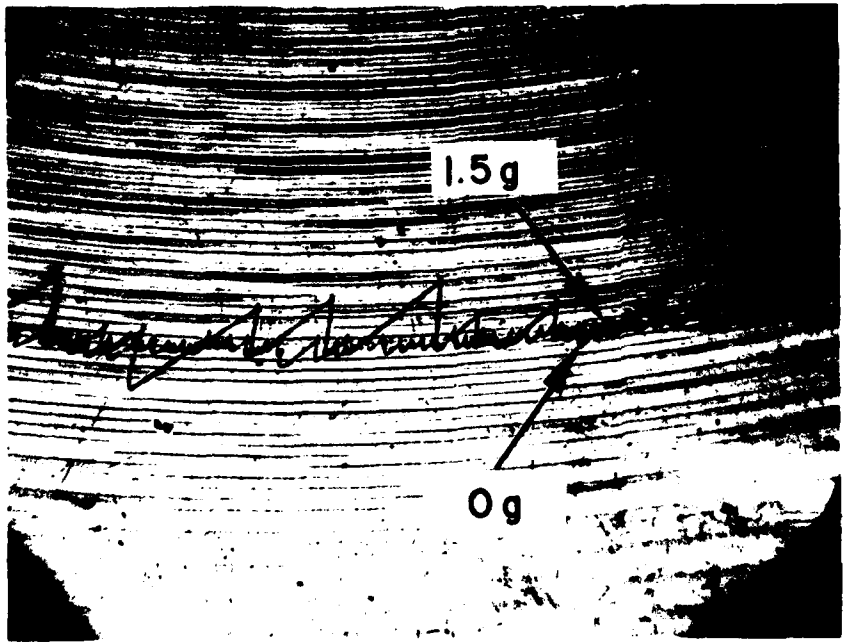


Figure 29. Photomicrograph Overlapped Scratch.

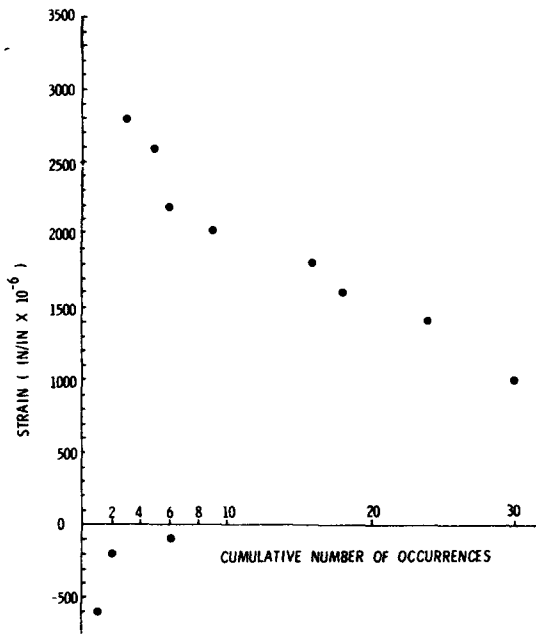


Figure 30. Strain Cumulative Occurrence Chart for Eight Hour Flight Program, Recorded by Gage "B".

The second manual approach used to reduce the data required the use of a calibrated microscope. By employing this type of setup, it was also possible to analyze a trace using the level crossing count method.

The reading tolerance using the calibrated microscope was again less than  $50 \mu\epsilon$  and usually within  $30 \mu\epsilon$  for the 6" gage.

To enhance the image of the scratch for measurement purposes, the scratch recorded face of the brass

TABLE IV  
FLIGHT NUMBER 5 MANEUVERS

Taxi	Recovery from Vertical and Inverted Flight
Take-off	Recovery from High Speed Dive
Split S	Slow Flight
Cuban 8	T.P. Stalls
Barrel - Roll	Left Spin
Cloverleaf	Right Spin
Immelmann	Maximum Performance Climbing Turn
Loop	Lazy 8
Aileron Roll	Single Engine Landing Touch and Go
Power on & Secondary Stalls	Normal Landing

disc was polished using a metallurgical specimen polisher. This reduced both the tarnish build up on the disc and also unwanted scratches which occurred through handling and manufacturing. Figure 31 shows the disc in its unpolished condition. This can be compared to Figure 32 which is the same portion of the disc in its polished condition. The effect of the polishing is evident and it obviously increases not only the ease by which the trace can be read, but also the accuracy of determining the true maximums and minimums of the strain cycles.



Figure 31. Photomicrograph of an Unpolished Disc.

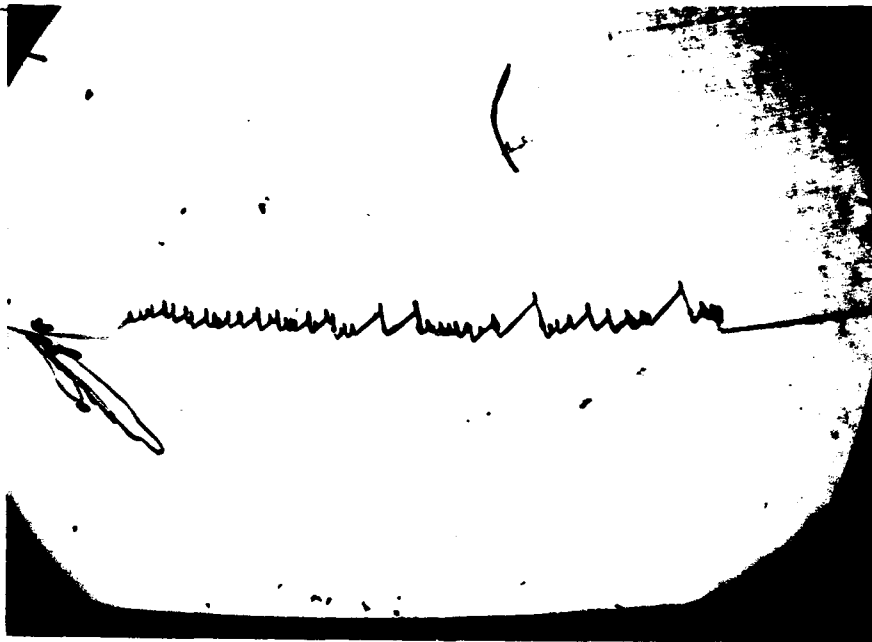


Figure 32. Photomicrograph of A Polished Disc.

*Data Correlation*

The main effort of correlating scratch gage data against electric gage data of the flight test program was centered around flight No. 5. Of the 30 electrical resistance gages installed on the lower right spar cap, No. 16 and No. 17 were used to correlate strains because of their proximity to the scratch gage (Figure 33). Electrical resistance strain gage data was recorded on a light beam oscillograph trace. The data comparison was performed mainly on a point-by-point basis.

The scratch gage readings used in the strain correlation were obtained merely from the 6" gage on the lower side of the right wing (Fig. 16, B).

Flight No. 5 consisted of the maneuvers shown in Table IV, performed in the order listed. The maneuvers

caused various loadings ranging from zero to a positive 5.5 g. Although all strain values were read from the oscillograph output for every maneuver, only a few typical individual occurrence points are presented. The variation of strain between gages 16 and 17, was very small; therefore, only one of the gages, No. 16, was used for reference purposes. The values recorded by No. 16 along with the corresponding scratch gage readings for the same load occurrences are shown in Table V. This is a small data sample presentation from all the strain readings recorded.

In order to convert the recorded scratch to an actual strain value, the scratch length was divided by the effective spanning length of the gage. This length is somewhat arbitrary due to adhesive width. For the purpose of this study the effective length was chosen as the distance between the centroids of the adhesive area (B, Fig. 34). If other choices; i.e., A, Fig. 34, are made, variations of 6% may result for the six-inch gage.

Figure 33. Location of Gages on Right Lower Spar Cap.

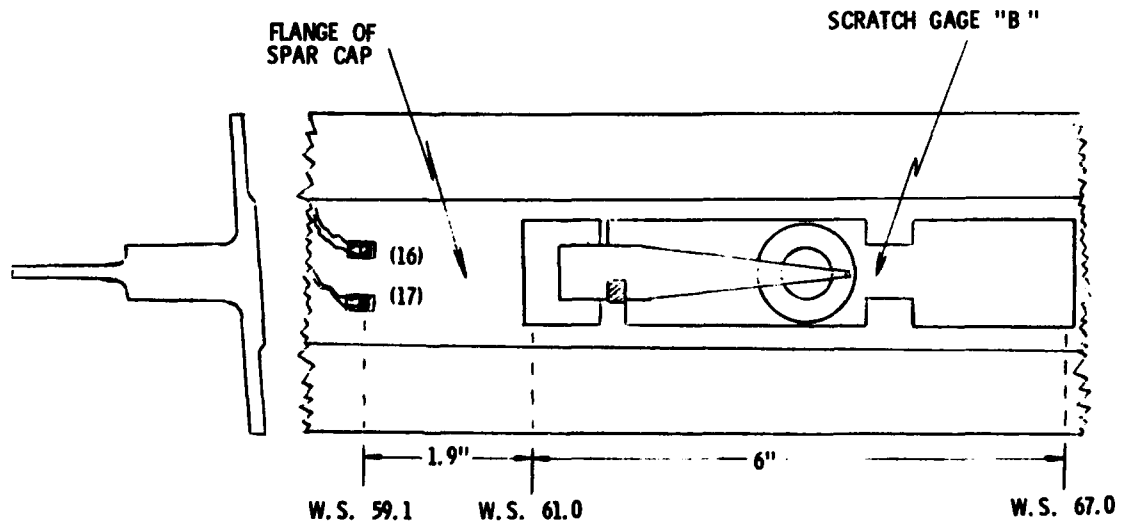


**TABLE V**  
**COMPARISON OF SCRATCH STRAIN GAGE READINGS**  
**TO ELECTRIC STRAIN GAGE READINGS**

MANEUVER	L = 6.19		$\Delta$
	ELECTRIC	SCRATCH	
CUBAN - 8	530	560	30
	1340	1320	-20
	490	560	70
	1220	1290	70
	300	380	80
	1060	1110	50
BARREL ROLL	1190	1210	20
	550	640	90
	1550	1550	0
	710	690	-20
IMMELMANN	1390	1380	-10
	290	400	110
	940	1000	60
RECOVERY FROM INVERTED FLIGHT	1320	1350	30
	-30	40	70
	690	740	50

It must be remembered that the scratch gage records an extension or contraction over a pre-set length; in this case, 6 inches. Therefore, the gage records not a unit strain, but an average strain value computed over the spanning length. Thus, installations should be avoided where large strain gradients exist over the gage length.

The correlation between the three-inch scratch gage and the electrical resistance gage No. 16 was very erratic for asymmetric maneuvers due to the fact that the gages were on opposite wings. The accuracy of the three-inch gage is shown by the correlation of data of a symmetric maneuver (Table VI).

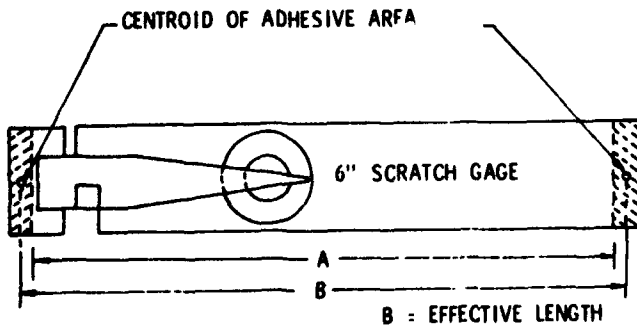


**Figure 34. Illustration of Effective Spanning Length of Gage.**

**TABLE VI**  
**MAXIMUM AND MINIMUM STRAIN DATA**  
**CORRELATION BETWEEN THREE-INCH SCRATCH**  
**GAGE AND ELECTRICAL RESISTANCE GAGE**  
**NO. 16 FOR A SYMMETRIC MANEUVER.**  
 ( $\Delta$  = Scratch Minus Electric)

ELECTRIC GAGE	SCRATCH GAGE	$\Delta$
$\mu\epsilon$	$\mu\epsilon$	$\mu\epsilon$
1380	1330	-50
540	520	-20
1450	1290	-160
180	150	-30
1320	1210	-110
-30	-30	0

### V. FINDINGS

The major results and significant observations of the laboratory and flight test programs can be summarized as follows.

- (1) The recording disc capacity depends upon the magnitude of the strains, the frequency of their application, and the length of the gage. Under normal operation, the six-inch gage disc rotated approximately one-half revolution for the mission profile application which simulates a flight of one hour and a half duration.
- (2) Either side of the brass disc may be used for recording.
- (3) The gage records all strain values (tension and compression).
- (4) Strain cycles are distinguished when rotation of the disc is present.
- (5) Rotation is produced by the contraction portion of the strain cycle.
- (6) A threshold or minimum amount of contraction is needed to produce rotation. This amount has been suggested as 0.004 inch by the manufacturer. Test results from this program indicate that 0.002 inch is sufficient.
- (7) Thus, for a properly installed gage, minimum threshold strain range of 0.002 inch/L inch may be recorded and distinguished.
- (8) Gage sensitivity is the minimum strain range capacity of the gage (the minimum value which will produce rotation).
- (9) Gage sensitivity is dependent upon the gage length.
- (10) Proper gage installation requires the installed gap to be less than some prescribed value in order that rota-

tion capabilities of the gage remain constant. For the conditions of this investigation, this value has been determined to be 0.056 inch, and should be the same for any gage length.

(11) Thus, the installation is sensitive to mean strain since this effectively changes the initial gap.

(12) The maximum strain value,  $\epsilon_{\text{max}}$ , below which a properly installed gage is sensitive, may be determined with the aid of the following empirical formula

$$\epsilon_{\text{MAX}} = (K - GG) / L$$

where  $K = 0.056$  inch

$GG =$  gage gap (inch)

$L =$  spanning length of the gage (inch)

(13) The random sampling of the flight test results presented herein indicates that the gage is capable of recording all maximum and minimum strain values produced by typical fighter aircraft maneuvers.

(14) All damaging strain range cycles can be detected and recorded with a proper choice of gage length. ( $L \geq 0.002 / \Delta\epsilon$ ).

(15) It appears to be reasonable and is recommended that the gage spanning length be taken as the distance between the centroids of the glue strips (B, Fig. 34).

(16) Individual strain readings as large as  $2400 \mu\epsilon$  were recorded during the flight program. Maximum recording limit values of  $5000 \mu\epsilon$  (tension) and  $4000 \mu\epsilon$  (compression) were possible with the 6" gage. The three inch gage had twice this capacity.

(17) If the recordings of individual small maneuvers (less than 2 g) and gust strains are not necessary for damage calculations, the three-inch gage would be adequate and would allow a minimum of 30 hours flight time in between disc replacement. If the recording of the small loads was necessary, a six inch gage would be required and the flight time recording capacity would be reduced to approximately eight flight hours per one revolution of the brass disc.

(18) Laboratory tests have been conducted and have shown that the strain recording capacity of the gage is not affected by variable frequency strain cyclic loading from 0 cps to 4 cps.

## VI. SYSTEM APPLICATION

As an illustration of fleet usage, the instrumentation of an entire jet trainer aircraft fleet is considered. The program would involve 800 individual aircraft located at 12 Air Force Bases, and would be concerned with the wing spar and carry-through structures only. (This is not to say that the strain data collected could not be used in some manner for the tail section fatigue calculations). The number of gages per aircraft would be determined by the previously conducted fatigue tests. One gage might be sufficient if appropriate stress transfer functions could be determined for each fatigue-critical location. The stress monitoring of the critical locations on the front spar and carry-through structure of the jet trainer in question, Figure 35, could likely be accomplished using one scratch gage carefully located. If this is impossible, or if it is necessary to separate symmetric maneuvers from non-symmetric maneuvers, then two or more gages per aircraft would be required.

The points of installation would be dependent on the stress transfer function, the size of gage (3-inch or 6-inch) and the accessibility of the installation area. If the gage was to be installed on the exposed flange of the spar cap (lower

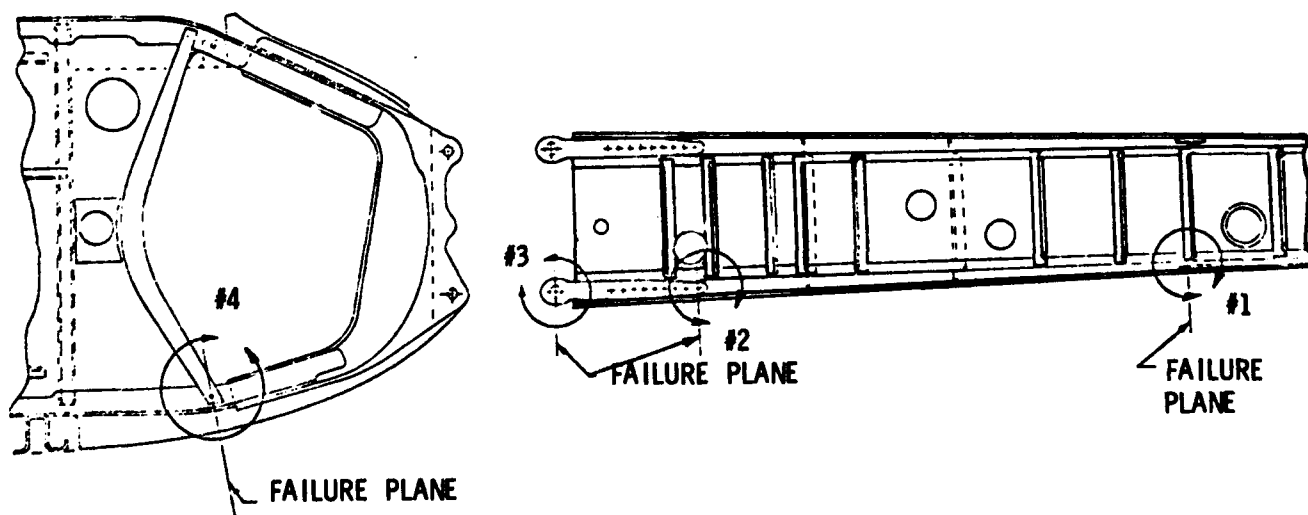


Figure 35. View of Wing and Fuselage Front Spar, Depicting Location of Critical Areas in Fatigue (L.H. Side Looking Aft).

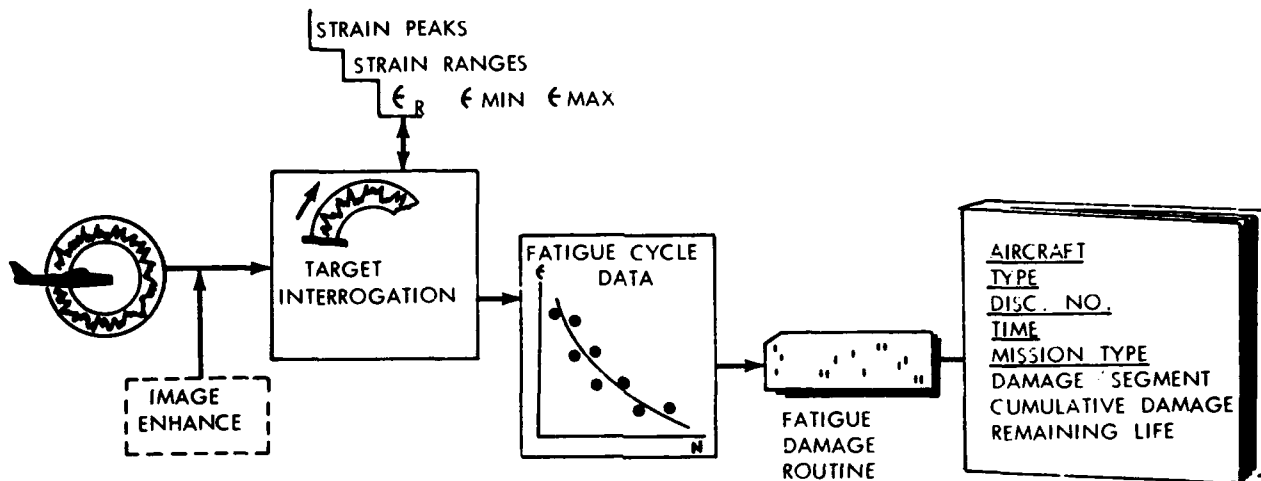


Figure 36. Tail Number Fatigue Life Monitoring System for Fighter Aircraft.

or upper) as in the flight test, a more sophisticated cover design would be necessary. The gage could also be bonded or clamped to an internal structural member thus precluding any necessity for a gage cover. It must, however, be near an access hole of some sort since periodical gage inspection and disc replacement is inherent to the program.

Based on flight test data presented previously in this paper, a recording disc would make one revolution in a three-inch gage for 30 hours of flight time. A flight time usage figure for the aircraft in consideration is 55 flight hours per month per aircraft. Therefore, to insure no overlapping of the scratch trace on the brass disc, (one revolution), replacement should be made at least once every two weeks. This operating procedure would produce two discs per month for each aircraft in the fleet or 1600 discs per month. If two or more gages are installed on each aircraft, the disc data output would be increased proportionally.

This abundance of recorded scratch data suggests the need for an automatic disc interrogation and data retrieval system on a regularly scheduled basis which would be required for an efficient and economical damage monitoring program. In its ultimate sense, such a system would, in a minimum number of operations, transpose target information into an increment of fatigue damage sustained during the operational time period contained on the disc. Figure 36 is a schematic of such a system.

The basic steps of this type of system would be the following:

- (1) Instrumentation of fighter and/or trainer aircraft on a fleet-wide basis.
- (2) Electronically and automatically reduce the data contained on the discs by digitizing it using the various counting methods.
- (3) Tabulate data and code in a format suitable for inclusion as basic input into a computer routine for calculating fatigue damage.
- (4) Catalog computer output according to individual aircraft tail numbers for use in remaining life predictions.

The automatic disc interrogation and data reduction could be handled at one central base, thereby keeping equipment costs to a minimum and at the same time minimizing catalog procedural problems. If, however, the number of aircraft and the number of bases involved becomes exceptionally large, the use of individual disc interrogation machines at each base might be warranted with the digitized output being sent to a central computer facility.

## CONCLUSIONS

The program of individual aircraft tail number fatigue damage monitoring for trainer aircraft is an illustration



of a potential system application of the Prewitt Scratch Gage.

An optimum system to accomplish fleet damage monitoring would rely on direct measurement of the complete cyclic strain history at the critical location. An alternate approach would be to sense strains at remote locations and to convert these into critical values with appropriate transfer functions.

The mechanical device summarized in this paper could be utilized effectively in this respect either as a direct strain sensor mounted in the general vicinity of a fatigue critical location or as a load factor or event monitor attached

to a remote but sensitive member (i.e. landing gear, stores pylon, etc).

For fatigue life monitoring, automatic data reduction is envisioned, and it is suggested that the trace not be allowed to overlap. Target capacity is a direct function of the total strain excursions experienced and with careful consideration the amount of target utilized over a specific period might be the initial indication of the aircraft usage. Although not currently available, automatic disc interrogation equipment utilizing optical scanning principles could produce exceedance data for specified levels of strain. These results, when input into a fatigue damage computer program, could provide damage values for the period of life recorded on the disc.

#### REFERENCES

1. G.J. Roth, J.P. Ryan, and J.C. Sliemers, *Parametric Fatigue Analysis of USAF Aircraft*, AFFDL-TR-67-89, Air Force Flight Dynamics Laboratory, Wright-Patterson AFB, Ohio (1967).
2. T.L. Haglage and H.A. Wood, *Scratch Strain Gage Evaluation*, AFFDL-TR-69-25, Air Force Flight Dynamics Laboratory, Wright-Patterson AFB, Ohio (1969).
3. T.L. Haglage, *Flight Test Evaluation of a Scratch Strain Gage*, AFFDL-TR-69-116, Air Force Flight Dynamics Laboratory, Wright-Patterson AFB, Ohio (1969).
4. J.A. Finlason, *T-37 Flight Test Evaluation of Stress Levels in the Forward, Lower Spar Cap*, Rept. 318-6971-013, Cessna Aircraft Company, Wichita, Kansas.

**AIRFRAME ENVIRONMENT DESIGN CONSIDERATIONS – THE SHAPE OF THE  
TURBULENCE SPECTRUM AND PROBABILITIES OF ENCOUNTERING  
GIVEN PEAK GUSTS AND RMS VALUES**

by

Jerry W. Jones\*

The Boeing Company  
Wichita, Kansas

**NOMENCLATURE**

Symbol		Subscripts	
C	= A factor appearing in the gust velocity spectra expressions suggested by Lumley, Panofsky and Busch.	B	= Busch and Panofsky equation
cpf	= Cycles per foot	D	= Dryden equation
fps	= Feet per second	K	= von Karman equations
F(x)	= Cumulative probability of x. $P(X \geq x)$	L	= Lappe equation
k	= Spatial frequency in cycles/foot	P	= Panofsky and Lumley equation
L	= Integral scale length of turbulence in feet	T	= Truncated
u	= Longitudinal gust velocity in fps	t	= Time series
v	= Lateral gust velocity in fps	u	= From longitudinal gust velocity time series
w	= Vertical gust velocity in fps	v	= From lateral or vertical gust velocity time series
$\mu$	= Arithmetic mean	1	= Lower frequency limit of truncated spectrum
$\sigma$	= Standard deviation	2	= Upper frequency limit of truncated spectrum
$\Phi$	= One dimensional gust velocity power spectral density in $(\text{feet/sec.})^2/(\text{cycles/ft.})$		

**INTRODUCTION**

Atmospheric turbulence considerations in aircraft design requirements are of growing interest and concern to the Air Force and to aircraft manufacturers. Operational speeds and structural flexibility of aircraft have continued to increase through the years as large strides in improved performance have been achieved. With this evolution, the role of atmospheric turbulence has become a significant consideration in aircraft design. Older generation aircraft, due to their relatively slow speeds, had to cope mainly with the low power, high frequencies of tur-

bulence. The high speeds of modern aircraft cause their response frequencies to be coincident with the high power, low frequencies of turbulence. It appears that future higher-speed aircraft will be responsive to turbulence of very low frequencies where little is known about turbulence power characteristics. The use of higher-speed aircraft, coupled with the military requirement for low-level contour flying, results in greater fatigue and in the need for an accurate model of low altitude atmospheric turbulence environment.

Such a model for atmospheric turbulence at low

<sup>1</sup>Research supported by USAF Contract Nos. AF33(615)-3724 and F33615-68-C-1468.

\*The views expressed herein are those of the author and do not necessarily reflect the views of the U.S. Air Force or Department of Defense.

altitude is being developed by The Boeing Company<sup>1</sup> in cooperation with the United States Air Force during an extensive Low-Level Critical Air Turbulence (LO-LOCAT) research program. The LO-LOCAT Program consists of three phases of testing. Phases I and II, using four C-131B aircraft as instrumentation platforms, have been completed. Turbulence wavelengths up to 7,000 feet were measured during that portion of the program. The purpose of Phase III is to extend the statistical definition of the turbulence environment and define wavelengths up to 14,000 feet by using a higher-speed (T-33A) airplane as the instrumentation platform.

Although low-level atmospheric turbulence characteristics have been studied previously, the data obtained have been limited due to inadequate topographical and meteorological coverage and turbulence wavelength resolution. The LO-LOCAT Program has been designed to obtain turbulence intensity and meteorological data at altitudes less than 1,000 feet above the ground over a wide range of geophysical conditions and utilizes improved data acquisition, processing, and analysis techniques.

Data are being analyzed with respect to variations in terrain, altitude, atmospheric stability, time-of-day, season, and geographic location. The probabilities of encountering specific magnitudes of turbulence and the shapes of the turbulence power spectra for various meteorological and geophysical conditions being determined during the LO-LOCAT Program are discussed in this paper.

#### DATA ACQUISITION

LO-LOCAT Phases I and II atmospheric turbulence data were obtained over a 15-month period. Each C-131B aircraft was located at a different base within the United States and was flown over a test route near the base. The routes, located in California, Colorado, Kansas, and New York were established to give a wide range of topographical and climatological conditions. Each route consisted of eight straight legs, each of which was approximately 20 nautical miles in length. The legs were traversed in the same direction on each flight. LO-LOCAT Phase III data were obtained during a 10-1/2-month flight period. Phase III consisted of flying the faster T-33A airplane over essentially the same routes as established for Phase I and II. All legs were extended to a length of 30 nautical miles to obtain a data recording time interval similar to that of Phases I and II. Some legs were relocated due to the extension in length.

Normally, three missions were scheduled every other day during all three phases of testing: one at dawn, one at mid-morning and one in the afternoon. This schedule was varied as necessary when weather conditions, aircraft maintenance problems, or other factors interfered. The airplane was flown at two flight altitudes, 250 feet and 750 feet absolute altitude to record the gust data. The pilot followed the terrain contour, as closely as safety al-

lowed, using a radar altimeter to maintain a constant absolute altitude. Only one altitude was used for any one flying day and the test altitude was alternated on successive flight dates.

Five and one-half minutes (Phases I and II) and four and one-half minutes (Phase III) of information, recorded while flying over each leg, constituted a turbulence sample. The variation of gust velocity with time was computed from these data. In the calculations, airplane motion effects were removed giving three orthogonal, space oriented gust velocity components. High-pass numerical filtering of the gust velocity time function was used to ensure valid data, especially for the lower frequencies. Dynamic calibration of all measurements used in the gust velocity computation ensured validity of the data.

The instrumentation system and data processing methods used for this program were developed to cope with the difficulties normally encountered in turbulence measurement. Frequency response of the gust probe was evaluated during wind tunnel testing. It was found that the response was different from 1.0 in the frequency range of interest. The frequency response characteristics obtained were compensated for during gust velocity calculations.

#### DATA CATEGORIZATION

Individual samples cannot be used to establish a turbulence model because of the random nature of atmospheric turbulence. The analysis then, to be meaningful, must be carried out in a statistical manner. The idea of categorizing each sample and performing statistical comparisons only on data of like characteristics (categories) was employed to aid in the statistical analysis. This is pictorially described in Figure 1. The categorization sequence is arranged to place the categories in an order of anticipated pertinence from top to bottom.

Categorization by topography is aided by establishing a terrain index for each leg of each route. The terrain index consists of a roughness factor determined from the terrain profile. Radar altitude was subtracted from airplane pressure altitude to yield this profile. The terrain roughness factor, after linear trends are removed, is then computed as the standard deviation of the terrain. Lapse rate is determined from temperature data measured at the 100 and 1,000 feet altitude above the terrain. The atmospheric stability category which applied to each sample is then established based on the following definitions:

Atmospheric Stability	Lapse Rate °F/1000 Ft.
Very Stable	< 2
Stable	≥ 2 < 5
Neutral	≥ 5 < 6
Unstable	≥ 6

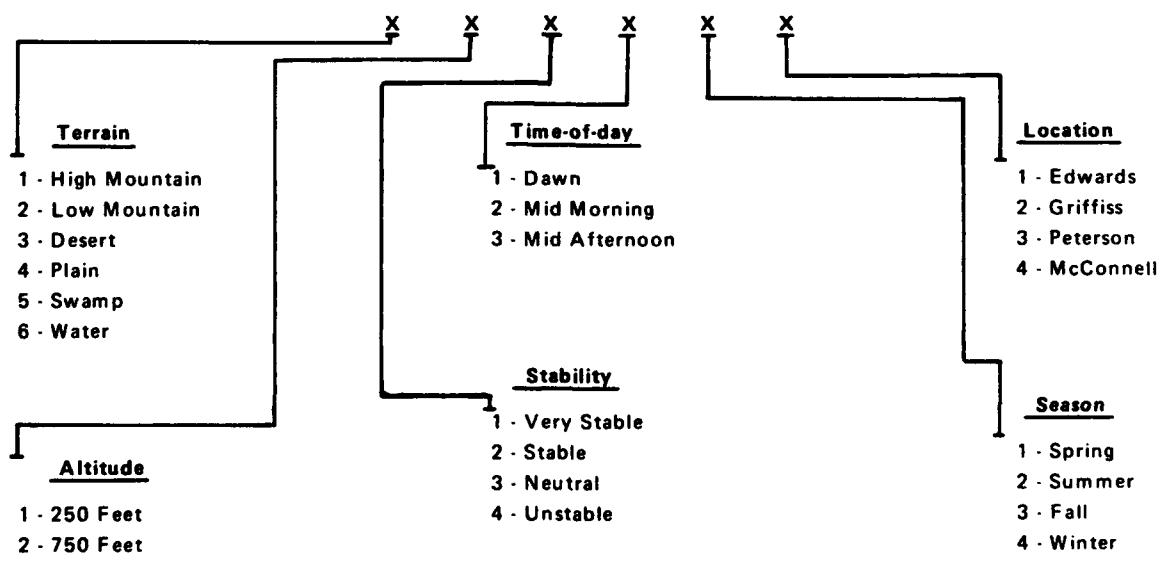
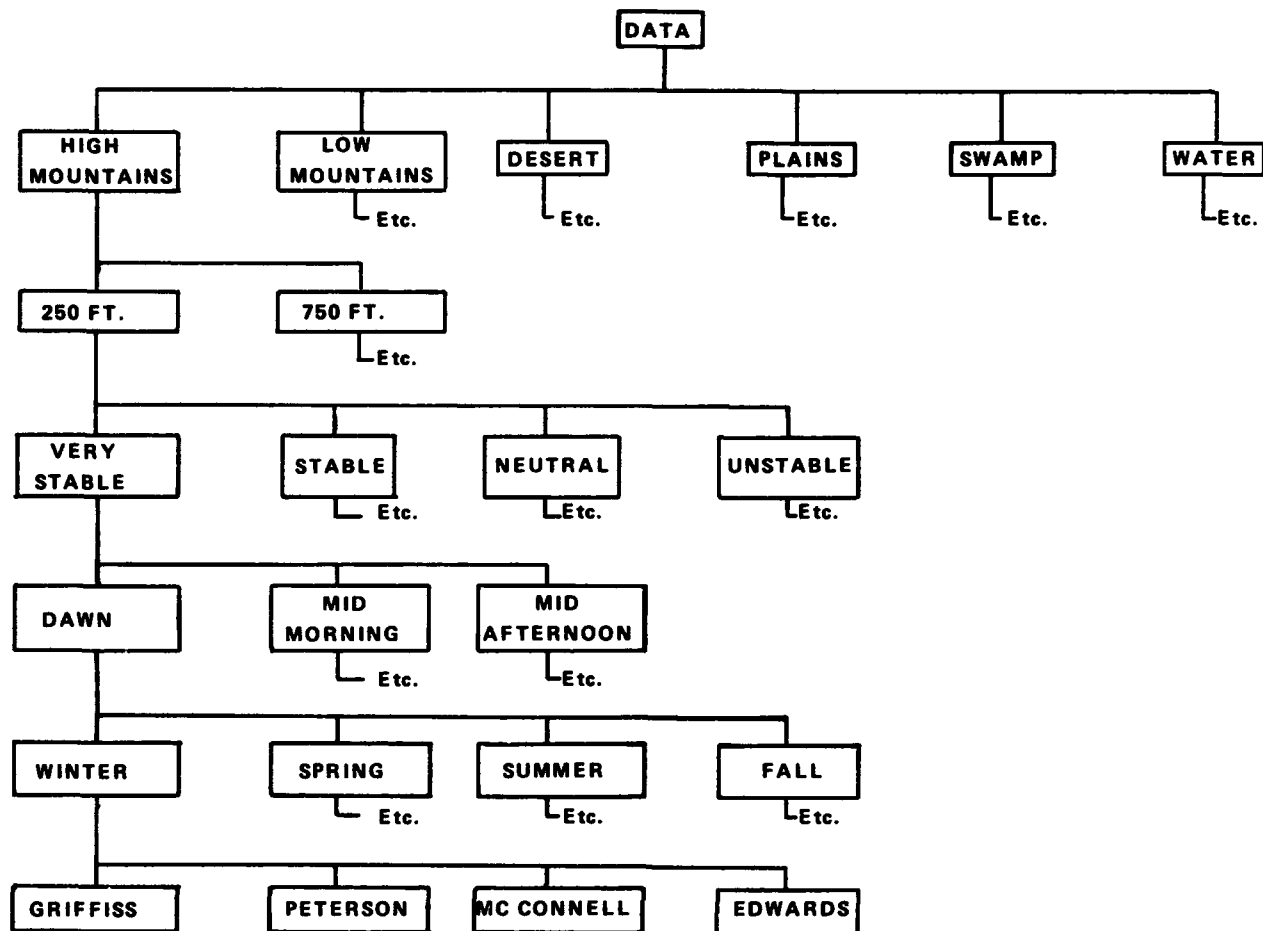
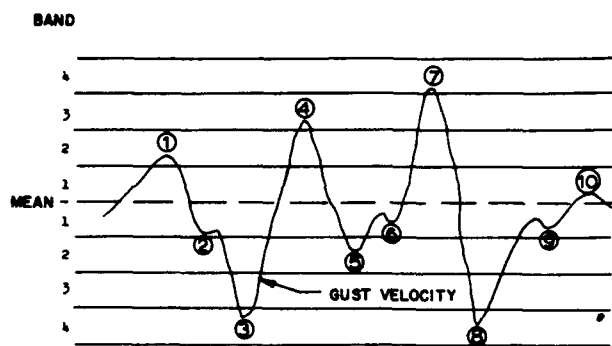


Figure 1. Data Categorization.



Band No.	Plus Peak Ident.	Minus Peak Ident.
1	⑩	
2	①	⑤
3	④	
4	⑦	③ ⑧

② ⑥ ⑨ = Secondary Peaks  
= Not Counted

Figure 2. Peak Count Example.

#### Gust Velocity Time Series Model

Computed gust velocity is being analyzed using amplitude and peak count techniques. Individual gust velocities are computed at 100 samples per second. A normalized cumulative distribution is computed to show the number of gusts encountered equal to or greater than a given magnitude per mile for peak count data. The cumulative probability distributions are calculated to permit comparison between the different sets of data.

In the peak count procedure, Figure 2, the number of primary peaks which fall in each 2 fps wide amplitude band are counted. Each maximum positive or negative excursion between adjacent crossings of the mean is defined as a primary peak. Secondary peaks are not considered. High frequency, low amplitude data are inherently counted in this process as primary peaks in the lowest band. As a result, this causes an excessive accumulation of data points in the lowest bands which are not representative of primary peak count data in the higher bands. Since the distribution must terminate at a probability equal to 1.0 at zero gust velocity, the higher frequency peaks in the lowest bands are removed by extrapolation. Figure 3 shows a peak count distribution and illustrates how it was extrapolated to eliminate the peaks in the lowest band. The shaded points indicate the cumulative number of peaks in

the lowest band as they were originally counted. The unshaded points are the extrapolated values. This curvilinear extrapolation is based on the shape of the distribution curve.

The amplitude count technique was also used to determine probability functions of computed gust velocity. Each component was computed at 100 samples per second. In this technique, amplitude bands 2 fps wide are placed on either side of the mean. The number of samples which occur in each band is determined, then corresponding positive and negative bands are added together. This technique is illustrated in Figure 4. The distributions of the primary peak count and the amplitude count were very similar. The cumulative probability of the peaks was always slightly higher for a given gust velocity value than the cumulative probability of the amplitude count.

The relationship between the peak count distribution curves for the three gust velocity components accumulated over 130,000 miles is shown in Figure 5. In this paper, cumulative probability is defined as the probability of encountering a value (rms, peak gust, etc.) equal to or greater than the value shown by the abscissa. The peak count distribution of the lateral component is slightly higher than either the vertical or the longitudinal. This relationship was similar for all categories investigated except for some slight changes in the vertical at very low probabilities. This appeared to be a function of altitude. The maximum gust velocity measured during Phases I and II was 55 fps. During Phases I and II, the high mountains in

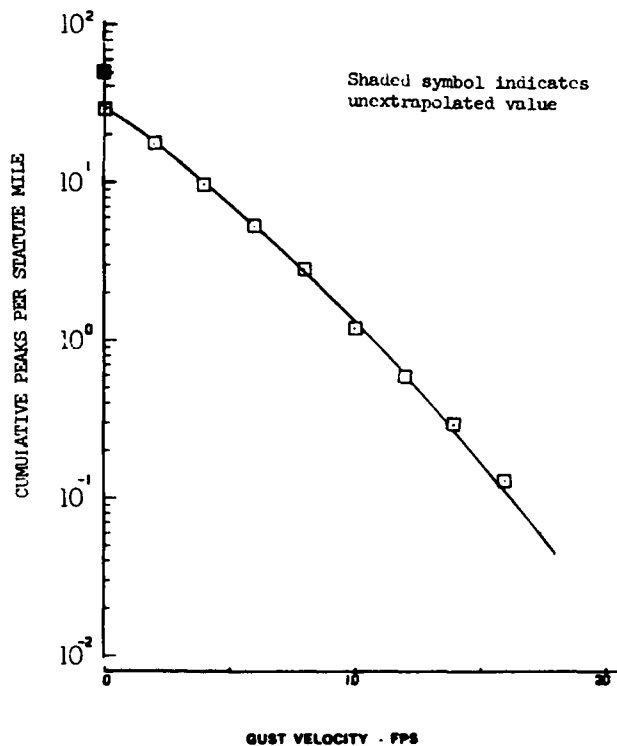
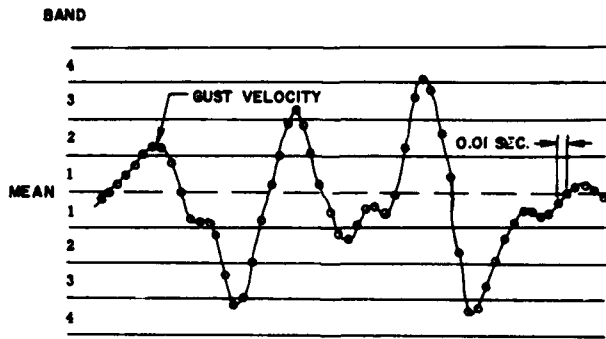


Figure 3. Peak Count Extrapolation Technique.



Band No.	Occurrences
1	31
2	16
3	6
4	4

Figure 4. Amplitude Count Example.

Colorado were not contour flown at low level due to flight safety reasons, otherwise, larger gusts probably would have been encountered. Those high mountain data are not included in any of the cumulative probability data shown. During Phase III, gust velocities in excess of 75 fps were obtained.

The lateral component is used to illustrate the effect of the various geophysical conditions on the Phases I and II peak count distributions as shown in Figure 6. These data were obtained at an altitude of 250 feet and include all stabilities except for very stable. The mountain data has the highest distribution with plains, desert, and water following in that order. The plains data has a higher distribution than desert even though the terrain roughness for the desert is generally higher than for the plains. This is attributed primarily to the fact that the wind velocities were generally much higher over the plains.

The effects of altitude are shown in Figure 7. These data were obtained over mountainous terrain and include all stabilities except very stable.

The distributions for the stability categories of stable, neutral, and unstable were very nearly equal and are combined in Figure 8 for clearer presentation. The distribution curve for the very stable situation is quite a bit lower than for the other stabilities. These data were ob-

tained over the mountains at 250 feet altitude, and are representative of the terrain-altitude combination studied.

An equation was derived for the gust velocity primary peaks recorded during contour flight. It was based on (1) all lateral peak data, and (2) on the data category which gave the greatest probability of encountering given peak values. The maximum gust velocity category involved lateral peaks recorded over both high and low mountains at the 250-foot altitude with all atmospheric stabilities other than very stable. These data are in close agreement to the lateral data presented in Reference 1. The following equations were obtained using the composite Gaussian procedure:

For all peaks -

$$F(x) = [0.927 \exp. (-0.477x)] + [0.073 \exp. (-0.274x)] \quad (1)$$

For maximum peaks -

$$F(x) = [0.921 \exp. (-0.339x)] + [0.079 \exp. (-0.228x)] \quad (2)$$

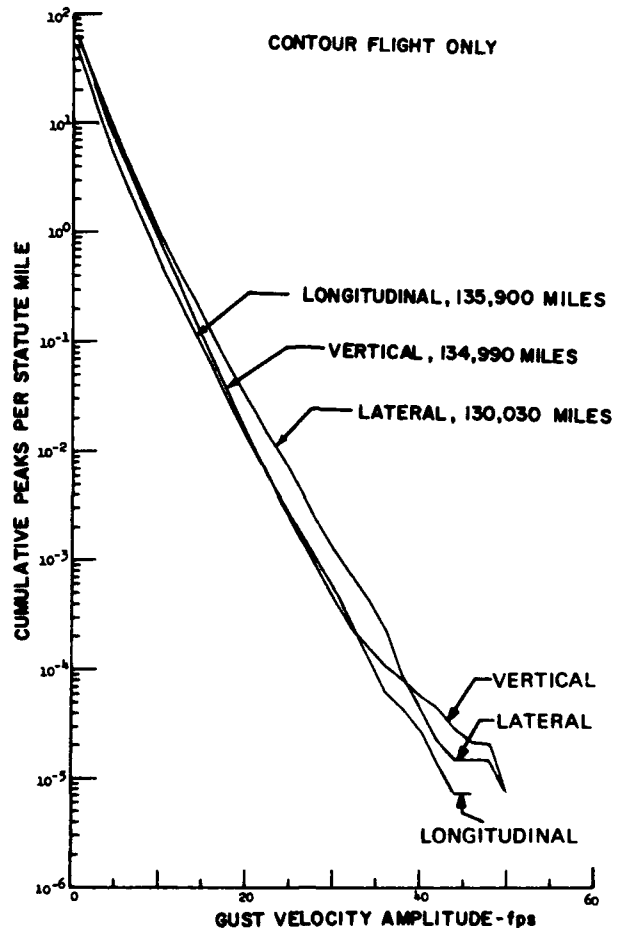


Figure 5. Comparison of Gust Velocity Component Peaks.

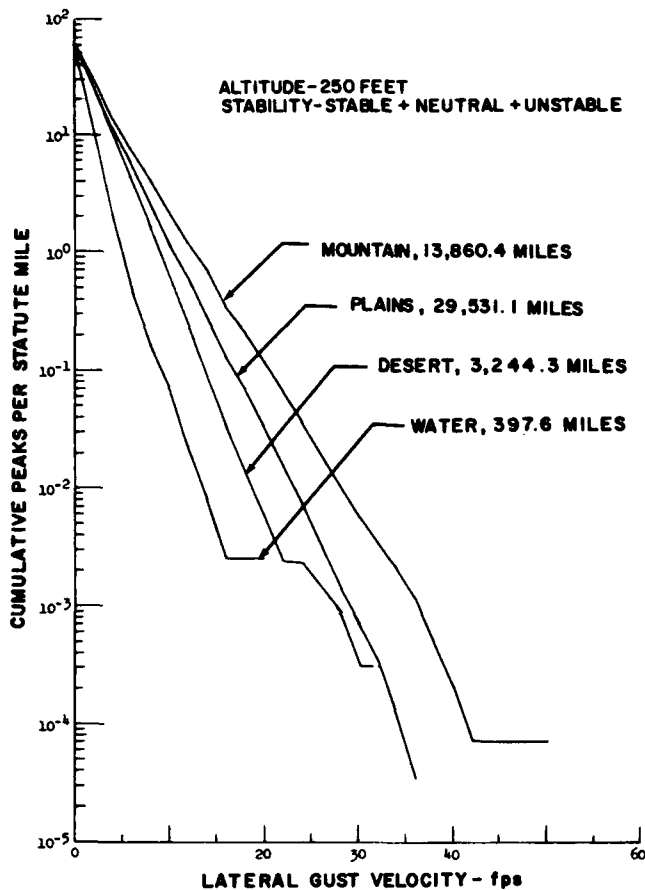


Figure 6. Terrain Effects on Lateral Gust Velocity Peaks.

Comparison of the observed distributions to Equations (1) and (2) is given in Figure 9.

Generally, the relationship between Phases I and II and Phase III statistical distributions is similar. However, Phase III distributions tend to level off at the higher gust velocities. This is attributed to the higher speed of the Phase III airplane which permitted measurement of longer wavelength turbulence. This will be discussed in detail later.

The standard deviation (rms) of the gust velocity time functions was calculated for each turbulence sample. Figure 10 shows the cumulative probability distributions for Phases I and II and Phase III data. The distribution characteristics of the rms values were very similar to those of the peak count and amplitude count during Phases I and II. That is,

- The lateral component had the highest probabilities.
- Highest probabilities occurred over the mountains, followed by plains, desert, and water.
- Higher probabilities occurred at 250 feet rather than 750 feet.

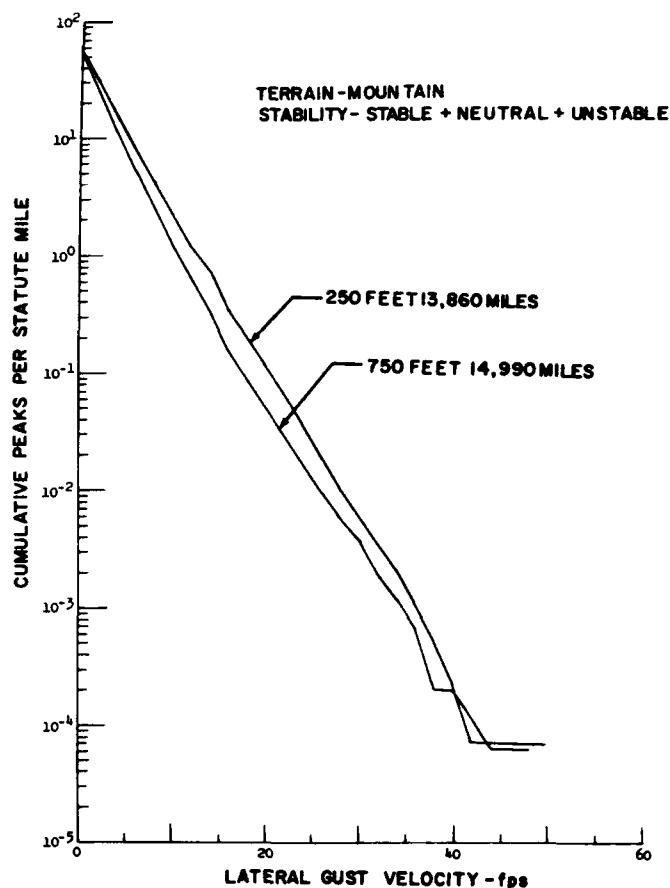


Figure 7. Altitude Effects on Lateral Gust Velocity Peaks.

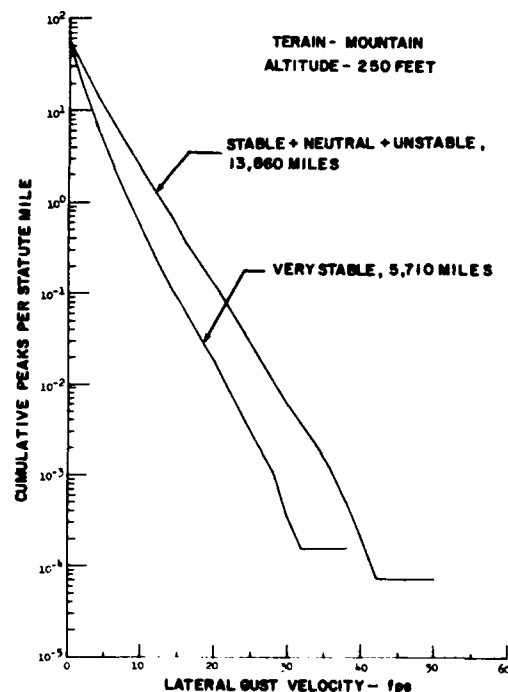


Figure 8. Atmospheric Stability Effects on Lateral Gust Velocity Peaks.

- Higher probabilities occurred when the atmosphere became more unstable.

The distributions of all Phases I and II rms gust velocity components greater than 1.0 fps can be approximated with a truncated normal distribution. Using this approximation gives a representation of the cumulative probability of the data within a value of 1.5 percent of the actual cumulative probability for all bands of rms gust velocity values. An example of the agreement of the truncated normal distribution in the form of the probability density is shown in Figure 11. Due to low signal-to-noise ratio,

which occurred when the rms values were less than one, no attempt was made, for this paper, to describe the shape of the distribution in the range from zero to one fps.

At the high values of rms gust velocity, the truncated normal distribution underestimated the observed data by a cumulative probability difference of 1.5 percent or less. Therefore, mathematical expressions were derived to represent the observed data by summing terms of two normal distribution equations. The first represents the data within 1.5 percent probability, the second accounts for the

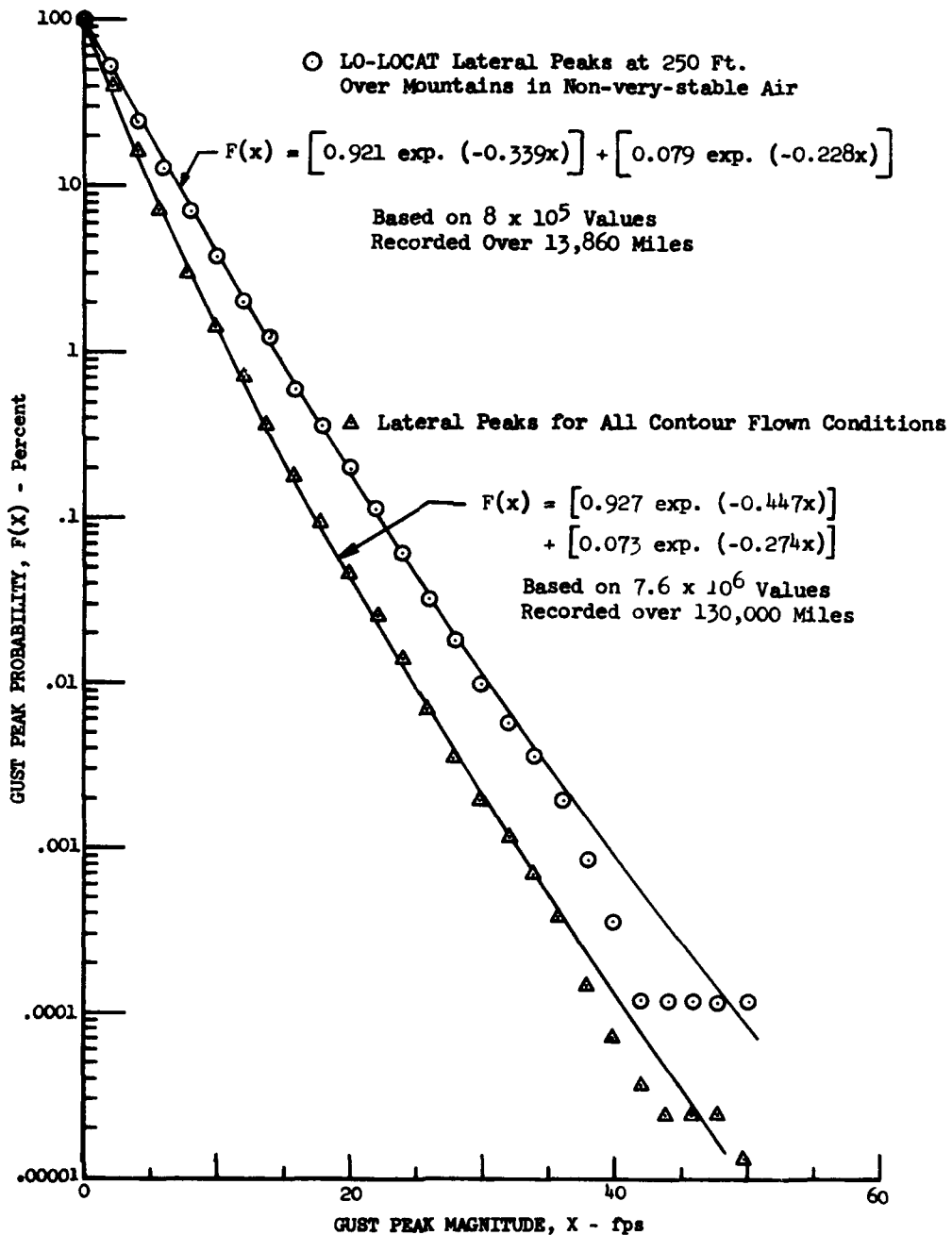
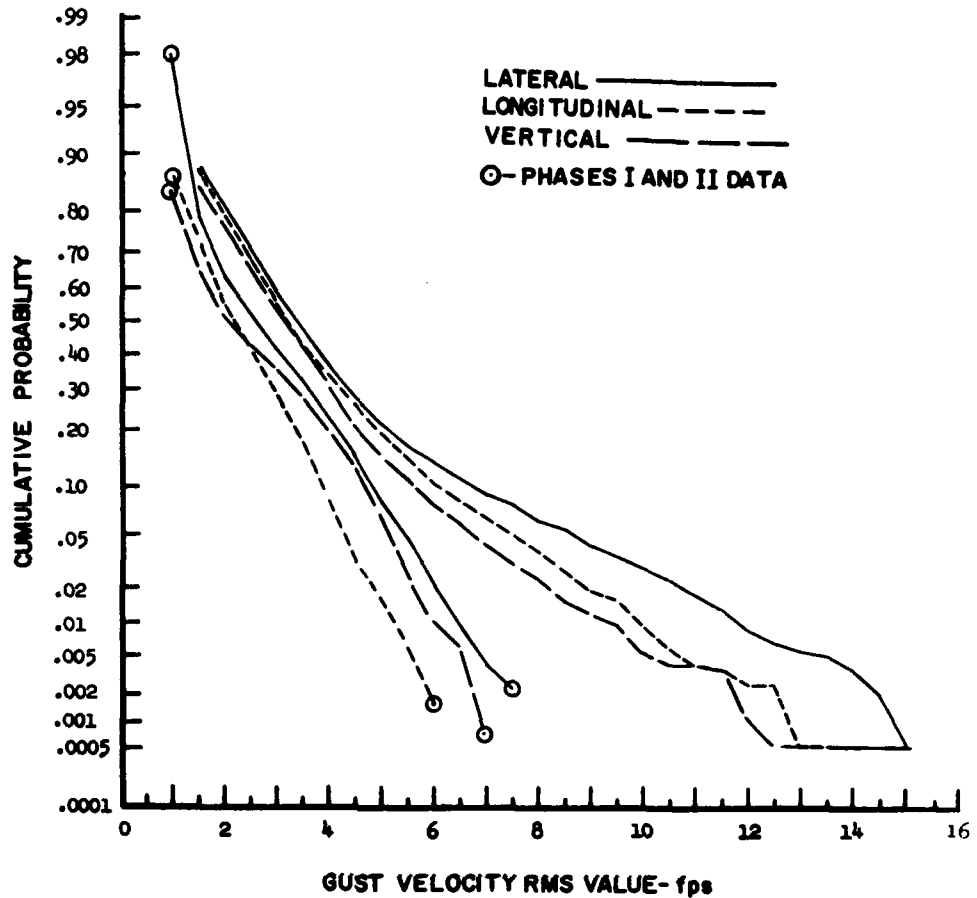


Figure 9. Gust Primary Peak Mathematical Model (Phases I and II).



Figure 10. RMS Gust Velocity Cumulative Probability.



underestimation at the higher values. The general form of this cumulative probability distribution is:

$$F(x) = \frac{1}{\sqrt{2\pi}} \left[ \frac{1}{\sigma_2} \int_{i=1}^a \exp. - \frac{1}{2} \left( \frac{x_i - \mu_2}{\sigma_2} \right)^2 dx + \frac{1}{\sigma_3} \int_{n=a}^b \exp. - \frac{1}{2} \left( \frac{x_n - \mu_3}{\sigma_3} \right)^2 dx \right] \quad (3)$$

Constants for Equation (3) are given in Table 1. Other distribution expressions such as logarithmic-normal, Chi-square, and Rayleigh were evaluated to determine how well they fit the experimental data. In all cases these expressions did not represent the rms gust distributions as well as Equation (3).

As discussed previously, the probability of encountering a given value of rms gust velocity is highest for rough terrain, 250 feet, and atmospheric stabilities other than very stable. Therefore, as was done in the case of gust primary peak distributions [see Equation (2)], the mathematical expression for the lateral rms gust velocity was derived for the geophysical category involving high and low mountains,

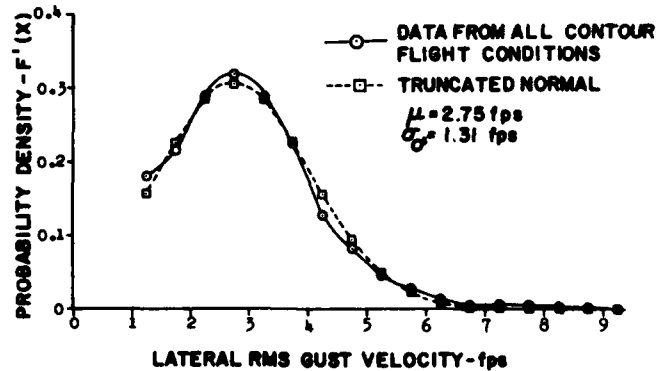


Figure 11. RMS Probability Density Compared to a Truncated Normal.

**TABLE I.**  
**RMS GUST VELOCITY DISTRIBUTION CONSTANTS**

	GUST VELOCITY COMPONENT		
	u	v	w
a	4.39	4.65	6.33
$\mu_2$	2.53	2.75	2.59
$\sigma_2$	1.18	1.31	1.30
$\mu_3$	1.31	1.29	0.00
$\sigma_3$	1.97	2.31	2.19
b	9.00	9.50	9.00

the 250-foot altitude, and the non-very stable atmospheric stabilities. The general form of this expression is also represented by Equation (3). In this case, the first term in the expression represents the data within a cumulative probability of two percent. The constants for the equation are as follows:

$$\begin{aligned} a &= 4.62 & b &= 9.50 \\ \mu_2 &= 3.81 & \mu_3 &= 3.20 \\ \sigma_3 &= 1.26 & \sigma_3 &= 2.18 \end{aligned}$$

The relationship of the lateral gust velocity cumulative probability distribution for this category to all Phases I and II data is shown in Figure 12.

Comparison of rms data from Phases I and II and Phase III has not shown any significant variation in how turbulence is associated with each category. However, the average Phase III rms value is always greater than obtained during Phases I and II. This difference is attributed to two things: (1) Phases I and II do not include any high mountain data from the Peterson route whereas Phase III does,

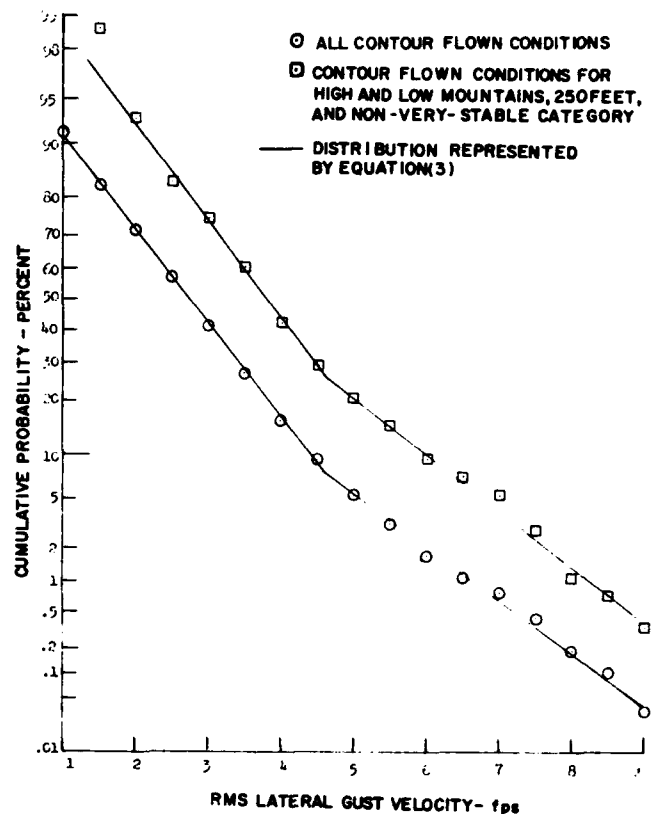


**Figure 12. RMS Gust Velocity Cumulative Probability Distributions.**

and (2) turbulence exists at longer wavelengths than could be resolved during Phases I and II due to a combined effect of the data filtering processes and the lower speed of the Phases I and II airplane. The filtering is required to remove high amplitude-low frequency drift in calculated gust velocity.

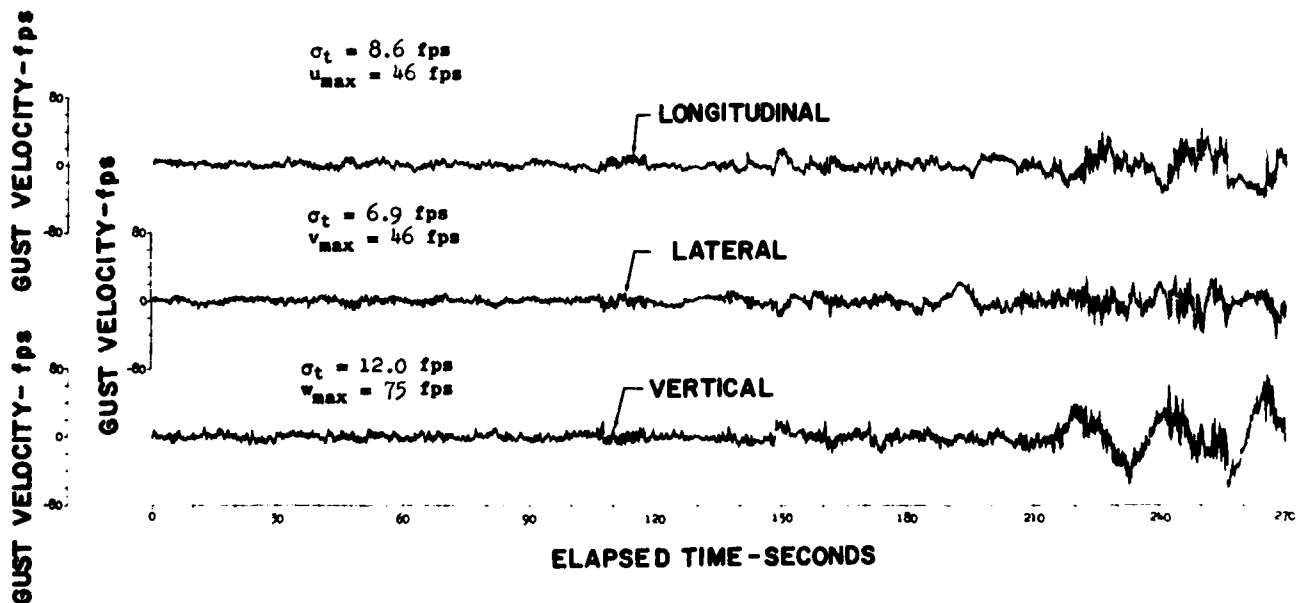


**Figure 13. Time History of Gust Velocity Components; Severe Turbulence Encounter.**

The vertical gust velocity time history in Figure 13 was recorded during Phase III and depicts long wavelength turbulence of approximately 14,300 feet containing gust velocities exceeding 74.0 fps. The long wavelength component appears at a frequency of approximately 0.04 cps in the time history. This same long wavelength turbulence, if encountered during the Phases I and II testing, would have appeared at a frequency of 0.02 cps due to the lower speed at which the C-131 aircraft were flown. Phases I and II gust velocity measurements in this frequency realm would have been attenuated approximately 80 percent by the data filtering techniques utilized to alleviate the effects of instrumentation drift. This is a cogent example of the fact that there is turbulence at low altitudes that contains wavelengths longer than 7,000 feet. This is the reason why, in comparing Phase III results with Phases I and II for equivalent categories, that (1) the probability distributions of peak gust velocities are higher, (2) the probability distributions for rms gust velocities are higher, and (3) the integral scale lengths are larger.

#### Gust Velocity Power Spectra Model

In recent years, the usage of power spectral techniques in aircraft design has continued to increase. Indications are that future design work will rely even more on this technique, requiring a detailed knowledge of the power spectral density of atmospheric turbulence in the design frequency range. Once this is known, aircraft response spectra may be computed using applicable transfer functions.

Measured spectra are compared to a number of mathematical expressions to define the atmospheric turbulence spectral model. This analysis is also accomplished on a geophysical category basis involving terrain roughness, altitude, and atmospheric stability.

The observed spectra are being compared to turbulence spectra expressions suggested by Theodore von Karman, J.L. Lumley and H.A. Panofsky, H.L. Dryden, and U.O. Lappe. During Phase III the Busch-Panofsky equation was included. The expressions are as follows:

von Karman

$$\left[ \frac{\Phi_v(k)}{\sigma_{t_v}^2} \right]_K = \frac{L_{Kv} \left[ 2 + 377.5 (L_{Kv} k)^2 \right]}{\left[ 1 + 70.78 (L_{Kv} k)^2 \right]^{11/6}} \quad (4)$$

$$\left[ \frac{\Phi_u(k)}{\sigma_{t_u}^2} \right]_K = \frac{4L_{Ku}}{\left[ 1 + 70.78 (L_{Ku} k)^2 \right]^{5/6}} \quad (5)$$

Busch-Panofsky

$$\left[ \frac{\Phi_v(k)}{\sigma_{t_v}^2} \right]_K = \frac{0.644 C_v}{1 + 1.5 C_v^{5/3} k^{5/3}} \quad (6)$$

Lumley-Panofsky

$$\left[ \frac{\Phi_u(k)}{\sigma_{t_u}^2} \right]_B = \frac{11800}{C^2 \left[ 1 + (2950 k)^{5/3} \right]} \quad (7)$$

Dryden

$$\left[ \frac{\Phi_v(k)}{\sigma_{t_v}^2} \right]_D = \frac{L_{Dv} \left[ 2 + 6 (2\pi L_{Dv} k)^2 \right]}{\left[ 1 + (2\pi L_{Dv} k)^2 \right]^2} \quad (8)$$

$$\left[ \frac{\Phi_u(k)}{\sigma_{t_u}^2} \right]_D = \frac{4L_{Du}}{1 + (2\pi L_{Du} k)^2} \quad (9)$$

Lappe

$$\left[ \frac{\Phi(k)}{\sigma_t^2} \right]_L = \frac{2\pi L_L}{(1 + 2\pi L_L k)^2} \quad (10)$$

Equations (4), (6), and (8) represent both the vertical and lateral components of turbulence and Equations (5), (7), and (9) represent the longitudinal component. Equation (10) has been suggested for all three components.

Good agreement has been found between the observed spectra and the von Karman equations. Equations (6) and (7) are also giving a good representation of the observed data. Equations (8), (9), and (10) have not exhibited a good representation of the observed data, especially at the higher frequencies. The basic disagreement has been in the turbulence inertial subrange where these expressions have a -2 logarithmic slope rather than the -5/3 slope of the data which is contrary to Kolmogorov's theory.

Typical spectra comparisons are shown in Figures 14 and 15. In each case, the computed spectrum values have been divided by values from the mathematical expression in question and these ratios plotted against frequency. Comparisons of the observed spectra with the Lappe ex-

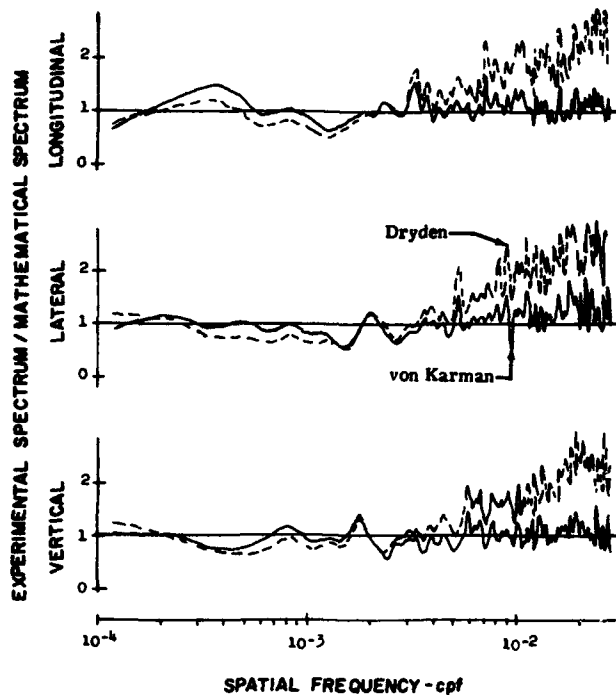


Figure 14. Typical Comparison of Experimental Spectra with von Karman and Dryden Mathematical Expressions.

pression have given results essentially the same as those for the Dryden expressions.

Although the von Karman expressions provided the most accurate fit, indications are that they slightly underestimate the actual power at the very long wavelengths. This is illustrated in Figure 16 which is a plot of spectra normalized by  $\sigma_t^2 L$  and plotted versus  $kL$ . This method of normalizing eliminates the variables  $\sigma_t^2$  and  $L$  which are known to vary with geophysical conditions. Average data points are shown at specific values of  $kL$  for all Phase III data.

#### Scale Length

The atmospheric turbulence scale length  $L$  is an indication of the average eddy size associated with the longitudinal turbulence component. Disagreements have occurred in the past concerning the choice of scale lengths to be used in design applications. Estimations of this parameter have varied from 500 to 5,000 feet. In the LO-LOCAT Program, scale lengths are being analyzed statistically for various geophysical conditions. Since the von Karman spectra is a valid model, scale lengths based on the von Karman expressions represented by the following equations are being analyzed thoroughly.

$$L_{Kv} = .110 \left( \frac{\sigma_t^3}{\sigma_T^3} \right) \left( \frac{1}{k_1^{2/3}} - \frac{1}{k_2^{2/3}} \right)^{3/2} \quad (11)$$

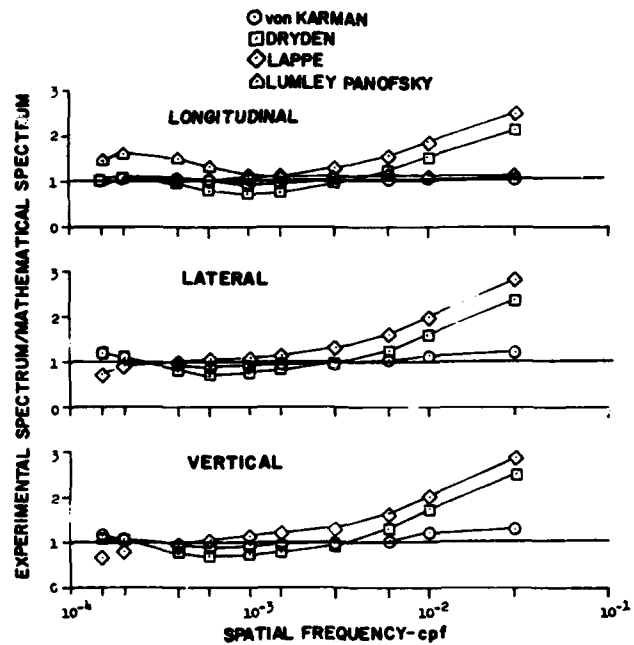


Figure 15. Experimental/Mathematical Spectra Comparisons.

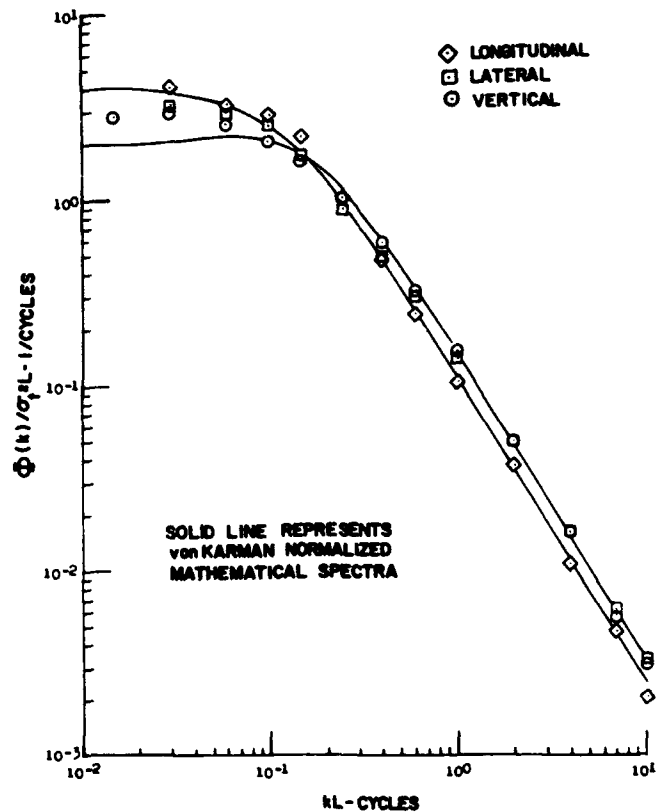


Figure 16. Gust Velocity Average Power Spectra Normalized by  $\sigma_t^2 L$ .

Figure 17. Variation of von Karman Longitudinal Scale Length with Altitude and Terrain.

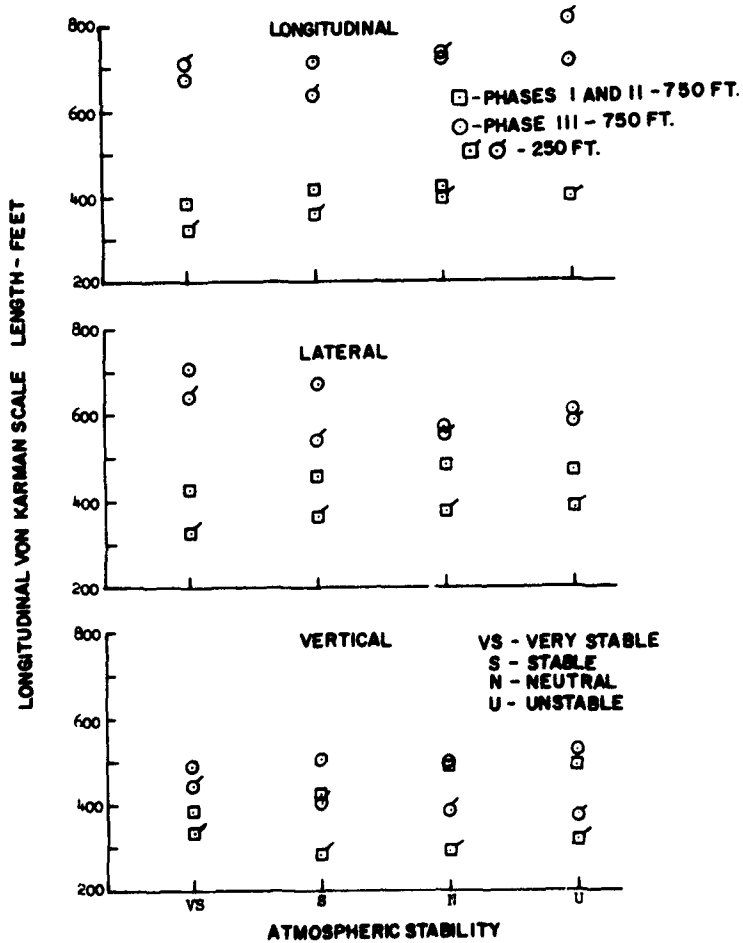
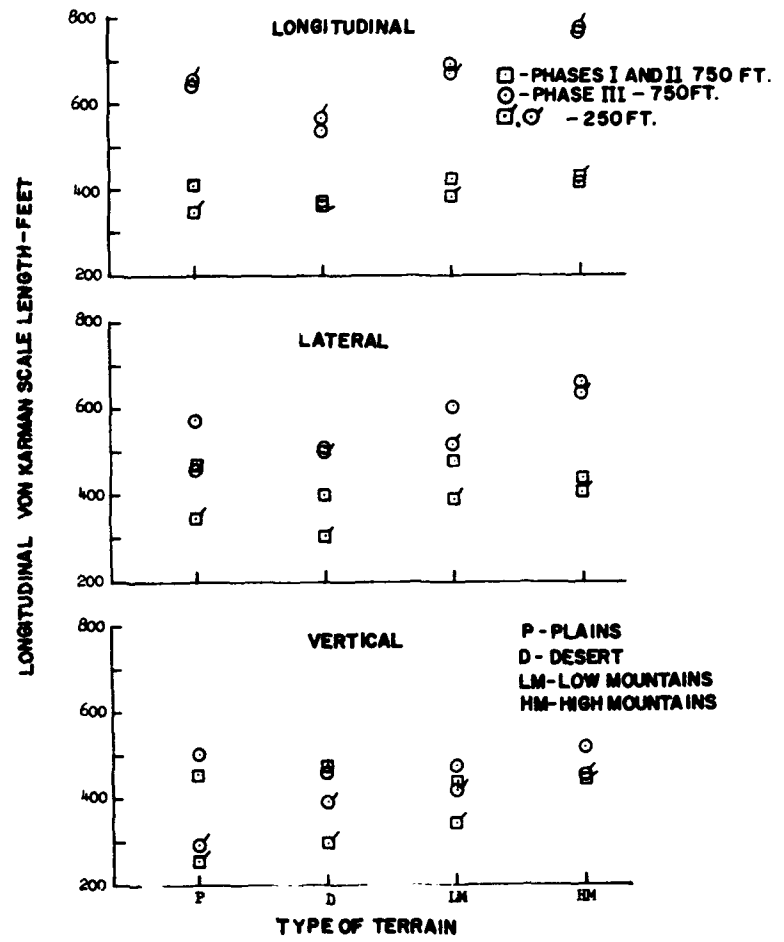


Figure 18. Variation of von Karman Longitudinal Scale Length with Altitude and Stability.

$$L_{Ku} = 0.0717 \left( \frac{\sigma_t}{\sigma_T} \right)^3 \left( \frac{1}{k_1^{2/3}} - \frac{1}{k_2^{2/3}} \right)^{3/2} \quad (12)$$

Equations (11) and (12) were derived from Equations (4) and (5), respectively considering a standard deviation ( $\sigma_T$ ) based on the area under the truncated spectrum in the inertial subrange.

During Phases I and II of the LO-LOCAT Program, scale length was found to be affected by terrain roughness, height above the ground, and atmospheric stability. At the 250-foot altitude, scale length was found to increase with increasing terrain roughness. At the 750-foot altitude, atmospheric stability appeared to have an effect on scale length. As the atmosphere became more unstable, scale length showed a tendency to increase in magnitude. These trends were more evident for scale length computed from the vertical component than from the other two components.

Preliminary Phase III data are shown for the same types of trends. Figure 17 shows variations of average scale length values with terrain and altitude. Scale lengths at the

250-foot altitude tend to increase with terrain roughness, while those recorded at 750 feet are somewhat inconsistent with relationship to terrain.

The mean values of scale length shown in Figure 18 are plotted as a function of atmospheric stability for each of the test altitudes.

The average scale length values recorded during the Phase III Program are 715, 598, and 450 feet as computed from the longitudinal, lateral, and vertical components, respectively. Average corresponding values for all data recorded during Phases I and II were 387, 409, and 367 feet. As mentioned previously, the values of  $\sigma_t$  being recorded during Phase III are greater in magnitude than the values recorded during Phases I and II. This is due to the longer wavelength turbulence being measured during Phase III. These larger gust velocity rms values increase the scale length values appreciably.

The data presented and conclusions reached in this report are preliminary. At the conclusion of Phase III, data from all three phases of the LO-LOCAT Program will be analyzed collectively to provide an even larger and more encompassing statistical sample.

## REFERENCES

1. W.H. Austin, Jr., *Environmental Conditions to be Considered in the Structural Design of Aircraft Required to Operate at Low Levels*, SEG-TR-65-4, Systems Engineering Group, Wright-Patterson AFB, Ohio (1965).

The following is reference material in which the contents of this paper are discussed in detail:

- J.D. Gault, *Low Altitude Atmospheric Turbulence (LO-LOCAT) Mid-Term Technical Data Analysis*, SEG-TR-67-35, Systems Engineering Group, Wright-Patterson AFB, Ohio (1967).
- G.W. Jones, J.W. Jones, and K.R. Monson, *Interim Analysis of Low Altitude Atmospheric Turbulence (LO-LOCAT) Data*, ASD-TR-69-7, Aeronautical Systems Division, Wright-Patterson AFB, Ohio (1969).
- D.E. Gunter, G.W. Jones, J.W. Jones, and R.H. Mielke, *Low Altitude Atmospheric Turbulence (LO-LOCAT) Phases I and II*, ASD-TR-69-12, Aeronautical Systems Division, Wright-Patterson AFB, Ohio (1969).
- K.R. Monson, G.W. Jones, and R.H. Mielke, *Low Altitude Atmospheric Turbulence (LO-LOCAT) Phase III Interim Report*, AFFDL-TR-69-63, Air Force Flight Dynamics Laboratory, Wright-Patterson AFB, Ohio (1969).
- G.W. Jones, J.W. Jones, and R.H. Mielke, *Low Altitude Atmospheric Turbulence (LO-LOCAT) Phase III*, AFFDL-TR-70-10, Air Force Flight Dynamics Laboratory, Wright-Patterson AFB, Ohio (1970).

**SESSION 3A**

**FRACTURE I**

*Chairman*

**Dr. H. Liebowitz**  
**The George Washington University**

# THREE-DIMENSIONAL STRESS-STATE IN A CRACKED PLATE

by

G.C. Sih

Professor of Mechanics  
Lehigh University, Bethlehem, Pa.

## INTRODUCTION

Fracture mechanics has received considerable attention in recent years, both theoretical and experimental, so that by integrating both aspects a better understanding of the subject has been made possible. From a theoretical viewpoint, models have been proposed in an attempt to characterize the fracture behavior of engineering materials. Because of the complicated nature of the physics of the crack problem, simplifying but plausible assumptions must often be made so as to reduce the analysis to manageable proportions. The objective is then to develop effective analytical crack models which presumably could simulate reality with a reasonable degree of accuracy.

The present understanding of fracture mechanics relies heavily upon the planar analyses such as those advanced by Inglis<sup>1</sup>, Griffith<sup>2</sup>, and others. They have been highly successful in predicting the fracture behavior of specimens in which the stress state is essentially two-dimensional. Loosely speaking, if the crack length is small in comparison with the thickness of the specimen, the deformation of a large portion of the body at some distance away from the surfaces is independent of the coordinate in the thickness direction. Such type of deformation is commonly known as "plane strain". On the other hand, if the crack length is large as compared to the specimen thickness, then without substantial error the transverse shear and normal components of stress can be assumed to vanish throughout the thickness of the specimen and the other three in-plane stress components remain practically constant over the specimen thickness. In this case, a state of "generalized plane stress" prevails. It is now well known that the forces  $G$  (named after Griffith) required to drive a crack for the two special cases mentioned above are given by

$$G = \frac{\pi k^2}{E} \quad , \quad (\text{generalized plane stress})$$

and

$$G = \frac{\pi(1-\nu^2)k^2}{E} \quad , \quad (\text{plane strain}) \quad (1)$$

in which  $\nu$  is the Poisson's ratio and  $E$  the Young's modulus of the material. Here,  $G$  is assumed to be constant along the straight crack front which extends through the thickness of the specimen. The factor  $k$  for a uniformly ex-

tended specimen whose in-plane dimensions are much larger than the crack length, say  $2a$ , can be determined from the equations of the theory of elasticity and is equal to  $\sigma\sqrt{a}$  for both plane strain and generalized plane stress, where  $\sigma$  is the uniform tensile stress. It should be pointed out that whenever the applied loads on the crack surface are self-equilibrating<sup>†</sup> or zero, the  $k$ -factor for two-dimensional problems is independent of the elastic properties of the material and the  $G$ -force for plane strain and generalized plane stress differs only by a factor of  $1 - \nu^2$ .

In many plate-like structural members, however, the crack length may be of the same order of magnitude as the plate thickness. In such instances, the in-plane stresses can no longer be assumed to remain constant across the thickness direction since the free surfaces of the plate can exert appreciable influence on the stress distribution in the plate. As a result, the crack driving force  $G$  will vary along the crack front and the problem becomes three-dimensional. In discussing the three-dimensional aspects of the fracture thickness problem, it is natural to inquire whether the two-dimensional results of plane strain and generalized plane stress could serve as appropriate bases or limiting cases for the three-dimensional analysis. In this respect, it should be made clear that the generalized plane stress equations are only approximately true because they do not satisfy all the three-dimensional equations of elasticity. The assumption that  $\sigma_{xx}$ ,  $\sigma_{yy}$  and  $\sigma_{xy}$  are function of  $x$  and  $y$  only and the stresses on all  $z$ -planes vanish violates, in general, some of the Beltrami-Michell compatibility equations (in the absence of body forces)

$$\nabla^2 \sigma_{ij} + \frac{1}{1+\nu} \frac{\partial^2 \sigma_{kk}}{\partial x_i \partial x_j} = 0 \quad (i, j, k = 1, 2, 3) \quad (2)$$

where the summation convention on  $i, j, k$  is used and hence  $\sigma_{kk} = \sigma_{11} + \sigma_{22} + \sigma_{33}$ . Adopted also are the notations  $x_1 = x$ ,  $x_2 = y$ ,  $x_3 = z$  and  $\sigma_{11} = \sigma_{xx}$ ,  $\sigma_{12} = \sigma_{xy}$ , etc. The symbol  $\nabla^2$  in Eq. (2) is the Laplace operator in three dimensions. Now, to illustrate that the generalized plane stress solution cannot be exact in general, it suffices to show that Eq. (2) can be satisfied only for a very special distribution of stress in the plate. Introduce the Airy stress function  $F(x, y)$  such that

$$\sigma_{xx} = \frac{\partial^2 F}{\partial y^2} \quad , \quad \sigma_{yy} = \frac{\partial^2 F}{\partial x^2} \quad , \quad \sigma_{xy} = -\frac{\partial^2 F}{\partial x \partial y} \quad (3)$$

<sup>†</sup> The dependency of  $k$  on the Poisson's ratio arises only when the applied loads on the crack are unbalanced. For more details, refer to the work of Sih and Liebowitz.



and consider the three expressions obtainable from Eq. (2) by letting  $i = j = 1$ ,  $i = j = 2$  and  $i = 1, j = 2$ . By adding and subtracting, the first two of the foregoing compatibility equations together with the third yield

$$\frac{\partial^2}{\partial x^2} (\nu^2 F) = 0, \quad \frac{\partial^2}{\partial y^2} (\nu^2 F), \quad \frac{\partial^2}{\partial x \partial y} (\nu^2 F) = 0$$

which imply that

$$\nu^2 F = Ax + By + C = \sigma_{xx} + \sigma_{yy} \quad (4)$$

where A, B and C are constants of integration. While the stress state in Eq. (4) is an exact solution of the equations of elasticity<sup>†</sup>, it is of little practical importance as it restricts  $\sigma_{xx} + \sigma_{yy}$  to be a linear function of x and y.

Turning to the solution of the crack problem, note should be made of the consequence of the approximation involved in the generalized plane stress assumption. From Ref. 3, the asymptotic expansion of the transverse strain near the crack vertex on the positive side of the x-axis is

$$\epsilon_{zz} = \frac{\nu w_z}{r^2} = -\frac{2\nu k}{r} \cos \frac{\theta}{2} + \dots \quad (5)$$

where r is the radial distance measured from the crack tip and  $\theta$  the angle from the x-axis. The transverse displacement  $w_z$  may be obtained by a simple integration. Note that  $w_z$  becomes unbounded at the crack tip  $r = 0$ . This is contrary to most elasticity solutions involving geometric singularities where the displacements are bounded.

In view of the comments just made, the generalized plane stress solution will not be a limit of the three-dimensional solution. Furthermore, it is incorrect to refer to the stress distribution on the surface layer of a plate with or without a crack as being in a state of "generalized plane stress".

The problem of plane strain does represent an exact special case of the more general three-dimensional problem. In fact, such a condition has been known to prevail in a region close to the crack border interior to the plate. This was first shown by Sih et al<sup>5</sup> in a three-dimensional analysis of the crack problem. Briefly, they carried out an eigenfunction expansion using the three biharmonic functions originally introduced by Galerkin and concluded that for a bounded displacement field at the crack edge the in-plane and transverse normal stresses were found to be proportional to  $r^{-1/2}$  while the transverse shear stresses are finite throughout the plate. Explicit expressions for the crack-border stresses and displacements were determined. The familiar condition of  $\sigma_{zz} = \nu (\sigma_{xx} + \sigma_{yy})$ , which arises in the two-dimensional problem of plane strain, is also shown to be satisfied in the three-dimensional case, except on the free surfaces of the plate. The intensity of the local stress field

may be a function of the thickness coordinate. The finite thickness plate solution presented in Ref. 5 may not be complete in that a knowledge of the order of the stress singularity, if any, on the surface layers where the crack penetrates through the plate is lacking. Because of this, additional complication arises due to the fact that the correctness of solution can no longer be guaranteed by the mere satisfaction of boundary conditions and differential equations, since the classical uniqueness theorem of Kirchhoff in the theory of elasticity does not apply to problems with geometric discontinuities such as a through crack in a thick plate.<sup>††</sup>

Having mentioned the analytical difficulties involved in solving the thickness problem, it can be said that the available mathematical tools can at best yield the qualitative character of the three-dimensional singular stresses in an exact manner. The quantitative part of the solution may be obtained either by resorting to a numerical analysis such as the finite element technique (without knowing the accuracy) or by developing approximate three-dimensional theories based on variational principles in such a way that the essential features of the thickness problem are still retained.

In what follows, a theoretical treatment of the thickness problem will be given. Starting with a three-dimensional eigenfunction expansion of the components of the displacement vector, the crack-border stress field for general loading conditions is found to depend on three intensity-parameters each of which is a function of the thickness coordinate. For special loadings on the cracked plate, they can be identified with the stress-intensity factors in plane extension, plate bending and anti-plane shear problems. For comparison purpose, the simplest type of theories which assume the stress variation across the plate thickness to be known are examined. These were due to Reissner<sup>6</sup> and Goldenweizer<sup>7</sup> for the bending of thin plates. Thus, for plates free from surface tractions  $\sigma_{zz}$  is taken to be zero everywhere. In Ref. 6, the bending stresses are assumed to be a linear function of the thickness coordinate z and the transverse shear stresses a parabolic function of z independent of the plate thickness. Goldenweizer's theory is slightly more general in that no restrictions are placed on the mode of stress distribution in the z-direction. Nevertheless, this distribution function must be pre-assigned to depend on the plate thickness, a shortcoming of all existing plate or shell theories. The results based on the theories proposed in Refs. 6 and 7 show that the magnitude of the bending stresses near the crack edge is drastically changed when the plate thickness increases from zero to some finite, but small, value. This is evidenced by the high elevation of the local moments as the ratio of plate thickness to crack length is perturbed slightly from zero.

† There exists a special class of problems referred to as "plane stress" which should be distinguished from "generalized plane stress". In plane stress, the in-plane stresses  $\sigma_{xx}$ ,  $\sigma_{yy}$  and  $\sigma_{xy}$  are permitted to be functions of x, y and z. The stress variation across the plate thickness turns out to depend on  $z^2$  (Ref. 4).

†† The same situation is encountered in the part-through surface flaw problem in which the surface stress singularity is not known. In this connection, the solution obtained from a numerical analysis is always in question.

A further improvement of the plate theory for extensional and bending loads can be made by assuming that all the six stress components in a cracked plate are function of  $x$ ,  $y$  as well as  $z$ . On the basis of variational principles, a more refined theory of thick plates is derived with the allowance that the  $z$ -distribution function can be determined from the condition  $\sigma_{zz} = \nu (\sigma_{xx} + \sigma_{yy})$  in the vicinity of the crack as suggested from the exact three-dimensional analysis<sup>5</sup>. A system of three simultaneous partial differential equations is obtained and solved for the problem of a pressurized crack in a finite thickness plate of infinite extent. Stress variations across the thickness are found explicitly with the exception of those in a thin layer near the plate surface and discussed in connection with the stress-intensity parameter used in the linear theory of fracture mechanics. A still better approximation of the three-dimensional thickness problem can be made by admitting a more general representation of stress state. This is discussed briefly as possible future work.

Finally, the question of verifying the analytical results on the thickness effects warrants some remarks. Experimental measurements on the fracture strength of a few selected metals have been made by Irwin<sup>8</sup>, Srawley and Beachem<sup>9</sup>, and others. There appears to be an optimum thickness for which the fracture resistance of a given material is maximum. It should be pointed out that this feature is the cause of the interaction of plastic deformation with the plate thickness and hence will not show up in any elastic analyses such as those presented in this work. Thus, caution must be exercised in comparing analytical results based on idealized continuum theories with experimental data obtained by testing the actual material.

### ASYMPTOTIC EXPANSIONS IN THREE DIMENSIONS

Let an elastic medium be bounded by two parallel planes  $z = -h/2$  and  $z = h/2$  which will be referred to as a plate. A rectangular crack of height  $h$  extends from the origin  $x = y = 0$  to negative infinity along the  $x$ -axis as indicated in Fig. 1. In describing the crack as a plane of discontinuity, it is convenient to adopt the cylindrical polar coordinates  $(r, \theta, z)$ . The  $z$ -axis is placed along the straight crack front and the coordinates  $r, \theta$  are used to define the position of an element in the plane of the plate, Fig. 2. Now, denote the components of the displacements in the radial and tangential directions by  $u_r, v_\theta$  and the component in the  $z$ -direction by  $w_z$ . The corresponding stress components are  $\sigma_{rr}, \sigma_{\theta\theta}, \dots, \sigma_{r\theta}$ .

The solution for the displacement vector will be sought in the form of a power series in  $r$  as  $r^{\lambda_m+n}$  multiplied by a vector function depending on both  $\theta$  and  $z$ , where  $n$  is an integer and  $\lambda_m$  ( $m = 0, 1, 2, \dots$ ) are the eigenvalues in the crack problem. A rigorous mathematical deduction on the values of  $\lambda_m$  has been made by Hartranft and Sih<sup>10</sup> who showed that the displacements can be represented by power series involving one-half and integer powers of  $r$ . For the present purpose of obtaining the singular stresses,

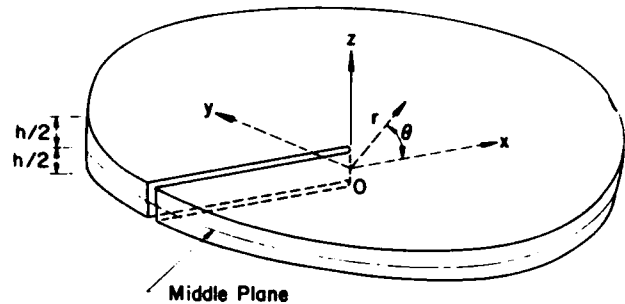


Figure 1. A Through-the-Thickness Semi-Infinite Crack.

it suffices to consider those terms in the displacement field with one-half powers of  $r$ , i.e.,

$$2\nu[u_r, v_\theta, w_z] = r^{1/2} [f_1(\theta, z), g_1(\theta, z), h_1(\theta, z)] + r^{3/2} [f_2(\theta, z), g_2(\theta, z), h_2(\theta, z)] + O(r^{5/2}) \quad (6)$$

where  $\mu$  is the shear modulus of elasticity. Substituting Eq. (6) into the strain-displacement relations in Appendix I yield the strain components in power series as

$$\begin{aligned} 2\nu \epsilon_{rr} &= r^{-1/2} (\frac{1}{2} f_1) + r^{1/2} (\frac{3}{2} f_2) + O(r^{3/2}) \\ 2\nu \epsilon_{\theta\theta} &= r^{-1/2} [f_1 + (\partial g_1 / \partial \theta)] + r^{1/2} [f_2 + (\partial g_2 / \partial \theta)] + O(r^{3/2}) \\ 2\nu \epsilon_{zz} &= r^{1/2} (\partial h_1 / \partial z) + r^{3/2} (\partial h_2 / \partial z) + O(r^{5/2}) \\ 4\nu \epsilon_{r\theta} &= r^{-1/2} [(\partial f_1 / \partial \theta) - \frac{1}{2} g_1] + r^{1/2} [(\partial f_2 / \partial \theta) - \frac{1}{2} g_2] + O(r^{3/2}) \\ 4\nu \epsilon_{\theta z} &= r^{-1/2} (\partial h_1 / \partial \theta) + r^{1/2} [(\partial g_1 / \partial z) + (\partial h_2 / \partial \theta)] + O(r^{3/2}) \\ 4\nu \epsilon_{zr} &= r^{-1/2} (\frac{1}{2} h_1) + r^{1/2} [(\partial f_1 / \partial z) + \frac{3}{2} h_2] + O(r^{3/2}). \end{aligned} \quad (7)$$

Note that the leading terms possess the inverse square root singularity except for the transverse normal strain  $\epsilon_{zz}$  which remains finite at the crack edge. This is different from the generalized plane stress solution shown in Eq. (5). Making use of the generalized Hooke's law for an isotropic, homogeneous elastic body given in Appendix I, the stress components are found:

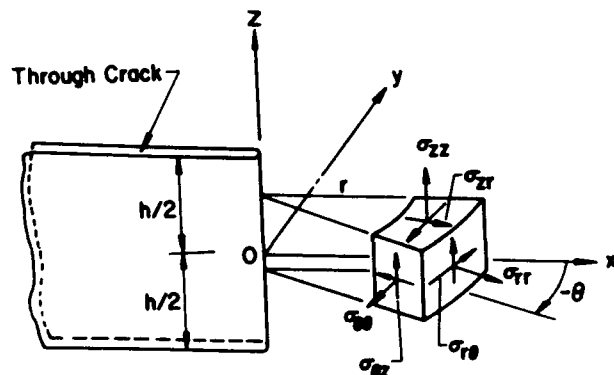


Figure 2. Notation of Stresses in Polar Coordinates on an Element Ahead of Crack.

$$\begin{aligned}
(1-2\nu) \sigma_{rr} &= r^{-1/2} [\nu(\partial g_1/\partial \theta) + \frac{1}{2}(1+\nu)f_1] + r^{1/2} \\
&\quad \nu[(\partial g_2/\partial \theta) + (\partial h_1/\partial z) + \frac{1}{2\nu}(3-\nu)f_2] \\
(1-2\nu) \sigma_{\theta\theta} &= r^{-1/2} [(1-\nu)(\partial g_1/\partial \theta) + \frac{1}{2}(2-\nu)f_1] + r^{1/2} \\
&\quad \nu[(\partial h_1/\partial z) + (1-\nu)(\partial g_2/\partial \theta) + \frac{1}{2}(2+\nu)f_2] \\
(1-2\nu) \sigma_{zz} &= r^{-1/2} \nu[(\partial g_1/\partial \theta) + \frac{3}{2\nu}f_1] + r^{1/2} \\
&\quad \nu[(\partial g_2/\partial \theta) + \frac{5}{2}f_2 + \frac{1-\nu}{\nu}(\partial h_1/\partial z)] \\
2\sigma_{r\theta} &= r^{-1/2}[(\partial f_1/\partial \theta) - \frac{1}{2}g_1] + r^{1/2}[(\partial f_2/\partial \theta) + \frac{1}{2}g_2] \\
2\sigma_{\theta z} &= r^{-1/2}(\partial h_1/\partial \theta) + r^{1/2}[(\partial g_1/\partial z) + (\partial h_2/\partial \theta)] \\
2\sigma_{zr} &= r^{-1/2}(\frac{1}{2}h_1) + r^{1/2}[(\partial f_1/\partial z) + \frac{3}{2}h_2] \quad (8)
\end{aligned}$$

where terms with order  $r^{3/2}$  or higher are neglected. In the three-dimensional case, the coefficients of  $r$  in Eq. (8) will be coupled through the equations of equilibrium. This is unlike the two-dimensional eigenfunction expansion method<sup>11</sup> in which they are independent of each other. The detailed structure of the functions  $f_1, f_2$ , etc. may be determined by appealing to the equations of equilibrium in Appendix I. By setting the coefficients of  $r^{-1/2}$  and  $r^{-3/2}$  equal to zero, there results a system of six simultaneous partial differential equations in the variables  $\theta$  and  $z$ :

$$\begin{aligned}
\frac{1}{2}(5-8\nu)(\partial g_1/\partial \theta) - (1-2\nu)(\partial^2 f_1/\partial \theta^2) + \frac{3}{2}(1-\nu)f_1 &= 0 \\
-\frac{1}{2}(3-8\nu)(\partial g_2/\partial \theta) + (1-2\nu)(\partial^2 f_2/\partial \theta^2) + \frac{5}{2}(1-\nu)f_2 + \frac{1}{2}(\partial h_1/\partial z) &= 0 \\
-(7-8\nu)(\partial f_1/\partial \theta) - 4(1-\nu)(\partial^2 g_1/\partial \theta^2) + \frac{3}{2}(1-2\nu)g_1 &= 0 \\
(9-8\nu)(\partial f_2/\partial \theta) + 4(1-\nu)(\partial^2 g_2/\partial \theta^2) + \frac{5}{2}(1-2\nu)g_2 + 2(\partial^2 h_1/\partial \theta \partial z) &= 0 \\
(\partial^2 h_1/\partial \theta^2) + \frac{1}{4}h_1 &= 0 \\
2(1-2\nu)(\partial^2 h_2/\partial \theta^2) + \frac{9}{2}(1-2\nu)h_2 + 3(\partial f_1/\partial z) + 2(\partial^2 g_1/\partial \theta \partial z) &= 0. \quad (9)
\end{aligned}$$

These equations may be solved in an exact manner the details of which are given in Appendix II. The results for the problem symmetric<sup>†</sup> in  $\theta$  defined as

$$f_1, f_2, h_1, h_2 \text{ even in } \theta; \quad g_1, g_2 \text{ odd in } \theta \quad (10)$$

are given by

$$\begin{aligned}
f_1(\theta, z) &= B(z) \cos(\theta/2) + C(z) \cos(3\theta/2) \\
g_1(\theta, z) &= -\frac{7-8\nu}{5-8\nu} B(z) \sin(\theta/2) - C(z) \sin(3\theta/2) \\
h_1(\theta, z) &= A(z) \cos(\theta/2) \quad (11)
\end{aligned}$$

and

$$\begin{aligned}
f_2(\theta, z) &= D(z) \cos(\theta/2) + E(z) \cos(5\theta/2) - \frac{1}{3} A'(z) \cos(\theta/2) \\
g_2(\theta, z) &= \frac{9-8\nu}{3-8\nu} D(z) \sin(\theta/2) - E(z) \sin(5\theta/2) - \frac{1}{3} A'(z) \sin(\theta/2) \\
h_2(\theta, z) &= F(z) \cos(3\theta/2) - \frac{2}{5-8\nu} B'(z) \cos(\theta/2). \quad (12)
\end{aligned}$$

In order to prepare for the satisfaction of the free crack surface conditions

$$\sigma_{\theta\theta} = \sigma_{r\theta} = \sigma_{\theta z} = 0 \quad \text{at} \quad \theta = \pm \pi \quad (13)$$

it is first necessary to calculate for the quantities

<sup>†</sup> The skew-symmetric problem which requires  $f_1, f_2, h_1, h_2$  odd in  $\theta$ ;  $g_1, g_2$  even in  $\theta$  may be solved in the same way.<sup>10</sup>

$$\begin{aligned}
[\sigma_{\theta\theta}, \sigma_{r\theta}, \sigma_{\theta z}] &= r^{-1/2} [\sigma_{\theta\theta}^{(1)}, \sigma_{r\theta}^{(1)}, \sigma_{\theta z}^{(1)}] + r^{1/2} \\
&\quad [\sigma_{\theta\theta}^{(2)}, \sigma_{r\theta}^{(2)}, \sigma_{\theta z}^{(2)}] + \dots \quad (14)
\end{aligned}$$

in which  $\sigma_{\theta\theta}^{(1)}, \sigma_{r\theta}^{(2)}$ , etc. stand for

$$(1-2\nu)\sigma_{\theta\theta}^{(1)} = \frac{4-2\nu}{5-8\nu} B(z) \cos(\theta/2) - \frac{1}{2}(1-2\nu) C(z) \cos(3\theta/2)$$

$$\sigma_{r\theta}^{(1)} = \frac{1}{2(5-8\nu)} B(z) \sin(\theta/2) - \frac{1}{2} C(z) \sin(3\theta/2)$$

$$\sigma_{\theta z}^{(1)} = -\frac{1}{4} A(z) \sin(\theta/2)$$

and

$$(1-2\nu)\sigma_{\theta\theta}^{(2)} = -\frac{1}{6}(1-4\nu) A'(z) \cos(\theta/2) + \frac{15}{2} \left(\frac{1-2\nu}{3-8\nu}\right) D(z) \cos(\theta/2) - \frac{3}{2}(1-2\nu) E(z) \cos(5\theta/2)$$

$$\sigma_{r\theta}^{(2)} = \frac{3}{2(3-8\nu)} D(z) \sin(\theta/2) - \frac{3}{2} E(z) \sin(5\theta/2)$$

$$\sigma_{\theta z}^{(2)} = \frac{3-4\nu}{5-8\nu} B'(z) \sin(\theta/2) - \frac{1}{4} [2C'(z) + 3F(z)] \sin(3\theta/2).$$

The conditions in Eq. (13) can be satisfied by taking

$$A(z) = 0, \quad B(z) = -(5-8\nu) C(z)$$

$$D(z) = -(3-8\nu) E(z), \quad F(z) = -\frac{2}{3} (7-8\nu) C'(z). \quad (15)$$

Thus, the displacement functions  $f_1, f_2$ , etc. in Eq. (6) may be expressed in terms of two independent quantities  $C(z)$  and  $E(z)$  as follows:

$$f_1(\theta, z) = C(z) [-(5-8\nu) \cos(\theta/2) + \cos(3\theta/2)]$$

$$f_2(\theta, z) = E(z) [-(3-8\nu) \cos(\theta/2) + \cos(5\theta/2)]$$

$$g_1(\theta, z) = C(z) [(7-8\nu) \sin(\theta/2) - \sin(3\theta/2)]$$

$$g_2(\theta, z) = -E(z) [(9-8\nu) \sin(\theta/2) + \sin(5\theta/2)]$$

$$h_1(\theta, z) = 0$$

$$h_2(\theta, z) = C'(z) [-\frac{2}{3}(7-8\nu) \cos(3\theta/2) + 2 \cos(\theta/2)]. \quad (16)$$

Following the same procedure, other functions such as  $f_3, f_4$ , etc. associated with  $r^{5/2}, r^{7/2}$ , etc. may also be obtained without difficulty. In fact, by setting up the recurrence relations the solution may be written down in closed form<sup>10</sup>. It follows from Eqs. (6) and (16) that the asymptotic expansions of the displacements become

$$2u_r = r^{1/2} C(z) [-(5-8\nu) \cos(\theta/2) + \cos(3\theta/2)]$$

$$+ r^{3/2} E(z) [-(3-8\nu) \cos(\theta/2) + \cos(5\theta/2)] + \dots$$

$$2u_\theta = r_{1/2} C(z) [(7-8\nu) \sin(\theta/2) - \sin(3\theta/2)]$$

$$- r^{3/2} E(z) [(9-8\nu) \sin(\theta/2) + \sin(5\theta/2)] + \dots$$

$$2u_z = r^{3/2} C'(z) [2 \cos(\theta/2) - \frac{2}{3}(7-8\nu) \cos(3\theta/2)] + \dots \quad (17)$$

and they are all bounded at the crack edge with  $w_z$  being one order higher than the leading terms for  $u_r$  and  $v_\theta$ . The corresponding stress components for the symmetric problem of in-plane extension and out-of-plane bending are

$$\sigma_{rr} = r^{-1/2} C(z) [-\frac{5}{2} \cos(\theta/2) + \frac{1}{2} \cos(3\theta/2)]$$

$$+ r^{1/2} E(z) [-\frac{9}{2} \cos(\theta/2) + \frac{3}{2} \cos(5\theta/2)] + \dots$$

$$\sigma_{\theta\theta} = -r^{-1/2} C(z) [\frac{3}{2} \cos(\theta/2) + \frac{1}{2} \cos(3\theta/2)]$$

$$- r^{1/2} E(z) [\frac{15}{2} \cos(\theta/2) + \frac{3}{2} \cos(5\theta/2)] + \dots$$

$$\begin{aligned}
\sigma_{zz} &= -r^{-1/2} C(z) [4\nu \cos(\theta/2)] - r^{1/2} E(z) [12\nu \cos(\theta/2)] + \dots \\
\sigma_{r\theta} &= -r^{-1/2} C(z) \left[ \frac{1}{2} \sin(\theta/2) + \frac{1}{2} \sin(3\theta/2) \right] \\
&\quad - r^{1/2} E(z) \left[ \frac{3}{2} \sin(\theta/2) + \frac{3}{2} \sin(5\theta/2) \right] + \dots \\
\sigma_{\theta z} &= r^{1/2} C'(z) (3-4\nu) [\sin(\theta/2) + \sin(3\theta/2)] + \dots \\
\sigma_{zr} &= -r^{1/2} C'(z) [(1-4\nu) \cos(\theta/2) + (3-4\nu) \cos(3\theta/2)] + \dots
\end{aligned} \tag{18}$$

To be noted is that as  $r \rightarrow 0$  the stresses  $\sigma_{rr}$ ,  $\sigma_{\theta\theta}$ ,  $\sigma_{zz}$  and  $\sigma_{r\theta}$  all tend to infinity like  $r^{-1/2}$  while  $\sigma_{\theta z}$  and  $\sigma_{zr}$  remain bounded. Eq. (18) also indicates that the relation  $\sigma_{zz} = \nu(\sigma_{rr} + \sigma_{\theta\theta})$  holds in a small cylindrical region centered around the crack front. The anti-plane type of deformation is not included in Eq. (18). Otherwise, the transverse shear stresses  $\sigma_{\theta z}$  and  $\sigma_{zr}$  would be singular. Thus far the  $z$ -distribution in the plate is still arbitrary and no conditions have been imposed on the functions  $C(z)$  and  $E(z)$ . This will be left for discussion in the next section.

### TRIAxIAL CHARACTERISTICS OF LOCAL STRESSES

Mathematical analysis of crack problems has continuously played a key role in the development of the theories of crack propagation and in the understanding of the mechanics of fracture. A good example of this is the two-dimensional elliptical cavity solution of Inglis<sup>1</sup> without which the Griffith theory of fracture would be incomplete. The work of Sneddon<sup>12</sup> on the stress distribution around a penny-shaped crack has enabled Irwin<sup>13</sup> to identify the energy release rate of Griffith with the coefficient of the  $r^{-1/2}$  term in the local stress field. As a consequence, it has cleared the way for a more general application of the linear elastic theory of fracture mechanics in two dimensions. The same, however, cannot be said for the three-dimensional theory of thickness fracture. Progress in the understanding of thickness fracture has been inhibited by the lack of mathematical descriptions of conditions prevailing near the crack border.

Recently, some important advances (Refs. 5, 10, and 14) have been made in obtaining the general character of the three-dimensional stress state near the crack border. Under the most general loading conditions, those stresses which become unbounded at the crack border (see Fig. 2) are found to be

$$\begin{aligned}
\sigma_{rr} &= r^{-1/2} A_1(z) \left[ \frac{1}{2} \cos(3\theta/2) - \frac{5}{2} \cos(\theta/2) \right] \\
&\quad + r^{-1/2} A_2(z) \left[ \frac{1}{2} \sin(3\theta/2) - \frac{5}{2} \sin(\theta/2) \right] \\
\sigma_{\theta\theta} &= -r^{-1/2} A_1(z) \left[ \frac{1}{2} \cos(3\theta/2) + \frac{3}{2} \cos(\theta/2) \right] \\
&\quad - r^{-1/2} A_2(z) \left[ \frac{1}{2} \sin(3\theta/2) + \frac{1}{2} \sin(\theta/2) \right] \\
\sigma_{zz} &= -r^{-1/2} 4\nu [A_1(z) \cos(\theta/2) + \frac{1}{3} A_2(z) \sin(\theta/2)]
\end{aligned}$$

<sup>†</sup> In the three-dimensional theory of elasticity, there is no need to introduce moments and transverse shear force quantities as it is done in the approximate plate theories. The stress state in accordance with Eq.(22) simply requires the in-plane stresses to be odd in  $z$  and the transverse shear stresses even in  $z$ .

$$\begin{aligned}
\sigma_{r\theta} &= -r^{-1/2} A_1(z) \left[ \frac{1}{2} \sin(3\theta/2) + \frac{1}{2} \sin(\theta/2) \right] \\
&\quad + r^{-1/2} A_2(z) \left[ \frac{1}{2} \cos(3\theta/2) + \frac{1}{6} \cos(\theta/2) \right] \\
\sigma_{\theta z} &= r^{-1/2} A_3(z) \left[ \frac{1}{4} \cos(\theta/2) \right] \\
\sigma_{zr} &= r^{-1/2} A_3(z) \left[ \frac{1}{4} \sin(\theta/2) \right]
\end{aligned} \tag{19}$$

where  $A_1(z)$  is equal to  $C(z)$  in Eq. (18). Those terms in Eq. (19) associated with  $A_2(z)$  and  $A_3(z)$  can be determined by the same asymptotic expansion method described earlier.

So far no effort has been made to satisfy the free stress conditions on the faces of the plate, namely

$$\sigma_{zz} = \sigma_{\theta z} = \sigma_{zr} = 0 \quad \text{for } z = \pm h/2. \tag{20}$$

A quick glance at Eq. (19) reveals that the conditions specified by Eq. (20) can be satisfied if and only if the coefficients  $A_j(z)$  ( $j = 1, 2, 3$ ) vanish for  $z = \pm h/2$ . Hence, all the stresses and displacements on the plate faces near the crack are zero, a result which is suspect on physical grounds. A possible explanation of this could be that the surface displacements and stresses near the crack edge are described by terms of order higher in  $r$  than those given in Eq. (19). The author has attempted to resolve this disturbing feature of the thickness problem but so far without success.

Nevertheless, the stress state in Eq. (19) as functions of  $z$  does permit the crack driving force to vary along the crack front. In principle, the coefficients  $A_j(z)$  ( $j = 1, 2, 3$ ) can be evaluated from the boundary conditions of the crack problem. A normal procedure for accomplishing this is to separate the three-dimensional problem into two parts as follows:

(1) The first part called "stretching" concerns with deformation where the plane layers of the plate experience extension (or compression). Consequently, the displacements  $u_r$  and  $v_\theta$  are even functions and  $w_z$  is an odd function of  $z$ , i.e.,

$$\frac{\partial u_r}{\partial z} = 0, \quad \frac{\partial v_\theta}{\partial z} = 0, \quad w_z = 0 \quad \text{for } z = 0. \tag{21}$$

(2) The second part, referred to loosely as "bending"<sup>†</sup>, deals with deformation which displaces the plate out of its original plane. Here, the displacements  $u_r$  and  $v_\theta$  are odd functions and  $w_z$  is an even function of  $z$ ; hence

$$u_r = 0, \quad v_\theta = 0, \quad \frac{\partial w_z}{\partial z} = 0 \quad \text{for } z = 0. \tag{22}$$

The sum of these two parts represents the general mode of deformation of the plate. On account of the complexity of the three-dimensional equations of elasticity, only a limited number of crack problems can be solved. As of this date, the author is aware of only one example in which  $A_j(z)$  ( $j = 1, 2, 3$ ) are determined explicitly. This is the case

of an infinite body containing a half-plane crack opened out by isolated forces<sup>3</sup>. Moreover, no rigorous solution of the finite thickness problem for non-trivial loading cases has been obtained. Because of this, one is forced to limit considerations to weaker boundary conditions such as those assumed in the approximate theories of thin plates and to allow partial contradiction of the compatibility conditions.<sup>†</sup> The simplifying assumptions regarding the stress or strain distribution are made in such a way that the three functions  $A_j(z)$  ( $j = 1, 2, 3$ ) do not occur simultaneously in a given problem. In this connection, there are three distinct classes of practical problems whose solutions can be obtained in a relatively simple manner.

### (1) In-Plane Extension

By expressing the stress variations across the plate thickness in the  $z$ -direction as products of those in the plane of the plate, simplified theories of plates may be derived by means of variational principles. For this class of problems,  $A_1(z)$  and  $A_2(z)$  are even functions of  $z$  and  $A_3(z) = 0$ , i.e.,

$$A_1(z) = -\frac{k_1(z)}{2\sqrt{z}}, \quad A_2(z) = \frac{3k_2(z)}{2\sqrt{z}}, \quad A_3(z) = 0 \quad (23)$$

where  $k_1(z)$  and  $k_2(z)$  are respectively the stress-intensity factors associated with the opening and edge-sliding mode of fracture.

### (2) Out-of-Plane Bending

On the basis of the approximate plate bending theories advanced by Reissner<sup>6</sup>, Goldenweizer<sup>7</sup> and others,  $A_1(z)$  and  $A_2(z)$  are odd functions of  $z$  and can be identified with the bending stress-intensity factors  $K_1(z)$  and  $K_2(z)$  referred to symmetrical and skew-symmetrical loadings, respectively.

$$A_1(z) = -\frac{K_1(z)}{2\sqrt{z}}, \quad A_2(z) = \frac{3K_2(z)}{2\sqrt{z}}, \quad A_3(z) = 0 \quad (24)$$

### (3) Anti-Plane Shear

This is perhaps the simplest group of boundary-value problems to solve mainly because the governing differential equation is of the Laplace type in two-dimensions and its solution is well understood. In this special case, both of the displacement components  $u_r$  and  $v_\theta$  are taken to be zero while  $w_z$  is restricted to depend only on  $x$  and  $y$ . Hence,

$$A_1(z) = A_2(z) = 0, \quad A_3(z) = 2\sqrt{z} k_3 \quad (25)$$

in which  $k_3$  is the stress-intensity factor for the tearing mode of fracture.

The definition of the stress-intensity factors in Eq. (23) and (24) is a generalization of the conventional ones

which are independent of  $z$ . In relation to the energy consideration of Griffith, it might be informative to calculate for the input work rates for crack extension averaged through the plate thickness as

$$\begin{bmatrix} G_1 \\ G_2 \end{bmatrix} = \lim_{\delta \rightarrow 0} \frac{1}{\delta} \int_{-h/2}^{h/2} \int_0^\delta \begin{bmatrix} \sigma_{yy}(\delta-\rho, 0, z) \\ \sigma_{xy}(\delta-\rho, 0, z) \end{bmatrix} \begin{bmatrix} u_y(\rho, \pi, z) \\ u_x(\rho, \pi, z) \end{bmatrix} d\rho dz \quad (26)$$

and to compare them with those found from the two-dimensional theory of plane strain or generalized plane stress.

## APPROXIMATE THEORIES OF PLATE BENDING

In the standard theory of thin plates under bending, it is customary to assume that the bending stresses are distributed linearly over the thickness of the plate:

$$[\sigma_{xx}, \sigma_{yy}, \sigma_{xy}] = \frac{12z}{h^3} [M_{xx}, M_{yy}, M_{xy}] \quad (27)$$

In Eq. (27),  $M_{xx}$  and  $M_{yy}$  are the bending couples, and  $M_{xy}$  the twisting couple defined by

$$[M_{xx}, M_{yy}, M_{xy}] = \int_{-h/2}^{h/2} [\sigma_{xx}, \sigma_{yy}, \sigma_{xy}] z dz.$$

From the differential equations of equilibrium, the transverse shear stresses which satisfy the free plate surface conditions can be shown to vary parabolically in the following manner

$$[\sigma_{xz}, \sigma_{yz}] = (3/2h) [1 - (2z/h)^2] [V_x, V_y] \quad (28)$$

where  $V_x$  and  $V_y$  are the shear stress resultants given by

$$[V_x, V_y] = \int_{-h/2}^{h/2} [\sigma_{xz}, \sigma_{yz}] dz.$$

Refer to Fig. 3 for notations of  $M_{xx}$ ,  $M_{yy}$ , etc. and the stress variations of  $\sigma_{xx}$ ,  $\sigma_{yy}$ , etc. across the plate thickness. In the absence of normal loads, the thin plate theory assumes  $\sigma_{zz}$  to be vanishingly small throughout the plate.

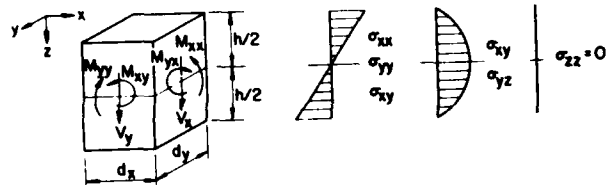


Figure 3. Notation of Moments and Shear Stress Resultants and Stress Variation Over Plate Thickness.

<sup>†</sup> Violation of this kind can lead to absurd results for the displacement field. For instance, the classical Poisson-Kirchhoff theory of plate bending gives a multi-valued displacement field for the problem of a through crack subjected to bending loads.<sup>15</sup>

Earlier investigations (Refs. 16, 17, and 18) on the bending stresses near the crack ends were based on the classical Poisson-Kirchhoff theory. The number of boundary conditions satisfied along the crack face turned out to be fewer than that can in reality be prescribed. If the crack is placed along the x-axis, three physical boundary conditions consisting of  $M_{yy}$ ,  $M_{xy}$  and  $V_y$  should be specified on the edge  $y = 0$ . The exclusion of the transverse shear deformation in the classical theory, however, led to the contraction of the three conditions ( $M_{xx}$ ,  $M_{xy}$ ,  $V_y$ ) into two of the so-called Kirchhoff conditions

$$M_{yy} \quad \text{and} \quad V_y + \frac{\partial M_{xy}}{\partial x} \quad (29)$$

which are the bending moment and the sum of vertical shear force and edgewise rate of change of twisting moment. Because of this reduction in the number of boundary conditions, the stress distribution obtained from the classical theory is erroneous in the boundary layer, i.e., local to the crack ends and faces. The inaccuracy of the classical solution may be seen from Ref. 16.

$$\begin{aligned} \sigma_{rr} &= (2r)^{-1/2} (z/h) K_1^* \frac{7+\nu}{2(3+\nu)} \left[ \left( \frac{3+5\nu}{7+\nu} \right) \cos(\theta/2) - \cos(3\theta/2) \right] \\ &\quad + (2r)^{-1/2} (z/h) K_2^* \frac{5+3\nu}{2(3+\nu)} \left[ \sin(3\theta/2) - \left( \frac{3+5\nu}{5+3\nu} \right) \sin(\theta/2) \right] \\ \sigma_{\theta\theta} &= (2r)^{-1/2} (z/h) K_1^* \frac{7+\nu}{2(3+\nu)} \left[ \cos(3\theta/2) + \left( \frac{5+3\nu}{7+\nu} \right) \cos(\theta/2) \right] \\ &\quad - (2r)^{-1/2} (z/h) K_2^* \frac{5+3\nu}{2(3+\nu)} \left[ \sin(3\theta/2) + \sin(\theta/2) \right] \\ \sigma_{zz} &= 0 \\ \sigma_{r\theta} &= (2r)^{-1/2} (z/h) K_1^* \frac{7+\nu}{2(3+\nu)} \left[ \sin(3\theta/2) - \left( \frac{1-\nu}{7+\nu} \right) \sin(\theta/2) \right] \\ &\quad + (2r)^{-1/2} (z/h) K_2^* \frac{5+3\nu}{2(3+\nu)} \left[ \cos(3\theta/2) - \left( \frac{1-\nu}{5+3\nu} \right) \cos(\theta/2) \right] \\ \sigma_{\theta z} &= (2r)^{-3/2} \frac{h^2 - 4z^2}{2h(3+\nu)} \left[ K_1^* \sin(\theta/2) - K_2^* \cos(\theta/2) \right] \\ \sigma_{zr} &= -(2r)^{-3/2} \frac{h^2 - 4z^2}{2h(3+\nu)} \left[ K_1^* \cos(\theta/2) + K_2^* \sin(\theta/2) \right]. \end{aligned} \quad (30)$$

The parameters  $K_1^*$  and  $K_2^*$  are functions of the load and geometry. For the case of an infinite plate with a through crack owing to uniform bending moment  $m_0$  and twisting moment  $n_0$ , these parameters are of the forms

$$K_1^* = (6m_0/h^2) \sqrt{a}, \quad K_2^* = (6n_0/h^2) \sqrt{a}.$$

Eqs. (30) imply that the angular variation of the stresses is a function of the Poisson's ratio of the plate. This is inconsistent with the more exact solution in Eq. (19). Another serious defect is that both  $\sigma_{\theta z}$  and  $\sigma_{zr}$  are singular of the order  $r^{-3/2}$  at the crack ends whereas the result of the three-dimensional analysis given in Eq. (18) requires  $\sigma_{xz}$  and  $\sigma_{zy}$  to be finite as  $r \rightarrow 0$ .

It is apparent that the approximate Kirchhoff conditions are not adequate for determining asymptotic solutions of the stresses and displacements near the crack. For this reason, the available stress solutions on cracks in spherical and cylindrical shells which incorporate conditions of the type in Eq. (29) are misleading. A more refined analysis of a spherical cap containing a finite crack will soon be completed by Sih and Hagendorf<sup>19</sup>. In their work, the

effect of transverse shear deformation is included in the shell theory and as a consequence five boundary conditions can be satisfied on the crack instead of four as in the standard thin shell theory.

The first attempt to resolve the inaccuracies caused by the Kirchhoff conditions connected with the crack problem was made by Knowles and Wang<sup>20</sup> for an initially flat plate of zero thickness. They used the Reissner's<sup>6</sup> sixth order bending theory which admits three rather than two boundary conditions on an edge. The analysis was later generalized by Hartranft and Sih<sup>21</sup> to include the effect of plate thickness. The resulting stress state takes the same form as Eq. (19) with  $A_j(z)$  ( $j = 1, 2, 3$ ) specialized according to Eq. (24) in which

$$K_1(z) = (12z/h^3) + (1) m_0 \sqrt{a}, \quad K_2(z) = (12z/h^3) + (1) n_0 \sqrt{a}. \quad (31)$$

The equivalent shear difficulty is now negated since  $\sigma_{rz}$  and  $\sigma_{\theta z}$  are no longer singular. Further, the Reissner theory does predict the correct  $r$ - and  $\theta$ -dependence of the bending stresses in spite of the simplified assumptions made in Eq. (27) and (28). This dependence coincides with that of the stretching of thin plates. Hence, it is consistent with the view that each layer of the plate experiences extension or compression, with the aggregate of layers producing bending.

The functions  $\Phi(1)$  and  $\Psi(1)$  in Eq. (31) can be computed numerically from integral equations of the standard type based on the Reissner's sixth order bending theory. The mathematical details are given elsewhere<sup>21</sup>. For a vanishingly thin plate,  $\Phi(1)$  reduces to  $(1 + \nu) / (3 + \nu)$  which corresponds to the limiting case treated in Ref. 20. The variation of  $\Phi(1)$  with the plate thickness to crack length ratio  $h/a \sqrt{10}$  is illustrated graphically in Fig. 4 for Poisson's ratio of  $\nu = 0.0, 0.3, 0.5$ . The magnitude of the

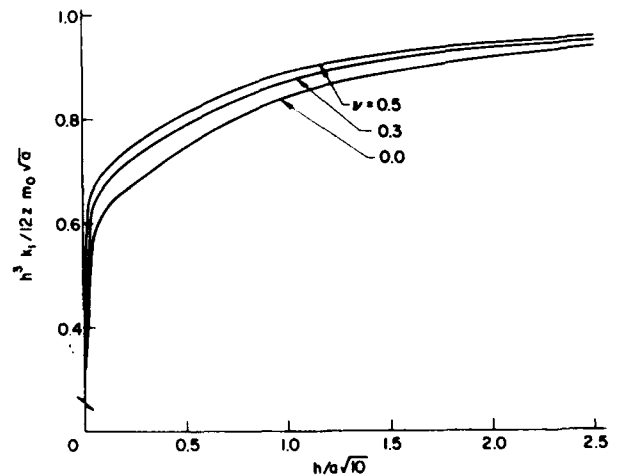


Figure 4. Normalized Stress-Intensity Factor versus Plate Thickness to Crack Length Ratio in the Reissner Theory.

normalized  $K_1(z)$  - factor in Eq. (31) is seen to increase rapidly as the plate thickness changes from zero to some small value. With a crack length that is ten times greater than the plate thickness,  $K_1(z)$  is approximately 65% beyond the value corresponding to  $h = 0$  and  $\nu = 0.3$ . In fact, the slope of the curves in Fig. 4 becomes unbounded in the limit as  $h \rightarrow 0$ . The influence of plate thickness on  $K_2(z)$  or  $\Psi(1)$  for the case of applied twisting moment is not as pronounced as in the symmetric problem. Incidentally, Wynn and Smith<sup>20</sup> have recently performed a series of experiments on the combined extension and cylindrical bending of plates. Good agreements were found for the analytic results of Hartranft and Sih<sup>21</sup>. Since the mathematical analysis does not account for crack closure on the compressive side of the plate, experimental data should be interpreted accordingly.

A way to improve Reissner's thin plate theory is to take a more general assumed distribution of stress in the thickness direction. The functions which express the various stresses are of the form  $f(z)g(x,y)$ , i.e.,

$$\begin{aligned} [\sigma_{xx}, \sigma_{yy}, \sigma_{xy}] &= (4/h^2)f''(2z/h) [M_{xx}, M_{yy}, M_{xy}] \\ [\sigma_{xz}, \sigma_{yz}] &= -(2/h)f'(2z/h) [V_x, V_y] \\ \sigma_{zz} &= 0 \end{aligned} \quad (32)$$

The physical boundary conditions are expressed in terms of the moments  $M_{xx}, M_{yy}, M_{xy}$  and transverse shear forces  $V_x, V_y$ , per unit length of the edges. On this basis, Goldenweizer<sup>7</sup> derived a system of equations governing the un-

knowns  $M_{xx}, M_{yy}$ , etc. which are very similar to those appearing in the Reissner theory<sup>6</sup>. The basic difference between the two theories is that the stress variation in the  $z$ -direction characterized by  $f(2z/h)$  in Eq. (32) can depend on the plate thickness to crack length ratio whereas in Ref. 6 the  $z$ -dependence of the stresses is restricted as indicated by Eq. (27) and (28). The plate is still assumed to be sufficiently thin so that  $\sigma_{zz} = 0$  if the lateral loads were not present.

The function  $f(z/2h)$  can be selected arbitrarily or determined experimentally. Sih<sup>23</sup> has proposed to expand  $f(z/2h)$  in a trigonometric series

$$f'(2z/h) = b_0 - \sum_{n=1}^{\infty} (-1)^n b_n \cos[(2\pi n z/h)] \quad (33)$$

which satisfies the conditions that  $\sigma_{xz} = \sigma_{yz} = 0$  on the planes  $z = \pm h/2$ , i.e.,  $f'(\pm 1) = 0$ . In Eq. (33),  $b_0$  and  $b_n$  are given by

$$b_0 = \sum_{n=1}^{\infty} (-1)^n b_n, \quad b_n = [1 + (a\pi n/h)^2]^{-1} \quad (34)$$

Approximately one hundred terms were taken in the summation series of Eq. (33) and (34) for the calculation of  $f'(2z/h)$ . The numerical results on the variations of the in-plane stresses  $\sigma_{xx}, \sigma_{yy}, \sigma_{xy}$  and transverse shear stresses  $\sigma_{xz}, \sigma_{yz}$  plotted against the nondimensional thickness coordinate are shown in Fig. 5. In plate bending,  $\sigma_{xz}$  and  $\sigma_{yz}$  are even in  $z$  and presumably they achieve greater magnitudes as the plate thickness is increased.

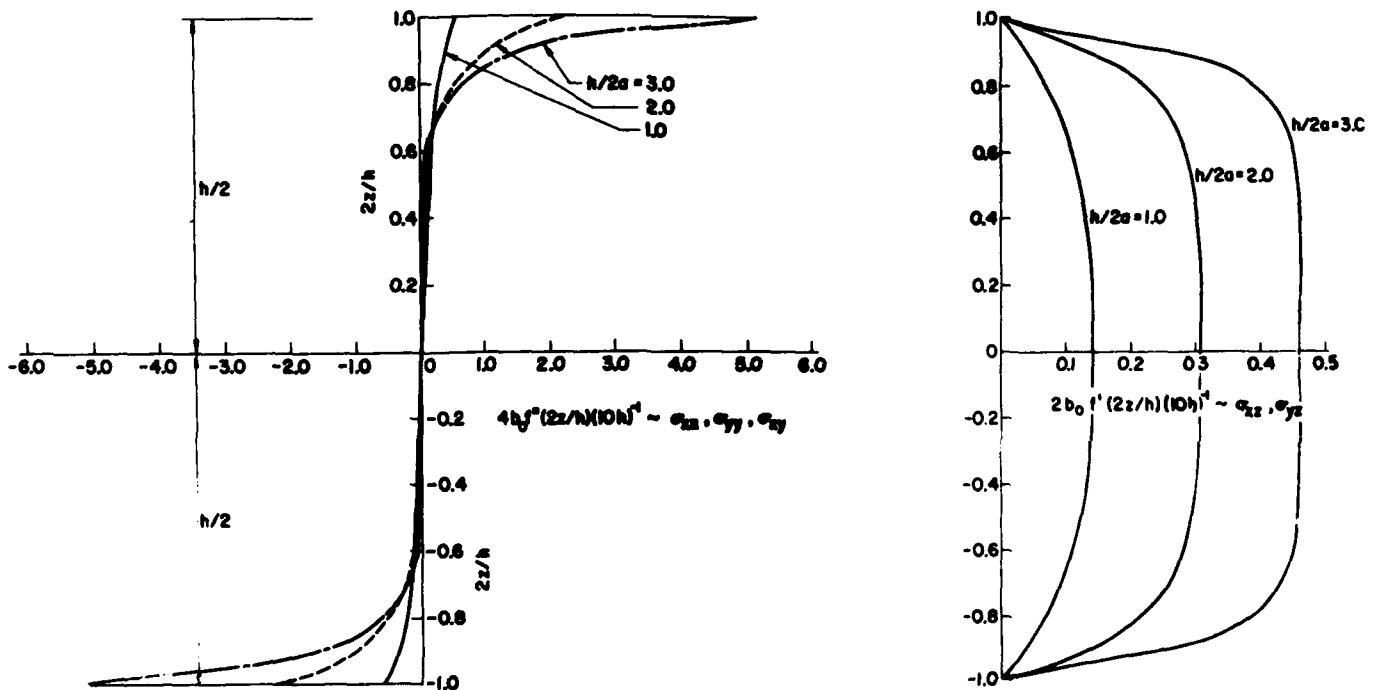


Figure 5. Assumed Stress Variation Across Plate Thickness.

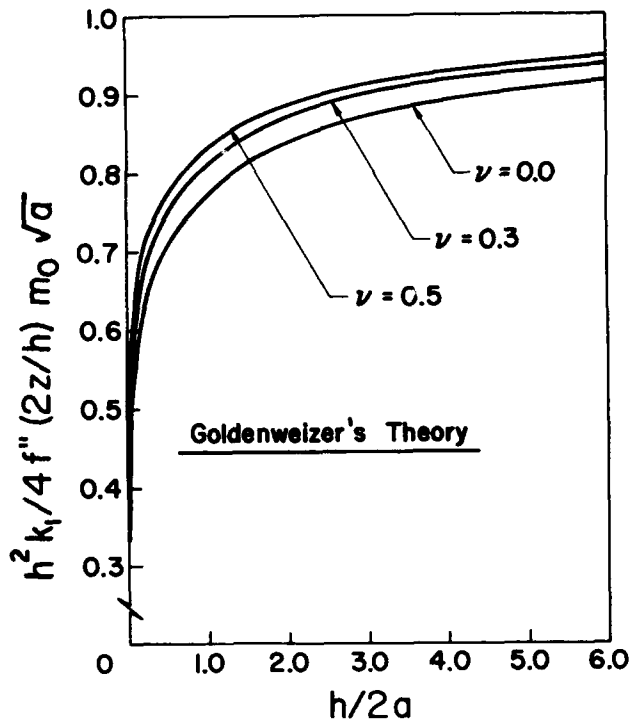


Figure 6. Dimensionless Stress-Intensity Factor as a Function of Plate Thickness in the Goldenweizer Theory.

Using the theory developed in Ref. 7 and Eq. (33), Sih<sup>23</sup> has solved the problem of an infinite plate with a crack of length  $2a$  upon which uniform bending moments are applied. The detailed structure of the bending stresses is again the same as the three-dimensional case with  $\sigma_{xz}$  and  $\sigma_{yz}$  remaining finite at the crack ends. The intensity of the local stresses is governed by

$$k_1(z) = (4/h^2) f''(2z/h) \Lambda(1) m_0 \sqrt{a} \quad (35)$$

where  $m_0$  is the magnitude of the applied moment. This quantity  $\Lambda(1)$  evaluated at the crack vertex  $x = a, y = 0$  is calculated numerically for various values of  $h/2a$  and  $\nu = 0.0, 0.3, 0.5$ . Fig. 6 displays the normalized stress-intensity factor as a function of  $h/2a$ . The curves are seen to climb sharply at first and then level off gradually for thicker plates. Physical interpretation of the numerical results in Fig. 6 for large values of  $h/2a$  is not meaningful as the bending theory of Goldenweizer is valid only for thin plates. The asymptotic value of all the curves may be viewed simply as a mathematical limit. For thin plates, it is informative to note the rise of  $K_1(z)$  as the plate thickness to crack length ratio is varied, say from 0 to 1/5. The amount of increase for the bending stress-intensity factor is approximately 95% for  $\nu = 0.0$ , 77% for  $\nu = 0.03$ , and 68% for  $\nu = 0.5$ .

#### PROPOSED THEORY OF PLATES

One of the shortcomings of the existing plate

theories is that  $\sigma_{zz}$  is assumed to be negligible throughout the plate and hence the condition  $\sigma_{zz} = \nu(\sigma_{xx} + \sigma_{yy})$  ahead of the crack cannot be satisfied. It is proposed to construct a new theory of plate stretching or bending such that the essential features of the three-dimensional characteristics of the solution to the crack problem are retained. As a simplification of the three-dimensional problem, the following form of stress state is taken<sup>24</sup>:

$$\begin{aligned} [\sigma_{xx}, \sigma_{yy}, \sigma_{xy}] &= (4/h^2) f''(2z/h) [S_{xx}, S_{yy}, S_{xy}] \\ [\sigma_{xz}, \sigma_{yz}] &= -(2/h) f'(2z/h) [Z_x, Z_y] \\ \sigma_{zz} &= f(2z/h) S_{zz} \end{aligned} \quad (36)$$

The quantities  $S_{xx}, S_{yy}$ , etc. in Eq. (36) depend on  $x$  and  $y$  only and  $f(2z/h)$  will not be assigned arbitrarily but determined from the known condition  $\sigma_{zz} = \nu(\sigma_{xx} + \sigma_{yy})$ . The differential equations and boundary conditions for the new theory in terms of  $S_{xx}, S_{yy}$ , etc. can be best found by requiring the complementary energy of the system to be a minimum with the admitted equilibrium of stress state as given by Eq. (36). This enables the reduction of the three-dimensional equations of elasticity to a system of equations involving only two variables  $x$  and  $y$ . The conditions that

$$\sigma_{zz} = \sigma_{xz} = \sigma_{yz} = 0 \quad \text{for} \quad z = \pm h/2$$

leaving the faces of the plate free of tractions can be satisfied by taking

$$f(\pm 1) = f'(\pm 1) = 0. \quad (37)$$

The application of the minimum energy principle in the calculus of variations requires the adoption of the generalized displacements  $U_x, V_y, W_z$  which are the weighted averages of the actual displacements  $u_x, v_y, w_z$ , through the plate thickness, i.e.,

$$\begin{aligned} U_x &= \frac{2}{h} \int_{-1}^1 f''(\zeta) u_x(x, y, h\zeta/2) d\zeta \\ V_y &= \frac{2}{h} \int_{-1}^1 f''(\zeta) v_y(x, y, h\zeta/2) d\zeta \\ W_z &= - \int_{-1}^1 f'(\zeta) w_z(x, y, h\zeta/2) d\zeta \end{aligned} \quad (38)$$

with  $\zeta$  being the normalized thickness coordinate  $2z/h$ . Without going into the mathematical details, the minimum principle yields a system of simultaneous partial differential equations. The three essential ones governing  $W_z, Z_x$  and  $Z_y$  are

$$\begin{aligned} \alpha^2 [1 + \beta^2 / (1 - \nu^2)] \nabla^4 W_z - 2\alpha^2 \nabla^2 W_z + W_z &= 0 \\ Z_x - \alpha^2 \nabla^2 Z_x &= \frac{1}{\alpha^2} \frac{\partial Q}{\partial x} \\ Z_y - \alpha^2 \nabla^2 Z_y &= \frac{1}{\alpha^2} \frac{\partial Q}{\partial y} \end{aligned} \quad (39)$$



provided that

$$Q = \frac{D}{1+\nu} [(1-\nu) (W_z - \alpha^2 \nu^2 W_z) + (\alpha \beta c)^2 \nu^2 W_z]$$

and

$$\alpha^2 = \frac{h^2}{8} I_2, \quad \beta^2 = \frac{3}{2} (1_1/I_2^2) - 1, \quad \kappa^2 = \frac{1-\nu}{1+\nu}, \quad D = \frac{Eh^3}{12(1-\nu^2)} \quad (40)$$

in which  $I_1$  and  $I_2$  represent the integrals

$$I_1 = \int_{-1}^1 [f'(c)]^2 dc, \quad I_2 = \int_{-1}^1 [f''(c)]^2 dc.$$

Once  $W_z$ ,  $Z_x$  and  $Z_y$  are obtained, the remaining six unknowns follow directly from

$$U_x = -\frac{\partial W_z}{\partial x} + \frac{2\alpha^2}{(1-\nu)D} Z_x, \quad V_y = -\frac{\partial W_z}{\partial y} + \frac{2\alpha^2}{(1-\nu)D} Z_y$$

and

$$\begin{aligned} S_{xx} &= -D \left( \frac{\partial^2 W_z}{\partial x^2} + \nu \frac{\partial^2 W_z}{\partial y^2} \right) + \frac{Q^2}{1-\nu} \left[ (2-\nu) \frac{\partial Z_x}{\partial x} + \nu \frac{\partial Z_y}{\partial y} \right] \\ S_{yy} &= -D \left( \frac{\partial^2 W_z}{\partial y^2} + \nu \frac{\partial^2 W_z}{\partial x^2} \right) + \frac{Q^2}{1-\nu} \left[ (2-\nu) \frac{\partial Z_y}{\partial y} + \nu \frac{\partial Z_x}{\partial x} \right] \\ S_{xy} &= -D(1-\nu) \frac{\partial^2 W_z}{\partial x \partial y} + \alpha^2 \left( \frac{\partial Z_x}{\partial y} + \frac{\partial Z_y}{\partial x} \right) \\ S_{zz} &= \frac{\partial Z_x}{\partial x} + \frac{\partial Z_y}{\partial y} \end{aligned} \quad (41)$$

These equations apply to problems of either stretching or bending of elastic plates depending upon whether  $f(2z/h)$  is even or odd in  $z$ .

The newly developed theory may be regarded as an improvement over that of generalized plane stress which has been used in almost all the current theories of fracture dealing with the stretching of elastic plates. In order to have an understanding of what the new theory predicts, the problem of a uniformly pressurized crack in an infinite plate is considered. If the crack extends from  $x = -a$  to  $x = a$ , then the problem possesses one-quarter symmetry. In other words, it is sufficient to consider the mixed boundary conditions on the quarter plane  $x > 0$  and  $y > 0$  by specifying

$$U_x(x,0) = 0, \quad x > a \quad \text{and} \quad S_{yy}(x,0) = -S_0, \quad x < a$$

and

$$S_{xy}(x,0) = Z_y(x,0) = 0 \quad \text{for all } x.$$

With the aid of Fourier transforms, the above conditions lead to a set of dual integral equations

$$\begin{aligned} \int_0^{\infty} s H(s) \cos(sx) ds &= 0, \quad x > a \\ \int_0^{\infty} s^2 p(s) H(s) \cos(sx) ds &= -\frac{\pi S_0}{\alpha^2 \beta} \end{aligned} \quad (42)$$

solving for the unknown  $H(s)$  and  $p(s)$  is a known function depending upon the parameters  $\alpha, \beta$ , etc. Eq. (42) may be manipulated and reduced to a single Fredholm equation of the second kind. Asymptotic expansions of the stresses near the crack tip give

$$\begin{aligned} \sigma_{xx} &= (2r)^{-1/2} k_1(z) [\cos(\theta/2) - \frac{1}{2} \sin \theta \sin(3\theta/2)] + O(1) \\ \sigma_{yy} &= (2r)^{-1/2} k_1(z) [\cos(\theta/2) + \frac{1}{2} \sin \theta \sin(3\theta/2)] + O(1) \\ \sigma_{xy} &= (2r)^{-1/2} k_1(z) [\frac{1}{2} \sin \theta \cos(3\theta/2)] + O(1) \\ \sigma_{zz} &= (2r)^{-1/2} k_1^*(z) [2\nu \cos(\theta/2)] + O(1) \\ \sigma_{xz} = \sigma_{yz} &= O(1) \quad \text{as } r \rightarrow 0 \end{aligned} \quad (43)$$

in which

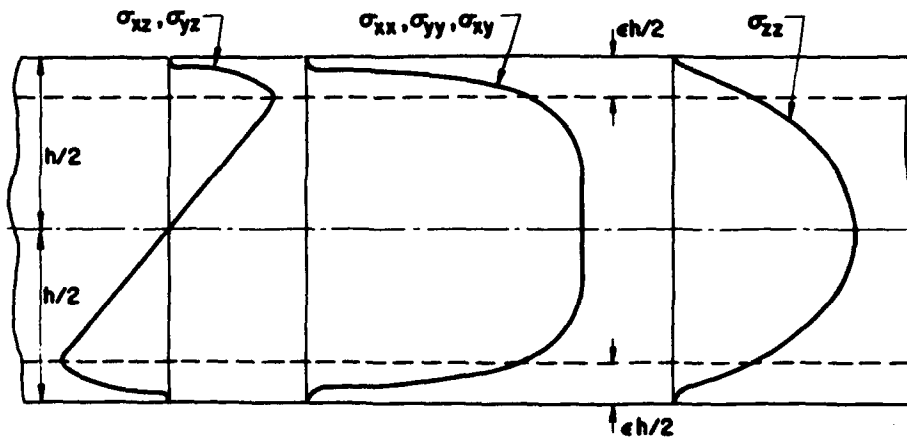
$$k_1(z) = (4/h^2) f''(c) n(1) S_0 \sqrt{a} \quad (44)$$

and

$$k_1^*(z) = -[1/\alpha^2(1+\beta^2)] f'(c) n(1) S_0 \sqrt{a}. \quad (45)$$

In Eq. (44) and (45), the intensity factors  $k_1(z)$  and  $k_1^*(z)$  vary along the crack front in the  $z$ -direction and are functions of  $\nu, h/a$ , etc. through  $\Omega(1)$  which is the limit of  $\Omega(\xi)$  as the dimensionless  $\xi$ , normalized against the half crack length, approaches unity, i.e., the crack tip. It should be emphasized that the stress distribution in the surface layers of the plate is not determined by this approximate analysis. Only the interior solution is correct. This point will be discussed later on.

Figure 7. Stress Distribution in a Stretched Plate as a Function of the Thickness Coordinate.



A possible way of finding  $f(\xi)$  in Eq. (44) and (45) is to apply the condition  $\sigma_{zz} = \nu(\sigma_{xx} + \sigma_{yy})$  prevailing near the crack front interior to the plate as dictated by the exact three-dimensional solution<sup>5</sup>. The appropriate stress components in Eq. (43) may be combined to render the differential equation

$$f''(\xi) + \frac{h^2}{4a^2(1+\beta^2)} f(\xi) = 0, \quad |\xi| < 1-\epsilon \quad (46)$$

whose solution is

$$f(\xi) = \text{const.} \cos \left[ \frac{h\xi}{4a\sqrt{1+\beta^2}} \right], \quad |\xi| < 1-\epsilon \quad (47)$$

since  $f(\xi)$  must be an even function of  $z$  for plane extension problems. The quantity  $h/2\alpha\sqrt{1+\beta^2}$  in the argument of the cosine function can be related to  $f(\xi)$ :

$$\frac{h}{2\alpha\sqrt{1+\beta^2}} = \left( \int_{-1}^{-1-\epsilon} [f'(\xi)]^2 d\xi + \int_{-1}^{-1-\epsilon} [f(\xi)]^2 d\xi \right)^{1/2}. \quad (48)$$

From Eq. (47) and (48),  $f(\xi)$  can be computed for  $|\xi| < 1-\epsilon$ , where  $eh/2$  is used to denote the thickness of the boundary layer close to the plate surface within which the plane strain condition is not satisfied. This layer is introduced with the intent of emphasizing that the stress state for  $(1-\epsilon) < |\xi| < 1$  is not determined by the present theory. Near the plate surface,  $f(\xi)$  is constructed arbitrary with the only requirements that  $f(\xi)$  and its first and second derivatives are continuous at  $|\xi| = 1 - \epsilon$  and that the free-surface conditions  $f(\pm 1) = f'(\pm 1) = 0$  are satisfied. A typical set of curves showing the variations of the in-plane stresses  $\sigma_{xx}$ ,  $\sigma_{yy}$ ,  $\sigma_{xy}$ ; the transverse shear stresses  $\sigma_{xz}$ ,  $\sigma_{yz}$ ; and the transverse normal stress  $\sigma_{zz}$  through the plate thickness is illustrated in Fig. 7. The function  $f(\xi)$  depicted in Fig. 7 gives nearly constant value of the in-plane stresses in the  $z$ -direction,

deviating from the constant only in a layer of thickness  $eh/2$  measured from the plate surface. Similar interpretations apply to  $\sigma_{zz}$  and  $\sigma_{xz}$ ,  $\sigma_{yz}$ .

The requisite numerical results are obtained by solving the integral equation for  $\Omega(\xi)$ :

$$\Omega(\xi) + \int_0^1 G(\xi, n) \Omega(n) dn = \sqrt{\xi}, \quad 0 < \xi < 1$$

where the kernel  $G(\xi, n)$  is

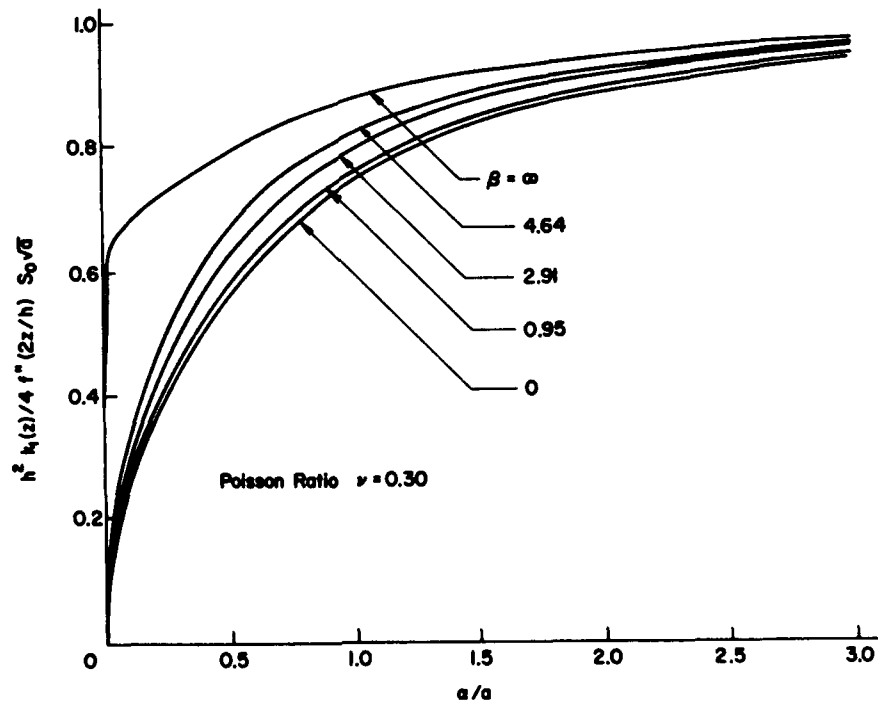
$$G(\xi, n) = \sqrt{\xi n} \int_0^1 s q(s/a) J_0(\xi s) J_0(ns) ds, \quad 0 < \xi \leq 1; 0 < n \leq 1$$

and  $J_0$  is the zero order Bessel function of the first kind. These computations are carried out for  $\nu = 0.3$  and different values of  $\beta$ . The results are summarized graphically in Fig. 8. The normalized stress-intensity factor  $k_1(z)$  in Eq. (44) is plotted against  $a/a$  by varying  $\beta$  from zero to infinity. Each value of  $\beta$  corresponds to a particular set of curves for the  $z$ -variation of the stresses as in Fig. 8. In general, as  $a/a$  departs from zero, all the curves increase in magnitude very sharply at the beginning and then level off steadily as  $a/a$  continues to grow. To be noted is that for small values of  $a/a$  or thin plates, a significant change in the  $k_1(z)$ -factor is observed for a slight variation of  $\beta$  which is a function of the boundary layer thickness  $eh/2$ .

## DISCUSSION

To reiterate, the complexity of the three-dimensional equations of elasticity prohibits any effective analytical solution for the problem of a crack in a finite thickness plate. Although asymptotic expansions of the three-dimensional stress and displacement fields interior to the plate can be obtained, the state of affairs in a boundary layer close to the plate surface remain unknown. As a matter of

Figure 8. Stress-Intensity Factor versus the Thickness Parameter in the Proposed Theory.



practical interest, one is forced to use the approximate theories of plates derived from minimum principles in the calculus of variations. The objective of such an approach is of course to relax the system of equations in the three-dimensional theory of elasticity by reducing the number of independent variables from three to two. Hopefully, the resulting plate equations can be solved explicitly for the finite-thickness crack problem. This has been accomplished in the present paper with the additional provision for finding the stress distribution across the plate thickness. For the first time, an analytical solution of the cracked plate problem has been obtained which accounts for the thickness effect. The local intensity of the stress field is found to depend very sensitively on the change in plate thickness in the range where the width of the rectangular crack is much larger than its height. There remains, however, a considerable amount of work yet to be done. Leaving aside the uncertainty of the perturbed stress state on the plate surface, some immediate improvements on the plate theory presented in this work can be made.

A better approximation of the three-dimensional stress state is to take a series expansion

$$\sigma_{ij}(x,y,z) = f_1^{(ij)}(z) S_{ij}^{(1)}(x,y) + f_2^{(ij)}(z) S_{ij}^{(2)}(x,y) + \dots$$

The corresponding system of differential equations may be derived from the minimum principles. A finite number of the functions  $f_k^{(ij)}(z)$  ( $k = 1, 2, \dots$ ) could perhaps be determined from the conditions preassigned to various discrete regions at different distances away from the crack. One of these conditions described earlier is the requirement that  $\sigma_{zz} = \nu(\sigma_{zz} + \sigma_{yy})$  for the near-field solution. Further work along this line is being continued.

Another crucial question of the through crack problem which remains unanswered is the plate surface stress state near the crack ends without which the accuracy of any numerical solution is in doubt. This part of the problem is very difficult and requires additional investigation.

An understanding of thickness fracture in common metals will of course further complicate the situation where interaction of plastic deformations local to the crack with

the free plate surfaces takes place. Experimental evidence indicates that the plastic enclave surrounding the leading edge of the crack does vary in the thickness direction. For thinner plates in which the magnitude of the transverse displacement is appreciable, localized necking or dimpling of the crack has been observed. In somewhat thicker plates, the crack front adopts the shape of a thumb-nail when fractured. All these observations are indicative of the effect of triaxiality associated with thickness fracture.

Data of fracture toughness versus plate thickness have been recorded experimentally (Refs. 8 and 9). The strength of cracked plates with moderate thickness is found to decline with increase of plate thickness. This can be related to a ductile-brittle transition of the fracture mode. Interior to the plate, the hydrostatic tension predominates and causes cleavage fracture such that the fractured surface is in a plane normal to the applied stress. In very thick plates, a large portion of the crack front is in a state of plane strain and the fracture resistance is usually very low. Near the outside surface of the plate, there is extensive shear deformation occurring on the maximum shear plane. Thus, the fracture surface lies in a plane inclined at  $45^\circ$  to the applied stress. This region is referred to as the "shear lip". As the thickness decreases, the plane strain region is reduced and the fracture strength rises reaching a maximum when the shear lip occupies the full thickness of the plate. Additional reduction of the plate thickness tends to exert constraint on the plastic enclave causing it to elongate in a narrow region. This confinement leads to localized necking accompanied by extensive plastic deformation and damages the material along the crack path. As a consequence, the fracture toughness of the cracked plate is reduced. To be emphasized is that the occurrence of a maximum fracture toughness value is strictly due to the interplay between plate thickness and plastic deformation. Such a peak phenomenon is not expected to occur in purely brittle materials.

#### ACKNOWLEDGEMENT

This paper describes work performed at Lehigh University for the National Aeronautics and Space Administration under Grant NGR-39-007-025 through the Lewis Research Center. The author is indebted to Dr. J.E. Srawley for his constant interest and encouragement in this work.

## REFERENCES

1. C.E. Inglis, "Stresses in a Plate due to the Presence of Cracks and Sharp Corners," *Trans. Inst. Naval Architects (London)*, 60:219-230 (1913).
2. A.A. Griffith, "The Phenomena of Rupture and Flow in Solids," *Phil. Trans. Roy. Soc. London*, 221:163-198 (1921).
3. G.C. Sih and H. Liebowitz, "Mathematical Theories of Brittle Fracture," pp. 67-190, *Mathematical Fundamentals of Fracture*, Vol. II, Academic Press, New York (1968).
4. S. Timoshenko and J.N. Goodier, *Theory of Elasticity*, pp. 241-244, 2nd ed., McGraw-Hill, New York (1951).
5. G.C. Sih, M.L. Williams, and J.L. Svedlow, *Three-Dimensional Stress Distribution Near a Sharp Crack in a Plate of Finite Thickness*, AFML-TR-66-242, Air Force Materials Laboratory, Wright-Patterson AFB, Ohio (1966).
6. E. Reissner, "The Effect of Transverse Shear Deformation on the Bending of Elastic Plates," *J. Appl. Mech.*, 67:A69-77 (1945).
7. A.L. Goldenweizer, "On Reissner's Plate Theory," *Izv. Akad. Nauk SSSR, OTN* 4:102-109 (1958).
8. G.R. Irwin, "Fracture Mode Transition for a Crack Transversing a Plate," *J. Basic Eng.*, 82:417-423 (1960).
9. J.E. Srawley and C.D. Beachem, *Resistance to Crack Propagation of High-Strength Sheet Materials for Rocket Motor Casings*, NRL-5771, Naval Research Laboratories, Washington, D.C. (1962).
10. R.J. Hartranft and G.C. Sih, "The Use of Eigenfunction Expansions in the General Solution of Three-Dimensional Crack Problems," *J. Math. Mech.*, 19:123-138 (1969).
11. M.L. Williams, "On the Stress Distribution at the Base of a Stationary Crack," *J. Appl. Mech.*, 24:109-114 (1957).
12. I.N. Sneddon, "The Distribution of Stress in the Neighborhood of a Crack in an Elastic Solid," *Proc. Roy. Soc. London*, 187:229-260 (1946).
13. G.R. Irwin, "Analysis of Stresses and Strains Near the End of a Crack Transversing a Plate," *J. Appl. Mech.*, 24:361-364 (1957).
14. M.K. Kassir and G.C. Sih, "Three-Dimensional Stress Distribution Around an Elliptical Crack Under Arbitrary Loadings," *J. Appl. Mech.*, 33:601-611 (1966).
15. G.N. Savin, *Stress Concentration Around Holes*, English ed., Pergamon Press, New York (1961).
16. M.L. Williams, "The Bending Stress Distribution at the Base of a Stationary Crack," *J. Appl. Mech.*, 28:78-82 (1961).
17. G.C. Sih and J.R. Rice, "The Bending of Plates of Dissimilar Materials with Cracks," *J. Appl. Mech.*, 31:477-482 (1964).
18. G.C. Sih, "Flexural Problems of Cracks in Mixed Media," pp. 39-409, *Proc. 1st Int. Conf. Fracture*, Vol. 1, Japanese Society for Strength and Fracture of Materials, Sendai, Japan (1965).
19. G.C. Sih and H.C. Hagendorf, *On the Theory of Spherical Shells with Cracks*, Research Report, Lehigh University, Bethlehem, Pennsylvania, to be published.

## REFERENCES (Continued)

20. J.K. Knowles and N.M. Wang, "On the Bending of an Elastic Plate Containing a Crack," *J. Math. Phys.*, 39:223-236 (1960).
21. R.J. Hartranft and G.C. Sih, "Effect of Plate Thickness on the Bending Stress Distribution Around Through Cracks," *J. Math. Phys.*, 47:276-291 (1968).
22. R.H. Wynn and C.W. Smith, "An Experimental Investigation of Fracture Criteria for Combined Extension and Bending," *J. Basic Eng.*, in press.
23. G.C. Sih, *Bending of a Cracked Plate with Arbitrary Stress Distribution Across the Thickness*, ASME Paper 69-WA/PVP-2. *J. Eng. Ind.*, 92/2:350-356 (1970).
24. R.J. Hartranft and G.C. Sih, *An Approximate Three-Dimensional Theory of Plates with Applications to Crack Problems*, *Int. J. Eng. Sci.*, in press.

## APPENDICES

### I. Basic Equations in the Theory of Elasticity

#### (1) Strain-Displacement Relations.

$$\begin{aligned}
 \epsilon_{rr} &= \frac{\partial u_r}{\partial r}, & \epsilon_{r\theta} &= \frac{1}{2} \left( \frac{1}{r} \frac{\partial u_r}{\partial \theta} + \frac{\partial v_\theta}{\partial r} - \frac{v_\theta}{r} \right), \\
 \epsilon_{\theta\theta} &= \frac{u_r}{r} + \frac{1}{r} \frac{\partial v_\theta}{\partial \theta}, & \epsilon_{rz} &= \frac{1}{2} \left( \frac{\partial u_r}{\partial z} + \frac{\partial w_z}{\partial r} \right), \\
 \epsilon_{zz} &= \frac{\partial w_z}{\partial z}, & \epsilon_{z\theta} &= \frac{1}{2} \left( \frac{\partial v_\theta}{\partial z} + \frac{1}{r} \frac{\partial w_z}{\partial \theta} \right).
 \end{aligned} \tag{49}$$

#### (2) Hooke's Law.

$$\begin{aligned}
 \sigma_{rr} &= 2\mu \left[ \left( \frac{\nu}{1-2\nu} \right) \nu + \epsilon_{rr} \right], & \sigma_{r\theta} &= 2\mu \epsilon_{r\theta}, \\
 \sigma_{\theta\theta} &= 2\mu \left[ \left( \frac{\nu}{1-2\nu} \right) \nu + \epsilon_{\theta\theta} \right], & \sigma_{rz} &= 2\mu \epsilon_{rz}, \\
 \sigma_{zz} &= 2\mu \left[ \left( \frac{\nu}{1-2\nu} \right) \nu + \epsilon_{zz} \right], & \sigma_{z\theta} &= 2\mu \epsilon_{z\theta},
 \end{aligned} \tag{50}$$

where  $\nu = \epsilon_{rr} + \epsilon_{\theta\theta} + \epsilon_{zz}$ .

#### (3) Equations of Equilibrium.

$$\frac{\partial \sigma_{rr}}{\partial r} + \frac{1}{r} \frac{\partial \sigma_{r\theta}}{\partial \theta} + \frac{\partial \sigma_{rz}}{\partial z} + \frac{\sigma_{rr} - \sigma_{\theta\theta}}{r} = 0,$$

APPENDICES (Continued)

$$\frac{\partial \sigma_{rz}}{\partial r} + \frac{1}{r} \frac{\partial \sigma_{\theta z}}{\partial \theta} + \frac{\partial \sigma_{zz}}{\partial z} + \frac{\sigma_{rz}}{r} = 0, \quad (51)$$

$$\frac{\partial \sigma_{r\theta}}{\partial r} + \frac{1}{r} \frac{\partial \sigma_{\theta\theta}}{\partial \theta} + \frac{\partial \sigma_{\theta z}}{\partial z} + \frac{2\sigma_{r\theta}}{r} = 0.$$

II. Determination of the Displacement Functions.

From the fifth of eqs. (9),  $h_1$  takes the form

$$h_1(\theta, z) = A(z) \cos(\theta/2) \quad (52)$$

which suggests the product solution for  $f_1$  and  $g_1$  as

$$f_1(\theta, z) = B(z) \cos(\lambda_1, \theta), \quad g_1(\theta, z) = B_1(z) \sin(\lambda_1, \theta) \quad (53)$$

The parameter  $\lambda_1$  can be evaluated by putting  $f_1$  and  $g_1$  into the first and third of eqs. (9) resulting in

$$\begin{aligned} [2(1-2\nu)\lambda_1^2 + 3(1-\nu)] B(z) + (5-8\nu)\lambda_1 B_1(z) &= 0 \\ (7-8\nu)\lambda_1 B(z) + [4(1-\nu)\lambda_1^2 + \frac{3}{2}(1-2\nu)] B_1(z) &= 0 \end{aligned} \quad (54)$$

For a non-trivial solution, the determinant of the coefficients of  $B(z)$  and  $B_1(z)$  must vanish. This gives the characteristic value equation

$$\lambda_1^4 - \frac{5}{2} \lambda_1^2 + \frac{9}{16} = 0$$

whose roots are  $\lambda_1 = \pm \frac{1}{2}, \pm \frac{3}{2}$ . Hence, eqs. (53) become

$$f_1(\theta, z) = B(z) \cos(\theta/2) + C(z) \cos(3\theta/2)$$

$$g_1(\theta, z) = B_1(z) \sin(\theta/2) + C_1(z) \sin(3\theta/2)$$

with

$$B_1(z) = - \left( \frac{7-8\nu}{5-8\nu} \right) B(z), \quad C_1(z) = - C(z).$$

APPENDICES (Continued)

In a similar fashion,  $f_2$  and  $g_2$  can be found. With the help of eqs. (52),  $h_1$  in the second and fourth of eqs. (9) may be eliminated:

$$(3-8\nu) (\partial g_2 / \partial \theta) - 2(1-2\nu) (\partial^2 f_2 / \partial \theta^2) - 5(1-\nu) f_2 = A'(z) \cos(\theta/2) \quad (55)$$

$$(9-8\nu) (\partial f_2 / \partial \theta) + 4(1-\nu) (\partial^2 g_2 / \partial \theta^2) + \frac{5}{2} (1-2\nu) g_2 = A'(z) \sin(\theta/2)$$

First, consider the homogeneous solution

$$f_2^{(h)}(\theta, z) = D(z) \cos(\lambda_3 \theta), \quad g_2^{(h)}(\theta, z) = D_1(z) \sin(\lambda_3 \theta) \quad (56)$$

in which  $\lambda_3$  can be obtained from the equations

$$\begin{aligned} [2(1-2\nu)\lambda_3^2 - 5(1-\nu)] D(z) + (3-8\nu)\lambda_3 D_1(z) &= 0 \\ (9-8\nu)\lambda_3 D(z) + [4(1-\nu)\lambda_3^2 - \frac{5}{2}(1-2\nu)] D_1(z) &= 0 \end{aligned}$$

Solving the determinant for  $\lambda_3$  leads to

$$\lambda_3^4 - \frac{13}{2} \lambda_3^2 + \frac{25}{16} = 0$$

and  $\lambda_3 = \pm \frac{1}{2}, \pm \frac{5}{2}$ . It follows that

$$\begin{aligned} f_2^{(h)}(\theta, z) &= D(z) \cos(\theta/2) + E(z) \cos(5\theta/2) \\ g_2^{(h)}(\theta, z) &= D_1(z) \sin(\theta/2) + E_1(z) \sin(5\theta/2) \end{aligned} \quad (57)$$

and

$$D_1(z) = \left(\frac{9-8\nu}{3-8\nu}\right) D(z), \quad E_1(z) = -E(z)$$

The particular solutions of eqs. (55) are simply

$$f_2^{(p)}(\theta, z) = -\frac{1}{3} A'(z) \cos(\theta/2), \quad g_2^{(p)}(\theta, z) = -\frac{1}{3} A'(z) \sin(\theta/2) \quad (58)$$

APPENDICES (Continued)

Adding eqs. (57) and (58) yields the complete solutions to eqs. (55):

$$f_2(\theta, z) = f_2^{(h)}(\theta, z) + f_2^{(p)}(\theta, z), \quad g_2(\theta, z) = g_2^{(h)}(\theta, z) + g_2^{(p)}(\theta, z).$$

The governing equation for  $h_2$  is found by inserting eqs. (53) into the sixth of eqs. (9):

$$\partial^2 h_2 / \partial \theta^2 + \frac{9}{4} h_2 = - \left( \frac{4}{5-8\nu} \right) B'(z) \cos(\theta/2)$$

which yields

$$h_2(\theta, z) = F(z) \cos(3\theta/2) - \left( \frac{2}{5-8\nu} \right) B'(z) \cos(\theta/2)$$

This completes the determination of the displacement functions associated with  $r^{1/2}$  and  $r^{3/2}$ . Other terms in the series expansions corresponding to  $r^{5/2}$ ,  $r^{7/2}$ , etc. may be obtained in the same way.



# BUCKLING IN THIN CRACKED SHEETS\*

by

R.L. Carlson, G.F. Zielsdorff and J.C. Harrison

School of Aerospace Engineering  
Georgia Institute of Technology

## INTRODUCTION

The problem of buckling in thin cracked sheets is well known. It can occur when the stress distribution in a thin sheet includes a region of compression adjacent to the crack. It is reasonable to expect, therefore, that some out-of-plane deflections may develop in the vicinity of the crack lip as loading progresses. Correspondingly, at some point in the loading process buckling is said to occur. A precise specification of the stress at which buckling takes place has been avoided in most of the work which has been reported. For example, Dixon and Strannigan<sup>1</sup> have studied the problem of a sheet with a tensile load applied perpendicular to the crack direction and they have chosen to select an upper and lower bound for buckling from their average stress versus bending-strain curves. These bounds differ substantially in magnitude.

The importance of buckling upon the static strength and fatigue characteristics of cracked sheets has not as yet been fully resolved. For instance, in static strength tests on aluminum alloy sheet, reductions of about 10% were noted by Dixon and Strannigan<sup>1</sup>, by Walker<sup>2</sup>, and by Trotman<sup>3</sup> when buckling was not restrained, while Kuhn<sup>4</sup> observed reductions of about 25%. Forman<sup>5</sup> found reductions of up to 40% on AM355CRT steel sheet.

For fatigue characteristics there appear to be remarkable variations in the observed effect of buckling. Rooke<sup>6</sup> and others noted very little effect when buckling was unrestrained in their experiments on the rate of growth of fatigue cracks in aluminum alloy sheet. Cricklow and Wells<sup>7</sup> conducted tests on titanium sheet and observed crack growth rates in unrestrained specimens which were ten times greater than in the restrained specimens. It should be noted, however, that no reference is made about how close the mean stress was in the above experiments to the buckling stress.

An indication that the possibility of buckling should not be overlooked in any work involving cracks in thin sheets is obtained from Dixon and Strannigan's photoelastic analysis of the elastic stress distribution adjacent to the crack. They demonstrated that the maximum stress at the crack tip was higher when buckling was unrestrained than it was

when buckling was restrained. This led to correspondingly larger stress concentration factors.

The result of a semi-empirical analysis of the buckling problem has been used by a number of workers. It may be expressed as

$$\sigma = kE \left(\frac{t}{L}\right)^2,$$

where  $\sigma$  is the applied traction stress necessary to cause buckling,  $E$  is Young's modulus,  $t$  is the sheet thickness and  $L$  is the crack length. A value of  $k$  of about 10 has been suggested by Mansfield<sup>8</sup>. When based on experimental data, the value of  $k$  has been observed to vary from about 2 to about 7. The value of  $k$  would thus appear to depend on material properties, the geometry of the models, and very likely upon the manner in which the critical stress is defined. It is apparent, then, that there is a need for standardizing the definition of critical or buckling stress so that experimental investigations can be planned and interpreted in a uniform manner. One of the objectives of the studies described in this paper was to develop a rational definition which has a basis in the classical theory of stability.

As may be surmised from the preceding discussion, the problem of buckling in a cracked sheet possesses several features which cause it to be particularly difficult to analyze. Treated as a classical stability problem in which the sheet is assumed to be perfectly flat until a critical value of load is achieved, it may be noted that the prebuckle stress state is nonuniform. Although some work has been done on problems of this type, it is not too extensive because exact solutions are difficult.

Another feature which should be recognized arises from the fact that because of the small radius at the tip of a crack, a plastic zone will be developed upon the application of even a small load. Buckling, therefore, involves an elastic-plastic process.

## EXPERIMENTAL PROGRAM

### Plan of Program

The problem selected for the experimental investigation was that of the thin sheet with a tensile load applied

\*The work described is supported by the U.S. Army Research Office - Durham under Contract No. DAHC04 68 C 0004.

across a central, simulated crack which was aligned normal to the direction of loading. In one series of experiments, tests of the type conducted by Dixon and Strannigan<sup>1</sup> were performed. These consisted of progressively increasing the tensile load and monitoring the change of curvature along the edge of the crack. These were essentially standard tests and they provided a reference or basis for comparison with the additional, specialized experiments which were conducted.

Because of the difficulties associated with most stability problems which involve an inelastic response, the corresponding elastic problem is normally examined first. In the case of the column the difference between the Euler load and the tangent modulus load can be quite large, so the elastic analysis is of little value if the column of interest is in the inelastic buckling range. It is of interest to note, however, that the transition from the elastic to the inelastic classification can, at least in principle, be shifted to smaller values of column slenderness ratio by increasing the proportional limit of the column material by precompressing it while restraining it from buckling. This process consists of a preconditioning in which the structural element is modified to insure an elastic response in a subsequent stability test.

Although a process of the type outlined above would

not be useful for studying column behavior, the possible application to the crack problem was considered to be worthy of consideration. Whereas inelastic buckling involves loading of the entire structural element into the inelastic range for the column, the inelastic zone in the cracked sheet problem is relatively small and removed from the region of buckling. The difference between the so-called classical buckling for the "elastic" cracked sheet and the "elastic-plastic" or real cracked sheet may, therefore, be small. If this difference is small, it follows that a buckling stress obtained from an elastic analysis should be useful for predicting the value of load beyond which deflections can be expected to be significant.<sup>†</sup>

The method adopted for experimentally transforming the crack buckling problem to an elastic problem was to precondition the sheet specimens by applying a lateral pressure in the vicinity of the crack to insure a plane stress response, and then applying a tensile load which exceeded the expected buckling load. Upon unloading, a residual stress state was present, of course, but subsequent reloading without lateral restraint involves only an elastic response as long as the stresses achieved during the preconditioning process are not exceeded.<sup>††</sup> By this means the problem is experimentally transformed to an elastic problem. If only the elastic state superimposed on the initial reference state is con-

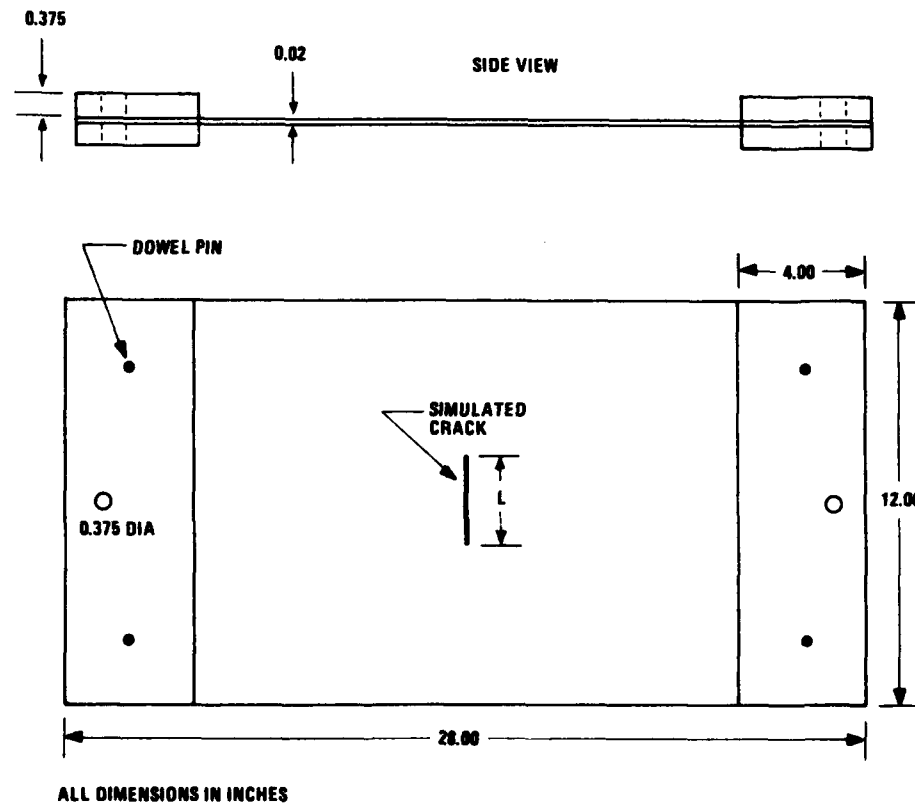


Figure 1.  
Sheet Specimen.

<sup>†</sup> In most stability problems in which the ultimate or failure load is substantially greater than the buckling load, the buckling load is of secondary interest. Here, however, the effect on fatigue behavior as bending becomes significant causes the buckling load to be of considerable interest.

<sup>††</sup> It is important to recognize that the presence of an initial stress within a region which can buckle can affect the value of load at which buckling occurs. Experimental results indicate that in the present problem the residual stress along the edge of the crack - the region of buckling - was small. This point is discussed in the section - DISCUSSION OF RESULTS.

**TABLE I.  
PRESTRESS LOADS**

CRACK LENGTH (INCHES)	PRESTRESS LOAD (POUNDS)
2.0	1800
2.2	1600
3.0	1000
4.0	500

sidered, then results based on an elastic analysis prove to be useful. Making use of these ideas, a preconditioning process was developed and a series of experiments was conducted. In these tests the specimens were free of lateral constraint; that is, they were free to buckle.

### Specimens

The specimen selected for experimental studies is shown in Figure 1. The design used permitted the introduction of an essentially uniaxial tensile field near the ends of the specimen. The material chosen for the experiments was 0.020 inch thick sheet of the aluminum alloy 2024-T3. Fifteen specimen blanks were machined to size, and of these, the seven specimens with the smallest deviation from flatness were selected for use. The 0.375 inch thick end plates were made from bar stock of the aluminum alloy 2024-T4, and they were bonded to the sheet specimens with a room temperature curing epoxy. Two dowel pins were used to assure proper alignment of the plates on the sheet.

Four values of crack length,  $L$ , were selected: 2.00, 2.20, 3.00 and 4.00 inches. A crack was simulated by use of a jeweler's saw with a blade width of 0.0063 inch. Access

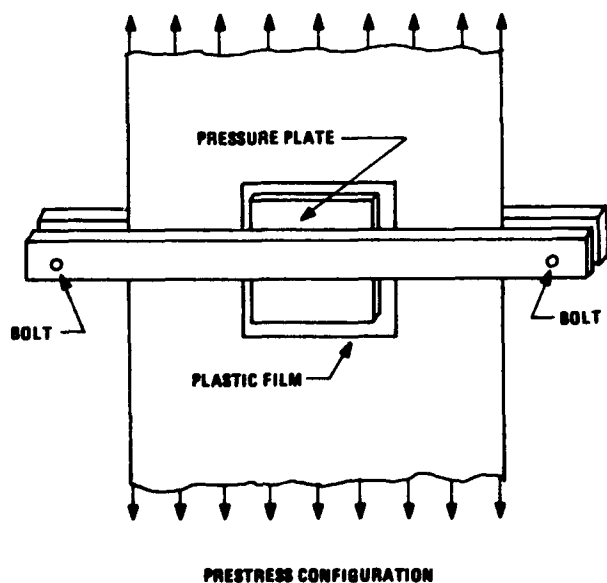


**Figure 2. Prestress Fixture.**



**Figure 3. Specimen in Testing Machine.**

for the blade was made by drilling a hole in the center of the specimen with a No. 74 carbon steel drill.

### Test Procedure

One specimen of each of the four crack lengths was prestressed in an Instron testing machine. A prestress load exceeding the expected buckling load was chosen for each specimen (see Table I). To prevent buckling lateral pressure was applied to the surfaces on each side of the crack during prestressing. The pressure was applied through two metal plates which were held in place by a frame assembly (see Figure 2). Mylar film was used to reduce friction between the plate and specimen surfaces as prestressing took place.

With the exception of the prestressing history, the virgin and the prestressed specimens were processed in the same manner. The instrumentation and the measurements obtained were identical. Metalfilm type C12-141B strain gages were mounted back-to-back with the strain sensitive direction being parallel to the crack edge as shown in Figures 3 and 4. The gage elements were at the center of the crack and as close to the edge as possible. With the use of the SR-4 strain measuring instrument, and a switching and balancing unit, the strain output of each gage and the strain difference of the two back-to-back gages was measured as loading proceeded.

Each specimen was loaded in the Instron machine with the load range being determined by the estimated



Figure 4. Simulated Crack.

magnitude of the buckling load, and the load increments being chosen to provide sufficient data for analysis.

### Test Results

The results of tests on the virgin specimens are presented in Figure 5 and the results on the prestressed specimens are given in Figures 6 and 7.

The load versus strain difference curves of Figure 5 indicate that an inflection point separates the initial region in which the slope decreases with increasing strain difference from a region in which the slope increases with increasing strain difference. The observed behavior describes the stiffening which occurs in the post-buckling region.

The load versus average strain curve of Figure 6 is linear up to the region in which second order, nonlinear effects due to bending become significant. The data on this transition in behavior are used in the analysis of the stability experiments.

The load versus strain difference data for the pre-

TABLE II.  
UPPER AND LOWER BOUND OF  
VIRGIN SPECIMEN BUCKLING LOAD

CRACK LENGTH (INCHES)	LOWER BOUND (POUNDS)	UPPER BOUND (POUNDS)
2.0	500	920
2.2	430	700
3.0	380	510

TABLE III.  
BUCKLING LOADS FOR  
PRESTRESSED SPECIMENS

CRACK LENGTH (INCHES)	LUNDQUIST ZERO LOAD (POUNDS)	BUCKLING LOAD (POUNDS)	BUCKLING STRESS (PSI)
2.0	200	1000	4180
2.2	160	850	3550
3.0	120	410	1710
4.0	30	270	1120

stressed specimens are presented in Figure 7. These data have been plotted with respect to initial values of load,  $P_0$ , and strain difference  $\Delta\epsilon_0$ , for convenience in the analysis of the data. The initial values of  $P_0$  are listed in Table III. This form of presentation will be discussed in detail in a subsequent section. The form of these curves is similar to that of the corresponding curves for the virgin specimens.

### ANALYSIS

In the section - Plan of Program - the use of a prestress procedure which transforms the crack problem into an elastic problem was described. Because the subsequent response of the sheet specimens was elastic, an application of elastic plate theory is possible.

The analysis of the problem of interest begins with a consideration of the coupled, nonlinear plate equations which arise from the need to satisfy in-plane compatibility and equilibrium in the transverse direction. From the compatibility requirement

$$\nabla^4 F = Et \left[ (w_{,xy})^2 - w_{,xx}w_{,yy} - (w_{0,xy})^2 + w_{0,xx}w_{0,yy} \right], \quad (1)$$

where  $\nabla^4$  is the two dimensional biharmonic operator, the comma subscript denotes differentiation with respect to the independent variables which follow, and  $w$  is the total transverse deflection. The function  $w_0$  describes the initial deviation from flatness in terms of the transverse deflection prior to loading. The quantity  $(w - w_0)$  is the deflection due to the applied load.  $E$  is Young's modulus,  $t$  is the plate

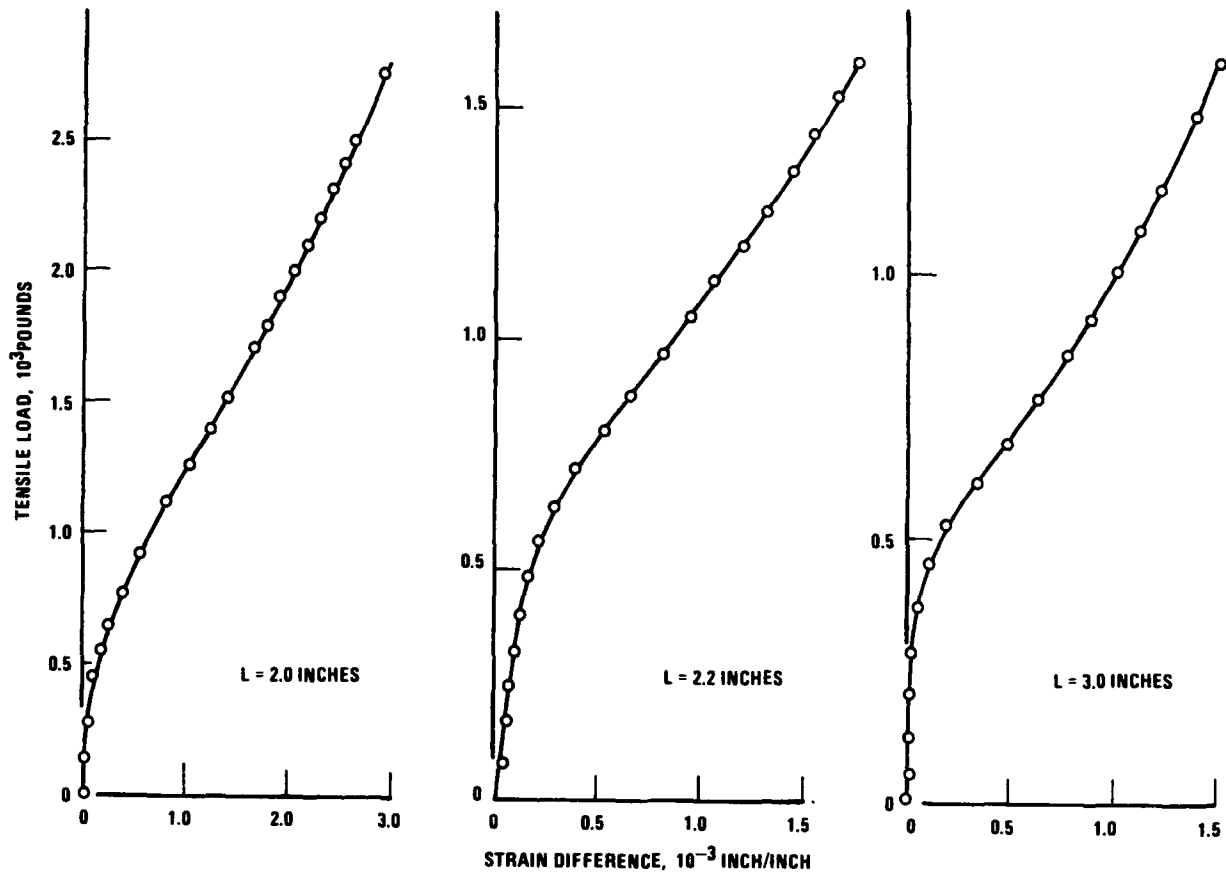


Figure 5. Tensile Load versus Strain Difference for Virgin Specimens.

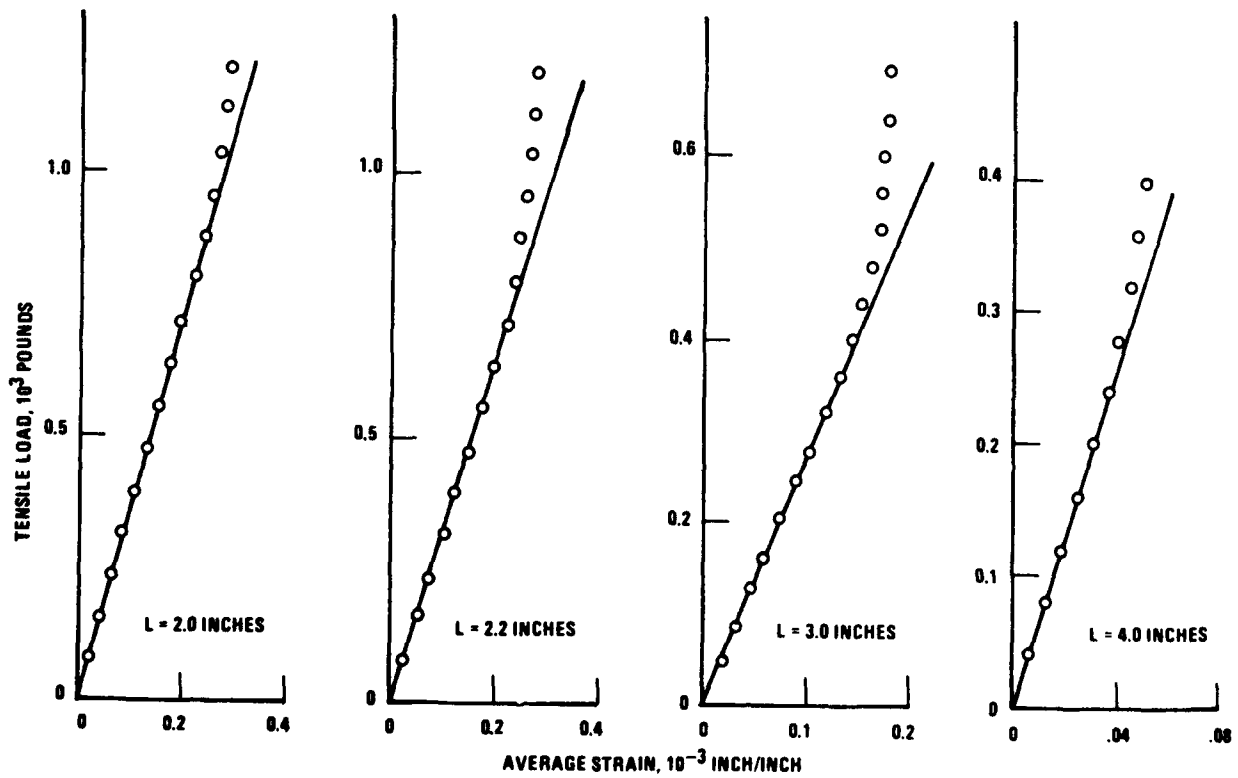


Figure 6. Tensile Load versus Average Strain for Prestressed Specimens.

thickness, and  $F$  is the stress function defined in terms of the in-plane stress as

$$N_x = F,_{yy} \quad , \quad N_y = F,_{xx} \quad , \quad \text{and}$$

$$N_{xy} = -F,_{xy} \quad . \quad (2)$$

From the equilibrium requirement,

$$D \nabla^4 (w - w_0) = F,_{xx} w,_{yy} - 2F,_{xy} w,_{xy} + F,_{yy} w,_{xx} \quad (3)$$

where

$$D = \frac{Et^3}{12(1-\nu^2)} \quad , \quad \text{and } \nu \text{ is Poisson's ratio.}$$

The boundary conditions consist of in-plane edge tractions and homogeneous conditions on  $w$  and its derivatives (e.g., conditions for fixed, hinged or free edges).

In a linearized theory the nonlinear terms on the right side of Eq. (1) are neglected, so that Eqs. (1) and (3) become uncoupled. To be able to adopt this procedure, however, it is necessary to examine the nature of the neglected terms.

Omission of the nonlinear terms in Eq. (1) implies that the in-plane stresses can be determined by a plane stress analysis, and that the effects of second order, nonlinear behavior due to bending can be neglected. It is also important to note that it follows that if this is a valid procedure,

the in-plane stresses will be linearly proportional to the applied, in-plane edge tractions.

At this point it is pertinent to recognize that the quantities

$$(w,_{xy})^2 - w,_{xx} w,_{yy}$$

and

$$(w_0,_{xy})^2 - w_0,_{xx} w_0,_{yy}$$

are, respectively, the Gaussian curvatures of the total deflection function and the initial deviation from flatness function. Since the Gaussian curvature of developable surfaces is zero, it follows that Eqs. (1) and (3) become uncoupled if these functions represent developable surfaces. That is, there are, for such surfaces, no second order nonlinear effects due to bending.

Apparently the first to recognize and to exploit this feature in plate buckling problems was Donnell<sup>9</sup>. He considered a plate with simple support on three sides and loaded by a uniform compression which acted parallel to the fourth edge which was free. The bent surface in this case is approximately a developable surface and, exploiting this fact, Donnell was able to derive a deflection-load relation of the Southwell type<sup>10</sup>. Donnell showed that test results analyzed by the Southwell method correlated well with theoretical calculations for the given loading and boundary conditions. Additional support for the applicability of the Southwell method for plate problems with bent surfaces which are approximately developable surfaces has also been provided

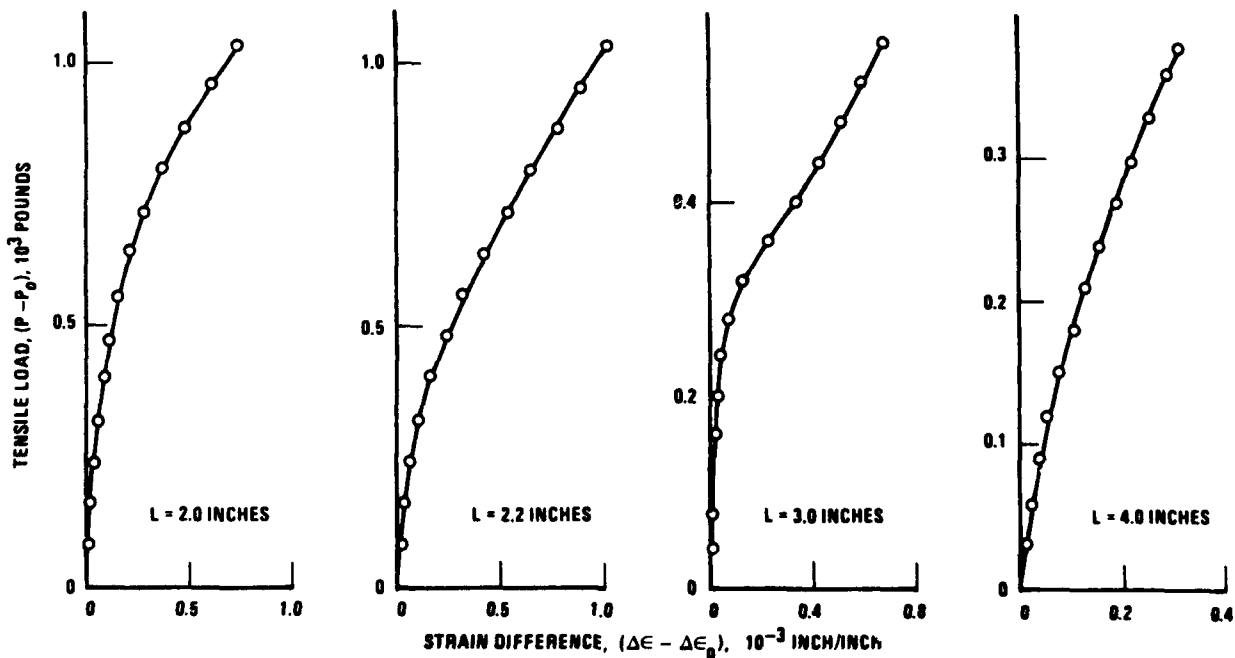


Figure 7. Tensile Load versus Strain Difference for Prestressed Specimens.

recently by Way<sup>11</sup>. The problem of the lateral buckling of a deep beam was studied by Way, and he obtained excellent correlation between the calculated theoretical buckling load and the buckling load obtained from a Southwell plot of experimental results.

Donnell also considered the problem of a square plate which was simply supported on all four sides and loaded in uniform compression in one direction. To account for middle surface, extensional strains in this problem, he used the appropriate nonlinear plate equations, and he concluded that the Southwell method would apply only if the imperfection amplitude and the deflection were small compared to the plate thickness.

Although Donnell analyzed only two plate problems, he was able to identify two features of plate behavior which affect the applicability of the Southwell method. That is, either the imperfection and the deflection must be small, or the bent surface must be very nearly a developable surface.

The interest of the authors in the Southwell method arose through a consideration of the stability problem in which a tensile field is applied to a sheet with a crack. In this problem, localized buckling can occur along a free edge normal to the direction of the applied load. This problem has one feature in common with Donnell's first problem; that is, there is a free edge. For the stability problem of interest here, however, the prebuckle stress state is nonuniform so a more general analysis than that of Donnell is required.

The derivation of a Southwell relation of the type obtained by Donnell for his first problem depends on the permissibility of neglecting the second order, nonlinear effects due to bending. Although some evidence has been cited which tends to support this assumption for some problems, it should be examined for applications of the type which are of interest in this paper. Fortunately, this requirement can be examined experimentally by monitoring the stress state as loading progresses; i.e., if  $\nabla^4 F = 0$ , a linear relationship should be observed between the applied load and the in-plane stress. Ultimately, a nonlinear response can be expected to emerge. If attention is confined to the linear range, however, the linearized, uncoupled versions of Eqs. (1) and (3) apply, and it is possible to proceed with an analysis of these simplified equations. The objective of the analysis which follows is to derive a Southwell type of relationship which can be used in the crack buckling problem.

The linearized versions of Eqs. (1) and (3) can be written as

$$\nabla^4 F = 0, \quad (1')$$

and

$$\begin{aligned} D\nabla^4 W - N_x W_{,xx} - 2N_{xy} W_{,xy} - N_y W_{,yy} = \\ N_x w_{o,xx} + 2N_{xy} w_{o,xy} + N_y w_{o,yy} \end{aligned} \quad (3')$$

where for convenience, use has been made of the substitution  $W = (w - w_o)$ . Eq. (1') must be solved subject to given in-plane edge tractions. With a solution for Eq. (1') and through use of Eq. (2), Eq. (3') may be obtained and solved subject to given homogeneous boundary conditions on  $W$  and its appropriate derivatives.

In view of the fact that for the stipulated conditions the in-plane stresses are linearly proportional to the applied load, a load intensity factor,  $\lambda$ , may be introduced such that

$$\begin{aligned} \frac{N_x}{D} = \lambda p_1(x,y), \quad \frac{N_y}{D} = \lambda p_2(x,y), \\ \frac{2N_{xy}}{D} = \lambda p_3(x,y) \end{aligned} \quad (4)$$

Then Eq. (3') may be expressed as

$$\begin{aligned} D\nabla^4 W - \lambda(p_1 W_{,xx} + p_2 W_{,yy} + p_3 W_{,xy}) = \\ \lambda(p_1 w_{o,xx} + p_2 w_{o,yy} + p_3 w_{o,xy}) \end{aligned} \quad (5)$$

If  $w_o = 0$  in Eq. (5) and if the applied loading can produce buckling, then the resulting eigenvalue problem generates eigenfunctions  $W_1, W_2, \dots$  and associated eigenvalues  $\lambda_1, \lambda_2, \dots$ . This eigenvalue problem can, in general, be difficult to solve. In this development, however, the primary objective is to examine and then make use of the properties of the governing equations.

If  $\lambda_1$  is the smallest eigenvalue, and if the initial deviation from flatness of the plate is well represented as

$$w_o = a_1 W_1, \quad (6)$$

then, using the properties of the solution of Eq. (5) when  $w_o = 0$ , and applying the homogeneous boundary conditions, the solution to Eq. (5) can be written as

$$W = \frac{a_1}{\left( \frac{\lambda_1}{\lambda} - 1 \right)} W_1 \quad (7)$$

Although this result can easily be recast into the form used for Southwell plots, it is of questionable origin because it depends on the applicability of Eq. (6). If Eq. (6) is not exact, there is no systematic method for judging the accuracy and hence the usefulness of Eq. (7).

Since the representation given by Eq. (6) is not acceptable as a basis for examining the properties of solutions to Eq. (5), a more general representation should be de-

veloped. The eigenfunctions are linearly independent, so this suggests that the smooth, continuous deviation from flatness function might be well represented by the expression

$$w_o = \sum_{k=1}^m a_k W_k, \quad (8)$$

where the admissible  $w_o$  are restricted to those having the same boundary conditions as the eigenfunctions  $W_k$ . To represent  $w_o$  by such a sum, it is necessary, of course, to specify a scheme for computing the coefficients  $a_k$ .

One method for computing the  $a_k$  is to make use of some of the properties of eigenfunctions cited by Mikhlin<sup>12</sup>. To describe this procedure it is convenient to introduce the operators

$$L_1 = D \nabla^4,$$

and

$$L_2 = p_1 \frac{\partial^2}{\partial x^2} + p_2 \frac{\partial^2}{\partial y^2} + p_3 \frac{\partial^2}{\partial x \partial y}.$$

If the operators  $L_1$  and  $L_2$  are positive definite, then for the eigenvalue problem described by the equation

$$L_1 W - \lambda L_2 W = 0$$

and the homogeneous boundary conditions, the eigenfunctions are orthogonal to the functions obtained by applying the operator  $L_2$  to the eigenfunctions.

For the operators  $L_1$  and  $L_2$  to be positive definite Mikhlin<sup>12</sup> specified that a positive constant  $\gamma^2$  exist such that

$$\int_A W L_1 W dS \geq \gamma^2 \int_A |W|^2 dS,$$

and

$$\int_A W L_2 W dS \geq \gamma^2 \int_A |W|^2 dS,$$

where integration is over the region of the given problem. Making use of the orthogonality property cited above, the coefficients  $a_k$  of Eq. (8) can be computed by use of the formula

$$a_k = \frac{\int_A w_o L_2 W_k dS}{\int_A W_k L_2 W_k dS}. \quad (9)$$

Although this could be expected to provide a very satisfactory basis for obtaining the desired representation for  $w_o$ , its use depends, in each problem, on the properties of the opera-

tors  $L_1$  and  $L_2$  and the given boundary conditions. It is, therefore, desirable to be able to specify a method for computing the  $a_k$  which does not have as a prerequisite the satisfaction of the conditions necessary for the development of Eq. (9).

A procedure based on the use of the method of least squares can be adopted for this purpose. Thus, it may be required that the integral of the error squared be a minimum. The requirement that

$$I = \int_A e^2 dS = \int_A \left[ w_o - \sum_{k=1}^m a_k W_k \right]^2 dS \quad (10)$$

be a minimum generates the conditions

$$\frac{\partial I}{\partial a_k} = 0 \quad \text{for } k = 1, 2, \dots, m. \quad (11)$$

Eqs. (11) provide a system of linear, nonhomogeneous equations for computing the coefficients  $a_k$ . Since the theoretical implications of the development and not the practical difficulties associated with computing the unknowns are of interest,  $m$  may be as large as is necessary to provide a good representation of  $w_o$ .

If Eq. (8) provides a good representation of  $w_o$ , a good solution to Eq. (5) can be developed. Because of the homogeneous boundary conditions, the solution is the particular solution

$$W = \frac{a_1}{\left( \frac{\lambda_1}{\lambda} - 1 \right)} W_1 + \sum_{k=2}^m \frac{a_k}{\left( \frac{\lambda_k}{\lambda} - 1 \right)} W_k \quad (12)$$

A comparison of Eqs. (7) and (12) reveals that they differ only in the summation term on the right side of Eq. (12). If the eigenvalues are well separated, the term involving the first eigenfunction and the first eigenvalue tends to become dominant on the right side of Eq. (12). Then it follows that Eq. (12) tends to the Southwell form. If this dominance develops as  $\lambda$  increases, it should manifest itself in an emerging linearity of a plot of  $W/\lambda$  versus  $W$  at a station on the plate. It is of interest to note that if the measurement station is selected to be at a point at which  $W_2$  is zero (a node line), the contribution of the summation in Eq. (12) is shifted to terms for which  $k > 2$ . These terms, because of the ordering of the  $\lambda_k$ , naturally tend to be progressively smaller as  $\lambda$  increases. The judicious choice of a



measurement site can, therefore, be used to suppress the contribution of the higher modes.

The derivation of Eq. (12) satisfies the objectives of the analytical part of the work presented here. The application of this analysis to the problem of interest will be examined in the next section of the paper.

## DISCUSSION OF RESULTS

In the discussion which follows the principle features of the experimental results for both the virgin specimens and the prestressed specimens will be described. The analytical results of the preceding section will be applied and the relation of these results to those obtained in other investigations will be discussed.

The results presented in Figure 5 for virgin specimens depict the variation of tensile load with the change in curvature along the edge of the simulated cracks. The forms of these curves are similar to those obtained by Dixon and Strannigan<sup>1</sup>, and following their procedure, upper and lower bounds for the buckling load have been obtained. The lower limit corresponds to a proportional limit of a stress-strain curve. An upper limit has been selected as the point at which the curves merge with a straight line which is tangent to the curve in the region in which the curvature changes. The bounds obtained are presented in Table II. Additional reference will be made to these results at another point in this section of the paper.

Before proceeding, however, it should be noted that the maximum loads achieved in the specimens with 3.0 inch and 2.2 inch cracks were of the order of the loads used to precondition the prestressed specimens. For these virgin specimens the zero shifts in the average strain readings upon unloading were, respectively, 5 microinches per inch and 10 microinches per inch. This indicates that the initial stresses along the crack edges of the corresponding prestressed specimens were of the order of 50 psi. and 100 psi., respectively. These initial stresses are both less than 4 percent of the crack edge stresses achieved at the buckling loads for these specimens.

It can be concluded, then, that relatively small initial stresses were present in the regions in which buckling occurred (above and below a crack) in the prestressed specimens. The buckling behavior observed in the prestressed specimens should, therefore, very closely represent the buckling behavior of the type specified; i.e., the elastic analysis should be valid for the prestressed specimens.

The load versus average strain curves for the prestressed specimens are presented in Figure 6. Since a uniaxial stress state exists at the crack edges, these data indicate the relation between the applied tensile load and the compressive stress developed along the crack edges. It can readily be seen that the relationship is linear initially, but that eventually, a nonlinear behavior emerges. The

nonlinearity observed is in the direction which would be associated with middle surface stretching due to bending. The departure from linearity, then, represents the point beyond which the nonlinear terms on the right side of Eq. (1) begin to become significant and can no longer be neglected. Correspondingly, the substitution of Eq. (4) in Eq. (3'), and the derived results summarized by Eq. (12) can be utilized only within the linear ranges of Figure 6. The curves of Figure 6, therefore, provide data on the range over which a Southwell type of analysis can be applied.

The load versus strain difference data for the prestressed specimens are presented in Figure 7, and in form, they are similar to the curves of Figure 5. The variables of Figure 7, however, are presented in a form which is more suitable for use in the modified Southwell plot usually referred to as a Lundquist plot. Lundquist<sup>13</sup> observed that though column data were frequently erratic immediately after loading, they usually developed the behavior predicted analytically after a certain value of load had been exceeded. This type of behavior is often observed in experiments and various procedures are commonly adopted to compensate for the spurious initial behavior. Lundquist showed that the Southwell relation could be modified to allow for this behavior. In terms of the analysis presented here, the Southwell relation has the form

$$\lambda_1 \left[ \frac{W(x_1, y_1)}{\lambda} \right] = W(x_1, y_1) + a_1 W_1(x_1, y_1),$$

where  $(x_1, y_1)$  represent a point on the plate and the variables plotted are

$$\frac{W(x_1, y_1)}{\lambda} \quad \text{and} \quad W(x_1, y_1).$$

In a modified form of the Lundquist type, the basic relation is of the form

$$(\lambda_1 - \lambda_0) \left[ \frac{W(x_1, y_1) - W_0(x_1, y_1)}{\lambda - \lambda_0} \right] = \left[ W(x_1, y_1) - W_0(x_1, y_1) \right] + \left[ a_1 + W_0(x_1, y_1) \right] W_1(x_1, y_1).$$

Reference to the definition of  $\lambda$ , and use of the relation between strain and curvature readily reveals that the above Lundquist relation can be written in terms of the strain difference at a point, and the applied load. If the strain dif-

ference is defined as  $\Delta\epsilon$  and the load as  $P$ , the variables to be plotted are

$$\frac{\Delta\epsilon - \Delta\epsilon_0}{P - P_0} \quad \text{and} \quad (\Delta\epsilon - \Delta\epsilon_0)$$

The inverse of the slopes of the lines of Figure 8 may then be identified as the quantity  $(P_1 - P_0)$ , where  $P_1$  is the load value corresponding to the smallest eigenvalue. The values of  $P_1$  for the different crack lengths are presented in Table III as Buckling Loads. The Buckling Stress values are based on the use of the area away from the crack; i.e., the thickness times the width of 12 inches.

An examination of the Lundquist plots in Figure 8 reveals that the linearity sought is observed. There is an initial deviation from linearity in each case. This is commonly observed in such plots and it can be attributed to the extreme sensitivity of the ratio variable to slight errors in the mea-

sured initial values, and to some extent to the possible contribution of higher modes at the lower load values.

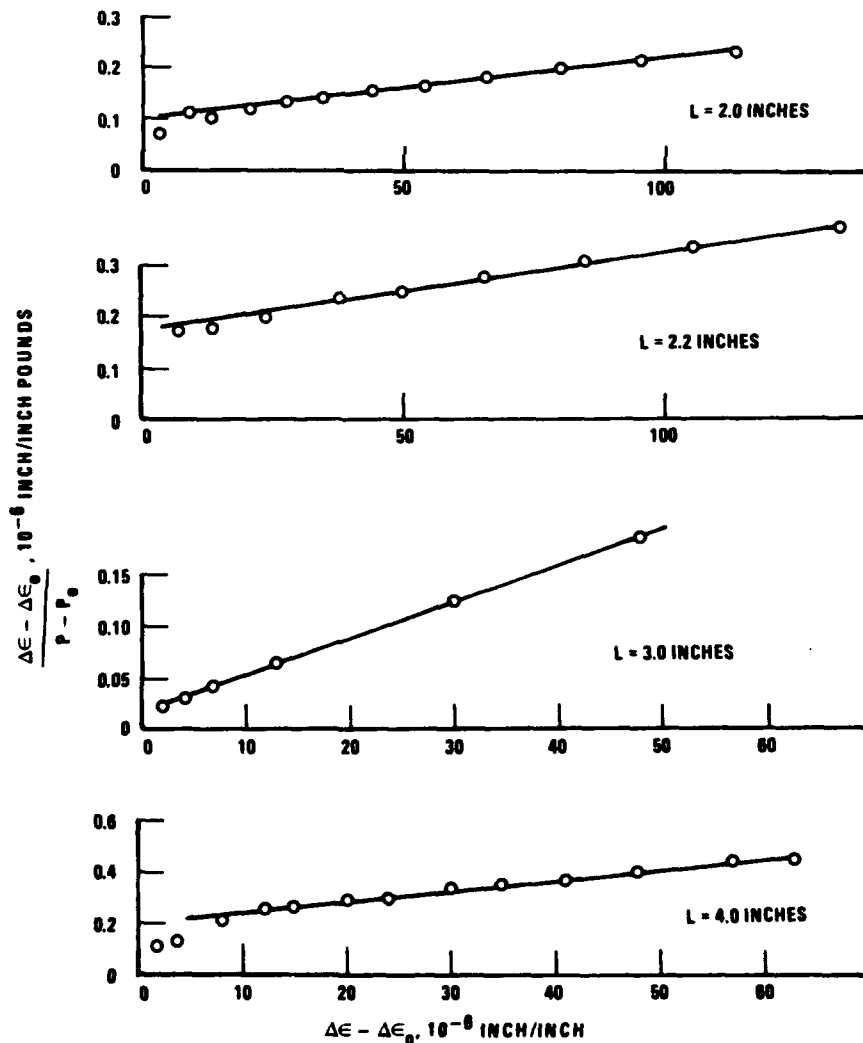
It should be noted that the Lundquist plots were discontinued at load values corresponding to the beginning of a deviation from linearity for the curves presented in Figure 6. A continuation of the use of data beyond these loads exhibited a consistent tendency for the additional points to lie below the linear Lundquist plots. This is in the direction which would be expected for the behavior observed; i.e., as the second order, nonlinear effects emerge, the load increment necessary for a given increase in curvature increases and the value of the Lundquist ratio decreases.

It was noted in the introduction that previous workers had made use of the buckling formula

$$\sigma = kE \left(\frac{t}{L}\right)^2$$

In order to examine the validity of this relation a plot was

Figure 8. Lundquist Plots for Prestressed Specimens.



made in Figure 9 of  $\sigma/E$  versus  $(t/L)^2$ . As can be seen, the Lundquist data for the prestressed models conform well to a linear relationship for these variables. Also appearing in Figure 9 are the points representing the upper and lower bounds of the critical stresses of the virgin specimens as determined by the method of Dixon and Strannigan<sup>1</sup>. It is significant that the upper bound stresses are all close to the straight line. This correlation between the two methods of defining buckling indicates that when applied to data on the prestressed specimens, the elastic analysis provides relevant information about this buckling problem.

The data have been plotted in another form in Figure 10. The curve in Figure 10 was obtained by transferring points from the line of Figure 9. Figure 10 corresponds to the critical stress versus slenderness ratio plot used for Euler columns. This illustrates the similarity in the buckling behavior of the elastic column and the cracked thin sheet.

The upper bound stress cited above would appear to be of basic value for correlating the effect of buckling on fatigue behavior, because at this level of load, bending due to buckling can be expected to be a significant factor. To obtain a valid correlation of such effects on two different materials, it is essential that specimens be examined for comparable conditions, and that the buckling effect in both be significant. The use of the upper bound as a reference value, would seem to satisfy these requirements. It follows, then, that the observed correlation between the upper bound load and the critical loads obtained from the prestressed specimens is of particular interest.

It is also of interest at this point to examine the role of the quantity  $k$  in the equation

$$\sigma = kE (t/L)^2$$

It is seen that the value of  $k$  is the slope of the straight line of Figure 9. For the present work  $k = 4.0$ . As pointed out

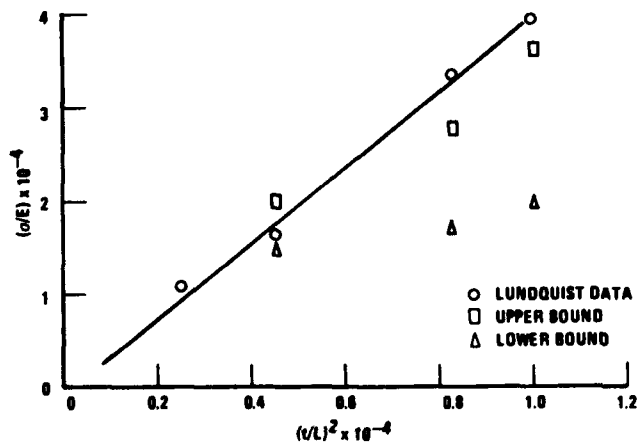


Figure 9. Linear Plot of Buckling Data.

earlier, however, the value of  $k$  has not been observed to be a constant under all conditions. Dixon and Strannigan<sup>1</sup> report values of  $k$  equal to 2.28 and 5.12 for aluminum alloy sheets of 0.079 and 0.037 inch thickness, respectively. A review of data from several sources (1, 2, 14, 15), in fact, seems to indicate that  $k$  is not actually a constant.

Some insight into why  $k$  varies, can be obtained from a consideration of the stress distribution in the vicinity of the crack. Dixon and Strannigan<sup>1</sup>, by use of photoelastic models, showed that for crack length to sheet width ratios of less than 0.6 the magnitude of the compressive stress along the crack edge is equal to the magnitude of the uniform tensile stress far removed from the crack. Theoretical support for this observation has also been given by Neuber<sup>16</sup> in an analysis of the stress distribution around elliptical cracks. The observed equality of these quantities provided a basis for a derivation<sup>1</sup> of the formula for critical stress. It should be expected, however, that when the crack length to sheet width ratio is greater than 0.6, the sheet width should appear explicitly in the formula for buckling.

The possible difficulty cited above cannot, however, be used to explain all of the discrepancies which can be found. There also appears to be a sheet thickness effect which is not accounted for in the simple buckling relationship cited above. A possible explanation for the difficulty may be found in recognizing that the strip of material at the edge of the crack has properties which are more complex than those of the simple column which has been used as a model to derive the buckling formula. In particular, another analogy proposed by Walker<sup>2</sup> might be visualized by considering a column on an elastic foundation. For such a column the buckling stress may be written in the form

$$\sigma = CE \left(\frac{t}{L}\right)^2 (1 + F),$$

where  $C$  is a constant and the quantity  $F$  depends on the

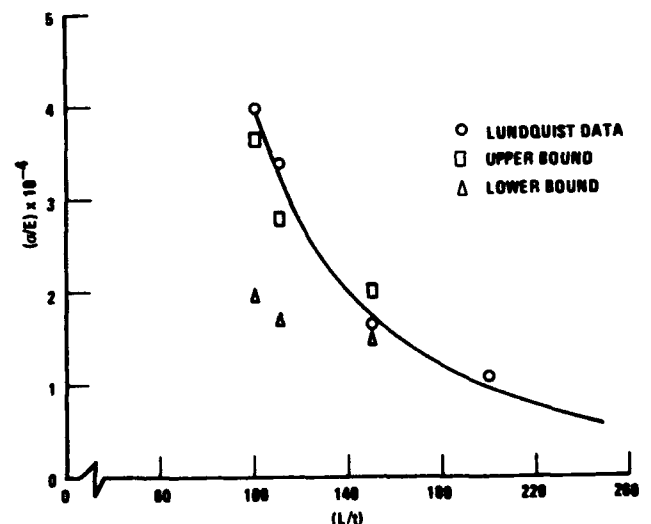


Figure 10. Nonlinear Plot of Buckling Data.

column length, the area moment of inertia of the cross section of the column, Young's modulus and the foundation stiffness. Naturally, if the foundation stiffness decreases sufficiently, the simple column formula is approached as a limiting case. If the quantity  $C(1 + F)$  is now redefined as  $k$ , it is readily seen that the value of  $k$  will be constant only for a limiting condition; i.e., it is not a true constant.

The objective of the preceding discussion was not to suggest that the column on an elastic foundation be used as a model for the crack buckling problem. The objective was to illustrate how a complex system can have buckling properties which cannot be completely described by the type of formula which applies for a simple column.

It is important to emphasize at this point that the method which has been described in this paper for determining the buckling stress is *not* based on the existence of such a simple formula. As a consequence, it should be possible to design and to conduct a parametric experimental study which would provide a basis for developing a relationship which does not have the deficiencies of the simple formula. This would merely require a systematic extension of the studies described in this paper.

#### CONCLUSIONS

The experimental and analytical results presented in the preceding sections describe a number of the features of the problem of buckling in thin cracked sheets. Four principle conclusions follow from the results which have been presented and they are summarized below.

1. Although the problem involves an elastic-plastic response, it is possible, by properly prestressing test specimens, to study a related elastic problem. Since the residual or initial stresses produced in the zone in which subsequent buckling occurs are small compared to the stress

necessary to cause buckling, the results of an elastic stability analysis can be applied to the prestressed model.

2. The application of a Southwell method of analysis to plate stability problems must be restricted to behavior which is described by the linearized plate equations. The point at which second order nonlinear effects become significant can be detected experimentally, however, so the range over which the Southwell method applies can be specified and used to determine the buckling load for the elastic, cracked sheet problem.

3. The upper bound on the buckling stress, as defined by Dixon and Strannigan<sup>1</sup>, provides a rational reference stress for correlations of the effect of buckling on fatigue because it represents a level of loading beyond which the deflection and the bending due to buckling become large. The critical stresses obtained by the prestress - Southwell method developed here correlate well with the upper bound stresses. This suggests that the fundamental buckling behavior is not substantially modified in going from the elastic-plastic to the elastic model. The correlation of these responses is probably due to the separation of the zones in which buckling and plastic deformation occur.

4. The simple buckling stress relation

$$\sigma = kE \left( \frac{t}{L} \right)^2,$$

which has been used by a number of investigators has been critically evaluated. The variation of  $\sigma$  with  $(t/L)$  is shown to be properly described in this formula, but a review of data from the literature indicates that  $k$  is not a true constant. It depends on sheet thickness and it can be expected to become dependent on specimen width as the crack length increases. The techniques developed in the present paper could be used to conduct a parametric study in which these effects are more fully investigated.

#### REFERENCES

1. J.R. Dixon and J.S. Strannigan, "Stress Distribution and Buckling in Thin Sheets with Central Slits," *Proc. 2nd Int. Conf. Fracture*, Chapman and Hall, London (1969).
2. E.K. Walker, *A Study of the Influence of Geometry on the Strength of Fatigue-Cracked Panels*, AFFDL-TR-66-92, Air Force Flight Dynamics Laboratory, Wright-Patterson AFB, Ohio (1966).
3. C.K. Trotman, "Discussion," pp. 538-539, *Proc. Crack Propagation Symp.*, College of Aeronautics, Cranfield, England (1966).
4. P. Kuhn, *The Prediction of Notch or Crack Strength Under Static or Fatigue Loading*, SAE Paper 843C, Society of Automotive Engineers, New York (1964).

## REFERENCES (Continued)

5. R.G. Forman, *Experimental Program to Determine Effect of Crack Buckling and Specimen Dimensions on Fracture Toughness of Thin Sheet Materials*, AFFDL-TR-65-146, Air Force Flight Dynamics Laboratory, Wright-Patterson AFB, Ohio (1965).
6. D.P. Rooke, N.J. Gunn, J.T. Ballet, and F.J. Bradshaw, *Crack Propagation in Fatigue: Some Experiments with DTD 5070A Aluminum Sheet*, RAE-TR-64025, Royal Aircraft Establishment, Farnborough, England (1964).
7. W.J. Cricklow and R.H. Wells, "Crack Propagation and Residual Static Strength of Fatigue-Cracked Titanium and Steel Cylinders," in *Fatigue Crack Propagation*, ASTM-STP-415, American Society for Testing and Materials, Philadelphia, Pennsylvania (1967).
8. E.H. Mansfield, *On Theoretical Plasticity and Crack Propagation*, ARC-CP-568, Aeronautical Research Council, London (1961).
9. L.H. Donnell, "On the Application of Southwell's Method for the Analysis of Buckling Tests," pp. 27-38, *Stephen Timoshenko 60th Anniversary Volume*, McGraw-Hill, New York (1938).
10. S. Timoshenko and J.M. Gere, *Theory of Elastic Stability*, p. 190, McGraw-Hill, New York (1961).
11. E. Way, *The Lateral Instability of a Simply Supported Deep Beam Subjected to a Concentrated Load at Its Centroid*, Engineers Thesis, Stanford University, Dept. of Aeronautics and Astronautics, Stanford, California (1967).
12. S.G. Mikhlin, *Approximate Methods for Solution of Differential and Integral Equations*, p. 195, American Elsevier, New York (1967).
13. E.E. Lundquist, *Generalized Analysis of Experimental Observations in Problems of Elastic Stability*, NACA-TN-658, National Aeronautics and Space Administration, Washington, D.C. (1938).
14. B.L. Clarkson, "The Propagation of Fatigue Cracks in a Tensioned Plate Subjected to Acoustic Loads," in (N.J. Trapp and D. Forney, Eds.), *Acoustical Fatigue in Aerospace Structures*, Syracuse University Press, Syracuse, New York (1965).
15. R.L. Carlson and S.C. Bailey, *On the Analysis of Column and Plate Stability Experiments*, Report 68-6, Georgia Institute of Technology, School of Aerospace Engineering, Atlanta, Georgia (1968).
16. H. Neuber, *Theory of Notch Stresses: Principles for Exact Stress Calculations*; F.A. Raven, Translator, DTMB-Trans.-74, p. 56, David Taylor Model Basin, Washington, D.C. (1945).

**THE EFFECT OF RIVETED AND UNIFORMLY SPACED STRINGERS  
ON THE STRESS INTENSITY FACTOR OF A CRACKED SHEET**

by

C.C. Poe, Jr.

NASA Langley Research Center  
Hampton, Virginia

**LIST OF SYMBOLS**

$A_{ij}$	= displacement of the $i$ th rivet due to a force of unity at the $j$ th rivet	$r, \theta$	= plane polar coordinates
$a$	= half crack-length	$S$	= applied uniaxial stress
$B_i$	= displacement of the $i$ th rivet due to an applied uniaxial stress of unity	$t$	= thickness
$b$	= stringer spacing	$v$	= $y$ component of displacement
$C$	= stress intensity correction factor, $k/S\sqrt{a}$	$w$	= stringer width
$d$	= rivet diameter	$x, y$	= Cartesian coordinates
$E$	= Young's modulus	$x_0, y_0$	= rivet coordinates
$F$	= maximum force in a stringer	$\mu$	= ratio of stringer stiffness to total stiffness
$k$	= stress intensity factor	$\nu$	= Poisson's ratio
$\bar{k}$	= stress intensity factor coefficient for rivet forces	$\sigma_{xx}, \sigma_{yy}$	= normal stress components
$L$	= stringer load concentration factor	$\tau_{xy}, \tau_{xz}, \tau_{yz}$	= shearing stress components
$p$	= rivet spacing	Subscripts:	
$Q_j$	= rivet force at the $j$ th rivet	max	= maximum
		s	= stringer
		Superscripts:	
		s	= stringer

**INTRODUCTION**

The design of a complex structure to have maximum residual strength and maximum resistance to fatigue crack propagation requires a quantitative knowledge of the stress state in stiffened panels containing cracks. Stress analyses of cracks have been performed only on simple configurations and panels with one or two stringers (Refs. 1-10). Existing knowledge of the effect of multiple stringers on the stresses in a cracked sheet is limited to experiments with box beams and tension panels (Refs. 11-15).

The present paper examines the effect of multiple stringers on the stresses in a cracked sheet with crack

lengths up to six times the stringer spacing. The stringers were assumed to be uniformly spaced and attached to the sheet by means of uniformly spaced rivets. The unknown rivet forces were determined by requiring the displacements at the rivets in the sheet and stringers to be equal. The stress intensity factor for the cracked sheet was determined by superimposing the stress intensity factors for the rivet forces and for the applied uniaxial stress. The stress intensity factor and forces in the most highly loaded rivet and stringer plotted against crack length are presented for various values of rivet spacing and stringer stiffness. More complete results are given in Reference 16, along with the equations used to calculate the displacements in the sheet and stringers.

## FORMULATION OF PROBLEM

### Unknown Rivet Forces

The sketch in Figure 1 shows a sheet stiffened with stringers of uniform size and spacing. The stringers are attached to the sheet with equally spaced rivets, and the stringers and sheet are subjected to the uniaxial stresses  $S$  and  $S_E^E$ , respectively, which produce equal straining at large distances from the crack. The sheet contains a crack which extends equally on both sides of a stringer center line.

The next sketch, Figure 2, shows the rivet forces acting symmetrically with respect to the crack and in opposite directions on the sheet and stringer as required by equilibrium. The row of rivets coincident with the crack is not shown because those rivets exert no force due to symmetry. The forces in the sheet and stringers are assumed to be coplanar.

The equations necessary to determine the unknown rivet forces  $Q_j$  were obtained by requiring the displacements at the rivets to be equal in the sheet and stringers. The displacements were written in terms of influence coefficients defined as follows: Let the influence coefficients  $A_{ij}$  and  $B_i$  be the displacements at the  $i$ th rivet in the sheet due to unit values of  $Q_j$  and  $S$ , respectively,

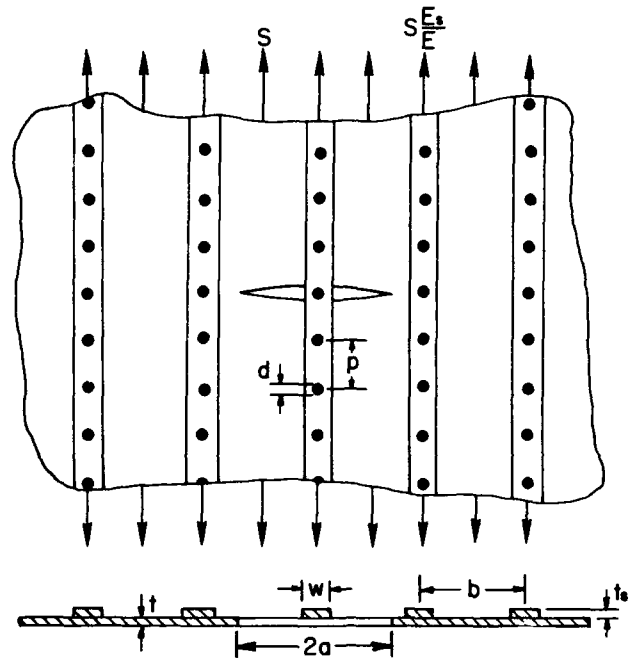


Figure 1. Sheet Stiffened with Stringers of Uniform Size and Spacing, Attached to Sheet with Equally-Spaced Rivets.

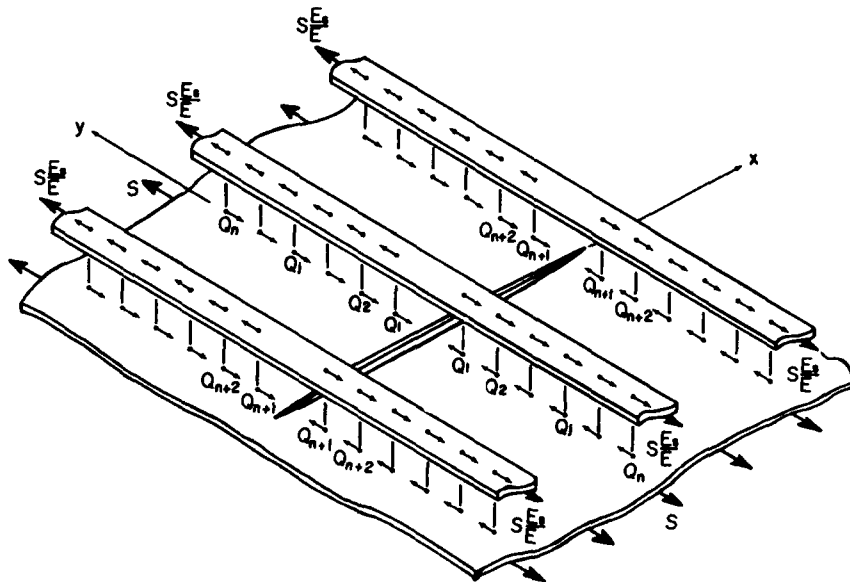


Figure 2. Rivet Forces Acting Symmetrically with Respect to Crack .

and  $A_{ij}^s$  and  $B_i^s$  the displacements of the  $i$ th rivet in the stringers due to unit values of  $Q_j$  and  $\frac{SE_s}{E}$ , respectively. Then the displacement of the  $i$ th rivet in the sheet and stringers can be written.

$$v_i = - \sum_j A_{ij} Q_j + B_i S \quad (1)$$

and

$$v_i^s = \sum_j A_{ij}^s Q_j + B_i^s \frac{E_s}{E} S \quad (2)$$

respectively, where the summation over  $j$  includes all rivets. The negative sign was introduced in Eq. (1) because the rivet forces act in opposite directions on the sheet and stringers. Equating equations (1) and (2) and collecting terms,

$$\sum_j (A_{ij} + A_{ij}^s) Q_j - \left( B_i - \frac{E_s}{E} B_i^s \right) S = 0, \quad (i = 1, 2, 3, \dots) \quad (3)$$

A truncated set of these simultaneous coupled equations was solved for the unknown rivet forces. The equations used to compute the influence coefficients in equations (3) are given in Reference 16.

### STRINGER LOAD CONCENTRATION FACTOR

For a stringer that spans the crack, the rivet forces oppose the opening of the crack and thus transfer load

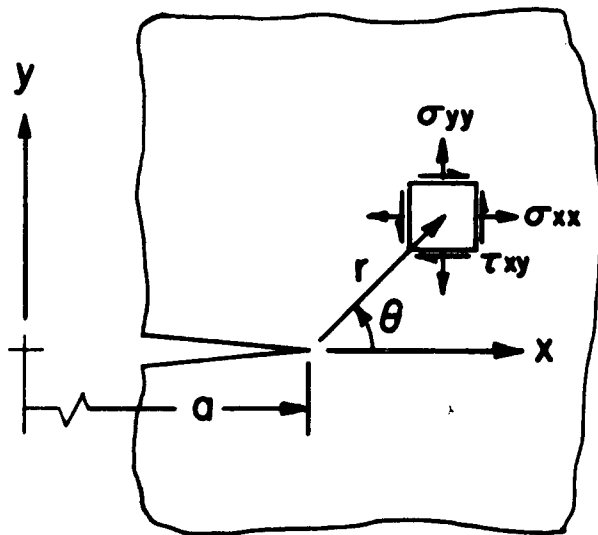


Figure 3. Stresses Near Crack Tip.

from the sheet to the stringer. Therefore, the sum of the rivet forces represents an increase in the stringer force above the applied force so that the maximum force in the stringer becomes

$$F = \frac{wt_s SE_s}{E} + \sum_j Q_j \quad (4)$$

where the summation extends over all the rivets in that particular stringer. For convenience, a stringer load concentration factor  $L$  is defined as the ratio of the maximum force in the stringer to the force applied to the stringer at infinity. Thus, the maximum force is

$$F = L \frac{wt_s SE_s}{E} \quad (5)$$

Substituting equation (4) into (5) and solving for  $L$ ,

$$L = 1 + \frac{E}{wt_s SE_s} \sum_j Q_j \quad (6)$$

### Stress Intensity Factor for the Stiffened Sheet

The stresses in the vicinity of a crack tip are proportional to the stress intensity factor<sup>17</sup>. For the symmetrical case of plane extension (mode I) and neglecting higher powers of  $r$ , the stresses near the crack tip in Figure 3 are:

$$\begin{aligned} \sigma_{xx} &= \frac{k}{\sqrt{2r}} \cos \frac{\theta}{2} \left( 1 - \sin \frac{\theta}{2} \sin \frac{3\theta}{2} \right) \\ \sigma_{yy} &= \frac{k}{\sqrt{2r}} \cos \frac{\theta}{2} \left( 1 + \sin \frac{\theta}{2} \sin \frac{3\theta}{2} \right) \\ \tau_{xy} &= \frac{k}{\sqrt{2r}} \sin \frac{\theta}{2} \cos \frac{\theta}{2} \cos \frac{3\theta}{2} \\ \tau_{xz} &= \tau_{yz} = 0 \end{aligned}$$

Because both the uniaxial stress  $S$  and the symmetrical rivet forces  $Q_j$  produce only an opening mode of crack deformation, the stress intensity factors due to each can be superimposed. Thus, the total stress intensity factor is

$$k = S\sqrt{a} + \sum_j \bar{k}_j Q_j \quad (7)$$

where  $S\sqrt{a}$  is the component due to the uniaxial stress  $S$  and  $\sum_j \bar{k}_j Q_j$  is the component due to the symmetrical rivet forces  $Q_j$ . For the case of plane stress, the coefficient  $\bar{k}_j$  is given in Reference 18 for the symmetrical point forces shown in Figure 4 as

$$\bar{k} = \frac{\sqrt{a}}{\pi t} \left[ (3 + \nu) \xi_1 - (1 + \nu) \xi_2 \right] \quad (8)$$



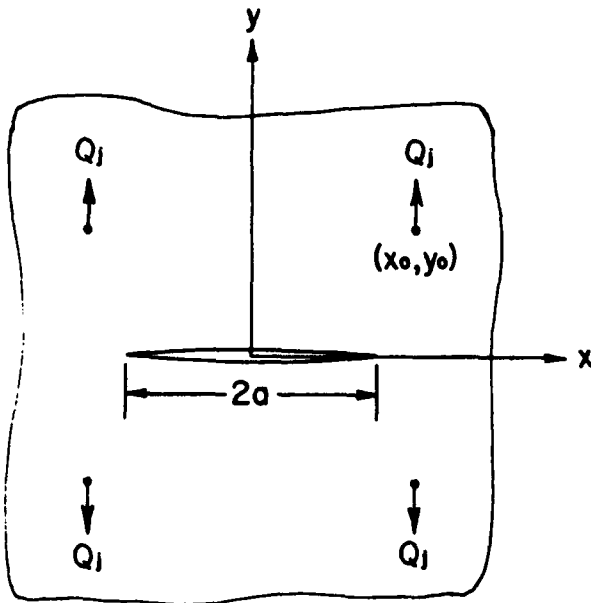


Figure 4. Symmetrical Point Forces.

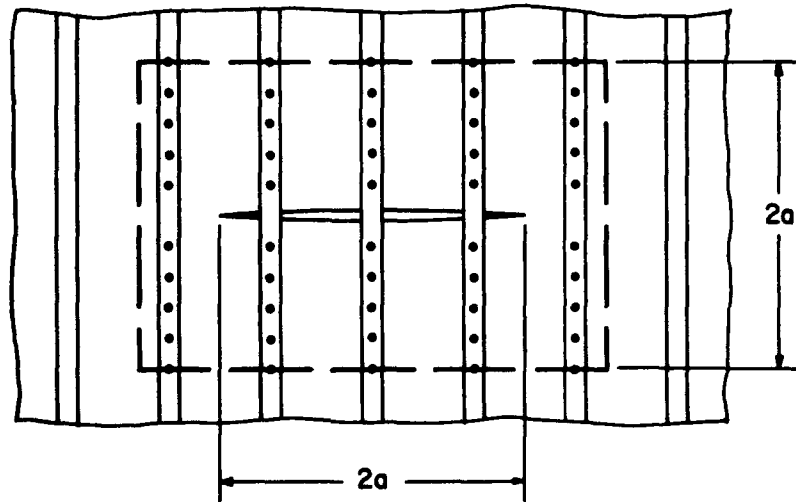
where

$$\xi_1 = \frac{\gamma}{\sqrt{(x_0^2 - y_0^2 - a^2)^2 + 4x_0^2 y_0^2}}$$

$\xi_2 =$

$$\frac{[(x_0^2 + a^2)y_0^2 + (x_0^2 - a^2)^2]y_0^2 + x_0^2 y_0^2 (x_0^2 + y_0^2 - a^2)}{\gamma [(x_0^2 - y_0^2 - a^2)^2 + 4x_0^2 y_0^2]^{3/2}}$$

Figure 5. Rectangular Region Showing Rivets Included in Solution of Equation (3).



and

$$\gamma = \frac{1}{\sqrt{2}} \left[ \sqrt{(x_0^2 - y_0^2 - a^2)^2 + 4x_0^2 y_0^2} - (x_0^2 - y_0^2 - a^2) \right]^{1/2}$$

(An error in Ref. 18 has been corrected in  $\xi_2$  of equation (8).) For convenience, a stress intensity correction factor, C, is defined to be the ratio of the stress intensity factor for the cracked sheet with stringers to the stress intensity factor for the unstiffened sheet. Thus,

$$k = CS\sqrt{a} \quad (9)$$

Substituting equation (9) into (7),

$$C = 1 + \frac{1}{S\sqrt{a}} \sum_j \bar{k}_j Q_j \quad (10)$$

#### Numerical Solution

Because the stresses in the sheet at large distances from the crack are unaffected by the presence of the crack, the rivet forces are negligibly small except in the vicinity of the crack. In the present investigation only those rivets within the rectangular region shown in Figure 5 are included in the solution of equations (3). The height of the region was chosen to be equal to the crack length 2a or to include 20 rivets per stringer, whichever was larger. The width of the region extended beyond the crack tips to include the next stringers. Because of symmetry, only those rivets in one quadrant of this area were actually considered as unknowns in the solution of equations (3). From preliminary calculations, the computed value of the stress intensity correction factor C was found to be affected by less than 1 percent by increasing the size of this region.

## RESULTS AND DISCUSSION

### Stress Intensity Correction Factor

Figure 6 shows the stress intensity correction factor plotted against crack length for various values of rivet spacing in one graph and of stringer stiffness in the other. Both crack length and rivet spacing have been made nondimensional by dividing by the stringer spacing. The nondimensional stiffness parameter  $\mu$  is defined to be the ratio of stiffness of the stringers alone to the stiffness of the stringers and sheet. Thus, for stringers of uniform size and spacing

$$\mu = \frac{1}{1 + \frac{btE}{wt_s E_s}} \quad (11)$$

Variations in stringer width and rivet diameter were found to have only a small effect on the results; thus, the ratios  $d/p = 1/4$  and  $w/d = 5$  have been used for all the results presented.

For a given crack length, the effect of decreasing rivet spacing is to reduce the stress intensity factor. When the crack tip is not in the vicinity of a stringer, the curves appear to approach a lower bound as the rivet spacing becomes small. In the limit, this condition approaches the case of continuously attached stringers. Hence, these results should be applicable to the case of continuously attached stringers when the crack tip is not in the vicinity of a stringer. On the other hand, the minimum points, which occur in the curves when the crack tip is slightly beyond a stringer, continue to decrease in

value for decreasing values of rivet spacing. Thus, small values of rivet spacing enhance the effectiveness of stringers as crack arresters.

For a given crack length, an increase in the stringer stiffness also reduces the stress intensity factor. However, even for the case where the stringer stiffness is much greater than the sheet stiffness ( $\mu \rightarrow 1.00$ ), the stress intensity factor is not reduced to zero. Moreover, more than 80 percent of the maximum possible reduction in the stress intensity factor occurs for a value of  $\mu = 0.5$ . Therefore, an optimum value of  $\mu$  may exist when considering additional restraints such as minimum gages, buckling strength, fabrication costs, and so forth.

### Stringer Load Concentration Factor

The stringer load concentration factor can be shown to have a maximum value. Consider the case in which the crack has progressed entirely across the width of the sheet. The maximum force that must be transferred from the sheet to the stringers is  $btS$  per stringer. Thus the maximum force in a stringer becomes

$$F_{\max} = \frac{wt_s E_s S}{E} + btS \quad (12)$$

Substituting equation (12) into (5), the maximum value of  $L$  becomes

$$L_{\max} = 1 + \frac{btE}{wt_s E_s} \quad (13)$$

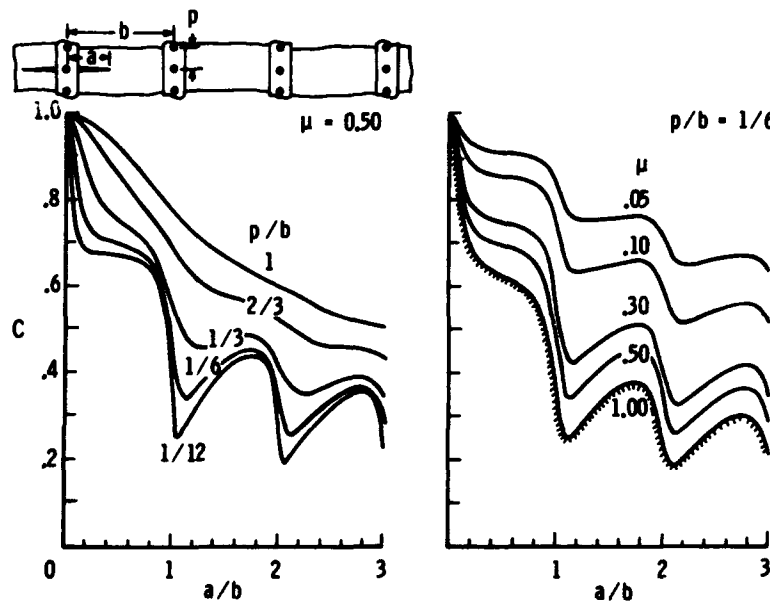


Figure 6. Effect of Rivet Spacing, Stringer Stiffness, and Crack Length on the Stress Intensity Correction Factor.

Figure 7. Effect of Rivet Spacing, Stringer Stiffness, and Crack Length on the Stringer Load Concentration Factor for the Most Highly Loaded Stringer.

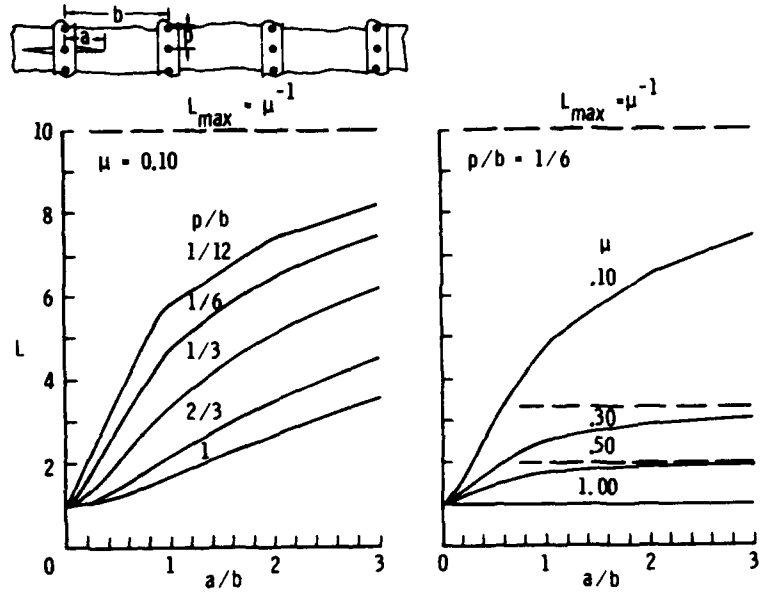
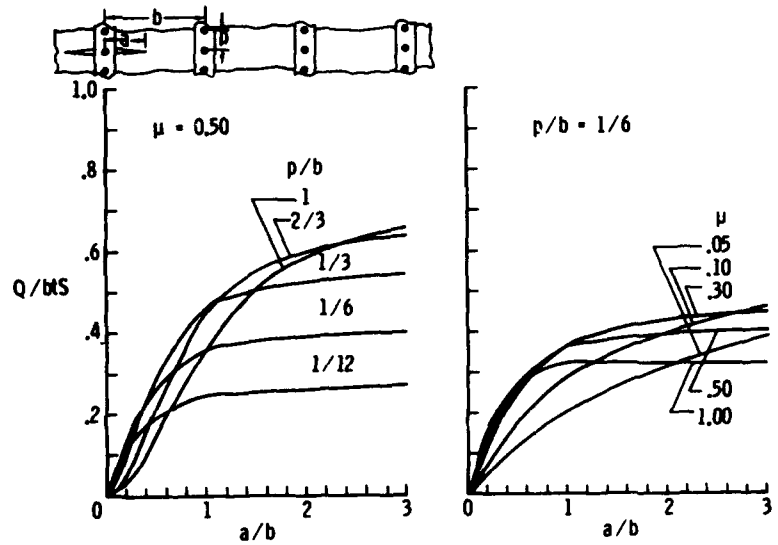


Figure 8. Effect of Rivet Spacing, Stringer Stiffness, and Crack Length on the Force in the Most Highly Loaded Rivet.



Substituting equation (11) into (13),

$$L_{\max} = \mu^{-1} \quad (14)$$

Thus the maximum value of  $L$  is the reciprocal of the stiffness parameter  $\mu$ .

Figure 7 shows the stringer load concentration factor  $L$  for the most highly loaded stringer plotted against crack length for various values of rivet spacing in one graph and stringer stiffness in the other. The most highly loaded stringer was always the middle stringer. For small values of crack length, the crack has little effect on the force in the stringer, and  $L$  is unity. For longer cracks, the curves for the various values of stringer stiffness increase and asymptotically approach the values of  $L_{\max}$  given by equation (14). For large values of rivet spacing,  $L$  reaches  $L_{\max}$  only for very long cracks.

#### Rivet Force

The force in the most highly loaded rivet is likewise limited in magnitude for very long cracks. The force in one of the rivets must be less than the maximum force  $btS$  that is transferred from the sheet to a stringer.

Figure 8 shows the force in the most highly loaded rivet plotted against crack length for various values of rivet spacing in one graph and stringer stiffness in the other. The rivet force was normalized by dividing by the maximum rivet force  $btS$ . The most highly loaded rivet was always the first rivet in the middle stringer. For very small cracks, the rivet force is essentially zero. For longer cracks, the force increases and the curves become asymptotic to values of  $Q/btS$ . The asymptotic values of  $Q/btS$  are smaller for smaller values of rivet spacing and larger values of stringer stiffness.

A simple relationship for the maximum values of  $Q/btS$  cannot be derived like that for  $L_{\max}$  in equation (14). However, the asymptotic values of  $Q/btS$  for various combinations of the values of rivet spacing and stringer stiffness were determined and are plotted in Figure 9 as a function of rivet spacing. For the smaller values of stringer stiffness and the larger values of rivet spacing, the asymptotes were estimated from solutions for values of crack length larger than  $\frac{a}{b} = 3$ . The curves show that the maximum value of  $Q/btS$  is smaller for smaller values of rivet spacing. The value approaches zero as indicated by the extrapolated portion of the curves because a fixed force must be shared by an increasingly large number of rivets for decreasing values of rivet spacing. For values of rivet spacing less than  $p/b = 1/2$ , the maximum value of  $Q/btS$  is also smaller for larger values of stringer stiffness. Values of  $p/b$  larger than one-half are of less practical significance.

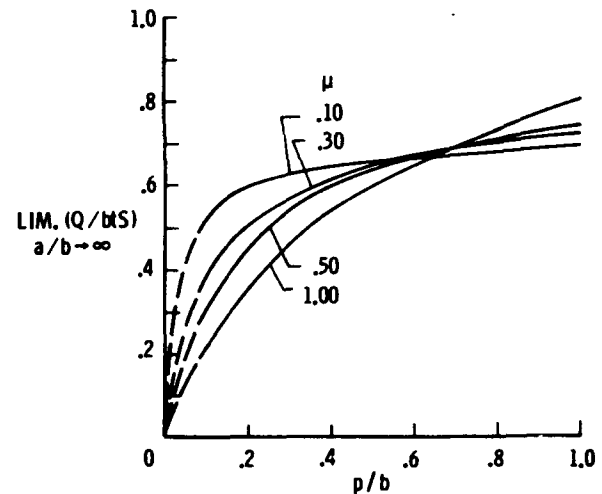


Figure 9. Effect of Rivet Spacing and Stringer Stiffness on the Maximum Force in the Most Highly Loaded Rivet.

#### CONCLUSIONS

The effectiveness of stringers in reducing the stress intensity factor depended primarily upon rivet spacing and stringer stiffness. For a given crack length, larger values of stringer stiffness and smaller values of rivet spacing resulted in lower values of the stress intensity factor. However, even when the stringers were very stiff and the rivet spacing was very small, the stress intensity factor was greater than zero. Rivet spacing had a pronounced effect on the stress intensity factor when the crack tip was in the vicinity of a stringer and is therefore an important parameter determining the effectiveness of stringers as crack arresters.

For large values of crack length, the forces in the most highly loaded rivet and stringer asymptotically approached limiting values. Also, these asymptotic values of force were smaller for larger values of stringer stiffness and smaller values of rivet spacing.

The stress intensity factor results indicate that the residual static strength and the resistance to fatigue crack growth of a stiffened sheet of a given weight can be significantly increased by using a larger proportion of material in the stringers and a smaller rivet spacing.

## REFERENCES

1. J.P. Romualdi, J.T. Frasier, and G.R. Irwin, *Crack-Extension-Force Near a Riveted Stiffener*, NRL-R-4956, Naval Research Laboratory, Washington, D.C. (1957).
2. J.L. Sanders, Jr., *Effect of a Stringer on the Stress Concentration Factor Due to a Crack in a Thin Sheet*, NASA-TR-R-13, National Aeronautics and Space Administration, Washington, D.C. (1959).
3. J.P. Romualdi and P.H. Sanders, *Fracture Arrest by Riveted Stiffeners*, AFOSR-TR-60-174, Carnegie Institute of Technology, Pittsburgh, Pennsylvania (1960).
4. M. Isida and Y. Itagaki, "Stress Concentration at the Tip of a Central Transverse Crack in a Stiffened Plate Subjected to Tension," *Proc. 4th U.S. Natl. Congr. Appl. Mech.*, 2:955-969 (1962).
5. H.A. Leybold, *A Method for Predicting the Static Strength of a Stiffened Sheet Containing a Sharp Central Notch*, NASA-TN-D-1943, National Aeronautics and Space Administration, Washington, D.C. (1963).
6. R. Greif and J.L. Sanders, Jr., "The Effect of a Stringer on the Stress in a Cracked Sheet," *J. Appl. Mech.*, 32:59-66 (1965).
7. M. Isida, *Effect of a Stringer on the Stress Intensity Factors for the Tension of a Cracked Wide Plate*, Lehigh University, Dept. of Mechanics, Bethlehem, Pennsylvania (1965).
8. M. Isida, Y. Itagaki, and S. Iida, *On the Crack Tip Stress Intensity Factor for the Tension of a Centrally Cracked Strip with Reinforced Edges*, Lehigh University, Dept. of Mechanics, Bethlehem, Pennsylvania (1965).
9. J.M. Bloom and J.L. Sanders, Jr., "The Effect of Riveted Stringer on the Stress in a Cracked Sheet," *J. Appl. Mech.*, 33:561-570 (1966).
10. I.E. Figge and J.C. Newman, Jr., *Prediction of Fatigue-Crack-Propagation Behavior in Panels with Simulated Rivet Forces*, NASA-TN-D-4702, National Aeronautics and Space Administration, Washington, D.C. (1968).
11. H.F. Hardrath, H.A. Leybold, C.B. Landers, and L.W. Hauschild, *Fatigue-Crack Propagation in Aluminum - Alloy Box Beams*, NACA-TN-3856, National Aeronautics and Space Administration, Washington, D.C. (1956).
12. H.F. Hardrath and R.E. Whaley, *Fatigue-Crack Propagation and Residual Static Strength of Built-Up Structures*, NACA-TN-4012, National Aeronautics and Space Administration, Washington, D.C. (1957).
13. H.F. Hardrath and H.A. Leybold, *Further Investigation of Fatigue-Crack Propagation in Aluminum-Alloy Box Beams*, NACA-TN-4246, National Aeronautics and Space Administration, Washington, D.C. (1958).
14. R.E. Whaley and P.R. Kurzhals, *Fatigue-Crack Propagation in Aluminum-Alloy Tension Panels*, NASA-TN-D-543, National Aeronautics and Space Administration, Washington, D.C. (1960).

#### REFERENCES (Continued)

15. H.A. Leybold, *Residual Static Strength of Aluminum-Alloy Box Beams Containing Fatigue Cracks in the Tension Covers*, NASA-TN-D-796, National Aeronautics and Space Administration, Washington, D.C. (1961).
16. C.C. Poe, Jr., *The Effect of Riveted and Uniformly Spaced Stringers on the Stress Intensity Factor of a Cracked Sheet*, M.S. Thesis, Virginia Polytechnic Institute, Blacksburg, Virginia (1969).
17. P.C. Paris and G.C. Sih, "Stress Analysis of Cracks," pp. 30-81, *Fracture Toughness Testing and Its Applications*, ASTM-STP-381, American Society for Testing and Materials, Philadelphia, Pennsylvania (1965).
18. P.C. Paris, *Application of Muskhelishvili's Methods to the Analysis of Crack Tip Stress Intensity Factors for Plane Problems, Part 3*, Lehigh University, Institute of Research, Bethlehem, Pennsylvania (1960).

# STRESS INTENSITY FACTOR FOR A STRAIGHT CRACK APPROACHING A CIRCULAR HOLE

by

A.S. Kobayashi and D.E. Maiden

University of Washington  
 Department of Mechanical Engineering  
 Seattle, Washington

## I. INTRODUCTION

A practical problem which occurs in riveted structures, such as an aircraft wing, is the study of the arrest capability of a stiffener or of a rivet hole in front of a crack propagating by fatigue or by rapid fracture. Such two-

dimensional structure analysis is not only complicated by the presence of a hole but also by the presence of stiffeners and rivets which form a redundant structure with stiffness varying with crack geometry.

Several investigators have considered this problem

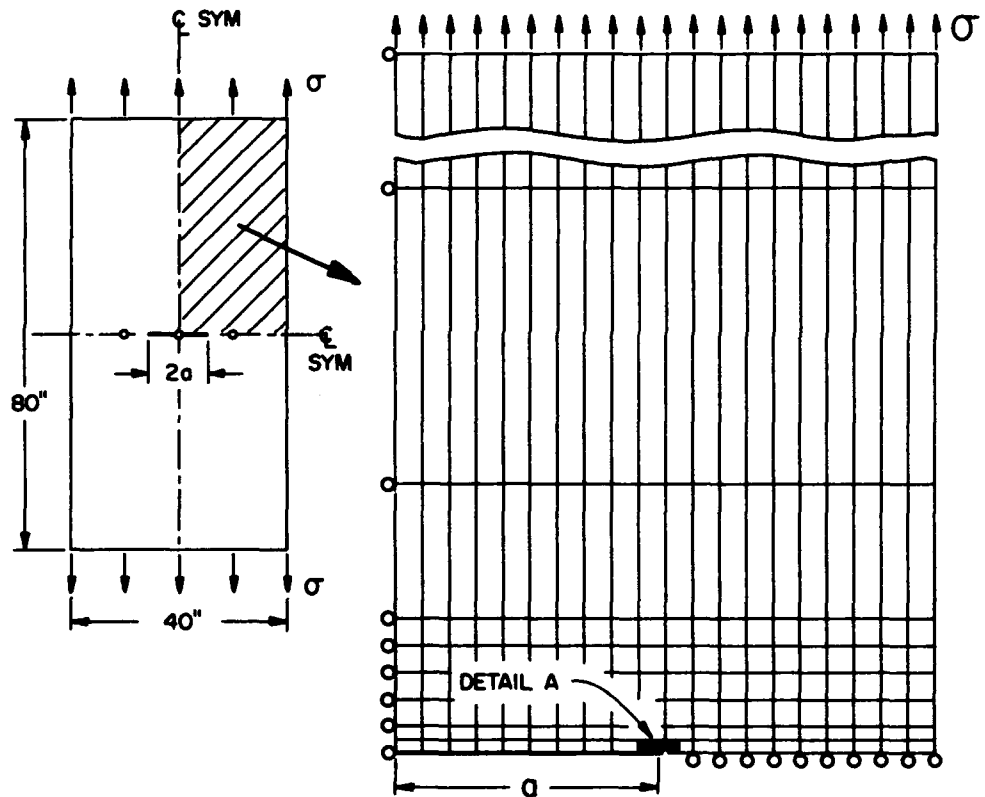
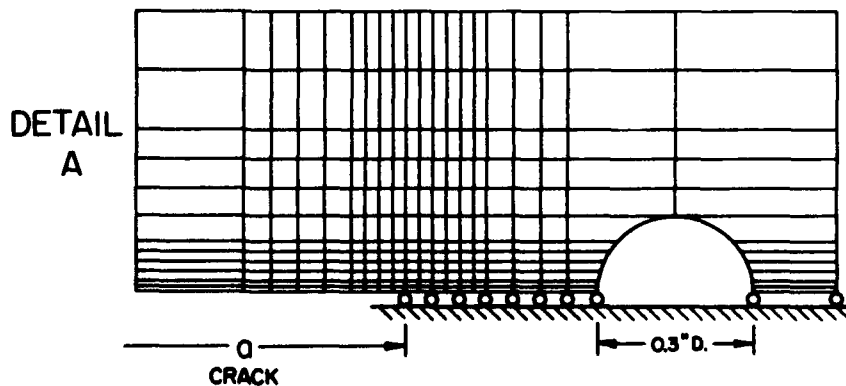


Figure 1. Centrally Cracked Plate with Rivet Holes, Subjected to Uniaxial Tension.

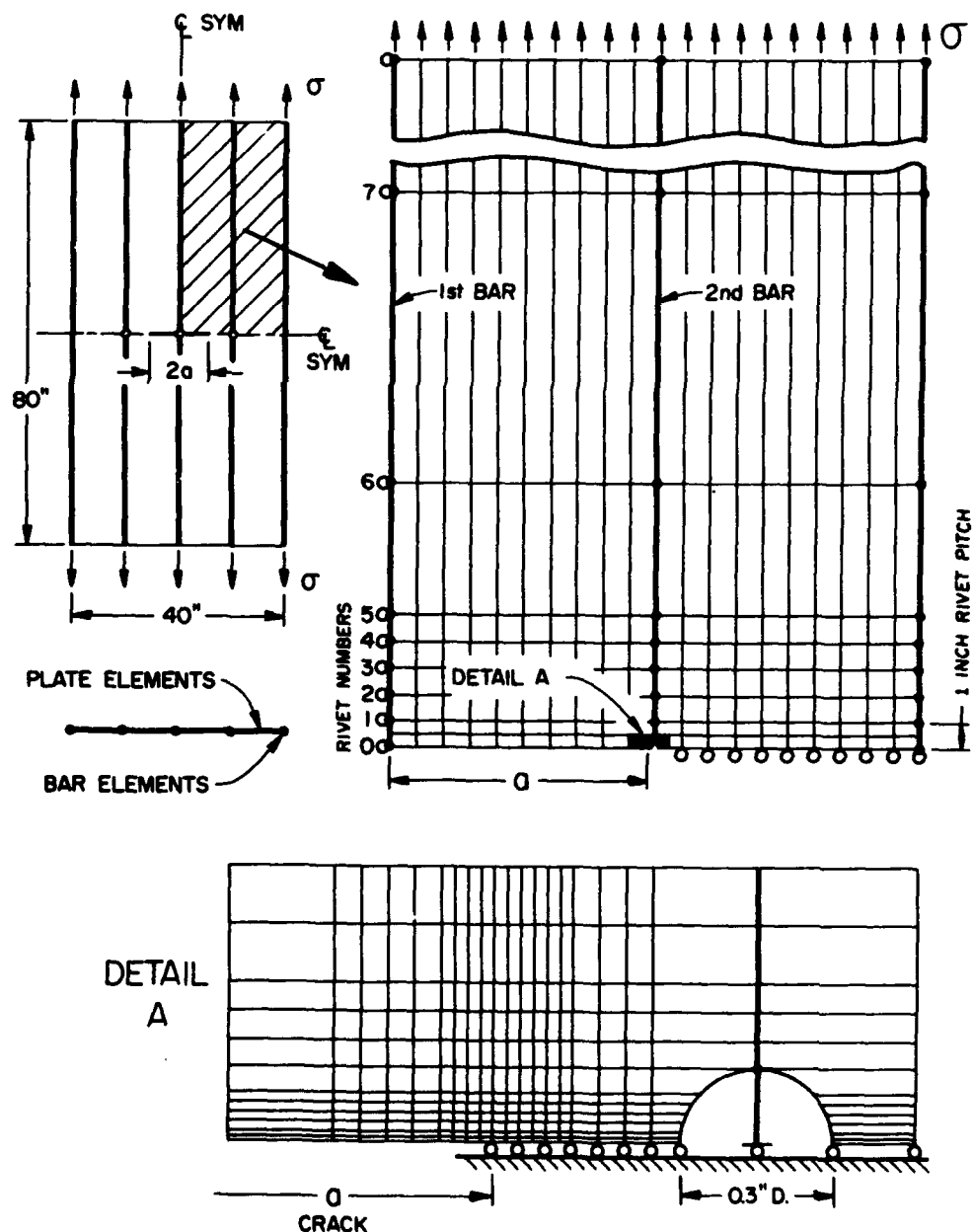


with various simplifying assumptions necessary for deriving elastic solutions. The pioneering work of Reference 1 was continued in References 2 and 3 by simulating the rivet forces on the stiffener with concentrated forces distributed along the stiffener but applied to a cracked infinite plate without rivet holes. In References 4, 5 and 6, the stiffener was considered to be continuously welded to the plate<sup>†</sup> and the effects of the stringer rigidity on the stress intensity factor of a central crack in the stiffened panel were studied. In all references cited above, the effect of the presence of holes was not considered due to the increased complexity which it would impose on this problem of elasticity.

In this paper, the fracture resistance of typical stringer reinforced panels of finite width and subjected to uniform tension was studied for the purpose of establishing a solu-

tion procedure. No attempt was made to organize a design manual on the fracture resistance of stringer reinforced panels. Typical panel structures with rivet holes used in this study are shown in Figures 1 and 2. The shearing forces between the stringers and the plate were assumed to be transferred only through tightly fitted rigid rivets and the friction force between stringers and the plate was ignored. Stringer stiffnesses of 0% (unstiffened panel as shown in Figure 1), 25%, 50% and 75% of the plate stiffness were considered. The two stringers on the edges of the plate were assumed to have one-half of the cross-section of the interior stringers so that the stringer reinforced panel could be considered as a portion of the total structural assembly. The rivet pitch of the panel was assumed to be 1 inch so that one can consider the problem as though all linear dimensions were normalized by the rivet pitch. The tensile load

Figure 2. Centrally Cracked Plate with Riveted Stiffeners, Subjected to Uniaxial Tension.



<sup>†</sup> This type of crack arresting stiffener is used in welded ship hulls.<sup>7,8</sup>



on the panel was assumed to be  $\sigma$  psi so that all stress values should be normalized with respect to the applied load. The crack was assumed to initiate at the rivet hole located at the center of the panel and to propagate symmetrically outwards towards its two neighboring rivet holes.

Linear fracture mechanics was used to assess the crack propagation rate and hence the possibility of fracture arrest in these panels. The stress intensity factors and the strain energy release rates were determined as the propagating crack tip approaches and jumps through adjoining rivet holes.

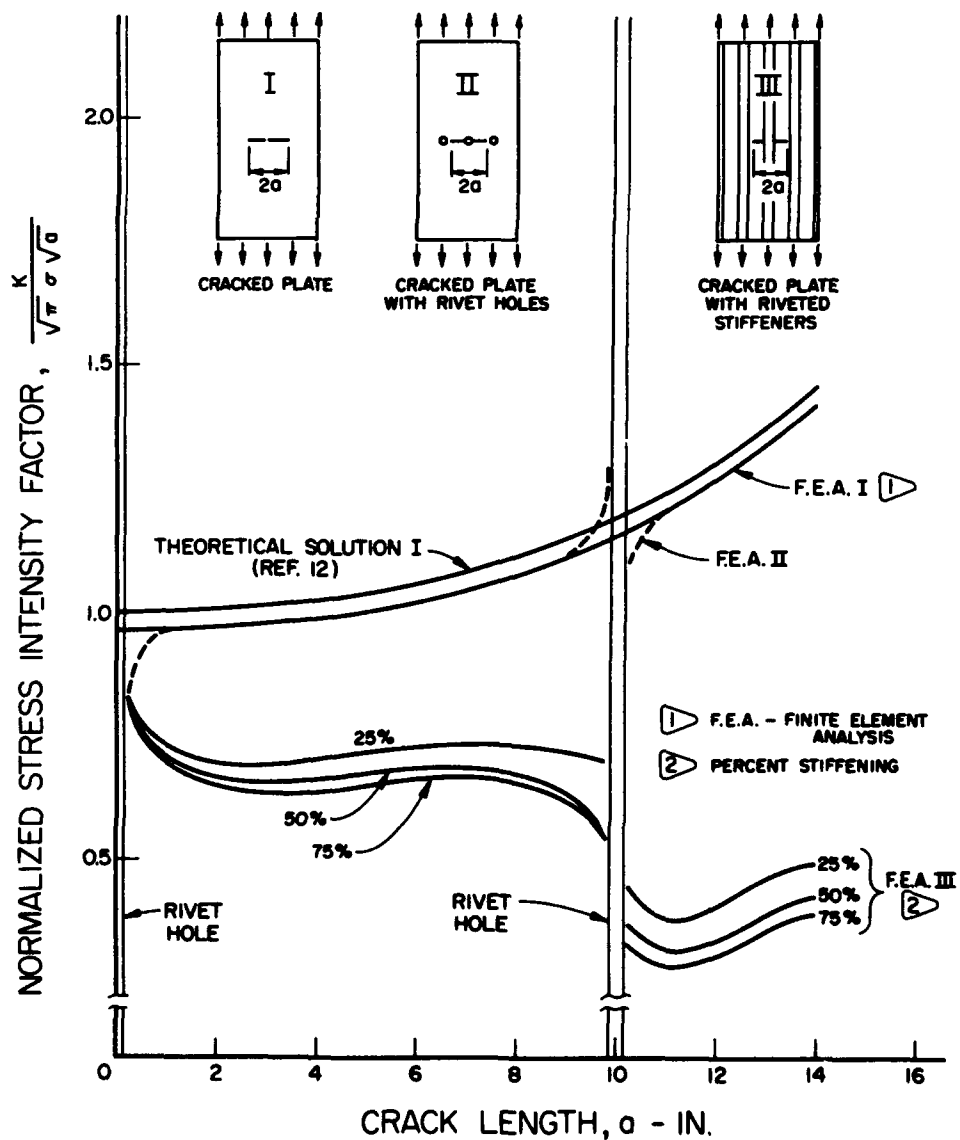
## II. METHOD OF APPROACH

As mentioned earlier, published and some unpublished literature regarding this subject is based on an approximate analysis by the use of two-dimensional theory in elasticity. The writers chose to use the numerical method of finite element analysis which allowed a more exact modeling of the actual cracked panel. No description of the method

of finite element analysis will be given here since the method is widely used and is well described in standard texts, such as Reference 9.

Due to symmetry of the problem, only a quadrant of the entire stiffened panel with appropriate symmetry requirements was necessary for analysis. Typical finite element idealizations of the centrally cracked panel thus considered are also shown in Figures 1 and 2. Note that rivets 5 inches away from the horizontal line of symmetry were no longer considered to exist at 1 inch intervals since the stiffener reaches the uniform state of the applied stress  $\sigma$  at this distance. Such simplification was necessary to reduce the number of finite element nodes in order to reduce the computational time involved. 1000 nodes were used for the plate and the vertical stringers were represented by bar elements between nodes (rivets) and with total cross sections of 25%, 50% and 75% of the plate cross section. The rivet holes in line with the propagating crack were assumed to be completely unloaded from symmetry requirement.

Figure 3. Stress Intensity Factor in Centrally Cracked Plates without Rivet Holes, with Rivet Holes, and with Riveted Stiffeners, all Cases Subjected to Uniaxial Tension.



The stress intensity factor of the crack tip was computed from the crack opening displacement ( $v$ ) following the procedure described elsewhere<sup>10,11</sup>. For this symmetric problem, only the opening mode exists and thus stress intensity factor of  $K_1$  was determined by the near field solution of the plane stress problem-as

$$K_1 = \frac{(1+\nu)G}{2} \sqrt{\frac{2\pi}{r}} v$$

where  $G$  and  $\nu$  are the shear modulus and Poisson ratio of the aluminum panel, respectively.

$r$  is the distance from the crack tip to the finite element node on the crack surface.

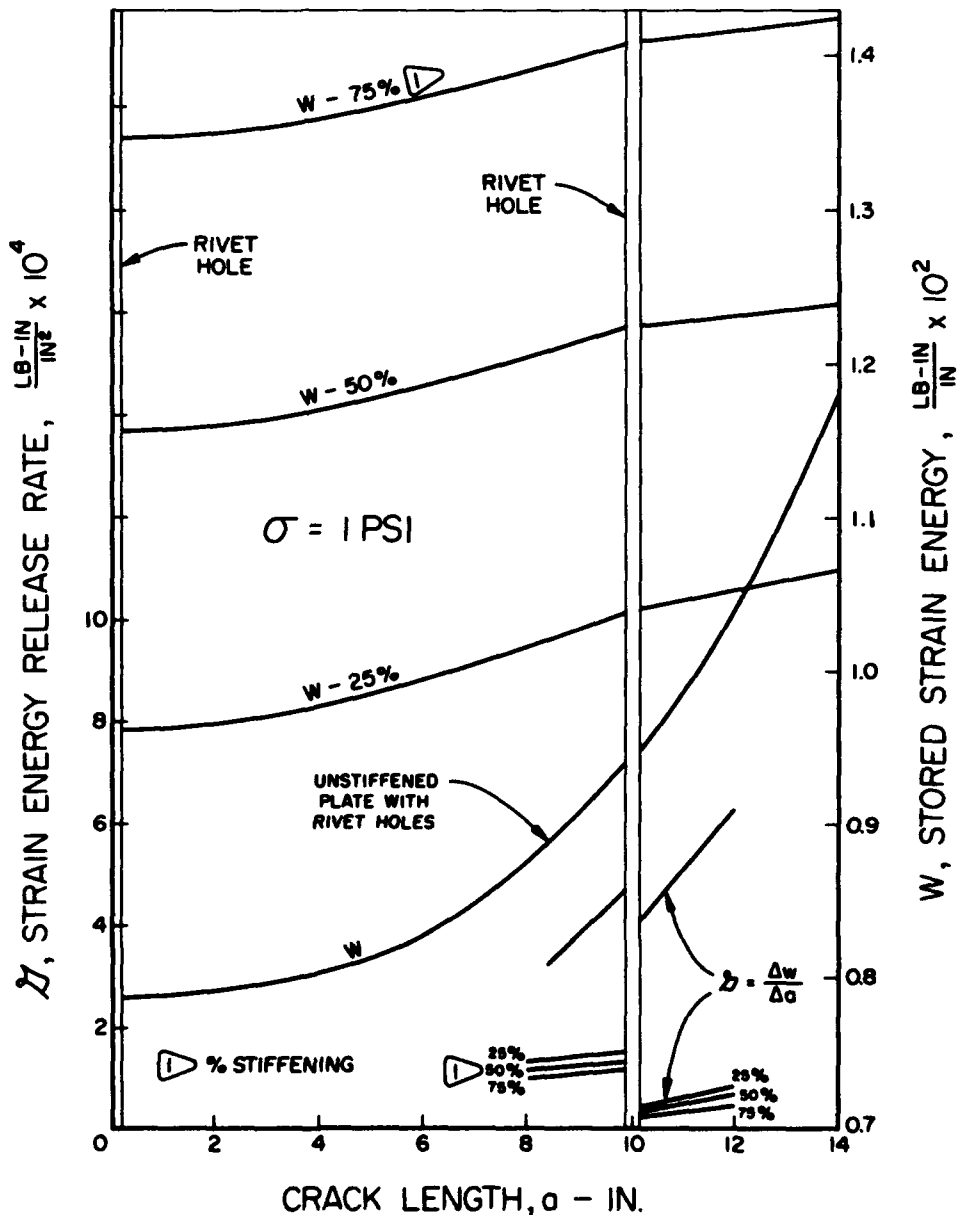
Also the strain energy release rate,  $\mathcal{G}$ , and the strain energy which is instantaneously released as the crack

penetrates its neighboring rivet hole and emerges from the other side of the hole, were computed. For this purpose changes in stored elastic energy with respect to extending crack length were determined. The above computation was continued across the rivet hole by assuming a pre-existing small flaw on the other side of the rivet hole and the stress intensity factors and stored strain energy were further computed. For elastic analysis of a cracked structure, the strain energy release rate can be determined with better numerical accuracy by using the relation of

$$\mathcal{G} = \frac{K_1^2}{E}$$

For a crack tip blunted by the rivet hole, the above relation could not be used and thus the change in the slopes of the extrapolated stored elastic energy curves on two sides of the rivet hole was determined. This quantity then represents the change in strain energy released by the crack jumping across the rivet hole.

Figure 4. Strain Energy Release Rate and Strain Energy in Plates With Rivet Holes and Plates With Riveted Stiffeners, All Subjected to Uniaxial Tension.



### III. RESULTS

Calculations were carried out for the following four cases of unstiffened panel, 25% stiffener, 50% stiffener, and 75% stiffener. Figure 3 shows the normalized stress intensity factor (normalized in terms of the equivalent stress intensity factor of an infinite plate with central crack and subjected to uniaxial tensile stress,  $\sqrt{\pi} \sigma \sqrt{a}$ ) with respect to crack length of  $a$  in the unstiffened and stiffened panels. Figure 4 shows the stored strain energies in the panels for various crack lengths as well as changes in strain energy release rates as the crack jumps across the rivet hole. Figure 5 shows the variations of stresses in the three stiffeners straddling the extending crack.

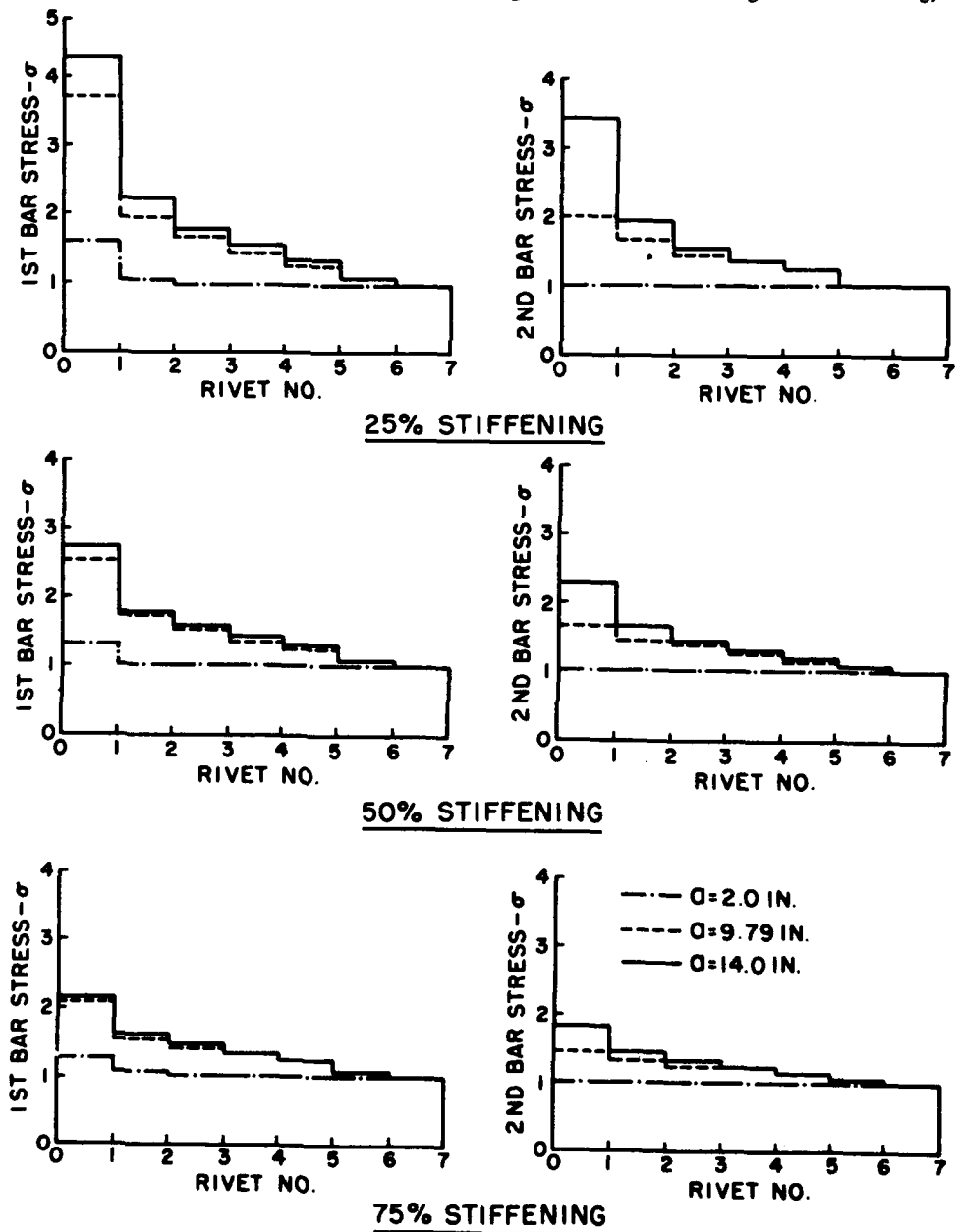
### IV. DISCUSSION OF RESULTS

Once the crack tip is sufficiently away from the

starter hole, the stress intensity factor for the unstiffened panel follows that of finite plate without rivet holes until the crack tip approaches the neighboring hole. The 3-4% mismatch between the theoretical curve<sup>12</sup> and the computed curve for an unstiffened plate in this region represents the numerical error involved in the finite element analysis. Theoretically, the stress intensity factor will then approach infinity as the crack is about to break through the hole. Our calculation also shows this trend but in real engineering materials such as aluminum the plastic yield zone ahead of an extending crack will connect through to the hole and will accelerate the crack extension rate as the crack tip approaches the hole.

In Figure 4, a discontinuity in the slope of the stored elastic energy and hence in the strain energy release rate is observed as the crack jumps across the hole. In order to estimate the significance of this change in strain energy re-

Figure 5. Stiffener Stresses As A Function of the Applied Stress  $\sigma$  for Various Crack Lengths -  $a$ .



lease rate, we will postulate that the dynamic stress intensity factor for a crack propagating with constant velocity in a brittle material is approximately 30 to 40% higher than the corresponding static stress intensity factor following our limited experimental evidences involving dynamic photoelasticity<sup>13,14</sup>. We can then deduce that the dynamic strain energy release rate for a running crack can be approximately 70% higher than the static values by the misuse of

$$\mathcal{G} = \frac{K_1^2}{E}$$

Figure 4 now represents the dynamic strain energy release rate within a scaling factor of, say, 1.7 for the running crack.

The arrest capability of the hole ahead of the running crack can be estimated by studying the drop of the strain energy release rate as the crack jumps across the hole. Again from our limited experimental evidences quoted above, the arrest strain energy release rate is approximately 45% lower than the critical strain energy release rate,  $\mathcal{G}_c$ . In the case of the unstiffened panel in Figure 4, this drop is only 10% of the strain energy release rate of the running crack so our theory predicts that there is no chance that the crack will be arrested when it penetrates through the hole. A larger hole would obviously increase the amount of this drop in strain energy release rate and therefore one could establish such minimum hole size by repeating this computational procedure for enlarged holes. For three cases of stiffened panel, the drop in strain energy release rate as the crack jumps across the rivet hole is approximately 75% of average strain energy release rate and thus the crack will be

arrested at the rivet hole and probably before it reaches the rivet hole.

Returning to Figure 3, the stress intensity factors for stiffened panels show marked decreases as the crack approaches the rivet hole, which is the reversed trend of an unstiffened panel. Simultaneously the stresses in the central stringer and the adjacent stringers increase rapidly with crack extension, as shown in Figure 5. Figure 3 shows that the crack will initially propagate rapidly, but then slow down to a constant rate and will be arrested as it approaches the hole. For real materials with the yield zone reaching the hole, the crack will still be arrested due to the large drop in strain energy release rate as described previously. Additional studies, such as the effect of loosely fitting rivets, can be studied by this procedure by assigning a free movement of the rivet node to move a prescribed displacement before loading the stringer. Comparison between the stress intensity factors of unstiffened and stiffened panels in Figure 3 indicates that the tightness in rivet fittings will have significant effects on the magnitude of stress intensity factors as the crack tip approaches the rivet hole as well as the arrest capability of the panel.

#### ACKNOWLEDGEMENT

This investigation was supported by the Office of Naval Research, Contract Nonr-477(39), NR 064 478. The writers wish to thank Mr. J.M. Crowley and Dr. N. Basdegas of ONR for their encouragement during the course of this investigation.

## REFERENCES

1. J.P. Romualdi, J.T. Frasier, and G.R. Irwin, *Crack Extension Forces Near a Riveted Stiffener*, NRL-4956, Naval Research Laboratory, Washington, D.C. (1957).
2. J.P. Romualdi and P.H. Sanders, "Fracture Arrest by Riveted Stiffeners," pp. 74-90, *Proc. 4th Midwestern Conf. Solid Mech.*, University of Texas, Austin, Texas (1959).
3. J.P. Romualdi, "Fracture Arrest Design Considerations," *Proc. Crack Propagation Symp.*, Vol. II, College of Aeronautics, Cranfield, England (1961).
4. M. Isida and Y. Itagaki, "Stress Concentration at the Tip of a Central Transverse Crack in a Stiffened Plate Subjected to Tension," *Proc. 4th U.S. Natl. Congr. Appl. Mech.*, 2:955-969 (1962).
5. R. Grief and J.L. Sanders, Jr., "The Effect of a Stringer on the Stress in a Cracked Sheet," *J. Appl. Mech.*, 32/1:59-66 (1965).
6. J.I. Bluhm, "Fracture Arrest," pp. 1-63; H. Liebowitz, Ed., *Fracture: An Advanced Treatise*, Vol. V, Academic Press, New York (1969).
7. H. Kihara, T. Kanazawa, K. Ikeda, et al., "Effectiveness of Crack Arresters - I," Paper 2-3, *Proc. Fall Meeting Japan. Soc. Naval Architect.* (1967).
8. H. Kihara, T. Kanazawa, K. Ikeda, et al., "Effectiveness of Crack Arresters - II," Paper 1-15, *Proc. Fall Meeting Japan. Soc. Naval Architect.* (1968).
9. O.C. Zienkiewicz and Y.K. Cheung, *The Finite Element Method in Structural and Continuum Mechanics*, McGraw-Hill, New York (1967).
10. A.S. Kobayashi, D.E. Maiden, B.J. Simon, and S. Iida, *Application of the Method of Finite Element Analysis to Two-Dimensional Problems in Fracture Mechanics*, ASME Paper 69-WA/PVP-12, American Society of Mechanical Engineers, New York (1969).
11. S. Iida and A.S. Kobayashi, *Crack Propagation Rate in 7075-T6 Plates Under Cyclic Tensile and Transverse Shear Loading*, ASME Paper 69-MET-J, American Society of Mechanical Engineers, New York (1969).
12. R.G. Forman and A.S. Kobayashi, "On the Axial Rigidity of a Perforated Strip and Strain Energy Release Rate in a Centrally Notched Strip Subjected to Uniaxial Tension," *J. Basic Eng.*, 86:693-699 (1964).
13. W.B. Bradley and A.S. Kobayashi, "An Investigation on Propagating Cracks by Dynamic Photoelasticity," *J. Exp. Mech.*, to be published.
14. W.B. Bradley and A.S. Kobayashi, *Fracture Dynamics -- A Photoelastic Investigation*. Presented at the 3rd U.S. National Symposium on Fracture, Lehigh University, Bethlehem, Pennsylvania, August 1969.

# AN EFFECTIVE STRAIN CONCEPT FOR CRACK PROPAGATION AND FATIGUE LIFE WITH SPECIFIC APPLICATIONS TO BIAXIAL STRESS FATIGUE

by

E.K. Walker

Materials Research Laboratory  
Lockheed - California Company

## LIST OF SYMBOLS

<p><math>a</math> = 1/2 crack length</p> <p><math>C</math> = A derived constant for a selected condition of biaxial stress</p> <p><math>d(2a)/dN</math> = Crack growth rate, micro-inches/cycle</p> <p><math>E</math> = Young's modulus, psi (kg/mm<sup>2</sup>)</p> <p><math>\bar{\Delta} K</math> = Effective stress intensity parameter, <math>\beta \bar{S} \sqrt{\pi a}</math>, ksi <math>\sqrt{\text{in.}}</math></p> <p><math>N</math> = Cycles of loading, crack growth; cycles to failure, fatigue life</p> <p><math>P_{x,y}</math> = Principal stresses, psi (kg/mm<sup>2</sup>)</p> <p><math>\Delta P_{x,y}</math> = Principal stress ranges, psi (kg/mm<sup>2</sup>)</p> <p><math>R</math> = Stress ratio, <math>S_{\min}/S_{\max}</math></p> <p><math>S</math> = A maximum or a minimum cycle stress, psi (kg/mm<sup>2</sup>)</p> <p><math>S_{\max}</math> = Maximum stress, psi (kg/mm<sup>2</sup>)</p> <p><math>S_{\min}</math> = Minimum stress, psi (kg/mm<sup>2</sup>)</p>	<p><math>\Delta S</math> = Stress range (<math>S_{\max} - S_{\min}</math>), psi (kg/mm<sup>2</sup>)</p> <p><math>\bar{S}</math> = Effective stress under uniaxial loading <math>\Delta S^m S_{\max}^{1-m}</math>, psi (kg/mm<sup>2</sup>)</p> <p><math>\bar{S}_v</math> = Volumetric effective stress <math>\frac{\bar{\epsilon}}{v} E</math>, psi (kg/mm<sup>2</sup>)</p> <p><math>\beta</math> = Width correction factor</p> <p><math>\Delta \gamma_o</math> = Octahedral shearing strain range, percent</p> <p><math>\Delta \gamma_{x,y,z}</math> = Principal shearing strain ranges, percent</p> <p><math>\epsilon_{x,y,z}</math> = Principal normal strains, percent</p> <p><math>\epsilon_T</math> = Total volumetric strain = <math>\langle \epsilon_x \rangle^1 + \langle \epsilon_y \rangle^1 + \langle \epsilon_z \rangle^1</math></p> <p><math>\bar{\epsilon}_v</math> = Effective volumetric strain, percent</p> <p><math>\nu</math> = Poisson's ratio</p> <p><math>b,c,n</math> = Exponents</p> <p><math>m</math> = An exponent derived empirically from either crack propagation or uniaxial loading fatigue data (<math>m \leq 1</math>).</p>
--	--

## INTRODUCTION

This paper deals primarily with an observed underlying similarity of the influences of maximum stress on the propagation rates of cyclic loaded macro cracks and on fatigue life of unnotched specimens under uniaxial and biaxial loadings. This similarity was emphasized in part in a recent paper on stress ratio effects in aluminum alloys<sup>1</sup>. In Reference 1 it was demonstrated that an effective stress of the form:

$$\bar{S} = (S_{\max})^{1-m} (\Delta S)^m \quad (1)$$

provided a simple means for correlating both cracking rate data and uniaxial load fatigue data. These crack propagation and fatigue data correlations will be briefly reviewed in terms of variations in induced triaxial stress states. This

review will establish necessary background for a more general concept of effective strain which permits the effects of maximum stress to be treated in a singular manner for macro crack propagation and for fatigue life under both uniaxial and triaxial stress states.

### Effective Stress Concept

The derivation of effective stress is based on the observations of several investigators 2,3,4 who have proposed expressions for the propagation of macro cracks having the form;

$$\frac{d(2a)}{dN} = f \left[ \beta \left( S_{\max} \sqrt{\pi a} \right)^c \left( \Delta S \sqrt{\pi a} \right)^b \right] \quad (2)$$

This expression can be rewritten

$$\frac{d(2a)}{dN} = f \left[ \beta \left\{ \left( S_{\max} \sqrt{\pi a} \right)^{1-m} \left( \Delta S \sqrt{\pi a} \right)^m \right\}^n \right]$$

where  $1 - m = \frac{c}{c + b}$

$$m = \frac{b}{c + b}$$

$$n = c + b$$

Since the product of the two stress terms now has the dimensions of stress, an effective stress,  $\bar{S}$ , can be defined (see Equation 1). An expression having the same form as Equation (2) can now be written using the effective stress.

$$\frac{d(2a)}{dN} = f \left[ \beta \left( \bar{S} \sqrt{\pi a} \right) \right] = f \left[ \bar{\Delta} K \right] \quad (3)$$

### Effective Stress Applications

Figure 1 shows data for crack growth in 2024-T3 and 7075-T6 aluminum<sup>2</sup> as plotted using the effective stress intensity  $\bar{\Delta}K$  (1). In Figure 1, the effective stress intensity was computed using  $m = 1/2$ . Figure 2 shows a similar plot for 301.1/2 H stainless sheet. Figure 2 data are from tests of 8-inch wide, 0.12-inch thick sheet cycled at 600 cpm. In Figure 2, a value of  $m = 2/3$  was used for computing  $\bar{\Delta}K$ . Values of  $m$  for Figures 1 and 2 were obtained for best fit using available computer routines. From data given in Reference 1, values of  $m$  of approximately 1/2 may be typical of aluminum alloys.

Crack propagation in Figure 1, occurred in both the tensile and shear modes. From data given in Reference 2, the transitions between tensile and shear mode cracking occurred near a  $\bar{\Delta}K$  of about 13 ksi  $\sqrt{\text{in}}$  for 2024-T3 aluminum. The transition of 7075-T6 aluminum was at a slightly lower  $\bar{\Delta}K$ . If the transition between tensile to

shear mode cracking is, as suggested in Reference 5, the change from a triaxial to biaxial state of stress near the crack tip, then, the value of  $m$  does not appear to be significantly influenced by this change in stress state.

Figure 3 shows data for unnotched fatigue coupons of 2024-T3 aluminum<sup>6</sup> as correlated with the effective stress  $\bar{S}$  (Reference (1)). These data for sheet coupons represent a nearly uniaxial stress condition. Figure 4 shows data for sharply notched round coupons of 2024-T3 aluminum<sup>7</sup>. The data of Figure 4 represent a highly triaxial stress condition and most likely a predominantly elastic notch stress strain behavior. In both Figures 3 and 4, the influence of maximum stress appears to be adequately predicted by an effective stress based on  $m = 1/2$ .

From the data shown for crack propagation and fatigue life under uniaxial loading, it is apparent that the effects of maximum stress are approximately the same over a wide range of stress states. These stress states include those of tensile and shear mode macro crack propagation, stress states of unnotched sheet fatigue coupons and stress states of sharply notched round fatigue coupons.

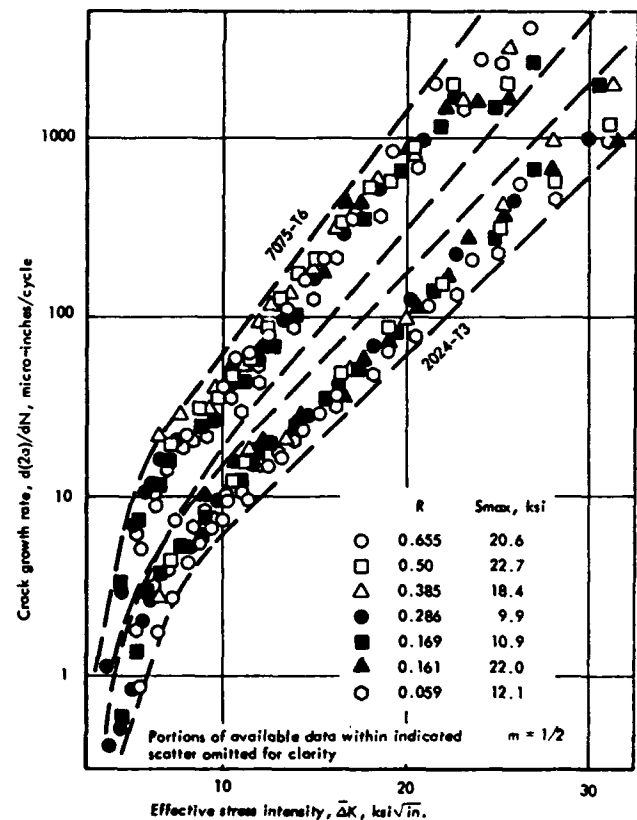
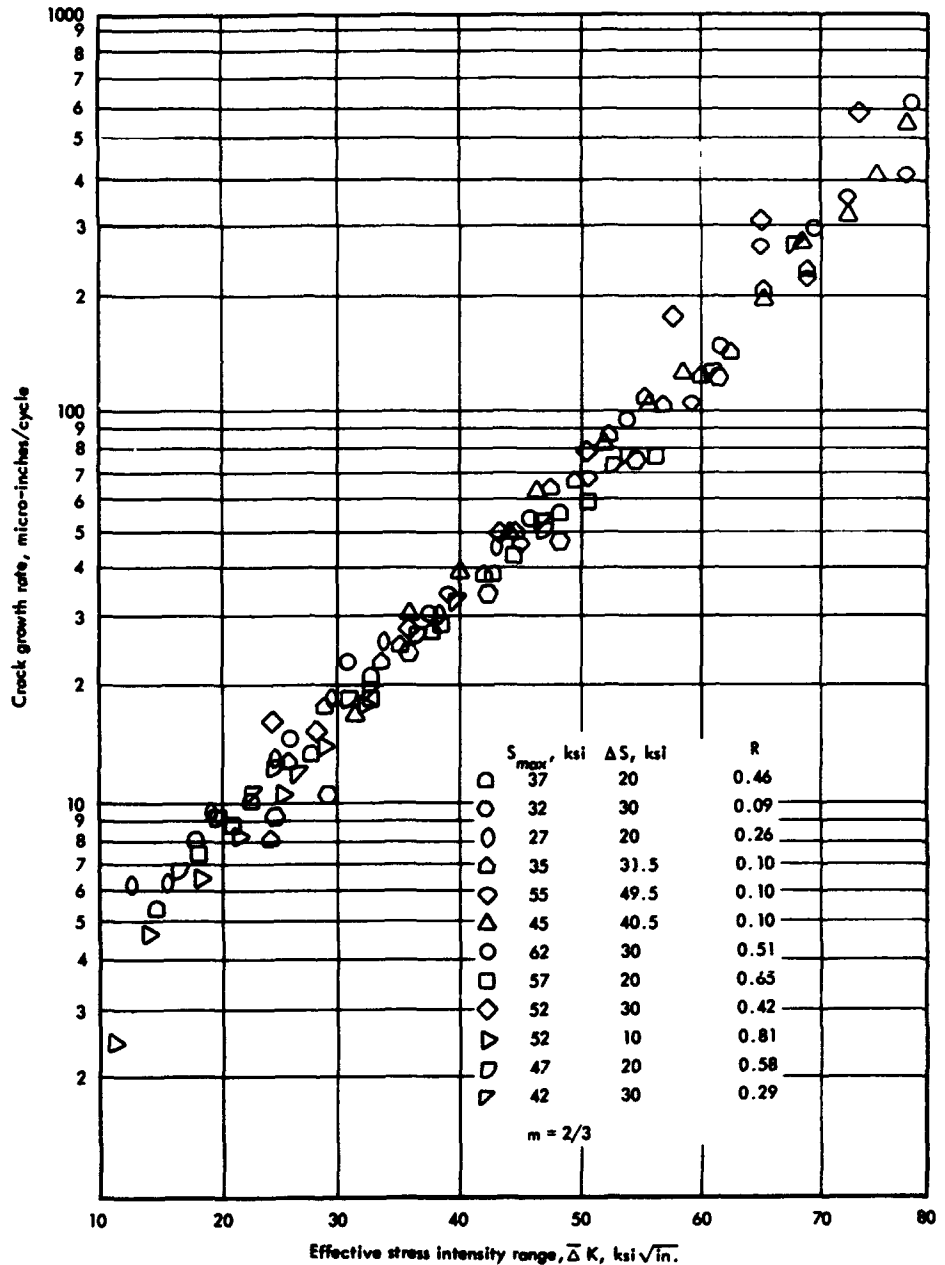


Figure 1. Crack Growth in 2024-T3 and 7075-T6 Aluminum.

Figure 2. Crack Growth in 301-1/2 H Stainless Steel.



## DISCUSSION

### Biaxial Loading Fatigue

From the observed independence of a  $m$  on stress state, the possibility that the exponent  $m$  might be of direct significance to fatigue under multiaxial loading is suggested. To explore the possibility of such a significance, the following ground rules were established:

1. The expression for effective stress  $\bar{S}$  should be generalized in a manner such that for a specific case of triaxiality, the expression would reduce to:

$$C (\Delta S)^m (S_{max})^{1-m}$$

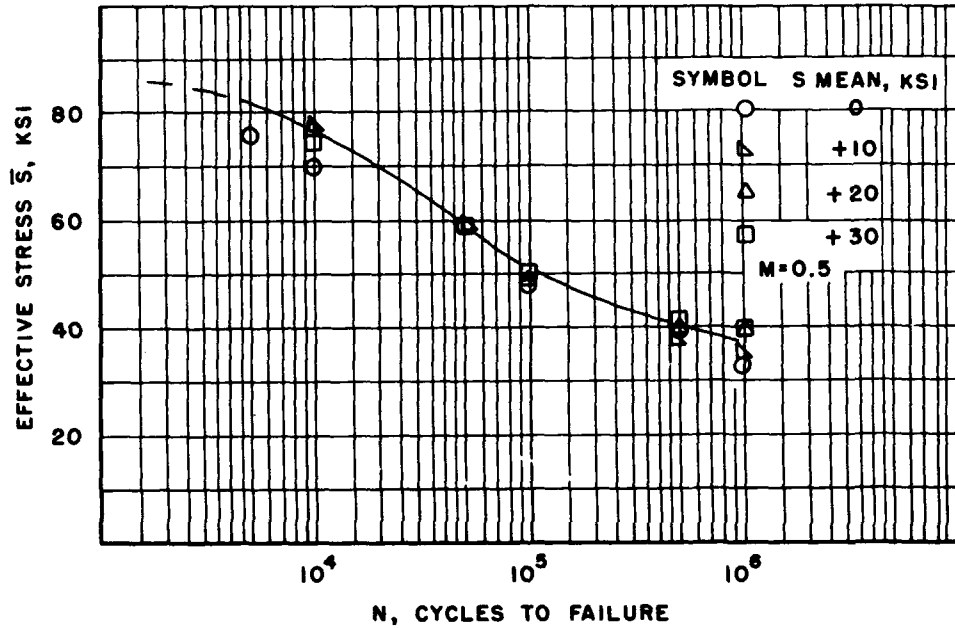
2. The only empirically derived parameter would be the exponent  $m$ .

3. The expression could employ easily obtained bulk properties such as moduli and Poisson's ratios.

With the foregoing ground rules, literature on multi-



Figure 3. Unnotched Fatigue, 2024-T3 Aluminum.



axial loading fatigue were reviewed.

The concept of relating fatigue under multiaxial loading to stress range and maximum stress parameters have been considered 8,9,10. However, the approach in these references is to add effects of stress range and maximum stress rather than to multiply these effects as suggested by Equation (1). Further, the coefficients resulting from these additive relationships are not constant when the effect of stress ratio is considered or alternately, are not constant with changes in fatigue life. From the papers reviewed, and with the established ground rules in mind, the concepts considered most promising were those proposed

by Sines<sup>8</sup> and Crossland<sup>9</sup> and by Shewchuk, Zamrik and Marin<sup>11</sup>.

Sines recommended modifying the alternating octahedral shear stress by an additive parameter involving the mean hydrostatic stress invariant. Crossland modified the alternating octahedral shear stress by the maximum hydrostatic stress. Shewchuk, et al, related biaxial stress fatigue to the octahedral shearing strain and introduced approximate solutions for combined elastic and plastic strains and for material anisotropy. The work of Shewchuk, et al, was limited to biaxial stresses between uniaxial and equal biaxial tension so that judging from the data summarized

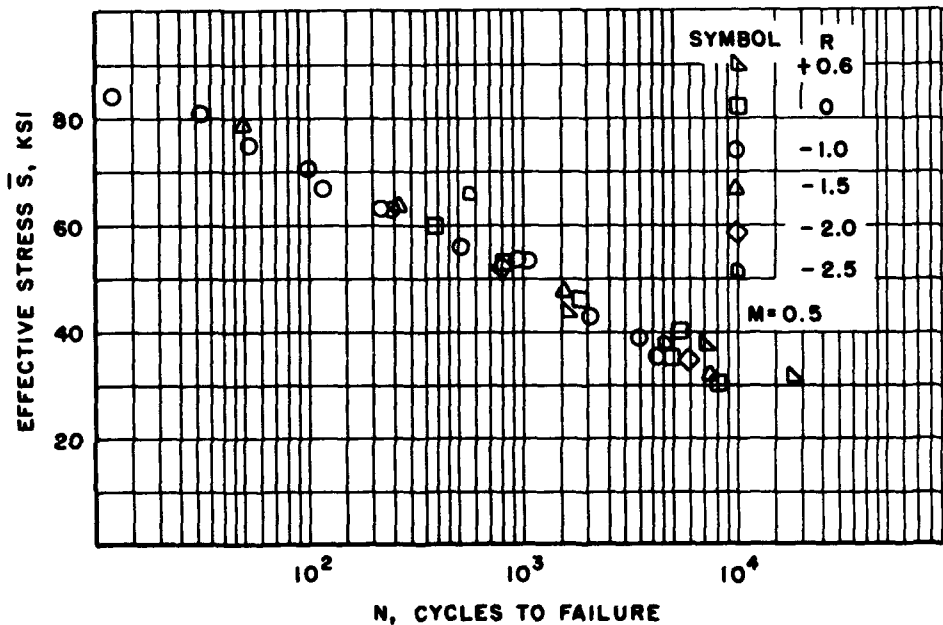


Figure 4. Fatigue Life for  $K_T = 5$  Notch Round Specimens, 2024-T3 Aluminum.

by Sines, the modifying effect of a mean hydrostatic stress or a similar term would be of little significance. Shewchuk et al did not consider the effects of mean or maximum stresses. From the above papers, it was decided that the most promising approach to providing a meaningful relationship for multiaxial stress fatigue would be to consider modifications of the octahedral shearing strain which would satisfy the established ground rules involving the exponent  $m$ .

### Effective Strain Concept

Possible adaptations of the octahedral shearing strain equation were studied by comparing the computed constants to constant life biaxial loading fatigue data summarized by Sines and as also used by Yokobori and Yoshimura<sup>12</sup>. From the study, one formulation demonstrated merit both for its simplicity and for agreement with data. This formulation defines an "effective volumetric strain"  $\bar{\epsilon}_v$ .

The effective volumetric fatigue strain = (Octahedral Shearing Strain Range) <sup>$m$</sup>  (Total Extensional Strain) <sup>$1-m$</sup> .

$$\bar{\epsilon}_v = (\Delta\gamma_o)^m (\epsilon_T)^{1-m}. \quad (4)$$

The effective volumetric fatigue strain  $\bar{\epsilon}_v$  is related to the effective volumetric fatigue stress  $\bar{S}_v$ :

$$\bar{S}_v = E \bar{\epsilon}_v. \quad (5)$$

The interpretation of Equation (4) can best be illustrated in terms of the simple case of biaxial stress fatigue in an isotropic elastic material. The loading cases considered in the example will be limited to those in which the loads are in phase i.e. principal strains reaching extreme values simultaneously).

For the conditions set forth for the example, the octahedral shearing strain range can involve both a change in principal strain magnitudes and in orientation of the octahedral shear plane. Perhaps the simplest way of treating this is to express  $\Delta\gamma_o$  as the vector difference between extreme values. This approximation implies that the fatigue behavior is not sensitive to the sequence of intermediate strains (path independent):

$$\Delta\gamma_o = \frac{2}{3} \sqrt{\Delta\gamma_x^2 + (\Delta\gamma_x - \Delta\gamma_y)^2 + \Delta\gamma_y^2}. \quad (6)$$

For the case of biaxial stress in an isotropic elastic material:

$$\Delta\gamma_o = \frac{2}{3} \frac{(1+\nu)}{E} \sqrt{\Delta P_x^2 + (\Delta P_x - \Delta P_y)^2 + \Delta P_y^2}. \quad (7)$$

The concept of total extensional strain is arrived at by considering compressive strains as having no effect. Whereas in normal mathematical treatment involving volume change, compressive strains mathematically cancel tensile strains, here as a first approximation of fatigue behavior, they are not considered to do so.

$$\epsilon_T = \langle \epsilon_x \rangle^1 + \langle \epsilon_y \rangle^1 + \langle \epsilon_z \rangle^1, \quad (8)$$

where

$$\langle x \rangle^1 = x; \langle -x \rangle^1 = 0; \langle 0 \rangle^1 = 0.$$

For the case of biaxial stress in an isotropic elastic material:

$$\epsilon_T = \frac{1}{E} \left[ \langle P_x - \nu P_y \rangle^1 + \langle P_y - \nu P_x \rangle^1 + \langle -\nu P_x - \nu P_y \rangle^1 \right]. \quad (9)$$

As will be shown, the concept of  $\epsilon_T$  is supported by the correlations with available biaxial fatigue data. It could also be supported by considerations of flaw growth during fatigue life.

Introducing Equations (7) and (9) and (5) as approximations for  $\Delta\gamma_o$ ,  $\epsilon_T$ , and  $E \bar{\epsilon}_v$  into Equation (4) will give an expression for biaxial stress fatigue in an isotropic elastic material

$$\bar{S}_v = \left[ \frac{2}{3} (1+\nu) \sqrt{\Delta P_x^2 + (\Delta P_x - \Delta P_y)^2 + \Delta P_y^2} \right]^m$$

$$\left[ \langle P_x - \nu P_y \rangle^1 + \langle P_y - \nu P_x \rangle^1 + \langle -\nu P_x - \nu P_y \rangle^1 \right]^{1-m} \quad (10)$$

For the quantity  $\Delta\gamma_o$  of Equation (10), it is not important which principal stress range is designated as  $\Delta P_x$  or  $\Delta P_y$  as all quantities are squared and additive. For  $\epsilon_T$  in Equation (10), it is important to select the extreme principal stress state yielding the maximum  $\epsilon_T$ . As the applied tensile loadings become small with respect to the compressive loadings, the compressive loadings will produce the maximum value of  $\epsilon_T$ .

For example, in the simple case of uniaxial tension the cross-over point as defined by equating values of  $\epsilon_T$  for the tensile and compressive extremes of stress is:

$$\frac{S_{\min}}{S_{\max}} = R = \frac{-1}{2\nu}.$$

For such cases as equal biaxial tension and 2:1 biaxial tension it is possible to relate  $\Delta P_x$ ,  $\Delta P_y$  and  $P_x$ ,  $P_y$  in terms of applied stress  $S$  and stress range  $\Delta S$ .

For these cases Equation (10) will reduce to:

$$\bar{S}_v = C \Delta S^m S^{1-m} \quad (11)$$

Table I shows values of C for typical cases of biaxial loading. The selection of  $m = \frac{1}{2}$  in Table I as possi-

bly typical for many materials is based on data given in Reference 1. The selection of  $m = \frac{2}{3}$  was based on calculations for a nickel-chromium-molybdenum steel (Figure 5) and on crack propagation data for 8-inch wide, center notched sheets of 301-1/2 H stainless (Figure 2). Values of C as shown in Table I are used in conjunction with Equation (11) for computing the influence of biaxial loading.

TABLE I. TYPICAL SOLUTIONS FOR CASES OF BIAXIAL STRESS

Principal Stress State	Assumptions $P, \Delta P$	General Solution for C in $\bar{S}_v = C \Delta S^m S^{1-m}$ $\nu = \frac{1}{3}$	Values of C $m = \frac{1}{2}$	Values of C $m = \frac{2}{3}$
Uniaxial Tension	$P_x = S_{\max}, \Delta P_x = \Delta S$ $P_y = \Delta P_y = 0$	$(\frac{8}{9})^m (2)^{m/2} \Delta S^m S_{\max}^{1-m}$	1.13	1.17
1:1 Tension	$P_x = S_{\max}, \Delta P_x = \Delta S$ $P_y = S_{\max}, \Delta P_y = \Delta S$	$(\frac{8}{9})^m (2)^{m/2} (\frac{4}{3})^{1-m}$	1.28	1.30
1:1 Tension Compression	$P_x = S_{\max}, \Delta P_x = \Delta S$ $P_y = -S_{\max}, \Delta P_y = -\Delta S$	$(\frac{8}{9})^m (6)^{m/2} (\frac{4}{3})^{1-m}$	1.70	1.86
1:2 Tension	$P_x = S_{\max}, \Delta P_x = \Delta S$ $P_y = 2S_{\max}, \Delta P_y = 2\Delta S$	$(\frac{8}{9})^m (6)^{m/2} (2)^{1-m}$	2.09	2.11
1:2 Tension Compression	$P_x = S_{\max}, \Delta P_x = \Delta S$ $P_y = -2S_{\max}, \Delta P_y = -2\Delta S$	$(\frac{8}{9})^m (11)^{m/2} (2)^{1-m}$	2.43	2.59
Uniaxial Compression	$P_x = -S, \Delta P_x = \Delta S$ $P_y = 0, \Delta P_y = 0$	$(\frac{8}{9})^m (2)^{m/2} (\frac{2}{3})$	.92	.98

## Effective Strain Application

Figures 5 and 6 show the correlation between a curve of constant  $\bar{S}_v$  for cases given in Table I and biaxial load fatigue data for zero to tension pressure loading of a hollow cylinder with superimposed longitudinal stress. These data are taken from the compilation of Sines<sup>8</sup>. Figure 7 shows a similar correlation for superimposed bending and torsion<sup>8</sup>.

From the correlations of Figures 5, 6, and 7, the shape of the curve of constant  $\bar{S}_v$  is reasonably close to the data trend except in the region of zero to compression cycling. In this region, the extensional strains are Poisson induced in the transverse and short transverse grain directions of the cylinders. It is thus difficult to assess whether the poor correlation is the result of assumed isotropy or the result of conceptual error.

In Figures 5 and 6, the selection of  $m = \frac{1}{2}$  was arbitrary. The value of  $m$  does not significantly affect the

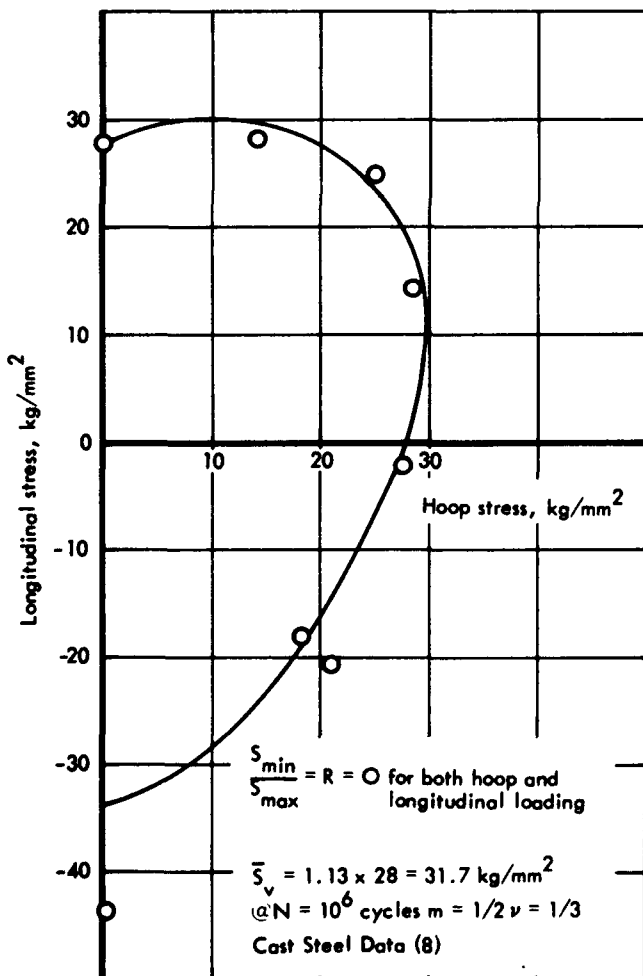


Figure 5. Combined Hoop Tension and Longitudinal Loading Fatigue of Cast Steel Cylinders.

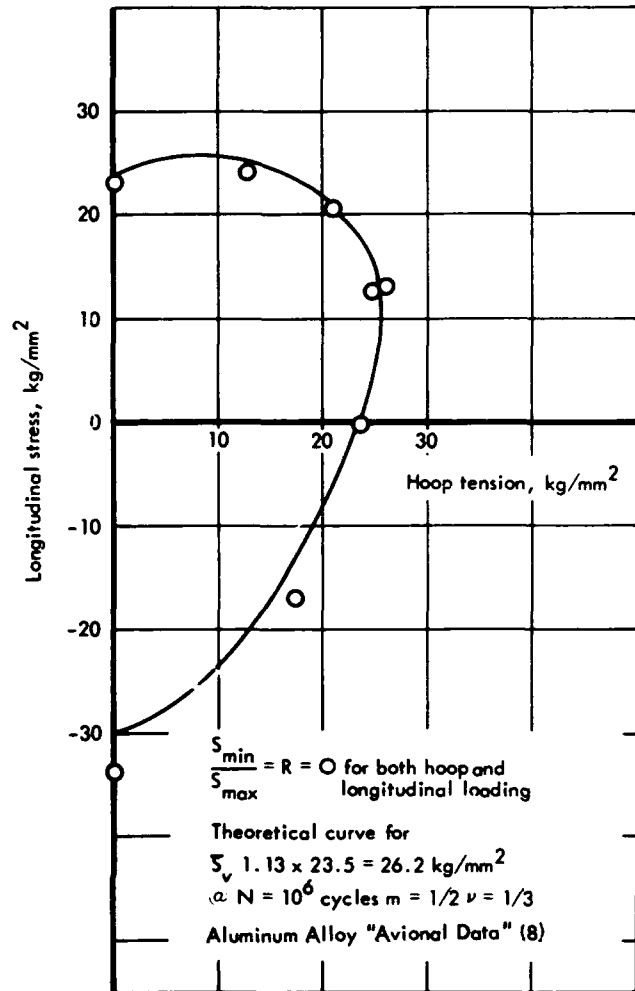


Figure 6. Combined Hoop Tension and Longitudinal Loading Fatigue of Aluminum Cylinders.

shape of the constant  $\bar{S}_v$  curve. In Figure 7 the selection of  $m = \frac{2}{3}$  was not arbitrary. This value of  $m$  was required to account for the shift in  $\bar{S}_v$  due to changes in mean stress. A value of  $m = \frac{2}{3}$  was independently found to fit cracking rate data for 301-1/2 H stainless steel (Figure 2). Thus, the possibility is presented that  $m$  may be constant for classes of materials. This deserves further study.

In Figures 1 through 4 showing macro crack propagation and uniaxial loading fatigue lives, no attempt was made to evaluate  $\bar{S}_v$ . These correlations therefore depend on  $C$  varying in a similar manner during crack propagation or during fatigue lives of similar geometry specimens. For macro crack propagation, a similar variation in  $C$  would require the transition from tensile to shear mode cracking to occur as a function of cracking rate. That this does in fact occur was noted by Broeck and Schijve<sup>2</sup>. This observation in a sense implies that cyclic plasticity ahead of a fatigue crack varies with  $\bar{\Delta K}$  and is thus responsive in a similar manner to any combination of max-

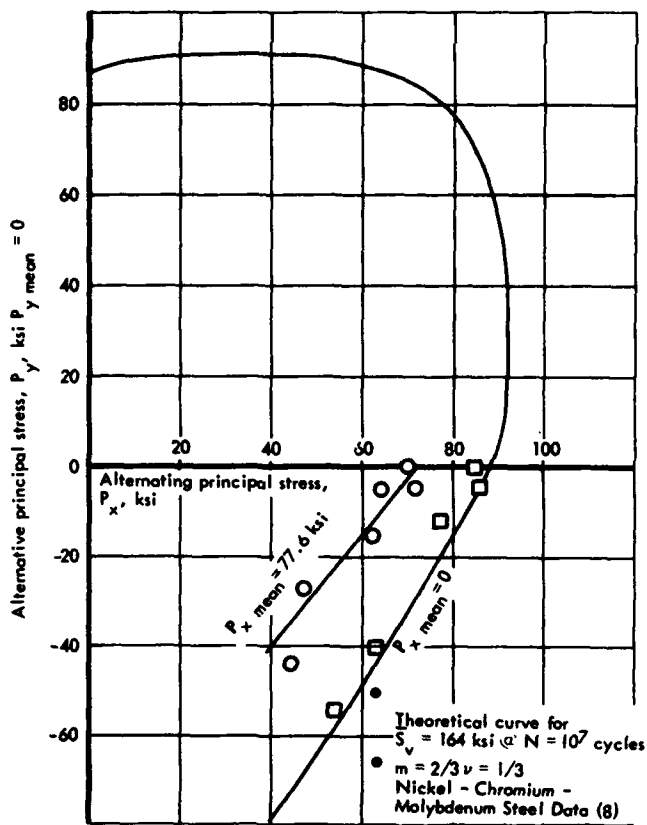


Figure 7. Combined Bending and Torsion Fatigue Showing Effect of Mean Bending Stress.

imum and alternating stress having a single value of  $\bar{S}$ . This point also deserves further study.

Figures 1 through 7 show a wide range of application of the effective strain concept and its simplified form effective stress. It has been demonstrated that the concept leads to relatively straight forward engineering calculations. Such possibilities as constant values of  $m$  for classes of materials, and relationships to cumulative cyclic strain naturally lead to speculation on fundamental significance. Such speculation while tempting is however premature. For the present the effective strain concept is offered for its unifying observations and for its obvious benefit to fatigue analysis.

### CONCLUSIONS

A concept of effective volumetric strain has been proposed and a working equation for biaxial loading fatigue has been derived. It has been shown that:

1. The concept is applicable to a wide range of fatigue phenomena including the propagation of macrocracks and uniaxial and biaxial loading fatigue.
2. The concept involves only one empirically derived parameter, the exponent  $m$ , which may prove to be constant for classes of materials.

## REFERENCES

1. K. Walker, "The Effect of Stress Ratio During Crack Propagation and Fatigue for 2024-T3 and 7075-T6 Aluminum," in *Fatigue - Effects of Environment and Dynamic Loading on Life Prediction*, ASTM-STP-462, American Society for Testing and Materials, Philadelphia, Pennsylvania (1968).
2. D. Broeck and J. Schijve, *The Influence of the Mean Stress on the Propagation of Fatigue Cracks in Aluminum Alloy Sheet*, NLR-TR-M.2111, National Lucht-en Ruimtevaartlaboratorium, Amsterdam (1963).
3. J.C. McMillan and R.M. Pelloux, *Fatigue Crack Propagation Under Program and Random Loads*, ASTM Paper 42A. Presented at the 69th Annual Meeting, June 1966.
4. F. Erdogan, *Crack Propagation Theories*, NASA-CR-901, National Aeronautics and Space Administration, Washington, D.C. (1967).
5. J. Schijve, *Analysis of the Fatigue Phenomenon in Aluminum Alloys*, NLR-TR-M. 2122, National Lucht-en Ruimtevaartlaboratorium, Amsterdam (1964).
6. H.J. Grover, S.M. Bishop, and L.R. Jackson, *Fatigue Strength of Aircraft Materials - Axial Load Fatigue Tests on Unnotched Sheet Specimens of 24S-T3 and 75S-T6 Aluminum Alloys and of SAE 4130 Steel*, NACA-TN-2324, National Aeronautics and Space Administration, Washington, D.C. (1951).
7. D.Y. Wang, *Effect of Stress Ratio on Fatigue Crack Growth and Mode of Fracture in 2024-T4 and 7075-T6 Aluminum Alloys in Low-Cycle Ranges*, AFML-TR-66-216, Air Force Materials Laboratory, Wright-Patterson AFB, Ohio (1966).
8. G. Sines, *Failure of Materials Under Combined Repeated Stresses with Superimposed Static Stresses*, NACA-TN-3495, National Aeronautics and Space Administration, Washington, D.C. (1955).
9. W.N. Findley, "A Theory for the Effect of Mean Stress on Fatigue of Metals Under Combined Torsion and Axial Loading on Bending," *J. Eng. Ind.*, 81:301 (1959).
10. B. Crossland, "Effect of Large Hydrostatic Pressure on the Torsional Fatigue Strength of an Alloy Steel," in *Proc. IME-ASME Conf. Fatigue*, American Society of Mechanical Engineers, New York (1956).
11. J. Shewchuck, Y. Zamrik, and J. Marin, "Low-Cycle Fatigue of 7075-TG51 Aluminum Alloy in Biaxial Bending," *Exp. Mech.*, 8:504-512 (1968).
12. T. Yokobori and T. Yoshimora, *A Criterion for Fatigue Fracture Under Multi-Axial Alternating Stress State*, Tohoko University, Research Institute for Strength and Fracture of Materials, Sendai, Japan (1966).

# FRACTURE AND FATIGUE GROWTH OF PARTIALLY EMBEDDED FLAWS

by

L.R. Hall and R.W. Finger

The Boeing Company  
Aerospace Group  
Seattle, Washington

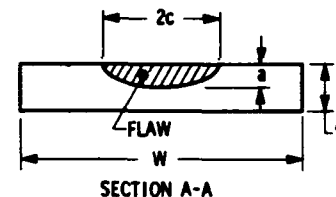
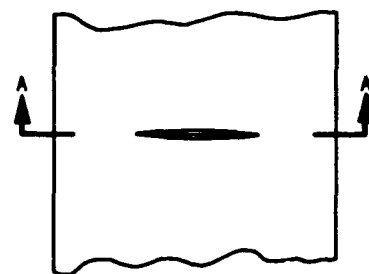
## INTRODUCTION

Many failures in aerospace structures have originated at partially or fully embedded flaws. Potential sources of such flaws include weld defects, rivet and bolt holes, geometrical discontinuities, and corrosion pits. Flaws usually initiate and grow under the influence of loads and environment. In aircraft structures, fluctuating loads are probably the most common cause of crack formation and propagation; environmental effects can markedly influence the rates of both crack formation and crack propagation. In spacecraft and booster structure, crack-like defects often present in the as-fabricated structure can grow under the influence of cyclic and invariant loadings, and environment.

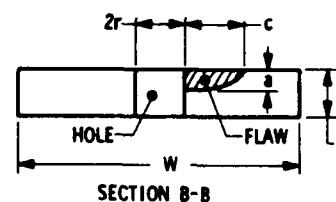
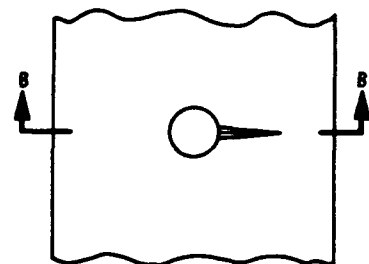
Partially or fully embedded flaws are often subjected to plane strain deformations in the vicinity of the flaw peripheries. Plane strain conditions result in minimum fracture toughness and minimum resistance to stress corrosion effects and are of considerable practical interest. Surface flaws (Figure 1a) are a significant example of flaws that can be subjected to plane strain crack tip deformations; they are commonly found in aerospace structure and are prone to both load and environmental effects. Hence, the testing of surface-flawed specimens provides a representative means of gathering data on the effects of fatigue loadings and environment on plane strain flaw growth. A second flaw geometry commonly encountered in aerospace structure is the partially embedded flaw growing from a rivet or bolt hole (Figure 1b). In relatively thick sections, such flaws can grow under plane strain conditions and become unstable before penetrating the section thickness.

The objective of this paper is to present the results of recent studies of fracture and fatigue induced flaw growth in both surface-flawed specimens and specimens containing partially embedded flaws originating at circular holes. Uniaxially stressed surface-flawed specimens of 2014-T62 aluminum and 6A1-4V(ELI) titanium are tested in ambient air, liquid nitrogen and liquid hydrogen environments; flaw growth rates determined by an end-point analysis are compared to rates calculated using continuous measurements of flaw-opening displacements at the surface of individual specimens. Uniaxially stressed specimens of 2219-T87 aluminum and 5A1-2.5Sn(ELI) titanium containing flaws

originating at holes are fractured in liquid nitrogen; an additional nine flaw-at-hole specimens are cycled to failure in liquid nitrogen and liquid hydrogen environments.



(a): SURFACE FLAW



(b): FLAW ORIGINATING AT HOLE

Figure 1. Flaw Geometries.

Linear elastic fracture mechanics principles are used to interpret test results. For surface flaws, an equation expressing plane strain cyclic flow growth rates is derived. For partially embedded flaws originating at holes, a semi-empirical failure criterion and methods of estimating fatigue life are developed. Results are applicable to material selection, design, and safe life prediction for structure in which embedded flaws can grow and fracture under conditions of plane strain.

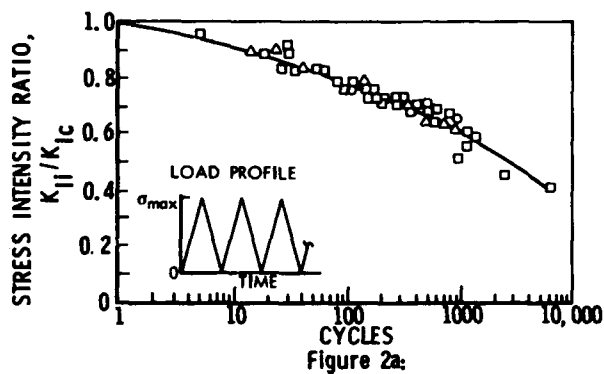
### BACKGROUND

It has been well substantiated that under certain restrictive conditions, crack instability occurs when the maximum stress intensity at a crack tip reaches the critical stress intensity for the material-environment-geometry combination under test. The restrictive condition is that the size of the zone of plastically yielded material at the crack tip must be small with respect to characteristic crack and specimen dimension. For conditions of plane strain in the immediate vicinity of the crack tip, the critical stress intensity is called the plane strain fracture toughness of the material. Plane strain fracture toughness is considered to be a form of material property in that it is independent of geometry and loading conditions, and varies from material to material in a manner similar to the yield stress. It has further been shown (Ref. 1 through 9) that the effect of fluctuating loads on fatigue crack growth rate can be correlated through the stress intensity parameter. Following the initial suggestion of Paris<sup>1</sup>, a number of investigators have proposed crack growth rate equations of the form

$$\frac{da}{dN} = G (\Delta K)^n \quad (1)$$

where  $da/dN$  is the crack growth rate,  $G$  is a function of relatively minor variables other than  $\Delta K$ , and  $\Delta K$  is the range in stress intensity applied to the crack tip during the loading cycle. Discussions of this type of crack growth rate correlation can be found in References 10, 11 and 12.

A practical approach to the problem of estimating crack growth rates and cyclic life for conditions of plane



LEGEND:  
 □ LONGITUDINAL & LONG TRANSVERSE  $K_{Ic} = 54.8 \text{ KSI} \sqrt{\text{IN}}$   
 ○ WELD (13-9 wire)  $K_{Ic} = 31.3 \text{ KSI} \sqrt{\text{IN}}$   
 △ SHORT TRANSVERSE  $K_{Ic} = 23.0 \text{ KSI} \sqrt{\text{IN}}$

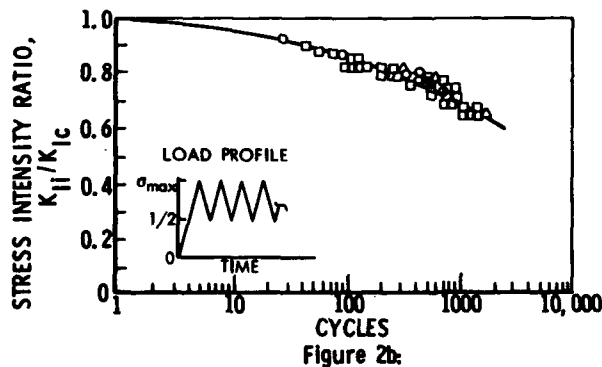


Figure 2. Round-Notched-Bar Fatigue Data (17-7 PH Steel Plate & Forging @ R.T.)

strain was proposed by Tiffany<sup>13</sup>. It was noted that cyclic lives for round notched bar and surface-flawed test specimens were primarily a function of maximum initial stress intensity applied to the tip of the flaw during the first loading cycle ( $K_{II}$ ) to the plane-strain fracture toughness of the parent material ( $K_{Ic}$ ). Accordingly, cyclic life data were plotted on  $K_{II}/K_{Ic}$  - versus-cycles-to-failure graphs where it was observed that data for particular material-environment combi-

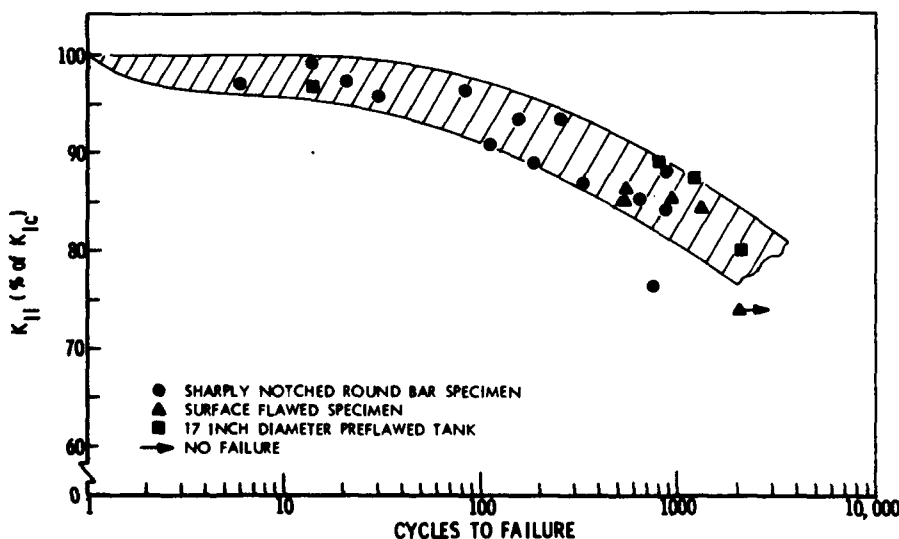
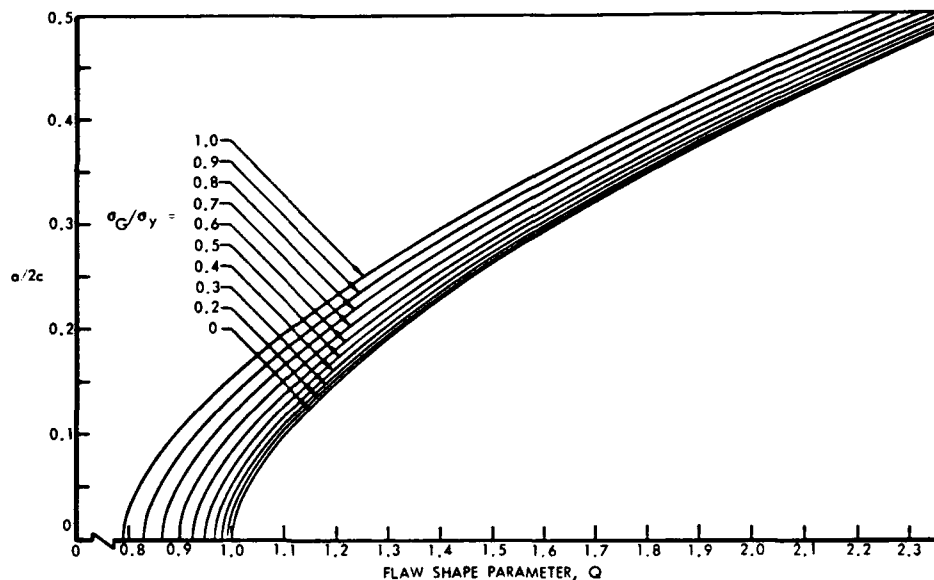


Figure 3. Combined Cyclic Flaw Growth Data of Ladish D6A-C Steel Plate (Tested at Room Temperature).



**Figure 4. Shape Parameter Curves for Surface and Internal Flaws.**



nations and test conditions could be reasonably represented by a unique curve. Flaw growth rates were computed using the slopes of the cyclic life curves. Since this approach required knowledge of only the initial and final conditions for each test, it was called an end-point analysis. Some of Tiffany's original data are included in Figure 2. Results of cyclic life tests for surface-flawed cylindrical tanks, uniaxially stressed surface-flawed specimens, and round notched bar specimens are compared in Figure 3. Good agreement between  $K_{II}/K_{IC}$  - cyclic life correlations are obtained for all three specimen types. The scatter band is unusually broad for this particular set of data because of eccentric flaw growth effects in the round notched bar specimens.

It can be shown (Ref. 12) that the end-point approach to correlating plane-strain crack growth rates and stress intensity is strictly valid only when the functional dependence of stress intensity on load and crack geometry is identical from specimen to specimen. However, since crack growth rate is proportional to approximately the fourth power of the applied stress intensity, the influence of initial stress intensity on cyclic life tends to predominate over influences due to differences in stress intensity-load-crack geometry relationships. This explains the good agreement observed between round notched bar and surface-flawed specimen test results evidenced in Figure 3. For surface-flawed specimens, Irwin<sup>15</sup> has shown that the relationship between stress intensity, load, and crack geometry is approximately the same for all specimens with flaw depths less than one-half the specimen thickness. Hence, the end-point analysis is applicable to surface-flawed test specimens in which flaw depths do not exceed one-half the specimen thickness. As flaw depths start to exceed this value, stress intensity is increasingly influenced by the stress-free back specimen face and the end-point method becomes increasingly inaccurate.

Surface-flawed specimen test results have also shown that a failure criterion applicable to embedded flaws for which the stress intensity varies along the crack periphery is

$(K_I)_{max} = K_{IC}$ .  $(K_I)_{max}$  is the maximum applied stress intensity along the crack periphery. For a semi-elliptically shaped surface flaw in a finite plate (Figure 1a), Irwin<sup>15</sup> has shown that the maximum value of stress intensity generated by a uniform tensile stress acting perpendicularly to the plane of the flaw occurs at the end of the semi-minor axes of the flaw and is given approximately by the expression

$$(K_I)_{max} = 1.1 \sqrt{\pi} \sigma (a/Q)^{1/2} \quad (2)$$

where  $\sigma$  is the uniform tensile stress, "a" is the flaw depth; Q is a shape parameter as given in Figure 4; and  $(a/Q)$  is the effective flaw size. Equation 2 is applicable to elastic stress

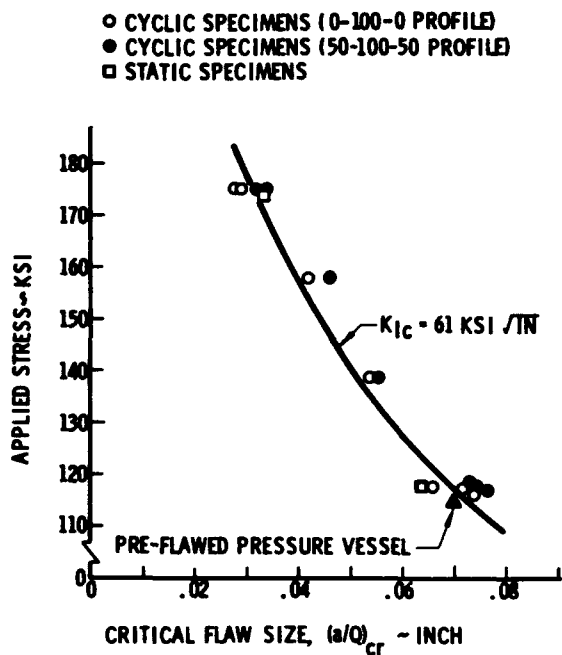


**Figure 5. Critical Flaw Size vs. Applied Stress (5 Al-2.5 Sn(ELI) Ti @ -320°F).**

**TABLE I  
CHEMICAL COMPOSITION OF MATERIALS**

ELEMENT (% By Weight) Except As Noted	2014-T6 ALUMINUM PLATE (1.0-Inch Thick)		2219-T87 ALUMINUM PLATE (1.0-Inch Thick)		5A1-2.5Sn (ELI) TITANIUM PLATE (0.375-Inch Thick)	6A1-4V (ELI) TITANIUM PLATE (0.375-Inch Thick)
	Min	Max	Min	Max		
Copper	3.9	5.00	5.8	6.80	--	--
Silicon	0.5	1.20	--	0.20	--	--
Manganese	0.4	1.20	0.20	0.40	--	--
Magnesium	0.2	0.80	--	0.02	< 0.01	--
Iron	--	1.00	--	0.30	0.19	0.11
Chromium	--	0.10	--	--	--	--
Zinc	--	0.25	--	0.10	--	--
Vanadium	--	--	0.05	0.15	--	4.40
Tin	--	--	--	--	2.50	--
Carbon	--	--	--	--	0.02	0.04
Nitrogen (ppm)	--	--	--	--	70	51
Oxygen (ppm)	--	--	--	--	940	750
Hydrogen (ppm)	--	--	--	--	94	38
Zirconium	--	--	0.10	0.25	--	--
Other Elements	Each	0.05	--	--	--	--
	Total	0.15	--	--	--	--
Titanium	--	0.15	0.10	0.20	Balance	Balance
Aluminum	Balance	Balance	Balance	Balance	5.10	6.20

levels and flaw depths less than one-half the parent plate thickness. Failure stresses are plotted as a function of flaw size at failure (critical flaw size) for 5A1-2.5Sn(ELI) titanium in Figure 5; data are included for uniaxially stressed surface-flawed specimens loaded either monotonically to failure (static specimens), or cyclically under both zero-to-tension (0-100-0) and half-tension-to-tension (50-100-50) loading cycles; one data point for a surface-flawed cylindrical tank cycled to failure under zero-to-tension loading profile is also shown. The failure criterion  $(K_I)_{max} = K_{Ic}$  is represented by the solid curve drawn through the data points. Good agreement is evidenced between test data and failure criterion.

### MATERIALS AND PROCEDURES

The 2014-T62 and 2219-T87 aluminum alloy test specimens were cut from 1.0-inch thick plates. Chemical compositions reported by the vendors are included in Table I. Mechanical properties are listed in Table II. The 6A1-4V (ELI) and 5A1-2.5Sn(ELI) titanium alloy specimens were cut from 0.375-inch thick plates from a single heat and rolling batch. Chemical compositions reported by the supplier are included in Table I and mechanical properties are listed in Table II.

All testing was conducted using uniaxially stressed pre-flawed specimens. Flaws were produced by growing a starter slot under low stress tension-tension fatigue loadings to the required final flaw dimensions. Starter slots with dimensions slightly less than the required final flaw dimensions were cut with an electrical discharge machine (EDM). The starter flaws were then grown to the required final flaw dimensions under low-stress fatigue, using maximum cyclic stress levels of 20 ksi and 50 ksi for the aluminum and

titanium alloys respectively. Flaw geometries for surface flaws and flaws originating from hole specimens are schematically illustrated in Figure 1. Crack surfaces were perpendicular to the rolling direction for the titanium alloys and the 2014-T62 aluminum alloy, and parallel to the rolling direction for the 2219-T87 aluminum alloy.

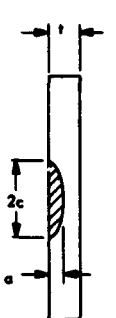
Tests at room temperature were conducted in laboratory air. Temperature and relative humidity were neither controlled nor measured. Ambient temperatures were very near 72°F for all tests. Relative humidities usually ranged from 40 to 80 percent. Tests at -320°F and -423°F were conducted in liquid nitrogen and liquid hydrogen respectively.

All cyclic loading profiles were sinusoidal with a cyclic frequency of 20 cycles per minute at ambient and

**TABLE II  
MECHANICAL PROPERTIES OF MATERIALS**

MATERIAL	TEMP. (°F)	ULTIMATE TENSILE STRENGTH (Ksi)	0.2% OFFSET YIELD STRENGTH (Ksi)	ELONGATION IN 2.0-INCH GAGE (%)	$K_{Ic}$ (Ksi√in.)
2014-T62 Aluminum (Long Grain)	70	69	62	9	See Table 6
	-320	83	72	12	
	-423	94	76	-	
2219-T87 Aluminum (Trans. Grain)	70	69	56	7	42
	-320	87	68	8	45
	-423	101	76	9	47
6A1-4V(ELI) Titanium (Long Grain)	70	125	122	15	See Table 6
	-320	198	193	6	
	-423	238	232	-	
5A1-2.5Sn(ELI) Titanium (Long Grain)	70	120	110	23	120
	-320	187	180	17	75
	-423	220	210	8	64

TABLE III  
TEST PROGRAM FOR SURFACE FLAWS

FLAW CONFIGURATION	MATERIAL	ENVIRONMENT	TEST TYPE	LOADING PROFILE	NUMBER OF TESTS
	2014-T62 Aluminum	Ambient Air	Static	0-100	3
			Cyclic	0-100-0	5
			Cyclic	50-100-50	5
		Liquid Nitrogen	Static	0-100	3
			Cyclic	0-100-0	5
			Cyclic	50-100-50	5
	Liquid Hydrogen	Static	0-100	3	
		Cyclic	0-100-0	5	
		Cyclic	50-100-50	5	
6Al-4V(ELI) Titanium	Ambient Air	Static	0-100	3	
		Cyclic	0-100-0	5	
		Cyclic	50-100-50	5	
	Liquid Nitrogen	Static	0-100	3	
		Cyclic	0-100-0	5	
		Cyclic	50-100-50	5	
Liquid Hydrogen	Static	0-100	3		
	Cyclic	0-100-0	5		
	Cyclic	50-100-50	5		

-320°F temperatures and two cycles per minute at -423°F. Static fracture loading rates were selected to result in failure at or near one minute after initial load application.

Testing of surface-flawed specimens was conducted according to the test program outlined in Table III. For each material-environment combination, thirteen specimens were tested. Three specimens were statically fractured; five specimens were cycled using a zero-to-tension loading profile; and five additional specimens were cycled under a half-tension-to-tension loading profile. For all material-environment combinations except titanium in room air, specimens were cycled to failure. For the titanium specimens tested in room air, static fracture tests showed that it would not be possible to effect failures under elastic stress levels using flaw depths less than one-half the specimen thickness; accordingly, these specimens were subjected to predetermined numbers of loading cycles using elastic peak cyclic stresses followed by low stress fatigue cycles and a static pull to failure to mark and reveal the resulting flaw growth.

For each loading profile in ambient and liquid nitrogen material-environment combinations, one cyclic specimen was instrumented to continuously measure relative perpendicular displacement of the flaw surfaces at the specimen face and on the flaw centerline. The elements of the instrumentation (excluding the recording equipment) are shown in Figure 6. Mounting platelets were micro-spot-welded to the specimen so that relative displacement of the platelets would be the same as maximum flaw-opening displacement being measured. The transducer was a single-strand constantan wire strain gage partially bonded using Duco cement. An unbonded length of 1.0 inch was used to avoid large local strains. Strains developed in the flaw-opening detection instrumentation were periodically measured throughout the duration of the instrumented cyclic tests. Gage outputs were recorded for both maximum and minimum cyclic loads at 50- to 200-cycle intervals.

Static fracture testing of specimens with flaws originating at circular holes was conducted according to the test program outlined in Table IV. One nominal specimen thickness of 0.375-inch was used for all titanium alloy tests. Three specimen thicknesses were used for the aluminum alloy tests: 0.90-inch, 0.80-inch and 0.70-inch for specimens with flaw depth to specimen thickness ratios of 0.20, 0.50 and 0.80 respectively. Specimen thickness was varied to avoid excessively large specimen dimensions and load requirements. Nine cyclic tests of specimens with flaws originating at holes were conducted. Three 2219-T87 aluminum specimens were cycled in liquid nitrogen and liquid hydrogen. With the exception of peak cyclic load, the same test variables were used in each set of three tests, i.e., a hole diameter-to-thickness ratio of 0.5, a flaw depth-to-thickness ratio of 0.20, and a flaw depth-to-length ratio of 1.0.

## RESULTS

### Surface-Flawed Tests

Tables V through X contain results for the six material-environment combinations tested. The first three specimens listed in each table were statically fractured; the next group of five specimens were cycled using a zero-to-tension loading profile; the last group of five specimens were cycled using a half-tension-to-tension loading profile. All

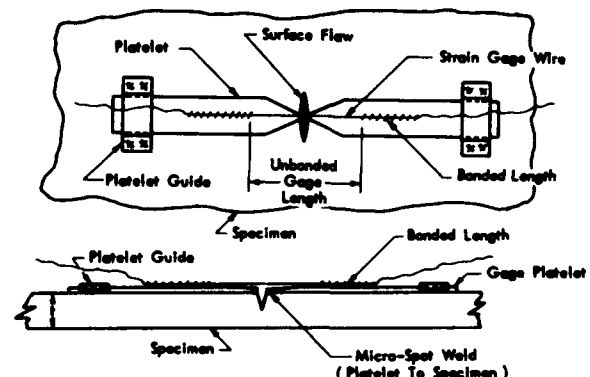
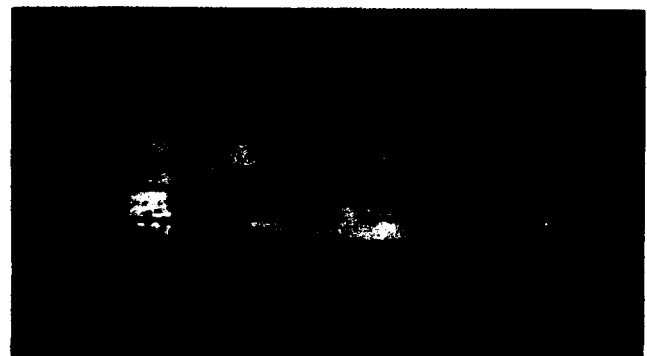
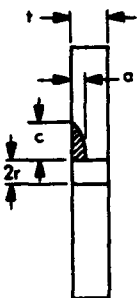


Figure 6. Instrumentation for Measuring Flaw Opening Displacements.

**TABLE IV  
TEST PROGRAM FOR FLAWS ORIGINATING AT HOLES**

FLAW CONFIGURATION	MATERIAL	TEST TEMP. (°F)	$\frac{2r}{t}$	$a/t$	NUMBER OF TESTS FOR $a/c =$		
					0.25	0.50	1.00
	2219-T67 Aluminum	-320	1.0	0.2	2	2	2
				0.5	2	2	2
				0.8	2	2	2
			0.5	0.2	2	2	2
				0.5	2	2	2
				0.8	2	2	2
Ti-5Al-2.5 Sn (ELI)	-320	1.0	0.2	2	2	2	
			0.5	2	2	2	
			0.8	2	2	2	
		0.5	0.2	2	2	2	
			0.5	2	2	2	
			0.8	2	2	2	

**TABLE V  
FRACTURE TOUGHNESS AND CYCLIC LIFE DATA FOR  
2014-T62 ALUMINUM BASE METAL IN AMBIENT AIR**

SPECIMEN				CYCLIC EXTENSION OF EDM FLAW			FLAW SIZE BEFORE TEST RUN			TEST			FLAW SIZE AT FAILURE			STRESS INTENSITIES			CYCLES TO FAILURE	
Identification	Configuration	Gage Thickness (in)	Gage Width (in)	Temperature (°F)	Max. Cyclic Stress (Ksi)	Number of Cycles In Thousands	Flaw Depth, $a_1$ (in)	Flaw Length, $2a_1$ (in)	Flaw Size, $(a/Q)^{1/2}$ (in)	Temperature (°F)	Max Cyclic Stress (Failure Stress, Ksi)	Min. Cyclic Stress (Ksi)	Max Cyclic Stress Yield Stress	Flaw Depth, $a_2$ (in)	Flaw Length, $2a_2$ (in)	Flaw Size, $(a/Q)^{1/2}$ (in)	$K_{II}$ (Ksi $\sqrt{\text{in}}$ )	$K_{Ic}$ (Ksi $\sqrt{\text{in}}$ )		$K_{II/K_{Ic}}$
AC-1	Fig. 1	0.615	5.81	Room	15.0	10.0				Room	51.2		0.82	0.230	0.83	0.163		40.3		
AD-1	Fig. 1	0.448	6.06	Room	15.0	7.0				Room	56.3		0.90	0.160	0.63	0.123		38.5		
AE-1	Fig. 1	0.595	6.02	Room	15.0	10.0				Room	60.1		0.96	0.128	0.55	0.106		38.1		
RAO-1*	Fig. 1	0.601	4.50	Room	12.0	15.0				Room										
RAO-2	Fig. 1	0.902	5.00	Room	20.0	5.0	0.120	0.430	0.084	Room	48.5	0	0.78	0.425	1.10	0.233	27.5	45.7	0.60	1900
RAO-3	Fig. 1	0.897	5.63	Room	18.0	17.0	0.145	0.515	0.101	Room	48.5	0	0.78	0.410	1.10	0.230	30.0	45.3	0.66	1302
RAO-4	Fig. 1	0.922	5.65	Room	15.0	7.0	0.200	0.780	0.146	Room	48.5	0	0.78	0.390	1.10	0.229	36.2	45.2	0.80	388
RAO-5	Fig. 1	0.904	5.65	Room	15.0	9.0	0.225	0.810	0.154	Room	42.0	0	0.67	0.475	1.63	0.317	32.1	45.9	0.70	834
RAS-1	Fig. 1	0.927	4.51	Room	20.0	7.0	0.130	0.500	0.097	Room	55.0	27.5	0.88	0.300	0.88	0.185	33.4	46.1	0.72	2189
RAS-2	Fig. 1	0.900	5.00	Room	18.0	8.0	0.148	0.500	0.100	Room	48.5	24.3	0.78	0.397	1.22	0.249	29.9	46.8	0.64	4877
RAS-3	Fig. 1	0.903	5.65	Room	18.0	8.0	0.135	0.550	0.101	Room	48.5	24.3	0.78	0.390	1.16	0.238	30.1	46.2	0.65	4260
RAS-4	Fig. 1	0.928	5.65	Room	15.0	7.0	0.205	0.800	0.151	Room	48.5	24.3	0.78	0.375	1.18	0.239	36.7	46.2	0.79	2332
RAS-5	Fig. 1	0.889	5.65	Room	15.0	8.5	0.220	0.785	0.150	Room	42.0	21.0	0.67	0.480	1.60	0.312	31.7	45.9	0.69	3588

\* Failed in Grip

**TABLE VI**  
**FRACTURE TOUGHNESS AND CYCLIC LIFE DATA FOR 2014-T62 ALUMINUM BASE METAL IN LIQUID NITROGEN**

SPECIMEN				CYCLIC EXTENSION OF EDM FLAW			FLAW SIZE BEFORE TEST RUN			TEST				FLAW SIZE AT FAILURE			STRESS INTENSITIES			CYCLES TO FAILURE
Identification	Configuration	Gage Thickness (in)	Gage Width (in)	Temperature (°F)	Max. Cyclic Stress (Ksi)	Number of Cycles In Thousands	Flow Depth, $a_1$ (in)	Flow Length, $2c_1$ (in)	Flow Size, $(a/Q)_1$ (in)	Temperature (°F)	Max Cyclic Stress (Failure Stress, Ksi)	Min. Cyclic Stress (Ksi)	Max Cyclic Stress Yield Stress	Flow Depth, $a_{cr}$ (in)	Flow Length, $2c_{cr}$ (in)	Flow Size, $(a/Q)_{cr}$ (in)	$K_{II}$ (Ksi $\sqrt{in}$ )	$K_{Ic}$ (Ksi $\sqrt{in}$ )	$K_{II}/K_{Ic}$	
AC-2	Fig. 9	0.603	6.07	Room	15.0	7.0				-320	52.5		0.73	0.218	0.63	0.157		40.5	Shear Tests	
AD-2	Fig. 9	0.586	6.06	Room	15.0	5.0				-320	56.6		0.80	0.160	0.65	0.121		38.4		
AE-2	Fig. 9	0.604	6.09	Room	15.0	12.0				-320	64.0		0.89	0.125	0.55	0.102		39.8		
NA0-1	Fig. 9	0.604	4.997	Room	20.0	10.0	0.085	0.300	0.060	-320	63.0	0	0.88	0.18	0.57	0.118	30.2	42.3	0.71	773
NA0-2	Fig. 9	0.604	4.304	Room	15.0	25.0	0.090	0.335	0.064	-320	56.0	0	0.78	Delaminated						
NA0-3	Fig. 9	0.602	4.996	Room	15.0	4.0	0.110	0.500	0.087	-320	53.0	0	0.74	0.32	0.83	0.174	30.5	43.2	0.71	1976
NA0-4	Fig. 9	0.597	4.992	Room	15.0	12.0	0.150	0.570	0.109	-320	56.0	0	0.78	0.23	0.86	0.165	36.0	44.4	0.81	288
NA0-5	Fig. 9	0.603	4.994	Room	15.0	15.0	0.160	0.600	0.113	-320	49.0	0	0.68	Delaminated						
NA5-1	Fig. 9	0.577	4.998	Room	15.0	16.0	0.110	0.400	0.080	-320	63.0	31.5	0.88	0.23	0.80	0.162	34.7	49.4	0.70	5905
NA5-2	Fig. 9	0.603	4.493	Room	15.0	15.0	0.139	0.555	0.103	-320	56.0	28.0	0.78	Delaminated						
NA5-3	Fig. 9	0.602	4.502	Room	12.0	15.0	0.198	0.685	0.123	-320	56.0	28.0	0.78	Delaminated						
NA5-4	Fig. 9	0.596	4.989	Room	15.0	13.0	0.160	0.630	0.119	-320	56.0	28.0	0.78	0.27	1.10	0.204	37.6	49.3	0.76	2107
NA5-5	Fig. 9	0.604	4.500	Room	12.0	40.0	0.180	0.690	0.129	-320	50.0	25.0	0.70	Delaminated						

**TABLE VII**  
**FRACTURE TOUGHNESS AND CYCLIC LIFE DATA FOR 2014-T62 ALUMINUM BASE METAL IN LIQUID HYDROGEN**

SPECIMEN				CYCLIC EXTENSION OF EDM FLAW			FLAW SIZE BEFORE TEST RUN			TEST				FLAW SIZE AT FAILURE			STRESS INTENSITIES			CYCLES TO FAILURE
Identification	Configuration	Gage Thickness (in)	Gage Width (in)	Temperature (°F)	Max. Cyclic Stress (Ksi)	Number of Cycles In Thousands	Flow Depth, $a_1$ (in)	Flow Length, $2c_1$ (in)	Flow Size, $(a/Q)_1$ (in)	Temperature (°F)	Max Cyclic Stress (Failure Stress, Ksi)	Min. Cyclic Stress (Ksi)	Max Cyclic Stress Yield Stress	Flow Depth, $a_{cr}$ (in)	Flow Length, $2c_{cr}$ (in)	Flow Size, $(a/Q)_{cr}$ (in)	$K_{II}$ (Ksi $\sqrt{in}$ )	$K_{Ic}$ (Ksi $\sqrt{in}$ )	$K_{II}/K_{Ic}$	
SAH-1	Fig. 9	0.450	4.993	Room	15.0	10.0					68.1		0.90	0.136	0.636	0.114		44.9	Shear Tests	
SAH-2	Fig. 9	0.465	4.982	Room	12.0	18.0					72.8		0.96	0.155	0.696	0.130		51.2		
SAH-3	Fig. 9	0.456	4.998	Room	12.0	10.0					64.3		0.85	0.206	0.778	0.151		48.8		
HA0-1	Fig. 9	0.455	4.997	Room	20.0	15.0	0.065	0.427	0.063	-423	70.0	0.7	0.92	0.213	0.672	0.141	34.4	51.3	0.67	549
HA0-2	Fig. 9	0.450	4.989	Room	20.0	15.0	0.103	0.410	0.078	-423	64.0	0.7	0.84	0.235	0.711	0.148	34.9	48.0	0.73	302
HA0-3	Fig. 9	0.457	4.998	Room	18.0	16.0	0.059	0.514	0.060	-423	64.0	0.7	0.84	0.254	0.939	0.184	30.6	53.5	0.57	1019
HA0-4	Fig. 9	0.459	4.999	Room	15.0	18.0	0.104	0.652	0.097	-423	64.0	0.7	0.84	0.274	1.028	0.200	38.9	55.9	0.69	536
HA0-5	Fig. 9	0.453	4.987	Room	15.0	12.0	0.107	0.677	0.098	-423	58.0	0.7	0.76	0.254	1.099	0.197	35.3	50.3	0.70	392
HA5-1	Fig. 9	0.453	4.990	Room	18.0	15.0	0.109	0.603	0.100	-423	70.0	35.0	0.92	0.194	0.822	0.156	43.1	53.9	0.80	1048
HA5-2	Fig. 9	0.452	4.982	Room	18.0	10.0	0.104	0.607	0.095	-423	64.0	32.0	0.84	0.226	0.888	0.170	38.4	51.5	0.74	1995
HA5-3	Fig. 9	0.454	4.996	Room	15.0	22.0	0.103	0.690	0.098	-423	64.0	32.0	0.84	0.231	0.894	0.172	39.1	51.8	0.75	1258
HA5-4	Fig. 9	0.446	4.998	Room	15.0	27.0	0.135	0.774	0.122	-423	64.0	32.0	0.84	0.202	0.875	0.161	43.6	50.0	0.87	613
HA5-5	Fig. 9	0.456	4.987	Room	15.0	23.0	0.135	0.777	0.119	-423	58.0	29.0	0.76	0.266	1.129	0.205	39.1	51.2	0.76	1498

**TABLE VIII**  
**FRACTURE TOUGHNESS AND CYCLIC LIFE DATA FOR 6A1-4V (ELI) TITANIUM BASE METAL IN LIQUID NITROGEN**

SPECIMEN				CYCLIC EXTENSION OF EDM FLAW			FLAW SIZE BEFORE TEST RUN			TEST				FLAW SIZE AT FAILURE			STRESS INTENSITIES			CYCLES TO FAILURE
Identification	Configuration	Gage Thickness (in)	Gage Width (in)	Temperature (°F)	Max. Cyclic Stress (Ksi)	Number of Cycles In Thousands	Flow Depth, a <sub>f</sub> (in)	Flow Length, 2c <sub>f</sub> (in)	Flow Size, (a/Q) <sub>f</sub> (in)	Temperature (°F)	Max Cyclic Stress (Failure Stress, Ksi)	Min. Cyclic Stress (Ksi)	Max Cyclic Stress Yield Stress	Flow Depth, a <sub>cr</sub> (in)	Flow Length, 2c <sub>cr</sub> (in)	Flow Size, (a/Q) <sub>cr</sub> (in)	K <sub>II</sub> (Ksi√in)	K <sub>Ic</sub> (Ksi√in)	K <sub>II</sub> /K <sub>Ic</sub>	
SNT-1	Fig. 2	0.379	3.00	Room	30.0	5				-320	121.3	-	0.63	0.128	0.590	0.100		75		Static Tests
SNT-2	Fig. 2	0.371	2.00	Room	50.0	1				-320	152.1	-	0.79	0.100	0.260	0.059		72		
SNT-3	Fig. 2	0.370	2.00	Room	30.0	1				-320	127.6	-	0.67	0.130	0.325	0.068		65		
NT0-1	Fig. 2	0.373	2.00	Room	50.0	5	0.029	0.152	0.025	-320	158.0	0	0.82	0.084	0.220	0.047	48.8	66.7	0.73	358
NT0-2	Fig. 2	0.373	2.00	Room	50.0	8	0.026	0.146	0.023	-320	143.0	0	0.75	0.101	0.279	0.058	42.0	67.2	0.62	621
NT0-3	Fig. 2	0.371	2.00	Room	50.0	4	0.039	0.230	0.035	-320	143.0	0	0.75	0.087	0.283	0.057	51.9	66.4	0.78	256
NT0-4	Fig. 2	0.368	2.00	Room	50.0	1	0.062	0.371	0.055	-320	143.0	0	0.75	0.080	0.383	0.065	65.5	71.2	0.92	74
NT0-5	Fig. 2	0.376	2.00	Room	50.0	2	0.060	0.358	0.052	-320	128.0	0	0.67	0.110	0.412	0.077	57.1	69.4	0.82	115
NTS-1	Fig. 2	0.365	2.00	Room	50.0	5	0.035	0.189	0.031	-320	158.0	79.0	0.82	0.072	0.236	0.048	54.0	67.5	0.80	624
NTS-2	Fig. 2	0.369	2.00	Room	50.0	4	0.037	0.217	0.033	-320	143.0	71.5	0.75	0.106	0.314	0.064	50.5	70.7	0.71	1154
NTS-3	Fig. 2	0.373	2.00	Room	50.0	2	0.046	0.268	0.041	-320	143.0	71.5	0.75	0.081	0.289	0.056	56.2	66.0	0.85	542
NTS-4	Fig. 2	0.365	2.00	Room	50.0	1	0.072	0.394	0.062	-320	143.0	71.5	0.75	0.080	0.394	0.066	69.5	71.6	0.97	86
NTS-5	Fig. 2	0.373	2.00	Room	50.0	1	0.063	0.398	0.056	-320	128.0	64.0	0.67	0.094	0.398	0.071	59.1	66.4	0.89	310

**TABLE IX**  
**FRACTURE TOUGHNESS AND CYCLIC LIFE DATA FOR 6A1-4V (ELI) TITANIUM BASE METAL IN LIQUID HYDROGEN**

SPECIMEN				CYCLIC EXTENSION OF EDM FLAW			FLAW SIZE BEFORE TEST RUN			TEST				FLAW SIZE AT FAILURE			STRESS INTENSITIES			CYCLES TO FAILURE
Identification	Configuration	Gage Thickness (in)	Gage Width (in)	Temperature (°F)	Max. Cyclic Stress (Ksi)	Number of Cycles In Thousands	Flow Depth, a <sub>f</sub> (in)	Flow Length, 2c <sub>f</sub> (in)	Flow Size, (a/Q) <sub>f</sub> (in)	Temperature (°F)	Max Cyclic Stress (Failure Stress, Ksi)	Min. Cyclic Stress (Ksi)	Max Cyclic Stress Yield Stress	Flow Depth, a <sub>cr</sub> (in)	Flow Length, 2c <sub>cr</sub> (in)	Flow Size, (a/Q) <sub>cr</sub> (in)	K <sub>II</sub> (Ksi√in)	K <sub>Ic</sub> (Ksi√in)	K <sub>II</sub> /K <sub>Ic</sub>	
SHT-3	Fig. 12	0.370	1.10	Room	50.0	20.5				-423	101.3	-	0.41	0.125	0.310	0.063		80		Static Tests
SHT-4	Fig. 12	0.374	1.10	Room						-423	132.5	-	0.53	0.057	0.234	0.041		57		
SHT-5	Fig. 12	0.374	1.10	Room						-423	140.5	-	0.57	0.057	0.227	0.041		53		
HT0-1	Fig. 12	0.372	1.10	Room	50.0	20.4	0.025	0.092	0.017	-423	120.0	3.7	0.48	0.099	0.268	0.054	30.4	54.3	0.56	802
HT0-2	Fig. 12	0.367	1.10	Room	50.0	20.3	0.021	0.090	0.016	-423	170.0	3.7	0.68	0.040	0.119	0.024	41.9	51.5	0.81	133
HT0-3	Fig. 12	0.369	1.10	Room	50.0	20.4	0.030	0.131	0.022	-423	120.0	3.7	0.48	0.099	0.244	0.030	34.9	52.3	0.67	392
HT0-4	Fig. 12	0.360	1.10	Room	50.0	19.8	0.030	0.208	0.036	-423	120.0	3.7	0.48	0.104	0.234	0.048	44.4	51.4	0.86	133
HT0-5	Fig. 12	0.367	1.10	Room	50.0	20.3	0.044	0.208	0.033	-423	100.0	3.7	0.40	0.138	0.336	0.068	35.6	51.0	0.70	396
HTS-1	Fig. 12	0.372	1.10	Room	50.0	20.5	0.040	0.151	0.028	-423	140.0	70.0	0.56	0.074	0.166	0.035	45.4	50.7	0.90	45
HTS-2	Fig. 12	0.373	1.10	Room	50.0	20.7	0.039	0.147	0.027	-423	120.0	60.0	0.48	0.130	0.293	0.060	38.2	57.5	0.66	3281
HTS-3	Fig. 12	0.370	1.11	Room	50.0	20.5	0.043	0.200	0.033	-423	120.0	60.0	0.48	0.113	0.298	0.040	42.3	57.4	0.74	1542
HTS-4	Fig. 12	0.374	1.10	Room	50.0	20.6	0.047	0.204	0.035	-423	130.0	60.0	0.48	0.086	0.272	0.053	43.5	53.7	0.81	230
HTS-5	Fig. 12	0.369	1.11	Room	50.0	20.4	0.049	0.207	0.035	-423	105.0	52.5	0.42	0.130	0.320	0.064	38.5	52.5	0.73	1990

**TABLE X**  
**FRACTURE TOUGHNESS AND CYCLIC FLAW GROWTH DATA FOR**  
**6A1-4V (ELI) TITANIUM BASE METAL IN AMBIENT AIR**

SPECIMEN				CYCLIC EXTENSION OF EDM FLAW			FLAW DATA BEFORE TEST RUN				CYCLIC TEST			FLAW DATA AFTER TEST RUN				STATIC FRACTURE TEST DATA					RESULTS					
Identification	Configuration	Grope Thickness (in)	Grope Width (in)	Temperature (°F)	Max Cyclic Stress (Ksi)	Number of Cycles In Thousands	Flaw Depth, $a_i$ (in)	Flaw Length, $2c_i$ (in)	Flaw Size, $(a/Q)_i$ (in)	$K_{II}$ (Ksi $\sqrt{in}$ )	Temperature (°F)	Max Cyclic Stress (Ksi)	Min Cyclic Stress (Ksi)	Max Cyclic Stress/Yield Stress	Flaw Depth, $a_f$ (in)	Flaw Length, $2c_f$ (in)	Flaw Size, $(a/Q)_f$ (in)	$K_{II}$ (Ksi $\sqrt{in}$ )	Temperature (°F)	Flaw Depth, $a_{st}$ (in)	Flaw Length, $2c_{st}$ (in)	Failure Stress (Ksi)	Failure Stress/Yield Stress	Apparent $K_{Ic}$ (Ksi $\sqrt{in}$ )	Number of Applied Loading Cycles, N	$\Delta(a/Q)$ (in)	$\Delta(a/Q)/N$ Micro-in/Cycle	$(K_{II} + K_{Ic})/2$ (Ksi $\sqrt{in}$ )
SRT-1	Fig. 2	0.378	3.00	Room	40.0	1.0													Room	0.185	0.740	114.1	0.88	84				
SRT-2	Fig. 2	0.372	3.00	Room	30.0	4.0													Room	0.190	0.740	106.0	0.82	78	Static Test			
RT0-1	Fig. 2	0.369	2.00	Room	30.0	6.0	0.129	0.560	0.102	65.3	Room	105.0	0	0.81	0.145	0.560	0.107	67.0	Room	0.145	0.560	122.9	0.95	80.2	61	0.005	89	66.2
RT0-2	Fig. 2	0.364	2.00	Room	30.0	5.0	0.124	0.560	0.097	54.6	Room	90.0	0	0.69	0.136	0.560	0.101	55.9	Room	0.136	0.560	124.4	0.96	79.8	80	0.004	52	55.3
RT0-3	Fig. 2	0.369	2.00	Room	40.0	3.0	0.103	0.440	0.080	49.6	Room	90.0	0	0.69	0.133	0.470	0.091	52.8	Room	0.133	0.470	126.5	0.98	76.5	400	0.011	1	51.2
RT0-4	Fig. 2	0.371	2.00	Room	30.0	20.0	0.075	0.335	0.058	42.4	Room	90.0	0	0.69	0.092	0.340	0.064	44.5	Room	0.092	0.340	134.0	1.03	69.2	300	0.006		43.4
RT0-5	Fig. 2	0.374	2.00	Room	40.0	4.5	0.084	0.340	0.045	34.5	Room	75.0	0	0.58	0.132	0.410	0.081	41.6	Room	0.132	0.410	127.0	0.98	75.6	1500	0.019	1	39.1
RT5-1	Fig. 2	0.371	2.00	Room	30.0	5.0	0.125	0.560	0.101	64.9	Room	105.0	52.5	0.81	e	e	-	-	Room	-	-	105.0	0.81	-	235	0.052	22 <sup>b</sup>	72.5 <sup>b</sup>
RT5-2	Fig. 2	0.374	2.00	Room	30.0	6.0	0.120	0.570	0.094	54.4	Room	90.0	45.0	0.69	0.130	0.570	0.100	55.5	Room	0.130	0.570	126.0	0.97	81.1	630	0.004	6.1	54.9
RT5-3	Fig. 2	0.375	2.00	Room	40.0	2.0	0.101	0.440	0.078	49.4	Room	90.0	45.0	0.69	0.121	0.440	0.084	51.5	Room	0.121	0.440	128.1	0.99	76.4	1100	0.007	6.5	50.5
RT5-4	Fig. 2	0.365	2.00	Room	40.0	4.0	0.080	0.340	0.045	43.8	Room	90.0	45.0	0.69	0.121	0.380	0.076	48.4	Room	0.121	0.380	130.3	1.00	72.7	2400	0.014	5.8	46.1
RT5-5	Fig. 2	0.370	2.00	Room	40.0	9.0	0.072	0.340	0.054	34.6	Room	75.0	37.5	0.58	0.136	0.385	0.078	40.8	Room	0.136	0.385	127.1	0.98	71.9	8000	0.022	3.6	37.7

e Not Detectable  
b Estimated Using  $K_{Ic} = 80 \text{ KSI } \sqrt{in}$

stress intensity values were calculated using the Irwin<sup>15</sup> approximate expression for maximum stress intensity factor at the tip of surface flaws in finite thickness plates subjected to uniform tension  $\sigma$ , i.e., Equation (2).

All aluminum specimens and titanium specimens tested in liquid nitrogen and hydrogen were cycled to failure. The resulting data are shown on semi-log graphs of cycles to failure versus  $K_{II}/K_{Ic}$  in Figures 7 through 11. Individual  $K_{Ic}$  values were used in the calculation of all  $K_{II}/K_{Ic}$  ratios.

Titanium specimens tested in room air were not cycled to failure but, rather, over limited ranges of applied stress intensity. The resulting data in Table X are plotted in Figure 12 on log-log graphs of average stress intensity versus average flaw-growth rate. Average growth rates were computed for each specimen by dividing the total flaw growth,  $\Delta(a/Q)$ , by the number of the applied loading cycles; the corresponding average stress intensities are the arithmetic averages of the initial and final maximum stress intensities at the tip of each flaw.

**Figure 7. Cyclic Flaw Growth Curves for 2014-T62 Aluminum Base Metal in Ambient Air.**

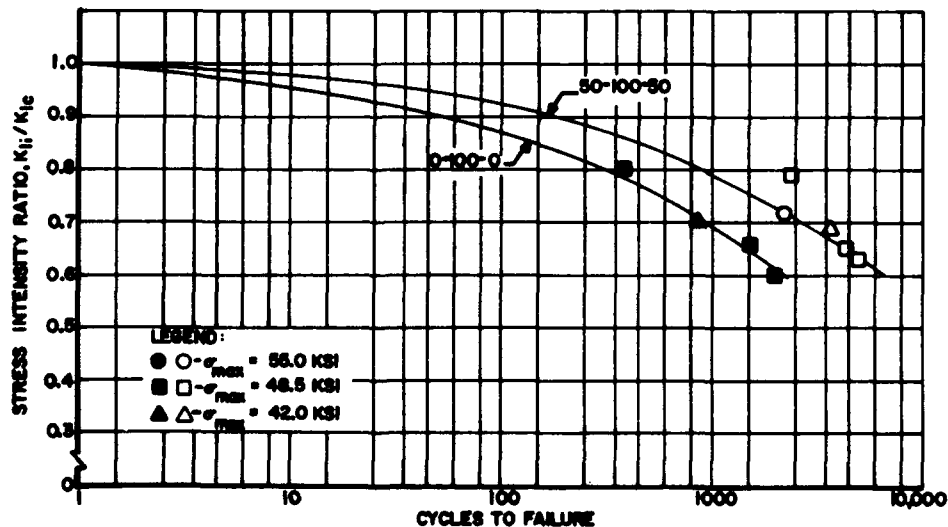


Figure 8. Cyclic Flaw Growth Curves for 2014-T62 Aluminum Base Metal in Liquid Nitrogen.

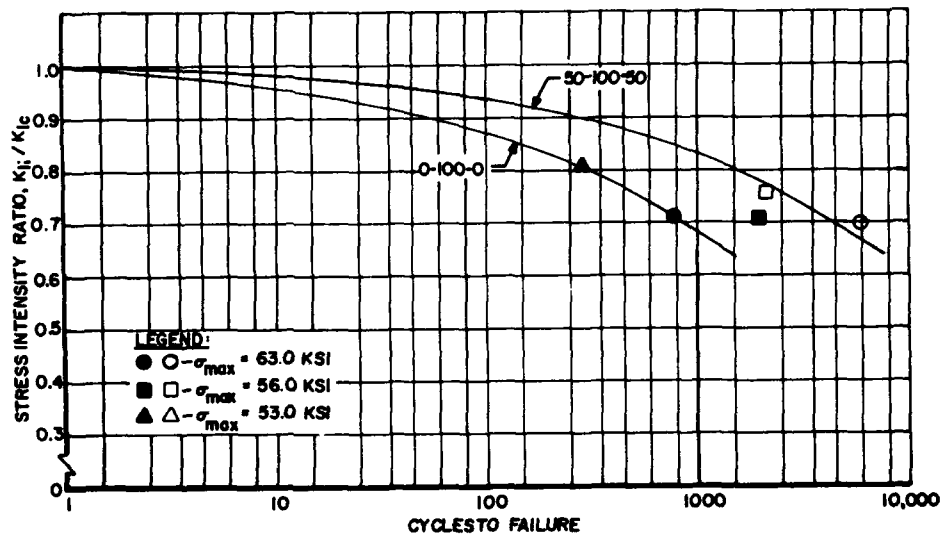


Figure 9. Cyclic Flaw Growth Curves for 2014-T62 Aluminum Base Metal in Liquid Hydrogen.

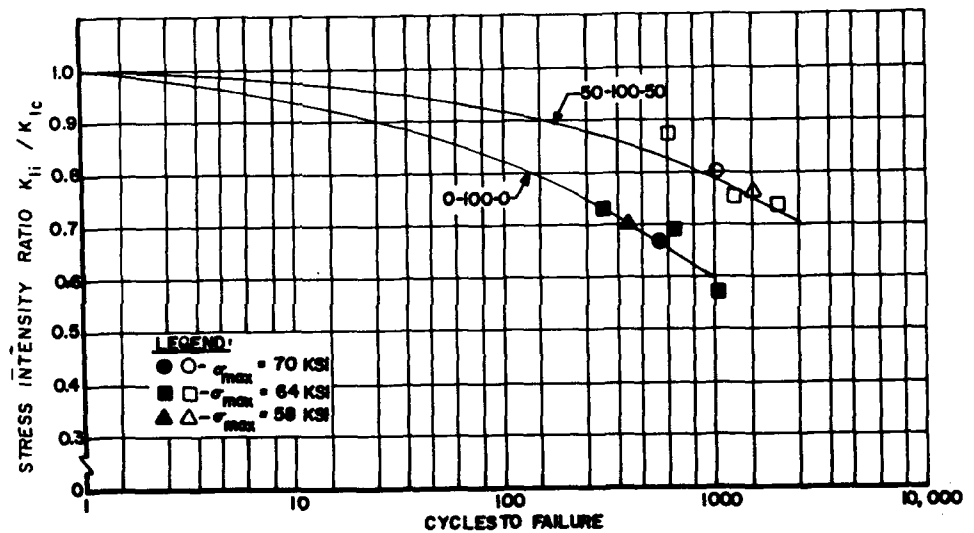
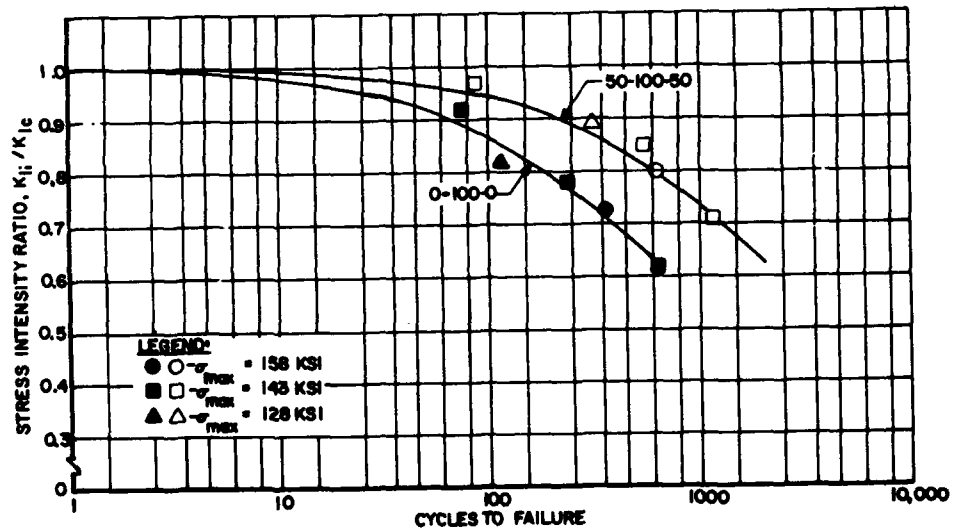
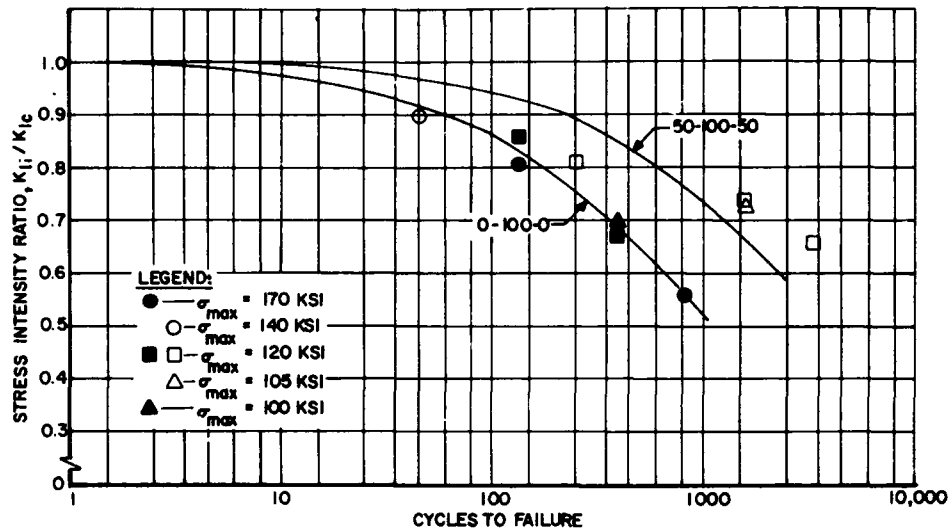


Figure 10. Cyclic Flaw Growth Curves for 6A1-4V (ELI) Titanium Base Metal in Liquid Nitrogen.





**Figure 11. Cyclic Flaw Growth Curves for 6A1-4V (ELI) Titanium Base Metal in Liquid Hydrogen.**



Figures 13 through 18 contain graphs of flaw-opening strain versus cycles for six specimens that were instrumented to measure flaw-opening displacement. Each data point represents an individual reading of strain at the peak cyclic stress level. For specimens that were cycled to failure, the rate of increase of flaw-opening strain was so large during the last few loading cycles that it was not possible to take strain readings. The last strain measurements were taken some 50 to 100 cycles prior to failure.

When the single-strand constant wire strain gages were partially bonded to the mounting platelets (as illustrated in Figure 6) some slack was unintentionally introduced into the gage wire over the unbonded length. Due to the slack, some fixed value of flaw-opening displacement had to be effected before the gage was strained. Hence, the strains measured were not a result of the total flaw opening but only partial values thereof. Since the flaw-opening displacement required to initiate straining of the gage wire should be the same for each loading cycle, it was concluded

that the shape of the curves in Figure 13 through 18 was not affected by the initial slack in the gage wires; rather, the curves were shifted downward by an unknown constant value.

**Flaw-At-Hole Tests**

Tables XI through XIV summarize test variables and gross fracture stress values for the seventy-two fracture tests of specimens with flaws originating at circular holes. Failure stresses are plotted in terms of flaw depth-to-length ratio in Figure 19. Separate plots are included for each material and for each hole diameter-to-thickness ratio tested. The effect of hole diameter on failure stress is illustrated in Figure 20 where it can be seen that the effect is reasonably constant for all a/c and a/t ratios and both materials. All failures originated at the flaw and under elastic net section stresses. After the flaw became unstable and crack propagation had completely severed the flawed half of the specimen, the remaining unflawed ligament underwent an ultimate strength failure. Fracture surfaces on the flawed side of all test

(Text Continued on Page 250)

**Figure 12. Flaw-Growth-Rate Curves for 6A1-4V (ELI) Titanium Base Metal in Ambient Air.**

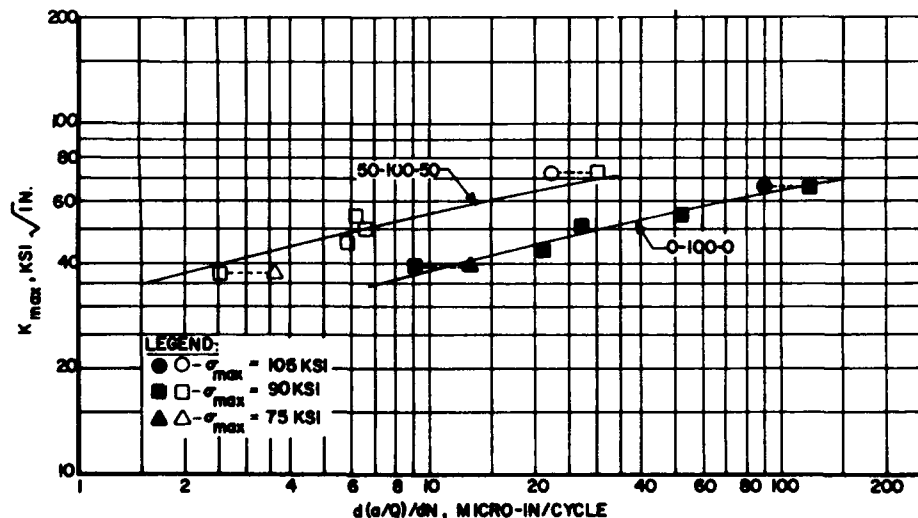


**Figure 13. Flaw-Opening Strain vs. Cycles for 2014-T62 Aluminum Specimen RA0-2.**

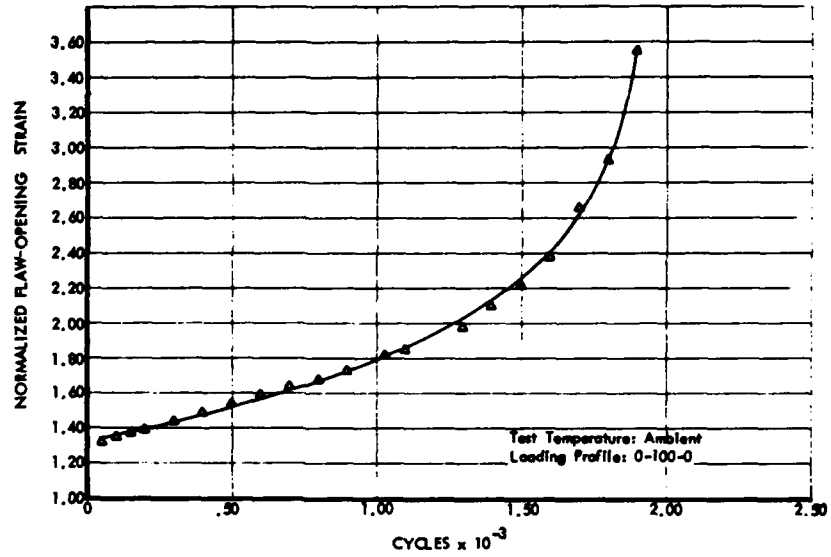


**Figure 14. Flaw-Opening Strain vs. Cycles for 2014-T62 Aluminum Specimen RA5-2.**

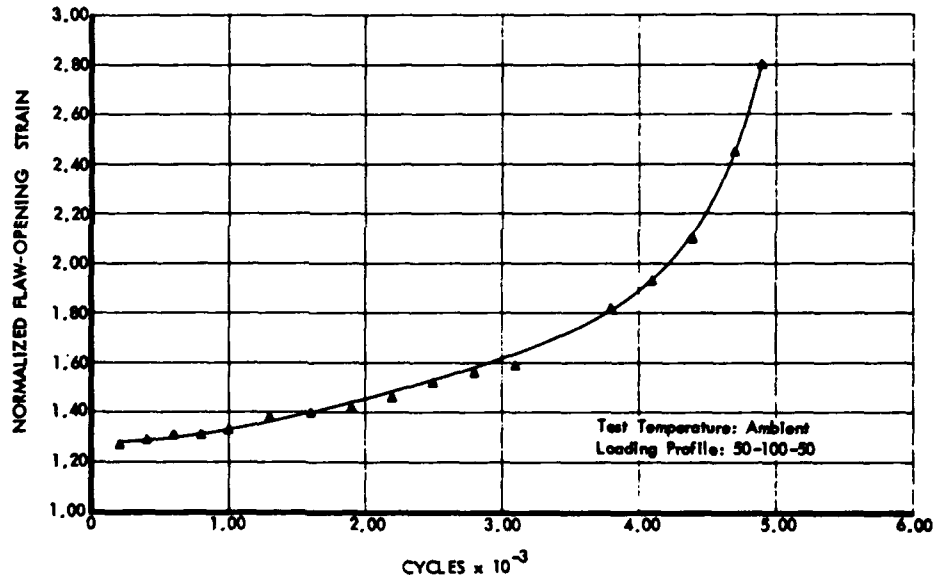


**Figure 15. Flaw-Opening Strain vs. Cycles for 6A1-4V (ELI) Titanium Specimen RT0-5.**

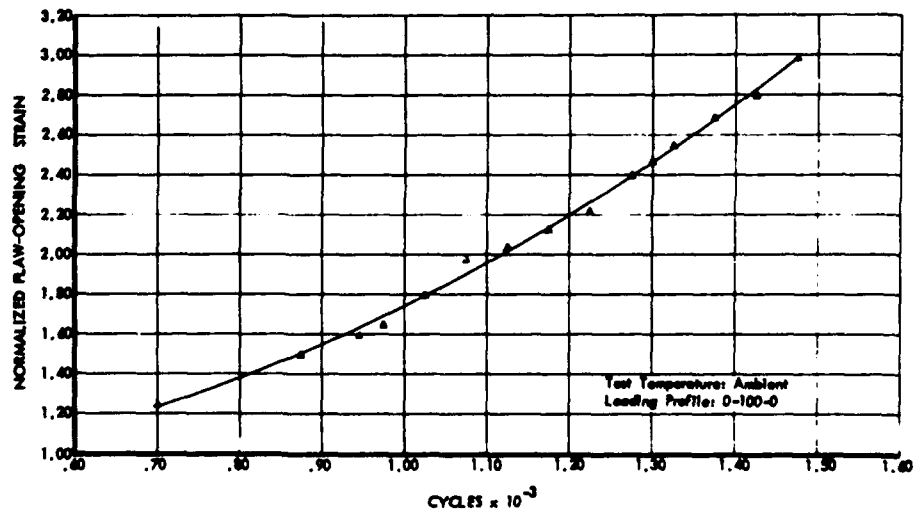


Figure 16. Flaw-Opening Strain vs. Cycles for 6A1-4V (ELI) Titanium Specimen RT5-5.

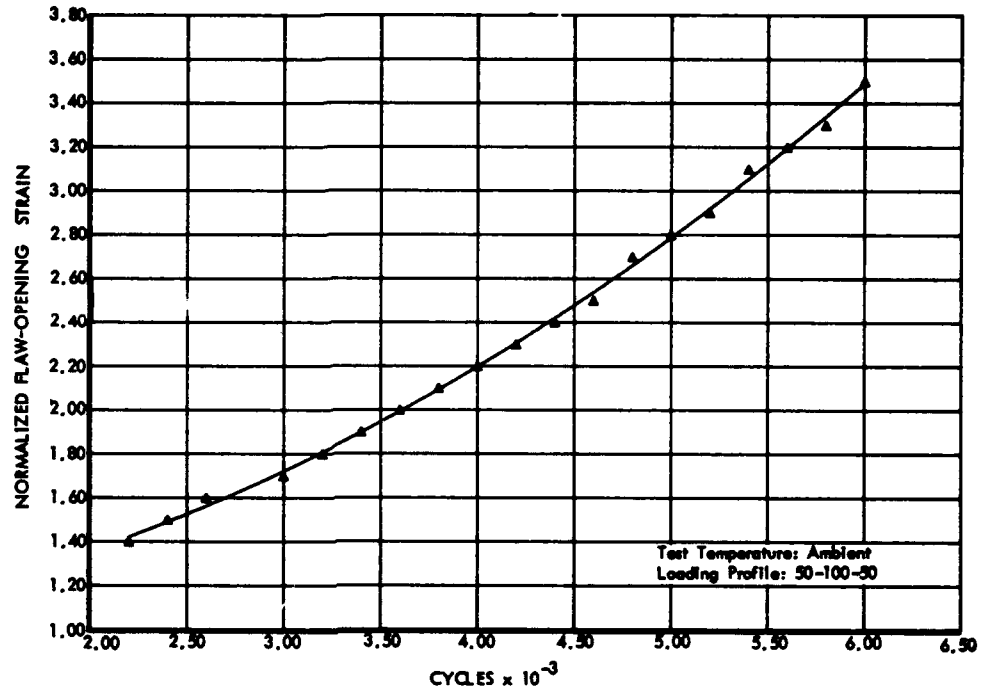


TABLE XI  
FRACTURE DATA FOR 2219-T87 ALUMINUM  
WITH FLAWS ORIGINATING AT HOLES

Identification	SPECIMEN		ENVIRONMENT		HOLE		FLAW VARIABLES				GROSS FAILURE STRESS (Ksi)
	Gage Thickness (Inch)	Gage Width (Inch)	Medium	Temperature (°F)	Diameter, 2r (Inch)	2r/t	Flaw Depth, a (Inch)	Flaw Length, c (Inch)	a/t	a/c	
5HA22-1	0.9002	4.0005	LN <sub>2</sub>	-320	0.4495	0.499	0.190	0.710	0.211	0.268	47.6
5HA22-2	0.8995	4.0025	LN <sub>2</sub>	-320	0.4505	0.501	0.190	0.710	0.211	0.268	47.5
5HA25-1	0.9002	3.9965	LN <sub>2</sub>	-320	0.4500	0.500	0.205	0.356	0.228	0.576	48.5
5HA25-2	0.9010	3.9992	LN <sub>2</sub>	-320	0.4495	0.499	0.178	0.348	0.198	0.511	52.2
5HA21-1	0.9002	4.0012	LN <sub>2</sub>	-320	0.4500	0.500	0.166	0.166	0.184	1.000	52.9
5HA21-2	0.9005	3.9970	LN <sub>2</sub>	-320	0.4503	0.500	0.200	0.180	0.222	1.111	52.7
5HA52-1	0.7985	7.5040	LN <sub>2</sub>	-320	0.4000	0.501	0.400	1.610	0.501	0.248	39.6
5HA52-2	0.8002	7.5010	LN <sub>2</sub>	-320	0.3998	0.500	0.396	1.700	0.495	0.233	38.6
5HA55-1	0.7990	5.0045	LN <sub>2</sub>	-320	0.4002	0.501	0.388	0.710	0.486	0.546	42.5
5HA55-2	0.8005	5.0000	LN <sub>2</sub>	-320	0.4012	0.501	0.388	0.710	0.485	0.546	45.0
5HA51-1	0.6994	4.0036	LN <sub>2</sub>	-320	0.3994	0.571	0.430	0.455	0.615	0.945	50.6
5HA51-2	0.6995	4.0025	LN <sub>2</sub>	-320	0.4002	0.572	0.408	0.410	0.583	0.995	45.2
5HA82-1	0.6995	9.0050	LN <sub>2</sub>	-320	0.3500	0.500	0.525	2.170	0.751	0.242	30.2
5HA82-2	0.6999	9.0030	LN <sub>2</sub>	-320	0.3492	0.499	0.565	2.230	0.807	0.253	28.7
5HA85-1	0.6998	9.0060	LN <sub>2</sub>	-320	0.3500	0.500	0.520	1.060	0.743	0.491	43.6
5HA85-2	0.6980	9.0040	LN <sub>2</sub>	-320	0.3513	0.503	0.550	1.050	0.788	0.524	37.4
5HA81-1	0.7998	4.0001	LN <sub>2</sub>	-320	0.3500	0.438	0.575	0.560	0.719	1.027	43.1
5HA81-2	0.7993	4.0005	LN <sub>2</sub>	-320	0.3495	0.437	0.555	0.550	0.694	1.009	43.7

**TABLE XII**  
**FRACTURE DATA FOR 2219-T87 ALUMINUM WITH FLAWS ORIGINATING AT HOLES**

SPECIMEN			ENVIRONMENT		HOLE		FLAW VARIABLES				GROSS FAILURE STRESS (Ksi)
Identification	Gage Thickness (Inch)	Gage Width (Inch)	Medium	Temperature (°F)	Diameter, 2r (Inch)	2r/t	Flaw Depth, a (Inch)	Flaw Length, c (Inch)	a/t	a/c	
1HA22-1	0.9000	4.9985	LN <sub>2</sub>	-320	0.8995	0.999	0.216	0.685	0.240	0.315	39.0
1HA22-2	0.8995	5.0025	LN <sub>2</sub>	-320	0.9005	1.001	0.190	0.660	0.211	0.288	42.0
1HA25-1	0.8990	5.0015	LN <sub>2</sub>	-320	0.9008	1.002	0.192	0.340	0.214	0.565	41.8
1HA25-2	0.8992	5.0002	LN <sub>2</sub>	-320	0.9008	1.002	0.196	0.350	0.218	0.560	42.7
1HA21-1	0.8995	3.9993	LN <sub>2</sub>	-320	0.9004	1.001	0.186	0.172	0.207	1.081	43.5
1HA21-2	0.8995	4.0015	LN <sub>2</sub>	-320	0.8995	1.000	0.176	0.158	0.196	1.114	42.3
1HA52-1	0.7990	7.5020	LN <sub>2</sub>	-320	0.7998	1.001	0.396	1.530	0.496	0.259	31.0
1HA52-2	0.8001	7.5000	LN <sub>2</sub>	-320	0.7995	.999	0.370	1.620	0.462	0.228	35.1
1HA55-1	0.8000	7.5000	LN <sub>2</sub>	-320	0.7998	1.000	0.400	0.710	0.500	0.563	35.5
1HA55-2	0.8004	7.5000	LN <sub>2</sub>	-320	0.8003	1.000	0.395	0.685	0.494	0.577	35.5
1HA51-1	0.7985	3.9975	LN <sub>2</sub>	-320	0.8001	1.002	0.410	0.400	0.513	1.025	36.3
1HA51-2	0.7995	4.0005	LN <sub>2</sub>	-320	0.8004	1.001	0.404	0.400	0.505	1.010	37.0
1HA82-1A	0.6990	9.0110	LN <sub>2</sub>	-320	0.7005	1.002	0.550	2.130	0.787	0.258	21.6
1HA82-2	0.6995	9.0050	LN <sub>2</sub>	-320	0.6995	1.000	0.520	2.230	0.743	0.233	25.8
1HA85-1	0.7008	9.0020	LN <sub>2</sub>	-320	0.7005	1.000	0.520	0.965	0.742	0.539	33.7
1HA85-2	0.7010	9.0010	LN <sub>2</sub>	-320	0.7001	0.999	0.540	1.000	0.770	0.540	33.0
1HA81-1	0.7000	3.9972	LN <sub>2</sub>	-320	0.6990	0.999	0.565	0.550	0.807	1.027	32.7
1HA81-2	0.6996	4.0024	LN <sub>2</sub>	-320	0.7000	1.001	0.560	0.560	0.800	1.000	35.3

**TABLE XIII**  
**FRACTURE DATA FOR 5A1-25Sn(ELI) TITANIUM WITH FLAWS ORIGINATING AT HOLES**

SPECIMEN			ENVIRONMENT		HOLE		FLAW VARIABLES				GROSS FAILURE STRESS (Ksi)
Identification	Gage Thickness (Inch)	Gage Width (Inch)	Medium	Temperature (°F)	Diameter, 2r (Inch)	2r/t	Flaw Depth, a (Inch)	Flaw Length, c (Inch)	a/t	a/c	
5HT22-1	0.3858	1.9988	LN <sub>2</sub>	-320	0.1860	0.482	0.092	0.260	0.238	0.354	134.8
5HT22-2	0.3905	2.0028	LN <sub>2</sub>	-320	0.1860	0.476	0.098	0.268	0.251	0.366	116.4
5HT25-1	0.3775	2.0004	LN <sub>2</sub>	-320	0.1840	0.487	0.066	0.136	0.175	0.485	147.6
5HT25-2	0.3833	2.0014	LN <sub>2</sub>	-320	0.1840	0.480	0.074	0.140	0.193	0.529	139.3
5HT21-1	0.3920	2.0002	LN <sub>2</sub>	-320	0.1860	0.474	0.076	0.084	0.194	0.905	144.7
5HT21-2	0.3812	1.9971	LN <sub>2</sub>	-320	0.1880	0.493	0.074	0.066	0.194	1.121	155.6
5HT52-1	0.3815	4.0010	LN <sub>2</sub>	-320	0.1920	0.503	0.192	0.750	0.503	0.256	78.4
5HT52-2	0.3705	4.0008	LN <sub>2</sub>	-320	0.1880	0.518	0.192	0.750	0.518	0.256	77.9
5HT55-1	0.3880	2.0005	LN <sub>2</sub>	-320	0.1850	0.477	0.176	0.384	0.454	0.458	100.5
5HT55-2	0.3885	2.0006	LN <sub>2</sub>	-320	0.1850	0.476	0.190	0.352	0.489	0.540	97.8
5HT51-1	0.3835	1.9982	LN <sub>2</sub>	-320	0.1860	0.485	0.182	0.200	0.475	0.910	112.2
5HT51-2	0.3877	1.9984	LN <sub>2</sub>	-320	0.1860	0.480	0.180	0.180	0.464	1.000	121.3
5HT82-1	0.3700	5.4495	LN <sub>2</sub>	-320	0.1860	0.503	0.300	1.200	0.811	0.250	64.8
5HT82-2	0.3748	5.5014	LN <sub>2</sub>	-320	0.1880	0.502	0.300	1.180	0.800	0.254	62.5
5HT85-1	0.3824	2.7492	LN <sub>2</sub>	-320	0.1860	0.486	0.288	0.620	0.753	0.465	80.4
5HT85-2	0.3920	2.7514	LN <sub>2</sub>	-320	0.1850	0.472	0.300	0.620	0.765	0.484	81.1
5HT81-2	0.3868	1.9970	LN <sub>2</sub>	-320	0.1860	0.481	0.306	0.280	0.791	1.093	97.2
5HT81-2	0.3874	2.0000	LN <sub>2</sub>	-320	0.1860	0.480	0.280	0.308	0.723	1.100	100.7

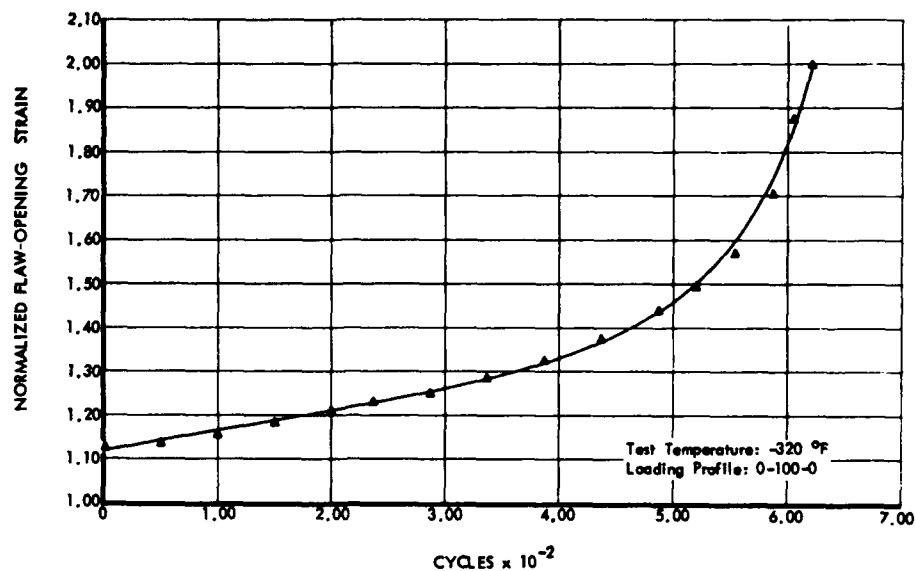
**TABLE XIV**  
**FRACTURE DATA FOR 5A1-2.5Sn (ELI) TITANIUM WITH FLAWS ORIGINATING AT HOLES**

SPECIMEN			ENVIRONMENT		HOLE		FLAW VARIABLES				GROSS FAILURE STRESS (Ksi)
Identification	Gage Thickness (Inch)	Gage Width (Inch)	Medium	Temperature (°F)	Diameter, 2r (Inch)	2r/t	Flaw Depth, a (Inch)	Flaw Length, c (Inch)	a/t	a/c	
IHT22-1	0.3875	2.7497	LN <sub>2</sub>	-320	0.3740	0.965	0.076	0.285	0.196	0.267	107.9
IHT22-2	0.3901	2.7485	LN <sub>2</sub>	-320	0.3735	0.957	0.090	0.290	0.231	0.310	99.8
IHT25-1	0.3870	1.9980	LN <sub>2</sub>	-320	0.3760	0.972	0.086	0.132	0.222	0.652	99.8
IHT25-2	0.3794	1.9965	LN <sub>2</sub>	-320	0.3740	0.986	0.080	0.132	0.211	0.606	105.7
IHT21-1	0.3805	2.0006	LN <sub>2</sub>	-320	0.3750	0.986	0.072	0.070	0.189	1.029	122.2
IHT21-2	0.3835	1.9982	LN <sub>2</sub>	-320	0.3750	0.978	0.074	0.068	0.193	1.088	110.9
IHT52-1	0.3855	5.5025	LN <sub>2</sub>	-320	0.3745	0.971	0.182	0.725	0.472	0.251	69.5
IHT52-2	0.3821	5.5018	LN <sub>2</sub>	-320	0.3745	0.980	0.190	0.725	0.497	0.262	67.3
IHT55-1	0.3830	2.7470	LN <sub>2</sub>	-320	0.3740	0.977	0.190	0.350	0.496	0.543	78.9
IHT55-2	0.3835	2.7495	LN <sub>2</sub>	-320	0.3740	0.975	0.180	0.380	0.469	0.474	79.2
IHT51-1	0.3795	1.9980	LN <sub>2</sub>	-320	0.3735	0.984	0.182	0.178	0.480	1.022	89.9
IHT51-2	0.3740	1.9998	LN <sub>2</sub>	-320	0.3730	0.997	0.204	0.196	0.545	1.041	87.4
IHT82-1	0.3737	5.5015	LN <sub>2</sub>	-320	0.3735	0.999	0.300	1.170	0.803	0.256	55.9
IHT82-2	0.3854	5.5015	LN <sub>2</sub>	-320	0.3730	0.968	0.300	1.170	0.785	0.256	62.3
IHT85-1	0.3824	2.7492	LN <sub>2</sub>	-320	0.3745	0.979	0.288	0.620	0.753	0.465	68.1
IHT85-2	0.3920	2.7514	LN <sub>2</sub>	-320	0.3755	0.958	0.300	0.620	0.765	0.484	71.0
IHT81-1	0.3755	2.7480	LN <sub>2</sub>	-320	0.3730	0.996	0.308	0.276	0.820	1.116	77.2
IHT81-2	0.3926	2.7485	LN <sub>2</sub>	-320	0.3750	0.955	0.296	0.296	0.754	1.000	79.0

**TABLE XV**  
**CYCLIC DATA FOR SPECIMENS WITH FLAWS ORIGINATING AT HOLES**

SPECIMEN				HOLE		FLAW SIZE BEFORE TEST RUN				ENVIRONMENT		GROSS CYCLIC STRESS (Ksi)	CYCLES TO FAILURE
Material	Identification	Gage Thickness, t (Inch)	Gage Width (Inch)	Diameter, 2r (Inch)	2r/t	Flaw Depth, a <sub>i</sub> (Inch)	Flaw Length, c <sub>i</sub> (Inch)	(a/c) <sub>i</sub>	(a/t) <sub>i</sub>	Medium	Temperature (°F)		
2219-T87 Aluminum	HACH-1	0.800	4.00	0.402	0.503	0.166	0.150	0.208	1.107	LH <sub>2</sub>	-423	45.5	98
	HACH-2	0.800	4.00	0.402	0.503	0.168	0.144	0.210	1.167	LH <sub>2</sub>	-423	41.0	339
	HACH-3	0.80	4.00	0.402	0.503	0.176	0.148	0.220	1.189	LH <sub>2</sub>	-423	41.0	446
5A1-2.5Sn (ELI) Titanium	HTC-7H	0.367	2.00	0.185	0.504	0.075	0.075	0.204	1.000	LH <sub>2</sub>	-423	81.7	539
	HTC-8H	0.372	2.00	0.185	0.497	0.071	0.075	0.191	0.947	LH <sub>2</sub>	-423	80.5	471
	HTC-9H	0.371	2.00	0.185	0.498	0.082	0.076	0.221	1.079	LH <sub>2</sub>	-423	71.3	1191
	HTC-4N	0.368	2.00	0.185	0.503	—	—	—	—	LN <sub>2</sub>	-320	115.0	382
	HTC-5N	0.365	2.00	0.185	0.507	—	—	—	—	LN <sub>2</sub>	-320	115.0	374
	HTC-3R	0.368	2.00	0.185	0.502	0.075	0.075	0.204	1.000	LN <sub>2</sub>	-320	95.0	1734

**Figure 17. Flaw-Opening Strain vs. Cycles for 6A1-4V (ELI) Titanium Specimen NTO-2.**



specimens were very flat and exhibited only very small shear lips. The fracture surface of one aluminum specimen (1HA52-2) exhibited extensive delamination along the flaw periphery. Fracture surfaces of several other aluminum specimens (1HA22-2, 5HA22-1, and -2, and 1HA51-2) exhibited small amounts of delamination along the flaw periphery.

Table XV summarizes test variables and cyclic lives for nine specimens containing flaws originating at holes that were cycled to failure. Flaw size at fracture was difficult to determine accurately and so only initial flaw sizes are reported. It did appear that all failures occurred before the flaw depth penetrated the specimen thickness.

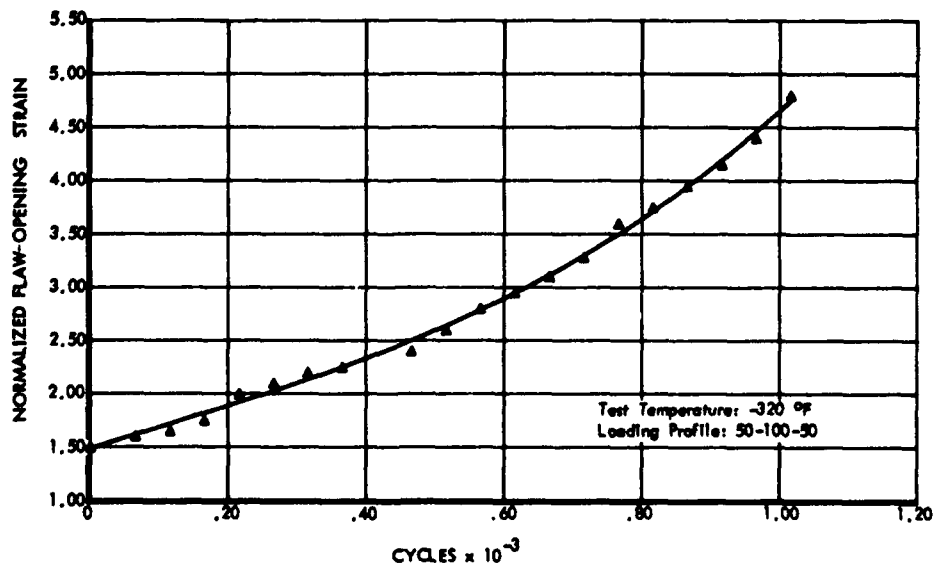
### ANALYSIS AND DISCUSSION

#### Fracture at Surface Flaws

Plane strain fracture toughness ( $K_{Ic}$ ) values were

calculated for the tested materials using Equation 2 and the assumption that fracture initiated under the influence of the maximum applied stress intensity at the tip of the flaw. The resulting  $K_{Ic}$  values are summarized in Table XVI for both 2014-T62 aluminum and 6A1-4V(ELI) titanium alloys. Within the usual experimental scatter, reasonably constant values of  $K_{Ic}$  were calculated for given material-environment-test conditions. Furthermore, there is good agreement between  $K_{Ic}$  values for both statically and cyclically tested 6A1-4V(ELI) specimens. Similar results have been obtained on a number of previous investigations (Ref. 14, 16, 17) in which surface-flawed specimens have been tested. For the 2014-T62 aluminum alloy,  $K_{Ic}$  values for statically tested specimens were slightly less than corresponding values for cyclically tested specimens. The discrepancy was more pronounced at ambient and  $-320^{\circ}\text{F}$  temperatures than at  $-423^{\circ}\text{F}$  and is probably largely due to difference in conditions at the critical flaw peripheries between the two groups of specimens. Flaw growth in cyclically tested specimens was irregular in nature and resulted in flaws with very rough

**Figure 18. Flaw-Opening Strain vs. Cycles for 6A1-4V (ELI) Titanium Specimen NT5-2.**



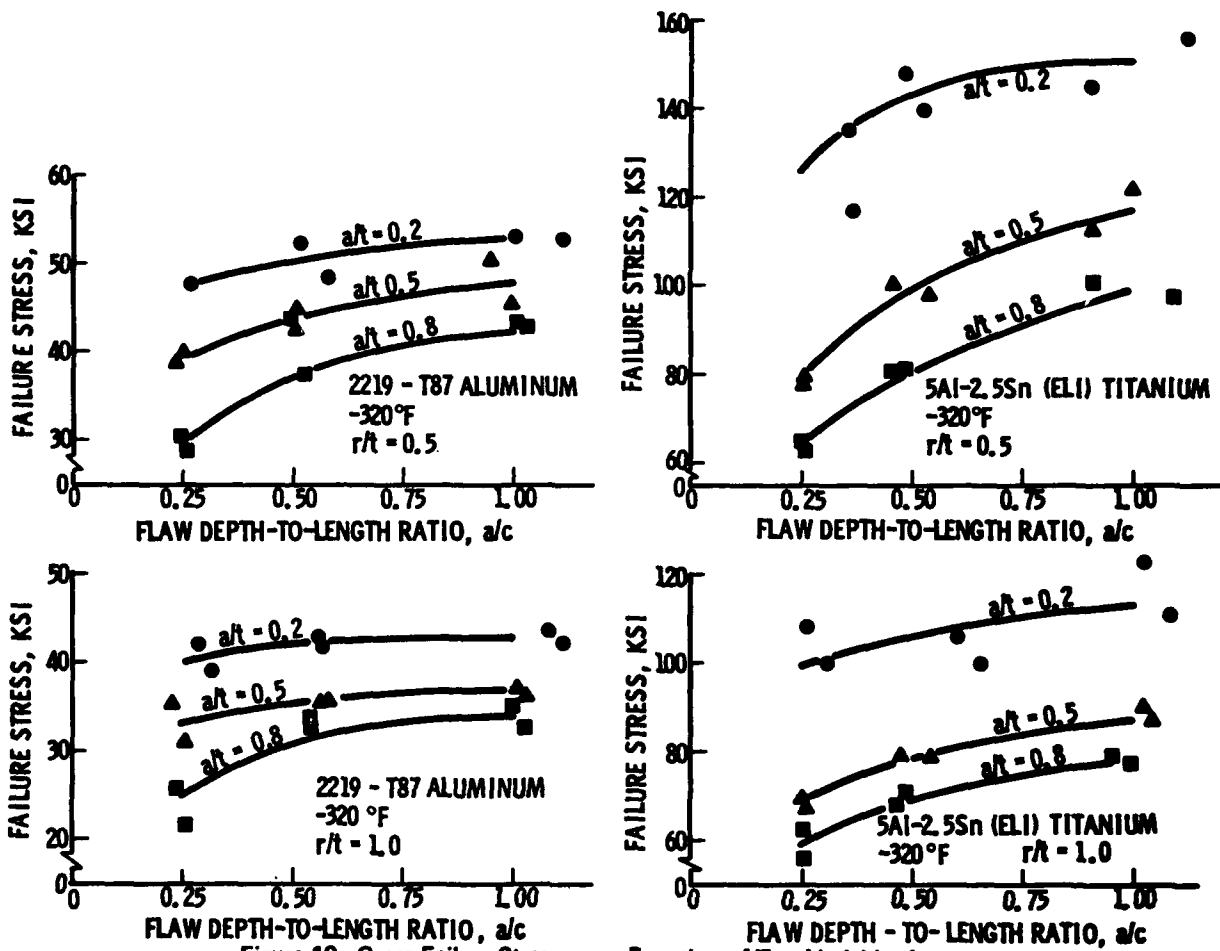


Figure 19. Gross Failure Stresses as a Function of Test Variables for Specimens with Flaws Originating at Holes.

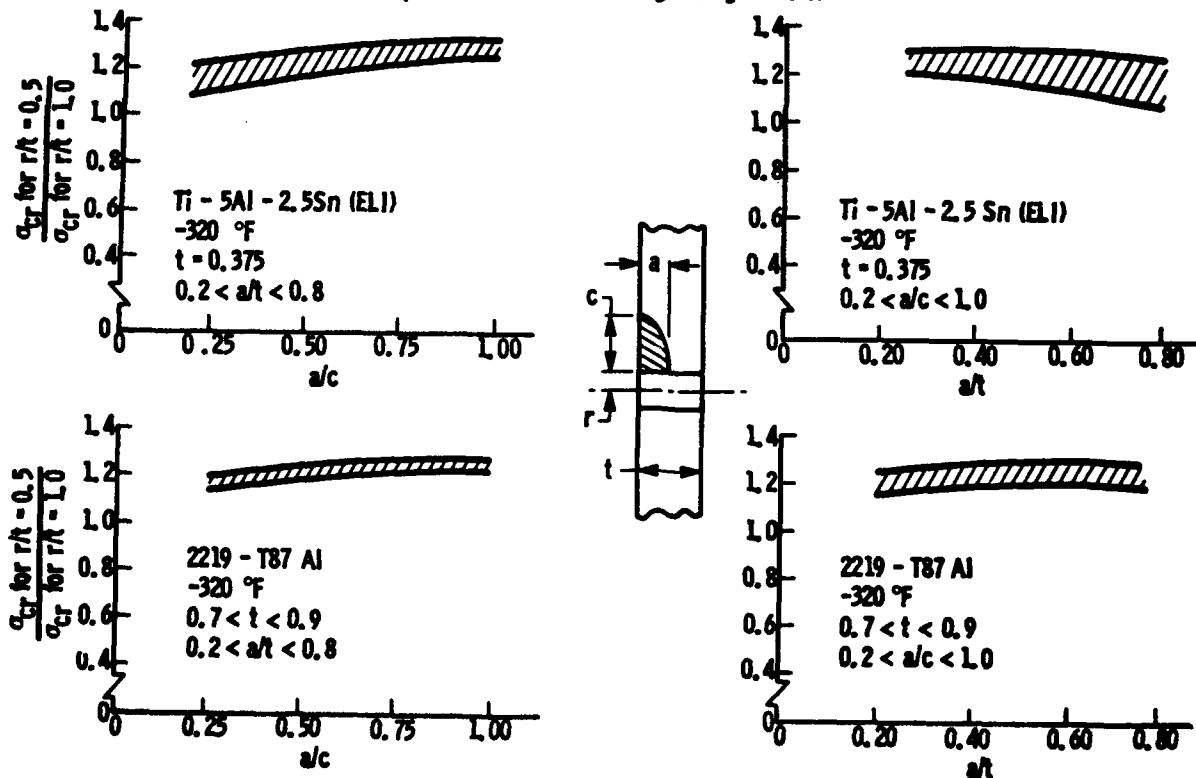


Figure 20. Effect of Hole on Failure Stress for Specimens with Flaws Originating at Holes.

**TABLE XVI**  
**PLANE STRAIN FRACTURE TOUGHNESS VALUES**  
**FROM SURFACE FLAW TESTS**

MATERIAL	TEST TYPE	TEST TEMP. (°F)	NUMBER OF TESTS	AVERAGE $K_{Ic}$ (Ksi/√in)	RANGE OF $K_{Ic}$ (Ksi/√in)
2014-T62 Aluminum Base Metal (Long Grain)	Static	Amb.	3	39	38-40
		-320	3	40	38-41
		-423	3	48	45-51
	Cyclic	Amb.	9	46	45-47
		-320	5	46	42-49
		-423	10	52	48-56
6Al-4V(ELI) Titanium Base Metal (Long Grain)	Static	Amb.	2	81	78-84
		-320	3	71	65-75
		-423	3	52	50-55
	Cyclic	Amb.	0	-	-
		-320	10	68	66-72
		-423	10	53	51-58

surfaces and peripheries that appeared quite jagged when viewed with the naked eye. On the other hand, flaws in statically tested specimens were very flat and regular to the naked eye and more closely resembled the mathematical model of a flat, planar, regular crack for which Equation 2 was developed.

The afore described fracture test results are consistent with the view that, for surface flaws having depths less than half the parent structure thickness, failure initiates at the maximum flaw depth when the applied stress intensity reaches the plane strain fracture toughness of the parent material. For cracks with very irregular peripheries, the critical stress intensity value may be slightly higher than the plane strain fracture toughness.

#### Fatigue Growth of Surface Flaws

An analysis was undertaken to determine if a flaw-growth-rate equation could be derived to represent the cyclic life and flaw-growth-rate data developed in this investigation. An equation of the form

$$d(a/Q)/dN = C(\sigma_o/\sigma)^2 (1 + \lambda)^m (\Delta K)^n (1 - K_{max}/K_{Ic})^{-p} \quad (3)$$

was chosen where:

$C$  = a constant for a particular material-environment combination;

$\sigma$  = peak cyclic stress level;

$\sigma_o$  = an arbitrarily chosen peak cyclic stress level for which the value of  $C$  is derived;

$K_{max}$  = peak stress intensity at the tip of the flaw during the loading cycle;

$K_{min}$  = minimum stress intensity corresponding to  $K_{max}$ ;

$$\Delta K = (K_{max} - K_{min});$$

$$\lambda = K_{min}/\Delta K;$$

$m, n, p$  = exponents to be experimentally evaluated.

In Equation 3,  $C$  represents the effect of material properties, environmental conditions, and minor variables (such as frequency) on flaw-growth rate. Lambda ( $\lambda$ ) is a modified value of the Roberts and Erdogan<sup>6</sup> ( $\beta$ ) that accounts for the effect of mean-applied  $K$  during the loading cycle;  $\lambda = 0$  for a zero-to-tension loading cycle and 1.0 for a half-tension-to-tension loading cycle. The  $(\Delta K)^n$  term expresses the dominating effect of stress intensity range in the manner originally suggested by Paris<sup>1</sup>. The flaw-opening measurements in Figure 13 through 18 show that flaw growth rates increase rapidly as  $K_{max}$  approaches  $K_{Ic}$ . Accordingly, the  $(1 - K_{max}/K_{Ic})^{-p}$  term was included to account for this observed behavior. Finally, the stress ratio  $(\sigma_o/\sigma)^2$  was used to express the experimental result that the cyclic life data for specimens cycled to failure at different elastic peak cyclic stress levels can be represented by a unique  $K_{Ii}/K_{Ic}$  - or  $K_{Ii}$  - versus-cycles-to-failure curve. This result implies that flaw-growth rates are inversely proportional to the square of the peak cyclic stress (Ref. 16). Although no systematic investigation of the stress-level dependence of plane-strain flaw-growth rates has been undertaken over large ranges of peak cyclic stress, the data herein and in References 16 through 18 show that it is experimentally justified to consider flaw-growth rates to be stress-level dependent for the ranges of peak cyclic stress normally encountered in spacecraft pressure vessels.

Preliminary calculations showed that  $n \approx 4$  for all material-environment combinations tested in this program. Values of  $p$  were found to be  $\approx 1.0$  for aluminum and  $\approx 0.2$  for titanium in all environments. Accordingly, the value of  $n = 4$  was chosen for all materials and values of  $p = 1.0$  and  $0.2$  were used for aluminum and titanium, respectively. Having selected values for  $n$  and  $p$ , values of  $C$  were calculated using the experimental data for the zero-to-tension loading profile ( $\lambda = 0$ ). Finally, values of  $m$  were calculated using the experimentally established ratios of cyclic life for the zero-to-tension profile to cyclic life for the half-tension-to-tension profile. The resulting values of  $C$  and  $m$  are summarized in Table XVII.

The growth-rate expressions in Table XVII were integrated to construct the cyclic life curves included in Figures 7 through 11, where the test results can be compared to the fitted curves. In Figure 12, where Equation 3 is compared with experimentally determined flaw-growth rates, the equation was evaluated for the intermediate peak cyclic stress level ( $\sigma_o$ ) used in each set of tests; data for the maximum and minimum peak cyclic stress levels were multiplied by the square of the ratio of the actual to intermediate peak cyclic stress, i.e.,  $(\sigma/\sigma_o)^2$ , to make all data applicable to a single  $\sigma_o$  level; the calculated and actual data points are joined by dashed lines in Figure 12.



**TABLE XVII**  
**EXPERIMENTALLY EVALUATED CONSTANTS FOR GROWTH RATE EQUATION**

MATERIAL	TEMP. (°F)	AVERAGE OF APPARENT CYCLE $K_{IIc}$ (Ksi $\sqrt{In.}$ )	$\sigma_o$ (Ksi)	$\frac{d}{dN} \left( \frac{a}{Q} \right) = C \left( \frac{a_o}{\sigma} \right)^2 (1+\lambda)^m (\Delta K)^n \left( 1 - \frac{K_{max}}{K_{Ic}} \right)^p$			
				C	m	n	p
2014-T62 Aluminum Base Metal	+70 -320 -423	46 46 52	50	$1.20 \times 10^{-5}$ $1.20 \times 10^{-5}$ $2.70 \times 10^{-5}$	2.3 1.7 1.3	4.0 4.0 4.0	1.0 1.0 1.0
6Al-4V (ELI) Titanium Base Metal	+70 -320 -423	80 68 52	100	$4.87 \times 10^{-6}$ $2.03 \times 10^{-6}$ $2.03 \times 10^{-6}$	1.9 2.3 2.3	4.0 4.0 4.0	0.20 0.20 0.20
2014-T62 Aluminum 0.5-Inch Welds	+70 -320 -423	20 -- --	20	$1.49 \times 10^{-4}$ -- --	-- -- --	4.0 -- --	1.0 -- --
2014-T62 Aluminum 0.6-Inch Welds	+70 -320 -423	20 -- --	20	-- -- --	-- -- --	-- -- --	-- -- --
6Al-4V (ELI) Titanium As-Welded Welds	+70 -320 -423	60 50 45	100	$6.33 \times 10^{-6}$ $5.65 \times 10^{-6}$ $24.7 \times 10^{-6}$	-- -- 2.4	4.0 4.0 4.0	0.20 0.20 0.20
6Al-4V (ELI) Titanium Stress Relieved Welds	+70 -320 --	71 54 --	100	$5.32 \times 10^{-6}$ $2.80 \times 10^{-6}$ --	-- -- --	4.0 4.0 --	0.20 0.20 --

In general, there is good agreement between Equation 3 and test data over the entire range of  $K_{II}$  values used in each set of tests; one notable exception is Ti-6Al-4V (ELI) base metal in liquid hydrogen subjected to a half-tension-to-tension loading profile (Figure 11). A smooth curve could be drawn to very closely represent this data; however, such a

curve would have an unusually flat slope and would intersect the zero-to-tension data curve at  $K_{II}/K_{Ic} = 0.85$ . In view of the agreement between the zero-to-tension cyclic life curves for the titanium base metal in liquid nitrogen and liquid hydrogen, the half-tension-to-tension data for the liquid hydrogen environment were represented by the corresponding liquid nitrogen curve in Figure 11.

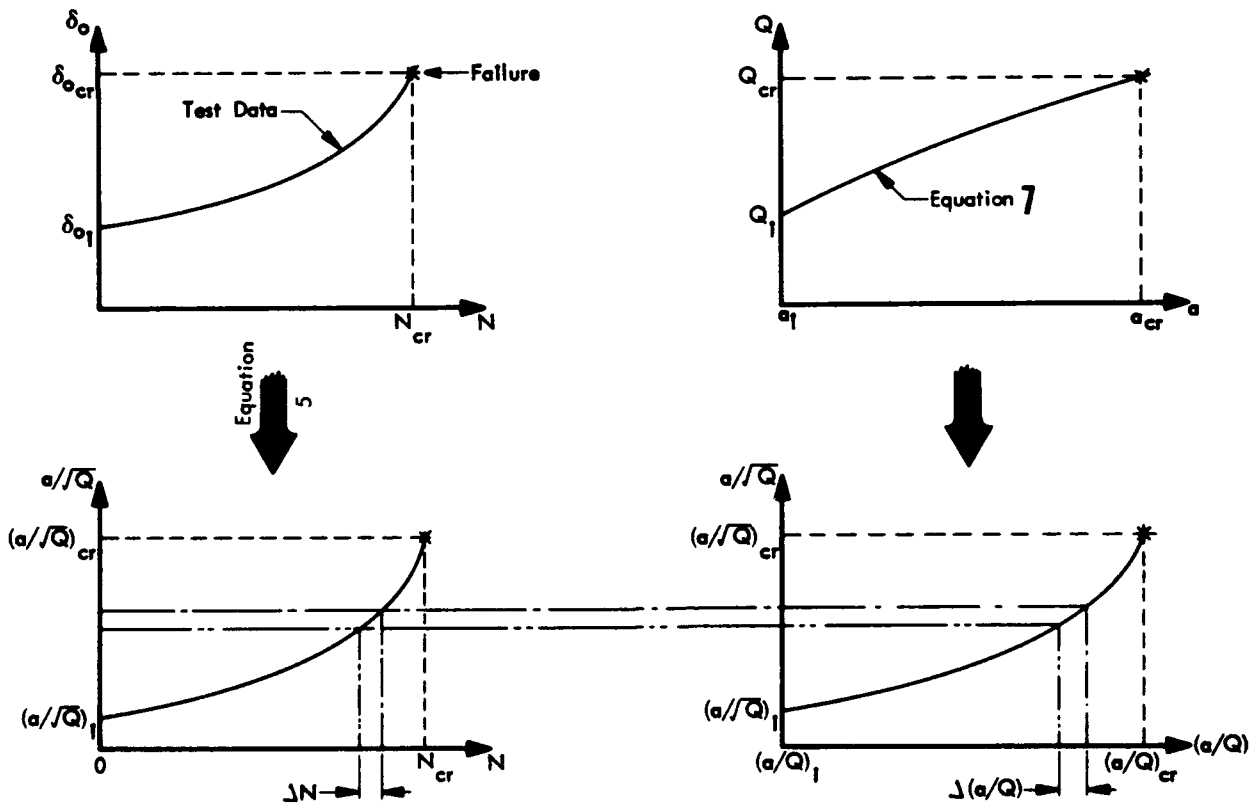
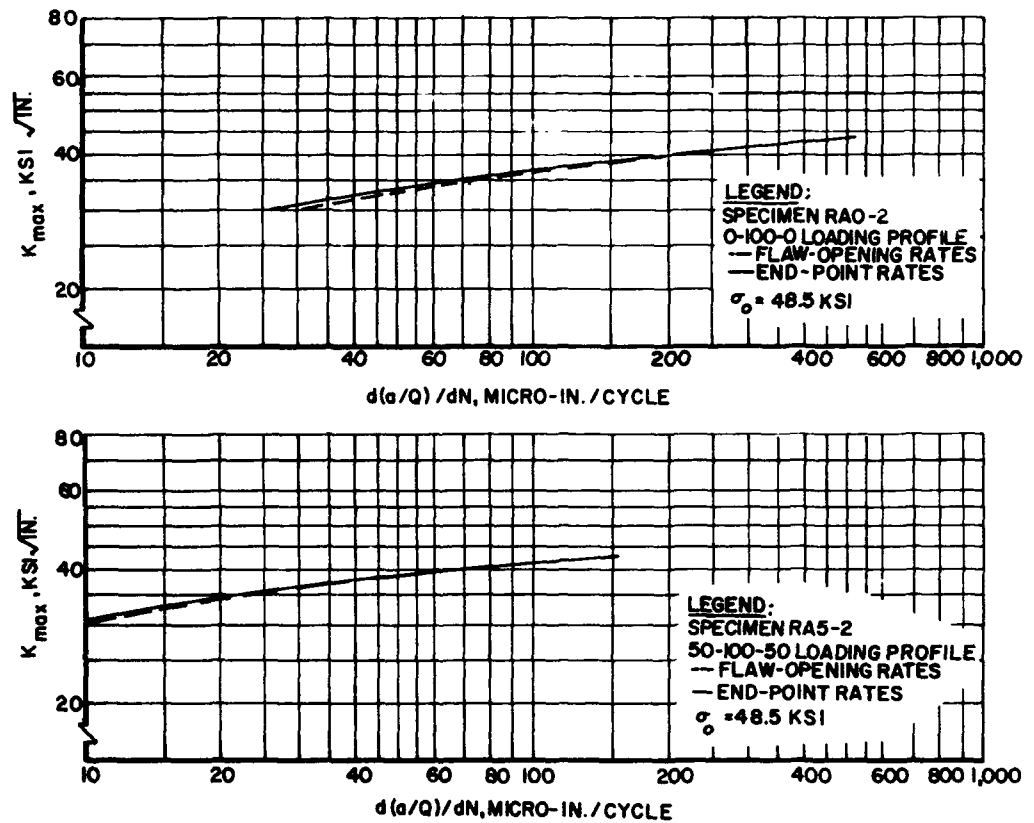


**Figure 21. Schematic Representation of Flaw-Opening Flaw-Growth-Rate Analysis.**

Figure 22. Comparison of End-Point and Flaw-Opening Growth Rates for 2014-T6 Aluminum Base Metal in Ambient Air.



It is interesting to note that the value of  $n = 4$  derived for Equation 10 is the same as the  $n$ -value that Paris<sup>2</sup> found to be in agreement with test results obtained from through-the-thickness cracks growing under conditions of plane stress in a number of metallic materials (steel, aluminum, titanium, and molybdenum). It can be speculated that  $n = 4$  will also be in agreement with test results for surface flaws growing under conditions of plane strain for metallic materials other than those tested in this program.

A second analysis was undertaken to calculate flaw growth rates using the experimentally established flaw-opening versus applied loading cycle curves (Figure 13 through 18). First, an approximate relationship between flaw opening and flaw dimensions was established. Use was made of an expression for the opening displacement of a completely embedded elliptical flaw in an elastic solid subjected to a uniform tension normal to the crack surface and at infinity (Ref. 19). The maximum opening displacement,  $\eta_o$ , occurs at the diametral center of the crack and is expressed by the equation

$$\eta_o = \frac{4(1-\nu)^2}{E} \frac{\sigma a}{\Phi}; \quad (4)$$

$\nu$  is Poisson's ratio and  $\Phi$  is a complete elliptic integral of the second kind. There is no solution available for flaw-opening displacement for a semi-elliptical surface flaw but such displacements should also be proportional to  $\sigma$  and  $a/\Phi$  for elastic materials. Following Irwin's analysis (Ref. 15) to account for the effect of plastic yielding, the maximum

flaw opening displacement,  $\delta_o$ , can be approximated by

$$\delta_o = C \sigma \sqrt{\frac{a}{Q}} \quad (5)$$

where  $C$  is a constant.

Values of  $C$  can be estimated for a given test specimen from the equation

$$\delta_{of} - \delta_{oi} = C \sigma [(a/\sqrt{Q})_f - (a/\sqrt{Q})_i] \quad (6)$$

where the subscripts  $i$  and  $f$  refer to initial and final values, respectively.

Since Equation (5) relates flaw-opening displacement to the parameter  $a/\sqrt{Q}$ , whereas flaw size is expressed in terms of  $a/Q$ , a relationship between  $a$  and  $2c$  is required so that values of  $a/\sqrt{Q}$  can be converted to flaw size values. Flaw lengths were not continuously monitored in these tests and so a relationship between flaw depth and flaw width had to be assumed. Two particular points on this relationship are obtained from the known initial and final flaw sizes. Intermediate points were estimated using the simple assumption that  $2c$  varies linearly with respect to "a", i.e.,

$$\frac{a - a_i}{a_f - a_i} = \frac{2c - 2c_i}{2c_f - 2c_i} \quad (7)$$

Unreported tests conducted at The Boeing Company in

Figure 23. Comparison of End-Point and Flaw-Opening Growth Rates for 6A1-4V (ELI) Titanium Base Metal in Ambient Air.

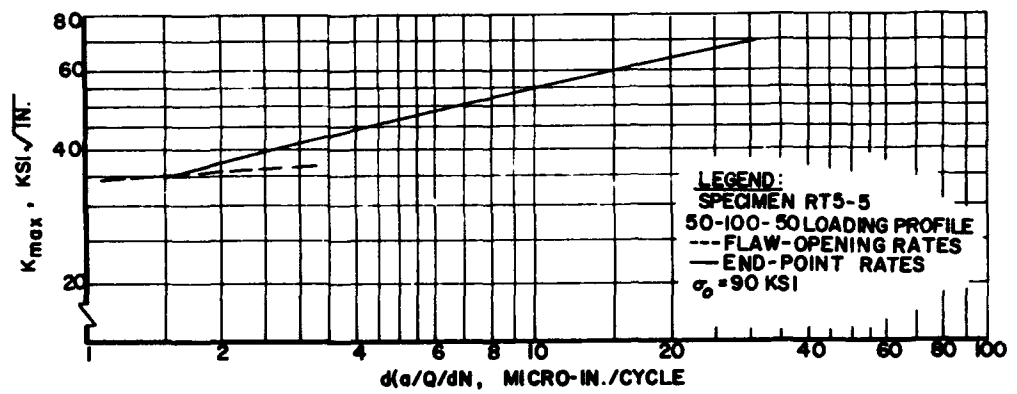
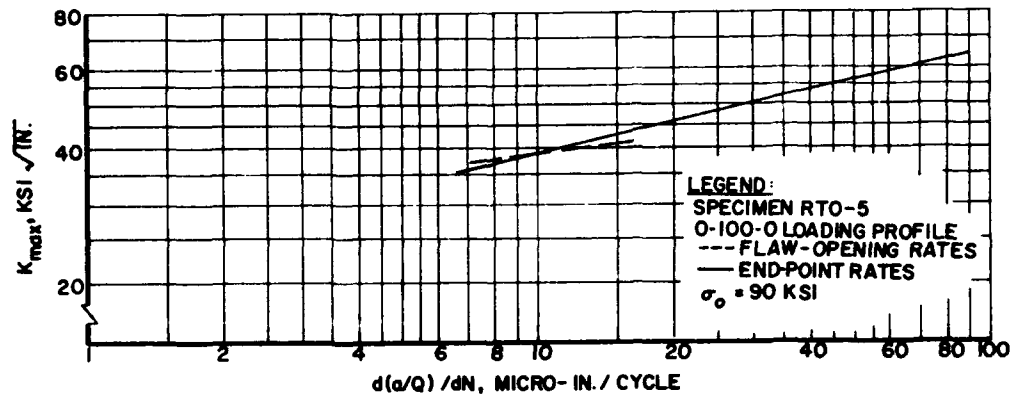


Figure 24. Comparison of End-Point and Flaw-Opening Growth Rates for 6A1-4V (ELI) Titanium Base Metal in Liquid Nitrogen.

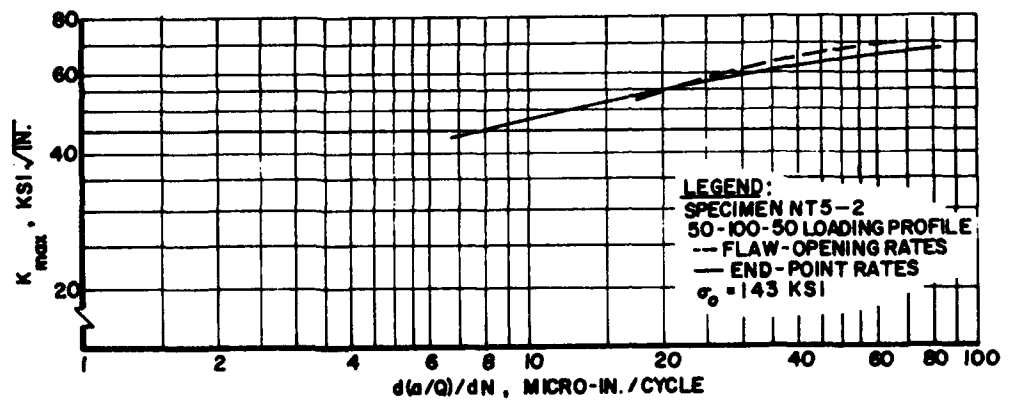
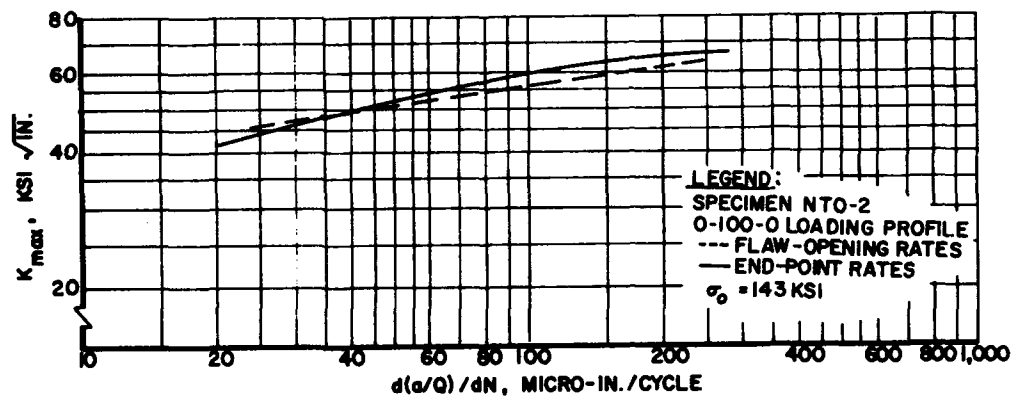
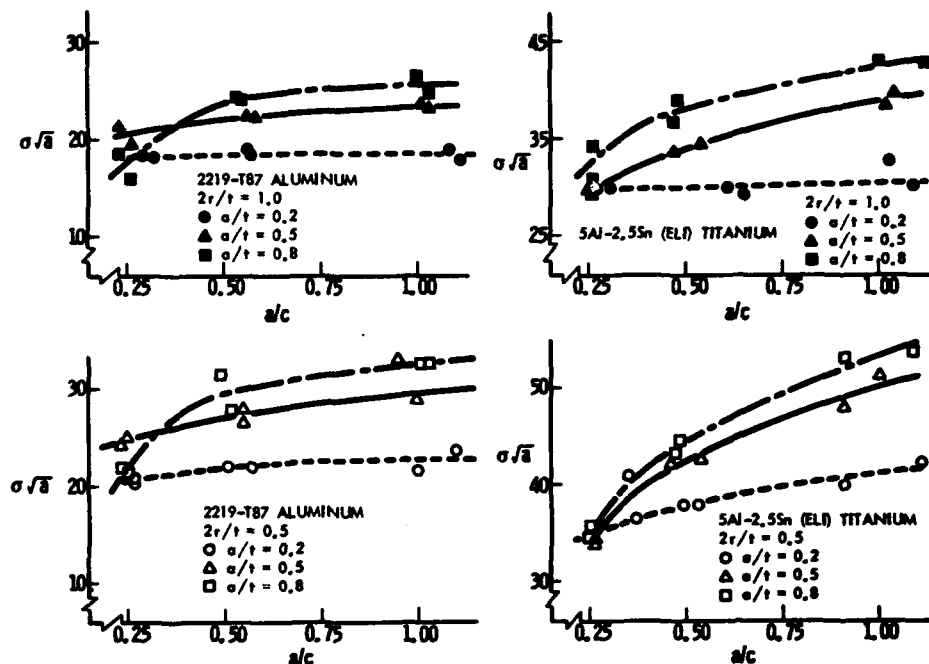


Figure 25.  $\sigma \sqrt{a}$  vs.  $(a/c)$  For Specimens with Flaws Originating at Holes.



which surface-flaws were intermittently cycled and marked have shown that Equation (7) is a good assumption.

Best-fit curves were then drawn through the flaw-opening strain-versus-cycles data with the aid of a digital computer. Results are shown in Figures 13 through 18. The program used isolates and analyzes the prominent geometric characteristics of the data and prescribes an appropriate fitting function with similar geometric characteristics. Least-square curves of polynomials and rational functions are fitted and the curve showing the least error is selected. For specimens that were cycled to failure, rational functions provided the best fit for the data; for specimens cycled over limited  $K_I$  ranges (titanium in ambient air), polynomials provided the best data fit. For those specimens that were cycled to failure, the mathematical expressions for the fitting curves were used to estimate the maximum flaw-opening strain on the cycle prior to fracture. Flaw-growth rates were then computed, as illustrated in Figure 21. Equation (7) was used to establish, in turn,  $Q$  versus  $a$  and  $a/\sqrt{Q}$  relationships. Equation (6) was used in conjunction with the test data to establish a relationship between  $a/\sqrt{Q}$  and applied loading cycles,  $N$ . Flaw-growth rates were calculated by dividing increments of  $a/Q$  by corresponding increments of  $N$ . All computations were carried out on a digital computer and the resulting flaw-growth rates for aluminum in room air, titanium in room air, and titanium in liquid nitrogen are related to  $K_{max}$  by the dotted curves in Figures 22 through 24.

Flaw-growth rates determined through the use of the flaw-opening instrumentation are in good agreement with corresponding end-point rates except for the titanium base metal at room temperature. For this material-environment combination, specimens were cycled over only small  $K_I$  ranges due to limitations imposed by material thickness: it is believed that the curves used to fit the data for the limit-

ed  $K_I$  ranges tested exhibited geometric properties different from those that would have characterized the corresponding part of a curve representing the average behavior for a much greater range of  $K_I$ .

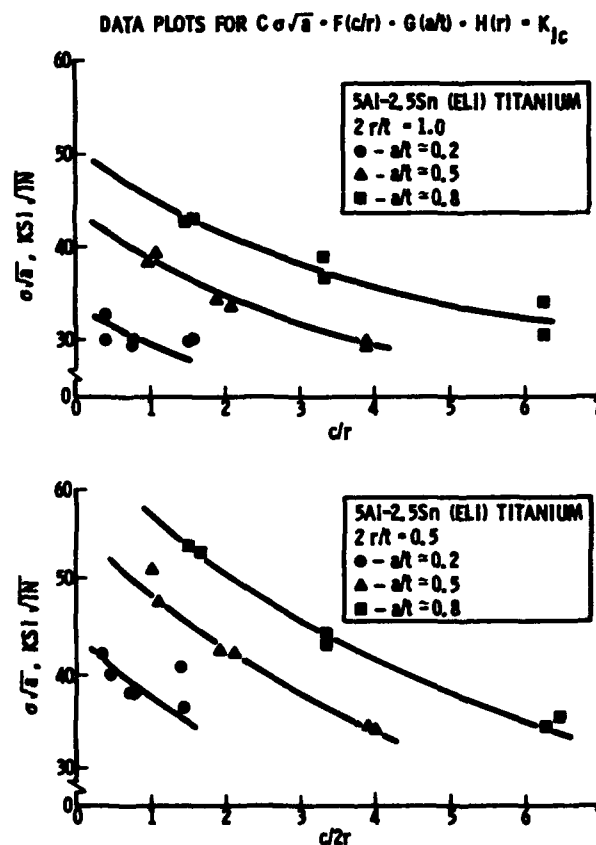


Figure 26.  $\sigma \sqrt{a}$  vs. Flaw Length to Hole Size Ratios for Titanium Specimens With Flaws Originating at Holes.

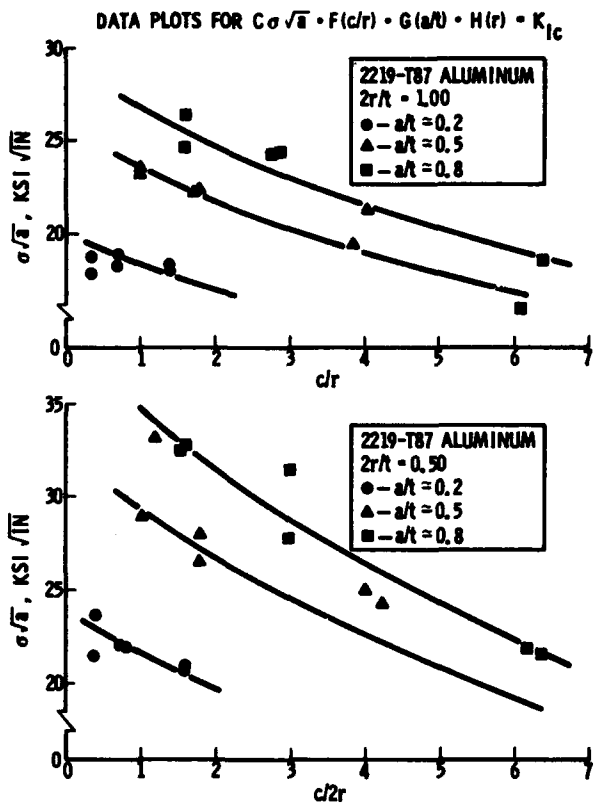


Figure 27.  $\sigma\sqrt{a}$  vs. Flaw Length to Hole Size Ratios for Aluminum Specimens with Flaws Originating at Holes.

#### Fracture at Flaws Originating From Holes

An attempt was made to develop a failure criterion for partially embedded flaws originating at holes using linear elastic fracture mechanics principles. It was assumed that failure originated along the peripheries of the flaws under

conditions of plane strain and at the location of maximum applied stress intensity,  $K_{max}$ . It is believed that the test specimens were sufficiently wide to eliminate specimen width effects so specimen geometry effects could be expressed in terms of the thickness ( $t$ ) only. Flaw size and shape are dependent on  $a$  and  $c$  and hole size is expressed by  $r$ . Hence, the failure criterion took the form

$$K_{max}(a, c, r, t) = K_{Ic} \quad (8)$$

Because of the combined stress concentrations of hole and flaw in the vicinity of the intersection of the flaw periphery and hole surface, it was felt that failure would very likely initiate near that intersection and the most significant flaw variable would be "a". Dimensional considerations then led to the following specialization of the Equation (8) criterion:

$$\sigma\sqrt{a} \cdot F(a, c, r, t) = K_{Ic} \quad (9)$$

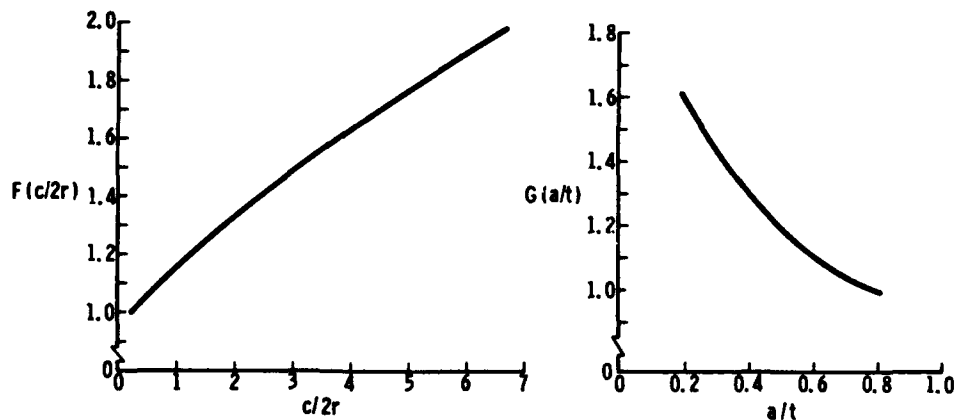
To gain insight into the form of  $F(a, c, r, t)$  values of  $\sigma\sqrt{a}$  were plotted in terms of different independent variables in Figures 25 through 27. It was at first thought that it might be possible to modify the failure criterion for surface flaws (Ref. 20) to predict failure stresses for flaws originating from holes. Under certain restrictive conditions (Ref. 20), the surface flaw failure criterion assumes the form

$$C\sigma\sqrt{a} \cdot F(a/c) \cdot G(a/t) = K_{Ic} \quad (10)$$

where  $G(a/t)$  is both material and  $(a/c)$  dependent. However, the  $\sigma\sqrt{a}$  versus  $(a/c)$  data plots in Figure 25 show that any attempts to modify Equation 10 to account for hole effects would not be successful. Data plots of  $\sigma\sqrt{a}$  against  $c/r$  in Figures 26 and 27 expressed the test results in a very orderly manner. Accordingly, a failure criterion of the form

$$C\sigma\sqrt{a} \cdot F(c/2r) \cdot G(a/t) \cdot H(r/t) = K_{Ic} \quad (11)$$

Figure 28. Failure Criterion for Flaws Originating at Holes.



$$K_{Ic} = 1.1 \sigma\sqrt{a} \cdot F(c/2r) \cdot G(a/t) \sqrt{4r/t}$$

was evaluated. Calculations showed that with the values of  $F(c/2r)$  and  $G(a/t)$  shown in Figure 28 and with  $H(r/t) = \sqrt{4(r/t)}$ , failure stresses could be calculated for all test specimens (excepting the delaminated aluminum specimen 1HA52-2) that differed from the actual failure stress by not more than  $\pm 9\%$ . In view of the complex geometry of the test specimens, the wide range of flaw sizes and shapes tested, and the usual  $\pm 5$  to  $10\%$  scatter in plane strain fracture toughness values, the success of Equation 11 is remarkable.

A review of the results obtained using the Equation 11 failure criterion led to the observation that the decreasing trend of  $G(a/t)$  with increasing  $a/t$  was an unanticipated

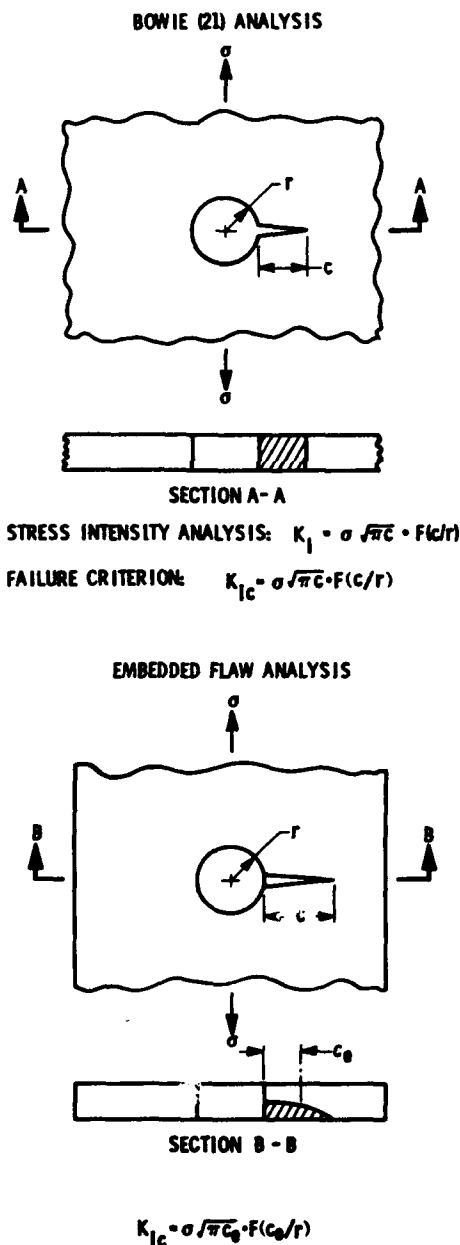


Figure 29. Comparison of Failure Criteria for Through-The-Thickness and Embedded Flaws Originating at Holes.

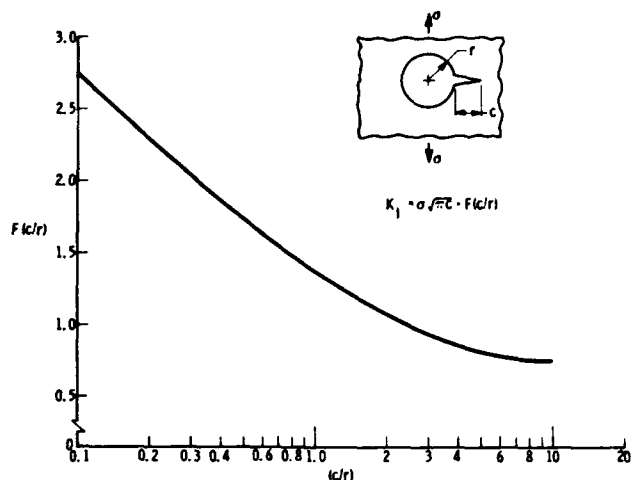


Figure 30.  $F(c/r)$  for Flaws Originating From Hole Failure Criterion.

result. For comparison, the Equation 10 surface flaw failure criterion for conditions under which fracture initiates at the maximum flaw depth contains a  $G(a/t)$  function that increases with increasing  $(a/t)$ . A second unanticipated result was the marked effect of  $c/r$  on fracture stress. In addition, it was noted that the effect of hole size on fracture strength decreased as flaw length increased. These observations led to

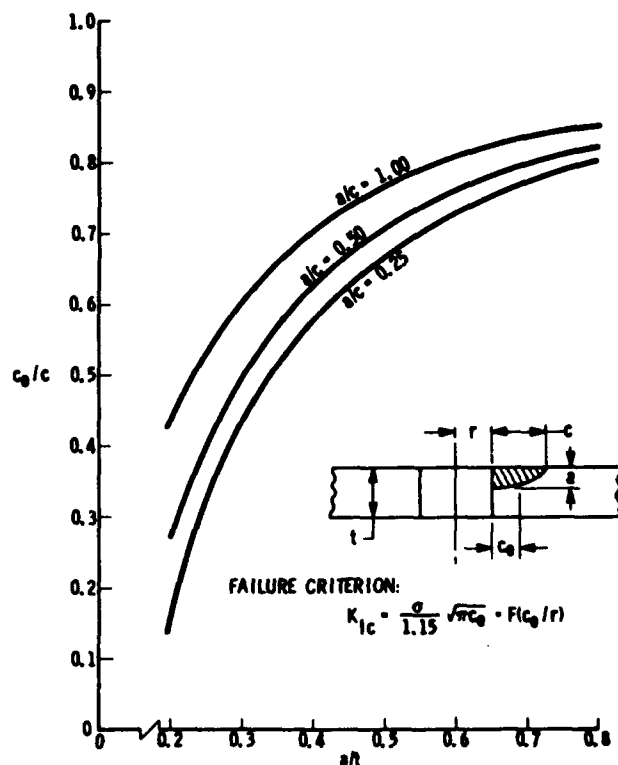
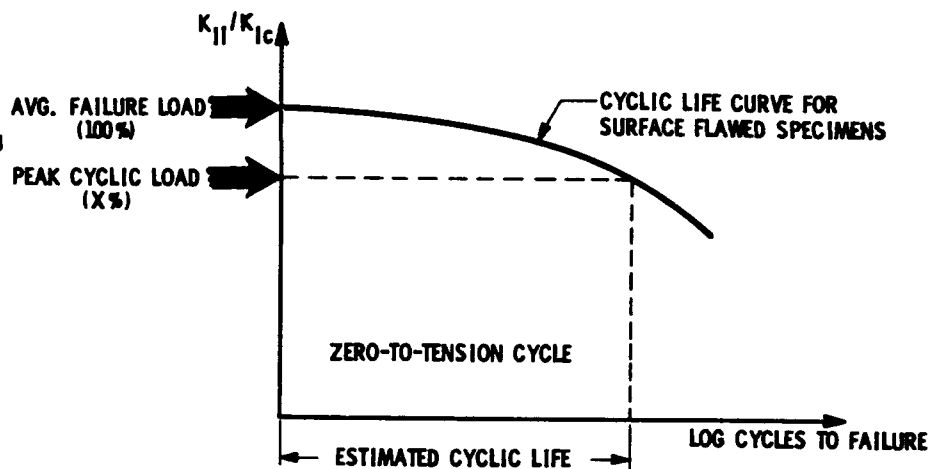


Figure 31. Values of Effective Flaw Length for Flaws Originating at Holes.

Figure 32. Method of Estimating Cyclic Life for Specimens with Flaws Originating at Holes.



$K_{II}$  - MAXIMUM STRESS INTENSITY APPLIED DURING INITIAL LOADING CYCLE  
 $K_{Ic}$  - PLANE STRAIN FRACTURE TOUGHNESS OF MATERIAL

the speculation that an orderly set of effective embedded flaw lengths could be calculated which, when substituted into Bowie's<sup>21</sup> stress intensity solution for through-the-thickness cracks originating at a hole, could be used to calculate failure stresses for embedded flaws. This approach is illustrated in Figure 29 where geometry, stress intensity, and failure criterion for the Bowie analysis is compared with the geometry and speculated failure criterion for the embedded flaw tests under discussion. Values of the function  $F(c/r)$  from the Bowie solution are included in Figure 30. Assuming a failure criterion of the form

$$K_{Ic} = C\sigma\sqrt{\pi c_e} \cdot F\left(\frac{c_e}{r}\right) \quad (12)$$

calculated values of  $(c_e/c)$  were found to relate to  $(a/c)$  and  $(a/t)$  in a very orderly manner for a value of  $C = 0.87$ . The curves are material independent for the two tested materials. Failure stresses calculated using the Equation 12 failure criterion and the curves in Figures 30 and 31 differed

from actual failure stresses by less than 10% for all but four specimens, 5HT22-1, 1HT82-1, 1HA52-2, and 1HA82-1. The actual failure stresses for 5HT22-1 and 1HA52-2 were higher than calculated due to inadequate crack sharpening in the titanium specimen and delamination in the aluminum specimen. The failure stresses for specimens 1HT82-1 and 1HA82-1A were lower than the comparable calculated values by 11 and 19% respectively. No reason could be found for the poor agreement of the 1HA82-1A test result. For comparison, the failure stress for the duplicate specimen of 1HA82-1A (1HA82-2) was approximately 4% lower than the calculated value.

In view of the highly empirical approach to the subject fracture problem, it is natural to question the applicability of the failure criteria to material and flaw geometries other than those tested. However, the agreement between the criteria and the results of the wide range of flaw geometries and two distinctly different materials tested implies that the criteria might be applicable to other materials and flaw shapes.

Figure 33. Cycle Life Results for 5A1-2.5Sn (ELI) Titanium @ -320°F.

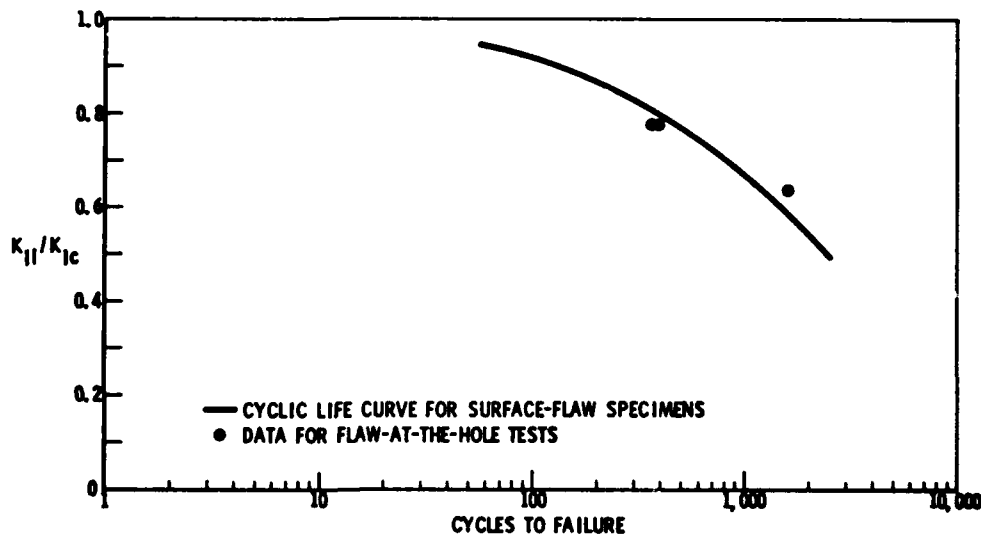
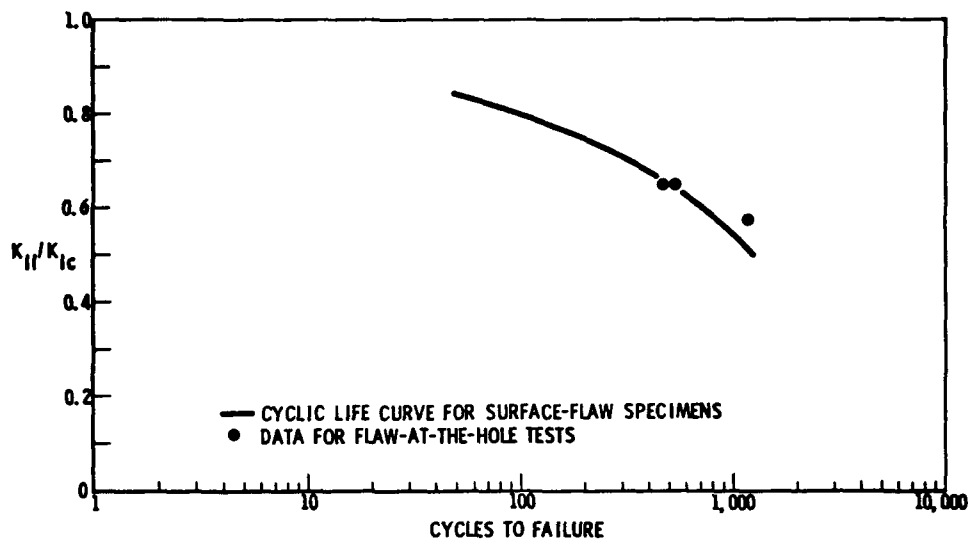


**Figure 34. Cycle Life Results for 5A1-2.5Sn (ELI) Titanium @ -423°F.**



**Fatigue Growth of Flaws Originating From Holes**

Prior to the cyclic testing of the nine specimens containing flaws emanating from holes, estimates of cyclic life were made for each specimen using an end-point analysis and previously developed (Ref. 16) cyclic life curves from tests of surface-flawed specimens. The estimates were made as schematically illustrated in Figure 32. The average failure load for corresponding statically tested specimens was taken as the load for which  $K_{Ii} = K_{Ic}$  on the ordinate of the surface flaw cyclic life curve. A peak cyclic load equal to X% of the average failure load was chosen to fail the specimen before the flaw depth completely penetrated the specimen thickness. The estimated cyclic life was then taken as the abscissa of the point on the cyclic life curve having an ordinate of X%. The success of this method for the nine tested specimens is illustrated in Figures 33 through 35 where good agreement is evidenced between predicted and actual cyclic lives. It appears the end-point method of estimating cyclic life is applicable to a wide range of partially embedded flaw geometries.

**CONCLUSIONS**

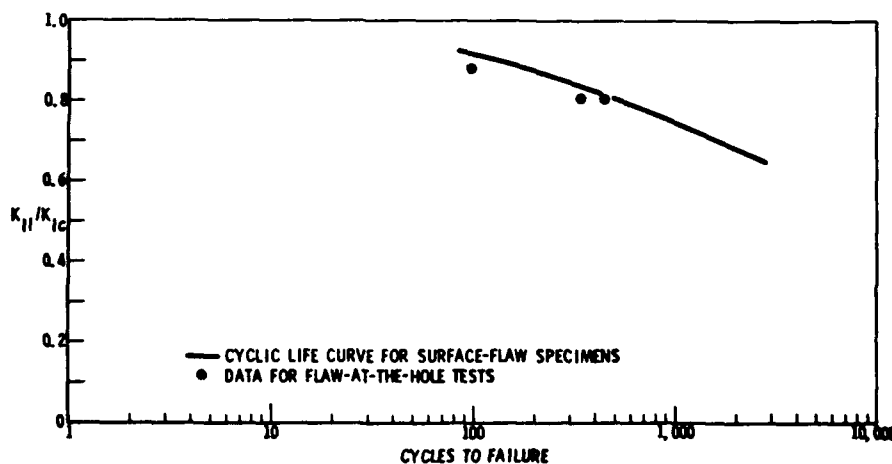
1. Fatigue growth of surface flaws can be considered a continuous process proceeding at rates expressed by  $d(a/Q)/dN$  (the rate of change of effective flaw size per cycle) and the following equation:

$$d(a/Q)/dN = C(\sigma_o/\sigma)^2 (1 + \lambda)^m (\Delta K)^n (1 - K_{max} / K_{Ic})^{-p}$$

where values of C, m, n, and p are experimentally evaluated constants.

2. For given material-environment combinations tested under uniform cyclic loading conditions, cyclic lives for tension loaded surface-flawed specimens that fail at flaw depth less than one-half the parent material thickness can be represented by a unique  $(K_{Ii}/K_{Ic})$  - versus-cycles-to-failure curve (cyclic life curve).

**Figure 35. Cycle Life Results for 2219-T87 Aluminum @ -423°F.**





3. It appears that cyclic life curves for surface-flawed specimens can be used in conjunction with an end-point approach to make reasonable estimates of cyclic life for structure containing more complex partially embedded flaw geometries. This method successfully predicted cyclic life for nine test specimens containing partially embedded flaws originating at a hole. It is believed that the method is applicable to the flaw-at-hole geometry as long as failure occurs before the flaw depth penetrates the thickness of the structure.

4. A failure criterion developed for 2219-T87

aluminum and 5A1-2.5Sn(ELI) titanium structure containing partially embedded flaws originating at a circular hole is very likely applicable to other materials in which such flaws could become unstable under conditions of plane strain.

#### ACKNOWLEDGEMENT

The authors wish to acknowledge the financial support of the National Aeronautics and Space Administration's Lewis Research Center through Contracts NAS3-7993 and NAS3-12016 under the administration of Mr. Gordon T. Smith.

#### REFERENCES

1. P.C. Paris, M.P. Gomez, and W.E. Anderson, "A Rational Analytic Theory of Fatigue," *Univ. Washington Trends Eng.*, 13/1 (1961).
2. P.C. Paris, *The Growth of Cracks Due to Variations in Loads*, Ph.D. Dissertation, Lehigh University, Bethlehem, Pennsylvania (1962).
3. D.R. Donaldson and W.E. Anderson, "Crack Propagation Behavior of Some Airframe Materials," pp. 375-441, *Proc. Crack Propagation Symp.*, Vol. II, College of Aeronautics, Cranfield, England (1961).
4. D. Broeck and J. Schijve, *The Influence of the Mean Stress on the Propagation of Fatigue Cracks in Aluminum Alloy Sheet*, NRL-TN-M.2111, National Aero- and Astronautical Research Institute, Amsterdam (1963).
5. D. Broeck and J. Schijve, *The Effect of the Sheet Thickness on the Fatigue Crack Propagation in 2024-T3 Alclad Sheet Material*, NLR-TR-M.2129, National Aero- and Astronautical Research Institute, Amsterdam (1963).
6. R. Roberts and F. Erdogan, *The Effect of Mean Stress on Fatigue Crack Propagation in Plates Under Extension and Bending*, ASME Paper 67-WA/MET-2, American Society of Mechanical Engineers, New York (1967).
7. H.W. Liu, "Crack Propagation in Thin Metal Sheets Under Repeated Loading," *J. Basic Eng.*, 83/1: 23-31 (1961).
8. H.W. Liu, "Fatigue Crack Propagation and Applied Stress Range - An Energy Approach," *J. Basic Eng.*, 85/1:116-122 (1963).
9. R.G. Forman, V.E. Kearney, and R.M. Engle, *Numerical Analysis of Crack Propagation in Cyclic-Loaded Structures*, ASME Paper 66-WA/MET-4, American Society of Mechanical Engineers, New York (1966).
10. P.C. Paris and F. Erdogan, "A Critical Analysis of Crack Propagation Laws," *J. Basic Eng.*, 85/4: 528-534 (1963).
11. J.R. Rice, "The Mechanics of Crack Tip Deformation and Extension by Fatigue," p. 247, *Fatigue Crack Propagation*, ASTM-STP-415, American Society for Testing and Materials, Philadelphia, Pennsylvania (1967).
12. H.H. Johnson and P.C. Paris, "Sub-Critical Flaw Growth," *Eng. Fracture Mech.*, 1:3-45 (June 1968).

#### REFERENCES (Continued)

13. C.F. Tiffany and F.A. Pall, *An Approach to the Prediction of Pressure Vessel Minimum Fatigue Life Based Upon Applied Fracture Mechanics*, D2-22437, Boeing Company, Seattle, Washington (1963).
14. C.F. Tiffany and P.M. Lorenz, *An Investigation of Low-Cycle Fatigue Failures Using Applied Fracture Mechanics*, AFML-TDR-64-53, Air Force Materials Laboratory, Wright-Patterson AFB, Ohio (1964).
15. G.R. Irwin, "Crack Extension Force for a Part-Through Crack in a Plate," *J. Appl. Mech.*, 29:651-654 (1962).
16. C.F. Tiffany, P.M. Lorenz, and L.R. Hall, *Investigation of Plane Strain Flaw Growth in Thick-Walled Tanks*, NASA-CR-54837, National Aeronautics and Space Administration, Washington, D.C. (1966).
17. C.F. Tiffany, P.M. Lorenz, and R.C. Shah, *Extended Loading of Cryogenic Tanks*, NASA-CR-72252, National Aeronautics and Space Administration, Washington, D.C. (1967).
18. J.N. Masters, *Cyclic and Sustained Load Flaw Growth Characteristics of 6A1-4V(ELI) Titanium*, NASA-CR-92231, National Aeronautics and Space Administration, Washington, D. C. (1968).
19. A.E. Green and I.N. Sneddon, "The Distribution of Stress in the Neighborhood of a Flat Elliptical Crack in an Elastic Solid," *Proc. Camb. Phil. Soc.*, 46:159-163 (1950).
20. J.N. Masters, W.P. Haesc, and R.W. Finger, *Investigation of Deep Flaws in Thin Walled Tanks*, NASA-CR-72606, National Aeronautics and Space Administration, Washington, D.C. (1969).
21. O.L. Bowie, "Analysis of an Infinite Plate Containing Radial Cracks Originating at the Boundary of an Internal Circular Hole," *J. Math. Phys.*, 35:60-71 (1956).

**SESSION 3B**  
**FUNDAMENTALS II**

*Chairman*

Prof. R.A. Heller  
Virginia Polytechnic Institute

# ON THE CRITERION OF LOW-CYCLE SHEAR FRACTURE

by

F.D. Ju, J.T.P. Yao, and T.T. Liu

The University of New Mexico  
Albuquerque, N.M.

## NOMENCLATURE

- $i$  = Number of application of shear load
- $j$  =  $j^{\text{th}}$  specimen
- $m(p)$  = Sample mean of the cumulative damage  $[X_j(p)]$  at a given value of  $p$
- $n$  = Number of cycles before fracture
- $N$  = Number of samples
- $p$  = Exponential parameter for damage per cycle
- $s(p)$  = Sample standard deviation of the cumulative damage at a given value of  $p$
- $X_j(p)$  = Cumulative damage at fracture for  $j^{\text{th}}$  sample
- $\Delta\gamma_i$  = Increment plastic deformation at  $i^{\text{th}}$  shear cycle
- $\gamma_u$  = Plastic deformation at fracture for single shear load

## INTRODUCTION

During the past three decades, the problem of low-cycle fatigue has been studied by many investigators. Most of these investigations are concerned with quasi-static loading conditions. In reality, much of the repeated loads are dynamically applied, for instance, gust loads on aircraft structures. Therefore, it is desirable to study the behavior of metals subjected to small numbers of repeated loads which are dynamically applied. The objective of this investigation is to establish the fracture criterion for specimens subjected to low-cycle reversed shear deformations. For comparison, two loadings were studied. One was statically applied loading; the other was dynamic shock loading.

The choice of shear fracture is due to the fact that the hydrostatic loading does not readily lead to failure and that most materials failed under low-cycle loading usually follows the maximum distortion theory. The configuration of a reversed shear specimen (Figure 1) is referred to an earlier work by Ju, Baker and Yao<sup>1</sup>. In the course of determining the characteristic empirical value in low-cycle

dynamic loading, a specially designed reverse shock loading machine is employed, Ju and Shanon<sup>2</sup>.

The survey of works concerning the behavior of metals under low-cycle static loading conditions is referred to Ju and Baker<sup>3</sup> Yao and Munse<sup>4</sup> and Coffin<sup>5</sup>. However, a brief review is pertinent for some selected literature on both dynamic behavior of materials and the low-cycle failures.

For dynamic loading, Campbell<sup>6</sup> reported that, for a steel rod subjected to the longitudinal impact, the stress necessary to cause a given plastic strain was greater than that to cause the same strain in a static test. Characteristically, the dynamic stress causing 0.1 percent set is 15 to 18 percent higher than that in the static test. More recently, Martin and Murphy<sup>7</sup> made comparison of a number of investigations to show that the dynamic fracture strengths were higher than the static fracture strength by the order of 1.1 to 25. They further concluded that in general, it is inadequate to predict fracture due to dynamic loads by the state of stress or strain; rather it is necessary to know some additional property of materials, for instance the load duration for complete fracture. In low-cycle loading, Benham<sup>8</sup> reported that the total plastic strain increased as the number of cycles increased, following a linear log-log relationship up to  $10^5$  cycles. However, the total number of cycles prior to failure depends on the nature of loading which he experimented with one under constant-load cycles and another under constant strain cycles. Wilkins<sup>9</sup> studied the rotating bending tests to an aluminum alloy conforming to British Standard L 65. He found that the cumulative sum of damage varied from 1.11 to 1.29. Miner<sup>10</sup> proposed a linear cumulative damage theorem for long-life fatigue, in which the fatigue damage is expressed as the ratio between the number of cycles at each stress level and the corresponding fatigue life. Fatigue failures are assumed to occur when the linear sum of all ratios for all stress levels reaches unity. Experimentally, these sums are found to range from 0.5 to 3.0.<sup>11</sup> In a fatigue test of mild steel cantilever specimens subjected to repeated lateral impulse loads, Tanaka<sup>12</sup> found the cumulative damage follows the Miner's hypothesis<sup>10</sup>. These results have verified Crede's prediction of fatigue failure for a material subjected to repeated impulse loads<sup>13</sup>. Yao and Munse<sup>14</sup> expressed the low-cycle fatigue damage as a power function of plastic deformations and used the linear cumulative damage criterion. In their experimental study, the cumulative sum for axially loaded specimens was found to be ranging from 0.94 to 1.08, which

was much closer to the predicted value of unity than those values for long-life fatigue.

In general, the shape of the load-time curve of the load cycle is found to be an important factor in low-cycle fatigue<sup>4</sup>. However, its effect will be reduced in dynamic cases. Very recently, Coffin<sup>15</sup> studied the effect of high temperature to the low-cycle fatigue behavior of 'A' nickel. He pointed out the importance of the loading rate in low-cycle fracture criterion.

### LOW-CYCLE SHEAR FRACTURE CRITERION

The damage per loading is expressed as a power function of plastic shear deformations.

$$(\text{damage per loading})_i = \left( \frac{\Delta\gamma_i}{\gamma_u} \right)^p \quad (1)$$

where the fracture parameters  $\Delta\gamma_i$  are the change in plastic shear strain at  $i^{\text{th}}$  loading,  $\gamma_u$  the ultimate shear strain (single loading) and  $p$  an empirical constant. The value of  $p$  is dependent of material and loading rate. The present investigation will demonstrate the experimental method of determining the value of  $p$ , as well as showing the effect of loading rate.

Suppose that the material and geometry of specimens are fixed,  $p$  should be affected by the loading rate. In addition, because the equation must satisfy the single load fracture condition, the limiting value has to be one. Hence, the criterion for low-cycle shear fracture is then,

$$\sum_{i=1}^n \left( \frac{\Delta\gamma_i}{\gamma_u} \right)^p = 1.0 \quad (2)$$

To evaluate  $p$  experimentally, the following procedure is used. Specimens are repeatedly deformed plastically with reversed constant shear load until fracture. Plastic shear deformations are measured and shear strains are computed. A set of arbitrary values for the exponent  $p$  in the power function as given by Equation (1) is assumed. For each value of  $p$ , a cumulative damage  $X_j(p)$  at fracture is computed for the  $j^{\text{th}}$  specimen as follows:

$$X_j(p) = \sum_{i=1}^n \left( \frac{\Delta\gamma_i}{\gamma_u} \right)^p \quad (3)$$

where  $n$  is the total number of loadings before fracture. For a total of  $N$  specimens tested, the sample mean of the cumulative damage,  $m(p)$ , is computed as follows:

$$m(p) = \frac{1}{N} \sum_{j=1}^N X_j(p) \quad (4)$$

Also, the sample standard deviation of the cumulative damage,  $s(p)$ , is computed as follows:

$$s(p) = \frac{1}{N} \sum_{j=1}^N [X_j(p) - m(p)]^2$$

By imposing the low-cycle shear fracture criterion (2), one obtains the value of  $p$  for  $m(p) = 1$ . Then the corresponding standard deviation at the value of  $p$  can also be found.

### EXPERIMENTAL DETERMINATION OF THE EXPONENTIAL PARAMETER 'p'

Two series of experiments with reversed constant shear loads were conducted, using 27 specimens. One series was for static loadings, and the other for dynamic shock loadings. Specimens used in this study were made from 0.031 inch 6061-T6 aluminum alloy sheet. The geometrical configuration is one of double shear reversed loading model<sup>1</sup> as shown in Figure 1. The plastic shear strain was measured

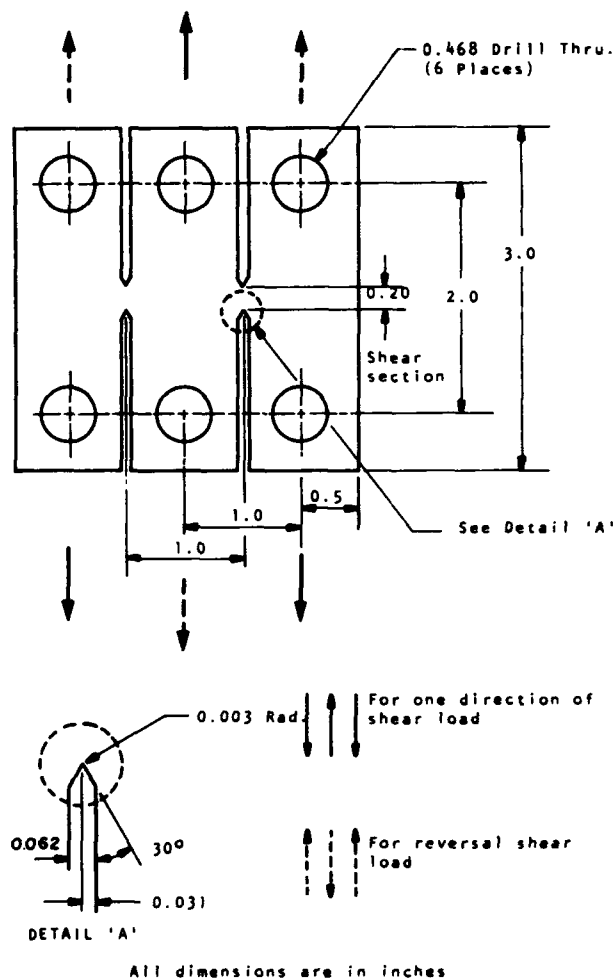


Figure 1. Shear Specimen Configuration.

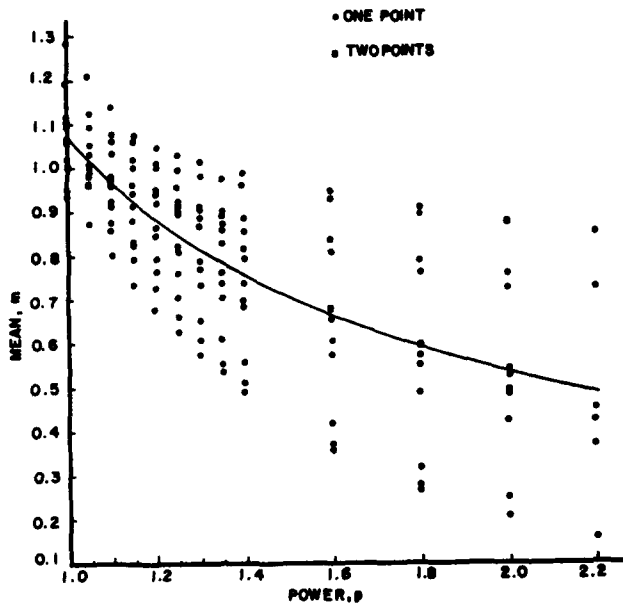


Figure 2.  $m(p)$  in the Center Part of Critical Shear Section for Static Test.

by the permanent angular set at the center part of the shear after each loading.

In the static experiment the plastic shear strain of each cycle  $\Delta\gamma_i$  remained essentially constant before full fracture. Equations (3), (4), and (5) are then used to evaluate  $p$  experimentally. With the use of a digital computer, the sample mean and the standard deviation,  $m(p)$  and  $s(p)$ , are plotted as shown in Figures 2 and 3. The power  $p$  was found to be 1.06 for  $m(p)$  to be unity, therefore

$$\sum_{i=1}^n \left( \frac{\Delta\gamma_i}{\gamma_u} \right)^{1.06} = 1.0 \quad \text{for static test} \quad (5)$$

At the value  $p = 1.06$ , the cumulative-damage varied from 0.87 to 1.20 with the minimum sample standard deviation equal to 0.093.

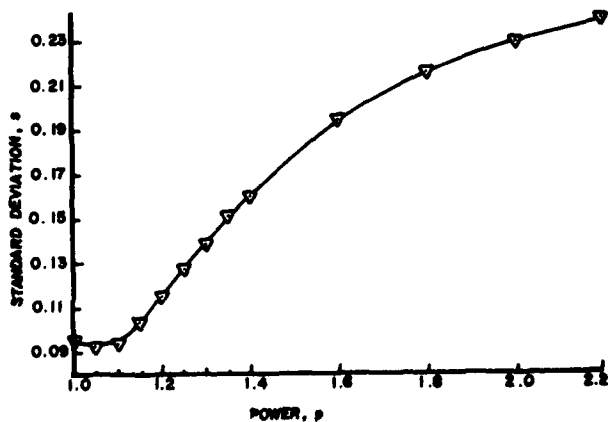


Figure 3.  $s(p)$  in the Center Part of Critical Shear Section for Static Test.

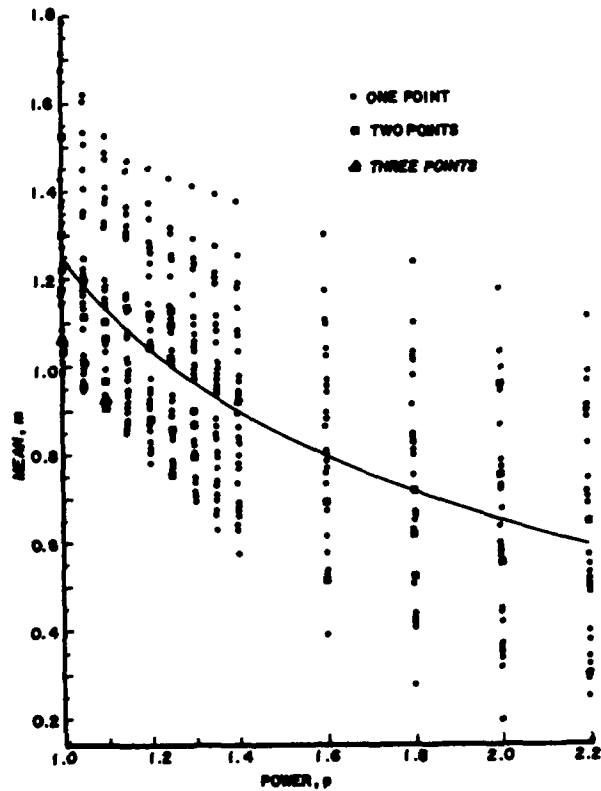


Figure 4.  $m(p)$  in the Center Part of Critical Shear Section for Dynamic Test.

For the dynamic test,  $\Delta\gamma_i$  is not a constant for  $i \leq 7$ . However, for  $i \geq 10$ ,  $\Delta\gamma_i$  is approximately a constant. By use of the digital computer,  $m(p)$  and  $s(p)$  are shown in Figures 4 and 5; the power  $p$  is 1.26 for the summation of cumulative damage to be unity.

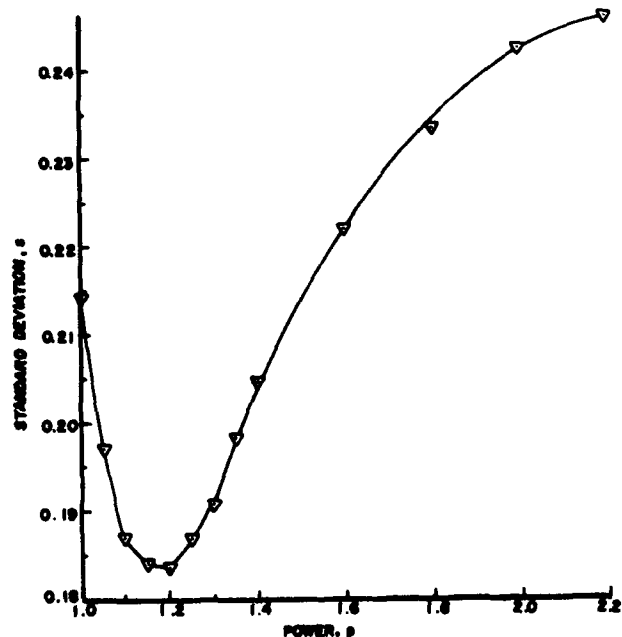


Figure 5.  $s(p)$  in the Center Part of Critical Shear Section for Dynamic Test.

$$\sum_{i=1}^n \left( \frac{\Delta \gamma_i}{\gamma_u} \right)^{1.26} = 1.0 \text{ for dynamic test} \quad (6)$$

At  $p = 1.26$ , the cumulative damage varied from 0.75 to 1.43 with the sample standard deviation equal to 0.1875. This shows that plastic deformation in dynamic tests is slightly higher than in static tests.

### CONCLUSION

The cumulative-damage criterion due to reversed low-cycle shear loading is expressed as a power function of plastic shear deformations. The empirical equation for both dynamic and static low-cycle shear fracture is established to be:

$$\sum_{i=1}^n \left( \frac{\Delta \gamma_i}{\gamma_u} \right)^p = 1.0 \quad (7)$$

where  $p$  is an empirical constant. For the given configuration of specimens of aluminum alloy, the power  $p$  was found to be 1.26 for dynamic tests and 1.06 for static tests. This phenomenon indicates that the specimen can withstand more cycles of dynamic loads than corresponding static loads.

### ACKNOWLEDGEMENTS

The work described in this paper was conducted in the Department of Mechanical Engineering at the University of New Mexico, and supported by the Air Force Office of Scientific Research.

The authors wish to express their thanks to the late J.G. Baker for his assistance in several phases of this work.

## REFERENCES

1. F.D. Ju, J.G. Baker, and J.T. Yao, "A Specimen for Reversed Shear Deformations," *Mater. Res. Stand.*, 7/12:517-523 (1967).
2. F.D. Ju and M.J. Shannon, *The Dynamic Low-Cycle Testing Machine - Design and Calibration*, AFOSR-66-0568, Air Force Office of Scientific Research, Washington, D.C. (1967).
3. F.D. Ju and J.G. Baker, *Preliminary Study of Pure Shear Fracture Model*, AFOSR-64-0568, Air Force Office of Scientific Research, Washington, D.C. (1965).
4. J.T. Yao and W.H. Munse, "Low-Cycle Fatigue of Metals: Literature Review," *Welding J. Res. Suppl.*, 41:182s-192s (1962).
5. L.F. Coffin, Jr., "Low-Cycle Fatigue: A Review," *Appl. Mater. Res.*, 1/3:129-141 (1962).
6. S.D. Campbell, "An Investigation of the Plastic Behavior of Metal Rods Subjected to Longitudinal Impact," *J. Mech. Phys. Solids*, 1:113-123 (1953).
7. C.W. Martin and G. Murphy, "Model Prediction of Fracture Due to Explosions," *J. Eng. Mech. Div. ASCE*, 89 (EM2):133-150 (April 1963).
8. P.P. Benham, "Fatigue of Metals Caused by a Relatively Few Cycles of High Load or Strain Amplitude," *Met. Rev.*, 3/11:203-234 (1958).
9. E.W. Wilkins, "Cumulative Damage in Fatigue," pp. 321-332, *Colloquium on Fatigue*, International Union of Theoretical and Applied Mechanics, Copenhagen (1955).
10. M.A. Miner, "Cumulative Damage in Fatigue," *J. Appl. Mech.*, 12:A159-A164 (1945).
11. M.A. Miner, "Estimation of Fatigue Life with Particular Emphasis on Cumulative Damage," in *Metal Fatigue*, McGraw-Hill, New York (1959).
12. S. Tanaka, "On Cumulative Damage in Impulse Fatigue Tests," *J. Basic Eng.*, 85:535-538 (1963).
13. C.E. Crede, "The Effect of Pulse Shape on Simple Systems Under Impulse Loading," *Trans. ASME*, 77:957-961 (1955).
14. J.T. Yao and W.H. Munse, "Low-Cycle Axial Fatigue Behavior of Mild Steel," pp. 5-24, *Fatigue of Aircraft Structures*, ASTM-STP-338, American Society for Testing and Materials, Philadelphia, Pennsylvania (1962).
15. L.F. Coffin, Jr., "Predictive Parameters and Their Application to High Temperature, Low-Cycle Fatigue," pp. 643-654, *Proc. 2nd Int. Conf. Fracture*, Chapman and Hall, London (1969).



# THE EFFECT OF THE SURFACE LAYER AND ENVIRONMENT ON CYCLIC BEHAVIOR AND FATIGUE OF METALS

by

I. R. Kramer

Martin Marietta Corporation  
Denver, Colorado

## INTRODUCTION

An investigation was conducted to determine the influence of the surface layer on cyclic work-hardening, work-softening cyclic creep, and the fatigue resistance of aluminum 7075-T6, titanium (6 al/4V), copper and aluminum 1100. For annealed copper and aluminum, tested in air and in vacuum under alternating tension-compression at fixed plastic strains, the specimens work harden, and the increase in the applied stress at the terminal strain limits was found to be equal to the increase in the surface layer stress. For prestrained specimens which soften when cycled, the decrease in the surface layer stress was equal to the decrease in the surface layer stress. The surface layer stress of aluminum was measured as a function of strain in air and in vacuum. At the same strain, the surface layer stress in the vacuum case was less than that in air. The cyclic hardening was also less in vacuum. Cyclic creep was found to be due to plastic flow associated with the relaxation in the surface layer stress. Because of the lower surface layer stress, cyclic creep was less in vacuum than in air.

The fatigue life of aluminum 7075-T6 and titanium (6 al/4V) was influenced strongly by the surface-layer stress. Increasing the surface layer stress caused the fatigue life to decrease and decreasing the surface layer stress increased the fatigue resistance.

In a number of papers we have reported that during unidirectional plastic deformation a surface layer is formed which opposes the motion of dislocation. Further, for some metals such as polycrystalline high-purity aluminum and copper the surface layer can relax rather rapidly even at low temperatures. The fractional decrease in the surface layer stress was found to be independent of strain and followed the relationship.<sup>1</sup>

$$\frac{\Delta \sigma_s}{\sigma_s(0)} = bt^m \quad (1)$$

where  $\Delta \sigma_s$  is the decrease in the surface layer stress,  $\sigma_s(0)$  is the initial surface layer stress and  $b$  and  $m$  are constants. It was also shown<sup>2</sup> at temperatures of

35°C and below, for aluminum, dislocation obstacles associated with the interior did not relax. Our most recent work on copper (OFHC) has shown that interior dislocation obstacles are not relaxed until the temperature is in excess of about 150°C. The decrease in surface layer stress, as a result of relaxation, was accompanied by an increase in the activation volume<sup>3</sup> and indicates that the dislocation density in the surface layer is decreased.

Based upon the observations on the formation and relaxation of the surface layer, this investigation was directed toward determining the influence of the surface layer stress in cyclic creep, cyclic hardening and softening and fatigue by measuring the change in the surface layer stress as a function of the number of cycles. A number of investigations were conducted at reduced pressures as an aid in separating internal from surface layer dislocations reactions during cyclic hardening, creep, and fatigue.

## EXPERIMENTAL PROCEDURE

The aluminum (99.97%) and copper (OFHC) specimens had a nominal diameter of 0.15 in. and a gage length of 2 in. for the cyclic creep tests; for tension-compression tests the gage length was 0.3 in. Before testing, the specimens were annealed in vacuum ( $10^{-5}$  torr) at 350 C for 2 hr. for the aluminum and at 450 C for 1 hr. for the copper. The fatigue specimens had a gage length of 0.3 in. and a diameter of 0.15 in. After machining, the 7075-T6 aluminum was solution treated at 470 C for one hr., water quenched and aged for 24 hrs. at 120 C. The titanium specimens (6 al/4V) were annealed in vacuum ( $10^{-5}$  torr) at 760 C for 2 hr. Prior to testing, aluminum and copper specimens were electrochemically polished in a methyl alcohol-nitric acid solution and the titanium in a nitric-hydrofluoric acid until the diameter was reduced by 0.004 in. The tests were conducted in an electrohydraulic machine (MTS) and for the cyclic creep and hardening experiments an extensometer was mounted across the specimen. The sensitivity of the measurements was such that 1 in. of chart was equal to a strain of  $10^{-5}$ , and on the load scale 1 in. of chart was equal to 100 lb.

The surface layer stress was measured by the difference between the maximum stress after straining and the

initial flow stress upon reloading after the removal of the surface layer. The surface layer was removed by electrochemical polishing about 0.01 in. from the diameter. The surface layer stresses reported in this paper are given at  $\bar{\sigma}_s = \Delta L/A$  instead of  $\sigma'_s = \Delta L/A_s$  where  $\Delta L$  is the decrease in load after removal of the surface layer,  $A_0$  is the cross-sectional area of the specimen, and  $A_s$  is the cross-sectional area of the surface layer. From previous measurements<sup>4,5</sup> the depth of the surface layer for aluminum single crystals and iron,  $\bar{\sigma}_s \approx 10\bar{\sigma}_s'$ . The use of  $\bar{\sigma}_s$  instead of  $\bar{\sigma}_s'$  simplifies Eq. 2 and eliminates the necessity of determining  $A_s$ .

Schematic drawings and appropriate definitions of the three types of cyclic tests are given in Figure 1. Figure 1 (A) shows the creep behavior for specimens cycled between two stress values, in this case between 0 and  $\sigma_{max}$ . Figures 1 (B) and 1 (C) represent typical cyclic work hardening and work softening curves, respectively.

## EXPERIMENTAL RESULTS

### Cyclic Creep

Typical cyclic creep curves for polycrystalline aluminum cycled between stress limits of 5,000 and 6,700 psi at 300°K and at 5,055 psi at 192 K are presented in Figure 2. As may be expected the cumulation of plastic strain increases with decreasing strain rate (Figure 3.) A cyclic creep curve for copper, representing data from 4 specimens is given in Figure 4. These data, as well as those for aluminum, appear to give a linear relationship when plotted on a log-log basis.

The change in the surface layer stress,  $\bar{\sigma}_s$ , as a function of the number of creep cycles is given in Figures 5 and 6, for aluminum and copper, respectively. These data were obtained under the same conditions as those presented in Figures 3 and 4 and interrupted after 1, 2, 5, 12, and 20 cycles for aluminum and after 10, 20, 30, and 40 cycles for copper to measure the surface layer stress. The bar denotes true stress. Included in these figures are the computed value for  $\bar{\sigma}_i$ , the average stress required to move dislocations through obstacles in the bulk material. This value was obtained from the equation<sup>4-7</sup>

$$\bar{\sigma}_a = \bar{\sigma}_0 + \sigma_i(N) + \bar{\sigma}_s(N) + \bar{\sigma}^* \quad (2)$$

where  $\bar{\sigma}_a$  is the applied,  $\bar{\sigma}^*$  is the average stress required to move dislocations at a given velocity commensurate with the strain rate and  $\bar{\sigma}_0$  is the stress below which dislocation generation does not occur. For convenience in this paper, we have taken the proportional limit as a limiting value for  $\bar{\sigma}_0$ . The values of  $\bar{\sigma}^*$  were measured before and after cycling by the strain rate cycling method and the data indicated that  $\bar{\sigma}^*$  was

essentially constant. Therefore, from Equation 2, during the cycling  $\Delta \bar{\sigma}_i = -\Delta \bar{\sigma}_s$ .

The data in Figures 5 and 6 show that during cyclic creep the surface layer stress initially decreases very rapidly and then decreases at a slower rate. For copper subjected to 40 cycles at a stress,  $\bar{\sigma}_{max} = 21,600$  psi the surface layer stress decreased from 2,400 to 1,200 psi and for aluminum subject to 4,300 cycles at a stress,  $\bar{\sigma}_{max} = 4,420$  psi the surface layer stress was reduced from 650 to

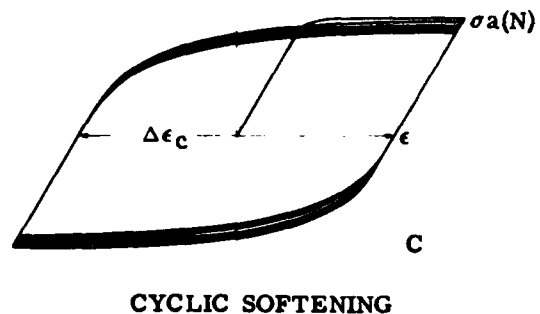
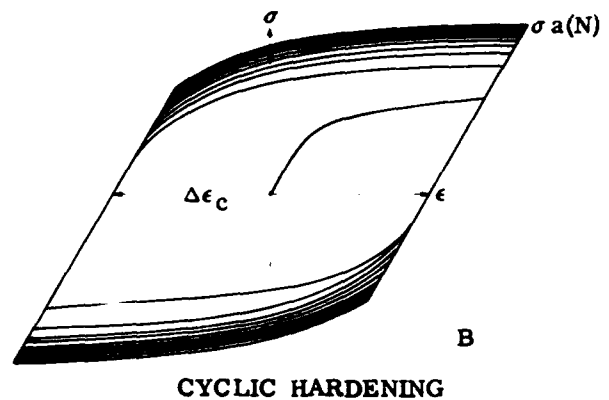
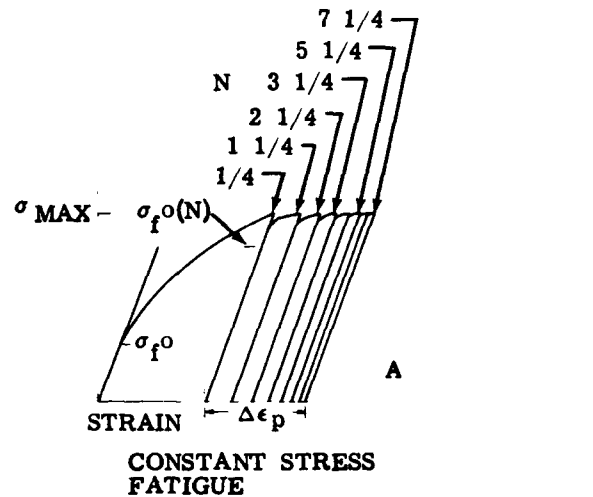


Figure 1. Schematic Diagrams of the Various Cyclic Stress-Strain Tests.

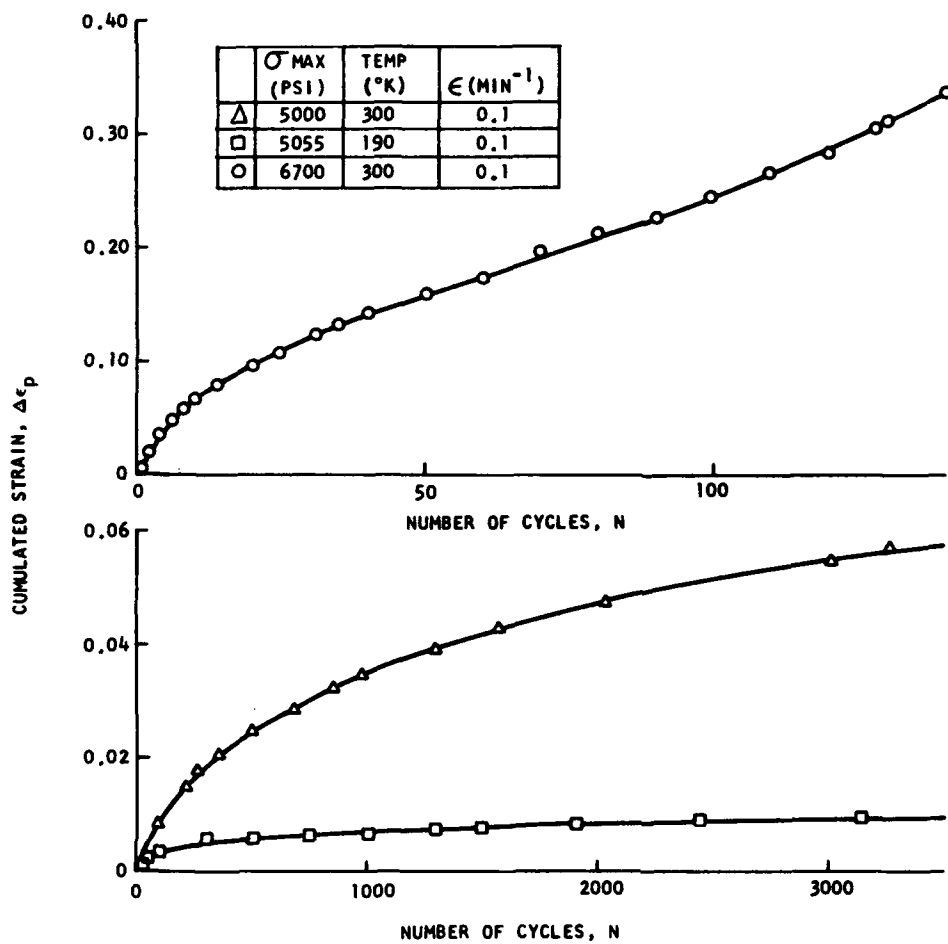


Figure 2. Cumulative Strain During Constant Stress Cycling as a Function of Stress and Temperature for Polycrystalline Aluminum .

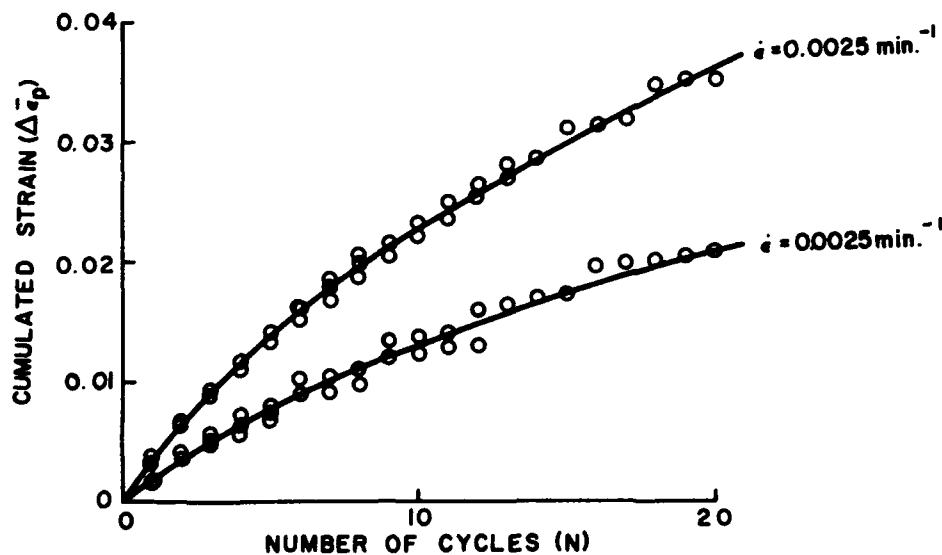


Figure 3. Cumulative Strain,  $\Delta \epsilon_p$ , as a Function of Strain Rate,  $\dot{\epsilon}$ , for Polycrystalline Aluminum.  
 $\bar{\sigma}_{max} = 5,910 \text{ psi}$ ,  
 $T = 300\text{K}$ .

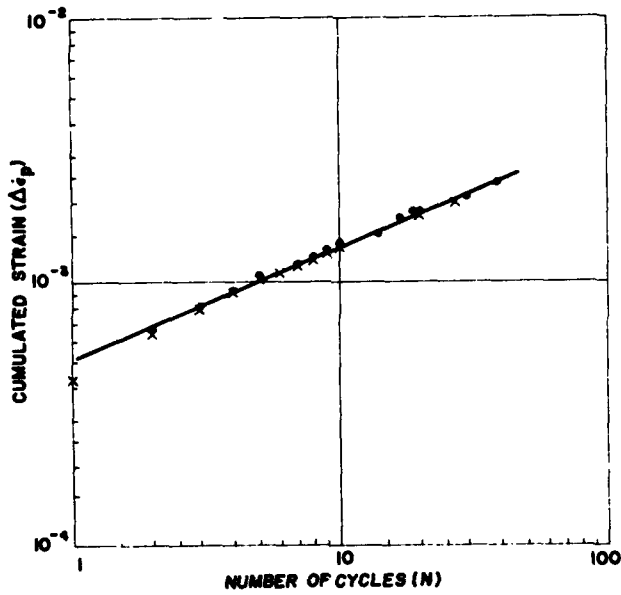


Figure 4. Cyclic Creep of Polycrystalline Copper (OFHC).  $\bar{\sigma}_{max} = 23,000$  psi,  $T = 300K$ ,  $c/s = 0.01$ .

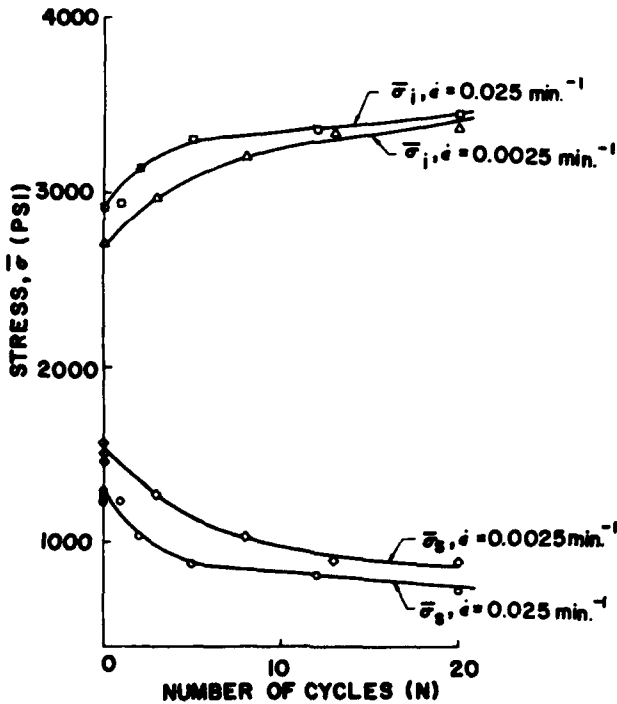


Figure 5. Relationship for Polycrystalline Aluminum Between  $\bar{\sigma}$  and  $\bar{\sigma}_i$  as a Function of Stress Cycles (N) for Strain Rates, 0.0025 and 0.025  $min^{-1}$ .  $\bar{\sigma}_{max} = 5,910$  psi,  $T = 300K$ .

55 psi. There is a striking parallel between the decrease in the surface layer stress and the increase in creep strain. The creep strain is large during the early portion of the cycling period and the surface layer decreases rapidly, later, the creep strain per cycle is low and the surface layer stress also decreases slowly.

To demonstrate in another manner that cyclic creep is caused by the relaxation of the surface layer stress, a series of experiments were conducted wherein aluminum specimens were cycled and then held at zero load to allow more time for relaxation. Under these conditions only  $\bar{\sigma}_s$  relaxes and  $\bar{\sigma}_i$  is unchanged.<sup>2</sup> The data show that immediately on recycling after the relaxation period the cyclic creep rate increases rapidly (Figure 7). In Figure 7 the numbers below the curve indicate the relaxation time. The rate of relaxation of the surface layer stress for aluminum is given in Figure 8.

It may be expected because of the smaller surface layer stress that cyclic creep would be less in vacuum than in normal atmospheres. To test this postulate the surface layer stress was measured at pressures of  $2.5 \times 10^{-5}$  torr (Figure 9). Specimens were placed in tensile vacuum apparatus and the system was evacuated before straining. The load was removed and the specimens were allowed to relax for 18 hours and then restrained in vacuum. The data show the surface layer stress as a function of strain at  $2.5 \times 10^{-5}$  torr is definitely lower than that under atmospheric conditions. The cyclic creep behavior of high purity aluminum and commercially pure aluminum (1100) at  $2.5 \times 10^{-5}$  torr and in air is presented in Figure 10. Compar-

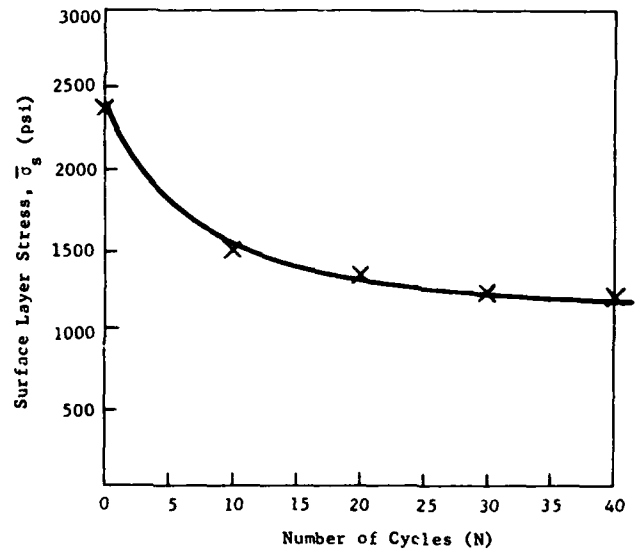


Figure 6. Relationship for Polycrystalline Copper (OFHC) Between Surface Layer Stress and Number of Stress Cycles,  $\bar{\sigma}_{max} = 23,000$ ,  $c/s = 0.01$ .

Figure 7. Effect of Relaxation on Cumulative Strain  $\Delta \epsilon_p$  for Polycrystalline Aluminum.  $\bar{\sigma}_{max} = 4,420$  psi,  $T = 300K$ .

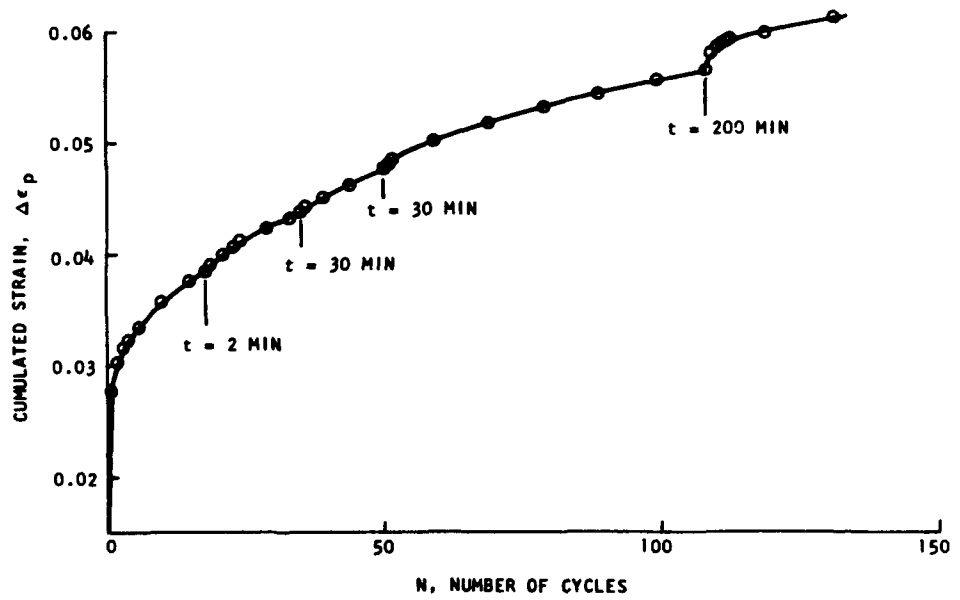
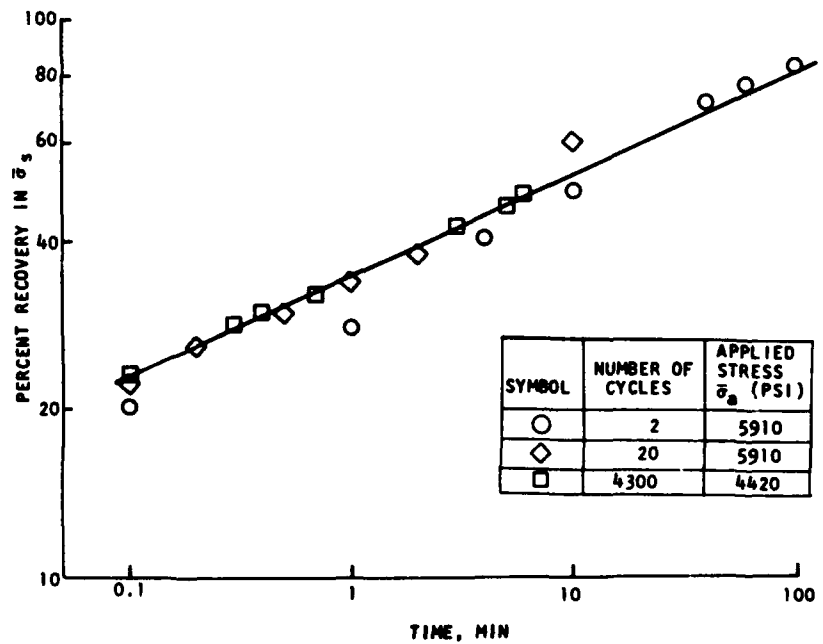
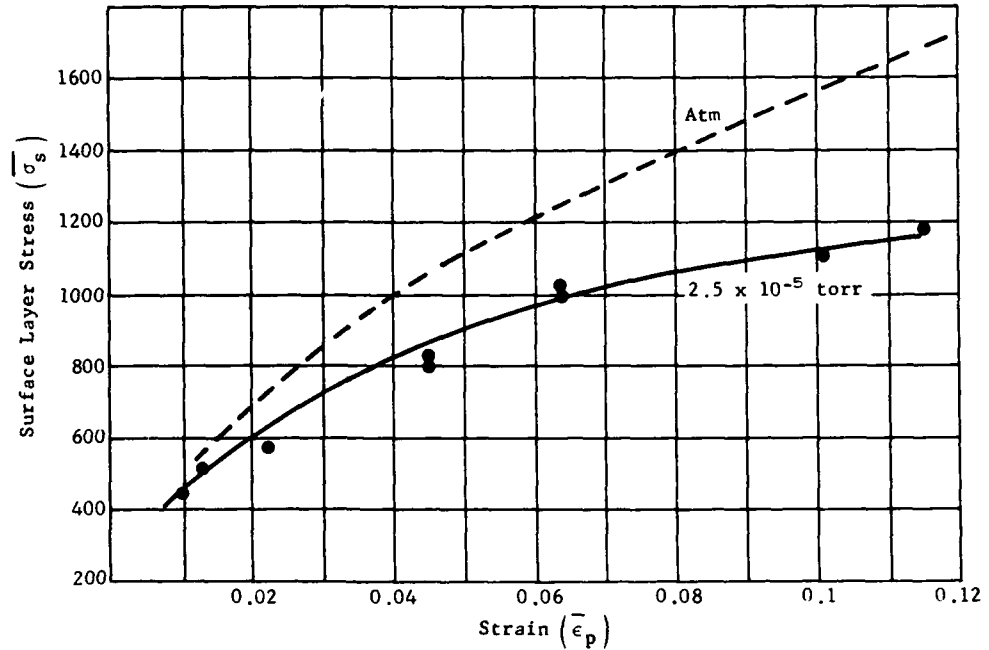


Figure 8. Recovery Rate of the Surface Layer Stress,  $\bar{\sigma}_s$  for Polycrystalline Aluminum.  $T=300K$ . Solid Line Represents Previously Established Recovery Curve (1).



**Figure 9. Surface Layer Stress of High Purity Aluminum Specimens Deformed at  $2.5 \times 10^{-5}$  Torr and Atmospheric Pressure.**



isons of curves 1 and 2, 3 and 4, and 5 and 6 show that there is less cyclic creep in vacuum than in air.

#### Work Hardening in Tension-Compression

Curve A presented in Figure 11 is typical of the behavior of an annealed specimen that has been cycled in tension-compression. In this particular case, aluminum specimens were cycled within a plastic strain range of  $\Delta \epsilon_c = 0.003$  at a rate of 0.2 cpm. The data appear to follow a relationship of

$$\sigma_a(N) = CN^r \quad (3)$$

where, in this case  $C = 1,950$  psi and  $r = 0.3$ .

Figure 12 shows the values for the increase in the surface layer stress and applied stress measured after  $1\frac{1}{4}$ ,  $2\frac{1}{4}$ ,  $5\frac{1}{4}$ ,  $8\frac{1}{4}$ , and  $20\frac{1}{4}$  cycles at  $\Delta \epsilon_c = 0.003$ . Both the surface removal and relaxation methods were used in determining the surface layer stress. It is seen that the increase in the applied stress,  $\Delta \bar{\sigma}_a$ , is equal to the increase in the surface layer stress. <sup>a</sup> After about eight cycles, for this value of cyclic strain, the specimen was fully work hardened as indicated by the lack of change in  $\Delta \bar{\sigma}_a$  and  $\Delta \bar{\sigma}_s$ .

#### Work Softening in Tension-Compression

For the study of the relationship between the change in the surface layer stress and the work softening characteristics of previously strained metals subjected to tension-compression forces, aluminum specimens were pre-strained to 0.03, 0.04, 0.05, and 0.06; and then cycled

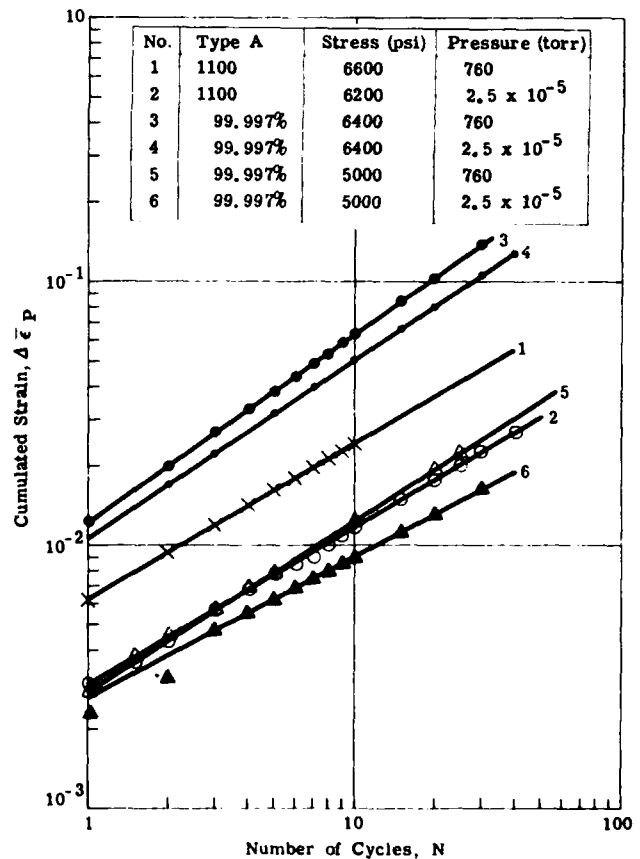


**Figure 10. Effect of Reduced Pressures on the Cyclic Creep Rate of High-Purity and Al-1100.  $T = 300K$ .**

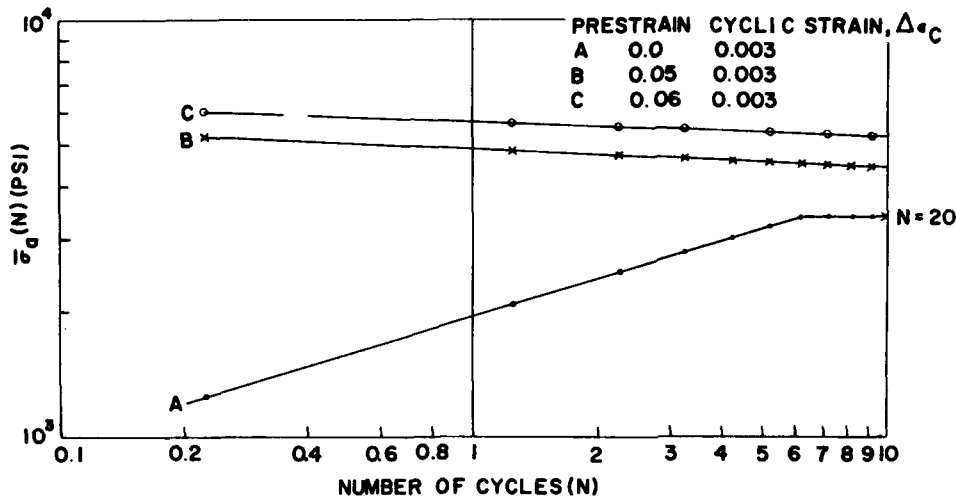


Figure 11. Cyclic Hardening and Softening of Polycrystalline Aluminum at Various Prestrains.  $T = 300K$ .

between plastic strain limits,  $\Delta \epsilon_c = 0.003$ , until there was no further decrease in the applied stress at the terminal strain limits. The surface layer stress was then measured. After saturation, the surface layer stress was about 180 psi and equal to that obtained in a unidirectional tensile test at a strain of 0.0015.

As shown in Figure 11 curves B and C, for specimens prestrained 0.05 and 0.06 the decrease in the applied stress as a function of the number of cycles appears to follow a log-log relationship. For the four strain conditions studied, 0.03, 0.04, 0.05, 0.06, the curves were approximately parallel and displaced downward with decreasing prior strain.

The decrease in the applied stress at saturation and the corresponding decrease in the surface layer stress are shown in Figure 13. The decrease in the surface layer stress was obtained by measuring its value after prestraining and after cycling to saturation. As in previous cases, the data show that the decrease in the applied stress is equal to the decrease in the surface layer stress.

#### Cyclic Hardening after Surface Layer Removal

A critical experiment was performed to demonstrate that cyclic hardening is associated with the surface layer and not the bulk. If cyclic work hardening is due to hardening within the bulk of the specimen, then removing the surface layer after prestraining would not cause any changes in the subsequent cyclic behavior. If, however, the surface layer is responsible for cyclic work hardening, then the surface removal treatment should alter the subsequent cyclic behavior.

Of interest are the experiments on three prestrained copper specimens that were strain-cycled after the surface layer had been removed. The data presented in Figure 14 are for copper specimens that have been cycled be-

tween constant plastic strain limits,  $\Delta \epsilon_c$ , of 0.008 and 0.02, where  $\Delta \epsilon_c$  is the width of the hysteresis loop. Curve A (Figure 14) was obtained when annealed specimens were cycled at  $\Delta \epsilon_c = 0.008$ , and is typical in that hardening occurs. Curves B and C are for specimens that had been prestrained, 0.03 and 0.05, respectively and then strain-cycled after the surface layer was removed by electrochemical polishing an amount of 0.01 in. from the diameter of the specimen. Instead of work softening, as is usually the case for prestrained specimens, the specimens work hardened. These data confirm our statement that cyclic work hardening is associated only with the surface layer and not with the bulk properties of the specimen.

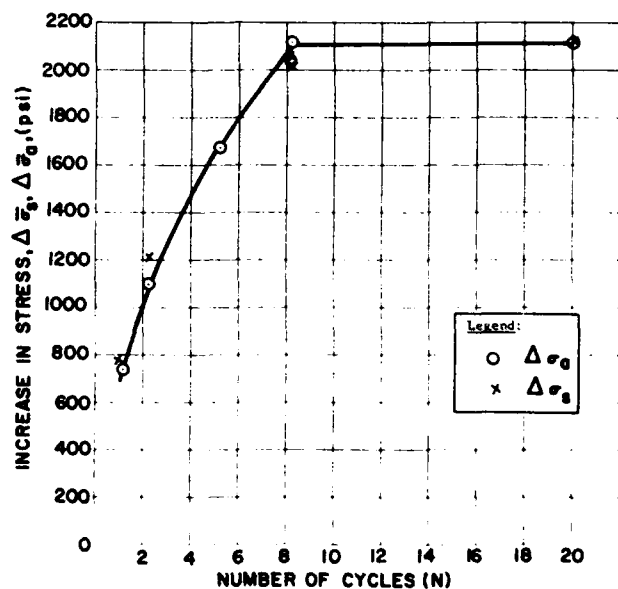


Figure 12. Relationship Between Increase in Applied Stress and Surface Layer Stress as a Function of Number of Strain Cycles at  $\Delta \epsilon_c = 0.003$ .

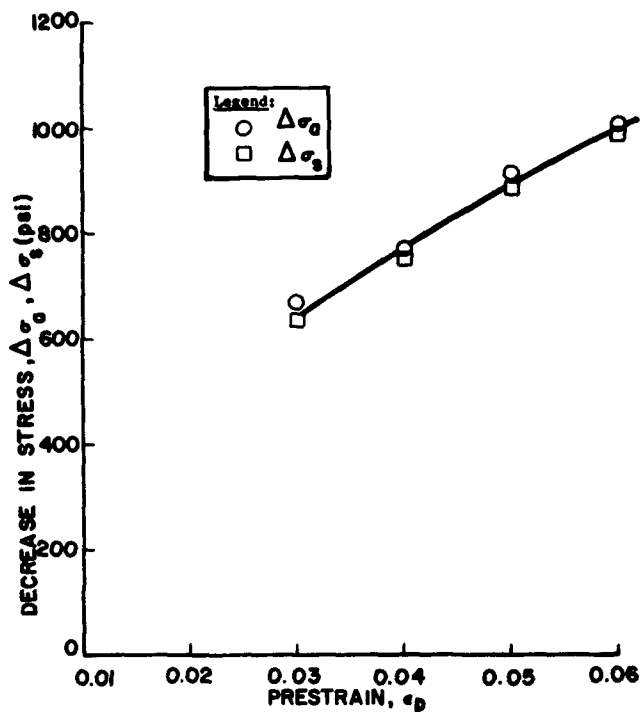


Figure 13. Decrease in Applied and Surface Layer Stress at Saturation as a Function of Prestrain.

Subsequent work showed that the cyclic process does precondition the specimen so that the formation of the surface layer stress is enhanced when a specimen is cycled and then strained an additional amount. This enhancement may be shown by the following considerations. When a specimen is prestrained unidirectionally and the surface layer removed, upon restraining, the stress-strain curve always rejoins the virgin stress-strain curve. To determine whether this same behavior is followed after cyclic hardening, copper specimens were strain-cycled six times at  $\Delta\epsilon_c = 0.008$ , the surface layer was removed, and the specimen was then restrained in tension. The resulting stress-strain curve coincided at the higher strains with the extension of the stress-strain curve of the sixth cycle and not that of the first cycle. During the cyclic period, the stress increase,  $\Delta\sigma_a$ , was 9,100 psi and, from measurements after the removal of the surface layer, the increase in surface layer stress,  $\Delta\sigma_s$ , was 8,450 psi. These data again show that cyclic hardening is due to the surface layer. To determine whether the increase in the flow stress after cyclic hardening and surface removal was due to the increase in the surface layer stress, copper specimens were subjected to six strain cycles at  $\Delta\epsilon_c = 0.008$ , the surface layer removed and then strained to 0.015. Measurements of the surface layer stress after this treatment showed that  $\bar{\sigma}_s = 9,075$  psi. From Eq. 2 the value of  $\Delta\sigma_s$  after cycling and strain-

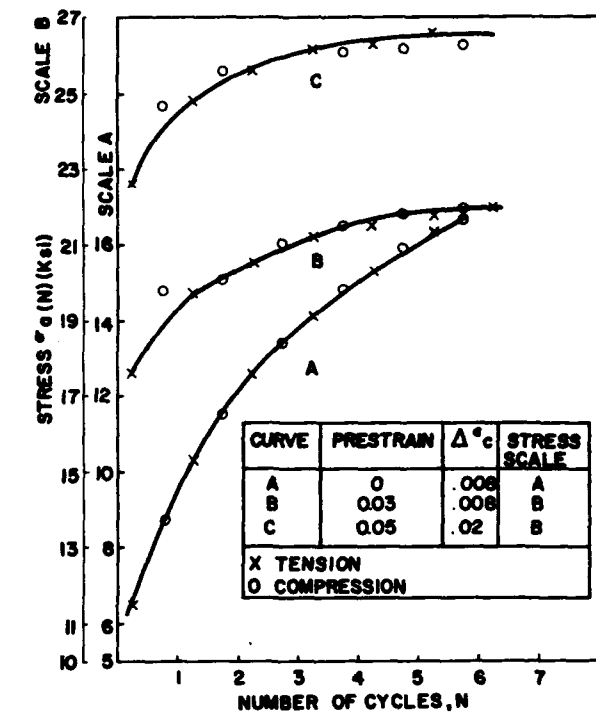


Figure 14. Cyclic Work Hardening of Copper (OFHC). (A) Annealed Condition; (B) and (C) Prestrained 0.03 and 0.05, Respectively and Cycled After Removal of Surface Layer.

ing to 0.015 can be calculated. Assuming  $\bar{\sigma}^* = 0$ , which will maximize  $\bar{\sigma}_i$ , at a strain of 0.008,  $\bar{\sigma}_i + \bar{\sigma}_o = 6,650$  psi, the  $\bar{\sigma}_a$  value minus  $\bar{\sigma}_s$ . At 0.015 strain  $\sigma_a = 17,400$  psi,  $\sigma_s = 9,075$  psi, and, therefore,  $\bar{\sigma}_i + \bar{\sigma}_o = 8,325$  psi. Since  $\sigma_o$  is a constant the increase in  $\sigma_i$  due to cycling and straining is 1,700 psi. Therefore, this increase in  $\bar{\sigma}_i$  cannot account for the 9,100 psi increase in  $\bar{\sigma}_a$  during cycling.

Thus, the data show that strain cycling of annealed specimens preconditions the specimens so that the formation of the surface layer stress is greatly enhanced.

#### Activation Volume After Cyclic Hardening

The relative increase in the dislocation density of the surface layer and the bulk material was determined by measuring the change in the activation volume of copper specimens cyclic hardened at  $\Delta\epsilon_c = 0.004$  and 0.008. Using the strain rate change technique the activation volume as a function of strain was obtained on annealed specimens. Specimens were then cycled until the hardening was virtually completed and then immediately afterwards the activation volume was measured. Care was taken to obtain values as close to the onset of plastic flow as possible. The data show (Figure 15) that



activation volume decreased markedly as a result of the strain hardening. In Fig. 15,  $\gamma = 2.3\epsilon$  and  $\tau = 0.435 \sigma$  was used for conversion to shear strain and shear stress. These tests were then repeated except the surface layer was removed before measuring the activation volume. In this case the initial value of the activation volume was about equal to that for the annealed specimens. With further straining the activation volume decreased and finally became equal to that of specimens which had only been cycled. This latter observation is to be expected in view of our previous statement that after cyclic hardening and surface removal, upon subsequent straining, the stress-strain curve becomes coincident with that of the extrapolated portion of the last cyclic hardening curve. The observation that the activation volume after cyclic hardening and surface removal is the same as that of the annealed specimens shows that the dislocation density increased in the surface layer and the bulk dislocations were unaffected. Of further interest are the activation volume measurements after specimens were cyclic hardened, strained during the strain rate sequence and then allowed to relax for 66 hrs at  $\gamma = 0.1$ . As may be seen in Figure 15, after relaxation of the surface layer stress, the activation volume is somewhat larger than that for the annealed specimen. This increase is to be expected<sup>3</sup> because in the an-

nealed specimen the dislocation density is an average of the density in the surface layer and the bulk, while in the relaxed specimens the dislocation density of the bulk and the surface region are essentially equal.

#### Formation of the Surface Layer at Small Strains

In our previous investigations, measurements of the surface layer stress were always made at strains within the plastic range. However, it is known that within the so-called linear region of the stress strain curve for polycrystalline metals, plastic deformation does occur. Since it is expected that a surface layer will form whenever plastic deformation is present, it was decided to investigate, in a preliminary manner, the formation of the surface layer stress at low strains. Instead of measuring the surface layer stress in the usual manner, it was decided to take advantage of the observation that the surface layer stress increases when a specimen is subjected to alternating stresses. Specimens of 7075-T6 were cycled at  $\pm 40,000$  psi for 500 times and then pulled in tension. The initial flow stress (proportional limit) after cycling increased from 53,845 to 58,120 psi. Companion specimens were also cycled and pulled in tension after polishing 0.01 inch from the diameter to remove the surface layer. The initial flow stress

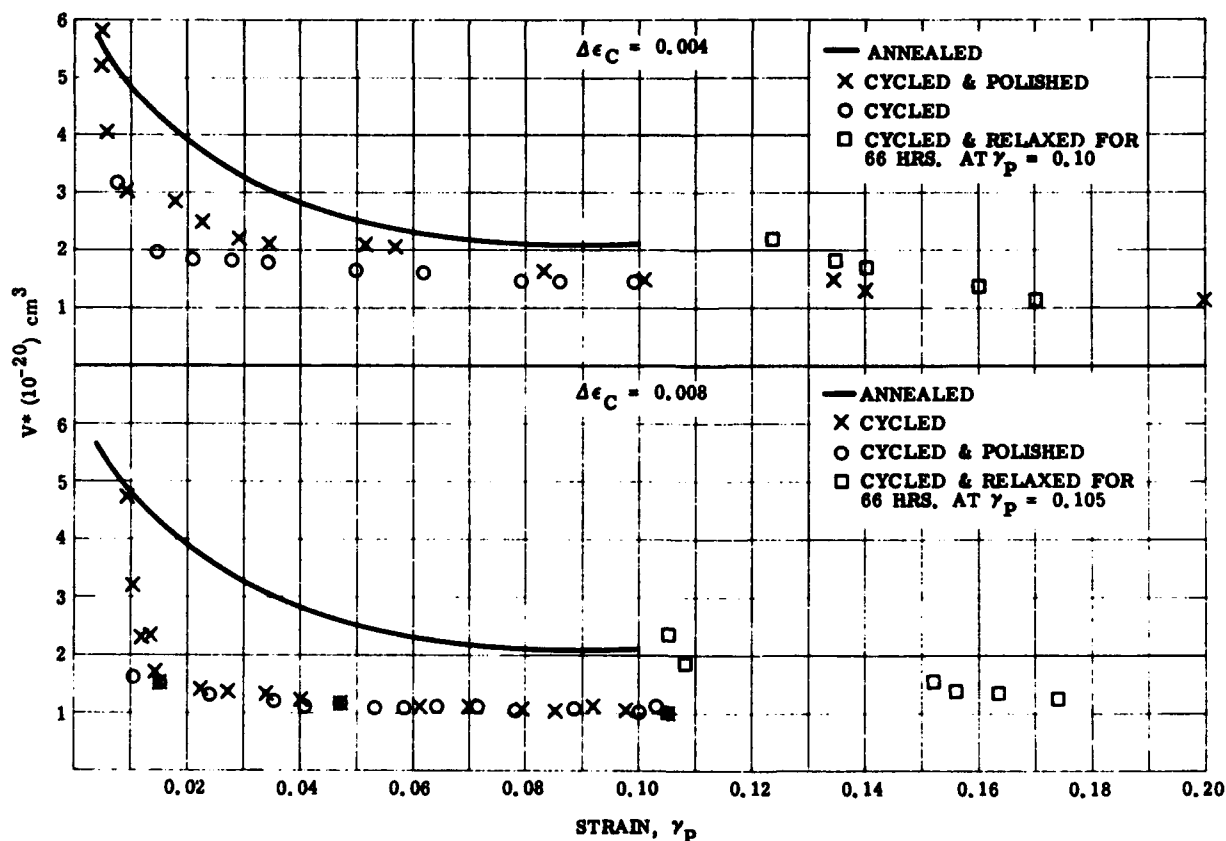


Figure 15. Activation Volumes,  $V^*$ , of Cyclic Hardened Copper (OFHC).

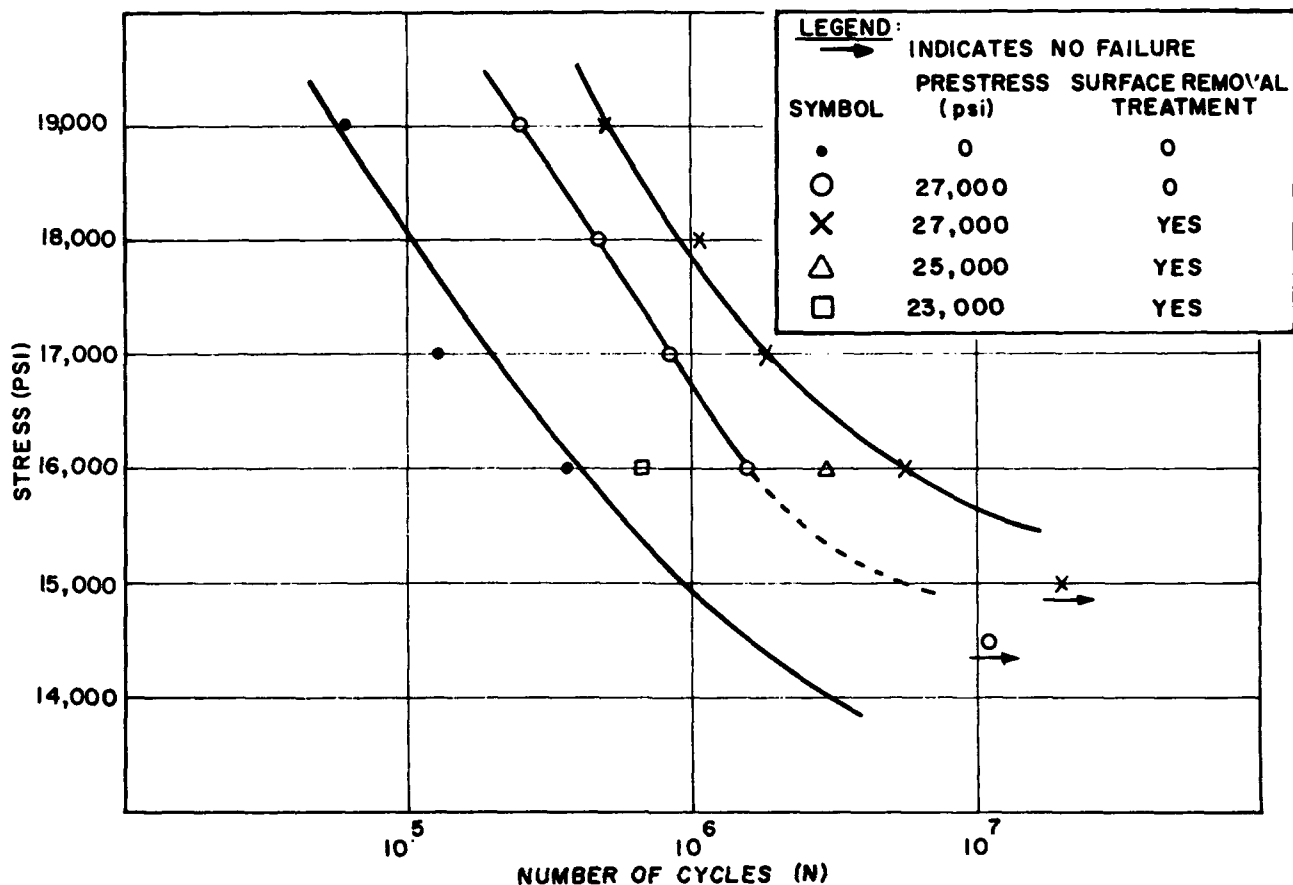


Figure 16. Effect of Removal of Surface Layer on the Fatigue Life of OFHC Copper. Tested in Tension-Compression.

was 54,140 and, within 295 psi, was equal to the initial flow stress of the virgin material. The observation that the initial flow stress, after removal of the surface layer, decreased to that of the virgin material shows that the work hardening is due to an increase in the surface layer stress; in this case about 3980 psi. In similar type tests, specimens were prestrained to 40,000 psi and the surface layer was removed before cycling at  $\pm 35,000$  psi. After cycling 1000 times the specimens were pulled in tension. No change in the initial flow stress was found. It is of interest to note that the endurance stress of fatigue specimens treated in this manner is also about 35,000 psi (Figure 17).

#### Influence of the Surface Layer on Fatigue Life

In previous publications<sup>8,9</sup> it was suggested that the surface layer plays a fundamental role in the fatigue resistance of metals. This hypothesis was advanced on the premise that the probability of starting a crack would be larger in the surface region because of its high dislocation density. The following data support this point of view. To show the effect of the surface layer stress on fatigue life, OFHC copper specimens were tested in tension-compression at constant stress amplitudes after three precon-

dition treatments (Figure 16). In one, the specimens were tested in the annealed condition; in the other the specimens were prestrained and the surface layer formed during the prestraining operation was removed by electro-chemically removing about 0.01 inch from the diameter. For comparison purposes to determine the effect of prestrain alone, a series of specimens were prestrained and tested without removing the surface layer. As a preliminary means of determining the effect of removing the surface layer, specimens were prestrained at 23,000, 25,000 and 27,000 psi and fatigue-tested at 16,000 psi. In Figure 16, it may be seen that the fatigue life improved with increasing prestress up to 27,000 psi. This stress is near the ultimate tensile strength and the prestress could not be raised without causing necking. Accordingly, the remainder of the fatigue tests were conducted by prestressing at 27,000 psi. From Figure 16 it is seen that while prestressing alone increases the fatigue life, removing the surface layer after prestressing causes a further increase. It was observed that the hysteresis loop during the fatigue testing of the copper specimens was very wide and showed that plastic flow occurred during the first compression cycle. This plastic deformation causes a surface layer to form; however, the stress associated with this layer would be less

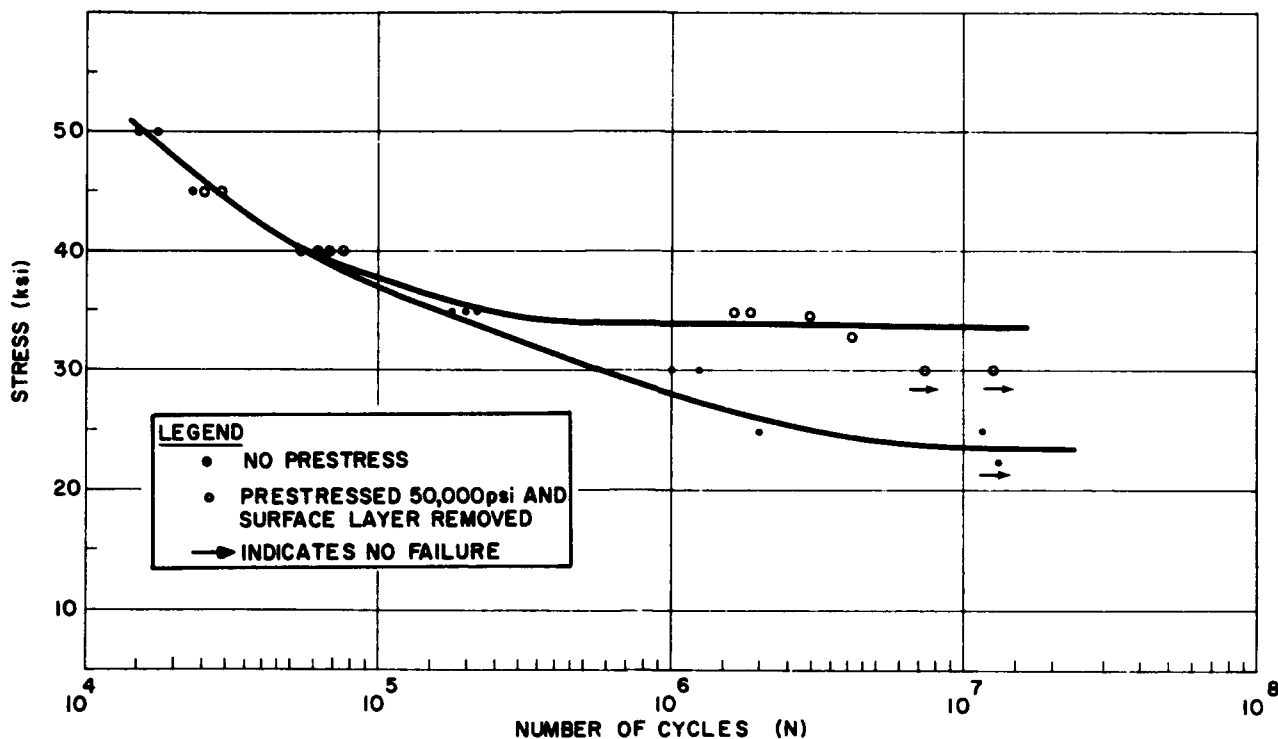


Figure 17. Effect of Removal of Surface Layer on the Fatigue Life of 7075-T6 Aluminum. Tested in Tension-Compression.

than that formed by the prestressing operation.

The effect of prestressing and removal of the surface layer on specimens of 7075-T6 aluminum tested in tension-compression is shown in Figure 17. After establishing the baseline fatigue curve, specimens were prestressed in the range of 40,000 to 80,000 psi and fatigue tested at 35,000 psi after removing the surface layer. The optimum improvement in fatigue life was obtained by prestressing at 50,000 psi. Prestressing in the plastic flow region caused the fatigue life to be less than that of the unstressed material. As shown in Figure 17, the 50,000 psi prestress and surface removal treatment increased the endurance limit at  $10^7$  cycles from 23,000 to 34,000 psi, an increase of about 48 per cent. At stresses above 40,000 psi the two curves coincide. From observations of the widths of the hysteresis loops during the fatigue tests, it was apparent that some plastic flow occurred at stresses above 34,000 psi. The width of the loop increased with increasing stress and it follows that the surface layer was partially reformed.

The fatigue curves for 7075-T6 aluminum for specimens tested in tension-tension are shown in Figure 18. In this case, the prestraining and surface removal treatment increased the fatigue at the higher stress; however, the endurance at  $10^7$  cycles is not affected. Several data points

were obtained by fatiguing the specimens immediately after prestressing to 60,000 psi. As shown in Curve C, Figure 18, the fatigue life is less than that indicated by the baseline curve.

The effect of the surface layer on the fatigue life of titanium (6 al/4V) is given in Figure 19. For the annealed specimens the endurance limit is about 77,000 psi, however, when the specimens were prestressed to 100,000 psi and the surface layer was removed before fatigue testing the endurance limit is about 85,000 psi. The fatigue life in the high stress region appears to be increased by a factor of two. Similar to the data for 7075-T6 aluminum, prestressing the titanium alloy in the plastic range did not improve the fatigue life.

#### Effect of Aging on Fatigue Life of 7075-T6 Aluminum

From observations on the hysteresis loops during the fatigue cycling, it was apparent that some plastic flow had occurred at stresses above the endurance limit. This plastic flow could be a result of a Bauschinger effect in the case of the tension-compression fatigue test and/or an unpinning of dislocations during the prestraining operation. Because diffusion at room temperature is extremely low, these unpinned dislocations could be available to aid

in the reformation of the surface layer upon subsequent stressing. To determine whether the fatigue resistance could be enhanced further by aging, specimens were aged at 120C for 1.5 hours after the prestress and surface removal treatment. These specimens were tested in tension-tension to avoid the Bauschinger effect. Although the data are limited, it is seen in Figure 18 that the aging treatment increased the fatigue life at about 50,000 psi by a factor of 10. Aging after prestressing without the surface removal lowered the fatigue lift.

From the data presented in Figure 18, it may be seen again that decreasing the surface layer stress causes an increase in the fatigue life. When 7075-T6 aluminum specimens are prestressed, those grains with a favorable orientation will undergo plastic deformation and a surface layer will be formed. In addition, some dislocations will be unpinned and will become mobile. Upon subsequent deformation, some of these dislocations will move to the surface and aid in the reformation of the surface layer. It is proposed that the aging treatment causes a repinning of the dislocations to render them immobile. From the observations in Figure 18 that the fatigue life of the prestressed and aged specimens is approximately the same as that of the prestressed specimens, it appears that the aging treatment does not cause the surface layer to recover. In an attempt to verify this point, specimens of 7075-T6 aluminum were prestressed to 60,000 psi and then aged at 120C for various time periods up to 5 hours. When tested in tension, the initial flow stress was higher than that of similarly pre-

stressed specimens that were not aged. A decrease would be expected if the surface layer stress recovered. The data, however, indicate that aging occurred to re-pin the dislocations. These tests alone do not show that the surface layer was not recovered by the aging treatment because it is possible that the combination of the hardening by precipitation and the softening by relaxation of the surface layer stress could result in an overall strengthening. However, if we examine both the fatigue results and these tensile tests, we may tentatively conclude that the surface layer was not recovered appreciably.

## DISCUSSION

The experimental data show that during cyclic creep the surface layer stress decreases. The amount of creep increases with the initial value of the surface layer stress and the time allowed for relaxation between cycles. To account for cyclic creep in terms of surface layer stress, it is proposed that during the unloading and reloading portion of the cycle a partial recovery of the surface layer occurs. This recovery would allow plastic flow to occur at a stress equal to  $\sigma_{max} - \Delta \sigma_s$ , where  $\Delta \sigma_s$  is the decrease in the surface layer stress. Upon continued straining to reach  $\sigma_{max}$  both  $\sigma_i$  and  $\sigma_s$  would be increased, however, from Eq. (2), with  $\sigma_a$ ,  $\sigma_o$ , and  $\sigma^*$  as constants,  $\sigma_s$  must decrease with each cycle. This process of partial recovery and reformation of the surface layer as a result of plastic deformation continues until the specimen fractures or until Eq. (2) is satisfied when

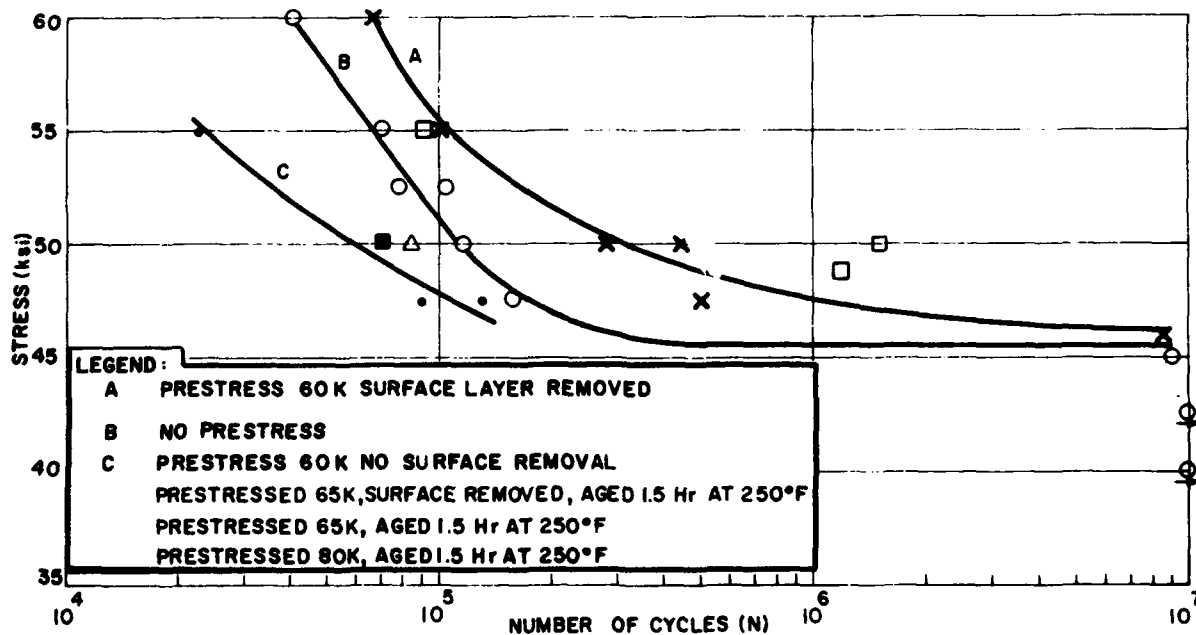
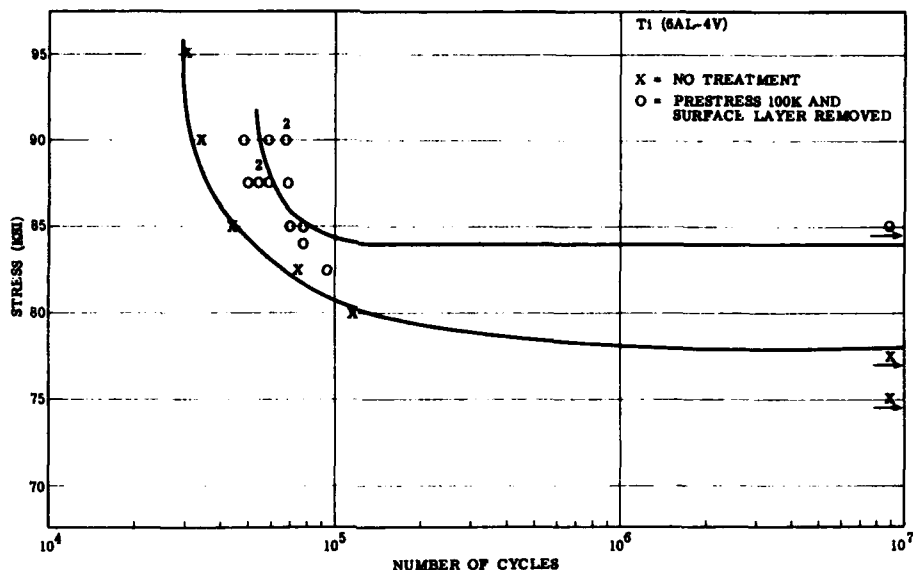


Figure 18. Effect of Removal of Surface Layer on the Fatigue Life of 7075-T6 Aluminum. Tested in Tension-Tension.

Figure 19. Effect of Removal of Surface Layer on the Fatigue Life of Titanium (6 al/4V). Tested in Tension-Compression.



$\bar{\sigma}_i$  is increased by an amount equal to the initial surface layer stress. The recovery of  $\bar{\sigma}_s$  would follow the relationship given in Eq. (1) where  $\bar{\sigma}_s(0)$  would decrease with each cycle.

The data presented in Figures 12 and 13 show that cyclic work hardening and softening is accompanied by corresponding changes in the surface layer stress. The observations that prestrained specimens harden instead of soften if the surface layer is removed before cycling also demonstrate that cyclic hardening is associated with the surface layer and not with the dislocation obstacles in the bulk material. It may be shown that work softening of prestrained specimens is primarily due to the relaxation time involved and cycling, per se, does not exert a large influence. For aluminum specimens prestrained 0.05 the surface layer stress was 1060 psi. After 10 cycles at  $\Delta \epsilon_c = 0.003$  equivalent to 50 minutes, the surface layer stress was 180 psi, a decrease of 83%. According to Figure 8, for a relaxation period of 50 minutes the surface layer stress would relax 75%.

The evidence that fatigue failures are associated with dislocation interactions in the surface layer is contained in Figures 16, 17, 18 and 19. The curves show that when the surface layer is reduced, the fatigue life is increased. Further, when the surface layer stress was increased (Figure 18), the fatigue life decreased.

When the specimens were prestressed both  $\sigma_i$  and  $\sigma_s$  were increased to a value dictated by the stress-strain relationships. Upon removal of the surface layer,  $\sigma_i$  was unchanged and  $\sigma_s = 0$ . Ideally, during the fatigue cycling at a stress lower than  $\sigma_a - \sigma_s - \sigma^*$  [see Eq. (2)], the specimen should behave essentially elastically on a macroscopic scale. However, on a micro-

scopic scale, some grains with a favorable orientation will deform plastically and a surface layer will be formed locally. These grains will become sites for the nucleation of cracks. The surface layer stress and the number of plastically deformed grains will be larger in those specimens that were not prestressed than in the prestressed and polished specimens. This condition arises because  $\sigma_i$  in the first case is lower than that of the second case, and according to Eq.(2) the surface layer stress for the same applied stress must differ correspondingly. The evidence that a surface layer is formed when specimens are fatigued at stresses within the so-called linear region of the stress-strain curve is in the observation that the increase in the proportional limit of cycled specimens may be eliminated by removing the surface layer.

Additional evidence that fatigue failures are associated with the surface layer may be found in the observation that the fatigue life is increased greatly when the tests are conducted in vacuum ( $\sim 10^{-5}$  torr). The surface layer stress of high purity aluminum at  $2.5 \times 10^{-5}$  torr was found to be lower than that in atmospheric air. The rate of relaxation of the surface layer stress was also higher in vacuum than in air. In addition, the rate of cyclic work hardening in vacuum was considerably smaller. Thus, for a given number of fatigue cycles, before failure, the surface layer stress would be less in vacuum than in air. From the evidence accumulated from fatigue behavior in vacuum and by purposely increasing or decreasing the surface layer stress, a hypothesis for fatigue failures may be formulated. This hypothesis is based upon dislocation reactions that take place within the surface layer. It is proposed that during fatigue cycling the surface layer stress increases, and when it reaches a value in a local region equal to the fracture strength a crack will be initiated.

Since there is a gradient of stress in the surface layer, the crack will propagate until the stress in front of the crack tip is less than the fracture strength. During the next cycle(s) the surface layer stress will be increased and the crack will again propagate. This process will give rise to steps on the fractured surfaces in accordance with observations. On the basis of this proposed hypothesis, the endurance limit would be that stress amplitude at which the surface layer did not form, or the rate of increase of the surface layer stress is very small and does not build

up to a critical value during the fatigue test.

#### ACKNOWLEDGMENTS

This research was supported in part by the U.S. Air Force under Contract Number F33615-68-C-1363 monitored by the Aerospace Research Laboratory at Wright-Patterson Air Force Base, and by Contract AF49 (638)-1455 monitored by the Air Force Office of Scientific Research.

#### REFERENCES

1. I.R. Kramer, "The Effect of the Surface Layer Stress on the Transient Creep of Polycrystalline Aluminum," *ASM Trans. Quart.*, 60:310 (1967).
2. I.R. Kramer and C.L. Haehner, "Low Temperature Recovery of Polycrystalline Aluminum," *Acta Met.*, 15:199 (1967).
3. I.R. Kramer, "Effect of the Surface on the Activation Energy and Activated Volume for Plastic Deformation of Fcc Metals," *Trans. Met. Soc. AIME*, 230:991 (1964).
4. I.R. Kramer, "Influence of the Surface Layer on the Plastic Flow Deformation of Aluminum Single Crystals," *Trans. Met. Soc. AIME*, 233:1467 (1965).
5. I.R. Kramer, "Surface Layer Effects on the Plastic Deformation of Iron and Molybdenum," *Trans. Met. Soc. AIME*, 239:199 (1967).
6. I.R. Kramer, "Role of the Surface Layer on the Plastic Deformation of Aluminum," p. 127, *Environment Sensitive Mechanical Behavior*, Gordon and Breach, New York (1967).
7. I.R. Kramer, "Surface Layer Effects on the Plastic Deformation of Iron and Molybdenum," *Trans. Met. Soc. AIME*, 239:520 (1967).
8. H. Shen, S.E. Podlaseck, and I.R. Kramer, "Vacuum Effects on the Tensile and Creep Properties of Aluminum," *Trans. Met. Soc. AIME*, 233:1933 (1965).
9. H. Shen and I.R. Kramer, "Fatigue in Vacuum Environment," *Trans. Int. Vacuum Met. Conf.*, P.263 (1967).

# MECHANISMS OF FATIGUE IN FILAMENT-REINFORCED METALS\*

by

J. R. Hancock

Center for Applied Research on Materials  
Midwest Research Institute  
Kansas City, Missouri

## I. INTRODUCTION AND REVIEW

Relatively few detailed studies have been carried out on the fatigue behavior of filamentary metal-matrix composites and still fewer on the effects of filament-matrix interfaces on fatigue properties. The fatigue behavior of filamentary composites is complex and depends on the mechanical properties of both constituents, the length, diameter, and volume fraction of the reinforcements and their orientation with respect to direction of load application, the interfacial bond strength and microstructure, the residual stresses, and the type of fatigue test conducted.

Forsyth et al.,<sup>1</sup> found that the rate of fatigue-crack propagation in an aluminum alloy could be reduced substantially by imbedding small numbers of continuous steel wires in the alloy. A number of investigators have found that reinforcement with unidirectionally aligned filaments raised the endurance limit of the composite for either oscillating tensile stresses<sup>2-5</sup> or reversed-bending tests.<sup>6-8</sup> In studies of copper reinforced with brittle tungsten filaments, Ham and Place<sup>2</sup> concluded that the tension-tension fatigue behavior could be improved if a matrix were used which would not fatigue-harden under service conditions. They concluded that fatigue hardening at the tip of cracks propagating in the matrix could build up sufficiently large stress concentrations to cause premature and abrupt fracture in adjacent filaments. Similarly, Morris<sup>9</sup> and Toth<sup>5</sup> have explained the higher endurance limit for 6061 Al matrix over 2024 Al matrix, each reinforced with continuous boron filaments, on the basis of differences in cyclic work-hardening rates in the matrix. The higher work-hardening rate of 2024 Al was associated with more rapid buildup of stress concentrations at crack tips which resulted in premature fracture of nearby filaments. Toth<sup>5</sup> has also shown that the endurance limit is lower when boron filaments are oriented at an angle to the direction of cyclic load application (off-axis tests) and for cross-piled filament (boron) orientations. Other work<sup>10</sup> using ductile beryllium filaments has shown that cross-piled filament orientations suffer no reduction in endurance limit relative to unidirectional filament orientations.

The only study published on the effect of interface conditions on the fatigue behavior of filament-reinforced

metals showed that the reverse-bending fatigue life was highest when specimens of aluminum reinforced with stainless-steel wires were fabricated (diffusion bonded) at  $T \approx 510^\circ\text{C}$ .<sup>8</sup> Lower and higher fabrication temperatures resulted in shorter fatigue lives. The ease with which cracks propagated along interfaces for the lower fabrication temperatures was minimized by the presence of an intermetallic compound at the interface formed during fabrication at  $510^\circ\text{C}$ . The resulting improvement in fatigue life was attributed to improved mechanical keying between the filaments and matrix, rather than to higher bond strength, and to the resulting difficulty of crack propagation along the irregular interface.<sup>11</sup> This supposition is supported by microscopic observations that a mechanical bond existed between stainless-steel filaments and the intermetallic-compound reaction product.<sup>12</sup> The decrease in fatigue life of aluminum-stainless steel composites for fabrication temperatures  $T > 510^\circ\text{C}$  was attributed to the ease with which the brittle intermetallic compound at the interface cracked during fatigue.<sup>8,11</sup>

The fatigue properties of composites are not thought to be very sensitive to surface imperfections, and cracks often initiate internally.<sup>3,13</sup> The prevention of broken filaments during fabrication is a particularly difficult problem when brittle reinforcements are used. The initiation of fatigue cracks at the ends of discontinuous or broken filaments appears to be well-established. Detailed studies, however, have not been made on fatigue-crack initiation in composites reinforced with axially aligned, continuous ductile filaments.

Generally, at low cyclic stress amplitudes, cracks are deflected around filaments. Cook and Gordon<sup>14</sup> proposed that maximum toughness can be achieved in a composite system by providing a weakly bonded interface, which will split under the influence of large tensile stresses ahead of an advancing crack. Crack-tip stresses are thereby relieved and crack growth impeded or arrested by a blunting mechanism. Completely notch-insensitive composites have been produced by this mechanism.<sup>15</sup> As higher stress amplitudes are applied, particularly for the case of brittle reinforcements, crack-tip stresses become large enough to fracture nearby filaments, and filaments no longer function as crack stoppers.<sup>2,5,9</sup> The composite behaves in a more

\* This research was supported by the Air Force Materials Laboratory under Contract No. F33615-67-C-1547.

brittle fashion, the higher the interfacial bond strength.<sup>14,15</sup>

In summary, previous work has shown that reinforcement with strong, stiff filaments can reduce the rate of crack propagation and raise the endurance limit. Work-hardening effects at crack tips in the matrix have been found to be damaging to fatigue properties of specimens reinforced with brittle filaments, and filament-matrix-interface conditions have been shown in at least one case to affect fatigue performance. Lacking gross internal discontinuities, such as broken filaments or fractured interfacial reaction products, the mechanisms of fatigue-crack initiation and growth in filament-reinforced metals are not clear. Finally, it is not presently possible to predict the number of cycles to failure or to predict quantitatively the fatigue performance with increasing vol. % of reinforcement in filament-reinforced metals. Although composite materials add new complexities to understanding fatigue behavior, the results of years of mechanisms research on the fatigue of metals provide invaluable guidance for the study of these problems (for a recent, comprehensive review of fatigue mechanisms in metals, see Grosskreutz<sup>16</sup>).

It was clear from consideration of the above results that further research was needed to clarify the role of the interface in composite fatigue behavior and to develop methods of predicting the fatigue performance of composites. Accordingly, some results are presented below on an investigation which has as its goals (1) the determination of the effects of mechanical interlock at interfaces on the low-cycle fatigue behavior of filamentary metal-matrix composites, and (2) the development of methods to predict the fatigue behavior of filamentary metal-matrix composites.

Two series of composite specimens reinforced with ductile filaments were investigated; one series was pure aluminum reinforced with as-drawn beryllium wires (rough wire surface), and the second series was pure aluminum reinforced with electropolished beryllium wires (smooth wire surface).

To our knowledge, all previous investigations of the fatigue behavior of filament-reinforced metals have employed cyclic bending tests, oscillating tension tests or cyclic torsion tests. For most structural applications, it is important to evaluate the fatigue performance of filamentary composites under uniform stresses which include compressive stresses as well as tensile stresses. Rosen<sup>17</sup> has shown that large uniform compressive strains are likely to result in the buckling of filaments in plastic-matrix composites. These results, however, do not apply to the present experiments since the relatively small ratio of filament to metal-matrix elastic moduli results in a critical compressive strain (for filament buckling) which is much larger than the cyclic strains which we use.<sup>17</sup> Strain-controlled, axial fatigue tests were therefore conducted, and the results were correlated with high-resolution observations in the electron microscope, with fractographic studies in a scanning electron microscope, and with conventional metallographic observations.

## II. EXPERIMENTAL

### A. Materials

Continuous lengths of as-drawn and electropolished beryllium wire (99.37 wt. % Be)<sup>†</sup> were used to reinforce pure aluminum (99.35 wt. % Al). The average diameter of the as-drawn beryllium wire was  $0.00474 \pm 0.00004$  in., and the maximum depth of surface disparities was approximately  $5 \mu$  (microns). For the fabrication of specimens reinforced with electropolished wire, continuous lengths of beryllium were electropolished at 25°C,  $\approx 0.6$  amp/cm<sup>2</sup> in a solution containing 133 ml. ethanol, 67 ml. ethylene glycol, 10 ml. nitric acid, 2 ml. hydrochloric acid, and 2 ml. sulfuric acid.<sup>††</sup> The final average wire diameter was  $\approx 0.00435$  in.  $\pm 0.00004$  in.

Figure 1 shows the surfaces of as-drawn and electropolished beryllium wire, and Table I is a summary of the tensile properties for as-drawn, electropolished, and annealed

TABLE I  
AVERAGE TENSILE PROPERTIES OF BERYLLIUM WIRE

SPOOL	CONDITION	GAGE LENGTH (IN.)	UTS (PSI)	FRACTURE STRAIN (%)	No. OF SPECIMENS
1	As-drawn	15	151,840	7.9	9
2	As-drawn	15	152,775	6.8	4
3	As-drawn	15	151,900	11.5	2
3	Electropolished	15	148,390	6.3	10
1	Electropolished	15	149,900	4.1	1
1	Electropolished	2	150,500	8.6	1
3	As-drawn, annealed	2	121,033	17.4	3
1	Polished, annealed	2	124,300	15.4	1

<sup>†</sup> Beryllium Corporation Lot 169NC; provided by the Advisory Group for Aerospace Research and Development, North Atlantic Treaty Organization.

<sup>††</sup> This electrolyte should be considered potentially explosive. Explosions have occurred recently in other laboratories while using a composition containing twice the acid concentration given above.





(a) As-Drawn Beryllium Wire



(b) Electropolished Beryllium Wire

Figure 1. Surface of (a) As-Drawn Beryllium Wire, and (b) Electropolished Beryllium Wire. Arrow shows a large BeO inclusion.

(475°C, 2 hr.,  $\approx 10^{-6}$  torr vacuum) beryllium wire for a strain rate of  $\approx 5-6 \times 10^{-5} \text{ sec}^{-1}$ . A change in the strain rate by a factor of  $\pm 2$  altered the UTS (ultimate tensile strength) by  $\approx \pm 2.3\%$ . A sharp yield point occurred in the annealed wire at  $\approx 97,500$  psi.

### B. Composite Fabrication

Each series of composite specimens, containing  $\approx 34$  vol. % of unidirectionally aligned beryllium wires (Figure 2), were fabricated by filament-winding and vacuum-diffusion-bonding methods (475°C,  $\approx 10^{-6}$  torr, 6,000 psi, 2 hr.). After the wire was wound on a mandrel at a predetermined spacing, a thin layer of 4% polystyrene in toluene was sprayed on the wire mats to maintain wire alignment and spacing during sectioning and composite layup. Wire mats were alternately stacked with wire-brushed aluminum sheets (0.0038 in. and 0.0040 in. thick for electropolished wire and as-drawn beryllium wire, respectively) for diffusion bonding. During heatup in vacuum, the polystyrene binder evaporated at  $\approx 300^\circ\text{C}$ ; full bonding pressure was applied at 425°C.

The volume fraction of beryllium wires in composite specimens was determined by counting the number of wires in photomicrographs of specimen cross sections.

Aluminum control specimens were prepared by dif-

fusion bonding 0.0050 in. thick sheets at 475°C,  $\approx 10^{-6}$  torr, 4,000 psi, for 2 hr.

### C. Fatigue Tests

A gage section, 0.250 in. long, was machined in each composite specimen and in aluminum control specimens by electric-discharge machining; the final cross section

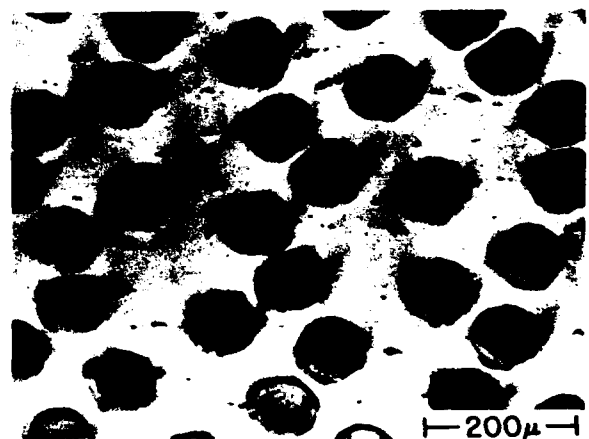


Figure 2. Cross Section of a Composite of Aluminum Reinforced with 34 vol. % of Beryllium Wire.

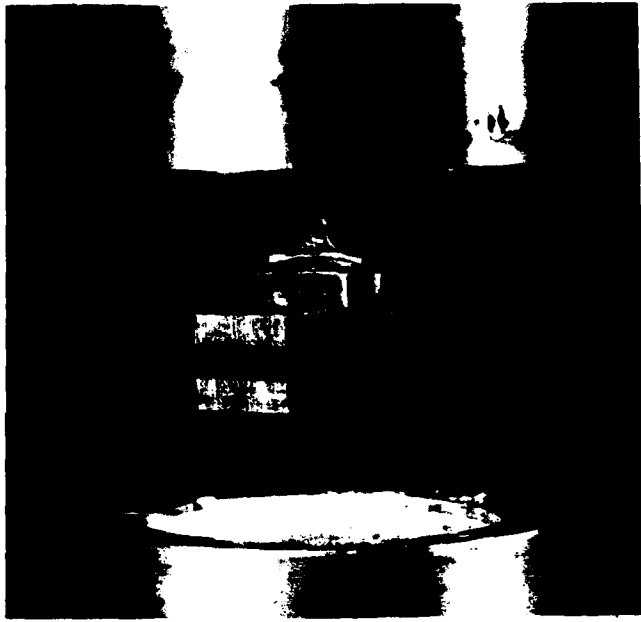


Figure 3. Gripping Arrangement for Testing Composite Specimens.

of the gage length after electropolishing was  $\approx 0.120$  in.  $\times$  0.060 in. Steel tabs were epoxied to the fatigue specimens to provide a mechanical grip when immersed in Wood's-metal (melting point  $\approx 75^\circ\text{C}$ ) grips on an Instron testing machine. The grips and specimen size were designed to limit the cyclic shear stress on the epoxy bonds to  $< 0.1$  of the ultimate shear strength. Figure 3 shows the gripping arrangement. This mounting technique facilitated specimen alignment, precluded accidental straining of the specimen during mounting, and eliminated large compressive gripping stresses. The gripping arrangement gave a linear stress-strain response when tested with an elastic control specimen at a cyclic load well in excess of that required for the composite tests.

Low-cycle axial fatigue tests were conducted on an Instron testing machine under conditions of zero-to-tension, controlled, cyclic strains at  $\approx 8$ -15 cycles/min for composites and for aluminum control specimens. Figure 4 shows a typical hysteresis loop for a composite specimen during the first cycle and illustrates the type of test conducted. The strain was measured on composite specimens by temperature-compensated foil strain gages cemented to either side of the specimen. Strain gages were not cemented to aluminum control specimens because it was felt that their presence might perturb crack growth and fatigue lives. For both aluminum and composite specimens, the total strain range was measured (in addition to the measurements with strain gages on the composite specimens) with a dual linear-variable-differential-transformer extensometer and controlled through calibrated limit switches on a Daytronic 300CL/62 instrument. Zero-to-tension, controlled-strain tests were con-

ducted to evaluate composite performance under compressive as well as under tensile stresses, and to help alleviate buckling in the specimen, since the compressive stress was initially less than the tensile stress and only gradually built up to a push-pull stress condition.

The first cycle of strain was applied at the slower strain rate of  $5 \times 10^{-4} \text{ sec}^{-1}$  to obtain Young's modulus,  $E$ , of the composite. The measured values of  $E$  were expected to be high due to end constraints and the short gage lengths which were necessary to avoid buckling during the compressive half cycle. The average value of  $E$  ( $22.9 \times 10^6$  psi) was 6-17% higher (strain sensitivity of  $\approx 1 \times 10^{-4}$ ) than predicted by the "rule of mixtures,"<sup>†</sup> using the extreme values of modulus ( $38$ - $44 \times 10^6$  psi) which have been reported for drawn beryllium wire<sup>19</sup>.

Load-controlled, oscillating tensile-stress fatigue tests were performed on electropolished and annealed (2 hr.,  $475^\circ\text{C}$ ) beryllium wire on an Instron testing machine. The wire ends were wrapped with aluminum foil and mounted in pin-vise grips for testing.

A dial micrometer was used to measure crosshead motion and indicate strain over the 2-in. gage length. Axial stresses were calculated on the basis of the original cross-sectional area.

#### D. Electron Microprobe Analysis

Electron microprobe analyses of filament-matrix interfacial regions were performed on specimens from each

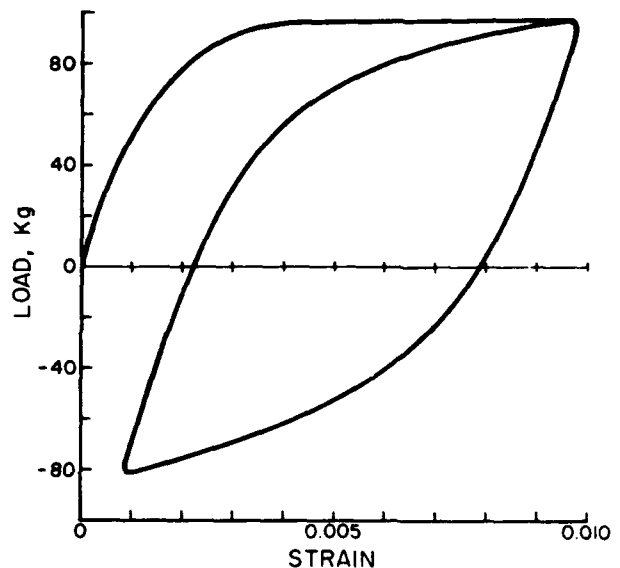


Figure 4. Hysteresis Loop for the first Cycle for an Aluminum-Beryllium Composite Cycled Between  $\approx$  Zero and a Positive Strain Limit.

<sup>†</sup> The "rule of mixtures" is a simple volume weighting of the constituent moduli to give the modulus of the composite, i.e.,  $E = V_1 E_1 + V_2 E_2$ ; Voigt<sup>18</sup> first proposed the uniform strain assumption to calculate the elastic constants of polycrystals.

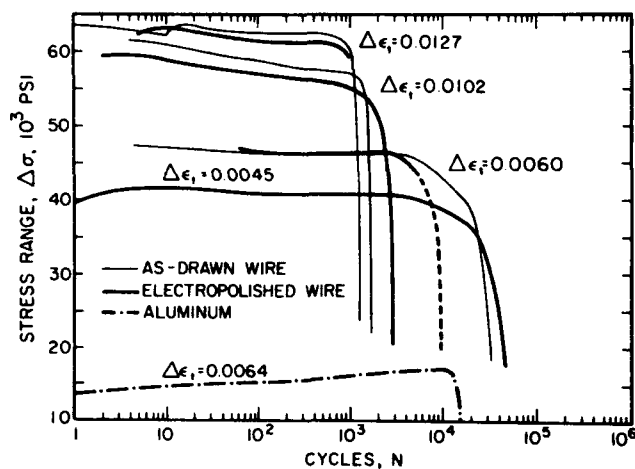


Figure 5. Stress Range vs. Number of Elapsed Cycles for Aluminum - 34 vol. % Beryllium Composites and Pure Aluminum.

of the two series of composites.<sup>†</sup> No diffusion penetration of aluminum into the beryllium filaments was detected (sensitivity 0.5 wt. %), nor was segregation of impurities (Fe, Si, Cu) at interfaces detected.

### E. Microscopy

Metallurgical and dislocation structures in the matrix, filaments, and interfacial regions were examined in an Hitachi HU-11 electron microscope at 100 KV. Sections of as-fabricated and fatigued composite specimens were electrothinned to perforation in standard Disapol electrolyte A-2 (70 m. ethanol, 12 ml. distilled water, 10 ml. butylcellosolve, 7.8 ml. perchloric acid) at 13 volts, -5°C.

Fracture surfaces of composite specimens were studied in the scanning electron microscope<sup>††</sup> to determine fracture modes, crack-path morphology, and to evaluate qualitatively the interfacial bond strength.

Longitudinal sections of fatigued composites were metallographically polished and examined in a light microscope to determine the extent of crack nucleation and growth away from the fracture surface and to identify crack nucleation sites.

## III. RESULTS

### A. Low-Cycle Fatigue

Representative curves of stress range vs. number of elapsed cycles (fatigue hardening or softening curves) are plotted in Figure 5 for pure aluminum and for composite specimens reinforced with as-drawn beryllium wire and with electropolished beryllium wire. Pure aluminum continued to harden throughout the test until failure was imminent,

<sup>†</sup> Electron microprobe analyses were performed by E.F. Fullam, Inc., Schenectady, New York.

<sup>††</sup> JEOL scanning electron microscope at E.F. Fullam, Inc., Schenectady, New York, and a Cambridge Stereoscan scanning electron microscope at Massachusetts Institute of Technology, Cambridge, Massachusetts.

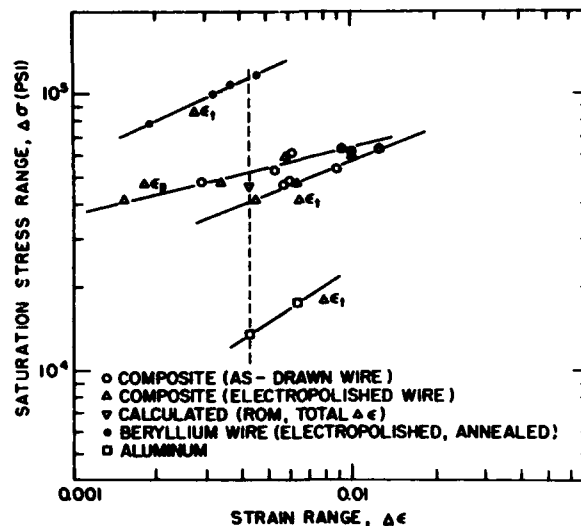


Figure 6. Cyclic Stress-Strain Curves for Aluminum - 34 vol. % Beryllium Composites, Pure Aluminum, and Beryllium Wire.

while little or no cyclic hardening occurred in the composite specimens. The differences in cyclic stress range developed between the two series of composite specimens at the two highest strain levels are approximately 2-4% and are not significant, owing to slight differences in the controlled strain ranges. The sharp increase in stress range at  $N = 10$  cycles,  $\Delta\epsilon_t = 0.0127$ , for the composite reinforced with as-drawn beryllium wire is a result of "resting" the specimen at zero stress for three days before resuming the test.

The results of all fatigue tests are presented in terms of cyclic stress-strain curves (Figure 6), Manson-Coffin plots<sup>20,21</sup> (Figure 7), and S-N curves (Figure 8).

The saturation values of stress range in Figure 6 were taken from the flattest part of the curves in Figure 5 at  $N \approx 400$  cycles. The cyclic stress-strain curves for the two series of composite specimens are identical (plotted both in terms of total strain range,  $\Delta\epsilon_t$  and plastic strain range,  $\Delta\epsilon_p$ ). The power-law relationship for the cyclic stress-strain curve is

$$\Delta\sigma = K\Delta\epsilon^\beta \quad (1)$$

where  $\Delta\sigma$  is the stress range,  $\Delta\epsilon$  is the strain range, and  $K$  and  $\beta$  are constants. Using plastic strain range,  $\Delta\epsilon_p$ , the values for the constants  $K$  and  $\beta$  are given in Table II. These results demonstrate that mechanical keying at the interface had no effect on the cyclic-load transfer capability. It is also noteworthy that the cyclic strain-hardening exponents,  $\beta$ , for the composites, bulk beryllium, and 1100 aluminum are identical. Data for control specimens of aluminum and beryllium wires are plotted in Figure 6 in terms of total strain range,  $\Delta\epsilon_t$ , since accurate measurements of  $\Delta\epsilon_p$  were not obtained.

TABLE II  
MATERIAL FATIGUE CONSTANTS

MATERIAL	CYCLIC STRESS-STRAIN CONSTANTS		MANSON-COFFIN CONSTANTS		REFERENCE
	K (PSI)	$\beta$	$a$	$c$	
Al-Be (as-drawn)	200,750	0.24	0.35	0.10	-
Al-Be (electropolished)	203,500	0.25	0.50	0.34	-
Bulk beryllium	-	0.23	0.35	-	22,23
1100 aluminum	-	0.23	0.69	-	23

It may be questionable whether the results of load-controlled fatigue tests for the beryllium wire are directly comparable with the results for strain-controlled tests of aluminum and composite specimens. In making such comparisons, we have made the *a priori* assumption that the saturation stress in a strain-controlled test is equivalent to the stress in a load-controlled test.<sup>24,25</sup>

A rule-of-mixture calculation for  $\Delta\epsilon_t = 0.0043$  (dotted line in Figure 6) gives a composite saturation stress range which is  $\approx 11\%$  higher than was observed. Moreover, the calculated saturation stress range should be even higher, since the data for beryllium wire were not corrected for the change in cross section resulting from plastic extension.

Manson-Coffin curves (strain range vs. fatigue life) are shown in Figure 7. Unusually large uncertainties in the experimental data are indicated in the figure. The specimen reinforced with as-drawn beryllium wire and tested at  $\Delta\epsilon_t = 0.0058$  was observed to buckle during testing and the arrow indicates that the fatigue life should perhaps be longer than indicated. With the exception of composite specimen AB5 ( $N_f = 2,469$  cycles), cracking appeared to initiate at or near the Wood's-metal grips. For the lower strain ranges studied, the majority of crack growth and the

resulting fracture surface occurred well beyond the grips. At the highest strain ranges ( $> 0.010$ ), cracks tended to propagate directly across the specimen with considerably less crack growth along interfaces (see Section III, C).

The Manson-Coffin curves show that at the lower strain ranges studied, substantially longer fatigue lives were observed for composites reinforced with as-drawn beryllium wire. The constant strain fatigue lives of both series composites were of the same order as pure aluminum, but were about two orders of magnitude longer than that of beryllium wire.

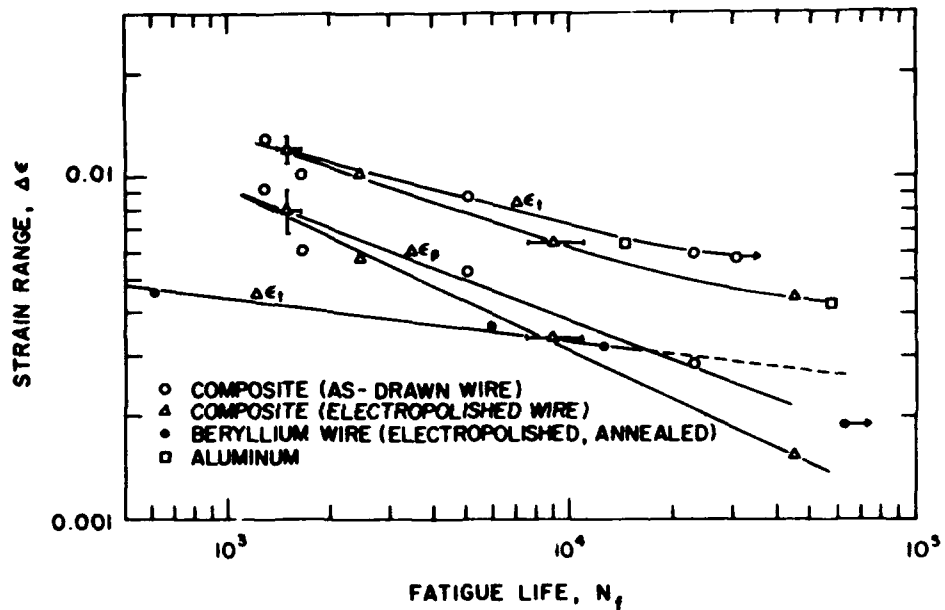
The Manson-Coffin relationship is given by

$$\Delta\epsilon_p N_f^a = c, \quad (2)$$

where  $N_f$  is the fatigue life, and  $a$  and  $c$  are constants. Values of  $a$  and  $c$  are given in Table II for both series of composites and for bulk beryllium and 1100 aluminum. The value of  $a$  for beryllium wire is expected to be nearly the same as for bulk beryllium since the Manson-Coffin curves are in good agreement.<sup>22</sup>

Several effects of filament-surface roughness on

Figure 7. Manson-Coffin Curves for Aluminum - 34 vol. % Beryllium Composites, Pure Aluminum, and Beryllium Wire.



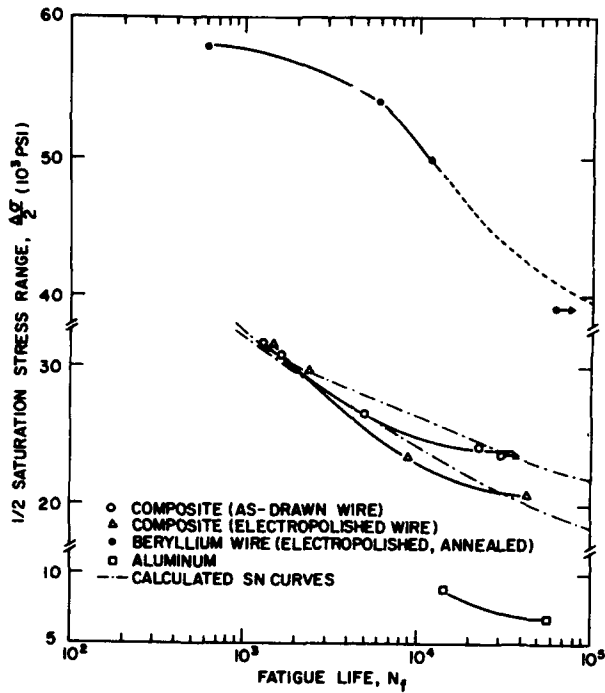
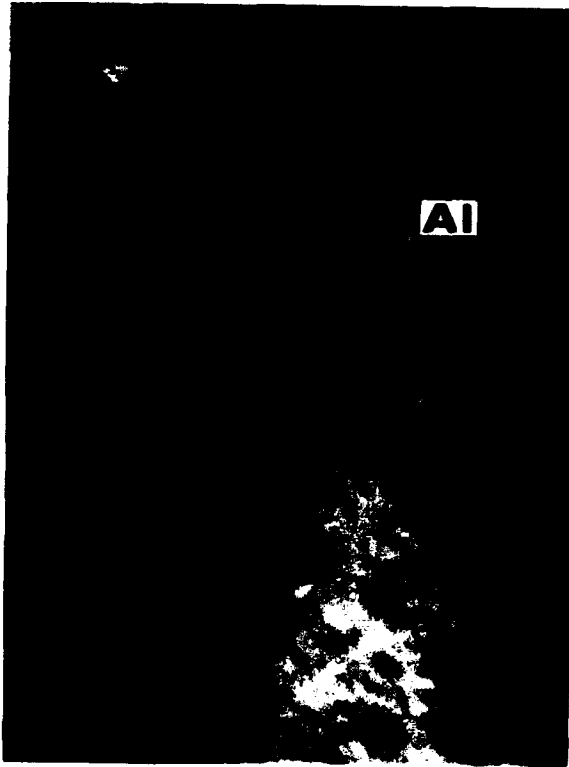


Figure 8. S-N Curves for Aluminum - 34 vol. % Beryllium Composites, Pure Aluminum, and Beryllium Wire.

composite performance are immediately apparent: (1) fatigue lives are prolonged and the endurance limit is apparently raised by the rough filament surfaces; (2) since the overall effect of rough surfaces is to extend the fatigue life, surface disparities do not give rise to harmful notch effects; and (3) interface conditions have a strong influence on the fatigue performance of metals reinforced with ductile filaments.

The fatigue data are presented in the form of S-N curves in Figure 8. The stress plotted for the composites and for aluminum is one-half the saturation stress range, whereas the data for beryllium wire is of the type normally taken for S-N curves, i.e., for load-controlled tests. Equations (1) and (2) were combined to obtain an expression for the S-N curves in terms of the cyclic material constants (Table II). These are shown as dashed lines in Figure 8. The discrepancies between the individual points and the calculated curves represent both a measure of the scatter in the data, and/or inaccuracies in the relationships assumed between stress, strain, and fatigue life. It would be of interest to know whether the S-N curve for composites determined by conventional load-controlled tests would fit these derived data, so that one could obtain the S-N curve as well as the cyclic material constants in Table II from strain-controlled tests.



(a) Metallurgically bonded interface in a fatigued composite.

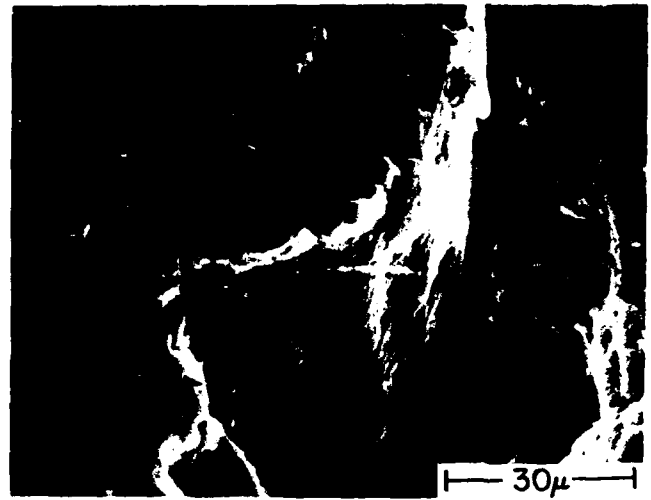


(b) Interface in an as-fabricated composite showing a nonmetallic interface phase (arrow).

Figure 9. Interfaces in Aluminum-Beryllium Composites.



(a) Electropolished Beryllium Wires



(b) As-Drawn Beryllium Wires

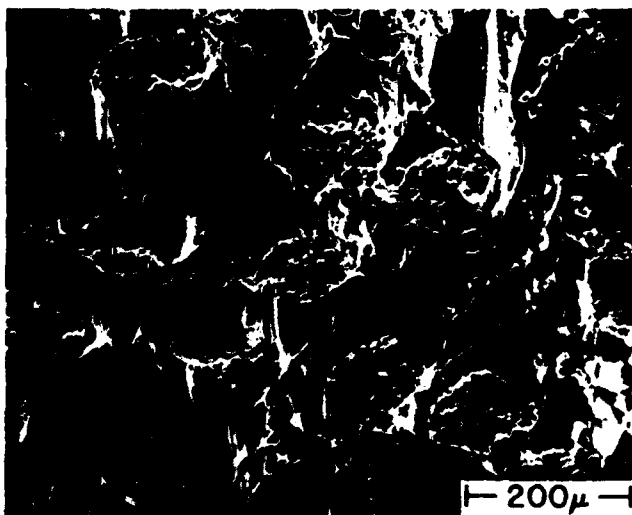
Figure 10. Interfacial Areas on Fatigue Fracture Surfaces of Aluminum Reinforced With (a) Electropolished Beryllium Wires; and (b) As-Drawn Beryllium Wires; (45° tilt).

### B. Interface Characterization

Observations in the electron microscope indicate that the filament-matrix interface was coherent and metallurgically bonded (Figure 9a). Only the beryllium side of the interface is electron transparent in Figure 9a. No evidence was found that recrystallization occurred around the periphery of filaments due to solute diffusion, nor was diffusion of aluminum into beryllium detected by electron microprobe analysis (see Section II, D). It may therefore be assumed that the strength of beryllium wire in the composites is that measured for annealed beryllium wire (Table I). Figure 9b shows an interface in the same composite specimen in the as-fabricated condition. The perforation occurred

directly at the interface and an interfacial phase, presumably an oxide layer (arrow), extends across the perforation. The interfacial phase was  $\approx 0.06 - 0.10 \mu$  thick. Some interface contamination may also have occurred from the incomplete removal of the polystyrene used to bind wire mats together for composite layup. In either event, this non-metallic phase may result in a mechanically weak interface or may be a site for easy crack initiation.

Fractographic observations were made in a scanning electron microscope to reveal how interfaces respond to cyclic loading and to judge qualitatively the strength of the interfacial bond. Figures 10a and 10b show interfacial areas on the fatigue fracture surface in composites rein-



(a) Typical area of fracture surface illustrating that filament pullout did not occur



(b) Interfacial area showing aluminum adhering to filament

Figure 11. Fracture Surfaces on a Tension-Test Specimen of Aluminum Reinforced With As-Drawn Beryllium Wires; (45° tilt).



**Figure 12. Dislocation Structure in Aluminum Matrix in an As-Fabricated Composite.**  
 (Fe, Si, Cu) -rich inclusions (arrow) were commonly observed in the matrix.

forced with electropolished and with as-drawn beryllium wire, respectively. The magnification in the direction normal to the magnification marker on micrographs tilted  $45^\circ$  to the electron beam is 0.707 times the indicated magnification due to foreshortening. The micrographs in Figure 10 illustrate that the extensive crack growth, which occurred approximately parallel to interfaces, was in most instances crack growth in the aluminum matrix, roughly parallel to and very near to the interface. Aluminum was observed to adhere to most of the filaments, although areas could be found which resembled decohesion at the original interface. An example of the latter is shown in the arrow in Figure 10b.

The fracture surface on a tension-test specimen show-



**Figure 13. Typical Grain Size ( $3-4 \mu$  diameter) in Beryllium Filaments in an Aluminum-Beryllium Composite.**

ed that filament pull-out did not occur and was not expected for ductile filaments, but rather large shear deformations in the aluminum occurred near the filaments (Figure 11a). In areas where the filaments separated from the matrix by local necking, aluminum still adhered to the filaments (Figure 11b).

The above observations lead to the following qualitative characterization of interface structure and strength. For the fabrication conditions employed, the interface was metallurgically bonded and the bond strength generally exceeds the shear strength of the aluminum matrix. Isolated, locally weak areas may be present, however, as a result of thin oxide layers or other contaminants.



**Figure 14. Fatigue Fracture Surface of Aluminum Reinforced with Electro-Polished Beryllium Wires**  
 ( $\Delta\epsilon_f = 0.006$ ;  $N_f \approx 9,000$  cycles; 50X,  $\approx 0^\circ$  tilt).

### C. Deformation Structures

**Fabrication.** The dislocation density in as-fabricated composite specimens was typically high (Figure 12), as a result of the differential thermal contraction between aluminum and beryllium during cooling from the fabrication temperature. The fact that the matrix was already in a mildly work-hardened condition partially accounts for the small extent of cyclic hardening observed in composite specimens.

Figure 13 shows the typical grain size ( $\approx 2.4 \mu$  diameter) in the beryllium filaments as viewed parallel to the filament axis. The grain size of as-drawn beryllium ingot wire (0.005 in. nominal diameter) has been reported previously to be  $2 \mu$  average diameter by  $6 \mu$  long<sup>26</sup>.

**Tension.** The fracture surface of the tension-test specimen exhibited features typical of ductile fracture in the aluminum matrix. Failure in the aluminum by the nucleation and coalescence of voids is clearly shown in Figure 11. As pointed out earlier, filament pullout did not occur and filament fractures were not found away from the fracture surface. Measurement of the diameter of beryllium filaments on the fracture surface indicated that the local fracture strain was approximately 20%. Since little localized necking was apparent, the fracture strain of the composite is apparently near that for annealed beryllium wire (Table I).

Comparison of the tensile- and fatigue-fracture surfaces on beryllium filaments in composite specimens is made below.

**Fatigue.** Figure 14 shows micrographs which when

viewed in stereo reveal the overall topographical features of a composite fatigue-fracture surface. The topography was extremely irregular, and extensive crack growth in a direction parallel to the filament axes (henceforth referred to as "vertical" cracks) was characteristic. Vertical crack growth in the aluminum matrix was the more extensive the lower the applied cyclic strain range, and vertical cracks exhibited a pronounced tendency to extend across the specimen in the short transverse direction (perpendicular to the plane of aluminum sheets in the composite layup). Figure 15a shows a typical area of the above fracture surface in greater detail. The surface of a vertical crack is shown in Figure 15b, which is intersected by another vertical crack (arrow) inclined to it.

Longitudinal sections of specimens which had been cycled to failure were examined metallographically to obtain a preliminary estimate of the distribution of cracking, the extent of cracking at regions remote from the fracture surface, and, if possible, to determine where cracks were nucleating. Filament fractures were not found in the tension-test specimen except those directly at the fracture surface. A few transverse cracks were observed in beryllium filaments in regions well removed from the fracture surface for  $\Delta\epsilon_f \approx 0.010$ , but these had not propagated into the aluminum matrix. Most filament cracks found near the fracture surface were associated with vertical matrix cracks. An example is shown in Figure 16; the crack emanated from the fracture surface on the right of the micrograph. Several vertical cracks were found (lower portion of Figure 16) which typically grew parallel to interfaces in the aluminum matrix, supporting earlier observations in the scanning electron microscope that cracking parallel to the interfaces occurred primarily in the aluminum matrix.



(a) Typical topographic features.



(b) Surface of vertical crack (center) and intersecting vertical crack (arrow).

Figure 15. Fatigue Fracture Surface of Aluminum Reinforced with Electro-Polished Beryllium Wires ( $\Delta\epsilon_f = 0.008$ ;  $N_f \approx 9,000$  cycles;  $45^\circ$  tilt).





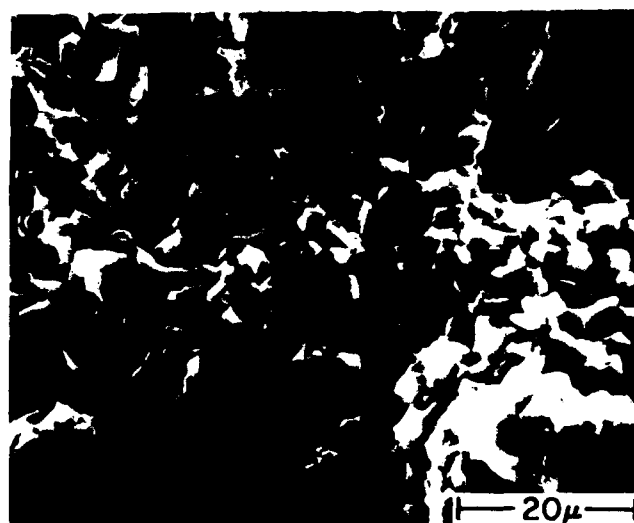
Figure 16. Fatigue Crack in Aluminum-Beryllium Composite;  $\Delta\epsilon_t = 0.006$ ;  $N_f = 30,897$  Cycles.

The fatigue fracture surface of virtually all filaments was normal to the filament axis, and displayed characteristic "directional" features as shown by the arrow in Figure 17a. The clear distinction between fatigue fractures and tensile fractures (Figure 17b) left no doubt that the beryllium filaments failed by the progressive growth of transverse cracks during the composite fatigue tests. The directional features observed on the beryllium filaments may be analogous to fatigue-crack growth striations, commonly observed, for example, in aluminum alloys. In Figure 17a, the "growth striations" would indicate a crack growth rate of  $\sim 5-10 \mu/\text{cycle}$ .

Most of the small facets on the tensile fracture surface in Figure 17b are  $\approx 2-5 \mu$  diameter, which strongly suggests a correlation with grain size (Figure 13) and the occurrence of intergranular fracture. Furthermore, the fracture mechanisms and surface appearance were no doubt influen-



(a) Fatigue fracture;  $\Delta\epsilon_t = 0.0045$ ;  $N_f = 45,432$  cycles; arrow shows possible crack growth direction.



(b) Tensile fracture; fracture strain  $\approx 20\%$ .

Figure 17. Fracture Surfaces of Beryllium Filaments in an Aluminum Matrix ( $0^\circ$  tilt).

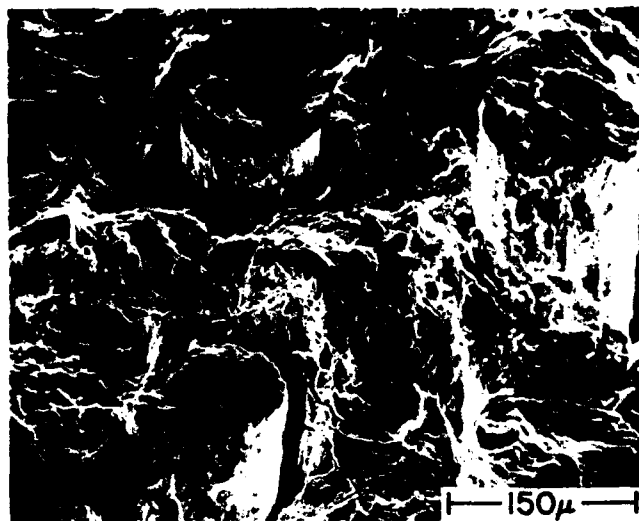
ced by the pronounced fiber texture of the drawn wire (prismatic fiber texture with  $\langle 10\bar{1}0 \rangle$  directions parallel to the wire axis and basal planes randomly oriented in radial and tangential directions<sup>26</sup>).

Evidence of fatigue-crack growth striations in the aluminum matrix is shown in Figure 18. The arrows in Figures 18a and 18c show the location of Figures 18b and 18d, respectively. Both examples occurred on surfaces oriented approximately normally to the loading direction and appear to link adjacent vertical shear cracks. The majority of evidence currently available suggests that the occurrence of fatigue striations in aluminum is strong evidence that crack growth occurred under Stage II, plane-strain conditions. The measured crack growth rates,  $da/dN$ , in Figures 18b and 18d are approximately  $5 \mu/\text{cycle}$  and  $7.5 \mu/\text{cycle}$ , respectively, and are in good agreement with observed crack-growth rates in other materials cycled at a constant total strain range of 0.0127.<sup>27</sup>

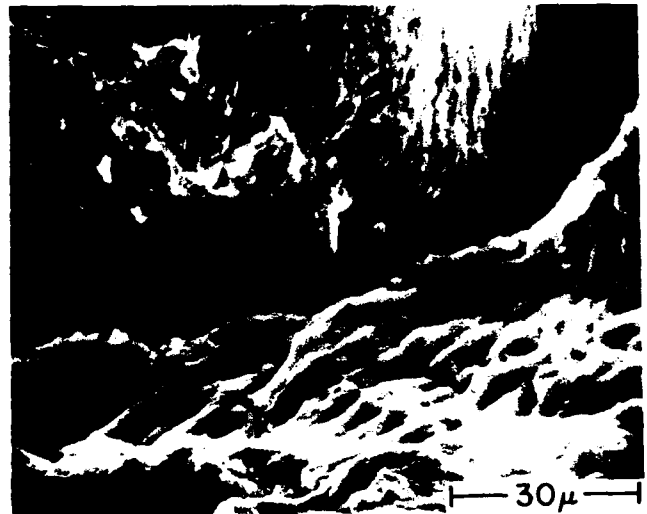
No evidence of cracking at aluminum-aluminum diffusion bonds was found in the tension-test or fatigue specimens; however, transmission electron microscopy revealed that some of the aluminum-aluminum bonds may have been contaminated with the polystyrene binder. Figure 19a shows such a contaminated bond (arrow) in a fatigued composite specimen. A dislocation cell structure typical of high-amplitude fatigue tests developed in the aluminum matrix for cyclic tests at  $\Delta\epsilon_t = 0.006$  (Figure 19b).

#### IV. DISCUSSION

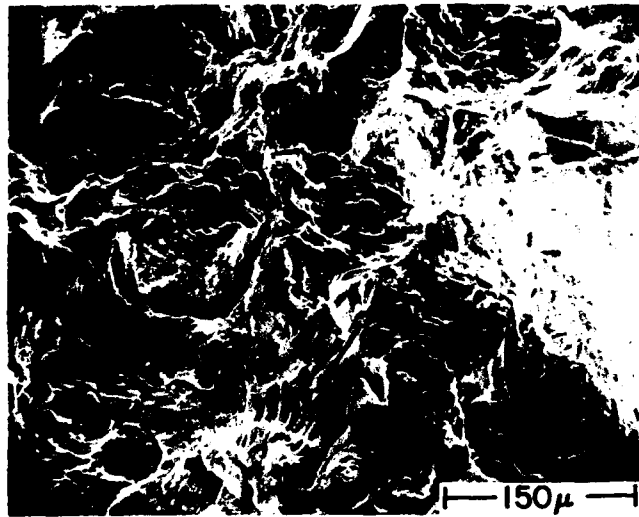
The fatigue performance of aluminum-beryllium composites was well behaved in terms of the well-known power-law relationships for the cyclic stress-strain curve and the Manson-Coffin curve. In view of the good metallurgical bond achieved at interfaces, it was not surprising that the



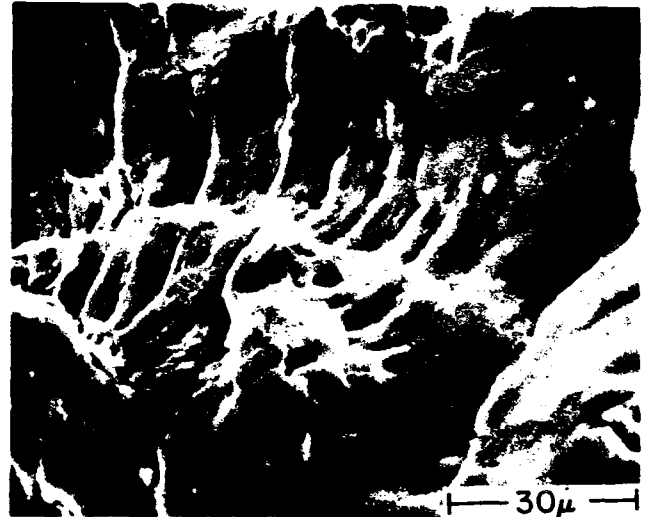
(a)



(b)



(c)



(d)

**Figure 18. Fatigue Fracture Surface of Aluminum Reinforced with As-Drawn Beryllium Wires Showing Fatigue-Crack Growth Striations in Aluminum Matrix, ( $\Delta\epsilon_f = 0.0127$ ;  $N_f = 1,304$  cycles;  $45^\circ$  tilt). (a,b)  $da/dN \approx 5 \mu/\text{cycle}$ ; (c,d)  $da/dN \approx 7.5 \mu/\text{cycle}$ .**

cyclic load-carrying capacity of the composite was not affected by filament surface roughness. The deviation observed between experimental and calculated values of composite saturation stress indicate that a simple rule-of-mixtures relationship between the constituents and composite saturation stress ranges is not accurate. Possible reasons for this deviation may be related to the difference in the work-hardening characteristics of the aluminum when constrained between the filaments,<sup>28</sup> and to complexities in cyclic composite plastic behavior due to Bauschinger effects in the filaments and matrix.

The principal result of altering interface conditions was to extend the fatigue life and possibly to raise the endurance limit of composites reinforced with filaments having

rough surfaces. As a result of grip effects on fatigue crack initiation and the tendency, for  $\Delta\epsilon_f > 0.010$ , for fracture surfaces to be flatter and therefore nearer the grip, it is possible that the slopes,  $\alpha$ , of the Manson-Coffin curves for the two series of composites do not actually differ as much as the data indicate. Thus, it is possible that the Manson-Coffin curves for the two composite series should be nearly parallel but displaced as a result of interface effects.

Correlation of the macroscopic fatigue behavior of aluminum-beryllium composites with microscopic observations on metallurgical and deformation structures lead to the following phenomenological description of fatigue-crack initiation and growth.

We can assume that crack initiation is rapid for low-



(a) An Aluminum-Aluminum Diffusion Bond (arrow) Approximately  $5 \mu$  from a Filament-Matrix Interface in a Fatigued Aluminum-Beryllium Composite.



(b) Dislocation Cell Walls Terminated and Pinned at an Inclusion in the Aluminum Matrix ( $\Delta\epsilon_t = 0.006$ ;  $N_f = 30,897$  cycles; reinforced with as-drawn beryllium wire).

Figure 19.

cycle fatigue in general and in the present case because of the grip effect in crack initiation, and that crack growth accounts for most of the fatigue life in the composite specimens. The early decrease in stress range with continued cycling (Figure 5) supports this view. Thus the major questions are, "where might internal cracks nucleate?" and "what is the early crack-path morphology?" First, consider the following:

(1) While aluminum-beryllium interfaces are generally well-bonded, there exist isolated regions of weakness (Figures 9, 10).

(2) Fatigue fracture surfaces of beryllium filaments (Figure 17) suggest that the rate of crack growth is extremely rapid in the beryllium filaments.

(3) Metallographic evidence has shown that isolated cracks can develop in the beryllium filaments during cyclic straining.

(4) For a given strain range, the fatigue lives of the composites are  $\sim 2$  orders of magnitude longer than the fatigue life of beryllium wire and about the same as for aluminum.

The evidence therefore suggests that crack initiation occurs internally at randomly located, weakly bonded interface regions (exclusive of surface grip effects), and cracks rapidly grow across the beryllium filaments. Apparently, growth of transverse filament cracks into the aluminum matrix is impeded. Zak and Williams<sup>29</sup> have shown that, given a crack in the stiffer phase (beryllium in the present case) at a bi-metallic interface, the maximum principal stresses at the crack tip occur along the interface, thus leading to the observed crack growth parallel to interfaces.

Since significant differences in fatigue life occur only at the lower strain ranges studied (when interface cracking

is most prominent), and since the difference in composite properties must be associated with interface properties, then one concludes that crack initiation at interfaces and/or crack growth along interfaces are the factors which account for the difference in fatigue lives between the two series of composites. The initiation of cracking at the grips probably ensures that initiation is equally rapid in both series of composites. Thus, if there is no significant difference in the rate of crack initiation between the two series of composites, then crack growth along interfaces is the controlling factor and the situation is analogous to that described by Baker<sup>8</sup> for stainless-steel-reinforced aluminum; i.e., the disparities on the as-drawn beryllium wire present effective impediments to crack growth along interfaces. The fatigue-hardening data (Figure 5) can be interpreted to support this last assumption, and considering that low-cycle fatigue tests are being conducted, the assumption seems reasonable. In order for as-drawn beryllium wire to be effective in impeding interfacial crack growth and in prolonging the fatigue life of composites, cracks must propagate within  $\approx 5 \mu$  (maximum depth of surface disparities on as-drawn beryllium wire) from the interface. The observations in the scanning electron microscope support that this does indeed occur (Figure 20). Failure finally occurs then as a result of an accumulation of filament fractures and interface cracks, and the linking up of these by a shear mode of crack growth or by normal Stage II crack growth in the aluminum matrix.

At the largest strain ranges studied where plastic flow and concomitant cyclic work-hardening is more extensive, cracks grow directly across the matrix with little or no interfacial crack growth. In this case, cyclic work-hardening and crack-tip stresses dominate, as described for composites reinforced with brittle filaments.<sup>2,5,9</sup>

Since crack growth in the aluminum matrix accounts for most of the fatigue life, the Manson-Coffin curves for the composites should be expected to be nearer that for aluminum than for beryllium, as observed. Others have ob-

tained similar results for aluminum-beryllium composites.<sup>10</sup> Thus, the crack-growth resistance of the matrix is of major importance in determining the fatigue life of composites. This should not, of course, be interpreted to mean that filamentary reinforcement is not beneficial. The cyclic load-carrying capacity of the composite will normally be considerably higher than that of the matrix alone.

The fatigue behavior of metals reinforced with brittle or with ductile filaments is similar in that cracks largely originate at filament fractures. In the case of ductile beryllium filaments, however, broken filaments in as-fabricated composites are readily avoided and local overloads do not cause sudden catastrophic failure of filaments. Ductile beryllium filaments fractured by the progressive nucleation and growth of fatigue cracks. In view of the poor fatigue performance of beryllium wire in terms of resistance to cyclic strains, it may be possible to improve the fatigue performance of the composites by improving the fatigue resistance of beryllium; e.g., by prolonging the time necessary for crack nucleation by surface treatments and/or by controlling the metallurgical structure of the beryllium wire to produce a larger cyclic strain-hardening exponent,  $\beta$ .<sup>30</sup> These possibilities may be limited, however, by the resistance of the matrix to cyclic strains. Improved composite performance may also be achieved by the use of filaments having variable cross sections, designed to inhibit interfacial crack growth. Finally, the design of interfaces to impede interfacial crack growth, particularly in the high-cycle fatigue realm, should also be effective when brittle reinforcements are used.

## V. SUMMARY

The major observations made in this study are summarized below:

1. Relatively little cyclic hardening occurred in composite specimens.
2. The cyclic-load-transfer capability was unaffected by filament surface roughness.
3. Deleterious notch effects due to filament-surface roughness were not observed.
4. Fatigue life was enhanced in the lower strain region by reinforcement with filaments having rough surfaces.
5. The filament-matrix interfacial bond strength generally exceeded the shear strength of the aluminum matrix.
6. The lower the applied strain range, the greater was the tendency for cracks to propagate along interfaces.

7. Aluminum-beryllium composites obey the usual power-law relationships for the cyclic stress-strain curve and the Manson-Coffin curve.

## VI. CONCLUSIONS AND RECOMMENDATIONS

Two major conclusions were drawn from the results of this study:

1. The observed increase in fatigue life in composites reinforced with ductile filaments having rough surfaces was a result of impeding the growth of cracks, primarily through the aluminum matrix, along interfaces. Interface conditions and the crack-growth resistance of the matrix are therefore important considerations in the design of fatigue-resistant filament-reinforced metals.

2. The Manson-Coffin and cyclic stress-strain power-law analyses of fatigue behavior apply to metals reinforced with ductile filaments.

The present results emphasize the need for further research on the optimum design of composite materials. Many opportunities exist for the improvement of composite performance through the development of optimum geometry, metallurgical structure, and interfacial bond strength. The advantages of plastically deformable filaments should be examined closely in terms of improved composite toughness and reliability. A compromise between filament strength and ductility or the use of a combination of ductile and brittle filaments in a composite may produce maximum fatigue resistance.

For the development of methods of predicting composite fatigue behavior, either from constituent properties or from composite behavior itself, detailed fatigue studies need to be conducted as a function of vol. % reinforcement.

## ACKNOWLEDGEMENT

I would like to acknowledge the support of the Air Force Materials Laboratory and the interest and encouragement of Mr. Walter Trapp and Dr. Walter Reimann. I would like also to thank Professor M. Brull, U.S. Representative for the Advisory Group for Aerospace Research and Development, NATO, who provided the beryllium wire for this study; my colleagues, Dr. J.C. Grosskreutz and Mr. Gordon Gross, for their continued interest, encouragement, and help; and Dr. R.M.N. Pelloux and Dr. N.J. Grant, who made available to us a scanning electron microscope for the fractographic studies.

## REFERENCES

1. P.J.E. Forsyth, R.W. George, and D.A. Ryder, "Some Preliminary Tests on Aluminum Alloy Sheets Reinforced with Strong Wires," *Appl. Mater. Res.*, 3:223 (1964).
2. R.K. Ham and T.A. Place, "The Failure of Copper-Tungsten Fiber Composites in Repeated Tension," *J. Mech. Phys. Solids*, 14:271 (1966).
3. A.W.H. Morris and E.A. Steigerwald, "An Investigation of the Fatigue Behavior of Tungsten-Reinforced and Steel-Reinforced Silver Composites," *Trans. Met. Soc. AIME*, 239:730 (1967).
4. A. Toy, "Mechanical Properties of Beryllium Filament-Reinforced Aluminum Composites," *J. Mater.*, 3:43 (1968).
5. I.J. Toth, *An Exploratory Investigation of the Time Dependent Mechanical Behavior of Composite Materials*, AFML-TR-69-9, Air Force Materials Laboratory, Wright-Patterson AFB, Ohio (1969).
6. R.V. Williams and D.J. O'Brien, "The Reinforcement of Metals with Metal Wires," *Appl. Mater. Res.*, 3:148 (1964).
7. A.A. Baker and D. Cratchley, "Metallographic Observations on the Behavior of Silica Reinforced Aluminum Under Fatigue Loading," *Appl. Mater. Res.*, 3:215 (1964).
8. A.A. Baker, "The Effect of Fiber Volume Fraction and Interfacial Bond on the Fatigue of Aluminum Reinforced with Stainless Steel Wires," *Appl. Mater. Res.*, 5:143 (1966).
9. A.W.H. Morris, unpublished work. (Cited by Ref. 5)
10. *Beryllium Wire - Metal Matrix Composites Program*, EDR-5950, General Motors Corp., Allison Division, Indianapolis, Indiana (1968).
11. A.A. Baker, "The Fatigue of Fiber-Reinforced Aluminum," *J. Mater. Sci.*, 3:412 (1968).
12. J.R. Hancock and J.C. Grosskreutz, "Plastic Yielding and Strain Distribution in Filament-Reinforced Metals," p.134, *Metal Matrix Composites*, ASTM-STP-438, American Society for Testing and Materials, Philadelphia, Pennsylvania (1968).
13. R.G. Gates and W.A. Wood, "Evaluating Potential Fatigue Performance of Composites (Cu/W and Cu/Mo) from Microstructural Behavior," p. 218, ASTM-STP-438. (See Ref. 12)
14. J. Cook and J.E. Gordon, "A Mechanism for the Control of Crack Propagation in All-Brittle Systems," *Proc. Roy. Soc. London*, 282A:508 (1964).
15. G.A. Cooper and A. Kelly, "Tensile Properties of Fiber-Reinforced Metals: Fracture Mechanics," *J. Mech. Phys. Solids*, 15:279 (1967).

## REFERENCES (Continued)

16. J.C. Grosskreutz, "Fatigue Mechanisms in the Sub-Creep Range," to be published.
17. B.W. Rosen, "Mechanics of Composite Strengthening," p. 37, *Fibre Composite Materials*, American Society for Metals, Cleveland, Ohio (1965).
18. W. Voigt, *Lehrbuch der Kristallphysik*, p. 716, Tuebner, Leipzig (1928).
19. H.S. Schwartz, *Mechanical Behavior of Beryllium Wire Reinforced Plastic Composites. Part 1, Static Mechanical Properties*, AFML-TR-66-404, Air Force Materials Laboratory, Wright-Patterson AFB, Ohio (1967).
20. S.S. Manson, *Behavior of Materials Under Conditions of Thermal Stress*, NACA-TN-2933, National Aeronautics and Space Administration, Washington, D.C. (1954).
21. L.F. Coffin, "A Study of Cyclic Thermal Stresses in a Ductile Metal," *Trans. ASME*, 76:931 (1954).
22. R.W. Smith, M.H. Hirschberg, and S.S. Manson, *Fatigue Behavior of Materials Under Strain Cycling in Low and Intermediate Life Range*, NASA-TN-D-1574, National Aeronautics and Space Administration, Washington, D.C. (1963).
23. B. Tomkins, "Fatigue Crack Propagation - An Analysis," *Phil. Mag.*, 18:1041 (1968).
24. T.H. Alden, "The Determination of an S-N Curve from Cyclic Strain Hardening Data," *Trans. Met. Soc. AIME*, 224:1287 (1962).
25. J.R. Hancock and J.C. Grosskreutz, "Mechanisms of Fatigue Hardening in Copper Single Crystals," *Acta Met.*, 17:77 (1969).
26. J.P. Denny and G.E. Meyer, "Beryllium Ingot Wire," *Wire and Wire Prod.*, 41:1640 (1966).
27. T.W. Crooker and E.A. Lange, "Low-Cycle Fatigue Crack Propagation Resistance of Materials for Large Welded Structures," p. 109, *Fatigue Crack Propagation*, ASTM-STP-415, American Society for Testing and Materials, Philadelphia, Pennsylvania (1967).
28. S.W. Tsai, *Mechanics of Composite Materials. Part 1, Introduction*, AFML-TR-66-149, Air Force Materials Laboratory, Wright-Patterson AFB, Ohio (1966).
29. A.R. Zak and M.L. Williams, "Crack Point Stress Singularities at a Bimetallic Interface," *J. Appl. Mech.*, 30:143 (1963).
30. J.C. Grosskreutz, *Fatigue Mechanisms and the Development of Fatigue-Resistant Materials*. Presented at the Air Force Conference on Fatigue and Fracture of Aircraft Structures and Materials, Miami Beach, Florida, December 1969.

# THE EFFECT OF FREQUENCY ON HIGH-TEMPERATURE, LOW-CYCLE FATIGUE

by

L.F. Coffin, Jr.

General Electric Research and Development Center  
Schenectady, New York

## INTRODUCTION

The prediction of long life behavior of metals subjected to elevated-temperature, low-cycle fatigue is of considerable interest to designers of high temperature power generating equipment. Lifetimes for this equipment may range from a few hundred hours to twenty years or longer, and may involve up to 50,000 cycles of start and stop operation. Most often designs must be of very high reliability, as in the case of aircraft gas turbines. Fatigue failures which result in removing the equipment from service for extended and expensive repair are obviously highly undesirable.

An important problem facing the designer is how best to use laboratory material information to predict failure in extended service. This information is generally obtained over short time periods, because of limited testing facilities, the cost of extended testing, but primarily because the designer needs the information before the component is built. This places heavy emphasis on the ability to extrapolate short time results to long time service. As an example, there have been developed over the years a number of methods to predict long time creep behavior from short time test results. The same need is now present for high-temperature, low-cycle fatigue.

Increasing attention is being given to this problem, as is evidenced by the mounting literature on the subject.<sup>1</sup> One approach has been proposed by Manson and Halford<sup>2</sup> and involves the extension of Manson's method of universal slopes<sup>3</sup> to elevated temperature. A set of criteria is established which determines a lower bound life which is 10% of the life predicted in the methods of Ref. 3, or a still lower life based on the inclusion of the frequency, the slope of the stress rupture line, the fraction of the time the material is subjected to maximum stress in the cycle, and certain characteristics of the creep-rupture curve. A new method<sup>4</sup> by the same authors substitutes a cyclic creep-rupture test where the rupture life of the material is obtained by cycling between equal tensile and compressive stresses to failure.

Coffin<sup>5</sup> proposed the use of temperature and time or temperature and strain rate parameters to modify the constant C in the relationship  $N_f^\alpha \Delta \epsilon_p = C$ . The method considered  $\alpha$  to be  $\frac{1}{2}$ , a highly restrictive assumption, since

there is a considerable amount of data indicating  $\alpha > 0.5$  at elevated temperatures.

Wood<sup>6</sup> has proposed a fractional damage concept to account for hold times under steady stress in which the fatigue damage term  $N_c/N_f$  is assumed to be inversely linear to the creep-rupture term  $t_c/t_f$ . Here  $N_f$  is the room temperature life at a given strain range,  $N_c$  is the elevated temperature life at the same strain range,  $t_c$  is the total time under creep at a given stress level and  $t_f$  is the time-to-failure by creep rupture at a stress comparable to that for the hold time applied.

Eckel<sup>7</sup> and more recently Coles and Skinner<sup>8</sup> have proposed the use of a frequency-time parameter of the form  $\nu^k t$  in expressing fatigue behavior. Here  $\nu$  is the frequency,  $t$  is the failure time and  $k$  a material constant. Coles et al<sup>9</sup> have applied this parameter to data where the total strain range is maintained constant.

More recently Coffin<sup>10</sup> has developed an approach based on the concept of the "frequency modified fatigue life." Using results from A-nickel at three temperatures and several crosshead rates, it was determined that the equation  $\nu^k t = C_1$  applied for all data at one temperature and a specific plastic strain range. Here again  $\nu$  is the frequency,  $t$  the total time of the test and  $k$  an exponent shown to be independent of the plastic strain range. The term  $C_1$  or  $\nu^k t$  can also be expressed as  $N_f \nu^{k-1}$  where  $N_f$  is the life, and is called the frequency modified fatigue life. It was then shown that when  $\nu^k t$  was plotted against  $\Delta \epsilon_p$  on logarithmic coordinates, a straight line resulted, expressed as

$$C_1 \beta \Delta \epsilon_p = C_2 \quad (1)$$

The constants  $C_1$ ,  $\beta$  and  $C_2$  were determined for several materials subjected to continuous cyclic straining at elevated temperatures including A-nickel, AISI 304 stainless steel,<sup>11</sup> a Mo-V steel<sup>12</sup> and a manganese steel and indicated a good fit for the various frequencies and strain ranges of the experimental information available.

Another interesting feature of Equation (1) was

its representation at different test temperatures. It was argued that  $\beta$  was a function of temperature, increasing with increasing temperature, and was the result of the changing mode of fracture from transgranular to intergranular with increasing temperature. For a particular material at several temperatures the straight lines converge at a value of  $C_1$  of approximately 25 (when time is expressed in minutes), and blend into a single upper bound line at lower values of  $C_1$ . The upper bound curve is determined from the short time tensile ductility and  $\beta = 1/2$ .

One advantage of combining fatigue life with frequency is to permit time extrapolation. For a given  $\nu^k t$ , a particular frequency and life are paired, so that low-frequency, long-time results are equivalent to higher frequency, short time laboratory experiments. Another possible advantage of the frequency-modified life is that other wave forms could be considered, providing the period remains constant. Hopefully cyclic programs in which hold times were introduced could be predicted by the frequency modified fatigue life concept.

In the present paper the concept of the frequency modified fatigue life is extended to include the elastic strain range as well as the plastic strain. Combining the two terms, one determines a total strain range or pseudo-stress range (elastic modulus times the total strain range). These quantities can be directly related to design and hence permit a means for designing for long life from short time laboratory results. Included also in the paper is a comparison of predicted life to that actually determined under hold time conditions for three materials, such that a judgement can be made of the usefulness of the approach.

### EFFECT OF TEMPERATURE AND FREQUENCY ON PLASTIC STRAIN RANGE-LIFE RELATIONSHIPS

The concept of the frequency modified fatigue life referred to above is considered here in more detail. In the earlier paper<sup>10</sup> it was shown that, for specific temperatures, a single-valued relationship existed between plastic strain range and a combination of frequency,  $\nu$ , and total time-to-failure,  $t$ , (or cycles to failure,  $N_f$ ), having the form  $\nu^k t$  (or  $N_f \nu^{k-1}$ ). A generalized representation of the plastic strain range vs. this parameter for a variety of test temperatures is shown in Figure 1. Several comments can be made with respect to this figure.

1. The abscissa  $N_f \nu^{k-1}$  is a logarithmic scale and represents a combination of frequency and cycles to failure such that, for a specific temperature, frequency effects are accounted for in the parameter. The quantity  $k$  is a function of temperature.

2. The ordinate  $\Delta \epsilon_p / \epsilon_f$  is also a logarithmic scale and is the plastic strain range divided by the short time

\*  $\beta$  is actually the exponent of  $N_f \nu^{k-1}$ .

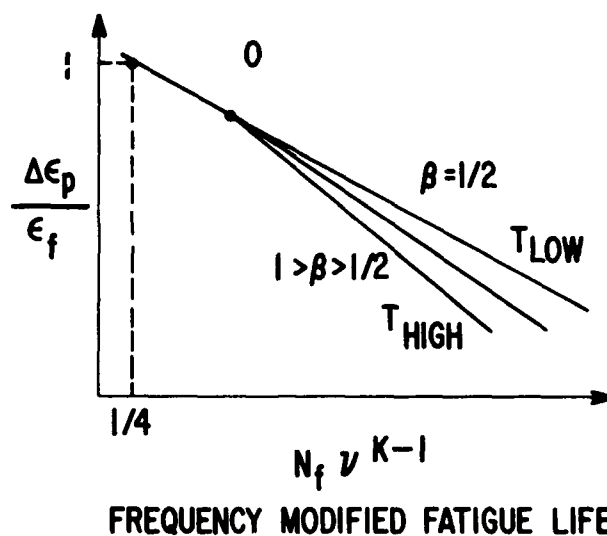


Figure 1. Generalized Representation of Plastic Strain Range vs. Frequency Modified Fatigue Life.

tensile ductility of the material. This normalized quantity permits consideration of several temperatures in a single diagram.

3. An upper-bound curve is envisaged which is obtained by cycling at high frequency such that the fatigue failure process occurs by a ductile, transgranular mode. The physical picture for this will be considered later. It would be anticipated, that no matter what the circumstances, a point of fatigue failure could not fall outside of this line. The exponent which represents the slope of this line is assumed to be 0.5.

4. For specific test temperatures, straight lines are constructed whose slope is represented by  $\beta^*$ , such that  $\beta$  increases with increasing temperature. At low temperatures where the fracture mode is ductile, the upper bound curve applies. At higher temperatures all curves converge at 0.

Experimental evidence indicates that the frequency-modified fatigue life at 0 is of the order of 25-100 when  $\nu$  is in cycles per minute. For the upper bound curve (low temperature), frequency effects are assumed to be small and  $k = 1$ . The equation for this line then is

$$\frac{\Delta \epsilon_p}{\epsilon_f} \cdot N_f^{0.5} = C \quad (2)$$

By letting  $N_f = 1/4$  and  $\Delta \epsilon_p = \epsilon_f$ ,  $C = 1/4$ . The equation for any specific elevated temperature is given by

$$\Delta \epsilon_p = C_2 N_f^{-\beta} \nu^{(1-k)\beta} \quad (3)$$

where  $C_2$  depends on  $\epsilon_f$  and the specific location of 0.

5. The quantity  $k$  is determined from tests at a given temperature and a constant plastic strain range, but at



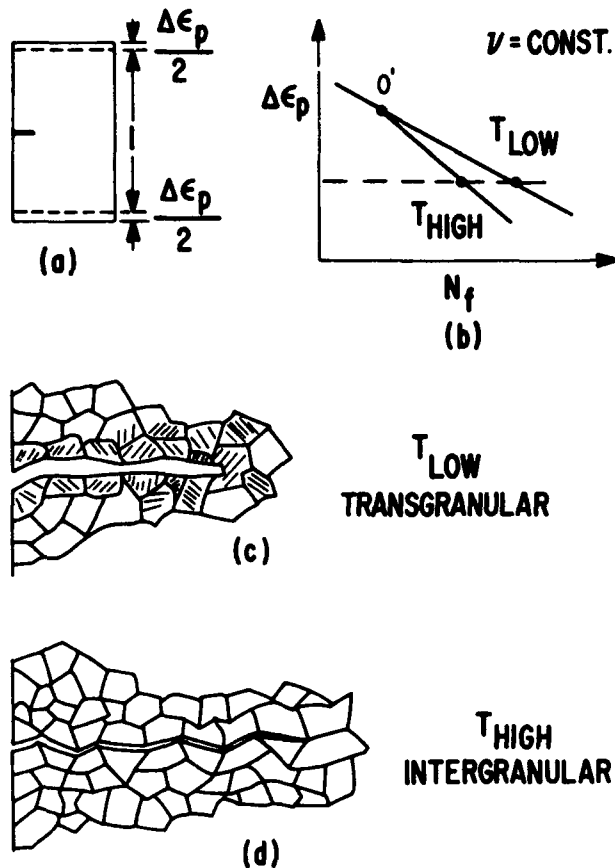


Figure 2. Model of Effect of Temperature on Low Cycle Fatigue Crack Propagation.

different frequencies. Using logarithmic coordinates,  $k$  is the exponent of  $\nu$  and represents the slope of a straight line drawn as the plot of  $\nu$  vs.  $t$ .

#### PHYSICAL SIGNIFICANCE OF PLASTIC STRAIN RANGE RELATIONSHIP

The physical interpretation of Figure 1 and Eq. (3) is based largely on the well-substantiated fact that low cycle fatigue failure in laboratory test specimens is largely a crack propagation process.<sup>13</sup> This is particularly so at elevated temperatures, where, among other factors, oxidation has been shown to enhance crack nucleation.<sup>14</sup> Assuming that uniaxially loaded test specimens are being considered in this discussion, crack propagation is occurring with a plastic zone at the crack tip which extends across the entire cross section of the specimen. Under such circumstances many factors influence crack propagation, relating either to the localized strain at the crack tip, or the capacity for deformation there. In the former category are included strain hardening and strain rate effects; in the latter, ductility and environment.

A simple model can be used to show how these various effects act together to affect low cycle fatigue life. Referring to Figure 2(a) and assuming the frequency to be

constant, a volume of material acted on by a plastic strain range,  $\Delta \epsilon_p$ , is assumed, which contains a single small crack. The mode of propagation of this crack then determines the low cycle fatigue life. For a specific plastic strain range and two temperatures, low and high, it is assumed that the mode of crack propagation changes from a ductile transgranular mode at low temperature to a brittle, intergranular mode at high temperature. These two situations are shown schematically in Figures 2(c) and 2(d), for the same number of cycles. Because of its brittle nature, the intergranular crack is considerably further advanced. Now referring to Figure 2(b), failure has occurred in fewer cycles for the intergranular crack.

Again assuming the same frequency, but increasing the plastic strain range, the brittle mode of failure at high temperature can be expected to gradually transform to a more ductile mode. This is because of the influence of the increased strain rate on the fracture mode, as seen from the relationship

$$\dot{\epsilon}_p = 2 \nu \Delta \epsilon_p \quad (4)$$

With a sufficiently large plastic strain range, the strain rate is high enough to cause a completely transgranular fracture, identified as point  $O'$ . Hence the break in the  $N_f - \Delta \epsilon_p$  line at high temperature results from a change in fracture mode at the crack tip.

Keeping the plastic strain range and the temperature constant, but considering the effects of a low or high frequency, one can produce the results shown schematically in Figure 3. Decreasing the frequency lowers the plastic strain rate and according to the above arguments, shortens the life. The fact that the low frequency line parallels the high frequency line is explainable by the frequency-modified fatigue life concept.

#### EXPERIMENTAL SUPPORT OF PLASTIC STRAIN RANGE RELATIONSHIP

Some experimental support for the model presented

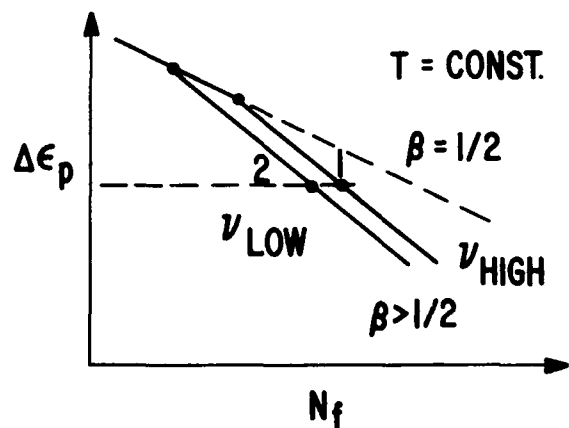
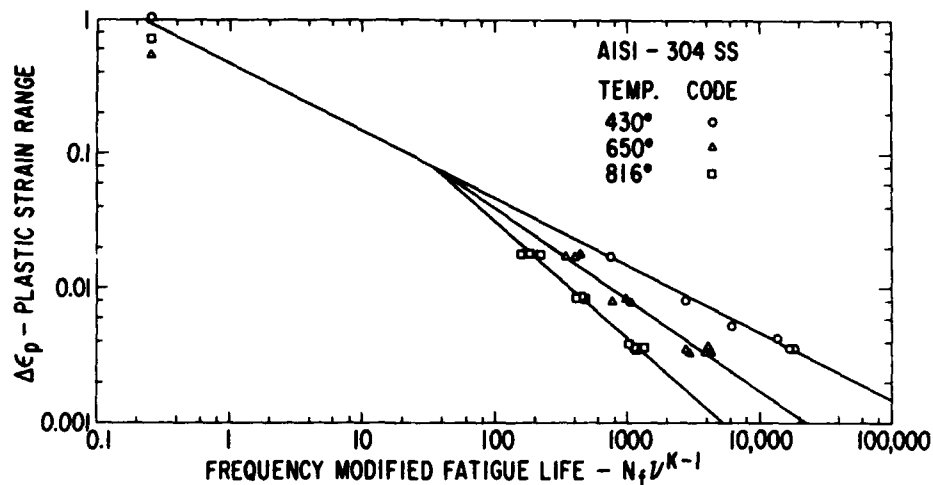


Figure 3. Schematic View of the Effect of Frequency on Fatigue Life.

Figure 4. Plastic Strain Range vs. Frequency Modified Fatigue Life for AISI 304 Stainless Steel at Three Temperatures . After Berling and Slot.



above was given in the earlier paper.<sup>10</sup> Figure 5 of that paper is replotted to conform with the present Figure 1, and is shown as Figure 4. Here the plastic strain range is plotted vs. the frequency modified fatigue life for AISI 304 stainless steel at three temperatures, the data coming from the work of Berling and Slot.<sup>11</sup> The value of  $\beta$  for the lowest temperature is 0.5. Tensile ductility values are shown at a life of 0.25. Agreement with the model representation for plastic strain range is favorable.

Experiments were also conducted on annealed AISI C1010 steel at 600°C following the procedures given in Reference 1. Both large and small values of plastic strain range were applied to uniaxially loaded hour-glass shaped specimens subjected to controlled diametral strain. For small strains the specimen diameter was 0.25" and the hour-glass radius was 1.5". For large strains the diameter was reduced to 0.125" and the radius to 0.5" to reduce buckling. Three frequencies were used for strains less than 0.2 so that the frequency modified fatigue life could be determined, as shown in Figure 5. For these smaller strains  $\beta$  was found to be 0.79. For the larger strains a single intermediate fre-

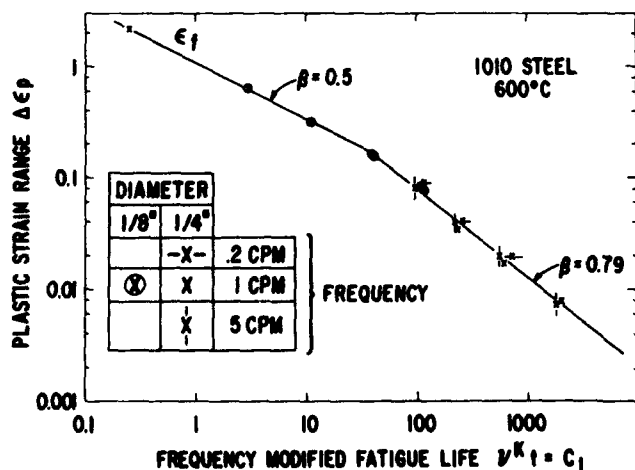


Figure 5. Plastic Strain Range vs. Frequency Modified Fatigue Life for C1010 Steel at 600°C.

quency was used and  $\beta$  was found to be 0.5. The short time tensile ductility is seen to fall on this latter line. A well-defined break in the plot of the data is found at a life of 40 cycles, in support of the plastic strain model described above. Unfortunately the severe oxidation of the steel at these temperatures prevented any observation of the change in fracture mode associated with the discontinuity.

#### EFFECT OF FREQUENCY ON THE ELASTIC STRAIN RANGE

Laboratory low cycle fatigue tests on metals at room temperature have led to the development of a relationship between the applied plastic strain range and the resulting stress range.<sup>15</sup> Thus

$$\Delta\sigma = A (\Delta\epsilon_p)^n \quad (5)$$

where A is the stress range for a plastic strain range of unity, and n is the cyclic strain hardening exponent. Use of Equation (5) generally neglects consideration of the frequency of cycling. At elevated temperatures the frequency would be expected to influence the stress range at a given plastic strain range. This effect can be accounted for in a simple manner by modifying Equation (5), so that

$$\Delta\sigma = A (\Delta\epsilon_p)^n \nu^{k_1} \quad (6)$$

For a frequency insensitive material,  $k_1 = 0$ . To obtain the elastic strain range the stress range in Eq. (6) is merely divided by E, the elastic modulus. From Eq. (6) the term "the frequency modified stress range" can be introduced as  $\Delta\sigma'$  where

$$\Delta\sigma' = \Delta\sigma \cdot \nu^{-k_1} \quad (7)$$

#### EXPERIMENTAL SUPPORT FOR EQUATION (6)

To verify Equation (6) further experiments were made on AISI C1010 steel, at 600°C in which the plastic strain range was held at a constant value of 0.00312 and the frequency varied from 0.0016 to 22 cpm. Because cyclic

TABLE I.  
MATERIAL CONSTANTS FOR EQ. (8)

MATERIAL	TEMP.	K	C <sub>2</sub>	β	A	E x10 <sup>6</sup>	n	k <sub>1</sub>
AISI C1010	600°C	0.763	3.0	0.79	53,300	23.3	0.22	0.118
AISI 304	650°C	0.81	1.10	0.70	150,000	23.0	0.257	0.20
Rene 41	760°C	0.80	0.398	0.65	552,000	24.8	0.185	0
1 Cr-Mo-V	565°C	0.9	1.31	0.75	94,900	24	0.15	0

hardening was a function only of plastic strain range but not of cycles of strain at this temperature, a single specimen was used. Results are shown in Figure 6. The slope of this line is the exponent k<sub>1</sub> in Eq. (6), and is tabulated, along with other constants, in Table I.

Other experiments were carried out on this and other specimens in which the frequency was fixed and the strain range varied. Three frequencies were employed, namely, 5 cpm, 0.2 cpm and 0.008 cpm. As seen in Figure 7 all three frequencies give equivalent slopes on the log stress range vs. log plastic strain range representation, in further support of Eq. (6). From these plots and the k<sub>1</sub> determined from Figure 6, the constants A and n are found.

Equation (6) can also be verified by plotting the frequency modified stress range Δσ' vs. Δε<sub>p</sub> for the various frequencies and strain ranges. This is seen in Figure 8. Included are the results for C1010 steel at 600°C and some recent work on A286 at 1100°C.

### THE GENERALIZED FATIGUE EQUATION

The total strain range Δε can be found by summing the plastic strain range, Δε<sub>p</sub>, and the elastic strain range Δε<sub>e</sub>. Combining equation (3) with the elastic strain range Δσ/E, found from Eq. (6), and eliminating Δε<sub>p</sub>, gives

$$\Delta \epsilon = \frac{AC_2^n}{E} N_f^{-\beta n} k_1 + (1-k)\beta n + C_2 N_f^{-\beta} (1-k)\beta \quad (8)$$

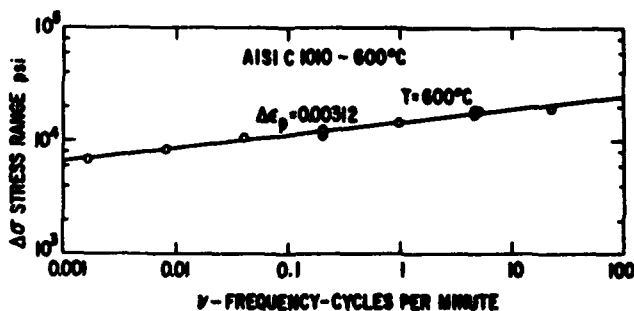


Figure 6. Stress Range vs. Frequency for AISI C1010 Steel at 600°C.  
Δε<sub>p</sub> = 0.00312

Following procedures employed for low temperature, low-cycle fatigue design<sup>16,3</sup> Equation (7) can be used directly in design, when a strain analysis of the part in question has been made. The pseudo-stress amplitude σ<sub>a</sub> = E Δε/2 may also be used when a stress analysis has been employed.

Equation (8) may be regarded as a generalized fatigue equation applicable to both high and low temperatures. At high temperatures specific values for the several constants A, C<sub>2</sub>, n, β, k and k<sub>1</sub> must be determined for each temperature. At low temperatures Equation (8) can be directly converted to Manson's<sup>3</sup> method of universal slopes or that proposed by Langer.<sup>16,17</sup> Assuming no frequency effects at low temperature, k = 1 and k<sub>1</sub> = 0. Letting β = 0.6, n = .2, C<sub>2</sub> = D<sup>0.6</sup> where D is the tensile ductility, and A = 3.5 σ<sub>u</sub>/D<sup>1.2</sup>, where σ<sub>u</sub> is the ultimate strength, there results

$$\Delta \epsilon = \frac{3.5 \sigma_u}{E} N_f^{-.12} + D^{0.6} N_f^{-0.6}, \quad (9)$$

which is Manson's equation. Again letting k = 1 and k<sub>1</sub> = 0, β = 0.5, n = 0, C<sub>2</sub> = 0.5D and A = 2σ<sub>e</sub> where σ<sub>e</sub> is the endurance limit of the material, there results

$$\Delta \epsilon = \frac{2 \sigma_e}{E} + \frac{\epsilon_f}{2N_f^{0.5}} \quad (10)$$

the low cycle fatigue equation proposed by Langer.<sup>16</sup>

Equation (8) is useful for evaluating the performance of materials subjected to high-temperature, low-cycle fa-

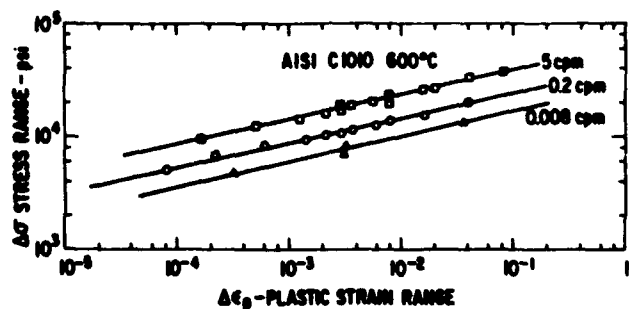


Figure 7. Stress Range vs. Plastic Strain Range for C1010 Steel at 600°C. Three Frequencies as Indicated.

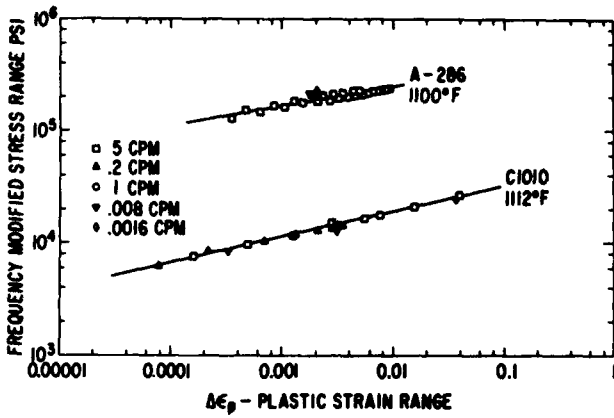


Figure 8. Frequency Modified Stress Range vs. Plastic Strain Range for A286 at 1100°F and AISI C1010 Steel at 1112°F.

tigue. Each of the constants has physical significance being either directly or indirectly related to other better known physical properties. As indicated earlier,  $\beta$  is a function of temperature, ranging from 0.5 at low temperatures to 1 at very high temperatures. The exponent  $n$  is the cyclic strain hardening exponent and relates to the monotonic strain hardening coefficient of the material.<sup>15</sup> The quantity  $C_2$  is related to the tensile ductility of the material as indicated in Eq. (3) and Fig. 1.

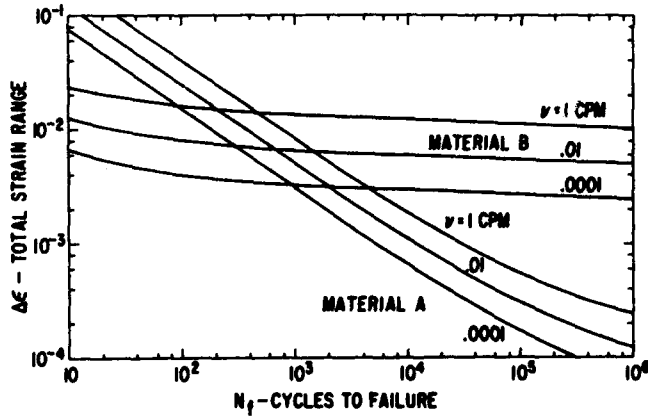


Figure 9. Effect of Frequency on Total Strain Range vs. Cycles to Failure for Hypothetical Materials A and B. Ductility vs. Strength.

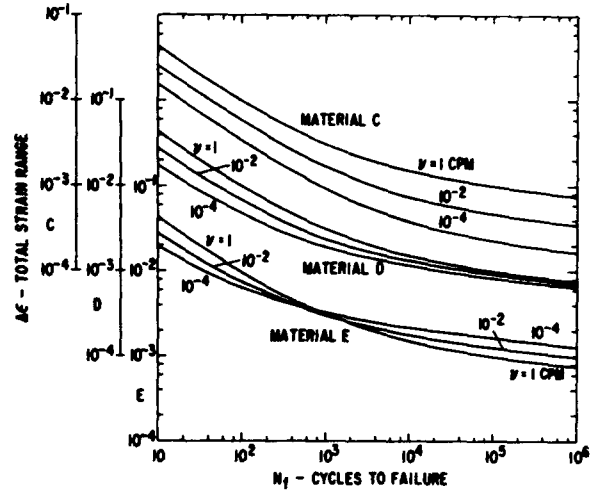


Figure 10. Effect of Frequency on Total Strain Range vs. Cycles to Failure for Hypothetical Materials C, D and E - Various  $k_1$ 's.

The strength of the material is reflected in the constant  $A$ , and is the stress range when  $\nu = 1$  cpm and  $\Delta\epsilon_p = 1.0$  from Equation (6). The time dependent effects are introduced by the quantities  $k$  and  $k_1$ .  $k$  modifies the plastic strain range at a given frequency as seen in Equation (3). Hence  $k$  reflects a time dependent ductility loss attributable to such factors as creep or other diffusional processes leading to grain boundary fracture, or to environmental influences such as a stress-oxidation interaction at the crack tip.<sup>18</sup> In the absence of time-dependent ductility changes,  $k = 1$ . Finally,  $k_1$  modifies the stress range as seen in Eq. (6), and hence relates to the time dependent strength of the material. It closely approximates the strain rate sensitivity exponent  $m$ , employed in monotonic time-dependent deformation analysis. It may be a positive or negative quantity depending on the degree of strain and time aging occurring in the alloy. For metals unalloyed for creep strength,  $k_1$  is a high positive number ( $\sim 0.2$ ).

To show the effect of the various material constants on the shape of the  $\Delta\epsilon$ - $N_f$  relationship given in Eq. (8) some hypothetical materials are assumed. The constants for these alloys are listed in Table II. First a comparison is made between a very ductile, low strength at high tempera-

TABLE II.  
HYPOTHETICAL MATERIAL CONSTANTS FOR EQ. (8)

MATERIAL	TEMP.	$k$	$C_2$	$\beta$	$A/E \times 10^{-6}$	$n$	$k_1$
A	High	0.85	1.0	0.7	800	0.15	0.15
B	High	0.85	0.04	0.7	20,000	0.05	0.15
C	High	0.85	0.2	0.7	4,000	0.15	0.15
D	High	0.85	0.2	0.7	4,000	0.15	0
E	High	0.85	0.2	0.7	4,000	0.15	-0.075

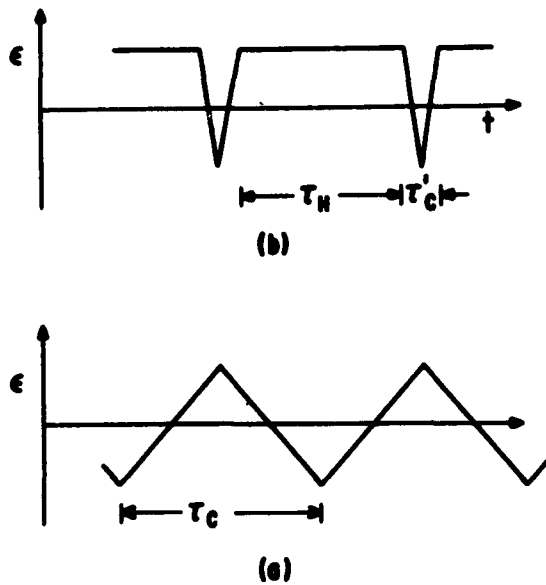


Figure 11. Strain Program (a) Triangular Wave Form, (b) Tensile Hold.

ture alloy (A) with a low ductility high creep strength high temperature alloy (B). Thus alloy A has a high  $C_2$  and  $n$ , and a low  $A$ , while alloy B has a low  $C_2$  and  $n$  and a high  $A$ . Other constants,  $\beta$ ,  $k$  and  $k_1$  are the same in each alloy. The results are seen in Fig. 9. Of particular interest is the large difference in slope between the two alloys, and the effect of frequency on life at particular total strain ranges. Alloy B is shown to be extremely frequency sensitive, alloy A much less so.

Another analysis can be made for a material in which  $k_1$  is varied. An intermediate strength, intermediate ductility material is assumed as identified in Table II in which three values of  $k_1$  are employed, namely 0.15, 0 and -0.075. Note in Fig. 10 the large difference in the effect of frequency at long lives, indicating how a low or even negative value of  $k_1$  can improve the long life fatigue behavior at low frequencies.

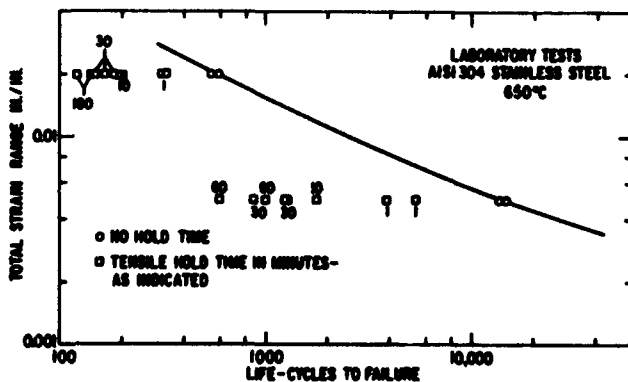


Figure 12. Effect of Hold Times on Life. AISI 304 Stainless Steel - 650°C - After Berling and Conway.

## DETERMINATION OF THE CONSTANTS

While an approximate determination of the constants can be assumed in terms of other physical constants, exact determination can be made only by experimentation. For a specific material and temperature, a minimum of nine fatigue tests are required to determine  $C_2$ ,  $k$  and  $\beta$ . Three frequencies and plastic strain ranges are selected and procedures outlined earlier<sup>10</sup> are followed. To determine  $A$ ,  $n$  and  $k_1$ , the necessary information can be derived from a single specimen, as discussed above.

## APPLICATION TO HOLD TIME TESTS

The derivation of Eq. (8) and the material constants in that equation come from laboratory tests involving controlled strain limits and cyclic strain with no hold times. If closed-loop control is used, constant strain rate cycling can be employed as seen in Fig. 11a. While the results of these tests and the subsequent determination of Eq. (8) are of interest, the value of this work is of more significance if it can be shown to apply more generally. Of particular interest is the possible application of this approach to hold time test results. Laboratory hold time tests generally involve a strain-time program shown in Figure 11b. Here a fully reversed strain of period  $\tau_c'$  is imposed together with a tensile strain held for a time  $\tau_H$ , such that the total period is  $\tau_c' + \tau_H$ .

If one now assumes that wave shape does not influence the fatigue results, hold time results could be predicted from triangular wave shape tests. Referring to Figure 11, if  $\tau_c$  is the period of the triangular wave shape in Fig. 12a, then when

$$p = \frac{1}{\tau_c' + \tau_H} \quad (11)$$

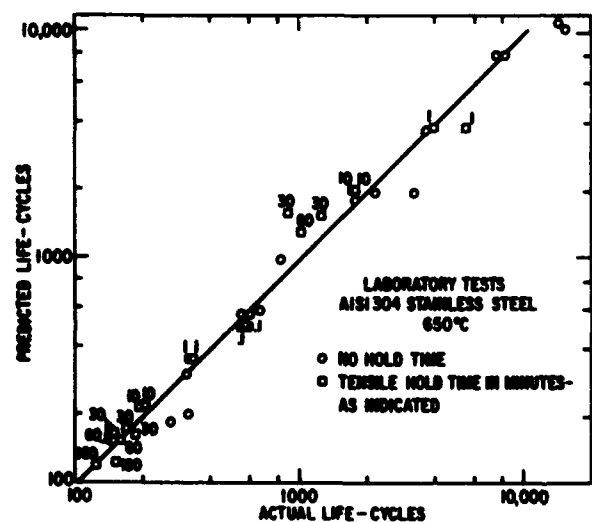


Figure 13. Comparison of Actual and Predicted Life with Hold Times - AISI 304 Stainless Steel - 650°C.

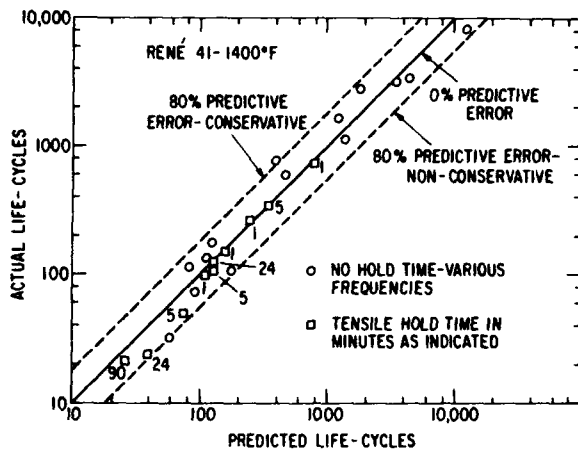


Figure 14. Comparison of Actual and Predicted Life with Hold Times - Rene 41 at 1400°F.

the fatigue results would be the same. It is of particular interest to determine the experimental support for such an assumption from available hold time results.

#### AISI 304 Stainless Steel at 1200°F

Berling and Conway recently published results of hold times on 304 stainless steel at 1200°F.<sup>19</sup> While their tests included equal hold times in tension and compression, compression hold times only, and tensile hold times, only the tensile hold time results will be considered here. Figure 12 shows their results for different tensile hold times compared to continuous cycling results at a strain rate of  $4 \times 10^{-3} \text{ sec}^{-1}$ . A large decrease in life is noted, particularly for the longer hold times. To compare these results with those predicted by Eq. (8), Eq. (11) is assumed and the appropriate constants for the use of Eq. 8 determined. Values of  $\beta$ ,  $C_2$  and  $k$  for this material were reported earlier,<sup>10</sup> as obtained from the work of Berling and Slot.<sup>11</sup> Sufficient data is also given in that report to evaluate  $A$ ,  $n$  and  $k_1$ . These values are listed in Table 1. With these constants and the assumptions of Eq. (11) the predicted life given in (8) is compared to the test data of Berling and Conway. This comparison is shown in Figure 13, both for hold time and no hold time test results. With the exception of one point, the error in predicted hold time results are within 30% of the actual lives.

#### Rene 41 at 1400°F

Cammett has reported elevated temperature low cycle fatigue test results of Rene 41 including several hold time tests in an internal General Electric Company report.<sup>20</sup> His most extensive results were carried out at 1400°F. Appropriate constants for these results are given in Table 1. No trend was observed in the plot of stress range vs. frequency at constant plastic strain range. Hence  $k_1$  was assumed to be zero. Comparison of actual vs. predicted life is shown in Figure 14 for both hold and no hold time tests.

Results are seen to fall within a band indicating less than  $\pm 80\%$  error in life.

#### 1 Cr-Mo-V Steel at 565°C

Coles et al<sup>9</sup> investigated the effect of tensile hold times on several steels including a 1% Cr-Mo-V steel at 565°C. From information given in Figures 17 and 18 of that paper, the constants  $k$ ,  $\beta$  and  $C_2$  could be determined directly. From their Fig. 14,  $k_1$  was assumed to be zero and  $n = 0.15$ , from which  $A$  could be calculated. All the constants are given in Table 1. Determining the frequencies from Eq. (11) actual lives are compared with those predicted by Eq. (8), and the results are shown in Fig. 15.

#### DISCUSSION

The approach taken in this report is to introduce the effect of time in both the elastic and plastic strain range components by means of the frequency of cycling. While time effects are usually accounted for through the strain rate of the material in monotonic deformation, there are certain complications to this approach when considering fatigue. As indicated earlier, it is assumed that low cycle fatigue failure is largely a crack propagation process, where the principal concern is the degree of crack advance with each cycle. Strain rate as a variable becomes almost meaningless since the strains and strain rates around the crack tip are so highly localized that there is at best a complex relationship between the average strain rate and these localized effects. The time per cycle or the frequency assumes more meaning, since here, at least, the entire body is subjected to the same time interval. If attention is focussed on the crack tip, the cycle time relates to metallurgical and

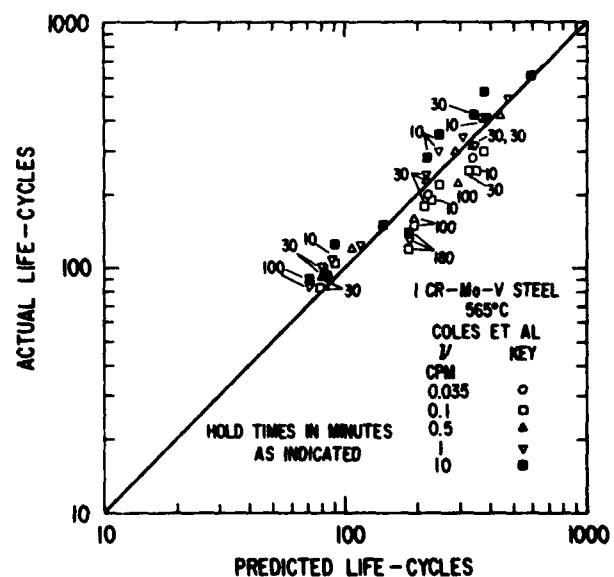


Figure 15. Comparison of Actual and Predicted Life with Hold Times - 1 Cr-Mo-V Steel at 565°C.

environmental changes at the crack tip during the interval and contribute directly to the crack propagation rate.

It is seen in Eq. (8) that the frequency effects are introduced through the quantities  $k$  and  $k_1$ , where  $k$  determines the high strain response to frequency and  $k_1$  the low strain. As indicated earlier the two  $k$ 's have different physical significance, one relating to time dependent ductility changes, the other to strain rate effects on strength. Thus the frequency effects will be different at high and low strains, as seen in Figure 10. This fact is of importance when considering the findings of Coles et al.<sup>9</sup> Referring to their Fig. 20 a much more pronounced spread in life due to different hold times occurs when the total strain range is 0.015 than when the strain range is 0.04. While part of this effect is due to the decreasing slope of the  $\Delta\epsilon-N_f$  curve with increasing life, consideration must also be given to the different effects of  $k$  and  $k_1$ .

Referring to Table I, it was assumed that Rene 41 and the 1 Cr-Mo-V steel had a  $k_1$  of zero. This will influence the life prediction at high life. The techniques for obtaining  $k_1$  described earlier were not used for these two materials. Undoubtedly there is a frequency effect at high life and this fact may account for some of the scatter on Figures 14 and 15.

Krempf and Walker,<sup>21</sup> in considering the hold-time effects at 1000°F of a Cr-Mo-V steel, heat treated to produce a high and low rupture ductility, showed that the hold-time effect was greater for the low ductility heat treatment. This behavior is not surprising if one considers the two materials to be somewhat like those shown in Fig. 9, which compares a high ductile, low strength material to a low ductility, high strength material. Under the assumption that the  $k$  and  $k_1$  values are the same, the low ductility, high strength material shows a much greater frequency (and hence hold time) effect.

An assumption of the present work is that the fatigue life is independent of the wave shape providing the period of the cycle is the same. Berling and Conway have shown that this is not the case for a 304 stainless steel at 1200°F. Considering, for the same total strain range, hold-time programs of tension only, compression only, and mixed tensions and compressions, the life was most detrimentally affected by hold times in tension. These tension results are shown here as Figure 12. But, following the methods described above, in which the frequencies of such

experiments are determined and the lives evaluated on the basis of the frequency modified fatigue life, good agreement with the short time continuous cycling results are achieved. With hold periods in compression, the prediction of the present work would be conservative. It is interesting to note that the continuous cycling tests used as a basis for predicting the hold time failed in a few hours. The hold-time tests lasted as long as 1000 hours giving an indication of the time extrapolation involved in the results shown in Figure 13.

## SUMMARY

A relatively simple description of the high-temperature, low cycle fatigue process is presented through the introduction of the frequency-modified fatigue life. An exponential relationship is shown to exist between this quantity and the plastic strain range, the exponent depending on the temperature. Further, a frequency-modified stress range is introduced which is also an exponential function of the plastic strain range and leads to the determination of the elastic strain range. This total strain range can then be found, which has direct application to design.

By extrapolation of the frequency to low values, long life fatigue prediction from short life laboratory tests is possible. In particular, assuming that life is independent of wave shape, test results involving hold-time can be predicted. Fatigue lives obtained from hold-time experiments on three materials, 304 stainless steel, Rene 41 and 1 Cr-Mo-V steel are compared with those determined from the generalized equation and good agreement is found.

Since the various constants of the generalized equation can be related to other physical properties, fatigue curves constructed for any combination of the constants can be related to other properties. As a consequence a qualitative judgement of the appropriate physical properties necessary to construct a desired fatigue curve can be made.

## ACKNOWLEDGEMENT

The author wishes to acknowledge the help of D.C. Lord in the performance of the experimental aspects of this report. He is indebted to the Materials and Processes Technology Laboratory and Mr. J.T. Cammett for permission to use the unpublished data on Rene 41.

## REFERENCES

1. E.G. Ellison, "A Review of the Interaction of Creep and Fatigue," *J. Mech. Eng. Sci.*, 11:318 (1969).
2. S.S. Manson and G. Halford, "A Method for Estimating High-Temperature and Low-Cycle Fatigue Behavior of Materials," in *Int. Conf. Thermal and High Strain Fatigue M/R-32*, Metals and Metallurgy Trust, London (1967).
3. S.S. Manson, *Thermal Stress and Low Cycle Fatigue*, Chapter 4, McGraw-Hill, New York (1966).
4. S.S. Manson, G. Halford, and D.A. Spera, "The Role of Creep in High-Temperature, Low-Cycle Fatigue," in *The A.E. Johnson Memorial Volume*, submitted for publication.
5. L.F. Coffin, "Cyclic Strain and Fatigue Study of a 0.1 C-2 Mo Steel," *Trans. Met. Soc. AIME*, 230:1690 (1964).
6. D.S. Wood, "The Effect of Creep on the High-Strain Fatigue Behavior of a Pressure Vessel Steel," *Welding J. Res. Suppl.*, 45:92s (1966).
7. J.F. Eckel, "The Influence of Frequency on the Repeated Bending Life of Acid Lead," *ASTM Proc.*, 51:745 (1951).
8. A. Coles and D. Skinner, "Assessment of Thermal Fatigue Resistance of High Temperature Alloys," *J. Roy. Aeron. Soc.*, 69:343 (1965).
9. A. Coles, G.J. Hill, R.A. Dawson, and S.J. Watson, "The High Strain Fatigue Properties of Low-Alloy Creep Resisting Steels," in *Int. Conf. Thermal and High Strain Fatigue M/R-32*, Metals and Metallurgy Trust, London (1967).
10. L.F. Coffin, "Predictive Parameters and Their Application to High-Temperature Low-Cycle Fatigue," *Proc. 2nd Int. Conf. Fracture*, Chapman and Hall, London (1969).
11. J.T. Berling and T. Slot, "Effect of Strain Rate on Low Cycle Fatigue Resistance of AISI 304, 316, and 348 Stainless Steels at Elevated Temperatures," in *ASTM-STP-459*, American Society for Testing and Materials, Philadelphia, Pennsylvania (1969).
12. P.G. Forrest, "The Use of Strain Cycling Tests for Assessing Thermal Fatigue Resistance," *Appl. Mater. Res.*, 4:239 (1965).
13. R.C. Boettner, C. Laird and A. McEvily, "Crack Nucleation and Growth in High-Strain, Low-Cycle Fatigue," *Trans. Met. Soc. AIME*, 233:379 (1965).
14. L.F. Coffin, "Cyclic Strain-Induced Oxidation of High Temperature Alloys," *ASM Trans. Quart.*, 56:339 (1963).
15. J. Morrow, "Cyclic Plastic Strain Energy and Fatigue of Metals," p. 45, *Internal Friction, Damping, and Cyclic Plasticity*, ASTM-STP-378, American Society for Testing and Materials, Philadelphia, Pennsylvania (1965).
16. B.F. Langer, "Design of Pressure Vessels for Low-Cycle Fatigue," *J. Basic Eng.*, 84:389 (1962).
17. J.F. Tavernelli and L.F. Coffin, "Experimental Support for a Generalized Equation Predicting Low-Cycle Fatigue," *J. Basic Eng.*, 84:533 (1962).



#### REFERENCES (Continued)

18. C.J. McMahon and L.F. Coffin, *Mechanisms of Damage and Fracture in High-Temperature, Low-Cycle Fatigue of a Cast, Nickel-Based Superalloy*, General Electric Company, Research and Development Center, Schenectady, New York (1969).
19. J.T. Berling and J.B. Conway, *Effect of Hold-Time on the Low-Cycle Fatigue Resistance of 304 Stainless Steel at 1200°F*. Presented at the 1st International Conference on Pressure Vessel Technology, Delft, Holland, 1969.
20. J.T. Cammett, *Elevated Temperature Low-Cycle Fatigue Behavior of René 41*, R69AEG-332, General Electric Company, Aircraft Engine Group, Cincinnati, Ohio (1969).
21. E. Krempl and C.D. Walker, "The Effect of Creep-Rupture Ductility and Hold-Time on the 1000°F Strain Fatigue Behavior of a 1 Cr-1Mo-0.25V Steel," in ASTM-STP-459. (See Ref. 11).

# A KINETIC MODEL FOR CRACK GROWTH PREDICTIONS

by

Phillip H. Graham

Atlantic Research Corporation  
A Division of The Susquehanna Corporation  
Alexandria, Virginia

## INTRODUCTION

In recent years, there has been an increasing effort within the aerospace industry, in particular, to refine existing experimental and analytical techniques for prediction of failure in aircraft structures and materials. While considerable progress can be cited, the effort has been hampered by the fact that an analysis of the state of stress and strain existing throughout a structure does not provide the desired information without the application of a suitable criterion for fracture.

Depending upon the structural material and its application, the criterion for failure might be defined in several manners. Most frequently cited failure criteria are the occurrence of irreversible deformations accompanying yielding or drawing processes and ultimate fracture failure. The increased use of polymeric plastic compositions have forced consideration of crazing and reinforcement-matrix separations as additional criteria.

The description and prediction of failure requires the definition of a mathematical model which for prescribed loading functions, i.e., stress, strain and temperature as functions of current and prior history, defines a unique time or distribution of times to fail. These models are arrived at through consideration of the material and its known behavior, the boundary conditions imposed in the structural problem, and the background and interests of the investigator. Ultimately, the comparison of prediction and performance defines the procedure of choice. In this paper, an approach to material fracture based upon the kinetic concept is outlined. The kinetic concept of fracture considers fracture as a process developing in a body under load and that the extent of accumulated damage in the body is a function of prior history. The basic processes leading to the ultimate fracture are the thermofluctuation ruptures of interatomic bonds. It is through the progressive rupture of these bonds that cracks are initiated and subsequently propagated.

## BACKGROUND

For the past thirty-five years, numerous workers have investigated the application of the fundamental concepts of a model for molecular displacement processes

based upon the principles of absolute reaction rate theory. The model has been explored in some detail and it has been demonstrated that the viscoelastic properties of many real materials can be described through use of the basic concepts. The phenomena of stress relaxation and creep as well as the behavior of many materials under dynamic and extrusion conditions are explained.

Of particular importance, has been the extension of the Tobolsky-Eyring reaction rate approach to include a model for prediction of the life-time of materials under dead load creep. Although Tobolsky and Eyring<sup>1</sup> only reported experimental correlation for certain failure data obtained from tests of polymeric threads, Zhurkov<sup>2</sup> recently reported that creep rupture data for 50 widely different materials including metals, alloys, nonmetallic crystals and polymers are described by the reaction rate model.

At Atlantic Research Corporation, studies of polymer failure and fracture phenomena conducted with both in-house and contract support have demonstrated an excellent correlation with the predictions of the simple Tobolsky-Eyring model. Specific examples include polymer crazing phenomena, drawing and yielding behavior and ultimate fracture of widely differing compositions. Recent studies of the failure of highly filled composite solid rocket propellant<sup>3,4</sup> and certain reinforced plastic compositions<sup>5</sup> have shown that both the matrix-filler bond failure and ultimate fracture behavior are predictable by this model. These facts indicate that the reaction rate approach to fracture prediction may be quite general.

At this point, we should like to point out that the University of Utah is conducting some studies<sup>6</sup> patterned after the work of Zhurkov<sup>2</sup> utilizing electron paramagnetic resonance (EPR) to detect the number of broken bonds under application of mechanical stress. This present work uses Nylon 6 and Nylon 66 because of the relatively larger number of free radicals released during fracture at room temperature. Constant load, constant loading rate, and fatigue (cyclic) tests have been imposed, and the number of broken bonds measured agrees well with the theoretical predictions. Thus, it appears that there is a very close connection between the kinetic model envisioned by Tobolsky-Eyring and the experimental measurements of Zhurkov and Devries-Williams.

The original development was given as follows:<sup>1</sup>

Suppose that specimen failure, i.e., rupture, is due to bond slippage or displacement in the direction of applied stress. If the number of such bonds per unit area is  $N$ , the rate of breaking of such bonds under stress, assuming repair is possible is:

$$-\frac{1}{N} \frac{dN}{dt} = \frac{2kT}{h} \exp\left(-\frac{\Delta F^\ddagger}{RT}\right) \sinh\left(\frac{\sigma\lambda}{2NkT}\right) \quad (1)$$

where  $\Delta F^\ddagger$  is the activation free energy, i.e., energy barrier, for the process and  $\lambda$  is the "jump distance" or distance projected in the direction of applied stress that the bond must displace for the process to occur. The  $k$ ,  $h$  and  $R$  are, respectively, Boltzmann's constant, Planck's constant and the universal gas constant. When  $N$  equals zero, failure will have occurred since the number of remaining bonds is zero.

For large values of the argument of the hyperbolic sine where the relative frequency of bond repair is quite low, expression (1) reduces to:

$$-\frac{1}{N} \frac{dN}{dt} = \frac{kT}{h} \exp\left(-\frac{\Delta F^\ddagger}{RT}\right) \exp\left(\frac{\sigma\lambda}{2NkT}\right) \quad (2)$$

An approximate integrated solution of (2) for time to failure,  $\tau$ , was given by Tololsky and Eyring: This solution can be written in the form:

$$\ln \tau T \sigma = A + \frac{B}{T} - C\sigma \quad (3)$$

where:

$$A = \ln \frac{h}{kC} - \frac{\Delta S^\ddagger}{R}$$

$$B = \frac{\Delta H^\ddagger}{R} \quad \text{and} \quad C = \lambda/2N_0 kT$$

By regression analysis, the coefficients of equation (3) are readily available from constant stress (load) creep failure data determined over a suitable temperature range. In principle, at least, three measurements of  $\tau$  under independent conditions of temperature and stress level are sufficient for a given material.

In applying the reaction rate theory to experimental creep data for metals and plastics, observers have consistently found that the argument of the hyperbolic sine is independent of temperature. This corresponds to a proportional increase with temperature of the ratio,  $\lambda/N$ . Denoting  $N_0$  as the number of unbroken bonds per unit area in the unstressed material, a material constant,  $C = \lambda/2N_0 kT$ , is obtained which is independent of temperature. Defining  $U$  as the ratio of  $N$  to  $N_0$ , the differential expression becomes:

$$-\frac{d \ln U}{dt} = \frac{kT}{h} \exp(-\Delta F^\ddagger/RT) 2 \sinh \frac{\sigma C}{U} \quad (4)$$

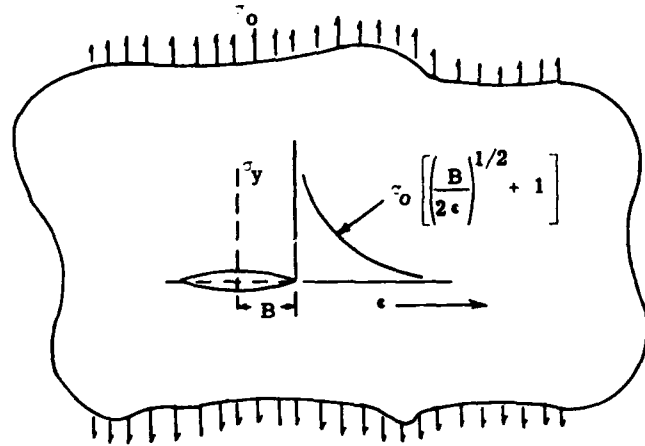


Figure 1. Crack Model Schematic.

This equation is readily applied in differential form for even the most complex loading function,  $\sigma(t)$ , by converting to finite difference form and using computerized integration.

By combination of these expressions with an assumed form for the stress distribution in the vicinity of an isolated crack, a crack growth model is developed.

The derivation of model is patterned for the analysis reported by M.L. Williams<sup>7</sup>: Consider a narrow elliptical crack of half-length,  $B$ , located in a thin infinite sheet of material. A stress,  $\sigma_0$ , is applied at infinity normal to the axis of the crack. As seen in Figure 1, the maximum principal stress,  $\sigma_y$ , varies from infinity at the crack edge ( $\epsilon = 0$ ) to  $\sigma_0$  at infinity, ( $\epsilon = \infty$ ). For our simple model, we wish to analyze the crack growth under the following conditions:

a. The maximum principal stress,  $\sigma_y$ , will be used as input to the reaction rate analysis subroutines in a computer program.

b. The quantity,  $\epsilon$ , will be defined in  $J$  finite elements of size  $\delta$ , i.e.,  $\epsilon = J\delta$  (see Figure 2.) By this procedure, the maximum principal stress,  $\sigma_y$ , becomes an average value,  $\bar{\sigma}_y$ , over each element given by:

$$\bar{\sigma}_{y1} = \sigma_0 \left[ \frac{2B}{\delta} \frac{1}{2} + 1 \right] \quad (5)$$

$$\bar{\sigma}_{yJ} = \sigma_0 \left[ \frac{B/\delta}{2J-1} \frac{1}{2} + 1 \right] \quad (6)$$

Since the values of  $\bar{\sigma}_y$  in the above expressions depend both upon the magnitude of the ratio,  $\frac{B}{\delta}$ , and the instantaneous value of  $B$ , the use of a parameter  $N$  defined as  $B_0/\delta$  and specifying  $B_0$  as 1 permits the expressions (5) and (6) to be written as follows:

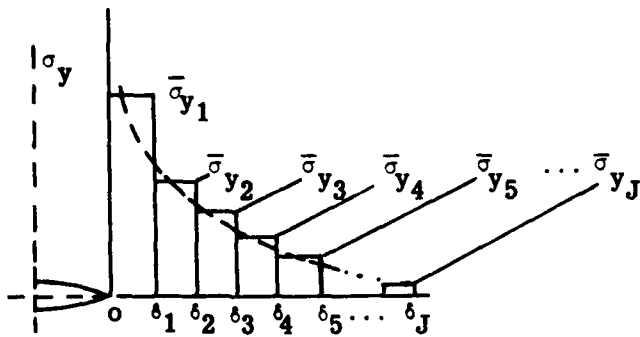


Figure 2. Crack Element Distribution.

$$\bar{\sigma}_{y1} = \sigma_0 \quad 2(N+K-1) \frac{1}{2} + 1 \quad (7)$$

$$\bar{\sigma}_{yJ} = \sigma_0 \quad \frac{N+K-1}{2J-1} \frac{1}{2} + 1 \quad (8)$$

where  $K$  is a counter to indicate the number of the element at the crack tip.

c. At the start of experiment,  $J$  elements on the midplane of crack propagation contain  $N_0$  bonds. Since it is both desirable and reasonable to limit consideration to the more rapidly failing elements, the failure of  $M$  elements is to be monitored continuously. Choice of the value for  $M$  probably depends on the absolute accuracy desired and the value selected for  $N$ . The following table based on an assumed value of 10 for  $N$  shows the effect of choice of  $M$  on the ratio of crack line stress to imposed structural stress. Examination of Table I suggests that a valid  $M$  would lie between 10 and 25 since the change in stress concentration is slight per unit  $J$ .

TABLE I.  
STRESS CONCENTRATIONS FOR ELEMENT  
 $M$  for  $N = 10$ .

$M$	$\bar{\sigma}_y / \sigma_0$
1	5.46
5	2.06
10	1.72
25	1.45
50	1.32
100	1.22

With the above conditions in mind, consider a constant load experiment. At zero time, a constant load,  $\sigma_0$ , induces concentrated stresses in elements near the crack. Utilizing the differential form of the Tobolsky-Eyring reaction rate expression and material parameters determined from separate constant load creep-to-failure experiments, the failure time,  $\tau_{K1}$ , for the first element is computed. The change in bonds per unit element for elements  $2-M$  as reflected by change in the parameter,  $U$ , is determined by integration in time from zero to  $\tau_{K1}$ .

Failure of the first element transfers the peak stress to the second element and increases the stress concentration on the remaining elements. The  $M+1$  element is evaluated and becomes the  $M$  element during the second step of failure propagation.

The fracture propagation will accelerate slightly at this point since the  $2-M+1$  elements were slightly damaged during the first time period. In addition, the increase in crack length from  $B = 1$  to  $B = 1 + \delta$  increases the stress concentration factor slightly. The failure time,  $\tau_{KJ}$ , is computed and the change in elements  $3-M+1$  is determined.

This process of stepwise crack growth is continued

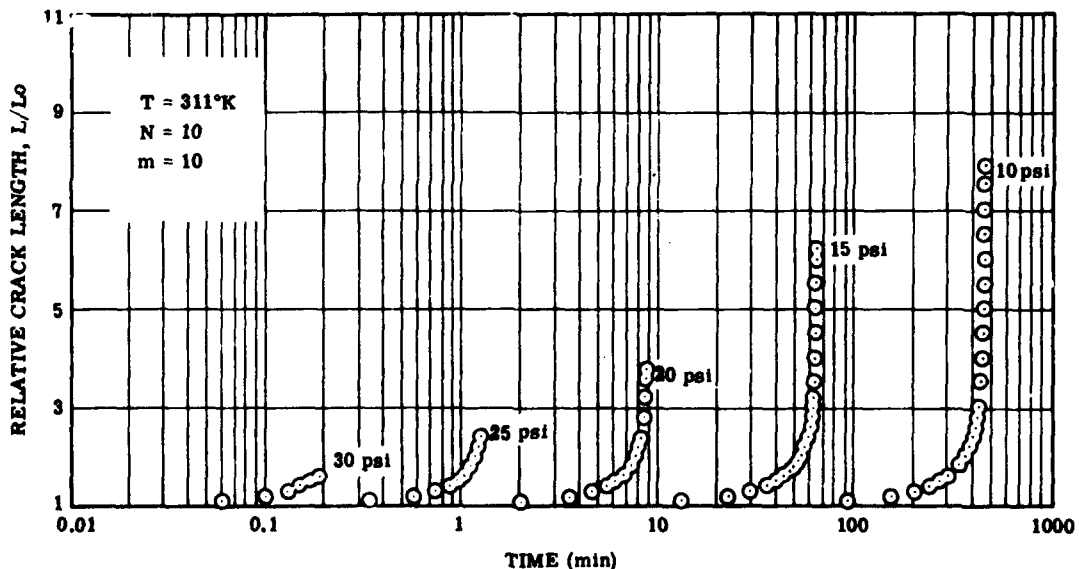


Figure 3. Relative Crack Length Versus Time as Function of Stress.

until the failure time for a unit element,  $\tau_{KJ}$ , approaches a limiting velocity. Studies<sup>8</sup> of the maximum crack velocity in a variety of materials possessing a wide range of sound velocities has indicated an approximate proportionality to the form:

$$V_c \approx 0.31V_s \quad (9)$$

where  $V_c$  is the maximum crack velocity and  $V_s$  is the sound velocity.

From the kinetic rate model, the estimate of maximum crack velocity would be given approximately by the expression:

$$V_c \approx \frac{\lambda}{\tau_0} = \frac{\lambda k \Delta H}{hR} \exp(\Delta S/R) \quad (10)$$

This model has been formulated and tested on the computer using reasonable parameters and conditions of constant load, constant loading rate and cyclic loading. Various combinations of the parameters in the model have been considered and the results of the analysis have proven quite interesting. In the studies to date, an arbitrary critical failure time of 0.01 minutes for an element was assumed i.e., calculations were terminated when the time for element failure,  $\tau_{KJ}$ , was less than 0.01 minute. For an element size of 0.1B, this represents a crack velocity of 10 crack lengths per minute.

## DISCUSSION

### Constant Stress Studies

*a. Effect of Stress Level* - The first set of studies was to determine the effect of varying stress levels,  $\sigma_0$ , on calculated crack growth. The material constants used were those for a composite rocket propellant formulation. The temperature was constant, N was selected as 0 (equivalent to an element size equal to 1/10 of the half crack length),

and M was set at 10. The results of these calculations are plotted in Figure 3.

The results illustrate several features of the model.

(1) Induction Period - An induction period, i.e., delay before initial crack extension, is observed. This reflects the reaction rate contribution to the model. Examination of plots of stress level versus induction time showed  $\ln t_0$  approximately proportional to  $1/\sigma$ .

Qualitatively similar behavior was suggested by Williams in his model for crack propagation. (see reference 7, p. 183) in the expression

$$t_0/\tau \approx -\ln \left( 1 - \frac{\epsilon^* \sqrt{2} \delta/b}{\sigma_0/E_v} \right) \quad (11)$$

for a "bundle of fibers" of dimension  $\delta$  and a rate-independent critical strain,  $\epsilon^*$ .

(2) Crack Growth Rate - The crack growth rate, once the induction period has passed, depends upon the level of stress. This observation, contrary to the predictions of the simple Griffith Theory which implies that a crack does not grow until a critical stress is achieved and then propagates catastrophically, is interesting. Zhurkov<sup>2</sup> reports "... the rate of crack growth increases with the stress monotonically." He has also observed that "... at a given stress, the time required for a crack to initiate is much less than the time of its growth to the fracture of the specimen." This is in complete agreement with our calculations.

As the crack extends in this model, one finds an approximately exponential relationship between crack length and time. This agrees qualitatively with the predictions of Williams (Reference 7, p. 187) where the following is cited:

$$\frac{s}{b} \approx \frac{1}{4} \exp \left( \frac{\pi}{2\sqrt{2}} \frac{\sigma_0/E_v}{\epsilon^*} \frac{t}{\tau} \right) \quad (12)$$

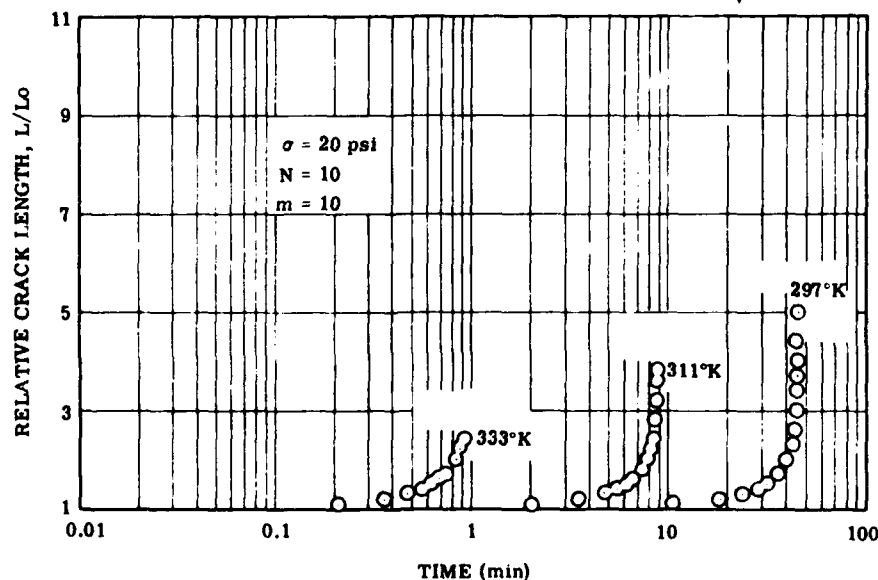


Figure 4. Relative Crack Length Versus Time as Function of Temperature.

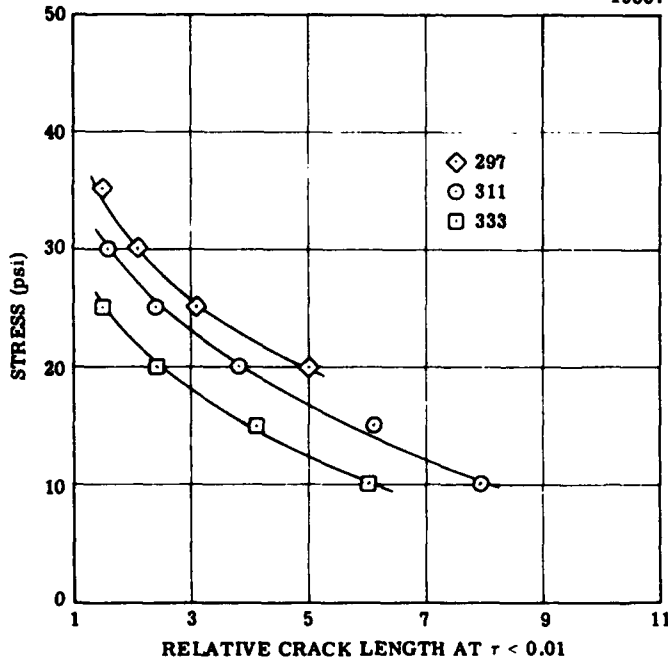


Figure 5. Relative Crack Length at  $\tau = 0.01$  Versus Applied Stress.

where  $s$  is the distance the crack has traveled through the material with initial crack length,  $b$ , under stress,  $\sigma_o$ .

(3) Crack Criticality - Examination of the curves reveals that as the stress decreases, the crack length at which the crack growth proceeds at the "critical speed",  $\tau_{KJ}$  per element, increases. This reflects the fact that the absolute rate of crack propagation depends both upon the stress level and the instantaneous crack size.

b. Effect of Temperature - For this study, the stress was held constant at 20 psi and temperature was varied.

Figure 4 represents the results.

It can be observed that the induction period, crack growth rate and crack length at  $\tau_{KJ}$  depend upon the temperature. The result is as expected.

When both stress and temperature were varied, it was possible to obtain a "Griffith-like" plot of stress levels versus crack length at criticality. The curves are very similar to those predicted by the Griffith expression,  $\sigma = K\sqrt{\frac{E\gamma}{c}}$ . This is illustrated in Figure 5.

c. Model Scaling Parameters - In the analysis of crack growth using the reaction rate model, one must determine appropriate values of  $N$  and  $M$  which would provide the most precise answers.

The parameter,  $N$ , relates the size of the reaction element to the crack length, i.e., it dimensions the hypothetical bundle of bonds which constitutes a unit of crack extension. As such, it determines the absolute rate of crack length extension for a given failure time per element. Since the increment of crack extension,  $\delta$ , is defined as  $B/N$ , larger values for  $N$  give smaller crack extensions per failed element.

At the same time, however, since the average initial element stress increases as  $\delta$  decreases, the rate of crack extension increases as  $N$  increases.

Figure 6 illustrates the effect of choice of  $N$  on crack extension behavior. As can be observed, the crack propagation rate and induction period depend on the value selected for  $N$ .

An empirical method for determining the best value for  $N$  would consist of determining the crack length versus time curve at constant temperature for constant stress load-

Figure 6. Relative Crack Length Versus Time as Functions of Element Size.

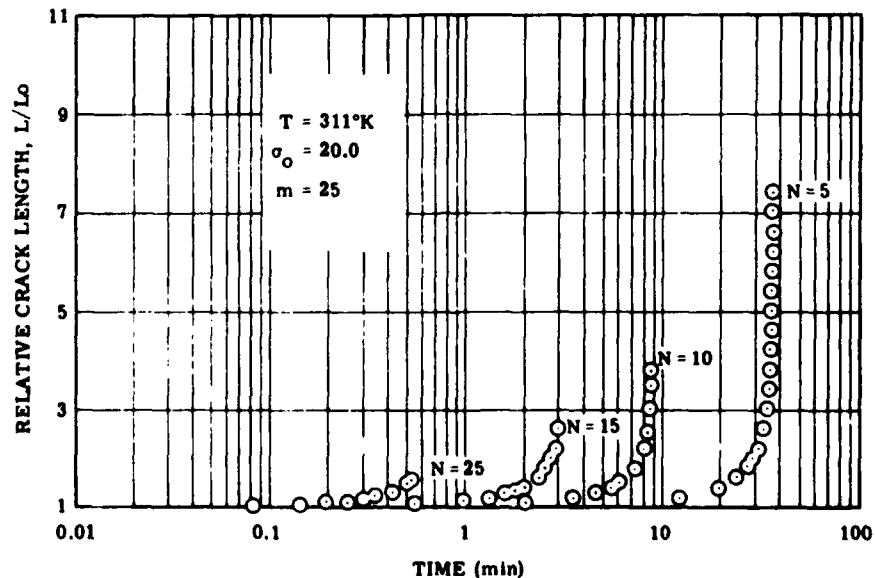
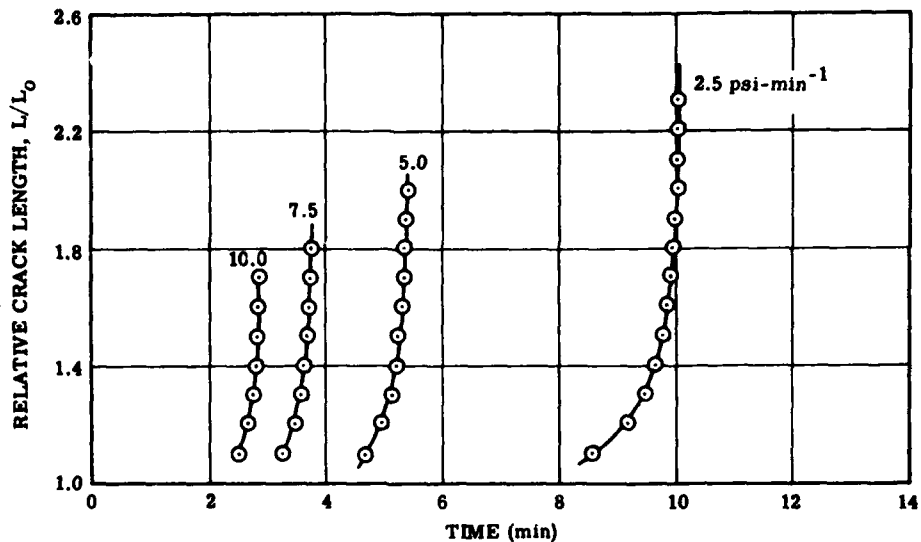


Figure 7. Relative Crack Length Versus Time under Constant Stress Rate.



ing and graphically or numerically determining the best  $N$  value to fit the data to curves calculated for the creep-determined reaction rate parameters.

A more sophisticated approach to this problem could involve an element scaling technique employing the Dugdale hypotheses<sup>9</sup>. Physically this seems to be a reasonable postulate for application to certain composites and to many elastic and viscoelastic materials which exhibit "yielding" behavior. Wnuk and Knauss<sup>10</sup> have described the application of such an analysis for the study of the behavior of cracks in glass-like high polymers.

#### Crack Growth Under Variable Loading Histories

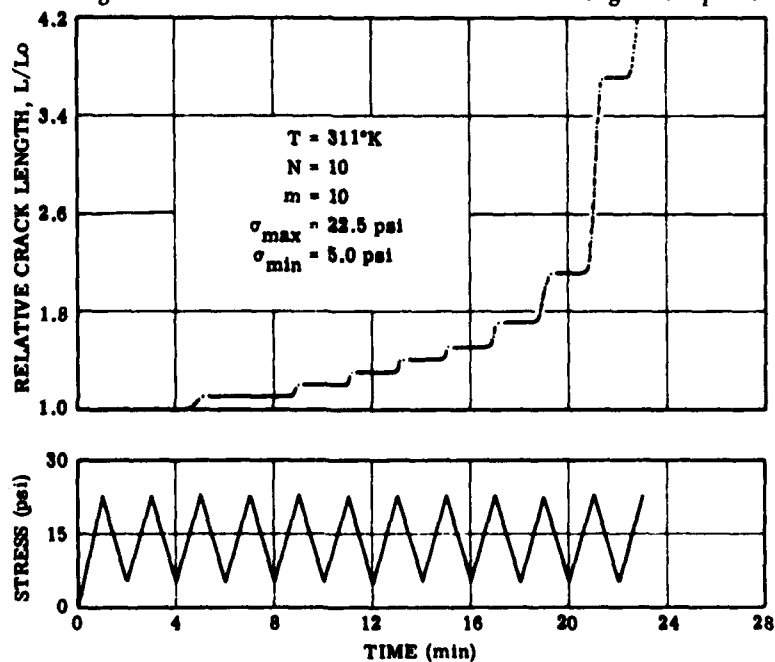
This model, which readily lends itself to computerized analysis, has been examined for conditions of variable stress histories. The specific conditions to be described are constant stress rate and cyclic stress loadings.

a. *Constant Stress Rate* - Figure 7 illustrates the relative crack length as a function of time for a constant stress rate loading history. The crack can be seen to grow sooner and at a more rapid rate under higher stress rate loading. This might have been anticipated after examination of the crack growth behavior under constant stress loading.

b. *Cyclic Stress Loading Histories* - In Figure 8, a cyclic stress loading history has been analyzed for a cracked specimen cycled between 5.0 psi and 22.5 psi with a cycle time of 2.0 minutes. Temperature was considered constant and  $N$  and  $M$  were set at 10.

One observes that the calculated curve for relative crack length versus time exhibits initially the typical "growth-rest" periods similar to those described by Williams, Knauss and Wagner<sup>11</sup>. It is observed that the initial crack extension does not occur until the third loading peak. The growth behavior is more or less gradual up to the 8th cycle. Beyond

Figure 8. Calculated Crack Growth for Isothermal Cyclic Stress Loading.



this point, however, the growth rate accelerates rapidly.

Additional studies of the model under cyclic loading have shown that the behavior is dependent upon the peak stress of loading as well as the frequency or period of loading. The results seem to indicate that the time under higher stresses controls the propagation behavior. This seems logical since rate of bond breakage and hence the crack propagation rate is directly proportional to an exponential function of the stress in this model.

#### SUMMARY AND CONCLUSIONS

This model, based on the kinetic concept of fracture, affords an opportunity for a unified treatment of the initiation and subsequent propagation of fracture. From

parametric evaluation, the predictions of the model have been shown to be consistent with the experimental observations of other workers.

The significant potential for this approach lies in its ability to account for the effects of stress level, temperature and prior history through the use of a minimum number of easily accessible material parameters. This differs from certain other approaches where the effects of accumulated damage are not easily defined.

#### ACKNOWLEDGEMENTS

The author gratefully acknowledges the enlightening discussions and suggestions of Mr. Frank Moore during the development of this model.

#### REFERENCES

1. A. Tobolsky and H. Eyring, *J. Chem. Phys.*, 11:125 (1943).
2. S.N. Zhurkov, *Int. J. Fracture Mech.*, 1:312 (1965).
3. P.H. Graham, C.N. Robinson, and C.B. Henderson, *Int. J. Fracture Mech.*, 5:57(1969).
4. P.H. Graham and C.N. Robinson, *Applications of Reaction Rate Theory to Polymer Fracture*. Presented at the 7th Annual PIA Conference, Stevens Institute of Technology, Hoboken, New Jersey, November 1969.
5. Atlantic Research Corp., Alexandria, Virginia, unpublished studies.
6. K.L. De Vries and M.L. Williams, *Electron Paramagnetic Resonance and Morphology of Fracture*, UTEC-DO-69-029, University of Utah, Salt Lake City, Utah (1969).
7. M.L. Williams, "The Fracture of Viscoelastic Material," p. 157, *Fracture of Solids*, John Wiley, New York (1963).
8. J.J. Gilham, *J. Appl. Phys.*, 27:1262 (1956).
9. D.S. Dugdale, *J. Mech. Phys. Solids*, 8:100 (1960).
10. M. Wnuk and W. Knauss, *Delayed Fracture in Viscoelastic-Plastic Solids*, GALCIT-SM-68-8, Graduate Aeronautical Laboratories, California Institute of Technology, Pasadena, California (1968).
11. M.L. Williams, W.G. Knauss, and F.R. Wagner, *Bull. 5th Meeting ICRPG Working Group Mech. Behavior*, 1:681 (1966).



**SESSION 4A**

**FRACTURE II**

*Chairman*

**Prof. H.T. Corten  
University of Illinois**

# STATISTICAL VARIATION IN FRACTURE TOUGHNESS DATA OF AIRFRAME MATERIALS\*

by

A.F. Liu

Lockheed-California Company  
Burbank, California

## NOMENCLATURE

F	= fracture strength, ksi	2L	= length of a center-cracked panel, inch
V	= volume of test specimen, inch <sup>3</sup>	F <sub>NET</sub>	= net section fracture stress, ksi
m	= an empirically determined constant in the Weibull distribution function (The Weibull slope)	F <sub>TY</sub>	= tensile yield strength, ksi
G <sub>c</sub>	= fracture toughness, in.-lb/inch <sup>2</sup>	F <sub>g</sub>	= gross area fracture stress, ksi
K <sub>c</sub>	= critical stress intensity factor, mixed mode, ksi $\sqrt{\text{in.}}$	X <sub>i</sub>	= observation, data point
K	= stress intensity factor at crack tip, ksi $\sqrt{\text{in.}}$	$\bar{X}$	= sample mean
K <sub>Ic</sub>	= critical stress intensity factor, plane strain, ksi $\sqrt{\text{in.}}$	S	= sample standard deviation
$\sigma'_g$	= loading rate, pound or psi/sec.	$\gamma$	= a location parameter in the log-normal distribution function
t	= thickness of a plate, inch	X <sub>u</sub>	= a location parameter in the Weibull distribution function
a	= half crack length in a center cracked panel or crack length in notched bend and double cantilever beam specimens, inch	X <sub>o</sub>	= a scale parameter in the Weibull distribution function
W	= specimen width, inch	$\sigma$	= population standard deviation (assumed)
		$\bar{X}_{\alpha/\sigma}$	= tolerance for the mean
		$\alpha$	= selected reliability level (%)

## INTRODUCTION

In design of a fail-safe aircraft structure, it is important to select materials having high residual strength properties for the major members in the structure. Searching of available fracture toughness data, and conducting of residual strength tests on candidate alloys are required prior to final design of the aircraft. Usually, when considering a certain type of mechanical property data, e.g., tensile strength or fracture toughness of an alloy, two statistical parameters, namely, standard deviation and the mean value are of common interest to the user and the manufacturer. An additional parameter, the guaranteed minimum value, which is based on a certain degree of reliability (the so called MIL-HDBK-5 A and B values), is of particular interest to the user. To establish reliable values for these parameters, it is necessary to know the frequency distribution of the data.

Probability density functions which fit test data such as static tensile strength and notch tensile strength for metals, composites and ceramics, fatigue and stress rupture properties of metals, etc., have been thoroughly studied by various investigators (e.g., References 2 to 9). However, statistical analysis for fracture toughness data of engineering alloys are rare. It is the aim of the present work to discuss the feasibility of applying statistical treatments to fracture toughness data, and to estimate the statistical parameters for some commonly used airframe materials.

## THE NATURE OF FRACTURE TOUGHNESS DATA

Prior to discussing the statistical variation or scatter in fracture toughness data, it is worthwhile to briefly review some fracture theory, fracture phenomena and variables that affect the fracture toughness of materials.

\* The major portion of the work was accomplished while the author was associated with the Boeing Company, Renton, Washington, and has been released as a Boeing document (Reference 1). Permission for presentation was granted by The Boeing Company, and is gratefully acknowledged.

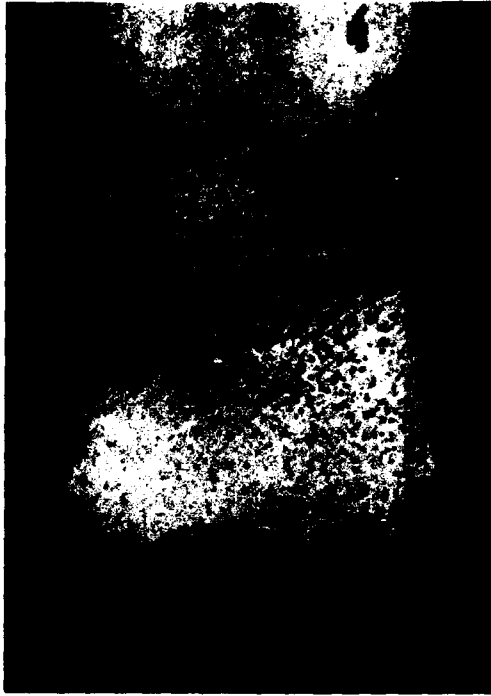


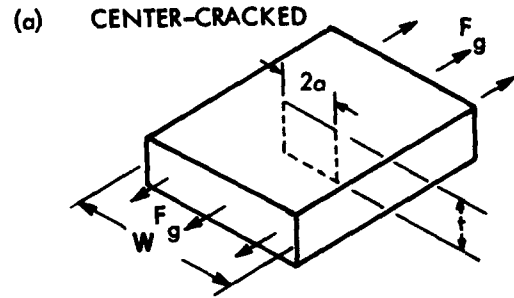
Figure 1. Section Through the Neck Area of a Tensile Specimen of Copper Showing Cavities and Crack Formed at the Center of the Specimen as the Result of Void Coalescing. (From K. Puttick, Reference 10).

When conducting a tensile test it has been found that prior to fracture, small voids are formed in the center of the specimen inside the necked area. These voids then coalesce and join together to form a microscopic crack. At the same time more small cavities are formed and distributed over the remaining cross section of the specimen. Inhomogeneities such as point defects, inclusions and second phase particles, etc., increase the probability of forming these voids. Figure 1 is a photograph taken from Reference 10, showing a cross section of a tensile specimen containing numerous voids at a stage between necking and final fracture. The fracture process consists of joining up these voids on the plane perpendicular to the loading direction and coalescing into a central crack. This crack grows until it approaches the surface of the specimen, then propagates along localized shear planes at roughly 45 degrees to the surface of the specimen as predicted by strength of materials.

According to Weibull's statistical theory of fracture (References 8 and 9), the number of imperfections in a specimen increases with increasing specimen size. The probability of having a larger initial cavity, or flaw (a weakest link), present in the material also increases as the size of the specimen is increased. Consequently, the fracture strength will decrease with increasing specimen size. This theory has been expressed as

$$\frac{F_2}{F_1} = \left( \frac{V_2}{V_1} \right)^{-\frac{1}{m}} \quad (1)$$

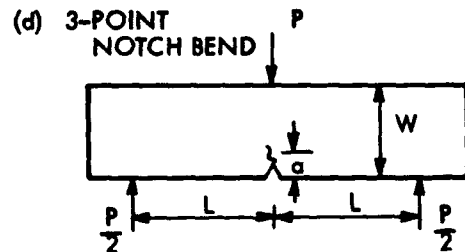
where  $F$  is the fracture strength of a specimen having a test volume  $V$ , and  $m$  is an experimentally determined factor in Weibull's distribution function which will be discussed



$t$  = THICKNESS



$t$  = THICKNESS



$t$  = THICKNESS

Figure 2. Specimen Configurations for Fracture Toughness Testing.

in subsequent sections. Thus, a large size effect is predicted for materials having a low  $m$  values while no effect will be predicted for homogeneous materials with an  $m$  value equal to infinity.

The size effect is also applied to materials which do not form voids during fracture. For some materials, such as glass, dangerous cracks or flaws are usually formed on the specimen surface and its fracture strength will depend upon the specimen surface area instead of the volume. For special material forms, such as wire and fiber stocks and glass tubing, the tensile strength may depend on the length of the specimen (see Reference 11).

In the case of testing metallic materials using a pre-cracked specimen microcracks are also found in the area adjacent to the major crack front (see Reference 12); however, the mechanics of crack propagation differs from that discussed above in that the location of the failure is predetermined (i.e., the crack tip vicinity) and therefore size effects, under certain condition, may be of limited importance. Consider a plate containing a through-the-thickness-crack loaded uniformly perpendicular to the crack. The term fracture toughness ( $G_C$ ) is defined to be a measure of the energy (inch-pounds per square inch) required to create a unit area of crack surface at onset of rapid fracture. Elastic analysis has shown that the fracture toughness is proportional to the critical stress intensity factor ( $K_C$ , ksi  $\sqrt{\text{inch}}$ ) at the crack tip (Reference 13). The stress intensity factor ( $K$ ) is a function of crack length, applied load level, specimen geometry and loading condition. Elas-

tic solutions for  $K$  are analyzable for any specimen geometry under any loading condition that can be specified in terms of suitable stress functions and boundary conditions.

Fracture toughness data used in the present analysis were generated from the four types of specimens shown in Figure 2. The center-cracked panel (Figure 2a) is usually used for conducting plane stress or mixed mode fracture toughness ( $K_C$ ) tests for thin sheets and plates. The other specimens (Figures 2b to 2d) are used for evaluating the plane strain  $K_{IC}$  fracture toughness values. Fracture toughness values measured from these specimens are usually affected by many variables as indicated in Table I. Wherever possible, these factors should be kept constant when a mass of data are subjected to statistical analysis.

Adequate fracture toughness values depend on control of metallurgical factors as shown in Table I. Valid fracture toughness data may be obtained by controlling the other variables (except  $t$  for center cracked panels). A large amount of fracture toughness data is given in Reference 14. Upon reviewing these data, the following statements can be made:

- Loading rate does not affect fracture toughness of common aluminum alloys.

TABLE I.  
FACTORS THAT AFFECT FRACTURE  
TOUGHNESS VALUES

	$K_{IC}$ TESTING	$K_C$ TESTING (CENTER-CRACKED PANELS)
1	Metallurgical variables: grain direction, product form, heat treat cycles, foreign atoms (e.g., inter- stitials), specimen surface conditions, etc.	Metallurgical variables
2	Environment: temperature, cor- rosive medium, etc.	Environment
3	Loading rate	Loading rate
4	Type of loading: 4 point bend, axial load, etc.	Buckling restraint for thin sheets
5	Specimen configuration: notched bend, surface flaw, etc.	Geometry of the panel: • thickness of the panel • crack length to panel width ratio • panel width • panel length

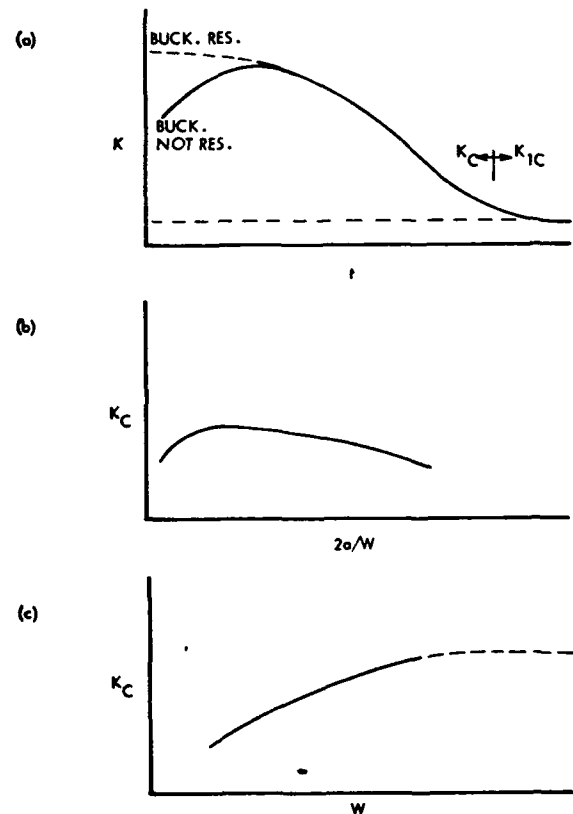


Figure 3. Schematic Representation of Geometrical Variables that Affect Fracture Toughness.

- An increase in stress rate results in lower  $K_C$  values for low carbon steels and higher  $K_C$  values for  $\alpha + \beta$  type titanium alloys.

- An increase in test temperature normally results in increased  $K_C$  values. However, for some exceptional cases, dependent on the alloy and the associated heat treatment, such as AM 350 and HP 150 steels,  $K_C$  values will decrease with an increase in test temperature.

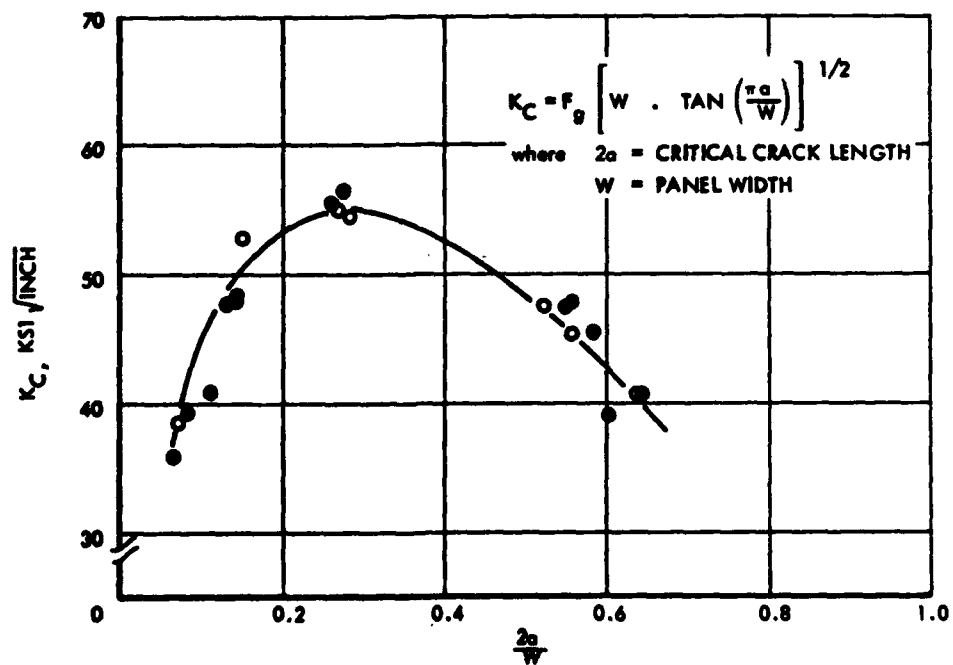
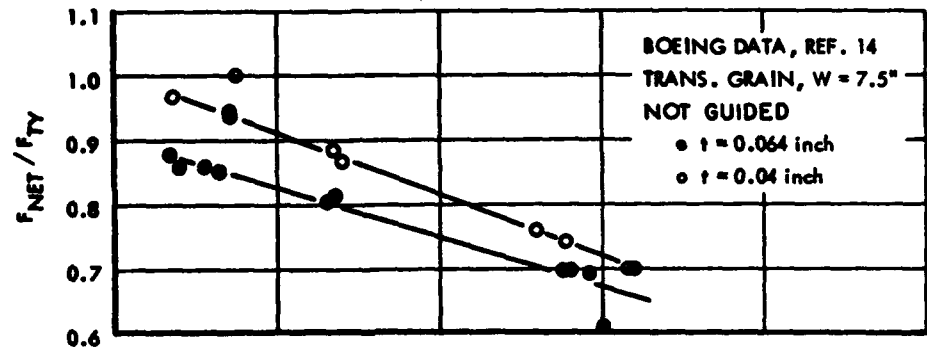
- Although fracture toughness of a given alloy is often found to be inversely proportion to its yield strength (or ultimate tensile strength), opposite cases are also present. Furthermore, test panels fabricated from a given alloy which have similar yield strengths after undergoing different heat treatments, e.g., underaged versus overaged, might exhibit different fracture toughness properties.

In fracture testing of center-cracked panels, the  $K_C$  value is often affected by the dimension of the test panel. General trends are schematically illustrated in Figure 3 to show how the geometrical variables affect  $K_C$  test results. A decrease in  $K_C$  with increasing thickness of the panel in-

dicates that the state of stress at the crack tip changed gradually from plane stress to plane strain. In other words, the triaxial state of stress increases with increase in plate thickness. Also, a decrease in  $K_C$  is observed for extremely thin sheets. Local plasticity and crack opening displacement have been taken into account to explain this phenomena (see Reference 15). However, this behavior may also be due in part to sheet buckling. Higher  $K_C$  values would normally be obtained if buckling guides were attached to the test panels.

In addition to the effect of thickness, the  $K_C$  values are sometimes affected by the free edges of the panel in front of the crack tip. Schematic illustrations are given in Figures 3b and 3c. Figures 4 to 8 show some of the actual test data. Note the trends shown in Figure 3 are independent of the other variables. That is, loading rate, environment and metallurgical variables will only shift or change the shape of these curves. For example, Figures 4 and 5 show the effects of  $2a/W$  and  $W$  on the  $K_C$  values for 2024-T3 aluminum. Figure 6 shows that 7075-T6 aluminum is less susceptible to panel width effects as compared to the data shown in Figure 5 for 2024-T3. The susceptibility to panel width

Figure 4. Effect of Crack Length to Panel Width Ratio on Fracture Toughness for Clad 2024-T3 Sheets.



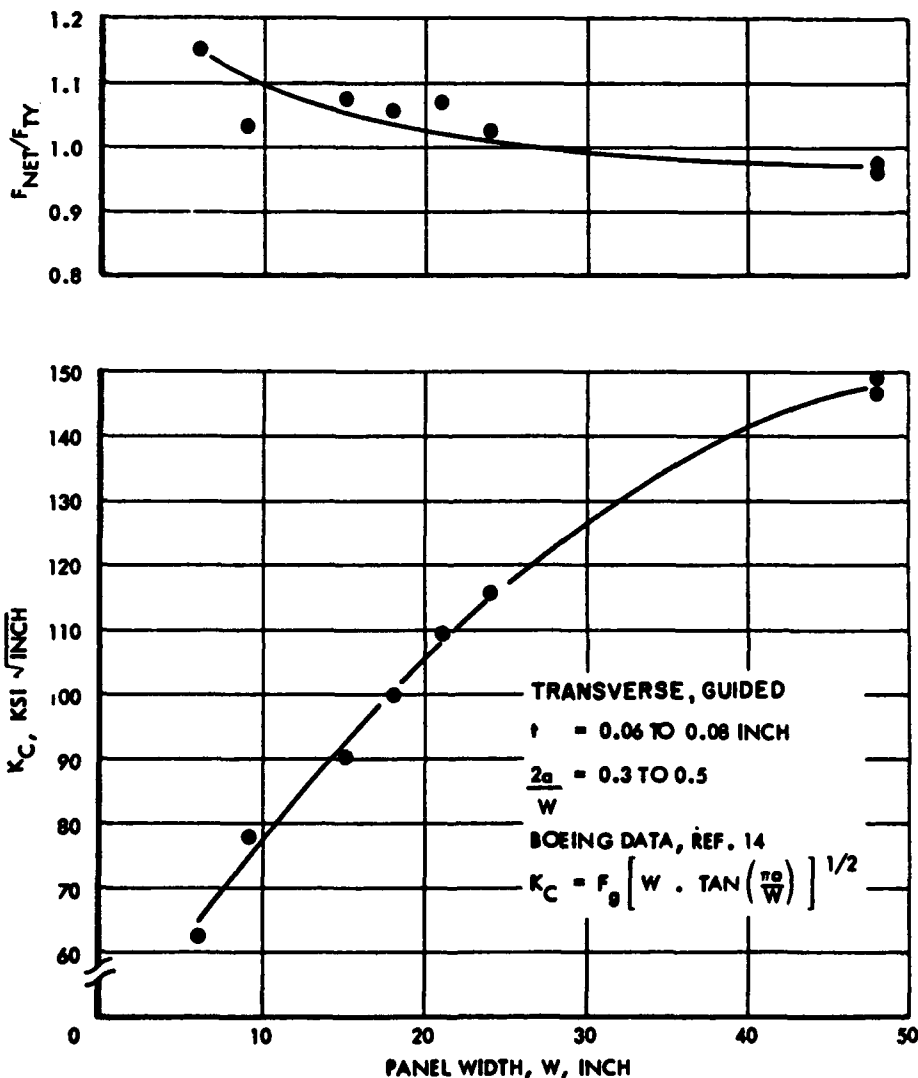
effects for 7075-T6 is further decreased (see Figure 7) as the panel thickness is increased. Furthermore, for brittle material like 7178-T6 aluminum, neither panel width nor crack length to panel width ratio will affect the  $K_C$  test results (Figure 8).

One more geometrical factor which significantly affects the  $K_C$  value, is the panel length. When remote loading is applied to the center-cracked panel as shown in Figure 2a, the crack surfaces are free of applied load and the panel edges parallel to crack are subjected to a uniform normal tensile stress. The load paths have to pass around the crack tip. Consequently, when the crack becomes long in relation to the distance between the crack and the loading grips abrupt changes in crack tip stress field occurs. This condition has been analyzed by Fichter (Reference 16) as shown in Figure 9. Test data for 7075-T6 aluminum and AM 355 steel support the trend developed by the elastic analysis (Figures 10 and 11).

### METHODS FOR DETERMINING FREQUENCY DISTRIBUTION FOR FRACTURE TOUGHNESS DATA

In many applications of the theory of probability, it is necessary to find the probability that a given error or variation will lie within certain limits. In such cases we utilize the principle that the probability of an error lying within given limits is equal to the area under the probability density curve between those limits. In other words, the definite integral of a given probability function would yield the result of interest. The most commonly used probability density function (p.d.f.) is the Gaussian, or the so called normal distribution. Figure 12 shows this p.d.f. has a symmetrical bell-shaped form. To determine the frequency distribution for a given set of engineering data, it is often assumed that the data fit one of the available probability distribution functions, and the choice of such a distribution is based on experience.

Figure 5. Effect of Panel Width on Fracture Toughness for Bare 2024-T3 Sheets.



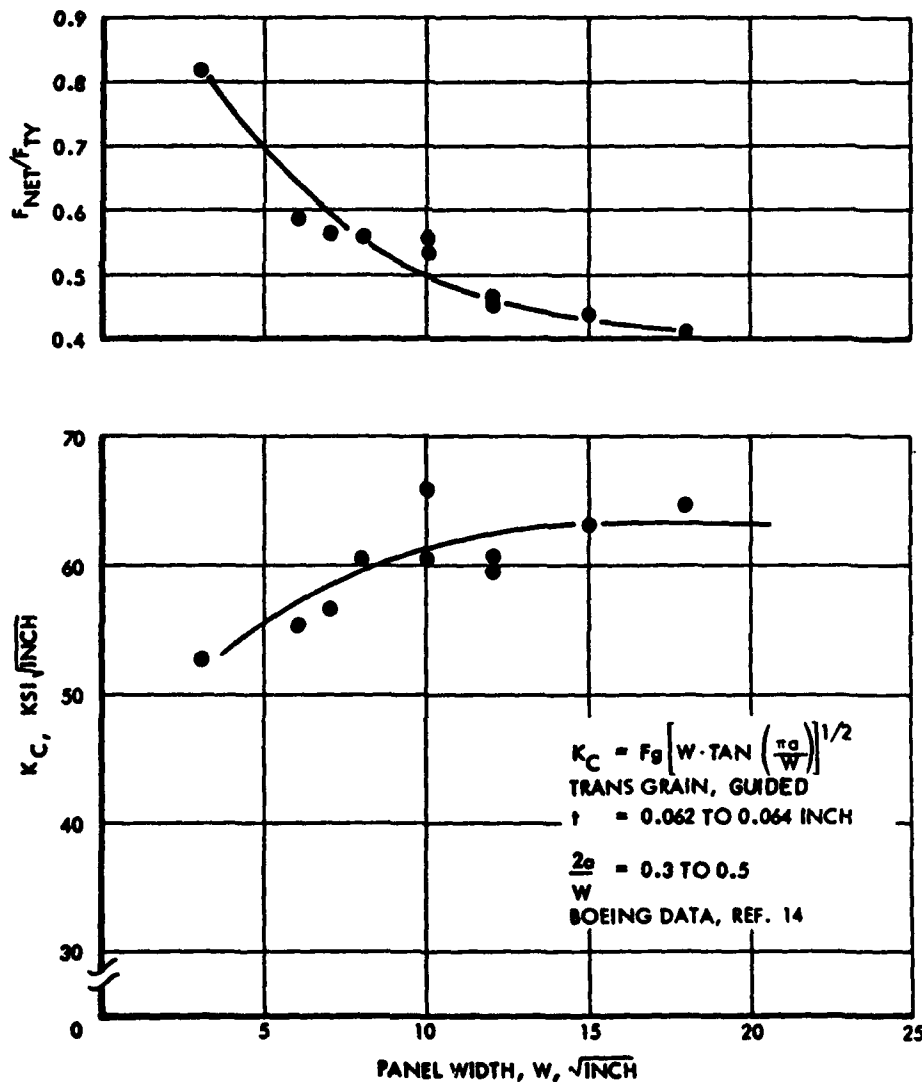
One way to solve the problem of deciding whether or not an assumed p.d.f. is acceptable consists of estimating the statistical parameters and checking the obtained goodness of fit by the Chi-square test. However, the Chi-square test technique does not have the capability of showing the degree of fitness, i.e., which p.d.f. fits the data better if more than one acceptable function is available. Furthermore, to perform Chi-square tests requires very large sample sizes. Therefore, it does not appear to be practical to use the Chi-square test in the evaluation of fracture toughness data because this type of data is very costly to obtain. The problem then is to search for a practical engineering procedure for determining the goodness of fit between data points and an assumed p.d.f.

In general, a p.d.f. may be characterized by its location, scale and shape parameters. Some p.d.f.'s, such as Gaussian, do not have shape parameters, because the Gaussian has a fixed shape. Using the technique of linear transformation, the probability or cumulative frequency scale can be

arranged to develop a linear relationship with the observed data points. In other words, on probability paper with the cumulative frequency scale as the ordinate and the observation scale as the abscissa, a straight line with positive slope represents a cumulative distribution function with some location and scale parameters. Therefore, one may plot a set of data on the constructed probability paper for a rough test of goodness of fit by fitting a straight line through the data points and obtain an estimate of the statistical parameters. A typical plot for a Gaussian distribution is shown in Figure 13.

When considering a p.d.f. for fracture toughness data, there are two objectives that have to be considered. First, the possibility that the p.d.f. will fit the data. Second, that the function can be used to construct probability paper. The Weibull distribution has been widely applied to the analysis of data for fracture of materials, especially ceramics and fatigue data. The normal distribution has been applied to many kinds of engineering data, e.g.,

Figure 6. Effect of Panel Width on Fracture Toughness for Bare 7075-T6 Sheets.



tensile and stress rupture properties of engineering alloys, and the error in many kinds of physical measurements. In many cases, a better fit is obtained if the observations are transformed to a logarithmic scale. This type of presentation is called a log-normal distribution. The log-normal distribution has generally been applied to fatigue data.

The mathematical formula and the general shape of three p.d.f.'s are shown in Figures 12, 14 and 15. As shown in Figures 14 and 15, both the log-normal distribution function and the Weibull distribution function contain a location parameter,  $\gamma$  and  $X_0$ , respectively. In many cases, these location parameters are assumed to be zero and the distribution functions still exhibit satisfactory results. Therefore, in this paper fracture toughness data are examined to determine if the data fits one of five distribution functions. These functions are:

1. Normal distribution function

2. Log-normal distribution function, two-parameter
3. Log-normal distribution function, three-parameter
4. Weibull distribution function, two-parameter
5. Weibull distribution function, three-parameter

Typical probability paper plots for log-normal and Weibull distributions are shown in Figures 16 and 17, respectively.

A computer program was developed for performing linear transforms to construct probability paper for any particular p.d.f.. The method of transform and plotting is similar to that of Reference 17. Ordered observations,  $X_i$ , data points, from the lowest to the highest are plotted on the X axis. Two or more consecutive points will be assigned for identical observations. The cumulative frequency scale is plotted on the y axis. A best-fit straight line is de-

Figure 7. Effect of Panel Width on Fracture Toughness for 7075-T6 Plates.

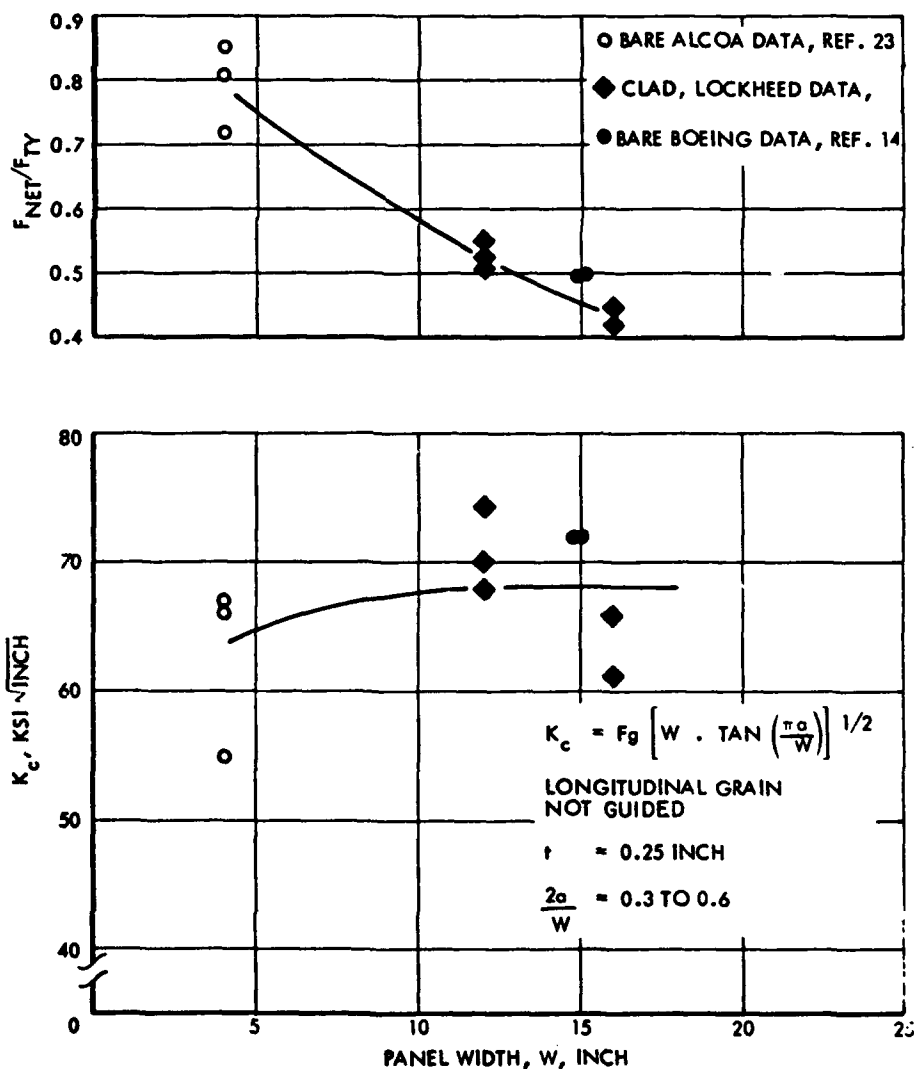




Figure 8. Effect of Crack Length to Panel Width Ratio on Fracture Toughness for Bare 7178-T6 Sheets.

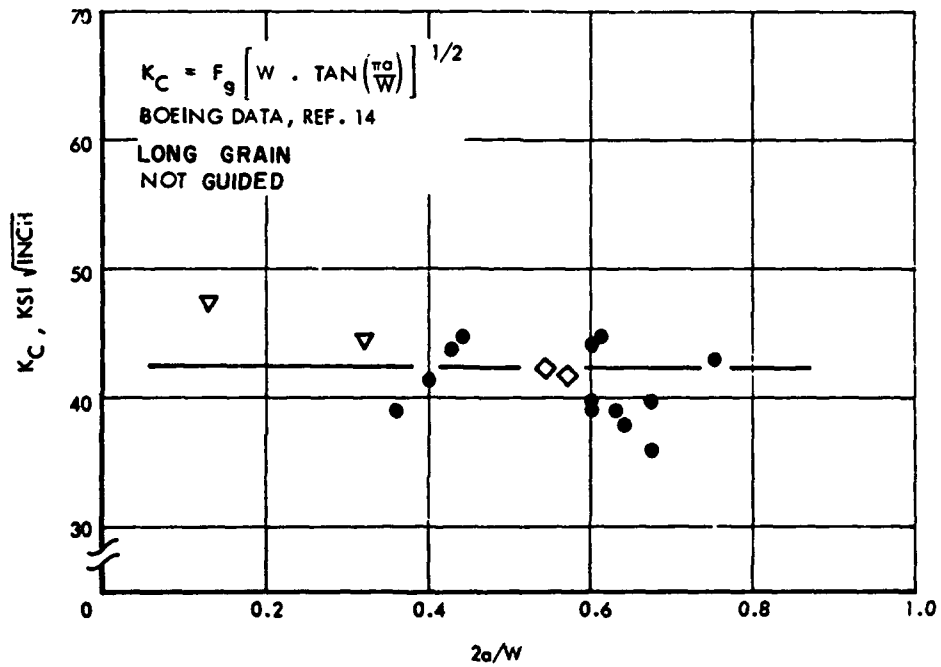
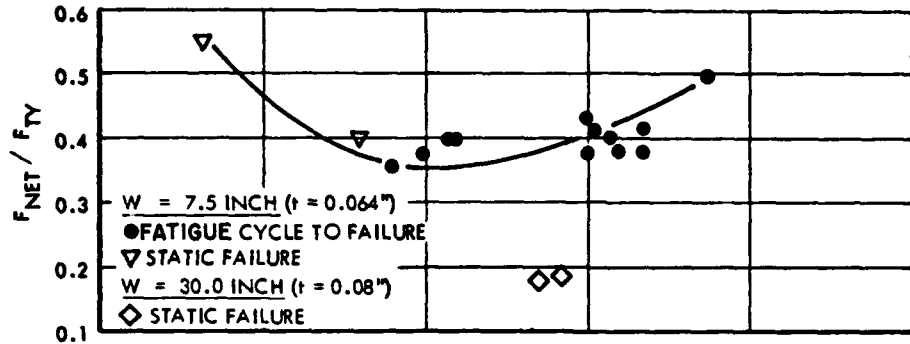


Figure 9. Panel Length Effects on Crack Tip Stress Intensity for Center Cracked Panels, Elastic Analysis (After Fichter, Reproduced from Ref. 16).

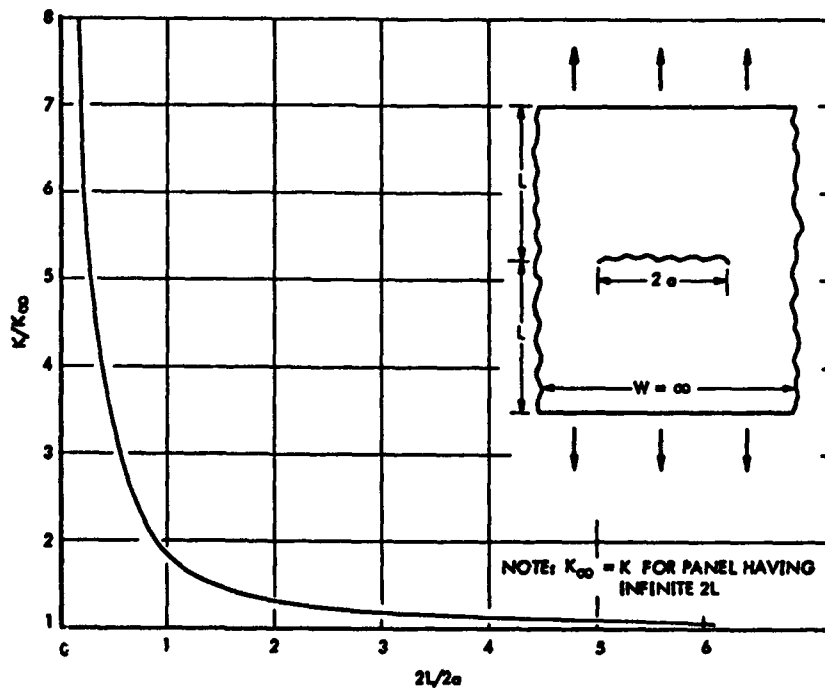
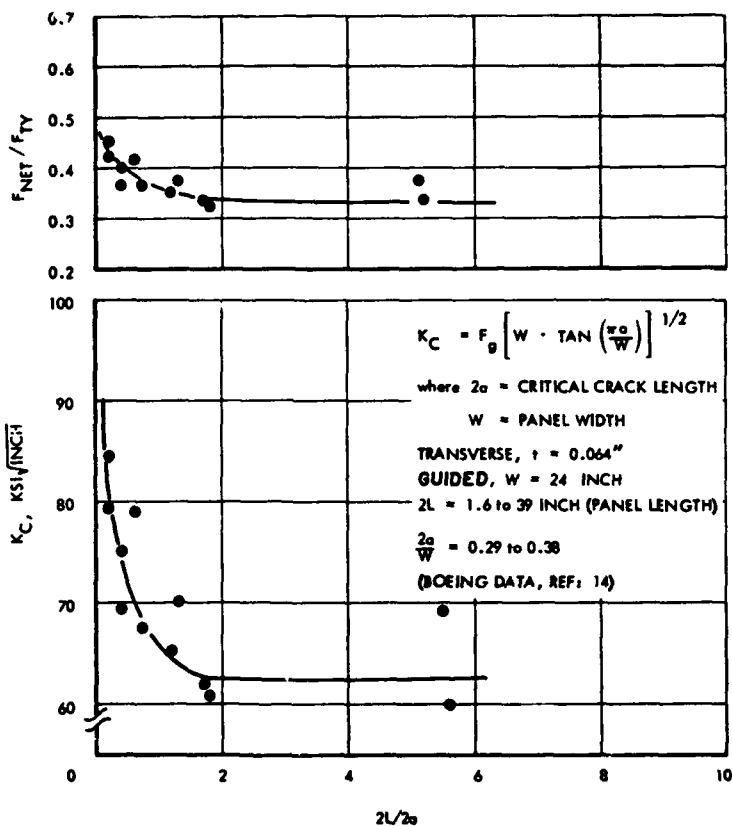


Figure 10. Effect of Panel Length on Fracture Toughness for Bare 7075-T6 Sheets.



terminated by the method of least squares. Fifty trials were performed on each data set. In each plot, the straight line which exhibits the minimum root mean square (RMS)

difference, is considered to be the best fit of the data.

To compare the best fit among several p.d.f. plots,

Figure 11. Effect of Panel Length on Fracture Toughness for AM355 CRT Sheets.

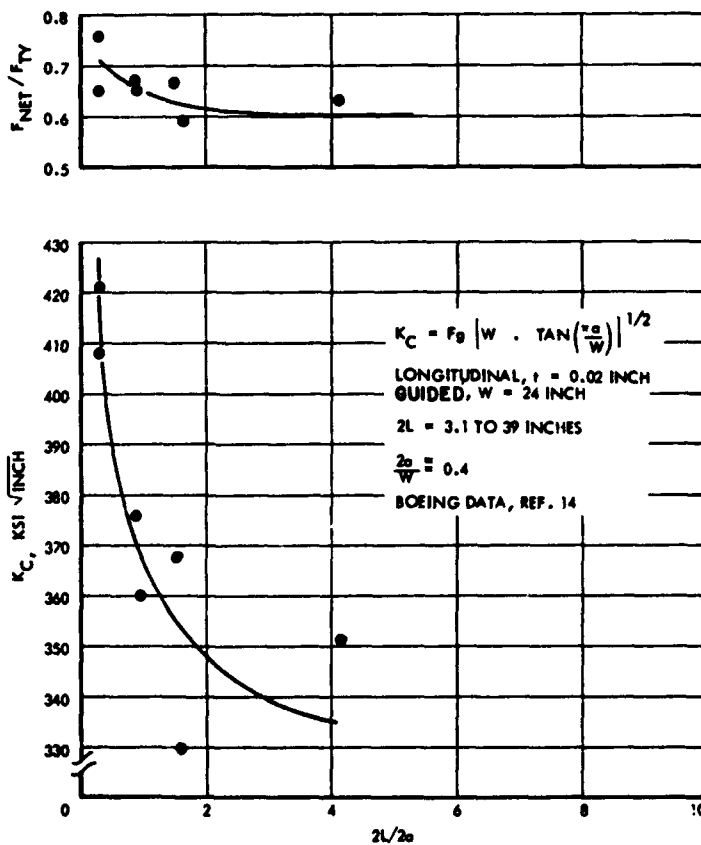
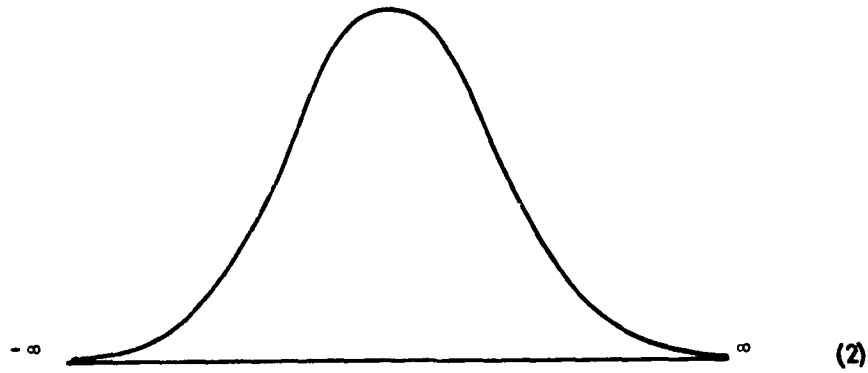


Figure 12. Normal Probability Function.



$$f(x) = \frac{1}{S\sqrt{2\pi}} \text{EXP} \left[ -\frac{1}{2} \left( \frac{x - \bar{X}}{S} \right)^2 \right]$$

with  $-\infty < x < \infty$

where  $S$  = sample standard deviation  
a scale parameter

$\bar{X}$  = sample mean  
a location parameter

simply compare the RMS values for the best fit straight lines. However, because the data points were plotted to different scales for the different probability density functions, these minimum RMS deviations need to be trans-

formed to a common scale before direct comparison can be made. The recalculated RMS values for the best fit curves in common scale then provide an indication of the degree of fit between the p.d.f. and the observed data.

Figure 13. Normal Probability Paper (Typical Plot).

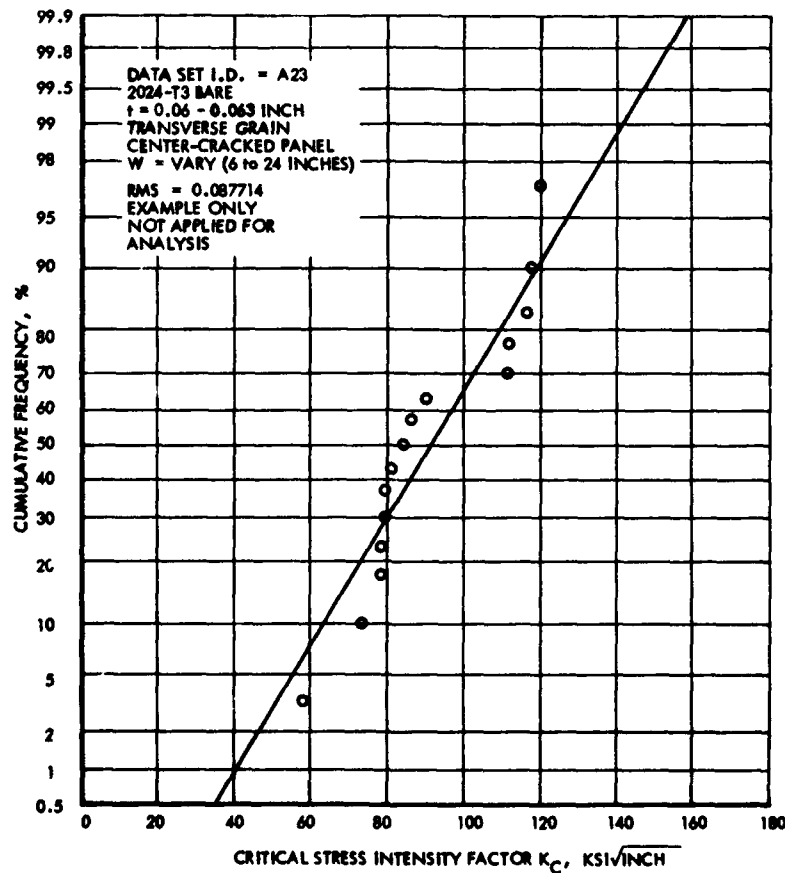
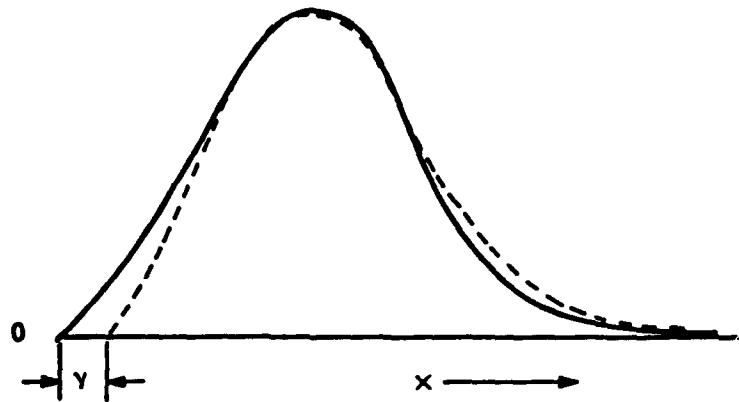


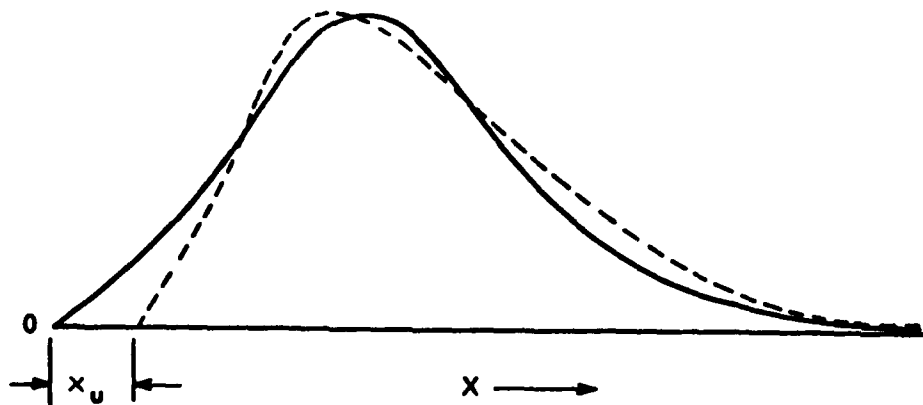
Figure 14. Logarithmic-Normal Probability Function.



$$f(X) = \frac{1}{(X-Y) S \sqrt{2\pi}} \text{EXP} \left[ -\frac{1}{2} \ln^2 \left\{ \left( \frac{X-Y}{e^{\bar{X}}} \right)^S \right\} \right] \quad (3)$$

with  $X \geq Y$   
 for  $Y = 0$  or  $Y > 0$   
 where  $S$  = sample standard deviation  
           a shape parameter  
 $\bar{X}$  = sample mean  
           a scale parameter  
 $Y$  = a location parameter

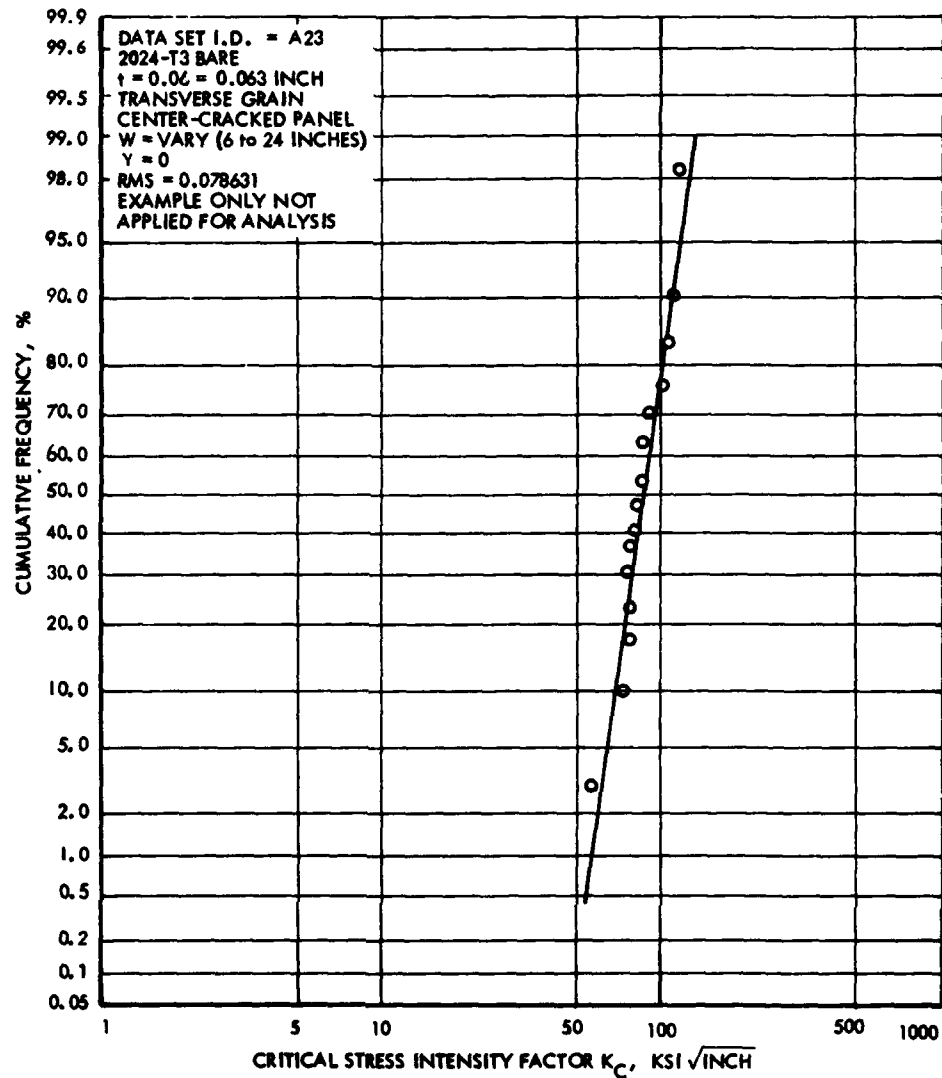
Figure 15. Weibull Probability Function.



$$f(X) = \frac{m}{X_0} (X - X_u)^{m-1} \text{EXP} \left[ -\frac{(X-X_u)^m}{X_0} \right] \quad (4)$$

with  $X \geq X_u$   
 for  $X_u = 0$  or  $X_u > 0$   
 where  $X_u$  is a location parameter  
 $X_0 (>0)$  is a scale parameter and  $m (>0)$  is a shape parameter and are empirically determined constants.

Figure 16. Log-Normal Probability Paper (Typical Plot)



As can be seen in the cumulative frequency plots, Figures 13, 16 and 17, the two-parameter log-normal and the Weibull distributions fit the given data set well, but the normal distribution exhibits a poor fit. However, when the data is subjected to the computerized curve fitting process, as noted in Figures 13, 16 and 17, the RMS value for the normal distribution is 0.088 and the RMS value for the other two functions are 0.079 for the log-normal and 0.095 for the Weibull distribution. Thus it is concluded that among these three functions, the log-normal p.d.f. fits the data best and the Weibull distribution exhibits a poor fit although the overall departure between each p.d.f. is insignificant. Therefore, it is felt that the computerized technique offers a more accurate measurement over conventional hand plotting procedure.

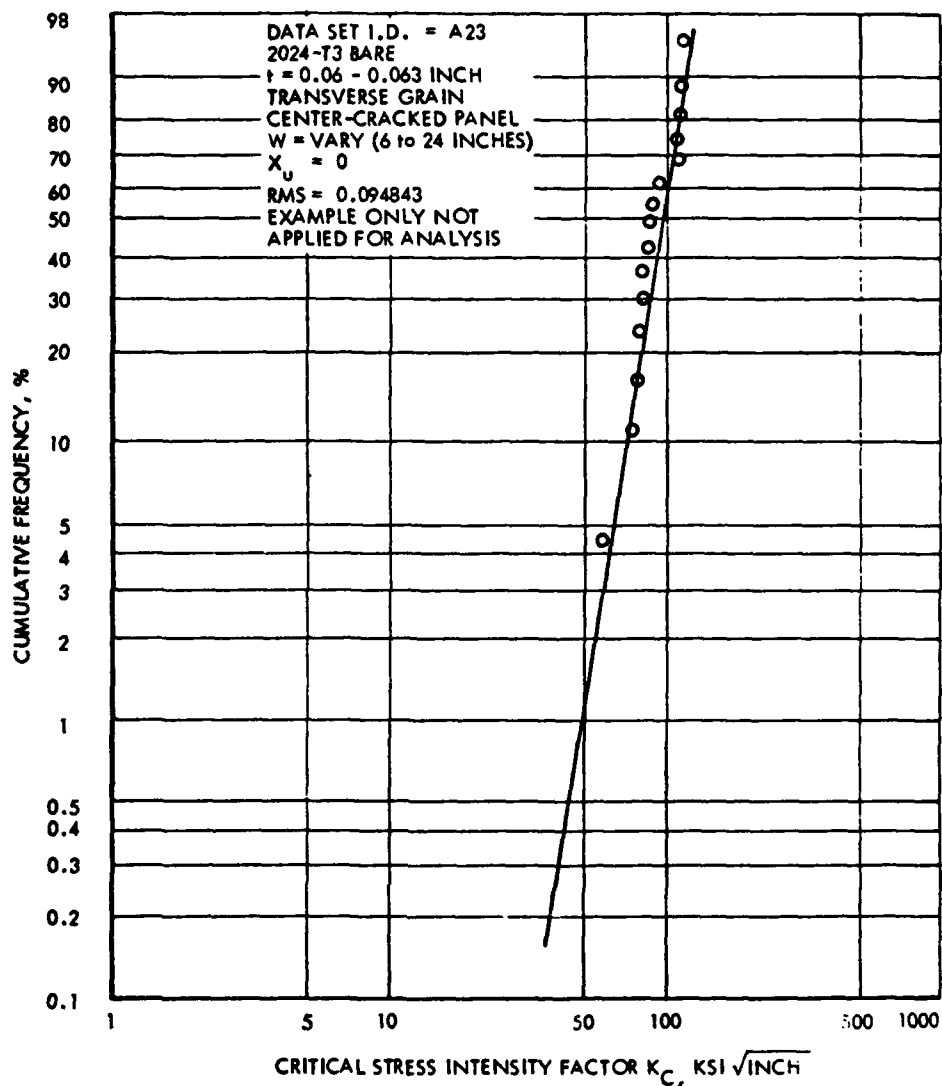
Recently, Weibull proposed a graphical method similar to the present work for evaluating the acceptability and the goodness of fit for assumed distribution functions (see Reference 18). Weibull introduced the "maximum number of runs" concept. This concept sets to count the number of runs required for an assumed p.d.f. (with assumed

parameters) to pass through a set of data points. The degree of fit is then evaluated based on the corresponding least square deviations. Although Weibull's method was developed on a more rigorous statistical basis, it is anticipated that the present graphical method will serve as a useful tool for solving most engineering problems.

#### PRESENTATION AND DISCUSSION OF RESULTS

Fracture toughness data were chosen from References 14, 19, 20 and 21. The data were divided into 91 sets by considering the nature of the testing technique, the environmental conditions and materials. Among the 91 sets of data, 79 sets contained  $K_{Ic}$  data obtained from center-cracked panel tests for steels, titanium, aluminum and nickel base super alloys at various test temperatures and 12 sets contained  $K_{Ic}$  data on notched bend specimens for steels and titanium alloys. In addition, two sets of  $K_{Ic}$  data (Reference 22) from double cantilever beam specimens for magnesium oxide, were selected for analysis. The data for the magnesium oxide were considered to be very suitable

Figure 17. Weibull Probability Paper (Typical Plot).



for plane strain evaluations due to the high degree of brittleness of the material and the fact that a crack line load testing technique was used. The data, 54 observations in one set and 104 observations in another set, provided enough data points for determining the frequency distribution.

The present investigation is divided into two parts. The first part is an analysis and comparison of the goodness of fit between data sets and the assumed probability functions. The second part is an evaluation of the statistical parameters based on the result of the first part.

### I. Distribution Analysis

First, the curve fitting results were reviewed to identify general trends of the distribution of data, especially to determine if there was an effect due to test temperature and material. Tables II and III present some typical examples of the curve fitting results for  $K_C$  and  $K_{Ic}$  data, respectively. The value of the RMS differences, shown in Tables II and

III reflect the closeness of fit between the distribution function and the test data. A majority of the  $K_C$  data exhibited a better fit with the three-parameter distribution functions. The effects of testing temperature and materials does not appear to be significant.

To normalize the sample size effect, the RMS differences for each  $K_C$  data set (79 sets total where each set contains six observations or more) were weighted according to the sample size of each data set, that is, the contribution of each set was weighted in proportion to the number of observations contained in the set and the average RMS difference was computed. As a further check on the sample size effect, 34 sets of data, which had 10 or more observations in each set, were selected for comparison from the total of 79 data sets. The results of these computations are summarized in Table II. As shown in Table II, the trends on the closeness of fit developed for both cases were the same. This can probably be attributed to the effect of the normalization procedure; however, data sets containing

**TABLE II.**  
**FREQUENCY DISTRIBUTION ANALYSIS RESULTS FOR  $K_C$  DATA,**  
**TYPICAL EXAMPLES AND SUMMARY**

Alloy	t (Inch)	Temp. (°F)	Grain Dir.	ROOT MEAN SQUARE DIFFERENCES					Remarks	Sample Size	Data set I.D.	Data Source
				Normal	2-Parameter Log-Normal	3-Parameter Log-Normal	2-Parameter Weibull	3-Parameter Weibull				
7178-T6 Bare	0.16-0.17	RT	L	0.036	0.032	0.032	0.044	0.031	Not guided	47	A32	Ref.14
7178-T6 Bare	0.17	RT	L	0.104	0.106	0.106	0.102	0.102	Not guided	7	A31	Ref.14
									Machine Mill on One Side, Fatigue Cycle to Failure			
7075-T6 Bare	0.04	RT	L	0.120	0.129	0.129	0.115	0.115	Not guided	7	A27	Ref.14
7075-T6 Bare	0.09	RT	L	0.05	0.047	0.029	0.062	0.027	Not guided	6	A28	Ref.14
2024-O-HT-T4	0.04	RT	L	0.05	0.059	0.059	0.042	0.042	Not guided	12	A9	Ref.14
2024-T3 Clad	0.064	RT	L	0.093	0.086	0.038	0.106	0.041	Not guided	16	A20	Ref.14
									Material Stretched 6%			
2024-T3 Clad	0.064	RT	L	0.121	0.117	0.069	0.127	0.068	Not guided	12	A15	Ref.14
									Material Stretched 2.5%			
Ti,6Al-4V, M.A.	0.025	-110	T	0.111	0.104	0.045	0.117	0.054	Guided	6	D51	Ref.21
Ti,8Al-1Mo- 1V T.A.	0.025	-110	T	0.099	0.100	0.100	0.092	0.092	Guided	6	D41	Ref.21
									BNA			
Ti,6Al-4V, M.A.	0.05	RT	L	0.081	0.062	0.062	0.060	0.086	Guided	8	51	Ref.20
Ti,8Al-1Mo-1V D.A.	0.05	RT	L	0.048	0.044	0.034	0.061	0.033	Guided	8	41	Ref.20
									BNA			
Ti,8Al-1Mo-1V T.A.	0.025	RT	T	0.046	0.045	0.045	0.055	0.046	Guided	18	D42	Ref.21
Ti,6Al-4V,M.A.	0.025	400	T	0.081	0.080	0.079	0.092	0.080	Guided	6	D55	Ref.21
Ti,8Al-1Mo-1V T.A.	0.025	400	T	0.120	0.120	0.067	0.125	0.073	Guided	6	D48	Ref.21
Ti,6Al-4V,M.A.	0.025	650	T	0.056	0.062	0.062	0.040	0.040	Guided	18	D56	Ref.21
Ti,8Al-1Mo-1V T.A.	0.025	650	T	0.037	0.033	0.024	0.062	0.026	Guided	18	D44	Ref.21
PH 15 - 7 Mo	0.025	-110	T	0.091	0.083	0.056	0.096	0.054	Guided, RH 1100	6	D11	Ref.21
PH 14 - 8 Mo	0.025	RT	L	0.082	0.083	0.083	0.076	0.076	Guided	6	BNA	Ref.20 11
AM350 SCT	0.025	RT	L	0.032	0.028	0.020	0.052	0.023	Guided	8	BNA	Ref.20 21A
AM350 CRT	0.025	RT	T	0.045	0.044	0.045	0.062	0.046	Guided	18	D22	Ref.21
PH 15 - 7 Mo	0.025	400	T	0.062	0.053	0.044	0.073	0.047	Guided, RH 1100	6	D13	Ref.21
PH 15 - 7 Mo	0.025	650	T	0.047	0.041	0.040	0.063	0.040	Guided, RH 1100	18	D14	Ref.21
Rene 41	0.025	-110	T	0.081	0.074	0.068	0.090	0.070	Guided	6	D31	Ref.21
Rene 41	0.025	RT	T	0.045	0.045	0.045	0.055	0.048	Guided	17	D32	Ref.21
INCO 718 CRA	0.025	RT	L	0.057	0.053	0.051	0.072	0.054	Guided	15	BNA	Ref.20 31

**TABLE II. (Continued)**  
**FREQUENCY DISTRIBUTION ANALYSIS RESULTS FOR K<sub>C</sub> DATA,**  
**TYPICAL EXAMPLES AND SUMMARY**

Alloy	t (Inch)	Temp. (°F)	Grain Dir.	ROOT MEAN SQUARE DIFFERENCES					Remarks	Sample Size	Data set I.D.	Data Source
				Normal	2-Parameter Log-Normal	3-Parameter Log-Normal	2-Parameter Weibull	3-Parameter Weibull				
Rene 41	0.025	400	T	0.069	0.057	0.057	0.065	0.060	Guided	6	D33	Ref.21
Rene 41	0.025	650	T	0.056	0.056	0.056	0.063	0.056	Guided	18	D34	Ref.21
Rene 41	0.025	1400	T	0.092	0.088	0.075	0.106	0.078	Guided	6	D36	Ref.21
Average of 79 sets data (sample size >8)				0.065	0.065	0.058	0.069	0.055	[ 1 ]	859	-	-
Average of 34 sets data extracted from 79 sets having sample size >10				0.054	0.056	0.049	0.059	0.046	[ 1 ]	559	-	-

[ 1 ] avg. RMS Diff =  $\frac{\sum RMS_i \cdot N_i}{\sum N_i}$

where N<sub>i</sub> = sample size of a single data set

RMS<sub>i</sub> = RMS for that particular set

**TABLE III.**  
**FREQUENCY DISTRIBUTION ANALYSIS RESULTS FOR K<sub>IC</sub> DATA**

ALLOY	WELDMENT	LOADING COND.	GRAIN DIR.	ROOT MEAN SQUARE DIFFERENCES					REMARKS	SAMPLE SIZE	DATA SET I.D.	DATA SOURCE
				NORMAL	2-PARAMETER LOG-NORMAL	3-PARAMETER LOG-NORMAL	2-PARAMETER WEIBULL	3-PARAMETER WEIBULL				
250 Grade Maraging Steel	MIG weld	3 pt load	-	0.102	0.089	0.073	0.111	0.078	Center of Weld NRL Plate 5	12	K2	Ref. 19
	TIG weld	3 pt load	-	0.044	0.045	0.045	0.050	0.046	C.O.W. Plate 2	18	K3	Ref. 19
	TIG weld	3 pt load	-	0.043	0.044	0.044	0.046	0.043	C.O.W. Plate 1	17	K4	Ref. 19
	TIG weld	3 pt load	-	0.042	0.042	0.042	0.049	0.041	C.O.W. NRL Plate 6	19	K11	Ref. 19
	Short Arc weld	3 pt load	-	0.039	0.037	0.039	0.045	0.036	C.O.W. NRL Plate 11	19	K15	Ref. 19
	Short Arc weld	3 pt load	-	0.042	0.041	0.041	0.052	0.038	Heat Affected Zone NRL Plate 11	18	K16	Ref. 19
	TIG weld	3 pt load	-	0.037	0.033	0.033	0.047	0.034	H.A.Z. Plate 2	10	K7	Ref. 19
	TIG weld	3 pt load	-	0.047	0.050	0.050	0.053	0.052	Diffusion Zone Plate 1	10	K10	Ref. 19
	NO	3 pt load	L	0.080	0.070	0.046	0.097	0.055	Plate 1	26	K1	Ref. 19
NO	3 pt load	T	0.046	0.048	0.048	0.041	0.040	Plate 2	24	K2	Ref. 19	
Ti <sub>1.4</sub> Al-3 Mo-1V	NO	4 pt load	T	0.060	0.057	0.052	0.079	0.055	BETA STA 1150°F	10	T8-B	Ref. 14
Ti <sub>1.6</sub> Al-4V	NO	4 pt load	T	0.091	0.087	0.060	0.102	0.047	BETA STA 1250°F	22	T5	Ref. 14
MO	--	Crack line load	-	0.076	0.051	0.050	0.073	0.052	---	54	CARN TECH-1	Ref. 22
MO	--	Crack line load	-	0.104	0.075	0.063	0.107	0.081	Titanium Doped	104	CARN TECH-2	Ref. 22



**TABLE IV.**  
**STATISTICAL VARIATIONS IN FRACTURE TOUGHNESS OF ALUMINUM ALLOYS**

Alloy	t (inch)	Temp. (°F)	Grain Dir.	K <sub>IC</sub> - Data (Ksi√In.)			log S	log σ	σ̄ <sub>g</sub> /σ	Min. K <sub>IC</sub> Est./In.	Buckling Res.	t <sub>g</sub> Ksi/sec	W (inch)	Remarks	Sample Size	Data Set ID
				Min.	X	Max.										
2024-T3 Bare	0.06-0.063	RT	T	86.4	106.8	118.5	0.057	0.08	95.2	70.3	No	Slow	24	Center Cracked Panels	7	A-23-A
2024-T3 Clad 2.5% Stretched	0.04	RT	L	40.3	50.1	60.3	0.065	0.08	45.5	33.6	No	Slow	7.5	Center Cracked Panels	10	A13-A
	0.04	RT	T	36.4	47.8	63.8	0.071	0.08	43.5	32.1	No	Slow	7.5		10	A17-A
	0.064	RT	T	42.2	51.4	59.8	0.050	0.08	46.7	34.5	No	Slow	7.5		10	A16-A
	0.064	RT	L	44.5	54.1	71.5	0.082	0.08	49.1	36.3	No	Slow	7.5		10	A15-A
2024-T3 Clad 6% Stretched	0.04	RT	T	36.6	46.7	55.2	0.062	0.08	42.4	31.3	No	Slow	7.5	Center Cracked Panels	10	A21-A
	0.04	RT	L	27.6	49.3	60.0	0.100	0.08	44.8	33.1	No	Slow	7.5		10	A35-A
	0.064	RT	T	45.7	51.9	58.7	0.047	0.08	45.9	33.9	No	Slow	7.5		6	A19-A
	0.064	RT	L	43.3	50.1	64.0	0.059	0.08	46.2	34.2	No	Slow	7.5		14	A20-A
2024-O-RT-T4	0.04	RT	L	34.8	44.5	52.1	0.060	0.08	40.5	31.1	No	Slow	7.5	Center Cracked Panels	10	A9-A
	0.04	RT	T	34.9	44.1	51.1	0.056	0.08	40.1	30.9	No	Slow	7.5		10	A5-A
	0.064	RT	L	29.0	45.9	58.0	0.090	0.08	41.7	32.1	No	Slow	7.5		10	A7-A
	0.064	RT	T	31.2	45.1	53.8	0.073	0.08	41.0	31.6	No	Slow	7.5		10	A10-A
7178-T6 Bare	0.16-0.17	RT	L	34.5	44.2	61.0	0.053	0.09	40.7	29.0	No	Slow	9	Machine Mill on One Side, Fatigue Cycling to Failure. Fatigue cycling to Failure	17	A32-B
	0.16-0.17	RT	L	30.8	46.4	72.2	0.089	0.09	42.7	30.4	No	Slow	15		17	A32-C
	0.16	RT	T	39.1	44.9	52.7	0.047	0.09	40.3	28.6	No	Slow	9		10	A33-A
	0.17	RT	L	44.2	50.5	58.1	0.043	0.07	45.7	35.1	No	Slow	15		7	A31
	0.064	RT	L	30.7	41.0	45.2	0.030	0.07	38.1	29.2	No	Slow	7.5		13	A34-A
7075-T6 Bare	0.04	RT	T	38.2	50.9	59.4	0.060	0.08	45.3	33.5	No	Slow	6	Fatigue cycling to failure	7	A26
	0.04	RT	L	38.9	50.3	54.7	0.052	0.08	44.9	33.2	No	Slow	6		7	A27
	0.09	RT	L	60.3	64.6	70.6	0.027	0.08	57.1	42.2	No	Slow	5		6	A28
7075-T6 Clad	0.064	RT	L	32.8	42.0	48.8	0.057	0.07	39.3	30.1	No	Slow	7.5	Fatigue cycling to failure	16	A30A

△ All are Center - Cracked Panels, Tangent Width Correction Used

larger sample sizes seemed to exhibit a closer fit. The data in Table II shows that there is a better fit with the three-parameter distribution functions. The two-parameter Weibull distribution does not offer a good fit with the data when compared with the other distribution functions. However, the numerical departure in closeness of fit between all five distribution functions is not significant.

Four types of K<sub>IC</sub> data are shown in Table III. The K<sub>IC</sub> data for maraging steel weldments fits well for all five distribution functions. The closeness of fit between distribution functions and K<sub>IC</sub> data for maraging steel, titanium alloy and magnesium oxide can be rated as follows: The three-parameter Weibull and the three-parameter log-normal distributions exhibit the best fit, the two-parameter log-

**TABLE V.**  
**STATISTICAL VARIATIONS IN FRACTURE TOUGHNESS OF TITANIUM ALLOYS**

Alloy	t (inch)	Temp. (°F)	Grain Dir.	K <sub>IC</sub> - Data (Ksi√In.)			log S	log σ	σ̄ <sub>g</sub> /σ	Min. K <sub>IC</sub> Est./In.	Buckling Res.	t <sub>g</sub> Ksi/sec	W (inch)	Remarks	Sample Size	Data Set ID	
				Min.	X	Max.											
Ti, 6Al-3Mo-1V Beta 87A 1150°F	0.48	RT	T	84.6	90.1	96.4	0.019	0.08	86.5	77.2	-	-	1.5	4 point load, K <sub>IC</sub>	8	T8-A	
Ti, 6Al-3Mo-1V Beta 87A 1000°F	0.48	RT	T	99.9	108.4	106.5	0.011	0.08	99.3	88.6	-	-	1.5	4 point load, K <sub>IC</sub>	8	T9	
Ti, 6Al-4V Beta 87A 1250°F	-	RT	T	96.3	105.1	117.3	0.034	0.08	98.4	78.4	-	-	1.5	4 point load, K <sub>IC</sub>	12	T3-A	
Ti, 6Al-4V Mill Ann.	0.025	80	T	120.7	109.3	112.8	0.018	0.05	101.2	83.7	Yes	1.25	8	σ <sub>ys</sub> = 197.2 Ksi σ <sub>ys</sub> = 138.2 Ksi σ <sub>ys</sub> = 129.9 Ksi	6	D94	
	0.025	80	T	100.8	116.7	125.4	0.056	0.05	108.0	89.3	Yes	1.25	8		6	D93	
	0.025	80	T	151.0	175.3	186.6	0.087	0.05	162.3	134.3	Yes	1.25	8		6	D98	
	0.05	RT	L	150.3	199.7	172.0	0.024	0.05	149.3	123.6	Yes	100	24		8	88A51	
	0.05-0.07	RT	T	133.0	193.2	169.0	0.082	0.05	141.8	117.3	Yes	1.1, 1.0	12		Center Cracked Panels	6	T10-A
		400	T	126.5	134.3	143.5	0.018	0.05	124.3	102.8	Yes	1.25	8			6	D55
	0.025	650	T	100.1	118.0	130.3	0.08	0.05	112.8	93.3	Yes	1.25	8		18	D96	
	0.05	650	L	195.6	230.4	245.8	0.034	0.05	214.5	177.5	Yes	750-1000	24		7	88A52	
	0.025	-110	T	96.9	108.8	140.8	0.063	0.07	97.6	74.9	Yes	1.25	8		6	D51	
	0.05	-110	T	135.3	190.1	165.9	0.035	0.07	134.7	103.3	Yes	-	8		6	88A54	
Ti, 6Al-1Mo-1V Duplex Ann.	0.05-0.07	RT	T	164.2	169.5	174.2	0.01	0.05	154.4	123.0	Yes	-	8	Center Cracked Panels	6	T6-A	
	0.05	RT	L	185.2	207.7	244.0	0.04	0.04	198.6	152.7	Yes	100	24		8	88A41	
	0.05	650	L	187.0	202.6	245.2	0.036	0.05	202.5	161.3	Yes	1000	24		7	88A42	
Ti, 6Al-1Mo-1V Triplex Ann.	0.025	80	T	110.5	119.9	128.7	0.023	0.04	115.7	99.5	Yes	1.67	8	Center Cracked Panels	18	D42	
	0.025	-110	T	120.0	127.9	134.6	0.026	0.04	120.3	103.4	Yes	1.67	8		6	D41	
	0.025	400	T	123.6	129.5	144.4	0.028	0.04	121.7	104.6	Yes	1.67	8		6	D43	
	0.025	650	T	140.3	134.2	125.7	0.025	0.04	110.2	94.7	Yes	1.67	8		18	D44	

△ Tangent Width Correction Used

**TABLE VI.**  
**STATISTICAL VARIATIONS IN FRACTURE TOUGHNESS OF**  
**STEELS AND NICKEL BASE SUPER ALLOYS**

Alloy	t (inch)	Temp. (°F)	Grain Dir.	K <sub>IC</sub> - Data (Ksi √in.)			log S	log σ	σ <sub>o/e</sub>	Min. K <sub>IC</sub> Ksi √in.	Buckling Res.	σ <sub>g</sub> Ksi/sec	W (inch)	Remarks	Sample Size	Data Set ID
				Min.	X	Max.										
18 Ni, maraging steel (grade 250)		RT	L	69.5	76.8	93.1	0.025	0.03	75.2	67.1	—	—	—	3 point load, K <sub>IC</sub>	26	K1
		RT	T	75.4	84.3	94.5	0.020	0.03	82.3	73.5	—	—	—	3 point load, K <sub>IC</sub>	24	K2
4330M (200-220)	0.08	RT	L	224.0	231.6	241.0	0.014	0.05	211.1	168.1	No	-	5	Center cracked panels	6	E2
PH14-8 Mo	0.025	RT	L	209.9	221.8	230.4	0.019	0.05	202.1	161.1	Yes	300-1000	24	Center cracked panels	6	MM11
		650	L	170.0	182.7	198.8	0.022	0.05	167.6	133.5	Yes	700-1000	24	Center cracked panels	7	MM12
PH15-7Mo (RH 1100)	0.025	80	T	101.3	112.4	133.8	0.035	0.05	105.6	84.9	Yes	1.25	8	Center Cracked panels	18	D12
		-110	T	85.1	103.1	131.8	0.021	0.10	88.4	60.5	Yes	1.25	8		6	D11
		400	T	89.2	99.4	120.6	0.032	0.05	90.6	72.2	Yes	1.25	8		6	D13
		650	T	76.3	89.0	101.6	0.037	0.05	84.3	67.2	Yes	1.25	8		18	D14
AISI 50 CRT	0.025	80	T	142.8	163.5	198.2	0.04	0.05	155.0	123.5	Yes	1.67	8	Center Cracked panels	18	D22
		-110	T	96.2	95.9	150.0	0.166	0.10	83.0	56.8	Yes	1.67	8		6	D21
		400	T	142.1	156.4	170.2	0.033	0.05	142.6	113.6	Yes	1.67	8		6	D23
		650	T	116.3	129.7	138.4	0.028	0.05	122.9	97.9	Yes	1.67	8		18	D24
AISI 50 BCT	0.025	RT	L	236.0	310.9	332.0	0.043	0.05	283.4	225.8	Yes	100	24	Center cracked panels	6	MM21
		RT	L	212.8	284.4	378.0	0.07	0.05	262.5	209.1	Yes	300-1000	24		8	MM21-A
		650	L	225.2	264.1	282.0	0.035	0.05	240.0	191.9	Yes	0.95	24		6	MM22
INCO 718 CRA	0.025	RT	L	316.0	349.2	395.0	0.024	0.04	335.8	288.6	Yes	-	24	Center cracked panels	15	MM31
		RT	T	236.1	262.2	285.4	0.028	0.04	249.3	214.2	Yes	-	24		9	MM32-A
		650	L	308.7	334.0	353.6	0.025	0.04	315.4	271.1	Yes	-	24		17	MM34
INCO 41	0.025	80	T	143.1	184.8	222.4	0.032	0.05	174.9	139.3	Yes	1.25	8	Center cracked panels	17	D32
		-110	T	144.3	164.9	208.9	0.033	0.05	150.0	119.5	Yes	1.25	8		6	D31
		400	T	143.0	164.5	196.6	0.031	0.05	149.9	119.4	Yes	1.25	8		6	D33
		650	T	132.9	165.0	208.0	0.033	0.05	156.4	124.6	Yes	1.25	8		18	D34
		1000	T	125.6	153.7	176.8	0.034	0.05	140.1	111.6	Yes	1.25	8		6	D35
		1400	T	102.2	109.8	121.7	0.025	0.05	100.1	79.7	Yes	1.25	8		6	D36

△ Tangent Width Correction Used

normal distribution ranked close second, and the normal and the two-parameter Weibull distributions are rated last.

In summarizing, it is anticipated that the two-parameter log-normal distribution function will satisfy both K<sub>IC</sub> and K<sub>IC</sub> testing data. The three-parameter functions, although they exhibited somewhat better results, contain the location parameter which when introduced into these functions causes difficulties in calculation of statistical parameters. Consequently it is not desirable to use these functions if another choice is available.

## II. Statistical Parameters for Fracture Toughness Data for Some Engineering Alloys

By making use of the two-parameter log-normal distribution, the sample mean ( $\bar{X}$ ) and sample standard deviation (S), for some airframe materials are computed and listed in Tables IV, V and VI. Notice that the sample standard deviation, calculated from the data sets, exhibited a considerable variation from one set of data to another set of data for the same material tested under the identical conditions. In such cases, it is common to use the sample mean and an assumed population standard deviation for determining the guaranteed minimum fracture toughness. The minimum fracture toughness values, Min. K<sub>IC</sub> or Min.

K<sub>IC</sub>, were estimated based on taking 95 percent tolerance on the mean and 95 percent reliability level on the standard deviation (one-sided for both cases). Calculated values are also tabulated in Tables IV, V and VI.

## SUMMARY

The nature of the fracture toughness testing and factors that affect the test results were reviewed. Emphasis has been placed on the fact that without paying close attention to the physical phenomenon involved, conclusions drawn from any statistical analysis would have little meaning. A graphical method was adopted for evaluating the closeness of fit between given probability density functions and fracture toughness data. It is concluded that those probability functions commonly used to fit material mechanical properties data, are also applicable for fitting the fracture toughness data.

## ACKNOWLEDGEMENTS

The author wishes to thank S.L. Barter for preparation of the computer program. Special acknowledgements are due to Mr. J.P. Butler of the Boeing Company and to Mr. J.C. Ekvall of the Lockheed-California Company for their constructive support in the preparation of the paper.

## REFERENCES

1. A.F. Liu, *Statistical Variations in Fracture Toughness Data of Airframe Materials*, D6-15784 TN, Boeing Company, Seattle, Washington (1968).
2. J.P. Butler, "Fatigue Scatter and a Statistical Approach to Fatigue Life Prediction," in *Proc. Symp. Fatigue of Aircraft Structures*, WADC-TR-59-507, Aeronautical Systems Division, Wright-Patterson AFB, Ohio (1959).
3. E.Y. Robinson, *Engineering Application of Weibull Statistics*, ASME Paper 65-MET-21, American Society of Mechanical Engineers, New York (1965).
4. V. Weiss, G. Schaeffer, and J. Fehling, *Effect of Section Size on Notch Strength*, ASME Paper 66-MET-4, American Society of Mechanical Engineers, New York (1966).
5. V. Weiss, *Application of Weibull's Statistical Theory of Fracture to Sheet Specimens*, ASME Paper 62-WA-270, American Society of Mechanical Engineers, New York (1962).
6. P.M. Scop and A.S. Argon, "Statistical Theory of Strength of Laminated Composites," *J. Compos. Mater.*, 1:92 (1967).
7. R.A. Wallhaus, *A Statistical Study of Factors Influencing the Strength of Glass Fibers*, T/AM-217, University of Illinois, Urbana, Illinois (1962).
8. W. Weibull, "A Statistical Theory of the Strength of Materials," *Proc. Roy. Swed. Inst. Eng. Res.*, 193/151 (1939).
9. W. Weibull, "A Statistical Distribution Function of Wide Applicability," *J. Appl. Mech.*, 18:293-297 (1951).
10. K.E. Puttick, "Ductile Fracture in Metals," *Phil. Mag.*, 4:964 (1959).
11. E. Orowan, "Fracture and Strength of Solids," *Phys. Soc. Prog. Repts. (London)*, 12:185-232 (1949).
12. C.F. Tipper, "The Study of Fracture Surface Markings," *J. Iron Steel Inst. (London)*, 185:4-9 (1957).
13. G.R. Irwin, *Relation of Stresses Near a Crack to the Crack Extension Force*. Presented at the 9th International Congress of Applied Mechanics, University of Brussels, Belgium, September 1957.
14. S.H. Smith and A.F. Liu, *Fracture Mechanics Application to Materials Evaluation and Selection for Aircraft Structure and Fracture Analysis*, D6-17756, Boeing Company, Seattle, Washington (1966).
15. A.S. Tetelman and A.J. McEvily, *Fracture of Structural Materials*, p. 137, John Wiley, New York (1967).
16. W.B. Fichter, *Stress at the Tip of a Longitudinal Crack in a Plate Strip*. Presented at the 5th U.S. National Congress of Applied Mechanics, University of Minnesota, Minneapolis, Minnesota, June 1966.
17. J.H.K. Kao, "Characteristic Life Patterns and Their Uses," W. Ireson, Ed., *Reliability Handbook*, McGraw-Hill, New York (1966).

#### REFERENCES (Continued)

18. W. Weibull, *A Criterion for the Acceptability of Assumed Distributions*, AFML-TR-69-124, Air Force Materials Laboratory, Wright-Patterson AFB, Ohio (1969).
19. J.A. Keis, H.L. Smith, H.E. Romine, and H. Bernstein, "Fracture Testing of Weldments," in *Fracture Toughness Testing and Its Applications*, ASTM-STP-381, American Society for Testing and Materials, Philadelphia, Pennsylvania (1965).
20. *Fracture Toughness and Tear Tests*, AFML-TDR-64-238, Air Force Materials Laboratory, Wright-Patterson AFB, Ohio (1964).
21. *Notch Resistance and Fracture Toughness Characteristics of High Strength Metals*, AFML-TDR-63-494, Air Force Materials Laboratory, Wright-Patterson AFB, Ohio (1963).
22. G.W. Groves and D.A. Sholl, *The Fracture Toughness of Impure MgO Crystals*, TR-2, Carnegie Institute of Technology, Dept. of Metallurgy and Materials Science, Pittsburgh, Pennsylvania (1966).
23. *Fracture Characteristics of Aluminum Alloys*, TP-18, ALCOA Research Laboratories, New Kensington, Pennsylvania (1965).

# FATIGUE AND FRACTURE OF METAL-MATRIX COMPOSITES

by

I.J. Toth

and

TRW, Inc.

K.D. Shimmin

Air Force Materials Laboratory

## I. INTRODUCTION

### 1.1 General Considerations

Composites are of interest in present day technology because they offer the opportunity to "tailor make" a material with a combination of properties that is not available in any single material. Considerable advances have been made in the development of the fabrication technology of unidirectionally-reinforced, metal-matrix composites, particularly with respect to the utilization of the high strength, high modulus filaments, such as boron and silicon carbide. Little work has been done, however, on the efficient tailoring of the laminate to specific strength and stiffness requirements. Therefore, there is a need for tailoring in the form of cross-plying in order to insure for adequate transverse properties in case of composites, such as aluminum-boron, especially at elevated temperatures for applications, such as compressor blades. Satisfactory performance in static tensile tests is frequently used as the criterion for further development of a composite system for use as a structural or semi-structural material. However, in actual service, the failure of a component is frequently determined either by its response to alternating or fluctuating stresses; i.e., fatigue, or its behavior under sustained load at elevated temperatures; i.e., creep. Therefore, prior to the acceptance of a metal-matrix composite system as a structural material for many applications, it is necessary to evaluate thoroughly the fatigue and creep characteristics of that particular system. In particular, the fatigue behavior of both unidirectional and cross-plyed composites must be thoroughly understood. Presently available data on some unidirectional composites serve not only to indicate the potential of composite materials, but also to illustrate the complexity of their behavior. From a knowledge of the factors influencing the fatigue behavior of homogeneous materials and basic principles and properties of filament reinforced materials, it is possible to predict several factors which may influence the fatigue behavior of composites. Such factors as residual stresses due to differential thermal contraction of the matrix and filament during fabrication, interfacial bond strength, stress concentrations in the matrix at in situ filament fractures, filament ends in the case of discontinuous reinforcement, and mode of deformation will be important. In addition to these, there can be several other factors with cross-plyed materials. In fabricating cross-plyed materials by hot pressing procedures, points of high pressure and deformation occur at crossover points be-

tween filaments in successive layers. Such points of close proximity of filaments raise serious questions as to the fatigue behavior of cross-plyed material.

### 1.2 Technical Background

Relatively few data have been reported in the literature on the fatigue behavior and mechanism of fatigue failure of unidirectional metal-matrix composites and practically none are found for cross-plyed composites. In a study of fatigue crack propagation in steel-wire-reinforced aluminum and tungsten wire-reinforced aluminum, Forsyth, et al.<sup>1</sup> found that the incorporation of small number of filaments suitably dispersed were capable of substantially reducing the rate of fatigue crack propagation. For this purpose, the strength of the filaments appeared to be more important than the aspect ratio (length-to-diameter.) Further, it was reported that the parallel filaments were not the most favorable orientation for increased strength. Williams and O'Brien<sup>2</sup> have demonstrated a considerable improvement in fatigue strength in reversed bending of a steel-wire-reinforced aluminum alloy composite. The influence of interfacial bonding on the fatigue behavior of a composite has been studied by Baker<sup>3</sup> who reports significant improvements in strength in the steel-aluminum composite system. Baker has also studied the effect of fiber diameter and discontinuous fibers on the fatigue of steel reinforced aluminum composite.<sup>4</sup>

In contrast to these encouraging results, Ham and Place<sup>5</sup> found that although tensile properties are improved greatly by filament reinforcement, the reinforcement of copper with continuous brittle tungsten wires up to 23 volume percent was comparatively ineffective against fatigue. The authors attribute the poor fatigue properties of these composites to fatigue hardening of the matrix at the tips of the matrix cracks, which can build up stress concentrations sufficiently large to fracture proximate filaments. Similarly, Baker and Cratchley<sup>6</sup> did not observe marked improvements in the reversed-bending fatigue life of silica reinforced aluminum. This study was complicated by the complex behavior to be expected during the compressive half-cycles imposed in this type of loading. The composite failure occurred by delamination, and a significant contributing factor was the presence of aluminum oxide at the matrix-filament interface.

Boller<sup>7</sup> has made an extensive study of the fatigue properties and failure mechanisms in "S" glass-reinforced

plastic laminates. One of the most significant findings was that laminates with alternate plies  $\pm 5^\circ$  to the load axis exhibited superior fatigue properties to those having plies parallel to the load axis.

The initial phase of the present Air Force Program at TRW was designed to contribute to a fundamental understanding of the characteristics and mechanism of failure of fiber reinforced metal-matrix composites subjected to fatigue and creep loading conditions. The objective was facilitated by studying model composite systems of tungsten-reinforced silver and steel-reinforced silver with both continuous and discontinuous aligned reinforcement. Significant increases in the tension-tension fatigue strength, comparable to the enhancement of the tensile strength, were observed by Morris and Steigerwald<sup>8</sup> in composites of silver reinforced with continuous or discontinuous aligned filaments of tungsten or steel. It was also found that the mode of failure changed markedly at approximately 12 v/o volume percent reinforcement in the tungsten-silver composite system. At less than 12 v/o, extensive random filament fractures were noted throughout the composite. In contrast, at filament loadings of greater than 12 v/o, filament fractures were only observed in the primary composite failure plane. This behavior was interpreted in terms of the stress concentrations at in situ filament fractures and the extent of overlap of such perturbations onto proximate filaments. Further, the mode of composite deformation was found to depend on the relative elastic moduli of the components. More precisely, the degree of strain in the composite, and hence the degree of plastic strain in the matrix, which for a given load decreases as the elastic modulus of the reinforcement increases with respect to the matrix modulus, controls the fatigue behavior and deformation of the matrix. In the two systems involved, tungsten-silver and steel-silver, the elastic moduli were  $56 \times 10^6$  for the tungsten,  $30 \times 10^6$  for the steel, and  $10 \times 10^6$  for the silver. These differences were manifested in the degree of matrix fatigue cracking which was significantly greater in the steel-silver system.

Limited fatigue data are available for boron-reinforced aluminum. Toy et al.<sup>9</sup> have investigated the tension-tension axial fatigue behavior of boron-reinforced X7002-T6 aluminum alloy. An appreciable increase in the fatigue strength of the alloy was noted on reinforcement with 24 v/o boron, the endurance limit for  $10^7$  cycles being 38,000 psi and 25,000 psi respectively for composite and alloy. The same authors reported significant improvements in the fatigue properties of X7002-T6 aluminum at room temperature and 500°F when reinforced with beryllium filaments. In the 500°F tests, the matrix was almost completely overaged after one hour which corresponds to approximately  $10^5$  cycles. A reverse cantilever bending technique was used by Krieder and Leverant<sup>10</sup> to determine the high cycle fatigue behavior of boron-reinforced aluminum and age-hardened 2024 aluminum matrices. Specimens were vibrated at resonance frequency. The amplitude of vibration was maintained constant, the frequency being adjusted with time

as structural changes occurred within the composite. Significant improvements in fatigue properties were again attributable to fiber reinforcement.

The fatigue behavior of continuous, aligned, boron-reinforced pure aluminum and 2024 aluminum has been investigated by Morris.<sup>11</sup> The fatigue strength of the matrix materials was observed to be improved significantly by the incorporation of boron filaments, the degree of improvement being an increasing function of volume fraction reinforcement. The fatigue strength of boron-reinforced aluminum was observed to be greater than the comparable boron-reinforced 2024-0 or 2024-T6 aluminum composites.

To date, little attention has been given to the effect of filament orientation on the tensile strength of filament reinforced metal-matrix composites. Indeed, no published data are available concerning the effect of this parameter on the time dependent mechanical behavior of composite materials.

The effect of filament orientation on tensile strength has been treated theoretically by Stowell and Liu,<sup>12</sup> and Tsai,<sup>13</sup> and Kelly and Davies.<sup>14</sup> Three possible failure mechanisms in a material reinforced with long, unidirectionally-aligned filaments are postulated, viz. filament failure, matrix failure in shear, or matrix failure in plane strain. The operative mechanism is dictated by the angle between the filament direction and the direction of applied stress.

Jackson and Cratchely<sup>15</sup> have measured the ultimate tensile strength of aluminum reinforced with silica or stainless steel filaments as a function of filament orientation. They have found a marked decrease in ultimate tensile strength at an orientation of approximately  $5^\circ$ , in agreement with theory. The use of laminated composites enabled retention of the  $0^\circ$  orientation strength to a greater off-axis angle, but to the detriment of the composite  $0^\circ$  tensile strength.

Experimental verification of the theoretical predictions has also been reported by Cooper<sup>16,17</sup> in a study of monolayer tungsten-reinforced copper composites. The tapes were fabricated by electrodeposition to ensure a weak filament-matrix bond. This was considered desirable on the basis that weakly bonded material may prove to be insensitive to sharp notches by virtue of their ability to delaminate and blunt the notch. The resultant data compared with the theoretical predictions and indicates best overall agreement with the continuous function proposed by Tsai.

The materials selected for the investigation to be reported herein were 6061 aluminum alloy reinforced with nominally 4-mil diameter boron filament. The 6061 aluminum alloy was selected as the matrix material for the following reasons: (1) The investigators as well as others had demonstrated ease of bonding of the 6061 alloy, (2) this alloy was readily available in the required thin foil form, and (3) the relatively lower work hardening characteristics

of 6061 alloy in comparison with 2024 alloy gave promise of better fatigue performance of the composite.

The anisotropy of properties of the 6061 aluminum alloy-boron composite as well as other aluminum boron composites requires some form of off-axis strengthening to improve transverse properties. This strengthening could take the form of cross-plying or matrix strengthening procedures. Initially, in this effort, cross-plying techniques were investigated. Efforts at matrix strengthening were investigated later and are reported subsequently.

## II. MODEL BORON-ALUMINUM SYSTEM-TENSILE AND FATIGUE BEHAVIOR OF 25% BORON REINFORCED 6061 ALUMINUM ALLOY

### 2.1 Selected Composite Types

The initial material selected for investigation of on and off-axis properties of unidirectional and multidirectional boron reinforced composites is considered a model boron-aluminum composite because filament loadings were kept constant at 25 nominal volume percent. This amount of reinforcement is not sufficient to make the composite attractive as a practical system, but filament loadings were maintained at a low level for two reasons: (1) The state of the art of composite technology at the start of the program was such that high quality composites could not be consistently produced at higher volume fractions and (2) in fabricating multidirectional or cross-ply composites there was no danger, at this relatively low filament content, of developing mechanical damage at filament cross-over points.

In many applications, such as compressor blades, the direction of the predominately axial peak load may fluctuate slightly, hence the use of a  $\pm 5^\circ$  cross-ply configuration may serve an advantage. In order to improve the torsional strength of potential composite components, such as shafts, torsion tubes, and compressor blades, cross-plying of the  $\pm 45^\circ$  type may well be advantageous. Therefore, multiple ply layers of these types of 6061 Al-B composites selected for this investigation are shown in Table I.

In the case of the unidirectional composite material supplied by another Air Force Contract (produced by Harvey Aluminum Co.) was also tested.

### 2.2 Composite Preparation

The most significant problem in the preparation of composite specimens is in obtaining reproducible, representative composite samples. The high-strength, high modulus boron filaments are very sensitive to mechanical damage. For the consolidation of aluminum-boron composites, the diffusion bonding technique was selected. Since the attainment of uniform alignment and separation of reinforcing filaments is necessary for high quality and reproducible composites, improved filament handling and alignment

TABLE I.  
SELECTED TYPES OF 25 v/o B-6061 A1 COMPOSITES

COMPOSITE TYPE	LOADING DIRECTION		SOURCE
		(DEGREES)	
Unidirectional	A	0	TRW
	B	5	
	C	20	
	D	45	
$\pm 5^\circ$ bidirectional	E	0	TRW
	F	15	
	G	25	
$\pm 45^\circ$ bidirectional	H	0	TRW
	I	45	

techniques were developed at the start of this program. This was achieved on a modified lathe winding machine. The 6061 Al foil was prepared by etching in a mixture of nitric and hydrofluoric acids and then scrubbing with steel wool to produce a finely scratched surface. The prepared foil, having a thickness of about 4.7 mill, was taped to the winding drum, and the filaments wound at 145 filaments-to-the-inch so as to obtain a tape containing a nominal boron volume fraction of 25 percent. In winding the filament, it was coated with a film of polystyrene-trichlorethylene solution just before it contacted the drum. After the polystyrene dries, it acts as a temporary foil-filament bond; then the tape can be removed from the drum and cut to the required size (4 x 3.75") in the desired filament orientation, without damaging the filaments or the uniformity of this alignment.

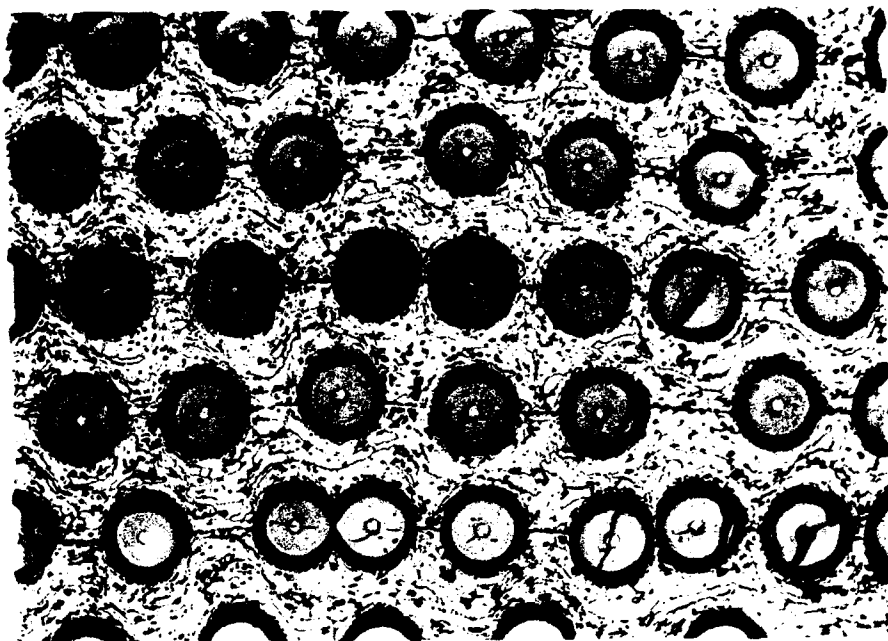
The required type of composite panels were produced by diffusion bonding a stack-up of ten monolayer filament-matrix foil tapes and a cover sheet of matrix foil. In the production of cross-ply composites alternate plies at  $\pm \theta^\circ$  to the common axis were used. The diffusion bonding was performed in the vacuum hot press where the polystyrene is allowed to volatilize before hot pressing. The bonding parameters were 975°F for 1 hour under 6,700 psi. A typical photomicrograph illustrating filament distribution of a unidirectional composite is shown in Figure 1 and that of a cross-ply composite shown in Figure 2.

The filament contents of some composite specimens were checked metallographically by area count of specimen cross-sections. The values obtained were in the range of 23.9 to 27.4 volume percent.

Some of the composites were prepared in the 0 and T6 heat treated conditions. The 0 heat treated condition was considered to be the as-hot-pressed composite state. The T6 condition was obtained by solution treating at 975°F for 1/2 hour and water quenching, followed by aging at 350°F for 8 hours.

The fabricated composites were ground, using a

Figure 1. Typical Photomicrograph of a Unidirectional Composite (Type A). Magnification 100X.



silicon carbide wheel, to the tensile specimen geometry in Figure 3. The geometry of the fatigue specimens is a modification of the tensile specimens as shown in Figure 4. It is realized in the selection of specimen configurations that the influence of specimen size on the off-axis mechanical behavior cannot be ignored. Therefore, some preliminary checks were made. In order to determine the effect of specimen width, the off-axis tensile strength was measured of a  $45^\circ$  filament oriented unidirectionally composite. Specimen widths of 0.1, 0.25, 0.5, and 1.0 inch have been tested using a constant gage length of 1.0 inch and a thickness of 0.080 inch. The tensile strength was found to increase with specimen width (20,100; 22,400; 22,800; and 23,000 psi) only very slightly.

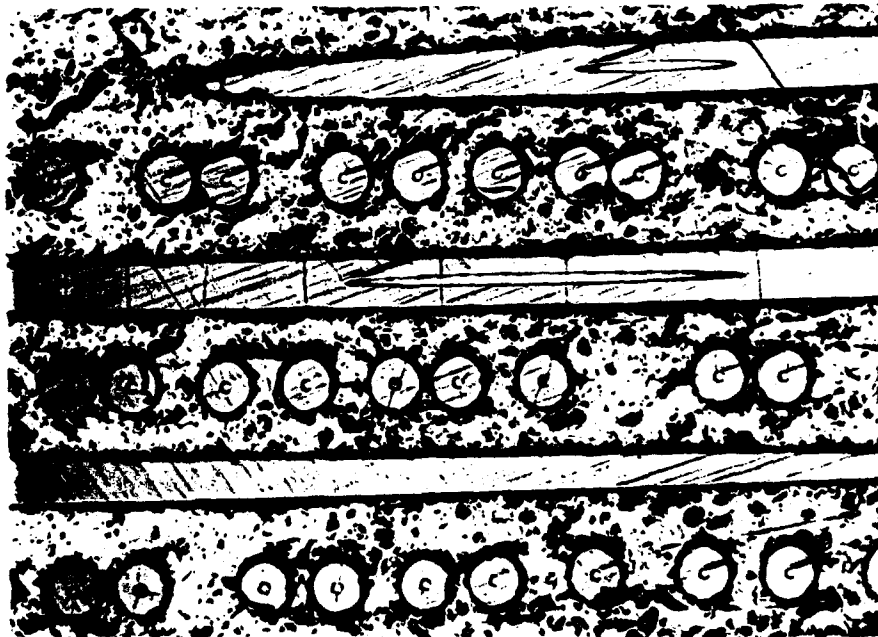
### 2.3 Testing Methods

The room temperature tensile properties of the

filaments, the unreinforced matrix, and the composite materials were determined in tests performed on an Instron testing machine at a strain rate of 0.020 - 0.040 in/in/min. To determine the static properties of boron, the filaments were epoxied into accurately aligned grooves in stainless steel tabs. A one-inch gage length was used and the modulus of elasticity was obtained by assuming that the strain in the filament could be determined from the crosshead movement of the Instron testing machine.

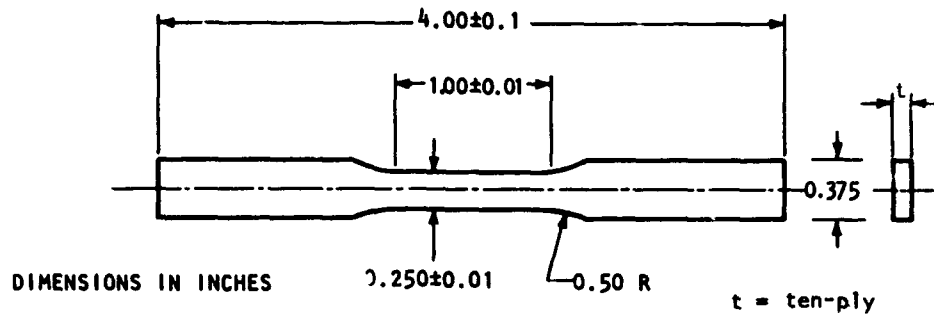
The fatigue behavior of the composite was determined in axial loading tension-tension fatigue tests performed in a standard Baldwin-Sonntag Unit (frequency 1800 cpm) under constant load conditions. A ratio of static-to-dynamic load of 3:2 is employed throughout this work, giving a sine wave loading pattern with an R factor of 0.2. The tests were conducted at stress levels such as to

Figure 2. Typical Photomicrograph of a Cross-Plied Composite (Type T). Magnification 75X.





**Figure 3. Tensile and Creep Specimen Geometry.**



establish the S/N curves to  $10^7$  cycles, using actual fracture as the failure criterion.

**2.4 Tensile Behavior of 25% Boron-6061 Aluminum Alloy Composites**

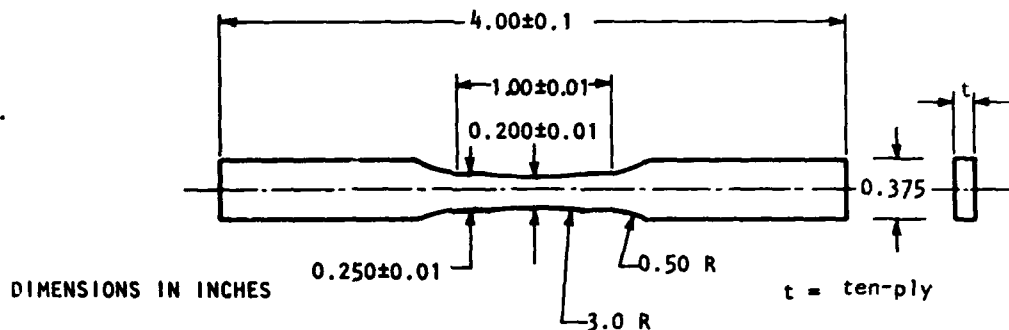
The room temperature tensile strength and elastic

modulus have been measured for all of the spools of boron filaments received from United Aircraft. Four tensile specimens were cut consecutively from the beginning of each spool. The values obtained are presented in Table II, together with the values quoted by United Aircraft. These results show that the filaments, at least at the beginning of

**TABLE II.  
TENSILE DATA FOR BORON FILAMENTS**

TEST NO.	UNITED AIRCRAFT TEST				INTERNAL TESTS		
	SPOOL DESIGNATION	DIAMETER IN.	UTS PSI	ELASTIC MODULUS PSI X $10^6$	DIAMETER IN.	UTS PSI	ELASTIC MODULUS PSI X $10^6$
1 2 3 4	S-2686	0.00400	439,000	62.6	0.0042	445,500	52.3
					0.0042	372,600	45.4
					0.0041	452,300	42.0
					0.0041	468,200	40.9
5 6 7 8	S-2687	0.00403	470,000	61.8	0.0040	463,000	46.0
					0.0040	467,000	47.6
					0.0040	299,500	48.5
					0.0040	517,100	52.7
9 10 11 12	S-2688	0.00399	436,000	60.0	0.0040	472,600	47.5
					0.0040	507,600	51.7
					0.0040	463,000	45.7
					0.0040	342,900	47.2
13 14 15 16	S-2697	0.00405	481,000	61.2	0.0042	517,000	46.0
					0.0041	501,500	47.6
					0.0042	500,400	46.0
					0.0041	501,500	47.6
17 18 19 20	S-2711	0.00405	442,000	60.0	0.0041	458,300	45.1
					0.0041	439,400	46.2
					0.0041	420,500	38.5
					0.0041	436,400	44.6
21 22 23 24	S-2712	0.00400	482,000	60.0	0.0042	488,800	44.3
					0.0042	463,500	42.5
					0.0042	480,900	43.5
					0.0042	460,600	46.0

Figure 4. Fatigue Specimen Configuration.



each spool, were of high quality. In all cases, the average filament strength was above 400,000 psi. The 6061-aluminum alloy exhibits typical mechanical properties in annealed condition of 18,000 psi ultimate tensile strength, 8,000 psi yield strength, elongation of about 25%, and a modulus of elasticity of  $10 \times 10^6$  psi. In the solution treated and aged (T6) condition, the properties are 45,000 psi ultimate tensile strength, 40,000 psi yield strength, elongation of about 12% but no change in the modulus of elasticity.

It is known that the condition of the matrix plays an important role in the behavior of the composite. Therefore, in study, the effect of filament orientation on the room temperature tensile properties of unidirectional 25

v/o B-6061 Al in both 0 and T6 conditions was determined. The results are listed in Table III and shown graphically in Figure 5. In this figure, the values of ultimate tensile strength as a function of filament orientation are superimposed on the predicted curves that were calculated using the analyses given by Kelly and Davies.<sup>14</sup> It can be seen that the "as-pressed" material follows closely the predictions whereas the "solution-treated-and-aged" composite appears to have very low efficiency of reinforcement. It is known that a complex stress state can develop in the matrix on cooling from the fabrication and/or solution treating temperature.<sup>18</sup> This is mainly due to the large difference in the thermal expansion coefficients of the two component materials - 16.0 micro-in/in/ $^{\circ}$ F for aluminum<sup>19</sup> and only

Figure 5. Effect of Heat Treatment on Off-Axis Tensile Strength of 25 v/o B-6061 A1 Unidirectional Composite.

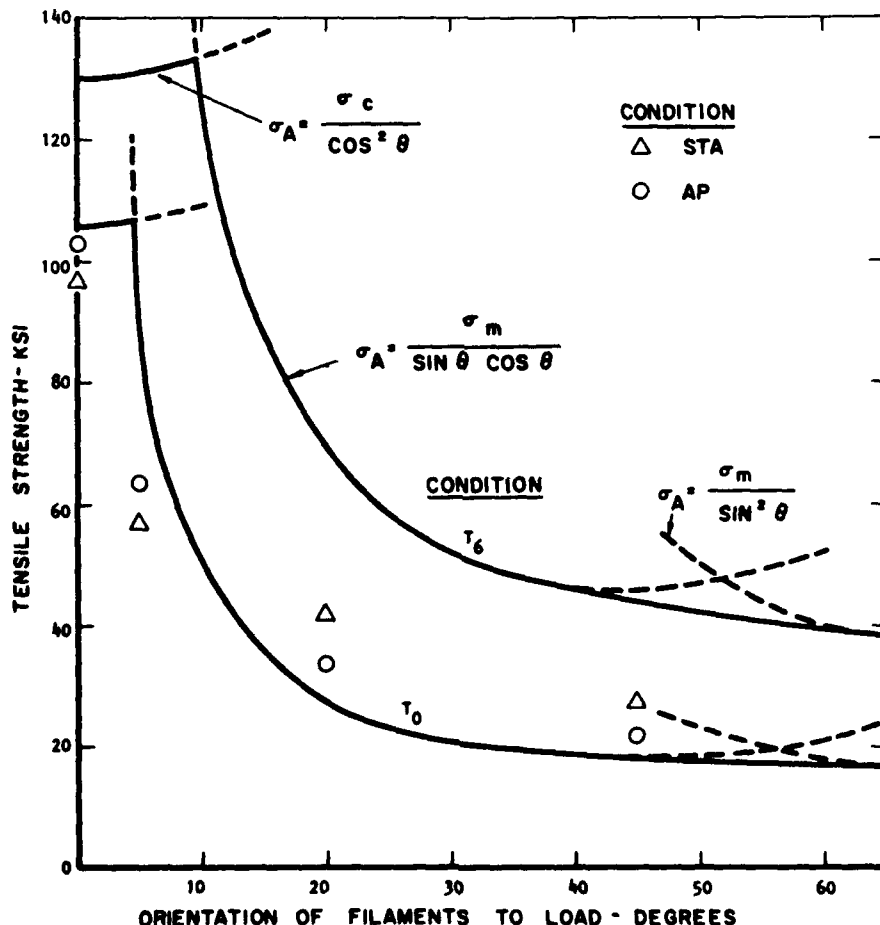


**TABLE III.**  
**EFFECT OF HEAT TREATMENT ON THE TENSILE BEHAVIOR**  
**OF 25 V/O B-6061AL UNIDIRECTIONAL COMPOSITE**

Sp. No.	(A) Condition	Tension Filament Axis (°)	ACTUAL				PREDICTED (B)		σ <sub>m</sub> ' at Failure Strain KSI (C)
			UTS KSI	0.2 YS KSI	Strain to Failure in./in.	E 10 <sup>6</sup> PSI	UTS KSI	E 10 <sup>6</sup> PSI	
1A-3	AP	0	100.2	-	0.0055	19.8			
1A-4	AP	0	100.0	-	-	23.4			
1A-7	AP	0	108.7	-	0.0062	19.2			
4A-4	AP	0	106.5	-	-	21.9			
(AVG)			103.9			22.1	106.0	22.5	
1A-1	STA	0	100.9	-	0.0065	16.6			
1A-2	STA	0	95.5	-	-	21.4			
(AVG)			98.2			19.0	130.0	22.5	
1B-3	AP	5	66.3	63.4	0.0106	21.6			
1B-4	AP	5	59.9	-	-	21.4			
(AVG)			63.1			21.5	88.0	12	
1B-1	STA	5	60.5	57.1	0.0045	27.0			
1B-2	STA	5	54.5	-	-	17.5			
(AVG)			57.5			22.2	131.0	40	
1C-3	AP	20	32.3	19.8	0.0226	16.0			
1C-4	AP	20	35.2	-	-	16.9			
(AVG)			33.8			16.4	27.0	14	
1C-1	STA	20	44.8	37.2	0.0094	19.4			
1C-2	STA	20	45.6	-	-	21.2			
(AVG)			44.2			20.3	70.0	40	
1D-3	AP	45	22.7	-	-	11.3			
1D-4	AP	45	20.9	13.4	0.0838	11.1			
(AVG)			21.8			11.2	18.0	18	
1D-1	STA	45	27.8	22.7	0.0280	12.5			
1D-2	STA	45	28.6	-	-	9.4			
(AVG)			27.2			10.9	44.0	40	

(A) AP = As pressed  
 STA = 975°F, 1/2 Hr. - H<sub>2</sub>O Quench  
 + 350°F, 8 Hrs - Air Cool

(B) Based On: σ<sub>f</sub> = 400 ksi;  
 σ<sub>m</sub>' (AP) 6061 Al = 8-18 ksi (see Table)  
 σ<sub>m</sub>' (STA) 6061 Al = 40 ksi  
 E<sub>f</sub> = 80 x 10<sup>6</sup> psi  
 E<sub>m</sub> = 10 x 10<sup>6</sup> psi

(C) Estimated

T<sub>m</sub> (AP) 6061 Al = 12 ksi  
 T<sub>m</sub> (STA) 6061 Al = 30 ksi

Using the analysis of Kelly and Davis (20)

2.7 micro-in/in/°F for boron.<sup>20</sup> Thus, on cooling, the aluminum matrix in the composite tends to contract about six times as much as the boron. The boron filaments resist this contraction producing tensile strain, and a corresponding tensile stress, parallel to the filaments in the aluminum. Under certain conditions of cooling rate, it is con-

ceivable that the peak residual stress intensity may be sufficiently high that plastic yielding will occur in the matrix on cooling. Shimezu, et al.,<sup>21</sup> proposed that this residual stress effect, which promotes early matrix yielding on loading, also limits the total strain capacity of the composite and produces composite fracture at a strain

below the basic fracture strain of the reinforcing filaments. The magnitude of the residual stresses will be higher in the solution-treated condition due to the faster cooling rate employed. Thus, the large residual stresses present in the matrix make the latter appear unresponsive to conventional heat treatment. Therefore, because of the lack of a suitable heat treatment schedule for composites of this type, only "as-pressed" composites, having a more predictable behavior, were studied initially.

As a prerequisite to fatigue testing and also as a means of composite quality check, the tensile behavior of the various types of 25 v/o B-6061 Al composites were determined. The tensile results at both ambient and elevated temperatures for the unidirectional (U-D) composites are presented in Table IV. The room temperature strength and modulus measurements of the 0-degree composite indicated a calculated filament stress at failure of approximately 390,000 psi, and a rule of mixture modulus. These values characterize the composites were of reasonably high quality in the light of the state-of-the-art in Al-B composite fabrication.

The experimental off-axis strength values are superimposed, in Figure 6, on the predicted strength curve which was calculated from Tsai's equation. This equation for prediction of unidirectional composite strength as a function of filament orientation is as follows:

$$\frac{1}{(\sigma_1)^2} = \frac{m^4}{X^2} + \frac{(1-m^2)^2}{(S^2 - X^2)} + \frac{n^4}{Y^2}$$

Where:  $\sigma_1$  = composite strength at angle ( $\Theta$ ) filament orientation

X = composite strength at 0° filament orientation

Y = composite strength at 90° filament orientation

S = ultimate shear strength of matrix

m = Cos  $\Theta$

n = Sin  $\Theta$

The experimental values are in very good agreement

TABLE IV.  
TENSILE BEHAVIOR OF 'AS PRESSED'  
25 V/O B-6061 Al UNIDIRECTIONAL COMPOSITE

SP. NO.	ORIENTATION AXIS (°)	TEST TEMP. °F	UTS KSI	0.2% YS KSI	STRAIN TO FAILURE IN./IN.	MODULUS E 10 <sup>6</sup> PSI
1A-3	0	75	100.2	-	0.005	19.8
1A-4	0	75	100.0	-	-	23.4
1A-7	0	75	108.7	-	0.006	19.2
4A-4	0	75	106.5	-	-	21.9
5A-3	0	400	82.8	-	0.006	19.7
4A-6	0	400	89.0	-	0.006	22.9
1A-5	0	600	80.4	-	0.004	16.0
4A-7	0	600	78.7	-	0.005	13.5
1B-3	5	75	66.3	63.4	0.010	21.6
1B-4	5	75	59.9	-	-	21.4
2B-1	5	400	76.2	-	0.007	13.6
2B-7	5	400	84.1	-	0.006	15.7
2B-3	5	600	61.8	61.1	0.009	12.5
1B-9	5	600	Grip Failure	-	-	-
1C-3	20	75	32.3	19.8	0.023	16.0
1C-4	20	75	35.2	-	-	16.9
1C-5	20	400	33.4	27.8	0.032	13.9
1C-7	20	400	29.8	25.6	0.013	12.5
3C-4	20	600	12.0	11.0	0.090	8.6
3C-5	20	600	12.9	12.0	0.080	9.4
1D-3	45	75	22.7	-	-	11.3
1D-4	45	75	20.9	13.4	0.084	11.1
1D-5	45	400	16.0	13.1	0.054	11.2
1D-8	45	400	16.2	13.1	0.105	9.3
2D-5	45	600	8.5	7.9	0.055	8.9
2D-7	45	600	10.6	8.1	0.085	7.8
1V-2	90	75	14.7	13.4	0.087	11.8
1V-5	90	75	14.9	14.0	0.081	-

TABLE V.  
TENSILE BEHAVIOR OF PANEL HA-328 - 25 V/O B-6061 AL UNIDIRECTIONAL COMPOSITE

SP. NO.	ORIENTATION AXIS, DEGREE	UTS KSI	0.2% Y.S. KSI	STRAIN TO FAILURE, IN/IN	MODULUS, E 10 <sup>6</sup> PSI
J-3	0	44.8	-	0.0035	24.1
J-6	0	47.5	-	0.0043	22.9
J-9	0	48.5	-	0.0046	16.5
K-3	5	45.9	-	0.0041	27.8
K-5	5	43.9	-	0.0046	16.3
K-7	5	45.0	-	0.0039	25.6
L-2	20	30.5	24.4	0.0144	17.2
L-9	20	31.1	24.5	0.0126	13.9
M-2	45	22.8	13.7	0.1480	11.5
M-6	45	22.3	14.4	0.1250	10.7
W-1	90	15.4	13.4	0.0091	12.8
W-3	90	15.4	13.6	0.0096	8.6

with the predicted curve, except the 5° orientation (type B) which shows appreciably lower than predicted values. In connection with this, it is interesting to note that this latter composite type has a higher tensile strength at 400°F than at room temperature. Since this "strengthening" phenomenon was not observed in the case of the other types of com-

posites investigated thus far, it suggests that the residual stresses in this type (B) composite have the most severe effect on properties. As the filament orientation decreases from 45 to 0 degrees the aluminum matrix is strengthened from 18 to 570 percent at room temperature and from 220 to about 2000 percent at 600°F. In other words, the

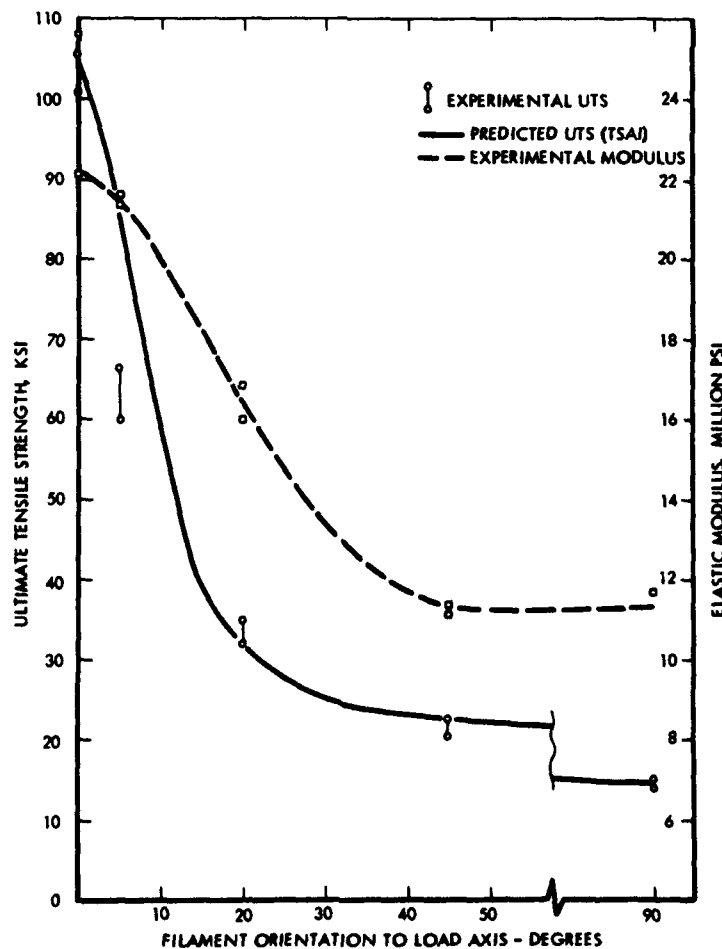


Figure 6.  
Correlation of  
Off-Axis Tensile  
Values with  
Predicted  
Curve Using  
Tsai Analyses.

extent of reinforcement is more pronounced at higher temperatures.

For the purpose of comparison, the room temperature tensile behavior of a 25 v/o B-6061 Al unidirectional composite supplied by the Government (panel HA-328 from Harvey Aluminum Co.) is summarized in the 0- 5- 20- 45- and 90- degree filament orientations in Table V. In the 0- and 5- degree orientations, where the filaments control the composite tensile behavior, the strength and fracture strain values are significantly lower than was found for similar composites (Table IV) which were fabricated at TRW. Strength and modulus measurements of the 0- degree composites at room temperature indicate a calculated filament strength utilization of only about 150,000 psi for the HA-328 panel as compared to about 390,000 psi for the TRW-fabricated composites. As can be expected at 20- 45- and 90- degree orientations, where the matrix controls the composite behavior, there is negligible difference in properties between the composites from the two sources.

The tensile behavior of the cross-ply (C-P), or laminated, composites is presented in Table VI. In comparing the fracture surface of Figures 7a and 7b, it can be seen that cross-plying has changed the fracture mode from pure shear of the matrix along the filament axis to predominately plane tensile failure of both matrix and filament. Therefore, it must be noted that the elongation values measured for the 1-inch gage length of the 45° U-D and ± 45° C-P specimens are not really comparable. In the first case, the shear failure of the matrix was preceded by a very highly

localized plastic deformation, whereas in the latter case, the predominately tensile failure was preceded by a rather uniform deformation throughout the gage length, mostly because filament rotation could take place in a balanced manner without causing specimen misalignment.

It is interesting to note in Figure 8 that the fracture mode of the 20-degree unidirectional (type C) composite is progressively changing from simple tensile at room temperature, to shear plus tensile at 400°F, and to pure shear at the test temperature of 600°F. Similarly in Figure 9, the fracture mode of the 5-degree unidirectional (type B) composite is shown to have changed from simple tensile to predominately shear failure. However, by using this same filament orientation in an alternating cross-ply (± 5°) configuration (composite type E), the fracture mode remains at all test temperatures predominately tensile in nature.

In summary, the tensile results of these composites were as anticipated. In the case of unidirectional composites, the angle of the filament from the load axis at which the failure mode changes from tensile to shear becomes progressively smaller with increasing test temperature, because the shear strength of the matrix is decreasing. However, in the case of cross-plyed composites where the previously operative shear path is reinforced with filaments, failure is restricted to be mainly tensile in nature. This restricted fracture path results in a rather extensive elongation of the specimen during tensile straining when accompanied by a large degree of filament rotation.

TABLE VI.  
TENSILE BEHAVIOR OF 'AS PRESSED' 25 V/O B-6061 Al CROSS-PLY COMPOSITE

SP. NO.	TYPE	TENSION TO FILAMENT COMMON AXIS (°)	TEST TEMP. °F	UTS KSI	0.2 YS KSI	STRAIN TO FAILURE IN./IN.	MODULUS E 10 <sup>6</sup> PSI
2E1	± 5° Cross-Ply	0	75	79.9	-	0.005	21.1
2E5		0	75	75.1	-	0.005	21.8
2E2		0	400	66.1	-	0.008	15.4
2E7		0	400	72.9	-	0.007	18.3
1E1		0	600	61.5	-	0.006	15.1
2E6		0	600	63.4	-	0.005	11.7
2F-1		15	75	37.5	-	0.014	18.8
2F-5		15	75	41.8	-	0.007	18.7
1G-4		25	75	25.0	20.2	0.013	15.2
1G-8		25	75	28.0	17.5	0.016	
2H-4	± 45° Cross-Ply	0	75	18.9	12.7	0.043	12.0
2H-7		0	75	19.3	13.1	0.050	10.9
1H-2		0	400	15.8	9.5	0.210	8.4
2H-6		0	400	15.7	11.2	0.150	9.6
2H-2		0	600	10.6	8.1	0.280	9.2
2H-5		0	600	8.5	7.2	0.310	8.9
1T-6		45	75	58.2	35.4	0.011	16.0
1T-7		45	75	64.1	44.1	0.011	18.6

**Figure 7. Comparing Tensile Fracture Surfaces of (a) 45° U-D, and (b) and (c) ± 45° C-P Composites, Tested at RT, and at 600°F.**



**(a) R.T.**



**(b) R.T.**

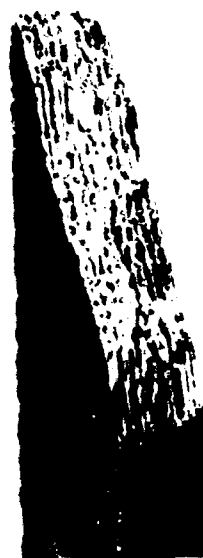


**(c) 600°F**

**Figure 8. Effect of Test Temperature on Tensile Fracture Mode of 20° U-D (type C) Composite.**



**(a) R.T.**



**(b) 400°F**



**(c) 600°F**

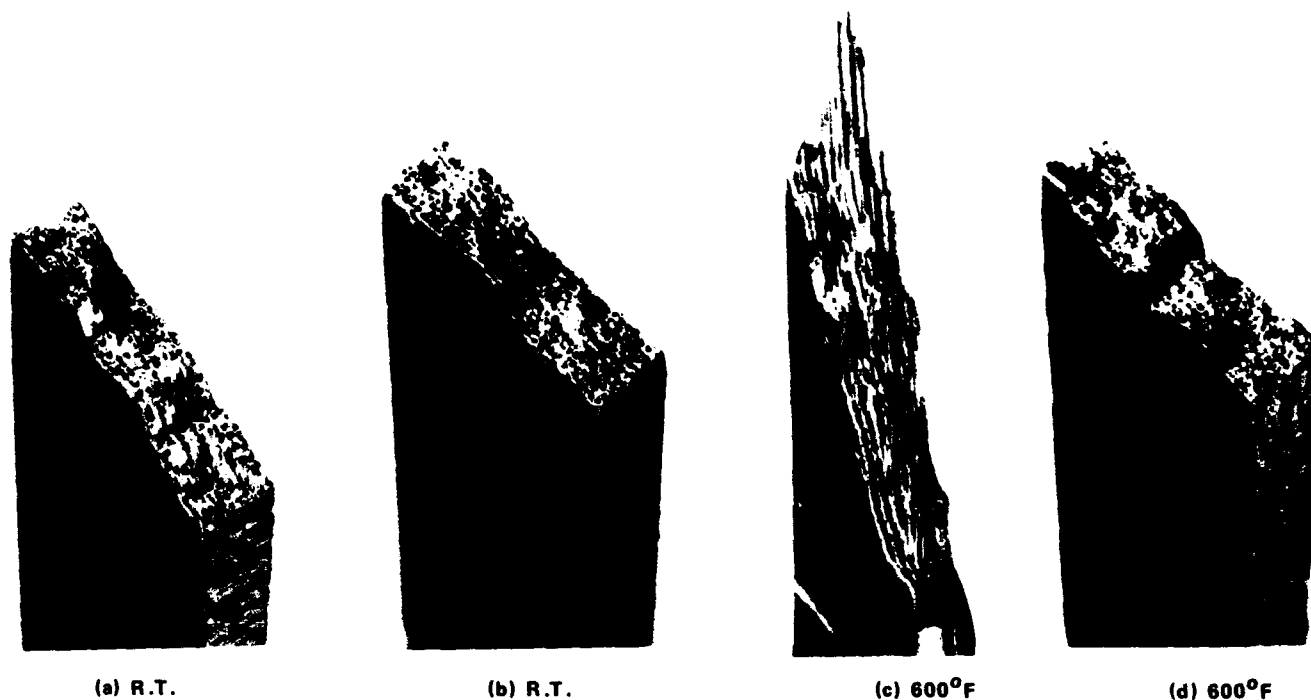


Figure 9. Comparing Tensile Fracture Surfaces of (a) and (c)  $\pm 5^\circ$  C-P with (b) and (d)  $5^\circ$  U-D Composites at Two Test Temperatures.

TABLE VII.  
FATIGUE BEHAVIOR OF TRW'S 25  
V/O B-6061 AL UNIDIRECTIONAL COMPOSITES

FILAMENT ORIENTATION	CODE	MAX. STRESS PSI	NO. OF CYCLES TO FAILURE $\times 10^3$
$0^\circ$	4A8	74,000	49
	4A5	70,000	244
	3A2	66,000	3,884
	1A11	63,000	10,008*
	1A6	62,000	10,104*
$5^\circ$	6B4	55,000	67
	6B6	52,000	134
	6B7	51,000	380
	2B4	50,500	3,511
	2B5	50,000	10,072*
	2B8	48,000	10,014*
$20^\circ$	3C1	28,000	42
	3C7	27,500	89
	3C6	27,000	456
	3C8	26,500	6,769
	3C2	26,000	10,184*
$45^\circ$	2D3	20,000	9
	3D3	18,000	104
	2D1	17,000	1,820
	3D7	16,000	10,660*

\* Terminated Prior to Failure.

## 2.5 Fatigue Behavior of 25% Boron-6061 Aluminum Alloy Composites

The results of the fatigue behavior investigation on 25 v/o B-6061 Al composites under conditions of axial tension-tension loading using an R factor of 0.2 are summarized in Tables VII, VIII, and IX. It is interesting to note in Figure 10, where the present S/N curve is compared to S/N curves obtained in the prior investigation for  $0^\circ$  unidirectional composites, that the 6061 Al matrix composite has the highest endurance limit.

Morris<sup>11</sup> suggested that the reason for the higher fatigue strength of the 1100-Al over the 2024-Al matrix composite may be found in the difference of work hardening characteristics of the two matrices. The higher work hardening rate of 2024-Al is assumed to be related to higher failure in the 2024-Al composite. Alloy 6061-Al, having a lower work hardening rate, was thus selected over 2024-Al as a matrix material. It is therefore argued that the superior fatigue strength of the 6061-Al matrix composite is associated with its lower work hardening rate. However, it must be noted that the latter composite has also shown a significantly higher tensile strength. This cannot be related to a difference in work hardening characteristics, but is a direct result of improved composite fabrication techniques. In this case, the degree of enhancement in fatigue behavior is, therefore, more meaningful when the results are con-



**TABLE VIII.**  
**FATIGUE BEHAVIOR OF HARVEY'S 25**  
**V/O B-6061 AL UNIDIRECTIONAL COMPOSITES**

FILAMENT ORIENTATION	CODE	MAX. STRESS PSI	NO. OF CYCLES TO FAILURE x 10 <sup>3</sup>
0°	1J2	43,000	21
	1J10	42,500	9
	1J8	42,000	130
	1J4	41,000	770
	1J1	40,000	10,389*
5°	1K10	39,000	3
	1K9	38,000	55
	1K1	37,500	5,191
	1K4	37,000	9,999
20°	1L4	30,000	5
	1L7	29,000	111
	1L1	28,000	4,547
	1L10	27,000	10,035*
45°	1M3	20,000	10
	1M5	19,000	98
	1M1	18,000	173
	1M8	17,000	1,459

\* Terminated Prior to Failure.

sidered in terms of the ratios of endurance limit (at 10<sup>7</sup> cycles) to ultimate tensile strength. These ratios were obtained as 0.63, 0.76, and 0.42 for 6061-Al 25 v/o B, 1100-Al 25 v/o B, and 2024-Al 20 v/o B respectively.

The results of the fatigue investigation of some unidirectional and cross-plyed specimens are presented for comparison in Figure 11. It can be seen that the fatigue behavior of these composites are characterized by a rather flat S/N curve. In comparing the unidirectional and the

**TABLE IX.**  
**FATIGUE BEHAVIOR OF TRW'S 25**  
**V/O B-6061 CROSS-PLYED COMPOSITES**

Specimen Type	Tension to Filament Common Axis (°)	Code	Max. Stress Psi	No. of Cycles to Failure x 10 <sup>3</sup>
± 5° Cross-Ply	0	1E4	60,000	52
	0	2E3	57,000	154
	0	2E4	56,000	258
	0	1E5	56,000	309
	0	1E6	55,000	4,409
	15	2F8	33,000	28
	15	1F5	32,000	84
	15	1F3	31,000	1,873
	15	2F4	30,000	11,080*
	25	1G3	21,000	12
	25	1G2	20,000	99
	25	1G5	19,000	439
± 45° Cross-Ply	25	1G9	17,500	11,312*
	0	3H4	19,000	8
	0	1H7	18,000	414
	0	3H3	17,000	7,829
	0	2H1	16,000	10,012*
	45	1T1	46,000	50
	45	1T2	46,000	73
	45	1T3	45,000	133
	45	1T4	43,000	172
	45	1T5	40,000	106
	45	1T9	38,000	4,801

\* Terminated Prior to Failure.

cross-plyed composites at 5 and 45 degree filament orientations to the load axis, it is evident that at 25 v/o reinforcement the anticipated higher than normal stress field at fila-

**Figure 10. Effect of Matrix on the Fatigue Property of B Reinforced Unidirectional Composites.**

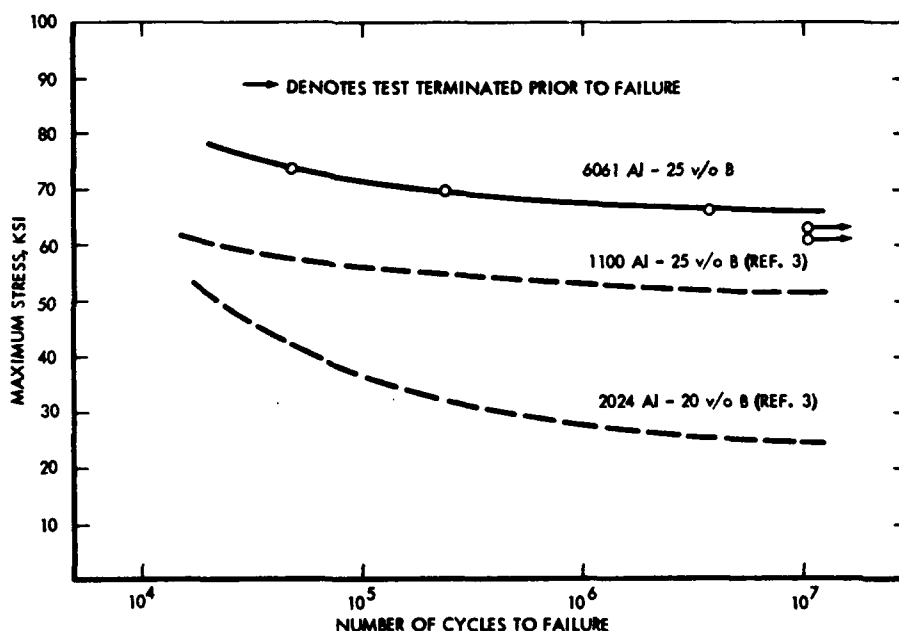
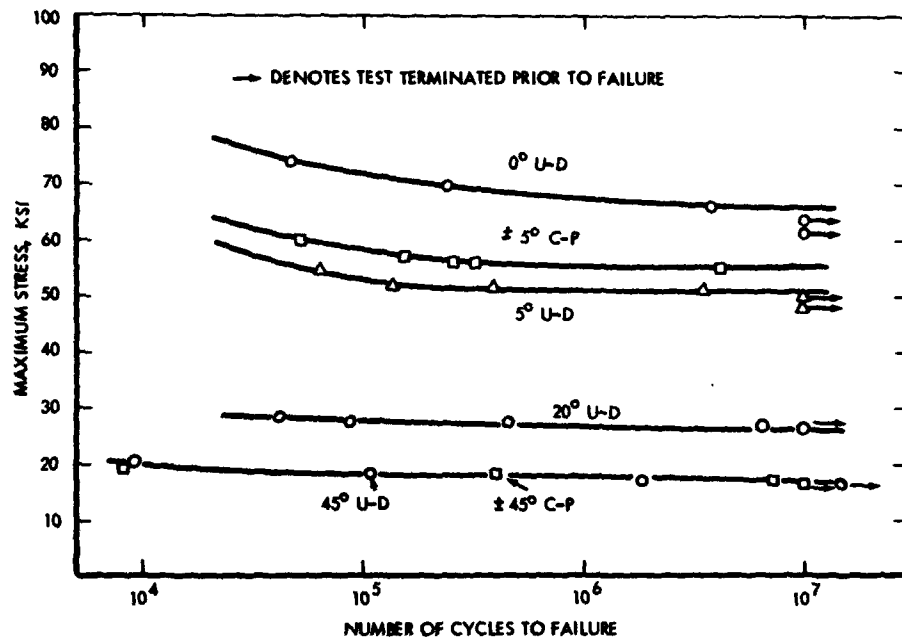


**Figure 11.**  
**Fatigue Data**  
**for Unidirectional**  
**(U-D) and Cross-**  
**Plyed (C-P) 6061**  
**AL-25 v/o B**  
**Composites.**



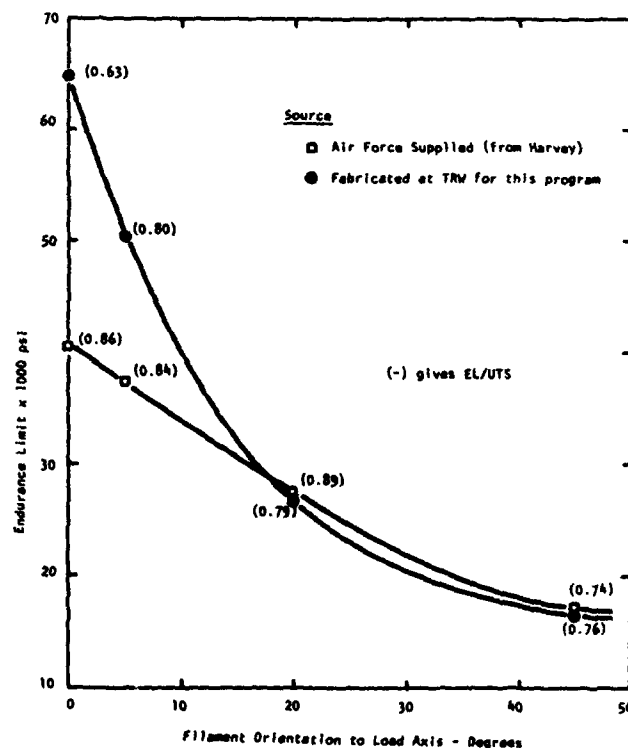
ment crossover points have no detrimental effect on composite fatigue behavior.

The effect of off-axis loading on the endurance limits ( $10^7$  cycles) with respect to filament direction is presented for two sources of unidirectional composites in Figure 12, for orientations of 0, 5, 20, and 45 degrees. The ratios of endurance limit to ultimate tensile strength are given in parentheses. These ratios, being in the range of 0.63 to 0.80 for the TRW material and 0.74 to 0.89 for the

Harvey material, show no significant trend with filament orientation. In fact, the effect of off-axis loading on the fatigue behavior of boron reinforced aluminum is similar to that noted for their tensile properties.

A comparison of endurance limits of unidirectional and cross-plyed 25 v/o B-6061 Al is shown in Figure 13. In considering the off-common-axis behavior of the cross-plyed composites it must be pointed out that they are not comparable directly to the off-axis behavior of unidirectional

**Figure 12.**  
**Fatigue Endurance**  
**Limits as a Function**  
**of Filament**  
**Orientation of Two**  
**Sources of**  
**Unidirectional**  
**25 v/o B-6061 AL.**



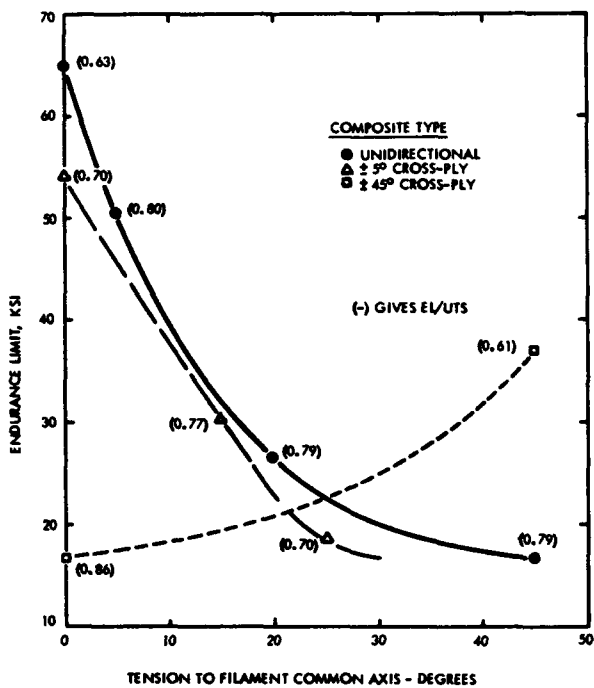


Figure 13. Comparison of Endurance Limits of Unidirectional and Cross-Plied 25 v/o B-6061 AL Composites.

composites, since in the first case, there are two filament orientations each of which represents 12.5 v/o B, and, in the second case, all of the 25 v/o B filaments are in one direction. Thus, it appears from Figure 13, that the fatigue characteristics of say the  $\pm 5^\circ$  C-P material, when tested at 25 degrees to the common axis, is inferior to the unidirectional composite that is tested at a similar off-axis angle. But in case of this cross-plied material, it is only the 12.5 v/o B which is actually at 20 degrees to the load axis that probably controls its load bearing behavior.

A better appreciation of the effect of cross-plying can be obtained in comparing the fatigue fracture surfaces in Figure 14 of two typical cross-plied composites with their corresponding unidirectional partners. It can be clearly seen that even at  $5^\circ$  filament orientation, the fracture mode of the unidirectional material contains some areas of shear failure, whereas the cross-plied material fails entirely in tension. The difference in failure mode, as expected, is more pronounced at 45 degree filament orientation, where the unidirectional composite fails by fatigue cracking and shear within the matrix parallel to the filament direction, whereas in the cross-plied material the fracture path appears to be tensile in nature. The fracture paths of some fatigue-tested specimens are shown in Figure 15 in direct relation to filament orientation. Specimen type A ( $0^\circ$  U-D) shows a typical fatigue fracture path where filament fracture is the controlling failure mechanism. Specimen type G ( $\pm 5^\circ$  C-P) was tested at 25 degrees to the

common axis. This specimen together with the 20-degree unidirectional specimen (not shown here) indicates that even at a filament orientation of 20 degrees the failure mode is basically matrix fatigue and shear failure. In the case of cross-plied materials, however, the fracture path must run through one-half of the filaments in the specimen cross-section. Specimen type H ( $\pm 45^\circ$  C-P) shows, adjacent to the fracture surface, some filament rotation towards the load axis. Specimen type D ( $45^\circ$  U-D) indicates failure of the matrix parallel to the filament direction, but closer examination of this under the optical microscope reveals that some filament fracture has also occurred.

In an attempt to find differences in the mechanism of filament fracture under various test conditions, the fracture surface of a number of tensile, fatigue, and creep tested specimens, having lower than 20-degree filament orientation to the load axis, were examined metallographically focusing on the filaments themselves. Basically four types of filament fracture modes were observed. These are shown in Figure 16 as having origins of fracture at: (a) The filament surface, (b) the boron-tungsten core interface, (c) an inclusion in the boron, (d) and the site of a pre-existing crack. At first it is thought that filament fracture mode type (a) is a typical fatigue fracture until it was found to exist in tensile and creep tested specimens as well. In a qualitative way, the degree of occurrence of the various filament fracture modes under tensile or fatigue loading conditions is given below.

TYPE OF FRACTURE	a	b	c	d
TENSILE	few	some	MANY	few
FATIGUE	SOME+	some	some +	none

Thus there is a definite indication that filament fracture mode type (a) is mainly found in fatigue and type (c) is mainly found in tensile tested composites. However, the difference in their occurrence is too small, as well as their distribution over the fracture surface is too random, to allow the conclusion that the filaments really fracture by a different mechanism under the different testing conditions. The metallographic investigation of these composite fracture surfaces, therefore, suggests that under the conditions studied, the filaments have fractured basically in a tensile manner. But this then implies that boron filaments are not susceptible to fatigue damage. If the filaments are not susceptible to fatigue damage and if they control the fatigue behavior of the composite, a horizontal S/N curve may be anticipated. However, if it is assumed that the matrix relaxes in cyclic loading so that its contribution to fatigue strength can be completely disregarded, the endurance limit for the 25 v/o B-6061 Al ( $0^\circ$  U-D) composite should still be 97,000 psi (which is 25 percent of the filament strength utilization found in tensile). The actual endurance limit of this composite, however, is only 65,000 psi. It is therefore obvious that the matrix has a significant effect on the fatigue behavior of this composite, even when tested para-

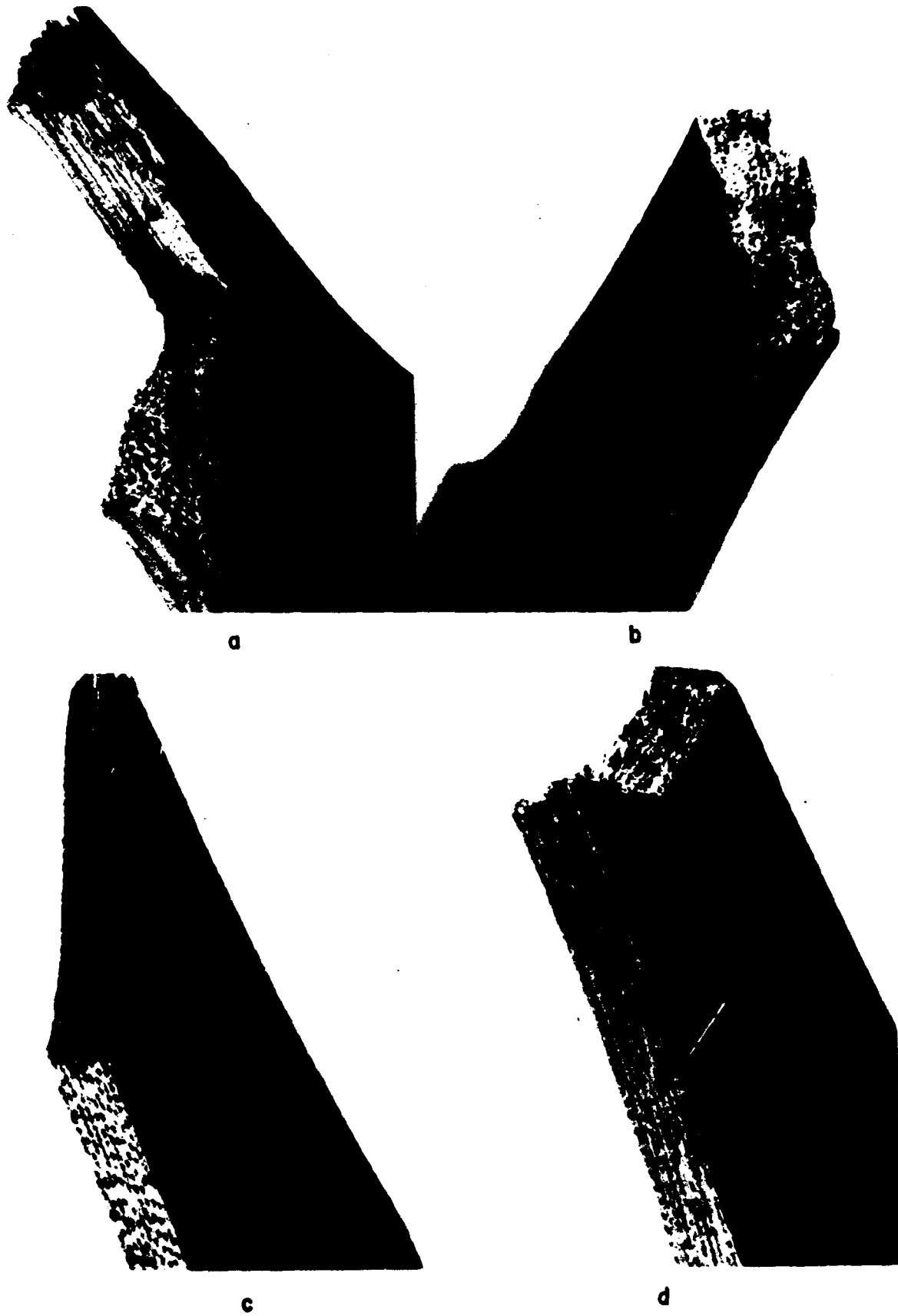


Figure 14. Comparing Fatigue Fracture Surfaces of (a) 5° U-D, (b) ±5° C-P, (c) 45° U-D, and (d) ±45° C-P.

lled to the filament direction.

In the light of the above discussion, it is pertinent to consider the fatigue behavior of the unreinforced matrix. The endurance limit at  $10^7$  cycles of the 6061 aluminum matrix, using an R factor of 0.2, is about 16,000 psi in the T-0 condition, and about 30,000 psi in the T6 condition. For this investigation, the matrix has not been heat treated and, hence, it is assumed to be in the T-0 condition. Actually, the ultimate tensile strength of an 11-layer diffusion-bonded (under similar conditions used for the composite) 6061 foil was found to be 22,000 psi which is somewhat higher than expected for annealed material. Nevertheless, using the endurance limit of 16,000 psi and the tensile strength of 22,000 psi gives an endurance/tensile ratio of about 0.73 for the matrix material. It is interesting to note that this value is very close to the ratios shown in Figure 13 for the composite materials, despite the high internal stresses known to exist in the composite. The closeness of these ratios suggests that the matrix controls the fatigue behavior

of the composite. No evidence, however, was found for extensive fatigue damage in the aluminum matrix, as shown in Figure 17 for a  $0^\circ$  U-D composite.

Some interesting observations were recently presented by Cooper<sup>16,17</sup> on the fracture toughness of metal matrix composites. Most relevant was the observation that in a composite of copper reinforced with brittle tungsten filament, cracking occurs only in the filaments. The mechanism of failure postulated is that the crack propagating in the filament is arrested at the filament-matrix surface. However, as a result of redistribution of the load in the composite, the stress concentration in the matrix at the point of filament fracture is sufficient to cause fracture of the next filament immediately ahead of the existing line of filament breaks. Thus, the crack advances through the composite by bridging the matrix and breaking only filaments as it propagates. This mechanism is directly applicable to the situation arising during the fatigue of boron reinforced aluminum composites but there is one important exception.

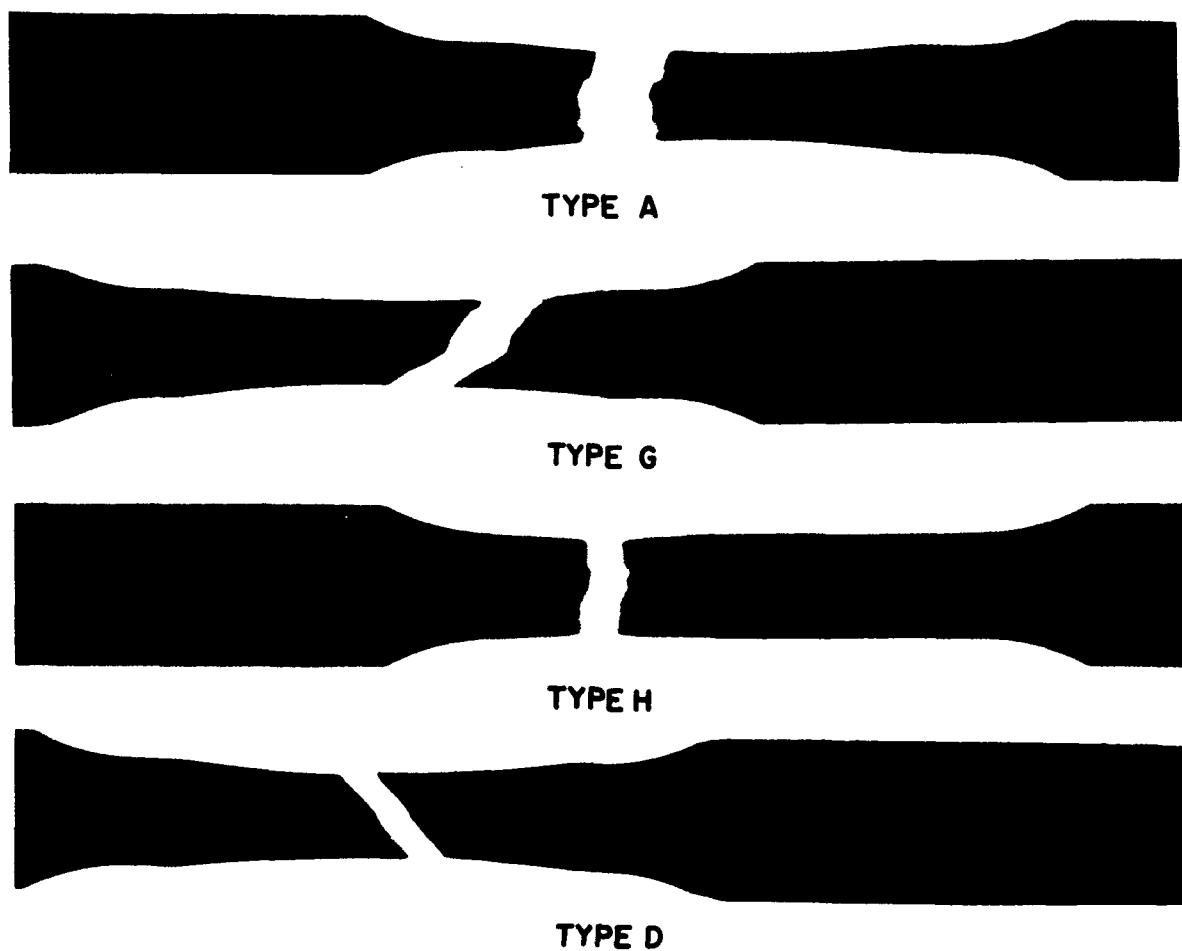
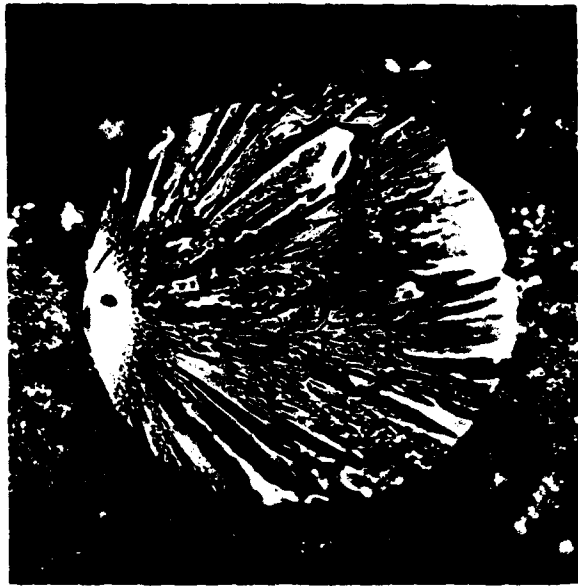


Figure 15. Radiography of Some Fatigue Tested 25 v/o B-6061 A1 Composites.



Type (a) Fracture Originates at Filament Surface.



Type (b) Fracture Originates at B/W Core Interface.



Type (c) Fracture Originates at An Inclusion.



Type (d) Fracture Originates at Site of Preexisting Crack.

Figure 16. Typical B Filament Fracture Surfaces in a 6061 AL Matrix. 500X.

The exception is that the boron filaments fracture not by a fatigue mechanism, and hence, as shown in Figure 17, the filament breaks are not lined up as in the copper-tungsten system.

In Figure 18, the photomicrograph of a fatigue tested 0-degree unidirectional composite shows that the matrix can work harden to the extent that in certain areas, it even reaches its fatigue limit. The fact that very few such matrix fatigue cracks are observed in the composites indi-

cates that such an extent of matrix fatigue hardening is not necessary to build up sufficient stress concentrations to fracture proximate filaments.

In summary of the above discussions, it was tentatively suggested that failure, for a 0-degree of low angle 25 v/o B-aluminum composite under tension-tension cyclic loading, occurs in the following manner:

1. Initial filament fracture arises from basically

Figure 17.  
Photomicrograph  
of a  $0^\circ$  U-D  
Composite adjacent  
to Fatigue Fracture.  
100 X.



three sources: (a) Filament breaks developed during composite fabrication, (b) filament fragmentation near the surface during specimen preparation by grinding, and (c) initial filament breaks occurring at points of weakness during actual fatigue loading.

2. Stress concentrations in the matrix resulting from above filament breaks grow in magnitude with time under cyclic loading as a result of matrix work hardening and some fatigue damage.

3. Cracks initiate at matrix-filament interface at

site of proximate filaments when magnitude of stress concentration is high enough. The stresses involved are higher for matrices having higher work hardening rate, and hence result in earlier crack initiation.

4. The nucleated cracks propagate by a shear mechanism along matrix-filament interface to a point where the existing stress level exceeds the filament tensile fracture stress and results in filament fracture.

This failure mode of fracturing proximate filaments can continue in a localized plane until the effective compo-

Figure 18.  
Photomicrograph  
of a Fatigue  
Tested  $0^\circ$  U-D  
Composite Showing  
that the Matrix at  
Certain Areas has  
Reached its Fatigue  
Limit. 250 X.



site area in that plane is reduced enough for composite tensile failure to occur.

Having postulated that the matrix was the controlling element in determining the fatigue behavior of boron-aluminum composites, a further study was desirable to establish the precise role of the matrix in the fatigue process. The most practical approach in studying the influence of the matrix is by changing its behavior through suitable thermal-mechanical treatments. An investigation of internal stresses and matrix strength level of the composite is beneficial, not only for this study, but for general property enhancement as well. The attainment of the highest strength level in the matrix is of importance for good general performance of the composite in the non-reinforced directions, however, it may prove to be disadvantageous for good fatigue behavior. This may be the case due to the higher work hardening rate of the stronger matrix. In order to further establish the role of work hardening rate elevated temperature tests would be of particular significance.

Since potential users of composites are not particularly interested in the 25 volume percent reinforcement selected for the initial phase of this work and since the technology of boron-aluminum composite production had advanced considerably in the year since the effort was initiated, more practical composites with higher volume percent reinforcements would be selected for further investigations.

### III. PRACTICAL BORON-ALUMINUM COMPOSITES

#### 3.1 Specific Objectives

The objectives of this program are to investigate the time-dependent mechanical behavior of practical boron filament reinforced 6061 aluminum composites. This study includes the evaluation of the relative roles of the matrix metal and filament reinforcement in fatigue strength and failure mechanisms by using variables such as strength level and residual stress in the matrix and volume fractions and orientations of filaments in multi-ply composites.

Specifically the program involves the following phases:

*Phase 1.* Optimization of filament content of multi-directional composites.

*Phase 2.* Thermo-mechanical conditioning of the matrix.

*Phase 3.* Determination of room temperature fatigue behavior of composites.

*Phase 4.* Determination of elevated temperature fatigue behavior of composites.

*Phase 5.* Investigation of the fatigue behavior of boron filament for correlation with composite behavior.

#### 3.2 Composite Materials Fabrication and Test Procedures.

All composites were fabricated at TRW as part of this program from a matrix foil of 6061 aluminum and continuous filaments of boron. Two batches of boron filaments were procured from Hamilton Standard. The first batch, with average spool strength values of 371, 355, 359, 365, and 371 ksi, was procured in February, 1969 and was used for the completion of Phases 1 and 2 and the initiation of Phases 3 and 5 of this program. The second batch, with average spool strength values of 431, 413, 403, 422, 428, and 532 ksi, was procured in August, 1969 and was used for the remainder of the program to date.

Composite fabrication was essentially the same as that used in the previous phase of the effort. However, the thickness of the aluminum alloy foil and the feed rate of the filament winding lathe were varied as shown in Table X to produce the various composites.

Tensile specimens were the same as those in the early work. However, the initial fatigue tests conducted on the 60 v/o B-6061 Al composites resulted in excessive matrix fatigue shear cracking due to the non-uniform transfer of load from grips to interior of the specimen as shown in Figure 19a. The fatigue specimen was modified as shown in Figure 19c to incorporate matrix cover sheets to improve load transfer into the composite resulting in fatigue failures as illustrated in Fig. 19b.

To determine the optimum filament content in multi-directional composites the following techniques were utilized:

(a) Chemical dissolution of matrix and counting of full-length filaments to evaluate percentage of filament breakage resulting in fabrication.

(b) Evaluation of tensile strength as a function of filament content in a direction parallel to one of the filament orientations where strength is controlled by filament integrity.

(c) Examination of filament distribution by metallography.

The results of the above examinations permitted the selections of physically sound cross-ply composites for further evaluation.

TABLE X.  
FILAMENT WINDING PARAMETERS

VOLUME PERCENT BORON	FOIL THICKNESS MILS	FEED RATE MILS/TURN
30	3.8	6.9
40	2.9	5.7
50	2.2	5.2
60	1.7	4.8
73	1.0	4.2





Figure 19 (a and b). Fatigue Failure Characteristics when using (a) Initial, (b) Modified Fatigue Specimen Geometry.

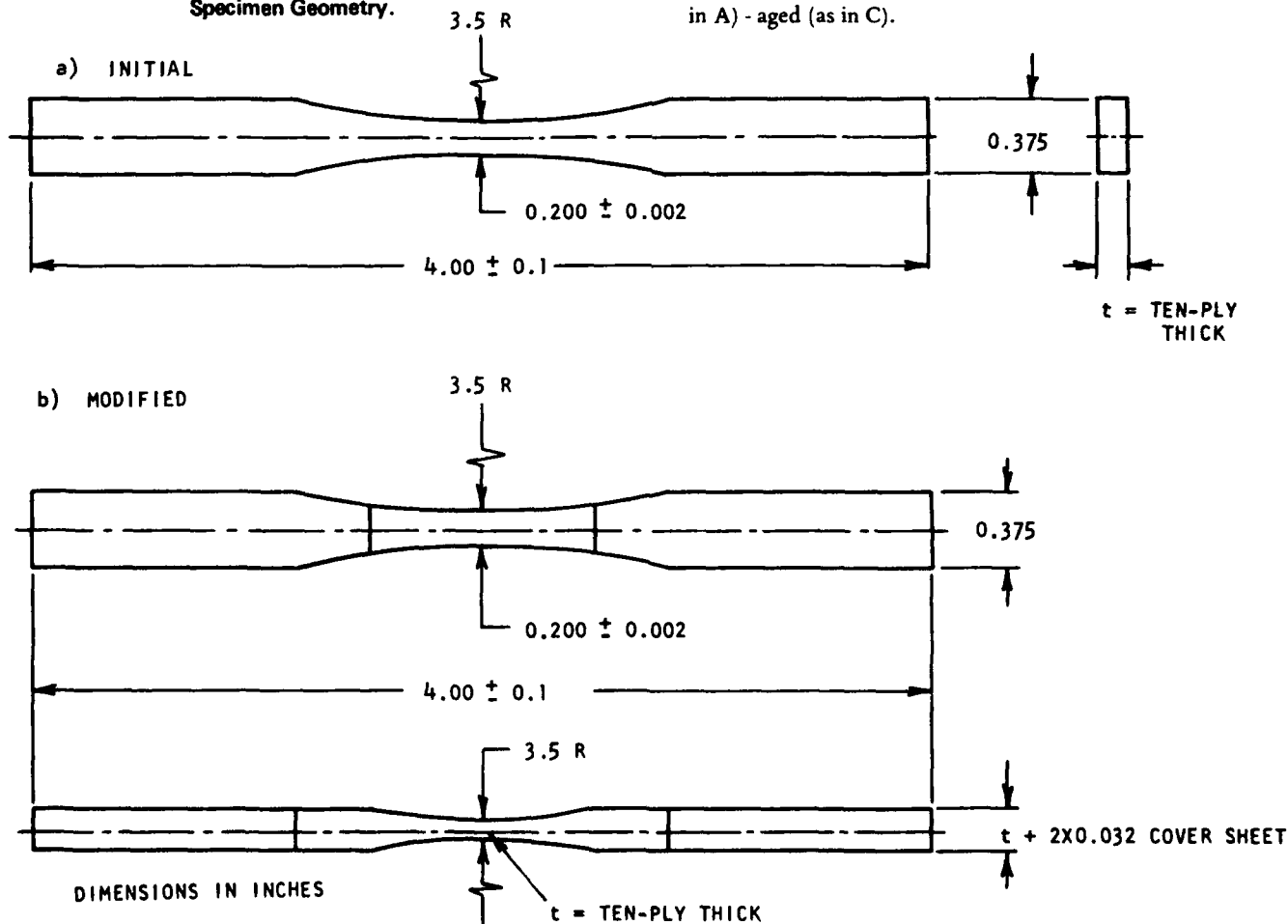


Figure 19c. Initial and Modified Fatigue Specimen Configurations.

The application of various treatments to the composites that may improve matrix properties especially in the non-reinforced directions were briefly explored. Mechanical deformation by rolling to stress-relieve (plastically) the matrix was found to be suitable for U-D composites but was found to be unworkable for C-P composites due to the bi-directional reinforcement inhibiting matrix plastic flow without excessive filament breakage. Therefore, this method of matrix conditioning was abandoned.

Specimens of U-D and C-P composites were subjected to the following heat treatments:

(O) As pressed. All of the composite panels were slow-cooled from the fabrication temperature, thus this condition can be called the annealed treatment.

(A) Sub-zero treated (i.e. cooled to  $-320^{\circ}\text{F}$  for 10 minutes.)

(C) Solution treated and aged using the modified treatment condition which was found to give the highest transverse strength in U-D Boron-Aluminum by Davis<sup>22</sup> of Harvey Aluminum (i.e. Heat to  $930^{\circ}\text{F}$  for 1 hour. - water quench - age at  $340^{\circ}\text{F}$  for 6 hours.)

(B) Solution treated (as in C) - Sub-zero treated (as in A) - aged (as in C).

The room temperature tensile properties on the reported composite materials were determined in tests performed on an Instron testing machine at a constant cross-head movement of 0.020 in/min. Strain measurements were made using a one-inch strain gage extensometer.

In order to obtain good load alignment and to reduce end constraints on off-axis test specimens a specially designed ball joint type grip fixture, shown in Figure 20, was used for both tensile and fatigue tests.

The fatigue behavior of the composite is determined in axial loading in a Budd, Model 5K-DDS, fatigue machine (frequency 1500 cpm) with the tension-tension fatigue load superimposed upon a static load. A ratio of static-to-dynamic load of 3:2 is employed throughout this work, giving a sine wave loading pattern with an R factor of 0.2. Most of the tests are conducted at stress levels such as to establish the S/N curve to  $10^7$  cycles, using actual fracture as the failure criterion. The elevated temperature tension-tension fatigue tests will be performed at a temperature of 400°F.



Figure 20. Ball Joint Type Grip Fixture.

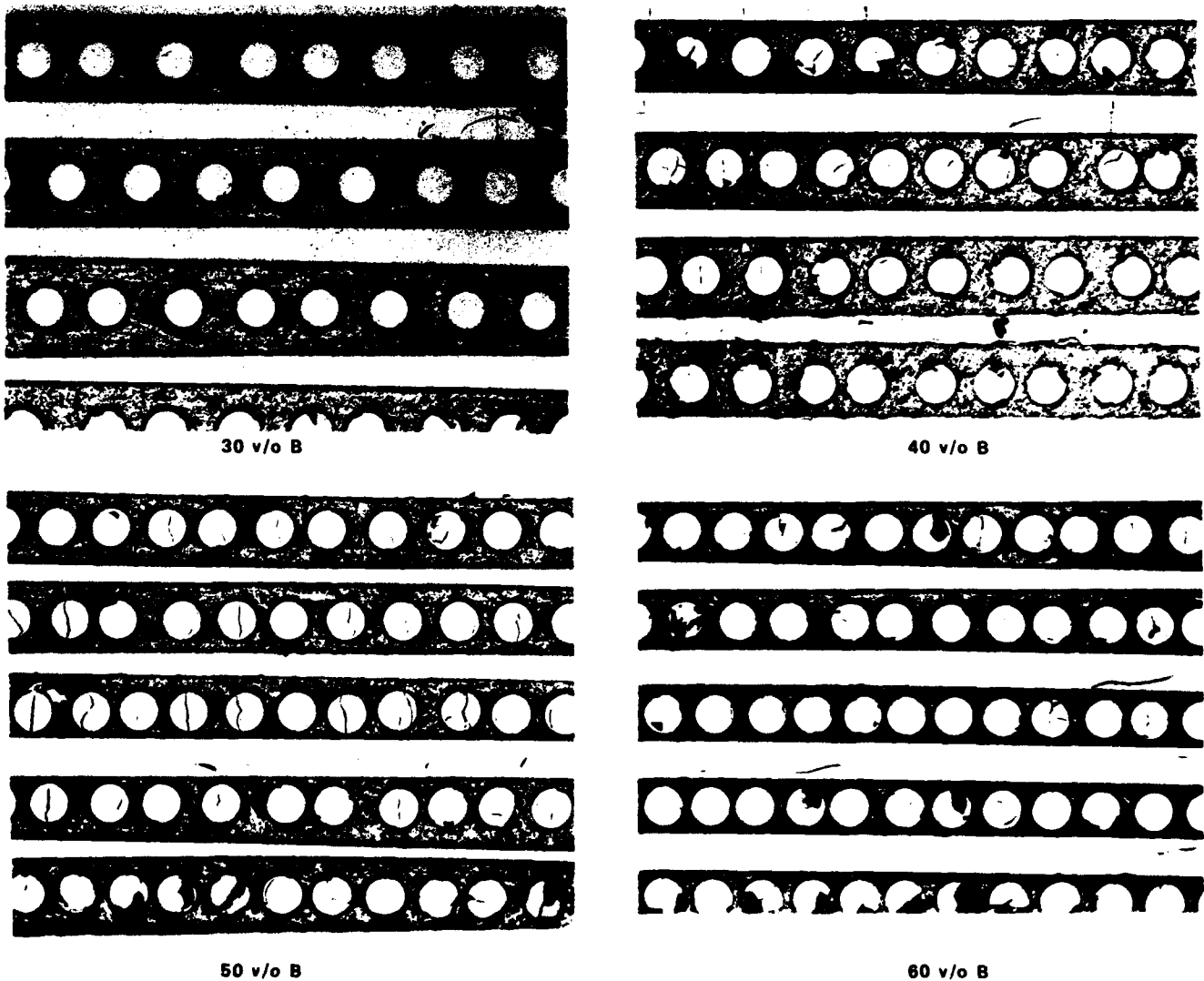


Figure 21. Photomicrographs of Cross-Plied B-6061 AL at Four Levels of Reinforcement. 75X, Reduced 10% for Reproduction,

### 3.3 Filament Content Optimization (Phase 1)

For the purpose of establishing optimum (or maximum useful) filament content and the selection of a suitably lower filament content in cross-plyed composites for further evaluation nominal filament levels of 30, 40, 50 and 60 v/o B were investigated. The criteria used for the optimum filament content selections were: (a) No touching at filament-filament cross over points, (b) small filament breakage during fabrication, and (c) maximum useful tensile strength of the composite.

Examination of the filament distribution by metallography, as shown by typical photomicrographs in Figure 21, indicates that in the investigated cross-plyed composites there is good filament separation (i.e. no touching at filament-filament cross over points) even at 60 v/o B reinforcement.

The percentage of filament breakage resulting in fabrication was evaluated by chemical dissolution of matrix on full-size tensile specimens and counting the number of unbroken filaments, expressed as percentage of the theoretical number of full length filaments in Figure 22 for the various levels of boron. It is evident that even at 60 v/o B the filament breakage attributable to composite processing is only 8%.

The above cross-plyed composites were tensile tested in a direction parallel to one of the filament orientation axes where behavior is normally controlled by filament integrity. The tensile strength results are presented in Figure 22 as a function of filament content. It can be observed that the highest strength advantage is obtained at 60 v/o B.

Based on the above results 40 and 60 v/o B composites were selected for further investigation.

### 3.4 Conditioning of Matrix (Phase 2)

The main objective of this phase of the program was to study thermal and mechanical means of improving the strength contribution of the matrix and thus to achieve a better overall composite performance especially in non-reinforced directions. Based on tensile behavior, two matrix conditions (i.e. two strength levels) were to be selected for the fatigue investigation (Phase 3) part of the program.

Mechanical deformation by rolling to remove residual thermal stress (plastically) and to work harden the matrix was the first method considered for matrix conditioning. Preliminary work indicated that this technique was suitable for U-D composites (by transverse rolling) but was found unworkable for C-P composites due to the bi-directional reinforcement inhibiting matrix plastic flow without excessive filament breakage. Therefore, this method of matrix conditioning was abandoned early in the program in favor of the more promising thermal methods.

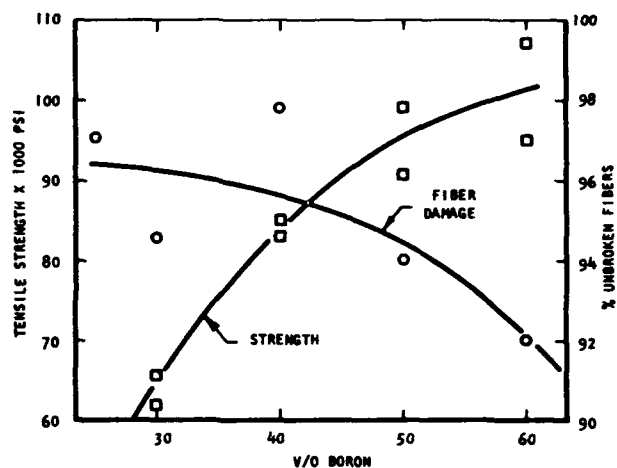


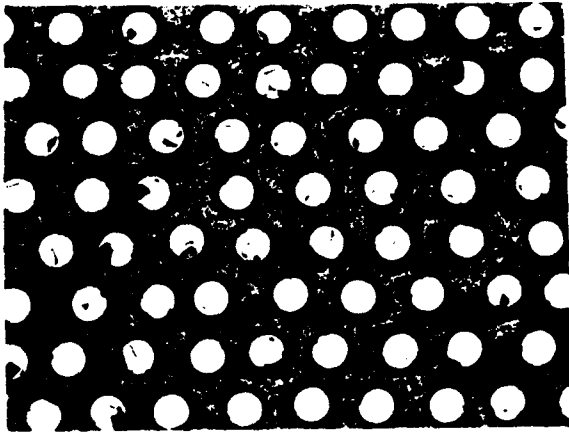
Figure 22. Effect of Filament Content on Filament Breakage and Tensile Strength in "As-Fabricated" 0-90 Deg. C-P Boron-6061 AL.

### 3.5 Tensile Behavior of Practical Boron-Aluminum Composites

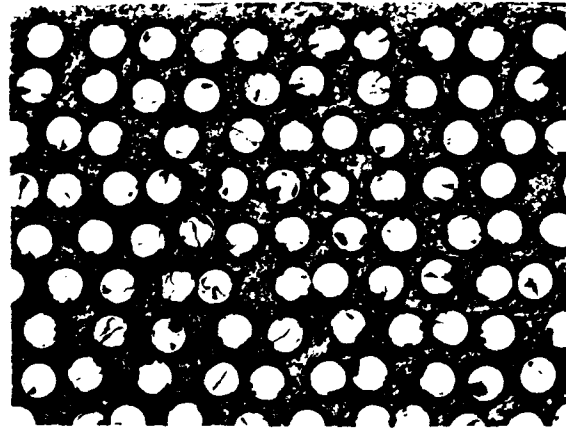
The tensile behavior of U-D and C-P composites in four different conditions of heat treatments were investigated. These heat treatments coded as O, A, C, and B are fully identified in Section 3.1. In general, treatments O and A leave the matrix in the annealed or soft condition, whereas treatments C and B are both designed to render the matrix in the precipitation hardened conditions. Typical photomicrographs for the U-D composites are shown in Figure 23. It is evident that good filament distribution was obtained even at 73 v/o B.

The 0-degree tensile properties of U-D boron 6061 aluminum in the four heat treatment conditions are summarized in Table XI. As anticipated, of the two precipitation hardened matrix conditions the (B) treatment is the more effective one. The strength of this latter type is compared graphically with that of the annealed (O) type in Figure 24. It is interesting to note that the (B) treatment or modified T6 condition resulted in a composite strength improvement of about 30,000 psi at all levels of reinforcement. This is surprising since the (B) treatment can only strengthen the matrix, hence the composite strength improvement should decrease with decreasing matrix content. Another interesting feature of Figure 24 which cannot be explained currently, is that there is a break in both curves at about 50 v/o B, suggesting a different failure mode beyond this filament content. The tensile results of the (A) treated composites being similar to that of the (O) treated composites suggests that the latter was cooled slow enough to avoid residual stress build-up.

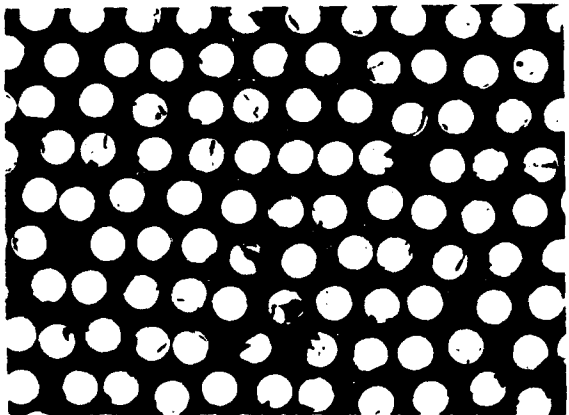
The effect of heat treatment on the transverse tensile properties of the U-D composites are summarized in



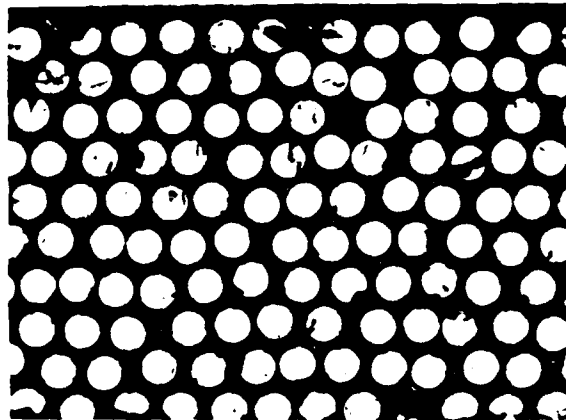
**30 v/o B**



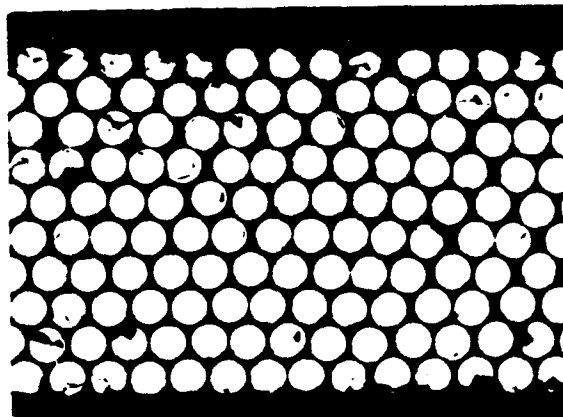
**40 v/o B**



**50 v/o B**



**60 v/o B**



**73 v/o B**

**Figure 23. Photomicrographs of Unidirectional B-8061 AL Composites at Five Levels of Reinforcement. 75X.**

**TABLE XI.**  
**EFFECT OF HEAT TREATMENT AND FILAMENT CONTENT**  
**ON TENSILE BEHAVIOR OF 0-DEG. U-D BORON 6061 ALUMINUM**

Specimen Code	Treatment*	Nominal v/oB	UTS ksi	Elastic Modulus x10 <sup>6</sup> psi		Strain To Failure Micro In/In	
				E <sub>1</sub>	E <sub>2</sub>		
3A	3/2	0	30	103.1	24.7	17.8	6500
3A <sup>o</sup>	3/6	0	30	112.0	22.1	17.5	7400
4A <sup>o</sup>	3/2	0	40	151.0	27.7	19.8	8000
4A <sup>o</sup>	3/6	0	40	140.1	30.7	23.7	6300
5A <sup>o</sup>	10/2	0	50	176.3	33.4	27.2	6600
5A <sup>o</sup>	10/6	0	50	192.2	31.8	24.2	7700
6A <sup>o</sup>	2/2	0	60	192.1	35.2	30.3	6500
6A <sup>o</sup>	2/6	0	60	204.1	39.9	31.8	7000
7.3A <sup>o</sup>	2/2	0	73	225.1	45.7	42.2	5800
7.3A <sup>o</sup>	2/4	0	73	219.1	43.5	40.5	5100
3A	3/1	A	30	99.3	19.1	18.5	6100
3A <sup>a</sup>	3/5	A	30	114.0	22.0	16.2	6500
4A <sup>a</sup>	3/1	A	40	154.6	31.7	N.D.	6300
4A <sup>a</sup>	3/5	A	40	158.1	31.3	N.D.	7300
5A <sup>a</sup>	10/1	A	50	174.4	30.1	21.9	6900
5A <sup>a</sup>	10/5	A	50	195.9	N.D.	N.D.	N.D.
6A <sup>a</sup>	2/1	A	60	200.8	35.7	28.8	6600
6A <sup>a</sup>	2/5	A	60	194.2	N.D.	N.D.	N.D.
3A	3/4	C	30	127.5	18.1	16.1	7000
3A <sup>c</sup>	3/7	C	30	120.1	22.8	15.2	8000
4A <sup>c</sup>	3/4	C	40	157.2	28.4	21.1	7000
4A <sup>c</sup>	3/7	C	40	145.4	30.8	21.6	6500
5A <sup>c</sup>	10/4	C	50	189.2	34.3	27.7	7100
5A <sup>c</sup>	10/7	C	50	199.0	32.6	31.1	7400
6A <sup>c</sup>	2/4	C	60	208.7	38.2	31.2	6500
6A <sup>c</sup>	2/7	C	60	210.6	34.4	30.0	7300
3A	3/3	B	30	138.7	21.1	16.6	7500
3A <sup>b</sup>	3/8	B	30	142.4	23.9	19.7	7500
4A <sup>b</sup>	3/3	B	40	166.9	29.1	22.4	6700
4A <sup>b</sup>	3/8	B	40	169.1	30.0	26.3	6200
5A <sup>b</sup>	10/3	B	50	213.3	35.5	26.7	7500
5A <sup>b</sup>	10/8	B	50	214.2	34.3	31.0	7200
6A <sup>b</sup>	2/3	B	60	215.8	40.2	30.1	6700
6A <sup>b</sup>	2/8	B	60	225.7	35.9	31.2	7700
7.3A <sup>b</sup>	3/1	B	73	254.0	46.3	38.1	6400
7.3A <sup>b</sup>	3/2	B	73	248.7	45.6	41.5	6200

(\*) 0 = As Fabricated (slow cooled)  
A = Cooled to -320°F for 10 mins.  
B = Heat to 930°F for 1 hr. - Water Quench - Cool to -320°F for 10 mins.  
Age at 340°F for 6 hrs.  
C = Heat to 930°F for 1 hr. - Water Quench - Age at 340°F for 6 hrs.

there is no further decrease. It is interesting to note that the (B) and (C) treatments are giving similar results. Thus only the (C) condition is compared graphically in Figure 25, with the annealed (O) condition.

Transverse tensile fracture surfaces of the U-D composite specimens in both the annealed (O) and solution treated and aged (C or B) conditions, were examined under the microscope for fracture modes. The results of the frac-

ture surface studies are presented in Table XIII in terms of estimated percentages of total fracture area for filament splitting, filament matrix debonding and matrix failure. It appears that the transverse tensile fracture of all the annealed composites (low matrix strength level) is controlled by the failure strength of the matrix, in contrast to all the solution treated and aged composites (high matrix strength level) where failure is controlled by the transverse strength of the filaments. Photomicrographs of transverse

**TABLE XII.**  
**EFFECT OF HEAT TREATMENT AND FILAMENT CONTENT ON**  
**TRANSVERSE TENSILE BEHAVIOR OF U-D BORON-6061 ALUMINUM.**

Specimen Code	Treatment	Nominal v/oB	UTS ksi	E x 10 <sup>6</sup> psi	Strain to Failure Micro In/In	
3F	2/2	0	30	14.6	14.7	7900
3F <sup>o</sup>	2/6	0	30	14.3	11.4	7500
4F	2/2	0	40	13.8	17.3	6100
4F <sup>o</sup>	2/6	0	40	14.3	15.4	4000
5F <sup>o</sup>	1/1	0	50	13.7	N.D.	N.D.
5F <sup>o</sup>	1/3	0	50	14.8	N.D.	N.D.
6F <sup>o</sup>	1/1	0	60	14.9	N.D.	N.D.
6F <sup>o</sup>	1/3	0	60	15.4	N.D.	N.D.
7.3F <sup>o</sup>	2/2	0	73	13.2	19.9	1100
7.3F <sup>o</sup>	2/4	0	73	13.7	24.2	930
3F	2/1	A	30	14.8	12.2	4700
3F <sup>a</sup>	2/5	A	30	15.3	9.9	7600
4F <sup>a</sup>	2/1	A	40	14.2	14.7	2200
4F <sup>a</sup>	2/5	A	40	15.2	17.8	3100
5F <sup>a</sup>	1/1	A	50	15.0	15.1	2800
5F <sup>a</sup>	1/2	A	50	15.0	15.6	2500
6F <sup>a</sup>	1/1	A	60	16.3	21.1	3800
6F <sup>a</sup>	1/2	A	60	13.7	19.7	2000
3F	1/1	C	30	31.9	15.4	2400
3F <sup>c</sup>	1/2	C	30	30.4	12.5	3100
4F <sup>c</sup>	2/7	C	40	21.9	15.9	1700
4F <sup>c</sup>	2/4	C	40	26.4	13.0	1900
5F <sup>c</sup>	1/1	C	50	23.2	18.3	3500
5F <sup>c</sup>	1/2	C	50	22.2	15.3	4300
6F <sup>c</sup>	1/1	C	60	17.4	16.3	2200
6F <sup>c</sup>	1/2	C	60	19.7	19.5	2800
7.3F <sup>c</sup>	2/1	C	73	18.6	20.2	1800
7.3F <sup>c</sup>	2/3	C	73	21.6	20.1	1500
3F	1/1	B	30	29.5	13.2	2200
3F <sup>b</sup>	1/2	B	30	31.5	14.4	2500
4F <sup>b</sup>	2/8	B	40	23.2	15.1	1700
4F <sup>b</sup>	1/2	B	40	23.9	16.3	3000
5F <sup>b</sup>	1/1	B	50	20.3	N.D.	N.D.
5F <sup>b</sup>	1/2	B	50	20.7	N.D.	N.D.
6F <sup>b</sup>	1/1	B	60	17.0	N.D.	N.D.
6F <sup>b</sup>	1/2	B	73	17.2	N.D.	N.D.

(\*) 0 = As-Fabricated (slow cooled)

A = Cooled to -320 for 10 mins.

B = Heat to 930°F for 1 hr. - Water Quench - Cool to -320°F for 10 mins.  
Age at 340°F for 6 hrs.

C = Heat to 930°F for 1 hr. - Water Quench - Age at 340°F for 6 hrs.

fracturing in a solution treated and aged composite are shown in Figure 26. It is evident that the transverse tensile cracks can propagate in the filaments as easily as in the matrix.

The effect of heat treatment on the tensile properties of 0-90 deg. cross-plyed composites is summarized in Table XIV and the tensile strength values are presented graphically in Figure 27. The large difference in behavior of the two solution treated and aged composites (C and B)

can be explained in terms of residual stresses resulting from the differential thermal contraction of the matrix and filament on cooling from the solutionizing temperature. The magnitude of the residual stresses involved can be appreciated by considering the thermal expansion coefficients ( $\alpha$ ) of the matrix ( $\alpha_m = 16.0$  micro-in/in<sup>o</sup>F) and the filament ( $\alpha_f = 2.7$  micro-in/in<sup>o</sup>F). Thus on cooling from the solutionizing temperature (940°F) the matrix tends to contract 13,760 micro-in/in and the filament only 2,322 micro-in/in, producing a possible net axial thermal strain in the

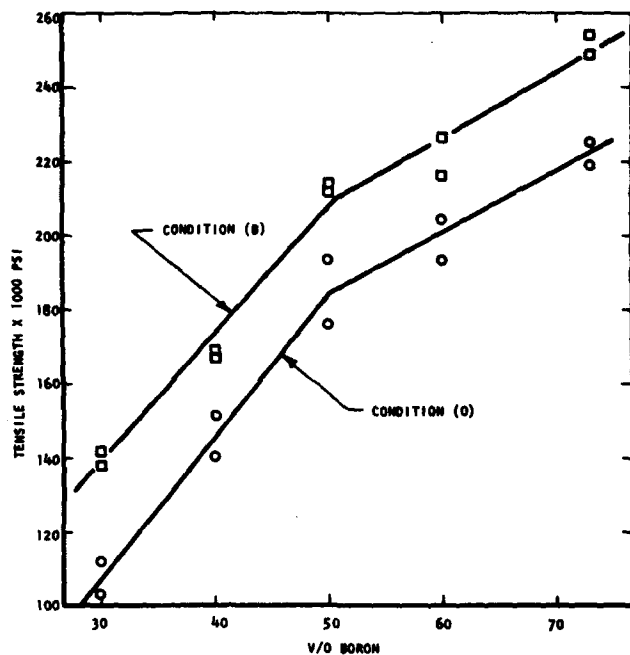


Figure 24. Tensile Strength of 0-Deg. U-D Boron-6061 Aluminum in the Annealed (O) and Modified T6 (B) Conditions.

composite of 11,438 micro-in/in. The stiff boron filaments resist this contraction producing a tensile strain, and a corresponding tensile stress parallel to the filaments in the aluminum. Reactively, a compressive strain, and a corresponding compressive stress is generated in the boron filaments. The elastic strain limit of the nonprecipitation hardened matrix is only about 800 micro-in/in, even at room temperature. Thus, most of the composite thermal strain will be taken up by plastic flow of the matrix. This plastic flow apparently is much more difficult in the C-P material than in the U-D one, due to the bi-directional constraint of the matrix. The bi-directional reinforcement of the C-P composite introduces large triaxial residual stresses in the matrix.

In general, increased triaxial stresses result in increased fracture stress and decreased fracture strain for a material. This decreased fracture strain as shown in Table XIV was very much in evidence in case of the (C) treated composite material. In other words, as the residual triaxial stress state of the matrix is increased by additional filaments, resulting in more bi-directional constraint of the matrix, the fracture strain of the composite has decreased. Thus it appears that when the matrix is in a high residual triaxial stress state (as in Type C) premature fracture is initiated in or induced by the matrix.

In the (B) treated composite the large triaxial residual stress, developed during water quenching from the solutionizing temperature was significantly decreased or eliminated by the employment of stress relief treatment prior to aging. Actually, in the sub-zero stress relieving treatment an additional net axial thermal strain of 5177

TABLE XIII.  
TRANSVERSE TENSILE FRACTURE MODE OF  
U-D B-6061 AL

Matrix Condition	Fracture Mode	Percent Fracture Mode Area				
		30v/oB	40v/oB	50v/oB	60v/oB	73v/oB
Annealed	Filament Splitting	15	25	30	30	15
	Filament-Matrix Debonding	15	15	10	10	15
	Matrix Failure	70	60	60	60	70
Solution Treat and Age	Filament Splitting	50	60	55	55	50
	Filament-Matrix Debonding	0	5	5	5	10
	Matrix Failure	50	35	40	40	40

micro-in/in is generated in the composite during cooling. Assuming that the solution treated matrix at room temperature has already had a residual strain equivalent to its flow stress, then most of this additional thermal strain was dissipated by plastic flow of the matrix. But the flow stress of the matrix is increasing with decreasing temperature, therefore, some of this additional strain will be absorbed elastically by the filaments. Thus it is fair to assume that the filament axial compressive strain has slightly increased on cooling to minus 320°F. Now, on heating to room temperature, the previously operating differential contraction process is changed to a differential expansion process. The matrix tends to expand 6240 micro-in/in and the filament only 1063 micro-in/in, hence the stiffer boron filaments re-

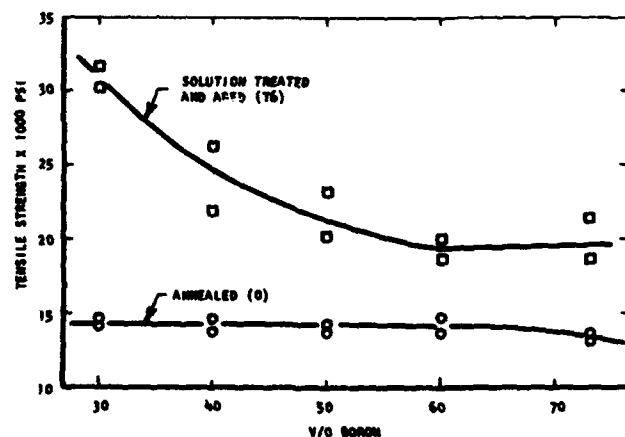
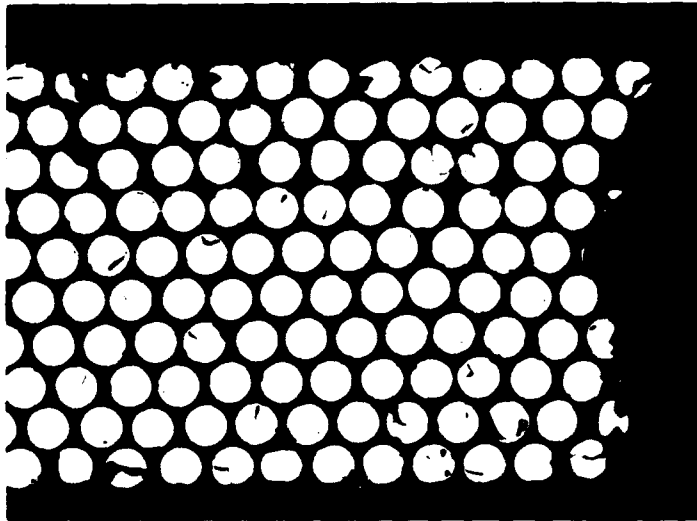
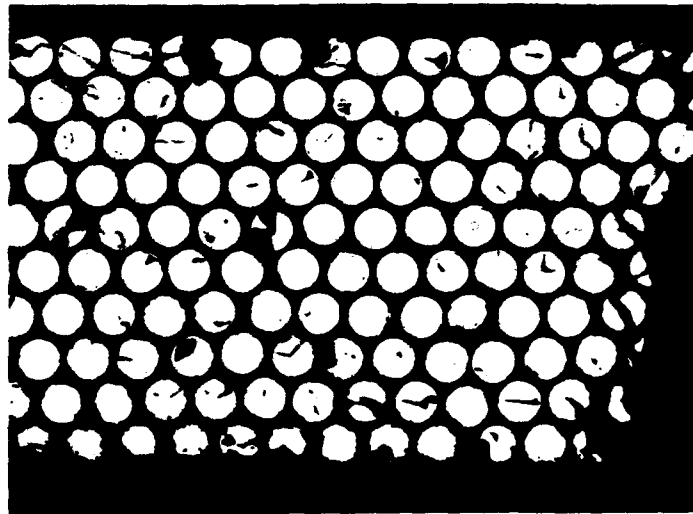


Figure 25. Transverse Tensile Strength of Boron-6061 AL as a Function of Filament Content for 0 and T6 Conditions.



**A. Annealed Condition. Matrix Strength Controlled Failure.**



**B. Solution Treated and Aged Condition. Filament Transverse Strength Controlled Failure.**

**Figure 26. Effect of Matrix Strength Level on Transverse Fracture Mode of Boron 6061 AL. 100X.**

sist the matrix expansion. Thus the sub-zero treatment is capable of not only relieving the axial tensile strain of the matrix but it may even change it to axial compressive strain. In any case the selected sub-zero treatment prior to aging was found to be very desirable especially in the case of the C-P composite, not only to utilize the higher matrix strength but also to retain utilization of the filament strength.

Based on the above results, the selected two matrix conditions for the fatigue behavior investigation

were conditions (O) and (B).

### **3.6 Fatigue Behavior at Ambient Temperature of Selected Composites (Phase 3)**

The objective of this phase is to evaluate the fatigue behavior of 40 and 60 v/o B-6061 Al unidirectional composites under loading conditions of 0, 5, 15, 45, and 90 degrees to the reinforcement direction and bi-directional multiply composites tested under  $\pm 45$  degree and 0-90 degree loading. These composites will be evaluated both



**TABLE XIV.**  
**EFFECT OF HEAT TREATMENT AND FILAMENT CONTENT**  
**ON TENSILE BEHAVIOR OF 0-90 DEG. C-P BORON-6061 ALUMINUM**

Specimen Code	Treatment*	Nominal v/oB	UTS ksi	Elastic Modulus x 10 <sup>6</sup> psi		Strain to Failure Micro In/In
				E <sub>1</sub>	E <sub>2</sub>	
3T <sup>o</sup> 2/1	0	30	61.9	15.0	9.7	5500
3T <sup>o</sup> 2/5		30	66.0	16.0	9.3	7300
4T <sup>o</sup> 2/4		40	85.0	16.5	13.0	6400
4T <sup>o</sup> 2/6		40	83.0	16.0	11.1	7200
5T <sup>o</sup> 2/1		50	99.1	20.1	14.5	7100
5T <sup>o</sup> 2/5		50	90.0	18.4	14.1	6300
6T <sup>o</sup> 2/3		60	107.5	25.3	17.4	5800
6T <sup>o</sup> 2/5		60	95.1	23.9	17.2	5100
3T <sup>c</sup> 2/7	C	30	54.5	16.7	9.4	4300
3T <sup>c</sup> 2/8		30	53.8	16.5	13.5	4300
4T <sup>c</sup> 2/7		40	44.8	16.3	11.9	3300
4T <sup>c</sup> 2/8		40	54.8	18.3	12.2	4100
5T <sup>c</sup> 2/7		50	49.7	25.1	14.1	3000
5T <sup>c</sup> 2/8		50	52.7	20.1	13.4	3400
6T <sup>c</sup> 2/7		60	34.3	19.6	15.7	2300
6T <sup>c</sup> 2/8		60	43.0	16.5	13.8	2900
3T <sup>b</sup> 2/2	B	30	81.0	16.8	10.1	6500
3T <sup>b</sup> 2/6		30	80.1	14.7	9.4	6900
4T <sup>b</sup> 2/1		40	91.8	17.8	13.0	6300
4T <sup>b</sup> 2/3		40	107.5	17.3	13.0	7800
5T <sup>b</sup> 2/2		50	115.3	19.2	14.3	7400
5T <sup>b</sup> 2/6		50	114.1	18.5	13.9	7400
6T <sup>b</sup> 2/2		60	114.5	20.6	16.4	6800
6T <sup>b</sup> 2/6		60	101.2	23.7	17.0	6000

(\*) 0 = As-Fabricated (slow cooled)

C = Heat to 930°F for 1 hr. - Water Quench - Age at 340°F for 6 hrs.

B = Heat to 930°F for 1 hr. - Water Quench - Cool to minus 320°F for 10 mins. Age at 340°F for 6 hrs.

in the as-pressed (O) condition and the sub-zero modified T-6 (B) condition. This paper presents a report of the current status of the effort. Thus far the 40 and 60 v/o composites have been evaluated in the 0 degree U-D and the 0-90 C-P configurations in the as-pressed condition.

The fatigue results obtained on the 0-deg. unidirectional 40 v/o B-6061 Al composite are summarized in Table XV. Specimens from two panels containing different "batches" of reinforcing filament were evaluated, and the effect of filament strength on fatigue behavior is illustrated. The composite tensile strength of the two panels was found to be 145 and 180 ksi, respectively. The fatigue behavior of the two panels is characterized by parallel flat S/N curves, as shown in Figure 28 giving an endurance limit to ultimate tensile strength ratio of about 0.75. This tends to confirm the fact that the ratio of fatigue properties to tensile properties is a function only of the matrix.

The fatigue results obtained on 0-degree unidirectional 60 v/o B-6061 Al composites in the (O) condition are summarized in Table XVI. Here too, two strength levels of composites are evaluated and the fatigue results are illustrated in Figure 29. Again the two S/N diagrams are essentially parallel and give an endurance limit to ultimate strength ratio of about 0.80.

It is interesting to note that increasing the filament content has apparently increased the ratio of endurance limit to ultimate strength in these composites, since the 25 v/o composite has an E.L./U.T.S. ratio of 0.63, the 40 v/o composite ratio was 0.75, and the 60 v/o composite ratio was 0.80. Examination of the data indicates that there has been a linear increase in fatigue strength with increasing reinforcement while the increase in static strength at higher filament contents has tended to taper off due to increasing damage to filaments during fabrication or some change in

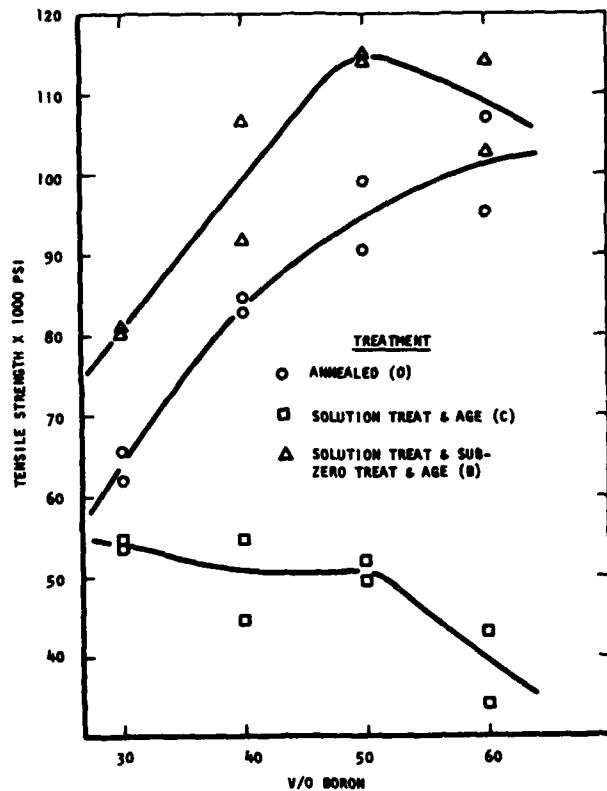


Figure 27. Effect of Heat Treatment on Tensile Strength of 0-90-Deg. C-P Boron-6061 AL Composites.

mode of static fracture at higher filament contents. This is another indication of the primary role of the matrix in determining fatigue behavior.

The fatigue behavior of 0-90 degree cross-ply composites of 40 and 60 v/o boron are presented in Table XVII

Figure 28. Fatigue Data for 0-Deg. U-D 40 v/o B-6061 AL Composite.

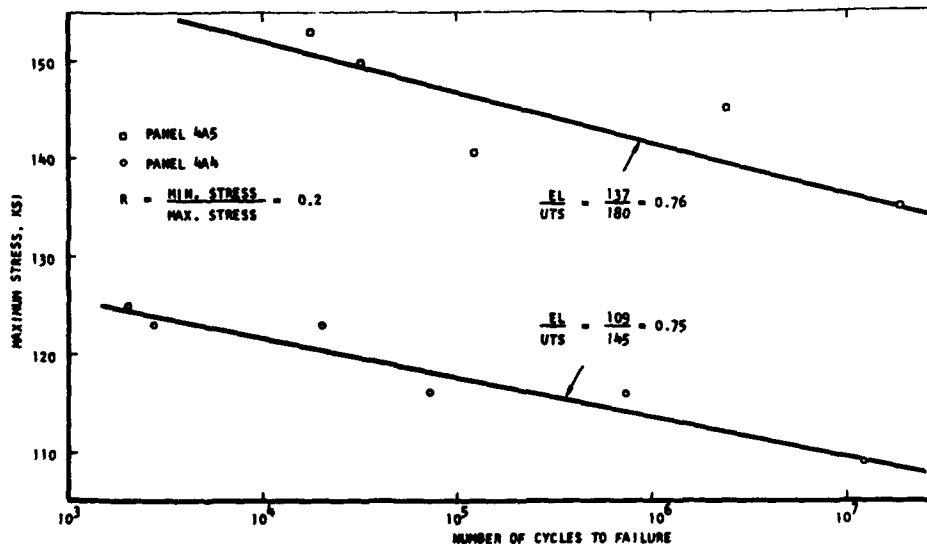


TABLE XV. FATIGUE BEHAVIOR OF 0-DEG. U-D 40 v/o<sup>(a)</sup> B-6061 AL<sup>(b)</sup>

CODE	MAX. STRESS PSI	NO. OF CYCLES TO FAILURE
4A4-6	125, 000	2, 100
4A4-7	123, 000	2, 700
4A4-8	123, 000	20, 700
4A4-3	116, 000	71, 900
4A4-9	116, 000	781, 300
4A4-2	109, 000	11,911, 600
4A5-4	153, 000	18, 100
4A5-8	149, 400	33, 400
4A5-3	144, 900	2,431, 200
4A5-7	140, 400	125, 700
4A5-2	135, 000	18,579, 100

(a) The ultimate strength of panel 4A4 is 145.5 ksi utilizing boron of 371 ksi uts. The strength of panel 4A5 is 175 ksi using 431 ksi boron.

(b) Both composites are in the (O) treated condition.

and are compared with the earlier results on the 25 v/o composite in Figure 30. Here again the S/N diagrams are essentially parallel and relatively flat. When the endurance limits of these composites are compared with endurance limit of 16,000 psi for 6061 Aluminum in the T-0 condition it appears that the 40 and 60 v/o fit a linear relationship between fatigue strength and reinforcement content while the 25 v/o results are lower than would be expected. At this time these results can only be attributed to the change in the state-of-the-art of composite technology during the interval between investigations.

#### IV. WORK IN PROGRESS

Effort on this program is continuing so as to establish the off-axis fatigue behavior of the 40 and 60 v/o

**TABLE XVI.**  
**FATIGUE BEHAVIOR OF 0-DEG U-D 60**  
**v/o<sup>(a)</sup> B-6061 AL<sup>(b)</sup>**

CODE	MAX. STRESS PSI	NO. OF CYCLES TO FAILURE
6A7-7	246,300	19,800
6A7-3	243,000	247,700
6A7-8	239,500	789,300
6A6-2	221,000	300
6A6-3	221,000	200
6A6-6	220,000	3,800
6A6-1	216,000	20,900
6A6-8	215,000	1,136,600
6A6-5	210,000	1,540,100
6A6-7	205,000	6,293,900

(a) Ultimate tensile strength of 6A7 panel is 283 ksi and that of 6A6 panel is 275 ksi.

(b) Composite is in the (O) treated condition.

B-6061 Al composites in the (O) condition at room temperature. In addition to these efforts, a complete study of the on and off-axis fatigue behavior of unidirectional and bidirectional 40 and 60 v/o B-6061 Al composite in the modified T-6 condition is being conducted. The elevated temperature fatigue behavior of the selected composites is being determined at 400°F. (Phase 4).

An investigation of the fatigue behavior of the boron filaments, used in the composite program, has been initiated at the Air Force Materials Laboratory to provide base line data for analysis of the composite behavior. This investigation is being conducted utilizing an electromagnetic axial-load fatigue testing device which was designed and built at AFML. Preliminary results in this effort have given data with an excessive amount of scatter which apparently indicates a temporal relationship with the testing schedule.

**Figure 29. Fatigue**  
**Data for 0-Deg.**  
**U-D 60 v/o**  
**B-6061 AL**  
**Composite.**

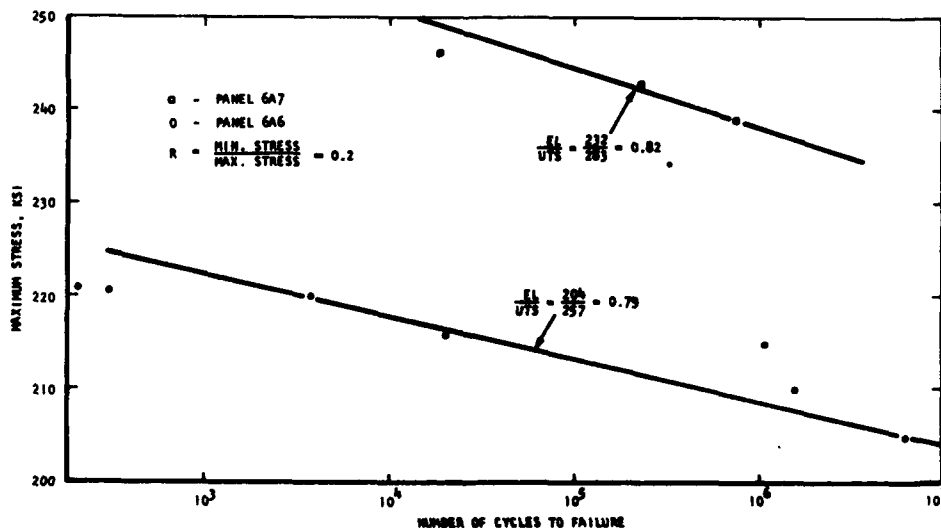


**TABLE XVII.**  
**FATIGUE BEHAVIOR OF 0-90 DEG C-P**  
**COMPOSITES OF 40% AND 60%**  
**B-6061 AL**

CODE	v/o BORON	MAX. STRESS	NO. OF CYCLES TO FAILURE
4T4-3	40	84,300	1,200
4T4-8	40	81,600	900
4T4-6	40	78,700	69,100
4T4-2	40	76,900	411,600
4T4-7	40	76,900	703,500
4T4-4	40	70,400	2,891,400
4T4-1	40	66,200	2,905,900
6T3-3	60	87,400	6,800
6T3-8	60	84,600	1,590,300
6T3-6	60	83,900	443,100
6T3-2	60	78,700	2,913,700

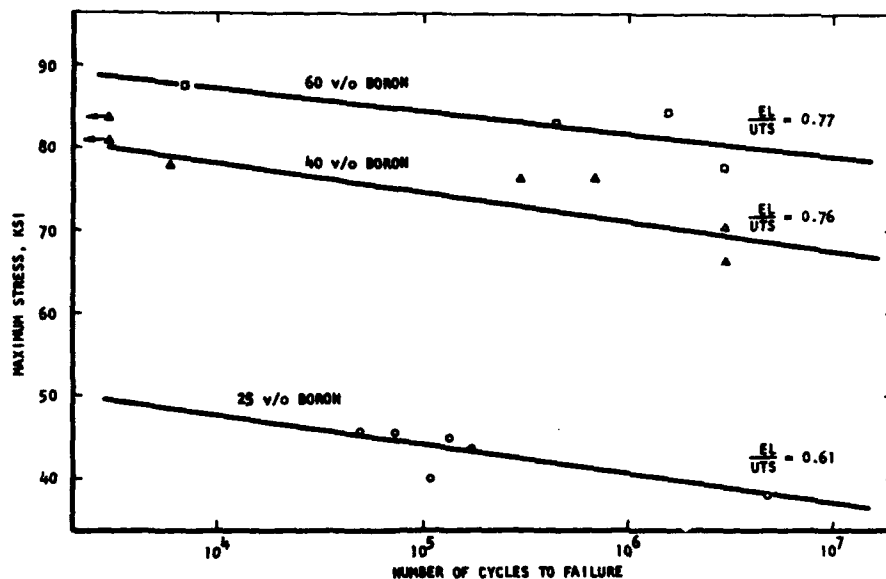
Two possible causes for the results have been postulated i.e., (1) interrelation between the sampling technique and variation in properties along the length of the boron filament and (2) possible environmental effects on fatigue behavior of boron filament. Because of these problems, it was decided to redesign this experiment, and results are presented in the next section.

The overall effort in this program involves an investigation of the creep behavior of boron-aluminum composites under various loading conditions, which has not been discussed in this paper, and this work is continuing.

## V. FUTURE PLANS

In the next year's effort on this program's additional aspects of the fatigue behavior of boron reinforced 6061 aluminum will be investigated as follows:

Figure 30. Fatigue Data for 0-90 Deg. C-P Composites of B-6061 AL.



### Phase 1 - Fatigue Damage Analyses

The mechanism of fatigue damage accumulation in both annealed and solution treated and aged composites will be investigated at both the high cycle and low cycle fatigue life regimes. The damage analyses will include evaluation of residual tensile strength of the composite and of extracted filaments subsequent to prior fatigue history and measurement of filament breakage during the fatigue process.

### Phase 2 - Effect of A-Ratios on Fatigue Behavior

The effect of superimposed static stresses on the room temperature axial fatigue behavior of unidirectional (0°) and cross-plyed (+45° and 0-90°) composites will be evaluated by obtaining data to supplement the information obtained at an A-ratio (dynamic stress/static stress) of 0.67 in the previous phase of the program. Thus additional fatigue data will be obtained at A-ratios of 0.25, 1.5, and 4.0 using at least four maximum load levels. For this work one matrix condition (annealed or solution treated and aged) and one filament volume fraction (40 or 60 v/o B) will be selected. The data obtained will be utilized to establish modified Goodman diagrams.

### Phase 3 - Notched Fatigue Behavior

The notch sensitivity in fatigue of 0° and 0-90° orientational composites will be investigated by means of axial fatigue tests on double notched specimens. Apart from filament orientation, the main variable will be a notch-radius. To establish fatigue strength reduction for discontinuities, ranging from that typical of bolt holes to sharp notches, notch-radii of 0.2, 0.02, and 0.002 inch will be utilized.

### Phase 4 - Fatigue Behavior under Non-Axial Loading

The influence of state of stress on fatigue behavior

of composites will be determined by bending fatigue experiments. The bending fatigue behavior of composites ranging from mono-layer tape through various multi-ply configurations will be evaluated and the failure modes obtained in the tests will be compared with results obtained in axial loading in other phases of the program.

### Phase 5 - Elevated Temperature Fatigue Behavior

The investigation of elevated temperature fatigue behavior of boron-6061 aluminum composites will be extended to obtain information at two elevated temperatures (e.g. 500 and 600°F). This information will supplement that obtained at 400°F in the previous phase of this effort. The results of these tests together with additional analytical tests will enable the establishment of fatigue failure mechanism as affected by temperature.

The investigation of fatigue behavior of filaments will be continued as follows:

1. A statistical sampling plan will be developed to eliminate the effect of filament property variation on the results of the fatigue tests.
2. The fatigue behavior of bare filaments in air will be determined.
3. An investigation of the fatigue behavior of boron filament with a vapor deposited aluminum coating to protect against environmental effects will be made.
4. The effect of a thick coating of aluminum in which fatigue cracks may initiate on filament fatigue will be investigated.
5. Elevated temperature fatigue properties of the filament will be determined at the temperatures used in the composite investigation.

6. Residual strength of fatigue tested filaments will be studied.

The goal of this effort is to provide sufficient infor-

mation on the time dependent mechanical behavior of metal matrix composites so that predictions of performance may be made and so that designers may have confidence in the ability of these materials to perform satisfactorily in service.

#### REFERENCES

1. P.J.E. Forsyth, R.W. George, and D.A. Ryder, *Appl. Mater. Res.*, 3:223-228 (1964).
2. R.V. Williams and D.J. O'Brien, *Appl. Mater. Res.*, 3:148-150 (1964).
3. A.A. Baker, *Appl. Mater. Res.*, 5:143-153 (1966).
4. A.A. Baker, *Appl. Mater. Res.*, 5:210-217 (1966).
5. R.K. Ham and T.A. Place, *J. Mech. Phys. Solids*, 14:271-280 (1966).
6. A.A. Baker and D. Cratchley, *Appl. Mater. Res.*, 3:215-222 (1964).
7. K.H. Boller, *Fatigue Strength of Plastic Laminates Reinforced with Unwoven "S" Glass Fiber*, Forest Products Laboratory, Madison, Wisconsin (1964).
8. A.W. Morris and E.A. Steigerwald, *Exploratory Investigation of the Time Dependent Mechanical Behavior of Composite Materials*, AFML-TR-66-255, Air Force Materials Laboratory, Wright-Patterson AFB, Ohio (1966).
9. A. Toy et al., *Development and Evaluation of the Diffusion Bonding Process as a Method to Produce Fibrous Reinforced Metal Matrix Composite Material*, AFML-TR-66-350, Air Force Materials Laboratory, Wright-Patterson AFB, Ohio (1966).
10. K.G. Krieder and G.R. Leverant, "Boron-Aluminum Composite Fabricated by Plasma Spraying," in *Symp. Advanced Fibrous Reinforced Composites*, Vol. 10, Society of Aerospace Material and Process Engineers, Los Angeles (1966).
11. A.W. Morris, *An Exploratory Investigation of the Time Dependent Mechanical Behavior of Composite Materials*, Air Force Materials Laboratory, Wright-Patterson AFB, Ohio (1967).
12. E.Z. Stowell and T.S. Liu, *J. Mech. Phys. Solids*, 14:177-186 (1961).
13. S.W. Tsai, NASA-CR-224, National Aeronautics and Space Administration, Washington, D.C. (1965).
14. A. Kelly and G.J. Davies, *Mater. Rev.*, 10:1-77 (1965).
15. P.W. Jackson and D. Cratchley, *J. Mech. Phys. Solids*, 14:49-64 (1966).
16. G.A. Cooper, *J. Mech. Phys. Solids*, 14:103-111 (1966).
17. G.A. Cooper, *Metals Mater.*, 1:109-115 (1967).
18. J. Haener and N. Ashbaugh, "Three Dimensional Stress Distribution in a Unidirectional Composite," *J. Compos. Mater.*, 1:54 (1967).
19. *ALCOA Aluminum Handbook*, Aluminum Company of America, Pittsburgh, Pennsylvania (1967).

#### REFERENCES (Continued)

20. F.E. Warner, "Boron Filaments," Chapter 10; L.J. Broutman and R.H. Krock, Eds., *Modern Composite Materials*, Addison-Wesley, Reading, Massachusetts (1968).
21. H. Shimizu, J.F. Dolowy, Jr., R.J. Taylor, and B.A. Webb, *Metal-Matrix Composites Behavior and Aerospace Applications*, SAE Paper 670861, Society of Automotive Engineers, New York (1967).
22. L.W. Davis, "Factors Affecting Transverse Properties of Metal Matrix," in *Composite Materials: Testing of Design*, ASTM-STP-460, American Society for Testing and Materials, Philadelphia, Pennsylvania (1969).

# THE EFFECT OF STRAIN RATE ON THE FRACTURE OF ADVANCED FIBER-REINFORCED COMPOSITES

by

F.Y. Soliman and J.S. Wallace

Lockheed-Georgia Company  
Aerospace Sciences Laboratory  
Marietta, Georgia

## INTRODUCTION

The advantages of advanced composites as aircraft structural materials are well known to the Air Force as well as the aerospace companies. They are being clearly demonstrated by structural applications of boron and graphite composites in several types of airplanes and helicopters.

The behavior of composites is under continuous investigation by many workers to predict the composite structural response under various types of loads as generated from actual aircraft missions. However, although considerable advances have been accomplished in this field, some important questions remain to be answered.

During abrupt maneuver or due to severe gust environment, the airloads on an aircraft element rise in the order of seconds. The performance of the structure is dependent on the behavior of the basic composite material from which it is fabricated. Routine testing procedures provide a significant amount of basic information that is mainly pertinent at slow rates of deformation. The behavior of the material can differ significantly if it is experiencing a high-speed loading different from that used in the basic design of the structure. In general, the mechanical response of any material, and particularly advanced composites, cannot be obtained from static tests. Vibration tests can provide more insight into the dynamic characteristics of the material, but they are limited to small strains only. The recent availability of high-speed testing machines enables the scientist to investigate the behavior of structural materials under loading rates approaching those encountered in aircraft operations.

The effect of the rate of straining on the behavior of conventional aircraft structural materials has been investigated theoretically and experimentally<sup>1-6</sup>. Also, various types of studies in the fatigue characteristics of different types of graphite composites<sup>7-8</sup> have been conducted. An investigation concerned with the behavior of a filled elastomer at high strain rates has been published recently<sup>9</sup>.

The primary aim of the investigation described here was to determine the influence of the rate of loading on the response of advanced composites and its effect on the mode

of failure. A particular type of graphite composite was used in the experimental investigation. Various laminae orientations were introduced to obtain the effect of fiber orientation on the strain-rate sensitivity of the composite. A particular digital computer with a high-speed data storage was used to monitor the experiments. Photomicrographs were used to investigate the type of fracture mechanisms in various types of laminates.

The following sections present a summary of the constituents and manufacturing method of the composite system considered. Experimental procedures and the equipment used in different tests are also summarized. The experimental results are discussed in the light of the performance of conventional metallic materials. The last section presents conclusions and recommendations based on the available test results.

## COMPOSITE MATERIAL

The experimental work was carried out on graphite fiber-reinforced composites. The graphite fiber was Thornel 50 with a Young's modulus of  $47.7 \times 10^6$  psi and ultimate tensile strength of  $252 \times 10^3$  psi. The matrix was ERL-2256 epoxy resin with 19.2 PHR MPDA curing agent. Thirty percent by weight acetone was added to the resin bath during filament winding to adjust the viscosity. The tensile strength and modulus of the resin system were  $9.1 \times 10^3$  psi and  $0.507 \times 10^6$  psi, respectively, whereas the flexural strength and modulus were  $16.4 \times 10^3$  psi and  $0.597 \times 10^6$  psi.

The composite laminae were prepared by filament winding. Each lamina was B-staged by heating for 15 minutes at 95°C, followed by 25 minutes at 105°C. Laminates were formed by hand lay-up of the B-staged laminae in the desired orientation. The laminates were press-cured on the following cycle:

30 minutes at 70°C and 90 psi.

30 minutes at 100°C and 180 psi.

60 minutes at 160°C and 180 psi.

The laminae were removed from the mold after it cooled, and were post-cured for 120 minutes at 160°C. The

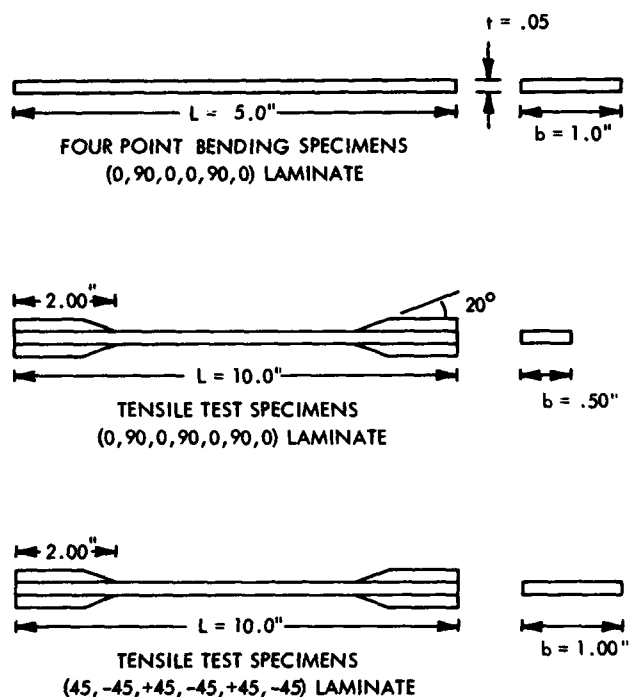


Figure 1. Specimen Configurations Used.

resulting laminates represented typical graphite composites fabricated in a laboratory environment.

The composition of the composite system was aimed at 50 percent fiber volume in a plate form with nominal thickness of 0.05 inch. Fiber analysis of the formed composite plates indicated some variation in fiber volume content from one plate to another. The fiber volume content within one plate, however, was almost constant. A summary of the chemical analysis ( $\text{HNO}_3$  digestion analysis) for all composite plates is in the Appendix of this paper.

Plates with laminae oriented at  $0^\circ/90^\circ$  were formed for tension and bending tests, whereas plates with  $\pm 45^\circ$  fiber orientation were made for tension tests alone. Specimens of the configurations shown in Figure 1 were cut with a diamond saw from each plate, to a nominal cross section as indicated. A slight deviation from the standard test specimen dimensions as recommended in the Air Force Structural Design Guide for advanced composite applications was necessary so that the ultimate loads of specimens tested at high loading rates would be low enough relative to the rigidity of the machine.

## EXPERIMENTAL PROCEDURES

The objective of the test program was to determine the effect of the rate of loading on the mechanical behavior and ultimate strength and stiffness of advanced composites such as graphite fibers reinforcing epoxy matrix. The experimental procedure was to subject the test specimens to constant rate of loading in a relatively stiff machine, and to record the machine input and the composite response. Special emphasis was placed on accurate measurements of

ultimate strength, load-time, average deformation-time, and local strain-time responses of the composite. The test specimens were thin enough to warrant variations in the strain-rate and/or the stress gradient along the tested specimens.

Loading rates between 0.005 and 2 inches per minute were obtained using a Model TTCL Instron universal testing machine with fixed cross-head speed. The Instron was calibrated and the load and head travel were measured using standard recorders on the Instron testing machine. The initial effective gauge length of the test specimens was used for the calculation of the overall average strains from the cross-head displacement of the Instron. Local electric resistance strain gauges, however, were placed on each side of the specimens surface at mid-span, and the strain response was monitored on an x-y plotter.

The equipment used for the high-speed loading rates from 0.15 in/min. to 3000 in/min. was a 10K, closed-loop, hydraulic, universal testing machine manufactured by MTS. The maximum applied load on the specimens was not to exceed 3000 pounds. The selected loading rates were 0.15, 60, 120, 180, 300, 600, 1500, and 3000 inches per minute. The loading piston on the lower plateau of the MTS machine and the load cell on the upper fixed head were calibrated and checked periodically for alignment. A special joint was attached to the load cell on the upper jaw of the testing machine to secure a self-alignment device for the loading fixture. The lower side of the specimens was attached to a slack joint on the MTS machine to allow the piston to build up to maximum constant speed before loading the specimen. A silicone rubber ring 1/8 inch thick was used in the slack joint as a shock absorber. The load cell was also insulated from the testing machine by a rubber cushion. These precautions helped reduce any ringing due to the contact of the slack grips, and prevented fixture bouncing, especially at high loading rates. It also aided in reducing the transmission of machine vibration to the specimens.

Extreme care was taken in clamping each specimen in the jaws so as to minimize any bending and twisting of the specimen. A special spacer was used in the jaws to ensure that the specimens were parallel to the loading axis. The jaws also were checked to ensure perfect alignment.

Figure 2 is a functional block diagram of the MTS test apparatus and the hook-up of the recording equipments. The hydraulically driven piston, with all attachments, was arranged to allow a travel of 0.25 inch before contacting the lower grip of the specimen. A storage oscilloscope was used to record the load versus time and head displacement versus time, and Polaroid pictures were taken for all stored data.

Two strain gauges, one affixed to each side of test specimens, were attached to two signal conditioners with built-in calibration resistors. Six-volt batteries were used as



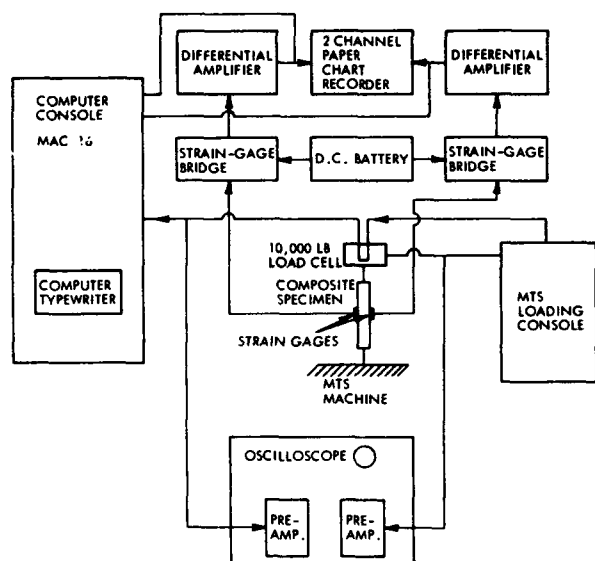


**Figure 2. Schematic of Test Set-up and Recording Equipments.**

the bridge excitation. From the signal conditioners, the strain outputs were relayed through two Sanborn 8875A Differential Amplifiers and then sent to the MAC 16 computer for processing. The same signals were input to a Sanborn 322 Dual Channel D.C. Amplifier-Recorder. The strain as a function of time was thus recorded on the H.P. Recorder for "real time" analysis, and was used to check the results obtained by the MAC 16. However, because of recording speed, this H.P. Recorder could be used only at load rates slower than 120 in/min.

The load signal was taken from the MTS and put into one channel of a Dual Trace Tecktronix Storage Oscilloscope. The deflection of the piston was recorded with the other channel of the scope. The load and deflection outputs were also input to the MAC 16 for processing and more manipulations. The load was calibrated using a Digital Volt Meter, and the deflection of the MTS was set at one inch full deflection. The scope was then calibrated to 0.25 inch deflection per centimeter. These calibrations were checked frequently throughout the tests and before the start of testing any group of specimens. The computer system (MAC 16) was triggered and started sampling the data at the loading instant of the MTS machine by means of a step-function generator. The oscilloscope was triggered after a 50-pound load increase from the loading instant.

The high-speed data acquisition system used in this experiment consisted of a Lockheed Electronics MAC-16 digital computer, an ASR 33 Teletypewriter with paper tape reader and punch, and a Datawest analog-to-digital converter and multiplexer. The MAC-16 is a one-microsecond cycle time, 16-bit word, general purpose computer with 4096 words of core memory. The datawest ADC is a 100 KHz, 15-bit resolution converter with a full-scale reading at  $\pm 10$  volts. Five channels were used in this experiment to

monitor the MTS load cell, head displacement, and the output of two strain gauges as installed on each side of the composite specimen and a starting trigger.

A special computer program was written such that it occupied 640 words of memory (the remainder of memory was used for data storage) and operated as follows:

- 1) Memory was cleared and a request made for identification and specification data about each specimen in terms of specimen dimensions, fiber content and orientation, and calibration data.
- 2) After type-in of all pertinent data, these data were punched out on paper tape in a format compatible with the IBM 360/50 'RAX' remote-access computing system.
- 3) Calibration data were then requested and stored for each channel.
- 4) The program then cycled on the triggering channel (which was connected to the start button on the MTS unit), awaiting a level change.
- 5) After triggering, the program commenced sampling on all four data channels once every 100 micro-seconds, testing the load channel for an incremental change of 0.5 percent of full-scale load (i.e.,  $\pm .05$  volt). Only samples which exceeded this increment were stored. The full-scale load was a function of the laminae orientations within every specimen.
- 6) Data samples were punched on paper tape in a format compatible with the RAX System.
- 7) The program returned to step 1 above.

Each recorded sample contained two 16-bit data words for a 100 micro-second interval clock, and one 16-bit word for each of the four data channels. The maximum load rate (3000 in/min.) saturated the sampling time such that all samples taken were recorded, resulting in 40 to 50 samples per channel. On the other hand, the slowest load rate (0.15 in/min.) resulted in approximately 100 points per channel per specimen. It should be noted that the whole spectrum of load rates, including specimen types and other variables, was processed using exactly the same computer program.

The average stresses were calculated from the load-time history as recorded on the oscilloscope and the computer, using the original geometrical dimensions of each specimen. The average strain and strain rates were obtained from the records of the head-deflection time history records as stored on the oscilloscope and the computer. The local strain and strain rate were obtained from the strain-gauge output records stored on the MAC 16 computer. The adhesively bonded strain gauges were used for precise local

strain measurement. Since the life of bonded strain gauges was unpredictable, especially at high strains beyond 10 percent, the machine head-deflection records were used as an indication for continuous strain observation. Thus, the stress-strain/strain-rate data could be obtained from the stress-time and strain-time history as recorded on two parallel systems. The computer output, however, was more accurate than the scope data, and the photographs collected from the scope were used mainly as a back-up and a checking system for the computer.

The deflection-time records and the strain-time records were generally smooth, indicating continuous deformation to failure. The load-time records were also continuous except at high load rates of 3000 in/min., where some irregularities and fluctuation in the records were observed for some specimens. Every experimental condition, however, was repeated at least three times to ensure reproducibility and to reduce the scatter of the test data.

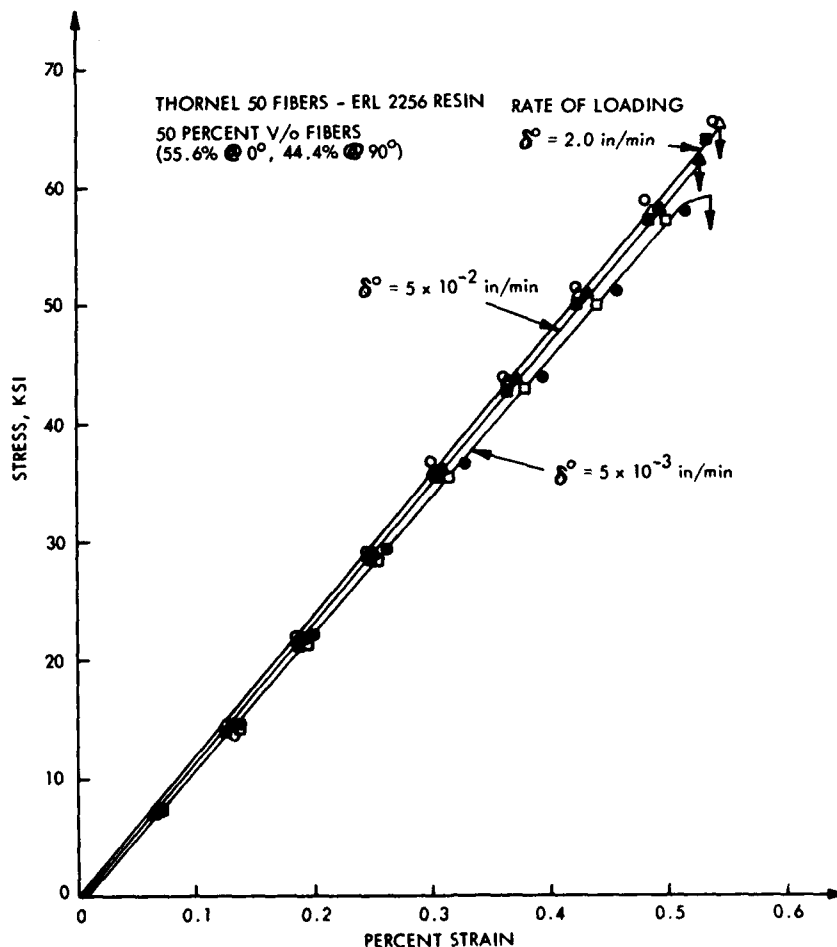
### EXPERIMENTAL RESULTS AND DISCUSSION

Stress-strain curves obtained from constant rate of loading tests are shown in Figures 3 to 6 for laminates with plies oriented at  $(0^\circ/90^\circ)$ . These curves represent the average of a number of experiments conducted under iden-

tical conditions. As shown in Figure 3, the elastic modulus of the material changes slightly due to the rise in the rate of loading from 0.005 in/min. to 2 in/min. The tests conducted at 0.05 in/min., which represent static testing, show a typical value of elastic modulus and strength for this type of composite with the particular fiber orientation used. Figure 4 represents the same observation as shown in Figure 3, but for different fiber-volume content for the same composite. Again, a slight increase in the strength and stiffness of the composite is evident due to the increase in the speed of loading. The maximum strain at failure in both figures occurred at about 0.55 percent.

The effect of the loading speed becomes more evident in Figure 5, where tests were conducted at rates up to 180 in/min. A comparison between the strength and stiffness of the composite tested at 180 in/min. to that tested under static conditions shows a gain in the strength of about 30 percent, whereas the modulus increased by about 14 percent. These percentages represent the gain in strength and modulus, respectively, based on 56-percent fiber volume content. It should be noticed, however, that the basic response of the composite is linear under loading speeds from 0.005 in/min. to 180 in/min. No significant change in the basic characteristics of the  $(0^\circ, 90^\circ)$  laminates is noticed, except in a gain in the strength and modulus

Figure 3. Effect of Loading Speed on Stress-Strain Curves for Graphite Composites.



of the material. However, the criterion of linearity changes at significantly high rates of loadings.

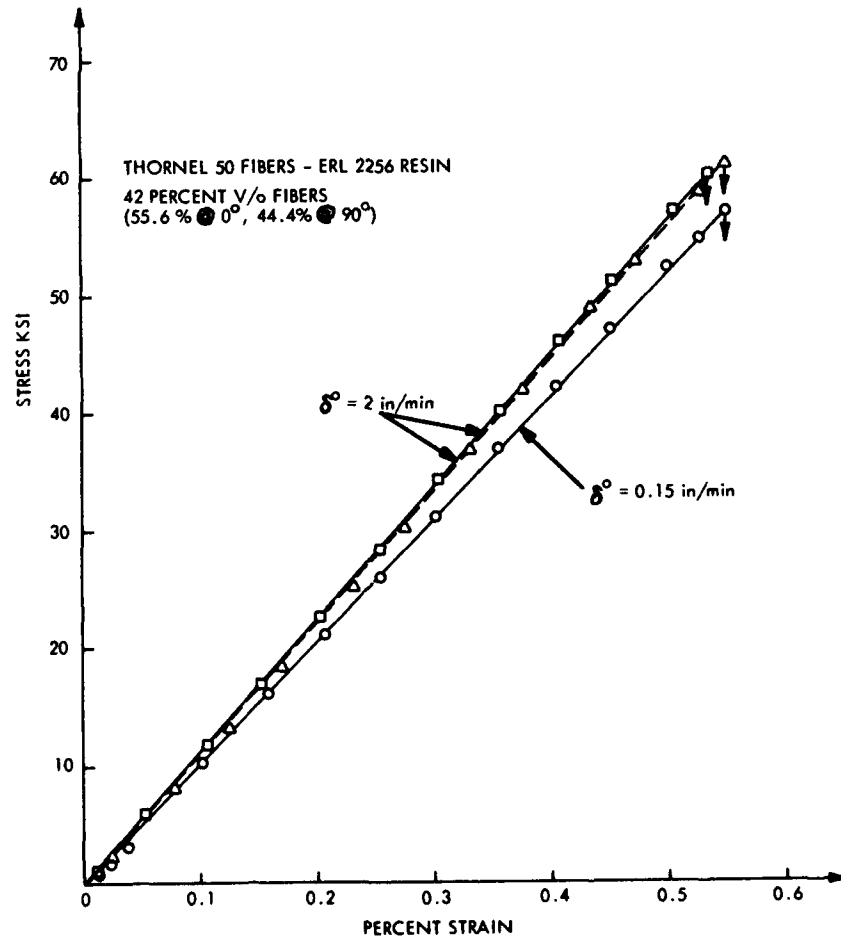
Figure 6 represents the stress-strain diagram for tests conducted at loading rates of 1500 in/min. and 3000 in/min. Although the general behavior of the material is continuous, there were two distinct slopes, one at low strain levels up to 0.35 percent and the other is beyond 0.35 percent strain and up to failure. Again, a slight increase in the failure strain was observed, whereas the gain in the fracture stress was significantly pronounced as compared to the static results at 0.05 in/min. rate of loading. A significant rise in the elastic modulus of the composite can be observed.

The mechanism of load transfer from one fiber to another through the bonding matrix plays a significant role in the behavior of the overall composite under these high rates of loading. The basic viscoelastic characteristics of the bonding matrix and its dependence on the loading time as well as the interlaminar shear behavior between the various plies are reflected in the overall strength and stiffness of the composite specimens. This phenomenon was even more pronounced for composites with laminae not oriented in the principal direction of loading, as will be described later.

The stress-strain curves can be replotted as stress versus rate of loading or strain rate for different strain levels (Figures 7 and 8). The experimental results can be approximated by a set of straight lines, and it can be observed that a change in the slopes from low to high strain rates tests can be deduced. At low strain rates, the stresses increase up to a specific rate of loading, and then a decreasing slope occurs. The experimental points from several specimens, as obtained from the same original composite plate, indicate the existence of a point of change in slope which could be considered the critical strain rate or critical loading speed. This can be observed in Figure 7 for (0°, 90°) laminates tested at rates from 0.15 in/min. up to 600 in/min. A summary of the fracture strength of all composite specimens tested at rates from 0.005 in/min. up to 3000 in/min. is presented in Figure 9 for (0°, 90°) laminates.

Some scatter in the strength of the Thornel 50 fibers from spool to spool to form the various test panels contributed significantly to the test results. Also, due to the variability in the composite material studied in terms of controlled fabrication procedures, controlled fiber-volume content, and void content, some of the experimental results could not be confidently evaluated. Thus, these experi-

**Figure 4. Effect of Loading Speed on Stress-Strain Curves for Graphite Composite.**



mental data points cannot be reasonably discussed until a detailed investigation is completed to explain their malfunction. The average of three to four experiments conducted under the same test conditions and from the same panel originally fabricated are thought to be representative of the trend of the results and are used for the data presentation in this paper.

In Figure 9, the average of experimental points as well as some individual results are plotted. The individual test points in the domain of loading rate between 100 and 1000 in/min. seemed to be necessary to observe the change in the slope of the fracture strength versus rate of loading curve. In general, all experiments showed such a trend. However, the fiber-volume content and the final thickness of the fabricated panels caused some discrepancy in the test results. Figure 9 indicates a continuous and gradual increase in the fracture strength of the composite as the speed of loading increased. In the neighborhood of 200 in/min. to 300 in/min., the test result showed an abrupt

change in the slope of the fracture strength versus rate of straining curve. Such an abrupt change in this type of curve was not clearly observed in conventional metallic materials as used for aircraft structures.

The results of a similar investigation conducted at Lockheed<sup>2</sup> on bare aluminum 7075-T6 and 1010 steel are shown in Figure 10, combined with data for normalized 4130 steel sheet material<sup>1</sup>. The results for titanium<sup>1</sup> are shown in Figure 11. The well-known behavior of a continuous and gradual increase in the fracture strength as the rate of loading increases for all three structural materials can be easily detected. The tensile strength of the four metallic materials considered in Figures 10 and 11 varies as a function of the logarithm of the rate of loading. The degree of dependence on the strain rate, however, varies from one material to another. For example, the two types of steel considered (1010 and 4130) have a strain-rate dependence which is more pronounced as compared to that in the aluminum 7075-T6 alloy, where the strain-rate effect is not very

Figure 5. Effect of Loading Speed on Stress-Strain Curves for Graphite Composite.

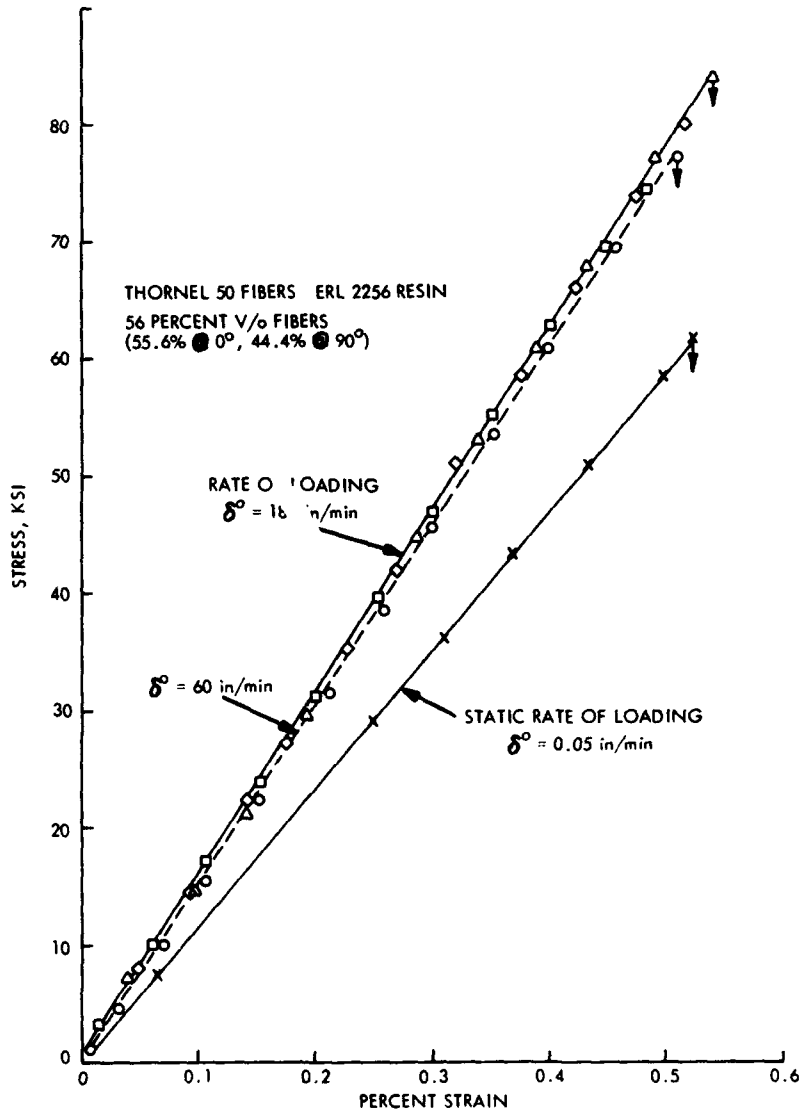
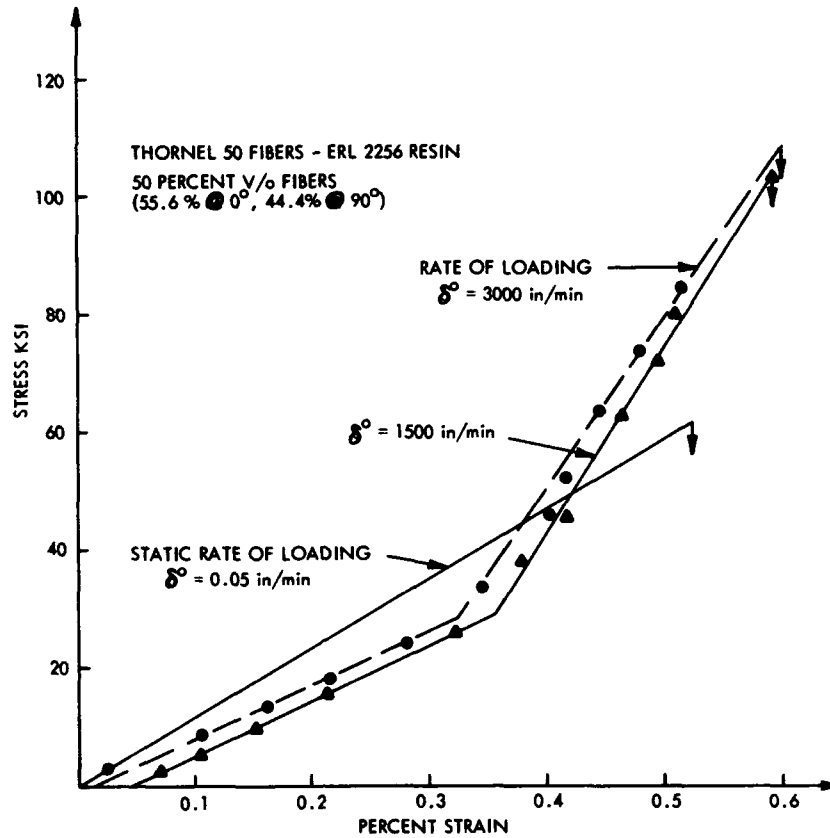


**Figure 6. Effect of High Loading Speeds on the Stress-Strain Curves for Graphite Composite as Compared to Static Values.**



evident. The effect of the strain rate on the aluminum, however, is more pronounced in cases where there is an induced stress concentration in the tested specimens<sup>2</sup>. (The sensitivity of these four materials to strain rate is also highly dependent on temperature, a subject which is beyond the scope of this paper.)

The basic stress-strain curves for the three metallic materials are affected by the rate of straining, not only in terms of the proportional limit or the yield point as based on 0.2 percent strain offset, but also in the degree of ductility and the percent strain at failure. For completeness, some typical stress-strain curves for aluminum, titanium, and

**Figure 7. Stress versus Rate of Loading for Graphite Composite.**

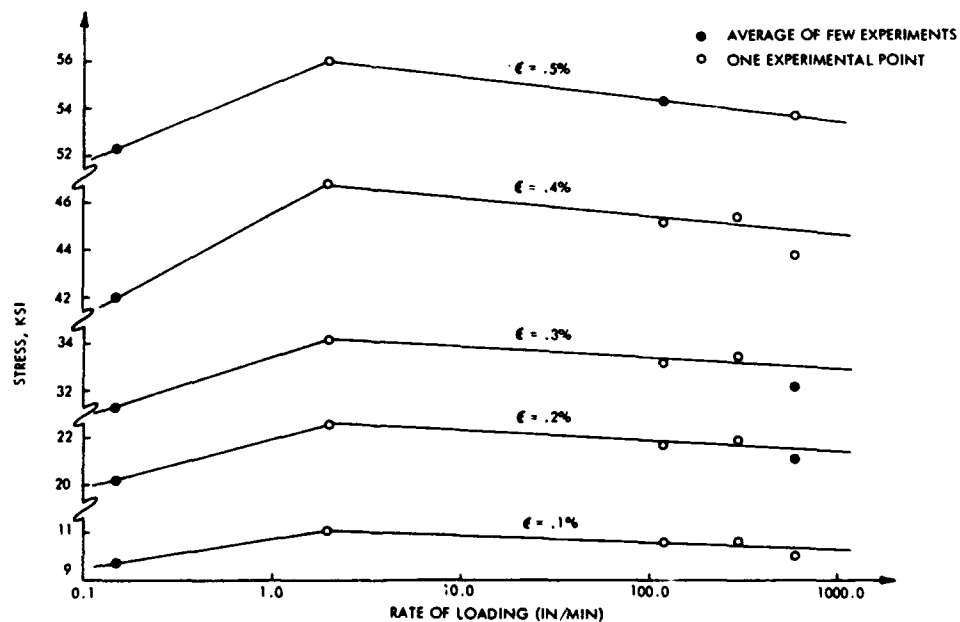
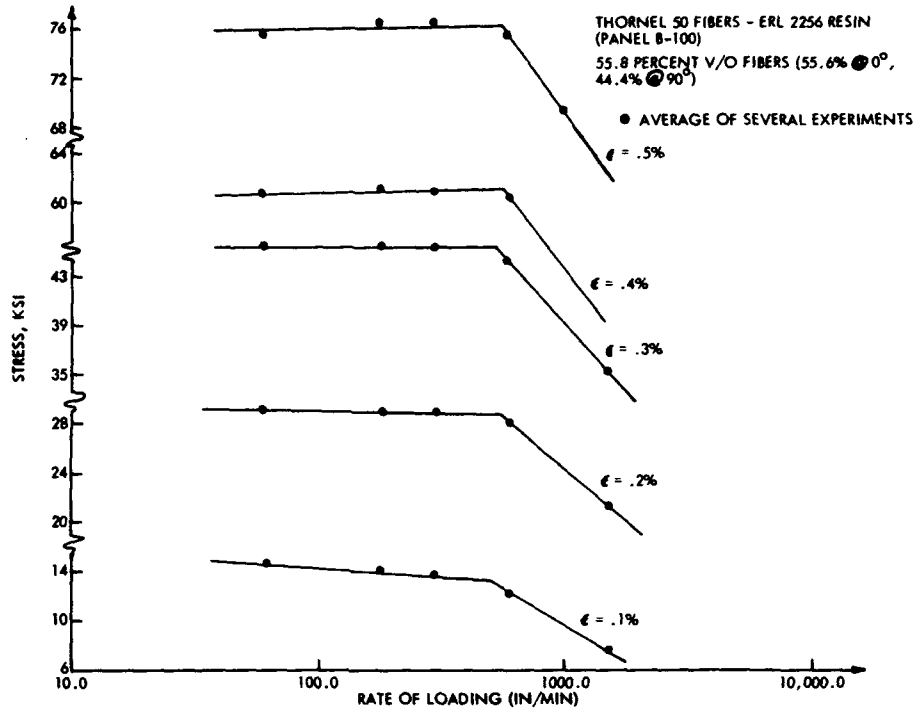


Figure 8. Stress versus Rate of Loading for Graphite Composite.



steel<sup>1</sup> are shown in Figure 12. A comparison of the curves in Figures 5 and 12 shows some distinct difference between the composite and the metallic structural material. This is mainly in terms of the linear behavior of the composite up to failure, whereas most conventional aircraft metals indicate a high degree of plasticity beyond their proportional limits which occur at very low strains.

Figure 13 represents a comparison between various ultimate tensile strength versus rate of loading curves for metallic aircraft structural materials and the particular graphite composite used in this investigation. It is to be noted that the lower overall strength of the composite is

mainly attributed to the lower percentage of laminae oriented in the load direction and the low percentage of fiber content in the composite. Based on these results, one can expect superior performance from the composite as compared to 4130 steel and 7075 aluminum if all fibers are aligned in the load direction. One of the main observations to be gained from this figure is the crossing of the graphite curve with the aluminum curve at a loading rate of about 1000 in/min. Thus, even at a low percent of fiber content within the panels and with about 50 percent of the plies oriented perpendicularly to the load direction, the composite appears to offer more strength as compared to aluminum at high rates of loadings. The same figure

Figure 9. Effect of the Rate of Loading on the Tensile Fracture Strength of Laminated Thornel 50 Graphite Fibers - ERL 2256 Resin Composite.

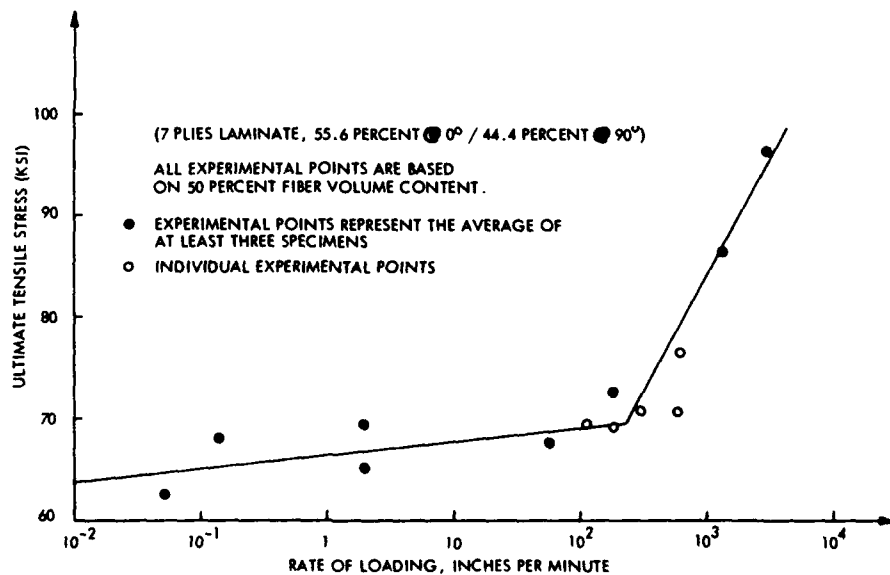
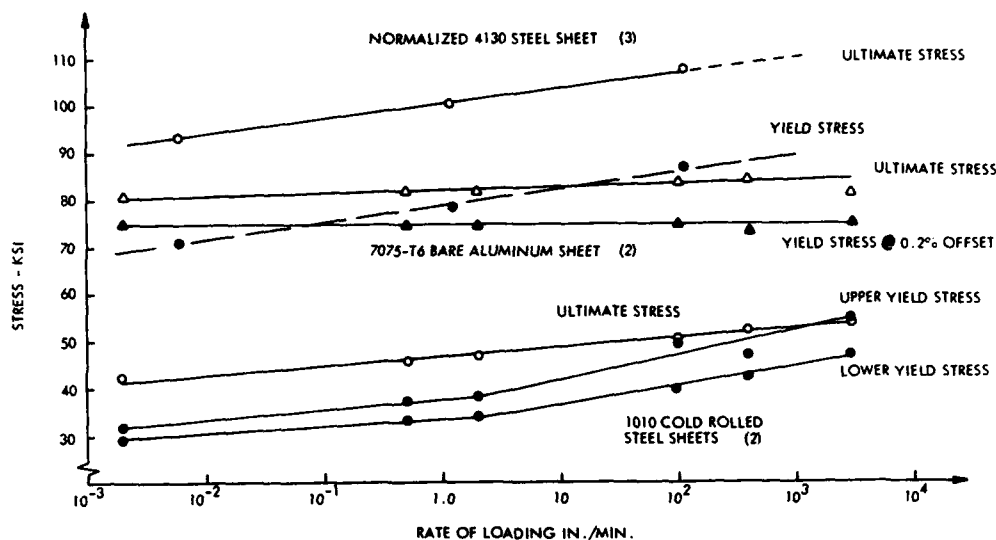


**Figure 10. Effect of the Rate of Loading on the Yield and Ultimate Stresses of Some Aircraft Structural Materials.**



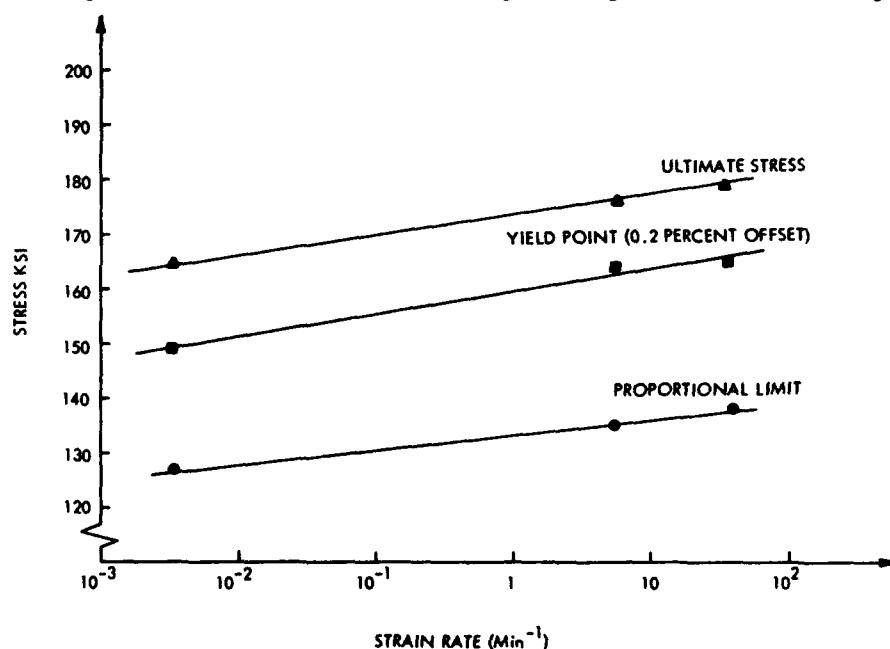
also shows the better performance of the composite as compared to the 1010 clad, rolled-steel sheets.

The effect of the rate of loading on the elastic modulus of graphite composite and aircraft metallic materials is shown in Figure 14. A linear increase in the modulus as function of the logarithm of the rate of loading is quite evident. In the case of titanium 6AL-4V, a slight increase in the elastic modulus up to a rate of loading equal to about 1.2 in./min., followed by a continuous decrease in the modulus below the static values of the basic alloy. This response can also be detected in the basic stress-strain curves as shown in Figure 12, where the plastic deformation in the alloy under the same stress level is higher in the high rate of straining tests ( $60 \text{ min}^{-1}$ ) as compared to  $0.6 \text{ min}^{-1}$  strain rate tests. The same response can also be observed in the case of the 7075 aluminum (Figures 12 and 14).

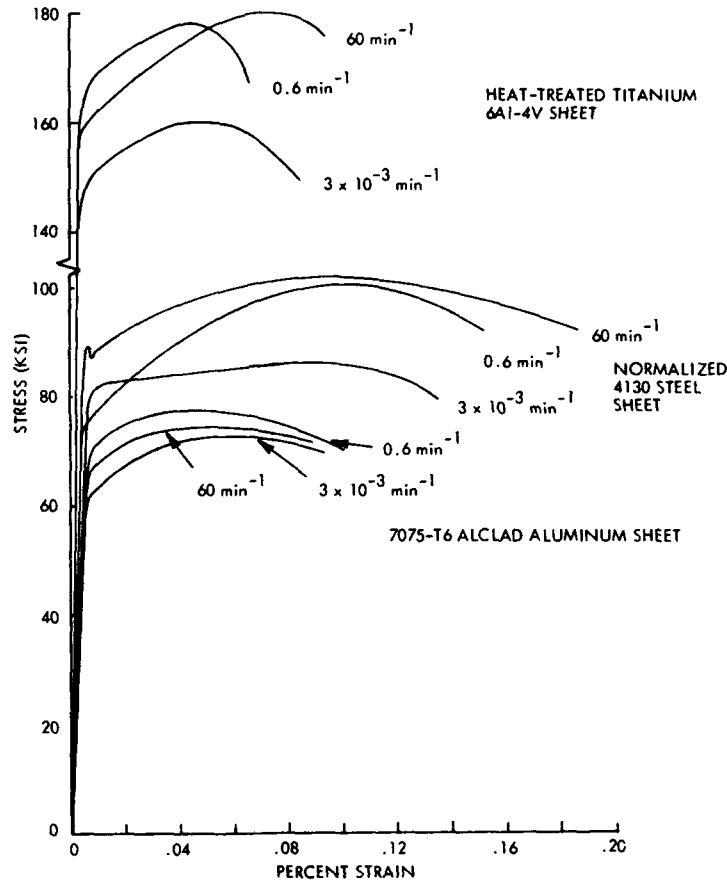
For the 4130 steel sheets, under a constant total strain, the stresses increase as the rate of straining increases, and thus a continuous rise in the elastic modulus is expected as the rate of loading increases. However, the elastic modulus of this type of steel decreases as the rate of straining increases. This has been observed in data collected from Reference 6.

The same phenomenon was also observed in the flexural strength and stiffness of the same composite, as shown in Figure 15. Again, a continuous gradual increase in the ultimate flexural strength of the composite was noted as the rate of loading increased. An abrupt increase in the strength showed up at loading speeds of about 120 in./min., which is consistent with observations reported in the uniaxial tensile test data. The absolute value of the ultimate flexural strength was higher than the tensile strength due to

**Figure 11. Effect of Strain Rate on the Ultimate Stress, Yield Stress and Proportional Limit for Heat-Treated 6Al-4V Titanium Alloy Sheet.**



**Figure 12. Effect of Strain Rate on the Stress-Strain Curves of Heat-Treated 6Al-4V Titanium Alloy Sheet, Normalized 4130 Steel Sheet, and Alclad 7075-T6 Aluminum Alloy Sheet<sup>1</sup>.**



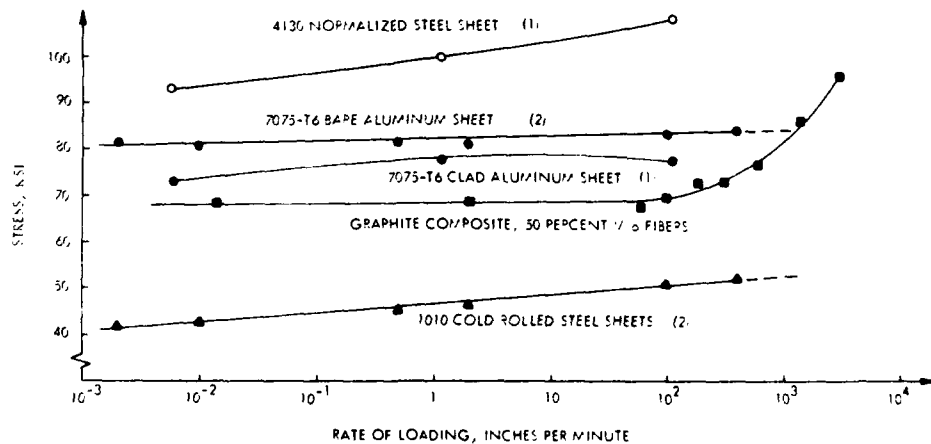
the increased number of plies oriented in the direction of the applied flexural loads. This, in turn, eliminated some of the effects caused by the interlaminar shear behavior of the composite at high rates of loading, which is mainly controlled by the resin system.

Figure 16 presents typical stress-strain curves for

the graphite composite with plies oriented at  $\pm 45^\circ$  with respect to the tensile loading axis. This figure covers rates of loading from 60 in/min. to 600 in/min. As expected, a distinct difference in the basic stress-strain curves is evident in comparison with the stress-strain curves for the (0°, 90°) laminates shown in Figures 3 through 6. A continuous and linear behavior is shown up to 50 percent of the ultimate

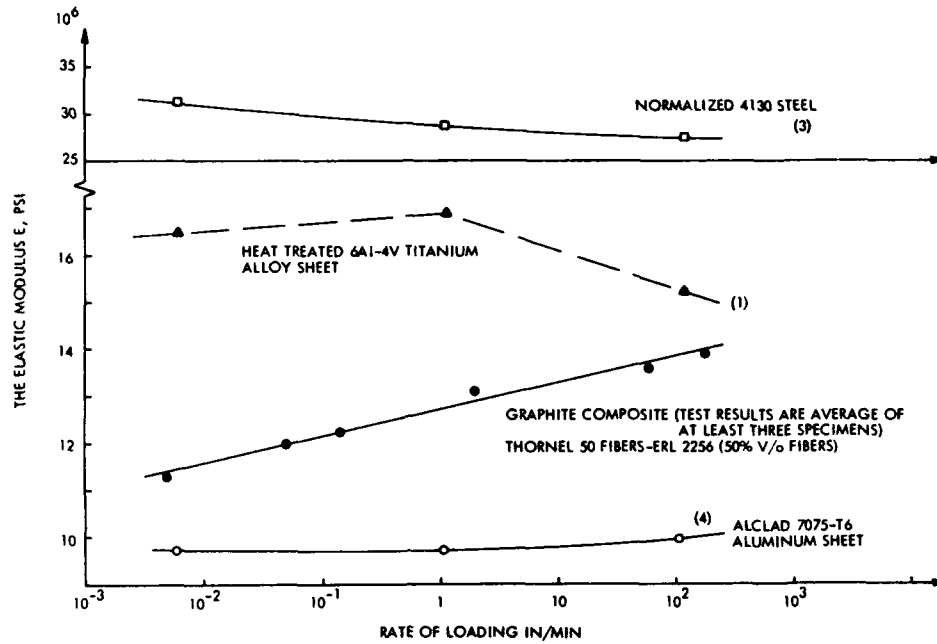
- 7075-T6 BARE ALUMINUM SHEET, ULTIMATE TENSILE STRESS
- ▲ STEEL 1010 COLD ROLLED SHEETS, ULTIMATE TENSILE STRESS
- GRAPHITE COMPOSITE, 50 PERCENT  $\pm 45^\circ$  FIBERS (55.6°: ● 0°, 44.4°: ● 90°)

**Figure 13. Ultimate Tensile Stress as a Function of Loading Speed for Composite and Metallic Materials.**





**Figure 14. Effect of Rate of Loading on the Elastic Modulus of Graphite Composite and other Metallic Materials.**



load accompanied with low strain levels. This is followed by a continuous and nonlinear response for higher strains and up to failure. At these rates of loadings, the (0°, 90°) laminates indicated a continuous and linear response up to failure.

The basic phenomenon of increased strength and stiffness due to rise in the rate of loading is still evident. The elastic modulus for this type of laminae orientation based on 0.2 percent strain still shows a continuous increase in the modulus as the rate of loading increases. The same

concept is manifested in Figure 17 for specimens tested at loading rates from 0.15 in/min. to 3000 in/min. Again, an apparent increase occurs in the fracture strength and the elastic modulus of the specimens as the rate of loading increased. Also, the linearity of the stress-strain curves followed by a nonlinear response at high strains is consistent for all tested specimens.

A summary of the stress versus rate of loading at constant strains is shown in Figure 18 for this type of laminate configuration. The data deduced from the computer

(6 PLYS LAMINATES, 66.67 PERCENT 0° / 33.33 PERCENT 90°)

**Figure 15. Effect of the Rate of Loading on the Bending Fracture Stress of Laminated Thornel 50 Graphite Fibers - ERL 2256 Resin Composite.**

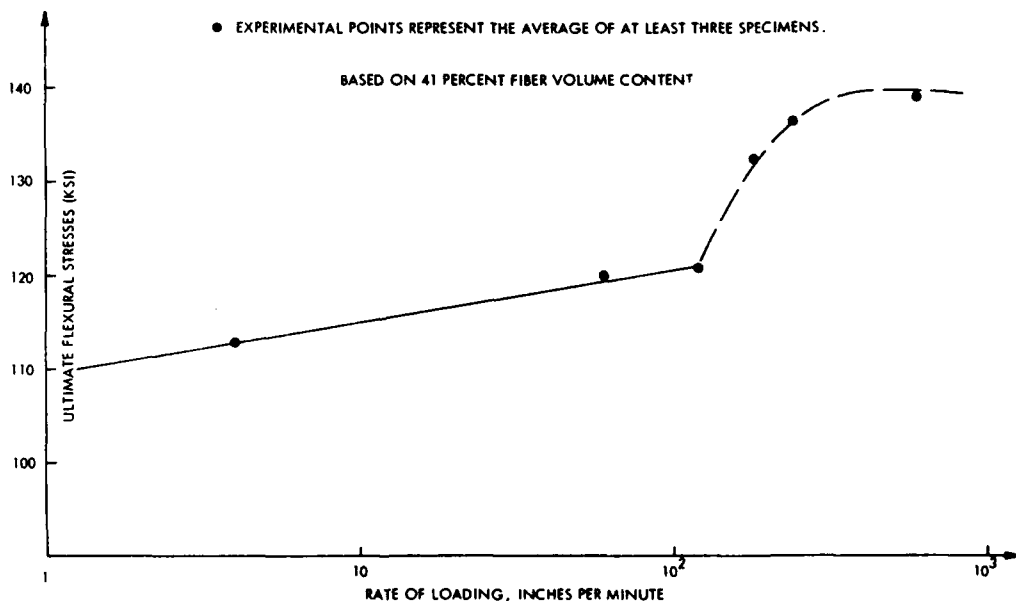
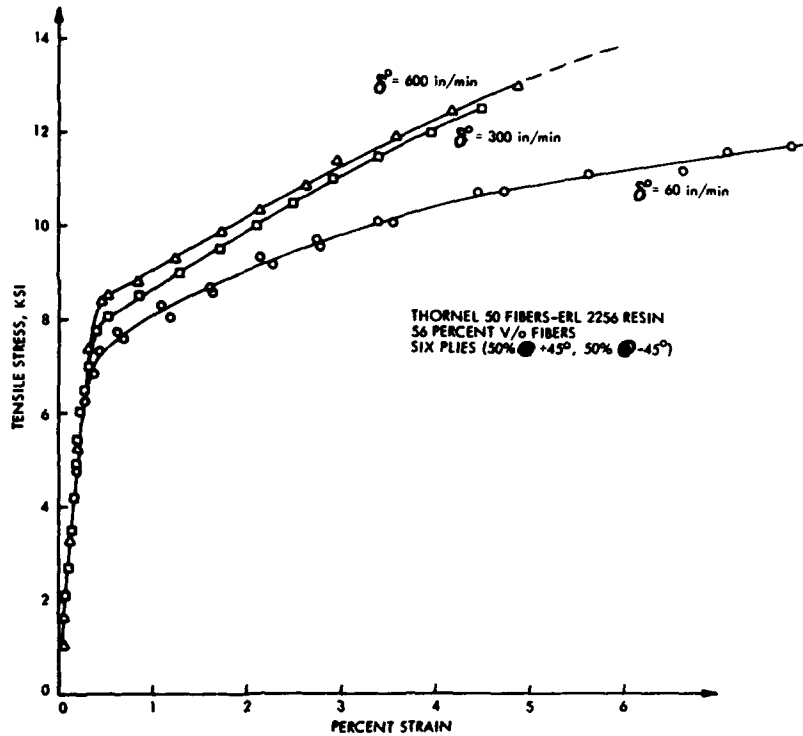


Figure 16. Stress-Strain Curves at Various Rates of Loading for (+45°, -45°) Graphite Composite Laminates.



output represent a fairly linear relation between the stress and the rate of loading at constant strain levels. One can also observe (Figure 18) that the change in the slope of the stress versus the rate of loading line occurs at a critical speed between 200 in/min. to 300 in/min.

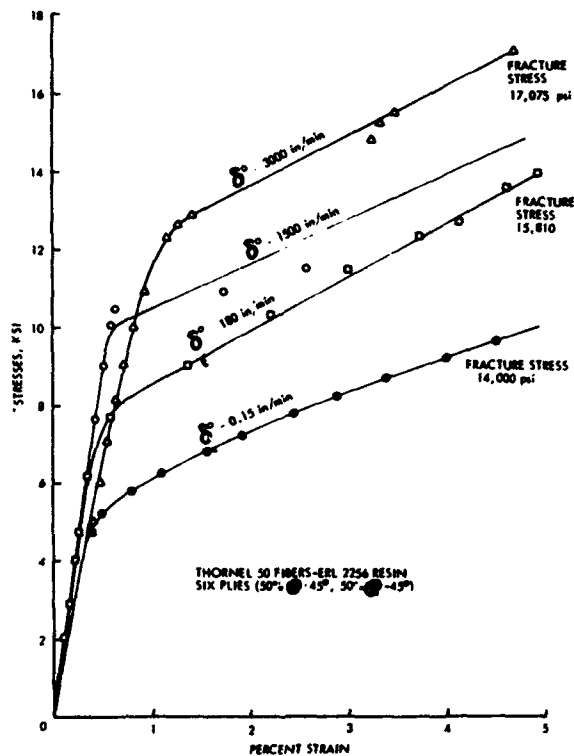


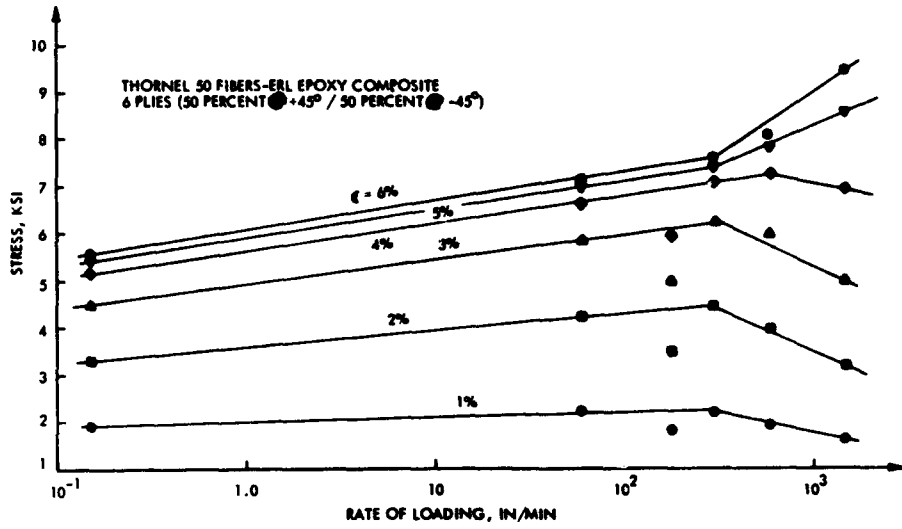
Figure 17. Stress-Strain Curves at Various Rates of Loading for (+45°, -45°) Graphite Composite Laminates.

At a loading rate below the critical rate of loading and for a constant strain level up to 3 percent, the slope of the stress versus rate of loading line increases as the rate of loading increases. Beyond the critical speed of loading, the slope of the line decreases. This trend, however, changes at high strain levels beyond 4 percent, and a continuous increase in the stress is observed as the rate of loading increases. This observation can be attributed directly to a slippage mechanism between the various plies in a laminate and an inelastic extension of the bonding matrix within the laminae. In the fiber orientation used in this laminate configuration, all loads transferred from the machine head to the specimen are controlled by the bonding matrix. The load is transferred from one ply to another by interply shear stresses and within the same lamina, it is transferred from one fiber to another by shear stresses in the bonding matrix.

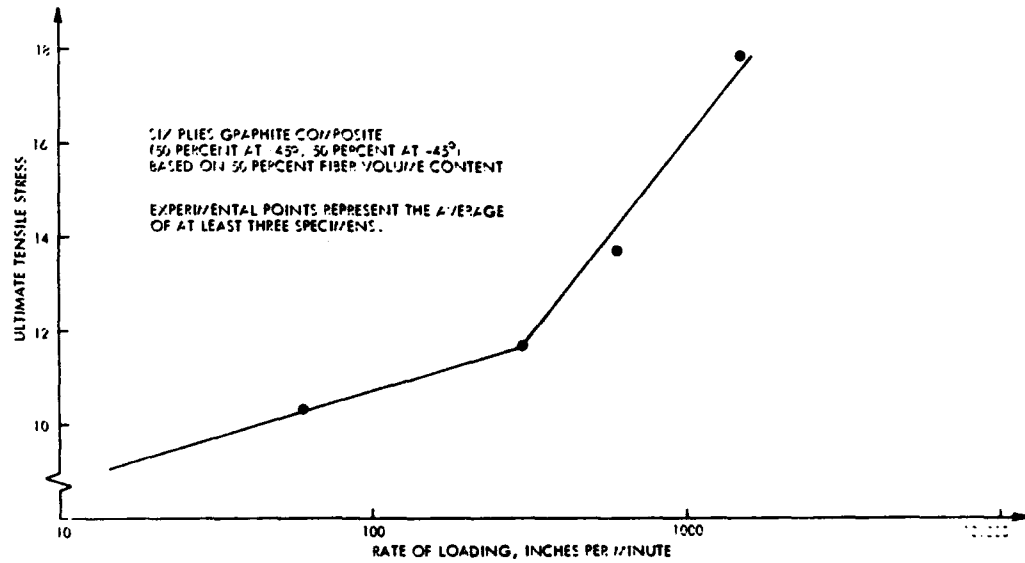
Figure 19 shows the ultimate tensile stresses versus rate of loading for this type of laminae orientation. The same significant increase in the ultimate stress as function of the rate of loading can be observed. The critical rate of loading point is also evident and is consistent with what has been observed in the (0°, 90°) laminate configuration.

A comparative representation of the accumulated failure strain for the graphite composite is shown in Figure 20, with documented data for steel and aluminum. This

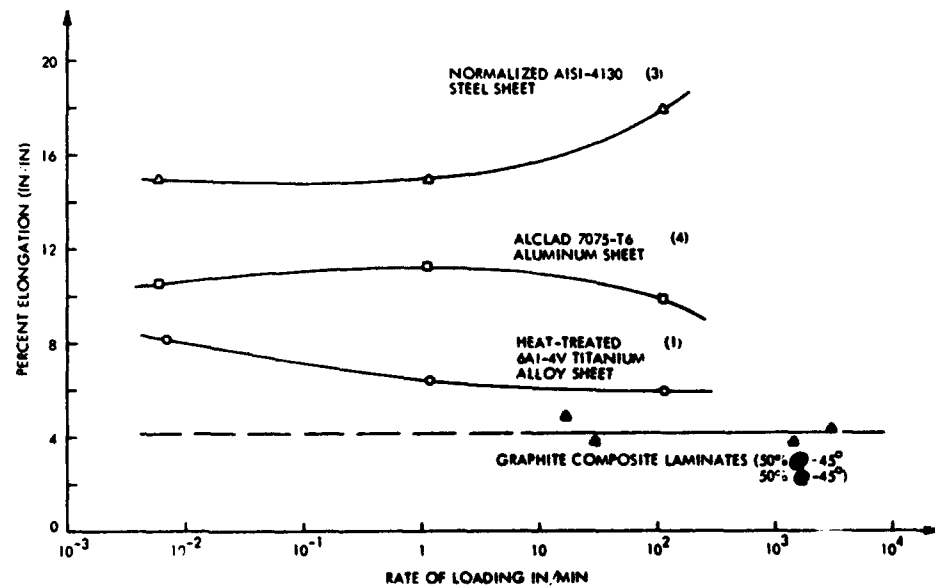
**Figure 18. Stress versus Rate of Loading for Constant Strains.**



**Figure 19. Effect of the Rate of Loading on the Fracture Stress of Laminated Graphite-ERL 2256 Resin.**



**Figure 20. Effect of Loading on the Elongation of Metallic and Composite Materials.**



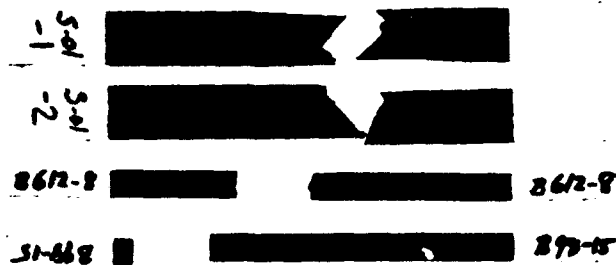


Figure 21. Typical Tensile Specimens ( $0^\circ$ ,  $90^\circ$ ) and ( $45^\circ$ ,  $-45^\circ$ ).

Figure 20 presents the failure strain for composite laminates with ( $\pm 45^\circ$ ) laminac orientation. The failure strain for specimens with ( $0^\circ$ ,  $90^\circ$ ) fiber orientation did not exceed 0.55 percent strain and is not shown. A basic comparison between the failure strain of conventional material and that accumulated in laminates with the  $\pm 45^\circ$  fiber orientation indicate that the composites have almost a constant total elongation over the loading range tested. The titanium 6AL-4V and the aluminum 7075-T6, however, show a reduction in total elongation as the rate of loading increases. Also, the percentage of the total elongation in the composite is lower than that in any of the metallic materials shown in Figure 20.

The fracture pattern of some typical tensile specimens is shown in Figure 21. In some cases, one can observe the change in the fracture mode due to the rise in speed of specimens loading. Some of the tensile specimens showed, however, two distinct modes of failure, depending on the ply orientations within a laminate. A shear failure mode was dominant in the case of the ( $\pm 45^\circ$ ) laminates, whereas a clear tensile failure mode was observed in the ( $0^\circ$ ,  $90^\circ$ ) laminates. Some of the specimens were examined under a light microscope to detect the penetration of cracks throughout the width of the specimens.

In Figure 22, the fracture mode of a bidirectional reinforced specimen at ( $0^\circ$ ,  $90^\circ$ ) showed a combination of tension and shear failure modes. It is also interesting to notice the penetration of the interlaminar shear failure between the plies and the propagation of this type of failure along the specimen length.

Figures 23 and 24 represent the fracture mode of ( $\pm 45^\circ$ ) bidirectional laminates tested at two different rates of loading: 300 in /min. and 600 in /min. As shown in these figures, a predominately shear failure was observed in all tested specimens. No major crack-penetration along the specimen length was observed. However, near the fractured surface, shear failure cracks were noticed in the outer plies of the tested laminate. This type of crack plus a slight interlaminar shear failure were assumed to create the controlling fracture mechanism in this type of laminate stacking and orientation.

The fractographic features associated with the com-

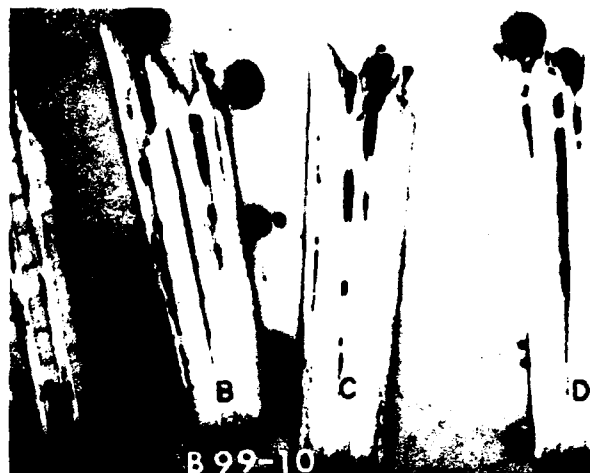


Figure 22. Photomicrograph of a ( $0^\circ$ ,  $90^\circ$ ) Bidirectional Composite Tested at 60 in/min (10 X Reduced 25%).

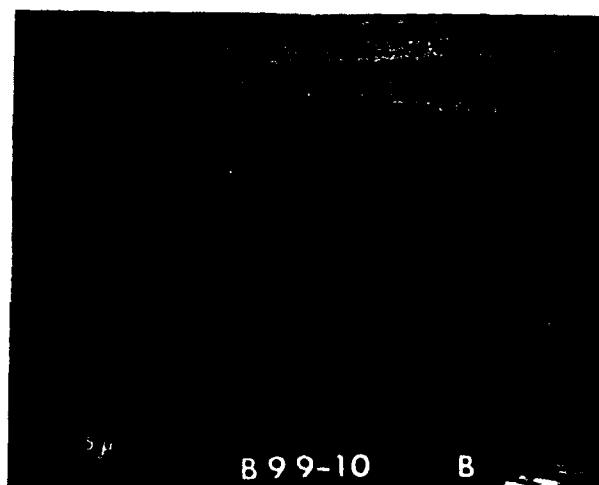
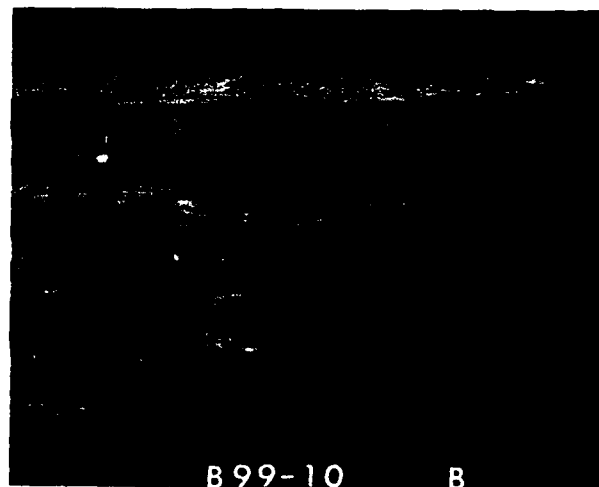


Figure 22b. Photomicrograph of a ( $0^\circ$ ,  $90^\circ$ ) Bidirectional Composite Tested at 60 in/min, Magnification of Section B (200X Reduced 25%).

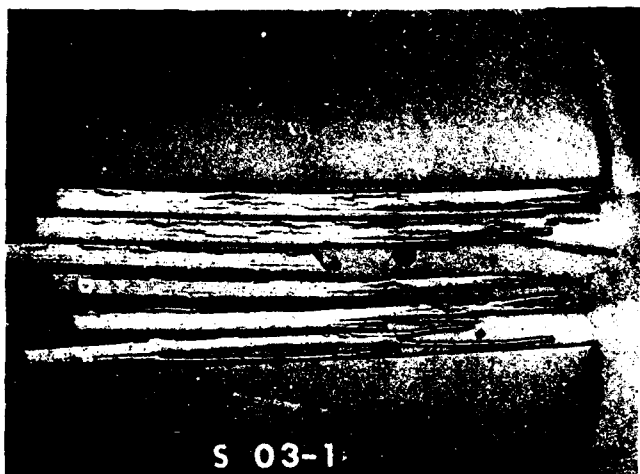


Figure 23. Photomicrograph of a (45°, -45°) Bidirectional Composite Tested at 300 in/min (5X Reduced 25 %)

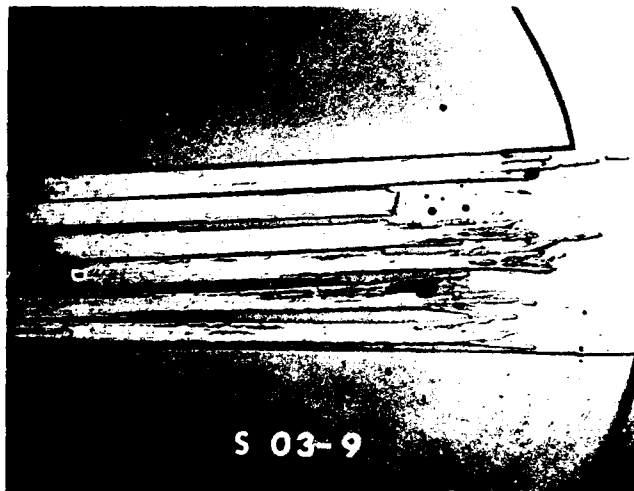


Figure 24. Photomicrograph of a (45°, -45°) Bidirectional Composite Tested at 600 in/min.

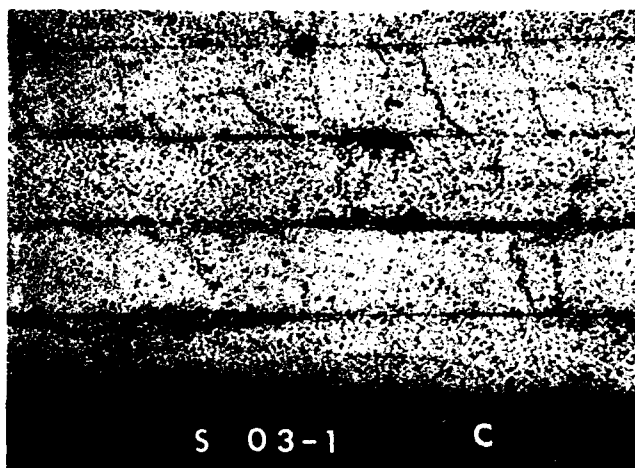


Figure 23b. Photomicrograph of a (45°, -45°) Bidirectional Composite Tested at 300 in/min, Magnification of Section C (100X Reduced 25%).

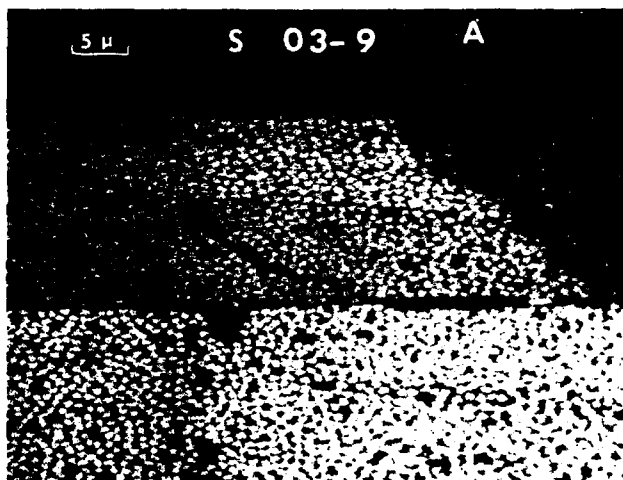


Figure 24b. Photomicrograph of a (45°, -45°) Bidirectional Composite Tested at 600 in/min, Magnification of Section A (50X, 200X Reduced 25%).

posite failure can be correlated with the fracture mechanics concepts to describe the stress conditions at the origin of fracture. Such a concept has been applied to various metallic materials<sup>8</sup> with a reasonable degree of success.

### EFFECT OF COMPOSITE RESPONSE ON THE SAFETY ANALYSIS OF COMPOSITE STRUCTURES

The safety analysis of any structure depends on a particularly assumed failure mechanism. This is usually based on an adopted failure criterion in conjunction with the deformational response of the structure, which is a direct function of the mechanical response of the basic material and the geometry of the particular structure considered. Some investigators e.g., Ref. 11, suggested the use of the material failure or the material instability due to inelastic deformations as alternative structural failure mechanisms. Thus, the inelastic response of the structural material is a significant parameter in the selection of the design condition of a structure.

In the case of a composite structure formed from laminates with simple stacking sequence and orientation, such as (0°, 90°) or (0°) laminates, the material usually exhibits a linear response up to failure, and in general, it can be represented by an elastic brittle medium. Thus, the critical failure mechanism of the structure can be characterized by the statistical dispersion of the failure resistance<sup>11</sup>. This can be accomplished by replacing the constant physical parameters, such as the moduli of elasticity and the coefficients of viscosity, in the governing structural equations by the probability density functions of the material response. In this case, the basic material is considered to be a random medium, and the governing structural equations with stochastic coefficients. The distribution of failure resistance in this case can be deduced from simplified assumptions of known statistical variation of local strength. This approach has been thoroughly studied<sup>12</sup>.

Under a uniform applied tensile stress, the distribution of the resistance to failure of this type of laminate configuration has been suggested in<sup>11</sup> to be in the form of the third asymptotic distribution of extreme (smallest) values (Weibull distribution<sup>13</sup>). There are indications that such a distribution correlates well with experimentally observed effects of size, geometry, and stress distribution<sup>11</sup>. This theory also provides the resistance to failure in bending from knowledge of the resistance to failure in pure tension, based on the same level of probability of failure.

For a composite system with nonlinear response due to the basic properties of the laminae or due to the stacking sequence and fiber orientation of the plies, as in the case of the  $\pm 45^\circ$  laminates, the established theories of linear elasticity and viscoelasticity are not applicable. Thus, the introduction of stochastic distributions of the material response in the formulation of the constitutive equations or in the governing structural equations is precluded. Experi-

mental data obtained from this investigation will be used in the formulation of failure-resistance analysis for graphite composite with various laminae stacking and orientation, and will be reported in a forthcoming publication.

### SUMMARY AND CONCLUSIONS

The basic response of a graphite composite system has been thoroughly investigated under various levels of loading rates. Different types of laminae orientations with respect to the loading axis have been used to examine the influence of fiber orientation on the dynamic response of the composite system as a function of loading rates.

Based on the results obtained from this investigation, one can conclude that the speed of loading has a significant effect on graphite composites, and this can be used as a measure of the sensitivity of various composites to the rate of load application. Two main concepts have been observed: the increase in the fracture strength as the rate of loading increased, and the increase in the stiffness as the rate of loading increased.

The percentage increase in the strength and stiffness of the composite due to the rise in the rate of loading is a direct function of the laminae orientation. For unidirectional or bidirectional composite laminates, the response was linear up to failure; for off-axis laminates, a non-linear behavior was clearly observed.

At loading rates close to the static rate, 0.05 in./min., both the strength and stiffness of the composite improve slightly. The increase becomes more evident for higher rates of loading beyond 600 in./min. The ultimate tensile stress of bidirectional laminates increases as a linear function of the logarithm of the rate of loading. At a critical speed, there is an abrupt change in the relation between fracture strength versus the logarithm of loading rate.

Results observed with composites have been compared to conventional material such as titanium, aluminum and steel to obtain a basic comparison between the two types of aircraft structural materials. Based on the low percentage of fiber content in the composite used, it can be stated that the graphite composite shows better performance under high rates of loadings, compared to the conventional metallic materials. This performance is measured by the strength and stiffness of the composite in comparison to the metallic materials.

Fractographic techniques were used to examine the fracture pattern and failure modes in the composite as a function of rate of loading and fiber orientation. These techniques were also used to determine the penetration of surface cracks throughout the specimens. Consideration was given to the importance of defining a consistent failure criterion and developing the basic mechanical response of the composite in any failure analysis or fatigue failure analysis of composite structures. Further evaluation of the effect of composite properties on a general failure analysis is still

under investigation.

These results are quite important in designing composite structures with minimum weight as subjected to impact or dynamic loading conditions. Such information is still lacking in the "Structural Design Guide for Composite Structures," where the sensitivity of various advanced composites to high loading rates is not reported.

### ACKNOWLEDGEMENTS

The authors wish to extend their special gratitude to Mr. T.D. Neill of the Systems Sciences Laboratory, Lockheed-Georgia Company, for his writing of the computer programs and assistance in the hookup of the computer to the experimental setup. We also wish to thank J.M. Colt for his help in preparation of the tests and the reduction of data, and R.C. Waugh for preparation of the composite panels. Special thanks are extended to J.H. Sams, III, for his support and encouragement during the conduct of the study.

### APPENDIX

Chemical Analysis of the Composite Plates by HNO<sub>3</sub> Digestion

PLATE IDENTIFICATION	FIBER ORIENTATION	Volume Percent of Fiber		
		MAX.	MIN.	AVERAGE OF 60 SAMPLES
B-98	7 plies ( 4 @ 0° 3 @ 90°)	43.70	40.10	42.15
B-99	7 plies ( 4 @ 0° 3 @ 90°)	48.00	44.84	46.80
B-100	7 plies ( 4 @ 0° 3 @ 90°)	56.34	54.55	55.80
B-612	7 plies ( 4 @ 0° 3 @ 90°)	50.7	49.2	49.7
S-01	6 plies @ (± 45°)	43.6	42.0	42.7
S-02	6 plies @ (± 45°)	48.620	46.74	47.30
S-03	6 plies @ (± 45°)	58.33	55.85	56.77

## REFERENCES

1. H.E. Dedman, E.J. Wheelahan, and J.R. Kattus, *Tensile Properties of Aircraft Structural Metals at Various Rates of Loading After Rapid Heating*, WADC-TR-58-440, Aeronautical Systems Division, Wright-Patterson AFB, Ohio (1958).
2. H.S. Pearson, *Effects of Strain Rate on Mechanical Properties of Metals in the Presence of Stress Concentrators*, ER-10244, Lockheed-Georgia Company, Marietta, Georgia (1969).
3. J.D. Morrison and J.R. Kattus, *Tensile Properties of Aircraft Structural Metals at Various Rates of Loading After Rapid Heating*, WADC-TR-55-199, Aeronautical Systems Division, Wright-Patterson AFB, Ohio (1956).
4. C.L. Dotson and J.R. Kattus, *Tensile Properties of Aircraft Structural Metals at Various Rates of Loading After Rapid Heating*, WADC-TR-55-199, Aeronautical Systems Division, Wright-Patterson AFB, Ohio (1955).
5. R.C. Bates and W.G. Clark, "Fractography and Fracture Mechanics," *ASM Trans. Quart.*, 62:380-389 (1969).
6. A. Rosen and S.R. Bodner, "The Influence of Strain Rate and Strain Aging on the Flow Stress of Commercially-Pure Aluminum," *J. Mech. Phys. Solids*, 15:47-62 (1967).
7. M.P. Hanson, *Tensile and Cyclic Fatigue Properties of Graphite Filament-Wound Pressure Vessels at Ambient and Cryogenic Temperatures*, NASA-TN-D-5354, National Aeronautics and Space Administration, Washington, D.C. (1969).
8. R.J. Dauksys, N.N. Pagano, and R.G. Spain, *Graphite Fiber/Epoxy Resin Matrix Composites*, AFML-TR-67-367, Air Force Materials Laboratory, Wright-Patterson AFB, Ohio (1968).
9. T. Nicholas and A.M. Freudenthal, "The Mechanical Behavior of a Filled Elastomer at High Strain Rates," *Trans. Rheol. Soc.*, 13/3:323-333 (1969).
10. G.S. Tomkins and J. Warcing, "The Effect of Material Stress-Strain Properties on Fatigue Failure," *Proc. 2nd Int. Conf. Fracture*, Chapman and Hall, London (1969).
11. A.M. Freudenthal, *Combination of the Theories of Elasticity, Plasticity, and Viscosity in Studying the Safety of Structures*, International Association for Bridge and Structural Engineering (1968).
12. G.R. Irwin, *Encyclopedia of Physics*, Vol. VI, Springer-Verlag, Berlin (1962).
13. W. Weibull, "A Statistical Theory of Strength of Materials," *Proc. Ing. Vetenskaps Akad. (Stockholm)*, No. 151 (1939).



# FRACTURE TOUGHNESS STUDIES USING THICK ACRYLIC MATERIALS

by

H.L. Smith, F.R. Stonesifer, and K.R. McKinney

Ocean Technology Division  
Naval Research Laboratory

## I. BACKGROUND

A number of years ago a military specification was drawn up stating the fracture toughness requirements for acrylic material for aircraft transparencies<sup>1</sup>. The need for tougher canopy materials, as well as a reliable quantitative method for evaluating the fracture strength of material was made known by the Naval Bureau of Aeronautics and by the Air Force Materials Laboratory. A number of pilots and aircraft had been lost in the Korean Conflict due to explosive decompression of aircraft cockpits when their canopies were pierced by gunfire fragments. Loss of cabin pressure was so rapid in some cases that the pilot was actually pulled out of the plane. The Naval Research Laboratory, who was working in the area of the fracture strength of materials, was asked to work on this problem.

Fracture mechanics was only in the formative stages at this time. Dr. George Irwin had written several papers suggesting modifications to A.A. Griffith's brittle fracture theory<sup>2,3</sup>. These modifications extended fracture mechanics to cover finite plates and to deal with plastic flow at the crack tip, but very limited data existed verifying Dr. Irwin's theories. In July 1951, attention was called to work by Wolock, Axilrod and others at the National Bureau of Standards who had discovered that stretching of polymethyl methacrylate, just above the second order transition temperature, could enhance its resistance to crazing<sup>4</sup>. It was reasoned by Mr. J.A. Kies of the Naval Research Laboratory, that stretching should also increase the fracture strength of the material. The wide sheet tensile specimen was being used to some extent at NRL to determine the limiting stress which could be maintained, without fracture, when a central crack was initiated in some manner such as by a 22 calibre penetration. This test was now modified by cutting a central slot through the sheet perpendicular to the principal stress prior to imposing a load on the specimen. Natural cracks were then placed in each end of the slot by tapping with a sharp knife. The load and corresponding crack length was used to calculate the energy required for crack propagation. This was referred to as  $dW/dA$  or the work per unit area required to propagate a crack. The critical value, at which rapid unstable fracture occurred, was referred to as a critical  $dW/dA$ . More recently this term is referred to as  $\mathcal{G}$  or  $\mathcal{G}_c$ . The load at instability is obtained from either the load dial or load extension curve and the unstable crack length is distinctly seen on the Plexi-

glas fracture surface<sup>5,6</sup>. (See Figure 1).

As cast polymethyl methacrylate was found to have a critical  $dW/dA$  value of from 4 to 5 in-lb/in<sup>2</sup>. Some stretch

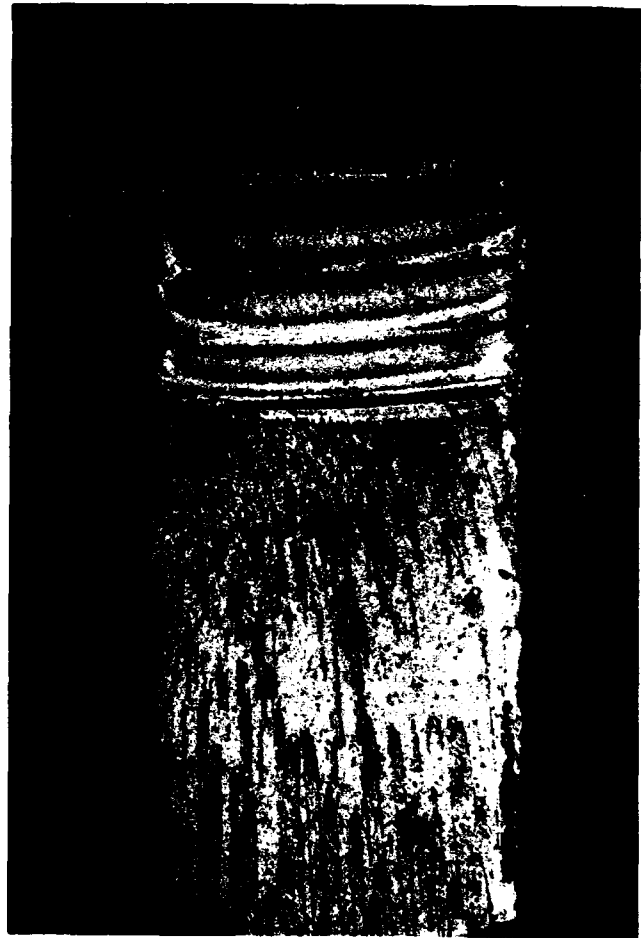
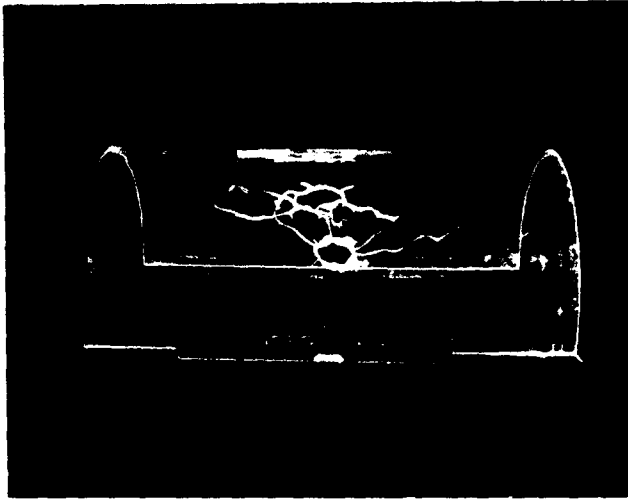
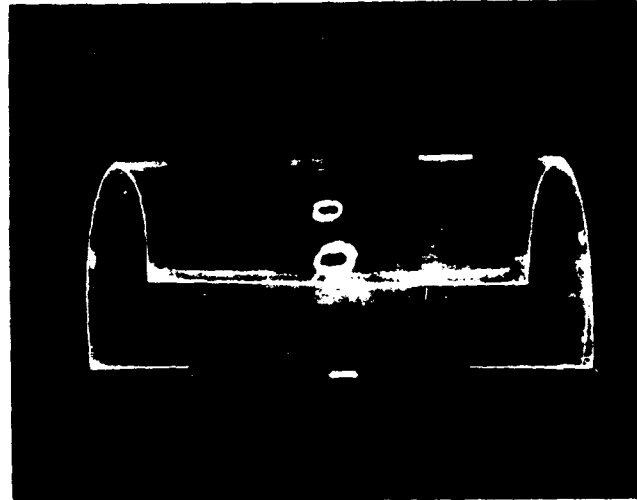


Figure 1. Surface Markings on As-cast Polymethyl Methacrylate.



AS-CAST - 2 psi



90% STRETCHED - 20 psi

0.25" MIL-P-5425 - SHOT WITH 1.375" LONG YAWED DART AT +160°F

Figure 2. Stretched versus As-cast Canopy Models.

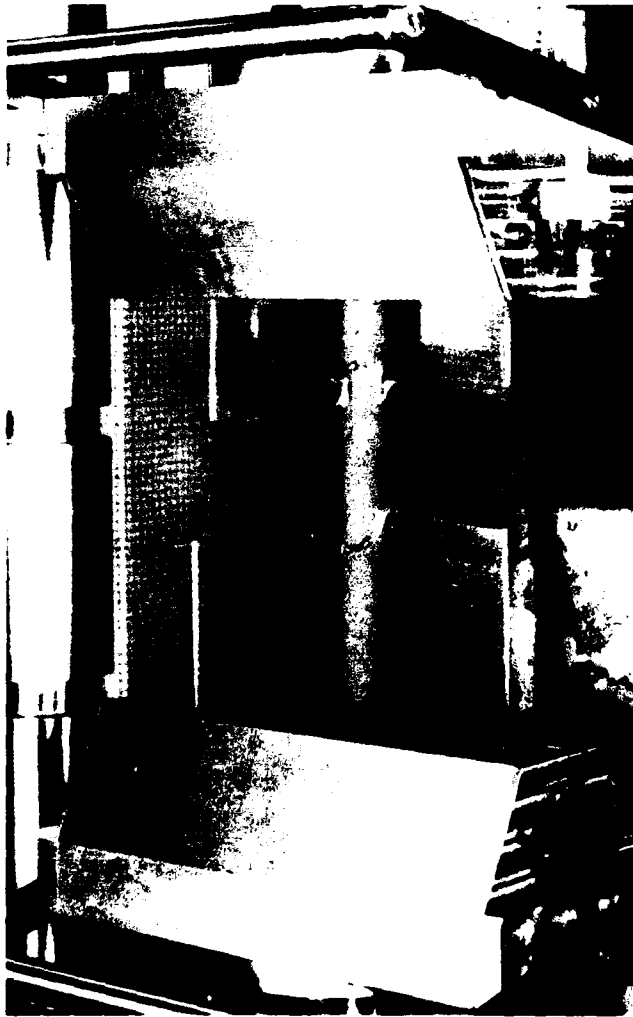


Figure 3. Heavy Wide Plate Grips for Center Notch Tensile Tests.

oriented Plexiglas obtained from the National Bureau of Standards, as well as some Plexiglas hot-pressed at NRL, was found to have a critical  $dW/dA$  value of more than 10 in-lbs/in<sup>2</sup>. A cooperative program was begun between the Navy, the Air Force, and Rohm and Haas in which a stretching machine was built at Rohm and Haas to investigate optimum stretching parameters for Plexiglas I, II, and 55. Critical fracture toughness,  $dW/dA$ , values of 20 to 30 in-lbs/in<sup>2</sup> were found to be feasible for polymethyl methacrylate under optimum stretching conditions<sup>7</sup>. Several aircraft companies cooperated in a further development of stretched acrylic material. It was found that stretching could be used to enhance the crack propagation resistance of plastic materials which were not appreciably cross-linked in molecular structure. Figure 2 is an example of the improvement afforded a stretched canopy model over an as-cast model<sup>8</sup>. As a result of these several efforts, most military and civilian planes now incorporate the use of stretched polymethyl methacrylate for the load bearing member of their transparencies. Perhaps more fracture toughness tests have been made on aircraft transparencies than on any other application, running as high as several hundred thousand for one company alone.

## II. RENEWED INTEREST

Interest in the hot stretching of transparent plastics has been renewed in the past few years<sup>9</sup>. With the introduction of larger and faster aircraft it has become necessary to use stretch-oriented polymethyl methacrylate in thicknesses approaching one inch. Such a finished stretched thickness, combined with overall canopy size, requires a large thick casting. Successful stretching is somewhat limited in final percent stretch, resulting in less than an optimum toughness which could be realized if a larger amount of stretching were

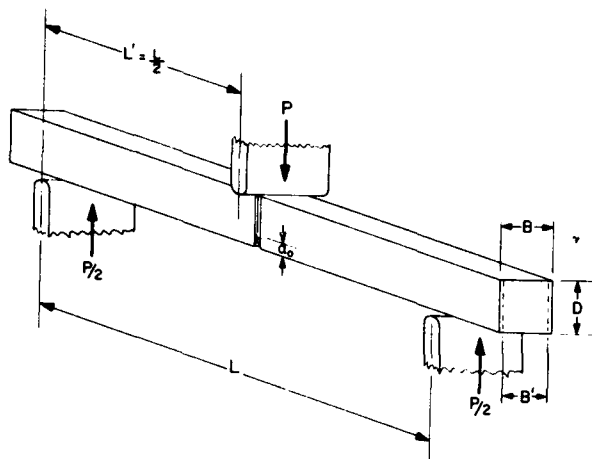


Figure 4. Single-Edge-Cracked 3-Point Bend Bar.

feasible. These thicknesses of material also require larger test specimen sizes than desired if one uses the initial specification requirement of a centrally notched tensile test to evaluate fracture toughness. Early publications on metals indicated that a central notch tensile specimen should be at least 16 times as wide as it is thick and the length should be 2-1/2 to 3 times the width. Specimens of this size become expensive to test, requiring large quantities of stretched material and large test grips such as those shown in Figure 3. In addition to the aircraft transparency requirements, one might mention that a number of deep diving vehicles now have camera and human viewing ports several inches in thickness which might benefit from the use of stretch oriented plastic material.

Experience in the fracture testing of metals suggests that one go to a different type specimen such as the bend bar or the compact tension specimen to evaluate these thicker acrylic materials. We chose to study the advantages and disadvantages of the three-point bend specimen as shown in Figure 4. An additional benefit over material savings to be realized from the bend test is that the induced bending stresses more nearly model the actual case for many transparent acrylic enclosures such as windows, windshields, and two-piece canopies which design analysis treat as plates in bending<sup>10</sup>. In order to give one confidence in the bend test it is necessary to show that it gives comparable fracture toughness values with the central notch tensile test. It was decided to evaluate stretched and as-cast Plexiglas to see what difficulties one might encounter and how one might deal with these difficulties.

### III. EVALUATION OF STRETCHED PLEXIGLAS 55

#### A) 0.9" Thick, 59 to 63% Stretched Plexiglas 55

The Goodyear Aerospace Corporation kindly supplied us with four pieces of stretched Plexiglas 55 for our studies. These four pieces of material were 12" x 26" by

approximately 0.90" in thickness. Shrink back measurements were made on several pieces of the material which were found to be stretched from 59%\* to 63%. Figure 5 shows two of the stretched pieces, one prior to and one after holding in an oven at 145°C for 21 hours.

Two types of fracture toughness measurements were made on these stretched plates. First, a central notch was placed in three plates perpendicular to the 26" length and cracks inserted at each end of the notch by tapping on a sharpened knife. The 2" long central slot was increased in length to approximately 2 1/4". The specimens were loaded in tension until failure occurred giving a tensile, central notch, K or  $\mathcal{G}$  value. One plate was cut into bend specimens approximately 0.9" thick by 1.8" wide by 9" long. The specimens were notched at mid-length approximately half way through the 1.8" dimension and a crack inserted at the notch root with a sharpened knife. The specimens were broken in a 3-point bending test giving additional K or  $\mathcal{G}$  values. The crack was not required to propagate through the thickness of the acrylic material but rather in the plane of the plate. One group of specimens were longitudinal and one group transverse to the original 26" plate length. In each case the fatigue crack popped sharply through the specimen giving a reliable  $K_{Ic}$  value. The modified Kies bend test formula

$$K_{Ic} = 1.90 \left[ \frac{1}{(1-a/D)^3} - (1-a/D)^3 \right]^{1/2} PL'/BD^{3/2} \quad (1)$$

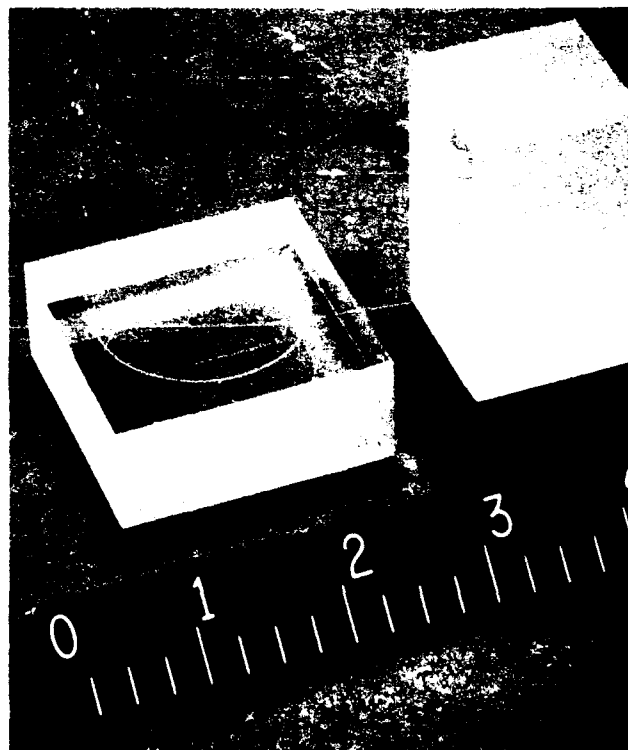


Figure 5. Shrink Back of Stretched Plexiglas 55.

TABLE I.  
K<sub>IC</sub> VALUES FOR 0.90" THICK STRETCHED PLEXIGLAS 55

CENTER NOTCH TENSILE TEST - % STRETCH VARYING FROM 59 TO 63				
SPECIMEN NUMBER	MAXIMUM LOAD (LBS)	CRACK LENGTH (IN.)	K <sub>IC</sub> (PSI √ IN. )	
1	9,100	2.34	1950	
2	10,630	2.24	2000	
3	14,040	2.42	3130	
			Ave. 2360	
BEND TEST - SPECIMENS PARALLEL TO 59% STRETCH DIRECTION				
SPECIMEN NUMBER	MAXIMUM LOAD (LBS.)	CRACK LENGTH	K <sub>IC</sub>	K <sub>IC</sub> (COR.)
		(IN.)	(PSI √ IN. )	(PSI √ IN. )
L1	236	0.93	1933	1938
L2	294	0.89	2265	2274
L3	267	0.88	2021	2027
L4	247	0.92	1998	2004
L5	231	0.91	1814	1819
			Ave. 2006	2012
BEND TEST - SPECIMENS PARALLEL TO 63% STRETCH DIRECTION				
SPECIMEN NUMBER	MAXIMUM LOAD (LBS.)	CRACK LENGTH	K <sub>IC</sub>	K <sub>IC</sub> (COR.)
		(IN.)	(PSI √ IN. )	(PSI √ IN. )
T1	349	0.90	2747	2763
T2	288	0.89	2245	2253
T3	301	0.90	2387	2397
T4	272	0.93	2233	2242
T5	298	0.92	2440	2451
T6	271	0.89	2112	2119
			Ave. 2360	2371
			Std. Dev. 223	226

where P = total load

L' = half span length

D = bar depth

B = bar width

a = crack depth

was used to calculate the 3-point bend K<sub>IC</sub> values. The tangent formula

$$K_{IC}^2 = \frac{S E}{(1 - \nu^2)} =$$

$$\frac{w \sigma^2}{(1 - \nu^2)} \tan \frac{\pi a}{w} \quad (2)$$

where E = elastic modulus

σ = gross stress

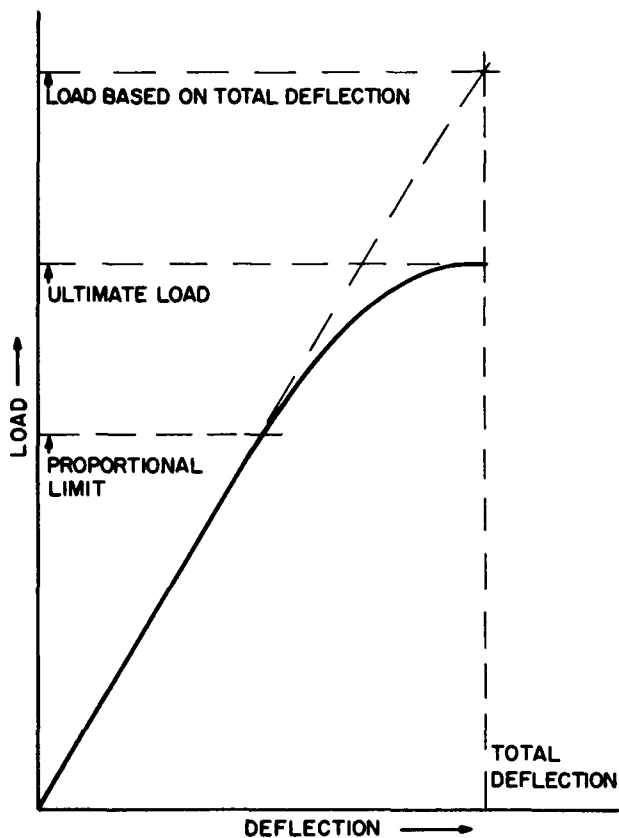
ν = Poisson's ratio

a = half crack length

w = specimen width

was used to calculate the tensile K<sub>IC</sub> values. Agreement between the two methods was very good as shown in Table I. Some small amount of plastic flow occurred in the bend tests. For plane strain fracture Irwin<sup>11</sup> recommends a Δa increase in the actual crack length to allow for plastic flow where

$$\Delta a = \frac{1}{6\pi} \left( \frac{K_{IC}}{\sigma_{ys}} \right)^2 \quad (3)$$



LOAD-DEFLECTION CURVE FOR PRE-CRACKED  $K_{Ic}$  BEND BAR SPECIMEN

Figure 6. Scaling Concept for Plasticity Corrections.

This formula was used to make the  $K_{Ic}$  plasticity corrections shown in Table I. J.A. Kies has published a graphical method for making this plasticity correction<sup>12</sup>.

In connection with work at NRL on very tough steels in the 150 to 200 ksi yield strength range we have

found success in using what we term a scaling factor concept as shown in Figure 6. This is based on the premise that the specimen would not have yielded prior to crack propagation had the specimen been of sufficient size. One merely uses in the  $K_{Ic}$  formula the load represented by the intersection of the extended elastic portion of the load-extension curve and a line through the maximum load perpendicular to the deflection or strain axis<sup>13</sup>.

#### B) 0.25" Thick, 75% Stretched, Plexiglas 55

A small piece of 1/4" thick, 75% stretched, Plexiglas 55 was on hand at NRL which had been stretched a number of years ago by the Rohm and Haas Company. This material had been tested in the wide sheet, central notch, tensile test and found to have a critical stress intensity parameter of approximately 3000 psi  $\sqrt{\text{in}}$ . Two bend specimens 1/4" thick x 1/2" wide x 2.5" long were cut from this material and tested in the three-point bend test. Again the specimens were notched and pre-cracked approximately halfway through each specimen. When loaded in three-point bending, the two  $K_{Ic}$  values were found to be 2940 and 2960 psi  $\sqrt{\text{in}}$ , which were corrected by the scaling factor technique to give values of 3150 and 3070 psi  $\sqrt{\text{in}}$ . These higher values were expected since the material was biaxially stretched 75%, an amount which had been determined earlier to be near the optimum stretch for Plexiglas 55. Good agreement is seen to exist between the two test methods for both the 0.9" thick stretched Plexiglas 55 and the 0.25" thick 75% stretched Plexiglas 55.

### IV. EVALUATION OF AS-CAST PLEXIGLAS II UVA

#### A.) Wide Plate Central Notch Tensile Test

As-cast Plexiglas II UVA was selected to study since it was available in stock thicknesses up to two inches. Again in order to arrive at a fracture toughness value which

Figure 7. Specimens for Size Effect Studies of As-cast Plexiglas II UVA.

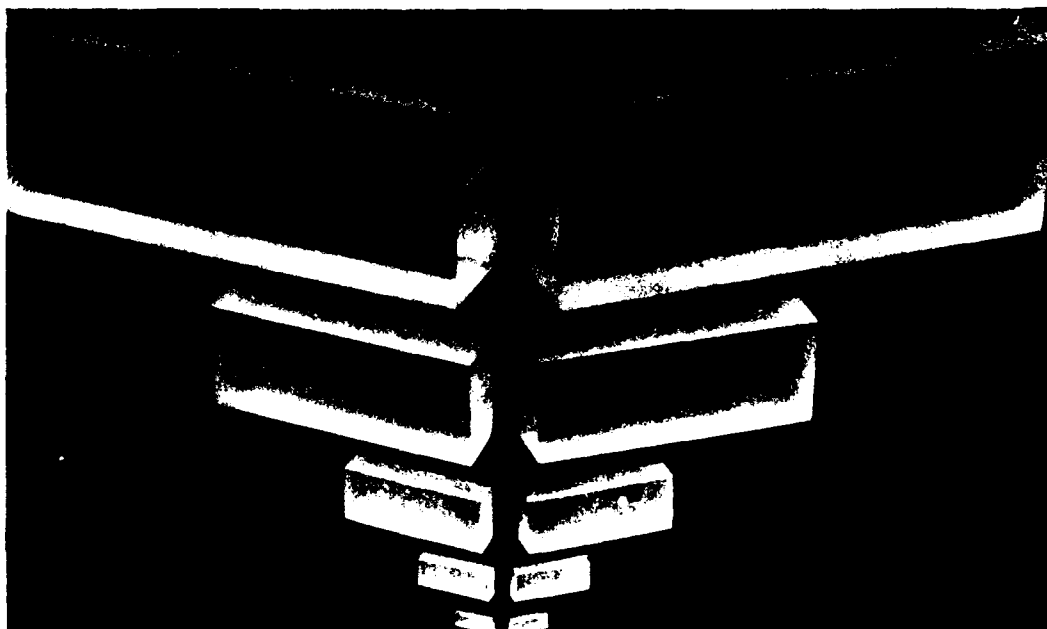


**TABLE II.**  
**K VALUES FOR AS-CAST PLEXIGLAS II UVA**

CENTER NOTCH TENSILE TEST					
SPECIMEN NUMBER	MAXIMUM LOAD (LBS.)	CRACK LENGTH (IN.)	$\frac{K_{Ic}}{(PSI \sqrt{IN.})}$		
1	6,100	3.41	1257		
2	5,950	3.87	1330		
3	5,750	4.20	1325		
4	6,170	3.78	1363		
			Ave.	1319	

BEND TESTS - CONSTANT STRAIN RATE					
SPECIMEN DEPTH	MAXIMUM LOAD (LBS.)	CRACK LENGTH (IN.)	K (PSI $\sqrt{IN.}$ )	K (COR.) (PSI $\sqrt{IN.}$ )	
1/4"	6.7	0.143	1507	1536	
1/2"	20.5	0.243	1180	1185	
1"	42.4	0.518	941	943	
2"	154.0	0.910	1007	1008	
4"	464.0	1.709	995	996	

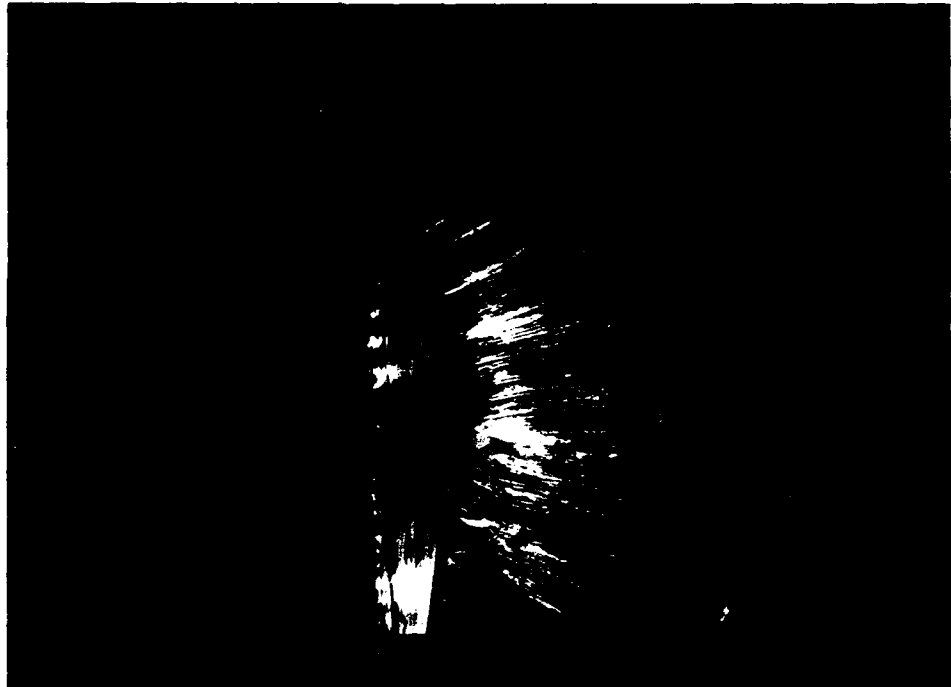
BEND TESTS ON 1" x 2" SPECIMENS - VARYING LOADING RATE					
LOADING RATE (LBS/MIN)	MAXIMUM LOAD (LBS.)	CRACK LENGTH (IN.)	K (PSI $\sqrt{IN.}$ )	K (COR.) (PSI $\sqrt{IN.}$ )	K (SCALE F) (PSI $\sqrt{IN.}$ )
20	126	1.059	962	963	1054
60	162	0.909	966	967	1079
100	192	0.853	1112	1113	1198
120	180	0.969	1176	1178	1320
140	185	0.982	1100	1101	1182
180	178	0.894	1041	1042	1162
220	197	0.914	1201	1202	1313
250	189	0.859	1064	1065	1171
275	203	0.872	1199	1201	1295
300	204	0.904	1262	1263	1355
400	183	0.935	1260	1261	1386
500	197	0.891	1266	1268	1358
600	188	0.893	1218	1219	1338
700	180	0.913	1199	1200	1291
800	196	0.880	1247	1248	1291
1000	200	0.851	1230	1231	1276
1200	195	0.915	1309	1311	1421

one had confidence in, the wide plate central notch tensile specimen was chosen to obtain standard  $K_{Ic}$  values. Four specimens 12" wide by 1" thick by 26" long were prepared with 2" long central cuts extended to approximately 2.25". Each plate was loaded in tension until it failed by sudden, rapid, crack propagation. The crack length and load at instability was used to calculate the  $K_{Ic}$  value using the tangent formula. These results are given in Table II. An average  $K_{Ic}$  value of 1319 psi  $\sqrt{in.}$  was obtained.

**B.) Size Effect Studies Using the Bend Test**

Bend test specimens were also made from Plexiglas II UVA material using the standard two-t depth or width, a one-t thickness, and a ten-t length. The centrally located edge notch extended approximately halfway through the two-t depth. Five sizes were chosen on which to do size effect studies to determine the usefulness of the bend test method for determining the fracture toughness of as-cast

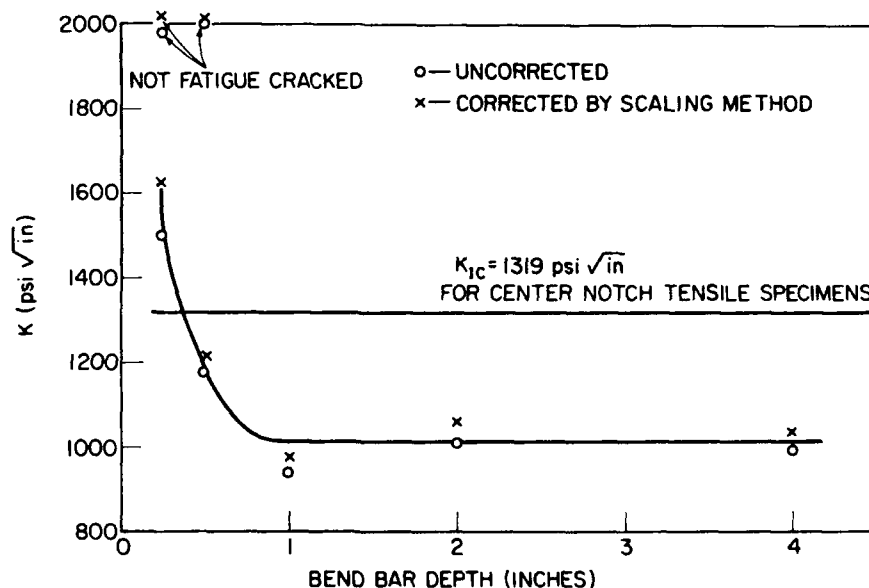
**Figure 8. Fracture Surface of 2" Thick As-cast Plexiglas II UVA.**



Plexiglas. Each size specimen was kept in similitude with the above dimensions, with sizes varying from 1/8" to 2" in thickness. Figure 7 shows a broken specimen from each of the five sizes. Figure 8 shows the fracture surface of one of the 2" thick as-cast bend bars. Fracture markings show the leading edge of the crack to depart from a straight line, with the farthest advance to be in the center. An average crack length value was used in computing fracture toughness values. One could straighten out the crack front by notching the sides of the specimen. An optimum notch depth must be experimentally determined since too deep a notch would result in the crack front leading at the two plate surfaces. We did not side notch our specimens since the small improvement in accuracy would not warrant the additional cost of side notching.

It was known that Plexiglas is strain rate sensitive, so each size specimen was loaded at such a rate as to cause failure in approximately three minutes. Results are listed in Table II with the data plotted in Figure 9. Each point represents the average of four specimens. The first difficulty encountered in the laboratory was that the crack propagated through the specimen slowly without reaching instability for the three larger size specimens. As a result a critical fracture toughness value was never reached. The velocity of crack propagation was directly related to the applied  $\dot{\sigma}$ . A definite instability was obtained for the 1/4" bar depth size with uncertainty existing in the case of the 1/2" bar depth, one specimen definitely going unstable at a K value of 1349 psi  $\sqrt{\text{in}}$ . Such results are of little value in assigning a critical fracture toughness value to an as-cast plate of

**Figure 9. Bend Bar Depth versus K for Scaled Specimens of As-cast Plexiglas II UVA.**



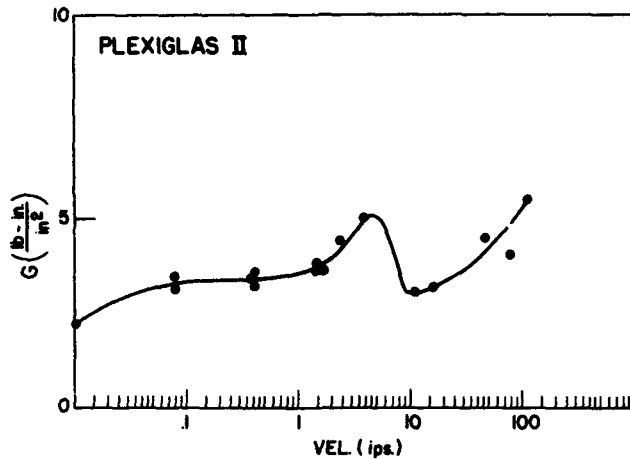


Figure 10.  $S$  versus Crack Velocity in As-cast Plexiglas (Mast and Mulville Data).

Plexiglas. If one accepts the tensile  $K_{IC}$  results of  $1319 \text{ psi} \sqrt{\text{in}}$ , one sees that bend test specimens below approximately  $3/8$ " in depth or  $3/16$ " in thickness would also give erroneous results even though the crack goes unstable. Using the equation

$$\text{Min. dimension} = (\text{Factor}) (K_{IC}/\sigma_{ys})^2 \quad (4)$$

and using  $3/16$ " as the minimum dimension one arrives at a factor of approximately 10. This is in contrast to the factor of 2.5  $(K_{IC}/\sigma_{ys})^2$  generally recommended for metal testing.

#### C.) Natural Crack Requirement

An additional point of difficulty is seen in the excessively high K values obtained for the two smaller size specimens when the root of the notch did not terminate in a natural crack. Some work has been published on notched bend specimens of glass which indicate fatigue cracking is not necessary in order to give correct  $K_{IC}$  values. We have a limited amount of data at NRL verifying this point. However, our notches were ground in the glass bend bars and close examination shows a large number of tiny cracks present at the root of the notch induced by the grinding. Such cracks could easily serve the purpose of a fatigue crack in glass. For Plexiglas a more pronounced fatigue crack or a crack driven ahead of a sharp knife blade indentation such as was used in our studies is necessary.

#### D.) Strain Rate Studies

It was decided to look further into the influence of strain rate on applied K in as-cast Plexiglas. Work by Mast and Mulville of the Naval Research Laboratory<sup>14</sup> shows crack velocity to vary with  $S$  in the manner shown in Figure 10. In their study they used a closed-loop servo-controlled mechanical test system to drive a crack under a constant  $S$  along a narrow double cantilever type specimen. They found stable crack propagation to occur with  $S$  increasing as crack velocity increased until a sharp maximum was seen to occur around five inches per second.

This is taken to mean that a crack in as-cast Plexiglas will propagate without going unstable below this velocity. The change to unstable fast fracture implies a maximum  $S$  value has been reached. Other work by Vincent and Gotham<sup>15</sup> and by Gurnee and Hunt<sup>16</sup> on as-cast polymethyl methacrylate shows a broader maximum in  $S$  at a crack speed of approximately 0.4 in/sec. Williams, Rodon and Turner<sup>17</sup> also find a maximum in  $S$  to occur at a crack speed of approximately 1 in/sec.

A number of bend specimens 1" wide by 2" deep by 10" long were made from Plexiglas II UVA. The specimens were notched, fatigue cracked, and loaded at various loading rates from 20 lbs/min. to 300 lbs/min. The resulting K values as a function of loading rate are given in Table II and Figure 11. The maximum load and the extent of the knife induced crack is used in computing K. Additional tests were made using loading rates up to 1200 lbs/min. These data are shown in Table II but are not included in Figure 11. Both visual observation and load extension curves show that the crack does not reach general instability below approximately 300 lbs/min. loading rate. However, some local instability is seen to exist at just those loading rates which give the higher K values; namely, 120 and 220 lbs/minute. The K values obtained at loading rates of 120, 220 and above 300 lbs/minute do agree with the wide plate center notch tensile  $K_{IC}$  values of approximately 1319  $\text{psi} \sqrt{\text{in}}$ . These data indicate that one must be sure that fast fracture instability does occur. It indicates further that if one obtains a local pop-in in a bend test one can rely on the computed  $K_{IC}$ . Instabilities which result in exhaustion of stored strain energy prevent a general or complete instability with the crack arresting.

Rough measurements indicate average crack velocities to vary from 0.03 in/sec to 0.30 in/sec at loading rates below 300 lbs/min. These velocities are below those found in References 14 thru 17 at which a sharp drop occurs in the applied  $S$  or K. NRL's experience with the testing of various length central notch aluminum sheets had shown only the longer sheets to go unstable because of the increased

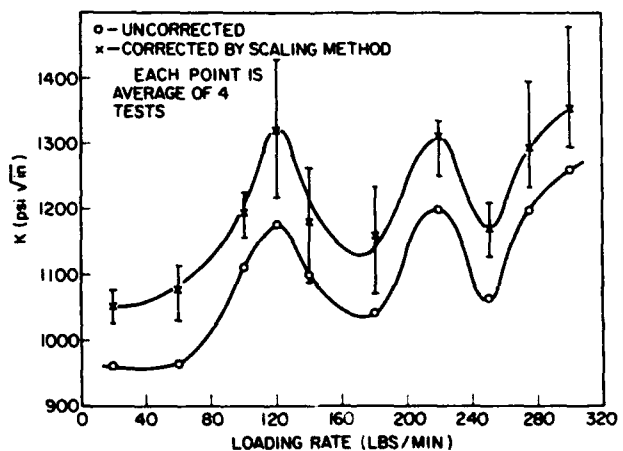
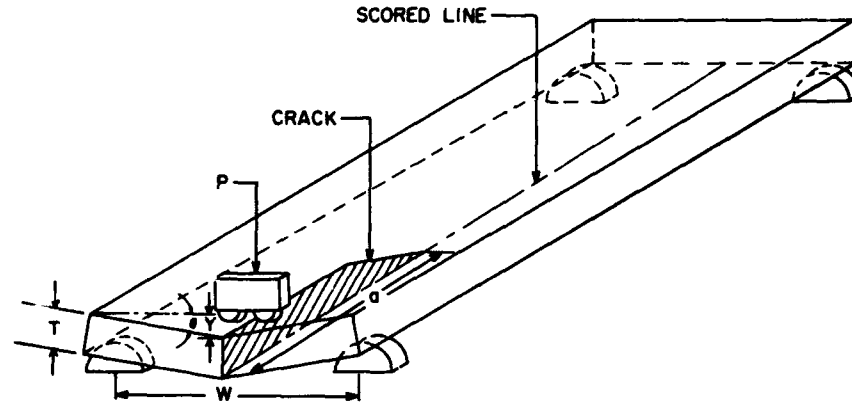


Figure 11. Loading Rate versus K for As-cast Plexiglas II UVA.



Figure 12. The "Outwater" Specimen. Designed to Maintain Constant  $\dot{\epsilon}$ .



strain energy present. The possibility was suggested that instability could be made to occur in the bend test at the slower loading rates by going to longer specimens. Accordingly 1" wide by 2" deep specimens of Plexiglas II UVA were made up in 26" lengths. A loading rate of 250 lbs/min. which did not produce instability previously was chosen to study the influence of loading span. Results show that for duplicate specimens instability was achieved in both specimens broken on the 24" span, in one specimen at 20" and 16" spans, and in neither specimen at the 12" span. At a loading rate of 20 lbs/min. one specimen on 24" span went unstable and one did not. These data indicate that one can introduce unstable conditions by a sufficient increase in breaking span but it may be more practical to simply increase the loading rate.

Work at NRL by Krafft on a ship steel, a line pipe steel and on a pressure vessel steel showed a periodicity to exist between  $K_{Ic}$  and strain rate somewhat like that shown here for as-cast Plexiglas at the lower loading rates. His explanation for crystalline metals involved dislocation mobilities as they relate to the moving crack tip plastic zone<sup>18,19</sup>.

In seeking the condition necessary for instability, it was decided to measure the stored elastic energy in each specimen at maximum load, just before instability. It was found from the load extension curve that recoverable strain energy or elastic energy amounted to approximately 2.0 in.-lbs for the longer span or the faster strain rate on those specimens which went unstable. For those which did not go unstable, less than half that amount, 1 in.-lb., was stored in the specimen. In most cases instability did not result in complete fracture for the 1" wide by 2" deep bend specimens. The uncracked region was approximately one square inch in area and should require about 4.0 in.-lbs of energy for complete fracture. Since only 2.0 in.-lbs was present, the crack arrested after a travel of approximately 1/2 inch. However, the fracture area could exceed 1/2 square inch since we know that  $\dot{\epsilon}$  drops at instability.

### V. SLOW GROWTH OF CRACKS IN AS-CAST PLEXIGLAS

Failure can, of course, occur under lower than critical fracture stresses given sufficient time. Data was obtained for crack velocity versus applied  $\dot{\epsilon}$  for 1/2" thick Plexiglas

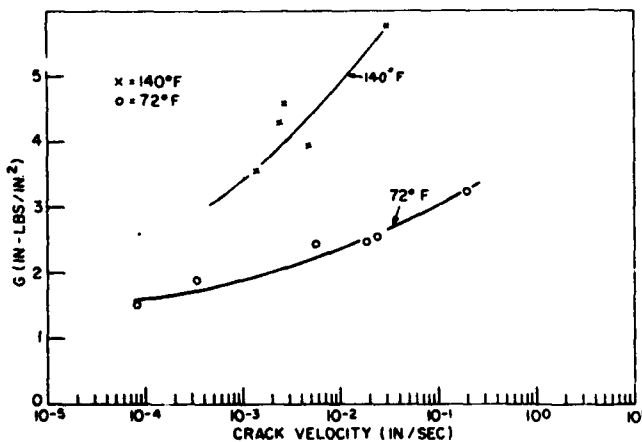


Figure 13. Crack Speeds in 1/2" Thick Plexiglas II UVA versus Applied  $\dot{\epsilon}$  at 15% Relative Humidity.

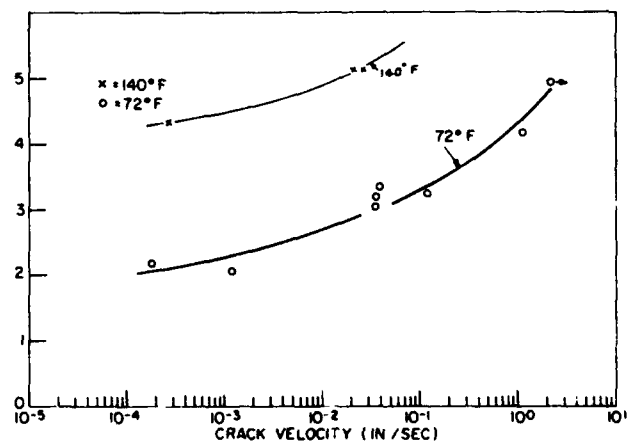


Figure 14. Crack Speeds in 1/2" Thick Plexiglas II UVA versus Applied  $\dot{\epsilon}$  at 90% Relative Humidity.

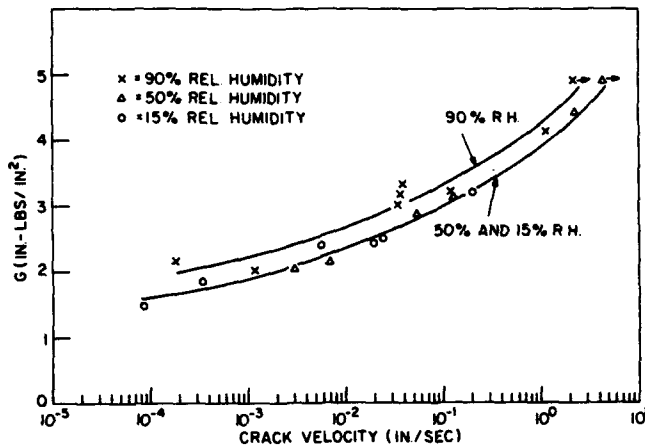


Figure 15. Crack Speeds in 1/2" Thick Plexiglas II UVA versus Applied  $G$  at 72°F.

II UVA as a function of temperature, humidity and method of loading. The test method used for this study was one originated by Professor Outwater of the University of Vermont as shown in Figure 12. The mechanics is such that a constant  $G$  is maintained over the entire specimen length with the exception of small end effects.

#### A.) Temperature and Humidity Studies

Figure 13 is a plot of applied  $G$  versus crack velocity for data taken at 15% relative humidity. For a given  $G$  level one sees a distinct decrease in velocity as the test temperature is raised from 72°F to 140°F. Figure 14 shows a similar decrease in velocity with increase in test temperature at 90% relative humidity. Figures 15 and 16 show  $G$  versus crack velocity taken at 72°F and at 140°F, respectively. For a given  $G$  level a small decrease in velocity is seen with increasing relative humidity. This is probably due to moisture at the crack tip either softening the material surrounding the tip or an actual blunting or rounding out of the crack tip.

#### B.) Low Cycle Fatigue

Cyclic loading may be more damaging to a material or to a structure than continuous static loading. This would be true under conditions in which the material surrounding the crack tip flows plastically, first on loading and then again on unloading. So-called low cycle fatigue was looked at for one temperature, 72°F, and a relative humidity of 50%. The specimen was loaded to a particular  $G$  value and held for 10 seconds, then unloaded for 10 seconds, then re-loaded etc. Results for the very limited data are plotted in Figure 17 in which crack velocities relate to total time under maximum  $G$ . Little difference is noted between crack velocities for static and fatigue loading at the lower applied  $G$ 's. However, the crack speed for fatigue loading is somewhat faster than that for static loading at the higher applied  $G$  values, indicating an increasing difference between the two loading methods as  $G$  is increased. This difference in crack speed must be due to

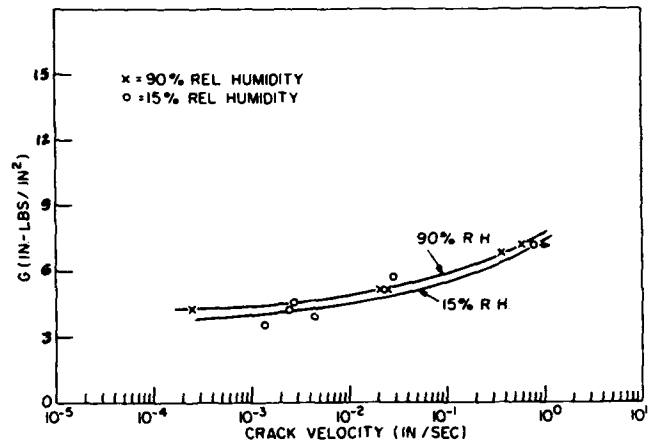


Figure 16. Crack Speeds in 1/2" Thick Plexiglas II UVA versus Applied  $G$  at 140°F.

damage in the crack tip plastic zone during cycling since the additional time for the effects of humidity alone to act would result in a decreasing crack velocity for cyclic loading.

When the crack tip was immersed in water during cycling at 72°F it was necessary to raise the applied  $G$  to 7.8 in.-lb/in.<sup>2</sup> before the crack began to move; however, rapid crack propagation or instability then occurred.

## VI. CONCLUSIONS

1) The three-point bend test may be employed to give an accurate  $G_{Ic}$  or  $K_{Ic}$  value for stretched polymethyl methacrylate. An actual crack is required in the test bar and minimum size test specimen dimensions should be met. Where doubt exists results may be checked against the central-notch, wide-plate, tensile test.

2) Using the three-point bend test to measure critical fracture toughness values of as-cast polymethyl methacrylate

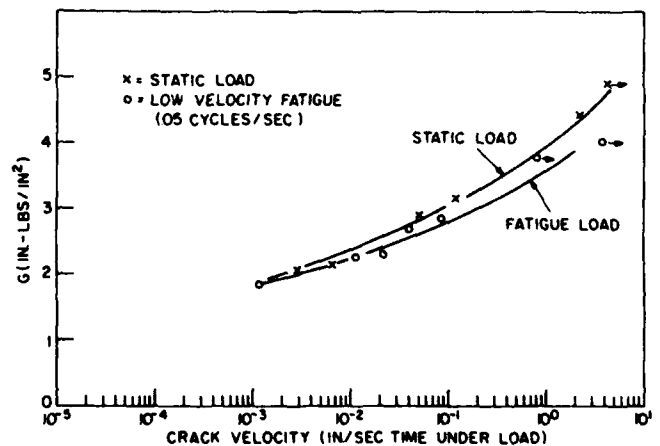


Figure 17. Crack Speeds in 1/2" Thick Plexiglas II UVA versus Applied  $G$  at 72°F and 50% Relative Humidity.

requires close scrutiny to assure that an actual instability does occur. Again results may be checked against the central-notch, wide-plate tensile test.

3) For the environmental conditions investigated here a threshold fracture toughness parameter,  $K$ , of approximately  $700 \text{ psi} \sqrt{\text{in.}}$  exists for onset of slow cracking in as-cast Plexiglas II UVA. If one wishes to predict safe replacement times for this material one must make sure that imposed  $K$  values are below this level or one must obtain crack propagation rates for the actual service conditions of concern.

4) If the  $K_{Ic}$  fracture toughness values obtained

for the 59% to 63% stretched Plexiglas 55, namely, 2000 to  $2370 \text{ psi} \sqrt{\text{in.}}$ , are not sufficiently high to satisfy service requirements, then some method to obtain additional stretch is required.

## VI. RECOMMENDATIONS

It is recommended that the bend test be allowed for evaluating the fracture toughness of stretched polymethyl methacrylate and that crack velocity studies be made on stretched material of interest under realistic test conditions. Such studies would provide information as to the remaining useful life of stretched material or structures in the presence of known flaws.

## REFERENCES

1. *Plastic, Sheets, and Parts, Modified Acrylic Base, Monolithic, Crack Propagation Resistant*, MIL-P-25690A, Department of Defense, Washington, D.C. (1960).
2. G.R. Irwin, "Fracture Dynamics," in *Fracturing of Metals*, American Society for Metals, Cleveland, Ohio (1948).
3. H.L. Smith, J.A. Kies, and G.R. Irwin, "Rupture of Plastic Sheets as a Function of Size and Shape," *Phys. Rev.*, 83/4:872 (1951).
4. B.M. Axilrod, M.A. Sherman, V. Cohen, and I. Wolock, *Effects of Moderate Biaxial Stretch-Forming on Tensile and Crazing Properties of Acrylic Plastic Glazing*, NACA-TN-2779, National Aeronautics and Space Administration, Washington, D.C. (1952).
5. J.A. Kies, A.M. Sullivan, and G.R. Irwin, "Interpretation of Fracture Markings," *J. Appl. Phys.*, 21:716-720 (1950).
6. H.L. Smith, J.A. Kies, and A.B. Clark, *Toughness in Plastics Based on Fracture Surface Appearance*, NRL-MR-1863, Naval Research Laboratory, Washington, D.C. (1968).
7. J.A. Kies and H.L. Smith, *Toughness Testing of Hot Stretched Acrylics*. Presented at the Joint Conference of the Aircraft Industries Association and the Research and Development Command, Wright-Patterson AFB, Ohio, March 1955.
8. H.L. Smith and W.E. Anderson, *Fracture Studies of Transparent Aircraft Materials*, WADD-TR-60-176, Aeronautical Systems Division, Wright-Patterson AFB, Ohio (1960).
9. *Study of Hot Stretching of Transparent Plastics*, Contract DA19-129-AMC-844 (N), Lowell Technological Institute Research Foundation, Lowell, Massachusetts (1967).
10. D.C. Cully and J.D. Locke, *Criteria for Toughness ("K" Factor) Requirement of Transparent Materials*, GER-14408, Goodyear Aerospace Corp., Akron, Ohio (1969).
11. G.R. Irwin, J.A. Kies, and H.L. Smith, "Fracture Strengths Relative to Onset and Arrest of Crack Propagation," *ASTM Proc.*, 58:640 (1958).

#### REFERENCES (Continued)

12. J.A. Kies, H.L. Smith, and F.R. Stonesifer, *Graphical Methods for Plasticity Corrections in Fracture Mechanics*, NRL-R-6918, Naval Research Laboratory, Washington, D.C. (1969).
13. F.R. Stonesifer and H.L. Smith, "Fracture Toughness Measurements on 12% Ni Maraging Steel Weldment," *J. Hydronautics*, 3/1:54-57 (1969).
14. J.A. Kies, unpublished lecture. Presented to the British Iron and Steel Research Association, London, April 1965.
15. P.I. Vincent and K.V. Gotham, *Nature*, 210:1254 (1966).
16. C. Gurney and J. Hunt, *Proc. Roy. Soc. London*, 299A:508 (1967).
17. J.G. Williams, J.C. Radon, and C.E. Turner, "Designing Against Fracture in Brittle Plastics," *Poly. Eng. Sci.*, 8/2:130-141 (1968).
18. J.M. Krafft, "A Rate Spectrum of Strain Hardenability and of Fracture Toughness," pp. 61-16, *Report on NRL Progress*, Naval Research Laboratory, Washington, D.C. (January 1966).
19. J.M. Krafft, "Plastic Flowing," pp. 13-15, *Report of NRL Progress*, Naval Research Laboratory, Washington, D.C. (June 1968).

**SESSION 4B**

**PHENOMENA I**

*Chairman*

**R.E. Herfert  
Northrop Corporation**

# REVIEW OF THEORIES AND LAWS OF FATIGUE CRACK PROPAGATION

by

R.M. Pelloux

Metallurgy and Materials Science Department  
Massachusetts Institute of Technology  
Cambridge, Massachusetts

## INTRODUCTION

A general law of fatigue crack propagation should take into account the five following factors:

- 1) geometry (crack length, specimen dimensions);
- 2) loads (magnitude and direction of the forces, for instance, uniform, wedge or edge forces);
- 3) material properties (yield and ultimate strength, modulus of elasticity, ductility);
- 4) time (number of cycles, stress rate and strain rate);
- 5) environment (temperature, pressure, media).

Most of the fatigue crack propagation equations which have been derived so far take into account only the geometry and loads factors. The materials properties, the environment and time factors have been difficult to analyze and to fit into a mathematical equation; consequently, these factors are usually included in a constant called the "Material constant". However, since the main function of a fatigue crack propagation equation is to permit the extrapolation of fatigue test data, it will be important to know how to take into account these last three factors. For reason of simplicity, in this paper we will assume that the fatigue crack growth rates under consideration are independent of temperature, time and environment.

In order to review briefly the different theories of fatigue crack propagation it is necessary to group them into classes on the basis of the approach taken for their derivation. There are four types of fatigue crack growth laws or theories:

- 1) theoretical laws based on dimensional analysis;
- 2) theoretical equations derived from a work hardening and fatigue damage model;
- 3) theoretical equations relating the growth rate to the crack tip opening displacement;

- 4) semi-empirical laws.

In this paper we shall attempt to review the theories from a materials selection point of view, that is, how the materials properties enter into a fatigue crack propagation law. (See Table I for the notation of materials properties.) For a more detailed analysis of the mechanical and mathematical derivations the reader should consult the reviews by Paris<sup>1</sup> and Rice<sup>2</sup>.

## DIMENSIONAL ANALYSIS THEORIES

Considering a transverse crack of length  $2l$  in a sheet of infinite width Frost and Dugdale<sup>3</sup> and later Liu<sup>4</sup> showed that on the basis of dimensional analysis and geometrical considerations

$$\frac{dl}{dn} = A(\sigma) \cdot l$$

This equation supposes that the factors controlling crack extension remain geometrically similar as the crack progresses. They assume that the strain distribution ahead of the crack is the controlling factor. Frost<sup>5</sup> found empirically that  $A(\sigma) = B\sigma^3$  leading to Frost's law

$$\frac{dl}{dn} = B\sigma^3 l \quad (1)$$

Liu<sup>6</sup> on the basis of a concept of total hysteresis energy absorbed at failure found that  $A(\sigma) = B\sigma^2$  leading to Liu's law

$$\frac{dl}{dn} = B\sigma^2 l \quad (2)$$

Equations (1) and (2) show that on the basis of simple dimensional analysis the growth rate should be proportional to the crack length.

More recently Yang (7) derived, also by dimensional analysis, a law of the type

$$\frac{dl}{dn} = f(K) \quad (3)$$

where  $K$  is the stress intensity factor. At this point it is

important to mention that most of the fatigue crack growth theories assume  $\sigma_{\max} = \Delta\sigma$  (the stress range) and  $\sigma_{\min} = 0$ . This assumption leads to  $K_{\max} = \Delta K$  (range of stress intensity factor).

Rice<sup>8</sup> in a discussion of Yang's derivation objects to the selection of strain rate as an independent variable. Rice<sup>8</sup> also shows that by using the surface energy term  $S$  (dimensions: force/length) as a variable one can get from dimensional analysis a law of the following type:

$$\frac{d\ell}{dn} = \frac{S}{C} f \left( \frac{K^2}{CS} \right) \quad (4)$$

$C$  being a material constant with dimensions force/length<sup>2</sup>. A more general expression also derived by Rice<sup>2</sup> gives

$$\frac{d\ell}{dn} = \left( \frac{\Delta K}{Y} \right)^2 f \left[ \left( \frac{\Delta K}{\rho Y} \right)^2, \epsilon_y, \epsilon_F, N \right] \quad (5)$$

$f$  is a dimensionless function and  $Y$  is the yield strength of the material.

The main problem in the derivation of a crack propagation law by dimensional analysis lies in the difficulty of listing all the variables that may influence the crack growth rate. However, equations (1) and (2) and (5) show that, ideally, the crack growth rate under constant nominal stress should be proportional to the crack length and inversely proportional to the square of a material strength parameter.

#### FATIGUE CRACK PROPAGATION THEORIES DERIVED FROM WORK HARDENING MODELS

Head<sup>9</sup> derived the first fatigue crack propagation law. It is based on a model made of rigid-work hardening elements which represent the plastic zone at the tip of the crack. The fracture criteria is the fracture stress of each element. After correction for the proper dependence of the plastic zone size on crack length, Head's crack propagation law is

$$\frac{d\ell}{dn} = \frac{\beta}{12E} \frac{\sigma^2 \ell}{(U - Y) Y} \quad (6)$$

$\beta$  is the work hardening coefficient of the element.

McClintock<sup>10</sup> proposed a more detailed work hardening analysis based on the accumulation of fatigue damage under increasing plastic strain amplitudes in a process zone of size  $\rho$  at the tip of the crack. McClintock's derivation is based on the following assumptions.

1) The plastic strain amplitude  $\epsilon_p$  at a distance  $r$  from the tip of the crack, within the plastic zone of size  $R$ , is

$$\epsilon_p = \epsilon_y \left( \frac{R}{r} - 1 \right) \quad (7)$$

where  $\epsilon_y$  is the yield strain. This equation is an exact solution for the plastic strain distribution for mode III of crack opening. It is assumed valid for mode I of crack opening.

2) The fatigue damage law is based on Coffin's law (11) of low cycle fatigue,

$$N^{1/m} \epsilon_p = \frac{\epsilon_F}{2}$$

where  $\epsilon_F$  is the true fracture strain for monotonic fracture. The fatigue damage function is  $4 (\epsilon_p/\epsilon_F)^m dn$  and fracture occurs when

$$\int_0^N 4 \left( \frac{\epsilon_p}{\epsilon_F} \right)^m dn = 1 \quad (8)$$

Taking  $m = 2$  McClintock obtained the following expression for  $R \gg \rho$ :

$$\frac{1}{\rho} \frac{d\ell}{dn} = 7.5 \left( \frac{\epsilon_y}{\epsilon_F} \right)^2 \left( \frac{R}{\rho} \right)^2 \quad (9a)$$

where  $1/\rho \cdot d\ell/dn$  gives a dimensionless growth rate. By replacing  $R = (\Delta K/2Y)^2$  and  $\epsilon_y = Y/E$  where  $Y$  is the yield stress and  $E$  is the modulus of elasticity, we obtain

$$\frac{1}{\rho} \frac{d\ell}{dn} = \frac{7.5}{16} \frac{(\Delta K)^4}{\epsilon_F E^2 Y^2 \rho^2} \quad (9b)$$

The merit of McClintock's derivation is that it takes into account the material mechanical properties  $\epsilon_F$ ,  $E$  and  $Y$ . (It should be pointed out that since most of the derivations refer to high strength materials the factors  $E$  and  $Y$  can be interchanged because a rough estimate of the flow stress  $Y$  is  $0.01E$ .)

The use of Coffin's law as a fatigue damage law is not completely justified since Coffin's law is essentially a law of low cycle fatigue crack propagation. However, a more accurate damage law would not change the results markedly. When the Coffin exponent  $m$  is taken equal to 1.5, which is closer to the average values observed for many materials, the derivation yields a growth rate

$$\frac{d\ell}{dn} = A (\Delta K)^{3/2} \quad (10)$$

It can be seen that the growth rate is strongly dependent upon the Coffin's exponent which also depends on the cyclic stress-strain hardening exponent as shown by Tomkins<sup>12</sup>.

An exact solution of McClintock's theory (see figure 5 of reference 10) predicts that a crack will not propagate when the plastic zone size is equal to the process zone size  $\rho$ . In view of recent observations of a  $\Delta K$  threshold for nonpropagating fatigue cracks<sup>13</sup> the application of McClintock's theory to very low growth rates should be reviewed.

For instance, for the aluminum alloys considered the  $\Delta K$  threshold is of the order of 5 ksi which corresponds to a process zone size of 25 microns, that is, less than a grain size.

Tomkins<sup>12</sup> assumes that the plastic zone can be represented by two bands of plastic shear of length  $R$  acting at  $\pm 45^\circ$  from the crack plane at the crack tip. The rate of fatigue crack growth is assumed to be

$$\frac{d\ell}{dn} = R\Delta\epsilon_p \quad (11)$$

$\Delta\epsilon_p$  is the applied plastic strain range, which is related to the cyclic stress by the cyclic stress-strain hardening relationship

$$\Delta\sigma = k\epsilon_p^\beta \quad (12)$$

Using the plastic zone size given by Bilby<sup>14</sup>

$$R = \ell\sqrt{2} \left[ \sec\left(\frac{\pi}{Y} \frac{\Delta\sigma}{2}\right) - 1 \right] \quad (13)$$

Tomkins derives two crack propagation laws, one for low cycle fatigue and one for low stress crack growth.

a) low cycle fatigue

$$\frac{d\ell}{dn} = \frac{\pi^2}{8} \left(\frac{k}{2Y}\right)^2 \Delta\epsilon_p^{(2\beta+1)} \cdot \ell \quad (14)$$

and Coffin's law is derived from that expression:

$$\Delta\epsilon_p N_f^{1/(2\beta+1)} = C \quad (15)$$

$$\text{with } 2\beta + 1 = m$$

b) low stress fatigue crack growth

On the basis of a cyclic work hardening behavior at low plastic strains expressed by

$$\Delta\sigma = k\Delta\epsilon_p^\beta$$

$$\text{with } \beta = 0.5$$

the same type of assumption and derivation gives

$$\frac{d\ell}{dn} = \frac{\pi^2}{4} \frac{1}{(kY)^2} \Delta\sigma^3 \sigma_m \cdot \ell \quad (16)$$

Tomkins can also reconcile his derivation with Paris's law on the basis that  $\Delta\epsilon_p$  is a net section (uncracked) plastic strain range. A conversion of  $\Delta\epsilon_p$  to gross section stress range gives

$$\frac{d\ell}{dn} = \beta(\Delta K)^4$$

Tomkins' theory is based on equation (11) which expresses the crack growth rate in terms of an equivalent

plastic crack tip opening displacement. The expression used for  $R$  is a simplified solution to an elastic-plastic problem and it is not valid for the fully plastic problem considered by Tomkins. However, the results of the derivation yield a good correlation with the experimental data on low cycle fatigue.

In the low stress case the work hardening law used for the small plastic strain amplitudes has not been firmly established. Furthermore in the case of the small scale yielding ( $\sigma \ll Y$ ) the net plastic strains should be equal to zero.

Erdogan<sup>15</sup> also based a crack growth theory on the assumption that  $d\ell/dn$  is proportional to the dislocation density  $m$  within the plastic zone [ $m = f_1(R_{\max})$ ] and to the fraction  $\phi$  of dislocations which contribute to crack extension.

$$\phi = f_2(R_{\text{reversible}})$$

The general expression is

$$\frac{d\ell}{dn} = A(R_{\max})^{\alpha_1} (R_{\text{rev}})^{\alpha_2} \quad (17)$$

The model used by Erdogan is oversimplified and too vague.

Krafft<sup>16</sup> derives a crack propagation law by using a tensile ligament instability model, the growth rate per cycle being equal to one process zone diameter. The law is

$$\frac{d\ell}{dn} = \frac{A \cdot f(\Delta K/K_{\max})}{E^3 K_{IC}^2 n} \cdot K_{\max}^4 \quad (18)$$

The  $K_{IC}$  term is introduced when Krafft assumes that the ratio of the fatigue process zone size  $d_f$  to the tensile zone size  $d_F$  is

$$\frac{d_f}{d_F} = \frac{K_{\max}^2 - K_{\min}^2}{(K_{IC})^2}$$

This law takes into account  $n$ , the work hardening exponent, which represents the tensile strain applied to the ligament before necking occurs.

#### MODELS BASED ON A CRACK TIP OPENING DISPLACEMENT

Weertman<sup>17</sup> applied the Bilby, Cottrell and Swinden<sup>18</sup> crack theory of continuously distributed infinitesimal dislocations to the crack growth problem. Weertman takes a fracture criterion which states that fatigue crack extension takes place when a total crack tip displacement  $D$  is reached. The crack growth equation derived is

$$\frac{d\ell}{dn} = \frac{(\Delta\sigma \sqrt{\ell})^4}{2\gamma G Y^2} \quad (19)$$

where  $\gamma$  is a plastic work term and  $G$  the shear modulus.



TABLE I.  
NOTATION OF MATERIALS  
PROPERTIES

Y	tensile yield stress (unless specified, the monotonic and cyclic flow stresses are assumed to be equal)
U	ultimate tensile strength
$\beta$	cyclic work hardening coefficient
$\epsilon_F$	tensile fracture strain $(\ln \frac{A_0}{A_f})$
$\epsilon_y$	yield strain
E	modulus of elasticity

McEvily<sup>19</sup> modified equation (19) empirically and proposed the following equation:

$$\frac{d\ell}{dn} = A \frac{(\Delta\sigma \sqrt{\ell})^4}{\frac{(Y+U)EU^2}{2} \epsilon_F} \quad (20)$$

where U is the ultimate tensile stress and  $\epsilon_F$  the monotonic fracture strain. McEvily found that this equation fits the data of a wide variety of materials (steels, aluminum and nickel alloys, brasses).

Lardner<sup>20</sup> also derived a dislocation model of fatigue crack growth following Bilby's theory. Lardner assumes that crack extension can take place during unloading, which is contradicted by all observations. The growth rate obtained by Lardner is:

$$\frac{d\ell}{dn} = \frac{(1-\nu)}{4GY} (\Delta K)^2 \quad (G \text{ shear modulus}) \quad (21)$$

Lardner assumes that the oxide film at the crack tip contributes to the resistance to dislocation motion near the tip, in order to account for the critical stress intensity below which a crack will not propagate.

Frost and Dixon<sup>21</sup> have presented a fatigue crack growth theory based on a continuum model of crack tip extension. The main assumption is that the crack growth rate is equal to the increase in crack length of the ellipse perimeter, representing the crack boundary, between the loaded and unloaded condition. This increase in length is taken

TABLE II.  
DEPENDENCE OF THE FATIGUE GROWTH RATE ON  
MATERIAL PROPERTIES IN DIFFERENT THEORIES

	$\frac{d\ell}{dn} = A (\Delta K)^n$	
	Reference	Constant A
McClintock	10	$[E^2 Y^2 \epsilon_F \rho^2]^{-1}$
McEvily	19	$[EU^2(Y+U)\epsilon_F]^{-1}$
Krafft	16	$[E^3 K_{IC}^2 n]^{-1}$
Frost	21	$(E^2 Y)^{-1}$
Pearson	22	$[E]^{-3.6}$
Miller	29	$(EYK_{IC})^{-1}$
Head	9	$[E(U-Y)Y]^{-1}$

over the length of the boundary which is under a tensile tangential stress. The result is

$$\frac{d\ell}{dn} = \frac{\Delta\sigma^2 \ell}{E^2} \ln \left( \frac{4E}{\Delta\sigma} - 1 \right) \quad (22)$$

After a plasticity correction the growth rate equation gives

$$\frac{d\ell}{dn} = \frac{32\Delta\sigma^3 \ell}{E^2 Y} \quad (23)$$

The derived equation fits the data reported by Frost and also it matches the empirical law of Pearson<sup>22</sup>.

$$\frac{d\ell}{dn} = 3.43 \times 10^7 \left( \frac{K}{E} \right)^{3.6} \quad (24)$$

McClintock<sup>23</sup> also suggested that the rate of crack growth could be related to the crack tip opening displacement by a proportionality constant C giving

$$\frac{d\ell}{dn} = C(2u_y)$$

and with C taken to be 0.5.

$$\frac{d\ell}{dn} = 2 \frac{\Delta\sigma^2 \ell}{EU} \quad (25)$$

McClintock found that this equation correlated fairly well with striations spacings reported by Pelloux<sup>24</sup>.

## SEMI-EMPIRICAL LAWS OF FATIGUE CRACK PROPAGATION

These laws are called semi-empirical because they are an attempt to fit the test data by means of fundamental parameters such as the stress intensity factor. The law obtained by Paris<sup>25</sup>,

$$\frac{d\ell}{dn} = C (\Delta K)^m \quad (26)$$

is a typical semi-empirical law. A value of  $m = 4$  gives a good fit with the data over five orders of magnitude of growth rates (from  $10^{-8}$  to  $10^{-3}$  inches/cycle).

Broek and Schijve<sup>26</sup> found an empirical law of the form

$$\frac{d\ell}{dn} = C_1 \frac{(\Delta K)^3}{1-R} \exp(-C_2 R) \quad (27)$$

$$\text{with } R = \sigma_{\min}/\sigma_{\max}.$$

Forman proposed (27)

$$\frac{d\ell}{dn} = \frac{C(\Delta K)^n}{(1-R)K_c - \Delta K} \quad (28)$$

Some recent work of Hudson<sup>28</sup> comparing the validity of the Paris and Forman empirical equations for 7075T6 and 2024T3 aluminum alloys showed that Paris's equation produced a good fit to the data for a given value of  $R$  except at higher growth rates. Forman's equation produced an excellent fit to the data for both 2024 and 7075. The data from all the tests at negative  $R$  values fell into a narrow scatter band with the data from  $R = 0$  showing that the compression part of the cycle did not affect growth rate markedly. For positive  $R$  values the data of rate against stress intensity falls within discrete bands. For a given value of  $\Delta K$  the higher the stress ratio the higher the rate of crack propagation.

Miller<sup>29</sup> has recently attempted to measure the scatter in the parameter  $n$  in the expression

$$\frac{d\ell}{dn} = A (K_{\max})^n$$

The average of sixty-nine values of  $n$  investigated is 3.5 and the standard deviation 0.65. Also using data obtained with 4340 steel, Miller evaluated the dependence of the constant  $A$  on the mechanical properties. After comparing the fit of the data with the equations given by McClintock, McEvily, Krafft, and Pearson (see Table II), Miller concluded that the best fit was given by

$$\frac{d\ell}{dn} = \frac{B}{EYK_{IC}} (K_{\max})^n \quad (29)$$

## DISCUSSION

This short review of fatigue crack growth theories shows that the variety of possible theories is endless. It is therefore necessary to use as a basis for a theory what is presently known about the micromechanisms of fatigue crack growth. We shall limit our discussion to the case where crack growth is by regular striation formation, neglecting tearing around large inclusions. Recent work<sup>30</sup> has confirmed that crack extension occurs essentially by shear or sliding off. As a consequence  $d\ell/dn$  should be directly related to the crack tip opening displacement. This observation is further confirmed by all the results of programmed loads tests: when the load amplitude is changed, the amount of crack extension is changed immediately without delay, at least when the load changes are not excessively large. (See the electron micrographs of reference 31.) Most of the work hardening theories cannot account for the results of the programmed load tests since they predict a gradual change of the growth rate by way of a damage criteria. This does not mean that the work hardening theories should be completely discarded since some gradual, second order changes of the growth rates are also observed after a sudden change of load<sup>32</sup>.

Consequently a crack growth theory should attempt to relate the crack tip opening displacement (CTOD), which is a function of  $(\ell, \Delta\sigma, \sigma_{\max})$ , to the growth rate  $d\ell/dn$ . In a first approximation we can write

$$\frac{d\ell}{dn} = 1/2 \text{ CTOD} = \frac{1}{8\pi} \frac{(\Delta K)^2}{YE} \quad (30)$$

Note that this derivation has  $d\ell/dn$  proportional to  $\ell$ , which is in conflict with most of the reported crack growth data. It is also found that in general the calculated CTOD is much larger than the growth rate<sup>33,34</sup>. Further experimental work will be needed to establish the exact relationship between CTOD and growth rate.

The next question is whether to introduce a ductility factor in the relationship between the CTOD and  $d\ell/dn$  to correct for the fact that a material with a high flow stress  $Y$  does not necessarily exhibit a low growth rate.

$$\frac{d\ell}{dn} = \frac{1}{8\pi} \frac{(\Delta K)^2}{YE} \frac{1}{\text{ductility}} \quad (31)$$

The ductility factor should represent a plane strain ductility. Miller<sup>29</sup> found that  $K_{IC}$  was a good measure of the triaxial ductility and gave a good fit for equation (31) with the mechanical properties of high strength steels. On the other hand, Hahn<sup>33</sup> shows that for a large variety of steels the growth rate is independent of the ductility, and also of the yield stress. Hahn's observation stresses the importance of determining the role, if any, of the monotonic mechanical properties on the fatigue crack growth rate. For instance, the flow stress  $Y$  used in the preceding equations should be a measure of the plastic behavior of the cyclically work hard-

ened plastic zone. Consequently,  $Y$  should be obtained from the cyclic stress-strain curve and will depend upon the cyclic history. The most difficult part of a theory will certainly be to take into account the influence of random loads by means of a damage criterion and/or a residual stress factor.

In summary the theoretical derivation of a fatigue crack propagation law as defined above requires:

1) an exact solution for the fatigue plastic zone size and shape and for the plastic strain distribution within the plastic zone for the different modes of elastic-plastic crack opening;

2) a law of cyclic stress-strain hardening of the material;

The reader interested in theoretical considerations to take into account the influence of the environment and temperature on the fatigue crack growth rate should consult the references by Wei<sup>35</sup> and Gittus<sup>36</sup>.

3) a failure criteria relating the crack tip opening displacement to the amount of crack extension.

This law should also account for nonpropagating fatigue cracks at low  $\Delta K$  values and for the influence of residual stresses.

So far the semi-empirical laws have been used as guidelines in the derivation of theoretical laws. It is felt at this time that a sound theory should start from a number of coherent physical observations and proceed on the basis of fundamental principles rather than attempt to fit the data. Nevertheless the empirical laws, which include some of the mechanical properties ( $E$ ,  $Y$ ,  $U$ ,  $K_{IC}$ ,  $\epsilon_F$ ) give a good account of the process of fatigue crack growth (at least in the case of small scale yielding) and should be used to guide materials selection and research for better fatigue resistant materials.

#### REFERENCES

1. P.C. Paris and F. Erdogan, *J. Basic Eng.*, 85/4:528 (1963).
2. J.R. Rice, "The Mechanics of Crack Tip Deformation and Extension by Fatigue," p. 247, *Fatigue Crack Propagation*, ASTM-STP-415, American Society for Testing and Materials, Philadelphia, Pennsylvania (1967).
3. N.E. Frost and D.S. Dugdale, *J. Mech. Phys. Solids*, 16:92 (1968).
4. H.W. Liu, *J. Basic Eng.*, 83:23 (1961).
5. N.E. Frost, *J. Mech. Phys. Solids*, 9:143 (1961).
6. H.W. Liu, *J. Basic Eng.*, 85:116 (1963).
7. C.T. Yang, *J. Basic Eng.*, 89:487 (1967).
8. J.R. Rice, *J. Basic Eng.*, 89:493 (1967).
9. A.K. Head, *Phil. Mag.*, 44:925 (1953).
10. F.A. McClintock, "On the Plasticity of the Growth of Fatigue Cracks," p.65, *Fracture of Solids*, John Wiley, New York (1963).
11. L.F. Coffin, *J. Basic Eng.*, 82:671 (1960).
12. B. Tomkins, *Phil. Mag.*, 18:1056 (1968).
13. J.A. Feeney, J.C. McMillan, and R.P. Wei, *Environmental Fatigue Crack Propagation of Aluminum Alloys at Low Stress Intensity Levels*, D6-60114, Boeing Company, Seattle, Washington (1969).
14. B.A. Bilby and K.H. Swinden, *Proc. Roy. Soc. London*, 285A:22 (1965).

#### REFERENCES (Continued)

15. F. Erdogan, "Crack Propagation Theories," p. 497, *Fracture: An Advanced Treatise*, Vol. II, Academic Press, New York (1968).
16. J.M. Krafft, *A Comparison of Cyclic Fatigue Crack Propagation with Single Cycle Crack Toughness and Plastic Flow*. Presented to Committee E24, American Society for Testing and Materials, September 1964.
17. J. Weertman, *Proc. 1st Int. Conf. Fracture*, Vol. I, Japanese Society for Strength and Fracture of Materials, Sendai, Japan (1965).
18. B.A. Bilby, A.H. Cottrell, and K.H. Swinden, *Proc. Roy. Soc. London*, 272A:304 (1963).
19. A.I. McEvily, *Proc. 1st Int. Conf. Fracture*, Vol. II, Japanese Society for Strength and Fracture of Materials, Sendai, Japan (1965).
20. R.W. Lardner, *Phil. Mag.*, 17:71 (1968).
21. N.E. Frost and J.R. Dixon, *Int. J. Fracture Mech.*, 3:301 (1967).
22. S. Pearson, *Nature*, 211:1077 (1966).
23. F.A. McClintock, ASTM-STP-415, p. 170. (See Ref. 2)
24. R.M. Pelloux, *ASM Trans. Quart.*, 57:511 (1964).
25. P.C. Paris, "The Fracture Mechanics Approach to Fatigue," p. 107, *Proc. 10th Sagamore Army Mater. Res. Conf.*, Syracuse University Press, Syracuse, New York (1964).
26. D. Broek and J. Schijve, NLR-TR-101-361, National Aero- and Astronautical Research Institute, Amsterdam (1963).
27. R.G. Forman et al., *J. Basic Eng.*, 89:459 (1967).
28. C.M. Hudson, NASA-TN-D-5390, National Aeronautics and Space Administration, Washington, D.C. (1969).
29. G.A. Miller and J.F. Throop, *Optimum Fatigue Crack Resistance*. Presented to Committee E9, American Society for Testing and Materials, Annual National Meeting, Atlantic City, New Jersey (1969).
30. R.M. Pelloux, *ASM Trans. Quart.*, 62:281 (1969).
31. J.C. McMillan and R.M. Pelloux, "Fatigue Crack Propagation Under Program and Random Loads," p. 505, ASTM-STP-415. (See Ref. 2)
32. R.W. Hertzberg, "Fatigue Fracture Surface Appearance," p. 205, ASTM-STP-415. (See Ref. 2)
33. G.T. Hahn, M. Sarrate, and A.R. Rosenfield, *Experiments on the Nature of the Fatigue Crack Plastic Zone*. Presented at the Air Force Conference on Fatigue and Fracture of Aircraft Structures and Materials, Miami Beach, Florida, December 1969.

#### REFERENCES (Continued)

34. R.N. Wright and A.S. Argon, *Fatigue Crack Growth in Silicon-Iron*, R-1058, Massachusetts Institute of Technology, Cambridge, Massachusetts (1969).
35. R.P. Wei and J.D. Landes, *Mater. Res. Stand.*, 9:25 (1969).
36. J. Gittus, "Theoretical Analysis of Dislocation Movements and Crack Propagation Under Tension-Tension Fatigue in a Material Exhibiting Time-Dependent Plasticity," *J. d'Automne*, Paris (October 1969).

# A MODEL STUDY OF THE CHARACTERISTICS OF FATIGUE CRACK EXTENSION

by

W.G. Fleck

Cleveland State University  
Cleveland, Ohio

R.B. Anderson

Carnegie-Mellon University  
Pittsburgh, Pennsylvania

## INTRODUCTION

Fatigue crack propagation is a complex process influenced by a multitude of factors including component geometry, loading characteristics, material properties, and environmental conditions. The relationship of the cyclic rate of extension of through-cracks in plates to these various parameters has been explored by many investigators. The literature is abundant in experimental crack extension data that demonstrate the dependence of cyclic growth rates in a given material on crack length, maximum and minimum cyclic load, plate thickness, temperature, and loading frequency. It has been shown previously (Reference 1) that the development of a model of the growth process provides some additional insight into relationships of the cyclic rate of growth to these parameters and to material tensile properties. The model has been used to correlate growth rate data for several materials under a variety of loading conditions.

This paper describes the application of the crack extension model to the study of damage accumulation near the crack tip, dependence of the cyclic rate of crack extension on certain tensile properties, transition from the flat mode to slant mode of growth, and the effect of plate thickness on the growth rate.

The cyclic crack extension model presented in Reference 1 describes the process of fatigue crack growth in terms of accumulation of damage in an element of material ahead of a growing crack. The derivation of an expression for the cyclic rate of crack extension in Reference 1 focuses on the damage history of the element subjected to increasing cyclic strain, as shown in Figure 1. The upper and lower curves represent, respectively, the strain distribution at maximum cyclic load and minimum cyclic load. As the crack grows the fatigue element is subjected to increasing values of maximum strain and strain range and the fatigue life of the element decreases. Damage is assumed to have reached the critical value when the crack has grown to the edge of the element, a distance  $\delta$  from its center.

As shown in Figure 1 the distance from the crack tip at which the strain range is equal to the endurance strain range is denoted by  $r_d$  and is referred to as the radius of the damage zone. When the fatigue element is farther than  $r_d$  from the crack tip, it is assumed to be unaffected by cyclic

loading. The distance from the crack tip at which the maximum strain is equal to the yield strain is referred to as the radius of the plastic zone and denoted by  $r_p$  in Figure 1. The distance from the crack tip at which the strain range equals twice the yield strain is  $r_R$ , and is referred to as the radius of the zone of reversed plastic deformation.

By employment of expressions for strain distribution near the crack tip, the linear cumulative damage rule, and a failure criterion, the rate of crack extension is derived in Reference 1 as a function of  $r_d$ ,  $r_p$ ,  $r_R$ ,  $\delta$ , and tensile properties including fatigue ductility ( $\epsilon_f^P$ ), yield strain ( $\epsilon_Y$ ), yield strength ( $\sigma_Y$ ), and the plastic zone radius at fracture ( $r_{pc}$ ).

The resulting expression for the average cyclic growth rate through the damage zone is

$$\frac{\bar{da}}{dn} = \frac{4 \left( \frac{r_R}{r_d} \right) \left( \frac{r_d}{\delta} \right)}{\left( \frac{\epsilon_f^P}{\epsilon_Y} + \gamma \right)^2} \left[ 1 - \frac{\delta}{r_d} - \frac{2}{A} \right. \tag{A-1}$$

$$\left. (1 - \sqrt{\delta/r_d}) \left( 2 - \frac{1}{A\sqrt{(\delta/r_d) - 1}} \right) \right. \tag{A-3}$$

$$\left. + \frac{2}{A^2} \ln \left( \frac{A-1}{A\sqrt{(\delta/r_d) - 1}} \right) \right] \tag{1}$$

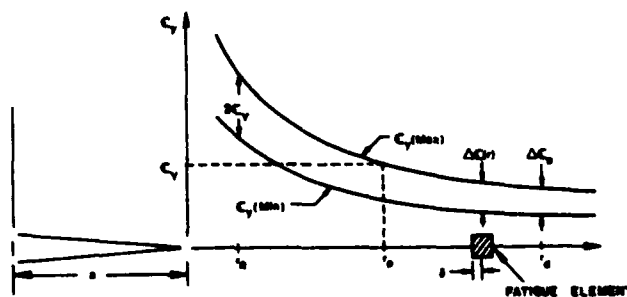


Figure 1. Cyclic Strain Distribution Near Fatigue Crack Front.

in which

$$A = \frac{\left( \frac{\epsilon_f^p}{\epsilon_Y} + \gamma \sqrt{\frac{r_d}{r_R}} \right)}{\gamma \sqrt{\frac{r_p}{r_R}} - 1} \quad (2)$$

and

$$\gamma = \frac{\frac{\epsilon_f^p}{\epsilon_Y} + \sqrt{\frac{r_R}{r_p}} \sqrt{\frac{r_{pc}}{\delta}}}{\sqrt{\frac{r_{pc}}{\delta}} - 1} \quad (3)$$

For small values of  $r_d$ ,  $r_p$ , and  $r_R$  relative to crack length, these parameters are related in Reference 1 to the maximum stress intensity factor, ( $K_{max}$ ), the stress intensity factor range ( $\Delta K$ ), the endurance strain range ( $\Delta \epsilon_e$ ), cyclic load ratio ( $R$ ), the endurance strength at zero mean stress ( $\sigma_{e0}$ ), and ultimate strength ( $\sigma_u$ ) as follows:

$$r_p = \pi/8 \left( \frac{K_{max}}{\sigma_Y} \right)^2 \quad (4)$$

$$r_R = \pi/32 (\Delta K/\sigma_Y)^2 \quad (5)$$

$$r_d = 4r_R \left( \frac{\epsilon_Y}{\Delta \epsilon_e} \right)^2 \quad (6)$$

$$\frac{\Delta \epsilon_e}{\epsilon_Y} = \frac{2 \sigma_{e0}/\sigma_Y}{1 + \left( \frac{\sigma_{e0}}{\sigma_u} \right) \left( \frac{1+R}{1-R} \right)} \quad (7)$$

A non-dimensionalized growth rate  $da/\delta/dn$  then can be expressed as a function of five non-dimensional quantities  $\frac{\Delta K}{\sigma_Y \sqrt{\delta}}$ ,  $\frac{\Delta K}{K_{max}}$ ,  $\frac{\epsilon_f^p}{\epsilon_Y}$ ,  $\frac{\Delta \epsilon_e}{\epsilon_Y}$ , and  $\frac{K_{cc}}{\sigma_Y \sqrt{\delta}}$  that are related, respectively, to load range, cyclic load ratio, ductility, endurance strain, and cyclic stress intensity factor at fracture.

#### Relationship of Growth Rate to Tensile Properties

The expression for cyclic growth rate generated by the model and given by equations (1) through (7) is depicted graphically in Figure 2, in which the non-dimensionalized growth rate is plotted as a function of a non-dimen-

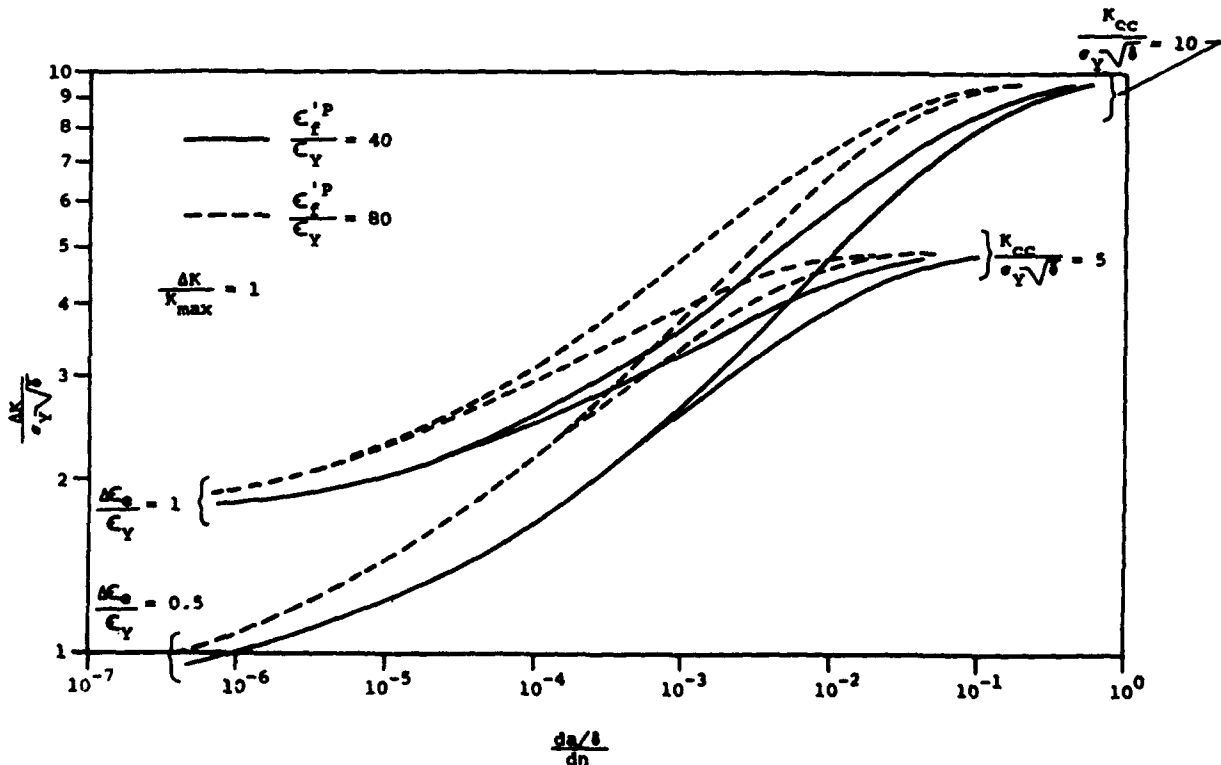


Figure 2. Non-Dimensionalized Growth Rate Curves Generated by the Model.

sional stress intensity factor for some arbitrarily selected values of material quantities.

It is apparent in Figure 2 that the critical stress intensity factor dominates the rate of crack growth at high stress intensities but has negligible influence at low stress intensities. The effect of ductility on growth rate is strong throughout, but appears to be most significant at intermediate stress intensities, as long as growth occurs in a single mode. As might be expected the influence of the endurance strength at low stress intensities is large but diminishes at high stress intensity values. It should be noted that equation (1) predicts a zero crack growth when the radius of the damage zone,  $r_d$ , equals the fatigue element radius  $\delta$ . The stress intensity factor range at this point is found from equations (5) and (6) to be

$$\Delta K_e = \frac{2\sqrt{2\delta}}{\pi} \Delta\sigma_e \quad (8)$$

Thus the stress intensity factor range below which the model predicts no growth is seen to be a function of the fatigue element radius and the endurance stress range.

An example of the relationship between the rate of crack extension and specific material properties is shown in Figure 3. In this figure the solid curve represents the cyclic growth rate of an arbitrary reference material, and the dashed curves indicate growth rates for hypothetical materials having values of either ductility, yield strength, critical stress intensity factor, endurance strength, Young's

modulus, or fatigue element radius equal to twice that of the reference material. The model indicates that ductility and Young's modulus have equal influence on the growth rate and the effect of either of these parameters is strongest for intermediate values of  $\Delta K$ . The critical cyclic stress intensity factor is seen to have a large effect at high stress intensities and negligible effect at low stress intensities. The yield strength has little effect on crack extension rate over the entire range of growth. Both the fatigue element radius and the endurance strength strongly influence growth rates at low stress intensities but have small effect at high stress intensities. The results for  $\delta$  and  $\sigma_{e0}$  are nearly identical and are represented as a single curve in Figure 3.

#### Accumulation of Fatigue Damage

The model characterizes fatigue crack growth as a process of cyclic damage in which the lifetime of a fatigue element ahead of the crack determines the rate of crack extension. As the crack grows, a fatigue element in the path of the crack is subjected to continually increasing values of mean strain and strain range. The method of summing the damage in the element at different strain levels that was assumed in the development of the model is the Palmgren-Miner linear damage rule expressed by

$$\sum_{i=1}^L \frac{n_i}{N_i} = 1 \quad (9)$$

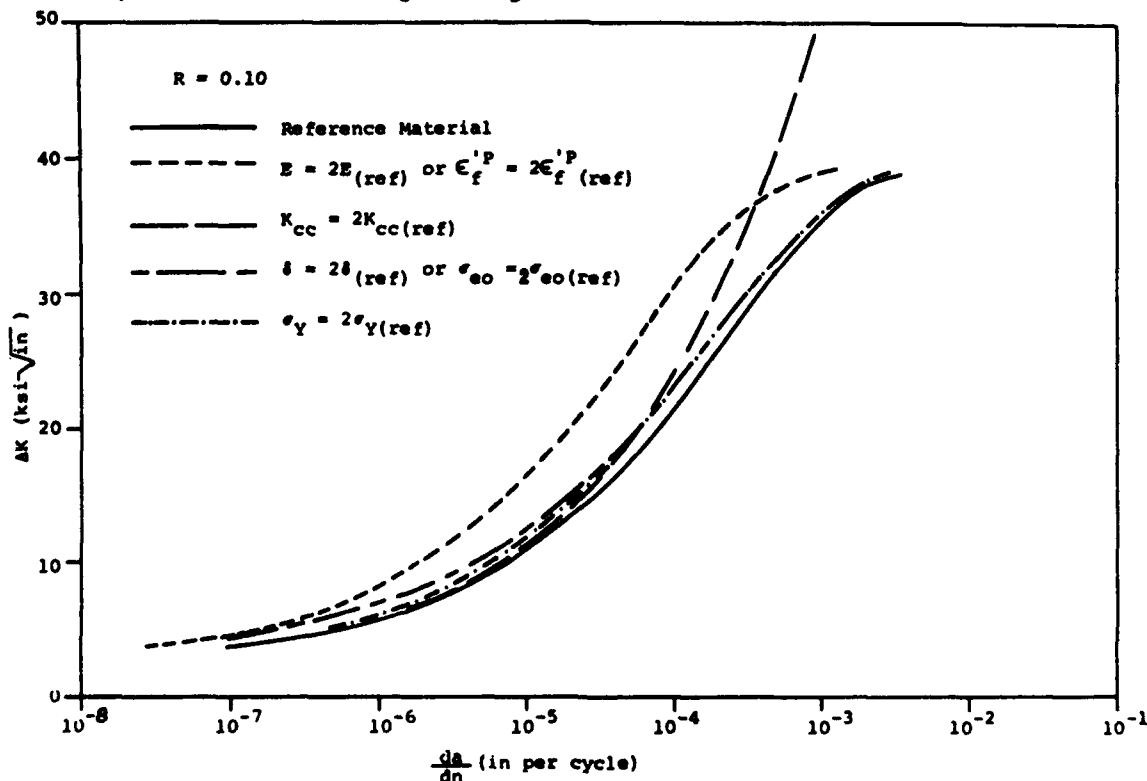


Figure 3. Example of Relationship of Mechanical Properties to Cyclic Growth Rates.



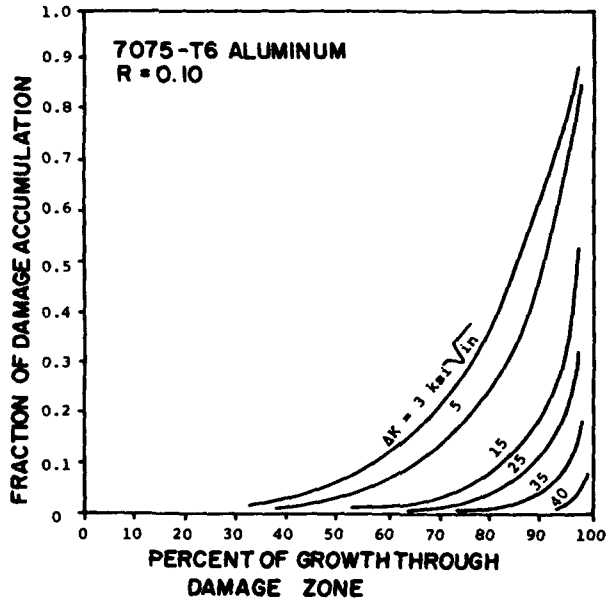


Figure 4. Effect of Stress Intensity Factor Range on Damage Accumulation.

In equation (9)  $L$  is the total number of different strain levels,  $n_i$  is the number of cycles at the  $i^{\text{th}}$  strain level, and  $N_i$  is the lifetime of the element at the  $i^{\text{th}}$  strain level. If the crack extends with each cycle of loading,  $n_i$  equals one and  $L$  equals the total number of cycles necessary to advance the crack through the damage zone.

When the fatigue element is within the damage zone, i.e. at a distance  $\hat{r}$  from the crack tip where  $\delta < \hat{r} < r_d$ , it is in a partially damaged state and equation (9) can be written

$$\sum_{i=1}^S \frac{n_i}{N_i} + \sum_{i=S+1}^L \frac{n_i}{N_i} = 1 \quad (10)$$

The terms  $\sum_{i=1}^S \frac{n_i}{N_i}$  represent the fraction of damage accumulated by the fatigue element during the  $S$  cycles required to extend the crack an amount equal to  $r_d - \hat{r}$ . The terms  $\sum_{i=S+1}^L \frac{n_i}{N_i}$  represent the fraction of damage which will be accumulated as the crack grows through the remaining distance  $\hat{r} - \delta$ . Denoting

by  $F$  and using the expression developed in Reference 1 for  $N_i$  in terms of  $r_i$ ,  $r_d$ ,  $r_p$ ,  $r_R$ ,  $A$ , and  $\gamma$  lead to an expression for the fraction of damage accumulated as the crack grows an amount equal to  $r_d - \hat{r}$  given by

$$F = \sum_{i=1}^S \frac{4}{\left(\gamma \sqrt{\frac{r_p}{r_R}} - 1\right)^2} \left( \frac{\sqrt{\frac{r_d}{r_i}} - 1}{A - \sqrt{\frac{r_d}{r_i}}} \right)^2 \quad (11)$$

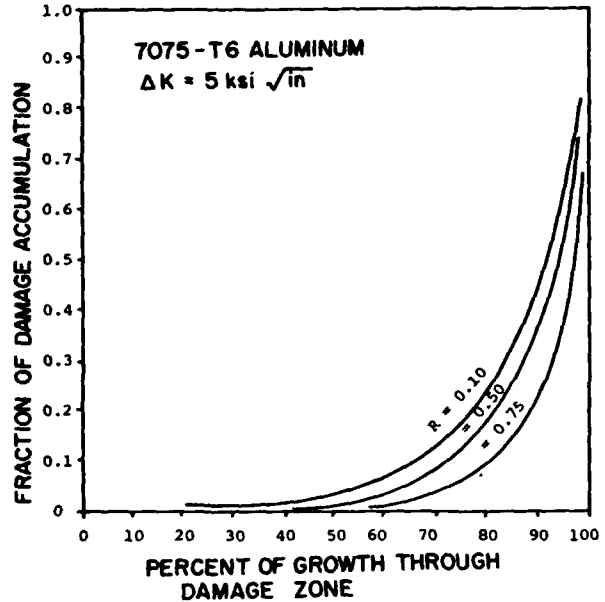


Figure 5. Effect of Cyclic Load Ratio on Damage Accumulation.

$$\text{in which } S = \frac{r_d - \hat{r}}{\bar{da}/dn}$$

Proceeding as in Reference 1, the summation in equation (11) is approximated by the integral

$$F = \int_{\hat{r}}^{r_d} \frac{4}{\left(\gamma \sqrt{\frac{r_p}{r_R}} - 1\right)^2} \left( \frac{\sqrt{\frac{r_d}{r}} - 1}{A - \sqrt{\frac{r_d}{r}}} \right)^2 dr \quad (12)$$

Equation (12) is plotted for a specific example in Figure 4 which shows the increase in damage accumulation in a fatigue element in 7075-T6 aluminum ahead of a growing crack. The properties of 1/16" thick 7075-T6 aluminum sheet are used in this example. The fraction of damage accumulated is plotted as a function of the fraction of the damage zone traversed by the crack for several values of  $\Delta K$ . The sharp increase in damage accumulation as the crack grows toward the fatigue element is related to the high strain gradient near the crack front. It is clear for this example that at higher values of stress intensity range the damage is concentrated in a smaller fraction of the damage zone.

Figure 5 shows the fraction of damage accumulated as a function of proximity of the fatigue element to the crack tip for several values of cyclic load ratio. For a given value of  $\Delta K$  the damage is more closely concentrated at the crack front at higher values of the cyclic load ratio.

It is apparent, then, that on a local scale fatigue crack extension is predominantly a low cyclic lifetime pro-

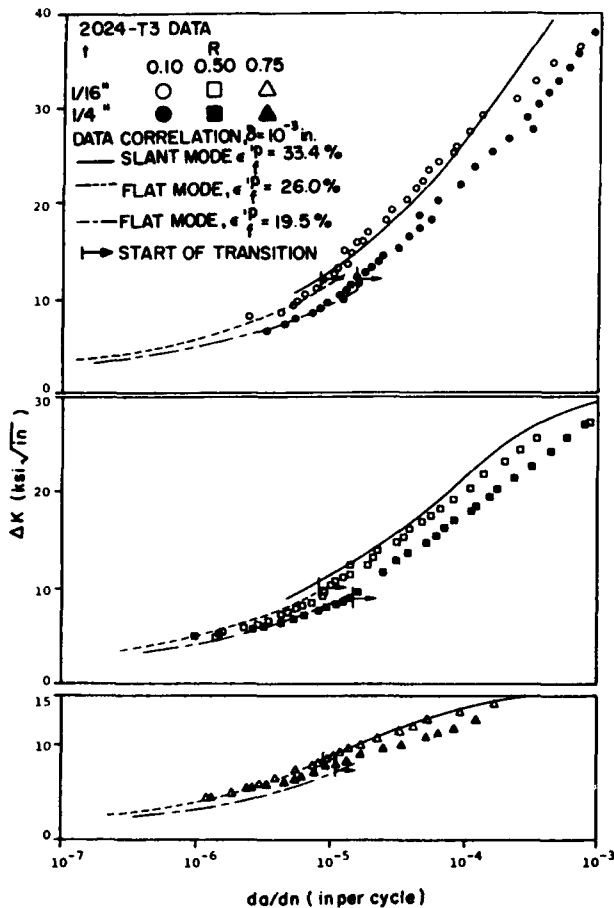


Figure 6. Crack Extension Rate Data and Model Correlation for 2024-T3 Aluminum.

cess. For the specific example, of 7075-T6 aluminum subjected to a  $\Delta K$  of 3 ksi  $\sqrt{\text{in}}$  at  $R$  equal to 0.1, the model indicates that about 66,000 cycles are required for the crack to traverse the damage zone. However, as shown in Figure 4, only about 14% or 9400 cycles are required to produce 50% of the damage. The behavior is similar at higher values of  $\Delta K$ . For example, at  $\Delta K$  equal to 25 ksi  $\sqrt{\text{in}}$  and  $R$  equal to 0.10, the crack grows through the damage zone in 1200 cycles, but 50% of the damage is done in the last 10 cycles.

#### Mode Transition and Sheet Thickness Effects

The effect of sheet thickness and the transition from the flat to slant mode of crack extension on the growth rate of through-cracks was investigated in a program of fatigue tests of pre-cracked sheet specimens. Centrally cracked, 1/16" and 1/4" thick sheets of 2024-T3, 6061-T6, and 7075-T6 aluminum were sinusoidally loaded in tension at constant load amplitude. The growth rate data derived from these tests are presented in Figures 6, 7, and 8. The curves represent correlation of the data by the crack extension model, and the arrows indicate the beginning of transition from the flat mode of growth to the slant mode. For the 2024-T3 and 7075-T6 alloys the growth rate is higher in the 1/4" sheet than in the 1/16" sheet before and during mode transition, but after transition the

thickness effect diminishes. In the 6061-T6 specimens growth was entirely in the slant mode. The data shows higher growth rates for the thicker specimens of 6061-T6 but the thickness effect is less pronounced than for the other alloys, which exhibited mode transition.

Figures 6, 7, and 8 also show the growth rate curves generated by equations (1) through (7) with use of the appropriate mechanical properties listed in Table I. The slant mode growth rate curves for each alloy are fit to the data by using the fatigue element radius as the correlating parameter.

The flat mode curves are fit by use of the same fatigue element radius used in the slant mode. A reasonable fit to the flat mode data, however, required the use of a lower ductility than that derived from static tensile tests. The higher growth rate in the flat mode before transition is associated empirically with a reduced fatigue ductility. The lower apparent ductility may be related to higher lateral constraint of the material near the crack tip when the crack is growing in the flat mode. The flat mode fatigue ductility is also lower for the thicker 7075-T6 and 2024-T3 specimens. This apparent reduction in ductility may be similarly associated with a higher degree of lateral constraint at the crack front in thicker sheets.

The conditions at the beginning of transition from the flat mode to the slant mode were observed in the testing program and are summarized in Table II. These re-

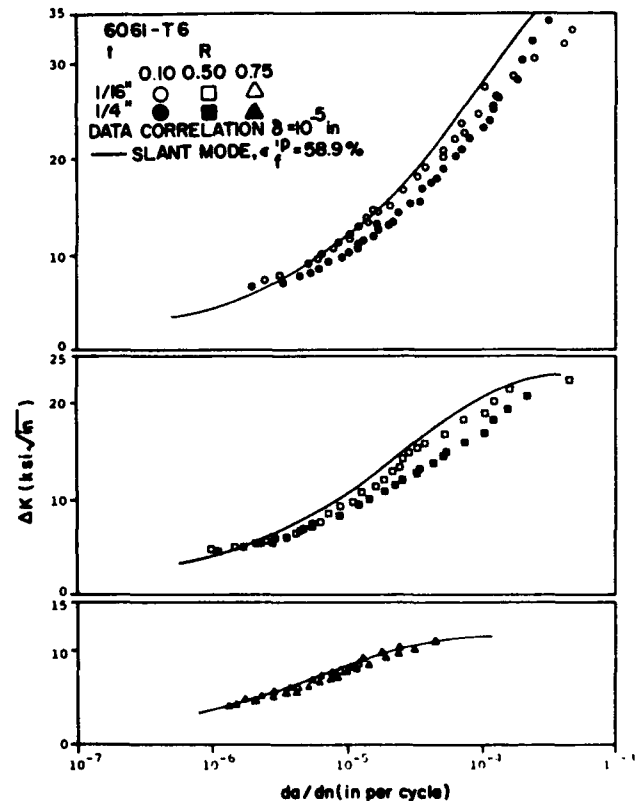


Figure 7. Crack Extension Rate Data and Model Correlation for 6061-T6 Aluminum.

TABLE I.  
MATERIAL PROPERTIES

MATERIAL	$\sigma_{eo}$ (ksi)	$\sigma_Y$ (ksi)	$\sigma_u$ (ksi)	E ( $10^6$ psi)	$\epsilon_f^p$ %	Grain Size (in.)	2 $\delta$ (in.)
1/16" 7075-T6 (clad)	12.5	69.2	76.1	10.0	34.6	0.003	0.0022
1/4" 7075-T6	23.0	77.8	86.1	11.0	26.7	0.003	0.0022
1/16" 2024-T3	20.0	53.0	70.5	11.2	33.4	0.002	0.002
1/4" 2024-T351	20.0	57.6	72.8	10.8	33.5	0.002	0.002
1/16" 6061-T6	13.5	43.4	47.5	11.0	58.9	0.002	0.00002
1/4" 6061-T6	13.5	44.7	48.3	10.3	56.2	0.002	0.00002

sults show that for a given alloy and a given R value, the stress intensity factors at transition are approximately equal for the 1/16" and 1/4" sheet specimens. Since the radius of the plastic zone is a function of the stress intensity factor (equation 4), the plastic zone radius at transition in these tests did not depend on the plate thickness. Similar observations have been reported in References 2 and 3. Apparently, the relationship between specimen thickness and plastic zone size at transition that is observed for monotonically loaded fracture specimens does not apply under cyclic conditions. The data in Table II also show that for a given material and thickness the growth

rate at transition is independent of R. This behavior has also been reported in References 4 and 5.

It is interesting to note in Table II that the radius of the zones of reversed plastic flow at transition computed from equation (5), although somewhat dependent on R, are of the same order of magnitude as the grain size of the material. This suggests that the extension of the region of reversed plastic flow beyond approximately one grain diameter may relax the lateral stress at the crack tip sufficiently to initiate transition from the flat mode to the slant mode of growth.

#### Cyclic Load Ratio and Critical Stress Intensity Factor

The critical values of the maximum stress intensity factor for the 7075-T6 specimens that fractured at values of net section stress less than the yield strength are listed in Table III. For the 1/4" sheet the critical cyclic stress intensity factors are within 5% of the static test value. For the 1/16" sheet data, however, the critical cyclic stress intensity factor decreases with decreasing cyclic load ratio. This reduction in  $K_{CC}$  for thin sheet may be due to more extensive cyclic damage of the material ahead of the crack associated with higher values of  $\Delta K$ . Cyclic damage may be less in the 1/4" sheets in which crack extension near the point of instability alternates between cyclic growth and rapid tunneling. Following a burst of rapid growth, the center portion of the crack front is observed to have advanced farther than the edges. During subsequent cyclic loading the displacement of the advanced crack front is inhibited by the trailing edges of unfractured material, resulting in a decrease in the stress at the advanced central portion of the crack and an increase in stress on the lagging edges. This behavior is consistent with observations of the fracture surface which show that the rate of fatigue growth after a rapid burst is much faster at the edges than in the center. The low stress over the central portion of the crack front results in little cyclic damage there and leaves the material in an essentially unaffected condition. At the point of final fracture the crack moves through this relatively undamaged material, which should have approximately the same toughness, or critical stress intensity factor, as that of an uncycled specimen.

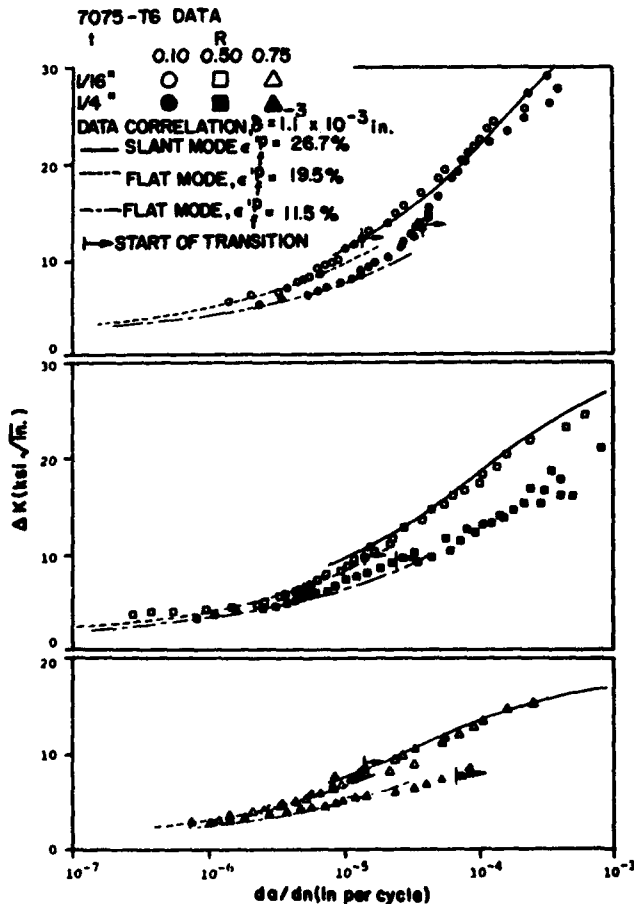


Figure 8. Crack Extension Rate Data and Model Correlation for 7075-T6 Aluminum.

**TABLE II.  
GROWTH MODE TRANSITION DATA**

MATERIAL	R	$K_{max}$ (ksi $\sqrt{in}$ )	$\Delta K$ (ksi $\sqrt{in}$ )	$r_p$ (in)	$r_R$ (in)	$da/dn$ (in. per cycle)
7075-T6 1/4"	0.10	15.9	14.4	0.017	0.0033	$4.0 \times 10^{-5}$
	0.50	18.8	9.38	0.023	0.0014	$2.5 \times 10^{-5}$
	0.75	30.3	7.52	0.060	0.0009	$6.6 \times 10^{-5}$
7075-T6 1/16"	0.10	13.6	12.3	0.015	0.0031	$1.5 \times 10^{-5}$
	0.50	19.8	9.88	0.032	0.0020	$1.5 \times 10^{-5}$
	0.75	32.0	7.93	0.084	0.0013	$1.5 \times 10^{-5}$
2024-T351 1/4"	0.10	13.6	12.3	0.022	0.0045	$1.7 \times 10^{-5}$
	0.50	18.4	9.20	0.040	0.0025	$1.6 \times 10^{-5}$
	0.75	31.7	7.83	0.119	0.0018	$1.1 \times 10^{-5}$
2024-T3 1/16"	0.10	13.5	12.1	0.026	0.0052	$8.9 \times 10^{-6}$
	0.50	18.2	9.13	0.047	0.0029	$8.3 \times 10^{-6}$
	0.75	33.5	8.30	0.157	0.0024	$9.0 \times 10^{-6}$

**TABLE III.  
CRITICAL CYCLIC STRESS INTENSITY FACTOR FOR 7075-T6 ALUMINUM SHEET**

THICKNESS (in)		1/4			
LOAD RATIO	Static Test	0.10	0.50	0.50	0.75
$K_c$ or $K_{cc}$ (ksi $\sqrt{in}$ )	48.5	50.3	46.9	46.5	50.7
THICKNESS		1/16			
LOAD RATIO	Static Test	0.10	0.50	0.50	0.75
$K_c$ or $K_{cc}$ (ksi $\sqrt{in}$ )	64.9	45.2	58.7	57.6	70.0

**SUMMARY**

A model of the process of fatigue crack extension has been used to examine the influence of certain material properties on the cyclic rate of crack growth. A parametric analysis indicates that the growth rate is most sensitive to ductility and Young's modulus at intermediate values of stress intensity factor range, to critical cyclic stress intensity at high stress intensities, and to the endurance strength at low stress intensities. For cases in which the plastic zone is small relative to the crack length the yield strength appears to have a minor influence on the growth rate.

An analysis of damage accumulation by use of the model indicates that cyclic crack extension is, generally, a low lifetime process on a local scale, and that most of the damage to a fatigue element in the path of the crack is done in a small fraction of the damage zone. At higher values of either the stress intensity range or the cyclic load

ratio damage is more closely concentrated near the crack front.

Experimental results show that the cyclic growth rate is higher in thicker sheets before transition from the flat mode of growth to the slant mode, and that after transition this thickness effect is diminished. Correlation of the experimental growth rate data by use of the model indicates that the higher growth rate in the flat mode and the higher growth rates in thicker sheets are associated with lower fatigue ductilities.

For a given cyclic load ratio and a given material, the stress intensity factor range at the beginning of mode transition was found to be the same for the two sheet thicknesses tested. Also for a given material and a given thickness the growth rate at the beginning of transition was found to be independent of the cyclic load ratio. The radius of the zone of reversed plastic deformation at the start of transition was computed to be of the same order of

magnitude as the grain size of the material.

For cases in which fracture occurred in the slant mode the critical cyclic stress intensity factor decreased with decreasing cyclic load ratio.

#### ACKNOWLEDGEMENTS

This work was partially supported through the NASA-ASEE Summer Faculty Fellowship Program and a grant from the National Science Foundation.

#### REFERENCES

1. W.G. Fleck and R.B. Anderson, "A Mechanical Model of Fatigue Crack Propagation," Paper 69, *Proc. 2nd Int. Conf. Fracture*, Chapman and Hall, London (1969).
2. S.R. Swanson, F. Cicci, and W. Hoppe, "Crack Propagation in Clad 7079-T6 Aluminum Alloy Sheet Under Constant and Random Amplitude Fatigue Loading," p. 312, *Fatigue Crack Propagation*, ASTM-STP-415, American Society for Testing and Materials, Philadelphia, Pennsylvania (1967).
3. D. Broek and J. Schijve, *The Effect of Sheet Thickness on the Fatigue Crack Propagation in 2024-T3 Alclad Sheet Material*, NRL-TR-M. 2129, National Aero- and Astronautical Research Institute, Amsterdam (1965).
4. D. Broek and J. Schijve, *The Influence of the Mean Stress on the Propagation of Fatigue Cracks in Aluminum Alloy Sheet*, NRL-TN-M.2111, National Aero- and Astronautical Research Institute, Amsterdam (1963).
5. D. Broek, P. DeRijk, and P.J. Severhuysen, *The Transition of Fatigue Cracks in Alclad Sheet*, NRL-TR-M.2100, National Aero- and Astronautical Research Institute, Amsterdam (1962).

# EXPERIMENTS ON THE NATURE OF THE FATIGUE CRACK PLASTIC ZONE

by

G.T. Hahn, M. Sarrate\*, and A.R. Rosenfield

Battelle Memorial Institute  
Columbus Laboratories  
Columbus, Ohio

## INTRODUCTION

Until recently, few generalizations could be made about fatigue crack growth. Although much of the data have been expressed as a power relation<sup>†</sup>:  $\frac{da}{dN} = A(\Delta K)^m$ , neither of the curve-fitting parameters is, in general, a constant. Both  $m$  and  $A$  depend on the stress range, the material, the test environment, and the exact details of the testing procedure. In the absence of correlations, it has been difficult to identify the metallurgical influences on the fatigue crack growth resistance.

Now, with the accumulation of more test data,<sup>1-27</sup> patterns are beginning to emerge. The compilation in Appendix A contains evidence of two growth rate regimes within which many alloys display striking similarities. Progress is also being made on the analytical front; see Rice<sup>28</sup> for a comprehensive review and more recent treatments by Rice and Johnson<sup>29</sup>, Erdogan<sup>30</sup>, and Liu and co-workers<sup>22,31</sup>. These analyses hinge on the two mechanisms of crack advance that have been proposed: (1) irreversible plastic blunting<sup>32-34</sup> and (2) Manson<sup>35</sup>-Coffin<sup>36</sup> type damage accumulation. They also depend on descriptions of the strain distribution in the locale of the fatigue crack<sup>34,37,38</sup>.

The experimental work described in this report deals with the plastic zone of a growing fatigue crack and its relation to the zone of a monotonically loaded, stationary crack. This subject is virtually unexplored because of the experimental difficulties, and only one set of measurements, by Liu and Iino<sup>22</sup> are known to the authors. The present study examines ways of applying two techniques: etch pitting and interferometry, to reveal the plastic zones produced by fatigue cracks under plane strain and plane stress conditions. Preliminary results are reported and these indicate that the plastic deformation generated by each loading cycle is similar to the zone of a stationary crack loaded monotonically.

On this basis, theoretical treatments of the monotonically loaded crack are tentatively extended to the fatigue crack problem. Simplified formulations of the plastic

blunting and damage accumulation are obtained in this way. The efficiency of the blunting mechanism and the number of plastic strain cycles experienced by material in front of the crack is estimated. This shows that both mechanisms can account for the value of the stress intensity exponent,  $m \approx 2$  observed in Regime No. 1 (the high cycle-low stress portion of the crack growth spectrum). While neither mechanism easily accounts for the invariance of crack growth rates in Regime No. 1, the existing observations are more easily rationalized in terms of blunting. A possible explanation is offered for the higher  $m$ -values and growth rates of Regime No. 2 (the low cycle-high stress range). Implications with respect to the metallurgical origins of the cyclic crack growth resistance and the prospects of improving it are discussed.

## EXPERIMENTAL PROCEDURE

### Plane Stress

Plastic zones under plane stress were revealed in an 0.00175 in. thick, cold rolled, mild steel foil - yield strength: 105,000 psi and toughness:  $K_c = 34 \text{ Ksi}\sqrt{\text{in}}$  - whose fracture behavior has been reported on before<sup>39-40</sup>. The behavior of the foil approximates two idealizations: elastic-perfectly plastic behavior and plane stress deformation. Because plane stress conditions are approached, the deformation within the plastic zone ahead of a crack is mainly transverse to the surface and easily measured.

The foil specimen was 4.0" long by 3.9" wide with a centrally located notch 0.220" long cut in by spark machining. It was prepolished to give a smooth surface and mounted in a small tensioning device which could be placed on the stage of an interference microscope. The strain distribution could thus be detected under load as well as after unloading. The specimen was loaded by means of a screw-and-lever arrangement, the load being monitored with an electric resistance strain gage (more detailed descriptions of the experimental methods are given in References 39 and 40). The fatigue loading corresponds to cycling between stress-intensity levels of  $K/\sigma_y = 0.025 - 0.25 \sqrt{\text{in}}$ .

†  $\frac{da}{dN}$  is the cyclic crack growth rate,  $\Delta K$  is the cyclic stress intensity variation,  $A$  is a materials parameter and  $m$  is a numerical constant.

\* Now with Argentine Atomic Energy Commission.

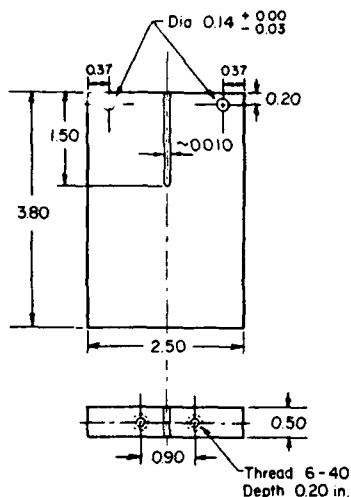


Figure 1. Cantilever Fracture Toughness Specimen.

After varying numbers of cycles, the loading was interrupted and interference patterns of the strain distribution at maximum and minimum loads were made.

#### Plane Strain

Studies of plastic zones under plane strain employed 1/2 in.-thick, Fe-3Si steel plates as the model material<sup>†</sup>. Descriptions of the material and the procedure for revealing zones on the surface and on interior sections by etching, as well as the zones displayed by virgin, stationary cracks in this steel after one cycle load-unload are given in Reference 41. Unlike the earlier work, the present studies were conducted with the DCB (double cantilever beam) specimen shown in Figure 1. Stress intensity values were calculated from the Mostovoy relation<sup>42</sup> and checked against compliance measurements. In an effort to avoid cleavage, the tests were carried out at 100 C, but this strategy was only partially successful. Cleavage can probably be avoided in future experiments by lowering the silicon content. The tensile properties of the steel at 100C, in Figure 2, show that the yield stress is 54,000 psi at this temperature.

In the first experiment fatigue crack growth was simulated by cutting in a sharp slit under load with intermittent unloading. The specimen was first loaded to a predetermined stress intensity level,  $K = 0.7 \sqrt{\text{in}}^{\dagger\dagger}$  in a horizontal tensile testing machine. Then the slit was extended 0.0008 in. by spark machining\* under load. At this point, the specimen was unloaded, and reloaded to  $K = 0.7 \sqrt{\text{in}}$ , and the sequence of steps, cutting, unloading, and re-loading repeated 50 times in quick succession. Effects of

the stress reversals within zone and the plastic region left behind the growing slit were discerned by comparisons with the zones produced by:

(i) A virgin slit subjected to one cycle of loading, and by

(ii) A slit cut in under load with the load controlled to produce a constant stress intensity at the crack tip which are described more fully elsewhere.<sup>43</sup>

In the second type of experiment, actual fatigue cracks were generated in pre-slitted DCB specimens and grown by cycling between a small preload and a maximum load and deflection controlled to give a fixed stress intensity range of  $\frac{\Delta K}{\sigma_Y} = 0.7 \sqrt{\text{in}}$ . These experiments were performed at 10 cps in a standard hydraulic fatigue testing machine. The zones associated with these cracks were then revealed by etching.

## RESULTS

#### Plane Stress

Figure 3 illustrates the condition of a sample under load after the first 1/2-fatigue cycle and the information derived from the interferometric fringe pattern (Figure 3a)\*\*: No crack growth was discernible in the steel foil after the

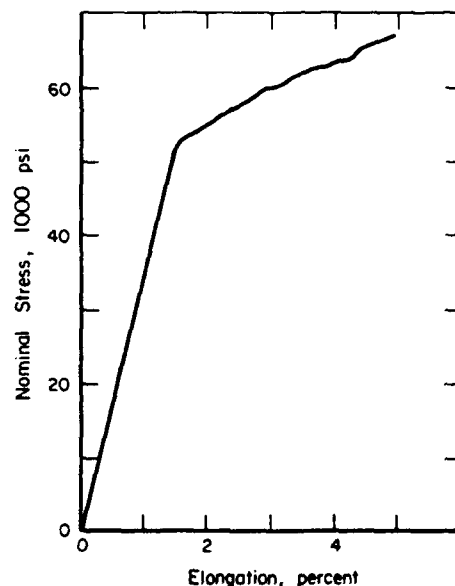


Figure 2. Stress-Strain Characteristics of the Fe-3Si Steel at 100 C.

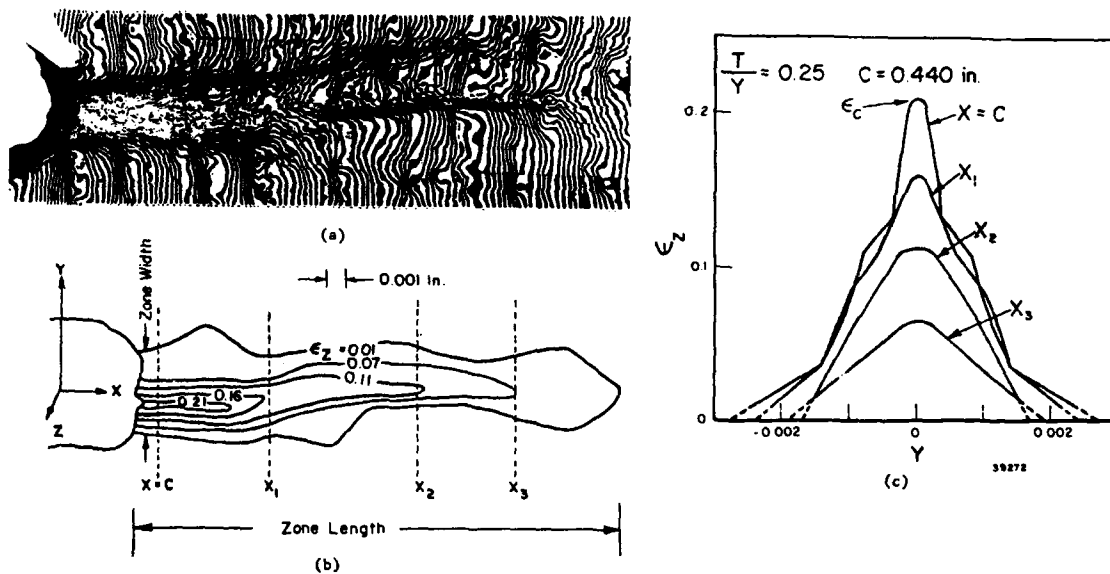
<sup>†</sup> Nominal Composition Si: 3.4%, C: 0.02%, remainder Fe.

<sup>††</sup>  $K$  is the stress intensity, and  $\sigma_Y$  is the yield stress.

\* The slits were spark machined with a 0.005 in. diameter copper wire which produces a slit  $\sim 0.005$  in. root radius.

\*\* The pattern reflects the distribution of the through-the-thickness strain  $\epsilon_z$ , and this can be converted into an isostrain contour map (Figure 3b) which shows the general shape of the zone, the zone length and the zone width at the crack (or slit) tip, as well as the distribution of strain within. Since the patterns are difficult to interpret right at the crack (or slit) tip, (See next page.)

**Figure 3. Strain Distribution Ahead of a Slit Revealed Under Load by Interferometric Fringe Pattern:** (a) fringe pattern displayed by sample with  $c = 0.440$  in. loaded to  $T/Y = 0.25$ ,  $K/Y = 0.30 \sqrt{\text{in.}}$ , (b) the isostrain contours derived from the fringes, and (c) the  $\epsilon_z$  strain profile at four points along the plastic zone. (a) and (b) 150X, reduced 70%.



tenth cycle of loading, but when the fatiguing was interrupted for zone measurement after twenty cycles the crack had extended slightly at either end (Figure 4a). Eventually, the growth rate settled down to a roughly constant value of  $\sim 2 \times 10^{-4}$  in/cycle.<sup>†</sup> This rate is not unlike those reported for high strength structural alloys at comparable  $\frac{\Delta K}{\sigma_Y}$  levels. It also appears that the initial growth rate is slightly larger than during steady-state growth.

Qualitatively, the plastic zone had the same long, narrow shape after many cycles of loading as it did after the first cycle before crack growth was observed. Both the zone length and the zone width increase as a result of cyclic loading. The zone length after one cycle is within the range (but somewhat on the high side) of our previous measurements. During the first few cycles of loading, the length remains roughly constant and only appears to increase upon the onset of crack growth (Figure 4b). During crack growth, the length again remains relatively constant at a value  $\sim 60\%$  greater than the original value. On the other hand, the zone appears to broaden even before crack growth starts. However, the width also attains a saturation value which is  $\sim 60\%$  greater than after the initial cycle (Figure 4c).

The on-load and off-load strain profiles of the first

fatigue cycle, including the COD and  $\epsilon_c$ , appear to be identical within the experimental error (see Figure 5a). This result as well as the disparate behavior of the two ends of the crack are puzzling. While the crack tip strain profile on the right end assumed the steady state value prior to the fifth cycle (Figures 5b and 5d), the profiles on the left end appeared to be unaffected up to the onset of crack extension sometime between the 10th and 20th cycle. More experiments are needed to establish the significance of these results which may have been affected by heterogeneities in

**TABLE I.**  
**SUMMARY OF COD AND CRACK-TIP STRAIN VALUES**

TYPE OF CRACKING	$\frac{K}{\sigma_Y}$ (in%)	COD ( $10^{-4}$ in)	$\epsilon_c$
Stable crack growth under monotonic loading <sup>40</sup>	0.32 - 0.35	2.6	0.24
Fatigue Crack Growth			
1st Cycle, Load-on	0.25	2.0	0.20
1st Cycle, Load-off	0.025	1.7	0.17
20th-100th Cycle, Load-on	0.25	3.9	0.31
20th-100th Cycle, Load-off	0.025	2.3	0.185

values attributed to the crack tip, i.e. at  $x = c$ , were always measured 0.001 in. from the tip. The  $\epsilon_z$ -profile at a particular distance from the crack tip can also be constructed (Figure 3c). The peak strain displayed by the profile at the crack tip,  $x = c$ , is referred to here as the crack-tip strain or  $\epsilon_c$ . The area within this profile, i.e.,  $-2 \int_{-c}^0 \epsilon_z dY$  represents the COD, or crack opening displacement. The fact that the zones are necked largely precludes inplane strain:  $\epsilon_x = 0$ . This and the constancy of volume give the result:  $\epsilon_Y = \epsilon_z$  (see Figure 4b for coordinates). Consequently, the COD (the total Y-displacement at the crack tip arising from plastic deformation) is:  $\text{COD} = 2 \int \epsilon_Y dY = 2 \int \epsilon_z dY$ . Note that the zone in Figure 3 represents the deformation produced by the first half of a single load-unload cycle involving a stress intensity range  $\frac{\Delta K}{\sigma_Y} = 0.3 \sqrt{\text{in.}}$ , the zone corresponding to the first half of the cycle employed in the fatigue experiments  $\frac{\Delta K}{\sigma_Y} = 0.25 \sqrt{\text{in.}}$  was similar in character but about 15% smaller.

<sup>†</sup> The possibility of intermittent crack growth is not precluded due to the small number of data points.



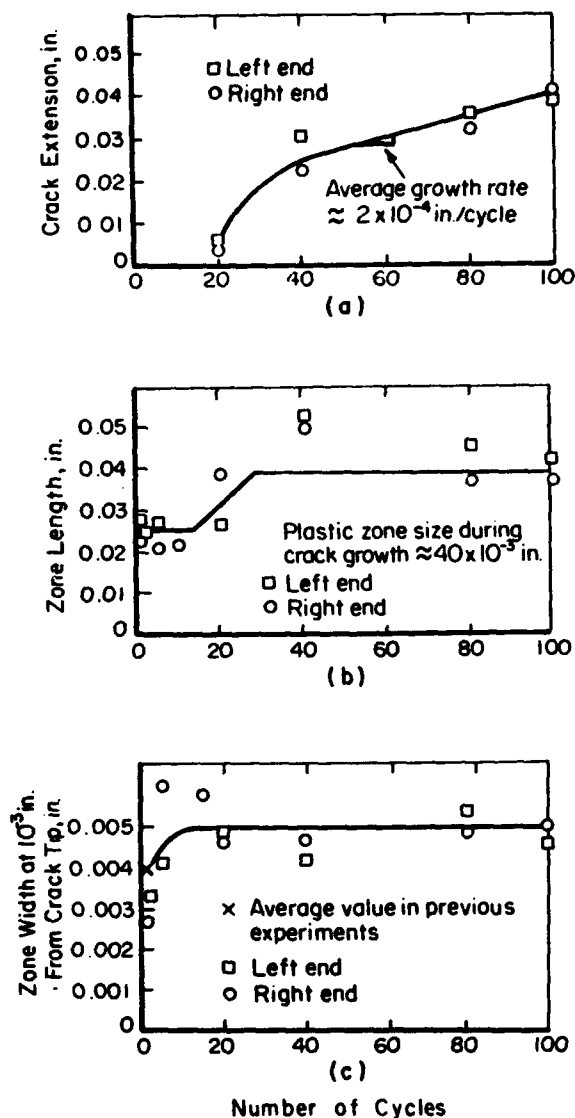


Figure 4. Influence of Cyclic Loading,  $\frac{\Delta K}{\sigma_Y} = 0.225 \sqrt{\text{in.}}$ , on the Steel Foil: (a) crack length, (b) plastic zone length, and (c) plastic zone width.

the foil, asymmetry of loading, and possibly, some tendency for the foil to buckle.

The results obtained after the onset of cracking appear to be more consistent. Figures 5b and 5d illustrate that a steady state was achieved quickly. Steady state values of the offload COD and  $\epsilon_c$  (which remained essentially unchanged throughout) were  $\sim 60\%$  of the on-load values (see Figure 5c and Table I). The on-load values were about 50% larger than those attending crack extension and stable crack growth during monotonic loading. Both the larger zones and the enhanced ductility may be connected with the cyclic softening<sup>33</sup> of the cold worked steel foil, an effect that has been observed on other materials. While these observations also lend support to the idea that fatigue crack growth proceeds with a constant value of COD, they also suggest that this COD need not be the same as the value associated with the ordinary crack extension.

In the present experiments the material directly in front of the crack experienced about 200 cycles of reverse plastic strain.<sup>†</sup> Since the maximum strain range per cycle =  $2 \cdot [\epsilon_c (\text{on-load}) - \epsilon_c (\text{off-load})] = 0.25$  at the crack tip (see Table I), the average plastic strain range over the entire zone length is about 1/2 this value, or  $\Delta \epsilon_p \sim 0.1$ , since the strain gradient is nearly linear<sup>40</sup>. Thus, the total plastic strain accumulation prior to cracking,  $\Delta \epsilon_p n \sim 20$  (85 times the value, 0.24, associated with failure under monotonic loading). Such strains could be accumulated if the material in front of the crack in the steel foil obeys a Manson-Coffin-type fatigue damage law<sup>35-36</sup>. Furthermore, a strain range  $\Delta \epsilon_p \sim 0.1$  is roughly consistent with expectations for a life of  $\sim 100$  cycles based on unnotched tests on a large number of materials<sup>44</sup>.

#### Plane Strain

The plastic zone produced in the DCB-specimen by the fatigue simulation procedure is shown in Figure 6. It can be compared with the zone of a stationary slit after one load-unload cycle reproduced in Figure 7 and with the zone of a slit cut-in under load at constant K without intermittent cycling.<sup>43</sup> The size of the zone at the crack tip is essentially the same in all three cases (see Table II<sup>††</sup>). On the basis of the relation between zone size and COD shown to exist for simplified elastic plastic models\*, the COD's and near tip strain distributions should also be similar. This is in accord with the close-ups of the etched tip of the stationary slit and the one cut-in at constant-K.\*\* However, when the slit (or crack) is subjected to cyclic loading, the deformation from a number of zones will be superimposed at the crack tip (depending on the growth per cycle relative to the forward extent of the zone). The zone produced by

(Text Continued on Page 435.)

† The number of plastic strain cycles  $N = \rho \left( \frac{da}{dN} \right)^{-1}$ , where  $\rho$  is the plastic zone length and  $\frac{da}{dN}$  the crack advance per cycle. At steady state,  $\rho = 0.040$  in., and  $\frac{da}{dN} = 2.10^{-4}$  in.

†† For convenience, the quantity  $\rho$ , which is referred to as the zone size is defined here as the furthest extent of the etched region from the slit on the plate midsection measured normal to the plane of the slit.

\*  $\text{COD} = \left( \frac{E}{\sigma_Y} \right) \rho$ , where  $\rho$  is the zone size,  $E$  is the elastic modulus and  $\sigma_Y$  is the yield stress<sup>43</sup>. This relation is valid at relatively low nominal stress levels  $\sigma$ :  $\sigma < 0.7 \sigma_Y$ .

\*\* When the Fe-3Si Steel is strained more than  $\sim 5\%$ , it no longer etches dark. The interface between the dark and light etching region at the slit tip can be regarded as an isstrain contour corresponding to about 5%.

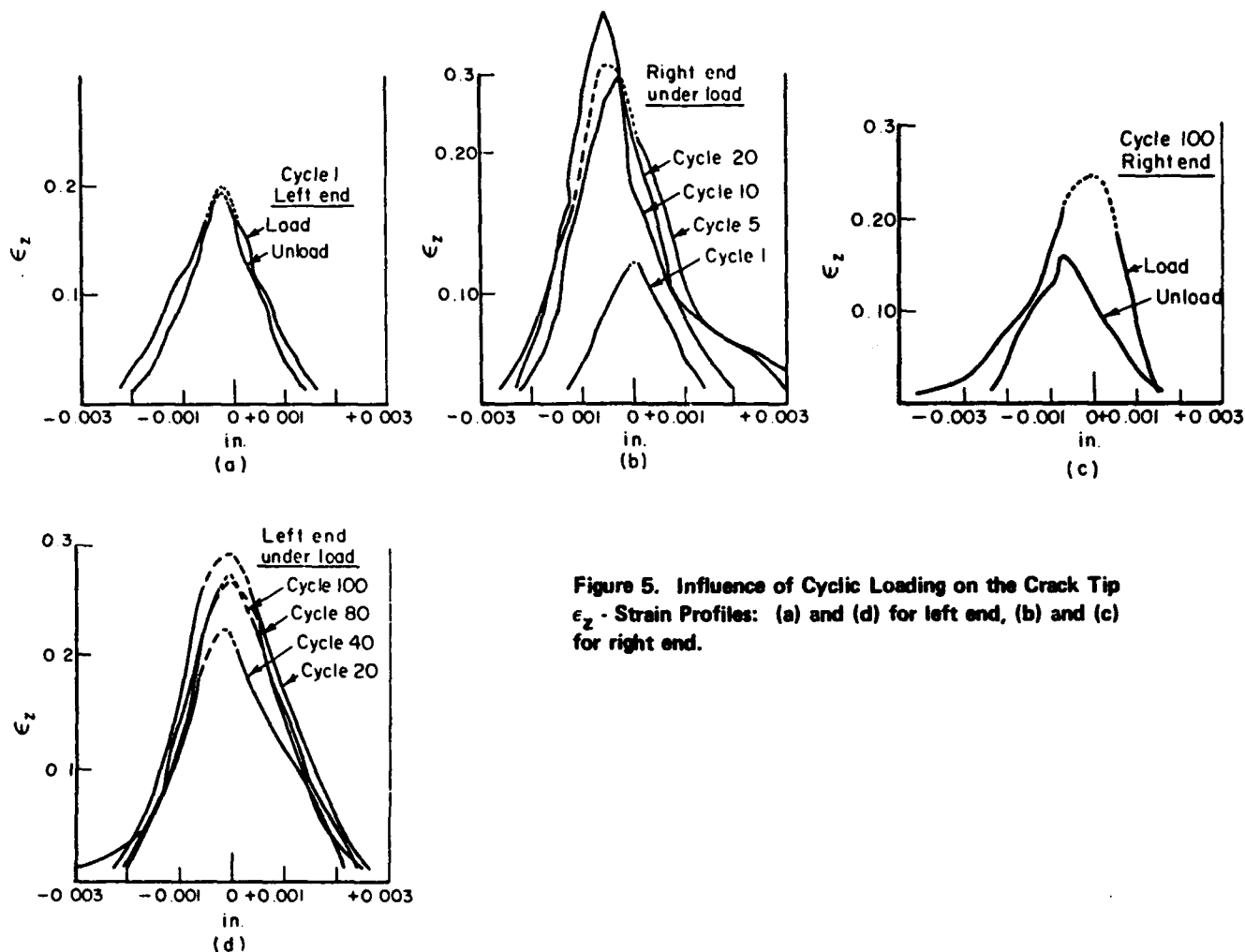


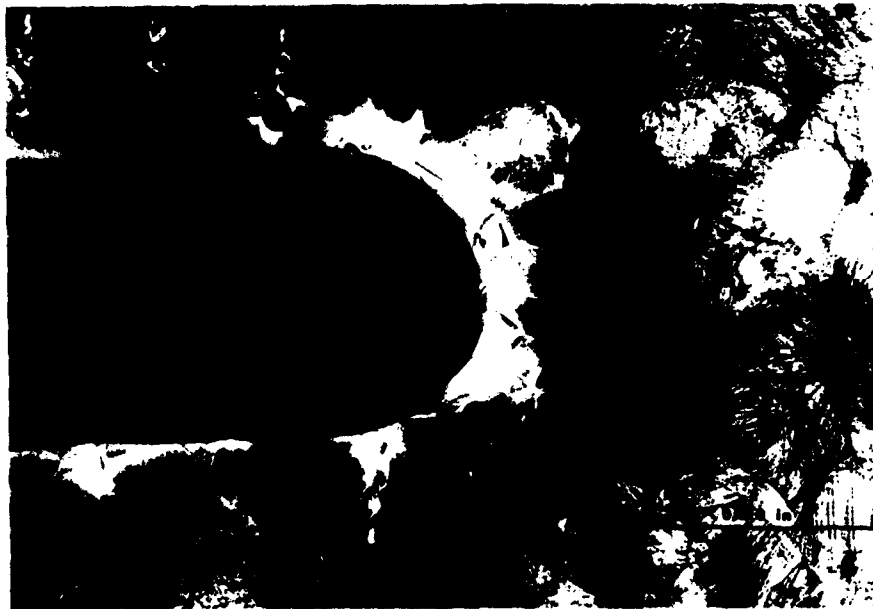
Figure 5. Influence of Cyclic Loading on the Crack Tip  $\epsilon_z$  - Strain Profiles: (a) and (d) for left end, (b) and (c) for right end.

TABLE II.  
SUMMARY OF PLASTIC ZONE SIZE-VALUES OBTAINED FROM ETCHING EXPERIMENTS

SPEC. NO.	DESCRIPTION OF EXPERIMENT	$K_{\sigma_Y}$ (in $^{1/2}$ )	CYCLIC GROWTH RATE (IN)	ZONE SIZE, $\rho$ (IN)	
				PLATE SURFACE	PLATE MIDSECTION
3P-18	Pre-cut slit subjected to one load-unload cycle	0.7	—	0.058	0.075
3P-23	Pre-cut slit subjected to one load-unload cycle	0.7	—	0.053	0.069
3P-18	Slit cut-in under load at constant stress intensity	0.7	—	0.055	0.074
3P-20	Slit cut-in under load with intermediate load cycling	0.7	$8 \cdot 10^{-4}$	0.058	0.070
3P-24	Fatigue Crack Growth	0.7	$\sim 2 \cdot 10^{-5}$	0.065	0.070
3P-25	Fatigue Crack Growth	0.7	$1.2 \cdot 10^{-5}$	0.046	0.060



(a)



(b)

Figure 6. Plastic Zone Produced in the Interior of Specimen 3P-20 by the Fatigue Simulation Procedure. The slit was cut-in under loads corresponding to  $\frac{K}{\sigma_Y} = 0.7\sqrt{\text{in.}}$  in 50–0.0008 in. increments with intermediate unloading:

- (a) zone revealed on specimen midsection, and
- (b) close-up of slit tip.

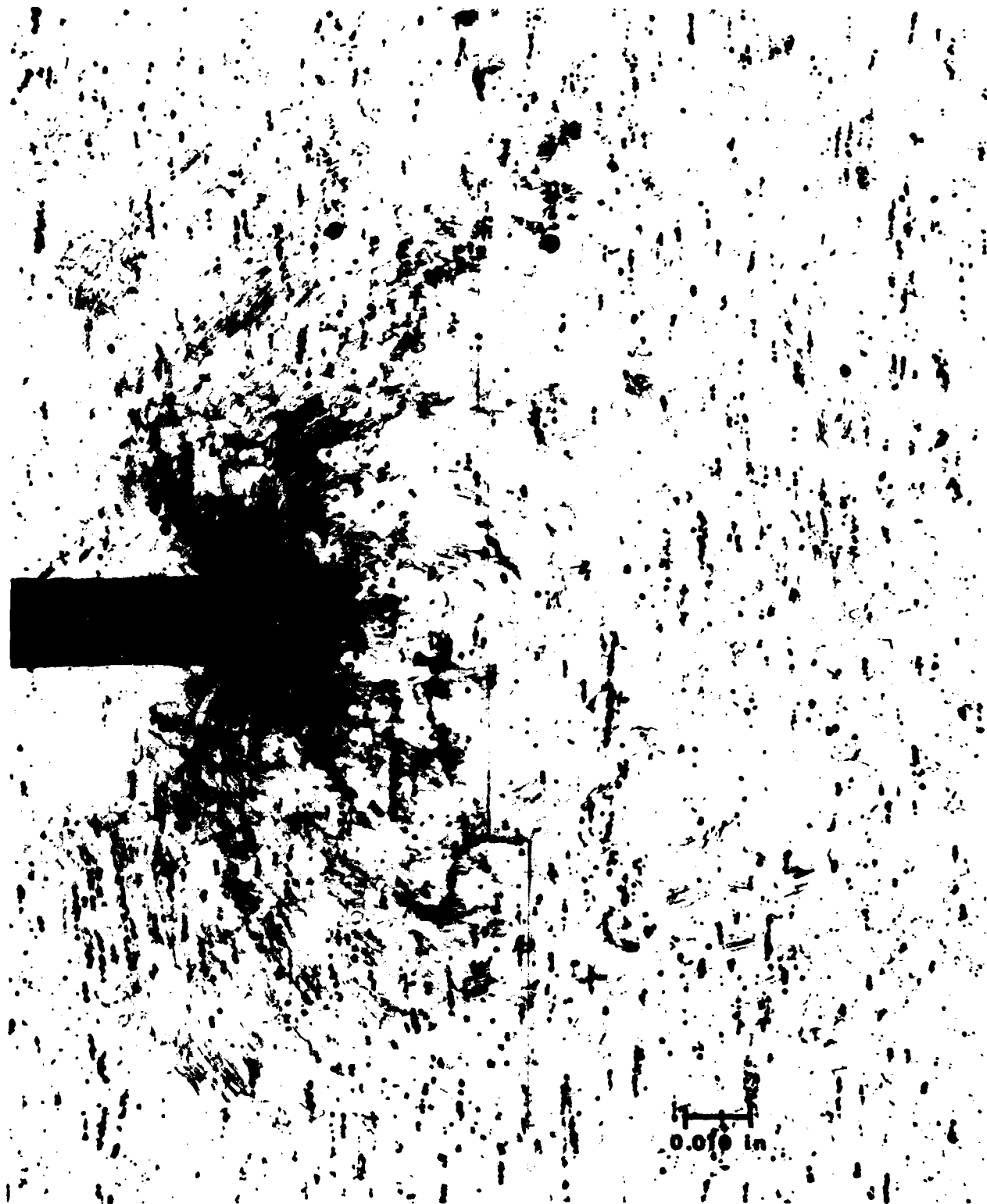


Figure 7. (Part A) Plastic Zone Produced in the Interior of Specimen 3P-19 by One Load-Unload Cycle. Pre-cut, virgin slit was loaded once to  $\frac{K}{\sigma_Y} = 0.7 \sqrt{\text{in}}$  and unloaded: (a) zone revealed on specimen midsection, and (b) close-up of slit tip.



Figure 7. (Part B) Plastic Zone Produced in the Interior of Specimen 3P-19 by One Load-Unload Cycle. Pre-cut, virgin slit was loaded once to  $\frac{K}{\sigma_Y} = 0.7\sqrt{\text{in}}$  and unloaded: (a) zone revealed on specimen midsection, and (b) close-up of slit tip.



(a) plastic zone revealed on specimen surface

Figure 8. Plastic Zone of a Mixed Fatigue-Cleavage Crack Produced in Specimen 3P-25 by 9930 Cycles with a Stress Intensity Range  $\Delta K = 0.7 \sqrt{\text{in}}$  (Cleavage portions are labeled C).



(b) plastic zone revealed in the interior on the specimen midsection

Figure 8. Plastic Zone of a Mixed Fatigue-Cleavage Crack Produced in Specimen 3P-25 by 9930 Cycles with a Stress Intensity Range  $\frac{\Delta K}{\sigma_Y} = 0.7 \sqrt{\text{in}}$  (Cleavage portions are labeled C).

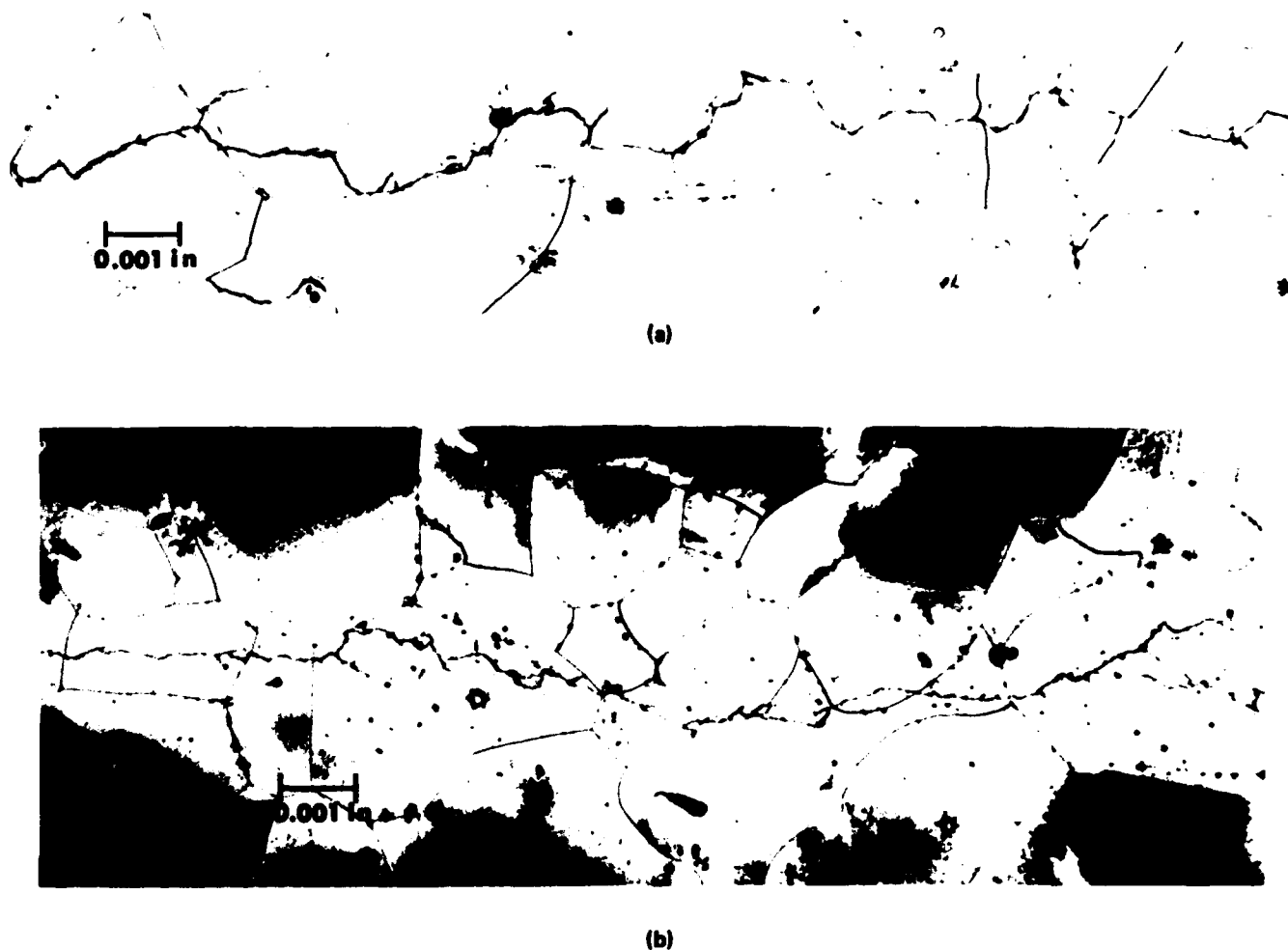


Figure 9. Profile of the Fatigue Crack on the Specimen Midsection:  
(a) Specimen 3P-24, (b) Specimen 3P-25.

cutting-in with intermittent unloading (Figure 6b) does, in fact, show a larger light etching zone at the crack tip<sup>†</sup> consistent with this picture.

The plastic zones and fracture morphologies of cracks produced by actual cyclic growth are shown in Figures 8-10. It is apparent from the pictures of the plate midsections, Figure 8, that the cyclic growth process was accompanied by some cleavage cracking. The fatigue portions of the failures are characterized by extensive light-etching regions on either side of the crack reflecting the superposition of deformations and resulting strain accumulation, and by the very ragged, irregular crack path with numerous instances of branching (see Figure 9). In some places the photos show irregularities on the crack path on a scale approaching the crack advance per cycle:  $\sim 2.10^{-5}$  in. The crack branches seem to have an included angle  $\sim 90^\circ$  and are in all cases at least 10 x larger than the average crack growth per cycle, a sign that the branches represent not merely nucleation but many cycles of growth. The branches suggest there are two alternate and symmetric sites near the

tip of the main fatigue crack for the cyclic growth, and that the two sites occasionally operate simultaneously. Similar observations have been reported and are discussed by Laird<sup>33</sup>. It is also interesting to note that some of the branches were arrested at grain boundaries (see Figure 9).

Table II illustrates that the fatigue crack plastic zone size is essentially the same as that displayed by the slits that were loaded to the same peak stress intensity level. Previous experience shows that the size of the zone attending a sharp crack is essentially the same as the slit zone-size (when the extent of the zone is much larger than the slit radius). Thus, the result derived from actual fatigue cracks and simulation experiment are the same: namely, there does not seem to be a significant difference in the plastic zone size of a cyclically loaded, growing crack and the monotonically loaded crack under plane strain conditions.

Figure 10 compares the near-tip strain distributions of a fatigue zone with a monotonic zone<sup>41</sup> at comparable

<sup>†</sup> When the Fe-3Si Steel is strained more than  $\sim 5\%$ , it no longer etches dark. The interface between the dark and light etching region at the slit tip can be regarded as an isotrain contour corresponding to about 5%.





Figure 10. Comparison of Fatigue Crack - and Stationary, Virgin Crack-Near-Tip Plastic Zones: (a) tip of fatigue crack of Specimen 3P-25 growing at  $\sim 10^{-5}$  in. per cycle at  $\frac{\Delta K}{\sigma_Y} \sim 0.5 \sqrt{\text{in.}}$ , and (b) virgin crack loaded to  $\frac{K}{\sigma_Y} = 0.4 \sqrt{\text{in.}}$  and unloaded<sup>41</sup>.

NOTE: The light etching region near the crack tip is the region strained plastically in excess of 5%. This region has essentially the same shape in both cases including the small protuberance directly in front of the crack. Taking into account the difference in stress intensity levels, the 5%-strain-region surrounding the fatigue crack is still substantially larger as a result of the accumulation of plastic strain during reverse cycling.

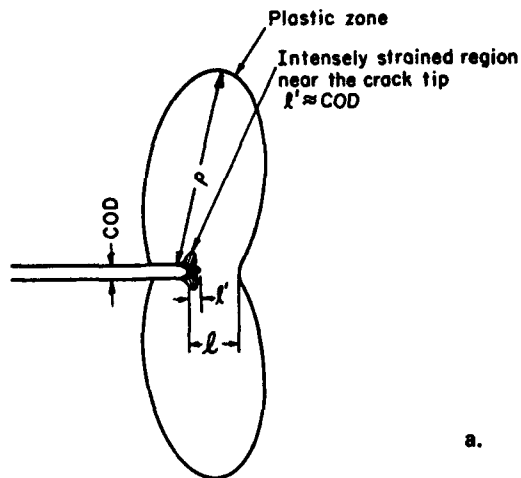
stress levels<sup>†</sup>; It can be seen that the light etching regions of both the fatigue and the monotonic zone display small protuberances directly in front of the crack. It seems likely that these are manifestations of the intensely strained region near the tip of the crack (see Figure 11a) recently treated by Rice and Johnson<sup>29</sup>. The shape of light etching region near the tip can be rationalized in terms of the slip line field and the superposition of the two symmetric enclaves directly in front of the crack as shown in Figure 11b. The existence of protuberances in both zones is further evidence that the basic character of the strain distribution is not altered by cycling. The fatigue zone does display a larger light etching

region and this is consistent with the superposition and accumulation of deformation from successive cycles.

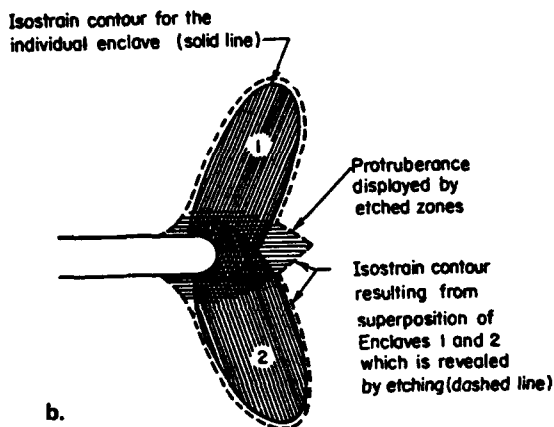
## DISCUSSION

The main finding here is there are no striking differences between fatigue crack zones -- those produced in the foil and in the Fe-3Si plate by simulation and actual cracking -- and the corresponding monotonic zones. While no radical differences were anticipated, the result is at odds with the expectation, discussed by Rice<sup>28</sup> that the steady-state

<sup>†</sup> The stress intensity level associated with the fatigue crack tip on the specimen midsection is less than the applied stress intensity level  $\frac{\Delta K}{\sigma_Y} = 0.7 \sqrt{\text{in}}$  because the crack tunneled. The value quoted in Figure 12:  $\frac{\Delta K}{\sigma_Y} \sim 0.5 \sqrt{\text{in}}$  is estimate based on the actual size of zone, and  $\frac{\Delta K}{\sigma_Y}$  - zone size relation developed for this DCB-specimen configuration<sup>45</sup>.



a.



b.

Figure 11. Schematic of Monotonically Loaded Crack Tip Plastic Zone:

- (a) plastic enclave identifying dimensions,  
(b) near tip, high strain contours.

cyclic zone is 1/4 the size of the stationary monotonic zone.<sup>†</sup> The discrepancy may simply be a consequence of the yield stress reduction affected by cycling (Bauschinger effect in the Fe-3Si steel and cyclic softening in the cold worked foil). Cyclic stress-strain measurements for these materials are needed to establish whether the reductions are large enough to account for the zones.

While questions remain, the observed similarities in size, shape and strain distribution do support the practice of applying the monotonic functional relations to the cyclic growth problem. For example, previous calculations and etching experiments indicate that the dimensions  $\rho$ ,  $l$ ,  $l'$ , and COD under plane strain (see Figure 11) can be approximated by the following expressions<sup>28,29,41,46</sup>.

<sup>†</sup> For cycling between zero stress intensity and a peak value.

<sup>††</sup>  $\eta' \sim 5$  for  $\frac{da}{dN} = 10^{-5}$  and  $Y = Y_c$ , and  $\Delta\bar{\epsilon}_p$ , the weighted average strain range close to the crack tip corresponds to the average strain in the monotonically loaded zone at distances smaller than the COD and is  $\sim 0.7^{29}$ .

MONOTONIC ZONE

CYCLIC ZONE

$$\rho \approx 0.2 \frac{K}{Y} \dots (1A) \quad \rho \sim 0.2 \left( \frac{\Delta K}{2Y} \right)^2 \dots (1B)$$

$$l \approx 0.03 \left( \frac{K}{Y} \right)^2 \dots (2A) \quad l \sim 0.03 \frac{\Delta K}{2Y_c} \dots (2B)$$

$$l' \approx \text{COD} \quad (3) \quad l' \sim \text{COD} \quad (3)$$

$$\text{COD} \approx \frac{K^2}{2EY} \dots (4A) \quad \text{COD} \sim \frac{\Delta K^2}{4EY_c} \dots (4B)$$

where  $K$  is the stress intensity,  $Y$  is the uniaxial yield stress,  $E$  the elastic modulus,  $\Delta K$  the stress intensity range,  $Y_c$  the cyclic yield stress and COD the crack opening displacement. The observation that  $\rho$  (monotonic)  $\approx \rho$  (cyclic) for the Fe-3Si Steel (see Table II) suggests that  $Y \approx 2Y_c$ . As will be discussed later, this is only likely to be true in the lightly strained region that controls the outward reach of the plastic enclave, and not in the heavily deformed region that affect the value of  $l'$  and COD. The number of cycles of plastic straining experienced by material in front of the crack is:

$$\eta = \frac{l}{\frac{da}{dN}} \sim \frac{0.03\Delta K^2}{\frac{da}{dN} 4Y_c^2} \sim \frac{0.03\Delta K^2}{\frac{da}{dN} Y^2} \quad (5)$$

$$\eta' \approx \frac{l'}{\frac{da}{dN}} \sim \frac{\Delta K^2}{\frac{da}{dN} 4EY_c} \quad (6)$$

where  $\eta$  is the total number of cycles of plastic strain, and  $\eta'$  the number of cycles of large plastic strains located within the intensely strained near tip region.<sup>29</sup> Estimates obtained in this way, assuming either  $Y_c = Y$  and  $Y_c = 2Y$ , are listed in Table III for three different materials. The relative invariance of the calculated values of  $\eta$  and  $\eta'$  is an indication that crack growth rates are scaled to the dimensions of the plastic zone. A crude estimate of the total accumulated plastic strain can also be derived:  $2\Delta\bar{\epsilon}_p \eta \sim 7^{††}$ . This suggests that the flow stress for deformation near the crack tip could be raised substantially by strain hardening, and for this reason, estimates are also given in Table III for  $Y_c = 2Y$ .

TABLE III.

ESTIMATES OF  $\bar{n}$  AND  $\bar{n}'$ , THE NUMBERS OF PLASTIC STRAIN CYCLES AND  $\beta$ , THE RATIO OF CRACK GROWTH PER CYCLE TO CRACK - OPENING DISPLACEMENT

Material	Y (Ksi)	Reference	$\frac{da}{dN}$ in/cycle	$\Delta K$ Ksi $\sqrt{\text{in}}$	$Y_c = Y$		$\beta$	$Y_c = 2Y$		$\beta$
					$\bar{n}$	$\bar{n}'$		$\bar{n}$	$\bar{n}'$	
7075-T6	~ 72	Liu and Iino <sup>22</sup>	10 <sup>-3</sup>	37	10 <sup>(a)</sup>	~ 1 <sup>(a)</sup>	1.0	5 <sup>(a)</sup>	~ 1	> 1
			10 <sup>-4</sup>	24	30	2	0.5	15	~ 1	~ 1
			10 <sup>-5</sup>	11	70	4	0.25	35	2	0.5
			10 <sup>-6</sup>	4.6	120	7	0.1	60	4	0.3
HY-130	~ 140	Barsom, et al. <sup>24</sup>	10 <sup>-3</sup>	140	30 <sup>(a)</sup>	~ 1 <sup>(a)</sup>	1.0	15 <sup>(a)</sup>	~ 1	> 1
			10 <sup>-4</sup>	83	110	4	0.25	55	2	0.5
			10 <sup>-5</sup>	29	130	5	0.2	65	3	0.4
			10 <sup>-6</sup>	10	150	6	0.2	75	3	0.3
10Ni-Cr-Mo-Co	~ 190	Barsom, et al. <sup>24</sup>	10 <sup>-3</sup>	165	20 <sup>(a)</sup>	~ 1 <sup>(a)</sup>	1.0	10 <sup>(a)</sup>	~ 1	> 1
			10 <sup>-4</sup>	85	60	3	0.3	30	2	0.7
			10 <sup>-5</sup>	35	100	5	0.2	50	3	0.4
			10 <sup>-6</sup>	13	140	7	0.1	70	4	0.3
			10 <sup>-7</sup>	5	200	11	0.1	100	5	0.2

(a) Probably an underestimate because plane strain conditions not satisfied.

Equations (1) - (4) are used in Appendix B to derive simplified expressions of the growth rates implied by the two mechanisms of crack advance that have currency:

(1) Irreversible Plastic Blunting (Kinematic Irreversibility)<sup>32-34</sup>. The crack advances because the deformation attending the unloading part of the cycle is not an exact reversal of the deformation that blunts the crack during loading:

$$\frac{da}{dN} \sim \beta \frac{\Delta K}{4EY_c} \quad (7)$$

and 
$$\left\{ \begin{array}{l} \frac{da}{dN} \sim 4 \left( \frac{\Delta K}{E} \right)^2 \\ \text{for } Y_c = 0.01E, \beta = 0.15 \end{array} \right. \quad (7A)$$

(2) Damage Accumulation<sup>22,31</sup>. The actual rupture of regions damaged by the succession of plastic strain cycles experienced by material in front of the crack:

DAMAGE ACCUMULATION

Large Strains:  $\frac{da}{dN} \sim \frac{\Delta \epsilon P^2}{4B^2 EY_c} \Delta K^2$  (8)      Small Strains:  $\frac{da}{dN} \sim \frac{0.1}{B^2} \left( \frac{\Delta K}{E} \right)^2$  (9)

$$\left\{ \begin{array}{l} \frac{da}{dN} \sim 25 \left( \frac{\Delta K}{E} \right)^2 \\ \text{for } \frac{\Delta \epsilon P^2}{B^2} = 1, Y_c = 0.01E \end{array} \right. \quad (8A) \left\{ \begin{array}{l} \frac{da}{dN} \sim 0.2 \left( \frac{\Delta K}{E} \right)^2 \\ \text{for } B^2 = 0.5 \end{array} \right. \quad (9A)$$

The quantity  $\beta \equiv \frac{da}{dN}/\text{COD}$  is the efficiency of the blunting process, B is a measure of ductility, and  $\Delta \bar{\epsilon}_p$ , the weighted average plastic strain range per cycle. These expressions are similar to the empirical growth rate law obeyed by a wide range of alloys in Regime No. 1 (see Appendix A and Tables IV and A-1):

$$\frac{da}{dN} \approx A' \left( \frac{\Delta K}{E} \right)^2 \quad (10)$$

where  $A' \sim 8$ . The experiments thus provide a way of examining the two mechanisms critically:

a. *Stress Intensity Dependence.* Both mechanisms can account for the experimentally observed stress intensity exponent:  $m \approx 2$ , which applies to both the microscopic growth rate and the striation spacing in Regime No. 1. (See results of Broek<sup>21</sup> on 7075-T6 and Miller<sup>26</sup> on 4340 and 18 Ni-Maraging Steel in Table A-1.

b. *Absence of a Yield Strength Dependence.* Tables IV and A-1 illustrate that crack growth rates in Regime No. 1 are independent of the yield stress level for a wide range of materials. At first glance this result appears to favor the "small strain" damage accumulation argument since the other two treatments predict a dependence on  $Y_c$  [Equations (7) and (8)]. However,  $Y_c$  is not the ordinary yield stress but the cyclic yield or flow stress. Evidence is presented in Appendix C, that the COD is most strongly influenced by the value of flow stress appropriate for the heavily strained material close to the crack tip. Since the rate of strain hardening varies inversely with strength level, it is possible that the cyclic flow stress at high strains ap-

TABLE IV.

SUMMARY OF SELECTED CYCLIC CRACK GROWTH RESISTANCE VALUES FOR A GROWTH RATE  $\frac{da}{dN} = 10^{-5}$  IN.  
(SEE TABLE A-1 FOR ENTIRE COMPILATION.)

MATERIAL	Y (Ksi)	$\Delta K_{10^{-5}}$ (Ksi $\sqrt{\text{in}}$ )	$\frac{\Delta K_{10^{-5}}}{E}$ $10^{-3}\sqrt{\text{in}}$	A'	$\Delta K_{1-2}$ (Ksi $\sqrt{\text{in}}$ )	REFERENCE
Fe-3Si	54	~38	1.3	6.2	-	Present Study
3Ni-Mo-V	93	39	1.3	5.9	-	Bates and Clark <sup>15</sup>
HY-80	95	33	1.1	8.3	-	Barsom, et al. <sup>24</sup>
HY-130	140	29.5	1.0	10.3	92	Barsom, et al. <sup>24</sup>
4340 (Q & T at 1000°F)	163	33	1.1	8.3	80	Miller <sup>18,26</sup>
10Ni-Cr-Mo-Co	191	35	1.2	7.4	86	Barsom, et al. <sup>23</sup>
18Ni-Maraging	218	31	1.0	9.4	80	Miller <sup>18,26</sup>
18Ni-Maraging	246/252	36	1.2	7.0	80	Wei, et al. <sup>12</sup> and Carman and Katlin <sup>8</sup>
H11	242	34	1.1	7.8	-	Carman and Katlin <sup>8</sup>
D6AC	241	32	1.1	8.8	~70	Carman and Katlin <sup>8</sup>
				Avg. 7.9		
5456-H321	37	12	1.2	7.0	-	Bates and Clark <sup>15</sup>
2024-T3	50	9.5/13	1.0/1.3	11/ 5.9	29	Forman, et al. <sup>9</sup> , Donaldson and Anderson <sup>4</sup> , McEvily and Illg <sup>2</sup> , Hudson and Hardrath <sup>5</sup> , Weibull <sup>1</sup>
2024-T3	50	10.5	1.1	9.1	16	Broek and Schijve <sup>6</sup>
2024-T3	50	14	1.4	5.1	-	Broek <sup>21</sup>
7075-T6	70	10	1.0	10.0	20	Broek <sup>21</sup>
7075-T6 (Argon)	70	14.5	1.5	4.8	-	Wei and Landes <sup>27</sup>
7075-T6	70	7.5	0.8	17.8	22	Wei and Landes <sup>27</sup>
7079-T6	65	12	1.2	7.0	-	Bates and Clark <sup>15</sup>
				Avg. 9.3		
Ti-6Al-4V	127	15	0.9	11.4	-	Bates and Clark <sup>15</sup>
70-30 Brass	18	14	0.9	13.0	-	McEvily, et al. <sup>7</sup>
70-30 Brass	92	14	0.9	13.0	-	McEvily, et al. <sup>7</sup>

$$\Delta K_{10^{-5}} \equiv \Delta K @ \frac{da}{dN} = 10^{-5} \text{ in}$$

$$A' \equiv 10^{-5} \left( \frac{\Delta K_{10^{-5}}}{E} \right)^{-2}$$

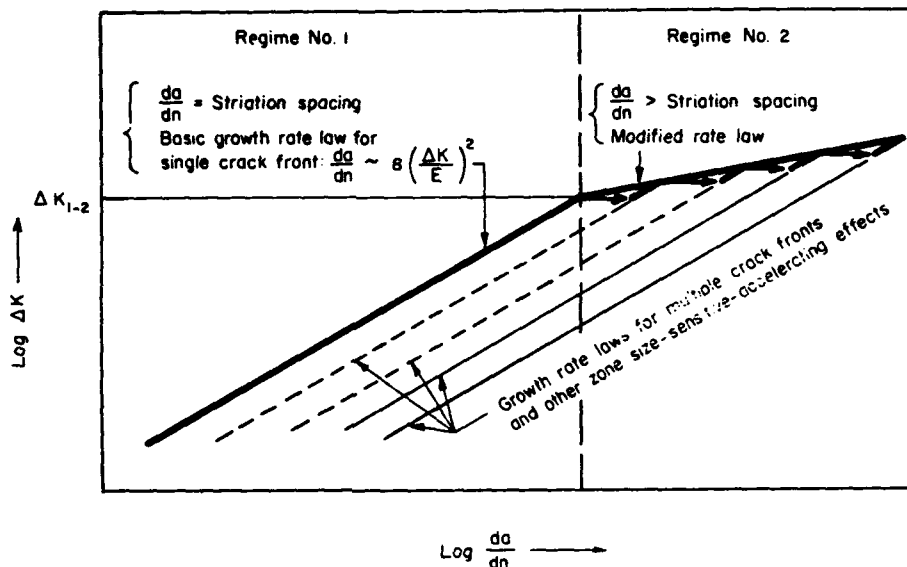
proaches a common level, e.g.,  $Y_c \sim \frac{E}{100}$ , for all materials. By way of this argument, which was suggested by Laird<sup>47</sup>, the absence of a yield stress dependence can be rationalized with either mechanism [see Equations (7A) and (8A)].

c. *Modulus Dependence.* Table IV illustrates that when the resistance cyclic crack growth is normalized with respect to modulus in Regime 1, the  $\frac{\Delta K_{10^{-5}}}{E}$  values are

nearly the same irrespective of alloy system. This feature, noted earlier by Bates and Clark<sup>15</sup>, is consistent with both mechanisms provided  $Y_c$  is a fixed fraction of E [see Equations (7A), and (8A)].

d. *Absence of a Ductility Effect.* Table IV shows that steels known to possess different levels of ductility still display the same resistance to crack growth. This seems

Figure 12. Simplified Schematic Representation of the Origin of Regimes No. 1 and No. 2.



to be inconsistent with the damage accumulation mechanism. However, it can also be argued here that the ductility in question is not the ordinary smooth bar value, but the value for a highly localized region under a complex state of stress, and this could be relatively invariant.

e. *Efficiency of the Blunting and Damage Accumulation Mechanisms.* Relatively little is known about the efficiency (degree of irreversibility) of the blunting process. A value of  $\beta \approx 0.15$  can be deduced directly in one case – from photographs of a relatively short, highly strained crack in a polyethylene sheet published by McEvily and co-workers<sup>49</sup> – which define both the COD and  $\frac{da}{dn}$ . This value is reasonably close to the  $\beta$ -values calculated for three alloys in Table 3 for  $Y_c = Y$ . The higher value,  $Y = 2Y$ , associated with the heavily strained hardened region, implies a greater efficiency, e.g.,  $\beta = 0.3 - 0.4$ . Such an efficiency may well be unrealistic, but this is not significant since the calculations of COD could well be in error by a factor of 2. Viewed in this light there is reasonably good agreement between the absolute prediction of the blunting mechanism and experiment [between Equations (7A) and (10)]. By the same token, the predictions derived from the “large strain” damage accumulation treatment, Equation (8A) are also reasonable, although the values of  $\Delta\bar{\epsilon}_p$  and B are at present very poorly defined. While the “small strain” damage accumulation treatment is least satisfactory for plane strain, it is roughly in accord with the results for the steel foil as pointed out in a preceding section.

f. *Transient Crack Growth Rates.* The damage accumulation mechanism implies that the material in front of a crack is conditioned by a number of plastic strain cycles. Consequently, the crack advance per cycle at a given  $\Delta K$  should increase gradually and only approach the steady state value after some number of stress cycles. Similar transients should be observed whenever  $\Delta K$  is increased abruptly; a gradually decreasing rate when  $\Delta K$  is abruptly reduced. This

expectation is not confirmed by photographs of the striations produced by programmed loads that have been published by McMillan and Pelloux<sup>50</sup> and Christensen and Harmon<sup>51</sup> which show no signs of transients. This probably is the strongest argument against the damage accumulation mechanism. To the extent that strain accumulation from successive cycles contributes to the value of  $Y_c$ , transients having the opposite character should be associated with the blunting mechanism. While the striations mentioned above provide no clear-cut evidence of such transients either, the experiments of Hardrath<sup>52</sup> do show that a high pre-stress can retard the crack growth rate, and this is consistent with the expectation for blunting.

g. *Environmental Effects.* The results of Barsom<sup>23</sup> on 12Ni-5Cr-3Mo and Wei and Landes<sup>27</sup> on 7075-T651 in Table A-1 show that certain “aggressive” environments greatly enhance the crack growth rate in Regime No. 1. This effect is difficult to understand in terms of the environments’ effect on the flow stress and blunting and easier to rationalize in terms of rupture, and thus, damage accumulation.

#### Regime No. 1.

The preceding paragraphs show that the main features of the low stress-high cycle portion of the growth rate spectrum can be explained either in terms of the plastic blunting or the damage accumulation mechanism. While neither mechanism is entirely satisfactory, irreversible blunting seems to be consistent with more observations at the present time.

#### Regime No. 2.

The mechanism of growth in Regime No. 2, the high stress-low cycle range is not well defined. A possible clue is the observation that macroscopic (or average) crack

advance per cycle exceeds the striation spacing<sup>15,21,26</sup>. This can begin to occur when brittle particles or other weak interfaces well in advance of the main crack front, come under the influence of the plastic zone and rupture. These ruptures not only contribute to the crack advance per cycle, but may be sources of secondary fatigue cracks as suggested by the work of Erhardt and Grant<sup>53</sup>. Thus the same mechanism operating in Regime No. 1 when augmented by an increasing length of active crack front (making  $A$  a stress dependent term) can account for (1) higher growth rates, (2) a greater stress dependence, and (3) the discrepancy between growth rate and striation spacing (see Figure 12). Accordingly,  $\Delta K_{1-2}$ : the stress intensity range at the transition from Regime No. 1 to Regime No. 2 should depend on the spacing and properties of specific microstructural features which may vary from alloy to alloy and heat to heat. Consistent with this, the  $\Delta K_{1-2}$ -values listed in Tables IV and A-1 are not constant and do not seem to correlate with yield strength. At higher stress intensity levels, the approach to general yielding and transition from plane strain to plane stress may also accelerate the crack growth rate.

This admittedly tentative picture could have important implications with respect to the metallurgical factors and alloy development. To the extent that environmental effects are not involved, neither Equation nor the compilation of  $\Delta K'$  values shows any systematic effects of composition, microstructure, or the usual thermal-mechanical treatments. It is true that metallurgical contributions amounting to  $\sim \pm 20\%$  of  $\Delta K_{10^{-5}}$  (corresponding with  $\sim 50\%$  change in total life) could be obscured by the scatter of the data. Beyond this, the prospects of improving crack growth resistance in *Regime No. 1* by the usual techniques do not seem bright. It is possible that large improvements could be realized by metallurgical changes that are designed to eliminate susceptibility to aggressive environments. Special microstructures, such as composites with interfaces normal to the crack front that delaminate preferentially, may offer advantages. The micrographs in this report contain some evidence that fatigue cracks are impeded by grain boundaries, but it is not clear whether enough boundaries can be introduced to affect the average crack growth increment significantly<sup>54</sup>.

In contrast, the behavior in Regime No. 2, especially the value of  $\Delta K_{1-2}$ , could be quite sensitive to the microstructure, to the strength and spacing of hard particles and to other metallurgical factors if the explanation offered here is correct. Furthermore, significant improvements in total life can be achieved simply by increasing  $\Delta K_{1-2}$  and postponing the higher growth rates generated in Regime No. 2. To test this possibility, it would be useful to compare  $\Delta K_{1-2}$ -values obtained for a single phase alloy with modifications involving different distributions and morphologies of hard particles.

## CONCLUSIONS

1. The interferometric technique applied to the steel

foil and the etching technique for Fe-3Si can provide useful insights to the size of the fatigue crack plastic zone and the strain distribution within it. Preliminary results show that cyclic loaded zone in the foil (plane stress) and in the Fe-3Si (plane strain) are essentially the same size as the corresponding "monotonic" zones. This result suggests that the cyclic flow stress at small strains is roughly 1/2 of the ordinary tensile yield stress consistent with the Bauschinger effect.

2. The observed similarities in the size, shape and strain distribution within the cyclic and monotonic zones lend support to the practice of adapting functional relations for the monotonic case to the fatigue problem. Estimates of the monotonic zone size and crack-tip displacement indicate that the material in front of a fatigue crack is subjected to about 50-150 cycles of reverse plastic deformation, of which about 2-7 cycles involve the large plastic strains experienced within the intensely deformed near-tip region. The crack advance per cycle is estimated to be 10-50% of the crack opening displacement.

3. The compilation of cyclic crack growth-rate measurements for steels, aluminum alloys and a titanium alloy, provides evidence for 2 growth-rate regimes. Regime No. 1 involves the low stress intensity values and low growth rates usually  $< 10^{-4}$  in. per cycle which correspond with the striation spacing, and a stress exponent  $m \approx 2$ . Regime No. 2 is the high stress-high growth rate portion of the spectrum usually  $> 10^{-5}$  in. per cycle and a larger stress exponent,  $m \gtrsim 4$ .

4. The cyclic crack growth resistance in Regime No. 1 is roughly proportional to the elastic modulus but relatively insensitive to yield strength, composition and ductility. Growth rate measurements on a variety of steels, aluminum alloys and Ti-6Al<sub>4</sub>V can be approximated by the expression  $\frac{da}{dN} \approx 8 \left( \frac{\Delta K}{E} \right)^2$ , where  $E$  is the modulus. While neither the blunting or damage accumulation mechanisms easily account for all of the features of Regime No. 1, more of the existing observations can be rationalized by blunting.

5. Some of the features of Regime No. 2 can be explained by the mechanism responsible for Regime No. 1 together with the idea that crack growth is further enhanced by an increasing length of active crack front. This is thought to occur when the plastic zone is large enough to produce cracks at hard particles and other weak interfaces ahead of the main crack front which then also extend by cyclic growth and connect with the main crack. Accordingly, improvements in fatigue life could be realized by postponing the transition from Regime No. 1 to No. 2, and this may be related to metallurgical factors.

## ACKNOWLEDGEMENTS

The authors are grateful to W.J. Trapp, A.W. Brisbane and F. Ostermann for their encouragement and sup-

port of this work. They are indebted to H. Mindlin for assistance in conducting the fatigue tests, P. Mincer for the metallographic work and to C. Pepper for her work on the

manuscript. They also wish to thank C. Laird, R. Hoagland, and J. Barsom for stimulating and useful discussions.

#### REFERENCES

1. W. Weibull, *The Propagation of Fatigue Cracks in Light-Alloy Plates*, SAAB-TN-25, Svenska Aeroplan Aktiebolaget, Linköping, Sweden (1954).
2. A.J. McEvily and W. Illg, *The Rate of Crack Propagation in Two Aluminum Alloys*, NACA-TN-4394, National Aeronautics and Space Administration, Washington, D.C. (1958).
3. W. Illg and A.J. McEvily, *The Rate of Fatigue-Crack Propagation for Two Aluminum Alloys Under Completely Reversed Loading*, NASA-TN-D-52, National Aeronautics and Space Administration, Washington, D.C. (1959).
4. D.R. Donaldson and W.E. Anderson, "Crack Propagation Behavior of Some Airframe Materials," pp. 375-441, *Proc. Crack Propagation Symp.*, Vol. II, College of Aeronautics, Cranfield, England (1961).
5. C.M. Hudson and H.F. Hardrath, *Effects of Changing Stress Amplitude on the Rate of Fatigue Crack Propagation in Two Aluminum Alloys*, NASA-TN-D-960, National Aeronautics and Space Administration, Washington, D.C. (1961).
6. D. Broek and J. Schijve, *The Influence of the Mean Stress on the Propagation on Fatigue Cracks in Aluminum Alloy Sheet*, NRL-TN-M.2111, National Aero- and Astronautical Research Institute, Amsterdam (1963).
7. A.J. McEvily, R.C. Boettner, and A.P. Bond, "On Cold Work and Fatigue Crack Propagation in  $\alpha$ -Brass," *J. Inst. Metals*, 93:481 (1965).
8. C.M. Carman and J.M. Katlin, *Low Cycle Fatigue Crack Propagation of High Strength Steels*, ASME Paper 66 - MET-3, American Society of Mechanical Engineers, New York (1966).
9. R.G. Forman, V.E. Kearney, and R.M. Engle, *Numerical Analysis of Crack Propagation in Cyclic Loaded Structures*, ASME Paper 66-WA/MET-4, American Society of Mechanical Engineers, New York (1966).
10. S.R. Swanson, F. Cicci, and W. Hoppe, "Crack Propagation in Clad 7079-T6 Aluminum Alloy Sheet Under Constant and Random Amplitude Fatigue Loading," p. 312, *Fatigue Crack Propagation*, ASTM-STP-415, American Society for Testing and Materials, Philadelphia, Pennsylvania (1967).
11. T. Yokobori, M. Tanaka, et al., "Fatigue Crack Propagation Behavior of Mild Steel and High Strength Steels," *Rept. Res. Inst. Strength Fracture Mater. (Tohoku Univ., Sendai, Japan)*, 3:39 (1967).
12. R.P. Wei, P.M. Talda, and C. Li, "Fatigue Crack Propagation in Some High Strength Steels," p. 460, ASTM-STP-415. (See Ref. 10)
13. T.W. Crooker, L.A. Cooley, et al., *Subcritical Flaw Growth in 9Ni-4Co-0.25 C Steel: A Fatigue and Fractographic Investigation and Its Relationship to Plane Strain Fracture Toughness*, NRL-6698, Naval Research Laboratory, Washington D.C. (1968).

## REFERENCES (Continued)

14. R.C. Schwab, *The Use of Tapered Double-Cantilever-Beam Specimens for Fatigue Crack Growth Studies*, NSRDC-2689, Naval Ship Research and Development Center, Washington, D.C. (1968).
15. R.C. Bates and W.G. Clark, Jr., *Fractography and Fracture Mechanics*, 68-1D7-RPAFC-P1, Westinghouse Research Laboratories, Pittsburgh, Pennsylvania (1968).
16. T.W. Crooker and E.A. Lange, *Fatigue Crack Growth in Three 180-Ksi Yield Strength Steels in Air and in Saltwater Environments*, NRL-6761, Naval Research Laboratory, Washington, D.C. (1968).
17. L.R. Hall, *Plane-Strain Cyclic Flaw Growth in 2014-T62 Aluminum and 6A1-4V (Z1) Titanium*, NASA-CR-72396, National Aeronautics and Space Administration, Washington, D.C. (1968).
18. G.A. Miller, "The Dependence of Fatigue-Crack Growth Rate on Stress Intensity Factor and the Mechanical Properties of Some High-Strength Steels," *ASM Trans. Quart.*, 61:442 (1968).
19. D.F. Mowbray, W.R. Andrews, and A.J. Brothers, *Fatigue-Crack Growth-Rate Studies of Low-Alloy Pressure-Vessel Steels*, ASME Paper 68-PVP-23, American Society of Mechanical Engineers, New York (1968).
20. S.H. Smith, T.R. Porter, and W.D. Sump, *Fatigue Crack Propagation and Fracture Toughness Characteristics of 7079 Aluminum Alloy Sheets and Plates in Three Aged Conditions*, NASA-CR-996, National Aeronautics and Space Administration, Washington, D.C. (1968).
21. D. Broek, "The Effect of Intermetallic Particles on Fatigue Crack Propagation in Aluminum Alloys," *Proc. 2nd Int. Conf. Fracture*, Chapman and Hall, London (1969).
22. H.W. Liu and N. Iino, "A Mechanical Model for Fatigue Crack Propagation," *Proc. 2nd Int. Conf. Fracture*, Chapman and Hall, London (1969).
23. J.M. Barsom, *Investigation of Subcritical Crack Propagation*, M.S. Thesis, University of Pittsburgh, Pennsylvania (1969).
24. J.M. Barsom, E.J. Imhof, and S.T. Rolfe, *Fatigue-Crack Propagation in High-Strength Steels*, ARL-B-23103, U.S. Steel Corp., Monroeville, Pennsylvania (1968).
25. C.M. Hudson and J.T. Scardina, "Effect of Stress Ratio on Fatigue-Crack Growth in 7075-T6 Aluminum Alloy Sheet," *Eng. Fracture Mech.*, 1:429-446 (April 1969).
26. G.A. Miller, "Fatigue Fracture Appearance and the Kinetics of Striation Formation in Some High Strength Steels," *ASM Trans. Quart.*, 62:651-658 (1969).
27. R.P. Wei and J.D. Landes, "The Effect of D<sub>2</sub>O on Fatigue-Crack Propagation in a High Strength Aluminum Alloy," *Int. J. Fracture Mech.*, 5:69 (1969).
28. J.R. Rice, "Mechanics of Crack Tip Deformation and Extension by Fatigue," p.247, ASTM-STP-415.(See Ref. 10)



## REFERENCES (Continued)

29. J.R. Rice and M.A. Johnson, *The Role of Large Crack Tip Geometry Changes in Plane Strain Fracture*. Inelastic Behavior of Solids, McGraw Hill, N.Y. (1970).
30. F. Erdogan, "Crack Propagation Theories," p. 497, *Fracture: An Advanced Treatise*, Vol. II, Academic Press, New York (1968).
31. K.R. Lehr and H.W. Liu, "Fatigue Crack Propagation and Strain Cycling Properties," *Int. J. Fracture Mech.*, 5:45 (1969).
32. R.M. Pelleux, "Mechanisms of Formation of Ductile Fatigue Striations," *ASM Trans. Quart.*, 62:281 (1969).
33. C. Laird, "The Influence of Metallurgical Structure on the Mechanisms of Fatigue Crack Propagation," p.131, ASTM-STP-415.(See Ref. 10)
34. F.A. McClintock, "On the Plasticity of the Growth of Fatigue Cracks," p. 65; D.C. Drucker and J.J. Gilman, Eds., *Fracture of Solids*, John Wiley, New York (1963).
35. S.S. Manson, *Behavior of Materials Under Conditions of Thermal Strain*, NACA-TN-2933, National Aeronautics and Space Administration, Washington, D.C. (1953).
36. L.F. Coffin, Jr., "A Study of the Effects of Cyclic Thermal Stresses in Ductile Metals," *Trans. ASME*, 76:931 (1954).
37. J. Weertman, "Rate of Growth of Fatigue Cracks Calculated from the Theory of Infinitesimal Dislocations Distributed on a Plane," *Int. J. Fracture Mech.*, 2:460 (1966).
38. J. Weertman, "Growth of Fatigue Cracks Under Combined Static and Cyclic Stresses," *Int. J. Fracture Mech.*, 5:13 (1969).
39. M.F. Kanninen, A.K. Mukherjee, A.R. Rosenfield, and G.T. Hahn, "The Speed of Ductile-Crack Propagation and the Dynamics of Flow in Metals," p. 96; U.S. Lindholm, Ed., *Mechanical Behavior of Materials Under Dynamic Loads*, Springer-Verlag, New York (1968).
40. G.T. Hahn, M. F. Kanninen, and A.R. Rosenfield, "Ductile Crack Extension and Propagation in Steel Foil," *Proc. 2nd Int. Conf. Fracture*, Chapman and Hall, London (1969).
41. G.T. Hahn and A.R. Rosenfield, *Plastic Flow in the Locale of Notches and Cracks in Fe-3Si Steel Under Conditions Approaching Plane Strain*, SSC-191, Ship Structure Committee, Washington, D.C. (1968).
42. S. Mostovoy, P.B. Crosley, and E.T. Ripling, "Use of Crack-Line Loaded Specimens for Measuring Plane-Strain Fracture Toughness," *J. Mater.*, 2:661 (1967).
43. G.T. Hahn, A.R. Rosenfield, and M. Sarrate, *Observations of Yielding Accompanying Crack Growth*, Inelastic Behavior of Solids, McGraw Hill, N.Y. (1970).

## REFERENCES (Continued)

44. J.F. Tavernelli and L.F. Coffin, Jr., "A Compilation and Interpretation of Cyclic Strain Fatigue Tests on Metals," *ASM Trans. Quart.*, 51:438 (1959).
45. *Fracture Strain Program Progress Letter to Ship Structure Committee*, July 2, 1969.
46. B.A. Bilby and K.H. Swinden, "Representation of Plasticity at Notches by Linear Dislocation Arrays," *Proc. Roy. Soc. London*, 285 A22 (1965).
47. S.S. Manson, "Fatigue: A Complex Subject - Some Simple Approximations," *Exp. Mech.*, 5/7:193 (1965).
48. C. Laird, private communication.
49. A.J. McEvily, R.C. Boettner, and T.L. Johnston, "On the Formation and Growth of Fatigue Cracks in Polymers," p. 95, *Proc. 10th Sagamore Army Mater. Res. Conf.*, Syracuse University Press, Syracuse, New York (1964).
50. J.C. McMillan and R.M. Pelloux, "Fatigue Crack Propagation Under Program and Random Loads," p. 505, ASTM-STP-415. (See Ref. 10)
51. R.H. Christensen and M.B. Harmon, "Limitations of Fatigue-Crack Research in the Design of Flight Vehicle Structures," p. 5, ASTM-STP-415. (See Ref. 10)
52. H.F. Hardrath, "Cumulative Damage," p. 345, *Proc. 10th Sagamore Army Mater. Res. Conf.*, Syracuse University Press, Syracuse, New York (1964).
53. K. Erhardt and N.J. Grant, "Behavior of 2024 Aluminum in Low Cycle Fatigue at Low Strain Rates as a Function of Temperature," p. 702, *Proc. 2nd Int. Conf. Fracture*, Chapman and Hall, London (1969).
54. D.W. Hoepfner, "The Effect of Grain Size on Fatigue Crack Propagation in Copper," p. 486, ASTM-STP-415. (See Ref. 10)
55. H.W. Liu, "Fatigue Crack Propagation and the Stresses and Strains in the Vicinity of a Crack," *Appl. Mater. Res.*, 7:229 (1964).
56. H.H. Johnson and P.C. Paris, "Subcritical Flaw Growth," *Eng. Fracture Mech.*, 1:3-45 (1968).
57. G.T. Hahn and A.R. Rosenfield, "Local Yielding and Extension of a Crack Under Plane Stress," *Acta Met.*, 13:293 (1965).
58. A.R. Rosenfield, P.K. Dai, and G.T. Hahn, "Crack Extension and Propagation Under Plane Stress," pp. 223-258, *Proc. 1st. Int. Conf. Fracture*, Vol. I, Japanese Society for Strength and Fracture of Materials, Sendai, Japan.

## APPENDIX A

### Compilation of Cyclic Crack-Growth Rate Measurements

Noticeable departures from a simple exponential crack growth relation  $\frac{da}{dN} = A (\Delta K)^m$  were noted by Liu<sup>55</sup> as early as 1964. In the interim, most workers have tended to gloss over irregularities and have attributed a single mechanism,  $m \sim 4$  to the entire growth rate spectrum<sup>56</sup>. However, the recent work of Bates and Clark<sup>15</sup>, and Barsom, et al.<sup>24</sup> and measurements of the stress dependence of the striation spacing<sup>15,21,26</sup> offer good evidence for two regimes of the behavior:

*Regime No. 1.* This is the low stress-low growth rate portion of the spectrum, e.g., usually less than  $10^{-4}$  in. per cycle, where the macroscopic growth rate coincides with the striation spacing<sup>15,21,26</sup>. As shown in Tables A-1 and IV, growth rates for a wide range of alloys are approximately described by the following empirical expression:

$$\frac{da}{dN} \approx A' \left( \frac{\Delta K}{E} \right)^2 \quad (A-1)$$

where  $A' \sim 8$ .

*Regime No. 2.* This is the high stress-high growth rate position of the spectrum, e.g., usually more than  $10^{-5}$  in. per cycle. In this range growth rates tend to exceed the striation spacing and displays a greater stress sensitivity, e.g.,  $m \gtrsim 4$ .

These two regimes are shown schematically in Figure A-1 which also defines the symbols used here to characterize the two regimes and the transition. The compilation of crack growth rate measurements in Table A-1 represents a conscious effort to identify two types of behavior and to assign them to Regimes No. 1 and No. 2 on the basis of the exponent. In some cases, neither a clear-cut change in behavior nor a characteristic  $m$  could be detected, and the Regime assignment is arbitrary. The compilation is mainly for growth rate measurements in air, with  $R \sim 0$ , but Barsom's<sup>23</sup> measurements for 12Ni-Scr-3Mo Steel in NaCl and Wei and Landes<sup>27</sup> results for 7075-T651 in Argon and  $H_2O$  are included to illustrate the potency of "aggressive" environments.

It should be noted that when the coefficient  $A$  is evaluated empirically, it involves the exponent  $m$ :  $A \equiv \left( \frac{da}{dN} \right)_i \Delta K_i^{-m}$  (where  $\left( \frac{da}{dN} \right)_i$  is the growth rate corresponding to  $\Delta K_i$ ). Since  $m$  is frequently not known with precision, uncertainties in  $m$  are magnified in  $A$  even where  $\Delta K_i$  is established accurately. For this reason  $\Delta K_i$  is a more reliable index of performance than  $A$ , and  $\Delta K_i$  and  $m$  (rather than  $A$  and  $m$ ) are used here to characterize the growth rates and for purposes of comparison.

**Figure A-1. Schematic of Stress-Intensity-Growth Rate Spectrum with Two Regimes and Definitions of Terms in Table A-1.**

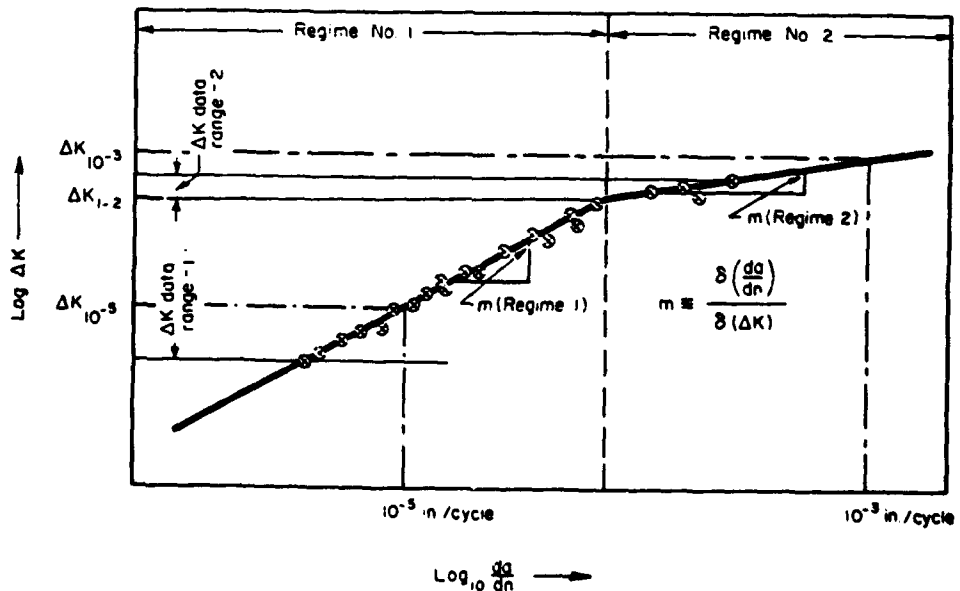


TABLE A-1. SUMMARY OF CYCLIC CRACK GROWTH DATA

MATERIAL	Y (KSI)	REGIME NO. 1		TRANSITION		REGIME NO. 2		REFERENCES
		DATA RANGE (KSI√in)	ΔK 10 <sup>5</sup> (KSI√in)	ΔK <sub>1/2</sub> (KSI√in)	ΔK <sub>1/2</sub> Y (KSI√in)	DATA RANGE (KSI√in)	ΔK 10 <sup>3</sup> (KSI√in)	
PART 1. STEELS								
Fe-36	64	-	36	-	-	40-120	~165	Present Study <sup>19</sup>
A-302B (a)	66	-	-	-	~40	40-110	~130	Mooney, et al. <sup>19</sup>
A-302B (b)	66	-	-	-	~40	40-90	~200	Mooney, et al. <sup>19</sup>
A-302B (c)	67	-	-	-	~40	60-110	~150	Mooney, et al. <sup>19</sup>
A-333	73	30-100 <sup>(a)</sup>	30/10 <sup>(a)</sup>	2.1/2.2 <sup>(a)</sup>	-	-	-	Bates and Clark <sup>15</sup>
SAE-4140	83	30-150	34	~1.85	-	-	-	Bates and Clark <sup>15</sup>
HY-40	87	21-61	33	2.48	-	-	-	Bennett, et al. <sup>24</sup>
HY-40	96	23-60	33	2.54	-	-	-	Bennett, et al. <sup>24</sup>
HY-100	136	5.2-26	20/23	2.3/2.6	-	-	-	Yokobori, et al. <sup>11</sup>
HY-130	140	19-68	28	2.16	-	-	-	Bennett, et al. <sup>24</sup>
HY-130	140	42-62	29.5	2.13	-	-	-	Bennett, et al. <sup>24</sup>
4340 (ANNEALED)	80	14-20/25	20	2.2/2.6	92	92-150	~140	Bennett, et al. <sup>24</sup>
4340 (I & T @ 1400F)	63	20-80	35	2.4/2.26 <sup>(a)</sup>	20/26	20/25-36	~120	Lu and Yip <sup>22</sup>
4340 (I & T @ 1000F)	163	20-80	33	~80	~80	80-110	~120	Miller <sup>18,26</sup>
4340 (I & T @ 800F)	221	20-80	33	~80	~80	80-90	~86	Miller <sup>18,26</sup>
4340 (I & T @ 200F)	163	20-80	33	2.6	~80	20-46	~50	Miller <sup>18,26</sup>
SAE-4140-2	160	-	-	-	-	40-100	~90	Miller <sup>18,26</sup>
SAE-4140-2	175/160	45-80	~34	~1.85	-	86-140	~165	Chooker, et al. <sup>13</sup>
1018-C-Mn-Co (a)	191	5.2-26	2.25	2.25	88	86-140	~165	Bates and Clark <sup>15</sup>
1018-C-Mn-Co (b)	162	30-60	30	2.24	-	-	-	Bennett, et al. <sup>24</sup>
1218-SC-Si-Mn (a)	184	21-60	31	2.16	-	-	-	Bennett, et al. <sup>24</sup>
1218-SC-Si-Mn (b)	184	25-60	28	2.16	-	-	-	Bennett, et al. <sup>24</sup>
1218-SC-Si-Mn	184	32-60	33	2.3	80	80-105	~130	Bennett, et al. <sup>24</sup>
1218-SC-Si-Mn (NAC1,800CPH)	184	19-53	25	~2.0	-	-	-	Schwab <sup>23</sup>
1218-SC-Si-Mn (NAC1,800CPH)	184	16-55	23	~2.0	-	-	-	Bennett, et al. <sup>24</sup>
1218-SC-Si-Mn (NAC1,800CPH)	184	20-47	16	~2.0	-	-	-	Bennett, et al. <sup>24</sup>
1218-Manganese	180	25-100	25	2.3	-	-	-	Bennett, et al. <sup>24</sup>
1218-Manganese	180	42-60	~16	2.3	-	-	-	Chooker and Lange <sup>16</sup>
1218-Manganese	218	20-80	31	2.2/2.1 <sup>(a)</sup>	~80	80-100	~110	Chooker and Lange <sup>16</sup>
1218-Manganese	246	20-100	36	2.2/1.7 <sup>(a)</sup>	~80	80-100	~150	Miller <sup>18,26</sup>
1218-Manganese	246/252	20-80	36	2.4	80	80-100	~150	Wei, et al. <sup>12</sup> and Carman and Kurlin <sup>8</sup>
1218-Manganese	286/288	18-60	35	2.6	-	21-29	~50	Wei, et al. <sup>12</sup> and Carman and Kurlin <sup>8</sup>
H 11	208	-	34	-	-	21-29	~50	Carman and Kurlin <sup>8</sup>
H 11	242	-	34	-	-	21-29	~120	Carman and Kurlin <sup>8</sup>
D6AC	241	32-80	32	~2.8	~70	21-60	~4.0	Carman and Kurlin <sup>8</sup>
PART 2. ALUMINUM ALLOYS								
7075-T6	70	5-22	7.5	2.3	22	22-42	~30	Forman, et al. <sup>9</sup> McEvily and Ilig <sup>2</sup>
7075-T6	70	6-24	10	2.4	24	24-66	~40	Forman, et al. <sup>9</sup> Hudson and Hargrave <sup>5</sup>
7075-T6 (R = 0.3)	70	6-18	8	2.8	18	18-22	~24	Forman, et al. <sup>9</sup> Brook and Schijve <sup>6</sup>
7075-T6	75.5	6-13	6	2.76	13	13-30	~22	Hudson and Scardine <sup>3</sup>
7075-T6	70	5-20	10	2/2 <sup>(a)</sup>	20	20-28	~33	Brook <sup>21</sup>
7075-T681 (Argon)	70	6-16	14.5	3.6	-	-	-	Wei and Linder <sup>27</sup>
7075-T681 (H <sub>2</sub> O)	70	6-16	8	3.6	-	-	-	Wei and Linder <sup>27</sup>
2024-T3	60	7-29	9.5/13	2.6/3	29	29-70	~40	Donaldson and Anderson <sup>4</sup> McEvily and Ilig <sup>2</sup>
2024-T3 (R = -1)	60	5-22 <sup>(f)</sup>	10.6 <sup>(f)</sup>	2.9	22 <sup>(f)</sup>	22 <sup>(f)</sup> , 26 <sup>(f)</sup>	~33 <sup>(f)</sup>	Hudson and Hargrave <sup>5</sup> Webb <sup>11</sup>
2024-T3 (R = 0.3)	60	4-16	8	4-16	16	16-22	~24	Ilig and McEvily <sup>3</sup>
2024-T3 (R = 0.26)	60	6-16	10.6	2.9	16	16-22	~24	Forman, et al. <sup>9</sup> Brook and Schijve <sup>6</sup>
2024-T381	60	4-12	6	2.6	12	12-20	~36	Brook and Schijve <sup>6</sup>
2024-T3	66	5-26	14	2.5/2 <sup>(a)</sup>	-	26-33	~38	Lu and Ilig <sup>20</sup>
7075-T6	66	8-30	12	2.6/2.1 <sup>(a)</sup>	-	13-20	~20	Brook <sup>21</sup>
7075-T6	68	6-13	~7	2.7	13	13-20	~20	Bates and Clark <sup>15</sup>
7075-T6	70	16-60	10/15	~3	13	13-20	~20	Swanson, et al. <sup>10</sup>
6466-H321	37	9-20	12	2.1/2.1	-	-	-	Smith, et al. <sup>20</sup>
PART 3. TITANIUM ALLOYS								
Ti-6Al-4V	127	13-35	15	3.2 <sup>(a)</sup>	-	-	-	Bates and Clark <sup>15</sup>
Ti-6Al-4V	121	40-68	38	~4	-	-	-	Hall <sup>1</sup>
PART 4. MISCELLANEOUS ALLOYS								
70-30 Brass (Annealed)	18	-	14	~8	-	-	-	McEvily, et al. <sup>7</sup>
70-30 Brass (Cold Worked)	62	-	14	~8	-	-	-	McEvily, et al. <sup>7</sup>

(a) 1-in. thick plate  
 (b) 2-in. thick plate  
 (c) Thickness direction  
 (d) Axial direction  
 (e) Based on section spacing  
 (f) Values quoted represent 1/2 the value reported because R = -1  
 (g) Based on section spacing

## APPENDIX B

### Simplified Formulations of the Cyclic Crack Growth Mechanisms

*A. Irreversible Plastic Blunting.* This process can be formulated approximately by noting that  $\frac{da}{dN}$ , the crack advance per cycle will be a fraction  $\beta$  of the COD [Equation (4B)]:

$$\frac{da}{dN} = \beta \cdot \text{COD} \approx \beta \cdot \frac{\Delta K^2}{4EY_c} \quad (\text{B-1})$$

where  $\beta$ , the efficiency (or degree of irreversibility) of the blunting process is regarded as constant to a first approximation.

*B. Damage Accumulation.* This mechanism is described in essentially the same way as proposed by Lehr and Liu<sup>31</sup> by combining Equations (5) and (6) with the Manson-Coffin fatigue damage law<sup>35,36,47</sup>:

$$n^{1/2} \Delta \bar{\epsilon}_p = B \quad (\text{B-2})$$

where  $\Delta \bar{\epsilon}_p$  is regarded as the weighted average plastic strain range and  $B$  the fracture strain for monotonic loading: This gives two results:

Small Strain: 
$$\frac{da}{dN} \approx \frac{0.03 \Delta \bar{\epsilon}_p \Delta K^2}{4B^2 Y_c^2} \sim \frac{0.1}{B^2} \left( \frac{\Delta K}{E} \right)^2 \quad (\text{B-3})$$

Large Strain:

$$\frac{da}{dN} = \frac{\Delta \epsilon_p^2 \Delta K^2}{4B^2 Y_c} \quad (\text{B-4})$$

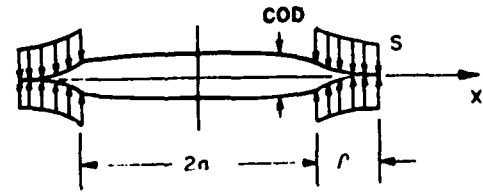
In the first,  $\Delta \bar{\epsilon}_p^2$  is the strain range averaged over all cycles, which Lehr and Liu estimate as  $\Delta \bar{\epsilon}_p \approx 4 \frac{Y_c}{E}$  and is consequently a relatively small strain, e.g.,  $\Delta \bar{\epsilon}_p \approx 0.02$ . In the second, only the number of cycles involving large strains is considered and  $\Delta \bar{\epsilon}_p \sim 0.5^{29}$ .

APPENDIX C

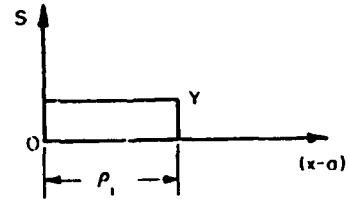
Augmented Dugdale Model

At the tip of a fatigue crack there exists a very heavily strained region where  $Y_c$ , the cyclic yield stress, may be greatly in excess of  $Y$ , the yield stress for ordinary monotonic loading. Simultaneously,  $Y_c$  may be less than  $Y$  in the remaining, lightly strained region of the plastic zone as a result of the Bauschinger effect. A model of this behavior is given in Figure C-1. Figure C-1a shows the Dugdale Model with the tips of the crack being pressed together by a traction denoted  $S$ . The region  $-a < x < a$  represents the crack,  $a < x < a + \rho$  the plastic zone. Usually  $S$  is set equal to a constant yield stress as in Figure C-1b. For the case of the fatigue crack, the distribution shown in Figure C-1c is postulated.

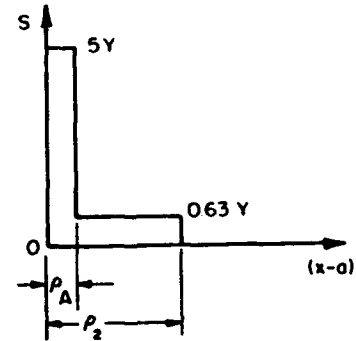
The two  $Y_c$ -levels represent the small heavily strained region where  $Y_c = 5Y$  and the lightly strained region where  $Y_c = 0.63Y$ . According to the calculation, which was made by methods outlined in References 57 and 58, COD (Case 2) = 1/5 COD (Case 1) when  $\rho_1 = \rho_2$ ,  $\rho_2/\rho_A = 5.5$  and  $T/Y = 0.25$ , where  $T$  is the nominal applied stress. Thus, there is a large difference in COD even though the plastic zones are the same size. Also the COD for the fatigue crack model is comparable to a much stronger material even though the heavily strained region occupies a small part of the total plastic zone. The model illustrates that the COD is strongly influenced by the value of  $Y$  appropriate for material closest to the crack tip.



a Dugdale Model



b Case 1 - Constant Flow Stress



c Case 2 - Model of Flow Stress Distribution for Fatigue Crack

Figure C-1. Augmented Dugdale Crack Model.

# FATIGUE CRACK GROWTH AND THE STRAIN INTENSITY FACTOR

by

A.J. McEvily, Head

Department of Metallurgy  
School of Engineering  
University of Connecticut

## INTRODUCTION

In recent years it has been shown that stress intensity factor,  $K_G$ , can be used to correlate fatigue crack growth data.<sup>1</sup> However, there are inherent limitations to this approach; the principal one being that the net section stresses must remain in the elastic range. Since in many cases crack growth occurs at net section stresses above yield as in low cycle fatigue, it is of interest to develop means of analyzing crack growth data at such stress levels. The development of such a method is a main concern of this paper.

## THE STRAIN INTENSITY FACTOR

Figure 1 provides an example of the typical dependence of the rate of fatigue crack growth<sup>2</sup> in a sheet specimen on the stress intensity factor,  $K_G$ . For an applied stress  $\sigma$  and a crack of length  $2c$  in a sheet wide with respect to  $c$ , this factor is defined as

$$K_G = \sigma \sqrt{c} \quad (1)$$

The basic premise involved in the use of this factor is that the

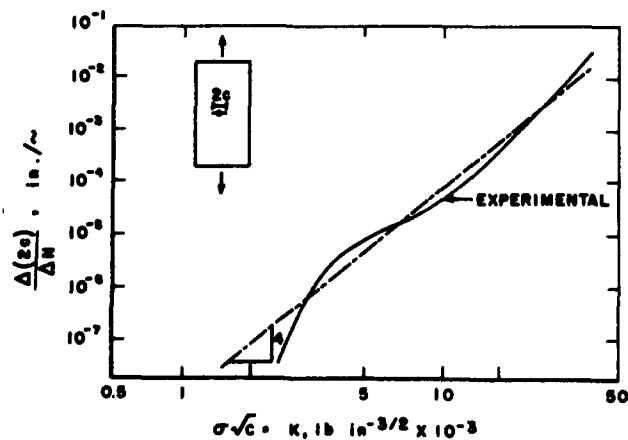


Figure 1. The Rate of Fatigue Crack Growth as a Function of the Stress Intensity Factor in a 12-inch Wide Sheet Specimen of the Aluminum Alloy 7075-T6.<sup>2</sup>

details, and hence the rate of the crack growth process, must depend upon the intensity of the stress field outside of the crack-tip plastic zone. This stress field intensity is linearly dependent upon the stress intensity factor.

From Figure 1 it can be deduced that a finite value of  $K_G$  is required for crack growth. The inflection observed at a growth rate of about  $10^{-5}$  inches per cycle results both from a change from flat to slant fracture in sheet specimens, as well as from environmental effects. Wei<sup>3</sup> has recently concluded that environmental effects may be the more dominant of the two. Environmental effects may therefore be more pronounced in the flat mode of growth than in the slant mode.

For tests beyond the elastic range, sheet specimens are usually not used and, in fact, there has been little work on crack growth in this range. However, it is known that most of the lifetime in low cycle fatigue of unnotched cylindrical specimens is spent in crack growth,<sup>4</sup> and from the fatigue striation spacing a measure of crack growth rate can be obtained. Such data have been obtained for OFHC copper and analyzed as shown in Figure 2.<sup>5</sup> Here a new pa-

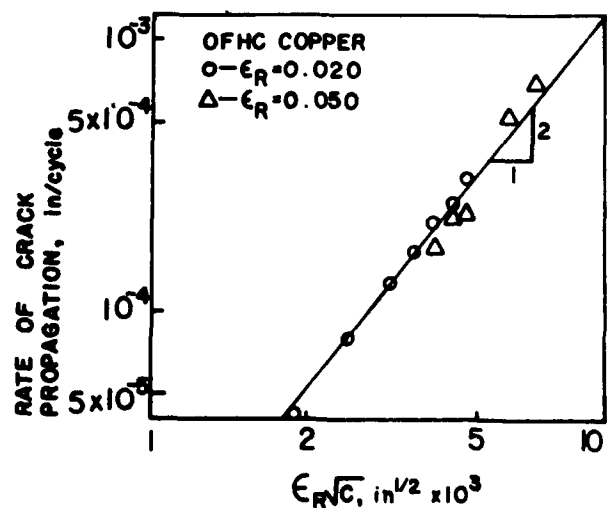


Figure 2. The Rate of Fatigue Crack Growth in Low Cycle Fatigue as a Function of the Strain Intensity Factor  $\epsilon_R \sqrt{c}$ .<sup>5</sup>

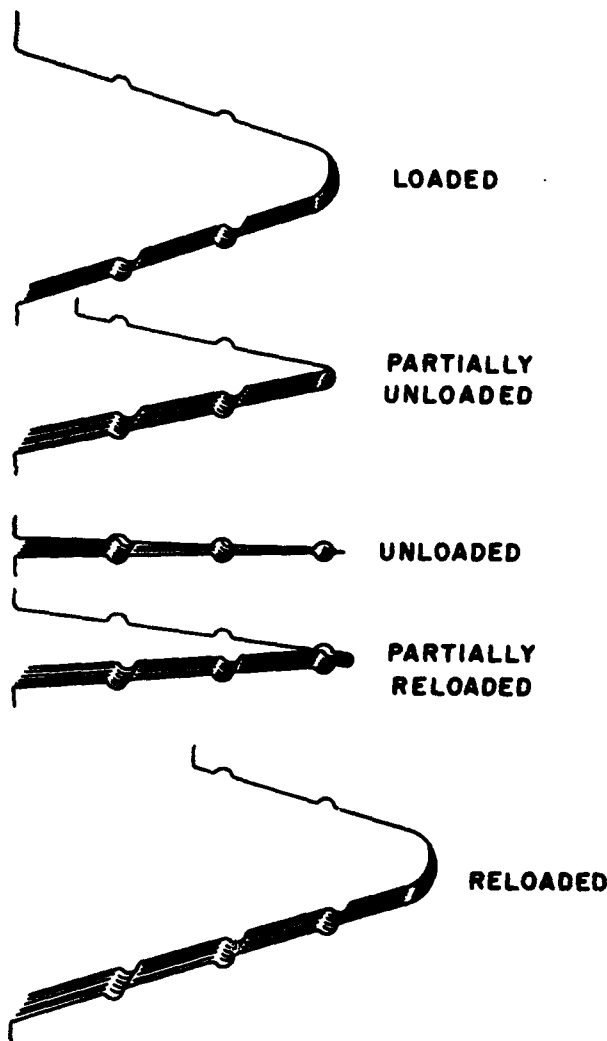


Figure 3. Schematic Illustration of the Deformation at a Fatigue Crack Tip During One Loading Cycle.<sup>6</sup>

parameter, the strain intensity factor,  $K_{\epsilon}$ , or simply  $\epsilon_R \sqrt{c}$  where  $\epsilon_R$  is the total strain range, is introduced. The philosophy behind the use of the strain intensity factor is similar to that employed in justifying the use of the stress intensity factor. We know that the crack tip deformation processes as shown in Figure 3<sup>6</sup> depend upon the strain conditions in the surrounding material, and it is postulated that these strain conditions relate to the strain intensity factor. For consistency with analysis in the elastic range, the total strain range, i.e. both elastic and plastic, should be used in analyzing the low cycle fatigue data; however, the small correction to include elastic strain has not been included in Figure 2.

It can be seen from Figure 2 that the strain intensity approach effects a reasonable correlation of data for two strain amplitudes. It is also of interest that integration of the expression

$$dc/dN = A (\epsilon_R \sqrt{c})^2 \quad (2)$$

leads to a form of the Manson-Coffin law. However, if this approach is to be more generally applicable, then it must be capable of bringing into a unified scheme crack growth data obtained with various types of test specimens. At present, results from tests as in Figures 1 and 2 are treated quite independently and there is no method available to provide an overall approach.

### NEW TESTS AND RESULTS

In order to relate results obtained with notched sheet specimens to those obtained with unnotched cylindrical specimens it is necessary to extend the experimental strain range beyond the usual limits. Further, since cylindrical specimen tests are run under fully reversed plastic strain, it is desirable that the tests on the sheet specimens be carried out under similar reversed loading. Tests on 2-inch wide, centrally notched sheet specimens of OFHC copper were therefore carried out under fully reversed loading conditions with the specimens equipped with loosely fitting guide plates to prevent lateral buckling. A small window in the guide plates allowed the cracks to be observed.

For purposes of some initial comparisons the results of these tests are given in Figure 4 as a function of the stress intensity factor. At low applied stress levels a satisfactory correlation of the data can be obtained, as expected.

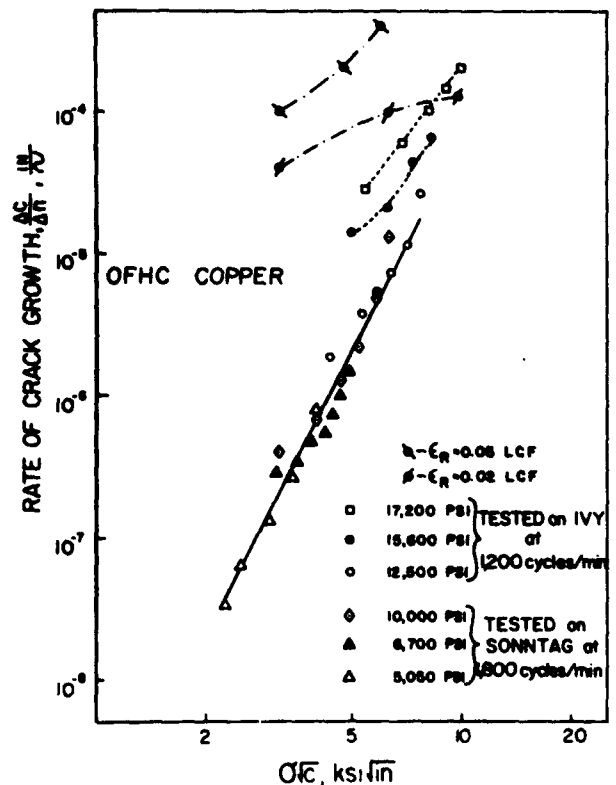


Figure 4. The Rate of Fatigue Crack Growth in Sheet and Cylindrical (LCF) Specimens of OFHC Copper as a Function of the Stress Intensity Factor.



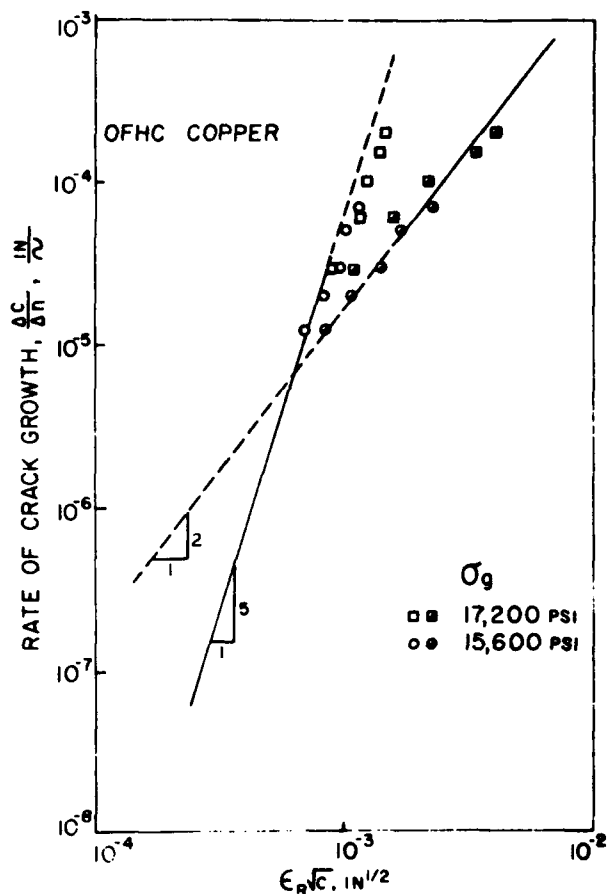


Figure 5. The Rate of Fatigue Crack Growth in Sheet and Cylindrical (LCF) Specimens of OFHC Copper as a Function of the Strain Intensity Factor. Open symbols:  $\epsilon_R$  calculated for the gross section. Half-filled symbols:  $\epsilon_R$  calculated for the net section.

At higher stress levels the rate of growth is no longer a single valued function of the stress intensity factor. It can easily be seen why the correlation is nonexistent in this range. Consider an ideal elastic-plastic material containing a crack of a given length. We can vary the plastic strain amplitude at will without changing the initial stress intensity factor. The initial crack growth rates will vary considerably, but will each have the same stress intensity factor, hence no correlation is to be expected.

It is of interest to note in Figure 4 that no inflection as in Figure 1 is present, which indicates an insensitivity on the part of copper to environmental effects. Also it is noted that throughout the range of stresses employed the fracture mode was always flat despite high values of the quantity,  $\left(\frac{\sigma \sqrt{c}}{\sigma_y}\right)^2$ , where  $\sigma_y$  is the yield stress. The absence of slant fracture may relate to the low yield strength and high ductility of the OFHC copper. In Figure 4, the results of the low cycle fatigue tests on cylindrical specimens are also shown.

Figure 5 shows the results of Figure 4 now plotted in terms of the strain intensity factor. For clarity, only the data for the copper sheet at high stress levels are plotted. For present purposes it is assumed that the multiplying factor on the stress and strain intensity factors is the same for both specimen types. A straight line of slope 5 represents the lower stress data, for the two figures in this range are related through Young's modulus. In the upper part of the figure a line of slope 2, taken from Figure 2, is shown. For the first time two rather disparate types of data are on the same graph in an orderly manner, and we can see the trends of crack growth behavior from very low rates which approach the nonpropagating level to those high rates at which the specimen is on the verge of static fracture. However, the rate of crack growth is no longer a single valued function of the strain intensity factor at high growth rates, and for this reason it is not a straightforward matter to express the rate of growth as a sum of elastic and plastic rate components.

The data points for the sheet specimens have been analyzed in two ways. The first involved the use of gross-section stresses which do not change during a test. These stresses were converted to equivalent strains by the use of the cyclic stress-strain curves shown in Figure 6.<sup>7,8</sup> (The lower curve was used as it is from a recent, carefully carried out test program. The upper curve from an older investigation is quite similar and is included to show the reproducibility of such curves.) The elastic strain equivalent to the applied stress range was added to the plastic strain range to give the value of the total strain range,  $\epsilon_R$ . This quantity multiplied by the square root of the semi-length of the central crack gives the strain intensity factor,  $\epsilon_R \sqrt{c}$ .

On this basis there is a fair correlation of data, but the trend is toward a lower slope than in the elastic range.

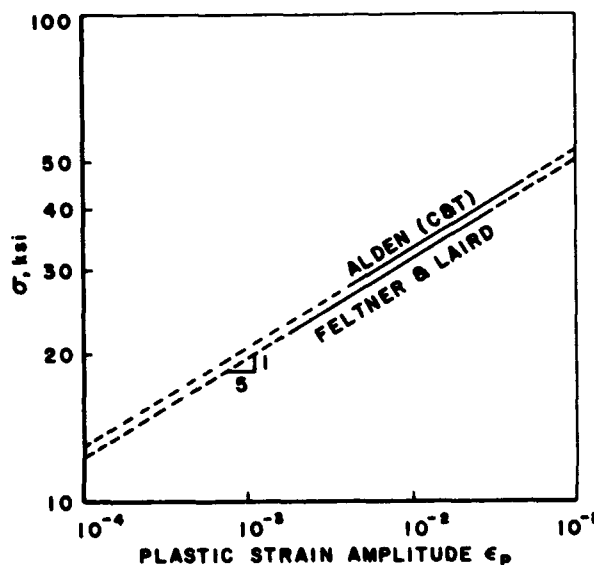


Figure 6. Cyclic Stress Plastic Strain Curves for OFHC Copper.<sup>7,8</sup> The designation (C&T) refers to the data of Coffin and Tavernelli.<sup>14</sup>

However, no agreement with the results for cylindrical specimens is obtained. It seemed reasonable to analyze the data in terms of the net section rather than gross section properties. For net section stresses in the elastic range it has been shown<sup>9</sup> that the peak elastic stress is related to the  $k_0$  by:

$$K_N \sigma_{NET} \sim \sigma \sqrt{c} \quad (3)$$

where  $K_N$  is a Neuber stress concentration factor,  $\sigma_{NET}$  is the net section stress, and  $\sigma$  is the gross stress. As a crack extends, the value of  $K_N$  decreases because of finite width effects, whereas  $\sigma_{NET}$  increases. These mutually compensating effects allow the product to be expressed in terms of the gross stress. For net section stresses in the plastic range there is no such mutual compensation. Plastic strains increase rapidly as the net section is reduced, and it seems preferable to analyze the data in terms of net section strains. This means that for each selected crack length a net section stress is determined which through Figure 6 is converted to a plastic strain range to which is added an elastic component to yield the total strain range,  $\epsilon_R$ . The results for the sheet specimens when analyzed on this basis are seen in Figure 5 to be in reasonable agreement with those obtained independently on cylindrical specimens.

#### DISCUSSION

In the foregoing a new method based upon the strain intensity factor,  $\epsilon_R \sqrt{c}$ , has been presented which provides a unified means for analyzing fatigue crack growth data in both the elastic and plastic ranges. Such an approach appears to be reasonable on the basis of known aspects of the growth mechanism which is largely strain controlled. In fact, a first-order correlation of growth data in the elastic range for some alloys of differing moduli can be obtained by dividing the stress intensity factor by Young's modulus (this, of course, gives the strain intensity factor). This of itself is an interesting observation for it suggests that details of metallurgical structure are only secondary in the growth process. They may, of course, be of more importance in the final fracture stage.

One important aspect of the growth process to be discussed has to do with the reasons for the various slopes observed. In the elastic range the reported slopes vary from 2 to more than 6 (in the present case  $\frac{dc}{dN} = 7 \times 10^{10} (\epsilon_R \sqrt{c})^5$  in/cycle). For the plastic range a value of 2 was deduced from Figure 2 ( $\frac{dc}{dN} = 16.7 (\epsilon_R \sqrt{c})^2$  in/cycle). A number of proposals have been advanced to account for these slopes. Among the possibilities are tearing, tearing accompanied by blunting, or kinematically irreversible blunting. Each of these would affect the crack opening displacement (COD), which as shown in the blunting model of Figure 3 controls the extent of growth per cycle. Analyses of the process based upon geometrical considerations alone usually lead to a second power dependence of the rate of growth in the stress intensity factor which is usually not observed. Ex-

perimental verification has been obtained for a second power dependency by determining the COD in the plane stress region for specimens containing 0.006-inch slits rather than fatigue cracks.<sup>10</sup> In a recent study by Rooke and Bradshaw<sup>11</sup>, the COD for *fatigue cracks* in high strength aluminum alloys were determined. Their results are plotted in Figure 7 in terms of  $(\sigma \sqrt{c})^2$ . If a curve is drawn as shown, then the COD is proportional to  $(\sigma \sqrt{c})^4$ . This interpretation is consistent with the observation that in this type of alloy the growth rate can be expressed as fourth power of the stress intensity factor. However, the correlation is more apparent than real, for Rooke and Bradshaw, by making a plastic zone correction to the crack length ( $c' = c_0 + r_p$ , where the radius of the plastic zone equals  $r_p = \frac{\sigma^2 c'}{2\sigma_y}$ ), obtained good agreement with experimental

COD values through the use of the following expression for the COD:

$$COD = \frac{4\alpha^2}{E\sigma_y} \left[ 1 - \frac{\alpha^2 \sigma^2}{2\sigma_y^2} \right]^{-1} \sigma^2 c_0 \quad (4)$$

where  $c_0$  represents the initial crack length at the start of monotonic loading and  $\alpha$  is a finite width correction the value of which will be taken as unity in this discussion. The loads involved in their experiments were three to five times greater than the peak fatigue load used to grow the crack, and some crack extension occurred during monotonic loading. In applying their results to fatigue crack propagation it is considered that prior stress history effects are negligible.

If we assume that the rate of fatigue crack propa-

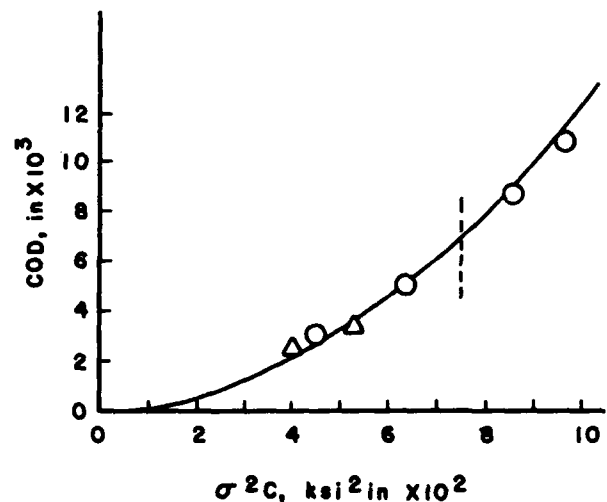


Figure 7. The Crack-Opening Displacement (COD) of Fatigue Cracks in Two High Strength Aluminum Alloys as a Function of the Square of the Stress Intensity Factor. The dashed line separates the regions of plane strain and plane stress. Based on the data of Rooke and Bradshaw.<sup>11</sup>

gation,  $\frac{dc}{dN}$ , is proportional to the COD, we can write

$$\frac{dc}{dN} = \frac{4D}{E\sigma_y} \left[ 1 - \frac{\sigma^2}{2\sigma_y^2} \right]^{-1} [\sigma^2 c_o - (B\sigma^2 c_o)_o] \quad (5)$$

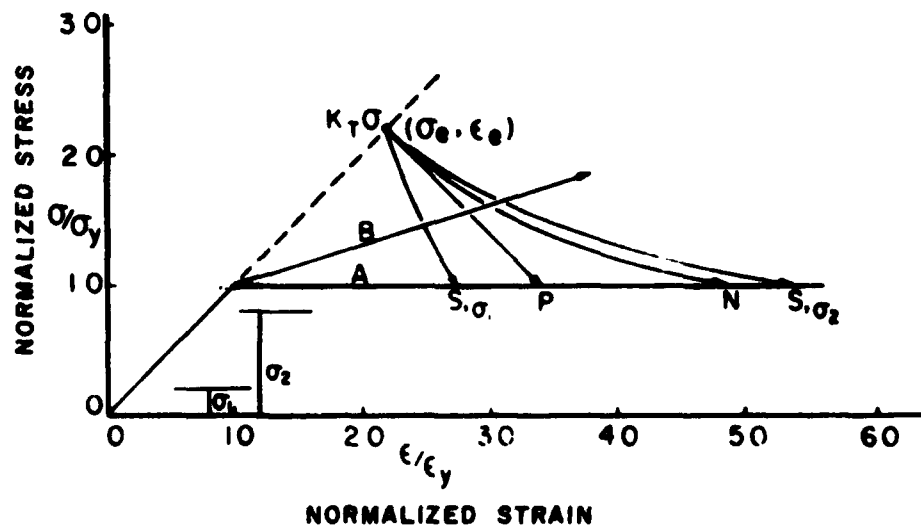
where  $(\sigma^2 c_o)_o$  relates to a critical COD which must be exceeded before the crack will advance,  $D$  is a scaling factor, and  $B$  is a constant which reflects both plane strain conditions and environmental effects which are important at low values of the stress intensity factor. The experimental curve shown in Figure 1 can be approximated by such an expression if  $D$  is assigned a value of 0.05, and  $(B\sigma^2 c_o)_o$  is  $11\text{Ksi}^2\text{in}$ . From equation (5) it is seen that at high values of  $\sigma/\sigma_y$  the rate of growth is no longer a single valued function of the stress intensity factor. With respect to the present results, the apparent straight line fit of Figure 4 should be modified in accord with equation (5). It will be of interest in future work to determine the general applicability of equation (5).

A related approach to the role of crack opening displacements in fatigue crack growth is to consider that the displacements depend upon the tip strain and the gauge length,  $l$ , over which this strain acts, or

$$\text{COD} = \epsilon_{\text{tip}} \cdot l \quad (6)$$

Let us examine the matter of the COD further with the aid of information concerning plastic deformation at the root of large notches, wherein changes in  $l$  are negligible.

Figure 8. Predictions of Plastic Strain at Root of Notch of Theoretical Stress Concentration Factor  $K_T$ .  $\sigma_0$  and  $\epsilon_0$  are the local stress and strain levels if the material were completely elastic.  $\sigma_1$  and  $\sigma_2$  are applied stress levels which affect the Stowell (S) prediction. The Neuber (N) and perpendicular estimates depend only upon the product  $K_T\sigma$ . Effect of strain hardening can be seen by comparing intercepts on curves A and B.



Two methods for calculating the associated plastic strains are due to Stowell<sup>13</sup> (modified by Hardrath and Ohman<sup>12</sup>) and Neuber<sup>15</sup>. The modified Stowell equation is

$$K_P = 1 + (K_T - 1) \frac{E_{\text{sec}}}{E} \quad (7)$$

where  $K_P$  is the plastic stress concentration factor,  $K_T$  is the theoretical stress concentration factor, and  $E_{\text{sec}}$  is the secant modulus associated with the stress-strain state at the notch root. For an applied stress  $\sigma$ , the total strain at the notch root can be expressed as

$$\epsilon_{PT} = \frac{\sigma_e - \sigma}{E(1 - \sigma/\sigma_p)} \quad (8)$$

where  $\epsilon_{PT}$  is the total strain at the tip of the plastically deformed notch,  $\sigma_e$  equals  $K_T\sigma$ , and  $\sigma_p$  is the local tip stress after plastic deformation.

Neuber has proposed that

$$K_T^2 = K_{\sigma P} K_{\epsilon P} \quad (9)$$

where  $K_{\sigma P}$  is the stress concentration factor after plastic deformation, and  $K_{\epsilon P}$  is the corresponding strain concentration factor. This relation leads to

$$\epsilon_{PT} = \frac{\sigma_e \epsilon_e}{\sigma_p} = \frac{\sigma_e^2}{E\sigma_p} \quad (10)$$

Figure 8 compares the nature of these predictions and also indicates a third approximation for  $\epsilon_{PT}$  given by the intersection of the perpendicular to the elastic line and the stress-strain curve. The equation associated with this line is

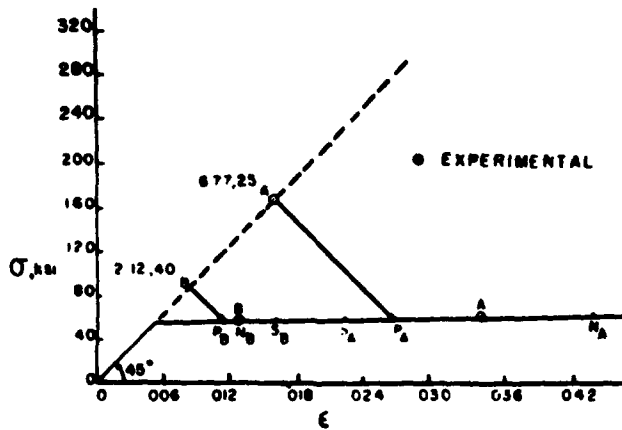


Figure 9. Comparison of Experimental and Predicted Values of Stress-Strain State at Root of Notch After Yielding for Two Notches ( $K_T = 2.12$  and  $6.77$ ) at Two Applied Stress Levels (21.0 and 25 Ksi). N is the Neuber prediction, S is the Stowell prediction and P is the intercept of the perpendicular from the elastic line to the stress-strain curve. Data from Crews.<sup>16</sup>

$$\epsilon_{PT} = \frac{2\sigma_e - \sigma_p}{E} \quad (11)$$

Figure 9 shows how experimental and predicted values compare. For large strains the Neuber prediction overestimates the strain, whereas the Stowell prediction and the perpendicular method underestimate it. An average of the perpendicular and Neuber methods would make a better prediction and would be given by

$$\epsilon_{PT} = \frac{\sigma_e^2 + 2\sigma_e\sigma_p - \sigma_p^2}{2E\sigma_p} \quad (12)$$

For  $\sigma_e \gg \sigma_p$ , equation (12) indicates that the strain would be 1/2 that predicted by the Neuber relationship. For the present then let us assume the modified Neuber relationship to be valid and also that elastic strains are small compared to plastic strains, so that

$$\epsilon_{PT} = \epsilon_p = \frac{\sigma_e^2}{2E\sigma_p} \quad (13)$$

For an ideally elastic-plastic material,  $\sigma_p = \sigma_Y$ , and

$$\epsilon_p = \frac{\sigma_e^2}{2E\sigma_Y} \quad (14)$$

Figure 10, which is based on the data of Crews<sup>16</sup>, indicates that such a relation is a reasonable approximation.

For the specific case of an elliptical slit in a sheet specimen, equation (14) can be written as

$$\epsilon_p = \frac{[(1 + 2\sqrt{\frac{c}{\rho}})\sigma]^2}{2E\sigma_Y} \quad (15)$$

where  $\rho$  is the tip radius of the ellipse. The stress intensity factor,  $K_\sigma$ , can be defined as

$$K_\sigma = \lim_{\rho \rightarrow 0} (\sigma_e) \frac{\sqrt{\rho}}{2} \quad (16)$$

As  $\rho \rightarrow 0$ , equation (15) becomes

$$\epsilon_p = \frac{K_\sigma^2}{2E\sigma_Y\rho_e} \quad (17)$$

where  $\rho_e$  is a material constant. The numerator of equation (17) is not material-dependent, whereas the denominator is. If  $\rho_e$  is independent of the value of  $K$ , the COD can be expressed as

$$\text{COD} = \frac{K_\sigma^2}{E\sigma_Y\rho_e} l \quad (18)$$

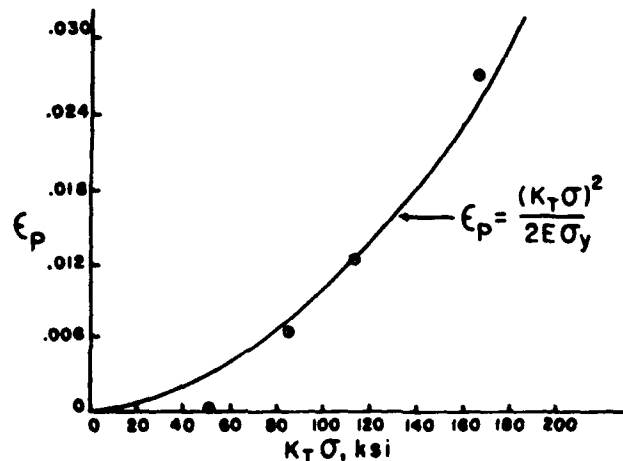


Figure 10. Plastic Strain at Root of Notch as a Function of the Parameter  $K_T\sigma$ , where  $K_T$  is the Elastic Stress Concentration factor and  $\sigma$  is the Applied Stress. ( $\sigma_Y$  taken as 52 Ksi,  $E$  as  $10.5 \times 10^3$  Ksi.) Data from Crews.<sup>16</sup>

For  $\ell$  of the same order as  $\rho_e$ , the usual dependence of the COD on  $K_{\sigma}^2$  is found. For the blunting process, comparison with equation (4) suggests that  $\ell$  is equal to

$$4\rho_e [1 - \sigma^2/2\sigma_y^2]^{-1},$$

which will give rise to the apparent fourth power dependency of the rate of fatigue crack growth on the stress intensity factor.

A concluding point has to do with the decrease in slope in Figure 5 as the yield level is exceeded. From Figure 8 it can be seen that the greater the difference between the elastic modulus and tangent modulus in the plastic region, the greater the local strain. Further, in the elastic range where the elastic moduli of the notch tip and net section are equal, the smallest variation results. Similarly when the net section stresses applied are well into the plastic range, the difference between tip strain and net section strain will be minimized, and, as in the elastic range, the tip strain will become proportional to the applied strain. The COD can be expressed as

$$\begin{aligned} \text{COD} &= \epsilon_{\text{tip}} \cdot \ell \\ &= A \epsilon_R \sqrt{c} \cdot \ell \end{aligned} \quad (19)$$

Comparison with equation (2) indicates that  $\ell$  must in effect be proportional to  $\epsilon_R \sqrt{c}$ .

### CONCLUDING REMARKS

1. A method based upon the strain intensity factor has been described for correlating fatigue crack growth data in both the elastic and plastic ranges.
2. The method has been shown to be applicable to data obtained with OFHC copper specimens. Further work is needed to determine the general applicability of the approach.
3. Through consideration of the crack opening displacement (COD) and crack tip deformation processes it has been possible to rationalize certain aspects of the fatigue crack growth process.

### ACKNOWLEDGEMENT

The author is indebted to the following for helpful correspondence and discussions: D.P. Rooke, F.J. Bradshaw, G.T. Hahn, R.M. Wetzel, C. Wells, and H. McI. Clark; and to R. Kumble for his assistance in the experimental phase of the work. It is appropriate to acknowledge the support of this study by the Air Force Office of Scientific Research under Contract F44620 69C011, Project Themis.

## REFERENCES

1. P. Paris, *Fatigue*, Syracuse University Press, Syracuse, New York (1964).
2. A.S. Tetelman and A.J. McEvily, *Fracture of Structural Materials*, John Wiley, New York (1967).
3. R. Wei, private communication.
4. C. Laird and G. Smith, *Phil. Mag.*, 7:847 (1962).
5. R.C. Boettner, C. Laird, and A.J. McEvily, *Trans. Met. Soc. AIME*, 233:379 (1965).
6. A.J. McEvily, R.C. Boettner, and T.L. Johnston, *Fatigue*, Syracuse University Press, Syracuse, New York (1964).
7. C.E. Feltner and C. Laird, *Acta Met.*, 15:1621 (1967).
8. T.H. Alden, *Trans. Met. Soc. AIME*, 224:1287 (1962).
9. H.F. Hardrath and A.J. McEvily, *Proc. Crack Propagation Symp.*, Vol. I, College of Aeronautics, Cranfield, England (1962).
10. G.T. Hahn and A.R. Rosenfield, *Acta Met.*, 13:293 (1965).
11. D.P. Rooke and F.J. Bradshaw, *Proc. 2nd Int. Conf. Fracture*, p. 46, Chapman and Hall, London (1969).
12. H.F. Hardrath and L. Ohman, NACA-TN-2566, National Aeronautics and Space Administration, Washington, D.C. (1951).
13. E.Z. Stowell, NACA TN-2073, National Aeronautics and Space Administration, Washington, D.C. (1950).
14. L.F. Coffin and J.F. Tavernelli, *Trans. Met. Soc. AIME*, 215:794 (1959).
15. H. Neuber, *J. Appl. Mech.*, 28:544 (1961).
16. J.H. Crews, Jr., NASA-TN-D5253, National Aeronautics and Space Administration, Washington, D.C. (1969).

# PREDICTION OF FATIGUE LIFETIME BY COMBINED FRACTURE MECHANICS AND ACOUSTIC EMISSION TECHNIQUES\*

by

D.O. Harris and H.L. Dunegan

A.S. Tetelman

Lawrence Radiation Laboratory,  
Livermore,  
California

School of Engineering, UCLA  
University of California,  
Los Angeles, California

## LIST OF SYMBOLS

<p><math>a</math> = Crack length for through crack, crack radius for penny-shaped crack</p> <p><math>a_0</math> = Initial crack length</p> <p><math>A</math> = Proportionality constant in N-K relation (Equation 1)</p> <p><math>B</math> = Specimen thickness</p> <p><math>C</math> = Proportionality constant in crack growth relation (Equation 2)</p> <p><math>D</math> = Proportionality constant between plastic volume and acoustic emission counts (Equation 14)</p> <p><math>F</math> = Tensile load on wedge-opening-loading fracture toughness specimen</p> <p><math>G</math> = Parameter in equation for stress intensity factor for WOL specimen (Equation 8)</p> <p><math>K</math> = Stress intensity factor</p> <p><math>\hat{K}</math> = Range of stress intensity factor (<math>=K_{\max} - K_{\min}</math>)</p> <p><math>K_{Ic}</math> = Plane strain fracture toughness</p> <p><math>K_p</math> = <math>K</math> at the proof load</p> <p><math>K_w</math> = <math>K</math> at the working load</p>	<p><math>m</math> = Exponent in N-K relation (Equation 1)</p> <p><math>n</math> = Number of fatigue cycles</p> <p><math>n_f</math> = Remaining number of fatigue cycles (cycles to failure)</p> <p><math>N</math> = Number of acoustic emission counts</p> <p><math>N_t</math> = Total number of acoustic emission counts observed during proofing</p> <p><math>q</math> = Exponent in crack growth relation (Equation 2)</p> <p><math>r_y</math> = Plastic zone size</p> <p><math>W</math> = Specimen width</p> <p><math>\alpha</math> = <math>a/W</math></p> <p><math>\alpha_0</math> = <math>a_0/W</math></p> <p><math>\beta</math> = Proportionality term in stress intensity factor equation (Equation 17)</p> <p><math>\hat{\sigma}</math> = Range of stress during fatigue loading (<math>=\sigma_{\max} - \sigma_{\min}</math>)</p> <p><math>\sigma_p</math> = Proof stress</p> <p><math>\sigma_w</math> = Working stress</p> <p><math>\sigma_{ys}</math> = Yield stress</p>
---	--

## INTRODUCTION

The need for efficient and lightweight designs in modern structures, coupled with severe environments (such as cyclic loading or corrosive atmospheres), has

resulted in the increased need for reliable techniques for the prediction of the safe operating lifetime of structures. One such method, based on a combination of acoustic emission and periodic proof testing, is described in this paper. This technique can be applied to

\*Work performed under the auspices of the U.S. Atomic Energy Commission.

cyclic loading, stress corrosion cracking, or hydrogen embrittlement with equal ease, but only the case of fatigue will be considered here.

Low-level acoustic emission is the term applied to the sound emitted by a material when it is plastically deformed, either by an external stress or an internal process, such as a martensitic phase transformation. The early work of Kaiser<sup>1</sup> in Germany, and Schofield<sup>2,3</sup> and Tatro<sup>4</sup> in this country has led to greatly increased interest in this field in recent years. Since this paper is concerned with the application of acoustic emission to the detection of the presence and growth of fatigue cracks, attention will be focused on the acoustic emission characteristics of flawed materials. Reference 5 provides a summary of work conducted on unflawed materials.

Investigations of acoustic emission from flawed specimens can be divided into three categories:

1. Monotonically rising load, with no stable crack growth (except for pop-in type behavior).<sup>6-9</sup>
2. Constant load, with subcritical cracks growing in a stable manner.<sup>10,11</sup>
3. Intermittent overstressing of a cracked specimen subjected to fatigue loadings.<sup>12</sup>

This paper is of the last category, and is an extension of the results contained in an earlier investigation.<sup>12</sup>

The results of monotonically rising load tests<sup>6,7</sup> have shown that the total number of counts of acoustic emission signals  $N$ , resulting from dislocation motion in the plastic zone at the crack tip, can be directly related to the stress intensity factor  $K$ , through a relationship of the form<sup>†</sup>

$$N = AK^m \quad (1)$$

where the exponent  $m$  is a constant for a given material of a particular thickness. A simplified model<sup>6</sup> that relates the acoustic emission counts to the volume of the plastic zone at the crack tip, and the plastic zone size to  $K$  predicts a value of 4 for  $m$ ; experimental values of 4 to 8 have been observed.<sup>6,7</sup>

Equation (1) suggests that acoustic emission could be applied to the detection of cracks and their subcritical growth by continuous monitoring of a structure. However, excessive background noise during service, such as would probably occur in aircraft, and the

expense involved eliminates this procedure in most cases of practical interest. As an alternative to continuous monitoring, a procedure which takes advantage of the *irreversibility* of acoustic emission is possible.

If a cracked structure is loaded to a particular value of  $K$  and then unloaded, emission will not occur during reloading until this previous value of  $K$  is exceeded. It is possible to take advantage of this *irreversible* nature to determine whether or not a crack has grown during cyclic loading at a stress  $\sigma_w$ , by periodically overstressing (proof-testing) the structure at a stress  $\sigma_p (>\sigma_w)$  while monitoring for acoustic emission. If flaws have grown at  $\sigma_w$  since the previous overstress, then the stress intensity factor during proof testing [ $K_p \approx \sigma_p (\pi a)^{1/2}$ ] will have increased, and emission will be observed during the proof test. Alternatively, if no crack growth occurred at  $\sigma_w$ ,  $K_p$  would remain the same as during the previous proof test and no *new* plastic deformation (and hence no acoustic emission) would occur.

A model to analytically predict the number of acoustic emission counts observed during the proof test as a function of the number of cycles at the working stress was presented in an earlier paper.<sup>12</sup> An outline of the derivation of this relationship will be presented here for completeness, and a comparison with experimental data obtained on 7075-T6 aluminum will be presented. The acoustic emission observed while holding at the proof stress is also of interest and provides information on how close the structure is to failure. The information gathered during the proof test can be used in conjunction with the fatigue crack propagation behavior of the material to predict the optimum number of cycles until the next proof should be conducted.

All previous work relating the acoustic emission to the stress intensity factor has been limited to the case of through cracks in plates, which is a two-dimensional planar problem. The acoustic emission can be directly related to the stress intensity factor in this instance, and no reference to the flaw size is necessary. This paper extends the previous analysis to penny-shaped cracks, which are often more representative of the type of flaws actually occurring in structures. The penny-shaped crack results show that it is no longer possible to directly relate the acoustic emission and stress intensity, but reference must also be made to the flaw size itself.

## THEORY

The rate of fatigue crack growth increases with in-

<sup>†</sup> $K$  is a parameter which completely determines the magnitude of the stresses near a crack tip in an elastic material.<sup>13</sup> It is of primary interest in the discussion of the stress analysis and propagation of cracks.



creasing stress intensity factor according to the relation,<sup>14</sup>

$$da/dn = CK^q \quad (2)$$

for a wide range of K; values of q from 2-6 are experimentally observed. For simplicity, the case of an infinite plate with a through crack of length 2a, subjected to a uniform stress at infinity, will be considered first. The stress intensity factor for this case is<sup>13</sup>

$$K = \sigma(\pi a)^{1/2} \quad (3)$$

Substituting this result into Eq. (2) and solving the resulting differential equation leads to the following result:

$$a = a_0 \left( 1 - \frac{q-2}{2} a_0^{(q-2)/2} C \sigma_w^q \pi^{q/2} n \right)^{-\frac{2}{q-2}} \quad (4)$$

Combining Eqs. (1), (3) and (4) leads to the following relationship between the number of fatigue cycles, n, and the total number of acoustic emission counts observed during the proof cycle, N<sub>t</sub>:

$$N_t = A \left[ K_p^m - K_w^m \right] = A \left\{ \left[ \sigma_p(\pi a)^{1/2} \right]^m - \left[ \sigma_w(\pi a)^{1/2} \right]^m \right\} = A \pi^{m/2} \sigma_p^m \left[ 1 - \left( \frac{\sigma_w}{\sigma_p} \right)^m \right] a_0^{m/2} \left[ 1 - \frac{q-2}{2} a_0^{(q-2)/2} C \sigma_w^q \pi^{q/2} n \right]^{-\frac{m}{q-2}} \quad (5)$$

The number of counts that would have been observed at K's lower than K<sub>w</sub> have been subtracted out because of the irreversibility of the acoustic emission phenomenon. This expression is greatly simplified if m and q are both equal to the commonly observed values of 4,

$$N_t = A \pi^2 a_0^2 \left( \sigma_p^4 - \sigma_w^4 \right) \left[ 1 - a_0 C \sigma_w^4 \pi^2 n \right]^{-2} \quad (6)$$

(for m = q = 4) ,

which agrees with Eq. (9) of Ref. 12\*. Equation (6) shows that N<sub>t</sub> increases with increasing  $\sigma_p/\sigma_w$  (larger proof stress for a given working stress) and number of fatigue cycles.

In practice, the relationship between the load, crack size, and stress intensity factor will be more complicated than Eq. (3). It will still be possible to theoretically calculate the (N<sub>t</sub> - n) relation, provided that the stress intensity factor equation is known. The special case of a wedge-opening-loading (WOL)<sup>15</sup> specimen will be worked out as a typical example. Figure 1 is a drawing of a standard specimen. The stress intensity relation for this geometry<sup>15</sup> is

$$K = \frac{F a^{1/2}}{BW} G(a/W) = \frac{F}{BW^{1/2}} \alpha^{1/2} G(\alpha) \quad (7)$$

where

$$G(\alpha) = 100 (0.296 - 1.855\alpha + 6.557\alpha^2 - 10.17\alpha^3 + 6.389\alpha^4) \quad (8)$$

Combining this expression with Eq. (2) leads to

$$\frac{da}{dn} = W \frac{d(a/W)}{dn} = W \frac{d\alpha}{dn} = CK^q = CK_w^q = C \left[ \frac{F_w}{BW^{1/2}} \alpha^{1/2} G(\alpha) \right]^q \quad (9)$$

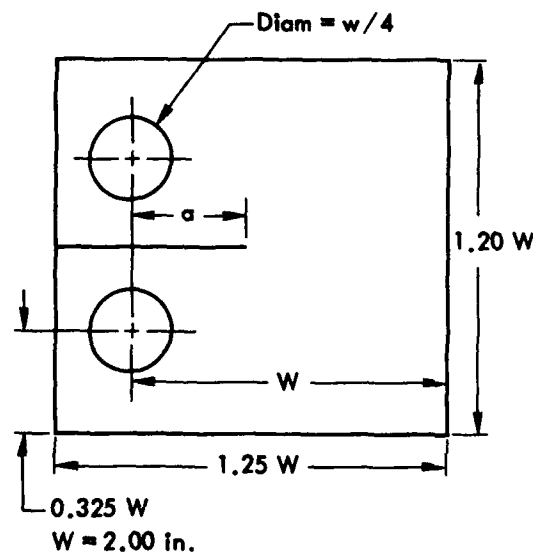


Figure 1. WOL Fracture Toughness Specimen Used in Experiment.

\* Note that there is a typographical error in Eq. (9) of Ref. 12; there should be brackets around the  $1 - C \sigma_w^4 \pi^2 n a_0$  term in the denominator.

Solving this differential equation by separating variables and integrating (as was done in the first case considered) leads to the following expression:

$$n(\alpha) = \eta(\alpha) \left/ \left[ \frac{C}{W} \left( \frac{F_w}{BW^{1/2}} \right)^q \right] \right. \quad (10)$$

where  $\eta(\alpha)$  is the following integral, which must be evaluated numerically:

$$\eta(\alpha) = \int_{\alpha_0}^{\alpha} \frac{dx}{\left[ x^{1/2} G(x) \right]^q} \quad (11)$$

The value of  $N_c$  corresponding to the crack length  $a = \alpha W$  and number of fatigue cycles can be calculated by determining  $K$  for the known crack length [Eq. 7], and substituting this relationship into the N-K relation [Eq. (1)].

Turning now to the penny-shaped crack analysis, it is assumed that the number of acoustic emission counts is proportional to the volume of the plastic zone at the crack tip. A more sophisticated assumption is used in the original derivation in Ref. 6, but this simplified one leads to the same end result. The plastic zone size  $r_y$  is related to the stress intensity factor by the following expression<sup>16</sup>:

$$r_y = \frac{1}{4\pi(2)^{1/2}} \left( \frac{K}{\sigma_{ys}} \right)^2 \quad (12)$$

for plane strain. Assuming the plastic zone to be a circle, the plastic volume is given by the following expression:

$$V_p = B\pi r_y^2 = \frac{B}{32\pi\sigma_{ys}^4} K^4 \quad (\text{through crack})$$

$$V_p = 2\pi a \pi r_y^2 = \frac{a}{16\sigma_{ys}^4} K^4 \quad (\text{penny-shaped crack}). \quad (13)$$

Now using the assumption that  $N$  is proportional to  $V_p$ ,

$$N = DV_p = \frac{DB}{32\pi\sigma_{ys}^4} K^4 \quad (\text{through crack})$$

$$N = \frac{Da}{16\sigma_{ys}^4} K^4 \quad (\text{penny-shaped crack}). \quad (14)$$

Equation (14) shows that the emission from a through crack depends only on the stress intensity factor  $K$ , and no reference to the flaw size is necessary. This is advantageous; fracture occurs when  $K$  reaches a critical value  $K_{Ic}$ , and  $K$  varies linearly with load. Hence, if  $K_{Ic}$  and  $K$  for a given load are known, the failure load can be easily determined directly. The same situation does not occur for penny-shaped cracks, since it is not possible to directly determine  $K$  from the acoustic emission without also knowing the flaw size.

The N-K relation for a semicircular surface flaw can easily be obtained from Eq. (14) by noting that  $V_p$  is simply one-half as large as for a complete penny-shaped crack. Hence, for a given  $K$ , only half as many counts will be observed. Extension of these results to embedded and surface elliptical flaws is straightforward.

## EXPERIMENTAL PROCEDURE

A detailed description of the acoustic emission instrumentation is contained in previous reports.<sup>6,7</sup> Briefly, a "differential" PZT transducer<sup>17</sup> resonant at 145 kHz was taped to the side of the specimen and coupled to the specimen with viscous resin. The output of the transducer was amplified 80 db and passed through a band-pass filter set to pass frequencies between 90 and 170 kHz. The signals were then fed into a digital counter set to sum all incoming signals (accumulation mode). The analog of this digital data was obtained from a digital-to-analog converter and displayed on the Y axis of an XY plotter. The voltage from the load cell of the testing machine was used to drive the X axis of the plotter, thereby giving a direct plot of acoustic emission counts versus load.

WOL specimens, as shown in Fig. 1, with  $W = 2$  in. and  $B = 0.48$  in., were prepared from 7075-T6 plate stock. Three types of tests were conducted:

1. *Rising load fracture toughness tests.* These tests were conducted to determine  $K_{Ic}$ , the fracture toughness of the material, in the conventional manner. A fatigue crack was introduced into the specimen prior to the test. Acoustic emission and notch opening displacement were monitored during the test. These tests provided the information necessary to evaluate the constants in the N-K relation [Eq. (1)].

2. *Straight fatigue-to-failure tests.* These tests consisted of cycling the specimen between 0.05 and 0.80 kips and measuring the crack length as a function of the number of fatigue cycles. No acoustic emission data were taken during these tests. These tests provided the crack

growth data needed to evaluate the constants in the crack growth equation [Eq. (2)].

3. *Fatigue with intermittent proof.* These tests consisted of introducing a 0.70-in. fatigue crack into the specimen by cycling at 0.80 kips. This was taken to be the point of zero fatigue cycles. The specimen was then cycled between 0.05 and 0.80 kips, and was proofed to 1.2 kips every 3000 cycles. Acoustic emission and notch opening displacement were monitored during the proofing, and the amount of acoustic emission observed (before it decreased to background) while holding at the proof load was noted.

### EXPERIMENTAL RESULTS AND COMPARISON WITH THEORETICAL PREDICTIONS

Table I provides a summary of the tests conducted in this investigation, along with the  $K_{Ic}$  results for each specimen. As expected, it is seen that  $K_{Ic}$  was the same for each of the three types of tests conducted. Figure 2 shows the acoustic emission and notch opening displacement results for the three rising load fracture toughness tests. Jumps in the displacement curve, or "pop-in" type behavior, was observed prior to final failure. The acoustic emission data of Fig. 2 was replotted for selected data points on log-log paper as a function of  $K$  to determine the constants in the N-K relationship. The log-log plot is presented in Fig. 3, which shows the

fair linearity and agreement between tests. The slope of the line provides the value of the exponent  $m$  in Eq. (1), and the coefficient  $A$  is easily calculated. The following N-K relation was found:

$$N = 2.46 \times 10^{-5} K^7 \quad (15)$$

where  $N$  is in counts and  $K$  in  $\text{ksi-in.}^{1/2}$ .

The crack length - fatigue cycle data obtained in the straight fatigue tests (specimens 4 and 5) was graphically differentiated to determine  $da/dn$ . This was plotted as a function of  $K$  on log-log paper (Fig. 4 shows the results). The dashed straight line was drawn through the data points and the equation of this line was determined to obtain the  $(da/dn - \hat{K})$  relation,

$$da/dn = 2.52 \times 10^{-8} \hat{K}^{2.69} \quad (16)$$

where  $a$  is in inches,  $n$  in cycles, and  $\hat{K}$  in  $\text{ksi-in.}^{1/2}$ . The crack growth data presented in Fig. 4 agrees well with that presented for 7075-T6 in Ref. 18 (page 369). Crack growth data from the intermittent proofing tests (Specimens 6 and 7) are also presented in this figure.

TABLE I. SUMMARY OF TESTS CONDUCTED, AND  $K_{Ic}$  RESULTS.  
All Specimens 7075-T6 Aluminum,  $W = 2$  inches

Spec. No.	Test type	$F_c$ (kips)	$a_c$ (in.)	$B$ (in.)	$K_{Ic}$ ( $\text{ksi-in.}^{1/2}$ )
1	Rising load fracture toughness	2.685	0.71	0.487	25.6
2	Rising load fracture toughness	2.825	0.70	0.485	26.8
3	Rising load fracture toughness	1.14	1.23	0.481	24.1
4	Straight fatigue to failure, no acoustic emission, $F = 0.75$	0.80	1.42	0.469	29.0
5	Straight fatigue to failure, no acoustic emission, $F = 0.75$	0.80	1.40	0.485	25.0
6	Fatigue with intermittent proof	1.154	1.206	0.481	23.3
7	Fatigue with intermittent proof	1.00	1.272	0.481	23.2

Table II provides a summary of the results of the fatigue with intermittent proofing tests. Figures 5 and 6 present the acoustic emission as a function of load for each of the proofing tests; the crack length at each proof cycle is indicated. The amount of acoustic emission observed while holding at the proof load of 1.2 kips is shown by cross-hatching. Notch opening displacement measurements were also made during each proof cycle, but are not included in Figs. 5 and 6 in the interest of clarity. The opening displacement data were relatively devoid of interest. "Pop-in" type behavior was observed only on the proof cycle in which failure occurred and during the preceding proof.

Table III provides the results of the theoretical calculations predicting the total number of counts observed during the proof cycle as a function of the number of fatigue cycles. These data are plotted in Fig. 7, and the results of the intermittent proofing tests are also presented in order to facilitate a direct comparison between the theoretical and experimental results. Figure 8 is a plot of the number of counts observed while holding at the proof load as a function of the corresponding stress intensity factor.

### DISCUSSION AND APPLICATION OF RESULTS

At least three indicators of impending failure were

Figure 2. Summation Acoustic Emission and Opening Displacement for Rising Load Fracture Toughness Tests.

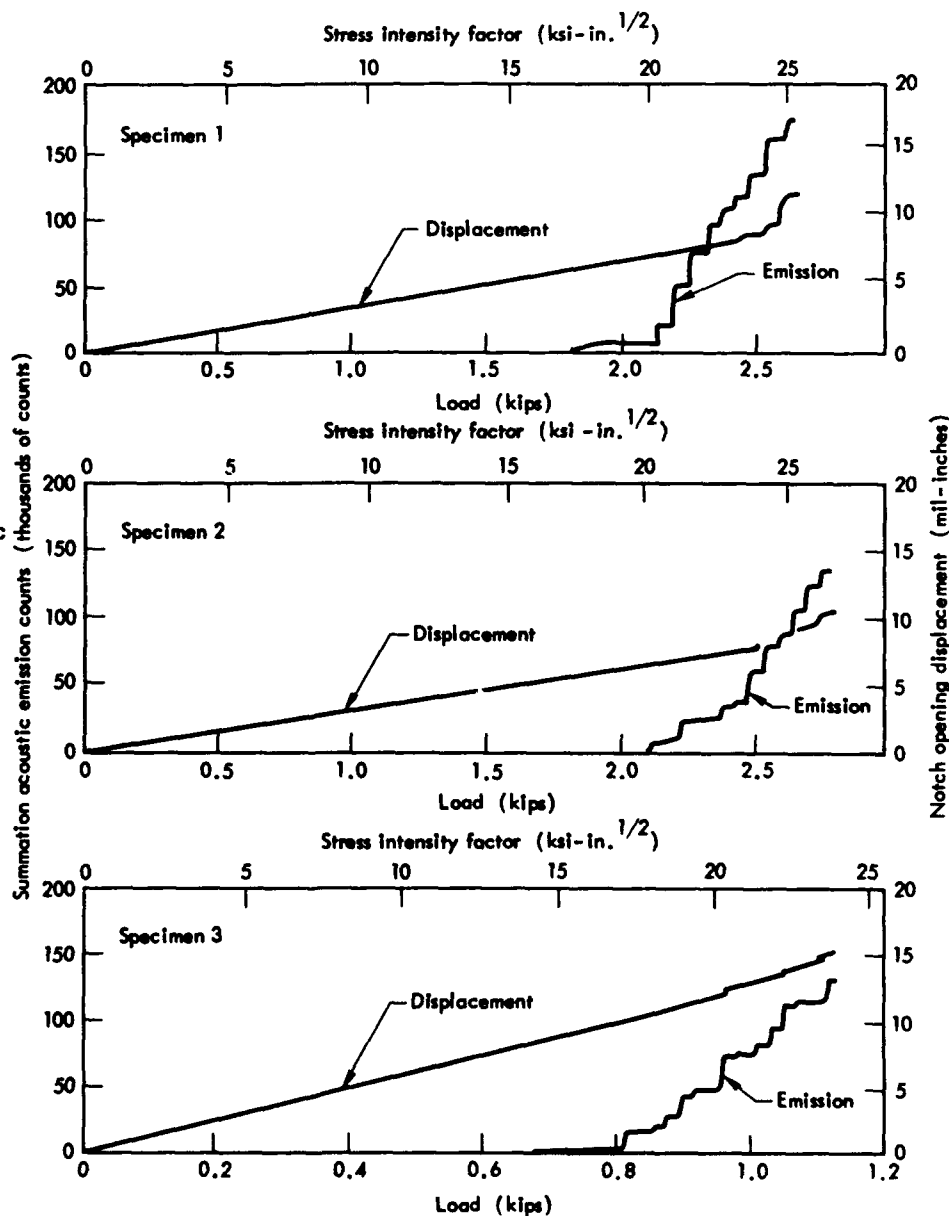


TABLE II. RESULTS OF INTERMITTENT PROOFING TESTS.

No. of fatigue cycles (thousands of cycles)	Specimen 6			Specimen 7		
	Crack length (in.)	Total counts to 1.2 kips (counts)	Counts during hold at 1.2 kips (counts)	Crack length (in.)	Total counts to 1.2 kips (counts)	Counts during hold at 1.2 kips (counts)
0	0.700	360	0	0.700	305	0
3	0.719	165	0	0.725	158	0
6	0.746	429	0	0.749	121	0
9	0.781	454	0	0.771	185	0
12	0.815	750	0	0.792	83	0
15	0.841	353	0	0.810	115	0
18	0.878	720	0	0.830	491	0
21	0.919	911	0	0.855	304	0
24	0.965	934	0	0.885	429	0
27	1.028	1040	1000	0.909	488	0
30	1.100	33,780	15,300	0.941	600	12
33	1.206	158,000 <sup>(a)</sup>	(a)	0.975	1350	100
36	—	—	—	1.021	5200	50
39	—	—	—	1.078	9390	8
42	—	—	—	1.159	41,400	9000
45	—	—	—	1.272	46,600 <sup>(a)</sup>	(a)

<sup>a</sup>Broke before reaching maximum load during proof cycle.

noted from the results of the proofing tests:

1. "Pop-in" type behavior of the notch opening displacement measurements was observed on the proof cycle immediately before the one in which failure occurred. This provided warning of impending failure in these laboratory tests, but would not be too useful in practical applications since displacement measurements must be made very close to the crack itself.

2. The amount of acoustic emission observed while holding at the proof load increased greatly during the last couple of proof tests, thereby indicating that the specimen was approaching final failure. As shown in Fig. 8, the value of  $K$  at the proof load,  $K_p$ , was about 20 ksi-in.<sup>1/2</sup> or greater for cases in which emission was observed during the hold. This is fairly close to the critical

value,  $K_{Ic}$ , which is about 24 ksi-in.<sup>1/2</sup> for this material (see Table I). Hence, if acoustic emission is observed at constant load in a structure of this material, there is a crack present whose  $K$  is greater than about 80% of  $K_{Ic}$ , and the structure is nearing failure.

3. The amount of acoustic emission observed during the rising load portion of the proof test ( $N_t$ ) increased with each succeeding proof, thereby indicating that a fatigue crack was present and growing. The amount of emission observed provided early warning of impending failure. Both tests showed considerable acoustic emission activity at least 9000 cycles before failure.

The agreement between the theoretical and experimental results shown in Fig. 7 is encouraging, when the amount of scatter usually observed in both acoustic

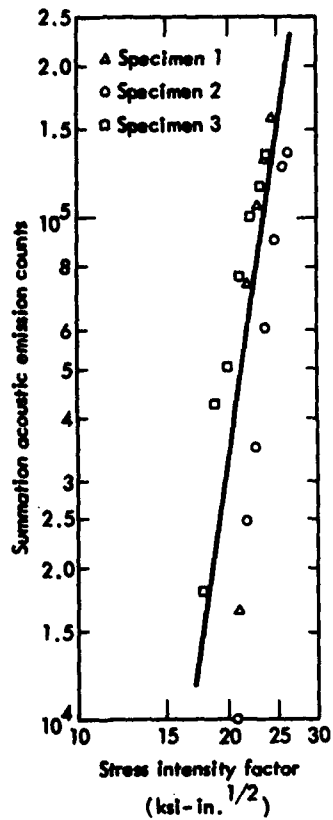


Figure 3. Summation Acoustic Emission Counts as a Function of the Stress Intensity Factor for the Rising Load Fracture Toughness Tests.

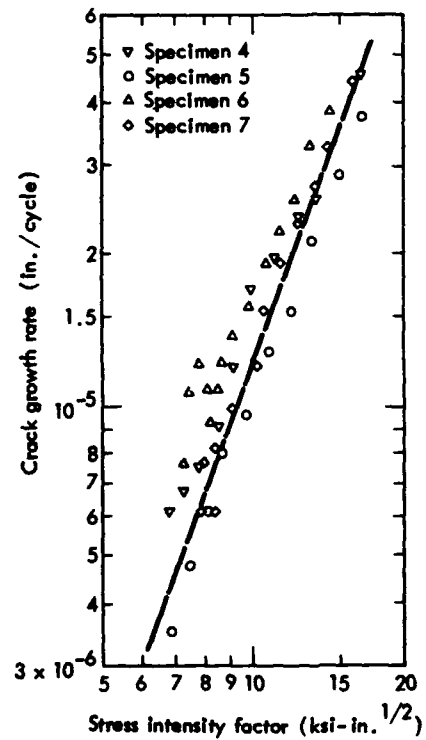


Figure 4. Crack Growth Rate for Cyclically Loaded Specimens.

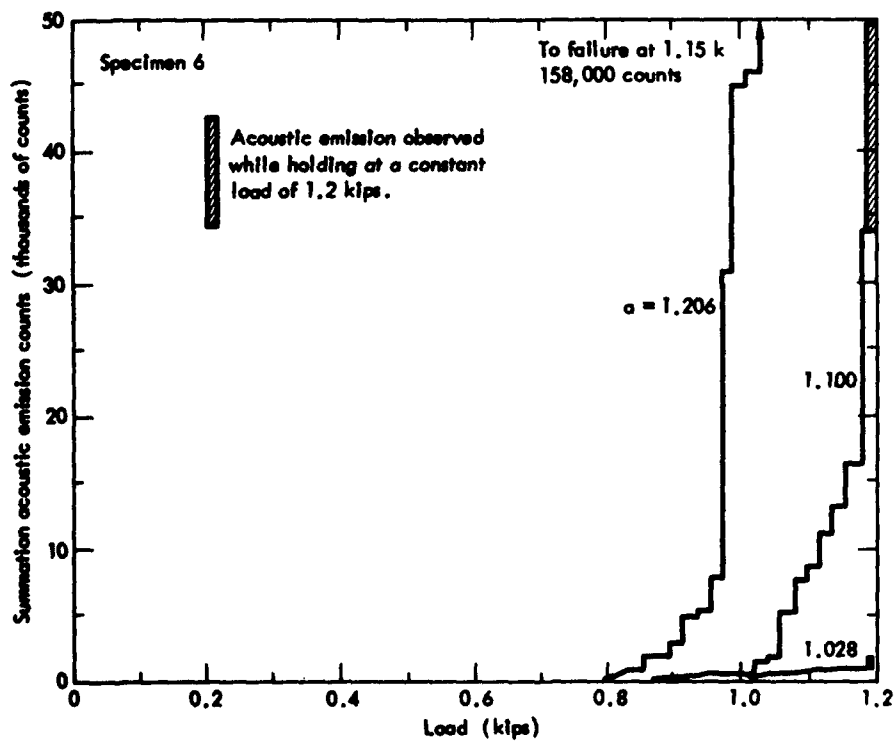
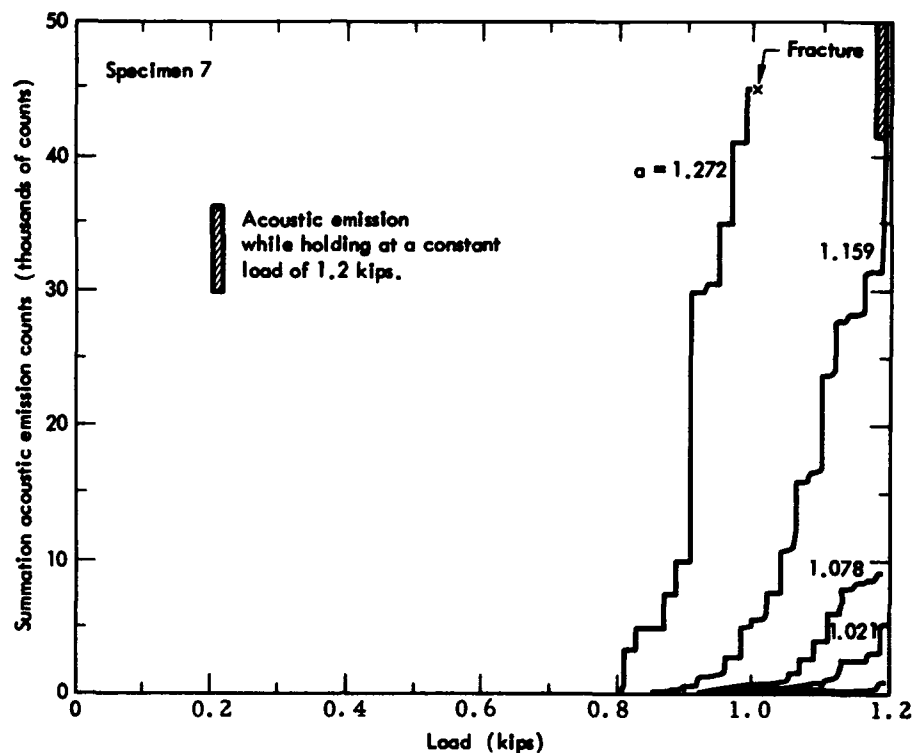


Figure 5. Summation Acoustic Emission as a Function of Load for Intermittently Proofed Cyclically Loaded Specimen.

Figure 6. Summation of Acoustic Emission as a Function of Load for Intermittently Proofed Cyclically Loaded Specimen.



emission and fatigue crack growth data is taken into consideration. Specimen 6 did break sooner than predicted by the theory, but did provide ample warning.

To check the integrity of a structure in practical applications, it would only be necessary to periodically proof and monitor the structure to form a curve such as the ones shown in Fig. 7. When it was found that conditions corresponded to the ascending portion of the curve (such as would be indicated by a rapid increase in  $N_t$  or  $dN_t/dn$ ) failure would be impending and only a few

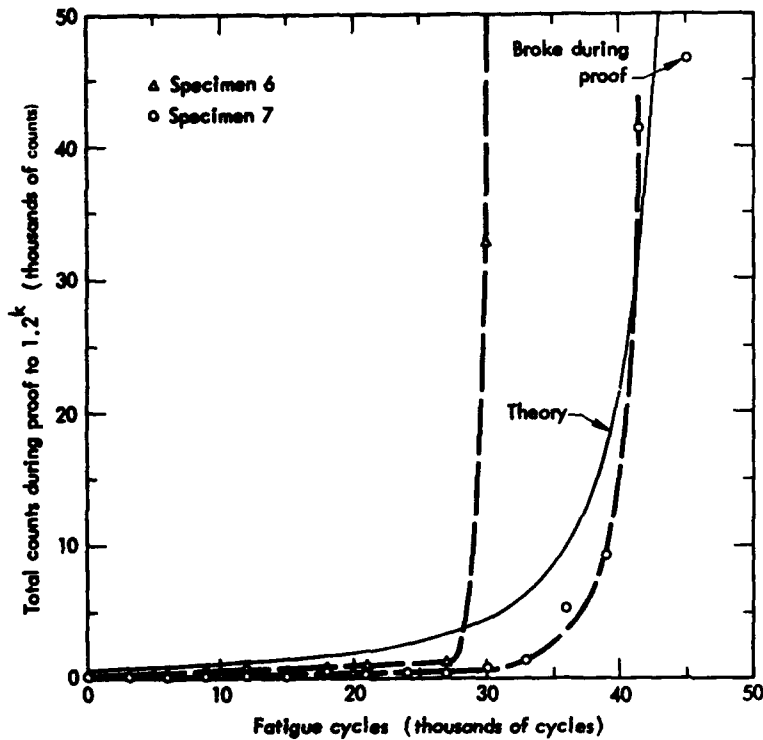
thousand cycles of life would be remaining. Hence, the structure should be removed from service.

If it were desired to retain the structure in service, the remaining lifetime could be estimated in two ways: (1) Using the procedure suggested by Tiffany and Masters,<sup>19</sup> and (2) using the results of emission observed while holding at the proof load. If it is assumed that  $K_p = K_{Ic}$  (a conservative assumption) then  $K_i$  (initial  $K$  for remaining portion of test) will be  $K_w$  and  $K_w/K_{Ic}$  ( $=\sigma_w/\sigma_p$ ) will be equal to 2/3. The data of  $K_i/K_{Ic}$

TABLE III. THEORETICAL RESULTS

$\alpha$	a (in.)	$\eta$	n (cycles)	$K_p$ (ksi-in. <sup>1/2</sup> )	$N_t$ (counts)
0.35	0.70	0	0	11.46	639
0.40	0.80	$2.791 \times 10^{-4}$	16,250	12.92	1,478
0.45	0.90	$4.787 \times 10^{-4}$	27,880	14.71	3,663
0.50	1.00	$6.117 \times 10^{-4}$	35,970	16.94	9,853
0.55	1.10	$7.107 \times 10^{-4}$	41,390	19.87	30,030
0.60	1.20	$7.695 \times 10^{-4}$	44,820	23.89	109,200
0.65	1.30	$8.041 \times 10^{-4}$	46,830	29.60	489,800
0.70	1.40	$8.228 \times 10^{-4}$	47,920	37.80	$2.71 \times 10^6$

Figure 7. Comparison of Theoretical and Experimental Results for Intermittent Proof Tests.



versus cycles to failure presented by Tiffany and Masters<sup>19</sup> suggests that the remaining lifetime is from 500 to a few thousand cycles. A more accurate estimate of the remaining lifetime could be made if  $K_i/K_{IC}$  versus cycles-to-failure data were available for this material.

The second procedure utilizes the observation that if emission is observed while holding, then a flaw with a  $K$  of 20 ksi-in.<sup>1/2</sup> or greater is present. The remaining cycles to failure can be calculated using the crack growth law and stress intensity factor equation, and using the  $K$  equation in the form

$$K = \beta \sigma a^{1/2} \quad (17)$$

where  $\beta$  is a geometry-dependent proportionality term, given below for several geometries:

- $\beta = \pi^{1/2}$  : through crack in infinite plate
- $\beta = 2/\pi^{1/2}$  : penny-shaped crack in infinite body
- $\beta = 2.24/\pi^{1/2}$  : semicircular surface flaw in semi-infinite body.

Solving for  $a$  in Eq. (17) and substituting this result into the crack growth equation leads to the following differential equation:

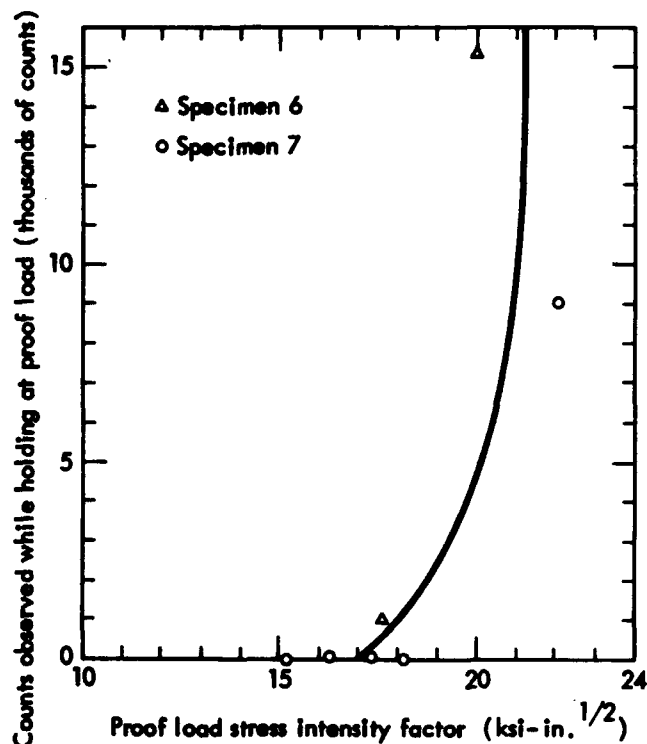
$$\frac{2\hat{K}}{\beta^2 \hat{\sigma}^2} \frac{d\hat{K}}{dn} = C\hat{K}^q \quad (18)$$

Now, if  $K_p = 20$  ksi-in.<sup>1/2</sup> (established by presence of emission during hold), then  $K_w = 2/3 (20) = 13.3$  ksi-in.<sup>1/2</sup>. If the remaining lifetime is considered to be the number of cycles to grow the crack out to the critical length at the working load, then  $n_f$  (remaining lifetime) can be calculated using Eq. (18) and the limits on  $K$ ,

$$n_f = \int_0^{n_f} dn = \frac{2}{\beta^2 \hat{\sigma}^2 C} \int_{13.3}^{24} \hat{K}^{1-q} d\hat{K} \quad (19)$$



Figure 8. Counts Observed While Holding at Proof Load as a Function of the Corresponding Stress Intensity Factor.



Using  $q = 2.69$  and  $C = 2.52 \times 10^{-8}$  [see Eq. (16)]:

$$n_f = \frac{7.94 \times 10^7}{\beta^2 \hat{\sigma}^2} \frac{1}{0.69}$$

$$\left[ \frac{1}{13.3^{(0.69)}} - \frac{1}{24^{(0.69)}} \right] = \frac{6.52 \times 10^6}{\beta^2 \hat{\sigma}^2} \quad (20)$$

where  $\hat{\sigma}$  is in ksi.

*This number of cycles would also be the optimum number of cycles between proofing tests, since proofing at this interval would guarantee that if emission during hold was not observed, then failure would not occur before the succeeding proof.*

Considering the case of a through crack [most severe of the cases listed after Eq. (17)] with  $\hat{\sigma} = 36$  ksi (half the yield stress for this material),  $n_f$  is found to be 1750 cycles, which shows that the structure must be monitored often under these conditions, and that if emission was observed during the hold then failure would be very close. This small number of cycle results from the closeness of the 20 ksi-in.<sup>1/2</sup> threshold for emission during hold to the critical value of 24 ksi-in.<sup>1/2</sup>. If these two stress intensities were further apart,  $n_f$  would

be larger. Also if  $\hat{\sigma}$  and  $\beta$  were smaller,  $n_f$  would be increased. For instance, considering  $\hat{\sigma} = 18$  ksi and  $\beta = 1/\pi^{1/2}$  (penny-shaped crack)  $n_f$  would be 64,000 cycles — a much more desirable proofing interval.

Crack growth data for fatigue with intermittent proof which was obtained on Specimens 6 and 7 was plotted as a function of  $K$  in Fig. 4, along with data from the straight fatigue tests. The data show that the crack growth behavior was not effected by the intermittent proof, which indicates that the occasional overload did not adversely affect the crack propagation behavior.

It would be possible to eliminate the proofing cycle, and just monitor the acoustic emission while holding at the working load. This would allow the determination of whether or not there were flaws present with a  $K$  greater than 20 ksi-in.<sup>1/2</sup>. This procedure would not give as early a warning, and it eliminates the double check provided by monitoring the emission while loading between the working and proofing loads.

## CONCLUSIONS

The following are the major conclusions to be drawn from the results of this investigation:

1. The use of acoustic emission in conjunction with periodic proof stressing provides a means of detecting the presence and growth of fatigue cracks.

2. The technique of periodic proofing can be used to detect impending failure by two methods: Observation of increasing number of counts during loading between the working and proofing loads; and observation of acoustic emission while holding at the proof load.

3. This technique provides ample and early warning of impending failure, and would therefore be of value in practical applications.

4. Good agreement was observed between experimental results and theoretical predictions made from a model for analysis of fatigue crack growth with intermittent proofing and acoustic emission monitoring.

5. Acoustic emission from a penny-shaped crack can not be directly related to the stress intensity factor, but reference must be made to the flaw size. This differs from the case of through cracks, for which the acoustic emission can be directly related to the stress intensity factor.

6. The optimum number of cycles between proofing can be calculated if the crack growth law,  $K$  variation with crack length, the minimum  $K$  for emission during hold and  $K_{IC}$ , are known. Equation (20) is the relationship for the particular material used in this investigation (7075-T6 aluminum).

#### REFERENCES

1. J. Kaiser, *Untersuchungen über das auftreten Geräuschen beim Zugversuch*, Ph.D. Dissertation, Technische Hochschule, Munich, West Germany (1950); *Arkiv Eisenhüttenwesen*, 24: 43-45 (1953).
2. B.H. Schofield, *Acoustic Emission Under Applied Stress*, ASD-TDR-63-509, Part 1, Air Force Materials Laboratory, Wright-Patterson AFB, Ohio (1963).
3. B.H. Schofield, *Acoustic Emission Under Applied Stress*, ASD-TDR-63-509, Part 2, Air Force Materials Laboratory, Wright-Patterson AFB, Ohio (1964).
4. C.A. Tatro and R. Liptai, "Acoustic Emission from Crystalline Substances," pp. 145-158, *Proc. Symp. Phys. Nondestructive Testing*, Southwest Research Institute, San Antonio, Texas (1962).
5. H.L. Dunegan and C.A. Tatro, "Acoustic Emission Effects During Mechanical Deformation," R. Buhshah, Ed., *Techniques of Metals Research*, Vol. V, John Wiley, New York, in press.
6. H.L. Dunegan, D.O. Harris, and C.A. Tatro, "Fracture Analysis by Use of Acoustic Emission," *Eng. Fracture Mech.*, 1/1:105-122 (1968).
7. H. Dunegan and D. Harris, "Acoustic Emission - A New Nondestructive Testing Tool," *Ultrasonics*, 7/3:160-166 (1969).
8. W.W. Gerberich and C.E. Hartbower, "Some Observations on Stress Wave Emission as a Measure of Crack Growth," *Fracture Mech.*, 3/3:185-192 (1967).
9. C.E. Hartbower, W.W. Gerberich, and H. Liebowitz, "Investigation of Crack-Growth Stress-Wave Relationships," *Eng. Fracture Mech.*, 1/2:291-308 (1968).
10. W.W. Gerberich and C.E. Hartbower, *Monitoring Crack Growth of Hydrogen Embrittlement and Stress Corrosion Cracking by Acoustic Emission*. Presented at the Conference on Fundamental Aspects of Stress Corrosion Cracking, Ohio State University, Columbus, Ohio, September 1967.

#### REFERENCES (Continued)

11. H.L. Dunegan and A.S. Tetelman, *Nondestructive Characterization of Hydrogen Embrittlement Cracking by Acoustic Emission Techniques*. Presented at the ASM Annual Meeting, Philadelphia, Pennsylvania, October 1969.
12. H.L. Dunegan, D.O. Harris, and A.S. Tetelman, *Detection of Fatigue Crack Growth by Acoustic Emission Techniques*, (Presented at the Seventh Symposium) on Nondestructive Evaluation of Components and Materials in Aerospace, Weapons Systems, and Nuclear Applications, San Antonio, Texas, April 1969.
13. P.C. Paris and G.C. Sih, "Stress Analysis of Cracks," pp.30-81, *Fracture Toughness Testing and Its Applications*, ASTM-STP-381, American Society for Testing and Material, Philadelphia, Pennsylvania (1965).
14. P.C. Paris, "The Fracture Mechanics Approach to Fatigue," p. 107, *Proc. 10th Sagamore Army Mater. Res. Conf.*, Syracuse University Press, Syracuse, New York (1964).
15. E.T. Wessel, "State of the Art of the WOL Specimen for  $K_{Ic}$  Testing," *Eng. Fracture Mech.*, 1: 77-103 (1968).
16. F.A. McClintock and G.R. Irwin, "Plasticity Aspects of Fracture Mechanics," pp. 84-113, *Fracture Toughness Testing and Its Applications*, ASTM-STP-381, American Society for Testing and Materials, Philadelphia, Pennsylvania, (1965).
17. H.L. Dunegan, A.E. Brown, and P.L. Knauss, *Piezoelectric Transducers for Acoustic Emission Measurements*, UCRL-50553, Lawrence Radiation Laboratory, Livermore, California (1968).
18. A.S. Tetelman and A.J. McEvily, Jr., *Fracture of Structural Materials*, John Wiley, New York (1967).
19. C.F. Tiffany and J.N. Masters, "Applied Fracture Mechanics," pp. 249-308, *Fracture Toughness Testing and Its Applications*, ASTM-STP-381, American Society for Testing and Materials, Philadelphia, Pennsylvania (1965).

**SESSION 5A**

**PHENOMENA II**

*Chairman*

**S.S. Manson  
NASA – Lewis Research Center**

# THE PREDICTION OF FATIGUE LIFE IN RANDOM VIBRATION ENVIRONMENTS

by

John C. Bowman

Ryan Aeronautical Company  
San Diego, California

## INTRODUCTION

Methods for predicting expected (mean) time to failure of the fatigue type for complex structures in random vibration conditions depend largely on the type of available test information, or, stated differently, on the economic dictates of a pure test program, a part test and part analytical approach, or an all analytical effort. An extreme case is where the expected fatigue life is determined directly from the mean of a series of shake table destruction tests. Analytically this is a trivial approach, but by no means is it trivial experimentally or economically.

A suitable methodology should, of course, be general, but it also should be flexible, offering the engineer a choice of approaches to fit the particular economics at hand. It is with this flexibility in mind that the present approach was prepared.

The basic method is partly test, partly analytical. A first variation of the basic method trades off some of the test effort for increased analysis, and a second variation is minimally experimental and maximally analytical.

In the basic method, the following are required inputs:

1. The failure mode and region must first be identified, sometimes no small task.

2. A short-time experimental sample of the structural response to the known random forcing function is required. The forcing function is *not* required in the analysis portion of the basic method – only the response. This sample must, of course, be for the particular failure mode and region at hand, and the sample may be taken at reduced input levels. The sample output is usually in one or both of two forms, and the analysis details depend on which one:

- a. A real time magnetic tape record of response strain versus time, showing positive and negative strain spikes.
- b. A response strain density curve which we call the response strain density spectrum, derived from the real time tape. This

curve gives response strain density, ( $\mu$  in/in)<sup>2</sup>/CPS, versus frequency, CPS.

3. The static stress-strain curve for the material in the failure mode and location is required.

4. The S-N curve for the material in the failure mode and location is also required.

In the first variation of the basic method, a short-time sample of the response to the random forcing function is not required. Instead, the response strain density spectrum is constructed analytically from two inputs:

1. The power spectral density (PSD) curve of the random forcing function,  $g^2$ /CPS versus frequency, CPS. This curve represents the random vibration environment for which the expected fatigue life is to be determined.

2. The structural response function, ( $\mu$  in/in)/g, in terms of peak failure area strain. This function, the ordinary "response function", sometimes given the symbol  $|H(\omega)|$  in structural dynamics, is a function of forcing frequency. The response function is determined, in this approach, by a simple sinusoidal sweep test at reduced  $g$  levels.

In the second variation of the basic method, the short-time sample of the response to the random forcing function is, again, not required, and, again, the response strain density curve is constructed analytically from the PSD curve of the random forcing function and from the structural response function. However, in this approach, the response function is determined analytically rather than from a sinusoidal sweep test. The inputs to this work are mass, stiffness, and damping properties of a representative mathematical model of the actual system.

It is not the purpose of this present paper to discuss in detail the exacting task of analytically determining the response function. This difficult subject, primarily of interest to the specialist structural dynamicist, is well treated in the literature and is highly computerized. To cover the ground adequately in a short paper would be an impossibility. However, some remarks on this approach are offered in a later section.

## BASIC METHOD

The point of departure for the basic method is the response strain density curve, the response strain density spectrum. An example is shown in Figure 1.

The spectrum is divided by frequency into fatigue producing bands, which we call critical frequency bands, each band with a center frequency. We speak of frequency bands and later peak strain zones. As an aid to identifying the fatigue producing frequency bands, consider first an upper bound for fatigue producing strain density. Above this bound, the failure is not of the fatigue type. Rather, this failure is of the first excursion (immediate) type. Clearly, at some high strain density, failure must occur on the first strain peak. We call the upper bound of fatigue producing strain density, the first excursion boundary. This boundary is determined as follows:

At each center frequency we envision the strain density point ( $\mu$  in/in)<sup>2</sup>/CPS as representing the average rate, strain squared per CPS, over a specified frequency bandwidth, characteristic of the filter width used in reducing the real time strain data to strain density data. Thus, the RMS strain over the bandwidth, in the sense of average velocity multiplied by a time interval gives the distance traversed, is given by:

$$e_{RMS} = \sqrt{SD \cdot BW}$$

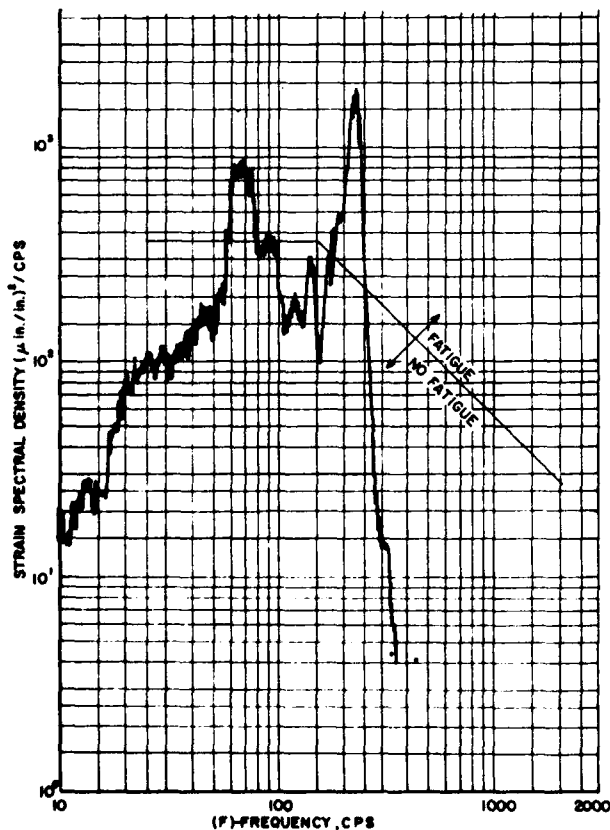


Figure 1. Response Strain Density Spectrum.

where

$e_{RMS}$  = RMS strain,  $\mu$  in/in

SD = Strain density, ( $\mu$  in/in)<sup>2</sup>/CPS

BW = Bandwidth, CPS

It is shown in Appendix 1 that  $e_{RMS} = e_{1\sigma}$ , a fundamental relationship that is used many times in this paper. The equality is based on the fact that the mean of the signed peak strains is zero. The significance of  $e_{1\sigma}$  is: If the amplitudes of the real time strain spikes in a time period are truly random, then they are normally (Gaussian) distributed, and 68.3% of the amplitudes are less than  $e_{1\sigma}$ . "Amplitude" means peak (maximum) value without regard to sign. " $1\sigma$ " means one standard deviation, here considered as a unit of strain size.

Let  $e_{tu}$ , corresponding to ultimate tensile stress  $F_{tu}$ , be the ultimate tensile strain for the material in the failure area. If the amplitudes of all of the real time strain spikes are less than  $e_{tu}$ , then first excursion failure does not occur. Conversely, if any of the strain amplitudes within the  $\pm 4\sigma$  domain are greater than  $e_{tu}$ , then it is assumed that first excursion failure theoretically occurs. "All" of the signed peak strains are assumed to be included between  $\pm e_{4\sigma}$ . The  $\pm 4\sigma$  limits are somewhat arbitrary. They are discussed in a later section of this paper.

Theoretically, a precisely normal distribution between  $\pm 4\sigma$  includes 99.996% of the strain peaks. Thus, the first excursion boundary is prescribed by the condition.

$$e_{4\sigma} = e_{tu}$$

We have  $e_{4\sigma} = 4e_{1\sigma} = 4e_{RMS} = 4\sqrt{SD_U \cdot BW} = e_{tu}$ , where  $SD_U$  is the required upper SD bound. Solving for  $SD_U$ , the first excursion boundary is given by

$$SD_U = (e_{tu}/4)^2/BW \quad (1)$$

For Figure 1, the material is K-1A cast magnesium alloy for which  $F_{tu} = 21,800$  psi and  $e_{tu} = 177,000$   $\mu$ in/in (see Figure 3). The bandwidth for Figure 1 is 50 cps for  $25 \leq f < 150$  CPS and 1/3 octave ( $1/3f$ ) for  $f \geq 150$  cps. Applying these data to equation (1) gives the first excursion boundary, presented in Table I.

TABLE I.  
FIRST EXCURSION BOUNDARY

f CPS	SD <sub>U</sub> , FIRST EXCURSION BOUNDARY ( $\mu$ in/in) <sup>2</sup> /CPS	
25 to 150	$3.92 \cdot 10^7$	Constant
150	$3.92 \cdot 10^7$	Straight line on
2000	$2.94 \cdot 10^6$	log-log plot

The first excursion boundary is well above the scale of Figure 1. Thus, first excursion failure is not a consideration in this example case.

There also is a lower bound for fatigue producing strain density. Let  $e_e$  be the strain corresponding to the endurance limit  $F_e$  for the material in the failure area. If the amplitudes of all of the real time strain spikes are less than  $e_e$ , then it is clear that fatiguing cannot occur, even for an indefinitely long time period. Thus, the lower strain density bound, which we call the fatigue boundary, is prescribed by the condition:

$$e_{4\sigma} = e_e$$

If the strain density is below the fatigue boundary, fatigue does not occur. The region on the strain density curve between the fatigue boundary and the first excursion boundary is the fatigue producing region, the region of interest in this paper. Again, we have  $e_{4\sigma} = 4e_{1\sigma} = 4e_{RMS} = 4\sqrt{SD_L \cdot BW} = e_e$  where  $SD_L$  is the lower SD bound. Solving for  $SD_L$ , the fatigue boundary is given by

$$SD_L = (e_e/4)^2/BW \quad (2)$$

For Figure 1,  $e_e = 3500/6.5 = 538 \mu \text{ in/in}$ , where the material is K-1A cast magnesium alloy with modulus of elasticity  $E = 6.5 \cdot 10^6 \text{ PSI}$  and endurance limit  $F_e = 3500 \text{ PSI}$  (See Figures 3 and 4). Again, the bandwidths are 50 CPS for  $25 \leq f < 150 \text{ CPS}$ , and  $1/3 f$  for  $f \geq 150 \text{ CPS}$ . Applying these data to equation (2) gives the fatigue boundary, presented in Table II.

TABLE II.  
FATIGUE BOUNDARY

f CPS	SD <sub>L</sub> , FATIGUE BOUNDARY ( $\mu \text{ in/in}$ ) <sup>2</sup> /CPS	
25 to 150	362	Constant
150	362	Straight line on
2000	27.2	log-log plot

The fatigue boundary is plotted in Figure 1. There are two critical frequency bands in Figure 1:

1. Center frequency 67 CPS, bandwidth 50 CPS, strain density  $800 (\mu \text{ in/in})^2/\text{CPS}$ .
2. Center frequency 225 CPS, bandwidth  $1/3 \cdot 225 = 75 \text{ CPS}$ , strain density  $1600 (\mu \text{ in/in})^2/\text{CPS}$ .

For any frequency band, the total number of cycles (total number of reversals, i.e., changes of sign of real time peak strains), is the center frequency of the band, in CPS, multiplied by the reference time period in seconds. We arbitrarily choose one hour (3600 sec.) as the reference time period.

Also characteristic of each frequency band is its  $1\sigma$  strain value, calculated from

$$e_{1\sigma} = e_{RMS} = \sqrt{SD \cdot BW}$$

It is assumed that the amplitudes of the real time strain spikes in the reference time period are truly random and thus are normally (Gaussian) distributed. Most of the strain spikes are low amplitude, some are medium amplitude, and very few are high amplitude. We break the amplitude range down into strain zones, in decimal parts of  $1\sigma$ , where the total number of cycles is normalized to unity. From a table of the probability distribution function for a normal distribution, e.g., Reference 1, we deduce the zonal probabilities given in Table III. The particular zonal breakdown chosen of course, is arbitrary.

TABLE III.  
ZONAL PROBABILITIES

ZONE	ZONE MIDPOINT	ZONAL PROBABILITY
0.0-0.1 $\sigma$	0.0 $\sigma$	0.079655675
0.1-0.3 $\sigma$	0.2 $\sigma$	0.156167170
0.3-0.5 $\sigma$	0.4 $\sigma$	0.147102078
0.5-0.7 $\sigma$	0.6 $\sigma$	0.133147773
0.7-0.9 $\sigma$	0.8 $\sigma$	0.115807054
0.9-1.1 $\sigma$	1.0 $\sigma$	0.096788129
1.1-1.3 $\sigma$	1.2 $\sigma$	0.077731153
1.3-1.5 $\sigma$	1.4 $\sigma$	0.059986567
1.5-1.7 $\sigma$	1.6 $\sigma$	0.044483477
1.7-1.9 $\sigma$	1.8 $\sigma$	0.031697806
1.9-2.1 $\sigma$	2.0 $\sigma$	0.021704278
2.1-2.3 $\sigma$	2.2 $\sigma$	0.014280621
2.3-2.5 $\sigma$	2.4 $\sigma$	0.009028889
2.5-2.7 $\sigma$	2.6 $\sigma$	0.005485383
2.7-2.9 $\sigma$	2.8 $\sigma$	0.003202321
2.9-3.1 $\sigma$	3.0 $\sigma$	0.001796420
3.1-3.3 $\sigma$	3.2 $\sigma$	0.000968358
3.3-3.5 $\sigma$	3.4 $\sigma$	0.000501590
3.5-3.7 $\sigma$	3.6 $\sigma$	0.000249659
3.7-3.9 $\sigma$	3.8 $\sigma$	0.000119407
3.9-4.1 $\sigma$	4.0 $\sigma$	0.000054878
SUM =		0.999958686

The zonal probabilities shown in Table III are interpreted as follows: Zonal probability  $\equiv$  Probability ( $z_0 \leq |u| \leq z_1$ )  $\equiv$  Shaded area (both sides) shown in Figure 2.  $u$  represents any standard normally distributed variable defined as follows: If  $x$  is the distributed variable, if  $\bar{x}$  is its mean, and if  $\sigma$  is its standard deviation, then  $u \equiv (x - \bar{x})/\sigma$ , dimensionless.  $z_0$  and  $z_1$  are also dimensionless, being decimal parts of  $1\sigma$ .

Note in Table III that the first zone is one half the width of the others. Also note that we treat here the values of the amplitudes of the real time strain peaks, which again are the peak strains without regard to sign, i.e., amplitudes are the absolute values of the signed strain peaks. It is the

TABLE IV.  
PREDICTED NUMBER OF REVERSALS VERSUS  
STRAIN LEVEL, FREQUENCY BAND 2

STRAIN AMPLITUDE $\mu$ in/in	PREDICTED NUMBER OF REVERSALS PER HOUR
0	64521.18
69.28204	126495.4
138.2820	119152.7
207.8461	107849.7
277.1282	93803.75
346.4102 (1 $\sigma$ )	78398.39
415.6922	62967.23
484.9743	48589.12
554.2563	36031.62
623.5384	25675.23
692.8204 (2 $\sigma$ )	17580.47
762.1024	11567.30
831.3845	7313.400
900.6665	4443.160
969.9486	2593.880
1039.231 (3 $\sigma$ )	1455.100
1108.513	784.3700
1177.795	406.2879
1247.077	202.2238
1316.359	96.71967
1385.641 (4 $\sigma$ )	44.45118
SUM=809966.7	

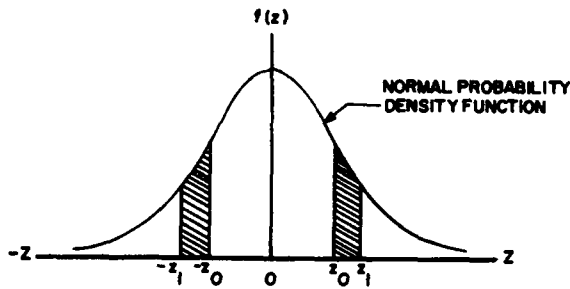


Figure 2. Basis for Zonal Probabilities.

signed peak values of the real time strain spikes that are normally distributed about a mean. This mean is zero in the cases treated here. (See Appendix 1). The signed peak strains range over  $\pm 4\sigma$ ; the strain amplitudes range over 0 to  $4\sigma$ .

As an example of the predicted number of reversals for various strain amplitudes zones, let us refer again to the example response strain density spectrum, Figure 1, and consider critical frequency band 2, the 225 CPS band. This band has more fatigue effect than band 1 since it has more reversals per hour (higher center frequency) and its strain density peak is further into the fatigue producing region of the strain density plot.

The total number of reversals for band 2 is  $f_{\text{MIDPOINT}} \cdot 3600 \text{ seconds} = 225 \cdot 3600 = 810,000$  for the one hour reference time period.

The RMS strain for band 2 is  $\sqrt{SD \cdot BW} = \sqrt{1600 \cdot 75} = 346.4102 \mu \text{ in/in}$ , which is also equal to the  $1\sigma$  strain.

Multiplying the  $1\sigma$  strain by the zone midpoints in Table III, and also multiplying the total number of reversals by the zonal probabilities in Table III, the predicted number of reversals as a function of strain amplitude level is obtained for the frequency band in question and for a one hour reference time period. These data are presented in Table IV. Note that the sum of reversals over the strain amplitude range 0 to  $4\sigma$  shows, theoretically, that 809966.7 reversals out of the total of 810,000 reversals for a one hour reference time period are accounted for, i.e., 33.3 reversals per hour remain theoretically outside the strain amplitude range 0 to  $4\sigma$ . This is the so called "tail" error.

The remainder of the procedure is simple. For each strain amplitude in Table IV, we enter the stress-strain curve for the material to obtain corresponding maximum stress (stress amplitudes). We then enter the S-N curve for the material at these stresses to obtain the allowable number of reversals to failure (100% cumulative damage) for each strain amplitude zone. We next divide the predicted number of reversals per hour for each strain amplitude zone by the corresponding allowable number of reversals to obtain

the incremental damage factor per hour for each strain amplitude zone. The sum of these increments gives the cumulative damage factor developed per hour for the frequency band (on the strain density curve) in question. The

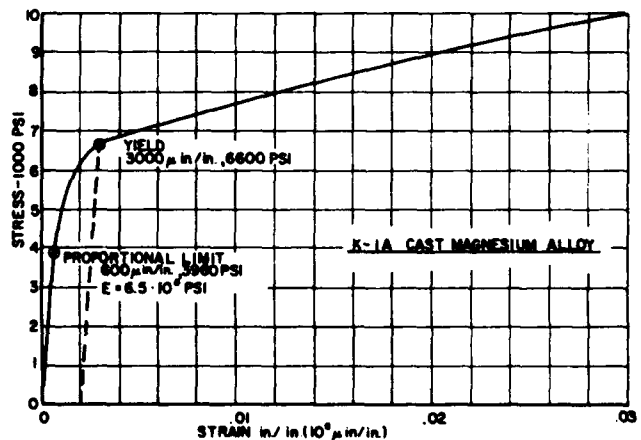
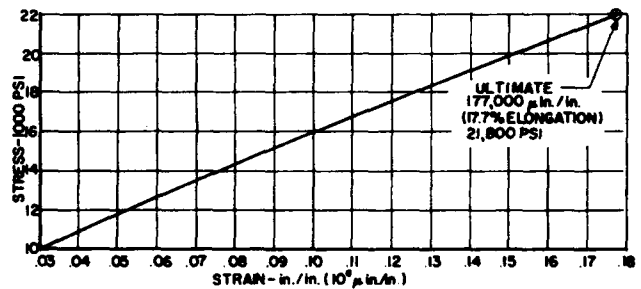


Figure 3. Stress-Strain Curve.



sum of cumulative damage factor per hour for the various critical frequency bands is the total cumulative damage factor developed per hour. Since a cumulative damage factor of 1.0 represents fatigue failure (100% damage is developed), the reciprocal of the total damage factor developed per hour is the required expected fatigue life in hours.

For the failure mode (bending fatigue) consistent with the example strain density spectrum, Figure 1, and for the failure area in question, a K-1A cast magnesium alloy region, the stress-strain and S-N curves are shown in Figures 3 and 4 respectively. The calculations giving the cumulative damage factor 0.2118909 for frequency band 2 are presented in Table V.

An important point is brought out by a consideration of the incremental damage factors illustrated in column 7 of Table V, namely, the reason for the  $4\sigma$  upper strain amplitude limit. Note that, with increasing strain amplitude the incremental damage factor grows rapidly to a maximum, and then tails off. This characteristic is typical of cases where the shape of the stress-strain and S-N curves are similar to those shown here, Figures 3 and 4, respec-

tively. It is typical that considerable damage remains at  $3\sigma$ , and that above  $4\sigma$  the incremental damage is negligible compared to the maximum incremental damage. For these reasons a  $4\sigma$  analysis was chosen.

Continuing with the example, the cumulative damage factor for frequency band 1 is 0.0015210, calculated similarly to that for band 2. The total cumulative damage factor is then  $0.2118909 + 0.0015210 = 0.2134119$ , and the expected fatigue life is  $1/0.2134119 = 4.69$  hours for the structure in question in the random vibration environment represented by the response strain density spectrum of Figure 1.

The calculation procedure for the basic method, applicable to a general case, has been prepared for computer processing. A FORTRAN IV program for the procedure is found in Appendix 2. The program is self explanatory.

For comparison purposes, and the comparison is offered with some apology, the actual measured fatigue life of the structure in question, nominally with the same response strain density spectrum as is shown in Figure 1, was 4.73

TABLE V.  
DAMAGE FACTOR PER HOUR, FREQUENCY BAND 2

1	2	3	4	5	6	7	
ZONE MIDPOINT TABLE 3	STRAIN AMPLITUDE, $\mu$ IN/IN = 346.4102 1	MAXIMUM STRESS, PSI FIGURE 3	ALLOW. REVERSALS H FIGURE 4	ZONAL PROBABILITY TABLE 3	PREDICTED REVERSALS PER HOUR 810,000 5	INCREMENTAL DAMAGE FACTOR PER HOUR 6 / 4	
0	0	Less than Endurance Limit (3500 PSI)	$\infty$	.079655675	64521.18	0	
0.2 $\sigma$	69.28204		$\infty$	.156167170	126495.4		
0.4 $\sigma$	138.2820			.147102078	119152.7		
0.6 $\sigma$	207.8461			.133147773	107849.7		
0.8 $\sigma$	277.1282			.115807059	93803.75		
1.0 $\sigma$	346.4102			.096788129	78398.39		
1.2 $\sigma$	415.6922			.077731153	62962.23		
1.4 $\sigma$	484.9743			$\infty$	.059986567	48589.12	0
1.6 $\sigma$	559.2563		3603.	$3.80 \cdot 10^6$	.044483477	36031.62	.009482005
1.8 $\sigma$	623.5384		3980.	.81	.031697806	25675.23	.03169781
2.0 $\sigma$	697.8204	4198.	.49	.021704278	17580.47	.03587851	
2.2 $\sigma$	762.1024	4410.	.33	.014280621	11567.30	.03505242	
2.4 $\sigma$	831.3845	4666.	.24	.009288889	7313.400	.03047250	
2.6 $\sigma$	900.6665	4822.	.18	.005985383	4443.160	.02468422	
2.8 $\sigma$	969.9486	4975.	.15	.003202321	2593.880	.01729253	
3.0 $\sigma$	1039.231	5130.	.12	.001996420	1455.100	.01212583	
3.2 $\sigma$	1108.513	5265.	.11	.000968358	784.3700	.007130636	
3.4 $\sigma$	1177.795	5380.	.10	.000501590	406.2879	.004062879	
3.6 $\sigma$	1247.077	5482.	.09	.000249659	202.2238	.002246931	
3.8 $\sigma$	1316.319	5568.	.08	.000119407	96.71967	.001208996	
4.0 $\sigma$	1385.641	5641.	$.08 \cdot 10^6$	.000054878	44.45118	.0005556398	
SUM =					809966.7	SUM = .2118909 (Damage Factor per Hour)	

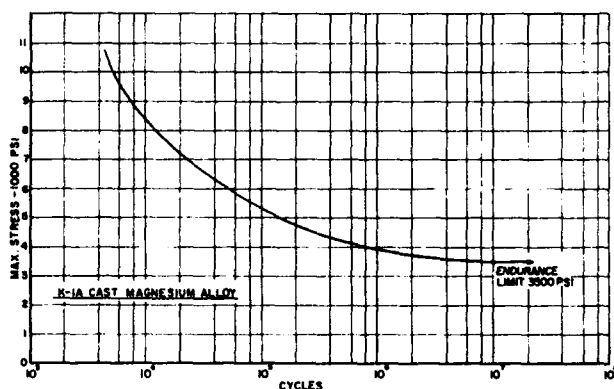


Figure 4. S-N Curve.

hours (one sample), as compared with the calculated expected (mean) value of 4.69 hours. The structure is an antenna subsystem, an extremely complex and expensive structure, part of the landing radar system for the lunar module (LM) used on Apollo missions. The landing radar system was designed and built by Ryan Aeronautical Company under subcontract to Radio Corporation of America (RCA).

It is cautioned that one should not draw important conclusions from this one sample "mean". Further work correlating a predicted mean to a valid experimentally determined mean is indicated. Also a study of the distribution of the experimental values of fatigue life about the mean, the standard deviation of fatigue life in particular, would be illuminating as regards such matters as confidence intervals for the predicted mean.

In the basic method, the point of departure treated so far is a response strain density curve. Figure 1 is an example. Instead, an alternative is offered by beginning with a real time record of response strain versus time from which the strain density spectrum may have been prepared. The real time record shows the positive and negative strain spikes over a relatively short time period.

In the case of a real time record of strain versus time, the number of strain spikes in various strain amplitude zones are counted directly. Positive and negative peaks are counted separately, either manually from a visual record, or electronically from a magnetic tape record. Electronic counting is accomplished with specialized equipment using gating circuitry. In each strain amplitude zone, the number of positive spikes and the number of negative spikes are averaged to give a zero mean, which must hold in the case of an indefinitely long time period. This average is, ratioed from the actual sample time up to the one hour reference time period, the predicted number of reversals per hour for each strain amplitude zone, each with a midpoint strain amplitude. Note that for each positive real time spike so averaged, there is a negative spike, one sign

reversal, one stress reversal. The ratioed up averages correspond to the predicted number of reversals per hour, Column 6 in Table V, which was estimated probabilistically from a point on the response strain density curve. However, in the present approach, in effect the entire spectrum is treated at once, rather than by identifying and considering separately only the fatigue procedure frequency bands of the spectrum as was done heretofore.

The remainder of this alternative approach to the basic method continues as before: For each midpoint strain amplitude, corresponding to Column 2, Table V, the maximum stress is determined from the stress-strain curve. These stresses correspond to Column 3, Table V. The S-N curve is entered at the maximum stresses to obtain the allowable number of reversals for each midpoint strain, corresponding to Column 4, Table V. For each midpoint strain amplitude, the predicted number of reversals is divided by the allowable number of reversals to obtain the incremental damage factor, corresponding to Column 7, Table V. The sum of the incremental damage factors gives the total damage factor per hour, and the reciprocal gives the required expected (mean) fatigue life in hours.

#### FIRST VARIATION OF BASIC METHOD, BY EXPERIMENTAL RESPONSE FUNCTION

In this variation of the basic method, instead of beginning with an experimentally determined response strain density curve, or a real time record of strain versus time, the response strain density curve is constructed analytically from:

1. The known power spectral density (PSD) curve for the driving function. The PSD curve represents the random vibration input to the structure.
2. The structural response function, failure area strain per g versus frequency for a sinusoidal input. The structural response function is obtained experimentally from a simple sinusoidal sweep test.

Basic to the present approach is the  $1\sigma$  strain integral

$$e_{1\sigma}^2 = \int_{f_1}^{f_2} \psi(f) |R(f)|^2 df \quad (3)$$

where  $e_{1\sigma} = 1_0$  strain level,  $\mu$  in/in

$\psi(f)$  = Input PSD,  $g^2/CPS$ , as a function of frequency, CPS

$|R(f)|$  = Structural response function, ( $\mu$  in/in)/g in terms of failure area strain. R is function of frequency, CPS.

$f_1$  and  $f_2$  = Lower and upper bounds respectively, of frequency band of interest, CPS.

Equation (3) is derived in Appendix 3.  $R(f)$ , in general, due to phase changes from damping, is complex valued. Its modulus (absolute value) is the structural response function required above. This modulus also is the ordinary response function measured experimentally in a sinusoidal sweep test.

Earlier we showed that

$$e_{1\sigma} = e_{RMS} = \sqrt{SD \cdot BW}$$

where  $SD$ ,  $(\mu \text{ in/in})^2/\text{CPS}$ , is the strain density over frequency bandwidth  $BW = f_2 - f_1$ , CPS.

Solving this equation for  $SD$ ,

$$SD = e_{1\sigma}^2 / BW \quad (4)$$

where  $e_{1\sigma}^2$  is given by equation (3).

To construct the response strain density curve, we choose a center frequency and bandwidth, from which  $f_1$  and  $f_2$  are determined. We perform the integration indicated in equation (3) over the bandwidth to obtain  $e_{1\sigma}^2$ , and divide by the bandwidth, according to equation (4), to obtain the strain density at the center frequency selected. We then choose another center frequency, with a corresponding bandwidth (which may or may not overlap the first bandwidth) and repeat the process for a number of center frequencies until the response strain density curve is well defined. Computer processing of the repetitive integrations is indicated.

Armed with the response strain density curve, the procedure for calculating the expected (mean) fatigue life follows precisely as indicated before for the basic method.

This approach, the first variation of the basic method, appears to yield, for complicated structures, the most results for the least time and money expenditure.

#### SECOND VARIATION OF BASIC METHOD, BY ANALYTICAL RESPONSE FUNCTION

In this variation of the basic method, the procedure parallels precisely that for the first variation, except that the structural response function  $|R(f)|$ ,  $(\mu\text{in/in})/g$ , is cal-

culated for an existing design rather than determined experimentally from actual or simulated hardware. The calculation of  $R(f)$ , complex valued, in the current state-of-the-art, is based upon superposition of normal modes with a lg sinusoidal driving function, and with representative damping. A lumped mass mathematical model in many cases is feasible. There are several all-purpose structural programs (FORMAT, SAMIS and the upcoming NASTRAN are three of them) that are aids in this work, but the mathematical modeling and calculation processing are extremely involved and exacting for useful results in complicated structures.

A full treatment of a modal analysis is beyond the scope of the present paper. However, a few remarks are offered. There are three major problem areas in modal analysis:

1. *The mathematical modeling.* Great skill, experience and judgement is required in this phase, and a relatively large budgetary expenditure in the mathematical modeling phase will pay off large dividends.

2. *Damping.* There are those who claim, because structural dampings are "small", that a single over-all equivalent viscous damping ratio can be assigned, more or less arbitrarily (or perhaps a series of such ratios, modal frequency dependent) and a straight-forward linear analysis can then proceed. In point of fact, this view holds only for the simplest of structures and for the simplest of dynamic loadings. Representative damping in complicated structures under random vibration environments is important and sophisticated. The subject deserves careful consideration.

3. *Computer implementation.* Computer aspects of engineering problems are often largely taken for granted, especially by those who have never actually solved a large problem by computer. Implementation of a modal analysis program such as segments of FORMAT or SAMIS (NASTRAN will be even more complicated), is a very difficult intricate task requiring great skill, patience and understanding of the inner workings of the program. It is not unusual to spend several months with SAMIS before beginning a problem for the first time. Computer implementation of large structural problems just cannot be done on a push button basis.

#### REFERENCES

1. *Handbook of Mathematical Functions*, pp. 966-972, NBS-AMS-55, U.S. Government Printing Office, Washington, D.C. (1965).
2. S.H. Crandall and W.D. Mark, *Random Vibration*, pp. 67-72, Academic Press, New York (1963).
3. E. Kreyzig, *Advanced Engineering Mathematics*, 2nd ed., pp. 759-762, John Wiley, New York (1967).

**APPENDIX 1**  
**THE EQUALITY OF  $e_{RMS}$  AND  $e_{1\sigma}$**

If  $x$  is a distributed variable having  $N$  discrete values  $x_i$ ;  $i = 1, 2, \dots, N$ ; then the root mean square (RMS) of  $x$  is defined by:

$$RMS = x_{RMS} = \frac{1}{N} \sqrt{\sum_{i=1}^N (x_i)^2}$$

and the standard deviation of  $x$  about its mean  $\bar{x} \equiv \frac{1}{N} \sum_{i=1}^N x_i$  is defined by:

$$\sigma = x_{1\sigma} = \frac{1}{N-1} \sqrt{\sum_{i=1}^N (x_i - \bar{x})^2}$$

If  $\bar{x}$  is *not* derived from the  $x_i$  values, but rather is specified, then the  $N-1$  in the denominator of the equation becomes  $N$  since the one statistical degrees of freedom lost in computing  $\bar{x}$  from the  $x_i$  values has been regained. Further, if  $\bar{x}$  is specified to be zero valued, then the  $\sigma$  equation becomes

$$\sigma = x_{1\sigma} = \frac{1}{N} \sqrt{\sum_{i=1}^N (x_i)^2}$$

Noting equality of the right hand sides of the RMS equation and the  $\sigma$  equation with  $\bar{x}$  specified zero, we have

$$x_{RMS} = x_{1\sigma}, \bar{x} = 0.$$

In the case at hand  $x$  is signed peak strain  $e$ , a discrete distributed variable. A large real time sample of strain versus time shows that the values of  $e$  are distributed symmetrically about a zero mean, that in any strain zone with interval  $(e_2 - e_1)$ ,  $e_2 > e_1$ , the number of positive values of  $e$  in the interval  $(e_2 - e_1)$  is found to be equal to the number of negative values of  $e$  in the interval  $-(e_2 - e_1)$ . Thus we specify  $\bar{e} = 0$  and  $e_{RMS} = e_{1\sigma}$ ,  $\bar{e} = 0$ .

In point of fact,  $e_{RMS}$  and  $e_{1\sigma}$  are defined by the same equation, for zero mean.

APPENDIX 2

FORTTRAN IV PROGRAM FOR BASIC METHOD

LEVEL 18 ( SEPT 69 )

05/360 FORTRAN H

DATE 70.217/07.59.55

COMPILER OPTIONS - NAME= MAIN,OPT=00,LINECNT=59,SOURCE,EBCDIC,NOLIST,NODECK,NOLOAD,MAP,NOEDIT,IO,XREF

C JOB NO 1008

C EXPECTED FATIGUE LIFE, RANDOM VIBRATION

C ROUTINE CALCULATES EXPECTED TIME TO FAILURE, GIVEN STRAIN DENSITY

C SPECTRUM IN FAILURE AREA, S-N CURVE FOR MATERIAL, AND STATIC

C STRESS-STRAIN CURVE FOR MATERIAL.

C DIMENSION DATEC(18),FR(20),SD(20),BW(20),RE(20),SS(20),SN(20),  
1ST(20),ET(20),PR(21),SX(1),EX(1),EZ(21),ZN(21),SZ(21),QN(21)

C ENTER PR VECTOR, INVARIANT CONSTANTS

ISN 0002 PR( 1)=7.965568E-02  
ISN 0003 PR( 2)=1.561672E-01  
ISN 0004 PR( 3)=1.471021E-01  
ISN 0005 PR( 4)=1.331478E-01  
ISN 0006 PR( 5)=1.156071E-01  
ISN 0007 PR( 6)=9.678813E-02  
ISN 0008 PR( 7)=7.773115E-02  
ISN 0009 PR( 8)=5.998657E-02  
ISN 0010 PR( 9)=4.448348E-02  
ISN 0011 PR(10)=3.169781E-02  
ISN 0012 PR(11)=2.170428E-02  
ISN 0013 PR(12)=1.428062E-02  
ISN 0014 PR(13)=9.028889E-03  
ISN 0015 PR(14)=5.485383E-03  
ISN 0016 PR(15)=3.202321E-03  
ISN 0017 PR(16)=1.796420E-03  
ISN 0018 PR(17)=9.683580E-04  
ISN 0019 PR(18)=5.015900E-04  
ISN 0020 PR(19)=2.496590E-04  
ISN 0021 PR(20)=1.194070E-04  
ISN 0022 PR( 21)=5.487800E-05

C PR-VECTOR OF ZONAL PROBABILITIES=PROBABILITIES THAT THE ABSOLUTE  
C VALUE OF A RANDOM STRAIN PEAK WILL LIE IN STRAIN ZONES 0 TO 0.1  
C SIGMA, .1 TO .3 SIGMA UP TO THE ZONE 3.9 TO 4.1 SIGMA. THE 1ST  
C ZONE IS HALF THE WIDTH OF THE OTHERS. A NORMAL (GAUSSIAN)  
C PROBABILITY DISTRIBUTION CURVE IS ASSUMED.

C STATISTICALLY, THE RMS STRAIN IN A SAMPLE IS EQUAL TO THE 1.0  
C SIGMA STRAIN, SINCE THE MEAN OF ALL POSITIVE AND NEGATIVE STRAIN  
C PEAKS IN A SAMPLE STATISTICALLY IS ZERO, AND THE NUMBER OF STRAIN  
C PEAKS IS LARGE.

C WRITE TITLES, READ AND WRITE INPUTS.

C 10 REAC(5,1000,END=5000) DATEC  
C 1000 FORPAT(18A4)

C WRITE(6,1010) DATEC

C 1010 FORPAT('JOB NO 1008, EXPECTED FATIGUE LIFE, RANDOM VIBRATION'///  
C 1 18A4///  
C 2 DENSITY, 5X, SAMPLE BANDWIDTH, 7X, RMS STRAIN/12X, CPS, 12X, (UI  
C 3N/IN)\*2/CPS, 10X, CPS, 16X, UIN/IN)

C THE LETTER U IS USED TO SIGNIFY 'MICRO', MEANING .10 TO THE MINUS  
C 6TH.

ISN 0024  
ISN 0025  
ISN 0026  
ISN 0027

SN 0028  
SN 0029  
C REAC(5, 1020) NF, NS, NT  
1020 FORMAT(3I10)  
C NF=NUMBER OF POINTS INPUTTED FROM STRAIN DENSITY SPECTRUM.  
C NS=NUMBER OF POINTS INPUTTED FROM S-N CURVE.  
C NT=NUMBER OF POINTS INPUTTED FROM STRESS-STRAIN CURVE.  
C NF, NS AND NT MUST NOT EXCEED 20 IN THE PRESENTLY DIMENSIONED  
FOR P. NS AND NT MUST BE AT LEAST 4, A REQUIREMENT OF SURROUTINE  
C SPLINE.  
C DO 30 I=1, NF  
ISN 0030 REAC(5, 1030) FR(I), SD(I), BW(I)  
ISN 0031 RE(I)=SQRT(SD(I)\*BW(I))  
ISN 0032 20 WRITE(6, 1040) FR(I), SD(I), BW(I), RE(I)  
ISN 0033 1030 FORMAT(1P3E20.6)  
ISN 0034 1040 FORMAT(1P4E20.6)  
ISN 0035  
C FR= VECTOR OF FREQUENCIES INPUTTED FROM STRAIN DENSITY SPECTRUM,  
C CPS. FR VALUES ARE MIDPOINT FREQUENCIES OF THE VARIOUS  
C FREQUENCY BANDS SAMPLED.  
C SD= VECTOR OF INPUTTED STRAIN DENSITIES, (UIN/IN)\*\*2/CPS,  
C CORRESPONDING TO FR VALUES.  
C BW= VECTOR OF INPUTTED BANDWIDTHS, CPS, CORRESPONDING TO FR VALUES.  
C IMPORTANT. SEE PROGRAM WRITEUP FOR INSTRUCTIONS ON CHOICE OF  
C POINTS AND BANDWIDTHS, AND HOW TO READ FR, SD AND BW VALUES FROM  
C THE STRAIN DENSITY SPECTRUM.  
C STRAIN DENSITY POINTS MAY BE INPUTTED IN ANY ORDER.  
C RE= VECTOR OF RMS STRAINS, UEN/IN, FOR THE VARIOUS FREQUENCY BANDS  
C SAMPLED. RE IS CALCULATED INTERNALLY.  
C  
C WRITE(6, 1050)  
ISN 0036 FORMAT(0'/'/' S-N DATA'/'7X,'PEAK STRESS S',4X,'ALLOWABLE REVERSAL  
ISN 0037 IS N'/12X,'PSI',13X,'DIMENSIONLESS')  
ISN 0038 REAC(5, 1060) SS(NS), SM(NS)  
ISN 0039 FORMAT(1P2E20.6)  
ISN 0040 WRITE(6, 1070) SS(NS), SM(NS)  
ISN 0041 FORMAT(1P2E20.6, 5X, 'ULTIMATE TENSILE')  
ISN 0042 NN=AS-2  
ISN 0043 DO 30 I=1, NN  
ISN 0044 J=NS-I  
ISN 0045 REAC(5, 1060) SS(J), SM(J)  
ISN 0046 30 WRITE(6, 1060) SS(J), SM(J)  
ISN 0047 REAC(5, 1060) SS(1), SM(1)  
ISN 0048 WRITE(6, 1080) SS(1), SM(1)  
ISN 0049 FORMAT(1P2E20.6, 5X, 'ENDURANCE LIMIT')  
C SS= VECTOR OF STRESSES INPUTTED FROM S-N CURVE, PSI.  
C SM= VECTOR OF INPUTTED N VALUES CORRESPONDING TO SS VALUES,  
C DIMENSIONLESS, FLOATING POINT. AN N VALUE IS THE ALLOWABLE  
C NUMBER OF STRESS REVERSALS AT A PARTICULAR PEAK SINUSOIDAL  
C STRESS LEVEL S.  
C THE FIRST S-N POINT MUST BE AT S=ULTIMATE TENSILE STRESS, WITH

```

C N=0.
C THE LAST S-N POINT MUST BE WHERE THE S-N CURVE FIRST BECOMES
C HORIZONTAL (AT S-ENDURANCE LIMIT).
C
C ALL S-N INPUT POINTS MUST BE ORDERED SEQUENTIALLY WITH RESPECT TO
C DECREASING STRESS (INCREASING N), A NATURAL ARRANGEMENT. S-N DATA
C READ AND WRITE INSTRUCTIONS ARE EXECUTED IN THIS ORDER.
C HOWEVER, INTERNALLY S-N DATA ARE STACKED AND PROCESSED IN REVERSE
C ORDER. SUBROUTINE SPLINE REQUIRES THAT THE INDEPENDENT VARIABLE
C BE IN INCREASING SEQUENTIAL ORDER. NEAR STATEMENT 140 STRESS SS
C IS THE INDEPENDENT VARIABLE, HENCE THE REVERSED ORDER OF S-N DATA.
C
ISN 0050 WRITE(6,1095)
ISN 0051 1085 FORPAT('0'/'/' STRESS-STRAIN DATA,'/8X,'STRESS, PSI',8X,'STRAIN, UI
IN/IN')
ISN 0052 DO 40 I=1,NT
ISN 0053 40 REAC(5,1060) ST(I),ET(I)
ISN 0054 WRITE(6,1090) ST(1),ET(1)
ISN 0055 1090 FORPAT(IP2E20,6,5X,'ORIGIN')
ISN 0056 WRITE(6,1100) ST(2),ET(2)
ISN 0057 1100 FORPAT(IP2E20,6,5X,'PROPORTIONAL LIMIT')
ISN 0058 NN=NT-1
ISN 0059 DO 50 I=3,NN
ISN 0060 50 WRITE(6,1060) ST(I),ET(I)
ISN 0061 WRITE(6,1070) ST(NT),ET(NT)
C
C ST=VECTOR OF STRESSES INPUTTED FROM STRESS-STRAIN CURVE, PSI.
C ET=VECTOR OF INPUTTED STRAINS CORRESPONDING TO ST VALUES, UIN/IN.
C
C THE 1ST STRESS-STRAIN POINT MUST BE AT THE ORIGIN (0,0).
C THE 2ND STRESS-STRAIN POINT MUST BE AT THE PROPORTIONAL LIMIT.
C THE LAST STRESS-STRAIN POINT MUST BE AT THE ULTIMATE TENSILE
C STRESS.
C ALL STRESS-STRAIN POINTS MUST BE ORDERED WITH RESPECT TO
C INCREASING STRESS(AND STRAIN), A NATURAL ARRANGEMENT.
C
ISN 0062 WRITE(6,1110)
ISN 0063 1110 FORPAT('0'/'/7X,'STRAIN DENSITY',6X,'DAMAGE FACTOR',8X,'POINT NUMBE
IR',5X,'PER HOUR')
ISN 0064 DF=C.
ISN 0065 KK=C
C
C DF=CUMULATIVE DAMAGE FACTOR. WHEN DF REACHES 1.0, FATIGUE FAILURE
C THEORETICALLY OCCURS. SEE BELOW NEAR STATEMENT 150 FOR FURTHER
C COMMENTS ON DF.
C KK=CONTROL NUMBER FOR 1ST EXCURSION TYPE FAILURE.
C
ISN 0066 EE=ST(2)/ET(2)
C
C EE=MODULUS OF ELASTICITY TIMES 10 TO THE MINUS 6TH.
C
C CALCULATE PARAMETERS UU AND WW.
C
C UU=NUMERATOR OF FATIGUE BOUNDARY EQUATION, STRAIN SQUARED.
C WW=NUMERATOR OF 1ST EXCURSION BOUNDARY EQUATION, STRAIN SQUARED.
C
C IF THE STRAIN DENSITY IS EVERYWHERE BELOW THE FATIGUE BOUNDARY,

```

```

C THEN FATIGUING DOES NOT OCCUR. IF THE STRAIN DENSITY IS
C SOMEWHERE ABOVE THE 1ST EXCURSION BOUNDARY, THE FAILURE IS OF
C THE 1ST EXCURSION (IMMEDIATE) TYPE. IN THIS CASE KK=1.
C OTHERWISE KK=0.
C
C IT IS REQUIRED THAT THE ENDURANCE LIMIT STRESS SS(1) BE LESS THAN
C THE PROPORTIONAL LIMIT STRESS ST (2) PHYSICALLY THIS CONDITION IS
C MET IN ALL KNOWN CASES.
C
C UU=(SS(1)/(4.*EE))**2
C WM=(ET(NT)/4.)***2
C
C ENTER MAIN (180) LOOP, CALCULATE AND ACCUMULATE INCREMENTS OF
C DAMAGE FACTOR DF.
C
C DO 100 I=1,NF
C DD=0.
C
C DC=DAMAGE FACTOR FOR STRAIN DENSITY POINT I.
C
C IF(SD(1).LE.UU/8M(1)) GO TO 160
C IF(SD(1).GE.WM/8M(1)) GO TO 170
C FA=3600.*FR(I)
C
C FA=TOTAL NUMBER OF CYCLES (REVERSALS) IN A FREQUENCY BAND SAMPLE
C FOR A 1.0 HOUR REFERENCE TIME PERIOD. FA IS SIMPLY THE
C MIDPOINT FREQUENCY OF THE SAMPLE, IN CPS, MULTIPLIED BY THE
C NUMBER OF SECONDS (3600) IN ONE HOUR.
C
C DZ=0.2*RE(I)
C XZ=0.
C DO 60 J=1,21
C EZ(J)=XZ
C ZN(J)=FA*PR(J)
C
C 60 XZ=XZ+DZ
C
C EZ=VECTOR OF MIDPOINT STRAINS (PEAK) FOR THE VARIOUS STRAIN ZONES
C OF THE NORMAL PROBABILITY DISTRIBUTION CURVE, UIN/IN.
C ZN=VECTOR OF EXPECTED NUMBER OF REVERSALS IN THE STRAIN ZONES,
C FOR A 1.0 HOUR REFERENCE TIME PERIOD. THE TOTAL OF ZN VALUES
C IS CLOSELY EQUAL TO FA.
C
C CALCULATE STRESSES SZ IN STRAIGHT LINE PORTION OF STRESS-STRAIN
C CURVE.
C
C SZ=VECTOR OF STRESSES (PEAK) CORRESPONDING TO ZONE MIDPOINT
C STRAINS EZ.
C
C DO 70 J=1,21
C IF(EZ(J).GT.ET(2)) GO TO 80
C SZ(J)=EE*EZ(J)
C
C 70 GO TO 110
C
C INTERPOLATE BY SPLINE FIT ON STRESS-STRAIN CURVE (ST AND ET
C VALUES) TO STRESSES SZ CORRESPONDING TO ZONAL MIDPOINT STRAINS EZ
C IN PLASTIC RANGE.
    
```

ISM 0067  
ISM 0068

ISM 0069  
ISM 0070

ISM 0071  
ISM 0073  
ISM 0075

ISM 0076  
ISM 0077  
ISM 0078  
ISM 0079  
ISM 0080  
ISM 0081

ISM 0082  
ISM 0083  
ISM 0085  
ISM 0086



```

C C SUBROUTINE SPLINE IS PART OF JOB NO. 1250.
C C
C C 80 L=J-1
C C J=22-J
C C DO 50 K=1,JJ
C C QN(K)=EZ(K+L)
C C CALL SPLINE(ET,ST,NT,QN,EZ,JJ)
C C
C C QN AND EZ ARE USED HERE AS TEMPORARY STORAGE VECTORS.
C C
C C DO 100 K=J,21
C C SZ(K)=EZ(K-L)
C C
C C INTERPOLATE BY SPLINE FIT ON S-N CURVE (SS AND SN VALUES TO
C C QN VALUES CORRESPONDING TO SZ VALUES ABOVE ENDURANCE LIMIT ONLY.
C C THOSE ZONES WHOSE SZ VALUES ARE LESS THAN OR EQUAL TO THE
C C ENDURANCE LIMIT DO NOT CONTRIBUTE TO DAMAGE FACTOR DF.
C C
C C QN=VECTOR OF ALLOWABLE NUMBER OF REVERSALS CORRESPONDING TO THOSE
C C ZONAL PEAK STRESSES SZ THAT ARE ABOVE THE ENDURANCE LIMIT.
C C
C C 110 DO 120 J=1,21
C C IF(SZ(J).GT.SS(1)) GO TO 130
C C 120 CONTINUE
C C GO TO 180
C C 130 L=J-1
C C JJ=22-J
C C DO 140 K=1,JJ
C C EZ(K)=SZ(K+L)
C C
C C EZ IS USED HERE AS A TEMPORARY STORAGE VECTOR.
C C
C C CALL SPLINE(SS,SN,NS,EZ,QN,JJ)
C C
C C ACCUMULATE DAMAGE FACTOR DF AND END MAIN (180) LOOP.
C C
C C THE INCREMENTAL DAMAGE FACTOR FOR EACH STRAIN ZONE IS THE EXPECTED
C C NUMBER OF REVERSALS Z: FOR THE ZONE DIVIDED BY THE ALLOWABLE
C C NUMBER OF REVERSALS QN FOR THE ZONE.
C C
C C DO 190 K=1,JJ
C C IF(QN(K).LE.0.) GO TO 170
C C 190 DC=CD+Z*(K+L)/QN(K)
C C DF=DF+DC
C C 160 WRITE(6,1120) I,DD
C C 1120 FORPAT(115,1PE23.6)
C C GO TO 180
C C 170 KK=1
C C WRITE(6,1130) I
C C 1130 FORPAT(115,13X,'FIRST EXCURSION FAILURE')
C C 180 CONTINUE
C C
C C IF(KK.EQ.1) GO TO 190
C C IF(DF.EQ.0.) GO TO 200
C C HRS=1./DF
C C WRITE(6,1140) HRS
C C 1140 FORPAT(0,'//',EXPECTED FATIGUE LIFE IS',1PE13.6,' HOURS.')

```

ISN 0087  
ISN 0088  
ISN 0089  
ISN 0090  
ISN 0091

ISN 0092  
ISN 0093

ISN 0094  
ISN 0095  
ISN 0097  
ISN 0098  
ISN 0099  
ISN 0100  
ISN 0101  
ISN 0102

ISN 0103

ISN 0104  
ISN 0105  
ISN 0107  
ISN 0108  
ISN 0109  
ISN 0110  
ISN 0111  
ISN 0112  
ISN 0113  
ISN 0114  
ISN 0115

ISN 0116  
ISN 0118  
ISN 0120  
ISN 0121  
ISN 0122

```

ISM 0123
ISM 0124
ISM 0125
    GO TO 10
    190 WRITE(6,1150)
    1150 FORPAT(0, '//', EXPECTED FAILURE IS OF THE FIRST EXCURSION (IMMEDIAT
    IE) TYPE. '// SEE TABLE IMMEDIATELY PRECEDING FOR IDENTIFICATION OF
    2CRITICAL STRAIN DENSITY POINTS. ')
    GO TO 10
ISM 0126
ISM 0127
ISM 0128
    200 WRITE(6,1160)
    1160 FORPAT(0, '//', STRAIN DENSITY SPECTRUM IS INSUFFICIENT TO CAUSE FAT
    1IGUE FAILURE, EVEN FOR AN INDEFINITELY LONG TIME PERIOD. ')
    GO TO 10
ISM 0129
ISM 0130
ISM 0131
ISM 0132
    5000 CALL EXIT
    STOP
    END

```

LEVEL 18 ( SEPT 69 ) OS/360 FORTRAN H DATE 70.217/08.00.26

COMPILER OPTIONS - NAME= MAIN,OPT=00,LINECNT=59,SOURCE,EBCDIC,NOLIST,NODECK,NOLOAD,MAP,NODEDIT,IO,XREF  
 SUBROUTINE SPLINE(XX,YY,P,XA,YA,N)

ISN 0002 C SUBROUTINE INTERPOLATES OR EXTRAPOLATES A GIVEN X,Y TABLE TO  
 C VALUES OF Y AT A GIVEN DIFFERENT SET OF X VALUES.  
 C  
 C METHOD IS BY SPLINE FIT, REFERENCE R.H. PENNINGTON, INTRODUCTORY  
 C COMPUTER METHODS AND NUMERICAL ANALYSIS, MACMILLAN 1965,  
 C PAGES 404-411.  
 C  
 C XX(I) IS ARGUMENT OF ITH VALUE YY(I) OF GIVEN FUNCTION, I=1 TO M.  
 C XA(K) IS GIVEN ARGUMENT OF KTH VALUE YAK) TO BE COMPUTED, K=1 TO N  
 C  
 C NEITHER XX NOR XA NEED BE AT EQUAL INTERVALS. HOWEVER, THE INPUT  
 C TABLE YY=F(XX) MUST BE ARRANGED IN INCREASING SEQUENTIAL ORDER  
 C WITH RESPECT TO XX. THE OUTPUT ARGUMENT XA MAY BE IN ANY ORDER.  
 C  
 C M IS NUMBER OF VALUES OR XX OR YY.  
 C N IS NUMBER OF VALUES OR XA OR YA.  
 C NEITHER M NOR N CAN EXCEED 100.

WARNING - THE EXTRAPOLATION MODE, DEPENDING ON THE FUNCTION BEING  
 TREATED, MAY BE GROSSLY IN ERROR FOR LARGE EXTRAPOLATION INTERVAL.

ISN 0003 C DIMENSION XX(100),YY(100),XA(100),YA(100),D(100),P(100),E(100),  
 C IC(4,100),A(100,3),B(100),Z(100)

COMPUTE COEFFICIENTS C OF SPLINE FIT SEGMENTS

ISN 0004 MN=M-1  
 ISN 0005 DO 2 I=1,MN  
 ISN 0006 D(I)=XX(I+1)-XX(I)  
 ISN 0007 P(I)=D(I)/6.  
 ISN 0008 2 E(I)=(YY(I+1)-YY(I))/D(I)  
 ISN 0009 DO 4 I=2,MN  
 ISN 0010 4 B(I)=E(I)-E(I-1)  
 ISN 0011 A(1,2)=-1.-D(1)/D(2)  
 ISN 0012 A(1,3)=D(1)/D(2)  
 ISN 0013 A(2,3)=P(2)-P(1)\*A(1,3)  
 ISN 0014 A(2,2)=2.\*(P(1)+P(2))-P(1)\*A(1,2)  
 ISN 0015 A(2,3)=A(2,3)/A(2,2)  
 ISN 0016 B(2)=B(2)/A(2,2)  
 ISN 0017 DO 6 I=3,MN  
 ISN 0018 A(I,2)=2.\*(P(I)-1)+P(I)-P(I-1)\*A(I-1,3)  
 ISN 0019 B(I)=B(I)-P(I-1)\*B(I-1)  
 ISN 0020 A(I,3)=P(I)/A(I,2)  
 ISN 0021 6 B(I)=B(I)/A(I,2)  
 ISN 0022 Q=D(M-2)/D(M-1)  
 ISN 0023 A(M,1)=1.+Q\*A(M-2,3)  
 ISN 0024 A(M,2)=-Q\*A(M,1)\*A(M-1,3)  
 ISN 0025 B(M)=B(M-2)-A(M,1)\*B(M-1)  
 ISN 0026 Z(M)=B(M)/A(M,2)  
 ISN 0027 MN=M-2  
 ISN 0028 DO 6 I=1,MN  
 ISN 0029 J=M-I  
 ISN 0030 6 Z(J)=B(J)-A(J,3)\*Z(J+1)

```

ISM 0031      Z(I)=A(I,2)*Z(2)-A(I,3)*Z(3)
ISM 0032      DO 10 I=1,M
ISM 0033      Q=1/(6.*D(I))
ISM 0034      C(1,I)=Z(I)*Q
ISM 0035      C(2,I)=Z(I+1)*Q
ISM 0036      C(3,I)=Y(I)/D(I)-Z(I)*P(I)
ISM 0037      C(4,I)=Y(I+1)/D(I)-Z(I+1)*P(I)

C
C
C      INTERPOLATE OR EXTRAPOLATE TO VALUES OF FUNCTION AT ARGUMENTS X A
DO 28 K=1,N
IF (XA(K)-XX(1)) 12,14,16
12 I=1
GO TO 26
14 YA(K)=YY(I)
GO TO 28
16 I=1
18 IF (XA(K)-XX(I+1)) 26,20,22
20 YA(K)=YY(I+1)
GO TO 28
22 I=I+1
24 IF (I-M) 18,24,24
24 I=I-1
26 YA(K)=(XX(I+1)-XA(K))*(C(1,I))*(XX(I+1)-XA(K))*2+C(3,I)
1+(XA(K)-XX(I))*(C(2,I))*(XA(K)-XX(I))*2+C(4,I)
28 CONTINUE
RETURN
END
ISM 0038
ISM 0039
ISM 0040
ISM 0041
ISM 0042
ISM 0043
ISM 0044
ISM 0045
ISM 0046
ISM 0047
ISM 0048
ISM 0049
ISM 0050
ISM 0051
ISM 0052
ISM 0053
ISM 0054

```

### APPENDIX 3 DERIVATION OF $e_{1\sigma}^2$ INTEGRAL

The usual derivation of the  $e_{1\sigma}^2$  integral, see for example Reference 2, follows from a knowledge of the autocorrelation function of the response, the spectral density of the response and the relationship between input and response spectral densities. In the present derivation we adopt a different less difficult point of view, and arrive at the same final equation.

Let  $\psi(f)$  be the given input power spectral density (PSD),  $g^2/\text{CPS}$ , a function of frequency  $f$ , CPS, defined over the limits  $f_1$  to  $f_2$  ( $f_2 > f_1$ ).

Also let  $|R(f)|$  be the measured structural (strain) response function,  $(\mu \text{ in/in})/g$  in terms of internal strains in a  $lg$  (peak) sinusoidal environment.  $|R(f)|$  is similar to the complex valued response function  $H(\omega)$  in theoretical structural mechanics.

For a continuous distributed variable  $x$ , the variance  $\sigma^2$  is defined, for example in Reference 3, by

$$\sigma^2 = \int_{-\infty}^{\infty} (x-\mu)^2 f(x) dx,$$

where  $f(x)$  is the probability density function of  $x$ , similar to  $f(z)$ , Figure 2.  $f(x)$  may be thought of as a weighting function for  $(x-\mu)^2$ .  $\mu$  is the mean of the continuous distributed variable  $x$ . For a symmetric distribution of  $x$  about  $x = 0$  which we assume here,  $\mu = 0$ .

In the case at hand,  $\sigma^2$ , which means  $(x = 1\sigma)^2$  or  $x_{1\sigma}^2$  is  $e_{1\sigma}^2$ .  $f(x)$  in the notation at hand is  $\phi(e)$ . We use  $\phi$  instead of  $f$  so as not to confuse the symbology with frequency  $f$ . Also  $x$  is signed peak strain  $e$ , here envisioned as a continuous distributed variable defined over the interval  $(e_2 - e_1)$ ,  $e_2 > e_1$ . The strain variance over the interval, with  $\mu = 0$ , then is

$$e_{1\sigma}^2 = \int_{e_1}^{e_2} e^2 \phi(e) de \quad (5)$$

The units of  $e_{1\sigma}^2$  are  $(\mu \text{ in/in})^2$ , and consistency of units gives

$$(\mu \text{ in/in})^2 = (\mu \text{ in/in})^2 \cdot \phi(e) \cdot (\mu \text{ in/in}).$$

Thus, the units of the probability density function  $\phi(e)$  are  $1/(\mu \text{ in/in})$ .

We now change the variable of integration from response strain  $e$  to input frequency  $f$ , noting that  $e$  is a

function of  $f$ , where the input is envisioned as sinusoidal. Equation (5) then becomes

$$e_{1\sigma}^2 = \int_{f_1}^{f_2} g(f) df \quad (6)$$

where  $g(f)$  is as yet undefined.

Dimensional consistency in equation (6) gives

$$(\mu \text{ in/in})^2 = g(f) \cdot \text{CPS}.$$

Thus the units of  $g(f)$  are  $(\mu \text{ in/in})^2/\text{CPS}$  which are also the units of strain density.  $g(f)$  is the instantaneous response strain density as can be seen by writing equation (6) in different form:

Let  $\bar{g}(f)$  be the average (mean) value of  $g(f)$  over the interval  $(f_2 - f_1)$ ,  $f_2 > f_1$ , defined by

$$\bar{g}(f) = \frac{\int_{f_1}^{f_2} g(f) df}{f_2 - f_1} = \frac{\int_{f_1}^{f_2} g(f) df}{\text{BW}}$$

$$\text{or} \quad \int_{f_1}^{f_2} g(f) df = \bar{g}(f) \cdot \text{BW}$$

Then equation (6) can be written

$$e_{1\sigma}^2 = e_{\text{RMS}}^2 = \bar{g}(f) \cdot \text{BW}, \quad \bar{e} = 0$$

or

$$e_{\text{RMS}} = \sqrt{\bar{g}(f) \cdot \text{BW}}$$

which is the familiar and fundamental response relationship

$$e_{\text{RMS}} = \sqrt{\text{SD} \cdot \text{BW}}$$

where  $\text{SD} = \bar{g}(f)$ , the average response strain density over the interval  $(f_2 - f_1)$ ,  $f_2 > f_1$ .

The instantaneous response strain density  $g(f)$  may also be expressed in terms of the measured output-input relationship by

$$g(f) = \psi(f) \cdot |R(f)|^2, \quad (7)$$

where  $\psi(f)$  is the input PSD,  $g^2/\text{CPS}$  and  $|R(f)|$  is the measured strain response function,  $(\mu \text{ in/in})/g$ , both defined previously.  $|R(f)|$  can be thought of as a transfer function and units changer. Note, by comparison of equations (5) and

(6), that the probability density function  $\phi(e)$  is "built into"  $|R(f)|$ . Dimensional consistency requires  $|R(f)|$  to be squared in equation 7, as follows:

$$\frac{(\mu \text{ in/in})^2}{\text{CPS}} \rightarrow \frac{g^2}{\text{CPS}} \cdot \left( \frac{\mu \text{ in/in}}{g} \right)^2 .$$

Thus, substituting equation (7) into equation (6), we obtain the  $e_{1\sigma}^2$  integral, equation (3) used previously.

$$e_{1\sigma}^2 = \int_{f_1}^{f_2} \Psi(f) |R(f)|^2 df$$

# IMPENDING FATIGUE FAILURE DETECTION BY OPTICAL CORRELATION

by

E. Marom and R.K. Mueller

Bendix Research Laboratories  
Southfield, Michigan

## INTRODUCTION

Material fatigue in structures remains the most common cause of service failure. Therefore, numerous investigations have been carried out for the purpose of developing methods that detect impending fatigue. However, no systematic methods could be found for this purpose since changes in the material microstructure during stress result in a "history" effect which in turn affects the specimen's life. The nonhomogeneity and the randomness of microstructures require a method that allows each specimen to be examined independently. In addition, the method must be sensitive enough to detect or evaluate the changes leading to fatigue and to predict impending catastrophic failure.

In the past, various methods for fatigue detection have been proposed. The most widely used method is the penetration technique, a mechanical test in which the inspected area is covered with a commercial penetrant. After proper development and surface cleaning, the penetrant accumulated in the cracks can be visually observed by means of ultraviolet irradiation. Other schemes involve the detection of infrared, ultrasonic, optical, microwave, or  $\gamma$ -ray radiation, which is scattered from an irradiated specimen or, in a passive mode, generated at propagating cracks.

The advent of the laser, with its capability to produce an intense coherent beam of light, has provided the means for improving and developing inspection techniques. Optical interferometry of diffuse arbitrary surfaces and optical correlation (pattern recognition) are the two schemes evolving from lasers and holography that will be treated here. This paper will deal mostly with the feasibility of using correlation measurements to detect impending fatigue failure.

## INTERFEROMETRY AND CORRELATION

Holography, the optical technique for wavefront reconstruction, can be used either to display interferometric fringes which are indicative of the similarity of two object waves (one holographically stored and the second directly viewed) or to display the correlation function of the two waves. The interferometric display results from the superposition of two mutually coherent waves: one

reflected (scattered) from the target, and the second generated from the hologram in the reconstruction process. In mathematical terms, we could describe this as

$$D_{fg}(x, y) = |f(x, y) + g(x, y)|^2 \quad (1)$$

where  $f(x, y)$  and  $g(x, y)$  describe the wavefronts to be compared. The discrepancies between these two coherent waves are displayed as a fringe pattern, which quite often is very difficult to interpret unambiguously.<sup>1</sup> However, this fringe pattern is essentially superposed on the image, so that the location of the region that suffers the most distortions is easily determined. Thus, it is quite difficult to quantitate the distortion (strain, displacement, rotation, in plane, out of plane, etc.), but it is easy to identify the region where it happens.

In another type of comparison (called correlation), the two wavefronts are convolved, i.e.,

$$C_{fg}(x, y) = \iint f(u, v) g^*(u + x, v + y) du dv \quad (2)$$

This correlation method has been developed<sup>2</sup> mostly for character (pattern) recognition or selection, but it has been successfully used<sup>3,4</sup> for monitoring slight changes in reflectivity (scattering), which may be due to crack formation, propagation, or fatigue.

Equation (2) indicates that the correlation display does not preserve the relationship between the target coordinates and the correlation function.

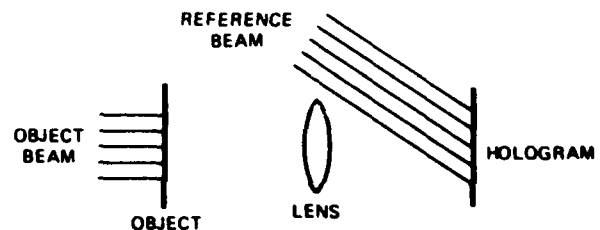


Figure 1. Construction of Hologram.

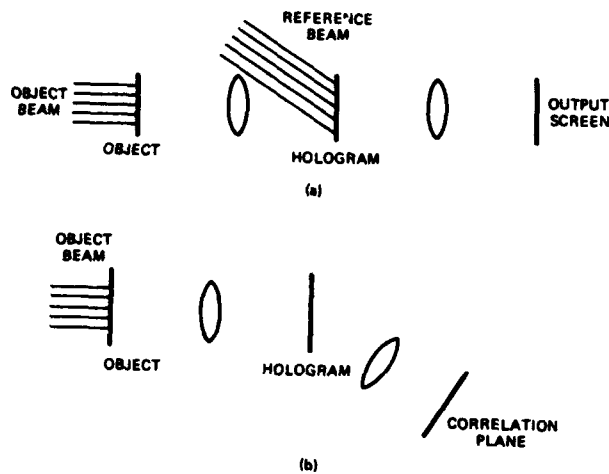


Figure 2. Holographic Interferometric Generation. (a) Interferometry Setup, (b) Correlation Setup.

Both interferometry and correlation can be displayed from a single hologram (obtained by the setup in Fig. 1) used to record and later to generate the  $g(x,y)$  function. Figure 2(a) indicates the configuration for interferometric measurements; both the reference beam and the object are illuminated, and the reconstructed image is superposed on the image of the object. In the correlation setup sketched in Fig. 2(b), only the object is illuminated and the scattered light is "filtered" by the hologram.

The surface of a specimen can be monitored by either interferometry or correlation. However, interferom-

etry requires interpretation, whereas correlation measurements are easily made and can even be automated. Thus, we will now discuss the feasibility of using optical correlation to detect surface changes leading to fatigue.

### CORRELATION COMPARISON

Two light distributions  $f_o(x,y)$  and  $f_k(x,y)$  of equal total intensity

$$\iint |f_o(x,y)|^2 dx dy = \iint |f_k(x,y)|^2 dx dy$$

are to be compared. After defining the measure of similarity of the functions as their mean-square average variation,

$$M_{ok} = \frac{1}{2} \iint_A |f_o(x,y) - f_k(x,y)|^2 dx dy \quad (3)$$

and after expanding the integrand, we obtain

$$M_{ok} = 1 - \text{Re} \iint_A f_o^*(x,y) f_k(x,y) dx dy \quad (4)$$

The integral in Eq. (4) represents the central value of the correlation function [as defined in Eq. (2)] which is already known<sup>2</sup> to be readily achievable by optical means. A practical implementation can be obtained with the apparatus sketched in Fig. 3. The scattered light from the specimen is recorded holographically. When this hologram is illuminated by the scattered light from the target-specimen, the diffracted light (propagating along the direction of the reference beam used in the holographic recording process) will display the correlation function. As indicated

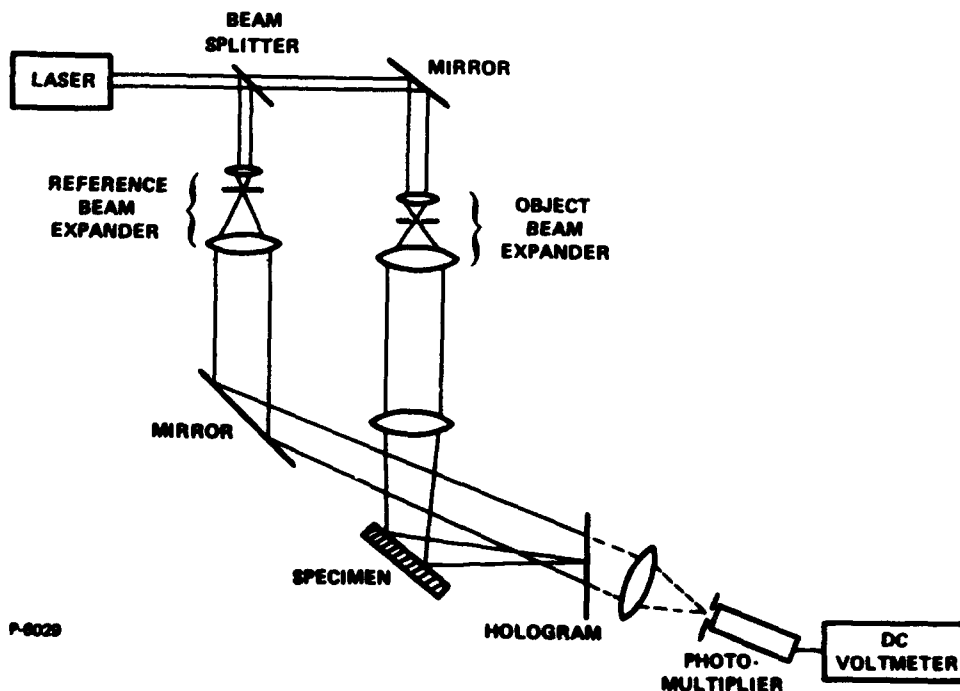
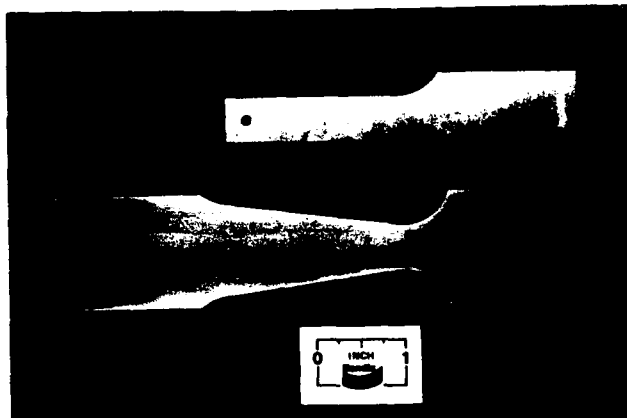


Figure 3. Schematic of Optical Correlation Apparatus.





**Figure 4. View of Cantilever Specimens Used in Fatigue Experiments.**

in Eq. (4), the central value of the correlation is of greatest significance for our comparison technique; thus, the experimental results discussed in the following sections will be based on these peak intensity values.

#### **Material and Specimen Preparation**

Specimens, of various commercial aluminum alloys, were prepared in two configurations: a T-shaped slab for stress gradient studies, and a tapered slab for uniform stress distribution (Fig. 4). Some specimens were tested as received, some were tested after being sandblasted, and some after being brightened or polished. A magnetic disc was attached to the free end of the cantilever - mounted aluminum specimen, and the specimen was then activated with an electromagnet. The frequency of the signal fed to the electromagnet was tuned to the resonant frequency of the

specimen-magnet, so that large vibrational amplitudes could be obtained with small power. The number of strain cycles was counted with an electronic counter, and the strain was calibrated with a gauge. Strain cycling was discontinued when a crack was observed under a 200 x magnification, or when the correlation intensity dropped to 20% of its initial value.

The photographic plate was accurately supported in a 3-axis micropositioner. After exposure and development, the plate was returned in its original position in the plate holder. Slight adjustments were always needed to correct for displacements, re-orientations, or distortions in the photographic process. The correlation measurements were made with a photomultiplier and with a pinhole which restricted the reading to the central peak. The pinhole was an electroformed hole of a diameter sufficiently large (0.1 mm) to permit passage of the peak of the correlation display. The layout of these various components is shown in Fig. 5.

#### **CORRELATION INTENSITY AS A MEASURE OF IMPENDING FATIGUE**

The incipient development of fatigue should be detectable by a careful monitoring of the surface state of a given material. The value of the correlation intensity peak, which provides a quantitative average value of all the changes that occur over the illuminated area, is the tool for this monitoring. Crack formation or propagation provide a continuous loss in correlation intensity; however, the location of the crack is quite difficult to determine from this type of measurement.



**Figure 5. View of Optical Correlation Setup.**

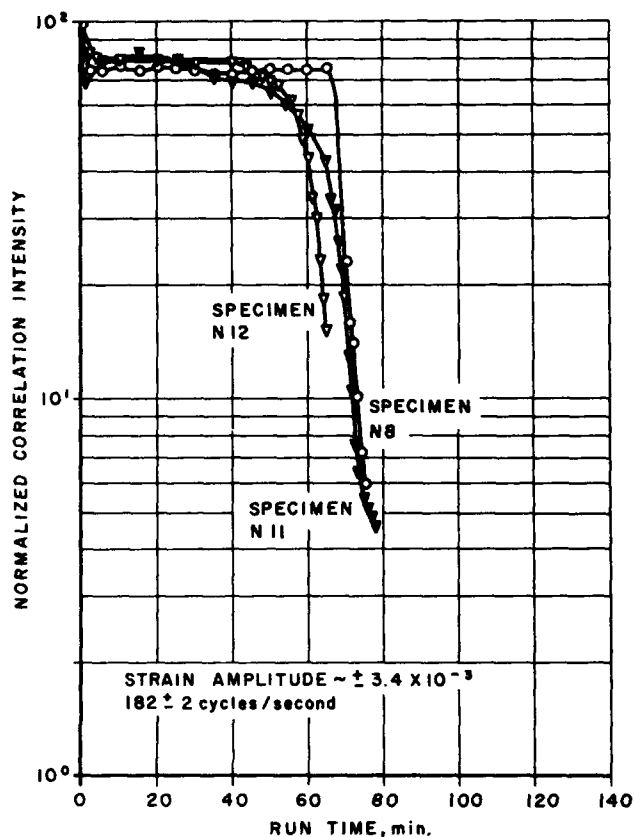


Figure 6. Correlation Intensity Versus Run Time for Specimens with Longitudinal Texture (As-Rolled Surfaces).

The correlation intensities measured for a number of aluminum alloy specimens subjected to a constant cyclic strain amplitude of  $\pm 3.4 \times 10^{-3}$  are shown in Figs. 6 and 7. Figure 6 shows a plot of the normalized correlation intensity versus run time for specimens in an as-rolled condition, while Fig. 7 shows the same for specimens whose surfaces were finished with No. 600 emery paper. Although there is considerable variation in the lives of the specimens, the curves show that the correlation decreases in three stages. The first stage is a decrease occurring in the first few seconds of run (a few thousand cycles), the second stage is a plateau extending for more than 60 minutes (up to several million cycles), and the third stage is a continuous loss of correlation which takes 15 minutes on the average. During this last stage, a crack about 1 mm in length would be usually detected when the correlation intensity decreased to less than 50 percent of the value it had at the outset of this stage.

#### Effects of Stress Levels on Fatigue Life

The effects of stress level on fatigue life, as detected by correlation measurements, are indicated in Fig. 8.

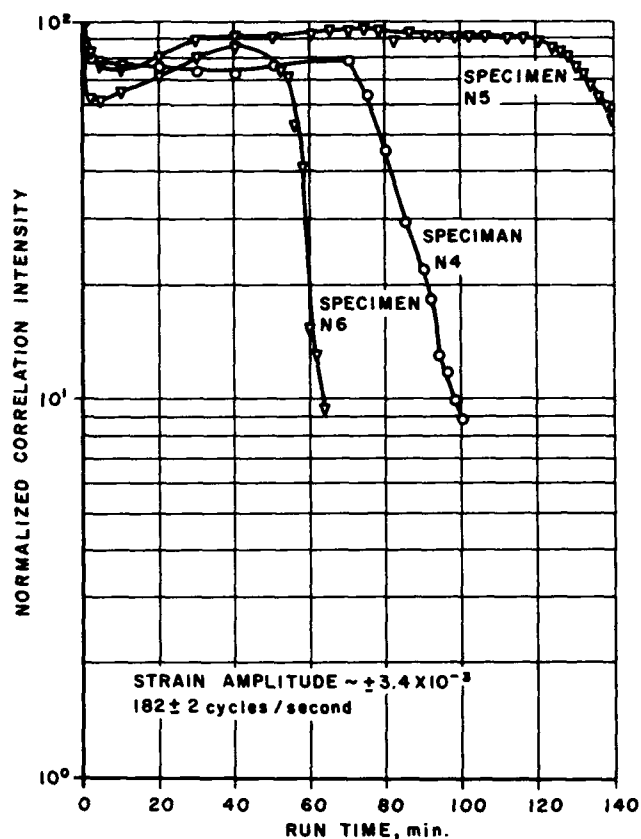


Figure 7. Correlation Intensity Versus Run Time for Specimens with Longitudinal Texture (Surfaces Finished with No. 600 Emery Paper).

As expected, the specimen subjected to the largest stress (strain amplitude) had the shortest life.

The first stage occurred within 1000 cycles regardless of the stress level. This phenomenon indicates that the first correlation drop results from the reorientation of very fine noise-like details in the target. The duration of the second stage was an inverse function of the strain applied to the specimen. In the last stage, the slope variations for the specimens subjected to strain less than  $3.4 \times 10^{-3}$  suggest that the crack propagation was not continuous.

The time chosen for hologram-filter preparation has no effect on the correlation curve. Figure 9 shows the correlation loss for a given specimen when various filters were made at several instances of time. The curve shows a continuously increasing slope, even though each filter exhibits an initially lower rate of loss which soon follows the trend.

#### Effects of Surface Finish

Specimens with polished, as-rolled, sanded, and chemically brightened surfaces were compared. The fa-

tigue life of as-rolled specimens appeared to be the shortest, while the mechanically polished specimens exhibited the longest life. However, the different surface conditions did not seem to affect the optical correlation. In the hologram-filters prepared for highly polished surfaces, the light intensity distribution is highly localized, and therefore the hologram exhibits strong attenuation for the strongest light components, as well as undesirable nonlinear optical effects. Bleaching the hologram greatly improves the performance of the filter. In general, specimens with roughened or as-is surfaces are preferred over polished specimens.

#### Metallographic Examination

All specimens were examined metallographically to relate surface deformation to loss in correlation. In general, the metallographic examination could reveal only large cracks which appear when the fatigue process is well under way. By comparing the photomicrographs of nonpolished specimens (Fig. 10) to those of polished-surface specimens (Fig. 11), one can observe the difficulty encountered in the visual determination of crack formation in the former.

However, when optical correlation was used, no difficulties were encountered in either case.

Although a quantitative relationship appears to exist between the correlation intensity and the crack length, a general relationship could not be established for all specimens (Fig. 12). Additional data are probably necessary to formulate this empirical rule.

Crack length, as observed from metallographic observations, does not appear to be a representative measure of fatigue damage. In fact, loss in correlation might be considered as a more representative evaluation of fatigue damage, since it may provide a continuous noncontacting monitor for deformation in targets which may be left in their assembly.

#### Selective Masking

Various features of crack development can be emphasized by a selective masking of either the target or the hologram filter.

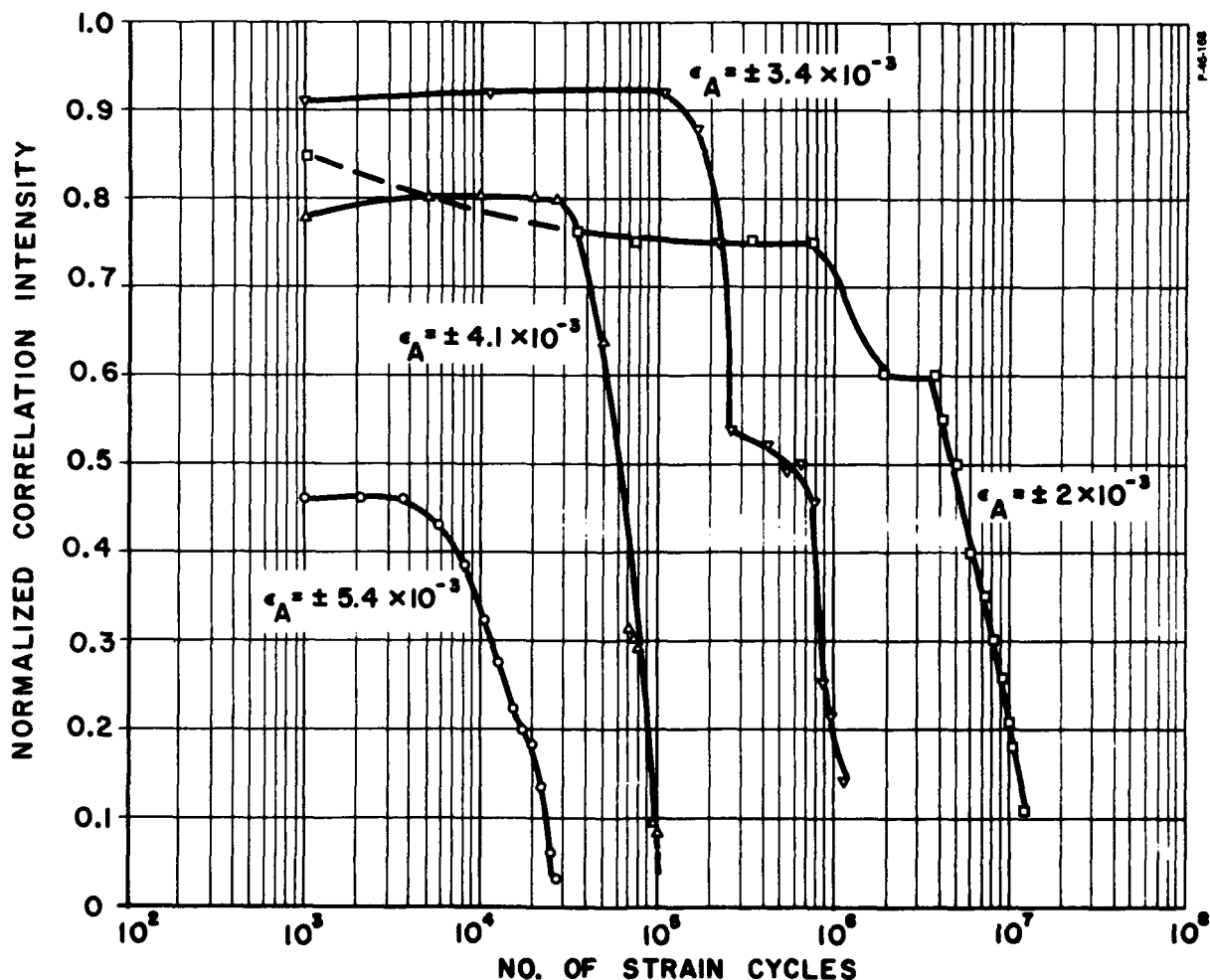


Figure 8. Effects of Stress Level on Fatigue Life.

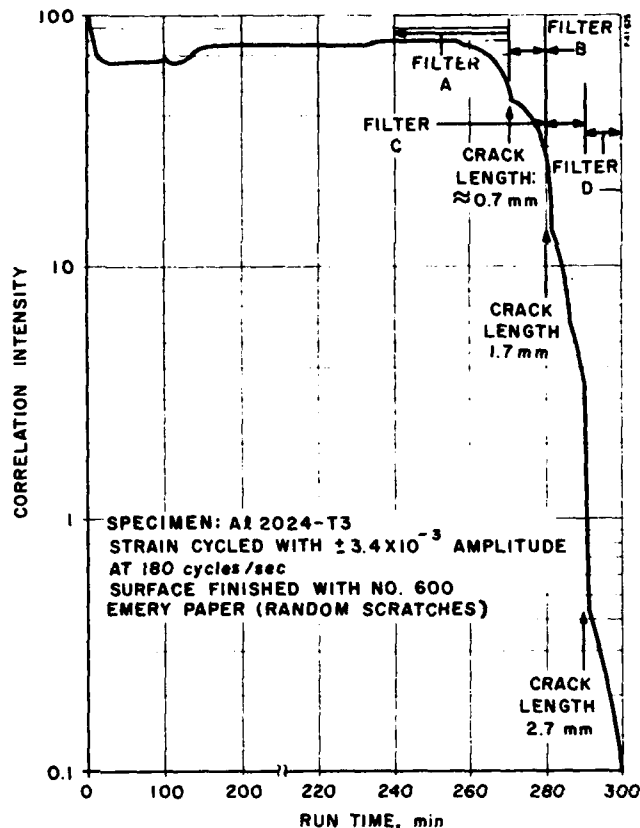


Figure 9. Correlation Intensity Versus Run Time Where a New Filter is Made After Each Significant Loss in Correlation.

As mentioned earlier, correlation measurements do not show the crack location; however, the approximate location would be found if the target is inspected section by section. Using the same filter, one can independently correlate certain selected areas by selective masking of the target. Figure 13 sketches this for a case where the critical area of the specimen has been divided into four regions. The correlation display of each region indicates that the fatigue failure starts in the first quadrant.

On the other hand, the hologram-filter can be selectively masked so that certain spatial frequencies could be emphasized. Thus, when the center of the filter is blocked, only high frequency components will contribute to the correlation; therefore, higher sensitivity is expected since fatigue cracks have primarily a high frequency effect. Also if the approximate orientation of the expected cracks is known, the sensitivity can be improved by observing only those directions perpendicular to the mean-propagation direction of the cracks.

#### CORRELATION AND HOLOGRAPHIC INTERFEROMETRY

A hologram filter made in the manner described

earlier can be used both for correlation measurements (as already discussed) as well as for interferometry. In the latter, both the hologram and the object are illuminated and care must be taken so that the object and the reconstructed image accurately superpose. Any discrepancies (or distortions) between the two images will show up as a fringe pattern. It is clear that this fringe pattern requires interpretation and thus cannot be used as an immediate evaluation of the state of the specimen's surface, whereas a correlation value can be. However, the fringe location and spacing indicate the localization of the crack.

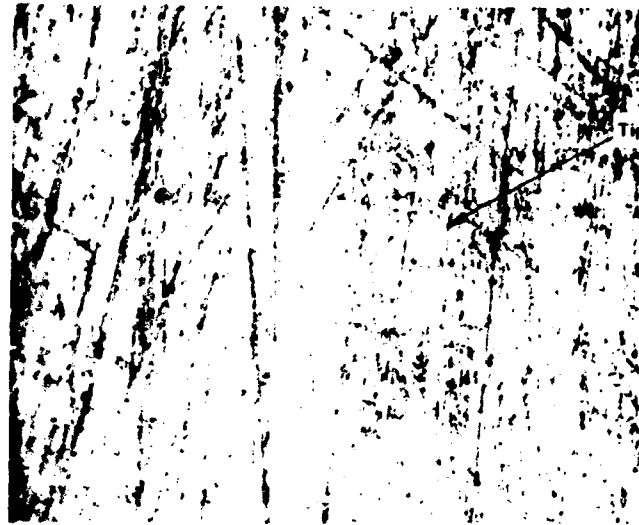
Because correlation provides an integral assessment of specimen changes, it is a more sensitive method for small deformation than holographic interferometry is. In the subfringe region, where partial fringes are very difficult to assess, the correlation method seems especially promising. In a simple comparison of the two methods, we recorded the light reflected from a membrane and then distorted the membrane by mechanically pushing its center. The correlation curve and the number of fringes counted as a function of target deformation are shown in Fig. 14. Thus, the greater usefulness of the correlation function seems to be in the early stages of the deformation.

#### Disturbance in the Beam Path

Optical correlation measurements can also be performed if an intervening disturbance (transparent obstacle, window, etc.) is in the beam path as long as the disturbance is static. Sometimes the disturbance is unavoidable particularly if there is a need to isolate the specimen (for instance when the specimen is in vacuum, in a toxic environment, or in a noisy environment). Correlation data have been successfully collected with window plates in the beam path but not with fiber optics bundles, even though rigidly supported. The minute displacements occurring within the bundle (because of slight temperature variations) erratically affected the measurements thereby making them unreliable.

#### Specimen Size Limitation

There is no theoretical limit to the size of the inspected area. It is plausible, however, that it will be easier to detect a small disturbance in a small illuminated area as opposed to a large one. Moreover, the sensitivity in the hologram-filter positioning is a direct function of the illuminated area. Thus, for both these reasons the inspected area should be limited. Therefore, one should inspect large areas by correlating the scattered light from several regions, each not larger than 2" in diameter (this value is chosen for setups where the separation between target and hologram is a few feet). The permissible inspected area increases with the distance between target and hologram, but then the detection of fine details of deformation targets is largely lost.



(1) 270 minutes  
100X



(2) 280 minutes  
50X



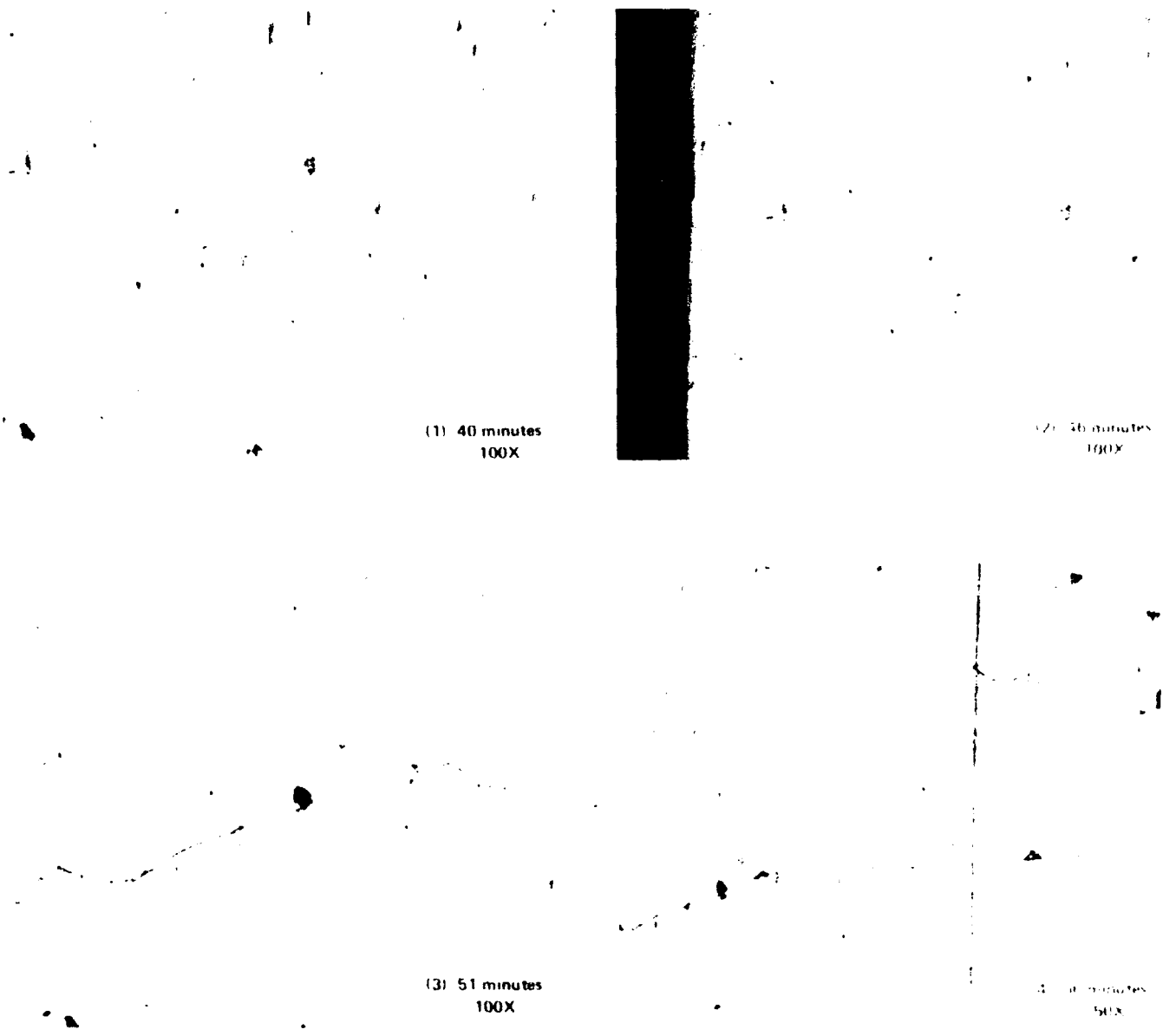
(3) 300 minutes  
50X

Figure 10. Photomicrographs Showing the Sequence of Crack Propagation  
In Specimen N9 Subjected to  $3.4 \times 10^3$  Strain Cycles  
(No. 600 Emery Paper - Random Scratches).

#### DISCUSSION

Experimental results obtained during the investigation have shown that the optical correlation technique can be used to detect incipient fatigue failure. In normal fatigue tests, the correlation intensity decreases very rapidly during the first few thousand strain cycles, but this change primarily represents the work-hardening which occurs in the metal. After the initial decrease, the correlation intensity remains nearly constant for a considerable number of strain cycles until incipient cracks form. This period

corresponds to saturation-hardening and is considered as the incubation period for crack nucleation. Once a crack exceeds the critical limit, it begins to propagate with each additional strain cycle, thereby causing the correlation intensity to decrease continuously. In investigating fatigue, one must differentiate between the decrease in correlation intensity occurring in the initial stage and that occurring in the last stage. Fortunately, this first stage lasts only a few thousand cycles at most, and the decrease in correlation intensity seldom exceeds 50 percent. If a material does not contain cracks in excess of the critical size,



**Figure 11. Photomicrographs Showing the Sequence of Crack Propagation In Specimen P5 Subjected to  $3.4 \times 10^3$  Strain Cycles (Polished Face).**

the correlation intensity reaches a steady-state condition after a few thousand strain cycles. If the correlation intensity begins to decrease again after only a few additional strain cycles, one can be certain that it will continue to decrease until complete failure occurs. Repeated tests show that a 50-percent decrease in correlation intensity, from its value at the beginning of the last stage normally indicates the occurrence of a crack on the order of 1 mm in length.

Since no two specimens deform in an identical man-

ner, it is not possible to establish a quantitative relationship between correlation intensity and crack size. However, the flaw size appears to be inversely proportional to the logarithm of the correlation intensity of a given specimen.

The roughness of the surface finish tends to decrease the fatigue life of a material in a manner similar to that produced by an increase in the stress level. However, these variables do not affect the use of the optical correlation technique for the detection of incipient failures. In other words, a 50-percent decrease in correlation intensity

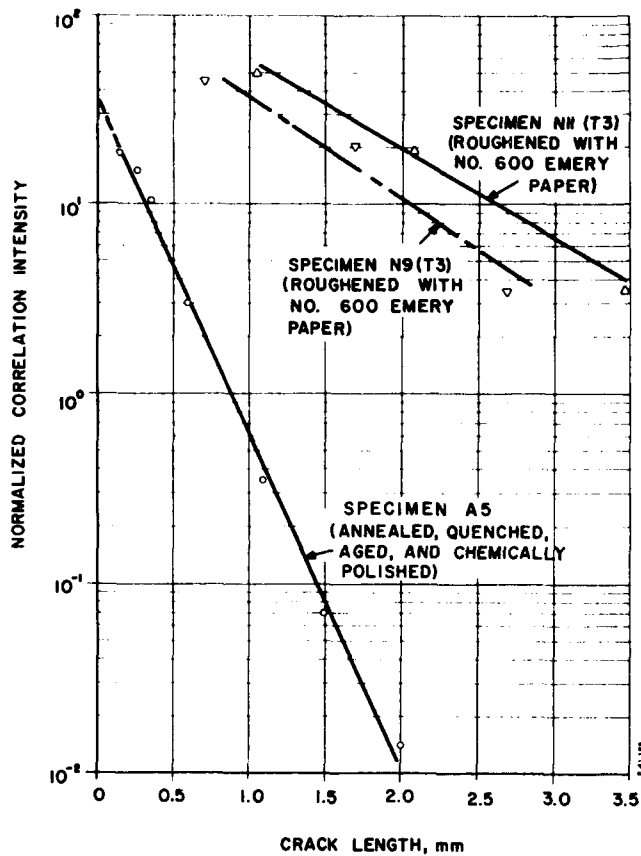


Figure 12. Correlation Intensity Versus Crack Length of Fatigued Specimens.

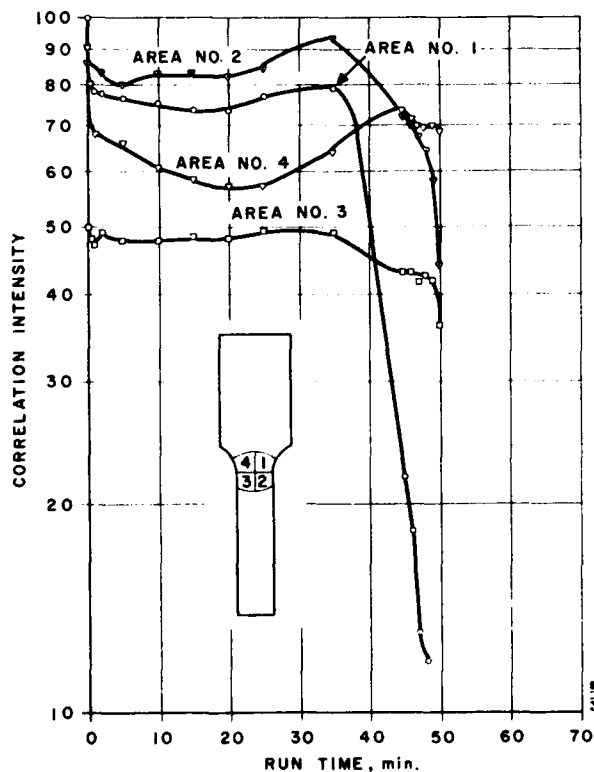


Figure 13. Correlation Intensity Versus Run Time Obtained by Selective Masking of the Specimen.

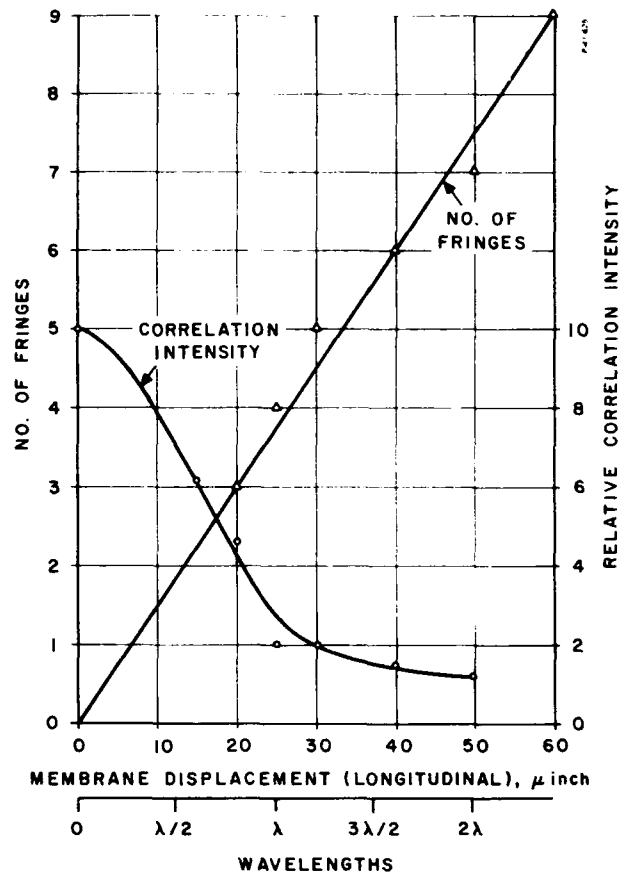


Figure 14. Comparison of Correlation Intensity Variations and the Number of Fringes for the Determination of Target Displacement.

during the last stage would indicate the occurrence of a flaw about 1 mm in length, regardless of the stress level or surface finish.

#### ACKNOWLEDGEMENTS

The authors would like to thank Dr. K.C. Chuang who performed some of the work described in this paper. The experiments described here were conducted under contract DAAJ02-68-C-0024 prepared for the U.S. Army Aviation Materiel Laboratories, Fort Eustis, Virginia and F33615-68-C-1475 for the Air Force Flight Dynamics Laboratory, Air Force Systems Command, Wright-Patterson Air Force Base, Ohio.

## REFERENCES

1. J.Ch.Viénot et al., *The Engineering Uses of Holography*, Cambridge University Press, London (1970).
2. A. Vander Lugt, *IEEE Trans. Inform. Theory*, IT-10:139 (1964).
3. E. Marom and R.K. Mueller, *Proc. 6th Symp. Nondestructive Evaluation of Aerospace and Weapons Systems Components and Materials*, p. 79, Western Periodicals, North Hollywood, California (1967).
4. E. Marom, *The Engineering Uses of Holography*, Cambridge University Press, London (1970).



# USE OF DAMPING TO REDUCE VIBRATION INDUCED FAILURES IN AEROSPACE SYSTEMS

by

David I.G. Jones and John P. Henderson

and

Ahid D. Nashif

**Air Force Materials Laboratory  
Wright-Patterson Air Force Base,  
Ohio**

**Research Institute  
University of Dayton  
Dayton, Ohio**

## INTRODUCTION

The problem of reducing vibration levels in structures or equipment arises throughout the entire spectrum of engineering activity. In many instances these problems are not fully recognized until a system is operational; indeed, many problems cannot be predicted because the mission profile of a system may change in the light of new requirements not even conceived at the design stage.

For problems in this category, quick effective solutions are, needless to say, demanded. The demands on engineers concerned with reducing or eliminating such unforeseen problems are therefore in some ways more pressing than they would otherwise be, as a result of the tight time schedules; but they are also eased in some other respects because fully optimized solutions, or the cheapest possible, are not then expected.

One of the most effective ways of rapidly coping with these "field" vibration problems is by means of additive damping designed to increase the overall damping of the affected structure or device by a factor varying between 10 and 100. While damping is not the panacea for all vibration problems, materials nonetheless exist which are capable of dissipating significant amounts of energy over substantial temperature ranges, and techniques have been developed to effectively utilize these materials<sup>1-8</sup>.

The materials most frequently used for damping are the so-called viscoelastic materials. It is the purpose of the present paper to describe an approach which has been successfully used to overcome some of the problems associated with the use of viscoelastic materials and which has led to satisfactory solutions of several practical problems. These problems and solutions are presented not because of their elegance but in the hope that they will encourage others faced with similar problems.

## APPLICATION OF DAMPING TO SPECIFIC PROBLEMS

### Approach

No general approach toward the solution of all vi-

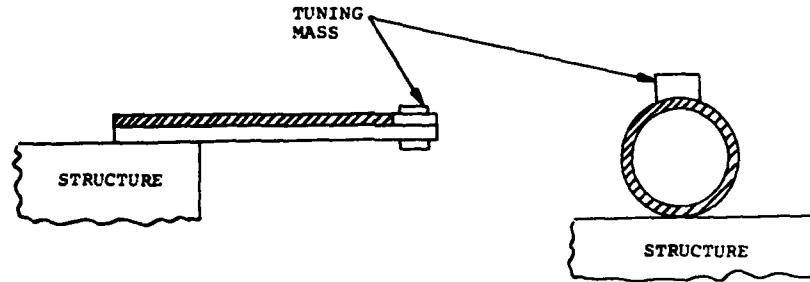
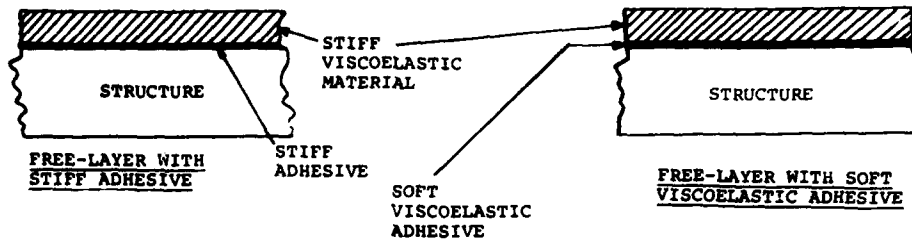
brational problems is possible, the actual approach depending on the complexity of the problem, the resources and materials available, the time schedule and so on. However, a certain minimum number of steps is unavoidable if one is not to resort to a very inefficient trial and error approach. These steps are:

- (i) Identify the problem.
- (ii) Define the environment, including excitation and temperature information.
- (iii) Idealize the structure as far as possible
- (iv) Measure response spectra and identify the important modes of vibration in the idealized structure, and in the actual structure for comparative purposes if possible.
- (v) Choose a damping treatment (Figs 1, 2) and damping materials<sup>9,10</sup>. This will depend on the response and modal surveys, the geometry of the structure and the damping materials available from commercial or other sources.
- (vi) Conduct response tests of the damping treatment in the idealized structural model over the operational temperature range, in order to optimize the treatment as far as possible.
- (vii) Conduct field tests if possible.

## Reduction of Vibration Damage in an IFF Antenna

The application of damping to reduce the severity of an operational vibration problem in the F-100 aircraft is first reviewed<sup>11</sup>. The problem involved failure of the rim of the dish-like inner surface of the antenna due to unexpectedly severe excitation from the cannon located near the antenna during firing. The problem was confined to the antenna itself, illustrated in Fig. 3, and the surrounding structure into which the antenna was bolted was sufficiently stiff to be unimportant except as an indirect excitation source.

**Figure 1. Typical Damping Techniques Using Stiff Viscoelastic Materials.**

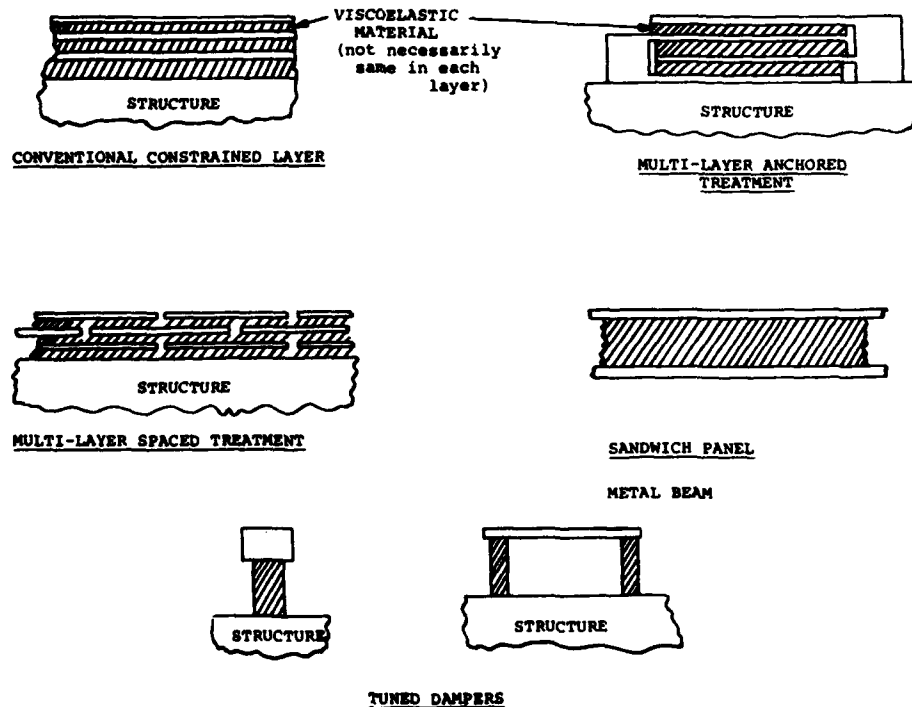


TUNED VISCOELASTIC DAMPERS

The antenna was tested at the Air Force Flight Dynamics Laboratory under shaker excitation simulating the field excitation spectrum, using a simple circular fixture, and the AFFDL tests showed that rapid failure occurred around the rim of the antenna in one to three minutes. Temperature rises of 30°F or more were observed in the vicinity of the electrical connector, probably because most of the energy was dissipated at that point.

Air Force Materials Laboratory tests using the same fixture, illustrated in Fig. 4, showed response spectra under harmonic excitation of the type shown in Fig. 5, with a resonant frequency around 485 Hz, and with no further response peaks up to several thousand cycles per second. The problem was clearly associated with this resonance, which appeared to involve high strains in the rim region and a diaphragmatic mode type.

**Figure 2. Typical Damping Techniques Using Soft Viscoelastic Materials.**



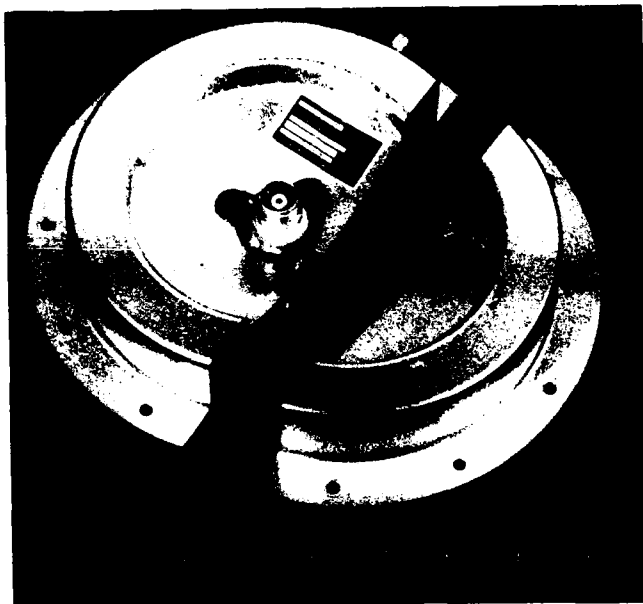


Figure 3. Sectioned View of Failed IFF Antenna (AT - 740/A).

A tuned damper consisting of a mass connected through a viscoelastic spring to an antinodal part of the vibrating structure was selected as the only feasible solution apart from complete redesign or relocation of the antenna, due to the geometry of the antenna and the ineffectiveness of layered damping treatments in the absence of large surface strains. The geometry of the antenna left room for a small tuned damper to be placed, in a ring-type configuration, around the electrical connector as shown in Figs. 4, 6 and 7. Several viscoelastic materials and damper configurations were evaluated and the response of the antenna measured, as a function of temperature, using miniature accelerometers. The final material was selected on the basis of the relatively slow variation of the damping properties with temperature (see Fig. 8) since this allowed the damper to remain turned over as wide a temperature range as possible. Other considerations were shear strength and bonding, since the damper had to withstand a very severe vibrational environment. Graphs of amplification factor in



Figure 4. Antenna/Damper Configuration on Test Fixture.

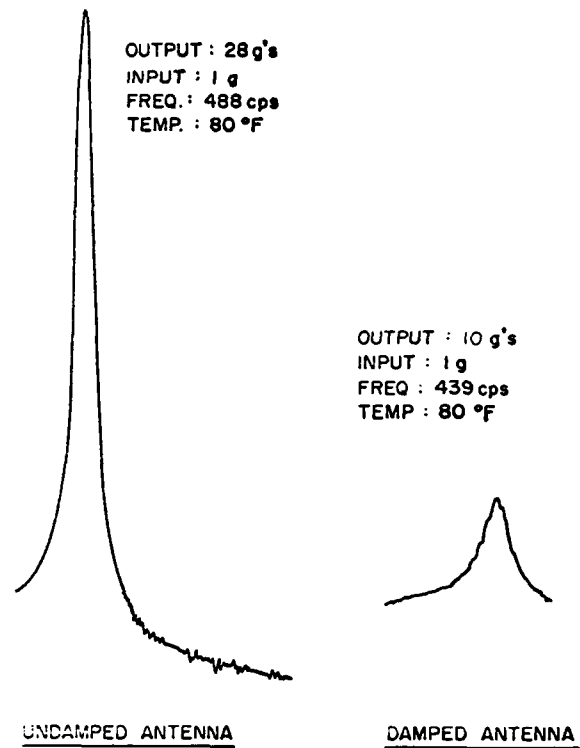


Figure 5. Typical Response Spectra.

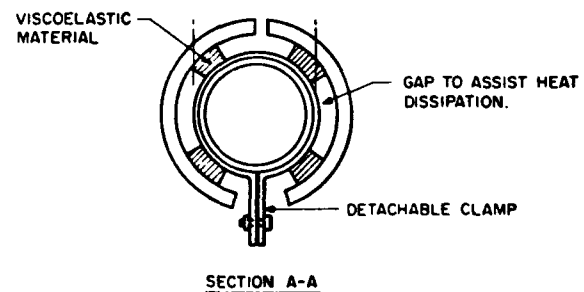
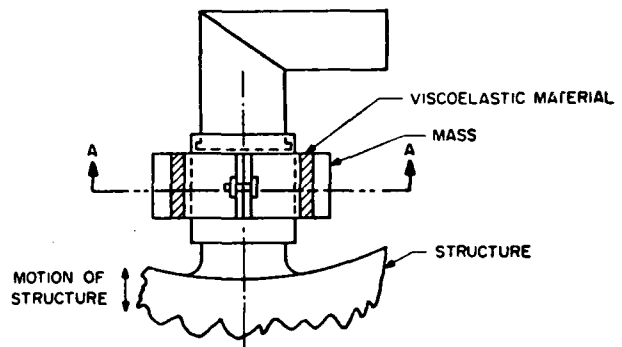
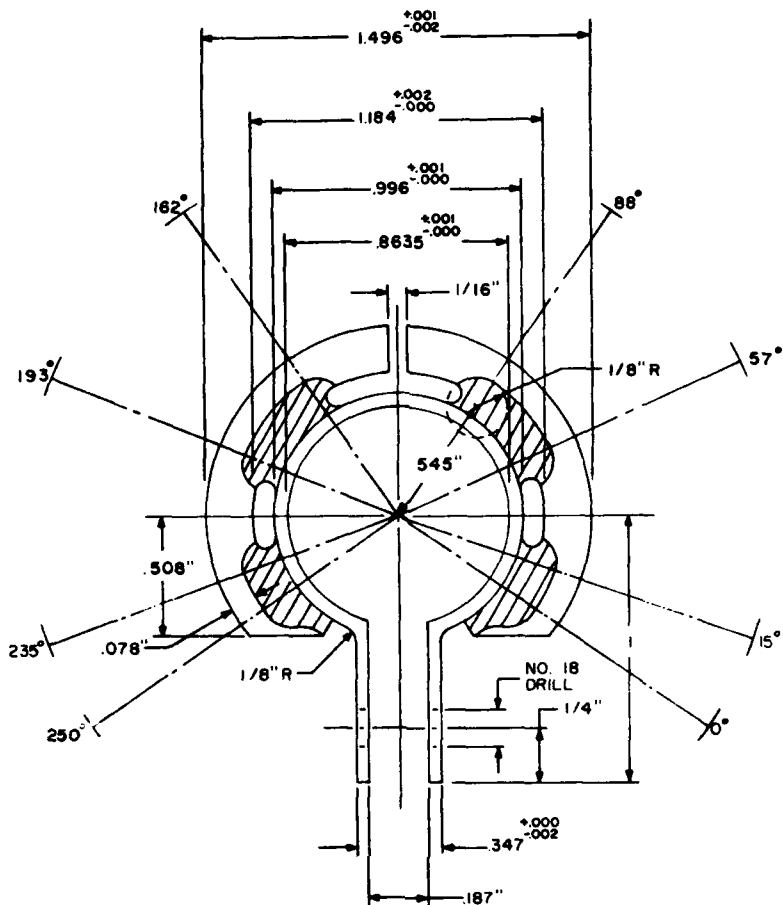


Figure 6. Damper Attachment to Electrical Connector.

Figure 7. Damper Geometry.



the antenna dish versus temperature, with this optimized damper attached, are shown in Fig. 9.

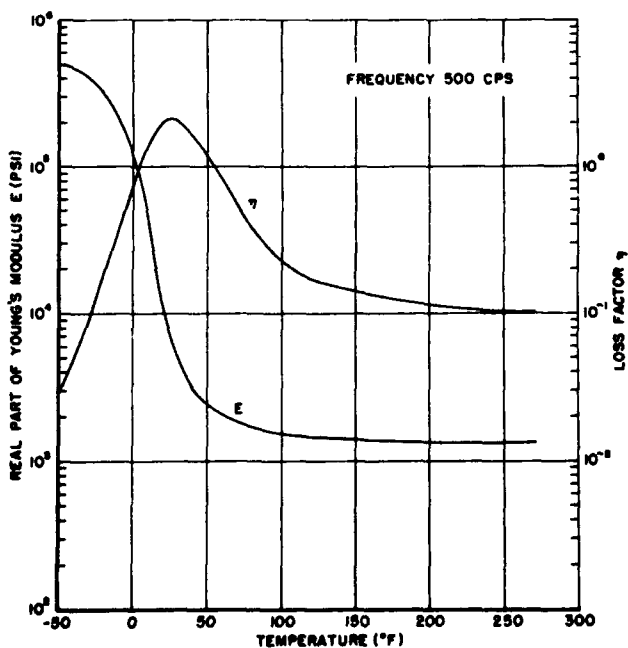


Figure 8. Complex Modulus versus Temperature for Paracril - BJ (U.S. Rubber Company, Air Force Materials Laboratory Data).

Tests of the antenna-damper combination under the simulated random vibration environment were carried out at room temperature in the AFFDL shaker facility to ensure that the dampers were satisfactory. This was a vital prelude to field testing because of the uniquely severe environment. It was observed that the test dampers failed in about one minute under continuous excitation, during which time the temperature of the viscoelastic material rose from about 90°F to about 175°F. Shear failure of the rubber occurred, probably due to falling shear strength with rising temperature until the damper eventually could not withstand the forces involved. Under half minute bursts of excitation, however, the dampers did not fail, probably because the temperature rises were far lower. Since the operational excitation due to gunfire bursts lasted even less than half a minute, it was concluded that the final damper design was satisfactory. The shaker tests under this excitation showed a four-fold increase in the life of the antenna. Field tests confirmed these results, showing an increase in life varying from four to twelve.

The improvement in operational effectiveness and cost reduction from the lower replacement needs amply justified the efforts involved in the development of the damper.

Reduction of Vibration Damage in a UHF Antenna

Failures also occurred in the UHF antenna on the

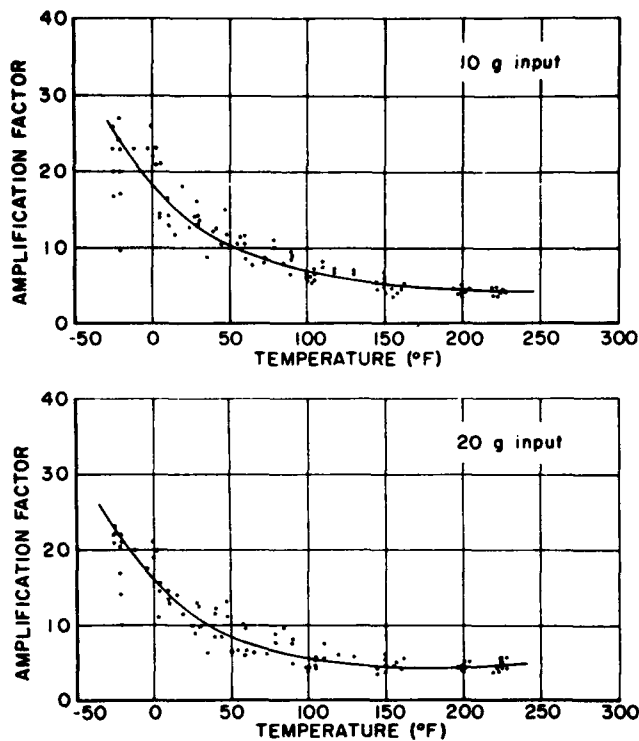
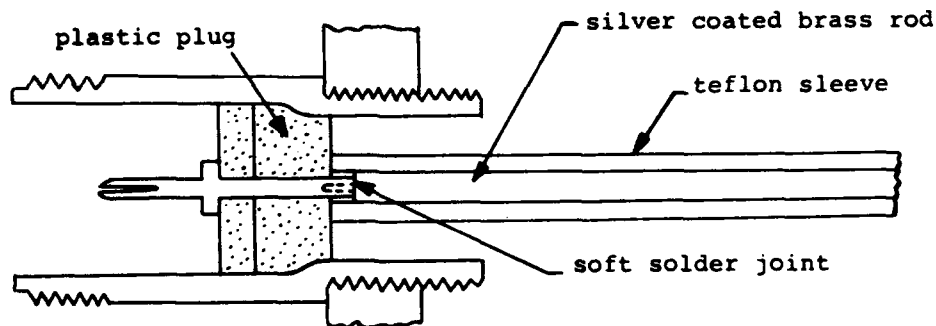


Figure 9. Amplification Factor at Resonance versus Temperature.

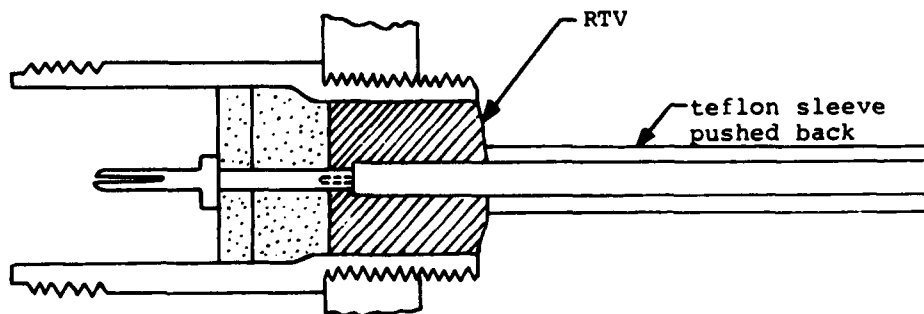
F-100 aircraft as a result of gunfire-induced excitation, and involved failure of the soft solder joint at the root of the radiating element or dipole as shown in Fig. 10.

In order to elucidate the vibrational characteristics of the basic antenna system, slots were machined in the surface of the aerodynamic shield protecting the radiating element, so that the element could be visually observed, as shown in Fig. 11. The frequency range from 100 Hz to 1000 Hz was slowly swept and the behavior of the radiating element observed by means of a stroboscope. At about 180 Hz, the entire antenna was observed to resonate in a sideways bending mode. At about 380 Hz, the first resonance of the radiating element within the aerodynamic shield occurred. The mode appeared to be almost pinned at the soft soldered joint and restrained by the shield at the other, since the outer end of the shield supported the outer half of the radiating rod. At a 5-g peak level of harmonic excitation, the maximum peak-to-peak amplitude at resonance appeared to be about 0.06 inches.

In order to reduce the failure problem, a damping treatment was needed to (i) increase the resonant frequency of the dipole to get it out of the area of greatest excitation, (ii) stiffen the root area to take some of the stress off the soft solder joint (ultimately, this joint was sometimes silver soldered as well as damped in the field) and (iii) add some damping.



UNFIXED DIPOLE



FIXED DIPOLE

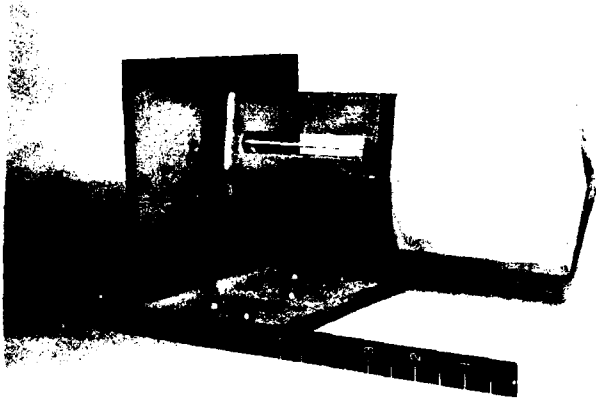


**Figure 11. Antenna in Fixture.**

A very simple means was found to achieve all of these objectives by pouring a suitable room temperature vulcanizing silicone rubber (RTV) into the cavity at the root of the dipole, as shown in Fig. 10. RTV's selected had to be pourable enough when uncured for simple field application and stiff enough when cured to achieve the desired increase in frequency.

Harmonic excitation tests of the damped dipoles showed that the resonant frequency was increased to about 480 Hz, the peak-to-peak amplitude at resonance dropped to about 0.02 inches and the mode shape changed, the root behaving more like a clamped end as would be expected.

Field testing of the fixed antennas showed a considerable increase in service life, by a factor of more than four. The fix was used under service conditions for a considerable period of time until the antenna was eventually relocated. In fact, for the cost of a few gallons of RTV, the F-100 fleet was spared this particular problem in its most severe form for nearly one year!

#### **Reduction of Vibration Damage in an Aircraft Dispenser**

A recent aircraft dispenser vibration problem is of considerable interest. The dispensers were attached under the wings and fuselage of the F-4 aircraft and the stores were held in the box-like cavities of the dispensers prior to re-

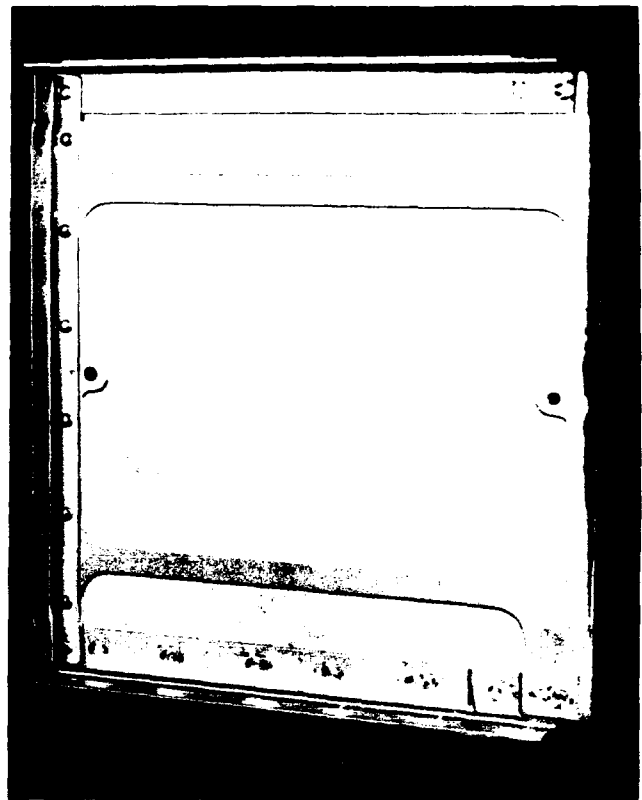
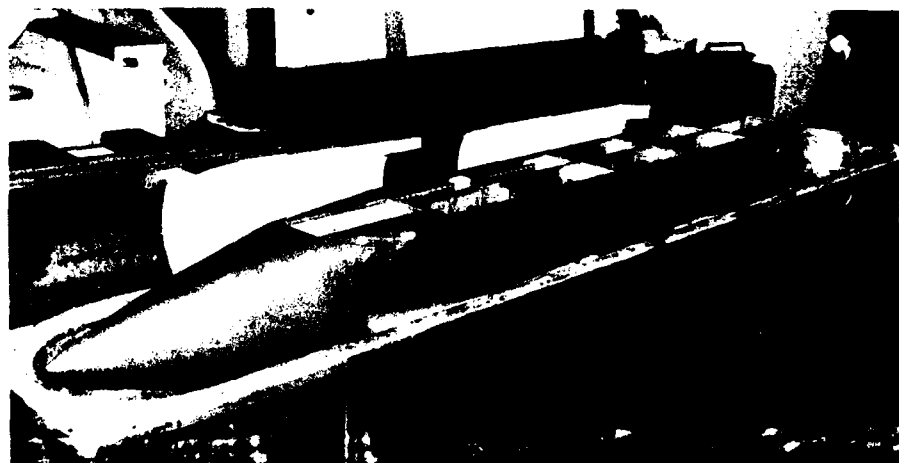


**Figure 13. Center Webs.**

lease, serving to maintain a smooth aerodynamic surface. Upon release, however, the cavities were in the open condition and cavity resonances were set up as the aircraft returned home at high speed, causing excessive vibration of the entire structure including the center webs, as illustrated in Figs. 12 and 13. The failure rate was so high that a dispenser barely lasted a single mission, a crack appearing at a stress raiser in the web, as shown in Fig. 14. It was considered that even a five-fold increase in life would be acceptable because field data indicated that other parts of the dispenser would fail first if any greater improvement were achieved for the center web.

The response of the center web under harmonic acoustic excitation was first examined in a horizontally oriented

**Figure 12. Dispenser in Inverted Position (SUU - 41).**



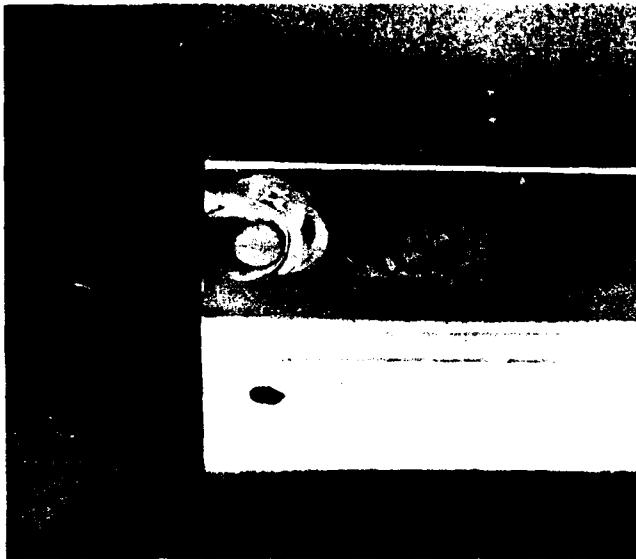


Figure 14. Crack in Center Web After a Mission.

dispenser using a stiff honeycomb "paddle" attached to a small shaker as an exciter. The various modes were excited as the frequency was varied and were observed by means of

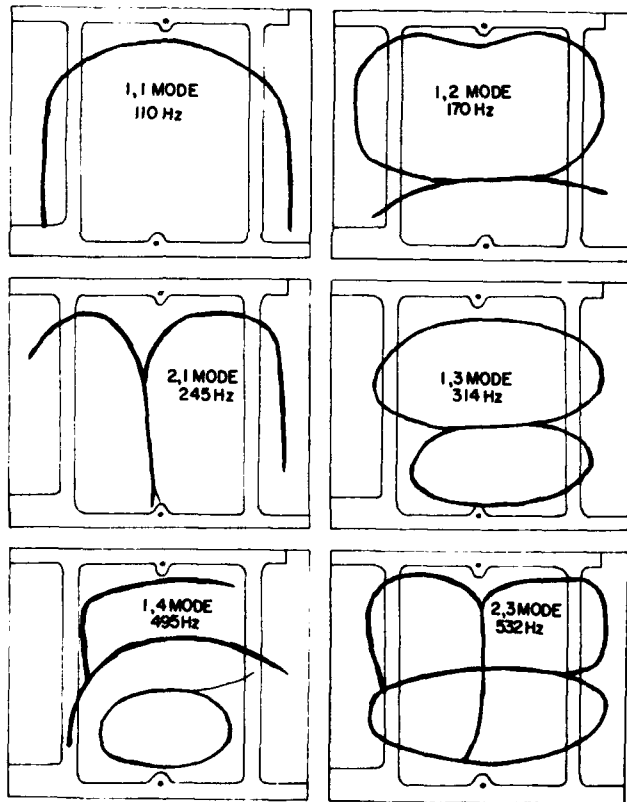


Figure 15. Nodal Patterns for Web in Dispenser.



Figure 16. Center Web in Fixture.

sand scattered on the horizontal web. Nodal patterns and frequencies observed are shown in Fig. 15. From these patterns and frequencies, it was clear that stiffening the structure would be unlikely to solve the problem because the cavity resonances would be likely to excite at least one mode and stiffening would at most simply change the mode or modes involved.

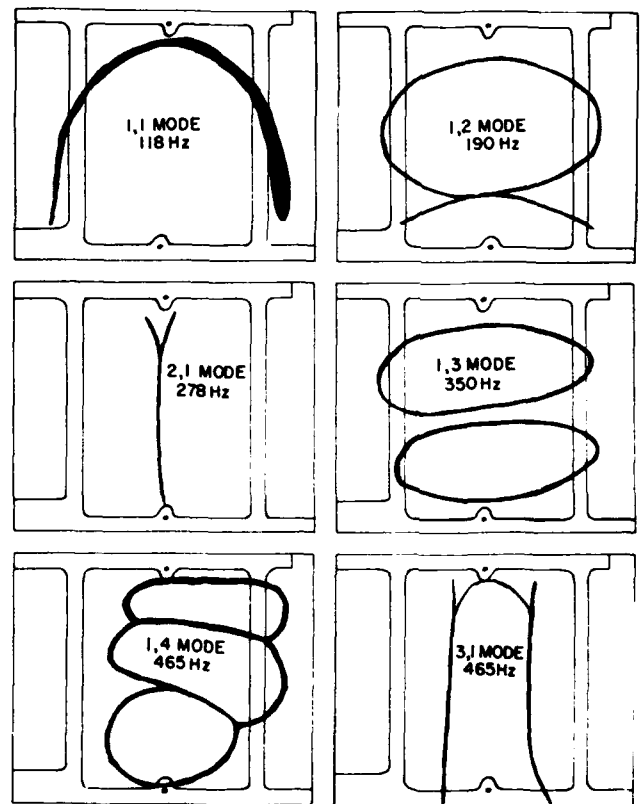


Figure 17. Nodal Patterns in Fixture.

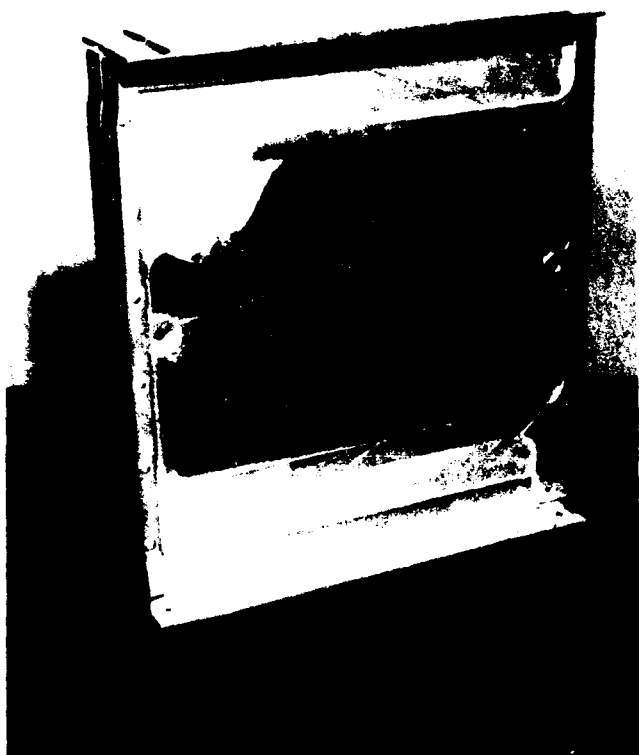


Figure 18. Damping Treatment on Center Web.

From these patterns, it was also apparent that the center webs were behaving somewhat as clamped-clamped-clamped-free plates, modified by the integral stiffeners, so that only the web itself would need to be tested if the appropriate boundary conditions could be reproduced to a reasonable degree of accuracy. This would eliminate the need for testing the entire dispenser, a task which would have been difficult in view of its size and the instrumentation available.

The next step taken was to excite a single center web specimen, supported by a suitable fixture as shown in Figure 16, on an electrodynamic shaker. In order to verify that the appropriate boundary conditions were being reproduced, sand pattern measurements were again made. The results are shown in Figure 17. It is seen that the nodal patterns and resonant frequencies are reasonably close to those observed in-situ for the same modes, so that the boundary conditions were taken to be acceptably reproduced.

The criteria which a damping treatment had to meet for this problem were (i) to operate within a clearance of at most 0.1 inches from the surface of the web in order to accommodate the stores, and (ii) to give high damping over an operating temperature range extending from about  $-30^{\circ}\text{F}$  to  $+200^{\circ}\text{F}$ . These figures were based on the best available estimates concerning the operational conditions. These limitations made it necessary to think in terms of a

layered damping treatment having a thickness of less than 0.1 inches, and occupying if at all possible only the central portion of the web between the integral stiffeners, as shown in Fig. 18, since this would ease problems of attachment. The desired temperature range imposed conditions on the choice of materials. This led to the choice of commercially available 3M-428 damping tapes.

The material was commercially available, an important factor in itself for any practical solution to a vibrational problem. It was available in the form of damping tapes comprising a thin layer of the viscoelastic adhesive backed by a thin sheet of aluminum, and gave high damping over an appropriate temperature range (Fig.19). It could be readily cut, worked, and placed in any number of layers on the surface of the web. The specific dimensions tested were 3M-428A, which had an aluminum thickness of 0.0055 inches and a viscoelastic adhesive thickness of 0.0025 inches; 3M-428B which had an aluminum thickness of 0.008 inches and viscoelastic adhesive thickness of 0.005 inches and 3M-428C which had aluminum thickness of 0.012 inches and viscoelastic adhesive thickness of 0.005 inches.

The first treatment seriously considered was a patchwork of adjacent sheets of 2.5 inch by 2.5 inch. 3M-428A tape laid up in five layers in the overlapping manner described by Plunkett and Lee<sup>6</sup>. The shaker testing was first carried out in order to determine whether this particular layered treatment would be effective at room temperature. The damping was measured in several modes, at several lo-

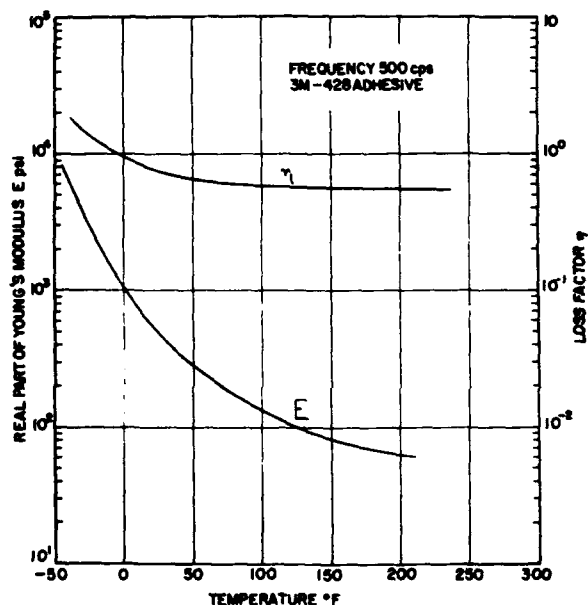
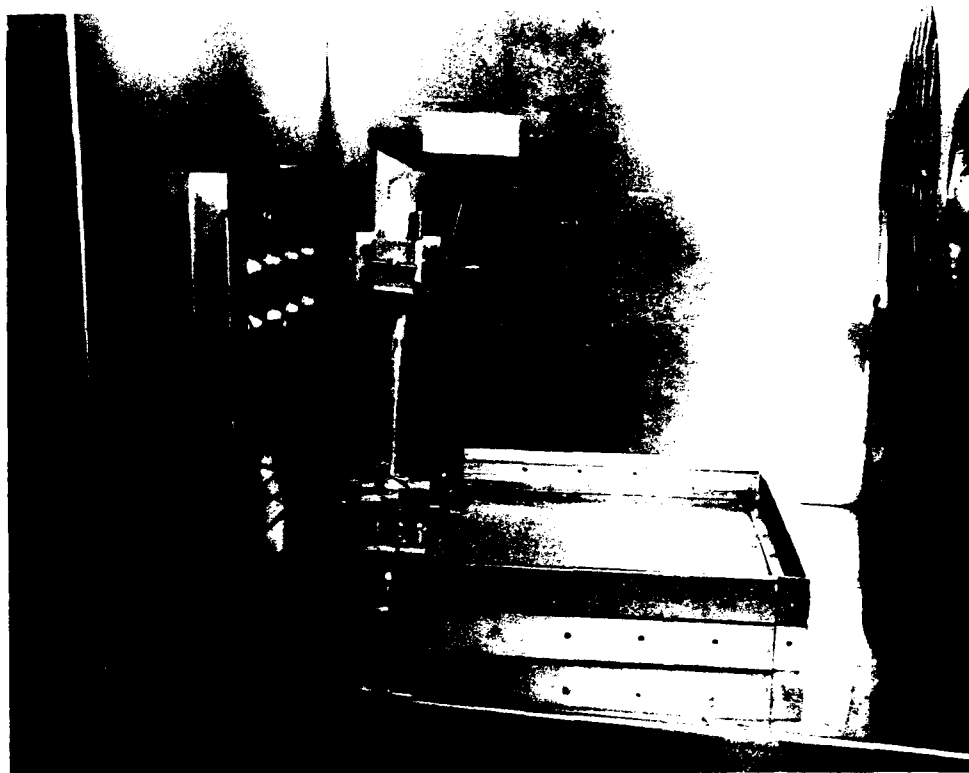


Figure 19. Complex Modulus versus Temperature for 3M-428 Adhesive (3M Company, Manufacturer's Data).



Figure 20. Point Excitation Setup.



cations on the web, by means of a miniature accelerometer. From the measured results, at about 85°F, the loss factor in each mode as determined by the "half-power bandwidth" method was over 0.027 compared with a figure of the order of 0.005 for the undamped panel. Since the transition temperature was near to 0°F, it was anticipated that greater damping would be attained at lower temperatures, which was desirable in view of the operational requirements. It was also determined, from the tests, that good measurement points for obtaining reliable and consistent results, and high amplitudes in as many modes as possible, were the points  $x = \pm 4$  in.,  $y = 0$  as shown in Fig. 13. This finding was very important because it was inconvenient to test all possible damping treatment combinations on the shaker over a wide temperature range. The points  $x = \pm 4$  ins.,  $y = 0$  were very suitable for excitation and pickup by means of magnetic transducers.

The web was next placed inside an environment chamber as shown in Fig. 20. It was no longer supported by the fixture because the boundary stiffeners were considered to be adequate under point excitation to reproduce the modes and frequencies observed in the dispenser. It was excited by a magnetic transducer at the point  $x = 4$  in.,  $y = 0$  and the response was picked up by another transducer at the point  $x = + 4$  in.,  $y = 0$ . Typical measured response spectra, for the undamped and for the damped structure, are shown in Fig. 21. The damping in each mode was measured, as before, by the "half-power bandwidth" method since the modes were in general sufficiently well separated for each to be individually identified and analyzed. Graphs of system

loss factor  $\eta_s$  versus temperature for a typical mode are shown in Fig. 22. In order to determine the effect of other treatment configurations on the damping, tests were also carried out on five layer configurations such as two-inch-wide strips of the same materials laid adjacent to one another with directions of alternate layers at right angles (90° crossply), parallel (unidirectional two-inch-wide strips along y-axis) and continuous (sheets occupying entire damped area). Results are shown in Fig. 22. It is seen that considerable scatter occurred but that no difference could be discerned between the damping effectiveness of the various configurations.

The configuration finally selected was a five-layer continuous layup of 3M-428A sheets to occupy the central area, between the integral stiffeners, on one side of the web. This configuration was forwarded for field testing and operational use. The field tests were successful and indicated a five-fold increase in service life, with the cracks propagating far more slowly and less catastrophically than in the undamped webs. The fix was implemented in the production and retrofit programs. The alternative course, namely the far more time consuming and expensive procedure of redesigning the entire dispenser, was abandoned as being unnecessary in view of the effectiveness of the fix. This must be one of the rare instances where a "short term" fix has actually made redesign unnecessary, and illustrates the fact that damping, when properly used for appropriate problems, can save time and money as well as solve an engineering problem.

One possible problem remained, namely the question of what would happen if the temperature should exceed about 150°F, where the present treatment is rather ineffective. The investigation was resumed to seek a means of adding some high temperature damping. This was accomplished by placing five continuous sheets of 3M-466 tape, having viscoelastic material thickness 0.002 inches and aluminum thickness 0.0055 inches, onto the center portion of the web as before. The properties of 3M-466 adhesive are shown in Fig. 23, and it is seen that the transition region occurs around room temperature, i.e. somewhat higher than for the 3M-428. The damping in a typical mode is shown in Fig. 24 as a function of temperature. In order to attain damping at high and low temperatures, one treatment was placed on one side of the web and the other treatment on the other wide. The measured damping is shown in Fig. 25

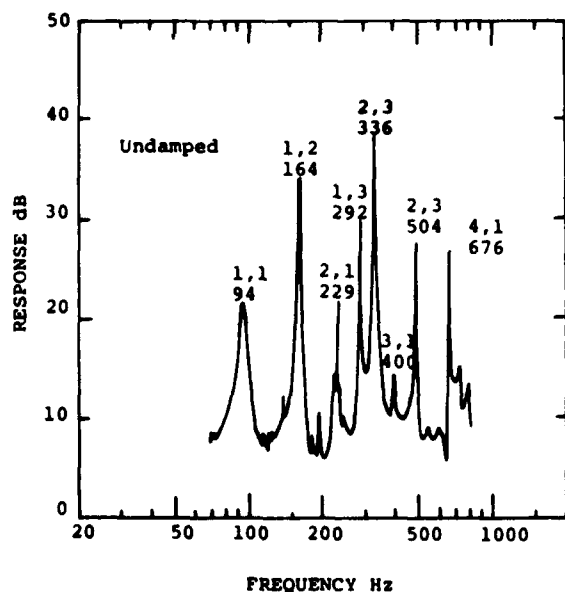
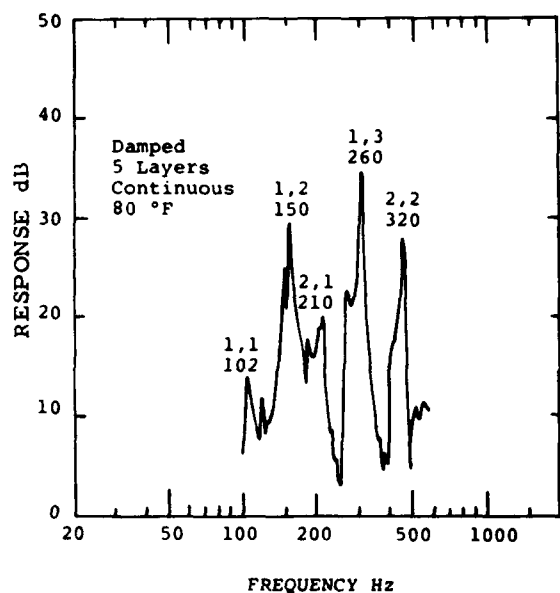


Figure 21. Typical Response Spectra.

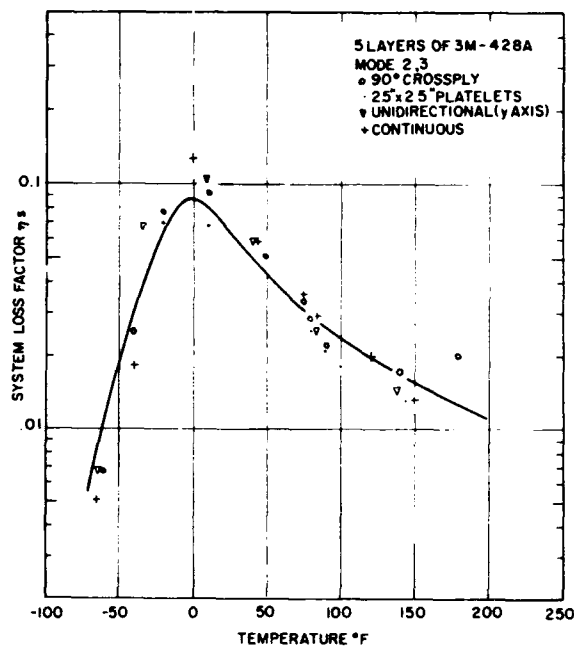


Figure 22.  $\eta_s$  versus Temperature for Five Layers of 3M-428.

as a function of temperature. The range of significant damping has clearly been considerably broadened. So far, no need has arisen for this higher temperature damping, but this situation is considered to be far better than having the need and no solution!

#### Reduction of Vibration Damage in a Remote Compass Transmitter

This problem involved the failure of a remote com-

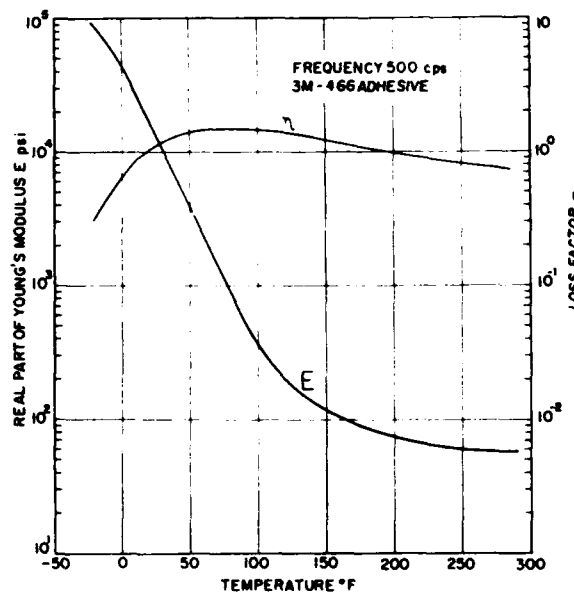


Figure 23. Complex Modulus of 3M-466 Adhesive versus Temperature (3M Company, Manufacturer's Data).

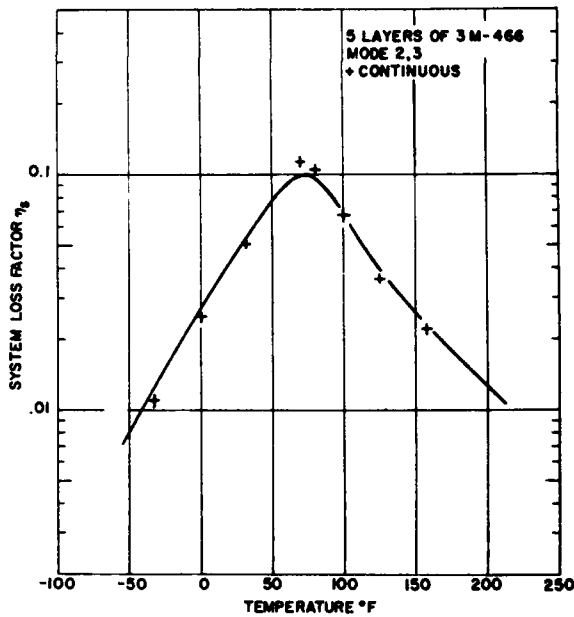


Figure 24.  $\eta_s$  versus Temperature for Five Layers of 3M-466.

pass transmitter located in the wing of the F/R-4 aircraft. The compass transmitter, which consists essentially of a pendulum suspended in an oil-filled brass bowl, was attached through a bracket to the upper surface of the wing, and the failure was associated with aerodynamically excited vibrations of the wing-bracket-compass system, leading to high

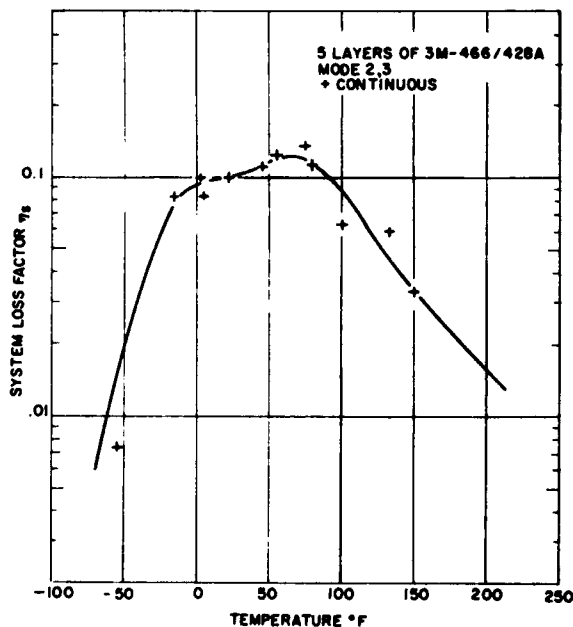


Figure 25.  $\eta_s$  versus Temperature for Five Layers of 3M-466 and Five Layers of 3M-428.

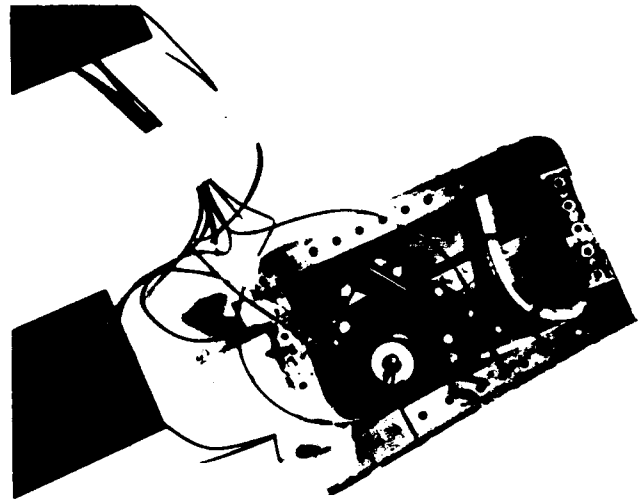


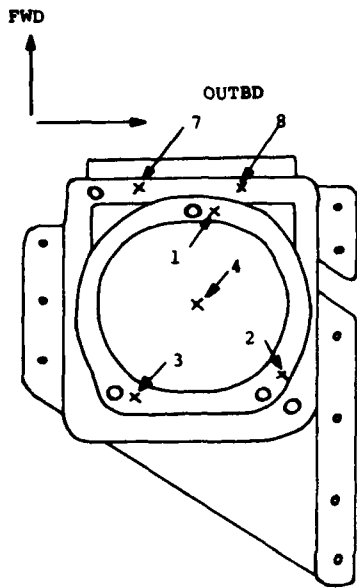
Figure 26. Remote Compass Transmitter in F-4 Wing.

dynamic stresses in the bowl of the compass and ultimate failure. The system is illustrated in Figs. 26 and 27.

The ensuing program to determine the main dynamic characteristics of the system, develop suitable structural models, and develop and test a fix, was a joint effort between the Air Force Materials Laboratory and the Dynamics Branch of the Deputy for Engineering, Aeronautical Systems Division, assisted by several other organizations and individuals. The present discussion is concerned with a brief outline only of one part of the total effort, namely the development of the damping fix and its evaluation under laboratory excitation. A report on the complete details of the effort, and particularly the characterization of the dynamics of the system, is planned for the future. It is sufficient for now to simply state that the response of the original transmitter and mounting was complicated by the effects of nonlinearities and dynamic instabilities. Tests performed to identify frequencies, mode shapes, and damping of the original and several modified configurations were, for the most part, conducted at low levels of excitation where the system appeared to be linear. The validity of the conclusions drawn from the low level tests was then verified by measuring the effect of the modifications on the response of the system when subjected to excitation more representative of the actual service environment.

Since the bracket for the remote compass transmitter was mounted on the fairly flexible skin-stringer structure of the wing, the first step taken was to investigate the dynamic compliances of the transmitter mounting system on the aircraft in the absence of the transmitter itself and then with it in place. Measurements were therefore made of the response at several points on the wing, bracket and compass resulting from a measured harmonic force applied at various points by means of a hand-held electro-mechanical driver. Data obtained from these measurements were used to generate frequency response plots and to identify important resonant frequencies and modes.

The dominant characteristic of the system, which became apparent from the frequency response plots, is that the lower frequency resonances were controlled by the flexibility of the mounting bracket. Typical response spectra for the undamped system are shown in Fig. 28. It is seen that significant peaks in the response occurred at about 185 Hz and 310 Hz. These spectra correlated with those observed during in-flight response measurements and laboratory tests, illustrated in Fig. 29, performed on the test fixture shown in Fig. 30.



Accelerometer locations and excitation points on compass and bracket.

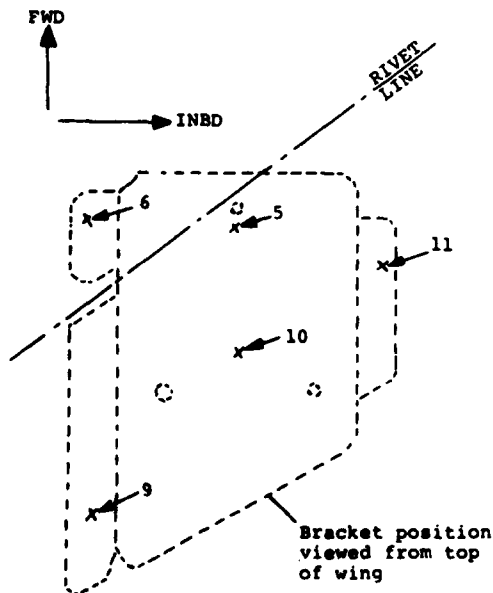


Figure 28. Measured Response Spectra in Wing.

After some preliminary testing, it became apparent that a significant improvement in the system response characteristics could be achieved by increasing the stiffness of the bracket and introducing significant additional damping into the system by means of a highly damped plate of the geometry shown in Figs. 31 and 32.

The first damped plate tested was of the geometry shown in Fig. 32a, comprising three layers of 0.014 inch thick 3M-466 viscoelastic adhesive sandwiched between three aluminum plates 0.031 inches thick and then attached to the properly cleaned bracket through the bottom layer of viscoelastic adhesive. The compass was then attached to the bracket by means of bolts through properly located holes in the damped plate. Graphs of measured system loss factor  $\eta_s$  versus temperature are shown in Fig. 33. Typical response spectra are shown in Fig. 29 for the damped system. It is seen that significant damping was achieved between about 0°F and 200°F, but that the damping below 0°F was rather low. This result was not surprising because the temperature of optimum damping of the 3M-466 adhesive is near room temperature.

This situation was remedied somewhat by adding a fourth layer of 3M-428 viscoelastic adhesive, 0.004 inches thick and another aluminum sheet 0.031 inches thick on top of the previous plate as shown in Fig. 32b. At temp-

Figure 27. Sketch of Remote Compass Transmitter in Wing.

eratures below 0°F, the 3M-428 adhesive would still give high damping and the now very stiff but lightly damped layers of 3M-466 would act as a spacer to some extent. Graphs of  $\eta_s$  versus temperature are shown in Fig. 33. This geometry was the one finally selected for the plate to be used as an operational fix.

Although time did not permit a complete field evaluation of the fix, it was demonstrated in laboratory tests simulating the actual service environment that dynamic stress levels in the compass transmitter were reduced by a factor of about two. It was then estimated that the service

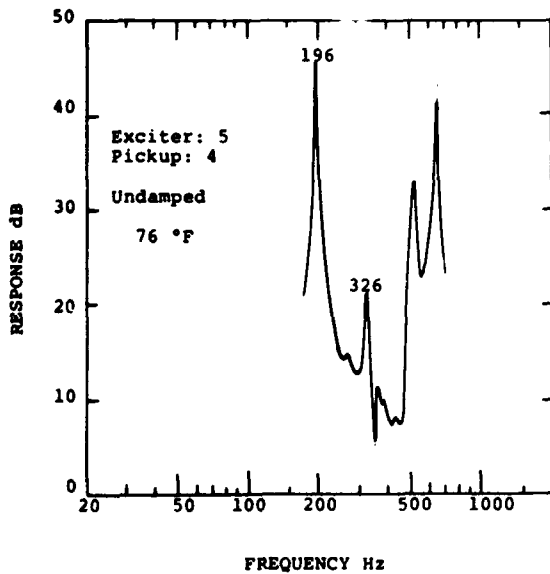
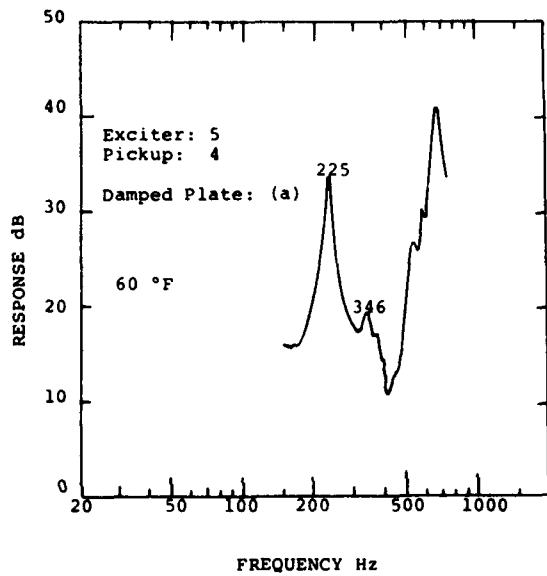


Figure 29. Typical Response Spectra Measured in Test Fixture.

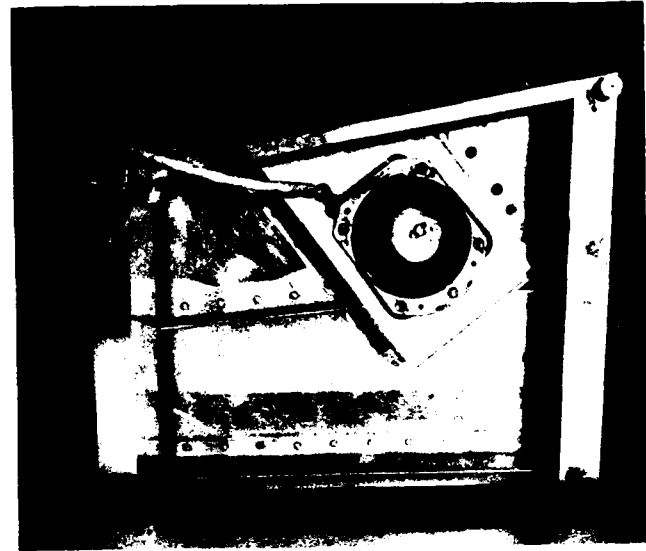


Figure 30. Remote Compass Transmitter in Test Fixture.

life of the compass should be extended by a factor varying from four to ten, resulting in considerable improvement in operational effectiveness and significant savings in maintenance and replacement costs. Current plans call for retrofit of all F-4 aircraft to incorporate this fix.

#### Damping of a Fan Blade

Vibration problems have arisen from time to time in jet engine fan, compressor, and turbine blades and various measures have been taken to reduce their severity, such as the use of "mid-span" shrouds in the fan stages, the payment of special attention to root design for high damping, and

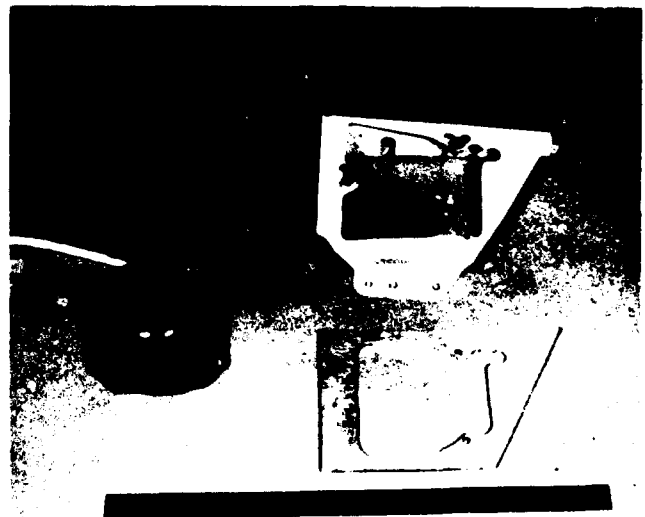


Figure 31. Compass, Bracket and Damped Plate.

careful design to avoid excitation of any modes at multiples of the rotational speed. With the coming of new generations of large and powerful jet engines, the sizes of the blades increase considerably and it becomes increasingly difficult to avoid vibrational problems. For this reason, means are being sought to introduce high damping into blades. This damping must meet at least the following criteria:

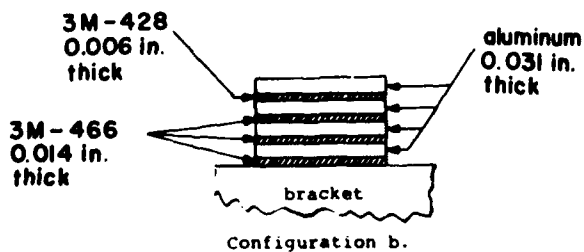
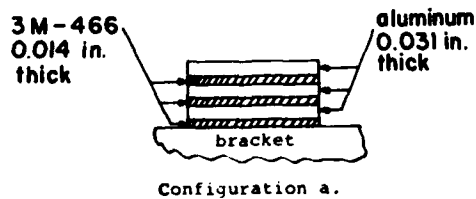
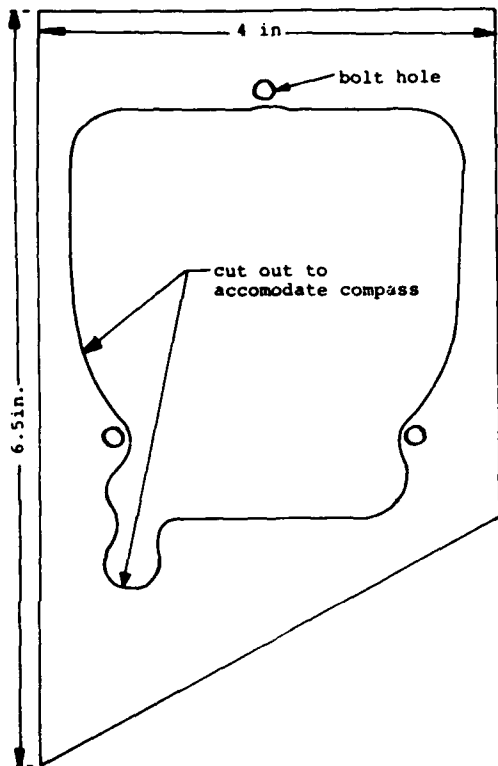


Figure 32. Damped Plate Geometry.

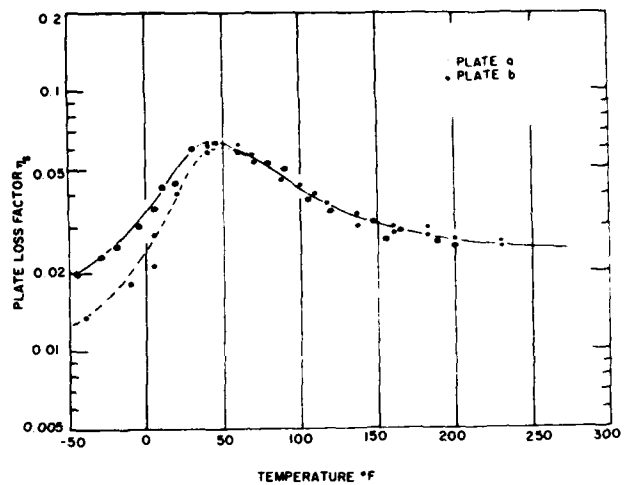


Figure 33.  $\eta_5$  versus Temperature for Two Plate Geometries.

- (i) Withstand very high "g" loads for significant periods of time without significant creep or failure.
- (ii) Be capable of effective operation at temperatures from  $-50^{\circ}\text{F}$  to  $+400^{\circ}\text{F}$  approximately for a fan blade and temperatures of over  $2000^{\circ}\text{F}$  for turbine blades.

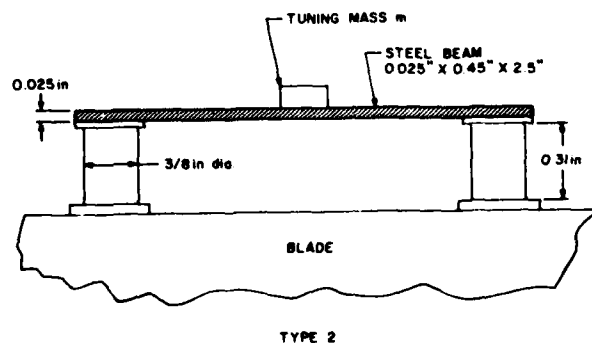
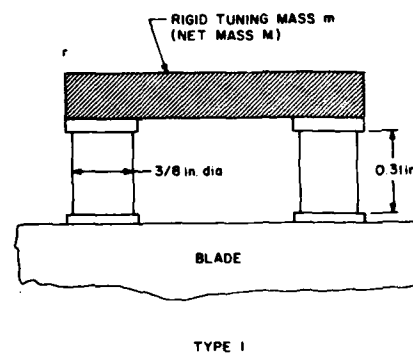


Figure 34. Test Damper Geometries.

- (iii) Be able to fit inside the blade.
- (iv) Be as reliable as the blade itself.
- (v) If possible, damp several modes of vibration of the blade.

No damping treatment or technique has yet been found to meet all these criteria. However, the fact that the modes of vibration of typical blades are well separated in frequency, the initial damping in still air is extremely small and the vibrational strain levels are small even for high vibrational displacement amplitudes leads one to the conclusion that a tuned damper of some kind would be very effective (at least in the laboratory) in damping any given mode and several dampers could be used to damp several modes, each damper being tuned to a specific modal frequency.

Investigation so far has been confined to demonstrating that high damping can be introduced into a fan blade by means of a very small and lightweight damper<sup>15,16</sup>.

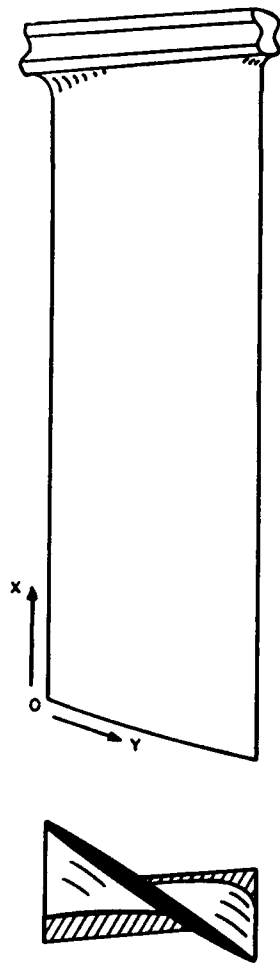


Figure 35. Sketch of Typical Fan Blade.

The damper geometries studied are shown in Fig. 34. These were placed first on a shaker table and vibrated to ascertain their resonant frequencies. They were then placed at various points on the fan blade sketched in Fig. 35. Typical response spectra observed for the first torsional mode are shown in Fig. 36. It is seen that very large reductions in response level, up to at least two orders of magnitude, were readily achieved. The damper frequencies were then varied and the response and damping, measured for the same mode, are shown in Fig. 37. It is seen that even quite large variations of the damper frequency do not reduce the damping significantly so that some variability in damper characteristic could be tolerated.

Many geometrical variations of the tuned damper would be capable of withstanding the high g-loads. Some are shown in Fig. 38. Engineering developments of such

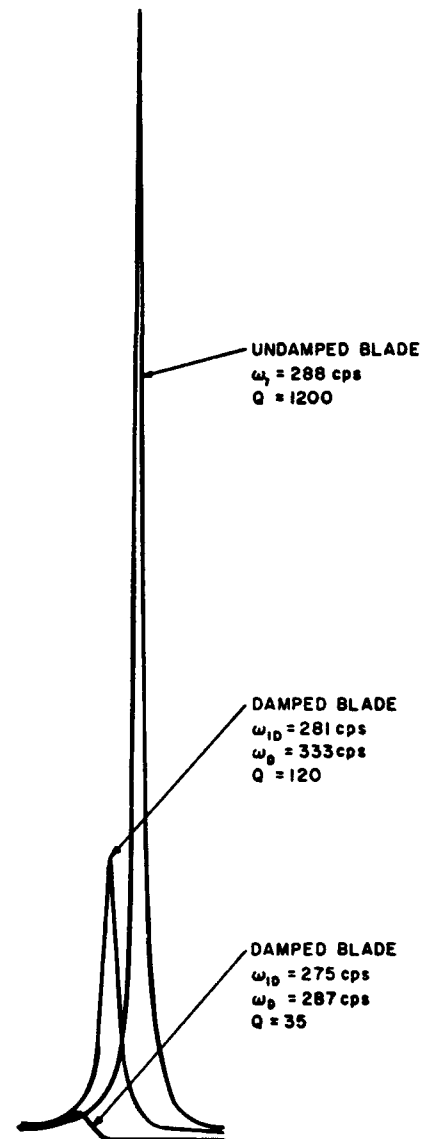


Figure 36. Typical Response Spectra.

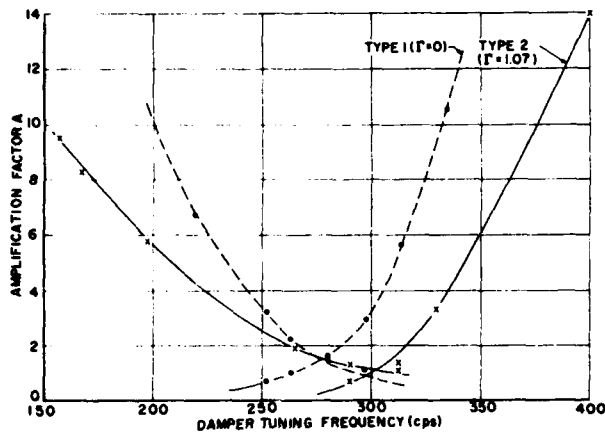


Figure 37. Variation of Amplification Factor Under Shaker Excitation with Damper Frequency.

dampers could be machined to close tolerances in an "encapsulated" form and inserted into specific points in a blade during manufacture. Needless to say, the development problems would be considerable but preliminary feasibility studies have indicated no apparently insuperable problems.

#### DISCUSSION

The main arguments usually advanced for not utilizing viscoelastic materials in reducing practical vibration problems in engineering are (i) their mechanical properties are not well understood, (ii) they are highly temperature-sensitive, (iii) even if materials were no problem, designers do not understand how to design damping treatments, (iv) their ageing characteristics are not always good and (v) they add weight.

It is hoped that the present paper has shown that, while these arguments are valid enough in the proper context, they should serve as a spur toward more careful evaluation of viscoelastic materials for damping rather than as an excuse for taking no action at all. Viscoelastic materials and treatments are often the most rational and ideal means of solving troublesome vibration problems and no engineer confronted with such a critical problem can afford to ignore the possibility that such a treatment may solve his particular difficulties far more easily and cheaply than the rather extreme solution of re-design.

#### ACKNOWLEDGEMENTS

Particular appreciation is due to the late 1/Lt G.H.

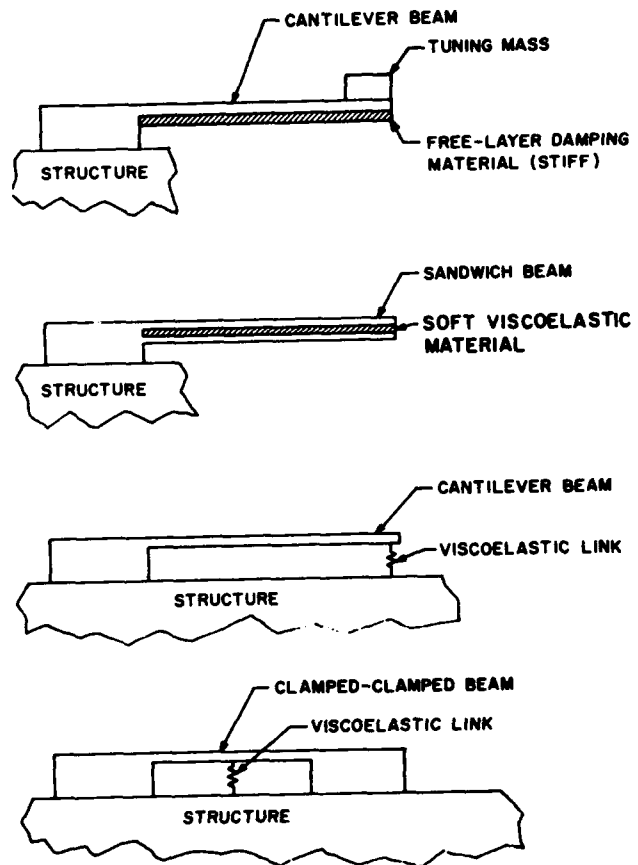


Figure 38. Possible Alternative Damper Configurations.

Bruns, III, for his vital contribution to our efforts in this area, and which led ultimately the work reported in this paper. Thanks are also due to W.J. Trapp, Chief of the Strength and Dynamics Branch, for his encouragement and support, J.R. Schmermund for expert assistance with electronic instrumentation, and Sally McLean for assistance with preparation of the manuscript. The authors wish to acknowledge the major efforts extended by W.G. Frost and P.H. Hermes of Aeronautical Systems Division (ASD) in the cooperative effort to develop the fix for the F-4 compass transmitter, the assistance of G.A. Plzak and V.C. McIntosh of Air Force Flight Dynamics Laboratory in the acquisition of response data on the F-4, the efforts of T.J. McDaniel of the University of Dayton in the analytical studies involving transfer functions, and the efforts of R. Sevy (AFFDL) in connection with the IFF antenna damper development. The work reported in this paper was sponsored by the U.S. Air Force under Project No. 7351, "Metallic Materials", Task No. 735106, "Behavior of Metals".



## REFERENCES

1. B.J. Lazan, A.F. Metherell, and G. Sokol, *Multiple Band Surface Treatments for High Damping*, AFML-TR-65-269, Air Force Materials Laboratory, Wright-Patterson AFB, Ohio (1965).
2. D. Ross, E.E. Ungar, and E.M. Kerwin, Jr., "Damping of Plate Flexural Vibrations by Means of Viscoelastic Laminae," pp. 49-87, *Structural Damping*, American Society of Mechanical Engineers, New York (1959).
3. P. Grootenhuis, "Vibration Control with Viscoelastic Materials," *Environ. Eng.*, 38:13-15 (1969).
4. J.E. Ruzicka, "Vibration Control," *Electro-Technol. Sci. Eng. Ser.*, No.56 (1963).
5. D. Birchon, "Hidamets - Metals to Reduce Noise and Vibration," *Engineer* (August 1966).
6. R. Plunkett and C.T. Lee, *Optimum Configurations for Damping by Constrained Viscoelastic Layers*, AFML-TR-68-376, Air Force Materials Laboratory, Wright-Patterson AFB, Ohio (1969).
7. H. Oberst and K. Frankenfeld, "Über die Dämpfung der Biegeschwingungen Dünner Bleche Durch Festhaltende Beläge," *Acustica*, 2/1:AB181-194 (1952); 4/2:433 (1954).
8. D.I.G. Jones, J.P. Henderson, and A.D. Nashif, "Reduction of Vibrations in Aerospace Structures by Additive Damping," *Shock Vibration Bull.*, 40 (1970).
9. D.I.G. Jones, "Material Damping," *J. Environ. Sci.*, 12/3:20-23 (1969).
10. A.D. Nashif and T. Nicholas, "An Analytical and Experimental Investigation of a Two-Layer Damping Treatment," *Shock Vibration Bull.*, 39/4 (1969).
11. D.I.G. Jones et al., *Development of a Tuned Damper to Reduce Vibration Damage in an Aircraft Radar Antenna*, AFML-TR-67-307, Air Force Materials Laboratory, Wright-Patterson AFB, Ohio (1967).
12. J.P. Henderson, "Energy Dissipation in a Vibration Damper Utilizing a Viscoelastic Suspension," *Shock Vibration Bull.*, 35/7:213-229 (1966).
13. *Dynamic Testing of Compass Transmitter of F-4 Phantom*, Structural Dynamics Research Corp., Cincinnati, Ohio (1969).
14. D.I.G. Jones and A.D. Nashif, "Damping of Structures by Viscoelastic Links," *Shock Vibration Bull.*, 36/4:9-24 (1967).
15. D.I.G. Jones and A.D. Nashif, "Damping of Blade-Like Structures," *Shock Vibration Bull.*, 39/4:19-29 (1969).
16. A.D. Nashif and D.I.G. Jones, "A Resonant Beam Tuned Damping Device," *J. Eng. Power*, 91:143-148 (1969).

# EFFECTS OF CORROSIVE ENVIRONMENTS ON FATIGUE LIFE OF ALUMINUM ALLOYS UNDER MANEUVER SPECTRUM LOADING

by

J.J. Gruff and J.G. Hutcheson

North American Rockwell Corporation

## INTRODUCTION

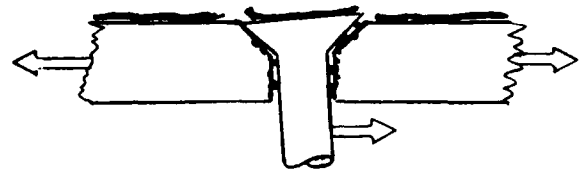
In recent years, aircraft manufacturers and operators have become increasingly aware of the necessity for establishing reliable methods for determining a safe service life for wing structures. For military aircraft, this is a particularly difficult task due to the fact that within any group of airplanes there may be wide variances in operational loadings and environments. Typically, the determination of wing service lives is based on a laboratory fatigue test of a full scale production wing to a maneuver load spectrum. Based on the fatigue life attained in the test - usually the last major failure which ends the program - a scatter factor is more or less arbitrarily applied to the test life to account for the expected scatter of fatigue life that could exist in a whole fleet of similar wing structures. Subsequently, actual service loadings experienced by the fleet are monitored on a periodic basis for comparison with the test load spectrum and service lives are modified for individual airplanes as their load history deviates from that applied to the test wing. Rarely, however, does the service life assessment take into account the degrading effects of severely corrosive environments to which service aircraft are often subjected.

High load factor military aircraft are generally fatigue-critical in their lower wing skins, which are typically aluminum alloy plate material with hundreds of countersunk holes for flush steel fasteners to attach the skins to spars and ribs. In service operation, as indicated in Fig. 1, these holes are particularly prone to corrosive attack as skin protective coatings and fastener platings break down from the fretting action due to relative motion occurring in the holes of the highly loaded fasteners. Foreign material and moisture enter between the fastener and hole surface by capillary action, providing an effective electrolyte for galvanic action between the steel fastener and aluminum wing skin. After prolonged operation, severe pitting and extensive exfoliation of some aluminum alloys can occur at critical holes. In Fig. 1 only the first two items are simulated in the actual laboratory fatigue test.

A variety of corrosion fatigue tests have been run over the years usually to study some particular corrosive effect on fatigue life. For example, specimens may be exposed to various corrosive environments and then tested to determine the environmental effect. Or they may be exposed during cycling to evaluate this effect. Or crack propagation and cracked strength in corrosive environments may be investigated. Each such study appears to indicate a new facet of corrosion fatigue and almost always

indicates that environmental effects are quite significant. Yet the applicability of the results to assessment of the service life of a fatigue critical aircraft structure often appears remote. One wonders - what if the specimen had had a stress concentration such as a hole with a fretted surface instead of being an unnotched polished material? What if the specimen had been a thicker plate material axially loaded instead of a simple rotating beam type or a thin sheet cantilever beam type? - What if the stress levels had been much higher such as experienced in military aircraft and, perhaps most of all, what if a maneuver spectrum type loading had been used which is after all the basis for the assessment of wing service life?

Maneuver spectrum loadings have been studied quite intensively in recent years and are known to have many complex effects not present in the constant amplitude test. For example, the few higher loads may produce favorable residual stresses to alleviate the effect of the more frequent lower loads. Reducing the minimum loads (in-



- Repeated variable amplitude tensile stresses.
- Repeated bearing stresses and relative fastener motion increasing  $K_T$  and fretting hole surface.
- Breakdown of paint, hole protective coating, and fastener plating allowing entrapment of dirt and moisture in the hole.
- Prolonged exposure to corrosive environments at tropical and seacoast airports and aboard aircraft carriers.
- Crevice corrosion and galvanic action accelerating corrosive attack on hole surface.
- Increasing surface pitting, and for some aluminum alloys intergranular attack and severe exfoliation.

Figure 1. Factors Affecting Wing Service Life.

creasing the amplitude) for "ground-air-ground" cycles will to a varying degree adversely affect life at all load levels, as will a periodic negative or compression load. Likewise the crack initiation and propagation phases of fatigue life and the crack size at failure can be completely different than in constant amplitude tests. All these factors appear important if service environments are to be evaluated for their effect on aircraft service fatigue lives.

Obviously, the combined effect of corrosive environments under a high stress spectrum loading is a complex integration of variables which will defy complete analysis for some time. However, some quantitative empirical appraisal of the combined effects appears necessary if there is to be real concern for the service life of operational aircraft in hostile environments as contrasted with the fatigue life demonstrated in the conventional laboratory test on new structure.

### TEST PROGRAM OBJECTIVES

One of the primary purposes of the subject pro-

gram was to study the fatigue behavior of 2020-T651 and 7075-T651 aluminum alloy plate materials under adverse environmental conditions such as may be experienced in service operation. These materials are used on the wings and tail surfaces of the RA-5C airplane, a Mach 2.0+ reconnaissance airplane which has had extensive usage in combat, aboard aircraft carriers, and at various geographic land bases. The materials are typically fatigue-critical at countersunk holes with flush steel fasteners for a maneuver type of spectrum loading. The basic program on these two materials was expanded to include similar evaluations of 7075-T73, 2024-T851, and 2024-T351 to test the general applicability of the results to these aluminum alloys which are in use on a number of military aircraft.

A related objective, especially for the 2020-T651 material, was to determine any difference that could be attributed to environment in the fatigue life of a new test wing and a surplus five year old test wing, which had two years of actual service and three years of exposed outdoor storage prior to test. In addition, an objective was to determine whether or not the use of water to simulate fuel

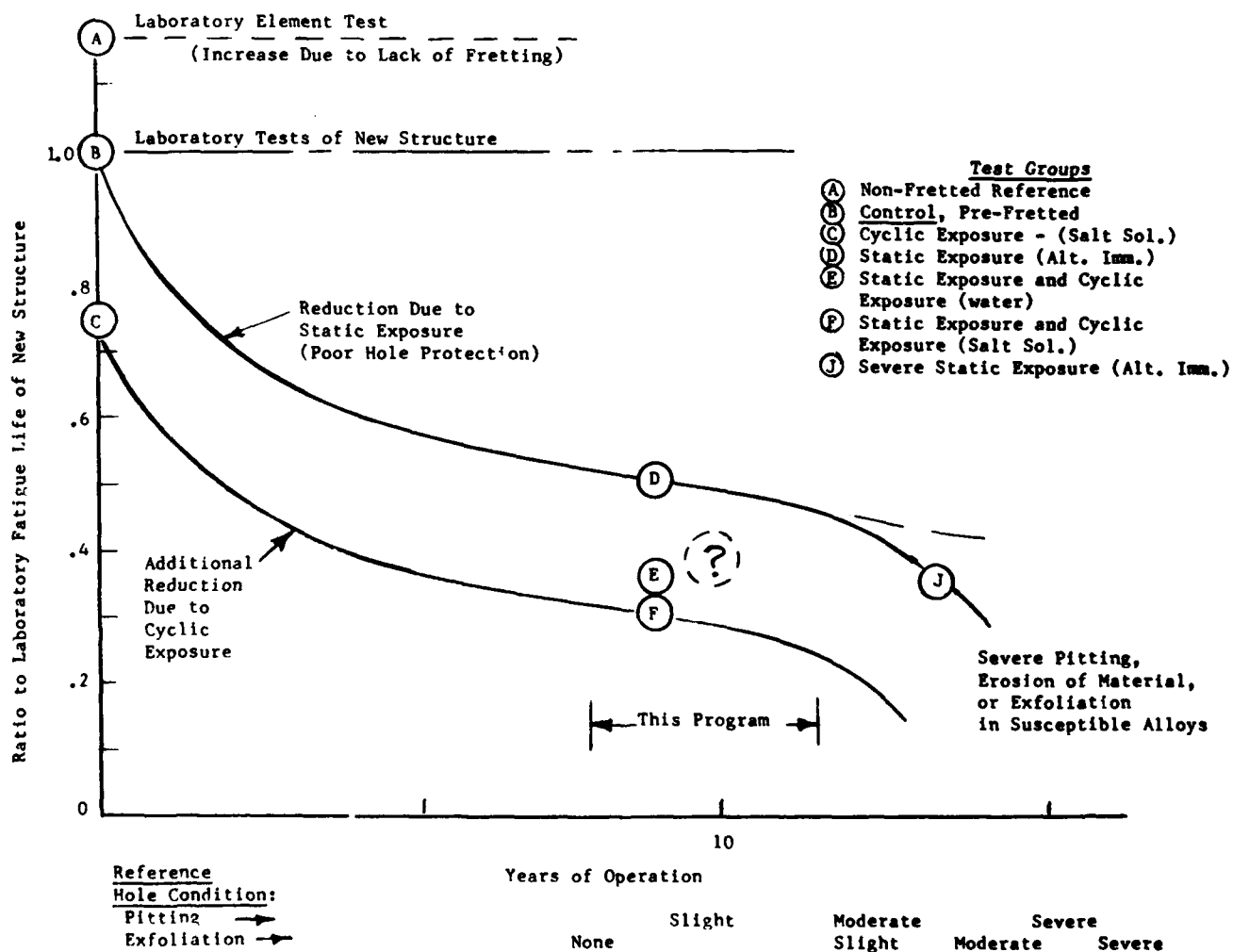


Figure 2. Effect of Corrosive Environments on Laboratory Fatigue Life.

pressures inside the test wing was also detrimental to fatigue life.

The subject program was performed on Phases IB and IIA of the RA-5C Extended Service Life Program under Contract N00019-68-C-0061 to the Naval Air Systems Command. Other phases of this program included full scale wing and fuselage fatigue tests of the RA-5C airplane, stress corrosion tests of complete wing components, and service life recommendations for critical components.

### TEST PROGRAM RATIONALE

Figure 2 illustrates, somewhat hypothetically perhaps, the anticipated reduction in wing fatigue life with years of service operation and exposure to corrosive environments. As protective coatings break down and the critical wing skin holes get increasing exposure to corrosive operational environments, hole surface conditions worsen, and fatigue life may be expected to be reduced as shown by the upper line on Figure 2. In Reference 1 correlations were obtained between the reduction in fatigue life and surface roughness or depth of pitting in 2024-T4 specimens. In addition entrapment of dirt, moisture, salt water, and various chemicals from the atmosphere or cleaning solutions between the fastener and wing skin material may cause the cyclic stresses to occur with adverse environments present further compounding the loss of fatigue life as shown by the lower line on the Figure. Numerous fatigue tests conducted with adverse environments during cycling without static exposure have demonstrated the reduction in fatigue life that can occur under these conditions. This would represent the loss of fatigue life at 0 years in the chart. Several studies, such as Ref. 2 have shown that even changes in laboratory humidity during cycling can significantly affect fatigue life. Similarly distilled water and salt solutions of increasing strength will progressively reduce fatigue life, although at a decreasing rate as was noted in Ref. 3. In relatively short time outdoor tests reported in Ref. 4, where static exposure and cyclic exposure were factors, bare 7075-T6 and 2024-T3 specimens experienced an appreciable drop in fatigue life.

After prolonged operation with poor hole protection and aluminum alloys which are susceptible to intergranular corrosion a further sharp drop in fatigue life may occur as indicated on Figure 2. References 5 and 6 are examples of test programs conducted on service parts "as is" with varying degrees of intergranular attack and exfoliation, which indicated large losses of fatigue life. If exposures to corrosive environments during cycling had also been simulated, it is likely that the loss of life would have been even greater.

Figure 2 is also used to set the stage for testing conducted under this program. The various encircled letters A through F on the Figure indicate what each test group is supposed to simulate. Group B is considered the control

group simulating results from a wing or component fatigue test on new structure where moderate hole fretting may occur at holes with fasteners. Group A is a reference to establish what fretting effects did to control Group B and may be considered similar to a laboratory element test of a hole type specimen where typical drilled hole finish exists. All groups except A include the pre-fretting effect. Group C then represents cyclic exposure only, Group D static pre-exposure only, and E and F static pre-exposure and cyclic exposure. The only difference between E and F is that group E specimens are dampened with distilled water and group F specimens are dampened with a 3-1/2% salt solution.

As indicated in Figure 2, the objective of this program was to make a first cut at bracketing what happens to fatigue life after a period of extended operation, but before hole conditions become noticeably poor. Some arguments should be advanced to defend the general shape of the static exposure curve in Figure 2, i.e., that the initial drop in fatigue life occurs early and remains stable for a considerable period of time until a drastic change in stress concentration occurs due to exfoliation or through erosion of material at the hole. If the curve is indeed stable for a long period then the choice of the static exposure period to be simulated by test is not too critical within the limits noted. For example, whether the accelerated laboratory static exposure period is say 20, 30, or 60 days is not particularly significant. Some admittedly circumstantial evidence for this situation is shown on Figures 3A and 3B. In Figure 3A, from Ref. 7, the maximum depth of pitting over 7 years of exposure to seacoast environments is plotted for a large variety of bare aluminum alloys in sheet form.

Similar curves on aluminum alloys are available for a variety of seacoast, industrial and rural geographic locations. The characteristic shape of these curves is generally the same. A rapid rise in the first year with a rapidly declining rate of corrosion in the following years. Fig. 3B plotted from data in Ref. 1, shows the effect on fatigue life of accelerated laboratory corrosive pre-exposures. Although exposures of up to 32 days in the 20% salt spray solution were simulated, the greatest drop in fatigue life occurred by the first day. It may not be clear from the Figure, but significant drops were also observed after only 4 hours and 8 hours of exposure. The Figure also shows that depth of pitting in the test increased rapidly in the first few days and then continued to increase slightly for the remainder of the test without much effect on fatigue after the first few days. It should be noted that the relative drop in fatigue life is large in these tests since unnotched specimens were used, but it appears to make the point very well for an initial early drop in life with relatively little change thereafter.

Figures 4A and 4B tell somewhat the same story. These were tests on 3/8 inch 7075-T651 plate specimens with 5/16 diameter countersunk hole conducted as part of

the present program. This is the same type specimen used for the majority of tests to be discussed later. The upper curve of Figure 4A shows that alternating exposure periods with cycling periods is less severe on fatigue life for the same total exposure than a single pre-exposure period for a comparable total exposure time. These exposures were made in the standard alternate immersion tank with 3-1/2% salt solution.

Figure 4B shows that even relatively short time exposures to moderate outdoor environments will produce a early drop in fatigue life. For reference purposes, the relative drops in life obtained in Group D 30-day alternate immersions pre-exposure tests on 7075-T651 specimen used in this test program are indicated at the far right of each Figure.

In the subject program the effects of cyclic exposure on fatigue life are bracketed for service evaluation purposes by testing static exposure specimens (Group D) without any corrosive environments during cycling and then with 100% of the cycling when dampened with distilled water (Group E) and separately with 100% of the cycling with 3-1/2% salt solution (Group F). In Ref. 3 it was noted that greatest per cent reduction in life occurred when tests were run in water relative to air, and increasing the salt concentrations of the water only produced a somewhat smaller increase in the fatigue life reduction. It would appear that precise choice of cyclic environment, whether moisture, salt water, or increased salt deposits is also not a critical factor.

**Figure 3A. Maximum Depth of Corrosion in Aluminum Alloys, Sea Coast United States (Ref. 7), Various Alloys.**

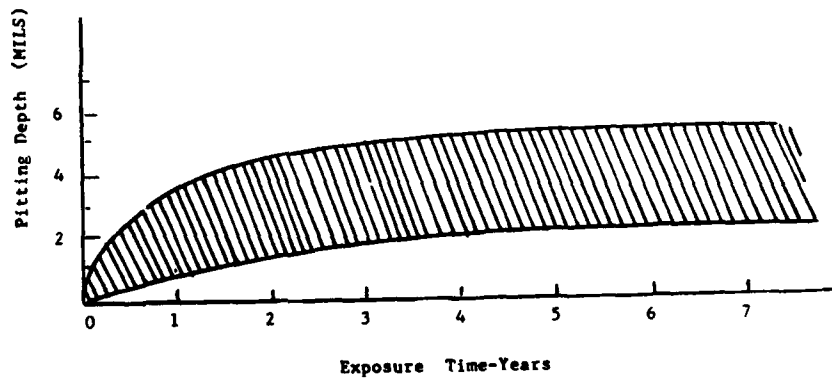


**Figure 3B. Effect of Exposure Time on Fatigue Life (Plotted from Ref. 1). 2024-T4 Unnotched Rotating Beam; Log Mean Life Unexposed: 5,598,000.**

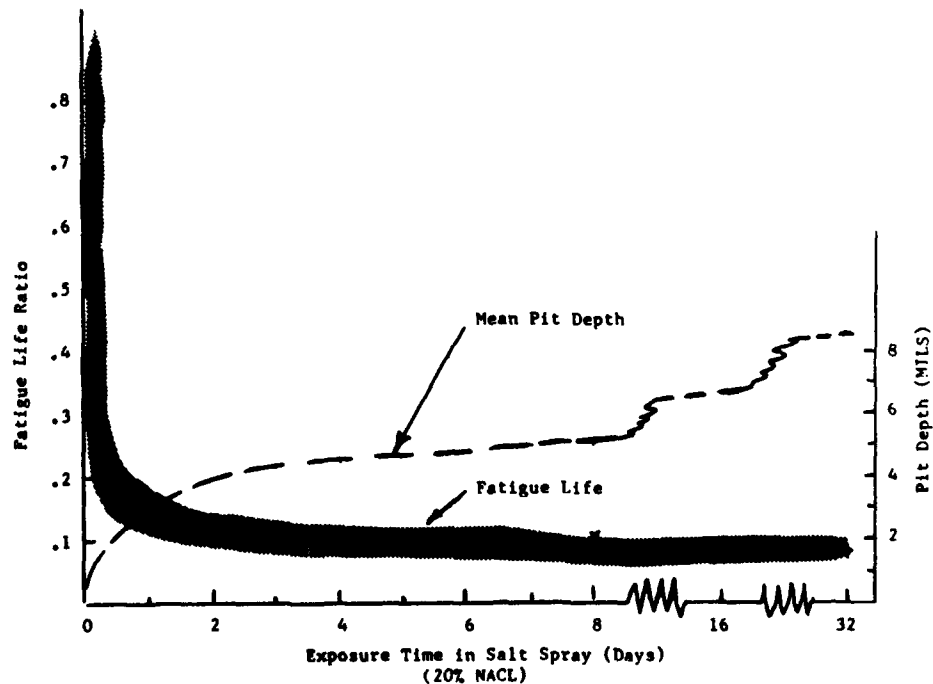


Figure 4A. Alternate - Immersion Exposure Constant Amplitude Tests 7075-T651. Control Specimen Mean: 4349 Cycles.

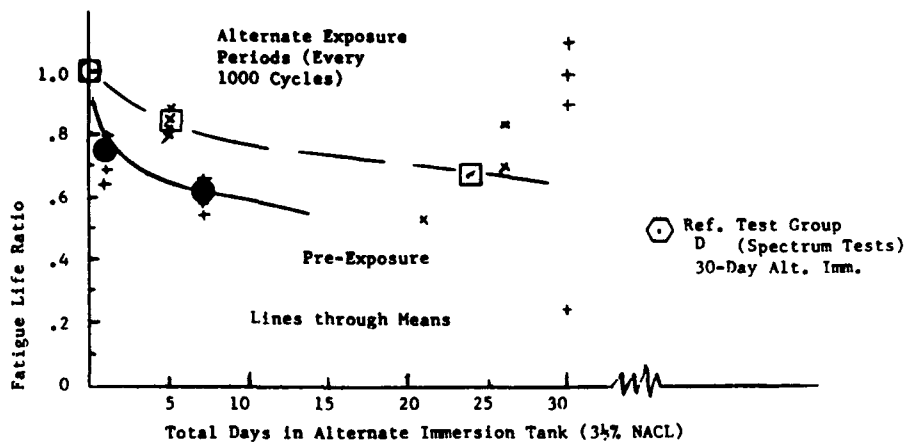
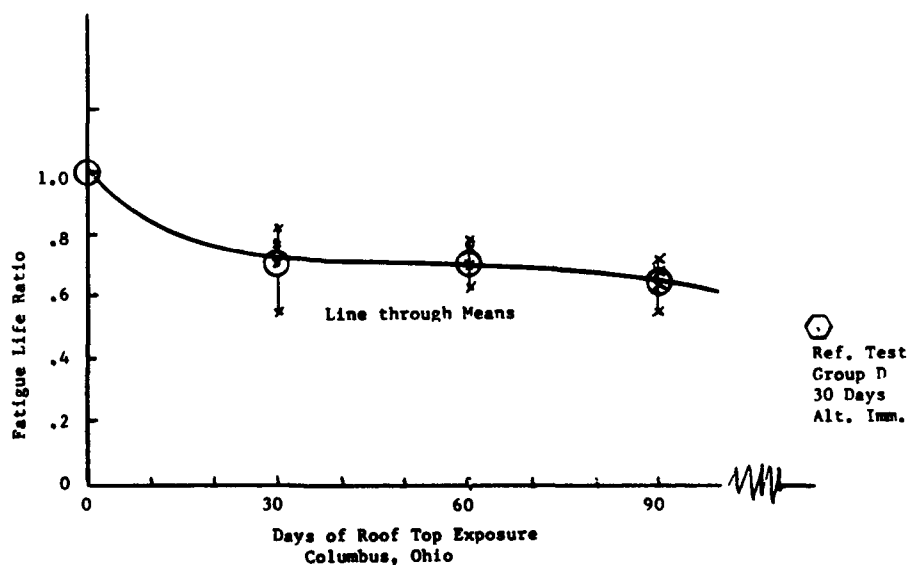


Figure 4B. Outdoor Environment Spectrum Tests - 7075-T651. Control Specimen Mean Life: 14,000 Hrs.



## TEST PROCEDURE

The test specimens and procedures used in this program are discussed in this section. Procedures are discussed in the chronological order used to conduct the tests where all procedures were required, as for Test Groups E and F.

### Materials

Table I lists the five aluminum alloy plate materials utilized in the subject program. The alloys represent a wide range of static and yield tensile strengths, tempers, chemical compositions, resistance to exfoliation and stress corrosion cracking, crack propagation resistance, and fracture toughness. None of the alloys, however, can be considered as having a high or special resistance to general or surface corrosion in the unclad or unplated condition

when exposed to outdoor or salt water environments.

### Specimen

The basic specimen is shown in Figure 5. Two holes were used in tandem since it was felt the unfailed hole would be useful for supplementary non-destructive inspections of an incipient failure condition after failure of the first hole had occurred. The test section holes were 5/16 inch diameter drilled and countersunk holes, as might be required for flush steel fasteners in a typical wing skin of this thickness. The stress concentration factor for the specimen was approximately 2.5.

Specimens were typically evaluated without any protective coating except that limited tests were also conducted on 2020-T651 and 7075-651 specimens with the holes given a brush "Alodine" treatment (MIL-C-5541) typical of that used on production RA-5C wing skins.

**TABLE I.  
SUMMARY OF MATERIAL PROPERTIES**

Mechanical properties are for the specific lots used in test program. Other properties are from the available literature on aluminum alloy plate materials.

MATERIALS		2020-T651	7075-T651	2024-T851	7075-T73	2024-T351
1 Original Plate Thickness		0.781	0.375	0.375	0.375	0.375
2 Condition		Artificially Aged	Artificially Aged	Artificially Aged	Over Aged	Naturally Aged
3 Principal Chemicals, % (Nominal)		Cu - 4.5 Li - 1.3	Zn - 5.6 Mg - 2.5 Cu - 1.6	Cu - 4.5 Mg - 1.5	Zn - 5.6 Mg - 2.5 Cu - 1.6	Cu - 4.5 Mg - 1.5
4 Mechanical Properties of Test Specimens	UTS-KSI	83.1	83.6	68.2	72.7	66.8
	YTS-KSI	75.0	74.7	59.8	58.8	48.2
	Elong %	6.3	14.0	9.7	13.7	17.0
5 General Corrosion Resistance (3-1/2% NaCl Alt. Immersion Exposure)		Fair	Fair	Fair	Fair	Fair
6 Exfoliation Resistance		High	Low	High	High	Low
7 Stress Corrosion Resistance (S.T. Grain Direction)		Very High	Low	Very High	Very High	Low
8 Crack Propagation Resistance (Est. relative order of resistance)		5*	3	4	2	1
9 Approximate Fracture Toughness (KSI $\sqrt{In}$ )						
K <sub>1c</sub> = Fat. Cr. (Long)		18	28	26	37	High
K <sub>c</sub> = 1/4 in. Thick (Long)		25	50	40	75	110

\* At high stress intensities; Approximately 2 for low stress intensities.

In order to determine the feasibility of reworking holes which were corroded and at incipient failure a separate Group K test series was conducted. These specimens were tested to determine the additional life which could be obtained if the corrosive test holes were reworked to remove cracks after detection. The original specimens were 2020-T651 which were fretted, alternately immersed for 30 days in 3-1/2% salt solution and tested in 3-1/2% salt solution until a crack or cracks were detected. The specimens were reworked by progressively reaming and etching the test holes until the cracks were completely removed. Additional 2020-T651 control specimens were machined to the same size test holes as the reworked specimens, and then both control and rework specimens were spectrum cycled in air until failure. The originally

exposed specimens of this group also indicated more severe corrosive effect than the specimens of Groups D, E, and F.

In an attempt to measure the corrosive effects of actual prior airplane service history an additional group of specimens called Group H were also prepared as shown in Figure 6. This Group consisted of ten upper and ten lower 2020-T651 wing skin specimens which had been removed from an A-5A wing with a history of approximately 750 flight hours and approximately 5 years of outdoor exposure. For both the upper and lower skin specimens, four were used as controls, three were tested in air, and three were tested in tap water as previously described. The "control" specimens were fabricated by reaming 0.015"

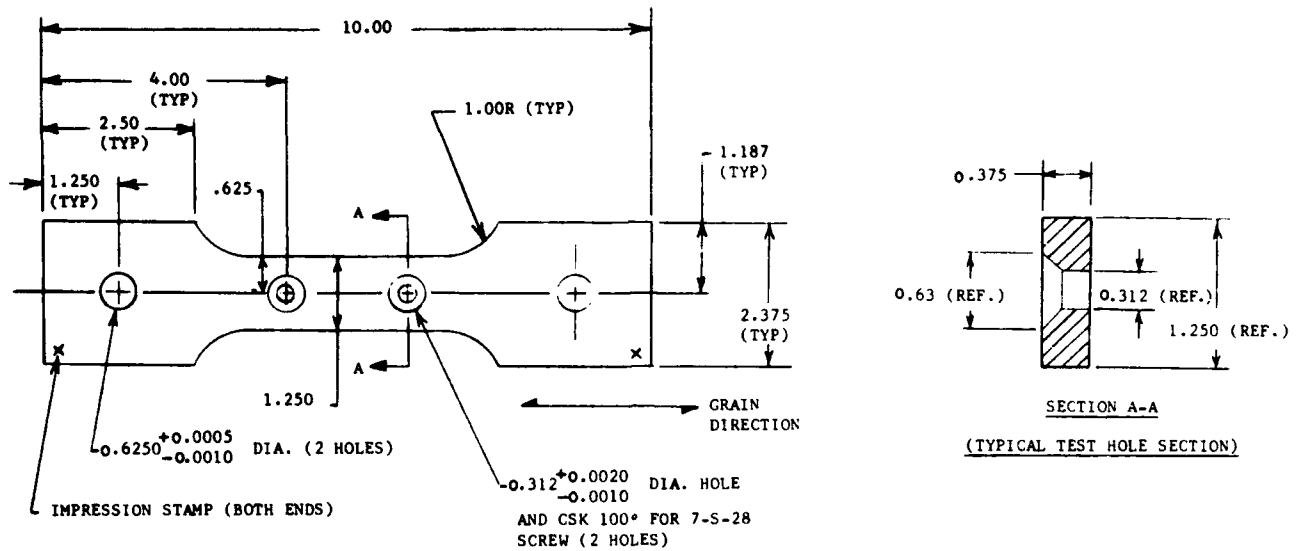


Figure 5. Test Specimens (All Groups Except H).

from all inside surfaces of the test hole (total of 0.030" on the diameter) in an attempt to remove all existing corrosive damage in the hole.

As indicated in Section A-A of the Figure, a significant feature of these wing specimens was that rubber "O" rings are typically used in the counter-bore to prevent fuel leakage and the point of fatigue origin in tests would be on the inside of upper and lower specimens, or in a protected location with respect to service exposure.

**Hole Pre-Fretting Procedure**

Except for reference Test Group A, the holes were given a pre-fretting procedure as shown in Figure 7, prior

to corrosion exposure and fatigue testing. The purpose of the pre-fretting procedure was to induce a moderate surface roughening of the hole inside diameters, as would be expected to exist in service due to repeated bearing stresses from a steel fastener. It was considered essential to avoid the polished type hole condition that frequently exists in perfectly prepared laboratory specimens if the effects of corrosive environments were to be realistically evaluated in terms of service usage. As indicated in the Figure, specimens were symmetrically loaded in pairs so that bearing stresses were distributed as uniformly as possible throughout the hole. This set-up permitted the application of high bearing stresses relative to tensile stresses as noted in the table on the Figure. The maximum tensile stress in

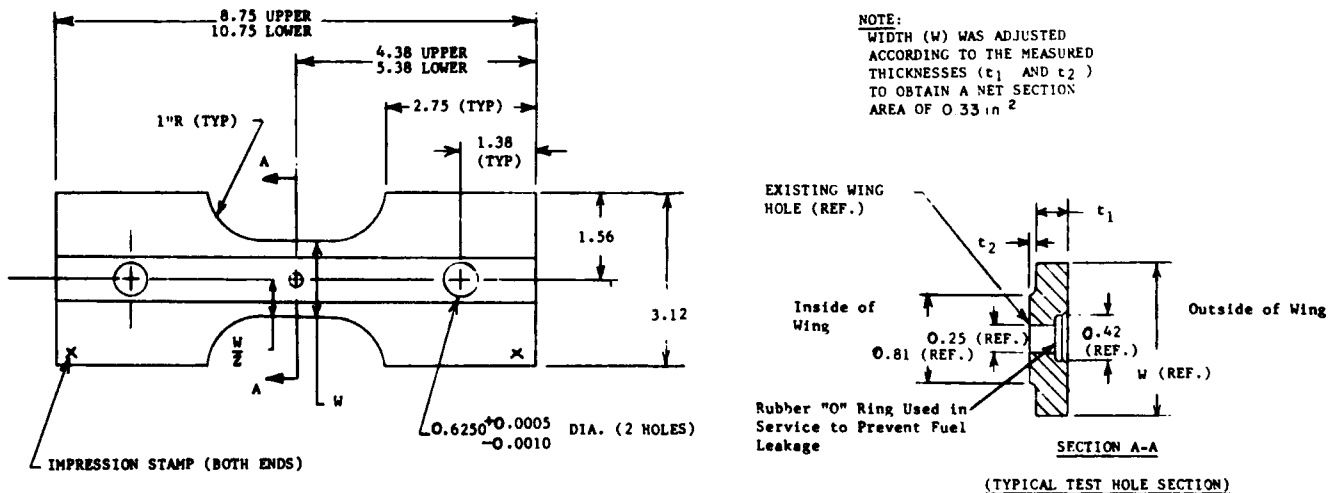
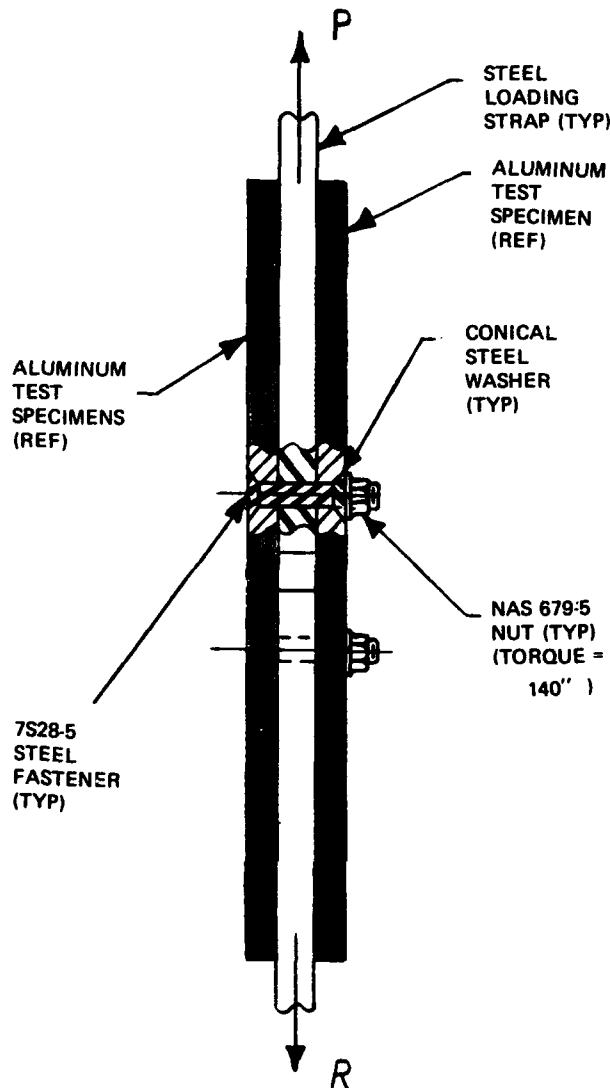


Figure 6. A-5A Wing Skin Specimens (Group H).





Pre-Fretting Loading

Order of Application	Load / Test Hole (Lbs.)	No. Cycles	Net $f_t$ (KSI)	NOM $f_{b_r}$ * (KSI)
1	3500	10,000	10.6	30
2	5250	500	15.9	45
3	7000	100	21.2	60

\* Includes countersink area; if all countersink area is neglected,  $f_{b_r}$  would be approximately 50% greater.

Figure 7. Pre-Fretting Procedure.

the pre-fretting procedure was less than the lowest stress applied in the fatigue spectrum, to be discussed in the next section, so that negligible fatigue damage would be induced by the fretting procedure. Any actual loss of life that can be attributed to the pre-fretting procedure must be considered the result of increased surface roughness in the hole.

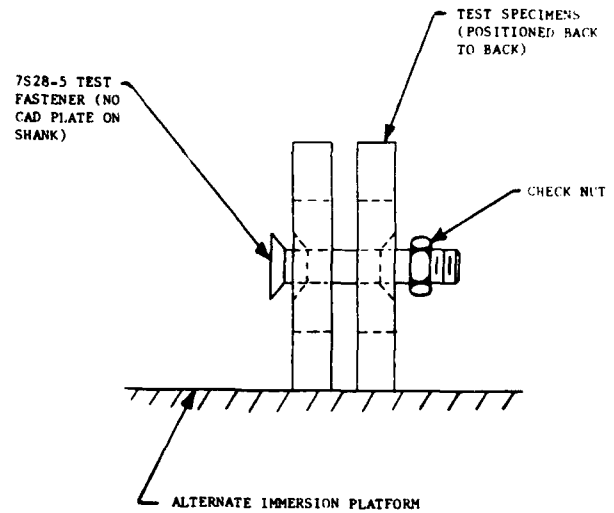


Figure 8. Typical Assembly for Static Exposure

### Static Exposure

After the pre-fretting procedure, specimens to be evaluated with static exposure to corrosive environments were given a 30 day exposure to the standard alternate-immersion test using a 3-1/2% salt solution in distilled water. During this exposure specimens are immersed in the solution for 10 minutes and allowed to dry for 50 minutes of each hour on a 24-hour, seven-day-week basis. A Ferris Wheel type apparatus was used to accomplish the immersion and drying cycle.

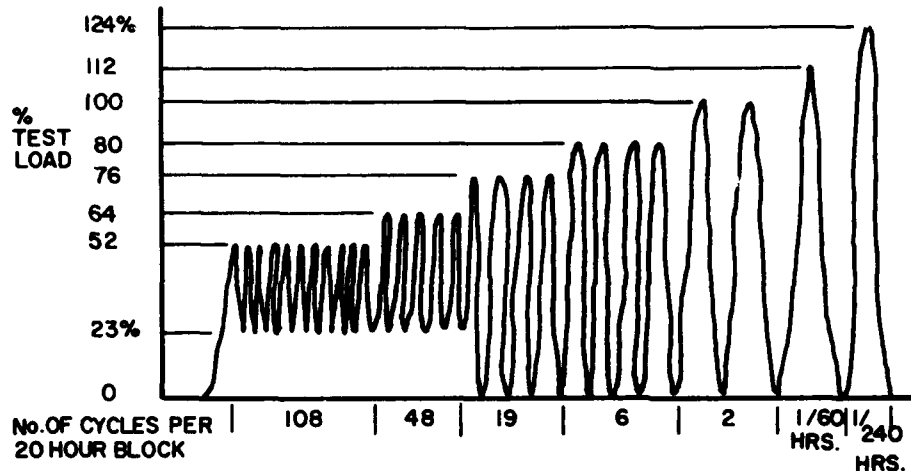
Specimens were prepared for the exposure by removing the cadmium plating from flush steel 7S28-5 fasteners used during the fretting program and assembling test specimens in pairs with the fasteners to promote galvanic corrosion in the test section holes as shown in Figure 8. Grip end holes were protected by wax coatings.

After the 30 day exposure period the fasteners were removed from the holes and thoroughly cleaned so there would be no additional corrosion prior to fatigue testing.

A few specimens which were being given the 30-day alternate-immersion exposure at a later time period than the other specimens unaccountably developed a considerably more severe exposure very early in the exposure period. These specimens which were 3 non-fretted 2020-T651 and 3 non-fretted 7075-T651 were placed in a separate Group J.

In addition to the 30-day alternate-immersion exposures, a group of specimens known as Group G were given outdoor exposures at Columbus, Ohio, at the North American plant in what might be called a "moderate industrial" environment. These additional 2020-T651 and 7075-T651 specimens were fretted, subjected to rooftop

100% Test Load = 45 KSI Net Tension  
Test Speed 120 CPM



% Load		Frequency Per 20 Hour Spectrum Block (Except as Noted)
Max.	Min.	
52	23	108
64	23	48
76	0	19
88	0	6
100	0	2
112	0	1/60 Hours
124	0	1/240 Hours

**NOTE:**

This spectrum was used for all materials tested except that for the 2024-T351 aluminum the 124% load was omitted because it exceeded the tensile yield strength for the material.

**Figure 9. Fatigue Spectrum.**

exposure and tested in air. The rooftop exposure consisted of assembly of the specimens in pairs with "stripped" 7S-28-5 fasteners, as was done with the alternately immersed specimens, and placing them on the rooftop for normal exposure to the elements. Specimens of each material were exposed for 30, 60 and 90 day periods.

**Fatigue Test Spectrum**

The test spectrum was based on the maneuver spectrum used for fatigue tests of the RA-5C wing and is shown in Figure 9. Maximum loads in the spectrum ranged from 52% to 124% of the 100% design condition load. Minimum loads were 23% for the two lower levels in the spectrum based on an assumed operational 1.0g load level, and zero for the higher load levels to account for the expected number of ground-air-ground cycles when the lower wing skin is essentially unloaded. A net tension stress level of 45 KSI at 100% test load was selected for the evaluations. This is a higher limit stress level than would be typical of high load factor military aircraft, but was required because the specimen stress concentration factor of approximately 2.5 was lower than would be typical of such wings. The theoretical peak stress at the hole edge, however, would correspond to an operational limit stress of say 32 KSI and a stress concentration of 3.5. The practical consequences of selecting a lower stress level for testing with this specimen would of course have been to add many months of fatigue cycling to the test program because of the need to cycle at the slowest practical rate for the corrosion evaluations and the high number of cycles that must be applied in spectrum loadings of this type.

An unfortunate result of the selection of the 45 KSI stress level was that at the 124% maximum load level the nominal net stress exceeded yield for the 2024-T351 specimen and it was considered necessary to eliminate this load level, which is applied only once every twelfth block,

when testing 2024-T351 specimens in the basic program. Comparative spectrum tests of 2024-T351 with and without the 124% load level in non-corrosive environments indicated that the fatigue life would have been reduced about 25% if this load level had been retained, in addition to producing noticeable yielding across the net section of the specimen. This difference in loading spectra should be kept in mind when comparing the absolute fatigue lives of 2024-T351 with the other alloys in the program; however, its relative performance in the various corrosion environment is considered valid.

As a number of investigators have observed, test speed is a critical parameter in corrosion fatigue testing, with slower cycle rates tending to show greater losses of life due to corrosive environments. In Ref. 3, for example it was noted that reducing the test speed from 2000 CPM to 1400 CPM and to 800 CPM caused progressive reductions in constant amplitude fatigue life over a wide stress range in 2024-T-4 specimens tested in a 3% NaCl solution. Maneuver loads in service to high load factors will be sustained for at least a few seconds and often for much longer times depending on the type of maneuver. Accordingly it was felt that testing at speeds much higher than 1 to 2 cycles per second might not be realistic for evaluation of a maneuver load spectrum in corrosion environments. A speed of 120 CPM was adopted for this program.

During the spectrum fatigue tests, inspections were conducted periodically to determine when crack initiation could first be detected in the hole and to determine the crack growth rate until complete fracture occurred. A "Micro-Mike" with 20X magnification was used with a flashlight for crack inspection. In nearly every specimen, fatigue cracks initiated at the base of the countersink in the hole and proceeded up the countersink as well as down into the hole. This situation proved fortunate for attaining a common base for evaluating crack initiation and propagation. By performing "non-stop" inspections at the

88% and 100% load levels in the spectrum, cracks could be fairly reliably detected when they reached 1/64 inches in length measured along the countersink. Liquid Zyglo penetrants were used on the non-corrosive environment specimens in Test Groups A and B to aid in the crack inspection, but only visual inspections were used in the corrosive environment tests to avoid the possibility of the penetrant inhibiting or accelerating the crack growth rate. Some limited constant amplitude tests on a 7075-T651 specimen with and without Zyglo penetrant, in non-corrosive environment, indicated that fatigue life was not affected by the use of the penetrant.

#### Test Setup for Fatigue Spectrum Loading

The basic loading system for all phases of this test consisted of a hydraulic actuator, a Baldwin-Lima-Hamilton load cell, and the test specimens installed in series by means of loading straps as shown in Fig. 10. Both loading systems were installed in a structural steel frame with Universal joints at each end of the assemblies to assure proper alignment of the specimens under load.

The loading systems were controlled by electro-hydraulic test equipment. Hydraulic pressure was supplied to the actuators, thru electrically controlled hydraulic systems, by a Denison hydro-pump. Each hydraulic system consisted of a control manifold, which regulated hydraulic flow to the actuator by means of a servovalve, and a by-pass manifold, which provided system pressure control and efficient fluid flow. Each servo-valve was electrically controlled by a separate servac unit incorporated in an M.T.S. Load Programmer. Automatically sequenced spectrum blocks were accomplished by programming the desired load levels on a closed loop tape system. Higher loads, which occurred less frequently than the number of spectrum blocks programmed on the tape loop, were applied by a Data Trak System. During all tests, the load cell signal was monitored on a calibrated Mark 280 recorder. Another Mark 280 recorder, which monitored the tape output and the composite signal of the electrical control system thru the load programmer, was used as a "trouble shooter". Any problems which developed in the control system could be isolated immediately.

Several devices were installed and servicing was performed prior to and during the test to minimize problems in the system which could cause deviation from the load program or even cause premature failure of the test specimens: A diode clipper was installed to eliminate an overload signal from the tape, a relay switch was installed to automatically "short out" the tape output signal as the tape splice passed thru the recorder head, error detectors were adjusted on the load programmer so that the loading system would be deactivated if a slight deviation from the desired signal occurred, the tape recorder head was cleaned after 8 hours of running time, gauze wipers were installed on the tape to minimize buildup of foreign elements on the head during operation, tapes were replaced after ap-

proximately 20,000 spectrum hours, micron filters in the servovalve were cleaned periodically, and the hydraulic oil in the system was analyzed for cleanliness on several occasions.



Figure 10. Typical Spectra Fatigue Test Setup.

### Cyclic Exposure

During the fatigue spectrum cycling described above for Test Groups C, E and F corrosive environments were simulated. For Groups C and F the specimen holes were filled with cotton which had been saturated with a 3-1/2% salt solution. The specimen test sections were then wrapped with cotton dampened with 3-1/2% salt solution. During cycling, additional solution was applied by a squeeze bottle to keep the cotton moist. A similar procedure was used for Test Group E except that distilled water was used in place of the salt solution. When cycling was stopped, at night or over weekends, the cotton was removed and the specimens were cleaned so that static exposure effects would be minimized in this phase of testing in which cyclic exposure effects were intended to be simulated.

### Summary

The test procedures applied in the basic program are summarized in Table II.

### SUMMARY OF TEST RESULTS

The test results are presented in Figures 11 through 18. In general all the aluminum alloy plate materials experienced significant and progressive reductions of mean fatigue lives for increasingly severe corrosive environments. Figure 11 shows the relative reduction in mean lives for the five alloys in various test groups compared to control

Group B and indicates the following:

1. The effects of the pre-fretting procedure itself on fatigue life are determined by comparing Groups A and B. This effect was generally less than 10% for all alloys except for 2020-T651 where a larger change due to pre-fretting alone was observed.

2. The 3-1/2% salt solution cyclic exposure of Group C produced a drop of about 25% in the median fatigue life of the alloys.

3. The 30 day alternate-immersion exposure prior to test of Group D produced a drop of nearly 50% in median fatigue lives when cycle tested in air. A much more severe exposure inadvertently experienced on 7075-T651 and 2020-T651 specimens exposed separately from the basic group and called Group J experienced a drop of almost 65% in fatigue life. The hole condition of these Group J specimens showed a severe pitted hole surface.

4. The combined effects of static exposure and 3-1/2% salt solution cyclic exposure of Group F produced an average drop in fatigue life of 70% for the five aluminum alloys. Group E tests on only 7075-T651 and 2020-T651 in which the cyclic exposure was distilled water instead of salt solution produced a similar drop of 70% for these two alloys, indicating only a small effect for the use of salt solution in place of distilled water.

Figure 12 shows the effects of the various environ-

TABLE II.  
SUMMARY OF TEST PROCEDURES

BASIC SEQUENCE		TEST GROUPS									
		A	B	C	D	E	F	G	H	J	K
1. PRE-FRETTED BY											
A. Fastener Bearing Stresses			X	X	X	X	X	X			X
B. "As Is" From Service Wing									X		
2. STATIC EXPOSURE											
A. 30 Day Alt. Immersion (3-1/2% NaCl)					X	X	X			X	X
B. Same, But Severely Corroded											
C. Outdoor (30/60/90 Days) Moderate Industrial Environment								X			
D. "As Is" From Service Wing									X		
3. SPECTRUM CYCLING IN											
A. Air		X	X		X			X	X	X	
B. Water Dampened						X			X		
C. 3-1/2% NaCl Solution Dampened				X			X				X
4. REWORKED PRIOR TO FAILURE AND TESTED IN AIR											X
		15	21	21	15	6	21	18	20	6	4
No. of Specimens @ Material (147 Total Specimens)	TOTAL PER GROUP	15	21	21	15	6	21	18	20	6	4
	2020-T651/W Alodine	3	3/3	3/3	3	3	3/3	9	20	3	4
	7075-T651/W Alodine	3	3/3	3/3	3	3	3/3	9	-	3	-
	7075-T73	3	3	3	3	-	3	-	-	-	-
	2024-T851	3	3	3	3	-	3	-	-	-	-
2024-T351	3	3	3	3	-	3	-	-	-	-	

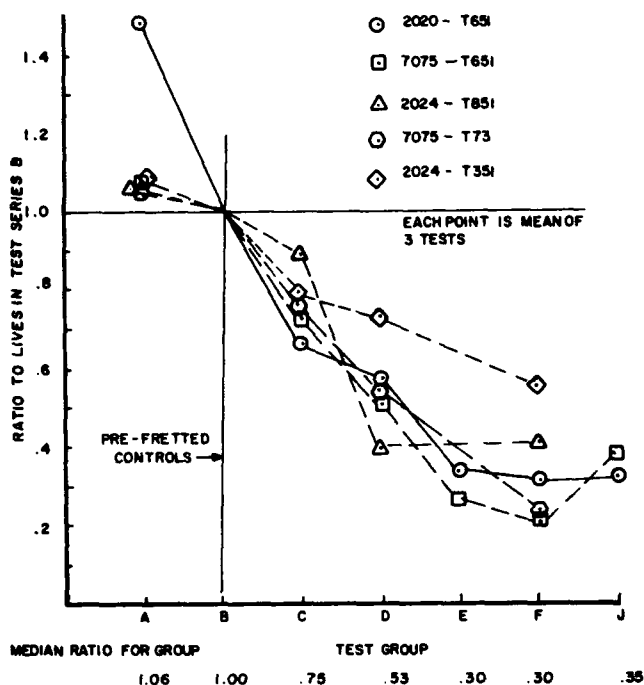


Figure 11. Relative Reduction in Fatigue Lives.

ments on time to crack initiation - defined here as the time for initiation of a 1/64 inch crack at the base of the countersink as shown in the Figure. As may be noted from this Figure cyclic exposures (Group C) and static exposure (Group D) when simulated separately each produced significantly earlier crack initiation. The combined effects

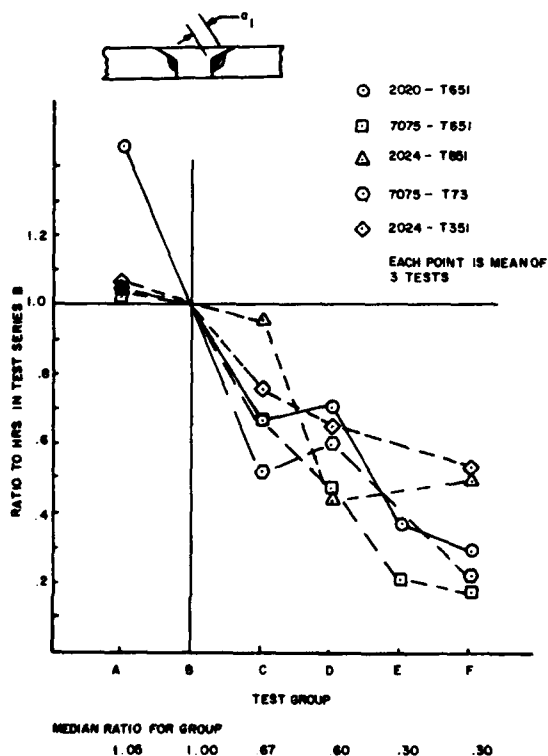


Figure 12. Relative Spectrum Hours to Crack Initiation (From 0 Hours to  $a_1 = 1/64''$ ).

of cyclic and static exposure likewise produced an average drop of 70% in the crack initiation period as noted for Groups E and F on the Figure.

Figure 13 shows the effects of the various environments on the crack propagation period - from 1/64" crack at the base of the countersink to complete fracture. Although the results are more diverse for the individual alloys, static exposures of Group D had a much greater effect on shortening the crack propagation period than did Group C cyclic exposures. In Group F four of the five alloys showed a remarkably close correlation each having about a 70% reduction in crack propagation period due to the effects of static and cyclic environment. Since crack length at fracture was not significantly affected by corrosive environments, as will be shown on the next Figure, the average crack propagation rate for the four alloys was approximately tripled by the static and cyclic corrosion environments.

Figure 14 shows the effects on residual cracked strength of the various corrosive environments. The effective crack length "2a" as measured after specimen failure appeared to be unaffected by environment for any of the alloys tested.

Figure 15 shows the effects on spectrum fatigue lives of the 2020-T651 and 7075-T651 specimens. The cross-hatched portion of each bar shows the crack propagation period as previously defined. The 7075-T651 specimens had the greatest control specimen life (Group B)

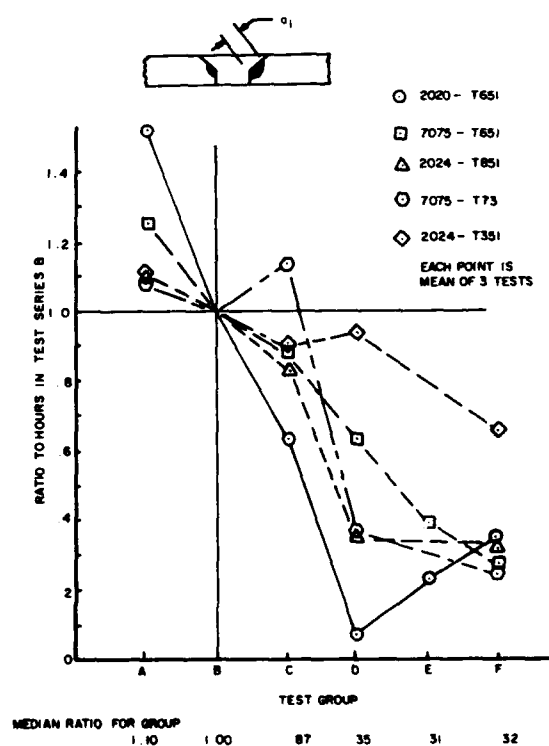


Figure 13. Relative Reduction in Crack Propagation Period -  $L_p$  (From  $a_1 = 1/64''$  to Failure).

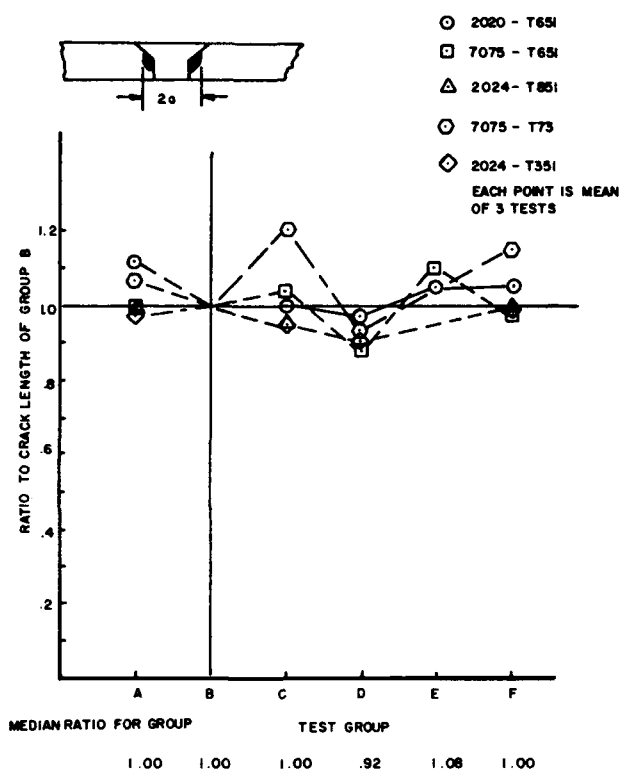


Figure 14. Residual Cracked Strength Based on Relative Crack Length at Failure - 2a.

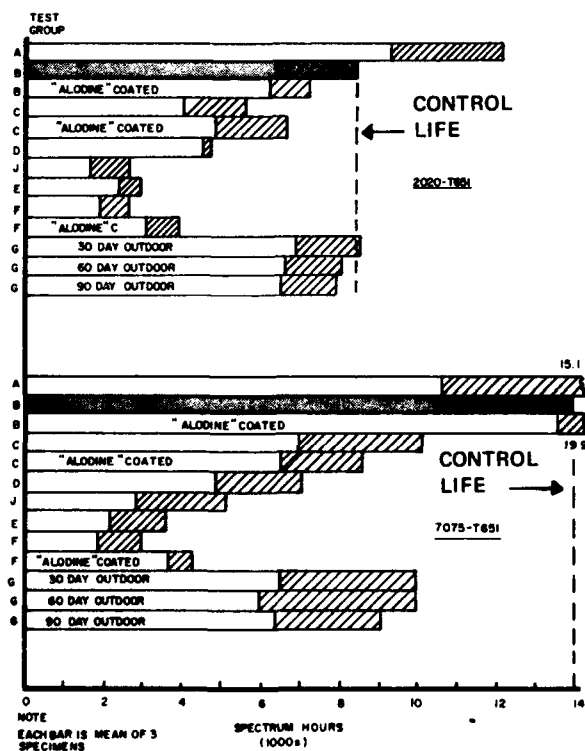


Figure 15. Mean Spectrum Fatigue Lives of 2020-T651 and 7075-T651 and Mean Crack Propagation Periods.

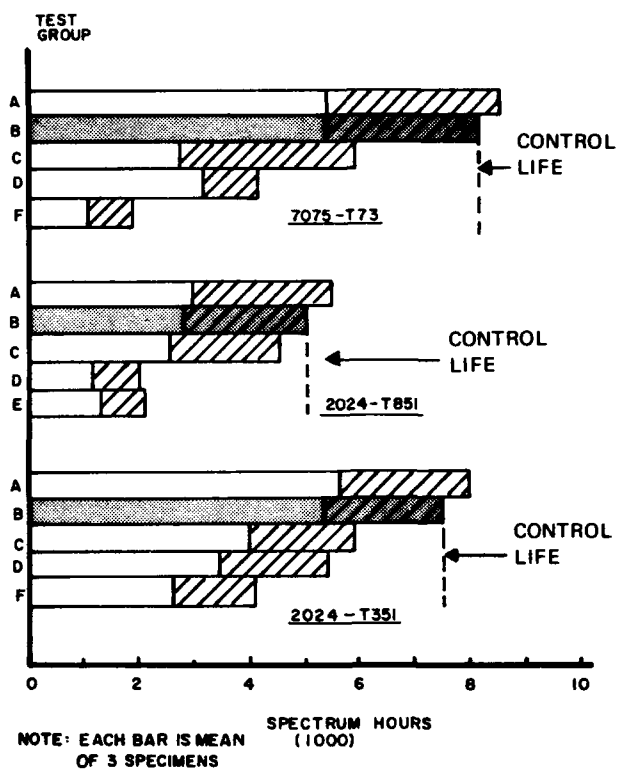


Figure 16. Mean Spectrum Fatigue Lives of 7075-T73, 2024-T851, and 2024-T351 and Mean Crack Propagation Periods.

of the five alloys, but also experienced the greatest relative reduction in life under static and cyclic exposure. This Figure also shows the overly-exposed mean life of Group J specimens which resulted in a further significant drop in life from comparable Group D specimens which received the normal 30-day alternate immersion exposure. The "Alodine" coated specimens of Group F appeared to offer some marginal benefit in preventing the loss of fatigue life in both materials. The relatively short outdoor exposures to 30, 60, and 90 days of moderate industrial environments (Group G) had a negligible effect on 2020 fatigue lives, but surprisingly even the 30 day exposure of the 7075 specimens reduced mean spectrum life about 30%.

Figure 16 shows the effects of the various Groups on mean spectrum fatigue lives of the 7075-T73, 2024-T851 and 2024-T351 specimens. The 2024-T351 specimens had the smallest relative reduction in fatigue life. The 7075-T73 specimens experienced almost identical relative drops in fatigue life to the 7075-T651 specimens although the -T651 specimens had approximately twice the fatigue life in each test group. Apparently such factors as increased fracture toughness and resistance to exfoliation and stress corrosion attacks are of no direct benefit for fatigue life in corrosive environments provided that significant exfoliation of the hole surface has not yet occurred.

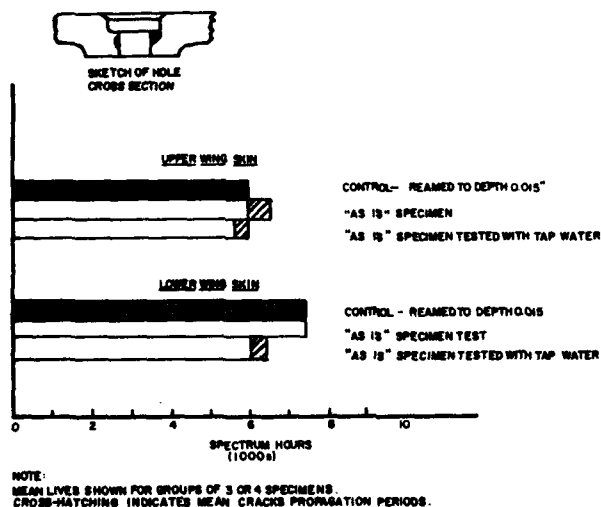


Figure 17. Mean Spectrum Fatigue Lives of 5-Year Service Wing Specimens (2020-T651) Group H.

Figure 17 shows the results of fatigue tests conducted on specimens cut from the upper and lower wing skins of an A-5A service wing with a total of five years of outdoor exposure. The existing holes in some specimens were reamed to remove possible corrosion and fatigue damage prior to test to create a control specimen. Other specimens were tested "as is", but were observed to be in excellent condition showing no evidence of fretting or corrosion damage. This condition is attributed to the relatively low bearing stresses on these holes and the rubber "O" rings used to prevent fuel leakage but which also apparently provide excellent corrosion protection of the hole. As may be observed from the Figure, no significant effect on fatigue life could be attributed to the prior service history on upper or lower wing skin specimens.

Tests were also run on "as is" specimens with tap water to determine whether the use of water inside the wing during full scale fatigue tests could have affected the laboratory test life. A small drop of approximately 10% on life may be attributed to this effect. In the basic program, larger reductions in life were indicated due to cyclic exposure but the difference may be attributed there to the use of prefretted holes with distilled water or 3-1/2% salt solution during cycling.

Ten specimens were originally planned to evaluate corrosion and fatigue rework procedures as Group K.

\* Nitric Hydrofluoric solution (Nitric acid 15-20% by weight, Hydrofluoric acid 3 ± 1% by weight, balance water).

Unfortunately, some of the specimens were inadvertently overloaded by a test machine malfunction during the fatigue cycling so that only limited data is presently available on the rework procedure. Two of the specimens were tested like Group J specimens until a detectable crack was observed in both of these severely corroded specimens at 1440 hours. In a step-by-step procedure, the holes were alternately reamed and etched\* until the crack was no longer detectable. Fatigue testing was then resumed and failures were obtained after 5040 and 6280 hours of additional testing. Two control specimens were also prepared by similar reaming and etching and then testing to failure at 9360 and 9600 hours. Based on these limited tests the rework procedure had restored about 2/3 of the life of the control specimens. Apparently all of the fatigue crack and corrosion damage was removed by the rework but not all fatigue damage.

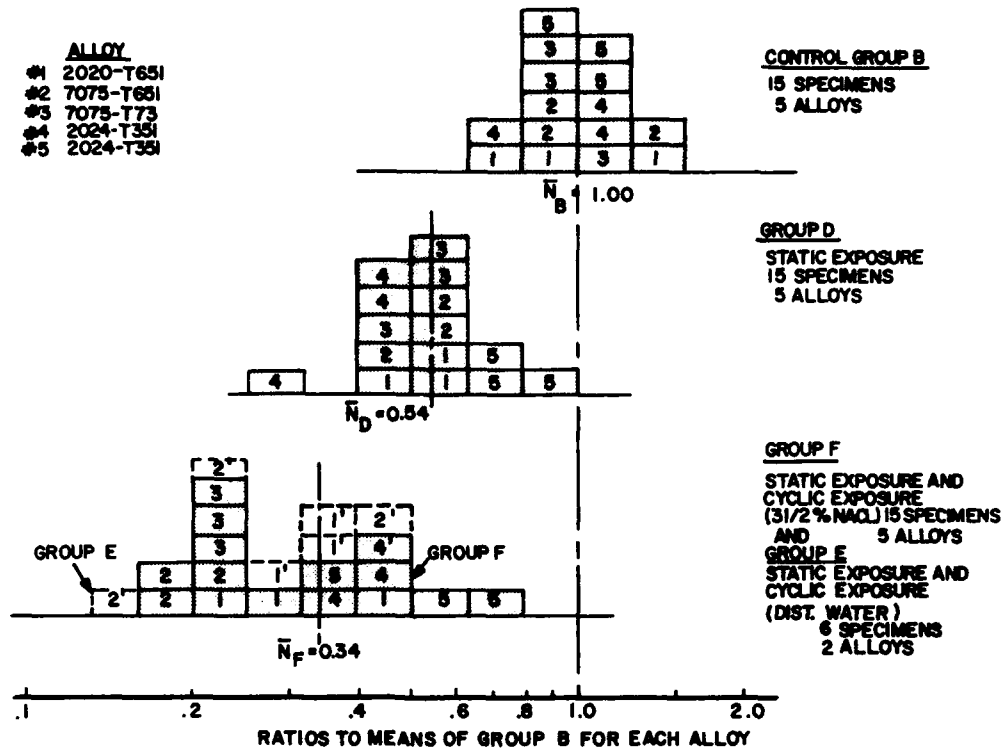
Figure 18 shows the distribution of individual specimen lives for Group B, D, and F plotted as ratios to Group B means.

#### APPLICABILITY OF SPECIMEN CORROSION TEST TO A FULL SCALE WING TEST

During the course of conducting laboratory wing fatigue development tests for the RA-5C airplane, a new wing structure had attained a satisfactory test spectrum life. Tap water under 10 PSI pressure was used during the test to simulate internal fuel pressures and evaluate fuel leakage. Subsequently an available surplus wing which had experienced two years of operation, including an aircraft carrier cruise, and three years of outdoor storage was fatigue tested to a somewhat modified spectrum. Again internal fuel pressures were simulated by tap water. This wing attained only 2/3 the life of the first wing. Comparative specimen tests of the original and modified spectrum produced about the same fatigue damage. Destructive inspection of holes in the high stress areas of both wings were performed to determine the size of fatigue crescents. In the first test wing the destructive inspection indicated that a number of wing skin holes along the rear spar which are countersunk for flush steel fasteners had fatigue crescents near critical crack length. In addition, countersunk and counter bored holes for "O" rings used at ribs and intermediate spar had fatigue crescents of near critical size. In the second test wing, which had had service exposure, the wing skin rear holes also had fatigue crescents near critical size but the holes where "O" rings were used had no evidence of fatigue cracks. Based on the specimen spectrum corrosion fatigue tests previously described the following conclusions were arrived at relative to the wing fatigue program:

1. Based on the 2020-T651 Group D (static exposure) tests, the apparent reduction in life for the wing skin rear spar holes could reasonably be attributed to its

Figure 18. Distribution of Individual Specimens for Test Groups B, D, E, and F.



five year exposure history. The Group D tests indicated a static exposure reduction to 0.57 of control specimen lives vs. the 2/3 reduction for the wing. This second wing fatigue test life at this area is considered a realistic basis for service life assessment of these holes.

2. Based on the 2020-T651 Group H tests of upper and lower wing skin specimens cut from a surplus wing with an identical exposure history to that of the second fatigue test wing in which no significant reduction of life was observed, it was concluded that the absence of fatigue crescents at these holes could be attributed to the "O" ring sealing feature which precluded a loss of life due to its exposure history. Accordingly it was further concluded, that service exposure effects on these holes are negligible and their service fatigue life is about 50% greater than the wing rear spar holes as indicated by the first test.

3. The effects of tap water used during both wing tests on each group of holes were evaluated as follows. The wing fuel sealing design is such that the test internal water under pressure would not normally wet the wing skin rear spar holes; however the high humidity prevailing at these holes during the test cycling could not be considered a non-representative cycling exposure compared to service operation. For the "O" ring holes, however, all cycling would take place with the fatigue critical portion of the hole fully immersed in tap water. This effect was considered unrealistic for service operation since the hole would be well protected from external moisture and probably be coated with jet fuel. Constant amplitude tests previously conducted had indicated that the fuel would be beneficial to fatigue life. Based on the Group H tests with tap water

	①	②	③	④	⑤	
<b>MATERIAL</b>	2020	7075	7075	2024	2024	Ave.
<b>TEMPER</b>	-T651	-T651	-T73	-T851	-T351	① ⑤
<b>GROUP D</b>	.57	.51	.52	.39	.73	.50
<b>GROUP F</b>	.31	.21	.23	.41	.55	.29
<b>AVE.</b>	.44	.36	.37	.40	.64	.40
<b>S.F.</b>	2.3	2.8	2.7	2.5	1.6	2.5*

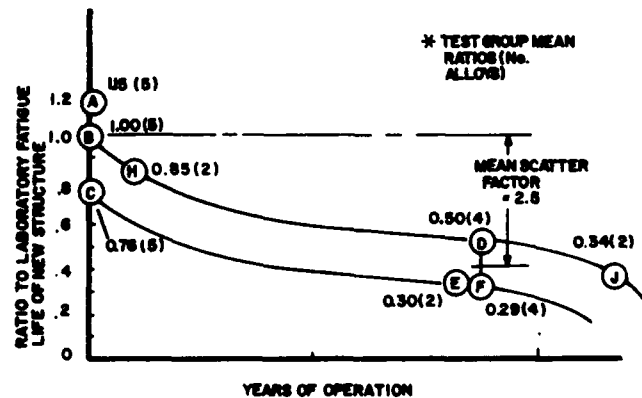


Figure 19. Approximate Environmental Scatter Factor Required on Tests of New Wing Structures When Hole Corrosion Protection is Considered Questionable (Based on ratios to control Group B).



it was concluded that the service fatigue life of the "O" ring type holes should be at least 10% higher than indicated by the first wing test.

The foregoing discussion was meant to show how the neglect of environmental effects during a laboratory wing fatigue test could result in unfair appraisals of wing service life.

### CONCLUDING REMARKS AND RECOMMENDATIONS

In these tests, simulated corrosive environments had a significant adverse effect on maneuver spectrum fatigue life for each of the five aluminum alloy plate materials tested. Although any quantitative correlation of results with long term operational service environments may not be possible, it is believed that results are at least indicative of the reduction in fatigue life that can occur in service operation when fatigue critical wing skin holes are not adequately protected. The use of a standard 30 day alternate immersion test with 3-1/2% salt solution to expose specimens with unplated steel fasteners installed cannot be considered overly severe when compared to the probable condition of a 10 year old service wing with the originally installed steel fasteners and hole protective coating. The use of concurrent exposure 100% of the time during cycling may be overly severe, however, since moisture with or without salt may only be present some of the time during actual maneuver loading. Perhaps a better approximation of long term corrosive effects on fatigue life may be obtained if the results of the Group D (30 day exposure, cycled in air) and Group F (30 day exposure cycled in salt solution) are averaged, as noted in the table on Figure 19. The 2024-T351 specimens are excluded from the average since its performance in these two test groups deviated significantly from the other four alloys. This may be due to the modified spectrum used for this alloy or may actually represent significantly better corrosion fatigue performance in this alloy as reported by a number of investigators. It may also be interesting to know what scatter factor would be required to account for operational environmental exposure if a service life is to be estimated from fatigue tests of a new wing or new wing specimen. These are also noted in the table. The necessary condition is, of course, that hole protection is considered inadequate for long time service operation. Of course the usual material scatter factors and individual airplane load spectrum scatter factors would still apply since the above factors are only averages to account for corrosive environments. Figure 19 also shows the original Figure 2 of the paper with Test Group mean ratios added.

The point of the foregoing for new designs is of course, not to arrive at additional arbitrary factors which would require prohibitive weight penalties but to select fasteners and/or protective coatings in fatigue-critical holes which are virtually immune from environmental effects. It appears likely for example, that rivet holes or interference type fastener holes would not be significantly affected by environmental effects. In the subject program fuel sealing type "O" rings apparently are very effective for corrosion protection on A-5 wings at multi-spar and rib attachments. It also is recommended that specimen corrosion fatigue tests of the wing skin material and fastener combinations be conducted early in the development program of a new design to determine whether any degradation of fatigue life may be anticipated in service so that this information may be incorporated early in the design. Such tests should be planned so that effect of environments on crack propagation rates and residual crack strength can be determined. However, since it is highly desirable that the first full scale wing fatigue test be completed at the earliest possible time, it will be unwise to complicate and lengthen the first test by inclusion of corrosion effects.

For airplanes that have been in service for some time, the practice of using a wing with a previous service history for additional fatigue testing is a good one from an environmental fatigue standpoint and should be followed even when a new production wing is available. In this way a more valid approximation of "service life", as distinguished from the laboratory fatigue life of unexposed structures, will be obtained. The conventional fatigue scatter factor is not intended to "scatter" enough to also include corrosive environmental effects which can be quite significant as demonstrated by this test program.

### ACKNOWLEDGEMENT

Testing discussed in the subject paper was performed as Phases IB and IIA of the RA-5C Extended Service Life Program under Contract N00019-68-C-0061 to the Naval Air Systems Command, Washington D.C. Technical monitors of the program were Mr. G. Gottschalk (AIR-530221) and Mr. S. Goldberg (AIR-52031C). North American Aviation, Columbus Division, Report NR69H-425, "Spectrum Corrosion Fatigue Tests of Various Aluminum Alloys, Phases I and II", August 1969, includes the test results obtained in these Phases of the Extended Service Life Program.

## REFERENCES

1. C.L. Harmsworth, *Effect of Corrosion on the Fatigue Behavior of 2024-T4 Aluminum Alloy*, ASD-TR-61-121, Aeronautical Systems Division, Wright-Patterson AFB, Ohio (1961).
2. J.A. Dunsby and W. Wiebe, "Effect of Atmospheric Humidity on Aircraft Structural Alloy Fatigue Life," *Mater. Res. Stand.*, 9/2:15-22 (1969).
3. W.M. Lorkovic, D. Varally, and R.D. Daniels, *Corrosion Fatigue of High-Strength Aluminum Alloys*. Presented at the NAEC Aeronautical Materials Laboratory Conference, Philadelphia, Pennsylvania, March 1963.
4. H.A. Leybold, H.F. Hardrath, and R.L. Moore, *An Investigation of the Effects of Atmospheric Corrosion on the Fatigue Life of Aluminum Alloys*, NACA-TN-4331, National Aeronautics and Space Administration, Washington, D.C. (1958).
5. P.J. Watts, E.C. Potere, and E. Phillips, *A 3D Corrosion Program*, Final Report, ES-40610, Douglas Aircraft Company, El Segundo, California (1962).
6. I.S. Shaffer and J.C. Sebastian, *Corrosion and Fatigue Evaluation of Spar Cap Specimens from HU-16 Wings*, NAEC-AML-2538, Naval Air Engineering Center, Philadelphia, Pennsylvania (1967).
7. F.L. McGeary, T.J. Summerson, and W.H. Ailor, *Atmospheric Exposure of Nonferrous Metals and Alloys - Aluminum Seven Year Data*, ASTM Paper 23, American Society for Testing and Materials, Philadelphia, Pennsylvania (1967).

# CORRELATION OF RESIDUAL STRENGTH OF BALLISTICALLY DAMAGED PANELS WITH FRACTURE TOUGHNESS THEORY

by

M.D. Campbell, J.F. Haskins, and J.E. Jensen

Convair Division of General Dynamics  
San Diego, California

## I. INTRODUCTION

In the past several decades, military attack and fighter aircraft performance requirements have resulted in the rapid evolution of design concepts and materials applications. The need to maximize parameters such as speed, range, and payload have required that structural weight be minimized and that maximum advantage be taken of high-strength materials. This has in turn created situations where materials of relatively low ductility and poor fracture properties are highly stressed in application, particularly in critical lower wing skins. The result of this is increased probability of major structural failure due to the propagation of cracks resulting from relatively minor battle damage. Figure 1 shows a typical example of a catastrophic failure in a stressed 7075-T651 aluminum alloy plate resulting from ballistic impact.

Although the designer has a number of alternatives to reduce the vulnerability of his design, such as choices of materials and the employment of less vulnerable configurations which arrest running cracks, for example, his difficulties in attempting to assess the vulnerability of a particular structural design are enormous. This is because of the apparently endless variety of damage patterns inflicted by various threats in individual materials and the resulting structural degradation. Solution of the designer's problems cannot be expected to be exact and straightforward because of the large number of critical parameters involved and the scatter generally experienced. For the same reasons, little useful information for designers can presently be gained from experimental evaluation of the behavior of full-scale structural configurations under the influence of ballistic damage.

The problem must be approached from a more basic point of view; one must understand and be able to predict the extent and significant characteristics of damage patterns resulting from individual threat-material-environment-configuration combinations and then be able to predict the resulting structural degradation.

Convair has attempted to develop both ballistic damage and residual strength prediction models to be used by the designer. Ballistic damage patterns have been characterized through ballistic testing, and characteristics of the

target and threat to which the resulting damage is sensitive have been identified (Ref. 1, 2, and 3). Damage models with specific, limited applications have been developed. Residual strength models have been based on application of fracture theory to analysis of structural members containing typical ballistic flaws. Limits of the applications require considerable dependence on analysis of empirical results.

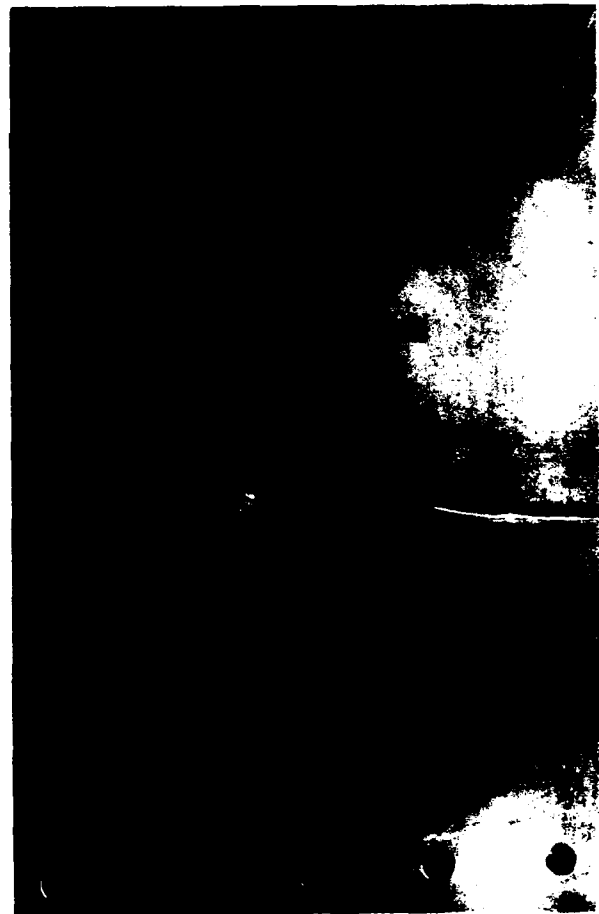


Figure 1. Catastrophic Failure of 0.25" 7075-T651 Test Panel.

**Figure 2. 35-foot  
Enclosed Range.**

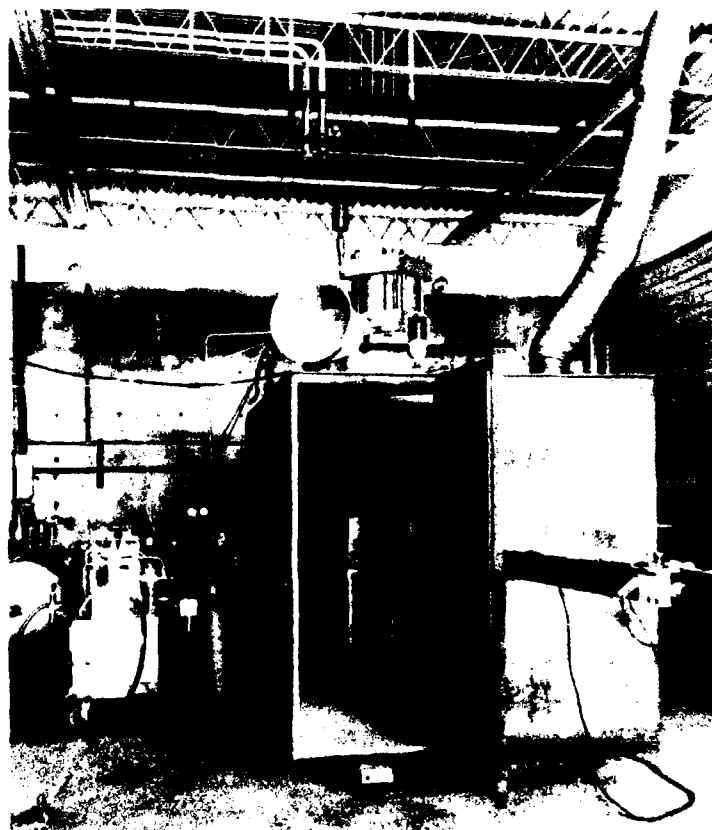


The following discussion deals with several aspects of fracture mechanics as they apply to ballistic flaws and the development of residual strength models. A large portion of the ballistic damage selected for treatment was typical of 7075-T651 alloy, and experimental data for the material was heavily relied on for comparison to theoretical

predictions. Emphasis has been placed on this alloy because of its applications in current military aircraft, its sensitivity to brittle fracture, and its usage in a great number of "classical" fracture studies.

The damage discussed below is that produced by

**Figure 3. Enclosed Target  
Box with 400,000-pound  
Specimen Loading  
Fixture.**



U.S. Cal. .50 armor-piercing (AP) projectiles. The energy and momentum of the Cal. .50 AP and the damage produced are in the midrange of nonexplosive projectiles normally encountered in military situations.

## II. EXPERIMENTAL FACILITIES AND METHODS

All gunfire damage testing conducted to develop Convair's damage models and produce residual strength test specimens was carried out in an indoor range at the Convair



Figure 4. Universal Specimen Mounting Fixture .

Kearny Mesa plant. The ballistic test facility is located in a reinforced-concrete walled area 30 by 100 by 18 feet. Full width and height access doors permit installation of large test specimens and fixtures. The 35-foot enclosed range shown in Figure 2 was used for the Cal. .50 firings on this program. Rifled barrels and the 35-foot flight path provided a stable projectile at impact. The fire-control tube contained a muzzle-blast suppressor and ports for photoelectric velocity timing.

Test specimens were mounted in a target box 6 by 6 by 14 feet. Preloaded specimens were positioned and loaded by the 400,000-pound tension fixture shown in Figure 3. Unloaded specimens were positioned by a fixture such as the one shown in Figure 4.

The high accuracy necessary to produce well centered hits in residual strength specimens, particularly at high obliquity angles, was maintained by bore-sighting with a small gas laser (Figure 5). Projectile velocity was controlled by variations in propellant charge. Numerous factors which influence muzzle velocity were controlled to produce velocity scatter as low as 0.1%.

Data analysis was assisted by the use of an SDS 930 computer. Fortran II programs were created for solution of conventional fracture mechanics relationships as well as the residual strength models presented in Section V.

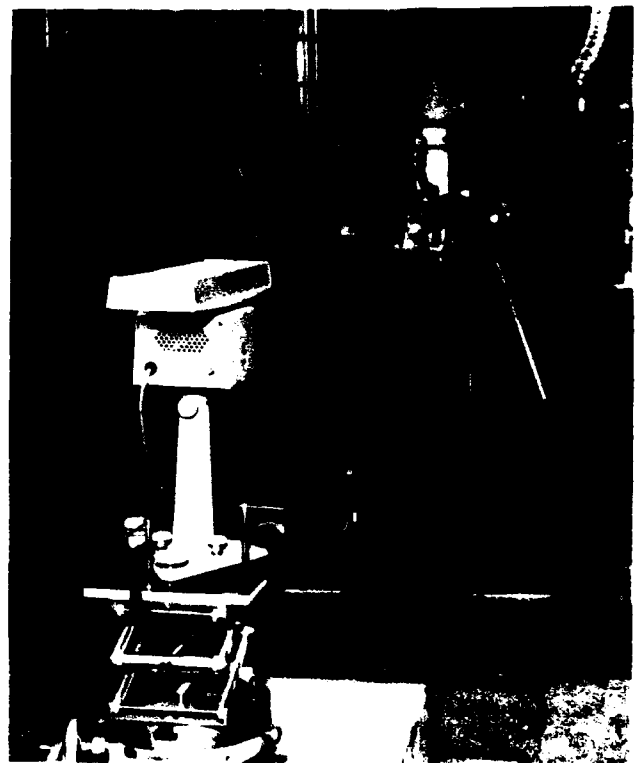


Figure 5. Bore-Sight Laser and Mount.

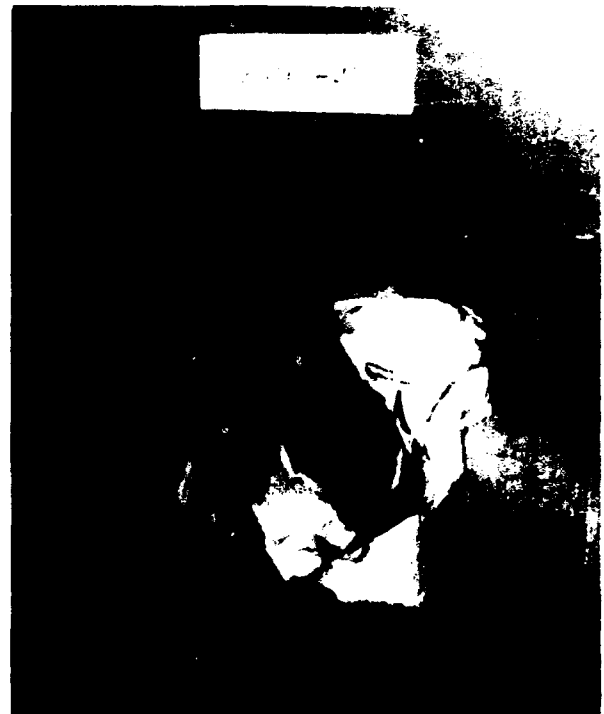
### III. BALLISTIC DAMAGE CHARACTERISTICS

Ballistic damage surveys performed by Convair in connection with model development have characterized the behavior of a number of structural materials.

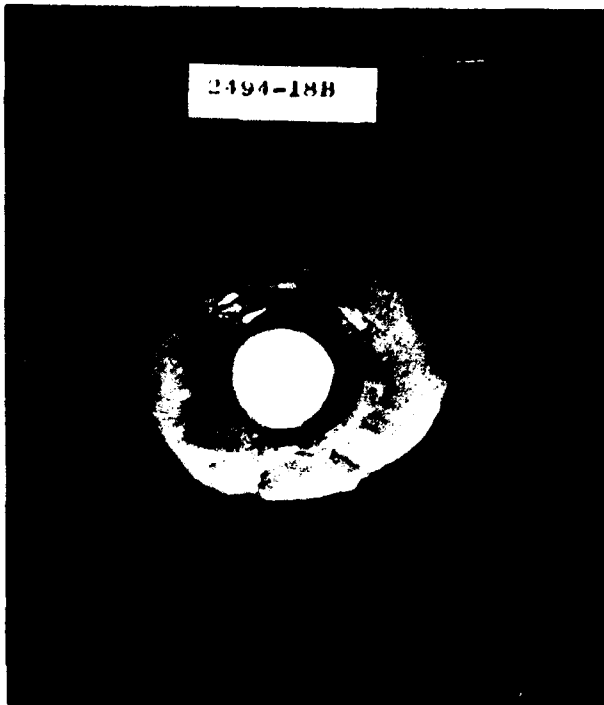
In order to mathematically treat the relationships involved, quantitative description of parameters common to the variations in damage patterns has been necessary. Descriptor systems have been developed to describe the extent and nature of spall, cracks, through-holes and out-of-plane



1/4 INCH



1/4 INCH



1/2 INCH



1/8 INCH

Figure 6. Ballistic Damage Variations in 7075-T651 Aluminum Alloy.

deformation. In the analysis of residual strength, the nature of the flaw introduced in the lateral direction (normal to load) is of particular interest. The following descriptors are the basis of a system to characterize the damage in this direction.

- $H_o$  = maximum lateral extent of through-hole
- $S_o$  = maximum lateral extent of spall
- $L_o$  = maximum lateral extent of cracking
- $D_o$  = maximum extent of lateral damage without regard to type

Subscripts f and b denote entrance and exit faces, respectively. The subscript e denotes an average of both faces. For example:

- $fS_o$  = maximum lateral extent of a spall on entrance face
- $eD_o$  = average of maximum lateral damage on entrance and exit faces

Other descriptors which will appear in the following discussion include:

- $\psi_i$  = crack tip angle of crack i (with respect to lateral direction).
- $\psi_m$  = minimum crack tip angle
- D = maximum damage without regard to type or direction

Examples of these descriptors and a more detailed discussion of the complete descriptor system may be found in Ref. 2.

The damage produced by Cal. .50 AP in 7075-T651 contains examples of all the basic damage types, and all can be extensive. Figure 6 illustrates several extreme variations

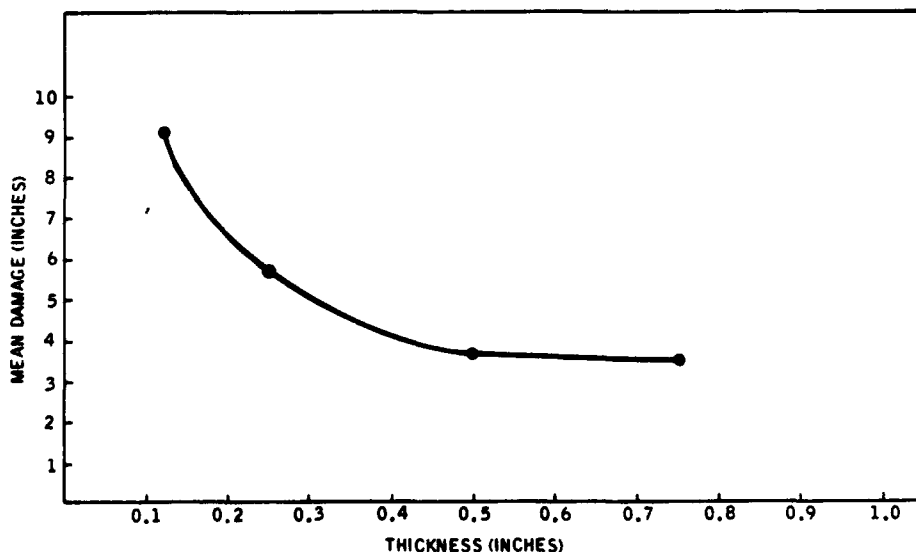


Figure 8. Mean Transverse Damage at Worst Obliquity and Velocity for Cal. .50 AP vs. 7075-T651 (Maximum Velocity = 3,000 ft./sec.).

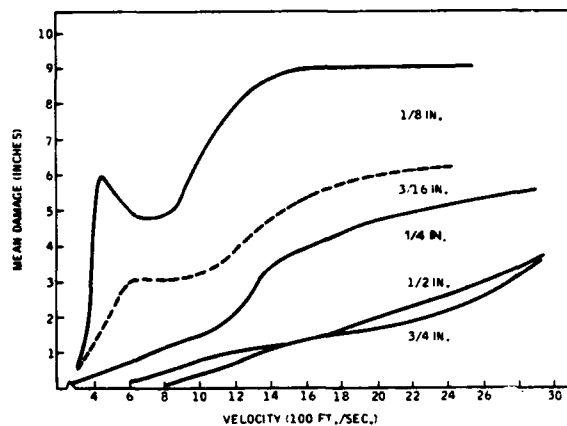


Figure 7. Mean Transverse Damage at Worst Obliquity as a Function of Velocity for Cal. .50 AP vs. 7075-T651.

which occur in thicknesses from 1/8 to 3/4 inch. If a mosaic were constructed of photos of typical damage near the maximum for a large number of thicknesses of 7075-T651, a smooth transition from in-plane tearing through cracking and irregular spalling to symmetric spalling would be seen as thicknesses went from below 1/8 to above 3/4 inch.

To illustrate the extent of the small caliber damage which can occur in structural materials, the maximum damage envelopes for Cal. .50 AP versus 7075-T651 are presented in Figures 7 and 8.

Projectile velocities up to 3,000 feet per second and obliquity angles ( $\theta$ ) from 0 to 85 degrees (obliquity plane parallel to transverse direction) are included in these presentations. Test specimens were unstressed. Damage in the transverse direction is most significant because it is the lateral direction in most design applications. Damage in the

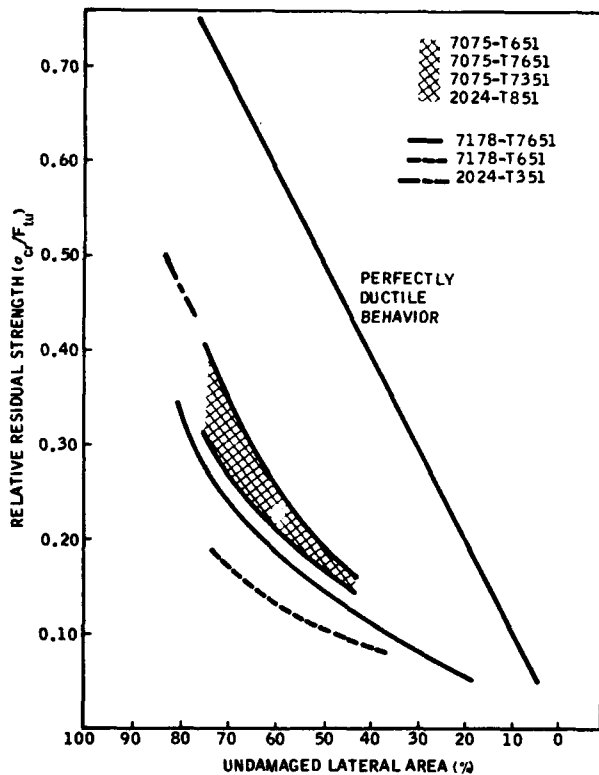


Figure 9. Relative Residual Transverse Strength vs. Undamaged Area for Aluminum Alloy Specimens.

longitudinal direction can exceed 20 inches under these conditions.

#### IV. APPLICATION OF FRACTURE TOUGHNESS TO RESIDUAL STRENGTH ANALYSIS

As will be shown in greater detail in Section V, the damage produced by ballistic impact in structural materials can produce brittle fracture under static stress. Figure 9 shows examples of deviations from ductile behavior determined experimentally.

Investigation of brittle fracture requires knowledge of the fracture toughness parameters and the characterization of the stress field of the material being studied.

The fracture theory, methods of measuring fracture toughness, and the experimental results for a number of metallic alloys have been the subjects of numerous technical papers. It appears that the characterization of fracture toughness of a given material is not altogether a simple task. Specimen geometry, measuring technique and analysis are clear cut for a number of materials; however, further formulation and understanding seems to be required for the more advanced materials and material systems. The understanding, application, and acceptance of fracture mechanics by materials, stress, and design engineers have made considerable

progress in recent years. However, fracture mechanics is still far from universal acceptance and use.

When one understands the difficulties involved in measuring fracture toughness under ideal laboratory conditions, it seems somewhat presumptuous to attempt to predict residual strength in panels damaged by small arms gunfire. However, by careful application of existing fracture mechanics theory one can examine damage and make a reasonable prediction about the panel's remaining strength. To do this we must have some elementary understanding of fracture mechanics and the boundary conditions which apply to our tests.

The terms common to plane stress testing and plane strain testing are designated as  $K_c$  and  $K_{Ic}$  respectively in the literature. It will be necessary for our purposes here to have a complete understanding of these terms and what their relation is to various type of flaws, specimen geometry, and applied loads.

It would be well to recall the leak-before-fail design for pressure vessels. For example, we know that in a thin-walled vessel it is possible for a surface flaw to grow to failure. In this situation the small flaw may grow in plane strain. It may, as the flaw deepens, depart from plane strain and require a correction term such as Kobayashi's magnification factor to make a proper calculation. For thin material, the flaw will grow through the thickness and reach a failure point, and the condition of plane stress will apply. As the thickness of the material is increased, the surface flaw reaches a size such that slow crack growth does not continue and a failure occurs in the plane strain condition. Discussions of this type are common in the literature, complete with pictures showing initial plane strain growth, a transition region, and final plane stress growth (Ref. 4). Discussion of this type leads to the design curve shown in Figure 10. This design curve is for 7075-T6 aluminum and is

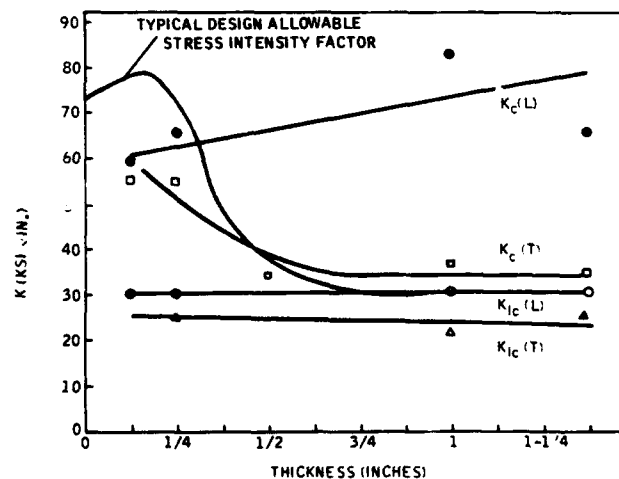


Figure 10. Typical Design Allowable Stress Intensity Factor and Summary of Kaufman et al., Data for 7075-T651.



**TABLE I.**  
**TENSILE AND TOUGHNESS DATA FOR 7075-T651 ALLOY**

THICKNESS (IN.)	LONGITUDINAL				TRANSVERSE			
	Ultimate (KSI)	Yield (KSI)	$K_{Ic}$ (KSI $\sqrt{IN.}$ )	$K_c$ (KSI $\sqrt{IN.}$ )	Ultimate (KSI)	Yield (KSI)	$K_{Ic}$ (KSI $\sqrt{IN.}$ )	$K_c$ (KSI $\sqrt{IN.}$ )
As machined 1/8	-	-	30.3	61.8	-	-	31.2	55.0
Fatigue cracked 1/8	-	-	32.0	59.1	-	-	30.2	51.2
1/4	83	77.3	25.4	54.8	84.8	74.2	24.8	40.5
1/4	85	78.8	30.1	67.0	85.8	75.4	24.2	52.4
1/4	83.9	78.2	32.8	65.6	84.0	72.0	27.3	54.9
1/2					87.0	77.2		33.4
1			30.2	82.3			21.7	36.2
1-3/8	83.9	76.6	30.2	82.2	82.9	73.6	27.1	36.2
1-3/8	86.3	80.3	30.9	65.5	85.6	77.4	26.1	30.9
1-3/8	86.0	78.5	31.2	64.7	86.6	76.0	27.8	34.4

given so that the reader may realize how careful one must be in using fracture mechanics to characterize residual strength of a damage panel. Typical data for aluminum alloy 7075-T651 generated by Kaufman et al. (Ref. 5) is also shown in Figure 10. These curves show the variation of both  $K_c$  and  $K_{Ic}$  with thickness for the longitudinal and transverse directions. This data is presented in greater detail in Table I. It is used here to represent how, using a through-crack specimen, one can generate both  $K_{Ic}$  and  $K_c$  data for thicknesses from 1/8 inch to one inch. The plane strain condition exists at pop-in, and  $K_{Ic}$  is determined from crack length and gross-section stress. As the crack length grows, a condition of plane stress develops and critical failure gives a measure of  $K_c$ .

The Kaufman paper uses Eq. (1) and (2) (based on the Irwin-Westergaard tangent relation) to make these calculations:

$$K_c^2 = w \cdot \tan\left(\frac{\pi a_0}{w} + \frac{K_c^2}{6w\sigma_{ys}^2}\right) \sigma_{Ic}^2 \quad (1)$$

and

$$K_c^2 = \sigma_c^2 w \tan \frac{\pi a}{w} \quad (2)$$

$\sigma_{Ic}$  = gross-section stress at initial unstable crack growth (pop-in), psi

$\sigma_c$  = critical gross-section stress (at onset of rapid crack growth), psi

$w$  = specimen width, inches

$2a_0$  = original crack length, inches

$2a$  = critical effective crack length (at onset of rapid crack growth), inches

$\sigma_{ys}$  = tensile yield strength, psi

The more accepted formula of today, recommended in ASTM STP 410 (Ref. 6),

$$K_I = Y \sigma a^{1/2}$$

where  $Y$  good to 1% is given by

$$Y = 1.77 \left[ 1 - 0.1 \left(\frac{2a}{w}\right) + \left(\frac{2a}{w}\right)^2 \right] \quad (3)$$

was not used in this work so that direct comparison could be made with data calculated using the Irwin-Westergaard tangent relation.

The flaws we are accustomed to considering usually start with a small imperfection not detectable by inspection of any kind. They may grow under load to some critical

size and as discussed earlier fail in either plane strain or plain stress depending on thickness. The instant through-the-thickness cracks provided by gunfire damage are not common in other problems involving thick structure. They cannot be produced from small surface flaws by slow growth of any type.

This work has shown that a projectile striking a panel generally causes one of two things to happen: a dent is made in the material for which there is no evidence of cracking; or the damage extends completely through the plate and may or may not have cracking associated with the damage. When we have through-damage with cracks, the cracks are often through the thickness cracks. This point is emphasized because in so many cases the analysis and thinking is aligned to small surface or embedded flaws which grow, originally at least, under conditions of plane strain. In measuring residual strength of panels damaged by gunfire, we are generally evaluating the strength under conditions of plane stress. To make calculations of residual strength of the panels damaged in this manner, then, the plane stress fracture toughness  $K_{Ic}$  is assumed applicable for all thicknesses used.

The residual strength calculations are then made by using  $K_{Ic}$  for the material involved, critical gross stress at failure, and the measured crack length corrected for plastic zone size. No attempt has been made to use  $K_{Ic}$  even though pop-in was observed and measured on a number of occasions.

To predict residual strength for damaged panels (again using aluminum as an example), we need to examine existing fracture toughness data for both the longitudinal and transverse directions and any thickness differences between the two. Figure 10 shows these differences as recorded

by Kaufman et al. for one alloy, 7075-T651. It is interesting to note the decay of  $K_{Ic}$  for the transverse direction as the thickness increases. Some clue to this may be supplied by the nature of the fractured surfaces of these various types of specimens. The shear lips for material loaded and failed in the longitudinal direction seem to be more pronounced than those loaded and failed in the long transverse direction.

Evidence of the failure occurring under conditions of plane stress is shown for titanium and two aluminum alloys in Figure 11. Shear lips are clearly shown for several thicknesses.

## V. RESIDUAL STRENGTH MODELS

Successful estimation of the residual static strengths of ballistically damaged panels has been accomplished by classifying damage patterns and formulating residual strength models based on elaboration of the assumptions made in Section IV. The following discussion presents several illustrations of models developed for specific cases. Model predictions and experimental data are presented for comparison.

### 5.1 Transverse Strength of Thin-Plate Aluminum Alloys Containing Longitudinal Cracks

The simplest case to consider is one that yields directly to fracture mechanics analysis. In such a case, the ballistic damage consists of through-cracks normal to the applied load in a material and thickness where the mode of failure can be accurately defined. Because of anisotropy in the high-strength alloys, ballistic cracks tend to propagate in the longitudinal direction of these materials. High-angle impacts with the obliquity plane in the longitudinal



Figure 11. Examples of Fracture Surfaces in Ballistically Damaged Panels.

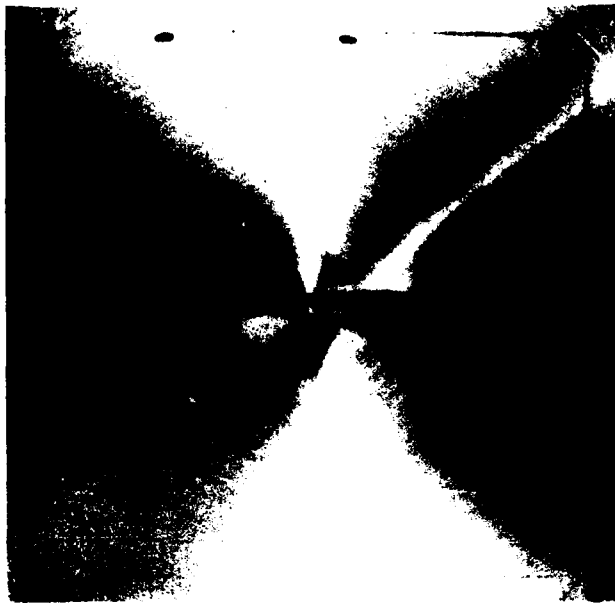


Figure 12. Example of Ballistic Damage Consisting of Transverse Cracks.

direction produce specimens with cracks predominantly, and often exclusively, in this direction. In 1/4-inch plate, cracks can be produced with little out-of-plane deformation.

Under the proper conditions, specimens containing such damage can resemble center-notch specimens used to determine  $K_{IC}$ . An example is shown in Figure 12. If the proper boundary conditions are met and crack-like ballistic damage affects the material similarly to machined notches and fatigue cracks, then residual strength should be predictable from  $K_{IC}$  data.

This hypothesis was tested for specimens of four aluminum alloys. Specimens 1/4 by 9 inches square of 7075-T651, 7075-T7351, 7178-T651, and 2024-T851 were impacted by Cal. .50 AP projectiles. Velocities and obliquity angles ( $\theta$ ) were varied to produce damage of varying degree. Obliquity planes were parallel to the longitudinal directions

TABLE II.  
COMPARISON OF PREDICTED AND MEASURED  
RESIDUAL STRENGTHS OF BALLISTICALLY  
FLAWED, 0.25-INCH TRANSVERSE  
ALUMINUM ALLOY SPECIMENS\*

MATERIAL	AVER. $D_0$ (IN.)	AVER. CRITICAL LOAD (1,000 LB.)		VARI- TION (%)
		PREDICTED	MEASURED	
2024-T851	3.07	46.9	46.4	+1
7178-T651	3.84	28.2	27.7	+4
7075-T7351	3.08	51.5	53.8	-4
7075-T651	3.67	43.7	46.5	-6

\*Specimens were 1/4 by 9 by 9 inches.

to initiate cracks in the longitudinal directions. Total damage extent in this direction ranged from 1.80 to 5.41 inches.

Residual strengths of the prepared specimens were then determined analytically. The method selected was based on the Irwin-Westergaard expression for plane-stress fracture toughness (Eq. 2). This was rearranged to:

$$\sigma_{cr} = \frac{K_{IC}}{\left(w \tan\left(\frac{\pi a}{w}\right)\right)^{1/2}}$$

Since the gross critical load =

$$P_{cr} = \sigma_{cr} (w \cdot t)$$

then

$$P_{cr} = \frac{K_{IC} (w \cdot t)}{\left(w \tan\left(\frac{\pi a}{w}\right)\right)^{1/2}} \quad (4)$$

One-half of the maximum lateral damage,  $D_0/2$ , does not exactly satisfy the expression if substituted for "a" directly.  $D_0/2$  differs from "a" by an amount equal to slow crack growth which occurs before the applied load becomes critical and by the effective plastic zone ahead of the crack tip (Ref. 6).

Slow crack growth was not routinely measured on specimens used to determine residual strength of panels containing ballistic damage. However, slow crack growth in the specimens was expected to be less than 5%. Therefore, the initial flaw size was assumed equal to the final crack length.

A correction for the plastic zone was accomplished using an iteration of  $P_{cr}$  similar to that used when calculating  $K_{IC}$  from a static strength test (Ref. 6).

Substituting  $D_0/2$  for "a", a preliminary value of the critical load was determined using:

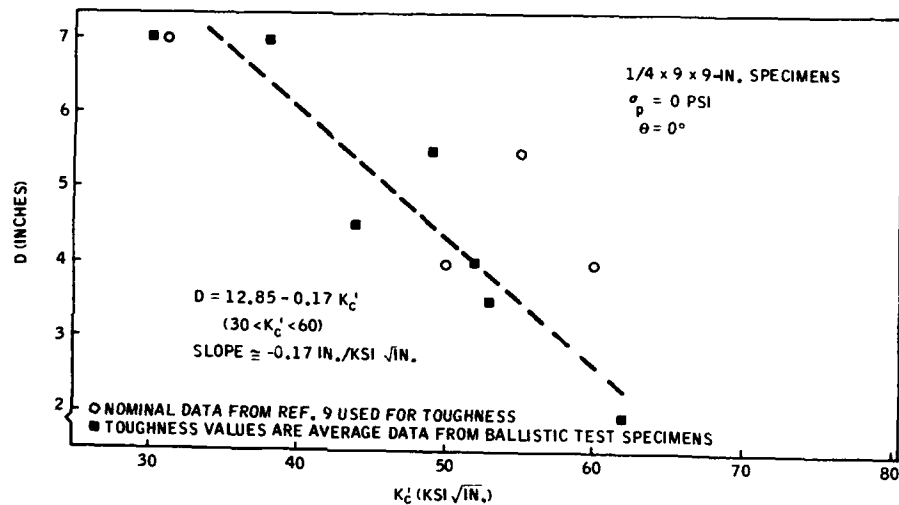
$$P_{cr} = \frac{K_{IC} (w \cdot t)}{\left(w \tan\left(\frac{\pi D_0}{2w}\right)\right)^{1/2}} \quad (5)$$

TABLE III.  
TRANSVERSE PLANE STRESS  
FRACTURE TOUGHNESS ( $K_{IC}$ )  
RESULTS FOR BALLISTICALLY  
DAMAGED SPECIMENS\*

MATERIAL	AVER. $2a_0$ (IN.)	AVER. TRANSVERSE $K_{IC}$ (KSI $\sqrt{IN.}$ )
7075-T651	2.77	53
7178-T651	4.09	38
2024-T351	1.80	62

\*Specimens were 1/4 by 9 by 9 inches.

**Figure 13. Maximum Damage as a Function of Transverse Fracture Toughness for Structural Aluminum Alloys – Cal. .50 AP M2.**



A correction to  $D_o$  for the plastic zone was made by:

$$a = \frac{D_o}{2} + \frac{(P'_{cr})^2 \cdot \tan\left(\frac{\pi D_o}{2w}\right)}{2\pi (\sigma_{ys})^2 (w \cdot t)^2} \quad (6)$$

$P_{cr}$  was finally calculated using Eq. (4).

The specimens were pulled to failure and the resulting residual strength compared with those predicted. The results are shown in Table II.

The small variations between the predicted and measured residual strengths indicate that these specimens can be treated with a center crack analysis. Specifically, the cracks comprising the assumed  $a_o$  are similar to those required for good  $K_c$  determinations. The results also confirm that the 1/4-inch-thick material fails in plane stress. This is evident in the fracture surface shown in Figure 11.

Evaluations were also made of specimens of 7075-T7651, 7178-T7651, and 2024-T351, for which good transverse  $K_c$  data was not available. In these cases the measured residual strengths could be used to calculate  $K_c$  if the same assumptions were used. Table III gives the values which resulted.

A very practical result of this analysis, applicable to many of the situations discussed here, is shown in Figure 13. The curve is a portion of a ballistic damage model which shows that the damage produced in the structural aluminum alloys is inversely proportional to toughness. Since residual strength for a given flaw size is also inversely proportional to toughness, the role of fracture toughness in structural vulnerability is compounded.

## 5.2 Longitudinal Strength of 2024-T851 Thin Plate Containing Smooth, Round Holes

High-velocity armor-piercing projectiles at near-zero degree obliquity produce smooth, round holes in thin plate.

An example of this is shown in Figure 14. In the illustration, there is little front or back spalling and no visible cracks on either face.

If there are no sharp notches around such a hole, the flaw can be shown to produce an elastic stress concentration of approximately 3 at the edge of the hole. A plate with a round hole will not fail at a net stress of  $1/3F_{tu}$ , however, since elastic and plastic deformation change the geometry as stress is applied. The ductility of even the high-strength aluminum alloys is sufficient to lower the stress concentration factor for rupture at a flaw to nearly 1.0 before failure occurs under static load.

The smooth, round hole produced by ballistic impact does not necessarily have to produce this behavior. If it contains unseen cracks or stress concentrations due to

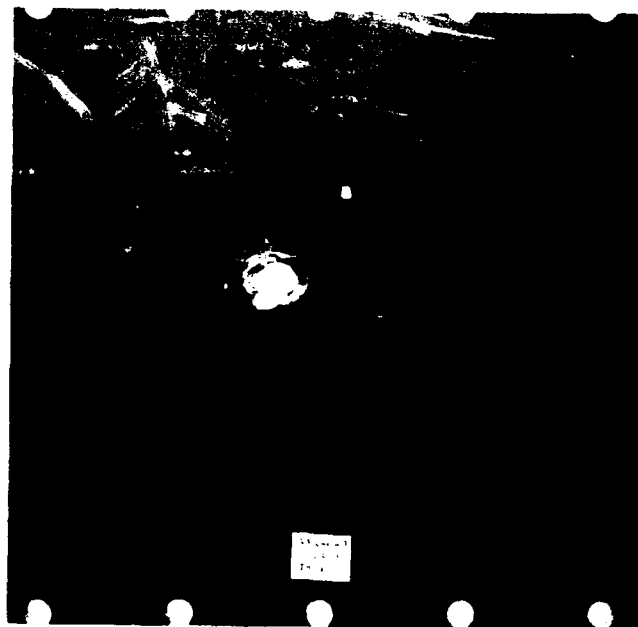


**Figure 14. High-Velocity Cal. .50 AP Damage in 2024-T851 0.25-Inch Plate.**

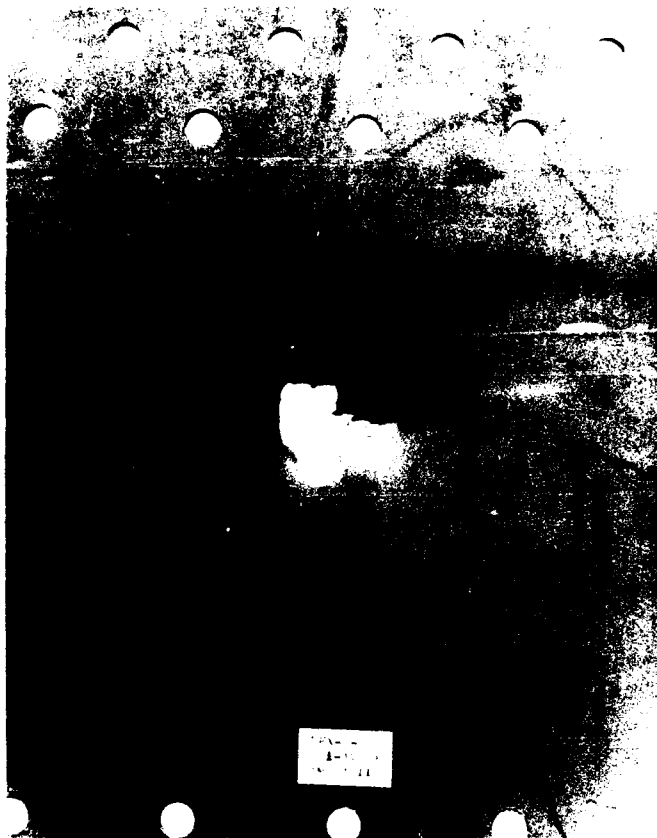


**Figure 15. High-Velocity Cal. .50 AP Damage in 6A1-4V Annealed 0.114-Inch Plate.**

composition or structure variations in localized areas created by the impact, brittle fractures could occur.

This occurrence was found not to be the case in at least one structural aluminum alloy, 2024-T851. Speci-

mens 1/4 by 9 by 9 inches containing smooth holes produced by Cal. .50 impacts were static-tested to failure in the longitudinal direction. The resulting net strengths were compared to the  $F_{tu}$  of the material. The average of  $F_{tu}/\sigma_{cr(net)}$  for six specimens was 1.02.

Hole diameters ranged from 0.650 to 1.570 inches, with the larger flaws produced by high-velocity oblique impacts being slightly elliptical. In these cases, major diameters were in the lateral direction. Damage of comparable extent but containing detectable cracks had significant effect on similar specimens of the material.

**5.3 Longitudinal Strength of 6A1-4V Annealed Thin Sheet Containing Cracks Radiating from a Ragged Through-Hole**

Typical design thicknesses of titanium alloys incur crack-like flaws when hit by high-velocity Cal. .50 AP projectiles. An example of 0.114-inch 6A1-4V annealed impacted by Cal. .50 at 2,250 feet per second is shown in Figure 15. The damage consists of a through-hole, much more ragged than those in the 1/4-inch 2024-T851 just discussed, with through-cracks extending in several directions.

The behavior of a series of specimens similar to this was analyzed. In these specimens, the ratio of hole radius to the one-sided crack length ( $H_o/2a$ ) varied from approximately 0.2 to 2.0. Specimens were nine inches wide, with the ballistic flaws ( $D_o$ ) extending from approximately 0.72 to 2.50 inches.

Although a number of models was applied, this combination was found to be best represented by the

**Figure 16. Crack Tip Angle Correction for Center Crack Residual Strength Analysis.**

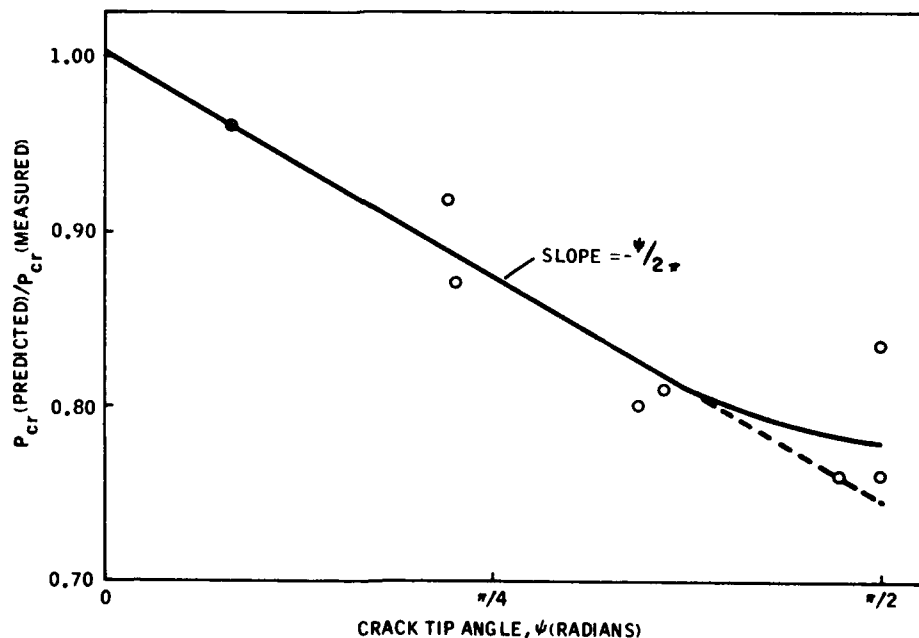


**TABLE IV.**  
**RESULTS OF RESIDUAL STRENGTH MODEL FOR BALLISTICALLY DAMAGED,**  
**0.114-INCH, 6A1-4V ANNEALED SHEET\***

SPECIMEN	D <sub>o</sub> (IN.)	ψ <sub>m</sub> (RAD.)	P <sub>cr</sub> (1,000 LB.)	
			PREDICTED	MEASURED
VFX-A-2	0.920	0.08 π	112	111
VFX-A-6	1.430	0.18 π	108	108
VFX-A-11	2.480	0.17 π	80.9	83.4
VFX-A-4	1.150	0.11 π	109	105
VFX-A-12	2.500	0.11 π	75.0	76.5
VFX-A-9	1.550	0.25 π	112	101
VFX-A-7	1.510	0.24 π	113	112
VFX-A-8	1.330	0.25 π	121	119

\* Specimens were 0.114 by 9 by 12 inches longitudinal.

simple center crack as used in the first example. However, it was necessary to correct the critical load predicted by the center-notch analysis to take the crack direction with respect to the load into account. Paris and Sik (Ref. 7) have suggested a correction of  $\cos^2\alpha$  for an inclined, linear through-crack with no hole. In the case being considered, the cracks radiating from the hole continually change direction as they progress.

To determine the proper correction for crack direction, values of critical load predicted using a center-crack analysis were compared to measured values. Ratios of the two were plotted as a function of the smallest crack tip angle found at the farthest damage extent.

The angle,  $\psi_m$ , was measured with respect to the lateral direction. In this case, the lateral direction was the transverse grain direction. In cases where the crack tip turned beyond  $\pi/2$  radians, the value was assumed to be equal to  $\pi/2$  radians. Figure 16 shows the relationship developed. The assumption that values of  $\psi$  greater than  $\pi/2$  have no further effect requires the slope of the curve to approach zero at  $\frac{\pi}{2}$  as shown. However, the straight line with slope =  $-\frac{1}{2\pi}$  is a good correction through  $\psi = \frac{\pi}{2}$ .

The resulting model using this correction has the form:

$$P_{cr} = \frac{K_c (w.t)}{\left(w \tan \frac{\pi\alpha}{w}\right)^{1/2} \left(1 - \frac{\psi_m}{2\pi}\right)} \quad (7)$$

The same iteration process used in the first example (Eq. 7) is used to determine a value for  $P_{cr}$  with a plastic zone correction.

Table IV compares the critical loads predicted by the model and measured values. The role of fracture toughness in structural vulnerability can again be exemplified by comparison of the results of this and the previous analysis. The damage in both the 2024-T851, 0.25-inch plate and the 6A1-4 annealed, 0.114-inch sheet was produced by the same threat: Cal. .50 AP at 2,200 feet per second. Furthermore,

the two sets of specimens were considered structurally equivalent, i.e., their thicknesses were in the same ratio as their design allowable stresses. They were also subjected to tensile preloading of the same force per unit width during ballistic impact.

Figure 17 shows residual strengths of the two specimen sets as a function of projectile obliquity angle. This is a structural vulnerability model for a specific case. Its importance to this discussion is that it shows the residual strength of the titanium alloy to be less than structurally equivalent 2024-T851 following impact by the same ballistic threat. The reason is primarily the nature of the damage. The smooth, round holes produced in the 2024-T851 were shown to result in a stress concentration factor for rupture of approximately 1.0. The damage in the 6A1-4V annealed, however, is crack-like and leads to brittle fracture with a marked decrease in gross strength.

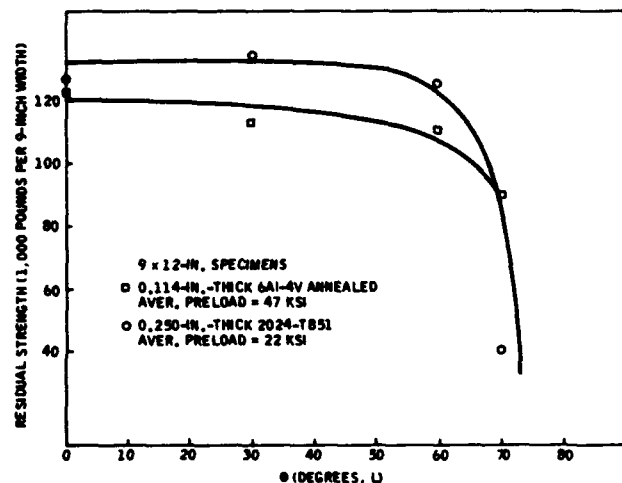


**Figure 17. Longitudinal Residual Strength for Structurally Equivalent 6A1-4V Annealed and 2024-T851 as a Function of Obliquity Angle, Cal. .50 AP M2 at 2,220 ft./sec.**

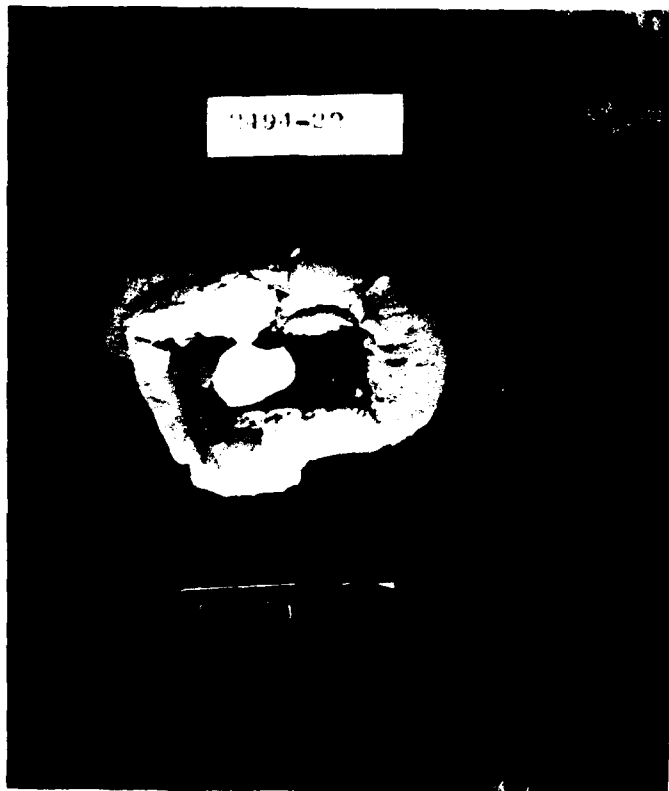
**TABLE V.**  
**RUPTURE STRESS CONCENTRATION FACTORS FOR BALLISTICALLY DAMAGED,**  
**0.50- AND 0.75-INCH, 7075-T651 PLATE**

SPECIMEN	THICKNESS (IN.)	WIDTH (IN.)	$P_{cr}$ (1,000 LB.)	RUPTURE STRESS CONCENTRATION	
				$w_e = w - H_o$	$w_e = w - D_o$
28A	0.754	8.08	392	1.25	1.08
29B	0.754	8.05	382	1.27	1.03
32B	0.754	8.05	377	1.31	1.03
33B	0.754	8.00	381	1.33	0.99
30A	0.754	8.13	354	1.43	1.09
34A	0.754	7.95	334	1.50	1.15
31B	0.754	8.03	313	1.59	1.29
67A	0.754	7.85	278	1.69	1.39
35A	0.754	7.90	265	1.79	1.39
18A	0.525	11.98	408	1.19	1.08
19A	0.525	8.00	255	1.23	1.06
17A	0.525	11.91	363	1.33	1.19
26A	0.525	11.91	335	1.37	1.19
20B	0.525	11.90	353	1.37	1.26
21A	0.525	11.90	322	1.45	1.33
22A	0.525	11.90	298	1.64	1.44
24A	0.525	11.90	259	1.84	1.67
23A	0.525	11.90	241	1.91	1.78

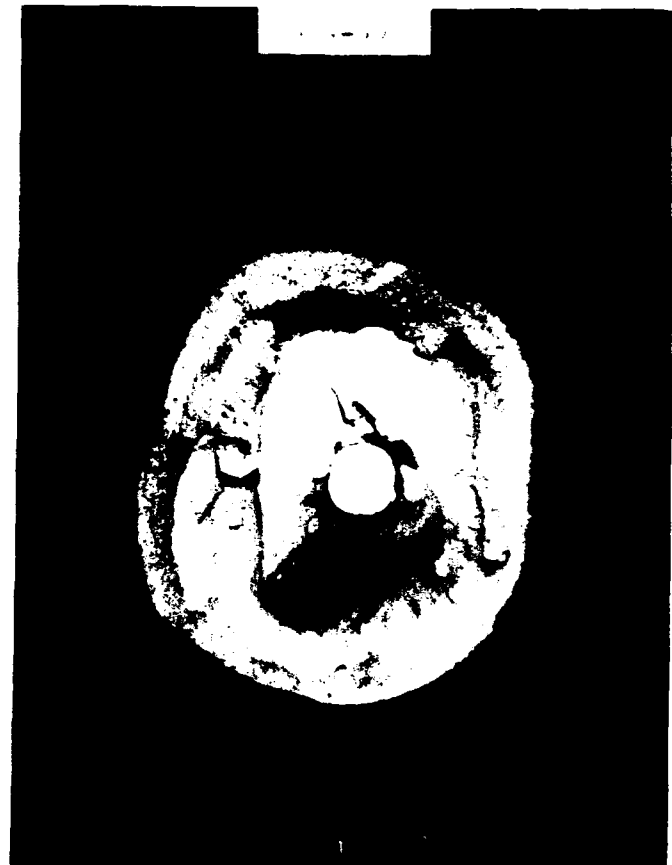
**TABLE VI.**  
**COMPARISON OF CENTER-CRACK RESIDUAL STRENGTH PREDICTIONS**  
**WITH MEASURED VALUES FOR BALLISTICALLY DAMAGED 7075-T651 PLATE**

SPECIMEN	THICKNESS (IN.)	$P_{cr}$ (1,000 LB.) PREDICTED			MEASURED
		$2a_o = H_o$	$2a_o = D_e$	$2a_o = D_o$	
28A	0.754	*324	215	185	382
29B	0.754	*331	213	175	392
32B	0.754	*341	221	182	377
33B	0.754	444	*213	176	381
30A	0.754	410	*218	181	354
34A	0.754	419	*211	182	334
31B	0.754	352	*235	195	313
67A	0.754	305	*212	184	287
35A	0.754	304	*210	173	265
18A	0.754	*331	261	219	408
19A	0.525	*231	169	143	255
17A	0.525	*243	249	210	363
26A	0.525	*254	-	176	335
20B	0.525	*349	265	231	353
21A	0.525	*278	212	204	322
22A	0.525	385	*206	203	298
24A	0.525	288	*223	202	259
23A	0.525	259	*-	204	241

\* Position of measured value in sequence.



1/2 INCH



3/4 INCH

Figure 18. Typical Maximum Cal. .50AP Damage in 0.50 Inch and 0.75 Inch 7075-T651 Plate.

#### 5.4 Longitudinal Strength of Thick-Plate 7075-T651 Containing a Through-Hole with Surrounding Spall

In 7075-T651 alloy plate 3/4 inch and thicker, the damage produced by Cal. .50 and smaller consists of a reasonably round through-hole with deep, round back-spalling. An example of this in 3/4-inch plate is shown in Figure 18.

Earlier in this section it was shown that a smooth hole has a rupture stress concentration factor of  $\sim 1.0$ . Since there are no visible cracks in the damage such as shown in Figure 18, the first look at these specimens was based solely on net strength. Because of the difference in damage extent on the front and back faces and the rough nature of the spalled face, it is difficult to estimate the load-carrying area. However, it is obvious that the effective amount of area removed by the damage is somewhat greater than the through-hole diameter.

Table V shows rupture stress concentrations calculated from the longitudinal residual strengths and the maximum and minimum effective areas. The first assumes that the lost area equals the through-hole diameter. The second assumes that the total area out to the maximum spall diameter is ineffective.  $W_e$  is the assumed load-carrying width. In no case did the first assumption yield an apparent stress concentration  $\sim 1.0$ . In only one case, the assumption that the entire damaged width was ineffective gave a value  $\sim 1.0$ .

Data also is included in Table 5 for 1/2-inch 7075-T651 plate. In this thickness, damage produced by Cal. .50 AP is similar to that in the 3/4 inch, except that the through-hole and back-spall are not necessarily circular and occasional cracks are visible. An example is also shown in Figure 18.

The high rupture stress concentration factors calculated for both thicknesses indicate the possibility of the ballistic damage containing crack-like flaws. To test this hypothesis, center-crack residual strengths were calculated for each specimen, assuming plane stress failure. Crack lengths were assumed to be equal to the hole diameter,  $H_o$ , the maximum lateral damage width,  $D_o$ , and an average of the front and back-face maximums,  $D_e$ . These results are shown in Table VI. The asterisks indicate where the measured values fall with respect to the predicted values.

In approximately half the cases, a value of  $2a_o$  less than  $H_o$  would be required for the predicted strength to be equal to the measured values. The others were bracketed by a crack equal to the mean between the front and back-face damage. This suggested that, contrary to the behavior of the thin titanium sheet, the stress concentration due to the presence of the hole was significant.

Therefore, the same specimens were analyzed using an expression based on Bowie's analysis (Ref. 8). The basic relationship is:



**TABLE VII.**  
**STRESS CONCENTRATION FACTOR FOR**  
**CENTER HOLE WITH LATERAL CRACKS**

$\frac{a}{r}$	$F_1$ (1 CRACK, UNIAX. STRESS)	$F_2$ (2 CRACKS, UNIAX. STRESS)
0.00	3.39	3.39
0.10	2.73	2.73
0.20	2.30	2.41
0.30	2.04	2.15
0.40	1.86	1.96
0.50	1.73	1.83
0.60	1.64	1.71
0.80	1.47	1.58
1.00	1.37	1.45
1.50	1.18	1.29
2.00	1.06	1.21
3.00	0.94	1.14
5.00	0.81	1.07
10.00	0.75	1.03
$\infty$	0.71	1.00

$$K_c = \sigma_{cr} \left( W \tan \left( \frac{\pi a}{W} \right) \right)^{1/2} F \left( \frac{a}{r} \right) \quad (8)$$

where  $F \left( \frac{a}{r} \right)$  is a factor determined for the ratio of crack length to hole radius.  $F_2$  is determined for a hole with cracks extending from both edges.  $F_1$  can be determined for a single crack. Values of  $F \left( \frac{a}{r} \right)$ , from Ref. 8, are given in Table VII.

For application to residual strength calculation,  $W$

was set equal to  $(w-H_0)$  and the equation was solved for  $P_{cr}$ . This resulted in

$$F_2 = \frac{K_c (w \cdot t)}{P_{cr} \left[ (w-H_0) \tan \left( \frac{\pi a}{(w-H_0)} \right) \right]^{1/2}} \quad (9)$$

The residual strength of each specimen was then used to determine the value of  $F_2$  necessary to satisfy Eq. (9). From the values of  $F_2$ ,  $H_0$ , and the data of Table VII, values were determined for the apparent crack length,  $a$ . These values are shown in Table VIII.

In all cases, the cracks necessary to satisfy the equation for residual strength were reasonably small and within the damaged area. With few exceptions, the predicted crack was less than 15% of the spalled area. The largest exceptions were in the 1/2-inch plate, where the damage was much more complex than in the 3/4 inch. In most cases, this region is within the disturbed material surrounding the through-hole.

These results indicate that typical small caliber damage in thick 7075-T651 plate can be treated by reducing the damage outside the through-hole to a set of cracks, one on each side of the hole. Where the damage is symmetrical and both the hole and spall are round, each crack can be assumed to be approximately 15% or less of the lateral damage outside the through-hole. In the 1/2-inch thickness, the more complex damage can be represented by the same model, but the effective crack length has to be assumed to be a larger percentage of the lateral damage.

**TABLE VIII.**  
**RESULTS OF CRACKED HOLE ANALYSIS OF BALLISTICALLY DAMAGED 7075-T651 PLATE**

SPECIMEN	THICKNESS (IN.)	$r$ ( $H_0/2$ ) (IN.)	$a$ (PREDICTED) (IN.)	$D_0/2$ (IN.)	$\frac{a}{D_0/2-r}$ (%)
28A	0.754	0.32	0.04	1.18	4.5
29B	0.754	0.33	0.04	1.06	5.5
32B	0.754	0.29	0.04	1.09	5.5
33B	0.754	0.15	0.09	1.15	9.0
30A	0.754	0.20	0.08	1.12	8.8
34A	0.754	0.17	0.13	1.07	15.
31B	0.754	0.27	0.10	0.95	14.
67A	0.754	0.35	0.12	1.02	18.
35A	0.754	0.36	0.13	1.16	16.
18A	0.525	0.31	0.04	0.83	7.3
19A	0.525	0.30	0.05	0.85	8.9
17A	0.525	0.30	0.06	0.90	9.7
26A	0.525	0.60	0.05	1.28	7.2
20B	0.525	0.29	0.06	0.73	14.
21A	0.525	0.49	0.06	0.95	13.
22A	0.525	0.23	0.24	0.96	34.
24A	0.525	0.42	0.20	0.97	35.
23A	0.525	0.57	0.14	1.07	28.

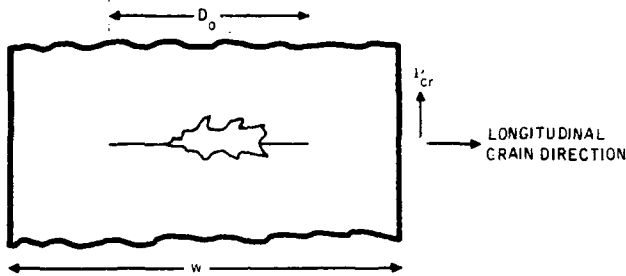
### 5.5 Additional Strength Analyses

Although the models and analysis discussed have not been tested for variables other than those specifically stated, it is expected that the applications include other materials and damage produced by projectiles other than Cal. .50 AP. Because of the difficulties in categorizing the many variables, analyses which have been performed on more complex damage patterns require detailed discussion beyond the scope of this paper. In many cases, residual strengths can be predicted for individual cases, but the analysis is too cumbersome for practical application.

### VI. MODEL SUMMARY

The following summarizes the residual strength models discussed in Section 5.

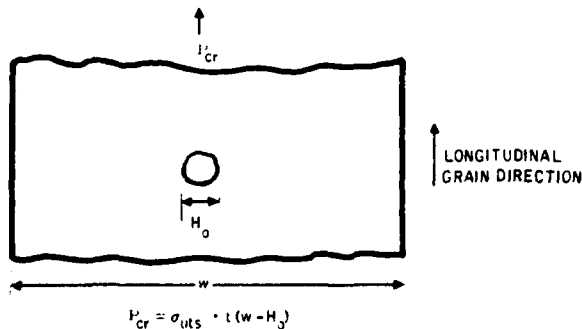
#### 6.1 Transverse Strength of Thin-Plate Aluminum Alloys Containing Longitudinal Cracks



$$P_{cr} = \frac{K_c (w \cdot t)}{\left( w \tan\left(\frac{\pi a}{w}\right) \right)^{1/2}}$$

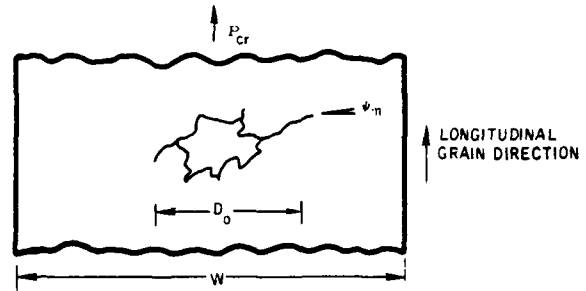
$$a = \frac{D_0}{2} - \frac{(P_{cr})^2 \cdot \tan\left(\frac{\pi D_0}{2w}\right)}{2\pi(\sigma_{ys})^2 \cdot w \cdot t^2}$$

#### 6.2 Longitudinal Strength of 2024-T851 Plate Containing Smooth, Round Holes



$$P_{cr} = \sigma_{UTS} \cdot t (w - H_0)$$

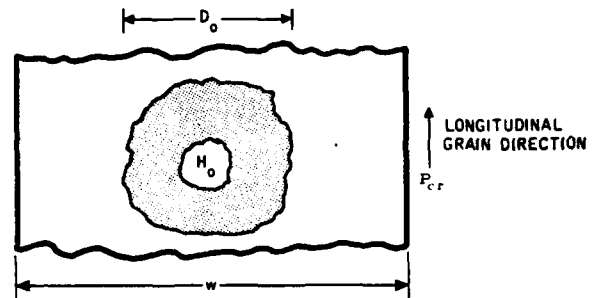
#### 6.3 Longitudinal Strength of 6A1-4V Annealed Thin Sheet Containing Cracks Radiating from a Ragged Through-Hole.



$$P_{cr} = \frac{K_c (w \cdot t)}{\left( w \tan\left(\frac{\pi a}{w}\right) \right)^{1/2} \left( 1 - \frac{1}{2} \psi_n \right)}$$

$$a = \frac{D_0}{2} + \frac{(P_{cr})^2 \tan\left(\frac{\pi D_0}{2w}\right)}{2(\sigma_{ys})^2 \cdot w \cdot t^2}$$

#### 6.4 Longitudinal Strength of Thick-Plate 7075-T651 Aluminum Containing Through-Hole with Surrounding Spall



$$P_{cr} = \frac{K_c (w \cdot t)}{F_2 \left[ (w - H_0) \tan\left(\frac{\pi a}{w - H_0}\right) \right]^{1/2}}$$

Note:  $F_2$  = stress intensity factor coefficient assuming  
 $a \approx 0.15 \left( \frac{D_0}{2} - \frac{H_0}{2} \right)$  for 3/4-inch plate;  
 $a \approx 0.30 \left( \frac{D_0}{2} - \frac{H_0}{2} \right)$  for 1/2-inch plate

### VII. ACKNOWLEDGEMENTS

The work described above was sponsored by Convair independent research and development programs 111-1238-911, 111-6806-156, and 111-6906, 159. A portion of the damage and residual strength data used in the analyses was developed on Contract N00156-68-C-2494 sponsored by the U.S. Navy Aerostructures Laboratory.

The authors wish to acknowledge the efforts of their co-workers who contributed to the success of the programs, particularly Mr. Gerald O'Barr, who was responsible for most of the ballistic testing.

## REFERENCES

1. M.D. Campbell, G.L. O'Barr, and G.E. Pynchon, *Development of Ballistic Test Facility and Evaluation of Vulnerability of Aircraft Materials*, ERR-AN-1134, General Dynamics Corp., Convair Division, San Diego, California (1967).
2. M.D. Campbell, G.L. O'Barr, and G.E. Pynchon, *Vulnerability of Aircraft Materials to Small Arms Gunfire*, ERR-1346, General Dynamics Corp., Convair Division, San Diego, California (1968).
3. J. Jensen, P. Thorndyke, and M.D. Campbell, *Aircraft Wing Structural Concepts with Improved Ballistic Damage Tolerance (U)*, GDC-DDG-69-002, General Dynamics Corp., Convair Division, San Diego, California (1969).
4. R.A. Rave and D.E. Schwab, *Lecture Notes for Safe-Life Design Practices: Practical Applications, Fracture Mechanics*, Douglas Paper 10230, McDonnell Douglas Corp., Long Beach, California (1969).
5. J.G. Kaufman et al., *Fracture Toughness, Fatigue and Corrosion Characteristics of 7075-T651, 7075-T7351, and 7079-T651 Aluminum Alloys*, AFML-TR-65-170, Air Force Materials Laboratory, Wright-Patterson AFB, Ohio (1965).
6. W.F. Brown and J.E. Srawley, *Plane Strain Crack Toughness Testing of High Strength Metallic Materials*, ASTM-STP-410, American Society for Testing and Materials, Philadelphia, Pennsylvania (1967).
7. *Fracture Toughness Testing and Its Applications*, ASTM-STP-381, American Society for Testing and Materials, Philadelphia, Pennsylvania (1965).
8. O.L. Bowie, "Analysis of an Infinite Plate Containing Radial Cracks Originating from the Boundary of an Internal Circular Hole," *J. Math. Phys.*, 35:60-71 (1956).
9. J.G. Kaufman and M. Molt, *Fracture Characteristics of Aluminum Alloys*, TP-18, ALCOA Research Laboratories, New Kensington, Pennsylvania (1965).

# COMBINED ENVIRONMENT SONIC FATIGUE TEST OF THE AFT FUSELAGE PANELS FOR A FIGHTER BOMBER AIRCRAFT

by

O.F. Maurer and R.M. Shimovetz

Air Force Flight Dynamics Laboratory  
Wright-Patterson Air Force Base, Ohio

## INTRODUCTION

The design of aircraft structural components to withstand sound induced fatigue, although being beyond the state of a mere qualitative approach, in many instances is lacking sufficient background such that reliable structures can be designed with a high degree of confidence based on readily available empirical information and analytical methods. Frequently, the basic structural design results from static load considerations and the sonic fatigue problem is taken into account by best available design criteria and design practices. A subsequent design and development test of the component in a simulated acoustic noise environment is conducted to verify or improve the basic design.

The problem is even more involved if other environments such as high temperatures act on the structure in combination with the acoustic noise excitation. In such cases the addition of thermal stresses or strains together with changes in the fatigue and other mechanical properties of the material<sup>1</sup> are not the only factors to complicate the problem, but also the resulting changes of the dynamic characteristics of the structure and the associated changes of the stress response statistics contribute to the complexity of developing an adequate structural configuration.

If high temperatures are involved, thermal strength considerations govern the selection of the material and the basic design and it appears that a subsequent development test in the combined environment will lead to suggestions as to necessary design changes. Such a test, the first of its type which was conducted in the AFFDL Sonic Fatigue Facility, is based on the following background:

During the development of a fighter bomber aircraft, it was anticipated that the fuselage aft centerbody would be exposed simultaneously to high temperatures and high level pseudo-acoustic loads. Both of these loads were expected to result essentially from the passing turbulent jet efflux. Calculations to determine these loads which were performed by the airframe manufacturer indicated that certain local structural surface areas would be exposed during parts of the mission profile to temperatures near 1300°F and overall sound pressure levels in the order of 165 decibels. A development test program was initiated to determine a structural configuration for the area which is predominantly ex-

posed to this combined load environment. The structural component primarily involved was a slightly curved stainless steel panel.

It was anticipated that, in sequence, various different design configurations would be investigated in the Sonic Fatigue Facility until a design was determined which would withstand at least 50 hours of the predicted environment.

## DESCRIPTION OF BASIC TEST ARTICLE AND TEST ARRANGEMENT

The general location of the structural area under consideration in the compound of the aircraft tail structure is shown in Figure 1. The approximate area which is exposed to the combined high thermal and sonic environment is marked in Figure 2. This area extends approximately over a length of 20 inches and a width of 10 inches. The skin, stringers, and frames of this structure consisted of stainless steel, AISI-321 (MIL-S6721A). The skin itself and the frames were made from 0.063 inch thick sheet material and the stringers were 0.032 inch sheet material. The size and configuration of the test panel had to be selected such that it very closely represented the actual structure and still could be adapted to the test section of the Sonic Fatigue Facility. The basic test panel, as shown in Figure 3, consisted of a rectangular 18" x 11.75" curved plate with

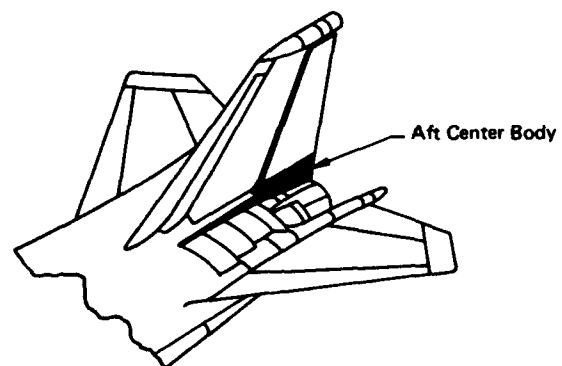


Figure 1. Aircraft Tail.

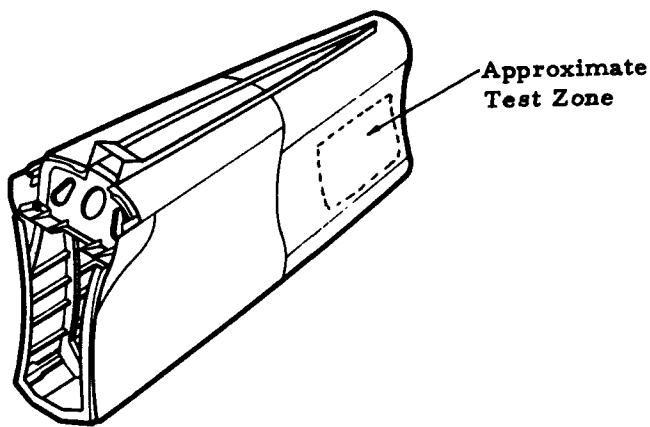


Figure 2. Aft Centerbody.

two Z stringers and two frame sections. The stringers were tied to the frame sections by angle clips. For the purpose of mounting the test articles into the test section a mounting frame of the same material (AISI-321) and thickness of the panel was riveted to the bulkhead sections and the skin as shown in Figure 4. This kind of mounting frame had the advantage of simulating to some extent the flexibility of the adjacent structure. For the purpose of fastening the panel to the side of the acoustic test section, holes were drilled into the flanges of the mounting frame, which were several times the diameter of the fastening bolts. It was expected that this would allow the panel to expand under the thermal load with a minimum restriction, if the bolts were only loosely tightened and if sufficient space for expansion were allowed between the surrounding test section and the panel. The two top center holes of Figure 4 were closely fitted with the bolts which centered the panel in position. Four different versions of this basic panel were tested. The differences existed mainly in the stringer construction and their connection with the frame sections. These will be described later.

The small chamber of the Sonic Fatigue Facility, which is shown in Figure 5 was selected for this test since it permitted the required very high intensity noise levels to be generated. Further information about this facility is contained in Reference 2. The sound was generated by two sirens which are located at the mouth and on top of the 12" by 12" test section. The test panels were fastened on the side of the test section. In order to reduce thermal conduction to the aluminum test section, thermal insulation material which consisted of a 1/2 inch thick compressed asbestos board was placed between the mounting frame and the test section. Additional cooling was provided by cooling coils such that no thermal distortion was introduced in the test section.

The panel was installed such that the concave side was excited by the sound waves and this required that the heat be induced from the convex side. A quartz lamp

radiative heater was constructed for this purpose. The 60 tubes of the heater supplied the heat to raise the temperature of the skin to 1250°F from as far away as 10 inches from the panel frame.

In the airplane, both the sonic load and the heat are acting on the panel from the concave side. This difference between the service and the test environment was expected to cause higher temperatures in the stringers than will be actually encountered in service. Therefore, some means had to be found to shield the stringers from the radiated heat. Since the service temperatures of the stringers were not known, an extra panel was heated on the concave side to the required skin temperature distribution, while the temperatures of the stringers which were located on the convex side were measured. It was found that in order to simulate the service heat distribution the stringers should be kept at 750°F to 800°F when the skin was at 1250°F. Several methods to shield the stringers from reaching excessive temperatures were tried. First a strip of "Marinite" board was used to shade the stringer tops as shown in Figure 6a. These strips "burned" down to a thin section within 2 hours and broke apart. Copper tubing using the waste cooling

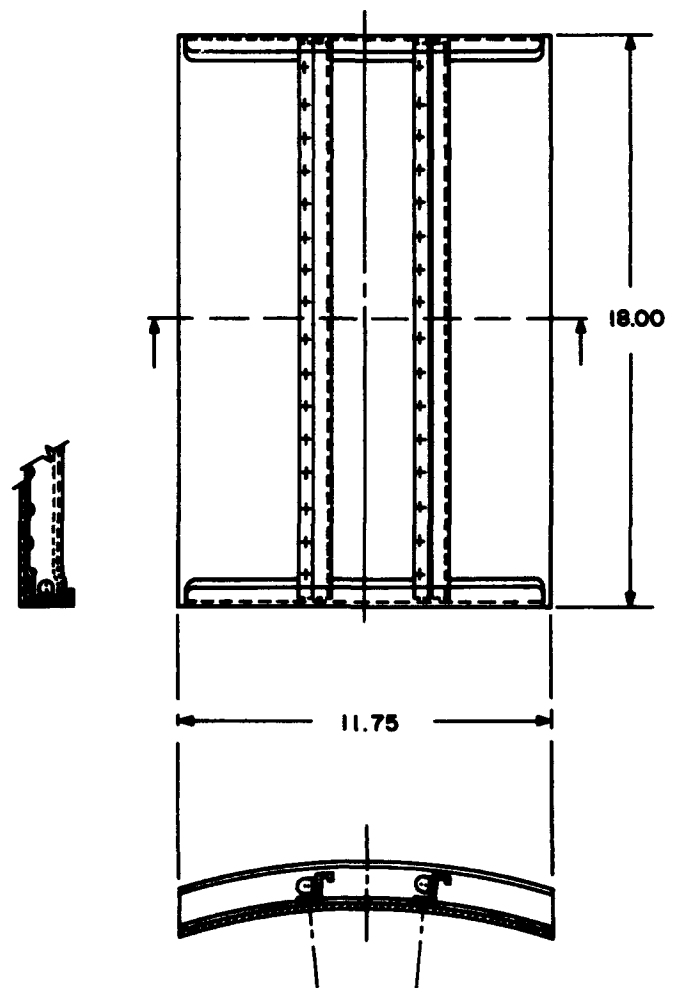


Figure 3. Basic Test Panel.



Figure 4. Test Panel with Mounting Frame.

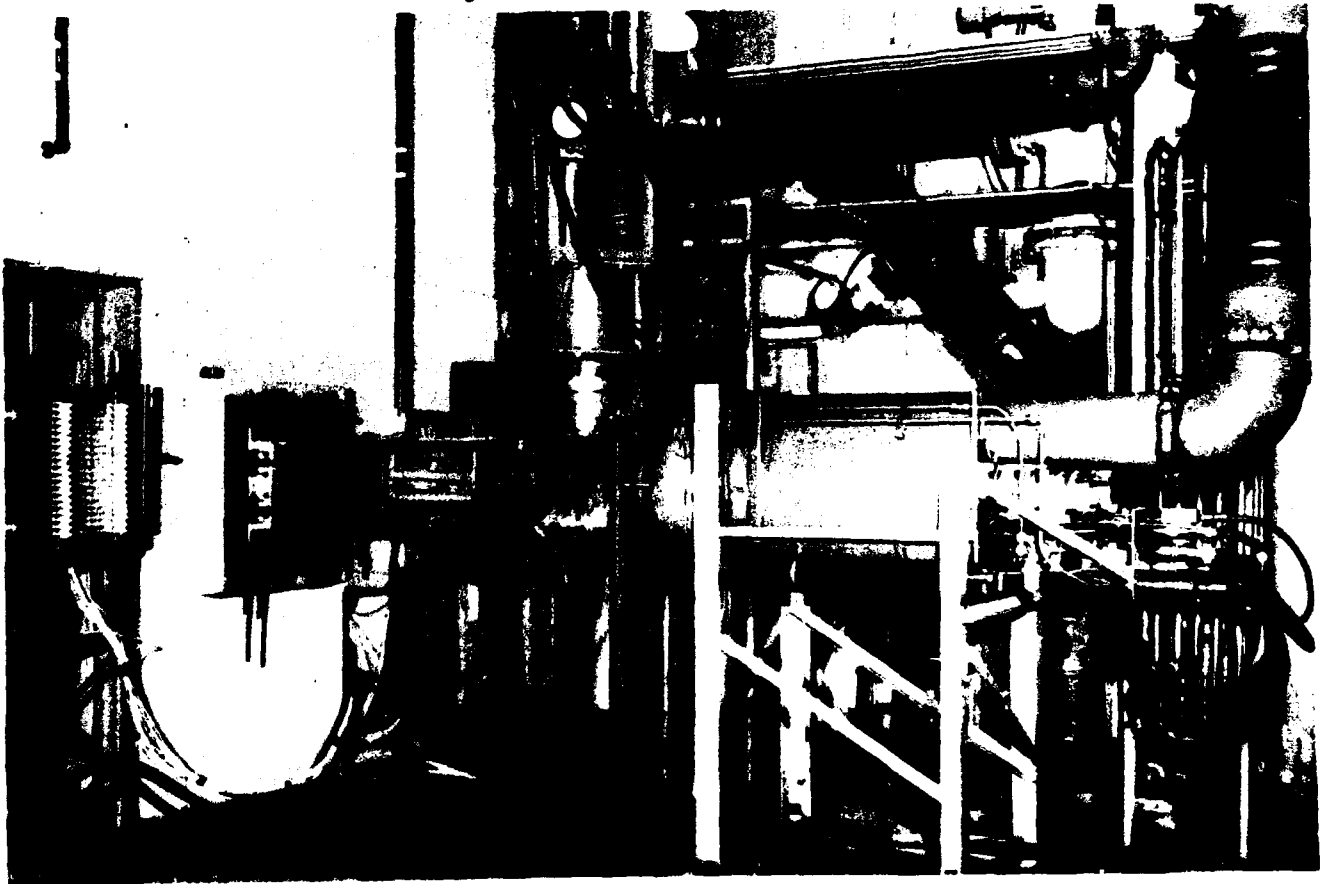
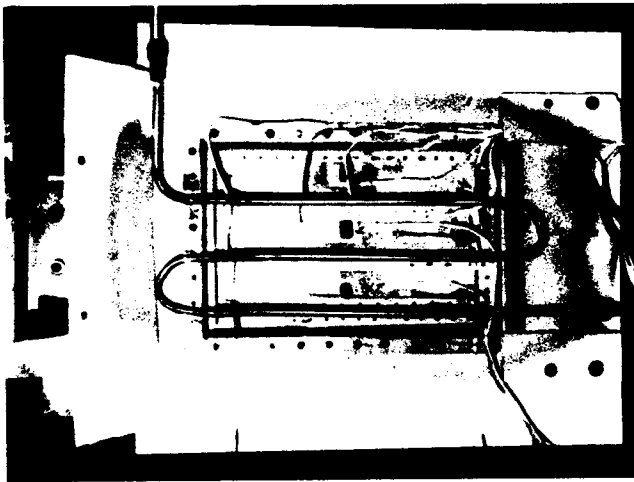


Figure 5. Siren Arrangement of Small Test Chamber.



A



B

Figure 6. Panel Installation with Stringer Cooler.



Figure 6C. Final Stringer Cooler.

water from the water-cooled heater reflector was laid above the stringers to shield them from the direct radiation of the lamps, Figure 6b. The copper tubing still permitted the stringer tops to reach temperatures 100°F to 150°F higher than required. The addition of curved shrouds which were bent from copper sheeting and soldered to the cooling tubes as shown in Figure 6c, successfully kept the stringer tops to near 300°F. Figure 7 shows the final installation of a panel with heater and stringer cooling arrangement.

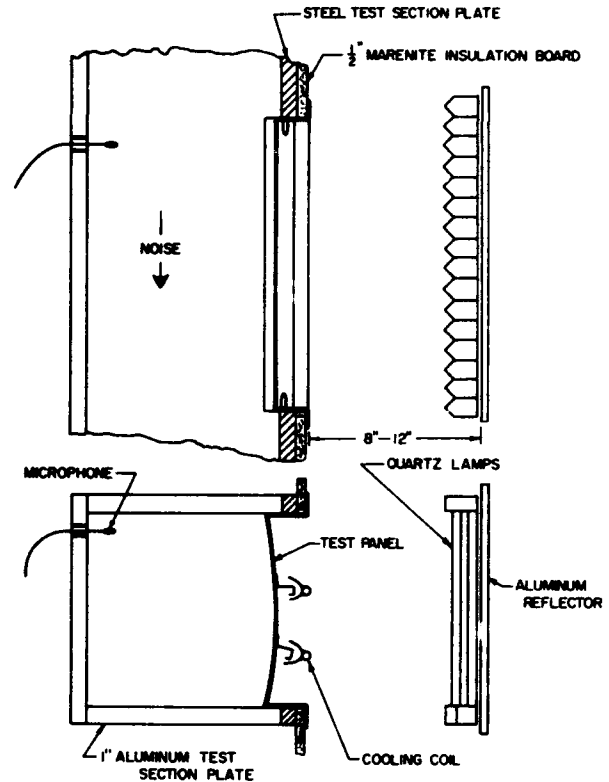


Figure 7. Test Panel Placed in Test Section.

The temperature distribution over the skin and stringers of the four test panels was monitored with 10 to 16 Chromel-Alumel thermocouples which were capacitive discharge welded to the panels directly. The location of these varied slightly from panel to panel. During the tests, frequent damage of the thermocouples was encountered. This prevented closed loop automatic control of the temperature distribution through the seven groups of tubes which made up the heater. Therefore, in order to maintain a set temperature distribution during a test run, the electrical power input to each group of tubes was recorded during the establishment of the temperature distribution and was manually maintained constant for each group during the test.

The two sirens of the facility which generated the random noise spectrum for the acoustic excitation of the panels are basically pure tone sirens. However, by programming the siren control systems for random amplitude and random frequency modulation a limited bandwidth of acoustic random noise can be obtained. The basic procedure of siren programming is described in Reference 3. The sound spectrum was monitored by a microphone which was placed into the wall of the test section opposite from the panel to be tested. During the tests, special care had to be taken not to exceed the allowable temperatures for this microphone.

#### PRELIMINARY EXPERIMENTS

The limitation in noise bandwidth which was posed

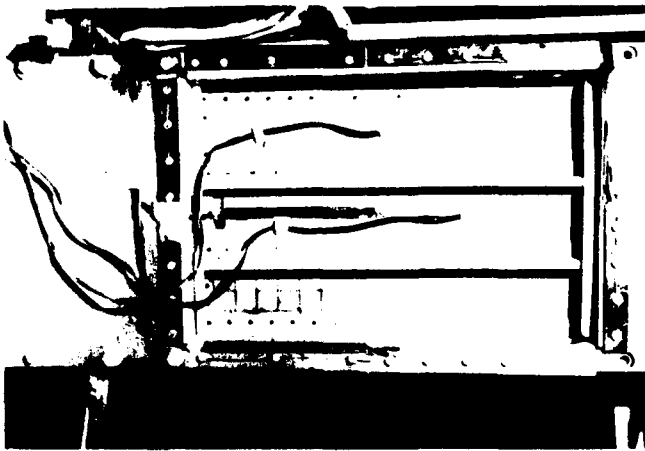


Figure 8. Panel Installation.

by the two sound sources, made it necessary to determine the predominant resonant frequencies of the panels, such that the excitation bandwidth could be placed over the range of these frequencies. By exploring the mode shapes

associated with these resonant frequencies, the location of maximum stress vibrations could also be found, which was necessary for the placement of strain gages. In order not to impair the fatigue life of the test specimen this was done with low sound pressure levels under the assumption that the stiffness of the panels, and with it their resonant frequencies, would shift approximately 20% downward under the actual test temperature. This assumption is based on data which are presented in Reference 4. With this knowledge it was expected that a limited, low level acoustic frequency survey of the panels under thermal loading would suffice to confirm the important resonances.

The acceleration mode shapes were mapped out by setting a siren to operate at the predetermined resonant frequencies. While the panel was excited at a natural frequency, one accelerometer was kept in a fixed position while a second accelerometer was placed at different locations on the grid which was laid out on the panel surface, Figure 8. The recorded accelerations and the relative

Figure 9a. Displacement Shapes at Room Temperature.

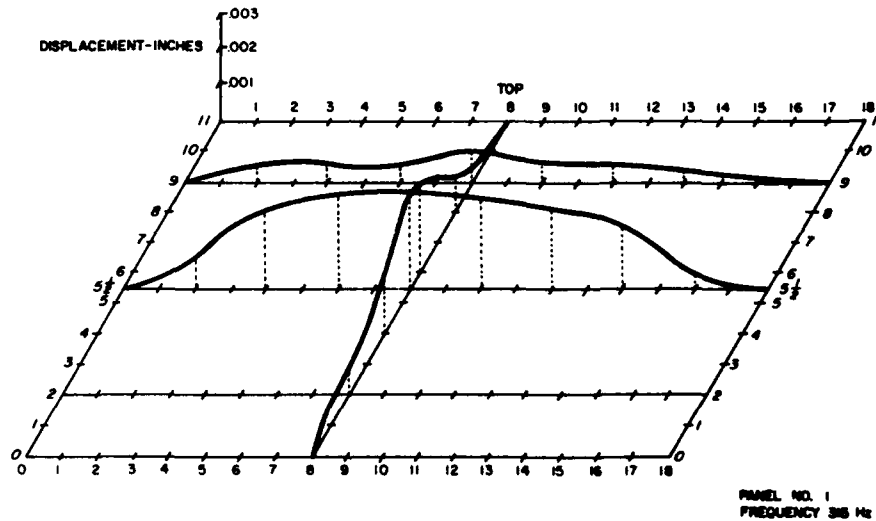
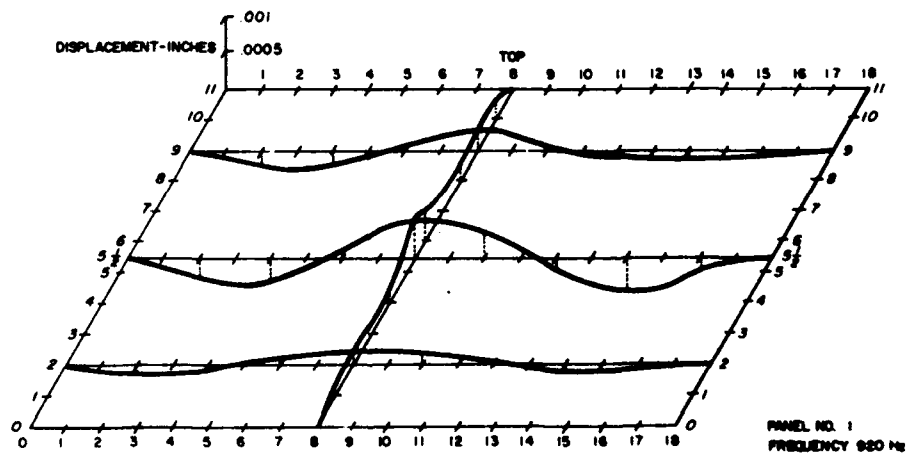


Figure 9b. Displacement Shapes at Room Temperature.





phase differences of the two accelerometers were used to determine the distribution of the acceleration across the panel surface. By known relationships these data were converted into displacement distributions, such as are presented in Figures 9a and 9b for the lowest observed mode at 315 Hz and for the highest measured mode at 920 Hz. Assuming pure bending and estimating minima of the second derivatives of the measured displacement curves served as guidelines for the placement of the strain gages. The modal surveys were conducted only for panels 1 and 2 because of the similarity of panels 3 and 4 with these first test articles.

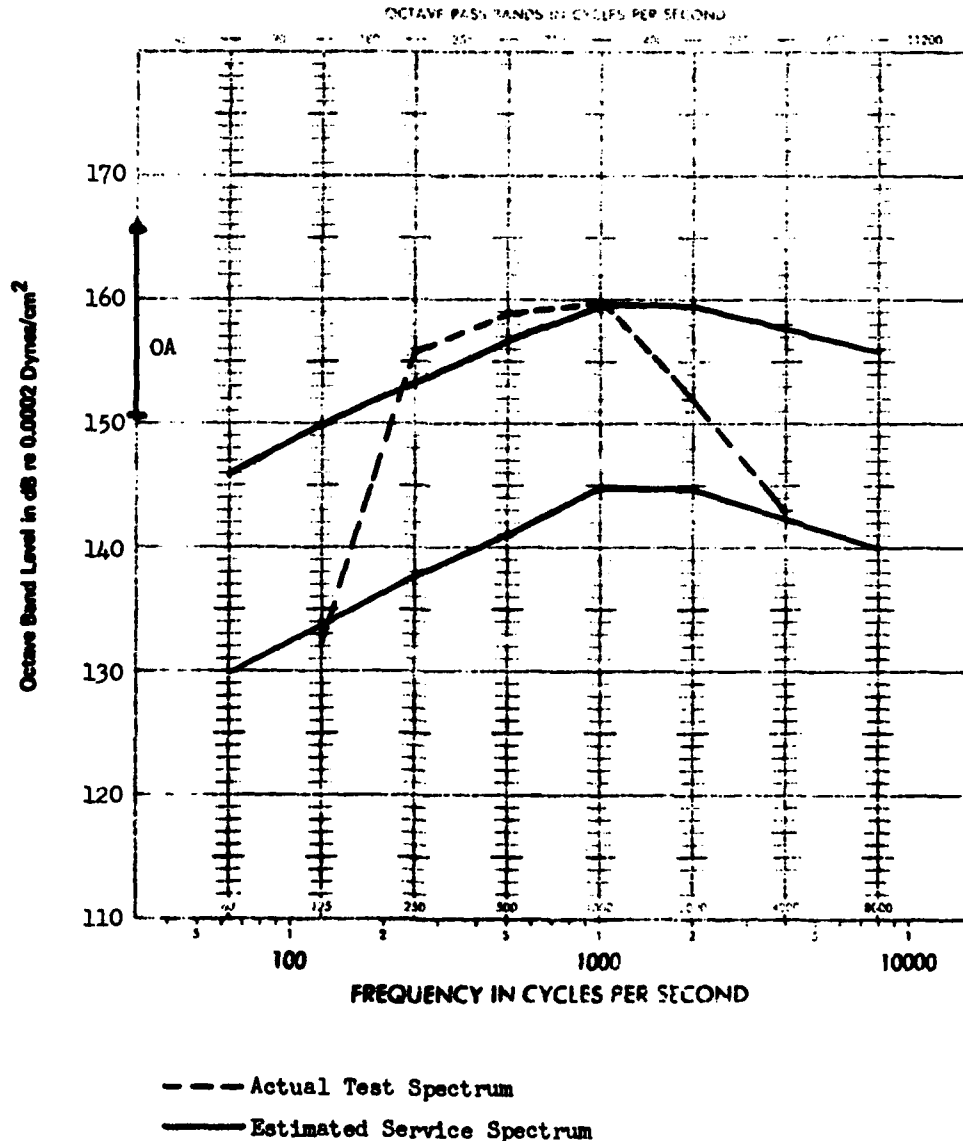
The strain gages which were selected are rated for usage at 1200°F; this range could possibly be extended to 1500°F. No information concerning gage properties under high frequency dynamic loading was available. Therefore, a limited survey was conducted by shaker experiments to obtain some information on the strain gage properties under the combined environment. It was found that the life of the

gages is very limited at the specified test temperatures and under cyclic loading.

### COMBINED HIGH TEMPERATURE SONIC FATIGUE TEST

The pseudo acoustic pressure levels expected on the skin were obtained by prediction methods which are outlined in Reference 5. The lower and upper limiting octave spectra of these pressures are presented in Figure 10. It was specified that the higher curve be applied during the test, however, due to the acoustic bandwidth limitation of the facility, some modifications were necessary in the test spectrum. The lower limit was approached in the octave band centered at 125 Hz. Between the center frequencies of 250 and 1000 Hz, the estimated upper service spectrum was exceeded by 2 dB and at 4000 Hz the lower limit was approached again. This placed the test spectrum well within the range of the predominant vibration modes of the panels which were previously determined. Slight variations of this

Figure 10. Service Noise Spectrum and Facility Test Spectrum.



basic spectrum were incurred during the various tests. Figure 11 displays a measured sound pressure level spectrum in 10 Hz bandwidths. Compromises were also necessary in the simulation of the thermal distribution in that the temperature gradient on the skin of the test panel shown in Figure 12 was not expected to be as steep as the actual structural surface. Both approximations in the simulated environment were expected to introduce some conservatism into the test. Slight variations from the temperature contours of Figure 12 were observed. Since no information was available about the rate with which the temperature would be introduced into the structural surface, a test thermal rate of 200°F/min to 250°F/min was arbitrarily selected to heat the panels to the equilibrium temperatures. Except for the first test run with the first panel when the heater was almost instantly turned on to full temperature, the above test rate was applied for all subsequent tests.

During the first test run, the temperature contours were also slightly more concentrated towards the center of the panels.

Within a few seconds, after both the random sound field and the heat distribution were acting on the first test article, no more strain signals could be received. It was determined that all strain gages had separated from the test

specimen. Using a different bonding technique cured the problem of gage separation, but the strain gages still failed within a short time from test start. The gage failure consisted mostly of breakage of the lead wires into the gages. This problem plagued the test over its complete duration such that insufficient strain data were acquired under exposure to the combined test environment and observation of panel failure yielded the only tangible test results.

### FAILURE DISCUSSION

It was originally planned that the number of visual inspections of the test article should be kept low, particularly in the beginning of the test, in order to reduce thermal cycling which resulted from each test stoppage. However, the first inspection of panel Nr. 1, which followed after two hours exposure to the combined environment, indicated extensive damage to the stringers already. This is shown on the top left of Figure 13 where the upper and lower stringers together with their frame connecting clips are drawn. The dotted lines indicate the cracks which were observed in this inspection. One notices that both top ends of the upper stringer and the left top of the lower stringer are missing. The cracks propagated down the web into the stringer base

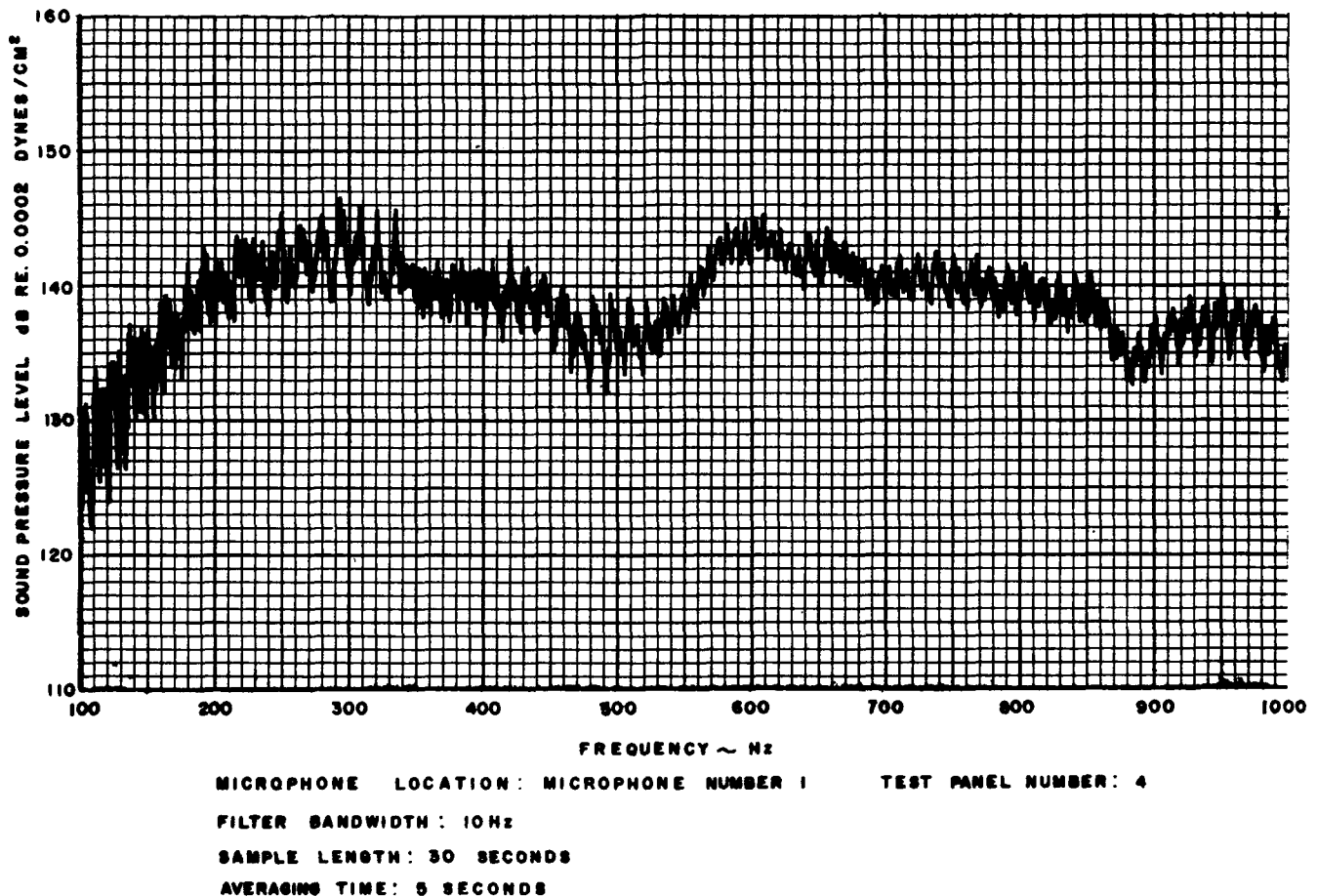


Figure 11. Sound Pressure Spectrum.

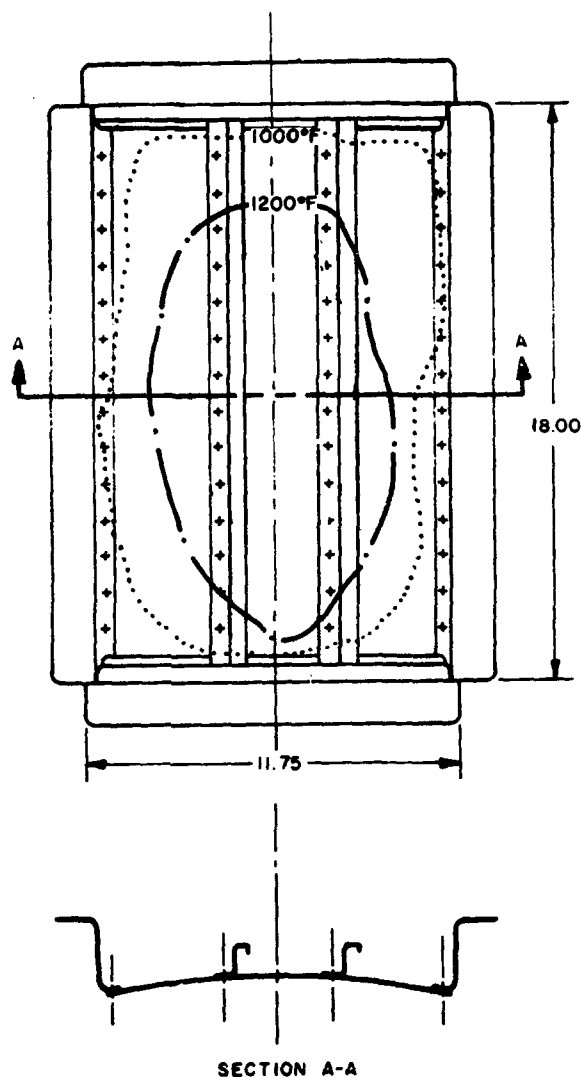


Figure 12. Test Temperature Distribution.

and a section on the left of the lower stringer broke off. Also the lower right angle clip showed damage near its bend. After one additional hour exposure time, the upper stringer was destroyed and the right angle clip was broken. Also the destruction of the lower stringer had progressed further. The failure pattern of the right top end being similar to the first observed failures is particularly noteworthy. The sixth inspection, after 4 hours and 46 minutes, revealed that besides the complete damage of both stringers, a progressive crack in the skin below the lower stringer occurred. At this point the test of the first panel was terminated. Figures 14a and 14b show the test article in its final condition.

It was suspected that the initial heat shock and the high thermal stresses due to the somewhat more concentrated pattern during the first hour of the test contributed heavily

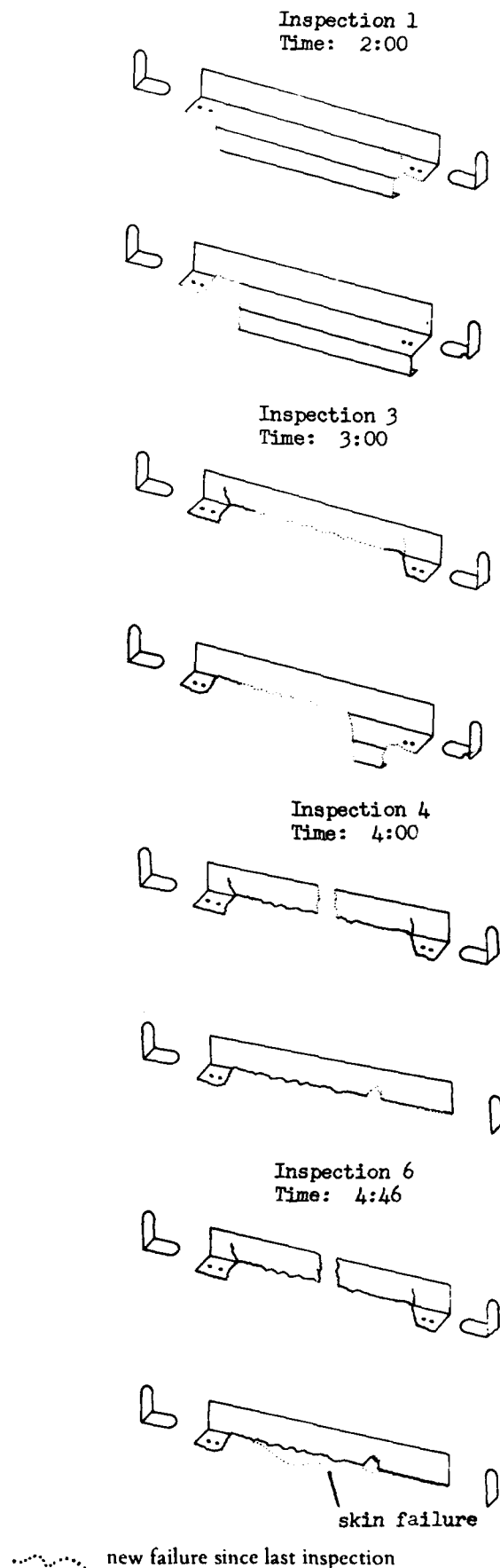


Figure 13. Failure Propagation of Panel Nr. 1.

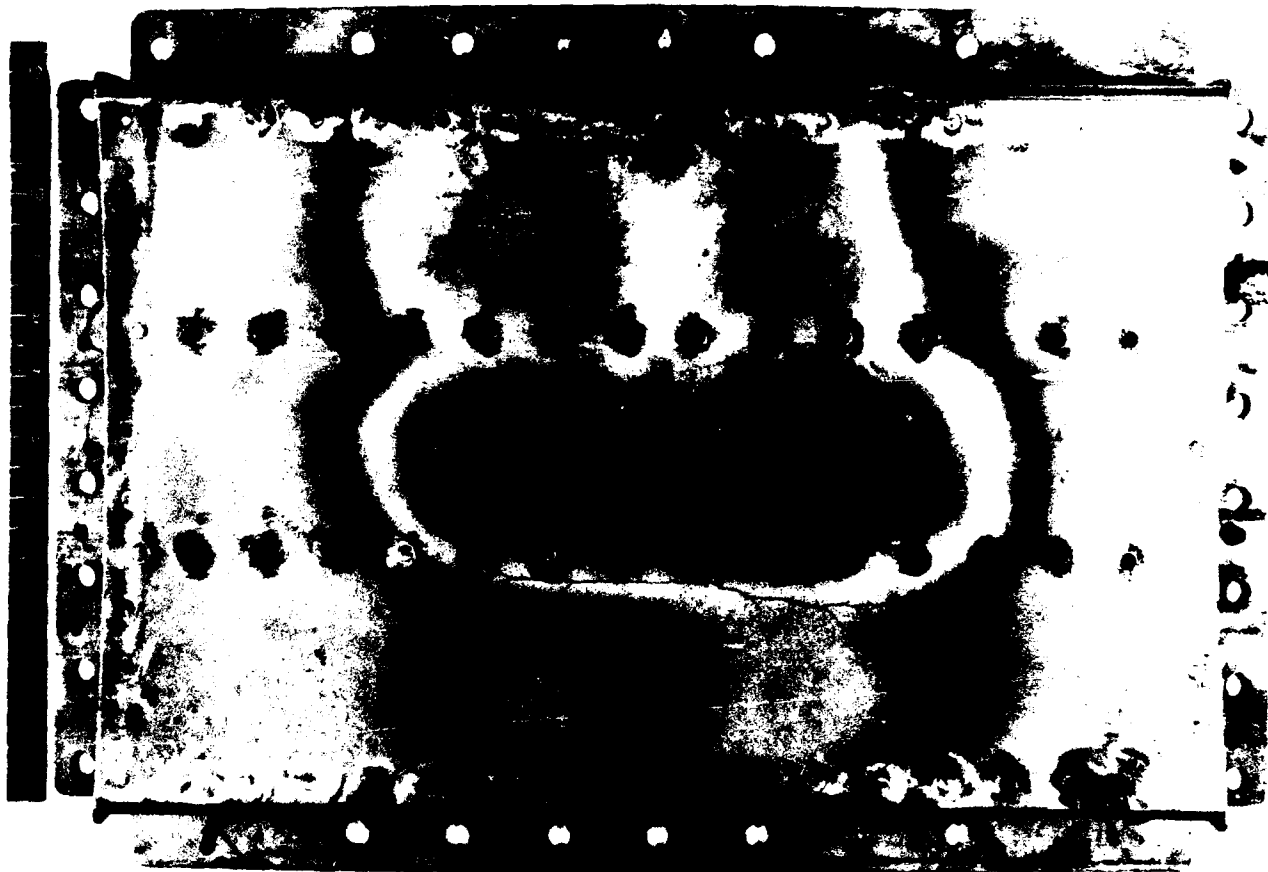


Figure 14a. Panel No. 1 After Test.

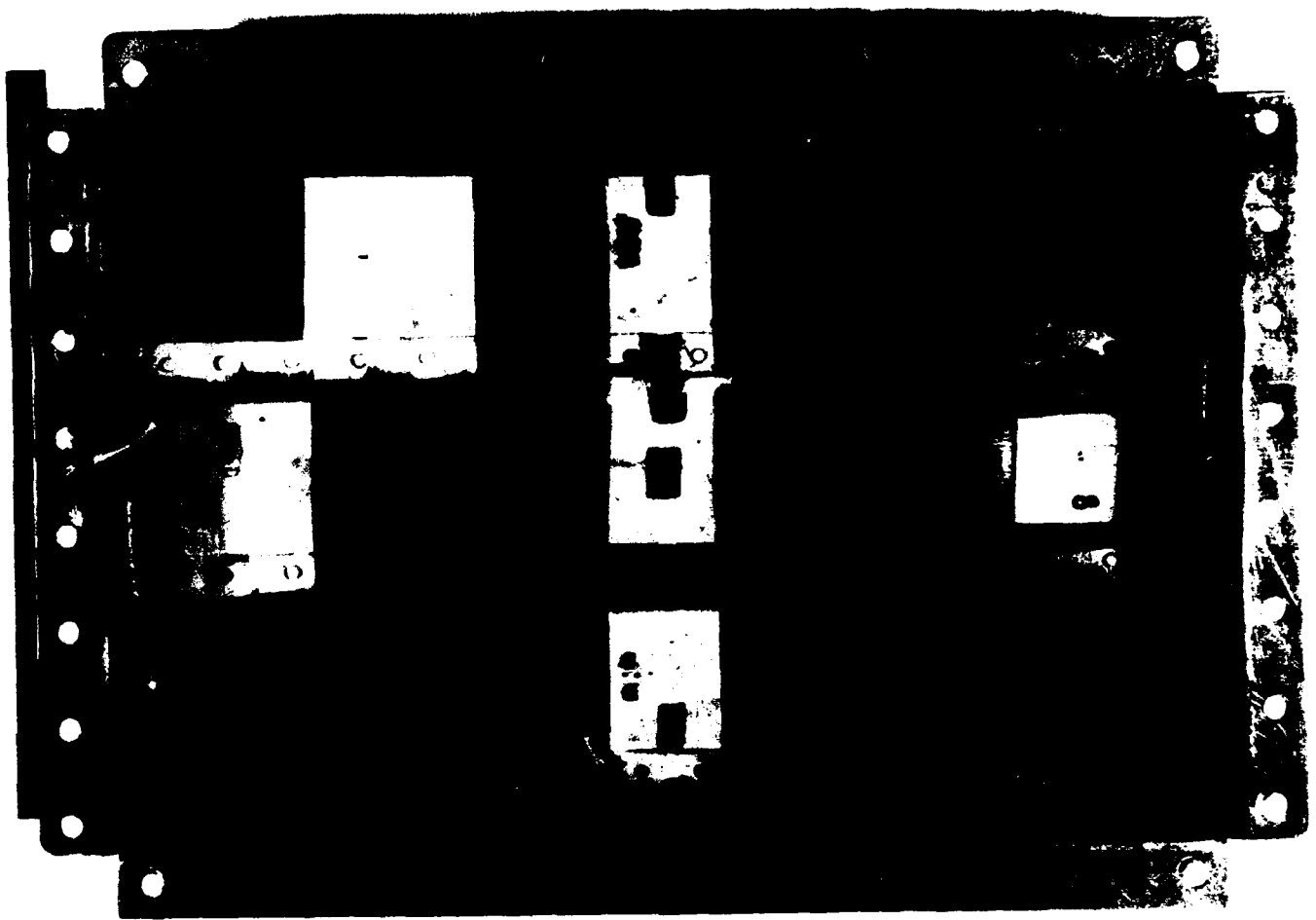
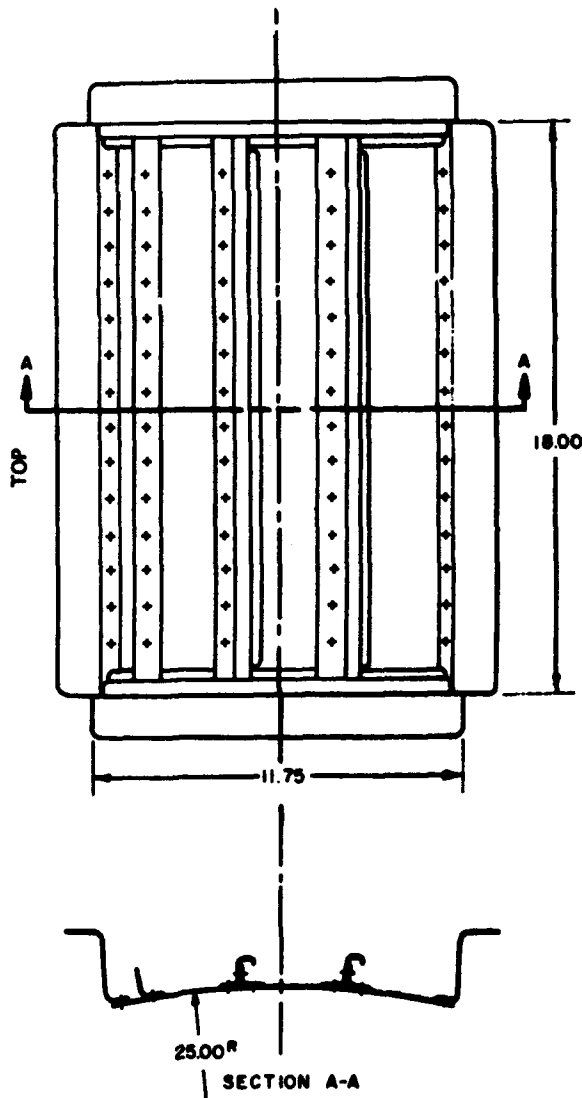


Figure 14b. Panel No. 1 After Test.



to the early failures on the stringers. However, comparatively large dynamic stresses must have also existed to cause the rapid damage. This possibly could be explained by a torsional buckling of the stringers which led to occasional "snap-through" motions with the associated high stresses near the connection to the frames. At this point it was suggested that in the following test panel the connection to the bulkhead section be removed and the stringers be replaced by heavier symmetrical sections. However, other considerations prevented this approach.

In the second version of the test panel the stringers were stiffened along the webs and the base as shown in

**NOTE**

Text continued on Page 572, following Figure 18c.

Figure 15. General Configuration of Panel No. 2.

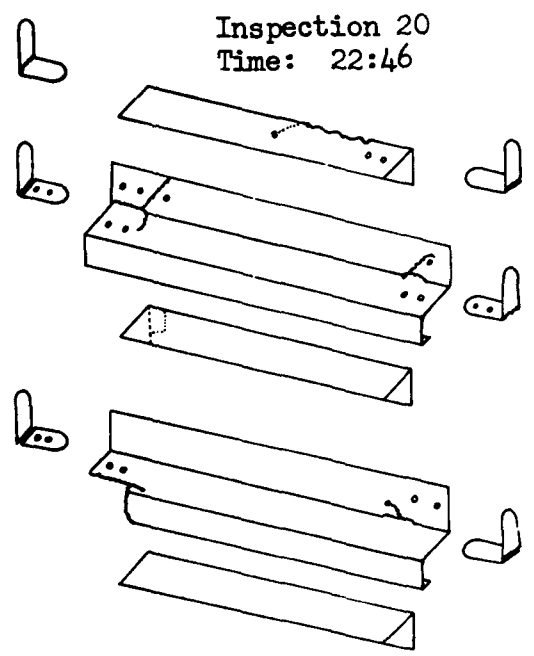
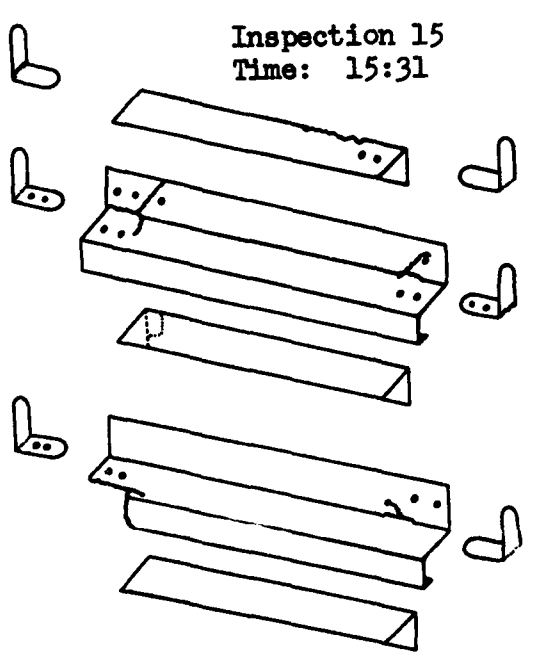
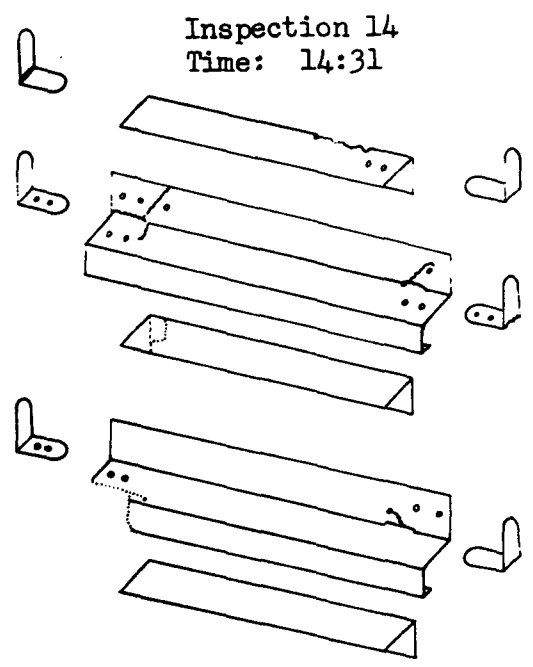
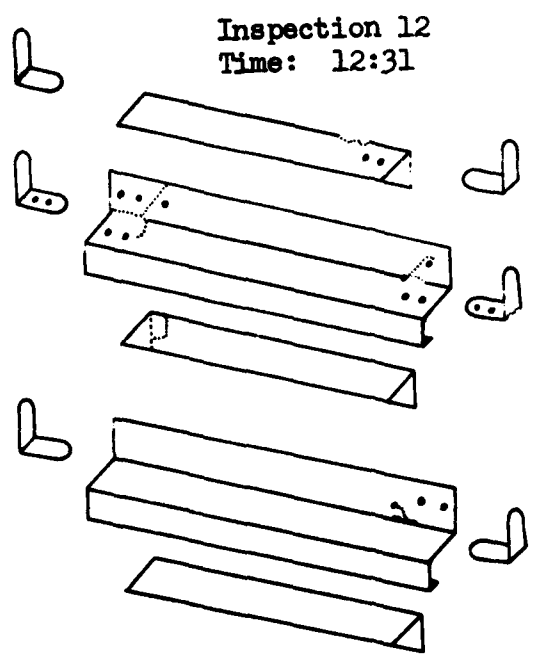


Figure 16a. Failure Propagation, Panel No. 2.

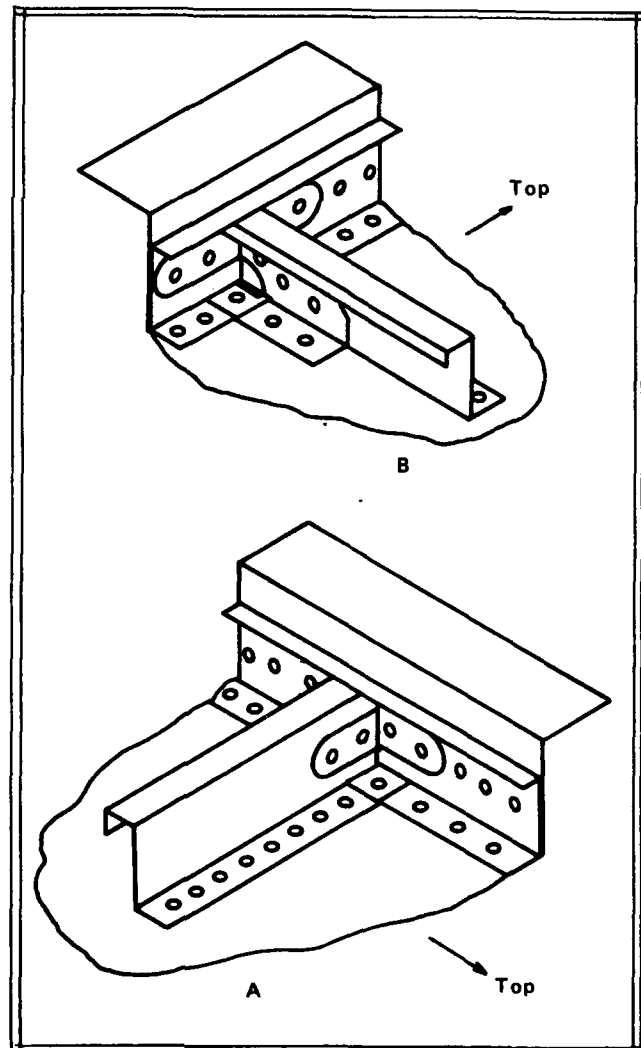
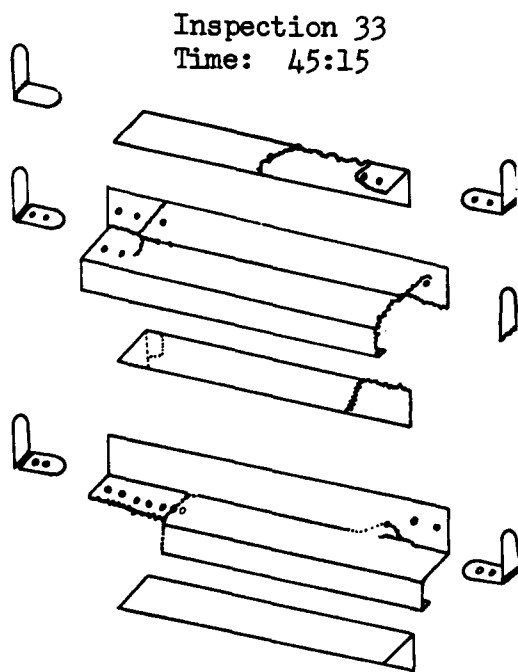
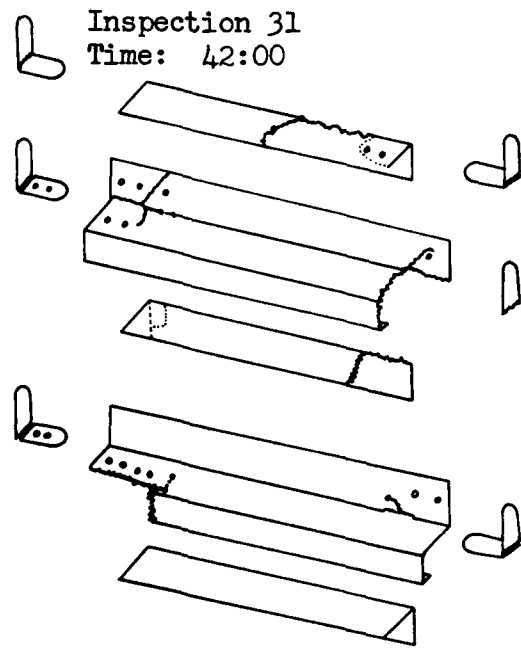
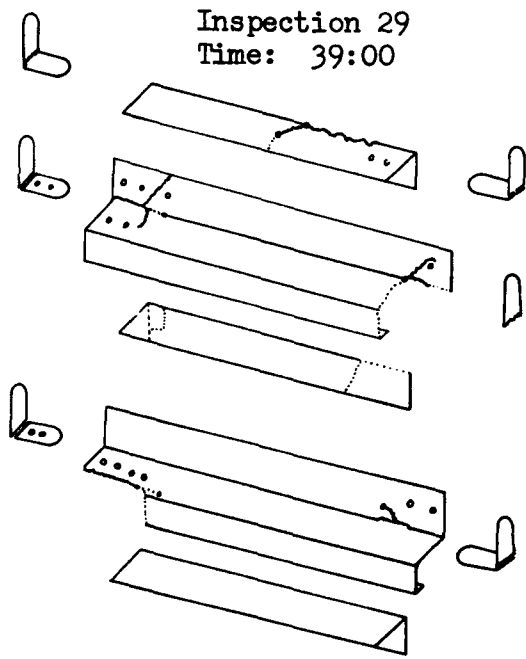
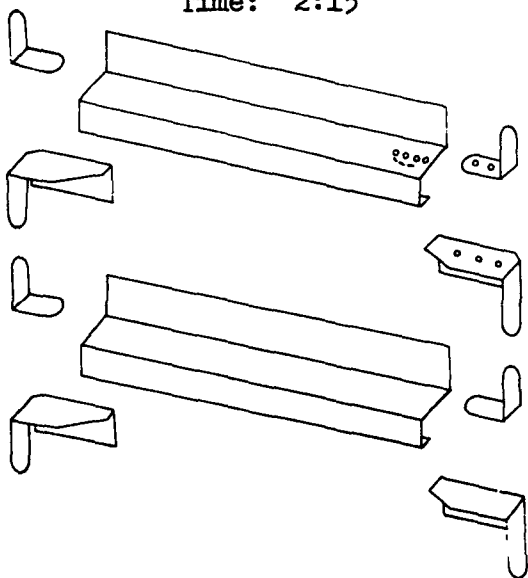


Figure 16b. Failure Propagation, Panel No. 2.

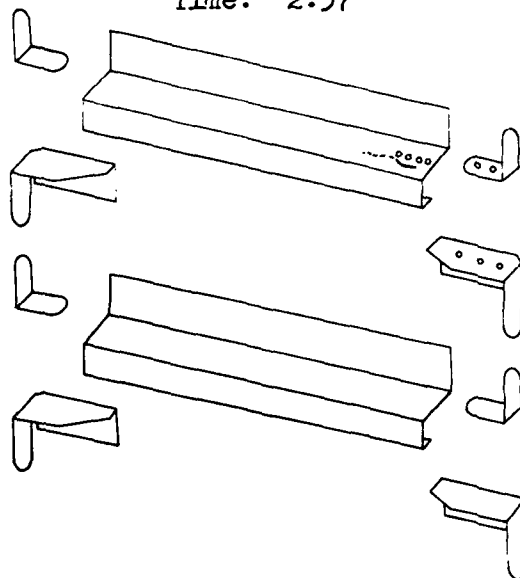
Figure 17. Schematic of Typical Stringer-Bulkhead Connection.



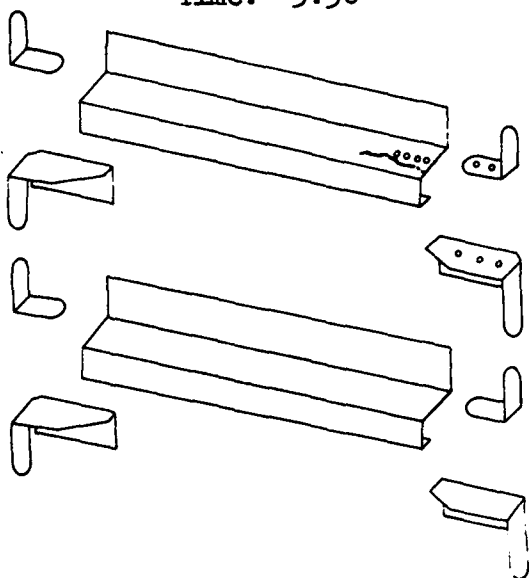
Inspection 4  
Time: 2:15



Inspection 5  
Time: 2:57



Inspection 6  
Time: 3:30



Inspection 9  
Time: 6:15

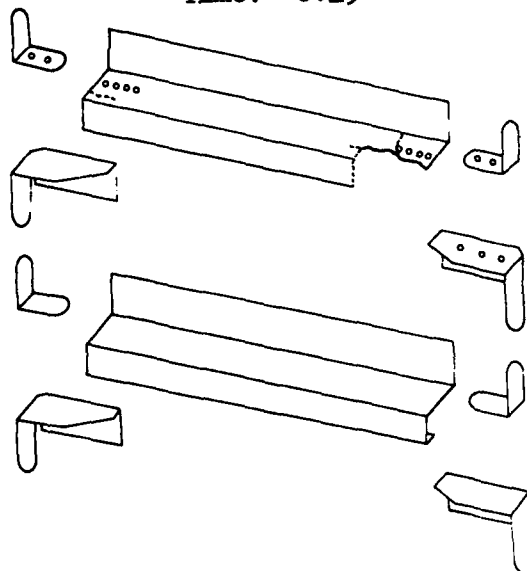
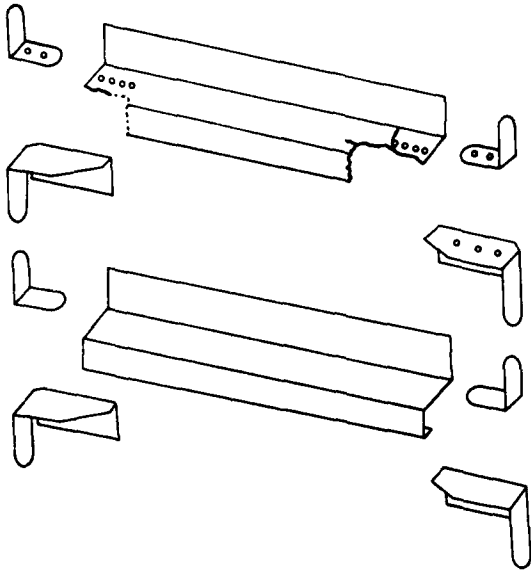
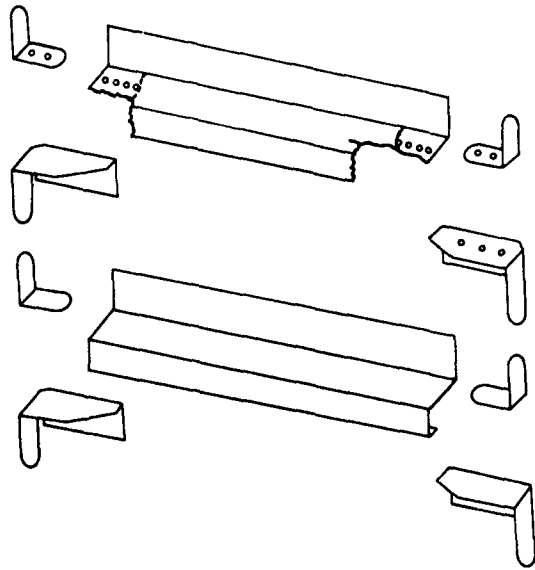


Figure 18a. Failure Propagation Panel No. 3.

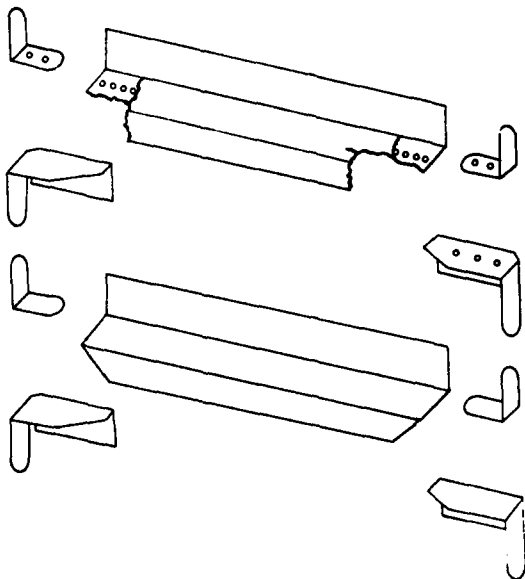
Inspection 12  
Time: 9:15



Inspection 13  
Time: 10:15



Inspection 16  
Time: 14:00



Inspection 30  
Time: 32:00

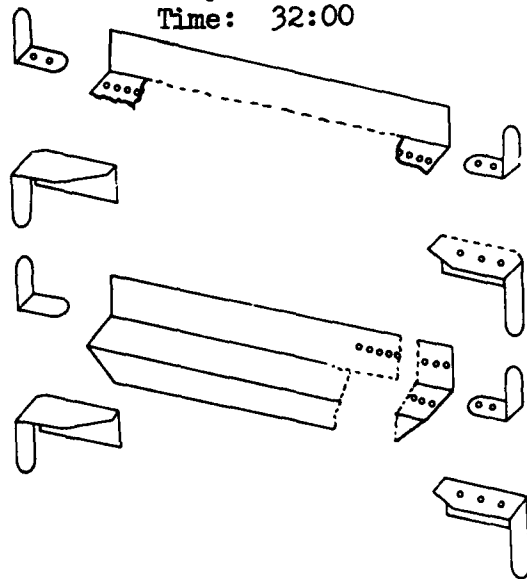


Figure 18b. Failure Propagation Panel No. 3.

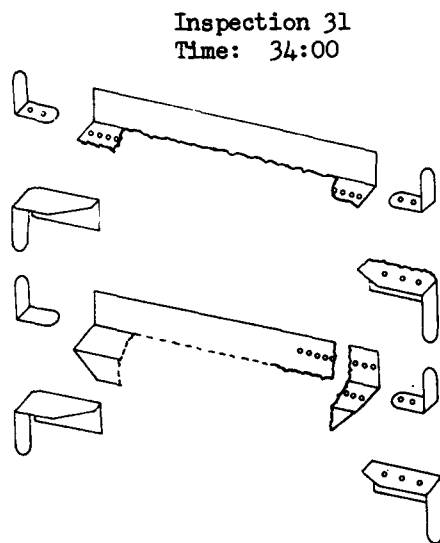


Figure 18c. Failure Propagation Panel No. 3.

Figure 15. An additional stiffener was riveted close to the skin upper edge.

The first cracks, originating in the base corner near the ends of the stringers, were detected after 12 hours and 31 minutes. This is shown in Figure 16a. Stop drilling of some of these initial cracks in the two main stringers was attempted and no essential further propagation of the cracks was observed until close to the completion of the test. However, after 14 hours, 31 minutes test time, the cap on the left hand side of the lower stringer had separated similarly to the first failures in panel Nr. 1. One hour later all angle clips were cut and no further propagation was observable until 36 hours accumulated test time. At the 29th inspection, after 39 hours test time, the right end of the upper stringer and of its added stiffener was disconnected. The panel completed the 50 hour test with additional failures in the web of the lower stringer as shown in Figure 16b.

The third test article resembled more closely the first panel with reinforcements of the stringer ends, which are shown in Figure 17. The damage development in Figure 18 indicates a first small crack near the right end of the upper stringer, which was detected after 2 hours and 15 minutes. It propagated further along the web and at 6 hours and 15 minutes test time the cap at the right end had disappeared. After an additional 4 hours a state of damage of the upper stringer was observed which closely resembled that of the first panel after 2 hours testing time. The lower stringer so far appeared undamaged, when it was decided to grind a wedge shaped piece from the cap on both ends as shown in

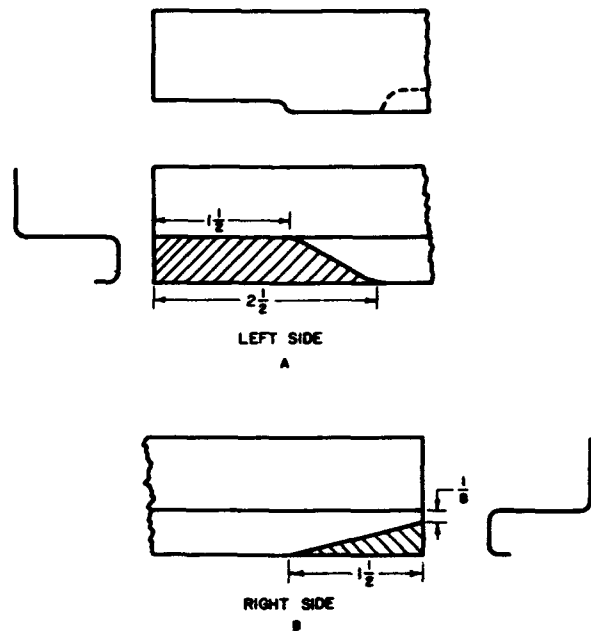


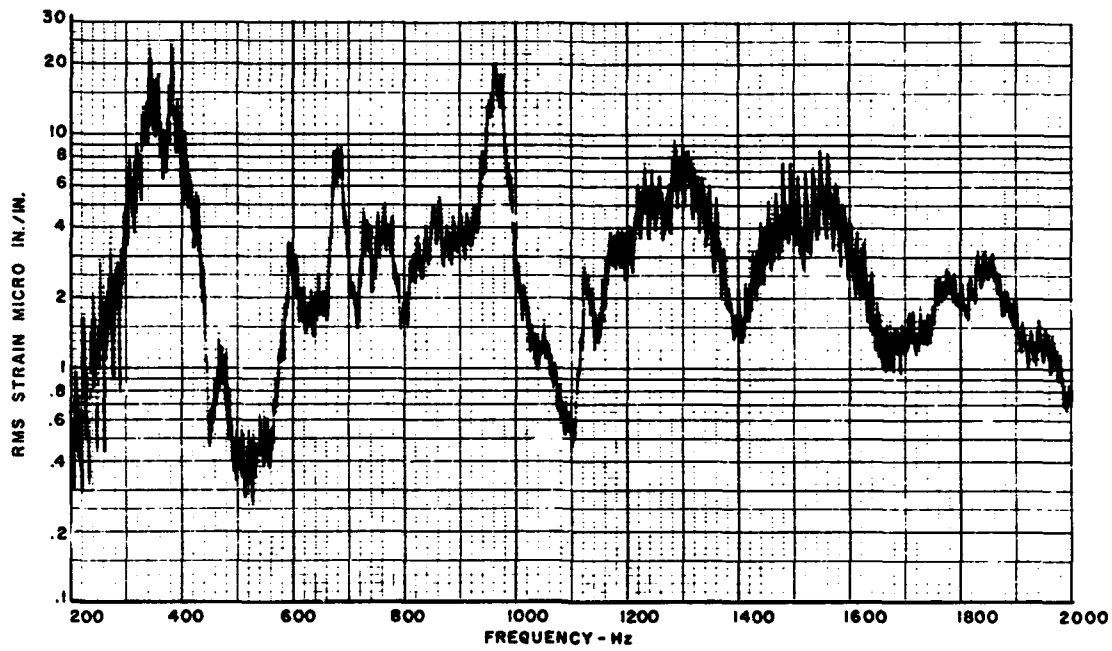
Figure 19. Modifications of Stringer Ends on Panel No. 4.

Figure 18b. This stringer withstood another 16 hours without visible cracking. However, at 32 hours extensive failure was observed. The test was terminated at 34 hours when both stringers had disintegrated similar to panel Nr. 1 after 3 hours test time.

The modifications of the second and third test article were incorporated in panel Nr. 4. In addition parts of the stringer caps were changed. At the left side of the stringers, the cap was completely removed for 1-1/2 inches, the end of the remaining cap was faired out as shown in Figure 19A. On the right stringer ends a wedge shaped section was ground off, similar to the previous panel with the dimensions as given in Figure 19B.

During the first heating of the panel, strain data could be recorded at various low temperatures, which resulted from the full sonic test level excitation. The largest dynamic strains in the stringers were found in the stringer foot and in the left side of the web close to the point where early failures were detected before. The two strain spectra of Figures 20a and 20b which were recorded at 400°F indicate the difference of stress level on the left and right end of the stringers. Particularly noteworthy is the low dynamic strain level which existed and which was not found markedly different at room temperature.

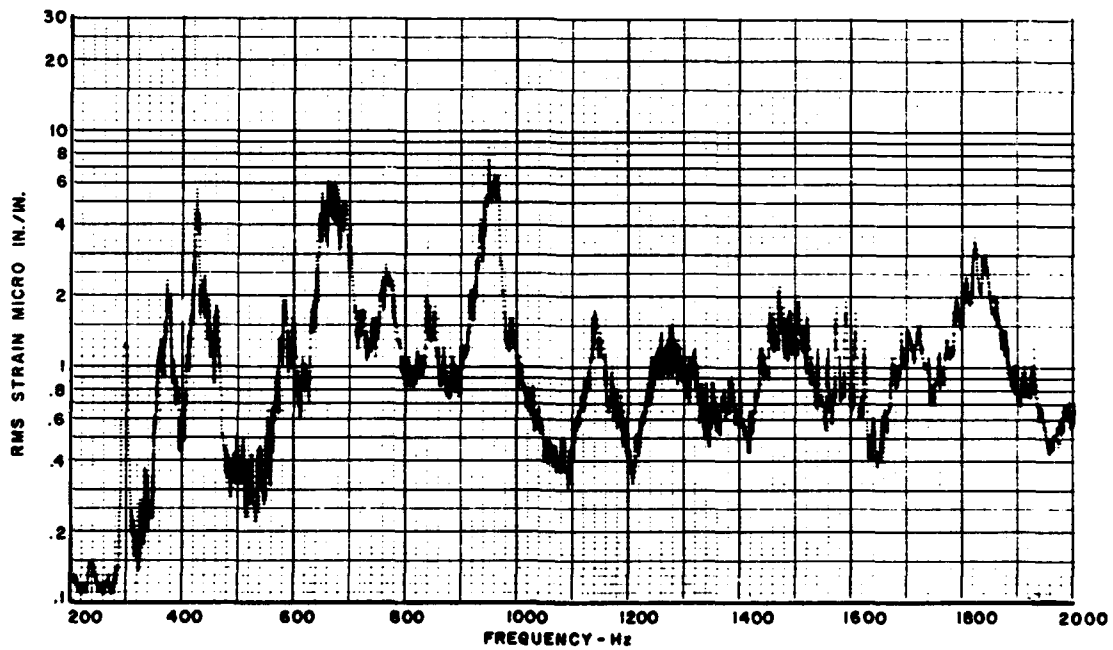
Before the start of the test a small notch was observed near the left end of the cap of the upper stringer. This most likely was introduced during removal of the cap. From this point the emergence of the first crack in the string-



FILTER BANDWIDTH: 10 Hz  
 SAMPLE LENGTH: 30 SECONDS  
 AVERAGING TIME: 5 SECONDS/FILTER

TEST PANEL NUMBER: 4  
 LEFT END STRINGER WEB  
 GAGE TEMPERATURE: 375°F

Figure 20a. Strain Spectrum.

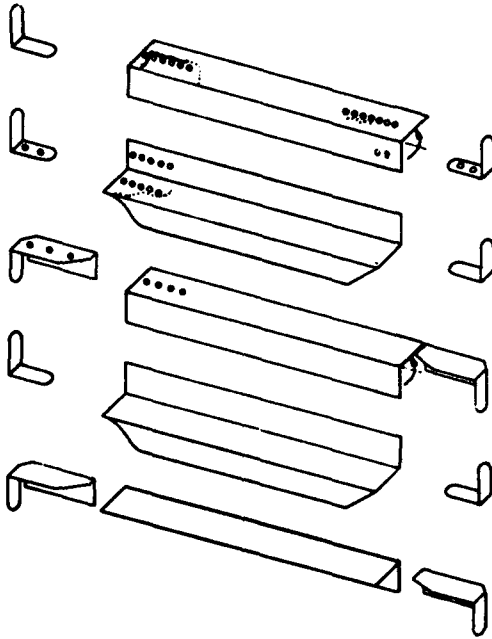


FILTER BANDWIDTH: 10 Hz  
 SAMPLE LENGTH: 30 SECONDS  
 AVERAGING TIME: 5 SECONDS/FILTER

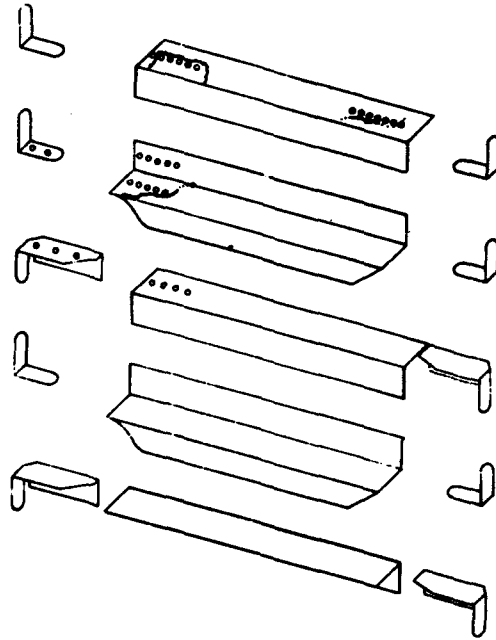
TEST PANEL NUMBER: 4  
 RIGHT END STRINGER WEB  
 GAGE TEMPERATURE: 400°F

Figure 20b. Strain Spectrum.

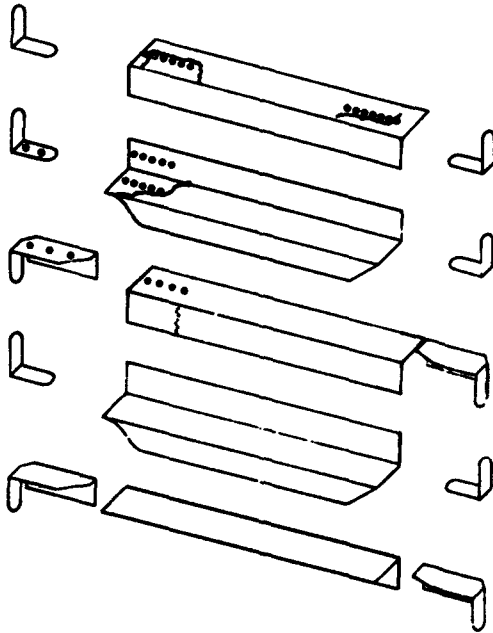
Inspection 16  
Time: 13:05



Inspection 19  
Time: 15:35



Inspection 20  
Time: 16:35



Inspection 26  
Time: 24:20

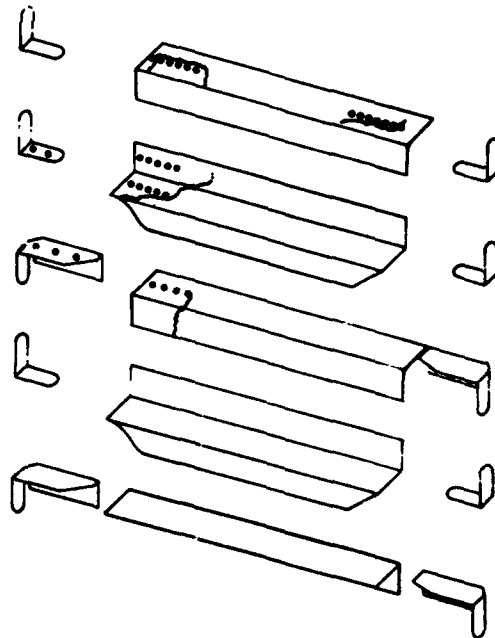


Figure 21a. Failure Propagation of Panel No. 4.

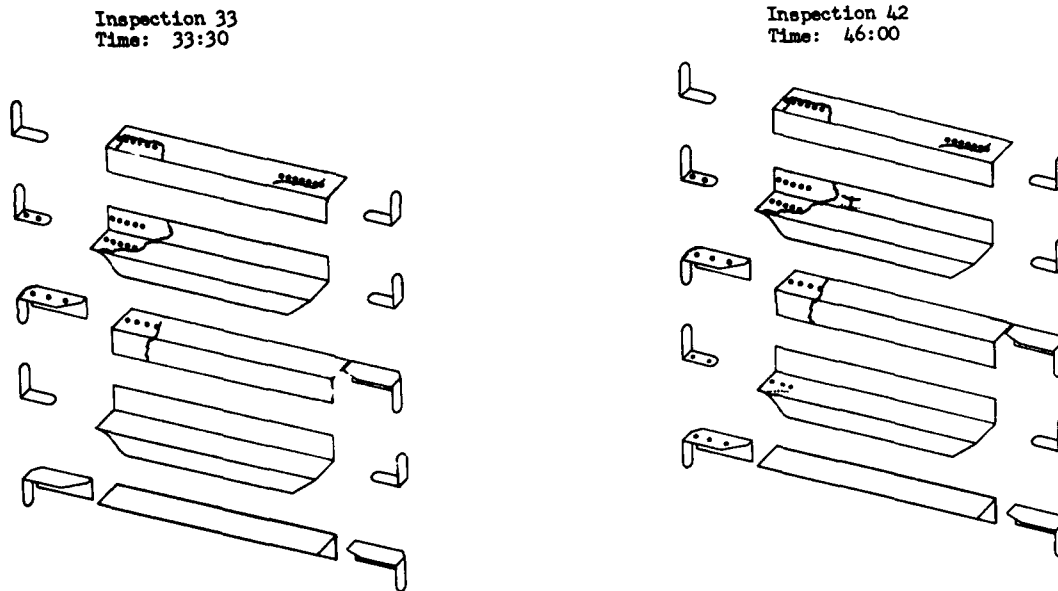


Figure 21b. Failure Propagation of Panel No. 4.

er was observed after 13 hours test time. This crack repeated itself after 46 hours in the lower stringer. The propagation of the first observed crack proceeded gradually for 33 hours into the foot of the stringer as shown in Figure 21. Also, the added stiffener of this stringer experienced some damage on the left side.

This panel completed the specified 50 hours of test time with the least damage of the four tested panels and was, therefore, with additional modifications recommended as the basis for a final design of this structural component.

#### CONCLUDING REMARKS

The series of tests led to some qualitative answers for the selection of a structural component design, which most likely would withstand the combined thermal-sonic environment for the specified time, but it also pointed out the limitations which at present exist in high temperature sonic fatigue testing. The rapid failure of strain transducers in the combined environment is a serious drawback in this type of experimentation. Thus all modifications of the panels had to be based on the location and progression of

the initial failures in combination with some assumptions as to the stress distribution in the panel. The vibrational strain data which were obtained at lower temperatures were not believed to be characteristic of those under high temperature conditions. There it was hypothesized, that occasional high dynamic stress cycles, resulting from "snap-through" motions or dynamic buckling, contributed strongly to the early failures particularly of the first tested panel. This problem which has been found in other sonic fatigue experiments to cause very rapid damage, requires further study in order to be accounted for in a quantitative manner, which more generally is also true for the high frequency random vibration problem under high temperature conditions.

Basic material fatigue data under high temperature conditions including low dynamic stress high frequency excitation are required for many materials used in aircraft construction.

Some of the above problems are pointed out in the hope that effort and progress will be stimulated, since similar and much larger scale experiments will be a requirement of the future.

## REFERENCES

1. S.S. Manson, *Thermal Stress and Low-Cycle Fatigue*, McGraw-Hill, New York (1966).
2. A.W. Kolb and H.A. Magrath, "RTD Sonic Fatigue Facility Design and Performance Characteristics," *Shock Vibration Bull.*, 37/Suppl. (1968).
3. O. Maurer, "Facility Sonic Fatigue Proof Testing," *Shock Vibration Bull.*, 37/Suppl. (1968).
4. A. Ives, T. Garrison, et al., *Short Time Elevated Temperature Tensile Properties of AISI 321 1/2 H Stainless Steel*, Report 8878-22, McDonnell Aircraft Corp., St. Louis, Missouri (1962).
5. K. Eldred et al., *Structural Vibrations in Space Vehicles*, WADD-TR-61-62, Aeronautical Systems Division, Wright-Patterson AFB, Ohio (1962).

**SESSION 5B**

**ANALYSIS**

*Chairman*

Prof. P.C. Paris  
Lehigh University



# STRUCTURAL RELIABILITY THROUGH DETAIL DESIGN AND DEVELOPMENT TESTING

by

Melvin Stone, Director

Douglas Aircraft Company  
McDonnell Douglas Corporation  
Long Beach, California

## INTRODUCTION

This paper describes an approach to design dependable long-life aircraft through the use of proper detail design and structural development testing. In discussing the aspects of structural fatigue, it is necessary to recognize past design practices based on static strength and present requirements on designing for fatigue strength due to advancements made in testing and analysis.

Today's commercial jet aircraft structure, except for landing gears, has been designed to be fail-safe. Fail-safe structure, by definition, can sustain reasonably high one-time flight loads with one or more failed elements within the structure. The fail-safe design concept allows the operation of an airplane to fully utilize the fatigue strength of the structure before it is retired from service for economic reasons.

Fatigue integrity and fail-safety cannot be calculated into a structure, it must be designed into the structure recognizing that fatigue indicates the initiation of a crack under application of repeated loads of varying magnitudes and frequencies. Fail-safety must consider the entire process of the crack propagation cycle, whereby a structural element will crack slowly, and then rapidly unless the detail design is such that it will retard or stop the crack. In any event, any crack must be detectable by simple inspection methods before it reaches a length to produce a failure. The designer has various methods at his disposal to assure high static strength and fatigue performance and still achieve minimum weight structure. One basic concept is to make the joint fatigue strength equal to or greater than that of the basic structure. The preferred method, which slightly increases the overall structural weight, is to add material locally to reduce stress levels in the area of the joint where high stress concentrations are known to exist. The basic structure, such as skin-longeron panel construction which is typical throughout the aircraft structure, constitutes the largest portion of the aircraft's structural weight.

The following principal items are discussed in this paper:

- Selection of Materials

- Design Practices
- Detail Design
- Detail Stress Analysis
- Fatigue Development Testing
- Scatter Factor

## SELECTION OF MATERIALS

The fatigue life, fail-safe, and corrosion resistance objectives are enhanced by the proper choice of materials consistent with strength, fracture toughness, and weight, but are more dependent on detail design practices developed during testing and substantiated by service experience.

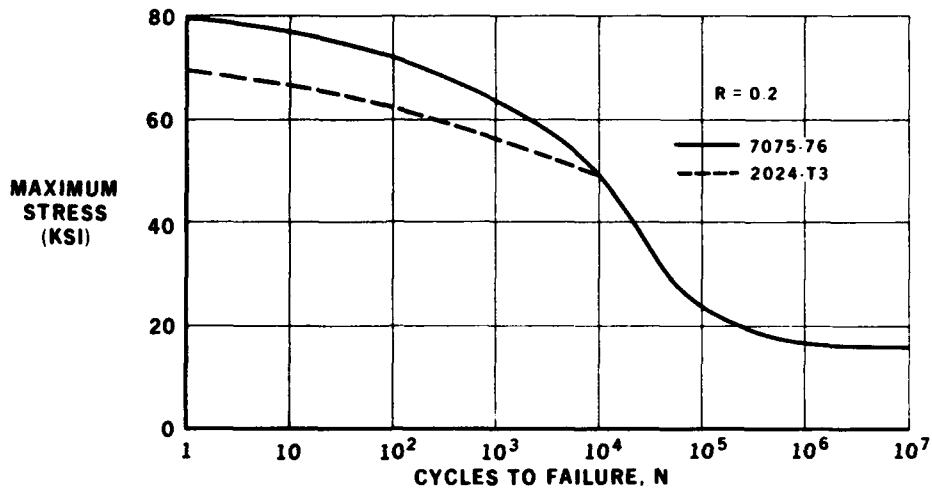
The results of over 1,000 constant amplitude component fatigue tests indicate, as shown in Figure 1, that the fatigue resistance of 7075 and 2024 material has been approximately equal for the range of stresses investigated at a  $K_T$  of 2.5. It is noteworthy that the DC-8 wing primary structure is constructed from 7075 material and a high-time aircraft has been operating in service with approximately 40,000 flight hours without any fatigue failures to date. The crack propagation and residual strength characteristics of a structure are also not dependent exclusively on the type of material used, but more sensitive to the proper detail design of redundant structure, the use of crack stoppers, and the manufacturer's attention to assembly details.

## DESIGN PRACTICES

Early airplanes were designed for static strength without consideration for longevity, as attested by the venerable DC-3. Since then, advancements in three areas can account for today's emphasis on designing for fatigue strength:

- There has been a significant increase in static ultimate strength of aircraft materials with little, if any, associated increase in fatigue strength.
- Loads on aircraft components are more ac-

**Figure 1. Fatigue Quality – Joints and Splices.**



curately derived through advanced analytical methods and on the basis of flight-loads airplane survey programs.

- Computerized analytical determination of stresses in redundant structure is far more realistic.

In today's competitive market the trend is to design to higher stress levels to take advantage of the higher strength allowables. Coupled with the actual increase due to the absence of conservatism in loads and predicted stress levels, the increase in working stress levels which the airplane will actually experience is most significant. For these reasons, it is mandatory that working stresses of current and future aircraft be established to gain desired longevities commensurate with the fatigue quality of the basic structural elements.

Basic structure working stress levels are carefully established using past performance as the primary measuring

stick while considering any features unique to the new design and advancement in technology that are available. The manufacturer's past successful basic standards and design concepts provide essential contributions to the new airframe design. Working stress levels on each new model can be cautiously increased only after earlier airplanes have exhibited reasonable longevity.

For assessment of fatigue life in transport aircraft working stress levels at  $1g + 0.4g$  provide a good basis of comparison. In the case of Douglas Aircraft, since 1956, the working stresses have been increased approximately 2,000 psi every four years. This increase has been accomplished with no derogation of airframe fatigue strength through improved knowledge of fatigue design and technological advancement.

Many past failures can be attributed to poor detail design, illustrated by the following:

**Figure 2. Fuselage – Detail Design.**

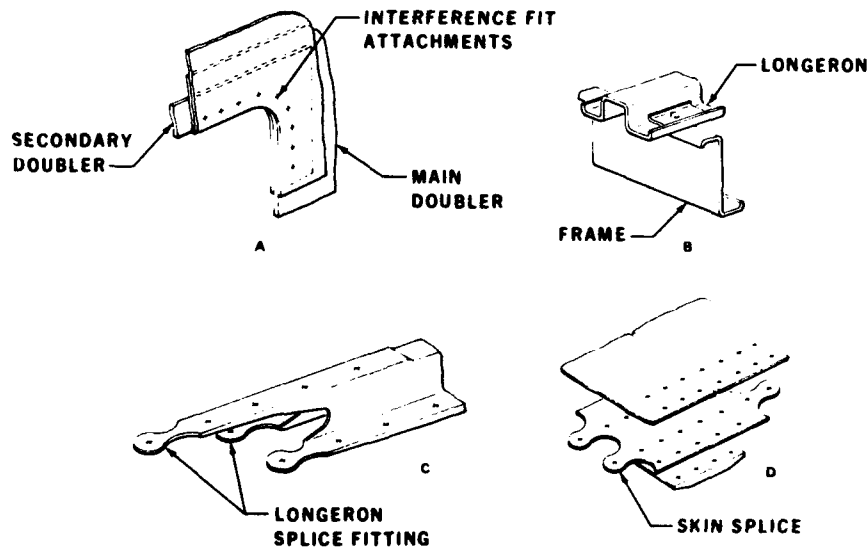
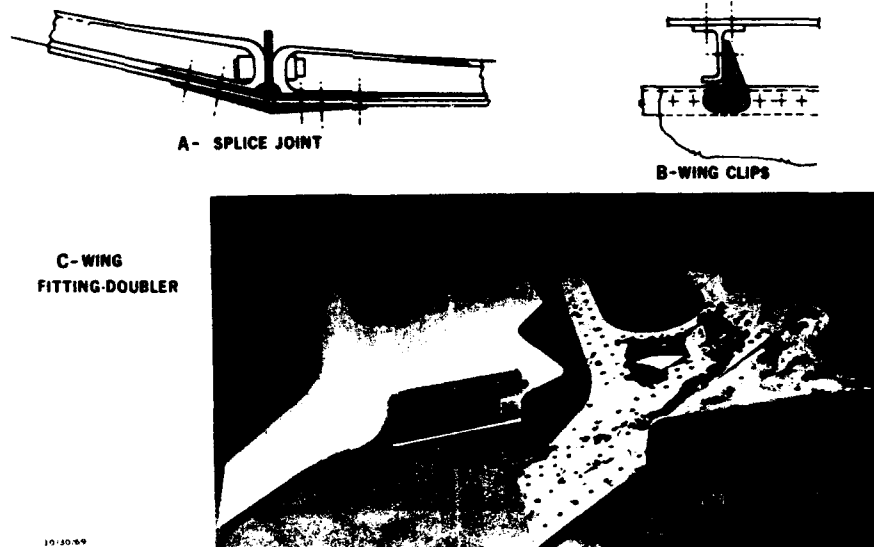


**Figure 3. Wing Design Detail.**



- Heavy spar cap construction.
- Omission of protective treatment - particularly at bolt holes.
- Superposition of stress concentrations at cut-outs.
- Noninterference fit fasteners.
- Abrupt changes in stiffness.
- Unnecessarily sharp corners and fillet radii.
- High bearing stresses.

**DETAIL DESIGN**

Good fatigue detail design means putting the structural material where it can be used most effectively. Most failures in the past designed aircraft can be directly associated with some deficiency that can be overcome through re-design of details to reduce local stress concentrations with no weight or cost penalty.

Based upon past experience, several areas must be given particular attention relative to design details, in order to provide fuselage and wing structure long-life, as Figures 2 and 3 demonstrate.

- Figure 2:

A The use of two properly tapered doublers around the fuselage door corners reduce stress concentrations.

B The addition of a local pad added to the fuselage longeron reduces stress concentration from bending between the longeron and frame connection.

C The fuselage longeron splice fitting tapered

ensures uniform load transfer and reduction of the first attachment load.

D A fuselage skin splice with tapered splice plate and finger doublers ensures uniform load transfer.

- Figure 3:

A By properly tapering and adding material locally at the wing splice joint the fatigue life at the discontinuity can exceed that of the basic structure.

B A properly designed wing clip of rib to stringer reduces eccentricity and local bending to increase fatigue life.

C An improperly designed wing fitting doubler with a sharp transition in local stiffness causes local high stresses and strains resulting in inadequate fatigue life.

**TABLE I.  
FATIGUE EVALUATION CHECK LIST**

<b>MATERIAL PROPERTIES</b>
GRAIN DIRECTION
SURFACE TREATMENT
WELDING NOT STRESS RELIEVED
HIGH TENSILE STRENGTH - HEAT TREATMENT
<b>STRESS RISERS</b>
SUDDEN CHANGE OF SECTION
FILLET RADII
OPEN HOLES
LACK CLOSE TOLERANCE HOLES
<b>RESIDUAL STRESSES</b>
FORMING
OVER TORQUE BOLT
INSUFFICIENT PRELOAD
<b>FRETTING</b>
RELATIVE MOTION OF FAYING SURFACES
LACK OF RADIUS EDGE
<b>STRESS CORROSION</b>
MISMATCHING
SUPERPOSITION OF NOTCHES

Figure 4. Wooden Model Vertical Stabilizer Spar Cap - Lower End of Upper Cap at Manufacturing Joint.



TABLE II.  
FATIGUE EVALUATION CHECK LIST

<b>JOINTS</b>
LACK GRADUAL CHANGES IN SECTIONS
ECCENTRICITY IN JOINTS
<b>SURFACE EFFECTS</b>
PLATING
DISSIMILAR METALS
HOLES, GROOVES, FILLETS
IMPROPER LOCATION
HIGH BEARING STRESSES IN RIVETED OR BOLTED MEMBER
SHARP EDGES
MIXED ATTACHMENT PATTERNS
<b>LOADING, LOAD PATHS</b>
DISCONTINUITIES
ECCENTRICALLY LOADED LUGS AND JOINTS
BUILDUP OF TOLERANCES
CLAMP UP STRESSES

Where locally adding material does not effectively reduce stresses at the discontinuities, other options are available to the designer. Interference fit attachments, Gemcor rivets, and Taperlok pins are also being used to improve the fatigue strength at fatigue critical hole locations. "Stress Coining" can be effectively used where open holes or clearance fit bolt holes are design requirements.

#### RECOGNITION OF PROBLEM AREAS

Successfully designing against fatigue failures depends on the recognition of fatigue critical areas. Once defined, sufficient attention can be given to the problem areas to improve their fatigue strength.

As mentioned earlier, all detail design must be closely scrutinized, detecting and minimizing local stress concentrations. The fatigue checklist presented in Tables I and II is used by designers, analysts, liaison engineers, inspectors, and fabricators to call attention to and improve potential sources of fatigue cracks. The checklist has been developed from data obtained from extensive test and service experience.

Regardless of the intentions to design a perfect structural part, the fact remains that some improvements can be made only when a complicated part can be visualized. The construction of a three-dimensional wooden model of the complicated parts will show undesirable features which enhances the fatigue life of the part. For example, Figure 4 shows a wooden full-scale mockup of a complicated vertical spar cap with integral fitting which allows proper load paths and area transitions to be visualized so that any neces-

sary changes can be made to the fitting prior to fabrication.

Experience has shown that if tests can be conducted early enough on large fittings and components, mandatory fatigue changes can be made and a considerable amount of weight saved before the first production parts are fabricated.

Photo stress tests, as shown in Figure 5, have been conducted on the main landing gear to determine the stress distributions and peak stress magnitudes in areas where stresses are difficult to predict. These tests were performed on full-scale aluminum models of the steel gears, because aluminum is easier to fabricate.

Cast photoelastic plastic material was cemented onto the landing gear components, and the stress distributions and magnitudes were measured by photoelastic techniques using polarized light and a polariscope while external loads were applied to the landing gear.

#### DETAIL STRESS ANALYSIS

To achieve fatigue strength with minimum weight, it must be recognized that the actual working internal loads must be predicted by accurate analytical methods.

With the advent of Fortran Matrix Abstraction Technique (FORMAT) analysis, an accuracy of 3 to 5 percent in predicting stress levels and deflections is achieved.

FORMAT<sup>1</sup> is an advancement in the state of the art which predicts accurate stress levels for fatigue analysis



Figure 5. Photoelastic Study of Main Gear Trunnion.

thereby allowing the structural material to be placed where it is most effective. This type of analysis allows the designer to save considerable weight in the basic structure and reserve some weight in significant fatigue critical areas. Douglas airframe structures are being completely optimized by using a computerized FORMAT analysis. In the past, airplanes using the Maxwell-Mohr computer methods have been analyzed using 2,000 forces and, in contrast, the latest aircraft have been analyzed using 100,000 forces per airplane. As a result, the latest structural elements are more thoroughly optimized than all past known aircraft.

The wing root idealization using FORMAT, a portion of the wing-fuselage intersection, is shown in Figure 6. Internal loads are calculated for all elements of skins, stringers, spar caps, bulkheads, ribs, doublers, and fittings.

Figure 7 shows a further detail analysis of the internal loads in the landing gear doubler, wing skin, bulkhead caps, and the shear in shear clips and bulkhead webs.

Internal loads in this detail are required to attain the fatigue quality of structures required of today's aircraft.

Preliminary fatigue analysis of the various structural elements is accomplished with the aid of computerized methods. This rapid preliminary evaluation is a tool used to

size test parts and to develop a test spectrum which will produce damage equivalent to that predicted for in-service operations. Structural elements investigated usually evolve from similar elements of earlier design. A library of test and service data from these similar elements are used to generate the S-N data necessary for the fatigue analysis (see Figure 8). Testing to the load spectra derived by the analysis in turn provides a check on the analytical methods. The iterative process improves the accuracy of both test and analytical evaluations. An automated computer program<sup>2</sup> is used that permits a rigid and extensive establishment of a loads spectrum based on a complete evaluation of the aircraft component.

### FATIGUE DEVELOPMENT TESTING

A development fatigue test program must be timely to permit the designer to incorporate the test findings into his design. Because of the costs involved in specific fabrication and test time, the program must be planned to utilize small inexpensive specimens which can be tested on high speed fatigue test machines.

#### Wing Tests

The initial single "bow tie" tests are used to screen candidate materials, types of fasteners, fatigue retardation

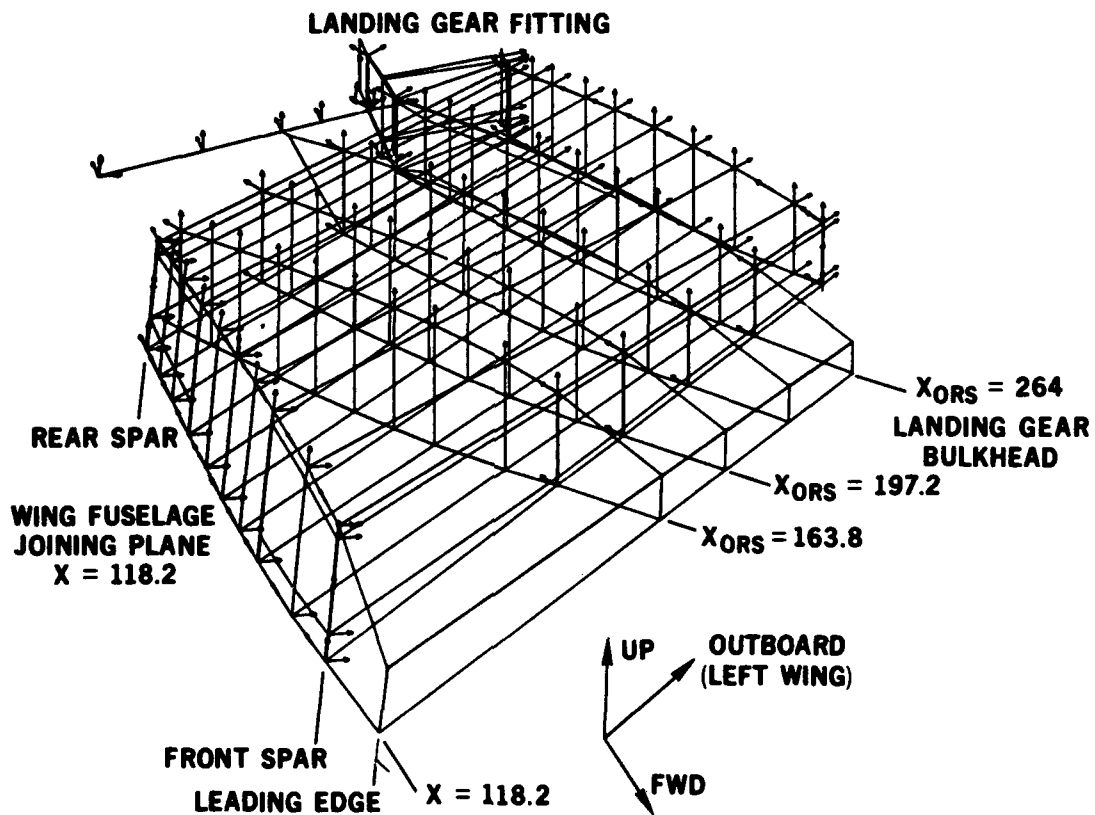
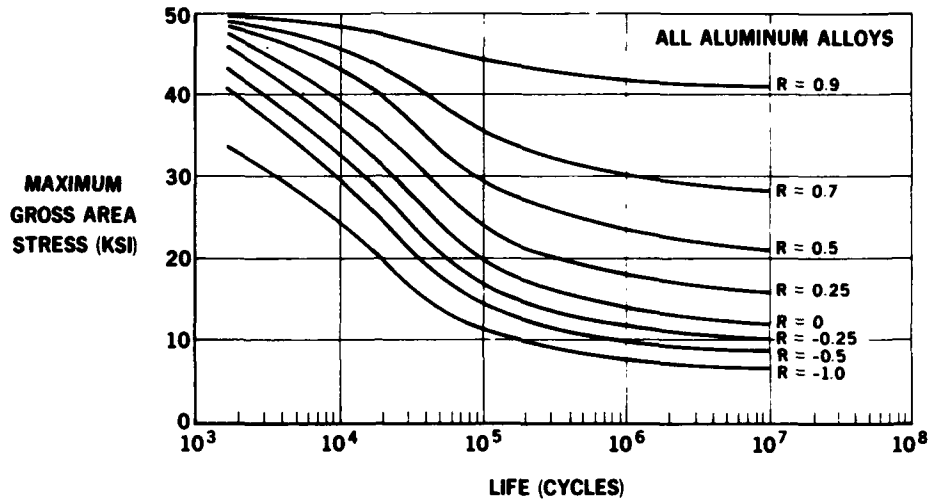


Figure 6. Wing Root Idealization.



Figure 8. S-N Diagram - Fuselage Splices - General.



processes such as stress coining, surface treatments, manufacturing processes, etc. Data from these tests are used to develop larger double bow-tie and simple joint splice specimens. Again this is a screening operation to further compare the various proposed design options. High speed fatigue machines are used with constant amplitude loading.

After completion of the second phase, full scale components are developed which incorporate the most promising features of the screening tests. The specimens are tested to both constant amplitude and variable flight-by-flight load spectra.

**Single Bow-Tie Tests**

The design engineer has always attempted to in-

crease the fatigue life of bolted joints and open holes without any weight penalty, and stress coining has been used to increase fatigue life by introducing residual compressive stresses that offset tensile stresses around holes. Single bow-tie specimen fatigue tests have been conducted to show the effects of stress coining on aircraft structure fatigue strength.

Test specimens shown in Figure 9 were fabricated from 7075-T651 and 2024-T351 aluminum bare plate in thicknesses from 0.125 through 0.500 inch. The test results of the 0.500-inch specimens are shown in Figure 10.

The test results also indicate that pad stress coining is equal to ring coining in thinner gages, but provides additional life in the thicker gages.

Figure 9. Single Bow-Tie Tests.

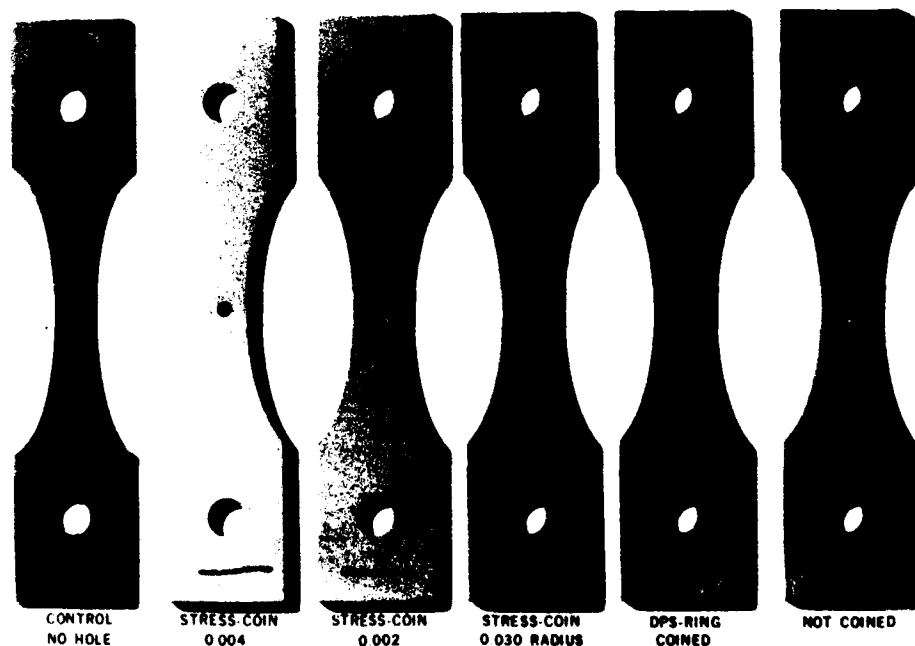
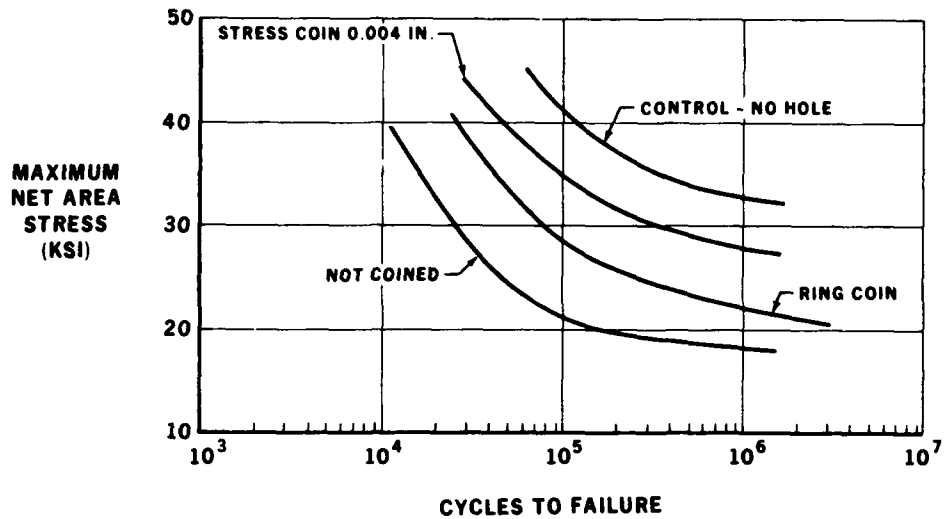


**Figure 10. Fatigue Test 0.500 7075-T651 Aluminum.**



Stress coining has been used successfully to improve the fatigue life of structural components for production aircraft and salvage rework by a factor of approximately four<sup>3</sup>.

Single bow-tie specimen fatigue tests have also been conducted to show the effect of materials, fretting surface finish, and open holes. When mating parts are clamped together and subjected to cyclic loads, fretting corrosion is initiated at the faying surface. The fretting generally interacts with the fatigue mechanism and causes failure to occur earlier than would otherwise be expected<sup>4</sup>. The effect of coining is not as pronounced at lower stress levels when fretting is introduced.

#### Double Bow-Tie Tests

Double bow-tie specimens, such as those shown in Figure 11, have been used extensively in a new design test

program to obtain reliable fatigue information in minimum time and at minimum expense. Results of specimens of this type have been found to correlate closely with results from more complex and expensive specimens composed of skin and stiffeners. The latter specimens are more difficult to design, fabricate, and test since the load line must be maintained at the composite section centroid to eliminate eccentricities. For the double bow-tie specimens, it is only necessary to duplicate the thicknesses of the skin and the flange of the stiffener which is attached to the skin. Eccentricities are eliminated since both plates are loaded by the same pin attachments. Tests of double bow-tie specimens in high speed fatigue machines permit rapid evaluation of various attachment types, hole sizes, hole preparation methods, materials, thickness effects, cladding, etc., on the fatigue life of basic structure. By varying the dimensions of the plates, load transfer through the attachments can be controlled to extend the usefulness of this type specimen to

**Figure 11. Double Bow-Tie Tests.**

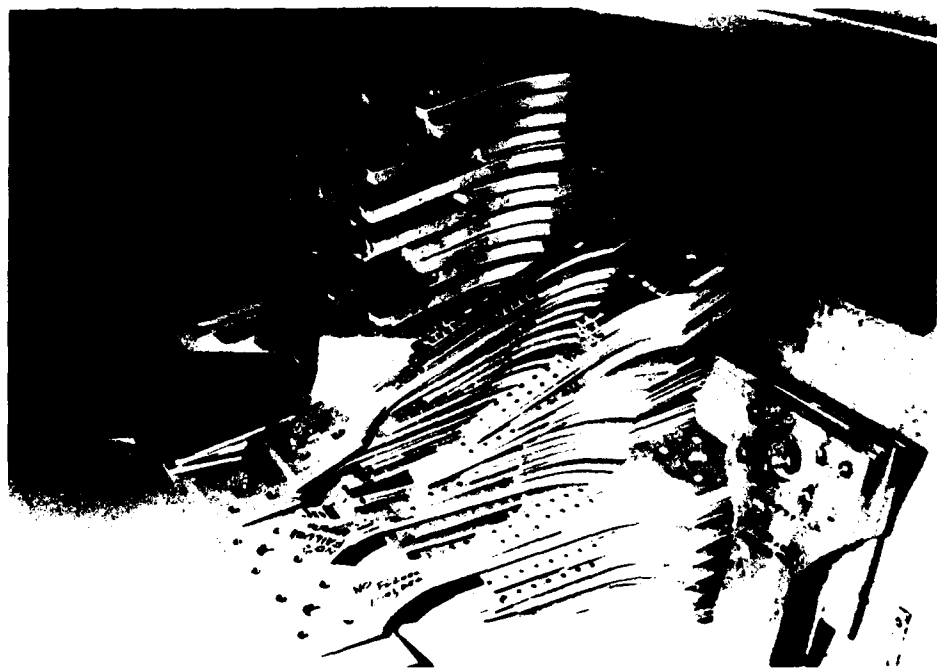
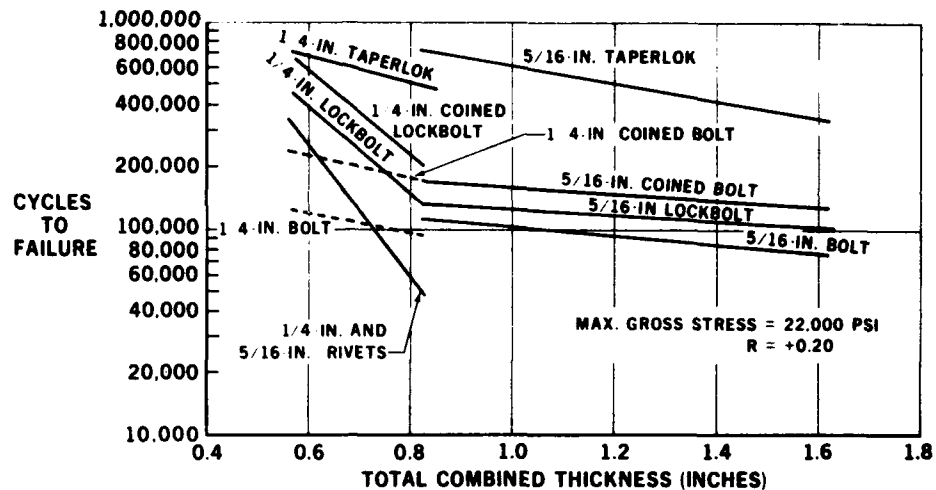




**Figure 12. Double Bow-Tie Fatigue Specimens Material Thickness vs Fatigue Life for Various Attachments.**



more applications.

In thick structure, the fatigue life of riveted attachments is reduced due to the insufficient swelling of the rivet inside the hole at the faying surfaces. Other attachments, such as Taperlok and hucklok fasteners were required to provide the proper interference fit and increase the overall joint fatigue life for thick material, as shown in Figure 12. Test results obtained from bow-tie specimens have been extremely valuable, for they can be obtained at a fraction of the cost, in time and material, that would otherwise be required.

**Splice Tests**

Bow-tie specimens cannot be used for all configurations; therefore, more typical simple wing skin splices, as shown in Figure 13, were used to further evaluate fasteners. These specimen tests were used to evaluate stress concentration effects of hole sizes, spacing, various fasteners, coining, hole expansion, fastener interference, material, and thickness.

Approximately 120 tests were conducted using two constant stress levels, 22,000 psi at R = 0.2 and 16,000 psi at R = -0.1. The latter value is being used to represent the wing ground-air-ground cycles. The faying surfaces were prepared dry, with oil and a sealant.

The results of these tests showed the superiority of Taperlok fasteners; the increase in fatigue life when interference fits were 0.002 and 0.004; and the effect of fretting fatigue failures.

**Wing Structural Component Tests**

Structural component development fatigue tests are conducted on the actual parts that will be used in the

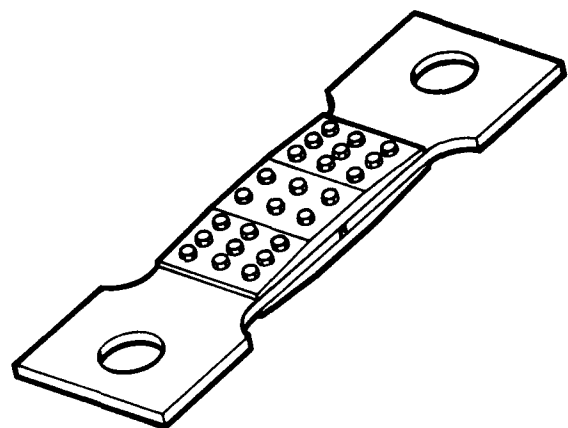


**Figure 13. Splice Tests.**

**TABLE III. WING STRUCTURAL COMPONENT FATIGUE TESTS**

STRUCTURAL COMPONENT	
INBOARD SWEEP BREAK SKIN-STRINGER JOINT	CENTER WING SPAR CAP JOINT AND SPAR CAP-SKIN BASIC STRUCTURE
OUTBOARD SWEEP BREAK SKIN-STRINGER JOINT	HEAVY BASIC SKIN-STRINGER STRUCTURE
INBOARD SWEEP BREAK SKIN-SPLICE STRINGER JOINT AND BASIC SKIN-SPLICE STRINGER	LIGHT BASIC SKIN-STRINGER STRUCTURE
OUTBOARD SWEEP BREAK SKIN-SPLICE STRINGER JOINT AND BASIC SKIN-SPLICE STRINGER	STRINGER TO COMMON STRINGER JOINT
SWEEP BREAK SKIN SPLICE AT REAR SPAR AND BASIC SKIN-SPAR CAP	SPLICE STRINGER TO FRONT SPAR JOINT
AERO BREAK SPAR CAP JOINT AND SPAR CAP-SKIN BASIC STRUCTURE	UPPER SURFACE ACCESS DOOR PANEL
	LOWER SURFACE ACCESS DOOR PANEL
	FUEL PUMP ACCESS AREA



Figure 14. Test Specimen - Inboard Skin-Stringer Joint Wing Lower Surface.

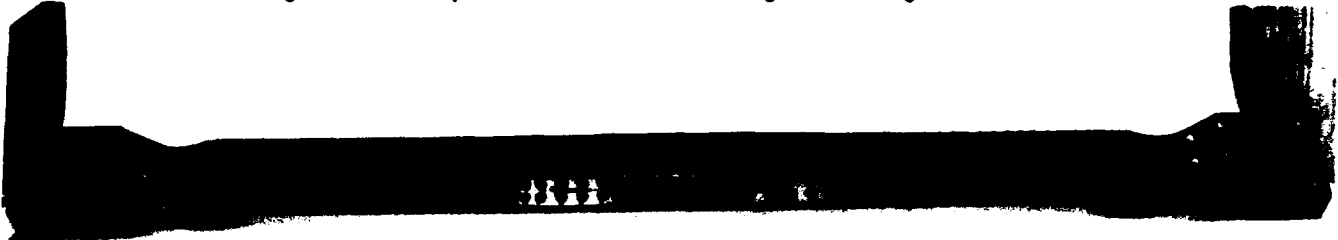


Figure 15. Test Specimen - Lower Rear Spar Cap Splice Wing Aerodynamic Break.

final aircraft design. All of the design knowledge gained through the bow-tie and other specimen testing is incorporated in the final structural components. Approximately 140 tests are conducted, as shown in Table III. Figures 14 through 16 show the test specimen in detail. The individual tests are continued and revised until at least 200,000 to 300,000 flight hours have been attained.

After the final configurations have been selected, flight-by-flight spectrum tests are conducted on each major component. This is in addition to the constant two-level amplitude tests noted previously. The value of the constant amplitude tests are two-fold: data for analytical S-N curves are obtained, and direct comparison can be made with test data of similar designs used on earlier airplanes. A typical wing lower surface skin-stringer joint at the side of the fuselage is shown in Figure 17. Note that the stringer is spliced by two shear-tension fittings which transfer load across the bulkhead tee through tension bolts. The skin is spliced internally by the bulkhead tee and externally by a splice plate. The specimen, as shown in Figure 17, was first stress coated and then loaded to failure to determine its

static strength. The numbers shown in the photograph refer to load levels at which the stress coating began to crack - the higher the number, the higher the load required to induce stress coat cracking. The specimen failed in the basic section at a gross stress level of 61,000 psi which matched the analytically predicted strength used in design.

A second specimen, identical to the one shown in Figure 17, was fatigue tested at a maximum gross tensile stress of 22,000 psi,  $R = +0.2$ . These cyclic loads are the same as those used in previous test programs and, therefore, provide a direct comparison of joint fatigue quality. The fatigue specimen failed after 220,000 cycles outside of the splice region in the basic section. The fatigue life of 220,000 cycles represents a fatigue quality comparable to that of DC-8 basic skin-stringer structure. The good fatigue quality of this joint is attributed primarily to the use of Taperlok fasteners and stress coining in the thick section, high load transfer regions of the splice. Two specimens, mounted in the 1.5-million-pound fatigue test machine at the laboratory test facility, are shown in Figure 18.

As previously noted, the wing sweep break skin

Figure 16. Test Specimen - Skin-Stringer Basic Structure Wing Lower Surface.





Figure 17. Static Test of Skin-Stringer Joint.

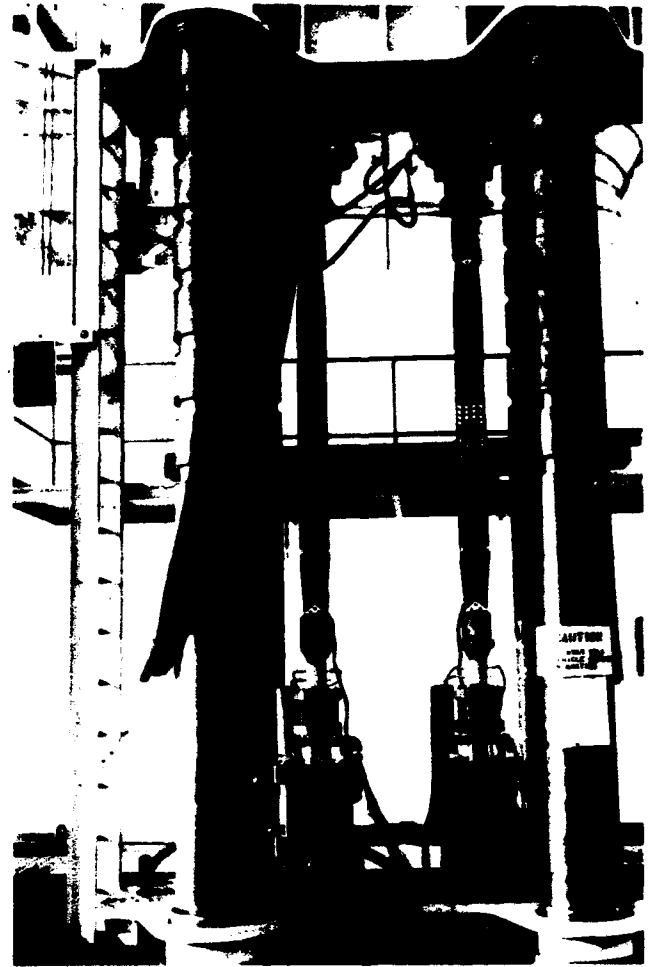


Figure 18. Test Setup.

stringer tests are typical of the other critical fatigue component tests.

Test results of this same fitting at both constant-level loadings and flight-by-flight loadings are shown in Figure 19.

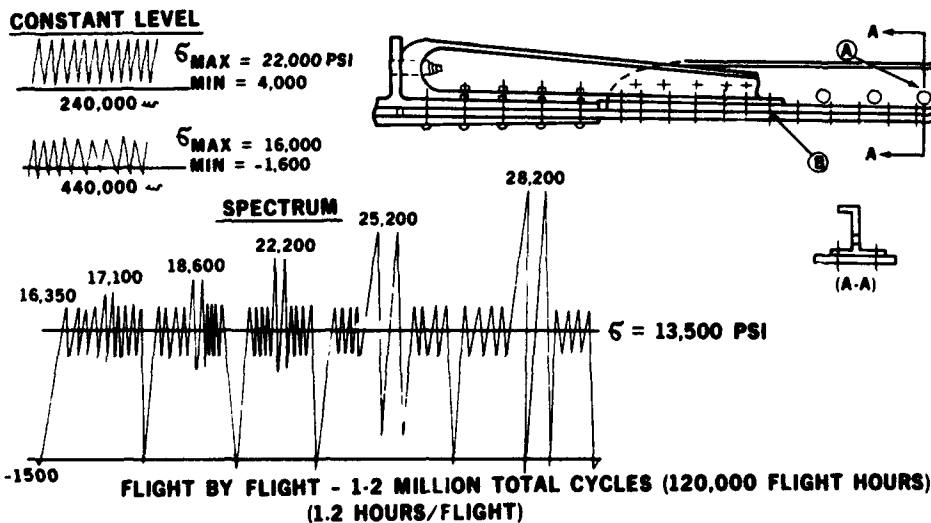
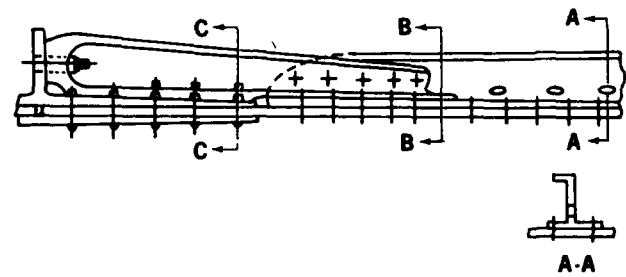


Figure 19. Fatigue Test Loads - Wing Sweep Break (Skin-Stringer).

The test loads have been increased slightly to account for manufacturing deviations. The first failures occur at point (A) in the basic stringer section and the next occur at point (B) in the same stringer section. Both of these failures do not occur in the complicated portion of the splice and are easily detectable.

The increase in area buildup at the joints, which accounts for the failures taking place in the basic structure, is shown in Figure 20. By increasing local structural areas, stresses are decreased providing maximum reliability and low maintenance with a minimum weight penalty.

Only after all fatigue component tests have been conducted, does the designer incorporate these components on the drawing which are identical and reflect the actual fatigue tests.



PERCENT AREA BUILD UP GROSS SECTION			
SECTION	TOTAL	SKIN	STRINGER
B-B	13%	2.5%	36%
C-C	39%	29%	61%

Figure 20. Drawings Reflect Test Results.

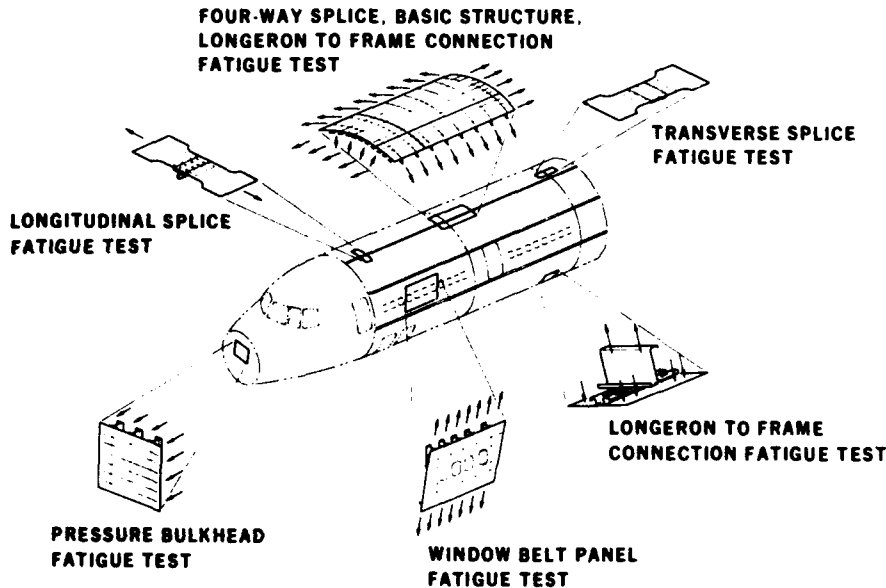


Figure 21. Fuselage Fatigue Development Tests.

### Fuselage Tests

The simple longitudinal and transverse splice, basic structure, and longeron-to-frame connection fatigue development tests, as shown in Figure 21, were conducted separately to evaluate and screen materials, fastener selection, surface treatments, etc. The design features obtained from these tests are then incorporated in a full-scale fuselage component, consisting of longerons, frames, splices, and attachments, then fatigue tested to the bi-axial loads, as shown in Figure 21. Additional fatigue tests are also conducted on window belt panels and pressure bulkhead panels. The pressure bulkhead panel fatigue test, shown in Figure 21, is typical of many other pressure panel tests.

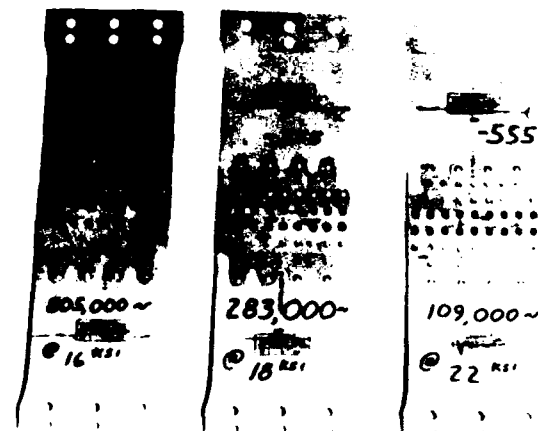


Figure 22. Transverse Splice - Ad Rivets and Lockbolts.

Figure 23.  
Longitudinal Splice.



#### Fuselage Basic Structure and Joint Development Tests

Tests were conducted to develop the various joints to be used in the fuselage design. Transverse and longitudinal skin splices and finger doubler designs were evaluated: twelve configurations each were evaluated for fatigue on various transverse skin and longitudinal splices.

The transverse skin splice fatigue tests are shown in Figure 22 for three different stress levels (16,000 psi, 18,000 psi, and 22,000 psi at  $R = +0.2$ ) with the various cycles to failure shown in the figure. The AD rivets and lockbolts are used as attachments in the splice areas.

The longitudinal skin splice fatigue tests are shown

in Figure 23 with their corresponding stress levels and cycles to failure.

#### Fuselage Component Tests

Curved fuselage panels (100 x 160 in.) have been tested. These panels represent sections of the fuselage with splices. These tests are conducted to determine the fatigue life under biaxial loads. Window belt panels are also included in these tests.

The biaxial loads, being applied to a curved fuselage panel, consist of 8 frames and 11 longerons with both transverse and longitudinal splices, as shown in Figure 24. The panels, as shown in Figure 25, are tested by air pres-

Figure 24. Fuselage Fatigue and Fail-Safe Test - View From Underneath Test Rig.



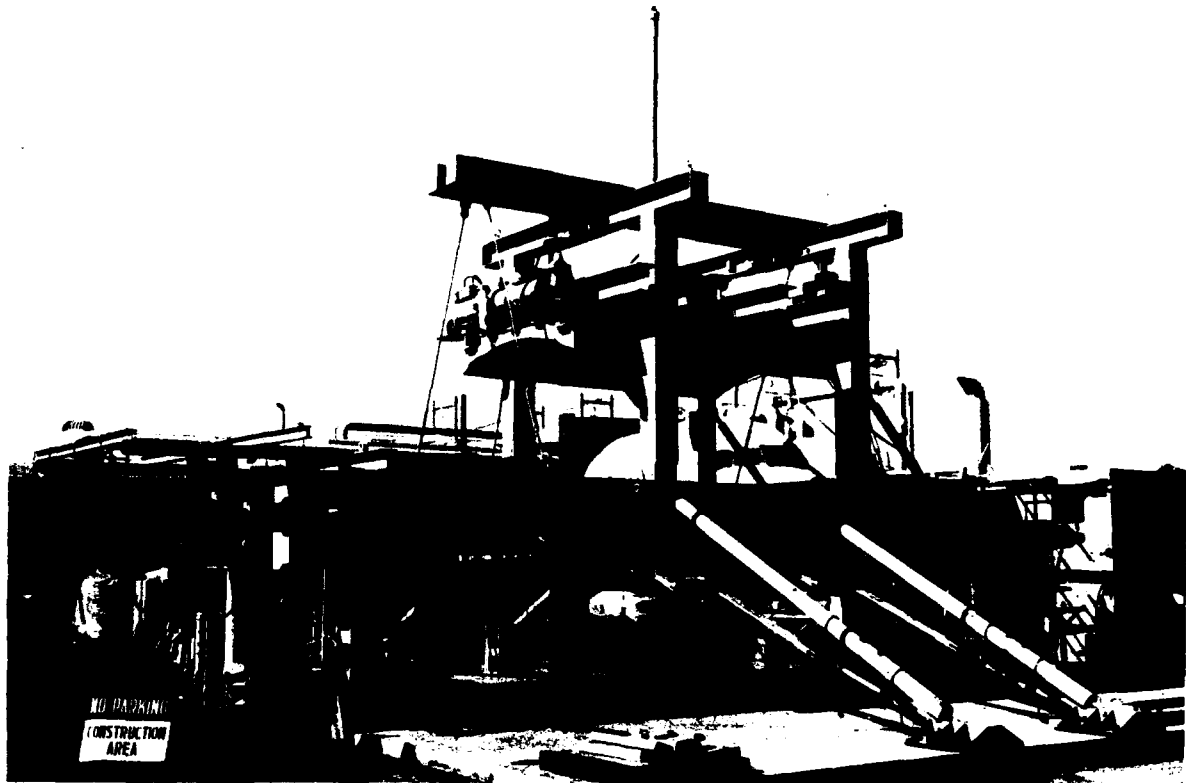


Figure 25. Fuselage Fatigue and Fail-Safe Tests – Vacuum-Rig Test Setup and Curved Panels.

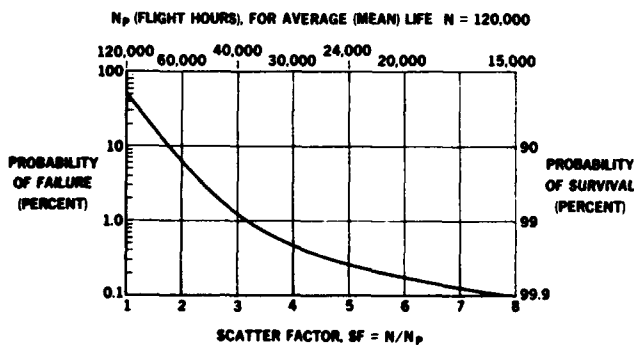


Figure 26. Fatigue Life Scatter Factors.

sure under vacuum, rather than in a water tank, whereby they can be inspected quite readily for cracks.

### SCATTER FACTOR

With our present knowledge of the fatigue mechanism, the complexity of structures to evaluate, and the dearth of test data available, there is no doubt that scatter factors must be applied to test results to ensure crack-free operation.

A statistical evaluation by itself does not provide the full story. For example, military aircraft demand reliability and a continuous state of readiness which preclude incipient cracking before repairs are made. Commercial aircraft, as long as the structure is fail-safe, can afford to

TABLE IV.  
PROBABILITY OF SURVIVAL

SF = $N/N_p$	PROBABILITY OF SURVIVAL (PERCENT)	$N_p$ (FLT HR) ( $N = 120,000$ )	$N_p$ (YEARS) (3,000 FLT HR/YEAR)
2.0	94.0	60,000	20
2.5	97.5	48,000	16
3.0	98.8	40,000	13.3
3.5	99.3	34,300	11.4
4.0	99.54	30,000	10.0

continue operation as long as it is economically feasible. Obviously the higher reliability requirement demands a higher scatter factor. New materials, new processes, and new design construction may reduce the confidence level, thus a higher scatter factor may be necessary.

The primary structure for present transport aircraft is designed for a fatigue life (average time to crack initiation) of approximately 120,000 flight hours, with the appropriate number of landings and pressurizations, depending on the intended usage of the aircraft. The structure, as a minimum, must equal this life under average utilization and loading conditions. Fatigue life scatter factors for an average of 120,000 flight hours are shown in Figure 26.

Based on this fatigue life scatter model, for a structure with an average life of 120,000 flight hours the probability of survival is shown in Table IV.

For a scatter factor of 2.0, which is representative of commercial aircraft designed to the fail-safe concept, the probability of survival is 94 percent, resulting in a crack-free structural life of 60,000 flight hours.

The structural integrity requirement of adequate component testing, proper detail design and maintenance, ease of crack detection, and good inspection procedures will usually provide fatigue strength in excess of the minimum design requirements.

## CONCLUSIONS

Safe long-lasting structure for commercial and military aircraft should be both fail-safe and fatigue resistant.

The development test program should be based on preliminary analysis using existing S-N data. Development component tests should then be conducted and completed before initiation of engineering detail design. These structural fatigue tests should be conducted by using constant level load testing for screening and establishing S-N data for analysis, and checking for structural reliability by spectrum load testing. After this, the designer should make the production drawing identical to the test parts.

Extra strength should be provided at joints so that any possible failures will occur in the basic structure, rather than the joints, to ease detection.

A sophisticated stress analysis (FORMAT or equivalent) is required so that detail stresses can be obtained within a 3 to 5 percent degree of accuracy.

The working stress levels of any new structural design should not exceed past stress levels by more than 10 percent.

Calculations and fatigue component tests should be made to account for manufacturing deviations.

Full scale tests should be conducted when necessary but in a manner such that the proper loads can be introduced into the structural components being fatigue tested.

## REFERENCES

1. D.S. Warren, *Applications Experience with the FORMAT Computer Program*, Douglas Paper 5095. Presented at the 2nd Air Force Conference on Matrix Methods, Wright-Patterson AFB, Ohio, October 1968.
2. P.R. Abelkis, *Fatigue Design Criteria and Life Prediction Computer Program for Aircraft Structures*, AFFDL-TR-66-197, Air Force Flight Dynamics Laboratory, Wright-Patterson AFB, Ohio (1967).
3. E.R. Speakman, *Fatigue Life Improvement Through Stress Coining Methods*, Douglas Paper 5516. Presented at the AIAA Aircraft Design and Operations Meeting, Los Angeles, July 1969.
4. E. Gassner, *On the Influence of Fretting Corrosion on the Fatigue Life of Notched Specimens of an AL-CU-NG 2 Alloy*, Pergamon Press, New York (1963).

# APPLICATION OF FRACTURE MECHANICS FOR FATIGUE LIFE PREDICTION

by

R.V. Sanga and T.R. Porter

The Boeing Company  
Commercial Airplane Group  
Renton, Washington

## I. INTRODUCTION

Fatigue cracks, visible or invisible, are a common occurrence in aircraft or similar structures subjected to varying degrees of stress amplitudes. Therefore, the evaluation of crack influence in terms of the fatigue life is of considerable concern in the design of damage-tolerant structures. The initial fatigue crack size, its growth rate, and the threshold stress-intensity-factor level for propagation are essential for estimating the fatigue life by fracture mechanics. Several authors have investigated the laws governing the crack propagation, non-propagation, repropagation, and residual strength characteristics of materials in terms of the stress levels. A brief review of the results of some of the investigators is given in Reference 3. Research per References 4 through 6 suggests that the fatigue crack growth rate is fully determined by the local elastic stresses around the crack tip. Since the fracture toughness parameter,  $K$ , determines the elastic stress field in the crack tip region, only  $K$  governs the rate of fatigue crack growth.

The purpose of this paper is to present the results of some Boeing 1965/1966 experimental work and subsequent analyses utilizing the principles of fracture mechanics for determining:

1. The endurance or threshold stress intensity levels,  $K_E$ , that will not propagate a crack.

2. The fatigue life variation with the stress level and specimen geometry by considering only the fatigue crack propagation characteristics.

This paper is divided into two parts. Part A describes an experimental determination of the threshold stress intensity factor level,  $K_E$ . Part B describes an analysis for determining fatigue life data by evaluating the required cycles to grow a fatigue crack from an assumed initial insignificant flaw size to failure. This is accomplished by using the available fatigue crack growth test data and also correlating with fatigue life test results of Reference 2. From these results, an estimate is also made of the threshold stress intensity factor level,  $K_E$ , for fatigue crack propagation.

## II. EXPERIMENTAL EVALUATION OF $K_E$ (PART A)

Fatigue tests are usually time consuming and expensive; therefore, the procedure developed in Reference 1 for establishing the endurance limit stress levels for round specimens of steel and aluminum alloys, labeled as an accelerated or a progressive fatigue test, is considered for determining the results of the above Item 1. Hence, a brief development of the technique is included in this paper. In the technique of Reference 1, the typical S-N curve is assumed to be hyperbolic in shape and the equation of the curve is written as

$$PN = C, \quad (1)$$

or in integral form denoted by

$$\int_0^N P \, dN = C \quad (2)$$

where

$P = (\sigma - \sigma_E)$  = the differential stress causing fatigue

$\sigma$  = stress in the specimen

$\sigma_E$  = endurance limit stress

$N$  = cycles

$C$  = constant

Subjecting the specimen to a progressively increasing stress level at a constant stress increase rate,  $\alpha_s = (\sigma/N)$ , the final expression between  $\sigma_{\max}$ ,  $\alpha_s$ ,  $\sigma_E$  and slope  $s$  is derived for experimental verification as

$$\sigma_{\max} = \sqrt{\alpha_s} \quad s + \sigma_E \quad (3)$$



By inputting the results of three tests for each specimen configuration, at three stress rates  $\alpha_s$ , Equation (3) establishes the endurance stress level  $\sigma_E$  at  $\alpha_s = 0$ .

A similar linear relationship is derived in this paper, but in terms of maximum stress intensity factor  $K_{max}$  instead of  $\sigma_{max}$ , stress intensity rate  $\theta$  instead of  $\alpha_s$ , slope  $S$  instead of  $s$ , and endurance threshold stress intensity factor level  $K_E$  instead of  $\sigma_E$  for an experimental determination.

Some of the previous investigators have represented crack growth rate by several types of functions such as: exponential, power and logarithmic (Reference 3). The relationships are in terms of crack length or net section stress or plastic zone ahead, or maximum tensile stress in cycle or stress concentration factor, respectively. In this investigation, the crack growth,  $\Delta a$ , or fatigue damage is attributed to the differential stress intensity factor level,  $K_D = (K - K_E)$  and the growth rate,  $(da/dN)$ , is represented by a similar power relationship.

Consider a centrally cracked panel under plane stress conditions, subjected to a stress ratio,  $\beta$  (maximum Stress/Minimum Stress) and a constant stress intensity factor rate,  $r = \Delta K / \Delta N$ . Under these conditions, fatigue damage or crack growth is continuously occurring for any stress intensity factor level  $K$  higher than the endurance stress intensity factor level,  $K_E$ . An expression for crack growth rate,  $da/dN$ , is written in terms of the semi-crack length,  $a$ , the differential stress intensity factor level,  $K_D$ , and the empirical constants  $n$  and  $M$  as:

$$da / dN = (K_D)^n / M. \quad (4)$$

In Equation (4),  $n$  is dimensionless and  $M$  is a material constant. Keeping  $r$  constant, and by progressively increasing the level of  $K$  in increments of  $\Delta K$ , the maximum stress intensity factor level  $K_{max}$  corresponding to a crack growth  $\Delta a$ , over a programmed number of cycles  $N$  causing the crack growth, can be written as:

$$K_{max} = K_E + \bar{N}r. \quad (5)$$

Making the necessary substitutions and integrating over  $\bar{N}$  cycles, the final expression for experimental verification is derived as follows:

$$da/dN = (K_E + \bar{N}r - K_E)^n / M \quad (6)$$

$$\Delta a = r^n \bar{N}^{(n+1)} / (M) (n+1) \quad (7)$$

$$(\Delta a) (r) = (\bar{N}r)^{(n+1)} / (M) (n+1) \quad (8)$$

$$X_{max} = K_E + [ (n+1) (M) (\Delta a) (r) ]^{1/(n+1)} \quad (9)$$

$$K_{max} = S\theta + K_E \quad (10)$$

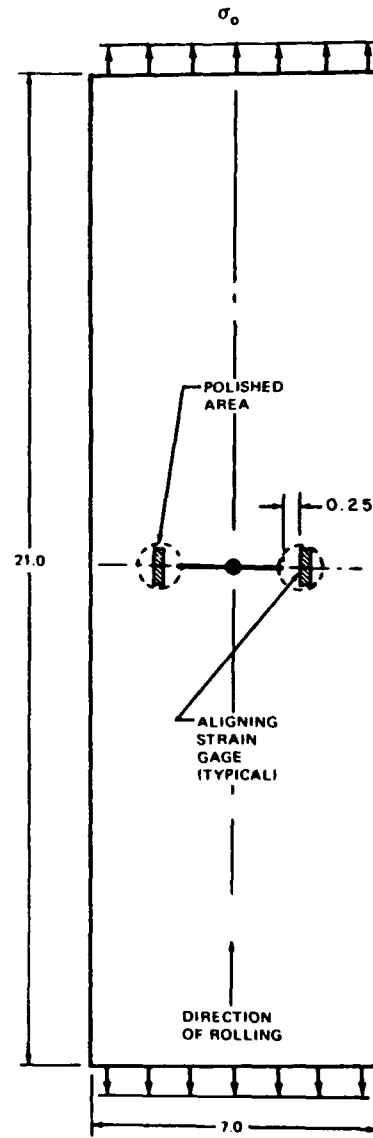
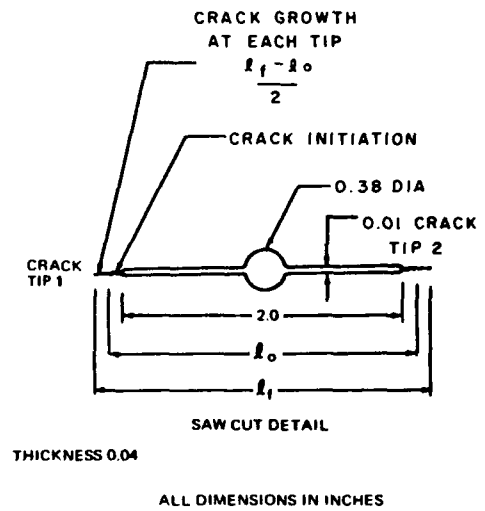


Figure 1. Test Specimen (Typical).

where

$$S = [(n+1)(M)(\Delta a)]^{\frac{1}{n+1}} \quad (11)$$

$$\theta = r^{1/(n+1)} \quad (12)$$

By conducting a minimum of three tests at three different values of  $r$ , the values of  $M$ ,  $n$ , and  $K_E$  satisfying the linear equation (10), can be evaluated for any value of  $\beta$ .

The geometry of a typical test coupon is shown in Fig. 1. All the specimens are made from sheet having a thickness of 0.04 in. A 2-in. saw cut is made with a jeweler's file. Four strain gages are installed on each specimen, two on either side 0.25 in. away from the crack tip for aligning purposes. Three values of  $\beta$  (5, 2, 1.5) are investigated and for each value of  $\beta$  three values of  $r$ , (0.00177, 0.00708, 0.0177) are considered. All the specimens are tested at 1800 cpm on the Sonntag, SF-1-U fatigue testing machine. Crack initiation is accomplished by cycling all the specimens at a high value of  $\beta = 20$ , at a  $K_{max}$  of 3 ksi

$\sqrt{in}$ , approximately. After the crack initiation, the crack growth characteristics ( $\Delta a$  versus  $N$ ) are determined for each specimen by increasing the  $K$  level in equal increments of  $\Delta k$  over a block of cycles  $\Delta N$ . For each value of  $\beta$ , the stress intensity rate  $r$  is maintained at a constant level. For each material a total of 9 tests are conducted. All crack growth data is obtained by a 50 power microscope with the specimen at rest and subjected to the mean load corresponding to the  $K$  level of the preceding step. The test setup is shown in Fig. 2.

The values of  $\beta$ , the number of loading steps; the cycles per step; the total number of cycles; the initial, incremental and final values of  $K$ ; the stress intensity rates; and the crack growth data for all the 2024-T3 and 7075-T6 tested specimens are shown in Table 1. Typical fatigue crack growth characteristic curves are shown in Figs. 3 through 8 for some of the specimens tested. In general, for specimens subjected to similar loading conditions for  $r$  and  $N$ , the crack growth is found to be a function of  $r$  when  $\beta$  is kept constant and vice versa. The crack growth in 7075-T6 is found to develop more suddenly than that in 2024-T3.

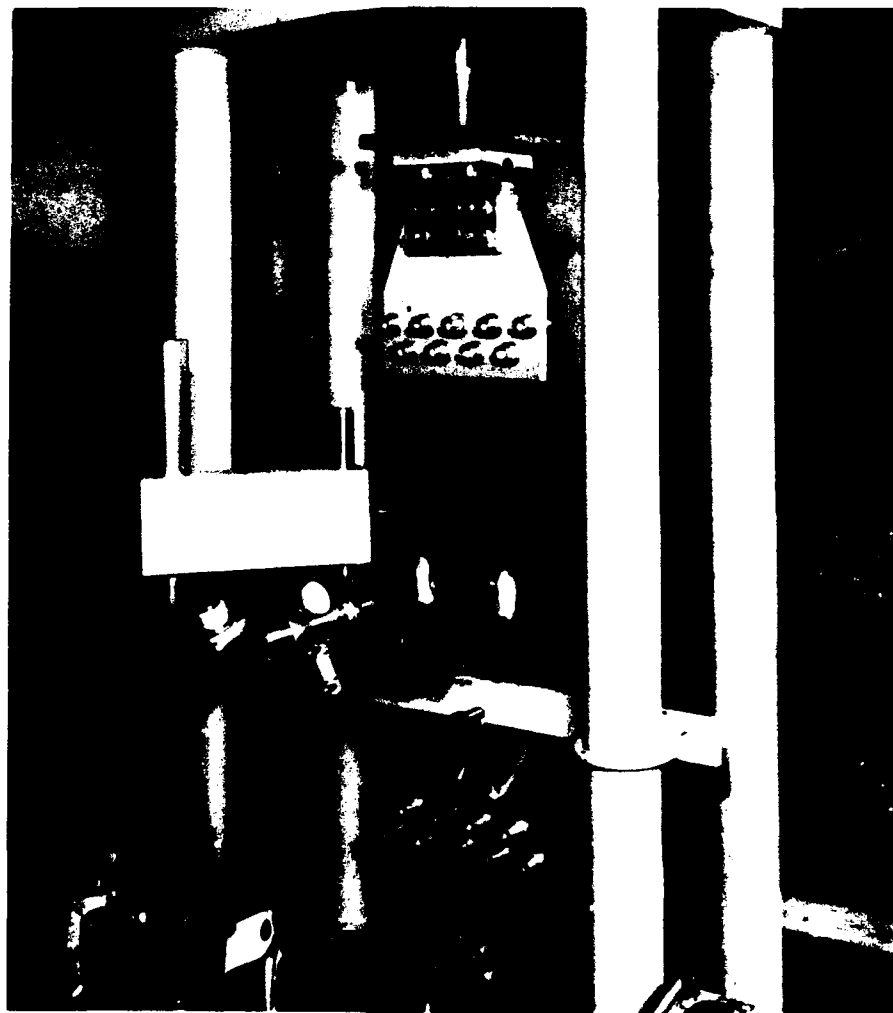
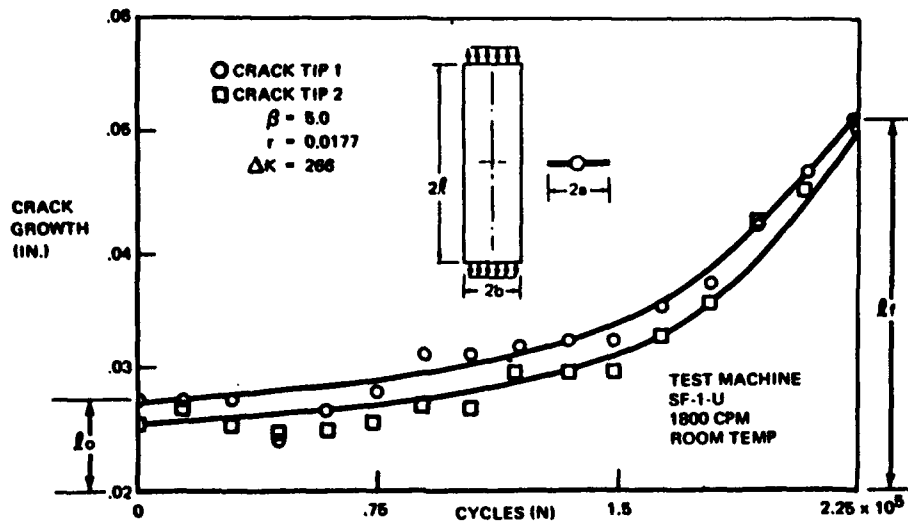


Figure 2. Test Setup.

Figure 3. Crack Growth (2024-T3).



From the fatigue crack growth characteristic data obtained from these tests, the linear relationship between  $K_{MAX}$  and  $\theta$ , necessary for evaluating the  $K_E$  level is established as follows:

1. Select the value of  $\beta$  for which  $K_E$  is required.
2. Select a value of  $n$  and evaluate  $\theta$  for the three stress intensity rates,  $r$ , used in the test for the value of  $\beta$  per step 1.
3. Check for possible linear relationship between the maximum  $K$  level the specimen is subjected to and the evaluated  $\theta$ ; if not linear, repeat step 2 for different values of  $n$ , until a satisfactory linear relationship is obtained.
4. The intercept at  $\theta = 0$  establishes the value of

$K_E$  for the established value of  $n$  for the material.

5. The value of the empirical constant  $M$ , satisfying the slope  $S$ , is evaluated from Equation (12).

The established linear relationship for evaluating the  $K_E$  level for 2024-T3 is shown in Fig. 9. In the case of 7075-T6 aluminum alloy, the test data exhibited a scatter characteristic, however, based on the postulated assumption and the derivation of linear relationship per Equation (10), straight lines are drawn to fit the data in the best possible way as shown in Fig. 10. The influence of  $\beta$  on these  $K_E$  levels is shown in Fig. 11. The values of the  $K_E$  levels for 2024-T3 and 7075-T6 aluminum alloys for  $\beta = 5$  are found to be  $1 \text{ ksi}\sqrt{\text{in.}}$  and  $2 \text{ ksi}\sqrt{\text{in.}}$  respectively.

An examination of the crack growth characteristic

Figure 4. Crack Growth (2024-T3).

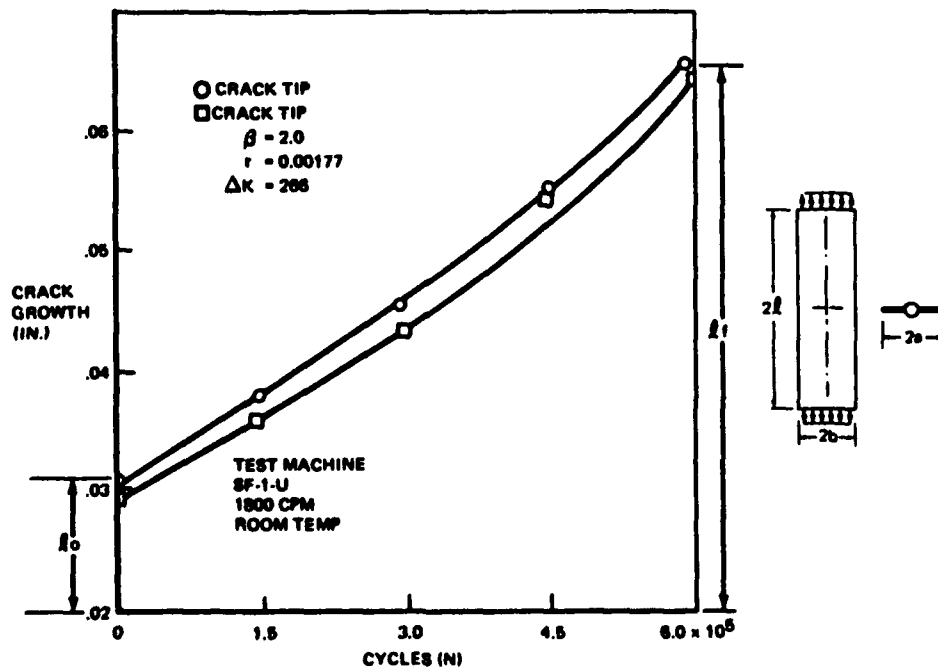


TABLE I.  
TEST RESULTS FOR 2024-T3 AND 7075-T6 SPECIMENS

SPECIMEN IDENT. NO.	SELECTED VALUE OF $\beta$ ( $\sigma_{MAX}/\sigma_{MIN}$ )	NO. OF LOADING STEPS	CYCLES $\times 10^5$		VALUE OF			STRESS INTENSITY RATE, $r = \Delta K/\Delta N$	CRACK GROWTH AT	
			PER STEP ( $\Delta N$ )	TOTAL (N)	INITIAL K	$\Delta K$	$K_{MAX}$		TIP 1	TIP 2
2024-T3 TEST SPECIMENS										
1	20	2	*	2.5	1777	177	3193	.00708	.0062	.0187
2	5	15	0.15	2.25	1777	266	5501	.01770	.0444	.0322
3	5	7	1.0	7.0	1777	177	2839	.00177	.0411	.0359
4	2	10	0.37	3.7	2660	266	5054	.00708	.0320	.0283
5	2	13	0.20	2.6	2660	354	6908	.01770	.0185	.0302
6	2	4	1.5	6.0	2660	266	3990	.00177	.0349	.0354
7	1.5	10	0.5	5.0	3540	354	6726	.00708	.0309	.0260
8	1.5	18	0.2	3.6	3540	354	9558	.0177	.0280	.0325
9	1.5	7	1.5	10.5	3540	266	5136	.00177	.0108	.0379
7075 T6 TEST SPECIMENS										
10	5	24	0.25	6.0	1240	177	5311	.00708	.0270	.0318
11	5	25	0.10	2.5	1240	177	5488	.01770	.0312	.0236
12	5	11	1.0	11.0	1240	177	3010	.00177	.0408	.0046
13	2	20	0.25	5.0	1770	177	6134	.00708	.0209	.0342
14	2	19	0.15	2.85	1770	266	6558	.01770	.0303	.01
15	2	18	1.0	18.0	1770	177	4779	.0177	.0343	.0454
16	1.5	13	0.37	4.81	2660	266	5852	.00708	.0302	.0211
17	1.5	17	0.2	3.40	2660	354	8324	.0177	.0313	.0247
18	1.5	9	1.5	13.5	2660	266	4788	.00177	.0331	.0232

\*CYCLED AT K VALUE OF 3193 FOR 150,000 CYCLES; 2485 FOR 100,000 CYCLES

data, after crack initiation, for 2024-T3 and 7075-T6 materials, Fig. 3 through 8, shows that the crack growth or fatigue damage in 2024-T3 assumes a continuously increasing characteristic, whereas the characteristic in 7075-T6 assumes two distinct zones. In all the 7075-T6 specimens tested, this trend of sudden crack growth rate (at high stress intensity factor levels) preceded by an insignificant damage rate, is found. Therefore, more vigilance is necessary for monitoring the growth of fatigue damage in 7075-T6 materials.

The root mean square method is used for the determination n for 7075-T6 material due to the scatter nature of the test data. The best value of n, satisfying the Equation

(10) is found to be 1.5 for 2024-T3 and 1.17 for 7075-T6 materials. The magnitude of the slope S is evaluated for the established linear relationship per Fig. 10 for 7075-T6 materials. Using this value coupled with the crack growth,  $\Delta a$ , per test, the value of M is calculated from Equation (12). The variation of M with  $\beta$  is shown in Fig. 12 for 2024-T3 material and the variation of M with  $\beta$  for 7075-T6 materials is drawn in Fig. 13 based on a similar characteristic even though much scatter is exhibited in the data. The estimated values of M based on these Figs. 12 and 13, for 2024-T3 and 7075-T6 are found to be  $25 \times 10^{10}$  and  $1.8 \times 10^{10}$  ( $k^n/in.$ ), respectively. A comparison of the variations of the material constant M with  $\beta$  for 2024-T3 and 7075-T6 materials (Figs. 12 and 13) indicates that the fatigue damage under high

Figure 5. Crack Growth (2024-T3).

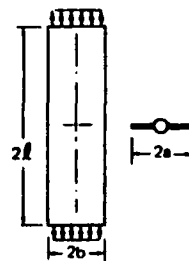
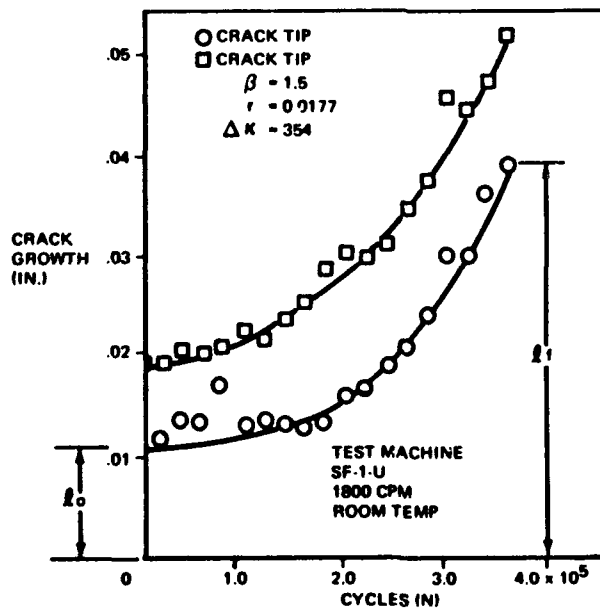
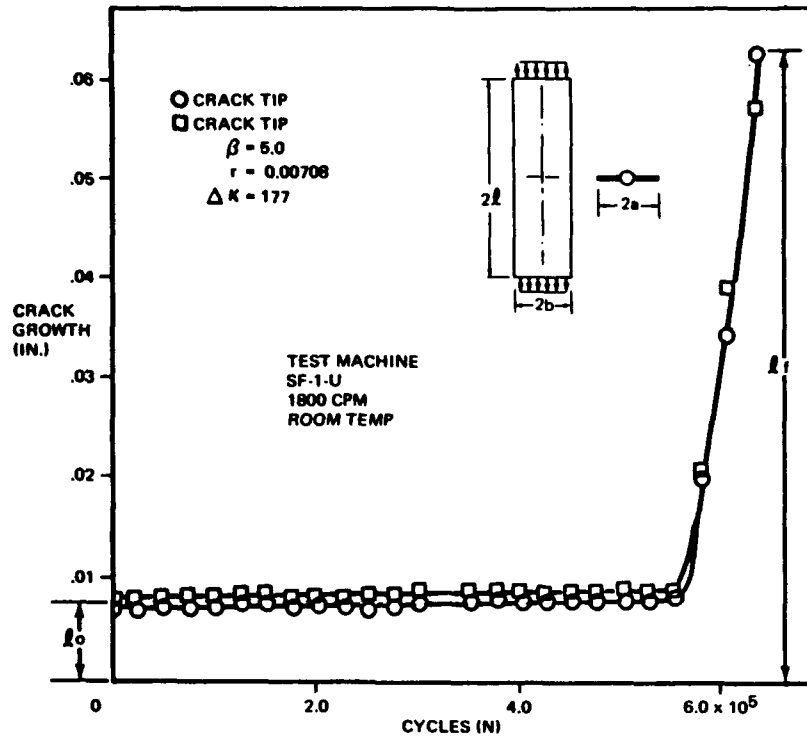


Figure 6. Crack Growth (7075-T6).



stress ratio conditions is higher than that for low stress ratios. For the considered test condition, this behavior has the right trend.

Having established the threshold stress intensity levels for nonpropagating fatigue cracks in 2024-T3 and 7075-T6 aluminum alloys, the allowable peak stress levels for non-propagating fatigue crack lengths, varying from 0.0004 to 1.0 in., are shown in Figs. 14 and 15 for 2024-T3 and 7075-T6 aluminum alloys, respectively. This is accomplished by using the expression for  $K$ , written in terms of the threshold stress intensity factor level  $K_E$ , the

endurance stress level  $\sigma_E$ , semi-crack length  $a$ , and the width correction factor  $\alpha$  as

$$K_E = \sigma_E (\pi a)^{1/2} \alpha \quad (13)$$

### III. FATIGUE LIFE AND $K_E$ LEVEL PREDICTIONS USING ANALYSIS TECHNIQUES (PART B)

Fatigue damage is frequently divided into four separate parts: (a) crack initiation, (b) micro-crack propagation, (c) macro-crack propagation, and (d) final failure. A technique for estimating the fatigue life is developed based

Figure 7. Crack Growth vs Cycles (7075-T6).

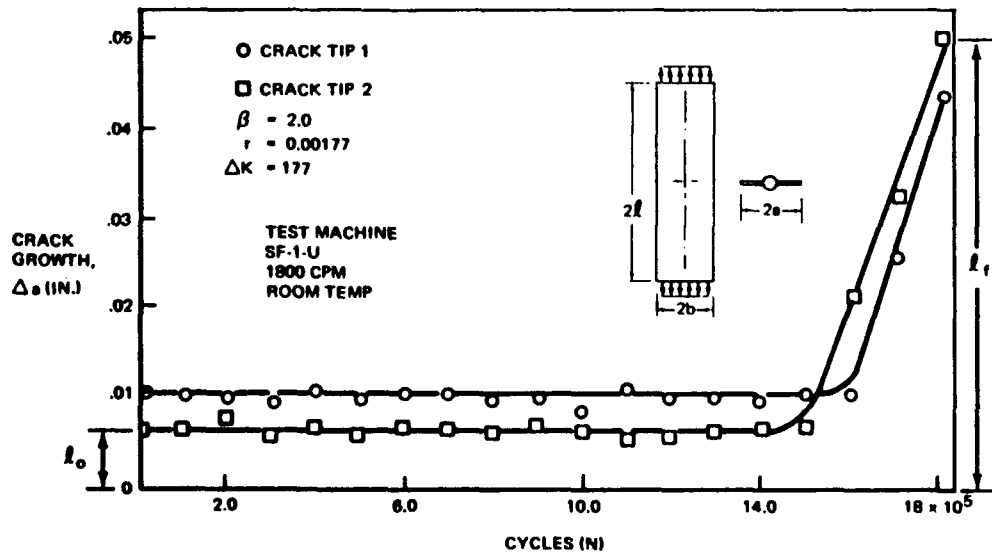
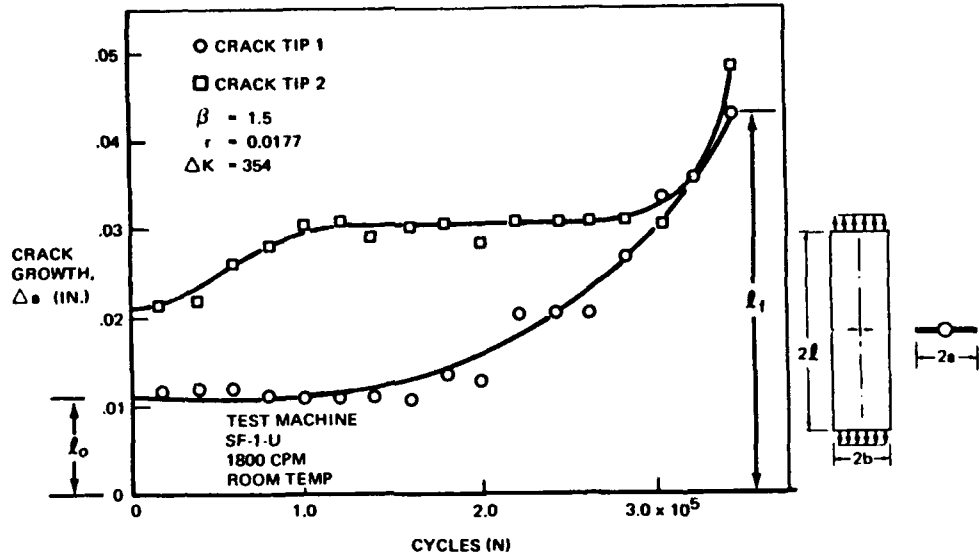


Figure 8. Crack Growth vs Cycles (7075-T6).



on the following assumptions:

1. Crack initiation, considered as a small fraction of the total fatigue damage.
2. Crack growth behavior in the micro-region is an extrapolation of behavior in the macro-region, and
3. Final failure occurring whenever the critical crack length is exceeded.

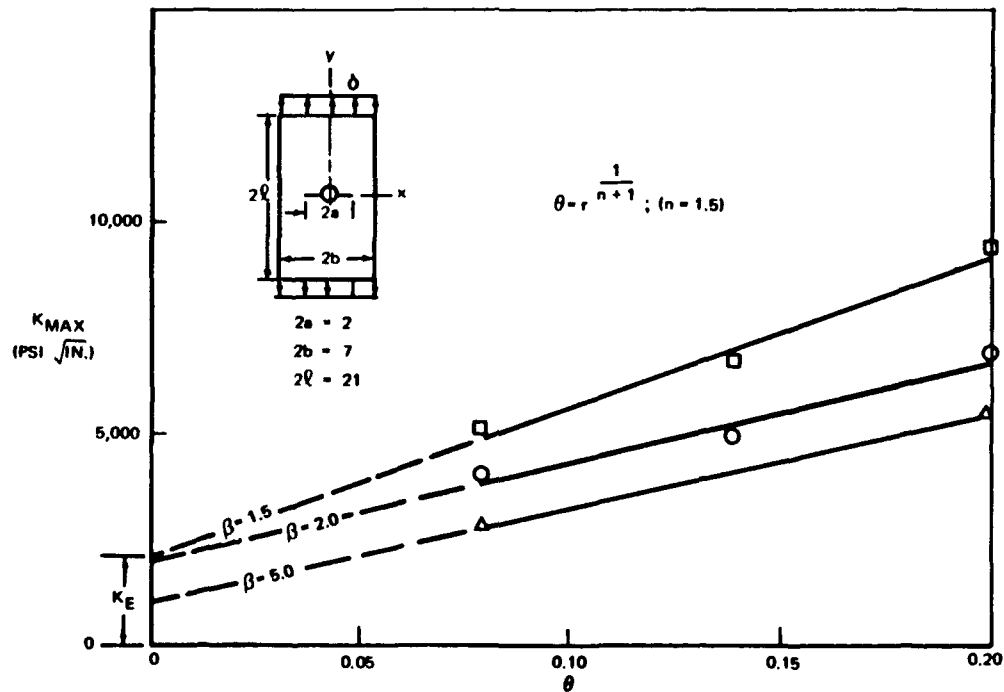
From these assumptions, the fatigue life is evaluated by considering the cycles required to grow a flaw from a small initial size to the critical length. Further, the assumed

initial fatigue crack length is constant for the material under investigation, giving due consideration to the specimen surface condition. This technique is applied to the fatigue test results given in Reference 2 for verification.

The fatigue crack growth relationship used in this development is based on the technique proposed per Reference 4. In this method, the fatigue crack growth rate is considered to be a function of the elastic stress field around the crack tip, as given by linear elastic fracture mechanics. This results in the crack growth rate being a unique function of K.

$$\text{i.e., } \frac{da}{dN} = G(K)$$

Figure 9.  $K_{MAX}$  vs  $\theta$ , (7075-T6).



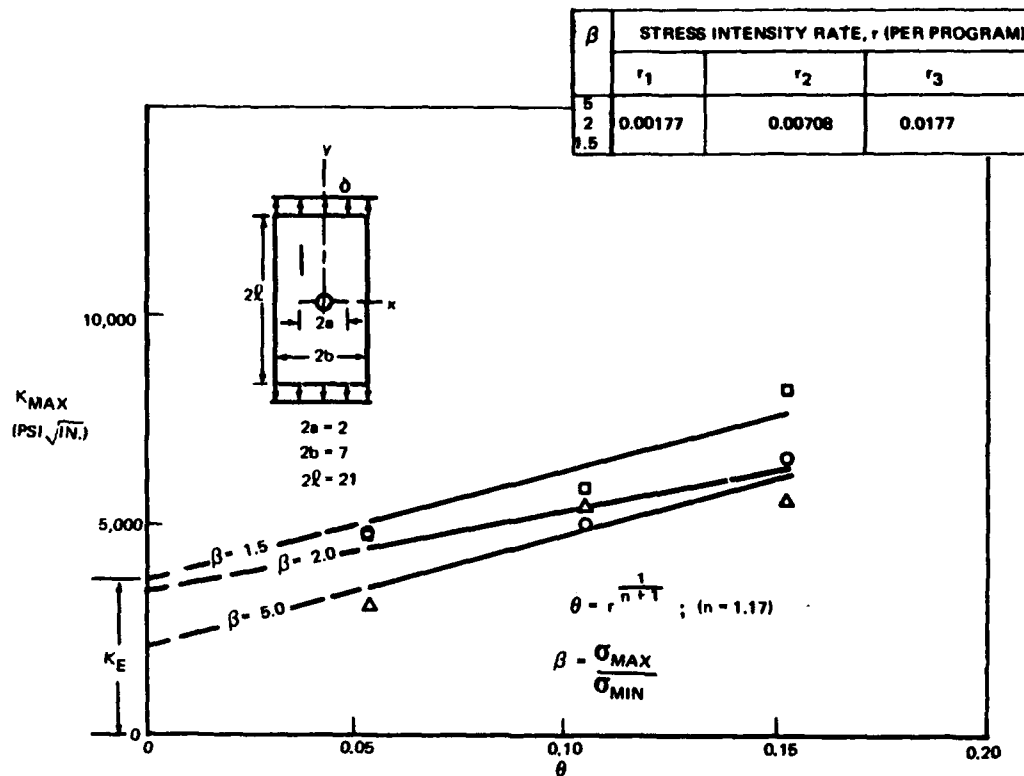


Figure 10.  $K_{MAX}$  vs  $\theta$ , (7075-T6).

where

$a$  = crack length, in.

$N$  = load cycles

$G$  = a function

$K$  = stress intensity factor,  $\text{ksi}\sqrt{\text{in.}}$

The relationship developed between  $K$  and crack growth rate over the macrorange is based on Boeing test data, whereas the crack growth rate in the microcrack (for low values of  $K$ ) region is based on the fourth-power relationship as given in Reference 5. Such a relationship, used in this analysis for 2024-T3 and 7075-T6 materials, is illustrated in Fig. 16.

Cycles to failure are estimated by numerically integrating the developed fatigue crack growth rate versus stress intensity factor relationship, Fig. 16, using an existing computer program. Inputs to the computer include the described crack growth rate versus stress intensity factor relationship and an applicable stress intensity factor versus crack length relationship for the specimen under investigation. The output gives a record of the crack length versus cycle behavior. From this output, the number of cycles required to propagate a crack between any two specified crack lengths can be determined.

This technique is applied to the carefully controlled test data presented in Reference 2 for the commonly used 2024-T3 and 7075-T6 aircraft materials. The several configurations investigated are shown in Fig. 17.

Figure 11. Variation of  $K_E$  with  $\beta$ .

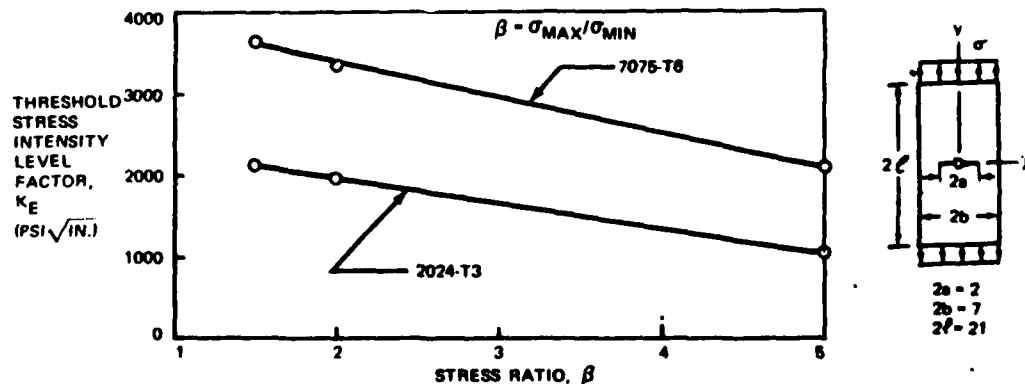


Figure 12. Variation of M with  $\beta$  (2024-T3).

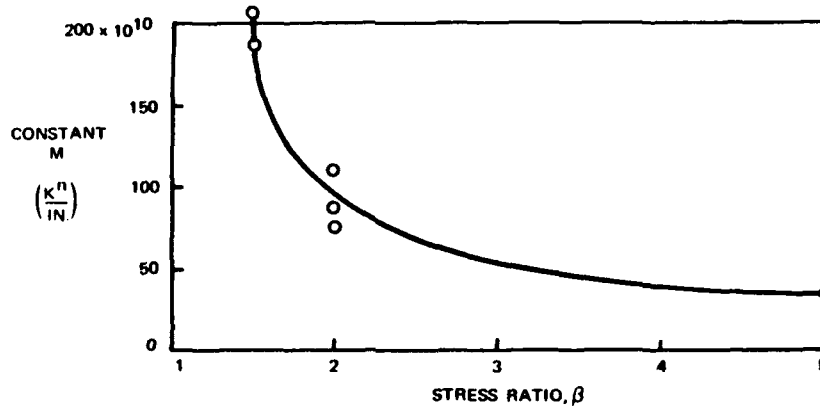
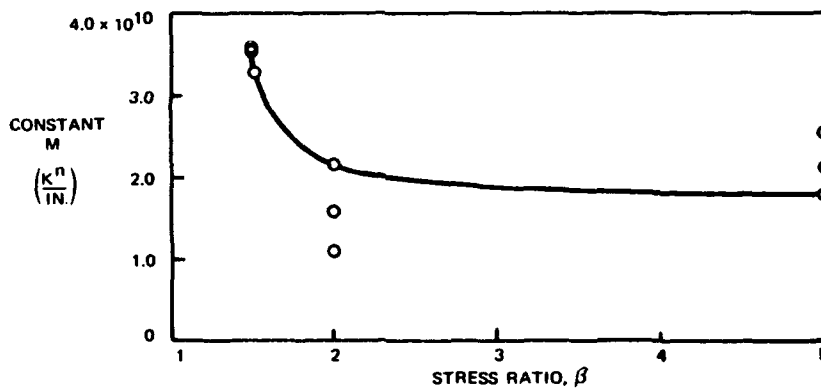


Figure 13. Variation of M with  $\beta$  (7075-T6).



The specimens per Reference 2 were cut from sheets with the rolling direction parallel to the longitudinal axis. The central holes are drilled in three steps for minimum distortion, and electropolished after machining. Testing was conducted in room air at a cyclic frequency of 1800 cpm. A few tests at the higher stress levels had a slower cycling rate. Only the tests conducted for  $\beta = \infty$  were considered for this application. The cycles to failure and the corresponding net area stress are used for all the investigated configurations of the test specimens per Reference 2.

Tests performed per Reference 7, on specimens similar to those under this investigation, have shown that cracks nucleate as quarter-circle flaws at the edge of the hole near the face of the specimen. The expression for the stress intensity factor, K, for such a surface flaw required for the application of the described technique, is written as:

$$K = \sigma \sqrt{\pi L} F \left(\frac{L}{R}\right) \text{M.F. } \alpha \quad (14)$$

Figure 14. Maximum Stress Levels for Nonpropagating Fatigue Cracks (2024-T3).

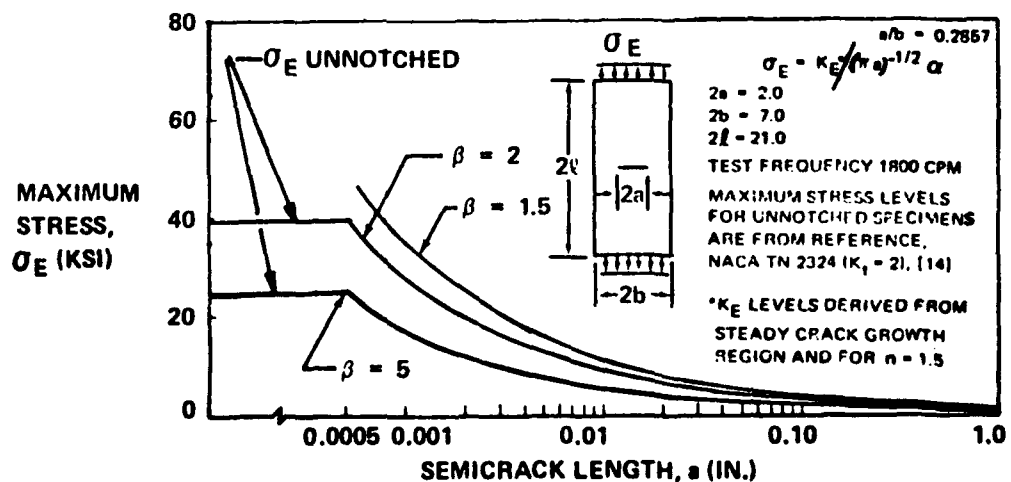
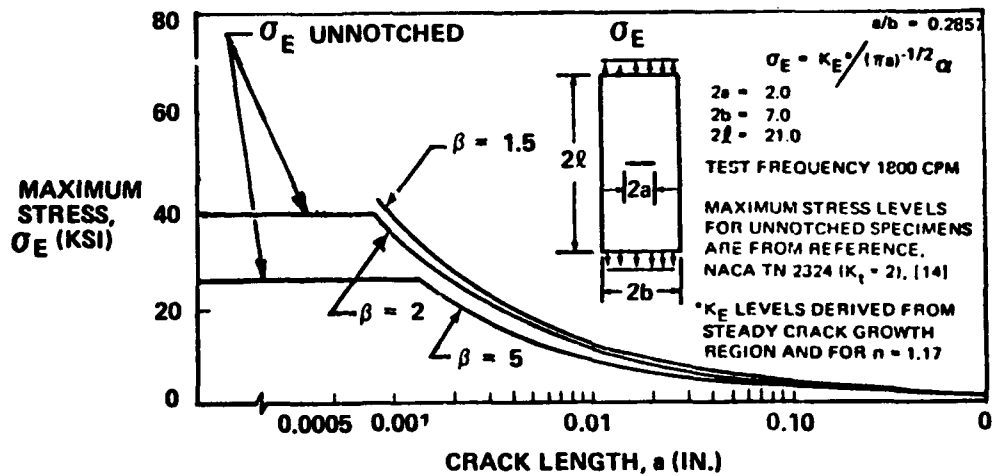




Figure 15. Maximum Stress Levels for Nonpropagating Fatigue Cracks (7075-T6).



where

- $\sigma_g$  = gross area stress, ksi
- L = surface crack length from the edge of the hole, in.
- R = radius of the hole, in.
- $F(\frac{L}{R})$  = correction factor due to the presence of the hole
- M.F. = modification factor for finite width
- $\alpha$  = correction factor for curved cracked front and material thickness.

The correction factor,  $F(\frac{L}{R})$ , for the hole, is that given per Reference 8. The finite width modification factor, M.F., used here, is based on the work given in Reference 9 and is evaluated as the ratio of the theoretical stress concentration factor for finite panels to that for infinite panels. This correction factor for the curved crack front and material thickness is written as:

$$\gamma = \frac{1.1}{\phi} \left( \frac{2t}{\pi L} \tan \frac{\pi L}{2t} \right)^{1/2}$$

for  $L \leq 0.050$  in.

or  $\gamma = 1$

for  $L > 0.050$  in.

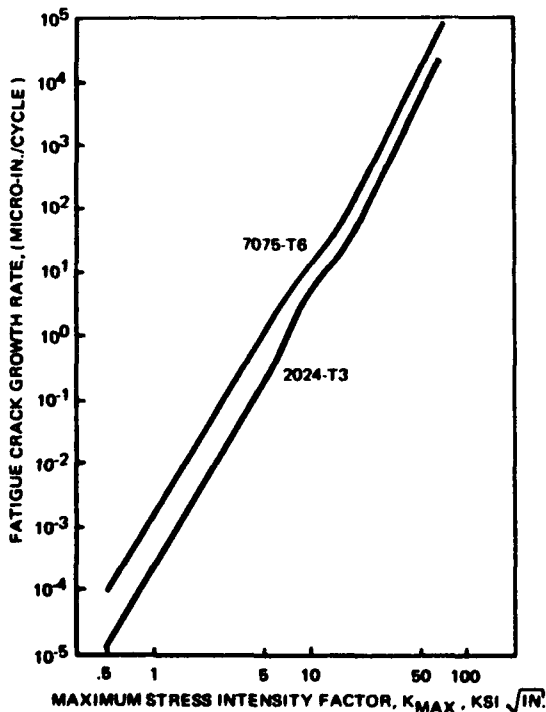
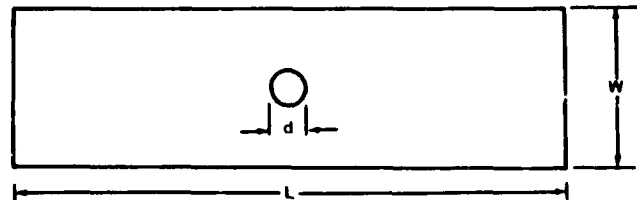


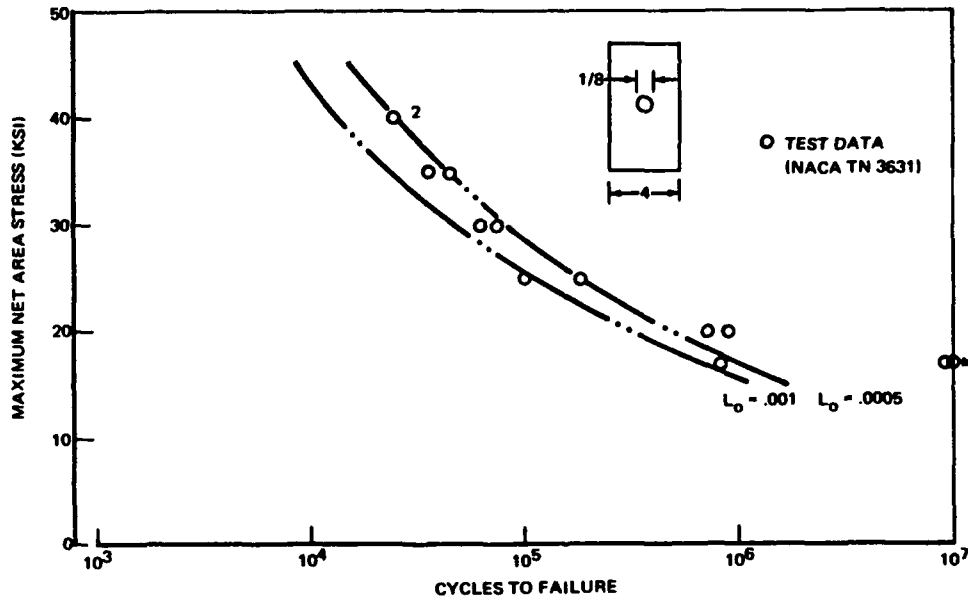
Figure 16. Assumed Fatigue Crack Growth Rate Behavior.



MATERIAL	HOLE DIAMETER, d (IN.)		
	W = 4 IN. L = 20 IN.	W = 2 IN. L = 20 IN.	W = 1/2 IN. L = 12 IN.
2024-T3 ALUMINUM ALLOY	1/8	1/16	1/32
	1/4	1/8	1/16
	1/2	1/4	1/8
	1	1/2	1/4
7075-T6 ALUMINUM ALLOY	2	1	1/4
	1/5	1/16	1/32
	1/4	1/8	1/8
	2	1	1/4

Figure 17. Test Specimen Details (NACA TN3631).

Figure 18.  
Estimated  
Cycles to  
Failure for  
2024-T3,  
W = 4, d = 1/8.



where

$\phi$  = complete elliptic integral of the second kind

$$\left( \frac{2t}{\pi L} \tan \frac{\pi L}{2t} \right)^{1/2} = \text{deep flaw correction factor}$$

$t$  = material thickness, in.

$L$  = surface crack length from the edge of the hole or flaw depth, in.

The deep flaw correction factor accounts for the stress intensity magnification for a flaw reaching the other surface. In this case, it is assumed to be the same as the finite width correction factor for center cracked panels, Reference 10.

Such correction factors have been applied for correlating surface flaw growth, Reference 11.

The failure criterion used in this analysis for all the investigated specimens is based on the critical crack length and the average stress in the uncracked area. Whenever this average stress exceeds 53 ksi for 2024-T3 and 65 ksi for the 7075-T6, the specimens are considered to have failed. This criterion is used instead of the fracture toughness limit because of the small specimen size.

Representative results of the fatigue life estimations for several specimen configurations are shown in Figs. 18 through 25. Each curve shows the estimated cycles to failure for the assumed initial flaw sizes of 0.0005 and 0.001 in. The test data of Reference 2 are shown for each specimen configuration for comparison purposes.

Figure 19.  
Estimated Cycles  
to Failure  
for 2024-T3,  
W = 4, d = 1/4.

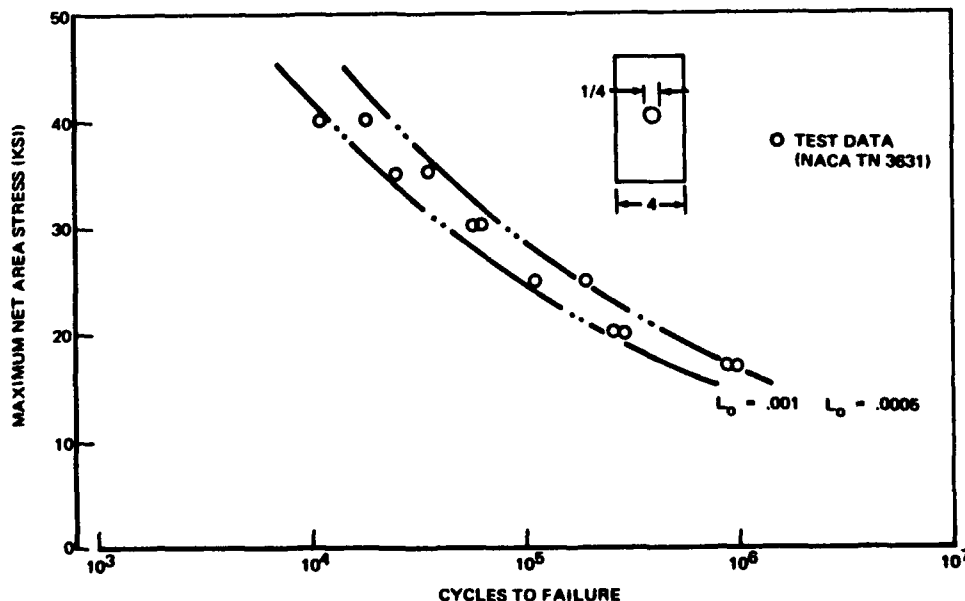


**TABLE II.**  
**EVALUATED THRESHOLD,**  
 **$K_E$  LEVELS FOR AN**  
**INITIAL FLAW SIZE OF**  
**0.0007 IN. BASED ON**  
**FATIGUE LIMIT TEST**  
**DATA OF NACA TN 3631**  
 $(\beta = \infty)$

MATERIAL	W	d (IN.)	FATIGUE LIMIT (KSI)	$K_E$ (KSI $\sqrt{\text{IN.}}$ )
2024-T3	4.0	1/8	15	1.6
		1/4	15	1.56
	1	1/2	14.5	1.42
		1	14	1.30
	4.0	2	17	1.35
		1/16	17	1.81
	2.0	1/8	15	1.55
		1/4	14	1.38
	2.0	1/2	14	1.26
		1	17	1.35
	.5	1/32	18	1.83
		1/16	19	1.85
	.5	1/8	20	1.78
		1/4	21	1.67
2024-T3	AVERAGE FOR ALL SPECIMENS-			1.55
7075-T8	4.0	1/8	17	1.81
		1/4	16	1.66
	4.0	2	19	1.51
		1/16	17	1.79
	2.0	1/8	17	1.76
		1	20	1.59
	.5	1/32	21	2.14
		1/8	19	1.70
	.5	1/4	22	1.75
		AVERAGE FOR ALL SPECIMENS-		

A comparison between the theoretical and experimental results shows varying degrees of agreement. In the majority of the cases, this data assumes a band falling within the two curves developed for the two theoretical sizes of flaws assumed. Whenever the maximum net area stress levels are higher than the test endurance limit levels, more test values fall within this band. It should be noted that the test specimens of Reference 2 did not have known flaws or cracks at the edges of the holes. For the stress levels in the vicinity of the endurance limit, a divergence is noticed. It appears that one possible explanation is due to the repre-

sentation of the crack growth rate relationship used in the life estimation technique where no consideration is given to the threshold stress intensity factor level for fatigue crack growth. If allowance is made for the non-propagating stress intensity level,  $K_{E_0}$ , for crack growth, a better correlation is possible. This then leads to the conclusion that the analysis model can be represented by a specimen having an initial flaw at the edge of the hole.

From a comparison of the fatigue life results above the endurance limit, an initial flaw size, say 0.0007

**Figure 20. Estimated**  
**Cycles to Failure For**  
**2024-T3, W = 2,**  
**d = 1/8.**

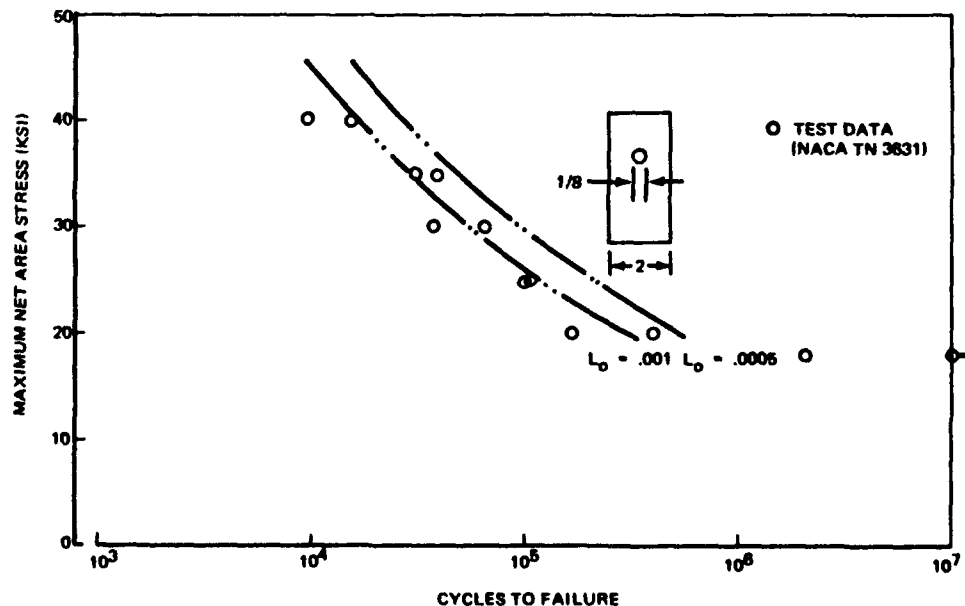
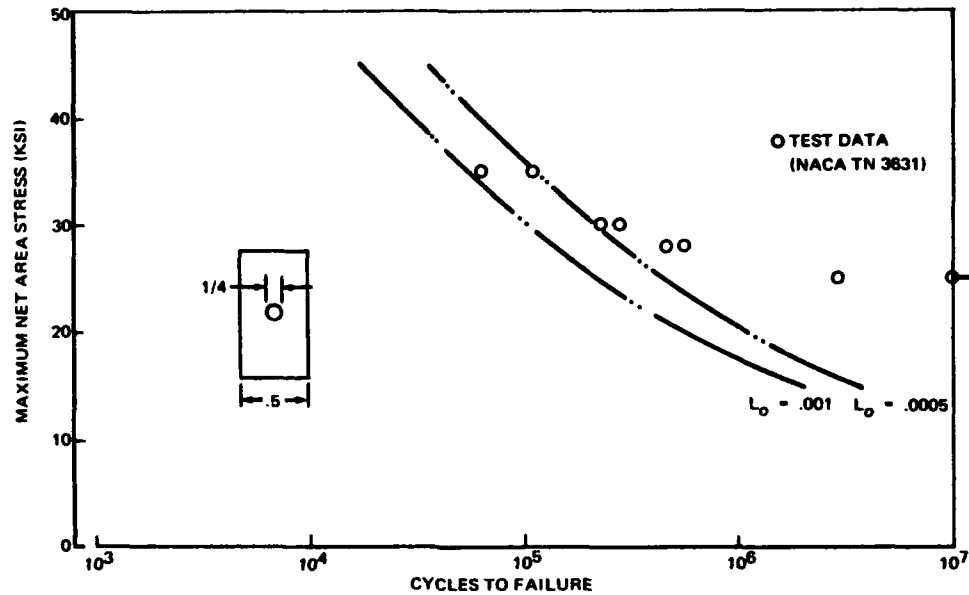


Figure 21.  
Estimated Cycles  
to Failure for  
2024-T3,  $W=0.5$ ,  
 $d=1/4$ .



in., lying between 0.0005 and 0.001 in., appears to be reasonable. Therefore, the threshold stress intensity factor levels for non-propagating fatigue cracks are calculated using the endurance limit stress from the test results of Reference 2 and a flaw length of 0.0007 in. in Equation (14). The threshold levels evaluated for all the investigated specimens are shown in Table II. The average values for  $\beta = \infty$  is found to be 1.55 and 1.75 ksi  $\sqrt{\text{in.}}$  for 2024-T3 and 7075-T6, respectively.

The comparison of the theoretical results to the test data per Reference 2 also suggests that the following are valid assumptions in the development of this fatigue life evaluation technique.

1. The effects on fatigue life due to crack nucleation are negligible;

2. The crack growth characteristic in the micro-range can be represented as an extrapolation of the characteristic in the macro-range;

3. The fatigue damage can be represented as a surface flaw instead of a through crack;

4. The stress intensity factor,  $K$ , incorporating the modification and correction factors as necessary for the simulation of a surface flaw type of crack, is applicable.

#### IV. DISCUSSION AND COMPARISON OF $K_E$ LEVELS

The threshold stress intensity factor levels  $K_E$ , as determined by an experimental investigation shown in Figs. 9 and 10 when compared with those deduced from the analy-

Figure 22.  
Estimated Cycles  
to Failure for  
7075-T6,  $W=4$ ,  
 $d=1/8$ .

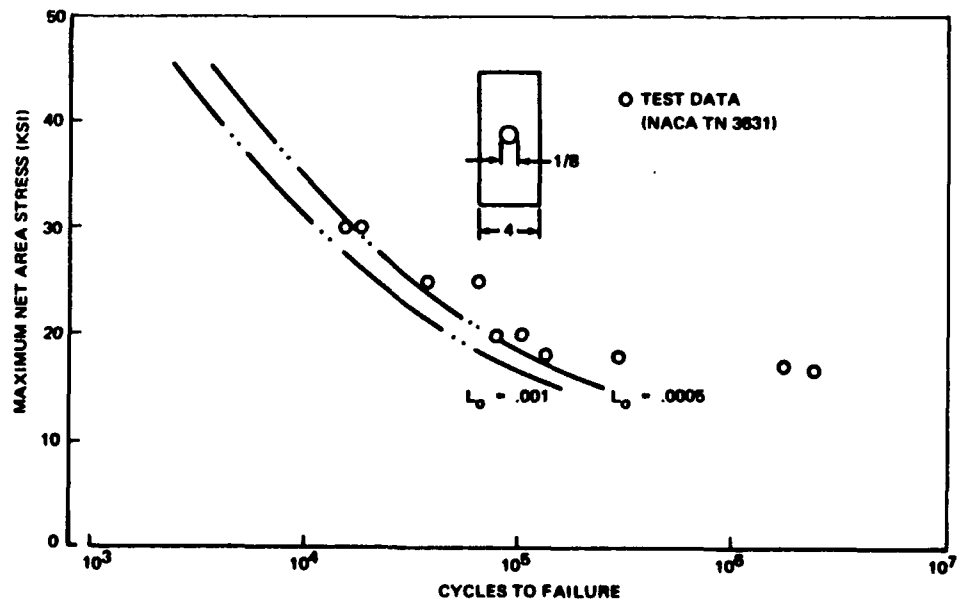
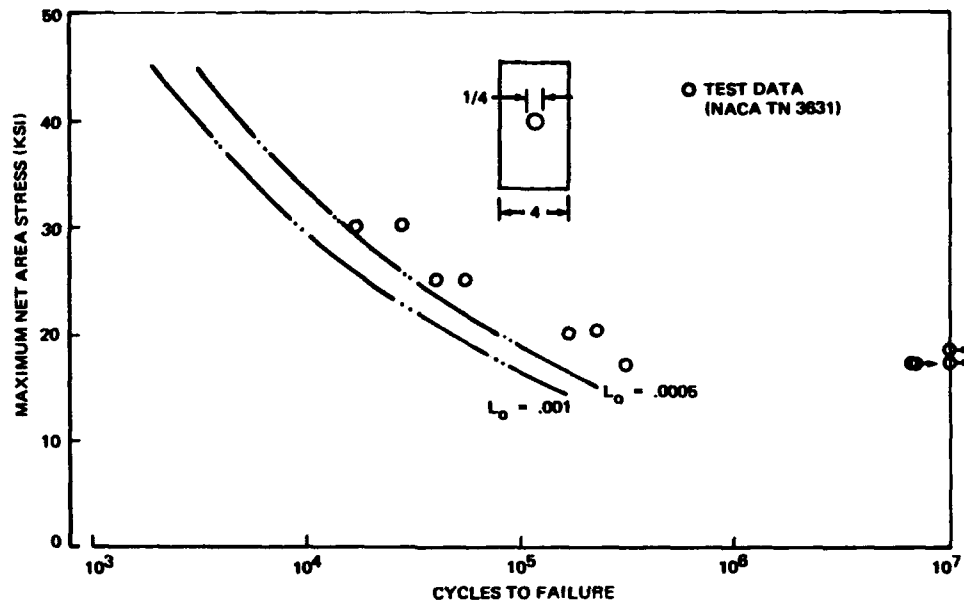


Figure 23.  
Estimated Cycles  
to Failure for  
7075-T6, W=4,  
d=1/4.



sis technique using the principles of fracture mechanics, as shown in Table II, appear to be in close agreement.

Based on crack growth studies per Reference 12, the stress intensity factor levels corresponding to the sub-critical crack growth regions (micro), in the vicinity of  $10^{-8}$  to  $10^{-10}$  in./cycle, for 7075-T6 aluminum alloys is reported to be in the vicinity of  $2 \text{ ksi} \sqrt{\text{in.}}$ . This value is in close agreement with that reported in Fig. 10 and Table II.

The results for the threshold stress intensity factor levels,  $K_E$ , determined for 2024-T351 and 7075-T6 materials with a different technique, namely, by progressively decreasing the stress intensity factor level from a high value to a low value and establishing the  $K_E$  levels as those values where no crack growth occurred, is demonstrated in

Reference 13. The magnitudes for both the 2024-T351 and 7075-T6 materials are found to be not only higher than the values determined per this paper but, the values for 2024-T351 are found to be higher than 7075-T6 material. As an example for  $\beta = 5$ ,  $K_E = 6 \text{ ksi} \sqrt{\text{in.}}$  versus  $1 \text{ ksi} \sqrt{\text{in.}}$  for 2024-T3 and  $K_E = 4 \text{ ksi} \sqrt{\text{in.}}$  versus  $2 \text{ ksi} \sqrt{\text{in.}}$  for 7075-T6. A possible explanation for this difference is that the application of a high stress intensity factor level followed by a lower level induces residual stresses comparable to the degree of the initial loading step. These stresses combined with the limited number of cycles allowed per step for establishing the crack growth or no growth characteristics and the ductile nature of the 2024-T3 material can be considered as the contributing factors. Therefore, the assumed representation of the crack growth rate as a power function of the damage causing stress intensity factor level,  $K_D = (K - K_E)$  and the

Figure 24.  
Estimated Cycles  
to Failure for  
7075-T6, W=2,  
d=1/8.

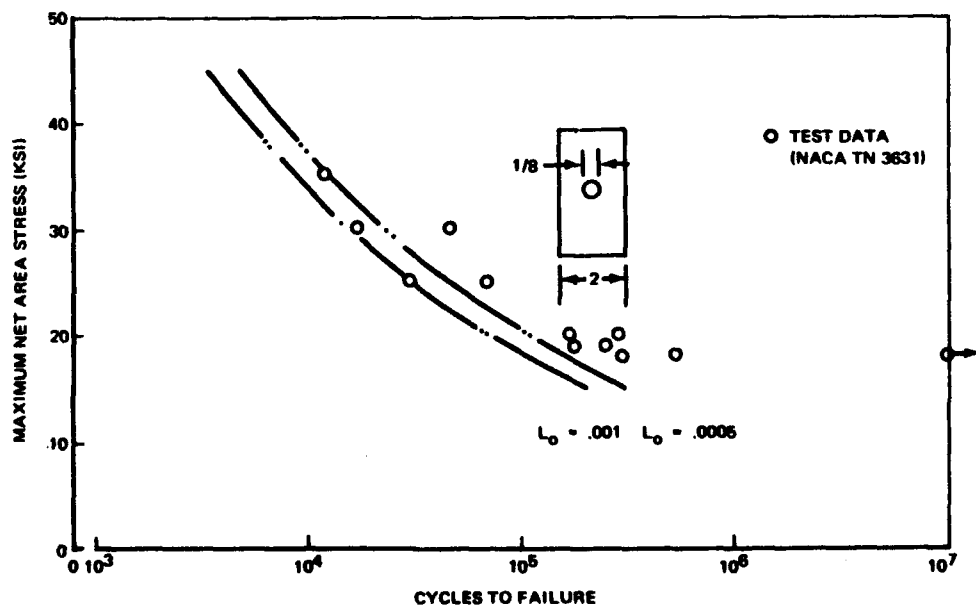
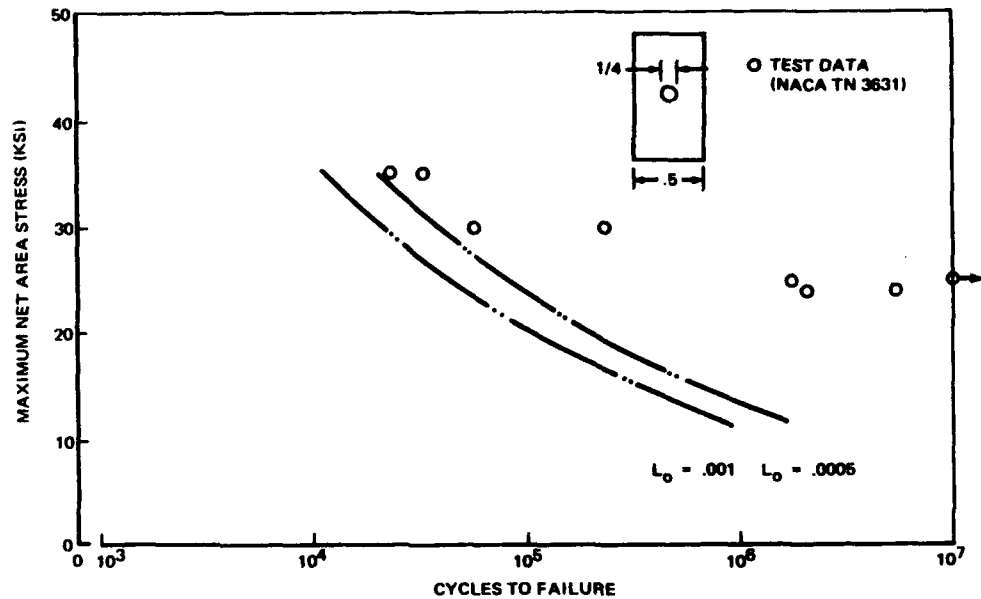


Figure 25.  
Estimated Cycles  
to Failure for  
7075-T6,  $W=0.5$ ,  
 $d:1/4$ .



material constant,  $M$  appear to be applicable.

### V. CONCLUSIONS

Based upon the results, comparisons, and discussions presented, the following conclusions are drawn:

1. The progressively increasing variable loading technique, similar to the Prot method, has been found feasible for establishing the threshold stress intensity factor levels,  $K_E$ , for non-propagating fatigue cracks.
2. Endurance stress intensity factor levels, referred to in this paper as the threshold stress intensity factor levels,  $K_E$ , do exist for non-propagating fatigue cracks in 2024-T3 and 7075-T6 aluminum alloys.
3. The determined values of these  $K_E$  levels are found to depend on the level of the stress ratio,  $\beta$ .  $K_E$  decreases with increasing values of  $\beta$ .
4. Within the investigated ranges of  $\beta$ , the values of  $K_E$  for 7075-T6 are found to be higher than those of 2024-T3.
5. In general, the fatigue crack growth in 2024-T3 material is found to be increasing steadily with increasing load, whereas the fatigue crack growth in 7075-T6 material is found to be negligible for a major portion of the programmed load and then appears to grow at a very fast rate at the higher load levels.
6. Constant amplitude fatigue performance data of test specimens with central holes can be simulated by the calculated cyclic life to grow a small initial fatigue crack to failure.
7. Using a corner crack at the edge of the hole for this fatigue model formulation, the initial corner flaw size is found to be about 0.0007 in. for both the 7075-T6 and the 2024-T3 aluminum alloys.
8. The threshold stress intensity factor levels,  $K_E$ , obtained by the increasing variable loading technique are comparable with those derived by using the endurance stress of the specimens with central holes and an initial flaw size of 0.0007 in.
9. It appears that  $K_E$  levels established by decreasing load testing with a cycles limit results in non-propagating crack stress intensity factors levels,  $K_E$ , somewhat greater than the increasing load technique.
10. It appears feasible to develop design guidelines for fatigue performance prediction after further extensive testing and analysis to encompass the several variables occurring in the fatigue phenomenon relating to crack growth and service potential of structures.

## REFERENCES

1. E.M. Prot, *Fatigue Testing Under Progressive Loading: A New Technique for Testing Materials*, WADC-TR-52-148, Aeronautical Systems Division, Wright-Patterson AFB, Ohio (1952).
2. C.B. Landers and H.F. Hardrath, *Results of Axial-Load Fatigue Tests on Electropolished 2024-T3 and 7075-T6 Aluminum Alloy Sheet Specimens with Central Hole*, NACA-TN-3631, National Aeronautics and Space Administration, Washington, D.C. (1956).
3. R.C. Thurston, *Propagating and Non-Propagating Fatigue Cracks in Metals*, Mines Branch Information Circular 1-C-115, Dept. of Mines and Technical Surveys, Ottawa (1960).
4. D.R. Donaldson and W.E. Anderson, "Crack Propagation Behavior of Some Airframe Materials," pp. 375-441, *Proc. Crack Propagation Symp.*, Vol. II, College of Aeronautics, Cranfield, England (1961).
5. P.C. Paris and F. Ergodan, "A Critical Analysis of Crack Propagation Laws," *J. Basic. Eng.*, 85/4:528-534 (1963).
6. H.H. Johnson and P.C. Paris, "Sub-Critical Flaw Growth," *Eng. Fracture Mech.*, 1:3-45 (June 1968).
7. J. Schijve and F.A. Jacobs, *Fatigue Crack Propagation of Unnotched and Notched Aluminum Alloy Specimens*, NRL-TR-M.2128, National Aero- and Astronautical Research Institute, Amsterdam (1964).
8. O.L. Bowie, "Analysis of an Infinite Plate Containing Radial Cracks Originating at the Boundary of an Internal Circular Hole," *J. Math. Phys.*, 35:60-71 (1956).
9. R.C. Howland, "On the Stresses in the Neighborhood of a Circular Hole in a Strip Under Tension," *Phil. Trans. Roy. Soc. London*, 229A (1930).
10. P.C. Paris and G.C. Sih, "Stress Analysis of Cracks," pp. 30-81, *Fracture Toughness Testing and Its Applications*, ASTM-STP-381, American Society for Testing and Materials, Philadelphia, Pennsylvania (1965).
11. B. Mukherjee, L.E. Culver, and D. J. Burns, "Growth of Part-Through and Through-Thickness Fatigue Cracks in Sheet Glassy Plastics," *Exp. Mech.*, 9:90-96 (1969).
12. B.M. Linder, *Extremely Slow Crack Growth Rates in Aluminum Alloys 7075-T6*, M.S. Thesis, Lehigh University, Bethlehem, Pennsylvania (1965).
13. J.J. Horsley, *Fracture Mechanics - Crack Initiation and Initial Growth*, D3-7660, Boeing Company, Wichita, Kansas (1969).
14. H.J. Grover, S.M. Bishop, and L.R. Jackson, *Fatigue Strength of Aircraft Materials: Axial Load Sheet Specimens of 24S-T3 and 75S-T6 Alloys and of SAE 4130 Steel*, NACA-TN-2324, National Aeronautics and Space Administration, Washington, D.C. (1951).

# FATIGUE CRACK PROPAGATION BEHAVIOR AND RESIDUAL STRENGTH OF BONDED STRAP REINFORCED, LAMELLATED AND SANDWICH PANELS

by

S.H. Smith, T.R. Portar, and W.L. Engstrom

The Boeing Company  
Commercial Airplane Group  
Renton, Washington

## SYMBOLS

<p><math>m_s</math> = Stress intensity factor reduction parameter under static condition, <math>IN^{1/2}</math></p> <p><math>m_d</math> = Stress intensity factor reduction parameter under cyclic condition, <math>IN^{1/2}</math></p> <p><math>K</math> = Crack tip stress intensity factor, <math>KSI \sqrt{IN}</math></p> <p><math>\Delta K_s</math> = Static stress intensity factor reduction, <math>KSI \sqrt{IN}</math></p> <p><math>\Delta K_d</math> = Cyclic stress intensity factor reduction, <math>KSI \sqrt{IN}</math></p> <p><math>K_c</math> = Plane stress critical stress intensity factor, <math>KSI \sqrt{IN}</math></p> <p><math>2c</math> = Surface fatigue crack length, IN.</p> <p><math>2a</math> = Fatigue crack length, IN.</p> <p><math>2a_{cr}</math> = Critical crack length, IN.</p> <p><math>\sigma_g</math> = Gross-area stress, KSI</p> <p><math>P</math> = Concentrated load, KIP</p> <p><math>P_T</math> = Load transferred into tear strap, KIP</p> <p><math>s</math> = Distance from crack line to concentrated forces P, IN.</p> <p><math>I_1, I_2</math> = Stress intensity factor coefficients, <math>IN^{-2}</math></p>	<p><math>\beta</math> = Coefficient in <math>I_1</math> and <math>I_2</math>, IN.</p> <p><math>b</math> = Distance from crack center-line to concentrated force, P, IN.</p> <p><math>\sigma_g'</math> = Effective gross-area stress, KSI</p> <p><math>\mu</math> = Poisson's ratio</p> <p><math>\alpha</math> = Finite panel width correction factor</p> <p><math>W</math> = Panel width, IN.</p> <p><math>W_s</math> = Tear strap width, IN.</p> <p><math>t</math> = Skin thickness, IN.</p> <p><math>t_s</math> = Tear strap thickness, IN.</p> <p><math>t_a</math> = Adhesive thickness, IN.</p> <p><math>t_c</math> = Honeycomb core thickness, IN.</p> <p><math>K_{MAX}</math> = Maximum cyclic stress intensity factor, <math>KSI \sqrt{IN}</math></p> <p><math>\sigma_{MAX}</math> = Maximum cyclic gross-area stress level, KSI</p> <p><math>R</math> = Ratio of minimum to maximum gross area cyclic stress levels</p> <p>UTS = Ultimate tensile strength of tear straps, KSI</p>
--	--

## I. INTRODUCTION

The "fail-safe" or "damage tolerant" concept of aircraft structural design provides that fatigue cracks which may occur during the lifetime of the structure will be safely contained. Fatigue cracks usually originate in areas of high stress concentration. Therefore, the structural designer is faced with the problem of designing the structure for minimum stress concentration and maximum crack growth containment without a severe weight penalty.

During the past ten years a considerable effort has been directed toward the collection and analysis of fatigue crack propagation behavior and residual strength properties of airframe metallic materials. These data and analysis methods have been developed using linear elastic fracture mechanics. Characterization of fatigue crack growth rate and fracture toughness or residual strength has been accomplished by laboratory testing of simple cracked specimens subjected to uniaxial or bending type loadings. Substantial effort is now being directed toward the application of linear



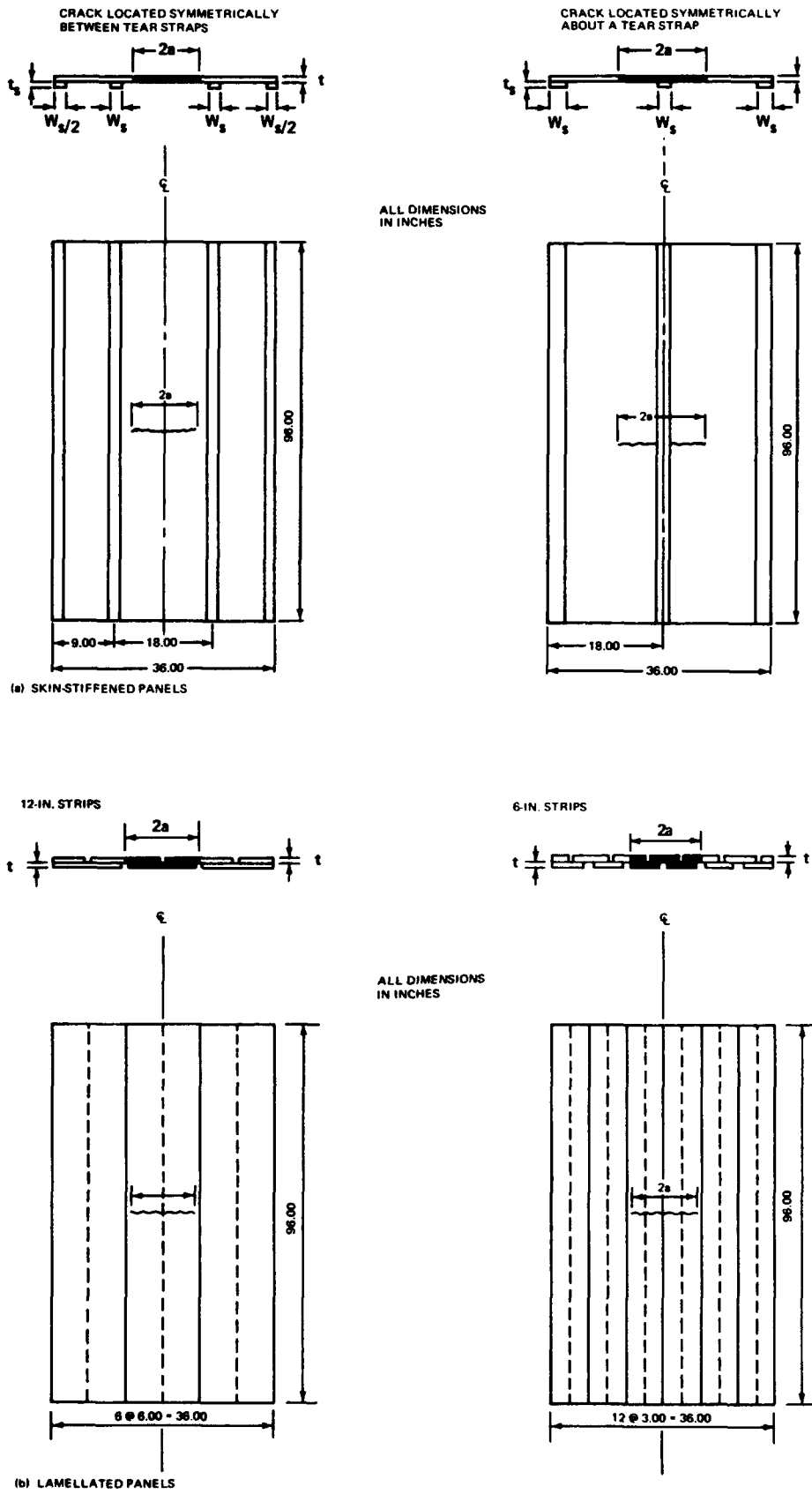


Figure 1. Schematic Diagram of Skin-Stiffened and Lamellated Panels.

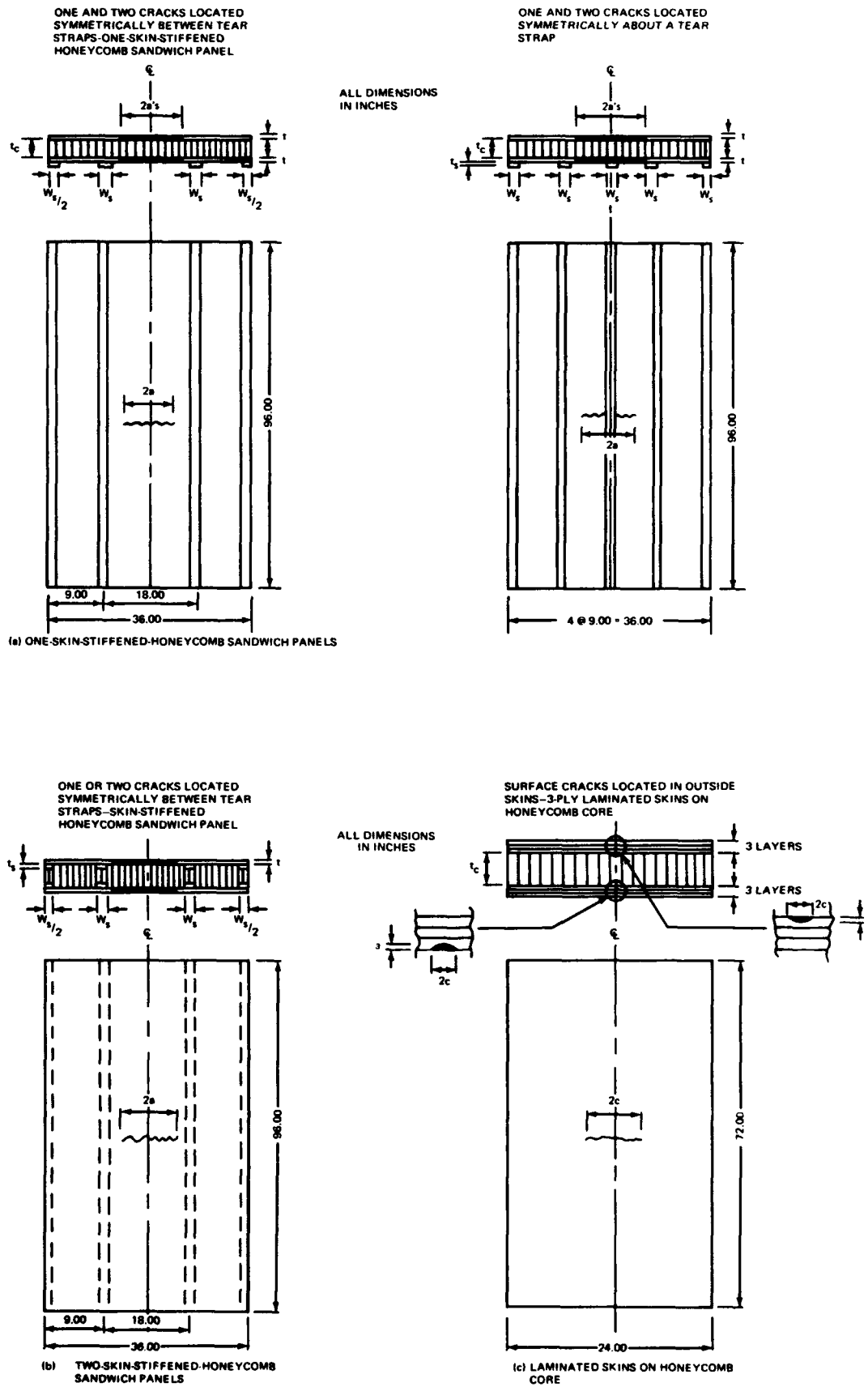


Figure 2. Schematic Diagram of Skin-Stiffened Honeycomb Panels and Laminated Panels.

elastic fracture mechanics techniques in treating the problems associated with the fatigue cyclic extension of cracks and the residual strength of complex, builtup aircraft structural components.

Structural bonding of primary aircraft structure with low modulus adhesives is becoming an area of increased interest. The potential fatigue and fail-safe benefits of bonded structure have long been recognized and are now within reach for primary structure by virtue of improved strength and reliability.

An exploratory testing program supplemented by linear elastic fracture mechanics was conducted to evaluate the "fail-safe" capability of bonded structure. The fatigue crack propagation behavior and residual strength of bonded strap reinforced simple, lamellated, and honeycomb sandwich panels were evaluated. Cyclic and static stress intensity factor reductions were the key parameters evaluated through variation of the geometrical, material, and test conditions of the structural panels.

## II. STRUCTURAL CONFIGURATIONS AND EXPERIMENTAL TECHNIQUES

The fatigue crack propagation behavior and residual strength properties of several types of adhesive bonded structural configurations were evaluated. Schematic diagrams of these structural panel configurations are given in Figs. 1, 2, and 3. The tear-strap-reinforced panels are subsequently referred to as skin-stiffened panels. Skin-stiffened panels with various tear strap widths for a constant percent stiffening, various adhesive thicknesses, various percent stiffening, and skin and tear strap alloys were evaluated. Lamellated panels were evaluated using strips of various widths. In the case of skin-stiffened panels, fatigue crack propagation behavior and residual strength were measured for cracks located symmetrically between and across tear straps. One- and two-skin stiffened honeycomb panels were evaluated. In these skin-stiffened honeycomb sandwich panels, 5052 aluminum core of 3.1 lb/cu. ft. density and 1/8 in. hexagonal cell size was used as the primary core material. In the two-skin stiffened panels,

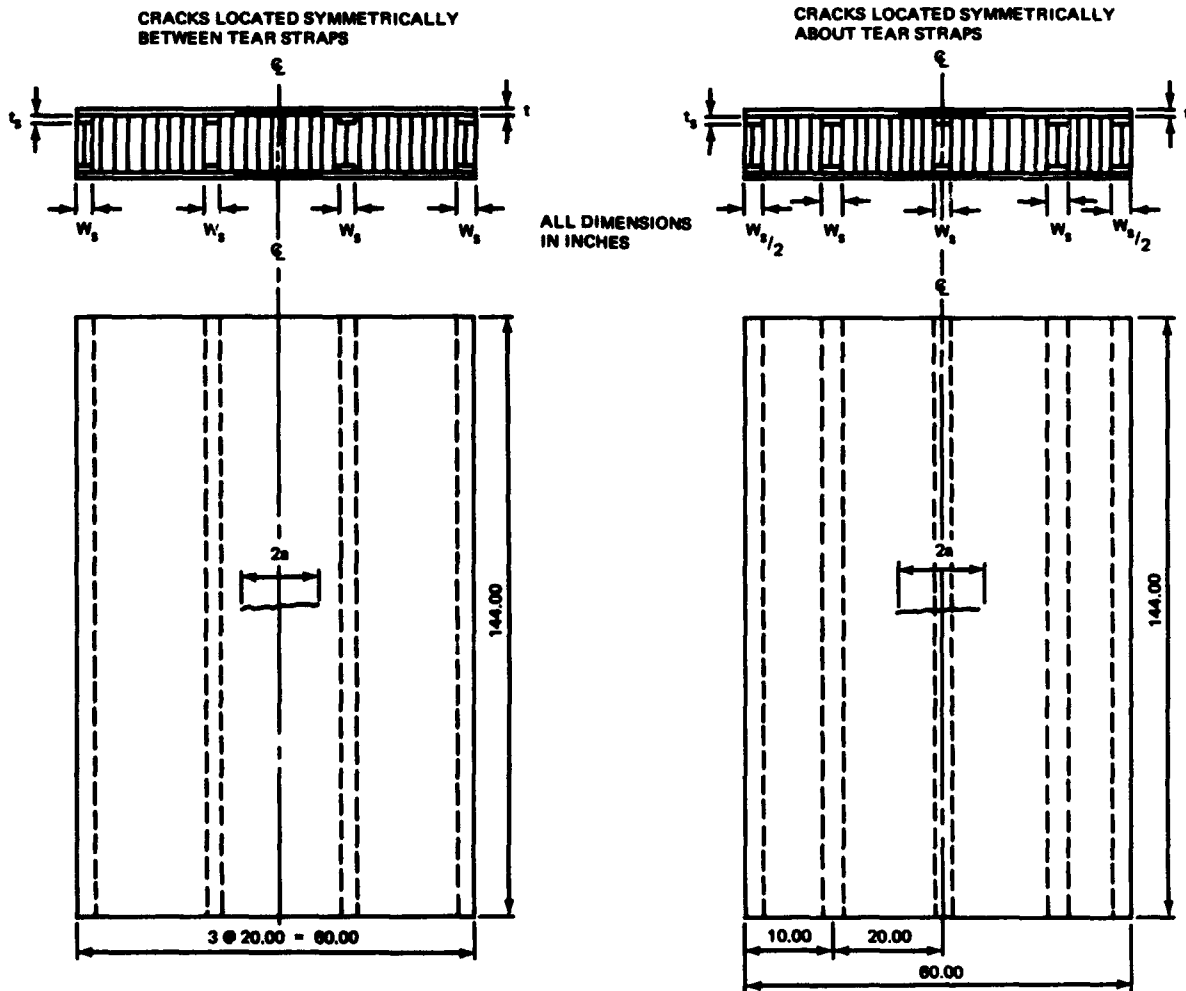


Figure 3. Schematic Diagram of Large Skin-Stiffened Honeycomb Panels.

12.0 lb/cu. ft. density core was used at the tear straps. All panels were bonded with an epoxy adhesive. Fatigue crack propagation behavior of skin-stiffened honeycomb sandwich panels was measured for various core thicknesses, bond-line void conditions, one and two skins cracked, percent stiffening, and applied gross-area cyclic stress levels. Following fatigue crack propagation testing, residual strength of the panels was determined. Fatigue crack propagation behavior of laminated skins on honeycomb core was measured by inducing surface flaws in the outside skins of each laminated face. Measurements of surface fatigue crack propagation were made in fatigue cycling the panels to failure.

Figure 4 shows the residual strength and fatigue crack propagation testing set-up. Pin-ended loading grips, which insured axial loading, were bolted to the ends of the specimens in preparing them for fatigue and fracture testing. The surface areas of all panels, along the line of expected crack propagation, were polished to facilitate the measuring of fatigue crack growth. A scale graduated in hundredths of an inch was attached to both sides of the panels to

measure fatigue crack growth. Surface fatigue crack progression was measured with the scales and with a surveyor's transit at various intervals during the fatigue crack propagation testing. Restraints were not used on the honeycomb sandwich panels to prevent skin buckling because of the stiffness of the thick honeycomb core. In testing the skin-stiffened panels, 3/4 in. plexiglas plates were clamped on each side of the panel to prevent out-of-plane buckling. Thin plastic spacers were used to fit the contours of the panels.

A photostress survey was conducted on one skin-stiffened panel under load to determine optimum strain gage locations for static load transfer determination. The panel was then instrumented with 25 axial gages and 55 rosette gages. Strain gage measurements were taken at various load levels and gage output was measured on a digital voltmeter. Maximum and minimum principal stresses and maximum shear stresses and the stress directions were determined by computer. All strain gage readings were temperature compensated.

**Figure 4. Residual Strength and Fatigue Crack Propagation Testing Setup.**



Constant amplitude fatigue crack growth cycling and fracture testing of the 24 by 72 in. panels and the 36 by 96 in. panels were performed in servovalve-controlled hydraulic test machines. Uniform gross-area stresses were applied hydraulically to the panels during fatigue cycling and controlled by single channel electronic load-control units. The skin-stiffened panels were fatigue-cycled at maximum gross area stress levels of 9 and 10 ksi and stress ratio, R, of 0.05. The skin-stiffened honeycomb sandwich panels were fatigue cycled at 10 ksi and stress ratio of 0.05. Fatigue crack propagation behavior of laminated skins on honeycomb core was evaluated at a maximum gross area cyclic stress level of 20 ksi and stress ratio of 0.05. Cyclic frequencies of 36 to 120 cycles/min. were used in fatigue-crack-growth testing. Test panels were statically pulled at a gross-area stress rate of 1,000 psi/sec. following fatigue crack propagation testing to evaluate residual strength. High speed photography at 1,000 fps was utilized to detect and measure slow crack growth during fracture testing. Ultimate load at fracture was obtained from load versus time records as produced by high-response galvanometers on an oscillograph during fracture testing of the panels.

Panels that were residual strength tested at -65°F and +130°F were also fatigue-crack-propagation tested at these temperatures. Panels tested at -65°F were equipped with a styrofoam chamber which enclosed the full width of the test panel. Fatigue crack propagation was monitored through thermally insulated plexiglass windows on each side of the chamber. Liquid nitrogen was introduced into the chamber to provide a test temperature of -65°F. The 130°F test temperature was provided by quartz crystal lamps surrounding the panel test area. Panels tested at -65°F and 130°F were instrumented with thermocouples to ensure constant temperature distribution throughout the test section. Thermostatic controls were used to maintain the test temperature within  $\pm 5^\circ\text{F}$ .

The 60 by 144 in. skin-stiffened honeycomb sandwich panels were tested in a 1200-kip-capacity universal test machine. Initial sawcuts were fatigued at a maximum gross area stress of 18.0 ksi and a stress ratio of 0.5 at a cyclic frequency of 2 cycles/min. A cold chamber similar to that used on the 36 by 96 in. panels was used during -65°F testing. These panels were also residual strength tested at a gross-area stress rate of 1,000 psi/sec. and high speed photography was used to measure slow growth.

The tensile specimens used to evaluate the base materials were all tested at room temperature in a 20-kip universal testing machine. An applied strain rate of 0.005 in./in./min. was used up to the proportional limits and allowed to increase until approximately 0.6% offset. Strain rate was then paced at 0.10 in./in./min. to failure.

All readout equipment and control systems were calibrated using primary or secondary standards traceable to the National Bureau of Standards.

### III. APPLICATION OF FRACTURE MECHANICS ANALYSIS TO STRUCTURAL PANELS

Linear elastic fracture mechanics is the analytical tool used in evaluating the fatigue crack growth and residual strength characteristics of the structural panels in this investigation. The static and cyclic stress intensity factor reduction due to load transfer into bonded tear straps are the key parameters used in analyzing the "fail-safe" capability and fatigue crack growth containment of the structural panels investigated.

*Fatigue Crack Propagation Behavior:* Basically, the elastic stress field "near" the fatigue crack tip is measured by the intensity of the stress intensity parameter, K. The rate of fatigue crack extension during cycling is controlled by the fluctuation of stress intensity and the maximum level (Reference 1, 2 and 3).

The stress intensity factor equation used for the unstiffened panel behavior from Reference 4 is:

$$K_{\text{MAX}} = \sigma_{\text{MAX}} \sqrt{\pi a} \left[ \frac{W}{\pi a} \tan \frac{\pi a}{W} \right]^{1/2} \quad (1)$$

The unstiffened  $K_{\text{MAX}}$  versus fatigue crack growth rate behavior of the skin materials is given in Figure 5.

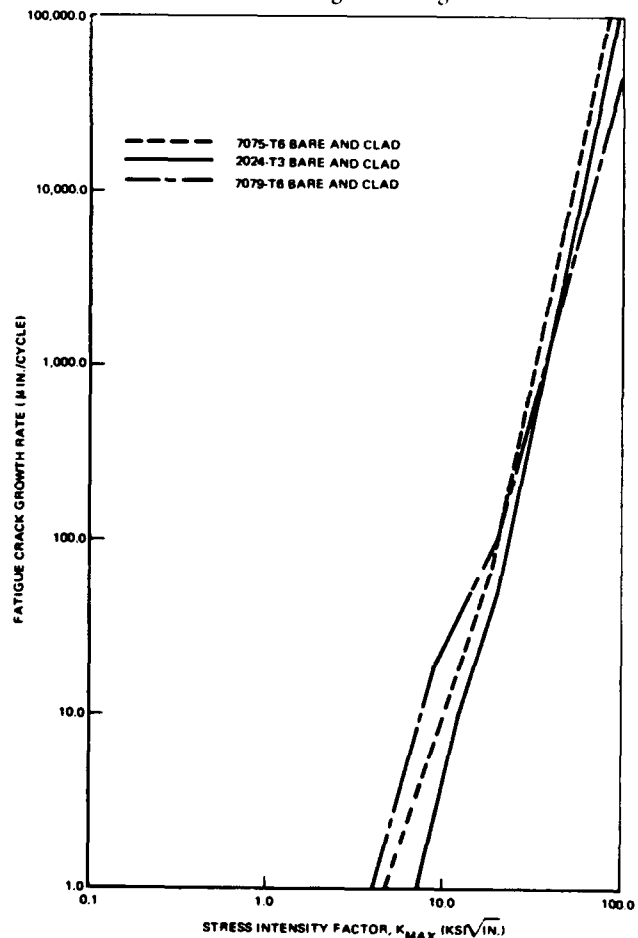


Figure 5. Rate of Fatigue Crack Growth vs. Stress Intensity Factor.

The technique used to evaluate the fatigue crack growth containment capability of the structural configurations tested is based on this concept of fatigue crack growth rate. From measured fatigue crack length versus cycles data, the rate of fatigue crack growth at a specific crack length was determined. The behavior of  $K_{MAX}$  versus fatigue crack length for the stiffened panels was compared to the behavior of  $K_{MAX}$  versus crack length for a corresponding unstiffened panel subjected to equivalent fatigue stress levels.

The difference between the stress intensity levels of

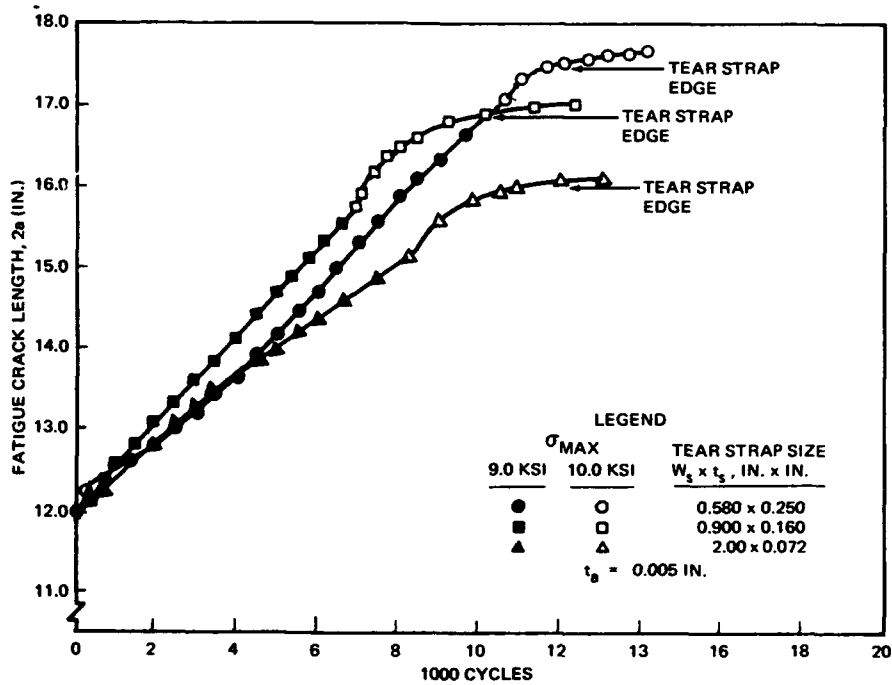
the stiffened and unstiffened panels at a given fatigue crack length is the cyclic stress intensity factor reduction,  $\Delta K_d$ . A cyclic stress intensity factor reduction parameter,  $m_d$ , is defined as

$$\frac{\Delta K_d}{\sigma_{MAX}}$$

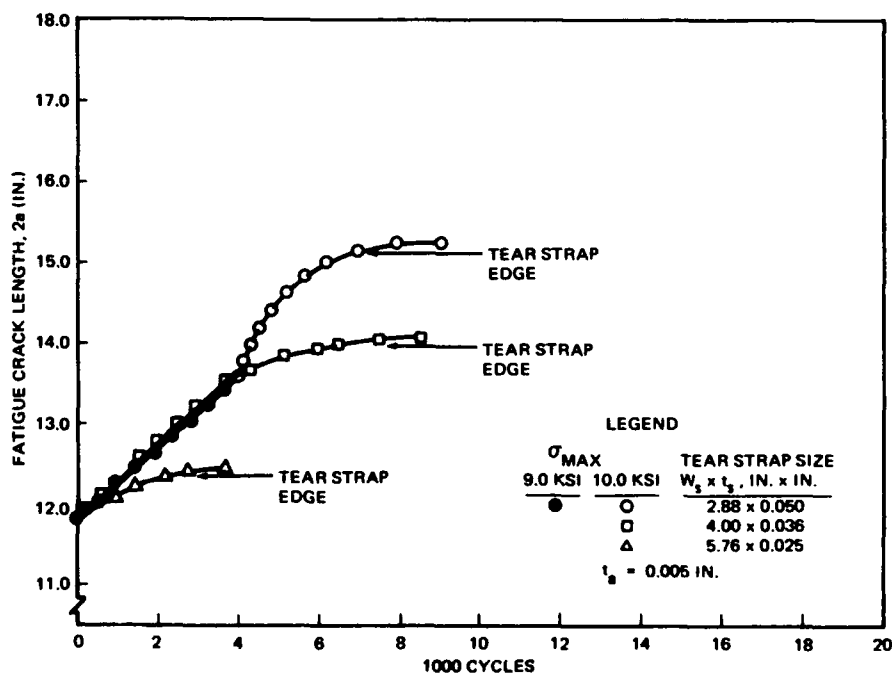
and is a function of fatigue crack length.

*Static Stress Intensity Reduction and Residual Strength:* For a skin crack located between bonded tear straps or located across and extending on both sides of a tear strap, load is transferred from the cracked skin into the

Figure 6. Fatigue Crack Propagation Behavior of Skin-Stiffened Panels of Various Tear Strap Widths.



(a) 2024-T3 CLAD SKINS AND 7075-T6 CLAD STRAPS, 20% STIFFENING



(b) 2024-T3 CLAD SKINS AND 7075-T6 CLAD STRAPS, 20% STIFFENING

tear straps. The amount of load transferred is a function of adhesive thickness, tear strap width, percent stiffening, skin crack length, tear strap spacing and panel temperature.

To accurately assess load transfer, the stress distribution along the tear strap length and width had to be known. The load transferred from the skin into bonded tear straps was measured by strain gages. Strain gage locations were selected judiciously to accurately measure loads, considering anticipated strain gradients.

Once the load transfer and its distribution were known, the reduction of the skin stress intensity factor level due to load transfer was calculated. The stress intensity factor formula for a pair of concentrated forces acting on a crack from Reference 5 is:

$$K = \frac{2Ps\sqrt{a}}{t\sqrt{\pi}} \left[ (3 + \mu) I_1 - (1 + \mu) I_2 \right] \quad (2)$$

$$I_1 = \frac{\beta}{s \left[ (s^2 + a^2 - b^2)^2 + 4b^2s^2 \right]^{1/2}} \quad (3)$$

$$I_2 = \frac{(a^2 + b^2)s^2 + \beta^2(a^2 - b^2)2 + b^2s^2(s^2 - a^2 + b^2)}{2s\beta \left[ (s^2 + a^2 - b^2)^2 + 4b^2s^2 \right]^{3/2}} \quad (4)$$

$$\beta = \frac{1}{\sqrt{2}} \left[ (s^2 + a^2 - b^2) + \sqrt{(s^2 + a^2 - b^2)^2 + 4b^2s^2} \right]^{1/2} \quad (5)$$

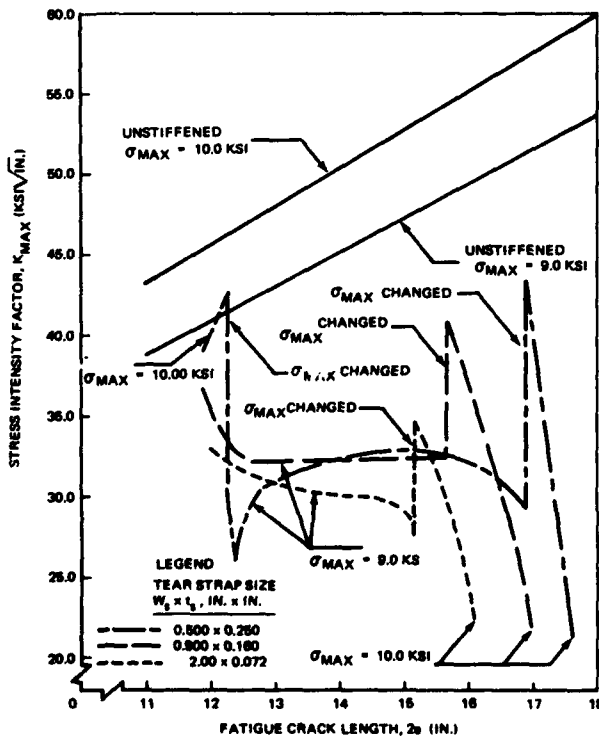
Superposition of the stress intensity factor values for a network of concentrated forces and the respective K values gave the total stress intensity factor reduction,  $\Delta K_s$ . A static stress intensity factor reduction parameter,  $m_s$ , is defined as

$$\frac{\Delta K_s}{\sigma_{MAX}}$$

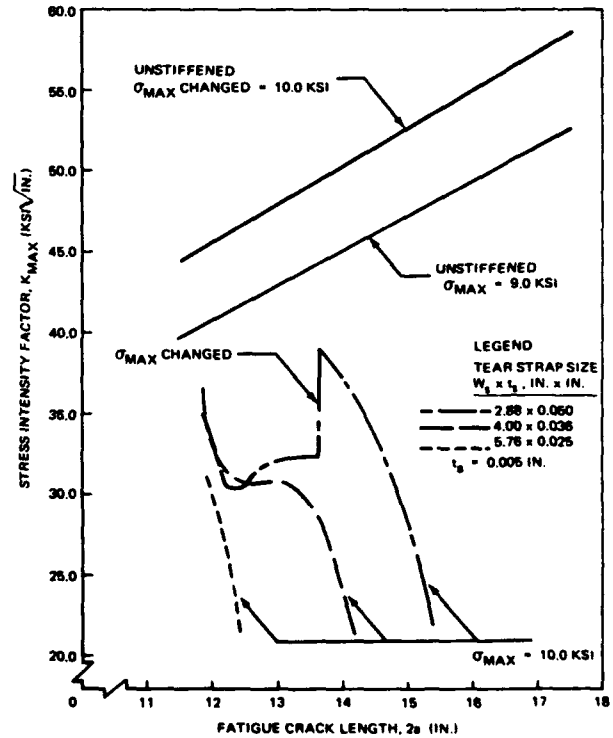
and is a function of fatigue crack length.

The concept described above could not be used for residual strength analysis at high stresses because strain gages on the strap adjacent to the crack yielded, resulting in non-linear behavior; therefore, a different approach had to be considered.

Residual strength of bonded tear strap panels was based on ultimate strength failure of the tear straps adjacent to the crack and the plane stress critical stress intensity level of the fatigue cracked skin. At failure, the ultimate load imposed on the panel consisted of the load for adjacent strap failure and the remaining load on the unfailed or unbroken ligament portion of the panel.



(a) 2024-T3 CLAD SKINS AND 7075-T6 CLAD STRAPS, 20% STIFFENING



(b) 2024-T3 CLAD SKINS AND 7075-T6 CLAD STRAPS, 20% STIFFENING

Figure 7. Stress Intensity vs. Fatigue Crack Length of Skin-Stiffened Panels of Various Tear Strap Widths.

The static stress intensity factor reduction for residual strength of a given panel configuration due to load transfer is determined by an effective stress concept. The remaining load on the unfailed portion of the panel is assumed to act as an effective gross area stress  $\sigma'_g$ . From the stress intensity factor solution for center-cracked panels and the plane stress critical stress intensity factor of the skin alloy, the static stress intensity factor reduction is given as:

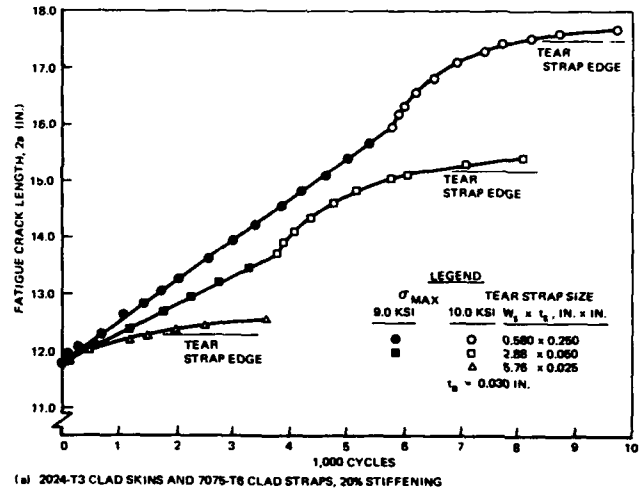
$$\Delta K_s = \sigma'_g \sqrt{\pi a} - K_c \quad (6)$$

#### IV. RESULTS AND DISCUSSION

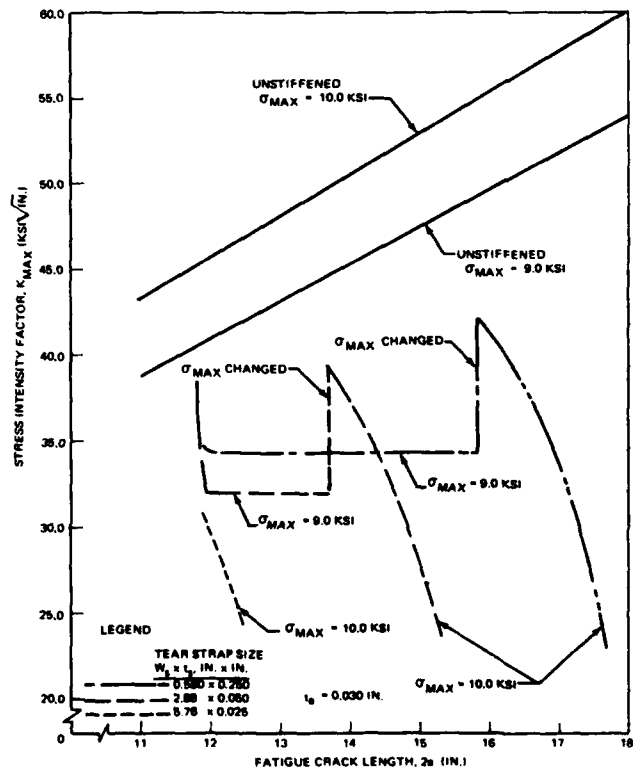
Fatigue crack propagation behavior, and cyclic stress intensity factor,  $K_{MAX}$  versus fatigue crack length curves for the simple skin-stiffened panels of various tear strap widths and designs, for a constant 20% stiffening are shown in Figs. 6 through 9. The effect of adhesive thickness,  $t_a = 0.005$  and  $0.030$  inches is also shown. The influence of variation of bonded tear strap width and thickness for a constant crack length of 12.4 in. shows a general trend of decreasing  $K_{MAX}$  values with increasing tear strap width and decreasing thickness. Laminated tear straps and the widest tear straps showed the smallest  $K_{MAX}$  values. Comparison of adhesive thickness is valid only for the adhesive thickness variation in given sets of panels (Table I) since crack length is not necessarily constant from set to set. The general trend of the comparison of adhesive thickness shows the  $K_{MAX}$  is smaller for the thinner adhesive thickness. Tear strap design comparison as shown in Fig. 9 is for 20% stiffening and  $t_a = 0.005$  in. The results show that the basic and laminated tear strap designs produce the lower  $K_{MAX}$  values than honeycomb tear straps with laminated tear straps slightly lower than basic tear straps.

The behavior of the skin stiffened panels compared in Figs. 6 through 9 is for the situation of a propagating fatigue crack located symmetrically between tear straps. Fatigue crack propagation behavior first showed a constant rate of growth and then a steadily decreasing rate of growth. This corresponds to a constant  $K_{MAX}$  and then a steadily decreasing  $K_{MAX}$  with fatigue crack length. Fig. 10 shows the results for a propagating fatigue crack located across a tear strap. These results show that the rate of fatigue crack propagation is first constant and then steadily increasing which results in a constant  $K_{MAX}$  and then a steadily increasing  $K_{MAX}$  with crack length. This contrast in growth rates for cracks between and across stiffeners is as expected.

Fatigue crack propagation behavior and cyclic stress intensity factor versus fatigue crack length curves for the two-skin stiffened honeycomb panels of various percent stiffening, honeycomb core thickness, bond void condition and applied gross-area stress levels are shown in Figs. 11 through 14. Fatigue crack propagation behavior was first measured with one skin cracked and then two skins and



(a) 2024-T3 CLAD SKINS AND 7075-T6 CLAD STRAPS, 20% STIFFENING



(b) 2024-T3 CLAD SKINS AND 7075-T6 CLAD STRAPS, 20% STIFFENING

Figure 8. Fatigue Crack Propagation Behavior and Stress Intensity vs. Fatigue Crack Length of Skin-Stiffened Panels With  $t_a = 0.030$  in.



TABLE I.  
RESIDUAL STRENGTH AND STATIC AND CYCLIC STRESS INTENSITY REDUCTION OF SKIN-STIFFENED PANELS

SKIN MATERIAL	STRAP MATERIAL	TEAR STRAP SIZE (t x w, IN.)	% STIFFENING	ADHESIVE THICK (IN.)	FATIGUE CRACK LENGTH (2a <sub>cr</sub> , IN.)	CRITICAL CRACK LENGTH (2a <sub>cr</sub> , IN.)	TEST FAILURE LOAD, KIPS	STRAP FAILURE STRESS (KSI, BASED ON ACTUAL UTS)	FAILURE NET-AREA STRESS IN SKIN AND OUTER STRAPS (KSI)	GROSS AREA FAILURE STRESS (KSI, TOTAL AREA)	NET AREA FAILURE STRESS (KSI, TOTAL NET AREA)	K <sub>c</sub> (KSI/IN.)	m <sub>s</sub> (IN. <sup>1/2</sup> )	m <sub>d</sub> (IN. <sup>1/2</sup> )
2024-T3 CLAD	7075-T3 CLAD	0.250 x 0.58	20	0.030	17.72	21.5	64.10	82.1	54.1	34.2	63.2	100.5	1.504	3.47
		0.250 x 0.58		0.005	17.70	23.2	60.23	82.1	53.8	32.1	62.9	100.5	1.169	3.78
		0.160 x 0.90		0.005	17.03	24.8	60.47	79.5	61.1	32.2	68.6	100.5	1.140	3.57
		0.072 x 2.00		0.005	16.12	19.5	61.17	77.0	43.2	32.6	55.7	100.5	1.096	3.24
		0.050 x 2.88		0.030	15.39	17.2	63.33	74.2	46.6	33.7	53.3	100.5	0.544	2.90
		0.050 x 2.88		0.005	15.31	16.0	65.92	74.2	46.8	35.1	53.3	100.5	1.440	3.30
		0.036 x 4.00		0.005	14.15	15.7	64.85	77.7	44.3	34.5	51.9	100.5	1.053	2.92
		0.025 x 5.76		0.030	12.55	14.5	57.42	77.9	34.9	30.6	44.3	100.5	0.1044	2.19
		0.025 x 5.76		0.005	12.47	13.1	62.11	77.9	37.5	33.1	45.8	100.5	0.528	2.42
2024-T3 CLAD		0.060 x 2.88		0.030	15.92	16.8	49.77	75.3	30.6	26.5	41.3	69.7	0.955	3.02
7075-T6 CLAD	7075-T6 CLAD			0.005	15.45	15.8	58.33	74.2	38.5	31.0	46.8	69.7	1.784	3.01
7075-T6 BARE	7075-T6 BARE			0.005	15.40	16.4	58.85	83.8	37.2	31.4	48.3	69.7	1.468	3.21
2024-T3 CLAD	2024-T3 CLAD			0.030	15.48	16.2	58.59	69.5	41.0	31.2	47.8	100.5	0.995	3.02
2024-T3 CLAD	2024-T3 CLAD			0.005	15.34	16.2	60.00	69.5	42.5	32.0	48.9	100.5	1.078	2.98
2024-T3 BARE	2024-T3 BARE			0.005	15.15	17.2	62.00	70.4	46.2	33.1	52.3	100.5	1.192	3.13
7079-T6 CLAD	7079-T6 CLAD			0.030	15.77	16.5	53.80	73.8	35.0	28.6	44.3	86.8	0.888	2.98
7079-T6 CLAD	7079-T6 CLAD			0.005	15.51	16.2	56.20	73.8	37.1	30.1	45.8	86.8	1.094	3.42
7079-T6 BARE	7079-T6 BARE				15.36	15.4	58.80	80.1	36.8	31.3	47.5	86.8	1.074	3.36
2024-T3 CLAD	7075-T6 CLAD	0.060 x 2.88			15.94	18.0	65.22	75.3	50.1	34.7	56.5	100.5	1.453	2.43
		LAMINATED			15.21	16.2	69.61	78.7	42.8	33.9	49.7	100.5	1.690	3.34
		0.060 x 2.88	20	0.005	17.99	28.0	44.10	74.4	71.9	23.5	58.6	100.5	0.714	3.08
		0.026 x 2.88	10	0.030	15.96	21.9	40.52	78.7	45.7	24.5	52.2	100.5	0.143	2.94
		0.025 x 2.88	10	0.005	15.45	23.4	37.86	78.7	45.9	22.8	52.7	100.5	—	2.92
		0.072 x 3.00	30	0.030	15.22	24.3	79.59	77.0	76.6	38.0	71.3	100.5	1.257	3.00
		0.072 x 3.00	30	0.005	15.10	24.2	82.92	77.0	72.0	39.6	74.0	100.5	1.446	3.28
2024-T3 CLAD					18.01	24.5	24.51	—	—	17.03	50.2	102.5	—	—
7075-T6 CLAD					18.01	23.7	19.59	—	—	13.60	39.8	81.8	—	—
2024-T3 CLAD					17.97	24.0	24.10	—	—	16.75	50.2	100.9	—	—
7075-T6 CLAD				0.005	18.12	24.0	21.12	—	—	14.63	44.1	88.3	—	—

1 0.125-IN. THICK CORE BETWEEN STRAPS 12 LB/FT<sup>3</sup>  
 2 LAMINATED STRAPS 3.00, 2.00, 0.76 x 0.025 IN.  
 3 CRACK LOCATED CENTRALLY ABOUT STRAP

PANELS 36 x 96 IN.  
 SKINS 0.040 IN. THICK  
 STRAPS ON 18-IN. CENTERS

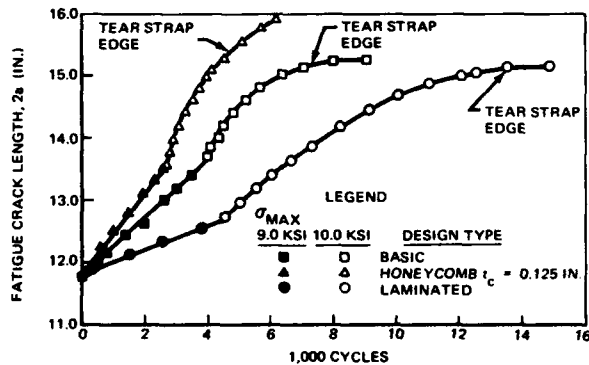
the core saw cut. Comparison of the influence of percent stiffening is supplemented by cyclic stress intensity factor reduction values shown in Table II. The results show generally that  $K_{MAX}$  is smaller for 20 percent stiffening than 10 percent stiffening. Results of 20 percent stiffened 7075-T6 clad skin and straps given in Fig. 12 show that  $K_{MAX}$  decreases with decreasing core thickness. That is, as the core thickness decreases, the load transferred into the tear straps increases.

Voids were intentionally induced in honeycomb sandwich panels in the area between skin and tear straps. These voids consisted of teflon strips 1/2 in. long and of width equal to the tear strap width. Evaluation of the influence of the voids showed that voids in four tear strap areas resulted

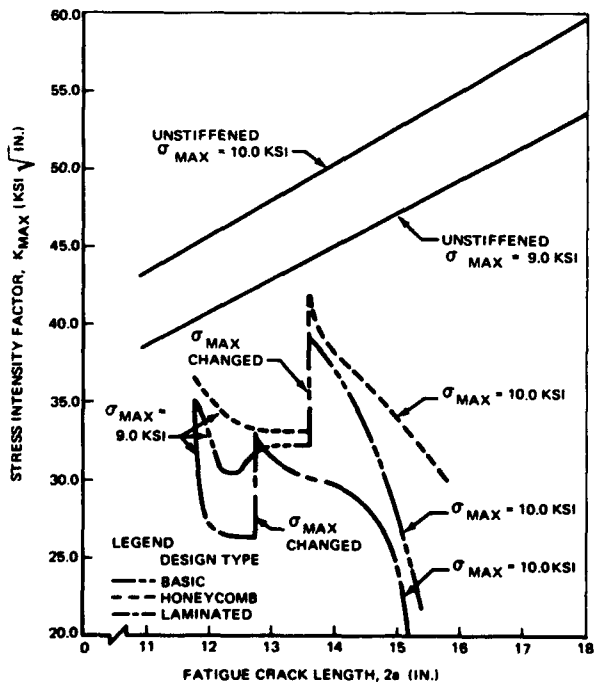
in the largest  $K_{MAX}$  value. The condition of no voids resulted in the smallest  $K_{MAX}$  value.

Fatigue crack propagation behavior and  $K_{MAX}$  versus fatigue crack length curves for skin-stiffened honeycomb sandwich panels fatigue cycled at 10.0, 18.0, 24.0 and 27.0 ksi maximum gross-area cyclic stress levels are shown in Fig. 14. The data trends of the 7075-T6 clad skins and straps for 20 percent stiffening and 0.25 in. thick 5052 core shows in general that  $K_{MAX}$  is directly proportional to  $\sigma_{MAX}$  for one skin cracked and not directly proportional to  $\sigma_{MAX}$  for two skins cracked.

Fig. 15 shows the fatigue crack propagation behavior and  $K_{MAX}$  versus fatigue crack length curves for one-skin

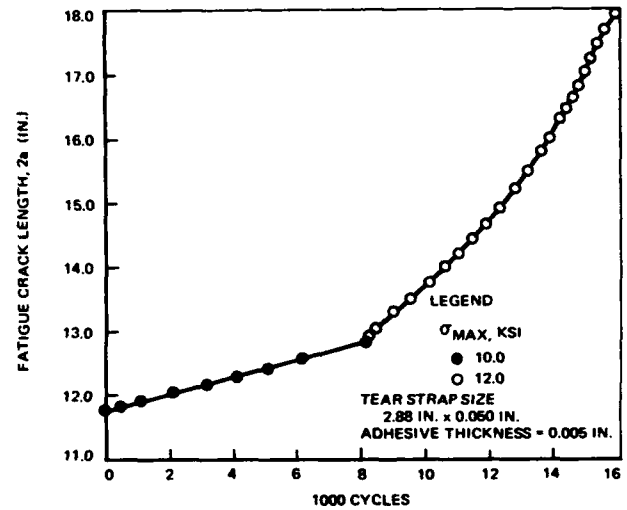


(a) FATIGUE CRACK PROPAGATION BEHAVIOR 2024-T3 CLAD SKINS AND 7075-T6 CLAD STRAPS

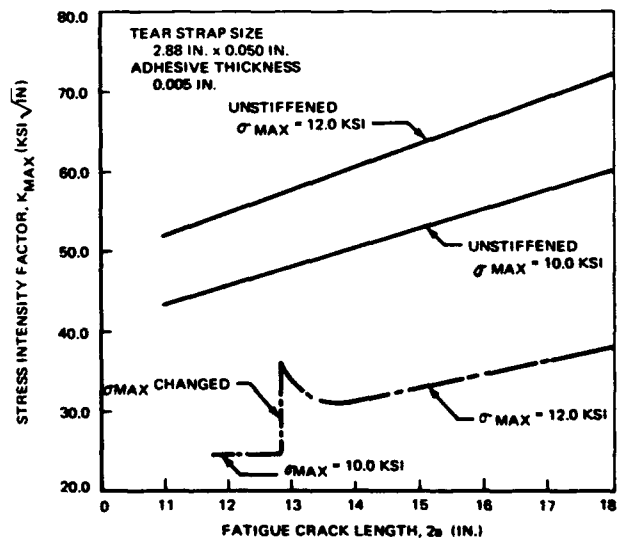


(b) STRESS INTENSITY FACTOR VERSUS FATIGUE CRACK LENGTH

Figure 9. Fatigue Crack Propagation Behavior and Stress-Intensity vs. Fatigue Crack Length of Skin-Stiffened Panels with Various Tear Strap Designs.



(a) FATIGUE CRACK PROPAGATION BEHAVIOR 2024-T3 CLAD SKIN AND 7075-T6 CLAD STRAP



(b) STRESS INTENSITY FACTOR VERSUS FATIGUE CRACK LENGTH

Figure 10. Fatigue Crack Propagation Behavior and Stress Intensity vs. Fatigue Crack Length of Skin-Stiffened Panel with Crack Located Symmetrically About A Strap.

TABLE II.  
RESIDUAL STRENGTH AND STATIC AND CYCLIC STRESS INTENSITY REDUCTION OF SKIN-STIFFENED HONEYCOMB SANDWICH PANELS

SKIN MATERIAL	PANELS 36 x 96-IN. (UNLESS NOTED) STRAPS ON 18-IN. CENTERS SKINS AND STRAPS ALL CLAD		(3.1 LB/FT <sup>3</sup> DENSITY CORE, 0.25 IN. THICK UNLESS NOTED, 1/8 IN. CELL SIZE, 5052 AL)		TEST FAILURE LOAD (KIPS)	STRAP FAILURE STRESS (KSI BASED ON ACTUAL UTS)	FAILURE NET-AREA STRESS IN SKIN & OUTER STRAPS (KSI)	GROSS-AREA FAILURE STRESS (KSI, TOTAL NET AREA)	NET-AREA FAILURE STRESS, TOTAL NET AREA	K <sub>c</sub> KSI IN.	m <sub>s</sub> (IN. <sup>1/2</sup> )	m <sub>d</sub> (IN. <sup>1/2</sup> )
	SKIN THICK (IN.)	TEAR STRAP MATERIAL	TEAR STRAP SIZE (IN. x IN.)	% STIFF								
2024-T3	0.025	7075-T6	0.025 x 1.80	10	52.13	77.9	35.8	25.1	41.8	106.5	0.279	2.36
2024-T3	—	—	0.025 x 3.60	20	68.94	76.6	32.3	29.4	42.7	106.5	0.000	2.58
7075-T6	—	—	0.025 x 1.80	10	46.90	76.5	31.3	22.70	38.3	85.3	0.541	3.53
—	0.025	—	0.025 x 3.60	20	59.52	73.8	27.6	25.45	38.4	85.3	0.0235	4-3
7075-T6	0.020	7075-T6	0.020 x 1.80	10	36.32	72.1	29.9	21.34	36.2	85.3	0.398	6-5
2024-T3	0.025	2024-T3	0.020 x 3.60	20	46.94	73.5	26.9	25.06	37.6	85.3	0.000	—
7075-T6	0.020	7075-T6	0.025 x 1.80	10	48.87	66.2	36.2	23.61	40.6	106.5	0.174	—
—	0.025	—	0.025 x 2.88	20	50.29	76.2	30.1	26.8	40.9	85.3	0.400	3.18
—	—	—	0.032 x 2.81	—	69.20	77.4	34.7	29.6	44.7	85.3	0.902	3.62
—	—	—	—	—	78.00	78.2	42.7	33.4	51.2	85.3	0.838	3.32
—	—	—	—	—	74.44	77.7	39.5	31.8	48.4	85.3	1.296	3.28
—	—	—	—	—	56.12	76.2	24.4	23.9	37.3	85.3	0.000	3.06
—	—	—	—	—	74.90	77.7	40.0	32.1	48.8	85.3	1.357	3.18
7075-T6	—	—	—	20	61.15	76.0	27.4	26.2	39.1	67.8	0.871	3.30
—	—	—	—	—	79.20	76.0	43.3	33.9	51.5	85.3	1.564	3.34
2024-T3	—	—	—	18	154.0	79.2	34.3	31.4	36.3	85.3	1.605	—
7075-T6	—	—	—	18	150.5	78.2	33.6	30.7	35.5	80.0	2.11	—
—	—	—	—	—	127.1	76.4	37.9	34.4	43.3	80.0	1.97	—
—	—	—	0.032 x 2.81	18	49.12	75.4	34.6	23.7	40.7	63.7	0.289	3.60
—	—	—	0.025 x 1.80	10	47.37	75.4	34.7	22.9	41.0	98.4	0.905	3.66
—	—	—	0.032 x 2.81	20	56.67	76.7	23.5	24.3	36.2	80.0	0.722	3.50
—	—	—	0.025 x 2.88	—	55.85	76.2	35.7	29.8	45.2	59.7	1.175	3.38
—	—	—	0.032 x 2.81	20	73.66	78.7	38.1	31.5	47.5	80.0	1.392	—
—	—	—	—	—	74.88	78.7	38.1	32.0	48.3	80.0	1.294	—
7075-T6	0.025	7075-T6	0.032 x 2.81	18	97.30	79.2	20.4	19.83	22.9	85.3	1.250	—

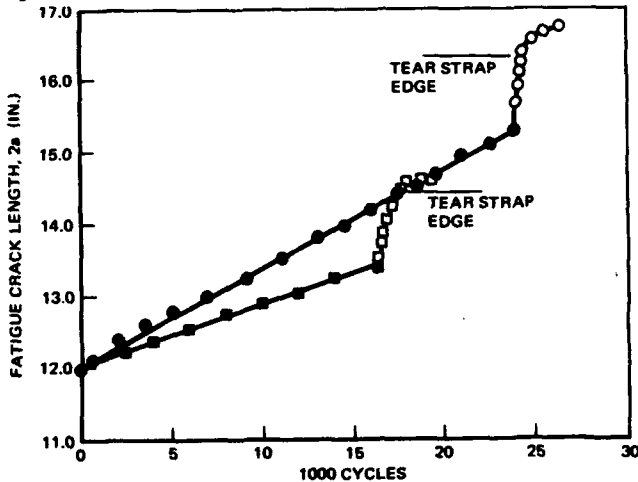
FLAG NOTES

- ① TESTED AT -66° F
- ② TESTED AT 130° F
- ③ PANEL SIZE 60 x 144-IN., TRANS. GRAIN DIRECTION, 20-IN. SPACING ON STRAPS
- ④ CRACKS LOCATED BETWEEN STRAPS
- ⑤ CRACKS LOCATED ABOUT STRAPS
- ⑥ TRANS. GRAIN DIRECTION
- ⑦ TWO SKINS

stiffened honeycomb sandwich panels for 14.8, 14.5 and 15.0% stiffening. These results show that the fatigue cracks in the unstiffened skins propagate at a steadily decreasing rate which implies that the honeycomb core transfers load.

Figure 16 shows the fatigue crack propagation results for three-ply 7178-T6 bare skins and 7075-T6 bare skins used as face skins on honeycomb core. These results are in terms of surface fatigue crack length versus cycles and shows an essentially constant rate of surface fatigue crack growth except the tail-end behavior of one face of the 7075-T6 panel. In monolithic panels (Reference 6), the observed surface fatigue crack growth behavior demonstrated a steadily increasing rate. This suggests that load is transferred from ply-to-ply as the fatigue crack propagates. In addition, this behavior demonstrates a constant  $K_{MAX}$ .

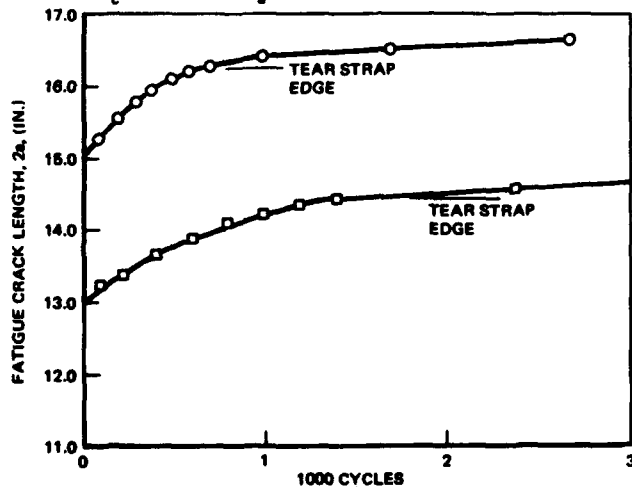
The fatigue crack propagation results are shown in Fig. 17 for 6 and 12 in. lamellated strip panels. These re-



(a) FATIGUE CRACK PROPAGATION BEHAVIOR—ONE AND TWO-SKINS CRACKED, 2024-T3 CLAD SKINS, 7075-T6 CLAD STRAPS

LEGEND			
ONE SKIN CRACKED	TWO SKINS CRACKED	PERCENT STIFFENING	TEAR STRAP SIZE, $W_s \times t_s$ , IN. x IN.
●	○	10.0	$1.80 \times 0.025$
■	□	20.0	$3.60 \times 0.025$

$t_c = 0.25$  IN.  $t_s = 0.005$  IN.

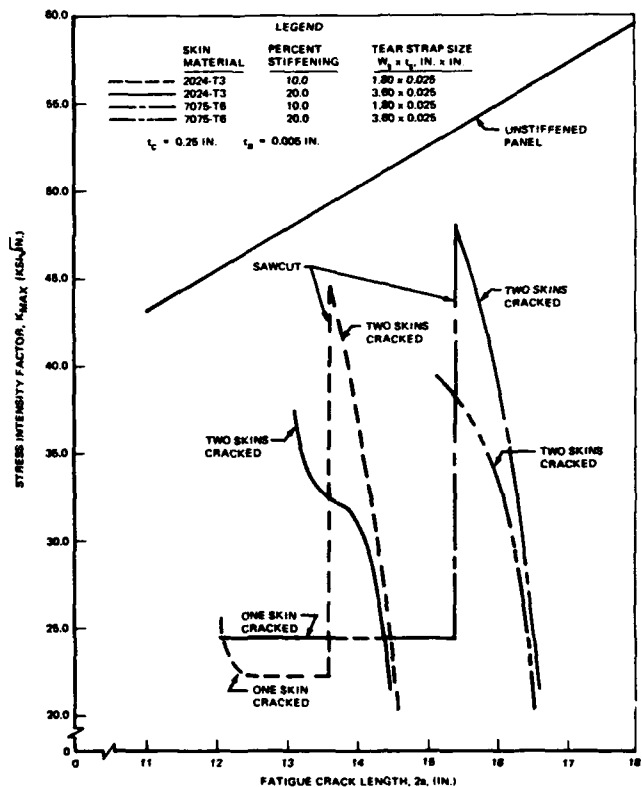


(b) FATIGUE CRACK PROPAGATION BEHAVIOR—TWO SKINS CRACKED, 7075-T6 CLAD SKINS AND STRAPS

Figure 11. Fatigue Crack Propagation Behavior and Stress Intensity vs. Fatigue Crack Length of Skin-Stiffened Honeycomb Panels with 10 and 20 Percent Stiffening.

sults show fatigue crack retardation, and that in the early cyclic period, 7075-T6 clad exhibited a slower rate of growth than 2024-T3 clad.

The static stress intensity factor reduction parameter  $m_s$  was experimentally measured on a skin-stiffened panel with  $t = 0.040$  in. and 2.88 by 0.050 in. 7075-T6 clad tear straps. Strain gage measurements were taken at fatigue crack lengths of 12.51, 13.71 and 15.48 inches at applied gross-area stress levels of 0, 3, 6, 9 and 12 ksi. Additional measurements were taken at 18 and 24 ksi for a crack length of 15.48 in. A typical example of the  $\sigma_y$  stresses from the strain gage measurements is shown in Fig. 18 for a crack length of 15.48 inches and  $\sigma_g = 12.0$  ksi. From the distribution of stresses, loads were determined at specific locations as shown in Fig. 19. The location of load transfer points utilized in  $\Delta K_s$  calculations are also shown in Fig. 19. The percent load transfer from the cracked skin into one strap versus applied gross-area stress



(c) STRESS INTENSITY FACTOR VS FATIGUE CRACK LENGTH

for the three different fatigue crack lengths is shown in Fig. 20. At the 15.48 in. crack length, the percent load transfer appears to be increasing with applied gross-area stress. The effect could be attributed to the peeling of the adhesive associated with the plastic deformation at the crack tip. Fig. 21 shows the  $\Delta K_S$  versus applied gross area stress as calculated by Eq's, (2) through (5).

Fig. 22 is a plot of the static stress intensity parameter,  $m_s$  versus final skin fatigue crack length for all of the skin stiffened panels with the same size tear strap and percent

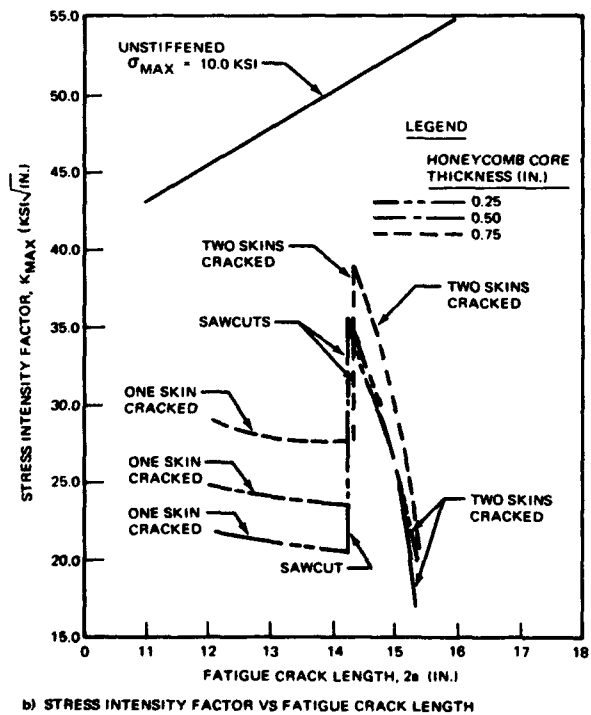
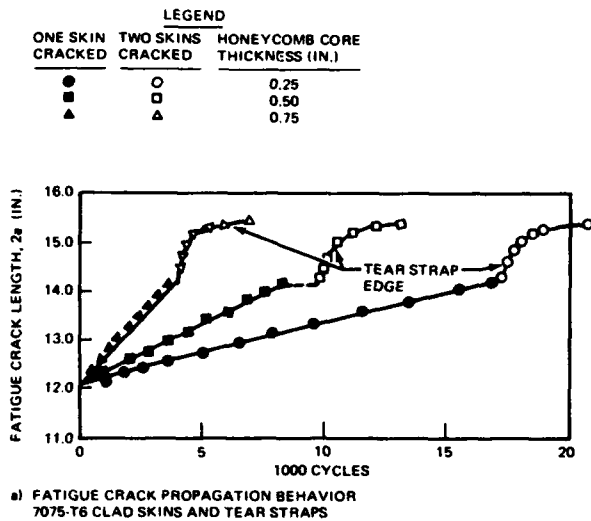


Figure 12. Fatigue Crack Propagation Behavior and Stress Intensity vs. Fatigue Crack Length of Skin-Stiffened Honeycomb Panels with Various Core Thickness.

stiffening. These data points include the strain gage measurements and  $m_s$  values for the residual strength tests as developed according to the failure criteria described previously. Fig. 23 shows the curve for 2.88 in. wide tear straps and data points for tear straps of other widths and thicknesses for a constant percent stiffening. The dashed curves are fitted through the data points and have a characteristic shape similar to the 2.88 in. wide tear strap curve.

There appears to be a failure envelope described by the data points. These results show that the 2.88 in. wide tear strap exhibited the highest residual strength. The three data points to the right for the narrow and thick tear straps resulted in unbonding failure of the straps the entire length of the panel. The data points for 2.88 in. wide tear straps

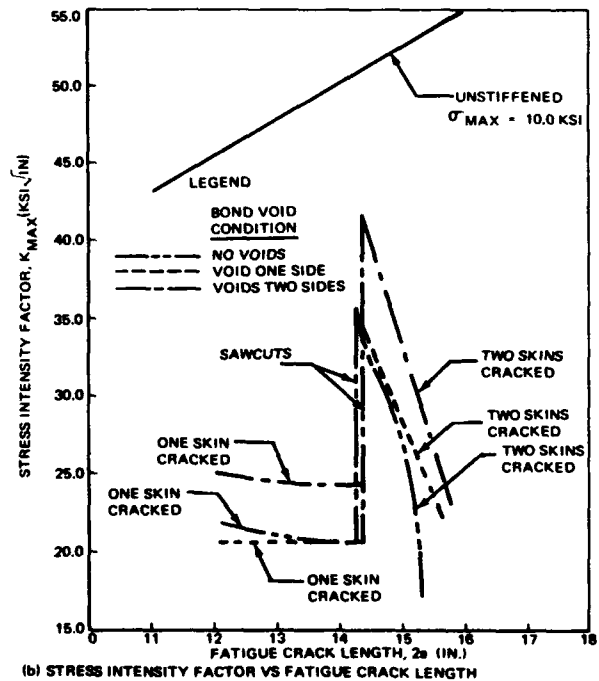
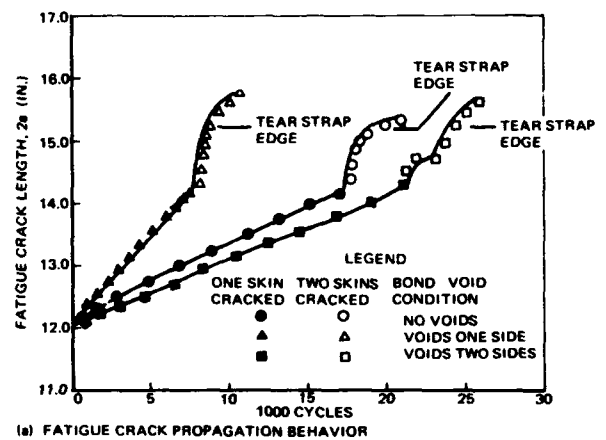


Figure 13. Fatigue Crack Propagation Behavior and Stress Intensity Factor vs. Fatigue Crack Length of Skin-Stiffened Honeycomb Panels with Voids.

**TABLE III.**  
**RESIDUAL STRENGTH OF ONE-SKIN-STIFFENED HONEYCOMB SANDWICH PANELS.**

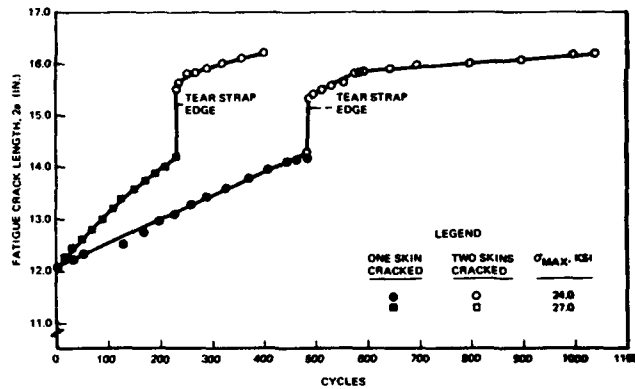
7075-T6 CLAD SKIN  
AND STRAPS

t (IN.) STIFFENED	t (IN.) UNSTIFFENED	TEAR STRAP SIZE (IN. x IN.)	% STIFF	FATIGUE CRACK LENGTH	CRITICAL CRACK LENGTH (IN.)	$\sigma_b$ KSI
0.032	0.032	2.16 x 0.077	14.5	15.80 (18.20)		26.7
0.020	0.040	2.02 x 0.080	15.0	15.96 (18.07)		22.7
0.040	0.020	2.03 x 0.079	14.8	15.96 (18.03)		28.4

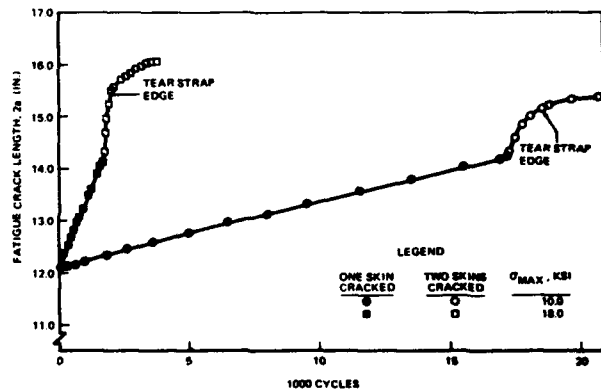
CRITICAL CRACK LENGTH NOT AVAILABLE

ON SKIN SIDE, CRACK GREW SLOWLY ACROSS ENTIRE PANEL WIDTH; ON STRAP SIDE, CRACK TIP WAS UNDER STRAPS

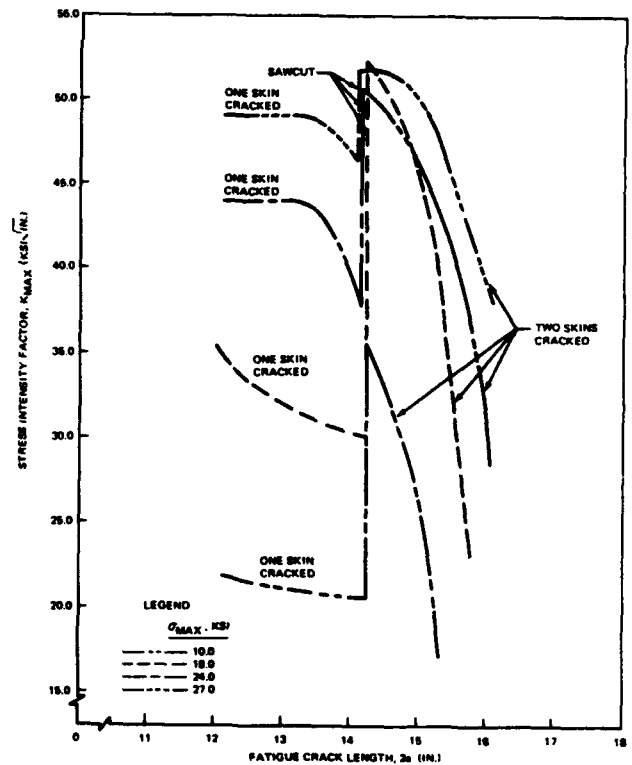
ON SKIN SIDE, CRITICAL CRACK LENGTH = 32.0 IN.; ON STRAP SIDE, CRACK TIP WAS UNDER STRAPS



(b) FATIGUE CRACK PROPAGATION BEHAVIOR AT  $\sigma_{MAX} = 10.0$  AND  $18.0$  KSI



(b) FATIGUE CRACK PROPAGATION BEHAVIOR AT  $\sigma_{MAX} = 24.0$  AND  $27.0$  KSI



(c) STRESS INTENSITY FACTOR VS FATIGUE CRACK LENGTH

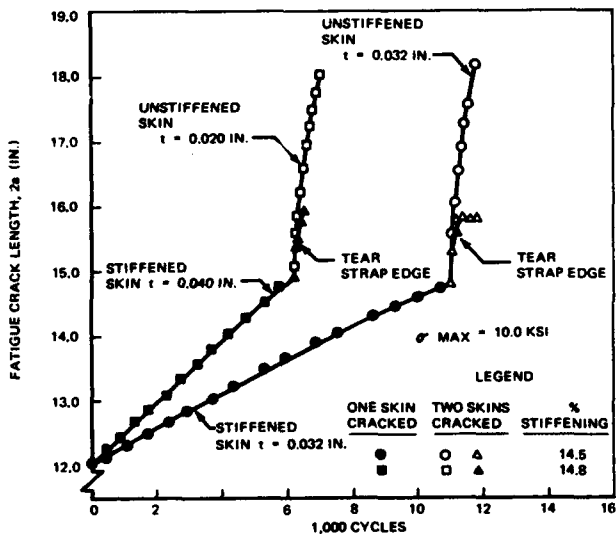
**Figure 14. Fatigue Crack Propagation Behavior and Stress Intensity vs. Fatigue Crack Length of Skin-Stiffened Honeycomb Sandwich Panels at Various  $\sigma_{MAX}$  Levels.**

and wider represent failure of the panels perpendicular to the applied load direction.

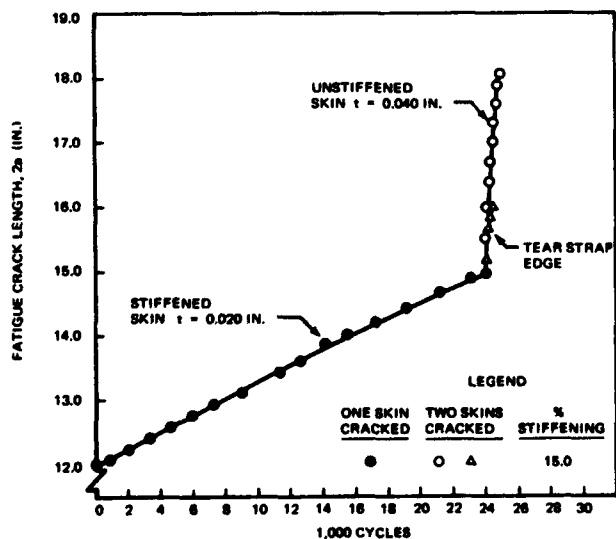
The magnitudes of  $m_s$  as determined from strain gages and  $m_d$  for a skin stiffened panel are compared. At crack lengths of 12.51, 13.71, and 15.48 in. the average  $m_s$  is 0.30, 0.42, and 1.52  $\text{in}^{1/2}$  and  $m_d$  is 1.29, 1.08, and 3.30  $\text{in}^{1/2}$ . These  $m_s$  values were determined using Eq's. (2) through (5). Residual-strength test of a duplicate panel at a fatigue crack length of 15.48 in. and application of Eq. (6) resulted in an  $m_s$  value of 1.44  $\text{in}^{1/2}$ . This shows a correlation of the  $m_s$  values.

Table III shows the residual strength results of one-skin stiffened honeycomb sandwich panels. The highest residual strength was obtained for 0.040 in. stiffened skin and 0.020 in. unstiffened skin.

Comparison of the static and cyclic stress intensity



(a) FATIGUE CRACK PROPAGATION BEHAVIOR



(b) FATIGUE CRACK PROPAGATION BEHAVIOR

Figure 15. Fatigue Crack Propagation Behavior and Stress Intensity vs. Fatigue Crack Length of One-Skin-Stiffened Honeycomb Sandwich Panels.

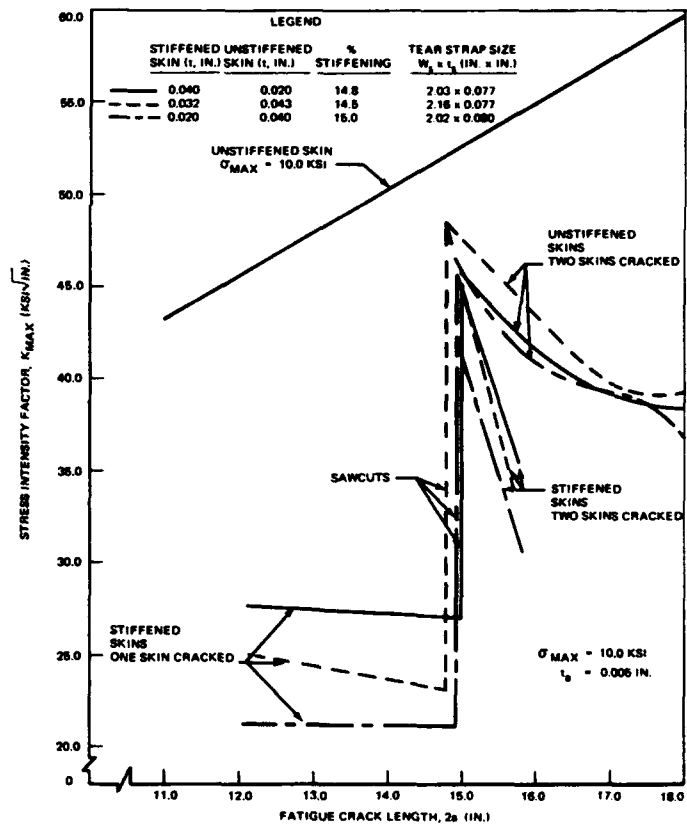
factor reduction parameter values in Table I and Table II are at the terminal fatigue crack and shows that the  $m_s$  values are much less than the  $m_d$  values for both the skin-stiffened and skin-stiffened honeycomb sandwich panels. The  $m_s$  values for the 60 by 144 in. skin-stiffened honeycomb sandwich panels were higher than the 36 by 96 in. skin-stiffened honeycomb panels.

The effect of test temperature showed an increase in  $m_s$  for increasing test temperature from  $-65^\circ\text{F}$  to room temperature and  $+130^\circ\text{F}$ . Comparison of grain direction showed higher  $m_d$  for transverse grain direction than for longitudinal grain direction as shown in Table II.

## V. CONCLUSIONS

Based on the analysis and results of this investigation, the following conclusions are reached:

Text continued following Figure 23.



(c) STRESS INTENSITY FACTOR VS FATIGUE CRACK LENGTH

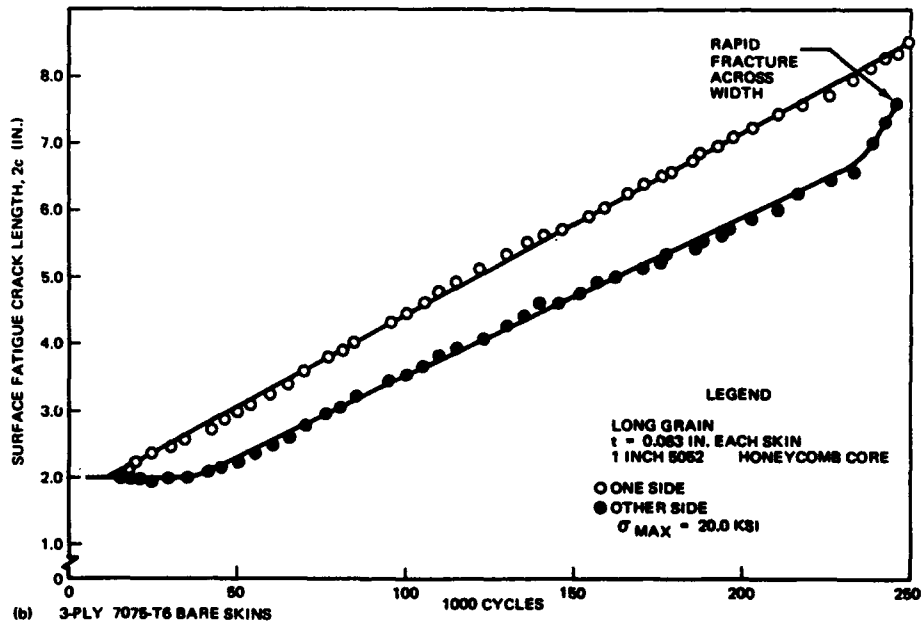
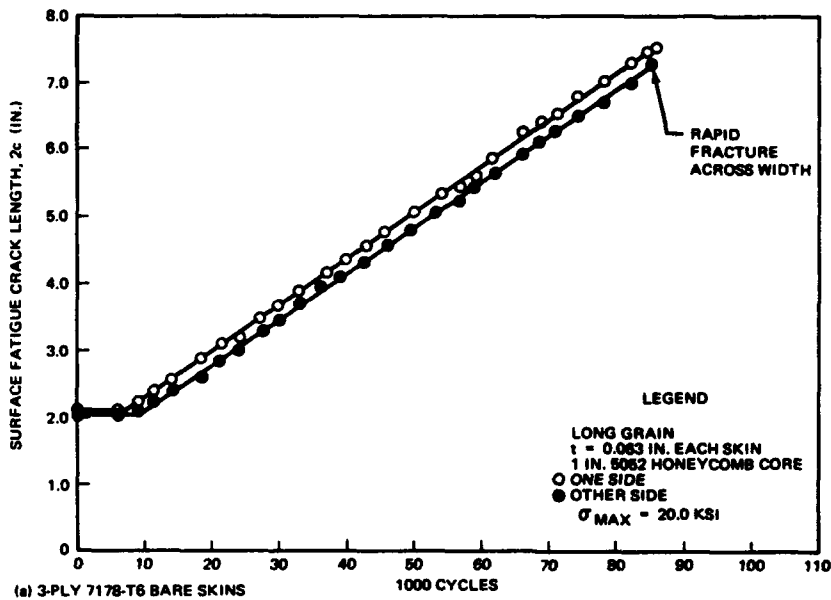


Figure 16. Fatigue Crack Propagation Behavior of Laminated Skins on Honeycomb Core.



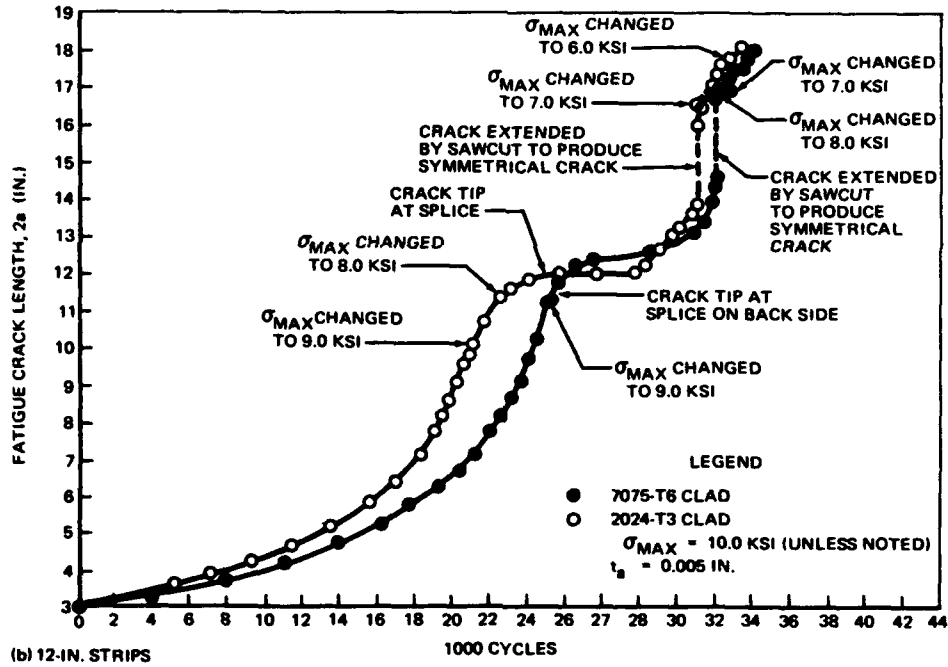
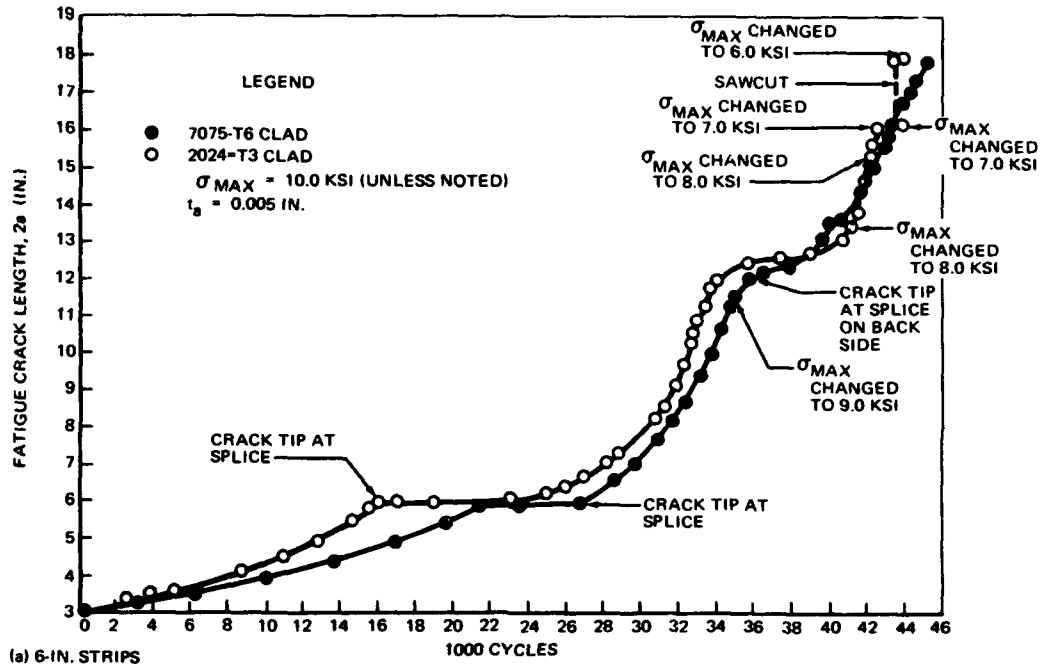


Figure 17. Fatigue Crack Propagation Behavior of Lamellated Panels.

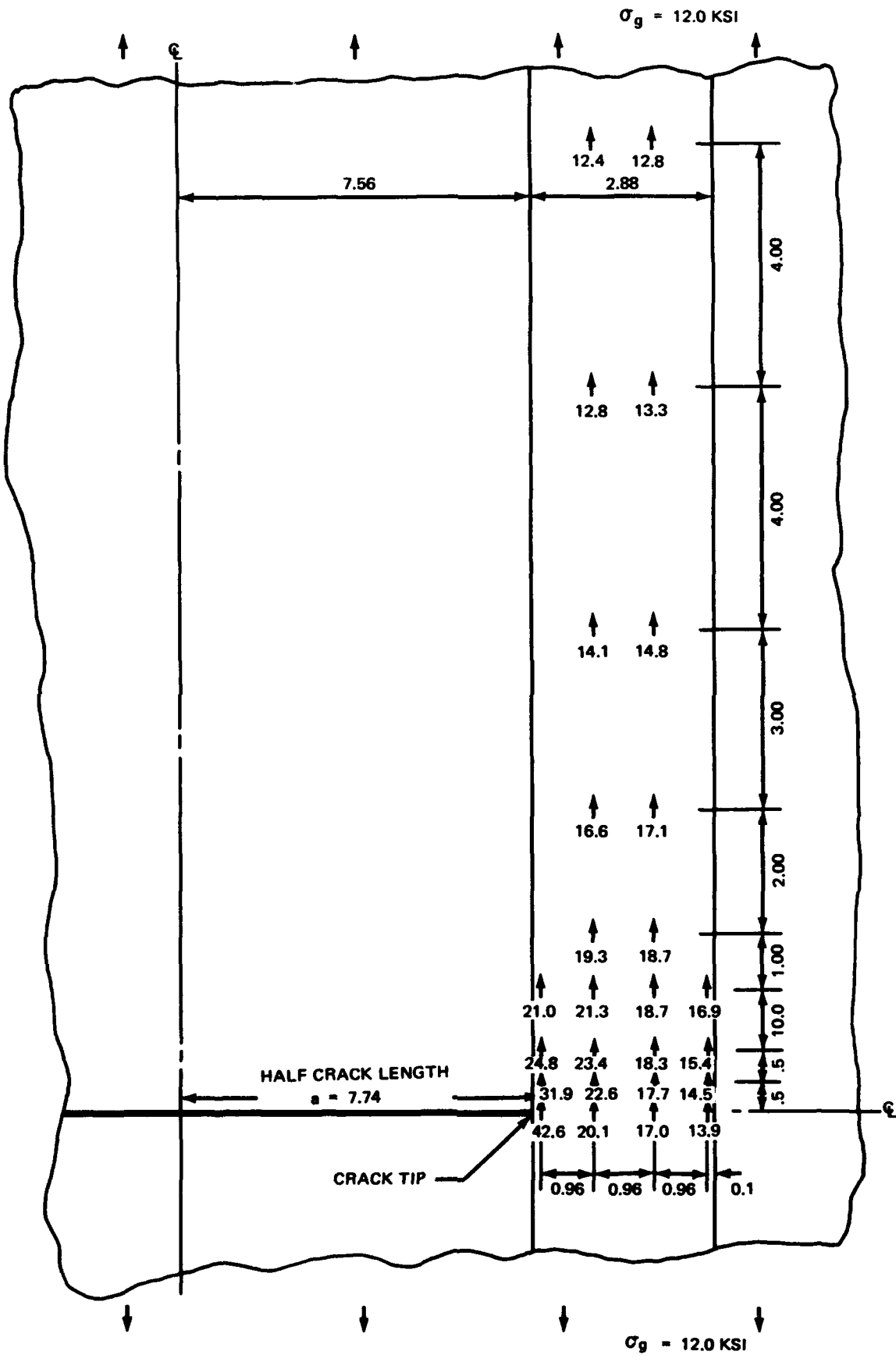


Figure 18.  $\sigma_y$  Stresses from Strain Gage Measurements.

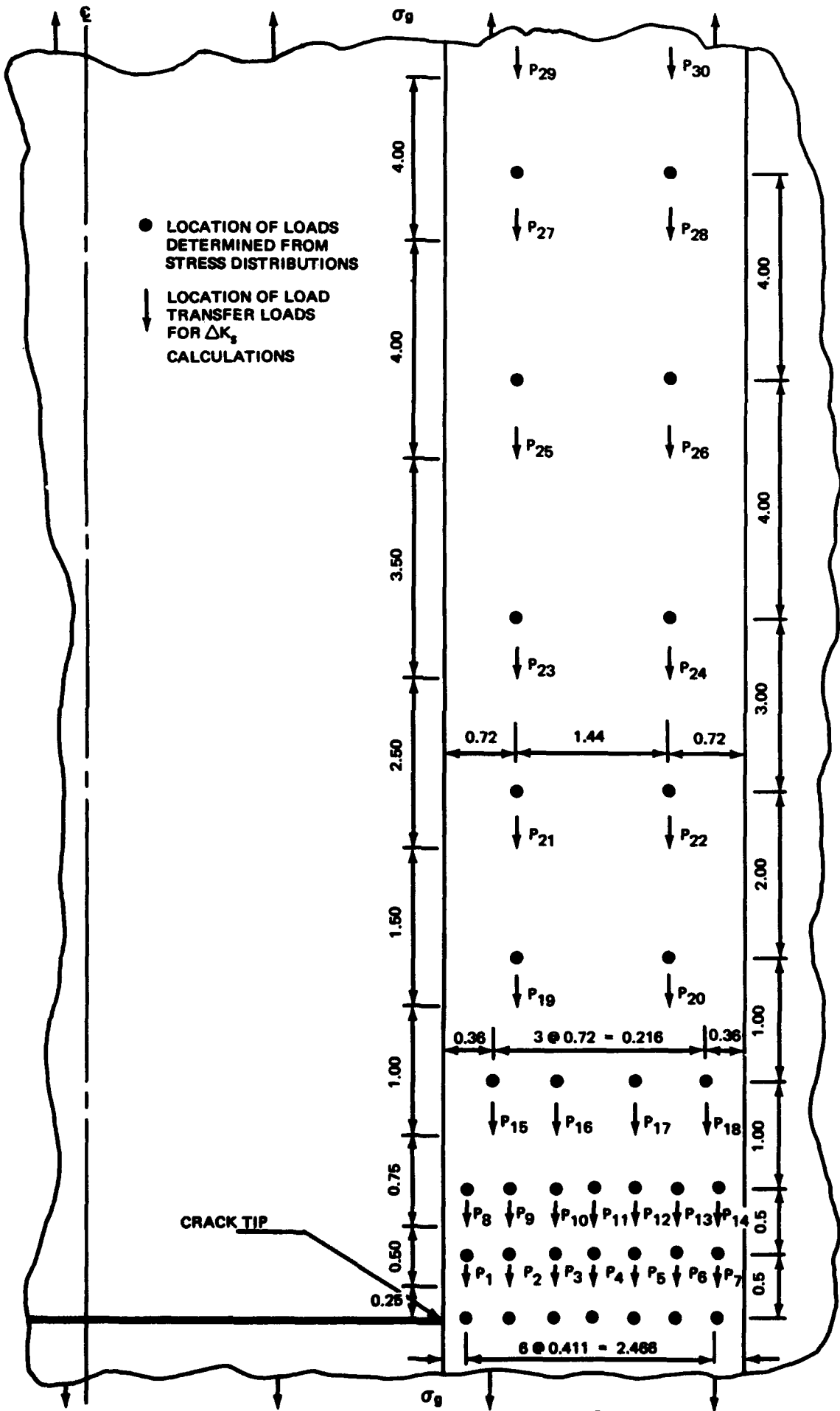


Figure 19. Location of Loads in  $\Delta K_s$  Calculations.

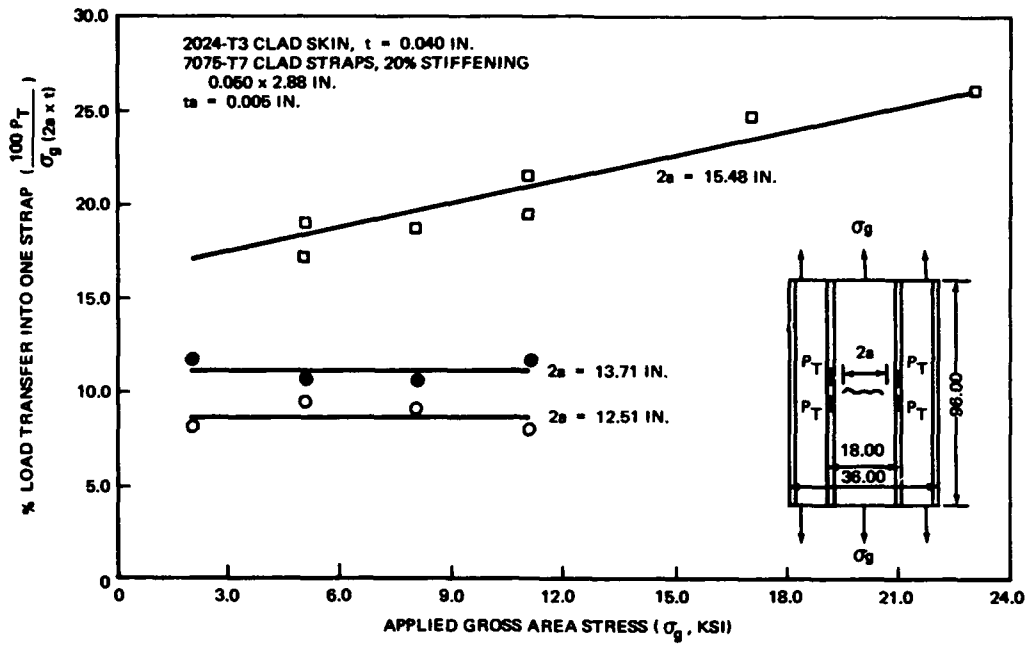


Figure 20. Percent Load Transfer from Cracked Skins into Tear Straps.

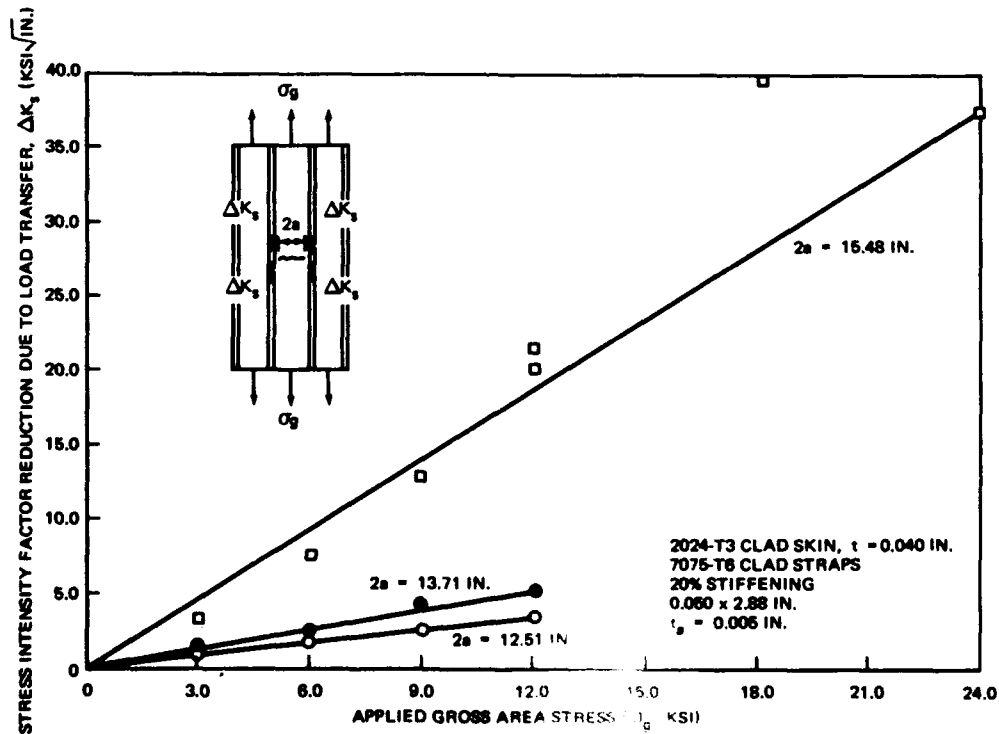


Figure 21. Stress Intensity Factor Reduction,  $\Delta K_s$ , Based on Load Transfer.

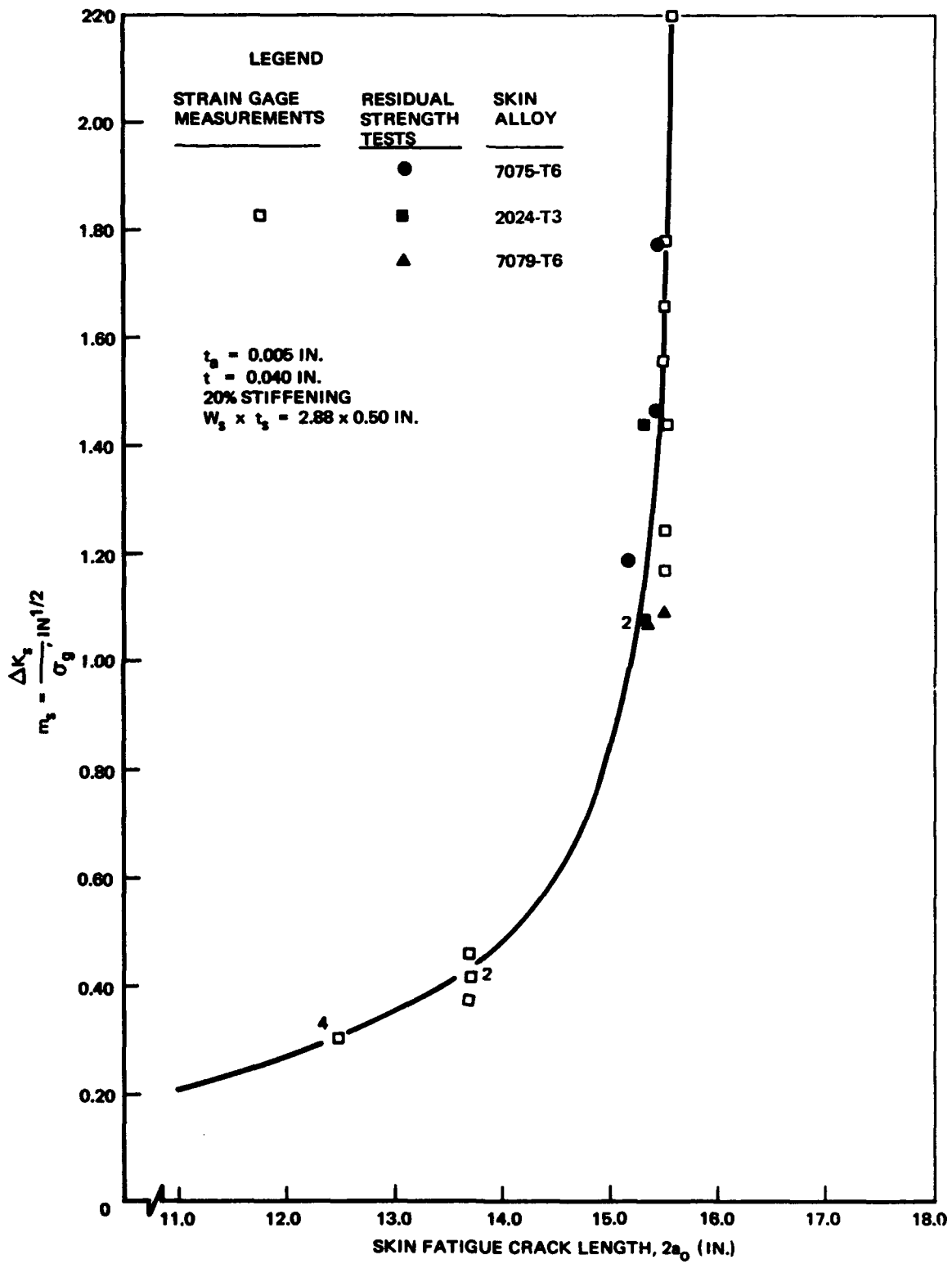


Figure 22.  $M_s$  vs. Crack Length Based on Strain Gage and Residual Strength Results.

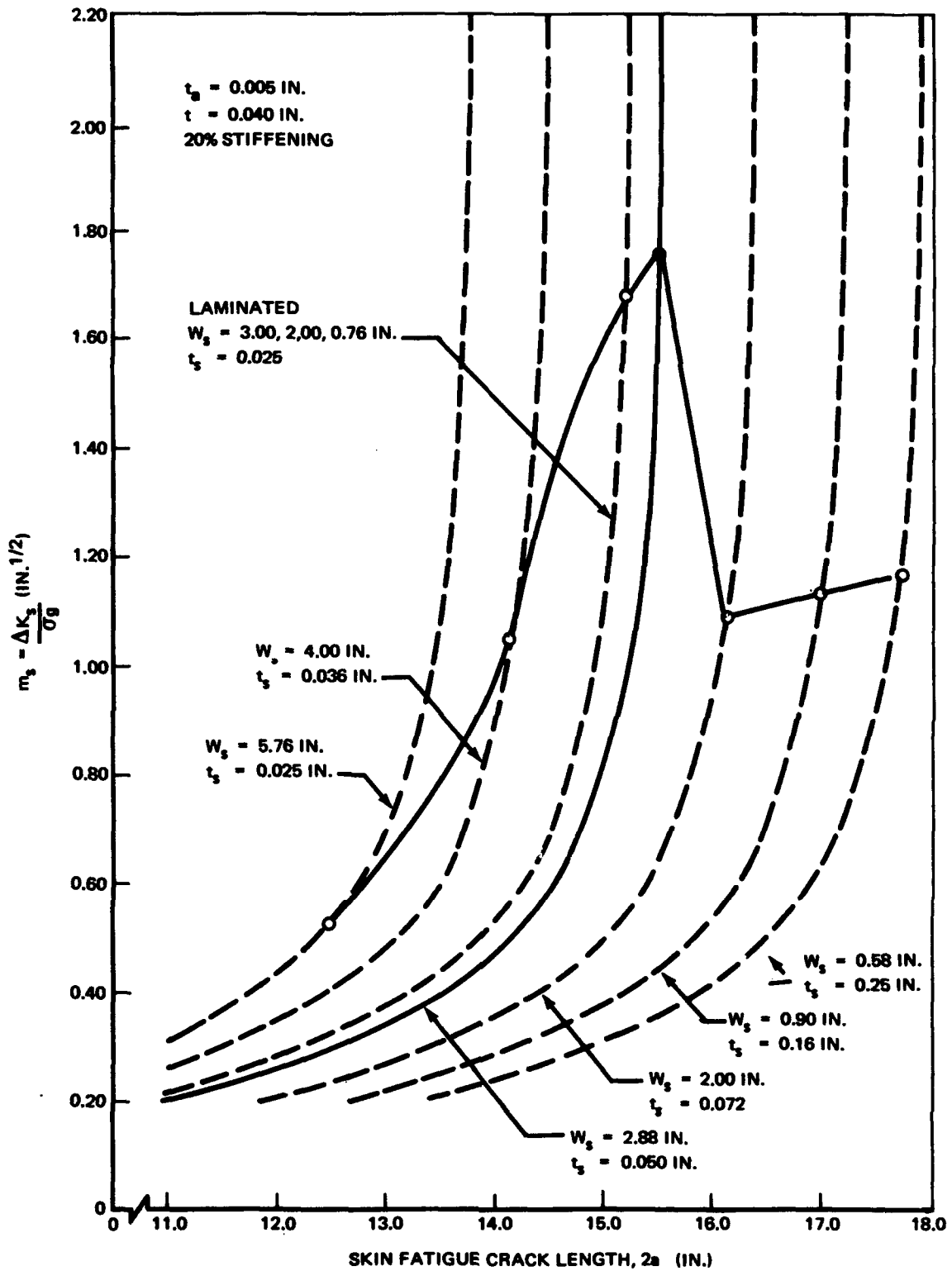


Figure 23.  $M_s$  vs. Crack Length for Various Tear Strap Widths and Thicknesses.

1. The static and cyclic stress intensity factor reduction can be used to quantitatively measure the fatigue crack growth containment and residual strength capability of adhesive bonded structure.

2. Comparison of the two adhesive thicknesses, 0.005 and 0.030 in. showed a generally lower  $K_{MAX}$  for the 0.005 in. thick adhesive than for 0.030 in. thick adhesive.

3. Tear strap evaluations showed that laminated tear straps and very wide tear straps produced the lowest  $K_{MAX}$  values.

4. The lowest  $K_{MAX}$  values did not vary appreciably for the thick adhesive for various percent stiffening. However, the  $K_{MAX}$  values decreased for the thin adhesive when the percent stiffening was increased from 10 to 20 and 30 percent.

5. Varying the honeycomb core thickness showed that  $K_{MAX}$  decreased as core thickness decreased.

6. The effect of test temperature showed that  $K_{MAX}$  decreased when the temperature was increased from  $-65^{\circ}\text{F}$  to room temperature and  $+130^{\circ}\text{F}$ .

7. When voids were intentionally induced between tear straps and skin in skin-stiffened honeycomb sandwich panels, the smallest  $K_{MAX}$  was found in the case of no voids in the bond line; the largest  $K_{MAX}$  resulted in the case of voids on two sides.

8. In varying the tear strap widths of skin-stiffened panels, the width of 2.88 in. showed the highest residual strength.

9. In comparing the  $K_{MAX}$  versus fatigue crack length behavior of a fatigue crack located symmetrically between tear straps and located symmetrically across a tear strap, the latter case resulted in a higher  $K_{MAX}$ .

10. Comparison of the static and cyclic stress intensity factor reduction parameters  $m_s$  and  $m_d$  showed that  $m_s$  values were lower than  $m_d$  values.

#### ACKNOWLEDGEMENT

The authors appreciate the assistance of Messrs. D.J. Hoffman, W.N. Westre, and J.M. Kelly of the Boeing Structures Staff Adhesive Bonding Development Group and Mr. S.C. Strehle of the Structures Laboratory.

#### REFERENCES

1. D.R. Donaldson and W.E. Anderson, "Crack Propagation Behavior of Some Airframe Materials," pp. 375-441, *Proc. Crack Propagation Symp.*, Vol. II, College of Aeronautics, Cranfield, England (1961).
2. P.C. Paris, M.P. Gomez, and W.E. Anderson, "A Rational Analytic Theory of Fatigue," *Univ. Washington Trends Eng.*, 13/1 (1961).
3. W.E. Anderson and L.A. James, *Estimating Structural Cracking Behavior from Substitute Tests*, BNWL-SA-2291, Battelle - Northwest Laboratories, Richland, Washington. Presented at the ASM-ASTME Western Metal and Tool Conference, Los Angeles, March 1969.
4. G.R. Irwin, "Analysis of Stresses and Strains Near the End of a Crack Transversing a Plate," *J. Appl. Mech.*, 24:361-364 (1957).
5. P.C. Paris, "A Handbook of Crack Tip Stress Intensity Factors," in *Fracture Mechanics Research at Lehigh University, 1960-1961*, D6-7960, Boeing Company, Seattle, Washington.
6. S.H. Smith, T.R. Porter, and W.D. Sump, *Fatigue Crack Propagation and Fracture Toughness Characteristics of 7079 Aluminum Alloy Sheets and Plates in Three Aged Conditions*, NASA-CR-996, National Aeronautics and Space Administration, Washington, D.C. (1968).

# VULNERABILITY CONSIDERATIONS IN THE DESIGN OF ROTARY WING AIRCRAFT STRUCTURES

by

M.J. Rich

Sikorsky Aircraft  
Division of United Aircraft Corporation  
Stratford, Connecticut

## LIST OF SYMBOLS

$a$ ,	= half crack length, inches	$R_s$ ,	= residual strength of damaged plate, fraction of ultimate strength
$C_L$	= lift coefficient	$S_{ult}$ ,	= ultimate strength of plate without damage, psi
$\frac{d(2a)}{dN}$	= crack propagation rate, inches/cycles	$S_{ys}$ ,	= yield stress, psi
$\frac{d(2a)^*}{dN}$	= crack propagation rate at intersect of two range approximation	$\Delta S$ ,	= stress range, $S_{max} - S_{min}$
$K$ ,	= stress intensity factor, $\text{psi}\sqrt{\text{in}}$	$V_d$ ,	= limit dive speed, kts
$\Delta K$ ,	= stress intensity range, $K_{max} - K_{min}$	$V_{max}$ ,	= maximum level flight speed, kts
$\Delta K^*$	= stress intensity at intersect of two range approximation	$W$ ,	= plate width, inches
$\bar{K}$ ,	= mean stress intensity	$X$ ,	= damage, fraction of plate width
$K_{Ic}, K_{Ic}$ ,	= plane strain and plane stress fracture toughness constants	$X_n$ ,	= crack size fraction at any subsequent time, $(2a)_n/W$
$n_1, n_2$	= slope of two range linear semi-log crack propagation	$X_o$ ,	= initial crack size fraction $(2a)_o/W$
$N$ ,	= cycles of loading	$\gamma$	= ratio of mean to range of stress intensity, $\bar{K} / \Delta K$
		$\rho$	= material density, $\text{Lb}/\text{In}^3$

## INTRODUCTION

The extensive use of rotary wing aircraft in a hostile combat environment adds an urgent need for new requirements in the structural design for such vehicles. The present experience of these vehicles in combat environment shows that the consideration of designing structures for survival of damage due to small arms

fire is of prime importance to further increase their combat efficiency. While present structural requirements and design practice result in a high degree of operational safety for noncombat utilization, it is becoming increasingly more questionable whether these past practices are sufficient to provide the desired combat capability. At the present time the rotary wing aircraft combat effectiveness with regard to structural design is only a by-product of the normal requirements.



In the present design of rotary wing structures, full consideration is given to the design operating requirements. Using the present military structural requirements,<sup>1</sup> the basic flight and ground loading conditions are satisfied. The mission and flight profiles are established from the detail specification of the specific helicopter. The result is that the full load spectra, both static and dynamic, can be established for structural design. Combining the structural configuration with the design loading spectra, materials are then chosen for an end product of an optimized minimum weight structure. However, there are no specific requirements that differentiate between combat and noncombat usage. In fact, the only difference between a commercial and military design is in the severity of loading spectra. Then the question arises as to what, if any, are additional requirements that should be included in the structural design for the military vehicle.

In addition to meeting the operating load levels, the rotary wing structures are designed to a considerable extent by fail-safe considerations.<sup>2</sup> The fail-safe design philosophy for rotary wing aircraft dynamic components, although similar, differs to an important degree from fixed-wing practice. The rotary wing aircraft airframe, being a multiredundant structure, is designed for loss of elements wherein the remaining structure is still capable of withstanding peak flight load maneuvers. Rotary wing dynamic components, however, are generally not redundant, and the fail-safe concept is really a safe residual life for the damaged structure. The types of damage considered are premature fatigue cracking, corrosion, or the incipient damage that may be caused in normal operation. Therefore, while the present structural requirements may not explicitly require consideration of combat damage, many components of a rotary wing aircraft have an appreciable built-in damage tolerance capability. The result of the fail-safe considerations provide considerable capability for survival from small arms fire.

The ability to stress-analyze and design rotary wing aircraft structures has been developed to a high level of confidence. The conventional airframe design is now considered to be in such a state of art that in many cases the usual static test substantiation has been bypassed. In general, the dynamic component structures subjected to a wide spectra of vibratory loading are considered to be the more important area of concentration. Even in these dynamic structures the level of confidence is extremely high. Verification testing is used more for establishing more accurate replacement times than for large redesigns. Thus, while there are still many questionable areas in design of fatigue-loaded structures, the current design and analysis can be considered to be an established procedure for present materials and configurations.

In essence, the capability to stress-analyze and design rotary wing aircraft structures is a well-developed procedure but is used mainly for normal design and material conditions. Some extensions have been made of

cracked and incipient damage conditions for the fail-safe considerations. The next logical step is to formulate the scope of structural combat damage to flight critical components and to include such effects in the structural design procedure. If such can be done, then a higher degree of combat damage tolerance can be built into the vehicle in its initial design stage. This requirement can be accomplished for a minimum weight increment over that for existing requirements.

The purpose of this paper is to examine the aspects of vulnerability in the structural design of rotary wing aircraft. The first step is to evaluate the requirements and to present, at least on a tentative basis, a rational conservative vulnerability design criterion. The aspects of such a vulnerability criterion must encompass both static and dynamically-loaded structure. Essentially, the requirement is a criterion for the residual strength and life for combat-damaged flight critical structures that affect the survivability of the vehicle. The next step is to review the means available to assess the effects of combat damage, particularly in regard to the use of fracture mechanics methods for assessing the residual static strength and the rate of damage growth in determining residual life. In reviewing the available data and methods, the information is to be catalogued in a usable manner with the viewpoint of applying such existing information.

Having established a design criterion and the methods of damage analysis, the next step to take is to analyze a typical rotary wing aircraft design and to assess vulnerability. On this basis, the critical design areas and material usage can point out the possible areas of improvement. The final consideration is to examine what, if any, are the questionable areas and to assure a procedure for vulnerability design and analysis.

## VULNERABILITY CRITERIA

Ideally, a vulnerability criteria should encompass the residual strength and life remaining after combat-induced damage as related to the mission usage of the rotary wing vehicle. The criteria in this respect would be similar to those requirements for fail-safe design such as proposed in References 2, 3, and 4.

The residual strength remaining after combat damage should be sufficient so that the significantly high peak loadings from combat maneuvers do not result in an unstable crack growth. Recognizing that significant combat damage should be readily inspectable, the tolerable damage criteria can be considered to be within a typical mission flight. In addition, the criteria should include consideration that the damaged strength requires a minimum of in-flight assessment. Furthermore, such damage should not impair the combat capability for the duration of the flight mission. There are various fail-safe criteria being used such as the tolerable damage be within the 80 percent of limit design load capability (FAA) or 50 percent of ultimate

load, which is 75 percent of limit load as specified in paragraph 3.1.14 of Reference 5 for fixed wing aircraft structures.

The question then arises as to the consideration of a spectra of flight loads or simply the use of one peak maneuver condition to represent a design criterion. In addition, there are considerations of the slow stable crack growth or the boundary of unstable crack propagation as being the limit on residual strength.

**Residual Strength:** It is proposed tentatively that a simple residual strength criteria for combat damage include the following features.

- a. Tolerable damage be limited to no unstable crack growth.
- b. The critical loading for combat damage include the peak maneuver for limit design conditions.

While this criteria is admittedly conservative, it simplifies the design problem to a single choice with a minimum of calculation.

Generally, there are margins of safety for the ultimate design load. For rotary wing aircraft dynamic components, these margins may be considerable since the specific component may be sized more by fatigue than by static considerations. Thus, the limit strength, with zero margin of safety, may permit considerably greater damage than would be predicted from the limit design load. The tolerable damage should be within the critical damage size as shown in Figure 1.

**Residual Life:** Rotary wing dynamic components are generally designed by fatigue considerations. As such,

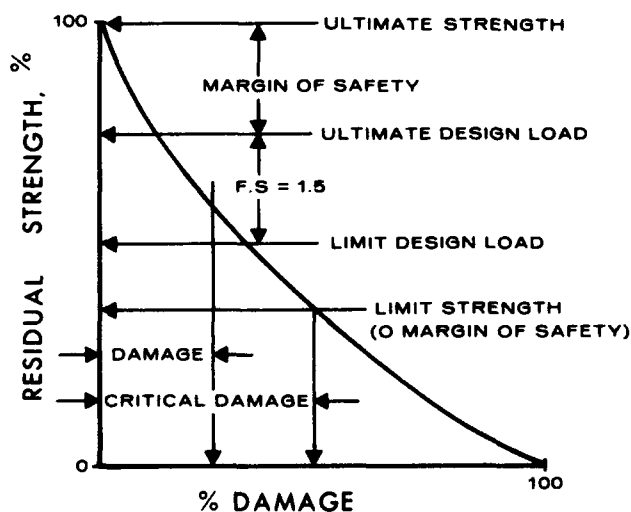


Figure 1. Residual Strength Criteria.

design requirements usually consider both the crack initiation and crack propagation in the selection of alloys. The crack propagation is usually considered to initiate from fatigue cracking and/or possible origins of corrosion. For battle damage from small arms fire, the initial damage would be more extensive, and the rate of crack propagation could be considerably higher than for small fatigue cracks. In any case, the size of the initial flaw or damage size has a considerable effect on the extent of the damage growth for the repeated loads.

For an initial damage size, the crack will grow at some rate depending upon the spectrum of vibratory loading imposed on the structure. In Figure 2, a residual life of the structure is shown for the load spectra imposed. The crack propagation of the battle-damaged structure will increase with time. The dynamic loadings are much lower than the peak static load, and the time to fatigue loading fracture does not represent the total picture of the problem. The limit on the fatigue crack growth is the critical size that causes an unstable condition at the limit design strength. Thus, as is illustrated in Figure 2, the time to fracture is limited by reducing the static residual strength required to that required for peak maneuvers.

As shown in Figure 2, the combat mission time should be less than the failure time as specified by both static and dynamic loadings. While the criteria may be conservative in that the probability of reaching limit loading is remote, the criteria does provide a consistent approach for combat requirements without requiring any precautionary action by the operating crew. Should the type of combat damage provide warning to the pilot, the criteria could then be modified by reducing effects of limit strength or by permitting slower crack growth time by reducing the flight load spectrum. It is also possible that in-flight monitoring of critical structures may permit greater survivability by warning the pilot to reduce his operating

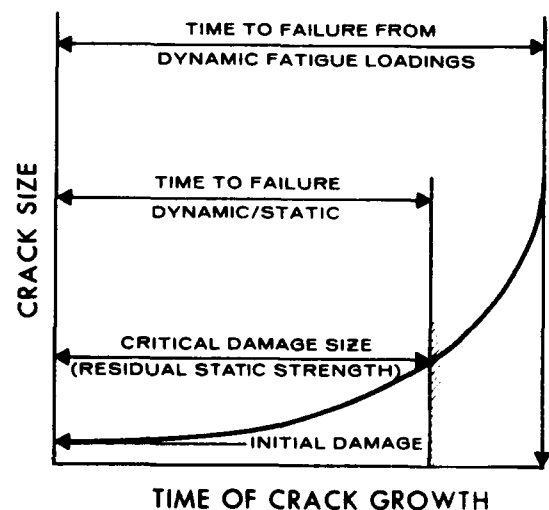


Figure 2. Residual Life Criteria.

loads. A study on the increase of survivability has been made and shows a considerable improvement for reduced operating levels for most flight critical components.<sup>6</sup>

### FRACTURE MECHANICS

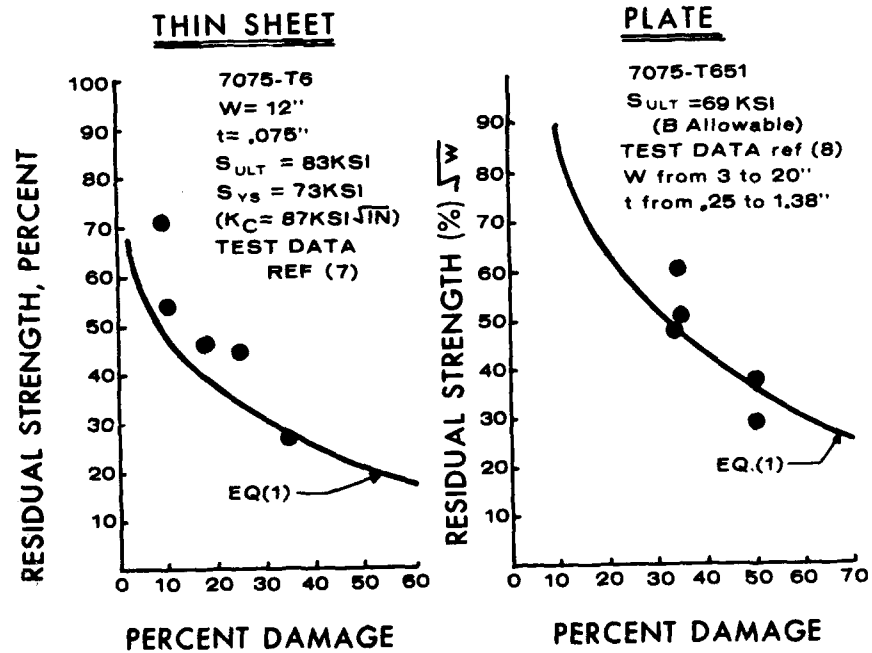
Having set forth the residual strength and life criteria, the means of damage assessment should be established. Fracture mechanics has developed to the stage that reasonable engineering assessments of effect of damage can be accomplished by the designer. Various methods are presently being used and will be reviewed for application.

**Residual Strength.** Using the fracture mechanics method wherein the stress intensity factor is related to the gross stress, the crack damage, the width of the plate, and is corrected for the plastic zone at the crack, a simple residual strength relationship can be formulated.

$$R_s = \frac{K_{Ic} \text{ (or } K_c)}{S_{ult} \left[ W \tan \left( \frac{\pi x}{2} + \left( \frac{K_{Ic}}{S_{ys}} \right)^2 / 2W \right) \right]^{1/2}} \quad (1)$$

- where
- $R_s$  = residual strength of damaged plate, fraction of ultimate strength
  - $W$  = plate width, inches
  - $x$  = damage, fraction of plate width
  - $S_{ult}$  = ultimate strength of plate without damage, psi
  - $S_{ys}$  = yield strength of undamaged plate, psi
  - $K$  = stress intensity factor
  - $K_{Ic}$  = fracture toughness constant of plate (plane strain)
  - $K_c$  = fracture toughness constant of thin plate or sheet (plane stress).

Figure 3. Residual Strength Correlation.



$K_{Ic}$  is selected as being most nearly representative of the types of structures involved with rotary wing dynamic components. For thin sheet material  $K_C$  (plane stress) would, of course, be used and is a higher fracture toughness value depending on the thickness involved. To be more exact, the fracture toughness value for the specific material and plate thickness should be used.

The residual strength fraction, Eq. (1), is compared to test results in Figure 3. The thin sheet comparison shows that the method is conservative for small fractional damage and is quite reasonable for the region of damage that would be considered in design (one-third to two-thirds range). For the plate thickness the correlation had to include a width parameter due to lack of data. Here again, the region of interest appears to be within acceptable accuracy, at least for this 7075-T6 material.

One problem that has been found in using fracture toughness values is the lack of data throughout the thickness range. As a start, the plane stress data on some

materials has been gathered and is shown in Table I. The toughest materials appear to be the low yield strength materials such as 6061-T6, 2014-T4, 4340 (150KSI) and Ti-6Al-4V (AN). The specific fracture toughness values show the relative effectiveness of the materials in terms of damaged strength.

The fracture toughness has been found to be much higher for thinner materials where plane stress conditions prevail.

For most of the materials shown in Table I, the increase in fracture toughness for thinner sections is academic since the critical thickness is less than those used in dynamic component design. The exceptions would be materials such as 6061-T6, 4340 (150 KSI) and titanium 6Al-4V (AN). It is therefore desirable that information be obtained on these types of materials to utilize their increased toughness for design applications. As examples of the increased toughness, the thickness effects are shown for 2024-T4 and 7075-T6 alloys in Figure 4.

TABLE I. FRACTURE TOUGHNESS CONSTANTS (ROOM TEMPERATURE)

Material	$S_{ULT}$ KSI	$S_{YS}$ KSI	$K_I$ KSI $\sqrt{IN}$	$K_{Ic}$ KSI $\sqrt{IN}$ LB/IN <sup>3</sup>	Test Thick. In.	Crit. (a) Thick. In.	Notes	Ref.
<b>Aluminum Alloys</b>								
6061-T6	— (b)	40 (b)	72	735	Unkn	Large	Round Bar	10
2024-T4	64 (c)	40 (c)	57	570	Large	Large	Plate	13
2024-T851	66 (b)	59 (b)	23	223	1 (min)	0.40	Plate (L)	9
7075-T651	78 (c)	70 (c)	28	278	0.5 (min)	0.40	Plate (L)	9
7075-T7351	69 (b)	57 (b)	32	317	1.38 (min)	0.78	Plate (L)	9
7079-T651	72 (b)	65 (b)	30	303	1.38 (min)	0.53	Plate (L)	9
7178-T651	85	76 (b)	26	255	1 (min)	0.28	Plate (L)	9
<b>Steel Alloys</b>								
4340 (150KSI)	150 (c)	132 (c)	150 (g)	531	Large	Large		17
4340 (210KSI)	210 (AV)	178 (c)	65	230	0.3 (min)	0.33	Round Bar	10
4340 (260KSI)	260	217 (c)	53	167	0.38 (min)	0.18	Plate (L)	9
4340 (260KSI)	260	217	70	248	0.3	0.26	Round Bar	10
<b>Titanium Alloys</b>								
6-4 (AN)	—	135 (d)	107 (d)	670	1	1.6"	Plate (L)	12
6-4 (STA)	169 (d)	155 (d)	47	293	0.25 (min)	0.23	Plate (L)	11
6-6-2 (Cond A)	161	159 (d)	29 to 40 (e)	177/243	0.25 (min)	0.16	Plate (L)	11
6-6-2 (STA)	184	177	31	189	0.25 (min)	0.08	Plate (L)	11

(a)  $t_{cr} = 2.5 (K_{Ic} / S_{YS})^2$

(d) Average Test Values

(g) Estimated

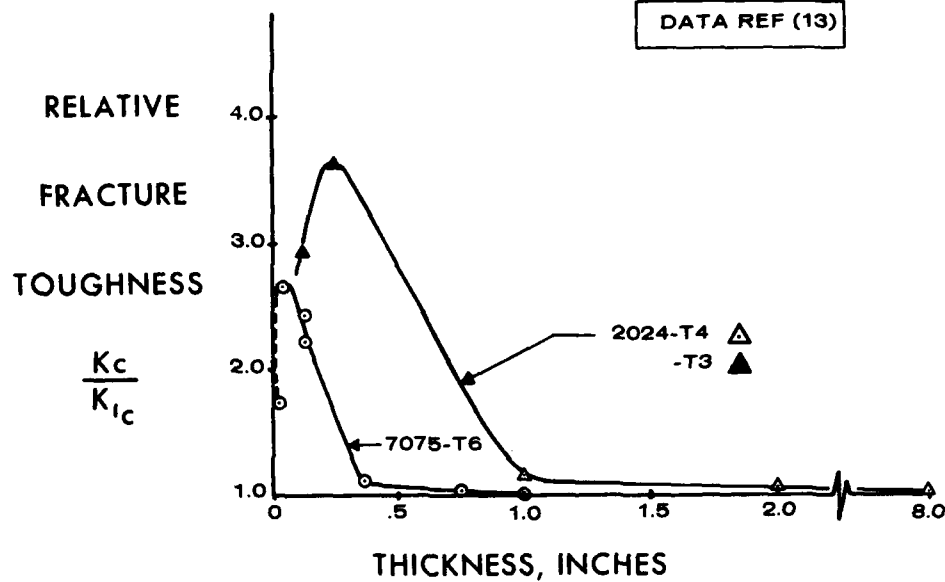
(b) REF 1 B Values

(e) Range of Results

(c) REF 1 S Values

(f) Without Plastic Zone Correction

Figure 4. Relative Fracture Toughness With Thickness.



If residual strength is to be considered in the initial design of the aircraft, then a most important factor is the specific damaged strength of the material. However, there can be tradeoff wherein ultrahigh strength material with lesser fracture toughness may be used at lower design stress loads for increased damage strength efficiency. The specific damaged strength would be:

$$\frac{S}{\rho} = \frac{K_{Ic} \text{ (or } K_c) / \rho}{\left[ W \tan\left(\frac{\pi x}{2}\right) + \left(\frac{K_{Ic}}{S_{ys}}\right)^2 / 2W \right]^{1/2}} \quad (2)$$

where  $\rho$  = material density, lb/in<sup>3</sup>.

Thus, specific fracture toughness ( $K/\rho$ ) is the major factor determining the specific damaged strength. However, Equations (1) and (2) are limited to strengths not exceeding the material allowables on the net section. For example, this would be the case for a material such as 6061-T6 where the fracture toughness is so high that the residual strength damage curve is the ideal straight line. Thus, Eq. (2) should be qualified by:

$$\frac{S}{\rho} \leq \frac{S_{ult}}{\rho} [1 - x] \quad (3)$$

**Residual Life:** Studies of fatigue crack propagation have shown that the crack growth rate ( $\frac{d2a}{dN}$ ) is a function of the stress intensity range ( $\Delta K$ ). One

characteristic form appears to be of the form shown in Figure 5 from Reference 14.

A simplified crack rate relationship from Reference 14 is of the form:

$$\frac{d(2a)}{dN} = C(\Delta K)^n, \quad (4)$$

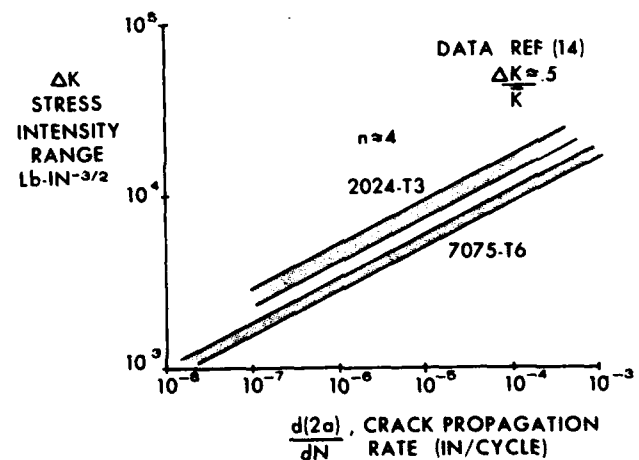


Figure 5. Crack Propagation Rates.

TABLE II. COMPARISON OF CRACK GROWTH TIMES

7075-T6 BARE SHEET	TEST CYCLES (REF 16)	CALCULATED RESULTS (CYCLES)	
		FROM EQ (6)	TWO RANGE SEMI-LOG METHOD
<b>High Crack Growth Case:</b> $X = 0.125, X_n = 0.50$ $\Delta S = 6280$ psi	64,000 ( $\gamma = 1.91$ )	12,900 ( $\gamma = 1.91$ )	66,400 ( $\gamma = 1.89$ to 2.08)
<b>Low Crack Growth Case:</b> $X = 0.163, X_n = 0.50$ $\Delta S = 2040$ psi	1,200,000 ( $\gamma = 1.89$ )	396,000 ( $\gamma = 1.89$ )	1,470,000 ( $\gamma = 1.89$ to 2.08)

where

- 2a = crack length, inches
- N = cycles of loading
- $\Delta K$  = stress intensity range  
 $K_{max} - K_{min}$ , ksi  $\sqrt{\text{in}}$
- n = the power.

A further extension of the rate method to correct for mean stress intensity has been made and is put into the following form:<sup>15</sup>

$$\frac{d(2a)}{dN} = B(1 + 2\gamma)^n (\Delta K)^n, \quad (5)$$

where

- B = material constant
- $\gamma$  = ratio of mean to range value of stress intensity,  $\bar{K}/\Delta K$ .

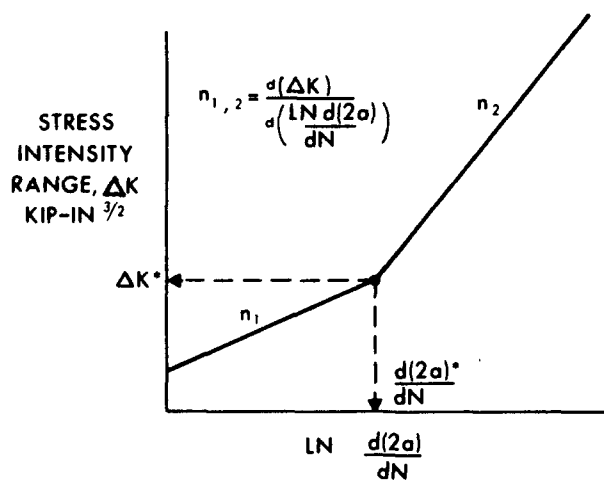


Figure 6. Two Range Semi-Log Approximation.

For the aluminum alloys, such as 2024-T3, and 7075-T6,  $m = 2$  and  $n=4$  appear to reasonably cover the test data ranges. Thus, a simple linear analysis to calculate crack propagation time would be obtained by integrating Eq. (5) to the following:

$$N = \frac{1}{B(1 + 2\gamma)^m W^{\frac{n-1}{2}}} \int_{x_0}^{x_n} \left[ \text{Tan} \frac{\pi}{2} x \right]^{\frac{n}{2}} dx, \quad (6)$$

where

- $x_0$  = initial fractional damage
- $x_n$  = fractional damage at any subsequent time
- N = cycle count from initial to a given damage size;
- and for  $m = 2$ , and  $n = 4$

$$N = \frac{2}{\pi B (1 + 2\gamma)^2 W} \left[ \text{CTN} \frac{\pi}{2} x_0 - \text{CTN} \frac{\pi}{2} x_n - (x_n - x_0) \right]. \quad (7)$$

However, comparisons have been made with crack rate growth curves of Reference 16, and they indicate that the linear log-log approximation is generally too conservative. It would appear to be more reasonable and accurate to integrate the crack growth for the semi-log two ranges as shown in Figure 6. A comparison of the methods with test results is shown in Table II.

The data for various aircraft materials is compiled in Table III.

In practice, the design data needed is an S-N plot of the damaged structure. A comparison of test S-N data of fatigue-cracked 6061-T6 blades with calculated results is shown in Figure 7. Along with the results of gunfire tests, the results indicate that the effect of residual stress and the type of crack induced by gunfire damage is such as to appreciably increase the damaged life. In any case, it would appear conservative to use the fracture mechanics method to predict the residual life of combat-damaged structures in lieu of specific test information.

TABLE III. CRACK PROPAGATION DATA CONSTANTS

MATERIAL	$\frac{\Delta K}{K}$	$+n_1$	$+n_2$	$\frac{\Delta K^*}{KSI\sqrt{IN}}$	$\frac{d(2a)^*}{dn}$ 10 <sup>-6</sup> in/cycle	REF.
6061-T6	1.5	0.45	10.8	12.1	5.3	18
2024-T3	0.42	3.7	7.1	8.8	6.4	15
	1.77	3.4	14.2	8.2	4.8	15
7075-T6	0.42	4.5	8.2	13.5	780	15
	1.77	9.6	16.6	25.6	760	15
Ti-6-4 (AN)	2.0	6.1	51.0	17.5	42	19
Ti-8-1-1 (Duplex AN)	2.0	3.2	23.7	9.6	5	19
4340 (175 KSI)	2.0	14.5	49.0	30	15	20

$+n = \frac{d(\Delta K)}{d \ln \frac{d(2a)}{dN}}$  constant in range 1 or 2

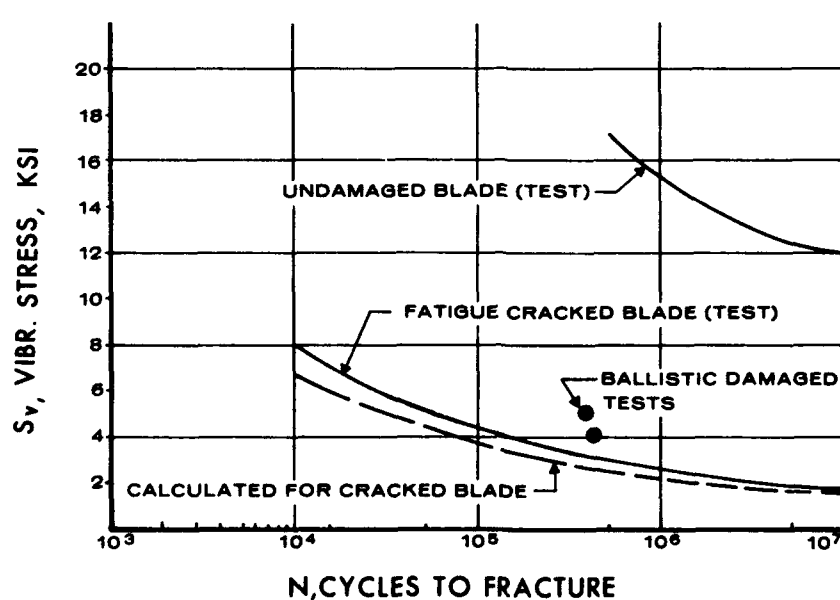


Figure 7. Test and Predicted Crack Propagation For a 6061-T6 Main Rotor Blade Spar.

## VULNERABILITY ANALYSIS

A combat vulnerability analysis of rotary wing aircraft starts with first assessing the flight-critical structural areas. As an example, a typical design was investigated.<sup>6</sup> The structural areas investigated are shown in the schematic diagram of Figure 8. The typical design investigated was a 190 knot (limit dive speed) 3g maneuver capability transport rotary wing vehicle.

The airframe components (1 through 10) are considered to be of conventional semimonocoque design with the usual redundancies and fail-safe design features. As such, the combat damage would be assessed on a residual strength basis. In Table IV are shown the design conditions for the airframe components, and in Figure 9 a summary is shown of the residual strength damage analysis of most critical elements.

TABLE IV. MAJOR AIRFRAME COMPONENTS

COMPONENT	DESIGN CONDITION
1. Stabilizer	$C_L$ (maximum at $V_d$ (190 knots))
2. Pylon	Maximum tail rotor thrust at 1g flight and $V_d$
3. Pylon Hinges	3g vertical takeoff and maximum tail rotor thrust at 1g flight and $V_d$
4. Tail Cone	3g vertical takeoff
5. Aft Fuselage	3g vertical takeoff, maximum tail rotor thrust for 1g flight at $V_d$
6. Center Fuselage	3g vertical takeoff, 3g autorotative pullup at $V_d$
7. Forward Fuselage	Same as No. 6 plus braked roll, nose gear obstruction and landing loads
8. Canopy	15 degree yaw at $V_d$
9. Transmission Frames	Forward Frame: 3g autorotative pullup at $V_d$ , 20g forward crash loads. Aft Frame: 3g vertic. pullup at $V_d$ 20g forward crash load
10. Transmission Beams	3g vertical pullup, 3g autorotative pullup at $V_d$ , 10g lateral crash loads

The stabilizer was considered to have a four-point attachment to the tail pylon, and the critical damage was the destruction of a single fitting. The tail pylon, being of much-reduced size in comparison to the main airframe, would not have the multiple redundancy normally evident in semimonocoque design. Therefore, the critical damage was the destruction of a cap on the forward or aft beam. The pylon fold joint critical damage was the destruction of one out of the four attachment fittings to the tail cone. The loss of a major longeron or a hit on a frame are the

critical damage considerations in the aft fuselage. A hit on a frame would not sever the element but would in effect cause a loss of bending continuity such as to consider that section to have only a shear-carrying capability (pin connection). A critical hit in the skin area of the aft fuselage would reduce the shear-carrying capability.

The main and tail rotor dynamic components are generally designed by fatigue considerations. Many of these components are of sufficient size and strength to defeat small arms fire in terms of residual strength although the damage may be sufficient to cause the initial "crack" to affect residual life. The design conditions for these components are shown in Tables V and VI. The most critical structure would be the main rotor blades, and the damage assessment is shown in Figure 10.

TABLE V. MAIN ROTOR DYNAMIC COMPONENTS

COMPONENT	DESIGN CONDITIONS
11. Blades	3g autorotative pullup at $V_d$ , limit power off rpm. 4g static ground conditions. Spectrum operation up to 3g and $V_d$ .
12. Cuffs	See blades, plus starting torque condition
13. Hinge	Spectrum of repeated loads from blade loads and cuff
14. Sleeve	Spectrum of repeated loads from blade loads and cuff
15. Spindle	Spectrum of repeated loads from blade loads and cuff
16. Vertical Hinge	Spectrum of repeated loads from blade loads and cuff
17. Horizontal Pin	Spectrum of repeated loads from blade loads and cuff
18. Lead Lag Damper	Spectrum of repeated loads from blade loads and cuff
19. Rotor Hub	Same as blades and cuff
20. Rotor Shaft	Same as blades and cuff

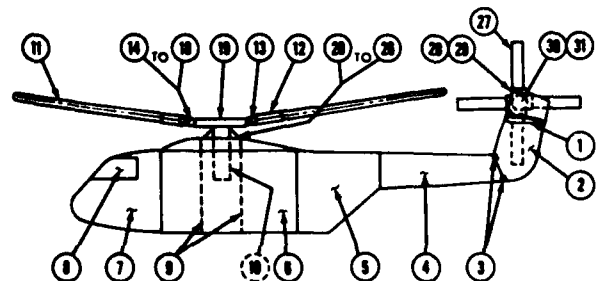


Figure 8. Schematic Diagram of Structural Areas.



Figure 9. Combat Damage Analysis of Airframe Components.

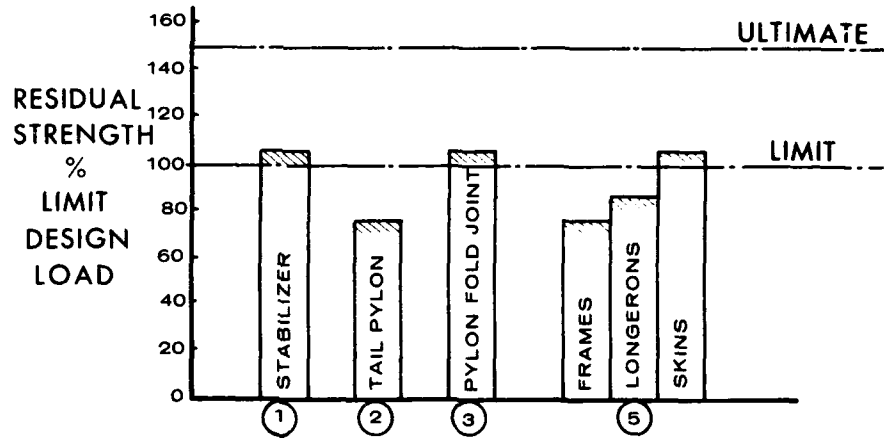
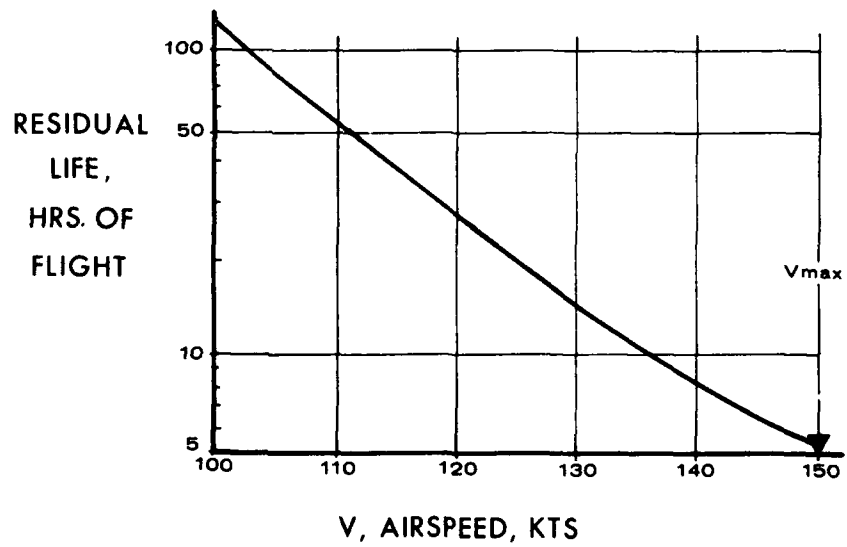


Figure 10. Combat Damage Residual Life of a Main Rotor Blade.



**TABLE VI. TAIL ROTOR DYNAMIC COMPONENTS**

COMPONENT	DESIGN CONDITIONS
27. Blades	Maximum yaw at $V_d$ , autorotation spectrum loading up to $V_d$ limit normal rpm
28. Cuffs	Same as blades
29. Sleeves	Same as blades
30. Spindle	Same as blades
31. Hub	Starting torque condition tie-down wind loads and blade conditions

The most critical structure would be the main rotor blades, and the damage assessment is shown in Figure 10.

The residual life curve of Figure 10 is based on an anticipated speed/stress for a typical blade and the results of limited ballistic tests. The residual life is greater than five hours for continuous operation at  $V_{max}$  (maximum level flight speed). It should be noted that bullet damage on a blade is probably not fed back to the pilot as rotor vibration. With inflight inspection of a blade, the

residual life could be amply increased; for example, a reduction to 120 knots would increase the residual life at least threefold.

The significant fact uncovered by ballistic tests on blade spars is that the crack propagation is delayed by the residual stresses in the localized area. The type of damage from ballistic impact is shown in Figure 11.

Additional ballistic tests on such components as the tail rotor spindle sleeve assembly showed at least fourteen hours flight time capability with 30-calibre damage. This indicates the heavier structures will function satisfactorily in flight for time sufficient enough to permit detection and removal.

Control rods and drive shafts are not specifically shown in Figure 8. However, these structures could be more sensitive to ballistic impact as the extent of initial damage is significantly a larger proportion of their size than that for other dynamic components. The main rotor control rod is designed principally for the vibratory loads from forward speed flight. In Figure 12 the results of fatigue testing are shown for 50-calibre damage. Testing of main rotor control system resulted in no failures after twenty to forty hours of testing with the exception of the results shown in Figure 12. In that particular case fracture was observed after nine hours of simulated flight.

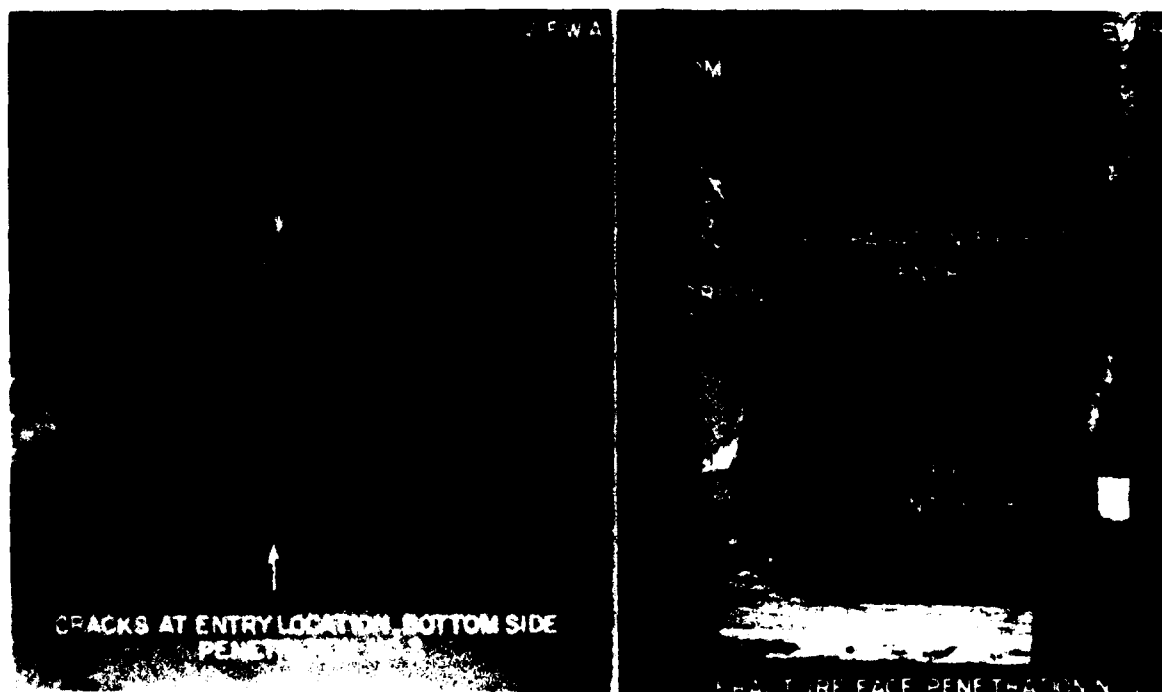


**Figure 11. Ballistic Damage to a Main Rotor Blade Spar.**

TABLE VII. SUMMARY OF COMBAT DAMAGED STRENGTH

MAJOR COMPONENT GROUP	MINIMAL RESIDUAL STRENGTH, % LIMIT LOAD	MINIMUM RESIDUAL LIFE	COMMENTS
Airframe	75% to 85%	Not critical	Compact fuselage structures having less redundancy and lighter (but primary) frames most critical. Design rather than material selection most important.
Dynamic Components	Not critical	> 5 hours at $V_{max}$	Blade spar structures most critical component. Residual stresses set up from bullet damage appear to extend residual life with respect to simply fatigue cracked blades.
Controls	Not critical	9 hours	Main rotor control systems most critical. Size of rods makes them more critical for residual life than residual strength on size helicopter investigated.
Drive Shafts	Not critical	> 3 hours	Thinner walled tubes most critical.

Testing of drive shafts with 50-calibre damage was also accomplished. All the structures evidenced greater than three hours of flight capability subsequent to the ballistic damage. The 2024-T3 aluminum drive shaft (2.0" O.D., 0.375" wall) test results shows flight capability for twenty hours after ballistic damage. In Figure 13 the results are shown for a thinner (and most critical) aluminum shaft (3.18" O.D., 0.092" wall) after three hours of simulated flight testing.

In summary, the combat damage assessment of the typical helicopter investigated is shown in Table VII.

The combat damage assessment made for this paper is considered to be a reasonable estimate for a typical large transport helicopter. The same assessment for a smaller vehicle may well reveal different results since the percentage damage will be greater. In addition, the selection of materials, geometry, and design philosophy may differ for each vehicle with resultant differences in residual life. However, the procedures and results of this assessment of a typical design does offer a perspective for what is generally the capability within present design practice.

In general, the airframe would be most critical for residual strength because of the inherent redundant nature of the structure. However, in certain areas, where the redundancy is at a minimum, the residual strength will fall below limit (design) strength. How critical this would be would depend on the capability and the frequency of reaching limit load conditions. By intent, the limit design load is such that it is not exceeded in the lifetime of the aircraft. But, again, this depends on the rotor capability of that specific machine. In general, 80 per cent of limit load



Figure 12. Main Rotor Control Rods.

**Figure 13. Aluminum Drive Shaft With Ballistic Damage After Three Hours of Testing.**



capability is considered fail-safe in fixed wing aircraft. In rotary wing vehicles the tendency has been to design for 100 per cent of limit load to insure safety. The latter design criteria is conservative and practically eliminates the statistical aspect.

It is clear from the assessment that only moderate changes in design would be needed to insure full flight capability of the airframe with small arms fire. This presumes, of course, that the fail-safe design philosophy is already built into the structure for the normal noncombat operation.

The dynamic components are more complex in that residual life is the critical aspect. In this regard the choice of both design and materials enters into the combat vulnerability. Most dynamic components do not have multiple load paths and in addition are designed by inflight fatigue loadings. Thus, the residual life must consider the crack propagation of the damaged part and how far that damage may progress until static failure will occur. The limited ballistic testing indicates that the damaged part does not progress to propagate a crack at once. The residual stress effects from the bullet appear to cause a considerable dwell period before the usual crack growth starts. This is of considerable importance in the blade spar because it means the difference between an acceptable residual life and an almost immediate type of failure. Again, the choice of materials and application of design principles using fracture mechanics may be able to further the residual life capability.

Control systems of the size investigated appear to give adequate residual life. But here again a greater capability may be desirable.

The drive shaft system may be the most critical area. The combination of high steady and vibratory loadings and the additional stress induced by the resultant unbalance. The rotating, thin-walled tubes appear to result in the lowest residual life structures.

In addition, increasing the flight duration time on the larger transport helicopters may require even greater attention to the residual life aspect. In particular, the use of inflight refueling may extend the flight duration time many-fold.

#### **DESIGN FOR COMBAT DAMAGE**

It is beyond the scope of this paper to go into all details for structural design for combat damage. However, the assessment does show up various areas for improvements that could readily be applied. Some ideas are shown schematically in Figure 14 and consist of the following:

*Airframe.* The use of design concepts may well be the answer for these structures. Frames should have multiple flanges, closer spacing of stringers in critical shear panel areas and multiple load paths in all sheet metal areas are some of the design concepts.

*Dynamic Components.* The design aspect should

include crack arresters to lower the stress intensity at the propagation of the crack. The use of double walled tubes or composite tubes for drive shafts and foam filled tubing for control rods would enhance the survivability for these structures. For example, the gunfire damage on a composite drive shaft (Boron Epoxy) of Figure 15 shows the extent of damage is much lower for composites than for metals. However, the use of hybrid structures such as shown in Figure 16 in non-redundant areas would be questionable due to extent of damage induced from metal flareout into the composite area.

*General.* The use of high fracture toughness material may well be the answer to improved survivability from small arms fire. The specific strength weight ratio for design should include concepts of damage.

## PROBLEM AREAS AND RECOMMENDED RESEARCH

Fracture mechanics has reached the state of the art that it should be used as a stress analysis tool in the design of structures. The residual strength method is considered to be adequate for use in the design of critical components for fail-safe design.

However, the residual life aspect, even for simple fatigue initiated crack propagation needs to have further research. The next area that needs further work is to relate the effects of ballistic damage to crack propagation rates and residual life. In addition, the means to use some accumulative damage rule or to develop load spectrum effects is needed.

A list of problem areas and recommended research work is given in Table VIII.

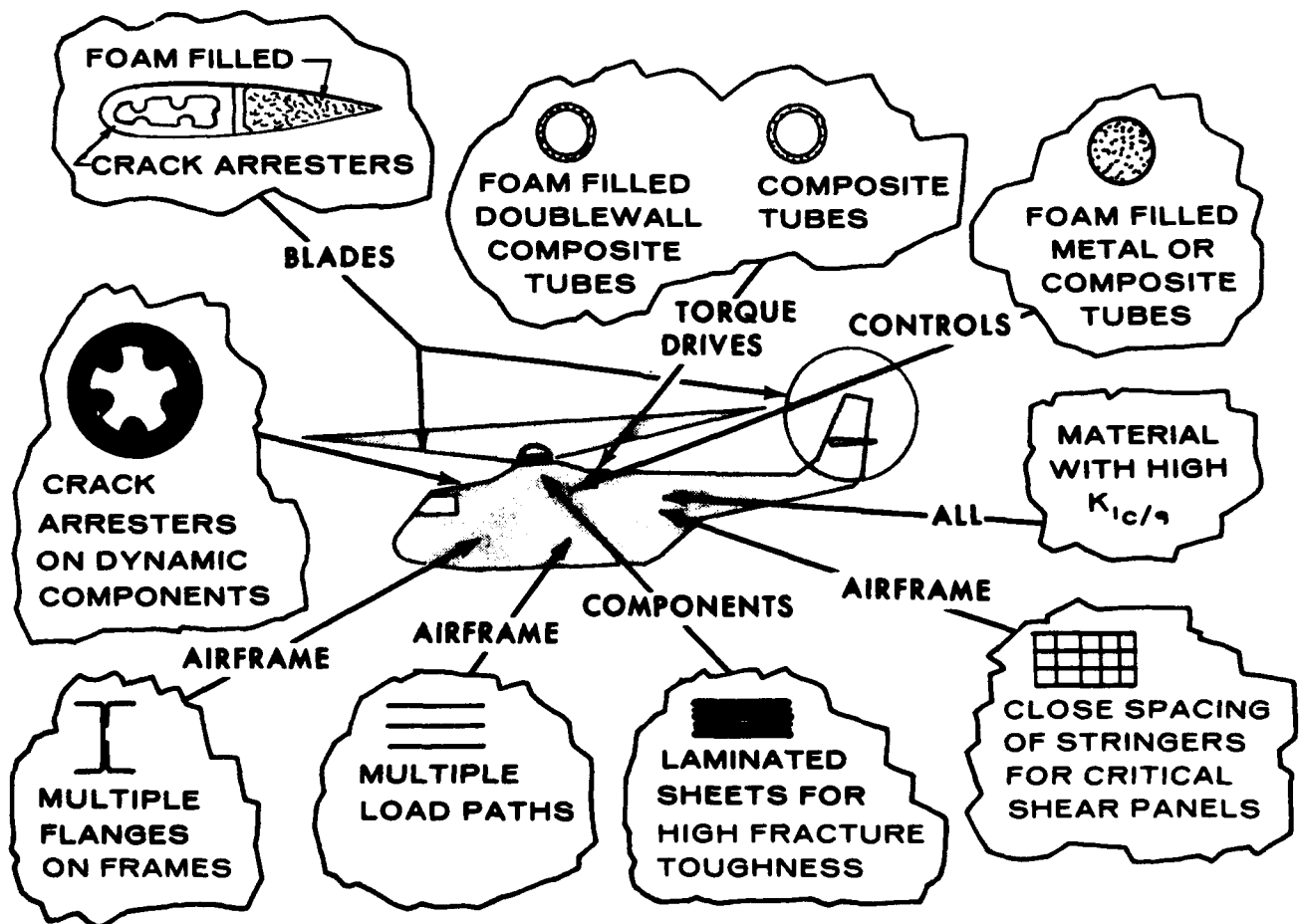


Figure 14. Design Improvements for Combat Damage.

Figure 15. .50 Caliber  
Damage to a Boron/Epoxy  
Drive Shaft.

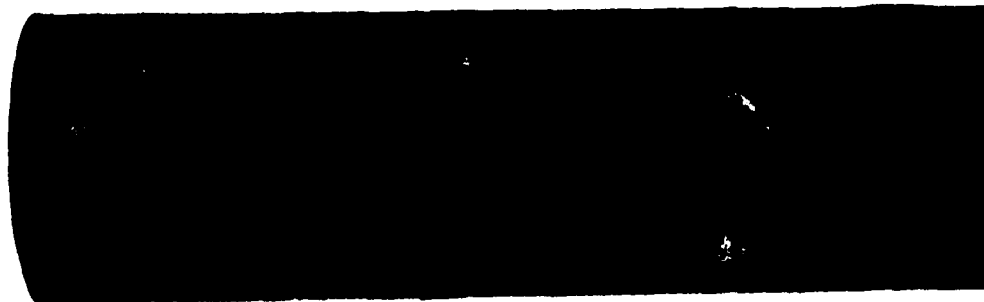


TABLE VIII. PROBLEM AREAS AND RECOMMENDED RESEARCH

PROBLEM AREA	RECOMMENDED RESEARCH	RESULT
1. Effect of mean stress on crack propagation rate.	Crack propagation rates experimentally determined with at least three ratios of mean to vibratory stress intensity range. Thin gage to plate thickness to be used to determine effects of thickness.	Goodman type of constant rate diagrams to be generated for different thickness.
2. Use of rate curves to determine crack propagation time.	Correlation studies using the Goodman rate diagrams of (1) above.	Empirical correction for crack propagation time analysis.
3. Effect of spectrum loadings.	Similar to (1) above, but using power spectrum vibratory stress intensity ranges.	Goodman type of constant rate diagrams but RMS stress intensities to be used.
4. Effect of bullet damage on crack propagation rate/time.	At least previous 1 and 2 items repeated for bullet damage and also checked for at least one RMS stress intensity range.	Empirical correction to using results of 1, 2, & 3.

### SUMMARY

The fracture mechanics methods of analysis provide the technical tool to evaluate combat damage. The residual strength portion appears to be well within the engineering accuracy to predict and design for the anticipated damage.

Further work needs to be done in the fracture mechanics approach to more accurately predict residual life, particularly with bullet damage. However, present

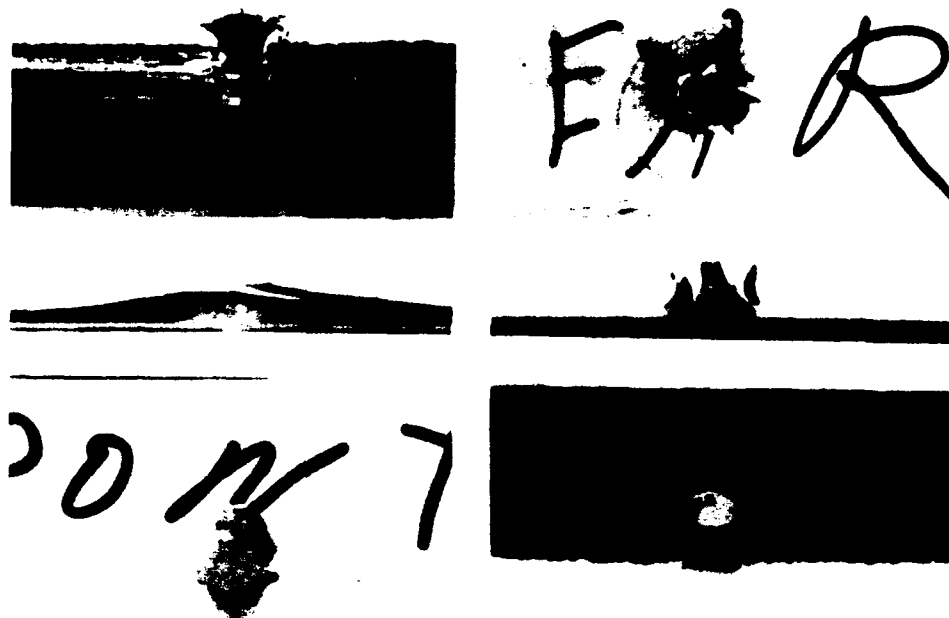
data may be sufficient to design conservatively for desired residual life.

An assessment of a typical transport helicopter indicates it is reasonable and practical to design for "vulnerability" against small arms fire.

### ACKNOWLEDGEMENTS

The contributions of Mr. L. Linzell, Senior Structures Engineer, Sikorsky Aircraft, in evaluating fracture mechanics methods are gratefully acknowledged.

Figure 16. .50 Caliber  
Damage to a Metal  
Reinforced With  
Boron/Epoxy.



#### REFERENCES

1. *Structural Design Requirements: Helicopters*, MIL-S-8698, Department of Defense, Washington, D.C.
2. H.T. Jensen, "The Evolution of Structural Fail Safe Concepts - Rotorcraft"; E. Gassner and W. Schutz, Eds., *Proc. 4th Symp. Int. Comm. Aeron. Fatigue*, Pergamon Press, New York (1969).
3. W.J. Crichlow, *The Materials-Structures Interface; A systems Approach to Airframe Structural Design*, Lockheed Aircraft Corp., Burbank, California. Presented at the 10th AIAA/ASME Structures, Structural Dynamics, and Materials Conference, New Orleans, Louisiana, April 1969.
4. M.J. Rich and L.E. Linzell, "Damaged" Static and Fatigue Stress Analysis of VTOL Structures, AIAA Paper 69-214, American Institute of Aeronautics and Astronautics, New York (1969).
5. *Airplane Strength and Rigidity Flight Loads*, MIL-A-8861, Department of Defense, Washington, D.C.
6. M.J. Rich, *Vulnerability and Crashworthiness in the Design of Rotary Wing Vehicle Structures*, SAE Paper 680673, Society of Automotive Engineers, New York (1968).
7. P. Kuhn and I. Figge, *Unified Notch-Strength Analysis for Wrought Aluminum Alloys*, NASA-TN-D-1259, National Aeronautics and Space Administration, Washington, D.C. (1962).
8. C. Federson, D. Moon, and W. Hyler, "Status of MIL-HDBK-5 Fracture Analysis," Item 64-16, *Minutes of the 31st Meeting*, MIL-HDBK-5 Committee, Department of Defense, Washington, D.C.
9. Anon., "Fracture Toughness Data," Item 64-16, *Minutes of the 35th Meeting*, MIL-HDBK-5 Committee (1968).

## REFERENCES (Continued)

10. G. Hanna and E. Steigerwald, *Fracture Characteristics of Structural Metals*, TAPCO-ER-5426, Bureau of Naval Weapons (RRMA-223), Washington, D.C. (1963).
11. A. Sommer and G. Martin, *Design Allowables for Titanium Alloys*, AFML-TR-69-161, Air Force Materials Laboratory, Wright-Patterson AFB, Ohio (1969).
12. C. Freed and R. Goode, *Correlation of Two Fracture Toughness Tests for Titanium and Ferrous Alloys*, NRL-6740, Naval Research Laboratory, Washington, D.C. (1969).
13. G. Irwin, "Fracture Mode Transition for a Crack Transversing a Plate," *J. Basic Eng.*, 82:417 (1960).
14. P.C. Paris, "The Fracture Mechanics Approach to Fatigue," p.107, *Proc. 10th Sagamore Army Mater. Res. Conf.*, Syracuse University Press, Syracuse, New York (1964).
15. R. Roberts and F. Erdogan, "The Effect of Mean Stress on Fatigue Crack Propagation in Plates Under Extension and Bending," *J. Basic Eng.*, 89:885-892 (1967).
16. S.H. Smith, *Random Loading Fatigue Crack Growth Behavior of Some Aluminum and Titanium Alloys*, ASTM Paper, American Society for Testing and Materials, Philadelphia, Pennsylvania (1965).
17. C. Tiffeny and J. Masters, "Applied Fracture Mechanics," in *Fracture Toughness and Its Applications*, ASTM-STP-381, American Society for Testing and Materials, Philadelphia, Pennsylvania (1965).
18. W. Degnan, P. Dripchak, and C. Matusovich, *Fatigue Crack Propagation in Aircraft Materials*, USAAVLABS-TR-66-9, Sikorsky Aircraft, Stratford, Connecticut (1966).
19. D. Wilhelm, "Investigation of Cyclic Crack Growth Transitional Behavior," p. 363, *Fatigue Crack Propagation*, ASTM-STP-415, American Society for Testing and Materials, Philadelphia, Pennsylvania (1967).
20. G. Miller, "The Dependence of Fatigue Crack Growth Rate on the Stress Intensity Factor and the Mechanical Properties of Some High-Strength Steels," *ASM Trans. Quart.*, 61:442 (1968).



**DAMAGE TOLERANT DESIGN – ANALYSIS METHODS  
AND TEST VERIFICATION OF FUSELAGE STRUCTURE**

by

T. Swift and D.Y. Wang

Douglas Aircraft Company  
McDonnell Douglas Corporation  
Long Beach, California

**LIST OF SYMBOLS**

$a$ = half crack length	$q_{csp}$ = shear flow in skin to crack stopper rivets
$a_c$ = half crack length at fast fracture	$r$ = distance ahead of crack from crack tip
$A$ = area	$R$ = number of rivet rows in crack stopper
$B$ = width of crack stopper	$R_{ct}$ = ratio of stress in the region of the crack tip in an un-stiffened panel to that in a stiffened panel at the same crack length
$C$ = finite panel width correction factor	$S$ = rivet spacing
$d$ = rivet diameter	$t$ = sheet thickness
$E_A$ = elastic modulus of aluminum	$t_{sp}$ = equivalent thickness of shear panel representing shear clip
$E_{cs}$ = elastic modulus of crack stopper material	$t_{csp}$ = equivalent thickness of shear panel representing skin to crack stopper rivets
$f$ = rivet stiffness parameter	$W$ = panel width
$G_a$ = shear modulus of aluminum	$x$ = distance from center of crack
$G_{sc}$ = shear modulus of shear clip	$y$ = width of skin simulating vertical bars in panel idealization
$h_{sp}$ = equivalent height of shear panel representing shear clip	$z$ = width of skin simulating horizontal bars in panel idealization
$h_{csp}$ = equivalent height of shear panel representing crack stopper to skin rivets	$\delta$ = rivet deflection
$h_b$ = thickness of adhesive bond	$\nu$ = Poisson's ratio
$K$ = stress-intensity-factor, $\text{psi}\sqrt{\text{in.}}$	$\sigma$ = gross area stress
$\Delta K$ = range of stress-intensity-factor ( $K_{max} - K_{min}$ ), $\text{psi}\sqrt{\text{in.}}$	$\sigma_h$ = hoop stress
$K_c$ = plane stress fracture toughness, $\text{psi}\sqrt{\text{in.}}$	$\sigma_R$ = gross residual stress
$K'$ = stress-intensity-factor, $\text{psi}$	$\sigma_p$ = principal stress
$K_c^*$ = plane stress fracture toughness including secondary effects, $\text{psi}\sqrt{\text{in.}}$	$\sigma_x$ = axial stress
$l$ = total crack length	$\sigma_y$ = local stress ahead of crack tip
$L$ = longeron spacing	$\sigma_{yct}$ = crack tip stress determined from lumped parameter analysis
$n$ = number of rivets between longerons	$\tau$ = shear stress
$N_x$ = axial load, $\text{lb/in.}$	
$P_{cs}$ = crack stopper load	

## INTRODUCTION

The fail-safe design of large transport aircraft has become increasingly important, particularly in pressurized fuselage shell structure. Since the design of the first jet transport aircraft, radial loading has more than doubled due to increases in fuselage size and higher cabin pressures. The fuselage shell would be even more susceptible to explosive failure than it was in earlier designs if refined techniques and improved materials were not used.

The main source of damage considered is due to skin cracks resulting from fatigue. Materials and stress levels are chosen so that cyclic crack growth rates are low and a propagating crack, prior to reaching a critical length, will be discovered within a certain inspection period. Furthermore, the structure must be designed to contain a fast fracture within reasonable damage tolerance limits so that rapid decompression of the cabin, resulting in injury to the passengers and crew, is prevented. Thrown engine parts, unnoticed damage from ground handling and battle damage, in the case of military aircraft, are all sources of failure which must be confined locally to avoid catastrophic failure.

An unstable fast fracture can be confined to a local area by providing a region of low stress ahead of the crack tip. Carefully designed stiffening elements such as frames with circumferential crack stopper straps provide effective redundant load paths. The crack tip stress is reduced as a large portion of the redistributed load is transferred to the stiffeners, resulting in crack arrestment and subsequent slow crack propagation in the vicinity of the stiffeners. The effectiveness of the stiffening elements, in reducing the crack tip stress, increases with stiffener cross-sectional area and rigidity of their attachment to the skin. The residual strength of damaged structure increases with increasing fracture toughness of the skin and effectiveness of the stiffeners.

The present paper describes a method of analysis to determine the effects of stiffening elements on the stress distributions in cracked panels of typical fuselage structure. The analytical results are combined with material fracture toughness constants to determine the residual strength of the damaged structure. A

method for analyzing fatigue crack propagation in the stiffened fuselage panels is developed. The influence of various secondary loads on fracture strength and crack propagation rate in the stiffened panels has been empirically evaluated. These loads, normally present in a fuselage shell, include shear, biaxial load, biaxial stress induced by lateral stiffeners, and bending stresses induced by a broken longeron.

A fatigue crack propagation and residual strength test program was conducted on a variety of test specimens to experimentally verify the analytical methods. The results of the tests also served to empirically evaluate the various secondary effects.

## ANALYSIS

### STRESS ANALYSIS OF CRACKED PANELS

A solution to the elastic stress distribution in an unstiffened plate containing a crack was developed by Westergaard.<sup>1</sup> The solution provides the distribution of longitudinal stress  $\sigma_y$  along the x axis which lies in the plane of the crack.

$$\sigma_y = \sigma \left[ 1 - \left( \frac{\sin \frac{\pi a}{W}}{\sin \frac{\pi x}{W}} \right)^2 \right]^{-1/2} \quad (1)$$

where

$\sigma$  = gross area stress

$a$  = half crack length

Equation (1) was derived for an infinitely wide plate with a series of cracks as shown in Figure 1(a).

When Equation (1) is used for the finite plate shown in Figure 1(b), a discrepancy exists along the boundaries of the plate. The lines AC and BD of Figure 1(a) are constrained to remain straight

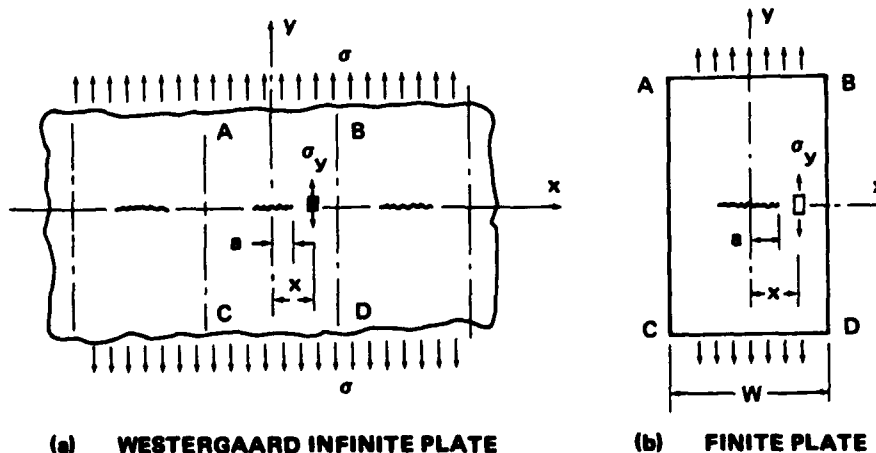


FIGURE 1. PANEL CONTAINING CENTRAL CRACKS

while those of Figure 1(b) are free to distort in the x direction. This discrepancy is reduced as the plate width increases. For an infinitely wide plate, Equation (1) is reduced to

$$\sigma_y = \frac{\sigma x}{a} \left[ \left( \frac{x}{a} \right)^2 - 1 \right]^{-1/2} \quad (2)$$

As x approaches a in Equations (1) and (2), the stress  $\sigma_y$  becomes infinite. In practice, however, this does not occur and a small plastic zone is formed at the crack tip.

The stress-intensity-factor equations to be used in this analysis are:

$$K = \sigma C \sqrt{W \tan \left( \frac{\pi a}{W} \right)} \quad (3)$$

and

$$K' = \sigma C \left\{ 1 - \left[ \frac{\sin \pi a/W}{\sin \frac{\pi}{W}(a+r)} \right]^2 \right\}^{-1/2} \quad (4)$$

where

K = stress-intensity-factor, psi  $\sqrt{\text{in.}}$

K' = stress-intensity-factor, psi

$\sigma$  = gross skin stress, psi

a = half crack length, in.

C =  $1.0 + 0.3 (2a/W)^2$

Equation (3), based on work by Irwin,<sup>2</sup> can be derived from Westergaard's expression, Equation (1). The finite panel width correction factor C, proposed by Allen,<sup>3</sup> is based on a series of calculations by Isida for specific cases as reported by Paris and Sih.<sup>4</sup> Stress-intensity-factor K' is the longitudinal stress  $\sigma_y$  at a distance  $1/2\pi$  from the tip of the crack [see Equation (1)]. It has been shown<sup>3</sup> that the values of K and K' are nearly equal for panel widths greater than 30 inches.

#### Lumped Parameter Analysis

The stresses from Equations (1) and (2) can be solved also by a "Lumped Parameter Analysis" of an idealized structure representing the panel. The method of analysis is based on the Force Matrix Method of Structural Analysis<sup>5,6</sup> and uses the Second Version of FORTRAN Matrix Abstraction Technique, FORMAT II,<sup>7</sup> as a tool through which the IBM 7094 computer solves the necessary matrix operations. A typical idealized structure is shown in Figure 2. The panel is divided into a series of discrete bars and panels. The bars carry axial load and the panels carry shear load. External loads and reactions are applied at the joints. Only one quarter of the panel requires consideration since the crack is assumed to propagate symmetrically about the centerline of the panel. The accuracy of the solution is dependent upon the fineness of the gridwork so that considerable detail is given to the area surrounding the crack. Economics prevents the use of such a fine grid in areas remote from the crack. The idealized structure

shown contains 209 redundancies and requires the solution of 540 joint equilibrium equations. The bar areas are determined as:

$$A_y = t(z_1 + z_2)/2 \quad (5)$$

$$A_z = t(y_1 + y_2)/2 \quad (6)$$

The shear panels have the same thickness as the plate. Loads are applied at the top of the panel and reactions are provided at the bottom. The external boundaries of the panel are free to deflect and unloaded vectors are provided along the vertical edge and in the vicinity of the crack so that deflections can be determined. Propagation of the crack is simulated by disconnecting the reactions one at a time from the center of the panel. Stress distributions throughout the panel are determined for each crack length. The crack tip stress is defined as the vertical bar stress adjacent to the simulated crack at the horizontal centerline of the panel (see Figure 2).

The net section stress  $\sigma_y$  obtained from this analysis is compared in Figure 3 to Westergaard's equations for two crack lengths, 7-inch and 19-inch. It can be seen that Westergaard's equations give slightly lower stresses.

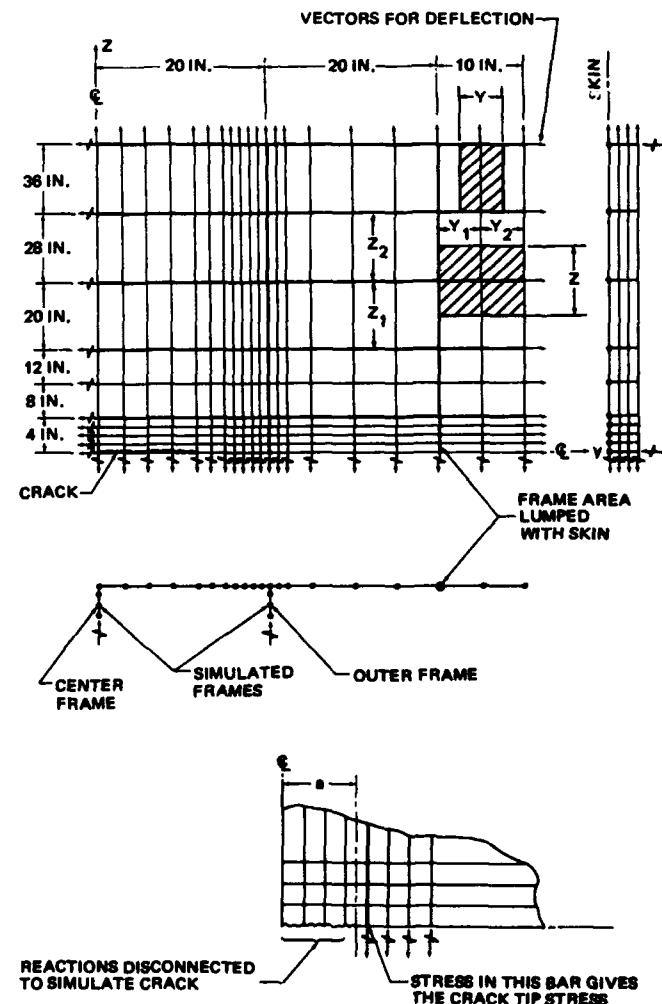


FIGURE 2. TWO-BAY LONGITUDINAL CRACK IDEALIZATION

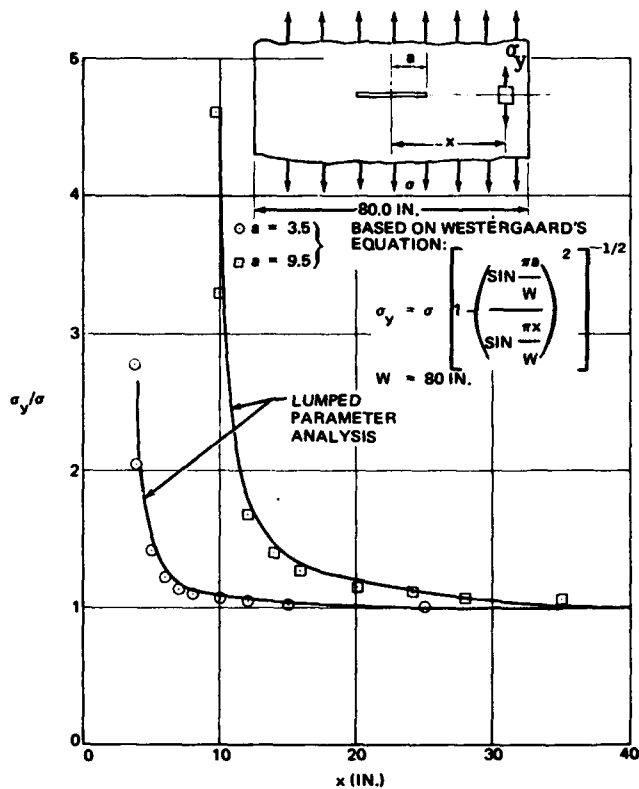


FIGURE 3. COMPARISON OF LUMPED PARAMETER ANALYSIS WITH WESTERGAARD'S EQUATION FOR FINITE PLATE WIDTH

### Stiffened Panels

The effects of stiffening, which would be extremely difficult to determine using the stress function methods of Reference 1, are relatively simple to solve using the Lumped Parameter Analysis. The stiffeners are lumped as additional bars and connected to the main panel by continuous shear panels. The crack tip stress in the stiffened panel is determined in the same manner as the unstiffened panel using an identical grid size. The effects of the stiffener on the crack tip stress as a function of crack length are expressed in a dimensionless ratio

$$R_{ct} = \frac{\sigma_{yct(a)} \text{ in unstiffened panel}}{\sigma_{yct(a)} \text{ in stiffened panel}}$$

Since Equation (1) can be so closely simulated by the Lumped Parameter Analysis, it is reasonable to assume that Equation (3) is also applicable for stiffened panels, provided the effects of stiffening are included.

$$\frac{K_{(a)} \text{ in unstiffened panel}}{K_{(a)} \text{ in stiffened panel}} = \frac{\sigma_{yct} \text{ in unstiffened panel}}{\sigma_{yct} \text{ in stiffened panel}} = R_{ct(a)}$$

Then for the stiffened panel, the stress-intensity-factor

$$K = \frac{\sigma C}{R_{ct}} \sqrt{W \tan \frac{\pi a}{W}} \quad (7)$$

$$\sigma = \frac{K R_{ct}}{C \sqrt{W \tan \frac{\pi a}{W}}} \quad (8)$$

The stress intensity at the tip of the crack and the net section stress are reduced when stiffeners are provided. As the crack extends, part of the load is transferred to the stiffeners and the remaining load is transferred to the net section of the skin, ahead of the crack tip (see Figure 4). The maximum reduction in crack tip stress occurs in the region of the stiffeners.

A comparison of stress distribution for an unstiffened and stiffened panel is shown in Figure 4 for a one-bay crack configuration.

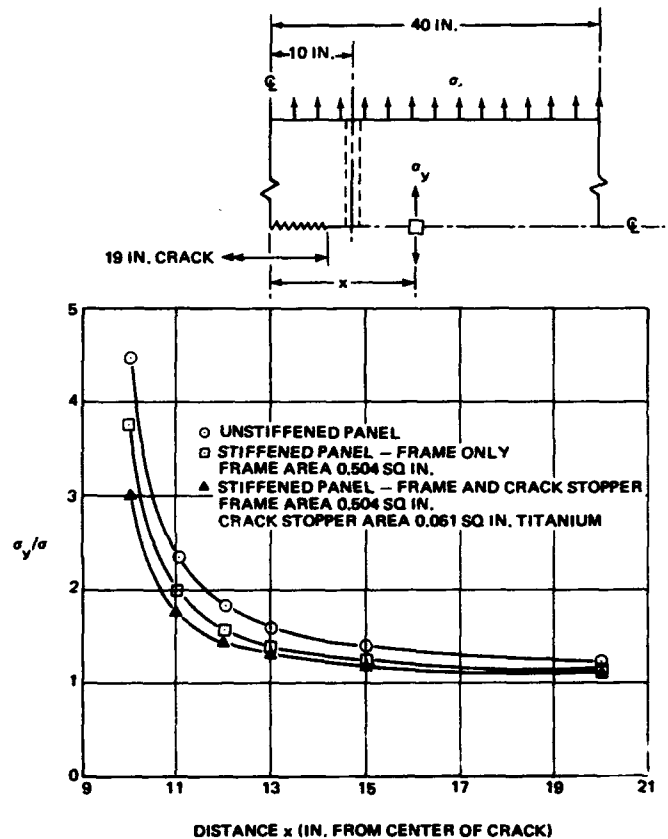


FIGURE 4. COMPARISON OF STRESS DISTRIBUTION AHEAD OF A CRACK IN UNSTIFFENED AND STIFFENED PANELS

### Fuselage Panel Idealization

Three types of crack considered for a typical fuselage shell and shown in Figure 5 are:

- A - One-bay longitudinal skin crack starting at the center of a bay
- B - Two-bay longitudinal skin crack starting at a frame
- C - Two-bay circumferential skin crack starting at a broken longeron

The panel sizes chosen for these configurations are shown in Figure 5; however, only one quarter of the panel is considered in the analysis.

A typical structural idealization is shown in Figure 2 for configuration B. Idealizations for configurations A and C are shown in Reference 8. Frame and longeron spacing is 20 inches and 8 inches, respectively. For types A and B, the longitudinal bars located at longeron positions in Figure 2 include longeron

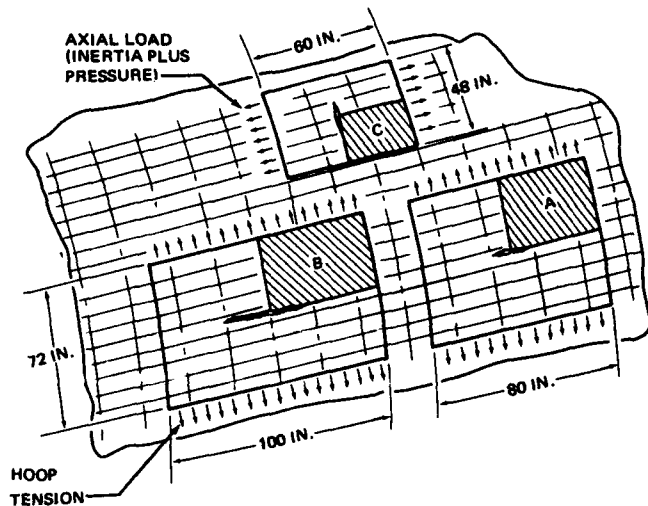


FIGURE 5. PANEL SIZES FOR THREE TYPES OF CRACK

area plus skin area from Equation (5). These areas are assumed to be in the plane of the skin. Vertical bars in the plane of the skin represent skin lumped area from Equation (6). The frames adjacent to the crack are simulated by three bars connected together and to the skin by continuous shear panels. For cases with crack stopper straps under the frame, the bar nearest the skin in the simulated frame represents the crack stopper and the remaining two bars represent the frame. For frames without crack stopper straps, the three bars are used to simulate the frames. A typical frame is shown in Figure 6. A skin crack directed towards the cutout in the shear clip as shown in Figure 6 is the most critical condition. The flange portion of the shear clip, connected to the skin, is relatively ineffective in picking up load from the cracked sheet for this condition and is not included in the section properties of the simulated frame section. However, if the crack is directed towards the center of the flange, then the shear clip will influence the crack tip stress and load will be transferred to the flange.

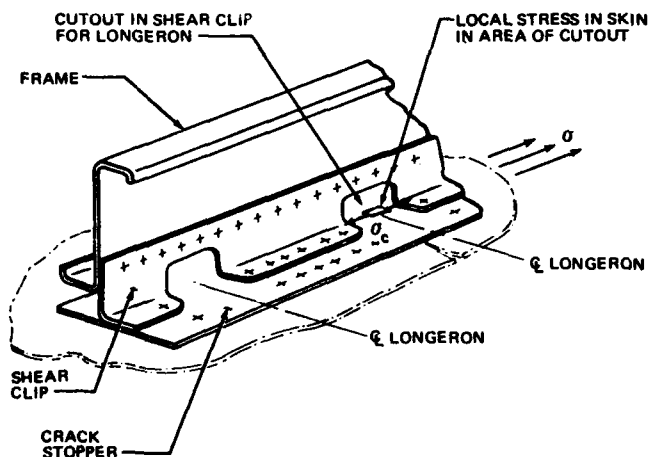


FIGURE 6. TYPICAL FRAME

Frames without crack stoppers are idealized as shown in Figure 9.

$$A_i + A_c + A_o = \text{total frame area}$$

where

$A_i$  = inner cap area

$A_c$  = center web area

$A_o$  = outer cap area

Frames with crack stoppers are idealized as shown in Figure 7. In this case,  $A_i + A_o$  is equal to the total frame area. The crack stopper is represented by a single bar with area:

$$A_{cs} = (\text{crack stopper net area}) \left( \frac{E_{cs}}{E_A} \right)$$

where

$E_{cs}$  = modulus of crack stopper material

$E_A$  = modulus of aluminum

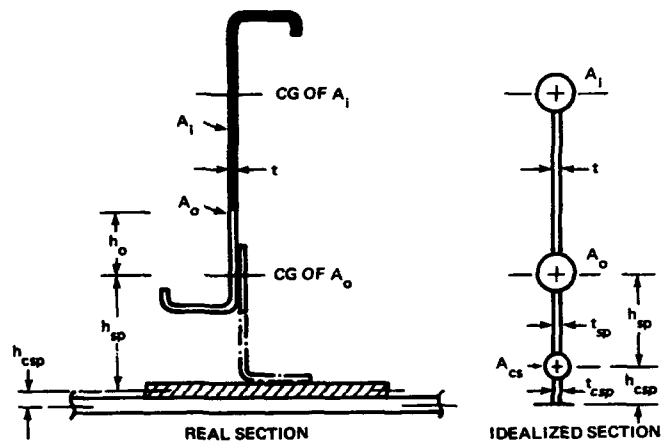


FIGURE 7. FRAME WITH CRACK STOPPER

The thickness of the simulated shear panels  $t_{sp}$  and  $t_{csp}$  is extremely important to the analysis. The amount of load transferred to the frame, and thus the crack tip stress, is influenced to a large degree by these thicknesses. Referring to Figure 7,  $t_{sp}$  is the thickness of a continuous shear panel of height  $h_{sp}$  having the same shear stiffness as the shear clip. The rivets connecting the crack stopper to the skin are simulated by a continuous shear panel of height  $h_{csp}$  and thickness  $t_{csp}$ .

Rivet shear deflection in aluminum alloy sheet can be expressed by

$$\delta = Pf/E_A d \quad (9)$$

where

$\delta$  = deflection

$P$  = applied load

$E_A$  = modulus of aluminum

$d$  = rivet diameter

$$f = 5.0 + 0.8 \left[ \frac{d}{t_1} + \frac{d}{t_2} \right] \quad (10)$$

and, for aluminum alloy rivets,

$t_1$  and  $t_2$  = thickness of joined sheets

For the shear clip to crack stopper and skin to crack stopper rivets,

$$f = 5.0 + 0.8 \left[ \frac{d}{t_1} + \frac{d}{t_2} \frac{E_{cs}}{E_A} \right] \quad (11)$$

where

$E_{cs}$  = modulus of crack stopper material

This equation, combined with Equation (9), has been substantiated by test for titanium crack stoppers.<sup>8</sup>

The shear clip shown in Figure 6 is idealized as shown in Figure 8.

In Figure 8, the thickness  $t_{sp}$  of the idealized shear panel B is determined to give the same shear deflection as A.

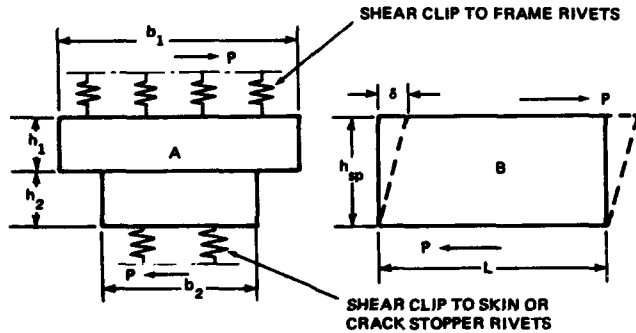


FIGURE 8. SHEAR CLIP IDEALIZATION

The shear deflection of system A is given by

$$\delta_A = P \left[ \frac{1}{E_A} \left\{ \left( \frac{f}{dn} \right)_F + \left( \frac{f}{dn} \right)_S \right\} + \frac{1}{t_{sc} G_{sc}} \left\{ \frac{h_1}{b_1} + \frac{h_2}{b_2} \right\} \right] \quad (12)$$

The shear deflection of the idealized panel B is given by

$$\delta_B = \frac{P h_{sp}}{L t_{sp} G_A} \quad (13)$$

$\delta_A = \delta_B$ ; therefore, equating Equations (12) and (13) and solving for  $t_{sp}$ :

$$t_{sp} = \frac{h_{sp}}{L G_A} \left[ \frac{1}{E_A} \left\{ \left( \frac{f}{dn} \right)_F + \left( \frac{f}{dn} \right)_S \right\} + \frac{1}{t_{sc} G_{sc}} \left\{ \frac{h_1}{b_1} + \frac{h_2}{b_2} \right\} \right]^{-1} \quad (14)$$

Equation (14) then gives the thickness of a continuous shear panel having the same stiffness as the shear clip-rivet combination

where

$L$  = longeron spacing

$n$  = number of rivets between longerons

$G_A$  = modulus of rigidity of aluminum alloy

$G_{sc}$  = modulus of rigidity of shear clip

$t_{sc}$  = thickness of shear clip

$t_{sp}$  = thickness of ideal shear clip

and

subscripts F and S refer to the shear clip to frame connection and the shear clip to crack stopper or skin connection, respectively.

In Figure 7, the thickness  $t_{csp}$  of the shear panel simulating the crack stopper to skin rivets is obtained in a similar way

$$t_{csp} = \frac{h_{csp} n E_A d}{L G_A f} \quad (15)$$

For the circumferential crack, type C of Figure 5, the frames are not included as a lumped area in the plane of the skin as were the longerons for types A and B. Load transfer to the frames is via a flexible shear clip arrangement and is not considered fully effective in picking up load in a transverse direction. The longeron is represented by two bars which are arranged to give the same section properties as the actual longeron. The rivets connecting the longeron to the skin are simulated to a continuous shear panel having the same shear stiffness as the rivets. Equations (9), (10) and (15) are used to determine the thickness of the shear panel.

In order to illustrate the effects of various typical stiffener configurations with different degrees of damage tolerance, five frame sections are considered for longitudinal cracks and four longeron sections for circumferential cracks. The frame and longeron idealizations considered are shown in Figures 9, 10 and 11. The cases considered for these configurations are listed in Table 1.

**Analysis Results** - In all of the cases included in Table 1, a uniform stress was applied to the upper boundary of the panel to both skin and stiffening elements. The ratio of unstiffened panel crack tip stress to stiffened panel crack tip stress  $R_{ct}$  is shown in Figure 12 as a function of crack length. Frame inner and outer cap stresses shown in Figure 13 are "unlumped" extreme fiber stresses. Bending moment and axial load are determined from axial loads in the idealized frame elements and applied to the actual frame cross section to determine "unlumped stresses." The longeron stresses shown in Figure 14 for circumferential cracks are direct bar stresses from the lumped parameter analysis. For the comparatively small sections considered, little accuracy is gained by unlumping. The stresses in the stiffening elements diminish rapidly with distance from the center of the crack. An example of this is illustrated in Figure 15 where the outer crack stopper stress and crack stopper to skin rivet shear flow is shown for case 3c of Table 1.

TABLE 1.  
DESCRIPTION OF ANALYSIS CASES

CASE NO.	CASE DESCRIPTION
1A	1-BAY LONGITUDINAL CRACK – FRAME WITHOUT CRACK STOPPER – .071 SKIN
1B	2-BAY LONGITUDINAL CRACK – FRAME WITHOUT CRACK STOPPER – CENTER FRAME INTACT – .071 SKIN
2A	1-BAY LONGITUDINAL CRACK – FRAME WITHOUT CRACK STOPPER – .080 SKIN
2B	2-BAY LONGITUDINAL CRACK – FRAME WITHOUT CRACK STOPPER – CENTER FRAME INTACT – .080 SKIN
3A	1-BAY LONGITUDINAL CRACK – FRAME WITH CRACK STOPPER – .071 SKIN
3B	2-BAY LONGITUDINAL CRACK – FRAME WITH CRACK STOPPER – CENTER FRAME AND CRACK STOPPER INTACT – .071 SKIN
3C	2-BAY LONGITUDINAL CRACK – FRAME WITH CRACK STOPPER – CENTER CRACK STOPPER FAILED – .071 SKIN
3D	2-BAY LONGITUDINAL CRACK – FRAME WITH CRACK STOPPER – CENTER CRACK STOPPER AND FRAME FAILED – .071 SKIN
3E	2-BAY LONGITUDINAL CRACK – FRAME WITH CRACK STOPPER – CENTER AND OUTER CRACK STOPPER AND CENTER FRAME FAILED – .071 SKIN
4	2-BAY LONGITUDINAL CRACK – FRAME WITHOUT CRACK STOPPER – CENTER FRAME REINFORCED – .071 SKIN
5	2-BAY LONGITUDINAL CRACK – FRAME WITH CRACK STOPPER – CENTER CRACK STOPPER FAILED – CENTER FRAME REINFORCED – .071 SKIN
6	2-BAY CIRCUMFERENTIAL CRACK – CENTER LONGERON FAILED – LIGHT HAT SECTION LONGERON – .071 SKIN
7	2-BAY CIRCUMFERENTIAL CRACK – CENTER LONGERON FAILED – HEAVY HAT SECTION LONGERON – .071 SKIN
8	2-BAY CIRCUMFERENTIAL CRACK – CENTER LONGERON FAILED – LIGHT TEE SECTION LONGERON – .071 SKIN
9	2-BAY CIRCUMFERENTIAL CRACK – CENTER LONGERON FAILED – HEAVY TEE SECTION LONGERON – .071 SKIN

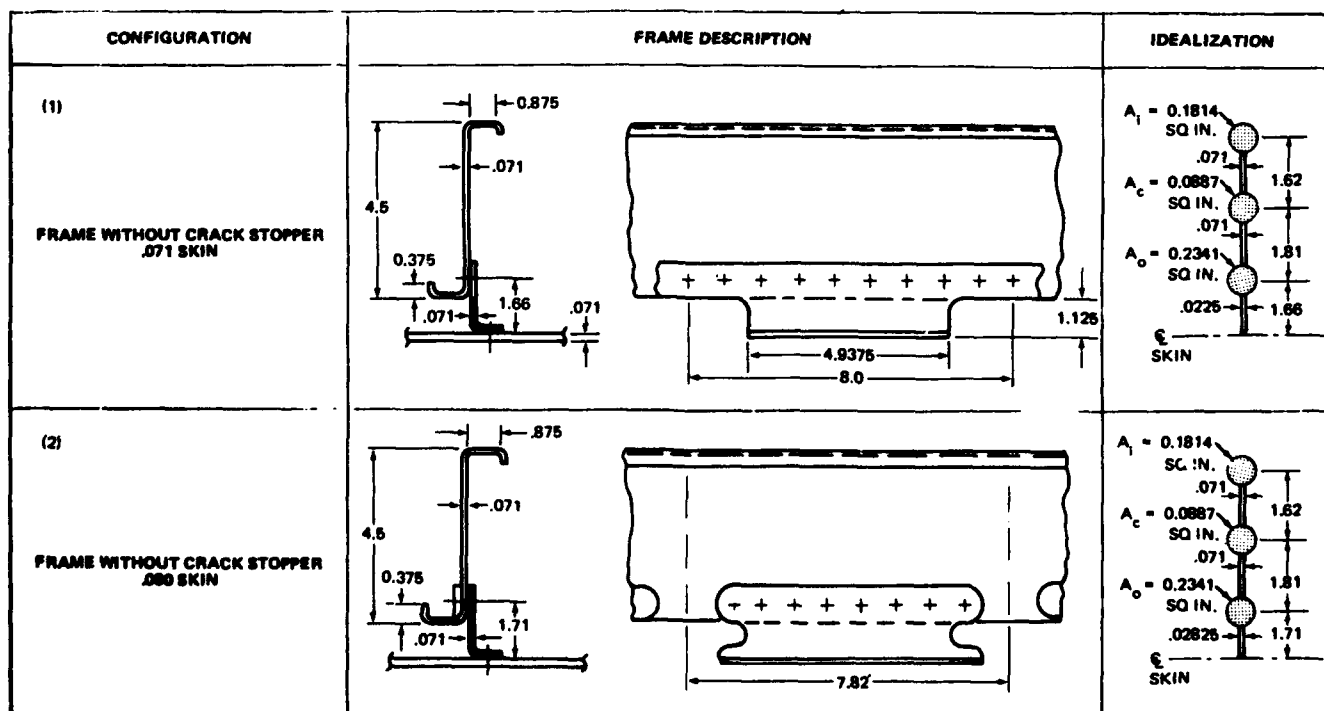


FIGURE 9. FRAME IDEALIZATION FOR THE PANEL CONTAINING LONGITUDINAL CRACKS

CONFIGURATION	FRAME DESCRIPTION	IDEALIZATION
(3) FRAME WITH CRACK STOPPER .071 SKIN	<p>FRAME 7075-T6</p> <p>SHEAR CLIP IDENTICAL TO CONFIGURATION (1)</p> <p>CRACK STOPPER TIT. 8-1-1 NET AREA 0.0609 SQ IN.</p> <p>25 3/16 RIVETS BETWEEN LONGERONS</p>	<p><math>A_1 = 0.2701</math> SQ IN.</p> <p><math>A_o = 0.2341</math> SQ IN.</p> <p><math>A_{cs} = 0.1035</math> SQ IN.</p> <p><math>\bar{c}</math> SKIN</p>
(4) FRAME WITHOUT CRACK STOPPER OUTER CAP REINFORCED	<p>FRAME 7075-T6</p> <p>CONFIGURATION IDENTICAL TO (1) EXCEPT FOR OUTER CAP REINFORCING</p> <p>REINFORCING AREA 0.158 SQ IN. ON CENTER FRAME ONLY</p>	<p><math>A_1 = 0.1814</math> SQ IN.</p> <p><math>A_c = 0.0887</math> SQ IN.</p> <p><math>A_o = 0.3921</math> SQ IN.</p> <p><math>\bar{c}</math> SKIN</p>
(5) FRAME WITH CRACK STOPPER OUTER CAP REINFORCED	<p>FRAME 7075-T6</p> <p>CONFIGURATION IDENTICAL TO (3) EXCEPT FOR OUTER CAP REINFORCING</p> <p>REINFORCING AREA 0.158 SQ IN. ON CENTER FRAME ONLY</p>	<p><math>A_1 = 0.2701</math> SQ IN.</p> <p><math>A_o = 0.3921</math> SQ IN.</p> <p><math>A_{cs} = 0.1035</math> SQ IN.</p> <p><math>\bar{c}</math> SKIN</p>

FIGURE 10. FRAME IDEALIZATION FOR THE PANEL CONTAINING LONGITUDINAL CRACKS

### Secondary Effects

There are several secondary effects that are not accounted for in the present analysis which can either increase or decrease the stress-intensity-factor  $K$ .

**Curvature and Pressure** – The analysis described so far is for flat panels loaded along the boundary to represent hoop tension or inertia loading as shown in Figure 5. For pressurized fuselage shells of large radius, such as those of modern large jet transport aircraft, the flat panel analysis is assumed to provide accurate stiffener stress distributions in view of their localized nature.

CONFIGURATION	LONGERON DESCRIPTION	IDEALIZATION
(6)	<p>1 ROW 3/16 ALUM. RIVETS 1-1/4 IN. PITCH</p>	<p>NET AREA 0.3029 SQ IN.</p> <p><math>A = 0.0916</math> SQ IN.</p> <p><math>A = 0.2113</math> SQ IN.</p>
(7)	<p>1 ROW 3/16 ALUM RIVETS 1-1/4 IN. PITCH</p>	<p>NET AREA 0.5121 SQ IN.</p> <p><math>A = 0.1733</math> SQ IN.</p> <p><math>A = 0.3388</math> SQ IN.</p>
(8)	<p>2 ROWS 3/16 ALUM. RIVETS 1-1/4 IN. PITCH</p>	<p>NET AREA 0.2895 SQ IN.</p> <p><math>A = 0.1875</math> SQ IN.</p> <p><math>A = 0.102</math> SQ IN.</p>
(9)	<p>2 ROWS 3/16 ALUM RIVETS 1-1/4 IN. PITCH</p>	<p>NET AREA 0.4865 SQ IN.</p> <p><math>A = 0.3885</math> SQ IN.</p> <p><math>A = 0.098</math> SQ IN.</p>

FIGURE 11. LONGERON IDEALIZATION FOR THE PANEL CONTAINING CIRCUMFERENTIAL CRACKS

Figure 15 shows how rapidly the loading diminishes in a crack stopper and its attachment to the skin. The skin stress-intensity-factor  $K$  at the crack tip, however, is affected by the bulging caused by the loss of hoop tension reaction along the edge of the crack. The bulging is required to maintain equilibrium of an element adjacent to the crack edge (see Figure 16). The induced local bending of the crack tip as a result of this condition increases the stress-intensity-factor  $K$ . The bulging is more severe when the crack is located adjacent to rather than midway between longerons.

**Buckling** – This condition is analogous to the curvature effect described above and is caused by a compressive stress along the edge of the crack theoretically equal to  $\sigma$  for the Westergaard unstiffened infinite plate. Lumped parameter analysis shows the compression stress to be  $1.7\sigma$  for a finite stiffened plate with stiffener configuration (7) of Figure 11. As a result, buckling of the thin sheet occurs similar to that shown in Figure 16, increasing the stress intensity at the tip of the crack.



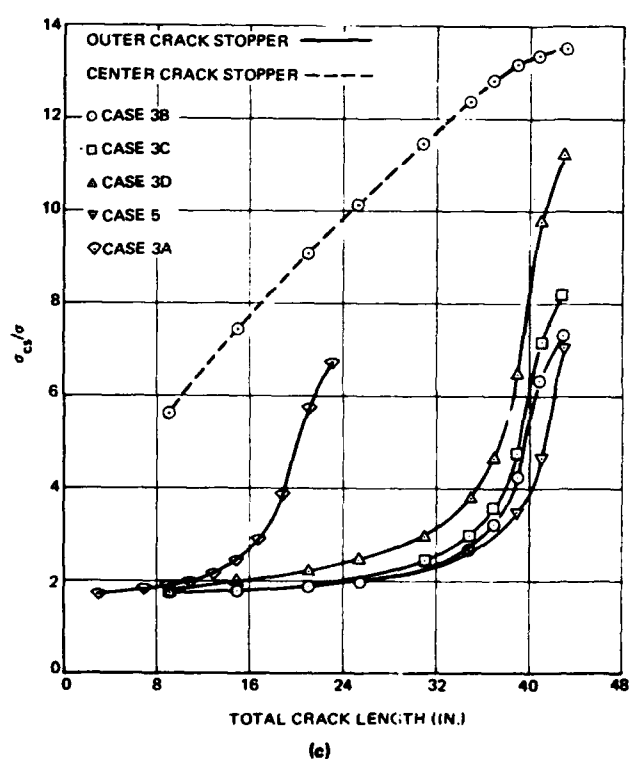
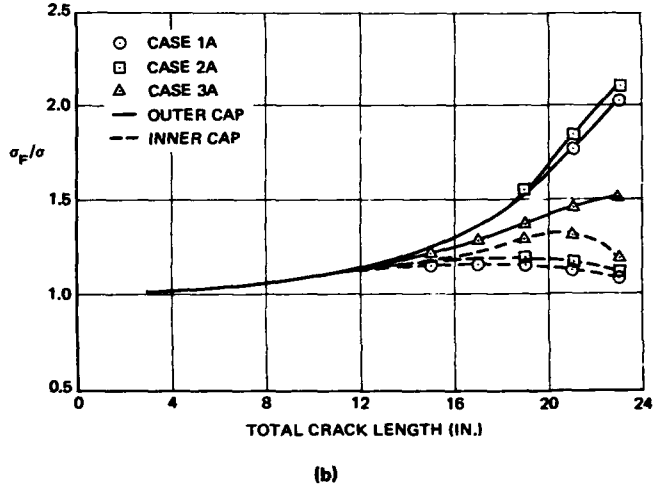
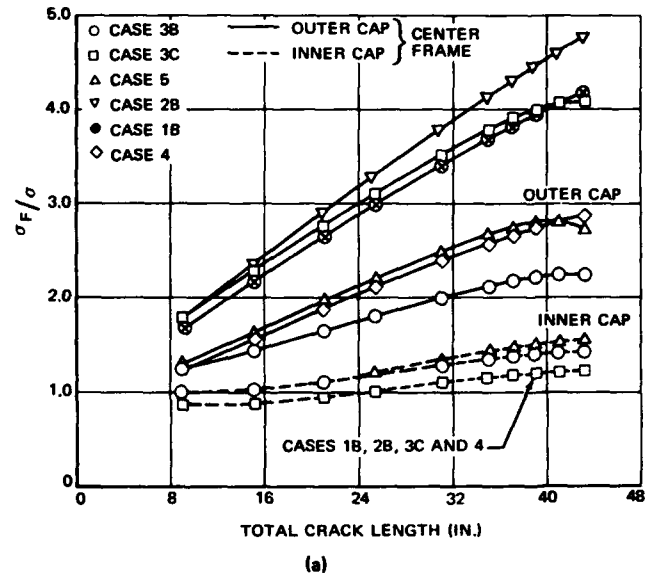
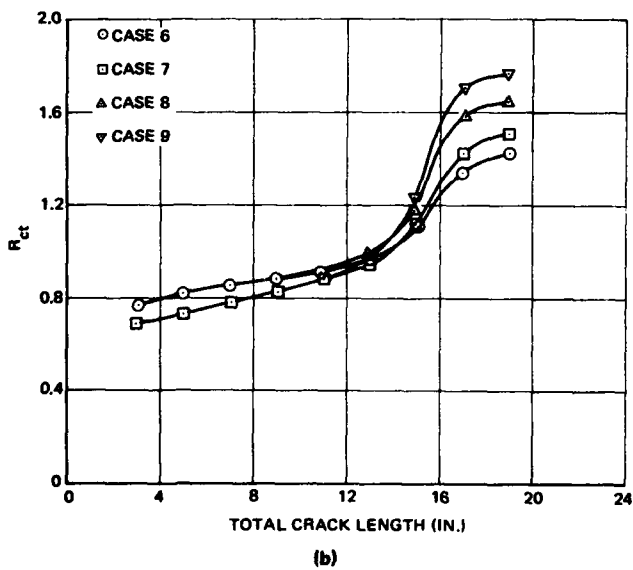
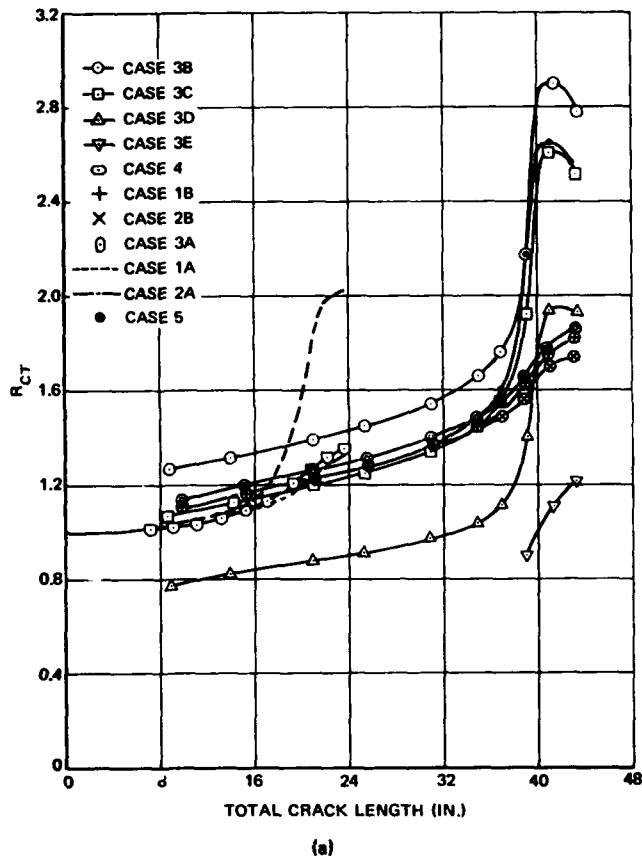


FIGURE 12. RATIO OF CRACK TIP STRESS IN UNSTIFFENED TO THAT IN STIFFENED PANEL,  $R_{CT}$ , VERSUS CRACK LENGTH

FIGURE 13. FRAME AND CRACK STOPPER STRESSES VERSUS CRACK LENGTH

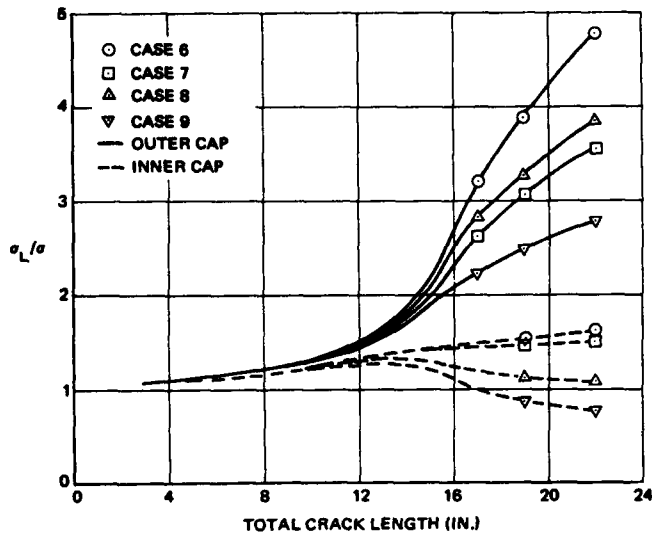


FIGURE 14. LONGERON STRESSES FOR CASES 6, 7, 8, AND 9

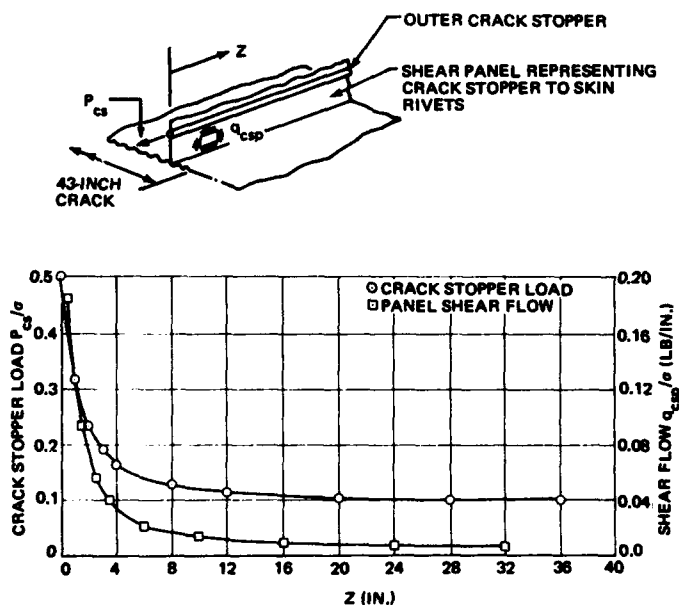


FIGURE 15. OUTER CRACK STOPPER AND SHEAR PANEL LOAD DISTRIBUTION FOR CASE 3c, TABLE 1

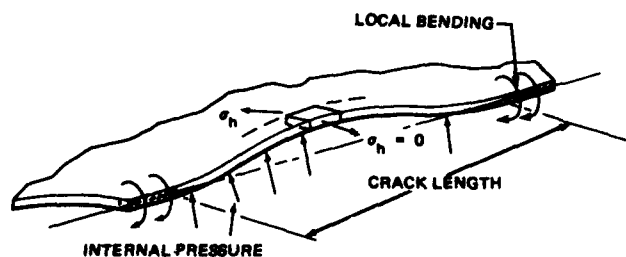


FIGURE 16. BULGING DUE TO PRESSURE

In the case of configurations (6) through (9) of Figure 11, the sheet deflection from buckling is increased by induced longeron bending caused by transfer of load from the longeron to the skin. Figure 17(a) shows that at some distance from the crack, the longeron load  $P$  is acting at the centroid of the section. This load is reacted by the skin ahead of the crack and is thus transferred a distance  $e$ . Again, the buckling induced causes an increase in stress intensity at the tip of the crack and is more severe when the crack is located adjacent to the lateral stiffening as shown in Figure 17(b). The longeron bending and thus the stress-intensity-factor  $K$  increases with longeron area. The induced bending in the center longeron for a uniaxial loading case causes the outer longerons to be loaded as shown in Figure 17(b). The resultant bending in the outer longerons tends to cancel out the bending caused by transfer of load from the cracked skin as indicated by the longeron stress curves of Figure 14. If, however, the panel section shown in Figure 17(b) were a section of a pressurized shell, then much of the inward bending of the center longeron would be relieved by the cabin pressure and the loading  $W$ , causing relief to the outer longeron bending, would not be present.

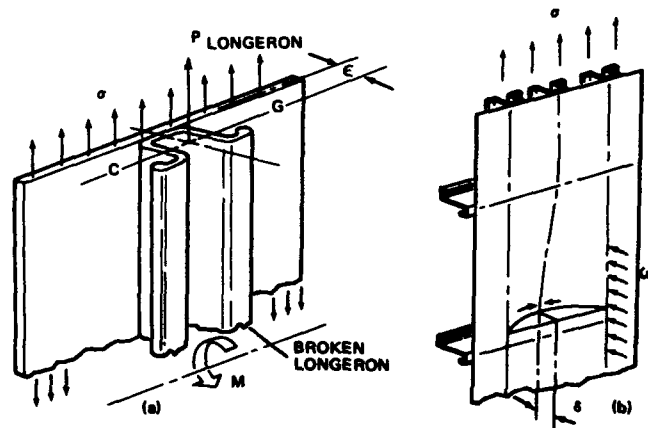


FIGURE 17. CENTER LONGERON BENDING

**Axial Tension** - The buckling caused by lateral compression stress and the bulging caused by pressure on a curved panel are relieved in a biaxial tension stress field. The tension stress parallel to the crack reduces or completely overrides the compression stress causing buckling. Thus the effective stress-intensity-factor  $K$  will not be as high in the presence of biaxial tension stresses. On the other hand, if the applied stress parallel to the crack is compressive, then the stress intensity factor will be increased.

**Lateral Stiffener Constraint** - A crack travelling parallel and adjacent to a stiffener in a uniaxial stress field is influenced by an induced biaxial tension stress  $\sigma_x$  in the skin in the vicinity of the stiffener. Under uniaxial tension loading, the lateral contraction  $\delta$  of an unstiffened panel will be:

$$\delta = \sigma \left( \frac{\nu}{E} \right) \left( \frac{W}{2} \right)$$

where

$\nu$  = Poisson's ratio

$W$  = panel width

$E$  = modulus of elasticity

The lateral stiffener only allows a deflection  $\delta_1$  as seen in Figure 18, thus placing the longeron in compression and inducing a local biaxial tension stress in the skin in the vicinity of the stiffener. The presence of the induced tension stress will relieve the compression stress causing buckling and thus reduce the stress-intensity-factor  $K$  at the crack tip.

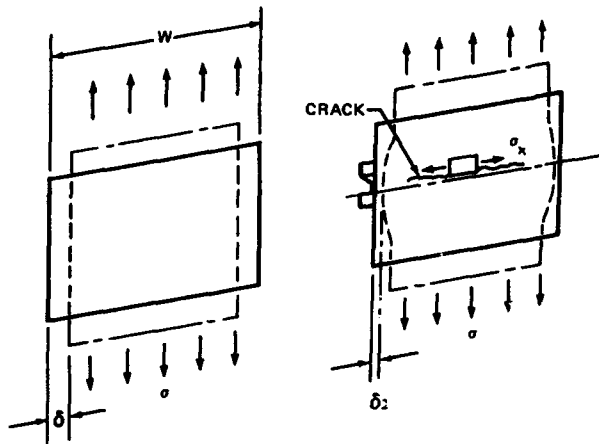


FIGURE 18. EFFECTS OF LATERAL STIFFENING

**Local High Stress Near a Shear Clip** – Where frames are attached to the skin with a shear clip as shown in Figure 6, a local discontinuity stress  $\sigma_c$  exists in the skin in the area of the cutout, which is higher than the applied stress  $\sigma$ . A crack approaching this area will be influenced by the higher stress and a higher stress-intensity-factor  $K$  will result. This effect, which has been shown to exist by strain gages, is not present when a crack stopper is used to provide continuity across the cutout.

**Variation in Crack Stopper Stress Across the Crack Stopper** – In the Lumped Parameter Analysis described, the crack stopper straps illustrated in Figure 6 are lumped into a bar and connected to the skin by a single shear panel. In fact, three rows of rivets are used for the attachment. The analysis, using this idealization, will not predict variations of stress across the crack stopper which do exist in practice. If adequate strength could be provided in one rivet row, then the crack stopper could be loaded only in a symmetrical manner.

**Shear Flow in Attachments** – The shear flow applied to the attachments connecting the crack stopper to the skin reaches a peak in the vicinity of the crack (Figure 15). The attachments adjacent to the crack are subjected to high loads which increase with the crack length. Local yielding of the attachments will cause a redistribution in load, resulting in a rounding off of both attachment shear flow and crack stopper load in the area of the crack. A reduction in crack stopper load locally will have the effect of increasing the crack tip stress and reducing  $R_{c1}$ .

**The Effects of Shear Stress Combined with Tension** – The stress intensity at the crack tip is increased when shear is combined with uniaxial tension. The values  $\sigma$  in Equation (7) is replaced by:

$$\sigma_p = \frac{\sigma}{2} + \sqrt{\left(\frac{\sigma}{2}\right)^2 + \tau^2}$$

where

$\sigma$  = tension stress normal to the crack

$\tau$  = shear stress

Axial tension stress is not included since its effect reduces the stress intensity at the crack tip where inclusion in the expression for  $\sigma_p$  would suggest that an increase in stress intensity takes place. The test program, which is to be discussed in Reference 8, was planned to provide data on all of the secondary effects listed above.

## FRACTURE STRENGTH OF PANELS CONTAINING CRACKS

### Skin Fracture Toughness Criterion

In unstiffened thin sheet panels containing cracks, fracture is usually governed by the plane stress fracture toughness  $K_c$ . When the stress-intensity-factor  $K$  of Equation (3) reaches the critical value for the material, fast fracture occurs. The residual strength of an unstiffened panel  $\sigma_R$  is given as

$$\sigma_R = \frac{K_c}{C \sqrt{W \tan\left(\frac{\pi a_c}{W}\right)}} \quad (16)$$

where

$\sigma_R$  = gross stress at fast fracture

$a_c$  = half the crack length at fast fracture

The consistency of the plane stress fracture toughness  $K_c$  as a material constant is not fully established for narrow test panels due to the presence of other variables, such as the amount of crack buckling in the thin sheet, adjustment for slow crack growth, and plastic zone size. Furthermore, Allen<sup>3</sup> indicates that when  $a$  is small, a fundamental assumption in the derivation of Equation (3) causes the equation to be inaccurate. The fracture toughness  $K_c'$  provides a more consistent material constant. The residual strength of an unstiffened panel then becomes

$$\sigma_R = \frac{K_c'}{C \left[ 1 - \left( \frac{\sin \frac{\pi a_c}{W}}{\sin \frac{\pi}{W} \left( a_c + \frac{1}{2\pi} \right)} \right)^2 \right]^{-1/2}} \quad (17)$$

However, for crack lengths of practical interest in panels with width greater than 30 inches, the values  $K_c$  and  $K_c'$  are nearly identical. The large 7075-T6 flat stiffened panel test results<sup>9</sup> show that  $K_c$  provides a reliable material constant for large panels because the influence of plastic zone size on  $K_c$  is small relative to a long crack length and the observed macro slow crack growth can be included in the final critical crack length,  $a_c$ .

In stiffened fuselage panels, the failure criterion of the damaged panel is either the ultimate tensile strength of the stiffeners or the fracture toughness of the skin. The stiffener tensile strength criterion is limited by the ultimate tensile strength or excessive yielding of the stiffener.

The skin residual strength of a stiffened panel  $\sigma_R$  is derived from Equation (8) by substituting  $K_c$  for  $K$ .

$$\sigma_R = \frac{K_c R_{ct(a)}}{C \sqrt{W \tan \frac{\pi a_c}{W}}} \quad (18)$$

where

$R_{ct(a)}$  = the ratio of the crack tip stress in the unstiffened panel to that in the stiffened panel at a given half crack length,  $a$

Figure 19 illustrates the residual strength versus crack length for a 120-inch wide unstiffened panel and two stiffened panels with configurations as noted for cases (1b) and (3b) of Table 1. Note the change in the direction and slope of the residual strength curves for the stiffened panels as the crack length approaches the spacing of the stiffeners. The maximum reduction of crack tip stress as expressed in terms of  $R_{ct(a)}$  occurs where the crack tip is in the region of the stiffeners (Figure 20). The characteristics of the fail-safe features in stiffened panels are shown in the residual strength curves of Figure 19. At crack length  $l_A$  and gross stress  $\sigma_{RA}$ , fast fracture will take place at A and the crack will be arrested at B. However, any fracture at a gross stress  $\sigma_R > \sigma_{RC}$  (the maximum residual strength of the panel with case 3b configuration) will not be arrested and would represent an explosive failure in a pressurized shell.

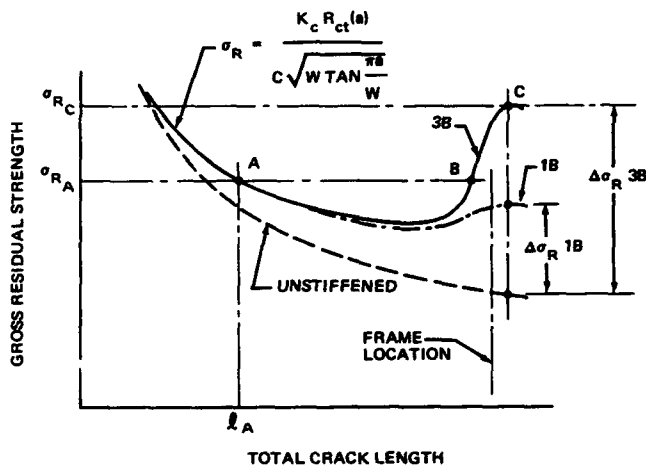


FIGURE 19. COMPARISON OF GROSS RESIDUAL STRENGTH CURVES FOR UNSTIFFENED AND STIFFENED PANELS - (CASES (1b) AND (3b))

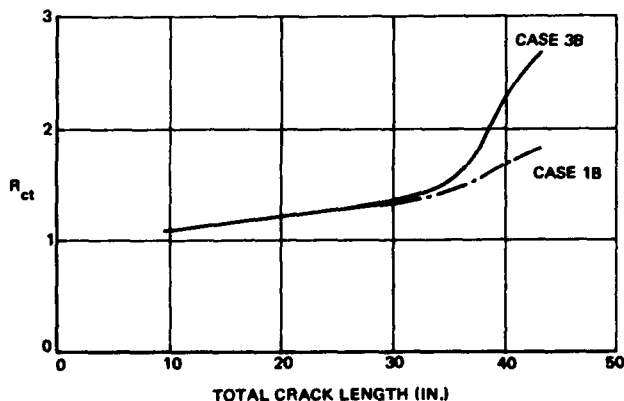


FIGURE 20.  $R_{ct}$  VERSUS CRACK LENGTH FOR PANEL CONFIGURATIONS (1b) AND (3b)

For a given panel width, the shape of the residual strength curve depends on the value of  $R_{ct}$  which in turn is determined by the design of the stiffener configuration. For a given area of the stiffener,  $R_{ct}$  increases with increasing shear rigidity of the stiffener attachment. For a given shear rigidity of attachment,  $R_{ct}$  increases with the area of the stiffener. An example of residual strength curves for the specific frame designs (cases 1b and 3b of Table 1) is shown in Figure 19. It is noted that the increase of residual strength,  $\Delta\sigma_R$ , for case 1b due to the stiffeners is not as great as for case 3b. The shear clip attaching the frame to the skin for case 1b is very flexible. The frame and shear clip of case 3b is identical to case 1b, but in addition it has a crack stopper strap connected directly to the skin with three rows of rivets which are comparatively stiff, resulting in a greater reduction of crack tip stress.

The gross residual stress  $\sigma_R$  is directly proportional to the fracture toughness  $K_c$  of the material, as shown in Equation (18) and Figure 19. The overall height of the residual strength curve varies directly with  $K_c$ .

### Stiffener Strength Criteria

The gross residual strength curve for skin criteria illustrated in Figure 19 is valid only as long as the stiffener remains intact. In certain cases, however, the stiffener may fail before the skin becomes critical. Stress distributions in frames, longerons and crack stoppers, as shown in Figure 13, must be defined to calculate the allowable based on stiffener critical criteria. In cases where the stiffening becomes critical, local yielding of the stiffener takes place before failure, resulting in an increase in skin crack tip stress and thus a decrease in  $R_{ct}$ . Stiffener failure and skin failure then occur at the same time, precipitated by stiffener yielding.

It has been indicated that increasing the attachment stiffness between the stiffener and the skin will increase the skin strength. This is due to a higher load transfer to the stiffener. If, however, the stiffness of the attachment is made too great, then the stiffener can become critical and the advantage gained in the skin criteria is lost due to stiffener failure.

### FATIGUE CRACK PROPAGATION

#### Growth Rate Equations

Recent investigations on fatigue crack propagation phenomena<sup>10, 11</sup> have shown that growth rate,  $da/dN$ , can be related to an exponential function of stress-intensity-factor range,  $\Delta K$ . The empirical rate equation in the general form is given as

$$\frac{da}{dN} = A \Delta K^n \quad (19)$$

where

$A$  = constant

$n$  = exponent, slope of  $\log \frac{da}{dN}$  vs  $\log \Delta K$  curve

The influence of load profile, environment, temperature, test frequency, state-of-stress, and material form on fatigue crack growth are not considered. However, the equation in the empirical form that is derived from the test data of a specific alloy in the gage and form used in the structure provides the necessary material property for a practical structural analysis within the framework of linear-elastic fracture mechanics. The presence of moisture accelerates fatigue crack growth rate only in

the plane strain state.<sup>12</sup> Therefore, the exponent  $n$  is expected to be higher at low values of  $\Delta K$ . In the other extreme, instability of crack growth occurs as  $\Delta K$  approaches  $K_c$ . The semi-empirical equation<sup>11</sup> is intended to compensate this condition and the effect of mean load.

$$\frac{da}{dN} = \frac{B \Delta K^n}{(1-R) K_c - \Delta K} \quad (20)$$

where

$B$  = a material constant

$K_c$  = fracture toughness of the material

$R$  = min-to-max stress ratio

The fatigue crack life prediction of  $a_1$  to  $a_n$  for an unstiffened panel can be computed by numerical or graphical integration of crack growth rate. The accuracy of the process depends on the reliability of test data used to derive the empirical equation. If the growth rate data derived from the sheet panels of a given material condition and width are applied to compute the life of an identical panel, the accuracy should be ensured within the scatter. The accuracy of using the empirical equation based on narrow panel test data to predict crack life in large panels or structure is not fully established. In Reference 9, the crack growth prediction curves for large 7075-T6 and 2024-T3 stiffened panels were found to be reasonably accurate using the semi-empirical equation derived from the narrow panel growth rate data. However, the effects of some variables, such as the variation in  $K_c$  with panel width and the secondary effects discussed in the section on secondary effects, were not considered. A significantly higher  $K_c$  for wide panels would greatly alter the accuracy of Equation (20) as  $\Delta K$  values approach  $K_c$ .

The relative fatigue crack propagation resistance of material can be represented by an empirical rate equation. Figure 21

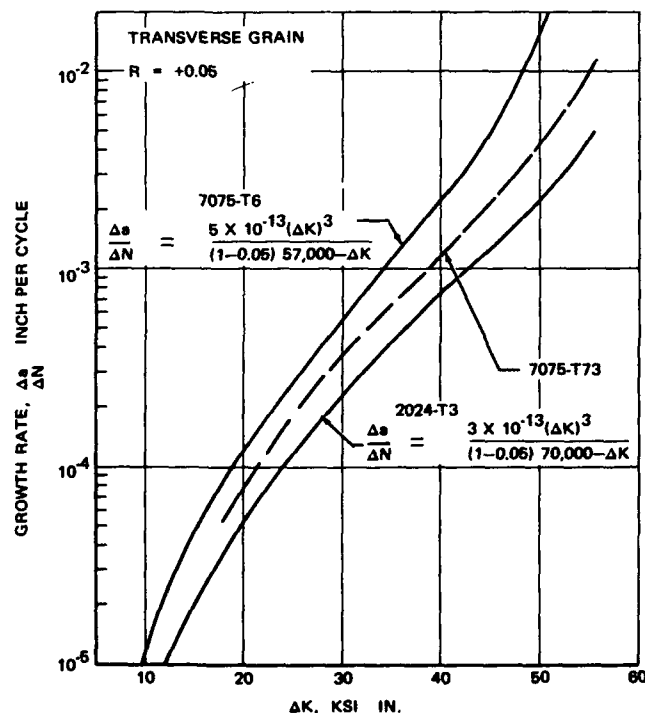


FIGURE 21. COMPARISON OF CRACK GROWTH RATE FOR 0.040 ALCLAD 7075-T6, 0.071 ALCLAD 7075-T73 AND 0.071 ALCLAD 2024-T3

illustrates the growth rate data for three alclad aluminum alloys: 7075-T6, 7075-T73 and 2024-T3. The data were derived from the test results of 30-inch-wide 0.071 unstiffened panels containing a central through-the-thickness crack.<sup>13</sup>

#### Analysis Method for Stiffened Panels

The method employs a simple graphical construction of fatigue crack growth curve; that is, crack length versus cycles of loading for stiffened panels. Figure 22 illustrates the steps involved in the process. First, the history of loading, in terms of applied maximum cyclic gross stress to a stiffened panel  $\sigma_{max}$  and stress ratio  $R$  versus half crack length,  $a$ , is to be defined. Then  $\sigma_{max}$  is transformed to an equivalent stress,  $\sigma$ , in an identical unstiffened panel which gives the same  $K_{max}$  as in the stiffened panel.

$$\sigma = \frac{\sigma_{max}}{R_{ct(a)}} \quad (21)$$

where

$R_{ct(a)}$  = ratio of crack tip stress in unstiffened panel to that in a stiffened panel

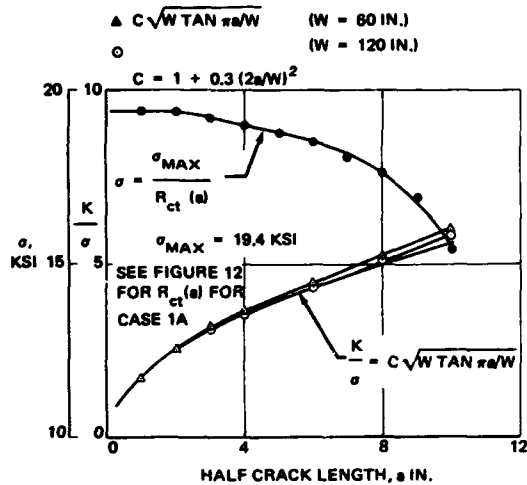
$\sigma_{max}$  = maximum cyclic gross stress in the stiffened panel

This equation is derived by equating  $K$  of Equation (3) and Equation (7). The values of  $\sigma$  versus half crack length are plotted in Figure 22(a). Second, the  $\Delta K$  versus half crack length curve plotted in Figure 22(b) is obtained by making several discrete computations at various crack lengths using the values of  $\sigma$  and  $C\sqrt{W \tan \pi a/W}$  provided in Figure 22(a).

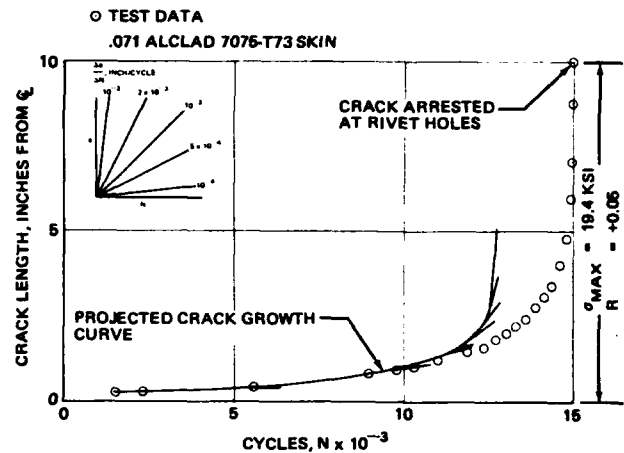
$$\Delta K = \sigma (1-R) C \sqrt{W \tan \frac{\pi a}{W}} \quad (22)$$

The fatigue crack growth curve is constructed by projecting a series of consecutive straight lines from initial crack length  $a_0$  to  $a_1$ ,  $a_1$  to  $a_2$ , ...  $a_{n-1}$  to  $a_n$  at a slope of the growth rate,  $da/dN(a = a_i)$ , as shown in Figure 22(d). The growth rate  $da/dN$  at crack length  $a_i$  is defined in the  $\Delta K$  versus  $da/dN$  curve of Figure 22(c), using the common cross-reference ordinate  $\Delta K$  in Figures 22(b) and (c). The growth rate curve of the skin material can be defined by a semi-empirical equation. The increment of projection,  $a_i$  to  $a_{i+1}$ , should be selected according to the rate of change of  $\Delta K$  with half crack length in Figure 22(b). For example, it is noted that at low values of  $a$ ,  $\Delta K$  varies greatly but not at longer crack lengths. Therefore, using small increments at small values of  $a$  and large increments at longer crack lengths will not cause inaccuracy.

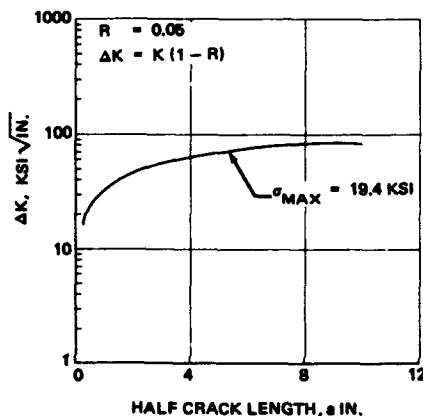
In a reverse process, the crack growth curve of the test results can be reduced to the  $\Delta K$  versus  $da/dN$  relation for the skin material. The test results may be analyzed to assess the effects of secondary variables which influence crack growth rate in a large stiffened panel. For example, the test results of Panel I in Figure 22(d), were reduced to derive  $\Delta K^*$  versus  $da/dN$  curves for 7075-T73 wide panels. Such curves were found to be significantly different from narrow panel curves at high values of  $\Delta K$ . A number of the secondary effects presented in the section on secondary effects can be evaluated from fatigue crack propagation test results of stiffened panels. For example, the effect of curvature and pressure on fatigue crack growth rate will be established by comparing the  $\Delta K$  versus  $da/dN$  curves for similar large stiffened flat and curved panels with the same skin material.



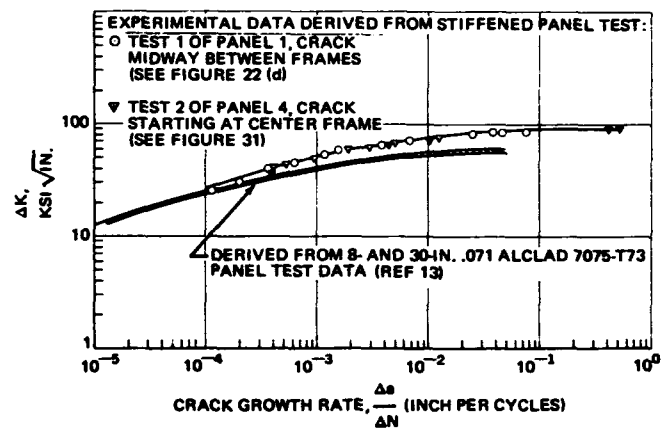
(a) TRANSFORMATION OF APPLIED GROSS STRESS IN STIFFENED PANEL TO EQUIVALENT GROSS STRESS IN AN IDENTICAL UNSTIFFENED PANEL



(d) GRAPHICAL CONSTRUCTION OF THE FATIGUE CRACK PREDICTION CURVE FOR PANEL 1 USING UNSTIFFENED PANEL DATA



(b) PLOT OF STRESS-INTENSITY-FACTOR RANGE,  $\Delta K$  VERSUS CRACK LENGTH



(c) PLOT OF STRESS-INTENSITY-FACTOR RANGE,  $\Delta K$  VERSUS FATIGUE CRACK GROWTH RATE,  $\frac{\Delta a}{\Delta N}$  FOR 0.071 ALCLAD 7075-T73

FIGURE 22. GRAPHICAL METHOD OF ANALYZING FATIGUE CRACK GROWTH CURVE FOR PANEL 1 CONTAINING A ONE-BAY LONGITUDINAL CRACK

### TEST PROGRAM

#### SPECIMEN DESCRIPTIONS

Four types of test specimens were chosen for the test program to assess typical damage in fuselage structure and to substantiate the analytical method.

#### Flat Panels Containing Longitudinal Cracks

Six large stiffened panels, typical of fuselage shell structure, were fabricated to experimentally evaluate a number of design features. All of the panels were made from .071-inch clad aluminum alloy sheet, 120 inches by 75 inches, and stiffened by frames and longerons. Principal variables in the designs, shown in Figure 23, are:

1. Skin material
2. Longeron spacing
3. Shear clip design
4. Frames with or without crack stoppers

The frames, spaced 20 inches apart on all of the panels, were formed from .071-inch 7075-T6 clad sheet with net area 0.5042 square inch and cross-sectional dimensions of configuration (1) shown in Figure 9. The longerons were made from 7075-T6

extrusion having a gross area of 0.312 square inch. The rivets attaching the crack stopper or shear clip to the skin were, in all cases, MS 20470DD6. During Test 3 of Panel 2 and Test 2 of Panels 5 and 6, the frame, central to a 2-bay crack, was reinforced with an angle 15 inches long as shown in Figure 10, configurations (4) and (5).

#### Flat Panels with Circumferential Cracks

Eight flat stiffened panels, 60 inches wide and 120 inches long, were fabricated to evaluate several different longeron configurations and two different skin materials. All of the panels, made from .071-inch clad aluminum alloy sheet were stiffened by longerons at 8-inch spacing and frames at 20-inch spacing. Longeron material for all of the panels was 7075-T6 extrusion and frame material was .071-inch 7075-T6 clad sheet of configuration (1) of Figure 9.

Principal variables in the panels were:

1. Longeron type
2. Longeron area
3. Skin material
4. Rivet configuration and type

A description of the panels is given in Table 2.

PANEL NUMBER	SKIN MATERIAL	LONGERON SPACING (IN.)	CRACK STOPPER MATERIAL	SHEAR CLIP DESIGN
1	7075-T73	6.5	-	
2	7075-T73	8.0	-	
3	7075-T73	6.5	-	
4 TEST 1	7075-T73	8.0	-	
4 TEST 2	7075-T73	8.0	-	
5	7075-T73	8.0	TITANIUM 8-1-1	
6	2024-T3	8.0	SINGLE ANNEALED	

FIGURE 23. PANEL CONFIGURATION FOR LONGITUDINAL CRACKS

TABLE 2.  
PANEL CONFIGURATION FOR CIRCUMFERENTIAL CRACKS

PANEL NUMBER	SKIN MATERIAL	LONGERON TYPE	LONGERON NET AREA (SQ IN.)	LONGERON TO SKIN ATTACHMENTS	CONFIGURATION NUMBER OF FIGURE 11
7	7075-T73	HAT SECTION	0.3029	NAS1097 DD6	6
8	7075-T73	HAT SECTION	0.5121	NAS1097 DD6	7
9	2024-T3	HAT SECTION	0.3029	RV5170-6 7075-T73	6
10	2024-T3	HAT SECTION	0.5121	NAS1097 DD6	7
11	7075-T73	TEE SECTION	0.2896	NAS1097 DD6	8
12	7075-T73	TEE SECTION	0.4866	NAS1097 DD6	9
13	2024-T3	TEE SECTION	0.2896	RV5170-6 7075-T73	8
14	2024-T3	TEE SECTION	0.4866	RV5170-6 7075-T73	9

### Curved Panel

One curved panel, 166 inches long by 104 inches wide, typical of fuselage shell structure with radius 118.5 inches, and stiffened by frames and longerons, was fabricated to determine the effects of pressure, curvature and biaxial tension loading. Skin material for this panel was .08-inch alclad 7075-T73 sheet. The frames, spaced 20 inches apart, having a net cross-sectional area of 0.5042 square inch, were formed from .071-inch 7075-T6 clad sheet to the dimensions shown in Figure 9, configuration (2). Longerons, spaced 7.82 inches apart, were made from 7075-T6 extrusion with a gross cross-sectional area of 0.312 square inch. The shear clips, attached to the skin by RV 5197-6 7075-T73 rivets, were designed as shown in Figure 9, configuration (2). Longerons were attached to the skin using RV 5121-6 rivets.

### EQUIPMENT AND PROCEDURES

The test procedure and load schedule for each panel were established to facilitate both the evaluation of the complete fail-safe capability of the panel design and the verification of the analytical method. To achieve these objectives, a flexible test schedule was adopted for each panel. Fatigue crack propagation, fast fracture, crack arrestment and residual failure strength of the stiffened panels were determined.

Test loads and crack lengths were chosen according to the analysis so that fast fracture was arrested at the highest possible stress level (see Figure 19). If the crack length chosen is too long, then fast fracture will occur at a stress level below the residual strength of the panel. On the other hand, if fast fracture occurs at a stress greater than the residual strength of the panel, total failure of the panel will occur. This difficulty could, of course, be minimized if several panels of one configuration were available to test at various stress levels. This is not economically feasible. The results of each test were assessed in conjunction with the analytical calculation to determine optimum stress levels for subsequent tests. One of the important practical characteristics evaluated was the dynamic effect at crack arrestment.

### Panels with Longitudinal Cracks

The 120-inch-wide flat panels were mounted in a servo hydraulic test rig. Uniaxial loading was provided by four 20-square-inch-area hydraulic jacks through a whiffletree arrangement attached to both skin and frames. Each jack load was monitored by a load cell and recorded by oscillograph. Loading was adjusted to allow for the whiffletree weight. The panels were subjected to a tension-tension cyclic loading with a minimum-to-maximum load ratio,  $R = 0.05$ , at a maximum cyclic rate of 24 cycles per minute. The system capability also extended to the application of incremental static loading. Six strain gages, installed on the panel, were continuously monitored by means of oscillograph recorders and several other gages were recorded at intervals.

Blue marking solution was uniformly sprayed over the area and lines describing an arc from the center of the crack were scribed on the skin at finite increments starting at the ends of the slot. The crack growth was observed by means of a telescope mounted approximately 10 feet from the specimen. Crack growth readings were taken with an accuracy of  $\pm 0.02$  at approximately 0.10-inch increments. The cyclic rate was adjusted periodically as the crack growth rate increased so that accurate data could be recorded. In some tests at predetermined crack lengths, the loading was increased statically in small increments until skin fast fracture occurred. The critical crack length, including slow growth and applied load at fast fracture, was accurately determined. Two tests were performed on Panels 1, 3, 4, 5 and 6, and three tests

on Panel 2. Repairs were made to the cracked area before proceeding to the next test. The crack positions were carefully chosen so that the repairs did not influence the subsequent test results.

A modification was made to the Lumped Parameter Analysis to evaluate the effects of the repaired areas on the test results. The effects were shown to be negligible for the crack locations chosen.

Seven positions for the initial crack starter slits in the tests of the six panels are shown in Figure 24. The slit location for each test is listed in Table 3. With the exception of crack positions 5 and 7 of Figure 24, all the cracks were placed one inch from the centerline of the longeron. Cracks 5 and 7 were placed midway between longerons. A typical 120-inch-wide panel mounted in the test fixture is shown in Figure 25.

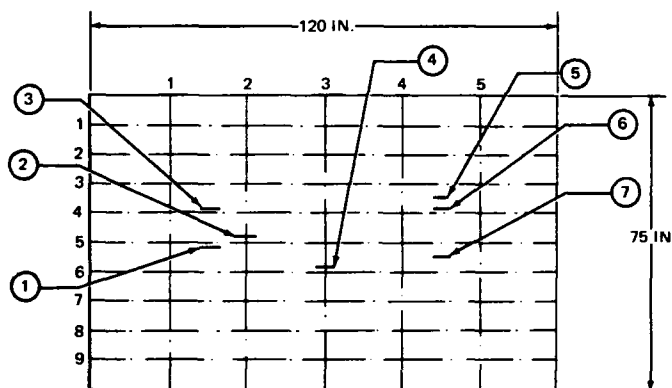


FIGURE 24. CRACK LOCATIONS FOR TESTS ON 120-IN. WIDE PANELS

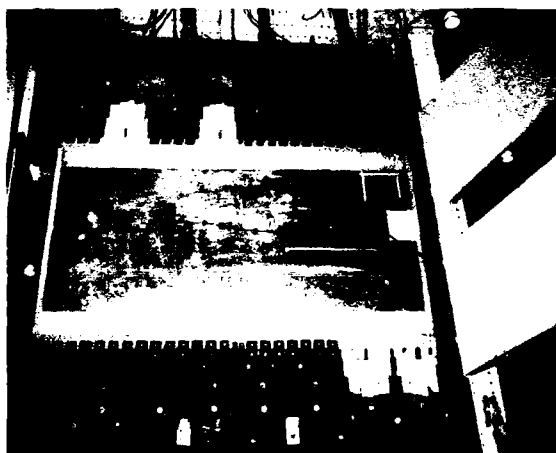


FIGURE 25. TYPICAL 120-IN. WIDE TEST PANEL MOUNTED IN THE TEST FIXTURE

### Panels with Circumferential Cracks

The 60-inch-wide panels were mounted in a 1.5-million-pound servo hydraulic testing machine. The capability existed to mount two panels side by side as illustrated in Figure 26. Uniaxial cyclic or static loading was applied to each panel by six 20-square-inch hydraulic jacks through a whiffletree arrangement attached to the upper and lower edges of the panel. The load was monitored by two load cells for each panel and continuously recorded by oscillograph.





FIGURE 26. TWO TYPICAL 60-IN. WIDE PANELS MOUNTED IN THE TEST FIXTURE

The testing procedure was similar to that used for the 120-inch-wide panels. Each skin crack starter slit was located over a completely cut longeron. Two tests were performed on each panel and the first consisted of propagating the skin crack to a predetermined length under uniaxial cyclic loading. Static loading was applied in increments to fast fracture the skin crack. In some cases, cyclic loading was applied to determine crack growth rate in the vicinity of the longeron. The second test was a repeat of the first except that after crack arrestment, the panel was loaded to failure. If after fast fracture the crack was arrested in rivet holes, cyclic loading was applied to restart a fatigue crack from the rivet hole prior to loading to failure.

The position of each crack starter slot is shown in Figure 27 and related to each test in Tables 5 and 6.

#### Curved Panel

The panel was mounted in a test rig specifically designed to test curved panels of 118.5-inch radius under cyclic pressure and axial tension loading. A schematic illustration of the rig is shown in Figure 28 and a photograph is presented as Figure 29.

The pressure source is provided by a vacuum chamber fitted to the outside of the skin. To start the test, the large rectangular chamber, fitted with a 2-inch-diameter rubber seal, was lowered onto the outer surface of the panel by means of a hydraulic jack. The seal is pressurized to approximately 5 psi and the chamber is evacuated by two large vacuum pumps through a plenum chamber so that pressure from the atmosphere is applied to the underside of the panel. The hoop tension loading induced is reacted by a set of whiffletrees attached to both skin and

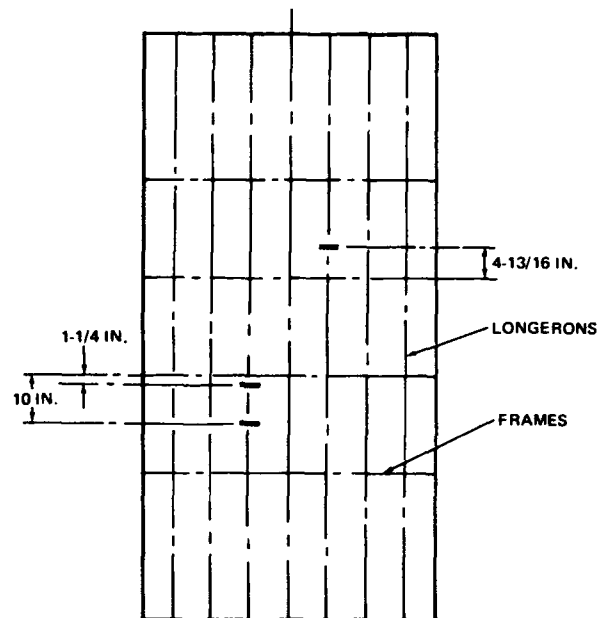


FIGURE 27. CRACK LOCATIONS FOR TESTS IN 60-IN. WIDE PANELS

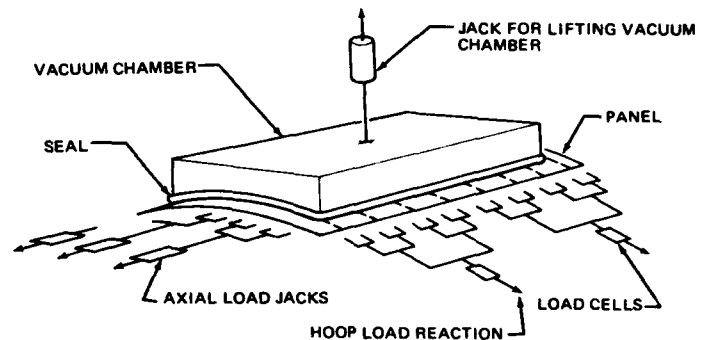


FIGURE 28. SCHEMATIC ILLUSTRATION OF VACUUM TEST RIG FOR CURVED FUSELAGE PANELS

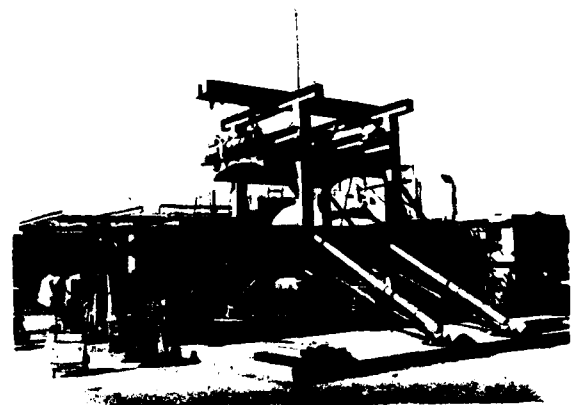


FIGURE 29. VACUUM TEST RIG FOR TESTING CURVED FUSELAGE PANEL UNDER COMBINED PRESSURE AND AXIAL TENSION LOADING

frames. Axial loading is applied simultaneously by a set of servo-controlled hydraulic jacks through a whiffletree arrangement to both ends of the panel. This arrangement ensures a minimum amount of longitudinal movement between the seal and the panel. Both hoop tension and axial loading are continuously monitored by load cells and recorded by oscillograph. A unique feature of the rig is that the panel can be observed from the underside during cyclic loading (see Figure 30). The upper surface of the panel can be inspected within minutes by lifting the vacuum chamber.

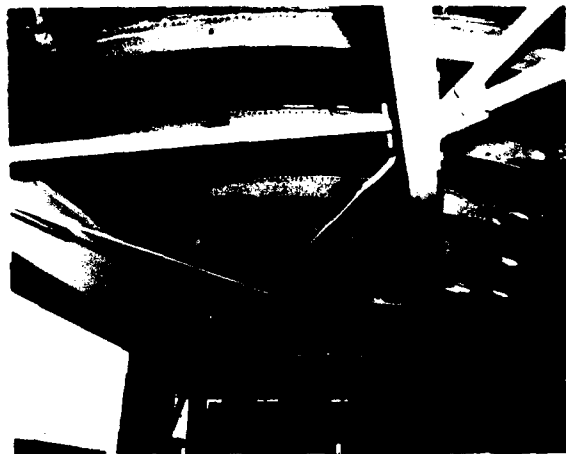


FIGURE 30. VIEW OF THE UNDERSIDE OF CURVED PANEL 15

Crack starter slots, similar to those used on the 120-inch-wide flat panels, were made in the skin. Crack growth was observed through an inclined mirror by means of a telescope mounted approximately 10 feet from the rig. Four tests were performed to determine the effects of pressure, curvature and biaxial tension:

1. One-bay crack with pressure load only
2. One-bay crack with pressure and axial load
3. Two-bay crack with pressure load only
4. Two-bay crack with both pressure and axial load.

For Tests 1 and 3, the crack was grown to a predetermined length under cyclic pressure loading at a minimum-to-maximum pressure ratio,  $R = 0.05$ . Static tests then were conducted to determine fast fracture and crack arrestment. In the static tests, the pressure was increased in increments until fast fracture occurred. In Tests 3 and 4, the cyclic test procedure was identical to that for Tests 1 and 2, except that the cyclic axial load was applied simultaneously with the cyclic pressure. For static tests, a predetermined axial load was applied to the panel; pressure was then increased in increments until fast fracture occurred.

## TEST RESULTS

### Flat Panels With Longitudinal Skin Cracks

The representative results from the cyclic and static tests in Panels 1 through 6 are plotted in Figures 22(d), 31, 32, 54, and 55. The static test results for fast fracture, crack arrestment and final residual strength are listed in Table 3. The load history in each test is indicated on the graphs. In some tests, such as shown in Figures 31, 32, and 55, static tests were performed on panels

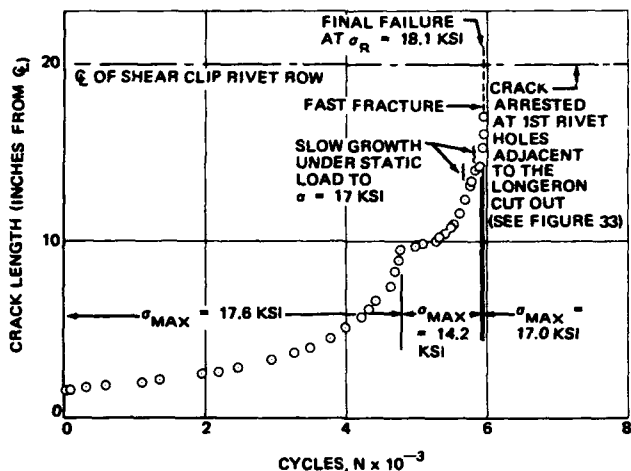


FIGURE 31. TEST RESULTS FOR TEST 2 OF PANEL 4

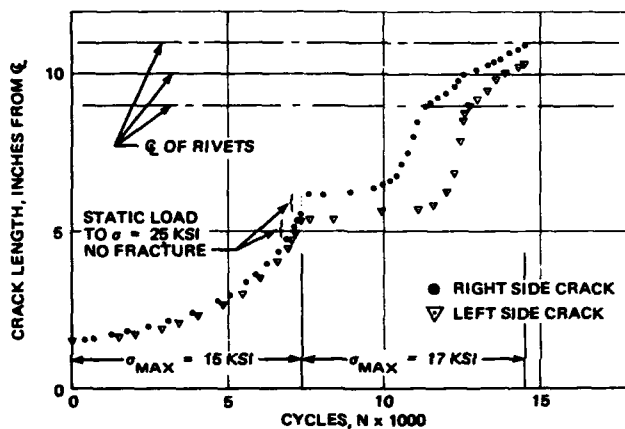


FIGURE 32. RESULTS OF TEST 1 FOR PANEL 6

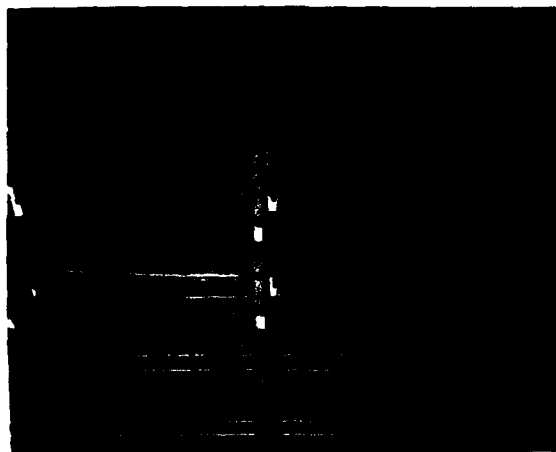


FIGURE 33. REAR VIEW OF PANEL 4. SHOWING ARRESTMENT OF A TWO-BAY SKIN CRACK

containing fatigue cracks of certain predetermined length to evaluate fast fracture arrestment capability and residual strength of the panels. Figure 31 shows the results of Test 2 for Panel 4. It is noted that a fast fracture occurred from a two-bay crack and was arrested in rivet holes at adjacent frames (see Figure 33). The fast fracture occurred under a cyclic maximum gross stress of 17,000 psi. Cycling was continued at a maximum gross stress of

TABLE 3.  
TEST RESULTS FOR 120-IN.-WIDE PANELS WITH LONGITUDINAL CRACK

PANEL NUMBER	TEST NUMBER	GROSS STRESS (PSI)	TOTAL CRITICAL CRACK LENGTH (IN.)	$R_{et}$	C	$K_c^*$ PSI $\sqrt{IN.}$	TYPE OF CRACK	CONDITION (1)	CASE (2)	CRACK LOCATION FIGURE 24
1	1	19,410	17.8	1.145	1.006	> 91,000	1 BAY	NF	1A	7
	2	19,410	17.8	1.145	1.006	> 91,000	1 BAY	NF	1A	1
2	1	22,000	17.8	1.145	1.006	> 103,137	1 BAY	NF	1A	5
	2	20,888	17.8	1.145	1.006	> 97,929	1 BAY	NF	1A	3
	3	17,300	33.2	1.430	1.023	92,000	2 BAY	FF	4	4
	3	18,476	42.95	1.858	1.038	90,400	2 BAY	FA	4	4
3	1	19,410	17.8	1.145	1.006	> 91,000	1 BAY	NF	1A	6
	2	19,124	24.1	1.250	1.012	96,200	2 BAY	FF	1B	2
	2	19,744	40.905	1.750	1.0349	98,500	2 BAY	FA	1B	2
4	2	17,000	35.0	1.435	1.0255	93,400	2 BAY	FF	1B	2
	2	18,100	41.93	1.78	1.0366	90,500	2 BAY	FA	1B	2
5	2	20,138	20.57	1.71	1.0088	96,700	2 BAY	FF	5	2
6	2	19,000	32.65	0.98	1.0222	> 145,500	2 BAY	NF	3D	2
	2	20,000	43.75	1.26	1.040	145,500	2 BAY	FF&FA	3E	2

(1) CONDITION FOR WHICH  $K_c^*$  IS EVALUATED  
 FF CRACK FAST FRACTURE  
 NF FAST FRACTURE DID NOT OCCUR  
 FA PANEL FAILURE

(2) CASE FOR WHICH  $K_c^*$  IS EVALUATED (SEE TABLE 1)

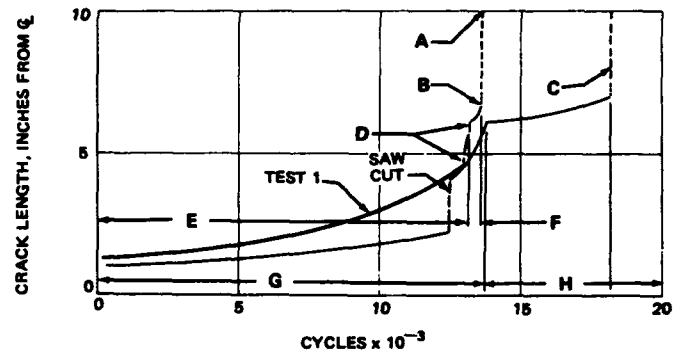
14,042 psi to restart a fatigue crack from the rivet holes. Failure of the panel occurred after loading in increments up to 18,100 psi. There was some evidence from strain gages that yielding of the center frame may have occurred (see Figure 48). In order to be sure that this had not caused failure, the center frame of Panel 2 was reinforced locally with an angle as shown in Figure 10, Configuration 4. Without yielding the center frame, final failure occurred at 18,476 psi (see Table 3). This stress level is almost the same as that which caused failure of Panel 4 and therefore it can be concluded that failure of both panels was due to skin fast fracture.

The static test results listed in Table 3 include  $K_c^*$  data for cases where fast fracture did not occur. The  $K_c^*$  listed for these cases is the maximum value applied without fast fracture at the most critical crack length.

It is of interest to note that for Test 2 of Panel 3, fast fracture and arrestment were achieved at 19,124 psi and final failure occurred from a stationary crack at 19,744 psi. This indicates almost no dynamic effect from fast fracture arrestment. Similarly, for Test 3 of Panel 2 and Test 2 of Panel 4, there is only 6 percent difference between stress levels at fast fracture arrestment and final failure from a stationary crack. It is hypothesized that as the crack approaches the frame and the frame starts to pick up load, the crack decelerates and gradually comes to rest. Figure 33 illustrates a typical view of a two-bay skin crack arrestment at the frame.

Curved Panel With Longitudinal Cracks

The results for Tests 1 and 2, and Tests 3 and 4 are plotted in Figures 34 and 35, respectively. The static test results are listed in Table 4. Load history for each test is indicated on the graphs and in Table 4 for static tests.



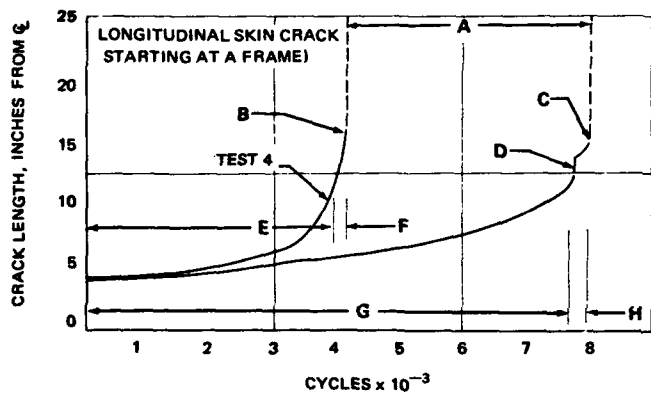
- A CRACK ARRESTMENT AT THE RIVET HOLES
  - B STATIC TEST: FAST FRACTURE AT P = 12.8 PSI  $\sigma_h = 14,912$  PSI
  - C STATIC TESTS: (1) P = 13.74 PSI  $\sigma_x = 28,796$  PSI NO FRACTURE (2) FRACTURE OCCURRED UPON REDUCTION OF  $\sigma_x$  TO 2500 PSI P = 13.38 PSI  $\sigma_h = 15,622$  PSI
  - D STATIC TEST: P = 13.36 PSI  $\sigma_h = 14,912$  PSI NO FRACTURE
  - E  $P_{MAX} = 10.2$  PSI  $\sigma_h = 11,883$  PSI  $\sigma_x = 0$
  - F  $P_{MAX} = 9$  PSI  $\sigma_h = 10,486$  PSI  $\sigma_x = 0$
  - G  $P_{MAX} = 10.2$  PSI  $\sigma_h = 12,960$  PSI  $\sigma_x = 16,371$  PSI
  - H  $P_{MAX} = 9$  PSI  $\sigma_h = 11,561$  PSI  $\sigma_x = 16,226$  PSI
- WHERE:  
 $N_x = 0.00865 L$   
 $L = \text{TOTAL AXIAL LOAD}$
- $P = \text{PRESSURE DIFFERENTIAL}$   
 $\sigma_x = \text{AXIAL STRESS} = 8.4 N_x + 121 P$   
 $\sigma_h = 1165 + 0.597 N_x$
- $\frac{P_{MIN}}{P_{MAX}} = \frac{\sigma_x MIN}{\sigma_x MAX} = +0.05$

FIGURE 34. RESULTS OF TESTS 1 AND 2 FOR PANEL 15, CURVED PANEL (LONGITUDINAL CRACK STARTING MIDWAY BETWEEN FRAMES)

TABLE 4  
TEST RESULTS FOR CURVED PANEL (PANEL NO. 15)

TEST NUMBER	PRESSURE AT FAST FRACTURE (PSI)	$\sigma_h$ (PSI) (1)	$\sigma_x$ (PSI) (2)	TOTAL CRITICAL CRACK LENGTH (IN.)	$R_{ct}$	C	$K_c^*$ PSI $\sqrt{IN.}$	TYPE OF CRACK	CONDITION (3)	CASE (4)
1	12.80	14,912	0	14.47	1.076	1.0023	66,460	1 BAY	FF	2A
2	13.36	15,622	2,500	16.1	1.095	1.0028	72,000	1 BAY	FF	2A
3	13.36	15,622	2,500	19.75	1.202	1.0043	73,106	1 BAY	AR	2A
3	10.8	12,600	0	24.2	1.210	1.0064	65,114	2 BAY	FF	2B
4	11.55	15,380	28,495	25.65	1.230	1.0072	80,573	2 BAY	FF	2B

(1)  $\sigma_h$  = HOOP STRESS NORMAL TO CRACK  
 (2)  $\sigma_x$  = AXIAL STRESS PARALLEL TO CRACK  
 (3) CONDITION FOR WHICH  $K_c^*$  IS EVALUATED { FF CRACK FAST FRACTURE  
 AR CRACK ARREST  
 (4) CASE FOR WHICH  $K_c^*$  IS EVALUATED (SEE TABLE 1).



- A CRACK ARRESTMENT AT RIVET HOLES UNDER SHEAR CLIP
- B STATIC TEST: FAST FRACTURE AT P = 11.55 PSI ( $\sigma_h = 15.38$  KSI)  $\sigma_x = 28.495$  KSI
- C STATIC TEST: FAST FRACTURE AT P = 10.8 PSI ( $\sigma_h = 12.582$  KSI)
- D STATIC TEST TOP = 11.9 PSI NO FRACTURE
- E  $P_{MAX} = 10.2$  PSI ( $\sigma_h = 12.96$  KSI)  $\sigma_{XMAX} = 16.371$  KSI
- F  $P_{MAX} = 9.5$  PSI  $\sigma_{XMAX} = 16.287$  KSI
- G  $P_{MAX} = 10.2$  PSI ( $\sigma_h = 11.883$  KSI)
- H  $P_{MAX} = 9.5$  PSI ( $\sigma_h = 11.068$  KSI)

FIGURE 36. RESULTS OF TESTS 3 AND 4 FOR PANEL 15, CURVED PANEL (LONGITUDINAL SKIN CRACK STARTING AT A FRAME)

One reason for the application of high axial stress during the static test for fast fracture was to determine if any tendency existed for the crack to turn 90 degrees and travel along the frame to the skin rivet line. This phenomenon has been observed in shells of smaller radius. Fast fracture occurred during Test 4 with axial stress 28,495 psi applied and no tendency of the crack turning was observed.

#### Flat Panels with Circumferential Cracks

The results from cyclic and static tests on Panels 7 through 14 are plotted in Figures 36 and 37. The static test results for fast fracture, crack arrestment and final residual strength are listed in

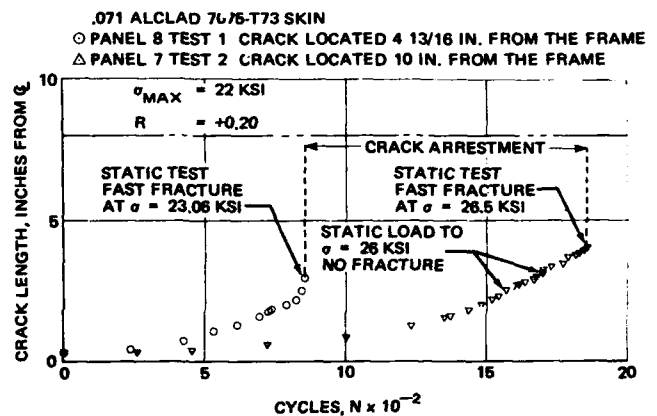


FIGURE 36. TEST RESULTS FOR PANEL 8 AND PANEL 7

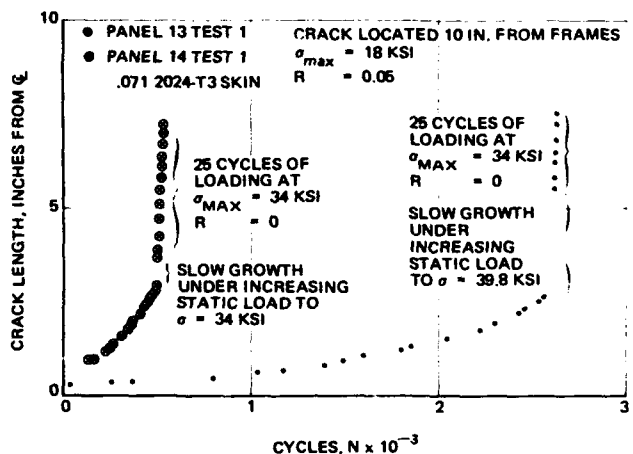


FIGURE 37. TEST RESULTS FOR PANEL 13 AND PANEL 14

Tables 5 and 6. Load history for each test is indicated on the graphs. Fracture toughness  $K_c^*$  is listed in Tables 5 and 6 for fast fracture, crack arrestment and final residual strength. Where fast fracture did not occur,  $K_c^*$  has been evaluated at the most critical crack length and is the maximum value applied without fast fracture.

In all of the tests listed in Tables 5 and 6 where the cracks were located midway between frames, crack propagation was always 90 degrees from direction of loading. Where the cracks were

**TABLE 5**  
**TEST RESULTS FOR 86-IN.-WIDE PANELS WITH CIRCUMFERENTIAL CRACK (HAT SECTION LONGERONS)**

PANEL NUMBER	CONFIGURATION NUMBER FIGURE 18	TEST NUMBER	DISTANCE Y (IN.) (1)	GROSS STRESS (PSI)	TOTAL CRACK LENGTH (IN.)	$R_{ct}$	C	$K_c^*$	CONDITION (2)
7	6	1	4-13/16	25,160	8.08	0.87	1.0064	104,358	FF
		2	10	26,540	8.246	0.875	1.0067	110,627	FF
				26,540	15.375	1.16	1.0197	117,266	AR
31,200	16.310	1.30	1.0222	128,286	FA				
8	7	1	4-13/16	23,060	6.550	0.77	1.0036	97,350	FF
		2	1-1/4	23,060	15.350	1.18	1.0196	100,940	AR
				23,100	7.250	0.78	1.0044	100,942	FF
23,100	15.200	1.15	1.0192	102,429	AR				
29,600	16.700	1.395	1.0232	114,598	FA				
9	6	1	10	34,000	13.000	0.97	1.0141	>164,284	NF
		2	4-13/16	40,000	12.410	0.95	1.0128	192,432	FF
10	7	1	10	29,800	12.400	0.92	1.0128	>147,869	NF
		2	4-13/16	34,000	12.400	0.92	1.0128	>168,631	NF

(1) Y IS THE DISTANCE FROM THE LATERAL STIFFENER (FRAME) TO THE CRACK LOCATION (SEE FIGURE 27)

(2) CONDITION FOR WHICH  $K_c^*$  IS EVALUATED

FF	CRACK FAST FRACTURE
AR	CRACK ARREST
FA	PANEL FAILURE
NF	FAST FRACTURE DID NOT OCCUR

**TABLE 6**  
**TEST RESULTS FOR 60-IN.-WIDE PANELS WITH CIRCUMFERENTIAL CRACK (TEE SECTION LONGERONS)**

PANEL NUMBER	CONFIGURATION NUMBER FIGURE 18	TEST NUMBER	DISTANCE Y (IN.) (1)	GROSS STRESS (PSI)	TOTAL CRACK LENGTH (IN.)	$R_{ct}$	C	$K_c^*$	CONDITION (2)
11	8	1	10	23,100	7.000	0.85	1.0128	91,760	FF
		23,100	14.750	1.15	1.0181	100,790	AR		
2	4-13/16	28,600	4.880	0.81	1.0020	98,213	FF		
		29,600	18.280	1.64	1.0278	102,266	FA		
12	9	1	10	24,000	3.720	0.685	1.0012	84,973	FF
		24,000	14.530	1.15	1.0176	103,795	AR		
2	4-13/16	24,800	3.210	0.67	1.0009	83,318	FF		
		27,800	17.620	1.745	1.0259	88,433	FF		
13	8	1	10	39,800	11.650	0.94	1.0113	>186,079	NF
		2	4-13/16	40,000	12.040	0.95	1.0121	>188,250	NF
14	9	1	10	34,000	12.200	0.92	1.0124	>166,034	NF
		2	4-13/16	40,000	12.200	0.92	1.0124	>195,393	NF

(1) Y IS THE DISTANCE FROM THE LATERAL STIFFENER (FRAME) TO THE CRACK LOCATION (SEE FIGURE 27)

(2) CONDITION FOR WHICH  $K_c^*$  IS EVALUATED (SEE TABLE 5)

located closer to a frame, the crack propagation was always in a direction away from the frame. A possible cause for this is the induced biaxial tension stress caused by the lateral stiffener constraint discussed in Item 4 of the section on secondary effects. The angle at which the crack propagates is illustrated in Figure 38 for Panel 8 after Test 1 where the initial saw-cut was located 4-13/16 inches from a frame. Figure 38 shows the crack arrestment between rivets after fast fracture on Panel 8, Test 1.

**Coupon Tensile Test Data**

Tensile tests were performed on coupons taken from the skins of Panels 1 through 15 and sections of crack stoppers on Panel 5. The properties are of typical values of the alloys.



**FIGURE 38. VIEW FROM SKIN SIDE OF PANEL 8 SHOWING CRACK ARRESTMENT BETWEEN RIVETS AFTER TEST 1**

## CORRELATION

### FRACTURE STRENGTH

#### Skin Fracture Toughness Criteria

The gross residual strength curve illustrated in Figure 19 completely describes the skin criterion as a mode of failure. The curve indicates the gross stress level and crack length at which fast fracture occurs. It will provide information on whether or not a crack can be arrested at a given stress level and crack length  $l_a$ . Gross residual strength, or the stress level at which failure will occur, is also indicated. The height of the curve is a function of the fracture toughness of the material as determined from test results. Ideally, the fracture toughness would be determined from unstiffened panels having the same width as the stiffened panels being analyzed; however, fracture toughness can be determined from stiffened panels of one configuration and used to derive gross residual stress curves for other configurations. The presence of secondary effects, described in the analysis section, make the determination of the true value of  $K_c$  as a material parameter extremely difficult. The secondary effects are evaluated empirically by replacing  $K_c$  in Equation (18) by  $K_c^*$ , which includes the secondary effects.

Flat Panels with Two-Bay Longitudinal Cracks - Evidence that  $K_c^*$  can be obtained from one panel and used for panels of other configurations is shown by Figures 39 and 40 where  $K_c^*$  has been

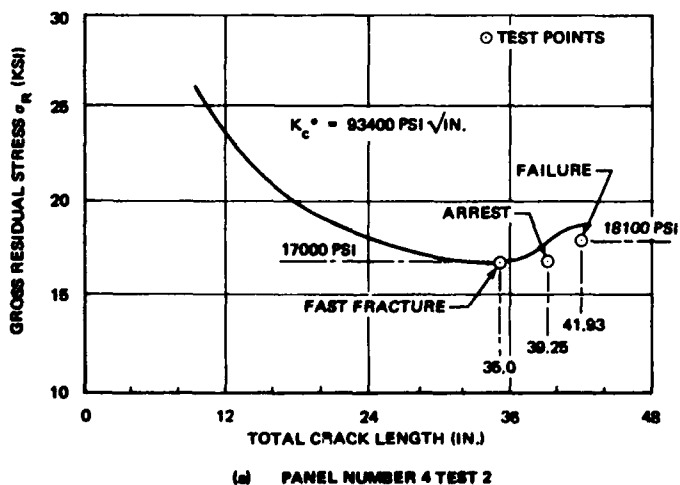
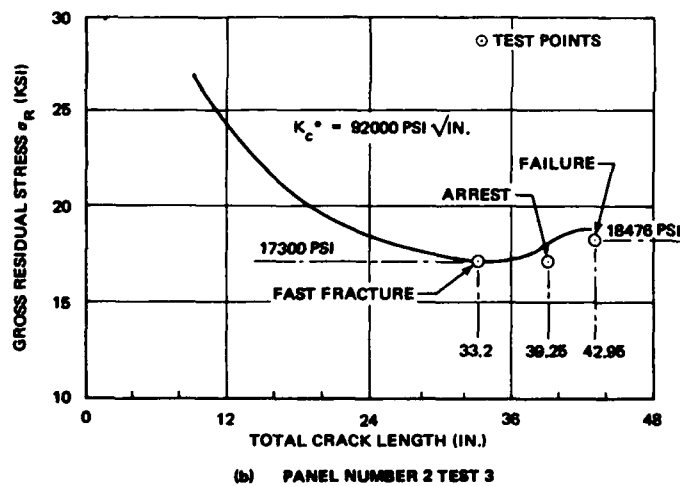


FIGURE 39. GROSS RESIDUAL STRENGTH CURVES FOR LONGITUDINAL CRACKED FLAT PANELS

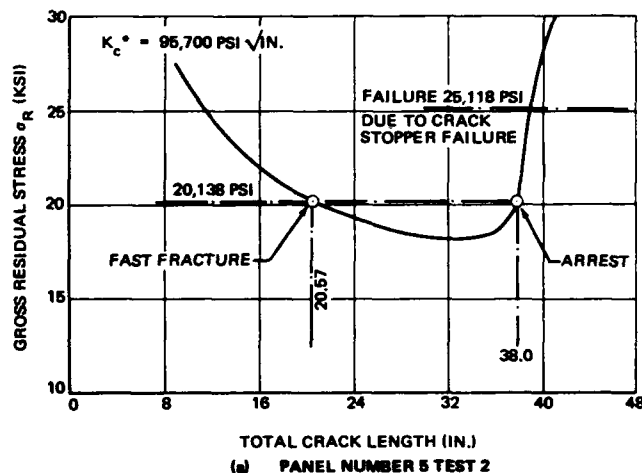
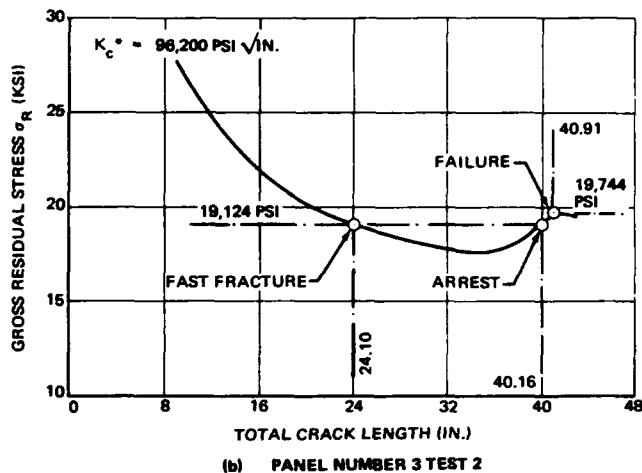


FIGURE 40. GROSS RESIDUAL STRENGTH CURVES FOR LONGITUDINAL CRACKED FLAT PANELS

determined from fast fracture in four panels containing longitudinal cracks. Each of the panel configurations is different and the stress levels and crack lengths at fast fracture are not the same, yet the spread in the value of  $K_c^*$  determined from the tests is within 4 percent. Panel 3, having the highest residual strength of Panels 2, 3 and 4, also has the highest fracture toughness  $K_c^*$ . It will be noted that only 2 percent variation in gross strength would be present between Panel 2 and Panel 3 if  $K_c^*$  had been the same for both panels.

Figures 39(a) and (b) and 40(b) show gross residual strength curves for panels without crack stoppers. It is noted that the test points at crack arrestment and final failure are below the curves for Panels 3 and 4 in Figure 39. This is due to the local high discontinuity skin stress in the vicinity of the cutout in the shear clip described in Item 5 of the section on secondary effects and illustrated in Figure 6. The Lumped Parameter Analysis assumes a constant applied stress level and does not account for local high stresses. However, the difference in strength between the test points and the analytical curve is within 5 percent. Figure 40(b) shows almost perfect correlation with fast fracture, crack arrestment and final failure for Panel 3. The different shear clip configurations of Panels 2, 3 and 4 do not significantly influence their residual strength.

Figure 40(a) shows excellent correlation of crack arrestment for Panel 5, which includes a titanium crack stopper. There is a significant increase in residual strength for this panel as indicated by the shape of the gross residual strength curve as compared to Panels 2, 3 and 4, where crack stoppers were not included. Final

failure of this panel was precipitated by crack stopper failure at the outer frame and occurred at 25,118 psi. The gross stress at final failure, based on skin criteria, would have been in excess of 30,000 psi if the outer crack stopper were not failed. In addition, the loading to produce a given gross stress level in Panel 5 is higher than that to produce the same stress in Panels 2, 3 and 4 due to additional crack stopper area.

Figure 41 shows gross residual strength curves for varying degrees of damage in Panel 6. The amount of damage for the three conditions shown is listed in Table 1 for analytical cases 5, 3d and 3e. All three curves are based on  $K_c^*$  determined at fast fracture, with Configuration 3e, where the center frame and outer crack stopper are intentionally cut. Fast fracture has previously been attempted at Point Y with the center frame cut only. The fact that this did not occur is the substantiation that the crack tip stress ratio  $R_{ct}$ , determined analytically for this point and condition, is at least of the correct order. This applies also to stress ratios calculated for case 5 since a fast fracture attempt was made at Point X with the center crack stopper broken.

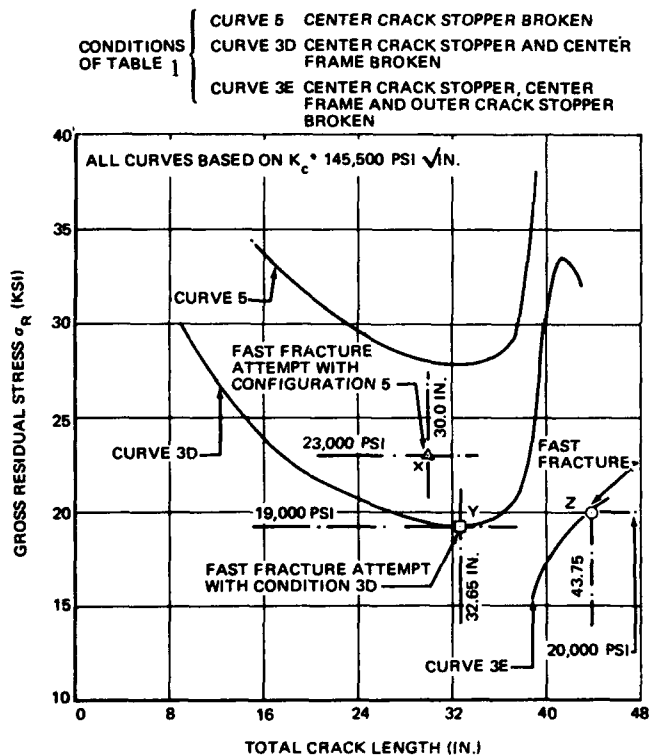


FIGURE 41. GROSS RESIDUAL STRENGTH CURVES FOR LONGITUDINAL CRACKED FLAT PANEL 6 WITH VARYING DEGREES OF DAMAGE

**Curved Panel With One- and Two-Bay Longitudinal Cracks** — Figure 42 shows gross residual strength curves for longitudinal cracks in curved Panel 15. Curves 42(a) for one-bay Tests 1 and 2 are derived using analytically determined crack tip stress ratios,  $R_{ct}$  for case 2a of Table 1 and  $K_c^*$  values determined experimentally at fast fracture. Curves 42(b), for two-bay crack Tests 3 and 4, are similarly derived using analytical case 2b of Table 1. The lower curves of Figures 42(a) and (b) were derived using  $K_c^*$  at fast fracture for the case where only pressure load was applied. The upper curves of Figures 42(a) and (b) are based on  $K_c^*$  determined with axial stress 2500 psi and 28,495 psi, respectively. Gross residual stress  $\sigma_R$ , for all of the the curves, is the hoop tension stress normal to the crack from pressure loading. In the Lumped Parameter Analysis of the flat panel, the influence

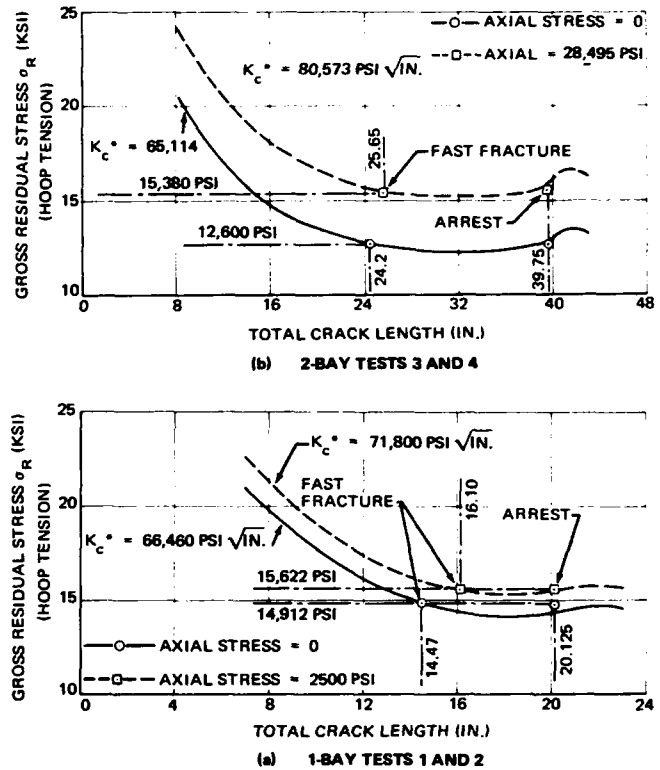


FIGURE 42. GROSS RESIDUAL STRENGTH CURVES FOR CURVED PANEL NUMBER 15

of biaxial load was not included. The effect of biaxial loading on gross residual strength of the curved panel is evaluated empirically by  $K_c^*$ .

The two  $K_c^*$  values, 66,460 psi  $\sqrt{\text{in.}}$  and 65,114 psi  $\sqrt{\text{in.}}$ , determined from the one- and two-bay tests where axial stress was zero, were evaluated using entirely different parameters. Stress levels, crack tip stress ratios  $R_{ct}$  and crack lengths were not the same, yet the variation between the two values is only 2 percent. This is further substantiation that  $K_c^*$  can be determined from one configuration and used to derive gross residual strength curves for other configurations, provided the crack tip stress ratio  $R_{ct}$  versus crack length has been analytically determined. All of the fast fractures for the four tests were arrested as predicted by the shape of the gross residual strength curve in the vicinity of the frame.

$K_c^*$  is shown to increase with axial stress due to cancellation of axial compressive stress along the edge of the crack. The upper value  $K_c^*$  for curved panels, however, would probably never be as high as that for flat panels. Some bulging will always exist to satisfy equilibrium of the element adjacent to the crack edge as illustrated in Figure 16. This is substantiated by the value of  $K_c^* = 80,573$  psi  $\sqrt{\text{in.}}$ , obtained with hoop tension stress 15,380 psi and axial stress 28,495 psi. The compressive stress parallel to the crack, theoretically equal to the gross stress normal to the crack from Westergaard's work on unstiffened panels, would be entirely cancelled out in this case by the axial tension stress of 28,495 psi, and yet the value of  $K_c^*$  obtained does not approach the values listed in Table 3 for flat panels with similar skin material. Further to this, crack bulging was observed during Test 4 of Panel 15 with axial tension stress of 28,495 psi and a pressure of 11.55 psi.

The derivation of hoop tension and axial skin stresses for the curved panel were based on the methods of Flugge.<sup>14</sup> When both

axial stresses and pressure are applied simultaneously, the skin is in a state of biaxial tension stress with longerons and frames uniaxially loaded. Under this state, the skin hoop tension and axial stresses are related by the equations:

$$\sigma_h = 1165P + 0.597 N_x \quad (23)$$

$$\sigma_{xs} = 8.4 N_x + 121P \quad (24)$$

where

$\sigma_h$  = hoop tension stress in the skin, psi

$\sigma_{xs}$  = axial tension stress in the skin, psi

$P$  = applied pressure, psi

$N_x$  = axial loading, lb/inch

The coefficients of Equations (23) and (24), calculated for the configuration of Panel 15, depend on frame and longeron area, shell radius and skin thickness. Skin stresses determined by the equations were substantiated by using biaxial strain gages on the skin. The variation of hoop tension stress between frames was quite small, particularly adjacent to a longeron where all of the skin cracks were located.

**Flat Panels With Circumferential Two-Bay Cracks** - This condition is intended to simulate a section of the fuselage shell, subjected to inertia shell bending stresses and axial stresses due to pressure as shown in Figure 5, Configuration C. Calculated values of the crack tip stress ratio  $R_{ct}$ , shown in Figure 12(b) for cases 6 through 9 of Table 1, are less than 1.0 for crack lengths up to 14 inches. This indicates a higher crack tip stress than the unstiffened panel for short crack lengths. The reason for this is illustrated in Figure 43 showing the concentrated load transfer from the broken longeron into the sheet at the center of the crack, which is in addition to the sheet gross applied stress.

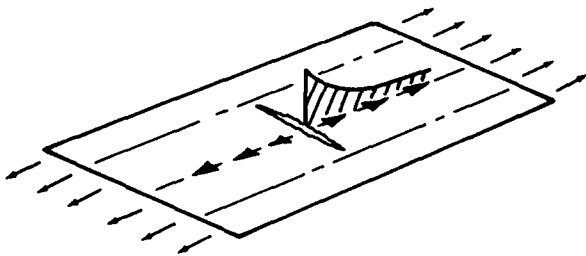


FIGURE 43. CONCENTRATED LOAD APPLIED TO THE SKIN FROM THE BROKEN LONGERON

This effect is reflected in the gross residual strength curves for Panels 7, 8, 11 and 12 shown in Figures 44 and 45, where crack lengths at fast fracture are comparatively short. All of the curves shown are based on  $K_{Ic}^*$  determined at fast fracture. Table 5 also shows values of the  $K_{Ic}^*$  calculated at crack arrestment and final failure.

Test 2 of both Panels 7 and 8 shows good correlation as illustrated in Figure 44 and by calculated  $K_{Ic}^*$  values at crack arrestment shown in Table 5. Crack arrestment is coincident with the curve, indicating that the calculated shape of the crack tip stress ratio curve  $R_{ct}$ , shown in Figure 12(b), is correct in this area. Final failure of Panels 7 and 8 occurred at crack lengths shorter than

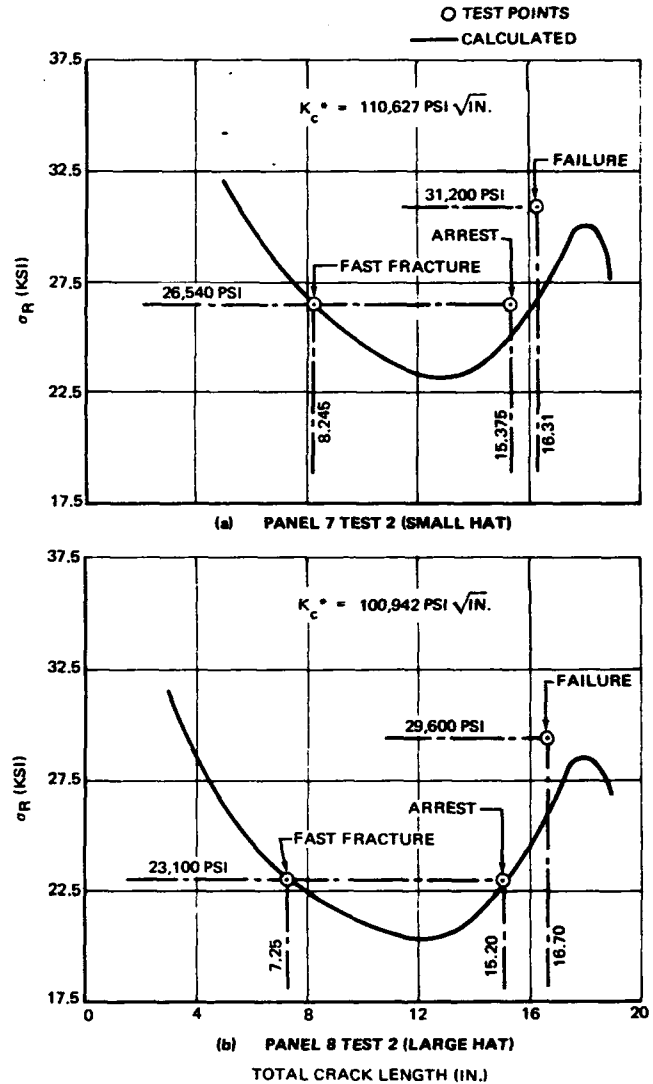


FIGURE 44. GROSS RESIDUAL STRENGTH CURVES FOR CIRCUMFERENTIAL CRACKED FLAT PANELS (HAT SECTION LONGERONS)

the curve predicts. The crack lengths at failure were 1.7 inches and 1.1 inches shorter than predicted for Panels 7 and 8, respectively, as shown in Figure 44. A possible remedy for this situation would be to refine the gridwork in the idealized analysis model by placing the vertical bars in the vicinity of the longeron closer together, thus increasing the accuracy of the stress distribution in this area.

The effect of center longeron bending, discussed under the second item of the section on secondary effects, should increase with longeron area because of a higher load transfer from the broken longeron to the skin. The tabulated  $K_{Ic}^*$  data listed in Table 5 verify this behavior. The  $K_{Ic}^*$  values evaluated from the panels with smaller "Hat" or "Tee" shaped longerons are considerably higher than those for panels with larger longerons.

The location of the crack in relation to the lateral stiffener also influences the stress intensity at the crack tip. The location of the crack for Panel 8, Test 2, was 1-1/4 inches from the lateral stiffener (frame) as indicated in Table 5. Longeron deflection for this case was greater than for Test 1 where the crack was located 4-13/16 inches from the frame. The length of unsupported longeron, 18.5 inches for Test 2 and 15-3/16 for Test 1, is the



main contributing factor for the increased deflection. However, the increase in stress intensity at the crack tip is offset by an induced biaxial tension stress caused by lateral stiffener restraint (and discussed under the fourth item of the section on secondary effects), resulting in a higher  $K_c^*$  for Test 2 than for Test 1. The fact that the biaxial tension stress is significant is made evident by Test 2 on the curved panel where a biaxial stress of 2,500 psi increased  $K_c^*$  by 8 percent (see Figure 42). All of the other panels were tested with cracks located 4-13/16 inches from the frame for one test and 10 inches for the other. Two out of three panels tested, where fast fracture occurred, gave slightly lower  $K_c^*$  values with the crack 4-13/16 inches from the frame. The exception of this is Panel 11 where  $K_c^*$  was higher with the crack located 4-13/16 inches from the frame.

Figure 45 shows crack arrestment at a shorter length than predicted after fast fracture for Panels 11 and 12. This is due to the influence of two rivet rows in the longeron. Although the rivet stiffness for the two rows was accounted for in the analysis, only one shear panel for each longeron was used to represent the two rows as illustrated in Figure 11. Rivet spacing was actually 1.0 inch for Panel 11 and 1.5 inches for Panel 12. This would have the effect of reducing the longeron spacing by 1.0 for Panel 11 and 1.5 for Panel 12. If Figure 45 is re-examined it will be noted that this is the order of the discrepancy. This effect, however, did not appear to influence the final failure where the

test points are quite close to the predicted values. Initial fast fracture was influenced by this effect, especially for the larger longeron of Panel 12 where  $K_c^*$  is shown to be lower than that determined from Panel 8 with large Hat section longerons having one rivet row. The crack tip stress will be influenced to a greater degree by the concentrated loads from the two rivet rows due to their closer proximity to the crack tip. This condition could be improved by including two shear panels to represent both rivet rows in the idealized analytical model.

Little correlation can be shown for fracture strength of the panels having 2024-T3 skin material. The  $K_c^*$  value for these panels was so high, fast fracture occurred only in Panel 13. However, in this case the crack was not symmetrically placed about the center longeron when static loading was applied. This condition was not considered as an analysis case. The values of  $K_c^*$  shown in Tables 5 and 6 are the maximum-stress-intensity factor  $K$  that the panels have been subjected to without fracture.

### Stiffener Strength Criteria

In most of the panels tested, strain gages were located in critical areas on the stiffening elements to measure stress as a function of crack length. Test data have been selected for a variety of configurations and correlated to calculated data from the Lumped Parameter Analysis. The panel selection was made not only to substantiate the analysis method but to point out certain discrepancies which exist and to suggest ways to improve the correlation.

**Flat Panels with One-Bay Longitudinal Cracks** - Figure 46 shows frame stress as a function of crack length for a typical panel containing one-bay longitudinal skin cracks. The frame cross section for these panels is shown in Figure 9 as Configuration 1 and the shear clip configurations are shown in Figure 23. The

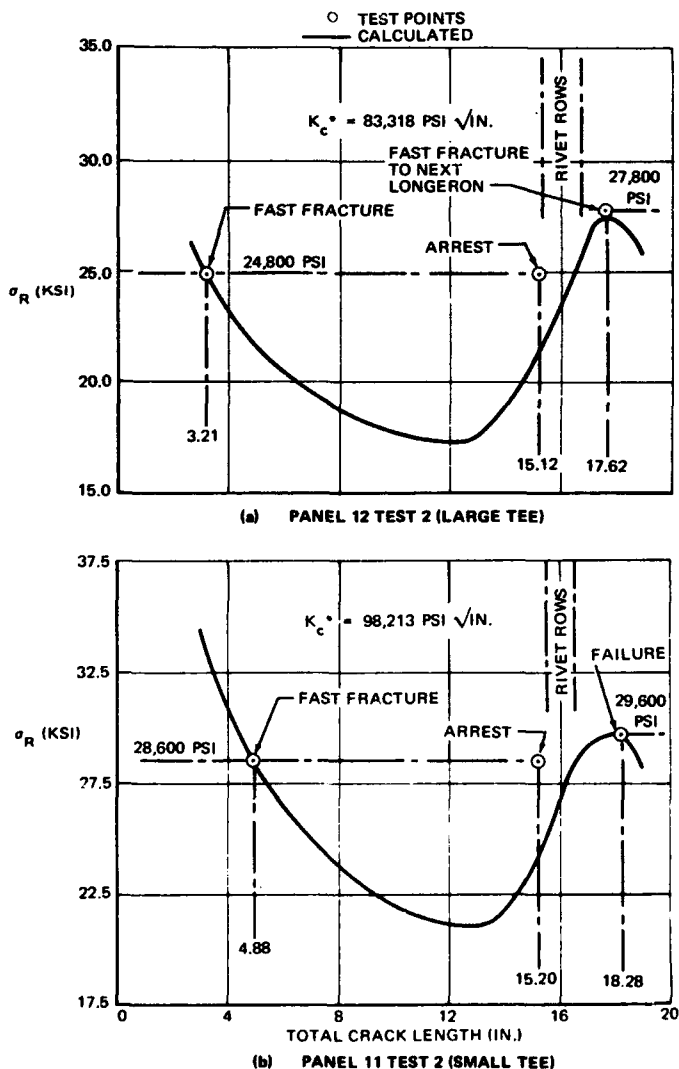


FIGURE 45. GROSS RESIDUAL STRENGTH CURVES FOR CIRCUMFERENTIAL CRACKED FLAT PANELS (TEE SECTION LONGERONS)

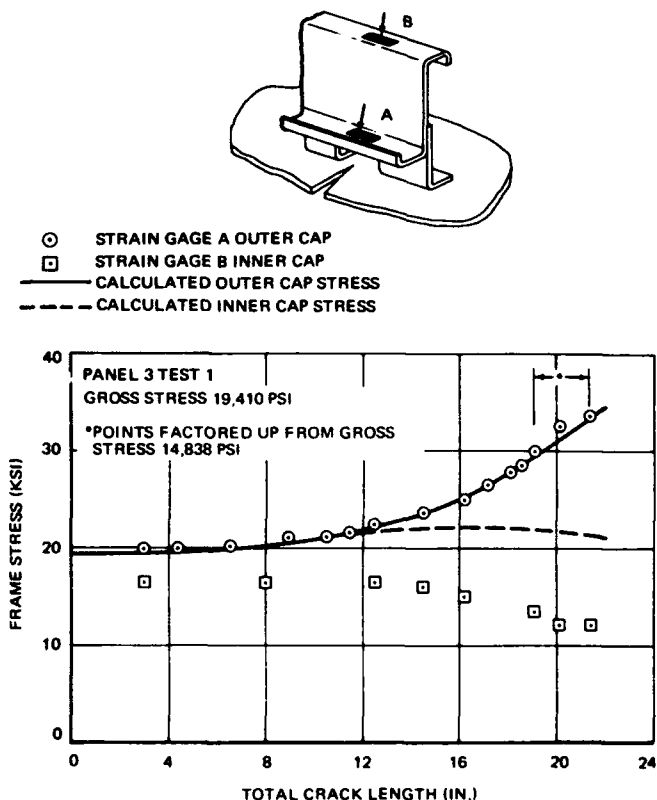


FIGURE 46. FRAME STRESS CORRELATION ONE-BAY CRACK TEST

calculated outer cap stresses, based on case 1a of Table 1, correlate quite well with strain gage data for most panels. The inner cap stress, however, is lower than the calculated value in both cases. This may be due to the reaction system initially chosen in the idealized analytical model. The reaction in the x direction at the crack location, shown in Figure 2, does not exist on the test panel. Although this reaction is small, it could affect the frame stress distribution. However, the frame outer cap is the most critical element and this correlates quite well with the existing idealization.

Figure 47(a) shows the crack stopper stress for Panels 5 and 6. It can be seen that the crack stopper is not symmetrically loaded. The stress on the side from which the crack is approaching is higher than on the other side. This effect is due to the three rows of rivets on the crack stopper. It may be noted that if adequate strength could be provided with one row, the crack stopper could only be loaded in a symmetrical manner. Plots of the average stresses are shown and correlate quite well with analysis, indicating that the load input to the crack stopper is accurate. The three rivet rows are represented in the analysis by a single shear panel so that only a uniform stress prediction in the crack stopper is possible. It is shown later that before failure of the crack stopper occurs, the stresses on both sides become equal. It would be possible, however, to refine the idealized model to include this variation but the number of joint equations would increase considerably.

Figure 47(b) shows frame stress for Panel 5 Test 1 which includes a crack stopper. Again, the outer cap frame stress correlates quite well but the inner cap stress is lower than predicted.

Flat Panels with Two-Bay Longitudinal Crack – The figure shows center frame outer cap stress correlation as a function of gross applied stress with a full two-bay crack in the skin. The gross residual strength curve for skin criteria is illustrated in Figure 39(a). Figure 48 indicates that some yielding in the center frame occurred as shown by the strain gage on the outer cap. It was not certain at this point if yielding of the center frame had precipitated the final failure. In view of this, the center frame was reinforced locally on Panel 2, and Test 3 (similar to the one performed on Panel 4) was conducted. The panel failed at almost the same gross stress as Panel 4 without center frame yielding. It was concluded that center frame yielding did not precipitate failure of Panel 4. A Lumped Parameter Analysis was performed to include the effects of local center frame reinforcement so that a correct crack tip stress ratio,  $R_{ct}$ , could be determined at failure. This is listed as case 4 of Table 1.

Figure 49 shows the outer frame outer cap stress correlation for Test 2 of Panel 5 as a function of applied gross stress for a full two-bay crack. The center frame on this panel had been reinforced so that a higher load could be applied to verify the increased gross residual strength of the skin due to the crack stopper. The analysis for this case, including the center frame local reinforcement, is listed as case 5 of Figure 9. Failure of this panel, as indicated by the analysis, was due to outer crack stopper tension failure. Failure occurred at a gross stress of 25,118 psi with a skin crack length of 40.19 inches. Considerable yielding in the skin at the crack tip was observed which caused a higher crack stopper load than was apparent from the elastic analysis. The plastic zone size was estimated, using Dugdale's method,<sup>15</sup> to be 0.3 inch. This was added to the visible crack

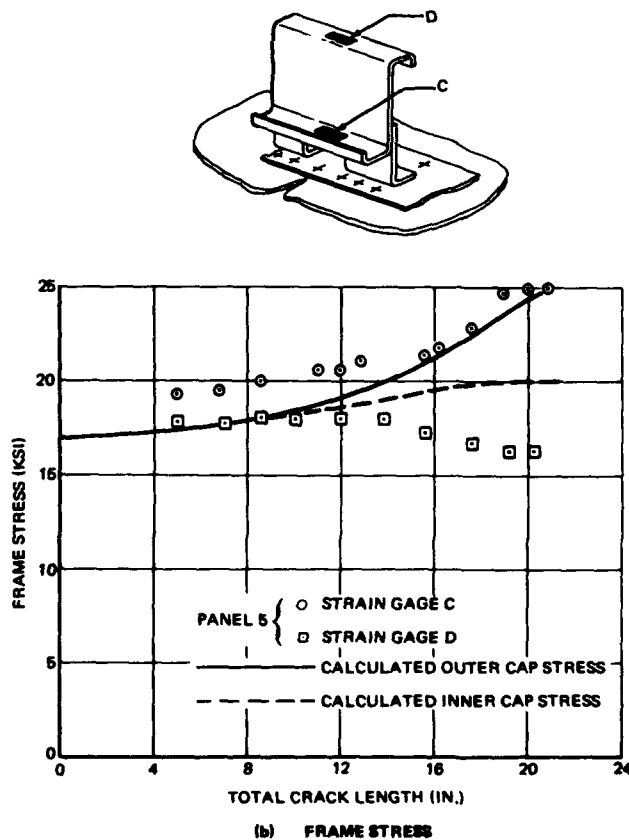
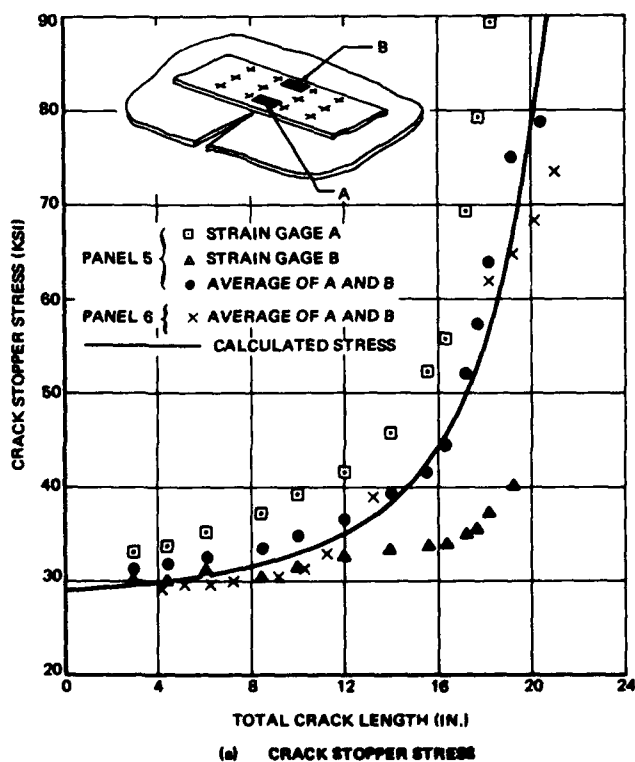


FIGURE 47. FRAME AND CRACK STOPPER STRESS CORRELATION ONE-BAY CRACK TEST PANELS 5 AND 6 TEST 1 GROSS STRESS 17,000 PSI

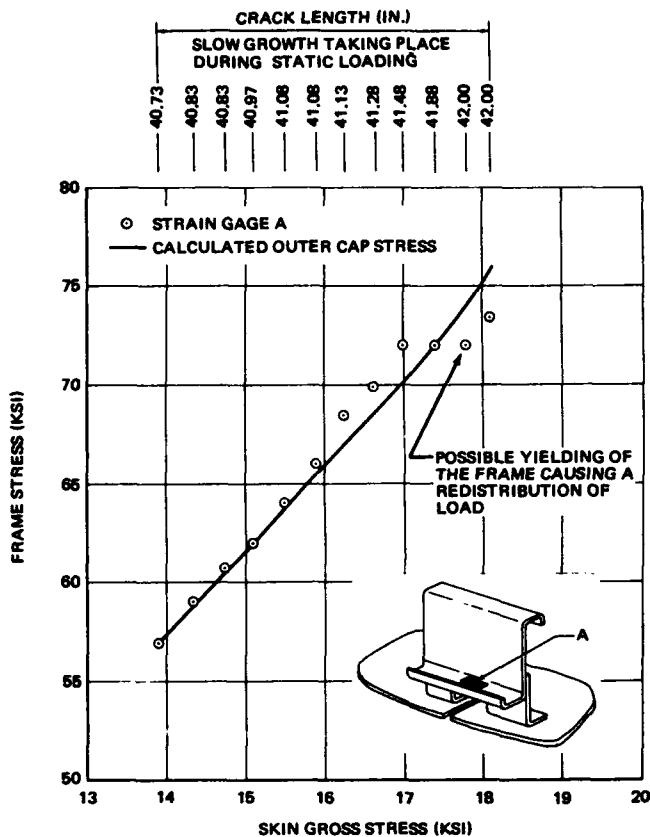


FIGURE 48. CENTER FRAME STRESS CORRELATION PANEL 4 TEST 2

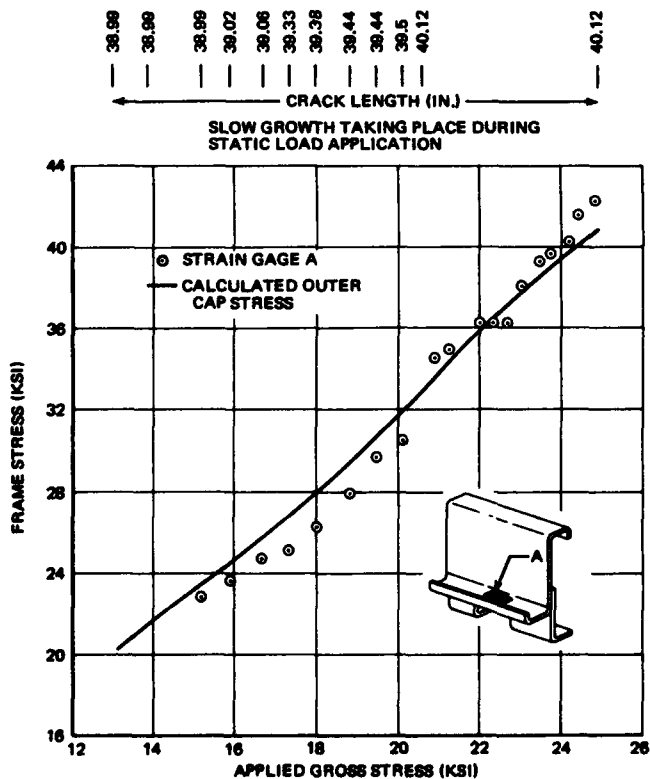


FIGURE 49. OUTER FRAME STRESS CORRELATION TWO-BAY CRACK TEST PANEL 5 TEST 2

length and the outer crack stopper load determined for a crack length of 40.79 inches from case 5 of Figure 13(c). The calculated crack stopper load at a gross stress of 25,118 psi was 10,150 lb. In order to substantiate this load, a complete section of each outer crack stopper was removed and loaded to failure in a tensile testing machine. Both sections of crack stopper failed at 10,100 lb.

Figure 50 shows stresses for the outer crack stopper of Panel 6 during the final failure test. The apparent irregularity of the calculated curve is due to slow crack growth during static load application. The existing damage to the panel at this time included an intentionally cut center frame and center crack stopper. It can be seen that the crack stopper stress is not uniform; the highest stress is on the side from which the crack is approaching. The stresses become uniform just prior to failure of the crack stopper, which occurred at a gross stress of 19,450 psi. Total failure of the panel occurred at 20,000 psi from a skin fast fracture. The average stress in the crack stopper is reasonably close to the prediction, indicating the load transfer from the skin is accurate.

Figure 51 illustrates the center frame stress for Panels 5 and 6 prior to reinforcement of the center frame. Again, the outer cap stress is close to the prediction but the inner cap stress is lower. In all the cases shown, the calculated stress in the critical stiffening element is substantiated by test, but the inner cap frame stress is always lower than predicted.

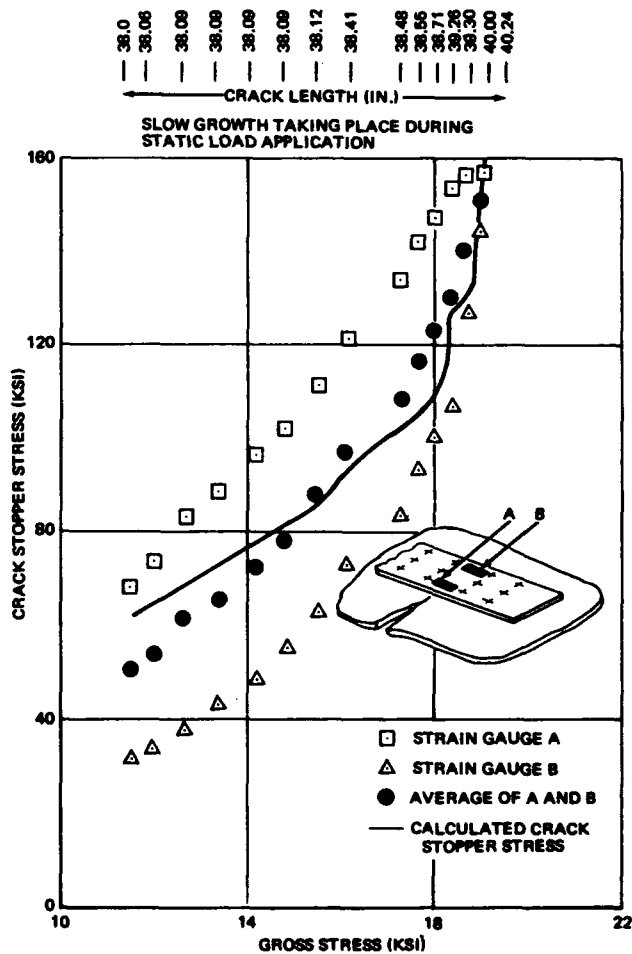


FIGURE 50. OUTER CRACK STOPPER STRESS CORRELATION TWO-BAY CRACK TEST PANEL 6 TEST 2

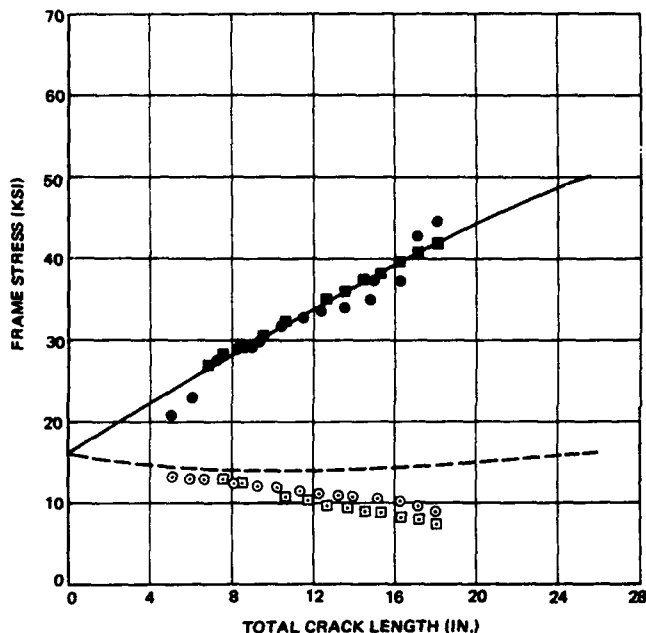
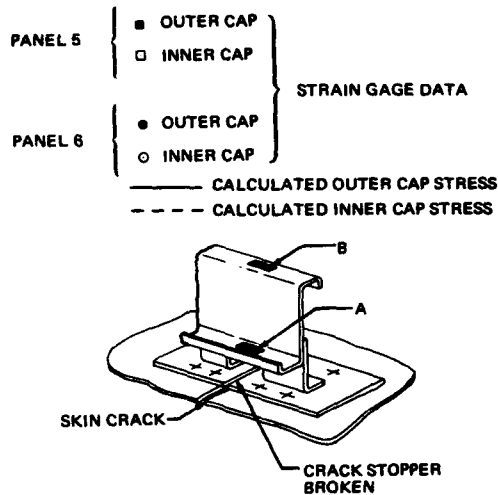


FIGURE 51. CENTER FRAME STRESS CORRELATION TWO-BAY CRACK TEST PANEL 5 AND 6 TEST 2 GROSS STRESS 16,400 PSI

**Flat Panels with a Circumferential Two-Bay Skin Crack** – In all of the panels tested for this condition, center longeron bending due to transfer of load from the cut longeron to the skin was present. This condition, described under the second item of the section on secondary effects and illustrated in Figures 17(a) and (b), almost completely cancels out the outer longeron bending stresses shown in Figure 14. Strain gage readings taken on the longerons indicated little or no bending. However, longeron load, determined by strain gage readings for Panel 10, is shown in Figure 52 as a function of gross panel stress for a full two-bay crack. The results show that the input of load to the longeron is accurate. Note the accuracy of the calculated load during the slow crack growth from 16.42 inches to 20.3 inches, illustrated in Figure 52. The crack in this case is extended 2 inches beyond each outer longeron. The accuracy of the load at this point also substantiates the rivet stiffness [Equation (9)] since the input of load into the longeron is a function of this stiffness.

The center longeron bending which occurred during the flat panel tests will not be present on curved pressurized panels. The pressure load applies a bending moment in the opposite sense which bends the longeron back into position. There is no

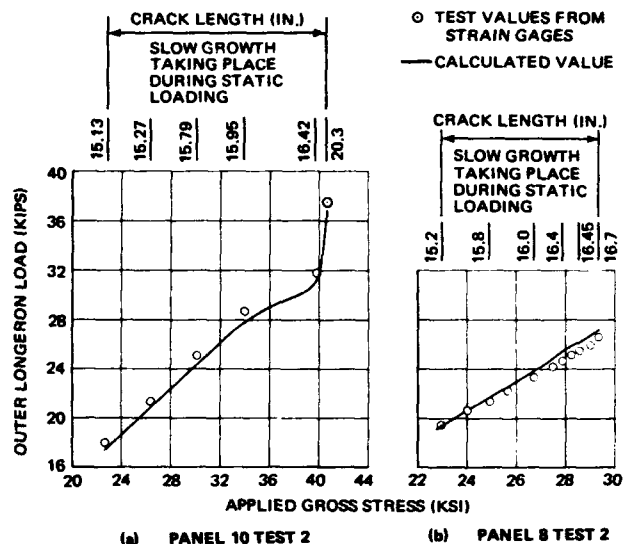


FIGURE 52. OUTER LONGERON LOAD. FLAT PANEL WITH CIRCUMFERENTIAL CRACK

tendency for the pressure to bend the longeron further than the neutral position since any additional outward deflection would be restrained by hoop tension in the skin. Recent testing for this condition, not reported herein, confirms this to be true. In view of this, the longeron stresses shown in Figure 14 would apply for a pressurized shell.

#### FATIGUE CRACK PROPAGATION

An accurate correlation between the analytical fatigue crack prediction curve and test results for a stiffened panel depends on the accuracy of the stress solution and the empirical crack growth rate equation for the skin material. Since the empirical crack growth rate equation derived from large unstiffened panels is not available, validity of using the rate equation of narrow unstiffened panels for large stiffened panels must be evaluated. The secondary effects which are not included in the Lumped Parameter Analysis will be evaluated empirically by replacing stress-intensity-factor  $K$  in Equation (3) by  $K^*$  which includes the secondary effects. The results for Panel 1 through Panel 6 containing longitudinal cracks are chosen to substantiate the analytical method because the secondary effects are small in these panels.

#### Fatigue Crack Growth Rate

Figure 22(d) presents the comparison of the predicted curve and the test results for Test 1 of Panel 1. The analytical curve was constructed by the graphical method developed here using the fatigue crack growth rate  $da/dN$  versus  $\Delta K$  data of the 7075-T73 narrow unstiffened panels. It is noted in Figure 22(d) that the correlation is poor as shown by the difference in slope (crack growth rate) of the two curves. This discrepancy is caused by the difference in the empirical growth rate,  $da/dN$  versus  $\Delta K$  curve for 7075-T73 narrow and wide panels as shown in Figure 22(c). The empirical crack growth rate relation for large stiffened 7075-T73 panels was reduced from the test results of Test 1 of Panel 1 and Test 2 of Panel 4. This was carried out by the reverse process of constructing a crack growth prediction curve. The empirical fatigue crack growth rate relation for 2024-T3 alclad large stiffened panels was derived from the results of Test 1 and Test 2 of Panel 6, using the same procedure as for Panels 1 and 4. The comparison of the  $da/dN$  versus  $\Delta K$  data derived from stiffened wide panels and the 30-inch-wide unstiffened panels is shown in Figure 53. It is noted that the difference in 2024-T3 is small as compared to that in 7075-T73.

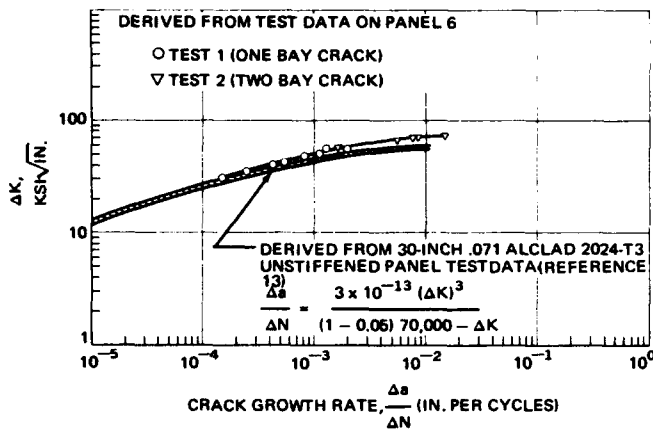


FIGURE 53. FATIGUE CRACK GROWTH RATE DATA DERIVED FROM THE RESULTS OF PANEL 6

The difference of  $da/dN$  versus  $\Delta K$  relation for large stiffened panels and narrow unstiffened panels of both 7075-T73 and 2024-T3 could be attributed to several factors. One factor is the difference in plane stress fracture toughness  $K_{Ic}^*$  for narrow and wide panels of 7075-T73 and 2024-T3. An increase of  $K_{Ic}^*$  value in the denominator of Equation (20) will greatly reduce the growth rate at  $\Delta K$  approaching the value of  $(1 - R)K_{Ic}^*$ . The  $K_{Ic}^*$  for both 2024-T3 and 7075-T73 is higher in wide panels than in narrow panels. For 7075-T73 sheet, the variation in thermal mechanical process of materials used for large panels and small panels may also contribute to the difference in fatigue crack growth resistance.

The comparison of fatigue crack growth rate  $da/dN$  versus  $\Delta K$  for alclad 2024-T3 and 7075-T73 wide panels in Figures 22(c) and 53, shows nearly the same resistance. The relative fatigue crack growth resistance of these two alloys is superior to that of 7075-T6 sheet as reported in Reference 9.

#### Prediction Curves for Stiffened Panels

The correlation of the analytical fatigue crack growth prediction curves and the test results for four panels of various configurations are shown in Figures 54 and 55. The analytical curves were derived by the simple graphical integration method presented in the section on Analysis. The curves for Panels 2, 4 and 5 were constructed using the  $da/dN$  versus  $\Delta K^*$  data for alclad 7075-T73 wide panels in Figure 22(c). It is noted in Figure 54 that the correlation is found to be excellent in crack length range

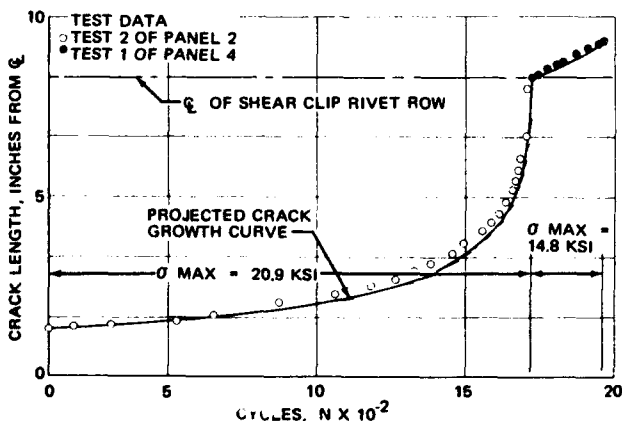


FIGURE 54. COMPARISON OF THE FATIGUE CRACK GROWTH PREDICTION CURVE AND RESULTS FOR TEST 2 OF PANEL 2 AND TEST 1 OF PANEL 4

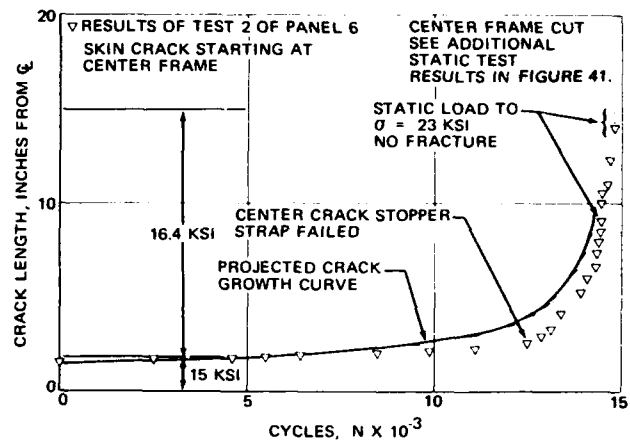


FIGURE 55. COMPARISON OF THE FATIGUE CRACK GROWTH PREDICTION CURVE AND RESULTS OF TEST 2 FOR PANEL 6

where  $da/dN > 10^{-3}$  inch per cycles. In the lower crack growth rate region, the correlation is not as good but is within the expected scatter. The correlation in Test 2 of Panel 6 with 2024-T3 skin, as shown in Figure 55, is also quite good. The analytical curve for Test 2 of Panel 6 was derived by using  $da/dN$  versus  $\Delta K^*$  data for alclad 2024-T3 wide panel in Figure 53.

If the empirical fatigue crack growth rate equations are derived from the test results for 120-inch-wide unstiffened panels, there is no doubt as to the validity of the correlation. To validate the correlation by using the  $da/dN$  versus  $\Delta K^*$  data which were reduced from the test results of other stiffened panels, the test load history and panel configurations selected to provide the referenced growth rate  $da/dN$  versus  $\Delta K^*$  data were sufficiently different from those of the panels being substantiated.

#### Secondary Effects on Fatigue Crack Propagation

Under the test conditions where the crack is subjected to significant secondary loads in addition to uniform uniaxial edge load, fatigue crack growth rate is expected to be different from that under uniaxial load. The secondary effects on fatigue crack growth rate are to be assessed by reducing the test results to  $da/dN$  versus  $\Delta K^*$  data. The empirical crack growth rate relation for the uniaxial loading case provides the reference for a particular loading case.

**Pressure and Biaxial Load on the Curved Panel** – The effect of pressure and curvature on fatigue crack growth rate is shown in Figure 56. These data are derived from the results of Test 1 and Test 3 of Panel 15 shown in Figures 34 and 35. It is noted that growth rate is greater in the curved panel than in the flat panel tests. The difference increases with  $\Delta K^*$  (or crack length), and there is no significant difference at short crack length. This is to be expected since the extent of crack bulge is a function of crack length. At a given growth rate, the difference between  $\Delta K^*$  for the flat panel and the curved panel increases with  $\Delta K^*$ , or more accurately, with crack length. This behavior is also substantiated by the fracture toughness  $K_{Ic}^*$  results in Table 4.

The fatigue crack growth rate  $da/dN$  versus  $\Delta K^*$  data for biaxial loading of Test 3 of Panel 15 are also plotted in Figure 56. The effect of biaxial loading reduces fatigue crack growth rate. In the low  $\Delta K^*$  range (or crack length), the rate is about the same as that in the flat panels, but it is higher than that in the flat panels at high  $\Delta K^*$ . This is caused by crack bulge in a long crack. The effect of crack bulge is not eliminated by biaxial tension load as observed in the test.

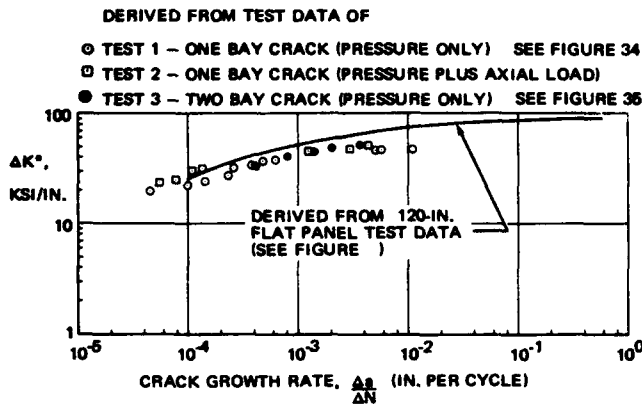


FIGURE 56. FATIGUE CRACK GROWTH RATE DATA DERIVED FROM TEST RESULTS OF PANEL 15 (CURVED PANEL)

**Bending Induced by the Broken Center Longeron** - In each of the tests for Panels 7 through 14, the secondary load induced by longeron bending on the crack tip, shown in Figure 17, must be considered. The effect on fatigue crack growth rate is illustrated in Figures 57 and 58. The growth rate  $da/dN$  versus  $\Delta K^*$  data for each panel were derived from the respective test results shown in Figure 37. For each panel, the growth rate is greater than that for the referenced unstiffened narrow panels except in the high growth rate region,  $da/dN > 4 \times 10^{-3}$  inch per cycle. The presence of longeron bending, which is not considered in the Lumped Parameter Analysis, increases the crack tip stress-intensity-factor. At a given crack growth rate,  $\Delta K^*$  is lower than that for unstiffened flat panels without longeron bending. The effect is expected to decrease as the crack length approaches the adjacent longerons which would relieve some of the bending load in the skin crack. Also must be considered is the factor that fracture toughness  $K_{Ic}^*$  is higher in the wide panel than the narrow panel as discussed earlier in growth rate. The effect of longeron bending should increase with the longeron area. This trend is substantiated by the growth rate data in Figures 57 and 58. In each case, the growth rate is higher in the panel with larger longerons.

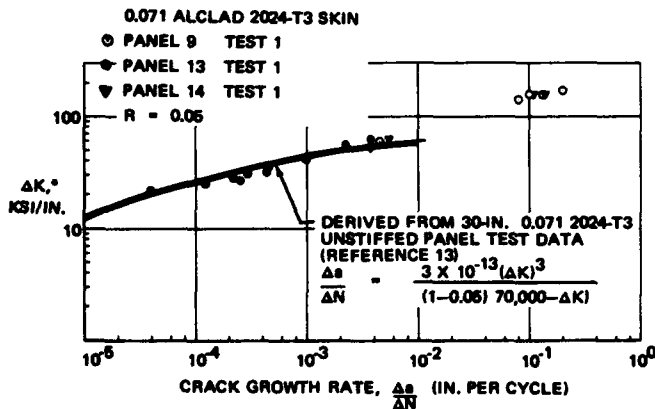


FIGURE 57. FATIGUE CRACK GROWTH RATE DATA DERIVED FROM THE RESULTS OF PANELS 9, 13 AND 14

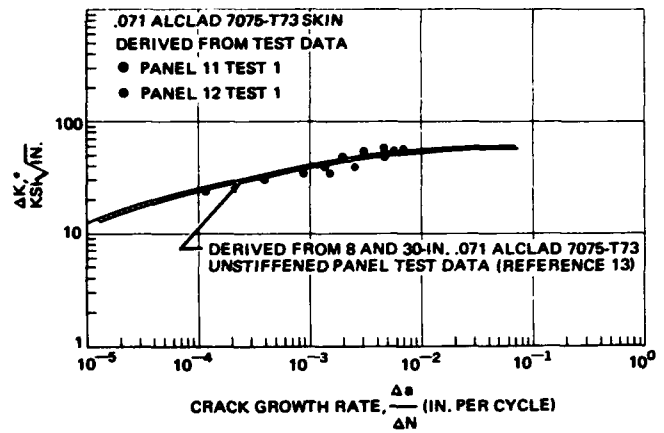


FIGURE 58. FATIGUE CRACK GROWTH RATE DATA DERIVED FROM THE RESULTS OF PANELS 11 AND 12

**Lateral Stiffeners** - The effect of biaxial tension stress induced by lateral stiffeners on fatigue crack growth rate is illustrated in Figure 18. The influence of biaxial tension stress field decreases with the distance from the lateral stiffeners. The results of Tests 1 and 2 of Panel 8 show that the rate of growth is lower in test 2 in which the crack is located closer to the adjacent frame (see Figure 59). It should also be noted that the crack growth rates for Test 2 of Panel 7 are not significantly different from those of Panel 8. The favorable influence of the biaxial stress field in the test of Panel 8 compensates for the greater longeron bending since Panel 8 has larger longerons than those in Panel 7. The influence of biaxial stress on direction of crack growth is shown in Figure 38.

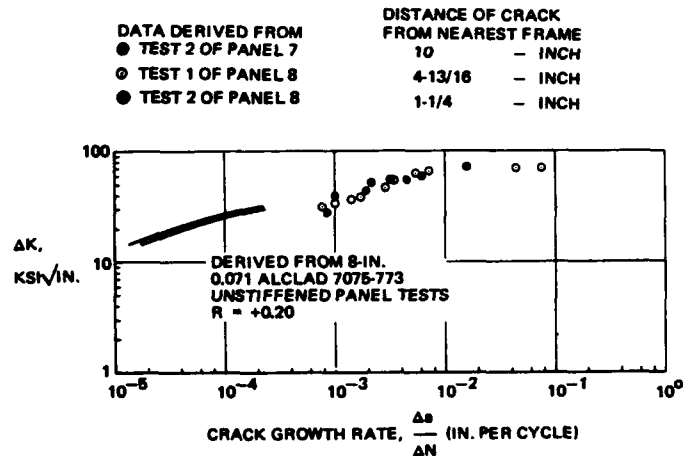


FIGURE 59. FATIGUE CRACK GROWTH RATE DATA DERIVED FROM THE RESULTS OF PANELS 7 AND 8

**Two Row Riveted Attachment** – In the Lumped Parameter Analysis, the longeron idealization for Configurations 8 and 9 of Figure 11 considers the two-rivet attachment in "Tee" shape longerons as a single centrally located shear panel. A closer point of load transfer from the broken longeron through the two rivets to the crack tip would cause a higher stress-intensity-factor than calculated, particularly when crack length is relatively short. This effect is observed by comparing the fatigue crack growth rate  $da/dN$  versus  $\Delta K^*$  data for Panels 9 and 13 in Figure 57. The rate of growth is higher in Panel 13 with "Tee" shaped longeron than in Panel 9 with approximately the same size "Hat" longeron.

## CONCLUSIONS

The correlation between analytical and test results for initial fast fracture, crack arrestment at the stiffeners, and residual strength of the full-scale damaged panels containing one- and two-bay skin cracks was excellent. The dynamic effect of fast fracture was

found to be negligible as shown by a small difference in the stress at crack arrestment and the residual strength of the panel.

The analytical method developed for predicting fatigue crack growth in the full-scale stiffened panels was found to be accurate within normal scatter.

The effect of typical secondary loads present in the fuselage structure on fracture strength and fatigue crack growth rate have been evaluated empirically. These effects, not considered in the analysis for uniaxial loading, include curvature and pressure, biaxial loading, biaxial stress induced by lateral stiffeners, shear, and bending stress induced by a broken longeron.

The rankings on fracture toughness  $K_{Ic}$ , and crack propagation resistance of aluminum alloy sheet as large structural panels are 2024-T3, 7075-T73, and 7075-T6. A great difference in the  $K_{Ic}$  exists for these alloys. The fatigue crack propagation resistance of 2024-T3 and 7075-T73 is nearly the same but is superior to that of 7075-T6.

## REFERENCES

1. Westergaard, H. M., "Bearing Pressures and Cracks," *Journal of Applied Mechanics*, June 1959
2. Irwin, G. R., "Analysis of Stresses and Strains Near the End of a Crack Traversing a Plate," *J. Applied Mechanics*, September 1957
3. Allen, F. C., "Stress Analysis of Centrally Cracked Plates," presented to ASTM Committee E24, March 1969
4. Paris, P. C. and Sih, G. C. "Fracture Toughness Testing and its Application," American Society for Testing Materials Special Publication No. 381, ASTM, Philadelphia, Pa.
5. Denke, P. H., "A General Digital Computer Analysis of Statically Indeterminate Structures," Douglas Paper 834, September 1959
6. Denke, P. H., "A Computerized Static and Dynamic Structural Analysis System; Part III, Engineering Aspects and Mathematical Formulation of the Problem," Douglas Paper 3213, presented to the SAE International Automotive Congress and Exposition, January 1965
7. Picard, J. and Morris, R. C., "Format II – Second Version of Fortran Matrix Abstraction Technique," AFFDL-TR-66-207, Volume I and Volume III
8. Swift, T. and Wang, D. Y., "Damage Tolerant Design – Analysis Methods and Test Verification of Fuselage Structure," McDonnell Douglas Report MDC-J0258, November 1969
9. Wang, D. Y., "An Investigation on Fatigue Crack Propagation and Failure Design of Stiffened Large Aluminum Alloy Panels with Various Crack Stoppers," Proc. 10th ASME/AIAA Structures, Structural Dynamics and Materials Conference, New Orleans, La., April 1969
10. Paris, P. and Erdogan, F., "A Critical Analysis of Crack Propagation Laws," *Journal of Basic Engineering*, Trans. of ASME, Series D, Vol. 85, December 1963
11. Forman, R. G., Kearny, V. E. and Engle, R. M., "Numerical Analysis of Crack Propagation in Cyclic Loaded Structures," *Journal of Basic Engineering*, Trans. of ASME, Vol. 89, September 1967
12. Wei, R. P., "Some Aspects of Environment-Enhanced Fatigue-Crack," preprint of a paper presented at the ASTM Fall Meeting in Atlanta, Ga., September 1968
13. Wang, D. Y., "A Study of Modeling Methods for Failure Design and Testing," McDonnell Douglas Report MDC-J0240, September 1969
14. Flugge, W., "Stress Problems in Pressurized Cabins," NACA T.N. 2612
15. Dugdale, D. S., "Yielding of Steel Sheets Containing Slits," *J. Mech. Phys. Solids*, Vol. 8, pp. 100-104, May 1960

# A RE-DEFINITION OF ENDURANCE LIFE DESIGN STRENGTH CRITERIA BY STATISTICAL METHODS

by

E.B. Haugen and J.A. Hritz

Aerospace and Mechanical Engineering Department  
The University of Arizona  
Tucson, Arizona

## INTRODUCTION AND DEFINITION OF PROBLEM

An often encountered problem in mechanical and structural design is the determination of the fatigue life and/or the allowable fatigue stress of proposed components. It is the purpose of this paper to establish a factual basis for defining the safe design criterion of a mechanical component subjected to an alternating tensile stress superimposed on a mean tensile stress, with the measure of reliability and fatigue life specified.<sup>††</sup> Attempts to solve this design problem in the past has often led to overdesign or unsafe design resulting from incomplete or incorrect definition of the applicable failure criterion.

## CONVENTIONAL COMBINED STRESS CRITERIA

Numerous attempts have been made to define safe combinations of biaxial and other stresses, usually depicted graphically as safe regions for design for specified cycles of life, as shown in Figure 1 (Ref. 1, p. 270).  $\sigma_a$  refers to the alternating stress magnitude and  $\sigma_m$  to the mean stress magnitude. The areas bounded by the X and Y axes and the Soderberg, Modified Goodman, Langer Modification, and Gerber lines presumably contain the points that define safe mean and dynamic stress combinations. Figure 1 also shows actual data points.

The earliest and most widely known combined-stress criterion was the Modified Goodman Line shown in Figure 1. This was a straight line connecting the endurance strength,  $S_e$ , plotted on the ordinate and the ultimate static tensile strength,  $S_u$ , plotted on the abscissa. Any combination of mean and alternating stresses that produced a point below the line was considered safe. The Modified Goodman Line was generally considered to be a conservative criterion for safe design. However, for the lower stress ratios ( $\sigma_a/\sigma_m \approx 1/10$ ) the mean stress,  $s_m$ , may exceed the yield strength,  $S_y$ .

The Modified Goodman Line and the other safe design definitions, noted in this section, apply to cycles of life from 1,000 to  $10^6$  or more cycles, where  $10^6$  cycles is considered to be the life at the beginning of the endurance strength for ductile steels. The Modified Goodman Line can be represented by the following equation;

$$\frac{\sigma_a}{S_e} + \frac{\sigma_m}{S_u} = 1. \quad (1)$$

The Gerber parabola, shown in Figure 1 was proposed to correct the conservatism of the Modified Goodman Line, since it fit existing data better, in the stress ratio

$$(\infty > \sigma_a / \sigma_m \geq 1),$$

than the Modified Goodman Line, see Figure 1. Yielding may occur in the area of stress ratios approximately 1/10 or less. The Gerber parabola\*

$$\frac{\sigma_a}{S_e} + \left( \frac{\sigma_m}{S_u} \right)^2 = 1. \quad (2)$$

The Soderberg Line shown in Figure 1, was proposed to eliminate the problem of exceeding the yield point at any stress combination defined as safe by terminating the line at the yield point,  $S_y$ , instead of the ultimate strength,  $S_u$ , on the abscissa. The Soderberg Line lies under the Goodman Line, and therefore is a more conservative design criterion (Ref. 9, p. 178). It is defined by

$$\frac{\sigma_a}{S_e} + \frac{\sigma_m}{S_y} = 1. \quad (3)$$

The Sines Line, shown in Figure 1 (Ref. 3, p. 125), is empirical and can be adjusted to fit the data for a particular material. This criterion is defined from zero mean stress to  $S_y$ , as shown in Figure 1. The equation is

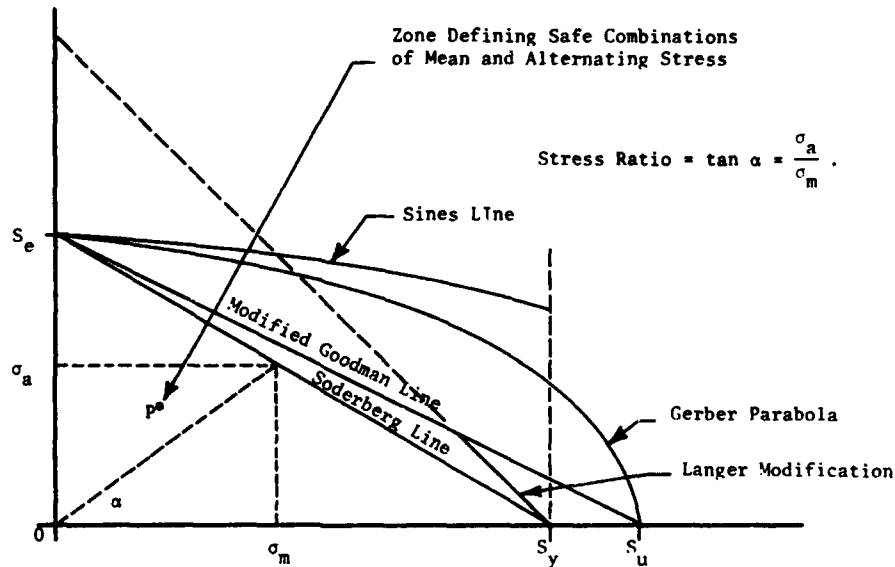
$$S_e - c \sigma_m = \sigma_a, \quad (4)$$

<sup>††</sup> The experimental research work that supports the conclusions in this paper was partially supported by the Office of Naval Research, Washington, D.C., under Contract No. N00014-67-A-0209-002, E.B. Haugen and D.B. Kecicoglu Co - Investigators.

\* See Figure 11, which shows the results of this study.



Figure 1. The Goodman, Gerber, Soderberg, Sines, and Langer Definitions of the Safe Design Region.



where  $c$  is a constant determined by testing.

The Langer Modification revises the Modified Goodman Line by excluding regions where the alternating stress plus the mean stress exceeds static yield strength, or where  $(\sigma_a + \sigma_m) > S_y$ . This criterion is subject to the same criticism as the Modified Goodman Line, at stress ratios ( $\infty > \sigma_a / \sigma_m \geq 1$ ) because the safe design area is defined as that below the line

$$\sigma_a + \sigma_m = S_y' \quad (5)$$

or below the Modified Goodman Line, as shown in Figure 1 (Ref. 4, p. 180).

The von Mises-Hencky or strain energy theory has been proposed for defining the safe design region for materials subjected to biaxial fatigue loading. Von Mises stresses, rather than the actual stresses, are plotted on the ordinate and the abscissa. The mean,  $\sigma'_m$ , and alternating,  $\sigma'_a$ , von Mises equivalent stresses<sup>†</sup> are given by (Ref. 9, p. 188).

$$\sigma'_m = \sqrt{\sigma_{xm}^2 - \sigma_{xm} \sigma_{am} + \sigma_{zm}^2 + 3\tau_{xzm}^2} \quad (6)$$

$$\sigma'_a = \sqrt{\sigma_{xa}^2 - \sigma_{xz} \sigma_{za} + \sigma_{za}^2 + 3\tau_{xza}^2} \quad (7)$$

The von Mises-Hencky theory was developed for static loads (Ref. 9, p. 184-185), and the theory applies only in the elastic range (Ref. 9, p. 153 of the material).

Because of the limitations and differences among the safe design criteria found in the literature, the experi-

<sup>†</sup> NOTE: In this study  $\sigma'_m = \sigma_m$  and  $\sigma'_a = \sigma_a$ , where both are tensile stresses.

<sup>††</sup> Manson defines low cycle fatigue as ( $1000 \leq n \leq 10^6$ ) cycles.

\* NOTE: Cycle life results in Table III.

mental research necessary to define a valid statistical fatigue strength envelope (including the mean value line) was undertaken.

## STATISTICAL METHODS

The Goodman, Soderberg, and Gerber Lines are deterministic models. It is now, however, an accepted fact that material fatigue life, either cycles-to-failure at fixed stress or stress at fixed cycle life, varies in a random fashion. Thus, fatigue life and/or strength are statistically distributed and cannot be described completely by discrete value models. The stress distributions developed experimentally in this study were plotted to define a safe design criterion as an allowable stress surface. (See Figure 11.)

## THEORY

The cycle range for low cycles, or short life, fatigue is  $1/4 \text{ cycle} \leq n \leq 1000 \text{ cycles}$ <sup>††</sup> (Ref. 4). Short life fatigue is defined as the conditions of metals subjected to high temperatures or to a stress condition that cause some plastic deformation in the material (Ref. 4). The second condition was useful, one purpose here being to test whether under certain stress conditions materials enter the short life fatigue condition.\*

Manson (Ref. 4, Chapter 4) postulates the possibility of predicting cycle life by measuring the amount of plastic strain in a material. Figure 2 shows that Manson refers to as the plastic strain range, such that

$$\epsilon_p = \epsilon_t - \epsilon_{el} \quad (8)$$

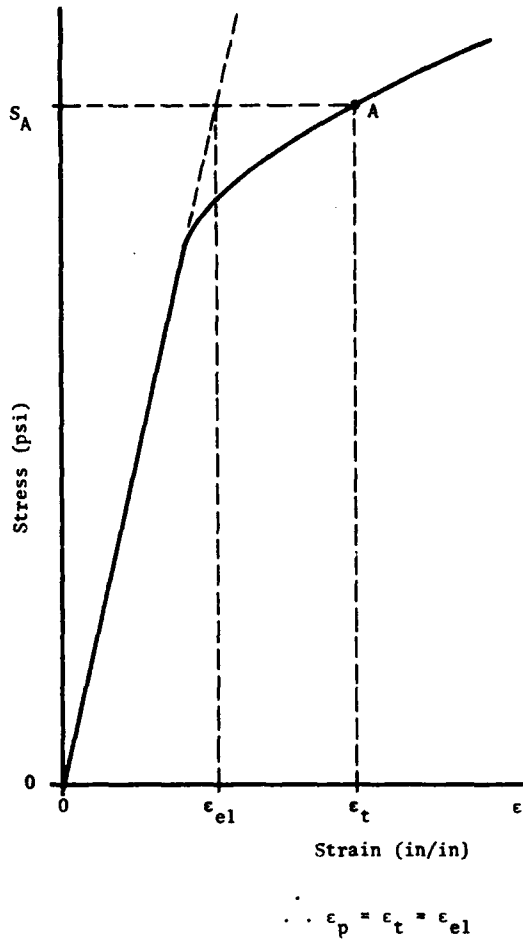


Figure 2. The Definition of Plastic Strain,  $\epsilon_p$ , in Relation to the Stress-Strain Diagram (Ref. 4, p. 132).

where  $\epsilon_p$  = plastic strain (in/in)

$\epsilon_t$  = total strain (in/in)

$\epsilon_{el}$  = elastic strain (in/in)

Manson proposed that

$$\epsilon_p = M \cdot N_f^z \quad (9)$$

where  $M$  and  $z$  are material constants determined by experimentation and  $N_f$  is the design cycles-to-failure of the material. When data is plotted on log-log paper, as shown in Figure 3, the desired constants can be obtained, leading to the conclusion that  $z$  is approximately  $-1/2$ . From equation (9):

$$N_f = \left[ \frac{\epsilon_p}{M} \right]^{1/z} = \left[ \frac{\epsilon_p}{M} \right]^{1 / - (1/2)} = \left[ \frac{\epsilon_p}{M} \right]^{-2}$$

or

$$N_f = \left[ \frac{M}{\epsilon_p} \right]^2 \quad (10)$$

The values of  $z$  or  $M$  are not important. It may be noted in equation 10 that for  $\epsilon_p = 0$ , cycle life is infinite, and for  $\epsilon_p > 0$  cycle life is finite. If  $\epsilon_p$ ,  $\epsilon_{el}$ , and  $\epsilon_t$  are plotted versus cycle life, the curve in Figure 4 results. As may be noted from Figure 4, plastic strain is dominant in predicting cycle life. Thus, reduction in plastic strain should result in increased cycle life. The Libertiny and Morrison papers, in agreement with the remarks above, (Ref. 5, p. 50) add more weight to the argument that plastic strain may indeed effect cycle life.

Based on these arguments, it seemed plausible to postulate that plastic strain imposes an important effect on cycle life. It was next necessary to show how this postulation might assist in defining a criterion (to be tested) for safe design of mechanical elements under alternating tensile stress superimposed on a mean tensile stress. Consider the magnitude of both alternating and mean stresses as shown in Figure 1, there were points in the Modified Goodman and Gerber safe design zones where the peak stress ( $\sigma_a + \sigma_m$ ) exceeded the static yield stress,  $S_y$ . Thus, there were situations in which short-life fatigue could be expected.

The static yield and the peak stress ( $\sigma_a + \sigma_m$ ) were utilized to construct a model that the experimental results would test. Figure 5 was divided into two regions, A and B; In region A, the sum ( $\sigma_a + \sigma_m$ ) was less than or equal to  $S_y$ , and in region B, the sum ( $\sigma_a + \sigma_m$ ) was greater than  $S_y$ , but less than or equal to  $S_u$ . Both regions were truncated at the mean endurance strength value,  $S_e$ . The question was whether region A provided the safe design region, region B

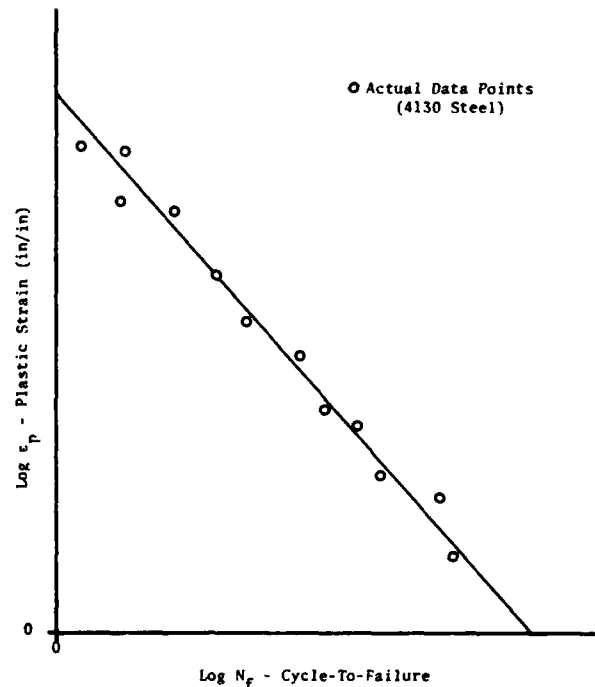
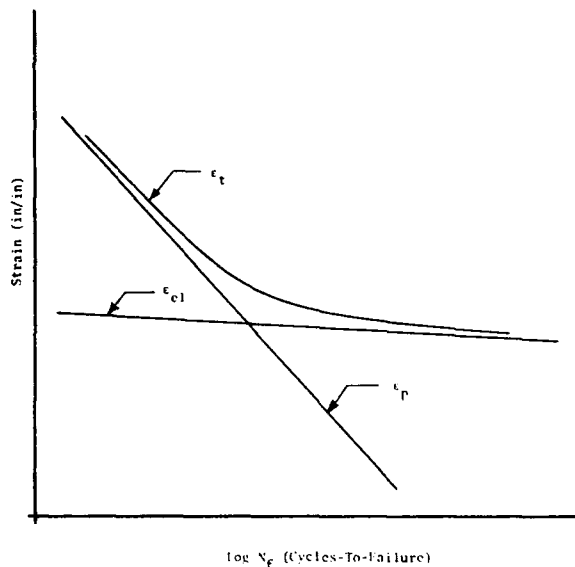


Figure 3. Cycles-to-Failure versus Plastic Strain (Ref. 4, p. 133).



**Figure 4. Cycles-to-Failure versus Plastic Strain,  $\epsilon_p$ , Elastic Strain,  $\epsilon_{el}$ , and Total Strain,  $\epsilon_t$ . (Ref. 4, p. 142).**

the short life region, and whether stress combinations outside regions A and B would result in certain failures. This postulation of two zones is subsequently referred to as proposed theory.

#### EXPERIMENTAL TEST PLAN AND METHOD

The test objective was to determine distributions of endurance strength, at enough significant stress ratios, to define an endurance strength envelope. At each stress ratio, enough values were obtained from tests to calculate the sample statistics of the strength distribution involved.

Figure 5 shows: lines 1, 2, 3, 4, 5, and 6, on which

distributions of endurance strength were obtained, the postulated regions A and B, the Modified Goodman Line, and the Gerber parabola. The strength distribution on line 1 anchored the strength surface at the alternating stress axis, and defined the mean truncation line for regions A and B. Distributions on lines 2 and 3 assisted in defining the shape of the strength surface at the higher values of  $s_a/s_m$ . Line 4 was needed because in this region the Modified Goodman Line predicts failure inside region A and the Gerber parabola in region B. Line 5 passes through an area in which both the Goodman and Gerber criteria predict safe design in region B (the short life region). The distribution on Line 5 helped establish the slope of the mean value line near the mean stress axis. Line 6 was necessary to locate the strength surface on the mean stress axis.

There were some available data from previous studies. These were cycle life distributions for fixed stress ratios. One set of data was clearly of finite life (plotted outside the endurance strength envelope), and the other set was near the threshold of infinite life, i.e.,  $10^6$  cycles. These distributions provided bounds on the location of the strength envelope mean value line. In this study, the cycle life was fixed at endurance. The testing procedure was determined by the staircase method (Ref. 11).

The mean value and the standard deviation estimators of the strength random variable at each stress ratio were calculated, the strength distributions were assumed normally distributed, as shown in previous studies, (Ref. 1, p. 351). Therefore, the mean and standard deviation were sufficient to uniquely define the strength distribution at each stress ratio. On lines 1, 3, 4, and 5, the staircase method of testing was used. The distribution on line 6 was determined from static tensile test data, developed using a Riehle Testing Machine, 0-60,000 lb. capacity and certified accurate within 0.2% of indicated load. The data was reduced by a computer program (Ref. 11). Enough specimens were tested at

**Figure 5. Graphical Representation of Test Plan.**

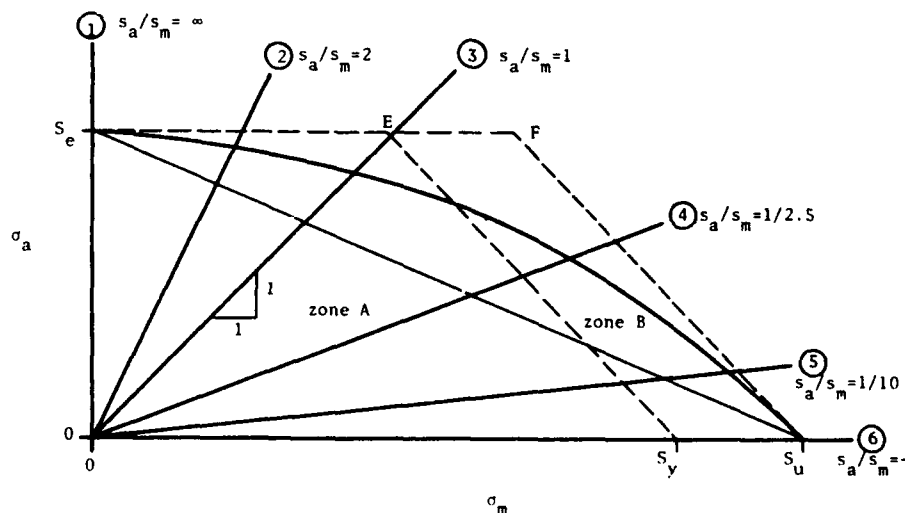


TABLE I.  
TEST PLAN PARAMETERS.

TEST NO.	STRESS RATIO ALTERNATING/ MEAN	SPECIMEN DIAMETER IN.	ASSUMED MEAN VALUES OF STRESS TO START STAIRCASE METHOD ANALYSIS	ASSUMED MEAN VALUES OF LOAD TO START STAIRCASE METHOD ANALYSIS	INCREMENT USED FOR STAIRCASE METHOD, STRESS LBS.	INCREMENT USED FOR STAIRCASE METHOD, STRESS LBS.
1	$\infty$	$d = .0620 \pm .0005$	$S_a = 59,000$	$L_a \approx 178$	$\Delta S_a = 4000$	$\Delta L_a = 12$
2	2	$d = .0740 \pm .0005$	cycles-to-failure	none	none	none
3	1	$d = .0695 \pm .0005$	$S_m = 48,000$	$L_m = 182$	$\Delta S_m = 3000$	$\Delta L_m = 12$
4	1/2.5	$d = .0645 \pm .0005$	$S_m = 80,000$	$L_m = 247$	$\Delta S_m = 3000$	$\Delta L_m = 9$
5	1/10	$d = .0645 \pm .0005$	$S_m = 100,000$	$L_m = 327$	$\Delta S_m = 2500$	$\Delta L_m = 8$
6	0	Diameter varied	Stress calculated for each specimen	none (static test)	none	none

\* $L_a$  is the alternating load and  $L_m$  is the mean load.

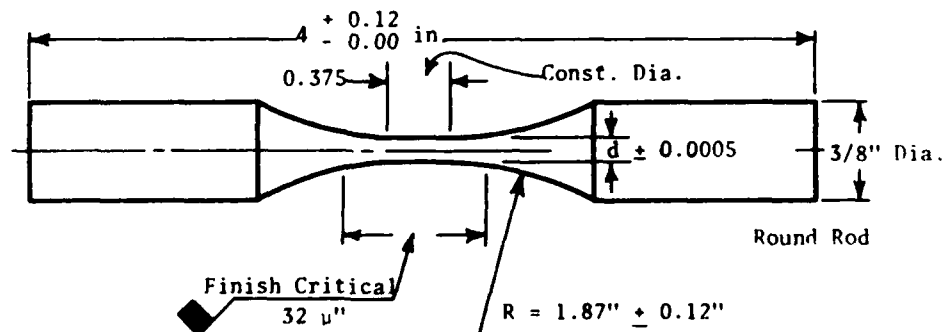
each stress ratio (24 or more) to insure meaningful statistical results. The test plan is given in Table I.

Loading, geometry, surface finish, and stress concentration were carefully controlled, to eliminate extraneous variables as much as possible.

The experimental testing program was carried out on a SF-01-U-Z Fatigue Testing Machine, Automatic Preload, Serial No. 040-2317 with the following operating characteristics:

- 1800 CPM repeated loading
- Axial Tension or Compression
- Load Capacity (B.L.H. Manual)
  - Alternating Force:  $0 \pm 200$  lbs.
  - Static Preload:  $\pm 200$  lbs. (Tension or Compression)
  - Accuracy:  $\pm 2\%$  of load or 1 lb.

Figure 6. Specimens for Axial Fatigue Machine Endurance Tests - Mean and Alternating Tensile Loading - Staircase Method.



NOTES:

1. Finish per ASTM specification for test specimens.
2. Stress level (see tabulation).
3. Tabulated loads and stresses are peak values.

**TABLE II.**  
**RESULTS FOR TEST SERIES 1.**

$$\sigma_a / \sigma_m = \infty$$

Specimen No.	Specimen Diameter In.	Cycles-to-Failure	Result	Alternating Load Lbs.
			Failure F Success S	
3	0.0618	294,000	F	178
34	0.0620	41,000	F	166
13	0.0621	124,000	F	154
19	0.0620	11,184,000	S	142
28	0.0616	1,190,000	S	154
18	0.0621	451,000	F	166
8	0.0620	2,231,000	S	154
32	0.0620	81,000	F	166
11	0.0615	247,000	F	154
38	0.0615	1,046,000	S	142
1	0.0623	1,246,000	S	154
2	0.0615	449,000	F	166
8'	0.0620	2,258,000	S	154
4	0.0621	141,000	F	166
31'	0.0620	2,762,000	S	154
2*	0.0618	67,000	F	166
7*	0.0617	300,000	F	154
38*	0.0623	2,589,000	S	142
14*	0.0616	189,000	F	154
35*	0.615	1,130,000	S	142
16*	0.0621	209,000	F	154
21''	0.0623	1,959,000	S	142
32''	0.0621	1,243,000	S	154
18''	0.0619	187,000	F	166
29''	0.0616	806,000	F	154
1''	0.0615	595,000	F	142
11''	0.0620	198,000	F	130
31 <sup>3</sup>	0.0624	2,268,000	S	118
13 <sup>3</sup>	0.0616	1,185,000	S	130
29 <sup>3</sup>	0.0625	1,868,000	S	142
30 <sup>3</sup>	0.0621	564,000	F	154
31 <sup>3</sup>	0.0617	2,786,000	S	142
28 <sup>3</sup>	0.0621	597,000	F	154
3 <sup>3</sup>	0.0615	577,000	F	142
28 <sup>3</sup>	0.0623	2,380,000	S	130
27 <sup>3</sup>	0.0616	377,000	F	142
36 <sup>4</sup>	0.0621	2,154,000	S	130
4 <sup>4</sup>	0.0620	1,541,000	S	142
23 <sup>4</sup>	0.0615	133,000	F	154
2 <sup>4</sup>	0.0615	697,000	F	142
12 <sup>4</sup>	0.0618	1,795,000	S	130
17 <sup>4</sup>	0.0621	2,795,000	S	142
26 <sup>4</sup>	0.0615	186,000	F	154
34 <sup>4</sup>	0.0616	782,000	F	142
14 <sup>4</sup>	0.0615	2,078,000	S	130
3 <sup>4</sup>	0.0615	611,000	F	142
20 <sup>4</sup>	0.0621	1,124,000	S	130
31 <sup>4</sup>	0.0618	1,215,000	S	142
8 <sup>4</sup>	0.0619	261,000	F	154
16 <sup>4</sup>	0.0620	1,863,000	S	142

The Fatigue Testing Machine was calibrated utilizing specimens with BLH variable resistance strain gages mounted on them and a BLH 120 C Digital Strain Indicator.

The design, machining, and finishing of test specimens was in accordance with the Manual on Fatigue Testing, Special Publication No. 91, ASTM, Baltimore, Maryland, 1949. Typical specimen design of those used in this testing

program is shown in Figure 6. The specific geometry and tolerances are given in Table 1.

**EXPERIMENTAL RESULTS**

The test data are presented in unreduced form in Tables II thru VII and Figures 7 through 10. Figure 5 relates the stress ratios studied to the Tables and Figures.

The approximate mean load values shown in Table I were obtained from Figure 1, and used as starting test values in the staircase method. The values were taken midway between the Modified Goodman Line and the Gerber parabola on the  $s_a/s_m$  line of the test. The step increments were approximate values from similar previous tests, and were between 1/2 and 2 standard deviations.

**TABLE III.**  
**RESULTS FOR TEST SERIES 2.**

$$\sigma_a / \sigma_m = 2$$

(Ref. 11, pages 166-167)

Specimen Diameter = 0.0740 inches Mean Load = 100 lbs. Alternating Load = 200 lbs.			
SPECIMEN NO.	CYCLES-TO FAILURE IN 10 <sup>3</sup> CYCLES	SPECIMEN DIAMETER IN.	REMARKS
26		0.0738	Stopped - 1.28 mil.
23	586	0.0743	
13	222	0.0737	
9	187	0.0736	
21	265	0.0745	
10	745	0.0737	
14		0.0745	test void
29	1,771	0.0739	stopped - 1.77 mil.
20	444	0.0735	
35	700	0.0742	
5	2,292	0.0745	stopped - 2.29 mil.
27	266	0.0743	
11	268	0.0743	
36	789	0.0742	
12	2,688	0.0743	stopped - 2.68 mil.
30	693	0.0736	
16	2,532	0.0743	stopped - 2.53 mil.
4	198	0.0732	tes' void
17	249	0.0735	
28	2,474	0.0737	stopped - 2.47 mil.
31	1,137	0.0738	stopped - 1.14 mil.
7	2,800	0.0740	stopped - 2.8 mil.
37	2,476	0.0738	stopped - 2.47 mil.
32	2,365	0.0743	stopped - 2.35 mil.
19	1,192	0.0738	stopped - 1.19 mil.
3	3,428	0.0735	stopped - 3.43 mil.

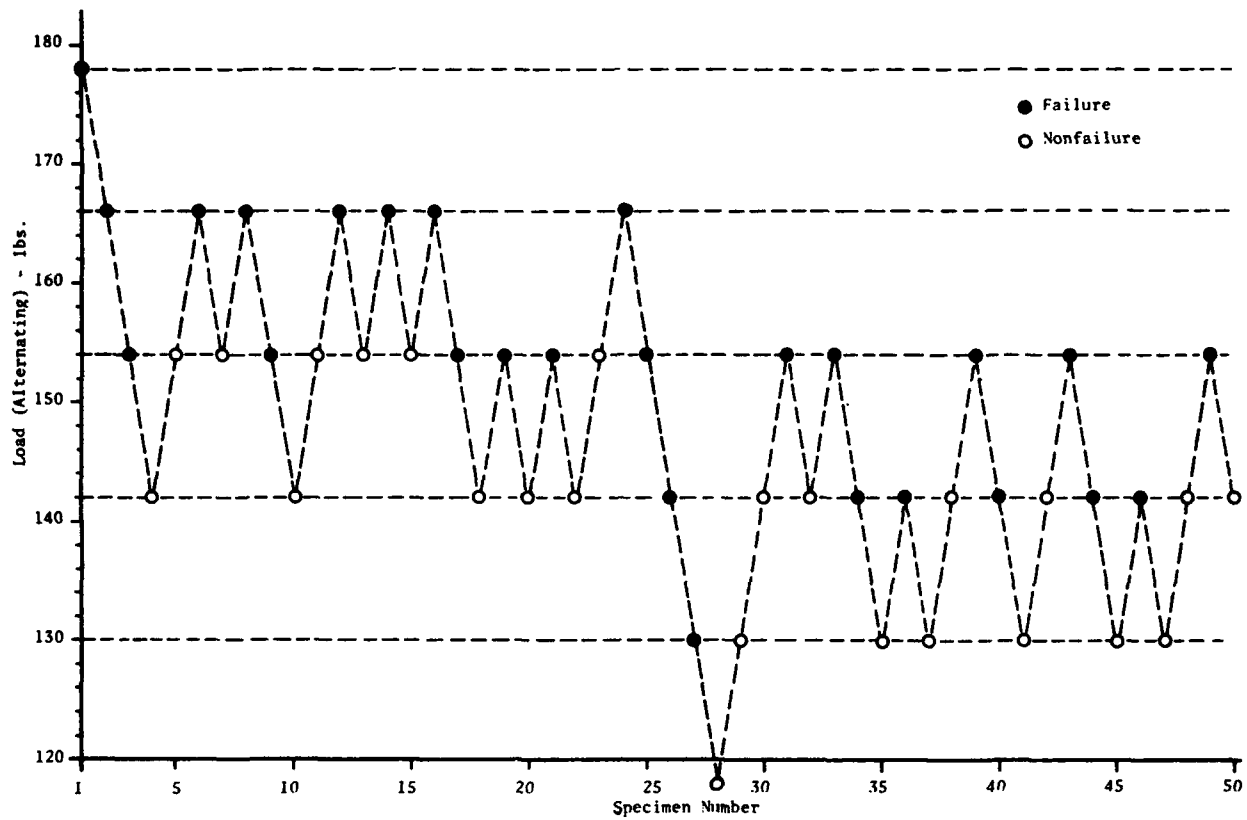


Figure 7. Graphical Representation of the Staircase Method Results (Test Series 1).  
For Strength Distribution Determination.

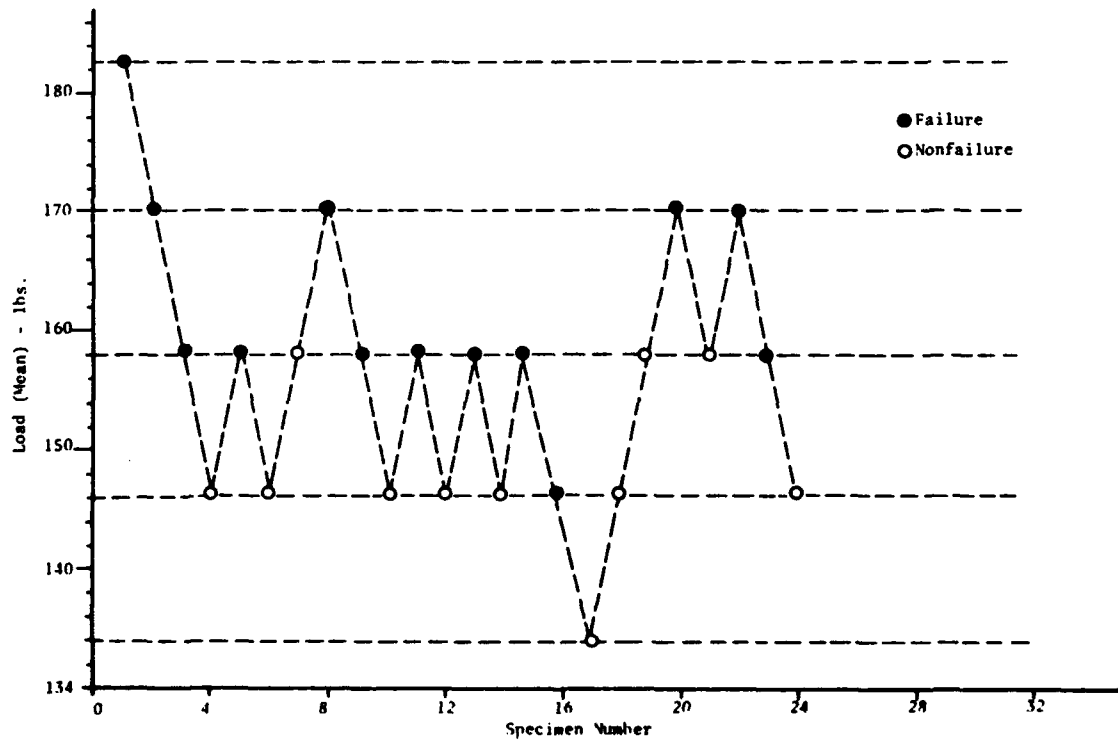


Figure 8. Graphical Representation of the Staircase Method (Test Series 3).

TABLE IV.  
RESULTS FOR TEST SERIES 3.  
 $\sigma_a / \sigma_m = 1.0$ .

Specimen No.	Specimen Diameter In.	Cycles to Failure	Result Failure F Success S	Alternating Load Lbs.
2	0.0695	130,000	F	182
33	0.0698	260,000	F	170
3	0.0693	365,000	F	158
8	0.0699	1,767,000	S	146
26	0.0679	280,000	F	158
29	0.0700	1,328,000	S	146
36	0.0695	1,036,000	S	158
7	0.0690	121,000	F	170
28	0.0696	130,000	F	158
20	0.070	1,038,000	S	146
33	0.0693	204,000	F	158
1	0.0690	1,163,000	S	146
16	0.0698	236,000	F	158
11	0.0700	1,568,000	S	146
38	0.0696	179,000	F	158
10	0.0700	465,000	F	146
19	0.0699	1,126,000	S	134
5	0.0690	1,013,000	S	146
35	0.0695	1,135,000	S	158
32	0.0700	437,000	F	170
9	0.0696	1,116,000	S	158
27	0.0694	118,000	F	170
12	0.0697	162,000	F	158
30	0.0696	1,862,000	S	146

TABLE V.  
RESULTS FOR TEST SERIES 4.  
 $\sigma_a / \sigma_m = 1/2.5$ .

Specimen No.	Specimen Diameter In.	Cycles to Failure	Result Failure F Success S	Alternating Load Lbs.
36	0.0645	433,000	F	99.8
13	0.0640	1,218,000	S	96.4
38	0.0646	523,000	F	99.8
10	0.0650	1,368,000	S	96.4
30	0.0642	579,000	F	99.8
26	0.0641	565,000	F	96.4
11	0.0650	1,186,000	S	93.0
37	0.0641	296,000	F	96.4
26	0.0641	2,186,000	S	93.0
1	0.0640	429,000	F	96.4
29	0.0644	527,000	F	93.0
16	0.0649	2,682,000	S	89.6
26	0.0648	9,000	F	93.0
33	0.0642	1,173,000	S	89.6
19	0.0643	1,283,000	S	93.0
27	0.0645	1,109,000	S	56.4
32	0.0640	409,000	F	99.8
9	0.0647	498,000	F	96.4
26	0.0640	1,032,000	S	93.0
17	0.0650	473,000	F	96.4
8	0.0644	1,127,000	S	93.0
34	0.0641	476,000	F	96.4
27	0.0645	1,105,000	S	93.0
4	0.0650	1,028,000	S	96.4
37	0.0647	289,000	F	99.8
17	0.0642	1,132,000	S	96.4
31	0.0650	443,000	F	99.8
21	0.0644	631,000	F	96.4
13	0.640	1,186,000	S	93.0

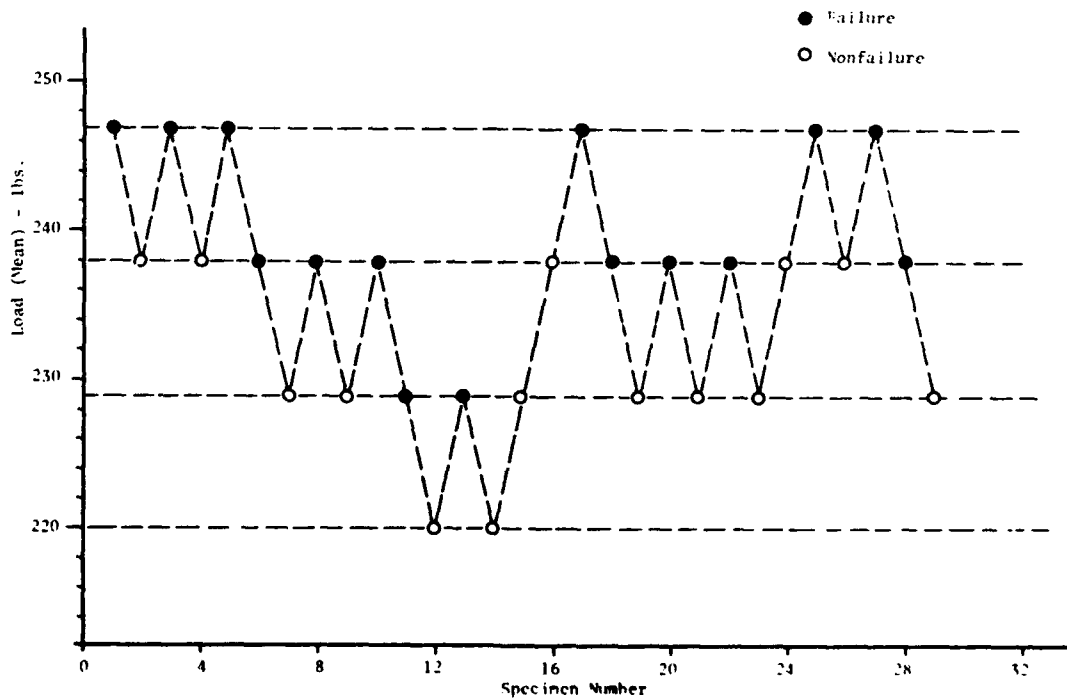


Figure 9. Graphical Representation of Staircase Method (Test Series 4).

TABLE VI  
RESULTS FOR TEST SERIES 5.  
 $\sigma_a / \sigma_m = 1/10$ .

Specimen No.	Specimen Diameter In.	Cycles to Failure	Result		Alternating Load Lbs.
			Failure F	Success S	
12	0.0646	88,000	F		32.7
23	0.0648	1,082,000	S		31.9
20'	0.0646	1,076,000	S		32.7
20	0.0643	1,000	F		33.5
1	0.0640	1,086,000	S		32.7
17	0.0645	1,106,000	S		33.5
30	0.0645	static	F	0	34.3
35	0.0641	$n < 1,000$	F		33.5
28	0.0648	1,000	F		32.6
31	0.0646	1,091,000	S		31.9
7	0.0642	1,393,000	S		32.7
18	0.0650	1,033,000	S		33.5
28'	0.0644	$n < 1,000$	F		34.3
4	0.0650	$n < 1,000$	F		33.5
14	0.0650	1,153,000	S		32.7
21	0.0647	1,051,000	S		33.5
17	0.0645	9,000	F		34.3
31	0.0649	1,623,000	S		33.5
19	0.0641	1,158,000	S		34.3
16	0.0650	5,000	F		35.1
37	0.0645	2,500	F		34.3
26*	0.0650	1,001,000	S		33.5
17*	0.0647	50,000	F		34.3
2*	0.0642	1,000	F		33.5
18*	0.0650	1,258,000	S		32.7
2''	0.0645	5,000	F		33.5
17''	0.0640	3,000	F		32.7
38''	0.0649	1,124,000	S		31.9
16''	0.0648	1,032,000	S		32.7
21''	0.0643	3,000	F		33.5

The staircase method consists of testing at different stress levels for a given number of cycles and recording either survival or failure for each specimen. If the specimen is a failure the stress level is decreased, if a survival the stress level is increased. The data appears as shown in Figure 7. This process is continued until a sufficient number of specimens have been tested to permit a proper statistical interpretation.

A special consideration is required in applying the staircase method in a combined-stress testing program. Since a ratio  $s_a/s_m = c$  must be maintained, both the mean and the alternating stress values must be increased or decreased such that the value  $c$  of the ratio is maintained constant.

In any experiment, the total number of successes will be approximately equal to the total number of failures and for the estimating of the mean,  $\mu$ , and the standard deviation,  $\sigma$ , only successes or failures are used, whichever is the smaller.

The estimate of the mean of the strength distributions is given by

TABLE VII.  
RESULTS FOR TEST SERIES 6.  
 $\sigma_a / \sigma_m = 0$ .

SPECIMEN NO.	SPECIMEN DIAMETER IN.	MEAN TENSILE LOAD (LBS)	CALCULATED MEAN TENSILE STRESS PSI
27	0.0593	308	111,500
32	0.0600	311	110,000
17'	0.0605	314	109,000
20	0.0599	298	105,800
29	0.0611	332	112,800
36	0.0596	302	108,300
31	0.0611	314	106,800
11	0.0607	319	110,500
20'	0.0610	319	109,200
8	0.0604	308	107,800
10	0.0603	300	105,200
21	0.0614	313	105,900
32	0.0611	342	116,500
12	0.0608	328	113,100
37	0.0601	334	117,800
35	0.0596	329	118,000
13	0.0611	332	113,000
7	0.0614	334	112,900
5	0.0610	335	114,800
26	0.0603	317	111,000
9	0.0606	318	110,200
33	0.0602	300	105,600
38	0.0608	310	107,200

$$\mu = y' + d \left[ \frac{A}{N} \pm \frac{1}{2} \right]$$

$n_0, n_1, n_2, \dots, n_k$  = number of successes or failures at each level.

$$\sum n_i = N$$

$N$  = total number of successes or failures

$$i = 1, 2, \dots, k$$

$$A = \sum i n_i$$

$$B = \sum i^2 n_i$$

use + when failures are counted as events  
and - when successes are counted.

$$\sigma = 1.620 d \left( \frac{NB - A^2}{N^2} + 0.029 \right)$$

where  $\mu$  = estimate of mean

$\sigma$  = estimate of standard deviation

$y'$  = lowest level on which the less frequent event occurred (normalized value)

$d$  = test interval



**TABLE VIII.**  
**TABULATION OF FINAL RESULTS.**  
(See Figure 11.)

TEST NO.	STRESS RATIO $\sigma_a / \sigma_m$	MEAN VALUE MEAN STRESS PSI	STD. DEV. MEAN STRESS PSI	MEAN VALUE OF ALTERNATING STRESS PSI	STD. DEV. ALTERNATE STRESS PSI	NO. OF SPECIMENS
1	$\infty$	0	0	48,700	4,440	50
2	2	23,250	-----	46,500	-----	24
3	1	40,600	1,845	40,600	1,845	24
4	1/2.5	72,100	2,160	28,900	865	29
5	1/10	101,200	3,010	10,120	301	30
6	0	110,560	1,300*	0	0	23

\*From (Ref. 11, p. 205).

The data reduction results are given in Table VIII. Table IX gives the sample calculations for test series 1. The data for test series 6 was reduced by means of an existing computer program for obtaining a stress distribution for static tensile ultimate strength.

#### UTILIZATION OF RESULTS

The results of the series of tests at the six stress ratios were plotted on the alternating tensile stress versus mean tensile stress diagram in Figure 11. The distributions

shown on stress ratio lines 1, 3, 4, 5, and 6 are shown as approximately normal distributions obtained directly from the reduced data. On stress ratio line 2, there was a point estimation of the mean value. As shown in Table III, the data at this level was an attempt to find the cycles-to-failure distribution at a given stress level of both the mean and alternating stresses. The mean stress level was inferred to pass either through point Q or very near it. See Figure 11. Also shown in Figure 11, stress ratio line 3 is from previously obtained data (Ref. 11), designated as P, that is definitely in the finite life zone ( $n \approx 120,000$  cycles). A summary of results is given in Table VIII.

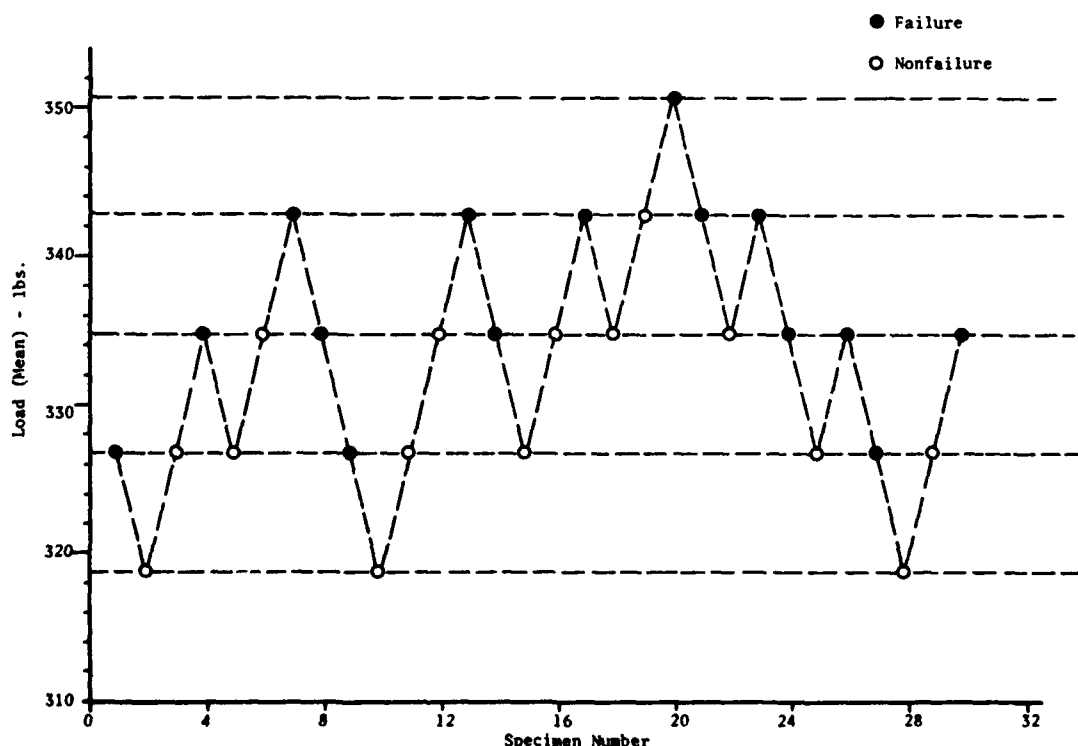


Figure 10. Graphical Representation of Staircase Method (Test Series 5).

$$\text{Equation (2): } \frac{S_a}{S_e} + \left( \frac{S_m}{S_u} \right)^2 = 1 \quad (\text{Gerber parabola})$$

$$\frac{S_a}{S_e \pm 3\sigma_{S_e}} + \left( \frac{S_m}{S_u \pm 3\sigma_{S_u}} \right)^2 = 1 \quad (+ 3\sigma \text{ Curves})$$

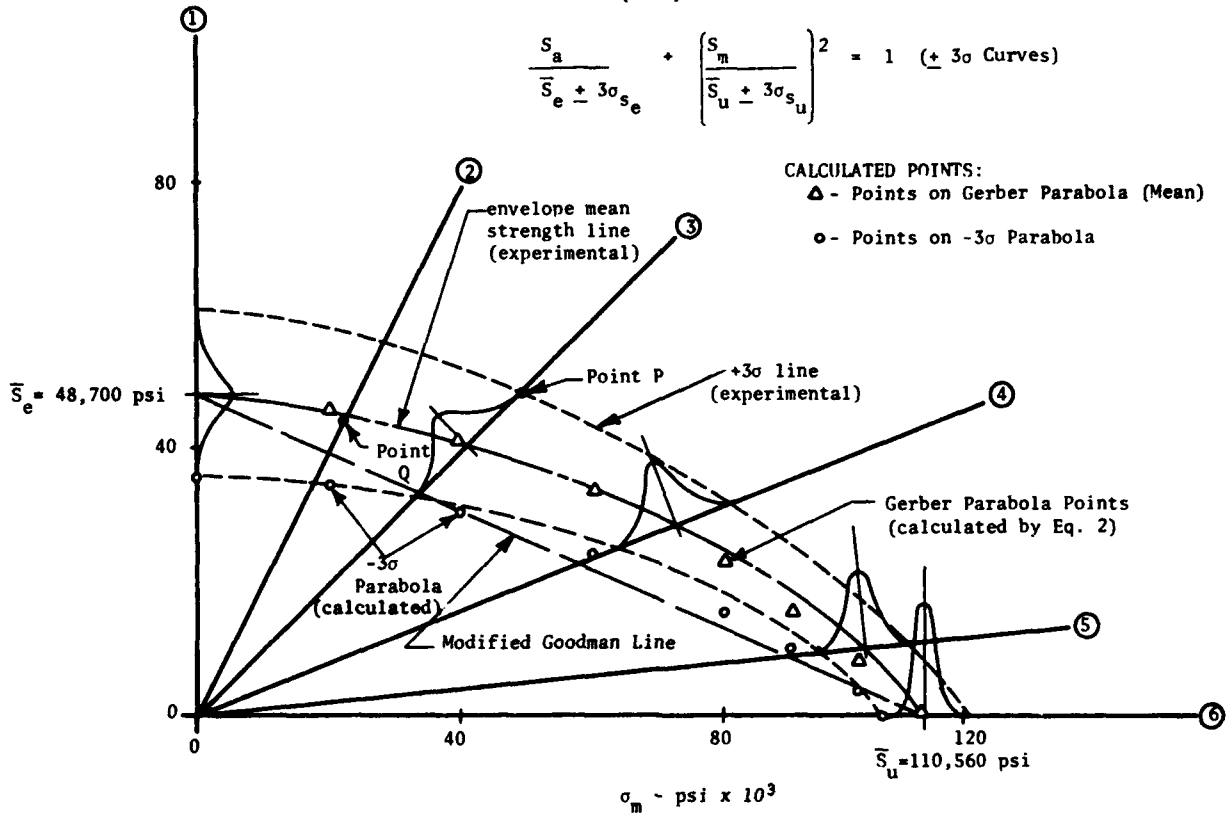


Figure 11. Resulting Endurance Stress Envelope from Test Program. (AISI 4340 Steel). (Results from Table VIII).

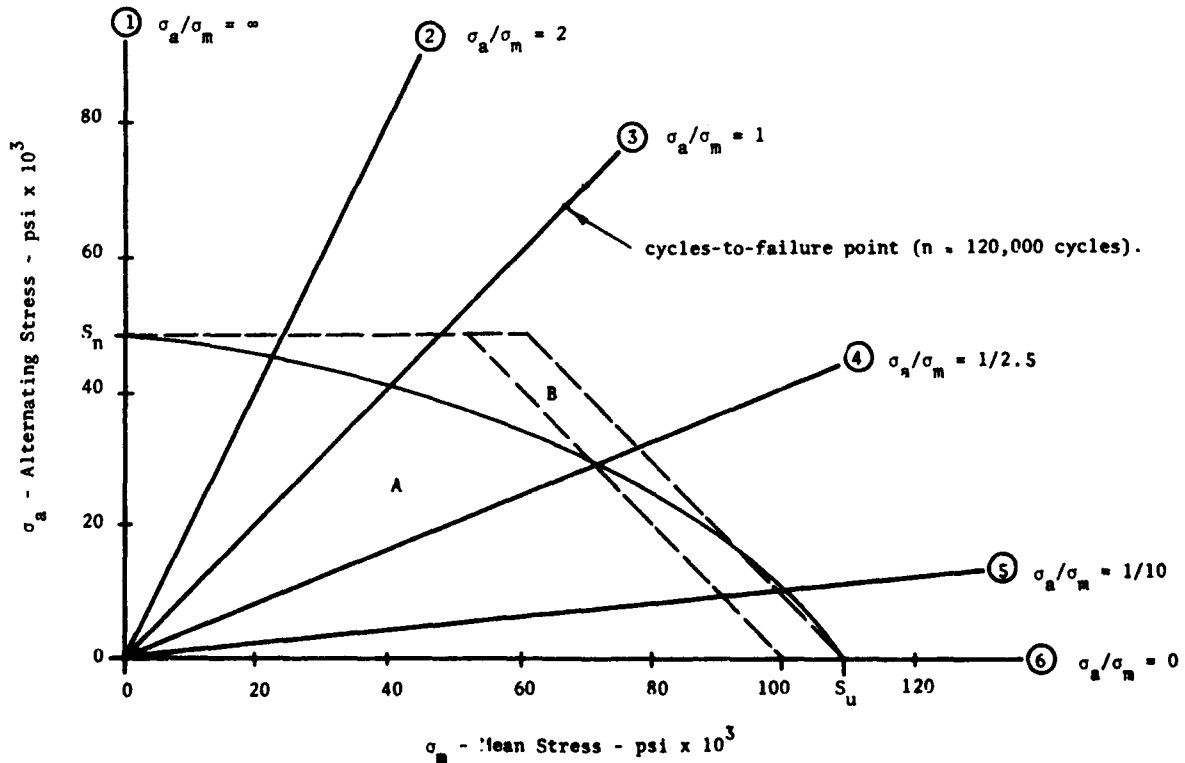


Figure 12. Mean Value Line (From Experimental Stress Surface) in Relation to the Proposed Safe Design and Short Life Regions.

TABLE IX.  
REDUCED DATA TEST SERIES 1.

Stress ratio = $\frac{\sigma_a}{\sigma_m} = \infty$				
26 failures				
24 nonfailures				
ALTERNATING LOAD (LBS.)	i	M <sub>i</sub> Nonfailures	im <sub>i</sub>	i <sup>2</sup> m <sub>i</sub>
154	3	6	18	54
142	2	11	22	44
130	1	6	6	6
118	0	1	0	0
		N = 24	A = 46	B = 104

$$\bar{X} = X_0 + d [A/N + 1/2]$$

d = test increment = 12 lbs.

X<sub>0</sub> = first stress level = 118 lbs.

$\bar{X}$  = mean value

$$\bar{X} = 118 + 12 [46/24 + 1/2] = 147 \text{ lbs.}$$

s = standard deviation estimator

$$s = 1.620 d [ (NB - A^2)/N^2 + 0.029 ]$$

$$s = 1.620(12) [ (24 \cdot 104 - 46^2)/24^2 + 0.029 ] = 13.40 \text{ lbs.}$$

$$\text{Area} = \pi(\text{specimen diameter})^2/4 = \pi(0.0620)^2/4 = 0.00302 \text{ in.}^2$$

$$\therefore \bar{X} = 147 \text{ lbs.}/0.00302 \text{ in.}^2 = 48,700 \text{ psi}$$

$$s = 13.4 \text{ lbs.}/0.00302 \text{ in.}^2 = 4,440 \text{ psi}$$

## DISCUSSION OF RESULTS

Figure 12 presents the locus of mean value points rather than distributions. The hypothesized safe and short life regions relative to the mean value line of the envelope can be clearly seen. The impression is that the data does not relate to the defined regions. The mean value points on lines 1, 2, 4, 5, and 6 fall in the boundary between the defined safe and unsafe design regions, eliminating the theory of two zones based on static yield strength. When the mean points on lines 3, 4, and 5 are considered in relationship to each other, the mean values for the stress ratios gravitate toward the safe region with increasing stress ratios. The existence of zone A describing a safe design region and zone B a short life region requires that the value of the yield strength must decrease as the stress ratio increases.

*t* = 1 · 10<sup>6</sup> cycles in this study.

## SUMMARY

The results of this study indicate the following, for the material studied at endurance<sup>†</sup> (AISI 4340 Steel).

1. The deterministic parabola (proposed by Gerber in 1874) very closely approximates the mean value locus of the strength envelope (see Figure 11), as determined experimentally in this study.

2. Theoretical parabolas closely approximate the +3σ and -3σ lines of the strength envelope, as experimentally determined.

3. It may be postulated (subject to confirmation) that the mean strength line of the strength envelope can be developed (to a good approximation) knowing the mean ultimate strength, S<sub>u</sub>, and the mean endurance strength S<sub>e</sub>, together with parabolic equation. As a further postulation, the ± 3σ lines may be developed (to close approximations) knowing  $\bar{S}_u \pm 3\sigma_S$  and  $S_e \pm 3\sigma_{S_e}$ , as is indicated in Figure 11, by using these values to write the parabolic equations.

4. If the endurance strength mean line follows a parabolic path, and  $\bar{S} \approx 0.5 \bar{S}_u$ , approximate strength envelopes can be developed from a knowledge of the distribution of S<sub>u</sub> only, and the fact that the ± 2σ endurance interval lies between 40% and 60% of S<sub>e</sub> (Ref. 1). Further investigation of this possibility is recommended.

5. The conservatism usually associated with the Modified Goodman Line, for endurance, is not valid near either the ordinate (σ<sub>m</sub> = 0) or the abscissa (σ<sub>a</sub> = 0), see Figure 11.

The actual locus appears to be parabolic, invalidating the shape of the Modified Goodman Line.

6. The Soderberg Line is indeed conservative in the region from σ<sub>a</sub>/σ<sub>m</sub> = 0 to 1, in which region it is under the -3σ line of the strength envelope.

7. The Langer Modification and the Sines Line do not appear to be of very much real significance.

8. The static yield strength does not lead to a meaningful criterion in determining safe or short cycle life. The value of the dynamic yield strength may provide a necessary modification, as suggested in Reference 6.

## RECOMMENDATIONS

Other steels and important non-ferrous materials should be studied and their endurance strength envelopes developed, to establish, reject, or restrict the parabolic shape of the mean value locus and of the ± 3σ lines of the combined-stress fatigue strength surface.

## REFERENCES

1. R.C. Juvinall, *Engineering Considerations of Stress, Strain, and Strength*, McGraw-Hill, New York (1967).
2. E.B. Haugen, *Probabilistic Approaches to Design*, John Wiley, New York (1968).
3. A.F. Madayag, Ed., *Metal Fatigue: Theory and Design*, John Wiley, New York (1969).
4. S.S. Manson, *Thermal Stress and Low-Cycle Fatigue*, McGraw-Hill, New York (1966).
5. J.L. Morrison and G.Z. Libertiny, *Notes on Fatigue*, University of Miami, Florida (1968).
6. M. Kawamoto and K. Nishioka, "Safe Stress Range for Deformation Due to Fatigue," *Trans. ASME.*, 77:631-634 (1955).
7. S. Timoshenko, *Strength of Materials*, Part 2, Van Nostrand, New York (1947).
8. D.B. Kececioglu, J.W. McKinley, and M.J. Saroni, *A Probabilistic Method of Designing Specified Reliabilities into Mechanical Components with Time Dependent Stress and Strength Distributions*, University of Arizona, College of Engineering, Phoenix, Arizona (1967).
9. J.E. Shigley, *Mechanical Engineering Design*, McGraw-Hill, New York (1963).
10. J. Marin, *Mechanical Behavior of Engineering Material*, Prentice-Hall, Princeton, New Jersey (1962).
11. E.B. Haugen and D. Kececioglu, *Interaction Among the Various Phenomena Involved in the Design of Dynamic and Rotary Machinery and Their Effects on Reliability*, University of Arizona, College of Engineering, Phoenix, Arizona (1969).
12. H. Schenck, *Theories of Engineering Experimentation*, McGraw-Hill, New York (1968).
13. R. Roeloffs and F. Garofalo, "A Review of Methods Employed in the Statistical Analysis of Fatigue Data," *ASTM Proc.*, 56:1081-1090 (1956).
14. M.N. Torrey and G.R. Gohn, "A Study of Statistical Treatments of Fatigue Data," *ASTM Proc.*, 56:1091-1123 (1956).
15. *A Guide for Fatigue Testing and the Statistical Analysis of Fatigue Data*, pp. 1-30, ASTM-STP-91-A, American Society for Testing and Materials, Philadelphia, Pennsylvania (1963).
16. F.R. Stulen, "On the Statistical Nature of Fatigue," pp. 23-40, *Statistical Aspects of Fatigue*, ASTM-STP-121, American Society for Testing and Materials, Philadelphia, Pennsylvania (1951).
17. R.E. Peterson, *Stress Concentration Design Factors*, John Wiley, New York (1953).
18. *Fatigue Testing Machine Automatic Preload*, Instruction Manual SF-01-U-2, Baldwin-Lima-Hamilton Corp., Dynamic Testing Dept., Waltham, Massachusetts (1957).
19. G. Sines and J.L. Waisman, *Metal Fatigue*, McGraw-Hill, New York (1959).

**SESSION 6**

**DESIGN AND SERVICE EXPERIENCE I**

*Chairman*

**G.F. Purkey**  
**Aeronautical Systems Division**

# SOME DEVELOPMENTS IN THE AIR FORCE AIRCRAFT STRUCTURAL INTEGRITY PROGRAM (ASIP)

by

Troy T. King

Aeronautical Systems Division  
Wright-Patterson Air Force Base, Ohio

## INTRODUCTION

The Air Force approach to structural fatigue certification was outlined during the 1959 Symposium on Fatigue of Aircraft Structures<sup>1</sup>. Due to the increasing number of fatigue failures/incidents that occurred during the 1950's, a large scale Air Force effort was conducted in 1958 to determine what steps were necessary to improve aircraft service life. The resulting program was presented during the Symposium.

Several changes have occurred in the Air Force approach to structural certification of aircraft since 1959. Of particular note are those changes in documentation, requirements, and philosophies. Also, it has become evident that the Air Force must convey to the aerospace industry the underlying reasons for the extensive effort that is contained in the present Air Force Aircraft Structural Integrity Program (ASIP). The Air Force situation is compounded by our imperative need to provide maximum operational readiness for the total life of our fleet in addition to the first requirement of providing flight safety.

This paper includes: (1) an outline of the current documentation for the Air Force ASIP, and (2) a discussion of the ASIP Flow Diagram which depicts current Air Force structural development requirements; with particular emphasis placed on reviewing (3) recent changes in structural testing practices and policies, (4) the actual usage monitoring efforts, and (5) the Air Force Fatigue Certification Program.

## DOCUMENTATION

Figure 1 lists the formal documentation for the Air Force Aircraft Structural Integrity Program (ASIP). This present documentation has evolved over the past 60 odd years of United States military aircraft procurement.

### AFR 80-13

AFR 80-13 (contained in the Appendix) has been the most recent addition to the documentation in this area. During the sixties, it became increasingly apparent that an Air Force directive covering ASIP was needed as the program had suffered from a lack of visibility and emphasis. The event that drew focus on the need for a regulation was a late 1968 study on Structural Testing for Aircraft Development

(Flax Study), which will be discussed in more detail later. Although an Air Force regulation had been drafted in 1967, the 1968 Study provided the needed impetus. AFR 80-13 was published 12 June 1969, and, in essence, it makes the structural development program outlined in ASD-TR-66-57 mandatory for Air Force aircraft. This regulation establishes broad policy, explains the Air Force aircraft structural integrity concept, and identifies responsibilities for implementing and conducting its requirements. The regulation gives recognition and emphasis to what has to be done and who is responsible for doing it. The various USAF commands are now in the process of preparing and issuing appropriate supplements which will identify their specific ASIP Responsibilities.

### ASD-TR-66-57

ASD-TR-66-57 is the next item for documentation for ASIP. This document explains and discusses the Air Force structural development practices; and specifies those requirements needed to ensure structural integrity of Air Force airplanes, or gives reference to the appropriate military specifications. Essentially, this document tells how all the pieces fit together, and has evolved through several earlier documents: ASD-TN-61-141 (1961), ARDC-AMC Program Requirements for the Structural Integrity Program for High Performance Aircraft (1959) and WCLS-TM-58-4 (1958).

Looking to the future, several changes will be made in the ASIP requirements document. Based on the findings and recommendations of the 1968 study, Hq USAF directed

- **AFR 80-13 & COMMAND SUPPLEMENTS**
- **ASD-TR-66-57 (ASIP REQUIREMENTS)**
- **MILITARY SPECIFICATIONS**
  - MIL-A-8860 THRU MIL-A-8862
  - MIL-A-8865 THRU MIL-A-8870
  - MIL-A-8871 (USAF)
  - MIL-A-8892 & MIL-A-8893 (PROPOSED)

Figure 1. Current ASIP Documentation.

that ASD-TR-66-57 be revised to include certain changes in requirements and philosophies. The revision effort has been completed and formal publication will be made as soon as Hq USAF release has been obtained. The next step is to place the contents of ASD-TR-66-57 into a USAF Military Standard in an attempt to provide a more formal document and to gain wider dissemination.

The Air Force is now preparing a limited (USAF) military standard requirements document for helicopters that will parallel ASD-TR-66-57 which applies to airplanes. We presently do not have a design and certification program for helicopters and similar VTOL vehicles. While the six major phases and some of the elements now defined for airplanes are applicable to other types of aircraft, specific documents are needed that detail those requirements necessary to ensure the structural integrity of each aircraft type.

### Military Structural Specifications

Next, and most basic in terms of requirements, are the various military specifications. The Air Force and Navy are in the process of revising and/or reorganizing the specifications listed in Figure 1 to reflect modern criteria and requirements. One basic change is that MIL-A-8870A will pertain to flutter and divergence alone while MIL-A-8892 and MIL-A-8893 will address vibration and acoustic phenomena, respectively. Although the revisions are still in the Air Force/Navy coordination process and have not been published to date, the essential requirements contained therein are being applied to current Air Force aircraft procurements.

### AIR FORCE STRUCTURAL DEVELOPMENT REQUIREMENTS

The basic philosophy underlying the ASIP is that the Air Force must provide and maintain maximum operational readiness for the total life of its weapon systems (Figure 2). The Air Force must be capable of going to war at any time without restrictions on the overall performance of the aircraft. Although overall performance includes all aspects of the weapon system, the basic integrity of the aircraft structure is of fundamental importance. Undesirable structural surprises that result in fleet grounding and/or restrictions cannot be tolerated. If a weapon system has an inherent failure area, this fact has to be uncovered through analyses and testing. Also needed is information on which aircraft will be affected first and what repair is adequate. In short, the Air Force must have the capability to predict and plan instead of observe and react. Admittedly, such an effort is very costly. This cost is justified though in view of the Air Force objective to develop a high-performance weapon system that can be utilized in varying, unpredictable mission roles and still retain the capability of maximum operational readiness. So, over the years, Air Force structures personnel with assistance from industry have instituted structural development requirements with the concept of maximum operational readiness foremost in mind.

### The National Defense Mission of the Air Force

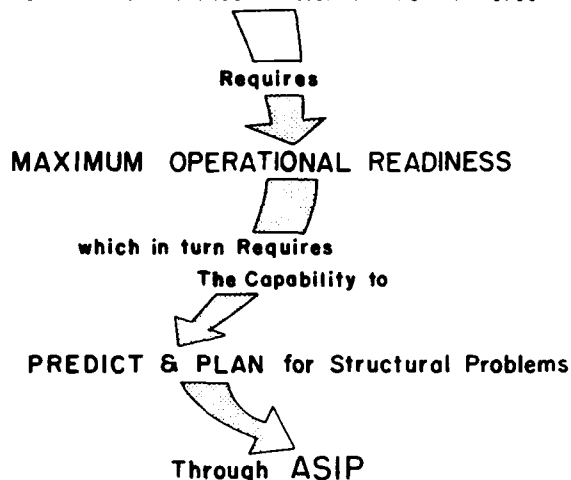


Figure 2. Function of ASIP.

Figures 3, 4, 5, and 6 contain the several steps in the chronological development of Air Force requirements for structural integrity. The program has grown from a set of "catch up" requirements to evaluate the fatigue life of systems already designed and built to an effort instituted concurrently with systems development to provide strength and service life. Attention will be focused on the latter program in the following paragraphs.

### Phase I - Design Information

First in any structural development program is the Design Information Phase (Figure 7). Although this phase has always been a part of the Air Force ASIP, the design criteria and predictions of aircraft usage are constantly improving as a result of actual usage data that is now being obtained on a continuous basis. The data recorded during flight operations have allowed significant improvements to be made in the definition of maneuver load factor for several types of aircraft. For example, Figure 8 presents the cumulative occurrence of normal load factor as a function of the design load factor for the Attack, Fighter, and Trainer Fighter class of aircraft. The important feature of these new curves is that the missions are separated into mission phases such as climb-out, cruise, bombing, gunnery, etc. Also, this information is significant since it is taken from actual combat experiences of several aircraft models. These curves and similar ones for other aircraft classes will allow the aircraft designer to develop better estimates of the fatigue loading spectra experienced by Air Force aircraft. Airborne flight recording programs have also enabled development of improved criteria for the turbulence environment (Figure 9). Special Air Force gust survey programs such as the B-66, F-106, and Allcat and actual usage efforts such as B-52, together with similar efforts throughout industry, have resulted in a better understanding of the phenomena of turbulence. Our present leaning towards the continuous turbulence analysis approach would not have been possible without these inflight recording programs.

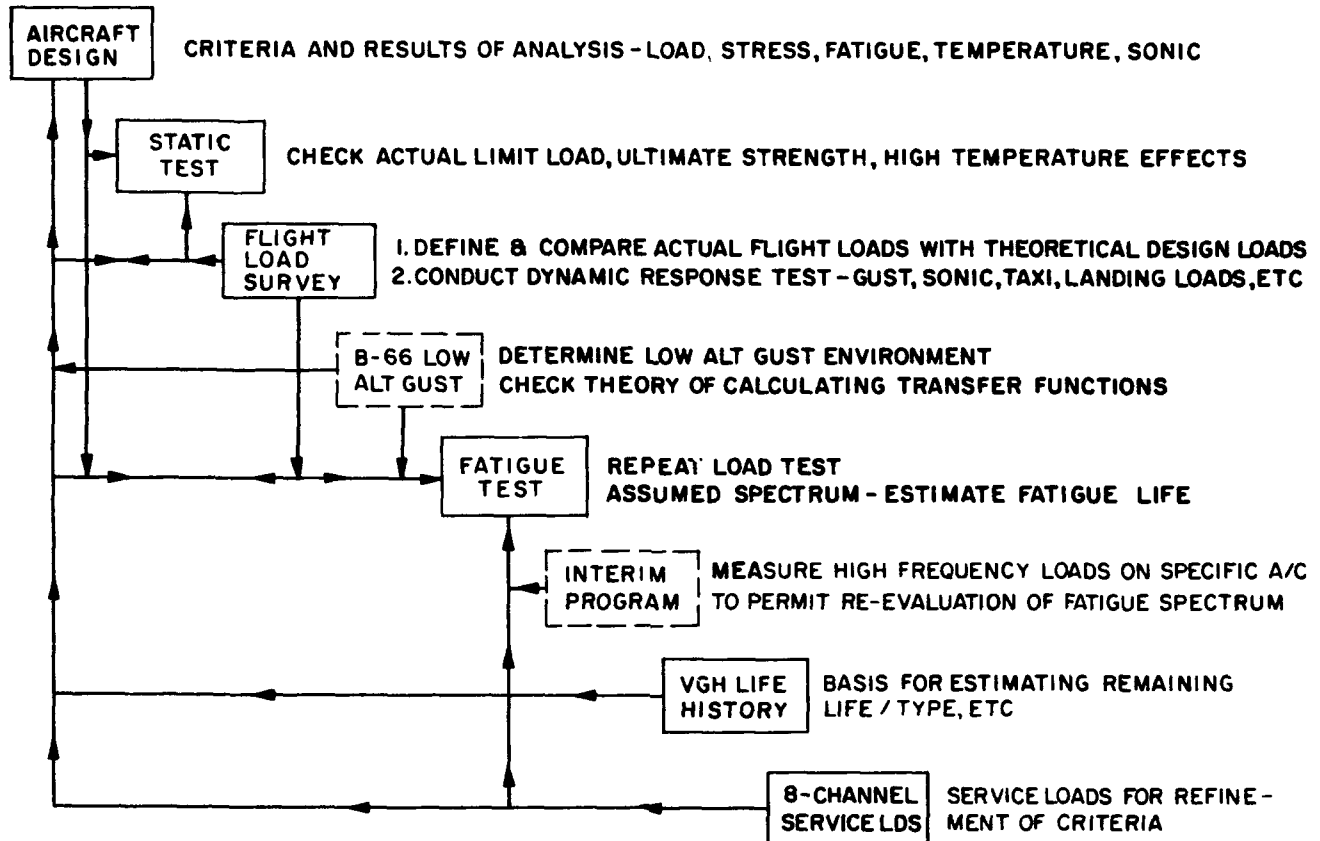


Figure 3. Structural Development Procedure.

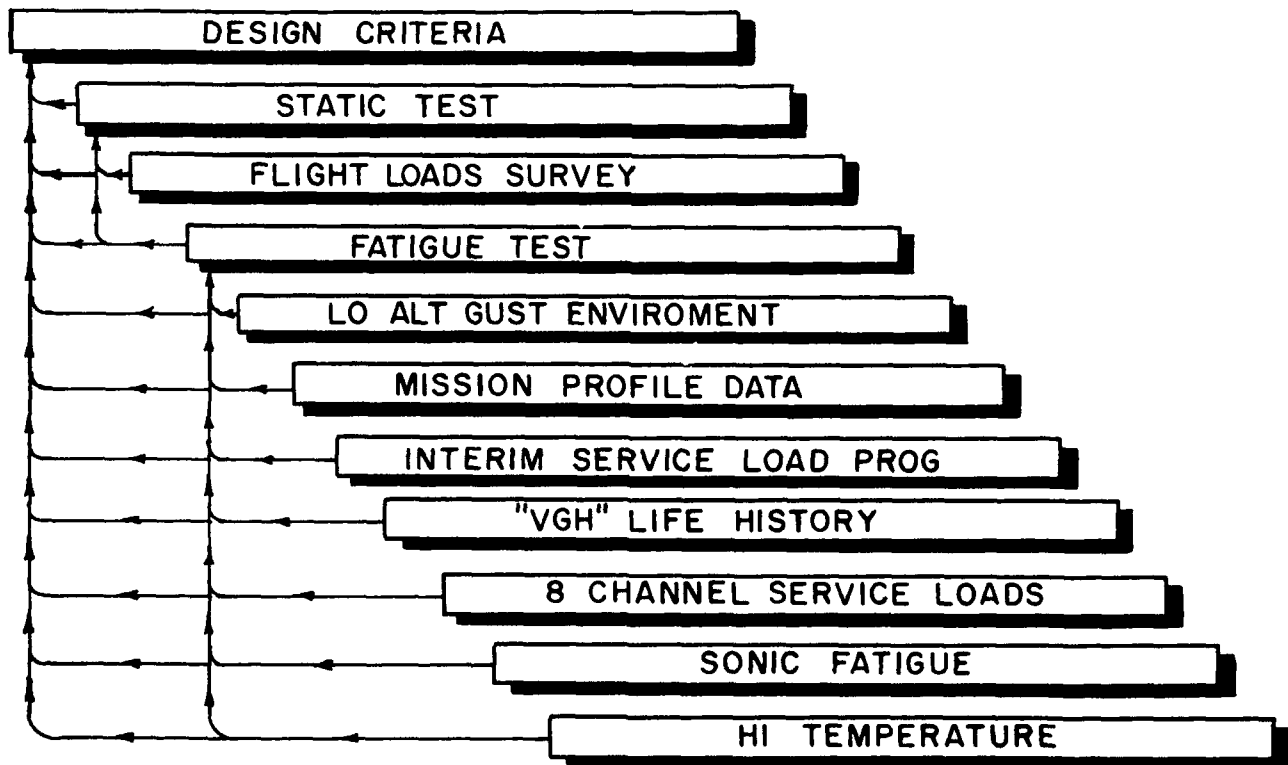


Figure 4. Steps to Improve Structural Integrity of High Performance Aircraft.  
(ARDC-AMC Program 1959).



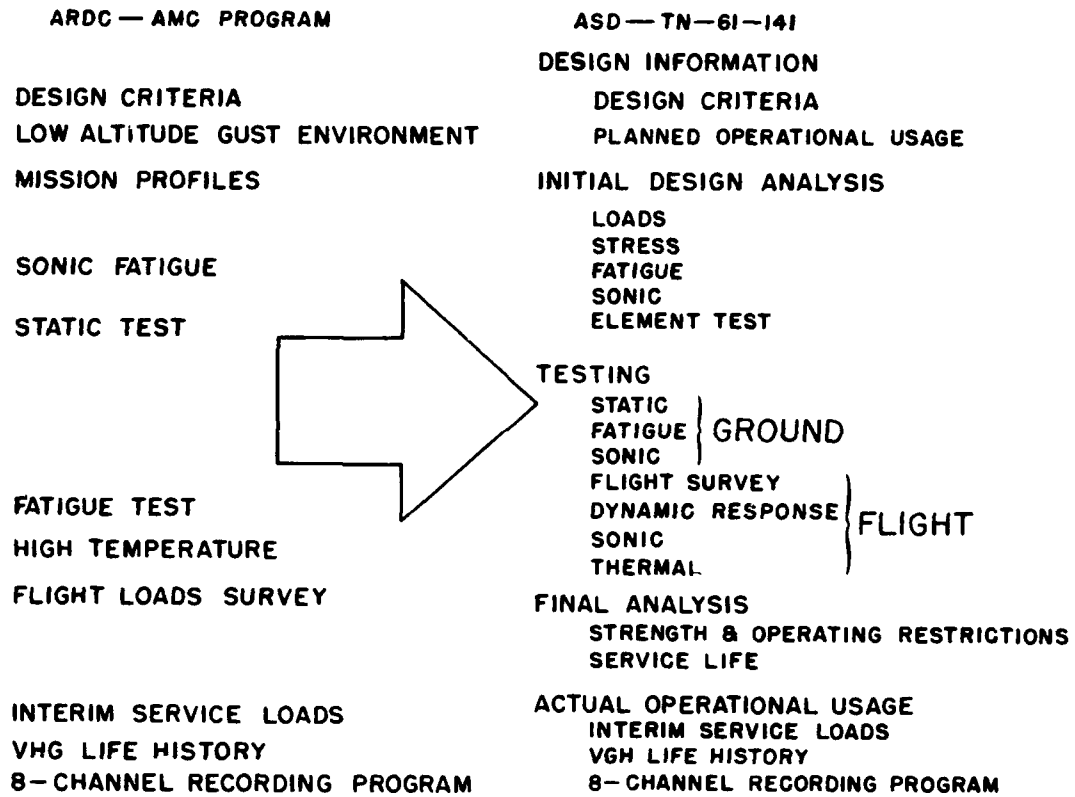


Figure 5. Elements of Aircraft Structural Integrity Program (ASD-TN-61-141).

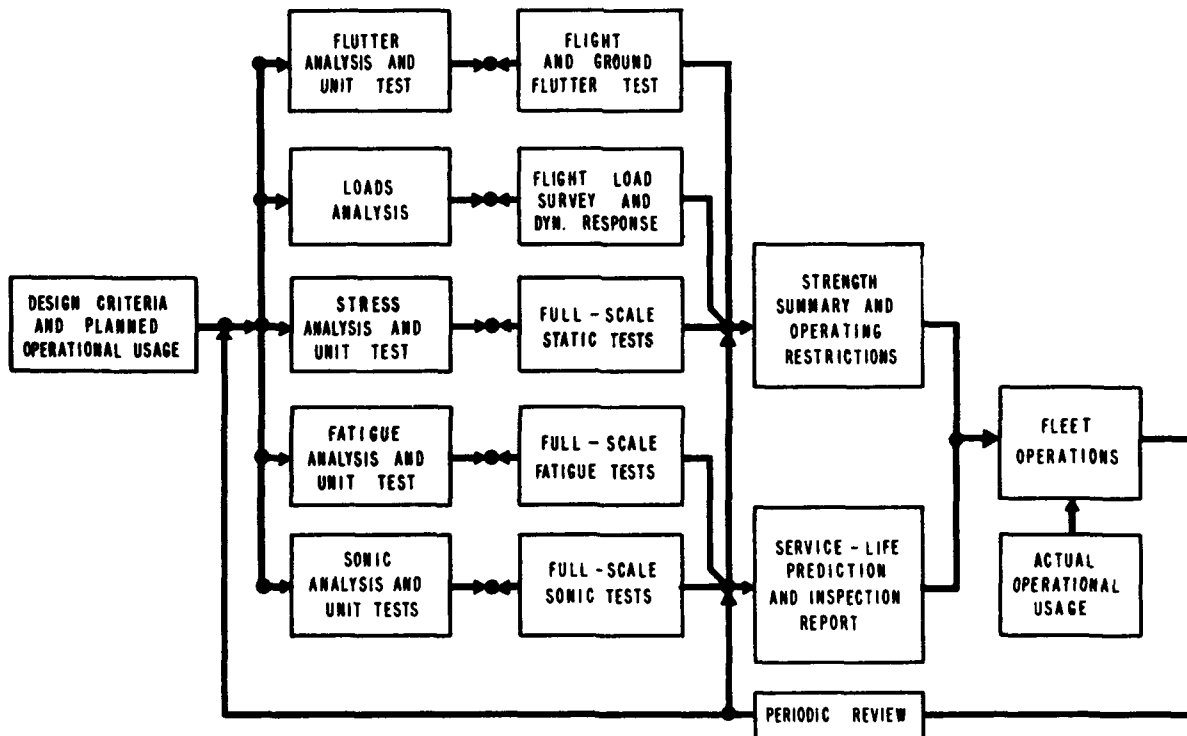


Figure 6. ASIP Flow Diagram (ASD-TR-66-57).

**PHASE I**  
**DESIGN**  
**INFORMATION**

**DESIGN CRITERIA AND**  
**OPERATIONAL USAGE**

**Figure 7. Current ASIP Requirements.**

These advances in criteria are being incorporated into the revised military specifications and improvements will continue to be made as more actual usage data are obtained from current and future service loads recording programs.

**Phase II - Initial Design Analysis**

After the criteria have been established, the next step in structural development is to calculate the loads to which the structure will be subjected together with the response of the structure to these loads (Figure 10). A chart was presented during the 1959 Fatigue Symposium<sup>2</sup> that identified a basic problem with the analysis capability (Figure 11). This chart is still appropriate. Due to the lack of knowledge of the basic phenomena of fatigue, there is

no accepted method that accurately predicts the cumulative effects of random loads. The capability to translate the results obtained from a controlled laboratory fatigue test to accurate predictions of future service experience is urgently needed. The problem of inadequate prediction techniques is the one big void in the analytical program and is further magnified by the inability to accurately predict in the design phase the usage that a system will experience in service.

**Phase III - Testing**

Next in the ASIP Flow Diagram is the Testing Phase (Figure 12). A recent development in this area occurred during the last quarter of 1968 when there was an in-house review of Air Force structural testing practices and policies. The review is referred to as the Flax Study; Dr. Flax being the (then) Assistant Secretary of the Air Force for Research and Development. Dr. Flax expressed concern over the fact that major static and fatigue test programs are not scheduled to be completed until long after production runs are under way, and that these structural tests are usually conducted even later than planned. Consequently, any defects discovered in the structural test program have resulted in the need for structural retrofit to production aircraft, often causing operational standdowns of the aircraft, and possibly en-

**I. FATIGUE MANEUVER SPECTRA**

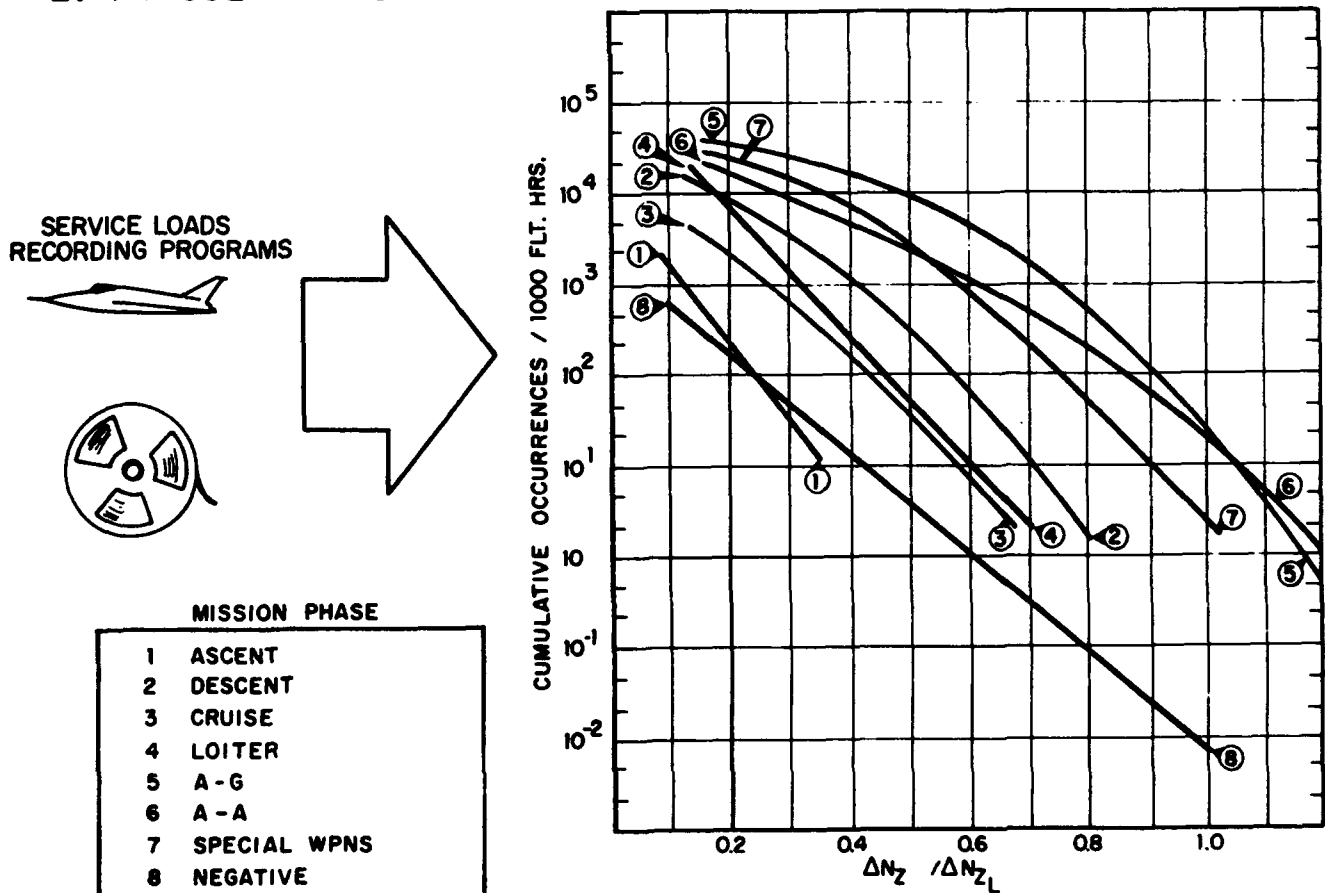


**Figure 8. Development of Improved Design Criteria.**

II. DESIGN STRENGTH PROCEDURE FOR GUSTS  
 III. FATIGUE GUST SPECTRA

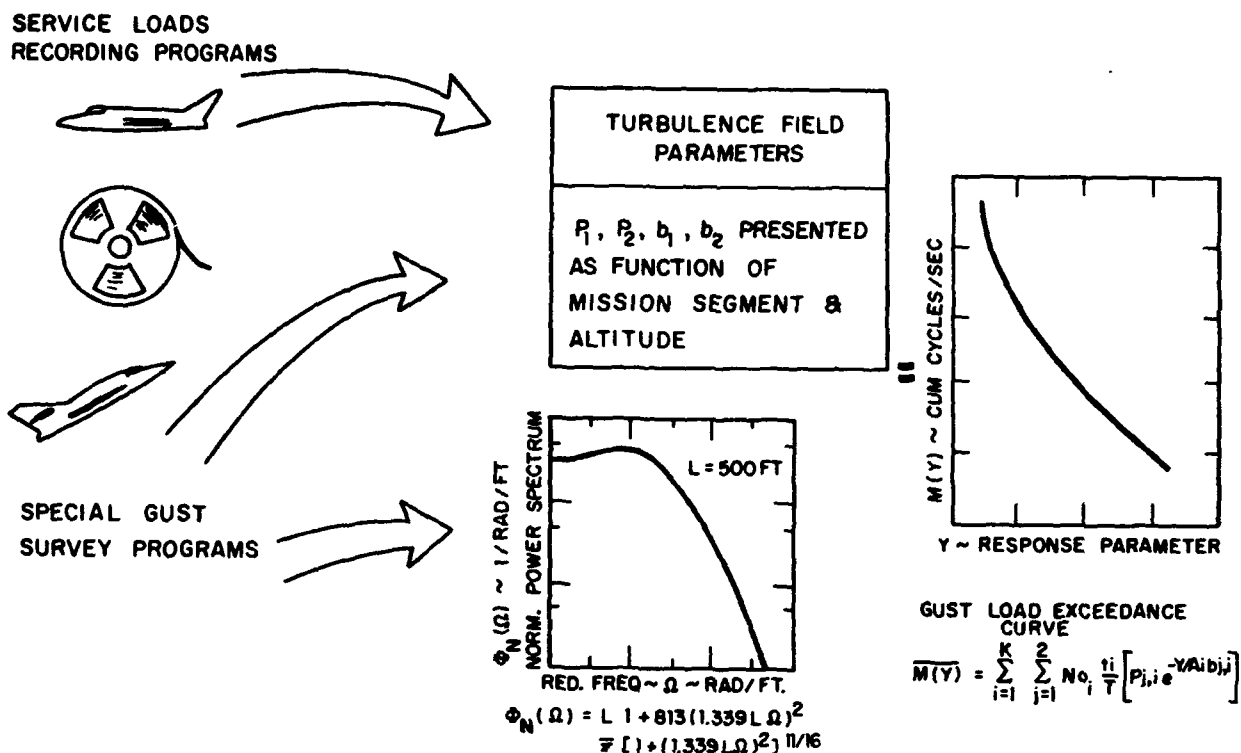


Figure 9. Development of Improved Design Criteria.

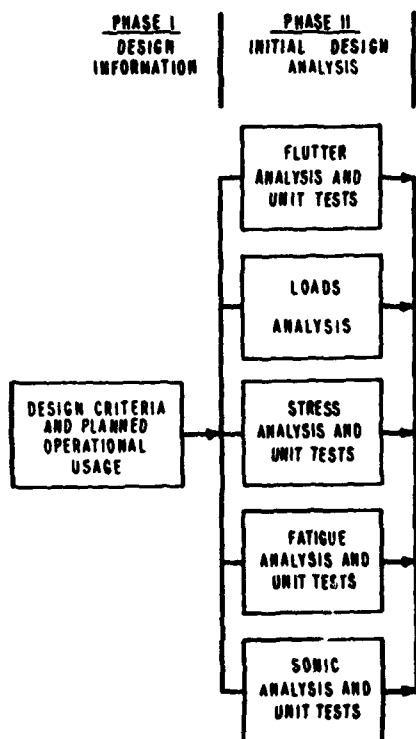


Figure 10. Current ASIP Requirements.

dangerous flight safety. Therefore, Dr. Flax requested that the Air Staff, in conjunction with AFSC and AFLC, review the matter in light of past experience and recommend appropriate revisions to present Air Force practices and policies for structural test verification of aircraft in development. In October 1968, a study group comprised of representatives of the Aeronautical Systems Division, Air Force Flight Dynamics Laboratory, and Air Force Logistics Command was convened to review the matter. The method of attack used in the study was to prepare case histories for both past and current weapon systems (Figure 13). Included were such data as original test schedules; specific airframes/aircraft allotted for static, fatigue, and structural flight tests; the actual milestones of the tests; reasons for deviations from the original schedules; and production buildup data. These case histories were then analyzed to establish trends and identify problem areas. A variety of problems were given visibility during the study (Figure 14):

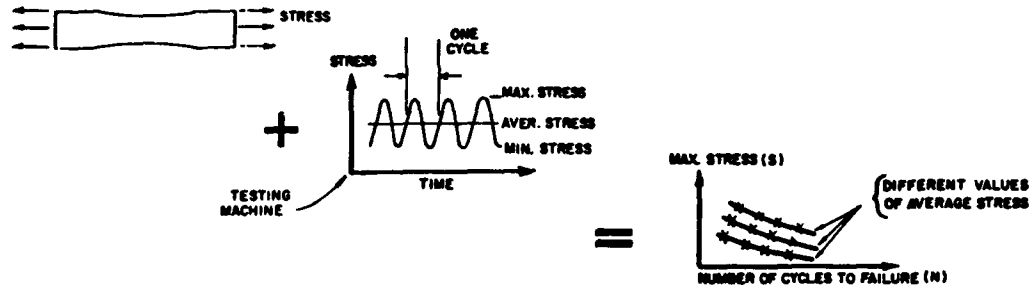
1. Test programs are being delayed as a result of structural redesigns.
2. Both static and fatigue tests almost always experience failures and, consequently, long downtimes.

# A BASIC PROBLEM:

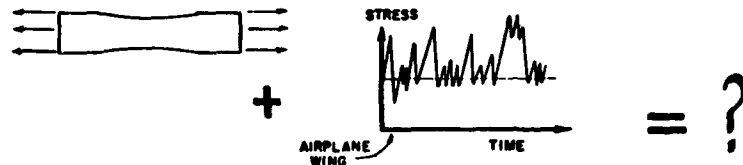
## WHAT IS THE CUMULATIVE EFFECTS OF RANDOM LOADING?

FOR EXAMPLE:

KNOWING THE RESULTS OF THIS PROBLEM



## WHAT IS THE ANSWER TO THIS PROBLEM?



"THIS IS THE CUMULATIVE DAMAGE PROBLEM FOR LOADING—IT IS COMPLICATED BY THE ADDITION OF MANY OTHER PARAMETERS IN THE TOTAL FATIGUE PROBLEM."

Figure 11. A Basic Problem.

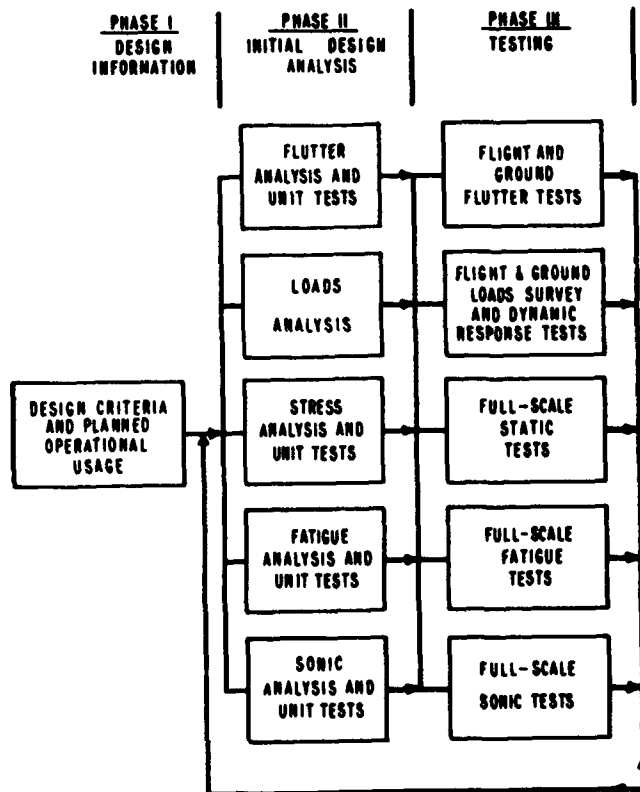
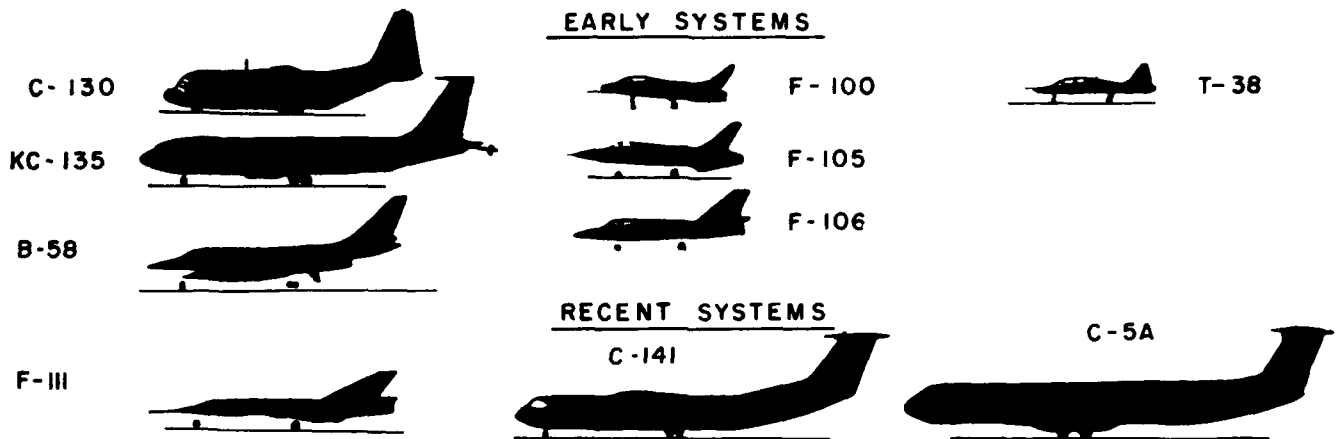


Figure 12. Current ASIP Requirements.

PREPARE CASE HISTORIES OF STRUCTURAL TESTING PROGRAMS FOR AIR FORCE AIRCRAFT



ASSESS CASE HISTORIES FOR OBSERVATION OF TRENDS AND IDENTIFICATION OF PROBLEMS

Figure 13. Method of Attack (Flax Study).

3. Fatigue tests are not usually scheduled to begin as early as static tests.
4. Fatigue tests take a long time to run.
5. One fatigue test is not always adequate, and second tests have seldom been conducted.

Several recommendations resulted from the study, and were accepted by Headquarters Air Force at all levels and also by Dr. Flax (Figure 15). One of the recommendations was that the full scale static test begin as early as possible. Although this has been the general approach in the past, the static tests have on occasion been delayed when redesigns were expected. Although the test article should be as representative as possible, it is also important to obtain early test results. In most cases, the effects of redesigns can be evaluated after the initial static test program by prudent use of component tests, by modification of the full-scale test article and subsequent retesting, and by analysis. Therefore, the ASD-TR-66-57 and MIL-A-8867 revisions now specify that the first airframe will be used for static test.

- STRUCTURAL REDESIGNS OFTEN DELAY MAJOR GROUND TESTS
- MAJOR GROUND TESTS ALMOST ALWAYS EXPERIENCE FAILURES
- FATIGUE TESTS ARE NOT SCHEDULED AS EARLY AS POSSIBLE
- FATIGUE TESTS TAKE A LONG TIME TO RUN
- A SINGLE FATIGUE TEST IS NOT OPTIMUM, AND SECOND TESTS ARE SELDOM CONDUCTED

Figure 14. Problems Highlighted During Flax Study.

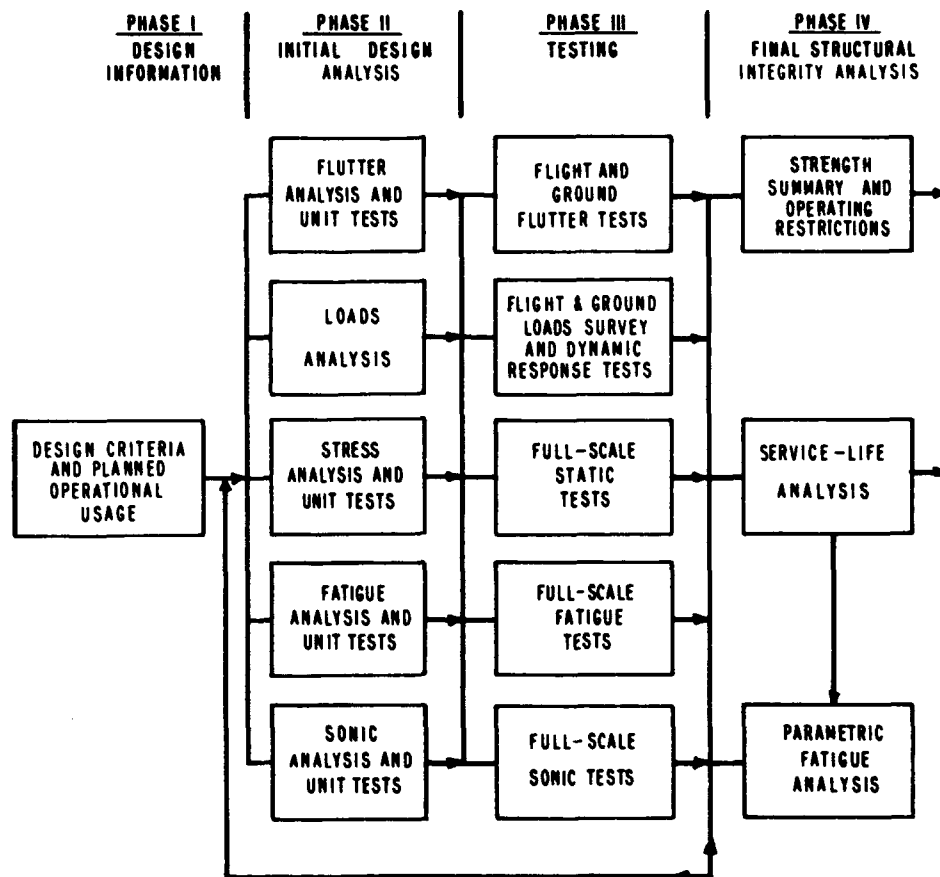
Another recommendation was that increased emphasis be placed on early pre-production component tests. The numerous failures in the full-scale test programs point up the need to conduct early tests on elements and components which are difficult to design and analyze to discover as many weak areas as possible before the major ground tests are conducted. Previously, identification and conduct of these engineering design type tests and developmental component tests were left to the discretion of the manufacturer. Bluntly speaking, the Air Force has been remiss by not providing sufficient direction and requirements in this important area. Therefore, ASD-TR-66-57 and MIL-A-8867 are being revised to place more emphasis on early pre-production component tests. The types of tests have been categorized for clarification and reporting procedures have been specified. Although the contractor will still retain full flexibility in determining the design development and pre-production verification test programs, the Air Force is, with this change, responsible for ensuring that the program is adequate in regard to both scope and schedule.

The next recommendation was that firm Air Force policy on fatigue testing be established. As discussed in the

- STATIC TEST AS EARLY AS POSSIBLE
- EMPHASIZE EARLY PRE-PRODUCTION COMPONENT TESTS
- ESTABLISH FIRM USAF POLICY ON FATIGUE TESTING
- CONDUCT COST EFFECTIVENESS STUDIES

Figure 15. Recommendations of Flax Study.

Figure 16. Current ASIP Requirements.



subsequent paragraph on the Air Force Fatigue Certification Program, it will be normal practice to conduct two full-scale fatigue tests on future aircraft development programs. When two fatigue tests are conducted, the first should be run as early as possible - at about the same time as the static test - and should be expedited through use of the earliest possible production airframe, timely formulation of the test spectra, rational compression of the test spectrum, rapid load application, and quick and gross repair of the test article when failures occur. A test of this kind should not be started until there is assurance of a second test since, although a gross test will locate most of the fatigue critical areas, it will not provide valid service life estimates for these areas. Therefore, firm programming decisions must be made before testing begins. This new testing philosophy, that of an accelerated early fatigue test plus a later refined test, has been incorporated into ASD-TR-66-57 and MIL-A-8867. Also, AFR 80-13 establishes the Air Force policy of normally conducting two fatigue tests.

A recommendation was made to conduct cost effectiveness studies to establish tradeoffs between development and production testing, and also between production buildup rates and possible structural retrofit. The main way the number of premature failures on the major structural ground tests can be reduced is to place more emphasis on early developmental testing. This may or may not be the cheapest way to go, and cost studies should provide the additional information needed to place the correct emphasis on these early tests. Cost studies are also necessary to establish trades between production buildup rates and structural ret-

rofit. Potential structural retrofit should impact production buildup plans. These studies will be made a part of the definition and/or acquisition contracts for new Air Force systems.

#### Phase IV - Final Structural Integrity Analysis

Phase IV of the flow diagram gives the results of all the extensive analyses and tests conducted during structural development (Figure 16). This final analysis phase summarizes both the strength and service life capabilities of the system, and is continually revised as required based upon the information gathered from the actual usage program.

An addition in this phase is the requirement for parametric fatigue analyses to identify those selected parameters that should be monitored on each aircraft for individual aircraft fatigue damage tracking. Years ago, it was realized that individual aircraft within a fleet could experience wide variations in damage accumulation, and that remaining service life could not be based on "logged" flight hours alone. The first Air Force concerted effort to monitor damage accumulation on individual aircraft was the B-52 "E" hour program. The actual flight hours were converted to "equivalent" hours by taking into consideration the mission deviation from the typical mission upon which the "E" hours were based. Next was the individual usage program for the B-58 fleet. This program is illustrating again that flight hours are not a valid indicator of the amount of service life that an aircraft has used. For example, Figure 17 illustrates that the actual damage for B-58 aircraft in the

PERCENT OF ACCUMULATED DAMAGE

	29	31	33	35	37	39	41	43	44	45	47	49	51	53	55	57	59	61	63	65	67	69	71	73	75	77
21																							1		1	
20																										
19															1											
18			1									1														
17							1							1	1	1	1									
16										1	2	3	2	3		1										
15							2		2	4	4	1	2	1	1											1
14							2		2	3	4	1		2		1										
13							2	2	1	2	3	1														
12				2	2		2	1	3		1															
11						1	2		2																	
10	1		1									1	1													

Figure 17. Bi-Variate Distribution, Percent Life Used vs. Flight Hours (B-58 Fleet).

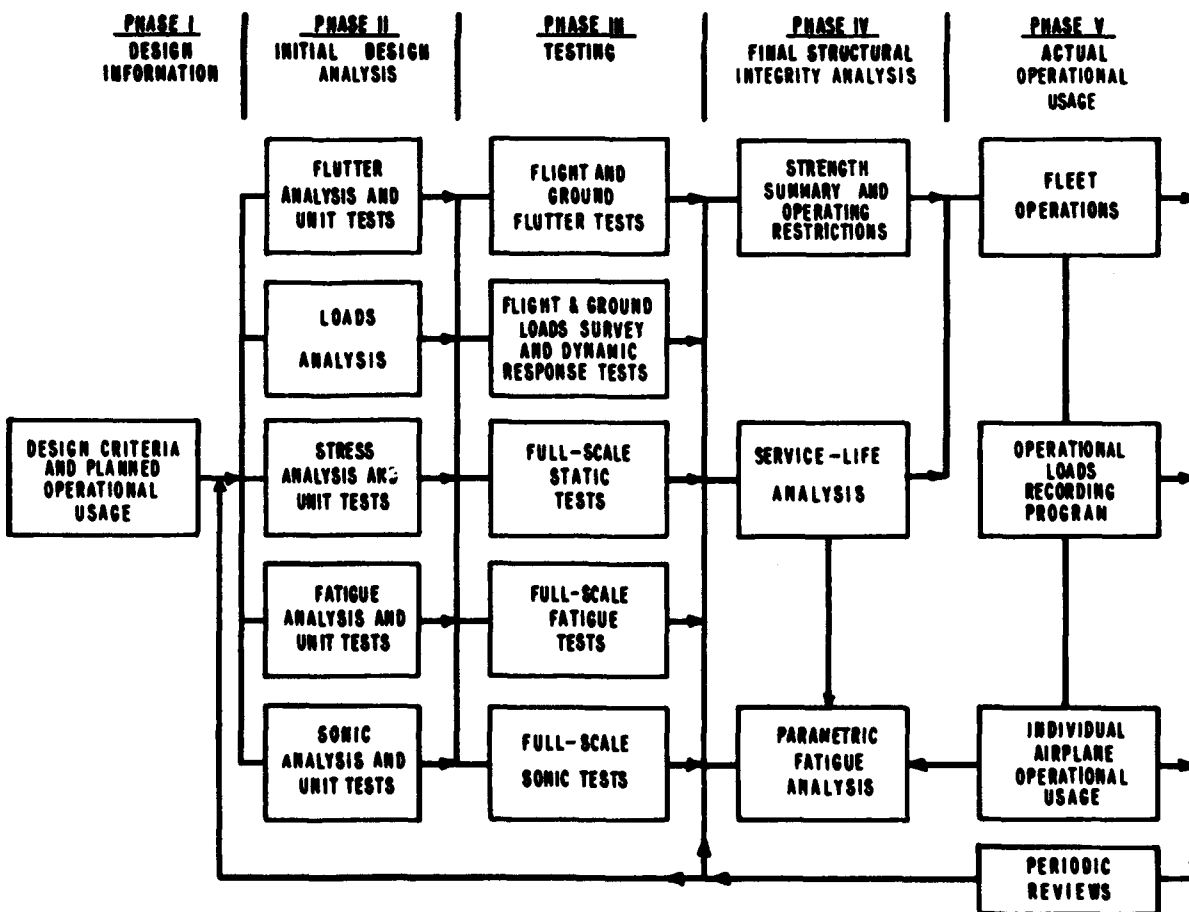


Figure 18. Current ASIP Requirements.

1500 hour flight time block ranges from 41% to 77%.

Out of these early findings has evolved the requirement for parametric fatigue analysis. By re-formatting the initial fatigue analysis, the parametric analysis presents damage per unit time as a function of certain critical parameters. These parameters are in turn gathered on each flight and for each aircraft by use of flight logs and/or some simple inexpensive flight recording device - normally exceedance counting accelerometers. The end result is that the aircraft in each fleet can be ranked in terms of accumulated fatigue damage, thereby providing the capability to schedule repairs, and replacement or rotation of aircraft.

#### Phase V - Actual Operational Usage

The single most important fact that years of structural development experience has taught the Air Force is this: Military aircraft designers cannot accurately predict either the environment or the utilization of a system throughout its operational life. Missions change, operating weights increase, modifications occur, multi-service procurement and therefore usage occurs; all of these can and do occur until the initial predictions regarding service life are incorrect. So, the Air Force has placed increasing emphasis on monitoring both the service environment and the utilization of its aircraft (Figure 18). The information gathered in the actual operational usage phase provides the capability to

reassess as the system ages the initial estimates regarding service life and to develop improved structural criteria for application to future systems.

For the Operational Loads Recording Program, the minimum flight recorded data requirements are velocity, normal acceleration, altitude, and time. In order to acquire sufficient data to develop load histories for components other than the wing, to develop revised criteria, and to react to specific fleet problems, the Air Force is approaching the effort from a true multichannel aspect. Although data in excess of the four (4) parameters listed above may not be needed on each airplane type, the multi-channel recorder provides the capability to monitor the additional data if required. The overall objective is to equip a percentage of the aircraft on each new system with continuous recording multichannel magnetic tape recorders. The number of channels to be recorded together with the number of aircraft in each system to be instrumented will depend on several considerations such as type of aircraft, mission requirements, total fleet size, etc. Each program will have to be tailored to fit the situation. In the individual usage program, the Air Force intends to account for the effects of different usages on fatigue damage by monitoring data on each flight of each aircraft for all new systems and for those older systems which have a sufficient data base to make the effort meaningful. Now for the problems and progress that have occurred in meeting these objectives.

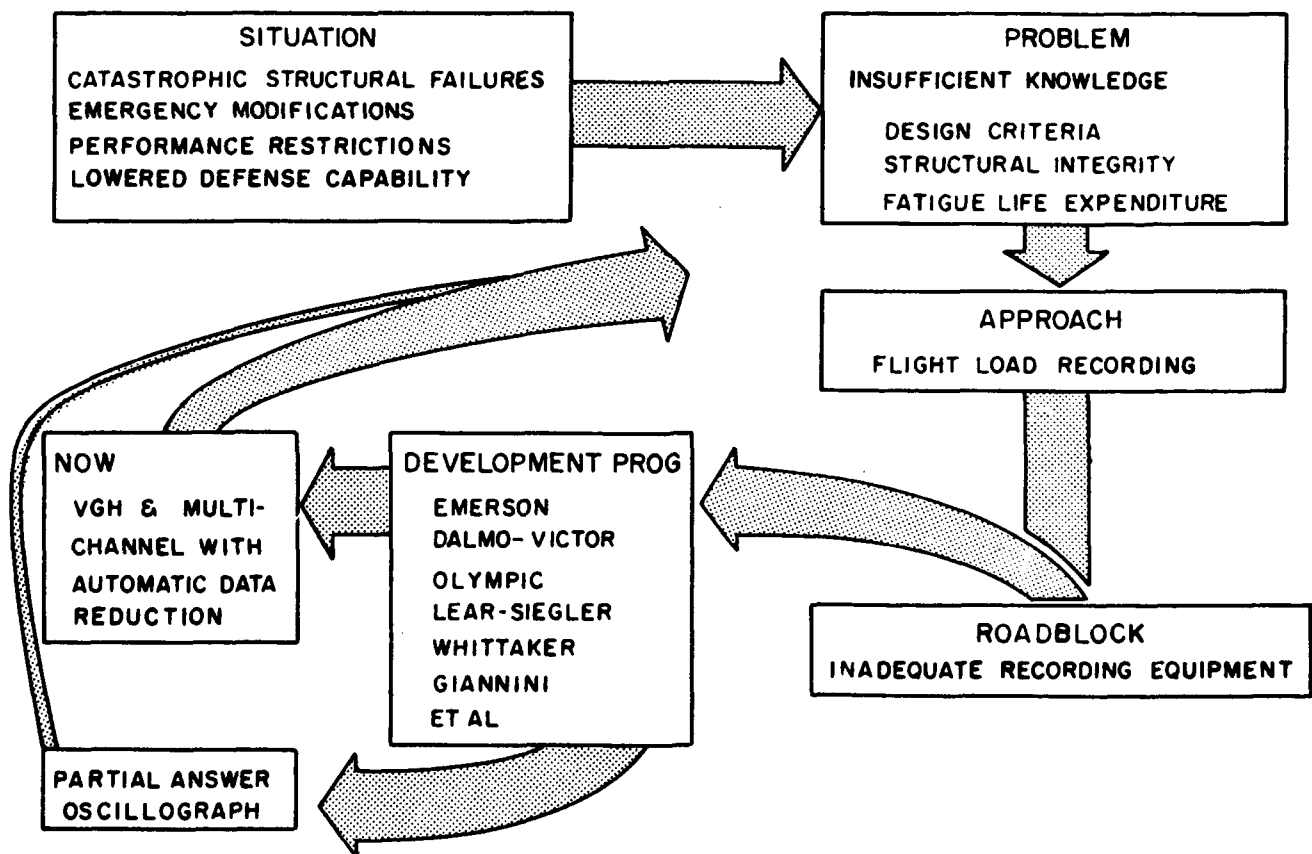


Figure 19. The Recorder Problem.



**TABLE I  
USAF RECORDER INVENTORY, 10-69**

MANUFACTURER	NO. OF UNITS	DESCRIPTION	DISPOSITION
CENTURY	70	9 CHANNEL, OSCILLOGRAPH, CONTINUOUS (# 409)	C-130, C-141, O-2
CENTURY	30	4 CHANNEL, OSCILLOGRAPH, CONTINUOUS (# 414)	IN STORAGE
CONRAC	550	4 CHANNEL, MAGNETIC TAPE, STATISTICALLY BLOCKED DATA	F-4 FLEET, F-4 THUNDERBIRDS, T-38, F-100, A-1, SPARES
CONRAC	12	240 SAMPLES/SEC., MAGNETIC TAPE, TIME COMPRESSED	ON LOAN TO A-37B FROM F-III
CONRAC	15	240 SAMPLES/SEC., MAGNETIC TAPE, CONTINUOUS	A-37B
WHITTAKER	107	240 SAMPLES/SEC., MAGNETIC TAPE, CONTINUOUS	F-III(100), AFFDL(4), PROTOT(3)
MAXSON	898	COUNTING ACCELEROMETER	F-4 FLEET
CONRAC	278	COUNTING ACCELEROMETER	F-4 FLEET
NOT IDENTIFIED	17	COUNTING ACCELEROMETER	F-4 FLEET

**TABLE II  
USAF REDUCED FLIGHT DATA, 10-69<sup>1</sup>**

TYPE	HOURS	STATUS <sup>2,3</sup>	Nz	MULTI-CHANNEL	MODEL DESIGNATION
A, F, TF	45000	C		X	F-84, F-86, F-94, <u>F-100</u> , F-101, F-102, F-104 F-105, F-106, <u>F-4</u> , F-5, A-1, <u>A-37</u>
	783870	C	X		F-80, F-100, <u>F-4</u>
BI BOMBER	3400	F		X	B-26K, B-57
BII BOMBER	50857	C		X	B-47, <u>B-52</u> , <u>B-58</u> , B-66
CARGO-ASSAULT	35747	C		X	<u>C-130</u>
CARGO-TRANSPORT	45904	C		X	C-135, <u>C-141</u>
REFUELING	1167	F		X	KC-135
TRAINER	12348	C		X	T-28, T-33, T-34, T-37, <u>T-38</u>
	1940	F	X		T-28
GROUND LOADS	2223	C		X	C-130, <u>C-141</u>

<sup>1</sup> SEE APPENDIX FOR MORE DETAILED PRESENTATION BY AIRCRAFT MODEL

<sup>2</sup> C INDICATES CONTINUING EFFORT; UNDERLINED MODELS ARE CURRENT RECORDING EFFORTS.

<sup>3</sup> F IN STATUS COLUMN INDICATES FINISHED EFFORT.

Although the obvious approach in 1958 was to obtain loads parameters by using inflight recorders, the roadblock was inadequate recording equipment (Figure 19). From 1958 to 1961 an unsuccessful effort was pursued to obtain a magnetic tape recorder manufactured by Emerson. In 1961 a development program was initiated with several companies. The Dalmo-Victor and Olympic were quick fixes to the Emerson development and they failed. As an interim solution, a development effort resulted in several oscillograph recorders. A longer lead time development program for a multi-channel recorder was with Whittaker and Lear-Siegler. Also, Conrac came in with a proposal for a new technique for the VGH recorder.

Although the success in developing flight recorders has been somewhat less than spectacular, the various development efforts have resulted in operational hardware (Table I). The Air Force has approximately 70 oscillograph recorders which are rotated through the fleet on an as required basis. More recently, 550 Conrac VGH magnetic tape recorders have been procured in support of the F-4, 100 Whittaker and 12 Conrac recorders for the F-111, and 15 Conrac recorders for the A-37B. Looking to the future, the Aeronautical Systems Division has firm plans to procure 30 flight recorders for the C-5 and the Air Force Logistics Command is undertaking a development program for a standard recorder to equip a percentage of their fleet. Eventually, this standard recorder will also be utilized in the acquisition phase. So, although the progress in obtaining recorders has been slow, advances are being made.

Since early in the 1950's, the Air Force has amassed a large quantity of recorded flight data (Table II). All of the early data and some of the current data are from the oscillograph recorders. The current recording programs are on

the F-100, F-4, A-37, T-38, C-130, C-141, and B-58. The F-111 recording program is starting now, and there are firm plans to initiate a C-5 recording effort. To date (Oct. 69) there is 45,000 hours of data on fighter operations; 54,000 hours on bombers; 12,350 hours on trainers; and 84,000 hours on cargo type aircraft. These are the data that were used to update the design criteria as previously mentioned.

Due to the increasing amount of data being obtained and the related impact on data reduction, the USAF is organizing a central facility that will manage the ASIP information in house. This concept is referred to as the Aircraft Structural Integrity Management Information System (ASIMIS). As shown in Figure 20, ASIMIS will provide for central management of the analyses, test, and recorded data as well as central reduction of all recorded flight data. These data will then be combined to provide information on loads environment, damage rates (both fleetwise and for individual aircraft), and modification requirements. More details concerning ASIMIS are contained in another paper being presented at this Conference (The Aircraft Structural Integrity Program in AFLC by H.B. Morrison, Jr., Colonel).

#### Phase VI - Inspections

The current flow diagram (Figure 21) gives proper recognition to the role that inspections play in achieving structural integrity. The information from the several test programs are used to establish what inspections are necessary and when, and this information is then published in the dash six (-6) T.O.. Most of these inspections can be made during the regularly scheduled IRAN's, or they may be conducted during the ACI (Analytical Condition Inspection) which is a periodic, systematic disassembly of an aircraft. Or, if the urgency of the inspection warrants, special inspec-

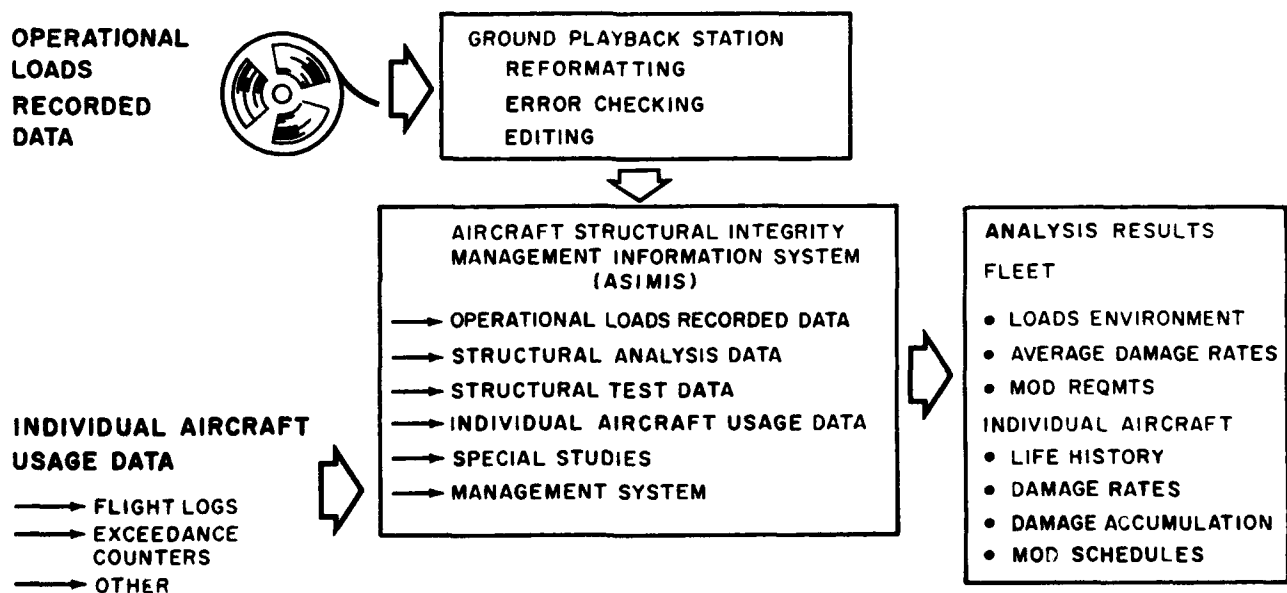


Figure 20. Aircraft Structural Integrity Management Information System (ASIMIS).

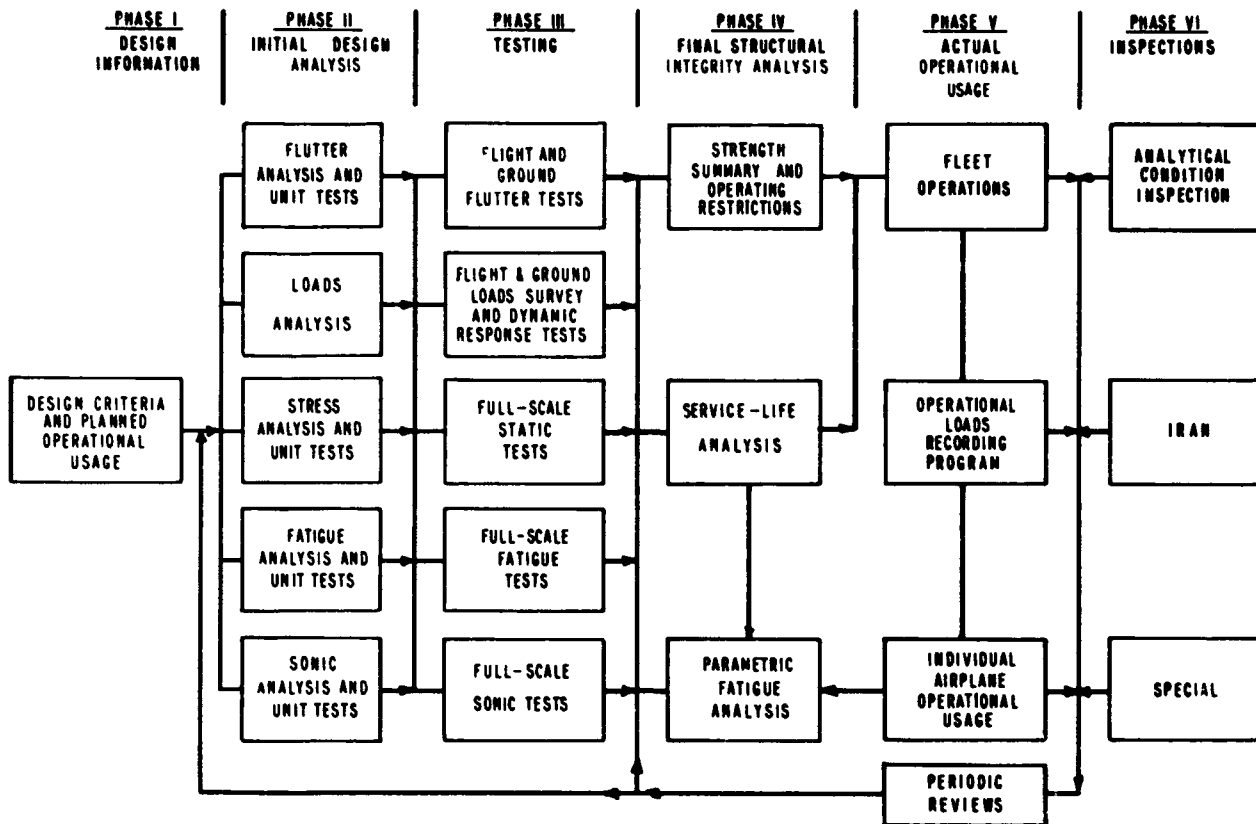


Figure 21. Current ASIP Requirements.

tions may be necessary. One thing should be kept in mind though; although inspections are often necessary to adequately monitor fatigue life, one of the goals of the structural integrity effort is to minimize the requirement for inspections (minimum number of inspections at maximum intervals).

### AIR FORCE FATIGUE CERTIFICATION PROGRAM

The main purpose of the ASIP Flow Diagram is to depict the total program requirements. Although the diagram adequately portrays the total picture, it does not show the interrelationships that exist in the Air Force Fatigue Certification Program. Figure 22 shows how the various elements of ASIP fit together to provide: (1) specified life capabilities for each aircraft system, (2) a rational method to schedule the aircraft for any required structural modifications in a manner that will achieve minimum downtime and loss of combat capability, and (3) the means to assess life trade-off requirements for various mission mixes and to make long range plans for aircraft replacement. This figure represents the maximum effort that can be made to meet above objectives.

As mentioned earlier, the requirement exists for two full-scale fatigue tests. The first test is needed to provide early flight safety and to allow any required structural changes to be made in production without incurring large and expensive retrofit programs. An early test will most likely not benefit from the results of the static test or the structural flight tests. Depending on what is learned from the early ground and flight tests and from the service loads recording program, a second fatigue test may or may not be necessary. Based on past experience, most of the time it *will* be required. If the early tests discover deficiencies that result in structural changes which have not been proven (fatigue wise) and if the recording effort reveals the test spectrum was inadequate, then a second fatigue test considerably downstream in the life cycle is required to refine the service life estimates. As mentioned earlier, firm plans must be made to conduct a second fatigue test before any commitment is made to an early, accelerated first fatigue test. If the requirement for two fatigue tests cannot be accepted, a tradeoff has to be made as in the past wherein the single fatigue test is not conducted until the significant portions of the flight loads survey and static test have been completed.

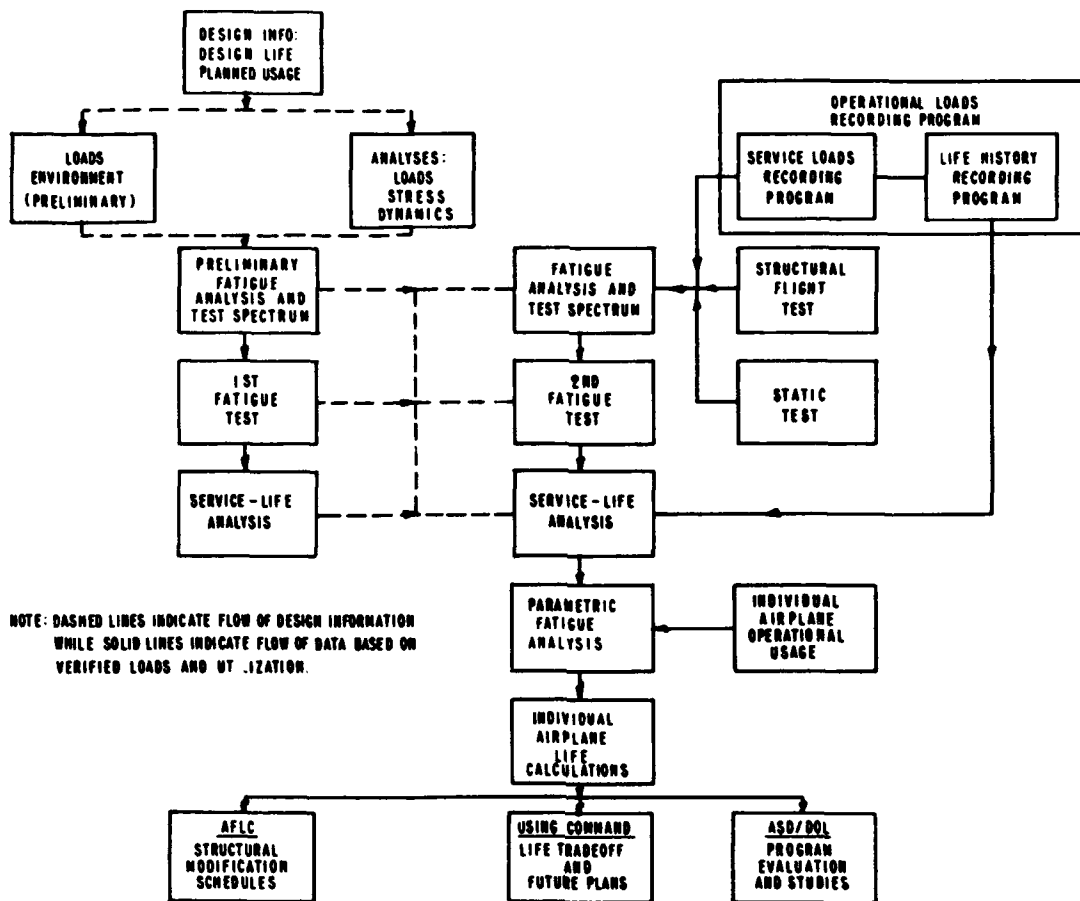


Figure 22. USAF Fatigue Certification Program.

**SUMMARY**

Due to the nature of the Air Force mission (national defense), each aircraft system must be kept in a state of maximum operational readiness throughout its operational life. Unscheduled fleet standdowns, and unscheduled and/or extensive maintenance cannot be tolerated. Extensive structural development effort as now contained in the Air Force ASIP (Figure 23) is necessary to achieve fleet readiness. This is the reason for the additional requirements of service loads recording, parametric analysis, and second fullscale fatigue test.

As in 1959, there are problems that must be solved before the maximum potential of the Air Force ASIP can be realized.

Maximum use must be made of the actual usage data to maintain up-to-date criteria.

Improved analysis methods must be developed that will allow accurate prediction of the cumulative effect of random loads on the fatigue life of the structure.

Firm Air Force policy on fatigue testing must be established. Early static and fatigue tests must be conducted which are given equal priority with other RDT&E tests. Also, provisions for a second fatigue test must be included in the event changes in configuration or service usage, or inaccuracies in the test spectrum make it impossible to relate the results of the early fatigue test to service experience.

A closing thought should be impressed on all of us:

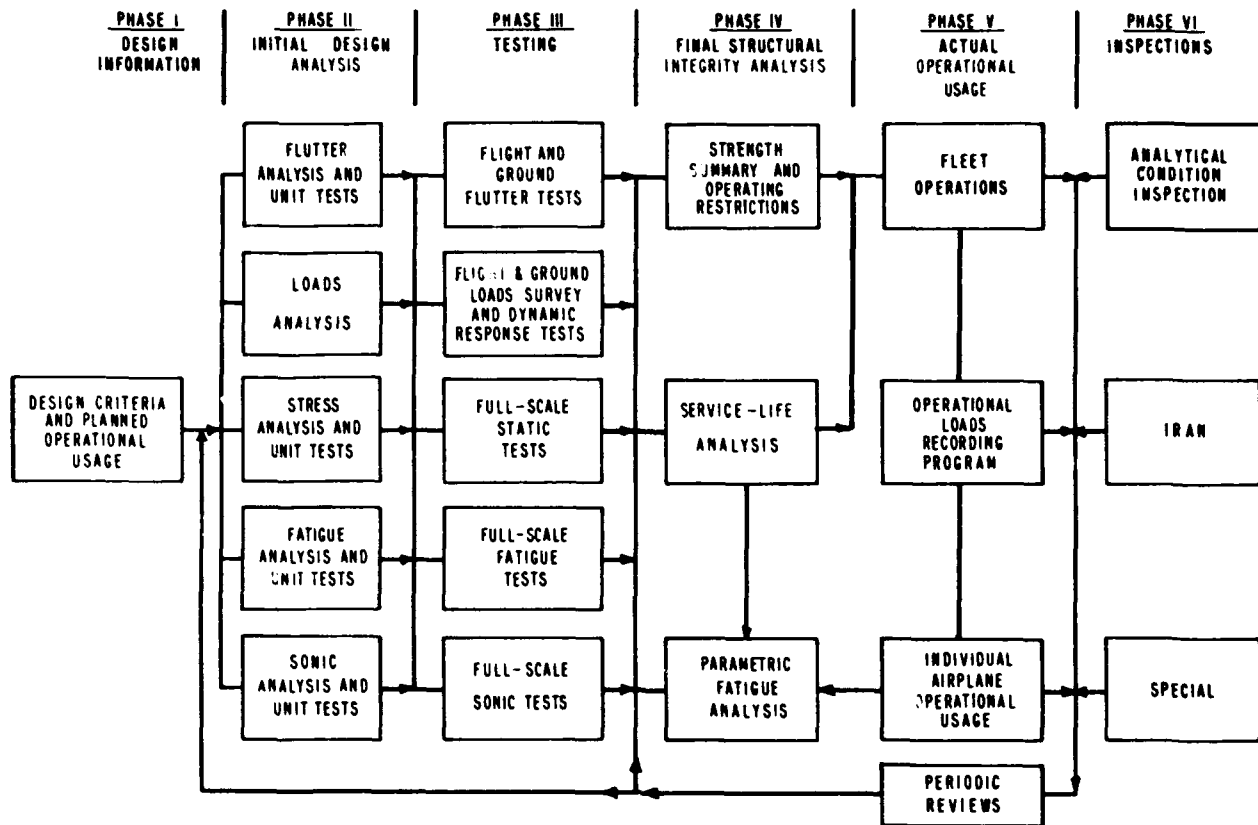


Figure 23. Current ASIP Requirements.

We must collectively acknowledge that if we the Air Force are going to be able to develop, procure, and operate our weapon systems in a wide role of missions over an extended life period, without costly unprogrammed retrofit and/or maintenance actions, we must be willing to pay for the complete ASIP and we must insure that it is implemented on a

timely basis. Anything short of this has not worked in the past - and will not work.

I challenge all of you who participate in these programs - both within DOD and the Industry - to fight for these objectives.

#### REFERENCES

1. J.P. Taylor, *Structural Integrity Program for High Performance Aircraft*. Presented at the Air Force Symposium on Fatigue of Aircraft Structures, Dayton, Ohio, August 1959.
2. Air Force Symposium on Fatigue of Aircraft Structures, Dayton, Ohio, August 1959.

#### APPENDICES

1. *Aircraft Structural Integrity Program*, AFR-80-13, Department of the Air Force, Washington, D.C. (1969).
2. List of USAF Reduced Flight Data by Aircraft Model, October 1969 (Table III).

DEPARTMENT OF THE AIR FORCE  
Headquarters US Air Force  
Washington DC 20330

AF REGULATION 80-13

12 June 1969

### Research and Development

## AIRCRAFT STRUCTURAL INTEGRITY PROGRAM (ASIP)

*This regulation establishes the Air Force aircraft structural integrity program, explains the concept, and outlines program objectives. It states policy, procedures, and responsibilities to be followed by appropriate major commands in conducting and implementing ASIP requirements.*

### 1. ASIP Explained:

a. The Aircraft Structural Integrity Program (ASIP) is a systematic procedure applied to an aircraft system to enhance design, diagnose potential or impending structural failure, provide a basis for corrective action, and predict operational life expectancy of the airframe.

b. ASIP insures that the critical structural tests (static and first fatigue test) are scheduled and completed as early as possible in the development cycle of new weapon systems. This will minimize the possibility of having to structurally modify a large number of production aircraft.

2. ASIP Phases: As currently developed, it consists of six interrelated phases:

Phase I. Design criteria and planned operational usage.

Phase II. Design Analysis (loads, stress, fatigue, flutter, and sonic analysis; and design development and pre-production verification tests).

Phase III. Testing (Structural component tests, full scale static, fatigue, flutter and sonic tests, flight loads survey and dynamic response).

Phase IV. Service Life Analysis (Strength summary and operating restrictions, service life prediction; parametric fatigue analysis).

Phase V. Operational Usage (Life history recording program; actual operational usage reports. This data feeds back into Phase IV studies and analyses to update and revise).

Phase VI. Inspections (Special inspections as required, analytical condition inspections, IRAN inspections).

3. ASIP Requirements Document. The structural integrity requirements for ASIP are contained in the current issue of ASD Technical Report TR-66-57. This report is unclassified and may be obtained from the Defense Documentation Center. The DDC number is AD 826-492.

### 4. ASIP Objectives:

a. Establish, evaluate, and substantiate structural integrity (airframe strength and service life) of aircraft systems.

b. Continually reevaluate the established structural integrity program, utilizing data inputs from operational usage.

c. Develop structural criteria and methods of design, evaluation, and substantiation for future aircraft systems.

d. Develop and apply statistical techniques for evaluating operational usage data, and provide logistic planning support (maintenance, inspections, supplies, etc.).

### 5. When to Apply ASIP:

a. Complete ASIP requirements will be applied to:

(1) All future aircraft systems developed by the Air Force.

(2) Aircraft systems currently in concept, definition, or acquisition phases.

b. ASIP requirements will be applied as necessary to assure flight safety and achieve the required service life to:

(1) Current operational first line aircraft.

(2) Aircraft systems not developed by the Air Force.

(3) Aircraft modified and directed to new missions.

OPR: AFRDDE

DISTRIBUTION: M

**6. Policy and Procedures.** The following guidances will govern the application of ASIP:

a. For cases specified in paragraph 5b, a modified ASIP will be submitted to HQ USAF for approval. Deviation from the ASIP requirements for the cases specified in paragraph 5 require HQ USAF approval.

b. ASIP management responsibility normally resides with the command, AFSC or AFLC, exercising engineering management responsibility for the system. In some instances, retaining responsibility for certain elements of the ASIP in AFSC after transfer of other engineering management responsibilities to AFLC may be advantageous. The transfer of management responsibilities normally occurs at the end of the system acquisition phase. The joint AFSC/AFLC engineering transfer agreement for each system will specifically document command ASIP responsibilities, as mutually agreed to by AFLC and AFSC, or as directed by HQ USAF.

c. ASIP requirements may not have been accomplished or only partially accomplished during system acquisition on older systems in the inventory. In these cases, AFLC will determine those elements of the ASIP appropriate and necessary to apply. Determination will be based on consideration of the design, operational usage, failure data, and planned future use of the aircraft.

d. Fatigue damage and airframe structural life depends on how an aircraft is used. Using commands, or HQ USAF will advise the AFSC/AFLC ASIP manager of any contemplated change in mission, and request the impact of such a change upon the structural integrity of the aircraft.

e. Budgeting and funding for ASIP requirements will be performed through command channels as stated in applicable DOD and Air Force directives.

f. ASIP data systems requirements will be documented as stated in AFR 800.3.

**7. Responsibilities of HQ USAF:**

a. Exercises surveillance over the ASIP, and provides guidance as appropriate.

b. Authorizes warranted deviations from the provisions of this regulation.

c. Approves ASIP for systems specified in paragraph 5b.

**8. Responsibilities of AFSC:**

a. Implements ASIP requirements in a timely manner as an integral part of the total aircraft weapon system contract definition and acquisition phases. The requirements of this regulation, ASD-TR-66-57 and the appropriate documents will be translated into meaningful requirements for each specific aircraft weapon system and will be specified in a Structural Integrity Master Plan. This Plan will be included as part of the procurement documentation for each weapon system in the definition and acquisition phase. It will be for the entire life span of the aircraft from contract definition phase through operational phase out. Included in the Master Plan will be the aircraft service life requirements, as well as a detailed ASIP data flow diagram which assigns specific data collection, reduction, dissemination, storage and analysis responsibilities. The Plan will be included as part of the procurement documentation for the contract definition phase and subsequent contracts.

b. Implements ASIP requirements for all Air Force weapon systems where engineering responsibility has not been transferred to AFLC. Specifies Air Force ASIP requirements when systems:

(1) Developed by another service are acquired by the Air Force for different usage (that is, F-4 and A-7).

(2) Developed outside the military establishment and are acquired by the Air Force.

(3) Are to be directed to new missions.

c. Provides and controls program funding to carry out a structural integrity program during the development and acquisition phase of each aircraft weapon system.

d. Maintains and revises ASD-TR-66-57 and referenced military specifications as appropriate to reflect advances or improvements in the state-of-the-art. Revisions to ASD-TR-66-57 will require prior HQ USAF (AFRDD) approval. Advises appropriate system program offices, AFLC Prime-AMA, commands and other management organizations of ASIP requirements.

e. Develops service load recorders. Procures and installs recorders in approximately 20 percent of selected operational aircraft during the acquisition phase.

f. Provides ASIP assistance to AFLC as required.

APPENDIX 1 (Continued)

12 June 1969

AFR 80-13

g. For systems for which AFSC has ASIP management responsibility, it:

(1) Advises HQ USAF and using commands of impact upon structural integrity of an aircraft when its proposed mission is changed.

(2) Prepares annual reports as of 30 June each year showing status, results of each individual aircraft ASIP, projected service life and modifications required. These reports will be prepared on AF Form 111, "Research and Development Management Report," RCS: HAF-R16, as stated in AFR 80-2 and in this regulation. They will be distributed to HQ USAF, AFLC and using commands.

**9. Responsibilities of AFLC:**

a. Implements ASIP requirements on all aircraft systems for which ASIP management responsibility has been transferred from AFSC.

b. For in-service aircraft for which ASIP requirements were not accomplished during the acquisition phase, and no ASIP Master Plan exists, determines the ASIP requirements essential for flight safety and required service life, prepares the Master Plan, obtains approval, and implements these requirements.

c. For in-service aircraft being modified and assigned to new missions, determines the new ASIP requirements, modifies the Master Plan, obtains approval, and implements these requirements.

d. Provides and controls program funding for the ASIP for each operational aircraft system.

e. Procures and installs recorders in approximately 20 percent of selected operational aircraft for which weapon system responsibility is assigned, if not previously accomplished during the acquisition phase.

f. For systems for which it has ASIP management responsibility, advises HQ USAF and using commands of the impact upon structural integrity of proposed

changes in mission from that for which the aircraft was designed.

g. Maintains, updates, and revises on a continuing basis the reports and analyses required by ASD-TR-66-57 and the Master Plan. For systems for which it has ASIP management responsibility, prepares annual reports as of 30 June each year showing status, results of each individual aircraft ASIP, projected service life and modifications required. These reports will be prepared on AF Form 111, RCS: HAF-R16, under AFR 80-2 and this regulation; and distributed to HQ USAF, AFSC and using commands.

**10. Responsibilities of Using Commands:**

a. Provide estimated system utilization data and life history utilization data to the ASIP manager for the system.

b. Install, remove, and process service loads recorder magazines as required.

c. Advise the ASIP manager for the system of contemplated changes in mission from that for which the aircraft was designed, and changes in operational environment.

d. Prepare and process actual operational usage data per technical order or other applicable instructions when required.

**11. Responsibilities of All Commands.** All commands involved with ASIP carry out the following duties:

a. Prepare and submit data, and perform analyses and tests as specified in this regulation, and as required by ASD-TR-66-57 for all Air Force developed aircraft weapon systems. Attachment 1 outlines command responsibilities.

b. Implement requirements of this regulation by issuing appropriate detailed documentation that will specify the command ASIP responsibilities and tasks. Each command will keep these documents current, and will coordinate all revisions to these documents with participating and/or management organizations.

BY ORDER OF THE SECRETARY OF THE AIR FORCE

OFFICIAL

JOHN F. RASH, Colonel, USAF  
Director of Administration

J. P. McCONNELL, General USAF  
Chief of Staff

1 Attachment  
ASIP Responsibilities for New Air Force  
Systems



APPENDIX 1 (Continued)

AFR 80-13

12 June 1969

**ASIP RESPONSIBILITIES FOR NEW AF SYSTEMS**

ASIP PHASES	AFSC	AFLC	USING COMMAND
<b>I Design Information</b>			
Design Criteria	I		
Operational Usage	I		D
Mission Profile	I		D
ASIP Master Plan	I	(I)	D
<b>II Initial Design Analysis</b>			
Load analysis	I		
Stress Analysis	I		
Fatigue Analysis	I		
Flutter Analysis	I		
Sonic Fatigue Analysis	I		
<b>III Testing</b>			
Ground Tests	I		
Flight Tests	I		
<b>IV Final Structural Integrity</b>			
Strength and Operating Restrictions Report	I		
Service-Life Analysis	I		D
Parametric Fatigue Analysis	I		D
<b>V Actual Operational Usage</b>			
Procure and Install Recorders	I	M	
FWD Recorder Magazines, Supporting Data, Etc.	I		D
Individual Aircraft Usage Program	I	(I)	D
Strength and Operating Restriction Report	I	M	D
Service-Life Analysis	I	M	D
Parametric Fatigue Analysis	I	M	D
Exceedence Counter Program (If Required)	I	M	D
<b>VI Inspections</b>			
		I	(I)

**NOTE:** I—Initiate and conduct tests and analyses, prepare reports and/or initiate contracts.  
M—Maintain and revise reports, or continue tests and analyses, and/or continue contracts.  
D—Provide and update data.  
(I)—Initiate if not previously initiated.

**Attachment 1**

APPENDIX 2.

Table III. USAF Reduced Flight Data (Oct. 69)

AIRCRAFT	HOURS	STATUS	COUNTER	MULTI-CHANNEL	OSCILL.	MAG. TAPE
F-80	360	F	X			
F-84	776	F		X	X	
F-86	1646	F		X	X	
F-94	350	F		X	X	
F-100	3308	F	X			
F-100	6236	F		X	X	
F-100	7568	9-69		X		X
F-101	2340	F		X	X	
F-102	2292	F		X	X	
F-104	2333	F		X	X	
F-105	8010	F		X	X	
F-106	3966	F		X	X	
F-4C	3573	F		X	X	
F-4C	780, 202	3-69	X			
F-4C	2166	9-69		X		X
F-5	2025	F		X	X	
F-111 <sup>3</sup>				X		X
A-1	430	F		X		X
A-37A	920	F		X		X
A-37B	400	9-69		X		X
T-28	121	F		X	X	
T-28	1940	F	X			
T-33	479			X	X	
T-34	426	F		X	X	
T-37B	2277	F		X	X	
T-38	3070	F		X	X	
T-38	5975	7-69		X		X
C-130	35747	10-69		X	X	
C-130 <sup>4</sup>	435	F		X	X	
C-135	8944	F		X	X	
KC-135	1167	F		X	X	
C-141	36960	9-69		X	X	
C-141 <sup>4</sup>	1788	9-69		X	X	
B-26K	2077	F		X	X	
B-47	620	F		X	X	
B-52	42113	F		X	X	
B-57	1322	F		X	X	
B-58	6000	4-69		X		X
B-66	2124	F		X	X	

- NOTES: 1. F in status column indicates finished effort  
 2. A date in the status column indicates a continuing effort  
 3. F-111 recorders being installed. Data collection to begin o/a January 1970.

# THE F-100 AIRCRAFT STRUCTURAL INTEGRITY PROGRAM (ASIP)

by

G.E. Fitch, Jr., R.E. Jackman, and W.P. Horsfall

North American Aviation/Los Angeles Division  
North American Rockwell  
Los Angeles, California

## INTRODUCTION

The F-100 Aircraft Structural Integrity Program (ASIP) is unique in the industry because it represents the application of the ASIP philosophy as embodied in MIL-A-8866 and ASD TR 66-57 to an aircraft system 10 years after the fact, i.e., to an aircraft with over 10 years of service history. The objectives of the program were, in this case, to provide verified modifications to the structure of the F-100 to extend its useful service life to the limit projected per Air Force logistic planning.

The F-100 airplane was designed prior to the establishment of the ASIP requirements which define a service life, and the aircraft was not fatigue tested to determine its life. In November 1958, a formal ASIP was established at ASD for the purpose of establishing, evaluating, and substantiating the structural integrity, both in static strength and fatigue life, of aircraft systems. Although fatigue was a consideration when the F-100 aircraft was designed, no requirement existed for a specific fatigue life. Historically, the succeeding generation of aircraft should have replaced the F-100 aircraft before it had reached a life of 2,000 hours. As it turned out, there was no timely replacement aircraft for the F-100, which necessitated its continued use.

In September 1965, the current F-100 ASIP, under Contract AF04(606)-14942, was begun at the North American Rockwell Los Angeles Division (NR/LAD). The requirements, as stated in Engineering Specification SMNE-65-131, are "... show proof of conformance as required by Specification MIL-A-8866, . . . as amended by this specification for a 5,500 flight hour service life, with or without airframe modifications . . ." This represents an operational life goal more than double its originally intended use.

## F-100 ASIP BACKGROUND

### F-100 History

The first request for a proposal to conduct a structural integrity program on the F-100 was received from SMAMA, McClellan Air Force Base, in October 1962 just 9 years to the month after Lt Col F.K. Everest set a new world's speed record of 755.149 miles per hour in the YF-100A exceeded Mach 1 in its initial flight.

The F-100A, the first of four models to be produced, was an air superiority fighter. The F-100C entered production in 1954, incorporating an integral fuel wing and special fighter-bomber provisions such as droppable fuel tanks and external stores under the wings. The F-100D is similar to the F-100C but incorporates systems to improve its fighter-bomber capabilities. The last Super Sabre, an F-100F two-place version, was completed in September 1959. In Southeast Asia, the F-100 is used exclusively as a fighter-bomber.

### U.S. Air Force Thunderbirds

For a period of 13 years, the USAF Air Demonstration Squadron was equipped with F-100 airplanes. (See Figure 1.) More than 1,000 shows were performed, in addition to countless numbers of practice flights during the period from 1956 through 1969. In June 1956, the squadron received their single-place F-100C airplanes plus one F-100F two-place airplane for VIP demonstration flights. In 1964, the F-100C's were replaced with F-105's for the remainder of the 1964 season. F 100D's were used by the squadron until April 1969.

### F-100 Structure Description

The wing outer panel (WOP) of the F-100 is multi-



Figure 1. F-100 Thunderbird Demonstration Aircraft.

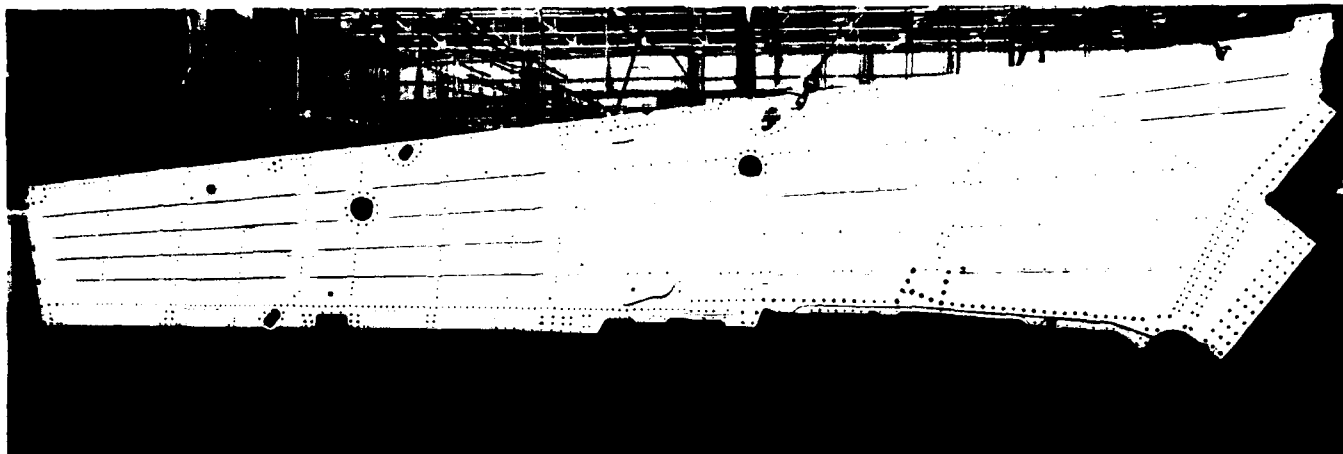


Figure 2. F-100 Aluminum Wing Outer Panel.

spar-plate construction from the root to wing canted station 217 and integrally stiffened multi-rib construction beyond to the tip. The upper and lower skins are sculptured from 1.75-inch 7075-T651 bare plates. (See Figure 2.) The maximum thickness of the lower skin is 1.50 inches and the minimum thickness is 0.070 inch in packet areas near the tip. The WOP is an integral fuel cell over the full span from front to rear spar.

Except for a heavy root rib which is made from a 2014-T6 forging, the wing utilizes 7075-T6 products.

The wing center section (WCS) is a box structure with upper and lower covers consisting of two skins each separated by spacer bars. (See Figure 3.) The skins are tapered from 0.25 inch at the front beam to 0.40 at the rear beam, and made from 7075-T6 rolled plate. There is a nonshear carrying stabilizing spar between the front and rear beams. The WCS contains fuel in self-sealing cells.

The fuselage is a conventional longeron-skin frame design with four longerons at most cross sections. Only 7075-T6 aluminum alloys are used forward of the field break, whereas titanium and steel are used extensively in the aft section.

### Three-Phase ASIP Program

The first two phases of a three-phase structural integrity program were initiated in September 1965. Phase I, Flight Load Survey, and Phase II, Fatigue Analysis, were concurrent, followed by Phase III, Full-Scale Fatigue Test.

Phase I, Flight Load Survey, involved 122 aircraft of three different instrumentation types and a "lead-the-fleet" concept of accelerated utilization on 22 aircraft to accumulate flight hours at a faster rate than the fleet. The primary purpose of Phase I was to obtain accurate loading spectra for each component of the structure to be used in Phase III fatigue test. The method of obtaining spectra made extensive use of calibrated strain gages on two of the aircraft to directly obtain wing, fuselage, and empennage bending moments. These data were supplemented by the usual velocity/load factor/altitude (VGH) type data collected on four of the flight test aircraft. The remaining Phase I airplanes contained statistical counters to record load factor exceedance levels.

In Phase II, Fatigue Analysis, element fatigue tests of critical areas were run to supplement a fatigue analysis of the primary structure of the airframe. The analysis

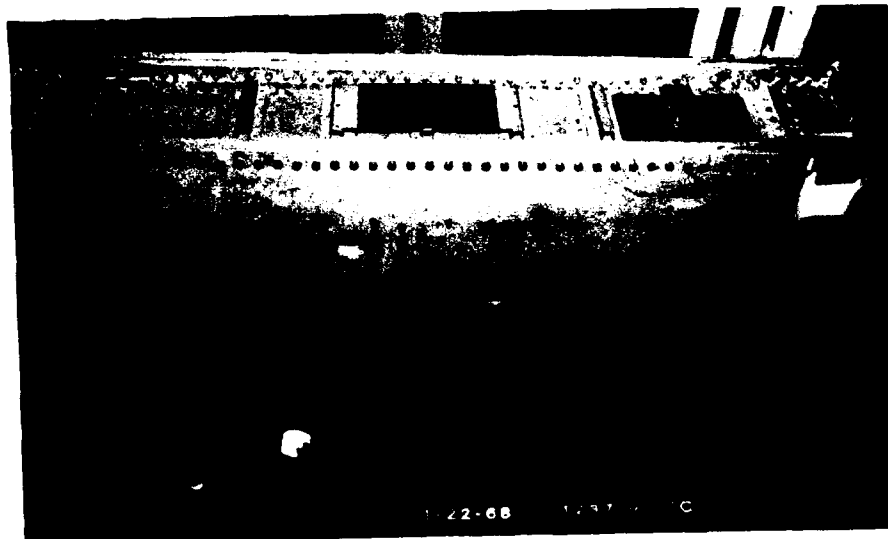


Figure 3. F-100 Wing Center Section.

consisted of determination of local stress spectra and a fatigue life prediction for the structural members. In this phase, modifications to the structure were designed where the life prediction indicated a possible life less than the life goal which had been determined to be 5,500 flight hours. To meet the criteria of 5,500 flight hours, a scatter factor of two for a total of 11,000 test hours was established.

In Phase III, Full-Scale Fatigue Test, proof of conformance spectra test were conducted on full-scale components: wing, fuselage, vertical tail, and landing gear. Tests were conducted initially on unmodified aircraft as furnished from the fleet by the USAF. Subsequent testing was performed on modified components as the modifications became necessary in order to meet the required life goal.

### Service Hour Statistics

Two studies of the service hour statistics were performed in the span of the ASIP program. The first of these studies summarized the status of the fleet as of 1 January 1965. This study<sup>1</sup> indicated that a total service life goal of 5,500 hours would cover 99.9 percent of the fleet aircraft projected through 1975. At that time, the fleet

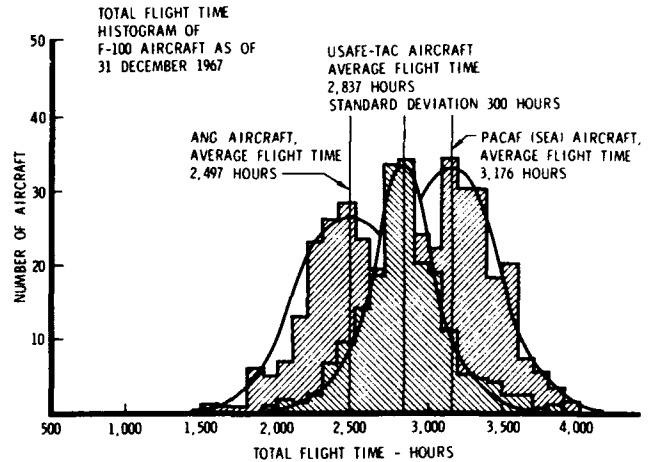


Figure 4. Total Flight Time Histogram for F-100 Aircraft.

average time was 1,988 hours, and the high-time aircraft had 2,800 service hours.

The study was repeated in 1968<sup>2</sup> when it became apparent that the utilization rates in Southeast Asia (SEA) far exceeded those which had been used for the 1965

TABLE I.  
PROGRAMMED UTILIZATION RATES - F-100 AIRCRAFT

FISCAL YEAR	QTR	USAFE and TAC		ANG		PACAF *	
		RATE	HOURS/MONTH	RATE	HOURS/MONTH	RATE	HOURS/MONTH
1968	1	73.5	24.5	76.4	25.5	123.8	41.3
	2	65.1	21.7	67.4	22.5	131.4	43.8
	3	69.5	23.2	68.4	22.8	131.4	43.8
	4	77.0	25.7	70.9	23.6	131.4	43.8
1969	1	83.6	27.9	71.2	23.7	131.4	43.8
	2	80.4	26.8	65.5	21.8	131.4	43.8
	3	80.0	26.7	66.2	22.1	137.7	45.9
	4	82.7	27.6	75.8	25.3	137.3	45.8
1970	1	74.1	24.7	69.5	23.2		
	2	86.2	28.7	55	18.6		
	3	87.1	29.0	56.5	18.8		
	4	91.3	30.4	67.6	22.5		
1971	1	90.6	30.2	69.4	23.1		
	2	87.6	29.2	60.0	20.0		
	3	114.8	38.3	41.8	13.9		
	4	101.3	33.8	55.4	18.5		
1972	1	103.9	34.6	51.5	17.2		
	2	126.5	42.2	39.7	13.2		
	3	84.8	28.3	41.4	13.8		
	4	69.4	23.1	48.7	16.2		
1973	1	69.4	23.1	49.5	16.5		
	2	69.4	23.1	42.1	14.0		
	3	69.4	23.1	42.3	14.1		
	4	69.4	23.1	51.0	17.0		

\* Actual rate between June and November 1967, 48.3 hours per month average.

statistical review for Tactical Air Command (TAC) aircraft in the United States and Europe.

By January 1968, the F-100 fleet had separated because of different utilization rates into three populations: TAC-USAFE, PACAF (SEA), and Air National Guard (ANG). Figure 4 is a histogram of the flight hours on the three populations of aircraft as of 31 December 1967. The first population consists of F-100 aircraft in TAC and USAFE. The data for the histogram were obtained from each using command for 470 aircraft stationed in the United States and Europe.

The third population is the ANG fleet. The histogram data for the flight time of 206 ANG aircraft was based on SMAMA information as of 31 December 1967.

#### Projection of the Flight Hours

The flight hours status of the aircraft population was projected for each population using the programmed rates shown in Table I, taken from Reference 3. Five utilization programs were considered as follows:

Program 1 - PACAF fleet is returned to TAC in the 4th quarter of FY 1969.

Program 2 - PACAF fleet is returned to TAC in the 4th quarter of FY 1970.

Program 3 - PACAF fleet is returned to TAC in the 4th quarter of FY 1971.

Program 4 - PACAF fleet is rotated into TAC in the 2nd quarter of FY 1969 and replaced by TAC aircraft which remains to the 4th quarter of 1970 and then returned to TAC fleet.

Program 5 - The PACAF and the TAC fleet remain unchanged for projection.

These projections are shown in Figure 5 for the 99 percentile coverage for 1972 and 1975.

#### Design Life Goal

From Figure 5, the 99 percentile PACAF fleet would exceed the initial life goal of 5,500 hours in November 1970 while the unrotated TAC-USAFE fleet would exceed 5,500 hours as of November 1973. Therefore, a revised design life goal for ASIP was necessary to cover the 99 percentile aircraft to retain F-100's in the inventory through FY 1975.

For example, the F-100 fleet in 1972 and 1975 would be separated into three service-hour populations if the rotation in program 4 was implemented. Program 4 assumes the present PACAF fleet is returned to TAC at the end of the second quarter of FY 1969. Part of the TAC fleet

replaces these aircraft from the second quarter of 1969 to the 4th quarter of FY 1970 and is then returned to the TAC fleet. The three populations and the 99 percent aircraft would have the following service hours in 1975:

Population	Service Hours
PACAF-TAC	6, 619
TAC-PACAF	6, 289
TAC-TAC	5, 965

#### Life Goal Redefined

As a result of the 1968 study, the service life goal was redefined as 7,000 hours total or 4,000 hours life extension after modification. At the same time, the design scatter factor was increased from 2.0 to 4.0. The original scatter factor of 2.0 was partially justified by the conservatism of the ASIP loading spectrum selected from the flight load survey. Later fatigue load surveys, particularly from SEA combat indicated increased severity of loading reducing the conservatism of the ASIP spectrum. The scatter factor for full-scale testing remained at 2.0.

#### Deficiency Summary

At the time of the program conception, there were no serious in-service fatigue failures to indicate that the airframe could not successfully attain 5,500 flight hours. A fatigue problem with the main landing gear trunion prior to 1960 was solved by a rework design and subsequently by a redesigned, beefed-up landing gear.

There were, however, design development fatigue tests performed prior to 1956 which indicated that certain wing structural areas might not be capable of attaining 5,500 hours, especially if a scatter factor on life of from 2.0 to 4.0 were required in demonstration.

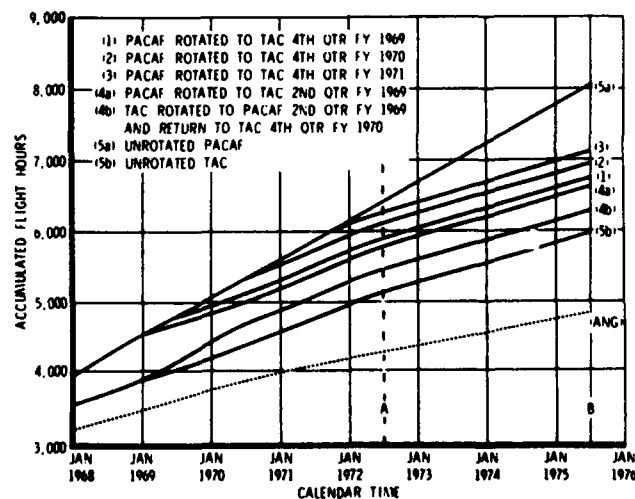


Figure 5. Flight Hour Projection, F-100 Fleet.

**TABLE II.  
IN-SERVICE CRACKS (POSSIBLE FATIGUE ORIGIN)**

A/C SERIAL NO.	DATE	A/C HOURS	LOCATION, SIZE, REMARKS
<b>F-100C THUNDERBIRD</b>			Skin fillet at root rib and diagonal spar
55-2724 (solo)	9-1-59	1, 080	RH lower skin, 8 in. long
55-2723 (solo)	2-17-64	2, 569	RH and LH lower skins, 8 in. long; RH upper skin, 1/4 in. long
55-2724	2-4-64	2, 418 A/C 1, 338 Wing	RH upper skin (192-14140) crack length 1/2 in.
55-2728	2-14-64	2, 800	RH and LH upper skin (192-14140), crack length 1/2 in.
55-2722	2-17-64	1, 661	RH upper skin (192-14140), crack length 1-1/2 in.
<b>F-100D AIRCRAFT</b>			
55-2874	1-28-66	2, 641	LH upper skin, 3/8 in. long (223-14140)
56-3153	3-25-66	2, 547	RH upper skin, 3/8 in. long (223-14140)
56-3038	5-16-66	2, 425	RH upper skin
56-3119	5-25-66	2, 605	RH upper skin
<b>F-100C AIRCRAFT</b>			
54-2075	7-6-66	2, 464	RH upper skin, 1/8 in. long
54-2039 (ANG)	7-23-66	2, 570	RH upper skin, two cracks 1/16 in. long
<b>F-100D AIRCRAFT</b>			
55-3639	2-25-66	2, 149	Skin rabbet at root rib and leading edge rib 96; L H upper skin 1-1/2 in. long; fus sta 257 (223-14140)
55-3558 (PACAF)	1965	Unknown	Rear spar main landing gear trunnion support
Unknown (French)	1964	Unknown	Rear spar main landing gear trunnion support
54-3561 (Thunderbird)	3-17-66	2, 233	Fuselage side skin fus sta 315, WL 12; RH side 8 to 10 in. long, terminates at upper longeron
<b>F-100D and F-100C</b>	Prior 5-6-65		65 cracked upper NLG drag links (180-34120), 12 condemned, 349 aircraft inspected and reworded per T.O.1F-100-964

Prior to initiation of the ASIP program, fatigue-type cracks occurred in wing skins in a critical structural section located in the wing root area. These cracks were first observed in F-100C Thunderbird aircraft which are subjected to a relatively severe flight load spectrum.

Table II is a list of the in-service failures which were of possible fatigue origin. A brief discussion of the important failures follows.

*Wing Station 33.875 Skin Fillet "Thunderbird" Crack*

Five of the listed failures occurred on the F-100C Thunderbird Aircraft. The cracks (Figure 6) were in a 3/4 inch-radius fillet in the upper and lower wing skins at the intersection of the root rib, butt plane 33, and the diagonal spar. The F-100C, D, and F wing skins are identical in this area; the upper skin being 0.781-inch thick and the lower skin being 0.821-inch thick. Lower tension skin cracks

**Figure 6. "Thunderbird"  
Fillet Crack in Wing  
Outer Panel Upper Skin.**



were encountered on two aircraft only. Both upper wing skins on one of these aircraft were also cracked. All other fillet cracks, including those six discovered in F-100C and F-100D fleet aircraft, have been in upper compression skins, and predominantly on the right-hand wing. A comparison of time to failure for fleet versus Thunderbird aircraft shows a wide range of hours (1,080 to 2,800) for Thunderbirds and narrow range for fleet aircraft (2,400 to 2,641 hours).

#### *Skin Rabbet Crack*

A skin crack has occurred on one occasion in the wing skin where it attaches to the root rib at fuselage station 257. The fracture occurred at a rabbet in the milled skin where the thickness steps from 0.188 inch to 0.343 inch in thickness with a 0.25-inch fillet radius. Fatigue beach marks were not apparent; the fractured surface was characterized by an acute angle between the fracture plane and the mid-plane axis of the skin.

#### *Rear Spar at Main Landing Gear Trunnion Failure*

There were two incidents of this failure. Fracture surface analysis was performed by SMAMA and NR on the two fractured halves of the rear spar on aircraft serial No. 55-3558. There was some discrepancy between the two pieces of the same fracture. SMAMA apparently found little or no evidence of surface corrosion, whereas the piece examined by NR showed definite signs of surface corrosion. It was conjectured that postcracking corrosion might have taken place in the several months that the part has been out

of service. However, intergranular corrosion was observed in both halves by both SMAMA and NR.

#### *Nose Landing Gear Upper Aft Drag Link Failure*

Failures of this part have occurred with the frequency reported in Table II. The failures were identified as fatigue and a Technical Order was used in the field to rework cracked drag links.

### **FLIGHT LOAD SURVEY**

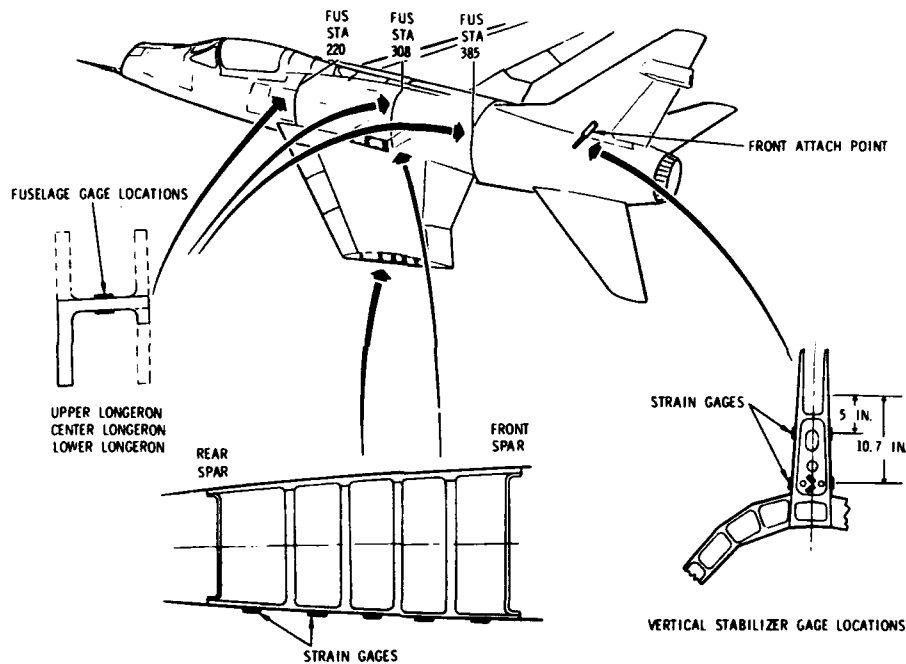
The objective of the flight load survey program was to provide loading spectra for all major components of the airframe for fatigue analysis and cyclic testing, primarily full-scale component testing. The methods used in the flight load survey were established from the concept, unique for ASIP programs, of measuring components bending moments in flight, along with load factor, and correlating bending moment with load factor so that load factor exceedance curves could be transformed directly to bending moment exceedance curves.

This method thus accomplishes, by direct measurement, what is normally derived analytically from VGH data. There was also the intent to derive R factor, ratio of minimum to maximum load, and data to establish the load reversal character of the load cycles, since they were found to be so important to fatigue by Nauman at NASA.<sup>4</sup>

A total of 122 aircraft were instrumented to obtain in-service fatigue load spectrum data. Four of the aircraft,



**Figure 7. Strain Gage Locations.**



code named "Yankee," contained digital tape recording systems and the remainder had only statistical accelerometers installed. Yankee No. 1 and No. 2 were equipped with calibrated strain gages to record bending moments at three wing stations, three fuselage stations, and one vertical tail station. Gages were also calibrated to measure vertical, side, and drag loads on the nose and main landing gear.<sup>5</sup>

#### Calibrated Strain Gages

Multiple sets of strain gages were required to define the bending moments for each station. (See Figure 7.) By the analysis of the calibration results, a circuit combining the strain gages and appropriate weighting factors, a resistor network was devised such that a single signal proportional to the total bending moment could be recorded on one channel of the digital recording system. This eliminates the necessity of reducing the data from each strain gage individually and the computations necessary to convert these several readings into bending moments.

The flight data collection period for the digital recorder instrumented aircraft was 6 months during 1966 and 1967, of which 172 flights were recorded including a variety of mission usages and external store configurations.

The data tape from each flight of the instrumented aircraft was played back through a ground station from which editing data tracks were made for selected parameters in flight. Editing data traces consisted of visually selecting the portions of the time histories with pertinent activity. These sections were then recompiled and a new condensed IBM tape was processed to give a tabulated time history for all parameters in proper engineering units and scaled

magnitudes.

A computer "peak cycle" program<sup>6</sup> was developed to analyze and classify the random data points for each trace of the condensed data tapes. Based on preset matrix levels, the data for each trace was classified in the following forms:

1. Maximum versus minimum peak (load factor or bending moment)
2. Load factor versus bending moment peaks

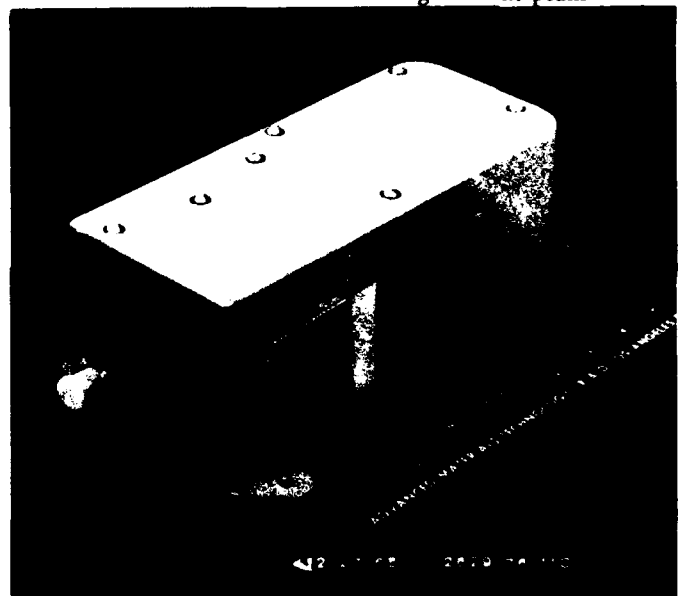


**Figure 8. Statistical Accelerometer Designed for F-100 ASIP Program.**

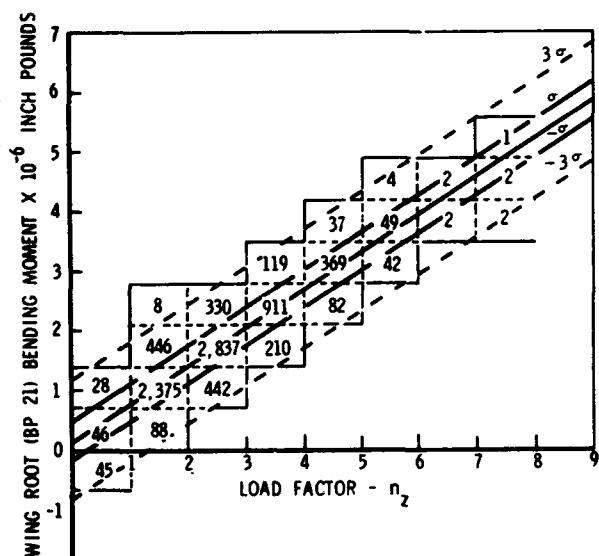


Figure 9. Graphic Illustration of Bending Moment, Load Factor Correlation.

3. Peaks versus speed, altitude (load factor or bending moment)

#### Statistical Accelerometer

The peak counting statistical accelerometer system (Figure 8), installed in 118 of the survey aircraft, was designed and developed at NR/LAD to record the significant peak vertical accelerations for 10 predetermined load factor intervals including two in the negative region. The system of logic was developed to duplicate, as closely as possible, the counting method used in the analysis of the flight data of the digital recorder instrumented aircraft. The counts were manually recorded before and after each flight on a supplemental data log sheet and then forwarded to NR/LAD for processing. Over 6,700 hours of flight load factor data were collected, and 3,300 hours were processed for the primary source of statistical load exceedance data.

#### Bending Moment Correlation

The correlation of bending moments with load factors is based on the total tabulation of the load factor versus bending moment matrix for each flight. A plot of load factor versus wing bending moment is shown in Figure 9. This data sample is used to define the statistical distribution of bending moments for the bending moment-load factor correlation. This distribution was attained by using a least square mean line and standard error of estimate lines, where the standard error of estimate lines are a measure of dispersion around the mean. It is assumed that the bending moments data in each load factor interval are normally distributed. Using standard statistical notation, the three sigma lines define the boundaries within which 99.7 percent of the data will fall for large samples of data and is used as the cutoff limits for the bending moment distribution for each load factor interval.

The distribution of occurrences in each of the bending moment intervals is determined from the total number of load factors in each load factor interval for the load factor spectrum considered. Summing the occurrences for each bending moment interval defines the frequency distribution of bending moment, and summing the occurrences from the largest to smallest values of bending moment defines the bending moment spectrum.

These bending moment spectra (Figure 10) for the wing spectrum for components to be tested were then adapted to a laboratory loading schedule for use with the automatic servo loading equipment used for the full-scale fatigue tests.

#### Southeast Asia (SEA) Combat Usage

As of July 1967, approximately 35 percent of the instrumented aircraft were located in SEA engaged in combat operations. A sampling of 1,000 flight hours of statistical accelerometer data was used to develop a load factor exceedance curve.<sup>7</sup> This curve is shown in Figure 10 in comparison to the exceedance curve representing peacetime usage (training base operations). The combat spectrum is slightly more severe than the peacetime spectrum. Comparative fatigue damage calculations indicated that up to a 13 percent reduction in fatigue life prediction would result from the increased severity.

#### Composite Spectrum

The fatigue specifications, MIL-A-8866 and ASD TR 66-57, permit the use of an average spectrum repre-

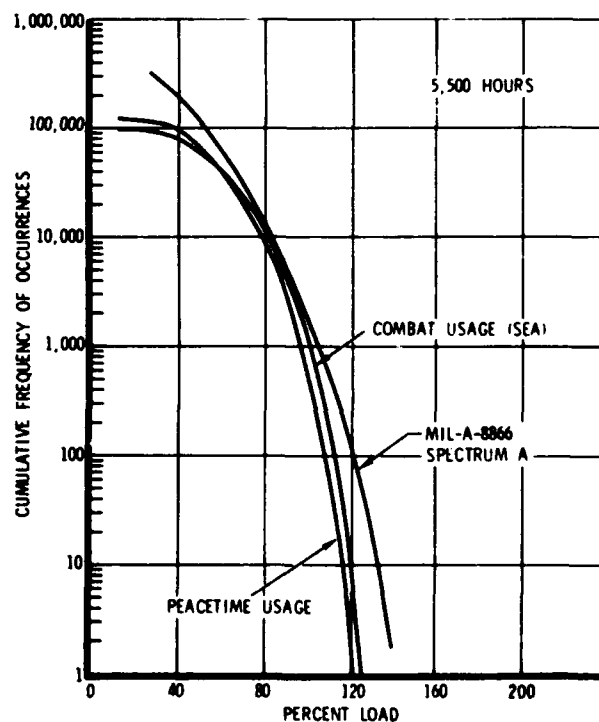


Figure 10. Wing Loading Spectrum for F-100 Aircraft.

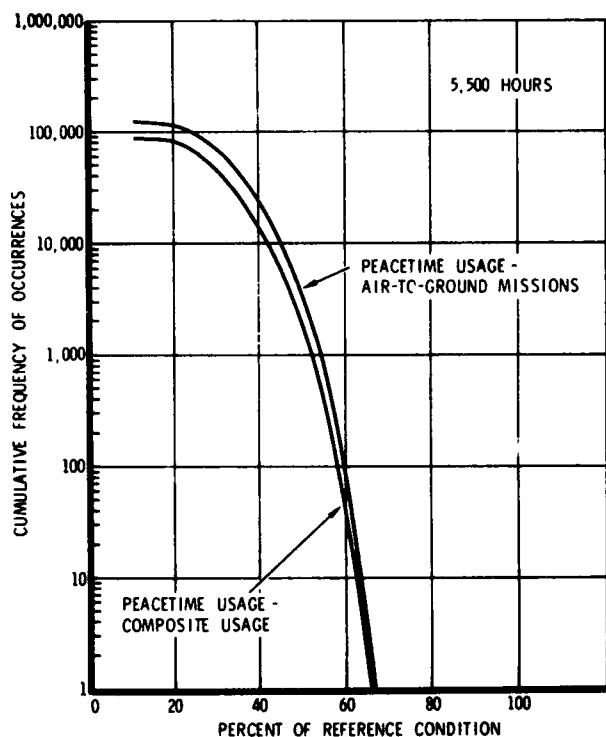


Figure 11. Comparison of Composite and Air-to-Ground Mission Type of Fuselage Loading Spectra.

senting a specified composite mix of the various missions which will be performed by the aircraft in service. No attempt was made in deriving the F-100 ASIP spectrum to arrive at an average spectrum. The spectrum was deliberately selected from the most severe usage, air-to-ground operations, ignoring all other types of mission.

A study was made using the data previously collected in Phase I of the program to determine the relative magnitude of a composite spectrum. Composite usage was defined as the expected average usage by mission type of all the operational aircraft in the fleet. Four missions, as described on pilot-crew chief reporting forms, were included and five aircraft each at six different bases were sampled to establish the current statistical mission mix. The composite spectrum resulting from this procedure is shown in Figure 11 taken from Reference 8. The composite spectrum is less severe than the Phase I ASIP spectrum by as much as 35 percent by comparative fatigue damage calculations based on Miner's linear cumulative damage.

#### VGH Recorders

Later in the program, in early 1968, VGH recorders, Conrac Model A/A24U-10, supplied by the USAF were installed in 28 aircraft. These aircraft were assigned to two bases in SEA and two in the continental U.S. Over 2,300 hours of VGH data was collected over a 6-month period ending in December 1968. This data was processed initially by Technology Incorporated, Dayton, Ohio, for analysis by North American<sup>9</sup> to provide bending moment exceedance

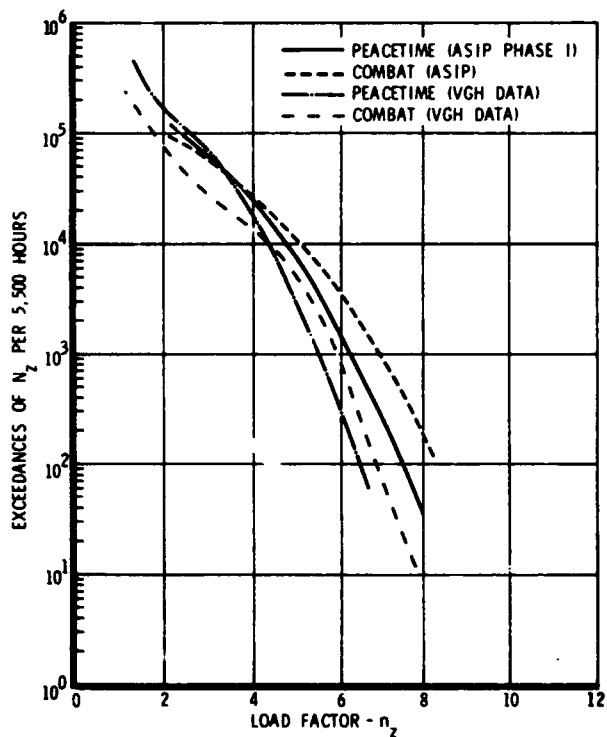


Figure 12. Peacetime and Combat Load Factor Spectra for VGH and F-100 ASIP Data, 5,500-Hour Life.

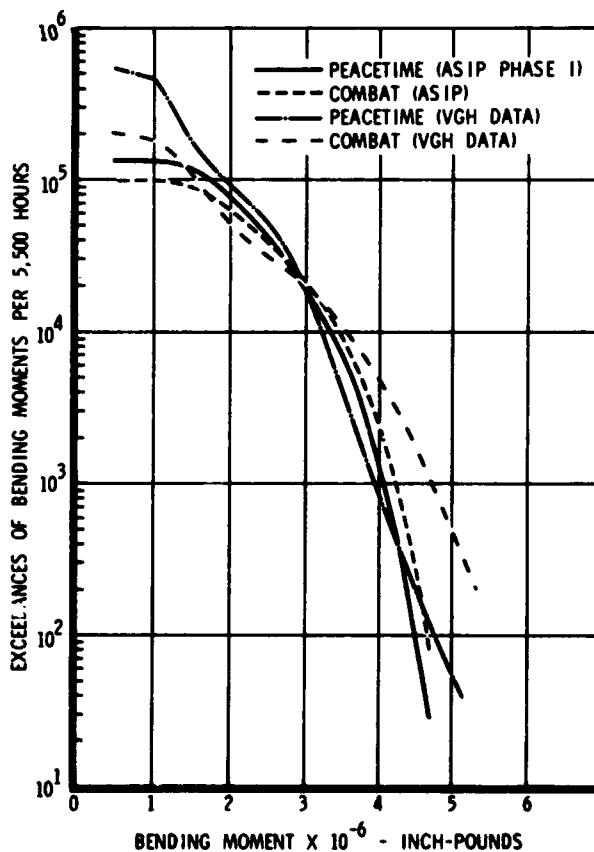
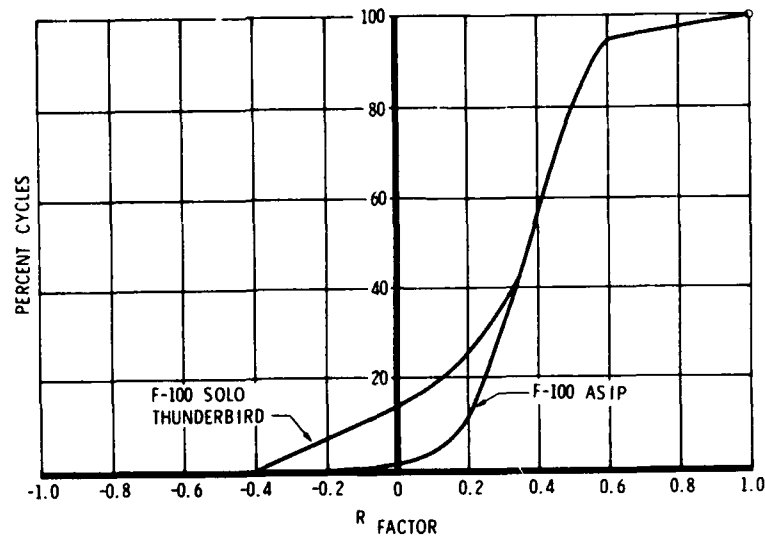


Figure 13. Peacetime and Combat Wing Bending Moment Spectra at Butt Plane 33.5 for VGH and F-100 ASIP Data, 5,500-Hour Life.

### R FACTOR DISTRIBUTION

**Figure 14. Revised R Factor Curve, Thunderbird Solo Aircraft.**



data similar to that derived from the strain-gaged aircraft. A comparison of the load factor exceedance data from the ASIP and VGH programs is shown in Figure 12. A comparison of the analytical bending moment exceedance curves with strain gage bending moment exceedance curves is shown in Figure 13. Whereas the load factor exceedance data from the VGH program is less severe than the original ASIP data, the bending moments derived analytically exceed those measured directly from the calibrated strain gage data. This was attributed to inclusion of higher gross weight flights with external stores in SEA operations. The difference in the two load factor curves was considered a systematic difference between the VGH recorder and the statistical accelerometer.

#### Thunderbird VGH

In-flight loads were recorded on Thunderbird demonstration aircraft for the first time in their operations as part of the VGH load collection program. Of primary interest in the Thunderbird operations was the negative load factor maneuvering of the solo and slot aircraft. The more frequent excursions into negative load factor regime is shown in Figure 14, taken from Reference 10. Of the positive maneuver cycles of the solo aircraft, 14 percent were followed by negative load factor valleys, while less than 2 percent are for fleet aircraft. The slot aircraft data indicated less severe maneuvers than for fleet aircraft. (See Figure 15.) Solo aircraft were shown by analysis of the spectrum to accumulate fatigue damage at about three times the rate of fleet aircraft. This study confirmed the previously formed conclusion that demonstration usage constituted "lead-the-fleet" type flying. Demonstration F-100's preceded the fleet in two important fatigue failures, the wing skin fillet (Figure 6) and the wing center section which will be discussed later.

#### Store Ejection Loads

One of the instrumented Yankee aircraft, with its

calibrated strain gages, was reactivated in 1968 to record the wing loads resulting from force ejection of various external store arrangements. This program came about as a result of combat losses of aircraft under circumstances which could be interpreted to implicate store ejection forces. Preliminary analysis of the effect of store ejection on the wing bending moment spectrum indicated no problems at the critical fatigue areas of the wing, near the root. Stores are ejected in normal delivery at or near 1 g so that excessive bending moments would not be expected. How-

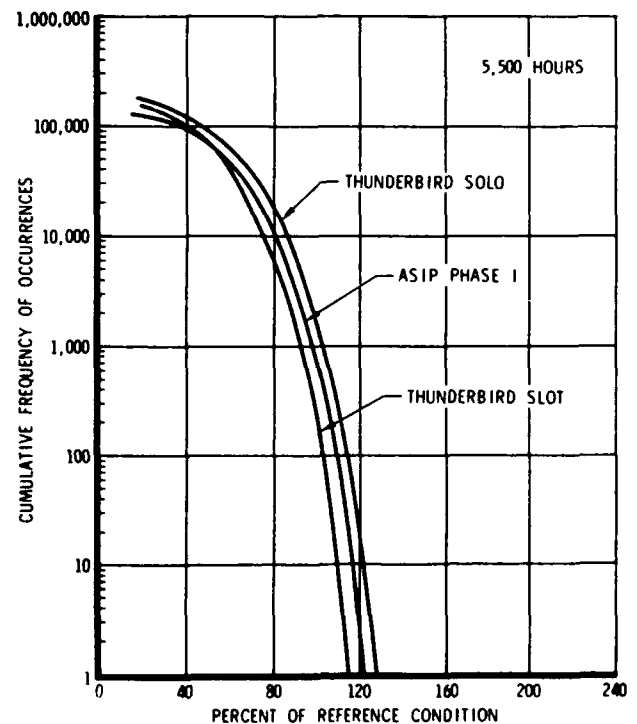


**Figure 15. Thunderbird Aircraft Wing Loading Spectra.**

ever, the preliminary analysis did indicate that bending moments for store ejection near the outboard store station exceeded those due to load factor maneuvering and that a possible problem existed although no fatigue critical cross-sections existed in that area of the wing outer panel. The preliminary analyses were based on a dynamic analysis of the wing subjected to the impulse loading of the explosive charge store ejection system.

The results of the in-flight data collection confirmed that:

1. The bending moments at the wing root due to store ejection were of a magnitude which would not increase the severity of the normal maneuver load spectrum.

2. The bending moments at the outboard store station were of sufficient magnitude to increase the severity of the fatigue loading spectrum.

However, when analyzed for its effect on fatigue life, a negligible, less than 2 percent loss, was calculated.<sup>11</sup>

### FATIGUE ANALYSIS AND ELEMENT TESTS

#### Critical Areas

During the first year of the program, while the flight load survey was being conducted, a fatigue analysis of the critical airframe components was performed. A preliminary fatigue loading spectrum derived from load factor exceedance curves from previous flight load survey data<sup>12</sup> was used for this analysis.

Critical areas were selected, and critical here means incapable of attaining 5,500 hours fatigue life to a scatter factor of 2.0, or 11,000 hours by:

1. Reviewing design development fatigue tests.
2. Reviewing the static stress analysis for high net stresses in combination with relatively high stress concentration factors
3. In-service failure reports

The structural elements selected for element fatigue testing are shown by diagram in Figure 16 and 17. The following items in the wing, fuselage, and landing gear were tested:

1. Wing center section (WCS) to wing outer panel (WOP) splice - lower skin
2. WOP upper and lower skin fillet butt plane 33 (wing root) - "Thunderbird" fillet
3. WOP lower skin at rear spar and root rib

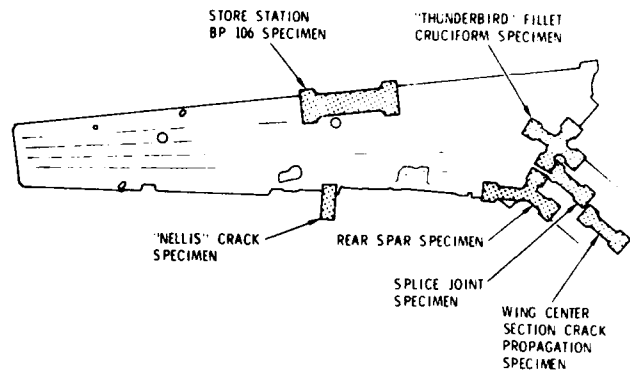


Figure 16. Location of Wing Skin Element Tests.

4. WOP lower skin butt plane 108 store station
5. WOP lower skin tab - aileron rib attach
6. Fuselage upper longeron for break splice, fuselage station 389
7. Nose landing gear upper aft drag link

#### Element Tests

The general approach followed during element testing was to use three specimens: two tested at constant load level cycles and one subjected to the realistic fatigue load spectrum. The objective of the constant load level tests was to provide supplemental S-N data points to be used with the basic material property S-N curve for the specific stress concentration,  $K_t$ , at the notch.

The single spectrum test was to provide an indication of the actual fatigue life and a preliminary estimate of the amount of error to be expected from cumulative damage fatigue life predictions.

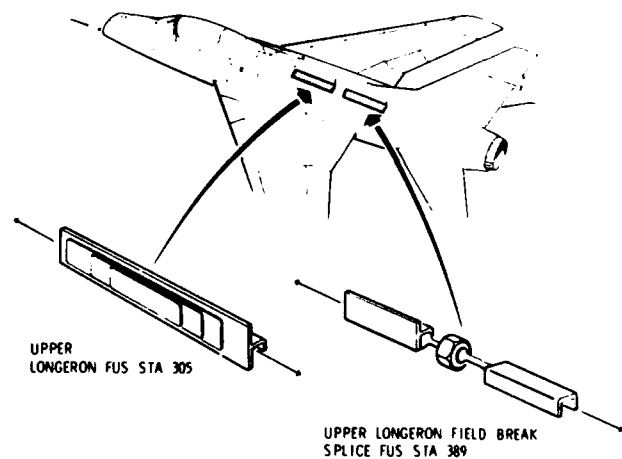


Figure 17. Fuselage Structural Element Tests.

**TABLE III.**  
**ELEMENT FATIGUE TEST RESULTS COMPARED TO**  
**PREDICTED LIVES**

STRUCTURAL ELEMENT	TEST LIFE (hours)	PREDICTED LIFE (hours)
<b>Wing</b>		
Lower skin fillet, wing station 33.875 ("Thunderbird" fillet)	5, 508	1, 280
Wing center section to wing outer panel splice joint lower skin	40, 750	18, 000
Wing outer panel lower skin at rear spar and root rib	22, 440	1, 770
Wing outer panel lower skin at butt plate 106 to 108	100, 000	42, 700
<b>Fuselage</b>		
Upper longeron field break splice, fuselage station 389	38, 450	27, 000
<b>Landing Gear</b>		
Upper aft drag link, nose landing gear	3, 977	5, 700
Above with rework No. 1	11, 275	
Above with rework No. 2	5, 520	

#### Fatigue Life Prediction

The fatigue life analysis consisted of a five-step procedure:

1. Calculation of the local stress level
2. Calculation of the stress concentration factor,  $K_t$
3. Selection and adjustment of S-N curves
4. Definition of the stress spectrum
5. Application of cumulative damage theory to predict fatigue life in airplane service hours

A computer program<sup>13</sup> based on Miner's rule of linear cumulative damage was prepared to perform the calculations. This program calculates the damage fractions for each spectrum, maneuver, ground-air-ground, etc., the total damage fraction and the predicted life in airplane service hours.

#### Comparison of Results

The element test and analysis results from Reference 14 are summarized in Table III. Note that some element test specimens endured up to 12 times the predicted fatigue life in hours. This was attributed to conservatism in the S-N data used, and conservatism of Miner's rule for high-load spectra typical of fighter aircraft maneuvers.

In previous fatigue programs at North American, such as the F-86 ASIP program,<sup>15</sup> Miner's rule has proved to be conservative by a factor of 2 or more for the typical fighter maneuver load spectrum. Also, element spectrum tests rarely prove to be as severe as full-scale component tests - largely due to inability to incorporate into the element test specimen secondary effects, eccentricities, etc, which increases the peak stress at the critical failure cross section.

#### Effectivity of the Fatigue Analysis

The analysis indicated that most of the areas considered critical had adequate fatigue life. Only one area, the WCS to WOP splice including the WCS lower skin, of those shown to have adequate fatigue life proved to be critical later during full-scale testing. The fuselage field break splice attained the required scatter factor of 2.0 in test, but failed in a later attempt to attain a scatter factor of 4.0. All areas indicated by analysis and element test to be critical did actually prove to be critical during full-scale testing. Full-scale testing revealed two critical fuselage areas and one wing area which had not been analyzed; i.e., had not been recognized as potential fatigue problem areas.

#### Element Tests of the "Thunderbird" Fillet

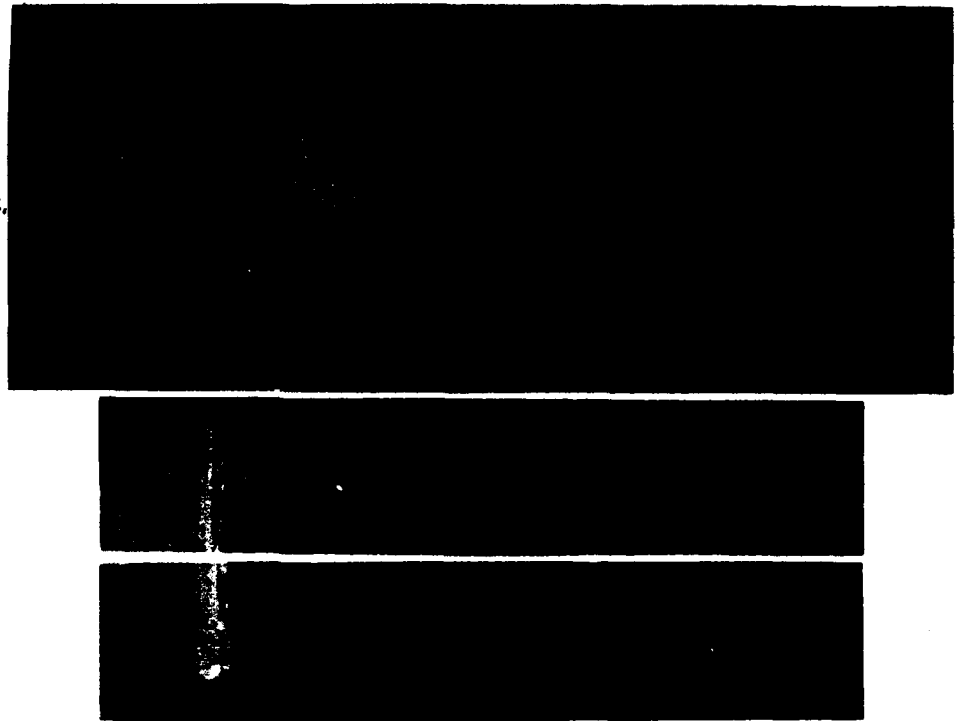
This element test specimen (Figure 18) replaces the cruciform in Figure 16 and was used to determine the effect on fatigue life of various processes:

1. Fillet radius enlargement
2. Shot-peening fillet
3. Periodic material removal in the fillet
4. External load cycling in compression only

Up to four normal lifetimes were obtained with specimens from which a small amount, 3 mils, of surface material in the fillet was removed by machining at the 75 percent expected life point as determined from the average of several specimens tested to failure without material removal.

Shot peening improved the fatigue life for both the original radius and the enlarged radius to reduce the stress concentration. All of these results are shown in Figure 19.

**Figure 18. "Thunderbird" Fillet Specimen, Compression Spectrum Loaded, 0.10-Inch Crack, Then Fractured in Tension at 18,450 psi.**



**Compression Fatigue**

Two of the fillet specimens were loaded in compression representing the upper wing skin. The spectrum element endured 70, 280 hours, the last 6,000 hours including

some small tension loads. The fracture surface is shown in Figure 18.

The second specimen was subjected to constant level load cycles of 30,000 psi compression on the net cross sec-

**Figure 19. "Thunderbird" Fillet Element Test Results.**

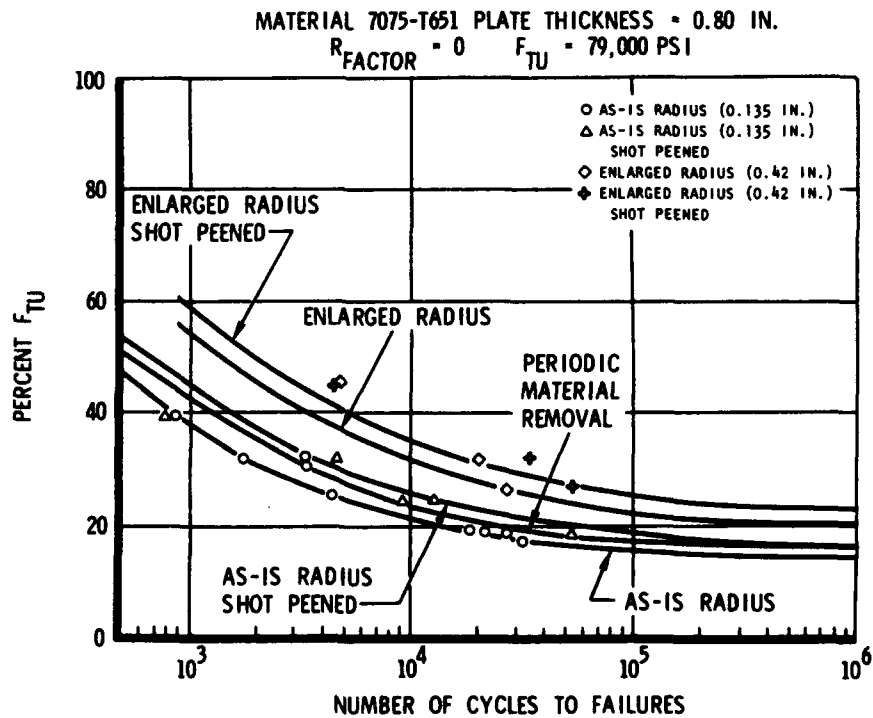
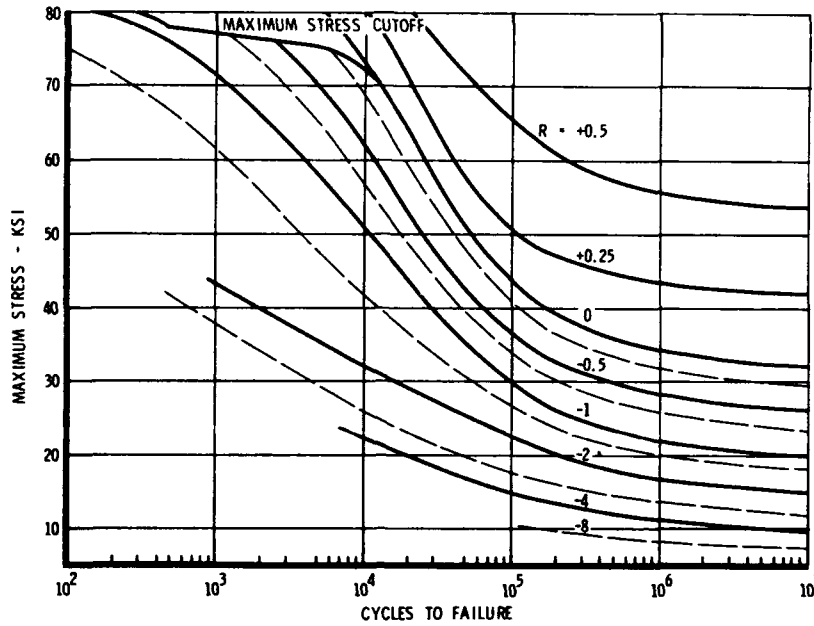


**Figure 20. S-N Data for 7075-T6 Aluminum at Various R Factors.**



tion. After 151,000 cycles, the cracks were visible with die penetrant visual inspection. The specimen was fractured statically to reveal the total extent of the fatigue crack. These tests prove that it is possible to produce a fatigue crack without external tension loads.

**Correction for Plasticity in Fatigue Life Prediction**

Plasticity was accounted for in performing the cumulative damage life prediction in order to analyze the compression skin fillet and to correct the simple Miner's rule solutions for tension loading.

In the cases where a fatigue test data point was available at  $R_{factor}$  of zero and constant load amplitude, the method of C.R. Smith<sup>16</sup> was used. This method is an empirical approach to the plasticity problem, making it unnecessary to calculate the stress concentration factor or the net stress at the notch, both of which are relatively difficult to calculate for complex parts. Having tested a specimen at  $R_{factor}$  of zero exactly duplicating the notch geometry, using the cycles to failure, a chart of S-N curves for unnotched specimens at various  $R_{factor}$  (Figure 20) is entered. At the intersection of the "cutoff" curve on the chart and the cycles to failure, the true  $R_{factor}$  and maximum stress at the base of the notch are determined. With the maximum stress known and the  $R_{factor}$ , a fatigue load spectrum can be transformed to a true stress spectrum. The fatigue life to initial cracking at the base of the notch can then be calculated by simple application of Miner's rule of cumulative damage.

Without a test data point, a similar correction can be made by calculating the stress concentration factor at the notch. This elastic stress concentration factor multiplied by

the net stress gives the apparent elastic stress at the notch. On a stress strain curve, the true plastic stress and strain can be determined. (See Figure 21.) It is then assumed that this high load was applied early in the life of the member, and the resulting residual stress was permanently imposed at the notch. The  $R_{factor}$  of the external load spectrum cycles can then be adjusted to give the true  $R_{factor}$  of the stress cycles at the notch.

The cumulative damage calculation is then in accordance with Miner's rule. It is required to have S-N data available for  $R_{factors}$  less than minus 1.0; i.e., where the

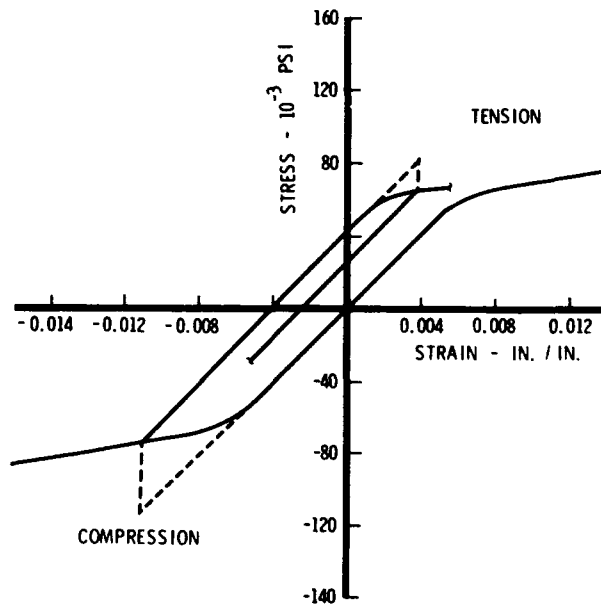


**Figure 21. Stress Strain Curve for 7075-T6 Aluminum Showing Plastic Strains Resulting in Residual Stresses.**



**TABLE IV.**  
**FATIGUE LIFE PREDICTION BY MINER'S RULE AND C. R. SMITH METHOD**

STRUCTURAL ELEMENT	SERVICE LIFE (hours)	ELEMENT LIFE (hours)	PREDICTED LIFE	
			MINER'S RULE (hours)	SMITH METHOD (hours)
Wing outer panel lower skin fillet, wing station 33.875 ("Thunderbird" fillet)	2,150	5,508	3,045 (1,280)*	4,460
Wing outer panel upper skin fillet, wing station 33.875 ("Thunderbird" fillet)	2,900	5,508	Does not Apply	12,670
Wing bolting bar	1,863	5,600	1,610	4,710

\* With more conservative S-N data.

compression peak of the cycles exceeds in magnitude the tension peak.

Table IV shows the results of such analysis performed on the tension and compression fillets of the WOP skin. Since the Smith method increased the life prediction magnitude, there is better agreement with test results which far exceed the Miner's rule life prediction.

**Fatigue Tests and Analysis of Taper-Lok Bolts in the Wing Outer Panel (WOP) to Wing Center Section (WCS) Lower Skin Splice**

Fatigue cracks developed in the WOP lower skin to the WCS splice on two wings during the full-scale F-100 ASIP testing at approximately 9,000 hours. These fatigue cracks were in the WOP lower skin progressing chordwise from the aft edge through the outboard row of fasteners. Since the splice exhibited insufficient fatigue life, it became necessary to modify the splice to be compatible with the redesigned skin fatigue life. The configuration of the splice area dictated that the geometry remain unchanged. Thus,

interference Taper-Lok fasteners were utilized to attain the life improvement required.

*Specimen Description*

The WOP to WCS splice consists of a three-row, double shear, step-tapered joint utilizing 7/16-inch and 1/2-inch bolts in 7075-T651 and 7075-T6 bare aluminum plate. During this program, this splice was simulated by element specimens 6.5 inches wide utilizing conventional as well as Taper-Lok fasteners. (See Figure 22.)

*Laboratory Test Results*

The WOP to WCS splice element test specimens were subjected to the same spectrum used for the full-scale component testing. In addition to the spectrum loaded specimens, there were five specimens with 1/2-inch conventional and 1/2-inch Taper-Lok fasteners which were cycled at a constant stress level with  $R_{factor}$  equal to zero. The results of the constant load cycling were used to establish the S-N curves shown in Figure 23 by the least

**Figure 22. Taper-Lok Bolt Splice Specimen.**

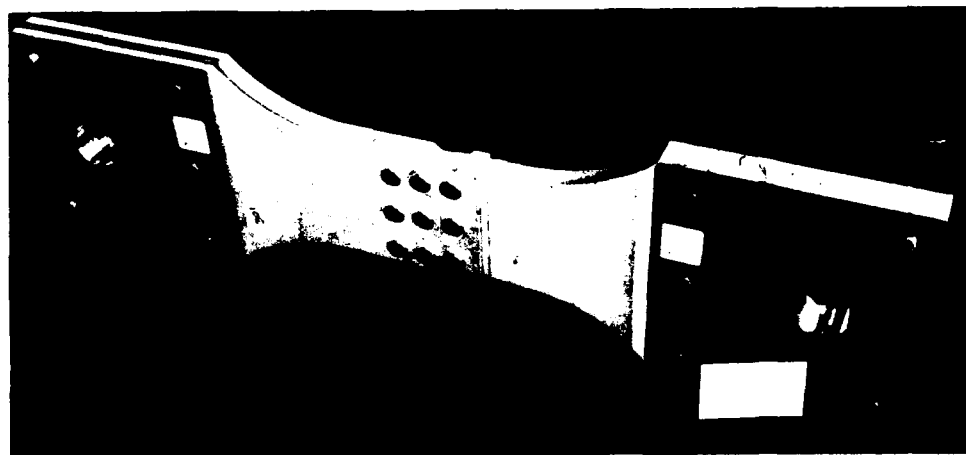
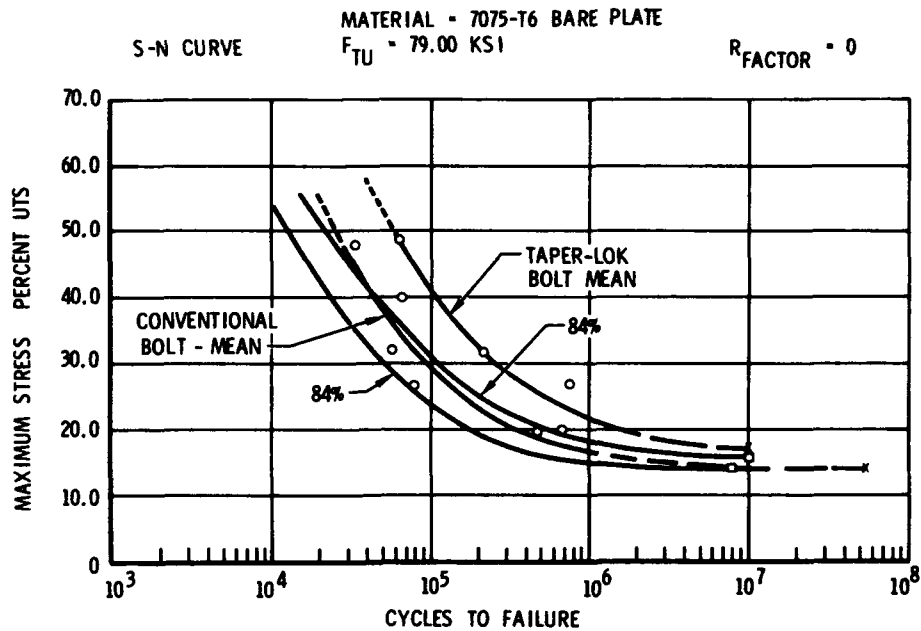


Figure 23. Taper-Lok Splice Test Results.



square fit technique of Reference 17. All of the results are shown in Table V, and they indicate a life improvement factor of approximately 2.0 for both constant level and spectrum tests. The spectrum test lives were greatly in excess of those obtained from the full-scale tests. Thus, the absolute magnitudes of fatigue life were not useful, but the life improvement factor of over 2.0 was used for projecting the full-scale life to obtain a life prediction for aircraft with Taper-Lok joints of over 18,000 hours. A comparison of type of failures is shown in Figure 24. The Taper-Lok specimens failed from fatigue cracks originating away from bolt holes.

**Additional Element Test Programs**

*Wing Center Section Lower Skin*

Subsequent to failures of the WCS in service and during full-scale test, a crack propagation test program was conducted on specimens taken from service aircraft. The center sections became available because modifications were designed and installed in fleet aircraft. The tension covers of the first 86 aircraft to be modified were subjected to a comprehensive inspection program to determine the extent of fatigue cracking in the fleet. The skins were then cut

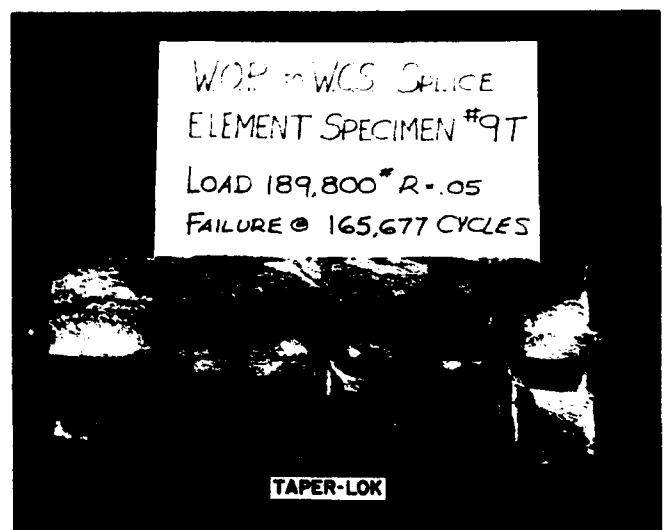
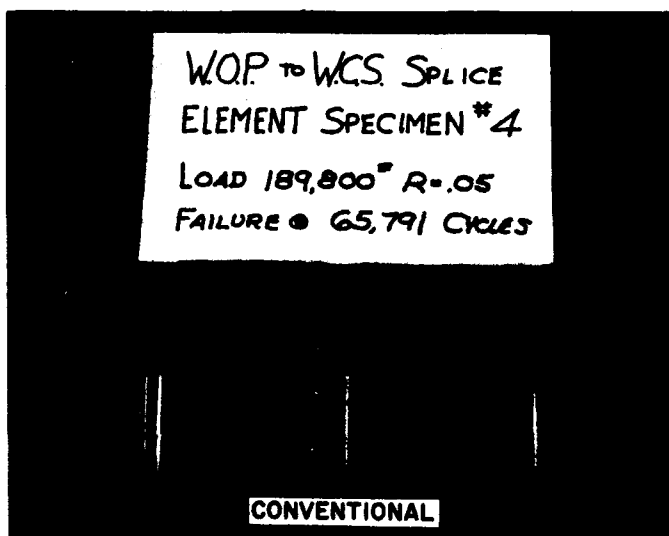


Figure 24. Contrasting Fracture Surfaces for a Splice with Conventional and Taper-Lok Bolts.

**TABLE V.  
TAPER-LOK BOLT SPLICE TEST RESULTS**

SPECI- MEN	LOAD TYPE	MAGNITUDE STRESS (PSI)	CONVENTIONAL	TAPER- LOK
			BOLTS (cycles or hours)	BOLTS (cycles or hours)
1	Constant	15,700	472,163	785,712
2	Constant	21,000	78,658	781,356
3	Constant	26,000	55,421	100,589
4	Constant	31,500	65,791	165,677
5	Constant	37,700	33,048	65,435
6	Spectrum	Standard 24,100 at 100%	132,000+	224,800+
7	Spectrum	Escalated 29,000 at 100%	62,400	147,200

into test coupons and subjected to crack growth tests, the results of which were primarily used to establish safe time limits for accomplishing the fleetwide modification program. The results of the test program were reported in Reference 18, a paper presented earlier in 1969 at a conference on crack propagation at SMAMA, McClellan AFB, and soon to be published. The most notable test result was that cracks in the boltholes which extended only part way through the thickness of the skin grew very slowly until they had extended through the thickness, at which time growth was rapid and finally catastrophic. In fact, specimens with part-through cracks had total fatigue lives of the same magnitude as test specimens without prior load history.

*Aileron Rib Lower Skin Tab Rear Spar at Wing Station 108*

Cyclic loads were applied to the aileron-flap support rib at wing station 108 in an attempt to simulate lower skin cracks encountered on service aircraft at this location. The tests proved that aileron-flap loads alone could not have caused the service cracks. Wing bending loads and main landing gear loads were to be applied to this area of the wing during full-scale testing so that no further action was required as a result of the element test.

*Upper Longeron at Fuselage Station 305*

Residual strength tests were conducted on longeron specimens reinforced with external straps to determine the ultimate strength capacity of the longeron in that configuration. The tests indicated that the straps were capable of restoring original static ultimate strength capacity to the longeron with the maximum extent of fatigue cracking observed in test or service.

**FULL-SCALE TESTING**

**Specimens**

The full-scale fatigue tests of the F-100 airframe were conducted on structural components from operational service aircraft with known service lives. The test aircraft were inspected for cracks in known critical areas to determine the condition of the structure prior to initiation of testing. The complete wing assembly, with the main landing gear installed, was tested as one item. The fuselage, with the nose gear installed, but with the vertical and horizontal stabilizer removed, was tested as a second item. The aft fuselage and vertical stabilizer assembly was tested as a third item. The horizontal stabilizer was not tested in this program, since it had demonstrated adequate fatigue life by tests during the design-development of the aircraft. Since the wing is attached to the fuselage by a nonredundant, for symmetrical loads, four-point system, there was no loss of accuracy in supporting the wing or fuselage on loading jigs. The tests were greatly expedited with the use of two load system setups allowing the two components to be tested simultaneously without impacting one component with the failures from the other. The numerous nuisance-type skin cracks incurred by the fuselage specimen would have needlessly prolonged the wing tests.

**Laboratory Loading Schedule**

The load programming equipment used for this test program utilized the curve following technique. The equipment offered the versatility required to apply a flight-by-flight load spectrum to the specimen consisting of flight maneuver loads, landing loads, and ground landing loads. A fair amount of randomness was possible with this program

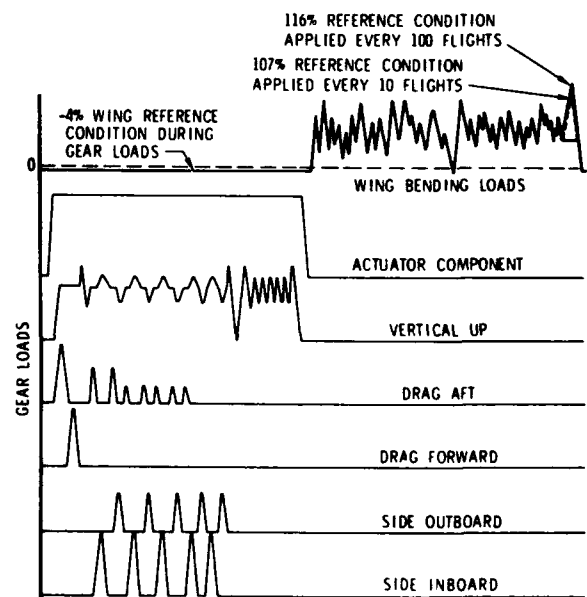


**Figure 25. A Typical Wing Load Sequence Representing One Flight.**

and modification of the load schedule could easily be accomplished with a minimum of effort.

The number of programming units for the loading system was determined by number of load conditions to be applied to the gear and the wing. Once this was established, the only restriction on the test spectrum was that each flight would be composed of a maximum of 30 flight load cycles and 30 gear load cycles.

The load spectrum applied to the wing and fuselage essentially consisted of the aforementioned flight-by-flight spectrum which represented 1.67 hours of flight. The flight loads consisted of approximately 30 cycles varying from negative to positive loads with various R factors selected on a random basis. The gear loads were also selected from one of three loading conditions. A typical flight sequence is shown in Figure 25 for the wing. A similar sequence exists for the fuselage. The loading sequence was repeated for 100 flights, after which the loading charts were changed to apply a different distribution of loading cycles. A total of 10 different distributions of load cycles and the distributions of gear cycles were used to make up the program. After 1,000 flights (1,670 test hours), the program was repeated.

For the vertical stabilizer installed on an aft fuselage, the loads were fully reversed and no significant ground-air-ground loads affected the spectrum. It proved more sat-

isfactory to use a block spectrum loading, with 400-hour blocks and 10 load steps per block. Sufficient randomness of loading was accomplished without resorting to flight by flight load sequences, since the stabilizer endured over 20,000 hours of test without failure.

#### Description of Test Setup

Both the wing and the fuselage were supported by jig work which picked up the four wing-to-fuselage attachment fittings using actual hardware. The aft fuselage and vertical stabilizer specimen was supported by jig work which picked up the longeron and frame fittings at the field break at fuselage station 389.

Load was applied to the front and rear spars of the wing and vertical stabilizer components through loading beams. This type of loading was chosen because of ease of setup and inspection. External surfaces were easily visible for observation with a minimum of teardown and setup rearrangement.

The load was distributed to the fuselage through steel straps riveted to the fuselage frames and hard points, such as horizontal stabilizer fittings and engine mount fittings.

Photographs of the test setup of the wing and fuselage major components are shown in Figures 26 and 27.

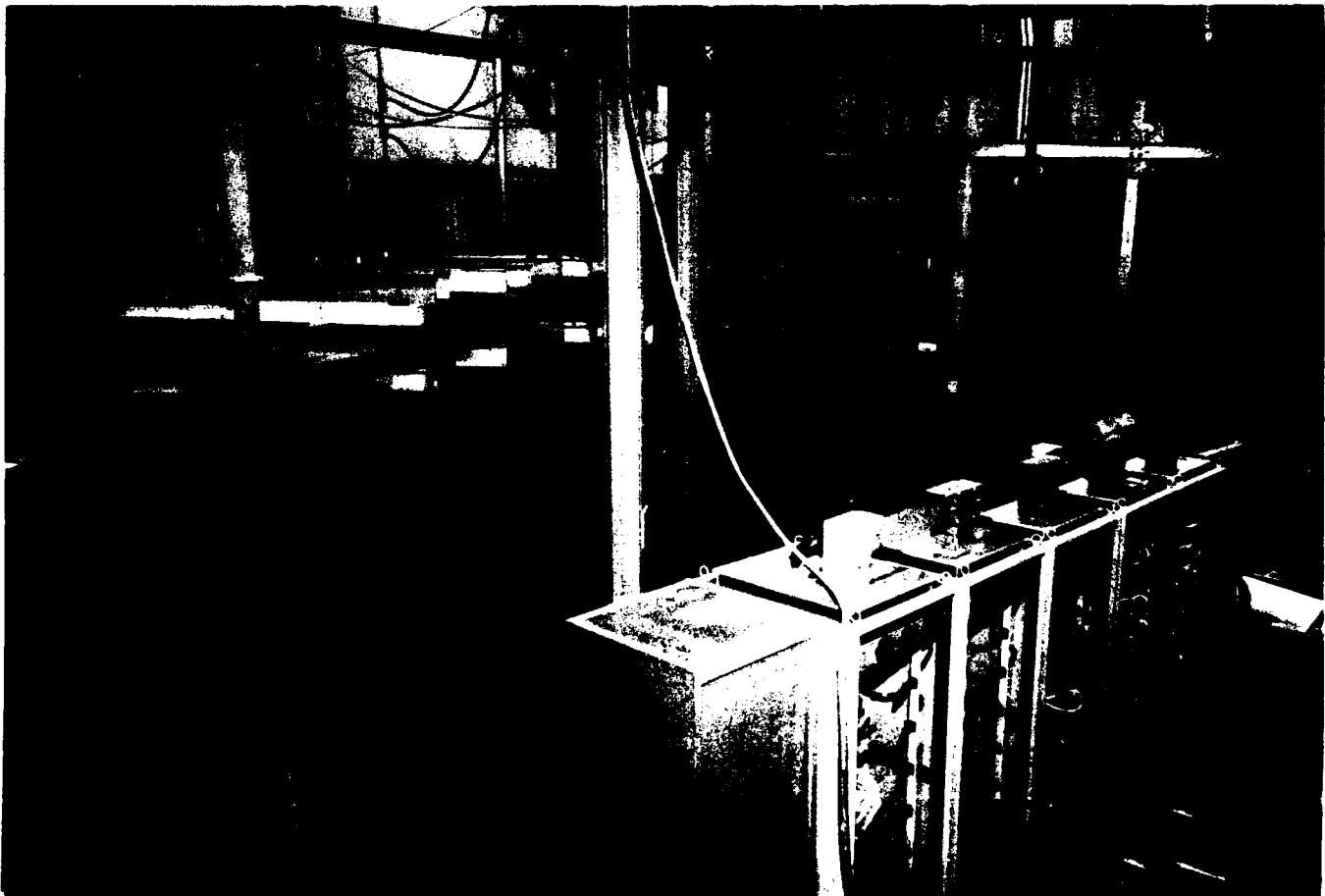


Figure 26. Wing Fatigue Test Setup.

The loads on all components were applied by hydraulic cylinders. The load output of each cylinder was controlled by a programmable closed loop-servo control.

Each system provides 24 channels of programmable closed loop servo control. The basic components of each system are nine MTS Data Traks, a 10-step matrix program selector for Data Trak sequencing control, and 24 MTS Servac Servo Controllers.

The Servac Servo Controllers control the load output of the hydraulic cylinders attached to the test component. A load transducer, installed in series with the hydraulic cylinder, produces a signal which is fed into the Servac. The Servac compares this load signal with the program input or command signal and generates a valve command to correct the error.

The system is programed by (1) plotting the prescribed spectrum waveform on each Data Trak Drum Chart, (2) setting up the matrix program selector to operate the desired Data Traks during the desired sequence steps, and (3) scaling the Servacs to provide the proper load magnitudes.

Several fail-safe circuits have been provided with the system. These circuits are as follows:

1. Servac Error Detector - These circuits are actuated whenever the load command signal error exceeds a preset percentage of the maximum programable Servac command

signal. There are two error detectors on each Servac; the first is usually preset to be activated before the second and provides a visual indication by lighting a light. Activation of the second error detector will (1) stop the program, (2) reduce all commands to zero, and (3) reduce the hydraulic system to a low-pressure bypass condition.

2. Differential Stroke Detector - Deflection transducers are mounted on each wingtip. The transducer outputs are compared in the differential stroke detector. If the difference between the outputs becomes greater than a preset limit, the system shuts down.

3. Absolute Deflection Limit Switches - Microswitches are mounted on each wingtip at an actuation level just above maximum wingtip deflection. If this deflection is exceeded and switch actuation occurs, the system will shut down.

A number of interlocks have been provided with the system to prevent an initial start in an unsafe condition. Examples: (1) valve pilot pressure must be on before primary pressure can be applied to the system, and (2) all Data Trak drums must be at the start (drum zero) before primary pressure can be applied to the system.

A continuous record of all applied loads was made. A separate strain gage bridge on the loading link was monitored on a Consolidated S-519 direct writing oscillograph. This procedure provided a check on the accuracy of



Figure 27. Fuselage Fatigue Test Setup.

**TABLE VI.  
FATIGUE LIFE SUMMARY**

<b>STRUCTURAL ELEMENTS</b>	<b>MAX SPECTRUM NET STRESS (hours)</b>	<b>STRESS CONC. FACTOR (<math>K_T</math>)</b>	<b>PREDICTED LIFE (hours)</b>	<b>FULL-SCALE TEST LIFE(1) (hours)</b>	<b>SERV. LIFE(1) (hours)</b>
Skin fillet, wing sta 33.875 wing outer panel, upper skin ("Thunderbird" fillet)	23,000	4.7	12,670	4,491	2,300
Skin fillet, wing sta 33.875 wing outer panel, lower skin ("Thunderbird" fillet)	23,000	4.7	4,460 (3)	5,508	2,530
Wing outer panel lower skin 51% spar bolt hole, wing canted sta 102	34,300	2.5 (2)	1,120	4,870	2,140
Wing center section lower skin	39,000	2.5	2,600	6,192	2,890 (T-Bird)
Wing center section to wing outer panel lower skin splice	25,000	3.4	30,000	9,116	No failures reported
Fuselage upper longeron, fus sta 305	25,500	3.2 (2)	91,000	12,224	2,580
Fuselage fitting, fus sta 222.5, wing-to-fuselage forward attach	-	-	No prediction made	13,227	No failures reported
Fuselage upper longeron, field break splice, fus sta 389	-	-	No prediction made	14,587	No failures reported

**NOTE:** 1. Where more than one failure occurred in service or in test, the life quoted is average.  
 2. Without consideration for fastener bearing.  
 3. C.R. Smith Method<sup>16</sup>.

loads and also was an aid in finding problem areas on the specimen or in the system when load "dumps" occurred. When major failures occurred, this load chart provided proof that failure did not result from an overload condition on the specimen.

**Inspection of Specimens**

Inspection procedure on the wing was set up on a regular schedule. Each 100 flights, a general visual inspection was made of all upper and lower surfaces paying particular attention to known critical areas. After each 500 flights, doors were removed and all accessible internal areas were inspected. Penetrant inspections, X-ray, eddy current, and ultrasonic inspection techniques were used, where applicable.

As the test program progressed and critical areas were identified, it became necessary to remove the bolts from both of the lower and upper surfaces of the wing and inspect the holes with both eddy current probes and a 30 power microscope. A visual check with the microscope was

used as the final check to determine the absence or presence and size of a crack.

**Summary of Fatigue Life Results**

The fatigue life of the critical items in the wing and fuselage are summarized in Table VI. The test lives are compared with service failures and calculated life by linear cumulative damage theory. The full-scale laboratory test failures occurred in approximately twice the hours to the average of the first failures in the fleet for wing failures. The actual ratio varies from 1.90 for lower skin fillet at wing station 33.875 ("Thunderbird" crack) to 1.56 for the upper skin fillet wing station 33.875. The 51 percent spar bolthole at canted station 102 had a 2.28 ratio of laboratory test life to service life while the wing center section lower skin had a ratio of 2.21. However, these laboratory failures include whatever service hours were on the specimen before test. When virgin wing specimens were tested, the test-to-service ratio approached 1.0. Refer to Table VII. For example, a lower skin fillet failure was produced on a "new"

**TABLE VII.**  
**FATIGUE LIFE COMPARISON, FULL-SCALE TEST SPECIMENS WITH**  
**AND WITHOUT PRIOR SERVICE HISTORY**

<b>STRUCTURAL ELEMENT</b>	<b>SERVICE LIFE (hours)</b>	<b>TEST LIFE INCL. SERV. LIFE (hours)</b>	<b>TEST LIFE EXCL. SERV. LIFE (hours)</b>	<b>TEST LIFE ON SPEC. W/O PRIOR SERVICE HISTORY (hours)</b>
Skin fillet, wing sta. 33.875, wing outer panel upper skin ("Thunderbird" fillet)	2,300	5,508	4,175	3,474
Skin fillet, wing sta. 33.875, wing outer panel lower skin ("Thunderbird" fillet)	2,530	5,508	4,175	2,105
Wing outer panel lower skin, 51% spar bolt hole, wing canted sta. 102	2,140	4,673	3,340	1,61
Wing center section lower skin	2,890	6,192	4,859	No test

(without service history) wing in 2,105 hours (see Figure 28). This is taken as an indication that the spectrum is indeed conservative, thus not a composite or average spectrum for which higher ratios of laboratory test to initial fleet failures would be expected, particularly for a large (over 1,000 aircraft) fleet exposed to a wide variety of missions. The calculated lives are less than the test lives in all cases except the compression fillet which life prediction depends upon the plasticity analysis, specifically upon the assumption of constant residual stress, to make the calculation. This indicates the conservatism of Miner's rule.

The fuselage upper longeron at fuselage station 305 required almost five times as many test hours to failure as service. This is interpreted in this case as failure to detect the early presence of the crack in the laboratory.

**Wing Station 33.875 Skin Fillet "Thunderbird" Crack**

The first serious structural fatigue failure to occur on the F-100 was the so called "Thunderbird" fillet. The cracks first appeared in the Thunderbird demonstration aircraft at as low as 1,000 hours. These cracks were reproduced in the laboratory full-scale tests at 5,500 hours.

**Upper Compression Skin Fillet**

The upper skin fillet cracks, as shown in Figure 6, occurred with greater frequency than in the lower skin fillet. This phenomena can be explained in terms of plasticity and residual tension stresses. The upper fillet crack progresses slowly and noncatastrophically, whereas the lower skin fillet crack generally extends at least to the first fastener hole at first detection.

The only other known documented case of compression loading fatigue cracking occurred in 1962 on the upper skin of a fighter wing, similar to the F-100 wing, during full-scale fatigue testing.<sup>19</sup> In this case, no wing load rever-

sals were included in the spectrum which was a typical fighter maneuver spectrum.

Various radius enlargements were attempted to obtain greater fatigue life in the fillet. The most generally satisfactory enlargement has been from the original 0.75-inch radius to 1.25 inches. The upper fillet crack appeared on the final full-scale wing fatigue specimen at 9,018 test hours. This crack was allowed to grow until it reached a size predetermined to be removable by remachining the fillet radius. The crack had grown from the original 0.11 inch to



**Figure 28. "Thunderbird" Fillet Crack Wing Outer Panel Lower Skin.**

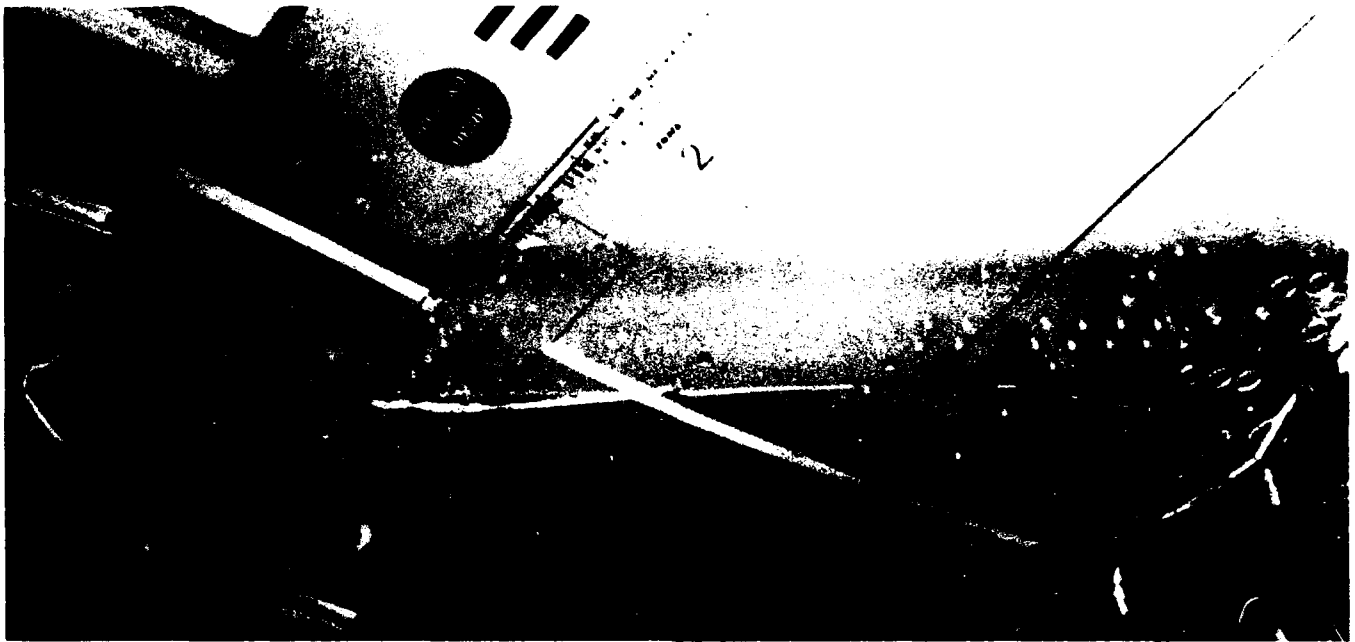


**Figure 29. Failure of Lower Skin at Wing Station 102, Left-Hand Wing Outer Panel.**

0.25 inch in a little less than 1,000 hours. The longest crack encountered in an upper skin fillet was approximately 1.50 inches and occurred in service on a Thunderbird aircraft.

#### **Lower Skin Fillet**

The longest crack observed in the tension skin occurred in service was approximately 8 inches, and no catastrophic failure has occurred in service or in the test laboratory. This has been attributed to the fact that the crack progresses along a general path of fasteners from the skin to the root rib flange. (See Figure 28.) The root rib flange

then provides an alternate load path for the wing bending loads in the skin.

During the investigation of various radius enlargements, the largest radius used was 2-1/4 inches. The crack, in this case, initiates at an adjacent fastener hole, rather than at the fillet. The progression of the crack was along a path which could have resulted in a full chord failure. That is, the crack progression was such that the root rib flange might not bridge across the fracture. Other methods for providing fail-safety were sought after this failure.

**Figure 30. Fracture Surface of Lower Skin at Wing Station 102, Left-Hand Wing Outer Panel, Test Specimen.**





**Figure 31. Fracture Surface of Lower Skin at Wing Station 102 Wing Outer Panel Service Aircraft.**



**Wing Canted Station 102 Lower Skin 51 Percent Spar Boltholes**

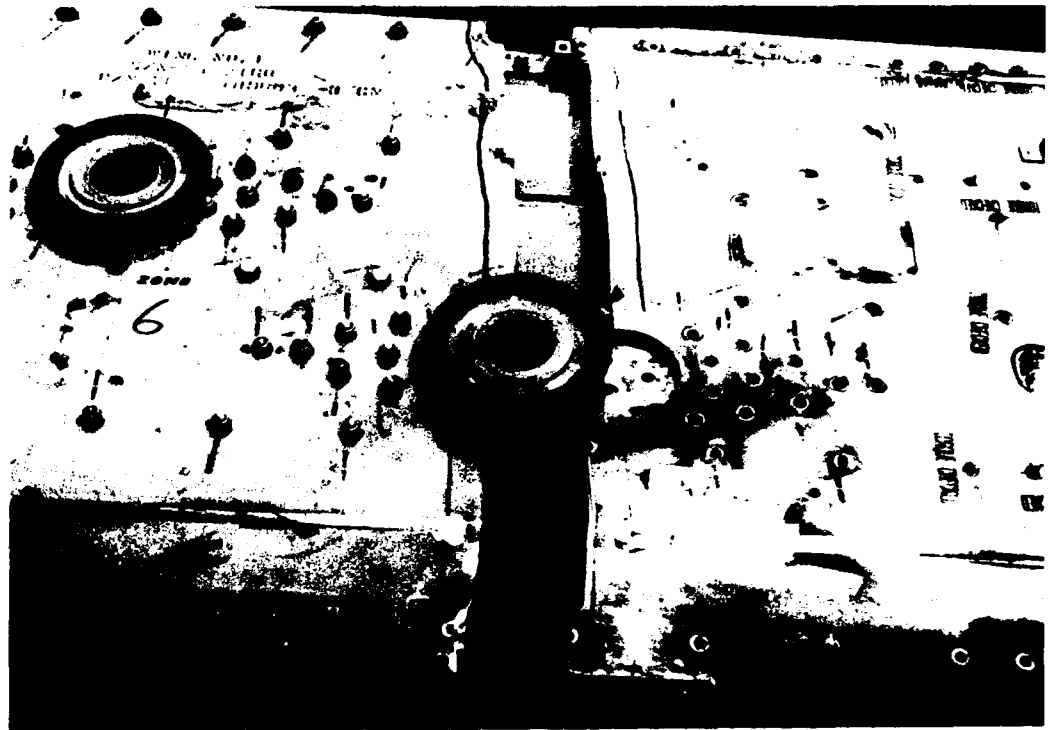
The full-scale wing fatigue test specimen failed in



**Figure 32. Failure of Wing Outer Panel Lower Skin Under Reinforcing Strap at Wing Station 102.**

4,674 hours total of test and service hours. The failure was completely across the wing structural box as shown in Figure 29. The fracture is shown in Figure 30, initiating at a fatigue crack which was approximately 0.75-inch long. The

**Figure 33. Failure of Wing Center Section Lower Skin.**



stress concentration at the fatigue crack was due to (1) standoff of the spar land to the basic skin thickness, (2) fastener bearing in hole, and (3) termination of spar cap.

A failure at the same location occurred in service at Nellis Air Force Base and the fracture is shown in Figure 31. Note the similarity of the laboratory-induced crack. Other fastener holes in the intermediate spars have similar stress concentrations. After reinforcing a full-scale wing test specimen with an external strap along the 51 percent spar, a full-chord wing failure occurred in 6,597 hours from a fastener hole under the strap. (See Figure 32). The bolthole involved is two holes inboard of the original wing canted station 102. Another full-chord laboratory failure occurred in 9,195 hours at the fourth bolthole outboard of the root rib along the 51 percent spar.

#### **Wing Center Section Lower Skins**

The test wing which had 1,333 hours of service life prior to test failed at 6,192 total hours test, plus service. (See Figure 33.) Only the outer of the two cover skins

failed shearing the common connecting bolts. The fracture surface showing the initiating fatigue crack is shown in Figure 34. The total crack length prior to rapid fracture was 0.90 inch.

A Thunderbird aircraft crashed during a demonstration flight at Laughlin Air Force Base, Del Rio, Texas. A subsequent investigation revealed a 1.50-inch fatigue crack in the WCS cover was the cause of the crash. The location of failure was at a bolthole, a few inches from the laboratory specimen failure.

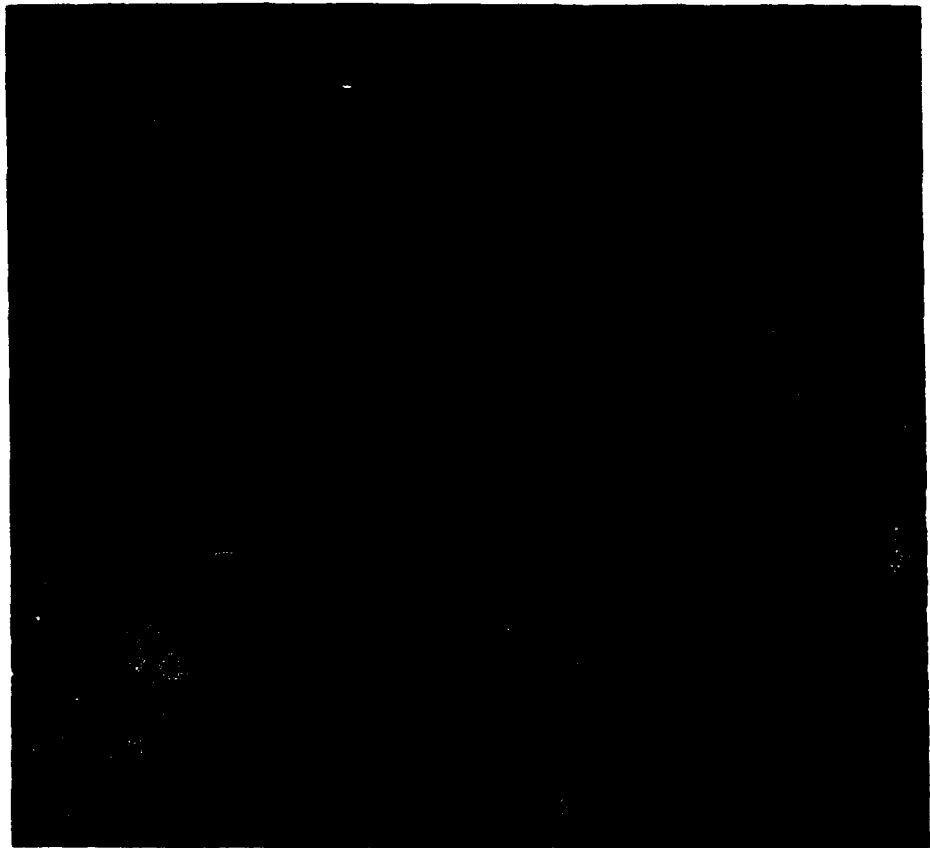
#### **Wing Outer Panel to Wing Center Section Lower Skin Splice**

The splice failed in fatigue of the outer panel skin in 9,275 hours as shown in Figure 35. Smaller fatigue cracks were found in the boltholes of the splice on two other specimens at 8,995 hours and 9,078 hours, showing consistency of fatigue life. These failures caused the redesign of the joint for Taper-Lok interference fit bolts.



**Figure 34. Failure of Wing Center Section Lower Skin.**

**Figure 35. Failure of Wing Outer Panel Lower Skin at Splice to Wing Center Section.**



**Upper Longeron, Fuselage Station 305.25**

The full-scale fuselage fatigue test specimen failed after 12,224 hours of simulated flight in both the upper

left- and right-hand longerons. (See Figure 36.) The left-hand crack stopped at the first fastener hole, whereas the right-hand crack progressed through 50 percent of the longeron area before stopping at a fastener hole. The

**Figure 36. Failure of Fuselage Upper Longeron at Fuselage Station 305.**





(A) Sawcut.



(B) First Crack Growth at 58 Percent Limit Load.



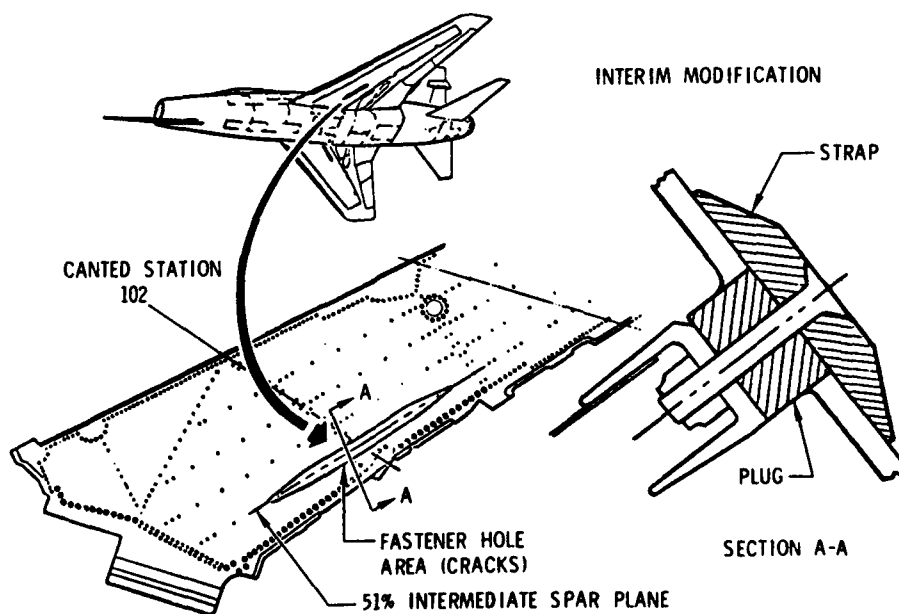
(C) Second Crack Growth at 130 Percent Limit Load.

Figure 37. "Thunderbird" Fillet Residual Test.

left-hand longeron crack, which had stopped at the first rivet, was machined out and a large radius provided; the longeron cracked again after 8,147 hours of additional testing.

The fleet has produced cracked longerons at 2,580 hours average, similar to those in the left-hand longeron of the test specimen.

Figure 38. Wing Modification - Wing Outer Panel Lower Skin, Canted Station 102.



## Residual Strength Tests

### Wing

A residual strength test was conducted on an F-100 wing to determine the effect of a crack in the forward lower surface fillet (tension) on the static strength of the wing. A saw cut, 1/4-inch long, was cut in both the right- and left-hand fillets. As the load was applied to the specimen, the crack jumped to the first bolthole (approximately 1-5/8 inches) on both the right- and left-hand fillet at 58 percent design limit load (DLL). At this time, an aluminum doubler was installed on the left-hand fillet. Load was again applied to the specimen. The crack on the right-hand fillet jumped to a second bolthole at 130 percent DLL. No change was noted in the left-hand fillet. The right-hand fillet was covered with a steel patch and load increased to 150 percent DLL, with no further failures. The crack progression on the right-hand fillet is shown in Figure 37.

### Fuselage

At the conclusion of 28,000 test hours on the fuselage, a residual strength test was conducted. Using the same flight load distribution as used in the fatigue test, the fuselage was loaded until catastrophic failure occurred. The fuselage withstood 231 percent of the maximum load applied during the fatigue test or 112 percent of the design ultimate load on the fuselage.

Prior to catastrophic failure, cracks in the upper shoulder skin occurred. In all instances, these originated in areas that had previous fatigue damage. Final failure occurred when the forward wing-to-fuselage attachment fittings fractured.

## FLEET MODIFICATIONS

Because of the service failures and full-scale test failures short of the desired life goal, modifications were designed; many were installed in service aircraft, and all were tested in the laboratory.

### Interim Modifications

Several designs were attempted to solve the cracking of the upper and lower skin fillet at wing station 33.875, "Thunderbird" fillet. The designs included enlarged fillets to reduce the stress concentration and doublers to reduce the net stress level. At least two fillet radius enlargement designs were applied to a limited number of fleet aircraft. Although no service failures have yet been recorded, all of these designs failed in full-scale test short of the desired life goal.

Because of the catastrophic failure at the 51 percent spar bolt hole at wing canted station 102 in service and test, an aluminum strap reinforcement (Figure 38) was installed in all fleet aircraft. Subsequent full-scale tests indicated that the strap was incapable of preventing full-chord failure of the wing skin from cracked bolt holes. (See Figure 32.) Furthermore, other bolt holes unprotected by the strap proved to have insufficient fatigue life to attain the total life goal of 7,000 hours.

### Final Modifications

A more comprehensive modification design was prepared for installation throughout the fleet and for final full-scale testing.

WING OUTER PANEL MODIFICATION  
(EXPLODED VIEW LH WING INVERTED)

Figure 39. Wing Outer Panel Modification.

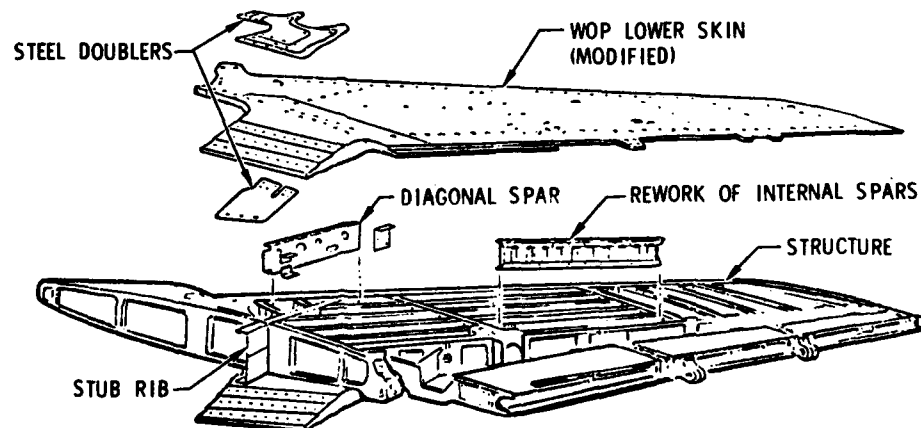
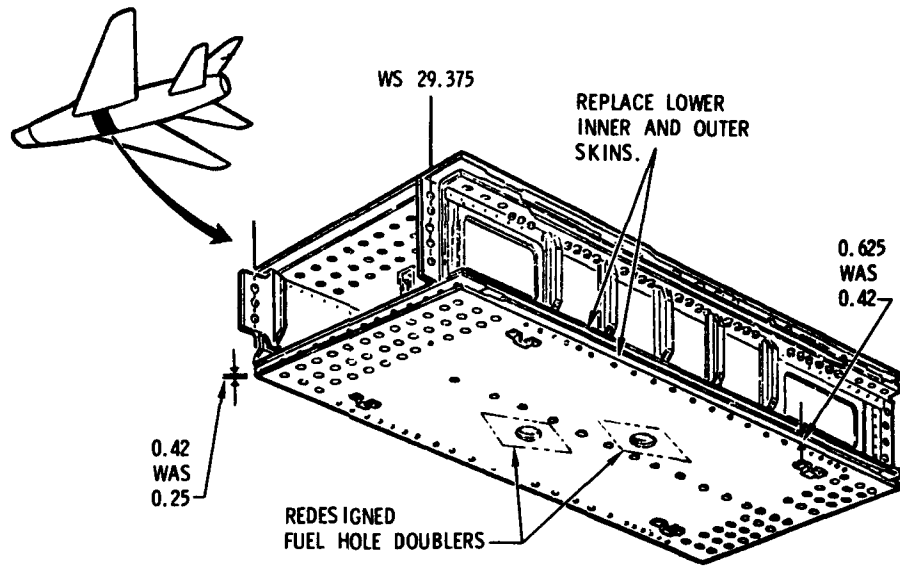


**Figure 40. Wing Center Section Modification.**



*Wing Outer Panel*

A new lower skin was provided which incorporated several changes:

1. A 0.188-inch thickness increase in the root rib area around the "Thunderbird" fillet
2. Wider spar lands and more generous runouts
3. Shot peening over the entire surface

Other changes to the wing assembly include heavy machined diagonal spars, replacing built-up sheet metal

spars as shown in Figure 39. Also, intermediate spar caps were machined to taper the cross section near their ends to reduce the effect of abrupt termination.

*Wing Center Section*

Following the failure of the wing center section in the laboratory and the Thunderbird demonstration failure, a new lower cover design was installed on wing center sections throughout the fleet. The two skins separated by spacer bars were increased in thickness at the forward beam from 0.25 to 0.44 inch and from 0.40 to 0.625 inch at the rear beam. (See Figure 40.) The doublers around the fuel cutouts were also redesigned with more taper to alleviate

**Figure 41. Fuselage Modifications.**

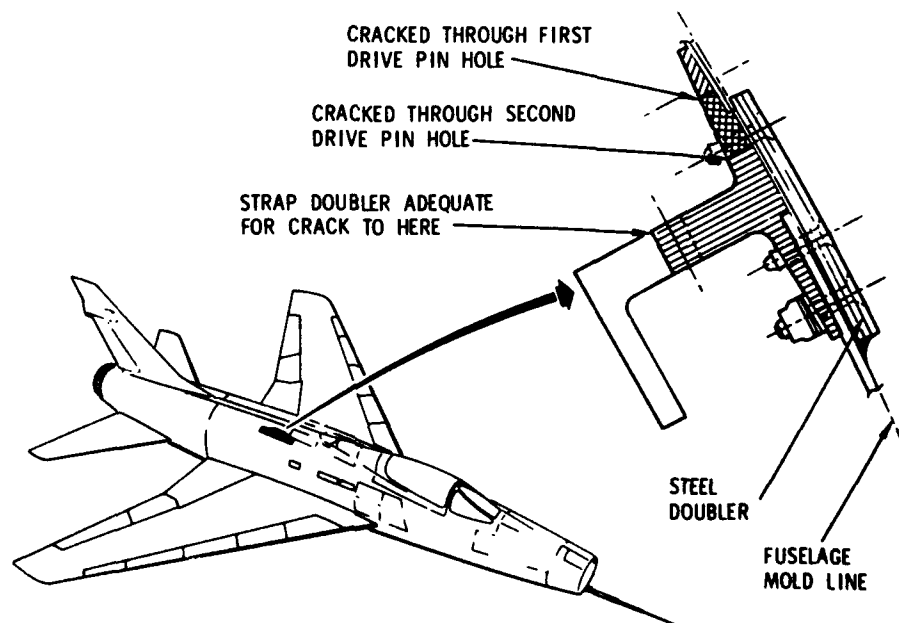


**TABLE VIII.**  
**SUMMARY OF FULL-SCALE FATIGUE TEST RESULTS COMPARING**  
**MODIFICATIONS TO UNMODIFIED STRUCTURE**

STRUCTURAL ELEMENT	SPECIMENS	AVERAGE HOURS TO FAILURE	HOURS WITH NO FAILURE
Skin fillet, wing station 33.875, wing outer panel upper skin ("Thunderbird" fillet)			
Unmodified	1	4,491	
Modified radius	1	9,018	
Remodified radius	1	6,012	
Skin fillet, wing station 33.875, wing outer panel lower skin ("Thunderbird" fillet)			
Unmodified	2	3,807	
Interim mod radius	2	5,644	
With aluminum doubler	2	7,244	
Final radius modifier with steel doubler	1		16,000
Wing outer panel lower skin bolt holes intermediate and diagonal spar			
Unmodified	3	6,370	
Modified	1	11,022	
Lower skin wing center section	1	6,192	
Modified	1	13,026	
Wing center section to wing outer panel lower skin splice joint			
Unmodified	2	9,156	
Modified	1		16,000

termination stresses. The new wing center sections have been installed throughout the fleet.

*Wing Center Section to Wing Outer Panel Splice*

The conventional bolts in the splice were replaced with interference fit Taper-Lok bolts of the same nominal size. Element tests, as previously discussed, had shown a life improvement of over 2.0.

*Fuselage Upper Longeron, Fuselage Station 305 to 314.*

A laminated steel doubler was installed externally as shown in Figure 41. This doubler was designed to replace approximately one-half the area of the original longeron and, in residual strength tests, demonstrated sufficient static strength to do so. Modification straps are now being released to the fleet for installation.

*Modification Test Summary*

Full-scale fatigue tests were concluded in November 1969 on production articles of the modified wing center section and both left- and right-hand wing outer panels. The test results are shown in Table VIII, and contrasted with average test lives of similar unmodified structure. A total of 16,000 hours was applied to the modified wing. Fatigue cracks were first found in the wing outer panel lower skin in

the region of the diagonal spar at 11,000 hours. (See Figure 42.) Similarly, fatigue cracks were found in the wing center section lower skins at 13,000 hours. The upper skin fillet modified by enlarging the fillet radius on the existing skin cracked at 9,018 hours and again at 15,030 hours, after removing the first crack with a deeper fillet radius cut.

The lower skin fillet has shown no evidence of cracking at 16,000 hours and the splice joint with Taper-Lok fasteners is crack-free.

The fuselage was subjected to a total of 28,000 hours of testing which included 16,000 hours on the longeron strap repair.

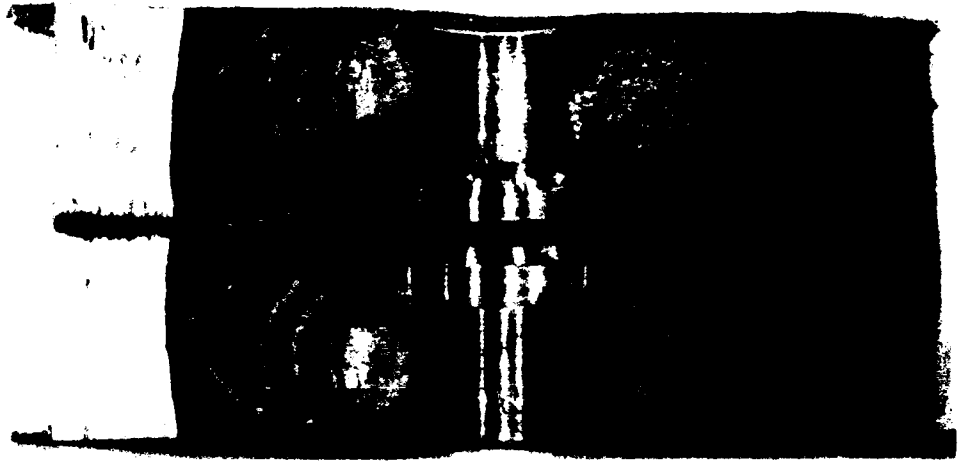
**PROGRAM RESULTS**

1. Conservative loading spectra were derived from flight load statistical data.
2. Full-scale tests on unmodified structure produced laboratory failures at approximately twice the fatigue life as the first failures at the same location in fleet aircraft.
3. Four critical cross sections of the wing and one in the fuselage were determined from the tests and analysis.

## LOWER SKIN

### WING NO. 5 RH DIAGONAL SPAR

**Figure 42. Lower Skin Crack, Modified Wing Specimen No. 5.**



### HOLE NO. 7 CORED OUT

4. Modifications were designed for these critical failure locations. The modifications were designed to attain 4,000 hours additional life with a scatter factor of 4.0 or 16,000 hours.

5. The modifications were tested and attained 11,000 hours on the wing outer panel, 13,000 hours on the wing center section, and 15,776 hours on the fuselage longeron strap.

### CONCLUSIONS

The principles embodied in the ASIP specifications, MIL-A-8866 as supplemented by ASD TR 66-57,<sup>20</sup> can be successfully applied to older aircraft to extend their useful service life.

With one exception, the "Thunderbird" fillet, fleet failures were preceded by full-scale test failures despite the

fact that the tests were initiated fully 12 years after the aircraft first became operational and also despite the lead-the-fleet nature of the Thunderbird demonstration aircraft.

The foregoing truly demonstrates the value of structural integrity programs and full-scale fatigue testing. For the future, individual aircraft usage programs, as presently conceived in ASD TR 66-57, would further benefit the reliability of operating large fleets of fighter aircraft through protracted service lives.

### ACKNOWLEDGEMENTS

The authors express thanks to Messrs. John Weber and Carmelo Guadagnino of SMAMA engineering for their guidance throughout the program, and, at North American Rockwell, to M. McGahey for loading spectra, J. Phillips for calculations, and W. O'Brien for project direction.

### REFERENCES

1. *Fatigue Analysis and Element Test Program. Phase 2 of F-100 ASIP Program*, NA-66-870, Vol. I, North American Aviation Corp., Los Angeles (1966).
2. *F-100 Life Goal Study and Modification Review of F-100 ASIP Program*, NA-68-131, North American Aviation Corp., Los Angeles (1968).
3. *Aerospace Vehicles and Flying Hours*, PA-69-4, Vol. I, Department of the Air Force, Washington, D.C. (1967).



#### REFERENCES (Continued)

4. E.C. Nauman, *Evaluation of the Influence of Load Randomization and of Ground-Air-Ground Cycles on Fatigue Life*, NASA-TN-D-1584, National Aeronautics and Space Administration, Washington, D.C. (1964).
5. *Phase 1 Lead-the-Fleet Flying Program. Final Report F-100 Structural Integrity Program*, NA-66-1213, North American Aviation Corp., Los Angeles (1966).
6. *Appendix C, Peak Cycle Program Description*, NA-66-1213, North American Aviation Corp., Los Angeles (1966).
7. *F-100 ASIP Special Report Covering Southeast Asia Usage*, NA-TFD-67-596, North American Aviation Corp., Los Angeles (1967).
8. *Average Loading Spectrum for Composite Usage of the F-100 Aircraft*, NA-68-341, North American Aviation Corp., Los Angeles (1968).
9. *First Interim Report - Analysis of F-100 VGH Data for the Period Ending December 31, 1968*, NA-69-641, North American Aviation Corp., Los Angeles (1969).
10. *F-100 Thunderbird Aircraft Fatigue Analysis Study Based on VGH Data*, NA-TFD-69-79, North American Aviation Corp., Los Angeles (1969).
11. *F-100 Yankee No. 1 Flight Program Store Ejection Flight and Load Analysis*, NA-69-52, North American Aviation Corp., Los Angeles (1969).
12. E. Titus, *Maneuver Load Data from F-100 Operations*, ASD-TDR-61-683, Air Force Flight Dynamics Laboratory, Wright-Patterson AFB, Ohio (1961).
13. R.M. Ault, G.E. Fitch, and J.T. Phillips, *Computer Program for Predicting Fatigue Life of Aircraft Structures Using Miner's Rule*, NA-66-334, North American Aviation Corp., Los Angeles (1966).
14. *Fatigue Analysis and Element Test Program. Phase 2 of F-100 ASIP Program*, NA-66-870, Vol. II, North American Aviation Corp., Los Angeles (1966).
15. *F-86F Structural Integrity Program. Phase 2 Fatigue Test Program Final Report*, NA-63-844, North American Aviation Corp., Los Angeles (1965).
16. C.R. Smith, *A Method for Estimating the Fatigue Life of 7075-T6 Aluminum Alloy Aircraft Structures*, NAEC-ASL-1096, Naval Air Engineering Center, Philadelphia, Pennsylvania (1965).
17. C.L. Davis, *Least Square Fit of Fatigue Data*, NA-65-906, North American Aviation Corp., Los Angeles (1965).
18. G.E. Fitch, *Crack Propagation of 7075-T6 Aluminum on the F-100 Airframe*, NA-69-346, North American Aviation Corp., Los Angeles (1969).
19. E.D. Bouchard, *A Fatigue Problem Encountered on the Upper Surface Compression Wing Skin During Repeated Load Testing on a High Performance Fighter Aircraft*, McDonnell Aircraft Corp., St. Louis, Missouri (1962).
20. *Air Force Structural Integrity Program Requirements*, ASD-TR-66-57, Aeronautical Systems Division, Wright-Patterson AFB, Ohio (1968).

# THE B-52G-H WING CYCLIC TEST PROGRAM

by

David F. Bryan

The Boeing Company  
Wichita Division

## INTRODUCTION

In 1961, the Strategic Air Command (SAC) estimates of projected usage for the B-52G-H fleet revealed a requirement for structural service life that significantly exceeded previous estimates. This requirement resulted in the design and installation of the ECP 1050 wing modification on all B-52G-H airplanes.

The B-52G-H ECP 1050 wing was designed to a specific service life requirement. A design usage of four times the SAC projected usage was used in the preliminary design stages to establish design stress levels. An extensive program of fatigue analysis and testing was conducted in connection with the ECP 1050 modification. This program was developed along the lines of Reference 1; the current Air Force Structural Integrity Program (ASIP) requirements

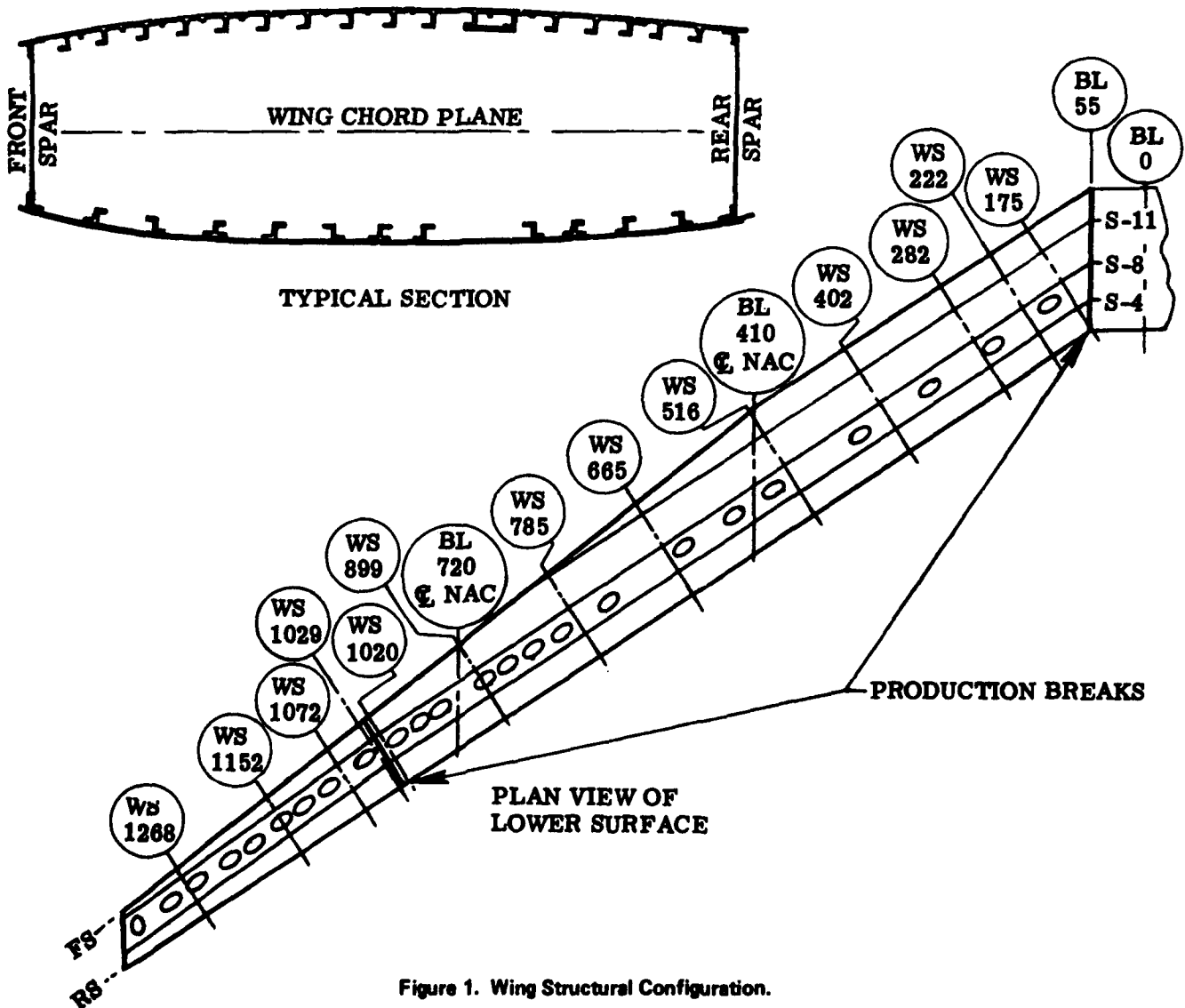


Figure 1. Wing Structural Configuration.

for military aircraft. The major elements of the B-52G-H structural service life program were:

- Preliminary (Design) Fatigue Analysis
- Preproduction Component Fatigue Tests
- Full-Scale Wing Cyclic Test
- Full-Scale Body and Empennage Cyclic Test
- Airplane Dynamic Response Tests (Flight Tests)
- Fleet Loads Recording (VGH)
- Periodic Updating Fatigue Analyses
- Fatigue Parametric Studies
- Fatigue Damage Monitoring on Individual Fleet Airplanes.

All elements of this program are complete with the exception of fatigue damage monitoring which, presumably, will continue as long as the B-52G-H fleet remains in service. The primary emphasis of this paper will be a discussion of the full-scale cyclic test of the B-52G-H wing.

#### FULL-SCALE WING CYCLIC TEST

The attainment of the service life objectives was assured during the design phase through control of the operating stress levels and the use of proven detail design practices. To verify that these objectives indeed had been met (and to provide a basis for timely incorporation of future modifications if they had not) the Air Force required a full-scale cyclic test. The objectives of the wing cyclic test were to:

1. Evaluate the fatigue life of primary structure.
2. Identify the locations of structural details where design improvements could be made to increase airplane service life by incorporation of "local" modifications.
3. Establish fleet inspection procedures and techniques for those structural locations found to be critical on the cyclic test article.
4. Investigate the crack propagation and fail-safe characteristics of the primary wing structure.

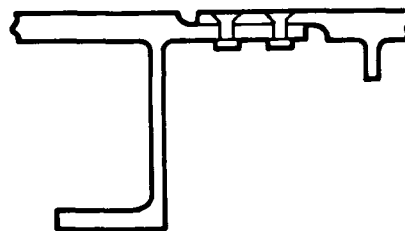
#### Test Specimen

The test specimen was assembled from B-52H airplane sections taken directly from the production lines. It consisted of a structurally complete wing, including secondary structure, and the forward, mid body, and aft body sections. The cyclic test wing specimen was equivalent to the tenth production article.

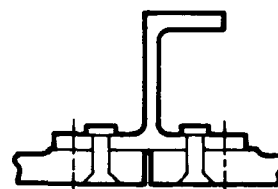
The B-52 ECP 1050 wing is a full cantilever, semi-monocoque, cellular beam tapering in planform and depth. The primary beam structure is a two-spar, tapered box beam with spanwise stiffeners and chordwise ribs at approxi-

mately 30-inch spacing as shown in Figure 1. The upper surface of the wing center section and the two upper surface inboard wing panels consist of integrally stiffened skin panels machined from extrusions. All other wing skins are machined from plate and are stiffened with "Z" sections. "J" sections are used for spanwise splices.

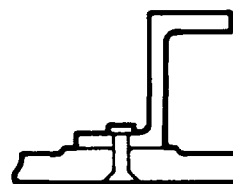
Some typical structural details are shown in Figure 2. The only chordwise splices in the primary structure occur at BL 55 and WS 1025. The structural materials used in



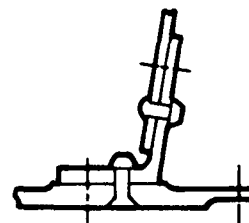
UPPER SURFACE SPANWISE SPLICE AND INTEGRAL STIFFENER



LOWER SURFACE SPANWISE SPLICE



LOWER SURFACE INTERMEDIATE STIFFENER



REAR SPAR LOWER CHORD AND SKIN ATTACHMENT

Figure 2. Typical Wing Structural Details.

**TABLE I**  
**ECP 1050 WING PRIMARY STRUCTURE MATERIALS**

LOCATION		CENTER SECTION AND INBOARD WING (W.S. 1025 INBD.)	OUTBOARD WING (W.S. 1025 OUTBD.)
UPPER SURFACE	SKIN	7075-T6 EXTR.	7178-T6 SHEET
	STIFFENERS	7075-T6 EXTR.	7178-T6 EXTR.
	FRONT SPAR CHORD	7178-T6 EXTR.	7178-T6 EXTR.
	REAR SPAR CHORD	7075-T6 EXTR.	7178-T6 EXTR.
LOWER SURFACE	SKIN	2024-T351 PLATE	2024-T351 PLATE
	STIFFENERS	7075-T6 EXTR.	7075-T6 EXTR.
	FRONT SPAR CHORD	7075-T6 EXTR.	7178-T6 EXTR.
	REAR SPAR CHORD	7075-T6 EXTR.	{ 7075-T6 to W.S. 1167 7178-T6 W.S.1167 OUTBD
FRONT SPAR WEB		7178-T6 PLATE	7178-T6 PLATE
REAR SPAR WEB		7178-T6 PLATE	7178-T6 PLATE

Figure 3a. Extended High Altitude Mission.

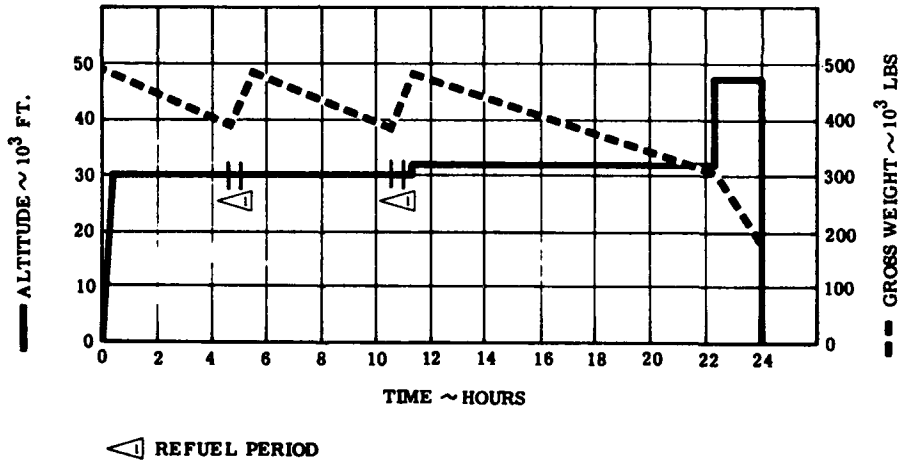


Figure 3b. Combat Crew Training Mission .

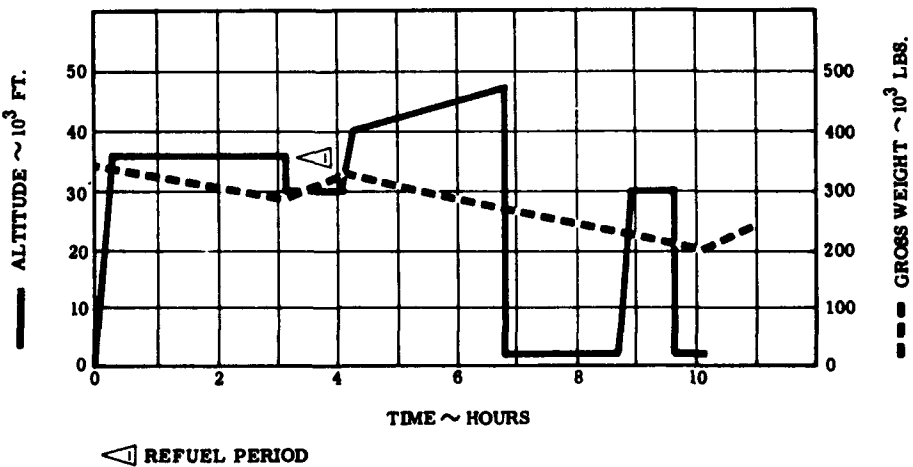
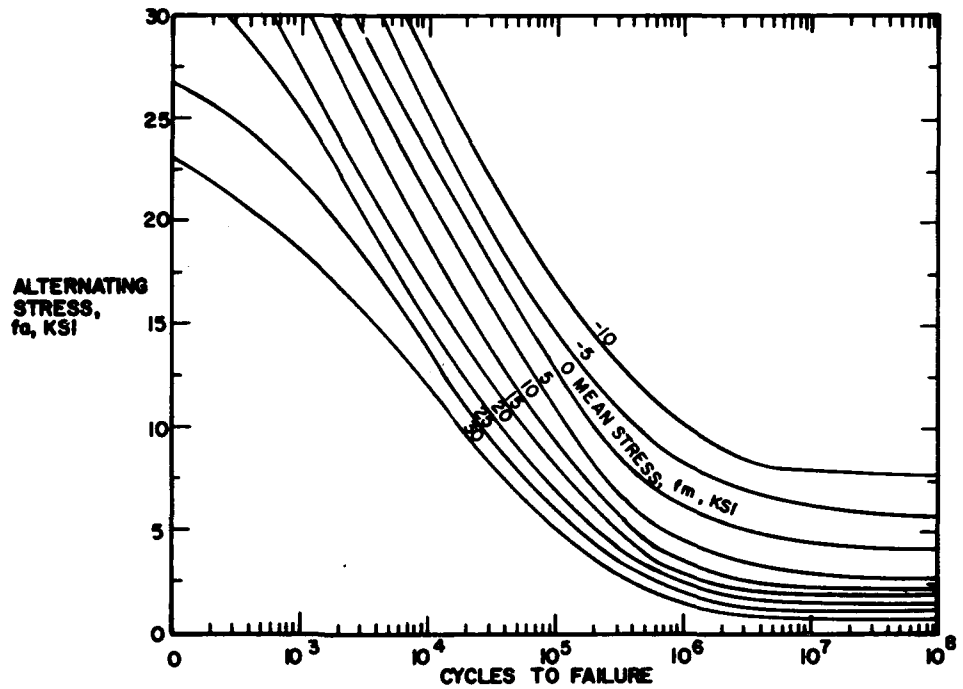


Figure 4. Stress Endurance Curves - Wing Lower Surface.



the various elements of the primary structure are given in Table 1. The secondary structure is cantilevered from the main beam box and includes the leading and trailing edge assemblies and the support structure for the flaps, spoilers, and nacelles.

**Preliminary Fatigue Analysis**

The first step in determining the cyclic test loads was to perform a fatigue analysis of the final structural configuration based upon the design usage and mission profiles furnished by the Air Force. The design usage consisted

of a mixture of Extended High Altitude (EHA) missions and Combat Crew Training (CCT) missions. The mission profiles are shown in Figures 3a and 3b. For analysis purposes, each mission profile was divided into approximately 20 phases with discrete values of gross weight, speed, and altitude.

Thirteen spanwise locations were selected for analysis. These locations are identified by wing station in Figure 1. Fatigue damage calculations were made at each analysis location for each design mission profile. The Linear Cumulative Damage Theory (Miner/Palmgren method) was used.

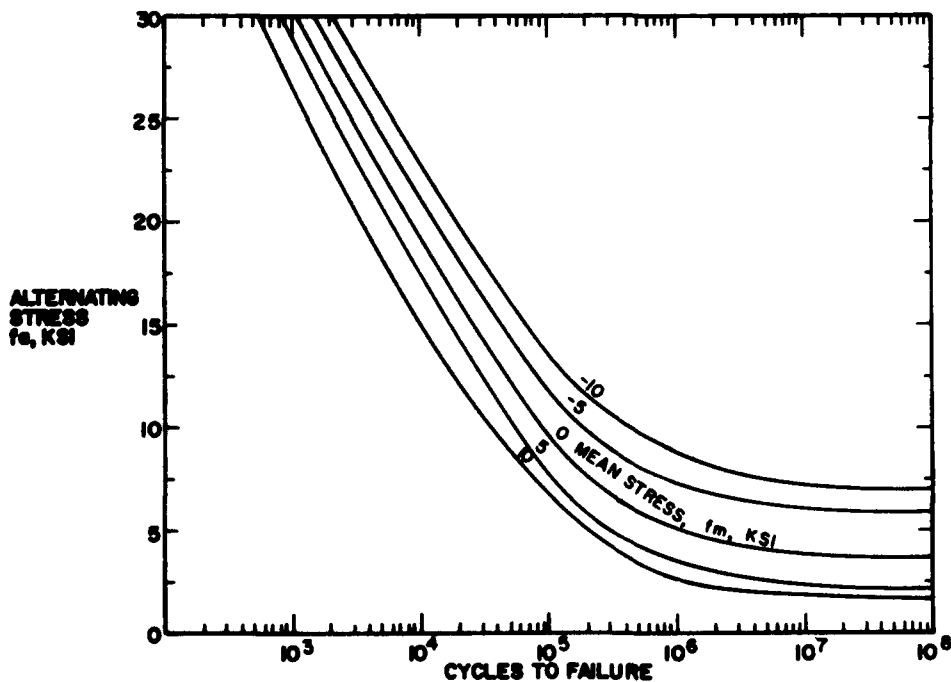
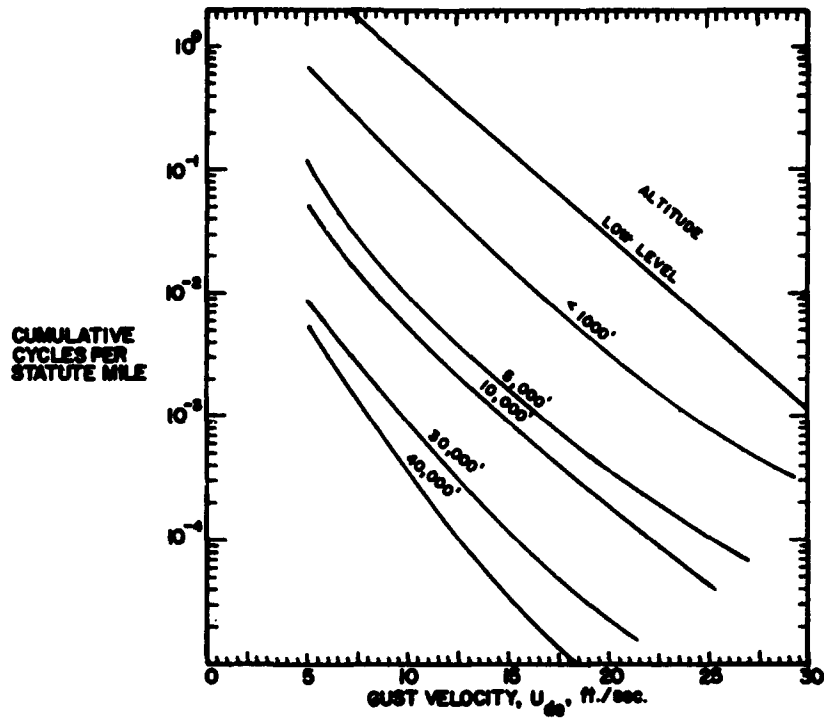


Figure 5. Stress Endurance Curves - Wing Upper Surface.

Figure 6. Atmospheric Gust Load Environment.



Stress excursions produced by the ground-air-ground cycle were included in the damage calculations.

The stress-endurance (S-N) curves for the lower and upper wing surfaces are shown in Figures 4 and 5, respectively.

These curves were derived using results from the fatigue tests of component panels representative of the wing structure. It was the intent of the design philosophy to configure structural discontinuities, such as splices, cutouts, and fitting attachments, to have a fatigue life at least as

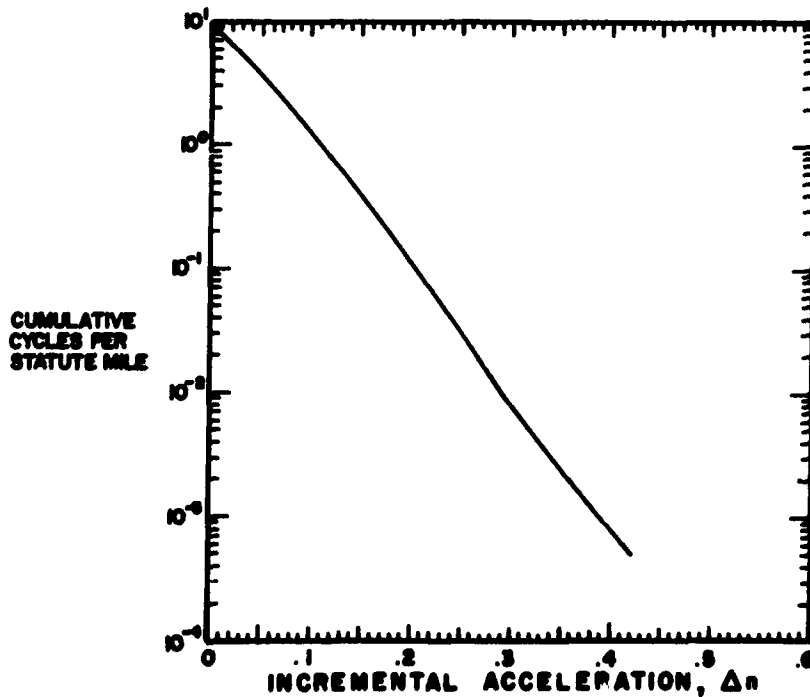


Figure 7. Refueling Load Environment.

good as the basic wing structure. Therefore, it was decided that the same set of S-N curves would be applicable for all lower surface analysis stations. The same approach was used for the upper surface analysis stations except that a different set of S-N curves was used.

The gust and maneuver load environment was defined in terms of derived equivalent velocity ( $U_{de}$ ). Examples of the gust curves are shown in Figure 6. The refueling load environment, Figure 7, was defined in terms of incremental load factor at the airplane center of gravity ( $\Delta n$ ). Dynamic response at the analysis stations was estimated using strain gage data collected on flight tests of earlier B-52 models. Power spectral density analysis methods were employed to convert this data for use on the ECP 1050 structural configuration.

The preliminary analysis provided the total stress experience and fatigue damage at each analysis station for each design mission profile. Examples of the fatigue analysis output for the two design mission profiles are shown in Figure 8.

A detailed discussion of the preliminary analysis is contained in Reference 2.

#### Development of Cyclic Test Loads Spectra

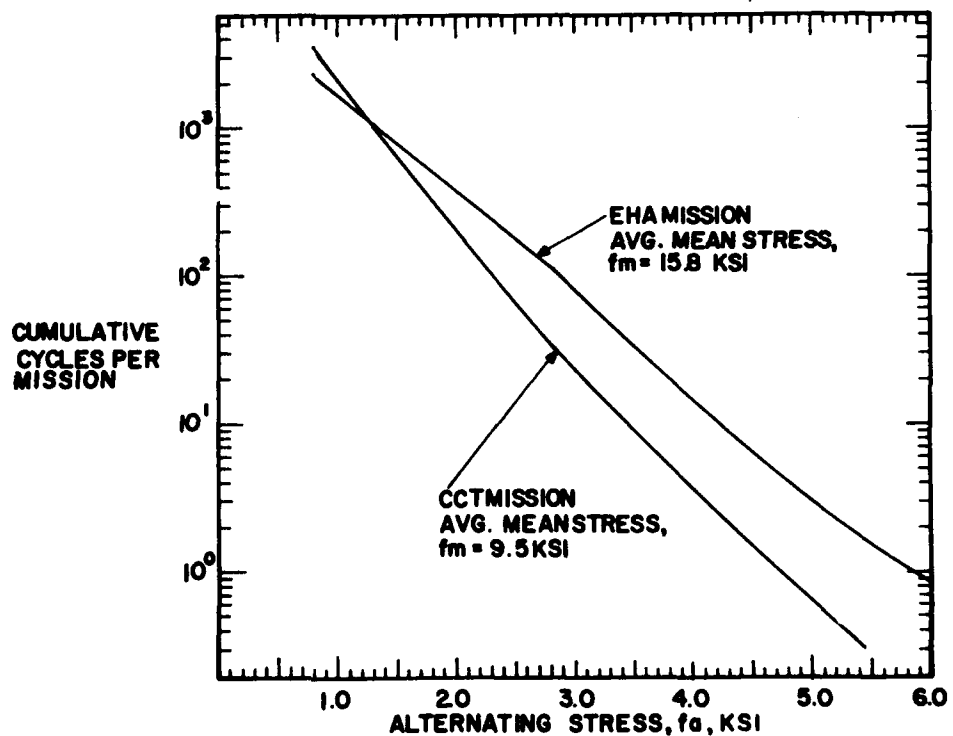
The cyclic test loads were derived to match the preliminary fatigue analysis damage and stress experience as close as possible and still keep testing time within practical

limits. Two cyclic test loading spectra were developed, one for the CCT mission and one for the EHA mission. Cyclic test stress spectra were developed for each analysis station. A study of the analysis fatigue damage and stress experience at the most critical location indicated that the following types of loading conditions would produce representative stress experience:

1. A ground condition producing the maximum load experienced during taxi
2. A spectrum of four alternating stress levels applied about an average one "g" stress to represent gust and maneuver loads
3. Varying engine thrust loads applied as they would occur during taxi, takeoff, cruise, and flaps down conditions
4. Representative flap loads for takeoff and landing conditions
5. Simulation of chordwise bending for cruise conditions
6. A 90 percent limit load applied periodically to represent relatively rare high load encounters.

A reference phase was selected for each mission to establish a single one "g" loading condition about which the alternating stresses could be applied. This selection was

Figure 8. Typical Fatigue Analysis Output - WS 785 Lower.



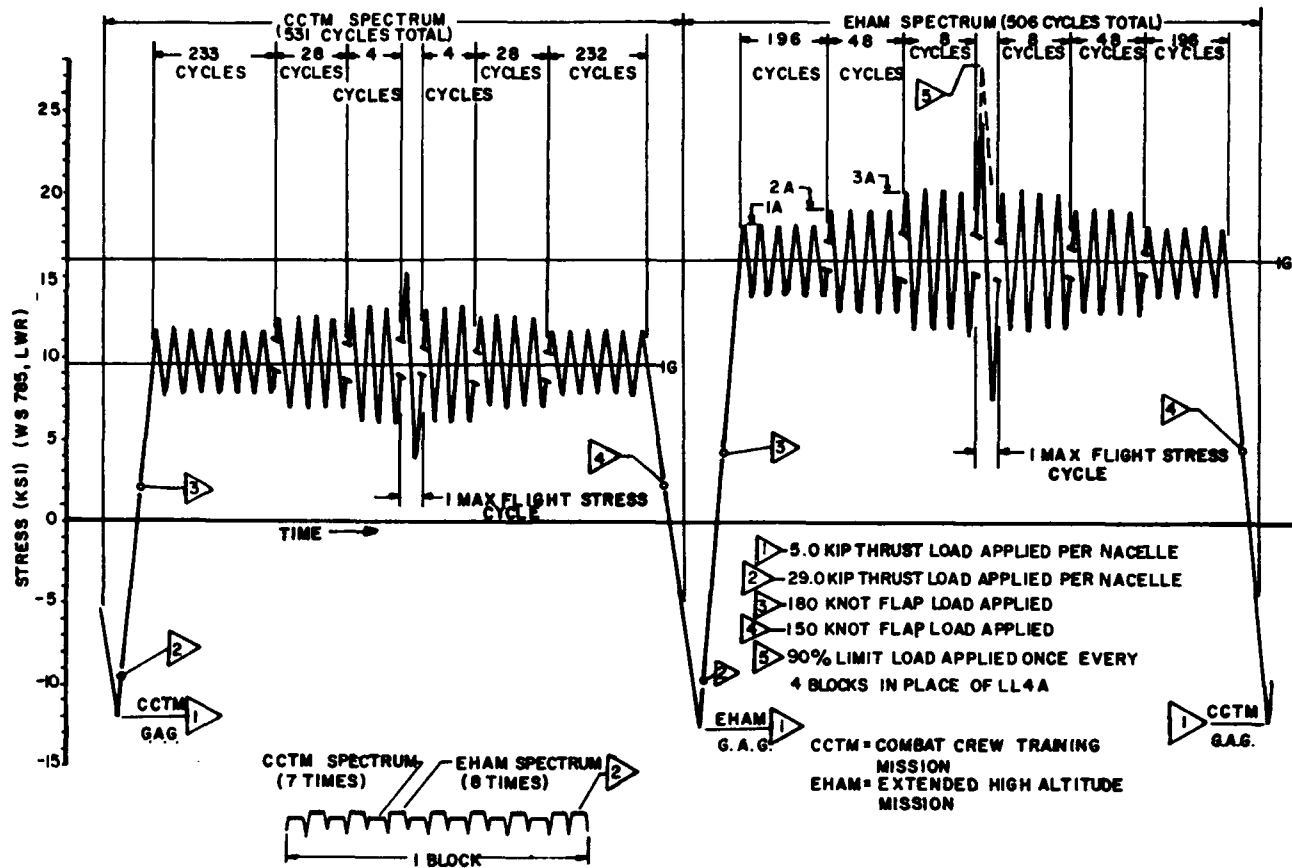


Figure 9. Cyclic Test Load Spectra at Typical Wing Station - EHA and CCT Missions.

based on averages of gross weight, speed, and altitude weighted according to gust damage.

The ground-air-ground (GAG) and maximum stress per flight cycle damage was accounted for inherently since these stress cycles were actually reproduced in the spectrum. The remaining mission damage (that due to gust and maneuver loads) was proportioned between three levels of alternating stress. The stress levels and number of occurrences at each stress level were selected to correspond with that derived in the fatigue analysis. The cyclic test stress spectrum for a typical analysis station is shown in Figure 9. Similar stress spectra were developed for each analysis station.

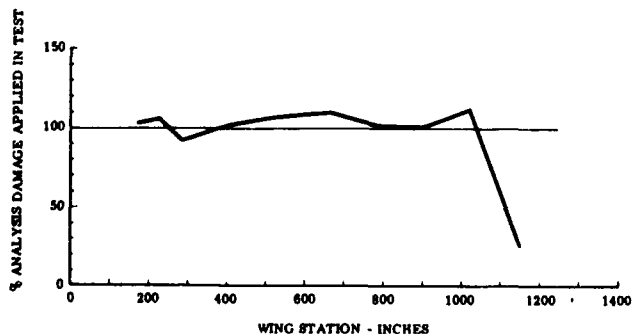


Figure 10. Comparison of Analysis and Test Damage.

A digital computer program was written to provide spanwise moment distributions and point loads at discrete spanwise locations along the front and rear spars of the wing. The object was to reproduce the desired stress spectrum at analysis locations as close as possible. The plot in Figure 10 shows the percent of analysis damage actually applied in cyclic test versus wing station.

See Reference 3 for more specific details concerning cyclic test load development.

### Test Setup

The test article was surrounded by steel towers, trusses, and beams to provide support for the test article and loading systems. An overall view of the test setup is shown in Figure 11. All loading was applied through direct cable or cable/sheave systems connected to servo controlled hydraulic rams. Seven individually controlled load systems were used on each wing for applying vertical loads. Two load systems for applying thrust and vertical loads were located at each engine nacelle. The location of the loading systems are shown in Figure 12.

A schematic diagram of the different types of loading systems are shown in Figure 13. The double throw systems for the  $W_1$ ,  $W_2$ , and  $W_3$  locations were required because of the large outboard wing deflections. The method of load block attachment to the wing surface is



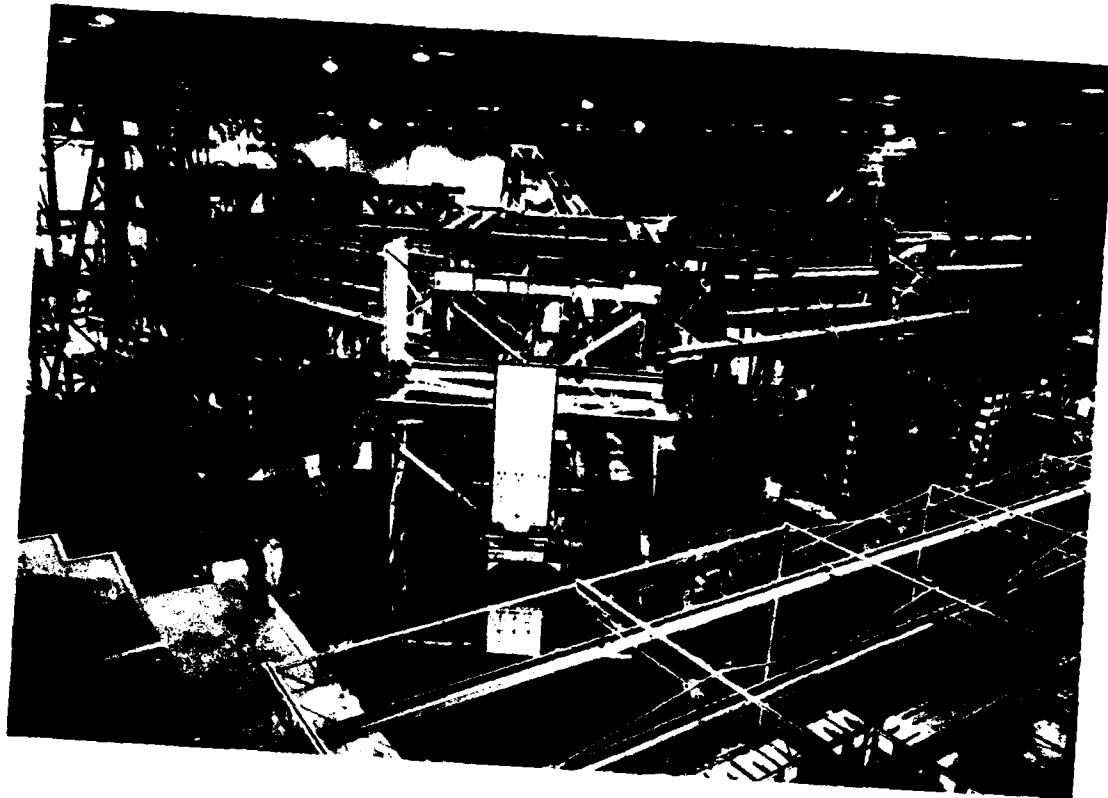


Figure 11. Front View of Cyclic Test Setup.

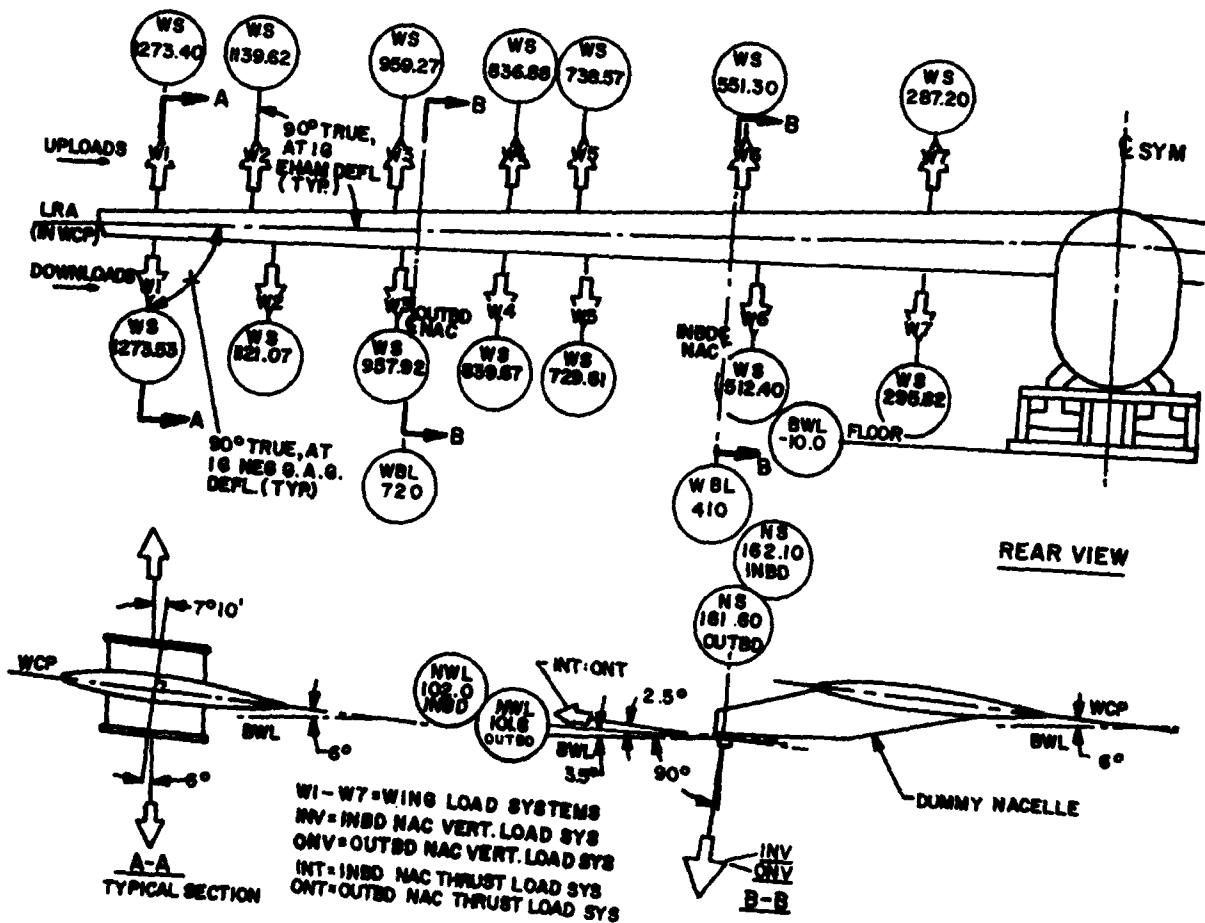
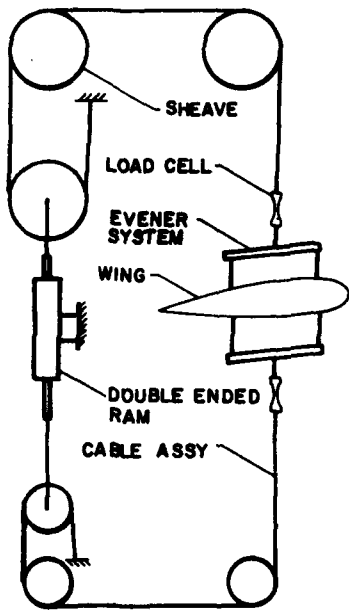
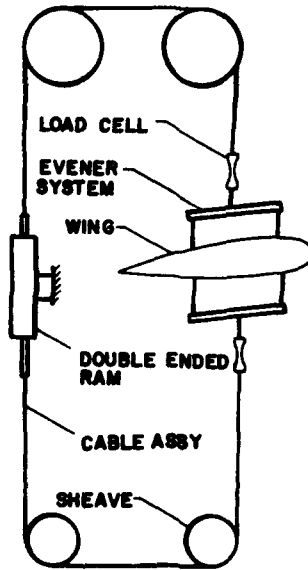


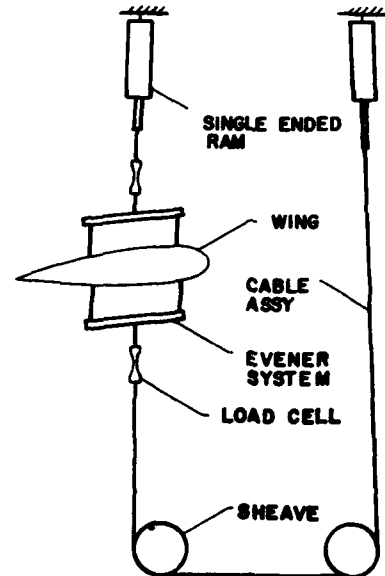
Figure 12. Wing and Nacelle Load Pull-Off Points.



**DOUBLE THROW SYSTEM**  
W1, W2 & W3

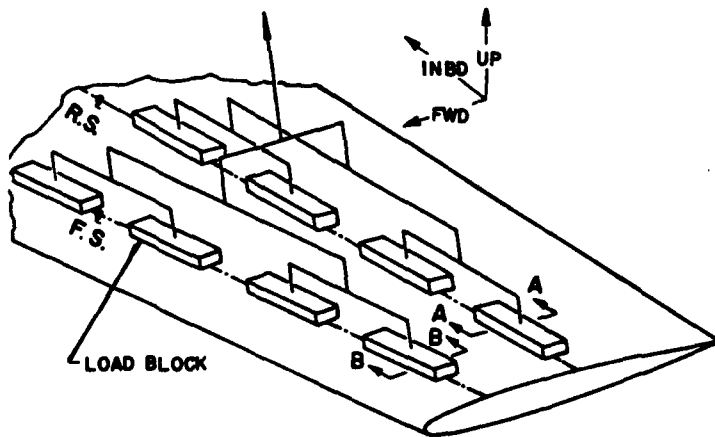


**SINGLE THROW SYSTEM**  
W4 & W5

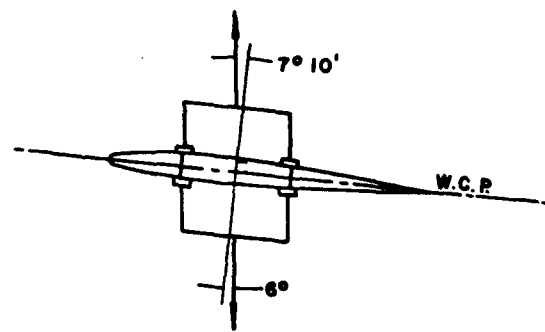


**DIRECT & SINGLE THROW SYSTEM**  
W6 & W7

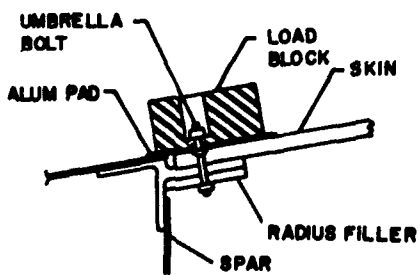
Figure 13. Typical Wing Loading Systems.



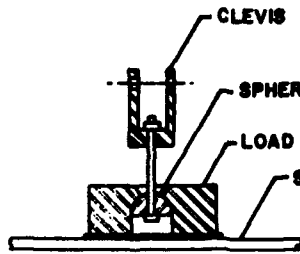
**TYPICAL WING LOADING - EVENER SYSTEM**  
LOWER SURFACE SIMILAR



**WING CROSS SECTION,**  
VIEW NORMAL TO L.R.A.



**TYPICAL LOAD BLOCK ATTACHMENT**  
A - A

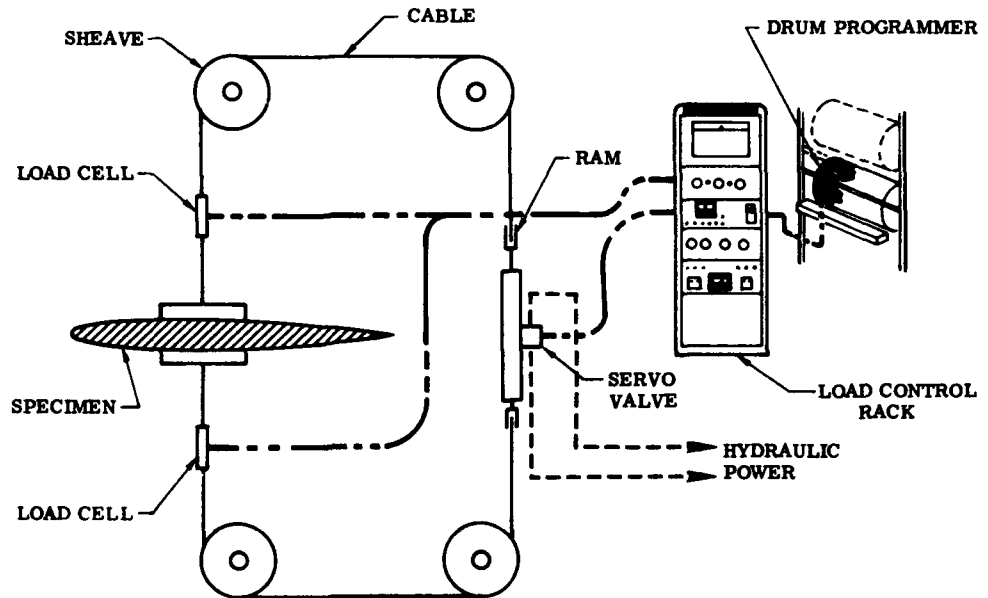


**TYPICAL PULL-OFF**  
B - B

L. R. A. = LOAD REF AXIS  
▨ - STEEL

Figure 14. Typical Wing Loading - Evener System.

Figure 15. Typical Load Control System.



shown in Figure 14. Separate systems for applying inboard and outboard flap loads were used.

Twenty-five automatic electrical hydraulic closed loop servo systems were used to apply loads to the wing. A schematic diagram of the servo control is shown in Figure 15. Loading rates and phasing between the different load-

ing systems were closely controlled to keep the test article balanced and to apply loads smoothly at all times.

Fail-safe circuitry was incorporated as an integral part of the automatic load control system to prevent test article damage due to malfunction of the electrical-hydraulic servo mechanisms or loading system failure. During



Figure 16. Cyclic Test Setup - View from R.H. Wing.

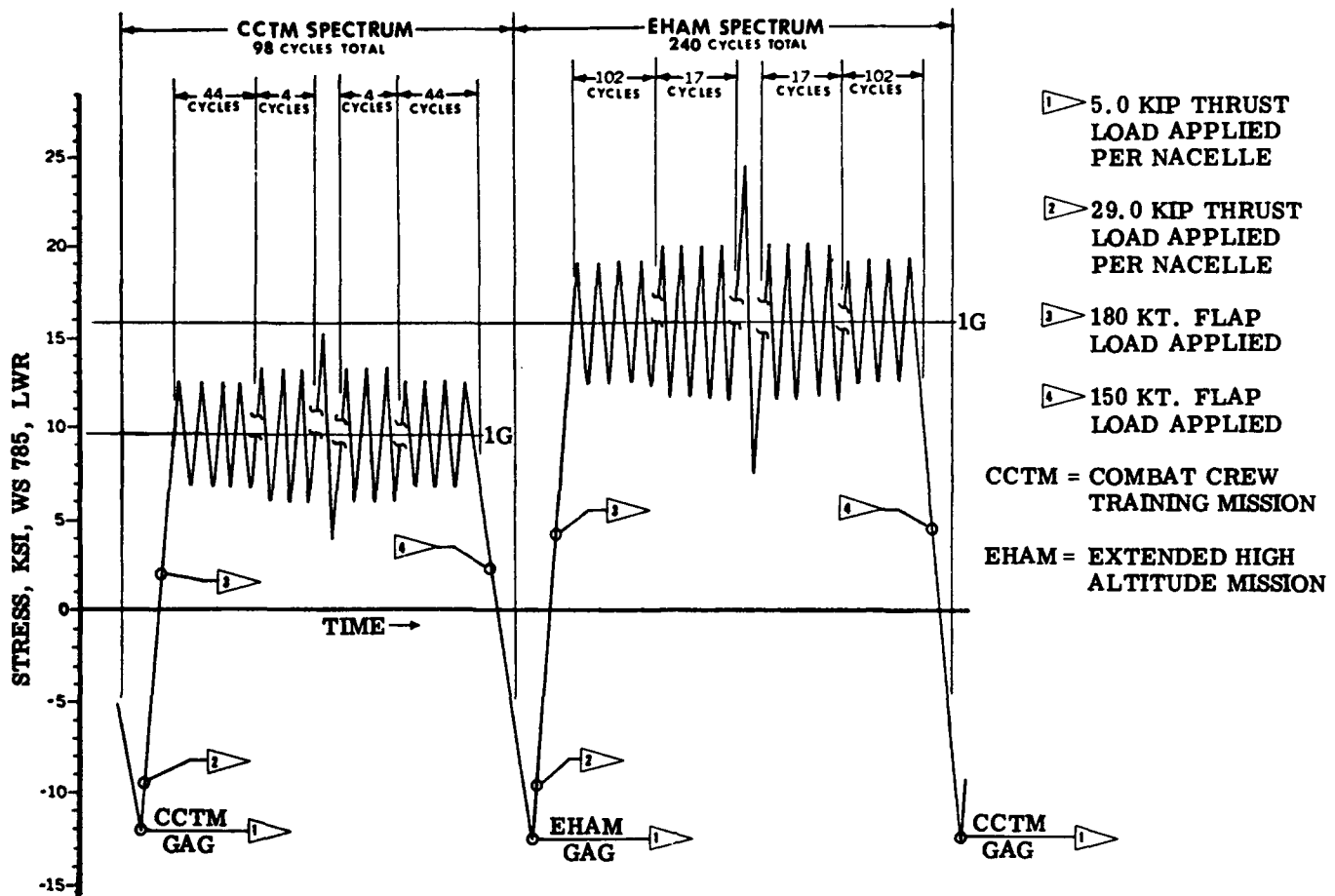


Figure 17. Typical Loading Spectra - Fifth and Sixth Lifetimes.

operation, the fail-safe system locked the loading rams in their existing positions at the instant of malfunction. Any of the following malfunctions would cause operation of fail-safe system:

1. Power failure
2. Drop in main hydraulic pressure
3. Excessive load or ram overtravel at any location
4. Programmer malfunction
5. Excessive error signal to servo valve
6. Actuation of the "panic" switch by the test operator.

A view of the test setup from the right hand wing is shown in Figure 16.

#### Test Procedure

Individual CCT and EHA loading spectra were applied in "blocks" of 15 as indicated in Figure 9. After the application of 44 "blocks", 36 additional spectra (18 CCT

alternated with 18 EHA) were applied. This was equivalent to one lifetime of loading.

At the end of four lifetimes of testing, no wing fatigue damage of a life-limiting nature was detected. It was recognized that the B-52G/H fleet might be required to remain in service beyond the time represented by the original design criteria. A decision was made to apply additional loading to determine by test the point at which fatigue cracking would occur over broad areas of the wing. Analysis indicated that this condition could occur between five and six lifetimes. An additional two lifetimes of cyclic loading were then applied. The loading spectra were altered during this phase of testing to reduce testing time. Figure 17 shows the loading spectra applied during the fifth and sixth lifetimes.

Extensive strain gage and fatigue crack detection wire instrumentation were employed to determine stress distribution at critical locations and to provide for early crack detection.

Over 100 scheduled inspections of the test article were performed throughout the testing period. About half of these inspections were considered major in that the interior and exterior structures were thoroughly inspected.

The remaining inspections were primarily external and less extensive. The principal inspection technique was visual examination with low power magnification. Dye penetrant methods were employed in suspected critical areas and to verify cracks discovered visually.

Additional details concerning the cyclic test setup and procedure are in Reference 4.

### Results and Discussion

As mentioned earlier, little significant fatigue damage was discovered during the first four lifetimes of testing. At approximately one lifetime, a crack was discovered in the web of a center wing section rib. A fleet modification was designed for this area and recommended for incorporation on fleet airplanes.

The only other wing damage found during the first four lifetimes of testing was limited to cracks in secondary trailing edge structure. These were not serious from a structural integrity standpoint. However, fleet modifications in these areas were recommended to reduce secondary structure maintenance. Also, if cracks in these areas were allowed to exist and propagate, this could eventually result in significant damage to the primary wing structure.

The first signs of general basic structure cracking occurred at 5.8 lifetimes in the wing lower surface. Figure 18 shows a comparison of the predicted and actual basic structure life. This plot shows that the life objective was exceeded by almost 50 percent. It will be noted that cracking was somewhat more extensive than predicted in a spanwise direction. This first appeared as cracks in stiffeners and spar chords at skin to stiffener attachment fasteners. Typical examples are shown in Figure 19. Cracks occurred at machine and hand driven rivet locations and taper bolt

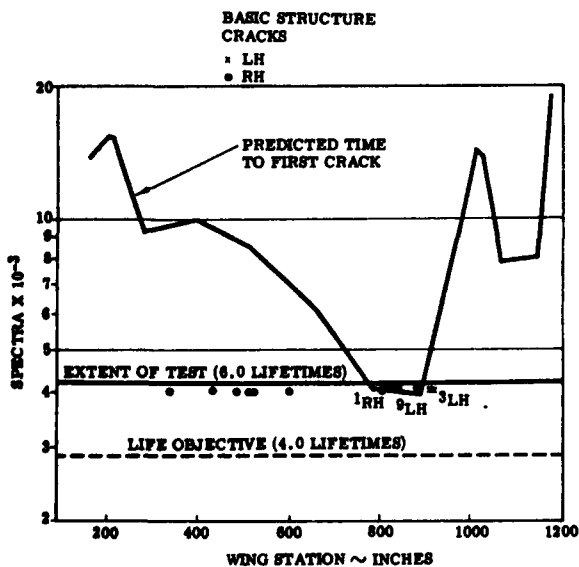


Figure 18. Predicted Life VS Cyclic Test Results - Wing Lower Surface.

fastener locations. In general, these kinds of details were common throughout the lower surface wing structure.

As the test progressed through six lifetimes and through the crack propagation phase, numerous other cracks were discovered in basic structure. More were found during the teardown inspection. An evaluation was made to define the basic structure life of the ECP 1050 wing.

Each wing experienced approximately the same number of fatigue cracks; however, the number in local areas varied to some extent. For this reason, a quantitative comparison of left hand and right hand wing skin and stiffener cracks was made. Figure 20 shows the number and locations for all known skin and stiffener cracks. Those in the stiffeners were distributed as shown in Table II.

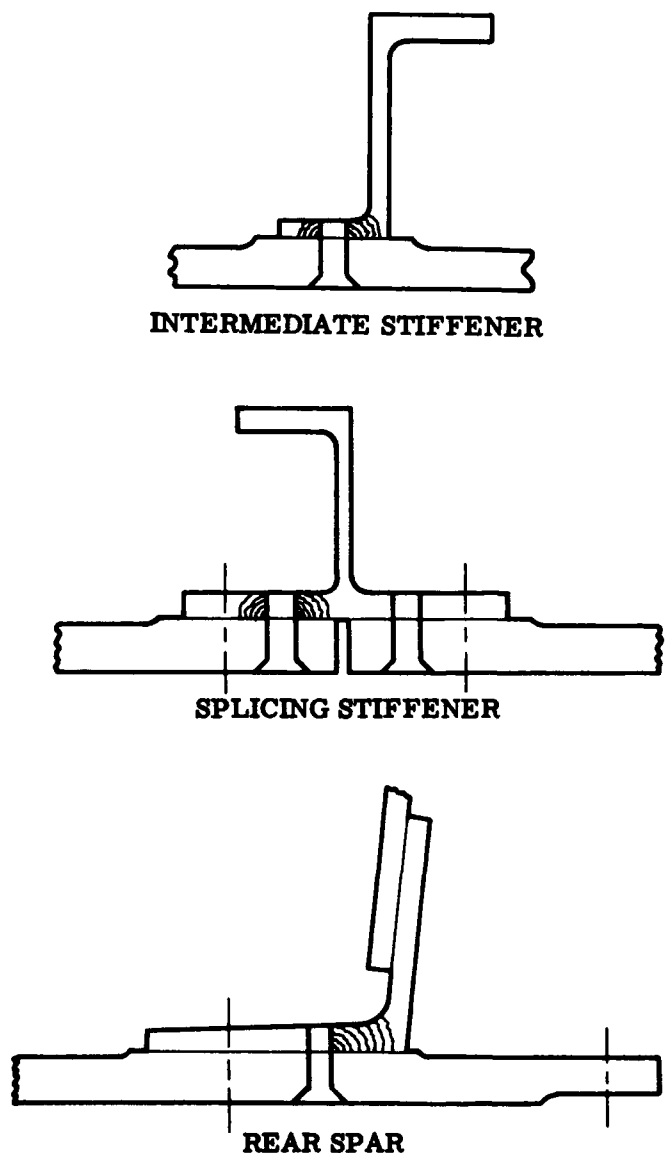
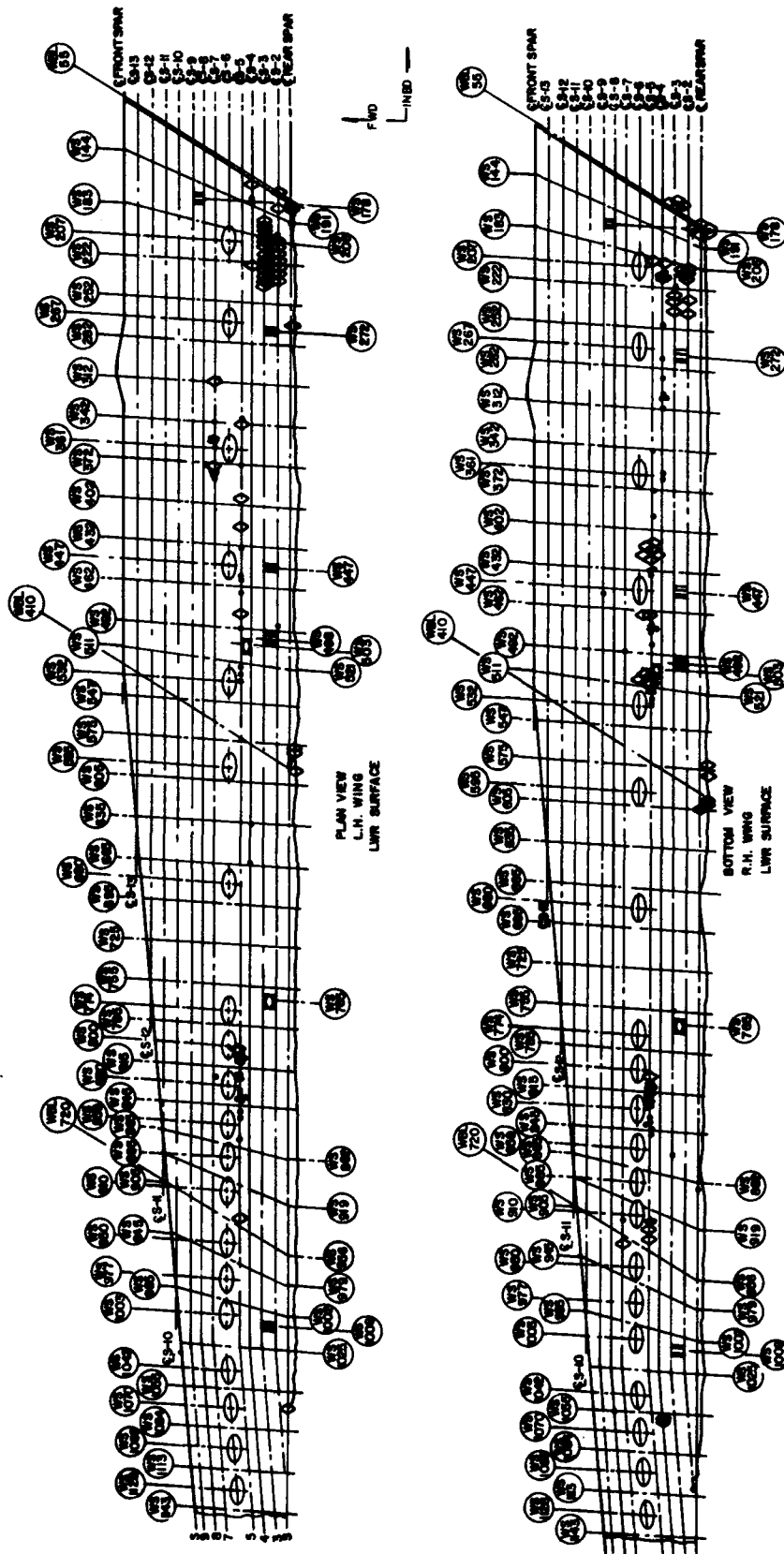


Figure 19. Typical Basic Structure Cracks - Wing.



NOTE: THESE VIEWS SHOW ALL KNOWN WING LOWER SKIN AND STIFFENER FATIGUE CRACKS FOUND DURING TESTING AND AFTER TEARDOWN.

LOCATION	NUMBER OF CRACKS		TOTAL
	LH WING	RH WING	
STIFFENERS	61	64	125
SKIN	51	45	96
TOTAL	113	109	222

Figure 20. Locations of All Skin and Stiffener Cracks.

**TABLE II  
BASIC STRUCTURE CRACKS IN STIFFENERS**

STIFFENER	CRACKS STARTING AT RIB CHORD ATTACH HOLE		CRACKS STARTING AT BASE FLANGE FASTENER HOLE	
	LH	RH	LH	RH
S-1	0	0	3	1
S-2	0	0	2	2
S-3	0	2	0	2
S-4	4	3	1	13
S-5	1	0	39	36
S-7	0	0	11	3
S-8	0	0	0	1
S-9	0	0	0	1
TOTAL	5	5	56	59

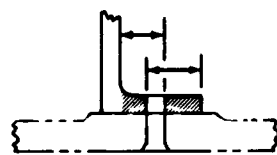
The number of cracks in left hand and right hand stiffeners was about the same except for base flange cracks in S-4 and S-7. A chemical analysis for composition of lower aft skin panel and all stiffeners inspected revealed no significant difference between the left and right wings. Since the difference in cracking patterns could not be attributed to unlike materials, it could have been the result of slight variations in fastener installation techniques. The S-7 stiffeners are attached with machine driven fasteners and would not be expected to show differences due to varying installation techniques. Stiffener S-4, being at the closure panel, had all hand-driven rivets which could account for more cracks in the right hand wing S-4. However, a close inspection of holes on the LH and RH wing revealed no noticeable differences in workmanship.

Since no apparent reasons were discovered for the scatter in these fatigue test results, it was assumed that they are representative of what can be expected on fleet airplanes.

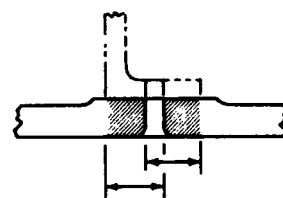
To clarify what is meant by cracked structure, it is necessary to define a condition which would have a reasonably high probability of detection during fleet inspections. A "detectable" crack is defined as one which would be found by close visual inspection with magnification during routine or depot level inspections. Some typical examples of what were judged to be minimum "detectable" lengths in cracked stiffeners and skins are shown in Figure 21.

A survey was performed of the inboard wing lower surface fastener installations to derive an average "detectable" length. The area of survey was from just outboard of the BL 55 splice to just inboard of the WS 1025 splice spanwise and from the rear spar chord to Stiffener S-8, inclusive. The distance from hole to edge plus hole diameter was determined for each fastener location. The average "detectable" length for the lower surface was found to be approximately 0.625 inches. Test and inspection results indicate that on fleet airplanes a stiffener cracked at a fastener may loosen the fastener such that sealing is lost and fuel seepage may occur. Conversely, a crack in the skin from a fastener hole probably would not cause fuel leakage until it had progressed beyond the faying surface of the attached stiffener or chord.

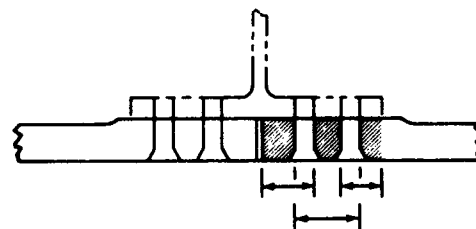
"Detectable" cracks included in this evaluation were selected from the ones occurring naturally and reported during the testing and teardown phases of the test. Only those found in basic structure were used since detail problem areas are monitored by lead-the-fleet inspections. Cracks found at faying surfaces, inside fastener holes, and other areas requiring teardown for access and cracks which were less than "detectable" length were not included.



STIFFENER OR SPAR CHORD



SKIN AT INTERMEDIATE STIFFENER



SKIN AT SPLICING STIFFENER

Figure 21. "Detectable" Crack Lengths.

← "DETECTABLE" LENGTH  
AVERAGE DETECTABLE LENGTH  $\approx 5/8"$

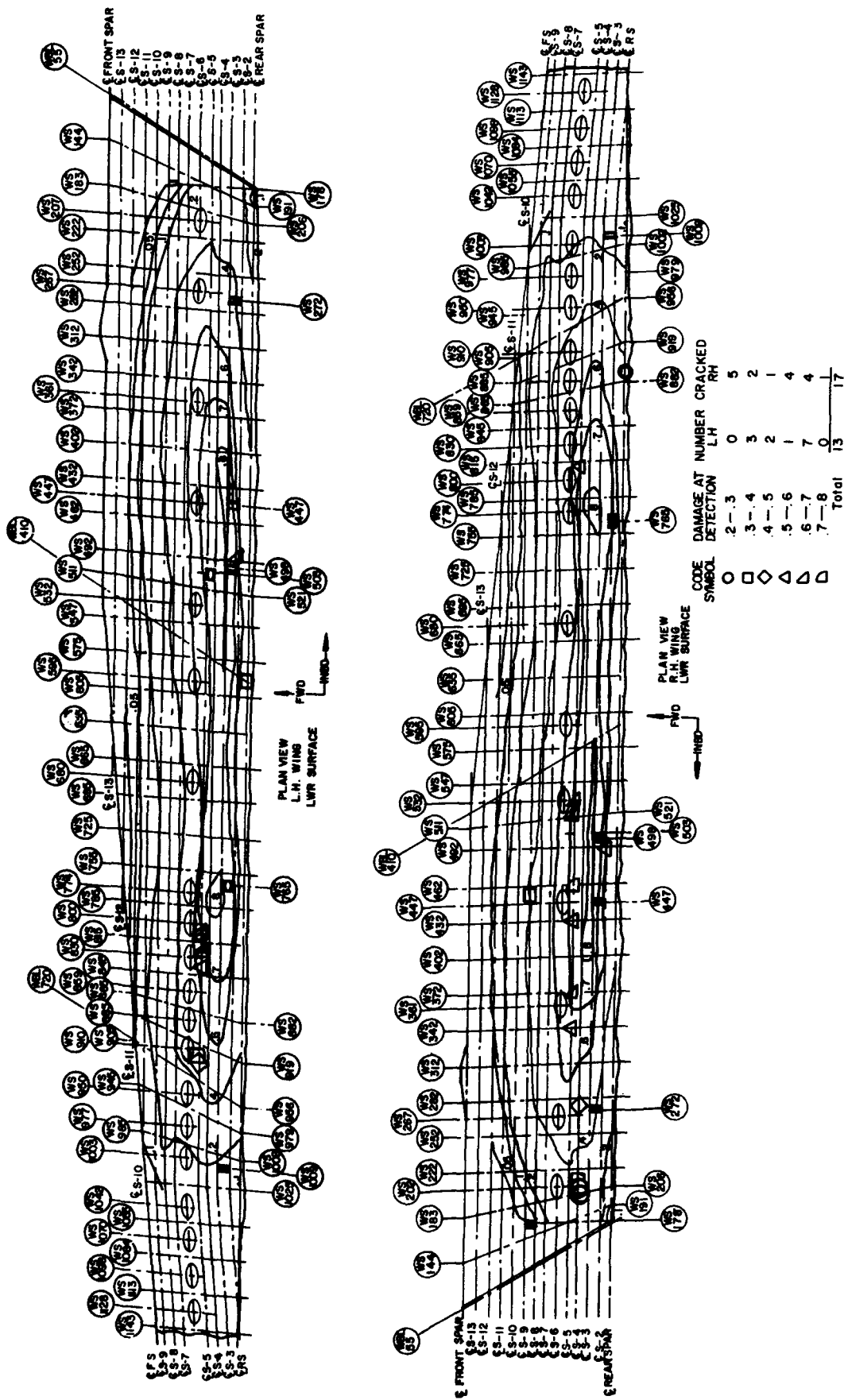


Figure 22. Detectable Crack Location:



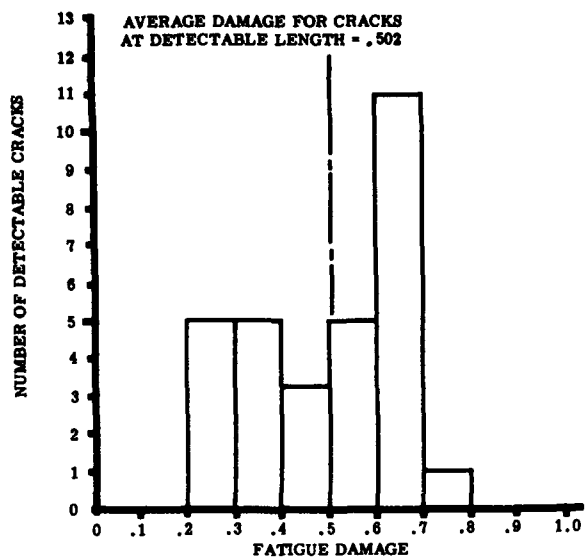


Figure 23. Damage Distribution of Wing Lower Surface Detectable Cracks.

Thirty cracks were considered as representative of basic structure "detectable" cracks.

Cyclic test stress values were derived from extensive strain gage data obtained during the early part of the test program supplemented with data from the crack propagation and fail-safe test phases.

The S-N curves used in the preliminary analysis of the wing lower surface, Figure 4, were developed from fatigue tests using 2024 plate for skins and 7075 extrusions for stiffeners. These curves also were used in this analysis to calculate fatigue damage.

Cyclic test fatigue damage was calculated using the linear cumulative damage theory. A damage value was calculated for each "detectable" crack location. Fatigue damage adjustments were made for all cracks longer than "detectable" length by subtracting that increment of damage experienced during growth from detectable length to length at discovery.

"Detectable" crack locations occurring on the left and right wings are shown in Figure 22. Also included on these planviews are contour lines representing total accumulated test damage.

Figure 23 shows the distribution of cracks within the damage bands at which they would become detectable. The average value of damage for all 30 cracks was calculated to be 0.502 with individual values ranging from about 0.25 to 0.75. This means that detectable cracks should occur at about half the life predicted using the S-N curves of Figure 4.

The damage values used in the Fleet Damage Monitoring Program were adjusted to account for the difference

between the analyses S-N curves and the cyclic test result. The occurrence of detectable stiffener cracks in fleet airplanes does not signify the end of useful life. The use of 2024 lower skin material gives confidence that the airplane can be flown beyond the detectable length stage without significantly compromising structural integrity.

Additional discussions of the results of the cyclic test program can be found in References 5 and 6.

### CRACK PROPAGATION AND FAIL-SAFE TESTING

The wealth of equipment, facilities, and experienced personnel available at the completion of the cyclic test presented a unique opportunity to conduct relatively economical crack propagation and fail-safe tests on a full-scale wing. Therefore, testing was continued with the objective of determining:

1. Crack propagation rates under cyclic loading
2. Capability of significantly cracked structure to withstand 90 percent limit load
3. Critical stress intensity factors, and
4. Fail-safe characteristics,

This portion of the test program was organized into four phases. Each phase consisted of observations of crack growths as they approached theoretical critical length. Large cracks were then repaired and the test proceeded to the next phase. The test article was loaded to destruction in the fourth phase.

Whenever possible, cracks that occurred naturally were used. However, in most instances, it was necessary to make sawcuts to initiate cracks for study.

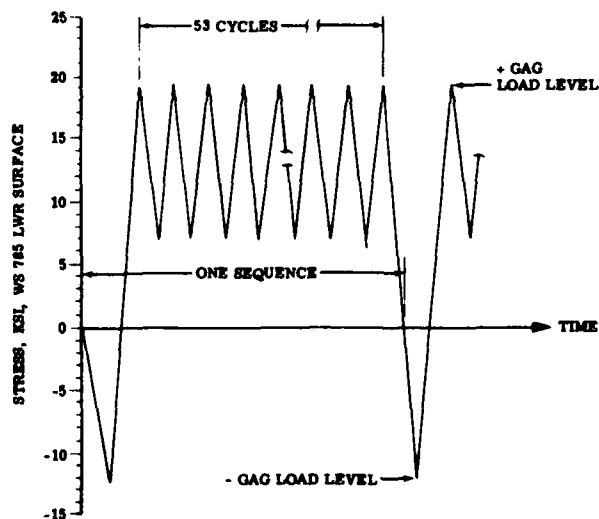


Figure 24. Loading Sequence - Crack Propagation and Failsafe Test.

Locations selected for study were strain gaged before sawcutting to establish the field stress. This field stress was used to predict crack propagation. Cracks were allowed to grow until they reached about 70 percent of the theoretical critical length for a 90 percent limit load condition. State-of-the-art fracture mechanics analysis techniques (1967) were used to predict growth and critical lengths. A discussion of these techniques can be found in Reference 6.

The load levels for crack propagation testing were selected to produce stresses which would propagate cracks at a rate commensurate with testing several areas of the wing within the allotted testing time. A loading sequence consisting of a ground-air-ground cycle and 53 cycles of an intermediate alternating stress was selected. The number of cycles per sequence was chosen to produce calculated fatigue damage equivalent to a composite of the EHA and CCT spectra used in the service life testing. The stress loading sequence for a representative wing station is shown in Figure 24.

#### Test Procedure

A typical location selected for crack growth study is

shown in Figure 25. A natural crack was found in the stiffener during earlier cyclic testing. This region of the wing experienced high analytical fatigue damage. The initial sawcut was made through the existing natural crack and for a length of 1.41 inches in the skin. Testing was then started and length measurements were taken periodically. When the crack reached 60 percent of the theoretical critical length, a 90 percent limit load was applied that produced a growth of 0.25 inches. Additional sequence loadings were applied until about 70 percent of theoretical critical length was reached. A second 90 percent limit load was applied which produced 2.22 inches of growth. Cycling was halted at this point and repairs were made to the test article.

#### Results and Discussion

The results of crack propagation analysis and test measurements at three typical locations are shown in Figure 26. The plots show length versus number of loading sequences. The  $2a$  length is the total crack length and includes the fastener hole diameter. Crack length was predicted using nominal gross area stress,  $\sigma$ , as well as  $1.1 \sigma$  and  $0.9 \sigma$ . These plots show generally good

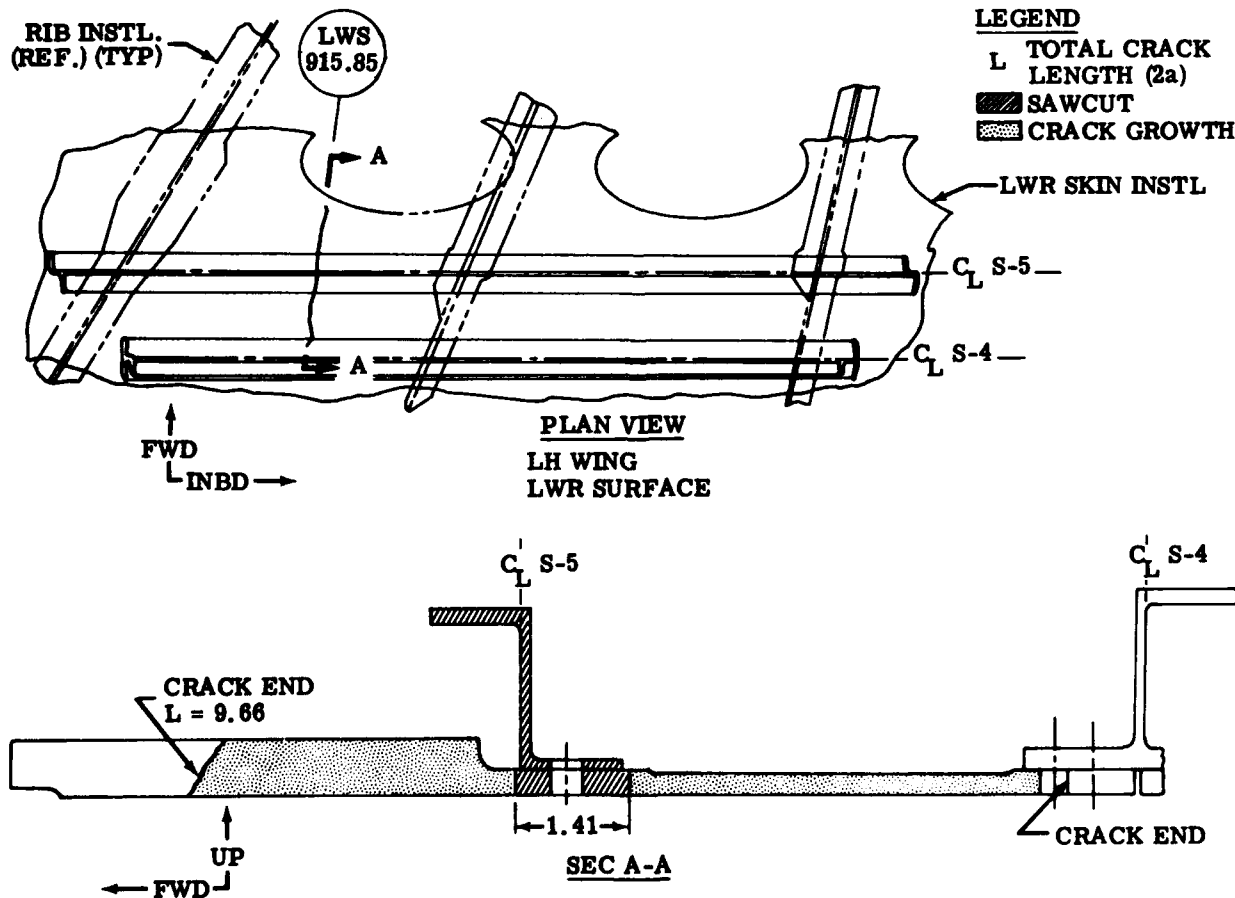


Figure 25. Details of Crack at LWS 915.85.

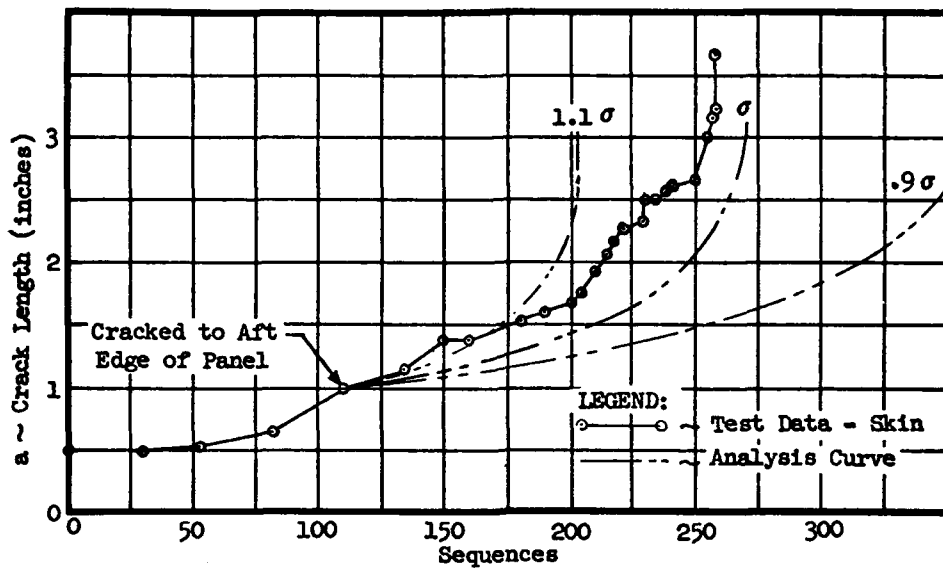


Figure 26a. RWS 600 Crack Propagation Curves.

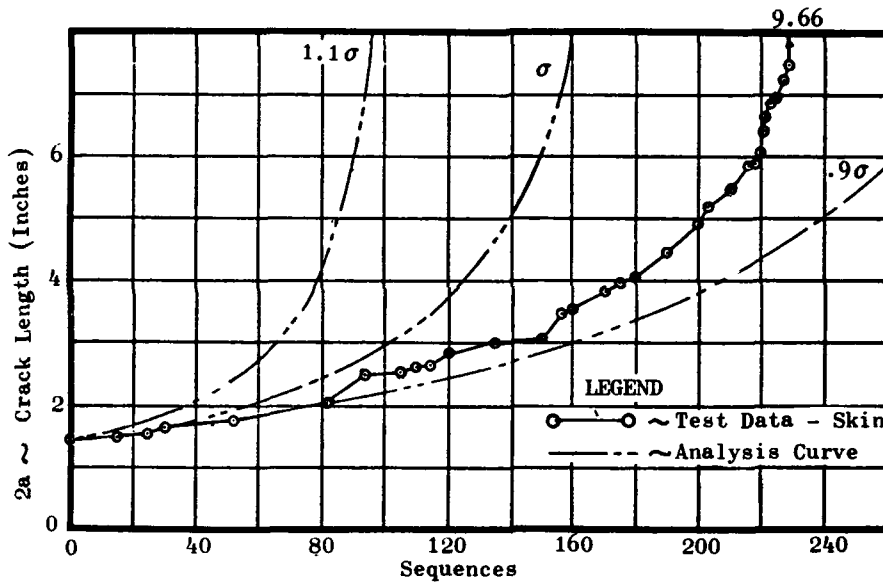


Figure 26b. LWS 915.85 Crack Propagation Curves.

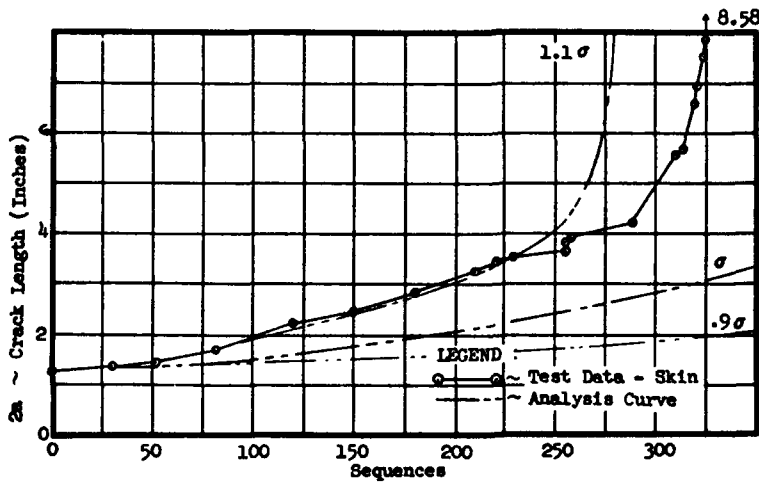


Figure 26c. RWS 1063.1 Crack Propagation Curves.

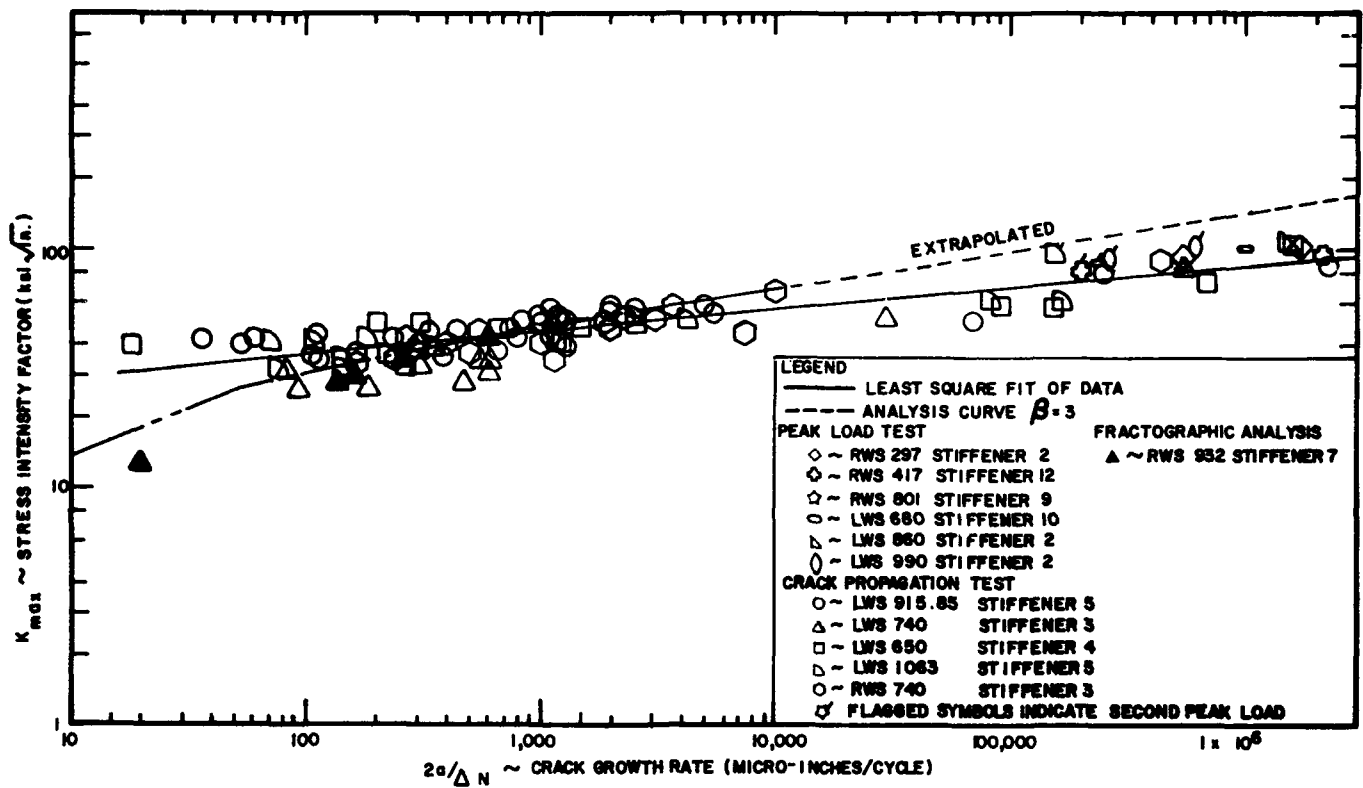


Figure 27. Stress Intensity Factor Versus Crack Growth Rate in 2024-T3 Material,  $\beta = 3$ .

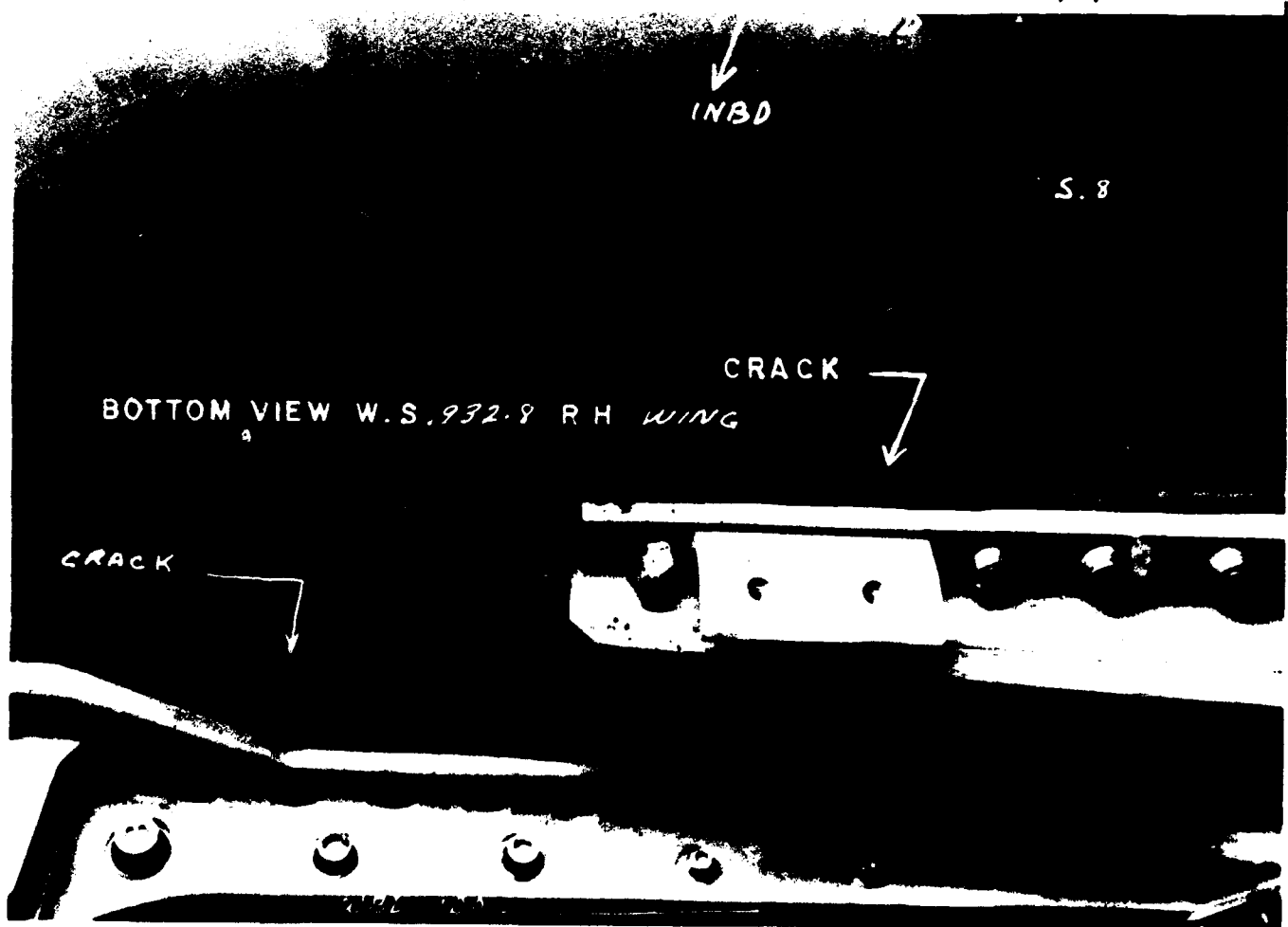


Figure 28. Fatigue Crack LWS 932.8, Lower.



**Figure 29. Photo Micrograph of Fracture Face for Sequence Loading. 4400 Magnification (Reduced 20%). Arrow shows direction of growth.**

agreement between predicted and measured values. The differences between the predicted growth curves for  $1.1 \sigma$  and  $0.9 \sigma$  show the high sensitivity of crack growth to stress level. This indicates the importance of accurate values of gross area stress.

Crack growth rate data obtained during the testing for 2024 material are shown in Figure 27. Stress intensity factor,  $K_{max}$ , is plotted against crack growth rate,  $\Delta 2a / \Delta N$ . The analysis curve, shown as a dash line, was developed using data from tests on flat panels tested at a maximum to minimum stress ratio,  $\beta$ , equal to 3.0. The solid curve represents a least squares fit through the data points.  $\beta$  for these data was approximately 3.

The test data are in close agreement with the analysis curve for the lower crack growth rates. This is in the region where previous test data was available. Greater differences are seen between the analysis curve and the present test data in the higher growth rate region. As seen in Figure 27, the analysis curve was extrapolated in this region since no previous test data were available.

An unexpected discovery was made early in the first

phase of the crack growth testing. Before application of the first 90 percent limit load, an inspection of the test article was scheduled. During this inspection, a 16-inch crack was discovered in the lower wing skin at RWS 932.8 as shown in Figure 28. The crack originated at an aft fastener hole in the outboard engine drag strut. The entire fracture face was removed from the test specimen and sent to the Metallurgical Laboratory for fractographic analysis. The laboratory was asked to construct a crack growth curve from evidence on the fracture face. A series of replicas was made at different locations along the fracture face and examined under the electron microscope.

Loading striations with a pattern similar to that shown in Figure 29 were found over much of the fracture length. This striation pattern was readily correlated to the sequence loading of Figure 23 since 53 striations were counted in each band.

The striation pattern for about 1.50 inches on either side of the hole at which the crack originated was found quite different as shown in Figure 30. This pattern was correlated with the spectrum loading of Figure 9 which placed the time of origin within the first six lifetimes of test-



Figure 30. Photo Micrograph of Fracture Face for Spectrum Loading. 5600 Magnification (Reduced 20%). Arrow shows direction of growth. Number of striations noted for each load level band.

ing. It was possible to count the number of spectra applied back almost to the origin and thus construct the history curve of Figure 31. Surprisingly, this study indicated the crack originated early in the second lifetime of loading. The crack progressed slowly until it reached a length of about two inches at which point more rapid propagation was observed. The crack was less than three

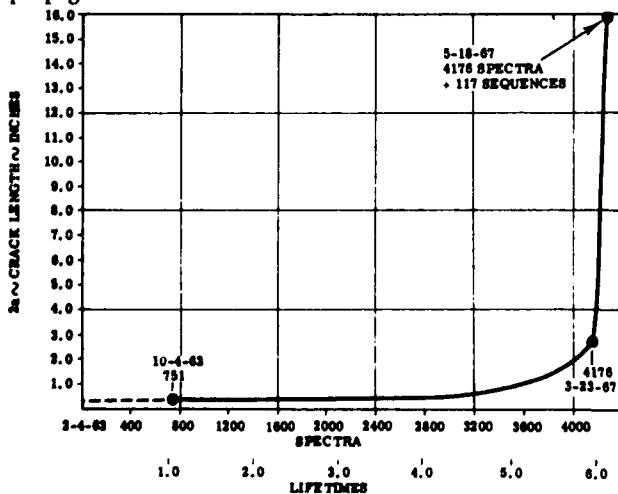


Figure 31. RWS 932.8 Crack History.

inches long at the beginning of the crack propagation phase of testing.

After completion of this phase of testing, the test article was still intact although many cracks were present. No critical stress intensity factor data had been gathered since no cracks had become unstable. At this point, it was decided to perform a test to destruction. Eighteen cracks ranging in length from about four to 19 inches were present in the wing structure prior to the first peak loading. At a peak load of 92.5 percent of limit load, some of the structure failed. The extent of structural failure is shown in Figure 32a. Two of the lower surface panels were failed completely and several rows of skin to stiffener fasteners were sheared outboard to about WS 665. A second peak load was applied which resulted in complete lower surface failure as shown in Figure 32b.

Since the final peak loading produced rapid fracture across complete panels, test data for calculating critical stress intensity factor ( $K_c$ ) were obtained. These data are plotted in Figure 33 for the 2024 skin failures. The analysis curve shown on the plot was constructed using data from tests on flat panels.

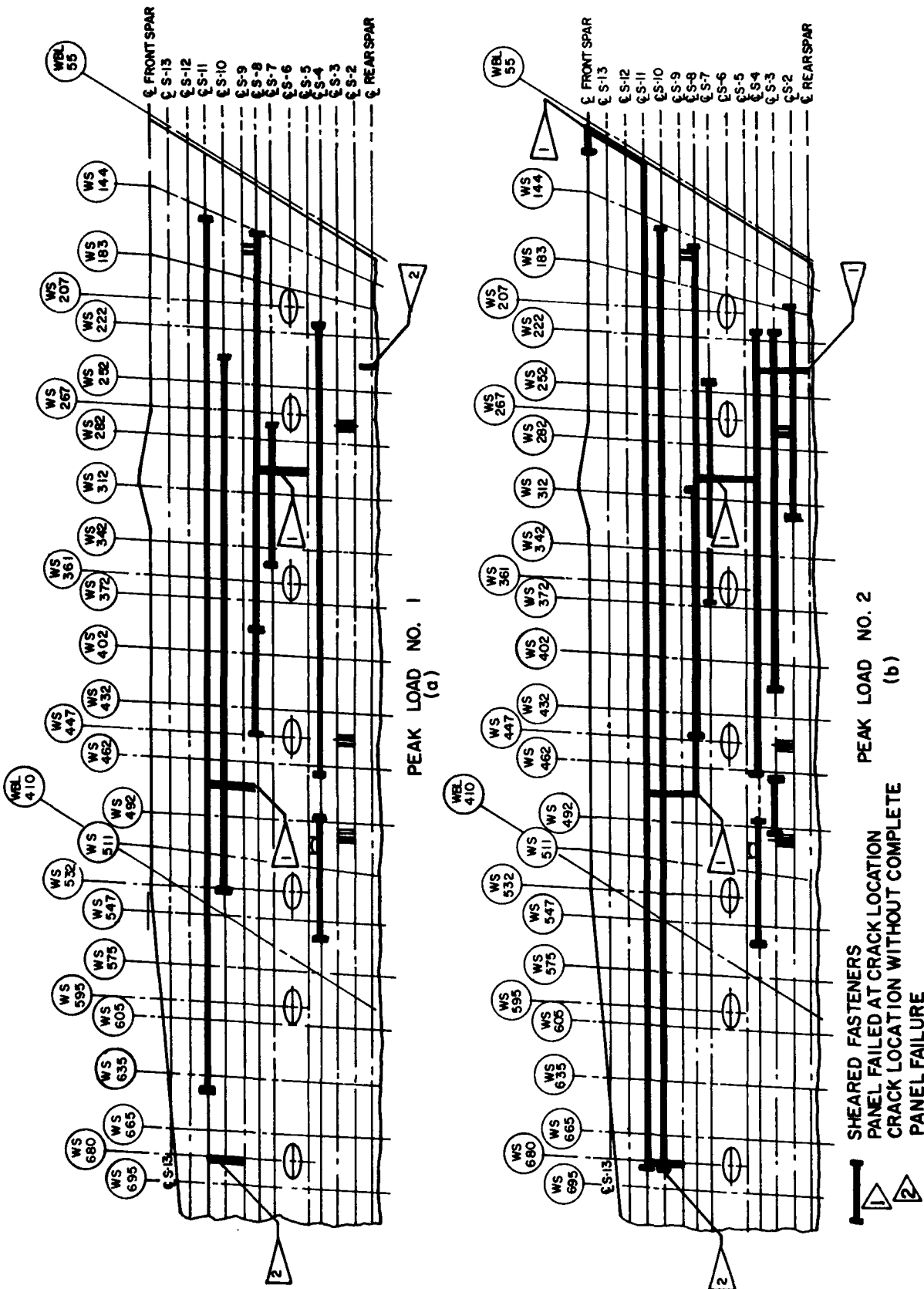


Figure 32. Sheared Fasteners on Left Hand Wing After Peak Loads.

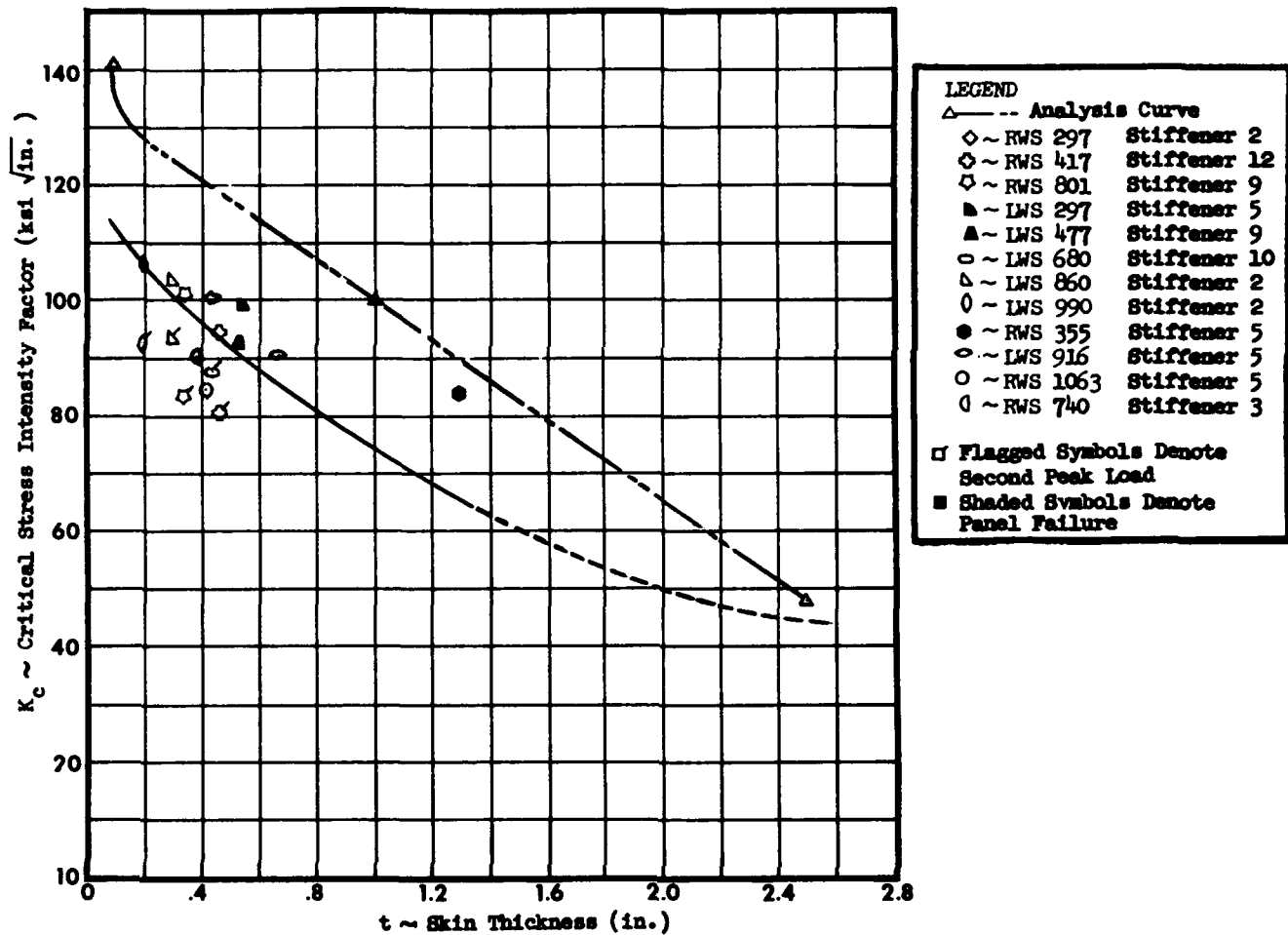


Figure 33. Critical Stress Intensity Factor Versus Skin Thickness, 2024-T3 Material.

Three of the cyclic test data points in Figure 33 represent actual failure values. The balance of the test points represent a value somewhat less than the true  $K_c$  value since the panels did not fail at this loading. Many of the unfailed locations were probably approaching criticality since the data points lie near and among the three failure values. The  $K_c$  test values are about 20 percent less than that predicted by the analysis curve.

Reference 6 contains additional data and discussion concerning the crack propagation and fail-safe tests.

#### CONCLUDING REMARKS

The B-52G-H ECP 1050 wing cyclic test furnished physical evidence that the design service life goal for the wing had been met and even exceeded. In addition, valuable crack propagation and fail-safe data were obtained which had been heretofore unavailable for full-scale structures of this type. Data from these tests, coupled with other elements of the structural service life program, made it possible to predict, with reasonable confidence, the useful service life of the B-52G-H airplanes under practically all usage conditions.



## REFERENCES

1. *Air Force Structural Integrity Program Requirements*, ASD-TR-66-57, Aeronautical Systems Division, Wright-Patterson AFB, Ohio (1968).
2. *B-52G ECP-1050 Preliminary Structural Fatigue Analysis, Volume I - Wing and Body*, D3-4374, Boeing Company, Wichita, Kansas (1962).
3. *Outline of Loads Requirements for Cyclic Test of Article No. 1, Volume I - Wing and Body(U)*, D3-3980, Boeing Company, Wichita, Kansas (1962).
4. *B-52G/H ECP-1050 Wing and Body Cyclic Test Outline*, D3-3981, Boeing Company, Wichita, Kansas (1965).
5. *B-52G/H ECP-1050 Structural Integrity and Service Life Analysis Summary*, D3-6625, Boeing Company, Wichita, Kansas (1965).
6. *Final Fatigue Analysis Summary and Fracture Mechanics Analysis, B-52G/H ECP-1050 Airplane*, D3-7709, Boeing Company, Wichita, Kansas (1968).

# A FATIGUE HISTORY OF THE F-105 AIRCRAFT

A Review of Results Obtained Through Analysis, Fatigue Testing, and Actual Usage  
of a  
High Speed Aircraft Subjected to Combined Peacetime and Combat Flying

by

Aaron M. Merkin

Fairchild Hiller Corporation  
Republic Aviation Division

## SYMBOLS AND DEFINITIONS

$n_z$  = normal load factor ( $n_{zL}$  = limit) .

$N_s$  = Service utilization factor, for positive load factors it is the number of times per flight hour that  $n_z \geq 2.0$ .

$g$  = Acceleration of gravity, feet/sec<sup>2</sup>.

$W$  = Weight of aircraft, pounds.

MAC = Mean aerodynamic chord.

C.G. = Center of gravity.

$\sigma_r$  = "Reduced" or equivalent value of stress amplitude in Shanley's method (psi).

$\sigma_e$  = Endurance limit stress (psi) - from S-N diagram.

$\sigma_{ult}$  = Ultimate tensile strength of material (psi).

$\sigma_{i_{max}}$  = Equivalent value of stress amplitude at fully reversed (R = -1.0) stress amplitude.

$\delta$  = Empirical constant derived as a function of the applied stress spectrum.

$d$  = Inverse slope of ( $\sigma_{i_{max}} - \sigma_{es}$ ) versus N curve plotted as a straight line on log-log paper.

$\alpha_i$  = Ratio of number of cycles applied at  $\sigma_{i_{max}}$  to total number of spectrum =  $n_i / \sum N_i$ .

M = Mach number.

$C_L$  = Lift coefficient.

VGH = Velocity, normal load factor ( $n_z$ ), altitude (ft).

$n_y$  = Lateral or side load factor.

$g$  = Pitch rate, degrees/second.

$p$  = Roll rate, degrees/second.

$r$  = Yaw rate, degrees/second.

$\dot{p}$  = Roll acceleration, degrees/sec<sup>2</sup>.

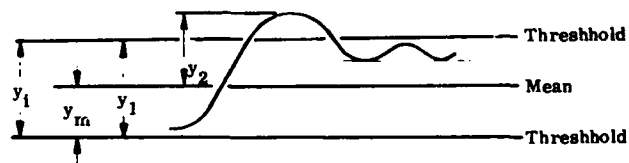
$\dot{q}$  = Pitch acceleration, degrees/sec<sup>2</sup>.

$\dot{r}$  = Yaw acceleration, degrees/sec<sup>2</sup>.

$pr$  = Roll-yaw coupling, degrees<sup>2</sup>/sec<sup>2</sup>.

$n_{ze}$  = Equivalent normal load factor =  $\frac{W_i}{W_d} n_z$ ; where  $n_z$  = normal load factor,  $W_i$  = instantaneous gross weight, and  $W_d$  = clean configuration supersonic gross weight (36,018# for 'D', 37,772# for 'F').

Peak = A peak is defined as a value greater than or equal to threshold for which the rise and fall of peak is equal to or greater than 50% of the incremental peak value and equal to or greater than the threshold increment. Mathematically, it is defined as follows:



A peak is defined at  $y_i$ , if:  $y_i \geq y_m$  and  $y_1$  and  $y_2 \geq 0.5y_m$ , and  $y_m$  where

$y_1$  = peak candidate  
 $y_m$  = threshold increment  
 $y_1$  and  $y_2$  = peak candidate rise and fall increment, respectively.

W.S. = Wing Station.

R.S.S. = Rear Spar Station.

## INTRODUCTION

The F-105 has been the object of one of the most extensive fatigue investigations conducted on military aircraft.

At the outset of the fatigue certification program, available spectra data was meager and inconclusive. As a consequence, early fatigue analysis and testing relied on semi-empirical military specification requirements and limited flight data from other aircraft, as a basis for development of flight spectra. In retrospect, this approach to fatigue evaluation is at best conservative. Yet it did serve a purpose. This early work helped locate fatigue-sensitive areas that had not been apparent through inspection of drawings and structural analysis. Therefore it will be discussed along with the more sophisticated approaches developed later.

In 1964, and again in 1967, the Air Force instituted statistical flight loads (VGH) programs to better verify the effects of changing fatigue environments on the F-105. The first program pertained strictly to the F-105D flying under peacetime conditions. Some 2500 hours of 3 channel VGH data, and 250 hours of 8 channel asymmetric data were recorded. The second program involved both 'D' and 'F' aircraft flying in a Southeast Asia (SEA) combat environment. 3000 hours of 3 channel VGH and 300 hours of 8 channel data were accumulated on the 'D', while 1000 hours of 3 channel VGH and 100 hours of 8 channel data were recorded on the 'F'.

Breakdown of resultant data led to a much more accurate picture of the flight maneuver and load spectra on the 'D' and 'F'. Utilizing these spectra, it became possible to better evaluate fatigue sensitive areas on the aircraft.

In addition, although they could only help minimize (not prevent) fatigue damage, field service records and Air Force U.R.'s have been constantly examined to see if, when, and where structural problems occurred in the process of actual usage. Since there are a number of F-105's still active, most of which have logged 2000 flight hours, and some approaching their initial required service life of 4000 hours, the reported structural problems are scrutinized to insure that fatigue is not the cause.

In brief, this history of the F-105 indicates need for a fatigue certification program at the outset\* of any new aircraft design, to evaluate very carefully the design philosophies. Such a program should be continued throughout the aircraft service life to account for varying conditions of usage. Also, by necessity, the program must include repeated fatigue analysis and testing so that problems revealed in the testing can be prevented on operational aircraft by taking corrective measures.

\* The original F-105 contract contained no requirement for a minimum aircraft fatigue life, or a fatigue certification program. However, the attention given to initial detail design has paid off by keeping fatigue problems at one of the lowest levels on high time service aircraft.

## DISCUSSION

### I. General Description of Aircraft

The F105 (See Figure 1) is an all metal, sweptback midwing turbojet-propelled supersonic fighter bomber. The aircraft is equipped with fully retractable tricycle landing gear. Its wings are dry since all internal fuel is carried in the fuselage. Besides carrying a fixed gatling gun in the fuselage nose, provisions exist on both the wings and fuselage for carrying varied armament stores as well as external fuel stores. Each wing has a fully controllable leading-edge flap, spoilers, trailing-edge flap, and aileron. The fuselage includes a supersonic engine-air-inlet duct, an area-rule design, a bomb bay, and an insulated and pressurized cockpit. The fuselage aft section supports a vertical fin and rudder, four clam shell speed brakes, a drag chute, arresting hook, and a one-piece maneuverable stabilizer. A cooling duct for the after-burner is located in the vertical fin.

There have been three production versions of the F105; the "B", the "D" and the "F". The "B" and "D" differ very little physically or structurally, with the "D" having a slightly longer nose radome. The main physical difference between the "F" and the other two is the presence of two cockpits where the "B" and "D" only had one, an additional 31" length of fuselage spliced in to make room for the second cockpit, and a larger vertical fin. Except for these areas, all three aircraft are very similar structurally.

### II. Structural Details Pertinent to Fatigue

#### A. Fuselage

The elliptical cross section fuselage (Figure 2) is of semi-monocoque construction except for a hinged nose radome housing radar and pitot-static system equipment. A field break point exists at station 633 to facilitate removal and installation of the engine. At this point all load carrying ability exists only through four cone bolts attaching to the upper and lower longerons. Fuselage bending strength is provided by longerons, stringers and effective external skin, while shear and torsional strength are provided by the sheet metal skin covering and by internal webs where applicable. For flight conditions the fuselage structure is considered a beam loaded by its own weight, engine and equipment loads, fuselage airloads, and tail loads. These loads, in turn, are balanced by wing loads which are applied to the fuselage at three distinct points; a link fitting at station 372, the front spar pickup frame at station 390, and the wing rear spar pickup frame at station 442. The latter two are considered the main fuselage frames or bulkheads. The attachment of the wing to the fuselage at frame station 442 is done in a rather unique manner. As can be seen from Figure 3, intersection of the wing rear spar and

transfer spar at this point creates a kick or pitching moment to be induced into the side of the fuselage. Since the frame is only designed for in-plane loads (wing rear-transfer spar shear and moment are reacted at this point), this kick moment is transmitted to a fuselage mounted side plate fitting, as horizontal couple loads, by adjustable wing retainers.

The side plate or wing root fitting then redistributes these loads into the fuselage side skin as horizontal skin shears and vertical frame reactions. This installation is shown in Figures 3 and 4. The adjustable retainer feature permits wing alignment and incidence corrections when required.

The entire bottom section of the fuselage between longerons has been made ineffective in carrying any load except torsion, by presence of doors in this region. Furthermore, from station 300 to 494, moveable bomb bay doors are completely ineffective in carrying primary loads, including torsion. In this area torsion is resisted by differential bending of the sides of the fuselage.

Above the upper longerons, beginning just aft of the cockpit, and running through to the fuselage breakpoint at station 633, there are provisions for fuel cells. Access is provided to these cells through holes in the structural top cover of the fuselage. (Figures 1 and 5.)

For landing and towing conditions the fuselage loads are due only to inertia forces. Reactions are provided by the wing at the three fuselage attachment points and by the nose gear. Nose gear loads are carried by nose beams into structural bulkheads in the forward fuselage.

Gun recoil loads are resisted by fuselage frames and redistributed into the semi-monocoque structure. The internally carried (by a displacing gear) bomb or fuel tank is supported on bulkheads at station 350 and 390 and beams which redistribute the loads into the main bulkheads.

The basic material of the fuselage skin, longerons, stiffeners and frames is 7075-T6 aluminum alloy. An exception is frame station 442, which is steel heat treated to 220 KSI.

#### B. Wing Group

The wing, which is fully cantilevered off the fuselage, consists of a main frame assembly, leading edge flap, trailing edge flap, trailing edge assembly, aileron, spoilers and wing tip. (See Figures 1 and 2.) The wing is swept back 45° at the 25% chord line. The panel has two main spars and a transfer spar attached to the fuselage by four pins which join the hinge fittings on the forward and transfer spars to mating fittings at fuselage stations 390 and 442. The wing is secured to the fuselage by a turnbuckle at its leading edge. Removable fairings cover the gap between the wing panel, wing stub and fuselage. The ailerons, spoilers,

and trailing edge flap are mounted on the aft spar. The leading edge flap is mounted essentially off the front spar. The main landing gear is suspended from forward and aft spars and retracts inboard to fit flush into the wheel well, where it is enclosed by fairings and doors. Supports are provided for attaching two pylons to the underside of each wing outboard of the landing gear. External fuel stores can be carried on the inboard pylon only; however, both pylons can be utilized as armament stores.

1. Main Frame Assembly. The wing frame assembly is composed of a forward, aft, and transfer spars; ribs, and skin. The method of analysis is along the lines of the two-spar "interaction" type, modified to account for the presence of the transfer spar. The box-like front spar acts in the nature of a propped cantilever fixed at fuselage frame 390, and supported at the transfer spar. The box-like rear spar and the forged transfer spar have a common point of origin, namely fuselage frame 442. They are treated as cantilever beams. The basic material of the wing structure is 7075-T6 aluminum alloy.

2. Spoiler (Considered secondary structure). The segmented spoiler (Figure 1) consists of five segments on each wing and is supported by a continuous hinge attached to the rear spar of the wing at the 70% line. Control linkages, actuated by a single 7075-T6 aluminum alloy, hydraulic actuator located in each wing, provide the means for deflection of the spoiler segments.

3. Leading Edge Flap (Considered secondary structure). The leading edge flap (Figure 1) forms most of the wing leading edge. It is deflected downward, rotating about a hinge line, to vary the camber of the wing. Maximum deflection is 20° dependent on indicated airspeed.

The leading edge flap is designed entirely from airloads and the interaction of wing and flap bending. The structure consists of a stiffened "D" tube supported at four points, three points of actuation and one idler. The main structure is a formed 7075-T6 aluminum alloy, channel spar with contoured 7075-T6 aluminum alloy forgings at the support points.

#### C. Main Landing Gear

The main landing gears (Figure 6) are mounted in the wing. Each gear assembly consists of an air-oil shock strut; a side brace; a wheel and brake assembly; an outboard door (made from a casting), and a built up sheet metal wheel fork fairing. Each main gear is attached to the wing by means of removable pins in the trunnion. The forward trunnion pin rotates in an eccentric assembly mounted in a trunnion fitting attached to the front spar. The aft trunnion pin rotates in a self-aligning bearing mounted in a support attached to the rear spar. When retracted, the main gear is enclosed in the wing by the outboard door, the fork fairing, and a hydraulically-operated inboard door mounted on the side of the fuselage. A door in the fork fairing provides ac-

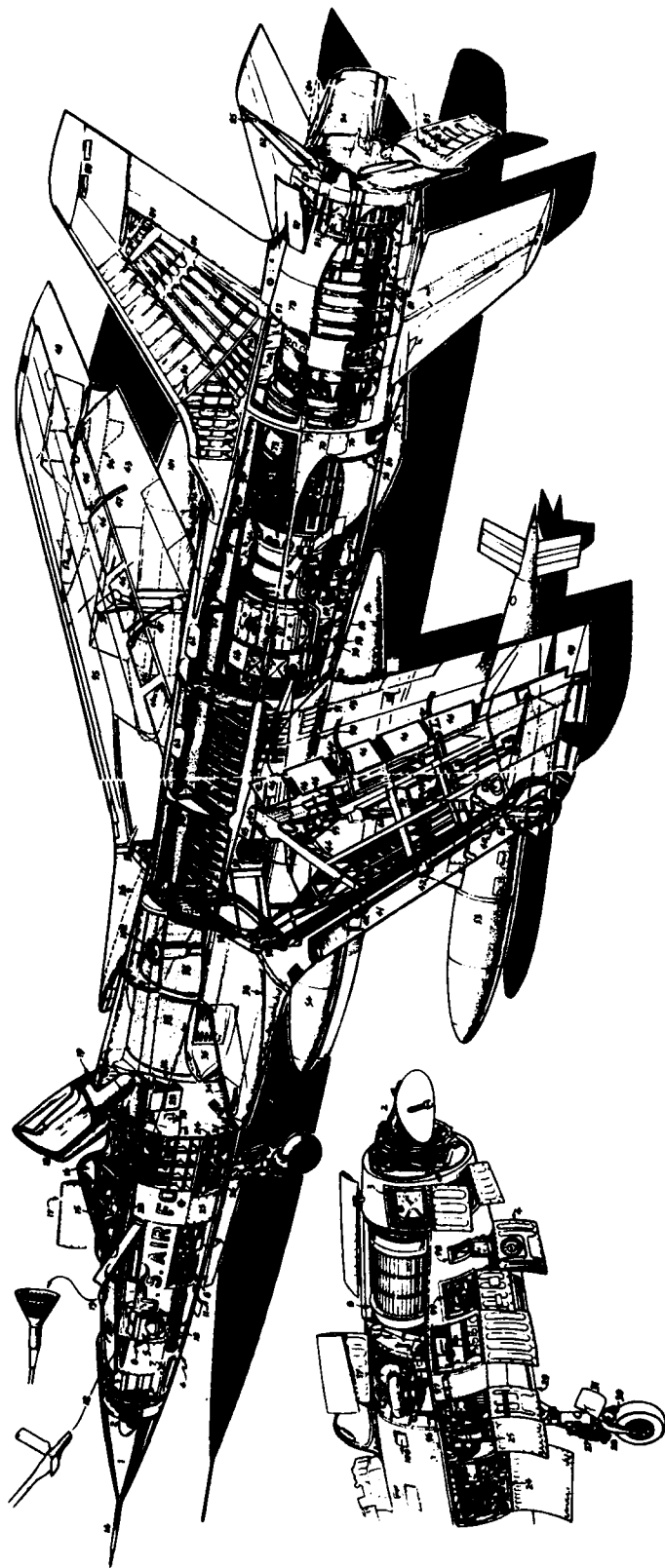


Figure 1. F-105D Cutaway View.

- 1 Dielectric nosecone: hinges to port
- 2 Radar antenna
- 3 NASARR R-14A radar
- 4 ADF antenna
- 5 Forward electronic pack
- 6 M-61 6-barrel 20mm gun: hyd. op.
- 7 Gun-port
- 8 Ammunition drum (beltless feed)
- 9 Cases retained
- 10 Lox converter
- 11 Lox filling point
- 12 Flight refueling socket for flying boom
- 13 Flight refueling probe and drogue
- 14 Pitot / static, electrically de-iced
- 15 Heated, bullet-resisting windshield
- 16 Sidepanels
- 17 Air-turbine unit driving AC generator and utility system hydraulic pump
- 18 Electrically operated canopy
- 19 Emergency canopy jettison button

- 20 Canopy external latch
- 21 Canopy jettison handle
- 22 Radar attack sight
- 23 Cockpit air-conditioning pack
- 24 Electronics compartments left and right
- 25 Hydraulics bay
- 26 Forward-retracting nosewheel
- 27 Torque-links
- 28 Hydraulic steering, electrically engaged
- 29 Anti-skid accumulator in nose-wheel bay
- 30 Taxiing light
- 31 Radar reflector
- 32 Production break
- 33 Cockpit floor-level
- 34 Variable-geometry intake
- 35 Boundary-layer fence
- 36 Intake duct to engine
- 37 Supplementary intake: gear-down only
- 38 Forged center section spar
- 39 Front wing attachment

- 40 Rear wing attachment
- 41 Leading-edge flap: max 20°
- 42 Actuators for 41
- 43 Fowler-type flap: max 34.5°
- 44 Forged bridge-member
- 45 Heavy machined wing-skin
- 46 Five-section flight spoilers (lateral control)
- 47 Guide rails for 43
- 48 Low-speed aileron: honeycomb
- 49 Aileron power unit
- 50 Aileron/spoiler mixer
- 51 Fuel lines from pylon tanks
- 52 Gravity fillers for pylon tank
- 53 450 US gal pylon tank: air bleed pressure feed
- 54 Republic "Buddy-Pack"
- 55 Forward fuel tank
- 56 Main fuel tank
- 57 Aft fuel tank
- 58 Fuel tank drains

Legend for Figure 1 Continued

- |  |  |  |
|--|--|--|
| 59 Main-gear anchorage   | 74 Cooling air to afterburner                    | 89 Buzz dampers                                  |
| 60 Breaker strut   | 75 Air discharge from 73                         | 90 Single-point pressure refueling               |
| 61 Multi-disc brakes with anti-skid                              | 76 Rudder disconnect                             | 91 Cartridge starter; two spares adjacent        |
| 62 Fuel tank access hatches                                      | 77 Rear-fuselage disconnect: four bolts          | 92 Water injection tank (stb'd) 36 US Gal        |
| 63 Pratt & Whitney J75-P-19W two-spool turbojet with afterburner | 78 Rudder power-unit compartment                 | 93 Primary hydraulic reservoir in wheel bay      |
| 64 Stainless-steel firewall                                      | 79 After-burner fuel injectors                   | 94 Bullpup missile on stb'd outer pylon          |
| 65 Johns-Manville "Tadpole" firewall                             | 80 Con-di nozzle actuators                       | 95 No fuel tanks in wing                         |
| 66 Compressor blow-off valve                                     | 81 Tailplane fulcrum                             | 96 100 Amp battery                               |
| 67 Engine oil tank 5% US gal                                     | 82 Four-petal speed brakes                       | 97 Ram-air turbine                               |
| 68 Engine oil drain  | 83 Speed-brake actuators                         | 98 Emergency and utility hydraulic accumulators  |
| 69 Oil filler  | 84 Horizontal petals open 19° or T/O thrust      | 99 Utility hydraulic reservoir and filler        |
| 70 Access to rail/roller engine mount                            | 85 Vertical petals travel-limited when gear down | 100 Exhaust from 17                              |
| 71 Accessory group (two doors under)                             | 86 Turbine danger-line                           | 101 Practice bomb dispenser on stb'd inner pylon |
| 72 Engine duct door  | 87 Braking parachute box                         | 102 "Bomb kicker"                                |
| 73 Compressor and turbine section shroud                         | 88 Access to aerial cable                        |  |

cess to the main landing gear wheel and axle when the gear is in the extended position. Analytically the main gear is considered as a beam column on a flexible support (the wing). Both deflections of wing and strut are accounted for. The side brace reacts a portion of inboard acting ground loads as axial load, while torque applied to the gear is transmitted through a scissors connecting the piston fork and outer cylinder.

Material for the gear is AMS 6427 steel, heat treated to 220 ksi minimum.

### III. Initial Fatigue Analysis - F105D

#### A. Basis for Analysis

As previously noted, initial F105 design and production contracts contained no fatigue requirements. Subsequently when the Air Force sought to verify the aircraft's ability to withstand 4000 flight hours, it became necessary to develop certain parameters to serve as a basis for determining the flight spectrum. These included:

1. Mission Profiles. The mission profiles for the fatigue analysis were based upon the Using Command's utilization of the airplane for pilot proficiency training. Only peacetime use of the airplane was considered. With these limitations, some twenty\* missions requiring five different configurations, were chosen as representing total fleet usage. Almost 70% of all the flight (spectrum) time involved missions requiring only clean aircraft configurations. Later studies and changed aircraft operation, indicated that most missions required carriage of external stores.†

2. Load Spectra. The load spectra were divided into four parts; a maneuver load spectrum, a ground-air-ground load spectrum, a component parts spectrum, and a gust spectrum.

- a. The maneuver load spectrum consisted of loads on the primary structure resulting from intentional maneuvers. In order to obtain this spectrum, statistical data was examined for frequency of the load parameters. It was decided to base exceedance curves for positive load factor‡ on a proposed Navy curve, which was a compromise between an NACA Standard probability curve, and the conservative requirements of MIL-A-8866. The Navy curve is shown in Figure 7(A). The service limit load factors were established to be the F105 design limit load factor,  $n_z = 8.67$  for subsonic flight and  $n_z = 7.33$  for supersonic conditions. The service utilization factor ( $N_s$ )  $\cong 26$ . The negative load factor spectrum was derived from flight test data on the F100A, C, D and E aircraft. Since examination of the data indicated that negative normal load factors generally occurred during symmetric maneuvers only, no negative load factors were

\* For explanation of actual mission profiles evaluated see Reference 1.

† A clean configuration requires higher balancing tail loads and aft fuselage bending moments than one with external stores. As a consequence, early analysis gave very conservative results on this portion of the aircraft.

‡ Load factor exceedance is the single most important parameter involved in load spectra development.

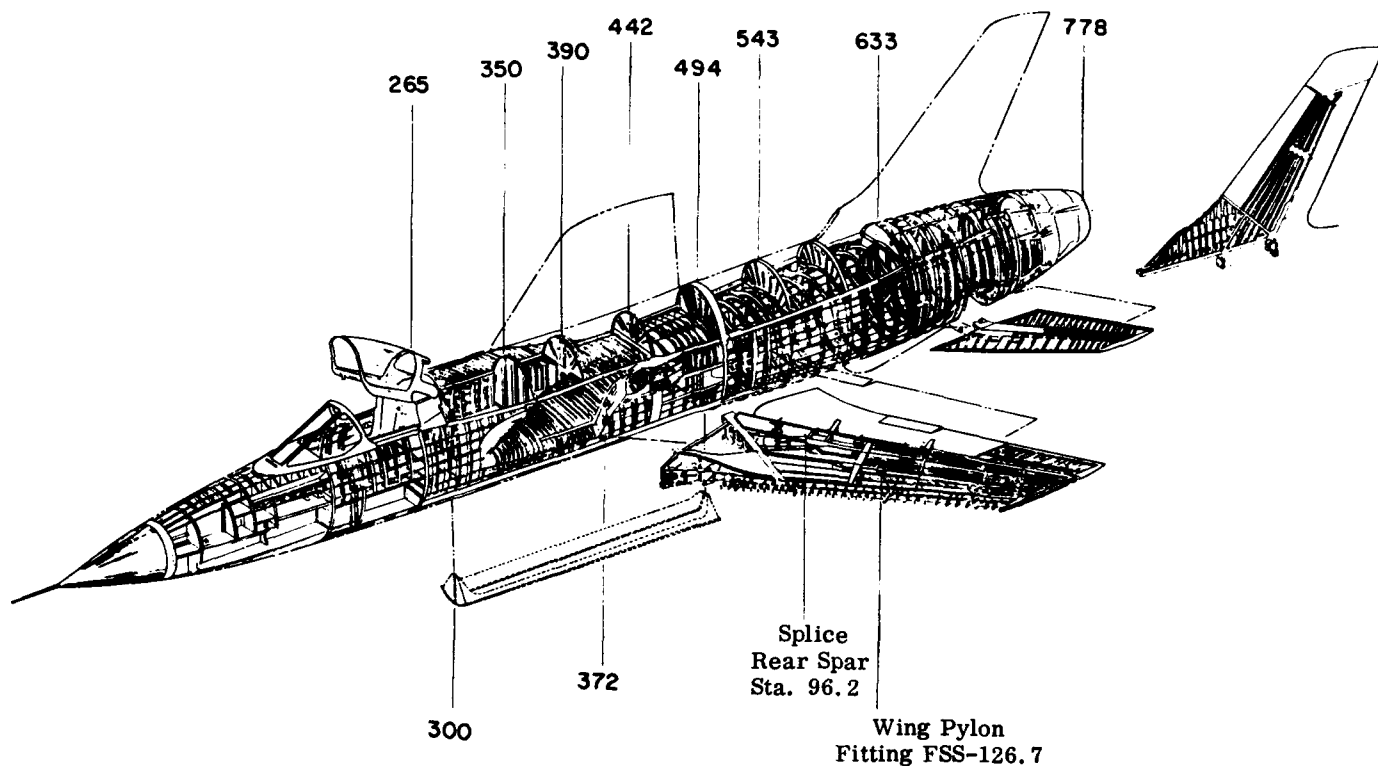


Figure 2. Pertinent Fuselage and Wing Stations.

included in the asymmetric spectrum. The exceedance curve for negative loads is shown in Figure 7 (B).

In order to relate the normal load factor ( $n_z$ ) spectrum to environment, a relation to speed and altitude was necessary. At the time the spectrum was prepared, the only available data giving speed and altitude relationships for jet fighter aircraft was flight data for 1577 hours of normal operational service of F86E and F aircraft and 971 hours of normal operational service of F100D and F aircraft. In addition, data on 165 flight hours of the F105B provided load factor-velocity correlations. Using these data, probability density curves were determined which permitted calculation of the probability of a load factor occurrence happening at any given speed and altitude. For purposes of analysis, three speeds and three altitudes were used to represent the entire regime. Using these conditions, it was then possible to establish the number of occurrences of each incremental load factor variation throughout the entire regime.

As stated above, all occurrences of negative load factor were assumed to be for symmetric conditions. Only balanced airplane conditions were considered. For the positive load factor conditions, however, flight data for five types of fully instrumented jet fighters indicated that approximately half of all occurrences between the load factors of 2.0 and 6.5 are asymmetric conditions. Therefore the positive load factor spectrum was separated into symmetric and asymmetric conditions by assuming for  $n_z/n_{zL} \leq .6$ , one half of all occurrences were symmetric; for  $n_z/n_{zL} = .7$ , three quarters of all occurrences were symmetric; and for

$n_z/n_{zL} \leq .8$ , all conditions were symmetric.

In order to select typical configurations for analysis, the maneuver history from the F-105 mission profiles was analyzed to establish the maneuver time in each mission and the total maneuver time in the life of the airplane. These maneuver times were then correlated with the load factors, speeds, and configurations shown in the mission profiles. Increments of 4000 pounds were used to establish typical gross weights for analysis. The maneuver time was correlated to the number of cycles for each condition, so that for each load condition the frequency of occurrence was proportional to the percent of total maneuver time.

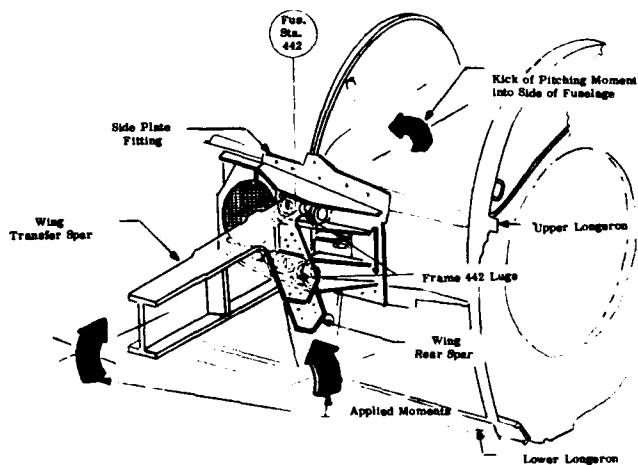


Figure 3. Side Plate - Transfer Spar Joint.

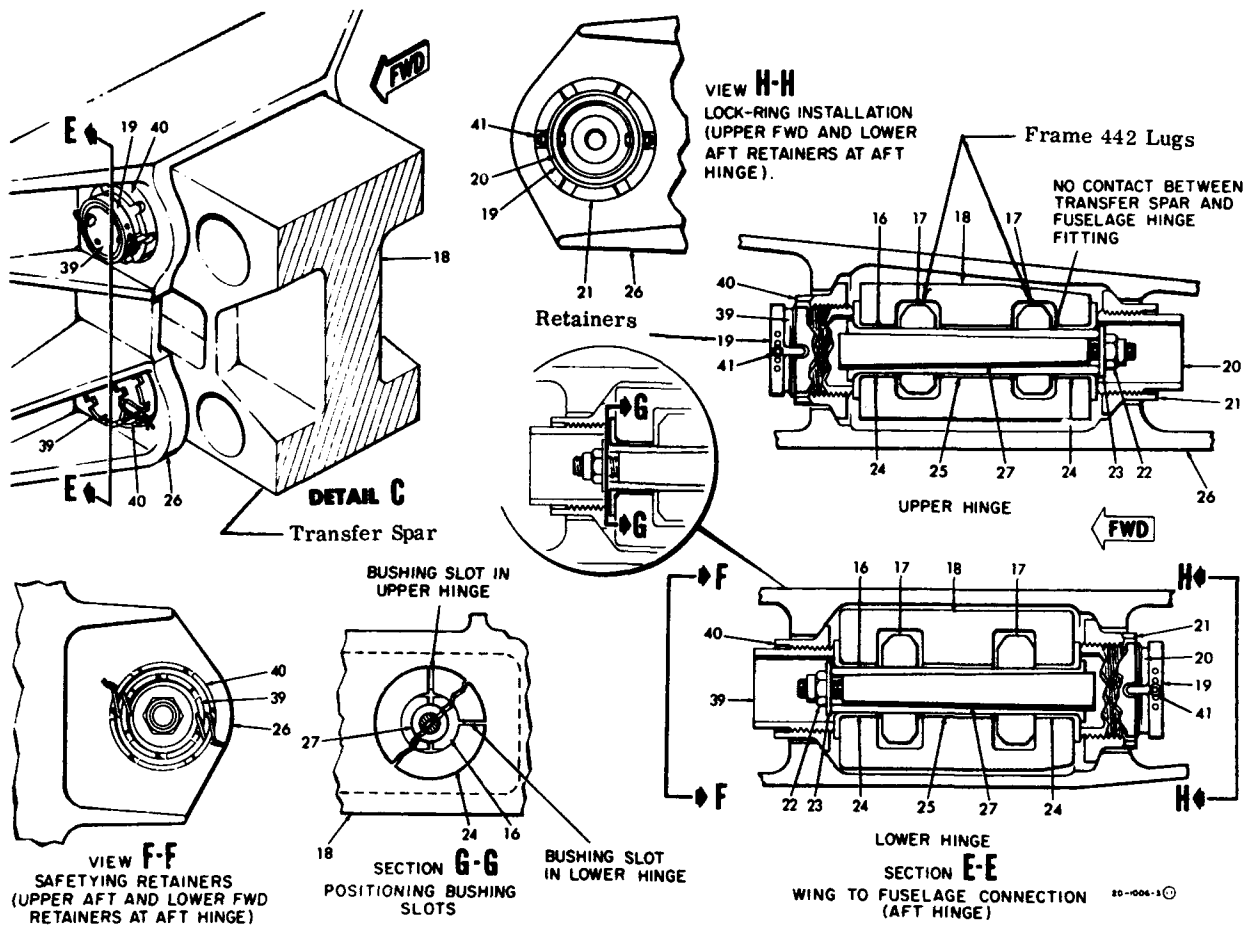


Figure 4. Wing Disconnects - Fus. Sta. 442.

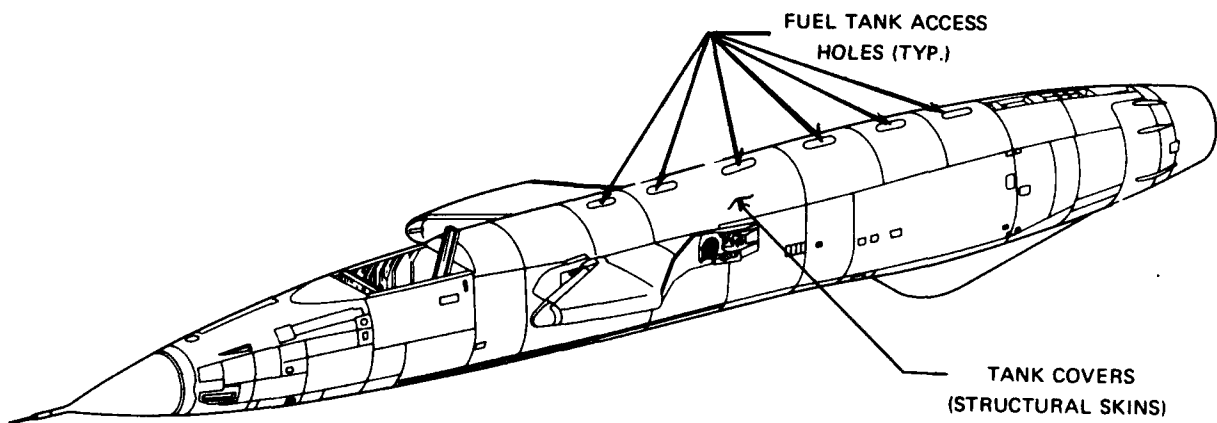
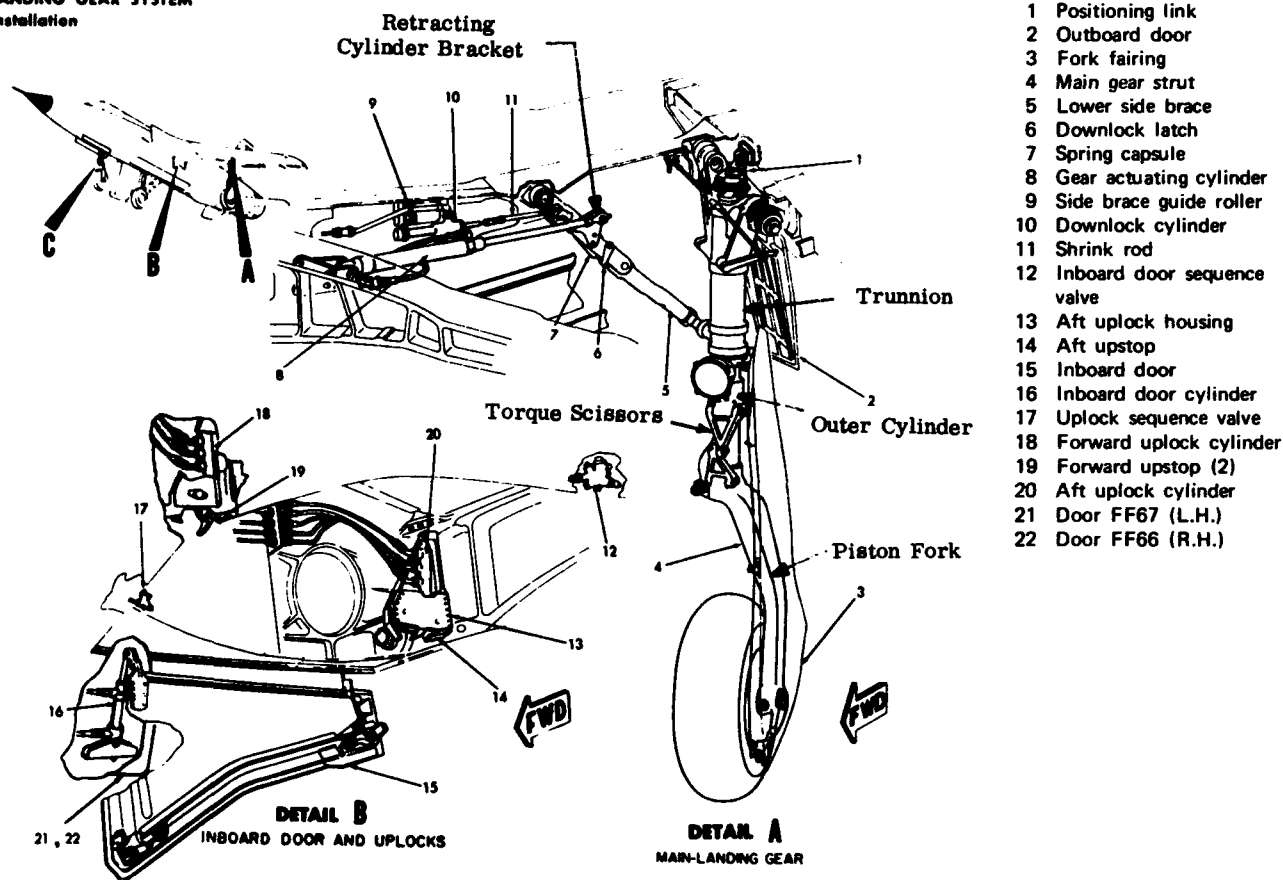


Figure 5. Fuselage Fuel Tank Access Holes.



**LANDING GEAR SYSTEM  
Installation**



**Figure 6. Landing Gear Strut and Door Installation.**

Since it was necessary to use specific values of load factor for the stress analysis, the exceedance curves were changed to discrete points by selecting increments of  $n_z$  and computing the number of occurrences for the variation of the normal load factor in the interval. This number of occurrences was then associated with the value of  $n_z$  in the middle of the interval. The increments selected started at 2g at low load factors, and were reduced as load factor increased above 4g, since the fatigue damage increases very rapidly with increases in load above the endurance limit. The number of occurrences in any increment were obtained as shown in Figure 7C.

For the airload distributions, balance loads were determined for a sufficient number of load factor and weight combinations so that the rest of the conditions could be obtained by scaling, using the ratio of  $n_z W$ , without appreciable error. In order to determine balancing tail loads, an average value of center of gravity equal to 29 percent MAC was used for all the weight configurations. Deviations of the center of gravity location from this average were insignificant.

The above procedure gave all necessary loadings for the balance conditions. However, for the dynamic conditions, it was not possible to construct exceedance curves from the limited amount of information then available. In order to establish a spectrum F84F flight test data was examined to determine envelope values of dynamic parameters. This data was compared to limited data available on the F2H-2, F-84G, F-86A, and F-94B aircraft. There was a strong similarity in the dynamic parameters for all these aircraft. Therefore, it was concluded that similar airplanes are flown in the same manner; and that statistical devices could and would be used for evaluation of the F-105. See Table I.

b. The ground-air ground spectrum affected both the landing gear and landing gear backup structure. The mission profiles chosen to represent flight usage allowed for only 2500 landings in 4000 hours of aircraft use; whereas detail Air Force requirements pertaining to structural fatigue certification programs, called for 5200 landings.

This conflict in criteria was resolved by a compromise; the landing gear was analyzed and tested for

3200 landings while its supporting structure was qualified for 4000 landings. In later analyses and tests, both gear and structure were qualified for 4000 landings. Included in this spectra were the effects of different aircraft sink rates,

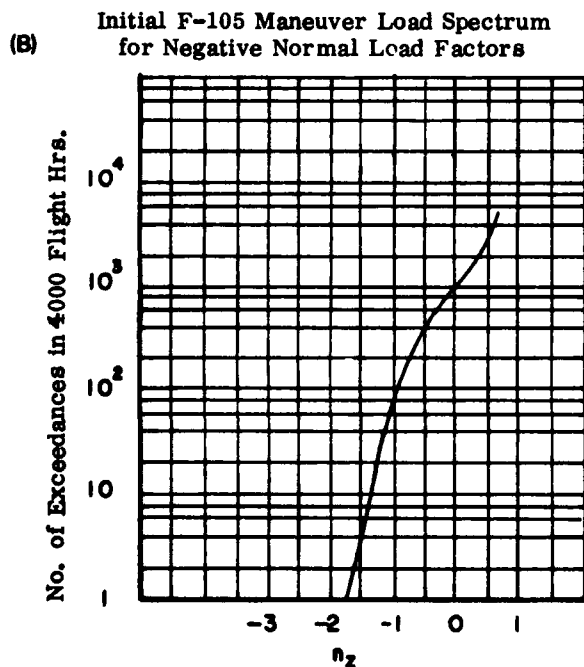
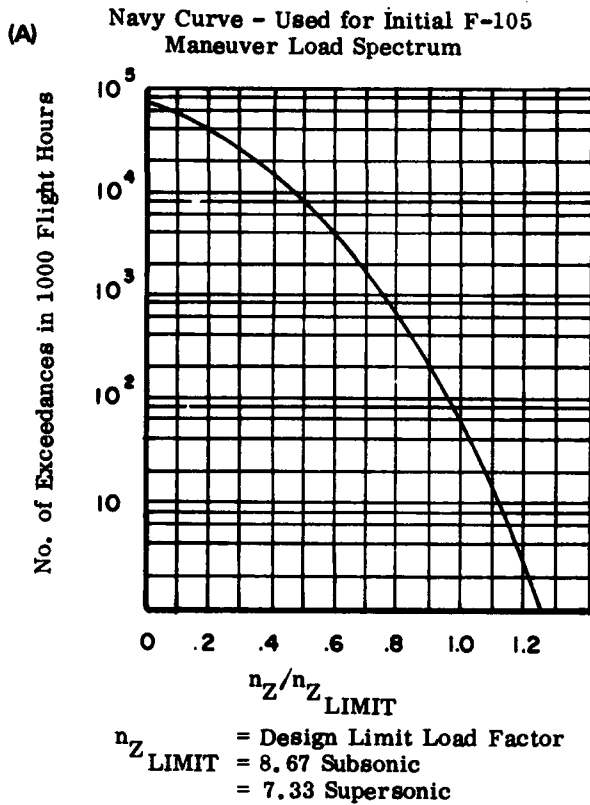
various degrees of braking, ground turning, and drift landings.

c. Component parts load spectrum. In addition to the primary loads resulting from flight and landing, it was necessary to evaluate the loads resulting from operation of the control surfaces and various major systems in the airplane. Eleven component parts were selected for evaluation, based on the existence of low static margins of safety and/or high stress concentration factors in the supporting structure. The supporting structure was analyzed rather than the components themselves, because the component parts can be readily inspected and replaced, while the backup structure cannot.

The spectra were developed from a study of the mission profiles, the primary maneuver load spectra, the envelope values of the dynamic parameters, and from discussions with pilots and the Using Command as to expected component usage in operational service.

Without getting into details involving derivation of each component spectrum (which is available in Reference 2), the components evaluated were aileron, leading edge flap, trailing edge flap, spoiler, rudder, speed brake, drag chute, engine mount, internal store displacement gear, bomb bay doors, and cockpit canopy.

d. The gust load spectrum consisted of the loads resulting from gusts. These loads were obtained by statistical analysis of gust frequencies, and elastic analysis of the aircraft structure to determine dynamic response. The spectrum was found to be non-damaging, with stresses below the endurance limit. For more details on the methods used, see Reference 3.



B. Points Investigated and Methods Used for Analysis

Analysis was performed for all items of fixed structure which were considered to have a possibility of being critical in fatigue. This included all areas of high stress determined by review of stress analysis reports, as well as all areas of high stress concentration determined by a review of major drawings and the airplane structure itself. All major

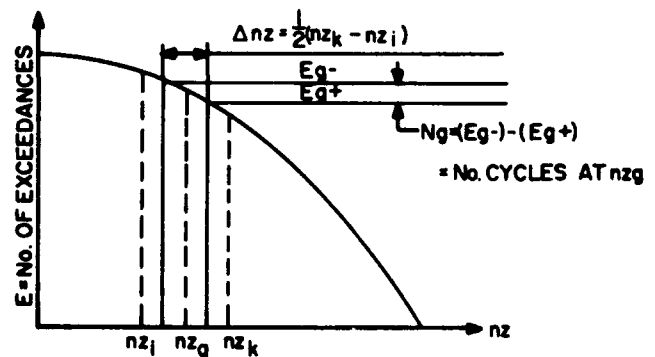


Figure 7. Exceedance Curves.

Figure 7C. Exceedance Curve

TABLE I.  
DYNAMIC PARAMETERS FOR ASYMMETRIC MANEUVER SPECTRA

MACH NO.	ALTITUDE	DYNAMIC PRESSURE	$n_z$	$n_y$	P	$\dot{P}$	q	$\dot{q}$	r	$\dot{r}$	DYNAMIC HORIZONTAL
											TAIL LOAD
											INCREMENT
		$q_D$	Normal Accel.	Lateral Accel.	Rolling Vel.	Rolling Accel.	Pitch Vel.	Pitch Accel.	Yaw Vel.	Yaw Accel.	$\Delta L_{HT}$
	FT.	Lbs/Sq.Ft.	g	g	Rad/Sec	Rad/Sec <sup>2</sup>	Rad/Sec	Rad/Sec <sup>2</sup>	Rad/Sec	Rad/Sec <sup>2</sup>	LBS.
0.6	10,000	367	1.0	-.42	2.73	-4.60	.33	-1.55	.17	± 1.11	14700
			2.5	-.45	2.92	-4.90	.38	-1.66	.18	± 1.18	15740
			3.0	-.43	2.78	-4.70	.38	-1.60	.17	± 1.13	15200
			3.5	-.40	2.56	-4.30	.36	-1.45	.15	± 1.04	13750
0.9	10,000	825	1.0	-.42	2.73	-4.60	.33	-1.55	.17	± 1.11	14700
			2.5	-.45	2.92	-4.90	.38	-1.66	.18	± 1.18	15740
			3.0	-.43	2.78	-4.70	.38	-1.60	.17	± 1.13	15200
			3.5	-.40	2.56	-4.30	.36	-1.45	.15	± 1.04	13750
			4.3	-.31	2.03	-3.40	.33	-1.15	.12	± .81	10900
			4.5	-.28	1.85	-3.10	.30	-1.05	.11	± .73	10000
			4.9	-.22	1.46	-2.45	.28	-.83	.09	± .59	7870
			5.5	-.15	.93	-1.58	.25	-.50	.06	± .39	4740
6.1	-.09	.55	-.85	.22	-.30	.03	± .23	2840			
1.2	20,000	980	1.0	-.42	2.73	-4.60	.33	-1.55	.17	± 1.11	14700
			2.5	-.45	2.92	-4.90	.38	-1.66	.18	± 1.18	15740
			3.0	-.43	2.78	-4.70	.38	-1.60	.17	± 1.13	15200
			3.5	-.40	2.56	-4.30	.36	-1.45	.15	± 1.04	13750
			4.3	-.31	2.03	-3.40	.33	-1.15	.12	± .81	10900
			4.5	-.28	1.85	-3.10	.30	-1.05	.11	± .73	10000
			4.9	-.22	1.46	-2.45	.28	-.83	.09	± .59	7870
			5.5	-.15	.93	-1.58	.25	-.50	.06	± .39	4740
6.1	-.09	.55	-.85	.22	-.30	.03	± .23	2840			

NOTES:

- (1)  $\Delta L_{HT}$  is to be added to balanced tail load.
- (2) For values of  $n_z$  other than shown, parameters are determined by extrapolation.

splices such as wing to fuselage, wing spar cap, fuselage, longeron, and skin splices were investigated. In addition areas of failure in static test were also included, which meant that the fuselage at station 494 (failed at 100 percent of ultimate load), and the vertical fin flag (which failed at 100 percent of ultimate load) also were checked.

In general, the fatigue life at a pre-selected point was calculated using a modified Shanley equation.\*

$$\frac{\sigma_r - \sigma_c}{\sigma_{ULT}} = \left[ \sum \alpha_i \left( \frac{\sigma_{imax} - \sigma_c}{\sigma_{ULT}} \right)^{\delta d} \right]^{1/\delta d} \quad (1)$$

A complete discourse on how to apply this equation is found in Reference 4. The only exceptions to its use were in areas where sufficient data was not available in a form that lent itself to easy substitution (spotwelds), and in the nose and main gear analysis. Both these areas utilized Miner's

Rule for determination of fatigue life. The early methods used in arriving at the stresses and cycles can best be demonstrated by examination of the sample tables shown in Appendix A.

C. Predicted Premature Failure Points (By Analysis)

A premature failure point is defined as one showing a life of less than 4000 hours under the initial design spectrum. No scatter factor is considered.

Some 40 points were analyzed on the fuselage, wing and empennage. All exhibited lives in excess of 4000 hours. While tests later confirmed the analytical results for those points, two points not considered did fail prematurely. (Section IV.) They failed because of unusually high stress concentrations, which were not properly evaluated in the original review of possible critical areas. After the failures, it was quite apparent that these were fatigue-sensitive areas.

\* For reasons why this method of determining fatigue life was chosen, see Reference 4.

Had they been suspect, some small scale testing could have been performed in order to determine the stress concentration factors, and analytical means would have predicted the test results.

#### IV. Initial Fatigue Test on an Entire F105D at Wright Field

Following the fatigue analysis, a test program was instituted to confirm the analytical conclusions, and to insure that all fatigue critical points on the aircraft had been properly evaluated.

##### A. Development of Test Spectrum

In formulating the spectrum for test of the complete airplane, it was necessary to minimize the number of test conditions and cycles, to keep the test to a reasonable length of time. A spectrum for testing was developed which was limited to a maximum of 80,000 cycles (actual cycles equalled 215,000) and five different conditions. Both active and inactive cycles were included because active cycles might have started a crack and inactive cycles propagated it. The shortened test spectrum was derived in the following manner.

An investigation of the analytical solutions indicated that the stress levels in the 26-32 KSI\* range alone accounted for over 50 percent of the anticipated useful life of each point analyzed. Further research determined the flight conditions which produced these stress levels, and a list was drawn up for each discrete point investigated. Invariably, a few conditions were found to contribute a major portion of the damage at the most critical + point. This led to a test spectrum consisting of:

1. Three balanced flight conditions which produced the most damage on the seven most critical points as shown by analysis.
2. A dynamic maneuver condition, chosen because of the high tail load associated with it, and which produced reversal of stresses in the aft fuselage.
3. A negative flight condition which produced stress reversals on the entire airplane.

Summarizing the test spectra consisted of the following five conditions:

- a. PC-09: A subsonic positive symmetrical maneuver at high load factor. Aircraft clean. This was a balanced condition.
- b. PC-12: A supersonic positive symmetrical flight maneuver. Aircraft clean. This was a balanced condition.

c. NC-12: A supersonic negative symmetrical flight maneuver. Aircraft clean. This was a balanced condition.

d. PC-1.2 (Dynamic): A supersonic positive symmetrical dynamic maneuver, two 450 gallon tanks on wing.

e. RPCSI-1.2: Rolling pullout, no external store, high load factor.

The number of cycles applied for each of these conditions was adjusted to match the total damage at each point.

Next, the actual damage due to the airplane flight spectrum was calculated, at each of the seven critical points selected. This damage was equilibrated in the reduced flight spectrum by varying the number of cycles at each stress level and flight condition producing damage. The inactive cycles were distributed by examining each condition and determining the number of inactive cycles per condition, or group of conditions. This number was applied to the total aircraft spectrum and a factor obtained. Applying this factor to the reduced spectrum, the inactive cycles were distributed within the test spectrum.

The damage at any point was defined by two parameters, number of cycles and stress amplitude. The S/N diagram plotted on log-log paper is a straight line. This line suggests that any point on it can be described as a stress ratio and a number of cycles. Thus two different points on the S/N diagram would have two different sets of values, but have the same damage. Thus the S/N diagram, in essence, is a line of equi-potential damage. At any pre-selected point the stress level and number of cycles were determined. This point was plotted on the proper S/N diagram. A line drawn through the point and parallel to the S/N diagram was line of equi-potential damage.

This concept led to a set of seven simultaneous equations developed from the Shanley equation using the seven critical airplane points as a basis for expansion. Rewriting the Shanley equation in a more useful form:

$$\Sigma \left[ \frac{\sigma_{i\max} - \sigma_c}{\sigma_{ULT}} \right]^{\lambda d} \frac{n_i}{N} = K \quad (2)$$

or total damage to match at a point =  $KN = K'$ ; where  $N$  = number of active cycles required. These values of  $K$  and  $N$  active were obtained from the actual tabular solution of each critical point.

In order to test to several stress levels, each flight condition that produced damage was subdivided into 60%, 80%, 100% and 115% of the balanced aircraft flight load.

\* The material was 7075-T6 aluminum alloy.  
 + Defined as points having lowest analytical fatigue lives.

The coefficients of the left hand side of the equation,

$$\left[ \frac{\delta_{i_{max}}' - \delta_e}{\delta_{ULT}} \right] \lambda d = \text{damage per cycle}$$

were computed for each load level of each test flight condition.

As stated previously, seven simultaneous equations were written. A typical equation is shown as follows:

$$\text{Let } \left[ \frac{\delta_{i_{max}}' - \delta_e}{\delta_{ULT}} \right] \lambda d = a$$

Then

$$\begin{aligned} K' = & (a) (60\%) (n_1) \text{ PC-09} \\ & + (a) (80\%) (n_2) \text{ PC-09} \\ & + (a) (100\%) (n_3) \text{ PC-09} \\ & + (a) (115\%) (n_4) \text{ PC-09} \\ & + (a) (60\%) (n_5) \text{ PC-1.2} \text{ ---} \\ & + (a) (115\%) (n_8) \text{ PC-1.2} \text{ ---} \\ & + (a) (60\%) (n_9) \text{ RPCSI-1.2} \text{ ---} \\ & + (a) (115\%) (n_{12}) \text{ RPCSI-1.2} \end{aligned}$$

Assigning values to  $n_i$ , the equations were iterated. The damage was closely approximated for all seven points.

#### B. Discussion of Premature Failures to Test Aircraft

1. Description of Test Vehicle Instrumentation. The test vehicle was instrumented to monitor areas of high strains. It was suspended in a test jig by means of counter-balance weights and cables such that there was zero "g" acting on the structure. The external loading, which simulated flight and inertia load distributions, was applied to the airplane by whiffle trees and tension pands. Other loading fixtures were designed to simulate concentrated loads on the structure caused by heavy equipment, and distributed loads due to fuel. These concentrated loadings were applied to the airplane by approximately 30 hydraulic cylinders from a 34-channel Fatigue Load Program and Control Loading System. The cylinder loads were distributed by means of the whiffle tree linkage system to aluminum tension pads bonded to the upper and lower surfaces of the wings and empennage, to shear straps bonded to fuselage side skins, and to the fixtures that simulated the concentrated loads due to equipment.

2. Loading System. The airplane was tested to the spectrum developed for the test. In addition to the basic airloads, it also included the application of engine thrust and

speed brake loads. The loadings were applied in 10 percent increments, with the load conditions in each 10 percent increment being random in order, so as to provide as close a simulation of actual airplane usage as possible. All test cycles for the positive steady state maneuver conditions were from 1g balanced airplane to the desired loading and return to 1g balance. For the dynamic tail condition the cycling range was from 0.4g to 2g and back to 0.4g, while the negative load condition was cycled from -0.2g to -1g and back to -0.2g.

3. Results. The fatigue test was stopped at 20% of the test spectrum, with the discovery of cracks on both the left and right sides of the lower outer flanges of the steel wing attachment frame forging at fuselage station 442\* (Figure 8). A large circumferential crack was also found in the radius of each of the left and right lower aft retainers\* (Figure 9). In addition, there were, what was assumed to be, secondary cracks in the wing root fitting, cracks in two formers forward of station 442, plus assorted shear failures in attachment rivets, and cracks in the wing-fuselage fairings.

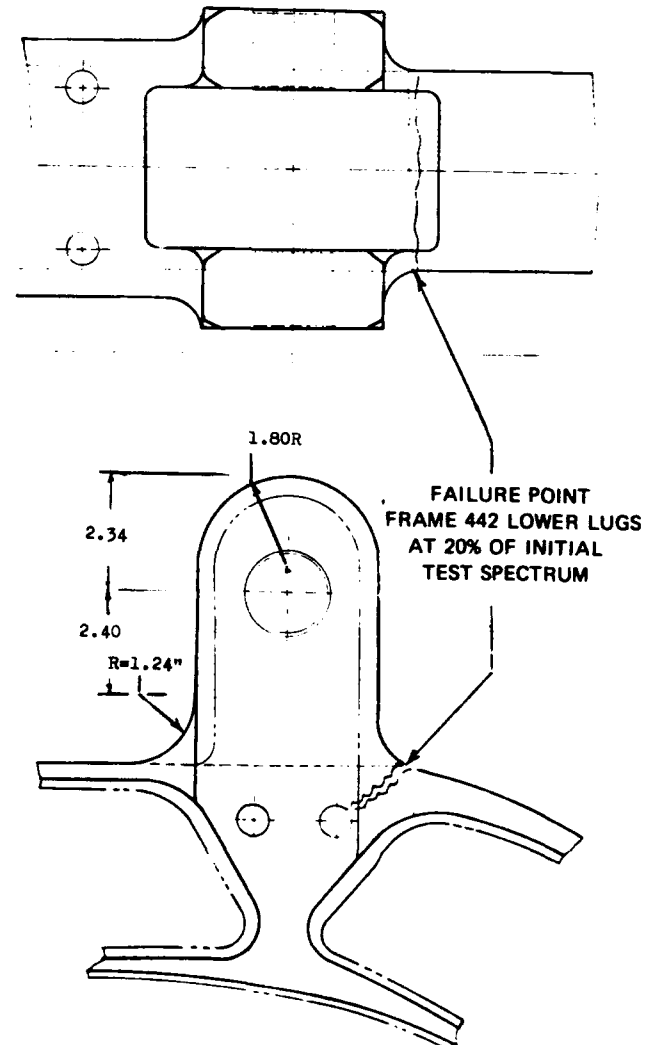
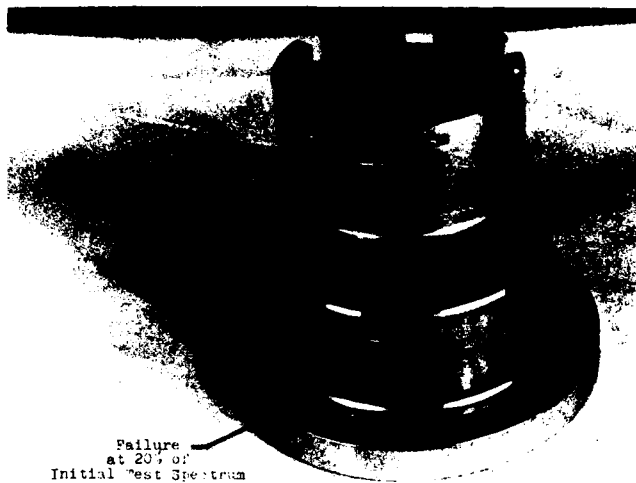


Figure 8. Original Design - Frame 442 Failure.

\* As explained in Section I, the frame at 442 carried vertical load and horizontal shear (due to bending moment) from the wing rear spar joint to the fuselage. The retainers and side plate transmitted torsion from this joint to the side of the fuselage (as pitching moment).



**Figure 9. F-105D Failure of Retainer Assembly.**

In both cases (the frame lugs and the retainers), the failures appeared to be due to high stress concentrations. In the case of the retainers, the problem was aggravated by non-uniform distribution of load between the retainer seat and the side plate fitting (thus causing high local stresses). See Figure 10.

#### V. Individual Component and Aircraft Testing at RAD Following Premature Failure at WPAFB Test Aircraft

##### A. Basis for Tests

With the failure of frame 442, and the wing retainers at the same station, a test program was initiated with three major objectives in mind:

1. To determine what load factors and safe life could be attained with the original production designed parts. This was necessary since there were already a large number of aircraft in service. It was hoped to permit flight use for up to 600 hours in the original configuration, after which rework would be accomplished.

2. To determine a practical way of reworking the frames and retainers in existing airplanes.

3. To design and test new production configurations for future airplanes. Simultaneous with the effort aimed at solving these problems, the initial fatigue spectrum was re-evaluated (and found to be conservative). Although the details of the re-evaluation will be discussed later on, it is necessary to bring this fact out now, since all of the testing that took place was influenced by the reduced spectrum that evolved from it.

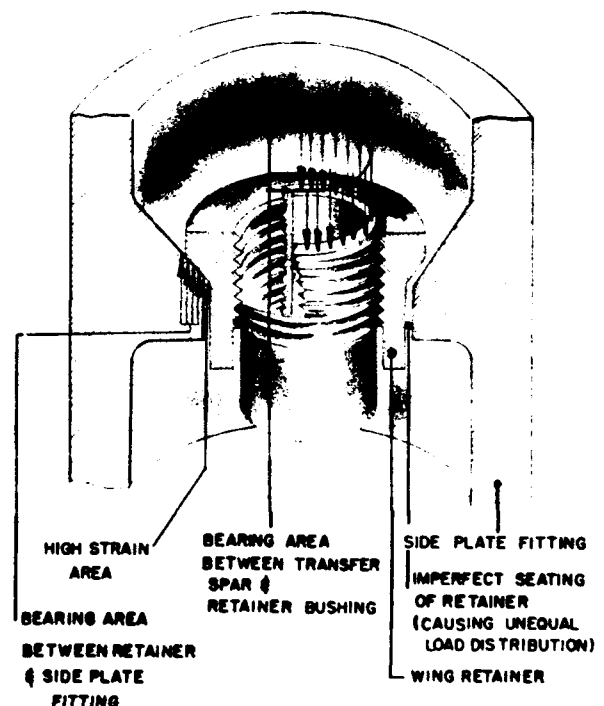
##### B. Small Scale Tests, Procedures and Equipment

1. Frame Testing. (See Figure 11.) All

component frame tests were conducted by applying in-plane loads to the frame lugs. Methods and equipment utilized for all frames tested were essentially similar. Loading was applied by means of hydraulic cylinders through a multiplying lever to steel beams. These beams mated with the frame lugs and were machined at the inboard ends to match the geometry of the transfer spar. The shear was reacted on simulated side plate fittings attached to the frame by six bolts which normally secure the frame to the actual side plate. This method of load take-out duplicated that which occurs on the airplane. Corrections in the applied load were made to allow for the dead weight of the loading beam. These corrections were such that the moments applied at the frame lugs were exact but the shear was approximately -4% in error. This error was negligible since the shear at the lugs contributes only about 10% to the frame stresses in the critical area.

Load cycling was achieved by coupling the cylinder supply and return lines through solenoid operated valves. These valves were controlled by a system of pressure switches and electrical relays. Load levels were monitored by strain gaged load cells read out on Baldwin SR-4 boxes. Normal procedures for monitoring loads were to control the high side of the load cycle off the cell on one side of the frame and the low side off the other. To ensure symmetry of loading, this process was reversed at least once during each load level in the block of the spectrum being applied.

A number of the frames tested were strain gaged in the area of the lower lugs (Figure 12A). The pur-



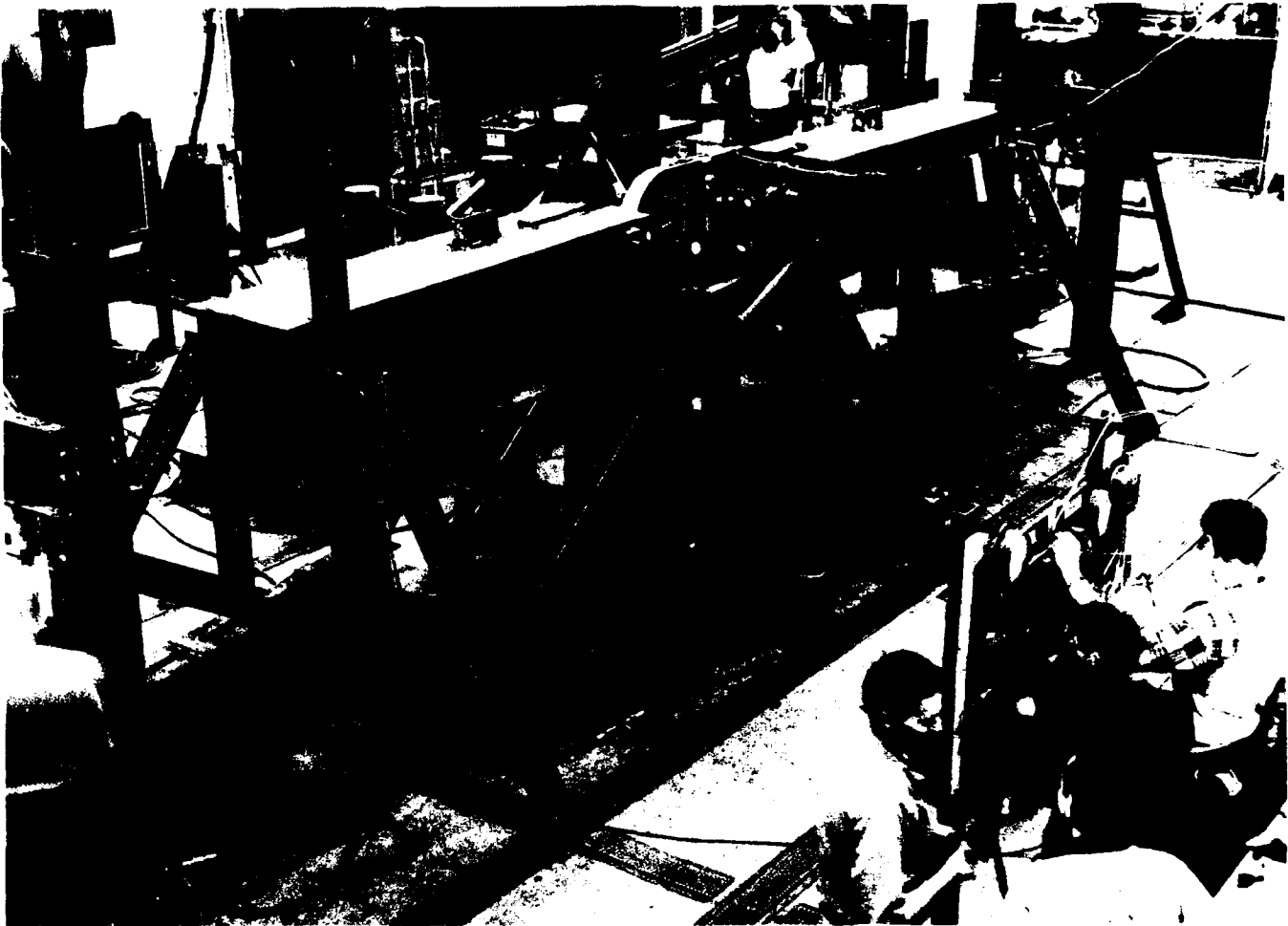


Figure 11. Component Frame Test at RAD.

pose of this instrumentation was initially to locate the stress concentration and in the later tests to assist in evaluating the various trial reworks.

2. Wing Retainer Tests. The wing retainers were fatigue tested in a fixture similar to that depicted in Figure 13A. This fixture consisted of two beams, each having a mechanical advantage, arranged so that the amplified load of each beam would be applied simultaneously and concurrently to the wing retainer. Beam stiffness was made high to minimize angular change in load application due to beam bending rotations in the plane of the test fixture.

As a further precaution against incorrect retainer load application, a spherical seat was provided in the head of the test fixture. This seat was bearing directly on a loading block that transferred load to the retainer. This arrangement insured full contact of the retainer with loading block during cycling.

Supporting seats for the wing retainers were designed and made to simulate the side plate forging in the areas of the lower aft, upper forward, lower forward and upper aft wing retainer supports. Seat deflections measured during center fuselage tests were found to be in reasonable agreement with deflections of the seat simulator used in re-

tainer component fatigue tests. The simulated support provided a spherical seat for the retainer, as well as approximating the local spring rate of the side plate forging.

All fatigue loads were applied with a 1/2 degree load eccentricity (Figure 13B). Based on a geometry

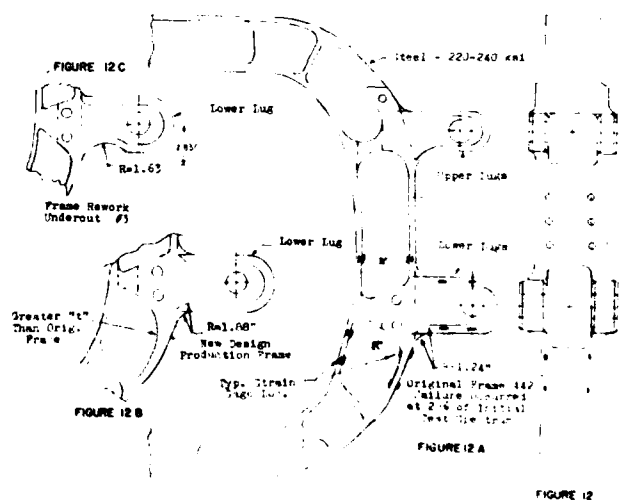


Figure 12. Original, Reworked and Redesigned Lugs - Fuselage Frame 442.

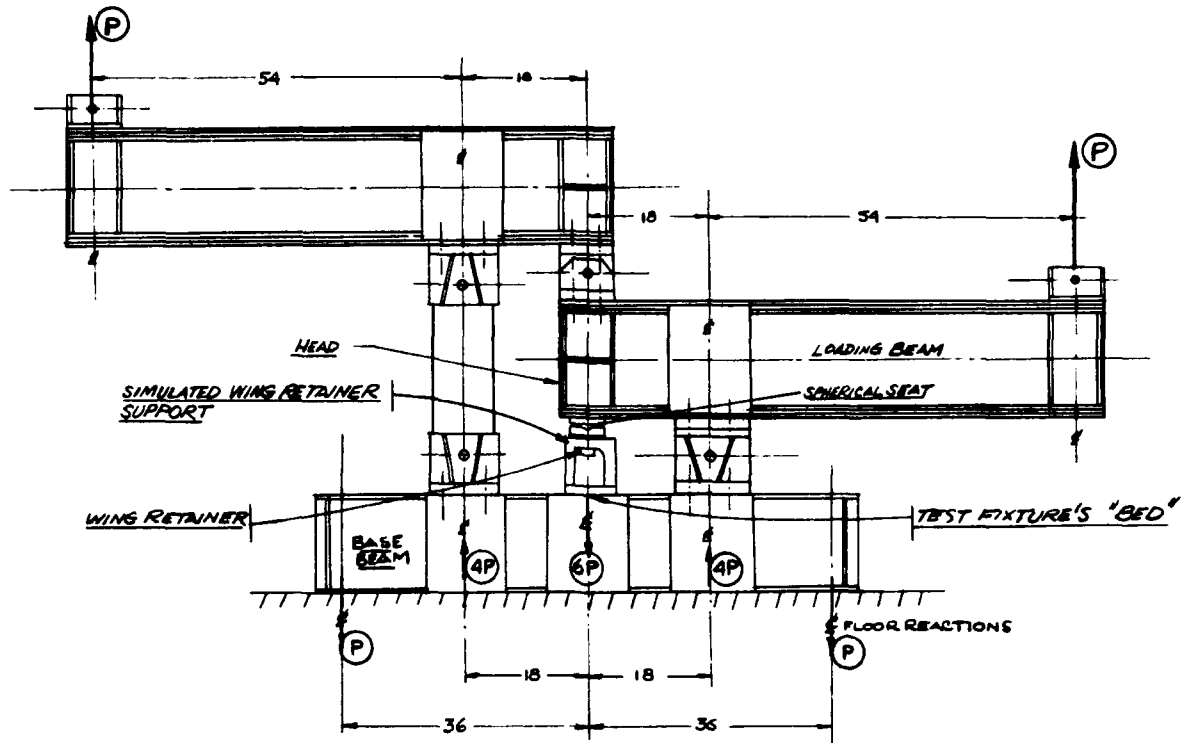


Figure 13A. Wing Retainer Fatigue Test Fixture  
(Mechanical Advantage: 6 to 1).

study of wing transfer spar engagement with the wing retainers, this angle represented maximum load angularity that could exist for an airplane installation. The simulated support block was positioned in the test fixture, with the retainer positioned concentrically with respect to the seat and so the  $1/2$  degree load eccentricity was maintained during cycling within ten minutes at the high load inputs.

### C. Rework and Redesign

1. Frame 442. The rework was based primarily on removing the area of high stress concentration and smoothing out the flow of load at the base of the lugs. Four undercuts at the base of the lug were tried, ranging in depth from shallowest at No. 1 to deepest at No. 4. An undercut of the outer frame flange near the lug, called undercut No. 5, was also tried. On the basis of the strain gage readings, and later confirmed by test, undercut No. 3, Figure 12c, was selected as giving the best promise of increased life. In addition to the undercuts, two attempts at reinforcing the frame by bolting on a plate and channels were made. However, the configuration of the frame is such that attachments were a major problem and neither rework gave improvements in life commensurate with the work involved. Shot peening was also tried but this process proved ineffective because of the high heat treat of the frame (220-240 ksi).

Redesign called for a revision to machining procedures in the area of the lug. This allowed more material and much larger radii in the critical area. See Figure 12B.

2. Retainers. (Refer to Figure 14.) Various attempts were made at eliminating fatigue in this part. Individual efforts were directed at increasing the wall thickness, changing the  $90^\circ$  fillet radius to an ellipse, smoothing the surface and tapering the flange (it was hoped that the center of resistance to load would be moved closer to the

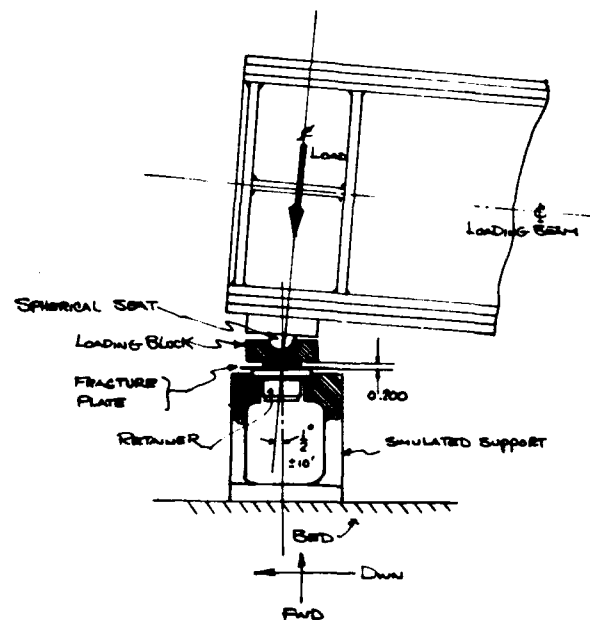
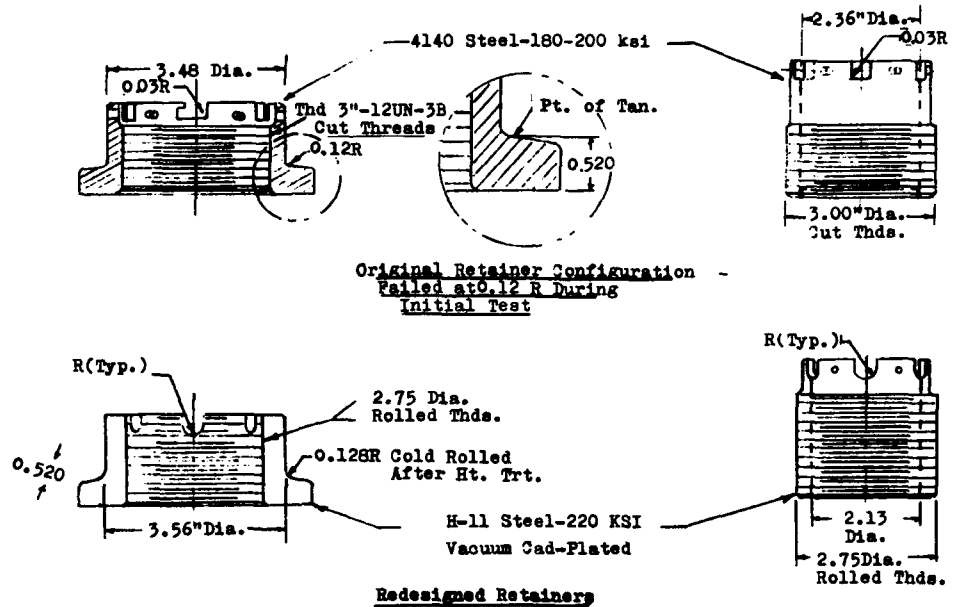


Figure 13B. Loading Geometry for Beam and Simulated Seat.



Figure 14. Original and New Design Wing Retainer Configuration - Fus. Sta. 442.



barrel of the retainer reducing the cantilever distance of load, and thereby reducing moment) while using the existing 4140 steel forging heat treated to 180 ksi minimum. Although each of these changes had some merit, the final solution required the following combinations: Material was changed to vacuum cad-plated H-11 steel heat treated to 220 ksi minimum, the fillet radius was cold rolled, the threads were rolled, the wall slots were rounded. See Figure 14. Only then were the retainers able to meet spectrum requirements. Without all of these features they continued to fail during fatigue testing.

D. Small Scale Test Results

The small scale tests accomplished their major objectives (See Table II):

1. They provided knowledge as to the ability of the original frame and retainer configurations to withstand a fatigue spectrum based on reduced subsonic and supersonic load factors, for a period of time that would allow them to be reworked or redesigned. Although 600 hours use at 80% load factor restriction was the life goal for the original frame configuration, Table II shows that the minimum test life of such frames was actually 1540 hours of the revised unrestricted spectrum. This high safety factor was built in, so as to minimize the effect of prior fatigue on the life after rework.

2. They demonstrated that an aircraft flying under restriction\* with the original configuration frame, could be reworked at its rated safe life (600 hours), then fly unrestricted for the rest of its required 4000 hour fatigue life.

3. They demonstrated the ability of reworked frames to withstand an unrestricted spectrum for the full airplane life.

\* Tests representing aircraft flying restricted and unrestricted used spectrums based on the revised less damaging data discussed under Item E.

TABLE II. SUMMARY OF FRAME 442 TEST RESULTS

ORIGINAL PRODUCTION	
FRAME SPECIMEN NO.	HOURS - REVISED SPECTRUM
1	1520
2	3700
3	4450
4	3700
5	3900
NO. 3 UNDERCUT	
FRAME SPECIMEN NO.	HOURS - REVISED SPECTRUM
1	8450
2	8450
3	6750
4 (Shot Peened)	8450
5	5050
6	9920
7	10360
8	11960
9	7960
10	9160
11	10840
REVISED MACHINING (NEW DESIGN)	
FRAME SPECIMEN NO.	HOURS - REVISED SPECTRUM
1	16000+
2	16000+

4. They demonstrated the ability of the redesigned frame lug and the new retainers to meet unrestricted spectrum requirements.

5. The retainers never did pose a serious problem since under the restricted load factor spectrum, tests demonstrated that the original configurations met the required 600 hour life of the unworked frame. At the time required for rework of the frame new, tested, full load capability retainers were available.

#### E. Discussion of Revised Spectrum

As previously noted, at the time of the frame-retainer failure at Wright Field, the original spectrum was reinvestigated and found to be conservative. These conclusions were based on newer data that was not available at the time the original program began. Items reconsidered were:

1. Service Utilization Factor ( $N_s$ ). It was found that operational usage on modern fighter bombers such as the F-100C, D, and F, and the F-105B gave values of  $N_s$  between 10 and 14, while older fighter bombers such as the F-84 series, and air-superiority fighters such as the F-86 and F-100A gave appreciably higher values. Therefore, it was decided that a value of  $N_s = 15$  would be a conservative, but reasonable, value to use for normal operational service. Previously  $N_s = 26$  was used (see Section II).

2. Service Limit Load Factor ( $n_{zL}$ ). Analysis of F-105B flight data showed that  $n_{zL}$  was approximately the same in both the subsonic and supersonic regimes, even though design limit load factors were not the same. It was agreed that  $n_{zL} = 7.33$  should be used for both subsonic and supersonic regimes. Previously the limit subsonic  $n_{zL}$  was 8.67.

3. Correlation between Load Factor Exceedances and Speeds and Altitudes. F-105B flight data showed that only 5% of the total number of exceedances occurred in the supersonic regime, while the original spectrum had 20% in the range. Furthermore, the probability curve for altitude used in the original spectrum was based on F-100D data, and the F-105 mission profiles called for more low level missions than the F-100D. In order to obtain a new correlation between load factor, speed, and altitude, the data was analyzed statistically to determine the relationships between the probabilities of occurrence of each of the three parameters. It was found that the parameters were statistically independent. As stated in Section II, the speed and altitude ranges had been divided into three portions each, giving nine combinations of speed and altitude. Since the parameters were found to be statistically independent, conditional probabilities for each of the nine regimes were obtained by multiplying the separate probabilities. However, the region  $0 < M < 0.75$  was found to be inconsistent with flight data, and therefore the occurrences for  $n_z \geq 4$  were apportioned to the  $0.75 \leq M \leq 1.0$  range.

By utilizing this data, a new, more realistic (but still quite conservative) and less damaging spectrum was evolved. It was this spectrum that was used as a basis for evaluating the results of various tests at RAD.

4. Aeroelastic Effects. The original loads analysis was conservatively based upon essentially linear variations of wing airload bending moments with load factor. After the failure of frame station 442 in the fatigue test article, flight test data from the F-105 structural integrity program was examined for correlation with the theoretical loads. It was found that aeroelastic effects unloaded the wing tips at high values of  $C_L$ , resulting in an inboard shift of the center of pressure, and thereby causing an appreciable decrease in the bending moment at frame 442.

In order to obtain more data to evaluate this tip stall effect, additional flight tests were performed. The tests consisted of several pull-ups to very high angles of attack at different Mach-altitudes, and provided a better picture of wing airload and bending moments under these conditions. Although a spectrum was developed to account for tip stall, it was never implemented in any of the testing at RAD because the proper bending moment values were not known at the time this testing was in progress.

#### F. Fatigue Test on an Entire Airplane at RAD

This test was run with components installed in an aircraft to demonstrate the validity of the jig-mounted component test results. It was not a total aircraft fatigue test, and was only intended to validate the fatigue strength of the previously failed area.

With the frame and retainers in their original configuration, the aircraft was tested to the revised, restricted spectrum, for a period (600 hours) representing the maximum time before frame rework and retainer redesign. Then the new design retainers were installed, the frame was undercut (No. 3), and the test continued using the revised 100% load factor spectrum. Failure of frame 442, duplicating that which occurred during the initial fatigue test at WPAFB, occurred at 114% of the combined spectrum (99% of revised unrestricted spectrum). Although the new retainers withstood the test with no cracks, the side plate fitting sustained damage similar to that incurred during testing at Wright Field. (Figure 15).

#### G. Fatigue Test of Side Plate Fitting and Supporting Structure

After the failure of frame 442 lugs, and the wing retainers during the initial fatigue test at WPAFB, and failure of frame 442 lugs in the airplane test at RAD it was noted that this fitting and its supporting structure were broken. Although it was believed that these failures were secondary in nature it was decided to demonstrate the inherent fatigue strength of these parts for the revised unrestricted spectrum.

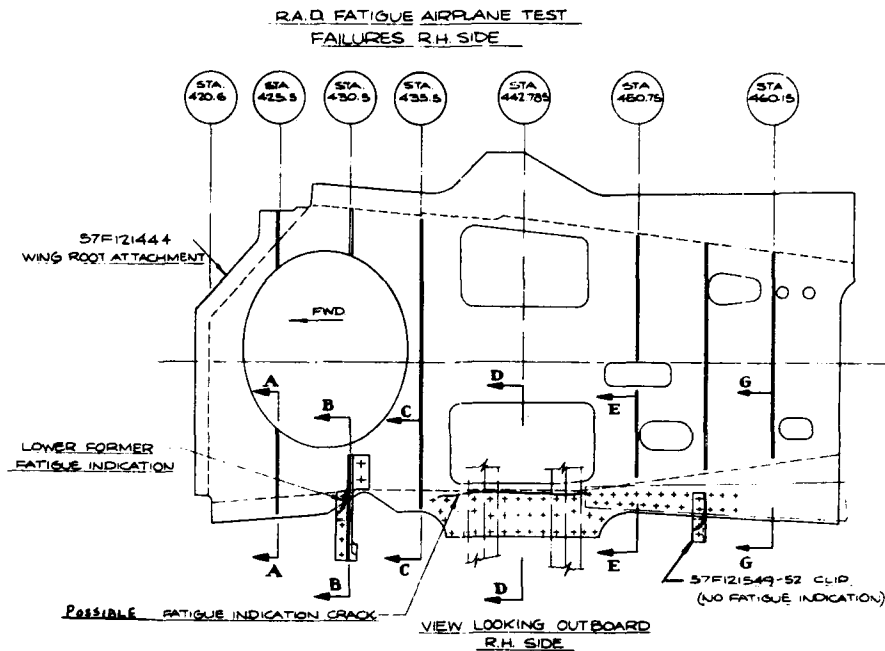


Figure 15. Side Plate Fitting

A specimen was constructed for the test using a production center (station 300-515) fuselage. The specimen consisted of all structural parts in this area, and therefore, gave an exact duplication of the load paths. Since the test was initiated in order to evaluate the side plate and supporting structure, a loading fixture was constructed to produce pitching moment at the transfer-rear spar attachment to the fuselage. The unreworked frame 442 lugs were only loaded by secondary effects due to side plate deflections and the test was not limited by their capability. The new, redesigned retainers were used during this test. Therefore, it became possible to demonstrate their capability to withstand 100% of the unrestricted spectrum when installed on an aircraft.

The results of the test were:

1. The wing root attachment fitting and its supporting structure sustained 400% of the revised unrestricted aircraft spectrum with no failures; and
2. The redesigned wing retainers, used for load transmission to the wing root attachment, sustained 400% of the revised unrestricted aircraft spectrum with no failure.

**VI. Second and Third Fatigue Tests on an Entire F105D at WPAFB - (to Revised Spectrum).**

*A. Second Test*

The initial test on an entire airframe (see Paragraph V-F) had resulted in failure of frame 442 and the wing retainers after 20% of, what was later identified as, a conservative spectrum. Once fixes to these components had been accomplished and the fatigue spectrum revised, it was nec-

essary to continue demonstration of the fatigue capability of the rest of the airframe. Therefore a second test was performed in the same jig with the airplane supported in the same manner as the first test. A new forward fuselage (forward of station 633) and set of wings were tested. The aft fuselage (station 633 aft) from the previous test was

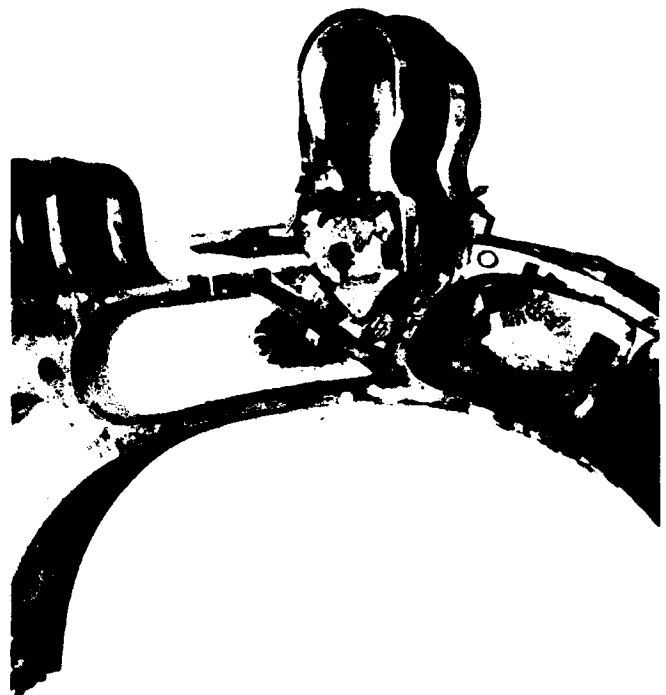
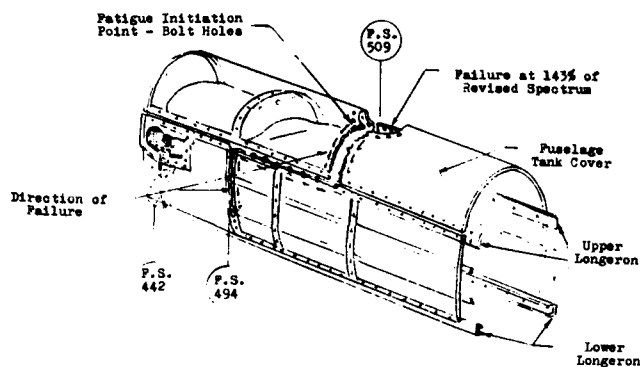


Figure 16. Failed Lower Lug - Undercut No. 3 - Frame 442 at 116% of Revised Test Spectrum.



**Figure 17. Fuselage Tank Cover Access Hole - Sta. 509.**

used because it was felt that this portion of the fuselage was not fatigue critical. The new fuselage frame 442 lugs had undercut No. 3. New production wing retainers were also used.

The aircraft was tested to the revised unrestricted spectrum. At 116% of the spectrum, failure occurred in the undercut No. 3 lug of frame 442 (Figure 16). As in previous tests, the spectrum did not include tip stall effects, a factor that could have raised frame life by another 35-40%.

#### B. Third Test

Completion of the second aircraft fatigue tests had demonstrated the ability of an F105 airframe, having reworked frame 442, to withstand better than 100% of the revised aircraft spectrum. Since late model D's and all F's were to be produced with the new design frame installed, a fatigue life for aircraft with this configuration was required. Therefore a new production frame was spliced into the airframe to permit such a test. (Two jig-mounted new production design frames withstood 400% of the revised spectrum without failure. Table II).

Starting from the stopping point of the second test (116% of the spectrum), testing continued until failure of the fuselage cross section occurred at 142%. Investigation of the failed area revealed evidence of progressive fatigue cracking of the fuel tank cover skin at fuselage station 509, starting at the rivet hole pattern surrounding the hatch cutout. (See Figure 17.)

Although aircraft life in this area exceeded the hoped for goal of 4000 hours, the combination of high induced stresses due to tail loads and stress concentrations from rivet holes around the cutout indicated a possibility of future trouble in this area. In addition, although no document required that scatter must be accounted for, its possible effect could not be ignored. Hence inspection procedures were developed to check both this and frame 442 reworked frames at regular time intervals.

During a normal inspection interval at 120% of the spectrum, two cracks were noticed emanating from the corners of the canopy latch cutout in the L&RH side skin at fuselage station 262. The 7/8 x 5 inch cutout had 0.061 inch fillet radii, and skin edges appeared to have been routed without any cleanup operation, leaving a jagged surface. (See Figure 18A). Small holes were drilled to stop the cracks, and the radius increased to 0.125 inches. The test was then continued with no further problems. Although these cracks could be considered "nuisance" cracks because of the light loading on this area, to avoid service problems all aircraft were reworked to a larger radius as described in Figure 18B. For those exhibiting cracks, rework is also described in Figure 18B.

#### VII. Conclusions Reached from Early Tests

Besides the obvious conclusion that the original frame 442 and retainer configurations were inadequate for the initial test spectrum, there were questions raised as to the ability of areas such as the undercut frame 442, and the fuselage tank cover at station 509, to withstand the revised fatigue spectrum, should scatter factors be taken into account. However, it must be emphasized that at the time these spectra were developed, meager data existed which could be considered directly applicable to the F105. Later

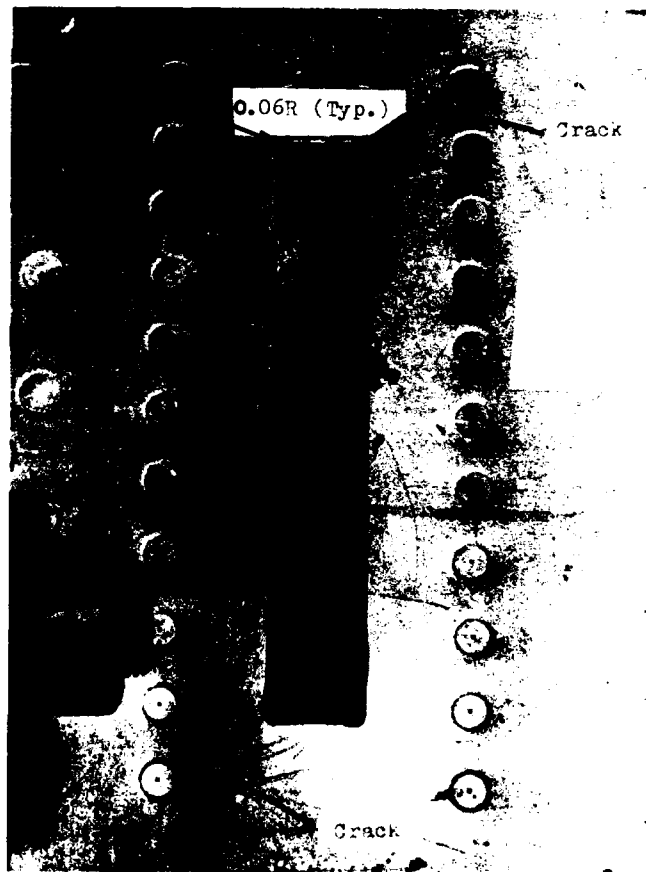
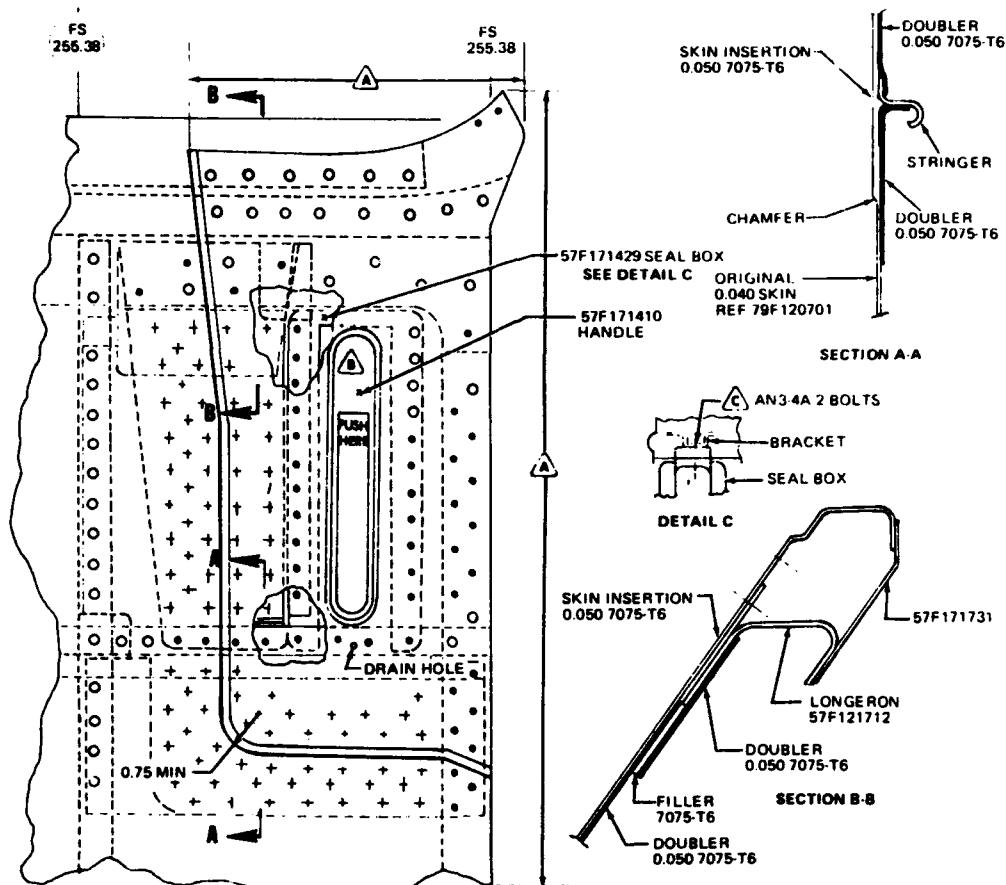


**Figure 18A. Canopy Latch Cutout at 120% of Revised Spectrum.**



**NOTES:**

- 1 A MINOR REPAIR CAN BE MADE BY STOP DRILLING CRACKS WITH A NUMBER 21 DRILL (0.150 INCH DIAMETER) THE CORNER RADIUS OF THE RECESS MAY BE ENLARGED TO 0.240 INCH RADIUS MAXIMUM TO ELIMINATE SMALL CRACKS.
- 2 DAMAGE REQUIRING A MORE EXTENSIVE REPAIR CAN BE REPAIRED BY FOLLOWING THE PROCEDURE OUTLINED BELOW.
- 3 REMOVE SECTION OF SKIN PANEL AS SHOWN; LOCATE THE CUT LINE ACCORDING TO THE RIVET PATTERN TO MAINTAIN MAXIMUM EDGE DISTANCE
- 4 FABRICATE DOUBLERS AND SKIN INSERTION FROM 0.050 THK 7075-0 CLAD, HEAT TREAT TO T6
- 5 DIMPLE HOLES IN SKIN INSERTION
- 6 COUNTERSINK FOR REPAIR FASTENERS IN ORIGINAL SKIN ONLY
- 7 MODIFY CUTOUT IN SKIN TO INCORPORATE A FULL RADIUS AS SHOWN AND GRIND 57F171410 HANDLE TO FULL RADIUS
- 8 COAT MATING SURFACES WITH SEALANT
- 9 FASTENERS:
  - REPLACE WITH SAME TYPE REMOVED
  - + MS20426AD5, 0.87 INCH SPACING
  - JO-BOLTS
- 10 VERIFY THAT THESE BOLTS ARE INSTALLED

Figure 18B. Repair of Skin Crack Canopy Latch.

discussions involving data gathered from in-service aircraft will show that these areas actually have more life than indicated by the early analyses and tests.

### VIII. Discussion of Service Aircraft Structural Failures Initiated by Fatigue Cracks

#### A. Background

Well after the conclusion of the fatigue tests at WPAFB, two aircraft broke up in the air due to what subse-

quent investigation attributed to fatigue-initiated failures. The most probable starting point of the failure was a cutout in the fuselage top cover splice at Station 350. This cutout provides clearance for the forward mounting lugs of the internal store displacement cylinder (Figures 1 and 19). The first aircraft was an F105B that was part of the Thunderbird Team; the second, an F105D-4.

#### B. Reason for Failure

The 7075-T6 alloy splice plate of the aircraft

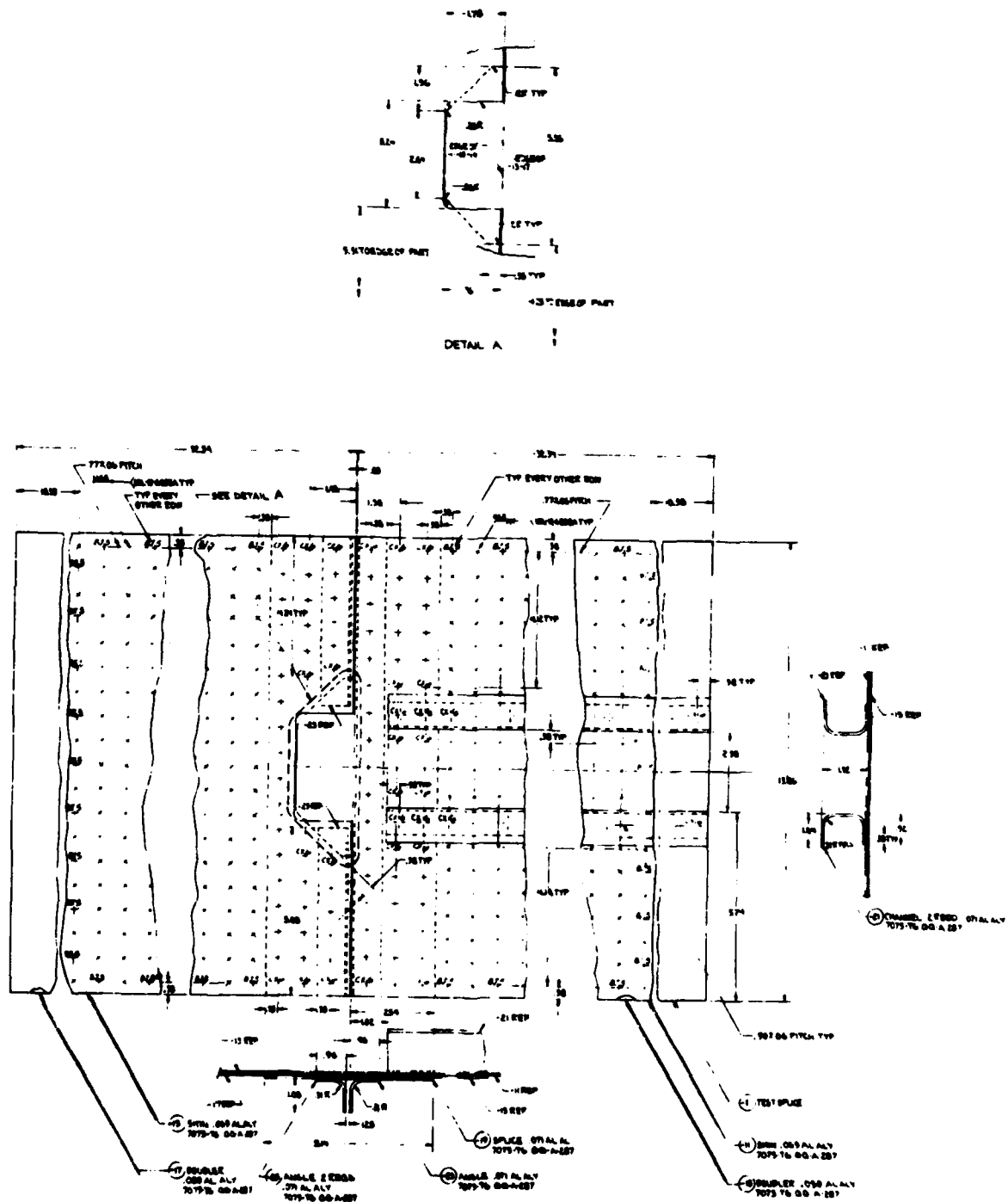


Figure 19. Test Splice, Tank Cover, F.S. 350 (Trapezoidal Cutout TS00-3160).

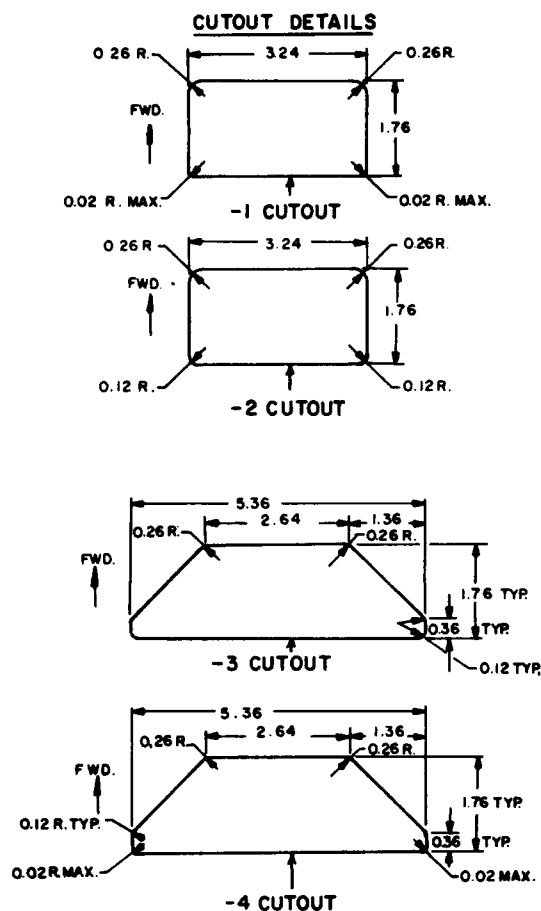


Figure 20. Details of Cutouts, FS 350 Test Program.

involved had a trapezoidal cutout, the dimensions and geometry of which is shown in Figure 20-3. Full details of the accident investigation and evidence leading to the conclusions reached are documented in Reference 5 and 6. Briefly, the evidence (which consisted of recovered parts from the aircraft) showed that the edges of the cutout were indented with file marks which extended around the radius where fatigue cracks appeared. Fracture analysis, and tests (see item C) showed that a small fatigue crack at this location was sufficient to initiate catastrophic failure at a load equal to half the static design load. It was known that both aircraft were in maneuvers well in excess of this value at time of failure.

Non-destructive inspection of F105B's and D's indicated this type cutout existed on the B's and early D's. All later production aircraft had been redesigned with a rectangular cutout (Figures 20-2 cutout and 21).

### C. Investigation of Fatigue Life and Strength of Structure in Cutout Area

A series of tests was undertaken to investigate the

fatigue life and strength of the structure in the cutout area. The initial tests were conducted on flat sheet specimens representative of the splice strap in this area. These sheet specimens were cycled at a constant stress level to obtain comparative lives of the trapezoidal and rectangular cutouts. Two variations of each shape were tested, i.e., trapezoidal and rectangular cutouts with 0.12 corner radii and similar configurations with sharp corners to represent the extreme case of file marks in the corner radius. Dimensions and geometry of these specimens are shown in Figure 22. Width of the specimens was adjusted to obtain the same stress levels in both the trapezoidal and rectangular configurations.

A second series of tests consisted of static and fatigue loadings on specimens designed to represent the actual airplane structure. The specimens were flat but the curvature of the section over the width involved is so slight that the flat configuration was considered fully representative. The static tests included tests on specimens with pre-cracked splice plates to obtain a comparison between the ultimate strength of sound splice plates and one in which a crack had been initiated. Eight builtup specimens, four of each basic configuration, were fabricated. Details of the specimens are shown in Figures 19 and 21. To obtain maximum information from these basic specimens, certain specimens were rebuilt after failure and retested. Of the original eight builtup specimens, three of each type were tested in fatigue and one of each type statically. The static specimens were then rebuilt, using the cracked splice plates from the flat sheet fatigue tests. The fatigue specimens with rectangular cutout (Figure 21) were also rebuilt using 0.080 thick splice plates, incorporating rectangular cutouts with sharp corners. See Figure 20-1. The purpose of these three specimens was to establish a minimum life for aircraft in which a cutout may have been inadvertently marked or the corner radii reduced during assembly. In addition, one of the three fatigue specimens with a trapezoidal cutout (Figure 19) was rebuilt incorporating a splice plate with a sharp cornered cutout. Thus a total of fourteen tests were obtained from eight basic specimens. An additional specimen similar in geometry to the trapezoidal type, but with a net cross-section width 1.82 times that of the basic design, and having a pre-cracked splice plate, was also static tested.

1. Test Loads and Fatigue Spectra. The flat sheet specimens were fatigued at a constant stress level. The high load limit was calculated to yield a stress of 25,000 psi on the net area of a section through the cutout. The specimens were tested tension-tension with the low limit 12 percent of the high.

The spectrum applied in fatigue testing of the built up specimens was the revised test spectrum used for the F105D airplane tests at WPAFB, with loads modified for the F105B airplane. All but three specimens tested were representative of the F105B airplane. The remaining three represented the F105D (0.080 splice plate versus 0.071

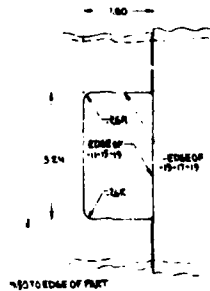
for the F105B). The builtup specimens were also tested tension-tension. The low limit load was 1.0g.

Since interest in the static tests centered on the failing loads for the specimens and the reduction of strength resulting from fatigue induced cracks, design ultimate loads were not applied. However the ultimate load, which is 32,700 pounds, has been used to calculate reserve factors and comparative strength of the various configurations.

2. Test Equipment and Procedures. The fatigue specimens were mounted vertically in a test fixture with

axial load applied by means of a hydraulic cylinder. Load cycling was achieved by coupling the cylinder supply lines through a solenoid operated valve controlled by a system of pressure switches and electrical relays. Load levels were continuously monitored by strain gaged load cells readout on SR-4 boxes. Two load cells were used in series with each specimen, one controlling the high side of the load cycle and the other, the low.

The flat sheet specimens with the trapezoidal cutout and sharp corners (cutout -4, Figure 20), failed at a relatively low number of cycles and therefore two of these



DETAIL A

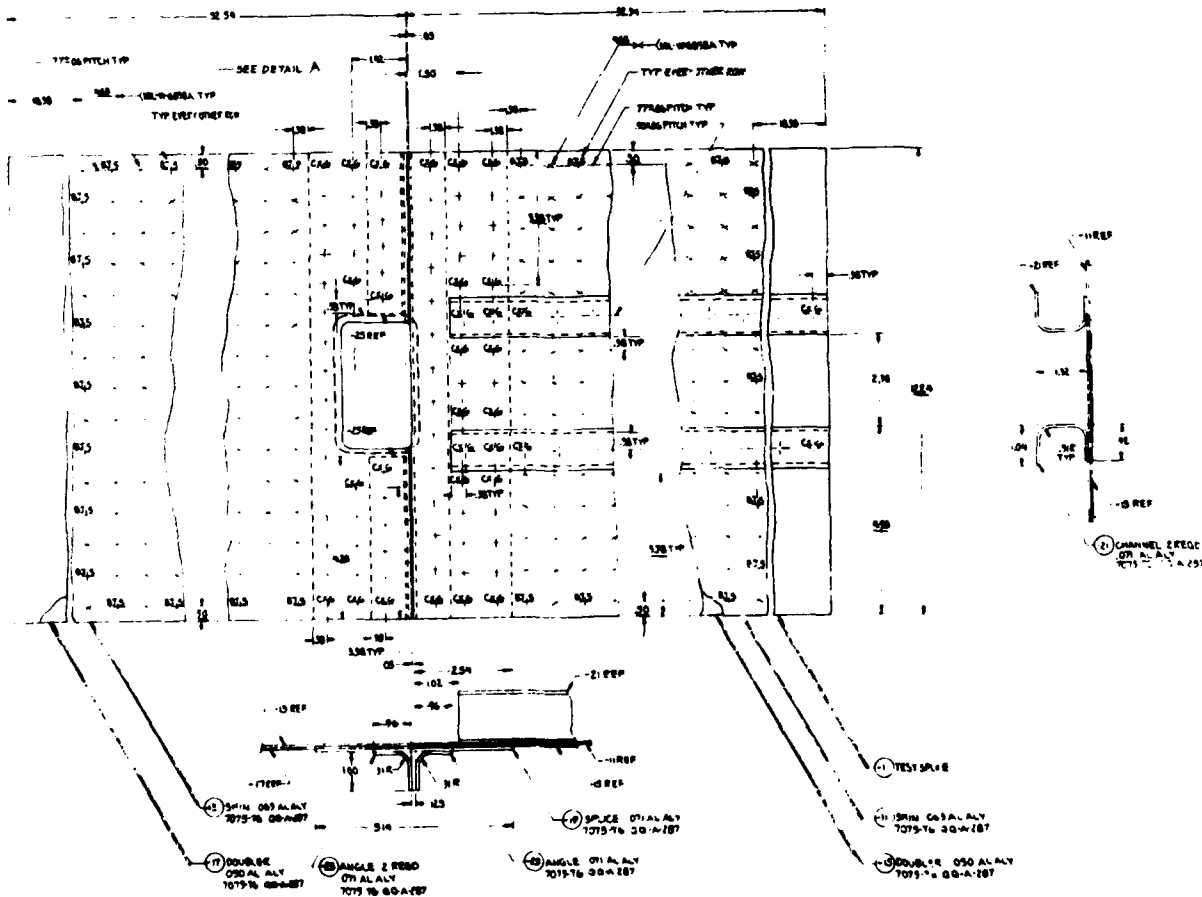
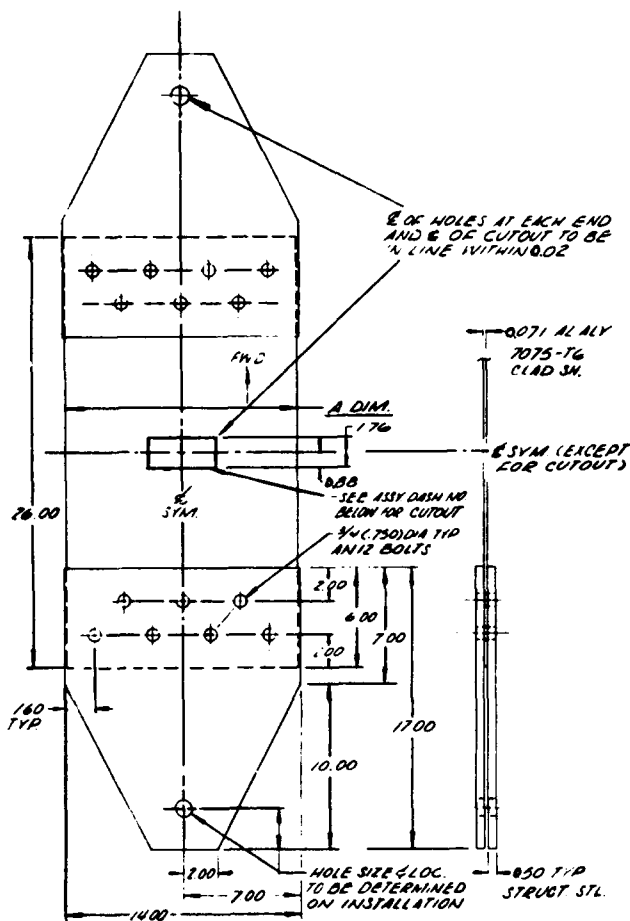


Figure 21. Test Splice, Tank Cover, F.S. 350 (Rectangular Cutout) TS00-3161.





SPECIMEN ASSY	A DIM.	CUTOUT DASH NO
-1	12.24	-1
-2	12.24	-2
-3	13.86	-3
-4	13.86	-4

Figure 22. Details of Flat Sheet Specimens, FS350 Test Program. (See Fig. 20 for details of cutouts.)

type specimen (Nos. 2 and 3, Table III) were tested by manual cycling in a Universal Test Machine.

### 3. Test Results.

#### a. Fatigue Tests

The test results obtained for flat sheet specimens are summarized in Table III. It will be observed that the trapezoidal cutout had a much shorter life than the rectangular cutout. Also the rectangular cutout showed a significant period of crack propagation and it was possible to observe crack indication prior to failure. The trapezoidal specimens failed shortly after the first crack initiation and detection of crack initiation was difficult. The mode of failure of all specimens was similar. Crack initiation occurred at the sharp corner or intersection of the 0.12 radius to the fore and aft edge of the cutout and propagated up to one inch in length prior to rupture. Figure 23 shows the crack propagation rates for a rectangular and trapezoidal cutout. It

will be observed that the rate of propagation of the trapezoidal is much higher than the rectangular.

The results of the fatigue tests for built-up specimens are noted in Table IV. It can be seen that the rectangular cutout had approximately four times the life of the trapezoidal, and the one trapezoidal specimen with sharp corners had a very low life. The fatigue crack initiated either at the sharp corner or at the bend of the corner radius to the fore and aft edge of the cutout. Rupture then occurred straight across the specimen. In cases where fatigue cracks occurred at both corners, the failure did not pass through the adjacent rivets. In cases where a fatigue crack occurred only at one corner, the failure was asymmetric, one side passing through the rivets and the other side straight out between the rivet rows (Figures 24 and 25). Examination of the failed surfaces showed the fatigue crack to be no longer than 1/8 inch. This contrasts with the flat specimens in which fatigue crack length usually exceeded one inch prior to failure. This is attributable to the fact that the fatigue specimens were tested to a spectrum including relatively high load levels and final failure always occurred during the high load factor cycles (static failures).

#### b. Static Tests

The prime purpose of the static tests was to determine the reduction in strength resulting from a

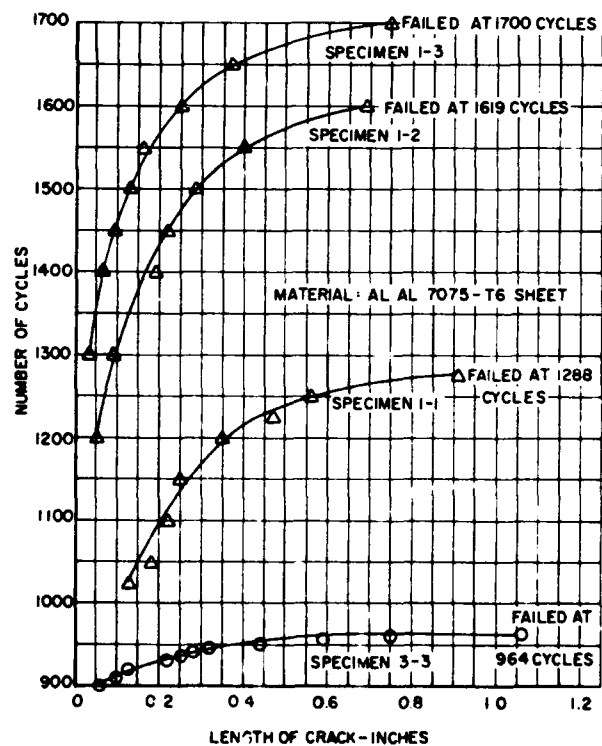


Figure 23. Crack Propagation Rates - Length of Crack vs. Number of Cycles (Cycled at 25,000 psi).

**TABLE III.  
TEST RESULTS OF FLAT SHEET SPECIMENS**

CUTOUT NO.	SPECIMEN NO.	NO. OF CYCLES WHEN CRACK FIRST DETECTED	NO. OF CYCLES AT FAILURE	REMARKS
1	1	1000	1288	
1	2	1200	1619	
1	3	1300	1712	
2	1	3010	-	The crack was 1/8" long after 4510 cycles at which time cycling was stopped and the specimen stored for future test.
2	2	3050	3534	
2	3	3000	4246	
3	1	-	1556	No crack detected at 1250 cycles.
3	2	-	895	No crack detected at 500 cycles.
3	3	900	964	
4	1	-	56	No crack detection checks were made.
4	2	-	111	No crack detection checks were made.
4	3	120	-	The crack was 0.07" long after 220 cycles at which time cycling was stopped and the specimen stored for future test.
4	7	900	-	21" wide specimen. Small crack was detected at 900 cycles at which time cycling was stopped and the specimen stored for future test.

**TABLE IV.  
TEST RESULTS OF TS-00-3160 AND TS-00-3161 SPECIMENS**

SPECIMEN TYPE	SPECIMEN NO.	TEST	% FATIGUE LIFE OR FAILING LOAD	REMARKS
TS-00-3160 Trapezoidal Cutout - 0.125R	1	Fatigue	23%	With 0.02 radius
	2	Static	34,900 lbs.	With 0.02 radius
	3	Fatigue	102%	
	4	Fatigue	46%	
	5	Static	23,100 lbs.	With precracked plate
	6	Fatigue	92%	
TS-00-3160 Modified	7	Static	41,000 lbs.	With precracked plate 21" wide
TS-00-3161 Rectangular Cutout - 0.125R	1	Fatigue	298%	
	2	Fatigue	Stopped at 464%	Cracks found
	3	Fatigue	386%	
	4	Static	39,400 lbs.	With uncracked plate
	5	Static	27,900 lbs.	With precracked plate
	6	Fatigue	145%	With 0.080 sheet, 0.02 radius
	7	Fatigue	96%	With 0.080 sheet, 0.02 radius
	8	Fatigue	85%	With 0.080 sheet, 0.02 radius

Figure 24. F.S. 350 Test –  
Failed Specimens –  
Trapezoidal Cutout.

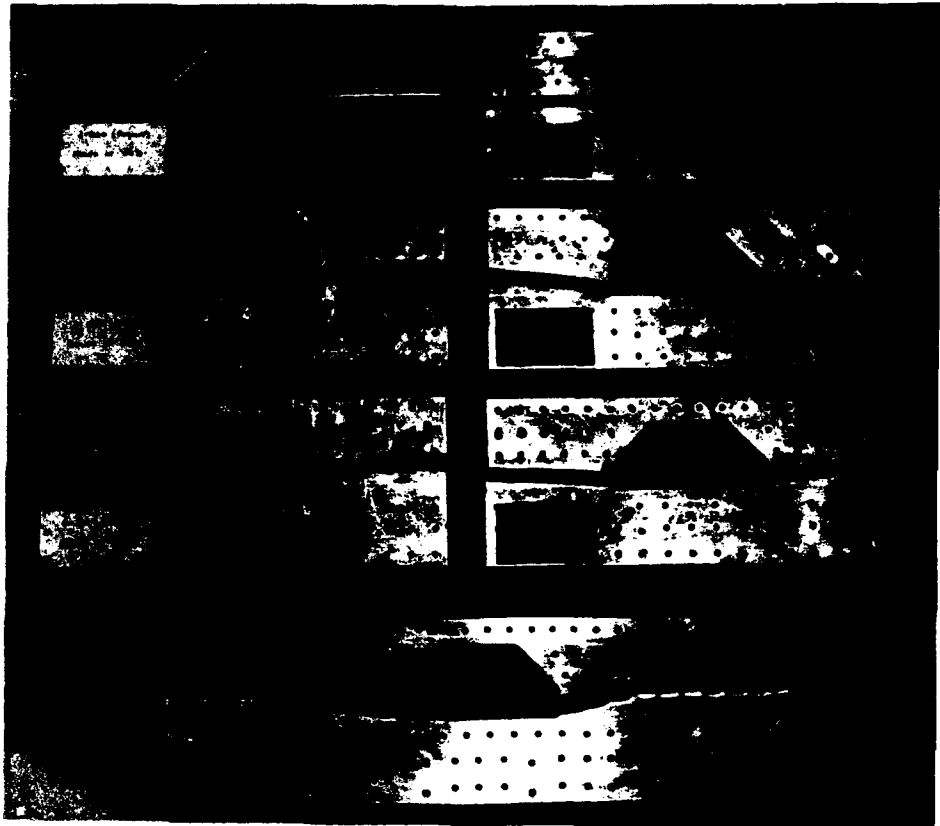
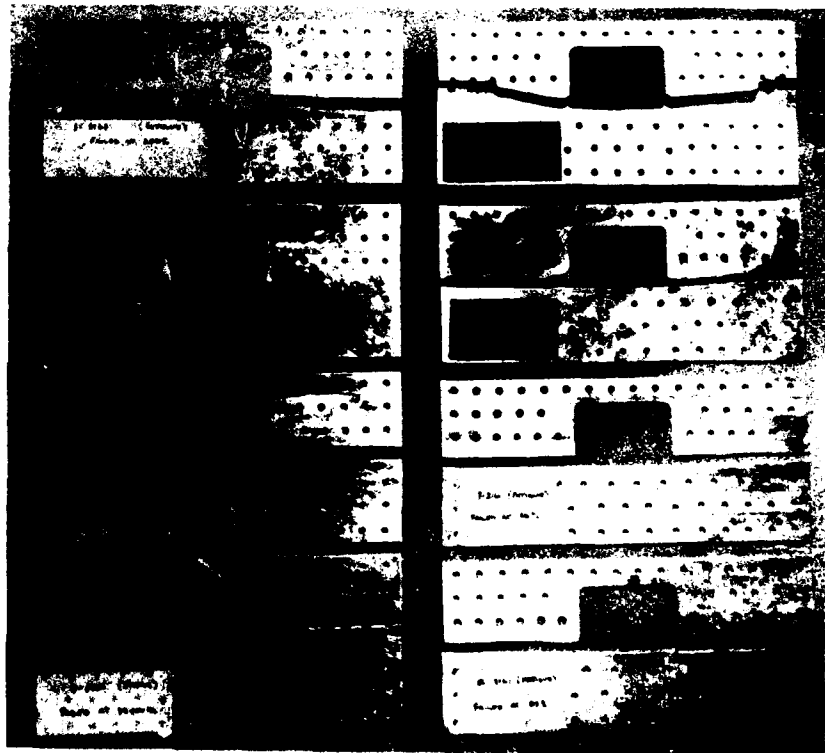


Figure 25. F.S. 350 Test –  
Failed Rectangular  
Cutout Specimens.



fatigue crack induced by previous service. The relative strengths of the uncracked and precracked specimens may be summarized in terms of reserve factor based on the ultimate load of 32,700 pounds.

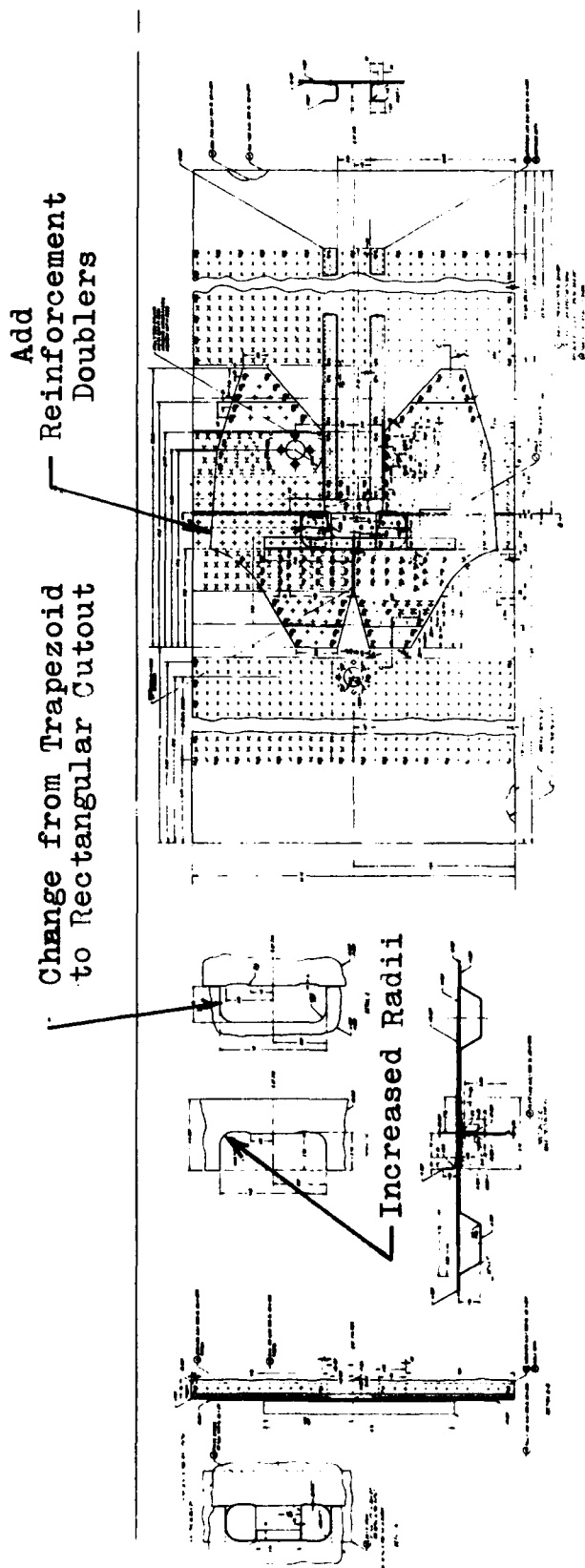


Figure 26. Rework of Trapezoidal Cutout - F.S. 350.

For the trapezoidal type (Table IV)

Uncracked specimen:

$$\text{Factor of Safety} = \frac{34,900}{32,700} = 1.07$$

Precracked specimen:

$$\text{Factor of Safety} = \frac{23,100}{32,700} = 0.705$$

Reduction due to crack = 34%

For the rectangular type (Table IV)

Uncracked specimen:

$$\text{Factor of Safety} = \frac{39,400}{32,700} = 1.21$$

Precracked specimen:

$$\text{Factor of Safety} = \frac{27,900}{32,700} = 0.953$$

Reduction due to crack = 30%

The purpose of testing the wide specimen was to assess if tests on the narrower specimens were representative, particularly for those with precracked splice plates. This wide-specimen had 1.82 times the net cross-section area of the basic trapezoidal specimen and failed at 41,000 pounds.

Therefore:

$$\text{Factor of Safety} = \frac{41,000}{32,700 \times 1.82} = 0.689$$

The value 0.689 compares favorably with 0.705 and is a confirmation that, in this range, the effect of specimen width on test results is negligible.

4. Conclusions. The results of these tests support the conclusion of References 5 and 6, which report the investigations of the two accidents. This conclusion was that initiation point of failure was at the trapezoidal cutout in the fuselage top cover splice at Station 350 and was directly due to fatigue cracks in the corner radius of the cutout.

D. *Reasons Why Neither Failure was Predicted by Analysis or Aircraft Fatigue Test*

The reason is quite simple. Both the fatigue analysis and the fatigue tests were performed on a production F105D. The 'D' production design had a rectangular cutout which was shown to be capable of at least four times the life of a trapezoidal cutout (Tables III and IV). This was well in excess of the required life of the 'D' aircraft. The difference in fatigue life due to the trapezoidal cutout in the earlier aircraft was not appreciated until the accident investigations pointed it out, because there had been no requirement to evaluate the fatigue life of 'B' aircraft

E. *Fixes to Eliminate the Problem Area*

1. Aircraft with Trapezoidal Cutouts. These aircraft were immediately reworked as shown in Figure 26.

This rework consisted of changing the cutout to a rectangular shape similar the 'D' but with radii of 0.76 inches instead of 0.12 inches, and adding two external 0.050 doublers over the area. The fix had the dual effect of reducing the notch sensitivity factor and lowering the basic stress level at this cross section of fuselage. Tests were run in a similar manner to those of Item C-3. No failures occurred at the time the test was stopped at 250 percent of the revised spectrum.

### 2. 'D' Aircraft with Rectangular Cutouts.

Since tests of the rectangular cutout had demonstrated a fatigue life in excess of four times that of the trapezoidal cutout, no immediate action was taken on these aircraft except to perform inspections to ascertain the radii did not have file marks in them. However, in the years that have followed the origin of this problem, life requirements and the type of flying has become more severe. Therefore the rectangular cutout has been reworked in a similar manner to the trapezoidal cutout (the corner radii were increased and doublers added).

3. 'F' Aircraft. At the time the problem appeared on the 'B' and early 'D's, the 'F' was still in its design stage. Therefore, it was possible to redesign the splice strap for the 'F'. This was done by changing the strap to one-half hard 301 stainless steel. The cutout maintained the rectangular shape originally used on the 'D' but radii were 0.25 inch minimum. Tests on specimens duplicating this configuration (actual test specimen radii were as low as 0.02 inches) indicated that this configuration was capable of withstanding 600 percent of the revised aircraft spectrum as applied to the 'F' airplane without failure (Reference 7). At test conclusion, a 0.25-inch crack was present in the radius of the splice plate. These cracks first became evident at 420 percent of the spectrum. This indicates a low crack sensitivity of 301 stainless steel, which was one of the reasons why it was chosen for this application. (See Figures 27 and 28).

## IX. F-105D/F Fatigue Strength Evaluation Based on "3 Channel" VGH and "8 Channel" Asymmetric Data

### A. Background

It should be apparent that in all analyses and tests previously discussed, little of the data used in evolving a spectrum for the F-105 was based on information derived from the F-105 itself. In the early evaluations, items such as mission profiles were based on contemplated use; while the expected relationship of velocity (V), vertical load factor ( $n_z$  or G), and altitude (H) was assumed, using data from older fighter aircraft as a guideline. Therefore, in 1964, the first of a series of VGH programs was undertaken to provide a better understanding of the fatigue environment the F-105 was exposed to. In addition to three channel VGH data, a second set of data designated "8 channel" was accumulated. Information gathered from this additional

\* 3 channel VGH data shall henceforth be denoted as 'VGH' only.

† Chronologically the "D" program preceded the "F" by one year.

data included: both lateral and longitudinal acceleration, static and dynamic pressures, and the angular rates around the three major orthogonal axes, that is; roll, pitch, and yaw rate and acceleration. This first program involved 27 D's operating under peacetime conditions. Nine operated from Germany, nine from Okinawa, and nine from Nevada. The first two were operational, the third a training base. Some 2500 hours of 3 channel VGH\*, and 250 hours of "8 channel", data were recorded. Data breakdowns included such supplemental information as air base, mission type, aircraft configuration (determined by the types and location of stores), flight data, barometric pressure, gross weight, time of takeoff and landing, and weight and drop time of stores. In addition, data reduction required measurement of peak values of each parameter and the simultaneous values of all other parameters. The recorded static and dynamic pressures were used to calculate airspeed, pressure, altitude, and Mach number.

In 1967 similar programs were instituted on the "D" and "F"† aircraft operating under Southeast Asia combat conditions. The number of aircraft and data collected included: (1) 19 D's, where 3000 hours of VGH and 300 hours of "8 channel" data were recorded, and (2) 10 F's where 1000 hours of VGH and 100 hours of "8 channel" data were recorded.

### B. General Discussion on Development of Flight Maneuver and Load Spectra

1. Mission Profiles. In the original F-105D fatigue analysis (Section III), it was necessary to formulate mission profiles based on contemplated use of the aircraft, since no operational data existed. These formulated mission

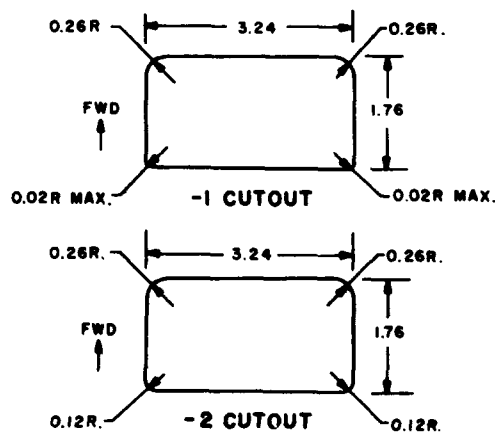


Figure 27. F105F Test - F.S. 350 Splice - 301 Corrosion Resistant Steel - 1/2 Hard.

profiles served as a base from which the percentage distributions of airplane configurations and gross weights were derived. The VGH data, however, made it possible to ascertain the distributions of gross weights and configurations directly within a particular mission (which could be defined because the airplane was in-service).\*

2. Mission Mix. In the peacetime program, the mission mix presented two problems: (a) The data were obtained from relatively few airplanes; did all the data collected represent the statistical sum of the entire fleet? and (b) Since there were three bases involved, two operational and one training, did the training base data have any meaning?

The first question was answered by employing missions data for entire wings at the bases where the instrumented aircraft were located, to determine the dis-

tribution of flight time among the various missions. This statement also holds for SEA usage.

The second question was answered by applying the following logic: Certainly, the analysis should include both training and operational data. However, since there were more operational bases than training bases, the data should be weighted to reflect these conditions. At the time the program was in progress there were a total of six operational and one training base. A mission mix was therefore employed in which a factor of three was applied to the operational data before combining with training base data.

3. Configurations. A large number of what will be called minor configurations were condensed down to approximately five major configurations. The basis for this reduction came from a number of preliminary investigations by the structural analysis group which determined: (a) that

\* The major difference between the original mission profile data and the VGH data is the small percentage (11%) of clean aircraft missions recorded during the VGH program. Almost all missions involved carriage of external stores. This in turn relieved after fuselage bending, and hence reduced fatigue damage.

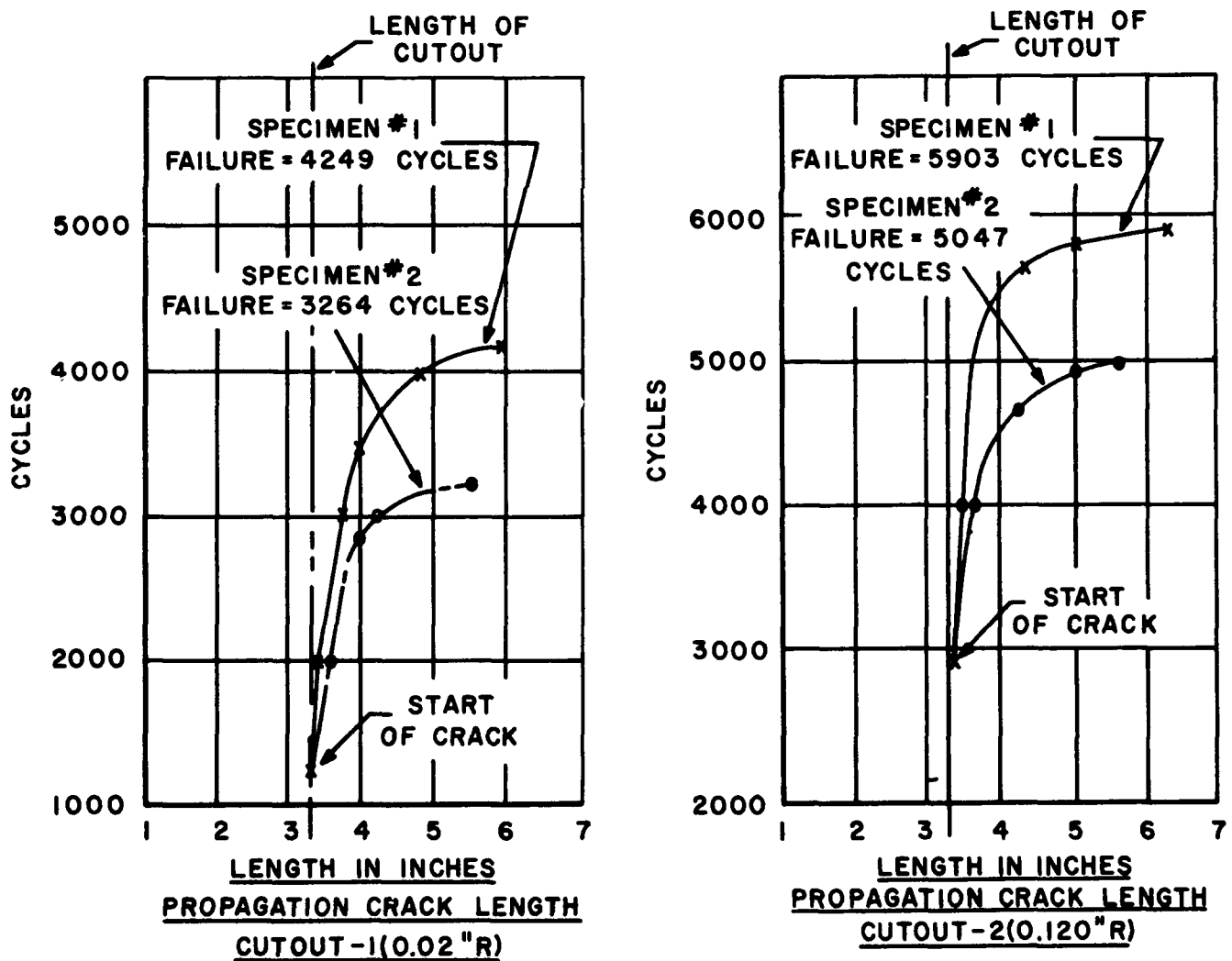


Figure 28. Crack Propagation Rates - F105F Splice Strap - F.S. 350-301 Corr. Res. Stl. - 1/2 Hard.

several different aircraft configurations at similar gross weights caused the same general stresses on critical points on the airframe structure, and (b) some store configurations caused such low additional stresses that the aircraft could effectively be considered clean.

Distribution of configurations with respect to missions was calculated from that portion of the VGH data which showed the number of flights per mission.

4. Gross Weights. Here again a large number of weight conditions (10), were reduced to six, separated at 2000 pound increments. Examination of  $n_z$  exceedances indicated these six to be the most actively used. All other weights were considered as acting within the ranges chosen.

5. Mach Numbers. The VGH data showed occurrences of  $n_z \geq 2.0$  at Mach Numbers at 0.1 intervals from 0.4 through 1.6 in the form of matrices of  $n_z$  vs. M. These data were processed to determine probabilities that exceedances of  $n_z$  occur in the designated Mach number.

In order to reduce the number of loading conditions and yet obtain a reasonable representation of Mach number conditions, the 13 Mach number regimes were combined and reduced to six weighted average values. For example, for  $M = 0.9 - 0.95$  the weighted average = 0.92; for  $M > 0.95$ , the weighted average = 1.2.

The following points should be noted regarding the selection of weighted average values:

a. Since the overwhelming majority of ( $n_z$ ) exceedances occurred in the speed range of  $0.6 \leq M \leq 0.95$ , only the exceedances outside these limits were combined. (i.e.,  $0.55 \leq M$  were combined at 0.55).

b. The above selection conservatively puts the 0.95 to 1.0 Mach number regime into the supersonic regime, and is based on the finding that the flight loads in this transonic range were nearly equal to the supersonic values.

c. The speed of Mach number 1.2, where the tail loads were highest, was chosen conservatively, to represent the entire supersonic range.

6. Altitudes (h). The VGH data showed occurrences of  $n \geq 2.0$  at ten altitudes starting from sea level to 50,000 feet. These data were processed to determine probabilities that exceedances of  $n_z$  occurred in designated ranges of altitude. (As an example of altitude range, exceedances listed for zero altitude pertain to the range from sea level to 2,000 feet.) The ten altitude regimes of the VGH data were condensed in the interest of practicality. Since less than 10% of all ( $n_z$ ) exceedances occurred above 15,000 feet, with the majority of those occurring near 20,000 feet, all the altitude ranges above 15,000 feet were combined at the 20,000 foot level. Using the weighted

ALTITUDE	MACH NUMBER				
	0.65	0.75	0.85	0.92	1.2
1000			⬡	⬡	
3000					
7000	⬡			⬡	⬡
12000		⬡	⬡		
20000			⬡	⬡	

Figure 29. Typical M-h Matrix for a Composite Mission on F105.

average concept led to five altitude ranges; i.e., for sea level to 2000 feet the weighted average was 1000 feet.

7. Normal Load Factors ( $n_z$ ). A normal load factor occurrence was defined as an  $n_z$  peak above or below the 1.0g level, bounded by rises or falls of 1.0g, or 50% of the incremental value of the peak, whichever is greater.

The VGH data showed occurrences of  $n_z \geq 2.0$  for the range from  $n_z = 2.0$  to  $n_z = 7.5$  in steps of 0.5. To reduce the number of loading conditions, the 12 ( $n_z$ ) regimes of the VGH data were reduced by considering the exceedances in the ranges of 2.0 thru 3.5 as a weighted average of 2.7. All other ranges maintained the 0.5 increment of  $n_z$ ; i.e., for  $n_z = 5.0 - 5.5$ ,  $n_z$  average = 5.2.

8. Symmetric Spectrum. This spectrum was derived using all of the data of Items 1-7. The spectra were presented in the form of matrices giving altitudes vs. Mach numbers, each such M-h matrix pertaining to a specific mission, configuration, gross weight, and load factor ( $n_z$ ). Utilizing these matrices and the total number of exceedances measured from the VGH data, and applying the theory of statistical independence with a digital computer program, the cycles were distributed to the spectrum of M-h matrices.

Inasmuch as the program distributed  $n_z$  exceedances to the flight regime without considering limitations on airplane capabilities due to wing life, gross weight, and tail power, the results obtained were reviewed to identify those exceedances which are impossible due to limitations on aircraft capabilities. Corrections to the spectra usually were accomplished by shifting such exceedances to the next highest Mach number at the same altitude at which aircraft capabilities were sufficient to apply the required  $n_z$ . M-h matrices, developed for a composite F-105 mission, are shown in Figure 29.

9. Asymmetric Spectrum. The asymmetric spectrum comprises the following three spectral components. (a) Dynamic parameters; (b) Maneuver cycles at  $n_z = 1.0$ ;

and (c) Maneuver cycles at  $n_z > 2.0g$ .

a. **Dynamic Parameters.** The dynamic parameters were derived from a study of "8" channel data. Since only a limited amount of this data was collected, parameter exceedance distributions at designated values of normal load factor, were not considered sufficiently representative of fleet usage. Therefore only envelope values, as derived from the recorded data were considered. These envelope values were assumed to be applied simultaneously with the normal load factors for asymmetric maneuvers.

b. **Maneuver Cycles at  $n_z = 1.0g$ .** The parameter ( $n_y$ ) lateral load factor, was considered the best indicator for ascertaining the frequency of asymmetric maneuvers inasmuch as  $n_y$  occurs in steady sideslip motion of the airplane when the roll control is neutral, as well as in rolling maneuvers when both the roll control (spoilers and ailerons) and the yaw control (rudder) are displaced. The total number of asymmetric maneuver cycles pertaining to  $n_z = 1.0$  was determined from the peak count of  $n_y$  for  $n_z < 2.0$ . The cycles were distributed among the Mach-number-altitude-configuration-gross weight regimes according to the probability distributions pertinent to the symmetric spectrum.

c. **Maneuver Cycles at  $n_z > 2.0$ .** The maneuver spectrum at  $n_z > 2.0$  was derived in the following manner: A total count of symmetric and asymmetric maneuver cycles, for  $n_z > 2.0$ , was determined from the 8 channel data. Next, the number of asymmetric maneuvers, i.e., the number of occurrences of  $n_y$  within this  $n_z$  range, was noted. A ratio of asymmetric to total occurrences was established. Applying this ratio, or asymmetric utilization factor, to the pure symmetric VGH data indicated that some 6-10% of all cycles in each Mach-altitude-weight-load factor category should be considered asymmetric.

10. **Additional Spectra.** Effects of speed brake, drag chute, and engine mount spectra were derived partly from data recorded on the F-105 and partly from other sources (Reference 8). Flight test load measurements were used where applicable. Such items as wing tip stall effects at high angles of attack, fuselage and wing airload distributions were in part derived using both this and wind tunnel data.

### C. Extrapolation of F-105D Data to Evaluate the F-105F

1. **Background.** At the time the peacetime VGH program was initiated, only the F-105D airplane had recorders installed. Since a fatigue picture of the F-105F was also required, the "D" data was used as a basis for initial development of "F" load spectra. (Eventually the "F" had VGH recorders installed in Southeast Asia.)

2. **Development of Load Spectra.** Basically the "F" spectrum was obtained from the digital computing

program for the "D" by introducing modifications to account for differences between "D" and "F" gross weights, airplane capabilities and Mach-altitude groupings. No change was made in the total spectrum cycles.

Gross weights for the "F" were estimated to be 2000 pounds higher than the "D". Consequently the "D" spectrum, as obtained by the digital computing program, was converted to the "F" spectrum simply by adding 2000 pounds to every gross weight in the "D" spectrum digital results. The Mach-altitude matrices obtained were reviewed to identify those exceedances which were impossible due to limitations on "F" airplane capabilities. Corrections were made, as in the case of the "D" spectrum, of Mach-altitude matrices, by shifting the "impossible" exceedances to the next highest Mach number at the same altitude at which aircraft capabilities were sufficient to apply the required  $n_z$ .

Dynamic parameters used for the "F" were the same as the "D". This was a rather conservative assumption since the "F" is a much more stable airplane than the "D".

### D. Analytical Procedures used in Determining Moments (Stresses) and Associated Cycles

Prior to the SEA VGH flight program, analysis leading up to damage calculations and life predictions, had literally been done by hand. (See Appendix A). Stresses used to calculate damage came primarily from bending moments (although such items as drag chute loads and speed brakes do contribute small axial stresses). Therefore it is possible to write two equations (one for symmetric loads, and one for asymmetric) expressing the total bending moment at any particular point on the aircraft as the sum of all the local bending moments affecting that point.

A computer program was written which calculates the bending moments produced at each point being analyzed by each load condition, using unit condition bending moments and multiplying factors. The computer then determines which bending moment range each condition falls into at each point, and adds the cycles for all the conditions that produce moments in each moment range. The calculation of unit condition bending moments was not included in this program because existing computer programs handled these computations adequately. The actual calculation of stresses from the final bending moments, and the fatigue life predictions themselves were not included in this program either, because the time required for these calculations is too short to warrant the use of a digital computer. Detailed discussion of this time saving computer program can be found in Appendix B.

### E. Results of Evaluation

1. **Peacetime VGH and "8 Channel" Data-F-105D.**



**TABLE V.**  
**UTILIZATION VALUES (PEAKS PER HOUR) FOR EACH PARAMETER BY AIR BASE,**  
**MISSION,  $n_z$  GROUP, GROSS WEIGHT, ALTITUDE, AND MACH NUMBER**

COMPOSITE	$n_x$	$n_y$	$n_z$	p	q	r	p	q	r	pq	qr	pr	HOURS
COMPOSITE	8.10	21.30	12.18	5.79	12.28	3.71	15.13	2.37	3.28	2.47	4.45	2.78	258.34
<b>AIR BASE</b>													
Bitburg	6.93	15.06	8.89	4.49	8.22	2.50	10.41	1.86	2.64	1.61	3.02	1.70	125.55
Kadena	7.97	13.26	10.63	5.43	10.66	2.96	11.84	1.26	2.22	1.81	3.18	2.55	36.44
Nellis	9.57	32.19	16.89	7.54	18.01	5.52	22.33	3.42	4.46	3.82	6.72	4.22	96.37
<b>MISSION</b>													
SWD	12.44	39.63	20.26	8.94	18.64	4.99	26.78	3.99	5.13	3.30	5.92	3.77	58.13
CBGG	17.08	31.68	29.61	8.60	33.85	7.03	22.17	4.58	2.51	3.11	11.99	3.17	31.83
AAG	13.86	24.54	24.16	16.48	15.36	7.12	32.40	2.25	7.12	5.81	4.12	8.62	5.34
AT	7.69	27.35	15.71	10.22	18.12	7.50	23.55	3.74	5.86	6.43	8.12	6.80	41.41
IN	3.21	7.23	1.79	1.37	1.24	0.60	3.62	0.49	1.19	0.30	0.39	0.44	115.17
TF	7.41	7.72	2.31	3.24	1.70	2.93	7.87	1.08	6.79	1.70	1.54	2.01	6.48
<b><math>n_z</math> GROUP</b>													
7.33	12.90	12.30	19.35	5.64	24.80	6.25	10.08	2.62	1.81	3.02	15.93	2.62	4.96
6.0	7.78	22.74	12.52	5.80	12.73	3.82	16.03	2.71	3.53	2.61	4.52	2.78	205.11
5.0	8.80	15.73	9.77	5.63	8.86	2.90	11.57	0.87	2.28	1.78	2.86	2.71	48.28
<b>GROSS WT.</b>													
28 - 34	8.61	25.60	15.00	7.00	16.60	5.03	21.93	3.66	4.62	3.79	6.63	3.97	79.45
34 - 36	10.16	25.61	15.47	7.73	15.72	5.06	19.08	3.12	4.25	2.83	5.50	3.38	56.33
36 - 38	8.07	25.80	15.31	6.98	13.16	3.94	14.98	1.79	2.91	2.59	4.50	3.08	51.18
38 - 40	5.61	11.08	5.21	2.52	4.71	1.23	5.45	0.61	1.31	0.90	1.45	0.90	45.59
40 - 50	5.92	6.42	1.68	0.81	2.28	0.39	1.94	0.88	0.97	0.00	0.27	0.31	25.81
<b>ALTITUDE</b>													
0 - 2	22.04	50.50	24.98	7.76	20.38	4.49	23.01	4.87	4.49	3.48	6.10	3.58	18.68
2 - 5	11.68	27.49	16.67	5.52	16.72	3.53	17.97	3.36	3.72	2.37	6.02	2.37	57.46
5 - 10	9.61	34.79	16.22	7.04	16.47	4.50	22.34	2.65	4.30	2.52	5.49	2.75	55.49
10 - 15	6.71	15.18	13.00	9.18	14.41	6.93	17.24	1.73	3.50	4.46	7.00	5.49	31.15
15 & Above	2.63	5.57	4.11	3.61	4.64	2.07	6.68	1.29	2.03	1.61	1.64	1.94	95.57
<b>MACH NO.</b>													
Below 0.6	11.78	23.35	14.28	8.18	20.10	6.77	19.41	3.06	3.69	3.74	9.40	4.06	78.95
0.6 to 0.7	7.73	17.88	11.11	4.08	10.64	2.14	10.93	2.57	2.35	1.76	2.62	1.75	82.88
0.7 to 0.8	6.78	20.21	12.69	5.82	9.07	2.88	14.45	1.74	2.79	2.27	2.49	3.07	45.79
0.8 to 0.9	3.96	27.65	11.63	5.38	6.22	2.48	17.27	1.56	4.91	2.15	1.67	2.51	35.83
0.9 to 0.95	3.43	17.16	5.39	3.19	3.02	1.55	12.42	1.31	4.00	0.90	0.49	1.14	12.24
0.95 & Above	3.38	0.38	1.88		0.75		0.38						2.66

a. Symmetric VGH Data - None of the instrumented aircraft produced data whose load factors reached the clean configuration subsonic or supersonic design limits of  $n_z = 8.67$  and  $7.33$  respectively. The highest recorded value was  $7.37g$  subsonic.

Although the "D" fleet was temporarily grounded during the program (due to a number of accidents apparently caused by fires), and it might have been expected that there would be some limiting of the pilot's maneuvering techniques after a grounding, the relative frequencies of the load factors after the grounding were actually higher than those before.

\* An  $n_z$  group consists of configurations having similar handbook  $n_z$  restrictions.

Airplanes whose store configurations placed them in the  $7.33 n_z$  group\* produced data having a relative frequency of  $n_z$  peaks considerably higher than that for the airplane in the other  $n_z$  groups. The relative frequency for the airplane in the  $6.0 n_z$  group was approximately the same as that for the  $5.0 n_z$  group. This indicates that when a store is cleared for flight, with no restrictions other than aircraft capability, it is used just that way.

As indicated in the curves for exceedance of  $n_z$  peaks per 1000 hours (Figure 30), the relative frequency of the peaks during conventional bombing and ground gunnery exceeded considerably the frequencies during the

TABLE VI.  
COMPARISON OF DYNAMIC PARAMETERS – ENVELOPE VALUES  
"D" Multi-Channel Data

$N_z$	PEACE TIME					SEA COMBAT				
	P	P	R	Q	$N_x$	P	P	R	Q	$N_x$
	<u>DEG</u> SEC <sup>2</sup>	<u>DEG</u> SEC	<u>DEG</u> SEC <sup>2</sup>	<u>DEG</u> SEC <sup>2</sup>		<u>DEG</u> SEC <sup>2</sup>	<u>DEG</u> SEC	<u>DEG</u> SEC <sup>2</sup>	<u>DEG</u> SEC <sup>2</sup>	
2.2	100	75	5	22.5	-.4	80	90	19	15	-.8
2.7	100	45	15	22.5	-.4	80	60	20	60	-.8
3.2	60	45	5	37.5	-.6	80	60	10	45	-.8
3.7	100	45	15	22.5	.....	120	60	10	30	-.8
4.2	100	45	25	22.5	-.2	120	30	30	30	-.8
4.7	100	45	15	22.5	.....	120	60	20	30	-.6
5.2	60	45	15	22.5	.....	80	60	20	30	-.6
5.7	100	15	15	22.5	.....	120	30	20	30	-.6
6.2	60	15	5	7.5	.....	40	30	10	15	-.4
6.7	60	15	5	7.5	.....	80	30	10	15	-.4
7.2	20	15	5	22.5	.....	40	30	10	30	-.4
7.7	60	15	5	7.5	.....	40	30	10	15	-.4

other mission types. The relative frequency during special weapons delivery was next largest. This second relative frequency was then closely followed by the frequencies during

air tactics, test flights, and air-to-air gunnery. Finally, the relative frequency for instruments and navigation was considerably less than that for air-to-air gunnery.

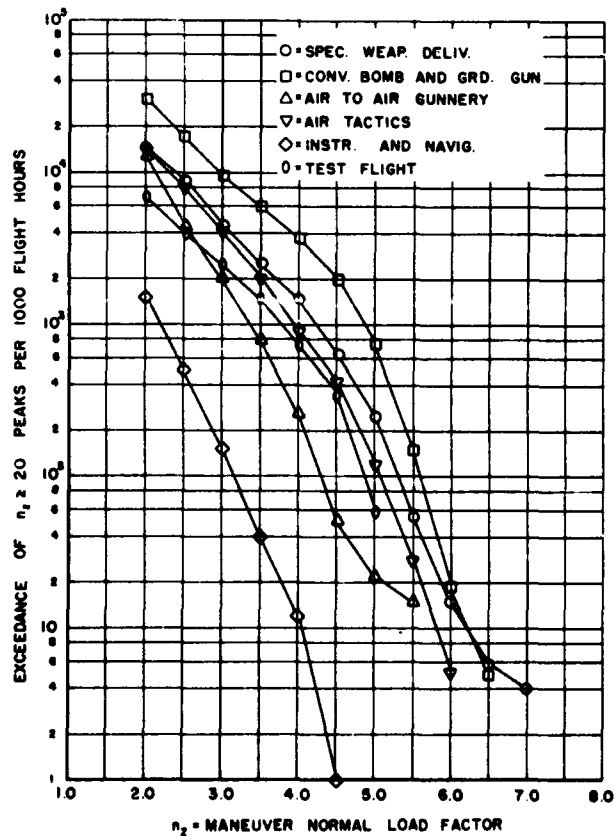


Figure 30. Comparison of Mission Data from Peacetime VGH Data.

b. F-105D Asymmetric Data (8 Channel) –

None of the F-105D airplanes instrumented during the 8-channel program produced data whose load factors reached the clean configuration subsonic Mach number design limit of  $n_z = 8.67g$  since the largest was  $5.73g$ .

Of the data recorded at the three air bases, the data from Nellis (a training base), revealed the highest utilization values (number of peaks per hour) for each of the twelve parameters.

In general, the mission types in order of highest to lowest utilization values are Conventional Bombing and Ground Gunnery, Air-to-Air Gunnery, Special Weapons Delivery, Air Tactics, Test Flights, and Instruments and Navigation.

A comparison of the angular rate utilization values indicates the pitch rate ( $q$ ) is much more dependent upon the type of mission flown than both roll rate ( $p$ ) and yaw rate ( $r$ ) - Table V.

The 7.33  $n_z$  group has the highest utilization values for  $n_z$ ,  $n_x$ ,  $q$ ,  $r$ ,  $pq$ , and  $qr$ . The 6.0  $n_z$  group has the highest utilization values for  $n_y$ , roll acceleration ( $\dot{p}$ ), pitch acceleration ( $\dot{q}$ ), yaw acceleration ( $\dot{r}$ ), and roll-yaw coupling ( $pr$ ). Table V.

Envelope values of recorded dynamic parameters are shown in Table VI along with aircraft design values (Table VII).

**TABLE VII.**  
**MAXIMUM ANGULAR RATES AND ACCELERATIONS**  
**F105D\***

	(1)	(2)	(3)	(4)
Normal Load Factor - $n_z$	8.67	6.1	1.0	0.5
Longitudinal Load Factor - $n_x$	1.5	1.0		
Lateral Load Factor - $n_y$		1.4		
Pitch rate - $q$ - deg/sec	$\pm 50$	$\pm 40$		$\pm 50$
Yaw rate - $r$ - deg/sec		30		65
Roll rate - $P$ - deg/sec		200	300	185
Pitch acceleration - $q$ - deg/sec <sup>2</sup>	-150	$\pm 75$		
Yaw acceleration - $r$ - deg/sec <sup>2</sup>		50		
Roll acceleration - $P$ - deg/sec <sup>2</sup>		300	600	

(1) is a sample of high load factor symmetric pull-up maneuver with abrupt check.

(2) is a sample of high load factor rolling pullout maneuver.

(3) is a sample of one "g" rolling maneuver with peak values.

(4) is a sample of a flat spin indicating some peak values.

\*NOTE: Rates and accelerations do not occur at the same time.

c. Fatigue Critical Areas by Analysis — As might be expected from looking at the exceedance curves of the two (Figure 31), the damage due to VGH peacetime usage was less than that due to the revised WPAFB test spectrum. In addition to the obvious reason of a generally lower load factor-cycle relationship, other factors aided in reducing the damage. Two of the more important factors were:

(1) Tip stall was taken into account.

This had a very desirable effect in that it tended to relieve wing root bending moments at the Mach-altitude-gross weight combinations at which it occurred. Furthermore it helped unload the undercut No. 3 lugs on frame 442.

(2) Reduced down tail loads. Evaluation of the VGH data indicated a greater percentage of time flown with heavy external wing stores than previously assumed. Although this meant more flight time at high gross weights, the presence of the stores produced an aft c.g. shift resulting in lower down tail loads. Since fuselage bending moments aft of fuselage station 442 are influenced by tail load, the reduced number of cycles at high tail load allowed for an increase in fatigue life at fuselage station 509, where failure had occurred at 142% of the test spectrum.

It is also important to note that a number of new points were subjected to analysis. They include: Fuel tank cover

\* Although no requirement existed for scatter, its effects were always considered. Hence, when lives are quoted as 10,000 hours with no scatter factor, these values were mentally divided by 4.

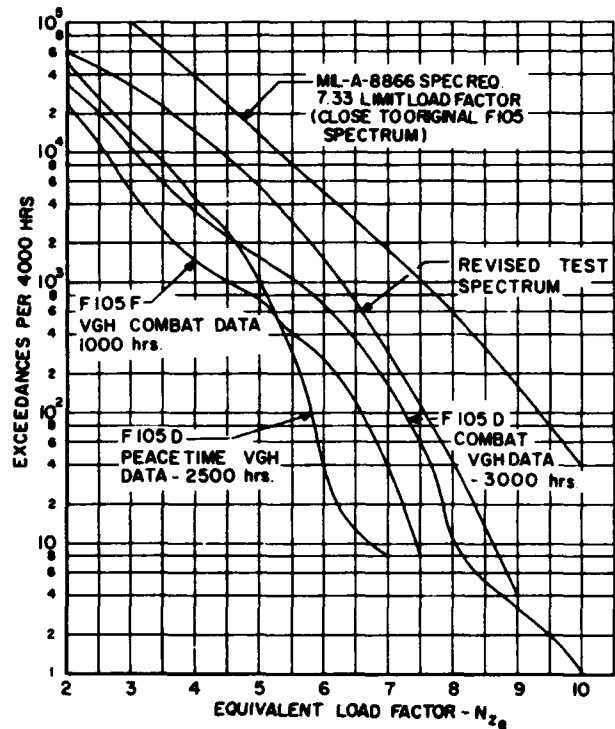


**Figure 31. Equivalent Normal Load Factor Exceedances for the F105D and F105F Using Various Spectra Data.**

cutout points on the fuselage similar in construction to the test failure point at station 509 (See Figures 5 and 17).

An additional wing point at the inboard pylon center post fitting (Figure 2) because the VGH data showed greater utilization of the aircraft with tanks than previously anticipated.

Specific points showing relatively low fatigue lives, with no scatter factor\*, under the "D" peacetime spectrum were:

- The tank cover skin splice at fuselage station 350 (Figure 21). This area which gave so much trouble when a trapezoidal cutout existed (Section VII), showed a predicted life of 10,400 hours for the rectangular cutout. The reinforcement designed at the time of the Thunderbird aircraft troubles, and shown in Figure 26, was recommended and accepted as a means of increasing the fatigue life of the "D" in this area.

- The tank cover skin splice at fuselage station 390 (Figure 32A). The splice and the rectangular cutout in it provide clearance for the aft end of the mounting lugs of the internal store displacement gear. It is a somewhat stronger splice, in that the radii were 0.25 inch minimum vs. 0.12 at station 350, the splice strap is thicker (0.112 vs. 0.080), and the skin plus a spotwelded doubler give a thickness of 0.130 vs. 0.080. As a consequence the predicted life was somewhat higher, 12,400 hours.

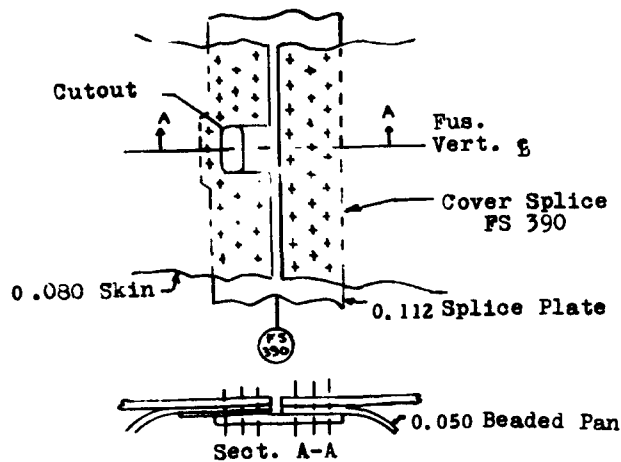
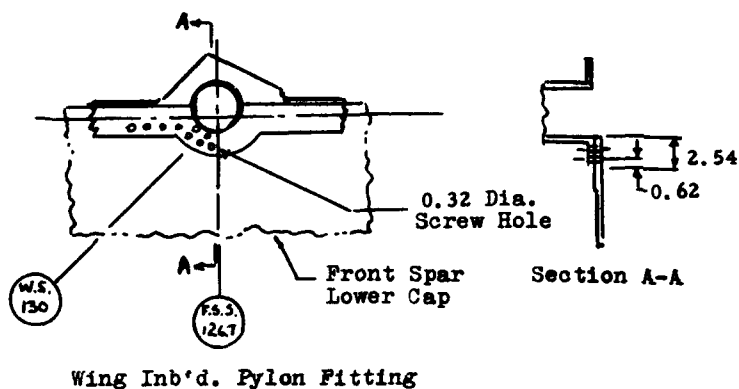


FIGURE 32 A



Wing Inb'd. Pylon Fitting

FIGURE 32 C

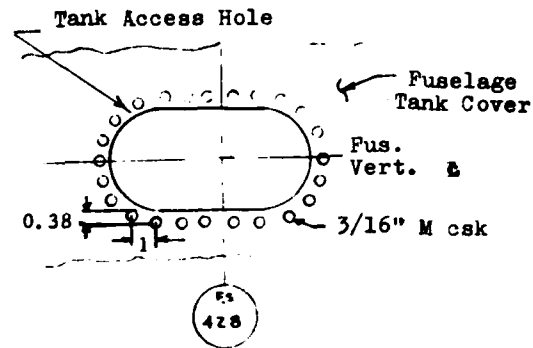


FIGURE 32 B

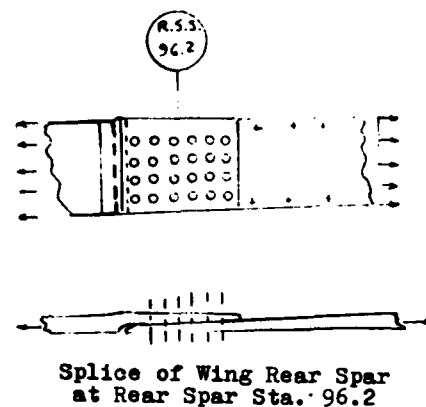


FIGURE 32 D

Figure 32. Fatigue Sensitive Areas Based on VGH Data.

- The tank cover skin at the fuel tank access door - fuselage station 428 (Figures 5 and 32B). This portion of the tank cover was critical along the edge of the fuel cell access cutout. It is almost an exact duplicate of the point of failure (station 309) in the third and final WPAFB fatigue test (Section V, Item B). Stress concentration is due to the line of attachment holes for the door along the edge of the cutout. Predicted life was 15,200 hours. This is lower than that at station 509, which was no longer critical, for reasons previously noted in Item (c-II).

- The wing inboard pylon fitting at front spar station 126.7 (Figure 32C). The fitting was analyzed for the effect of a fastener hole in the flange under the combined stresses existing at this point. These stresses include: net airload and inertia stress (primary stress), and the local stress due to introduction of couple loads into spar cap from pylon rolling moments. At the point investigated, the stress concentration is due to a number of holes around the flange. Predicted life was 21,400 hours.

- The splice of the wing rear spar forging to the outboard machined plate at rear spar station 96.22 (Figure 32D). The splice of the rear spar lower cap is accomplished

by six rows of attachments. Predicted life was 10,000 hours.

One final note about the use of the data for analysis: While there was a definite tendency toward an increase in load factor exceedances and damage, when evaluating data accumulated over a longer period of time (analysis was performed at 1,000 and 2,500 hours), a more important factor contributing to greater damage is the inclusion of asymmetric (8 channel) data at the 2500 hour check. At 1000 hours the data used was all symmetric.

2. Peacetime VGH and "8 Channel" Data - F-105F. In Item B it was stated that no such data was collected on the "F", but analysis of the "F" was performed based on modified "D" peacetime data. Primarily due to the fact that this was the first attempt at analyzing the "F" and because the way had been set by the "D" analysis, many more points were evaluated on the "F" than on the "D". Almost without exception points common to both aircraft were more critical on the "F". Using F-105D data to evaluate the F-105F may have been a reasonable way to go when no data existed for the "F" (this same concept was used in the original fatigue analysis and test) but

results based on this type of analogy should be used cautiously. Such factors as distribution and types of mission can increase or decrease fatigue damage to an aircraft. For the "F" analysis these were considered the same as the "D". Subsequent receipt of SEA combat VGH data on the "F" confirmed that the general mission configurations were the same, but their distributions different.

*Fatigue Critical Areas by Analysis - Essentially the predicted fatigue critical areas of the "D" were the fatigue critical areas of the "F". Table VIII shows the predicted lives for critical points on each aircraft. It was pointed out in the discussion of the rectangular cutout at station 350 (Section VIII, Item E-3) that the splice strap was changed to steel, and the radii increased on the "F". Therefore, for this point, because of the differing construction, no true comparison exists between the "D" and "F" fatigue damage.*

3. Combat SEA VGH and "8 Channel" Data - F-105D.

a. Symmetric VGH Data - The combat data is different from the peacetime data as follows:

(1) The combat data had longer flights (the average was 2.32 hours vs. 1.32 for peacetime), and fewer  $n_z$  peaks per hour in the lower  $n_z$  ranges. (Peacetime missions required more turns and other training maneuvers on much shorter flights - Figure 31); (2) The combat data had more  $n_z$  peaks over 5.5g's. (Figure 31); and (3) The combat flights were at much higher gross weights.

The combat data exceeded the F-105D design load factor envelope, with the highest  $n_z$  peak equal to 8.9g's at a gross weight of 41,591 pounds, yielding an  $n_{zc}$  of 10.3 g's.

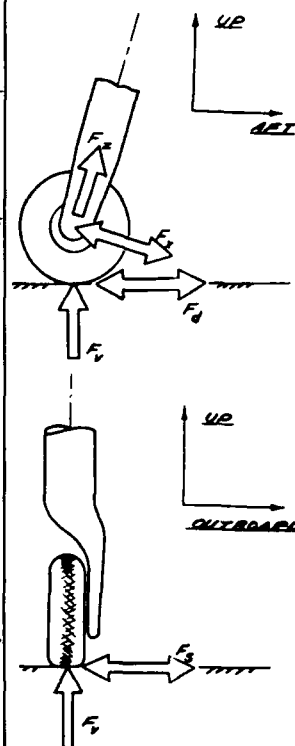
TABLE VIII.  
SUMMARY OF PREDICTED LIFE -- F105 D/F NO SCATTER FACTOR

POINTS OF INVESTIGATION	F-105-D		F-105-F	
	PEACETIME VGH DATA	COMBAT DATA	EXTRAPOLATED "D" PEACETIME VGH DATA	COMBAT DATA
	PREDICTED LIFE (HOURS)		PREDICTED LIFE (HOURS)	
1) Fuselage Station 350 - Tank Cover Skin Splice (Rectangular Cutout)	10,400*	6,100	17,800*	25,000
2) Fuselage Station 390 - Tank Cover Skin Splice	12,400	9,300	4,600	7,100
3) Fuselage Station 428 - Edge of Tank Cover Access Hole	15,200	10,100	5,500	8,700
4) Fuselage Station 509 - Edge of Tank Cover Access Hole	40,000	26,000	24,000	25,000
5) Frame 442 No. 3 Undercut - Attachment of Rear Spar to Fuselage	29,200	26,700	"F" frame is new design. Life is in excess of 40,000 hours.	
6) Wing Inboard Pylon Fitting Front Spar Station 126.7	21,400	7,700	13,000	17,000
7) Wing Rear Spar Forging Splice to Outb'd Plate Rear Spar Station 96.2	22,000	7,800	17,300	12,900

\*Splice strap is 7075-T6 aluminum alloy in "D", Steel in "F".

**TABLE IX.**  
**F-105B-20RE FATIGUE SPECTRUM FOR CYCLING OF MAIN LANDING GEAR**

Loading Configuration Number	Loading Configuration Title	Length of Strut Inches	Vertical Loads		Drag Loads				Total Number of Required Cycles Per 100%
			Pounds $F_z$	Pounds $F_v$	Pounds $F_x$		Pounds $F_d$		
					Forward	Aft	Forward	Aft	
			Side Loads Pounds $F_s$		Inboard	Outboard			
1	Hard Landing	81.22	19,000		15,100	12,800			360
2	Medium Landing	83.22	13,300		8,900	9,200			1,040
3	Mild Landing	83.22	9,800		5,300	5,500			2,880
4	Severe Braking Take-Off	80.88		21,480			0	7,520	3,200
5	Mild Braking Take-Off	80.88		21,480			0	4,300	9,000
6	Severe Braking Landing	80.88		14,380			0	5,030	3,200
7	Mild Braking Landing	80.88		14,380			0	2,880	12,000
8	Gear Walking	80.88		21,480	750	6,750			100
9	Gear Walking	80.88		21,480	2,400	3,600			19,000
10	Drift Landing	83.72		13,500	5,600	5,600			500
11	Turning	80.88		25,670	5,130	3,460			8,000



Ninety-six percent of the recorded F-105D SEA combat data was from one mission type (conventional bombing).

b. Asymmetric ("8 Channel") Data – The comparison of the combat and peacetime data shows that the former had: (1) Longer flights with much higher gross weights; (2) Fewer peaks per hour for all parameters except  $p$  and  $\dot{p}$ ; and (3)  $N_x$  and  $n_z$  peaks of higher magnitude and  $n_y$  peaks of lower magnitude.

Envelope values of recorded sea combat dynamic parameters along with recorded peacetime and aircraft design values are shown in Tables VI and VII.

Of the three recorded mission types\* instrumentation, navigation and test hops had the highest utilization values.

The increment of the longitudinal load factor induced by speed-brake operation was generally between 0 and -0.4g. Design envelope values are 0 to -0.8g.

\* Recorded mission types include: 1) ground gunnery; 2) conventional bombing; and 3) instrumentation, navigation and test hops.

The data indicated an overwhelming tendency of the combat aircraft to roll in on targets in one direction. Since this tactic allowed the enemy a definite defensive advantage, operational techniques were altered to eliminate it.

c. Fatigue Critical Areas by Analysis - From Figure 31, it is fairly evident that "D" combat operations were more damaging than those during peacetime. This is also demonstrated by viewing Table VIII. All areas previously designated as "possible critical areas" (without use of scatter factors) showed a reduction in life. For example at frame 442 with No. 3 undercut, predicted life dropped from a peacetime value of 29,200 hours to 26,720 hours in combat. Similarly the wing inboard pylon fitting, front spar station 126.7 dropped from 21,400 hours to 7,720 hours. Enough life existed at other points previously designated as being noncritical during peacetime, to remain in that category under combat use.

Combat damage calculations actually were based on the assumption that 15% of all flying during the

aircraft life would be under peacetime conditions with the remaining 85% combat flying. The peacetime flying contributed no more than 12% to the total of what is called "combat" damage.

4. Combat (SEA) VGH and "8 Channel" Data - F-105F. Comparison of the combat operational maneuver loads derived from the F-105F program with that derived from the F-105D program indicates that the load experience for the "F" was less severe. See  $n_z$  exceedance curve, Figure 31. No true comparison can be made between "F" peacetime data and "F" combat data since there was no peacetime program.

Comparison of combat operations maneuver load histories as well as aircraft utilization by mission type, indicates that the eight channel data samples were not representative of the VGH data samples. However, it should be recalled that only 100 hours of "8 channel" data was collected as compared to 1000 hours of VGH. Therefore, except for asymmetric data and dynamic parameters (not recorded on VGH aircraft), the results of the "8 channel" data should not be considered representative of "F" combat flying.

Critical Areas by Analysis - No Scatter Factor. Table VIII indicates that some of the areas previously noted as possibly being fatigue critical became more critical, while others showed improved life. These inconsistencies can only be attributed to the fact that the initial "F" peacetime evaluation was based on the "D" data, and that mission distributions recorded during "F" combat differed from those assumed for peacetime.

**X. Fatigue Analysis and Testing of the F105 Landing Gears**

One important area that has been thoroughly analyzed and tested, but not previously discussed, is the landing gear system. Both the 'B' and 'D' nose and main gears were subjected to analysis and test, with the only real problem occurring on the 'B' main landing gear. The reason for this is that the 'B' was the initially designed gear, and the 'D', which was designed later to accept higher design gross weights, included all the refinements to the 'B'. The 'F' gears are the same as the 'D'. A description of the landing gear is included under Section II. A picture of the gear is shown in Figure 6.

*A. Design Spectrum*

The F105 was designed to meet ANC 2A criteria for fighter aircraft. As a consequence, the static as well as fatigue load conditions covered landing loads, braking loads, gear walking loads (the F105 main gear is almost eight feet in length), and ground turning loads. The landing gear spectrum is shown in Table IX. Note that this spectrum did not include effects of pivoting, a factor which later plagued in-service aircraft (See Section XI).

*B. Discussion of Testing on 'B' Main Gear*

The main landing gear assembly evaluated was composed of the fork, outer cylinder assembly, and a trunnion. The trunnion was a new unused part; however, the fork and outer cylinder assembly had been subjected to 36 hard landings cycles during a landing gear stress investigation before commencement of the fatigue test.

Evaluation of the landing gear assembly utilized an actual F105 wing which was supported by steel structure in RAD's Engineering Research Laboratory. Except for a simulated wheel, the installation duplicated that of the aircraft.

The loads appearing in Table IX were applied by hydraulic cylinders. These cylinders were controlled by

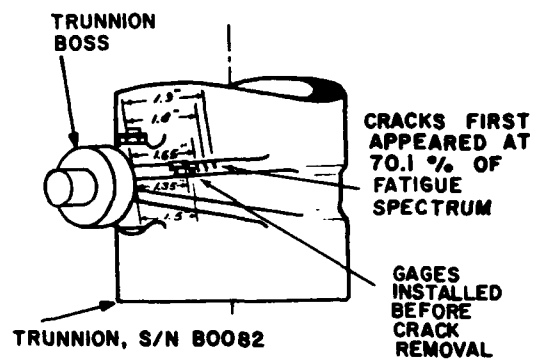


FIGURE 33-1

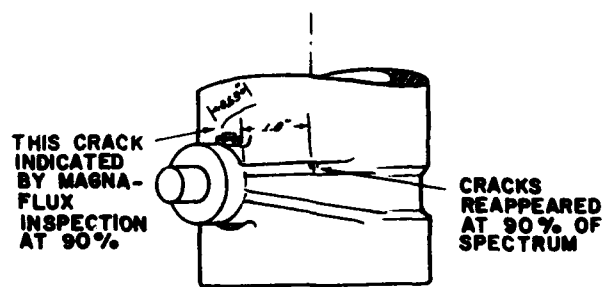


FIGURE 33-2

Figure 33. F105B Main Landing Gear Test.

pressure switches and manual valves for the cycled loads and the constant loads, respectively. Connected in series with each hydraulic cylinder assembly was a calibrated strain gage link indicating readings of tension and compression loads on an SR-4 box, which in turn, determined the pressure switch settings. The loading cylinders were reacted by various jigs mounted on the laboratory floor to provide the required geometry during the cycling.

The cycling pattern throughout the test required that the spectrum be repeated every ten percent of the total required number of cycles based upon 100 percent. This pattern provided for the frequent reapplication of each loading configuration to most accurately represent the actual loading cross section of the strut through its life.

Fatigue crack indications by dye checks first appeared in the top flange of the trunnion boss as shown in Figure 33-1, upon completion of 70.1 percent of the fatigue spectrum. Before removal of these cracks, strain gages were installed on the top flange. Hard landing loads were then applied in the forward direction, but were released upon excessive stress indications at 50 percent magnitude of the loads. Following removal of the gages, these cracks were treated by grinding operations at the installation until dye checks were negative. Then approximately 0.01 inches of additional material were removed and the cycling resumed.

Upon completion of 90 percent of the spectrum, cracks in the same area of the top flange were again indicated by dye checks (Figure 33-2). Removal of the gear assembly from the wing then permitted magnaflux inspections which indicated another crack 0.63 inches long as shown in Figure 33-2. This individual crack, after initial grinding, was characteristic of a lap of considerable depth in the material and was believed to contribute little or no influence toward a failure. Therefore, it received no additional treatment through the balance of the test. However, the reappearance of flange cracks required the removal of 0.09 inches of material as indicated in Figure 34-1 for a negative magnaflux inspection. The gear assembly was then returned to the wing installation with a strain gage installed on the top flange at the crack location. This strain gage indicated excessive stresses in agreement with previous findings for the same hard landing loads applied forward.

Cycling was resumed to complete 100 percent at which point cracks appeared in the top flange of, and at the base of, the trunnion boss as recorded in Figure 34-2. These new top flange cracks (which did not appear in the same place as previous ones), were again removed by controlled grinding to provide for a smooth surface transition into adjacent flange material. The crack indications in the thin-walled base of the trunnion boss, however, were not removed.

A crack, by dye check, appeared in the machined trunnion barrel as shown in Figure 35-1 after cycling through 100.1 percent of the spectrum.

Four cycles of hard landing were required to complete 120 percent of the spectrum when the outer cylinder failed as shown in Figure 35-2. It should be recalled that in addition to this percentage of fatigue cycling, this outer cylinder assembly was subjected to 36 cycles of hard landing loads. The fork and outer cylinder assembly were then replaced in order to determine additional trunnion life.

Dye checks upon completion of 140 percent of the spectrum produced crack indications in the radius where the top flange of the trunnion boss intersects the barrel (see Figure 35-3). Discovery of additional cracks by dye check of the trunnion barrel is also shown in Figure 36-1.

Cycling was continued until complete fracture of the upper trunnion barrel occurred at 143 percent of the fatigue spectrum. This trunnion failure as shown on Figure 36-3 terminated the fatigue test.

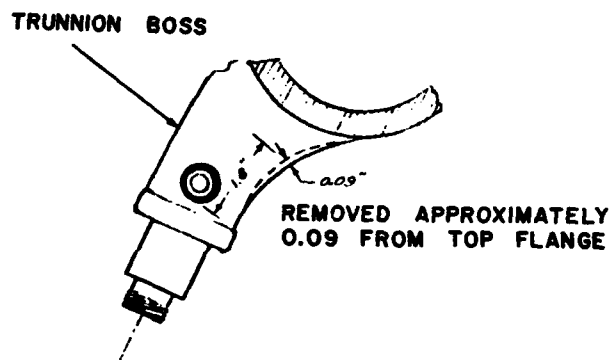


FIGURE 34-1

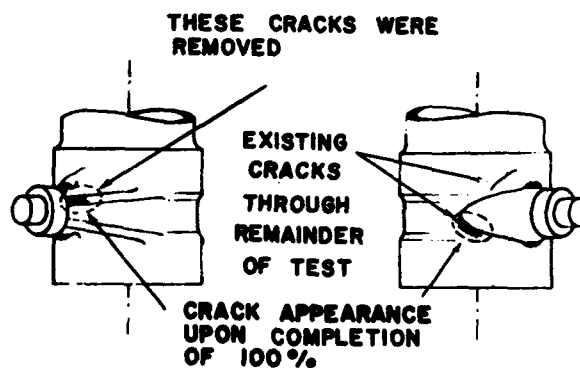


FIGURE 34-2

Figure 34. F105B Main Landing Gear Test.



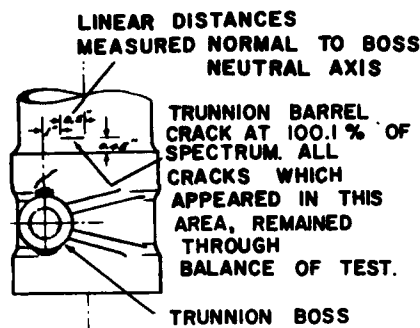


FIGURE 35-1

OBSERVER SEES FRONT VIEW OF OUTER CYLINDER

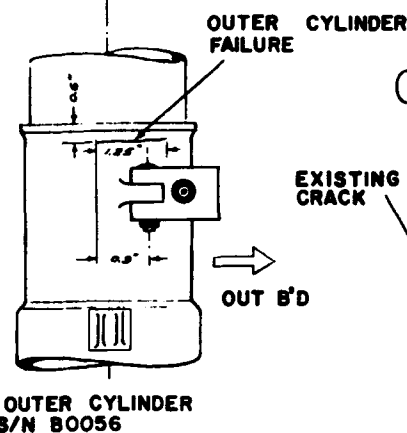


FIGURE 35-2

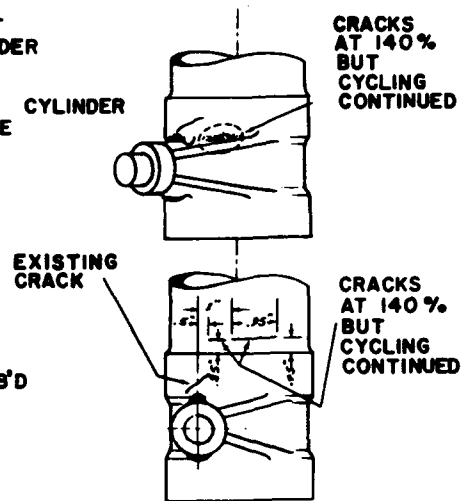


FIGURE 35-3

Figure 35. F105B Main Landing Gear Test.

It can be concluded from the test program that the F-105 main landing gear assembly was capable of sustaining its fatigue spectrum. It must be noted, however, that the gear might not have achieved the required life if the cracks observed during the spectrum had not been removed by grinding. The grinding operations were required for removal of the as-forged surface material in which the crack indications first became evident. (This surface material exhibited decarburization where mechanical properties were lower than the base metal.) The fatigue cracks in the gear assembly occurred in the as-forged skins of the trunnion and outer cylinder in all cases except as shown in Figure 35-1 and Figure 35-3. However, if these surfaces had been machined, it is probable that no fatigue cracks would have occurred prior to 100 percent of the spectrum. Subsequent to the fatigue test and prior to delivery of aircraft, all struts of the 'B' fleet were reworked like the test article, to insure meeting the prescribed life.

#### C. Analytical Results

Although analysis was performed, it must be stated that because the tests were completed first, it was possible to draw strongly from their results in the analytical work. The analysis, therefore, served mostly to make a tool available for evaluating the effects of changed aircraft usage.

#### D. Additional Tests

1. As previously noted, the F105D main gear was also tested. Since its design included all refinements for

eliminating fatigue problems learned on the 'B', and certain areas were beefed-up to account for heavier gross weights, the 'D' main gear sustained 150 percent of its spectrum with no problems. This test also paid the additional dividend of proving out the 'B' fixes.

2. The nose gear and its fuselage supporting structure sustained 400% of its fatigue life with no problems.

#### XI. Recorded Fatigue Failures (Service Results)

With the exception of the loss of the F-105B Thunderbird and F-105D-4 due to failure of the fuselage tank cover at station 350, the F-105 primary structure has been free of fatigue problems.

While there have been a few instances of failure in secondary structure these types of failure often occur, and can only be eliminated by attention to detail design. Since this is a history, and a discussion of the failures may aid others in avoiding similar problems, they will be described in some detail. In order of importance failed components include:

##### A. The F-105B Main Landing Gear Torque Scissors

This scissors transmits any torsion acting along the centerline of the strut from the fork-piston to the outer cylinder (Figure 6). They are made from AMS 6427 steel, heat treated from 220-240 ksi. At flight times varying from 600-1000 hours, cracks appeared in the lower torque

scissor radius (section A-A of Figure 37). Although it was obvious that a stress concentration existed at this point, there was some question as to why it had previously passed a fatigue test (Section IX). During the investigation into probable causes of failure, it was determined that actual usage required the aircraft to pivot and turn numerous times. Examination of the test spectrum showed no pivoting requirement, and only a minimal amount of turning. Hence the reason for failure. In order to eliminate the problem the scissors were redesigned as shown in Figure 37. This design eliminated the stress concentration.

**B. Main Landing Gear Retracting Cylinder Bracket**

This 7075-T6 aluminum alloy forged fitting is mount-

ed to the main landing gear side brace by four bolts. The main landing gear retracting cylinder attaches to it, permitting extension and retraction of the gear into the wing. Fatigue cracks appeared along radiused surfaces A-A and B-B as shown in Figure 38. Although fatigue tests demonstrated the capabilities of this bracket for handbook flight speeds, field reports indicated heavy ground usage for system check-out, along with marginal gear extension and retractions (there were incidents of gear stalls during retraction due to excessive air speeds). The fitting was redesigned using 7075-T73 aluminum alloy material, the pocket of Figure 38 was removed (reducing stress levels) and the basic radius increased. The fitting now has the capability to withstand excesses in use by a good margin.

**EXISTING CRACKS INDICATED BY MAGNA-FLUX INSPECTION UPON TRUNNION FAILURE**

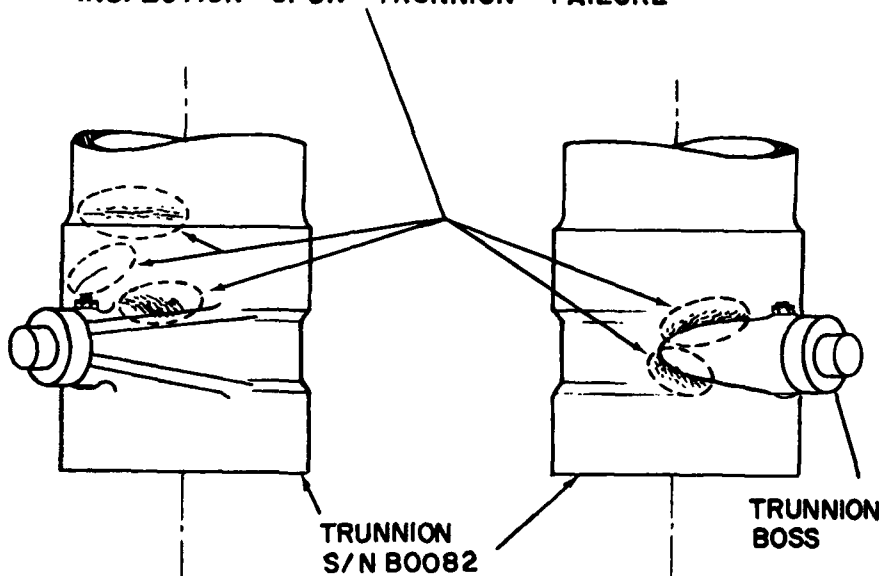


**Figure 36. F105B Main Landing Gear Test.**

**FIGURE 36-1**

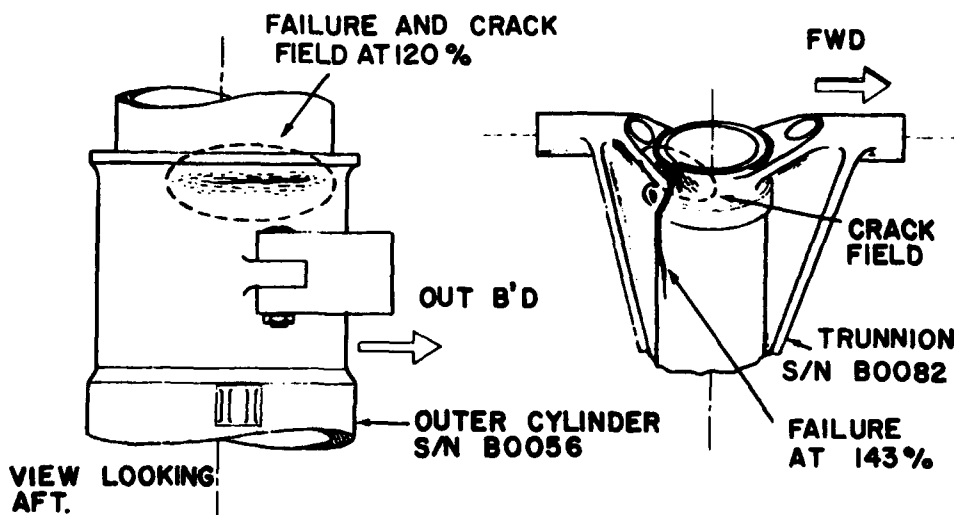


**FIGURE 36-2**

**FIGURE 36-3**

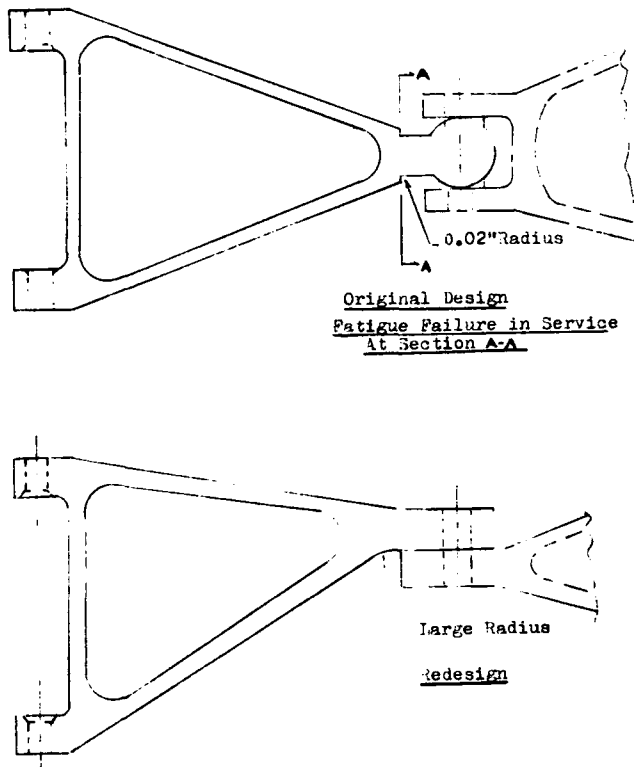


**Figure 37. Main Landing Gear Torque Scissors —**  
AMS 6427 Steel T.S. = 220-240 ksi .

#### C. Spoiler Actuator Cylinder

This cylinder operates the spoiler surfaces, and under initial design philosophies served as a stop for motion of these surfaces. The cylinder barrel, which was made of forged 7075-T6 aluminum alloy, exhibited cracks along the forging parting line where fatigue strength properties are lower than basic values. Although normal system pressure is 3000 psi, it was found that because this was a bottoming cylinder, surge pressures ran well in excess of 4000 psi. Furthermore, because of the nature of the control surface, it was in continuous use. In order to eliminate the problem, the cylinder barrel was redesigned utilizing 2014-T6 aluminum alloy material (with better fatigue properties than 7075-T6), heavier walls (reducing basic stresses), and most important, cylinder bottoming was eliminated (the system stops were moved elsewhere) thus reducing the internal surge pressures.

#### D. Leading Edge Flap Ribs

These 0.050 and 0.063 thick 7075-T6 aluminum alloy ribs (See Figure 39) beam airload shears on the L.E. flap skin surface to the flap spar and stiffen the skin structure against excessive deflection. The ribs experiencing cracks had an integral flange which attached to the spar web. This configuration necessitated a rib bend relief (stress concentration) at the junction of the spar and rib

flange. Aerodynamic studies indicated high frequency oscillations (70 - 100 cps) during severe maneuvering with L.E. Flaps extended. This phenomenon caused fatigue in the bend relief. Redesign consisted of ribs having a separate clip angle spliced to the spar web (eliminating the bend relief), a material change to 2024-T4 aluminum alloy, and an increase of flange bend radii from 0.063 to 0.125" (see Figure 39).

#### D. Climb Vent Boom

This welded corrosion resistant steel assembly (Figures 40-41), elliptical in cross-section was designed with a positive 26° rake angle as shown in Figure 40. The purpose of this boom is to maintain a positive pressure on the fuel cells to prevent them from collapse, and to permit fuel venting of the cells during refueling, (trapped air could cause overpressurization). Failure of the boom can result in a negative pressure, collapse of the cells, and complete overboard dumping of fuel.

Although no service failures occurred in any theater of operation, it was reported that strut welds on three booms had failed after 10 hours usage during special train-

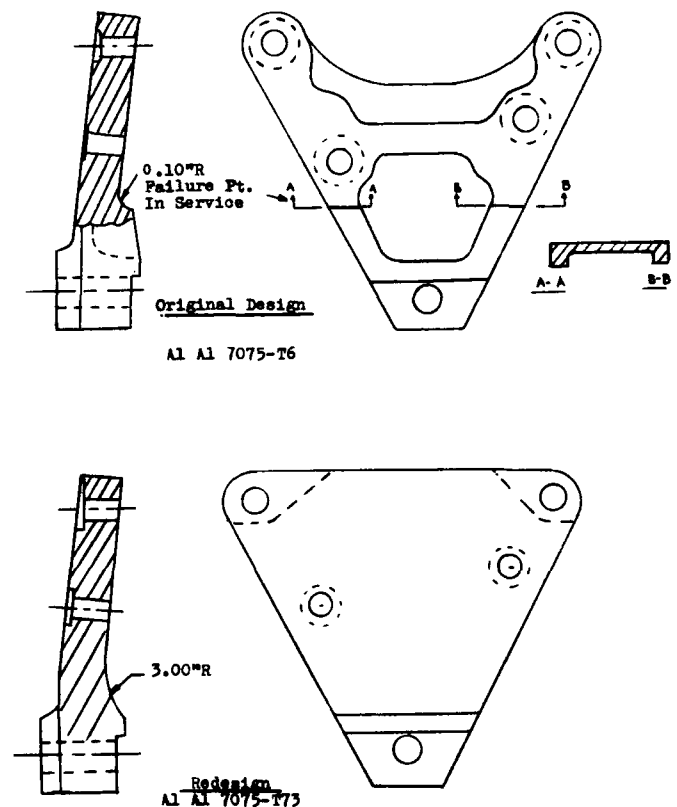


**Figure 38. Main Landing Gear Retracting Cylinder Bracket.**

ing tests at Nellis AFB. The failures which showed fatigue, and more important, led to negative rake angles, occurred due to severe turbulence. This turbulence was caused by a particular centerline stores configuration carried during repeated and sustained, high speed, low level (50 feet above ground) test missions. Since it was possible, at any time, to make this type of mission part of the operational requirements, preventative repairs were undertaken. These included the redesigns shown in Figure 41. Both tended to reduce weld and individual element stress levels below the material endurance limit.

**XII. Corrective Measures Taken to Prevent Fatigue Failures as Predicted by Analysis and Test**

As noted under Section VIII-C, the effects of both

\* Under the latest criteria the Air Force has requested that any reinforcements to the F-105, aimed at increasing fatigue life be based on 6000 hours with a scatter factor of four (4).

the peacetime and SEA combat VGH programs indicated a possible need to reinforce the fuselage tank cover from station 390 to 442 (station 350 was reinforced after the accidents), the wing in the area of the inboard pylon fitting at front spar station 126.7, and the rear spar cover splice at rear spar station 96.22 (Figure 32). The seriousness of this problem was brought to the attention of the Air Force in light of the fact that: (a) Scatter was not accounted for, and (b) The aircraft life requirement was being extended to 6000 hours. \*

Thus, the reinforcements that have been recommended for the fatigue critical areas are all based on this requirement (using a spectrum consisting of 15% peacetime and 85% SEA combat flying). They include:

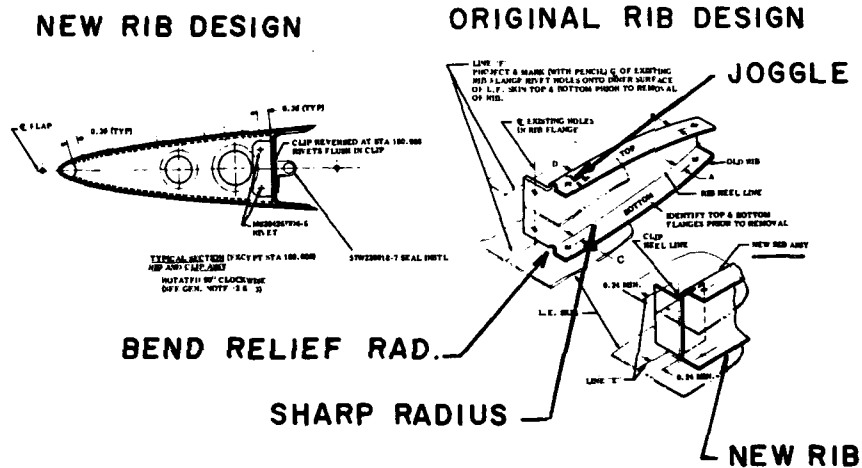
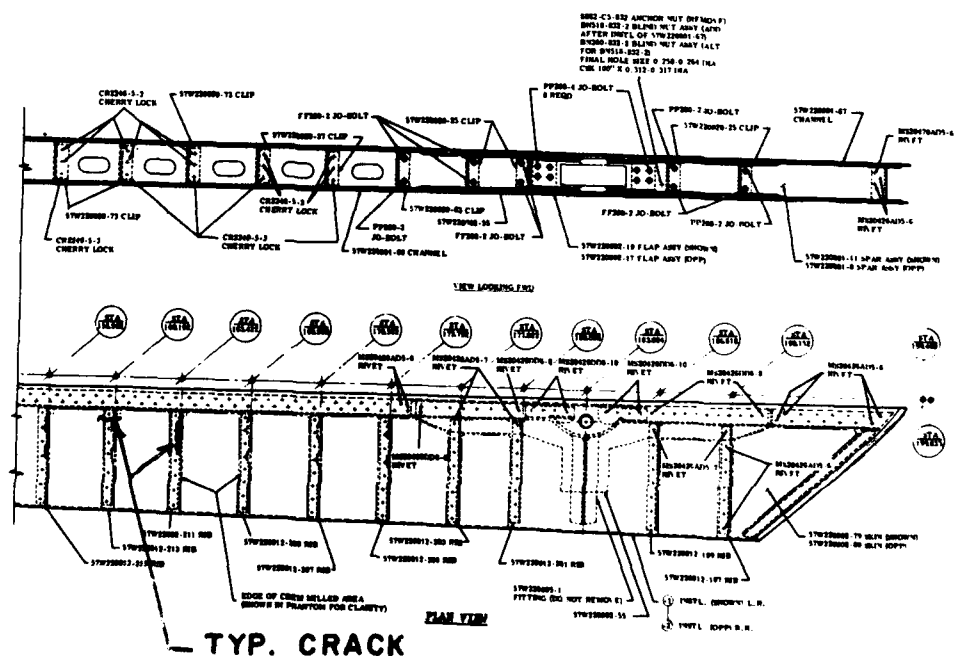


**Figure 39. Repair of Cracked Leading Edge Flap Ribs.**



1. Fuselage Reinforcement - This reinforcement commonly called "Strongback", and shown in Figure 42, consists of split doublers running along the spine of the aircraft from fuselage station 365 to 450 on the "D", and station 350 to 450 on the "F". These doublers effectively increased the moment of inertia of the fuselage cross-section, thus reducing the bending stresses in the critical areas for any applied moment. This in turn reduced fatigue damage.

2. Reinforcement - Wing inboard pylon fitting W.S. 126.7 and rear spar plate splice - R.S.S. 96.2 - Figure 43. These external reinforcements utilized the same concept as the "strongback" on the fuselage. By increasing the moment of inertia, bending stress and consequently fatigue damage was reduced.

### CONCLUSIONS

Although this paper dealt with the fatigue history of

the F105, the general conclusions reached can be applied to any aircraft. It is doubtful that these conclusions contain any new ideas on resolving the problem of fatigue; however, they do reaffirm existing concepts required for its prevention. Some of the more important conclusions are:

A. The importance of initial detail design cannot be overemphasized. All the certification programs in the world can't overcome fatigue-susceptible design. In areas of high cyclic load applications, design must not be compromised into creating a fatigue problem. Stress concentrations arising from holes or sharp radii, and rapid changes in cross section are to be avoided in such areas.

B. Designing against fatigue must be complemented by good manufacturing control practices. With the increased notch sensitivity of high strength materials, low quality workmanship cannot be tolerated.

C. A need exists for a fatigue certification program

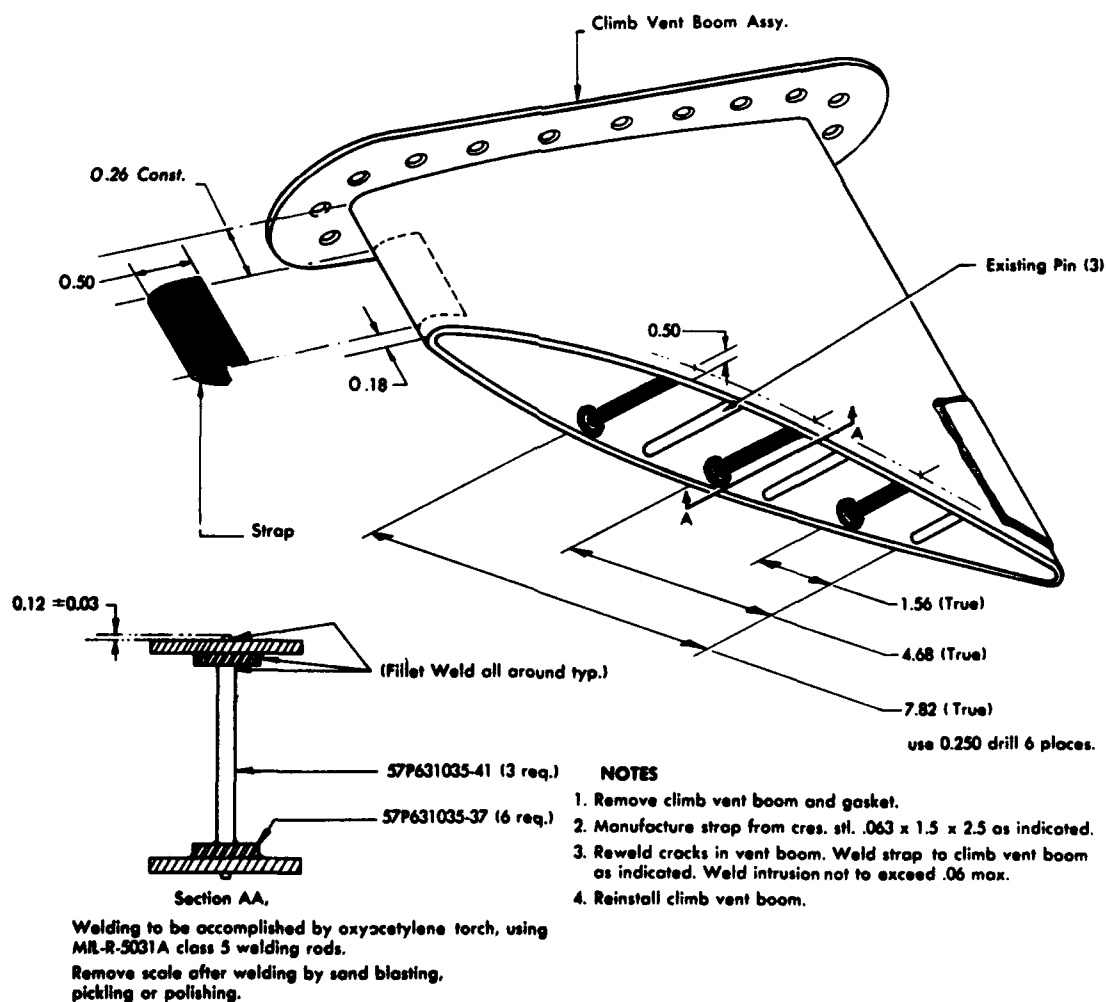


Figure 40. Climb Vent Boom Repair.

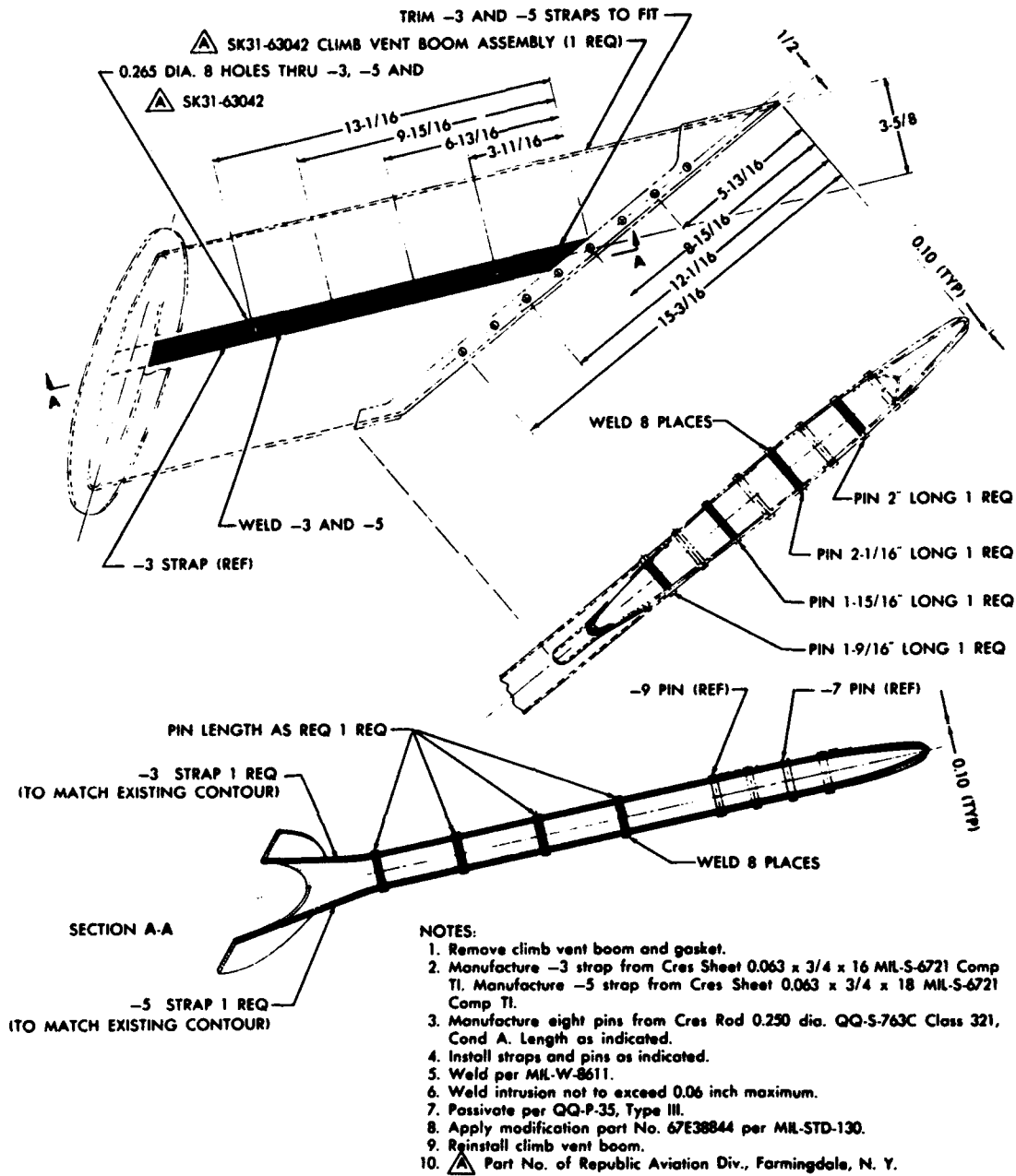


Figure 41. Climb Vent Boom Repair.

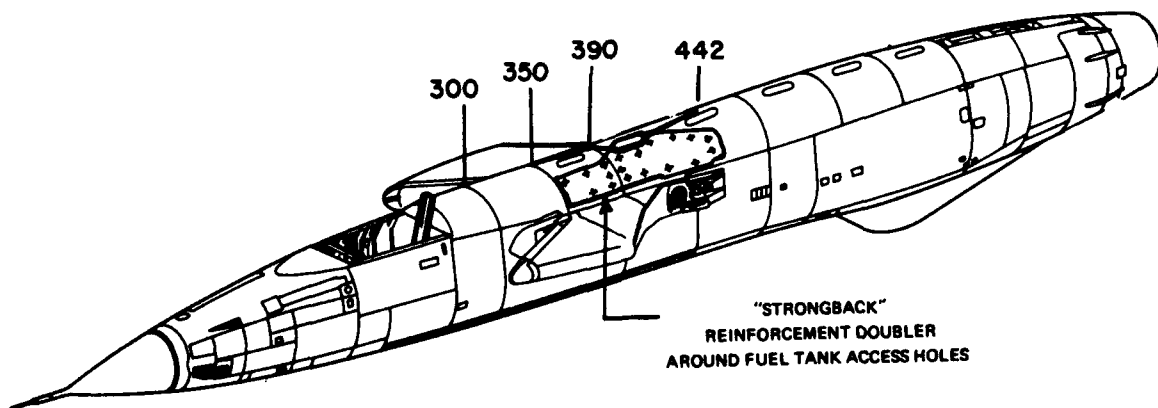
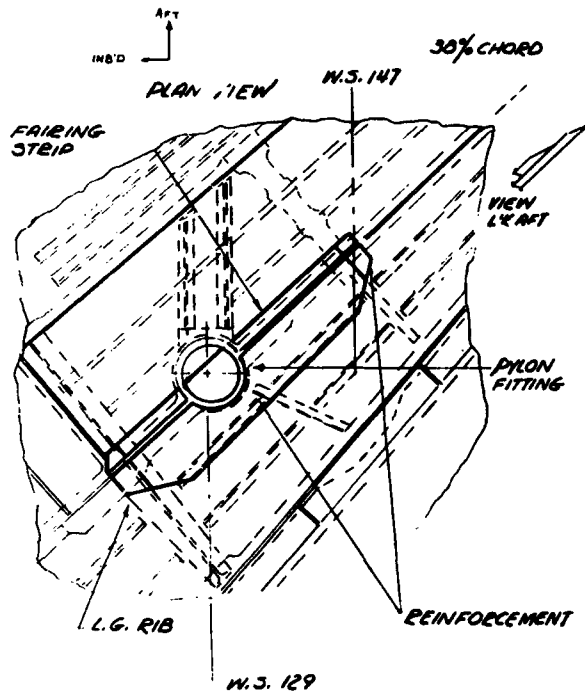


Figure 42. Fuselage Reinforcement to Increase Airframe Fatigue Life.



**Figure 43. Typical Wing Reinforcement.**

at the outset of any new aircraft design to evaluate very carefully the design philosophies. Such a program should

be continued throughout the aircraft service life to account for varying conditions of usage. Also, by necessity, the program must include repeated fatigue analysis and testing so that problems revealed in the testing can be prevented on operational aircraft by taking corrective measures.

D. Use of empirical data, and data extrapolated from one type aircraft to another, can lead to inaccurate evaluations. Such items as the percent time flown with and without stores, and varying mission requirements can create different flight maneuver spectra. While at the start of any new program it is necessary to use such data from other programs, data from the specific program itself should be obtained as soon as possible.

E. One limiting factor in evaluating fatigue test results is the amount of scatter possible in such results. While the ideal situation would be a requirement for numerous tests to account for such scatter, money is always a problem. Therefore, a single test with a scatter factor has to be accepted as sufficient.

These conclusions on control and prevention of fatigue do not guarantee that it will not occur. There are still too many variables that cannot be accounted for (with any degree of reliability) by analysis and test. The effects of such phenomena as corrosion fatigue and fretting are very difficult to evaluate or control. Even the basic assumptions of analysis and test are subject to argument. However, following the basic precepts just outlined greatly improves the chances for a fatigue-free structure.

## REFERENCES

1. *Summary Report - Fatigue Certification Program*, ESRT-15, RAC-1821 (1963).
2. J. Rosen and M. Pittel, *F-105D Airplane Fatigue Analysis Criteria - Load Spectra for Supporting Structure of Component Parts*, RAC-DR- 92-35, Part 3 (1962).
3. M. Chernoff and I. Stillman, *F-105D Airplane Fatigue Analysis Criteria - Loads Spectra due to Random Gusts*, RAC-DR-92-35, Part 4 (1963).
4. S. Saul, *Cumulative Damage in Fatigue*, ESAM-36 (1960; revised 1965).
5. V. Matulonis, *Structural Investigation of Accident to Thunderbird A/C S/N 57-5801*, ESAR-57-158, RAC-2779 (1964).
6. H. Bolton, *Engineering Safety Investigation - Accident to JF-105-05RE, Air Force S/N 58-1149 (RACD-4)* (1964).
7. R. Zebuda and A. Samet, *Fatigue Test - Station 350 Cutout, F-105F*, ESRT-91.
8. I. Stillman and R. Oliveto, *F-105D/F Airplanes Fatigue Analysis Criteria - Derivation of Load Spectra and Loads Based on VGH and Eight-Channel Data*, DR-105DF-1, FHR-3265 (1966).
9. *F-105D Statistical Flight Loads Program*, SEG-TR-66-16, Vols. I and II (1966).
10. *F-105D Combat Statistical Flight Loads Program*, SMNE-68-910, Vols. I and II (1968).
11. F. Dellosa, *F-105D Combat Fatigue Analysis Criteria*, SA105N1005, Section 1 (1967).
12. *F-105F Combat Statistical Flight Loads Program*, EFR-TR-82.4.1 (1969).
13. T. Whitiak and F. Dellosa, *F-105F Fatigue Analysis Criteria - Load Spectra and Loads Based on Southeast Asia Combat Data*, SA105M1007 (1969).

NOTE: All of the reports cited above were generated by the Republic Aviation Division (formerly the Republic Aviation Corporation), Fairchild Hiller Corporation, Farmingdale, New York.



TABLE A-1  
 TYPICAL FATIGUE LIFE PREDICTION - FUSELAGE  
 TOP TANK COVER SKIN - FUS. STA. 509  
 (REFER TO FIG. 17)

A-1 SECTION FUSELAGE STA. 509 TOP SKIN  
 JFM FLIGHT HISTORY & LIFE PREDICTION  
 10/21/76 AT 2000

1	2	3	4	5	6	7	8	9	10	11	12	13	14	15	16	17	18	19	20	21	23	24	25	26	27	28	29	30	31	32	33	34	35	36	37	38	39	40	41	42	43	44
1	2	3	4	5	6	7	8	9	10	11	12	13	14	15	16	17	18	19	20	21	23	24	25	26	27	28	29	30	31	32	33	34	35	36	37	38	39	40	41	42	43	44
1	2	3	4	5	6	7	8	9	10	11	12	13	14	15	16	17	18	19	20	21	23	24	25	26	27	28	29	30	31	32	33	34	35	36	37	38	39	40	41	42	43	44

## APPENDIX A

### Explanation of, and sample tables indicating early methods used in arriving at the stresses, cycles and damage at a particular point.

Referring to Table A-1:

Columns (1), (2), (3), (7), (8) and (9)

Definitions of conditions in the spectrum.

Columns (4) and (10)

Total fuselage bending moment for the basic reference flight conditions of the fatigue spectrum. The moment for all other conditions were obtained by prorating the load factor and weight at a particular speed.

Columns (5) and (11)

Stress due to  $M_{yy}$ , considering the basic analysis stress as unit solution =

$$M_{yy} \left( \frac{\sigma_{anal}}{M_{yyanal}} \right).$$

Columns (14) thru (32)

Columns of stress intervals above the endurance limit that were used in the damage calculations. The number

of occurrences, columns (6) and (12), for any condition was then written in the appropriate column. The summations at the bottom of the sheet show both symmetric and asymmetric cycles.

Columns (34) thru (43)

Tabular solution of the Shanley equation and determination of available life.

The only exception to this type analysis was frame 442. In this case an actual material stress-strain curve was developed by test. Spectrum stresses were obtained by determining all of the bending moments at the section in question, and then assuming a linear variation between moment and strain.

Predicted Critical Areas (by Analysis - No Scatter Factor)

A critical area is defined as one showing a life of less than 4000 hours under the initial design spectrum. No scatter factor is used (S.F. = 1).

## APPENDIX B

### Explanation of Computer Program for Determining Moments and Accumulating Cycles (SEA VGH Program)

#### LIST OF SYMBOLS

ALO	= total airload for unit airload curve (lbs)	N	= number of cycles for a load condition (cycles)
ARM	= bending moment due to one lb. on horizontal tail (in.)	$n_y$	= side load factor for a load condition (g)
BM	= equivalent bending moment for a load condition (in. lbs.)	$n_z$	= vertical load factor for a load condition (g)
BMAL	= bending moment due to unit airload curve (in. lbs.)	$n_x$	= longitudinal load factor for a load condition (g)
BMB	= bending moment due to unit load factor on 750 lb. bomb on outboard pylon (in. lbs.)	PA	= pitching acceleration for a load condition (rad/sec <sup>2</sup> )
BMIG	= bending moment due to 1g inertia (in. lbs.)	R	= upper limit of a bending moment range, R1 through R20 (in. lbs.)
BMP	= bending moment due to unit pitching acceleration (in. lbs./386 radians)	*SALO	= total airload for unit side airload curve (lbs.)
*BMSAL	= bending moment due to unit side load curve (in. lbs.)	SARM1	= bending moment due to one lb. load on vertical tail (in.)
BMSGEP	= bending moment at inboard pylon due to store gross effects (in. lbs.)	SARM2	= bending moment due to one lb. load on ventral fin (in.)
BMSGER	= bending moment at wing root due to store gross effects (in. lbs.)	SARM3	= bending moment due to one lb. load on fuselage carry through (in.)
BMSRMP	= bending moment at inboard pylon due to store rolling moment (in. lbs.)	*SF	= factor converting side bending moment to equivalent vertical moment
BMSRMR	= bending moment at wing root due to store rolling moment (in. lbs.)	*SL1	= load on vertical tail for a load condition (lbs.)
BMWL	= bending moment due to unit wing load distribution (in. lbs.)	*SL2	= load on ventral fin for a load condition (lbs.)
FAL	= fuselage airload for a load condition (lbs.)	*SL3	= load on fuselage carry through for a load condition (lbs.)
*FSAL	= fuselage side airload for a load condition (lbs.)	TL	= load on horizontal tail for a load condition (lbs.)
K1	= statement about 750 lb. bomb on outboard pylon (0 = no bomb, 1 = bomb)	WL	= total wing lift for a load condition (lbs.) (both sides)
K2	= bending moment due to BMSGEP (0 or 1)	WLO	= total wing lift for a unit wing load distribution (lbs.) (both sides)
K3	= bending moment due to BMSRMP (0 or 1.285)	*YA	= yawing acceleration for a load condition (rad/sec <sup>2</sup> )
K4	= bending moment due to BMSGER (0 or 1)	FALD	= airload drag on vertical tail (lbs.)
K5	= bending moment due to BMSRMR (0 or 1)	TALD	= total airload drag (including: fuselage, vertical tail, horizontal tail, with and without speed brakes) - lbs.

\* Asymmetric only.

Symbols Continued on Page 829

## LIST OF SYMBOLS, CONTINUED

BMSG96 = bending moment @ RSS962 due to store gross effects in. lbs.

$K_6$  = bending moment due to fin inertia (0 or -47719)

$K_7$  = bending moment due to airload drag on vertical tail (0 or 91.81)

$K_8$  = bending moment to total airplane airload drag = (0 or 30.7) (including fin, fuselage horizontal tail, and/or speed brake)

$K_9$  = bending moment due to BMSG96 (0 or 1)

### I. Discussion

This computer program was written to permit rapid calculation of the bending moments at each point being analyzed for each load condition in the SEA VGH program, determination of the moment range in which each condition belongs, and determination of the total number of cycles in each moment range. These operations are extremely simple mathematically, involving nothing more than cumulative multiplication and addition. However, in the previous peacetime VGH program, it was found that the huge number of load conditions created problems because of the volume of paper involved. Since the mathematical operations involved are so simple, in order to save time by use of a digital computer it was necessary to make the input procedures very simple. Therefore, some of the parameters which have fixed values at the points being analyzed were built into the program.

The computer nominally calculates bending moments at each point being analyzed. Actually, in order to account for asymmetric conditions on the fuselage, and local loadings due to axial loads, the computer calculates the equivalent moment about the horizontal axis that will give the same stress at the critical point of the section as the actual loading. Use of the computer to calculate the actual stresses for every condition is not warranted, because the damage per cycle for each moment range need be calculated only once in the program.

The input parameters can be divided into three groups: point description parameters whose values depend only on the points to be analyzed, unit condition parameters whose values depend on the unit condition (inertia or airload) and on the points being analyzed, and load condition parameters whose values depend only on the flight condition whose effect on the structure is being determined.

### II. Point Description Parameters

Using the F-105D as an example, the parameters ARM, SF, SARM1, SARM2, SARM3,  $K_2$  -  $K_9$  depend only on the point being analyzed and therefore are discussed with this group.

The most critical points chosen for analysis in the "D" SEA VGH program were:

POINT CODE	DESCRIPTION CODE	ITEM DESCRIPTION
01	F350	Fuselage top skin splice at the cutout - station 350
02	F390	Fuselage top skin splice spotwelding - station 390
03	F428	Fuselage top skin at access door - station 428
04	F509	Fuselage top skin at access door - station 509
05	W442	Wing attachment frame - station 442
06	WPYL	Wing inboard pylon fitting - front spar station 126.7

The values of the basic parameters at each of the points are given in Table B-1. The parameters ARM, SARM1, SARM2 and SARM3 represent the bending moments at each point due to the tail loads, and not the physical distance from the point to the tail. Therefore, these values are zero for the wing points and for the fuselage points forward of the wing rear spar attachment. Similarly, the parameter BMB, the bending moment due to a bomb on the outboard pylon, is zero at all fuselage points. The parameter SF, which converts a side moment to a vertical moment producing the same stress at the point being analyzed, is zero at F350 and F390 because the points being analyzed are on the vertical centerline, and therefore the effect of side moment at these points is zero.

The parameters  $K_2$ ,  $K_3$ ,  $K_4$  and  $K_5$  were introduced into the basic equation to make it easier to use existing procedures for calculating the effect of a store on the inboard pylon. Previous procedures used a separate computer program to calculate the effect of the store on each point on the wing. It was decided to simply add these store moments to the moments caused by the rest of the loads, and therefore the parameters  $K_2$  to  $K_5$  were given values of 0 or 1 so as to add the store moments at the correct points only. However, at the pylon fitting the stresses produced by the local effect of the store rolling moments were some 28% higher than the stresses produced by the same magnitude wing bending moments. The value of  $K_3$  was therefore

increased to 1.285. The moments calculated for point WPYL are therefore the equivalent wing moments that produce the same stresses at the pylon fitting as the combined effect of the actual wing moments and the local store rolling moments.

Similarly the parameters K6, K7, and K8 were introduced into the basic equation to account for the moment effect due to fin inertia, fin airload drag, and total airload drag respectively. As in the case of K2 through K5, it was decided to add these effects separately, where they exist. Thus K6 through K8 were given values or are zero.

Fixed input to the computer also included the upper limit of the moment ranges at each point. The lowest value quoted is the moment corresponding to the endurance limit stress at each point. All cycles of stress lower than the endurance limit are lumped together, because they theoretically contribute no fatigue damage. The remaining moments are spaced so as to make each moment range equal to a stress interval of approximately 2000 psi. This interval is considered to provide reasonable accuracy for the fatigue life calculations.

### III. Unit Condition Parameters

The parameters BMIG, BMP, BMWL, BMAL and BMSAL depend on both the points to be analyzed and the unit condition being used, and therefore, each parameter has a set of values at each point. These parameters represent the bending moment of each point being analyzed due to specific unit conditions. BMIG and BMP are the effects of inertia loading due to translational and pitching accelerations. Since the effect of rotational acceleration on the wing inertias are negligible, BMP = 0 on the wing points. The effects of stores carried on the wing pylons are calculated separately from the wing inertias.

The parameters BMAL and BMSAL, the effects of fuselage vertical and side airloads, are zero on the wing points. Similarly, the parameter of BMWL, the effect of wing airloads, is zero on the fuselage points from station 390 forward and from station 494 aft. The fuselage between stations 390 and 494 acts as the wing carry-through structure, and therefore BMWL is not equal to zero for fuselage points in this area.

The unit airload conditions cover the airload distributions throughout the range of angles of attack and Mach numbers of the F-105 flight regime. A relatively small number of unit conditions can thus be used to cover the entire spectrum of load conditions. To obtain the bending moment due to a load condition it is only necessary to multiply the bending moment due to the appropriate unit condition by the ratio of the total airloads of the load condition and the unit condition. The total airloads for the unit conditions are given by the parameters WLO, ALO and SALO. These parameters therefore have a single value for each unit condition, and are independent of the points being analyzed.

### IV. Load Condition Parameters

A load condition is defined by identifying the unit conditions of inertia and airload which best represents the distributions of the load condition, and applying multiplication factors to each unit condition.

The multiplying factors include the load factors ( $n_y$ ,  $n_x$  and  $n_z$ ), the rotational accelerations (PA and YA), the loads on the horizontal and vertical tails (TL, SL1, SL2, and SL3), and the total load of the distributed airloads (WL, FAL, FSAL, FALD, and TALD). In addition, conditions with a bomb on the outboard pylon are identified by the parameter K1, and conditions with stores on the inboard pylon include the bending moments due to store gross effects and store rolling moment (BMSGEP, BMSRMP, BMSGER, and BMSRMR).

To avoid carrying a lot of zeros for the asymmetric loads and factors when calculating symmetric conditions, each condition is identified as symmetric or asymmetric by a 0 or 1 in the first input condition. The computer then uses the appropriate formula, obviating the need for inputs of zero values for the asymmetric factors. The load conditions are identified by numbering in sequence (three digits are available), as the computer will associate the number of cycles (N) each condition with the condition number.

### V. Basic Equations

a) For each symmetric condition the bending moment (BM):

$$\begin{aligned} BM = & (n_z) \times (BMIG) + (PA) \times (BMP) \\ & + (FAL) \times \frac{BMAL}{(ALO)} + WL \times \frac{BMWL}{(ALO)} \\ & + (TL) (ARM) + (K_1) \times (BMB) (n_z) \\ & + K_2 \times (BMSGEP) + (K_3) \times (BMSRMP) \\ & + (K_4) \times (BMSGER) + (K_5) \times (BMSMR) \\ & + (K_6) (n_x) + (K_7) \times (FALD) \\ & + (K_8 \times (TALD) + (K_9) \times (BMSG96) \end{aligned}$$

b) For each asymmetric condition:

$$\begin{aligned} BM = & \text{symmetric bending moment} \\ & + (n_y) \times (SF \times BMIG) + (YA) \times (SF \times BMP) \\ & + (FSAL) \times \frac{SF \times BMSAL}{SALO} \\ & + (SL1) \times (SF) \times (SARM1) \\ & + (SL2) \times (SF) \times (SARM2) \\ & + (SL3) \times (SF) \times (SARM3) \end{aligned}$$

### VI. Computer Printout

At each point, separately, the computer determines

for each condition the bending moment, the moment range the condition belongs in, and its associated cycles. (See

table B-2). Finally, it accumulates all moments and cycles for all conditions as shown in table B-3.

**TABLE B-1  
INPUT DATA AT POINTS**

POINT CODE	DESCRIPTION	ARM	SF	SARM			BMB	K2	K3	K4	K5	K6	K7	K8	K9
				1	2	3									
01	F300	0	.682	0	0	0	0	0	0	0	0	0	0	0	0
02	F494	206	0	0	0	0	0	0	0	0	0	0	0	0	0
03	F428	0	.289	0	0	0	0	0	0	0	0	0	0	0	0
04	F633	67	1.34	57	0	0	0	0	0	0	0	-47719	+91.81	30.7	0
05	W442	0	0	0	0	0	-118828	0	0	1.0	1.0	0	0	0	0
06	WPYL	0	0	0	0	0	-22280	1.0	1.285	0	0	0	0	0	0
07	WR96	0	0	0	0	0	-29445	0	0	0	0	0	0	0	1.0
08	F350	0	0	0	0	0	0	0	0	0	0	0	0	0	0

**TABLE B-2  
TYPICAL IBM PRINTOUT  
BENDING MOMENT RANGE AND CYCLES**

**EXAMPLES:**

FLT CONDIN 417      ASYMM      K1 = C      CODES 141      1      109      206  
 CYC = 4      NZ = 2.7C      WL = 86710.0      FAL = 18600.0      TL = 1000.0  
 BMSGEP = 0.      BMSRMP = 0.      BMSGER = 0.      BMSRMR = 0.      PA = -0.52  
 NY = C.2C      YA = C.44      FSAL = 1430.C      SL1 = 5850.0      SL2 = 260.0      SL3 = 660.0

PT.	BENDING MOMENT	RANGE
6	0.32026923E 06	2
5	0.23829165E 07	1
4	0.37230431E 07	3
3	0.37778156E 07	3
2	0.27581415E 07	2
1	0.21911659E 07	2

**TABLE B-3**  
**MOMENT RANGE VS. CYCLES AT POINTS 1-6**

RANGE MOMENT	(FS 350) 01	(FS 390) 02	(FS 428) 03	(FS 509) 04	(F 442) 05	(WPYL) 06
1	1394	941	966	13363	18227	588
2	2150	1658	252	3570	57	1079
3	12155	8147	1946	1150	129	1853
4	1693	5676	8150	641	31	2686
5	1006	957	4666	396	44	6427
6	473	885	1513	421	46	4046
7	514	485	562	198	20	689
8	399	469	342	107	58	369
9	180	273	481	76	64	452
10	92	102	218	70	111	506
11	40	108	436	41	95	795
12	16	151	161	32	200	261
13	3	120	158	18	97	125
14	2	67	83	9	261	59
15	1	69	94	4	188	72
16	0	7	28	12	176	28
17	0	3	26	1	97	31
18	0	1	19	0	83	9
19	0	0	8	4	44	23
20	0	0	6	0	43	8
21	0	0	1	0	34	1
22	0	0	1	0	1	7
23	0	0	0	0	12	4
24	0	0	0	0	0	0
25	0	0	1	0	0	0
<b>TOTAL</b>	<u>20118</u>	<u>20118</u>	<u>20118</u>	<u>20118</u>	<u>20118</u>	<u>20118</u>

# THE DEVELOPMENT AND IMPLEMENTATION OF A FATIGUE MONITORING PROGRAM FOR A TRANSPORT AIRCRAFT

by

A.P. Shewmaker

Lockheed-Georgia Company  
Marietta, Georgia

J.A. Wagner

Warner Robins Air Material Area,  
Robins Air Force Base,  
Warner Robins, Georgia

## INTRODUCTION

The determination of the operational readiness of a single aircraft or a fleet of aircraft, when measured in terms of fatigue, requires an extensive and comprehensive structural integrity program. The most recent description of aircraft structural integrity programs outlined in Air Force Regulation 80-13, Reference 1, is discussed in detail as a six phase program in ASD Technical Report TR-66-57, Reference 2. These phases, in chronological order, are: Design Information, Initial Design Analysis, Testing, Final Structural Integrity Analysis, Actual Operational Usage, and Inspections. Each phase is further broken down into specific tasks involving either static or fatigue requirements. The phases, taken in order, supply data for each successive phase from the definition of requirements of the aircraft system, through design and testing and finally the service usage and monitoring of the aircraft system in terms of its operational parameters.

The C-130 aircraft was initially designed in accordance with structural requirements as defined by Specification MIL-R-1803, Reference 3. This specification did not contain requirements relating to fatigue, although limited testing was utilized in the design stage to insure that structural design concepts were compatible with the then current state-of-the-art. Subsequently, major fatigue certification programs were contracted for by the USAF, involving full scale testing and analysis of major airframe components, based on specific aircraft usages. These programs were after the fact in so far as design is concerned, and were initiated at a time when substantial quantities of the aircraft had already been produced. Data from these tests in the form of flight hours to crack initiation were utilized to establish special structural inspections for fleet aircraft. These inspection requirements were implemented by inclusion into Air Force Technical Manuals and were applied across the fleet independent of the actual operational usage. Inspection data feedback was extremely limited and in some cases non-existent. Since individual aircraft operational usage and structural inspection data were not monitored, the definition of the C-130 fleet operational readiness could be defined only in terms of fatigue analysis and tests results which were considered representative of a

specific usage. Major changes in operational usage were generally accounted for by updating the fatigue analysis, which may or may not have resulted in changes to the inspection requirements dependent upon prediction of time to crack initiation. This system of defining inspection requirements normally required a period of a year or more from the time the operational usage was defined until the inspection requirement could be implemented into the fleet. Again, it is emphasized that the inspection requirements were based on fleet averages and did not take into account individual aircraft experience. With the advent of the Vietnam war the C-130 took on the job as the major supply vehicle as ground transportation within Vietnam was subject to high fatality rates due to hostile forces. This role was conducive to accelerated fatigue damage since the aircraft generally operated from runways rougher than normal and flew at relatively low cruise altitudes with short duration flights.

Fatigue fracture data reported by field representatives and a sampling inspection of ten aircraft undergoing overhaul at WRAMA prompted an across-the-fleet inspection requirement of the C-130 center wing section. The results of this inspection revealed (1) that approximately 39% of fleet had already experienced initial fatigue cracking at one or more locations and (2) the variation in time to the specific cracking condition ranged from a minimum of 1200 flight hours to a maximum of 7600 flight hours. Furthermore, the missions that the aircraft were performing could not be terminated or delayed or taken on by other aircraft. This in effect dictated the continued operation of the aircraft with known visible damage. The damage tolerant design concept employed in the C-130 provided the necessary structural integrity to effect the continued usage of the aircraft in the visibly damaged unrepaired state. In order to cope with the overall structural condition of the fleet, it was necessary to implement a fatigue life monitoring program wherein individual aircraft could be monitored for both the current and future structural configurations. The basic objectives of the fatigue life monitoring program are to establish a procedure to provide an assessment of the structural integrity of the C-130 in terms of its past operational usage and to provide a means of quickly reacting to major changes in operational usage



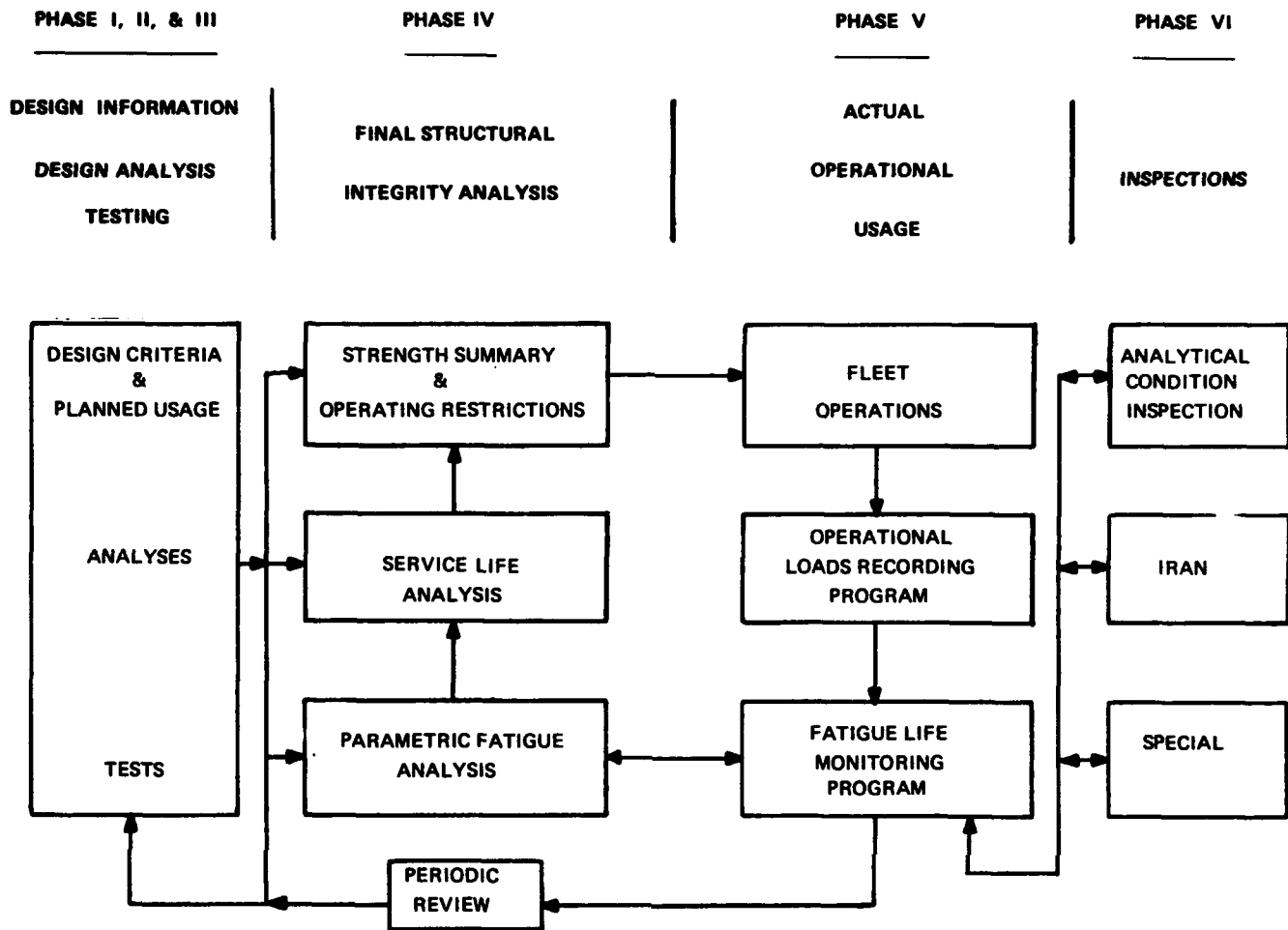


Figure 1. ASIP Flow Diagram.

throughout the service life of the aircraft. This implementation of the monitoring program on the C-130 completes the necessary link to describe a complete aircraft structural integrity program.

### DISCUSSION

#### Fatigue Monitoring Program Development

At the onset of development of the Fatigue Life Monitoring Program for the C-130, various phases of the Aircraft Structural Integrity Program were either completed or were in the process of being conducted. It was not until the monitoring program was implemented, however, that the various phases of ASIP were tied together to form a closed loop system for recording, transmitting, and evaluating structural information as it affects individual aircraft and/or the total C-130 fleet. Reviewing the ASIP flow diagram in Figure 1 as it existed prior to the implementation of the monitoring program, the following comments are made relative to status. Phases I, II, and III, Design Information, Initial Design Analysis, and Testing respectively, were complete except for a full scale fatigue test on the

C-130E wing which is in progress. Phase IV, Final Structural Integrity Analysis, also was complete except for performing the service life analysis for the C-130E wing and conducting a parametric fatigue analysis, both of which were tasks defined under the C-130E Fatigue Certification Program. No provisions existed for parametric fatigue analyses for other models of the C-130. Phase V, Actual Operational Usage, was probably the most incomplete of all phases. Fleet operations, although monitored, were not maintained by aircraft serial number and generally were available only for a prescribed base or wing. The Operational Loads Recording Program, better referred to here as an intermittently conducted VGH recorder program was used primarily to validate flight, gust, and maneuver data used in both static and fatigue studies. The individual airplane operational usage block was totally non-existent. Phase VI, Inspections, were being conducted and were based on data obtained from fatigue tests and service life analysis, representative of overall fleet averages and not geared to individual aircraft operational usage.

As may be deduced from the previous discussion all the basic elements required to operate a fatigue monitoring program were in some state of availability. Specific items,

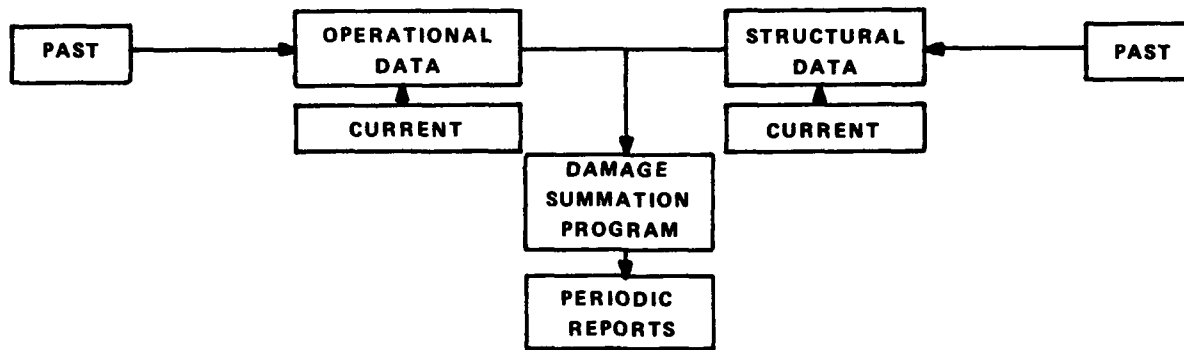


Figure 2. C-130 Fatigue Life Monitoring Program Flow Diagram.

however, such as individual operational usage data and the flow of data from one phase to another, were not in compliance with the ASIP flow diagram. The development and implementation of the fatigue monitoring program with its associated programs provided the closure block to effectively complete the data flow of the C-130 ASIP. Associated programs as used here refer to (1) completion of the parametric fatigue analysis for all series of the C-130, (2) an environmental loads recording program for aircraft located in Southeast Asia, (3) a specially instrumented aircraft for verifying statistical response data, and (4) implementation of a continuous life history recording program.

The basic ingredients of any individual aircraft fatigue life monitoring program include (1) the description of the operational usage of individual aircraft, (2) a method to convert this usage information into accrued damage, and (3) a means of assessing predicted versus actual damage values. The term damage as used herein refers to both fatigue, expressed in percent damage to crack initiation, and/or visible damage, expressed in crack length. Several methods are available and are presently in use by specific groups. These

various programs utilize crew data sheets, loads/acceleration recorders, or both, to define operational usage. In any case, however, these data must be subjected to analytical procedures to define accrued damage and must depend on inspection data to evaluate the predicted structural status.

The C-130 monitoring program, in its current operational stage, is shown in Figure 2. As noted, data items are listed as operational and structural and are further subdivided into past and current categories. The necessity of defining past historical data stems from the realization that the C-130 fleet aircraft had accrued flight time up to 10,000 hours and had experienced visible fatigue damage.

#### Operational Data

Past operational data was obtained utilizing data gathered from various sources. Individual aircraft possession records were used to define base assignments in terms of calendar time. Lockheed field service records supplied flight hour accumulations by calendar time. Mission profiles and utilizations were obtained from various using com-

TABLE I.  
MISSION DEFINITION, C-130 E

MISSION NUMBER	NAME	REMARKS
1	PROFICIENCY TRAINING	NORMAL ALTITUDE WITH S & G LANDINGS
2	BASIC TRAINING	NORMAL ALTITUDE WITH T & G LANDINGS
3	SHUTTLE	INCLUDES MULTIPLE SORTIES
4	SHORT RANGE LOGISTICS	>1.5 HRS. <4.5 HRS. DURATION
5	LONG RANGE LOGISTICS	>4.5 HRS. DURATION
6	AIRDROP	ALL MISSIONS WITH AIRDROP
7	STORM RECONNAISSANCE	SPECIFIC BASE ASSIGNMENT: > 8.0 HRS. DURATION
8	COMBAT TRAINING	LOW ALTITUDE WITH T & G OR S & G
9	LOW LEVEL	LOW ALTITUDE WITHOUT T & G OR S & G

S & G - STOP AND GO

T & G - TOUCH AND GO

mands again in terms of calendar time. The mission data from all commands was reduced into nine representative mission profiles as shown in Table I for each model series which were used to describe total past mission usage. The amalgamation of all these data resulted in a complete historical description of the operational usage of each C-130 in the inventory in terms of flight hours flown in each of the nine defined missions.

Current operational data is obtained in a much more precise manner. A crew data sheet designated AFTO Form 151, symbolically shown in Figure 3, is designed to record the more significant parameters involving damage accrual. Although the form is not discussed in detail a comprehensive review of it shows that a completed form contains sufficient data to describe fully the mission profile and aircraft operational loading. The problem encountered thus far with recording operational data is that the form flow rate has been well below 100%. That is to say, the form is not being completed on all aircraft for each flight. Figure 4 shows the flow rate of the form data in terms of calendar time. It may also be noted that the form data represents a sizeable package of information, approximately 10,500

forms per month, for a 100% flow rate, which requires considerable manpower to edit and transcribe to the computer. Various studies are underway designed to improve the flow rate and to reduce the processing effort and still record the required data. These include possible form modifications, review of the flow rate of the various bases, wings, and commands relative to each other, improved instructions on filling out the form, establishing the significance of the data to the using commands, etc. The implementation of the results of these studies should improve the flow rate toward the objective of 100% reporting and reduce the effort now required for processing.

*Structural Data*

Past structural data for each structural configuration was defined for each area considered in the monitoring program. The basic configuration for each serial was established by engineering drawing. Changes to the basic configuration as delivered from the factory were accounted for only when a specifically designed change was incorporated by a Technical Order and validated by a printout of the Technical Order Status Report. Attempts were made to de-

1. A/C Serial No.		2. Date Day-Month-Yr.		3. Command		4. Wing		5. Airframe Hrs.		Reports Control Sym.						
<b>TAXI AND TAKEOFF SEGMENT</b>																
6. Sortie No.	7. Takeoff Base	8. Gross Wt.	9. Fuel Wt.	10. Ext. Fuel Wt.	11. Taxiway					12. Taxi Time	13. Runway Type			14. Takeoff Type		15. Takeoff Time
					S	S	U	U	U		S	S	U	U	U	
1-																
1-																
<b>FLIGHT SEGMENT</b>																
16. Sortie No.	17. Clock Time	18. Segment Condition	19. Fuel Wt.	20. Ext. Fuel Wt.	21. Airspeed		22. Altitude	23. < 2000 Ft. AGL		24. Airdrop Wt.	25. Airdrop Time					
2-																
2-																
<b>LANDING SEGMENT</b>																
26. Sortie No.	27. Landing Base	28. Gross Wt.	29. Fuel Wt.	30. Ext. Fuel Wt.	31. Taxiway					32. Taxi Time	33. Runway Type			34. Landing Type		35. Landing Time
					S	S	U	U	U		S	S	U	U	U	
3-																
3-																
<b>TOUCH AND GO INFORMATION</b>																
4-																
4-																
<b>STOP AND GO INFORMATION</b>																
5-																
5-																

Figure 3. Operational Data Form, AFTO 151.

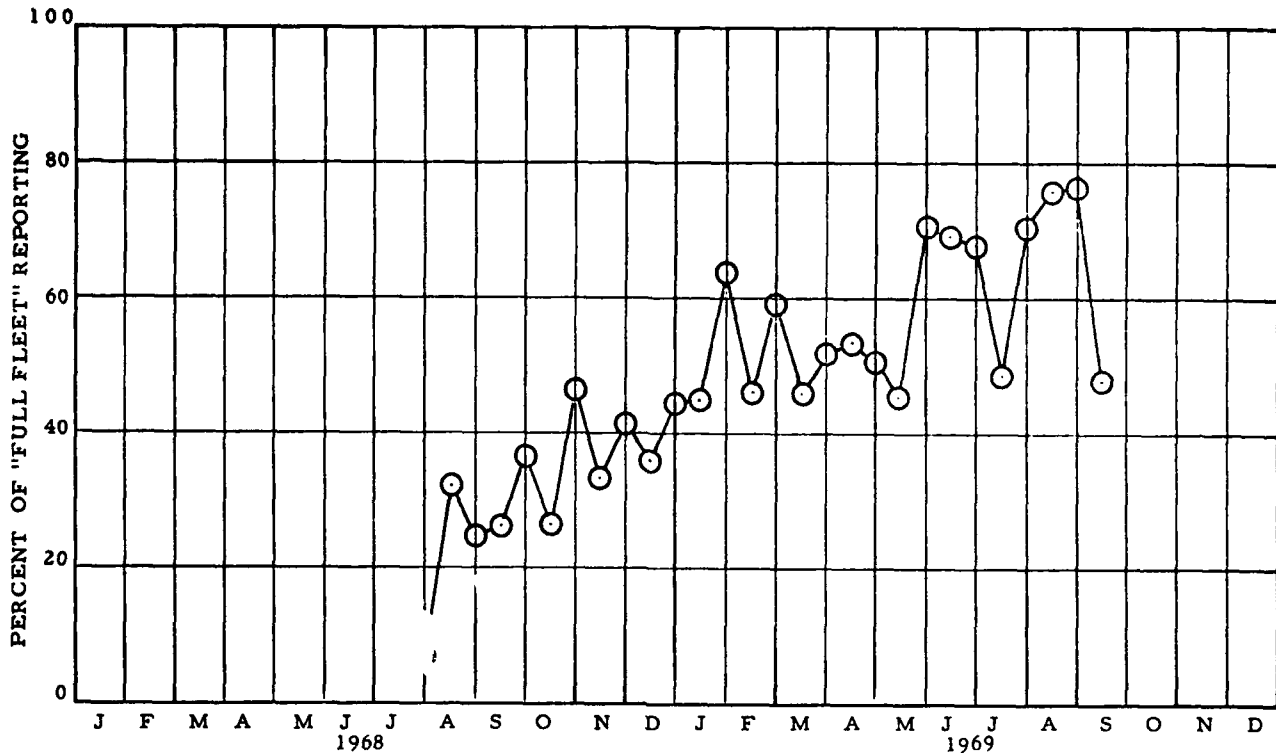


Figure 4. AFTO Form 151, Reporting Rate Vs. Calendar Time.

scribe the structure for non record type changes; however, the data concerning these changes was not of adequate quality. Therefore, modifications resulting from non record type T.O.s such as repairs or replacements were not accounted for.

Current structural data, as it pertains to structural configuration, is maintained by continuously updating the structure in accordance with the Technical Order Status Report. The structural condition, i.e., whether or not cracks exist, is monitored through reported special inspections which are accomplished at specified flight hour intervals. The results of special inspections are collected at WRAMA, where the data is stored on computer tape, then transmitted to Lockheed. This tape defines the crack length if one exists, the flight hours at the time of the inspection and the base location of the inspection. Additionally, an existing USAF maintenance reporting system has been modified that will provide similar type records for other structural locations. These data will hopefully reflect the overall aircraft structural condition and will provide data on crack locations not encountered in test. Repeated cracking conditions observed in fleet aircraft will provide the necessary data to statistically derive the structural performance factors required to monitor the aircraft.

**Damage Summation Program**

The damage summation program represents that portion of the monitoring program that converts fleet op-

erational usage data into accrued damage. This task is accomplished by performing a pseudo-fatigue analysis and/or fracture mechanics analysis at specific locations on individual aircraft based on the operational usage and structural configuration to define crack initiation and crack propagation respectively. The pseudo-analyses are accomplished through the use of a data blocking system wherein a constant damage rate is assigned to each data block. A data block provides a fixed value of damage for all combinations of significant loading parameters falling within specified regimes of those parameters. The data blocks cover the full range of operational usage. Tables II and III present the formatting of the data blocks for ground and flight operations respectively. The description of any particular data block is obtained by selecting a combination of the parameters, one in each column, that describes the operational usage. All possible combinations of each of these tables then describe the full operational capability of the aircraft. The operational usage forms are similarly reduced to data blocks of the same description. The total damage per mission or groups of missions is then defined as the summation of the matrix multiplication of the data block damage rates and the operational data blocks in terms of time or events. This is presented in equation form as follows:

$$D_{ij} = \sum_{l=1}^{l=n} (T_{i,l}) (R_{m,j,k,l})$$

TABLE II.

## DATA BLOCK LIMITS "GROUND"

DATA BLOCK NO.	EVENT	FUEL WEIGHT	CARGO WEIGHT	FIELD CLASS
1	NORMAL TAKE-OFF	0 - 10,000 LBS.	0 - 10,000 LBS.	SURFACED SMOOTH
2	MAX. TAKE-OFF	10 - 20,000 LBS.	10 - 20,000 LBS.	SURFACED ROUGH
3	NORMAL RUNOUT	20 - 33,000 LBS.	20 - 30,000 LBS.	UNSURFACED SMOOTH
4	MAX. RUNOUT	33 - 45,000 LBS.	30 - 40,000 LBS.	UNSURFACED ROUGH
5	NORMAL LDG. IMPACT	45 - 55,000 LBS.	) 40,000 LBS.	UNSURFACED
6	MAX. LDG. IMPACT	) 55,000 LBS		EXTRA ROUGH
7	TOUCH & GO			
8	GROUND-AIR-GROUND			
9	TAXI			

TABLE III.

## DATA BLOCK LIMITS "FLIGHT"

DATA BLOCK NO.	ALTITUDE	AIRSPD	FUEL WEIGHT	CARGO WEIGHT
1	CONTOUR	< 150 KIAS	0 - 10,000 LBS.	0 - 10,000 LBS.
2	0 - 2,000 FT. AGL	150 - 190 KIAS	10 - 20,000 LBS.	10 - 20,000 LBS.
3	2 - 5,000 FT. MSL	190 - 230 KIAS	20 - 33,000 LBS.	20 - 30,000 LBS.
4	5 - 10,000 FT. MSL	) 230 KIAS	33 - 45,000 LBS.	30 - 40,000 LBS.
5	10 - 20,000 FT. MSL		45 - 55,000 LBS.	) 40,000 LBS.
6	) 20,000 FT. MSL		) 55,000 LBS.	

where D = Total damage

i = Aircraft serial number

j = Specific structural location

T = Time or number of events in individual data block

l = Data block identification

R = Assigned data block damage value

m = Aircraft series code

k = Structural status code

n = Number of data blocks.

This equation, referred to as the damage summation equation, forms the heart of the fatigue monitoring program. It is used for predicting both crack initiation and propagation. Minor adjustments are required, however, to account for variable damage rates for crack propagations which are dependent upon initial crack length.

The fatigue damage values for the data blocks were obtained from a computer program developed to perform parametric fatigue studies. This program is referred to as "DART", an acronym denoting Damage Analysis in Rapid Time. DART has the capability of performing a fatigue analysis for any structural surface on the C-130 airframe. The program contains as stored data (1) loads tapes describing the full range of operational usage, (2), environmental parameters, and (3) S-N data. Input parameters are: (1) operational usage described by loading parameters such as fuel, cargo, altitude and velocity, (2) station definition, (3) relationship between loads and stress, and (4) structural quality level, "K", an effective stress concentration factor. By describing the operational usage either in terms of data blocks or missions together with the other input data, the program defines the mean and variable loads, converts them to stress and uses Miner's Theory of Cumulative Damage to arrive at a final damage value. The DART program has various optional outputs; however, for the fatigue monitoring program fatigue damage rates are computed for each data block for each station monitored on the airframe for specific structural configurations including known repairs, replacement or preventive modification.

The DART program also outputs stress occurrence

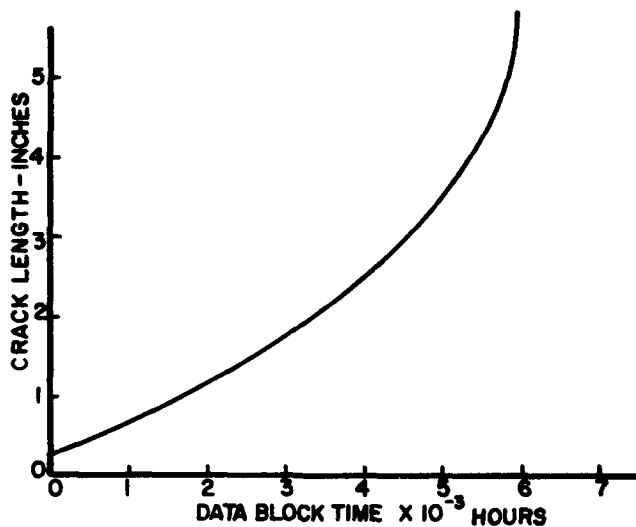


Figure 5. Crack Length Vs. Data Block Time.

data per data block which is used to determine damage rates for crack propagation. Crack propagation damage rates are accomplished using fracture mechanics equations adjusted to match test data obtained from panel tests conducted at Lockheed-Georgia Company. The equation in final form establishes the relationship between an applied stress spectrum and crack propagation. From the application of the equation a curve is established for each data block that relates crack extension versus time spent in the data block as shown in Figure 5. As in the case of crack initiation predictions, the total crack extension is determined by summing the individual predictions computed for each data block.

The allowable crack length for each specific area was established by a semi-empirical analysis that predicts crack instability as a function of the crack length and the applied stress level. The cutoff established for mandatory

repair requirements is defined as the maximum crack length for which repairs had been developed and/or the crack length at limit design stress that would result in the failure of the element under consideration whichever is less. In the case of the C-130, which incorporates damage tolerant structure, the failure of a single element will not result in the failure of the component or catastrophic failure of the aircraft for loads within the design range.

### Typical Program Output

Periodic damage reports that describe the structural condition of each individual aircraft in terms of crack initiation or crack propagation are submitted to WRAMA at quarterly intervals. The report is published as output from the Damage Summation Program and is controlled by the input parameters: operational usage, structural status, and the necessary stored data to define the remaining parameters in the damage summation equation. The report is presented in two sections. The first section is concerned with uncracked structural locations, whereas the second section relates to cracked locations. The criterion for tracking cracked locations is that the location must have been reported cracked by an inspection. In other words, the prediction of a crack in the first section has no influence on Section 2.

Figure 6 presents a facsimile of Section I of the damage report. Starting at the left margin, the various columns are defined as follows:

Column 1 lists the serial number of the specific aircraft.

Column 2 is a code that relates to the specific structural location on the airframe. A maximum of 16 stations are considered in the monitoring program and are currently based on critical areas defined by fatigue tests or analysis.

(1)	(2)	(3)	(4)	(5)	(6)	(7)		(8)	(9)	(10)
SERIAL NUMBER	CODE	CURRENT REPORT		TOTAL TO DATE		TIME TO CRACK INITIATION		PRED. RATE	REPAIR CODE	
		DAM.	FLT. HRS.	DAM.	FLT. HRS.	FLIGHT HOURS	MONTHS			
						CUR. RATE	PAST RATE			
6307836	1	5.0	179.0	100.0	7125.0	0.	0.	0.	0	
6307836	4	4.3	179.0	88.9	7125.0	460.	892.	5.	0	
6307836	3	4.4	179.0	86.9	7125.0	534.	1074.	6.	1	
6307836	7	3.8	179.0	75.4	7125.0	1155.	2328.	12.	0	
6307836	6	2.8	179.0	57.6	7125.0	2703.	5252.	29.	0	
6307838	1	THIS LOCATION CRACKED								
6307838	3	2.3	96.0	86.6	3639.0	533.	561.	6.	1	
6307838	6	2.4	96.0	84.7	3639.0	622.	655.	7.	0	
6307838	4	2.0	96.0	73.7	3639.0	1232.	1297.	13.	0	

Figure 6. Damage Accrual (Crack Initiation).

(1)	(2)	(3)	(4)	(5)	(6)	(7)	(8)	(9)	(10)
SERIAL NUMBER	STA.	LOC CODE	TOT	RPD	FLT. TIME	PRED.	TIME UNTIL REPAIR		MAX.
			FLT HRS	CRK. LGTH.		CRACK LGTH.	FLT. HRS.	MONTHS	TOTAL LGTH.
5800721			5183		237.0				
	120.5R	9F		.03		.06	1421	14	12.0
		9A		.09		.33			
		10F		.09		.33			
		10A		.03		.06			
	113.5R	91F		.50		.81	473	2	4.0
		91A		.50		.81			
		92F		.19		.24			
		92A		.00		.00			
	120.5L	39F		.00		.00	1421	14	12.0
		39A		.09		.21			
		40F		.15		.49			
		40A		.09		.21			
	181.0L	61F		.22		.88	726	5	8.0
		61A		.00		.00			
	160.0L	65F		.06		.36	1407	13	8.0
		65A		.00		.00			
	113.5L	75F		.00		.00	976	8	4.0
		75A		.09		.33			
		76F		.00		.00			
		76A		.06		.17			

Figure 7. Damage Accrual (Crack Propagation).

Columns 3 and 4 relate to the damage and flight hour accumulation during the current three-month reporting period.

Columns 5 and 6 present the total predicted damage at the station and the total flight hours on the airframe. It is noted that crack initiation is predicted at the value of 100% damage.

Columns 7, 8, and 9 headed by Time to Crack Initiation are predicted values in terms of flight hours or calendar months to crack initiation. Column 7 is presented in terms of the current operational data whereas Column 8 is presented in terms of the total past operational data. Column 9 is presented in calendar time in months until crack initiation and is based on current average flight hours per month for the base which the aircraft is assigned.

Column 10 is coded information which describes the structural condition of that station in terms of original structure, repair, replacements, etc.

The sample output for the crack monitoring portion of the damage report is shown in Figure 7.

The various columns of data are described as follows:

Column 1 lists the cracked aircraft serial number.

Column 2 defines the wing station location of the crack.

Column 3 is coded information detailing the exact rivet location of the crack.

Columns 4 and 5 define the flight hours and crack length observed at the last inspection respectively.

Column 6 lists the flight hours recorded during previous three months.

Column 7 lists the cumulative total flight hours on the aircraft.

Columns 8 and 9 are times to mandatory repair and the predictions are based on current usage data.

Column 10 is the maximum allowable total crack length that can be tolerated at the particular station.

In addition to the individual aircraft reporting as discussed above, supplemental data is presented simultaneously with the damage report that summarizes the fleet condition. These data provide the necessary information to define the operational readiness of the USAF C-130 fleet.

### Correlation of Predicted to Actual Damage Conditions

The damage tolerant design concept employed in the C-130 aircraft provides continued safe operation of the aircraft with cracks while operating within the design regime of operational usage.

This concept of design has, in the case of the C-130, allowed the aircraft to continue its operational role in an unrestricted manner, with visible damage. Two pronounced benefits have evolved from this method of operation:

1) The aircraft are allowed to continue normal operational usage in an unrestricted manner, although increased inspection requirements were imposed.

2) Data recorded and received through USAF inspections in relation to the areas being monitored provided

a means of assessing and correlating predicted structural status as presented in the periodic damage reports.

The benefits obtained from item 1) are noteworthy in several respects:

- The utilization of the aircraft is maintained.
- Repair kits were scheduled and applied at opportune down times.
- Crew confidence was maintained relative to the aircraft's capability.

The information obtained under item 2) provides the closing link in the fatigue life monitoring program by supplying the necessary data to correlate actual fleet structural conditions to that predicted by the monitoring program. Furthermore, by directly comparing these data,

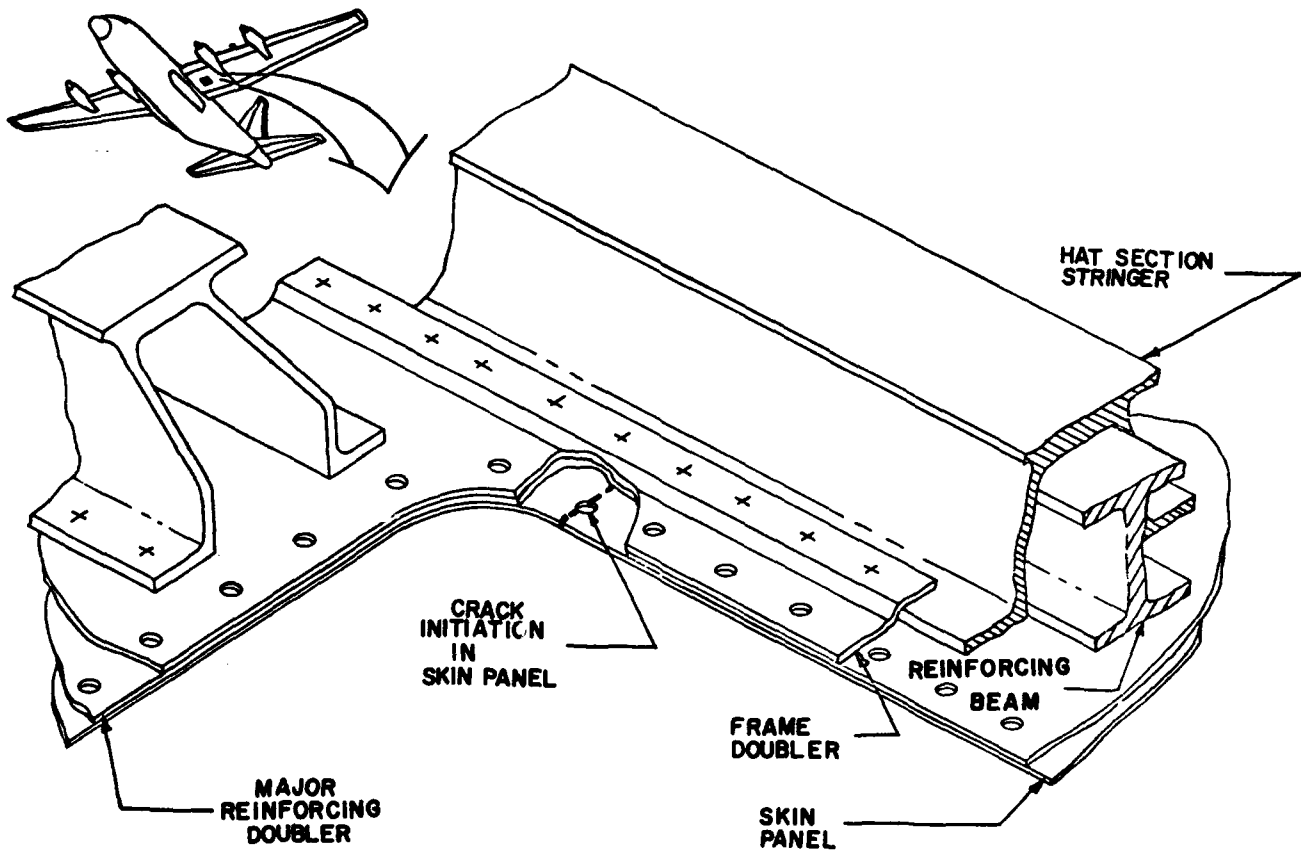
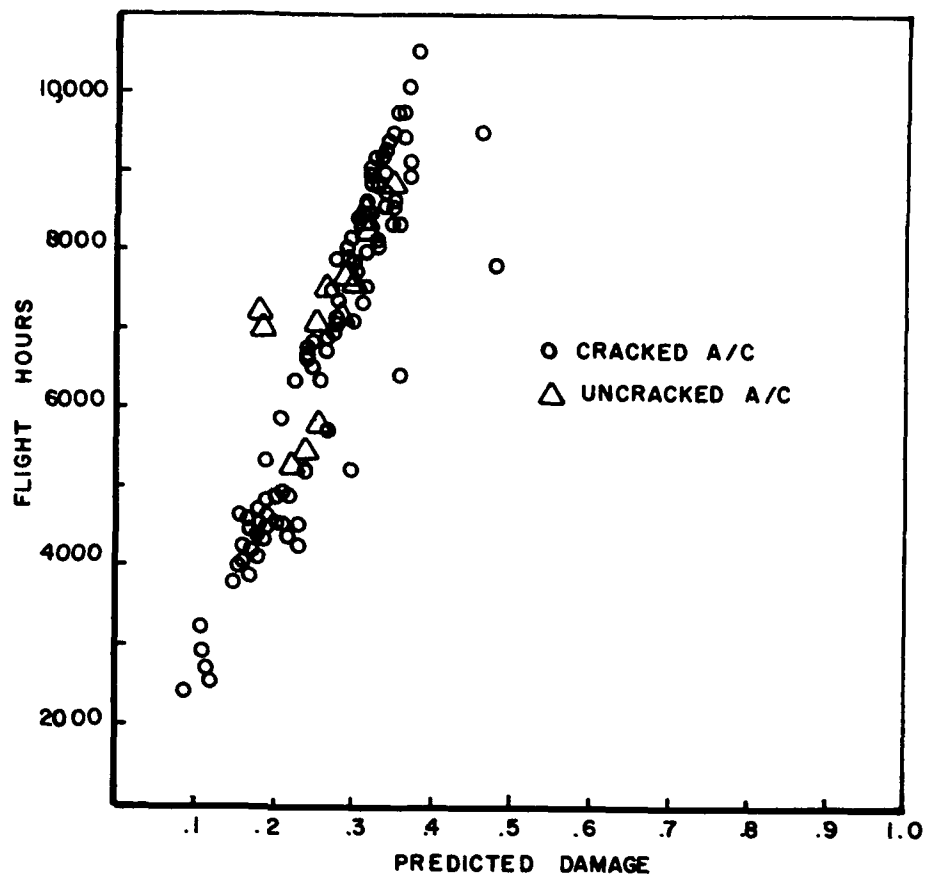


Figure 8. Structural Configuration at Corner of Wing Cutout, W.S. 120.5, Lower Surface.



Figure 9. Structural Status, Early Estimates - W.S. 120.5, Lower Surface.



various input parameters may be modified to improve overall fleet correlation.

In order to show these relationships, a station on the center wing lower surface of the C-130E is used for data comparisons. This station is used for several reasons: It is generally the first location on the lower surface to crack, thus providing a broad sample of data; the structural configuration is identical for the complete C-130E model production run; and finally, it is fairly typical of the individual station analysis.

An isometric sketch of this area is shown in Figure 8. The area involved is a cutout for access to the fuel bladder cells and is located at Wing Station 120.5 left and right. Cracks typically initiate at the fastener holes used to attach the closure door located at the tangency points common to the radius of the cutout and the spanwise axis. The cracks propagate in the chordwise direction. The construction of the center wing lower surface consists of three spanwise panels each 440 inches long and 26.7 inches wide fabricated from 7075-T6 aluminum alloy bare plate, reinforced by extruded hat section stringers spaced at 5.70 inch intervals.

Figure 9 is a graphical presentation of the structural status for the C-130E fleet for the wing lower surface cutout at W.S. 120.5. The data points shown in this figure in-

clude all C-130E aircraft for which crack initiation has been observed since the initial inspection and those aircraft that are currently uncracked. The figure relates for:

- cracked aircraft — the flight hours to crack initiation versus predicted damage.
- uncracked aircraft — the current total flight hours versus the predicted damage.

Reviewing this chart, various information can be determined such as:

- The variation in flight hours to crack initiation for cracked aircraft.
- The predicted status of uncracked aircraft.
- The relationship of predicted status between both cracked and uncracked aircraft.
- The variation in predicted damage for cracked aircraft.

The program input data to the damage summation equation as it relates to predicted damage values in Figure 9

is based on initial description of the past history in terms of the "Nine Mission Profiles" and damage rates as they were initially defined.

In an attempt to improve the correlation of predicted to actual damage, studies were initiated to evaluate the various parameters that were considered significant. Each of these are discussed as follows:

- Past operational data was the first parameter to be considered. It must be properly defined before the effects of scatter can be evaluated. Figure 10 presents an interesting aspect to scatter as it relates crack initiation between the left and right wing and is based on inspection data. It is recognized that the data may be biased to a degree, since if a crack were found on one side the individual would probably look very close on the opposite side. Nevertheless, it does indicate that regardless of the time to crack initiation a fairly narrow band exists between the left and right sides of individual aircraft. This tends to indicate that if the operational usage is properly accounted for scatter would be significantly reduced.

- Data block size and representative damage rates are probably one of the most important parameters to be considered for correlation purposes. Studies to date have been restricted to evaluating the mid point of the data block. That is, the initial constants were obtained for the data block by computing the damage corresponding to the mean operational values of each data block. These values change quite significantly when derived as the average damage for the corners of the data block. The size of the data block and the representation of the data block damages in terms of damage sources such as taxi, flight and ground-air-ground are currently under investigation.

- The effective stress concentration factor which is normally obtained from the fatigue test is being evaluated in terms of fleet cracking condition.

In other words the fleet aircraft are effectively being used as test specimens to define stress concentration values. This is accomplished by describing the applied loads or stresses that are applied to individual aircraft in accordance with its operational usage and determining from

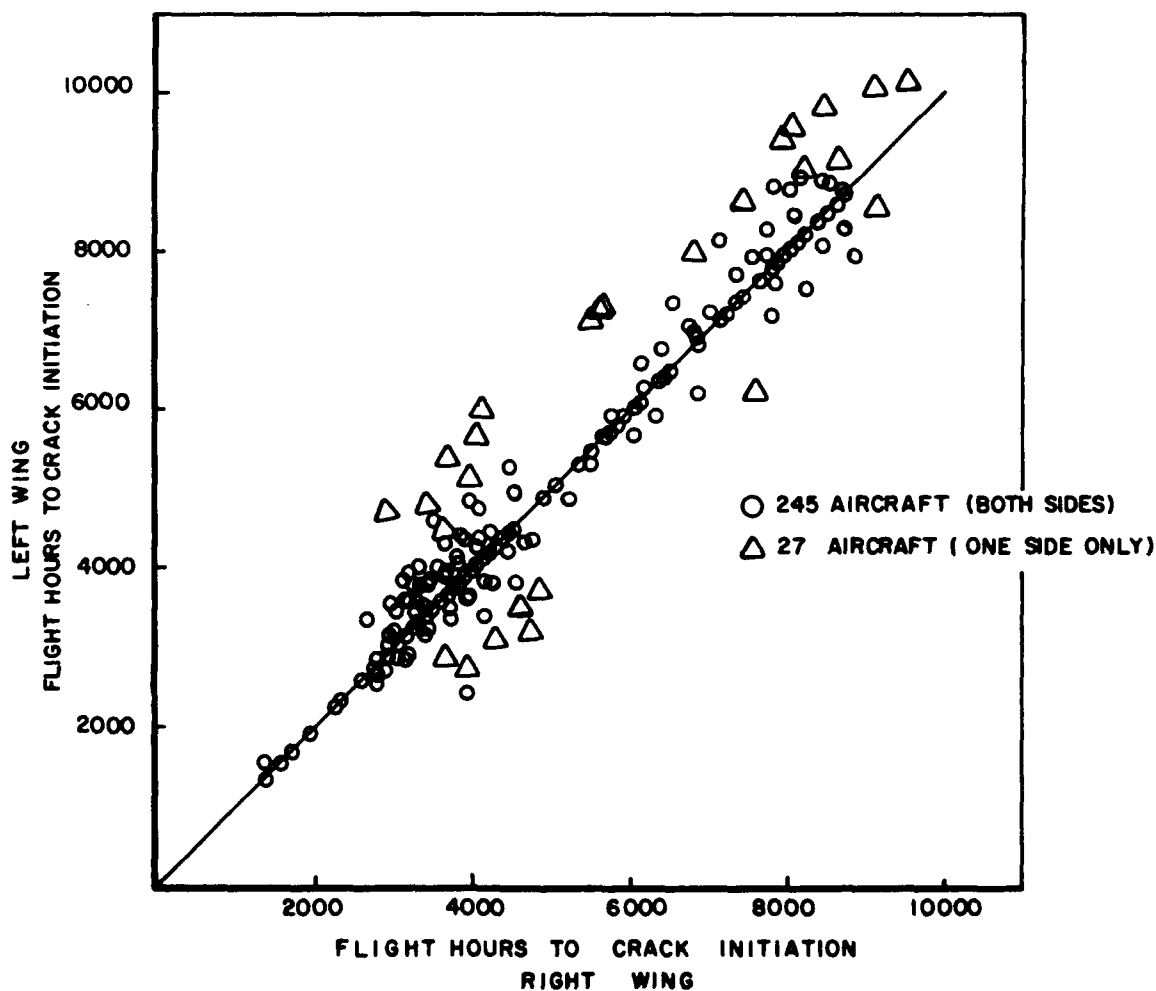


Figure 10. Crack Initiation, Left Wing Vs. Right Wing.

the S-N data which curve best describes crack initiation for that aircraft. This study is currently being conducted and therefore is not yet reflected in the damage status.

- Data being gathered from the recorder programs as earlier described will be evaluated in terms of environmental descriptions, load response information and stress to load relationship. Changes in data block damage rates resulting from these studies will be incorporated in the near future.

Figure 11 is a similar presentation of the data points shown in Figure 9 except that it reflects the changes in operational data and data block mid point damage values in terms of the predicted damage.

The correlation of predicted damage to actual damage is best shown in Figure 12 which presents that relationship as a function of cumulative percentage of the total aircraft. Reviewing this figure, which includes both the early and latest damage predictions, the following comments are made:

- The latest damage prediction curve represents better correlation than the early prediction curve.
- The band width of the latest prediction curve is narrower than the early prediction curve.

- The slope of latest damage prediction curve is flat over a wide range of the aircraft although it is offset from the correlation value of 1.0.

The effects of correlation with respect to crack propagation are in the initial stages of investigation. This study is being conducted on a statistical basis. That is, crack propagation described by fleet inspections is being statistically evaluated in terms of the operational data blocks. Preliminary results that are now available indicate that the rates as defined in the damage summation program are currently conservative. Attempts to improve correlation will be conducted along the same lines as the studies described for crack initiation.

### CONCLUSIONS

The Fatigue Life Monitoring Program for the C-130 in its current operational form is providing a means of assessing fleet structural damage in relation to operational usage. The implementation of this program has not been without problems such as the development of past operational data, the description of actual structural configurations for the in-service aircraft, the receipt of full flow data for current operational usage, and finally, the correlation of predicted to actual structural behavior. It is noted, however, that with continued review through evaluation of the various parameters, and the changes resulting from

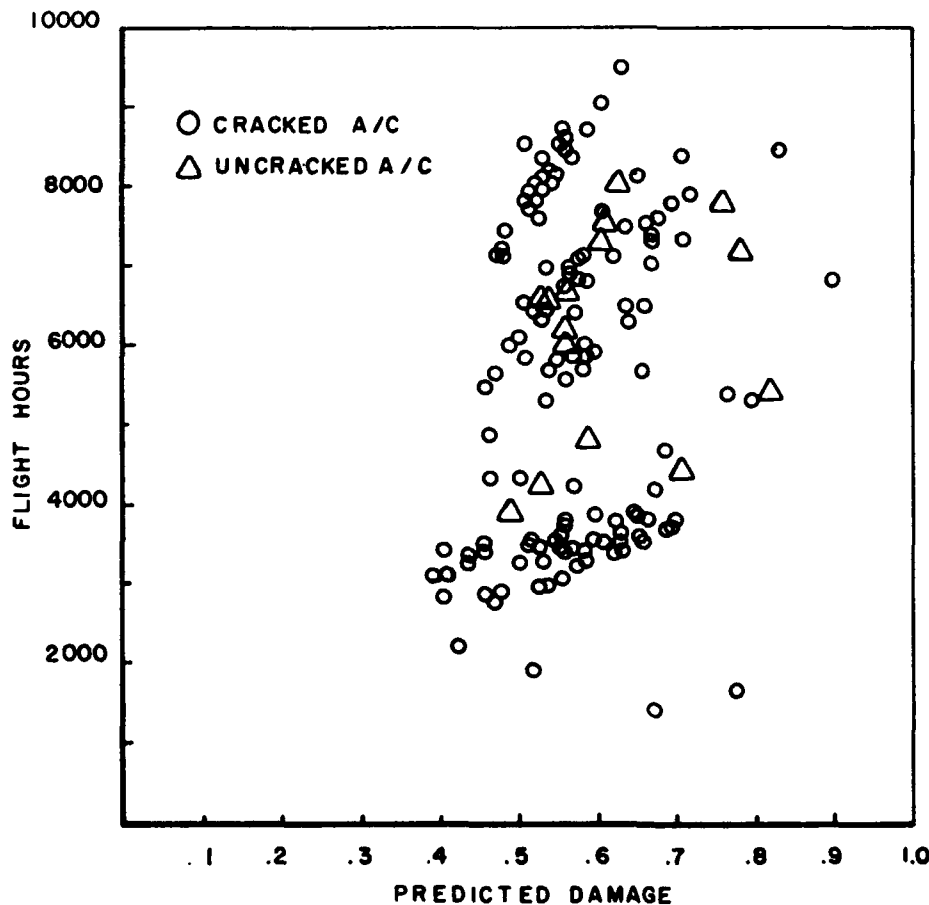
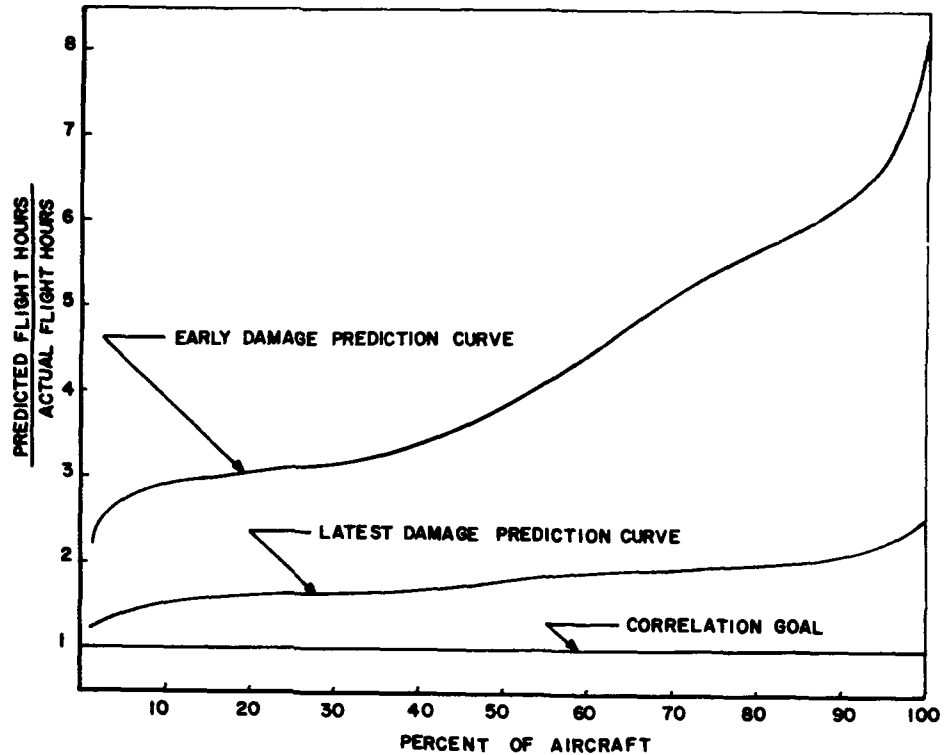


Figure 11. Structural Status, Latest Estimates - W.S. 120.5, Lower Surface.

Figure 12. Correlation Status of Predicted to Actual Time to Crack Initiation Vs. Percent of Aircraft Cracked, W.S. 120.5, Lower Surface.



these studies, improvement in the overall program may reasonably be expected. The Fatigue Life Monitoring Program in the present state, has the capabilities through judicious application of the data presented in the periodic damage reports to:

- Predict time to crack initiation and/or time for crack extension to a predetermined length for specific locations on individual aircraft.
- Describe operational changes to reduce current damage accrual rates for those aircraft which are experiencing unusually severe usage.
- Sort out specific missions that are highly damaging and make recommendations to reduce damage rates and still maintain mission capabilities.
- More objectively define special inspection requirements.
- Establish repair requirements such that lost utilization is held to a minimum.
- Establish long range planning for aircraft replacement in terms of fatigue damage accrual.

#### REFERENCES

1. *Aircraft Structural Integrity Program*, AFR-80-13, Department of the Air Force, Washington, D.C. (1969).
2. *Air Force Structural Integrity Program Requirements*, ASD-TR-66-57, Aeronautical Systems Division, Wright-Patterson AFB, Ohio (1968).
3. *Army Air Corps R-1803 Series Specifications*, Department of Defense, Washington, D.C. (1945).

# B-58 FLEET LIFE MONITORING AND USAGE EVALUATION BY CUMULATIVE FATIGUE DAMAGE METHOD

by

Dale H. Whitford and Robert J. Dominic

University of Dayton Research Institute  
Dayton, Ohio

## INTRODUCTION

The most generally used procedure for defining the age of an aircraft structure has been to assume that age is directly indicated by the cumulative number of flight hours that the structure has experienced in service. The basis for the structural life prediction was the observed number of flight hours to failure determined from cyclic fatigue test results which were modified by a scatter factor.

The validity of predicting the fatigue life of an aircraft structure solely in terms of cumulative flight hours has been questioned for some time. Structural fatigue is caused by the cyclic loads resulting from the interaction of the aircraft's usage with the flight environment. Because of the variability of atmospheric turbulence, piloting procedures, runway roughness, and the mission profiles used by a fleet of aircraft, no two aircraft experience the same load spectra during their lifetimes. Also, the load spectrum for a given aircraft varies from one flight to another.

The effect of this difference in experience from one aircraft to another was graphically portrayed by the data ob-

tained in the B-52 B-F service life monitoring program which was conducted in the early 1960's. In addition to the expected variation of the gust spectrum with altitude, the effects of geographical area and season were presented in Reference 1. For example, during low level flight over special low level, high speed courses, the average gust severity over the upper peninsula of Michigan was found to be 1000 times greater than the average severity over western New York. This large variation was for the average experience over these routes, and the spread of the individual flights would have been even greater.

Therefore, it has become obvious that a different parameter that is more clearly representative of the usage and environment experienced by individual aircraft is required in order for the various using commands and the Air Force Logistics Command (AFLC) to determine the age of the aircraft and the time at which the aircraft should be inspected and/or modified. This requirement is being met by the Air Force Structural Integrity Program (ASIP).

The Air Force Structural Integrity Program is a six-phase effort which is defined in ASD-TR-66-57 as

### PROGRAM ORGANIZATION AND RESPONSIBILITIES

#### SAN ANTONIO AIR MATERIEL AREA

- Overall Program Management
- Design and Installation of Oscillograph Recording System
- Quarterly Damage Summary

#### GENERAL DYNAMICS, FORT WORTH DIV.

- Past Usage Study
- Design and Installation of Strain Gages and FM Recording System
- Fatigue Damage Summary and Life Prediction Program Design
- Data Processing-Parametric Analysis Subsystem Coordination
- Recommend Structural Modifications

#### UNIVERSITY OF DAYTON RESEARCH INSTITUTE

- Instrumentation-Data Processing Sub-System Integration
- Instrumentation Consultation
- Data Acquisition
- Data Processing Design and Operation
- Data Analysis

#### SAAMA - GD/PW - UDRI

- Program Planning
- Parametric Analysis Modification

Figure 1. Organizational Responsibilities.

"... a systematic procedure applied to a particular aircraft system to enhance design, diagnose potential or pending failure, provide a basis for corrective action, and predict operational life expectancy of the airframe."<sup>2</sup> The six phases of the program are: design criteria, design analysis, testing, service life analysis, operational usage, and inspections.<sup>2</sup> Prior to 1965, the B-58 weapon system had benefited from Phases I, II, III, and VI, and part of Phase IV. The only work remaining was the updating of the parametric analysis by means of recorded operational spectra, initiation of a fleet tracking program, and the completion of the service life analysis of the fleet.

In view of this need, the San Antonio Air Materiel Area initiated a B-58 Fatigue Service Life Monitoring Program in the spring of 1965 in conjunction with an accelerated flying program called the Lead-the-Force Program.

The objectives of this program were to:

1. Verify or modify the B-58 design parametric damage rates,
2. Predict the service life of the fleet,
3. Provide a more reliable means for scheduling structural modification and for evaluating the added fleet life resulting from the modification,
4. Indicate the fleet life trade-off resulting from the different kinds of aircraft usage.

This paper describes the techniques used to achieve these objectives by defining the age of each B-58 aircraft in terms of the cumulative fatigue damage parameter at a number of fatigue critical points.

This program has been a good example of Government, Industry, and a University working together harmoniously toward a common goal, with each organization contributing in the areas in which each was the most competent. The organizations involved and their responsibilities are shown in Figure 1. In addition, automatic data processing was accomplished by use of the Analog-to-

Digital Conversion Facility and the 7094 Digital Computer Facility which were supplied, respectively, by the Directorate of Flight Test and the Deputy of Engineering, Aeronautical Systems Division, Wright-Patterson Air Force Base.

### TOTAL SYSTEM STUDY

The total system concept was used during the initial planning and development phases of this program. Basically, the use of this system concept is rather simple; however, many times it is overlooked in experimental investigations. A simple schematic of this system approach is given in Figure 2. To apply the system concept, the planning is done in reverse order from that in which the program is conducted.

The basic program requirements, established by SAAMA in Phase I, were to provide a rational method of analysis for predicting the structural fatigue life of each B-58 aircraft. Other specific objectives were those presented earlier in this paper.

After the objectives were established, the next step was to select an analysis technique and the appropriate data set which would satisfy the objectives. At the time the program was initiated, complete fatigue analyses, flight tests, dynamic stress analyses, and cyclic fatigue tests had been conducted on the airplane. In addition, a parametric fatigue analysis had been generated<sup>3</sup>. Since the parametric fatigue analysis had been based on original design spectra and limited flight test information, it was SAAMA's intention to verify the parametric analysis by obtaining a large sample of pertinent data from instrumented B-58 aircraft which were flying operational SAC missions. This information was to be used in various damage rate computations, and the results were to be compared directly with the damage rates of the original parametric analysis. The original damage rates were to be modified if significant differences in the comparisons were noted. Based on cyclic fatigue tests, approximately 22 known fatigue critical locations had been defined, and stress analysis data and S-N curves were available for all these points. Furthermore, General Dynamics had used PSD methods for converting load factor data from gust and maneuver spectra to stress at the various fatigue critical locations. Therefore, it was evident that all elements of a satisfactory analytical tech-

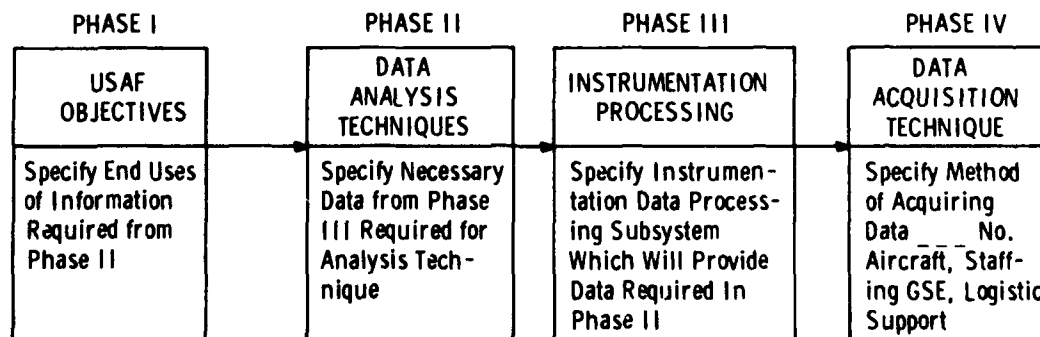


Figure 2. Total System Design Approach.

nique were available provided that measurements of load factor and the stress at or near the fatigue critical points were made. By this approach, not only would it be possible to measure the stresses directly and convert them to damage rates, but also it would be possible to check these damage computations by measuring gust and maneuver spectra and converting them to damage rates by PSD methods.

The third phase of the system analysis was to specify the instrumentation that would be used. Since the parametric analysis was presented in terms of damage rates vs. gross weight for various Mach-altitude combinations, and in view of the dual approach to computing damage mentioned in the previous paragraph, it was decided to measure normal load factor at the center of gravity, Mach number, pressure altitude, and stress at several fatigue critical locations. Because of the large amount of data that was to be collected and the complexity of the processing that was envisioned, it was decided to record the data on a magnetic tape recorder to permit the use of automatic data processing techniques. Data recording and data processing were to be accomplished during all mission segments from the time an aircraft left the ramp until the time it returned to the ramp after the flight.

The fourth and last phase of the system study required the specification of the data acquisition procedure. Since several structural modifications were being considered for the B-58, it was important that the existing parametric damage rates be verified as soon as possible. Consequently, it followed that the data acquisition system should maximize the amount of usable data acquired in a given time consistent with the high cost of magnetic tape recorders. To fulfill this requirement, it was decided to instrument all four of the Lead-the-Force (LTF) aircraft because they would be flying typical missions at twice the normal rate. In order to maximize the quality of the recorded data, a skilled electronic technician was assigned at each base and

was given complete responsibility for conducting the recording effort. Each base was equipped with a ground playback, quick-look system which would enable each technician to play back the tape, record the signals on an oscillograph chart, and visually monitor his instrumentation after each flight so that he could correct deficiencies with minimum loss of data.

In all four stages of developing this program, close coordination was maintained between all organizations involved. The one prime requirement of the data processing effort was that the parametric unit damage data generated must be directly comparable with the unit damage computations that had been generated by General Dynamics. The instrumentation design also was very closely coordinated to assure compatibility of the data with the previous analytical efforts that had been conducted. For example, all strain gage locations were specified to be identical to those which had been used for the cyclic test program, the static test program, and the various flight test programs conducted during the development stages of the B-58 aircraft. In this way, adequate back-up in the form of stress analysis and fatigue analysis was available for each of the various measured data points.

Thus, by approaching the problem in a systematic, careful way and by coordinating with all parties at every step, a total system was designed in which all components were compatible and were capable of assisting in the attainment of program objectives.

The technical approach to this program was divided into a unit damage rate analysis, a usage analysis, and a fatigue life analysis. These analyses are described in the following paragraphs.

### UNIT DAMAGE RATE ANALYSIS

Before discussing the procedure used to conduct the unit damage rate analysis, it would be well to describe the

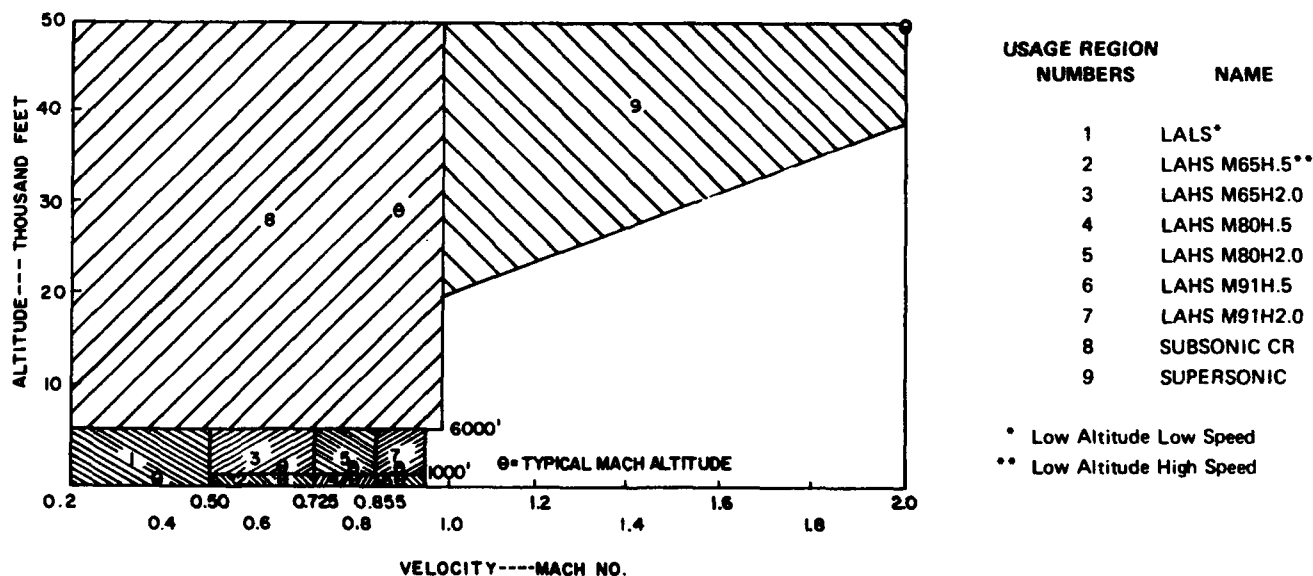


Figure 3. B-58 Usage Regions.

format of the B-58 parametric analysis. The normal flight environment of the B-58 aircraft is divided into nine distinct Mach-altitude regions.<sup>3</sup> A chart showing these Mach-altitude regions is presented in Figure 3. Each Mach-altitude region is defined by finite boundaries which were determined from studies of the various missions planned for the aircraft. By developing the gust and maneuver spectra for each of these Mach-altitude regions, damage rate curves for each critical fatigue point on the aircraft as a function of gross weight were computed. Other empirical data such as the mean stress of each fatigue point as a function of gross weight, Mach number, and altitude and the S-N curves for the various materials at the fatigue points were used in these damage rate computations.<sup>4</sup> The assumption basic to this analytical procedure was that the damage rate for a given fatigue point varies only with gross weight for all operation within a given usage region. Other damage rates generated were for miscellaneous usages such as the flight cycle, special maneuvers, taxi, take-off, touch-and-go landings, full stop landings, and landing gear retractions.

The Unit Damage Rate Analysis included the instrumentation and data processing tasks required to generate unit damage rates for these nine inflight regions and the seven miscellaneous usages. These tasks are described in the following paragraphs.

### Instrumentation

Four LTF aircraft were instrumented for this program. Two aircraft were located at Little Rock Air Force Base, and two were located at Grissom Air Force Base.

The complete instrumentation system included a Parsons AIR 2450 FM magnetic tape recorder with a 3600-ft tape capacity, a carrier amplifier and bridge balancing system manufactured by General Dynamics, and the various transducers. At a tape speed of 15/16 inch per second, a recording duration of over 12 hours was realized. Fourteen channels of analog data were recorded during each flight. Mach number and altitude were obtained from the central air data computer; normal load factor was obtained from an accelerometer mounted at the center of gravity; eight measurements of strain were obtained from strain gages mounted at fatigue critical locations; and three miscellaneous monitoring measurements also were obtained. These three measurements included a precision time reference; an event signal to indicate lift-off, refueling, and landing; and a tape speed compensation signal.

The location of the instrumentation is described in Reference 5 and is shown in Figure 4. The strain gage locations were: Fatigue Point 1 - the aft, inboard, wheel-

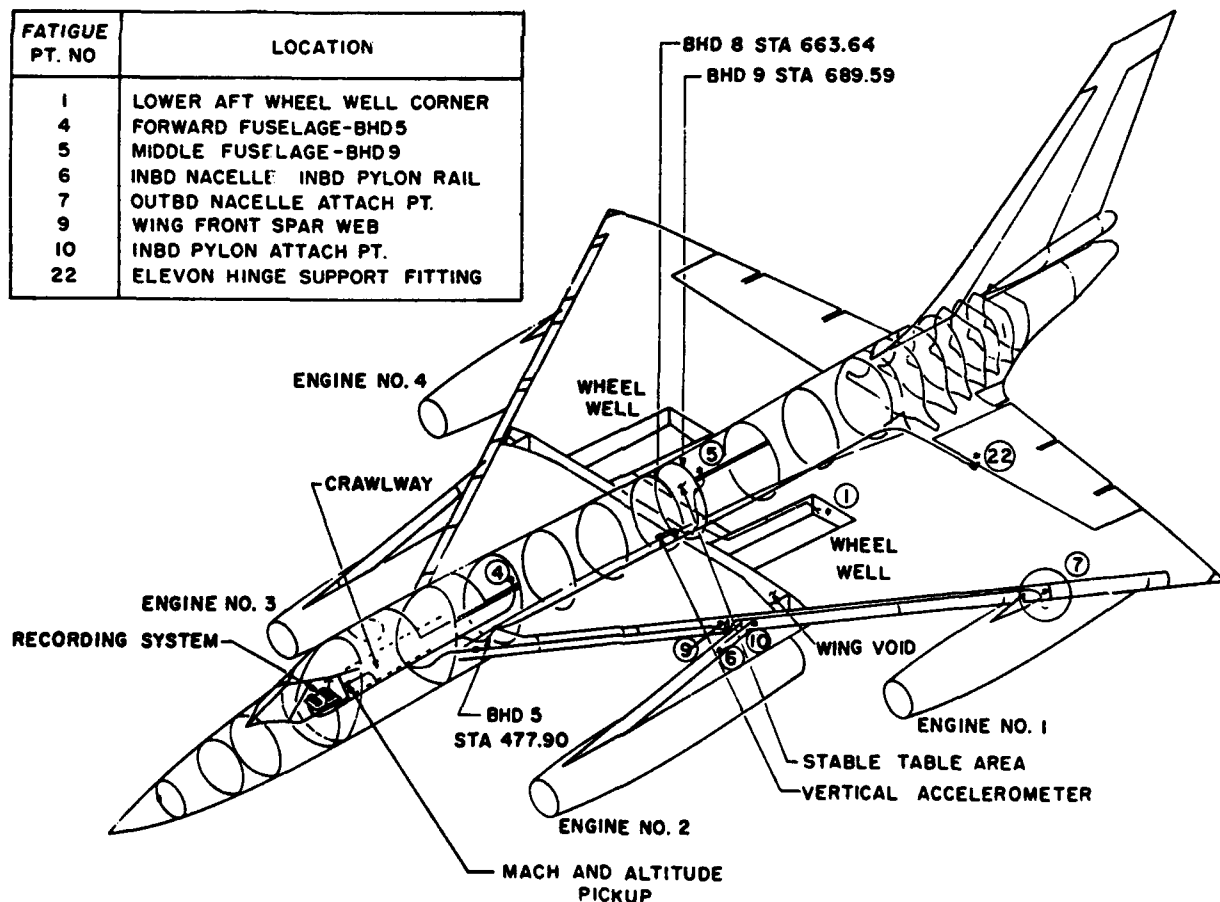


Figure 4. B-58 Instrumentation Locations.



well corner; Fatigue Point 4 -- the upper longeron at Fuselage Bulkhead 5; Fatigue Point 5 -- the upper longeron between Fuselage Bulkheads 8 and 9; Fatigue Point 6 -- the inboard nacelle pylon rail; Fatigue Point 7 -- the outboard nacelle attachment fitting; Fatigue Point 9 -- the wing front spar, inboard of the inboard pylon-to-wing intersection point; Fatigue Point 10 -- the lower surface wing panel outboard of the inboard pylon-to-wing attachment fitting; and Fatigue Point 22 -- the elevon hinge support fitting. The accelerometer for measuring normal load factor was located on the wing lower surface structure on the aircraft center line forward of Bulkhead 9. In order to determine the differences in response on the left side and the right side of the aircraft, and to determine whether or not pilot bias might enhance the stresses on one side, duplicate strain gage sets comprised of eight strain gage bridges per set were mounted on each side of the plane of symmetry of the aircraft. In order to insure against possible loss of data by loss of a strain gage, main and spare bridges were mounted at each fatigue critical location. Thus, a total of 32 strain gage-bridge systems were installed on each aircraft. Inasmuch as it was possible to record only eight measurements at one time, various combinations of left and right gages were recorded on the early flights to obtain comparisons of left and right damage rates and to determine relative sensitivities.

### Data Processing System

The overall flow chart of the data processing system is shown in Figure 5. Upon receipt of the data package, which includes the reel of magnetic tape, the oscillograph playback chart, and the pilot's logs, the data were inspected to be sure that no instrumentation malfunctions were missed by the field technician. Questionable data were sent to an instrumentation engineer for checking. When the data package was approved, the tape was processed by FM-to-digital conversion equipment at Wright-Patterson Air Force Base.

In this system, the FM signal from each of the fourteen tape tracks was converted to an analog signal which was filtered, digitized in an 11-bit format, and recorded on a reel of computer-compatible digital tape. In the meantime, historical information such as the date of the flight, the aircraft tail number, and other parameters recorded on the pilot's logs, which described the mission, were compiled and keypunched into IBM cards for later use in the data processing procedure.

The digitized tape was then input to the 7094 computer system at Wright-Patterson Air Force Base for editing and performing various computations. Approximately eight million data points were processed from each flight. Some of the functions performed by the editing program include the definition and selection of load factor peaks; the definition and selection of stress cycles; the computation of weight as a function of time including the effects of refueling; the determination of the mean stress history; the computation of Mach number and altitude; and the definition of mission segment (i.e., determining whether the aircraft was in ascent, cruise, descent, refueling, low level, or ground operations). Finally, the edit program categorizes the various load factor and stress cycles as either gust or maneuver cycles. Thus, a considerable amount of data condensation and computation was done in the edit program.

The output of the edit program was presented in both tabular and digital tape form. This tape was subsequently processed by another 7094 computer program which computed the ground-air-ground cycle damage and the unit damage for each fatigue point and tabulated statistical distributions of stress and load factor. These damage rates and distributions were coded in terms of Mach number, altitude, gross weight, mission segment, aircraft tail number, season, and other parameters by which the data can be categorized. The output of this computer program also is in the form of a computer tab and a magnetic tape. This tab in-

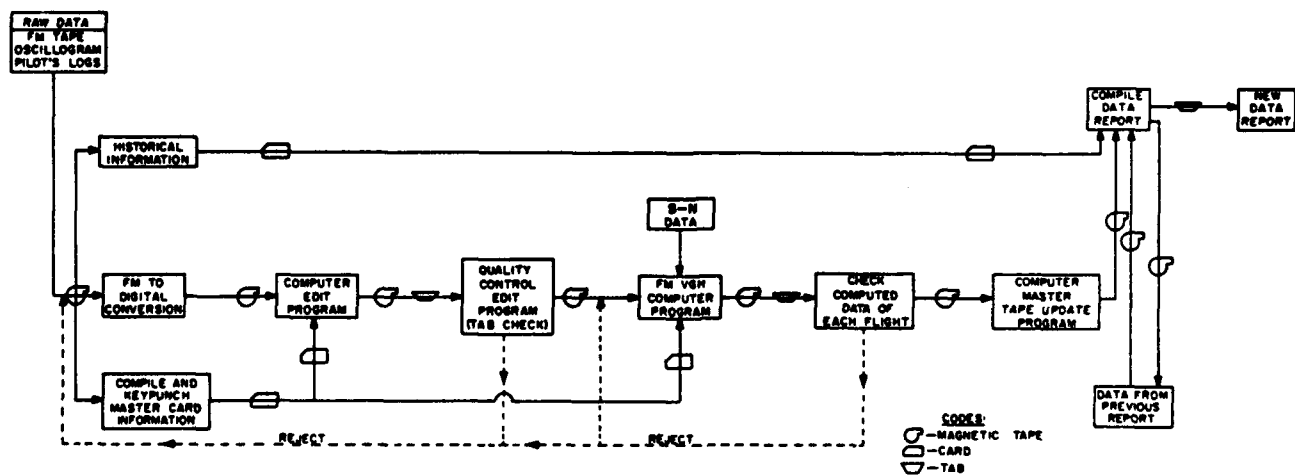


Figure 5. Data Processing Schematic.

cludes a chronological history of the entire flight including the Mach number, altitude, gross weight, and stress mean history for each stress measurement as a function of time. The tabular data is given a visual check to insure that valid computations have been performed and to verify that all of the instrumentation is operating properly. Rejected data are re-submitted for computation and checking. Upon approval, the data is stored on a master computer tape until a sufficient amount of data is gathered to warrant the generating of a composite periodic data report. Generally, this update compositing is done on a six-month basis.

The load factor peaks were defined according to the primary peak count criteria; that is, a peak is defined as that point which is the maximum (or minimum) between two successive crossings by the analog load factor signal of the 1-g signal level. Stress cycles were determined according to the cyclic stress criteria; that is; peaks and valleys of the stress trace were paired together in such a manner that the stress cycle defined would represent a 360-degree stress reversal.

In computing the damage, the mean and alternating stress from each stress cycle were computed, and then these stress values were used with the appropriate S-N curves to compute the damage for each individual cycle by Miner's method.

The ground-air-ground (GAG) cycle was determined from the mean stress history of each stress trace. Throughout the flight, the mean stress was computed over small increments of time and stored. Then, after the complete flight had been processed, the GAG cycle routine followed the various mean stress values, selected the maximum and minimum values for each fatigue point, and paired these values according to the cyclic stress criteria which was used for the strain gage data analysis. In some cases secondary GAG cycles superimposed on the primary GAG cycle were sufficiently large to contribute to the overall damage of a given flight.

In summary, a completely reduced data package would include gust and maneuver load factor spectra coded in terms of Mach number, altitude, weight, mission segment, flight number, aircraft serial number, and other parameters; bivariate stress spectra in terms of alternating stress vs. mean stress coded for all of the above parameters for each fatigue point; the ground-air-ground cycle damage and the ground operations damage for each fatigue point; and the computed unit damage rate vs. gross weight for each fatigue point coded by Mach-altitude usage region in the exact form of the original parametric analysis.

## USAGE AND FATIGUE LIFE ANALYSES

In order to determine how each aircraft has been utilized between the time of its first flight and a given time later, it is best to require that a Service Life Monitoring Program (SLMP) flight log be prepared by one of the aircrew members after each flight during the time period of interest.

## Current Usage

A reproduction of the B-58 SLMP flight log is presented in Figure 6. This log, known as AFTO Form 70, is completed by the aircrew immediately following each B-58 flight.<sup>6</sup> Note that all of the important parameters necessary for utilizing the unit damage data are on this chart. First, the various operations (mission segments) and their sequence are shown; i.e., take-off, cruise, refueling, etc. Note also the extra detail provided for the low altitude, high speed phase includes the name of the low altitude route, the number of entries or re-entries into that route, and the mode of low level flight (Terrain Avoidance or Constant Altitude). Other important information such as the configuration of the aircraft, the length of the mission, the takeoff gross weight, the landing weight, and the number and types of landings is also shown. The real heart of this form is found in Columns 9, 10, 11, and 12, which for each operation are, respectively, the Mach number, the pressure altitude, the gross weight at the beginning and the end of an operation, and the duration of each operation. When the data from each flight form is input into the computer and used in conjunction with the appropriate unit damage data, a computation of the total damage for each flight can be made.

## Past Usage

The flight log in Figure 6 was not used by the B-58 fleet until after the spring of 1965. Therefore, it was necessary to conduct a past usage study to determine the total usage of each aircraft prior to the initial use of AFTO Form 70. This past usage study involved an in-depth review of all available records that had been maintained by the airframe manufacturer and by the Strategic Air Command. Since the low altitude, high speed (LAHS) flight regime of this aircraft was considered to be one of the most severe usages, extra emphasis was placed on determining the amount of time flown in this usage region by each aircraft. Flight plans and mission accomplished records enabled the analysts to determine the number of LAHS missions that each aircraft had flown. Some mission duration information and other parameters useful in defining past LAHS usage were obtained from aircraft records at both Little Rock Air Force Base and Grissom Air Force Base. Reference 6 states, "... the composite of this data produced a good estimate of the low-altitude, high-speed time on each aircraft." Records maintained by General Dynamics logistics support personnel and results of previous usage studies were used to define gross weight and Mach number profiles of this previous usage.

Supersonic usage also was obtained from actual records kept by General Dynamics logistics support personnel, and aircraft gross weights for past supersonic flight were extrapolated from usage data that had been collected from current AFTO 70 forms by assuming that the past supersonic flight had been flown under the same gross weight conditions that presently were being experienced.

Inasmuch as the total flight time experienced by each

aircraft was recorded in a number of forms, one merely distributed the non-supersonic and non-LAHS usage among the low altitude, low speed and the subsonic cruise usage regions. Again, after a review of the available AFTO 70 forms had been conducted, it was determined that it was reasonable to estimate that past usage for each aircraft in the low- and high-altitude subsonic flight regimes occurred in the same proportion as similar usages on flights which were documented on the AFTO 70 forms. This assumption was considered to be sufficiently accurate because these usage regions were not nearly as damaging as the LAHS regions.

Take-off, landing, and taxi usage was extrapolated to the earlier flights based on the average usage of 100 flights per SAC base as recorded on the AFTO 70 records.

All unusual incidents (hard landings, near accidents, etc.) and special maneuvers on each aircraft had been tabulated since the first B-58 flight. Each incident had been studied and damage estimates for each fatigue point that would be affected by these incidents had been recorded.

Thus, the past usage study provided a reasonable

estimate of the service experience of each aircraft prior to the spring of 1965 by defining how much time each aircraft had spent in each gross weight, altitude, and Mach number usage category.

### Future Usage

The future usage of the fleet depends upon the mission mix that the Strategic Air Command is planning. If SAC plans to use the aircraft in the same manner as in the past, it merely is necessary to extrapolate the existing monthly damage trends of each fatigue point to determine the point at which wearout would occur. However, because of the recent installation of the redundant yaw damper modification which permits safer LAHS flight, SAC planned to resume operations in the LAHS usage regions. Therefore, from the time these flights were estimated to begin, it was necessary to generate new future damage trends for each fatigue point by computing the damage per month, which is the product of the modified unit damage rates and the respective values of the estimated future flight time per month in each usage region. The future damage trend resulting from this computation was considered to be the *average trend* for future flight. This average future damage trend for

1 AIRCRAFT SERIAL NUMBER		2 DATE OF FLIGHT		3 BASE OF OPERATION		4 FLIGHT NUMBER	
58-1021		050368		Little Rock AFB			
5 FLIGHT TIME		6		7		8	
HOURS		MINUTES		CENTERLINE PFD		EXTERNAL WEAPONS	
2690		06		X		UNDERWING WEAPONS	
9		10		11		12	
MISSION		NO. OF		GROSS WEIGHT (1000 POUNDS)		DURATION (HRS MIN)	
OPERATION		SEQUENCE OF OPERATION		ALTITUDE (FEET ABOVE TERRAIN)			
7.1 TAKE-OFF		1					
7.2 SUBSONIC CRUISE		2		91 20000		2+15	
7.3 INFIGHT REFUELING		3		80 25000		+10	
7.4 Subsonic Cruise		4		91 26000		2+00	
7.5 LOW ALTITUDE HIGH SPEED PHASE		5		59 As P16		1+43	
7.6 SUPERSONIC DASH							
7.7 CLASSIFIED MANEUVER							
7.8 ESCAPE MANEUVER							
7.9 SUBSONIC CRUISE		6		91 33000		1+37	
7.10							
7.11 LOW ALTITUDE - LOW SPEED		7		40 1600		+25	
7.12 TOUCH & GO LANDINGS							
7.13 FULL STOP LANDINGS							
7.14 NAME OF LOW ALTITUDE ROUTE		OB-3		Primary with Two Reentries		1	
7.15 TYPE OF LOW ALTITUDE OPERATION				PHASE 1, T.A. OR CON ALT		PHASE 2, T.A. OR CON ALT	
7.16							
7.17							
7.18							
7.19							
7.20							
7.21							
7.22							
7.23							
7.24							
7.25							
7.26							
7.27							
7.28							
7.29							
7.30							
7.31							
7.32							
7.33							
7.34							
7.35							
7.36							
7.37							
7.38							
7.39							
7.40							
7.41							
7.42							
7.43							
7.44							
7.45							
7.46							
7.47							
7.48							
7.49							
7.50							
7.51							
7.52							
7.53							
7.54							
7.55							
7.56							
7.57							
7.58							
7.59							
7.60							
7.61							
7.62							
7.63							
7.64							
7.65							
7.66							
7.67							
7.68							
7.69							
7.70							
7.71							
7.72							
7.73							
7.74							
7.75							
7.76							
7.77							
7.78							
7.79							
7.80							
7.81							
7.82							
7.83							
7.84							
7.85							
7.86							
7.87							
7.88							
7.89							
7.90							
7.91							
7.92							
7.93							
7.94							
7.95							
7.96							
7.97							
7.98							
7.99							
7.100							

INDIVIDUAL B-58/TB-58 AIRCRAFT USAGE

Figure 6. AFTO Form 70.

each fatigue point was multiplied by a safety factor, which is equal to the ratio of the *maximum* present damage trend in the fleet to the *average* present damage trend of the fleet, in order to obtain the *future maximum damage trend* which was used for the extrapolation.

**Fatigue Life Analysis**

The fatigue life analysis was the culmination of all of the work that had been done in the prior tasks. At this point the effort was a straightforward computer operation. Four times each year, a report was generated to indicate the life status of each aircraft. First, the past and present damage of each fatigue point of each aircraft was computed for the in-flight usage regions. Next, the past and present flight cycle damage and the taxi, take-off, landing, incident, and other miscellaneous damages were computed. Finally, all of the in-flight, ground, and miscellaneous damages were summed to obtain the total present damage for each fatigue point of each aircraft. The number of years from the time at which a given quarterly report was being generated until failure was predicted at each fatigue point on each aircraft was determined by using the current and future damage trends in conjunction with the appropriate time periods to determine the time required for Miner's damage ratio to equal 1.

**RESULTS**

The data presented in this paper is that which was

collected between May of 1965 through April of 1969. During this time, a total sample of 5,997 hours of data from 1004 flights has been reduced, analyzed, and incorporated into the various damage assessment reports.<sup>7</sup> A comparison of the measured low altitude and high altitude vertical gust spectra in the familiar form of  $\Delta n/A$  vs. cumulative probability is shown in Figure 7. One can see for both altitude ranges that there are significant decreases in the severity of the measured LTF spectra from those of the original design spectra. These results are typical of those obtained at other altitudes.

Some maneuver spectra comparisons for low and high altitude flight are shown in Figure 8. Data for a gross weight range of 100,000 lb. to 135,000 lb. are presented. The measured high altitude spectrum is much less severe than the corresponding design spectrum, whereas the low altitude spectrum is less severe at the more damaging, high-magnitude  $N_z$  levels but is more severe at the low-magnitude  $N_z$  levels.

Figure 9 is a comparison of the design and the measured values of 1-g trim stress vs. gross weight obtained at altitude ranges of 0-1000 feet and 20,000-40,000 feet for a given aircraft configuration.

The measurements of alternating and mean stress for each stress cycle for each of the eight monitored fatigue critical locations were converted directly to unit damage as a function of gross weight by using the S-N curves that had

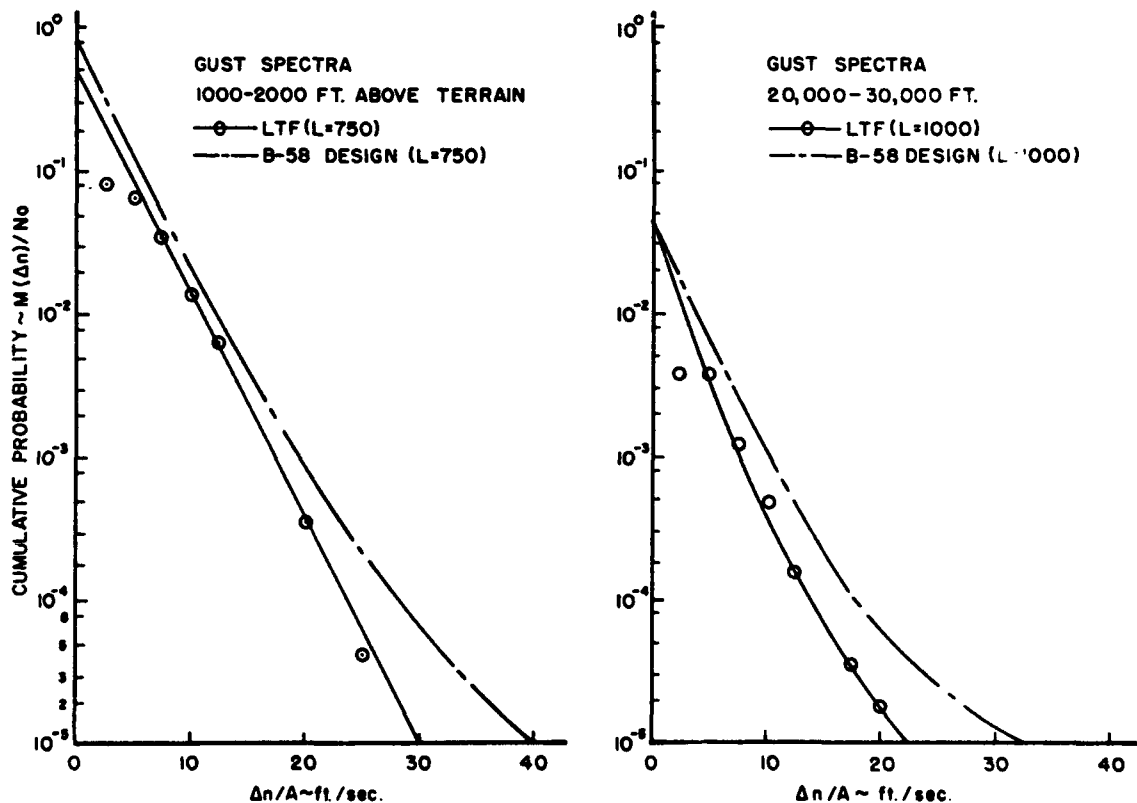


Figure 7. Gust Spectra Comparison.

been used for the original fatigue analysis of the B-58. These newly-derived unit damage rates were compared with those developed in the original parametric analysis. Typical results of these comparisons for low and high altitude usage regions are presented in Figure 10. Also included in Figure 10 are computed damage rates obtained by inputting the measured gust and maneuver spectra and the measured 1-g trim stress data into the same analytical model used to derive the original unit damage rates. Thus, two independent methods were used to determine the extent that the original unit damage data should be changed.

The data in Figure 10 are two of the nine unit damage vs. gross weight curves for Fatigue Point 1 (FP-1), the aft, inboard, wheel-well corner on the lower surface of the wing.<sup>7</sup> These curves represent operation in Usage Regions 2 and 8 (see Figure 3). The cumulative effects of the decreases in the spectra and the measured trim stresses from the design values resulted in a marked decrease in the damage rates derived from the computations in which these data were used. It also can be seen that the damage rates obtained from computations using the measured spectra agree well with the damage rates derived directly from measured stress for Usage Region 2; however, a considerable difference between these methods was observed in Usage Region 8. In view of the straightforward approach used in computing unit damage rates from measured stresses, this set of data is considered to be the best. The reason for the decrease in the damage rate at the high gross weight as shown by the measured stress data has not yet

been determined; however, the aircraft fly at this high gross weight so seldom that the effect of this data on aircraft life is negligible. Unit damage curves similar to those of Figure 10 were plotted for each usage region-fatigue point combination.

The variation of the damage rate of FP-1 caused by varying Mach number from 0.65 to 0.91 while flying at an altitude of 500 feet is indicated in Figure 11. The curve for Mach 0.65 is the same as that presented in Figure 10. The data in Figure 11 indicates that the damage at this LAHS usage region is so severe that only a few hours of flight in this region can be incurred before the structural life at FP-1 is expended. Note also the decrease of approximately a factor of 7 in Usage Region 6 unit damage rates that was made possible by the use of the measured LTF data. These modified damage rates are still very high; the reader should note that the numbers on the ordinate scale represent the number of *life times* expended per 1000 hours of flight in these usage regions.

Comparisons of the predicted and the measured damage during ground operations such as taxi, take-off, and landing and for the ground-air-ground cycle were also made. The ground-air-ground cycle damage comparison for FP-1 and FP-10 is presented in Table 1 for four different types of missions. The difference in the severity of the ground-air-ground damage between the LTF and design values is significant.

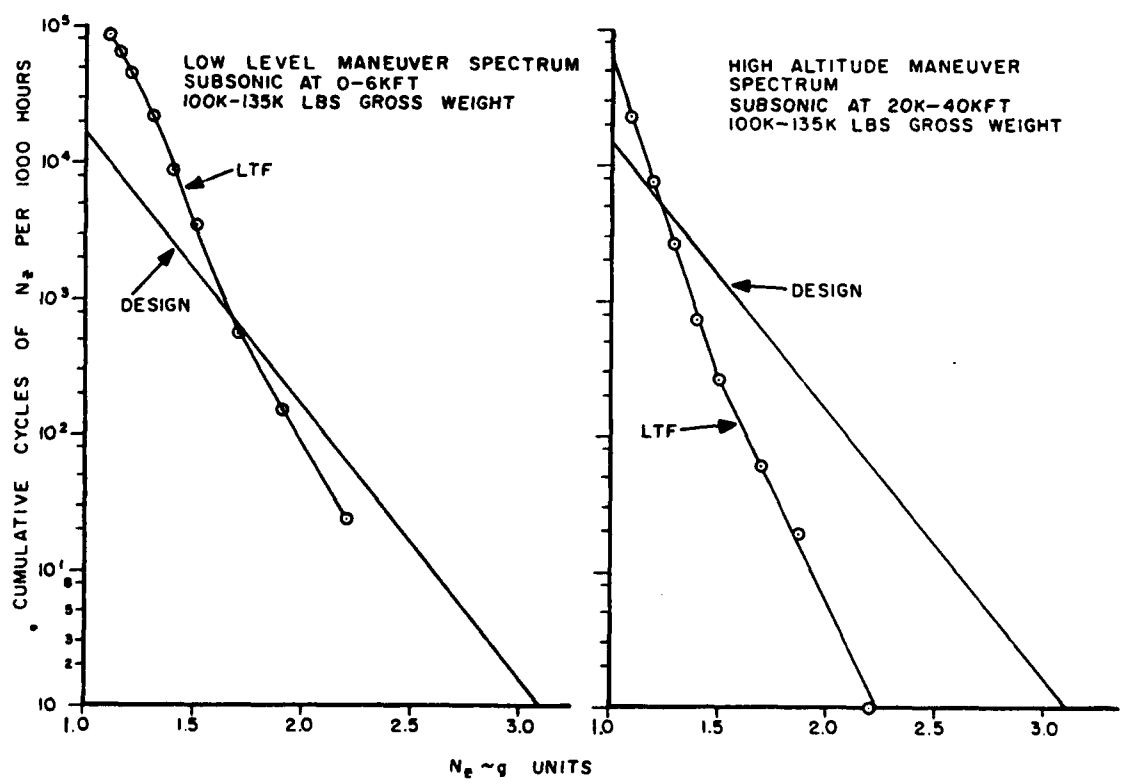


Figure 8. Maneuver Spectra Comparison, Usage Regions 2 and 8, Gross Weight 100,000 to 135,000 lbs.

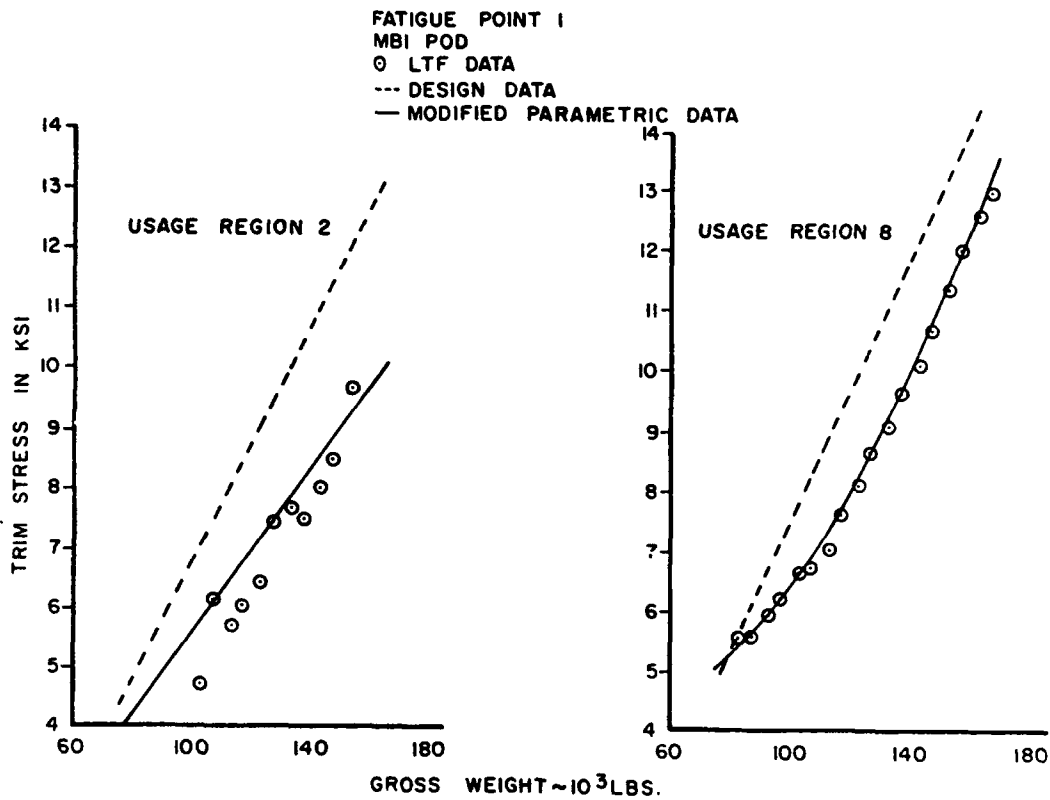


Figure 9. 1-g Trim Stress vs. Gross Weight Comparison, Usage Regions 2 and 8.

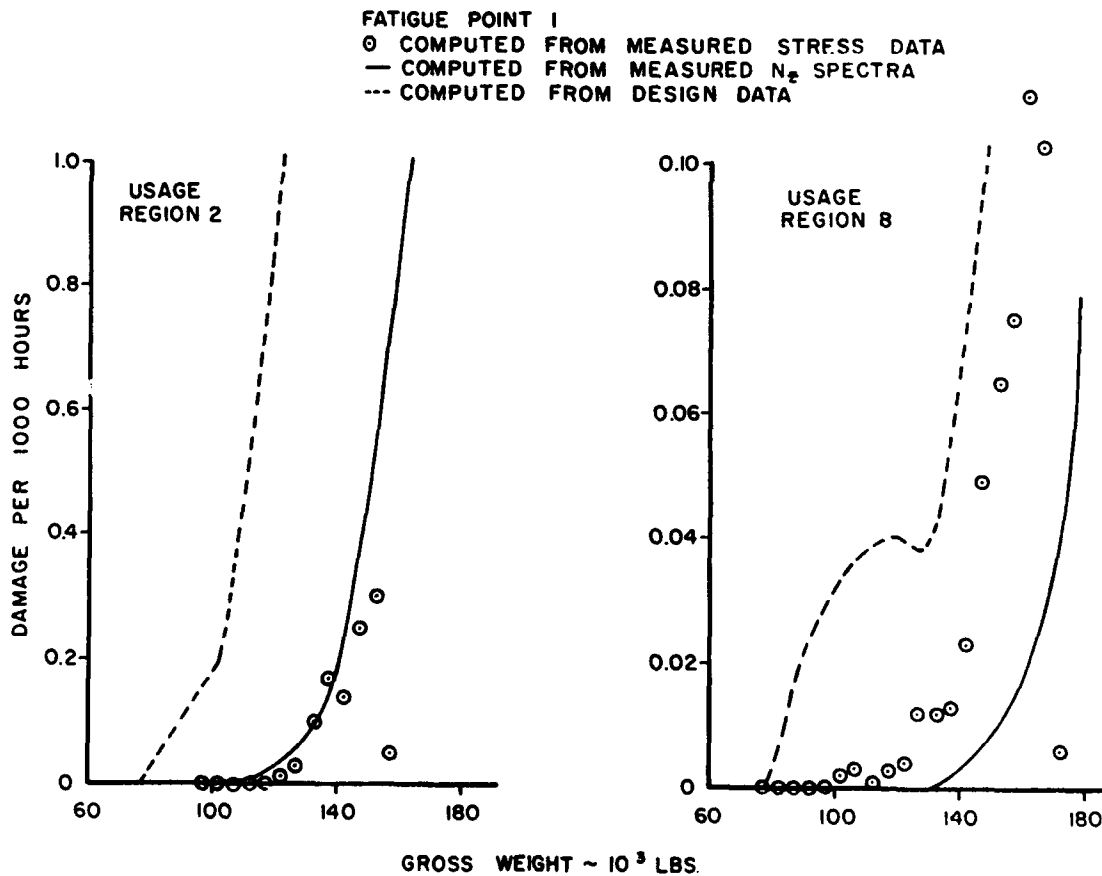


Figure 10. Unit Damage Rate vs. Gross Weight Comparison, Usage Regions 2 and 8.

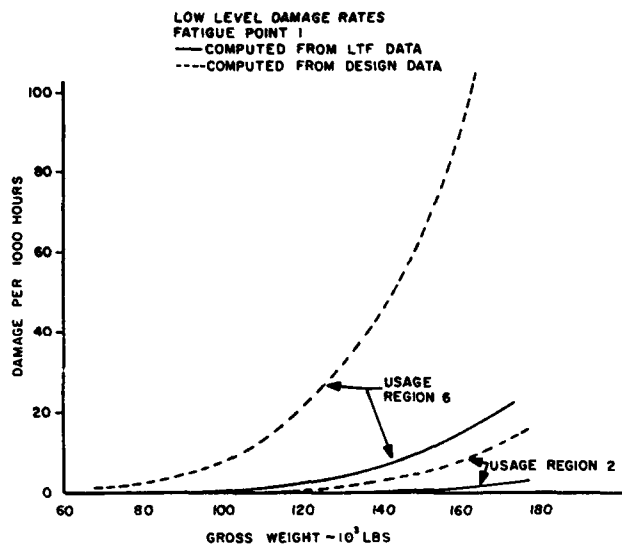


Figure 11. Variation of Unit Damage Rate with Gross Weight for Two Low Altitude Usage Regions.

TABLE I  
COMPARISON OF GROUND AIR-GROUND  
DAMAGE RATES

MISSION TYPE	AVERAGE DAMAGE PER FLIGHT X 10 <sup>6</sup>			
	FATIGUE POINT 1		FATIGUE POINT 10	
	DESIGN	LTF.	DESIGN	LTF.
A	250.0	101.0	65.6	275.4
B	250.0	56.2	65.6	409.4
C	250.0	103.1	65.6	210.0
D	215.0	89.7	111.3	197.4

Similarly, in Table II the comparisons of the design and LTF damage rates for the landing, take-off, and taxi mission segments are also presented. The data for Fatigue

TABLE II  
COMPARISON OF GROUND OPERATION DAMAGE RATES

USAGE	DAMAGE PER 1000 OCCURRENCES					
	FATIGUE POINT 1		FATIGUE POINT 4		FATIGUE POINT 5	
	DESIGN	LTF	DESIGN	LTF	DESIGN	LTF
LANDING	0.0016	0.00005	0.024	0.00589	0.66	0.11634
TAKE OFF	0	0.00041	0.060	0.00402	0.39	0.06898
TAXI *	0	0.00002	0	0.00015	0	0.00531

\* Damage Per 1000 Hours

TABLE III  
SUMMARY OF DAMAGE FOR FATIGUE POINTS 1, 5 AND 10

USAGE REGION	FATIGUE POINT 1		FATIGUE POINT 5		FATIGUE POINT 10	
	% TOTAL*	RANK	% TOTAL*	RANK	% TOTAL	RANK
Taxi	0	11	0.6	9	0.0	12
Takeoff	0.1	9	19.3	3	0.1	11
1	1.9	6	1.6	6	0.7	7
2	4.4	4	0.8	8	8.0	4
3	26.1	3	6.4	5	43.3	1
4	0.3	7	0.2	11	0.1	10
5	3.8	5	0.8	7	5.3	6
6	0	13	0	13	0	13
7	0	12	0.1	12	0.2	8
8	27.4	2	9.7	4	8.8	3
9	0.2	8	0.5	10	0.2	9
Landing	0	10	32.6	1	7.7	5
Gag	35.8	1	27.4	2	25.7	2

\*TOTAL DAMAGE IN SAMPLE OF 1004 FLIGHTS, 5997 HOURS

0.357

0.419

1.380

**TABLE IV**  
**QUARTERLY DAMAGE SUMMARY**  
**B-58 FATIGUE SERVICE LIFE MONITORING PROGRAM**

FATIGUE POINTS	AIRPLANE NUMBER 59/2449      B FLEET									
	01	02	03	04	05	06	07	08	09	10
Damage Qtrly	0.02	0.00	0.00	0.00	0.01	0.00	0.00	0.00	0.00	0.01
Cumulative	0.25	0.04	0.02	0.03	0.30	0.05	0.11	0.05	0.01	0.54
Remaining	0.75	0.96	0.98	0.97	0.70	0.95	0.89	0.95	0.99	0.46
Projected Wear-Out Years	5.2	26.6	24.2	52.8	5.6	25.4	14.8	27.9	58.5	2.3
Flights Remaining	428	3122	2834	5261	434	2072	1323	3095	6935	173

Points 1, 4, and 5 were selected because they were most representative of the variation of damage rates incurred by the various fatigue points for these types of usage. The damaging potential of these ground operations was essentially negligible for FP-1, whereas it was very significant for FP-5 and was quite significant for FP-4.

A review of the aircraft geometry readily indicates why FP-5 has such a high damage rate during landing (see Figure 4). This critical point, which is on an upper longeron of the fuselage at a fuselage station just aft of the main landing gear reaction point, receives a high tension stress caused by the down inertial loads of the aft wing-fuselage section during landing impact. These high tension stresses are sufficiently large to cause high-magnitude, alternating stress cycles which cause high damage for each landing.

It is interesting to note that the effect of taxi was found to be negligible for all of the fatigue points studied.

A summary of the damage rates for Fatigue Points 1, 5, and 10 (those which were found to be the most critical overall) are presented in Table III. The relative severity of these various usage regions or miscellaneous operations is normalized in terms of the percent of the total damage experienced during 1004 flights for each of these fatigue points. It should be noted that FP-10 received the highest total damage, and hence was the most critical point. It is also interesting to note that little or no damage was incurred in Usage Regions 6 and 7. At first one might think that this low damage is contradictory to the extremely high damage predicted in Figure 11. However, it should be recognized that the information in Figure 11 is unit damage rate data. Since the aircraft was restricted from flying in Usage Regions 6 and 7, no time was logged in these usage regions, and hence no damage was realized.

By the measurement of stresses at the fatigue critical locations and by the measurement of the load factor spectra, it was possible to obtain two independent computations of unit damage rates for each usage region in which the aircraft operated. These newly computed damage rates were compared with those originally determined from design and flight

test information, and the original rates were modified as required. During the course of this program, the unit damage rates were iteratively updated as a larger data sample was amassed. The updated unit damage data set was then input to a computer for use in future predictions of the life of each aircraft in the B-58 fleet in terms of its various fatigue critical locations.

A summary of typical results of these fleet life analyses for one aircraft is presented in Table IV. This table, obtained from Reference 8, indicates the damage that this aircraft accrued during the previous quarter, the cumulative damage to date, the damage remaining, and the projected years to wearout for each fatigue critical point on this aircraft. One damage summary chart like Table IV is generated four times a year for each aircraft in the fleet. To conserve space, damage is truncated at a resolution of only two decimal places. However, damages smaller than  $10^{-2}$  are retained in the computer and will be accumulated throughout the program. Note that the data in Table IV represents the fleet life predictions prior to the modification of the unit damage rates.

## DISCUSSION

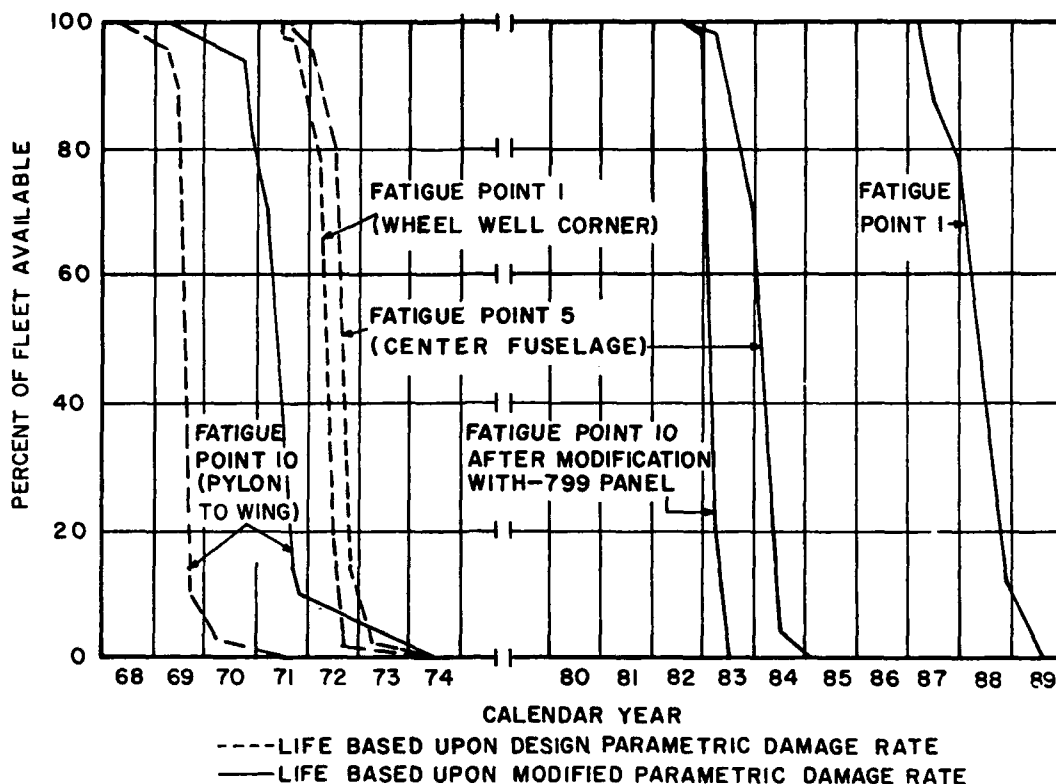
The following paragraphs contain a discussion of the various ways in which the data presented herein can be used and interpreted, as well as descriptions of some of the important by-products developed during the program.

### Analysis of the Fleet Life Prediction Data

By combining the data from all of the damage summary sheets of Reference 8 (one sheet for each B-58 aircraft in the fleet), one can plot the projected structural wearout trends of the fleet as shown in Figure 12. The data on Figure 12 is probably the most significant output of this program. One can see that Fatigue Points 1, 5, and 10 were the most fatigue-critical locations on the aircraft at the time Figure 12 was generated. Of these three locations, FP-10 was the most critical in that it governs the life of the fleet. The dashed curves in Figure 12 represent the life estimates based upon the original parametric damage rates<sup>8</sup>, whereas the solid lines represent the life based upon the modified parametric damage rates.<sup>9</sup>



Figure 12.  
Projected  
Structural Life,  
B-58 Fleet.



The first conclusion that one might draw from a study of Figure 12 is that the results of the Service Life Recording Program lengthened the estimated life of the fleet. Merely by the modification of the original parametric unit damage data, it was possible to predict an average fleet life increase of about 1-1/2 years based upon FP-10. Thus, without the expenditure of any funds or time for structural modifications, it was found that it was possible to rely on the B-58 fleet about 1-1/2 years longer than was originally anticipated. This extra time was available either to plan for modification, plan for inspection, or to provide additional lead time for the design and development for the aircraft which will be the successor to the B-58.

The curves of Figure 12 show the percent of the total fleet that remains in operation at a given time in terms of failure at three fatigue points. Based on this modified data the first B-58 aircraft will fail at FP-10 after the first quarter of 1969; 10% of the fleet will fail by the fourth quarter of 1970, and 90% of the fleet is expected to fail by the first quarter of 1972.

Another way in which Figure 12 can be used for management decisions is in determining the value gained by incorporating a structural modification. The predicted fleet wearout trend for FP-10 after the -799 wing panel modification is shown in Figure 12. Even though the fleet life was still limited by FP-10 after the -799 structural modification, the manager can see that the modification would extend the fleet wearout date approximately 12 years. From a cost/effiveness analysis, it was determined that this modification was justified, so the entire fleet was modified with the -799 wing panel. However, if in 1982 it was desired to extend the

fleet wearout date further, the manager can see that by modifying FP-10 again the fleet life would be limited by FP-5, and the cost of the new FP-10 modification would buy only about one more year of fleet life.

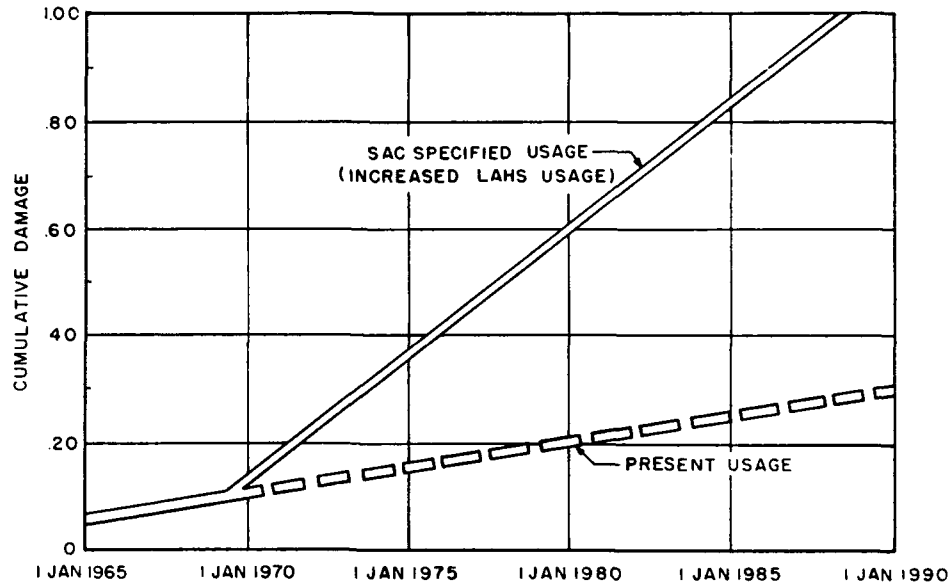
The data in Figure 12 was a major benefit of the program. The parametric damage rates for FP-1 and FP-5 were changed so greatly, and fleet wearout dates were extended so markedly, that there was no longer any need to purchase the FP-1 and FP-5 structural modifications that had been planned.

A third value of Figure 12 would be to assist in the scheduling of inspections and modifications. The reader should recall that the curves plotted on Figure 12 were obtained from individual damage summaries, such as Table IV, for each aircraft in the fleet. Thus, it is possible to plot a point on each fatigue point curve representing the time at which that fatigue point on each aircraft will fail. With this information, those scheduling inspections and modifications could first inspect those aircraft expected to fail first, and then schedule all succeeding aircraft inspections in order of estimated aircraft failure rather than in the order of serial number, flight hours, or any other criteria that has been used in the past. The data will also indicate the amount of lead time that is available to conduct inspections and to procure and install modification kits.

#### Damage Trends vs. Mission Type

Another valuable contribution of this program's results to quantitative decision-making is the information which would enable a manager to determine the structural life cost

**Figure 13. Effect of Two Types of Usage on Projected Life of Aircraft 59/2449, Fatigue Point 1.**



of various aircraft missions. An example of such information is presented in Figure 13. Two types of usage are represented in Figure 13: missions excluding flight in Usage Regions 6 and 7, and missions including flight in Usage Regions 6 and 7. By analyzing the slopes of the curves on Figure 13, one can determine that a significant decrease in the life of the fleet will result from scheduling appreciable amounts of low altitude flight at Mach numbers above 0.725 in the mission mix. With this information, the mission scheduling personnel can determine whether or not the value of the planned mission mix justifies such an expenditure of structural life. Similar curves can be generated from the unit damage data of the modified parametric analysis for all mission types being flown or expected to be flown. Inasmuch as the data are in parametric form, an estimate of the life expenditure of a new mission also could be estimated before the decision was made to incorporate that mission in overall utilization plans.

In actuality, the loss in fleet life shown in Figure 13 is academic, because both missions shown predict fleet lives beyond the planned phase-out date of the B-58 fleet. Nevertheless, the basic principles behind this type of data presentation are valid, and the mission planning that can be guided by this type of analysis can be an important factor in prolonging the life of the fleet without expending funds and time for structural modifications.

Unit damage data like that shown in Figure 11 actually was used for B-58 mission planning. Early in the program, before the unit damage rates had been decreased to agree with the LTF recorded data, it was noted from AFTO 70 forms that pilots had a tendency to fly the LAHS runs immediately after refueling, when the aircraft was at a high gross weight. It also was noted that the flights were being flown at Mach numbers greater than 0.725. Inasmuch as the design unit damage rates predicted higher values of damage per mission than were desired because of this high Mach

number, high gross weight, low altitude flight condition, pilots were instructed to reduce speed and fly low altitude runs at lower gross weights. Later, after the unit damage rates had been decreased, the speed restrictions were eased.

#### Cumulative Damage vs. Flight Hours

As a final analysis, we would like to compare the results of basing the age of a fleet on flight hours or on Miner's damage ratio. Reference 10 indicates that the variation in B-58 damage rate (damage per hour) caused by usage differences alone can vary by a factor of six. This finding indicated that in a given period of time, one aircraft was using its structural life six times faster than another. For a more highly fatigue-sensitive component than the one studied in Reference 10, the scatter would be expected to increase. The information obtained in Figures 10, 11, and 13 upholds the findings of Reference 10. There is a considerable difference in the damage incurred from flying one mission instead of another. The difference in damage trends shown in Figure 13 were caused primarily by the damage rate differences associated with low altitude flight at Mach 0.65 or Mach 0.91. There also is a considerable difference between the low altitude and the high altitude damage rates, as one would expect. Comparison of the damage rates for the low altitude and the high altitude usage regions in Figure 10 indicates that the Usage Region 2 damage rates are about ten times more severe than the high altitude cruise damage rates (based on strain gage data at 140,000 lb. gross weight). Also, by reviewing the variation in low altitude damage rates with gross weight for a given usage, one can see from Figure 10 that the low altitude damage rate for Fatigue Point 1 varies from zero to a little more than 0.3 as the gross weight increases from 100,000 pounds to 150,000 pounds.

The foregoing comparisons indicate it is reasonable to conclude that two aircraft can experience grossly different damage trends (caused by flying at different combinations

of gross weight, altitude, and Mach number), even if both vehicles have flown the same total number of flight hours. This conclusion is further borne out by comparing two B-58 aircraft that had accumulated about 1950 flight hours each. The first aircraft had accumulated a total damage at FP-1 of 0.30 and the second aircraft had a total accumulated damage of 0.80 at FP-1.<sup>8</sup> Upon study of the records, it was determined that the second aircraft was one of the older aircraft in the fleet that had been used extensively for early flights in Usage Regions 6 and 7 before the fleet had been restricted from flying in this regime. In fact, 34% of this aircraft's total fatigue life was expended while flying in these usage regions. The other aircraft had logged only 0.7 hours in this same region, and therefore had not sustained any appreciable damage from this usage.

Another interesting flight hour vs. damage example was noted from a comparison of the damages of two aircraft which were manufactured at the same time. Because of the difference of usage that these aircraft had realized, one had accumulated only 1300 flight hours whereas the other had accumulated a total of 2800 flight hours. In spite of this large difference in accumulated flight time, it was noted that the total cumulative damage of each aircraft was essentially the same.<sup>9</sup> This difference, again, was caused by a large amount of flight in Usage Region 6 by the aircraft that had flown only a total of 1300 hours, and consequently, the average damage per hour on this aircraft was considerably higher than that of the other aircraft.

These examples from this sample of B-58 data indicate that it is possible to incur large errors in aircraft life prediction if the predictions are based on flight hours, average damage per mission, or other gross averaging methods which have been used in most life analyses to date. By using the method presented herein, it is possible to predict an aircraft's age based upon the actual usage for each flight and on the average environment for each modular Mach-altitude region encountered. The average environment for each Mach-altitude region should be obtained from a large sample of recorded data from aircraft operating in the same geographical region, seasons, and mission mixes as the rest of the fleet. By subdividing this environmental data into small usage regions, the averaging errors are not as large as the errors of methods based on flight hours, etc. Therefore, it is believed that the use of a parameter such as Miner's cumulative damage ratio to indicate the life of each aircraft in a given fleet will provide much more realistic estimates of fleet life than the other methods that are in use today.

It is recognized that there are a number of uncertainties connected with Miner's theory and that scatter in fatigue experience is inevitable. It is emphasized that there is no substitute for periodic, carefully conducted inspections as planned for in Phase VI of the overall ASIP plan. Therefore, the fatigue damage parameter is not being recommended as the panacea for detecting all structural failures, but as a tool for indicating when inspections at potential failure locations should be scheduled for each aircraft in

the fleet. This cumulative damage information also can be used for scheduling modifications and for other long range planning by the using command and by AFLC.

### Strain Gage Experience

The results of this program have supported the University of Dayton's experience on the C-135 and B-52 service life monitoring programs that the strain gage is an excellent transducer that can be used with confidence on large-scale data acquisition programs, the nature of which precludes special handling of the strain gage systems. Instrumentation systems designed for ASIP programs must in themselves be reliable and must not interfere with the normal operational procedure of the using command. Therefore, the strain gage systems installed on the B-58 were designed to withstand the total aircraft environment. Once the gages were installed, wired, and waterproofed, no further attention or special handling was given to them by anyone at the two air bases. Our experience during the first 18 months of this B-58 program was that only five failures out of 128 gages occurred. Since most of these failures were not instantaneous, it was possible to detect them by analyses of the reduced data and then to switch the wiring from the main to the spare set of gages. This surveillance conducted by data processing personnel reduced the amount of data lost because of strain gage failures. Similarly, on the C-135 program, only two out of 24 gages were lost in one year, and on the B-52 B-F program in a two year period, only two out of 40 gages were lost. This reliability of the strain gage is either equal to or better than the reliability of pressure transducers or accelerometers that have been used over long periods of time on these and other flight loads programs conducted by the University of Dayton. Thus, we believe that the strain gage can be used reliably with minimal care in the same manner that accelerometers are used on flight loads programs.

From a cost standpoint, the strain gages also compare very favorably with the other transducers. Because of the high initial cost of pressure transducers, accelerometers, and rate gyros, and because of the high cost of purchasing spares and repairing these transducers, it is believed that the overall strain gage cost will actually be less. For example, it is estimated that the cost of installing main and spare strain gage bridges on one aircraft at four locations would be approximately \$375 per location. This price includes labor, materials, and travel costs. If two aircraft were to be instrumented in one trip, the cost per location would decrease to \$280. The strain gage circuit repair cost is variable and is often negligible when spare gages are switched into the circuit by the data acquisition technician. By comparison, the cost of an accelerometer installation, including the purchase price of the transducer, the cost of the mount, and the cost of installation is about \$500, and repair cost runs about \$190 per transducer. Other transducers vary in price up and down from these figures. To repair strain gages on a large ASIP program, one merely would provide a group of strain gage installation experts who would travel from one base to

another on an as-needed basis to install replacement strain gages on aircraft during normally scheduled phase inspections or modifications. Thus, as has been the University's experience, no flight time would be lost because of strain gage repair or installation. Inasmuch as the need for an expensive supply line of spare transducers would be minimized when strain gage systems are used, the cost/effectiveness index of strain gages would appear to be even more attractive when compared to other transducers.

Since the strain gages were used for measuring strain on the B-58 program and not for measuring loads, it was not necessary to provide load calibrations for the gages. Only the manufacturer's gage factor supplied with the gages is necessary. Therefore, the expensive cost of load calibration and aircraft down time would not be required when the strain gages are used as they were for this B-58 program.

### **Magnetic Tape Recorder Performance**

The FM tape recorder used for this program was satisfactory. Recording oscillographs were used to record the data from May 1965 until the tape recorders were delivered in December 1965. However, before the tape recorders were used solely on the program, one aircraft was equipped with a dual system in which one tape recorder and one oscillograph were used to record simultaneously the signals from one set of transducers. This dual recording system was utilized for a number of flights to obtain data for use in substantiating the validity of the tape recorder. The data comparison indicated that the digitized data from the FM tape recorder was superior, particularly in frequency response, to that obtained from the oscillograph. The ability to compare the FM data with that which was recorded in a visual chart form by the oscillograph also was very useful in developing and validating the various automatic data processing algorithms that were used. Studies conducted in parallel with this B-58 program indicated that adequate accuracy for load factor and fatigue-oriented data would be realized if the data to be processed were digitized to a resolution of 8 digital bits.<sup>11</sup> The B-58 data digital resolution was 11 bits.

### **Data Acquisition Effort**

The staffing of the data acquisition effort with experienced electronic technicians equipped with one quick-look, playback system at each base was a major factor in the high yield of good data that was realized. This method of operation provided the following advantages:

1. The data processing organization had direct line authority over the technicians in the field. Thus it was possible to exercise direct line control over the activities of these personnel and to obtain directly from them valuable information concerning current aircraft operations for use in the data analysis.

2. Excellent data yield was obtained. Since 1965

when the program was initiated, approximately 85% of the data that it was possible to record yielded valid information. Although the B-58 instrumentation system was considerably more complex than a conventional VGH system, the B-58 data yield rivaled that of oscillograph systems currently being operated by UDRI.

3. By meeting the plane after each flight, it was possible to bypass the current ASIP recorder specification requirement for a 30-hour recording duration between magazine changes.<sup>12</sup> This long duration recording period is placing a severe penalty on recording system design and on the maximum possible frequency response of the data by necessitating the use of extremely slow tape speeds and extremely high digital packing densities. The additional advantages accrued from meeting the aircraft after each flight were that the acquisition of flight logs was more reliable and it was possible for the technician to inspect his system more frequently.

4. By assigning the responsibility of data acquisition to an experienced technician, it is possible to reduce the number of spare units required because the technician was capable of making many minor repairs beyond those of merely changing units. This capability greatly reduces the resultant need for purchasing large stores of spare instruments required to maintain a smooth flow in a logistic supply line, and reduces the cost of maintaining a large repair depot.

5. By providing a ground-playback, quick-look system at each airbase, the need for tape magazines or cassettes was eliminated. Instead, after playback, during which the recorded tape is wound on a standard reel, the technician merely ships the reel of tape in a standard cardboard container. The quick-look system enabled the technician to evaluate instrumentation performance after each flight and to make repairs before a large amount of data was lost because of faulty instrumentation.

### **Automatic Data Processing System**

The automated data processing system proved to be more reliable and efficient than the previously-used manual systems, and yet it was capable of duplicating all of the manual processes. Experience gained from using the system indicated that the large quantities of data anticipated in future ASIP programs can be processed in a reasonable amount of time at a reasonable cost by currently available second generation computer systems. For example, studies indicated that two 7094 computers operating on a three-shift basis with normal amounts of maintenance time could process approximately 28,000 flight hours of data per month, which is the data reduction work load that AFLC anticipates when 433 recorders are being used in the ASIP program. Of course, one of the larger third generation computers could handle such a program more easily and would provide extra time for analysis.

The automated system vastly increased the amount of data that could be handled by a data processing group. For example, on the B-52 flight loads program, the University processed about 10 million data points manually over a two year period using an average of about 25 data processing clerks for the various manual and semi-automatic operations. On this B-58 program, a total of about 300 million data points per month (about 8 million data points per flight) are processed by one part-time technician and one data clerk. Of course, more high-level engineering and computer programming is required for the initial design of the automated system, but this initial effort soon will be amortized by the large data volume.

### CONCLUSIONS

This B-58 program has pioneered in developing techniques for modern Air Force Structural Integrity Programs and has yielded a number of state-of-the-art improvements in the service life recording field. This was the first program wherein large scale magnetic tape recording and automated data processing of multichannel structural integrity data was accomplished. It also was the first structural integrity program during which stress data were measured and converted directly to fatigue damage in parametric format. Inasmuch as both load factor and stress data were measured, it was the first program on which it has been possible to provide an independent check of the basic parametric damage rates by comparing the derived damage rates from the stress data with the derived damage rates obtained from the load factor data. Finally, the program has demonstrated the value and necessity of using the total system approach in designing an ASIP fleet-tracking program. The system approach is especially necessary to insure that the acquired data is compatible with the analysis techniques available and to assure compatibility of the instrumentation and data processing subsystems.

Major conclusions of this program are:

1. The program was highly successful and satisfied all objectives. The significant increases in time to failure resulting from modifying the original parametric damage rates provided the Air Force additional time to modify the most critical fatigue point and eliminated the need for two other modifications that were scheduled. The cost

savings from eliminated modifications more than paid for the cost of the B-58 Fatigue Service Life Monitoring Program.

2. Cumulative fatigue damage is a much better parameter than total flight hours for estimating the age and life of an aircraft and a fleet.

3. Parametric analyses based on design information must be verified by operational usage records, measured environmental information, and structural response data before reasonable estimates of fleet life can be made. The difference between design and operational data resulted in approximately a 1-1/2 year initial underestimate of the structural life of the B-58 fleet for the most critical location, and about a 12-year underestimate for the second most critical location.

4. The direct strain measuring approach of obtaining unit damage rates at known fatigue critical locations is more accurate than the computation of unit damage rates from measured load factor spectra because the strain approach is more direct and is independent of the load computations and stress analyses used during the developmental stages of the aircraft.

5. The use of strain gages was found to be a practical and relatively inexpensive method for monitoring stresses at fatigue critical locations. Strain gage bridges caused no more failures than accelerometers and pressure measuring transducers and did not require any special treatment or handling once they were installed.

### ACKNOWLEDGEMENTS

The authors wish to express their appreciation to each of the many people from the San Antonio Air Materiel Area, the Fort Worth Division of General Dynamics, the University of Dayton, and the Aeronautical Systems Division for their important contributions to the success of this program. Special thanks are due to Mr. T.J. White (SAAMA), Capt. H.R. McMillan (formerly with SAAMA, now with Headquarters, AFLC), Mr. W.R. Reeves (General Dynamics), Mr. John E. Hicks (Aeronautical Systems Division), and Mr. D.C. Zonars (Aeronautical Systems Division).

## REFERENCES

1. *B-52 B-F Flight Loads History Composite Report*, University of Dayton Research Institute, Dayton, Ohio (1964).
2. *Aircraft Structural Integrity Program*, AFR-80-13, Department of the Air Force, Washington, D.C. (1969).
3. *Final Cyclic Fatigue Analysis for Basic Airframe Structure of the B-58A and TB-58 Airplanes*, FZS-4-261, General Dynamics Corp., Fort Worth, Texas (1966).
4. *Final Cyclic Fatigue Flight Loads Spectra for the B-58A and TB-58A Airplanes, Revision A(U)*, FZS-4-257, General Dynamics Corp., Fort Worth, Texas (1966).
5. *Handbook of Operating and Maintenance Instructions for VGH/Strain Gage Recording System*, FSE-4-431, General Dynamics Corp., Fort Worth, Texas (1966).
6. *Implementation of B-58 Series Usage Report*, T.O. 1B-58-101, Department of the Air Force, Washington, D.C. (1964).
7. *Phase IV Fatigue Damage Analysis for the B-58 LTF Program*, UDRI-DR-69-07, University of Dayton Research Institute, Dayton, Ohio (1969).
8. *B-58 Fatigue Service Life Monitoring Program, 8th Quarterly Report*, FZM-4-2217-8, General Dynamics Corp., Fort Worth, Texas (1967).
9. *B-58 Fatigue Service Life Monitoring Program, 18th Quarterly Report*, RCS-AFLC-A38, San Antonio Air Material Area, Service Engineering Division, San Antonio, Texas (1969).
10. G.J. Roth, J.P. Ryan, and J.C. Sliemers, *Parametric Fatigue Analysis of USAF Aircraft*, AFFDL-TR-67-89, Air Force Flight Dynamics Laboratory, Wright-Patterson AFB, Ohio (1967).
11. G.J. Roth, *Sensitivity of Fatigue Damage Calculations to the Stress Increment Size and Digital Resolution of Load Factor Data*, ASD-TR-69-105, Aeronautical Systems Division, Wright-Patterson AFB, Ohio (1969).
12. *Military Specification Recorder, Signal Data MXU-553/A*, MIL-R-83165A, Department of Defense, Washington, D.C. (1969).

**SESSION 7**

**DESIGN AND SERVICE EXPERIENCE II**

*Chairman*

**M.S. Rosenfeld**  
**Naval Air Development Center**

# COMPARISON OF AIR FORCE FATIGUE PROBLEMS WITH PROBLEMS ON SIMILAR COMMERCIAL AIRCRAFT

by

Richard O. Schwake

Oklahoma City Air Materiel Area  
United States Air Force  
Tinker Air Force Base, Oklahoma

## INTRODUCTION

Today, as the state-of-the-art in aircraft design rapidly advances, it is easy to take for granted what has gone before. Yesterday's technical revolutions have become today's commonplace. High-performance, multi-engine jet aircraft are now in widespread usage by both the United States Air Force and by commercial operators worldwide. Two decades ago, aircraft the size and complexity of modern day jet aircraft were hardly imaginable. Likewise, the problems of fatigue certification, service life prediction, system reliability, and aircraft maintenance associated with today's jet aircraft were almost unheard of. As airplanes have become larger, more complex, and increasingly expensive, the science of airframe fatigue certification has become very important. In this paper, I will discuss one method used by the Oklahoma City Air Materiel Area to ensure adequate service life of first-line U.S. Air Force aircraft.

## AIRCRAFT STRUCTURAL INTEGRITY PROGRAM

Reliable, maintainable, on-line aircraft systems are a mandatory requirement of any air force. One major item of an aircraft system is the airframe structure, with the attendant mandatory requirement of structural integrity. The U.S. Air Force establishes, evaluates, and substantiates the structural integrity (airframe strength and service life) of its aircraft by employment of the Aircraft Structural Integrity Program (ASIP). By definition, the Aircraft Structural Integrity Program is a systematic procedure applied to a particular aircraft system to enhance design, diagnose potential or impending failure, provide a basis for corrective action, and predict operational life expectancy of the airframe. An objective of ASIP is to continually re-evaluate the initial structural integrity program of an aircraft by utilizing inputs from operational usage. By closely monitoring the operational usage inputs of an aircraft fleet, it is possible to determine the real-life conditions in the structural integrity of the fleet.

A thorough ASIP has been conducted on the KC-135 aircraft from the time of its initial development. As a result, this aircraft fleet has an impressive safety and reliability re-

cord. The KC-135 Stratotanker, built by The Boeing Company at Seattle, Washington, is the first-line jet tanker aircraft of the USAF Strategic Air Command. This four engine, swept-wing, multi-purpose tanker-transport aircraft provides high-speed, high-altitude refueling for both heavy bomber and jet fighter aircraft. The first KC-135 aircraft became operational on 18 June 1957, and there are now over 650 of these aircraft in use.

The KC-135 is sometimes referred to as the "military 707" as the two aircraft are somewhat similar in design. The KC-135, is, in fact, a variation or outgrowth of the original 707 prototype design. The planform and airfoil sections of the aircraft are the same, as is the location of stiffeners, spars, and ribs. There are, however, major differences in the two aircraft. Different materials are used in the wing structure and wing skin of the two aircraft. The 707 is a "fail-safe" airplane, whereas the KC-135 employs the "safe-life" design philosophy. Obviously, the usage of the two fleets also differs. With the various similarities and differences taken into account, it has been found in many cases that the two aircraft fleets experience fatigue problems in common or like areas. The purpose of this paper is to show how commercial fleet fatigue experience can be applied to a military fleet of similar design.

## DESIGN DIFFERENCES

The KC-135 was designed for SAC usage on a mission which consists of take-off, climb, cruise to rendezvous area, refuel a B-52, cruise back to base and land. The design mission time averages 5.1 hours with a yearly utilization of 450 hours. The 707 airplane was designed for a much greater yearly utilization and correspondingly greater fatigue life.

The primary difference between the fatigue design of military versus commercial aircraft stems from the degree of emphasis on "fail-safety." In providing structural reliability in aircraft structures, the aircraft industry has generally accepted two philosophic concepts—"safe-life" and "fail-safe." The concept of safe-life fatigue design demands that no fatigue failure occur during the operational life of the structure. If a fatigue failure does initiate, a safety problem exists and the service life of the structure is termi-



nated. In contrast to safe-life design, fail-safe design provides safety through damage containment, but trades maintenance cost for the service life gained beyond the initiation of fatigue damage. This provides an indefinite service life limited by economic factors rather than safety. Obviously, fail-safe structure must have a satisfactory level of fatigue performance if maintenance is not to become an economic burden. Structural reliability through fail-safe design must therefore be supported by an adequate level of fatigue performance.

The certification of the 707 was by the fail-safe philosophy, while the KC-135 fatigue analyses and maintenance programs are based on the safe-life concept. However, it should not be implied that either of the two designs was based on one of the two concepts exclusively. The structural designs of the two airplanes are very similar, with fail-safe structure used in both. The difference between the two airplanes with respect to fail-safe and safe-life design is the degree of fail-safety of one airplane compared to the other. Since the 707 was certified as fail-safe, this concept was emphasized to a greater degree than it was during the design of the KC-135.

The body of the 707 is a modification of that of the KC-135. There are structural and material differences, but basically the two bodies are quite similar. The 707 body has the same cross section as the KC-135 except the upper lobe of the fuselage which is slightly wider. The length of the 707-100 body is the same as that of the KC-135. The 707 body aft of station 1440 is identical with that of the KC-135, except that the refueling boom support structure has been eliminated. The 707 has more and also larger windows, with heavy skin and forged frames around them for reinforcement. Since the aerial refueling equipment is all on the lower deck of the KC-135, leaving the upper deck completely clear for cargo or troop carrying, only the upper lobe of the aircraft is pressurized. Both upper and lower lobes on the 707 are pressurized. The 707 has 2024 aluminum skin in the pressurized section, while the KC-135 has both 2024 and 7075 aluminum skin in this section. Both airplanes have 7075 aluminum stiffeners.

The wing planform and airfoil sections of the two aircraft are identical; however, there are differences in basic wing structure and type of material used. The lower surface of the KC-135 wing utilizes 7178 skin and stiffeners, whereas the 707 utilizes 2024 skin and 7075 stiffeners. The upper surface wing skin and structure of both the KC-135 and 707 employ identical materials, primarily 7178 aluminum. The ailerons, spoilers, and flaps of the two aircraft are also identical.

The fail-safe design philosophy of the 707 has resulted in the selection of damage tolerant materials and in redundant structure capable of sustaining cracks without failure. Examples of fail-safe structure on the 707 are the additional span-wise splices in some areas of the wing, and the internal circumferential tear straps in the fuselage.

Although the KC-135 aircraft is basically a safe-life design, it does possess some fail-safe features. For example, external circumferential tear straps ("belly bands") similar to the internal straps on the 707 have been added to the rear portion of the fuselage to limit the growth of longitudinal fatigue cracks. (See Figure 1.) Since the predominant design philosophy used in defining the fatigue requirements on USAF aircraft is the safe-life concept, the KC-135 is considered to be a safe-life airplane. Consequently, the fatigue integrity of the KC-135 is primarily dependent on the prevention of fatigue problem areas.

## COMPARISON OF USAGE

The service life of an aircraft fleet is a direct function of the type and amount of usage the fleet experiences. The usage of an aircraft fleet can be divided into a number of categories - the take-off gross weight, cruise altitude, cruise speed, length of flight (time), and per cent of time spent at low level flight. When comparing the usage of two aircraft fleets, all these categories must be considered. The comparison can be very complicated, especially when a military and a commercial fleet are being compared. The following comparison of KC-135 and 707 usage will therefore be general in nature. (See Figure 2.)

The usage of the KC-135 and the 707 fleets differs in many ways. To begin with, the take-off gross weight of the KC-135 is 297,000 pounds, as compared with 248,000 pounds for the 707. On an average SAC refueling mission, the KC-135 first climbs to and cruises at 34,000 feet, drops to 30,000 feet for refueling, and then climbs to and cruises at 45,000 feet. In comparison, the 707 cruises at 35,000 feet. The KC-135 cruises at approximately 0.78 Mach number, while the 707 normally cruises at 0.82 Mach number. The average air refueling mission for the KC-135 lasts 5.1 hours, whereas the average 707 flight lasts 2.04 hours. The per cent of flight time spent at low level for the KC-135 is approximately 10 per cent, as compared with approximately 5 per cent for the 707.

As can be seen, the usage of the two fleets differs in every respect. The length of the 707 mission is less than half that of the KC-135. As a result, the 707 must make more take-offs and landings, and undergo more ground-air-ground cycles than the KC-135. The fuselage of the 707 therefore undergoes many more pressurization-depressurization cycles than the KC-135, and, consequently, the fatigue accumulation on the 707 fuselage is greater than that for similar structure on the KC-135. The various usage categories affect different sections of the aircraft. For example, the difference in gross take-off weights of the two aircraft primarily affects the fatigue lives of the landing gear systems, but also has some effect on the fatigue lives of the wings and fuselage. Likewise, the difference in the cruise altitudes for the two aircraft primarily affects the fatigue lives of the wings and tail section. Since all of the above flight parameters are different for the KC-135 and the 707, the difference in the rates of fatigue damage accumulation

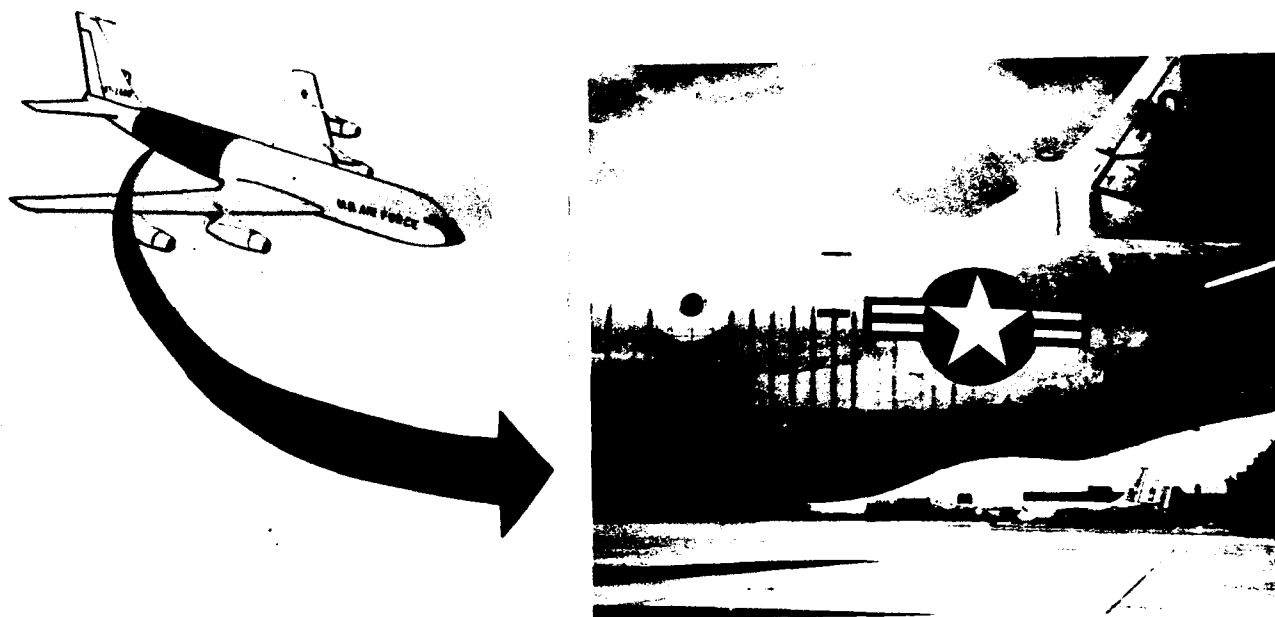


Figure 1. Circumferential Tear Straps on the KC-135.

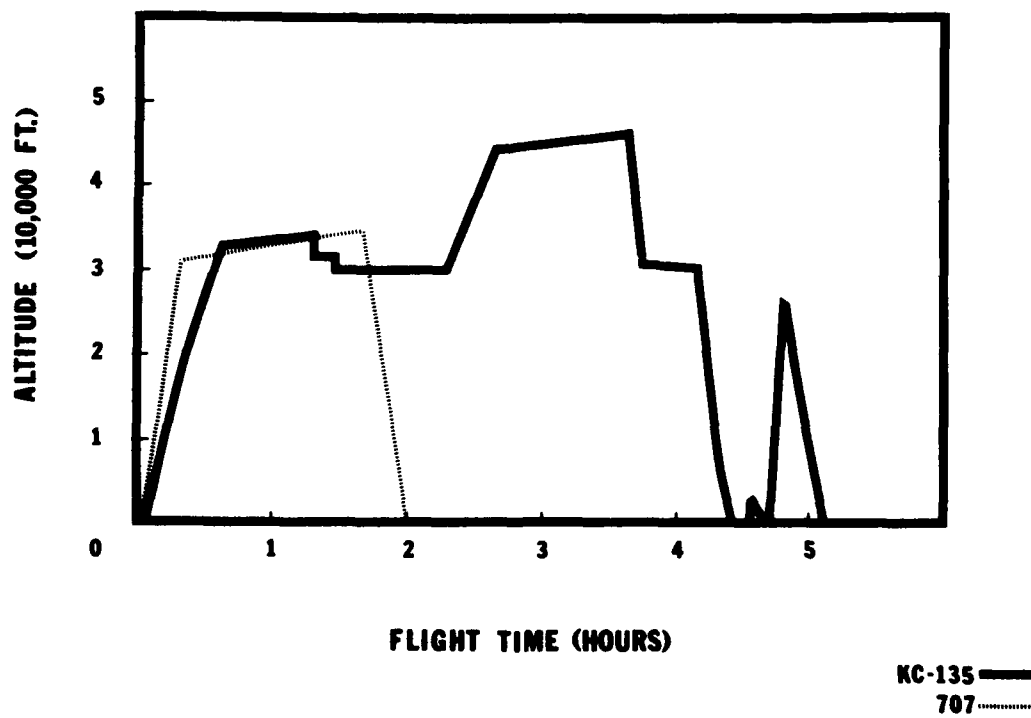


Figure 2. Typical Mission Profiles — KC-135 and 707 Aircraft.

cannot be attributed to a single flight parameter. Instead, the effect of the changes in various flight parameters can be determined only by an investigation of the effect of changes in each of the parameters independently.

The fatigue life of a particular structural detail depends upon the load environment, the materials used, and the "fatigue quality" of the detail design. The "fatigue quality" of a particular structural element is defined as the resistance to fatigue damage, or the fatigue tolerance of that element. Fatigue quality is a function of both design and the material used. In many cases, the fatigue quality of particular structural details of the KC-135 and the 707 is the same, as both airplanes use parts of identical design and materials. In these cases, the difference in fatigue lives of the structural details is caused by the different load environments of the two fleets. There are many structural elements on the two aircraft fleets that differ in design and/or materials. The difference in fatigue lives for these elements is a result of both the differences in fatigue quality and in load environment.

#### APPLYING COMMERCIAL EXPERIENCE TO MILITARY DESIGN

The procedure for applying 707 experience to the KC-135 fleet in order to predict the service life of a particular structural detail involves several steps. (See Figure 3.) First, the engineer must determine the commercial fleet experience of the detail in question. This includes the number of failures, the cause of the failures, and the flight hours at which each of the failures occurred. Next, a "usage factor" relating the severity of usage, or the rate of fatigue damage accumulation for the particular detail on the KC-135 versus the 707 must be determined. This factor, which is based on aircraft usage, can be expressed in terms of relative life. It is found by comparing usage data for the two fleets and determining what effect the various differences in usage have on the damage accumulation rate of the detail. A second factor, the "fatigue quality" factor, must also be determined. This factor relates the relative fatigue quality or fatigue tolerance of the structural detail for the two fleets. The "fatigue quality" factor can most accurately be determined from cyclic testing of the detail. However, cyclic test data is not always available and in most cases, time does not allow for a cyclic test program. Therefore, the "fatigue quality" factor must sometimes be estimated from available analyses and test data of a part of similar configuration and material. Once the "usage" factor and the "fatigue quality" factor have been determined, the estimated mean life of the structural detail for military usage can be calculated. This is done by multiplying the average hours at failure of the detail (commercial fleet experience) times the "usage" factor, times the "fatigue quality" factor. The safe life of the detail in the military fleet can then be found by dividing the estimated mean life by a "scatter" factor. The "scatter" factor is included to account for the inherent scatter in the fatigue performance of identical structures, and for USAF

usage must be a minimum of 4.0. The above procedure can be expressed in equation form:

$$\text{Commercial Experience} \times \text{Usage Factor} \times \text{Fatigue Quality Factor} = \text{Estimated Mean Life}$$

$$\text{Then, } \frac{\text{Estimated Mean Life}}{\text{Scatter Factor}} = \text{Safe Life}$$

It must be remembered that engineering judgment plays a very important role in the application of this procedure. When applying commercial fleet experience to a military fleet of similar design, the commercial experience must be evaluated and analyzed, the cyclic test data must be analyzed or estimated, and the "usage" and "fatigue quality" factors must be determined as accurately as possible, all of which require sound engineering judgment and expertise.

The procedure for applying commercial fatigue experience to a military fleet can be demonstrated by using the wing joint at Wing Station 360 on the 707 and KC-135 as an example. Based on an average 5.1 hour air refueling mission for the KC-135, the relative rate of fatigue damage accumulation at Wing Station 360 of the 707 is estimated to be 1.4 times that of the KC-135 wing joint. Based on flight hours, the "usage" factor is therefore 1.4. In comparing the fatigue quality of the two wing joints, it is noted that the two joints differ both in detail design and in materials utilized. On the 707, the wing stiffeners are machined from a large extruded section of 7075 aluminum to permit increased section and area at the end as an integral part of the stiffener. The stiffeners on the KC-135 wing are of constant cross section and are made of 7178 aluminum. The stiffener end attachments are made by the addition of separate machined angles. Comparative cyclic tests of the two wing joints at the same alternating stress level show the 707 wing joint will withstand 2.7 times the number of cycles taken by the KC-135 wing joint. Thus, the "fatigue quality" factor is  $1/2.7=0.37$ . By combining these two factors, the estimated mean life of the KC-135 Wing Station 360 wing joint is 0.52 times that of the 707 wing joint. The safe life of the wing joint can now be found by dividing the estimated mean life by a "scatter" factor (Figure 4.)

The KC-135 and 707 fleets have, on occasion, experienced fatigue problems in common or like areas. Since the yearly utilization rate for the 707 is approximately 3,000 hours/year compared with approximately 600 hours/year for the KC-135, fatigue-critical areas are usually first determined on the commercial fleet. Two examples of fatigue areas that have occurred on both fleets will now be discussed to illustrate how the KC-135 and 707 fleets experience similar fatigue problems. (See Figures 5a and 5b.)

The first example of a fatigue problem area that was common to both fleets is the Lower Trailing Edge Access Panel Hinge to Inspar Skin Attachment, BBL 70.5 to Wing Station 712. The fatigue problem existed in the area of the

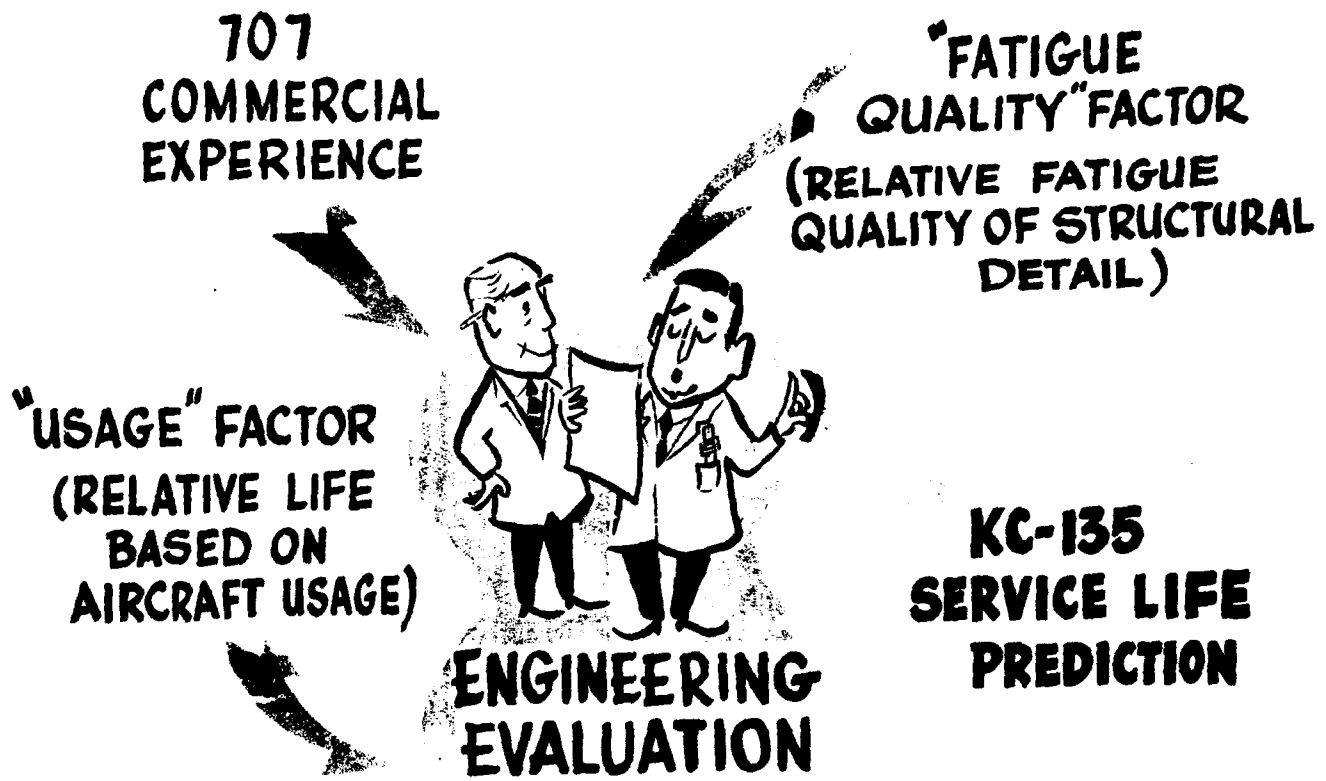


Figure 3. Procedure for Applying 707 Fleet Experience to the KC-135 Fleet.

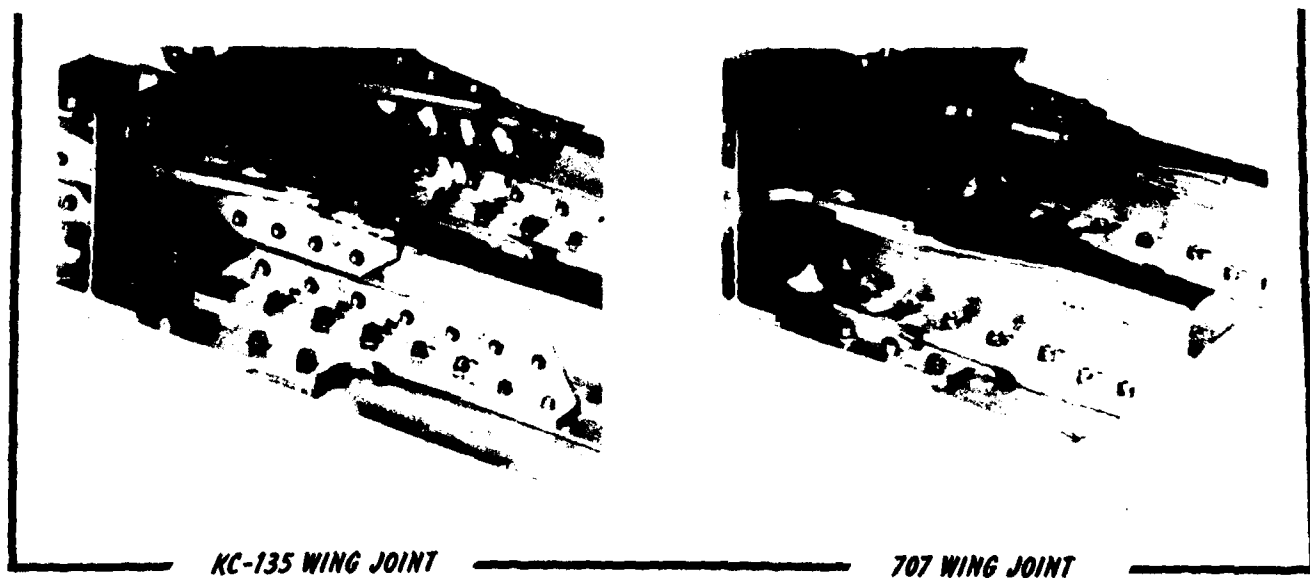


Figure 4. Comparison of KC-135 and 707 Wing Joint Detail.

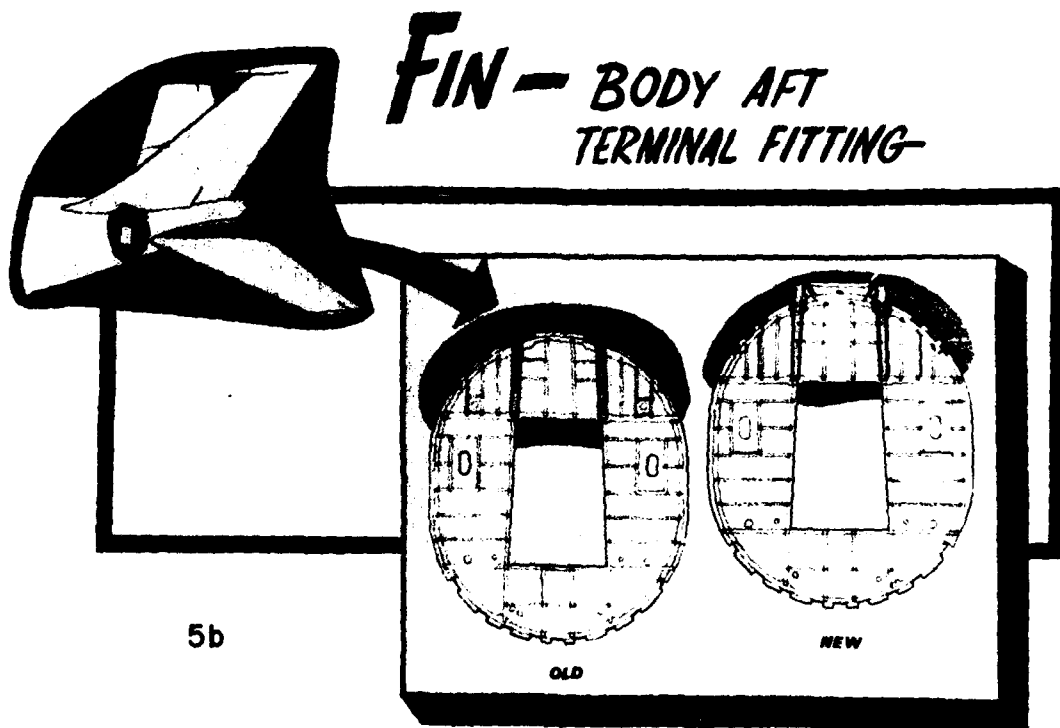
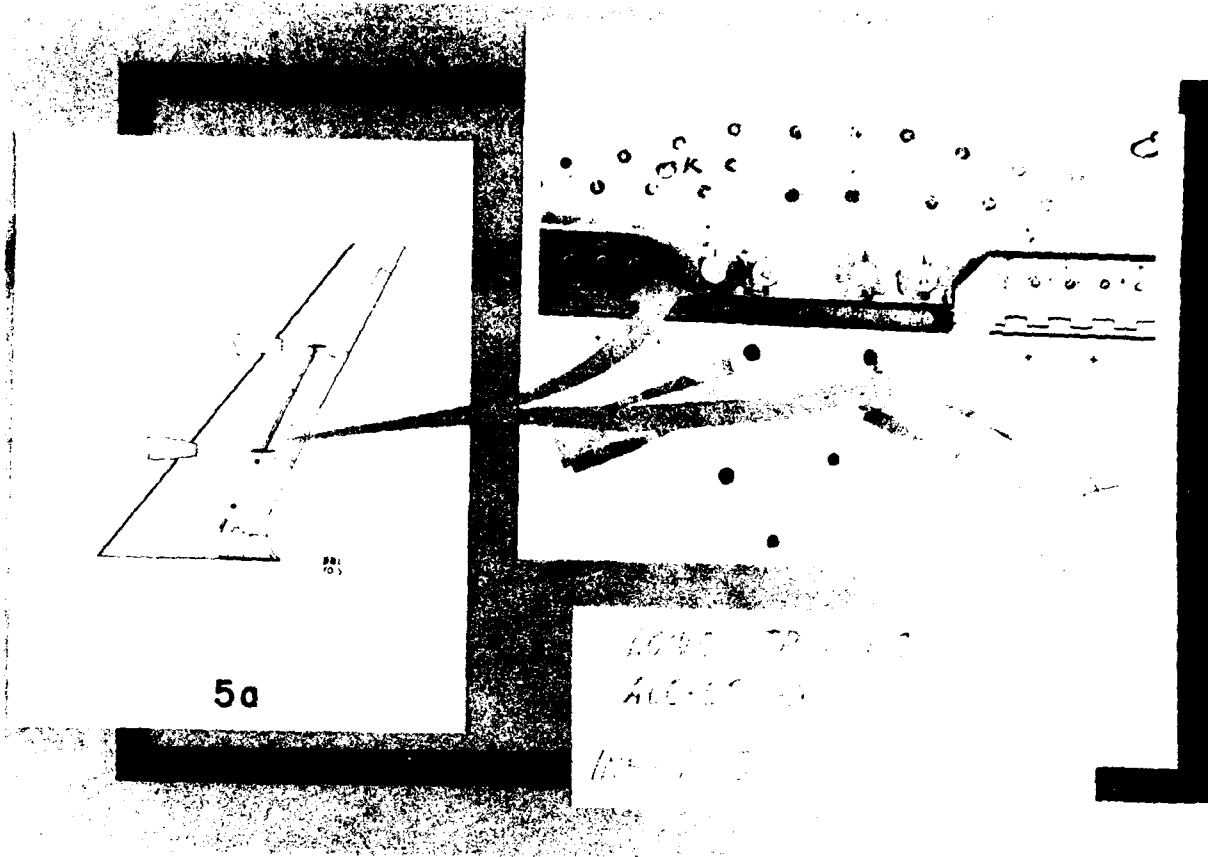


Figure 5. Areas of Similar Fatigue Failure Experience.

trailing edge access panel hinges which are attached to the aft edge of the wing lower skin by rivets. Because of the length of the hinge and the tight fit between the hinge attach rivets and the holes in the wing skin, the hinges carried a load imposed by wing flexure. This condition imposed a local stress concentration at the end fastener in the hinge and induced fatigue cracks in the wing skin. Altogether, there have been cracks of this type reported on five commercial 707 aircraft. The approximate time the cracks have occurred on the 707 has been 30,000 flight hours, although one crack was reported at approximately 15,000 flight hours. The same problem has occurred on the KC-135 fleet. There have been eleven cracks of this type reported, with the average time of occurrence being 4,000 flight hours. One crack was reported as early as 2,718 flight hours. The considerable difference between the flight hours at failure of the two fleets can be accounted for by the difference in materials and usage, as the detail design is identical for both fleets. The action taken to correct this problem consisted of enlarging the hinge fastener holes in the wing skin and of cutting the forward half of the hinges into two or three fastener segments. This cutting of the hinges and oversizing of the fastener holes prevents the hinges from being loaded. This fatigue problem was experienced first by the commercial fleet and later by the Air Force. The repair for the commercial fleet was adapted for use on the KC-135.

A second fatigue problem experienced by both fleets is the Fin-Body Aft Terminal Fitting at Body Station 1505. The commercial fleet first experienced this problem on three high-time aircraft, each with approximately 20,000 flight hours. Detailed examination of the fin-body aft terminal fittings on these aircraft revealed small fatigue cracks inside the bore of the upper outboard holes of the fittings. Because of these cracks, The Boeing Company issued a service bulletin calling for an inspection of the fin-body aft terminal fittings on all 707 aircraft with 12,000 or more flight hours. From the resulting large scale inspection, numerous other cracked terminal fittings were reported. The Boeing Company then reduced the inspection time to 7,000 flight hours, and later reduced it to 3,500 hours. For the terminal fittings found to be cracked, detailed instructions for an interim modification were issued. The modification consisted of reaming the holes until the cracks and additional material were removed, and installing bushings and/or bolts. Where it was impossible to remove the crack by reaming while maintaining sufficient edge distance (distance from the edge of the hole to the edge of the fitting), the fitting had to be replaced. The final modification for the fatigue-critical fin-body aft terminal fitting consisted of completely replacing the fitting and the 1505 bulkhead assembly with a newly designed fitting and bulkhead assembly.

When this problem was first encountered in the commercial fleet, it was believed that the problem would not immediately affect the military fleet, as the problem was occurring on commercial aircraft with very high flight hour accumulations. However, when the problem was found to

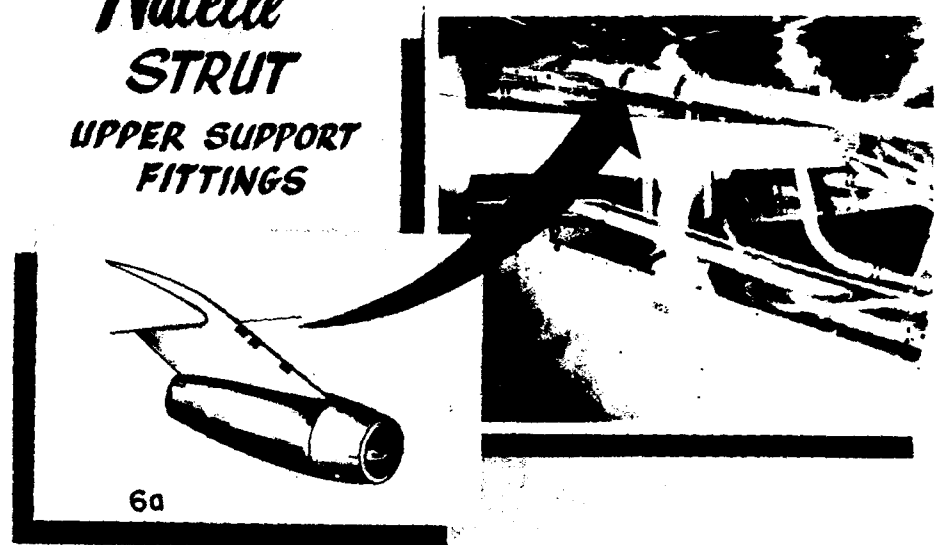
also occur on lower time commercial aircraft and the recommended inspection time had been subsequently lowered to 3,500 flight hours, OCAMA Engineering made the decision to inspect the military fleet. The decision was based primarily on commercial experience, since the KC-135 fleet had not yet experienced this problem. After an engineering evaluation of commercial terminal fitting data and a comparison of commercial versus military usage data, it was decided to inspect those KC-135 aircraft with 6,000 or more flight hours. This inspection time was higher than the commercial inspection time because of the difference in usage for the two fleets, especially with respect to the higher number of take-offs and landings the commercial fleet makes. A special inspection technical order was issued by OCAMA to inspect the top four bolt holes in each terminal fitting on all KC-135 aircraft with 6,000 plus flight hours. At this time, however, the commercial fleet was beginning to experience numerous cracked fittings and, as a result, the KC-135 inspection time and procedure was revised. The new inspection procedure included removing the top four bolts, reaming and eddy current inspecting the holes, and was to be accomplished on all aircraft with 4,500 or more flight hours. During the period in which the above inspections/rework were being accomplished, a technical order was approved for the KC-135 fleet which called for the replacement of the existing fin-body aft terminal fittings and portions of the 1505 bulkhead with a completely new design fitting-bulkhead assembly. The new fitting-bulkhead assembly design was identical to the commercial design.

Due to fatigue cracks detected in the aft terminal fitting on an attrited KC-135, a special technical order was issued to inspect and modify the entire KC-135 fleet. This technical order replaced the previous special inspection, and was an interim modification pending installation of the new design terminal fitting-bulkhead assembly. During this special inspection and modification, 50 fin-body aft terminal fittings were found to be either cracked or else had insufficient edge margin after reaming and had to be replaced. Commercial experience was very instrumental in this case, in revealing an impending problem in the military fleet that had not been previously detected.

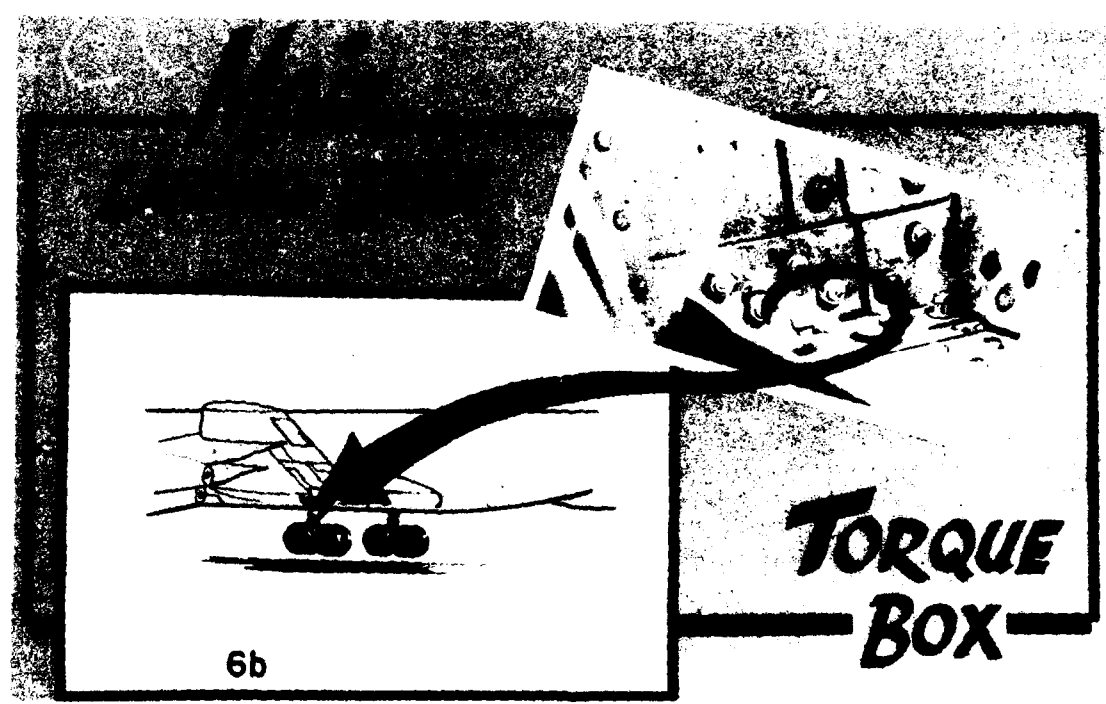
On many occasions, the commercial 707 fleet has provided the Air Force information concerning structural fatigue problems, which has in turn resulted in preventative maintenance or modifications to the KC-135 fleet. This commercial fleet experience has proved to be a valuable source of information for maintaining an effective Aircraft Structural Integrity Program on the KC-135 aircraft fleet. Examples of two cases where commercial 707 experience was utilized to prevent a fatigue problem in the military fleet will now be discussed. (See Figs. 6a and 6b.)

The first example is the Nacelle Strut Upper Support Fitting. On each nacelle strut there are several one-piece construction fairing attach clips, wiring support clips, a thermal anti-ice duct support bracket and, on the outboard struts only, a throttle control pulley bracket, all of which

*Nacelle*  
**STRUT**  
UPPER SUPPORT  
FITTINGS



6a



**TORQUE**  
**BOX**

6b

Figure 6. 707 Failures Which Resulted in KC-135 Maintenance or Modification.

are rigidly fastened to the upper and/or lower flanges of the strut upper support fitting. The tendency of these one-piece clips and brackets to absorb some fitting load induces stress concentrations which may initiate lateral fatigue cracks emanating from the fastener holes in the flanges of the fitting. These cracks, if allowed to progress, will ultimately result in failure of the fitting. Three instances have been reported of the cracking of the 707 nacelle strut upper support fitting. In order to eliminate this fatigue problem, a modification procedure to increase the fatigue life of the brackets was designed. The procedure included notching the brackets to minimize rigidity, enlarging fastener holes to remove fatigued metal, and adding rub strips between the brackets and the fitting flanges to prevent fretting. This modification has been incorporated by the Air Force, and as a result this problem has not occurred in the KC-135 fleet.

The second example is the Main Landing Gear Torque Box. During structural testing of several main landing gear support torsion boxes, and on some 707 aircraft in service, fatigue cracks were discovered at the attachment of the upper rib chord to the aft trunnion support fitting. It was subsequently found that the fatigue cracks were due to high working stresses. To strengthen the rib chord to trunnion support attachment and thereby improve the structural integrity of the landing gear support, a reinforcing angle was installed. Since the attachment is structurally the same on both the 707 and KC-135 aircraft, the identical

repair was accomplished on the KC-135 fleet, and the occurrence of this fatigue problem was prevented in the military fleet.

In conclusion, because the Air Force KC-135 and the commercial 707 aircraft have design similarities, the two aircraft sometimes experience similar structural fatigue problems. Since the commercial airliners fly considerably more hours per year than the military aircraft, fatigue problem areas are usually first determined on the commercial fleet. This commercial fleet fatigue experience has on several occasions provided advanced warning of a potential or impending structural fatigue problem for the military fleet. While commercial fatigue experience is not an infallible source of structural integrity program information for the military fleet, it has proved to be valuable when tempered with the knowledge of structural and usage differences. Commercial 707 fleet experience, therefore, provides a most valuable input for the USAF KC-135 Aircraft Structural Integrity Program.

#### ACKNOWLEDGEMENT

I wish to express my appreciation to Mr. L.L. Gore and Mr. Charles Harris of the Fatigue Group, The Boeing Company, Seattle, Washington, for their assistance in preparing this paper.

#### REFERENCES

1. *Air Force Aircraft Structural Integrity Program Requirements*, ASD-TR-66-57, Aeronautical Systems Division, Wright-Patterson AFB, Ohio (1969).
2. *C/KC-135 Series Aircraft History, Structural Integrity, Service Life*, Oklahoma City Air Material Area (OCNC), Oklahoma City, Oklahoma (n.d.).
3. A.C. Carlson, *Fatigue Comparison*, Boeing Company, Seattle, Washington (1962).
4. *Improvement of Lower T.E. Access Panel Hinge to Inspar Skin Attachment*, BBL 70.5 to W.S. 712, 707-100 and -200 Airplanes, Boeing Service Bulletin No. 2528, Boeing Company, Renton, Washington (1967).
5. *Lower Wing Skin Fatigue Strap Installation*, Boeing Service Bulletin No. 1662, Boeing Company, Renton, Washington (1962).
6. *Main Landing Gear Torque Box Reinforcement*, Boeing Service Bulletin No. 1602, Boeing Company, Renton, Washington (1962).
7. *Nacelle Strut Upper Support Fitting Inspection and Bracket Modification*, Boeing Service Bulletin No. 1798 (R-2), Boeing Company, Renton, Washington (1964).



# PARAMETRIC FATIGUE ANALYSIS MODELS FOR FIGHTER AIRCRAFT\*

by

Blaine S. West and George J. Roth

University of Dayton Research Institute  
Dayton, Ohio

## INTRODUCTION

The determination of the fatigue life of service aircraft is a problem of paramount importance to the Air Force. Evaluation of fleet average fatigue damage is necessary to provide the Air Force with data for long range planning, mission scheduling, and fleet life evaluation. The fatigue life monitoring of each individual aircraft in the fleet provides a means for scheduling structural modifications, aircraft deployment and aircraft retirement.

Aircraft can be classified into three general categories: (1) large cargo or bomber aircraft for which the fatigue damage can be attributed primarily to gust, (2) medium sized fighter-bomber aircraft subjected to both gust and maneuver loads of sufficient magnitude to produce damage, and (3) fighter aircraft for which all fatigue damage is due to maneuver loading. Historically, airframe hours have been used as an indicator of individual aircraft life for all classifications of aircraft. More recently, damage prediction techniques based on aircraft utilization have been used. It has been demonstrated that aircraft class and usage are important parameters in defining parametric models for fatigue damage accumulation. This paper is addressed to the problem of defining fatigue damage prediction techniques suitable for monitoring the accumulated damage on an aircraft tail number basis for fighter aircraft. Center of gravity load factor data collected in the Southeast Asia combat zone on F-5A, F-105D, and F-105F aircraft were used in the analysis. In addition, some peacetime data from the F-105D were used.

## ANALYSIS PROCEDURES

### Fatigue Damage Analysis

Analysis has shown that, in general, the load factor, gross weight, stores configuration, Mach number, and altitude are all important and independent variables affecting the fatigue damage to fighter aircraft. The relative importance of these parameters is dependent on both the specific aircraft characteristics and the utilization of the aircraft. The variation of fatigue damage with these parameters is illustrated for typical aircraft fatigue critical locations by Figures 1, 2, and 3.

\* This effort was sponsored by the Air Force Flight Dynamics Laboratory, Air Force Systems Command, United States Air Force.

The fatigue damages were computed treating each load factor occurrence as an independent stress cycle. The damages were then accumulated utilizing Miner's linear cumulative damage rule. This rule is stated mathematically as:

$$D = \sum_{i=1}^j \frac{n_i}{N_i}$$

where  $N_i$  = Number of cycles to failure under a specified cyclic loading condition

$n_i$  = Number of cycles experienced at a specified loading condition

$D$  = Accumulated damage

$j$  = Number of loading conditions experienced

Failure is expected when the accumulated damage,  $D$ , is equal to one.

The airborne portion of each flight was classified into the mission segments of ascent, cruise, refuel, maneuver, and descent. The accumulated fatigue damage was then classified by mission segment for each of the three aircraft. The results are presented in Table I. Approximately 99 percent of the total damage, exclusive of the ground-air-ground cycle, occurred during the maneuver mission segment. It was concluded that all damage exclusive of the maneuver mission segment and the ground-air-ground cycle could be regarded as insignificant for the SEA data samples under consideration.

The damage in the maneuver mission segment was separated into two categories: Maneuvering in the target areas and pull-up after weapon release for the F-105D and F-105F data samples. The results of these calculations are presented in Table II. In all cases, more than three-fourths of the total aircraft damage, exclusive of the ground-air-ground cycle, occurred during pull-up after weapon release. Analyses of the damage distribution were also performed on an individual aircraft basis yielding similar results.

TABLE I.

DISTRIBUTION OF FATIGUE DAMAGE BY MISSION SEGMENT

AIRCRAFT AND LOCATION	PERCENT DAMAGE	
	MANEUVER	ALL OTHER
F-105D at F.S. 442	99.6	0.4
F-105D at F.S. 509	98.9	1.1
F-105F at F.S. 442	99.3	0.7
F-105F at F.S. 509	99.4	0.6
F-5A at W.S. 26.6	97.7	2.3

TABLE II.

DISTRIBUTION OF FATIGUE DAMAGE OCCURRING DURING THE MANEUVER MISSION SEGMENT

AIRCRAFT AND LOCATION	PERCENT DAMAGE	
	PULL-UP AFTER WEAPON RELEASE	OTHER MANEUVERING
F-105D at F.S. 442	80.7	19.3
F-105D at F.S. 509	76.8	23.2
F-105F at F.S. 442	86.4	13.6
F-105F at F.S. 509	89.2	10.8

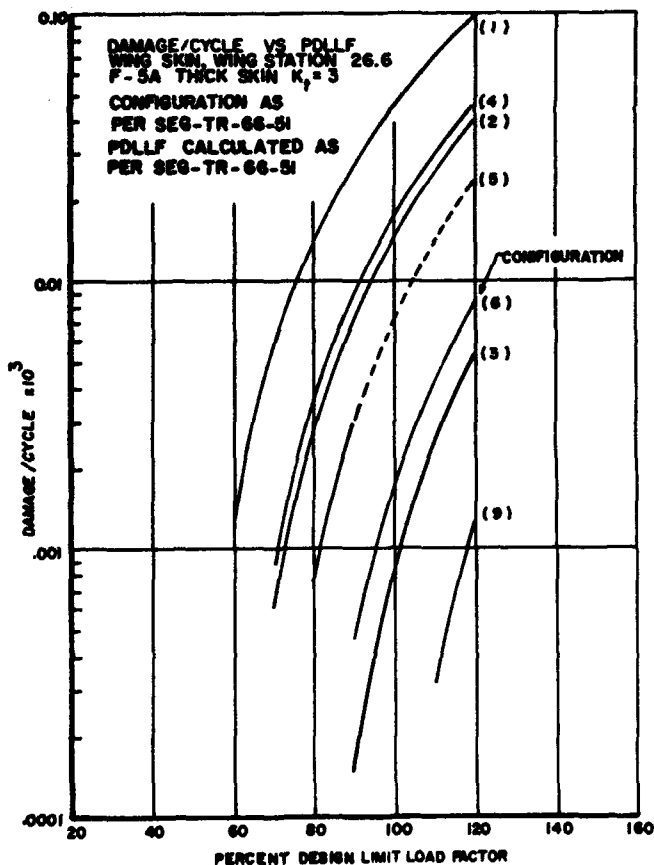


Figure 1. Fatigue Damage per Occurrence of Percent Design Limit Load Factor for Various Stores Configuration F5A Aircraft.

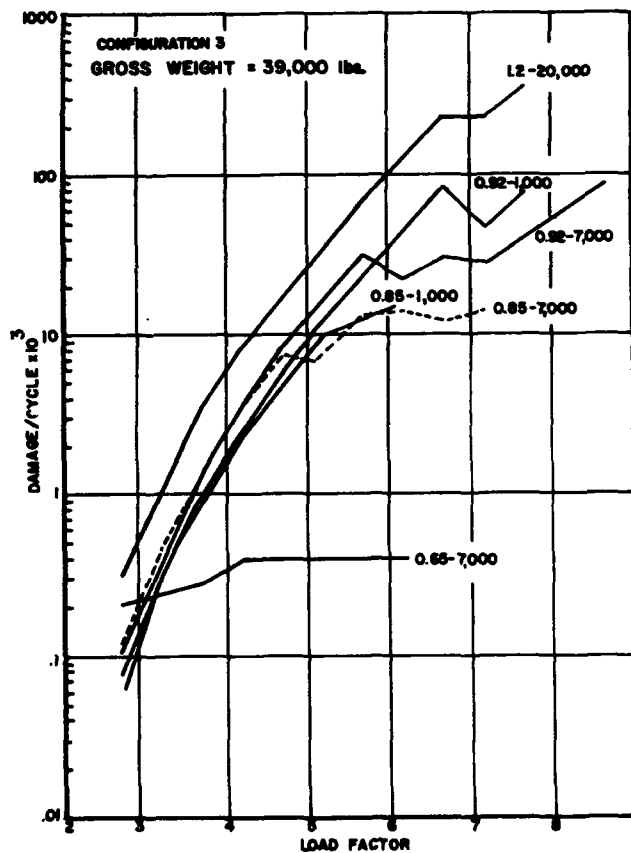


Figure 2. Damage per Cycle vs. Load Factor by Mach-Altitude Condition for the F-105D Transfer Spar at Fuselage Station 442.

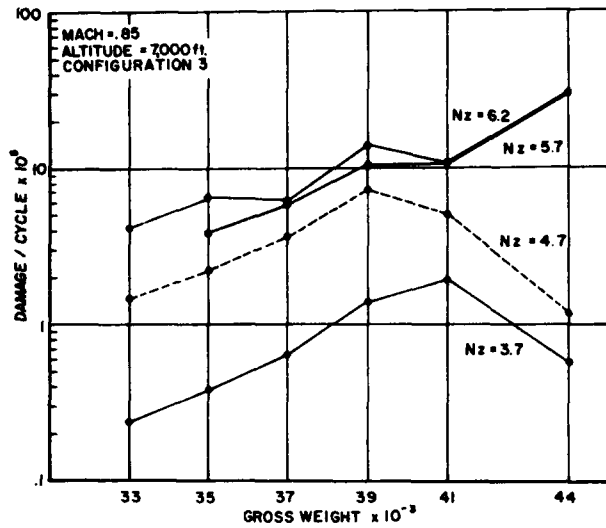


Figure 3. Damage per Cycle vs. Gross Weight by Load Factor for the F-105D Transfer Spar at Fuselage Station 442.

#### Damage Prediction Models

The four basic damage prediction models selected for evaluation are enumerated below.

- (1)  $(\text{Damage})_{\text{Hr.}} = \frac{\text{total damage basic data sample}}{\text{total hrs. basic data sample}}$  (Hrs. per aircraft)
- (2)  $(\text{Damage})_{\text{Flt.}} = \frac{\text{total damage basic data sample}}{\text{total flights basic data sample}}$  (Flights per aircraft)
- (3)  $(\text{Damage})_{\text{pU}} = \frac{\text{total damage basic data sample}}{\text{total pull-ups basic data sample}}$  (Pull-ups per aircraft)
- (4)  $(\text{Damage})_{\text{MA}} = \sum_{k=1}^{\ell} \sum_{i=1}^m \lambda_{ki} f_{ki}$

where:

$\lambda_{ki}$  = weighting factor = number of occurrences at each gross weight  $k$  and load level  $i$

$$f_{ki} = \sum_{j=1}^n p_{ij} d_{kij} =$$

predicted damage per occurrence at load factor level  $i$  and aircraft gross weight  $k$

$P_{ij}$  = probability of occurrence of Mach-altitude block  $j$  at load factor  $i$ .

$d_{kij}$  = damage at load factor level  $i$ , Mach-altitude block  $j$ , and gross weight  $k$ .

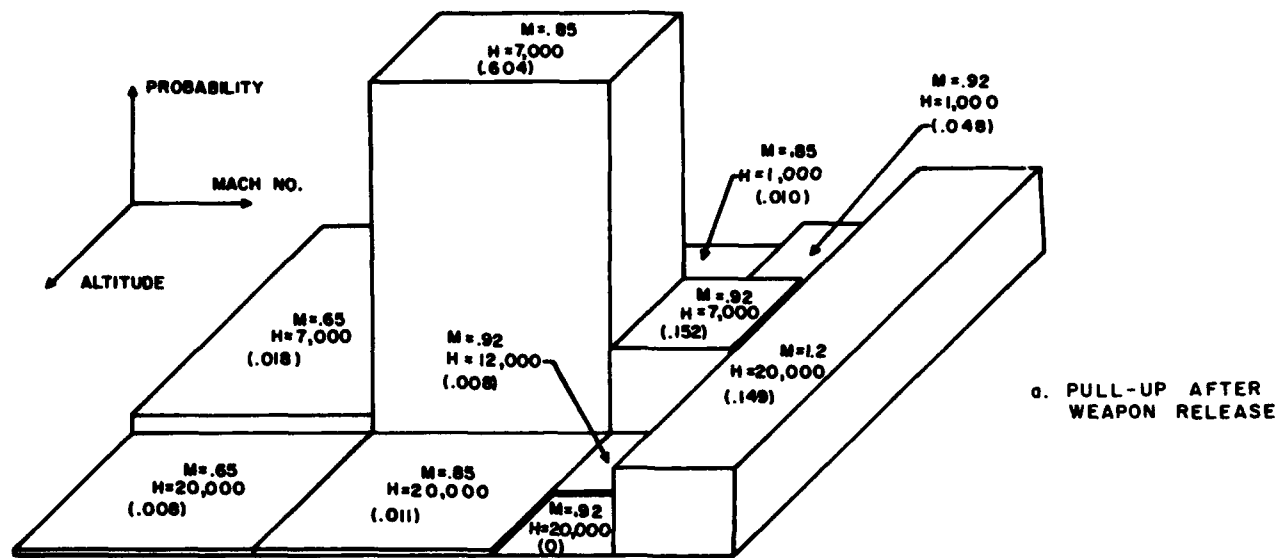
In general, the complexity of the calculations and the amount of information required increases in the order in which the models are listed. The first three models are self-explanatory; however, the fourth model warrants some additional comment.

The probability of occurrence,  $P_{ij}$ , is dependent on the classification of data included in the model. This model will be distributed differently depending on how the occurrences for inclusion are selected. Obviously, there is no point in including those occurrences in mission segments other than the maneuver mission segment since they cause no significant damage. In general, the occurrences during pull-up after weapon release were at a lower altitude and, higher Mach number than the other occurrences in the maneuver mission segment as shown in Figure 4. Also, the distribution with respect to load factor magnitude is quite different from these two groups as indicated in Figure 5. Therefore, the Mach-altitude probability model for use in damage prediction model (4) was based on only those occurrences which occurred during pull-up after weapon release.

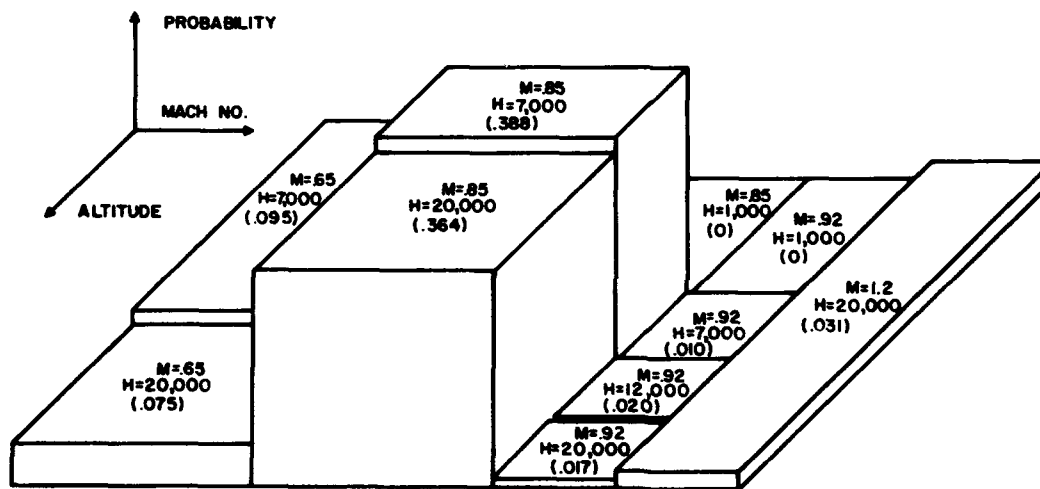
The results of applying the four damage prediction models to the F-105D data sample are presented in Table III. It should be noted that the numbers being compared in Table III. are not all based on the same data sample. The basic data sample for models (1) and (2) is the total data sample. The basic data sample for models (3) and (4) consists of the stores configuration three pull-up data (approximately 83 percent of the total pull-ups).

The fatigue damage analysis procedures described above for the F-105D are typical of what can be done for fighter type aircraft. Additional studies are reported in Reference 1 dealing with damage variation by airbase location, mission type, basic sample selection and other pertinent variables.

The relative merits of the various methods employed to predict fatigue damage to the F-105D aircraft are not easily defined. For the data sample analyzed, there was no significant difference in the ability of the various methods used. However, care must be exercised in generalizing these results to the total problem of evaluating the accumulated fatigue damage to the aircraft for all utilization. For example, the damage rate per hour would be quite sensitive to target location relative to the base. The damage rate per flight would be more sensitive to target type and the weapon delivery modes. The damage per pull-up would be sensitive to target topography and fortification as well as pilot reaction and time of day. This means that continuous flight load or strain recording would be necessary on a number of aircraft to provide a basis for establishing and revising damage rates or damage prediction models. This might be required on a squadron basis or an even finer breakdown, depending on the aircraft utilization.



a. PULL-UP AFTER WEAPON RELEASE



A/C 422  
294 OCCURRENCES  
ALL N<sub>2</sub>

b. NON-PULL-UP DATA

Figure 4. Comparison of Mach-Altitude Probability Plot for F-105D Aircraft for Pull-Up After Weapon Release with Non Pull-Up Maneuvers. Configuration 3 Data.

### DISCUSSION

The prediction of accumulated fatigue damage on a fighter aircraft presents a formidable problem. There are a multitude of parameters that affect the fatigue life. In the past, average values of damage per hour have been used to monitor the accumulated damage on each aircraft; however, the data presented here in the first column of Table III shows that this method may either overpredict or underpredict the damage by a factor of 2. Let us look at what causes these inaccuracies in the prediction. If one uses the average value of each parameter that determines the magnitude of the fatigue damage to calculate the average damage, he has assumed that during the life of the aircraft it will experience a distribution such that its average is the same as the average of the model. This may be true, but it does not insure a correct calculation unless all

of the parameters are dependent on each other. In the operation of fighter aircraft it was found that there was very little dependence of one parameter on another. For example, the altitude and Mach number are not a function of gross weight. The magnitude of the load factor is not a function of stores configuration, altitude, or gross weight. There was some dependence of load factor on Mach number but the scatter was rather large. When one uses the average value of damage, what he is really saying is that over the long term each aircraft will experience the same number of combinations of Mach number, altitude, weight, configuration, and load factor. This is a greater restriction than saying that each aircraft will experience the same spectrum of each parameter. Figure 6 is a plot of Mach-altitude probabilities of two of the F-105D aircraft and shows that these two aircraft did not have the same Mach-altitude spectrum. Figure 7 is a plot of the cumulative frequency of

TABLE III.

COMPARISON OF DAMAGE PREDICTION MODELS FOR F-105D AIRCRAFT

A/C	DAMAGE/HR.	DAMAGE/FLIGHT	DAMAGE/PULL-UP	M-A PREDICTED DAMAGE
	ACTUAL DAMAGE	ACTUAL DAMAGE	ACTUAL DAMAGE	ACTUAL DAMAGE
<b>Fuselage Station 509</b>				
130	.79	.77	.69	.91
160	1.13	1.17	1.61	2.07
240	2.50	2.20	1.82	1.12
357	1.10	.97	.83	.78
367	1.64	1.45	1.25	1.24
732	1.52	1.31	1.49	1.25
68	1.03	1.02	1.50	1.67
69	.64	.69	.72	.72
132	.49	.61	.74	.84
205	1.26	1.31	1.13	.87
378	.56	.60	.69	1.05
422	1.50	1.64	1.60	1.11
469	2.07	2.31	1.35	.84
$S^2 =$				
	.354	.311	.168	.148

<b>Fuselage Station 442</b>				
130	.64	.62	.66	.76
160	1.77	1.83	2.36	2.05
240	1.76	1.55	1.51	1.13
357	.76	.67	.68	.77
367	1.27	1.13	1.05	1.18
732	1.33	1.15	1.30	1.22
68	1.27	1.26	1.62	1.70
69	.68	.74	.76	.68
132	.57	.70	.81	.77
205	1.15	1.20	1.00	.82
378	.80	.85	.84	1.08
422	1.27	1.39	1.55	1.40
469	1.68	1.88	1.36	.86
$S^2 =$				
	.184	.183	.240	.168

$$S^2 = \frac{n \sum (x_i)^2 - (\sum x_i)^2}{n(n-1)}$$

load factor experience for five different F-5A aircraft and indicates that these aircraft did not have the same load factor spectrum. Figure 8 is a plot of the same data as Figure 7 but plotted in terms of percent design limit load factor. The difference in the relative position of the lines is due to the combinations of weight and store configuration that existed at the time the load factors were experienced.

The differences between Figures 7 and 8 point out the independent nature of the various parameters.

Efforts to predict the stress level encountered during operation of fighter aircraft are complicated by the wide latitude in usage. Loads encountered on a specific mission are affected by the pilot, the type and location of the target, enemy activity, visibility and weather conditions. Mission definition is dependent on base location, intensity of the conflict and military philosophy, and is subject to continuous redefinition. Therefore, it would seem that a fighter aircraft deployed in a combat zone could be expected to experience an unpredictable stress spectrum with regard to fatigue damage accumulation. Thus, in the authors' opinion, the use of statistical methods for predicting fatigue damage cannot rationally be expected to yield precise results for fighter aircraft. For purposes of accurately monitoring the fatigue damage to an individual fighter aircraft, it then becomes necessary to record data on each aircraft in the fleet.

FATIGUE MONITORING INSTRUMENTATION

A number of instruments and techniques have been proposed for the purpose of monitoring fatigue damage to structures. Three such systems are presented below. These systems are believed to be technically and economically feasible from the standpoint of fabrication, maintenance, reliability, and data reduction.

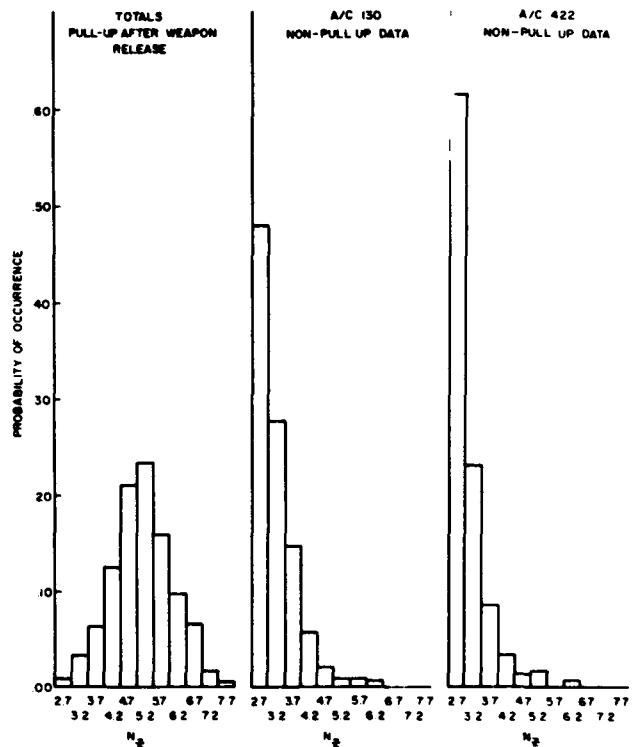


Figure 5. Distribution of Load Factors for Pull-Up and Non Pull-Up Data Samples for the F-105D Aircraft.

### Peak Counting Accelerometer

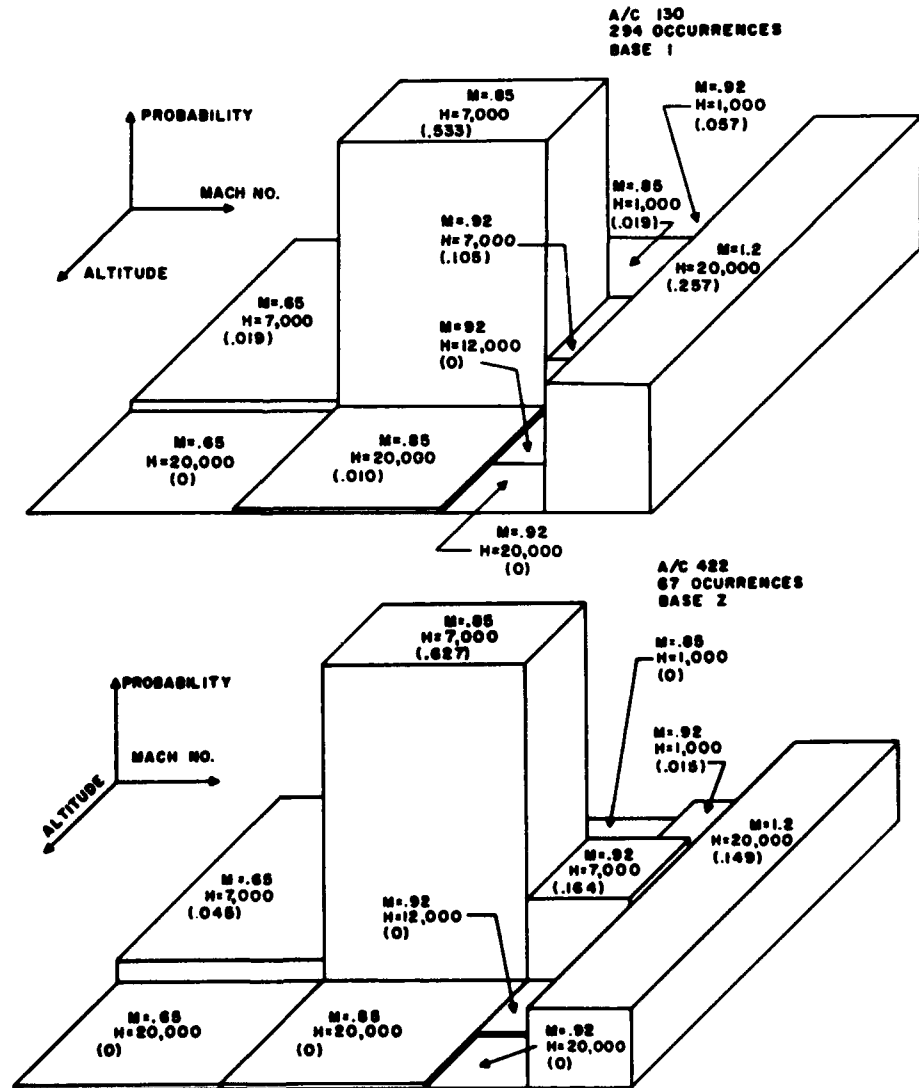
Peak counting accelerometers have been used by the British aircraft industry and the United States Navy for some time. The early installations recorded in registers the number of times that a given load factor was equaled or exceeded. These counts were independent of flight condition or aircraft configuration. Recently a new concept in counting accelerometers (References 3 and 4) was introduced for use with the F-111 aircraft. This new counting accelerometer separated the load factors by certain combinations of Mach number and wing sweep angle. This concept allows the calculation of different stresses for the same load factor level, depending on the aircraft's environment and configuration. The following presentation is a discussion of the design of a discriminating counting accelerometer.

A discriminating counting accelerometer can be visualized as an onboard data processing system. Its purpose is to provide a low-cost reliable system for accumulating

load factor data and correlating it to other variables. Historically, in performing a fatigue analysis of an aircraft fleet, the following calculations are performed: (1) simultaneous time history recordings of load factor, Mach number, and altitude are obtained; (2) these parameters are then blocked into class intervals and a report is prepared that presents the number of times that the load factor peak reached a certain value for each combination of class intervals of Mach number and altitude, along with other parameters such as weight and configuration; and (3) from the calculated curves or tables of stress peak counts, and the S-N data for a point on the aircraft, the fatigue damage is calculated.

An onboard counting accelerometer can be designed so that it has a series of accumulating registers which count the number of times that the load factor exceeds a certain value, with all the other parameters constant. This, in effect, is then a stress peak count. The principal disadvantage of this system is the large number of storage registers required to sort the load factor data by

Figure 6. Comparison of Mach-Altitude Probability Plots for Two F-105D Aircraft. Configuration 3 Pull-up Data.



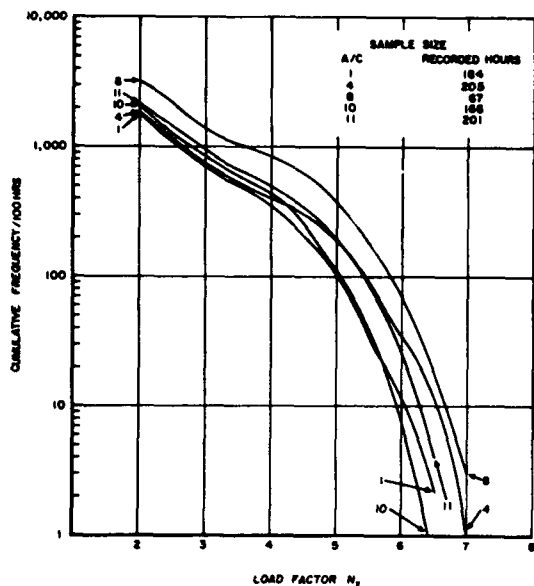


Figure 7. Cumulative Frequency Distribution of Load Factors for 5 Different F5A Aircraft.

combinations of Mach number, altitude, weight, and configuration. In the illustrated system (Figure 9), provision is made for sorting the g-data into three sub groups according to pre-defined conditions of other variables such as weight or configurations. The components required for this unit are conventional and commercially available; and the circuitry, namely the latching, sorting, and dropout circuitry, is well developed and reliable. The cost of the system hinges primarily on the choice of counters, which runs from \$20 per unit to \$70 per unit. In high quantity (10,000 counters) the price quoted by one manufacturer drops from \$70 to \$10 per unit.

The counting accelerometer operates as follows: as the acceleration level is increased from the normal 1-g level, contact is made by the acceleration transducer's wiper to successively increasing level contactors. Such contact, even if only momentary, brings the live supply voltage from the wiper to a given contact line and causes the latching relay for that level to momentarily operate. Operation of the latching relay closes a contact on the relay which connects the contact line to the live supply voltage by a route other than the accelerometer wiper. (This other route, for reset purposes, passes through the normally closed contacts of relay R.) Once this alternate route is established the latching relay is "latched on" and the contact line is live even after the accelerometer wiper leaves it. All levels operate in this manner.

To sort g occurrences with respect to weight or configuration, the five lines whether energized or not are routed to three counter banks through three banks of

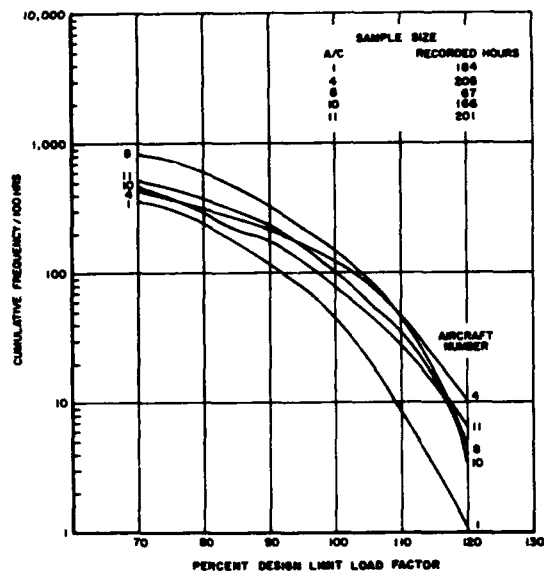


Figure 8. Cumulative Frequency Distribution of PDLFF for 5 Different F5A Aircraft.

ganged switches (three 5-pole relays). These operate from external commands shown here as configuration command buttons. The buttons would be replaced by two or three logic relays once the desired sorting function is established.

Upon return to the normal g-level or any established threshold, the reset contact is touched by the wiper contact, causing the reset relay R to de-energize all five latching relays, and re-establish the circuits to receive the next g-level signal.

Vibration and/or oscillation of the accelerometer are not counted, as neither are cycles in the g value which do not increase from the normal g level position or the established threshold level. This is accomplished by the latching relay mechanism, which holds any given tripped counter in the energized position until the reset contact is touched and relay R de-energizes all five latching relays. When a counter is held energized it is effectively locked, since it is during dropout of the counter solenoid that ratchet action occurs to permit counter advance upon the next energizing pulse. The counters, in effect, store the cumulative frequency of g levels equal to or greater than the level for that register.

#### Peak Counting Electro-Mechanical Optical Strain Transducer

The use of a peak counting accelerometer would still require calculations of the response of the aircraft structure to convert load factor magnitudes to stresses at various points on the aircraft. A more direct approach would be to record the number of times that a given strain

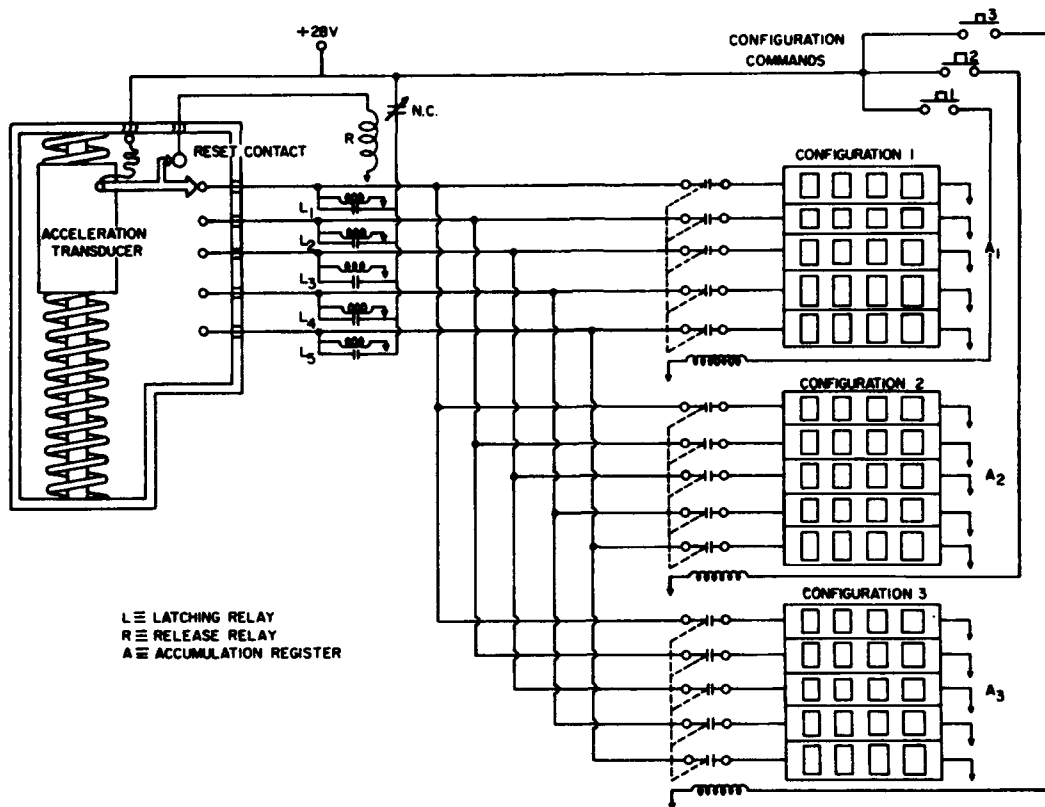


Figure 9. Schematic Diagram of Counting Accelerometer System.

level was equaled or exceeded at a particular point on the aircraft structure. If the exceedance spectrum of the stresses at a point could be known, it would not be necessary to know anything about the aircraft configuration, weight, or flight environment provided a constant 1-g trim stress could be assumed.

The components of a system to provide such knowledge can be grouped into three areas: (1) the accumulating registers; (2) the mechanical or electronic logic to sort the signal levels into bands; and (3) the strain transducer. The accumulating registers would be the same for all of the systems but the banding mechanisms would be dependent on the type of strain transducer.

One possible type of system would use a conventional dial indicator as the strain transducer with the indicating hand replaced by a drum with a small aperture and a light source inside the drum. Spaced around the outside of the drum would be photocells that would sense the amount of rotation of the drum, which would be proportional to the strain. Each photocell would be connected to a storage register so that every time a certain magnitude of strain was

equaled, the counter would index one count. The wiring diagram of the system is shown in Figure 10. The mechanism of the dial indicator is a rack and pinion with one set of step-up gears, so that for a rack travel of 0.0001 inches the dial rotates  $1.8^\circ$ . For a two-inch gage length, a stress of 1000 psi in aluminum would therefore cause a rotation of  $3.6^\circ$  and 36,000 psi would produce  $129.6^\circ$  of rotation.

If five class intervals were used to represent the stress exceedance curve from 12,000 to 36,000 psi, each class interval would be represented by  $21.6^\circ$  of rotation. This sensitivity would give a good resolution for positioning the photocells to distinguish one class interval from another. Assuming that only a peak count of the strains would be necessary, one additional photocell would be located at a threshold level. The strain level would have to decrease below this threshold level before a second peak could be recorded.

One strain channel of such a system is shown on the diagram. As strain increases the aperture slit rotates to illuminate successive photo-resistive cells which then ener-



gize their corresponding relay  $K_1$  —  $K_5$ . Energizing such a relay  $K_1$  —  $K_5$  closes the contact on that relay which brings current to the corresponding counter. This contact also brings an alternate current to the relay over a path other than through the photocell. This alternate current remains after the photocell is no longer illuminated and serves to latch the relay. This current, however, also passes through the normally closed contact of the reset relay  $K_0$  and de-energizes any and all given relays  $K_1$  —  $K_5$ , which had been latched. Reset occurs below the level of any desired strain level and hence there is never any conflict of the reset with the energizing and latching of any relay  $K_1$  —  $K_5$ . Of course, each strain level could be provided with its own reset level with the addition of four more relays. These new reset levels could be placed anywhere other than coincident with the level of the circuit that they are to reset.

There are several advantages to this type of instrument over a load factor recorder. The first and most important is that the accuracy of the fatigue analysis is not dependent on any usage parameters of the aircraft. No pilot log is required. The storage registers do not have to be read after each flight, but instead perhaps only once a month. The fatigue analysis performed with the strain data is independent of whether the loading was symmetric or asymmetric, provided the location of the sensor is such that the transfer factor is a constant for all types of loadings.

At the present time there are a few possible shortcomings of this system, mainly related to the strain transducer. The fatigue life and airworthiness of the dial indicator is unknown; however, any deficiencies should be minor and correctable with a minor effort. There may be some difficulties with transient temperature changes which could cause a differential thermal expansion between the aircraft structure and the dial indicator push rod. Another

consideration is that one complete system would be required for each fatigue critical location on the structure.

The remaining components of the system employ conventional and commercially available counters and relays. Cost of one channel would depend primarily on the price of the counters and the results of the dial indicator tests. The counters could run as high as \$70 each and the latching relays up to \$15 each. However, in large quantity these costs are expected to be more like \$10 and \$3, respectively.

### Resistance Strain Gage

Another method of monitoring the strain cycles is to use the analog output signal of a conventional strain gage bridge to operate relays at different signal levels. A circuit which would compare the output signal to reference levels is shown in Figure 11, along with a complete circuit diagram of the system.

The counting electrical resistive strain gage is essentially a system which blocks analog strain signals into five preset digital class intervals, and then registers the occurrence of each strain level into a counter as it occurs. The proposed system employs a resistive strain gage whose output signal is amplified and thus scaled up by a stable gain but low cost closed loop operational amplifier. The output of this amplifier is compared to a staircase of five voltage levels which are created by an appropriate stack of zener diodes. An alternative voltage staircase could be obtained by use of a resistive divider string. When the output of the amplifier exceeds the voltage level of a given tap on the staircase, the rectifier diode on that branch would become conductive and current would pass through the corresponding relay. A counter could be connected in parallel with this relay, as shown, or energized through a second

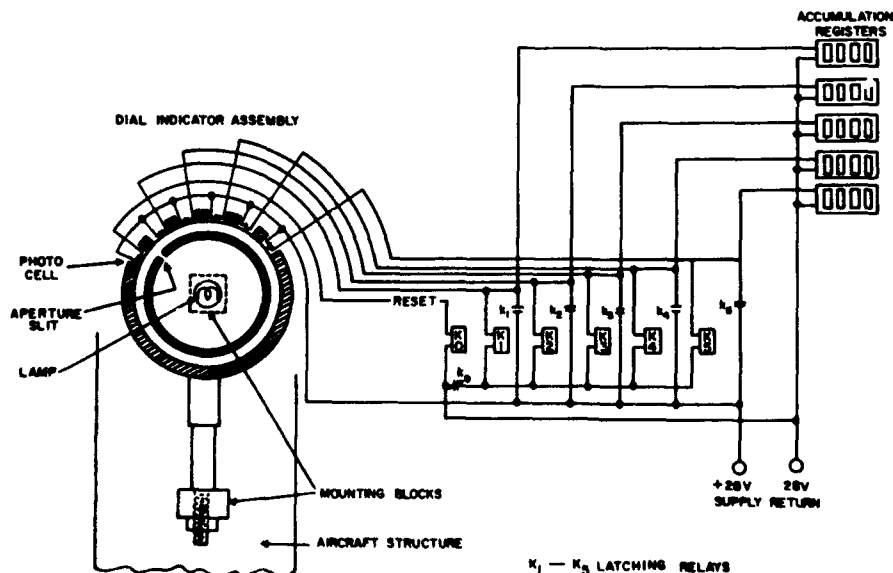
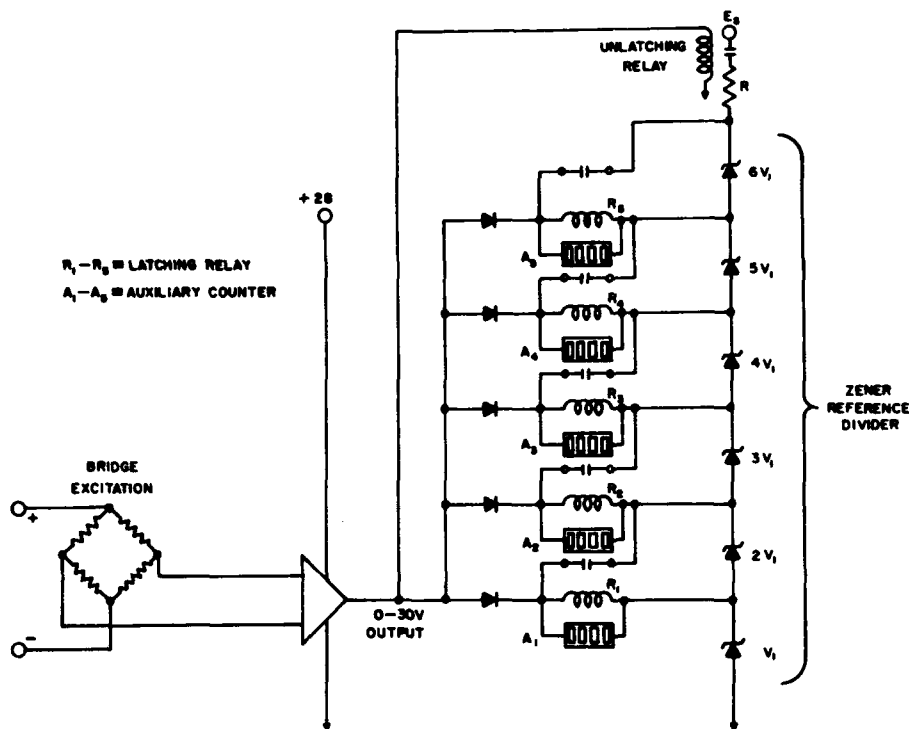


Figure 10. Schematic Diagram of Electro-Mechanical-Optical Peak Strain Counting System.

Figure 11. Schematic Diagram of Resistance Strain Counting System.



contact on the relay (not shown) for more reliability if required.

Energizing any given relay also closes the contact on that relay which connects the relay to a current from the staircase string. This latches it and holds it on, even if the amplifier output level changes to a lower level. When the output level drops to the reset level, the reset relay, which has contacts that are normally open, de-energizes and resets all latched relays. The reset relay is connected to the amplifier output and de-energizes only at near-zero levels of amplifier output and hence at near zero strain levels. This threshold level would be set near the 1-g trim stress level.

The components suggested in this system require some design considerations and in this regard the system is not as straightforward as an all-relay or electro-mechanical system. However, a proper design is reasonably certain, and once designed and tested, should be in every respect as reliable as an all electro-mechanical system.

### CONCLUSIONS

In view of the results presented here and in References 1 and 2, it appears that there are three alternatives available for monitoring the fatigue damage to fighter aircraft.

1. The first alternative would be the use of per hour, per flight, or per pull-up calculations. This would require instrumentation of a portion of the fleet to provide damage rates for the remainder of the fleet. Considering

the diverse utilization of fighter aircraft, this method has some obvious shortcomings as discussed previously and the confidence in the predicted damage, particularly on an aircraft serial number basis, would be low.

2. A second alternative would be to install a peak counting accelerometer on each aircraft, together with the necessary instrumentation and logic circuitry for determining Mach number, altitude, gross weight, and major configuration at the time of each load factor occurrence. The load factor occurrences would be segregated by these parameters and recorded in storage registers. The number of storage registers would be equal to the product of the number of bands required for each of the parameters. If the data were categorized by the five major configurations, 11 load factor levels, 6 gross weights, and the Mach-altitude breakdown defined for the F-105D data reduction program, a total of 3,310 storage registers would be required. For the SEA data sample analyzed during this study, the number of storage registers could be reduced to 396 with little loss in accuracy. This number could be pared even further by accepting some sacrifice in accuracy. For different usage or different aircraft, the number of registers might be reduced or increased. For example, the fatigue damage experienced by the F-5A for the data sample reported in Reference 1 could be adequately predicted using only 15 storage registers.

Although this method of monitoring fatigue damage eliminates the cost of recording and processing VGH time history data, it still requires a fairly sophisticated instrumentation and recording system. Also, while it is possible to eliminate or consolidate variables and thus reduce the

number of storage registers for a given data sample, this can only be done after an analysis of the VGH data.

3. The third alternative would be to eliminate the necessity for knowing parameters such as gross weight, configuration, airspeed, altitude, and load factor. This could be accomplished by using a strain amplitude cycle counter. The frequency at which selected strain levels were equaled

or exceeded could be sensed and recorded in accumulating storage registers. This strain exceedance data could then be used directly with an S-N curve to determine the cumulative damage at a fatigue critical location. Since only the magnitude of the strain peaks would be measured, a constant mean stress could be assumed or the mean stress could be expressed as a function of the aircraft gross weight and configuration. However, this added breakdown of the peaks would require additional storage registers.

#### REFERENCES

1. G.J. Roth and B.S. West, *Parametric Fatigue Analysis of USAF Fighter Aircraft*, AFFDL-TR-69-85, Air Force Flight Dynamics Laboratory, Wright-Patterson AFB, Ohio (1969).
2. G.J. Roth, J.P. Ryan, and J.C. Slicmers, *Parametric Fatigue Analysis of USAF Aircraft*, AFFDL-TR-67-89, Air Force Flight Dynamics Laboratory, Wright-Patterson AFB, Ohio (1967).
3. J.R. Sturgeon, *Fatigue Load Meters*, Mechanism Limited, Croydon, England.
4. *Maintenance Manual No. 61, Fatigue Recording System Type 25*, Mechanism Limited, Croydon, England.

## F-111 SERVICE USAGE RECORDER PROGRAM

by

Walter P. Dunn

Aeronautical Systems Division  
Wright-Patterson AFB, Ohio

### INTRODUCTION

During the early development stages of the F-111, a program to use airborne recorders on operational aircraft was established. The recorder program was designed to interface with and support the airplane structural fatigue program. Details of the counting accelerometer program were also being developed. It became evident that other structures oriented information related to airplane usage was needed. These other areas included strength considerations and actuator usage, in particular the actuator used to sweep the wing. These programs and aspects have been integrated together to yield the more general F-111 service usage recorder program, wherein the airborne recorder program is the more complex part.

Several organizations and companies within the Air Force and industry have been involved. Aeronautical Systems Division (ASD), Tactical Air Command (TAC), Strategic Air Command, (SAC) and Air Force Logistic Command (AFLC) organizations provide the government backbone for this effort. General Dynamics/Ft. Worth Div., Conrac Corp./ two divisions, Whittaker Corp./Dynasciences Div., General Time Corp., and other vendors have provided the hardware for the program. Since the program was considered to be a passive program, i.e. collection of usage data for later analysis, each organization strived to minimize the impact on the user of the airplane. Parameters were selected to yield information on such things as gross weight, configuration, etc. Equipment reliability was stressed, and a no flight-line maintenance goal other than removal and replacement of Line Replaceable Units (LRU's) was established. General Dynamics will ultimately use various data in the program to determine airplane fatigue life used and the number of operational flight hours remaining per airplane.

As the program has evolved two manufacturers of airborne recorder equipment have resulted. Conrac has provided an airborne recorder that operates in the time compression mode, i.e., the parameter data is recorded only when the parameter crosses from one data interval to another. Dynasciences is providing an airborne recorder which operates in the continuous mode, i.e., the parameter data is sampled and recorded at a fixed rate. Regarding the counting accelerometers, Conrac is providing a six load factor level device which contains an accelerometer transducer and two read-out indicators. One indicator is provided for the forward wing sweep usage of the airplane and one for the aft wing sweep usage. A second procurement is under way with General Time Corp. for additional counting

accelerometers which will have six load factor levels, three of which can be easily changed, and each read-out indicator will contain an elapsed time indicator. Pre-punched computer cards will be used at the flight-line level to provide auxiliary data and the counting accelerometer data as well as information to supplement the airborne recorder data.

The F-111 Systems Program Office (SPO) is the management focal point of the program and initially, will act as the USAF data reduction center. Other Air Force organizations are vitally involved in equipment procurement, implementation, maintenance, repair, data reduction, and other monitoring tasks. The program has evolved with the airplane, and is aimed at providing specific answers to particular problems. Those airframe components and areas shown to be significant strength and fatigue control points by analyses and tests will be individually monitored to ascertain the airplane service usage and flight hours remaining.

### BASIC PROGRAM

Aside from the program development and hardware procurement the F-111 service usage recorder program relies on four organizations interfacing and working together to provide the United States Air Force with positive feedback regarding the fatigue life and usage status of the F-111 airplanes. (See Fig. 1.) After the equipment has been installed in the airplanes the program functions basically as follows. The airplanes will be located at various bases and are being equipped with counting accelerometers and airborne recorders. All of the airplanes will have counting accelerometers, and approximately 20% will have airborne signal data recorders. Either recorder (Conrac or Dynascience) can be used in the airplane with a simple installation (tray) change. Magazines are used on both recorders which are transcribed onto computer magnetic tapes using the appropriate ground signal data converter. The transcribed magnetic tape is typical computer tape, 1.5 mil, 1/2-inch wide on 10 inch diameter reels. These tapes are then forwarded to the USAF data reduction center. The counting accelerometer data and general aircraft usage data will be forwarded to the data reduction center via use of prepunched computer cards. The data related thereon will consist of information on armament carried, airplane identification data, base, type of mission, and counting accelerometer data. The punched card data will also be used in support of reducing the data on the transcribed magnetic tapes.

Since it was desired to minimize the support impact on

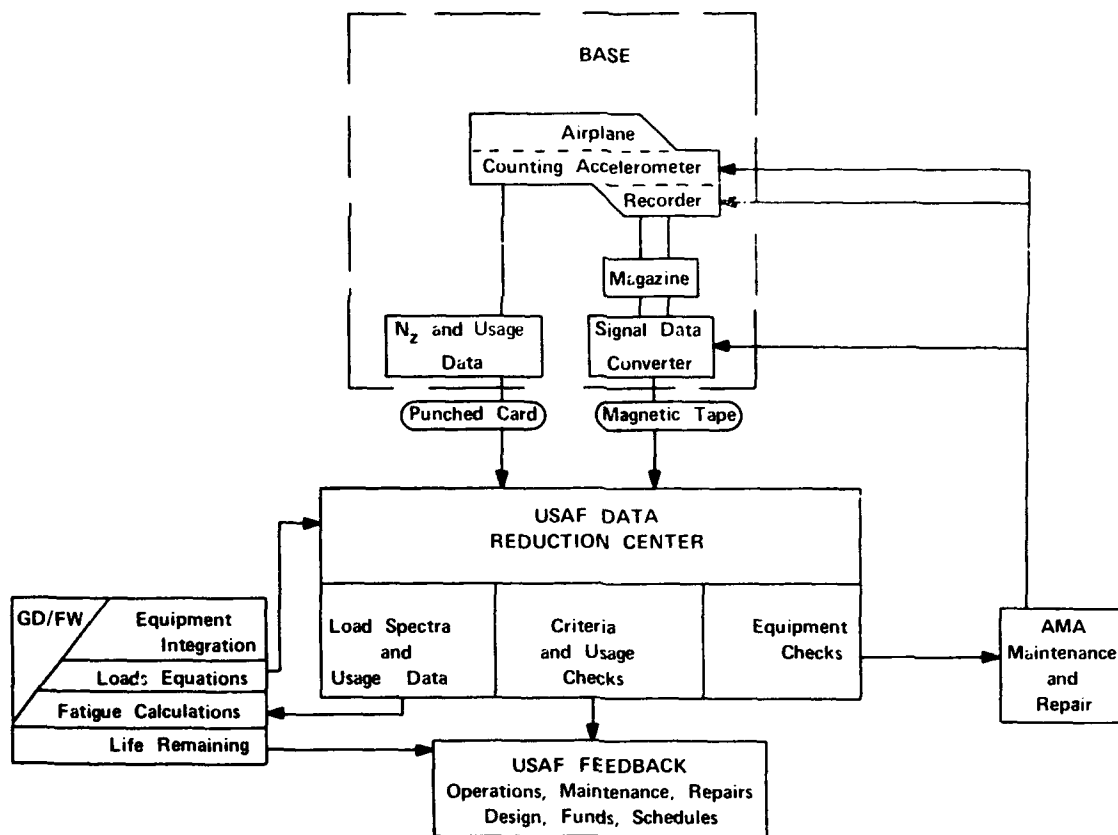


Figure 1. F-111 Service Usage Recorder Program.

the using command regarding the counting accelerometer and recorder installations, the program and equipment were established to minimize flight line maintenance. To accomplish this it was necessary to develop reliable equipment and to select parameters that would still provide the basic information even if malfunctions and some loss of data occurred. Therefore there is no routine flight-line maintenance regarding checkout and testing of the equipment. If the data reduction center determines that an unacceptable amount of data is being lost a decision will be made to remove and replace a LRU component or to request an Air Materiel Area (AMA) maintenance team to visit the base and correct the problem. This results in base personnel being required to perform a minimum number of tasks. One includes removal of the magazine from the airplane. The second involves transcription of the magazine to computer tape using the signal data converter. A third task involves marking the pre-punched computer cards with the appropriate data. The fourth and last task, as indicated above, is that of removal and replacement of LRU on an on-call basis.

The USAF data reduction center function, currently being performed by the F-111 SPO, is that of intermediate data reduction. Three basic data reduction functions are involved. The first is that of determining general airplane usage, mission load factor spectra, etc. The second involves determination of key peak load spectra and associated aircraft parametric data. The third function involves checking the equipment to assure that it is still functioning properly and reliably.

The load spectra data and aircraft usage data is forwarded to General Dynamics/Ft. Worth for inclusion in fatigue calculations. Those portions of the general aircraft usage information which are significant will be fed back into the USAF System to improve design criteria and etc. Results of the equipment checks will be reviewed to determine if organizational level personnel should remove particular LRU components or if the AMA maintenance teams should take action.

The General Dynamics/Ft. Worth Div. (GD/FW) is developing load equations for use by the USAF data reduction center in calculating key airplane locations loads spectra. Such equations will be used to compute horizontal tail loads, vertical tail loads, and wing pivot loads. The USAF data reduction center will determine the peak loads using these loads equations and other associated recorded data. These load data will be forwarded to General Dynamics for fatigue calculation purposes. Each critical fatigue location or component on the airplane will be evaluated based on the data available at General Dynamics/Ft. Worth and the data received from the F-111 service usage recorder program. The cumulative fatigue damage will be determined and the number of airplane operational flight hours will be calculated. The results will be reflected in the final fatigue analysis and also in periodic reports of the service life remaining for each individual airplane.

The remaining portion of the program involves maintenance and repair of the recorders and counting accelerometers.

PARAMETER	SAMPLES PER SECOND	SIGNAL SOURCE	ADDED FOR PROGRAM
1. Mach number	1	CADC	Modified
2. Pressure attitude	1	CADC	
3. Outside air temperature	1	Total temperature indicator	
4. Wing position	1	Wing sweep transmitter	
5. Acceleration, Z axis	30	} Three axis linear accelerometer	X
6. Acceleration, Y axis	15		
7. Acceleration, X axis	10		
8. Roll rate	15	} Flight control sensor set	
9. Yaw rate	15		
10. Pitch rate	15		
11. Flap position	1	Flap position transmitter	X
12. Landing gear position	1	From landing gear switch	
13. Sink Speed	5	Radar vertical velocity sensor	
14. LH horizontal tail position	15	LH horizontal tail transmitter	
15. RH horizontal tail position	15	RH horizontal tail transmitter	
16. Rudder position	15	Rudder transmitter	
17. Fuel flow, right engine	1	RH engine fuel flow transmitter	
18. Fuel flow, left engine	1	LH engine fuel flow transmitter	
19. True angle of attack	5	CADC	X
20. Right outboard spoiler position	30	RH spoiler transmitter	
21. Left outboard spoiler position	30	LH spoiler transmitter	
22. Left main landing gear oleo pressure	1	Pressure transducer	
23. Right main landing gear oleo pressure	1	Pressure transducer	X
24. Nose landing gear oleo pressure	15	Pressure transducer	X

Figure 2. F-111 Recorded Parameters.

ometer equipment. Once the data reduction center has flagged a malfunction and the base personnel have returned to the depot a defective LRU component, the depot level personnel become involved. Repair and calibration of defective components will be the depot's prime responsibility. Calibration and maintenance of the equipment after installation in the airplane will be secondary due to its reliability and design features. The counting accelerometers are ruggedized equipment which hold their calibration over a wide range of environment and a long period of time. The recorders are designed such that the electrical calibration plus the initial conditions of the parameters at the beginning of each flight result in the recorder being calibrated prior to each flight. Since most of the recorder parameter sensors are part of the prime airplane system they are maintained and calibrated by the flightline personnel during routine airplane maintenance.

### PARAMETERS

The parameters currently being recorded on the airborne recorders are shown in Fig. 2, "F-111 Recorded Parameters". The number of times the parameter is sampled per second is shown, as is the signal source and whether or not the sensor was added for the recorder program. Most of the available signal sources come from or are involved with the airplane flight control system.

It is apparent that the parameters can be grouped into sets for different purposes. One such grouping is used to de-

termine the airplane configuration, e.g. wing position, flap position, and landing gear position provide the basic information needed to determine the airplane's general configuration. Other groupings are made to monitor the airplane's mission, its control surface deflections, landing gear loads, gross weight and approximate cg, landing impact conditions, airframes loads, ground-operating and handling loads, and engine related conditions of thrust, incremental gross weight and engine out conditions.

In general the frequency response or samples per second required for each parameter were based on its use in one or more of the above groupings. However, the two spoiler position parameters were left at a relatively high frequency response to provide data positions if additional parameters need to be recorded in the future. The parameters selected reflect the basic design of the airplane, i.e. clean airplane usage; however the program parameters can be updated to include those necessary to cover store usage and other usage if desired.

Mach number was chosen as the speed parameter so that the results would be directly compatible with design and fatigue calculations. Pressure altitude and outside air temperature are needed to determine the flight region the airplane has been operating in. The three axes of acceleration and angular rates at the airplane cg provide a definition of the airplane's rigid body relative motion. Wing, flap, and landing gear positions data are useful in defining the airplane's configuration. Control surface deflections are provided by the left and right horizontal tail

COUNTER	CONRAC FOR F-111 A & E's g's	IN PROCUREMENT FOR F-111 D, F & FB's ~g's		
		Low	Nominal	High
1	0.5	.....	0.3	.....
2	3.0	.....	2.5	.....
3	3.5	-0.5	3.0	5.0
4	5.0	.....	4.0	.....
5	6.5	2.0	5.5	6.5
6	8.0	1.7	7.0	8.0
Pos. Reset	1.3	.....	1.3	3.5
Neg. Reset	0.7	.....	0.7	.....

Figure 3. F-111 Counting Accelerometer Load Factor Thresholds.

position indicators, the rudder position indicator and the left and right outboard spoiler position indicators. True angle of attack was added to the list to round out the group of parameters needed to predict the prime aerodynamic loadings on the airplane. To predict ground induced loads and ground handling data four additional parameters were added, i.e. three landing gear oleo pressure transducers and a landing vertical sink speed indicator.

The above parameters will be recorded on approximately 20% of the airplanes. As such, very detailed usage of the airplane

can be determined. However, detailed checks on a limited number of airplanes provide only a baseline for the fleet and do not provide a measure of the fatigue damage done on an individual airplane basis. Therefore this data must be augmented with selected data from each individual airplane. This is accomplished through the use of counting accelerometers and prepunched computer cards.

The counting accelerometers provide information on the vertical load factor exceedences of the airplane during operational usage. Six load factor levels were selected as being necessary to represent the  $N_z$  exceedence spectra. One level is used for negative maneuvers and five levels are used for positive maneuvers. The load factor levels for the Conrac device and also that device in procurement are shown in Fig. 3, "F-111 Counting Accelerometer Load Factor Thresholds". The load factor thresholds are given in terms of maneuver load factors with 1g load factor being level flight. The Conrac positive maneuver load factor reset level is 1.3g's and the negative maneuver reset load factor level is 0.7g's. Additional counting accelerometer devices are in procurement and will be used on the FB as well as the fighter aircraft. Since the additional counting accelerometers are to be used on both the FB and the fighter model of the F-111 it is apparent that the load factor levels must be different to accommodate the load factor range of the particular airplane. Therefore the device has a nominal load factor level setting and a choice of a low or high setting on three load factor levels. Jumper bars will be used within the accelerometer transducer to accomplish the load factor level change. Further, the low to nominal and high load factor level values were chosen so that four levels could be symmetric about the 1g level flight value.

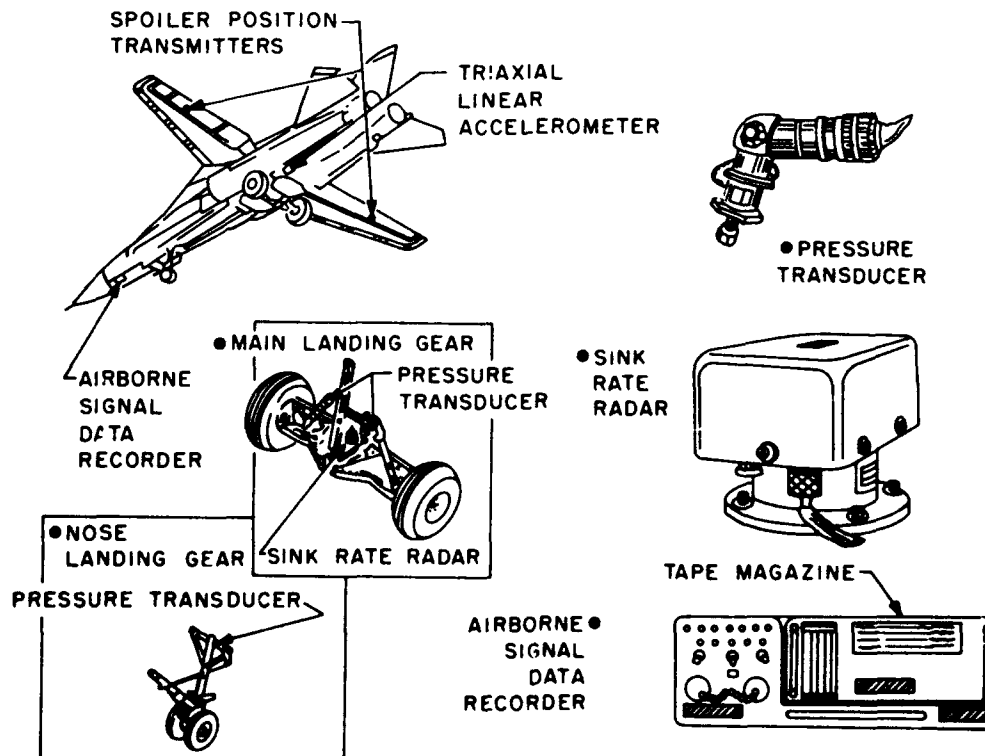
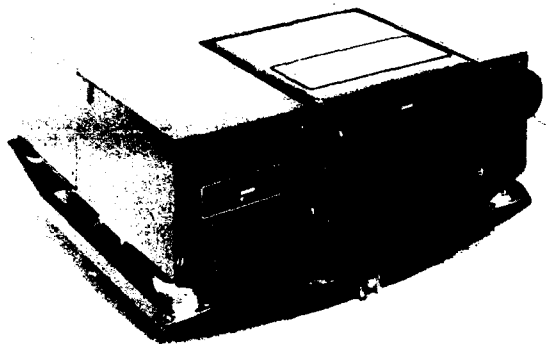


Figure 4. Location of Recorder and Added Sensors.



**Figure 5. Conrac Corp. Airborne Signal Data Recorder.**

Two levels below 1g and two levels above 1g provide the potential capability of being able to evaluate the symmetry of negative and positive maneuvers. The positive reset threshold level will also be changeable to allow for evaluation of high load factor secondary peaks. This versatility will provide the means of monitoring aircraft usage as necessary to support the fatigue damage and safe service life remaining calculations. Each counting accelerometer will have two six load factor level indicators. Only one indicator is operatable at a time depending on the wing sweep position and since the number of exceedences per flight hours is significant the additional accelerometer devices will incorporate an elapsed time indicator on each indicator.

#### **EQUIPMENT**

Placement of equipment in the airplane follows the general logical rules of placing the sensor where the parameter action is, and placing the recording device in the appropriate environment in the airplane. (See Fig. 4). The airborne signal

data recorder with magazine is located in the nose of the airplane in the right-hand forward electronics bay. When the equipment bay door is opened the tape remaining in the magazine can be easily determined. However, to facilitate flight-line schedules, the magazine will be removed and transcribed on a periodic basis rather than on a tape remaining basis which would require a closer scrutiny of the use of the tape. The oleo pressure transducers are integral with the oleo servicing connection and hence measure only the air curve pressures. The landing sink rate radar is mounted on the main landing gear and provides a direct read-out of the airplane vertical closing velocity with the ground prior to landing impact. The spoiler position transmitters are added to the outboard spoilers on each wing. The tri-axial linear accelerometer is mounted in the main landing gear wheel well as close to the nominal cg of the airplane as practical. The remaining parameter sensors are available on the airplane and only electrical taps are made into the devices.

Each of the three pieces of the counting accelerometer are mounted in the main landing gear wheel well. The two indicators are mounted on the side of the main landing gear wheel area in a position where they can be easily read when the airplane is parked on the ramp. The acceleration transducer is mounted in the center of the wheel well area on one of the main bulkheads therein.

The Conrac Corp. airborne signal data recorder is shown in Fig. 5. The associated signal data converter used to transcribe the data on the airborne magazine to computer tape is shown in Fig. 6. The Conrac recorder is approximately six inches high including shock mounts, 15 inches wide and 13 inches deep, and weighs approximately 40 pounds. The airborne magazine is hermetically sealed and contains the motor, magnetic tape, tape heads and associated circuitry. It also contains a percent of tape remaining and a three digit elapsed time indicator. Data from the Conrac recorder is placed on seven-track computer tape, six bits plus odd parity, by the signal data converter. The packing density is 200 BPI, and the record length is 192 characters long. A set of three characters contain the follow-

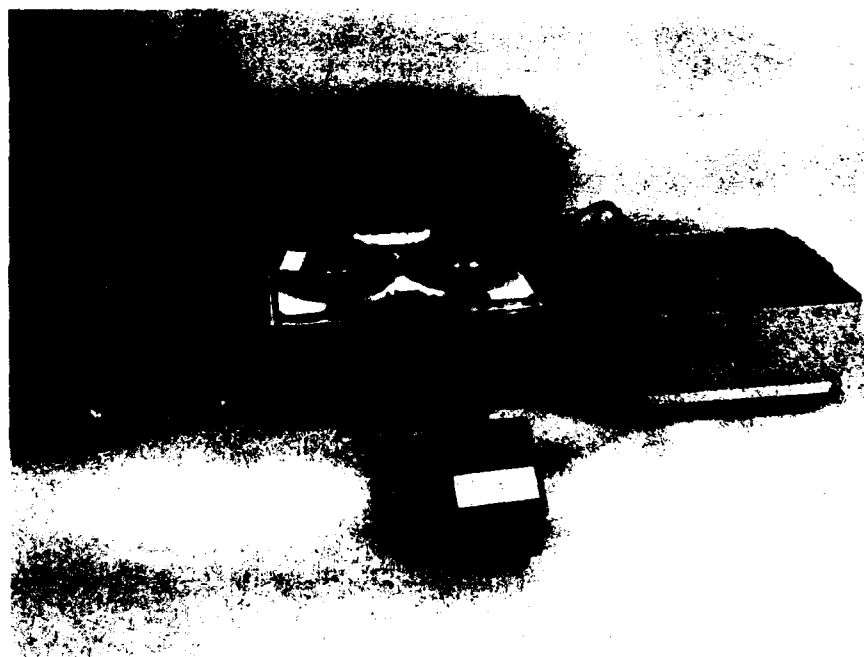


**Figure 6. Signal Data Converter Used with Conrac Recorder.**



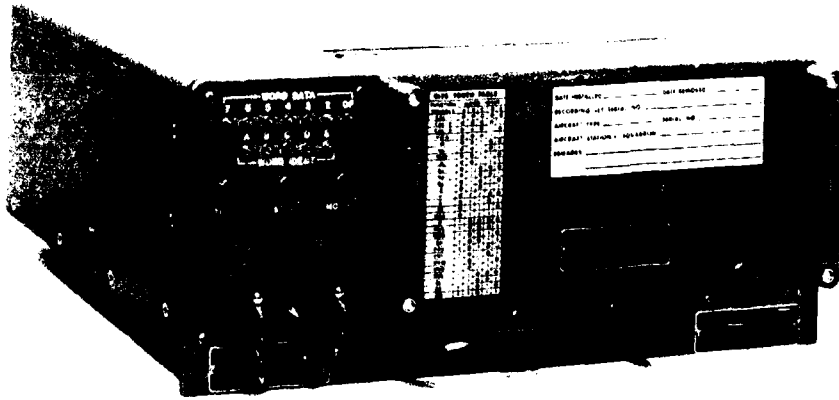


Figure 7. Dynasciences Airborne Signal Data Recorder.

ing information: Five bits are used as channel identification, six bits are used to reference time within a record, and seven bits are used to record the value of the parameter. This totals 18 bits or three characters. The last three characters of a record are used to record the record number and to identify the type of record. The record count is reinitialized to zero at the beginning of a flight. The different types of record are as follows, normal record, beginning of flight record, self test record, and acceleration exceedence record (three per flight are allowed). A normal record contains sixty-three parameter measurements plus record identification information. The sixty-three measurements have no specified order because of the comparison circuits used in the recorder. Even though each parameter is sampled a fixed number of times per second, each measurement is compared with the parameter value stored from a previous measurement and if it has not changed by a given amount the new measurement is not retained in the buffer memory. Sixty-three measurements comprise a full buffer memory of data which is recorded on the airborne magazine magnetic tape. The beginning of flight record allows for recorder warm-up and clearing of the buffer memory. The self test record provides information on the electrical calibration of the recorder at zero and full-scale for each parameter. The acceleration exceedence record is of value when a crash or break-up of the airplane is imminent, which is indicated by a sharp full-scale acceleration. This automatically places the available measurements in the buffer memory onto the airborne magazine magnetic tape. The Conrac recorder has built in test circuits to test the recording set separately from the remainder of the installation. A "go/no go" indication is provided on the front of the recorder which is also recorded on the magnetic tape.

The Dynasciences airborne signal data recorder is shown in Fig. 7, and the associated signal data converter for transcribing the airborne magazine recorded data onto computer magnetic tape is shown in Fig. 8. The Dynasciences recorder is approximately six inches high, seventeen inches wide and thirteen inches deep and is hard mounted in the airplane, and weighs approximately forty pounds. The Dynasciences airborne magazine is gasket sealed with the tape and heads mounted in the magazine and drive motors located in the recorder with mechanical

and electrical coupling between the two. Tape remaining is visible thru a window located in the airborne magazine. The recorder multiplexer samples each parameter at a fixed rate and records the value on the magnetic tape at six bits plus odd parity for each measurement. At the beginning of each flight, subsequent to recorder warm-up, electrical calibration of 10 percent, 50 percent and 90 percent full scale for each parameter is recorded. The airborne measurements are recorded continuously on the airborne magazine magnetic tape. The signal data converter is used to transcribe the data onto seven-track computer tape. The computer tape packing density is 800 BPI, and each record is 2,712 characters long. The last six characters of each computer tape record are used for record numbering. The record number is reinitialized to zero at the beginning of each airplane flight.

Both airborne signal data recorder systems contain signal conditioners and filters, multiplexer, analog to digital converter, programming and control circuits and magnetic tape magazine. The Conrac recorder has a comparator/buffer section which provides the capability of compressing the data while airborne. In both systems the data is recorded in a binary mode and the parameter input signals are filtered sufficiently to remove noise and unwanted high frequency signal information so that the signals are compatible with the sampling rates. Both recorder systems can be used on the F-111 and are turned on by a switch activated by the closing of the external power receptacle door and aircraft power is on the electrical system. The Dynasciences recorder has built in test equipment which can be used to check out the recorder and the airplane installation from the front of the recorder. This operation is manual and checks each of the parameters, the calibration signals, and power being provided to the recorder.

The Conrac Corp. counting accelerometer is shown in Fig. 9. Each indicator is approximately 3.5 by 5.5 by 6 inches and weighs approximately 4 pounds. The accelerometer transducer is approximately 1.7 by 2.5 by 4 inches and weighs approximately 1.0 pounds. The system is powered by 28 volts DC which is supplied to the appropriate indicator by a switch, the position of which is a function of the wing sweep position. The

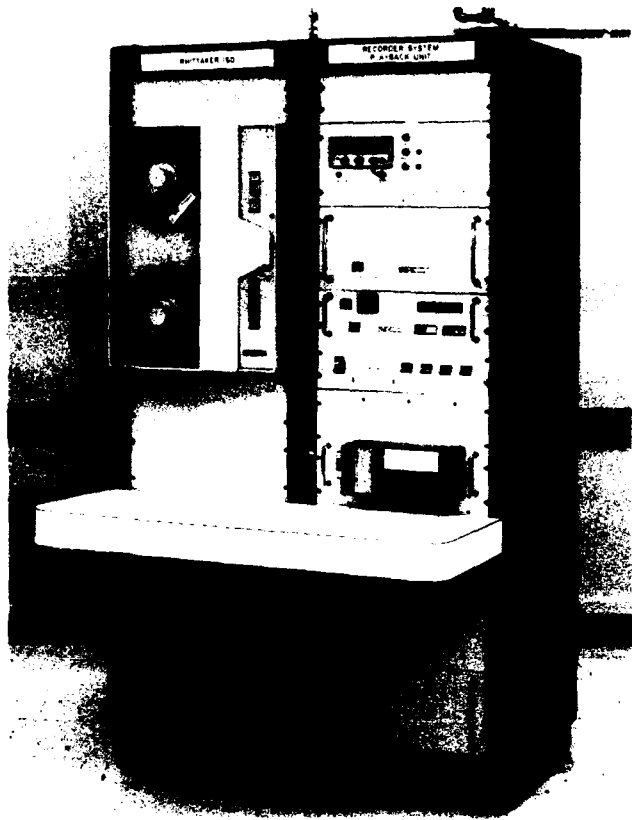


**Figure 8. Signal Data Converter  
Used with Dynasciences Recorder.**

system is entirely solid state and functions so that when a particular airplane cg load factor level is exceeded a count is recorded. No additional counts will be recorded by that particular load factor level until the airplane cg load factor has returned within the reset level. Therefore the device is a cumulative load factor exceedence counting device.

#### **GD/FW – PROGRAM INTERRELATIONSHIP**

The GD/FW Div. has designed, developed, and built the F-111 airplane. They are very much involved in the F-111 service usage recorder program. Two tasks are being performed by GD/FW which are as follows. First, they are installing in the airplane and checking out the airborne signal data recorder and sensor system and the counting accelerometer system. Secondly, the results obtained from operational usage of the airplane as recorded by the airborne signal data recorders and counting accelerometers will be used by GD/FW in fatigue damage calculations and safe service life remaining estimates.

GD/FW is providing equations which used in conjunction with the data recorded on the airborne recorder will predict operational loads induced in selected airplane components. Load spectra based on these equations and general airplane usage information will be provided to GD/FW by the data reduction center. These results will be combined with other available information at GD/FW to calculate the load environment as

sociated with selected components or areas throughout the airframe. These results will then be reflected in a final fatigue analysis, unit damage data report and safe service life remaining reports which are the desired outputs of the program.

Each airplane's fatigue life will be monitored, initially using design data and anticipated operational usage. As recorded data becomes available from the operational aircraft the load history will be upgraded and accumulated fatigue damage per individual airplane will be calculated. Parametric fatigue damage per mission segment will be used where practical and supported by airborne recorder, counting accelerometer data and pre-punched computer cards. An assessment will be made of the fatigue damage done by fleet, wing, squadron, and by individual aircraft. These results will be reflected in hours of safe service life remaining which represents the second major output of the program and will be reported every six months. The unit fatigue damage (parametric fatigue) and TAC/SAC usage definition will be updated as required on a yearly basis.

#### **TAC, SAC AND AMA – PROGRAM INTERRELATIONSHIP**

TAC and SAC will fly and use the airplane in performance of their prime missions. Anything which does not support the accomplishment of the prime missions must take a lower priority to that which does directly support the prime missions. The F-111 service usage recorder program is a long term support of their primary mission. However, use of TAC and SAC operational personnel to accomplish the recorder program must be held to a minimum. With this in mind a philosophy has evolved which requires no equipment trouble-shooting or check-out effort by flight-line personnel in support of the recorder program. Regarding the hardware, flight-line personnel will be required to only remove and replace defective LRU components as identified by the data reduction center. Regarding data handling, organizational personnel are needed to remove the airborne magazine and transcribe the data onto a computer tape using a signal data converter. The airborne magazine will be returned to the airplane and the computer tape will be mailed to the data reduction center. Organizational support for the counting accelerometers amounts to much the same thing, removal and replacement of LRU's and marking of pre-punched computer cards with the counting accelerometer data and pertinent airplane usage information. The marked computer cards will also be sent to the data reduction center. This concept places the responsibility of continued verification of the operation of the airborne equipment with the personnel at the data reduction center. Further repair and upkeep of the airborne recorder equipment is totally the responsibility of the cognizant AMA inventory manager.

Repair, overhaul, and maintenance of the equipment directly used in the F-111 service usage program, i.e. airborne recording equipment and signal data converters, will be the responsibility of depot personnel. Basically then, only one set of AGE need be procured for each particular piece of equipment. Portable testers, check-out equipment, and special calibration equipment normally provided each organization will not be

needed except at the depot. If the recording equipment or signal data converter needs to be checked out at the organizational level the depot personnel can take their equipment to the particular base having the problem and perform the task necessary with the equipment they take with them. An exception is made for those sensors which are common to the airplane system and parts of the recording system. In this case, the airplane AGE will be modified with adapters and indicators as necessary for use by depot personnel when at the base. Normally though, the data reduction center will identify malfunctioning components, which will be removed and forwarded by organizational personnel to the depot. The depot personnel will determine which components are repairable at the depot or vendor's factory and which components must be discarded. It is expected that the majority of the equipment can be completely overhauled and repaired by the depot personnel. It is further anticipated that they will be able to calibrate and check-out the equipment for return to Air Force supply. Since the signal data converters are large and are expensive to move, they will be maintained and serviced on site.

Supporting documentation is being developed and will be provided to assist the using command and the AMA's in supporting the program. Such documentation as TO's and training material will cover the airplane installation, removal and replacement of LRU's complete removal of recording equipment and securing the airplane for flying without the recording equipment, operation of the signal data converter, and maintenance and overhaul instructions for the equipment. Handbooks, manuals, mailing instructions, and program information are being provided to supporting organizations.

#### **SUPPLEMENTAL COMMENTS**

The F-111 service usage recorder program is a passive one. Current usage of the airplane is recorded to provide a baseline of loads spectra for comparison with results of labora-

tory fatigue tests. With little effort an overwhelming amount of technical data could be generated during the performance of this program. Therefore it is necessary that certain safeguards and ground rules be established for the program to prevent the volume of data from becoming the controlling factor. One such ground rule is that all data reduction and manipulation must be accomplished by electronic data processing and computer equipment. Only strength and fatigue sensitive areas will be monitored. No original data will be retained for longer than a one month time period. Only significant airplane usage and load spectra will be retained for further usage. The airborne recorder and counting accelerometer data will be extracted on a given schedule. Similarly, the removal and replacement of LRU components will be on a schedule to be accomplished only if the data reduction center deems it necessary. The data reduction center software programs will need to be very efficient and streamlined. Such programs will not be allowed more than 10 to 20 minutes for data reduction per 25 hours of airplane recorded data. The accumulated reduced service usage data will be forwarded to GD/FW on magnetic tape for further use in fatigue calculations.

Originally, emphasis was placed on recording clean airplane usage on the airborne signal data recorder. Some thought was given to recording additional parameters that would allow better definition of use of the airplane when carrying armament or other external stores. Such parameters would include presence of stores, stores released, roll accelerations, beta angle, total fuel remaining, heading, radar altitude, and speedbrake position or usage. Another parameter which could be hard-wired into the airplane or recorder which would facilitate data reduction would be an airplane-recorder ID number. At no time were auxiliary input boxes considered for the system because of the extra burden which would be placed on the flight-line and crew personnel. Further, such general information is needed in support of the counting accelerometer data and can be obtained along with the counting accelerometer data. The auxil-

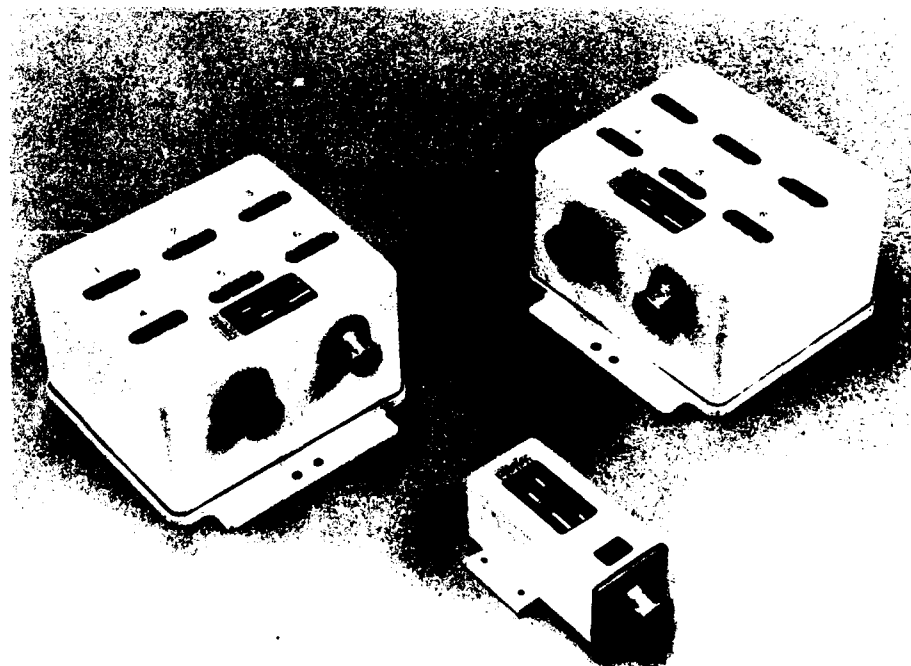


**Figure 9. Conrac  
Counting Accelerometer.**

ary information can then be correlated and used with the airborne signal data recorder information.

### SUMMARY

The F-111 service usage recorder program has been developed around the basic philosophy of minimizing the impact on the using organization, fully utilizing the data reduction center and available high speed data processors and electronic computers, and providing program results which will be meaningful in conserving and utilizing fully the potential of the F-111 airplane. The parameters were selected to minimize dependence on crew provided flight-logs and provide information on general

aircraft usage as well as provide information from which ground and flight-loads can be determined. A USAF data reduction center will provide for the basic data reduction of the airborne signal data recorded information as well as counting accelerometer data. This basic data will be provided GD/FW for determination of operational flight hours remaining on an individual aircraft basis as well as a squadron, wing and fleet basis. AGE equipment will be kept to a minimum by keeping the necessary equipment repair, overhaul, and maintenance at the depot level. Because of the size and complexity of the program all efforts must be streamlined and as efficient as practical. Growth potential for the program exists and is being considered to assure that all critical fatigue areas will be properly monitored on the airplane during its operational useful life.

# AIRCRAFT STRUCTURAL INTEGRITY PROGRAM IN AFLC

by

Col. Harry B. Morrison, Jr.

Hq. Air Force Logistics Command  
USAF

## INTRODUCTION

The implementation of Aircraft Structural Integrity Program (ASIP) in the Air Force Logistic Command (AFLC) falls into two distinct categories. The first category is that of continuing ASIP on relatively new aircraft that have had all the required elements accomplished from time of design. The second category is that of assessing structural integrity on older aircraft which lack the essential elements for a total program.

Two major subprograms of ASIP are presently being planned to support the aircraft in the first category. A recorder procurement is planned to support the recorder program requirements for the life monitoring portion of ASIP. In addition, an Aircraft Structural Integrity Management Information System (ASIMIS) is under development. ASIMIS will provide an in-house capability for the automatic data reduction of the recorder tapes and the means to monitor life on a tail number basis of aircraft which have ASIP implemented.

The aircraft in the second category present a greater problem and one on which comparatively little coordinated effort has been expended. The most obvious gap is in the technology required to establish a base line for fatigue life assessment of these aircraft. The large number of fleets in this category warrant a concerted effort to establish an after-the-fact procedure for structural integrity evaluation, utilizing inspection results, nondestructive inspection techniques and knowledge from the area of fracture mechanics.

## DISCUSSION

### ASIP for New and Future Aircraft

Many efforts are under way to improve the overall capability in the design and verification of structural integrity for our new and future aircraft. To enhance success in this area AFLC has taken several steps. First, we have established specific ASIP groups at each of the Air Material Areas (AMA) to provide the required focal point and necessary overall integration of the various technical disciplines on each weapon system. Secondly, we have initiated sub-programs of ASIP which we recognize as key requirements for the successful implementation of ASIP on any system. Specifically, two major sub-programs

have been initiated, the ASIMIS and the Recorder Program. Although these efforts are an integral part of ASIP, they must be handled as separate entities until they can be developed and assimilated into the total program.

### Recorder Program

One of the key elements in evaluating and advancing the state-of-the-art in the fatigue certification portion of ASIP is that of establishing a valid statistical estimate of the frequency and magnitude of the significant loads parameters. These data are not only required for accurate life assessment but also to refine present damage theories. Toward this end AFLC has efforts under way for the procurement of recorders which will provide a capability well beyond that existing today.

AFLC plans to procure a total recorder system to serve the needs of AF aircraft. The concept is to standardize as many components of the system as possible and will consist of all the system components including the sensors, recording equipment and ground equipment necessary to convert the recorder tape to a conventional computer compatible tape. At present, it appears that we can handle all of our current needs with one system that utilizes four different options on the signal data converter-multiplexer units. In other words, the same basic system can be used for a bomber or a fighter by simply changing the converter-multiplexer unit. This type of system will provide us with the flexibility of meeting the variety of space constraints, record times and parameters required by our present fleets. As can be seen from Figure 1, the general plan for procurement is a

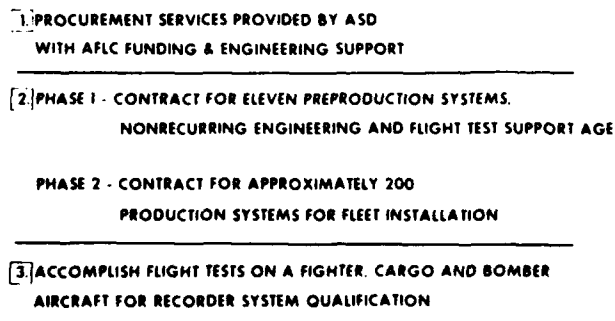


Figure 1. General Plan for Recorder Procurement.

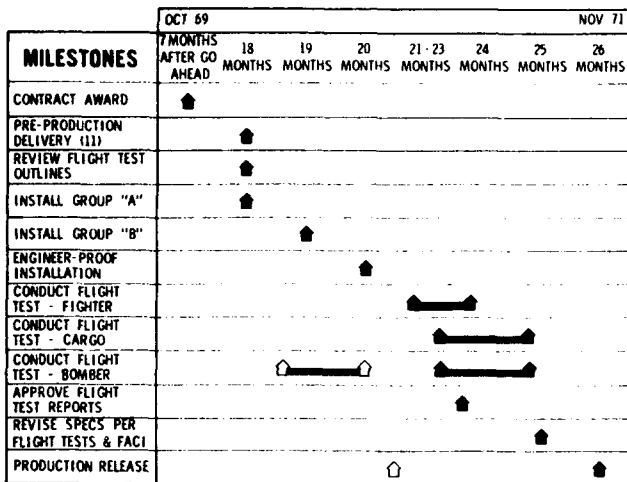


Figure 2. Recorder System Procurement Milestones.

coordinated effort between AFLC and Aeronautical Systems Division (ASD). The procurement will consist of two phases; the first phase will provide for the development of preproduction systems for flight and ground testing. The second phase will consist of the procurement of a number of production systems for fleet installation. Figure 2 presents the time frame of the major milestones until production release expected in late 1971. The three aircraft used for

flight testing represent a cross section of the type of requirements the recording system must meet in terms of space, recording time and parameters. The procurement of a recorder system of the type planned will fill a major gap in ASIP and simultaneously lay the groundwork for a rational and supportable ASIMIS.

*Aircraft Structural Integrity Management Information System (ASIMIS)*

Concurrent with the Recorder Program we have another major effort under way to support new and future aircraft. The final objectives of ASIP cannot be met unless we have the tools to provide a total management capability for all facets of structural integrity. Merely knowing the strength and life of a weapon system at a given time in its operational life is not sufficient. A weapon system undergoes constant change through modifications, improvements and operational requirements. Consequently, ASIP must be interfaced with other maintenance data systems if we are to remain current on the structural status and configuration of our fleet aircraft. AFLC is now in the process of developing the ASIMIS which will provide data automation support and services for ASIP and serve as the tool for total management.

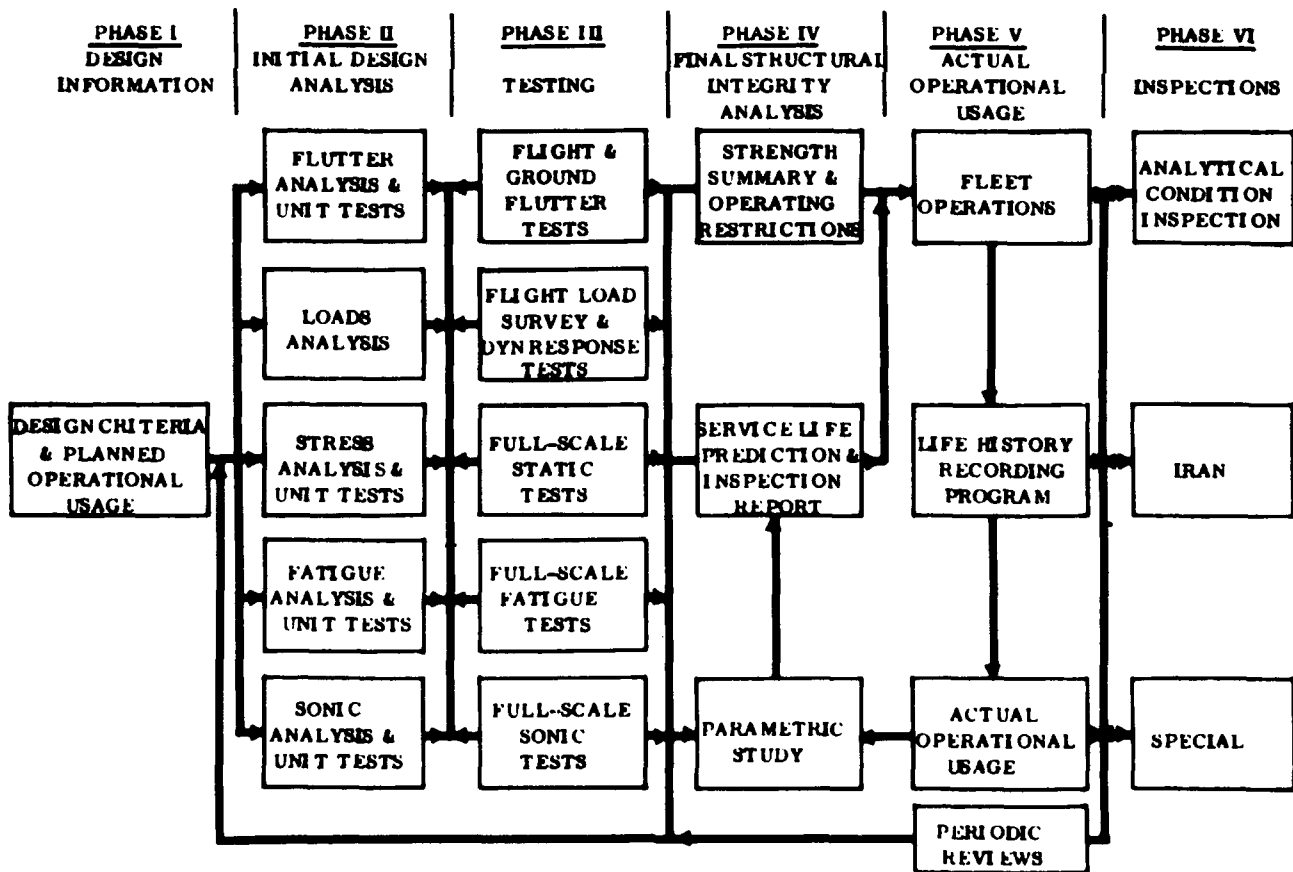


Figure 3. Current ASIP Requirements. (From ASD-TR-66-57, "Air Force Aircraft Structural Integrity Program: Airplane Requirements" by H.M. Wells, Jr. and T.T. King).

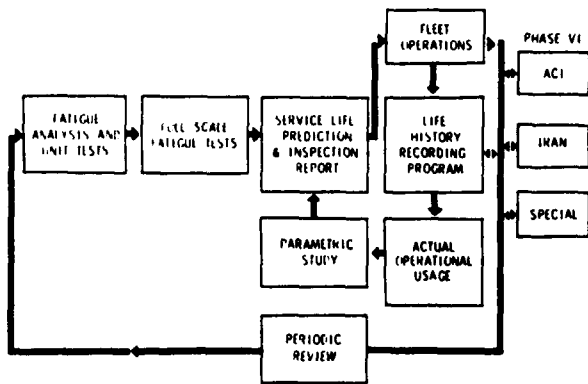


Figure 4. Fatigue Certification Program.

The flow diagram in Figure 3 shows the six phases and the various elements that provide for a complete ASIP. Figure 4 depicts the particular portion of the total ASIP which is addressed by ASIMIS. Phases I-IV are essential to the fatigue analysis and are represented by that element. The remaining elements are part of the fatigue certification portion of ASIP and comprise two loops. ASIMIS will provide support for the inside loop in terms of flight data reduction and operational usage, and for the outside loop in terms of computational programs, fatigue analysis and improvement of design criteria for future weapon systems.

Aircraft fatigue damage experience can be divided into two categories. One category consists of the environmental inputs such as gusts, maneuvers and ground loads. These inputs are primarily statistical in nature and can be predicted by mathematical models if sufficient data can be generated. The other category of damage experience is that of operational usage. This is a function of the actual missions flown and aircraft configuration. It is obvious that an air-to-ground combat mission for a fighter or a low level mission for a bomber would be more damaging than a navigational training mission for either aircraft. Also, the gross weight, stores configuration, geographical location, etc.,

can have a significant impact on the damage rate accumulated by an individual aircraft. Consequently, to successfully calculate the fatigue life of an aircraft, it is necessary to account for these variations from one airplane to another.

Figure 5 is a pictorial representation of the ASIMIS program and highlights the functional aspects of life monitoring. The Individual Aircraft Usage Record will provide data on each aircraft as to specific missions flown and pertinent operational parameters such as gross weight, aircraft configuration, time and altitude in mission phases, etc. These data are the primary sources for monitoring life on an individual tail number basis. Records from each aircraft will input operational parameters into the computer and will be translated into damage accumulation for each point determined to be critical for each aircraft. Simultaneously, the flight recorders will provide the inputs required to develop the statistical mathematical models of the environmental parameters. These data will then be analyzed for significant changes which must be reflected in the fatigue analysis, parametric analysis and final life calculations. The recorder data is also integrated into structural design criteria for future aircraft. The recorders will be installed on some percentage of the fleet based on type of aircraft and mission requirements. Recorder coverage of the total fleet is not economically feasible in light of the cost of recorders and data reduction. The outputs of the system will be interfaced with the Advanced Logistics System Computer Complex (ALS-X) which centralizes management for all logistics computer processes, thus providing the capability for controlling and monitoring the areas outlined in Figure 6.

- CONFIGURATION MANAGEMENT
- MODIFICATION MANAGEMENT
- MATERIAL IMPROVEMENT
- STANDARD AEROSPACE VEHICLE & EQUIPMENT STATUS (65-110)
- AIDS/MADARS

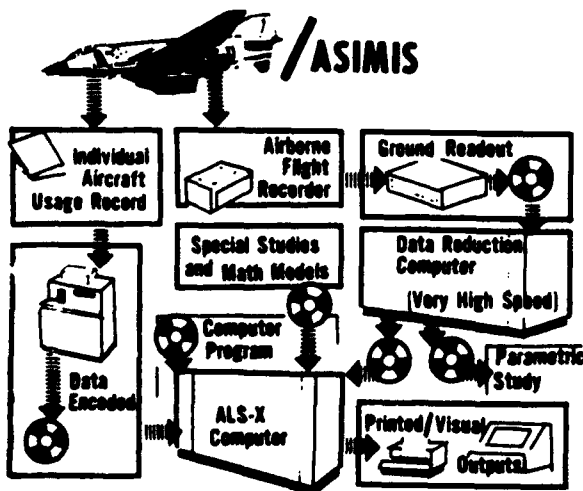


Figure 5. Aircraft Structural Integrity Management Information System (ASIMIS).

Figure 6. ASIMIS Interface with ALS Processes and Events.

In summary, the proper implementation of Air Force regulations together with the above subprograms will provide the tools required for total management of ASIP on new and future aircraft. Obviously, our final success in the utilization of these tools requires the full cooperation of all the people involved in the design, development, maintenance and use of the aircraft. Early implementation and continual application of the ASIP is a must if our objectives are to be achieved.

#### ASIP for Older Aircraft

The major problem facing AFLC today is that of

structural integrity assessment of our older aircraft. We have approximately fifty fleets in the Air Force inventory that can be considered in this category. Over the past years we have had numerous structural failures and enormously expensive modification programs on many of these fleets. The majority of the problems stem from fatigue failures, since none of these aircraft have been designed for a specific life and very few have any semblance of an ASIP as we know it today. Consequently, we are constantly put into the position of attempting to assure structural integrity with absolutely no base line from which to work. Some of the aircraft are serving first line mission roles in South East Asia (SEA) and have experienced 15 to 20 years of unknown usage history. To further complicate matters, restrictions have to be held to a minimum in order to achieve maximum mission effectiveness.

Imagine a real world problem of a catastrophic failure in a first line aircraft operating in SEA. The fleet consists of a couple of hundred aircraft serving a critical operational requirement. Imagine further that the aircraft are approximately 15 years old and no information on past usage or loads spectrum is available. A fatigue and static test was conducted quite a few years ago but available stress data is incomplete. Inspections reveal that cracks start in numerous fastener holes in the wing spar caps and show elongation and poor quality due to years of service. The immediate problem is to determine the safe operational envelope without grounding the fleet, and still maintain some rational degree of combat readiness. The long range problem is to develop a modification and installation schedule which has minimum operational impact and minimum risk to the fleet. In addition, the remaining safe life after modification installation is desired. One more complicating factor -- money is not available for any long term ASIP such as a full scale test or flight loads survey.

The first reaction to a problem of this nature is that a meaningful solution is impossible to find. Granted, our answers will not be as accurate as we would like, however, we are required to determine the best technical approach within the existing constraints. These types of problems are being faced by AFLC on a day-to-day basis on our older aircraft. In the above case, a positive attitude would be to consider the data that is available rather than worry about the lack of data. For instance, inspections revealed that approximately 15% of the fleet had spar cracking. This means that there is some reasonable time before a crack will propagate to catastrophic proportions; otherwise, these aircraft would have suffered catastrophic failure. The discovery of these failures also means inspections could be used to buy time for modification design and installation. In addition to the inspection results, the total flight hours on each aircraft in the fleet is known. This is not to imply that fatigue damage is necessarily a function of flight hours, but it is another bit of information. This is typical of the type of information that is available to arrive at a technical approach to solve the problem. We do our best but there is much room for improvement, both in safety and economy.

It seems that the knowledge which presently exists in several areas could be utilized to develop a rational pro-

cedure for assessing the structural integrity of older aircraft. The areas of fracture mechanics and mechanism of structural fatigue should be able to establish some useful facts from the analysis of a series of fleet failures. This information in conjunction with crack propagation rates and residual strength analyses could provide guidance in terms of restriction requirements, inspection intervals and modification design. Each of the contributing areas would have to be statistically analyzed to establish accuracy limits and a final estimate of confidence in the defined procedure. In conjunction with the above analytical approach, improvements in nondestructive inspection techniques are required. A capability to inspect relatively large and inaccessible areas in a short period of time is necessary for two reasons. First, we need this capability for inspecting large numbers of aircraft when a known problem exists. Secondly, we need this capability for a general inspection of the aircraft to help detect cracks that may be starting but have not yet made themselves known as a fleet problem. As time goes on it is obvious that we will have to depend more heavily on inspections to provide data for structural integrity assessment. If this increasing requirement is to be met, a concerted effort must be made now.

The above requirements for after-the-fact structural assessment may appear too ambitious, especially when viewed from the aspect of any one discipline. However, it must be realized that we are facing these problems today and are finding solutions to the best of our ability. So it isn't an academic exercise or study that is being requested, but a real world approach to a real world problem. It is emphasized that we are seeking a procedure, not an absolute and mathematically accurate theory. However, some measure of the accuracy of the answers derived from the procedure must be established in order to be useful in solving fleet problems. There is no doubt that a dedicated effort by experts such as those attending this conference could go a long way in developing a workable procedure. The major requirement is the continued interchange of ideas between the various disciplines and a recognition that these problems are here today. It only remains that we start an organized approach and refine it as we learn more.

#### SUMMARY

Efforts presently underway in AFLC will significantly improve the capability of implementing ASIP on new aircraft. The flight recorders and data reduction facility will provide a data base that will give us an insight into the limitations of our present procedures as well as refined life estimates on specific fleets. However, a larger percentage of the Air Force inventory is composed of aircraft which do not have sufficient testing and analysis on which to base service life estimates. The assessment of life on these aircraft requires the development of a new procedure. The problems associated with these aircraft are being solved by AFLC today on an individual basis. There is a critical need for experts from the areas of fracture mechanics, structural analysis and statistics to pool their efforts and develop a meaningful life assessment procedure for these older aircraft.



## INDEX OF AUTHORS

<i>Adair, A.M.</i>	87	<i>Liu, A.F.</i>	323
<i>Anderson, R.B.</i>	417	<i>Liu, T.T.</i>	265
<i>Bouton, I.</i>	117	<i>McEvily, A.J.</i>	451
<i>Bowman, J.C.</i>	475	<i>McKinney, K.R.</i>	395
<i>Bryan, D.F.</i>	755	<i>Maiden, D.E.</i>	217
<i>Butler, J.P.</i>	17	<i>Marom, E.</i>	493
<i>Campbell, M.D.</i>	539	<i>Maurer, O.F.</i>	557
<i>Carlson, R.L.</i>	193	<i>Merkin, A.</i>	779
<i>Coffin, L.F., Jr.</i>	301	<i>Morrison, H.B., Jr.</i>	899
<i>Coleman, T.L.</i>	123	<i>Mueller, R.K.</i>	493
<i>Coles, A.</i>	7i	<i>Nashif, A.D.</i>	503
<i>Dominic, R.J.</i>	847	<i>Pelloux, R.M.</i>	1
<i>Dunegan, H.L.</i>	459	<i>Poe, C.C., Jr.</i>	.07
<i>Dunn, W.P.</i>	889	<i>Popp, H.G.</i>	71
<i>Engstrom, W.L.</i>	611	<i>Porter, T.R.</i>	595
<i>Ferguson, J.</i>	5		& 611
<i>Finger, R.W.</i>	235	<i>Rich, M.J.</i>	635
<i>Fitch, G.E., Jr.</i>	723	<i>Roberson, J.A.</i>	87
<i>Fleck, W.G.</i>	417	<i>Ronay, M.</i>	99
<i>Frank, D.F.</i>	117	<i>Rosenfield, A.R.</i>	425
<i>Freudenthal, A.M.</i>	9	<i>Roth, G.J.</i>	877
<i>Graham, P.H.</i>	313	<i>Sanga, R.V.</i>	595
<i>Grosskreutz, J.C.</i>	47	<i>Sarrate, M.</i>	425
<i>Gruff, J.J.</i>	521	<i>Saunders, S.C.</i>	131
<i>Haglage, T.L.</i>	137	<i>Schwake, R.O.</i>	867
<i>Hahn, G.T.</i>	425	<i>Sheemaker, A.P.</i>	833
<i>Hall, L.R.</i>	235	<i>Shimmin, K.D.</i>	343
<i>Hancock, J.R.</i>	285	<i>Shimovetz, R.M.</i>	557
<i>Harris, D.O.</i>	459	<i>Sih, G.C.</i>	175
<i>Harrison, J.C.</i>	193	<i>Smith, G.C.</i>	113
<i>Haskins, J.F.</i>	539	<i>Smith, H.L.</i>	395
<i>Haugen, E.B.</i>	685	<i>Smith, S.H.</i>	611
<i>Henderson, J.P.</i>	503	<i>Soliman, F.Y.</i>	377
<i>Horsfall, W.P.</i>	723	<i>Stone, M.</i>	579
<i>Hritz, J.A.</i>	685	<i>Stonesifer, F.R.</i>	395
<i>Hunter, P.A.</i>	123	<i>Swift, T.</i>	653
<i>Hutcheson, J.G.</i>	521	<i>Tetelman, A.S.</i>	459
<i>Ito, Y.M.</i>	63	<i>Toth, I.J.</i>	343
<i>Jackman, R.E.</i>	723	<i>Trent, D.J.</i>	117
<i>Jensen, J.E.</i>	539	<i>Wagner, J.A.</i>	833
<i>Jones, D.I.G.</i>	503	<i>Walker, E.K.</i>	225
<i>Jones, J.W.</i>	159	<i>Wallace, J.S.</i>	377
<i>Ju, F.D.</i>	265	<i>Wang, D.Y.</i>	653
<i>King, T.T.</i>	701	<i>West, B.S.</i>	877
<i>Kobayashi, A.S.</i>	217	<i>Whitford, D.H.</i>	847
<i>Kramer, I.R.</i>	271	<i>Wood, H.A.</i>	137
<i>Lin, T.H.</i>	63	<i>Yao, J.T.P.</i>	265
<i>Lipsitt, H.A.</i>	113	<i>Zielsdorff, G.F.</i>	193

**AIR FORCE CONFERENCE**  
on  
**FATIGUE AND FRACTURE**  
of  
**AIRCRAFT STRUCTURES AND MATERIALS**

**Miami Beach, Florida**

*15 - 18 December, 1969*

**EXECUTIVE CO-CHAIRMEN**

Colonel Joseph R. Myers  
Commander  
Air Force Flight Dynamics Laboratory

Dr. A. M. Lovelace  
Director  
Air Force Materials Laboratory

**CONFERENCE CHAIRMAN**

H.A. Wood  
Air Force Flight Dynamics Laboratory

**TECHNICAL COMMITTEE**

H.A. Wood  
Chairman, Structures  
Air Force Flight Dynamics Laboratory

W. J. Trapp  
Chairman, Materials  
Air Force Materials Laboratory

R. M. Bader  
Air Force Flight Dynamics Laboratory

R. C. Donat  
Air Force Materials Laboratory

R. F. Hoener  
Air Force Flight Dynamics Laboratory

**ARRANGEMENTS COMMITTEE**

C. R. Andrews  
University of Dayton

A. J. Cannon  
Aeronautical Systems Division

J. M. Kelly  
Aeronautical Systems Division

Capt. J. M. Meiselman  
Air Force Flight Dynamics Laboratory

Lt. J. Altorfer  
Air Force Flight Dynamics Laboratory

UNCLASSIFIED  
Security Classification

DOCUMENT CONTROL DATA - R&D		
<i>(Security classification of title, body of abstract and indexing annotation must be entered when the overall report is classified)</i>		
1. ORIGINATING ACTIVITY (Corporate author) Air Force Flight Dynamics Laboratory (FBR) Wright-Patterson AFB, Ohio 45433		2a. REPORT SECURITY CLASSIFICATION Unclassified
		2b. GROUP N/A
3. REPORT TITLE Proceedings of the Air Force Conference on Fatigue and Fracture of Aircraft Structures and Materials		
4. DESCRIPTIVE NOTES (Type of report and inclusive dates) Proceedings of the Air Force Conference held 15-18 Dec, 1969 in Miami Beach, Fla.		
5. AUTHOR(S) (Last name, first name, initial) NONE		
6. REPORT DATE December 1970	7a. TOTAL NO. OF PAGES 916	7b. NO. OF REFS
8a. CONTRACT OR GRANT NO.	9a. ORIGINATOR'S REPORT NUMBER(S) AFFDL-TR-70-144	
b. PROJECT NO.		
c.	9b. OTHER REPORT NO(S) (Any other numbers that may be assigned this report)	
d.		
10. AVAILABILITY/LIMITATION NOTICES This document has been approved for public release and sale; its distribution is unlimited.		
11. SUPPLEMENTARY NOTES	12. SPONSORING MILITARY ACTIVITY AF Flight Dynamics Laboratory AF Materials Laboratory	
13. ABSTRACT The Air Force Conference on Fatigue and Fracture of Aircraft Structures and Materials, sponsored by the Air Force Flight Dynamics Laboratory (AFFDL) and the Air Force Materials Laboratory (AFML), Air Force Systems Command, was held on 15-18 December 1969 at the Carillon Hotel, Miami Beach, Florida. The purpose of the Conference was to discuss technological advancements in fatigue and fracture theory. The conference was comprised of ten technical sessions (including two panel discussions) entitled "The Role of Materials in Structures," "Fundamentals I & II," "Criteria;" "Fracture I & II;" "Phenomena I & II;" "Analysis;" "Design and Service Experience." A total of fifty-six (56) technical papers were presented.		

DD FORM 1473  
1 JAN 64

UNCLASSIFIED  
Security Classification

## Security Classification

14. KEY WORDS	LINK A		LINK B		LINK C	
	ROLE	WT	ROLE	WT	ROLE	WT
Structural Materials						
Fatigue Mechanisms						
Fracture Mechanics						
Fracture Analysis						
Crack Propagation						
Fracture Toughness						
Fatigue Life						
Structural Integrity						
Cumulative Fatigue Damage						
Fatigue Failures						
Residual Strength						
Fatigue Loadings						
Stress Intensity Factor						
Low Cycle Fatigue						
Fracture-Composites						

## INSTRUCTIONS

1. **ORIGINATING ACTIVITY:** Enter the name and address of the contractor, subcontractor, grantee, Department of Defense activity or other organization (*corporate author*) issuing the report.
- 2a. **REPORT SECURITY CLASSIFICATION:** Enter the overall security classification of the report. Indicate whether "Restricted Data" is included. Marking is to be in accordance with appropriate security regulations.
- 2b. **GROUP:** Automatic downgrading is specified in DoD Directive 5200.10 and Armed Forces Industrial Manual. Enter the group number. Also, when applicable, show that optional markings have been used for Group 3 and Group 4 as authorized.
3. **REPORT TITLE:** Enter the complete report title in all capital letters. Titles in all cases should be unclassified. If a meaningful title cannot be selected without classification, show title classification in all capitals in parenthesis immediately following the title.
4. **DESCRIPTIVE NOTES:** If appropriate, enter the type of report, e.g., *interim, progress, summary, annual, or final*. Give the inclusive dates when a specific reporting period is covered.
5. **AUTHOR(S):** Enter the name(s) of author(s) as shown on or in the report. Enter last name, first name, middle initial. If military, show rank and branch of service. The name of the principal author is an absolute minimum requirement.
6. **REPORT DATE:** Enter the date of the report as day, month, year, or month, year. If more than one date appears on the report, use date of publication.
- 7a. **TOTAL NUMBER OF PAGES:** The total page count should follow normal pagination procedures, i.e., enter the number of pages containing information.
- 7b. **NUMBER OF REFERENCES:** Enter the total number of references cited in the report.
- 8a. **CONTRACT OR GRANT NUMBER:** If appropriate, enter the applicable number of the contract or grant under which the report was written.
- 8b, 8c, & 8d. **PROJECT NUMBER:** Enter the appropriate military department identification, such as project number, subproject number, system numbers, task number, etc.
- 9a. **ORIGINATOR'S REPORT NUMBER(S):** Enter the official report number by which the document will be identified and controlled by the originating activity. This number must be unique to this report.
- 9b. **OTHER REPORT NUMBER(S):** If the report has been assigned any other report numbers (*either by the originator or by the sponsor*), also enter this number(s).
10. **AVAILABILITY/LIMITATION NOTICES:** Enter any limitations on further dissemination of the report, other than those

imposed by security classification, using standard statements such as:

- (1) "Qualified requesters may obtain copies of this report from DDC."
- (2) "Foreign announcement and dissemination of this report by DDC is not authorized."
- (3) "U. S. Government agencies may obtain copies of this report directly from DDC. Other qualified DDC users shall request through \_\_\_\_\_."
- (4) "U. S. military agencies may obtain copies of this report directly from DDC. Other qualified users shall request through \_\_\_\_\_."
- (5) "All distribution of this report is controlled. Qualified DDC users shall request through \_\_\_\_\_."

If the report has been furnished to the Office of Technical Services, Department of Commerce, for sale to the public, indicate this fact and enter the price, if known.

11. **SUPPLEMENTARY NOTES:** Use for additional explanatory notes.

12. **SPONSORING MILITARY ACTIVITY:** Enter the name of the departmental project office or laboratory sponsoring (*paying for*) the research and development. Include address.

13. **ABSTRACT:** Enter an abstract giving a brief and factual summary of the document indicative of the report, even though it may also appear elsewhere in the body of the technical report. If additional space is required, a continuation sheet shall be attached.

It is highly desirable that the abstract of classified reports be unclassified. Each paragraph of the abstract shall end with an indication of the military security classification of the information in the paragraph, represented as (TS), (S), (C), or (U).

There is no limitation on the length of the abstract. However, the suggested length is from 150 to 225 words.

14. **KEY WORDS:** Key words are technically meaningful terms or short phrases that characterize a report and may be used as index entries for cataloging the report. Key words must be selected so that no security classification is required. Identifiers, such as equipment model designation, trade name, military project code name, geographic location, may be used as key words but will be followed by an indication of technical context. The assignment of links, rules, and weights is optional.